ECCM

20

26-30 JUNE

2022

LAUSANNE

SWITZERLAND

Proceedings of the 20th European Conference on Composite Materials

COMPOSITES MEET SUSTAINABILITY

Vol 4 – Modeling and Prediction

Editors : Anastasios P. Vassilopoulos, Véronique Michaud

Organized by :

EPFL

Under the patronage of :

CCLAB Composite Construction Laboratory

LPAC Laboratory for Processing of Advanced Composites

ESCM EUROPEAN SOCIETY FOR COMPOSITE MATERIALS

ECCM 20
26-30 JUNE 2022
LAUSANNE SWITZERLAND

EPFL CCLAB Composite Construction Laboratory LPAC Laboratory for Processing of Advanced Composites

Proceedings of the 20th European Conference on Composite Materials ECCM20 26-30 June 2022, EPFL Lausanne Switzerland

Edited By :

Prof. Anastasios P. Vassilopoulos, CCLab/EPFL
Prof. Véronique Michaud, LPAC/EPFL

Oragnized by:

Composite Construction Laboratory (CCLab)
Laboratory for Processing of Advanced Composites (LPAC)
Ecole Polytechnique Fédérale de Lausanne (EPFL)

ISBN: 978-2-9701614-0-0
DOI: http://dx.doi.org/10.5075/epfl-298799_978-2-9701614-0-0

Published by :

Composite Construction Laboratory (CCLab)
Ecole Polytechnique Fédérale de Lausanne (EPFL)
BP 2225 (Bâtiment BP), Station 16
1015, Lausanne, Switzerland

https://cclab.epfl.ch

Laboratory for Processing of Advanced Composites (LPAC)
Ecole Polytechnique Fédérale de Lausanne (EPFL)
MXG 139 (Bâtiment MXG), Station 12
1015, Lausanne, Switzerland

https://lpac.epfl.ch

Cover:

Swiss Tech Convention Center
© Edouard Venceslau - CompuWeb SA

Cover Design:

Composite Construction Laboratory (CCLab)
Ecole Polytechnique Fédérale de Lausanne (EPFL)
Lausanne, Switzerland

©2022 ECCM20/The publishers

Disclaimer:

The ECCM20 organizing committee and the Editors of these proceedings assume no responsibility or liability for the content, statements and opinions expressed by the authors in their corresponding publication.

Editorial

This collection gathers all the articles that were submitted and presented at the 20th European Conference on Composite Materials (ECCM20) which took place in Lausanne, Switzerland, June 26-30, 2022.

ECCM20 is the 20th edition of a conference series having its roots back in time, organized each two years by members of the European Society of Composite Materials (ESCM).

The ECCM20 event was organized by the Composite Construction laboratory (CCLab) and the Laboratory for Processing of Advanced Composites (LPAC) of the Ecole Polytechnique Fédérale de Lausanne (EPFL).

The Conference Theme this year was “Composites meet Sustainability”. As a result, even if all topics related to composite processing, properties and applications have been covered, sustainability aspects were highlighted with specific lectures, roundtables and sessions on a range of topics, from bio-based composites to energy efficiency in materials production and use phases, as well as end-of-life scenarios and recycling.

More than 1000 participants shared their recent research results and participated to fruitful discussions during the five conference days, while they contributed more than 850 papers which form the six volumes of the conference proceedings. Each volume gathers contributions on specific topics:

Vol 1 – Materials

Vol 2 – Manufacturing

Vol 3 – Characterization

Vol 4 – Modeling and Prediction

Vol 5 – Applications and Structures

Vol 6 – Life Cycle Assessment

We enjoyed the event; we had the chance to meet each other in person again, shake hands, hold friendly talks and maintain our long-lasting collaborations. We appreciated the high level of the research presented at the conference and the quality of the submissions that are now collected in these six volumes. We hope that everyone interested in the status of the European Composites’ research in 2022 will be fascinated by this publication.

The Conference Chairs

Anastasios P. Vassilopoulos, Véronique Michaud

ECCM 20
26-30 JUNE 2022
LAUSANNE SWITZERLAND

Hosting Organizations

Composite Construction Laboratory (CCLab)
Laboratory for Processing of Advanced Composites (LPAC)
Ecole Polytechnique Fédérale de Lausanne (EPFL)

Venue

Swiss Tech Convention Center (https://www.stcc.ch)

Conference Chairs

Chair : Prof. Anastasios P. Vassilopoulos, EPFL, Switzerland
Co-Chair: Prof Véronique Michaud, EPFL, Switzerland

International Scientific Committee

Prof. Malin Åkermo SE
Dr. Emmanuel Baranger FR
Prof. Christophe Binetruy FR
Prof. Pedro Camanho PT
Prof. Konstantinos Dassios GR
Prof. Brian Falzon UK
Prof. Kristofer Gamstedt SE
Prof. Sotiris Grammatikos NO
Prof. Christian Hochard FR
Prof. Marcin Kozlowski PL
Prof. Stepan Lomov BE
Dr. David May DE
Prof. Stephen Ogin UK
Prof. Gerald Pinter AT
Prof. Silvestre Pinho UK
Prof. Yentl Swolfs BE
Dr. Julie Teuwen NL
Dr. Panayota Tsotra CH
Prof. Wim van Paepegem BE
Prof. Dimitrios Zarouchas NL
Dr. Andrey Aniskevich LV
Prof. Christian Berggreen DK
Dr. Nicolas Boyard FR
Prof. Valter Carvelli IT
Prof. Klaus Drechsler DE
Prof. Bodo Fiedler DE
Dr. Nathalie Godin FR
Prof. Roland Hinterholzl AT
Prof. Ian Kinloch UK
Dr. Thomas Kruse DE
Prof. Theodoros Loutas GR
Prof. Veronique Michaud CH
Prof. Alessandro Pegoretti IT
Prof. Joao Ramoa Correia PT
Prof. Jose Sena-Cruz PT
Prof. Antonio T. Marques PT
Prof. Thanasis Triantafillou GR
Prof. Albert Turon ES
Prof. Anastasios P. Vassilopoulos CH
Prof. Martin Fagerström SE
Dr. Alexandros Antoniou DE
Prof. Lars Berglund SE
Prof. Michal Budzik DK
Prof. Lucas Da Silva PT
Dr. Andreas Endruweit UK
Prof. Mariaenrica Frigione IT
Dr. Larissa Gorbatikh BE
Dr. Martin Hirsekorn FR
Prof. Vassilis Kostopoulos GR
Prof. Jacques Lamon FR
Prof. Staffan Lundstrom SE
Prof. Peter Mitschang DE
Dr. Soraia Pimenta UK
Prof. Paul Robinson UK
Dr. Olesja Starkova LT
Prof. Sofia Teixeira de Freitas NL
Dr. Stavros Tsantzalis GR
Prof. Danny van Hemelrijck BE
Prof. Michele Zappalorto IT
Dr. Miroslav Cerny CZ

Local Organizing Committee

Prof. Anastasios P. Vassilopoulos, EPFL
Prof. Véronique Michaud, EPFL
Angélique Crettenand and Mirjam Kiener, Lausanne Tourisme
And all those who helped, colleagues who reviewed abstracts and chaired sessions, and CCLab and LPAC students and collaborators who worked hard to make this conference a success.

ECCM 20
26-30 JUNE 2022
LAUSANNE SWITZERLAND

Sponsors

SHIMADZU
Excellence in Science

Bristol Composites Institute

JEC GROUP

suprem

Surface Measurement Systems
World Leader in Sorption Science

INSTRON

9T LABS

Anton Paar

DIA-STRON
DELIVERING MEASUREMENT SOLUTIONS

AELER

HRC

ICCM 23
BELFAST 2023
30 JULY – 4 AUGUST

TEIJIN

Functional Composite Materials

materials
an Open Access Journal by MDPI

ELSEVIER

Supporting partners

JEC

CertBond
COST Action CA18120

EsSENce

Switzerland Tourism.

SWISS

SBB CFF FFS

sampe
Switzerland

COMPOSITES UNITED | SWITZERLAND

canton de vaud

Lausanne

Contents

ON AN ORTHOTROPIC, ELASTO-PLASTIC MATERIAL MODEL TO SIMULATE THE CRASH OF A FRP GLIDER FUSELAGE

C. Rolffs[a], S. Scheffler[b], R. Rolfes[b]

a: Leibniz Universität Hannover, Institut für Statik und Dynamik, c.rolffs@isd.uni-hannover.de
b: Leibniz Universität Hannover, Institut für Statik und Dynamik

Abstract: *This article proposes an orthotropic elasto-plastic material model, which can be used as a numerically effective tool to evaluate the behavior of large structures made of fiber-reinforced plastics (FRP) in a crash scenario.*

Simulating the crash of a glider requires special consideration to the nonlinear material behavior. Like many other technical applications of fiber-reinforced plastic, the fuselage of a glider is built using quasi-orthotropic laminate stackings. In this contribution, a material model to describe the nonlinear material response of such laminates is presented. Orthotropic material parameters used in this model are derived from virtual tests, using only material parameters of unidirectional single plies as input. The authors believe that the presented material model and the used homogenization technique enables an accurate representation of the damage progression and the structural behavior of the glider fuselage in a crash scenario with acceptable numerical effort.

Keywords: FEM Simulation; material model; Plasticity; Crash

1. Introduction

Modern gliders have sophisticated structures designed to prevent damage to the pilot in the event of an accident. Their main tasks are, to ensure a survival space and influence the acceleration forces acting on the pilot [1]. Old aircraft, such as the Astir CS from the 1970s, are still widely used today due to their favourable flight characteristics for beginners and their price.

In order to develop retrofit modules that improve the crash characteristics of old aircraft a detailed understanding of the behaviour of the structure is needed. An efficient and detailed evaluation of different variants is only possible with a reliable and fast working FEM model. Since this simulation serves as a tool for the design of the geometry and the material, a short calculation time is of great advantage.

The theory of plasticity can be used to model materials that undergo permanent deformations that remain after applying and removing a certain load. This corresponds to a non-linear stress-strain response. Therefore, plasticity algorithms can be used as a closed formulation for nonlinear material responses of different causes.

The behaviour of FRP is dominated by the material response in fibre direction. This is usually considered transversely isotropic and linear-elastic, followed by brittle failure. However, using plasticity to simulate FRP structures has a number of advantages. Under tension in fibre direction, plastic straining reduces stress concentrations near holes, which improves the

  doi:10.5075/epfl-298799_978-2-9701614-0-0

accuracy of strength prediction in open-hole specimens [2]. Under compression and shear, the behaviour is more prominently influenced by the properties of the matrix material, which can be described as plastic [2] [3]. In a crash scenario, the governing failure mechanisms are crushing and delamination. After exceeding its compressive strength the material does not lose all of its integrity, but is still able to carry some loads [4]. This can be described as quasi-plastic behaviour.

Using a transversely isotropic elasto-plastic material model to simulate unidirectional layers in a laminate requires a lot of computational effort. Each ply has to be represented by at least one (ideally: three) element in thickness direction. Elements also have to be small, to ensure admissible aspect ratios. Using such a detailed model on large structures requires a great deal of computational effort.

Homogenisation of the whole laminate can help to reduce this effort. Approximating the behaviour of the whole laminate to that of one element of orthotropic symmetry leads to a loss of information. For instance, asymmetrically damaged laminates can not be depicted. However, the authors believe, that the overall behaviour of the structure is dominated by different aspects, like global buckling and crushing [5] [6]. These aspects can be modelled by the proposed model.

2. Orthotropic plasticity

2.1 Orthotropic plasticity algorithm

The described task requires a plasticity algorithm that differentiates between nine different types of loading: Tension and compression in all three main directions and three types of shear. For each of these types and all combinations of these, a yield criterion needs to be formulated. In order to establish the equations for this anisotropic elasto-plastic material model, the framework of invariant theory is used. Using the orthotropic invariants suggested by Vogler [7] the yield condition reads:

$$f = \alpha_1 I_1 + \alpha_2 I_2 + \alpha_3 I_3 + \alpha_4 I_4 + \alpha_{42} I_4^2 + \alpha_5 I_5 + \alpha_{52} I_{52}^2 + \alpha_6 I_6 + \alpha_{62} I_6^2 - 1 \quad (1)$$

$$\begin{aligned} I_1 &:= \tfrac{1}{2} tr(\sigma^{pind})^2 - a(\sigma^{pind})a - b(\sigma^{pind})^2 b \\ I_2 &:= a(\sigma^{pind})a \\ I_3 &:= b(\sigma^{pind})b \\ I_4 &:= tr\sigma - a\sigma a - b\sigma b \\ I_5 &:= \tfrac{3}{2} a\sigma^{dev} a \\ I_6 &:= \tfrac{3}{2} b\sigma^{dev} b \end{aligned} \quad (2)$$

For each stress state, a corresponding value for the yield condition f can be calculated. The value of f determines the nature of the step. Values smaller than zero indicate a purely elastic step, values equal to zero an elastic step. Values larger than zero are not permissible.

The current stress state can be decomposed. The invariants depend on the plasticity inducing stresses σ^{pind} and the deviatoric part σ^{dev}. They also depend on the structural vectors a and b, describing the orthogonal symmetry of the material. Each invariant is affiliated to a specific load case. I_1, I_2 and I_3 belong to shear loads in 12-, 13- and 23-direction. Invariants I_4, I_5 and I_6 belong

  doi:10.5075/epfl-298799_978-2-9701614-0-0

to uniaxial stresses in the main directions. Using also the square of these invariants enables differentiation between tension and compression.

The alpha parameters determine the hardening characteristics of the element after reaching the yield criterion. These parameters can be obtained by assuming a = [1,0,0]^T and b = [0,1,0]^T. To determine α_1, α_2 and α_3 the parameters corresponding to shear loads, the following pure shear stress states are presumed. Since Y_i are the initial yield strengths for shear in the respective direction, f should be equal to zero in each case:

Shear-12:

$$\sigma = \begin{bmatrix} 0 & Y_{12}^S & 0 \\ Y_{12}^S & 0 & 0 \\ 0 & 0 & 0 \end{bmatrix}$$

Shear-13:

$$\sigma = \begin{bmatrix} 0 & 0 & Y_{13}^S \\ 0 & 0 & 0 \\ Y_{13}^S & 0 & 0 \end{bmatrix}$$

Shear-23:

$$\sigma = \begin{bmatrix} 0 & 0 & 0 \\ 0 & 0 & Y_{23}^S \\ 0 & Y_{23}^S & 0 \end{bmatrix}$$

These stress states results in the following Invariants.

Shear-12:

$$I_1 = -(Y_{12}^2),\ I_2 = Y_{12}^2,\ I_3 = Y_{12}^2,\ I_4 = 0,\ I_5 = 0,\ I_6 = 0$$

$$\rightarrow \quad f \stackrel{!}{=} 0 = \alpha_1 I_1 + \alpha_2 I_2 + \alpha_3 I_3 - 1$$

Shear-13:

$$I_1 = 0,\ I_2 = Y_{13}^2,\ I_3 = 0,\ I_4 = 0,\ I_5 = 0,\ I_6 = 0 \quad \rightarrow \quad f \stackrel{!}{=} 0 = \alpha_2 I_2 - 1$$

Shear-23:

$$I_1 = 0,\ I_2 = 0,\ I_3 = Y_{23}^2,\ I_4 = 0,\ I_5 = 0,\ I_6 = 0 \quad \rightarrow \quad f \stackrel{!}{=} 0 = \alpha_3 I_3 - 1$$

Solving these three equations results in:

$$\alpha_1 = \frac{(Y_{12}^S)^2(Y_{13}^S)^2 + (Y_{12}^S)^2(Y_{23}^S)^2 - (Y_{13}^S)^2(Y_{23}^S)^2}{(Y_{12}^S)^2(Y_{13}^S)^2(Y_{23}^S)^2}$$

$$\alpha_2 = \frac{1}{(Y_{13}^S)^2}$$

$$\alpha_3 = \frac{1}{(Y_{23}^S)^2}$$

The same procedure can be used to obtain the rest of the alpha parameters.

The yield surface can also be written in a tensor-notation, which simplifies calculating the derivatives required by the newton-raphson scheme that is needed during the plasticity algorithm.

$$f(\bar{\sigma}, \mathbf{A}, \mathbf{B}, \bar{\varepsilon^p}) = \frac{1}{2}\sigma : \mathbb{K} : \bar{\sigma} + \mathbf{L} : \bar{\sigma} - 1 \tag{3}$$

In the first step of the implemented plasticity algorithm, linear elasticity is presumed. The subroutine receives strains from the main program and calculates the stresses using Hooks law. This stress state is then used to calculate f. If f is smaller than zero, a purely elastic step is

  doi:10.5075/epfl-298799_978-2-9701614-0-0

assumed and the stresses are returned to Abaqus. If f is larger than zero the stress state is not permissible.

To achieve a permissible stress state, the non-permissible stress state has to be projected back onto the yield surface, so that f equals zero. The direction of this projection can be done in different ways. The simplest being a radial return, from the non-permissible state, in a straight line towards the origin. To obtain accurate predictions of plastic Poisson coefficients this material model uses a non-associative approach [7]. A second surface, called plastic potential has been formulated similar to the yield surface.

$$g(\sigma, \mathbf{A}, \mathbf{B}) = \beta_1 I_1 + \beta_2 I_2 + \beta_3 I_3 + \beta_{42}^2 I_4^2 + \beta_{52}^2 I_5^2 + \beta_{62}^2 I_6^2 - 1 \tag{4}$$

In tensor notation with its derivatives with respect to σ:

$$g(\sigma, \mathbf{A}, \mathbf{B}) = \tfrac{1}{2}\sigma : \mathbb{M} : \sigma - 1 \tag{5}$$

$$\delta_\sigma g = \mathbb{M} : \sigma \tag{6}$$

$$\delta_{\sigma\sigma} g = \mathbb{M} \tag{7}$$

For the plastic flow parameters β_1, β_2, β_3, β_{42}, β_{52} and β_{62} the initial values of the respective yield surface parameters α_i have been used. In contrast to the yield surface, the plastic potential is not dependent on plastic strain but is constant. The tensor $\mathbb{M}$ gives us the direction perpendicular to the plastic potential surface.

The elastic-trial stress state has to be projected along the direction of $\mathbb{M}$ back to the yield surface. The new stress σ_{n+1} can be calculated as follows:

$$\sigma_{n+1}^k = \mathbb{F}_{n+1}^k : \sigma_{n+1}^{tr} \tag{8}$$

$$\text{with: } \mathbb{F}_{n+1}^k = [\mathbb{1} + \Delta\gamma_{n+1}^k \mathbb{C}_e : \mathbb{M}]^{-1} \tag{9}$$

A value for γ has to be found, where Eq. (10) is true.

$$f_{n+1}^k = \tfrac{1}{2}\sigma_{n+1}^k : \mathbb{K}_{n+1}^k : \sigma_{n+1}^k + \mathbb{L}_{n+1}^k : \sigma_{n+1}^k - 1 = 0 \tag{10}$$

Since the yield surface is not constant but changes its shape and size with ongoing plastic deformation, which is in turn dependent on the current stress state Eq. (10) has to be solved numerically.

In this material model, this is done using the newton-raphson algorithm. This algorithm produces a new estimate of γ using the following scheme:

$$\Delta\gamma_{n+1}^{k+1} = \Delta\gamma_{n+1}^k + \Delta^2\gamma_{n+1}^k \tag{11}$$

$$\Delta^2\gamma_{n+1}^k = \frac{f|_{n+1}^k}{(\frac{\delta f|_{n+1}^k}{\delta\Delta\gamma_{n+1}^k})} \tag{12}$$

Eq. (12) contains the derivatives of the yield function with respect to γ. This derivative can be determined as follows:

$$\frac{\delta f_{n+1}}{\delta\Delta\gamma_{n+1}} = \frac{\delta f_{n+1}}{\delta\sigma_{n+1}} : \frac{\delta\sigma_{n+1}}{\delta\Delta\gamma_{n+1}} + \frac{f}{\delta\mathbb{K}_{n+k}} : \frac{\delta\mathbb{K}_{n+1}}{\delta\Delta\gamma_{n+1}} + \frac{\delta f}{\delta\mathbb{L}_{n+1}} : \frac{\delta\mathbb{L}_{n+1}}{\delta\Delta\gamma_{n+1}} \tag{13}$$

  doi:10.5075/epfl-298799_978-2-9701614-0-0

2.2 Numerical implementation

The call of the subroutine for a Gauss point works as follows.

1. Abaqus passes the current deformation and the internal variables of the last step.
2. Elastic predictor: The step is assumed to be purely elastic and the trial stresses are calculated via hooks law.
3. Eq. (1) is evaluated using the trial stresses. If the result indicates an elastic step, the calculated trial stress is returned to Abaqus.
4. If it indicates a plastic step, the local Newton-Raphson iteration starts here.
    a. First, the tensor $\mathbb{M}$ gets calculated and $\mathbb{F}_{n+1}^{k}$ is set up according to eq. (9) as a function of γ. A new stress state σ_{n+1}^{k} is calculated using eq. (8).
    b. Depending on the current deformation, the hardening parameters α_i are determined via a table lookup.
    c. Eq. (1) is evaluated using σ_{n+1}^{k} and α_i determined in a. and b. If the value of f is smaller than a set tolerance, the iteration algorithm stops and the subroutine continues with step 5.
    d. The derivative of the yield surface with respect to gamma is set up according to eq. (13)
    e. A new γ is determined according to eq. (12)
5. The stress and the internal variables are transferred to Abaqus.

2.3 Homogenisation of non-linear material properties

The proposed material model is designed to simulate the response of a specific laminate. Carrying out experiments to determine the properties of each laminate stacking in a structure can be a tedious and expensive venture. An alternative is, to test a single unidirectional ply and derive the properties of different laminates from the results. The non-linear material behaviour cannot be analytically homogenised as easily as purely linear-elastic behaviour. Therefore, these properties are determined in a virtual experiment.

This homogenisation is done using a python script [2] that creates nine cubes made out of a prescribed ply stack. Periodic boundary conditions as described in [8] are applied to emulate unidirectional load on a representative volume element. The result of one of these simulations can be seen in figure 1.

  doi:10.5075/epfl-298799_978-2-9701614-0-0

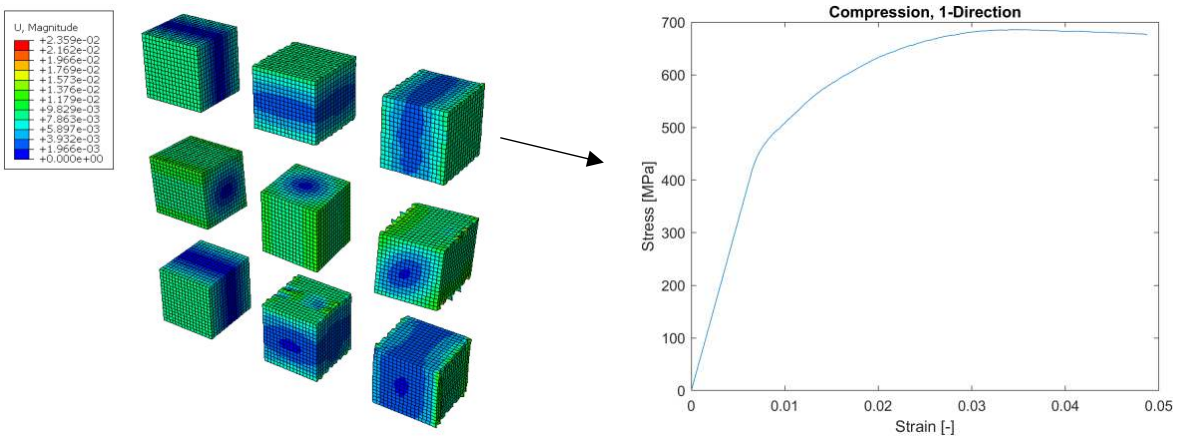

Figure 1. Results of a virtual test, to determine the nonlinear stress-strain response of a specific laminat

Another script evaluates these simulations and provides stress-strain diagrams as a result. These can be used to determine the elastic material properties as well as the plastic properties. Young's moduli and Poisson ratios describe the elastic realm. Hardening curves consisting of tables of one hundred pairs of stress-strain values per load type are used to describe the plastic behaviour.

3. Validating the material model

In order to validate the homogenisation and the reduction from a layer-based to a laminate-based material model, a series of experiments is carried out. In addition to the validation, these experiments are also used to generate material parameters of unidirectional material used in the Astir CS.

Three different laminate structures will be investigated. On the one hand, samples with fibres exclusively in fibre direction ([100,0,0]), on the other hand a 0°-dominated laminate ([50,40,10]) and a quasi-isotropic one ([25-50-25]).

Tests are carried out under compression- (according to ASTM D6641) and under tension-loading (ASTM D3039). Properties under shear loading are determined using V-notched-rail tests (ASTM D7078). Special attention is paid to recording the non-linear range of the stress-strain curve.

4. Crash simulation of a FRP glider fuselage

In a first step, the fuselage of an Astir CS was 3D scanned. A CAD model was created from the data generated by the scan and translated into a shell-model for Abaqus. This model was then compared with the manufacturer's construction plans and reduced to structurally relevant components. Material parameters are provided by literature. The first simulations were carried out with commercially available material models from Abaqus. Results of these simulations are shown in figure 2.

  doi:10.5075/epfl-298799_978-2-9701614-0-0

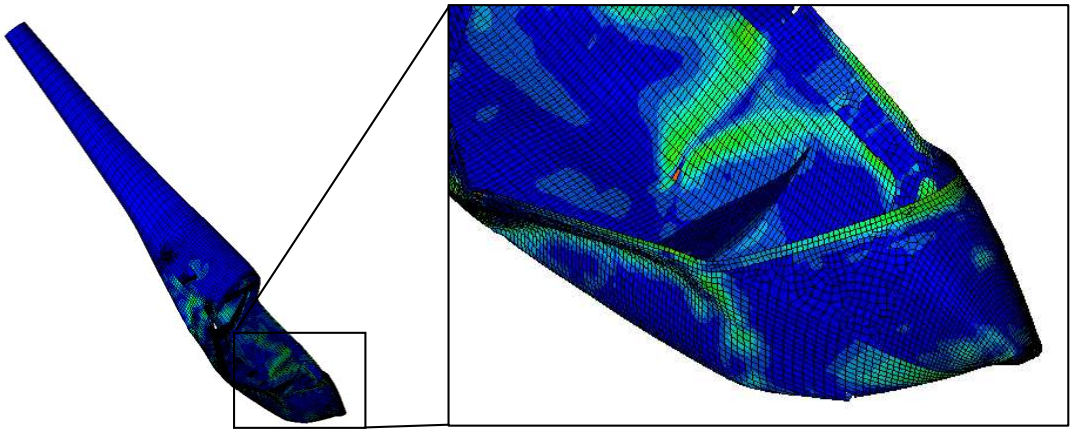

Figure 2. Crashsimulation of a FRP glider fuselage without plasticity

In a next step, the shell model was replaced by three dimensional elements. In a first attempt, each layer is represented by one element in thickness direction and a transversal isotropic elasto-plastic material model is represented. A damage routine has not yet been implemented. The results of such a simulation can be seen in figure 3. This preliminary simulation does not serve as a prediction for the crash event in this case. However, the plastic behaviour is clearly visible.

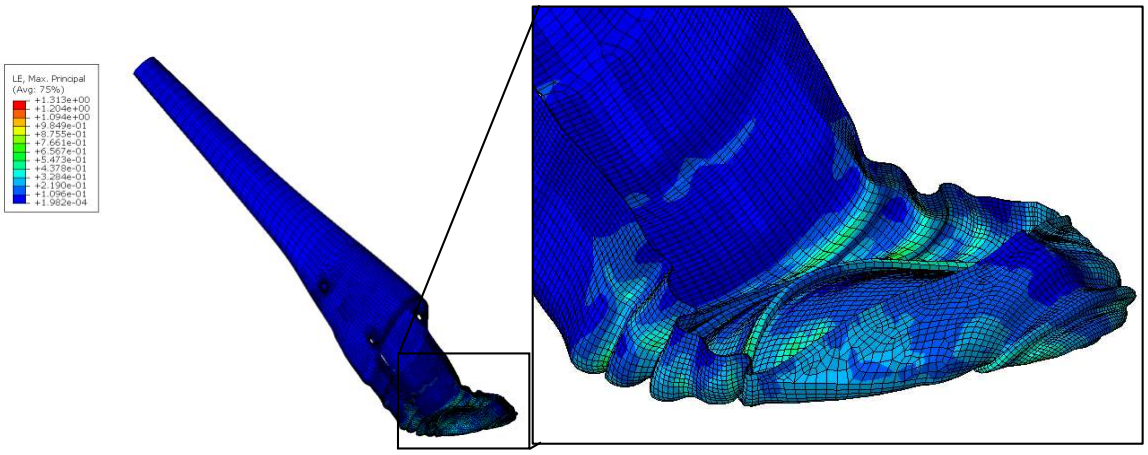

Figure 3. Crashsimulation of a FRP glider fuselage with plasticity

In a final step, the number of elements is reduced to one element in the thickness direction and the material model described in chapter 2 is applied. A fracture energy based continuum damage model will be implemented at a later stage.

5. Conclusion

The consideration of non-linear material behaviour when simulating FRP has the potential to improve the accuracy of crash behaviour prediction. However, this is done at the expense of a short computation time. The approach presented here, including the orthotropic elasto-plastic

  doi:10.5075/epfl-298799_978-2-9701614-0-0

material model developed for this purpose, makes it possible to contain this effect to a reasonable level. The accuracy of the prediction of processes that are not particularly relevant for the crash is given up in favour of faster computing time. However, effects that are relevant for the crash can be simulated accurately.

Using the proposed procedure the crash of a glider can be simulated in a short time. The simulation becomes an effective tool in the design of retrofittable crash modules for a glider. However, the process also has many potential applications beyond the task in this research project. Especially with regard to the layer structures used in rotor blades of wind turbines.

For a sufficient validation of the material model, further tests will be carried out on coupons, on smaller substructures and on large structures. After material parameters have been determined and the model has been calibrated on subcomponents, the crash of an aircraft is simulated in a full-scale test and compared with the simulation. An investigation of fundamentally different laminate structures is necessary to narrow down the range of application more precisely.

Acknowledgements

The funding of this research from the German "Federal Ministry for Economic Affairs and Climate Protection" within the framework of the Aviation Research Programme (LuFo) is gratefully acknowledged.

6. References

1. Belingardi G, Chiandussi G, Vehicle Crashworthiness Design – General Principles and Potentialities of Composite Material Structures, Impact Engineering of Composite Structures, Southern Illinois University, Carbondale, IL, USA; 2011; 193-260
2. Scheffler S, Ein neuer Modellierungsansatz zur systematischen numerischen Untersuchung des Versagensverhaltens von Verbindungen in FVK, Institut für Statik und Dynamik, 2018
3. Ernst G, Multiscale Analysis of Textile Composites – Stiffness and Strength -, Institut für Statik und Dynamik, 2009
4. Sokolinsky S, Numerical simulation of the crushing process of a corrugated composite plate, Composites: Part A 42; 2011; 1119-1126
5. Siromani D, Finite element modeling of the crushing behavior of thin-walled CFRP tubes under axial compression, Composites: Part B 64; 2014; 50-58
6. Thornton P.H., Energy Absorption in Composite Structures. J. Composite Materials Vol. 13, 1979: 247-262
7. Vogler M, Anisotropic Material Models for Fiber Reinforced Polymers, Institut für Statik und Dynamik, 2015
8. Sun CT, Vaidya RS Prediction of composite properties from a representative volume element. Composite Science and Technology, 1996; 56(2):171-179

  doi:10.5075/epfl-298799_978-2-9701614-0-0

NUMERICAL SIMULATION OF MICROSCALE CRACK PROPAGATION IN GLASS-EPOXY COMPOSITES USING DISCRETE FIBRES, MATRIX AND INTERFACE

Alexander Seidel[a], Anastasiia Khudiakova[a], Dennis Bublitz[a], Klaus Drechsler[a]

a: Chair of Carbon Composites, Department of Aerospace and Geodesy, TUM School of Engineering and Design, Technical University of Munich, Boltzmannstr. 15, 85748 Garching, Germany
E-Mail: alexander.seidel@tum.de

Abstract: *The material behaviour of an E-glass-fibre-reinforced epoxy is modelled on the microscale with discrete fibres, matrix and interface to predict the crack initiation and propagation process. Therefore, statistically relevant representative volume elements (RVEs) are generated using an adapted algorithm. An RVE fulfils periodicity in its geometry, mesh and its boundary conditions. Advanced material models are used for the matrix (Drucker-Prager plasticity with triaxiality-dependent damage) and the interfaces (Cohesive Zone Modelling). The model is calibrated with experimental data. The crack propagation is simulated for a tough and a brittle fibre-matrix interface. The results are considered qualitatively feasible.*

Keywords: Finite Elements; Microscale Simulation; Crack Propagation; GFRP; Abaqus

1. Introduction

The emission of greenhouse gases has to be significantly reduced in the coming years to minimise the negative impact on the environment. This goal can primarily be achieved by increasing the share of renewable energies, and in particular wind energy applications, in the total energy production. With the blades being one of the major structural parts of a horizontal axis wind turbine and those consisting dominantly of composites, understanding the mechanical behaviour of this material class will be crucial to designing new and optimising existing wind turbines. A main design criterion of wind turbine blades is to withstand extreme loads that would appear in the most unfavourable conditions during service. As fracture in composites starts at the scale of the individual fibres and subsequently leads to total failure, an investigation of the fracture behaviour of composites at this exact microscale can help to better understand the overall material response. Thus, in the scope of this work a Finite Element approach is presented to model the crack initiation and propagation in composite materials on the microscale in an E-glass-reinforced epoxy (glass-fibre reinforced polymer, GFRP) used in wind applications. This work focuses only on the material response transverse to the fibre direction, but by using solely three-dimensional elements, this method can easily be adapted to more complex load cases. The simulations are carried out using *Abaqus FEA* by *Dassault Systèmes Simulia Corp.* [1].

2. Numerical Model

2.1 Fibre Placement Procedure

The geometry of the microstructure of the GFRP is modelled using a representative volume element (RVE). Therefore, a statistically representative placement of the fibres is essential to

  doi:10.5075/epfl-298799_978-2-9701614-0-0

facilitate a correct material behaviour. An adapted version of the Random Sequential Expansion (RSE) algorithm described by Yang et al. [2] is utilised to generate such RVEs. The RSE algorithm is able to generate RVEs with a fibre volume content (FVC) of up to approximately 68 % [2]. The RSE algorithm adds circles representing the fibre cross sections to a domain of predefined size until the FVC in the current step exceeds the desired FVC. With this approach, the resulting FVC will differ slightly from the desired FVC. The adapted algorithm circumvents this by predefining the number of circles in the resulting RVE and from it calculating the size of the domain.

2.2 Mesh Generation

To perform a Finite Element Analysis of the RVE, the geometry has to be meshed. To allow for future investigations not only transverse to the fibre direction but also in fibre direction, an automated three-dimensional meshing workflow is implemented using *GMSH* [3]. The geometric information of the fibre placement procedure is used to reconstruct the geometry of the two-dimensional RVE. Subsequently, a layer of interface elements is inserted between the fibres and the matrix. To ensure that these interface elements are not distorted, the number of mesh points along the circle separating the interface from the fibre and the number of mesh points separating the interface from the matrix is set equal. Opposite sides of the two-dimensional region are defined to be periodic to facilitate not only a periodic geometry but also a periodic mesh. Subsequently, the two-dimensional geometry is meshed using dominantly four-noded rectangular elements. The resulting mesh is extruded along the fibre-direction. This way, a fully periodic mesh consisting of dominantly hexahedral and few prismatic elements is generated. The element types used are hexahedral elements with reduced integration and enhanced hourglass control (C3D8R) and prismatic elements (C3D6) for the fibres and the matrix and hexahedral cohesive elements (COH3D8) with a traction-separation response for the interfaces.

2.3 Model Definition

Periodic boundary conditions (PBCs) are applied quasi-statically to all sides of the RVE to ensure compatible displacements. For applying the PBCs, the *Abaqus* plugin *EasyPBC* by Omairey et al. [4] is utilised.

The glass fibres are not expected to show fracture under loading transverse to the fibre direction. In accordance with [5, 6], they are modelled as isotropic, linear elastic materials.

The matrix material model has to depict the complex material behaviour of an epoxy polymer. A main characteristic of epoxies is a triaxiality-dependent ductility. As was found in the literature [7, 8], epoxies show brittle behaviour when loaded in tension but ductile behaviour when loaded in compression. Models that have been used to predict this behaviour are the Mohr-Coloumb [9] and the related Drucker-Prager [5, 6, 10, 11] plasticity model. In the scope of this work, the linear Drucker-Prager plasticity model included in *Abaqus* was chosen because of its numerically beneficial simplicity compared to the Mohr-Coloumb plasticity model. The yield criterion for the Drucker-Prager model reads [1]:

$$F = t - p\tan(\beta) - d = 0 \text{ with } t = \frac{1}{2}q\left[1 + \frac{1}{K} - \left(1 - \frac{1}{K}\right)\left(\frac{r}{q}\right)^3\right]. \quad (1)$$

Herein, the following variables derived from stress invariants are used [1]: the equivalent pressure stress: $p = -1/3\, I_1$, the von Mises equivalent stress: $q = \sqrt{3 \cdot J_2}$ and the third

  doi:10.5075/epfl-298799_978-2-9701614-0-0 published under CC BY-NC 4.0 license

invariant of the deviatoric stress tensor: $r = J_3$. I_1 is the first invariant of the Cauchy stress tensor and J_2 and J_3 are the second and third invariant of the deviatoric stress tensor, respectively. β is the slope of the linear flow surface in the meridional (p-t) plane also referred to as friction angle, d is the cohesion stress and K is the flow stress ratio. To calculate β and K from experiments, the Drucker-Prager model can be matched to the Mohr-Coloumb model for the case of a triaxial test response [1, 5, 6]. This means that both models coincide under triaxial tension and compression. The Mohr-Coloumb model is defined using a cohesion stress c and a friction angle ϕ. Their relations to the tensile and compressive strengths $\sigma_{\mathrm{matrix},t}$ and $\sigma_{\mathrm{matrix},c}$ read [9]:

$$\sigma_{\mathrm{matrix},t} = 2c\frac{\cos\phi}{1+\sin\phi}\,,\ \sigma_{\mathrm{matrix},c} = 2c\frac{\cos\phi}{1-\sin\phi}\,. \tag{2}$$

Here, it has to be kept in mind, that the Mohr-Coloumb cohesion stress is not the same as the Drucker-Prager cohesion stress ($c \neq d$). The same applies for the Mohr-Coloumb friction angle and the Drucker-Prager friction angle ($\phi \neq \beta$). The relation follows as [1]:

$$\tan\beta = \frac{6\sin\phi}{3-\sin\phi}\,, K = \frac{3-\sin\phi}{3+\sin\phi}\,. \tag{3}$$

The cohesion stress d is dependent on the material hardening behavior. In this work, d is defined by the uniaxial tension yield stress $d = \big((1/\mathrm{K}) + (1/3)\tan(\beta)\big)\sigma_{\mathrm{matrix},t}$ [1]. The flow potential of the Drucker-Prager model is defined as $G = t - p\tan\psi$, with ψ being the dilational angle in the meridional plane [1]. The volume change of polymers in the yielding and in the post-yielding deformation regime are reported to be of minor influence [12], which means that polymers can be seen as approximately non-dilatant. Thus, $\psi = 0$ is chosen in the scope of this work. The Drucker-Prager yield surface is depicted in Figure 1. Material hardening is considered by extracting tabular data for true stress versus absolute plastic strain from tensile experiments. To include a triaxiality dependence not only during plastification but also during the onset of damage, a phenomenological ductile damage criterion proposed by Hooputra et al. is utilised [1, 13]. The criterion initiates damage as soon as the equivalent plastic strain at a material point $\bar{\varepsilon}_D^{pl}(\eta)$ reaches a critical value [1]. $\bar{\varepsilon}_D^{pl}$ is a function of the stress triaxiality η with $\eta = -p/q$ depending upon p and q as defined above. After damage initiated, the degradation of the material is modelled using the damage variable D. D can take values in the range $[0,1]$, where 0 represents an undamaged element and 1 represents a fully damaged element. D has a direct influence on the stiffness of the material and its yield stress. In the scope of this work, D is calculated based on the energy G_f dissipated during the damage process. For further information on the damage models used in *Abaqus*, the reader is referred to [1].

The fibre-matrix interface is modelled using a Cohesive Zone Modelling approach as pioneered for composites by González and Llorca. [14]. A single layer of cohesive elements has been inserted between the fibres and the matrix as described above. Their constitutive response is modelled using a bi-linear traction-separation law. This sets the traction vector acting on an element in relation to the separation displacement between its bottom and its top surface. The initial stiffness is defined by K. The onset of damage is determined by the quadratic nominal stress criterion [1]:

$$\left\{\frac{\langle t_n\rangle}{t_n^0}\right\}^2 + \left\{\frac{t_s}{t_s^0}\right\}^2 + \left\{\frac{t_t}{t_t^0}\right\}^2 = 1\,, \tag{4}$$

  doi:10.5075/epfl-298799_978-2-9701614-0-0 published under CC BY-NC 4.0 license

with ⟨ ⟩ as Macaulay brackets, t_n as normal traction stress, t_s and t_t as shear traction stresses along two directions and ^{0} denoting the peak values of the respective stresses. After the onset of damage, the material response is degraded using the damage variable D. This is applied without restriction to t_s and t_t, whereas t_n is only degraded in tension (no damage in compression). The displacement at failure δ_f is determined using the mode-independent fracture energy G_f. The traction-separation response is depicted in Figure 2.

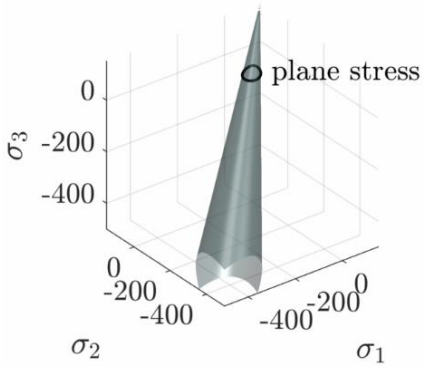

Figure 1: Drucker-Prager yield surface of the calibrated model for principle stresses.

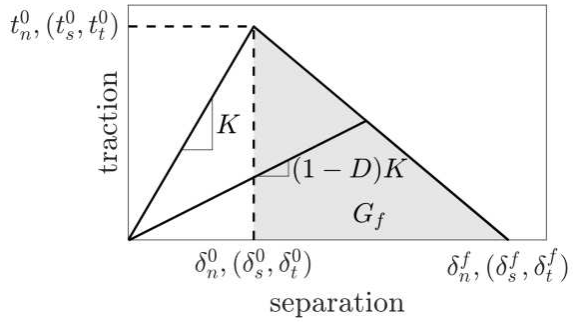

Figure 2:Traction-separation response. Recreated from [6].

3. Calibration of the Material Models

The materials used in the scope of this work are the resin *EPIKOTE™ Resin MGS™ RIMR 135 + EPIKURE™ Curing Agent MGS™ RIMH 137* from *Hexion Inc., Columbus, OH, USA* and the fibres *Hybon™ 2150* from *Nippon Electric Glass Co., Ltd., Ōtsu, Japan.* The geometric parameters needed for the RVE generation are extracted from a statistical evaluation of micrographs of unidirectional composites using this material pairing. The mean fibre diameter and the fibre diameter standard deviation result to $17.65\ \mu\text{m}$ and $1.41\ \mu\text{m}$. The interface thickness is set to $0.1\ \mu\text{m}$ as found in the literature, e.g in [5]. The total number of fibres in the RVE is set to 30 based on a separately carried out parameter study. With an FVC of $67\ \%$, the RVE size results to $106.45\ \mu\text{m}$. As the material response along the fibre direction is of no interest in this first step of investigation, the number of elements in fibre direction is kept small, namely 6, in order to reduce the computational workload. Nevertheless, for future investigations, this value can easily be increased. The resulting meshed geometry is depicted in Figure 3.

To determine the Young's modulus of the fibres, single fibres were tested under tensile load. It resulted to $E_{\text{fibre}} = 76469\ \text{MPa}$ and is in good agreement with values reported in the literature (e.g. $E_{\text{fibre}} = 74000\ \text{MPa}$ in [8]). The Poisson's ratio is expected to not vary to a significant degree for typical E-glass fibres. Therefore, the value of $\nu_{\text{fibre}} = 0.2$ is taken from [8].

The material parameters for the resin were determined by carrying out neat resin tensile tests (see Figure 4a) and neat resin compression tests (see Figure 4b) as well as neat resin V-notched rail shear tests (see Figure 4c). The resulting true stress versus true strain diagrams were used to extract the material parameters needed. As mentioned above, the hardening behaviour is defined using the tensile test results. As can be seen in Figure 4a, the material response under uniaxial tension does vary only to a small degree. Therefore, one representative specimen is chosen to extract the Young's modulus and the hardening behaviour. The difference of the sample's Young's modulus $E_{\text{matrix}} = 3019\ \text{MPa}$ compared to the averaged Young's modulus in

tension $\bar{E}_{\text{tens}} = 3041$ MPa and compression $\bar{E}_{\text{comp}} = 3056$ MPa is negligible. As can be seen in Figure 4a, the material softens slightly until final fracture. The difference in G_f when neglecting softening compared to considering softening for this material is $\Delta G_f \approx 0.8\,\%$. Thus, the fracture energy is set to a small value of $G_{f,\text{matrix}} = 0.001$ N/mm to cause element failure just after damage initiation as proposed in [5]. The values for the tensile strength $\sigma_{\text{matrix},t}$ and compressive strength $\sigma_{\text{matrix},c}$ of the matrix are extracted as averages from the tensile and compressive tests. With $\sigma_{\text{matrix},t} = 73.48$ MPa, $\sigma_{\text{matrix},c} = 93.53$ MPa and Equation (2), the Mohr-Columb cohesion stress and Mohr-Columb friction angle result to $c = 41.45$ MPa and $\phi = 6.89\,°$. Using Equation (3): $\beta = 14.04\,°$ and $K = 0.9230$. As already mentioned, non-dilatant flow is assumed ($\psi = 0$).

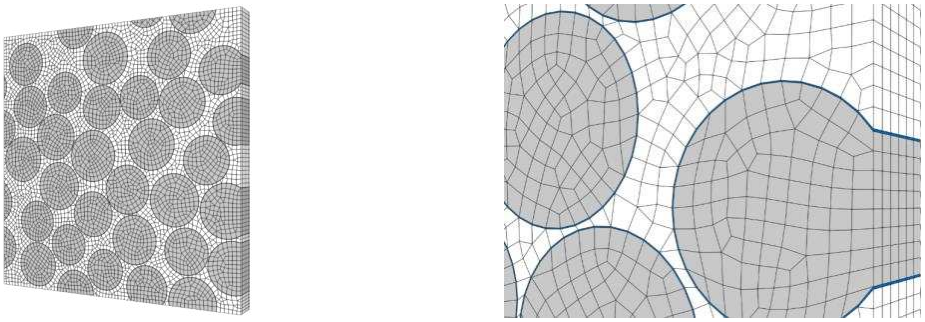

(a) Whole model. *(b) Detailed view of inserted elements.*

Figure 3: Meshed RVE. Fibres are depicted in grey, the matrix is depicted in white and the interfaces are depicted in blue.

As $G_{f,\text{matrix}} = 0.001$ N/mm for all triaxiality states, the onset of damage and final failure fall closely together. For that reason, the values for $\bar{\varepsilon}_D^{pl}$ for $\eta = -1/3, 0, 1/3$ are determined at the stage of ultimate failure (instead of onset of failure). Testing up to final failure under compression was not possible with the test setup used. For that reason, the following approach was chosen to introduce a relation $\bar{\varepsilon}_D^{pl}(\eta)$ (see Figure 4d). First, the equivalent plastic strain at the onset of failure is determined for $\eta = -1/3, 0, 1/3$ and an exponential function of form $\bar{\varepsilon}_D^{pl} = a\exp(-b\,\eta) + c$ is fitted to these three points obtained [10] (1). Secondly, the plastic strain difference from onset of damage to final failure for tension $\Delta\bar{\varepsilon}_t{}^{pl}$ is determined and the same exponential function is fitted to the three points shifted by $\Delta\bar{\varepsilon}_t{}^{pl}$ (2). Thirdly, the difference from onset of damage to final failure for shear $\Delta\bar{\varepsilon}_s{}^{pl}$ is determined. The difference from onset of damage to final failure for compression $\Delta\bar{\varepsilon}_c{}^{pl}$ is calculated as linear extrapolation of $\Delta\bar{\varepsilon}_t{}^{pl}$ and $\Delta\bar{\varepsilon}_s{}^{pl}$ (as it cannot be determined by the experiments). The same exponential function is fitted to the three new points (3). Lastly, as this scaled function yields unconventionally high values for $\eta = -1/3$, the final function is defined as a piecewise combination of the functions from step 2 and 3. If $\eta > 0$, $\bar{\varepsilon}_D^{pl}$ = function 3. Else, $\bar{\varepsilon}_D^{pl}$ = function 2 shifted upwards to fulfil continuity at $\eta = 0$ (4). The entire process with all its sub-functions is depicted in Figure 4d. The comparison between the experiments and the material model is depicted in Figure 4a – d.

The interface parameters are crucial for the overall RVE response [5, 9]. As the parameter values are difficult to determine experimentally, the stiffnesses are all set to a high value to ensure displacement continuity at the transition from fibres to matrix as commonly used for example in [5, 6, 15]: $K_{nn} = K_{ss} = K_{tt} = 1 \times 10^8$ N/mm^3. The peak traction stresses are all set to the cohesion of the resin as proposed by Totry et al. [15]: $t_n^0 = t_s^0 = t_t^0 = c = 41.45$ MPa. Two

  doi:10.5075/epfl-298799_978-2-9701614-0-0

different values are used to describe the damage evolution: $G_{f,\text{interface}} = 0.01$ N/mm (tough interface) and $G_{f,\text{interface}} = 0.002$ N/mm (brittle interface).

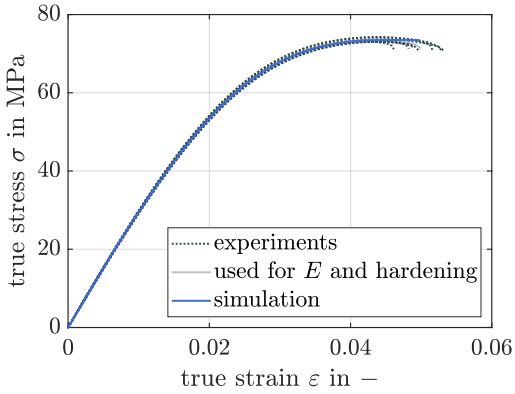

(a) Experiments and simulation for tension.

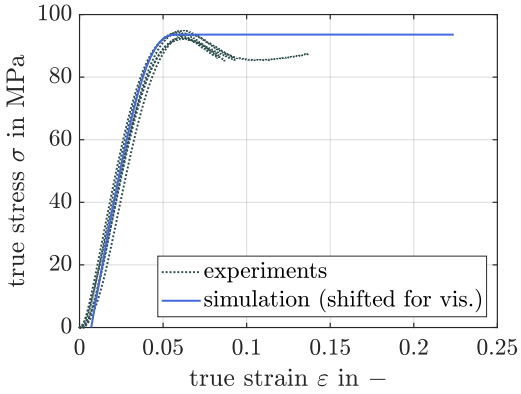

(b) Experiments and simulation for compression. Ultimate failure is not reached.

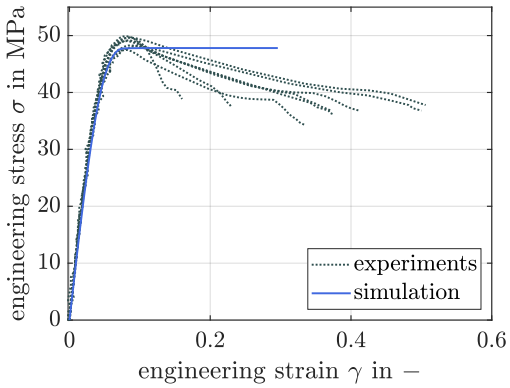

(c) Experiments and simulation for shear.

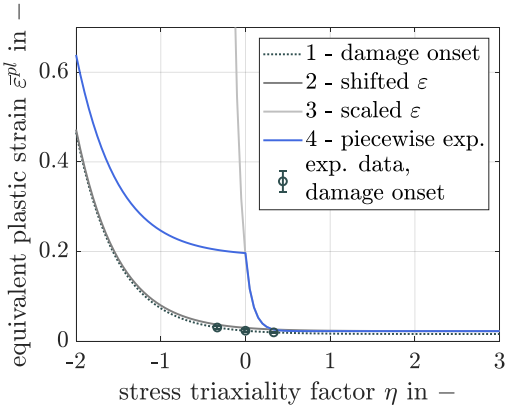

(d) Piecewise exponential triaxiality dependence for the onset of damage.

Figure 4: Calibrated material model.

4. Predicted Failure Modes by Crack Propagation

The RVE depicted in Figure 3 is loaded transverse to the fibre direction in uniaxial tension, uniaxial compression and pure shear for the case of a tough and a brittle fibre-matrix interface. The resulting failure modes are depicted in Figure 5.

5. Discussion

The material model for the fibres was calibrated directly with the Young's modulus and Poisson's ratio derived from experiments and the literature. Consequently, the material response is coherent with the experimental results. As can be seen in Figure 4a – c, the material model for the matrix can predict the material behaviour well up to the maximum strength for all investigated load cases (uniaxial tension, uniaxial compression, pure shear). The prediction quality remains high in the softening regime for uniaxial tension. For pure shear, the model does not predict the softening behaviour observed in the experiments. Nevertheless, the ultimate failure strain lies within the boundaries described by the experimental curves. For uniaxial compression, the experimental results lack data until ultimate failure. To accommodate for this, the material behaviour was extrapolated using a multi-step approach. A thorough investigation

in this regime cannot be carried out with the experimental data present. However, epoxies are expected to show a rehardening behaviour at higher strains and a high strain at ultimate failure in compression [11]. The model material behaviour is assumed to depict this behaviour in an averaged sense. As can be seen in Figure 5, the predicted failure modes for tough and brittle interfaces are qualitatively feasible for what is reported in the literature for fibre-reinforced polymers (e.g. in [9]). Tensile loading leads for both cases to the same crack path which is perpendicular to the loading direction. In compression, the crack paths differ for both cases. A tough interface leads to a linear path at an angle of approximately $45\ °$. A brittle interface shows a more complex path at a lower angle. Under shear loading, the crack path with a tough interface is comparable to the path observed under tension ($90\ °$). This could be an indicator, that the geometry of the RVE shows a preferred crack path direction because of favourable inter-fibre distances in this region. A brittle interface leads to a path at an angle of approximately $45\ °$.

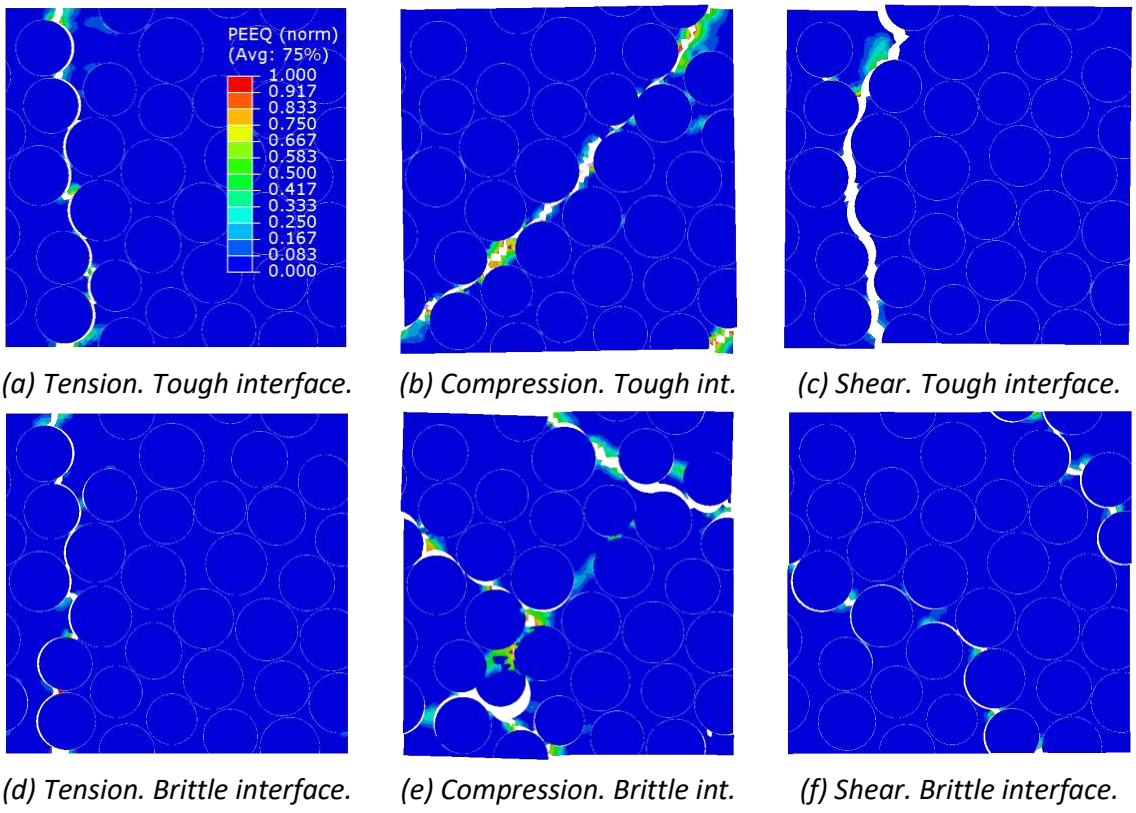

(a) Tension. Tough interface. *(b) Compression. Tough int.* *(c) Shear. Tough interface.*

(d) Tension. Brittle interface. *(e) Compression. Brittle int.* *(f) Shear. Brittle interface.*

Figure 5: Predicted crack propagation for tough and brittle interfaces. The RVEs are coloured by the equivalent plastic strain normalised to [0,1] for every simulation.

6. Conclusion

The crack initiation and propagation process in a glass-epoxy composite under loading transverse to the fibre direction was studied using Finite Element Analysis on the microscale. Therefore, representative volume elements were used to represent the bulk material. The results show a good qualitative agreement of the crack paths with fracture behaviour reported in the literature. Examining two different values of interface toughness shows that this property can have an influence on the crack path. Quantitative evaluations are still to be carried out and compared to experimental data of unidirectional specimens. Nevertheless, the presented model can be used for further investigating three-dimensional, multiaxial load cases of fibre-reinforced polymers.

  doi:10.5075/epfl-298799_978-2-9701614-0-0

7. Acknowledgements

The authors thankfully acknowledge the funding provided by the German Federal Ministry of Education and Research in the framework of the project *SensoTwin* (funding code: 13XP5121A).

8. References

1. Dassault Systèmes Simulia Corp. Abaqus Documentation Version 2017: Abaqus Materials Guide. 2017.
2. Yang L, Yan Y, Ran Z, Liu Y. A new method for generating random fibre distributions for fibre reinforced composites. Composites Science and Technology. 2013;76:14–20.
3. Geuzaine C, Remacle J-F. Gmsh: A 3-D finite element mesh generator with built-in pre- and post-processing facilities. Int. J. Numer. Meth. Engng. 2009;79:1309–31.
4. Omairey SL, Dunning PD, Sriramula S. Development of an ABAQUS plugin tool for periodic RVE homogenisation. Engineering with Computers. 2019;35:567–77.
5. Sharma A, Daggumati S. Computational micromechanical modeling of transverse tensile damage behavior in unidirectional glass fiber-reinforced plastic composite plies: Ductile versus brittle fracture mechanics approach. International Journal of Damage Mechanics. 2020;29:943–64.
6. Yang L, Wu Z, Cao Y, Yan Y. Micromechanical modelling and simulation of unidirectional fibre-reinforced composite under shear loading. Journal of Reinforced Plastics and Composites. 2015;34:72–83.
7. Asp LE, Berglund LA, Gudmundson P. Effects of a composite-like stress state on the fracture of epoxies. Composites Science and Technology. 1995;53:27–37.
8. Kaddour AS, Hinton MJ. Input data for test cases used in benchmarking triaxial failure theories of composites. Journal of Composite Materials. 2012;46:2295–312.
9. Vaughan TJ, McCarthy CT. Micromechanical modelling of the transverse damage behaviour in fibre reinforced composites. Composites Science and Technology. 2011;71:388–96.
10. Chevalier J, Camanho PP, Lani F, Pardoen T. Multi-scale characterization and modelling of the transverse compression response of unidirectional carbon fiber reinforced epoxy. Composite Structures. 2019;209:160–76.
11. Morelle XP, Chevalier J, Bailly C, Pardoen T, Lani F. Mechanical characterization and modeling of the deformation and failure of the highly crosslinked RTM6 epoxy resin. Mech Time-Depend Mater. 2017;21:419–54.
12. Lagattu F, Bridier F, Villechaise P, Brillaud J. In-plane strain measurements on a microscopic scale by coupling digital image correlation and an in situ SEM technique. Materials Characterization. 2006;56:10–8.
13. Hooputra H, Gese H, Dell H, Werner H. A comprehensive failure model for crashworthiness simulation of aluminium extrusions. International Journal of Crashworthiness. 2004;9:449–64.
14. González C, LLorca J. Mechanical behavior of unidirectional fiber-reinforced polymers under transverse compression: Microscopic mechanisms and modeling. Composites Science and Technology. 2007;67:2795–806.
15. Totry E, González C, LLorca J. Failure locus of fiber-reinforced composites under transverse compression and out-of-plane shear. Composites Science and Technology. 2008;68:829–39.

  doi:10.5075/epfl-298799_978-2-9701614-0-0

FATIGUE DAMAGE MODEL FOR COMPOSITE LAMINATES BASED ON A MORI-TANAKA FORMULATION

Matthias Drvoderic[a], Martin Pletz[a], Clara Schuecker[a]

a: Chair of Designing Plastics and Composite Materials, Department of Polymer Engineering and Science, Montanuniversitaet Leoben, 8700 Leoben, Austria;
matthias.drvoderic@unileoben.ac.at;

Abstract: *Unidirectional fiber reinforced composites develop matrix cracks in off-axis plies as the first form of damage in fatigue loading scenarios. Crack detection is used to quantify this form of damage and its resulting stiffness degradation is computed with a micromechanical model based on the Mori-Tanaka formulation. It is shown that the model predicts the stiffness degradation well when the calibration is based on the ratio of in-plane shear to transverse stress. Furthermore, a distinct separation into high and low dissipated energy of the fatigue cycles is found based on the in-plane to transverse stress ratio. This behavior links the dissipated energy to the two damage driving forces in Puck mode A stress space. All fatigue tests that show a high dissipated energy form a distinct cluster in SN diagrams whereas tests with low dissipated energy fall into a second cluster.*

Keywords: crack detection; fiber-reinforced polymers; fatigue damage model; composite fatigue; off-axis cracks

1. Introduction

The process of fatigue damage growth in multidirectional fiber-reinforced composite laminates comprises of distinct damage mechanisms which can be categorized into the characteristic damage states starting with matrix cracks followed by delamination and fiber failure [1]. Matrix cracks propagate along fibers and usually span the height of the whole ply as they grow in number and size during the fatigue life. The result of those cracks is a significant loss of ply-stiffness leading to a reduction of the global laminate stiffness [2–5]. For glass fiber-reinforced polymers (GFRPs), the density of matrix cracks can be directly computed from images of a specimen taken during fatigue tests. It is widely used as damage variable in progressive damage models or to calibrate numerical or phenomenological damage models [6–11]. Therefore, computing the crack density in an efficient way has become a vital part in experimental campaigns and algorithms have been developed to replace error prone and inefficient manual crack counting [12–14].

In the present work, Schuecker´s progressive damage model [9,15] which is based on Mori-Tanaka homogenization is used to compute the stiffness loss of a laminate due to off-axis cracks from fatigue loading. As shown in [16], the calibration of this model to experimental data can be done with standard fatigue tests combined with crack detection. However, the effect of off-axis cracks on the stiffness seems to depend on the microscopic crack type. Carraro et al. [17] have shown that off-axis matrix cracks are the result of two different damage driving forces. Local hydrostatic stress (LHS) or local maximum hydrostatic stress (LMPS) are identified as the critical stress depending on the biaxiality ratio of shear to transverse stress ($\lambda = \tau_{12}/\sigma_{22}$). This is also supported by fractographic images that show different crack patterns for off-axis cracks

  doi:10.5075/epfl-298799_978-2-9701614-0-0

depending on the level of in plane shear stress [18]. Therefore, the model has to be calibrated for both microscopic damage types. For this, the stiffness during fatigue tests as well as crack density is evaluated from an extended experimental campaign. The influence of the load level on the point of damage initiation is compared for different ratios of shear vs. transverse stress. The hysteresis of the fatigue cycles is also evaluated and compared against quasi-static stiffness data. Since the fracture surface is rather smooth for biaxiality rations smaller than one but shows shear cusps at biaxiality ratios higher than one, the dissipated energy should also be higher at higher biaxiality ratios since uneven fracture surface should result in more internal friction of the material.

2. Methods

2.1 Experimental Fatigue Data

Quasi-static stiffness, crack density and hysteresis cycles are evaluated from fatigue tests. The GFRP plates from which $\pm\theta_s$ specimen are cut were produced with vacuum pressing according to [19] with unidirectional (UD) glass fiber weave with an aerial weight of 220 g/m^2 (Porcher Industries Germany GmbH) and EPIKOTE™ MGS® LR160 as resin and EPIKURE™ MGS® LH160 as curing agent (Hexion Inc.). The stacking sequence of all specimens is $[+\theta_3/-\theta_3]_s$. All specimens except UD90° have a gauge length of 100 mm, a width of 20 mm and a thickness of 2 mm. For the UD90° specimen, a dogbone-like shape is used to prevent failure near the tabs with a gauge length of 200 mm [20].

To test different biaxiality ratios, $\pm$45°, $\pm$60°, $\pm$75° as well as UD90° specimen are tested at load levels from 50% to 85%. The load level is the ratio of the maximum load in the fatigue test to the static strength of the laminate computed by the Puck failure criterion [21]. For a detailed explanation of the load level, the reader is referred to [16]. The elastic stiffness from static tests as well as the transverse strength R_2 and in-plane shear strength R_{12} of the composite ply material which is needed for the computation of the load level is listed in Table 1.

The fatigue tests are performed with stress controlled sinusoidal load cycles with an R-ratio of 0.1 and a frequency of 3Hz for $\pm$45° specimen and 5Hz otherwise. The servo-hydraulic material testing system MTS 322 by MTS Systems Corporations is used for all tests. Additionally, the cycles had been periodically interrupted to perform displacement-controlled quasi-static tensile tests to track the degradation of the laminate stiffness. Images for the crack detection are made during the quasi-static tensile tests. Transilluminated white light imaging is used as imaging technique to achieve a high contrast between background and cracks.

Table 1: Elastic constants and strength of the composite ply material from static tests.

E_1 [GPa]	E_2 [GPa]	ν_{12} [-]	G_{12} [GPa]	R_2 [MPa]	R_{12} [MPa]
31.7	10.7	0.27	3.3	47.6	53.1

2.2 Crack Detection

The crack density as a function of the cycles is computed for each test according to

$$\rho_c = \frac{\sum_{i=1}^{n} L_i}{A} \tag{1}$$

  doi:10.5075/epfl-298799_978-2-9701614-0-0

with L_i as the length of the i^{th} crack and A as the evaluation area. This method also accounts for the length of cracks as it computes an average crack density weighted by the crack lengths instead of only accounting for the number of cracks. The algorithm form J.J. Bender [14] is used for the crack detection since it shows a high resilience against false detections or artefacts and showed good performance even near the point of crack saturation. The shift-distortion correction necessary for application of this algorithm as well as selecting the region of interest (evaluation region) is done with the python package *CrackDect* [13].

2.3 Damage model and calibration

The stiffness degradation part of Schuecker´s progressive damage model is used to compute the effect of the off-axis cracks based on experimentally obtained crack densities. The stiffness degradation is computed with a Mori-Tanaka homogenization where crack-like voids are used to mimic the effect of cracks in the ply-material. The Mori-Tanaka formulation for void inclusions is

$$E_{MTM,Void} = E^m \left[I + \frac{V}{1-V} (I - S)^{-1} \right]^{-1} \quad (2)$$

with E^m as the elasticity tensor for the ply material, V as the inclusion volume fraction of the crack-like voids and S as the Eshelby tensor. The aspect ratios for the crack-like inclusion are 100, 1, 10 in X, Y and Z-direction of the material coordinate system. This choice for the aspect ratios has shown to mimic the evolution of the engineering constants of the ply material as off-axis cracks grow [16].

Since the stiffness degradation of the damage model is based on a Mori-Tanaka homogenization, a calibration is necessary to map from the experimentally obtained crack density to the inclusion volume fraction of crack-like voids. For this, the crack density curves from the tests are fitted with a cumulative Weibull distribution function since the experimental curves show an S-like evolution when plotted over the logarithm of the number of cycles. The fitting approach with a correlation parameter μ from [16] is used since it has shown good results and is easy to automate. For the tests used in the calibration it is important that the crack density and the stiffness degradation correlate well and crack saturation is reached since the calibration incorporates an optimization routine which will yield wrong results otherwise. Therefore, the calibration curves are manually selected.

3. Results and Discussion

In Figure 1, the dissipated energy for the $\pm$45°, $\pm$60° and $\pm$75° laminate is shown for two load levels. There is a substantial jump in dissipated energy from the $\pm$75° and$\pm$60° to the $\pm$45° laminate. The biaxiality ratio λ for $\pm$45°, $\pm$60° and $\pm$75° is 1.7, 0.5 and 0.2, respectively. This jump could be a sign of the shift of damage driving force from LHS to LMPS. This corresponds to the findings of Quaresimin and Carraro [4], that for biaxiality ratios higher than 1, the damage driving force switches from LHS to LMPS and shear cusps start to develop resulting in an uneven and coarse fracture surface. This is expected to generate more internal friction with cyclic loading and therefore result in a higher dissipated energy. The dissipated energy also increases slightly with the applied load level, but this effect is much smaller than the gap between the $\pm$45° and $\pm$60° specimen.

  doi:10.5075/epfl-298799_978-2-9701614-0-0

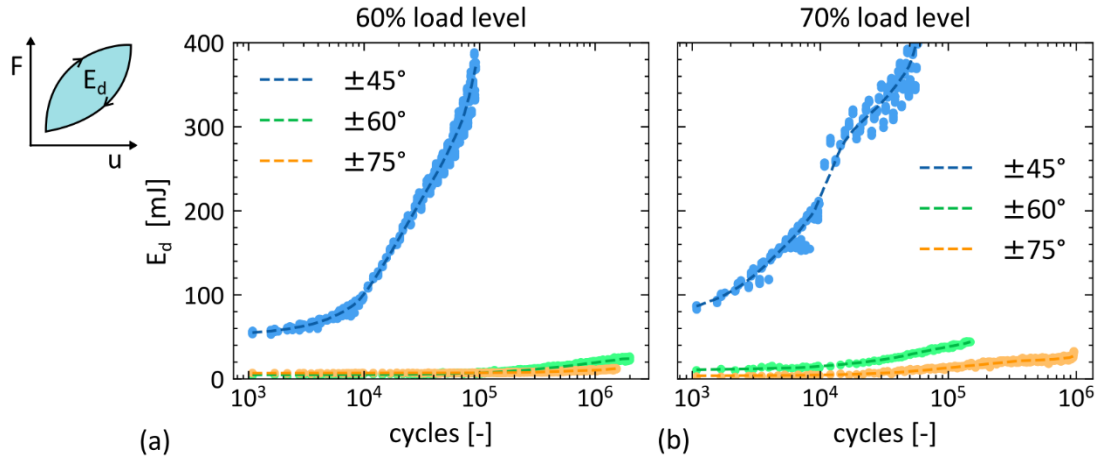

Figure 1: Dissipated energy E_d (scatter) for ±45°, ±60° and ±75° at 60% load level (a) and 70% load level (b) with overall trend for each test (dotted line). The pictogram shows the computation of the dissipated energy as integral over the hysteresis cycle.

Figure 2a shows the fitted curves for the crack detection for ±45° and ±60° tests at a load level of 55%, 60% and 70% as well as ±75° at 60% and 70% load level. Each series shows a clear trend to damage initiation at lower cycles counts for higher load levels. Also, the crack density curves show similar shape aside from ±60° at 55% and ±75° at 60% load level where the tests were stopped at 10^6 and $1.5 \cdot 10^6$ cycles, respectively. Figure 2b shows SN-data for damage initiation of the tests. The damage initiation is defined as the cycle where a crack density of 0.2 mm^{-1} is reached. It is clearly visible that the damage initiation for the ±45° tests and the other tests form two clusters in an SN-diagram. The SN-data for ±45° shows that no other tests fall into its scatter band (95% confidence interval) and all tests for ±60°, ±75° and UD90° form their own scatter band without interfering with the ±45° tests. This suggests that the dissipated energy can indeed be used as a criterion to separate the damage mechanism.

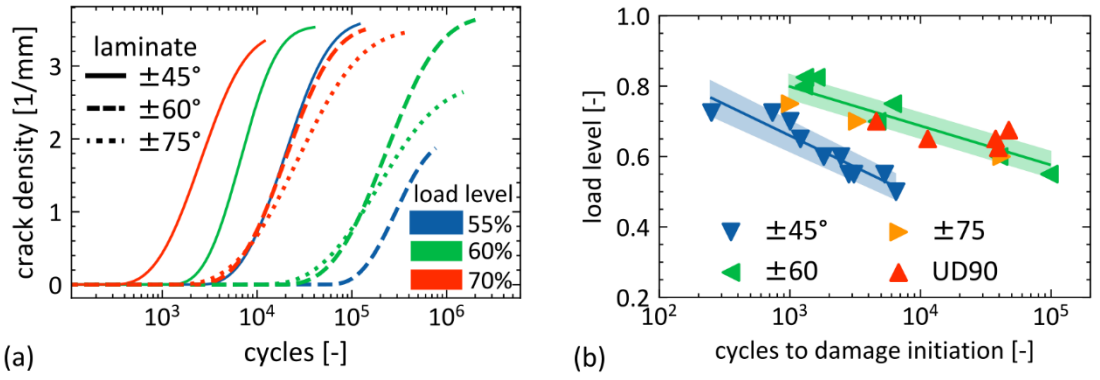

Figure 2: Fitted crack density curves (a) for ±45°, ±60° and ±75° laminates for various load levels and cycles to damage initiation (b).

To calibrate the stiffness degradation model, the method described in Section 2.3 is used. For the calibration one of the ±45° tests ($\lambda > 1$) and one of the UD90° tests ($\lambda < 1$) is selected which results in the calibration parameters $\mu_{45} = 0.012$ and $\mu_{90} = 0.004$. The correlation parameter μ_{45} computed for $\lambda > 1$ is similar to the one obtained for a different test series in [16] as $\mu_{45} = 0.011$

  doi:10.5075/epfl-298799_978-2-9701614-0-0

where the same matrix material and fibers had been used. Figure 3 shows the results of the stiffness degradation model and the experimental data for various load levels.

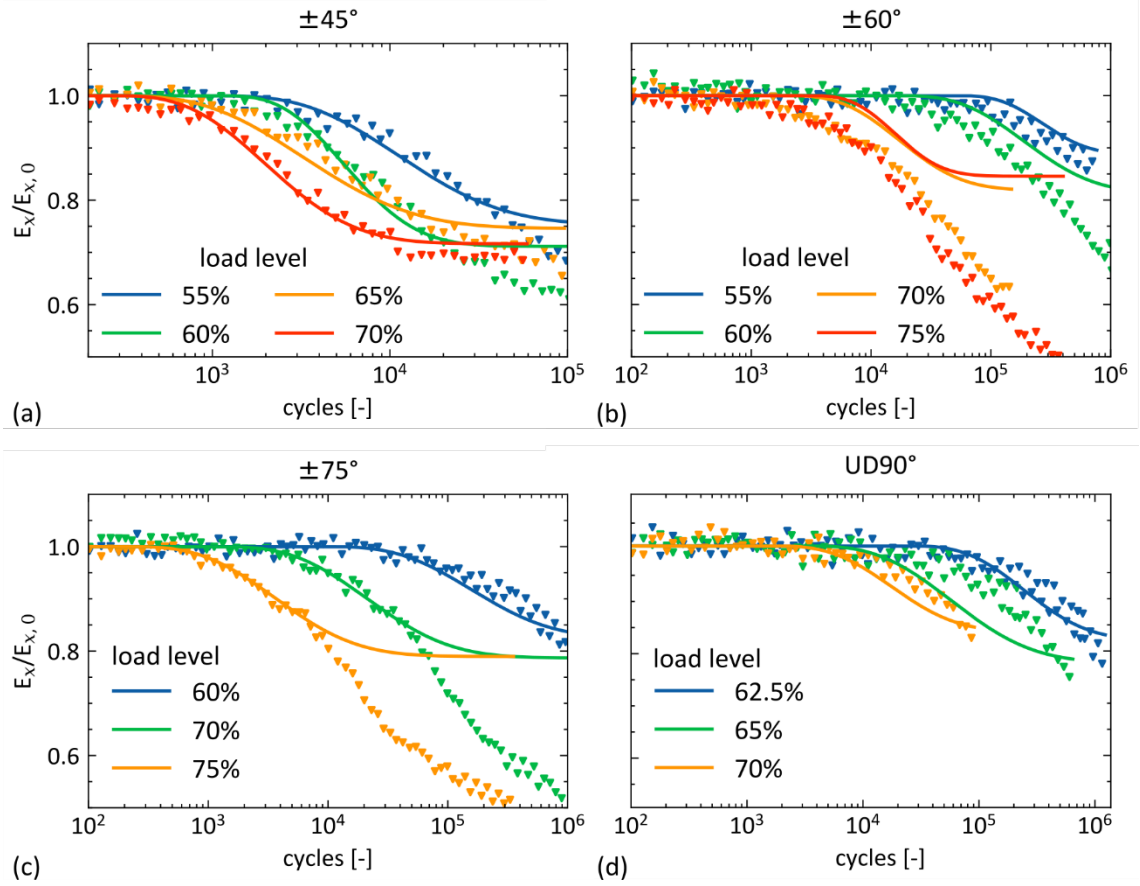

Figure 3: Experimental stiffness degradation (scatter) and computed stiffness degradation (lines) for the four tests for ±45° (a), ±60° (b), ±75° (c) and UD90° (d) at different load levels.

For the ±45° tests (Figure 3a), the computed and experimental degradation in stiffness fits well. A discrepancy between the model and experiments after crack saturation is visible. This is expected since other damage mechanisms like diffuse delamination will degrade the laminate further which is not accounted for in the model. The ±60° tests (Figure 3b) show a good model fit only for the load levels below 70%. At higher load levels, the discrepancy between model and experiments grows as the model underpredicts the stiffness degradation. In the ±75° tests (Figure 3c), the start of the computed stiffness degradation correlates well with experimental data but the experiments also show significant stiffness degradation after crack saturation. The model predicts the stiffness of the UD90° tests well. Note that the UD90° tests do not reach crack saturation due to prior failure of the specimen.

Figure 4a shows the predictions of the stiffness degradation model for the ±60° tests with μ_{90} used for load levels below 70% and and μ_{45} for higher load levels. It seems that for the ±60° tests, the separation by load level gives better predictions than the separation between the damage mechanisms based on the biaxiality ratio proposed from Quaresimin and Carraro [4].

Figure 4b shows the stress space of Puck mode A with the directions of the various laminates. As shown by the red dotted line, the separation of the damage modes intersects the ±60° tests

  doi:10.5075/epfl-298799_978-2-9701614-0-0

at a critical shear stress $\sigma_{12,c}$ whereas with a set biaxiality ratio (black dotted line), this is not possible. Using a critical shear stress $\sigma_{12,c}$ instead of the biaxiality ratio as a separation between the damage modes would mostly yield the same result. Low biaxiality ratios never reach $\sigma_{12,c}$ before the static strength is reached and the tests for high biaxiality ratios the separation is at very low load levels which is usually not tested since the fatigue life until damage initiation is extremely long or no damage starts to initiate at all. To further test this hypothesis, more experiments are necessary since it cannot explain the stiffness drop after crack saturation for the ±75° tests (see Figure 3c) and ±60° tests fall into the cluster for λ < 1 for the cycles to damage initiation (see Figure 2b) and not into both clusters.

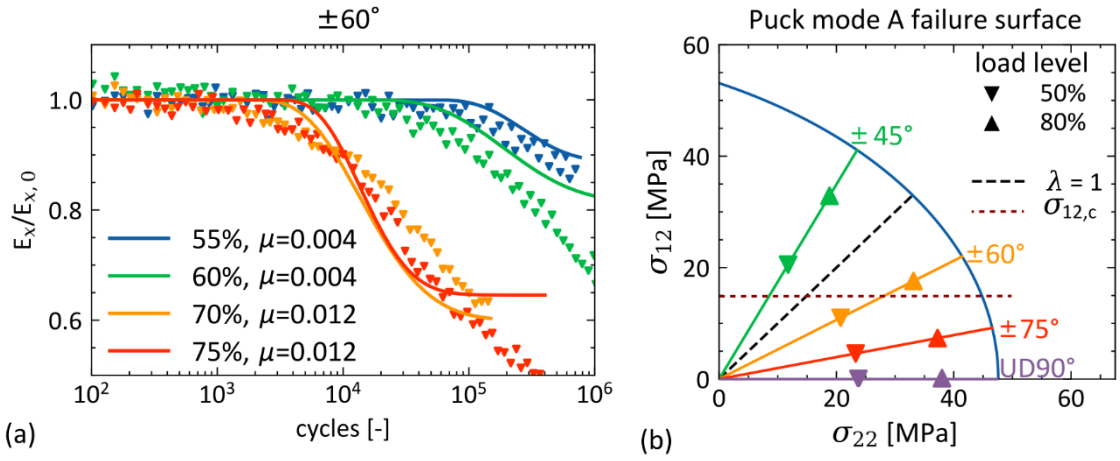

Figure 4: Experimental stiffness (scatter) vs. computed stiffness degradation (lines) for ±60° with the correlation constant for λ > 1 for load levels above 70% (a) and Puck mode A stress space (b) with the directions of the different laminates and the two criteria for the separation of the damage mode.

4. Conclusion

In this work, the effects of off-axis cracks in GRFP laminates are studied with automated crack detection of specimen in fatigue experiments. The dissipated energy is computed from hysteresis cycles and shows a substantial jump between ±60° and ±45° laminates, which correspond to a biaxiality ratio of 1.7 and 0.5, respectively, for the material used. SN-curves for damage initiation show two distinct clusters also separating the ±45° laminates from tests with a biaxiality ratio of less than 1. Quaresimin and Carraro [4] have shown that for positive transverse stresses combined with in-plane shear stress, the damage mechanism changes from in-plane shear dominated to transverse stress dominated at a biaxiality ratio of approximately 1. Our findings show that the dissipated energy is a useful tool to track the change between the damage mechanisms. A jump in dissipated energy for higher in-plane shear stresses also makes sense since fractographic images show shear cusps that result in an uneven and coarse fracture surface, which is expected to generate more internal friction in the fatigue loading cycles thus, a higher dissipated energy.

The stiffness degradation from Schuecker´s progressive damage model shows good prediction results when using different calibration parameters for λ > 1 and λ < 1. Nevertheless, it seems that the model underpredicts the stiffness degradation for the ±60° laminates at higher load

  doi:10.5075/epfl-298799_978-2-9701614-0-0

levels. The hypothesis, that the damage mechanism is only dependent on the in-plane shear stress and not the biaxiality ratio could explain this behavior but more experiments are needed to confirm it.

Acknowledgements

Special thanks go to the Chair of Materials Science and Testing of Polymers, Montanuniversitaet Leoben for providing the experimental data and images for the crack detection.

Part of this work has been performed within the COMET-project Experimental and numerical analysis of the damage tolerance behavior of manufactured induced defects and bonded repairs in structural aerospace composite parts (project-no.: VI-3.04) at the Polymer Competence Center Leoben GmbH (PCCL, Austria) within the framework of the COMET-program of the Federal Ministry for Transport, Innovation and Technology and the Federal Ministry for Digital and Economic Affairs with contributions by Montanuniversität Leoben (Chair of Designing Plastics and Composite Materials) and MAGNA Powertrain Engeneering Center Steyr GmbH CO KG. The PCCL is funded by the Austrian Government and the State Governments of Styria, Lower Austria and Upper Austria.

5. References

1. Reifsnider KL, editor. Fatigue of composite materials. Amsterdam ; New York: Elsevier; 1991. 519 p. (Composite materials series).
2. Wharmby A. Observations on damage development in fibre reinforced polymer laminates under cyclic loading. International Journal of Fatigue. 2003 May;25(5):437–46.
3. Tohgo K, Nakagawa S, Kageyama K. Fatigue behavior of CFRP cross-ply laminates under on-axis and off-axis cyclic loading. International Journal of Fatigue. 2006 Oct;28(10):1254–62.
4. Quaresimin M, Carraro PA. Damage initiation and evolution in glass/epoxy tubes subjected to combined tension–torsion fatigue loading. International Journal of Fatigue. 2014 Jun;63:25–35.
5. Tong J, Guild FJ, Ogin SL, Smith PA. On matrix crack growth in quasi-isotropic laminates—I. Experimental investigation. Composites Science and Technology. 1997 Jan;57(11):1527–35.
6. Nuismer RJ, Tan SC. Constitutive Relations of a Cracked Composite Lamina. 1987;16.
7. Zhang D, Ye J, Lam D. Ply cracking and stiffness degradation in cross-ply laminates under biaxial extension, bending and thermal loading. Composite Structures. 2006 Sep;75(1–4):121–31.
8. Adden S, Horst P. Stiffness degradation under fatigue in multiaxially loaded non-crimped-fabrics. International Journal of Fatigue. 2010 Jan;32(1):108–22.
9. Schuecker C, Pettermann HE. A continuum damage model for fiber reinforced laminates based on ply failure mechanisms. Composite Structures. 2006 Oct;76(1–2):162–73.
10. Glud JA, Dulieu-Barton JM, Thomsen OT, Overgaard LCT. Fatigue damage evolution in GFRP laminates with constrained off-axis plies. Composites Part A: Applied Science and Manufacturing. 2017 Apr;95:359–69.
11. Carraro PA, Quaresimin M. A stiffness degradation model for cracked multidirectional laminates with cracks in multiple layers. International Journal of Solids and Structures. 2015 Apr;58:34–51.

  doi:10.5075/epfl-298799_978-2-9701614-0-0

12. Glud JA, Dulieu-Barton JM, Thomsen OT, Overgaard LCT. Automated counting of off-axis tunnelling cracks using digital image processing. Composites Science and Technology. 2016 Mar;125:80–9.
13. Drvoderic M, Rettl M, Pletz M, Schuecker C. CrackDect: Detecting crack densities in images of fiber-reinforced polymers. SoftwareX. 2021 Dec;16:100832.
14. Bender JJ, Bak BLV, Jensen SM, Lindgaard E. Effect of variable amplitude block loading on intralaminar crack initiation and propagation in multidirectional GFRP laminate. Composites Part B: Engineering. 2021 Jul;217:108905.
15. Schuecker C, Pettermann HE. Constitutive ply damage modeling, FEM implementation, and analyses of laminated structures. Computers & Structures. 2008 May;86(9):908–18.
16. Drvoderic M, Pletz M, Schuecker C. Modeling Stiffness Degradation of Fiber-Reinforced Polymers Based on Crack Densities Observed in Off-Axis Plies. J Compos Sci. 2021 Dec 29;6(1):10.
17. Carraro PA, Quaresimin M. A damage based model for crack initiation in unidirectional composites under multiaxial cyclic loading. Composites Science and Technology. 2014 Jul;99:154–63.
18. Plumtree A. Fatigue damage evolution in off-axis unidirectional CFRP. International Journal of Fatigue. 2002 Apr;24(2–4):155–9.
19. Rieser R. Damage mechanics of composites under fatigue loads. [Austria]: Montanuniversität Leoben; 2016.
20. Drvoderic M. Probeneinflüsse bei der mechanischen Prüfung von Composites. [Leoben]: Montanuniversität Leoben; 2018.
21. Puck A. Festigkeitsanalyse von Faser-Matrix-Laminaten: Modelle für die Praxis. München: Hanser; 1996. 212 p.

  doi:10.5075/epfl-298799_978-2-9701614-0-0

A THREE-DIMENSIONAL VISCOUS-DAMAGE MODEL FOR POLYMER COMPOSITES UNDERGOING FINITE STRAINS

Igor A. Rodrigues Lopes[a,b], Federico Danzi,[a,b(*)],Pedro Ponces Camanho[a,b], Francisco M. Andrade Pires[a,b], Albertino Arteiro[a,b]

a: INEGI, Portugal – fdanzi@inegi.up.pt
b: DEMec, Faculdade de Engenharia, Universidade do Porto, Portugal
(*) Email: fdanzi@inegi.up.pt

Abstract: *Key ingredients for the constitutive modelling of polymer composites at finite strains are introduced in the present contribution. Invariant-based approaches are employed to describe the transversely isotropic elasto-plastic behaviour of unidirectional fibre-reinforced polymers. The dependency of the mechanical response on the strain-rate is introduced through viscous equations for both regimes. An additive deformation gradient decomposition is adopted to account for transverse matrix cracking in a smeared crack approach and longitudinal failure is predicted by a continuum damage model. Finite element simulations of 45^o off-axis compression demonstrate the ability of the constitutive equations to capture the experimentally observed behaviour. Numerical analyses of unidirectional open-hole-tension specimens with different fibre orientations illustrate that the finite strain damage modelling approach can predict the failure mechanisms correctly.*

Keywords: Fibre-reinforced polymers; Constitutive modelling; Finite Element Method; Strain-rate dependency; Damage.

1. Introduction

The use of polymeric fibre-reinforced composites in structural applications related to the transportation industries is particularly attractive due to the specific stiffness and strength properties, combined with the design possibilities, which allow obtaining high-performance behaviour with low weight. This aspect is even more important in the context of the restrictions dictated by the Green Deal. Composite laminates made of carbon-fibre reinforced epoxy resins have dominated the aeronautical industry, where computational tools are becoming essential to reduce development time and costs associated with the design and certification phases. Accurate and robust numerical models are required to obtain reliable predictions of the material and structural behaviour. The intrinsic nature of fibre-reinforced polymers makes their behaviour complex and, consequently, challenging to model. At the micro-scale, they consist of transversely isotropic fibres embedded in an isotropic polymeric matrix. Multi-scale modelling techniques are good candidates to model this kind of material, from a conceptual point of view, but their computational cost makes structural simulations unfeasible. Alternatively, when looking at the macroscopic level, e.g., the laminate level, the development of general constitutive equations that take the stacking sequence into account is a cumbersome task. Therefore, a compromise solution lies on the development of mesoscopic models that can be employed to model each of the unidirectional plies of a laminate [1,2].

  doi:10.5075/epfl-298799_978-2-9701614-0-0

Invariant-based approaches are well-suited to deal with the transverse isotropy of unidirectional composites in both elastic and plastic regimes [1]. The polymeric matrix makes the composite's response being dependent on the strain-rate. Modelling visco-plastic and visco-elastic effects has been addressed in [3,4] Continuum damage models and smeared crack approaches have been employed to model their progressive failure [2,5]. These models have been developed in the context of an additive decomposition of the strain tensor. Kinematic descriptions based on the deformation gradient, better suited for finite strains, are proposed in [6,7].

These approaches establish a framework for the constitutive modelling of fibre reinforced composites at finite strains, accounting for elastic and inelastic transverse isotropy, viscous effects, and failure mechanisms. They are reviewed and consistently adapted towards their unification in the present contribution. The features of each of these components are illustrated by means of numerical examples.

2. Constitutive modelling

2.1 Invariant-based visco-elastic-visco-plastic model at finite strains for transversely isotropic materials

A multiplicative decomposition of the deformation gradient is considered to distinguish its contribution for elastic ($\boldsymbol{F}^e$) and plastic deformations ($\boldsymbol{F}^p$). The constitutive equations are defined in the isoclinic configuration, where the fibres' alignment coincides to the reference one, being mapped from the initial configuration by $\widetilde{\boldsymbol{F}}^p$ and related to the general intermediate configuration through the rotation $\boldsymbol{\Phi}$:

$$\boldsymbol{F} = \boldsymbol{F}^e\boldsymbol{F}^p = \boldsymbol{F}^e\boldsymbol{\Phi}\widetilde{\boldsymbol{F}}^p. \tag{1}$$

The elastic stress-strain relationship is defined between the second Piola-Kirchhoff stress tensor and the Green-Lagrange strain tensors in the isoclinic configuration, based on the invariant theory:

$$\tilde{\boldsymbol{S}}_0 = \lambda\,\mathrm{tr}\big(\widetilde{\boldsymbol{E}}^e\big)\boldsymbol{I} + 2\mu_T\widetilde{\boldsymbol{E}}^e + \alpha\big[\mathrm{tr}\big(\widetilde{\boldsymbol{A}}\widetilde{\boldsymbol{E}}^e\big) + \mathrm{tr}\big(\widetilde{\boldsymbol{E}}^e\big)\widetilde{\boldsymbol{A}}\big]\boldsymbol{I} + 2(\mu_L - \mu_T)\big(\widetilde{\boldsymbol{A}}\widetilde{\boldsymbol{E}}^e + \widetilde{\boldsymbol{E}}^e\widetilde{\boldsymbol{A}}\big) + \beta\mathrm{tr}\big(\widetilde{\boldsymbol{A}}\widetilde{\boldsymbol{E}}^e\big)\widetilde{\boldsymbol{A}}, \tag{2}$$

with the structural tensor $\widetilde{\boldsymbol{A}} = \widetilde{\boldsymbol{a}} \otimes \widetilde{\boldsymbol{a}}$, and $\widetilde{\boldsymbol{a}}$ denoting the unit vector defining the fibres' orientation [7]. The elastic invariant parameters are related to the engineering elastic constants [1].

The yield function is expressed by

$$f = \alpha_1 I_1 + \alpha_2 I_2 + \alpha_3 I_3 + \alpha_{32} I_3^2 - 1 \leq 0, \tag{3}$$

where the invariants are expressed in terms of the symmetric part of the isoclinic Mandel stress tensor, decomposed into its plasticity and reaction components [7]:

$$I_1 = \frac{1}{2}\big(\mathrm{tr}\,\widetilde{\boldsymbol{\Sigma}}_s^{pind}\big)^2 - \mathrm{tr}\left(\widetilde{\boldsymbol{A}}\big[\widetilde{\boldsymbol{\Sigma}}_s^{pind}\big]^2\right), \qquad I_2 = \mathrm{tr}\left(\widetilde{\boldsymbol{A}}\big[\widetilde{\boldsymbol{\Sigma}}_s^{pind}\big]^2\right), \qquad I_3 = \mathrm{tr}\big(\widetilde{\boldsymbol{\Sigma}}_s\big) - \mathrm{tr}\big(\widetilde{\mathbf{A}}\widetilde{\boldsymbol{\Sigma}}_s\big). \tag{4}$$

The hardening parameters α_i are obtained from the material's response under distinct stress states [1,7].

  doi:10.5075/epfl-298799_978-2-9701614-0-0 published under CC BY-NC 4.0 license

The plastic potential is also expressed in terms of these invariants, with the parameters β_i being calibrated to achieve the material's plastic Poisson ratio [1]:

$$g = \beta_1 I_1 + \beta_2 I_2 + \beta_{32} I_3^2 - 1 = \frac{1}{2}\widetilde{\boldsymbol{\Sigma}}_s : \mathbb{M} : \widetilde{\boldsymbol{\Sigma}}_s. \tag{5}$$

The rate of plastic deformation is defined by

$$\widetilde{\boldsymbol{D}}^p = \dot{\gamma}\mathbb{M} : \widetilde{\boldsymbol{\Sigma}}_s, \tag{6}$$

where the plastic multiplier evolution, which introduces visco-plastic effects, is defined according to the Perzyna model [3], with the viscosity and non-dimensional parameters η and m, respectively:

$$\dot{\gamma} = \frac{\langle f^m \rangle}{\eta}. \tag{7}$$

Visco-elasticity is introduced by applying the finite strain theory of Kaliske [8] to the isoclinic configuration, leading to a stress response composed of an additional component $\tilde{\boldsymbol{S}}_1$:

$$\tilde{\boldsymbol{S}} = \tilde{\boldsymbol{S}}_0 + \tilde{\boldsymbol{S}}_1, \tag{8}$$

whose evolution is expressed by

$$\tilde{\boldsymbol{S}}_1^{n+1} = e^{-\frac{\Delta t}{\tau_1}} \tilde{\boldsymbol{S}}_1^n + \frac{1 - e^{-\frac{\Delta t}{\tau_1}}}{\frac{\Delta t}{\tau_1}} \gamma_1 \left(\tilde{\boldsymbol{S}}_{0,n+1}^{pind} - \tilde{\boldsymbol{S}}_{0,n}^{pind} \right). \tag{9}$$

The scalars γ_1 and τ_1 denote the relaxation parameter and relaxation time, respectively.

2.2 Smeared crack model for matrix cracking

Transverse matrix cracking is modelled by a smeared crack model [2], which has been extended to a finite strain framework by Leone [6] with an additive decomposition of the deformation gradient into the bulk and cracking components:

$$\boldsymbol{F} = \boldsymbol{F}_B + \nabla \boldsymbol{u}_c. \tag{10}$$

The transverse failure criterion has a similar invariant form, expressed by:

$$f_T = \zeta_1 \bar{I}_1 + \zeta_2 \bar{I}_2 + \zeta_3 \bar{I}_3 + \zeta_{32} \bar{I}_3^2 - 1 \leq 0. \tag{11}$$

The invariants $\bar{I}_i$ are obtained with the expressions in (4), but with the Cauchy stress tensor instead of the Mandel stress tensor, and the structural tensor defined in the final configuration. The parameters ζ_i are defined in terms of the material strength values for different loadings. When this criterion is verified, the crack plane orientation is estimated according to the stress state [9] and the initial traction vector acting on that plane is computed from the first Piola-Kirchhoff stress tensor and the unit vector normal to the crack plane, $\boldsymbol{e}_N$:

$$\bar{\boldsymbol{t}} = \boldsymbol{P} \cdot \boldsymbol{e}_N. \tag{12}$$

The cohesive tractions acting on the fracture plane evolve with the displacement jump $\boldsymbol{\omega}$, according to the traction-separation law defined as

  doi:10.5075/epfl-298799_978-2-9701614-0-0

$$\begin{cases} t_s = (1-d)\bar{t}_s, & if\ \omega_s \geq \omega_s^{max} \\ t_s = (1-d)\bar{t}_s \frac{\omega_s}{\omega_s^{max}}, & if\ \omega_s < \omega_s^{max} \end{cases} \tag{13}$$

for the shear component, with t_s denoting the shear component of the cohesive traction vector, $\bar{t}_s$ is its initial value, ω_s denotes the shear component of the jump and ω_s^{max} represents its maximum value. Note that the shear traction is co-linear to the shear jump component. For the normal components:

$$\begin{cases} t_N = (1-d)|\bar{t}_N|, & if\ \omega_s \geq \omega_s^{max} \\ t_N = (1-d)\bar{t}_N \frac{\omega_N}{\omega_N^{max}}, & if\ \omega_N < \omega_N^{max}. \\ t_N = k_N \omega_N, & if\ \omega_N < 0 \end{cases} \tag{14}$$

The evolution of the damage variable d is controlled by the equivalent jump, ω_{eq}, which is compared against the jump at failure estimated in mixed mode, ω_f^m [2]:

$$d^{n+1} = \max\left(\frac{\omega_{eq}}{\omega_f^m}, d^n\right), \qquad \dot{d} \geq 0, \qquad d \leq 1. \tag{15}$$

The displacement jump vector evolution, $\boldsymbol{\omega}$, is determined by establishing an equilibrium between the cohesive traction vector developing at the crack plane and the traction vector due to the bulk stresses:

$$\boldsymbol{R}_\alpha \boldsymbol{t} = \boldsymbol{P} \cdot \boldsymbol{e}_N. \tag{16}$$

The rotation matrix $\boldsymbol{R}_\alpha$ maps between the material and the crack plane coordinate systems. Note that only the bulk component of the deformation gradient contributes to the bulk stress, being related to the displacement jump through:

$$\boldsymbol{F}_B = \boldsymbol{F} - \nabla \boldsymbol{u}_c = \boldsymbol{F} - \boldsymbol{R}_\alpha \cdot \boldsymbol{\omega} \otimes \boldsymbol{l}, \tag{17}$$

where $\boldsymbol{l}$ denotes a vector with the appropriate characteristic length.

2.3 Continuum damage model for longitudinal failure

The present continuum damage model is based on the work of Maimí et al. [5], by considering only the damage variable in the longitudinal direction, d_1. For the present finite strain approach, the matrix representation of the relationship between the isoclinic Green-Lagrange strain tensor and second Piola-Kirchhoff stress tensor is defined by

$$\tilde{\mathbf{E}} = \mathbf{H}\tilde{\mathbf{S}}_0, \qquad \mathbf{H} = \begin{bmatrix} \frac{1}{E_{11}(1-d_1)} & -\frac{\nu_{21}}{E_{22}} & -\frac{\nu_{21}}{E_{22}} & 0 & 0 & 0 \\ & \frac{1}{E_{22}} & -\frac{\nu_{23}}{E_{22}} & 0 & 0 & 0 \\ & & \frac{1}{E_{22}} & 0 & 0 & 0 \\ & & & \frac{1}{G_{12}} & 0 & 0 \\ \text{sym} & & & & \frac{1}{G_{23}} & 0 \\ & & & & & \frac{1}{G_{12}} \end{bmatrix}. \tag{18}$$

The determination of the elastic invariant parameters employed in Eq. (2) is re-defined such that it recovers the relation expressed by

$$\tilde{\mathbf{S}}_0 = \mathbf{H}^{-1}\tilde{\mathbf{E}}. \tag{19}$$

The uncoupled maximum longitudinal strain criterion is adopted to define the fracture onset:

$$\frac{E_{11}}{X_T}\tilde{E}_{11} \leq 1, \tag{20}$$

with X_T denoting the longitudinal tensile strength. Failure under longitudinal compression is not considered in this contribution. The crack band model is employed to define the evolution of the damage variable, assuming a bi-linear softening law [2,9,10].

3. Numerical Results

3.1 Viscous effects

The simulation of a 45° off-axis compression is performed here, considering two different loading velocities, to illustrate both visco-elastic and visco-plastic effects. Damage is not considered in this example. The properties of carbon fibre-reinforced epoxy IM7-8552 are employed. The specimen's dimensions and loading conditions are in accordance with the work of Koerber et al. [3]. Their experimental stress-strain curves are compared to the numerical results obtained here, in Figure 1(a), where the accuracy of the numerical model to reproduce the strain-rate dependent behaviour of the material, in both elastic and inelastic regimes, is demonstrated. The initial slope of the curves captures the stiffer response associated with the higher strain-rate. The non-linear part of the curves related to onset and evolution of plastic strains is also affected by the strain-rate. In the case of the dynamic loading, a softening response is identified in the experimental results, which is not captured by the simulation. It is probably related to the onset of damage mechanisms that are not considered in these numerical analyses. The distribution of the equivalent von Mises stress in the specimen is illustrated in Figures 1(b) and (c), at the end of the simulations, where larger values are observed for the dynamic loading. This is consistent with the reaction curves obtained.

3.2 Damage mechanisms in open-hole-tension specimens

To illustrate the ability of the presented constitutive approaches to model damage at finite strains, the behaviour of open-hole-tension specimens is simulated. Viscous and inelastic effects are disregarded here, and only transversely isotropic elastic relations (Eq. (2)) coupled with transverse and longitudinal damage mechanisms (Sections 2.2 and 2.3) are considered. Two distinct situations are presented here: (i) a specimen with the fibres aligned with the loading direction (0°) and (ii) another specimen with the fibres at 40°. The mesh in the region near the hole is generated such that the finite elements become nearly aligned with the fibres [11]. The properties of the composite IM7-8552, reported in [2,9], are employed.

The reaction curves corresponding to both cases are presented in Figure 2(a) and (b), where softening behaviour due to the presence of damage mechanisms is obtained. The distribution of the smeared crack damage obtained at the maximum load is illustrated in Figure 2(c). In the 0° specimen, the longitudinal matrix splitting cracks are well captured. The evolution of the matrix cracking in a plane parallel to the fibres is clearly observed in the 40° specimen.

  doi:10.5075/epfl-298799_978-2-9701614-0-0

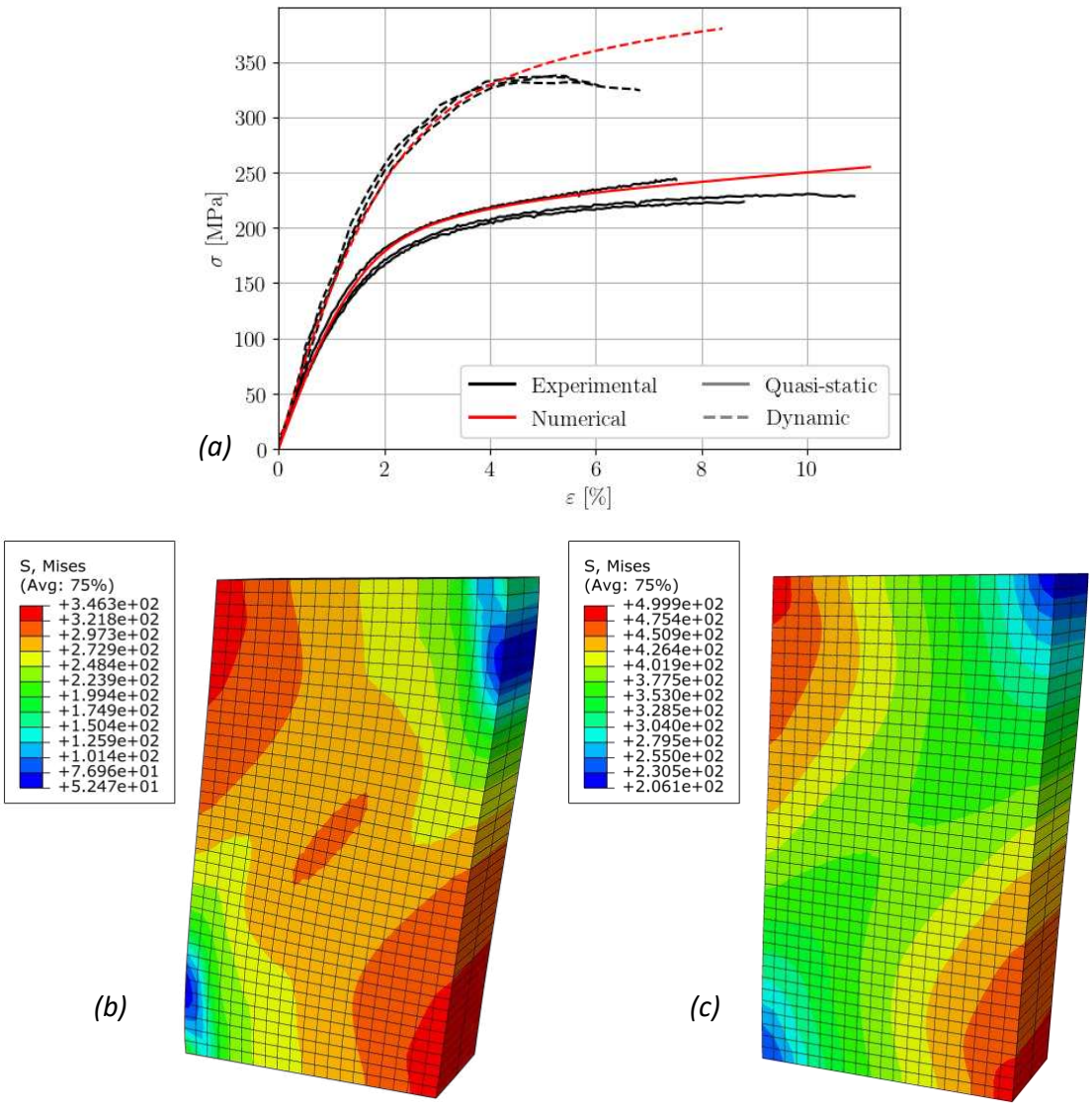

Figure 1: Numerical results. (a) Stress-strain curves. Distribution of the equivalent von Mises stress in the specimens subjected to (b) quasi-static and (c) dynamic loadings.

4. Conclusions

A set of constitutive equations for polymer composites has been formulated in a finite strain framework, in the present contribution. They allow modelling the transversely isotropic behaviour of fibre-reinforced polymers, in both elastic and plastic regimes, by employing an invariant approach for the elastic relationship, the yield function and the plastic potential. Visco-elasticity and visco-plasticity are also included to account for strain-rate dependency. A finite strain smeared crack approach based on the additive decomposition of the deformation gradient is employed to model transverse matrix cracking. Longitudinal tensile failure is introduced through a continuum damage model.

The simulation of 45° off-axis compression at two loading speeds, and the comparison against experimental results, shows the ability of the constitutive equations to capture viscous effects. Preliminary results of the finite strain implementation of the damage model illustrate that they can predict failure mechanisms observed in open-hole-tension specimens. In the future, the

  doi:10.5075/epfl-298799_978-2-9701614-0-0

invariant-based viscous equations will be coupled with the damage models. Moreover, finite strain equations will be developed to describe longitudinal failure under compression.

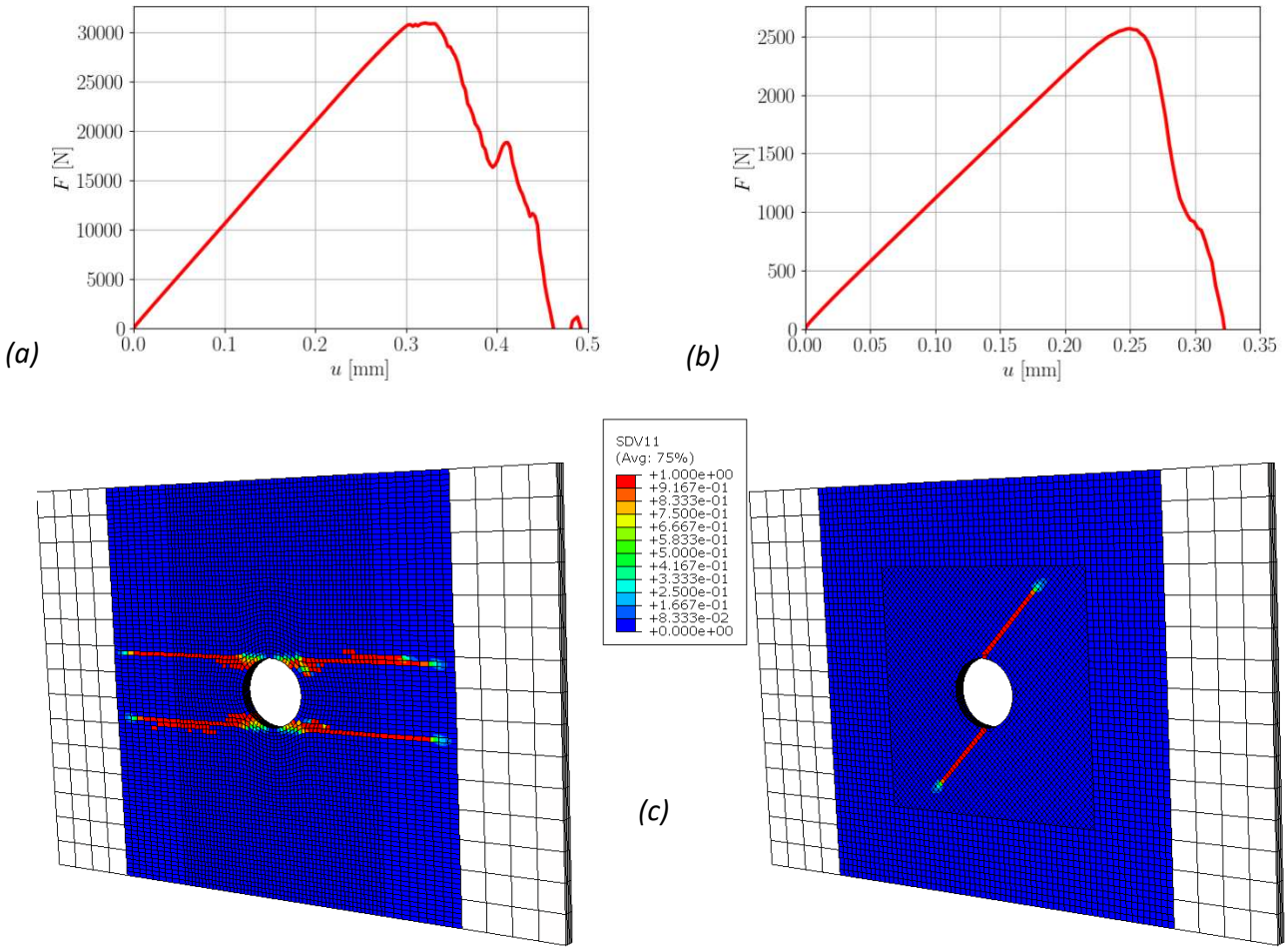

Figure 2: Numerical results of the open-hole-tension simulations. Reaction-displacement curves for (a) 0º and (b) 40º fibre's orientation, and (c) corresponding distributions of the smeared-crack damage variable at the maximum load.

Acknowledgements

The authors gratefully acknowledge the funding received from the Clean Sky 2 Joint Undertaking (JU), through the project TREAL — Thermoplastic material allowable generation using a reliability-based virtual modelling platform (Grant agreement No. 864723). The JU receives support from the European Union's Horizon 2020 research and innovation programme and the Clean Sky 2 JU members other than the Union. The present contribution reflects only the authors' view. The JU is not responsible for any use that may be made of the information it contains. Pedro P. Camanho acknowledges the support of FCT — Fundação para a Ciência e a Tecnologia, I.P., in the scope of the project UIDB/50022/ 2020.

  doi:10.5075/epfl-298799_978-2-9701614-0-0 published under CC BY-NC 4.0 license

5. References

1. Vogler M, Rolfes R, Camanho PP. Modeling the inelastic deformation and fracture of polymer composites-Part I: Plasticity model. Mechanics of Materials. 2013; 59:50–64.

2. Camanho PP, Bessa MA, Catalanotti G, Vogler M, Rolfes R. Modeling the inelastic deformation and fracture of polymer composites-Part II: Smeared crack model. Mechanics of Materials. 2013; 59:36–49.

3. Koerber H, Kuhn P, Ploeckl M, Otero F, Gerbaud PW, Rolfes R, et al. Experimental characterization and constitutive modeling of the non-linear stress–strain behavior of unidirectional carbon–epoxy under high strain rate loading. Advanced Modeling and Simulation in Engineering Sciences. 2018; 5(1).

4. Gerbaud PW, Otero F, Bussetta P, Camanho PP. An invariant based transversely-isotropic constitutive model for unidirectional fibre reinforced composites considering the matrix viscous effects. Mechanics of Materials. 2019; 138:103146.

5. Maimí P, Camanho PP, Mayugo JA, Dávila CG. A continuum damage model for composite laminates: Part I - Constitutive model. Mechanics of Materials. 2007; 39(10):897–908.

6. Leone FA. Deformation gradient tensor decomposition for representing matrix cracks in fiber-reinforced materials. Composites Part A: Applied Science and Manufacturing. 2015; 76:334–41.

7. Rodrigues Lopes IA, Camanho PP, Andrade Pires FM, Arteiro A. An invariant-based elasto-visco-plastic model for unidirectional polymer composites at finite strains. International Journal of Solids and Structures. 2022; 236–37:111292.

8. Kaliske M. A formulation of elasticity and viscoelasticity for fibre reinforced material at small and finite strains. Computer Methods in Applied Mechanics and Engineering. 2000; 185(2–4):225–43.

9. Zhuang F, Arteiro A, Furtado C, Chen P, Camanho PP. Mesoscale modelling of damage in single- and double-shear composite bolted joints. Composite Structures. 2019; 226:111210.

10. Maimí P, Camanho PP, Mayugo JA, Dávila CG. A continuum damage model for composite laminates: Part II - Computational implementation and validation. Mechanics of Materials. 2007; 39(10):909–19.

11. Falcó O, Ávila RL, Tijs B, Lopes CS. Modelling and simulation methodology for unidirectional composite laminates in a Virtual Test Lab framework. Composite Structures. 2018; 190:137–59.

  doi:10.5075/epfl-298799_978-2-9701614-0-0

FAILURE CRITERIA ASSESSMENT FOR COMPOSITE MATERIALS USING MICROMECHANICS MODELLING UNDER MULTIAXIAL LOADING CONDITIONS

Lei, Wan[a], Zahur, Ullah[a], Brain G., Falzon[a,b]*

a: Queen's University Belfast, Ashby Building, Stranmillis Road, Belfast, BT9 5AH, UK
–* l.wan@qub.ac.uk (Lei Wan)
b: School of Engineering, RMIT University, GPO Box 2476, Melbourne VIC 3001, Australia

Abstract: *This study assessed the widely used Tasi-Wu and Hashin failure criteria, using high-fidelity finite element-based analysis. Three-dimensional representative volume element models of IM7/8552 CFRP unidirectional composites subjected to biaxial loadings via periodic boundary conditions were constructed. The Drucker-Prager plastic damage constitutive model and cohesive zone model were utilised to simulate the mechanical response of the matrix and fibre-matrix interfaces, respectively. The RVE models were validated with experimental results from literature under uniaxial loadings and combined transverse and in-plane shear loads. Numerical simulations under (i) biaxial transverse and out-of-plane loadings and (ii) biaxial in-plane shear loading conditions, were selected in this paper for the assessment of these criteria and associated failure modes. Data-driven failure envelopes for composites under biaxial loadings were developed using a univariate spline function. It was found that micromechanics-based numerical modelling was an effective way to assess existing criteria with failure mode information.*

Keywords: Micromechanics analysis; Representative volume element; Multiaxial loadings; Failure criteria; Failure modes.

1. Introduction

Carbon Fibre Reinforced Polymer (CFRP) composites are increasingly used in a variety of industries where lightweight structures are needed, due to their excellent strength and stiffness per unit weight. Compared to isotropic materials used in structural engineering, CFRP composites are hierarchical with three different length scales (i.e. micro, meso and macro). Damage initiation and propagation mechanisms in different scales vary, and different approaches should be used. The failure analysis of composites under multiaxial loadings remains challenging in terms of both experimental and numerical approaches, considering the failure mode interaction and the characteristics of progressive failure of the constituent materials.

In industry, a high safety factor is often used in the initial design stage to account for a perceived lack of confidence in damage prediction. A large number of failure theories, criteria and models have been proposed in an attempt to provide better predictive capability in the failure of composite lamina/laminates. These failure criteria include but are not limited to strain-based [1], stress-based fully interactive criteria [2], stress-based non-interactive [3, 4], etc. These widely used failure criteria and theories were assessed and ranked in the 'World Wide Failure Exercises (WWFE)', according to their predictive capabilities of the failure strength of composite lamina/laminates under various loading conditions. The conclusion was that there are discrepancies between the predicted and experimental failure envelopes, and no failure theory

  doi:10.5075/epfl-298799_978-2-9701614-0-0

can handle all of the designed cases [5]. Nonetheless, most of these theories and models, such as Tsai-Wu and Hashin failure criteria, are still widely used in industry and taught to undergraduate students. Therefore, it is necessary to assess these failure criteria under multiaxial loadings before they are used to better understand their limitations under more complex loadings.

The availability of high performance computing and high fidelity numerical approaches has facilitated the failure analysis of composite structures under multiaxial loads when experiments are difficult to perform. A representative volume element (RVE) is widely used within the framework of the finite element method by considering the influences of the constituents (i.e. fibres, matrix and fibre/matrix interface) on the mechanical behaviour of composites. Recently, micromechanics-based modelling has been successfully applied to investigate the mechanical behaviour of composites and assess the abovementioned failure criteria and/or models under different combined loading conditions, such as combined transverse and out-of-plane shear [6], combined transverse and in-plane shear [7] and combined transverse compression and axial tension [8]. Totry et al. [6] investigated the failure mechanisms of CFRP composites under transverse and out-of-plane shear loadings with different interfaces (i.e. strong and weak interfaces) between the fibres and matrix. They assessed the Puck [3] and Hashin [4] failure criteria and found that the failure criteria agreed well with the numerical simulations for composites with a strong fibre-matrix interface but overestimated the composite strength when the interface was weak due to the interface dominated failure. They also pointed out that the interface fracture should be considered in the failure criteria. The same conclusion was made by Naya et al. [7], who performed the failure analysis of AS4/PEEK composite under transverse and in-plane shear loadings.

In this study, a computational micromechanics based RVE model with random fibre distribution is developed to predict the failure envelopes and failure modes of IM7/8552 UD CFRP composite laminae under multiaxial loading. The RVE model is built with three phases in which the fibres are modelled as linearly elastic and transversely isotropic, the mechanical behaviour of the matrix is modelled with a Drucker Prager plastic damage model accounting for the influence of hydrostatic pressure on the behaviour, and the interface is modelled as a bilinear cohesive law governed by the Benzeggath-Kenane damage propagation law for mixed-mode fracture. Biaxial transverse and out-of-plane loadings and biaxial in-plane shear loadings were considered using periodic boundary conditions. A detailed comparison is conducted between the failure prediction of two classical failure criteria (Tsai-Wu and Hashin) and micromechanical simulations.

2. Tsai-Wu and Hashin failure criteria

The Tsai-Wu failure criterion [2] is a phenomenological material failure theory for anisotropic composite materials. It is highly integrated and interactive since it considers all stress components in one equation. The general expression for the Tsai-Wu failure criterion is:

$$F_i\sigma_i + F_{ij}\sigma_{ij} = 1, (i, j = 1, 2, 3, 4, 5, 6), \quad (1)$$

where F_i, F_{ij} are the coefficients associated with the material strengths determined by experiments. For interfibre failure, the Tsai-Wu failure criterion reduces to:

$$F_2(\sigma_2 + \sigma_3) + F_{22}(\sigma_2^2 + \sigma_3^2) + F_{44}(\tau_{12}^2 + \tau_{13}^2) + F_{66}\tau_{23}^2 + (2F_{22} - F_{44})\sigma_2\sigma_3 = 1 \quad (2)$$

  doi:10.5075/epfl-298799_978-2-9701614-0-0

where

$$F_2 = \frac{1}{Y_T} - \frac{1}{Y_C}, F_{22} = \frac{1}{Y_T Y_C}, F_{44} = \frac{1}{S_{12}^2}, F_{66} = \frac{1}{S_{23}^2}, \quad (3)$$

with Y_T and Y_C being the tensile and compressive strengths of the material in the transverse direction, and S_{12} and S_{23} the shear strengths along and transverse to the fibres, respectively. These conventional strength properties of a typical UD composite are obtained from standard experiments under uniaxial or pure shear stress states. In this study, these were determined from experimentally validated numerical simulations.

Hashin proposed different failure criteria for the fibre and matrix by assuming a quadratic interaction between the tractions on the failure plane and it can distinguish between tension and compression [4]. Here only matrix failure is considered in the transverse and shear loading,

$$\left(\frac{\sigma_2 + \sigma_3}{Y_T}\right)^2 + \frac{1}{S_{23}^2}(\tau_{23}^2 - \sigma_2\sigma_3) + \frac{\tau_{12}^2 + \tau_{13}^2}{S_{12}^2} = 1. \ (\sigma_2 + \sigma_3 \geq 0) \quad (4)$$

$$(\frac{\sigma_2+\sigma_3}{2S_{23}})^2 + [\left(\frac{Y_C}{2S_{23}}\right)^2 - 1]\frac{\sigma_2+\sigma_3}{Y_C} + \frac{1}{S_{23}^2}(\tau_{23}^2 - \sigma_2\sigma_3) + \frac{\tau_{12}^2+\tau_{13}^2}{S_{12}^2} = 1. \ (\sigma_2 + \sigma_3 < 0) \quad (5)$$

where Y_T and Y_C are the transverse tensile and compressive strengths, respectively. S_{12} and S_{23} are the in-plane and transverse shear strengths, respectively.

3. Micromechanical modelling of composites

The computational micromechanical model is based on an RVE, which contains randomly distributed carbon fibres embedded in a polymer matrix. A total number of 50 fibres is used to capture the essential failure information of different constituents while maintaining reasonable computing efforts [9]. The experimentally measured average fibre diameter and fibre volume fraction are 7 μm and 60%, respectively. The final 3D RVE model of the composite lamina can be obtained by extruding the 2D model along the longitudinal direction. The RVE thickness is set to be 5 µm considering the balance between the aspect ratio of the mesh and the computational cost. Thus, the size of the RVE is $50\ \mu m \times 50\ \mu m \times 5\ \mu m$. Fibres and matrix in the RVE model were discretised with first-order hexahedral elements under a reduced integration scheme (C3D8R) and few tetrahedral elements (C3D6), while the interface was meshed with first-order cohesive elements (COH3D8). Fig. 1 illustrates the 3D RVE model of the composite with three constituents. The RVE model was discretised with around 50,000 elements in ABAQUS/Explicit [10] to capture the steep stress gradients between neighbouring fibres and ensure the balance between the accuracy and computational cost. To accelerate the simulation process, mass scaling is normally utilised in ABAQUS/Explicit and the stable time increment was selected as $5 \times 10^{-6}\ s$. The linear bulk viscosity and the quadratic bulk viscosity parameters were set to 0.06 and 1.2, respectively.

Carbon fibres were modelled to be linearly elastic and transversely isotropic. The polymer matrix was modelled as an isotropic elastoplastic material. The modified Drucker-Prager plastic damage model [10] was used to model the mechanical behaviour of epoxy under multiaxial stress states. The yield surface of the epoxy matrix is expressed by a modification of the Drucker–Prager yield function as,

  doi:10.5075/epfl-298799_978-2-9701614-0-0

$$\Phi(I_1, J_2, \sigma_I, \beta, \alpha) = \frac{1}{1-\alpha}\left(\sqrt{3J_2} + \alpha I_1 + B\langle\sigma_I\rangle\right) - \sigma_{myc} = 0 \quad (6)$$

where I_1 stands for the first invariant of the stress tensor, J_2 is the second invariant of the deviatoric stress tensor, α is the pressure-sensitivity parameter of the Drucker-Prager yield criterion, σ_I is the maximum principal stress, <> are Macaulay brackets and returns the argument if it is positive and zeroes otherwise, and B is a function of the tensile and compressive yield stresses (σ_{myt} and σ_{myc}), which is defined as,

$$B = \frac{\sigma_{myt}}{\sigma_{myc}}(1-\alpha) - (1+\alpha) \quad (1)$$

wherein α can be determined according to $tan\beta = 3\alpha$ from the internal friction angle of the material (β), which controls the hydrostatic pressure dependence on the plastic behaviour.

For the matrix behaviour under uniaxial tension, the quasi-brittle behaviour is controlled by an exponential cohesive law after damage onset, characterised by a single normalized scalar damage variable, to ensure the correct energy dissipation of the matrix G_m. For the matrix behaviour under uniaxial compression, perfect plasticity is assumed based on experimental findings [11]. For more details about the constitutive models and their numerical implementations, readers are referred to [10,11].

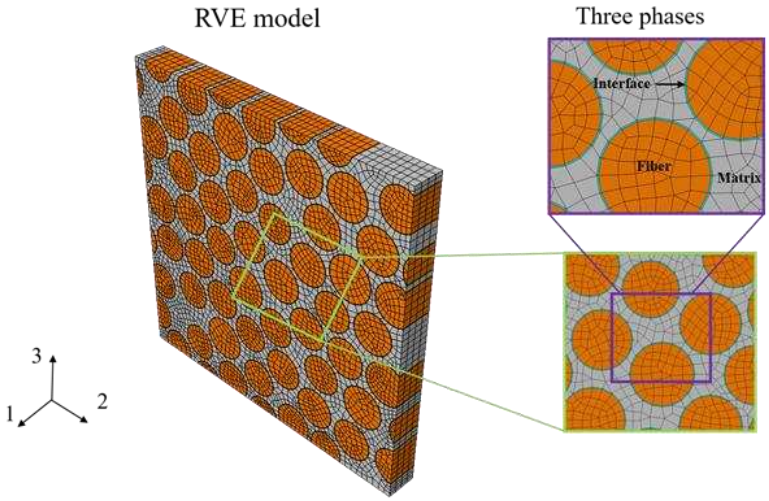

Figure 1. 3D micromechanics based RVE model with three constituents

Regarding the modelling of fibre/matrix interfaces, a cohesive zone model is used. Damage onset is controlled by a quadratic interaction criterion, and the damage occurs when the criterion involving the sum of nominal stress ratios reaches one. Damage evolution is defined based on the traction separation law, and the dissipated fracture energy is used to determine the separation displacement at failure. Once damage is initiated, traction starts to reduce based on the damage parameter, which monotonically increases from 0 (in the absence of damage) to 1 (at final failure). As previously mentioned, the energy-based Benzeggath-Kenane damage propagation criterion is adopted to capture mixed-mode fracture. The interface fracture energy in mode I, G_{IC}, could not be measured experimentally so it is assumed to be in the range of 2–5 J/m^2 [7]. In this study, the fracture energy of 2 J/m^2 in Mode I is adopted in the simulations, and due to the lack of experimental data, the interface fracture energies in the shear modes are

  doi:10.5075/epfl-298799_978-2-9701614-0-0

assumed to be equal to the matrix cracking fracture energy, 100 J/m^2. The material properties are given in Table 1.

Table 1. Material properties of the constituents [11]

IM7 fibre properties

E_1 (GPa)	E_2 (GPa)	υ_{12}	υ_{23}	G_{12} (GPa)	G_{23} (GPa)
287	13.4	0.29	0.48	23.8	7

8552 epoxy properties

E (GPa)	υ_m	σ_{myt}(MPa)	σ_{myc}(MPa)	G_m (J/m^2)
4.08	0.38	99	130	100

Interface properties

Thickness (mm)	K_{nn} (GPa/mm)	K_{ss}=K_{tt} (GPa/mm)	t_n^0 (MPa)	$t_s^0 = t_t^0$ (MPa)	G_{IC} (J/m^2)	G_{IIC}= G_{IIIC} (J/m^2)
0.0001	253	682	45	62	2	100

Periodic boundary conditions (PBCs) are imposed on the corresponding surfaces of the RVE using equations between the periodic nodes at opposite faces to guarantee the periodicity of the displacement and traction. The strains are computed from the imposed displacements divided by the corresponding lengths, while the predicted normal and shear stresses were computed from the resultant normal and tangential forces acting on the RVE faces divided by the cross-section area.

4. Results and discussions

Fig. 2 shows a comparison between numerical results of IM7/8552 and the prediction of Tsai-Wu and Hashin failure criteria under biaxial transverse and out-of-plane (σ_2, σ_3) loadings, and biaxial in-plane shear loadings (τ_{12}, τ_{13}). The numbers beside the failure point are the stress ratios. It can be seen in Fig. 2a (yellow square box) that the strengths of the composite predicted by both Tsai-Wu and Hashin failure criteria are smaller than the numerical results in the biaxial transverse tension loadings, especially when the stress ratio is close to 1. Failure strengths obtained from both Tsai-Wu and Hashin failure criteria agree with numerical results for the loading case with the stress ratio of –0.28. The comparison suggests that the predicted envelope from the Hashin criterion agrees well with the fitted envelope from numerical failure points until the infinite strength, while the predicted closed envelope from the Tsai-Wu criterion only agrees with the fitted envelope until a loading condition with a stress ratio of approximately 3.13. It is

  doi:10.5075/epfl-298799_978-2-9701614-0-0

still an open question whether the failure surface should be open or closed, especially under hydrostatic pressure. According to the numerical results, the fitted curve of the failure envelope under transverse compression and out-of-plane compression is open since the matrix is subjected to hydrostatic pressure under biaxial compressive loads and is constrained from fibres. The red squares in Fig.2b represent numerically generated data for curve fitting reasons, in which the negative τ_{12} means the opposite direction of its counterpart in the positive quadrant. It is clear from the fitted curve of the failure envelope that under biaxial in-plane shear the envelopes plotted with Tsai-Wu and Hashin failure criteria are in good agreement. Comparing the failure points obtained for $(+\tau_{12}, +\tau_{13})$ and $(+\tau_{12}, -\tau_{13})$, a slight difference was observed. The difference is mainly due to the randomly distributed fibres within the RVE, which changes the damage propagation during loadings, and this is explained in Fig. 4, in which the failure modes were discussed.

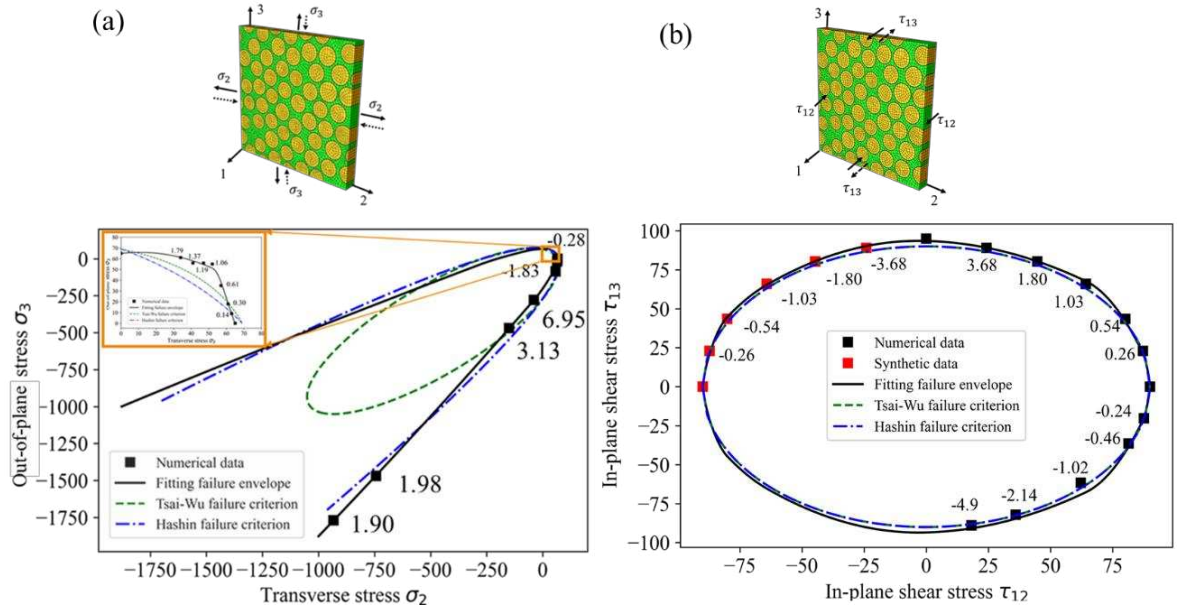

Fig. 2. Comparison between numerical results of IM7/8552 composite and prediction of failure criteria (Tsai-Wu and Hashin) under (a) biaxial transverse and (b) biaxial in-plane shear loadings

Fig. 3 shows the comparison of failure modes obtained from different stress ratios under biaxial transverse and out-of-plane loadings. These stress ratios correspond to the failure points in Fig. 2. 'T', 'CS' and 'No' besides these stress ratios represent the failure mode, which are matrix tensile failure, matrix shear failure caused by transverse compression and no matrix failure, respectively. The tensile failure and shear failure are quantified by DAMAGET and PEEQ in ABAQUS, respectively, as shown in Fig. 3 legends. DAMAGET represents the tensile damage variable which increases monotonically from zero when tensile damage initiates to one indicating complete failure; while PEEQ represents the equivalent plastic strain to quantify the plastic deformation. It can be seen that in the loading case of $(+\sigma_2, +\sigma_3)$, the failure modes are matrix tensile failure, and the fracture plane at a stress ratio of 0.3 becomes less apparent at a stress ratio of 0.6 until it disappears at a stress ratio of 1.06 due to the same values of transverse tensile stress and out-of-plane tensile stress. In the loading case of $(+\sigma_2, -\sigma_3)$, both failure modes are matrix shear failure caused by transverse compression with the fracture planes not being observed clearly. The same phenomenon was observed in the loadings case of $(-\sigma_2, -\sigma_3)$ with a ratio of 6.95, while beyond this point, no failure was observed in both homogenised

  doi:10.5075/epfl-298799_978-2-9701614-0-0

stresses during the biaxial loading process and the equivalent plastic strain field becomes random and severe due to the hydrostatic pressure on the matrix.

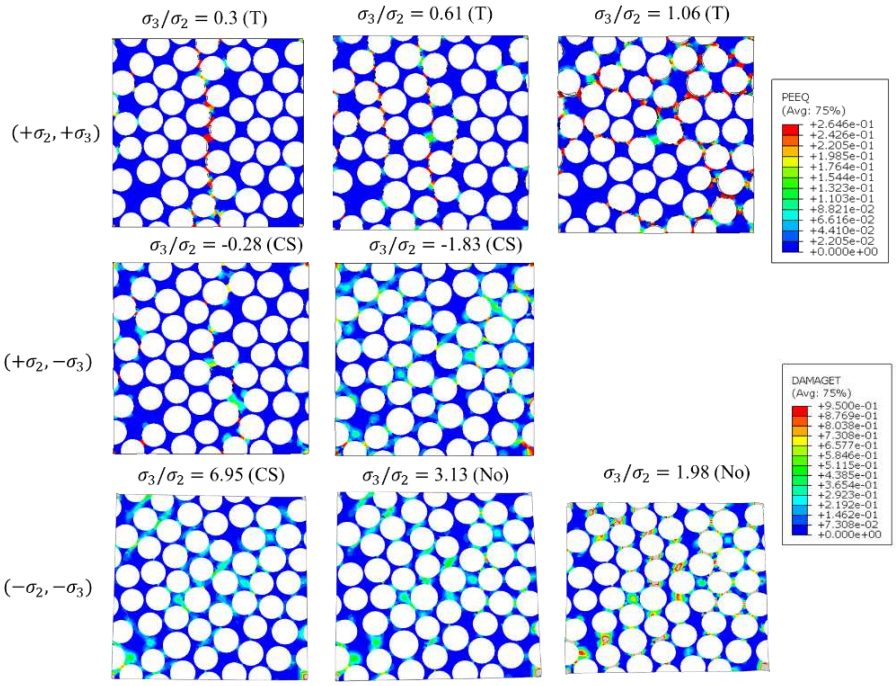

Fig. 3 Failure modes of IM7/8552 composite under biaxial transverse and out-of-plane loadings

Fig. 4 shows the comparison of failure modes with different shear stress ratios under biaxial in-plane shear loadings. 'SS' represents the matrix shear failure caused by the shear loadings, and the failure is quantified by the PEEQ field. It is shown that when the shear stresses are in the same direction (i.e. $\tau_{12} > 0, \tau_{13} > 0$) with a similar value, only one main shear plane with an angle of 45° inclined to transverse direction is formed, while two main shear planes are formed when τ_{13} is 3.68 times larger than τ_{12}. However, comapred to the loadings in the same direction, six parallel shear planes are formed when the shear stresses are in the opposite direction (i.e. $\tau_{12} > 0, \tau_{13} < 0$) with a similar value, and they decrease to four main planes when τ_{13} is 4.9 times larger than τ_{12}.

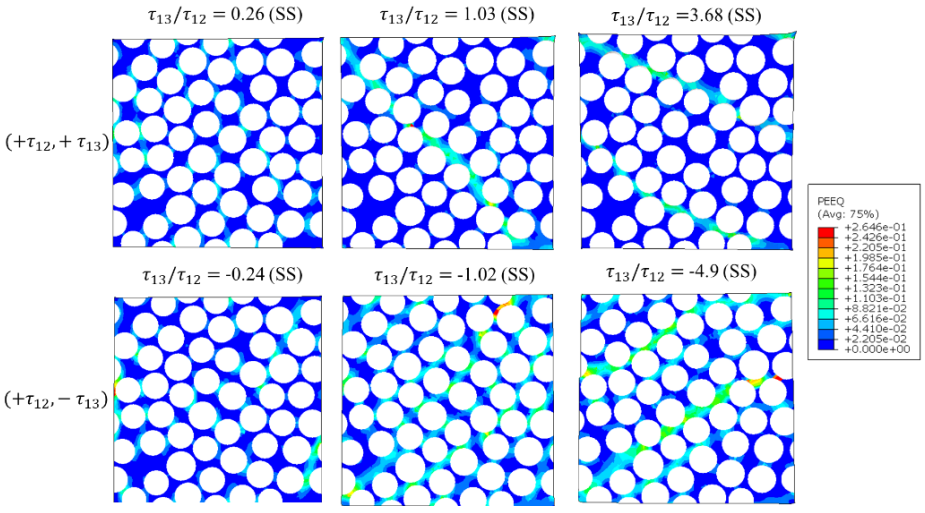

Fig. 4. Damage modes of the IM7/8552 composite under biaxial in-plane shear loadings

  doi:10.5075/epfl-298799_978-2-9701614-0-0

5. Conclusions

In the initial stage of composite structure design, simple failure criteria play a role in guiding the sizing of a structure. Tsai-Wu and Hashin failure criteria are widely used primarily for their simplicity of implementation. However, despite known limitations, they have never been fully assessed due to the limitations in testing certain load cases. The rapid development of computing power and storage capacity has enabled high fidelity computational micromechanics based modelling under multiaxial loading for damage/failure prediction and assessment. This study introduced a micromechanics based RVE model with random fibre distribution to predict the failure envelopes and failure modes of IM7/8552 UD CFRP composite laminae under biaxial loadings. The RVE model was built with three phases, including fibre, matrix and fibre/matrix interface. Biaxial transverse and out-of-plane, and biaxial in-plane shear loadings were considered using periodic boundary conditions. A detailed comparison was conducted between the failure prediction from the two classical failure criteria (Tsai-Wu and Hashin) and micromechanical simulations including the identification of failure modes.

Acknowledgements

This study was conducted as part of the Belfast Maritime Consortium UKRI Strength in Places project, '*Decarbonisation of Maritime Transportation: A return to Commercial Sailing*' led by Artemis Technologies, Project no. 107138.

6. References

1. Christensen RM. Tensor Transformations and Failure Criteria for the Analysis of Fiber Composite Materials. J Compos Mater. 2016 Jul 27;22(9):874–97.
2. Tsai SW, wu EM. A General Theory of Strength for Anisotropic Materials. J Compos Mater. 1971 Jul 27;5(1):58–80.
3. Puck A, Schürmann H. Failure analysis of FRP laminates by means of physically based phenomenological models. Compos Sci Technol. 2002;62(12–13):1633–62.
4. Hashin Z. Failure criteria for unidirectional fiber composites. J Appl Mech Trans ASME. 1980;47(2):329–34.
5. Kaddour AS, Hinton MJ. Maturity of 3D failure criteria for fibre-reinforced composites: Comparison between theories and experiments: Part B of WWFE-II. J Compos Mater. 2013;47(6–7):925–66.
6. Totry E, González C, LLorca J. Prediction of the failure locus of C/PEEK composites under transverse compression and longitudinal shear through computational micromechanics. Compos Sci Technol. 2008;68(15–16):3128–36.
7. Naya F, González C, Lopes CS, Van der Veen S, Pons F. Computational micromechanics of the transverse and shear behavior of unidirectional fiber reinforced polymers including environmental effects. Compos Part A Appl Sci Manuf. 2017;92:146–57.
8. Romanowicz M. A numerical approach for predicting the failure locus of fiber reinforced composites under combined transverse compression and axial tension. Comput Mater Sci. 2012;51(1):7–12.
9. Wan L, Ismail Y, Zhu C, Zhu P, Sheng Y, Liu J, et al. Computational micromechanics-based prediction of the failure of unidirectional composite lamina subjected to transverse and in-plane shear stress states. J Compos Mater. 2020;54(24):3637–54.
10. Dassault Systèmes. Abaqus 6.13 documentation; 2013.
11. Chen J, Wan L, Ismail Y, Ye J, Yang D. A micromechanics and machine learning coupled approach for failure prediction of unidirectional CFRP composites under triaxial loading: A preliminary study. Compos Struct. 2021;267:113876.

  doi:10.5075/epfl-298799_978-2-9701614-0-0

HIGH-SPEED THERMAL MAPPING AND IMPACT DAMAGE ONSET IN CFRP AND FFRP

Oscar Rodera Garcia[a], Guilherme Corrêa Soares[a], Farzin Javanshour[a], Nazanin Pournoori[a], Jarno Jokinen[a], Mikko Hokka[a], Mikko Kanerva[a]*

a: Faculty of Engineering and Natural Sciences, Tampere University, Finland
*corresponding author: oscar.roderagarcia@tuni.fi

Abstract:

The use of alternative, natural fibers instead of synthetic reinforcements in polymeric matrix composites, subjected to certain out-of-plane loads, requires a study on the susceptibility to damage. The aim of this work is to study the impact behavior and the stiffness reduction in flax and carbon fibre reinforced plastic laminates subjected to a 15 J drop-tower test. The detection of selected damage mechanisms was done by high-speed optical and infrared cameras monitoring the full-field deformation and temperatures on the composite surface. The elastic response of the laminates was modelled by a finite element method and ply failure was analyzed by the Hashin's and Puck's failure criteria. The results of thermal and strain measurements indicated the primary cracks due to the bending effect for the flax laminate. For the carbon laminate, the final fibre breaking was indicated. Numerical results showed the accuracy of the Puck's criterion about the prediction of first stages of the impact failure.

Keywords: biocomposites; impact; damage mechanics; infrared measurement; finite element method

1. Introduction

The growing interest in the using of bio-based materials in engineering applications might make them to be a part of primary structural components. In such a case, the substitution of synthetic fibres in polymeric composites is no longer the only justified selection; the structural integrity requires to be analyzed in all cases. The study of impact behaviour of fibre reinforced plastic (FRP) laminates involves complex failure mechanisms, such as delamination, matrix cracking, and fibre breakage. The interaction and onset of these mechanisms depend on the internal configurations of the structure and boundary conditions. All these complicate the analysis of the impact damage resistance and predictions.

Experimental investigations of stiffness of flax fibre reinforced plastic (FFRR) laminates subjected to impact have been recently studied [1]. However, the prediction of the involved failure mechanisms requires well-balanced optimization between experimental and numerical tools. Promising theories of failure prediction from the World-Wide Failure Exercise (WWFE) [2] allowed for the modelling of virtual impact testing by means of numerical simulations on the finite element (FE) basis. There, numerical predictions of intra and interlaminar failure were investigated for a carbon fibre reinforced plastic (CFRP) laminate [3, 4]. The related results were calibrated by experimental measurements made with ultrasonic C-scan inspections after the testing.

  doi:10.5075/epfl-298799_978-2-9701614-0-0

The current study carried out a combination of experimental measurements and numerical analysis of a 15 J drop-tower impact test for FFRP and CFRP laminate specimens. The detection of failure modes was done by means of the force-time response, deformation field (via Digital Image Correlation, DIC) and thermal dissipation (temperature field) on the rear side of the specimens. For that, high-speed infrared and optical cameras were used. The experimental measurements were complemented by the implementation of a FE model for the impact case. The model was run with two strength-based failure criteria, i.e., Hashin's and Puck's failure criteria.

2. Materials and methods

2.1 Materials, laminates, and test set-ups

The studied CFRP material was a AS4-3501-6 UD (Hexcel) unidirectional prepreg. It was stacked to form a quasi-isotropic laminate with a lay-up of $[0_3/-45/0/+45/-45/0/+45/0/0/-45/0/+45]_{SE}$ and a thickness of 0.1396 mm. Each lamina had a square shape of 58.1 × 58.1 mm^2. Table 1 shows the material properties for the lamina. The studied FFRP material was flax-epoxy composite with non-crimp unidirectional flax yarn fabrics (with an areal density of 300 g/m^2, Bcomp, Switzerland). The matrix polymer system was a standard epoxy Epopox A28 by Amroy Europe Oy (Lahti, Finland) and a Jeffamine D-23 polyether diamine hardener by Huntsman (Texas, USA) with 35 wt% hardener to resin ratio. The flax-epoxy composite was stacked in a cross-ply form with a lay-up of $[0/90/0/90/0/90]_{SE}$ and an average thickness of 0.42 mm. Each flax-epoxy lamina had a square shape of 60 × 60 mm^2. Table 2 shows the material properties for the lamina.

The impact tests were conducted mainly in compliance with the ASTM D5628-10 standard [5]. An impactor mass (comprising impactor and carriage) is set at a height that led to the impact energy of 15 J. The impactor had a hemispherical head with a diameter of 12.7 mm, made of steel (42CrMo4-QT). The total mass of the impactor and carriage was 2.87 kg. The contact force was measured using a load sensor (60 kN) between the head and the impactor structure.

Table 1. AS4-3501-6 UD lamina's elastic constants [6].

E_1 (GPa)	$E_2 = E_3$ (GPa)	$\nu_{12} = \nu_{12}$ (-)	ν_{23} (-)	$G_{12} = G_{13}$ (GPa)	$G_{12} = G_{13}$ (GPa)	$Density$ (kg/m^3)
142	9.2	0.25	0.29	6.1	3.6	1580

Table 2. Flax-epoxy UD lamina's elastic constants [7]. *Values equal the first in-plane direction.

E_1 (GPa)	$E_2 = E_3$ (GPa)	$\nu_{12} = \nu_{12}$ (-)	ν_{23} (-)	$G_{12} = G_{13}$ (GPa)	$G_{12} = G_{13}$ (GPa)	$Density$ (kg/m^3)
24.98	4.51	0.38	0.38*	5.21	5.21*	1210

2.2 Infrared thermal measurements and strain measurements

The full-field deformation and temperatures on the sample surface were monitored during the drop-tower impact test. A Photron Fastcam SA-X2 high speed optical camera (Photron, Tokyo,

  doi:10.5075/epfl-298799_978-2-9701614-0-0

Japan) with 100-mm lenses and a Telops Fast-IR 2 K high-speed infrared camera (Telops, Quebec City, Canada) with a 50-mm lens were used. The images were recorded at approximately 80 cm distance through a 50.8 by 50.8 mm unprotected gold mirror (PFSQ20-03-M03, THORLABS, Newton, United States) placed at an angle below the specimen to reflect IR electromagnetic radiation. The test was illuminated with Ultra-Bright cold LED modules (Visual Instrumentation Corporation, Lancaster, United States). The experimental setup used in the impact test is shown in Fig. 1.

The image acquisition of the optical and infrared cameras was synchronized by triggering them with a Keysight 33,500 B function generator (Keysight Technologies, Santa Rosa, CA, USA). The acquisition frequency on both systems was 10 kHz with a resolution of 768 × 624 pixels in the optical camera and 128 × 112 pixels in the infrared camera. The full-field strain was calculated by using a 2D DIC system with a commercial package (DaVis 10, LaVision, Göttingen, Germany). The optical images were processed with a subset size of 35 x 35 pixels, a step size of 11 pixels, and a virtual strain gauge (VSG) of 57 pixels. Matching process was carried by an affine shape function and a 6th order spline sub-pixel image interpolation scheme with zero-normalized sum of squared differences (ZNSSD) criteria.

The infrared camera measures radiometric temperature. Two different approaches exist to converting these radiometric temperature measurements to actual surface temperature. Here, a K-type thermocouple was attached to the surface of the CFRP specimen. Then, it was heated up to 200 ˚C, and the cooling process was monitored by both thermocouple and the infrared camera. Many calibration runs were used to construct a calibration curve to accurately convert the radiometric temperature to surface temperature. The second approach for the FFRP sample was based on partly painting a specimen with a paint with known emissivity in the temperature range of interest and a similar process of observing the cooling down of the material. Surface temperature was calculated using the determined emissivity (0.88) and that was related to the radiometric temperature measurements of the unpainted portion of the composite. Additional information about the high-speed optical and infrared systems can be found in published works [8, 9].

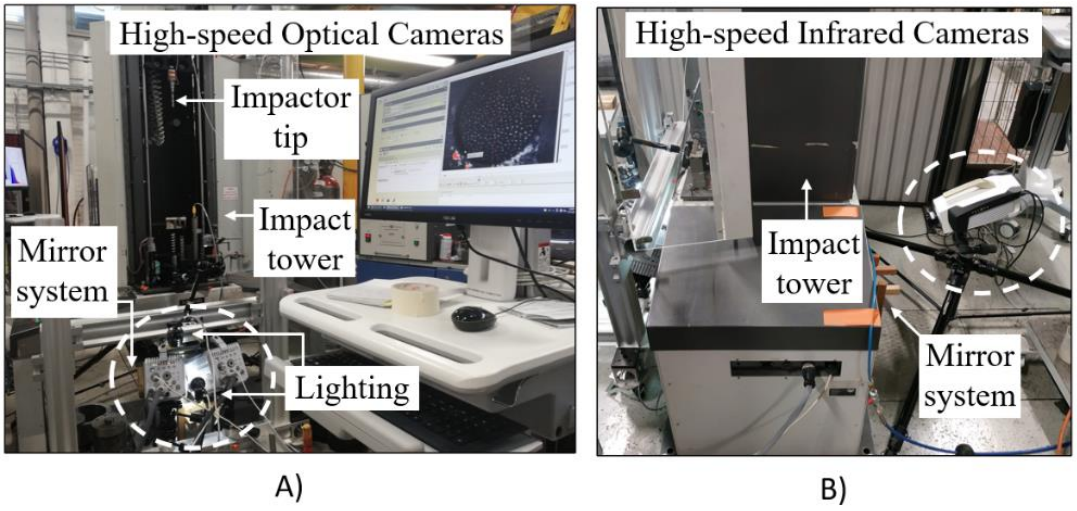

Figure 1. The experimental setup for the drop-tower impact test. A) The front view of the impact tower where high-speed optical camera are placed; B) the lateral view of the tower where high-speed IR camera is placed at the back part.

  doi:10.5075/epfl-298799_978-2-9701614-0-0

2.3 Impact damage model

The FE model for simulating the impact test was based on a transversally elastic constitutive model at the ply level. The simulation was run by using the Abaqus/Explicit. Two strength-based failure criteria were implemented through a user subroutine (VUMAT). The criteria were intended to indicate the onset of intra-laminar failure caused by the fibre and matrix related mechanisms. Fig. 2 shows the virtual test of the drop-tower impact for the carbon and flax model laminates.

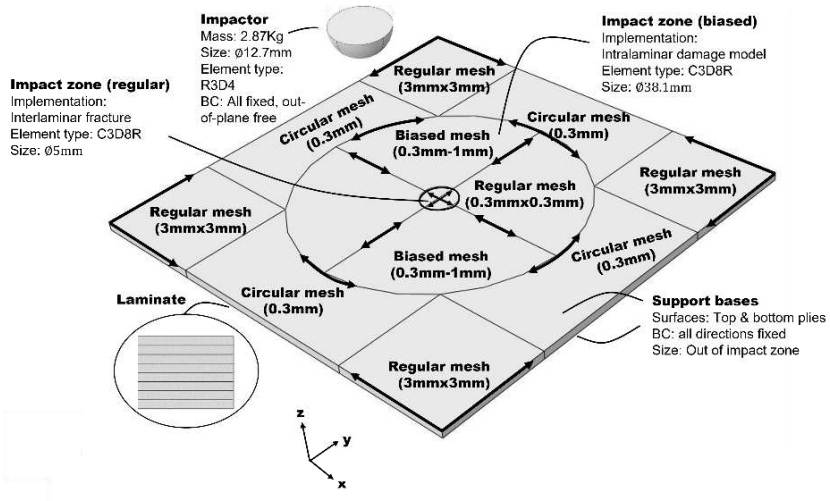

Figure 2. FE model of the simulated impact test and in-plane mesh structuring.

The impactor was modelled as a rigid body using 3D rigid elements (R3D4). The impactor contact model included normal and tangential constraints with a friction coefficient of 0.3 (steel-composite). The motion of the impactor was set in the out-of-plane direction, the rest of the degree of freedom was fixed. The laminate part was fixed (in all directions) at the outside area of the impact zone (see Fig. 2). The size of the FE laminate model was 58.1 × 58.1 mm^2 with a total thickness of 3.91 mm (5 mm for FFRP). The orientation of the plies followed the stacking sequences indicated in Section 2.1. The laminate mesh was defined with three-dimensional (3D) hexahedral continuum solid elements with eight nodes and reduced integration (C3D8R). The mesh size at the edge of the laminate was 3 mm. The impact zone was constructed with elements varying from 1 mm (the outer circle) to 0.3 mm (the inner circle) in size. The central zone was a refined regular mesh with the element size of 0.3 mm x 0.3 mm.

2.4 Failure criteria

The Hashin's and Puck's criteria [2] were used for the analysis of the failure onset related to the impact. The Hashin's criterion [10] is based on the Mohr-Coulomb failure theory. The criterion states that failure is caused by the stresses acting on a fracture plane. The formulation was developed based on this premise, but the (fracture) orientation angle was not able to be predicted due to computational limitations. The criterion distinguishes between fibre failure (FF) and inter-fibre failure (IFF) in tensile and compressive failure modes.

The Puck's criterion [11] was an extension of Hashin's criterion to formulate the failure analysis as a function of the oriented fracture plane. The calculation of the fracture angle was done through a maximization process of Puck's IFF functions [11]. For that, the stress tensor components were correlated to a fracture plane by means of the so-called 'action plane

  doi:10.5075/epfl-298799_978-2-9701614-0-0

stresses' ($\sigma_n(\theta)$, $\tau_{nt}(\theta), \tau_{nl}(\theta)$). The criterion distinguishes between tensile (IFF_+) and compressive (shear) matrix ($IFF\_$) failure IFF modes for the cracking phenomenon to transverse direction [9]. The criterion involves a third IFF mode, in which the fracture plane rotates about the longitudinal axis causing fibre breakage in adjacent UD layers, that was not studied in the current work. Rest of the formulation related to FF and IFF for both criteria can be found in a published work [12]. Table 3 presents the values of the material strengths for the CFRP and FFRP laminates.

Table 3. The strength parameters of a ply for the Hashin's and Puck's criteria [10, 11], and the values based on the experimental works [6, 7]. *Values equal the first in-plane direction. [2]Values taken from a work *[13].*

$Hashin's$	X_t	X_c	Y_t	Y_c	S_{12}	S_{13}	S_{23}
$Puck's$	-	-	$R_{\perp}^{+A}$	$2R_{\perp\parallel}^{A}(1+p_{\perp\perp}^{-})$	$R_{\perp\parallel}^{A}$	-	-
CFRP (MPa)	2172	1558	54	186	87	94	124
FFRP (MPa)	260	131[2]	18.58	18.58*	33.51	33.51*	33.51*

3. Results and discussions

Fig. 3 shows the experimental results of the force versus time for the CFRP and FFRP laminates. The damage threshold, F_d, at which the stiffness of the laminate presents a major change, was equal to the maximum force, $F_{\max}$, for the FFRP. For CFRP, the force grows after F_d.

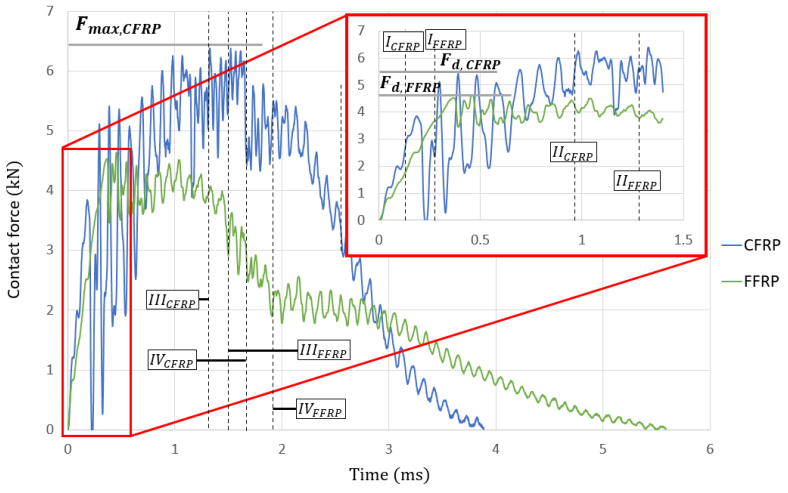

Figure 3. The force versus time history related to the 15 J impact tests for the CFRP and FFRP laminates.

A sequence of four IR spectra (time points) for each of the CFRP and FFRP laminate specimens are shown in Fig. 4. The IR results and force-time curve were correlated through time-steps of the test.

The CFRP laminate showed the highest temperatures at the almost final time-steps (1.56…1.66 ms). This phenomenon was due to fiber breaking. However, impact loading in CFRP was

  doi:10.5075/epfl-298799_978-2-9701614-0-0

characterized by the highest increase suspected delamination and anticipated intralaminar cracking at F_d. This type of behaviour is possible as reported in a published work [4]. The FFRP laminate presented the highest temperature values at the early time points of the force-time curve (but after F_d). It has been reported [1], that the primary cracks of flax-epoxy laminates can be due to bending during the impact test. The lower impact force (than for the CFRP laminate), have been suggested as consequences of lower bending stiffness [4].

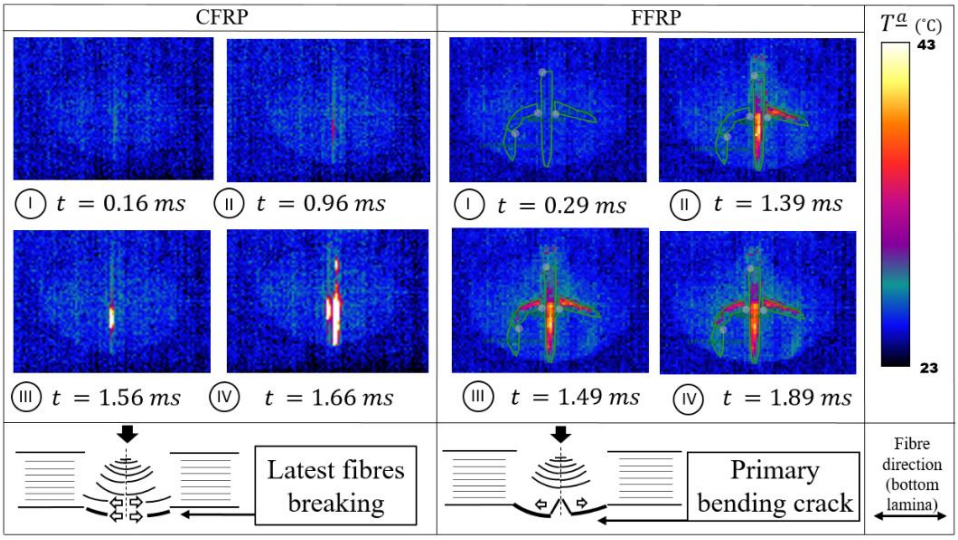

Figure 4. Surface temperature field recorded at the rear side of CFRP and FRP laminates. I-II-III-IV (sequences) were synchronized with the force versus time (see Fig. 1.)

Fig. 5 shows the full-field strains of the rear surface for the CFRP and FFRP laminates. As it can be observed, FFRP laminate experienced more deformation at the beginning of the impact. This is due to the FF what could affect the stiffness reduction at the F_d point [1].

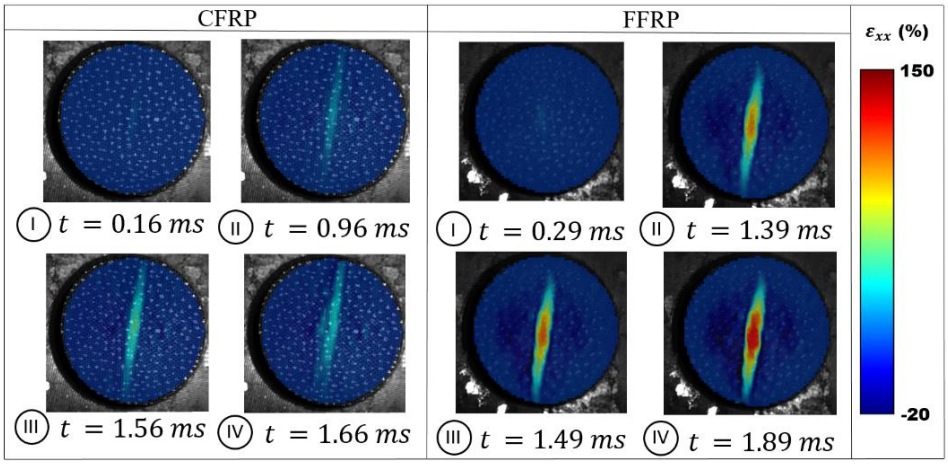

Figure 5. Full-field strain maps (DIC) of the fibre direction (ε_{xx}) on the bottom surface of CFRP and FFRP laminates. I-II-III-IV (sequences) were synchronized with theforce versus time (see Fig. 1.)

Fig. 6 shows the simulated von Mises stress and failure values by the Hashin's and Puck's criteria for the CFRP and FFRP laminates through the thickness direction. The results are shown at F_d.

The Hashin's failure criterion predicted a higher failure values in general. However, for the tensile IFF mode, Puck's criterion predicted a higher value. FFRP presented an IFF distribution in the thickness direction (by Puck), up to the rear side. This predicted the initiation of the

primary crack (for bending). This result was not predicted by the Hashin's criterion. For CFRP, the tensile IFF (Puck) was only predicted at the first layers of the laminate (with stiffness reduction at F_d). The Hashin's criterion only predicted failure initiation at the first (top) layer. The fracture plane for the Puck's criterion (IFF) modes resulted in (average) 55.5˚ (wrt. thickness direction). CFRP laminate did not reach fibre breakage at F_d, by predictions but both criteria showed failure (onset) at the first and middle plies.

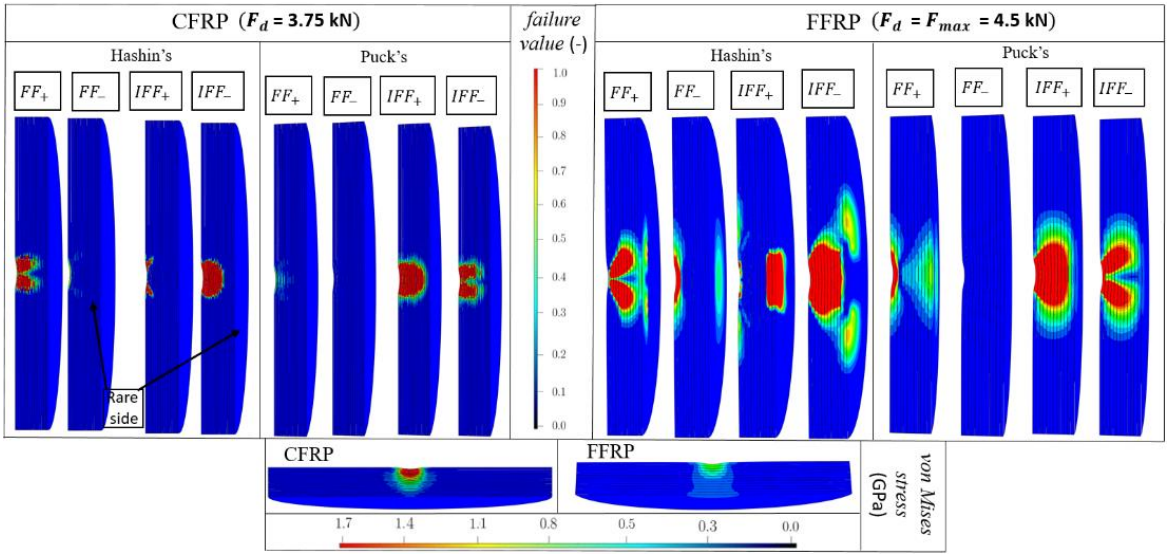

Figure 6. Predicted Von Mises stress and failure by Hashin's and Puck's criterion in CFRP and FFRP.

The IR measurement allowed for the observation of how (mechanical) energy turns into heat at the rear side during the testing. This enables a further interpretation of the failure mechanisms, as well as their evolution. In previous works [3, 4], it has been demonstrated, through ultrasonic C-scans, that delamination could be the main dissipative mechanism in some cases. In the current analysis, the IR spectra enabled to determine different projected areas of heat generated. This gives also further possibility to match the projected areas with the damage predicted (also inside the laminate). For future studies, it should be investigated whether the heat observed on the laminate surface is related to dissipation near the surface or damage inside the laminate. For damage inside, finite time is required for heat to be conducted to the surface.

4. Conclusions

The experimental methods of IR and strain measurements as fields, from the rear side of CFRP and FFRP laminate in this study, are a powerful tooling to analyze failure during the impact loads. Here, the thermal dissipation and strain fields together with the force versus time response indicated primary cracks due to the bending effect in the FFRP laminate. This damaging was predicted to be due to number of available interfaces and low material strengths based on numerical simulations.

The numerical impact simulations of the elastic response allowed understanding the effects of different damage modes. Also, they help to interpret the experimental results. The implementation of the Hashin's and Puck's failure criteria predicted the failure initiation for the FF and IFF modes at the F_d point of the impact. The numerical results demonstrated a higher precision by the Puck's IFF and FF modes in this study.

Acknowledgements

This research is partly based on the funding related to the ecosystem project SmartTram2 (5136/31/2019) for Tampere University funded by Business Finland.

5. References

1. Lawrence B., Fawaz Z., Bougherara H. Damage evolution in unidirectional and cross-ply flax/epoxy laminates subjected to low velocity impact loading. Composites Part A 2018; 112:452-467.
2. Hinton M. J., Kaddour A. S., Soden P.D. Failure Criteria in Fibre-Reinforced-Polymer Composites – The World-Wide Failure Exercise. Elsevier Ltd 2004; Edition 1.
3. González E.V., Maimí P., Martín-Santos E., Soto A., Cruz P., Martín de la Escalera F. et al. Simulating drop-weight impact and compression after impact tests on composite laminates using conventional shell finite elements. International Journal of Solids and Structures 2018; 144-145:230-247.
4. González E.V., Maimí P., Camanho P.P., Lopes C.S., Blanco N. Effects of ply clustering in laminated composite plates under low-velocity impact loading. Composite Science and Technology 2011; 71:805-817.
5. American Society of Testing and Materials, ASTM D5628-10 Standard Test Method for Impact Resistance of Flat, Rigid Plastic Specimens by Means of a Falling Dart (Tup or Falling Mass), ASTM International, 2010.
6. Skyttä V., Saarela O. and Wallin M. Progressive Failure of composite laminates; analysis vs experiments. Helsinki University of Technology, Laboratory of Lightweight Structures.
7. Javanshour F., Prapavesis A., Pärnänen T., Orell O., Lessa Belona M.C., Layek R.K. et al. Modulating impact resistance of flax epoxy composites with thermoplastic interfacial toughening. Composites Part A 2021; 150:106628.
8. Soared G. C., Hokka M. Synchronized Full-Field Strain and Temperature Measurements of Commercially Pure Titanium under tension at Elevated Temperatures and High Strain Rates. Metals 2022; 12:25.
9. Puornoori N., Soares G.C., Orell O., Palola S., Hokka M., Kanerva M. Adiabatic heating and damage onset in a pultruded glass fiber reinforced composite under compressive loading at different strain rates. International Journal of Impact Engineering 2021; 147:103728.
10. Hashin Z. Failure Criteria for Unidirectional Fibre Composites. Journal of Applied Mechanics 1980; 47:329–334.
11. Puck, A., Schürmann, H. Failure analysis of FRP laminates by means of physically based phenomenological models. In Failure criteria in fibre-reinforced-polymer composites, Elsevier Ltd 2002; 62:1633-1662.
12. Rodera Garcia O. Damage onset modelling of curved composite laminates, Master of Science thesis 2018, Tampere University of Technology.
13. Prapavesis A., Tojaga V., Östlund S., van Vuure A. W. Back calculated compressive properties of flax fibers utilizing the impregnated fiber bundle test (IFBT). Composites Part A: Applied Science and Manufacturing 2020; 135:105930.

  doi:10.5075/epfl-298799_978-2-9701614-0-0

HIGH TEMPERATURE FAILURE BEHAVIOR STUDIES OF CMC AND SUPERALLOY COUNTERSUNK BOLTED JOINT

Shuyuan Zhao[a], Qian Sun[b], Chao Lv[c]*

a: National Key Laboratory of Science and Technology for National Defense on Advanced Composites in Special Environments, Harbin Institute of Technology, Harbin 150080, China;
b: Shenyang Aircraft Design and Research Institute, Aviation Industry Corporation of China, Shenyang 110000, China;
c: China Academy of Aerospace Aerodynamics, Beijing 100074, China.
* Corresponding author (angel.zsy@126.com)

Abstract: *The strength analysis and design of C/SiC ceramic matrix composite countersunk head bolt joint structure play a vital role in improving bearing efficiency of joint structure and maintaining structural integrity, which have became a key technology in aircraft structural design. In this paper, a progressive damage process of 2D C/SiC composites and superalloy countersunk bolted joint under high temperature environment was simulated by using the ABAQUS finite element software. The effect of clearance level on high temperature tensile performance under different countersunk heights was studied for the CMC-superalloy bolted joint structures. The damage progression modes as the structure fails were discussed. Due to high temperature thermal mismatch effect and contact area variation between the superalloy bolt and ceramic matrix composite plate, the clearance fit accuracy of ceramic matrix composite and superalloy countersunk head bolt joint structure has less influence on the stiffness of the structure, whereas significant influence on the failure load of the structure under 750℃ working condition. When the countersunk height of the structure and the clearance fit accuracy are 1.7mm and 0.8%, respectively, the countersunk head bolt joint structure reaches the maximum bearing capacity. The present research provides theoretical guidance for design and application of CMC materials in aerospace and aeronautical fields.*

Keywords: *2D C/SiC composite; progressive damage analysis; tensile properties;bolted joint.*

1. Introduction

With extensive applications of joint structures in aerospace structures, countersunk fastening joints are of critical use due to their advantages in surface smoothness and load-transfer stability, especially for aircraft skin structures with aerodynamic shape and stealth performance requirements during operations [1-3]. However, the application of countersunk fasteners intensifies complicated stress concentration at the fastening area, which will reduce the joining efficiency of laminated composites. It is important to fully understand the mechanical behavior and failure mechanisms of countersunk bolted composite joints. In this paper, a progressive damage analysis of 2D C/SiC composites and superalloy countersunk bolted joint under high temperature environment was simulated by using the ABAQUS finite

  doi:10.5075/epfl-298799_978-2-9701614-0-0

element software. The effect of countersunk height on high temperature tensile performance under different clearance levels was studied for the CMC-superalloy bolted joint structures. The structural load bearing capacity and damage modes of the countersunk bolted joint at high temperatures will be discussed.

2. Progressive Damage Analysis Method

A finite element model was established to simulate quasi-statically tensile loading of the 2D plain woven C/SiC composite to superalloy countersunk bolted joint at high temperature via Abaqus/standard software, as shown in Fig.1. To address the nonlinear stress-strain relationship of C/SiC composites due to the progressive damage of matrix cracks, interface slipping and debonding, and fiber pull-out during tensile loading, a macroscopic constituent model was adopted here to characterize mechanical behavior of 2D plain-woven C/SiC composite materials. A 1000N preload was applied to the considered joints through Bolt load function in ABAQUS. Uniform temperature load of 750℃ was imposed to the entire joint structures. A user-defined subroutine UMAT including the nonlinear constitutive model, failure criterion and material degradation rule was developed, which was then embedded into the general package ABAQUS to implement a non-linear progressive failure analysis of C/SiC composite joint structure.

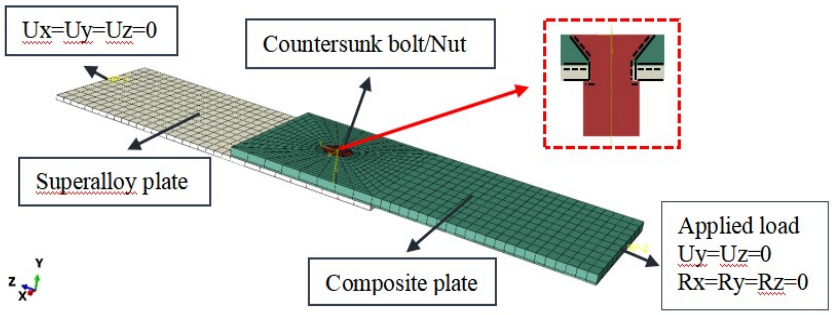

Figure 1. Finite element model of 2D C/SiC composite-superalloy countersunk bolted joint

3. Results and Discussion

The tensile failure loads of the joints under different countersunk heights and clearance fit accuracy are shown in Fig.2. As it can be seen, when the clearance fitting accuracy is 0.4%, the failure load of the structure decreases continuously from 2181.12N to 646.34N, while the failure load of the other two cases of clearance fitting accuracy increases first and then decreases with the increase of the countersunk height from 1.5mm to 2.1mm. Except for the case of countersunk height of 1.9mm, the failure load of the structure increases first and then decreases with the increase of clearance fit accuracy. When the clearance fit accuracy reaches 0.8%, the structure reaches the maximum failure load. For the countersunk height of 1.9mm case, the failure load of the connection structure with 0.8% clearance is 2956.19N, only slightly lower than the failure load of 3112.01N for the structure with 1.2% clearance. As the uniform temperature load of 750 ℃ was imposed to the structure, thermal mismatch effect

causes changes in clearance fit accuracy and pre-tightening force of the hybrid countersunk bolted joint. For the studied countersunk bolt joint of CMC and superalloy plates, the cylindrical part of the bolt undertakes the main tensile load. A smaller straight-edge region produces larger load eccentricity as it carries the majority of the load. Increasing the countersunk height of the bolt intensifies the initial stress concentration and results in complicated distribution of stress around the hole-edge area of the composite material plate. In addition, the increase of the countersunk height will improve the cross-section area of the bolt, which might reduce the stress increment caused by tension. And therefore, the failure load of the hybrid joint of CMC and superalloy plates shows diverse varying trends with the countersunk parameters. When the countersunk height of the structure is 1.7mm and the bolt-hole clearance is 0.8%, the carrying capacity of the head bolt connection structure reaches the maximum of 3134.89N.

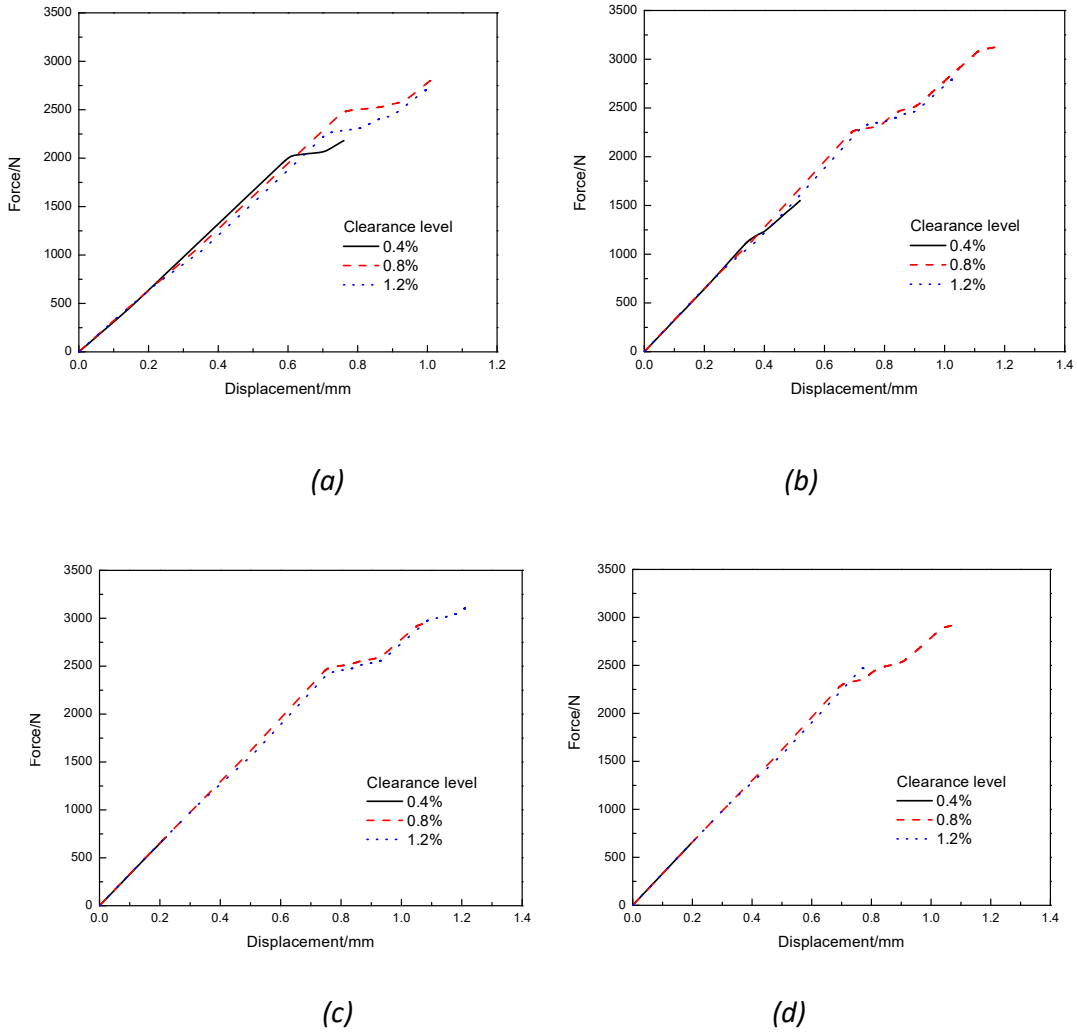

Figs.3 The load–displacements curves of the CMC/superalloy countersunk joints with different values of clearance level under given values of countersunk height (h) (a)h=1.5mm; (b) h=1.7mm; (c) h=1.9mm; (d) h=2.1mm

  doi:10.5075/epfl-298799_978-2-9701614-0-0

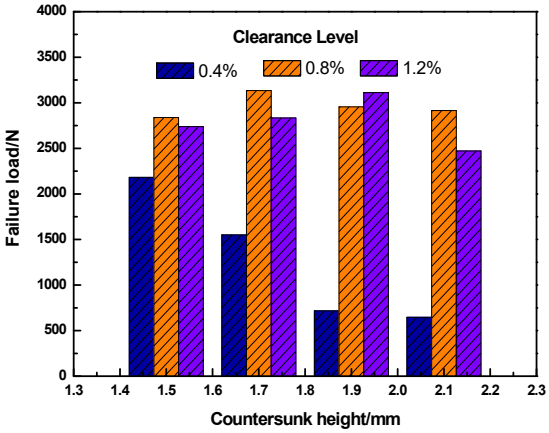

Fig.2 Effect of clearance level on the high temperature failure load of the joint structure under different countersunk heights

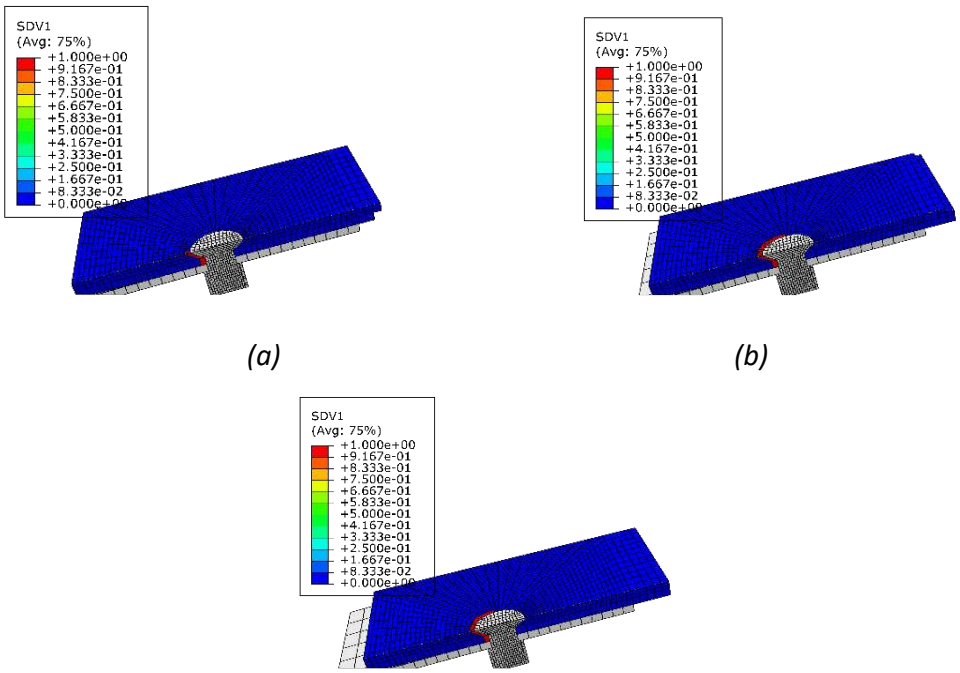

(a) *(b)*

(c)

Fig.4 Failure element distribution of the CMC/superalloy countersunk bolted joint with countersunk height of 1.7mm under different clearance levels (a) 0.4%; (b) 0.8%; (c) 1.2%

Failure element distribution of the CMC/superalloy countersunk bolted joint with countersunk height of 1.7mm under different clearance levels are shown in Figs. 4. The damage failure process of the connection structure generally occurs preferentially in the bottom elements on the left side of the ceramic matrix composite plate, and then gradually expands on the upward side, and the failure elements on the upper and lower sides runs through and then expands to the periphery, until the structure is completely damaged. As can be seen from Figure 4, the

damage failure of the ceramic matrix composite expands under the clearance level of 0.4%. The span range is small, mainly concentrated in a very narrow area of the left contact surface around the hole. The structure fails prematurely, while the bolt-hole clearance is 0.8% and 1.2%, the damage element expands in larger areas. When the accuracy is 0.8% and 1.2%, the damage unit is large. With the clearance accuracy of 0.8%, the failure load of the countersunk bolt joint structure reaches the maximum value.

4. Conclusions

In this paper, the high temperature tensile performance of the 2D C/SiC composites and superalloy countersunk bolted joint under varying clearance levels and countersunk heights were studied by using progressive damage analysis method. Due to high temperature thermal mismatch effect and contact area variation between the superalloy bolt and ceramic matrix composite plate, the clearance fit accuracy of ceramic matrix composite and superalloy countersunk head bolt joint structure has less influence on the stiffness of the structure, whereas significant influence on the failure load of the structure under 750℃ working condition. When the countersunk height of the structure and the clearance fit accuracy are 1.7mm and 0.8%, respectively, the countersunk head bolt joint structure reaches the maximum bearing capacity. The present research provides theoretical guidance for design and application of CMC materials in practical engineering area.

Acknowledgements

This work was supported by Pre-Research Foundation of Shenyang Aircraft Design and Research Institute, Aviation Industry Corporation of China (Grant No. JH20128255), supported by National Defence Basic Research Program (Grant No.JZ20180032) and supported by Pre-Research Foundation of Equipment Development Department of People's Republic of China Central Military Commission (Grant No. ZJJSN20200001).

5. References

1. T.L. Qin , L.B. Zhao, J.Y. Zhang . Fastener effects on mechanical behaviors of double-lap composite joints. Composite Structures 100 (2013) 413–423.
2. M. Chishti, C. H. Wang, R. S. Thomson, et al.. Numerical analysis of damage progression and strength of countersunk composite joints. Composite Structures 94 (2012) 643–653.
3. M. Chishti, C. H. Wang, R. S. Thomson, et al.. Experimental investigation of damage progression and strength of countersunk composite joints. Composite Structures 94 (2012) 865–873.

  doi:10.5075/epfl-298799_978-2-9701614-0-0

EXPERIMENTAL AND NUMERICAL STUDY ON THE TRANSVERSE CRACKING IN A COMPOSITE MATERIAL WITH A THERMOPLASTIC MATRIX

Frédéric Laurin[a], *Anne Mavel[a], Pascal Paulmier[a], Juan-Manuel Garcia[a], Mélanie Herman[b]*

[a] ONERA, DMAS, Université Paris-Saclay – frederic.laurin@onera.fr
[b] AIRBUS Operations, Airframe Engineering

Abstract: *The proposition of innovative and competitive designs of aeronautical structures manufactured with composite materials made of carbon fibres and thermoplastic matrix, presenting high potential for recyclability and interesting welding capabilities, cannot be performed without a deep understanding of the different sources of non-linearities specific to those high performance materials. The objective of the present study consists therefore in understanding the underlying physical phenomena leading to transverse cracking in a new generation of composite material with carbon fibres and thermoplastic matrix and in highlighting their specificities compared to a UD ply made of the same carbon fibres but associated with an epoxy matrix.*

Keywords: Composite with thermoplastic matrix; Multi-instrumented tests; Transverse cracking; Damage modelling; Fracture toughness

1. Introduction

Laminated composites constituted with unidirectional plies made of carbon fibres associated with a thermoplastic matrix are now being considered for the production of primary aeronautical structures due to the welding possibilities offered and the high potential for recyclability. In addition, these materials allow parts to be manufactured out-of-autoclave with an interesting production rate. Due to the recent development of these high performance materials, it is necessary to determine precisely their specificities; in terms of behaviour, damage mechanisms and fracture; compared to Carbon/Epoxy materials widely studied in the literature. This point is addressed in the present article from an experimental point of view. Indeed, in section 2, the experimental test campaign, designed to study the onset and evolution of transverse cracks, is presented. Some major differences have been observed between the test results obtained on this material and those obtained on a classical carbon/Epoxy material constituted with the same Carbon fibre but with an Epoxy matrix and different explanations have been experimentally investigated in section 3. Once this stage of understanding the specificities of damage mechanisms in a carbon/thermoplastic composite material been completed, the section 4 addresses the relevance of non-linear models, initially developed for carbon/epoxy composites, for thermoplastic matrix composites and to determine the modifications to be performed in such models in order to be consistent with the test results.

2. Experimental study of transverse cracking in a Carbon/Thermoplastic material

2.1 Presentation of the studied composite material

The laminated composite material, considered in this study, is made of T700GC carbon fiber associated with a TC1225 thermoplastic matrix supplied by Toray Advanced Composites with a

  doi:10.5075/epfl-298799_978-2-9701614-0-0

unidirectional ply architecture. The characterization specimens manufactured in this study ($[(45_m/-45_m)_n]_s$, $[(0_n/90_m)_p]_s$ cross-ply laminates, and $[(90/\pm45)_p]_s$, $[(45/90/-45/0)_p]_s$ multilayered plates) were produced at ONERA under a heated press in accordance with the curing cycle recommended by the manufacturer. The manufactured specimens were all controlled by C-Scan and microscopic observations to ensure the quality of the initial state of the specimens.

2.2 Experimental device and associated multi-instrumentation

The tensile tests have been performed at ONERA on a hydraulic testing machine with a maximal capacity equal to 100 kN, with associated hydraulic jaws.

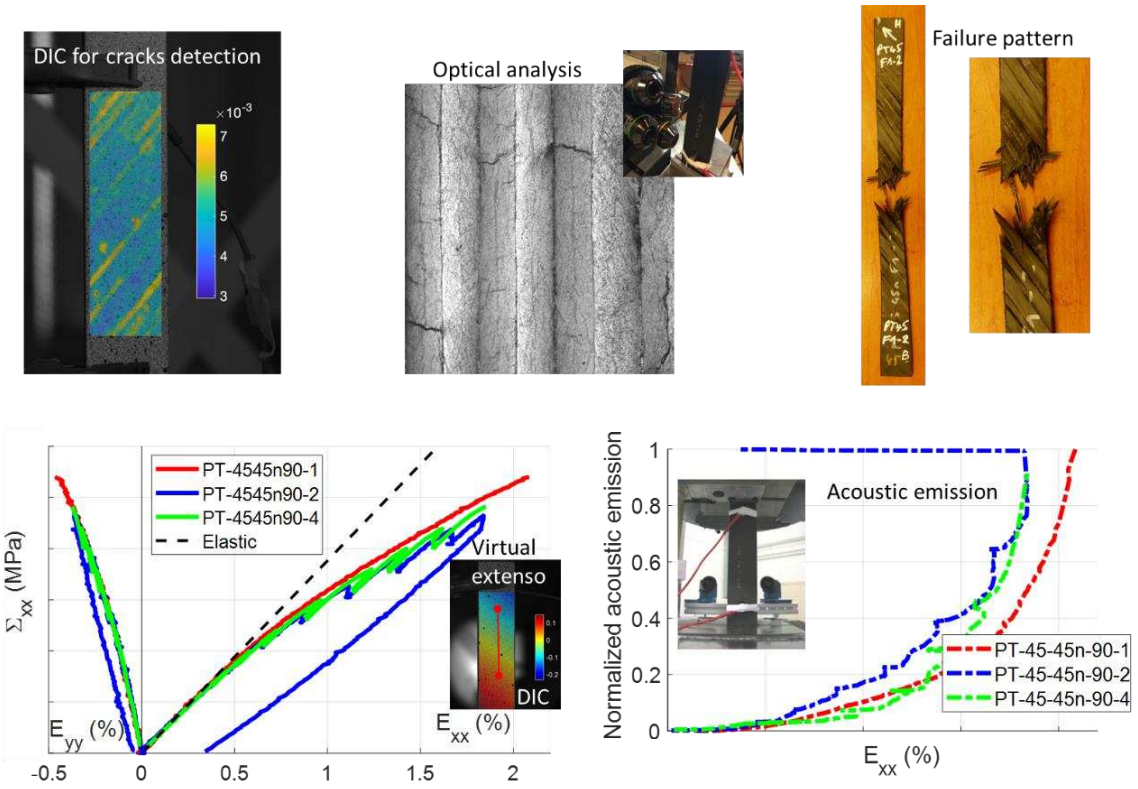

Figure 1: Presentation of the measurement techniques on tensile tests performed at Onera

Those tensile tests have been multi-instrumented, as reported in Figure 1, in order to understand the different sources of non-linearity encountered in such a new material, with :

- 1 acoustic emission (AE) sensor to monitor the evolution of damage [1] during the test. The acquisition system is the AEWin system supplied by MISTRAS and the acoustic sensor is a Nano80 sensor type.
- All the tests were monitored using stereo-correlation of digital images (DIC), carried out using Vic3D software [2]. Two 12bits cameras with 2000x2000 resolutions were used. A black and white speckle was made on the upper face of each specimen.
- For some specimens, a special attention has been paid to the transverse cracking evolution [3,4]. During those tests, after significant acoustic events, the applied displacement has been maintained while many pictures are taken with a CCD camera (12 bits with a resolution of 1379x1024 pixels) associated to a microscope with different objectives (x5 or x10). This

  doi:10.5075/epfl-298799_978-2-9701614-0-0

camera is fixed on a micrometre table with 3 axes which allows taking many pictures (between 20 and 50) on one edge of the specimen, previously polished. Then, these pictures are merged to obtain a large micrograph of the whole area of interest of the specimen as illustrated in Figure 2. The observed area is about 80 mm to be statically representative of matrix cracking in plies.

- Finally, the failure pattern of the different specimens were analysed optically and using SEM to confirm the ruin scenarios established using the other measurements.

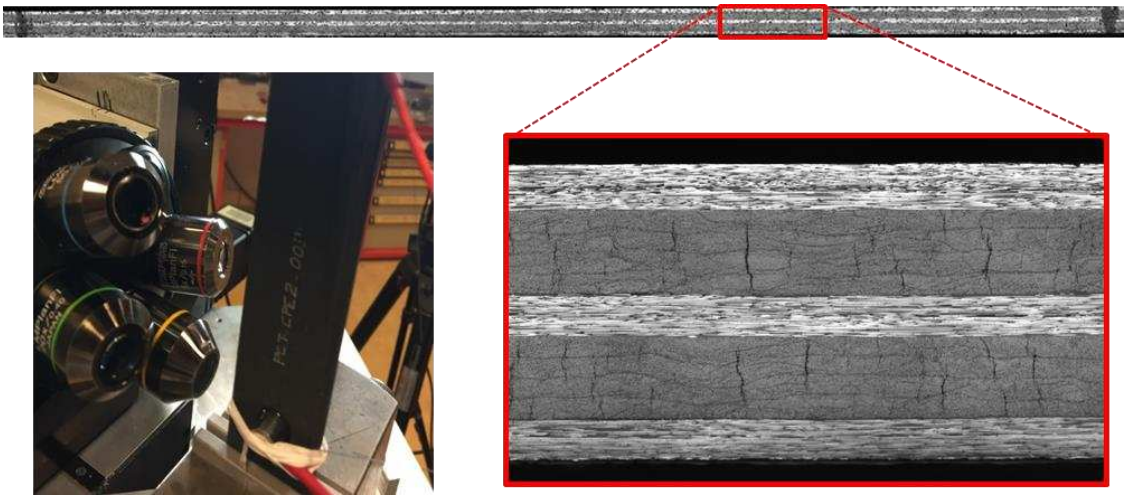

Figure 2: Fine observation of damage pattern in a T700GC/TC1225 cross-ply $[0_2/90_4/0]_s$ laminate

The damage onset and evolution of transverse cracking have been analysed through the analysis of tensile tests on two different stacking sequences. Cross-ply $[0/90_2/0/90_2/0]_s$ and $[0_2/90_4/0]_s$ laminates have been tested to determine the influence of the ply thickness on the apparent onset of damage but also on its evolution, as already observed on classical Carbon/Epoxy materials [3,5–7]. Figure 3a presents the macroscopic behaviour for the two cross-ply laminates which is almost linear, while lots of cracks are observed, due to the presence of 0° plies. The analysis of the acoustic emission allows determining the onset of damage, as reported in Figure 3b, which seems to be insensitive to the ply thickness. This point constitutes the first major difference with classical Carbon/Epoxy material.

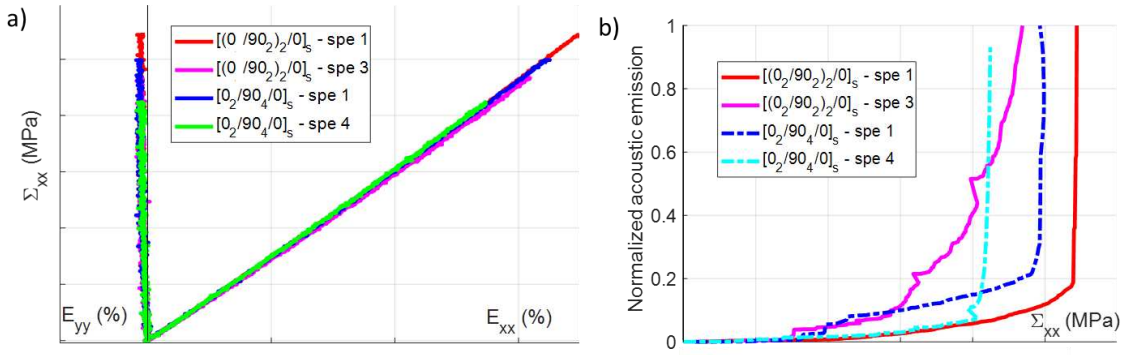

Figure 3: a) Macroscopic behavior of $[0/90_2/0/90_2/0]_s$ and $[0_2/90_4/0]_s$ laminates subjected to tensile loading and b) evolution of the cumulative acoustic energy as a function of the applied stress

The crack density evolution, monitored with AE and optical observation, seems to be sensitive to the ply thickness, as for the carbon/Epoxy materials. This point is confirmed considering the macroscopic failure stresses of these two laminates, which is higher for the thinnest 90-plies, because of lower loading report of less damaged 90-plies to the sane 0-plies.

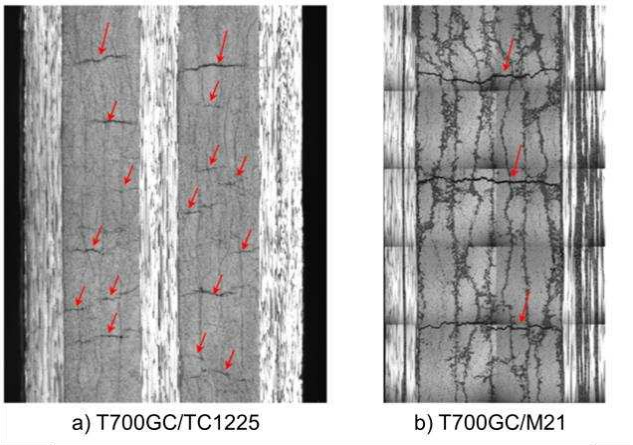

Figure 4: Comparison of damage patterns within cross-ply a) T700GC/TC1225 and b) T700GC/M21 $[0_n/90_m]_s$ laminates.

Finally, the damage patterns observed on T700GC/TC1225 laminates are carefully compared to those observed on other composite materials with thermoset matrix, as reported in Figure 4. Indeed, in cross-ply Carbon/Epoxy laminates made of T700GC fibre (same fibres) associated with an epoxy M21 matrix [3] proposed by Hexcel the transverse cracks propagate through the whole thickness of the ply whatever the thickness of the ply and local delamination at the tips of cracks are also observed. For the T700GC/TC1225 material, the cracks are spread over the ply thickness and present short lengths. A huge number of small cracks appear in the different plies prior the final failure, which is very specific and constitutes an original point of this study, which is discussed in the next section.

3. Explanation of specificities of the observed damage patterns

3.1 Possible physical explanations of diffuse cracking

As highlighted in the previous section, the damage pattern observed for the cross-ply T700GC/TC1225 laminates (but also for quasi-isotropic lay-ups presented in the sequel) is very specific compared to that observed on T700GC/M21 laminates. As proposed in [6,7], a mixed criterion can be relevant to explain the influence of the ply thickness on the onset of damage and on the damage pattern. It is assumed that a transverse crack can appear when a stress criterion (associated to the occurrence of local fibre/matrix deboundings), and an energy criterion (associated to the propagation of this micro-crack) are both fulfilled. As mentioned previously, tensile tests have been performed on $[90]_{16}$ plies to determine the transverse strength used in the stress criterion and the obtained value is very similar to that obtained on T700GC/M21 90° plies [3]. Therefore, the mode I fracture toughness used in the energy criterion has been experimentally investigated in the next section.

3.2 Experimental study of the fracture toughness in mode I

  doi:10.5075/epfl-298799_978-2-9701614-0-0

In order to determine the fracture toughness for mode I, Double Cantilever Beam (DCB) tests have been performed at ONERA on $[0_{12}]_s$ laminate containing a Upilex insert as a pre-crack with a length equal to 60 mm. The experimental device is illustrated in Figure 5a with the associated multi-instrumentation. A special attention has been paid to the development of an automated method, based on DIC, to measure the delamination crack length evolution during the loading. Moreover, few C-Scan analyses have been performed during interrupted DCB tests to control the crack front through the width and increase the confidence into the test results.

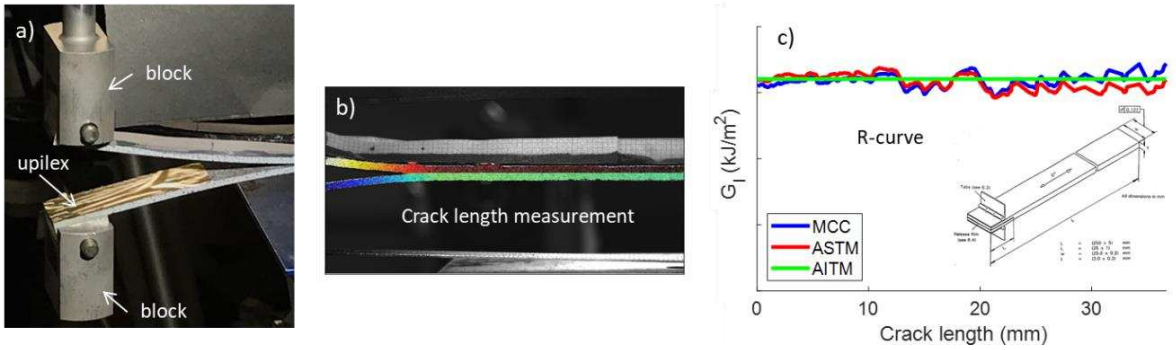

Figure 5: a) DCB experimental device, b) crack measurement length method with DIC and c) R-curve determined using different data reduction methods

In order to determine the R-curves and then the apparent fracture toughness from the knowledge of the displacement / load / crack length measurements, different data reduction methods, available in the literature [8,9], have been considered. Figure 5c presents the R-curves, estimated with the modified Compliance Calibration method and two other methods available in ASTM and AITM standards, which are consistent and allow estimating precisely the mode I fracture toughness. The measured fracture toughness of the Carbon/Thermoplastic material is 4.5 times higher than that of the Carbon/Epoxy material, as reported in Figure 6a.

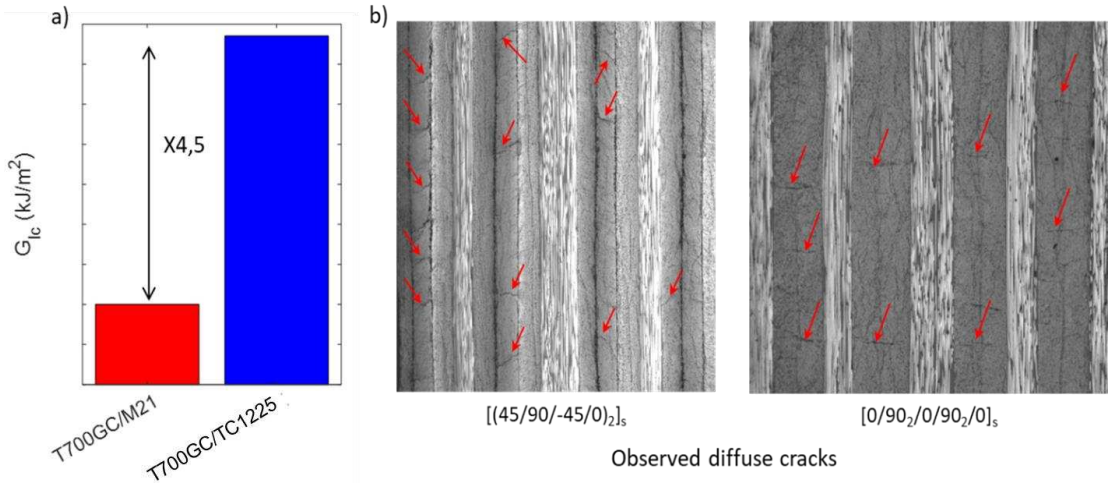

Figure 6: a) Comparison of the fracture toughness of T700GC/M21 and T700GC/TC1225 material and b) crack damage patterns observed on quasi-isotropic and cross-ply T700GC/M21 laminates

This very high fracture toughness may explain the short lengths of the observed transverse cracks and justifies probably the diffuse damage patterns, reported in Figure 6b for different

  doi:10.5075/epfl-298799_978-2-9701614-0-0

(quasi-isotropic and cross-ply) lay-ups, which is very different from those observed on Carbon/Epoxy materials presenting lower fracture toughness. It can be noted that plasticity, confined at the tips of the transverse cracks, can also partially explain the short lengths of the cracks and the diffuse damage pattern. Nevertheless, preliminary creep tests and measurements of permanent strains during regular unloading in tensile tests have not showed major differences in the non-linear behaviour prior cracks compared to the T700GC/M21 material.

To conclude this experimental study, diffuse damage patterns have been observed during tensile tests performed on different lay-ups which is a major difference compared to classical Carbon/Epoxy materials. Moreover, in-situ effect for the onset of damage, well established for carbon/epoxy materials, seems to be not relevant for this material probably due to the very high fracture toughness of the material in mode I.

4. A damage model for Carbon/Thermoplastic composites

4.1 Presentation of the damage and failure model

The objective of this section was to apply the existing Onera Progressive failure approach (OPFM), developed at Onera since many years for composite materials with thermoset matrix [10], to the T700GC/TC1225 in order to determine its advantages and drawbacks. The behaviour of the T700GC/TC1225 up to failure should be modelled considering the different sources of non-linearity (thermal residual stresses, viscosity, elastic non-linearity, intra-ply damage) at the ply scale using a laminate theory extended to non-linear behaviour. The prediction of the local non-linear mesoscopic behaviour up to the specimen failure is performed with the progressive failure approach proposed in [10], which is briefly summarized in this section. The present multiscale failure approach considers the unidirectional (UD) ply as the elementary entity of modelling and is predictive for different stacking sequences. It could be decomposed into four main steps. Firstly, in order to predict accurately the failure of a ply in a laminate, it is necessary to estimate correctly the mesoscopic stresses and strains. A non-linear thermo-viscoelastic behaviour has been proposed in Eq. 1.

$$\underline{\sigma} = \underline{\underline{\tilde{C}}} : \left(\underline{\epsilon} - \underline{\epsilon}^{th} - \underline{\epsilon}^{ve} - \underline{\epsilon}^{nl}\right) \quad (1)$$

where $\underline{\sigma}$ is the mesoscopic stress, $\underline{\underline{\tilde{C}}}$ the effective rigidity, $\underline{\epsilon}$ the total strain, $\underline{\epsilon}^{th}$ the thermal strain (in order to take into account the thermal residual stresses, which are essential to predict accurately the first ply failure), $\underline{\epsilon}^{nl}$ the non-linear elastic strain (in order to describe the hardening observed experimentally on UD plies subjected to longitudinal tensile loadings and especially on new generations of composite materials such as T700GC/M21 [3] or observed on the studied material), and $\underline{\epsilon}^{ve}$ the viscous strain. Secondly, the prediction of the ply failure within the laminate is performed with a failure criterion, based on Hashin's hypotheses [11], distinguishing the fibre failure mode and the in-plane interfiber failure mode and modelling separately the failure mechanisms in tension and in compression for each failure mode. The two main improvements of the fibre failure criterion, as compared to Hashin's criterion, are (i) the introduction of coupling between the intralaminar damage d_2 and the longitudinal tensile strength X_t (allowing to obtain conservative predictions for complex multiaxial loadings) and (ii) to take into account the influence of the in-plane shear on the ply failure in compression. The main improvement of the interfiber failure criterion is a better description of the reinforcement

of the apparent strength of the material for combined in-plane shear and transverse compressive loadings. Thirdly, when a ply within the laminate is broken in interfiber mode (*i.e.* when transverse cracks are present in the ply), its mechanical properties are progressively degraded using a thermodynamical degradation approach based on damage modelling already developed at Onera [10]. A continuum damage model is relevant for the T700GC/TC1225 due to the diffuse cracks observed within the ply. Fourthly, for a laminated unnotched coupon, the final rupture could be due to the first ply failure in fibre mode or in transverse compression.

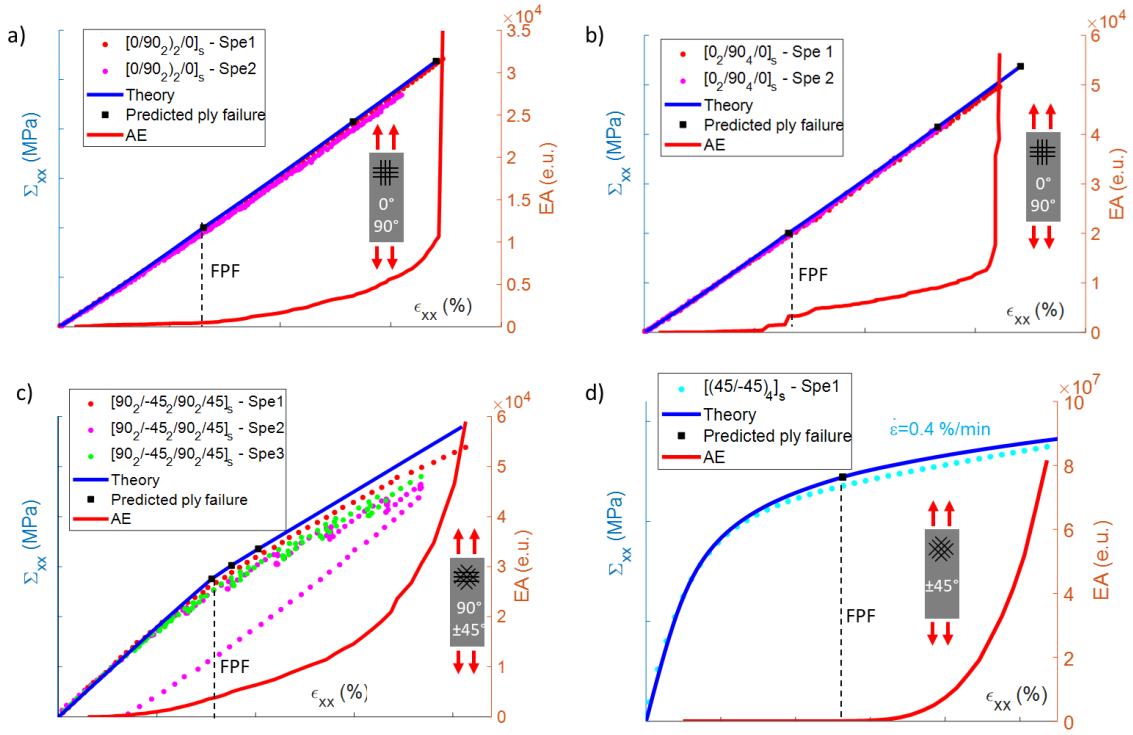

Figure 7: Comparisons between tests and model predictions for a [0/90$_2$/0/90$_2$/0]$_s$ laminate subjected to tensile loading, b) a [0$_2$/90$_4$/0]$_s$ laminate subjected to tensile loading, c) a [90$_2$/-45$_2$/90$_2$/45]$_s$ laminate subjected to tensile loading, and d) a [(45/-45)$_4$]$_s$ laminate subjected to tensile loading

Finally, the model has been identified on the available tests and applied successfully to other tests for validation. The tensile tests on 0° and 90° plies and [±45°]$_s$ laminate have been used for identification of the model. For the two considered cross-ply laminates, while the thickness of the 90-ply has been doubled, the apparent strength of the ply seems to remain constant, as reported in Figure 7. Additional test on cross-ply laminates will be performed soon. The predicted macroscopic behaviour for the [90$_2$/-45$_2$/90$_2$/45]$_s$ laminate is in rather good agreement with experimental data while the first ply failure is overestimated. Finally, the first ply failure within [(45/-45)$_4$]$_s$ laminate is accurately predicted by the model. Additional tests on laminates with different ply thickness should be performed soon to determine the ply thickness influence on apparent in-plane shear strength.

5. Conclusion / Perspectives

This study is a first step towards the characterization of the T700GC/TC1225 thermoplastic matrix material by trying to identify the similarities and differences with the carbon/epoxy

materials conventionally used in the aerospace industry. Particular attention was paid to the transverse cracking pattern presenting a diffuse nature of the damage within the plies, which constitutes a strong difference with the observations performed usually on carbon/epoxy materials. These diffuse damage patterns are probably due to the very high fracture toughness in mode I of the material (4.5 times higher than that of T700/M21). Finally, the Onera model, initially developed for thermoset matrix composites, was applied to the study material. Although the first simulations are in relatively good agreement with the test data, it seems necessary to take into account the plasticity of the matrix in the model and to introduce a particular management of the influence of the thickness of the plies on the transverse cracking (no influence on threshold but on the evolution law).

Acknowledgements

This study was carried out as part of the Clean Sky II project within the Large Passenger Aircraft platform in WP2.4.3 in collaboration with Airbus Operations.

6. References

1. N. Godin, S. Huguet, R. Gaertner, L. Salmon, Clustering of acoustic emission signals collected during tensile tests on unidirectional glass/polyester composite using supervised and unsupervised classifiers, NDT E Int. 37 (2004) 253–264.
2. F. Laurin, J.-S. Charrier, D. Leveque, J.-F. Maire, A. Mavel, P. Nuոez, Determination of the properties of composite materials thanks to digital image correlation measurements, Procedia IUTAM. 4 (2012) 106–115.
3. C. Huchette, Analyse multiéchelle des interactions entre fissurations intralaminaire et interlaminaire dans les matériaux composites stratifiés, Doctorate thesis, University of Paris VI, 2005.
4. N. Germain, Modélisation non locale de l'endommagement dans les structures composites, Doctorate thesis of Ecole des Mines de Paris, 2006.
5. A. Parvizi, K. Garrett, J. Bailey, Constrained cracking in glass fibre-reinforced epoxy cross-ply laminates, J. Mater. Sci. 13 (1978) 195–201.
6. G.J. Dvorak, N. Laws, Analysis of first ply failure in composite laminates, Eng. Fract. Mech. 25 (1986) 770.
7. P.P. Camanho, C.G. Davila, S.T. Pinho, L. Iannucci, P. Robinson, Prediction of in situ strengths and matrix cracking in composites under transverse tension and in-plane shear,Compos. Part A. 37 (2006) 165–176.
8. P. Prombut, Caractérisation de la propagation de délaminage des Stratifies composites multidirectionnels, Doctorate thesis, University of Toulouse, 2007.
9. T. Vandellos, Développement d'une stratégie de modélisation du délaminage dans les structures composites stratifiées, Doctorate thesis, University of Bordeaux I, 2011.
10. F. Laurin, N. Carrere, J.F. Maire, A multiscale progressive failure approach for composite laminates based on thermodynamical viscoelastic and damage models, Compos. Part Appl. Sci. Manuf. 38 (2007) 198–209.
11. Z. Hashin, Failure criteria for unidirectional fiber composites, J. Appl. Mech. 47 (1980) 329–334.

  doi:10.5075/epfl-298799_978-2-9701614-0-0

MODELLING THE PROGRESSIVE DAMAGE BEHAVIOUR OF THE FIBRE CEMENT BOARDS

V Y, Palagala[a], Nithyadharan, M[b]

a,b: Department of Civil and Environmental Engineering, Indian Institute of Technology Tirupati, India – ce18d502@iittp.ac.in

Abstract: *Fibre reinforced cement boards are widely used as sheathing in the walls and floors of cold formed steel (CFS) building systems. This boards serves as cladding and also acts as a structural element contributing to the strength and stiffness. A constitutive model of the board in progressive damage analysis format is essential to represent its behaviour in the finite element (FE) model of CFS sheathed wall and floor elements. In this paper, a constitutive model based on continuum damage mechanics (CDM) approach is developed for modelling the failure and damage behaviour of fibre cement board. The proposed model is implemented as user material subroutine, UMAT in FE analysis framework in ABAQUS software. The efficacy of the developed material model is validated with experimental response on (a) open-hole tension test, and (b) three-point bending test. The results show that the proposed model is able to capture the experimental response, and observed failure modes reasonably well.*

Keywords: sheathing; constitutive model; continuum damage mechanics; progressive damage analysis; UMAT

1. Introduction

The cold formed steel (CFS) wall panel building system is an assembly of CFS wall panels, floor panels, and roof [1]. The CFS wall panels are constructed with CFS (channel with lips) studs as framing members, cladded with single skin sheathing material made of wood, gypsum, cement or steel on both interior and exterior faces. CFS joists that spans between the wall panels are attached with sheathing on top face, acts as floor system in the CFS building. The sheathing is often connected to CFS framing members with self-drilling screws. In the recent days, the conventional wood and wood-based products such as plywood and oriented strand board (OSB) are gradually replaced with fibre cement board (FCB), gypsum plasterboard and calcium silicate boards (CSB). Among these, FCB are frequently preferred as outside cladding for perimeter wall panels in CFS wall panel building systems due to its excellent durability characteristics [2]. FCB is made of siliceous material and cement particles reinforced with non-hazardous cellulose fibres made from wood pulp. The longer and shorter direction of the board are considered as longitudinal (L) and transverse (T) directions, respectively. The current research on CFS walls and floors highlights that, the boards serves primarily as cladding and also enhances the (i) in-plane and out of plane buckling capacity of the CFS stud under gravity loading [3–5], (ii) resists the wind loading (between studs) acting normal to the wall panel by bending [6], (iii) offers lateral resistance under in-plane shear loading [7,8]. As the sheathing material contributes to strength and stiffness, a good constitutive model is essential to represent its behaviour in the FE modelling of CFS sub-systems, particularly walls and floor elements.

  doi:10.5075/epfl-298799_978-2-9701614-0-0

Very limited mechanical characterization studies on FCB for developing material models were reported in the literature. Recently, Jayesh 2020 [9], conducted a detailed mechanical characterization on FCB of 8mm, 10mm and 12mm thickness under tension, compression and shear loading as per ASTM standards along the longitudinal and transverse directions. This mechanical characterization study revealed that the board exhibits anisotropic material behavior. In the FE analysis of the CFS subsystems, the modelling of the CFS member considering geometric and material nonlinearity, and the nonlinear behaviour of the screw connections between CFS framing and sheathing have advanced to a mature state. Till date, the sheathing in the CFS sub-systems is modelled as an orthotropic lamina with linear elastic material properties. Telue and Mahendran, and Ye at el. [3,10] conducted FE studies on the CFS sheathed stud under axial compressive loading, where the sheathing material such as plasterboard, OSB, CSB and glass magnesium board were modelled with linear elastic constitutive law. Nithyadharan and Kalyanaraman [11] developed a FE model for the CFS wall panels sheathed with calcium silicate board (CSB) subjected to in-plane shear loading. In this study, the sheathing was modelled as linear elastic with Tsai-Hill failure criterion to study initiation of the damage in the sheathing material alone. The major limitation of the current FE studies on CFS sheathed studs/ joists reported in the literature are, the sheathing is modelled as linear elastic which eventually remains elastic even after the damage without experiencing strength and stiffness degradation.

To address the issue, this paper presents the development of constitutive model for the FCB in progressive damage analysis format, wherein the model captures the damage initiation and damage evolution, incorporating both strength and stiffness degradation similar to that observed in the experiments. The details about implementing the material model as user subroutine, UMAT in ABAQUS software [12] is explained subsequently. Further, a detailed validation study on (a) open hole tensile test specimen, and (b) three- point bending specimen are presented to demonstrate the efficacy of the developed material model.

2. Development of Constitutive Model for FCB

The constitutive model developed based on Continuum damage mechanics (CDM) approach is used widely for modelling the progressive damage behaviour of the fibre reinforced polymer composites [13–16]. Most of the commercial FE softwares has built-in material models based on CDM approach for modelling fibre reinforced composites. The failure criteria used to predict the damage initiation in fibre reinforced composites in the commercial softwares cannot be straightaway extended to FCB, though both the material possess anisotropic behavior. In this paper, a constitutive model for FCB based on CDM approach is developed which represents the experimental behavior with: (a) linear elastic behaviour up to onset of damage, (b) a strain-based failure criteria to predict the damage initiation, and (c) damage evolution to capture the post peak behavior.

The present CDM based constitutive model formulation is based on the ‘hypothesis of strain equivalence, where a constitutive equation of a damaged material is determined from the corresponding constitutive equation of a fictitious undamaged material merely by replacing the Cauchy stress tensor, σ by the corresponding effective stress tensor, $\hat{\sigma}$. The effective stress on the undamaged material will reach a fictitious stress at same strain state compared to the damaged material. The effective stress is calculated with the undamaged stiffness matrix and corresponds to the linear elastic behaviour without any damage. The effective stress tensor is related to Cauchy stress tensor by a damage operator M as given in Eq. (1).

$$\hat{\sigma} = M\sigma \tag{1}$$

where,

$$M = diag\left[\frac{1}{1-d_1} \quad \frac{1}{1-d_2} \quad \frac{1}{1-d_s}\right]$$

d_1, d_2 and d_s are damage variables along longitudinal, transverse and shear directions.

The constitutive relationship of the damaged material is given in Eq. (2),

$$\sigma = C_d\epsilon \tag{2}$$

The damaged stiffness matrix [C_d] is of form as given in Eq. (3) as below:

$$C_d = \frac{1}{D}\begin{bmatrix} (1-d_1)E_1 & (1-d_1)(1-d_2)v_{21}E_1 & 0 \\ (1-d_1)(1-d_2)v_{12}E_2 & (1-d_2)E_2 & 0 \\ 0 & 0 & D(1-d_s)G_{12} \end{bmatrix} \tag{3}$$

where,

$$D = 1-(1-d_1)(1-d_2)v_{12}v_{21}$$

$$d_s = 1-(1-d_1)(1-d_2)$$

$$d_1 = \begin{cases} d_1^t & if\ \hat{\sigma}_{11} \geq 0 \\ d_1^c & if\ \hat{\sigma}_{11} < 0 \end{cases} \quad ; \quad d_2 = \begin{cases} d_2^t & if\ \hat{\sigma}_{22} \geq 0 \\ d_2^c & if\ \hat{\sigma}_{22} < 0 \end{cases}$$

2.1 Damage Initiation

A strain-based failure initiation criteria is adopted here with 4 distinct failure modes/indexes (F_I): longitudinal tension and compression, transverse tension and compression (I=1t, 1c, 2t, 2c). Each failure index represents the damage initiation which is a function of strain applied as given in Eq. (4).

(i) Longitudinal tension (1-direction) (ii) Longitudinal compression (1-direction)

$$F_{1t}^2 = \left(\frac{\varepsilon_{11}}{\varepsilon_{1t}}\right)^2 ;\ if\ \varepsilon_{11} \geq 0 \qquad F_{1c}^2 = \left(\frac{\varepsilon_{11}}{\varepsilon_{1c}}\right)^2 ;\ if\ \varepsilon_{11} < 0$$

(iii) Transverse tension (2-direction) (iv) Transverse compression (2-direction) (4)

$$F_{2t}^2 = \left(\frac{\varepsilon_{22}}{\varepsilon_{2t}}\right)^2 ;\ if\ \varepsilon_{22} \geq 0 \qquad F_{2c}^2 = \left(\frac{\varepsilon_{22}}{\varepsilon_{2c}}\right)^2 ;\ if\ \varepsilon_{22} < 0$$

where, ε_{11} , ε_{22} are the strain applied along longitudinal, transverse directions, and ε_{1t}, ε_{1c}, ε_{2t}, ε_{2c} are the corresponding strain at the ultimate load along longitudinal and transverse directions under tension and compression loading.

2.2 Damage Evolution

Any of the failure index reaches the unit value, damage initiates in the material and on further loading causes strength and stiffness degradation, generally called as damage evolution. According to CDM model, the damage evolution is represented in terms of fracture energy dissipated (G_f) corresponding to each failure mode. The strain softening behaviour in the post peak response results in strain localization effects, leads to strong mesh dependency in the FE

analysis. This problem is alleviated by using the crack band model [17] by preserving the fracture energy and introducing a characteristic element length (L_c) as given in Eq. (5).

$$\varepsilon_f = \frac{2G_f}{\sigma_I^0 L_c} \tag{5}$$

The exponential degradation damage law proposed by [18] as given in Eq. (6) is adopted for modelling the damage behaviour of the FCB in post peak region for each individual failure mode.

$$d_I = 1 - \frac{1}{F_I} exp\left[(1 - F_I)\frac{L_c \sigma^0 \epsilon^0}{G_{fI}}\right] \tag{6}$$

where, F_I is the failure criteria corresponding to individual mode, and σ_0 , ϵ_0 are the ultimate stress and the corresponding strain experienced by the material, and G_{fI} is the fracture energy dissipated in each mode. To improve the convergence and to avoid numerical singularities, viscous regularization technique proposed by [19] is implemented, where it enables the tangent stiffness matrix of the softening material to be positive definite for small-time increments. The above material model is implemented as user material subroutine, UMAT in ABAQUS FE environment.

3. Validation studies

The constitutive law implemented as UMAT is validated in the FE framework with the experimental response of the board specimen subjected to in-plane tensile loading, and out-of plane (flexure) loading.

3.1 Open Hole Tension test

The experimental response of open hole tension (OHT) test specimen studied by [9] is considered for validating the UMAT model under in-plane loading. The test specimen is made of 10mm thick FCB cut along the longitudinal direction. The dimensions of OHT specimen are 44 mm (width) x 350 mm (length) with a circular hole of 10 mm diameter in the middle. The total test length of 250mm (excluding grip length) was subjected to tensile loading. Three linear strain gauges were attached adjacent to the vicinity of the hole at the net section to study the strain distribution along the width.

A FE model of the OHT test specimen is modelled in ABAQUS software using 4-noded S4R element and the material model is represented with UMAT. The constitutive properties and failure limits for modelling the FCB of 10mm thick is given in Table 1(a) [9]. The fracture energy dissipated corresponding to each mode is given in Table.1(b). At one end of the FE model all the translational and rotational DOFs are constrained to simulate clamped end conditions, and at other end, a uniform displacement of 1 mm is applied. The nonlinear equilibrium equations are iteratively solved by Newton-Raphson algorithm. Figure 1(a, b) shows the observed failure modes, i.e., tearing failure at the net section in both FE and experiment. A comparison of the load-displacement between the FEA and the experiment response is shown in Figure 2(a). The difference between the FEA and experiment, in terms of ultimate load and displacement are around 5%, clearly depicts the FCB behaviour is adequately modelled. Also, the comparison of strain distribution along the width at a particular load of 2kN obtained from the FE and experimental is shown in Figure 2(b). Overall, the comparison between the FE response and the experiment demonstrates the material model implemented for FCB works efficiently.

Table 1(a): Constitutive properties of FCB of 10mm thickness

t	E_{11}	E_{22}	G_{12}	υ	S_{11}^{+}	S_{22}^{+}	S_{11}^{-}	S_{22}^{-}	S_{12}
mm	N/mm²	N/mm²	N/mm²		N/mm²	N/mm²	N/mm²	N/mm²	N/mm²
10	9324.8	8292.7	5201.7	0.2	9.55	7.48	30.25	25.87	1.94

Table 1(b): Fracture energies for OHT coupon modelling

G_{f1t}[N/mm]	G_{f1c}[N/mm]	G_{f2t} [N/mm]	G_{f2c}[N/mm]
0.254	0.5	0.5	0.5

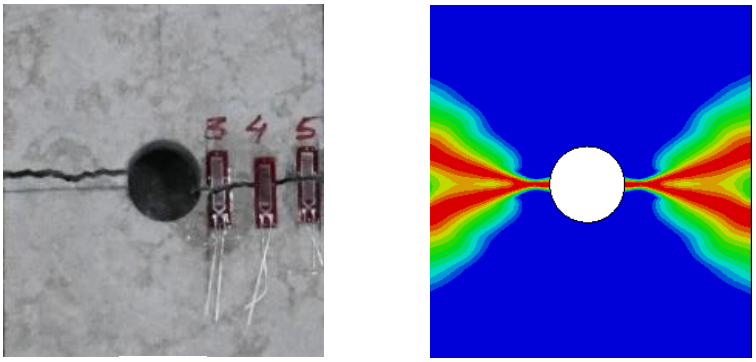

(a) (b)

Figure 1. Failure of open-hole tension test specimen (a) Experiment (b) FEA model

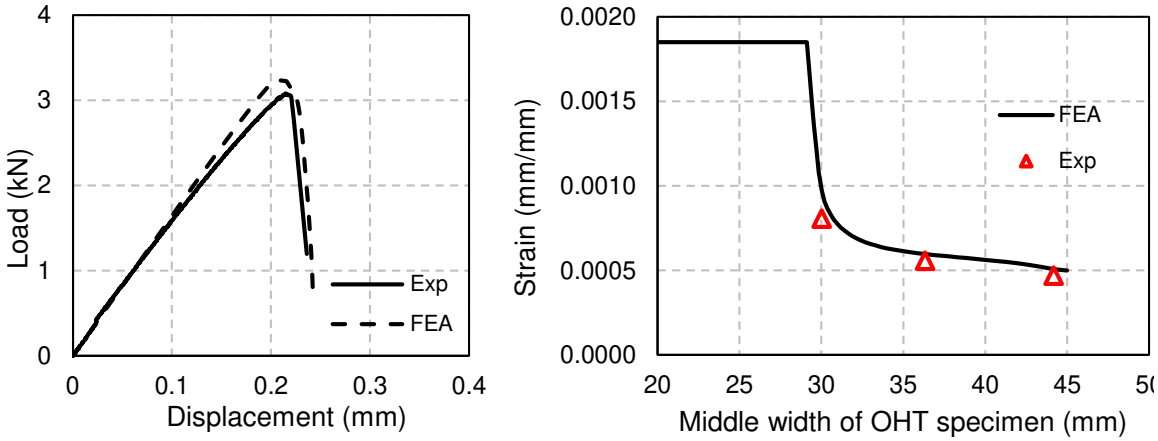

(a) (b)

Figure 2. (a) Comparison of load-displacement plot (b) Comparison of strain across the width between FE model and experimental response at 2kN load

3.2 Three-point bending test

Experimental studies on three-point bending test specimen are conducted as a part of this study to generate experimental response under out-of plane loading. The dimensions of the test specimen are 40mm (width) and 180mm (length) cut from the 12mm thick board along the longitudinal direction. The clear span between the supports at the bottom is 150mm with 15mm

overhang at both the ends. The test is performed under displacement-controlled mode at a loading rate of 0.25mm/min in 2.5kN Universal Testing Machine (UTM). The overall experimental setup is shown in Figure 3(a).

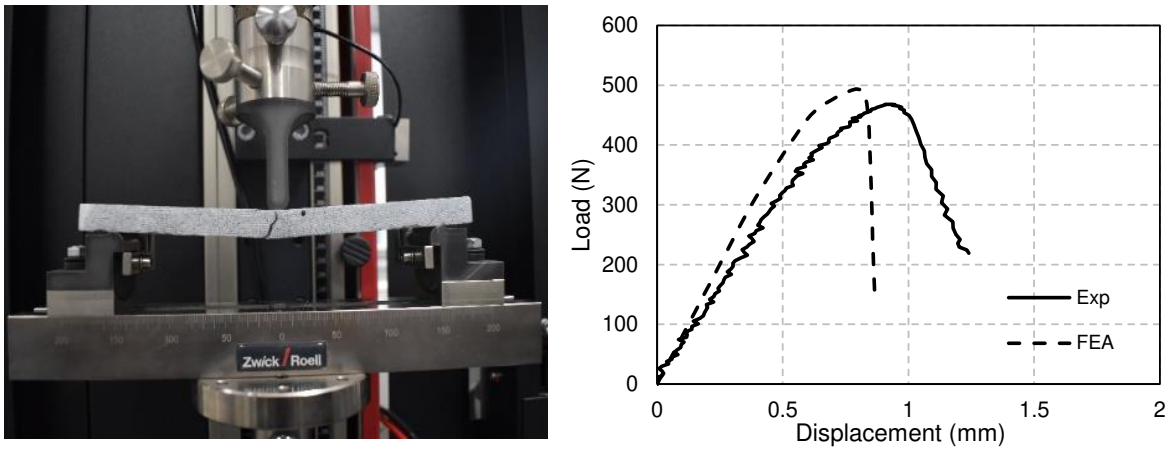

(a) (b)

Figure 3. (a) DIC test setup of three-point bending test (b) Comparison of load-displacement between DIC experimental and FE model

The FE model of the board test specimen is modelled in ABAQUS using S4R shell element with UMAT to model material behaviour. The roller supports and the loading points are modelled as discrete rigid element consisting of single notch edge as shown in Figure 4. The contact between test specimen and the supports/ loading points are modelled as contact pairs to simulate smooth surface to surface interaction and small relative sliding under the application of the load. The boundary conditions at support and loading wedge were applied at the reference points (RP) point in the discrete rigid surface. The RP at the supports were constrained with all translational and rotational DOF's. The displacement of 2mm is applied at the loading point along the Z direction with other DOF's constrained. The contact interactions between the shell element and the discrete rigid surfaces were modelled using hard contact for simulating normal interactions and a penalty method was used (with a friction factor of 0.1 and slip resistance of 0.005) for simulating the tangential behaviour. The constitutive properties and failure limits for modelling the FCB of 12mm thick is given in Table2(a) [9]. The fracture energy dissipated corresponding to each mode is given in Table2(b).

Table 2(a): Constitutive properties of FCB of 10mm thickness

t	E_{11}	E_{22}	G_{12}	υ	S_{11}^{+}	S_{22}^{+}	S_{11}^{-}	S_{22}^{-}	S_{12}
mm	N/mm²	N/mm²	N/mm²		N/mm²	N/mm²	N/mm²	N/mm²	N/mm²
12	9831.1	9566.5	5514.7	0.22	10.47	7.22	37.01	32.38	2.17

Table 2(b): Fracture energies for OHT coupon modelling

G_{f1t}[N/mm]	G_{f1c}[N/mm]	G_{f2t} [N/mm]	G_{f2c}[N/mm]
0.4	0.4	0.4	0.4

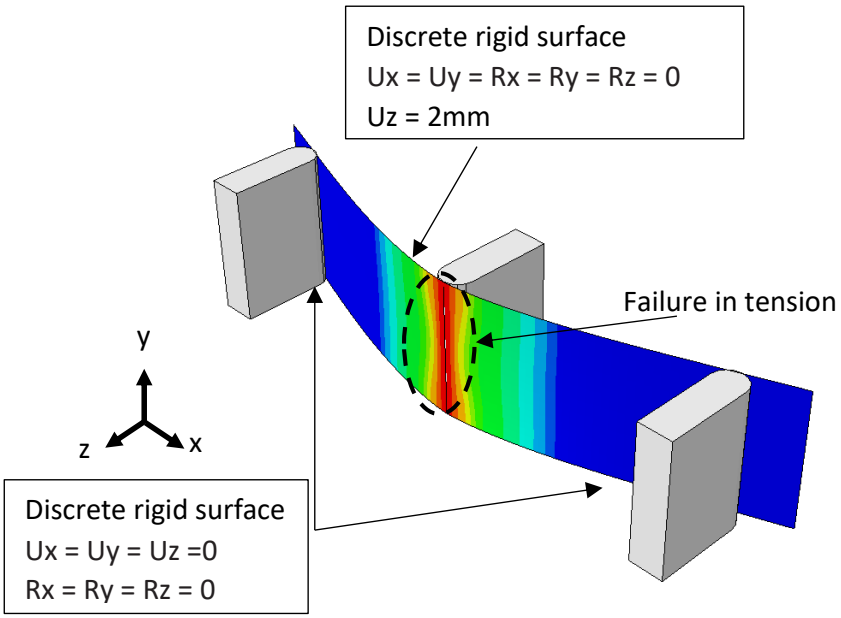

Figure 4. FE model of three-point bending test

The comparison of load-displacement response as obtained from the FE model and the experimental is shown in Figure 3(b). The linear elastic behaviour is captured well by the FE model with UMAT, and the ultimate load is over predicted by 6%. The comparison of ultimate displacement in FE simulation with test response is nearly 13% less. At present, the authors are working on improving the material model by incorporating the geometric nonlinear effects to predict the experimental response reasonably well.

4. Conclusion

A good constitutive model of sheathing is essential to represent its behaviour in the FE modelling of the CFS walls and floor sub-assemblages. The built-in material model library in commercial FE software lacks appropriate material models to simulate the behaviour of the FCB used in CFS building system. In this paper, a material model based on CDM approach is developed for FCB. The constitutive model adopts maximum strain-based failure criteria to predict the damage initiation, and an exponential degrading damage law for simulating the damage evolution in the post peak region. The efficacy of the developed material model (UMAT) is verified with open-hole tension test specimen and three-point bending test specimen. The comparison between the FE response and experimental results show that the proposed material model implemented in ABAQUS as UMAT, captured the failure mode and the load-displacement reasonably well.

Acknowledgments

The authors gratefully acknowledge the support of the research fund provided by Science and Engineering Research Board, Department of Science and Technology (DST), Government of India: (Grant No: CRG/2018/001893).

5. References

1 Grubb PJ, Gorgolewski MT, Lawson RM. Building Design using Cold Formed Steel Sections - Light Steel Framing in Residential Construction. Build Des using Cold Form Steel Sect. 2001;107.

2 Landolfo R. Lightweight steel framed systems in seismic areas: Current achievements and future challenges. Thin-Walled Struct. 2019;140(March):114–31.
3 Telue Y, Mahendran M. Behaviour and design of cold-formed steel wall frames lined with plasterboard on both sides. Eng Struct. 2004;26(5):567–79.
4 Peterman KD, Schafer BW. Sheathed Cold-Formed Steel Studs under Axial and Lateral Load. J Struct Eng. 2014;140(10):04014074.
5 Sonkar C, Mittal AK, Bhattacharyya SK. Comparative Study on Cold-Formed Steel Single-Stud and Multiple-Studs Wall Panels with Magnesium Oxide Sheathing under Axial Loading: Experimental and Analytical. Vol. 146, Journal of Structural Engineering. 2020. p. 04020224.
6 Bouterf A, Roux S, Hild F, Vivier G, Brajer X, Maire E, et al. Damage law identification from full field displacement measurement: Application to four-point bending test for plasterboard. Eur J Mech A/Solids. 2015;49:60–6.
7 Nithyadharan M, Kalyanaraman V. Behaviour of cold-formed steel shear wall panels under monotonic and reversed cyclic loading. Thin-Walled Struct [Internet]. 2012;60:12–23.
8 Mohebbi S, Mirghaderi SR, Farahbod F, Bagheri Sabbagh A, Torabian S. Experiments on seismic behaviour of steel sheathed cold-formed steel shear walls cladded by gypsum and fiber cement boards. Thin-Walled Struct [Internet]. 2016;104:238–47.
9 Jayesh B. Mechanical Characterization of Fibre Cement Board: Experimental Studies and Finite Element Validation. Thesis. Indian Institute of Technology Tirupati. 2020.
10 Ye J, Feng R, Chen W, Liu W. Behavior of cold-formed steel wall stud with sheathing subjected to compression. J Constr Steel Res. 2016;116:79–91.
11 Nithyadharan M, Kalyanaraman V. A new screw connection model and FEA of CFS shear wall panels. J Constr Steel Res [Internet]. 2021;176:106430.
12 ABAQUS [Computer software]. ABAQUS analysis user's manual, Version 6.8, Providence, RI, Dassault Systems Simulia.
13 Ladeveze P, LeDantec E. Damage modelling of the elementary ply for laminated composites. Compos Sci Technol. 1992;43(3):257–67.
14 Lapczyk I, Hurtado JA. Progressive damage modeling in fiber-reinforced materials. Compos Part A Appl Sci Manuf. 2007;38(11):2333–41.
15 Maimí P, Camanho PP, Mayugo JA, Dávila CG. A continuum damage model for composite laminates: Part I - Constitutive model. Mech Mater. 2007;39(10):897–908.
16 Matzenmiller A, Lubliner J, Taylor RL. A constitutive model for anisotropic damage in fiber-composites. Mech Mater. 1995;20(2):125–52.
17 Bazant ZP OB, Trandafirescu M. Bazant ZP, Oh BH. Crack band theory for fracture of concrete. Mater Struct 1983; 16(3):155–77. Acta Hortic. 2006;701 II:691–5.
18 Wang M, Song X, Gu X. Three-Dimensional Combined Elastic-Plastic and Damage Model for Nonlinear Analysis of Wood. J Struct Eng. 2018;144(8):04018103.
19 Duvaut G LJ. Duvaut G, Lions JL. Rigid visco-plastic Bingham fluid. In Inequalities in mechanics and physics 1976; 278-327. Springer, Berlin, Heidelberg.

STRESS CONCENTRATION STUDIES IN GLASS FIBER REINFORCED COMPOSITES CONSIDERING SHEAR NON-LINEARITY: EXPERIMENTS AND PROGRESSIVE DAMAGE MODELLING

P V Divakar Raju[a], M Nithyadharan[b], P Venkataraman[a]

a: Department of Mechanical Engineering, Indian Institute of Technology Tirupati, Tirupati, India-me19d506@iittp.ac.in
b: Department of Civil & Environmental Engineering, Indian Institute of Technology Tirupati, Tirupati, India

Abstract: *Progressive damage modeling of composite specimens considering non-linear stress-strain behavior is essential to accurately capture the macroscopic response in FE models. Hence, this paper presents a method for incorporating the shear non-linearity in the material model to predict the damage in composite laminates. Experimental studies are first carried out on unidirectional (UD) glass fiber reinforced laminates to evaluate the constitutive properties along fiber and matrix directions under both tensile and shear loading. Subsequently, a user-defined field (USDFLD), is used to modify the linear stress-strain behavior in Abaqus to simulate the nonlinear shear response. The proposed material model is demonstrated by simulating the response of the open-hole tension (OHT) specimen and validated with the experimental results on GFRP laminates. The results show that the proposed model can accurately capture the full-field strain response and the dominant failure modes, namely fiber breaking, and fiber-matrix shearing observed in experiments.*

Keywords: Progressive damage model; non-linear shear response; glass fiber reinforced composite; open hole tension specimen; digital image correlation.

1. Introduction

Composite components used in automotive and aerospace industries, are often connected through fasteners which are regions of stress concentration that cause premature failures. Hence, the development of a constitutive model capable of simulating the failure modes in composite laminates is essential for accurately predicting the macroscopic response of the structure under complex loading. Experimental studies show that there is an apparent non-linearity observed in the stress-strain response in GFRP laminate specimens when subjected to transverse tension and shear loading. The shear non-linearity is significant, which can influence the macroscopic response of composite specimens [1]. Hence, progressive damage modeling of composite structures requires this non-linear behavior to be accurately represented in the finite element model. However, available material models in commercial Finite Element (FE) software, ABAQUS consider the shear stress-strain response to be linear [2].

Hahn and Tsai [3] developed a theoretical formulation based on the complementary elastic energy density that accounts for the in-plane shear nonlinearity in the composite lamina, and later extended it to capture the behavior at the laminate level [4]. Their results showed good agreement with experimental results for uniaxially loaded specimens under tensile and compressive loading. Sun [5] developed a micromechanical model incorporating the

  doi:10.5075/epfl-298799_978-2-9701614-0-0 published under CC BY-NC 4.0 license

nonlinearity in matrix and linear elastic behavior of fiber, where a third-order strain term is included in the stress-strain response to represent the nonlinearity. Kenaga [6] developed a three-parameter orthotropic plasticity model to represent the nonlinear behavior of boron/aluminum composites and graphite/epoxy composites. The parameters of the plasticity model were obtained from experimental characterization studies performed under tension, compressive, and shear loading. Later, Sun and Chen [7] extended this work by considering a one-parameter model for the flow rule, knowing that for most unidirectional fiber composites the stress-strain relation in the fiber direction is linear.

Though, the above studies have considered the shear non-linearity in elasto-plastic formulations, there is a need for improving these models to include the damage evolution in the post peak region. Hence, the objective of this work is to develop a progressive damage model that considers the shear non-linearity in the material model. In the first phase, experimental studies on unidirectional glass fiber reinforced laminates are conducted to evaluate the constitutive properties in both fiber and matrix directions under tension and shear loading. Subsequently, the non-linear shear response is included in FE model through a user-defined field (USDFLD), using the model proposed by Chang and Lessard [1,8] . The developed material model was used to simulate the experimental response of the open-hole tension (OHT) specimen and validated with the experimental results.

2. Experimental investigation

2.1 Materials and specimen preparation

The GFRP composite laminates are manufactured by vacuum infusion technique from E-Glass plies of 1250 GSM and epoxy matrix. The characterization studies under tensile and shear loading are conducted in a 100 kN servo-hydraulic MTS Universal Testing Machine (UTM) at an ambient temperature of 25^{o}C. The strains in the specimens are measured both using 120Ω strain rosettes (TML, Japan) and Digital Image Correlation (DIC) for full-field strain measurement. The strain gauge is attached to the back of the specimen, and a random speckle is applied in the gauge section on the front face to measure the strains using DIC. The tests are conducted in displacement-controlled mode with a loading rate of 2 mm/min. The data from the strain gauges, MTS load cell and displacement transducer is acquired through a universal Data Acquisition System (DAQ) module (HBM, Germany), in a synchronous mode. The DIC setup includes a DSLR camera (Nikon D7500) placed in parallel to the specimen and a LED light for constant illumination.

2.2 Mechanical characterization – Tension and shear

The tension test is conducted as per ASTM D3039 [9]. The longitudinal test specimens of size (250×15 mm) are cut from the UD lamina using the CNC Router and tabs of 2.5mm thickness are attached to avoid the stress concentration at the grips. Similarly, transverse tensile specimens are also prepared from the UD lamina by cutting 90^{o} to the fiber direction. The dimensions of the transverse specimens are of size (175×25 mm) with end tabs of thickness 2.5 mm. The details of the test specimen and the observed failure modes are shown in Figure 1(a). The shear test is conducted as per ASTM D5379 [10]. The specimen is a rectangular strip of size (76×19 mm) with two v-notches as shown in Figure 1(b). The strains are measured using strain gauges pasted at ±45^{o} on the back of the specimen and full-field measurement using DIC. A total of 12 specimens, 4 each for tensile tests along longitudinal and transverse direction and 4 for the

  doi:10.5075/epfl-298799_978-2-9701614-0-0

shear loading are tested. The stress-strain response for tensile and shear loading are shown in Figure 1(c) and (d). The average stress-strain response of the group from individual curves are evaluated using equal arc segment method [11].

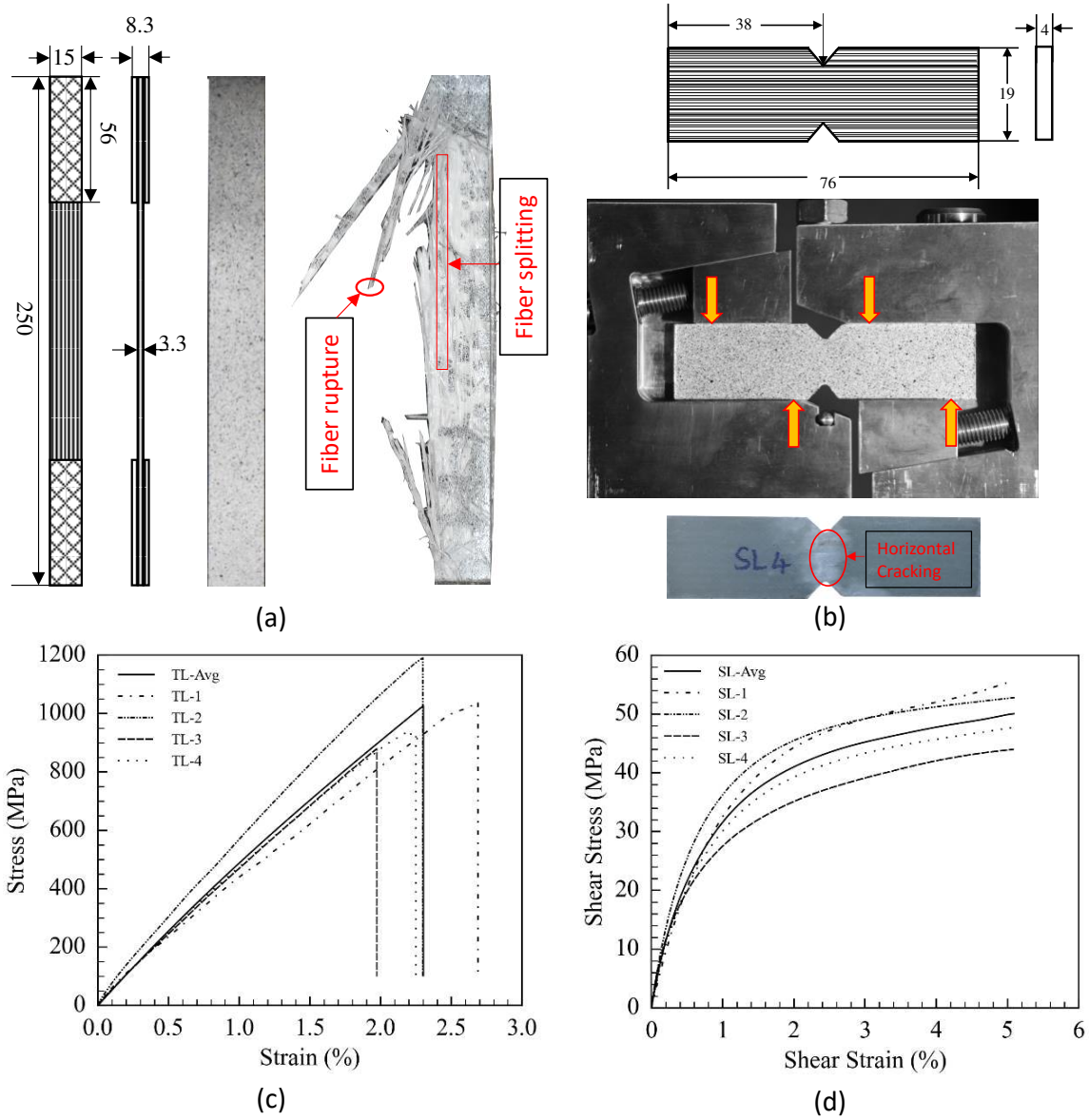

Figure 1:(a) Longitudinal tensile specimen and failure mode (b)Iosipescu shear test specimen and failure mode (c)stress-strain response of longitudinal specimen in tension (d) shear stress-strain response of iosipescu specimen

In the shear tests, the failure stress is evaluated at 5% strain as per ASTM standards. The mechanical properties of the individual specimens and their average values are summarized in Table 1. The tensile specimens show catastrophic fiber rupture at maximum load, while the shear specimens show horizontal cracking between notches. The non-linear shear stress-strain response is idealized with Hahn & Tsai model for use in the FE model.

2.3 Tension tests on open-hole specimens

In order to validate the proposed FE model, open hole tension tests are carried out as per ASTM D5766 [12]. Two sets of specimens of 3.3 mm thickness are tested: UD laminates of size (250×30 mm) with a 5 mm hole and balanced, symmetric laminate $[+45/-45]_s$ of size (250×36 mm) with a 6 mm hole.

Table 1: Mechanical properties evaluated through tensile and shear loading

Sample No.	E_{11} (GPa)	ϑ_{12}	X_t (MPa)	ε_{11} (%)	E_{22} (GPa)	Y_t (MPa)	ε_{22} (%)	G_{12} (GPa)	S_t (MPa)
Specimen 1	46.4	0.326	1040.1	2.69	19.4	52.8	0.85	4.2	55.7
Specimen 2	58.4	0.297	1190.5	2.30	18.1	53.6	1.15	5.1	52.8
Specimen 3	48.3	0.369	0879.6	1.97	16.1	41.4	0.96	3.6	44.0
Specimen 4	49.6	0.311	0941.2	2.25	-	-	-	4.2	47.8
Avg. Curve	51.6	-	1027.2	2.30	18.7	48.9	0.99	4.4	50.1
Average	50.9 ±4.6	0.33 ±0.03	1012.8 ±135.6	2.30 ±0.29	17.9 ±1.6	49.3 ±6.8	0.99 ±0.15	4.3 ±0.6	50.1 ±5.2

The width to the diameter ratio of 6, and diameter to the thickness ratio of 1.5 is maintained as recommended in the standard. The test is conducted in displacement-controlled mode with a loading rate of 2 mm/min, and the full field strain measurement is carried out using DIC. The failure in the UD and balanced symmetric laminate occurred at a load of 54 kN and 8 kN respectively, and the observed failure modes are shown in Figure 2.

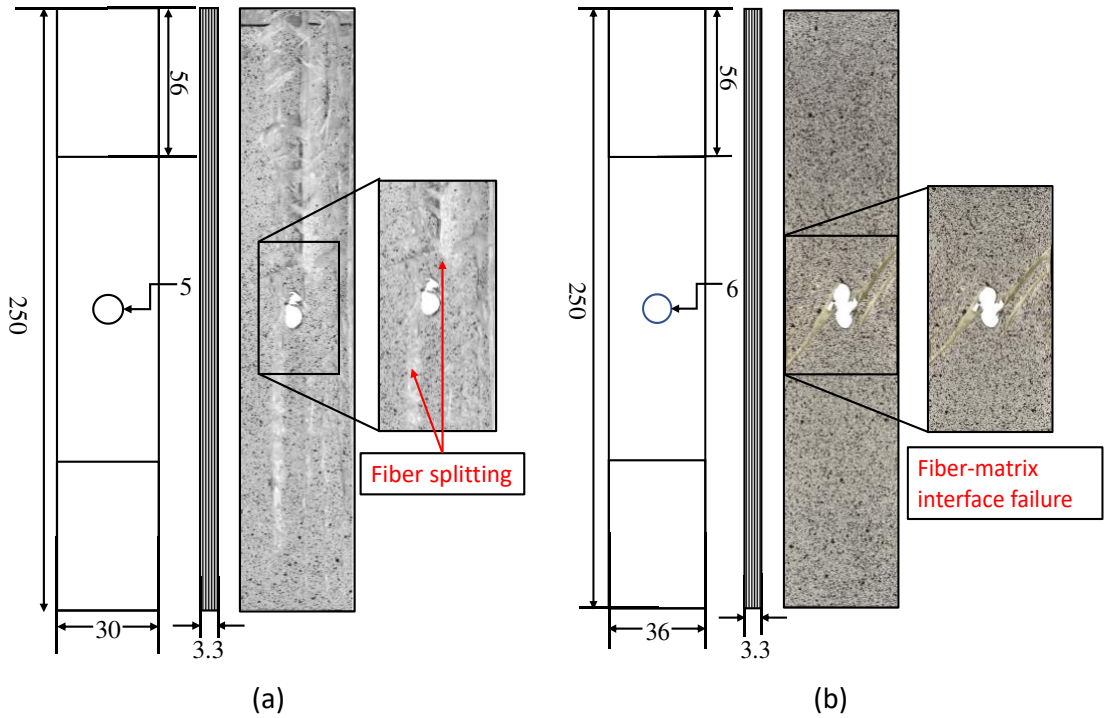

Figure 2: Specimen configuration and failure modes of (a) Unidirectional OHT specimen and (b) balanced-symmetric laminate

3. Finite element modeling

The OHT specimens with UD and balanced symmetric laminates are modeled in the Abaqus with linear shell element (S4R) with a ply thickness of 0.825 mm. The finite element model is shown in Figure 3. A radial refined mesh is used in the vicinity of the hole to capture the high stress gradient. In order to simulate realistic boundary conditions both the gripping zone are kinematically constrained to a reference node, and all the degrees of freedom are constrained at the left node and displacement is applied to the right node. The out of plane displacements and rotations are arrested in the remaining nodes.

  doi:10.5075/epfl-298799_978-2-9701614-0-0

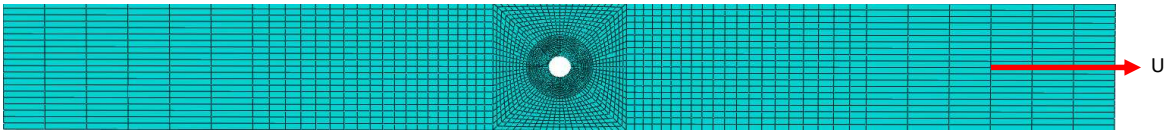

Figure 3:Finite element model with radial mesh in the vicinity of hole

The mechanical properties required for the material model are obtained from Table 1. The Hahn and Tsai model used to describe the nonlinear shear stress-strain response is given as

$$\gamma_{xy} = \frac{\sigma_{xy}}{G_{xy}} + \alpha {\sigma_{xy}}^3 \quad (1)$$

where, γ_{xy}, σ_{xy}, and G_{xy} correspond to the shear strain, shear stress and the modulus of rigidity respectively, and α is the parameter that characterizes the shear nonlinearity. In this study, the shear test data is used to obtain the value of alpha as 2.42×10^{-7} MPa^{-3}. In the stress based failure criteria proposed by Chang and Lessard [1] for modeling the progressive damage behavior of the composite laminate under compressive loading, the non-linear shear stress-strain response is implemented as an user-defined field (USDFLD) in Abaqus [8]. The USDFLD model can account for all major failure modes including matrix cracking, fiber matrix shear, fiber rupture, and fiber splitting. As the present study considers tensile loading, the existing USDFLD is modified using the strength parameters from obtained from tensile tests. The damage variable, *d* that represents the damage evolution in the non-linear shear stress regime is given as

$$d = \frac{3\alpha G_{xy} {\sigma_{xy}}^2 - 2\alpha {\sigma_{xy}}^3 / \gamma_{xy}}{1 + 3\alpha G_{xy} {\sigma_{xy}}^3} \quad (2)$$

Figure 4 and 5 shows a comparison between normal strain ε_{yy} and shear strain ε_{xy} contours obtained from DIC and the FE model for the UD OHT specimen at different loads on the same scale. The results show that there is a good agreement between the experimental and finite element model which validates the finite element model.

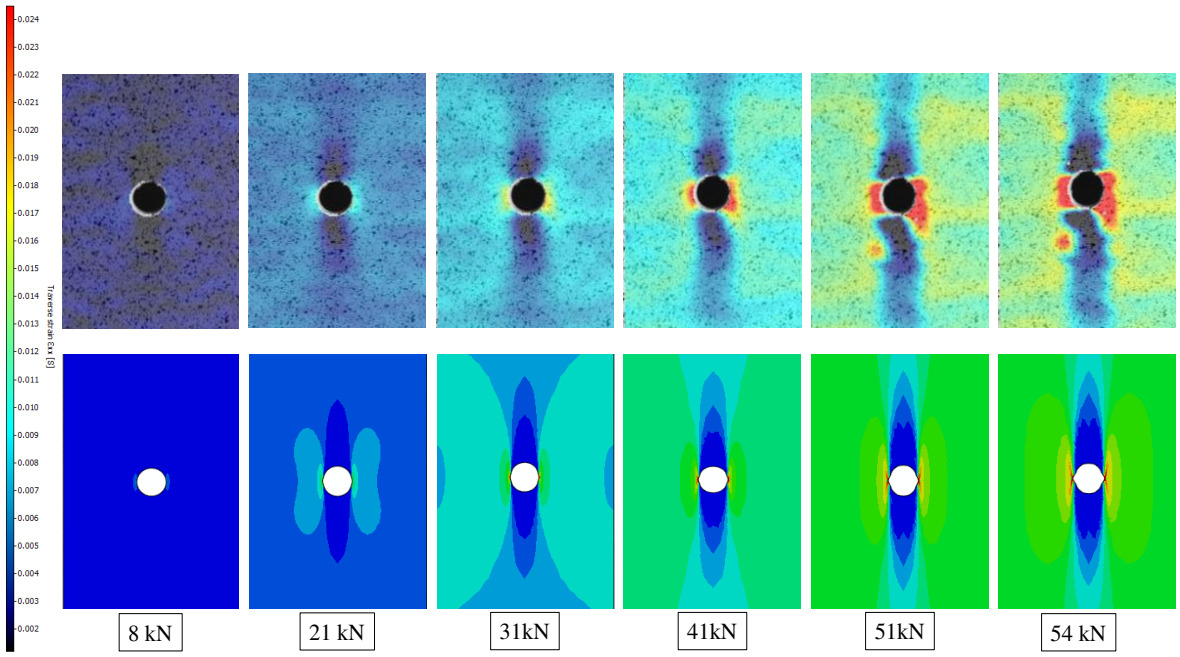

Figure 4:Comparison of normal strain (ε_{yy}) contours from DIC and FEA of UD OHT specimen

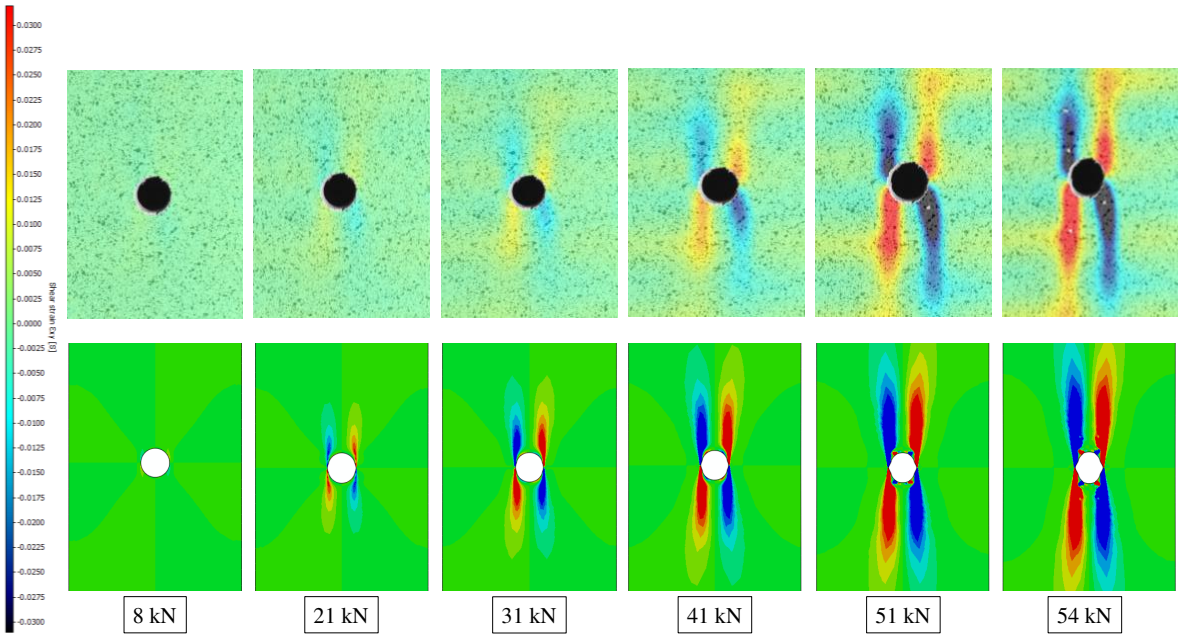

Figure 5: Comparison of shear strain (ε_{xy}) contours from DIC and FEA of UD OHT specimen

It may be observed that the damage initiates at diametrically opposite locations on the hole due to matrix cracking and propagates vertically along the fiber direction with increasing load, similar to what is observed in experiments Figure 2(a). The failure modes involved in this case are matrix cracking, fiber splitting, fiber fracture and fiber pull-out. Figure 6(a) and (b) shows the normal strain variation at the net-section along the width, from both experiments and FE model, which again show a good match with RMSE of 0.006.

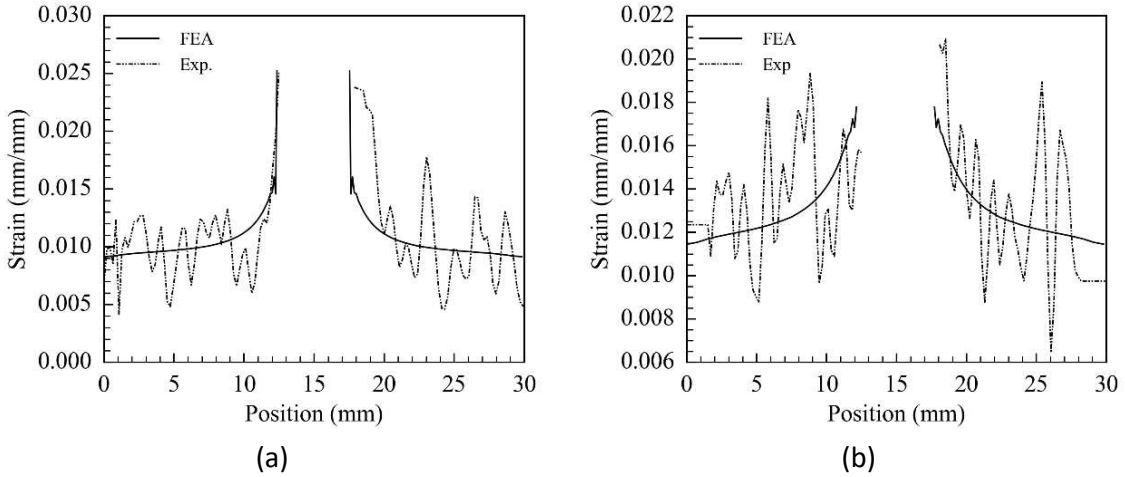

Figure 6:(a) normal strain ε_{yy} variation at net-section along the width at the loads of (a) 41.5 kN (b) at 51.3 kN of UD OHT specimen

The FE study is repeated for the balanced symmetric laminate under tensile loading. It is observed that the FE model is able to capture the failure modes, namely, crack initiation and propagation along the 45-degree plane qualitatively. The damage/crack initiates near the hole and propagates at an angle of 45 degrees to the loading axis along the fiber matrix interface. The strain variation at the net-section along the width for two different load cases are shown in Figure 7. In this case, it may be observed that the non-linear shear stress-strain behavior has a

significant influence on the observed normal strain response, which clearly highlights the need for developing a more accurate material model.

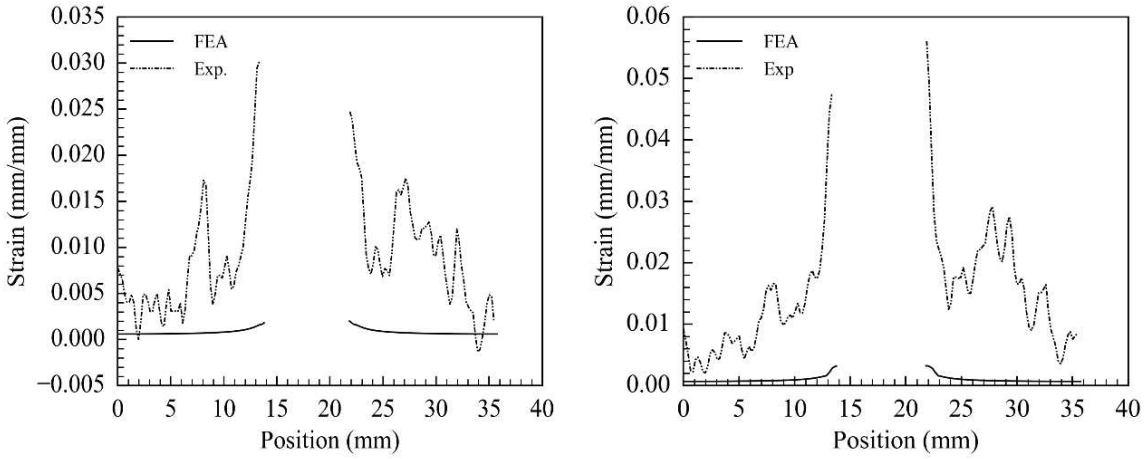

(a) (b)

Figure 7:(a) normal strain ε_{yy} variation at net-section along the width at the loads of (a) 6.1 kN (b) at 7.1 kN of balanced symmetric laminate.

4. Conclusions

This study investigates the influence of the non-linear shear stress strain behavior on the macroscopic response of GFRP laminates. Quasi-static tensile and iosipescu shear tests are performed on GFRP lamina to evaluate the strength and stiffness for developing the material model. The existing USDFLD subroutine in Abaqus is modified to capture the shear nonlinearity using the method proposed by Hahn and Tsai [3] for tensile loading case. The model is validated by comparing the strain response in both UD and $[+45/-45]_s$ specimens. The results show that good agreement in the case of UD specimens, but the predictions in the case $[+45/-45]_s$ laminate shows significant variation, which needs further investigation.

5. References

1. Chang F-K, Lessard LB. Damage Tolerance of Laminated Composites Containing an Open Hole and Subjected to Compressive Loadings: Part I—Analysis. J Compos Mater. 1991 Jan 24;25(1):2–43.
2. Hashin Z. Failure Criteria for Unidirectional Fiber Composites. J Appl Mech. 1980 Jun 1;47(2):329–34.
3. Hahn HT, Tsai SW. Nonlinear Elastic Behavior of Unidirectional Composite Laminae. J Compos Mater. 1973 Jan 27;7(1):102–18.
4. Hahn HT. Nonlinear Behavior of Laminated Composites. J Compos Mater. 1973 Feb 27;7(2):257–71.
5. Sun CT, Feng WH, Koh SL. A theory for physically nonlinear elastic fiber-reinforced composites. Int J Eng Sci. 1974 Nov;12(11):919–35.
6. Kenaga D, Doyle JF, Sun CT. The Characterization of Boron/Aluminum Composite in the Nonlinear Range as an Orthotropic Elastic-Plastic Material. J Compos Mater 1987 Jun 27;21(6):516–31.
7. Sun CT, Chen JL. A Simple Flow Rule for Characterizing Nonlinear Behavior of Fiber Composites. J Compos Mater. 1989 Oct 27;23(10):1009–20.
8. Abaqus [Computer software]. ABAQUS analysis user's manual, Version ABAQUS 2019, Providence, RI, Dassault Systemes Simulia.

  doi:10.5075/epfl-298799_978-2-9701614-0-0

9. ASTM D3039. (2014), Standard Test Method for Tensile Properties of Polymer Matrix Composite Materials, American Society for Testing and Materials, West Conshohocken, PA.
10. ASTM D5379. (2019), Standard Test Method for Shear Properties of Composite Materials by the V-Notched Beam Method, American Society for Testing and Materials, West Conshohocken, PA.
11. Zhong R, Wille K. Equal Arc Segment Method for Averaging Data Plots Exemplified for Averaging Stress versus Strain Curves of Pervious Concrete. J Mater Civ Eng [Internet]. 2016 Jan;28(1):04015071.
12. ASTM D5766. (2018), tandard Test Method for Open-Hole Tensile Strength of Polymer Matrix Composite Laminates, American Society for Testing and Materials, West Conshohocken, PA.

  doi:10.5075/epfl-298799_978-2-9701614-0-0

FAILURE OF LAMINATED COMPOSITE STRUCTURES WITH STRESS CONCENTRATIONS IN TENSION AND COMPRESSION

Christian, Hochard[a], Aldo, Cocchi[a] Olivier, Montagnier[b]

a: Laboratoire de Mécanique et d'Acoustique, Aix-Marseille-University, Marseille, France – hochard@lma.cnrs-mrs.fr
b: Centre de Recherche de l'Ecole de l'air, French Air Force and Space Academy, Salon, France

Abstract: *The failure of laminated composite structures is linked to the many mechanisms that can appear during degradation phase of the material under loading. The approach proposed here is to use the Continuum Damage Mechanics to describe the matrix degradation at the ply scale and a non-local criterion, the "Fracture Characteristic Volume (FCV)", to describe the failure in the fiber direction. The FCV is a cylinder with a circular shape of ply thickness. The criterion is defined by considering an average value, the stress in the fiber direction for example, over this volume compared to a maximum value. This approach is suitable for predicting failure for complex geometries with stress concentrations. The objective of this paper is to study the efficiency of this criterion on different laminates and types of concentration in the case of traction but also in compression.*

Keywords: Damage; Failure; laminate; stress concentration; compression

1. Introduction

Predicting the failure of laminated composite structures is still a fundamental issue. Its complexity is linked to the many mechanisms that can appear during degradation phase of the material under loading (diffuse damage, fiber-matrix debonding, transverse cracks, delamination, etc.) and the type of failure (tensile/compressive in the fiber direction,…). The approach proposed here is to use the *Continuum Damage Mechanics* (CDM) at the ply scale [1,2] to describe the matrix degradation and a non-local criterion [3,4], *the Fracture Characteristic Volume* (FCV), to describe the failure in the fiber direction. The FCV is a cylinder with a circular shape of diameter *d* and ply thickness *h*. The criterion is defined by considering an average value, the stress in the fiber direction for example, over this volume compared to a maximum value obtained on a flat specimen. The geometrical parameters of the FCV are identified from a tensile test on a specimen with a stress concentration, such as a notched plate. The model and the nonlocal failure criterion were implemented in Abaqus. This approach is suitable for predicting failure for complex geometries with stress concentrations. The objective of this paper is to study the efficiency of this criterion on different types of concentration in the case of traction but also in compression.

The model [5] is first recalled. Then, the material is presented and characterized in tension on flat hourglass shaped samples [6,7] (Figure 1a). To characterize the material in compression ASTMD695 tests are carried out but with original flat hourglass shaped samples [8](Figure 1b). In a second part, tests are carried out in tension and compression on various laminates and different types of stress concentrations (central hole, side saw cut,…). All the tests are compared

  doi:10.5075/epfl-298799_978-2-9701614-0-0

to non-linear simulations carried out with ABAQUS. The approach proposed here is well suited to predict crack initiation.

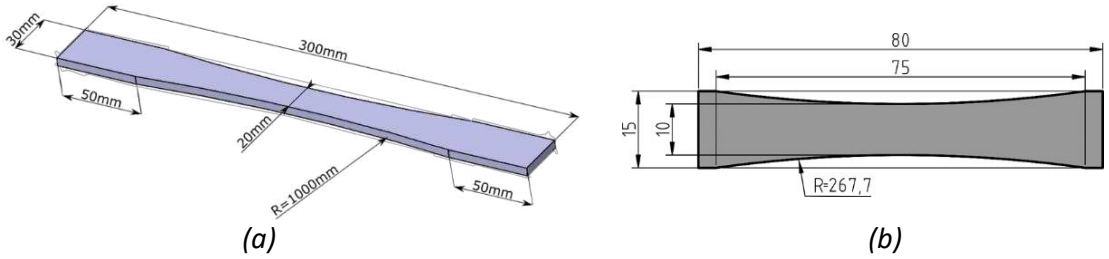

Figure 1. Hourglass shaped sample in tension (a) and compression (b)

2. CDM/FCV model parameters identification

2.1 CDM model at the Unidirectional ply scale

A model based on the *Continuum Damage Mechanics* (CDM) has been developed to describe the matrix damage evolution in composite material at the ply scale [5]. The damage is assumed to be uniform in the thickness of the ply. The CDM model describes the evolution of the matrix damage, consisting of small cracks running parallel to the fibers, which leads to a loss of stiffness in the transverse and shear directions. This model based on the work of P. Ladevèze [1] on *UniDirectional plies* (UD) has been extended to *woven plies* [2] and presented in several papers [4,5]. Even if the sizes of these cracks correspond to the thickness of the ply, they do not lead in general to the fracture of the laminate. On the other hand, the failure of one ply in the fiber direction is in general catastrophic for the laminate and the structure.

In the fiber direction, the UD ply shows an elastic behavior when applying a loading until the final brittle failure. A stress criterion can be used to model this brittle behavior. The model was applied to a Glass/Epoxy unbalanced woven ply. The woven ply was modelled by two UD plies with different thicknesses to take into account the different proportions of fibers in the warp and the weft directions, here 83% of fibers in the warp direction and 17% in the weft direction (Figure 2). The parameters of the elastic and damage laws of both UD plies were evaluated from the mechanical response of unbalanced woven ply laminates. The identification of the material properties required by the model is detailed in [2,5].

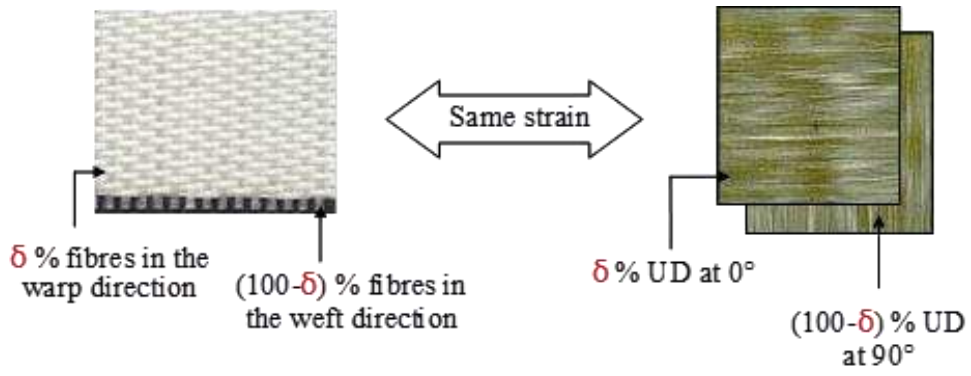

Figure 2. Assumption for woven plies

If in traction, the behavior is quasi-linear, it is not always the case in compression, in particular for carbon fiber. This non-linear behavior can be described by a decrease of the Young modulus depending on the strain [9]. For glass fibers, the behavior in compression is quasi-linear. The model has been identified on three tests (Figure 3). It should be noted that in the case of glass fibers, the behavior in compression is similar to tension.

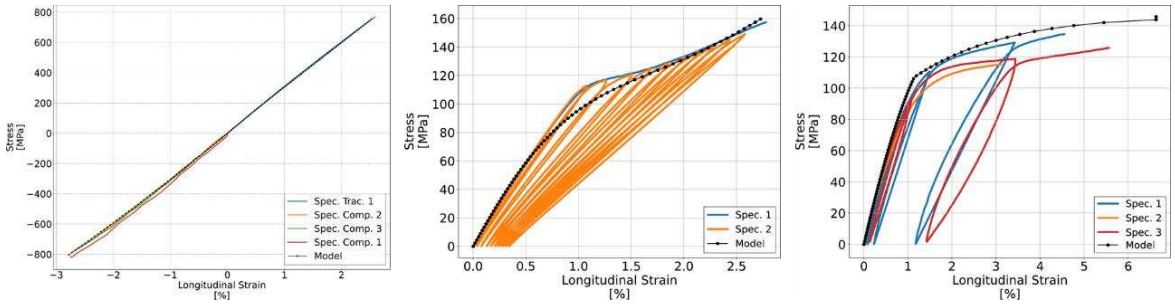

(a) *(b)* *(c)*

Figure 3. Model identification on $[0°]_{2ns}$ (a), $[90°]_{2ns}$ (b) and $[45°,-45]_{ns}$ (c) laminates

2.2 *Fracture Characteristic Volume* (FCV) criterion

Previous studies led to observe a strong underestimation of the failure strength when a local criterion was used to predict the failure of laminated structure with stress concentration. An original approach based on a *Fracture Characteristic Volume* (FCV) has been developed to account for the influence of stress concentrations [4,5]. The FCV is a cylinder defined at the ply scale as the volume $V = hS$, where h is equal to the thickness of the ply and S is the in-plane area (Figure 4).

The non local fracture criterion can be defined in the case of static loading as:

$$\overline{\sigma_{xx}} = \frac{1}{V}\int_V \langle\sigma_{xx}\rangle_+ \, dv \quad \text{and} \quad \overline{\sigma_{xx}} \geq X \quad \text{in tension} \qquad (1)$$

$$\overline{\sigma_{xx}} = \frac{1}{V}\int_V \langle\sigma_{xx}\rangle_- \, dv \quad \text{and} \quad \overline{\sigma_{xx}} \leq -X' \quad \text{in compression} \qquad (2)$$

where $\overline{\sigma_{xx}}$ *is* the mean stress, X is the maximal stress in tension and X' is the minimal stress in compression, material properties which need to be identified. In the case of glass fibers, the maximal stress X is equal to X'.

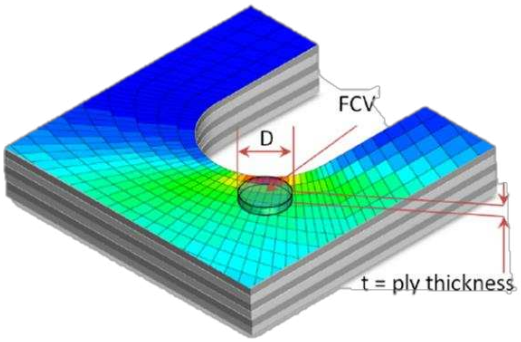

Figure 4. FCV non local criterion

3. Results for structures with stress concentrations in traction and compression

3.1 Identification and validation on $[0°,90°]_{4s}$ laminates

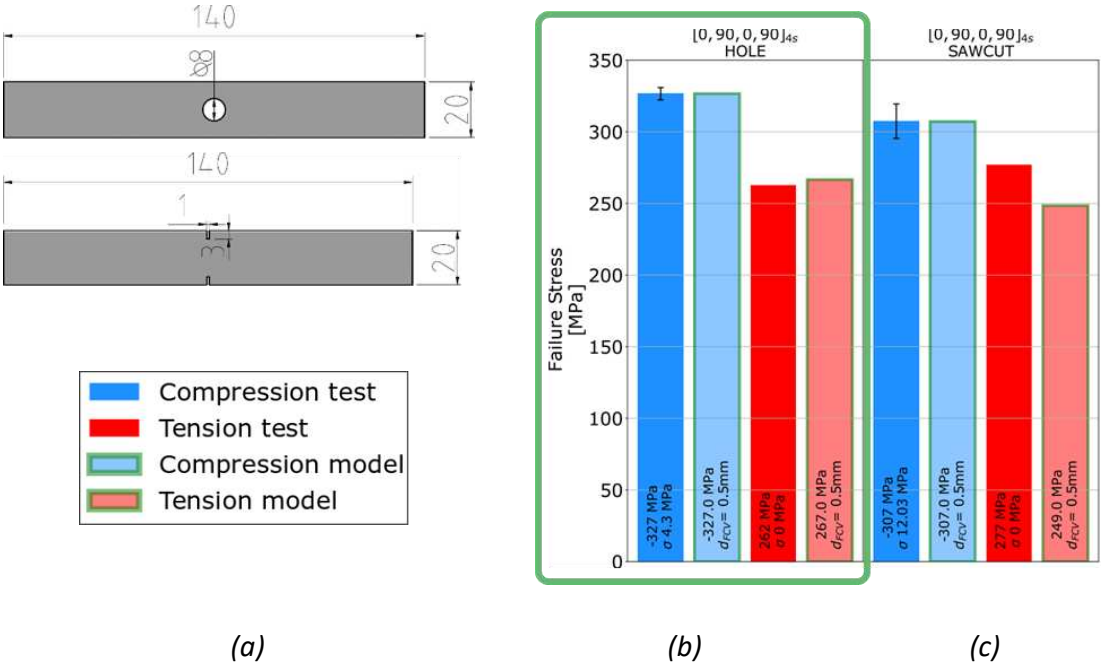

(a) *(b)* *(c)*

Figure 5. Samples with a hole (a) for the model identification on $[0°,90°]_{8s}$ (b), and validation on a sample with a sawcut (a and c)

To identify the diameter of the FCV, tensile and compression tests on laminated specimens $[0.90]_{8s}$ with a hole (Figure 5 a and b) are used. The diameter identified is the same in tension and in compression for glass fibers. For carbon fibers, the diameter is smaller in compression. It can be noted that even if the limits *X* and *X'* as well as the diameters of the FCVs are identical for the glass fibers, the compressive strength is higher for the $[0.90]_{8s}$ laminate. That is explained by the fact that the 90° plies are damaged in tension but not in compression, this mechanism is taken into account by the matrix damage model.

Still on this same $[0.90]_{8s}$ laminate, a validation test on a specimen with a saw cut (Figure 5a) was carried out and shows correct results in tension and compression with of course the same diameter for the FCV (Figure 5c).

3.1 Validation on $[0°,90°,45°,-45°]_{4s}$ and $[27.5,-67.5,67.5,-27.5]_{4s}$ laminates

Finally, still to validate the approach, other laminates were analyzed. Simulation results were compared to test results for a $[0°,90°,45°,-45°]_{4s}$ quasi-isotropic laminate with the two stress concentrations, hole and saw cut (Figure 6a), and for the same quasi-isotropic laminate but for tensile and compressive loads oriented at 22.5°, corresponding to tensile and compressive tests on a $[27.5,-67.5,67.5,-27.5]_{4s}$ laminate (Figure 6b). Once again, for all of these comparisons, the results are correct.

  doi:10.5075/epfl-298799_978-2-9701614-0-0

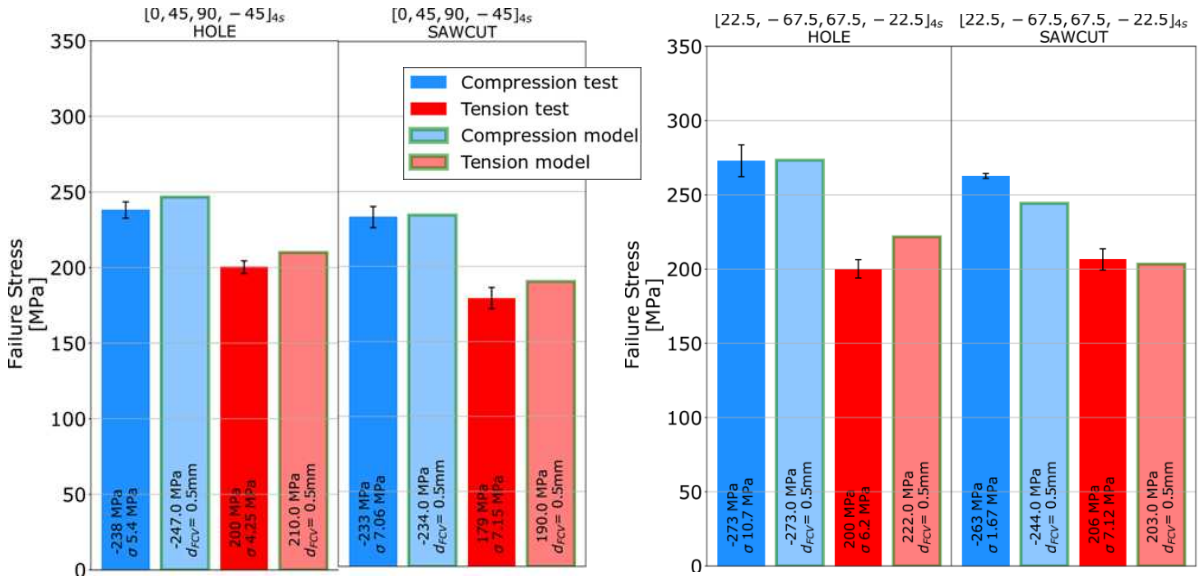

(a) *(b)*

Figure 6. Validation on $[0°,90°,45°,-45°]_{4s}$ (a) and $[27.5,-67.5,67.5,-27.5]_{4s}$ (b) laminates

4. Conclusions

A CDM model for the description of the matrix damage and a simple criterion based on a *Fracture Characteristic Volume* previously developed to predict the failure of laminated structure under tension loading was extended to the case of compression loading. Experimental tests on open hole and saw cut specimens were performed. The results obtained with the model matched the experimental data fairly well.

5. References

1. Ladevèze P, Le Dantec E. Damage modelling of the elementary ply for laminated composites. Composites Science and Technology 1992; 43(3):257–267.
2. Hochard C., Thollon Y. A generalized damage model for woven ply laminates under static and fatigue loading conditions. International Journal of Fatigue 2009;32(1):158-165.
3. Whitney JM, Nuismer RJ. Stress fracture criteria for laminated composites containing stress concentrations. Journal of Composite Materials 1974; 8(3):253–265.
4. Miot S, Hochard C, Lahellec N. A non-local criterion for modelling unbalanced woven ply laminates with stress concentrations. Composite Structures 2010; 92(7):1574–1580.
5. Hochard C., Miot S., Thollon Y., Lahellec N., Charles J.-P., Fatigue of laminated composite structures with stress concentrations, Composites Part B: Engineering, 65, pp. 11-16, (2014)
6. Payan J. , Hochard C. Damage modelling of laminated carbon/epoxy composites under static and fatigue loadings. International Journal of Fatigue 2002;24:299-306.

  doi:10.5075/epfl-298799_978-2-9701614-0-0

7. De Baere Y., Van Paepegem W., Hochard C., Degrieck J. On the tension–tension fatigue behavior of a carbon reinforced thermoplastic part II: evaluation of a dumbbell-shaped specimen. Polym Test 2011;30(6):663–672.
8. Cocchi, A., Montagnier, O., & Hochard, C., Study of hourglass-shaped specimens for the analysis of compression behaviour in fibre direction of FRP composites using compression and four-point bending tests. Composites Part A: Applied Science and Manufacturing, 2021 :144, 106332
9. Montagnier, O., & Hochard, C., Compression Characterization of High-modulus Carbon Fibers. Journal of Composite Materials, 2005;39(1):35-49

  doi:10.5075/epfl-298799_978-2-9701614-0-0

LOCAL STRESS ESTIMATION IN WOVEN COMPOSITES: A MULTISCALE MODEL

F. Lamon, P.A. Carraro, L. Maragoni, M. Quaresimin

Department of Management and Engineering, University of Padova
Stradella S. Nicola 3, Vicenza, 36100 (VI)
federico.lamon@phd.unipd.it

Abstract: *The work aims to provide a tool for predicting the static and fatigue crack initiation in woven composites. To this aim, the authors propose a multi-scale model for calculating the local stresses in the matrix of bundles. The model allows to move from the macro-scale to the micro-scale, passing through the meso-scale, by means of analytical and numerical models. First, the analytical meso-scale model is used to calculate the elastic properties and the mean stresses in bundles and pure matrix zones. Then, the stresses coming from the analytical meso-scale model are applied to 2D RVEs, where the microstructure of the bundle is represented, modelling the fibres with a real random distribution. The model is validated both experimentally, in terms of elastic properties, and numerically, in terms of mean and local stresses.*

Keywords: woven composites; elastic properties; stresses; analytical model; FE analysis

1. Introduction

Due to their high specific stiffness and strength properties, woven composites are excellent candidates for structural fatigue-driven applications. Cyclic loadings can cause different damage mechanisms, that result in a stiffness degradation of the composite part [1]. In woven composites, the first damage mechanism is the initiation and propagation of multiple cracks [2], that promote delaminations and fibre breakage, bringing the component to the final failure. The prediction of cycles to crack initiation is thus fundamental both in no-damage or stiffness driven fatigue design applications.

It has been proved by Carraro and Quaresimin [3], that the damage forces for crack initiation in unidirectional composites depend on the local stresses in the matrix. In particular, two damage parameters can be used, local hydrostatic stress (LHS) and local maximum principal stress (LMPS) depending on the loading conditions.

To extend the crack initiation criterion to woven composites, the local stress state in the matrix of bundles must be calculated. To this aim the authors propose a multi-scale model characterized by an analytical part, to calculate the mean stresses in the bundles and a numerical one to estimate the local stresses parameters.

2. The multi-scale model

The multi-scale model allows to calculate the local stresses in the matrix of the bundles. First, the global stresses applied to the laminate are used as an input for the analytical meso-scale model, allowing to calculate the elastic properties of the woven composite and the mean stresses in the bundles. Then, the stresses acting in the bundles are applied to microscale representative volume elements (2D-RVEs), characterized by a real fibre distribution.

  doi:10.5075/epfl-298799_978-2-9701614-0-0

The stress distribution in the matrix of the bundles and the damage forces for crack initiation are thus calculated by means of simple 2D-FE analyses.

2.1 The analytical meso-scale model

Starting from a solid knowledge of the material properties used as matrix and fibres, and of the geometry of the mesostructure, the analytical model aims to estimate elastic properties, mean stresses in the bundles and volume fraction of fibres in the bundles and in the overall laminate.

The bundles are considered homogeneous and orthotropic, characterized by a constant cross-sectional area, so fibre volume fraction. The waviness of each bundle is described accurately, also considering the possible differences in warp and weft directions. To this aim, a parametric function, defined piecewise imposing continuity and differentiability, is introduced to represent the midline of each bundle (Figure 1).

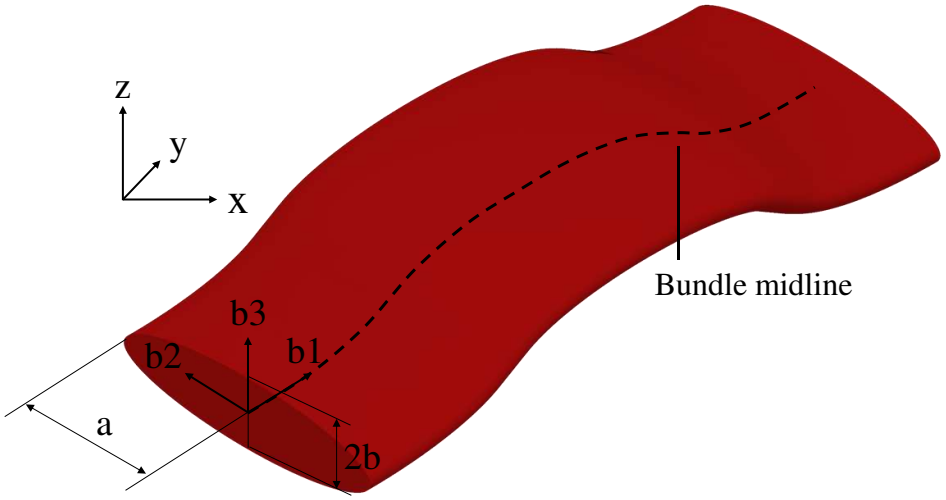

Figure 1. Half part of a homogeneous bundle: waviness in a periodic section.

The geometry representation together with the estimation of the global volume fraction, leads to the calculation of the fibre volume fraction in the bundles, so their elastic properties in the material coordinate system (m.c.s.).

The compliance matrix of the i-th bundle in the bundle coordinate system (b.c.s., b1-b2-b3 of Figure 1) $\left[S_{b-i}\right]$, is obtained through integral average along the midline of the infinitesimal elements of the bundle [4]:

$$S_{b-i\,u,v} = \frac{1}{l_{b-i}} \cdot \int_{s_{min}}^{s_{max}} S^{*}_{b-i\,u,v}(s)\,ds \qquad (u,v = 1-6) \qquad (1)$$

where s is the curvilinear coordinate along the midline, $l_{b\text{-}i}$ the length of the i-th bundle and $\left[S^{*}_{b-i}\right]$ the compliance matrix of each slice that form the bundle (in b.c.s.). The passages between different coordinate systems, so first from m.c.s. to b.c.s., reaching then the global coordinate system (g.c.s.) required different matrix transformations.

To calculate the engineering constants of the woven composite and the stresses distribution, the stiffness matrices of the constituents, so bundles and pure matrix zone, must be combined. A micromechanical approach is chosen, basing the model on the Mori-Tanaka's results [5]. The strain of the woven composite is represented as the volume average of the strains of bundles

and pure matrix zone. The bundles were considered as infinitely long cylinders of elliptic cross section. This allows to calculate the Eshelby's influence tensor for each bundle:

$$\left[A_{b-i}^{\infty}\right] = \left[I_6 + \left[\overline{B_{b-i}}\right]\left[\overline{Q_m}\right]^{-1}\left(\left[\overline{Q_{b-i}}\right] - \left[\overline{Q_m}\right]\right)\right]^{-1} \quad (2)$$

where $\left[\overline{B_{b-i}}\right]$ is the Eshelby's tensor, $\left[\overline{Q_{b-i}}\right]$ and $\left[\overline{Q_m}\right]$ the stiffness matrices respectively of the i-th bundle and the pure matrix zone, all expressed in the g.c.s..

Using the definitions of Eshelby's and Mori-Tanaka's influence tensors, it is possible to calculate the stiffness matrix of the woven composite. However, this leads to a non-diagonally symmetric stiffness matrix. To overcome the limitation, the authors adopted the modification introduced first by Ferrari [6] and then used by Dunn et al. [7] for the calculation of the woven composite stiffness matrix, and so the elastic properties:

$$\left[\overline{Q_c^{MT}}\right]_D = \left[\overline{Q_m}\right]I_6 + \sum_{i=1}^{n-bundle}\frac{V_{b-i}}{V_{GRU}}\left(\left[\overline{Q_{b-i}}\right] - \left[\overline{Q_m}\right]\right)\left[A_{b-i}^{MT}\right]_D \quad (3)$$

where $\left[A_{b-i}^{MT}\right]_D$ is the modified Mori-Tanaka's influence tensor, so defined:

$$\left[A_{b-i}^{MT}\right]_D = \left[\frac{V_m}{V_{GRU}}\left[A_{b-i}^{\infty}\right]^{-1} + \left(1 - \frac{V_m}{V_{GRU}}\right)I_6\right]^{-1} \quad (4)$$

V_{b-i} and V_m are the volumes of the i-th bundle and the pure matrix zone in a representative volume V_{GRU}.

The mean stresses in bundles and pure matrix zones are obtained in g.c.s. as follow:

$$\begin{cases}\left\{\overline{\sigma_{b-i}}\right\} = \left[\overline{Q_{b-i}}\right]\left[A_{b-i}^{MT}\right]\left\{\overline{\varepsilon_c}\right\} \\ \left\{\overline{\sigma_m}\right\} = \left[\overline{Q_m}\right]\left[A_{b-i}^{\infty}\right]^{-1}\left[A_{b-i}^{MT}\right]\left\{\overline{\varepsilon_c}\right\}\end{cases} \quad (5)$$

$\left[A_{b-i}^{MT}\right]$ is the Mori-Tanaka's influence tensor of the i-th bundle:

$$\left[A_{b-i}^{MT}\right] = \left[\frac{V_m}{V_{GRU}}\left[A_{b-i}^{\infty}\right]^{-1} + \sum_{j=1}^{n-bundle}\frac{V_{b-j}}{V_{GRU}}\left[A_{b-j}^{\infty}\right]\left[A_{b-i}^{\infty}\right]^{-1}\right]^{-1} \quad (6)$$

$\left\{\overline{\varepsilon_c}\right\}$ the strain tensor of the woven composite resulting from the stress state:

$$\left\{\overline{\varepsilon_c}\right\} = \left[\overline{S_c^{MT}}\right]_D\left\{\overline{\sigma_c}\right\} \quad (7)$$

where $\left[\overline{S_c^{MT}}\right]_D$ is the compliance matrix of the woven composite, obtained by inverting $\left[\overline{Q_c^{MT}}\right]_D$.

2.1 The numerical micro-scale model

The mean stresses in bundles are used as boundary conditions for micro-scale RVEs, allowing to obtain the local stress fields in the matrix of the bundles through 2D FE analyses. The RVEs are rectangular to represent the shape of the bundles. This allows to apply symmetric boundary conditions to their sides. A real-like fibre distribution is modelled, as explained by Maragoni et

al. [8]. From the stresses in the matrix of the bundles, LHS* and LMPS* parameters were calculated. They represent the average values of LHS and LMPS in a control volume of matrix (usually 1-10%) where the damage parameters reach their maximum values. This means in the zones where the cracks are expected to initiate.

3. Validation

3.1 Validation of the meso-scale model with experimental data

The analytical meso-scale model is validated through experimental data from literature [9] in terms of elastic properties. The validation referred to glass/epoxy and carbon/epoxy systems with plain architecture. A good agreement was found, as shown in Table 1.

Table 1. Experimental data from literature [9] and predictions from analytical meso-scale model.

Code	E_x [MPa]			
	Experimental	c.o.v. %	Predicted	Error %
CE1	62500	5.12	61675	1.34
CE3	49300	3.85	50008	1.42
GLE1	17500	5.71	17605	0.59
GLE2	20000	4.00	20250	1.23
GLE3	21500	4.65	20010	7.45
GLE4	20800	3.37	20329	2.32
GLE5	22800	5.26	24519	7.01
GLE6	22400	4.46	24382	8.13
GLE7	19600	6.63	19451	0.77

3.2 Validation of the multi-scale model with 3D FE analyses

The aim of the numerical validation is twofold. First the analytical meso-scale model is validated in terms of mean stresses in the bundles. Then, the results of the multi-scale model were proved. For the first objective, three-dimensional FE analyses were carried out, modelling plain architectures with different geometries in ANSYS 19.5. The bundles were considered as homogeneous, with an orthotropic behaviour. In the second validation, one of the homogeneous bundles, was replaced with a heterogeneous one, where the fibres are modelled with a real-random distribution, in a similar way as the 2D-RVEs. In both cases the validation regarded a representative unit of a single layer of woven (LRU).

Two different loading conditions were applied: a global normal stress σ_x, concentrating the validation on σ_2 and LHS*, and a global plane shear stress σ_{xy}, moving the validation on σ_6 and LMPS*.

The plain architecture was chosen, allowing to represent small LRUs with in-plane symmetric boundary conditions, reducing the computational effort compared to twill or satin architectures.

  doi:10.5075/epfl-298799_978-2-9701614-0-0

The symmetric out-of-plane boundary condition resulted the most suitable to represent the retrain of the out-of-plane movement caused by the shifting and nesting phenomena.

The results for different geometries when a global σ_x is applied are resumed below as example, respectively for the validation of the meso-scale (Figure 2) and the multi-scale model (Figure 3).

The numerical results from FE analyses are represented with blue bands, while red bands are associated with the predictions from the models. For the validation of the multi-scale model (Figure 3), the results are represented with a mean value (height of bands) and the single values from the multiple realisations of fibre distribution in the heterogeneous bundle. The accuracy in prediction of local stresses shows the possibility of incorporating the multi-scale model into a tool for estimating the life to crack initiation.

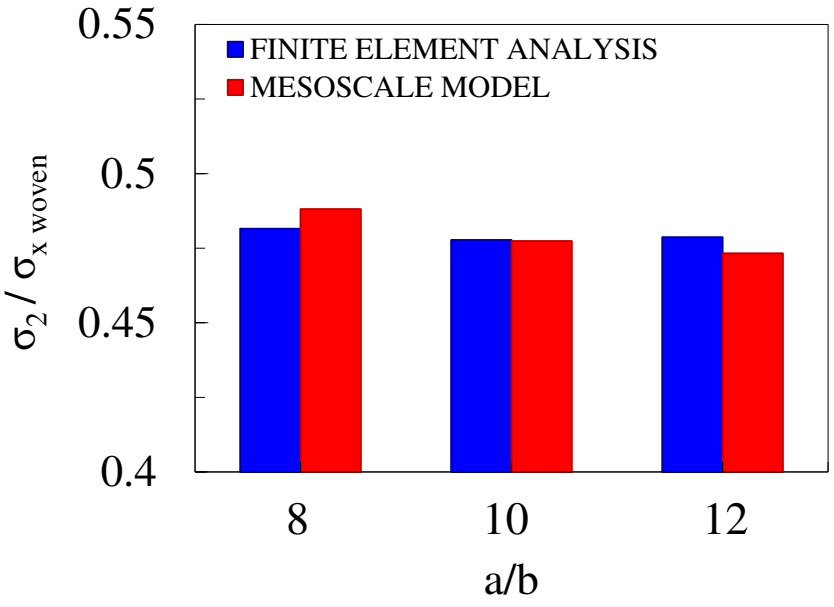

Figure 2. Prediction of σ_2 in transverse bundles, global σ_x applied.

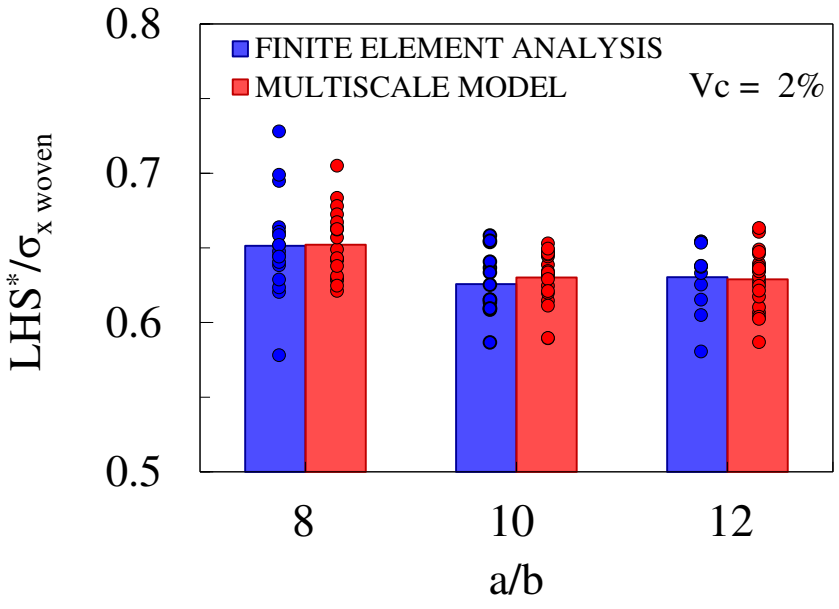

Figure 3. Prediction of LHS in the weft bundles under a global σ_x.*

4. Conclusions

A multi-scale model for woven composites is presented. The aim is to calculate the local stresses parameters in the matrix of bundles, proved to be the driving forces for crack initiation under fatigue. An analytical meso-scale model allows to calculate the elastic properties of the woven composite and the mean stresses in bundles and pure matrix zones, moving from the macro to the meso-scale. Then, the stresses are used as an input for the numerical micro-scale model. The robustness of the model was proved by means of double validation, experimental for the elastic properties and numerical for the prediction of mean and local stresses.

Acknowledgements

The authors wish to acknowledge the support and the computational resources made available by the High Performance Computing Lab at the Department of Management and Engineering (DTG), co-funded by the University of Padova in the framework of the program “Scientific research instrumentation 2015”.

5. References

1. Reifsnider KL. Fatigue of composite materials. Elsevier. 1991.
2. Naik NK. Woven-fibre thermoset composites. Fatigue in Composites. Elsevier. 2003, p. 296-313.
3. Carraro PA, Quaresimin M. A damage based model for crack initiation in unidirectional composites under multiaxial cyclic loading. Composites Science and Technology 2014; 99:154-63.
4. Byun J-H. The analytical characterization of 2-D braided textile composites. Composites Science and Technology 2000; 60:705-16.
5. Gross D, Seeling T. Micromechanics and homogenization. Fracture Mechanics. Springer. 2018.
6. Ferrari M. Composite homogenization via the equivalent poly-inclusion approach. Composites Engineering 1994; 4:37-45.
7. Dunn ML, Ledbetter H, Heyliger PR, Choi CS. Elastic Constants of Textured Short-Fiber Composites. J Mech Phys Solids 1996; 4:1509–41.
8. Maragoni L, Carraro PA, Quaresimin M. Development, validation and analysis of an efficient micro-scale representative volume element for unidirectional composites. Composites Part A: Applied Science and Manufacturing 2018; 110:268-83.
9. Naik NK, Ganesh VK. Thermo-mechanical behaviour of plain weave fabric composites: Experimental investigations. Journal of Materials Science 1997; 32:267-77.

  doi:10.5075/epfl-298799_978-2-9701614-0-0

STRAIN RATE DEPENDENT MODELLING OF IMPACT DAMAGE IN LAMINATED COMPOSITE PLATES

Darko Ivančević[a], Efthimis Giannaros[b], Luka Stanić[a]

a: Department of Aeronautical Engineering, Faculty of Mechanical Engineering and Naval Architecture, University of Zagreb, Zagreb, Croatia – divancevic@fsb.hr
b: Applied Mechanics Laboratory, Department of Mechanical & Aeronautical Engineering, University of Patras, Patras, Greece

Abstract: *The response of composite structures when subjected to impact damage differs significantly from those in static condition. The mechanical properties, which are determined by matrix behaviour, are a good illustration of this. Hence, a numerical methodology for laminated CFRP structures has been developed in this work to include strain rate effects into the impact damage simulation. The VUMAT subroutine has been used to implement the failure criteria and damage model developed for impact damage in laminated composite structures into Abaqus/Explicit. The implemented damage model is applicable for solid FE in three-dimensional stress state and can predict mesh-size-independent impact results for any target discretization, which allows usage of relatively coarse meshes thereby lowering computational cost. The methodology has been validated using latest experimental data.*

Keywords: composite materials; failure criteria; strain rate effects; impact damage; VUMAT subroutine

1. Introduction

Fibre-reinforced composites are increasingly being used in aerospace, automotive and other industries. Lack of knowledge on their overall properties, damage modes and evolution prevent the full exploitation of their full potential. Furthermore, constant need of the industry to reduce the cost of development and experiments leads to increased usage of numerical simulations. However, the influence of strain-rate is usually neglected in numerical simulations of impact loads, which can be attributed to difficulties in experimentally testing of composite mechanical properties at increased strain rates. In case of Carbon Fibre Reinforced Composites (CFRP), the influence of strain-rate is visible in the matrix dominated properties of composite and in shear and transverse load of layer, while carbon fibres are strain rate insensitive [1].

In this paper, a phenomenological-based, strain rate dependent failure theory for a three-dimensional stress state is used, where strain-rate effects on the material strength are applied by scaling functions. Furthermore, progressive damage of composite is added, based on the approach proposed in [2]. The model is implemented in Abaqus/Explicit using VUMAT subroutine and is mesh size independent enabling application in a wide range of engineering problems. The damage model uses three independent damage variables, one variable for tensile and compressive damage in the fibre direction and one variable for matrix damage. Damage propagation was modelled depending on the strain after failure initialisation and the strain value

  doi:10.5075/epfl-298799_978-2-9701614-0-0

at which the material was completely damaged based on the critical value of the strain energy release rate and the characteristic length of the finite element based on the approach proposed in [3].

2. Failure criteria

The following criteria for longitudinal failure, proposed in [2], are used.

Fibre tensile failure criterion is

$$\sigma_x^{t+\Delta t} > 0 \rightarrow f_{ft} = \left(\frac{\sigma_x^{t+\Delta t}}{X_t}\right) - 1; f_{ft} \geq 0, \tag{1}$$

where X_t represents tensile strength of composite in the fibre direction.

Fibre compressive failure criterion is

$$\sigma_x^{t+\Delta t} < 0 \rightarrow f_{fc} = \left(\frac{\sigma_x^{t+\Delta t}}{X_c}\right) - 1; f_{fc} \geq 0, \tag{2}$$

where X_c represents the compressive strength of composite in the fibre direction.

Matrix failure is a result of the combination of transverse, shear and through-thickness stresses. Unlike the fibre-dominated failure modes, the implemented model [2] assumes that the transverse response is determined by fracture plane orientation, which may not necessarily be normal to the loading direction. The fracture plane will always be oriented to maximize the value of the failure criterion, which for pure tensile load means that it will match the global coordinate system, while in case of pure transverse compression, the angle of the fracture plane is $\varphi_0 = 53°$. The fracture plane orientation is shown in Figure 1.

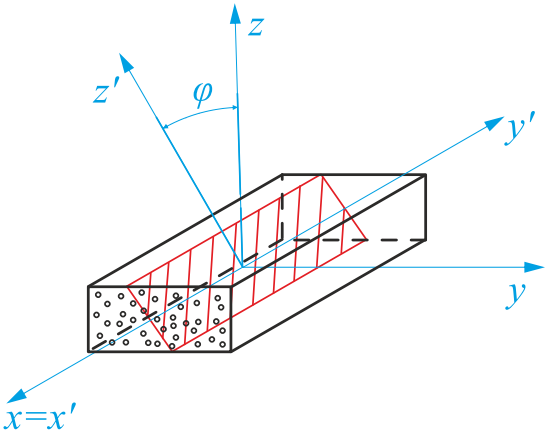

Figure 1. Definition of the fracture plane coordinate system

The failure initiation criteria for matrix tensile and compressive failure are

$$\left(\sigma_i^{t+\Delta t}\right) \xrightarrow{\perp x(\varphi)} \left(\sigma_{i'}^{t+\Delta t}\right), \tag{3}$$

$$\sigma_{y'}^{t+\Delta t} > 0 \rightarrow f_{mt} = \left(\frac{\sigma_{y'}}{Y_t}\right)^2 + \left(\frac{\tau_{xy'}}{k(\dot{\gamma}_{xy'})S_{xy}}\right)^2 + \left(\frac{\tau_{y'z'}}{k(\dot{\gamma}_{y'z'})S_{yz}}\right)^2 - 1; f_{mt} \geq 0, \tag{4}$$

$$\sigma_{y'}^{t+\Delta t} < 0 \rightarrow f_{mc} = \left(\frac{\tau_{xy'}}{k(\dot{\gamma}_{xy'})S_{xy} - \mu_l\sigma_{y'}}\right)^2 + \left(\frac{\tau_{y'z'}}{k(\dot{\gamma}_{y'z'})S_{yz} - \mu_t\sigma_{y'}}\right)^2 - 1; f_{mc} \geq 0, \tag{5}$$

  doi:10.5075/epfl-298799_978-2-9701614-0-0

where $\perp x(\varphi)$ represents 3D rotation around fibre direction axis (*X* axis) to account for the orientation of the fracture plane φ, Y_t is the matrix tensile strength and S_{xy} is the shear strength. The transverse friction coefficient, μ_t, is defined from the Mohr-Coulomb theory as

$$\mu_t = -\frac{1}{\tan(2\varphi_0)}. \tag{6}$$

The longitudinal friction coefficient, μ_l, can be calculated using shear strengths and transverse friction coefficient

$$\mu_l = \mu_t \frac{S_{xy}}{S_{yz}}, \tag{7}$$

where S_{yz} is the transverse shear strength, which is calculated from transverse compressive strength

$$S_{yz} = \frac{Y_c}{2\tan(\varphi_0)}. \tag{8}$$

The failure criteria consider the influence of the strain-rate using the scaling function, *k*, which is calibrated using in-plane shear strength data from quasi-static and dynamic tests. A second order polynomial is used to describe the scaling function obtained from normalized in-plane shear strength versus shear strain-rate

$$k(\dot{\gamma}_{xy}) = K_0 + K_1 \log_{10}\dot{\gamma}_{xy} + K_2 (\log_{10}\dot{\gamma}_{xy})^2. \tag{9}$$

3. Damage model

The damage model used in this work and proposed in [4] consists of three damage variables, fibre compressive damage, d_{Xc}, fibre tensile damage d_{Xt}, and matrix damage, d_m. The value of damage variables irreversibly increases from 0 to 1, depending on the strain after failure initiation. The relationship between failure strain, ε^f, fracture energy, Γ, onset failure stress, σ^0, and characteristic element length, *L*, is

$$\varepsilon^f = \frac{2\Gamma}{\sigma^0 L}. \tag{10}$$

Damage evolution is strain driven and the damage law, proposed in [3], is defined as

$$d^{t+\Delta t} = \max\left\{0, \min\left\{1, \varepsilon^f \frac{\varepsilon^{t+\Delta t,d} - \varepsilon^0}{\varepsilon^{t+\Delta t,d}(\varepsilon^f - \varepsilon^0)}\right\}\right\}, \tag{11}$$

where ε^0 represents equivalent initiation strain and $\varepsilon^{t+\Delta t,d}$ represents equivalent current strain. For fibre tensile and compressive damage modelling, equivalent stress and strain are given as stress and strain in fibre direction, while for matrix damage modelling equivalent stress and strain are calculated as

$$\sigma_m^0 = \sqrt{\langle\sigma_{y'}^{t+\Delta t}\rangle^2 + \left(\tau_{xy'}^{t+\Delta t}\right)^2 + \left(\tau_{y'z'}^{t+\Delta t}\right)^2}; d_m^{t+\Delta t} = 0, \tag{12}$$

$$\varepsilon_m^0 = \sqrt{\langle\varepsilon_{y'}^{t+\Delta t}\rangle^2 + \left(\gamma_{xy'}^{t+\Delta t}\right)^2 + \left(\gamma_{y'z'}^{t+\Delta t}\right)^2}; d_m^{t+\Delta t} = 0, \tag{13}$$

$$\varepsilon_m^{t+\Delta t,d} = \sqrt{\langle\varepsilon_{y'}^{t+\Delta t}\rangle^2 + \left(\gamma_{xy'}^{t+\Delta t}\right)^2 + \left(\gamma_{y'z'}^{t+\Delta t}\right)^2}; d_m^{t+\Delta t} > 0, \tag{14}$$

where $\langle x\rangle$ represents McCauley operator, defined as $\langle x\rangle = \max(0, x)$.

  doi:10.5075/epfl-298799_978-2-9701614-0-0

In the case of fibre tensile or compressive damage, failure strain is calculated as

$$f_{ft} \geq 0 \rightarrow \varepsilon_x^f = \frac{2\Gamma_{Xt}}{X_t l_x}, \tag{15}$$

$$f_{fc} \geq 0 \rightarrow \varepsilon_x^f = \frac{2\Gamma_{Xc}}{X_c l_x}, \tag{16}$$

where Γ_{Xt} and Γ_{Xc} are the intralaminar fracture toughness values for tensile and compressive modes and l_x corresponds to element length in *x*-direction in the global coordinate system. On the other hand, calculation of fracture energy in the mix-mode case is done using the quadratic interpolation function. In the case of delamination, i.e. $\varphi = 90°$ and tensile force, $\sigma_{y'} \geq 0$, matrix fracture energy is

$$\Gamma_m = \Gamma_I^m \left(\frac{\sigma_{y'}^{t+\Delta t | d_m^{t+\Delta t}=0}}{\sigma_m^0} \right)^2 + \Gamma_{II}^m \left(\frac{\tau_{xy'}^{t+\Delta t | d_m^{t+\Delta t}=0}}{\sigma_m^0} \right)^2 + \Gamma_{II}^m \left(\frac{\tau_{y'z'}^{t+\Delta t | d_m^{t+\Delta t}=0}}{\sigma_m^0} \right)^2, \tag{17}$$

where Γ_I^m is mode I matrix fracture energy and Γ_{II}^m is mode II matrix fracture energy. Furthermore, when tensile force acts on a fracture surface with $\varphi \neq 90°$ or in the case of matrix compressive damage, $\sigma_{y'} < 0$, the matrix failure energy is defined as

$$\Gamma_m = c_{num} \left[\Gamma_I^m \left(\frac{\sigma_{y'}^{t+\Delta t | d_m^{t+\Delta t}=0}}{\sigma_m^0} \right)^2 + \Gamma_{II}^m \left(\frac{\tau_{xy'}^{t+\Delta t | d_m^{t+\Delta t}=0}}{\sigma_m^0} \right)^2 + \Gamma_{II}^m \left(\frac{\tau_{y'z'}^{t+\Delta t | d_m^{t+\Delta t}=0}}{\sigma_m^0} \right)^2 \right]. \tag{18}$$

Contrarily to the original crack band model, where FE smaller than the distance between two intralaminar matrix cracks must be used to determine the exact amount of dissipated energy, this model uses the parameter c_{num}, which indicates the number of cracks per one element. It allows the use of coarser meshes and shorter simulation duration times. The c_{num} parameter is defined as a function of intralaminar matrix crack density, c_{dens}, and element dimension as

$$c_{num} = c_{dens} L_{yz}, \tag{19}$$

where L_{yz} is the characteristic element length, which in the case of matrix damage modelling is defined as

$$\varphi = 90° \rightarrow L_{yz} = l_z, \tag{20}$$

$$\varphi \neq 90° \rightarrow L_{yz} = \frac{l_y}{\cos(\varphi)}, \tag{21}$$

where l_y and l_z match the element lengths in *y* and *z* direction, respectively. Finally, by combining equations (18), (19) and (21) matrix damage failure strain is calculated as:

$$\varepsilon_m^f = \frac{2c_{dens} \left[\Gamma_I^m \left(\frac{\sigma_{y'}^{t+\Delta t | d_m^{t+\Delta t}=0}}{\sigma_m^0} \right)^2 + \Gamma_{II}^m \left(\frac{\tau_{xy'}^{t+\Delta t | d_m^{t+\Delta t}=0}}{\sigma_m^0} \right)^2 + \Gamma_{II}^m \left(\frac{\tau_{y'z'}^{t+\Delta t | d_m^{t+\Delta t}=0}}{\sigma_m^0} \right)^2 \right]}{\sigma_m^0 \cos(\varphi)}. \tag{22}$$

It can be noticed that characteristic element length faded away from the relation for matrix damage failure strain and was replaced by the parameter c_{dens}, that multiplies the matrix fracture energy and has the unit mm^{-1}. The disadvantage of the parameter c_{dens} is that it is determined inversely, so that the best match between the experimental and numerical force-time data is obtained.

  doi:10.5075/epfl-298799_978-2-9701614-0-0

Finally, the stresses are updated as

$$\left(\sigma_i^{t+\Delta t}\right) \xrightarrow{\perp x(\varphi)} \left(\tilde{\sigma}_{i'}^{t+\Delta t}\right) = \begin{bmatrix} \sigma_x^{t+\Delta t} \\ \sigma_{y'}^{t+\Delta t}\left(1-d_m^{t+\Delta t}\right)_{\sigma_{y'}^{t+\Delta t}>0} \\ \sigma_{z'}^{t+\Delta t} \\ \tau_{xy'}^{t+\Delta t}\left(1-d_m^{t+\Delta t}\right) \\ \tau_{y'z'}^{t+\Delta t}\left(1-d_m^{t+\Delta t}\right) \\ \tau_{z'x}^{t+\Delta t}\left(1-d_m^{t+\Delta t}\right) \end{bmatrix}, \tag{23}$$

$$\left(\tilde{\sigma}_{i'}^{t+\Delta t}\right) \xrightarrow{\perp x(-\varphi)} \left(\tilde{\tilde{\sigma}}_i^{t+\Delta t}\right) = \tilde{\sigma}_i^{t+\Delta t}\left(1-d_{X_t}^{t+\Delta t}\right)\left(1-d_{X_c}^{t+\Delta t}\right),$$

where $\tilde{\sigma}_{i'}^{t+\Delta t}$ is the stress vector in the fracture plane coordinate system with matrix damage and $\tilde{\tilde{\sigma}}_i^{t+\Delta t}$ is stress vector in global coordinate system with both matrix and fibre damage.

4. Low velocity impact simulation

The experimental results of the low velocity impact test from [5] are used for the model validation. Additionally, the numerical results obtained using LS-DYNA [5] are also used for comparison. The laminated plate, with total dimensions of 150 x 100 x 4.18 mm, was impacted at the centre by a 16 mm diameter spherical projectile with the mass of 3.22 kg. The applied impact velocity was 4.32 m/s, corresponding to a total kinetic energy of 30 J. The CFRP plate, made of TohoTenax IMS60 carbon fibres and Cycom 977-2 epoxy resin with the ply thickness of 0.174 mm, has the symmetric quasi-isotropic lay-up $[(+45/0/-45/90)_3]_s$ with 0° plies oriented in the direction of the longer side of the plate. The material properties of the laminated plate are given in Table 1.

Table 1. Mechanical properties of CFRP, after [2,5].

Property	Values
Elasticity properties	$E_{1,t}$=191 GPa; $E_{1,c}$=121 GPa; $E_{2,t}$=$E_{3,t}$=8.85 GPa; $E_{2,c}$=$E_{3,c}$=8.85 GPa; ν_{12}=ν_{13}=0.258; ν_{23}=0.33; G_{12}=4.41 GPa; G_{13}=4.22 GPa; G_{23}=3 GPa;
Strengths	X_t=3325 MPa; X_c=910 MPa; Y_t=68 MPa; Y_c=170 MPa; S_{12}=81 MPa
Fracture energies	Γ_I^m=347.1 J/m^2; Γ_{II}^m=571 J/m^2; Γ_{Xt}=Γ_{Xc}=40 kJ/m^2
Numerical parameters	c_{dens}=6.5 mm^{-1}; φ_0=53°; K_0=1.184; K_1=0.0609; K_2=0.003743

The specimen was placed on the rear supporting plate that has the same dimensions as the specimen plate, but with a 126 x 71.2 mm rectangular opening. The front side of specimen was clamped with four 13 mm diameter pins spaced 100 and 75 mm apart. The impactor, supporting fixture and clamps, shown in Figure 2., were modelled as rigid bodies.

  doi:10.5075/epfl-298799_978-2-9701614-0-0 published under CC BY-NC 4.0 license

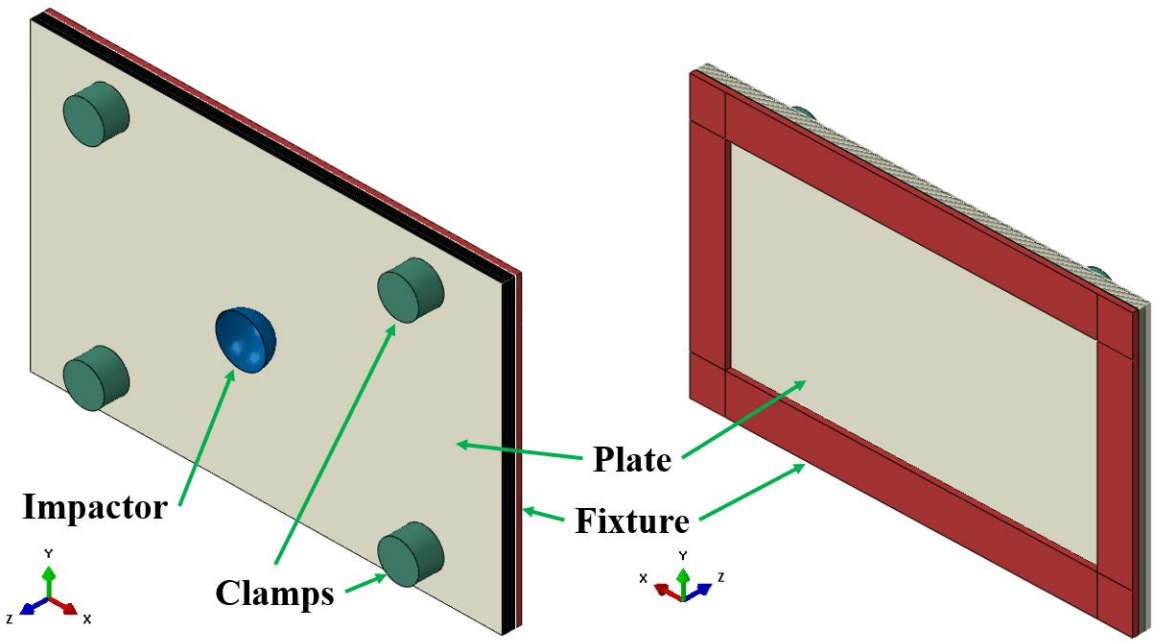

Figure 2. Numerical model

The laminated plate was discretized with 90000 elements, using 2 mm, one per ply, reduced integration linear solid elements. The c_{dens} parameter is determined iteratively to fit experimental force-time data and was set equal to 6.5 mm^{-1}. The contact between the plate, impactor, clamps and fixture was modelled using the general contact algorithm with friction being introduced between all contacting surfaces with a friction coefficient μ=0.3.

5. Results

Comparison of experimental and numerical force-time history and kinetical energy of the impactor are presented in Figure 3. and Figure 4.

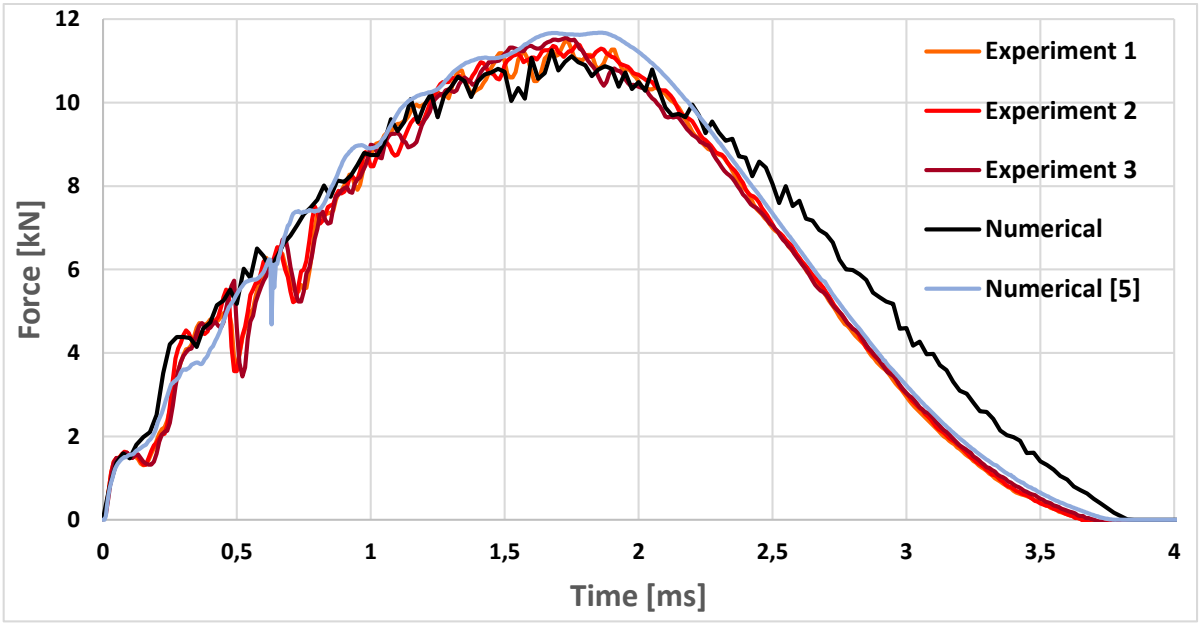

Figure 3. Force-time history

Before the time of 0.25 ms for the FE simulation and 0.3 ms for the test, the impact loads have a rapid growth that slows downs afterwards. The time of the end of load steep rise corresponds to the occurrence of matrix damage. The impact forces reach the maximum of 11.3 kN at the time of 1.75 ms for FE simulation and 11.5 kN at the time of 1.85 ms for the experiment in [5]. This time moment correspond to kinetic energy minimum of the impactor as shown in Figure 4.

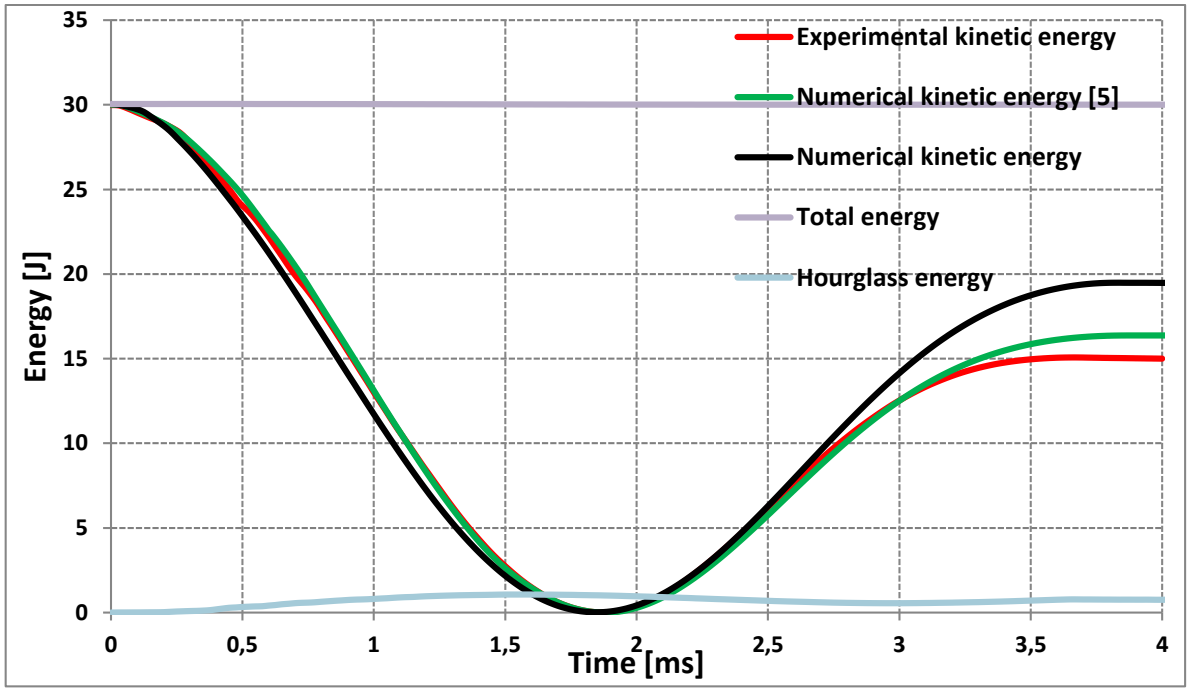

Figure 4. Energy history

The total energy of the model approximately remains constant during the impact process, which ensures the energy conservation in the model as shown in Figure 4. During the impact, the kinetic energy of the impactor is absorbed by the laminated plate. Most of the absorbed energy is transferred back to the impactor, while significant amount of energy is dissipated in form of matrix damage, fibre damage and friction. The amount of absorbed energy in the numerical simulation is less than in the experiment, as shown in Figure 4. The reason for this lies in the fact that much less matrix damage occurs in the numerical model compared to the experiment.

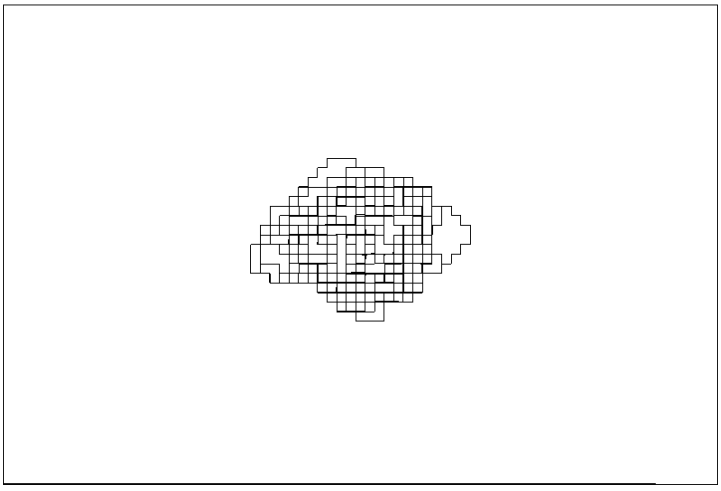

Figure 5. Matrix damage area

  doi:10.5075/epfl-298799_978-2-9701614-0-0

Figure 5. shows the matrix damage area of 1100 mm^2, developed after criteria (4) and (5) were satisfied, while in the experiment this area is 4334 mm^2. Furthermore, a smaller amount of absorbed energy is also manifested in a higher value of force during the repulsion of the impactor. The hourglass energy maintains low level, which guarantees the accuracy of the numerical calculation.

6. Conclusion

In the current work, a computationally efficient, phenomenologically based, failure criteria, which accounts strain-rate effects, and damage model for one integration point solid elements were presented and implemented into the Abaqus/Explicit using the VUMAT subroutine. By introducing the crack density parameter, the model becomes mesh-size-independent, which allows the application of coarser mesh and shorter simulation times. The numerical results are validated by experimental results of low velocity impact. The model showed good match between numerical and experimental contact force, but also deviation in the amount of absorbed energy and the area of matrix damage. In the future research it is necessary to examine the possible sources of discrepancies shown in the results. Furthermore, application of the failure criteria and the damage model in the case of high velocity impact will also be analysed. Further development of the VUMAT model described in this work will include the strain rate effects on the elasticity properties of the material. Additionally, a strain rate dependent cohesive zone model will be developed to accurately simulate the delamination failure mode at the impact loading.

Acknowledgements

The research is fully funded by the Croatian Science Foundation (HRZZ) within the project “COmputational modelliNg of COmposite stRuctures impact DamagE” (CONCORDE), grant number UIP-HRZZ-2020-02-9317.

7. References

1. Koerber H, Camanho PP. High strain rate characterization of unidirectional carbon epoxy IM7-8552 in longitudinal compression. Composites: Part A 2011; 42:462-470.
2. Raimondo L, Iannucci L, Robinson P, Curtis PT. Modelling of strain rate effects on matrix dominated elastic and failure properties of unidirectional fibre-reinforced polymer-matrix composites. Composite Science and Technology 2012; 72:819-827.
3. Bazant ZP, Oh BH. Crack band theory for fracture of concrete. Materials and structures 1983; 16:155-177.
4. Raimondo L, Iannucci L, Robinson P, Curtis PT. A progressive failure model for mesh-size-independent FE analysis of composite laminates subject to low-velocity impact damage. Composite Science and Technology 2012; 72:624-632.
5. Giannaros E, Kotzakolios A, Sotiriadis G, Kostopoulos V. A multi-stage material model calibration procedure for enhancing numerical solution fidelity in the case of impact loading of composites. Journal of Composite Materials 2021; 55(1):39-56.

  doi:10.5075/epfl-298799_978-2-9701614-0-0

MULTI-SCALE MODELLING OF POST-IMPACT HEALING IN FIBRE REINFORCED POLYMER COMPOSITE STRUCTURES

Dominik, Brezetić[a], Ivica, Smojver[a], Darko, Ivančević[a]

a: University of Zagreb, Faculty of Mechanical Engineering and Naval Architecture – dbrezetic@fsb.hr

Abstract: *A multi-scale framework for modelling of intrinsically self-healing FRP composite structures is presented in this work. At the microscale, matrix constituent is modelled using the previously developed and validated micro-damage-healing constitutive model. In this model damage variable reduces the material's elasticity modulus, whereas the healing variable causes its restoration. Reinforcing fibres are considered transversely isotropic and linear elastic. Hashin failure criterion and progressive damage model are used for modelling of fibre failure and post-failure behaviour. Inhere, the model is implemented in Abaqus/Standard user material subroutine UMAT and validated by means of three point bending (3PB) experiments presented in [1]. Subsequently, the validated model is implemented into Abaqus/Explicit user material subroutine VUMAT and used for numerical experiment of Low Velocity Impact (LVI). The results are presented in this work.*

Keywords: Abaqus/Explicit & Standard; multi-scale constitutive model; fibre reinforced polymer composites; micro-damage; healing.

1. Introduction

In this work a novel micromechanical micro-damage-healing constitutive model for intrinsically self-healing unidirectional (UD) Fibre Reinforced Polymer (FRP) composites is introduced. The intrinsic self-healing phenomenon is a property of the matrix constituent. Intrinsic self-healing means that the healing phenomenon results from processes such as polymer chain mobility and entanglement, reversible polymerizations, hydrogen bonding, softening of thermoplastic phases or ionic interactions. Thanks to the reversibility of these processes, the healing process is repeatable thus making these materials highly prospective for use in aeronautical structures.

Self-healing composite materials are experimentally well examined. Several works deal with investigation of fracture toughness of self-healing FRP composites: [2] where a Diels-Alder based thermoplastic copolymer was used as the matrix constituent or [3] where composite laminate was produced using bismaleimide (BMI) based prepregs. Furthermore, three-point bending tests were carried out in [1].

Numerical models for self-healing materials are based on foundations of Continuum Damage Mechanics (CDM). These foundations were used for establishment of Continuum Damage Healing Mechanics (CDHM), which was described in [4]. Most of self-healing constitutive models are developed for pure self-healing materials – polymers and asphaltic materials. In [5], an elasto-plastic micro-damage healing model for shape memory polymers is developed. On the other hand, in [6] it is dealt with development of micro-damage healing model of asphaltic materials at a macrolevel. Moreover, these phenomena are investigated at micro-scale in [7].

  doi:10.5075/epfl-298799_978-2-9701614-0-0

Finally, there are only few models for simulation of damage and healing phenomena in FRP composite materials. One of these models is [8] which is an analytical model using the shear-lag method and the classical lamination theory for prediction of residual stiffness of cracked cross-ply laminates. Three-point bending tests are used as a means for validation. Research in [9] deals with prediction of fracture and healing of plain woven composites using a micromechanical constitutive model where warp and weft yarns are approximated as UD plies.

The constitutive model developed and validated in this work couples von Mises linear isotropic hardening plasticity, micro-damage and healing models for the matrix constituent. The reinforcing fibres are modelled as linear elastic transversely isotropic material with Hashin failure criterion and progressive damage model. At the microscale, a micromechanical model based on the Rule of Mixtures is used for modelling of composite's structure. Experimental results taken from [1] are used as a means for validation.

2. Constitutive model description

The developed constitutive model is a micromechanical model. Thus, at the micro-scale, the reinforcing fibres and the matrix material are modelled separately. The transition from micro-scale to macro-scale, homogenisation, is enabled by applying the Rule of Mixtures. In the following text, modelling of the matrix material and the reinforcing fibres, along with homogenisation is described.

2.1 Micro-scale matrix material

The matrix constituent is modelled as an isotropic material using the developed elastic-plastic micro-damage healing constitutive model. Damage, healing and plasticity models are coupled using the concept of nominal and healing configurations and the strain equivalence hypothesis. After [6], evolution of the damage variable is given as

$$\dot{\phi} = \Gamma^{vd}\left(\frac{\bar{\bar{Y}}}{Y_{th}}\right)^{q}(1-\phi)^{2}\cdot\exp\left(k\cdot\bar{\bar{\varepsilon}}_{eff}\right), \tag{1}$$

where Γ^{vd} is the damage viscosity parameter that determines the rate of the damage variable evolution; $\bar{\bar{Y}} = \sqrt{\frac{3}{2}\bar{\bar{\boldsymbol{\sigma}}}'_{ij}\bar{\bar{\boldsymbol{\sigma}}}'_{ij}}$ is the damage driving force in the healing configuration, $\boldsymbol{\sigma}'_{ij}$ is the healing deviatoric stress tensor; Y_{th} is the threshold damage force; q and k are material parameters and $\bar{\bar{\varepsilon}}_{eff} = \bar{\bar{\boldsymbol{\varepsilon}}}_{ij}\bar{\bar{\boldsymbol{\varepsilon}}}_{ij}$ is the effective (equivalent) strain in the healing configuration. Damage initiation condition is defined as $\bar{\bar{Y}} \geq Y_{th}$. Healing evolution equation is defined as

$$\dot{h} = \Gamma^{h}(1-h)^{m}\,(1-\phi)^{m}, \tag{2}$$

where Γ^{h} is the healing viscosity parameter which determines the rate of the healing variable evolution and m is a material parameter which is determined experimentally. Healing initiates when the material is not being loaded i.e., when the strain rate is equal to zero, and when the material is damaged, meaning that the undamaged material cannot be healed. What is more, further damaging of previously healed specimen causes decrease of the healing variable. The variable that describes the influence both of damage and healing variables is referred to as effective damage variable and is defined as

$$\phi_{eff} = \phi(1-h). \tag{3}$$

  doi:10.5075/epfl-298799_978-2-9701614-0-0

Plasticity model employed to describe inelastic strain of the matrix material is the von Mises isotropic hardening plasticity model. The yield surface is defined as

$$f = \sigma_e - \left(\sigma_{y0} + \int H \cdot dp\right), \tag{4}$$

where σ_e is the von Mises equivalent stress, calculated as $\sigma_e = \sqrt{\frac{3}{2}\boldsymbol{\sigma}'_{ij}\boldsymbol{\sigma}'_{ij}}$, σ_{y0} is the initial yield stress, *H* is the linear isotropic hardening parameter, *dp* is the effective plastic strain increment and *p* is the effective plastic strain. Isotropic hardening i.e., the increase of the initial yield stress with each subsequent loading is defined as

$$\sigma_y = \sigma_{y0} + r(p) = \sigma_{y0} + \int H \cdot dp, \tag{5}$$

where *r* is the isotropic hardening variable. When $f > 0$, the materials actively yields.

2.2 Micro-scale – reinforcing fibres

As mentioned in the introduction, the reinforcing fibres are modelled as linear elastic transversely isotropic material with the Hashin failure criterion and progressive damage. Fibre damage evolution in the case of tension and compression is defined as

$$\phi_f^t = \frac{\delta_{eq}^f\left(\delta_{eq}^{T/C} - \delta_{eq}^0\right)}{\delta_{eq}^{T/C}\left(\delta_{eq}^f - \delta_{eq}^0\right)}, \tag{6}$$

where δ_{eq}^0 is the fibre initial equivalent displacement at which the initiation criterion for that mode was met; δ_{eq}^f is the equivalent displacement at which the material is completely damaged in this failure mode; $\delta_{eq}^{T/C}$ is the current fibre equivalent displacement – $\delta_{eq}^{T/C} = \delta_{eq}^T$ for the case of tension and $\delta_{eq}^{T/C} = \delta_{eq}^C$ for the case of compression. Fibre equivalent displacement for the case of tension, δ_{eq}^T, is calculated as

$$\delta_{eq}^T = L^C \sqrt{\left(\varepsilon_{11}^f\right)^2 + \left(\varepsilon_{12}^f\right)^2}, \tag{7}$$

where L^C is the characteristic element length and ε_{11}^f and ε_{12}^f are components of the fibre strain tensor. In case of compression, the displacement is calculated as

$$\delta_{eq}^T = L^C \sqrt{\left(\varepsilon_{11}^f\right)^2}. \tag{8}$$

2.3. Macro-scale – homogenised composite

The homogenisation is carried out using the principles of the Rule of Mixtures. These principles are defined with equations used for calculation of engineering constants of the homogenised composite material. Longitudinal elasticity modulus, E_{11}, transverse elasticity modulus, E_{22}, Poisson's ratio, ν_{12}, and in-plane shear modulus, G_{12}, of the homogenised composite material, are calculated as

$$E_{11} = E_{11}^f V^f + E^m(1 - V^f), \tag{9}$$

$$\frac{1}{E_{22}} = \frac{V^f}{E_{22}^f} + \frac{1 - V^f}{E^m}, \tag{10}$$

  doi:10.5075/epfl-298799_978-2-9701614-0-0

$$\nu_{12} = \nu_{12}^f V^f + \nu^m (1 - V^f), \tag{11}$$

$$\frac{1}{G_{12}} = \frac{V^f}{G_{12}^f} + \frac{(1-V^f)}{G^m}, \tag{12}$$

where G^m is the shear modulus of the matrix material; ν^m is the Poisson's ratio of the matrix material; E^m is the elasticity modulus of the matrix material; G_{12}^f is the in-plane shear modulus of the reinforcing fibres; ν_{12}^f is the Poisson's ratio of reinforcing fibres; E_{22}^f is the transverse elasticity modulus of reinforcing fibres; and E_{11}^f is the longitudinal elasticity modulus of reinforcing fibres. Components E_{33}, ν_{13}, ν_{23}, G_{23} and G_{13} are defined as

$$E_{33} = E_{22}, \tag{13}$$

$$\nu_{13} = \nu_{12}, \tag{14}$$

$$G_{13} = G_{12}, \tag{15}$$

while values of G_{23} and ν_{23} are determined experimentally or taken from the literature.

3. 3PB test validation

The constitutive model described in the previous section is implemented into Abaqus/Standard user material subroutine UMAT. Furthermore, it is validated using three-point bending experiments presented in [1]. Coupons used in the aforementioned research consist of thermally mendable bis-maleimide tetrafuran (2MEP4F) and unidirectional carbon fibres GA045. Achieved fibre volume fraction is 46 % with the [0/90/0] layup. In the experimental setup, an aluminium plate is inserted between the specimen and the loading nose to prevent fibre breakage. Mechanical properties of the matrix constituent, reinforcing fibres and the aluminium plate, used in numerical analysis, are given in Table 1.

Table 1: Mechanical properties of 2MEP4F, GA045 and aluminium.

2MEP4F		GA045		Aluminium	
E	4.14 GPa	E_{11}	228 GPa	E	70 GPa
ν	0.36	E_{22}	15 GPa	ν	0.33
σ_{y0}	118 MPa	ν_{12}	0.2	ρ_{Al}	2700 kg/m^3
ρ_{2MEP4F}	1310 kg/m^3	ν_{23}	0.4		
		G_{12}	15 GPa		
		G_{23}	7 GPa		
		X_t^f	4500 MPa		
		X_c^f	2000 MPa		
		$\rho_{CFRP} = 1276$ kg/m^3			

3.1. Finite element model description

In Figure 1a the experimental setup of the 3PB test is given along with boundary conditions and specimen, supports and load nose dimensions. The specimen is loaded three times and it is healed after the first and the second bending. Moreover, Figure 1a shows the discretization of the Abaqus model – specimen is discretized with 14400 C3D8R elements (19844 nodes),

  doi:10.5075/epfl-298799_978-2-9701614-0-0

aluminium plate with 4800 C3D8R elements (6804 nodes), whereas the load nose and each support are discretized with 400 R3D4 rigid elements (451 nodes). There are two healing periods in the experiment, first one is after the first bending. In the experiment, it lasts 1 h, and in the numerical analysis it is defined to last 1 s. Thus, healing model parameters are scaled during the healing period, as shown in Table 2. The second healing period is after the second bending. In the experiment it lasts 2h, and in the numerical analysis it lasts 2 s. The same scaled healing model parameters as in the first healing periods are used. Complete list of model parameters' values is given in Table 2.

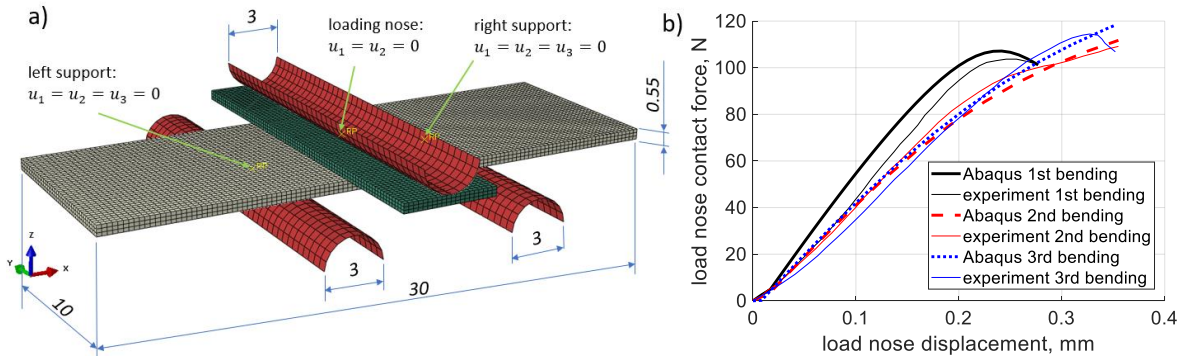

Figure 1: a) Discretized Abaqus model of the 3PB test experimental setup with dimensions in [mm], and boundary conditions – specimen discretized with 14400 C3D8R elements (19844 nodes), aluminium plate with 4800 C3D8R elements (6804 nodes), the load nose and each support are discretized with 400 R3D4 rigid elements (451 nodes); b) 3PB test validation results – comparison of force-displacement diagrams, experimental and analysis results.

Table 2: Constitutive model parameters used for numerical analysis of 3PB tests – damage, healing and plasticity model parameters.

Damage model		**Healing model**		**Plasticity model**	
Γ^{vd}	$5.61 \cdot 10^{-2}$ 1/s	Γ^{h}	0.0618 1/s	σ_{y0}	118 MPa
Y_{th}	3.1 MPa	m	2	H	1800 MPa
k	- 8	scaled healing parameters			
q	1	Γ^{h}_{3PB}	99.07 1/s		
		Γ^{h}_{LVI}	42 500 1/s		
		m	2		

3.2. Validation results

Force-displacement diagram showing experimental and analysis results for three bending cycles is given in Figure 1b and it shows good agreement of experimental and numerical results. It can be concluded that the developed constitutive model is able to predict both damaging and healing of intrinsically self-healing UD composite structures with good accuracy.

4. Low-velocity impact test – numerical experiment

After successful validation by means of 3PB tests, the model is implemented into Abaqus/Explicit user material subroutine VUMAT and used to predict damaging and healing in intrinsically self-healing FRP composite specimen after low-velocity impact. The experiment is a numerical test where the same matrix and reinforcing fibres materials (Table 1), with same constitutive model

parameters (Table 2) are used. The layup is $[45/0/-45/90]_S$ which is recommended in ASTM D7136, a standard for LVI tests.

4.1. Finite element model description

Abaqus model consist of a rigid base with a cut-out, a rigid spherical impactor and a rectangular specimen which is simply supported on the rigid plate, see Figure 2. The setup is discretized with 41,956 finite elements in total, out of which 1,140 R3D4, 40,760 C3D8R and 56 R3D3 elements.

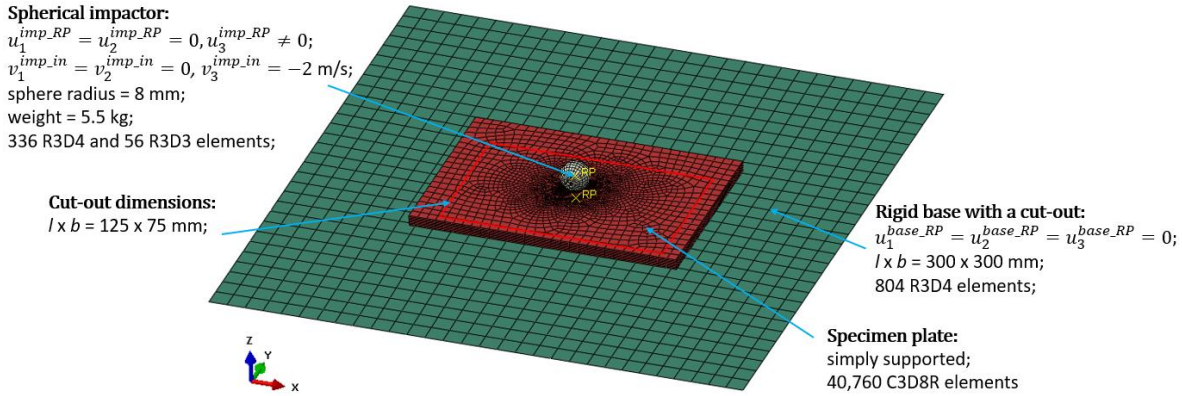

Figure 2: Abaqus model of the experimental setup with relevant dimensions, boundary conditions and number and type of elements; u^{base_RP}, base reference point displacement; $u_1^{imp\_RP}$, impactor reference point displacement; $v_1^{imp\_in}$, impactor initial velocity.

Composite specimen is impacted with a spherical impactor at 2 m/s – the analysis lasts until the rebound of the impactor, i.e. until it gets out of contact with the specimen. Then, the specimen is healed for 0.1 ms, and during that period, scaled healing viscosity parameter, Γ_{LVI}^h, given in Table 2, is used. This period is an equivalent to 1 h of healing with $\Gamma^h = 0.0618\ 1/\text{s}$.

4.2. Results and discussion

Due to the impact, both fibre and matrix damage occur in the specimen. However, the analysis did not predict fibre rupture. The critical failure mode is compressive fibre damage in the top ply (45˚) which is in direct contact with the impactor, and plies four (90˚) and five (90˚) in the impact zone, see Figure 3 where each of the mentioned plies is shown separately and magnified.

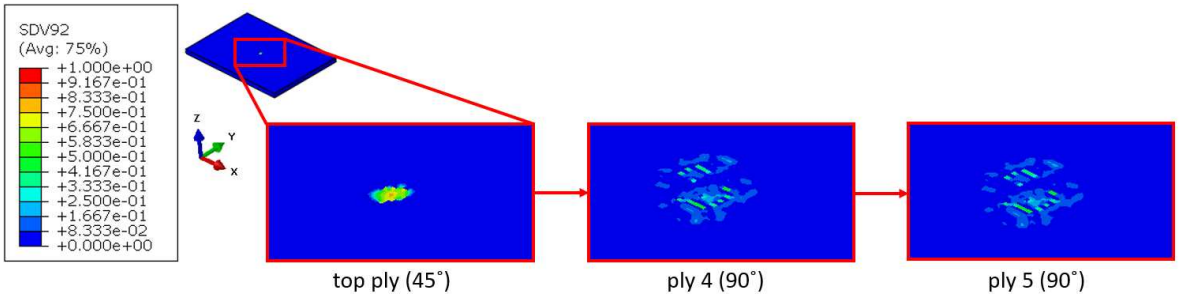

Figure 3: Compressive fibre damage after the first impact on the specimen in plies: 1 (top ply), 4 and 5.

On the other hand, matrix micro-damage is present throughout the specimen. Figure 4 shows a three-quarter section view of the specimen and the distribution of the effective damage variable, ϕ_{eff}, before and after the healing process. It can be observed that almost all matrix micro-damage is healed through the thickness of the specimen.

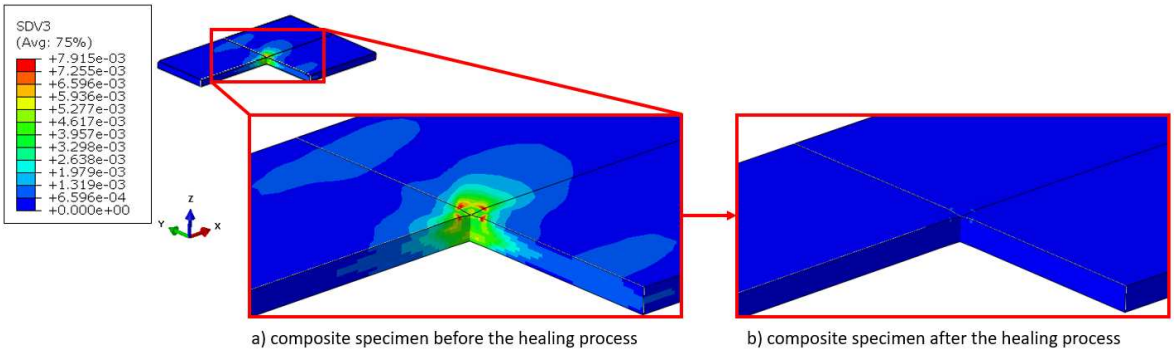

Figure 4: A three-quarter section view of the specimen and distribution of the effective damage variable, ϕ_{eff}: a) before the healing process; and b) after the healing process.

5. Conclusion

The micro-damage healing model for intrinsically self-healing unidirectional fibre reinforced polymer composites developed in this work is validated using experimental results available in [9]. Validation results have shown that the model is able to accurately describe both damaging and healing mechanisms of the investigated fibre reinforced polymer composite. Motivated by the successful validation, a pure numerical experiment is carried out to investigate the healing phenomenon and fibre damage after low velocity impact. The analysis predicts initiation of both fibre and matrix damage, where the fibre damage is localised in the impact zone of plies 1, 4 and 5. On the other hand, matrix damage is present through the thickness of the specimen. Analysis has shown that almost all matrix micro-damage can be healed.

Validation of the constitutive model for the case of the low velocity impact is a subject of further research when damaging-healing phenomenon and fibre damage will be investigated in detail.

Acknowledgements

Research presented in this work is funded by the Croatian Science Foundation (HRZZ) through the ACCESS (AdvanCed CompositE Selfhealing Simulation) project, grant number IP-HRZZ-2018-01-2248.

5. References

1. Park JS, Darlington T, Starr AF, Takahashi K, Riendeau J, Thomas Hahn H. Multiple healing effect of thermally activated self-healing composites based on Diels–Alder reaction. Composites Science and Technology 2010; 70: 2154–9.
2. Kotrotsos A, Tsokanas P, Tsantzalis S, Kostopoulos V. Healing of carbon fiber reinforced plastics by Diels–Alder based polymers: Effects of healing agent concentration and curing cycle. J Appl Polym Sci. 2019;136:1–12.
3. Kostopoulos V, Kotrotsos A, Tsantzalis S, Tsokanas P, Christopoulos AC, Loutas T. Toughening and healing of continuous fibre reinforced composites with bis-maleimide based pre-pregs. Smart Mater. Struct. 2016;25:1–12.

  doi:10.5075/epfl-298799_978-2-9701614-0-0

4. Barbero EJ, Greco F, Lonetti P. Continuum Damage-healing Mechanics with Application to Self-healing Composites. International Journal of Damage Mechanics. 2005;14:51–81.
5. Voyiadjis GZ, Shojaei A, Li G. A generalized coupled viscoplastic–viscodamage–viscohealing theory for glassy polymers. International Journal of Plasticity. 2012;28:21–45.
6. Darabi MK, Abu Al-Rub RK, Little DN. A continuum damage mechanics framework for modeling micro-damage healing. International Journal of Solids and Structures. 2012;49:492–513.
7. Davies R, Jefferson A. Micromechanical modelling of self-healing cementitious materials. International Journal of Solids and Structures. 2017;113-114:180–91.
8. Shabani P, Shokrieh MM, Saeedi A. A novel model to simulate the formation and healing of cracks in self-healing cross-ply composites under flexural loading. Composite Structures. 2020;235:1–11.
9. Udhayaraman R, Subramanian H, Mulay SS, Venkatachalam S. Multi-scale approach-based studies on the damage-healing and fracture behavior of plain woven textile composite. Mechanics of Advanced Materials and Structures. 2020:1–26.

  doi:10.5075/epfl-298799_978-2-9701614-0-0

Numerical Investigation of Compression-After-Lightning Strike Characteristics of Carbon/Epoxy Laminates

Darren Kong Kiat Lo[a], Xiaodong Xu[a], Juhyeong Lee[b]

a: University of the West of England, Coldharbour Lane, Bristol BS16 1QY, UK – darrenlo1997@gmail.com
b: Department of Mechanical and Aerospace Engineering, Utah State University, Logan, UT 84322-4130, USA

Abstract: The increasing use of composite materials in aircraft structures has emphasised proper investigation into the effects of lightning strike damage and the damage tolerance required to withstand such strikes. Testing laboratory-scale artificial lightning strikes to design lightning-resistant materials/structures is a costly endeavour, but this cost can be reduced with the use of finite element analysis available to the industry. The aim of this paper is to generate a model to predict the compressive failure of aerospace-grade carbon/epoxy laminates after a lightning strike. This is done using two user-defined material subroutines in ABAQUS to estimate the lightning strike damage and check for residual compressive strength. The main criterion used to determine lightning damage is the temperature levels after the lightning strike. The modelled laminate is compressed after being hit with 100 kA peak current Waveform D.

Keywords: Laminate; Strength; Compression-After-Impact; Lightning Damage

1. Introduction

The usage of composites in the aerospace industry has been growing significantly, with improvements in manufacturing techniques increasing the percentage of aircraft composite structures. Such an increase in composite usage would place emphasis on proper testing of lightning strikes on composite materials. International Air Transport Association (IATA) statistics has shown that an aircraft is struck by lightning every 1000 hours, equivalent to one strike per aircraft ever year (1). This means that it is only a matter of time for an aircraft to be struck by lightning. Therefore, investigation of damage tolerance of composite materials to lightning strikes is a matter of great concern due to the different behaviour of composites when struck by lightning as compared to metals.

A previous model has been created in ABAQUS to model the lightning effects on an AS4/3506 carbon/epoxy laminate (2). The paper characterized direct lightning effects by primarily focusing on the thermal effects of a 40 kA current lightning strike on carbon/epoxy laminates. While the paper (2) is comprehensive on establishing the physical effects of lightning strikes, it did not evaluate the residual strength of a lightning-struck laminate. It was addressed in the paper (3) in which a maximum current of 93.7 kA strike was used in accordance with the standardized Society of Automotive engineers (SAE) Aerospace lightning Waveform D (4). The paper (3) did not note the through thickness damage of the lightning strike, but only damage to the top layer and utilized a much thinner composite laminate. It also did not consider the temperature degradation in between the matrix damage, but only applying a single reduction factor to the element properties within the temperature boundaries. Regardless of if the element is at 301°C or 499°C, the amount of damage is set to be the same. Wang et al. (3) have also done the compression-after-lightning test with a specimen size of 500 mm x 250 mm x 2 mm, but they had undesirable failure modes such as compressive failure away from the

  doi:10.5075/epfl-298799_978-2-9701614-0-0

lightning damage. In this paper, a compression-after-lightning test has been modelled to evaluate the laminate's residual compressive strength. This paper mainly focuses on the lightning damage after a peak current strike of 100 kA and the subsequent compressive modelling using an ASTM standard compression-after-impact specimen (5).

2. Methodology

2.1 Dimensions, mesh size and properties

A composite laminate is modelled to meet the ASTM standard test method D1737/D1737M (5) for compressive residual strength of polymer matrix composite plates. The laminate is a flat rectangular plate with the dimensions of 150 mm x 100 mm x 4 mm. The finite element models are developed in two sequential steps: (a) the lightning strike model, after which the temperature field is transferred for (b) the compressive model. The composite laminate was discretized with 8-node linear brick coupled thermal-electrical elements (DC3D8E) in the lightning strike model, then converted 8-node linear brick stress/displacement elements (C3D8) in the subsequent compressive model. It is meshed using three-dimensional brick elements of 1.6 mm x 1.6 mm in-plane dimensions. A coarser mesh (2.5 mm x 2.5 mm) is also used in a mesh size study. The predicted lightning damage and the consequent predicted compressive strength were found to be not sensitive to the mesh size, and the results with the 1.6 mm element size are used for the rest of the paper.

The laminate is modelled as a ply-by-ply quasi-isotropic laminate with the layup of $[+45/0/-45/90]_{4s}$, totalling 16 layers on the top half of the laminate, with each layer simulated as a single orthotropic element with a thickness of 0.125 mm. The remaining 2 mm thickness on the bottom half of the laminate is modelled as a single homogenised quasi-isotropic element to reduce computational costs. The previous tests indicating that the lightning damage does not penetrate to the bottom half (6). The equivalent properties are calculated from orthotropic layer data.

Tables 1, 2 and 3 show the properties of the AS4/3506 carbon/epoxy laminate used in the lightning simulation. The values from the bottom half are the homogenised values.

Table 1: Composite thermal properties (7)

Temp	Density	Specific Heat	Thermal Conductivity$(W/mm*K)$		
(°C)	(kg/mm^3)	$(J/kg*K)$	Long	Trans	Thick
25	1.52E-06	1065	4.66E-02	6.83E-04	6.83E-04
350	1.52E-06	2100	2.47E-02	3.73E-04	3.73E-04
510	1.08E-06	2100	1.46E-02	1.79E-04	1.79E-04
1000	1.08E-06	5750	1.17E-02	1.32E-04	1.32E-04
3316	1.08E-06	5875	1.00E-04	1.00E-04	1.00E-04

Table 2: Composite electrical properties (7)

Temp	Electrical Conductivity(S/mm)		
(°C)	Long	Trans	Thick
25	35.97	1.15E-03	3.9E-06
350	35.97	1.15E-03	3.9E-06
510	35.97	2	2
1000	35.97	2	2
3316	35.97	2	2

Table 3 shows the elastic properties of AS4/3506 laminate at room temperature of 27°C.

Table 3: Composite elastic properties (7)

Top Half (Ply-by-ply)			Bottom Half (Homogenized)		
Engineering Constant	Unit	Values	Engineering Constant	Unit	Values
E1	[GPa]	130	E1=E2	[GPa]	49.8
E2=E3	[GPa]	7.7	E3	[GPa]	7. 7
G12=G13	[GPa]	4.8	G12	[GPa]	19.1
G23	[GPa]	3.8	G23=G13	[GPa]	3.8
v12=v13	-	0.3	v12	-	0.3
v23	-	0.35	v23	-	0.35

2.2 Lightning Simulation

The lightning simulation was conducted first in ABAQUS/Standard in two steps, a coupled thermal-electric step, where the lightning current is applied and a heat transfer step, where the initial lightning strike temperatures is allowed to propagate. The lightning damage is generated from a model previously developed by Lee (2). His model utilized subroutines to control the lightning current strike and flagged element failure based on their peak temperature. The lightning current has been increased to match standard SAE Waveform D at its peak current of 100 kA (4). All other boundary conditions and methods of calculating lightning damage has been kept the same as what was laid out in (2). The damage from the lightning strike is simulated by usage of a pre-defined temperature field. As laid out in (2), the damage boundary is between 300°C where the composite starts to degrade and 500°C where the composite is fully degraded. A solution dependent variable (SDV1) is monitored to estimate the degree of thermal damage in composite, with a zero value increasing from 300°C

  doi:10.5075/epfl-298799_978-2-9701614-0-0

noting the start of damage to one value noting 500°C or above where the element is considered to be fully damaged.

2.3 Compression After Lightning Simulation

The compression after lightning simulation is sequentially performed in ABAQUS/Standard. Using the results from the lightning simulation, the elements' elastic moduli were softened linearly from 300°C to 500°C where at 500°C, the properties of the composite are set to close to zero. The boundary conditions are set as per the ASTM compression-after-impact (CAI) test rig as seen in Figure 1. The base of the model has no Degree of Freedom (DoF) in the X, Y and Z directions to simulate the base being fixed in the test rig. The sides of the model have no DoF in the Y and Z directions but is allowed to translate in the X direction in the compression direction. The top of the model has no DoF allowed in the Y and Z direction and has a displacement linearly increased over a duration of 5 seconds up to 2 mm to simulate the applied compression. This displacement was chosen to apply a failure strain of 1.3%. Figure 2 shows the model with the boundary conditions applied, with the sides labelled.

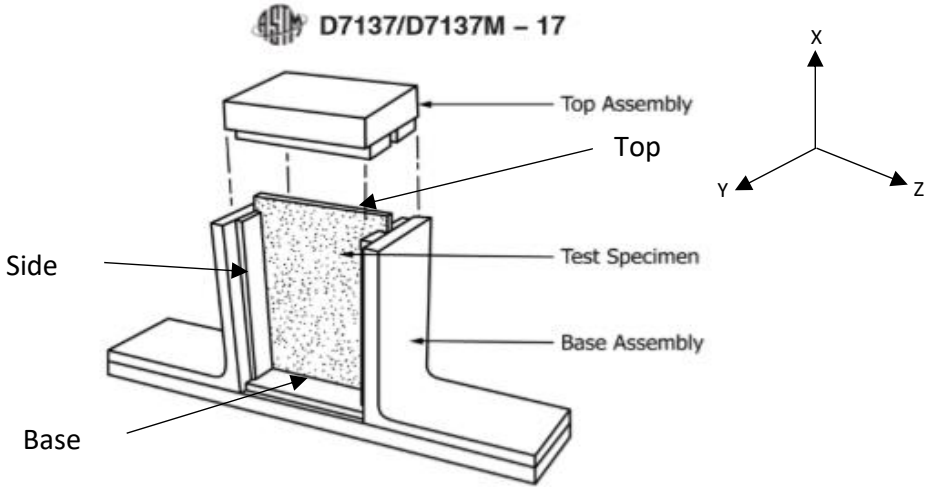

Figure 1 ASTM test rig with a plate in place

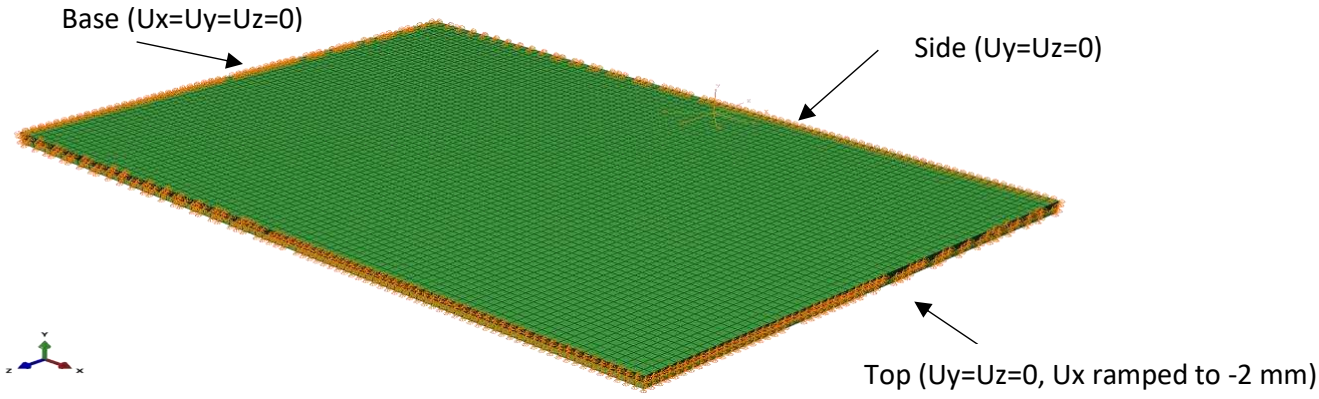

Figure 2 The FE model with the boundary conditions labelled

The residual strength of the composite is determined by the sum of the reaction force in the nodes at the bottom of the composite plate opposing the compressive force.

The compression-after-lightning simulation is controlled by a user subroutine created for this model. The stress and strain values are calculated over the time period (5 seconds) and upon hitting the failure point defined by the Hashin criteria (9), the element is flagged, and the elastic properties are set as close to zero. The most relevant criterion in this test is the compressive fibre failure criterion which is flagged as SDV 2. Equation 1 shows the failure criterion used when the stress in the fibre direction reaches the ultimate compressive strength of the ply ($S_{11} \leq 0$).

$$\left(\frac{\sigma_{11}}{S_{11}}\right)^2 \leq 1.0 \quad (1)$$

Where σ_{11} is the compressive stress in the fibre-direction, S_{11} is the compressive strength which is 1690 MPa as sourced from Hexcel's datasheet for IM7/8552 material (8). The reason for using two sets of material properties is due to the availability of the high temperature electric and thermal properties for AS4/3506, the availability of compression test results of IM7/8552 which will also be used as the future baseline material.

3. Results

3.1 Lightning Damage

Figure 2 shows the extent of the damage to the underlying layers of the composite. The lightning damage in red penetrated through 11 layers of the composite. Red elements are those hit temperatures at or above 500°C. The maximum width of the fully damaged elements is 16.5 mm (red) in the top layer, and the partially damaged elements span 38.4 mm in the top layer (blue).

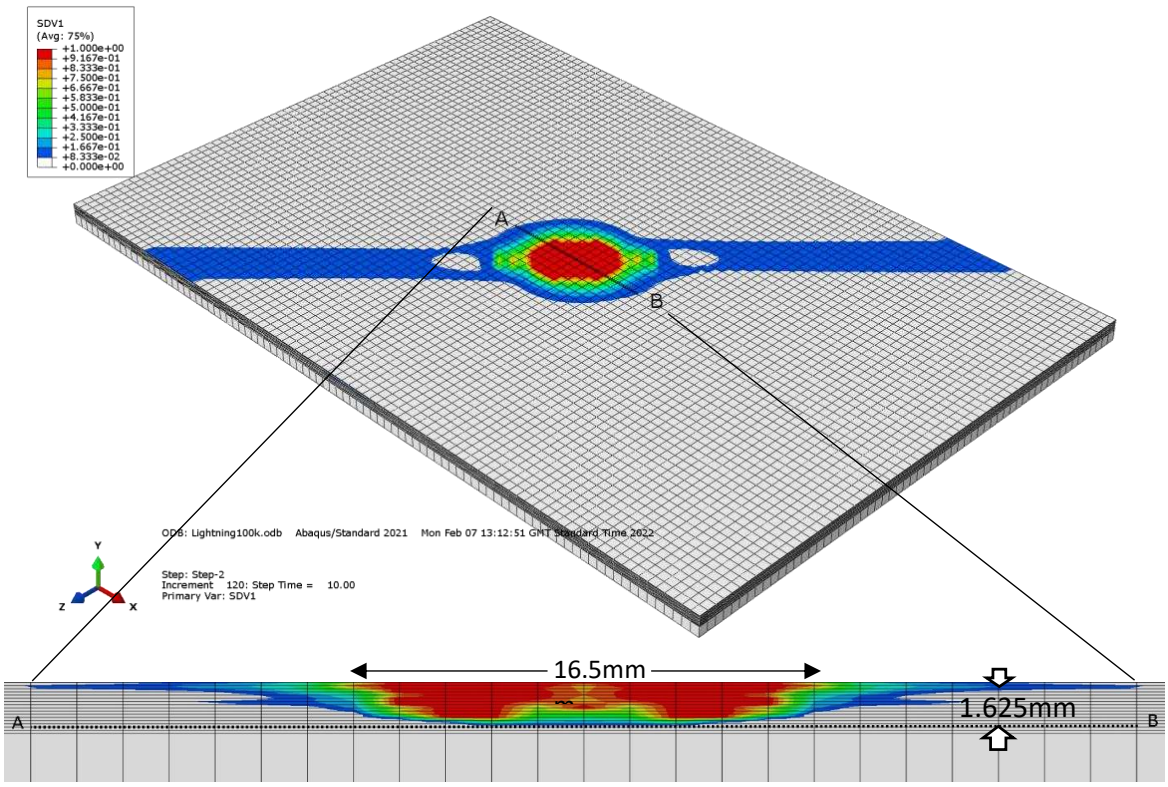

Figure 2 Lightning Damage

3.2 Compression after Lightning Response

Figure 3 shows the graph of the Compressive Stress vs Displacement of carbon/epoxy laminate subjected to 100 kA peak current. The peak compressive stress of the lightning damaged composite is 282 MPa. The load drop at a displacement of 1.908 mm mark (1.27% strain) indicates where the composite laminate is predicated to fail. The 2 mm mark is where the simulation is stopped. By close inspection of the compressive model, the lightning damage causes stress concentrations under compression. The 0° plies with the highest stress and stress concentration break first with the failed elements flagged and softened. The accumulation of the compressive damage quickly leads to the ultimate failure marked by the load drop in Figure 3.

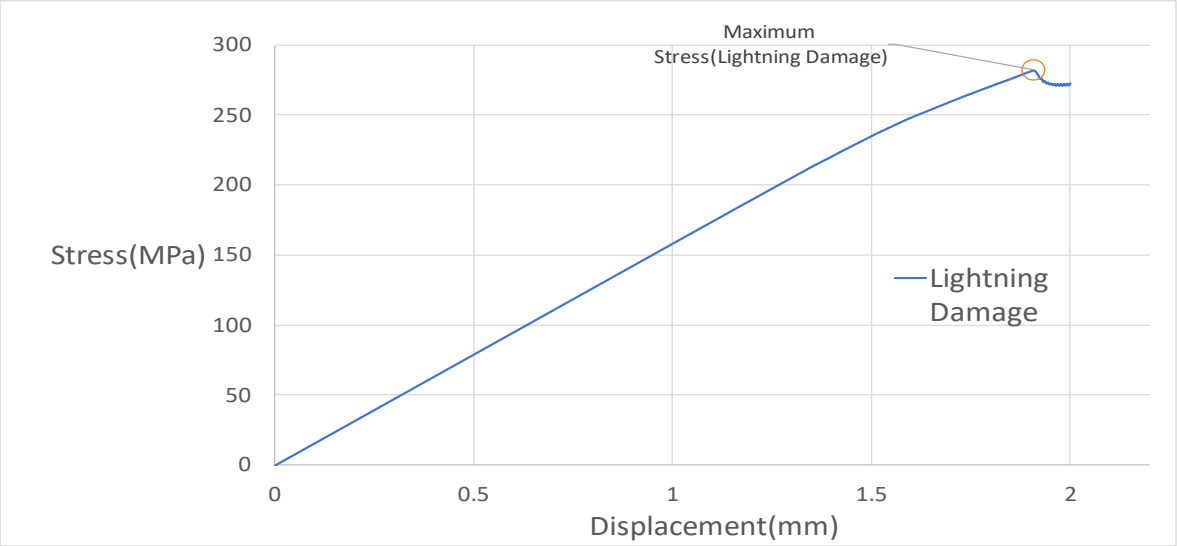

Figure 3 Stress vs. Displacement response in the compression model with lightning damage

4. Discussion

From the modelling results, the lightning damage has certainly reduced the compressive strength of the composite plate. The predicted compressive strength of 282 MPa for the lightning damaged laminate suggests that lightning damage may be equivalent to an open hole of a comparable diameter. For example, a 25.4 mm diameter hole in a 127 mm wide plate has a compressive strength of 285 MPa for the same layup and IM7/8552 carbon/epoxy material (10). These open-hole specimens were already successfully tested under compression (10) without undesirable global buckling and edge compressive failures as seen in other previous compression-after-lightning tests (3). Therefore, it is promising to conduct this compression test after 100kA maximum current lightning by cutting the lightning struck specimens down to these 150 mm by 100 mm by 4 mm standard CAI specimens.

5. Conclusion and future work

A compression-after-lightning model has been developed for the prediction of the residual strength of the lightning damaged laminate under compression. The modelling results

  doi:10.5075/epfl-298799_978-2-9701614-0-0

demonstrate that the lightning damaged laminate has a similar compressive strength to the measured values from the open-hole compression tests with a comparable damage size. This implies that expensive lightning tests may be represented by quasi-static tensile tests which are carefully selected by the numerical models. Future studies should look into the actual lightning and compression tests of the IM7/8552 laminates to validate the predicted lightning damage and residual compressive strength, and finally, the similarity in behaviour between the open-hole and the lightning struck composite laminate.

6. References

1. Zoriy V. Aircraft and lightning strikes: here is what the statistics say | Mainblades [Internet]. Mainblades. 2022 [cited 8 March 2022]. Available from: https://mainblades.com/article/aircraft-and-lightning-strikes-here-is-what-the-statistics-say/
2. Lee J, Lacy T, Pittman C, Mazzola M. Thermal response of carbon fiber epoxy laminates with metallic and nonmetallic protection layers to simulated lightning currents. Polymer Composites. 2017;39(S4):E2149-E2166.
3. Wang F, Yu X, Jia S, Li P. Experimental and numerical study on residual strength of aircraft carbon/epoxy composite after lightning strike. Aerospace Science and Technology. 2018;75:304-314.
4. SAE Aerospace. Aerospace Recommended Practice ARP5412B. 1999
5. Standard Test Method for Compressive Residual Strength Properties of Damaged Polymer Matrix Composite Plates [Internet]. Astm.org. 2022 [cited 8 March 2022]. Available from: https://www.astm.org/d7137_d7137m-17.html
6. Ogasawara T, Hirano Y, Yoshimura A. Coupled thermal–electrical analysis for carbon fiber/epoxy composites exposed to simulated lightning current. Composites Part A: Applied Science and Manufacturing. 2010;41(8):973-981.
7. Foster P, Abdelal G, Murphy A. Quantifying the Influence of Lightning Strike Pressure Loading on Composite Specimen Damage. Applied Composite Materials. 2018;26(1):115-137.
8. HexTow Laminate Properties in HexPly® 8552 [Internet]. Hexcel.com. 2022 [cited 8 March 2022]. Available from: https://www.hexcel.com/Products/Resources/1664/hextow-laminate-properties-in-hexply-8552
9. Hashin Z. Failure Criteria for Unidirectional Fiber Composites. Journal of Applied Mechanics. 1980;47(2):329-334.
10. Xu X, Paul A, Sun X, Wisnom M. An experimental study of scaling effects in notched quasi-isotropic carbon/epoxy laminates under compressive loads. Composites Part A: Applied Science and Manufacturing. 2020;137:106029.

  doi:10.5075/epfl-298799_978-2-9701614-0-0

CALIBRATING MACROSCALE MODELS OF 3D-WOVEN COMPOSITES: COMPLEMENTING EXPERIMENTAL TESTING WITH HIGH FIDELITY MESOSCALE MODELS

Carolyn Oddy[a], Ioannis Topalidis[b], Bassam El Said[b], Magnus Ekh[a], Stephen Hallett[b], Martin Fagerström[a]

a: Division of Material and Computational Mechanics, Department of Industrial and Materials Science, Chalmers University of Technology, Gothenburg, Sweden – carolyn.oddy@chalmers.se
b: Bristol Composite Institute, University of Bristol, Bristol, United Kingdom

Abstract: *Composites with 3D-woven reinforcement could help fill a growing need for lightweight materials with improved material integrity and out-of-plane performance. Developing efficient computational tools to predict their behaviour, however, is key to facilitating their widespread adoption in various industrial applications. Macroscale models are one such tool. They consider an approach where the material model is homogeneous and anisotropic. While macroscale models are computationally efficient, they also require large scale, complex and time consuming experimental testing campaigns to characterise the material response.*

One promising avenue that is explored in this work, is the development of a characterisation test matrix, in which material data is acquired through a combination of experimental testing and simulation of a high fidelity mesoscale representative volume element. In this collaborative project, both experimental testing and mesoscale simulations are carried out in order to calibrate a macroscale model for 3D-woven composites. The results are validated against off-axis experimental tensile tests, as well as multiaxial load scenarios applied to the mesoscale representative volume element.

Keywords: 3D-Woven Composite; Macroscale Model; Material Characterisation

1. Introduction

Composites with 3D-woven reinforcement are beginning to appear in a variety of industrial applications. The intertwining of yarns in 3D space creates a lightweight material with high out-of-plane stiffness and strength properties, damage tolerance and energy absorption capabilities, among other benefits. It also, however, creates a material which can show high levels of anisotropy. This anisotropy is not only found in the initial elastic material behaviour, but also in how different phenomena manifest themselves. The development of damage, permanent deformations, rate dependent mechanisms, final failure and softening all vary depending on the orientation of the reinforcement with respect to the loading direction.

The anisotropic behaviour of 3D-woven composites is due to the hierarchical nature of the internal fibre architectures. They are typically classified into three different scales: microscale, mesoscale and macroscale and are illustrated in Figure 1. Macroscale models, where the domain is assumed to be homogeneous, are computationally most efficient, in particular when trying to model structural components. However, full characterisation of a macroscale model requires a substantial number of experimental tests. Determining the initial elastic material parameters alone requires tensile, compressive and shear tests in various orientations relative to the woven

  doi:10.5075/epfl-298799_978-2-9701614-0-0

architecture. Additional complexity arises when damage, plasticity, rate dependence, final failure, and/or softening must be characterised. Further challenges can also appear if one wants to consider how various anisotropic couplings take place within these 3D-woven composites. Consequently, the full characterisation of 3D-woven composites in order to calibrate a macroscale model, has the potential to require a substantial and challenging testing campaign with a significant financial and time investment.

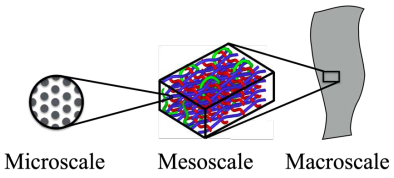

Figure 1. An illustration of the hierarchical nature of 3D-woven composites

As previously noted, these materials are hierarchical. Their macroscale behaviour is highly dependent on their subscale characteristics; from material choices to yarn geometries, weave architectures, yarn tensions etc. Any variation or change to the substructures, would largely invalidate previous experimental testing campaigns. Even for example material draping can lead to local regions with variations in macroscale properties.

This work proposes a collaborative approach to overcome the challenges discussed above. A workflow will be explored that combines the use of experimental testing with simulated material behaviour obtained from a high fidelity mesoscale models developed by Topalidis et al. [1]. The characterisation test matrix will therefore combine the acquisition of material data through both experimental testing and mesoscale simulations. In this way, experimental testing can be used to not only obtain some of the required parameters, but also to validate the mesoscale model under certain loading modes. By loading the RVE and experimental samples cyclically, under different effective deformation modes, it's possible to track how damage and permanent strains develop. In turn, this information is used to calibrate an orthotropic macroscale model including elasto-plasticity and damage developed by Oddy et al. [2].

2. Model Details and Proposed Calibration Scheme

There are several different classes of 3D-woven composites, all having one commonality: reinforcement yarns running through the thickness direction of the material. In this case the considered material is a carbon fibre reinforced epoxy, 3D-woven layer-to-layer interlock. A schematic of this type of weave is shown in Figure 2. It is characterised by warp yarns (running in the 1-direction) interlacing with and running in-between layers of weft yarns (running in the 2-direction).

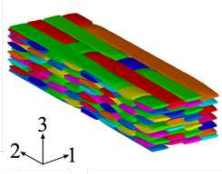

Figure 2. Schematic of 3D-woven layer-to-layer preform

A fully calibrated macroscale model for a 3D-woven composites of this nature, assuming complete anisotropy, could require hundreds of parameters, depending on the desired

  doi:10.5075/epfl-298799_978-2-9701614-0-0

complexity. This complexity can include anisotropic damage development, the unilateral character of damage, permanent strain development, rate dependent effects, and couplings between various deformation mechanisms. The ability to use mesoscale models to determine a portion of these parameters, would be very promising. In order to take steps to explore the viability of a calibration scheme involving both physical testing and mesoscale modelling, this work will be restricted to considering a material which is initially orthotropic and in which damage and plasticity develop in an orthotropic manner. Further, the restriction will here be made in this primary phase to only consider the tensile properties of the 3D-woven composite.

In the following section, the macroscale model developed by Oddy et al. is briefly introduced. Full details can be found in [2]. The model is thermodynamically consistent and allows for the inclusion of damage and inelastic phenomena in a modular fashion. Note also that the macroscale model is formulated and implemented in terms of structural tensors. This means that as the local reinforcement orientation varies over a potential component, there is no need for coordinate transformations at each material point. In this case however, the macroscale model is discussed in Voigt form where it is assumed that the local reinforcement directions align with the global coordinate axis. While the macroscale model is being introduced the required parameters for calibration are shown, and the test matrix involving experimental testing and mesoscale model simulations is developed and discussed. Finally, for continuity the mesoscale model developed by Topalidis et al. [1] is summarised.

2.1 Macroscale Model Details and Proposed Test Matrix

2.1.1 Elastic Material Properties

The starting point for the considered macroscale model, is the general assumption that the 3D-woven material can be described initially using an orthotropic stiffness tensor. This stiffness tensor in a coordinate system oriented based on the fibre architecture (i.e. the 123-system shown in Figure 2) is described in Voigt form by

$$\underline{\mathbb{E}} = \begin{bmatrix} \frac{E_1(1-\nu_{32}\nu_{23})}{\Delta} & \frac{E_1(\nu_{21}+\nu_{31}\nu_{23})}{\Delta} & \frac{E_1(\nu_{31}+\nu_{21}\nu_{32})}{\Delta} & 0 & 0 & 0 \\ \frac{E_2(\nu_{12}+\nu_{13}\nu_{32})}{\Delta} & \frac{E_2(1-\nu_{31}\nu_{13})}{\Delta} & \frac{E_2(\nu_{32}+\nu_{31}\nu_{12})}{\Delta} & 0 & 0 & 0 \\ \frac{E_3(\nu_{13}+\nu_{12}\nu_{23})}{\Delta} & \frac{E_3(\nu_{23}+\nu_{13}\nu_{21})}{\Delta} & \frac{E_3(1-\nu_{12}\nu_{21})}{\Delta} & 0 & 0 & 0 \\ 0 & 0 & 0 & G_{12} & 0 & 0 \\ 0 & 0 & 0 & 0 & G_{23} & 0 \\ 0 & 0 & 0 & 0 & 0 & G_{13} \end{bmatrix}, \tag{1}$$

where

$$\Delta = 1 - \nu_{12}\nu_{21} - \nu_{23}\nu_{32} - \nu_{31}\nu_{13} - 2\nu_{12}\nu_{23}\nu_{31}\,. \tag{2}$$

Therefore, 9 elastic engineering parameters are required, and the first set of entries in the test matrices shown in Table 1 and Table 2 can be considered.

Determining the in-plane Young's moduli and Poisson's ratios, i.e. E_1, E_2, ν_{12}, ν_{23}, ν_{13}, can be done with relative ease using standard tensile testing. In the case of a balanced weave the in-plane shear moduli can be determined using a 45^o off-axis tensile test. On the other hand, characterising the out-of-plane tensile and shear stiffness properties experimentally can be quite challenging. Manufacturing a tensile test sample with sufficient dimension is not a trivial task, and is commonly overcome by adding adhesively joined load introduction tabs. This is

  doi:10.5075/epfl-298799_978-2-9701614-0-0 published under CC BY-NC 4.0 license

further complicated given that the out-of-plane strength of a 3D-woven composite is substantially higher than the strength of adhesives. Similarly, while test methods for determining out-of-plane shear stiffness do exist, c.f. [3], the size of the unit cell again introduces complexities. The representative unit cells of 3D-woven composites are often more than one centimetre in length in at least one of the weave directions. Thus, ensuring that a representative number of unit cells exist in the gauge region of a physical test is not trivial and would require test rigs of an impractical size.

As one of the main benefits to 3D-woven composites, is their out-of-plane performance, characterising their out-of-plane parameters is important. It is therefore proposed that these be determined using results from mesoscale simulations. Further, by loading the mesoscale representative volume element (RVE) in six unique deformation modes, the full stiffness tensor can be determined. By combining this with the in-plane experimental tests, it provides a partial validation of the simulation results while also supplying additional information related to the out-of-plane properties. It also allows the primary assumption of orthotropy to evaluated.

2.1.2 Damage Development

The next set of material data that needs to be determined in order to calibrate the considered macroscale model describes how damage develops within the material. In the macroscale model developed by Oddy et al, a total of 4 damage variables are used: one in each reinforcement direction (d_1, d_2 and d_3) and one in shear (d_s). The damaged stiffness tensor, if reinforcement yarns are aligned in the local 123-coordinate system of the material, is expressed as

$$\underline{\underline{\mathbb{E}}} = \begin{bmatrix} \frac{(1-d_1)E_1(1-\nu_{32}\nu_{23})}{\Delta} & \frac{(1-d_1)(1-d_2)E_1(\nu_{21}+\nu_{31}\nu_{23})}{\Delta} & \frac{(1-d_1)(1-d_3)E_1(\nu_{31}+\nu_{21}\nu_{32})}{\Delta} & 0 & 0 & 0 \\ \frac{(1-d_1)(1-d_2)E_2(\nu_{12}+\nu_{13}\nu_{32})}{\Delta} & \frac{(1-d_2)E_2(1-\nu_{31}\nu_{13})}{\Delta} & \frac{(1-d_2)(1-d_3)E_2(\nu_{32}+\nu_{31}\nu_{12})}{\Delta} & 0 & 0 & 0 \\ \frac{(1-d_1)(1-d_3)E_3(\nu_{13}+\nu_{12}\nu_{23})}{\Delta} & \frac{(1-d_2)(1-d_3)E_3(\nu_{23}+\nu_{13}\nu_{21})}{\Delta} & \frac{(1-d_3)E_3(1-\nu_{12}\nu_{21})}{\Delta} & 0 & 0 & 0 \\ 0 & 0 & 0 & (1-d_s)G_{12} & 0 & 0 \\ 0 & 0 & 0 & 0 & (1-d_s)G_{23} & 0 \\ 0 & 0 & 0 & 0 & 0 & (1-d_s)G_{13} \end{bmatrix}. \quad (3)$$

Each damage variable must have an associated damage surface that controls its onset and development. These are denoted by $\phi_{d1}, \phi_{d2}, \phi_{d3}$ and ϕ_{ds}, respectively. The damage variables and their related surfaces can be calibrated using cyclic tensile testing in each reinforcement direction and in shear. By tracking how the stiffness of the material decreases at each unloading point under uniaxial loading (in each respective direction), the development of each damage parameter can be tracked. This is demonstrated in Section 3.2.

As with the case of the elastic parameters, determining the in-plane damage variables ($d_1, d_2, \phi_{d1}$and ϕ_{d2}) can be done with relative ease using experimental testing. Similarly, a promising avenue for evaluating out-of-plane tensile cyclic testing, and therefore the out-of-plane damage development (d_3 and ϕ_{d3}) is through mesoscale simulation. Finally, as the studied weave is relatively balanced, it is proposed that the in-plane shear damage behaviour (d_s and ϕ_{ds}) be characterised by a 45^o off-axis tensile test. The macroscale model proposed by Oddy et al. [2] assumes that all shear stiffnesses degrade equivalently under shear loading. Cyclic out-of-plane shear loading of the mesoscale RVE allows for that assumption to be verified. This is summarised in Table 1 and Table 2.

  doi:10.5075/epfl-298799_978-2-9701614-0-0 published under CC BY-NC 4.0 license

2.1.3 Plasticity

The final pieces of information required to calibrate the considered macroscale model are related to the development of permanent strains under different load orientations. The proposed testing plan is summarised in Table 1 and Table 2. As rate dependent effects are not addressed in this work and as the restriction has been made to determine only tensile properties of the 3D-woven composite, isotropic hardening is sufficient. Therefore, four yield surfaces with isotropic hardening are introduced. They control the onset and development of plastic strain in the three reinforcement directions and in shear and are denoted $\phi_{p1}, \phi_{p2}, \phi_{p3}$ and ϕ_{ps}, respectively. Once again, cyclic tensile testing in the warp direction, weft direction and at a 45^o off-axis angle provides information in order to characterise in-plane plastic strain development. The method for extracting hardening parameters is shown in Section 3.2. The development of out-of-plane plastic strains can be identified using the considered mesoscale RVE model.

2.1.4 Validation

In order to validate the macroscale model as well as explore the validity of such a proposed calibration scheme, multiaxial loading cases will be evaluated both experimentally and using the mesoscale RVE. Experimentally, off-axis test samples at both 15^o and 30^o to the warp direction will be loaded cyclically in tension. This will generate mixed in-plane tensile and shear loading. Multiaxial loading cases applied to the mesoscale RVE will also be evaluated.

Table 1: Proposed experimental test matrix.

	Elastic	Plasticity+Damage	Validation
Tensile cyclic load : Warp direction	E_1, ν_{12}, ν_{13}	$d_1, \phi_{d1}, \phi_{p1}$	
Tensile cyclic load : Weft direction	E_2, ν_{23}	$d_2, \phi_{d2}, \phi_{p2}$	
Off-Axis: 45°	G_{12}	$d_s, \phi_{ds}, \phi_{ps}$	
Off-Axis: 15°			
Off-Axis: 30°			

Table 2: Proposed simulation test matrix.

	Elastic	Plasticity+Damage	Validation
Stiffness tensor analysis	$E_1, E_2, E_3, \nu_{12}, \nu_{13}, \nu_{23}$		
Tensile cyclic load : Warp direction		$d_1, \phi_{d1}, \phi_{p1}$	
Tensile cyclic load : Weft direction		$d_2, \phi_{d2}, \phi_{p2}$	
Tensile cyclic load : Out-of-plane direction		$d_s, \phi_{ds}, \phi_{ps}$	
Shear cyclic loading: In-plane		$d_s, \phi_{ds}, \phi_{ps}$	
Shear cyclic loading: Out-of-plane		$d_s, \phi_{ds}, \phi_{ps}$	
Multiaxial loading			

2.2 Mesoscale Model Details

The mesoscale model used in this work has been developed by Topalidis et al., full details can be found in [1]. A schematic of the voxelised mesoscale finite element model is shown in Figure 3. Two distinct user-defined material subroutines have been developed, one for each material constituent, i.e. yarn and matrix.

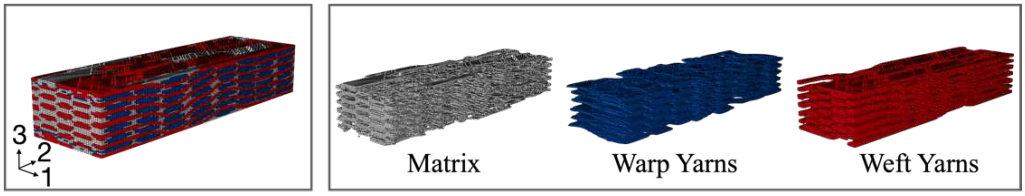

Figure 3. Schematic showing the voxelised RVE mesh and each material constituent within it

To summarise, the undamaged behaviour of a pure matrix element is assumed to have a non-linear shear and tensile response upon loading. Further, the matrix is assumed to unload linearly with the initial elastic slope. A criterion proposed by Tscheogl [4] is used to initiate damage. After damage initiation the stiffness is degraded according to the principal stress space. Figure 4 shows the behaviour of a single matrix element loaded in tension under uniaxial stress conditions and in shear. Under shear loading a plot of the driving stress and strain in the crack plane is shown. The crack is found to initiate at approximately 43°.

Similarly, the cyclic behaviours of a single yarn element loaded in tension in the fibre direction, and in the transverse direction under uniaxial stress conditions as well as in shear are shown in Figure 5. The yarns are assumed to be homogeneous and transversally isotropic, with initial elastic parameters based on an estimated inter-yarn fiber volume fraction according to the micro-mechanical model proposed by Chamis [5]. Failure is initiated according to criteria developed for unidirectional fibre composites. The yarn material is assumed to have a non-linear response in shear. Matrix cracking is predicted using a quadratic law developed by Catalanotti [6]. Both matrix failure criteria for the yarns require searching for a fracture angle which maximises the criterion. Fibre failure in the yarn element is initiated using a maximum stress criterion, and after initiation the full stiffness tensor is progressively degraded.

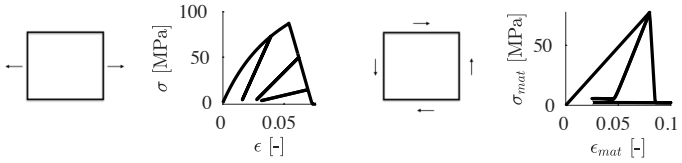

Figure 4. Behaviour of a single matrix element until various cyclic loads

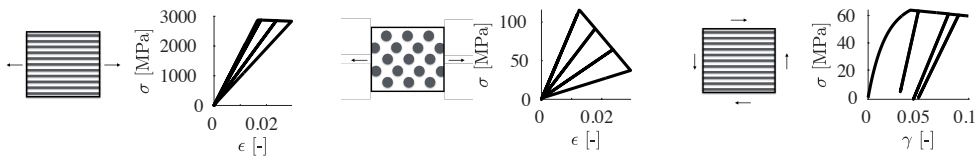

Figure 5. Behaviour of a single yarn element until various cyclic loads

3. Preliminary Results and Discussion

The generation of experimental as well as mesoscale simulation results is currently underway. Preliminary results are shown below.

3.1 3D-Woven Mesoscale RVE: Elastic Parameters

As a starting point, the assumption of elastic orthotropy for the consider 3D-woven composite has been validated. By loading the mesoscale RVE in six different uniaxial deformation modes, the homogenised stiffness tensor can be determined. The results of this initial analysis show that the symmetric elastic stiffness tensor is

$$\underline{\underline{\mathbb{E}}} = \begin{bmatrix} 77.5 & 6.37 & 4.18 & 0.008 & -0.001 & 0.003 \\ 6.37 & 67.8 & 4.91 & -0.0003 & -0.009 & -0.019 \\ 4.18 & 4.91 & 10.2 & -0.001 & -0.002 & -0.0004 \\ 0.008 & -0.0003 & -0.001 & 3.92 & -0.001 & -0.001 \\ -0.001 & -0.009 & -0.002 & -0.001 & 3.17 & -0.001 \\ 0.003 & -0.019 & -0.0004 & -0.001 & -0.001 & 3.71 \end{bmatrix} \text{[GPa]}. \quad (4)$$

As the magnitude of the values is minimal in the upper right and lower left quadrants of the stiffness matrix, the assumption of orthotropy for this material is found to be reasonable. Further, the associated elastic parameters for this stiffness tensor are summarised in Table 3.

Table 3: Elastic material properties generated using the mesoscale model.

Young's Moduli [GPa]	$E_1 = 75.7, E_2 = 65.2, E_3 = 9.66$
Poisson's Ratios [-]	$\nu_{12} = 0.06,\ \nu_{13} = 0.38,\ \nu_{23} = 0.46$
Shear Moduli [GPa]	$G_{12} = 3.92,\ G_{13} = 3.17,\ G_{23} = 3.71$

3.2 Extracting Damage and Hardening Parameters from Mesoscale RVEs

As a further starting point, the mesoscale material models discussed in Section 2.2 has been applied to a unit cell of a two-dimensional weave. As such, the validity of identifying parameters for the macroscale model by loading the mesoscale unit cell under cyclic loading can be shown. Full details on the proposed parameter identification routine can be found in Oddy et al. [2].

Figure 6 shows a resulting stress-strain curve when the mesoscale RVE for the 2D-woven composite is loaded cyclically in the warp direction. At each unloading segment, the stiffness is measured, which in turn indicates the macroscale damage behaviour. Note in this case, that at each unloading point an increase in stiffness is observed. This is likely due to geometric effects (e.g. yarn straightening in the mesoscale model). This increase in stiffness manifests itself as a negative damage parameter. In future work, if this behaviour is found, it may be more suitable to refer to this parameter by a different name. Further, the development of plastic strains with respect to an isotropic hardening stress can also be plotted. In this case the 'damage' parameter has been fit with an exponential curve with saturation. Similarly using isotropic linear hardening has been shown to be sufficient. Feeding this information for the development of damage and plastic strain, into the macroscale model discussed in Section 2.1 gives Figure 8.

The same process has been carried out in order to fit the stress-strain curve produced by loading the 2D-woven unit cell in shear. See Figure 7. In this case when identifying parameters for the macroscale model, both the damage and hardening behaviours were fit using exponentially saturating curves. Inputting this information into the macroscale model, gives that shown in Figure 8.

Acknowledgements

  doi:10.5075/epfl-298799_978-2-9701614-0-0

The project is financially supported mainly by Chalmers' Area of Advance in Materials Science under contract 2021-0037. M. Fagerström also gratefully acknowledges the financial support through Vinnova's strategic innovation programme LIGHTer (LIGHTer Academy grant no. 2020-04526). The simulations were performed on resources at Chalmers Centre for Computational Science and Engineering (C3SE) provided by the Swedish National Infrastructure for Computing (SNIC).

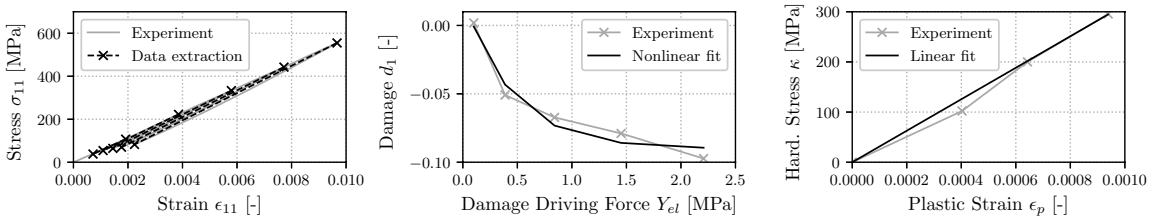

Figure 6. Parameter identification for tensile loading in the warp direction

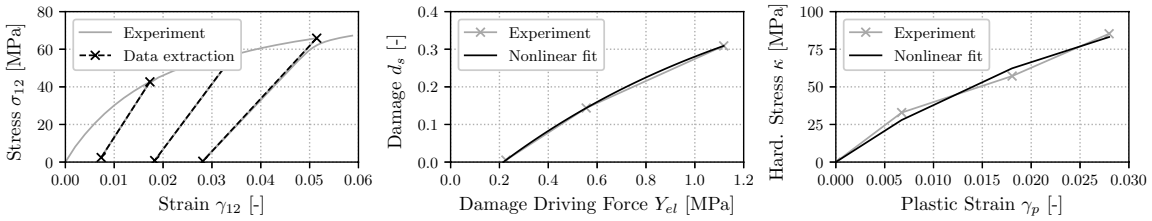

Figure 7. Parameter identification for shear loading

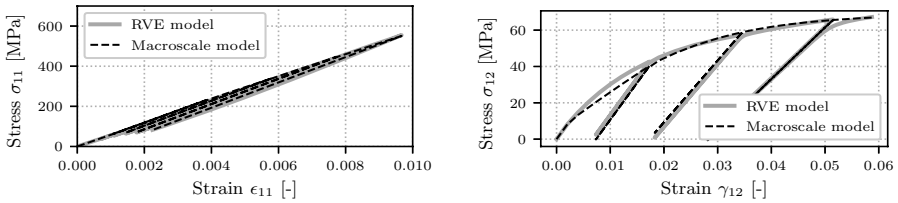

Figure 8. Macroscale model fit using parameters identified from mesoscale simulation

References

1. Topalidis I, El Said B, Thompson AJ, Keulen J, Hallett SR. A numerical study of the effects of draping on the mechanical properties of 3D woven composites. Proceedings of ICCM22 2019; Melbourne, Australia.
2. Oddy C, Ekh M, Fagerström M. Macroscale modelling of 3D-woven composites: Elasto-plasticity and progressive damage. International Journal of Solids and Structures. Under review.
3. Pettersson KB, Neumeister JM. A tensile setup for the IDS composite shear test. Composites: Part A 2006; 37:229-242.
4. Tschoegl NW. Failure surfaces in principal stress space. Journal of Polymer Science Part C: Polymer Symposia 1971; 32:239-267.
5. Chamis CC. Simplified composite micromechanics for hygral, thermal and mechanical properties. NASA Tech Memo 1983:19.
6. Catalanotti G, Camanho PP, Marques AT. Three-dimensional failure criteria for fiber-reinforced laminates. Composite Structures 2013; 95:63-79.

  doi:10.5075/epfl-298799_978-2-9701614-0-0

CONSOLIDATION OF HYBRID TEXTILES FOR AEROSPACE APPLICATIONS

V. Werlen[a,b], R. Vocke[c], P. Schwanemann[c], V. Michaud[b], C. Brauner[a], C. Dransfeld[d] , C. Rytka[b]

a: Institute of Polymer Engineering, University of Applied Sciences and Arts Northwestern Switzerland (FHNW), 5210 Windisch, Switzerland
vincent.werlen@fhnw.ch
b: Laboratory for Processing of Advanced Composites (LPAC), Ecole Polytechnique Fédérale de Lausanne (EPFL), CH 1015 Lausanne, Switzerland
c: Faserinstitut Bremen e. V. (FIBRE), 28359 Bremen, Germany
d: Aerospace Manufacturing Technologies Group, Faculty of Aerospace Engineering, Delft University of Technology, 2629 HS Delft, The Netherlands

Abstract: *Side-by-side hybrid textiles consist of layers of woven reinforcing fibres and flexible thermoplastic layers alternatively stacked on each other. They possess an elevated design freedom as many properties can be easily and locally changed. Side-by-side hybrid textiles can be consolidated with press molding to produce near-net shape final parts. Appropriate process parameters and local tailoring of the composite properties would enable to fully exploit their potential and create very high-performance, defect-free parts. However, the prerequisite for such an optimization approach is a three-dimensional consolidation model, which is not available yet. As a first step, we propose an impregnation model for hybrid textiles which considers air entrapment and dissolution and demonstrate that these two effects greatly influence impregnation. The model captures all relevant phenomena and is shown to be able to properly predict impregnation, and thus porosity.*

Keywords: Hybrid textiles; Impregnation; Press molding; Modeling; Thermoplastic Composites

1. Introduction

Fibre-reinforced thermoplastics (FRTP) display several advantages over the more widespread thermoset-based composites such as a potential for high volume production, better impact resistance and an ability to be recycled [1]. To produce FRTP, the base constituents are usually first architected to an intermediate material which is then consolidated in the final part in a subsequent step. The intermediate material can be classified according to its degree of mingling, for which film stacking, co-woven fabrics, commingled yarns and organosheets can be cited as examples with increasing degree of mingling.

As a rule of thumb, a higher mingling reduces the flow length and the cycle time but increases the costs. In addition, pre-consolidated materials and film stacking do not possess the drapeability inherent to textiles, which significantly decreases the geometrical complexity that can be achieved. Furthermore, the limited range of organosheets available on the market currently reduces the design freedom.

  doi:10.5075/epfl-298799_978-2-9701614-0-0

Hybrid textiles are an alternative intermediate material in which layers of woven reinforcing fibres and a flexible thermoplastic layer are alternatively stacked on each other as represented in Figure 1. The thermoplastic layer can take the form of a veil or woven thermoplastic fibres to conform to the drapeability of the reinforcing fibres. Recently, Reynolds investigated stamp forming with hybrid textiles based on veils and produced structural parts within a cycle time of 330 s. [2], proving the relevance of such a process for the industry.

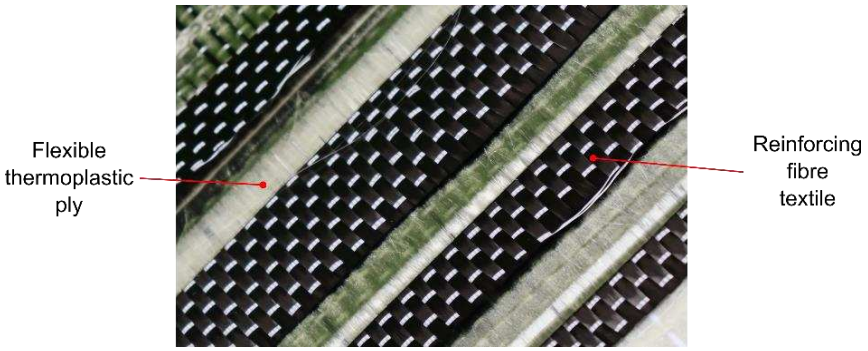

Figure 1: Picture of a partial cutaway of quasi-UD carbon / PEI hybrid textile manufactured at the Faserinstitut Bremen.

An advantage of hybrid textiles is their vast design freedom, as many parameters such as the fabric architecture, orientation or fibre volume fraction could be easily and even locally changed. An adequate selection of the parameters would therefore allow to locally tailor the composite properties and fully exploit their potential. We therefore propose press moulding of hybrid textiles to produce semi-complex shapes towards high-end applications.

This approach requires a consolidation model to avoid the formation of unwanted defects such as porosity or fibre disorientation, which is, however, not available yet. As a first step towards the creation of a complete consolidation model, an impregnation model must be selected and validated. Thereby, not only the overall impregnation behavior should be well described but also the remaining porosity as it has a detrimental impact on mechanical properties [3]. Several authors addressed the impregnation of fabrics, such as Kobayashi [4] and Grouve [5]. They both considered the impregnation of elliptical tows and based their approach on the model of Van West [6], thereby the air in the tows was assumed free to escape. Other authors proposed other similar approaches [7, 8], yet no one validated their model from the beginning to the very end of impregnation. This is unfortunate, as entrapped air mostly influences the end of impregnation and the residual void content as demonstrated by Rozant [9]. However, as the diffusion of air into molten thermoplastic was disregarded his model predicts a constant residual porosity while measurements showed a decay instead.

In this study, we propose to extend existing impregnation models with air entrapment and dissolution. We demonstrate that entrapped air dissolution needs to be considered to properly model the impregnation behavior. Glass quasi-unidirectional (UD) fabric and polypropylene (PP) or high-density polyethylene (HDPE) are chosen as model materials for the investigation in the form of film stacking, since once molten barely any difference is thought to remain when compared to other flexible thermoplastic plies. A validation of the model with high-temperature polymers and veils is planned as further step.

  doi:10.5075/epfl-298799_978-2-9701614-0-0

2. Materials and methods

A woven glass fibre fabric with a quasi-UD fabric architecture and an areal weight of 931 g m^2 provided by Tissa Glasweberei AG, as described and characterized in [10], was used in this study. The tows in the weave direction have 2400 tex with and a density of 3.5 tows cm^{-1}. Micrograph analysis was performed; the tow fibre volume fraction was measured to be 0.77 and the fibre diameter to be 9 µm with a standard deviation of 0.8 µm. The packing of the fibres can be overall well described with a hexagonal arrangement.

Two thermoplastics were investigated in this study, PP BJ100HP from Borealis and HDPE Lupolen 5031L from LyondellBasell. The technical datasheets specify that the PP has a melting temperature of 165 °C and a density of 906 kg m^{-3} in solid state while these values are respectively 131 °C and 952 kg m^{-3} for the HDPE. The polymers were obtained in the form of granulates and have been processed in 0.15 mm thick foils with a Collin FT-E20T-MP extruder.

5 plies of textiles were film stacked with two polymer foils between each layer and one on the top and bottom to target a final fibre volume fraction of 0.45. They were then pressed into 170 x 85 mm plates with a 200 kN Vogt hydraulic press. The mould was placed in the heated press with spacers to avoid pressure on the composite during heating up. Upon reaching the desired cavity temperature the spacers were removed and pressure was applied for different durations before cooling down under the same pressure. For each thermoplastic the experiment was repeated at different pressures as summarized in Table 1. The plates were then cut with a Compcut 200 circular saw and finally photographed to analyze the impregnation behavior over the whole surface. A precision ruler was photographed along each picture to determine the pixel size. The software ImageJ was used to manually select the dry areas and the whole tow and to measure properties such as the tow width, height, area, and impregnation degree. At least 30 measurements were performed for each plate.

Table 1: Summary of the test matrix

Thermoplastic	Cavity temperature [°C]	Cavity pressure [bar]	Press time [mn.]
PP	185	10.4 / 17.3	0/2/5/15/30/60
HDPE	155	35 / 69	0/2/5/15/30/60

3. Consolidation model

An analytical approach based on the model of Van West [6] is adopted, which propose to solve the impregnation for a cylinder equivalent to the ellipse as shown in Figure 2. The equivalent radius is given as:

$$R_{eq} = \sqrt{2}\ \frac{l_w\, l_h}{\sqrt{l_w^2 + l_h^2}} \tag{1}$$

Where l_w and l_h are the semi major and minor axis of the ellipse. The impregnation can be solved analytically for cylinders as follows:

  doi:10.5075/epfl-298799_978-2-9701614-0-0

$$r \ln\left(\frac{r}{R_{eq}}\right)\dot{r} = \frac{K_{tow}}{\eta\,(1-v_f)}\,(P_m - P_g) \tag{2}$$

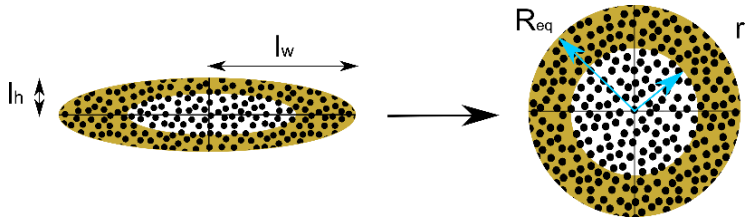

Figure 2: Representation of a partially impregnated tow and its equivalent cylinder according to Van West [6].

Where r is the radial distance to the impregnation front, R_{eq} the equivalent tow radius, K_{tow} the tow permeability, η the viscosity, v_f the tow fibre volume fraction, P_m the matrix pressure boundary on the periphery of the tow and P_g the gas pressure. The reader is redirected to [11] for more information. The tow permeability is predicted with the equation of Gebart for hexagonal packing [14] and the impregnation degree ξ is defined as:

$$\xi = \frac{R_{eq}^2 - r^2}{R_{eq}^2} \tag{3}$$

Assuming mechanical equilibrium between the applied pressure and full saturation of the inter-tow space, the fibre bed stress response and the matrix pressure yields:

$$P_{mat} = P_{applied} - \mathrm{A}\,\mathrm{e}^{v_f B} \tag{4}$$

Where P_{mat} is the matrix pressure, $P_{applied}$ the applied one and the term $\mathrm{A}\,\mathrm{e}^{v_f B}$ relates to the quasi-static stress response of the fabric, which was characterized in [11]. Following the ideal gas law, the air pressure is given as:

$$P_g = \frac{n\,R\,T}{V} = \frac{n\,R\,T}{A_{tow}(1-v_f)(1-\xi)} \tag{5}$$

Where A_{tow} is the tow surface and n the amount of gas in moles trapped in the tow per unit depth. Assuming that all the air in the hybrid textile is pushed inside the tows in the first moments of consolidation when the meso structure collapses as shown in Figure 3, the initial amount of air trapped in each tow reads:

$$n_0 = \frac{P_{atm} A_{tow}(1-v_0)v_f}{R\,T_0\,v_0} \tag{6}$$

Where it is assumed that the amount of air initially present in the hybrid textile and in a textile stack with the same number of layers of the reinforcing ply at rest are equal. In Equation (6) P_{atm} is the atmospheric pressure and v_0 is the fibre volume content of the textile stack at rest.

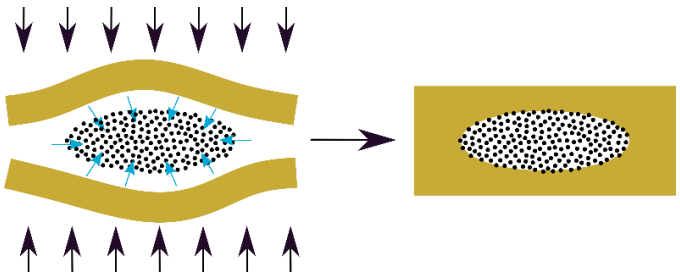

Figure 3: Schematical representation how additional air gets entrapped in the tow. The initial situation is represented in the left, as pressure is applied the molten thermoplastic fills the inter-tow space and pushes air into the tow.

The dissolution rate $\dot{n}$ is obtained by modifying the equation proposed by Epstein and Plesset [12] for bubbles in pure molten polymers by adding a correction factor G to the diffusivity to consider that the fibres are impermeable and disturb dissolution, as schematically represented in Figure 4. Thus:

$$\dot{n} = 2\,\pi\,r\,J = -2\,\pi\,r\,G\,D\,(C_s - C_\infty)\,(1 + \frac{r_i}{\sqrt{\pi G D t}}) \quad (7)$$

Thereby, J is the flux of species, D the diffusivity, t the time elapsed since the start of consolidation and C_s the saturation concentration at the bubble interface and C_∞ the initial concentration of the molten polymer which is assumed to be the saturation concentration at atmospheric pressure. The diffusivity of PP and PE, respectively 5e-9 and 6e-9 $m^2\,s^{-1}$, and Henry's constant, respectively 3.61e-5 and 4.28e-5 mol $Pa^{-1}\,m^{-3}$, were taken from [13].

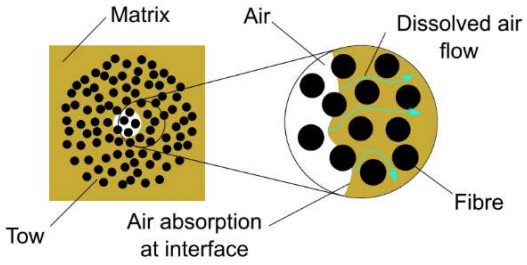

Figure 4: Schematical representation of air entrapment and dissolution. The air dissolves at the flow front interface and diffuses outwards, thereby the fibres obstruct the species flow.

4. Results

Figure 5 shows a photograph of partially impregnated plate cross-section, displaying regularly arranged tows surrounded in polymer without apparent porosity. One can distinguish between the impregnated and dry region of the tow, which has a darker shade. The impregnation front shape is overall centered in the tow with an elliptical shape, which corresponds quite well to the analytical predictions.

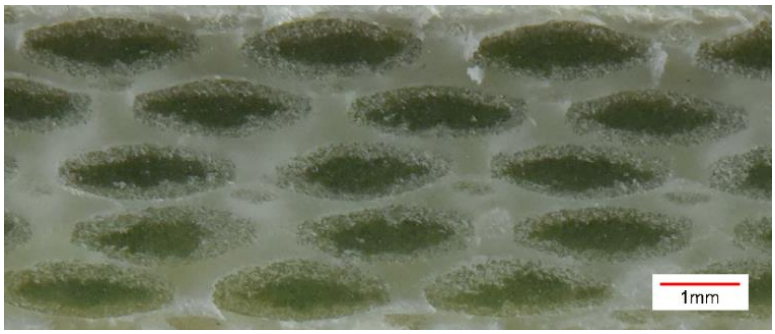

Figure 5: Picture of the cross-section of a PP plate pressed at 10.4 bar for 5 minutes.

It was observed that that the impregnation degree raises sharply at the beginning, then flattens significantly. This can be observed in Figure 6 where the measurements for PP pressed at 10.4 bar are displayed along with different predictions. Thereby, as the cooling time required for polymer solidification was measured to be 2 minutes, the total consolidation time is approximated as the press time plus one minute. The proposed model is found to satisfactorily predict the impregnation degree, thereby the parameter G was fitted using a simplex search method. Using the same model and neglecting air entrapment and dissolution, as many of the models available in literature do, results in a complete failure to predict impregnation as soon as flattening starts to occur. If diffusion is neglected and only the air originally in the tows is

entrapped, meaning that no air migrates from the inter-tow space into the tow, the predictions significantly overshoot. This tends to indicate that more air is trapped inside the tow to counteract impregnation and taking into account air migration is necessary.

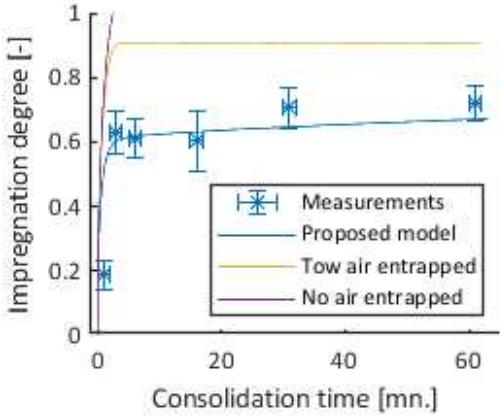

Figure 6: Measured impregnation degree in function of the time along with the predictions of the proposed model, the predictions of the same model if only the air originally in the tows is trapped without diffusion and the predictions if air entrapment is neglected.

The proposed model with appropriate parameter value describes the impregnation kinetics in a satisfactory manner. The value of G was found to be 8. 1e-4, meaning that the fibres do very significantly hinder diffusion or that the diffusion coefficient taken from the literature is overestimated. Figure 7 displays the results for the experiments with HDPE with the same value for G.

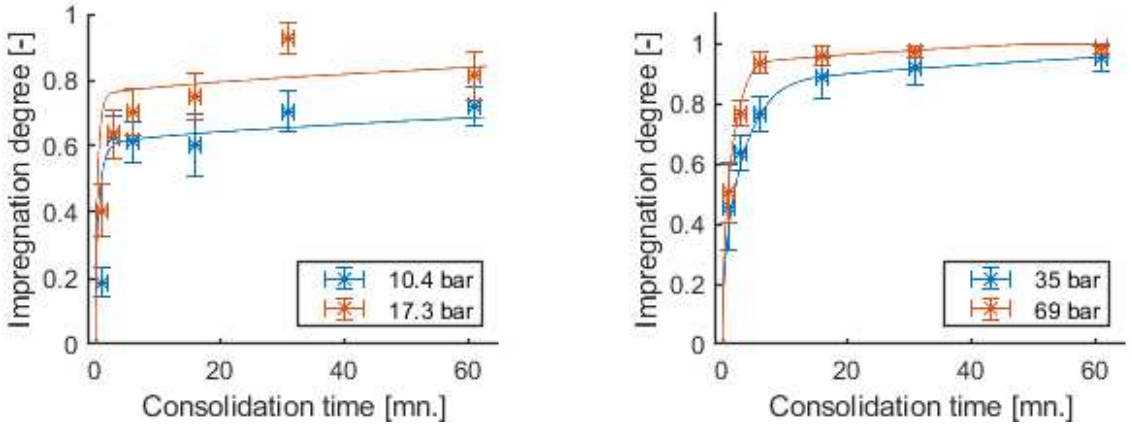

Figure 7: Measured impregnation degree in function of the time along with the predictions of the proposed model with PP as matrix in Figure 7a and HDPE as matrix in Figure 7b.

5. Discussion

The proposed model was found to be able to correctly describe the impregnation behaviour given appropriate parameter selection. The tow permeability predicted by the model of Gebart [14] was found to be well-suited to the measurements and the assumption that the whole air originally present in the textile remains trapped explains well the onset of the measured flattening of the impregnation degree. This effect coupled with diffusion can explain the large differences between the predicted time for full consolidation and those obtained in practice [5]. In this study the correction factor G for the reduced diffusion in porous structures was measured

  doi:10.5075/epfl-298799_978-2-9701614-0-0

empirically, however in future research the validity of existing approach for similar problems should be investigated [15].

This research sheds a new light on the underlying processes taking place during impregnation and allow a comprehensive understanding on how the different parameters affect it, which should be examined in detail. For instance, while previous models held that doubling the tow radius quadruples the impregnation time, it should be investigated this relation changes when air entrapment and dissolution are considered. Many of the parameters in this model depend on either pressure or temperature, not only the viscosity but also the saturation concentration and the diffusivity, which exponentially depends on temperature [13]. The optimal set of process parameters for impregnation is still unclear and should be investigated. Since entrapped air has such a predominant effect on residual porosity and on the impregnation time, air removal strategies and the possibility to press under vacuum should be evaluated.

In further work, the model will be validated with high-performance hybrid textiles and integrated into a three-dimensional consolidation model. Characterization of the solubility and diffusivity of gas in molten high-performance thermoplastics is completely lacking and should be performed as these values are required in the impregnation model.

6. Conclusion

This study investigated the impregnation behaviour of hybrid textiles made with a glass fibre quasi-UD textile and either PP or HDPE foils. We propose a novel impregnation model taking into account air entrapment and dissolution. We show that this is necessary for the correct prediction of the late-stage impregnation behaviour, which current impregnation models fail to predict. The proposed model was found to be able to correctly describe the impregnation behaviour with appropriate parameter selection of the diffusion reduction factor.

Acknowledgements

This work is part of the research project Consolidation of Thermoplastic hybrid yarn materials “ConThP” and is funded by the German Research Foundation [DFG Nr. 394279584] and the Swiss National Science Foundation [200021E / 177210 / 1]. We kindly thank Mr. Schneeberger and Tissa Glassweberei AG for providing the textiles and for their precious support.

1. References

1. Roux M, Eguemann N, Dransfeld C, Thiebaud F, Perreux D. Thermoplastic carbon fibre-reinforced polymer recycling with electrodynamical fragmentation: From cradle to cradle. J Thermoplast Compos Mater. 2017;30(3).

2. Reynolds N, Awang-Ngah S, Williams G, Hughes DJ. Direct Processing of Structural Thermoplastic Composites Using Rapid Isothermal Stamp Forming. Appl Compos Mater. 2020;27(1–2):107–15.

3. Dong C. Effects of Process-Induced Voids on the Properties of Fibre Reinforced Composites. J Mater Sci Technol. 2016;32(7).

  doi:10.5075/epfl-298799_978-2-9701614-0-0

4. Kobayashi S, Tsukada T, Morimoto T. Resin impregnation behavior in carbon fiber reinforced polyamide 6 composite: Effects of yarn thickness, fabric lamination and sizing agent. Compos Part A Appl Sci Manuf. 2017;101:283–9.

5. Grouve WJB, Akkerman R. Consolidation process model for film stacking glass/PPS laminates. Plast Rubber Compos. 2010;39(3–5):208–15.

6. Van West BP, Pipes RB, Advani SG. The consolidation of commingled thermoplastic fabrics. Polym Compos. 1991;12:417–27.

7. Phillips R, Akyüz DA, Manson J-AE. Prediction of the consolidation of woven fibre-reinforced thermoplastic composites. Part I. Isothermal case. Compos - Part A Appl Sci Manuf. 1998;395–402.

8. Jespersen ST, Wakeman MD, Michaud V, Cramer D, Manson J-AE. Film stacking impregnation model for a novel net shape thermoplastic composite preforming process. Compos Sci Technol. 2008;68:1822–30.

9. Rozant O, Michaud V, Bourban PE, Manson J-AE. A Model for the Consolidation of Warp-Knitted Reinforced Laminates. Polym Compos. 2001;22(3).

10. Werlen V, Rytka C, Michaud V. A numerical approach to characterize the viscoelastic behaviour of fibre beds and to evaluate the influence of strain deviations on viscoelastic parameter extraction. Compos Part A Appl Sci Manuf. 2021;143(October 2020):106315.

11. Bernet N, Michaud V, Bourban PE, Manson J-AE. An Impregnation model for the consolidation of Thermoplastic composites Made from Commingled Yarns. J Compos Mater. 1999;33(8):751–72.

12. Epstein PS, Plesset MS. On the stability of gas bubbles in liquid-gas solutions. J Chem Phys. 1950;18(11):1505–9.

13. Sato Y, Fujiwara K, Takikawa T, Sumarno, Takishima S, Masuoka H. Solubilities and diffusion coefficients of carbon dioxide and nitrogen in polypropylene, high-density polyethylene, and polystyrene under high pressures and temperatures. Fluid Phase Equilib. 1999;162(1–2):261–76.

14. Gebart BR. Permeability of Unidirectional Reinforcements for RTM. J Compos Mater. 1992;26(8):1100–33.

15. Dransfeld C, Utke I, Szmyt W, Guerra-nu C. Solving the inverse Knudsen problem : Gas diffusion in random fibrous media. 2021;620(April 2020).

Fatigue life prediction in viscoelastic materials

A. Vahid, Movahedi-Rad[a], Ghazaleh, Eslami[b], Thomas, Keller[c]

a : Composite Construction Laboratory (CCLab), École Polytechnique Fédérale de Lausanne (EPFL), Switzerland – abdolvahid.movahedirad@epfl.ch
b : Composite Construction Laboratory (CCLab), École Polytechnique Fédérale de Lausanne (EPFL), Switzerland.
c : Composite Construction Laboratory (CCLab), École Polytechnique Fédérale de Lausanne (EPFL), Switzerland.

Abstract: *This paper introduces a new fatigue life prediction methodology for viscoelastic materials in the tension-tension fatigue loading region. The model was established based on the total amount of energy dissipated during fatigue loading, and offers two main advantages with respect to existing models in the literature, i.e. it considers the creep effect on fatigue behavior and requires less input data. The model was applied to three different materials, an angle ply- and a cross ply glass/epoxy fiber-reinforced polymer composite as well as an epoxy adhesive. It was observed that the model predicted the fatigue life of the studied materials well at different stress ratios including those close to 1.0 where the creep effect was considerable. The model was used to plot constant life diagrams (CLDs), as well as to simulate cyclic-creep interaction and determine the cyclic- and creep-dominated regions in CLDs.*

Keywords: Fatigue; creep; energy dissipation; life prediction; cyclic-creep interaction;

1. Introduction

It is widely accepted that fatigue is one of the most common failure mechanisms in structural components, and pure static failure is rarely observed [1]. Among the different types of structural materials, viscoelastic materials such as polymers and polymer based-composites have attracted great attention on the part of researchers and designers because of their high stiffness-to-weight ratio, high corrosion resistance, and low thermal expansion coefficient. These materials are subjected to different cyclic loading patterns during their service life, including different loading levels and loading amplitudes, while their fatigue behaviors are highly dependent on the type of applied loading pattern [2]. The sensitivity of viscoelastic materials to the type of cyclic loading pattern is due to the fact that they possess two different groups of mechanical properties; namely, cyclic- and time-dependent mechanical properties [3,4,5,6,7]. It is well documented that the cyclic- and time-dependent phenomena can interact during cyclic loading, especially in polymers and matrix-dominated composites, even at room temperature, and the extent of their interactions depends on the material type, loading conditions, and environmental situations [4,5,6].

There are two approaches to model the fatigue behavior of viscoelastic materials. In the first case, which covers the majority of the existing models, they were formulated in a way that only the cyclic-dependent mechanical properties were taken into account. A main drawback of these models is that the effect of the time-dependent mechanical properties on fatigue life was ignored, and pure creep was thought of as fatigue with the stress ratio ($R = \sigma_{min} / \sigma_{max}$) of 1.0, which led to inaccurate fatigue life predictions as the stress ratio increased towards 1.0 [8]. In

  doi:10.5075/epfl-298799_978-2-9701614-0-0 published under CC BY-NC 4.0 license

the second approach, both cyclic- and time-dependent mechanical proprieties were considered in order to enhance the accuracy of the fatigue life prediction. Miyano et al. [3] introduced a model to predict the fatigue life at different stress ratios. To implement this model, two sets of *S-t* (stress-time) curves were required, one at the stress ratio of 1.0, obtained from a pure creep experiment, and another from a set of fatigue experiments at a stress ratio of 0.0. Reifsnider et al. in 2000 [9] suggested a new formulation based on the concept of the strength evolution integral (SEI) to calculate the remaining strength and life of composite materials and structures under mechanical, thermal, and environmental conditions that produce combinations of fatigue, creep, and stress rupture. Seven years later, Guedes [4] suggested a solution for SEI to predict the fatigue life for an arbitrary stress ratio. To make this model operational, the same two *S-t* curves as in Miyano's model are required as input data. In addition to *S-N* or *S-t* curves, a material's fatigue life can also be represented using constant life diagrams (CLDs) [8]. CLDs show the concurrent effect of mean stress (σ_m) and stress amplitude (σ_a) on the fatigue life of the examined material at different stress ratios. Existing CLD models offer a predictive tool for the estimation of the fatigue life of a material under loading patterns for which no experimental data exist; however, they have all been formulated based on only the cyclic-dependent mechanical properties [8].

According to the above review, the time-dependent mechanical properties should be considered in fatigue prediction methodologies for viscoelastic materials to enhance the prediction accuracy of the fatigue life at different stress ratios, especially those close to 1.0. In addition, it is well documented that many viscoelastic materials do not follow a linear cumulative damage law when cyclically loaded. Furthermore, due to the nonlinear nature of the interactions between time- and cyclic-dependent mechanical properties, fatigue behavior is nonlinearly dependent on the stress ratio [4]. Another unsolved aspect in the literature is the lack of knowledge regarding how much time- and cyclic-dependent mechanical properties participate in the overall fatigue behavior of the viscoelastic material, which is an important metric for a more application-dependent and reliable design in engineering structures. Therefore, a new method is needed to model the cyclic-creep interaction more accurately and consequently determine the creep- and cyclic-dominated stress levels and stress ratios.

The objective of this study is to present a novel model to predict the fatigue life of viscoelastic materials at different stress levels and stress ratios by introducing a new methodology based on the concept of the total dissipated energy (TDE). This model considers both cyclic- and time-dependent mechanical properties to predict *S-t* curves at different stress ratios including those close to 1, as well as pure creep. Unlike Miyano's model and the SEI model in which two sets of *S-t* curves were needed as input data, the proposed model requires only one *S-t* (or *S-N*) curve to predict the fatigue life at different stress ratios. The model is applied to different types of structural viscoelastic materials; namely, angle-ply composite, cross-ply composite, and epoxy adhesive. For each material, reference experimental results at the stress ratio of 0.1 were used as input data to predict fatigue behavior at two other stress ratios, i.e. 0.5 and 0.9 or 1.0. The accuracy of the predictions was evaluated by comparing them with experimental results obtained at the same stress ratios. The developed model is subsequently extended to simulate the cyclic-creep interaction at different stress ratios. Ultimately, the model serves to establish a new CLD formulation in which the creep- and cyclic-dominated regions are also determined.

  doi:10.5075/epfl-298799_978-2-9701614-0-0

2. Fatigue life prediction methodology

When cyclic loading is applied to a viscoelastic material, hysteresis loops are formed in the strain-stress coordinate system, see Figure 1a. The hysteresis area is a measure of the total dissipated energy per cycle (w_{diss}). During a load-controlled fatigue experiment, the hysteresis loops can shift under fatigue mean stress (σ_m), even at room temperature, indicating the presence of creep, and the evolution of the average strain per cycle (ε_m) can be monitored to describe this creep behavior [6].

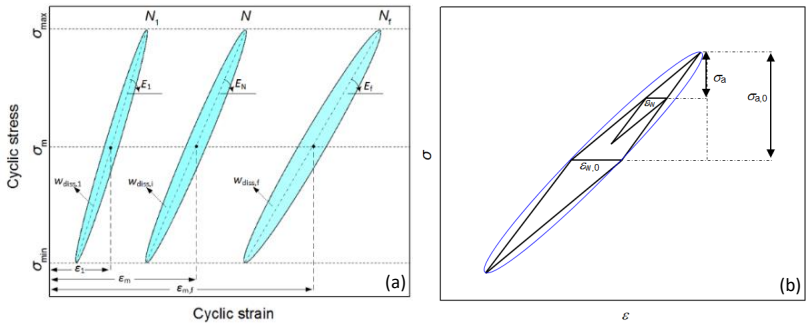

Figure 1. *(a) Schematic representation of hysteresis loops during tension-tension fatigue experiment, (b) Representation of hysteresis loop area and corresponding approximation of area by two triangles.*

The proposed prediction methodology was established based on the amount of the specimen's total dissipated energy (TDE), *W,* during its life under loading at the different stress levels and stress ratios. In fatigue experiments at the stress ratio of -1.0, energy dissipation was attributed to only the cyclic loading and therefore *W* was set equal to W_{cyclic}. At the stress ratio of 1.0, the origin of the energy dissipation was attributed to pure creep and TDE was set equal to W_{creep}. At other stress ratios, *W* was set equal to the algebraic sum of W_{cyclic} and W_{creep}, as follows:

$$W = W_{\text{cyclic}} + W_{\text{creep}} \tag{1}$$

W_{cyclic} was defined by the summation of all the individual stress strain hysteresis areas measured throughout the lifetime of the specimen [6,10].

$$W_{cyclic} = \sum_{i=1}^{N_f} w_{diss,i} \tag{2}$$

where $w_{diss,i}$ denotes the hysteresis area per cycle for the i^{th} cycle, and N_f is the number of cycles to failure. Since during a fatigue experiment, all the fatigue cycles cannot normally be recorded, W_{cyclic} was obtained here by calculating the area under the graph of w_i versus *N* from the first to the last cycle according to Eq. (3).

$$W_{\text{cyclic}} = \int_1^{N_f} w_{\text{diss}}(N)dN \tag{3}$$

The total creep energy in a viscoelastic material, E_{vis}, is equal to [11]:

$$E_{\text{vis}} = \int_0^t \sigma(\tau)\frac{\partial\varepsilon(\tau)}{\partial\tau}d\tau \tag{4}$$

where τ is the characteristic time. By solving this equation for a specimen loaded under σ_0 with a creep strain of ε_f at the moment of failure, $t = t_f$, W_{creep} was calculated by multiplying σ_0 by ε_f.

$$W_{\text{creep}} = \sigma_0\,\varepsilon_{\text{f}} \tag{5}$$

  doi:10.5075/epfl-298799_978-2-9701614-0-0

Due to the inherent power-law nature of fatigue-related phenomena in relation to fatigue life, the evolution of W_{cyclic} as a function of the fatigue maximum stress, σ_{max}, can be described by Eq. (6) in which α and β were the model parameters, as follows:

$$W_{\text{cyclic}} = \alpha\sigma_{\text{max}}^{\beta} \tag{6}$$

Another power-law equation was employed to show the variation of W_{cyclic} with respect to the fatigue life in which η and γ are model parameters, and $t_{\text{f,cyclic}} = N_f/f$, where f denotes the fatigue experiment frequency.

$$W_{\text{cyclic}} = \eta t_{\text{f,cyclic}}^{\gamma} \tag{7}$$

The variation of W_{creep} versus the constant applied stress and creep life was expressed by two separate power-law equations as shown in Eq. (8) and Eq. (9) respectively in which *a*, *b*, *g*, and *k* were model parameters:

$$W_{\text{creep}} = a\sigma_{\text{m}}^{b} \tag{8}$$

$$W_{\text{creep}} = g t_{\text{f,creep}}^{k} \tag{9}$$

To simulate the stress ratio effect on W_{cyclic}, a new function, $\psi_{\text{cyclic}}(R)$, was introduced in Eq. (7) in which $\psi_{\text{cyclic}}(R)$ was defined as the ratio of the hysteresis loop area at the stress ratio of *R* over the hysteresis loop area at a reference stress ratio (R_0).

$$W_{\text{cyclic}} = \psi_{\text{cyclic}}(R)\, \eta t_{\text{f,cyclic}}^{\gamma} \tag{10}$$

$$\psi_{\text{cyclic}}(R) = \frac{w_{\text{diss,i}}(R)}{w_{\text{diss,i}}(R_0)} \tag{11}$$

Hahn and R.Y. Kim [12] suggested an approximation to model the hysteresis loop area by using two triangles as shown in Figure 1b. They showed that the width of the triangle base, ε_{w}, was proportional to the stress amplitude, σ_{a}, and proposed the following equation to describe the fatigue hysteresis loop area:

$$w_{\text{diss}} = \varepsilon_{\text{w}}\, \sigma_{\text{max}}(1 - R)/2 \tag{12}$$

By implementing Eq. (12) into Eq. (11) for two stress ratios of R and R_0 at constant σ_{max}:

$$\psi_{\text{cyclic}}(R) = \frac{\varepsilon_{\text{w}}}{\varepsilon_{\text{w,0}}} \frac{(1-R)}{(1-R_0)} \tag{13}$$

By assuming that the cyclic stiffness would be comparable at different stress ratios and changes in cyclic stiffness would not significantly affect the hysteresis loop area, $\frac{\varepsilon_{\text{w}}}{\varepsilon_{\text{w,0}}}$ was calculated using Thales's theorem (Figure 3), and substituted in the previous equation, which yielded:

$$\psi_{\text{cyclic}}(R) = \left[\frac{(1-R)}{(1-R_0)}\right]^2 \tag{14}$$

To simulate the effect of the stress ratio on W_{creep}, a new function of $\psi_{creep}(R)$ was introduced in Eq. (9) in which $\psi_{\text{creep}}(R)$ is the ratio of W_{creep} at the stress ratio of *R* over W_{creep} at the stress ratio R_0 ($W_{creep,0}$).

$$W_{\text{creep}} = \psi_{\text{creep}}(R)\, g t_{\text{f}}^{k} \tag{15}$$

$$\psi_{\text{creep}}(R) = \frac{W_{\text{creep}}}{W_{\text{creep},0}} = \frac{\sigma_{\text{m}}\varepsilon_{\text{m,f}}}{\sigma_{\text{m},0}\varepsilon_{\text{m,f},0}} \tag{16}$$

In viscoelastic materials, a power function of stress has been widely used by various authors to express the stress-strain relationship, e.g. [13]:

$$\varepsilon_{\text{f}} \propto \sigma_{\text{m}}^{n} \tag{17}$$

where *n* is a material constant. Knowing $\sigma_{\text{m}} = \sigma_{\max}(1+R)/2$, $\psi_{\text{creep}}(R)$ was introduced as:

$$\psi_{\text{creep}}(R) = \left[\frac{(1+R)}{(1+R_0)}\right]^{1+n} \tag{18}$$

For the cyclic part, by equalizing Eq. (6) and Eq. (10), as shown in Eq. (19), the relationship between $t_{\text{f,cyclic}}$ and $\sigma_{\max}$ was obtained as a function of the stress ratio:

$$\alpha\sigma_{\max}^{\beta} = \psi_{\text{cyclic}}(R)\, \eta t_{\text{f,cyclic}}^{\gamma} \text{ or } t_{\text{f,cyclic}} = \left(\frac{\alpha}{\eta\, \psi_{\text{fatigue}}(R)}\right)^{1/\gamma} (\sigma_{\max})^{\beta/\gamma} \tag{19}$$

Concerning the creep part, $t_{\text{f,cyclic}}$ was determined by equalizing Eq. (8) and Eq. (15) (see Eq.(20)):

$$a\sigma_{\text{m}}^{b} = \psi_{\text{creep}}(R)\, g t_{f}^{k} \text{ or } t_{f,creep} = \left(\frac{a}{g\psi_{\text{creep}}(R)}\right)^{1/k} \sigma_{\text{m}}^{b/k} \tag{20}$$

To predict the *S-t* curve at an arbitrary stress ratio, Eq. (21) is proposed in which both $ln(t_{\text{f,cyclic}})$ and $ln(t_{\text{f,creep}})$, were taken into account via a linear interpolation:

$$ln(t_{\text{f}}) = \left(\frac{1-R}{2}\right) ln(t_{\text{f,cyclic}}) + \left(\frac{1+R}{2}\right) ln(t_{\text{f,creep}}) \tag{21}$$

where 0<R<1, and temperature as well as loading rate or frequency are constant.

3. Experimental data

The application and prediction accuracy of the suggested model were evaluated under tension-tension fatigue loading for three different materials: 1) a fully-cured angle-ply glass/epoxy fiber-reinforced polymer (FRP) composite with $[\pm 45]_{2s}$ layout (Material 1), 2) a cross-ply glass/epoxy composite with $[90,0]_{2s}$ layout (Material 2), both with a fiber content of 62% by volume, and 3) an epoxy-based resin with the commercial name SikaDur 330 (Material 3). Typical fatigue hysteresis loops of the studied materials at the selected stress levels are presented in Figure 2.

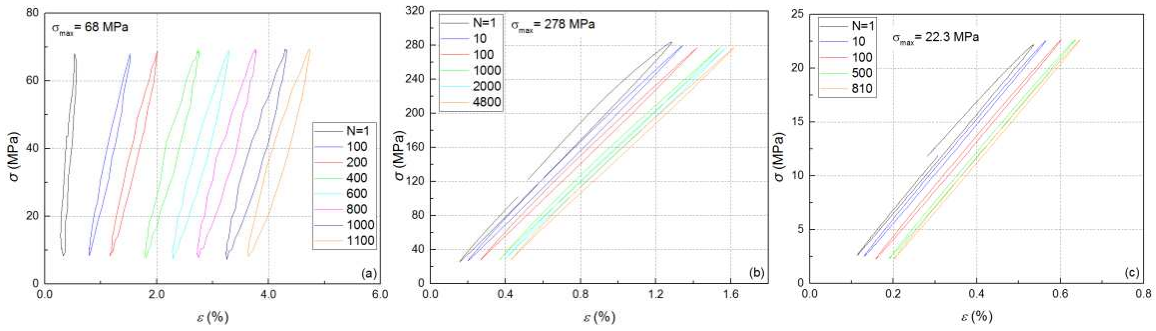

Figure 2. *Variation of hysteresis loops under cyclic loading at one selected stress level in different materials (a) Material 1, (b) Material 2, and (c) Material 3.*

4. Model application

The experimental data obtained at the stress ratio of 0.1 was used as the input data to determine the nine model parameters. Firstly, W_{cyclic} was calculated for all the experiments according to Eq. (3). Subsequently, the variation of the obtained W_{cyclic} was plotted against σ_{max} for all three materials. By fitting Eq. (6) to the experimental data points for each material, the two model parameters α, β were determined. Two other model parameters, η and γ, were estimated by fitting Eq. (7) to the experimental data points. W_{creep} was calculated at the stress ratio of 0.1 for all materials according to Eq. (5). By fitting Eq. (8) to the experimental data points, the two model parameters *a* and *b* were estimated. In order to determine the model parameters *g* and *k*, first the evolution of the W_{creep} against t_f in a double-logarithmic scale was plotted, and then Eq. (9) was fitted to the experimental data points. The last model parameter, *n*, was obtained by fitting Eq. (17) into the experimental data points. The model parameters of α, β, η, γ, *a*, *b*, *k*, *g*, and *n* obtained for Material 1 are 9.35×10^{22}, -11.48, 0.81, 0.82, 3.35×10^{-4}, 2.21, 2.22, -0.14, 1.21, respectively. Similarly, in Material 2, the model parameters are 6.88×10^{16}, -5.85, 2.06, 0.72, 1.03×10^{-2}, 1.01, 3.65, -0.11, 0.014, and finally in Material 3 they are 1.03×10^{7}, -4.72, 1.40×10^{-2}, 0.72, 3.11×10^{-4}, 1.99, 0.27, -0.22, 0.99.

5. Model validation

Figure 3 shows the *S-t* curve of the studied materials at the stress ratio of 0.1, which served as the input data, together with the predicted *S-t* curves at two selected stress ratios, i.e. 0.5 and 0.9 or 1.0. The predictions were validated by comparing them with the experimental results. Figure 3a and show that the proposed model predicted the fatigue life well at the stress ratio 0.5 for Material 1. At the stress ratio of 1.0, i.e. pure creep loading, the predicted *S-t* curve was in a similar good agreement with the experimental data points, although slightly overestimated. Figure 3b shows that the predicted *S-t* curves followed the experimental results well at both stress ratios of 0.5 and 0.9, although they were slightly overestimated at higher stress levels. In Material 3, the predicted *S-t* curves again corresponded well with the experimental data points at both stress ratios of 0.5 and 0.9 as shown in Figure 3c. It is noted that at stress ratio 0.9, runouts were observed at low stress levels, indicated with an arrow.

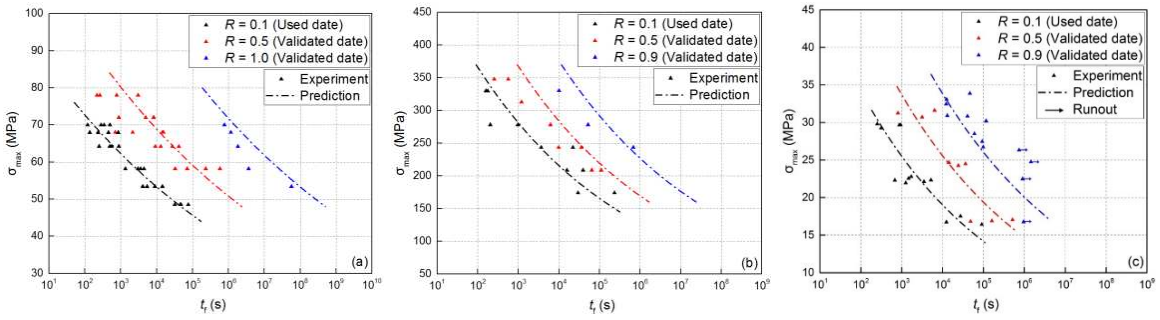

Figure 3. *S-t_f curves showing experimental results and predicted lifetime at different stress ratios in different materials (a) Material 1, (b) Material 2, and (c) Material 3.*

6. Modeling of CLD

The CLDs of the studied materials in the tension-tension sector were predicted according to Eq. (21) for the three studied materials and are shown in Figure 4. In each material, the constant life lines ranged between 10^3s and 10^6s. To implement the experimental data into the predicted

  doi:10.5075/epfl-298799_978-2-9701614-0-0

CLDs, power curve fitting was performed on all available experimental fatigue data at each stress ratio. In Material 1 (Figure 4a), at the stress ratio 0.5, there was a good agreement between the simulated constant life lines and the experiments; however, the prediction slightly underestimated the fatigue life at the low constant life line and overestimated it at the high constant life line. At the stress ratio 1.0, the predicted constant life lines slightly underestimated the fatigue life. In Material 2 (Figure 4b), at stress ratios of 0.5 and 0.9, the predicted constant life lines were in good agreement with the experiments at the high constant life line while they were underestimated at the low constant life line. The prediction results for Material 3 (Figure 4c) were in acceptable agreement with the experiments at the stress ratio of 0.5. At the stress ratio 0.9, at low constant life, the fatigue life prediction underestimated the fatigue life while at high constant life it was overestimated.

The participation of the cyclic and creep parts in the cyclic-creep interaction was set as equal to the total amount of energy dissipated by each, W_{cyclic} (Eq. (10)) and W_{creep} (Eq. (15)), respectively at different stress levels and stress ratios. Accordingly, if W_{cyclic} greater than W_{creep}, the fatigue behavior was cyclic-dominated while it was creep-dominated when W_{creep} was greater than W_{cyclic}. In this case, at the stress ratio R, W_{cyclic} might be equal to W_{creep} at $t_{f,trans}$, which was concluded that the fatigue behavior was equally governed by cyclic-dependent mechanical properties as well as time-dependent mechanical properties. In Figure 4, it can be seen that a major part of the CLDs was located in the cyclic-dominated region while the creep-dominated region was limited to the zone with higher stress ratios and lower constant life lines.

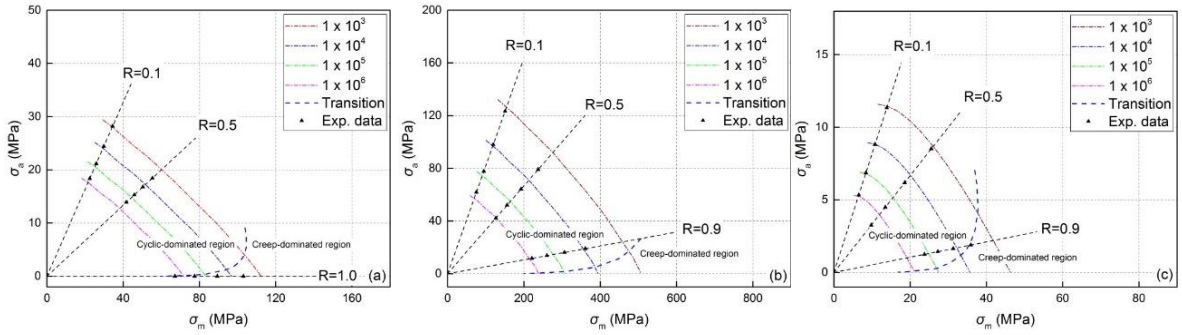

Figure 4. *Constant life diagrams (CLDs) for* $t_f = 10^3s - 10^6s$ *for different materials; (a) Material 1, (b) Material 2, (c) Material 3.*

7. Conclusions

In this work, a novel methodology to predict the fatigue life of viscoelastic materials in the tension-tension loading state was presented based on the total amount of energy that the materials dissipated during the cyclic loading (W_{cyclic}) and creep loading (W_{creep}). This model offers two main advantages with respect to existing models in literature, i.e. 1) the cyclic-creep interaction is considered to more accurately predict the number of cycles to failure at the different stress ratios, especially those close to 1.0, and 2) it requires less experimental effort. The experimental data obtained at the stress ratio of 0.1 was used as the input data to predict the fatigue life at other stress ratios. To evaluate the validity of the proposed model, the predicted results were compared with experimental results at the same stress ratios. It was observed that the predicted *S-t* curves were in good agreement with the experimental results. The developed model served as a new CLD formulation. The simulated constant life lines were compared with the experimental results and they were in good agreement at different stress

  doi:10.5075/epfl-298799_978-2-9701614-0-0 published under CC BY-NC 4.0 license

ratios, including those close to 1.0, as well as for pure creep. A new definition of cyclic-creep interaction was proposed, in which the participation of the cyclic and creep parts in the cyclic-creep interaction was set equal to the amounts of W_{creep} and W_{cyclic}, respectively. Finally, the cyclic- and creep-dominated regions were determined, and it was observed that the creep-dominated region was limited to the zone with higher stress ratios and lower constant life lines.

8. References:

[1] Samborsky D, Mandell JF, Miller DA. Creep/fatigue response of resin infused biaxial (Double bias) glass fabric laminates in reversed loading. In 32nd ASME Wind Energy Symposium. 2014.
[2] Brøndsted P, Lilholt H, Lystrup A. Composite materials for wind power turbine blades. Annual Review of Maters Research 2005; 35:505-538.
[3] Miyano Y, Nakada M, McMurray M K, Muki R. Prediction of flexural fatigue strength of CRFP composites under arbitrary frequency, stress ratio and temperature. Journal of Composite Materials 1997; 31(6):619-638.
[4] Guedes R M. Durability of polymer matrix composites: Viscoelastic effect on static and fatigue loading. Composites Science and Technology 2007; 67(11-12):2574-2583.
[5] Vieille B, Albouy W, Taleb L. About the creep-fatigue interaction on the fatigue behaviour of off-axis woven-ply thermoplastic laminates at temperatures higher than Tg. Composites Part B: Engineering 2014; 58:478-486.
[6] Movahedi-Rad AV, Keller T, Vassilopoulos AP. Fatigue damage in angle-ply GFRP laminates under tension-tension fatigue. International Journal of Fatigue 2018; 109:60-69.
[7] Movahedi-Rad AV, Keller T, Vassilopoulos AP. Creep effects on tension-tension fatigue behavior of angle-ply GFRP composite laminates. International Journal of Fatigue 2019; 123:144-156.
[8] Vassilopoulos, AP, Manshadi BD, Keller T. Influence of the constant life diagram formulation on the fatigue life prediction of composite materials. International journal of fatigue 2010; 32(4):659-669.
[9] Reifsnider K, Case S, Duthoit J. The mechanics of composite strength evolution. Composites Science and Technology, 2000; 60(12-13):2539-2546.
[10] Kliman V, Bílý M. Hysteresis energy of cyclic loading. Materials Science and Engineering 1984; 68(1):11-18.
[11] Guedes RM. Creep and fatigue in polymer matrix composites. Woodhead Publishing. 2019.
[12] Hahn HT, Kim RY. Fatigue behavior of composite laminate. Journal of Composite Materials 1976; 10(2):156-180.
[13] Findley WN, Davis FA. Creep and relaxation of nonlinear viscoelastic materials. Courier Corporation. 2013.

  doi:10.5075/epfl-298799_978-2-9701614-0-0

PREDICTING FLEXURAL PROPERTIES OF CARBON FIBRE REINFORCED THERMOPLASTICS SHEET MOULDING COMPOUNDS

Xiaodong Xu[a], Andre Jesus[a], Yi Wan[b], Qian Gao[b], Xiaohang Tong[b], Ruochen Xu[b], Zihao Zhao[b], Jun Takahashi[b]

a: University of the West of England, Coldharbour Lane, Frenchay Campus, Bristol BS16 1QY, UK– xiaodong.xu@uwe.ac.uk
b: Department of Systems Innovation, School of Engineering, The University of Tokyo
7-3-1 Hongo, Bunkyo ku, Tokyo 113-8656, JAPAN

Abstract: *In this paper, a stochastic morphological modelling framework previously developed for tension is further developed to predict flexural properties of Carbon Fibre Reinforced Thermoplastic Sheet Moulding Compound (CFRTP-SMC). The flexural modulus is predicted using a Monte Carlo simulation and classical laminate theory, and the flexural strength is predicted by using Weibull theory which accounts for fibre discontinuities. The results are validated against the experimental results from the Takahashi Lab of the University of Tokyo. The model will enable rapid designs of CFRTP-SMC structures with less testing, leading to potential cost reduction in structural applications.*

Keywords: Discontinuous reinforcement; Strength; Bending; Moulding compounds; Carbon Fibre Reinforced Thermoplastics (CFRTP)

1. Introduction

Carbon Fibre Reinforced Thermoplastics (CFRTP) materials have received substantial consideration from the automotive industry due to their high-performance characteristics, low weight and recyclability. An advanced material called Carbon Fibre Reinforced Thermoplastics Sheet Moulding Compounds (CFRTP-SMC) made of ultra-thin chopped carbon prepreg tapes has shown promising tensile properties [1] e.g. significantly improved tensile strength compared to the other SMCs. CFRTP-SMC material consistently exhibited fibre-dominant failures under tension and bending [2].

The “weakest-link” theory was originally introduced by Weibull [3] to explain size effects in solids. It assumes that when the weakest link in the chain breaks, the entire chain will fail, which makes it suitable for predicting brittle failures of solids. Weibull theory has been used to predict fibre failures in continuous fibre composites [4] but has not been adopted for discontinuous fibre CFRTP-SMC material.

A stochastic morphological modelling framework was established to predict the tensile behaviour of the CFRTP-SMC material [5]. Based on tape properties from their statistical distributions, the tensile properties such as Young’s modulus and tensile strength of a laminate were accurately predicted. The previous work was validated against the published results from the Takahashi Lab and demonstrated excellent accuracy and reliability of the proposed modelling framework.

In this paper, the existing modelling framework is further developed to predict flexural properties. The flexural modulus is predicted using a Monte Carlo simulation and classical

  doi:10.5075/epfl-298799_978-2-9701614-0-0

laminate theory, and the flexural strength is predicted by using Weibull theory which accounts for fibre discontinuities via a stress concentration factor. The results are validated against the experimental results from the Takahashi Lab [2]. The model is fast to run and is suitable for designs of structures made of CFRTP-SMC material.

2. Experiments

2.1 Material Fabrication

Geometrical and material properties used in the current work are shown in Table 1. The tapes are made of TR 50S carbon fibre tows (Mitsubishi Chemical Co., Japan) spread to form ultra-thin prepreg sheets 44 μm impregnated with DIAMIRON™ C polyamide-6 resin (Mitsubishi Chemical Co., Japan). The resulting CFRTP-SMC plate was processed by compression moulding at 250°C and 5 MPa pressure for 10 mins.

Table 1: Tape geometrical and material information [2, 5].

Property	Value	Property	Value
Orientation angle [°]	0 - 180	E_1 [GPa]	105
Tape width [mm]	5	E_2 [GPa]	4
Tape length [mm]	19	G_{12} [GPa]	1.2
Tape thickness [mm]	0.044	v_{12}	0.3
Tape volume fraction	54%	v_{21}	0.01

2.2 Four Point Flexural Test

The current CFRTP-SMC laminate with ultra-thin chopped carbon tapes, which was previously referred to as SM-CTT materials in the Takahashi Lab [1, 2], was cut into 6 off 125 by 35 by 3.1 [mm] specimens and tested on a four-point bending jig. They exhibited fibre-dominant failure at the tension side [2]. This is the same failure mode as what the current model was initially developed for under tension [5], so the same modelling framework is adopted to the new bending load case.

3. Models

The current stochastic morphological modelling framework is established in Matlab (MathWorks, US). The code is based on Monte Carlo methods and classical laminate theory. A novel Weibull failure criterion for discontinuous fibres is introduced, considering tape overlaps.

3.1 Laminate Generation

The moulding area, where chopped tapes are randomly distributed, is a rectangle offset by the length of one tape from the boundary of the laminate, as displayed in Fig. 1. The coordinates of each tape centre and its rotation angle follow uniform distributions. A total of 20 samples were randomly generated and run, which is significantly more than physical sample number of 6 [2].

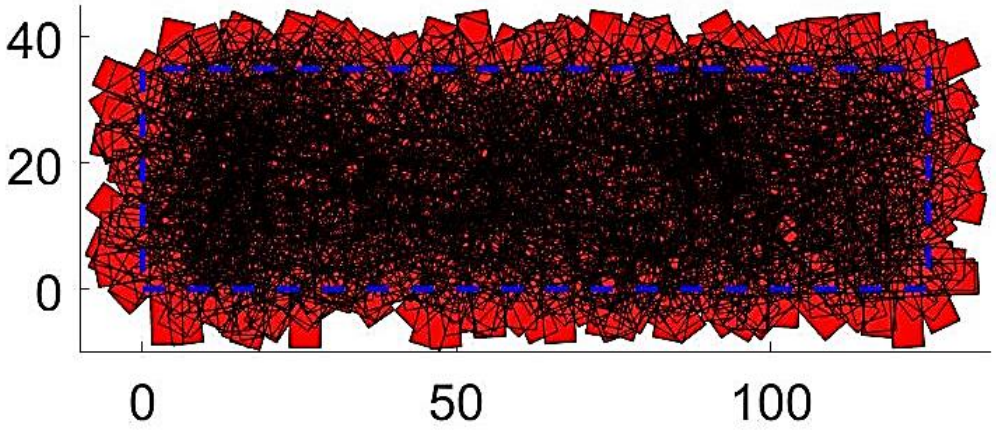

Figure 1. A laminate formed by random chopped tapes with the blue boxing indicating the size of the specimen

Although the current model is 2D, a "layer" concept is introduced to assist the calculation of flexural modulus and strength. The laminate is divided into multiple "layers", each of which has a thickness of 44 µm. A 3.1 mm thick laminate has approximately 70 "layers".

The elastic stiffness matrix of the laminate has been formulated using classical laminate theory

$$\mathbf{K} = \frac{1}{1-\upsilon_{12}\upsilon_{21}}\begin{bmatrix} E_{11} & \upsilon_{21}E_{11} & 0 \\ \upsilon_{12}E_{22} & E_{22} & 0 \\ 0 & 0 & G_{12}(1-\upsilon_{12}\upsilon_{21}) \end{bmatrix} \quad (1)$$

where the material elastic properties are listed in Table 1.

The transformed elastic matrix $\bar{\mathbf{K}}$ is computed by successive axes rotation and addition of the contribution from each individual tape according to Eq. (2).

$$\bar{\mathbf{K}} = \mathbf{T^{-1}KRTR^{-1}} \quad (2)$$

where **T** is the transformation matrix and **R** is the Reuter's matrix.

The sum of all transformed elastic matrix over all tapes are also calculated.

$$\bar{\mathbf{K}}_{\boldsymbol{t}} = \sum_{i=1}^{N_t} \mathbf{T^{-1}KRTR^{-1}} \quad (3)$$

where $\bar{\mathbf{K}}_{\boldsymbol{t}}$ is the total stiffness matrix, N_t is the total number of tapes.

A moment ***M*** per unit width is ramped up and applied to the laminate. It is related to its mid-plane strain ***ε*** curvature ***κ***.

$$\begin{Bmatrix} \mathbf{0} \\ \mathbf{M} \end{Bmatrix} = \begin{bmatrix} \boldsymbol{A} & \boldsymbol{B} \\ \boldsymbol{B} & \boldsymbol{D} \end{bmatrix} \begin{Bmatrix} \boldsymbol{\varepsilon} \\ \boldsymbol{\kappa} \end{Bmatrix} \quad (4)$$

where ***A***, ***B*** and ***D*** are the extensional, coupling and bending matrices, respectively. The ***A***, ***B*** and ***D*** matrices are normalised by the number of chopped tapes per "layer", to account for the average effect of randomly oriented tapes within the same "layer" height. They are directly related with the total stiffness matrix $\bar{\mathbf{K}}_{\boldsymbol{t}}$.

  doi:10.5075/epfl-298799_978-2-9701614-0-0

The mid-plane strain $\boldsymbol{\varepsilon}$ curvature $\boldsymbol{\kappa}$ are then converted into the fibre-direction stress of the chopped tapes, σ_u, according to Eq. (5) in which $\boldsymbol{z}$ is the location of the "layer" where the tapes are located.

$$\sigma_u = \bar{\mathbf{K}}\varepsilon + z\bar{\mathbf{K}}\kappa \tag{5}$$

The moment $\boldsymbol{M}$ is translated into an equivalent flexural stress σ_B, via Eq. (6) in which l_t is the laminate thickness. σ_B at failure will be compared against the experimental result.

$$\sigma_B = 6\boldsymbol{M}/{l_t}^2 \tag{6}$$

The elastic flexural modulus, E_B, is from $\boldsymbol{D}$ matrix according to Eq. (7). E_B will also be compared against the experimental result.

$$E_B = 12\boldsymbol{D}_{11}/{l_t}^3 \tag{7}$$

3.2 Weibull Failure Criterion

In the previous work [4], fibre failures in continuous fibre composites assumed an equal probability of survival between the 0° elements in the model and a unit volume of material, and the adopted criterion was a function of both the volume and the stress through the Weibull integration.

$$\sum_{i=1}^{\text{Number of } 0^\circ \text{elements}} \boldsymbol{V_i}\left(\boldsymbol{\sigma_{u,i}}/\boldsymbol{\sigma_{\text{unit}}}\right)^{\boldsymbol{m}} = \mathbf{1} \tag{8}$$

where $\sigma_{u,i}$ is the fibre-direction stress in the 0° elements, V_i is the volume of the 0° elements, σ_{unit} is the tensile strength of a unit volume of material and m is the Weibull modulus. When Eq. (8) is satisfied, fibre failure has been reached.

For the current CFRTP-SMC material which exhibits fibre-dominant failure, the same fibre failure criterion based on Weibull theory can be used. The fibre failure parameters are assumed as σ_{unit} = 3131 MPa and m = 41, based on similar IM7 fibres (Hexcel Co., US) reported by Xu et al. [6], but some modifications to Eq. (8) are required to address fibre discontinuities.

Chopped tapes with an angle smaller than 1° are identified Fig. 2(a). They are referred to as "critical tapes". One degree is chosen because it is the typical fibre misalignment angle in fibre composite structures. These "critical tapes" are expected to have the highest stress in the fibre direction, so most likely to fail. According to Weibull theory, the failures of these "critical tapes", i.e. the weakest link, will trigger the failure of the laminate.

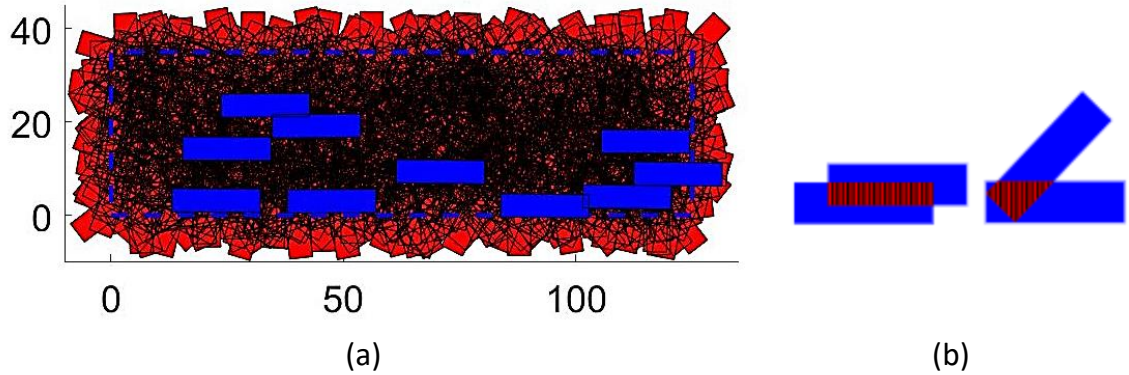

Figure 2. "Critical tapes" marked in blue (a) and their overlapped area with the other tapes (b)

Within the range of these "critical tapes", they are seen as continuous. The other angled tapes which touch these "critical tapes" in each layer are seen as discontinuous. The force carried by the other angled tapes therefore needs to be transferred to the "critical tapes". This results in an increase of stress in the "critical tapes" through a Stress Concentration Factor (SCF). The SCF is defined as the ratio between the resultant loading-direction stress taken by the "critical tapes" $\sigma_c + \sigma_a$, including those transferred from the overlapped angled tapes σ_a, and the fibre-direction stress in the "critical tapes" without considering force sharing σ_c, i.e. SCF = $(\sigma_c + \sigma_a)/ \sigma_c$. σ_a is calculated from the force shared through a overlapped area as shown in Fig. 2(b).

For each "critical tape", its fibre-direction stress, $\sigma_{u,}$ will be updated by multiplying the SCF and seen as a 0° element in Eq. (8). Then all "critical tapes" are integrated in as a failure check. Once the condition in Eq. (8) is fulfilled, the flexural strength of the laminate, σ_B, can be determined at the failure moment step according to Eq. (6).

4. Results

The predicted flexural modulus and flexural strength are compared against the experimental results reported by Nakashima et al. [2] as shown in Fig. 3. The preliminary modelling results show that the average flexural modulus is 3.4% higher and the average flexural strength is 12.9% higher than the average corresponding experimental results. The measured average flexural strength values from [2] always fall within the standard deviation of the simulations which is much larger than that in the tests. The agreement is reasonable considering the simplicity of the current modelling framework. It is also computationally efficient, with a run time of just over 8 minutes for each case.

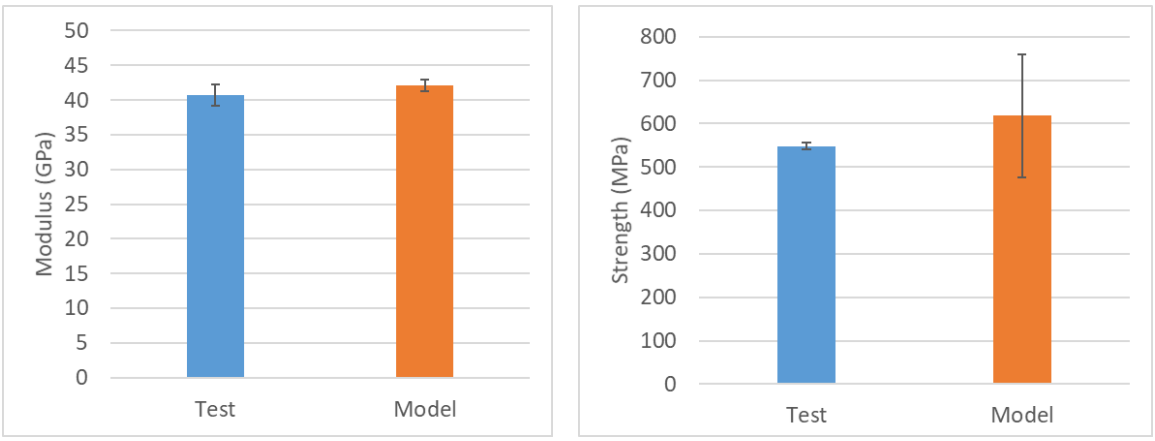

(a) (b)

Figure 3. Results comparison between tests and the model for flexural modulus (a) and flexural strength (b)

5. Discussion

The limitations of the current modelling framework are: 1) the model does not consider delamination or tape debonding failure mode, which may only be suitable for the thin-ply thermoplastic prepregs such as the current CFRTP-SMC; 2) the model has not been validated against different specimen thicknesses or tape sizes due to lack of experimental results.

There is scope to further develop the current model for different type of SMC materials and more loading scenarios such as compression, impact etc.

  doi:10.5075/epfl-298799_978-2-9701614-0-0

6. Conclusions

An existing stochastic morphological modelling framework originally for tension has been further developed to predict flexural properties of Carbon Fibre Reinforced Thermoplastic Sheet Mouding Compounds (CFRTP-SMC). The model is suitable for CFRTP-SMC material which exhibits fibre-dominant failures at the tension side under bending. For a simple model in a preliminary study, it captures the flexural modulus and flexural strength reasonably well. The model is computationally efficient so suitable for structural analyses.

Acknowledgements

This work was financially supported by the Vice Chancellor's Early Career Research Development Awards from the University of the West of England in the UK. The work was also partially funded by the Royal Society (IEC\R3\213017) and Japan Society for the Promotion of Science (JPJSBP 120225702).

7. References

1. Wan Y & Takahashi J, Tensile and compressive properties of chopped carbon fiber tapes reinforced thermoplastics with different fiber lengths and molding pressures, Composites: Part A 87 (2016) 271–281.
2. Nakashima Y, Suganuma H, Yamashita S & Takahashi J, Influence of strand dispersion method on mechanical properties of randomly orientated carbon fibre strand thermoplastic composites, 21st International Conference on Composite Materials, Xi'an, China (2017).
3. Weibull W. A statistical distribution function of wide applicability. Journal of applied mechanics 18 (1951) 293–297
4. Xu X, Wisnom MR, Li X, Hallett SR. A numerical investigation into size effects in centre-notched quasi-isotropic carbon/epoxy laminates. Composites Science and Technology 111 (2015) 32–39
5. Jesus A & Xu X, Rapid prediction of fibre-dominant tensile failure in randomly oriented strands, submitted (2022).
6. Xu X, Wisnom MR, Hallett SR. Deducing the r-curve for trans-laminar fracture from a virtual over-height compact tension (OCT) test. Composites Part A: Applied Science and Manufacturing 118 (2019) 162–170

  doi:10.5075/epfl-298799_978-2-9701614-0-0

Composites Meet Sustainability – Proceedings of the 20th European Conference on Composite Materials,
ECCM20. 26-30 June, 2022, Lausanne, Switzerland

RECENTLY PROPOSED FAILURE CRITERIA AND MODELING TECHNIQUES FOR FIBROUS COMPOSITES

Young Kwon[a], Carlos Diaz-Colon[b], Stanley Defisher[b]

a: Naval Postgraduate School, Monterey, California, USA – email) ywkwon@nps.edu
b: Naval Postgraduate School, Monterey, California, USA

Abstract: *This paper presents recently proposed failure criteria and modeling techniques for fibrous composites. One of them is a new set of failure criteria for fibrous polymer composites, which can be applied to specimens with or without any cutout such as cracks, circular or noncircular holes. The criteria have two parts. The first part is the stress condition which determines the locations for potential failure. The second part is the stress gradient condition which provides the failure path. For a material to fail at a critical location, both conditions must be satisfied simultaneously. A multiscale modeling technique is also presented for fibrous composites such that failure criteria can be applied to the fiber and matrix materials directly rather than the smeared lamina layer. The failure modes in this model are fiber break, matrix cracking, and fiber/matrix interface debonding.*

Keywords: Failure criteria; notches; multiscale modeling

1. Introduction

Prediction of failure in load-carrying structural members is critical for their reliable design. Laminated fibrous composites have many different failure modes so that various failure criteria have been proposed. Almost all of the failure criteria were developed for specimens without any hole or crack. If there is a crack, fracture mechanics has been used to predict crack growth. On the other hand, if there is a hole, other failure criteria have been proposed. Those criteria used a critical distance from the edge of the hole. If the stress at the critical location reaches the failure strength of the material, failure is considered to occur. Or the average stress from the edge of the hole to a critical distance was used for the failure criteria instead of the stress at the single critical location.

Very recently, a set of unified failure criteria were proposed for brittle materials regardless of whether a specimen has a crack, a hole, or none of them [1,2]. In addition, a multiscale technique was also presented to simulate progressive failure leading to final fracture. The multiscale approach links microscale (i.e., fiber and matrix materials) to macroscale (i.e., smeared composite materials) bidirectionally. Then failure criteria are applied at the fiber and matrix materials level in terms of their micro-stresses and micro-strains.

This paper presented both the unified failure criteria as well as the multiscale approach. They were applied to polymer composites, especially laminated carbon fiber composites. Analytical prediction of failure loads, failure modes, or failure locations using numerical modeling techniques were compared to the experimental results to validate the failure criteria and the modeling technique. The next two sections describe briefly the new failure criteria as well as the multiscale technique. Then, specimens with various kinds of holes were studied using the new

  doi:10.5075/epfl-298799_978-2-9701614-0-0

failure criteria. Finally, failure modes and failure locations were predicted using the multiscale approach for composite plates subjected to underwater shock loading.

2. Unified Failure Criteria for Brittle Materials

The newly proposed failure criteria have two parts. For failure to occur regardless of a hole or a crack, both criteria must be satisfied. The first part is based on the stress magnitude. For brittle materials, the maximum normal stress is used for the first part. In other words, the maximum normal stress must be equal to or greater than the failure strength of the material. This can be stated as

$$\left|\sigma_{\max}\right| \geq \left|\sigma_{fail}\right| \tag{1}$$

where $\sigma_{\max}$ is the maximum normal stress and σ_{fail} is the failure strength which is nominally obtained using tensile test coupons. The second part of the criteria is based on the stress gradient as stated below:

$$\sigma_{\max}^{3}\left|\frac{\partial\sigma_{\max}}{\partial s}\right|^{-1} \geq 2E\kappa_{fail} \tag{2}$$

where *E* is the elastic modulus, and κ_{fail} is the failure value which is another material property. The stress gradient $\left|\frac{\partial\sigma_{\max}}{\partial s}\right|$ is evaluated for all possible failure path from the location where the first criterion, Eq. (1), is satisfied. Then, the path that has the lowest stress gradient is the failure path, and Eq. (2) is applied to that direction whether the criterion is satisfied or not. Thus, the second part provides the failure path. In some cases, failure paths are known from symmetric conditions, but they may not be known in more general cases.

As the set of failure criteria are applied to a specimen without any notch like a tensile test coupon, Eq. (1) is the only criterion critical for failure. Because the stress gradient is zero, Eq. (2) is automatically satisfied. On the other hand, for a specimen with a line crack, Eq. (1) is always satisfied because of the stress singularity at the crack tip. In this case, Eq. (2) is used to determine the failure. For linear elastic fracture mechanics, the stress field at the crack tip is expressed for the first mode as below:

$$\sigma_{y} = \frac{K_{I}}{\sqrt{2\pi x}} \tag{3}$$

as the applied load is along the y-axis and the crack is oriented along the x-axis. The stress is inversely proportional to the distance *x* from the crack tip. Equation (3) is substituted into Eq. (2) to yield

$$\kappa_{fail} = \frac{K_{IC}^{2}}{2\pi E} \tag{4}$$

Thus, the failure value κ_{fail} is directly related to the energy release rate in fracture mechanics, and K_{IC} is the fracture toughness of mode I.

  doi:10.5075/epfl-298799_978-2-9701614-0-0

For a notch other than a line crack, stress singularity does not occur. In this case, none of the two criteria are satisfied explicitly. As a result, both criteria should be tested. However, further sudy showed that the second criteion is the dominant one for most hole sizes. In other words, failure stress easily exceeds the failure strength, which makes the first criterion is alerady satisfied before the second criterion is satisfied.

Let's consider an infinite plate with a circular hole or radius *R* and subjected to a uniform stress along the vertical (y-axis) direction. The stress along the y-axis at the edge of the hole is expressed in terms of the location along the x-axis as below because the failure would occur along the x-axis.

$$\sigma_y = \frac{1}{2}\left[2 + \frac{R^2}{x^2} + \frac{3R^4}{x^4}\right] \tag{5}$$

The stress gradient of Eq. (5) is

$$\left|\frac{\partial \sigma_y}{\partial x}(R)\right| = \frac{7}{R} \tag{6}$$

Substitution of Eq. (6) to the second failure criterion, Eq. (2) tells us that notch strength is inversely proportional to the one third power of the hole radius of the infinite plate.

3. Multiscale Analysis

Fibrous composite materials consist of fiber bundles embedded in a binding matrix material, and there are two different length scales. One scale is the microscale for the fibers, and the other is the macroscale for composite specimens or parts. At the macroscale, homogenized material properties are used for analysis, which are dependent on the fiber and matrix materials. Multiscale analysis is to link two different length scales bidirectionally as sketched in Fig. 1. As a result, there are two processes. One is the *upscaling process*, and the other is the *downscaling process*.

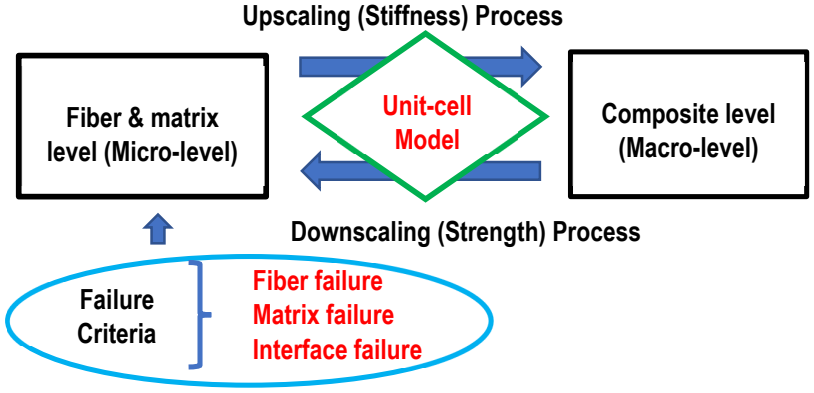

Figure 1. Multiscale analysis for fibrous composite materials and structures

The main function of the upscaling process is to compute the homogenized effective properties of the composites from the properties of the fiber and matrix materials. The downscaling process decomposes the composite material level stresses and strains into the fiber and matrix level stresses and strains. The latters are called microstresses and microstrains while the formers

  doi:10.5075/epfl-298799_978-2-9701614-0-0

are called macrostresses and macrostrains. Then, failure criteria are applied to the microstresses and/or microstrains instead of macrostresses and/or macrostrains. This is the key difference between the present multiscale based failure criteria and the traditional failure criteria which use macrostresses and/or macrostrains.

In order to make the multiscale approach computationally efficient, a unit-cell model was used to develop necessary equations for both upscaling and downscaling processes. The developed equations are analytical and do not require extensive computing power. As a result, the whole multiscale process is computationally very efficient. The details of the unit-cell model can be found in Ref. [3,4] and it was omitted here to save space.

Failure modes at the microscale are fiber fracture, matrix cracking, or fiber/matrix interface debonding. For example, interlaminar delamination and fiber splitting are matrix cracking and/or interface debonding. Hence, there are three failure criteria for three failure modes. The failure criterion for fiber failure is expressed in terms of the fiber stresses or fiber strains. The strain based failure criterion is

$$\left(\varepsilon_1^f\right)^2+\left(\gamma_{12}^f\right)^2+\left(\gamma_{13}^f\right)^2\geq\left(\varepsilon_{fail}^f\right)^2 \tag{7}$$

where superscript '*f*' indicates the strains in the fibers, and subscript '*1*' is the fiber direction. Fibers may have different strength in tension and compression, respectively. In that case, the failure strain ε_{fail}^f is different depending on the loading direction, i.e., either tension or compression.

The matrix material behaves like a brittle material. As a result, the maximum normal stress or strain criterion is used for the matrix material. Fiber/matrix debonding depends on the normal and shear stresses at the interface as shown in the failure criterion given below :

$$\left(\frac{\tau_{\text{inter}}+\sqrt{v^f}\left(\sigma_{\text{inter}}-\sigma_1\right)}{\tau_{\text{inter}}^{fail}}\right)^2+\left\langle\frac{\sigma_{\text{inter}}}{\sigma_{\text{inter}}^{fail}}\right\rangle\geq 1 \tag{8}$$

Here <> is the Macaulay operator, and v^f is the fiber volume fraction of the composite.

4. Results and Discussion

Laminated carbon fiber composite specimens containing various notches were tested to validate the proposed unified failure criteria. The specimens had the layer orientations $[0/90/+45/-45]_S$ which is called quasi-isotropic specimens. Each specimen was nominally 140 mm long, 24 mm wide, and 6 mm thick. Every notch was located at the center along the specimen length. Table 1 lists different sizes and shapes of notches tested for this study. The specimens had three different sizes of a circular hole, an elliptical shape of hole, or two same size holes. Figure 2 shows the local sections of the specimens with all different notches before and after tests with applied loading in the vertical direction.

Failed specimens showed that the layers with fiber orientations along the loading direction (outer layer) had the fiber failure and all other layers (inner layers) had either matrix or fiber/matrix interface failure. In this study, the theory used the smeared composite material properties to predict the failure at the notches. In other words, the lamination theory was used

to determine the effective material properties of the specimens. Finite element analyses were conducted to determine the stress gradient and the stress concentration factor using the effective material properties. The failure value of κ_{fail} used in the second failure criterion was obtained from the test data of the specimen with a 3 mm circular hole. That is why the theoretical failure stress is equal to the experimental failure stress in Table 1. Using the same failure value, all other specimens were predicted for their failure stresses. The theoretical failure stresses agreed well with the experimental values for all kinds of notches as seen in Table 1. The specimens with a single circular hole had the theoretical stresses within the scattered experimental data. The failure stress was determined as the failure load divided by the specimen cross-section without notches.

Table 1: Quasi-isotropic specimens of different notches

Speci. no.	Notch type	Notch size	Experi. Failure stress	Theoret. Failure stress
1	A circular hole	3 mm	560 MPa ± 16.2 MPa	560 MPa
2	A circular hole	6 mm	454 MPa ± 28.3 MPa	432 MPa
3	A circular hole	8 mm	386 MPa ± 17.7 MPa	372 MPa
4	Two circular holes	3 mm each	513 MPa ± 7.61 MPa	548 MPa
5	An elliptical hole	8 x 4 mm	354 MPa ± 11.9 MPa	341 MPa

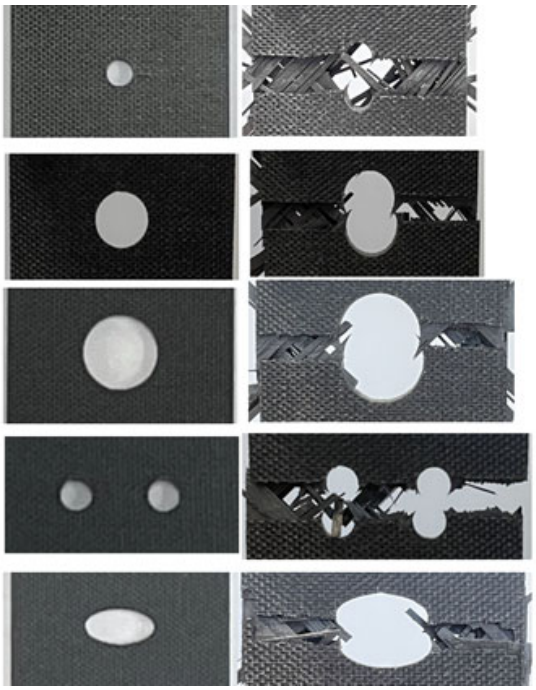

Figure 2. Quasi-isotropic carbon fiber composite specimens with various notches before and after failure

  doi:10.5075/epfl-298799_978-2-9701614-0-0 published under CC BY-NC 4.0 license

The next example was to predict failure of polymer composites using the multiscale approach. Cross-ply carbon fiber composite plates were subjected to underwater shock loading. Physical testing was conducted inside an anechoic water tank to simulate infinite water medium. Figure 3 shows the top view of the test setup under water. A plastic bottle containing liquid nitrogen, denoted LN2 in Fig. 3, was used as the shock loading. As liquid nitrogen evaporates and expands, pressure builds up inside the plastic bottle, which results in bursting the bottle and produces shock loading. Pressure gages were used to record the resultant shock pressure. Three pressure gages were used as denoted by P1 through P3 in Fig. 3. Two pressure gages were located at the same stand-off distance as the composite plate from the plastic bottle to determine what pressure would be applied to the composite plate under test. One pressure gage was placed closer to the plastic bottle to check the shock wave propagation. The stand-off distance was varied from a longer distance to a shorter distance until the composite plate failed.

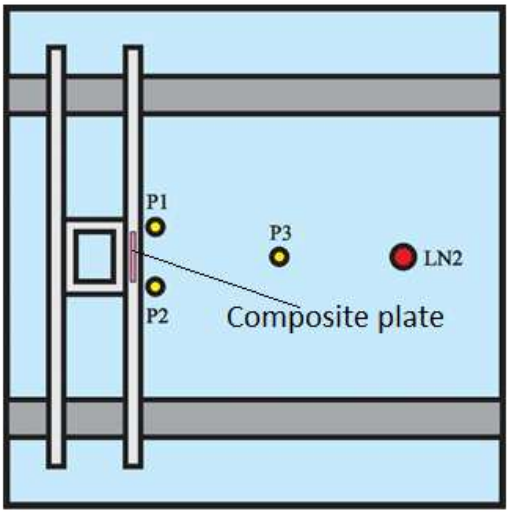

Figure 3. Top view of the test setup for underwater shock loading to clamped composite plate

Both air-back and water-back conditions were tested for comparison. The test results showed that greater shock pressure was required for failure of a composite with water-back than air-back. For the same shock loading, the stand-off distance to cause failure of the composite with water-back was about a half of that for the air-backed composite plate. However, a more interesting point was the failure pattern between the two different cases. The air-backed composite had failure around the whole plate while the water-backed composite had a very localized failure.

The numerical analysis used both multiscale and multiphysics modeling techniques. Multiphysics modeling was used for fluid-structure interaction between the composite plates and surrounding water where shock wave propagates. The water medium was modeled as an acoustic medium because the fluid motion and viscosity were neglected. The cellular automata technique was used to solve the acoustic equation. On the other hand, multiscale modeling was used for the composite plates to predict their failure.

Figure 4 shows failure of the tested plate with air-back and the predicted failure using the multiscale and multiphysics modeling technique. The clamped plate was teared along three

  doi:10.5075/epfl-298799_978-2-9701614-0-0

edges, top side and two sides. The cross-ply carbon fiber composites have fibers in the horizontal orientation at their outer layers. As a result, the major failure modes of the numerical study were the fiber failure at the left and right edge of the boundary as well as the matrix failure at the top and bottom edges. Therefore, the predicted failure modes agreed well with the experimental result.

The experimental and numerical results for the water-back case are shown in Figure 5. Failure was very localized in the composite plate. Only the right bottom location showed the major failure like fiber breakage in both studies that also confirmed the numerical prediction was quite reliable.

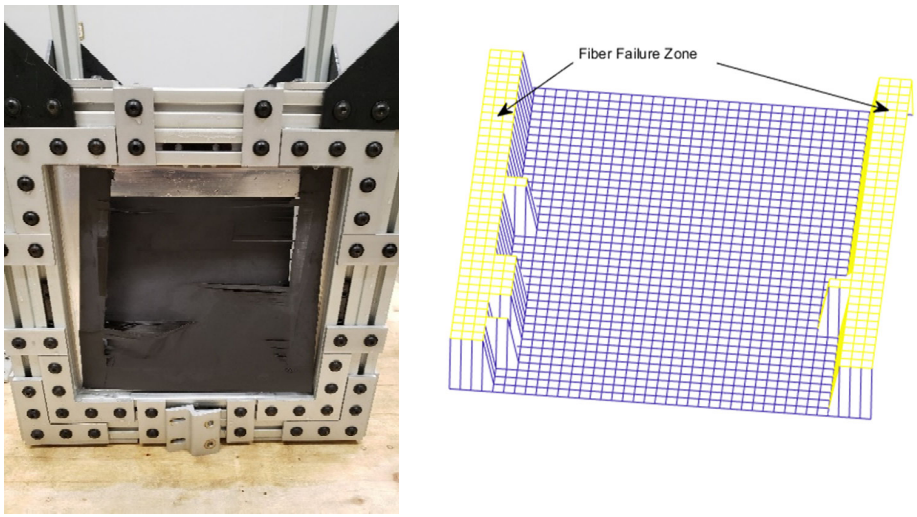

Figure 4. Failure of cross-ply composite clamped along edges with air-back. (left) experiment and (right) numerical prediction.

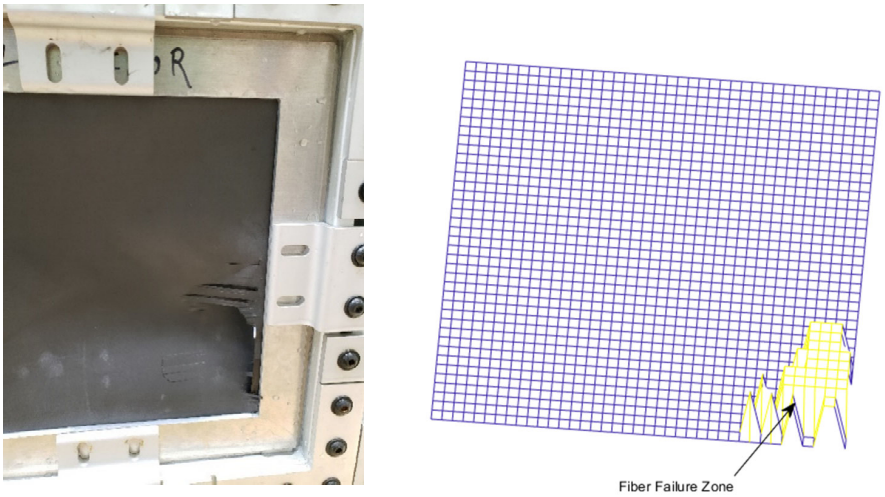

Figure 5. Failure of cross-ply composite clamped along edges with water-back. (left) experiment and (right) numerical prediction.

  doi:10.5075/epfl-298799_978-2-9701614-0-0

5. Conclusions

This paper presented newly proposed unified failure criteria as well as a multiscale approach to predict failure of polymer composites. The failure criteria can be applied to brittle materials regardless of any crack, hole, or none of them. The new failure theory was validated using analytical and experimental results. Furthermore, the multiscale and multiphysics modeling and simulation also predicted failure of air-backed or water-backed composite plates subjected to underwater shock loading, and the numerical results agreed well with the experimental result. The multiscale model used failure criteria based on microstresses and/or microstrains at the fiber and matrix material level.

Acknowledgements

The authors acknowledge the financial support from the Office of Naval Research.

6. References

1. Kwon YW, “Revisiting failure of brittle materials”, Journal of Pressure Vessel Technology, Vol. 143, December 2021, 064503.
2. Kwon YW, Diaz-Colon C, Defisher S, “Failure Criteria for Brittle Notched Specimens”, Journal of Pressure Vessel Technology, Vol. 144, No. 5, October 2022, 051506
3. Kwon YW, Darcy J, “Failure Criteria for Fibrous Composites Based on Multiscale Modeling”, Multiscale and Multidisciplinary Modeling, Experiments, and Design, Vol. 1, No. 1, 2018, pp. 3-17.
4. Kwon YW, Multiphysics and Multiscale Modeling: Techniques and Applications, CRC Press, 2015.

  doi:10.5075/epfl-298799_978-2-9701614-0-0

Composites Meet Sustainability – Proceedings of the 20th European Conference on Composite Materials, ECCM20. 26-30 June, 2022, Lausanne, Switzerland

MODELLING THE TEMPERATURE DEPENDENT VISCOELASTIC COMPACTION BEHAVIOUR OF UNCURED PREPREGS

*Siddhesh Kulkarni[a], Nora AlAhmed[a], *Kamran A Khan[b], Rehan Umer[b]*

a: Mechanical Engineering Department, Khalifa University of Science and Technology, Abu Dhabi, UAE
b: Aerospace Engineering Department, Khalifa University of Science and Technology, Abu Dhabi, UAE
kamran.khan@ku.ac.ae (*Corresponding/Presenting author)

Abstract: *In autoclave processes like ATL and AFP, and out-of-autoclave manufacturing processes like SQRTM, prepreg layers are compacted at temperatures higher than room temperature, for better flow of resin into the layers. For process modelling of such manufacturing techniques, there is a need to develop a model that can predict the thermoviscoelastic compaction response of prepregs at different temperatures. For experimental study, single step relaxation experiments for different rates and temperatures are carried out on a glass fiber/ epoxy resin matrix prepreg. A thermo-hyper-viscoelastic numerical model was developed within thermodynamics framework incorporating the traditional compaction model and temperature scaling function to capture rate dependent thermo-viscoelastic response during compaction and relaxation phenomena in uncured prepreg.*

Keywords: thermoviscoelastic, numerical model, prepreg

1. Introduction

Prepreg are resin matrix systems in which a sheet of fiber reinforcement is pre-impregnated with resin and semi-cured to be used at input stage for composite manufacturing. Prepregs not only obviates the need for resin infusion systems in manufacturing processes but also leads to high quality end component. Autoclave processes (1) like ATL and AFP, and Out-of-Autoclave(2) processes like VBO and SQRTM employed prepreg as raw material to their inherent processes. In these processes, compaction of prepreg at a temperature higher than room temperature, is a common and most important stage. This stage governs the clamping force required to hold the laminate in place as well the final volume fraction in laminate. Therefore, to model these processes for study and development, it is important to develop a model to capture time and temperature dependent stress response during compaction and thickness hold stage. Prepreg due to the fibre and resin present in its structure exhibit viscoelastic behaviour. This means that, not only prepreg's stress response depends on rate of compaction but it also experiences stress relaxation when held at constant thickness after compaction. Moreover, by increasing the temperature of prepreg during compaction, the resin in the laminate loses its viscosity and hence increases lubrication between fibres of prepreg. This leads to decrease in stress response in the laminate for the same deformation and rate of compaction (3). It was reported by Naresh et al (3) that by increasing the temperature by certain threshold resin bleeds out and the fabric loses the effect of its viscosity on fibres. As a result, to achieve higher volume fraction, the stress response started to increase at elevated temperatures for same compaction parameters. Therefore, for modelling purposes, such a threshold was kept in consideration while designing and running the experimental tests on prepreg.

  doi:10.5075/epfl-298799_978-2-9701614-0-0

The oldest known model to capture fabric's non-linear compaction stress response was proposed by Van Wyk (4) and later modified by Gutowski et al (5) which took into account elastic bending of fibre bundles. But such models did not take into account the effect of rate on stress response into the model and also failed to capture stress relaxation phenomena. To solve this problem, viscoelastic rheological Maxwell-Weichert model is adopted to model the fabrics compaction stress response. Ming Mei et al (6) incorporates the effect of temperature into the elastic modulus for spring only element of Maxwell-Weichert model and explores compaction and relaxation behaviour. But it considers compaction and relaxation case separately and considers temperature effect for only equilibrium stresses. Danzi et al (7) developed a unified expression for compaction and relaxation from Maxwell-Weichert model and later modified by Werlen et al (8) into a numerical model to capture compaction in dry and wet fabrics. Kulkarni et al (9) used a modified convolution integral model incorporating expressions for non-linear compaction model for fabrics to capture stress response during compaction and thickness hold for epoxy resin prepregs. The advantage of using a numerical model or an integral model is that the model whose parameters were calibrated from one loading history can be used to predict the stress response under different loading history. We assumed that the prepreg response was described by Maxwell-Weichert model. The finite viscoelasticity theory was used to capture the rate dependent compaction-relaxation response and the temperature scaling function was used to capture the effect of temperature on the overall thermo-viscoelastic response of prepregs.

2. Material and Sample Preparation

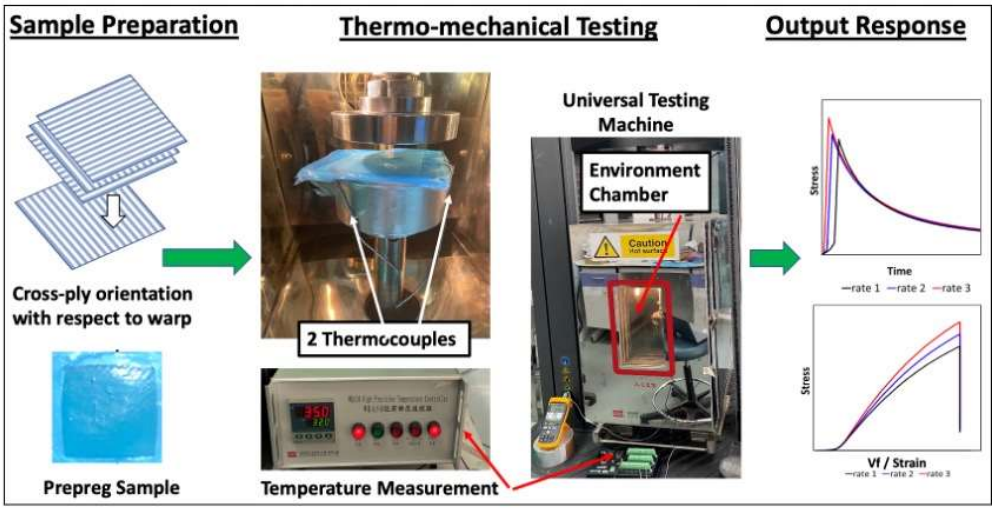

Figure 1: Experimental setup

For the experimental study, HexPly® M26T prepreg supplied by Hexcel® was chosen as the specimen. M26T prepreg is a 2/2 twill weave glass-fibre prepreg with epoxy resin as polymer matrix. The nominal thickness of single layer prepreg is 0.25mm. The density of the epoxy resin and the glass fiber in the prepreg is 1.29 g/cm^3 and 2.55 g/cm^3, respectively. The experimental setup is shown in Figure 1. The sheet was cut into a size of 70 mm x 70 mm and stacked into 4 layers in cross-ply orientation. MTS E45 testing machine equipped with environmental chamber was employed to conduct isothermal displacement-controlled compaction experiments. Before commencement of compaction tests, it was made sure that the platens and the sample had

  doi:10.5075/epfl-298799_978-2-9701614-0-0

reached the same temperature. A Campbell scientific data logger CR1000X was used to record the temperature while the mechanical testing data was obtained from MTS test suite software.

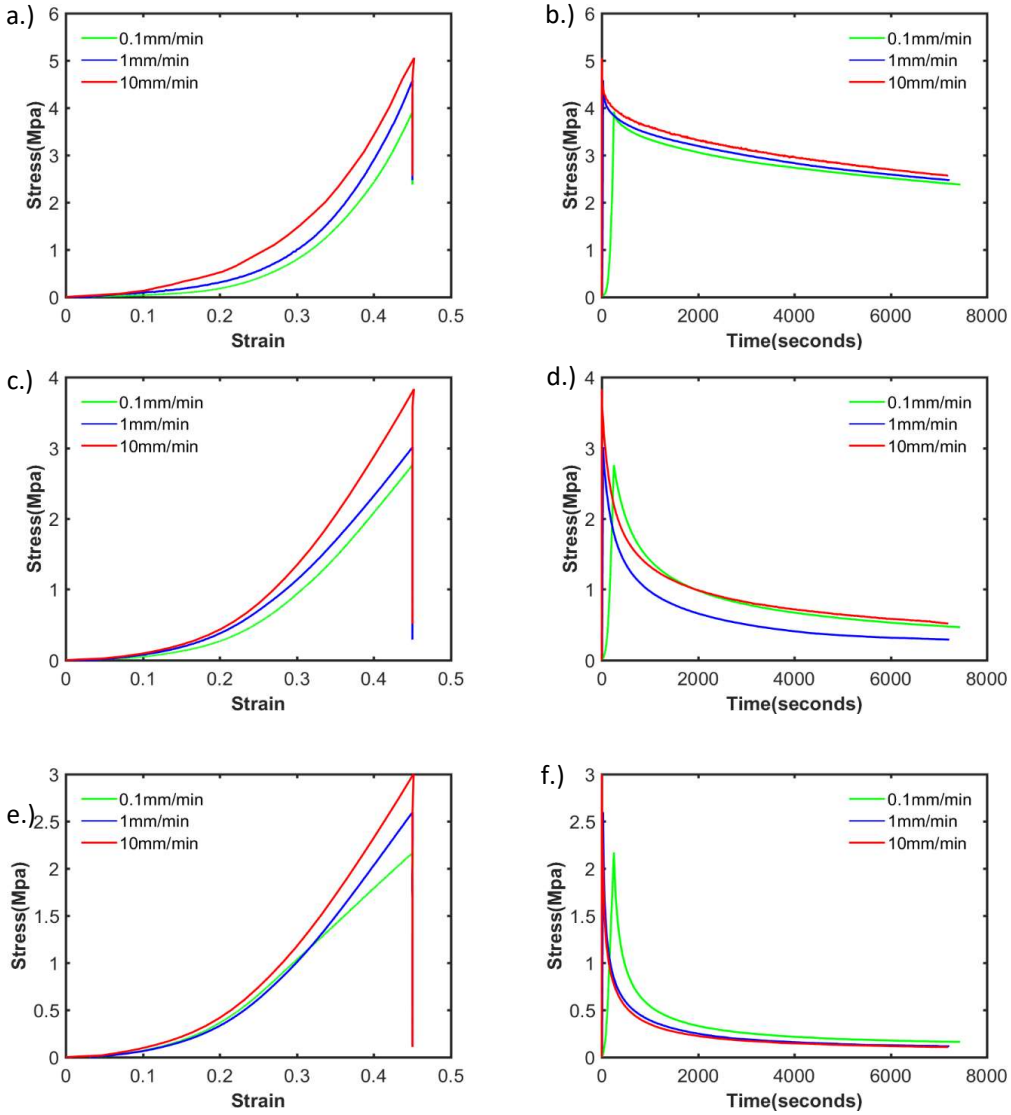

Figure 2: Single-Step Relaxation experiments for different rates in isothermal conditions; a,b at 25˚C; c,d at 35˚C; e,f at 45˚C

3. Experimental Program

The program consists of Single-step compaction-relaxation tests at isothermal conditions wherein, the specimen and the platens are ensured to be in isothermal conditions. The specimens were compacted at different predetermined displacement rate until a thickness corresponding to 45% strain was reached and then the specimen is held at that thickness for two hours to record stress relaxation. The tests were carried out for 0.1 mm/min, 1 mm/min and 10 mm/min displacement rates and at 25˚C (Room Temperature (fig. 2a and 2b)), 35˚C (fig. 2c and 2d) and 45˚C (fig. 2e and 2f) isothermal conditions.

4. Numerical Viscoelastic Modelling

  doi:10.5075/epfl-298799_978-2-9701614-0-0

From the experimental study, it was observed that the prepreg laminate exhibited highly non-linear viscoelastic compaction response. It was assumed that the deformation was uniaxial during the compaction and the material was continuous throughout the laminate and the response can be represented by Maxwell Weichert Model as shown in Figure 3.

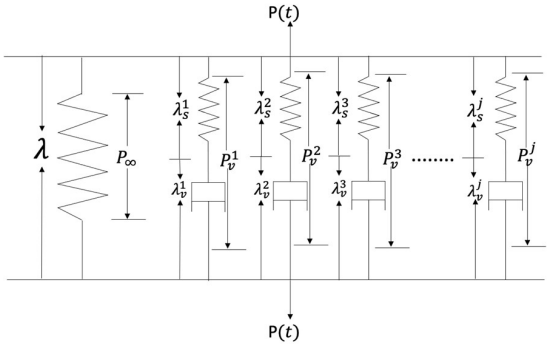

Figure 3. Maxwell Weichert Model

Following the finite strain viscoelastic theory, the deformation behavior can be described using the strain energy function $\psi(\boldsymbol{C}, \boldsymbol{H_j}, \Theta)$, where **C** is Cauchy green deformation tensor for overall deformation in the material, $\mathbf{H_j}$ is internal variable describing time dependent viscous behavior in the material and Θ is the temperature of the material. The strain energy function in a thermoviscoelastic material is expressed by,

$$\psi(\boldsymbol{C}, \boldsymbol{H_j}, \Theta) = T_\infty(\Theta) * \psi_\infty(\boldsymbol{C}) + \sum_{J=1}^{N} T_v^j(\Theta) * \psi_v^j(\boldsymbol{C}, \boldsymbol{H_j}) \quad (1)$$

where $\psi_\infty(\boldsymbol{C})$ represents the elastic energy in the material represented by the spring and $\psi_v^j(\boldsymbol{C}, \boldsymbol{H_j})$ represents the viscous energy in the material represented by the maxwell element j . $T_\infty(\Theta)$ and $T_v^j(\Theta)$ are temperature scaling functions with respect to a reference temperature Θ_0 for spring only element and maxwell element j respectively. $T_\infty(\Theta)$ and $T_v^j(\Theta)$ have values of 1 at Θ =Θ_0. Therefore, to derive stress response from the above energy function (eq.1), the second Piola Kirchhoff stress response is derived from the relation $S = 2\frac{\partial \psi}{\partial C}$ as follows,

$$\boldsymbol{S}(\boldsymbol{C}, \boldsymbol{H_j}, \Theta) = 2(T_\infty(\Theta) * \frac{\partial \psi_\infty}{\partial \boldsymbol{C}} + \sum_{J=1}^{N} T_v^j(\Theta) * \frac{\partial \psi_v}{\partial \boldsymbol{C}}) \quad (2)$$

Now instead of using a hyperelastic energy function for equilibrium or quasi-static stress response of the prepreg laminate, a modified Gutowski's model (5) was chosen and multiplied by $T_\infty(\Theta)$ to capture the equilibrium stress response as follows,

$$P_\infty(\lambda, \Theta) = T_\infty(\Theta) * A_s \frac{\left(\left(\frac{1}{\lambda}\right)^{\mathrm{m}} - 1\right)}{\left(\left(\frac{V_a}{V_{f0}}\lambda\right)^{\mathrm{m}} - 1\right)^{n}} \quad (3)$$

where P is first Piola Kirchhoff stress, A_s is the spring constant for the fibre, V_a is the maximum available fibre volume fraction, V_{f0} is the initial volume fraction and λ is stretch or length ratio of final thickness over initial. Values of m and n are generally 0.5 and 4 in the original Gutowski model but it had to be modified to fit the equilibrium stress response of the prepreg laminate.

  doi:10.5075/epfl-298799_978-2-9701614-0-0

Stretch (λ) is considered as hyperelastic or finite deformation measure. In compaction modelling, the value of Stretch (λ) is always equal to or less than one. To capture the viscous stresses in maxwell elements, hyperelastic energy functions were used to define its behavior and derive stress response for respective elements. Let $\boldsymbol{F_s}$ and $\boldsymbol{F_v}$ be the deformation gradient tensor for deformation in spring and dashpot element of a maxwell element respectively. Then the deformation of the total element is given by $\boldsymbol{F} = \boldsymbol{F_s F_v}$. Therefore, subsequent expressions that were obtained from this can be expresses as $\boldsymbol{C} = \boldsymbol{C_s C_v}$ and $\lambda = \lambda_s \lambda_v$. In an effort to model the nonlinear viscous behaviour of the fibre material, the maxwell elements are divided into Neo-Hookean spring maxwell elements and Yeoh spring maxwell elements. Therefore, the combined viscous energy function for maxwell energy function is given by,

$$\psi_v(\boldsymbol{C_s}, \Theta) = \sum_{J=1}^{S} T_v^j(\Theta) * a_{NH}^j(\boldsymbol{I_{1s}^j} - 3) + \sum_{J=S+1}^{N} T_v^j(\Theta) * a_Y^j\left(\boldsymbol{I_{1s}^j} - 3\right)^3 \tag{4}$$

where a_{NH}^j and a_Y^j are the fitting parameters for Neo-Hookean and Yeoh spring maxwell elements, $\boldsymbol{I_{1s}^j}$ is the first invariant of $\boldsymbol{C_s^j}$, s is the total number of Neo-Hookean spring maxwell elements and N is the total number of all maxwell elements. Therefore, the expression for first Piola Kirchhoff stress derived from Eq. (6) for unidirectional case is as follows (10),

$$P_v = \sum_{J=1}^{S} P_{v_{NH}}^j + \sum_{J=S+1}^{N} P_{v_Y}^j \tag{5}$$

$$P_v = \sum_{J=1}^{S} 2\, T_v^j(\Theta) * a_{NH}^j\left(\frac{\lambda}{\left(\lambda_v^j\right)^2} - \frac{\lambda_v^j}{\lambda^2}\right) + \sum_{J=S+1}^{N} 6T_v^j(\Theta) * a_Y^j\left(\frac{\lambda^2}{\left(\lambda_v^j\right)^2} + \frac{2\lambda_v^j}{\lambda} - 3\right)^2\left(\frac{\lambda}{\left(\lambda_v^j\right)^2} - \frac{\lambda_v^j}{\lambda^2}\right) \tag{6}$$

$\boldsymbol{C_v^j}$ or λ_v^j (for unidirectional case) is the unknown internal variable $\boldsymbol{H_j}$ responsible for the viscous behavior in the maxwell element. For a defined energy function, Koprowski et al (11) proposed an evolution law as follows,

$$\dot{\boldsymbol{C_v^j}} = \frac{4}{\eta^j}\frac{\partial \psi_v^j}{\partial \boldsymbol{I_{1s}^j}}\left(\boldsymbol{C} - \frac{1}{3}(\boldsymbol{C}{:}\left(\boldsymbol{C_v^j}\right)^{-1})\boldsymbol{C_v^j}\right) \tag{7}$$

where η^j is viscosity in the dashpot of the maxwell element j. Therefore, this evolution law was considered for unidirectional case for maxwell elements as follows,

For Neo-Hookean elements (j=1...s) is

$$\dot{\lambda_v^j} = \frac{4}{3\tau^j}\left(\frac{\lambda^2}{\lambda_v^j} - \frac{\left(\lambda_v^j\right)^2}{\lambda}\right) \tag{8}$$

where $\tau^j = \frac{\eta^j}{a_{NH}^j}$ and for Yeoh element (j= (s+1) .... N) is,

$$\dot{\lambda_v^j} = \frac{4}{\tau^j}\left(\frac{\lambda^2}{\left(\lambda_v^j\right)^2} + \frac{2\lambda_v^j}{\lambda} - 3\right)^2\left(\frac{\lambda^2}{\lambda_v^j} - \frac{\left(\lambda_v^j\right)^2}{\lambda}\right) \tag{9}$$

where $\tau^j = \frac{\eta^j}{a_Y^j}$ for j=(s+1) to N. By using Newton Raphson method for integration, λ_v^j values were evaluated for each maxwell element at each time step using the equation as follows,

$$\lambda_v^j(t) = \lambda_v^j(t-1) + \Delta t * \dot{\lambda_v^j}(\lambda_v^j(t), \lambda(t)) \tag{10}$$

Therefore, the total stress response for the Maxwell Weichert model is given by,

  doi:10.5075/epfl-298799_978-2-9701614-0-0

$$P(t,\Theta) = P_{\infty}(\lambda(t),\Theta) + P_{v}(\lambda(t),\lambda_{v}^{j}(t),\Theta) \quad (11)$$

Here, the reference temperature Θ_0 is taken as room temperature 25˚C or 298 K (in Kelvin temperature). The scaling functions and plot fits that are chosen use temperatures in their kelvin units but presented in Celsius for convenience.

5. Results

Table 1: Parameter values of elastic model (Modified Gutowski model)

Parameters	Values
A_s	0.508
V_a	0.899
m	0.3
n	1.58

Table 2: Parameter values for Maxwell Elements

Element no	Hyperelastic constants	Values	Tau Constants	Values
1	a_{NH}^{1}	0.088	τ_1	12433
2	a_{Y}^{2}	0.104	τ_2	751
3	a_{Y}^{3}	4.950	τ_3	0.36
4	a_{Y}^{4}	0.214	τ_4	233137

Table 3: Temperature Scaling functions for Maxwell elements and values of parameters

Element	Scaling function	Constant	Values
Spring only	$T_{\infty}(\Theta) = \exp\left(\left(\frac{\Theta_0}{\Theta_0 - 80}\right)^{C_{t0}} - \left(\frac{\Theta}{\Theta_0 - 80}\right)^{C_{t0}}\right)$	C_{t0}	6.44
Maxwell 1	$T_{v}^{1}(\Theta) = \exp\left(a_{t1} * \left(\frac{\Theta}{\Theta_0} - 1\right)\right)$	a_{t1}	15.67
Maxwell 2	$T_{v}^{2}(\Theta) = \exp\left(a_{t2} * \left(\frac{\Theta}{\Theta_0} - 1\right)\right)$	a_{t2}	14.50
Maxwell 3	$T_{v}^{3}(\Theta) = \frac{\exp\left(a_{t3} * \frac{\Theta_0}{\Theta}\log\left(\frac{\Theta_0}{\Theta}\right)\right) + b_{t3}}{1 + b_{t3}}$	a_{t3} b_{t3}	0.54 0.08
Maxwell 4	$T_{v}^{4}(\Theta) = \exp\left(1 - \left(\frac{\Theta}{\Theta_0}\right)^{C_{t4}}\right)$	C_{t4}	19.83

The developed numerical viscoelastic model was fitted to experimental data by using lsqcurvefit function in Matlab. The calibration of the constants was carried out in two stages. In the first stage, since the values of the Temperature scaling functions are 1 for reference temperature of 25˚C, the elastic model parameters A_s,m, n (Table 1) and viscous element model parameters a_{NH}^{j}, a_{Y}^{j} and τ^{j} (Table 2) are calibrated based on single step relaxation data for 25˚C. V_{f0} is found to be approximately the same for each experimental test which is 30%. It was found that 1 Neo Hookean element and 3 Yeoh elements fit well to the single step relaxation data for 25˚C. In the second stage, after the model constants are calibrated, single step compaction data for 35˚C and 45˚C are used to select the temperature scaling functions and calibrate the constants

in the temperature scaling functions (Table 3). The model fit for each temperature is compared for rates 0.1 mm/min (fig 4a and 4b), 1mm/min (fig 4c and 4d), and 10mm/min (fig 4e and 4f).

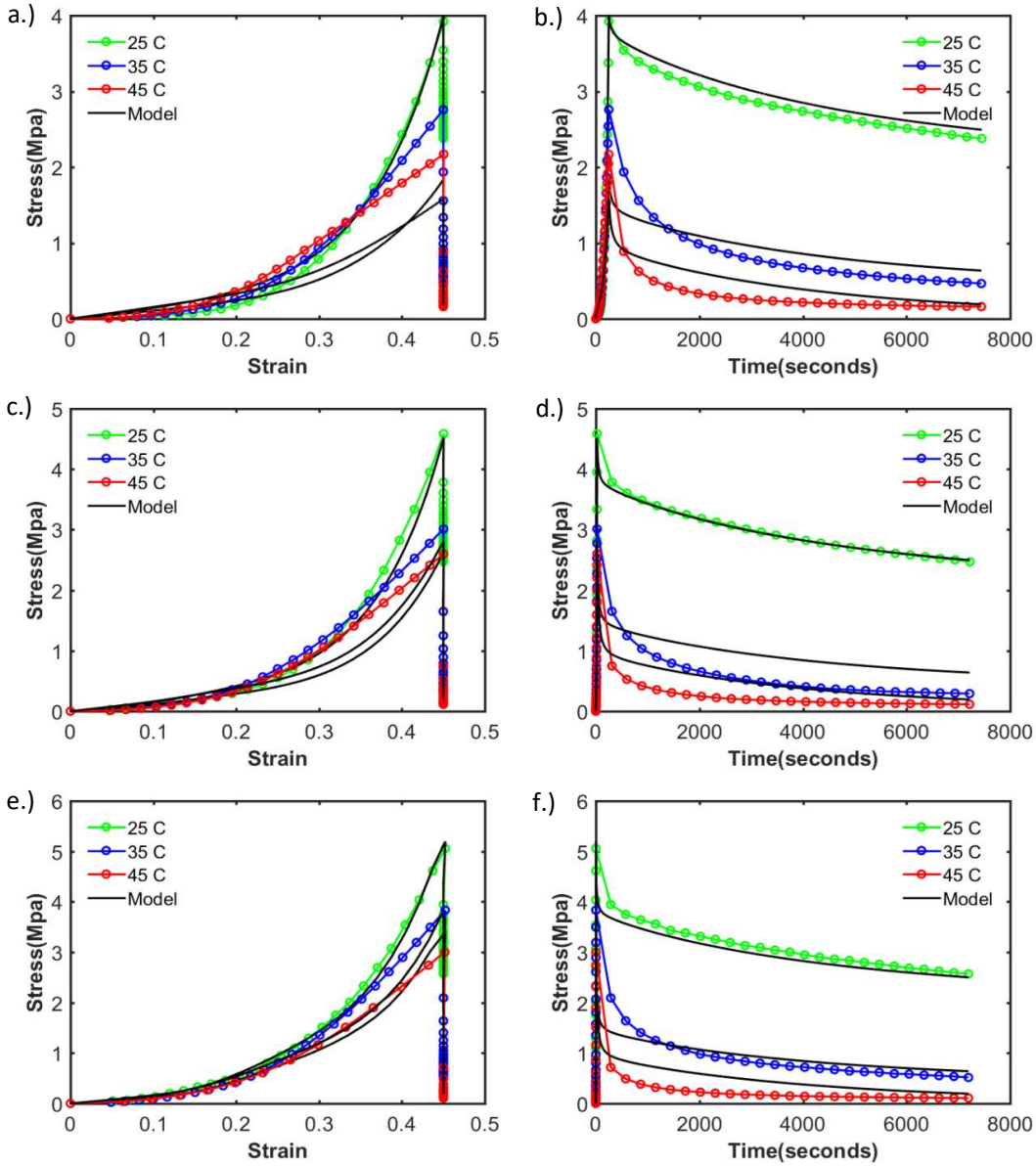

Figure 4: Comparison of model fit with experiments for different temperatures for rates 0.1 mm/min (a and b), 1 mm/min (c and d), and 10 mm/min (e and f)

6. Conclusion

The rate dependent thermo-mechanical single step compaction-relaxation experiments were conducted under three rates, i.e., 0.1 mm/min, 1 mm/min and 10 mm/min rates and under isothermal conditions at 25˚C (Room Temperature), 35˚C and 45˚C. A thermo-hyper-viscoelastic numerical model was developed within thermodynamics framework incorporating the traditional compaction model and temperature scaling function to capture rate dependent thermo-viscoelastic response during compaction and relaxation phenomena in uncured

prepreg. The model was able to capture reasonably well the rate dependent thermoviscoelastic behavior of prepreg under different rates and under different isothermal conditions.

7. References

1. K. Naresh, K.A. Khan, R. Umer, W.J. Cantwell. The use of X-ray computed tomography for design and process modeling of aerospace composites: A review. Materials and Design. 2020;

2. Naresh K, Khan KA, Cantwell WJ, Umer R. Rate and temperature dependent compaction-creep-recovery and void analysis of compression molded prepregs. Composites Part B: Engineering. 2022 Apr 15;235:109757.

3. Naresh K, Khan KA, Cantwell WJ, Umer R. Viscoelastic and cyclic compaction response of prepregs tested under isothermal temperatures and various compaction speeds. Polymer Composites. 2021;42(12):6928–40.

4. C. M. Van Wyk. Note on the Compressibility of Wool. Journal of the Textile Institute Transactions. 1946;285–92.

5. T. G. Gutowski, Z. Cai, S. Bauer, D. Boucher. Consolidation Experiments for Laminate Composites. Journal of Composite Materials. 1987;21:650.

6. Mei M, He Y, Wei K, Duan S, Li M, Yang X. Modeling the temperature-dependent viscoelastic behavior of glass fabric with binder in the compaction process. Polymer Composites. 2021;42(6):3038–50.

7. Mario Danzi, Christoph Schneeberger, Paolo Ermanni. A Model for the Time-dependent Compaction Response of Woven Fiber Textiles. Composites Part A. 2018;

8. Werlen V, Rytka C, Michaud V. A numerical approach to characterize the viscoelastic behaviour of fibre beds and to evaluate the influence of strain deviations on viscoelastic parameter extraction. Composites Part A: Applied Science and Manufacturing. 2021 Apr

9. Kulkarni SS, Khan KA, Umer R. Quasi-Linear Viscoelastic Modelling of Uncured Prepregs under Compaction. Proceedings of the American Society for Composites—Thirty-Sixth Technical Conference on Composite Materials. 2021;

10. Zisheng Liao, Mokarram Hossain, Xiaohu Yao, Markus Mehnert, Paul Steinmann. On thermo-viscoelastic experimental characterisation and numerical modelling of VHB polymer. International Journal of Non-Linear Mechanics. 2019 Sep;

11. N. Koprowski-Theiss, M. Johlitz, S. Diebels. Characterizing the time dependence of filled EPDM. Rubber Chemistry and Technology. 2011;147–65.

  doi:10.5075/epfl-298799_978-2-9701614-0-0

ACCOUNTING FOR LOCAL MORPHOLOGICAL FLUCTUATIONS IN THE PREDICTION OF THE TRANSVERSE ELASTIC BEHAVIOUR OF UD COMPOSITES

Sébastien, Joannès[a], Jennifer, Blondel[a,b], Eveline,Hervé-Luanco[a,c]

a: Mines Paris - PSL University (Evry, FR) – sebastien.joannes@minesparis.psl.eu
b: Manufacture Française des Pneumatiques Michelin (Clermont Ferrand, FR)
c: Université de Versailles, Saint-Quentin en Yvelines (Versailles FR)

Abstract: *While* unidirectional (UD) *materials are used for their excellent stiffness and strength in the fibre direction, they suffer from poor transverse properties. In the case of complex loadings, the first damage often appears in the transverse directions. While obtaining longitudinal properties is not a problem, transverse properties are still very difficult to measure reliably experimentally and the use of predictive models is often necessary. The main difficulty lies in taking into account the local morphological fluctuations which greatly influence the transverse behaviour. Using a recently developed model based on a Generalized Self-Consistent Scheme (GSCS) coupled with a Morphologically Representative Pattern (MRP), we propose to use the analytical solutions obtained to predict the effective transverse properties of different microstructural configurations. In a two-phase context, the robustness of the model is verified for phase contrasts up to 10^5, reinforcement volume fractions up to 70% or an incompressible matrix, which defeats many analytical models.*

Keywords: Micromechanical model; Homogenization; Interphase; Porosity; Hybrid

1. Introduction

On all the cross-sections in Figure 1, the phases involved are disconcertingly simple: fibres are perfectly aligned cylinders of revolution that the percolating matrix joins together.

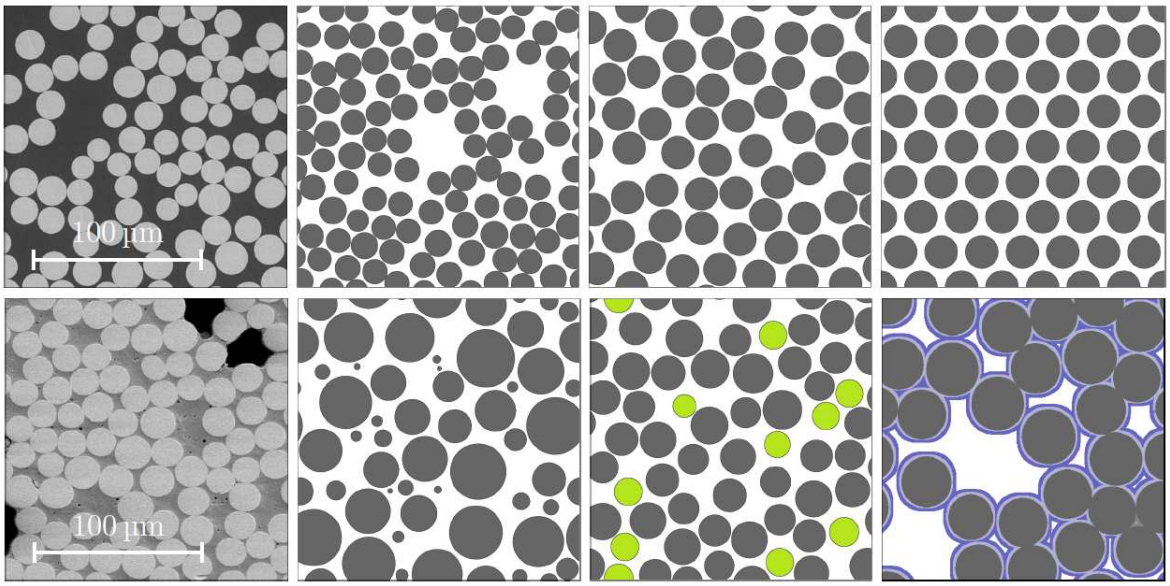

Figure 1. Cross-sections of real (with scale bars) and virtual unidirectional composite materials.

  doi:10.5075/epfl-298799_978-2-9701614-0-0

The UD discussed in this paper is the “elementary brick” used to build more complex composite structures. Whether it is a laminated composite, a woven-reinforced composite, or even a discontinuous-reinforced composite, these three configurations all result from the geometric assembly of UD “bricks”. The high anisotropy of UD is both a strength and a weakness. It is first of all an asset because the aligned arrangement of the fibres allows an optimal response to any longitudinal load. But it is also a weakness because the arrangement results also in poor mechanical strength in the plane of transverse isotropy. Real mechanical loadings are often complex, far from a uniaxial state of stress. The study of transverse properties is therefore as important as that of longitudinal properties.

For transverse properties, experimental characterisation is always a tedious procedure and the resulting uncertainties are often large. These complications provide a strong practical motivation for the development of models that can be used to predict material performance. However, this does not mean that the models eliminate the underlying difficulties. While the prediction of longitudinal properties of UD is rarely complicated, transverse properties are much more affected by interactions between constituents and the prediction of these properties is always a challenge. Indeed, although simple in nature, UD can exhibit a very wide variety of microstructures as suggested by Figure 1. If the longitudinal properties are only dependent (to the first order) on the intrinsic characteristics and the volume fraction of the phases, it is not the same for the transverse properties. Transverse properties are intimately linked to morphological fluctuations and the spatial distribution of the phases.

This paper builds on the results published in three papers [1-3], and aims to address the issue of model calibration to take into account local morphological fluctuations in the prediction of transverse behaviour of UD composites. After presenting the strategy on a simpler transport-diffusion problem, we propose in a second step to treat the mechanics problem and then to unify the approach.

2. Generalized Self-Consistent Scheme & Morphological Representative Patterns

The general framework of this work is best introduced by modelling the transport phenomenon in a multiphase transverse isotropic material. As an example, a UD brick of composite material is subjected to a molecular diffusion of water. It goes without saying that the present development is applicable to any other transport phenomenon and in particular to thermal diffusion. The strategy adopted in [1-2] allows the effective diffusivity of a composite medium to be predicted. While the components of the diffusivity tensor can be obtained by averaging the properties of the phases, the difficulty lies in how this averaging is carried out. If a simple law of mixtures is sufficient to accurately predict the longitudinal transport properties, a more refined model is required to deal with the transverse properties by taking into account morphological fluctuations. What distinguishes the different existing approaches, (while remaining within a mean-field modelling strategy), is the way they can handle (under undiluted conditions) local morphological fluctuations or a significant contrast between the properties of the phases involved. We have proposed to address these two challenges by exploiting a Generalized Self-Consistent Scheme [4,5] coupled with a morphologically representative model [6].

  doi:10.5075/epfl-298799_978-2-9701614-0-0

The GSCS part follows from the work in [7,8] which extends the initial 3 phase approach in [4] to the general case of "n" concentric phases. This work was revisited in [9] with a simplification of the formulation. The n-phases approach allows for example to consider problems of interphases or imperfect interfaces [10]. As mentioned above, in [1] the n-phase model has been coupled with a morphological pattern approach in order to capture transverse morphological fluctuations.

In [2], the model is implemented based on the microstructure and experimental results in [11,12]. In addition to the original 3 phase pattern, it was necessary to take into consideration the matrix areas trapped by an inverse pattern. Figure 2 illustrates this 2-phases/2-patterns model wrapped in the Equivalent Homogeneous Medium (EHM).

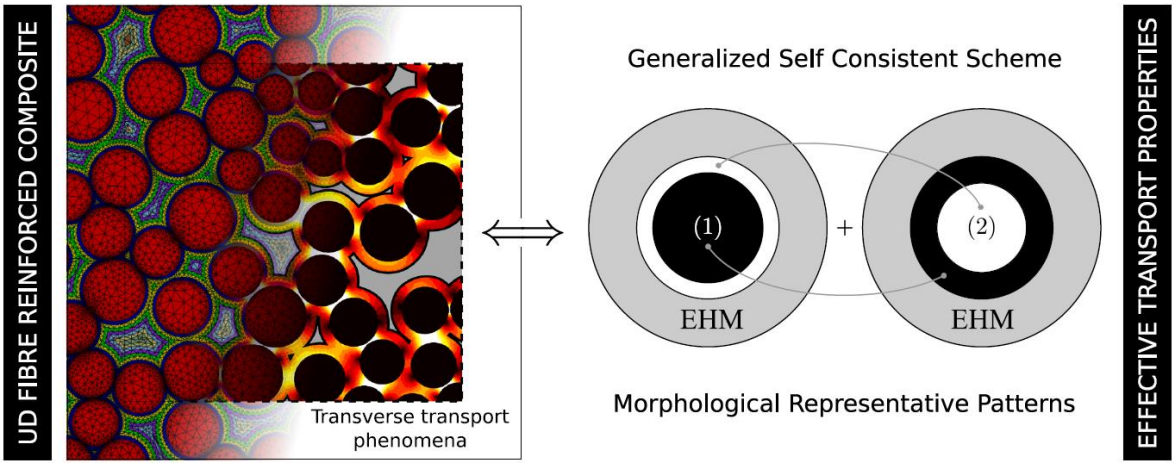

Figure 2. The composite medium (left) is modelled by a 2-phase/2-pattern approach (right). On the left, the flux norm is represented by a colour gradient from pale yellow to black (zero flux). The gray shaded areas correspond to the trapped matrix areas.

The behaviour of this particular case is governed by three morphological parameters: the volume fraction of reinforcement in the composite, f, the proportion of the original direct pattern, m, itself containing a concentration c of reinforcement. By defining f, it is possible to specify the range in which the effective transverse diffusivity can vary. The special case $c = f$ is relatively interesting as we will see in the forthcoming mechanical application, and, in this case:

$$\frac{D_T^{\text{eff}}}{D_T^{\text{matrix}}} = \frac{(1-f)(2m-1)}{(1+f)} \quad \text{if} \quad D_T^{\text{fibre}} = 0$$

By setting f, it is possible to specify the range in which the effective transverse diffusivity can vary (see Figure 3). The peak of the envelope curve corresponds to the classical GSCS model. The identification of the parameter m (and eventually c) remains an essential step. Several strategies based on the analysis of microstructure images have been experimented. Figure 3 shows the full predictive range of the proposed model and confirms the relevance of the proposed coupling between GSCS and MRP strategies.

  doi:10.5075/epfl-298799_978-2-9701614-0-0

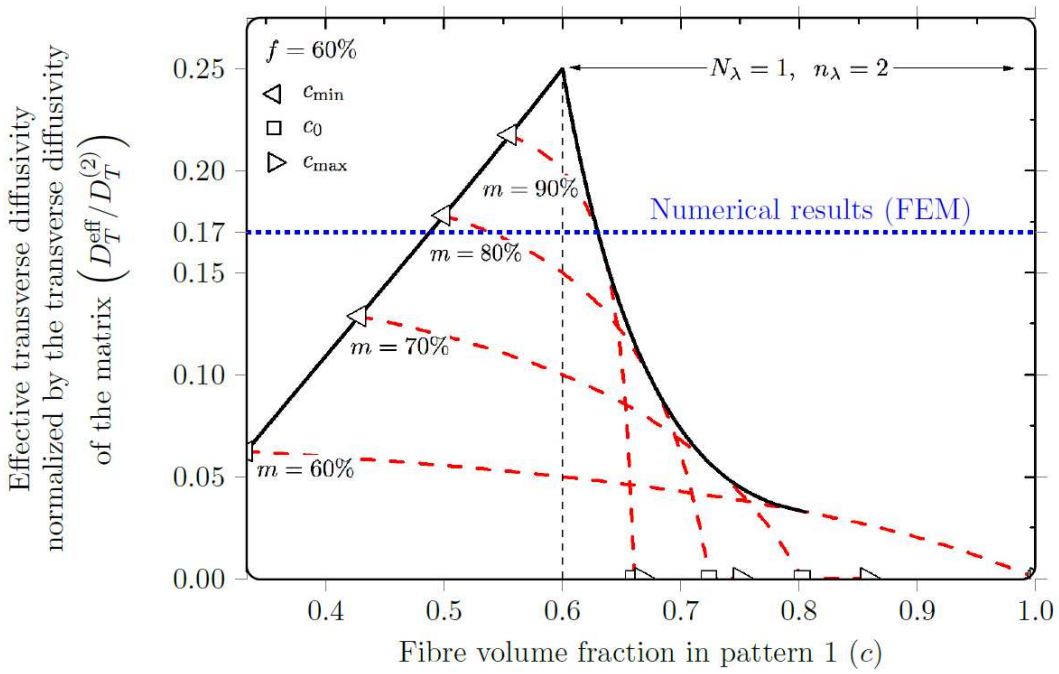

Figure 3. Envelope curve of the effective transverse diffusivity normalized by the matrix diffusivity

3. Extension of the model to mechanics

The previously described GSCS-MRP coupling has been extended to mechanics [3]. The focus was on k_{23}^{eff} and μ_{23}^{eff}, respectively the effective transverse bulk and shear moduli of the material. These two moduli are generally very difficult to obtain experimentally or with a very high uncertainty that makes structural calculations complex. The results [3] show a coupling between these two parameters, making the solution of the problem implicit.

As in the previous example, the model was also simplified to apply to the2-phases/2-patterns case with three parameters: f, m and c. In relation to diffusion, the first question raised was the existence of a unique (m, c) couple for the two elastic parameters studied. For this purpose, rather than very difficult experimental tests, full-field finite element numerical simulations have been carried out on representative microstructures. Uncertainties have been controlled through the use of tools such as the integral range method.

In Figure 4, the effective transverse shear modulus, normalized by the transverse shear modulus of the matrix is plotted as a function of phase contrast. The volume fraction of inclusions is $f = 0.6$; $\nu^{\text{fibre}} = 0.2$, $\nu^{\text{matrix}} = 0.3$. It can be seen from Figure 4 that the direct pattern of the original GSCS fails to capture the behaviour of representative random microstructures. For a given fibre volume fraction, f, but whatever the contrast of the properties between phases, we have shown that it is possible to define an optimised pair (m, c) allowing to predict with satisfaction and simultaneously k_{23}^{eff} and μ_{23}^{eff}. The sensitivity study has shown that in order to remain in a robust performance zone, it is nevertheless very profitable to choose $c = f$. In this case, the resolution remains implicit but the equations are much easier to handle.

  doi:10.5075/epfl-298799_978-2-9701614-0-0

Taking into account this configuration ($c = f$) and referring to the contrast conditions of the right part of Figure 4, the largest error for μ_{23}^{eff} is committed for the highest contrast ratio at 10^5 and is of the order of 5%; whereas the GSCS model leads to an error of more than 8% under the same conditions.

For k_{23}^{eff} (not shown on the figure), the error committed for the highest contrast ratio at 10^5 is less than 1%, which is much smaller than the GSCS model which leads to an error of the order of 8% also, under the same conditions. The question on the uniqueness of (m, c) pairs was then raised by extending the context of mechanics to the transport problem described above. By choosing $c = f$ and using the value of m optimised for mechanics, it is possible to predict with accuracy the values of k_{23}^{eff} and μ_{23}^{eff}, but also D_T^{eff}.

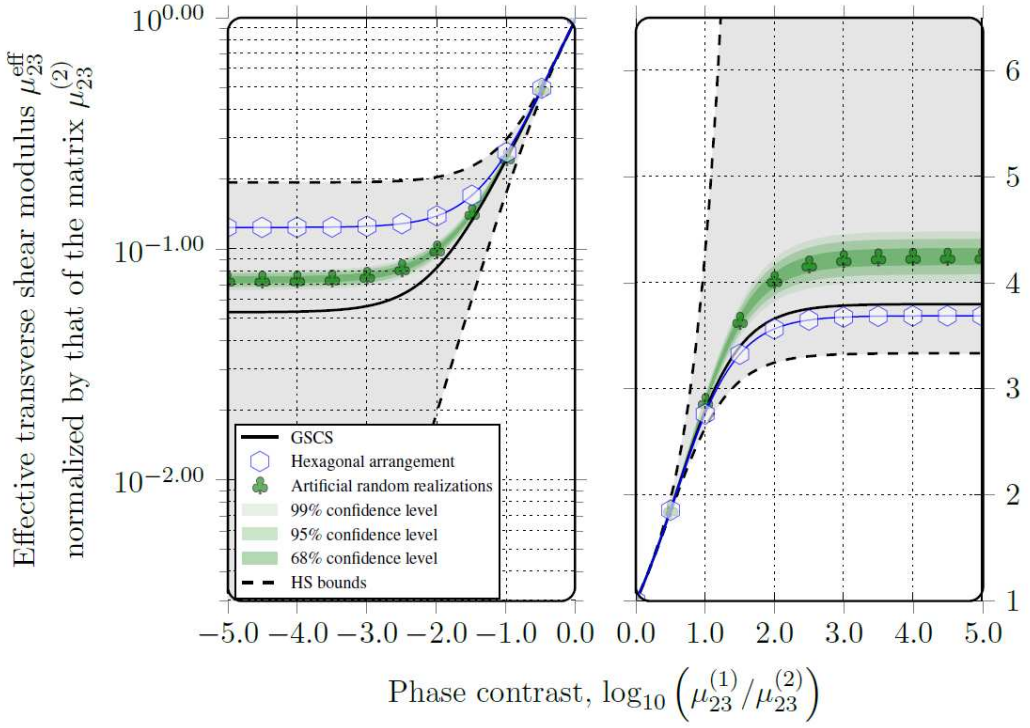

Figure 4. Effective transverse shear modulus, normalized by the transverse shear modulus of the matrix, plotted as a function of phase contrast.

4. Conclusion

The identification of m remains today the main challenge of this work and the use of the geometrical covariogram seems a very promising way. The present approach is appropriate to take into consideration the different microstructures illustrated in Figure 1. For some examples, however, the number of phases or patterns must be increased and the calibration strategy for the new parameters must be defined. For instance, the method has been used with success to model the porosity at different scales of the composite part of a high pressure cylinder. The application to hybrid composites is also a very interesting application and many others configurations are possible.

  doi:10.5075/epfl-298799_978-2-9701614-0-0

5. References

1. E. Hervé-Luanco et S. Joannès. “Multiscale Modelling of Transport Phenomena for Materials with n-Layered Embedded Fibres. Part I : Analytical and Numerical-Based Approaches”. International Journal of Solids and Structures 97-98 (2016), p. 625-636.
2. S. Joannès et E. Hervé-Luanco. “Multiscale Modelling of Transport Phenomena for Materials with n-Layered Embedded Fibres. Part II : Investigation of Fibre Packing Effects”. International Journal of Solids and Structures 97-98 (2016), p. 566-574.
3. J. Blondel, S. Joannès et E. Hervé-Luanco. “Analytical Modelling of the Effect of Morphological Fluctuations on the Transverse Elastic Behaviour of Unidirectional Fibre Reinforced Composites. International Journal of Solids and Structures 206 (2020), p. 436-455.
4. R. M. Christensen et K. H. Lo. “Solutions for Effective Shear Properties in Three Phase Sphere and Cylinder Models”. Journal of the Mechanics and Physics of Solids 27.4 (1979), p. 315-330.
5. Y. Benveniste. “Revisiting the Generalized Self-Consistent Scheme in Composites : Clarification of Some Aspects and a New Formulation”. Journal of the Mechanics and Physics of Solids 56.10 (2008), p. 2984-3002.
6. M. Bornert, C. Stolz and A. Zaoui. “Morphologically Representative Pattern-Based Bounding in Elasticity”. Journal of the Mechanics and Physics of Solids 44.3 (1996), p. 307-331.
7. E. Hervé et A. Zaoui. “N-Layered Inclusion-Based Micromechanical Modelling”. International Journal of Engineering Science 31.1 (1993), p. 1-10.
8. E. Hervé et A. Zaoui. “Elastic Behaviour of Multiply Coated Fibre-Reinforced Composites”. International Journal of Engineering Science 33.10 (1995), p. 1419-1433.
9. E. Hervé-Luanco. “Elastic Behaviour of Multiply Coated Fibre-Reinforced Composites: Simplification of the (n+1)-Phase Model and Extension to Imperfect Interfaces”. International Journal of Solids and Structures 196-197 (2020), p. 10-25.
10. E. Hervé-Luanco. “Elastic Behavior of Composites Containing Multi-Layer Coated Particles with Imperfect Interface Bonding Conditions and Application to Size Effects and Mismatch in These Composites”. International Journal of Solids and Structures 51.15 (2014), p. 2865-2877.
11. Y. Joliff, L. Belec et J. F. Chailan. “Modified Water Diffusion Kinetics in an Unidirectional Glass/Fibre Composite Due to the Interphase Area : Experimental, Analytical and Numerical Approach”. Composite Structures 97 (2013), p. 296-303.
12. Y. Joliff, W. Rekik, L. Belec et J. F. Chailan. “Study of the Moisture/Stress Effects on Glass Fibre/Epoxy Composite and the Impact of the Interphase Area”. Composite Structures 108 (2014), p. 876-885.

  doi:10.5075/epfl-298799_978-2-9701614-0-0

RATE DEPENDENT ADHESIVE MODELING OF DUCTILE ADHESIVE COMPOSITE JOINTS

Ghazaleh Eslami[a], A. Vahid Movahedi-Rad[b] and Thomas Keller[c]

a: Ph.D. candidate at Composite Construction Laboratory (CCLab), École Polytechnique Fédérale de Lausanne (EPFL), Switzerland – ghazaleh.eslami@epfl.ch
b: Guest researcher at Composite Construction Laboratory (CCLab), École Polytechnique Fédérale de Lausanne (EPFL), Switzerland
c: Full professor at Composite Construction Laboratory (CCLab), École Polytechnique Fédérale de Lausanne (EPFL), Switzerland

Abstract: *The mechanical behavior of flexible adhesives used in fiber-polymer composite joints under monotonic and cyclic loading is highly nonlinear and sensitive to displacement rate in particular. To simulate their rate-dependent mechanical behavior, a phenomenological model was developed consisting of a linear and a nonlinear Maxwell unit acting in parallel. The viscoelastic parameters were calibrated by the results obtained from experiments under tension monotonic and reversed cyclic loadings. The applicability of the derived model is presented by power-law relationships between 1) the monotonic viscoelastic parameters and the applied displacement rates, and 2) the cyclic viscoelastic parameters and the maximum cycle displacements. The relationships enabled the simulation of both the pre- and post-yield monotonic and cyclic response characteristics, such as stretching of molecular chains (strain hardening), and formation and accumulation of damage (softening).*

Keywords: Adhesive-composite joint; ductile adhesive; rate-dependent behavior; constitutive equation; cyclic response

1. Introduction

In a load-bearing structure composed of brittle members, such as composite laminates, pseudo-ductility can be obtained by using a pseudo-ductile adhesive in the joints [1]. Due to the relatively high stiffness of the laminates compared to the adhesive in pseudo-ductile joints, the joints' response to the applied displacement mainly depends on the behavior of the adhesive. The adhesives used for structural purposes are mostly thermoset polymers and exhibit viscoelastic behavior [2].

In thermoset polymers, viscoelastic behavior is a result of molecular chain movements, which are both strain rate- and temperature-dependent [3]. Different applied strain rates can result in different mechanical responses in the polymer, varying from brittle to pseudo-ductile, with different yield load and post-yield behavior [4]. The thermoset molecular chain structure consists of both primary bonds (in the chains and cross-links between the chains, mainly covalent bonds) and secondary bonds (van der Waals and hydrogen bonds), whose strength decreases as the distance between the chains increases. Under applied low strain rates, the coiled chains have sufficient time to uncoil. After the yield point, chains start to lose secondary bonds and subsequently become aligned or stretched [5]. The stiffness thus significantly decreases and the deformability significantly increases; stretching may result in a hardening behavior. On the other hand, under high strain rates, the chains do not have sufficient time to

  doi:10.5075/epfl-298799_978-2-9701614-0-0

rearrange and respond to the imposed displacement, and the molecular mobility of the chains is reduced. Consequently, the stiffness remains high and deformability low [6]. Broken primary and lost secondary bonds contribute to the initiation and propagation of damage and energy dissipation in viscoelastic polymers [7].

Comprehensive constitutive models are valuable assets for analysis and design purposes and a wide range of constitutive models has therefore been developed for viscoelastic materials. The simplest mechanical model for viscoelastic behavior consists of two elements, each representing a mechanical characteristic of the behavior: a spring and a dashpot (or damper). A linear spring is used for modeling the elastic behavior where the spring constant, S, is the modulus of elasticity. A linear viscous dashpot contains a fluid with a viscosity η is used to model the viscous behavior [8]. Spring and dashpot elements can be combined in a variety of configurations to produce a desired viscoelastic response. Maxwell and Kelvin are the most basic models that combine a Hookean spring with a Newtonian dashpot, in series and parallel, respectively [9]. The combination of a simple spring and a dashpot element has been long used for simulating the rate-dependent behavior of viscoelastic materials [10].

Bergström and Boyce performed a study on the large-strain time-dependent behavior of elastomeric materials [11]. They proposed that the mechanical behavior of elastomeric materials can be decomposed into an elastic and a time-dependent segment (viscous segment) and modeled with nonlinear springs and a dashpot. Liu et al. [12] found that the Bergström and Boyce model was unable to identify the damage accumulation in filled rubbers to capture their rupture under cyclic loading. To capture stress-softening, i.e. damage accumulation, Ayoub et al. [13] proposed a phenomenological model which comprised a nonlinear spring in parallel with a nonlinear Maxwell element. In their model, they identified the average length of the chains and the average number of chains per unit volume as the physical parameters and modified both by a variable damage parameter.

In this study, to allow for a representative simulation of the pseudo-ductile behavior of adhesively-bonded fiber-polymer composite joints under various applied displacement rates, a novel phenomenological model is developed for the viscoelastic behavior of pseudo-ductile adhesives. The phenomenological model consists of two parallel units: a Maxwell unit characterizing the linear viscoelastic behavior before the onset of adhesive chain stretching, and a modified Maxwell unit with a variable stiffness spring that characterizes the nonlinear viscoelastic behavior during the molecular chain stretching. Unlike in literature, a unique constitutive equation is proposed for modeling both the monotonic and reversed cyclic behavior of the pseudo-ductile adhesive. The model parameters were calibrated with the results of monotonic and reversed cyclic experiments, previously performed in [14].

2. General phenomenological model

Double-lap joint specimens consisting of fiber-polymer composite adherends and a ductile adhesive were subjected to a series of monotonic tension and reversed cyclic tension-compression experiments; details of the experimental work and its motivation can be found in [14]. The load-joint displacement responses of the adhesive joints under monotonic and reversed cyclic loading are summarized in Fig. 1. Since the laminate stiffness was significantly greater than the adhesive stiffness and the contribution of the laminates to the joint displacements was thus negligible [14], the measured joint displacements, shown in Figs. 1 were

directly used for modeling the viscoelastic behavior of the adhesive. Furthermore, the cyclic responses (Fig. 1 (b), (c), and (d)) between the two reversal points of each cycle [14], followed the same pattern as the monotonic responses (Fig. 1 (a)). Therefore, the derived phenomenological model for the monotonic responses was applicable to the cyclic responses.

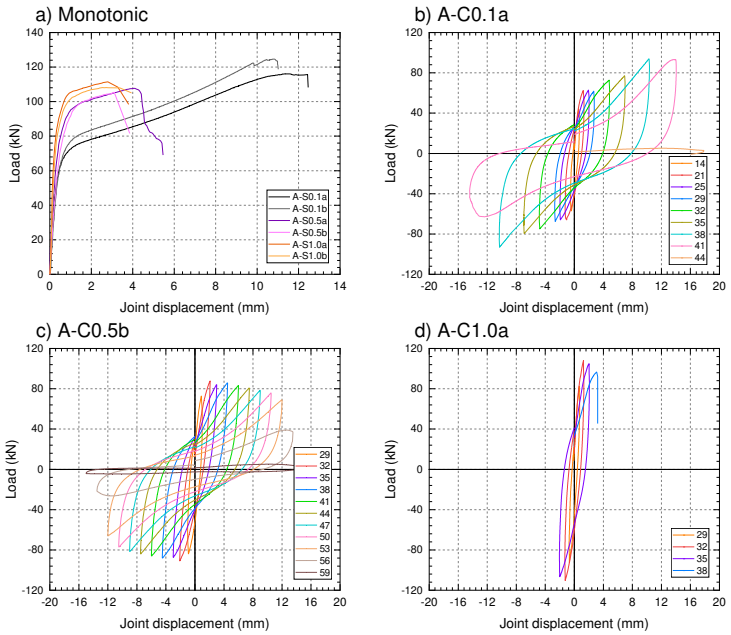

Figure 1. Load-joint displacement responses under a) monotonic loading under three displacement rates, and cyclic loading, primary cycles of b) A-C0.1a, c) A-C0.5b, d) A-C1.0a [14]

The investigated monotonic load-displacement curves were almost bilinear and thus consisted of two main branches, i.e., a pre-yield linear viscoelastic and a post-yield nonlinear viscoelastic branch, see Fig. 1 (a). Consequently, a phenomenological model composed of two dissimilar parallel Maxwell units was introduced, as shown in Fig. 2 (a). The first Maxwell unit includes a spring of constant stiffness and a dashpot in series, while the second unit consists of a spring with variable stiffness and a dashpot in series. The first Maxwell unit simulates the rate-dependent initial branch up to the yield point level as shown in Fig. 2 (b) (red line). The second Maxwell unit simulates the nonlinear stiffening due to the molecular chains' rate-dependent stretching up to the failure level, see blue line in Fig. 2 (b).

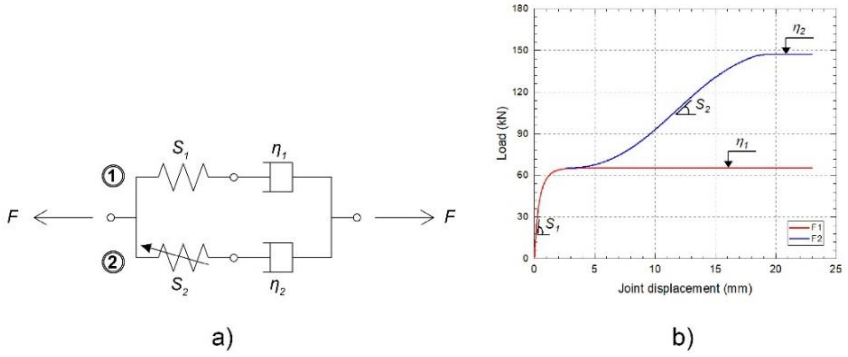

Figure 2. Rheological structure of phenomenological model

A mathematical model can be derived by combining the constitutive relationships of each Maxwell unit, considering force-displacement equilibrium and boundary conditions as follows:

$$X = X_1 = X_2 = \dot{X}t \quad (1)$$

$$F = F_1 + F_2 \quad (2)$$

where X is the total applied displacement, equal to the displacements of the first and second Maxwell units (X_1, X_2) in [mm], $\dot{X}$ is the applied displacement rate in [mm/s], and t is the time in [s]. Similarly, F is the total force, which is equal to the sum of the first and second Maxwell unit forces, F_1 and F_2, respectively, in [kN].

The force-displacement relationships in the Maxwell units can be expressed as follows [15]:

$$X_n = \left(\frac{1}{S_n} + \frac{1}{\eta_n \frac{\partial}{\partial t}}\right).F_n \ , \ n = 1,2 \quad (3)$$

where n is the number representing each of the Maxwell units. For the first Maxwell unit (n = 1), S_1 is the constant stiffness of the spring in [kN/mm], and η_1 is the viscosity coefficient of the dashpot in [kNs/mm]. For the second Maxwell unit (n = 2), S_2 is the variable stiffness of the spring to simulate the chain stretching effect on the load-displacement response, and η_2 is the viscosity coefficient of the second dashpot. Since the chain stretching causes a nonlinear increase in the adhesive stiffness, S_2 can be defined by a power-law relationship as follows [15]:

$$S_2 = \alpha \left(\frac{X}{\dot{X}}\right)^{\beta} \quad (4)$$

where α and β are fitting parameters defined for each cycle and displacement rate. By substituting the displacement equation (Eq. (1)) into the Maxwell unit relationships (Eq. (3) and (4)), the total load (Eq. (2)) can be calculated as follows:

$$F = \dot{X}\eta_1\left(1 - e^{-\lambda_1 t}\right) + \dot{X}\eta_2\left(1 - e^{-\frac{\lambda_2 t}{(\beta+1)}}\right) \quad (5)$$

where λ_1 and λ_2 are equal to S_1/η_1 and S_2/η_2, respectively. Parameters S_1, η_1, α, β, and η_2 are the considered viscoelastic parameters, to be determined for the development of the phenomenological model.

The optimization method used to estimate the viscoelastic parameters solved a nonlinear least-squares problem using the Trust Region Reflective (TRF) algorithm to apply error minimizing. The optimization task was performed using the Scipy.optimize library [16] in Python.

3. Monotonic and cyclic viscoelastic parameter results

3.1 Rate-dependent monotonic viscoelastic parameters

The load-displacement responses, obtained from the derived constitutive equation Eq. (5), are shown in Fig. 3 for the applied displacement rates of 0.1, 0.5, and 1.0 mm/s. The models agree well with the experimental results. The slight differences in the pre-yield linear segments of the phenomenological model and experimental curves were mainly due to the contribution of the laminate deformations, which became negligible after the yield points since the deformations in the adhesive increased significantly.

  doi:10.5075/epfl-298799_978-2-9701614-0-0

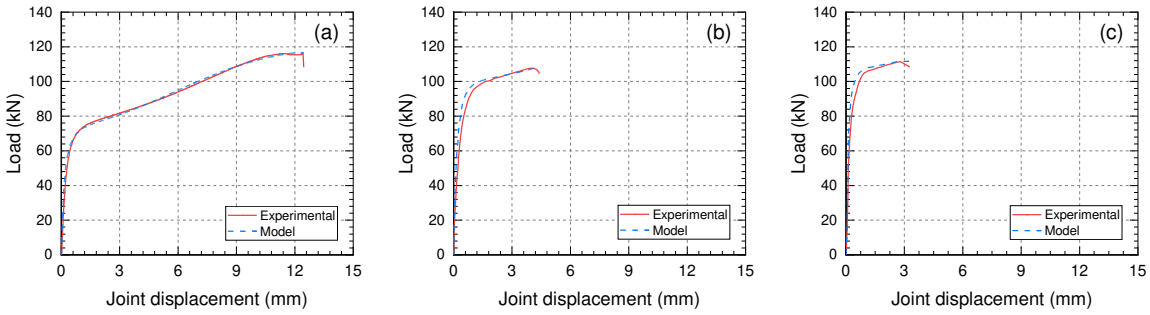

Figure 3. Phenomenological model and experimental load-displacement curves for displacement rates of: (a) 0.1 mm/s, (b) 0.5 mm/s, and (c) 1.0 mm/s.

The variations of the estimated viscoelastic parameters of the phenomenological model versus the applied displacement rates or joint displacement are shown in Fig. 4. The estimated values of S_1, η_1, and η_2, for the applied displacement rates of 0.1, 0.5, and 1.0 mm/s are shown with solid circles in Fig. 4 (a), (b), and (d) respectively, with added power-law fitted curves represented by dashed lines; the variable S_2 parameter is shown in Fig. 4 (c). By increasing the applied displacement rate, the S_1 parameter increased, while η_1, S_2, and η_2 decreased.

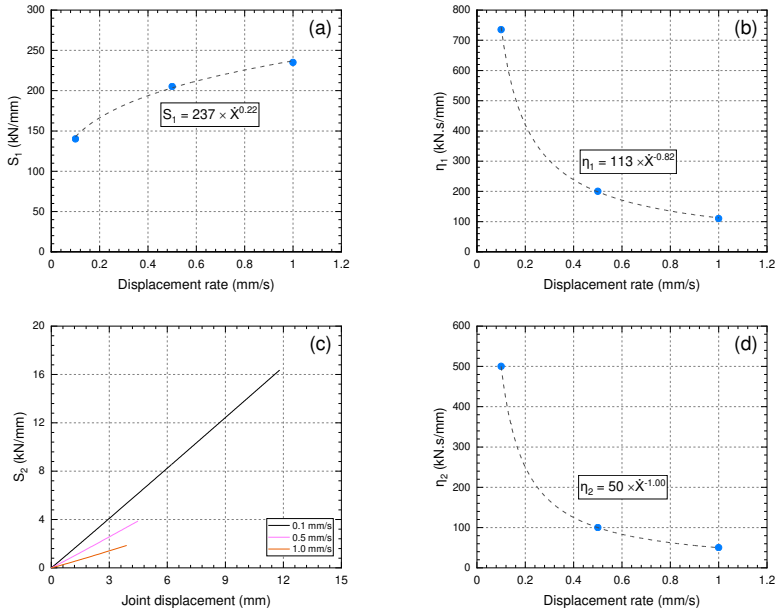

Figure 4. variation of monotonic viscoelastic parameters a) S_1, b) η_1, c) S_2, d) η_2.

3.2 Rate-dependent cyclic viscoelastic parameters

The cyclic responses of the specimens comprised primary and trailing cycles of which only the primary cycles are presented. Furthermore, by taking into account the different states of chains at the reversal points, each primary cycle response (Fig. 1 (b), (c), and (d)) was decomposed into T-P and P-P segments as 1) starting from the partially stretched state of the adhesive at the reversal point of the trailing cycle (T2) up to an almost fully stretched state at the first reversal point of the primary cycle (P1), and 2) starting from the latter (P1) to the also almost fully stretched state at the second reversal point of the primary cycle (P2) in the opposite direction.

The estimated viscoelastic parameters versus maximum cycle displacement (for S_1, η_1, and η_2) and cyclic displacement (for S_2), at each primary cycle, are shown in Fig. 5 for the applied

displacement rates, for partially and fully stretched states. The S_2 and η_2, parameters are not shown for the highest applied displacement rate of 1.0 mm/s due to the negligible amount of stretching.

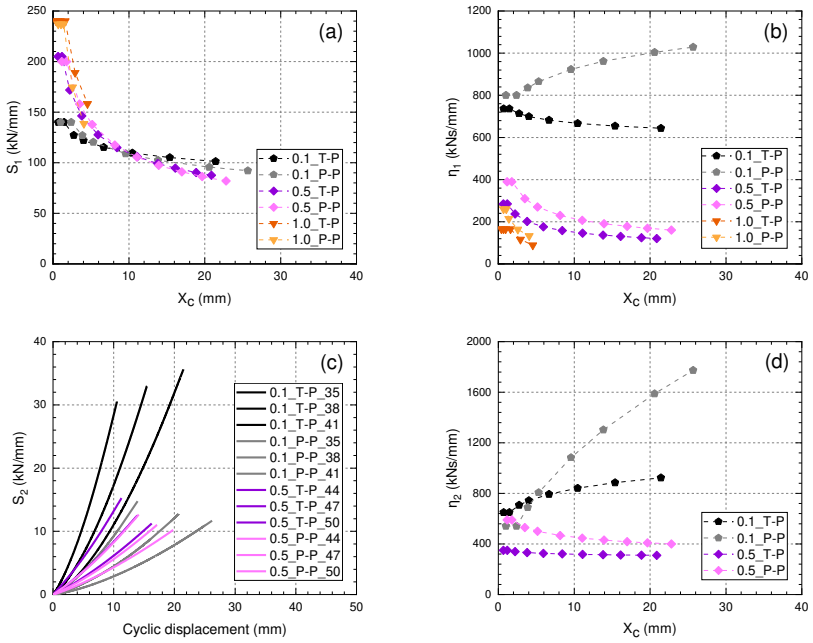

Figure 5. Variation of cyclic viscoelastic parameters, a) S_1, b) η_1, d) η_2, versus maximum cycle displacement, and c) S_2, versus cyclic displacement, under the applied displacement rates

The S_1 parameter values were initially higher at higher rates, see Fig. 5(a), but then decreased much faster than at the lower rate due to the higher loads (see Fig. 1), which increased damage formation and the associated softening. No significant differences could be observed for either of the states starting from partially or fully stretched materials.

The η_1 parameter values were higher at the lower rate and followed a decreasing trend with increasing applied maximum cycle displacements for all cases, except for the initially fully stretched material under the lowest 0.1 mm/s displacement rate, see Fig. 5(b). The accumulated damage generally decreased the viscosity parameters of the linear segment. In 0.1_P-P, however, the decreasing trend was reversed since the highly stretched chains at the reversal point first had to resist the reversed load until they ''buckled'', so to be realigned in the opposite direction.

The development of the S_2 parameter during each segment of the primary cycles is shown in Fig. 5(c). In all cases, the S_2 parameter exhibited an increasing trend due to an increasing number of aligned molecular chains with an increasing cyclic displacement. Under the lower applied displacement rate, due to the higher stretching in cycles with higher displacement, the maximum S_2 values increased in the T-P segments from each primary cycle to the next, while the slope of the curves decreased due to damage formation. In the P-P segments, the maximum S_2 values and slope of the curves (grey lines) were lower than in the T-P segments due to a delay in stretching. By increasing the cycle displacement, the delay in stretching in the opposite direction became more dominant and thus the S_2 maximum values decreased from each primary cycle to the next. At the higher applied displacement rate, much more damage was accumulated, which decreased both the S_2 maximum values and the slopes of the curves.

  doi:10.5075/epfl-298799_978-2-9701614-0-0

The η_2 parameter values were higher and increased for the lower 0.1 mm/s rate, and lower and decreased for the higher 0.5 mm/s rate (Fig. 5 (d)). The increasing-decreasing trends of the η_2 values were in line with the trends of the peak loads of each primary cycle (Fig. 1) since the former was determined from the latter (Fig. 2). The dominating hardening behavior at the lower rate increased the peak loads and thus η_2, while the dominating softening at the higher rate decreased the peak loads and η_2.

4. Model validation

The full cyclic responses of the experimental and phenomenological model under the displacement rate of 0.1 mm/s are compared in Fig. 6(a). The envelope curves of the experimental cyclic responses, shown in Fig. 1, and of the modeled cyclic responses, are further compared in Fig. 6(b). They were constructed by connecting the P1 peak loads. The comparison reveals that the hardening behavior under 0.1 mm/s and the softening behavior under 0.5 mm/s displacement rate were well represented in the model.

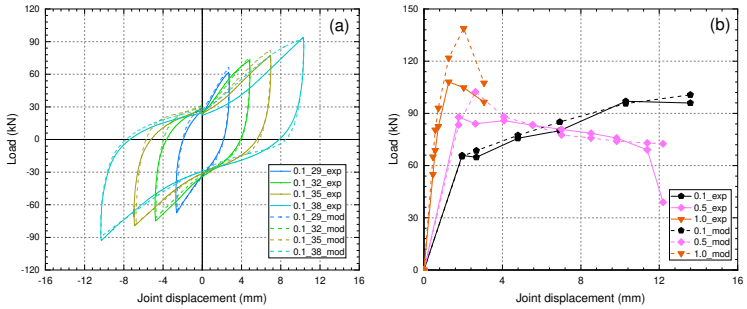

Figure 6. Experimental and modeled (a) load-displacement responses of full cycles for specimen A-C0.1a, and (b) envelope curves for specimen A-C0.1a and A-C0.5b at P1 reversal points

The comparison between the curves in Fig 6 validates the capacity of the phenomenological model to simulate the entire cyclic load-displacement behavior of the specimens.

5. Conclusions

A new phenomenological model was presented, allowing the simulation of the rate-dependent load-displacement responses of a pseudo-ductile adhesive joint under axial monotonic and cyclic loadings. By calibrating the viscoelastic parameters of the phenomenological model with the results from experimental monotonic and cyclic investigations, it could be concluded that:

1- The two Maxwell units of the phenomenological model were able to well simulate the rate-dependent pre- and post-yield branches of both monotonic and cyclic responses.

2- The viscoelastic parameters of the Maxwell units did capture well the physical characteristics of the adhesive in both monotonic and cyclic responses, such as stretching of molecular chains, and formation and accumulation of damage.

3- The effects of the applied displacement rate on the monotonic loading behavior were well represented by power-law relationships between the monotonic viscoelastic parameters and the applied displacement rates.

  doi:10.5075/epfl-298799_978-2-9701614-0-0

4- The proposed model could well predict the cyclic envelope curves, except for the final failure values of the last cycles. To also model the final chain scission, a third parallel unit could be added to the model, consisting of a dashpot element.

6. References

[1] Keller T, De Castro J. System ductility and redundancy of FRP beam structures with ductile adhesive joints. Compos Part B Eng 2005;36:586–96. https://doi.org/10.1016/j.compositesb.2005.05.001.

[2] Lancaster JF. The use of adhesives for making structural joints. Metall. Weld., Woodhead Publishing Series in Welding and Other Joining Technologies; 1999, p. 54–84. https://doi.org/10.1533/9781845694869.54.

[3] Ward IM, Sweeney J. Mechanical properties of solid polymers. vol. 1. 2013. https://doi.org/10.1016/0025-5416(67)90014-6.

[4] Angelidi M, Vassilopoulos AP, Keller T. Displacement rate and structural effects on Poisson ratio of a ductile structural adhesive in tension and compression. Int J Adhes Adhes 2017;78:13–22. https://doi.org/10.1016/j.ijadhadh.2017.06.008.

[5] Askeland DR, Wright WJ. The Science and Engineering of Materials. 7th Editio. Global Engineering: Timothy L. Anderson; 2014. https://doi.org/https://doi.org/10.1007/978-1-4899-2895-5.

[6] Foreman JP, Porter D, Behzadi S, Curtis PT, Jones FR. Predicting the thermomechanical properties of an epoxy resin blend as a function of temperature and strain rate. Compos Part A Appl Sci Manuf 2010;41:1072–6. https://doi.org/10.1016/j.compositesa.2009.10.015.

[7] Deblieck RAC, Van Beek DJM, Remerie K, Ward IM. Failure mechanisms in polyolefines: The role of crazing, shear yielding and the entanglement network. Polymer (Guildf) 2011;52:2979–90. https://doi.org/10.1016/j.polymer.2011.03.055.

[8] Brinson HF, Brinson LC. Polymer engineering science and viscoelasticity: An introduction, Second edition. 2015. https://doi.org/10.1007/978-1-4899-7485-3.

[9] Alfrey T, Doty P. The methods of specifying the properties of viscoelastic materials. J Appl Phys 1945;16:700–13. https://doi.org/10.1063/1.1707524.

[10] Schwarzl F, Staverman AJ. Time-temperature dependence of linear viscoelastic behavior. J Appl Phys 1952;23:838–43. https://doi.org/10.1063/1.1702316.

[11] Bergström JS, Boyce MC. Constitutive modeling of the time-dependent and cyclic loading of elastomers and application to soft biological tissues. Mech Mater 2001;33:523–30. https://doi.org/10.1016/S0167-6636(01)00070-9.

[12] Liu M, Hoo Fatt MS. A constitutive equation for filled rubber under cyclic loading. Int J Non Linear Mech 2011;46:446–56. https://doi.org/10.1016/j.ijnonlinmec.2010.11.006.

[13] Ayoub G, Zaïri F, Naït-Abdelaziz M, Gloaguen JM, Kridli G. A visco-hyperelastic damage model for cyclic stress-softening, hysteresis and permanent set in rubber using the network alteration theory. Int J Plast 2014;54:19–33. https://doi.org/10.1016/j.ijplas.2013.08.001.

[14] Eslami G, Yanes-Armas S, Keller T. Energy dissipation in adhesive and bolted pultruded GFRP double-lap joints under cyclic loading. Compos Struct 2020:112496. https://doi.org/10.1016/j.compstruct.2020.112496.

[15] Ferry JD. Viscoelastic properties of polymers. Third ed. John Wiley & Sons; 1980.

[16] Virtanen P, Gommers R, Oliphant TE, Haberland M, Reddy T, Cournapeau D, et al. {{SciPy} 1.0: Fundamental algorithms for scientific computing in Python}. Nat Methods 2020;17:261–72. https://doi.org/10.1038/s41592-019-0686-2.

  doi:10.5075/epfl-298799_978-2-9701614-0-0

INFLUENCE OF POLYMER MATRIX ON THE INDUCTION HEATING BEHAVIOR OF CFRPC LAMINATES

Thomas Hoffmann[a], Stephan Becker[a], Miro Duhovic[a], Peter Mitschang[a]

a: Leibniz-Institut für Verbundwerkstoffe GmbH, Erwin-Schroedinger-Str. 58, 67663 Kaiserslautern, Germany, www.ivw.uni-kl.de – thomas.hoffmann@ivw.uni-kl.de

Abstract: Within this study, the interaction of different matrix polymer systems with different reinforcing fabrics made of carbon fibers (CF) was analyzed experimentally and theoretically with respect to their heating behavior. For this purpose, an electro-technical model of a roving-roving cross-junction was developed. Additionally, this model was validated by means of induction heating tests. Compared to other laminate parameters, the dielectric properties of the polymer matrix has no significant influence on the induction heating behavior of fabric reinforced carbon fiber reinforced polymer composite (CFRPC). The heat dissipated at one cross-junction due to dielectric losses is up to twelve decades lower compared to the heat dissipated due to the contact resistance.

Keywords: carbon fiber reinforced polymer composite; thermoplastic resin; inductive heating; joule losses; dielectric polarization

1. Introduction

Induction heating is an effective method in particular for the processing of carbon fiber reinforced polymer composite (CFRPC). A major advantage of induction heating is the possibility of a fast and contactless heating, which is made possible by the high heating efficiency of this process. In induction heating of CFRPC laminates, a high-frequency alternating current (approx. 500 KHz) is applied to an inductor. The resulting alternating magnetic field induces eddy currents into the laminate, which results in heat generation within the material. As a prerequisite, the carbon fibers (CF) must allow the formation of electrical loops (e.g. through cross-junctions). The induced eddy current dissipates through electrical losses, which leads to rapid intrinsic heat generation within the laminate. However, it has not yet been validated, whether the type of polymer matrix, in particular its dielectric behavior, has an influence on the inductive heating behavior of CFRPC laminates. In order to investigate the influence of the used polymer matrix on the inductive heating behavior of CFRPC laminates, different polymers in combination with different reinforcing fabrics were investigated both experimentally and theoretically.

2. Heating mechanisms and analytical approach

In [1], an analytical approach was introduced in order to model the different heating contributions from different heat loss mechanisms during induction heating. This model can be visualized via the electric circuit as shown in Figure 1. The model differentiates between three different heat loss mechanisms as follows.

  doi:10.5075/epfl-298799_978-2-9701614-0-0

Joule losses within the fibers

When passing through the electrically conductive CF, losses due to the electrical resistance R_f of the CF occur [2]. The amount of generated heat P_f by these so called joule losses, depends on the electrical resistivity of the fibers ρ_f, the cross-sectional area of the fiber material A_f, the length of the path l_f (which the current passes) and the total current I_{total} that runs through the electrical loop (Eq. (1)).

$$P_f = {I_{total}}^2 * R_f = {I_{total}}^2 * \rho_f \frac{l_f}{A_f} \quad (1)$$

Contact losses at the cross-junctions

Since the current only runs along the electrically conductive fibers, it has to alternate between differently oriented rovings (0° and 90° direction). In these areas, heat generation occurs due to the contact resistance R_{jc} between the crossing rovings. The amount of dissipated heat due to contact losses P_{jc} depends on the contact area A_c of the crossing rovings, the contact resistivity ρ_c and the current I_{jc} passing through the cross-junction (Eq. (2)) [3, 4].

$$P_{jc} = {I_{jc}}^2 * R_{jc} = {I_{jc}}^2 \frac{\rho_c}{A_c} \quad (2)$$

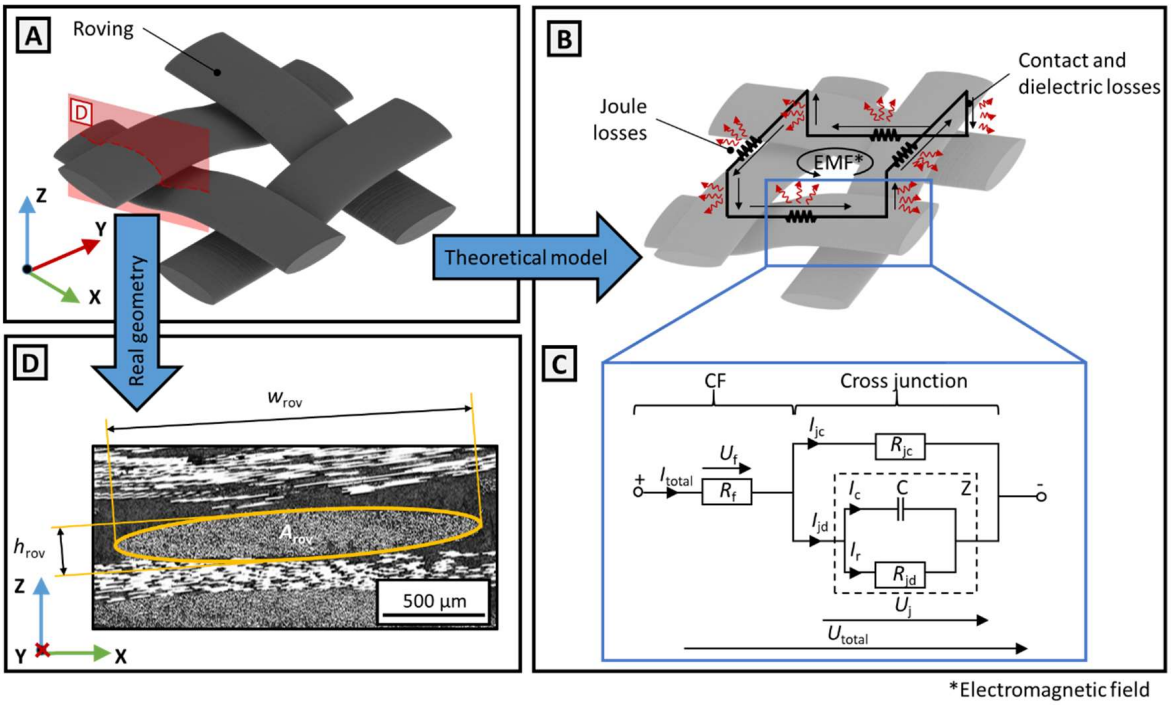

Figure 1: Schematic of a roving-roving junction (A), the resulting circuit loop with the position of the different loss mechanisms [2] (B), the electric circuit of a roving-roving junction [1] (C) and a micro-section of a roving-roving junction (D)

Dielectric losses at the cross-junction

At the cross-junctions, there is not always full physical contact between the crossing fibers within the rovings. In these areas, there is a thin polymer layer with the thickness *h* separating the fibers. In this case, the matrix polymer can act as a dielectric resulting in dielectric losses,

which lead to a heat generation P_{jd} at the cross-junctions [6,7]. According to Yarlagadda [2], the heat generation due to dielectric losses can be determined by Eq. (3).

$$P_{\mathrm{jd}} = {I_{\mathrm{r}}}^2 * R_{\mathrm{jd}} = {I_{\mathrm{r}}}^2 * \frac{h}{2\pi f A_{\mathrm{c}} \varepsilon_0 \, \varepsilon_{\mathrm{r}} \tan \delta} \tag{3}$$

The electric current I_r runs parallel to I_{jc} through the charged Area A_c. The frequency of the electro-magnetic field f, the relative permittivity ε_r, the permittivity of the vacuum with the value ε_0 (ε_0 = 8.8541878128 A*s/(V*m)) and the dissipation-factor tan(δ) of the matrix polymer further impact the dielectric losses at a cross junction.

R_{jc} and R_{jd} are strongly dependent on the contact conditions of the crossing CF within the rovings. To achieve a better understanding of how the matrix polymer, in particular the dielectric properties of the polymer, influence the inductive heating behavior, laminates based on three different polymers have been investigated experimentally and analytically.

3. Method

In order to investigate the single heat contributions, the variables introduced in Eq. (1) – (3) must be known. According to [2, 9], the resulting electrical loop in a cross-ply laminate can be simplified as a square. The length of the square sides are equal to the diameter of the induction coil. The sides of the square represent the areas, where the current runs through a roving along the fiber direction. Therefore, l_f equals the diameter of the inductor. For the calculation of the single heat contributions, the averaged cross-sectional areas of $\bar{A}_{rov}$ in 0° and 90° direction are used (Fig. 1 D)). As a further simplification, it is assumed that the contact area A_c and the charged area A_c are identical in size. A_c is determined via the product of the roving width in weft and warp direction W_{rov0} and W_{rov90}. With exception of the contact resistance R_{jc}, all resistances can be calculated with the previously introduced simplifications. However, there is a consensus in the literature [2-4], that the magnitude of the contact resistance between two rovings is in the range of $10^{-5}\Omega*m^2$. For all theoretical considerations, the parameter set of U_{total} = 1 V, h = 0.1 µm and $\rho_c = 10^{-5}\ \Omega*m^2$ is therefore used.

4. Materials

To investigate the influence of the polymer matrix on the induction heating behavior of CFRPC laminates, polypropylene (PP), polyamide 66 (PA66) and polyphenylene sulfide (PPS) were used as the polymer matrix. Since these polymers differ in their dielectric properties, a representative spectrum of polymer matrix systems is covered. All relevant properties of the used polymers are listed in Table 1.

  doi:10.5075/epfl-298799_978-2-9701614-0-0

Table 1: Overview of the relevant material properties of the used thermoplastic polymers PP, PPS and PA66.

Matrix	Manufacturer of the polymer	Density [a] ρ_m in g/cm³	Melting temp. [a] T_m in °C	Relative permittivity [b] ε_r	Dissipation factor [b] tan(δ)
PP	GEFO Folienbetrieb GmbH, Germany (Prop 402-1)	0.91	163	at 100 Hz 2.224 ± 0.0063 at 1 MHz 2.226 ± 0.0045	at 100 Hz 0.0063 at 1 MHz 0.00019
PPS	LITE GmbH, Austria (LITE P)	1.35	279	at 100 Hz 3.230 ± 0.028 at 1 MHz 3.227 ± 0.0045	at 100 Hz 0.0044 at 1 MHz 0.0005
PA66	BASF SE, Germany (Ultramid A4H)	1.11	260	at 100 Hz 3.02 ± 0.135 at 1 MHz 2.732 ± 0.069	at 100 Hz 0.0131 at 1 MHz 0.01817

[a] from suppliers' material data sheets [b] Measured according to DIN EN 62631-2-1 by the Institute of Polymer Technology of Friedrich-Alexander University Erlangen-Nuremberg, Germany

Additionally, these polymers were reinforced with different fabrics considering different contact conditions occurring in different fabric types. The name of each specimen is created by the fabric type and areal weight without units. All laminates were produced by means of film stacking with the textile parameters and laminate setups listed in Table 2. All laminates provide a laminate thickness h_{lam} of approximately 2.2 mm and a target fiber volume content (FVC) of 50 %. For every investigated matrix system, there were five specimens cut out of the previously manufactured laminates. To prevent edge effects, which may falsify the results of the induction heating experiments, the specimens were dimensioned accordingly (100 x 150 mm).

Table 2: Overview of the different reinforcement fabrics and laminate layups used in the studies

Name of specimen group	Plain 200	Twill 200	Twill 285	Satin 290
Fabric style	Plain	Twill 2/2	Twill 2/2	Satin 1/4
Area weight in g/m²	200	200	285	290
Thread-count in threads/cm	5	5	7	7
Number of cross-overs per cm²	13	6.5	12	11
Linear mass density ρ_{lin} in tex	200	200	200	200

5. Experimental setup

In order to conduct the induction heating experiments, each specimen was clamped vertically in a fixture (Fig. 2). Each specimen was inductively heated to a maximum temperature of 120°C with a pancake inductor (25 mm diameter, coupling distance a = 5 mm). The inductor was powered by a Powercube PW3-32/400 high-frequency generator from C.E.I.A. SpA (Italy) with the power output set to 40% and a frequency of approx. 480 kHz. The temperature was measured with a TIM 160 infrared camera (MICRO-EPSILON MESSTECHNIK GmbH & Co. KG, Germany). To provide an even emissivity of the measured laminate surface, an emissivity tape from TESTO SE & Co. KgaA, Germany with an emissivity of ε = 0.95 was applied to the laminate surface. The heating rates were calculated analogously to [5].

  doi:10.5075/epfl-298799_978-2-9701614-0-0

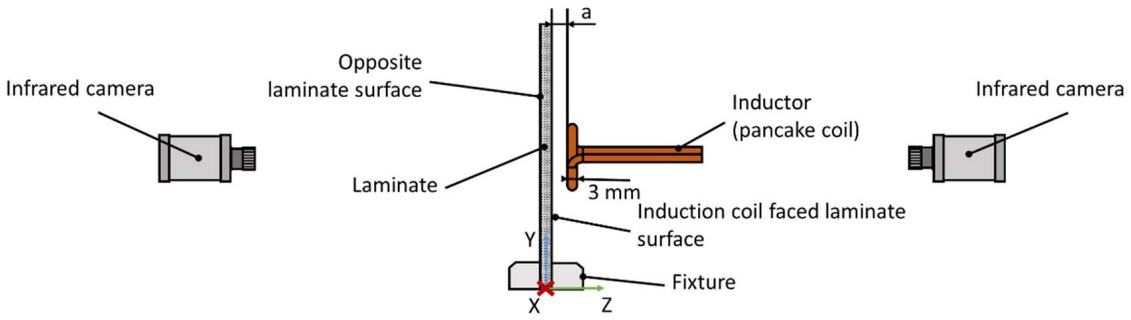

Figure 2: Schematic depiction of the experimental setup of the induction heating experiments.

6. Results and discussion

6.1 Investigation of roving geometries

In order to investigate the influence of the polymer matrix taking into account different roving geometries, laminates made with different matrix polymers and reinforcement fabrics are compared. Therefore, the roving heights h_{rov}, widths w_{rov} and cross sectional areas A_{rov} (Fig. 1 D) were determined via micro-sections of the investigated laminates. These measurements are additionally used to calculate the different heat contributions at a cross-junction. As the matrix polymer has no significant impact on the roving geometries, the values presented in Fig. 3 are averaged over all matrix polymers in weft and warp direction. The individual values used as input for the calculations can be found in [1].

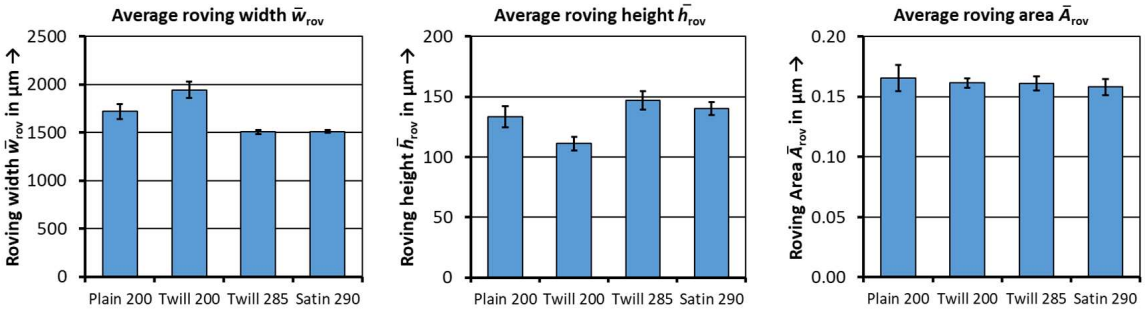

Figure 3: Comparison of the width $\bar{w}_{rov}$, height $\bar{h}_{rov}$, cross sectional area $\bar{A}_{rov}$ of the rovings depending on the fabric type averaged over all matrix polymers.

The cross-sectional area A_{rov} is the same for all investigated laminates. This is due to the linear density of the rovings ρ_{lin} being identical for all fabrics. The average width of the rovings is higher in laminates made of fabrics with lower areal weight (Plain 200, Twill 200).

6.2 Theoretical consideration of generated heat contributions at cross-junctions

Based on the theoretical cross-junction model introduced in section 2, the different heat contributions P_{jc}, P_{jd} and P_f were calculated for all previously introduced laminate configurations (Section 4). Using the parameter set presented in section 3 (in combination with the previously measured roving geometries), the heat contribution of the contact losses at the cross-junctions and the joule losses within the CF dominate (Fig. 4). The dielectric losses at the cross-junctions P_{jd} are up to twelve decades lower than the heat contributions P_f and P_{jc}. This further supports the conclusion drawn in the experiments, that the dielectric properties of the polymer have a negligible influence on the heat generation within the laminate.

  doi:10.5075/epfl-298799_978-2-9701614-0-0

The laminates with lower areal weights (Plain 200, Twill 200) produce a higher cumulated heat P_{total} than the laminates with higher areal weights (Twill 285, Satin 290). This is due to the lower contact resistances with an areal weight of 200 g/m^2 caused by the higher roving widths w_{rov} in these laminates [10]. A lower contact resistance R_{jc} leads to a lower total resistance of the electrical loop. In this case, this leads to an increased electric current and thus to a higher cumulated heat.

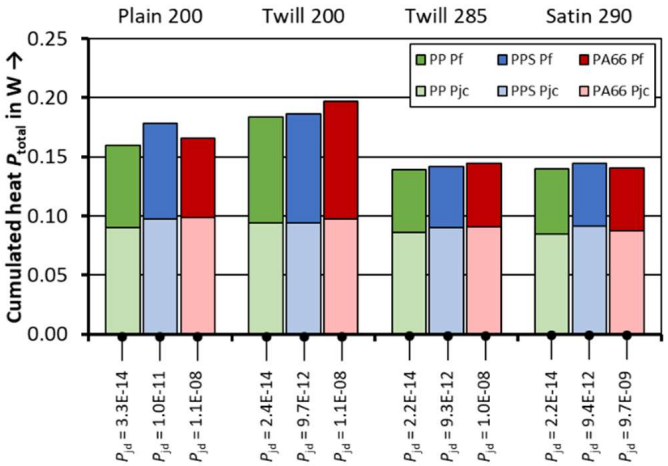

Figure 4: Comparison of the cumulated heat P_{total} at a roving-roving junction for the different matrix polymers in combination with different reinforcing fabrics. Due to the low contribution of dielectric losses in P_{total}, the P_{jd} values are listed separately below the graph.

6.3 Experimental validation

To investigate the influence of the matrix polymer on the inductive heating, the previously introduced laminates (Section 4) were heated up with the experimental setup described in section 5. The comparison of the resulting heating rates shows, that the matrix polymer has no significant influence on the heating rates (Fig. 5).

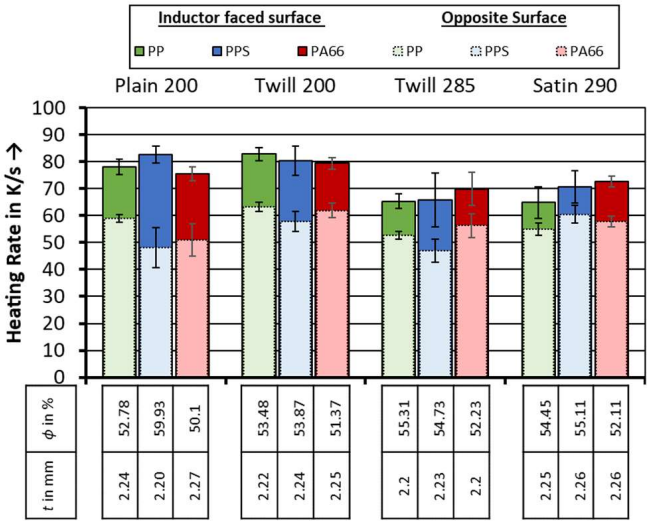

Figure 5: Comparison of the experimental induction heating rates in relation to polymer matrix and reinforcement fabric (coupling distance a = 5 mm, generator power P = 40 %)

  doi:10.5075/epfl-298799_978-2-9701614-0-0

The slight differences in heating rates can be caused by inhomogeneities, measurement uncertainties and light deviations in FVC and material thickness. Consequently, the dielectric behavior of the polymer matrix has no influence on the inductive heating rates of CFRPC laminates. The qualitative comparison of the calculated total heat contributions P_{total} (Fig. 4) with the heating rates of the corresponding laminates matches well.

6.4 Theoretical parametric study

Since the exact values of the contact resistivity ρ_c, the voltage U_{total} and the separation distance h are not known, these parameters were varied separately based on the basis parameter set introduced previously in section 3. The largest influence of the dielectric losses on the heating behavior can be detected with PA66 used as the matrix material. Therefore, PA66 in combination with the Twill 200 fabric was used for this study. Further combinations were investigated in [1].

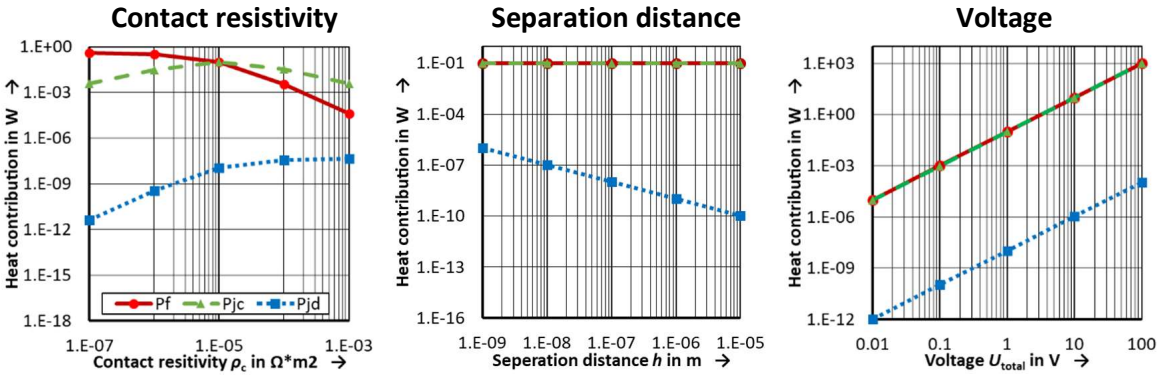

Figure 6: The heat contributions P_f, P_{jc} and P_{jd} in relation to the varied parameters (matrix polymer: PA66, fabric: Twill 200)

The increase of the contact resistivity, ρ_c results in an increase of the dielectric losses (Fig. 6). Since the electrical resistances R_{jd} (caused by the dielectric behavior of the matrix) and the contact resistance between the rovings R_{jc} run in parallel (Fig. 1 C), an increase of just R_{jc} will shift the electrical current and thus the heat contribution towards R_{jd}, which leads to an increase in the dielectric losses P_{jd}. When increasing the separation distance h, the opposite effect occurs. The resistance R_{jd} increases, which leads to a reduction of the dielectric losses P_{jd}. The increase of the voltage, U_{total} leads to a rise in all heat contributions, since the increase of the voltage leads to an increase of the electrical current in the electrical loop and thus to an increase in every single heat contribution. The heat contribution through dielectric losses however, remains relatively negligible.

7. Conclusion

The experimental heating rates and analytically determined heat contributions correspond well with one another. In fact, there is a heat loss, which can be attributed to the dielectric behavior of the polymer matrix. However, this heat loss is negligible compared to the other loss mechanisms that occur during the inductive heating process of fabric reinforced CFRPC laminates. The main contributors to the heating behavior in these types of laminates are joule losses within the fibers and contact losses at the roving cross-junctions.

Acknowledgements

This work has been conducted within the framework of the project “Process Optimization of Induction Welding of Continuous Carbon-Fiber Reinforced Thermoplastics by Process Simulation” which is funded by the Deutsche Forschungsgemeinschaft (DFG, German Research Foundation) – 272768988

8. References

1. Becker S, Michel M, Mitschang P, Duhovic M. Influence of polymer matrix on the induction heating behavior of CFRPC laminates. Composites Part B: Engineering. 2022;231:109561. doi:10.1016/j.compositesb.2021.109561.
2. Yarlagadda S, Kim HJ, Gillespie JW[J], Schevchenko NB, Fink BK. A Study on the Induction Heating of Conductive Fiber Reinforced Composites. Journal of Composite Materials. 2002;36:401–21.
3. Wang S, Kowalik DP, Chung DDL. Effects of the temperature, humidity, and stress on the interlaminar interface of carbon fiber polymer-matrix composites, studied by contact electrical resistivity measurement. The Journal of Adhesion. 2002;78:189–200. doi:10.1080/00218460210384.
4. Xu X, Ji H, Qiu J, Cheng J, Wu Y, Takagi T. Interlaminar contact resistivity and its influence on eddy currents in carbon fiber reinforced polymer laminates. 5NDT6 & E International. 2018;94:79–91. doi:10.1016/j.ndteint.2017.12.003.
5. Becker S, Mitschang P. Influence of thread count of carbon twill textile-reinforced polyamide 66 laminates on the inductive heating behavior. Journal of Thermoplastic Composite Materials. 2021;34:1135-1161. doi:10.1177/0892705719854493.
6. Fink BK, McCullough RL, Gillespie JW. A local theory of heating in cross-ply carbon fiber thermoplastic composites by magnetic induction. Polymer Engineering and Science. 1992;32:357–69. doi:10.1002/pen.760320509.
7. Loupy A, editor. Microwaves in organic synthesis. 2nd ed. Weinheim, Chichester: Wiley-VCH; 2006.
8. Fink BK, McCullough RL, Gillespie Jr JW. A model to predict the through-thickness distribution of heat generation in cross-ply carbon-fiber composites subjected to alternating magnetic fields. Composites Science and Technology. 1995;55:119–30. doi:10.1016/0266-3538(95)80024-7.
9. Miller AK, Chang C, Payne AGM, Menzel E, Peled A. The nature of induction heating in graphite-fiber, polymer-matrix composite materials. Sampe Journal. 1990;26:37–54.
10. Becker S, Mitschang P. Influence of thread count of carbon twill textile-reinforced polyamide 66 laminates on the inductive heating behavior. Journal of Thermoplastic Composite Materials 2021;34(8):1135-1161.

  doi:10.5075/epfl-298799_978-2-9701614-0-0

DO STANDARD DELAMINATION TESTS RELATE TO PLANAR DELAMINATION GROWTH?

René Alderliesten[a], Hajo den Ouden[a]

a: Structural Integrity & Composites, Department of Aerospace Structures & Materials, Faculty of Aerospace Engineering, TU Delft, The Netherlands: r.c.alderliesten@tudelft.nl

Abstract: *This paper discusses how standard unidirectional tests are to be related to planar growth, considering that these standard tests contain little to no information on transverse phenomena with respect to physical strain energy applied with loading. A concept is proposed to differentiate between applied work through the strain energy density, and the intrinsic material resistance through the strain energy release rate, to enable development of an overarching physics-based theory to relate standard unidirectional tests to planar delamination grow.*

Keywords: Delamination; Unidirectional; Planar; Physics; Fracture Mechanics

1. Introduction

Delaminations in fibre reinforced laminated composites comprise a damage type in which individual lamina in the laminate separate. This laminar decohesion can be induced by quasi-static, fatigue or (repetitive) impact loading, and is driven predominantly by peel and shear stresses at the interface, characterised as mode I and mode II opening.

Delamination growth in fibre reinforced polymer composites is generally evaluated with experiments that have been standardized for quasi-static load conditions. These tests characterize unidirectional delamination growth in mode I (DCB) [1,2], mode II (ELS [3] or ENF[4]) or mixed mode conditions (MMB) [5]. However, little attention is paid in literature to the applicability of these tests to in-service delamination problems that are generally characterized by planar delamination growth [6].

On top of that, there is only one standard available addressing fatigue delamination, which proposes to correlate for delamination onset the Strain Energy Release Rate (SERR) to a given number of applied load cycles [7]. Despite several attempts, there is yet no standard available to generate so-called fatigue resistance curves, i.e. the delamination growth rate plotted against some sort of similitude parameter based on the SERR concept. Several round robin exercises have been performed both within ASTM [8] and within ESIS-TC4 [9], with a second ESIS-TC4 round robin currently running [10]. The key obstacle to development of standard (fatigue) delamination testing appears the occurrence of fibre bridging in unidirectional tests, whereas the observations with in-service planar delaminations seems to indicate that this is merely a test artefact [11-14].

Hence this study investigated the relation between planar delamination growth, induced by transverse quasi-static and fatigue indentation loading, and these unidirectional delamination tests. To that aim, first planar delamination growth tests performed at EPFL [5], were analysed to identify up to what extent this planar growth could be correlated to the concepts of strain energy release and strain energy density. Secondly, an experimental setup was designed to

  doi:10.5075/epfl-298799_978-2-9701614-0-0

measure the delamination size through localising the delamination boundary during the transverse indentation loading of planar delamination specimens made of non-transparent carbon fibre reinforced polymer composites. With that set-up, quasi-static and fatigue planar delamination growth experiments were performed, to study the potential correlation between unidirectional standard tests and the performed planar tests. This paper presents the work performed and the experimental results measured, and discussed the applicability of standard unidirectional testing to the planar delamination problem.

2. Energy based concept for the determination of the delamination shape

2.1 Definition of planar delamination

Well-known sources of planar delamination in composite structures are initial laminar disbonds induced during manufacturing [5] or under impact loading [15]. While such initial delamination may not have severe consequences by its own, over time they can grow significantly thereby reducing the strength of the structure, potentially resulting in catastrophic failure.

Planar delaminations may grow in a planar fashion, as illustrated in Figure 1 (a), or they may propagate predominantly in a single transverse direction, as illustrated in Figure 1 (b). This difference appears to be related to the loading mode [16] or magnitude of loading applied, which is known from standard delamination testing to result in different material resistance to delamination growth measured [17]. The resistance expressed in terms of Strain Energy Release Rate (SERR) will vary along the entire planar delamination boundary [18], and potentially may be related to the strain energy locally available at the delamination tip, described using the Strain Energy Density (SED) [19].

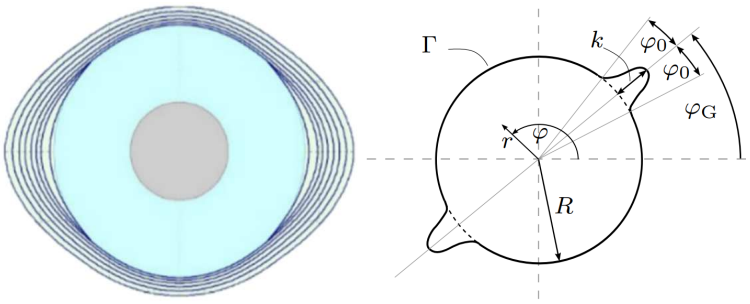

Figure 1. Illustration of planar delamination growth (a) and growth in a single transverse direction (b) [18]

2.2 Relation between strain energy release rate and strain energy density

Traditionally, prediction models developed in a fracture mechanics context relate parameters describing a 'driving force' to observed growth. Whereas, crack growth in metallic materials often was described using the Stress Intensity Factor *K*, delamination growth in composites often is described with the SERR *G*. Alternatively, this 'driving force' can be described by the SED, as proposed in other literature. However, to make the description of the delamination problem sounds from perspective of Physics, one need not only quantification of the 'driving force', but one also needs to quantify the intrinsic resistance of the material to fracture surface formation. Here, the authors propose to follow the concept outlined in [19], where the critical SED required to expand a delamination is considered 'driving force', and is related to the measured critical SERR as measure of resistance.

  doi:10.5075/epfl-298799_978-2-9701614-0-0

Daneshjoo et al. [19] developed this concept linking the SERR measured in a DCB test (mode I delamination) to the SERR measured in a ENF (mode II delamination) and MMB test, through equating the corresponding SED. This SED *S* is described by

$$S = D_1 \frac{G_I}{F_I} \tag{1}$$

where G_I is the mode I SERR, F_I is a constant derived from the constituent properties and D_1 is variable depending on the crack growth angle. The critical crack growth angle and the critical SED are determined to be at the point where the SED is at its minimum, which is the point of maximum amount of potential energy density at the crack front.

This relation between maximum potential energy density available at the crack front and the SERR forms the necessary framework to describe planar delamination growth. To illustrate this, consider the analogy with moving a box over the floor: the resistance counteracting the force is not a constant; it initially is constant (static friction) to turn into a dynamic force once the box is moving (dynamic friction).

2.3 Visible transverse delamination effects in planar specimen

In the current test standards (DCB, ENF & MMB) the various delamination modes are kept constant (pure mode I, pure mode II or a constant mix of two modes). In planar delamination growth, the (combination of) delamination modes can vary greatly along the delamination contour due to transverse effects. These effects influence how the planar delamination expands, but they in return are also influenced by the shape of the expanding delamination. The latter is the consequence of stress and strain redistribution campaigning the delamination shape change. This redistribution has an effect on the work applied, which can be observed when plotting the planar specimen compliance against the planar delamination expansion, as illustrated in Fig. 2.

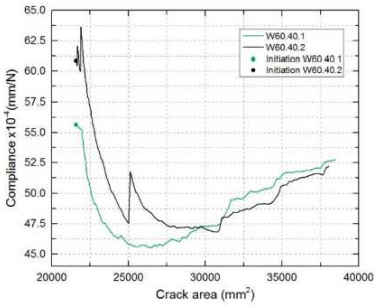

Figure 2. Compliance versus crack area of the composite mat with orthotropic properties [6]

2.4 Measuring planar delamination using the energy framework

While glass fibre reinforced composites are to some extent translucent, enabling the observation of planar delaminations [6], carbon fibre composites are opaque, which inhibits visual observation of internal delaminations. However, assuming that the SED at the delamination tip constitutes the 'driving force', the hypothesis is that through measuring strains on the thin panel surface, delaminations shapes can be visualized. Hence, Digital Image Correlation (DIC) was utilized to measure surface strains, which were transformed into the potential energy density through the classical laminate plate theory. The latter is required,

  doi:10.5075/epfl-298799_978-2-9701614-0-0

because the measured surface strains need transformation to strains at the plane or interface at which the delamination is. For example, if the delamination is at the centre of the laminate, the strains at the interface of delamination can be determined with

$$\varepsilon_{x0} = \varepsilon_{x,top} - \frac{h}{2}\kappa_x$$
$$\varepsilon_{y0} = \varepsilon_{y,top} - \frac{h}{2}\kappa_y \quad (1)$$
$$\gamma_{xy0} = \gamma_{xy,top} - \frac{h}{2}\kappa_{xy}$$

where the subscript 'top' indicate the measured surface strains. The average potential strain energy density was then determined with

$$u_\rho = \frac{1}{2}\left(A_{11}\varepsilon_{x,0}^2 + 2A_{12}\varepsilon_{x,0}\varepsilon_{y,0} + 2A_{16}\varepsilon_{x,0}\gamma_{xy,0} + A_{22}\varepsilon_{y,0}^2 + 2A_{26}\varepsilon_{y,0}\gamma_{xy,0} + A_{66}\gamma_{xy,0}^2\right) + \frac{1}{2}\left(D_{11}\kappa_x^2 + 2D_{12}\kappa_x\kappa_y + 2D_{16}\kappa_x\kappa_{xy} + D_{22}\kappa_y^2 + 2D_{26}\kappa_y\kappa_{xy} + D_{66}\kappa_{xy}^2\right) \quad (2)$$

which required the constituent properties from the ABD matrix.

3. Experimental observations on planar delamination growth

3.1 Test setup and equipment

A planar delamination test set-up was designed to comply to the following requirements:

- fixture should be sufficiently stiff to limit uptake of strain energy to max 1%,
- fixture can withstand 30 kN without yielding or buckling (twice the max test load),
- fixture should provide clearance to provide sufficient camera field of view.

To this aim a pyramid fixture was designed and manufactured, as illustrated in Fig. 3. In the design of specimen and clamping, it was considered that the panel's positioning allowed to test either pure mode II, or mixed mode I/II loading, analogue to the ELS specimen clamping [3], as schematically illustrated in Fig. 3.

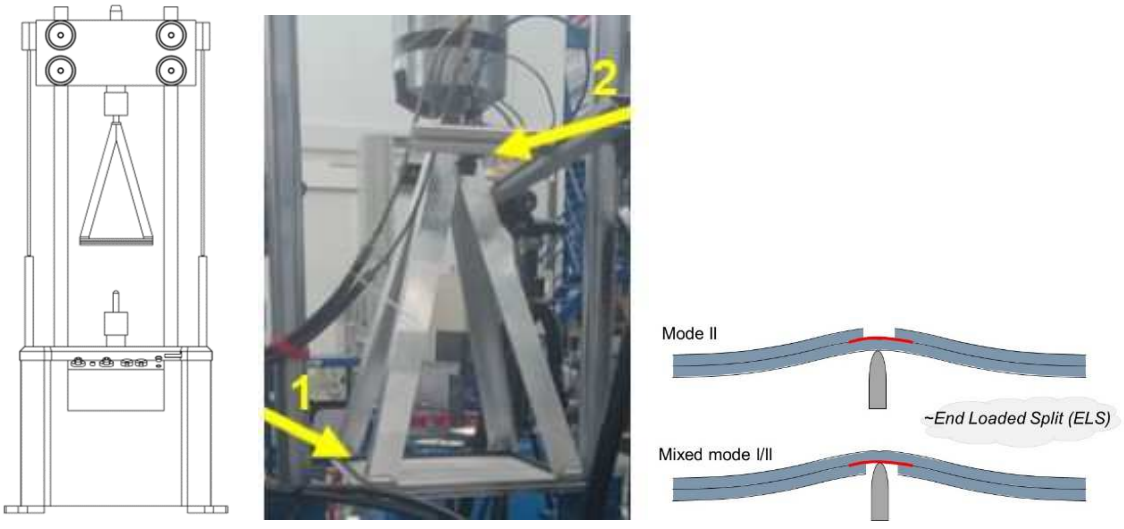

Figure 3. Fixture position in test machine (left), square specimen with speckle pattern (1) clamped in pyramid-shaped fixture, monitored with DIC camera (2); indenter is at actuator side below (centre), concept of tailoring the opening mode through specimen positioning (right)

3.2 Evaluating the work applied

The loads and cross-head displacements were recorded to quantify the work applied to the panel, which is described by the area underneath the load-displacement curve. Because the load-displacement curve was non-linear (quadratic with an offset), the area underneath the curve between minimum and maximum loading in fatigue was quantified with

$$U_n = P_1(\delta_2 - \delta_1) + \frac{1}{3}(P_2 - P_1)(\delta_2 - \delta_1) \quad (3)$$

3.2 Evaluation of delamination observations

The DIC surface strain measurements were used both to visualize the x/y curvature in the panel, and to formulate a bond state mapping criterion based on the strain energy density (SED). Both analysis techniques complement each other in visualizing the delamination shape, see Fig. 5.

To verify the delamination shape through the use of DIC surface strain measurement and CLT transformation, two additional non-destructive measurement techniques were utilized:

- Lock-in thermography
- Ultrasonic C-scanning

of which a C-scan is provided in Fig. 5 to illustrate the similarity in the observed delamination shapes.

To quantify the area of the measured delamination shapes, a shape function proposed by Köllner [18] was used

$$A_{del} = \pi R_p^2 + \frac{1}{4} k \phi_0 \left(8R_p + 3k\right) \quad (4)$$

of which Fig. 5 illustrates through an overlay with the bond state map the fit.

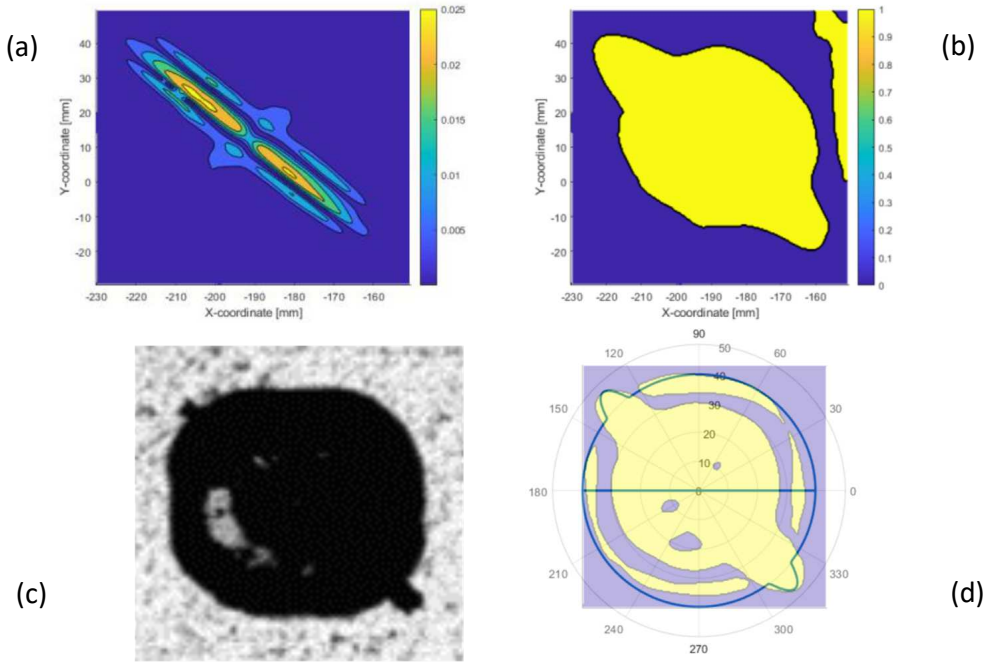

Figure 5. Comparison between the xy-curvature map (a), the bond state map (b), the corresponding C-scan result (c), and the overlay with the shape function (d).

3.3 Notable observations

With planar embedded delaminations two modes of delamination growth can occur: planar and transverse growth. Whereas literature solely spotted these two delamination modes separately, in this study both of these modes occurred in the same experiment, but in separate phases. In the initial phase of the test, the delamination area growth is increasing rapidly, as shown in Fig. 6 (a). Due the nonlinear relationship between delamination radius and area, the rapid areal increase occurs with a diminishing rate of radius increase. Once portions of the delamination contour are at their local delamination threshold, the delamination increase converges to the portion of the delamination front experiencing the least resistance. This transverse growth has a different relation to the panel's compliance increase, which results in substantially less energy dissipated with transverse growth, see Fig. 6 (b).

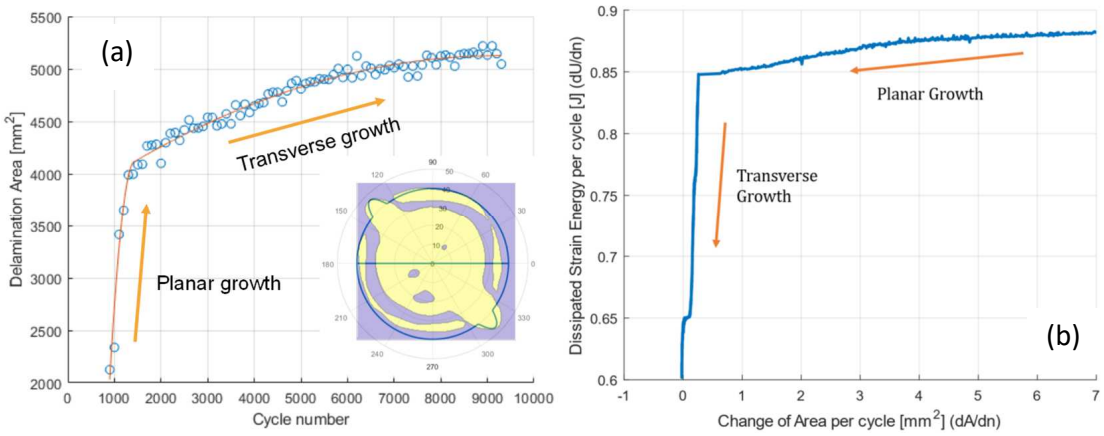

Figure 6. Fatigue delamination area growth curve exhibiting a transition from planar to transverse growth (a) and the dissipated strain energy associated to the areal growth (b)

4. Discussion on observations and the implications on current delamination framework

The planar delamination growth experiments [20] illustrate that when sufficient strain energy (work) is applied to the panel, the entire contour of delamination experience loading beyond the local threshold. The delamination grows in a planar fashion, experiencing local resistance related to fibre orientations relative to its growth direction. This variation in local resistance reveals itself by an overall change in areal delamination growth rate dA/dN, as shown in Fig. 6 (b). This variation in resistance in growth direction relative to the local fibre orientations, has been demonstrated in 1D experiments by Yao et al. [21,22]. Once local portions of the delamination contour reach their local delamination threshold, the extension becomes less planar, up to the extent that only very locally delamination increase is observed. This transverse growth occurs then only in the direction with the least resistance, which is known for low da/dN in fatigue to be less than at higher da/dN [17], and is associated here to planar growth. This explains the rapid decrease with energy dissipation, once only transverse growth is observed, see Fig. 6(b).

This variation along the entire delamination contour imposes some difficulty in prediction [23], because of the interplay between the local driving strain energy, influenced by the actual delamination shape, and the local resistance, related to the respective fibre orientations. The latter can be affected by fibre bridging [6], despite generally considered an artefact of

standard 1D DCB testing. However, insufficient evidence exists to draw firm conclusions, particularly, because in planar testing the effect of fibre bridging cannot be dissected well from the effect of in-plane stretching [6].

The different variation in strain energy density locally at the delamination contour relative to the variation in intrinsic local delamination resistance illustrates that a simple scaling law, i.e. Paris-type relation, based on one SERR parameter only is insufficient to describe planar delamination growth.

Hence concepts in which the driving work is characterised with SED, while the resistance is quantified in the physical SERR should be further developed in order to use 1D standard test data to predict planar delamination growth.

5. Conclusion

The current study illustrates that at the moment insufficient evidence exists in literature to apply standardized 1D tests results to planar 2D delaminations predictions, because

- 1D samples exhibit phenomena that yet have not been studied well for planar delaminations, like fibre bridging
- 1D samples lack transverse phenomena observed in planar delaminations
- 1D samples have one specific interface configuration (eg. 0°//0°), while planar delaminations in their circumference experience multiple fibre orientations with their intrinsic resistance and delamination features.

In addition, most methods only use simple scaling laws that relate growth to loading parameters allegedly describing similitude, which from perspective of physics is questionable. Instead, the base theory for delamination prediction should separate the applied loading from the intrinsic material resistance, through the use of respectively strain energy density and strain energy release. This would explain the observed different intrinsic delamination resistance in fatigue delamination growth, when transitioning from planar to transverse growth at low delamination growth rates.

6. References

1. ISO 15024. Fibre-reinforced plastic composites – determination of mode I interlaminar fracture toughness, GIC, for unidirectionally reinforced materials; 2001.
2. ASTM D5528-13. Standard test method for mode I interlaminar fracture toughness of unidirectional fiber-reinforced polymer matrix composites; 2013
3. ISO 15114. Fibre-reinforced plastic composites - Determination of the mode II fracture resistance for unidirectionally reinforced materials using the calibrated end-loaded split (C-ELS) test and an effective crack length approach; 2014.
4. ASTM D7905-14. Standard test method for determination of the mode II interlaminar fracture toughness of unidirectional fiber-reinforced polymer matrix composites; 2014.
5. ASTM D6671/D6671M-13, Standard test method for mixed mode I-mode II interlaminar fracture toughness of unidirectional fiber reinforced polymer matrix composites; 2006
6. Cameselle-Molares A, Vassilopoulos AP, Keller T (2018), Experimental investigation of two-dimensional delamination in GFRP laminates, Eng Fract Mech 203, 152-171.

  doi:10.5075/epfl-298799_978-2-9701614-0-0

7. ASTM D6115-97. Standard test method for mode I fatigue delamination growth onset of unidirectional fiber-reinforced polymer matrix composites; 2011.
8. Murri GB. (2014) Effect of data reduction and fiber-bridging on Mode I delamination characterization of unidirectional composites. J Compos Mater 48(19):2413–24.
9. Stelzer S, Brunner AJ, Argüelles A, Murphy N, Cano GM, Pinter G (2014), Mode I delamination fatigue crack growth in unidirectional fibre reinforced composites: Results from ESIS TC4 round robins, Eng Fract Mech, 116, 92-107.
10. Alderliesten RC, Brunner AJ, Determination of Mode I Fatigue Delamination Propagation in Unidirectional Fibre-Reinforced Polymer Composites, Test Protocol Version 3.2.
11. Alderliesten RC, Brunner AJ, Pascoe JA (2018), Cyclic fatigue fracture of composites: What has testing revealed about the physics of the processes so far?, Eng Fract Mech 203, 186-196.
12. Yao L, Alderliesten RC, Zhao M, Benedictus R. (2014), Bridging effect on mode I fatigue delamination behavior in composite laminates. Compos A Appl Sci Manuf 63, 103–109.
13. Jones R., Kinloch A.J., Michopoulos J.G., Brunner A.J., Phan N. (2017), Delamination growth in polymer-matrix fibre composites and the use of fracture mechanics data for material characterisation and life prediction, Composite Structures 180, 316–333.
14. Alderliesten R (2018). Fatigue delamination of composite materials: Approach to exclude large scale fibre bridging. IOP Conference Series: Materials Science and Engineering, 388(1), 012002.
15. Pascoe, J.A. (2021) Slow-growth damage tolerance for fatigue after impact in FRP composites: Why current research won't get us there, Theor Appl Fract Mech 116, 103127.
16. Nilsson K.F., Asp L.E., Alpman J.E., Nystedt L. (2001), Delamination buckling and growth for delaminations at different depths in a slender composite panel, Int Journal of Solids and Structures, 38, 3039-3071.
17. Amaral L, Yao L, Alderliesten RC, Benedictus R (2015), The relation between the strain energy release in fatigue and quasi-static crack growth, Eng Fract Mech 145, 86-97.
18. Köllner A, Forsbach F, Völlmecke C (2019), Delamination buckling in composite plates: an analytical approach to predict delamination growth, in Advanced Structured Materials, 241–255.
19. Daneshjoo Z., Amaral L., Alderliest R.C., Shokrieh M.M., Fakoor M. (2019), Development of a physics-based theory for mixed mode I/II delamination onset in orthotropic laminates, Theoretical and Applied Fracture Mechanics 103, 102303.
20. Planar delamination growth in carbon fibre reinforced composite panels, 4TU.ResearchData dataset, DOI 10.4121/19552078.
21. Yao L., Sun Y., Guo L., Alderliesten R.C., Benedictus R. (2018), Mode I fatigue delamination growth with fibre bridging in multidirectional composite laminates, Engineering Fracture Mechanics 189, 221-231.
22. Yao, L., Cui, H., Sun, Y., (...), Zhao, M., Alderliesten R.C. (2018), Fibre-bridged fatigue delamination in multidirectional composite laminates, Composites Part A: Applied Science and Manufacturing 115, 175-186.
23. Kölner A. (2021), Predicting buckling-driven delamination propagation in composite laminates: An analytical modelling approach, Composite Structures 266, 113776.

IMPACT OF COMPOSITE REPAIRS: INDENTATION, PLASTICITY, INTRALAMINAR AND INTERLAMINAR DAMAGE

Richard A. Brooks, Jun Liu, Zoe E.C. Hall, Haibao Liu, Bamber R.K. Blackman,

Anthony J. Kinloch, John P. Dear

Department of Mechanical Engineering, Imperial College London, Exhibition Road,
London, SW7 2AZ, UK – richard.brooks16@imperial.ac.uk

Abstract: *The present paper explores the impact behaviour of repaired carbon fibre-reinforced plastic (CFRP) composite laminates. In particular, the relationship between indentation size and the level and type of damage formed in continuous CFRP material under low-velocity impact loading is investigated. Repairs can be performed on previously impacted CFRP composite by removing the damaged material and bonding a patch of the same CFRP over the top of the damage hole. In some cases, a plug is added to fill the hole. Generally, an increase in indentation depth appears to correlate with an increased delamination damage area. This gives the potential for a quick and economical method to identify damage level in impacted components.*

Keywords: Polymer matrix composites; Impact damage; Delamination; Repair; Indentation

1. Introduction

Fibre-reinforced polymer composites (FRPs) are thought to be particularly susceptible to low-velocity impact damage. This can be caused by tool drop, collision of service vehicles and aircraft or runway debris. This type of damage is difficult to detect, hence it is referred to as barely visible impact damage (BVID). Special equipment and methods are required to identify and map the damage area. Although this damage may not cause immediate failure, it can weaken the structure significantly [1]. If the strength falls below the working load of the component, catastrophic failure could occur. Therefore, the effect of such damage on the structural integrity must be understood and corresponding action, such as repairing the structure, should be undertaken.

Under impact loading, the damage formed in CFRPs is dependent on factors including impact energy, impact speed, impactor hardness and impactor shape. Intuitively, higher impact energies lead to an increase in damage. Delamination damage is seen at low impact energies, with additional matrix damage and fibre damage observed at higher impact energies [1]. Matrix damage can occur under low-velocity impact, but is much more localised than the delamination damage, occurring directly beneath the impactor [2].

In some patch repair cases, a patch of composite material is adhesively bonded over the damaged area of composite. The adhesively bonded patch allows the applied load to be transferred around the damage, thus reducing the stress concentration at the edges of the damage [3]. In some other cases, the damage is cut out of the material and replaced with a plug of pristine material prior to patch adhesion. Plugs, attached to the material by an adhesive, are particularly advantageous under compression [4]. They can reduce the stress concentrations at the edge of the hole, as well as increasing the local stiffness in the area between the patches.

  doi:10.5075/epfl-298799_978-2-9701614-0-0

Therefore, plugs can improve the performance of a repair [4]. Finally, patch repairs are relatively straightforward to implement and can be completed in a fairly short time using only simple equipment [3,4].

Indentation on a composite panel after impact is commonly used by aircraft manufacturers to indicate damage severity [5]. However, Talreja and Phan [5] have criticised the practice of characterising BVID by dent depth as a physical relationship with impact damage severity has not yet been clarified. The indentation is mainly caused by local contact stresses and the indentation depth is affected by the strength and toughness of the surface ply. Therefore, it is an uncertain and unsubstantiated claim that the entire dent depth is attributable to ply cracks and delaminations. Furthermore, the assumption that dent depth correlates with cracks within the laminate and is therefore indicative of impact energy has not been supported by analysis or experiments [5]. Although little research has been undertaken into the relationship between indentation and damage, studies undertaken by Shuck as cited by Talreja and Phan [5] and by Panettieri et al. [6] do indicate a correlation between sample thickness and indentation depth. Furthermore, although the indentation depth may be strongly affected by the strength and toughness of the surface ply, it may also be somewhat affected by the plies beneath, up to a certain depth.

The current paper provides another examination of the relationship between material thickness and indentation depth. Furthermore, the intra- and interlaminar damage formed in samples of differing thicknesses is also compared.

2. Materials and Experimental Details

2.1 Materials

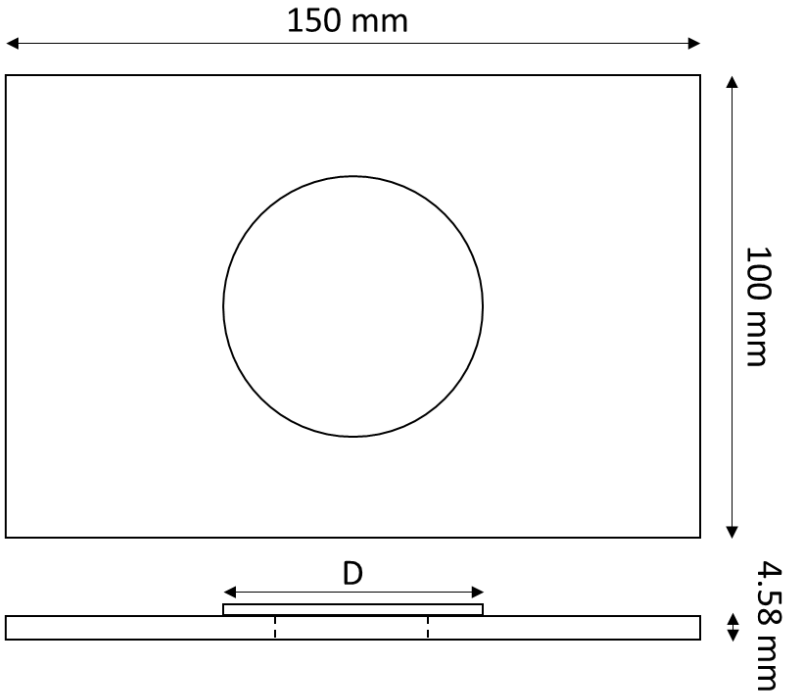

Figure 1: Plan- and side-view of repaired panel. D represents patch diameter.

  doi:10.5075/epfl-298799_978-2-9701614-0-0

The samples used in the present research were cut from quasi-isotropic CFRP laminates made from unidirectional pre-preg (MTC510-UD300-HS-33%RW) supplied by SHD Composites Ltd, UK. The pre-preg contained an epoxy matrix (MTC510) and T700 carbon fibres at a fibre volume fraction of 60%. Flat laminates were formed using an autoclave and cut into multiple samples of size 100 mm x 150 mm, in accordance with ASTM D7136 [7]. The quasi-isotropic lay-up of the panels was $[45_2/-45_2/0_2/90_2]_s$, with the 0° plies being aligned with the longer edge of the panels, giving a nominal thickness of 4.58 mm.

Patch-repaired samples were manufactured by removing a 40 mm diameter disc from the centre of a pristine panel. This hole represents the area of damage which would be caused by an impact at 7.5 J. A circular patch formed of quasi-isotropic CFRP with lay-up $[45/-45/0/90]_s$ (nominal thickness 2.3 mm) was then adhered over the hole using a single layer of MTFA-500 toughened epoxy-film adhesive of nominal thickness 0.25 mm, supplied by SHD Composites Ltd, UK, which was then cured. For patch + plug repaired samples, the same procedure was followed, but with the addition of a push-fit plug with an identical lay-up to the parent laminate being placed into the 40 mm hole prior to curing the adhesive. During the heating and curing process, the adhesive was able to flow into the gap between the plug and parent laminate, thus holding the plug in place beneath the patch. A schematic of a repaired panel is shown in Figure 1, where D represents the patch diameter. For this study, a 55 mm patch was used for the patch only sample and a 65 mm patch was used for the patch + plug sample.

2.2 Experimental Details

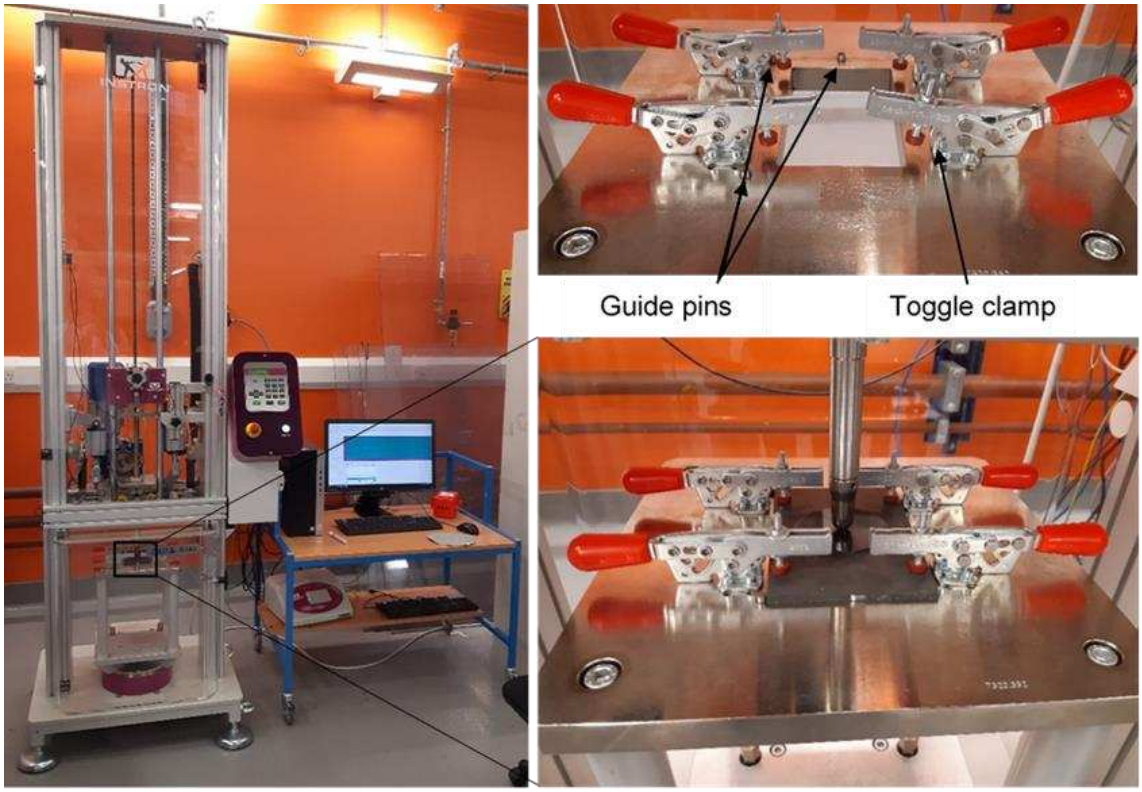

Figure 2: Drop weight machine and PC, showing window cut-out in impact zone with and without hemispherical impactor and clamped repaired sample.

  doi:10.5075/epfl-298799_978-2-9701614-0-0

Low-velocity drop weight testing was undertaken in accordance with ASTM standard D7136 [7] using an Instron CEAST 9340 drop weight tower, shown in Figure 2, fitted with a hemispherical stainless steel impactor of diameter 16 mm. 100 mm x 150 mm composite samples were clamped onto a steel picture frame using four rubber-tipped toggle clamps which prevented slippage of the sample during the impact test, see Figure 2. Three guide pins allowed the sample to be aligned in the centre of the impact zone, above a window cut-out of 125 mm x 75 mm. A load cell located in the forward section of the impactor, which sampled data at a rate of 500 kHz, measured force-time data. An anti-rebound system, which was able to catch the impactor after the first impact, was utilised to prevent multiple impacts. The drop weight tower was connected to a PC and was equipped with a CEAST DAS 64K data acquisition system, through which the tower was controlled and the data collected. Load-displacement and energy-time traces can also be calculated from the experimental data. This (a) allows the sample behaviour and (b) enables potential load drops, corresponding to damage initiation, to be identified.

Damage within the composite samples was examined using an ultrasonic C-scan technique. Scanning was undertaken both before and after the impact tests to allow damage accumulated during manufacturing, transport and storage to be identified and so separated from subsequent damage induced by the impact test. Scanning was undertaken using a portable 'Prisma 16:64 TOFD' ultrasonic C-scan device with a 5 MHz probe, supplied by Sonatest Ltd., UK. This phased array probe was attached to a 16 /mm encoder which measured the position of the probe along the scan axis. The resulting C-scan maps showed the delamination damage area present at different depths through the sample thickness and can be compared between samples.

Optical microscopy was undertaken to examine cross sections of the impacted samples. This allowed a detailed view of the intralaminar and interlaminar cracks to be achieved. Samples were first sectioned using a diamond saw, before being polished on a grinding wheel with silicon carbide grinding paper, followed by diamond suspension fluid on a polishing cloth.

Indentation depth was measured initially with a handheld digital depth gauge, followed by measurement using a Confocal microscope, to confirm accuracy in using the handheld gauge. Data from the Confocal microscope also allowed depth plots of entire indentations to be produced, as well as cross sections.

3. Results

3.1 C-scans

C-scans obtained after an impact at 7.5 J for a repaired sample with a 55 mm diameter 'patch only' and a repaired sample with a 65 mm diameter 'patch + plug' are shown in Figure 3. The delamination damage area is indicated and the different colours within the damage correspond to damage at different depths through the sample thickness, as indicated by the bar to the right of the scan. Red indicates damage close to the scanning surface whereas dark blue indicates damage close to the rear. Clearly, the damage area in the 'patch only' sample is much higher than that for the sample with a 'patch + plug'. More detailed discussion of these results can be found in [8, 9], along with examples of force-time and force-displacement graphs of the tests.

  doi:10.5075/epfl-298799_978-2-9701614-0-0

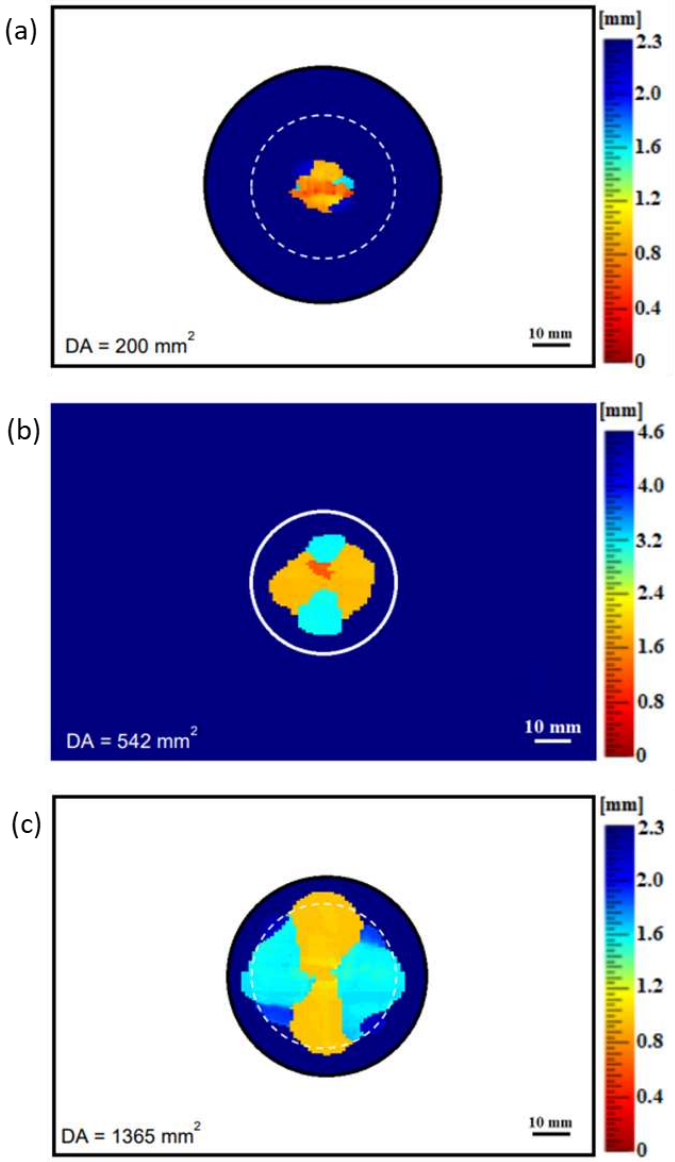

Figure 3: C-scan images of damage in (a) the patch in a 'patch + plug' repaired sample, (b) the plug in a 'patch + plug' repaired sample and (c) the patch in a 'patch only' repaired sample, along with their respective delamination damage areas after impact at an energy of 7.5 J.

3.2 Indentation

Following impact, an indentation was left on the patch surface at the point where the impactor hit the sample. The indentation depths on a 55 mm diameter 'patch only' and a 65 mm 'patch + plug' repaired sample were measured. The results obtained using the Confocal microscope generally supported those obtained using the handheld depth gauge. Therefore, measuring the indentation depth can be done accurately, simply and quickly on the current samples.

An example of a cross section which was produced for a 'patch only' repaired sample using the Confocal microscope data is shown in Figure 4. The vertical distance is the depth below the surface or zero condition (i.e. the indentation depth) and the zero condition for this data was chosen as the vertical distance well away from the indentation. The scan width was just over 7 mm, therefore, the maximum indentation depth (referred to simply as the indentation depth) is close to the centre of the scan at around 3.5 mm.

  doi:10.5075/epfl-298799_978-2-9701614-0-0

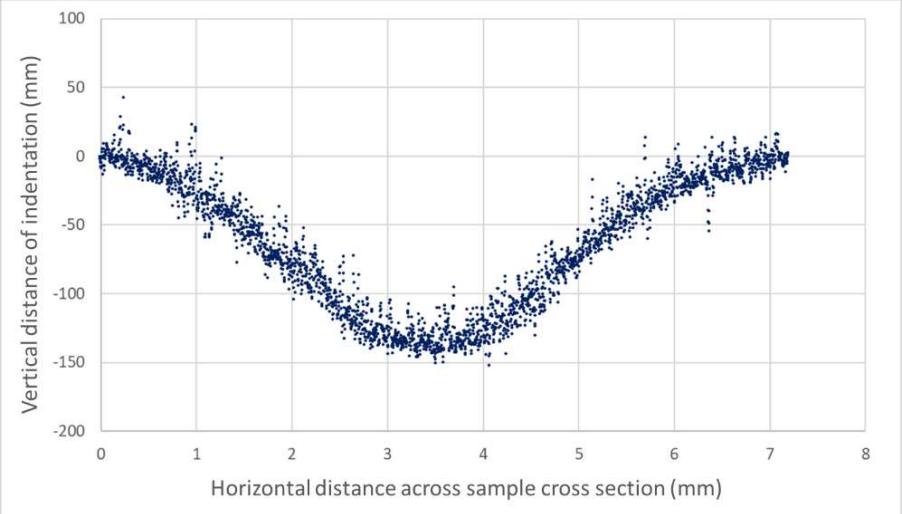

Figure 4: Example indentation cross section from Confocal microscope data for a 'patch only' repaired sample.

Previous indentation measurements undertaken for pristine samples of the same CF/Epoxy material indicate that the indentation depth reduces slightly after impact due to phenomena such as relaxation, but further changes are negligible after around 48 hours after impact. Now, indentation measurements were undertaken on the samples discussed in this study some months after they had been impacted. Therefore, the indentation depths recorded will be smaller than those which would have been recorded straight after impact. On an aircraft it is unlikely that an indentation would be measured immediately after impact. Therefore, working with indentations once the depth has plateaued is more appropriate for the aerospace industry.

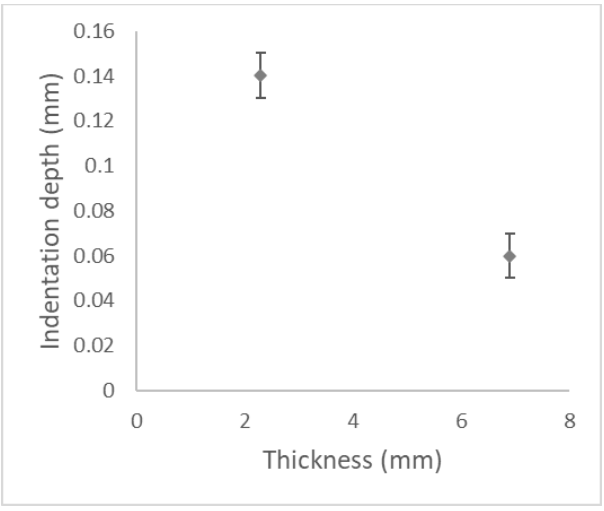

Figure 5: Indentation depth vs thickness for 'patch only' and 'patch + plug' repaired samples.

The measured indentation depths for the 'patch only' and 'patch + plug' repaired samples are shown in Figure 5. The points represent the depths measured using the handheld gauge and the error bars take into account both the variation following multiple measurements and the difference compared to the depth given by the Confocal microscope. The point at a thickness of 2.3 mm represents the indentation on the 'patch only' repair (the patch was 2.3 mm thick) and was measured to be around 140 microns. The point at thickness 6.9 mm is for the 'patch + plug' repair (2.3 mm patch + 4.6 mm plug thickness) and was measured to be around 60 microns.

  doi:10.5075/epfl-298799_978-2-9701614-0-0

3.3 Microscopy

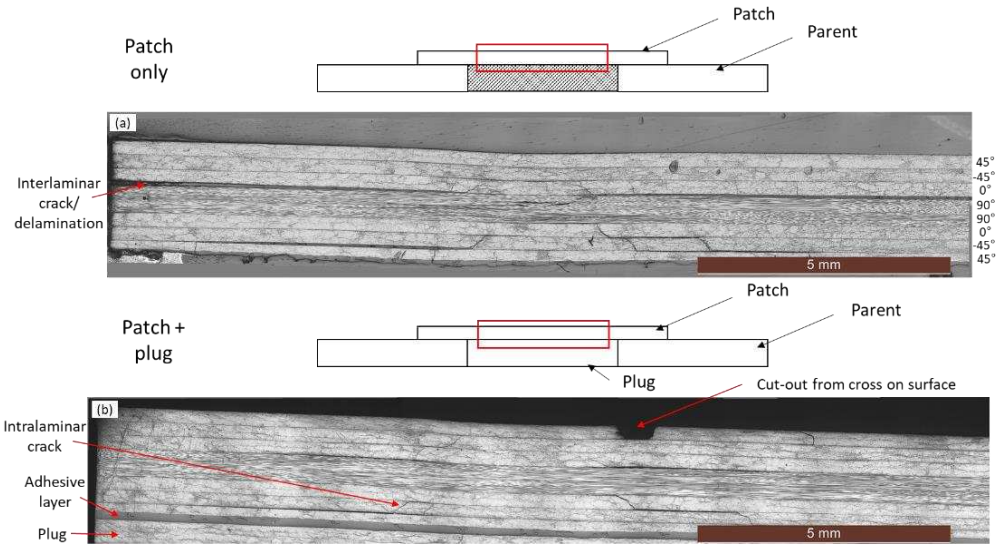

Figure 6: Optical microscope images of damage within the patch in (a) 'patch only' and (b) 'patch + plug' repaired samples. Schematics show position of images on sample cross sections.

Images taken using an optical microscope are shown in Figure 6(a) for a 'patch only' and Figure 6(b) for a 'patch + plug' repaired sample. The cross sections shown are at the centre of a sample, directly beneath the centre of the indentation, which is clearly visible at the top of each image. The cut-out visible in Figure 6(b) is from a cross cut into the surface of the patch during the repair procedure for this sample. It should be noted that the sample with plug shown in this section did show a slight dislodgement, in contrast to the sample for which the C-scan is shown in Section 3.1. However, both samples showed similar C-scans in the patch. Therefore, the microscopy images can be accurately compared. A C-scan was unable to be achieved for the plug in the dislodged sample due to the surface not being flat. The sample which showed no dislodgement was not cut apart for microscopy as it is required for future tests.

Intralaminar cracks radiate from near the indentation and propagate until they hit an interlaminar boundary. At this point, they are deflected along the inter-ply boundary, forming a delamination crack. This can cause intralaminar cracks to form in layers beneath, which leads to further delamination. By comparing Figure 6(a) with Figure 6(b), it can be observed that the damage map for intralaminar and interlaminar cracks within the patch for the two repairs is similar, with interlaminar cracks generally forming between the same layers in both samples.

4. Discussion

Indentation depth appearing to increase for a lower sample thickness suggests that a higher indentation depth could indicate a greater level of delamination damage. For example, the most delamination damage is seen in the 'patch only' repair (2.3 mm thick) and the least is seen in the 'patch + plug' repair (6.9 mm thick, or 7.1 mm including adhesive thickness). Therefore, although measuring indentation depth may be useful as a quick and economical way to estimate damage in an impacted CFRP material, other factors must be considered as the same trend may not apply when using a different impactor shape, impactor hardness, impact energy and impact velocity. Significant further research would be required before being able to apply this method on commercial aircraft, where safety is a key priority.

  doi:10.5075/epfl-298799_978-2-9701614-0-0

It appears that adding a plug may reduce the propagation of interlaminar cracks, hence, the delamination damage area is reduced. The delaminations in the patch appear to extend further from the impact zone in the 'patch only' compared to the 'patch + plug' sample. Therefore, the addition of a plug should lead to an improved residual strength of the repaired structure.

5. Conclusions

This paper has investigated the damage formed in repaired CFRP samples during impact and the relationship between indentation depth and the damage formed. Indentation depth appears to decrease with an increase in material thickness for the thicknesses tested in this study, i.e. 2.3 mm and 6.9 mm (7.1 mm including adhesive thickness). The addition of a plug to a patch repair appears to significantly reduce the delamination damage in the patch by giving better support to the patch. This has been shown through both C-scan and microscopy analyses of impacted samples. Therefore, greater indentation depth appears to be indicative of greater delamination.

Acknowledgements

The authors much acknowledge the Commercial Aircraft Corporation of China (COMAC) and Polar Manufacturing Ltd. For the purpose of open access, the authors have applied a Creative Commons Attribution (CCBY) licence to any Author Accepted Manuscript version arising.

6. References

1. Tuo H, Lu Z, Ma X, Xing J, Zhang C. Damage and failure mechanism of thin composite laminates under low-velocity impact and compression-after-impact loading conditions. *Compos Part B Eng*. 2019;163: 642–54.
2. Liu H, Liu J, Ding Y, Zheng J, Kong X, Zhou J, et al. The behaviour of thermoplastic and thermoset carbon fibre composites subjected to low-velocity and high-velocity impact. *J Mater Sci*. 2020;55: 15741–68.
3. Caminero MA, Pavlopoulou S, Lopez-Pedrosa M, Nicolaisson BG, Pinna C, Soutis C. Analysis of adhesively bonded repairs in composites: Damage detection and prognosis. *Compos Struct*. 2013;95: 500–17.
4. Soutis C, Duan DM, Goutas P. Compressive behaviour of CFRP laminates repaired with adhesively bonded external patches. *Compos Struct*. 1999;45(4): 289–301.
5. Talreja R, Phan N. Assessment of damage tolerance approaches for composite aircraft with focus on barely visible impact damage. *Compos Struct*. 2019;219: 1-7.
6. Panettieri E, Fanteria D, Montemurro M, Froustey C. Low-velocity impact tests on carbon/epoxy composite laminates: A benchmark study. *Compos Part B Eng*. 2016;107: 9-21.
7. ASTM International. Standard Test Method for Measuring the Damage Resistance of a Fiber-Reinforced Polymer Matrix Composite to a Drop-Weight Impact Event (D7136/D7136M−15) Annual Book of ASTM Standards West Conshohocken, PA, USA; 2015.
8. Hall ZEC, Liu J, Brooks RA, Liu H, Crocker JWM, Joesbury AM, Harper LT, Blackman BRK, Kinloch AJ, Dear JP. An investigation into the effectiveness of patch repairs to restore the impact properties of carbon-fibre reinforced-plastic composites for aerostructure applications. *Eng Fract Mech*. 2021. Submitted.
9. Liu H, Brooks RA, Hall ZEC, Liu J, Crocker JWM, Joesbury AM, Harper LT, Blackman BRK, Kinloch AJ, Dear JP. Experimental and numerical investigations on the impact behaviour of pristine and patch-repaired composite laminates. *Phil Trans A*, *Royal Soc*. 2022, in press.

  doi:10.5075/epfl-298799_978-2-9701614-0-0

AN IN-SITU DCB TEST USING XCT, SCRUTINIZING THE EFFECT OF INTERFACE FIBRE ORIENTATION ON INTER-LAMINAR FRACTURE TOUGHNESS OF CARBON FIBRE REINFORCED LAMINATES

Thanasis Chatziathanasiou[a], Jeroen Soete[a], Johan Vanhulst[a], Delphine Carrella-Payan[b], Anna Matveeva[b], Larissa Gorbatikh[a], Mahoor Mehdikhani[a]

a: Department of Materials Engineering, KU Leuven
Kasteelpark Arenberg 44 bus 2450, 3001 Leuven, Belgium
thanasis.chatziathanasiou@kuleuven.be
b: Siemens Industry Software NV
Interleuvenlaan 68, 3001 Leuven, Belgium

Abstract: *Test methods determining interlaminar fracture toughness of fibre-reinforced polymer composites typically rely on edge-monitoring techniques, such as edge microscopy and digital image correlation to locate the crack tip. Monitoring the crack tip in a 2D fashion implies that the crack front development inside the specimen and the likely associated toughening mechanisms are neglected. To facilitate a more comprehensive understanding of delamination initiation and propagation in carbon fibre-reinforced polymer composites, we implemented a novel in-situ double cantilever beam test, coupled with microfocus X-ray computed tomography. This methodology allowed for load-step dependent 3D crack visualisation. The effect of the interlaminar interface on interlaminar fracture toughness was explored by investigating two different layups, possessing* $0°//0°$ *and* $+45°//-45°$ *interlaminar interfaces.*

Keywords: Delamination; Fracture toughness; X-ray computed tomography; 4D analysis

1. Introduction

Delamination is a common, yet critical, failure mechanism in Fibre-Reinforced Polymer Composites (FRPCs). Its frequent dominance in fatigue and impact loading conditions, relevant to industrial applications of laminated structures, has triggered long-lasting efforts by industry and academia to unravel the factors influencing delamination resistance or Interlaminar Fracture Toughness (G_{IC}). These efforts gave rise to robust standardised methodologies, such as the standard double cantilever beam (DCB) test for mode I fracture toughness identification. In this test, the arms of a unidirectional (UD) bar-shaped specimen are pulled apart, and a tensile stress acts perpendicular to a pre-existing crack at the midplane. Despite its robustness, the standard approach is not suitable for multidirectional (MD) laminates, where unwanted toughening mechanisms come to prominence. Inherently, results from relevant studies are far from reaching a consensus both for initiation and steady-state propagation values of G_{IC} [1-4].

On top of the present toughening mechanisms, this lack of consensus can be partially attributed to the inaccuracy of the techniques used for real-time measurement of the delamination length. Current in-situ techniques monitor only the edge of the specimen in 2D. Consequently, they face difficulties detecting the exact initiation point and crack length. In contrast, microfocus X-ray computed tomography (micro-XCT) improves the quantitative

determination of G_{IC} by displaying the boundary line (instead of a point in edge monitoring techniques) between the starter crack and the composite laminate which can be used as a valid reference point for crack length measurements. Moreover, this technique enables a 3D characterisation of the crack front shape, while granting 3D insight into the development of toughening mechanisms.

In the current study, we explore the potential of in-situ micro-XCT to characterise the crack evolution during a DCB test. To the best of our knowledge, this study exhibits the first implementation of in-situ high-resolution micro-XCT for monitoring the crack front from initiation to steady-state propagation. This methodology is employed to identify the differences in delamination behaviour between two different interfaces. Comparative analysis is also performed using in-situ edge microscopy and digital image correlation (DIC).

2. Materials and methods

2.1 Specimen preparation

Automated tape laying followed by autoclave curing was used to produce aerospace-grade composite panels of UD prepreg tapes, at SABCA Limburg NV, Belgium [5]. The prepregs were produced by Cytec from Tenax® – E HTS40 F13 12K carbon fibres and a toughened epoxy resin, CYCOM® 977-2. A Teflon film of 12.5-µm thickness was embedded at the laminate mid-thickness interface to facilitate the starter crack [6]. To investigate the effect of fibre orientation at the delaminating interface, two composite layups were manufactured: $[0°]_{22}$ and $[(+45°/-45°)_5/+45°//-45°/(-45°/+45°)_5]$, with two distinct midplane interfaces: $0°//0°$ and $+45°//-45°$. The specimens are hereafter called with their interface type.

Three DCB specimens per layup were cut into the ASTM D5528 standard dimensions (length = 180 mm, width = 20 mm and thickness = 4.1 mm) using a rotating diamond blade. The initial crack length value was set at α_0 = 50 mm. To attain adequate surface quality for crack tip monitoring, the long edges of the specimens were grinded and polished using a Struers LaboSystem device. Subsequently, DCB loading blocks were glued on the specimens using the Araldite® 2011 epoxy adhesive and cured in an infrared oven at 97 ℃ for 45 min.

2.2 DCB testing with conventional crack monitoring tools

To facilitate a direct comparison to the novel in-situ DCB test coupled with micro-XCT, DCB tests were performed a priori, in conjunction with edge microscopy and mesoscale DIC. One long edge of the specimens was coated with a random speckle pattern, using black and white spray paint. Furthermore, a mm-scalebar was applied to the same edge, on which the initiation point (Teflon film tip) was indicated with a point marker.

The conventional tests were performed using an Instron 5567 universal testing machine (5-kN load cell) with displacement control, at a displacement rate of 2 mm/min [6]. For image acquisition, two CCD-cameras were placed parallel to the long edges of the specimen (Figure 1). Both cameras captured images at a rate of 1 frame per second. The first camera imaged the speckled side (mesoscale DIC), with a 40 × 30 mm field of view. The second camera, aimed at the other (unspeckled) edge of the specimen, was used for microscale analysis. It was mounted on a joystick-controlled machine to track the 6.66 mm × 4.98 mm field of view around the advancing crack tip.

The DIC software used for crack tip monitoring was VIC-2D by Correlated Solutions, through which a 21×21-pixel^2 subset size (pixel size ~ 0.025 mm) and a 2-pixel step size were selected. To measure the crack length, the strain localisation method was used, where the crack is detected by means of the transverse strain component ε_{yy} which exceeds zero at the crack tip [7]. The DIC resulting initiation point was compared to the point determined with the non-linearity (NL) point in the load-displacement curve, described in the ASTM D5528 standard [6]. Finally, to obtain the evolution of the G_{IC} with the evolving crack length, which forms the so-called resistance curve (R-curve), the Modified Beam Theory (MBT) was used.

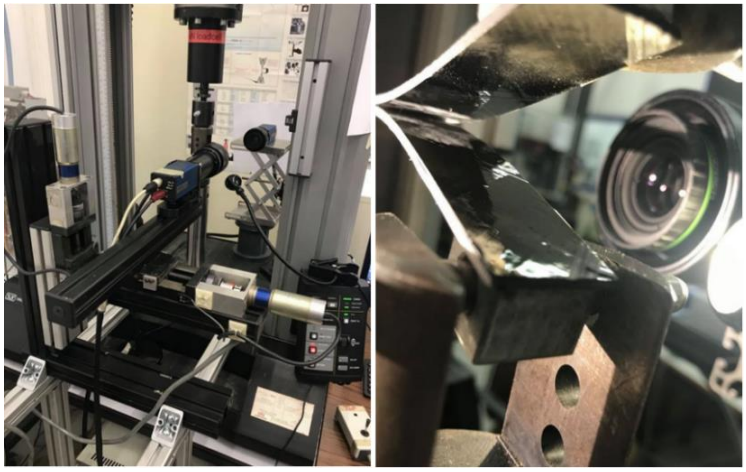

Figure 1 Setup for the conventional DCB test, coupled with edge microscopy and mesoscale DIC

2.3 DCB testing with in-situ micro-XCT

A TESCAN UniTOM XL scanner of the KU Leuven XCT Core Facility was used for the in-situ DCB tests. One specimen from each layup was mounted on an in-house developed in-situ DCB device. During testing one loading block remained stationary at its initial position while the other moved away to exert normal opening (mode I) load. The loading device was magnetically attached to the rotation stage inside the UniTOM XL scanner, ensuring minimum vibration during scanning (Figure 2). With a displacement rate of 2 mm/min (consistent with the preceding DCB tests), loading was applied in a stepwise manner to obtain intermediate in-situ scans, unravelling the evolution of the crack front. At each step once the desired force was reached, the testing was halted, and after a short period of stress relaxation, the crack tip was located and centred in live-view X-ray radiography for a 3D scan.

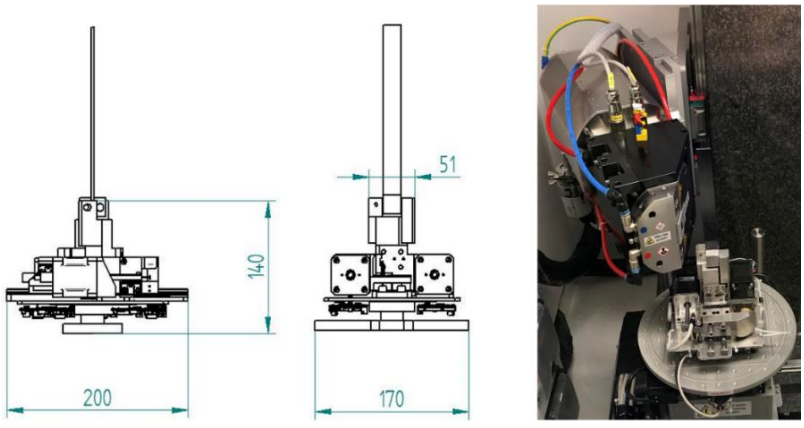

Figure 2 Orthographic drawings and in-situ view of the in-house developed DCB loading rig

The scanning parameters were optimised using static post-mortem scans performed on the pre-tested DCB specimens. The X-ray voltage was set to 120 kV, power to 15 W, exposure time to 100 ms, and the number of projections to 2000 with 3 times averaging. The voxel size was 15.6 µm. This led to a scan duration of approximately 12 mins. Subsequently, each scanned volume was reconstructed in the Acquila software package by TESCAN XRE. Post-processing of the reconstructed volumes was performed in the Thermo Scientific Avizo 2021.1 software by ThermoFisher.

3. Results and discussion

3.1 DCB with In-situ edge microscopy and DIC

Concerning the $0°//0°$ specimens, edge microscopy showed that the crack propagation was steady, and maintained along the interfacial mid-plane. No toughening mechanisms, i.e., fibre bridging, crack migration, secondary crack formation or intraply damage were evident. Thereafter, the R-curves were reconstructed using mesoscale DIC crack length measurements and MBT (Figure 3). The curves were relatively stable without any pronounced G_{IC} increase from initiation to steady-state propagation, which is reasonable considering the absence of any toughening mechanisms. The average initiation G_{IC} was found to be 423.68 $\pm$ 22.06 J/m^2 while the average steady-state propagation G_{IC} was 373.53 $\pm$ 7.97 J/m^2.

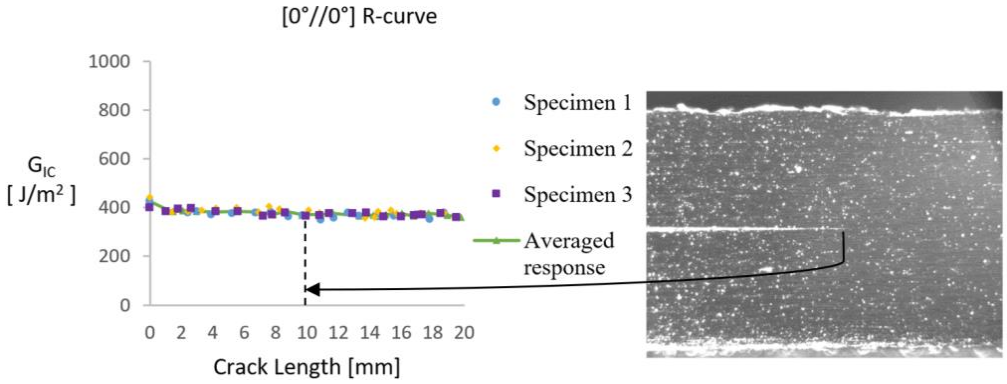

Figure 3 R-curve for the 0°//0° specimens along with a representative edge microscopy image exhibiting a straight and steady crack path in absence of any toughening phenomena

Concerning the $+45°//-45°$ specimens, it was possible to identify a combination of toughening mechanisms using edge microscopy. These can be clearly distinguished in a multi-step procedure consisting of: (1) pinning of the primary crack tip at the Teflon boundary, (2) secondary crack formation at the interface adjacent to the mid-plane, (3) ply bridging, (4) primary crack migration, (5) coalescence of the two cracks, (6) propagation in a tortuous path. The final step occurs in absence of any additional toughening mechanisms. This is conceptualised as the steady-state propagation G_{IC}.

The above steps correlate well with the R-curves obtained using DIC-measured crack lengths (Figure 4a). Initially, a pronounced increase from initiation G_{IC} occurs, corresponding to the migrated crack and ply bridging phenomenon (Figure 4b-c). Then, the curve reaches a plateau, which corresponds to the tortuous path followed after crack coalescence. This correspondence was validated using the edge microscopy images related to their respective R-curve points. Using the MBT, the average initiation G_{IC} was found to be 489 $\pm$ 43.56 J/m^2, while the steady-state propagation value reached 818.20 $\pm$ 39.10 J/m^2.

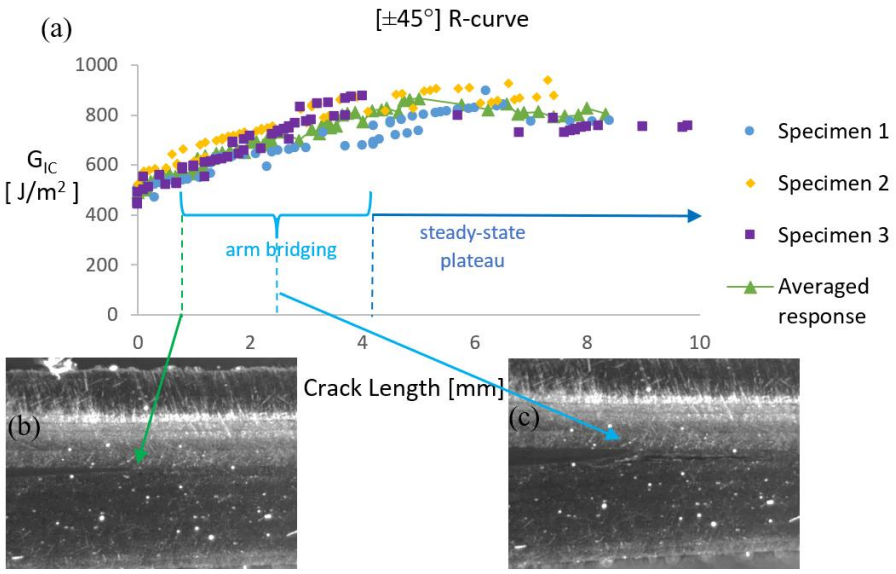

Figure 4 (a) R-curve for the $+45°//-45°$ specimens, edge microscopy image exhibiting (b) crack pinning and secondary crack formation and (c) ply bridging phenomena

3.2 In-situ micro-XCT

The in-house developed loading rig had a limit of 10 mm for the applied cross-head displacement. With this limit, seven scans were performed for the $0°//0°$ interface specimen and five for the $+45°//-45°$ specimen. Crack length was quantified in three different locations (two at the edges and one in the centre of the sample), using the 2D slices.

Despite anticipating a curved (due to the edge effects) but symmetric crack front for the $0°//0°$ specimen, initiation was found to occur first on one edge of the specimen. The crack front slowly evolves into the curved configuration but remains asymmetric even when the R-curve reaches the steady-state plateau (Figure 5a). However, quantification of the fracture toughness based on the crack lengths in the three different locations (using the MBT method) showed little difference (Figure 5b).

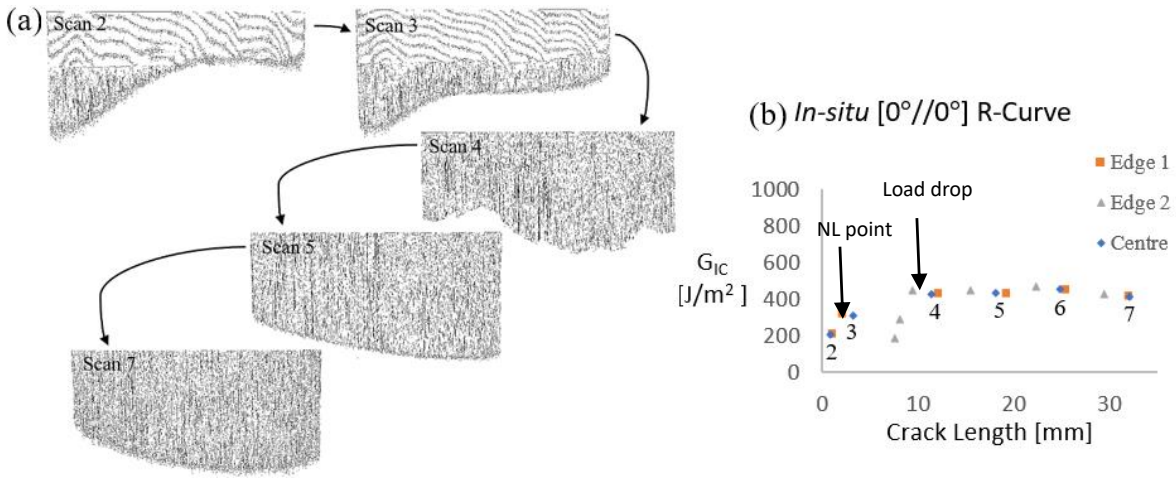

Figure 5 (a) 3D rendering of the in-situ load steps, showing the evolution of the crack front for the $0°//0°$ specimen and (b) the resulting R-curve exhibiting the dependency of G_{IC} on the chosen crack path (correspondence with the NL and load drop points shown at their respective scan number points within the R-curve)

Unfortunately, 10 mm cross-head displacement proved insufficient to cause any significant crack propagation for the $+45°//-45°$ specimens, and hence quantifying G_{IC} was not possible from this test. However, qualitative 3D analysis validated the crack migration and ply bridging phenomena observed under edge microscopy (Figure 6). These results were achieved by applying a manual wedge-driven opening to the specimen, extending beyond 10 mm cross-head displacement.

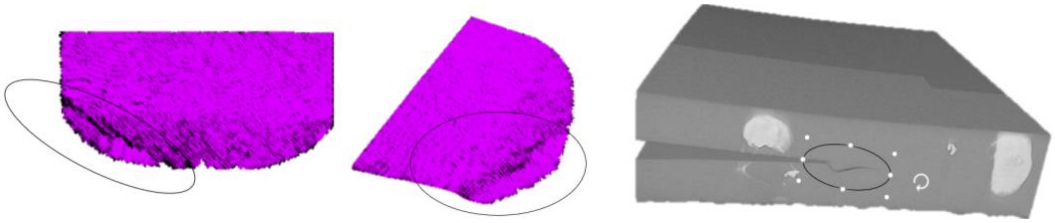

Figure 6 Micro-XCT visualisation of the $+45°//-45°$ interface specimen, exhibiting crack migration and ply bridging phenomena initiating from one edge of the specimens (wedge-driven opening)

An interesting observation, common for both types of interfaces, was the presence of partial crack initiation within the linear-elastic region of the force-displacement curve. This opposes the consideration that the NL point is being referred to as a conservative choice for initiation G_{IC} measurements. This leads us to believe that the initiation G_{IC} can be overestimated using conventional edge monitoring techniques to quantify crack lengths. This belief was quantitatively validated for the in-situ micro-XCT tested $0°//0°$ interface specimens, where an initiation G_{IC} value of 188.65 – 211.56 J/m^2 was recorded (Figure 5b). These values are much lower than those measured in the tests using 2D edge monitoring techniques (which was 423.68 $\pm$ 22.06 J/m^2 (Figure 3). On the contrary, the values measured using edge monitoring were much closer to those calculated at the load drop point (Scan 4) for the in-situ test, which fall within the range of 429.74 – 448.34 J/m^2, depending on the crack path observed (edges or centre).

4. Conclusions

A novel in-situ DCB test coupled with micro-XCT was performed, giving rise to a 3D analysis of the crack front development of carbon FRPC specimens, possessing two different interlaminar interfaces. DCB tests using conventional edge monitoring techniques, i.e., edge microscopy and mesoscale DIC were also performed, offering means of comparison. Vastly different crack paths were observed, giving rise to distinct R-curves for the two interface types, which were correlated to the present toughening mechanisms.

Acknowledgments

This study is supported by the KU Leuven Research Council (projects C14/21/076 and C24/17/052) and the FWO Postdoc Fellowship (project ToughImage - 1263421N). The study material was produced in the framework of the IBO project M3Strength supported by SIM (Strategic Initiative Materials in Flanders) and VLAIO (Flemish government agency for Innovation and Entrepreneurship. The FWO large infrastructure (project I013518N) is acknowledged for their financial support of the X-ray infrastructure and the KU Leuven XCT

  doi:10.5075/epfl-298799_978-2-9701614-0-0

Core facility is acknowledged for the 3D image acquisition and quantitative post-processing tools (https://xct.kuleuven.be/).

5. References

1. Bin Mohamed Rehan MS, Rousseau J, Fontaine S, Gong XJ. Experimental study of the influence of ply orientation on DCB mode-I delamination behavior by using multidirectional fully isotropic carbon/epoxy laminates. Composite Structures. 2017;161:1-7.
2. Pereira AB, de Morais AB. Mode I interlaminar fracture of carbon/epoxy multidirectional laminates. Composites Science and Technology. 2004;64(13-14):2261-70.
3. Nicholls DJ, Gallagher JP. Determination of GIC in Angle Ply Composites Using a Cantilever Beam Test Method. Journal of Reinforced Plastics and Composites. 1983;2(1):2-17.
4. de Morais AB. Double cantilever beam testing of multidirectional laminates. Composites Part A: Applied Science and Manufacturing. 2003;34(12):1135-42.
5. Mehdikhani M, Steensels E, Standaert A, A.M. Vallons K, Gorbatikh L, Lomov SV. Multi-scale digital image correlation for detection and quantification of matrix cracks in carbon fiber composite laminates in the absence and presence of voids controlled by the cure cycle. Composites Part B. 2018;154:138-47.
6. International A. D5528 - Standard Test Method for Mode I Interlaminar Fracture Toughness of Unidirectional Fiber-Reinforced Polymer Matrix Composites. ASTM; 2007.
7. Khudiakova A, Grasser V, Blumenthal C, Wolfahrt M, Pinter G. Automated monitoring of the crack propagation in mode I testing of thermoplastic composites by means of digital image correlation. Polymer Testing. 2020;82:106304.

  doi:10.5075/epfl-298799_978-2-9701614-0-0

CRACKING PREDICTION IN LAMINATES WITH PLY DISCONTINUITIES USING A VARIATIONAL STRESS ANALYSIS

M. J. Mohammad, Fikry[a], Vladimir, Vinogradov[b], Shinji, Ogihara[a]

a: Department of Mechanical Engineering, Faculty of Science and Technology, Japan – 7519705@ed.tus.ac.jp
b: School of Engineering, Newcastle University, UK

Abstract: *This study experimentally investigates and analytically evaluates the cracking behavior in resin pocket that existed due to ply discontinuity in a unidirectional laminate. Experimental observations revealed that several cracks formed in the resin pocket prior to the initiation of delamination cracks. The observed cracks typically occur within the resin pocket, rather than at the interfaces with the discontinuous ply, and are curved towards the center of the pocket. For the cracking prediction, a simple variational stress analysis based on the principle of minimum complementary energy is developed. By assuming a higher level of residual stresses due to chemical shrinkage of the resin during curing, it is shown that the crack locations are best determined using the principle of maximum energy release rate, while the curved crack path can be governed by the distribution of the maximum principal stress. The predicted cracking sequence and the crack curvatures agree well with experimental observations.*

Keywords: Ply discontinuity; Resin pocket; Crack behavior; Variational analysis, Energy release rate

1. Introduction

Ply termination is often used in composite structures to alter the laminate thickness or fiber orientation, accommodate changes in structural geometry, or create a hybrid composite by changing the ply material. When an internal ply is terminated, a resin-rich pocket is formed at the edge of the dropped ply. This discontinuity leads to stress concentrations and represents a source for damage initiation [1]. An illustration of a unidirectional laminate with a resin-rich region associated with ply discontinuity is shown in Fig. 1. The current work extends the applicability of the variational approach for analysis of a laminate with alternating material properties in the longitudinal direction of laminates based on the original variational model of Hashin [2].

The main motivation of this study is to elucidate the material properties and damage behavior of laminates with discontinuous plies. Ply discontinuities, resulting in formation of resin-rich regions, imply existence of more than one material in several regions along a ply, and requires the laminate to be subdivided in the longitudinal direction. Mathematical treatment of the problem required appropriate boundary conditions at each interface between the regions with different layups/materials. Here, the principle of minimum complementary energy and several mathematical means have been used to systematically determine the necessary boundary conditions and to approximate the stress distribution and effective Young's modulus of the laminate. Similar to Hashin [2, 3] an admissible stress field that satisfies equilibrium and all the appropriate boundary and continuity conditions was first constructed in each region. It is then

  doi:10.5075/epfl-298799_978-2-9701614-0-0

used in conjunction with the principle of minimum complementary energy to achieve the optimal stress state.

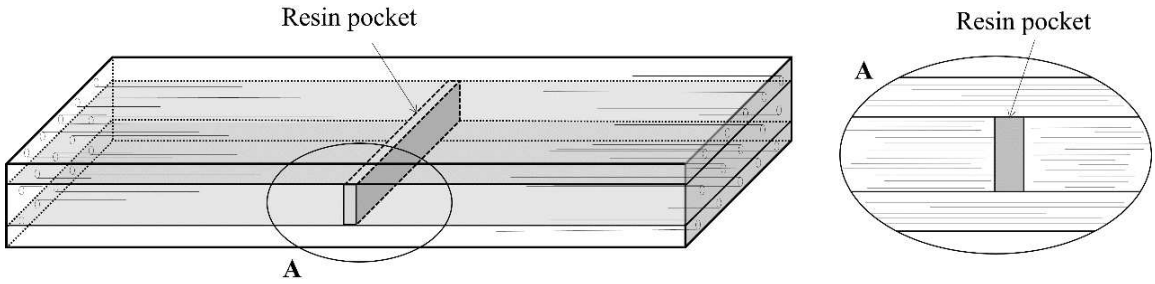

Figure 1. Formation of a resin pocket resulted from ply discontinuity

2. Experimental observation

A unidirectional (UD) $[0]_8$ laminates with four discontinuous plies in the middle were manufactured and tested in tension. The material was carbon fiber/epoxy unidirectional (UD) tape prepreg (Torayca, T700SC/2592). Monotonic tensile load was applied using a TENSILON RTF-1350 tensile testing machine at a crosshead speed of 0.5 mm/min. An optical microscope KEYENCE VH-Z100R was used for in-situ edge observation.

Fig. 2 shows a crack appearance in the resin pocket in a specimen having the length of the resin region of L_0 ≈ 1.24 mm. It is interesting to notice that the cracking pattern observed in these experiments is not intuitive. One would expect failure along the interfaces between the resin region and the discontinuous ply, where the resin is stressed to a higher degree, having stress concentrations/singularities in the corners. We assumed that this happened due to the chemical shrinkage of the resin during curing, where it was constrained by the surrounding UD plies, causes additional residual stresses in the pocket. From the observation, we also noticed that all cracks in the resin region are curved toward the center of the region, while successively formed cracks demonstrate higher curvatures (comparing the crack patterns at 451, 564, and 596 MPa in Fig. 2).

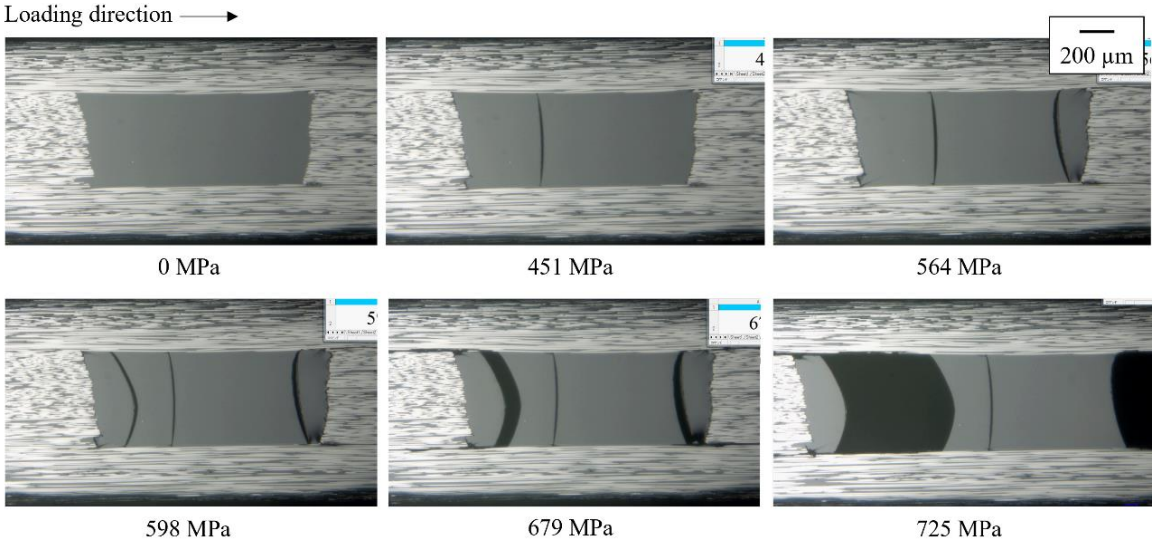

Figure 2. Crack occurrence in the resin pocket, (a) First crack at applied stress of 451 MPa, (b) Second crack at applied stress of 564 MPa, (c) Third crack at applied stress of 598 MPa

  doi:10.5075/epfl-298799_978-2-9701614-0-0

3. Variational stress analysis

3.1 Construction of admissible stress field

The analysis model used in this study is illustrated as in Fig. 3 where a two-ply system is considered, while a symmetry condition about the x-axis ($z = 0$) is applied. We first assume that the longitudinal normal stress σ_{xx} in each ply (m) varies only along the x-direction:

$$\sigma_{xx}^{(m)} = \phi_m(x), \tag{1}$$

where $\phi_1(x)$ and $\phi_2(x)$ are unknown functions to be determined. For the stress defined in Eq. (1) to be admissible for its use in the principle of minimum total complementary energy, stresses $\sigma_{xz}^{(m)}$, $\sigma_{zz}^{(m)}$, along with $\sigma_{xx}^{(m)}$ have to satisfy all equilibrium equations and traction continuity conditions.

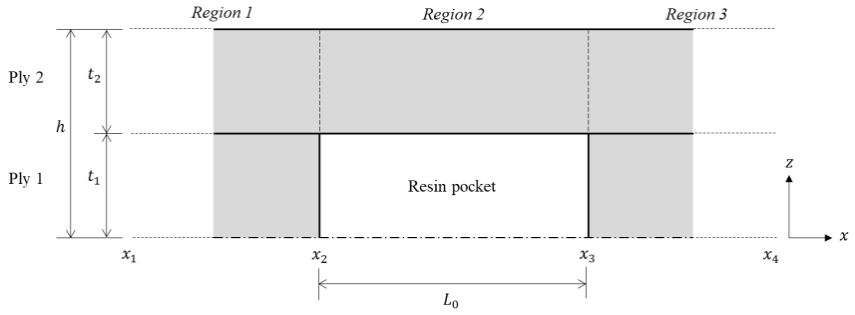

Figure 3. Analysis model

The resulting stresses of other stress components are:

$$\sigma_{xx}^{(1)} = \phi(x), \tag{2}$$

$$\sigma_{xx}^{(2)} = \frac{N_{xx}}{t_2} - \left(\frac{t_1}{t_2}\right)\phi(x), \tag{3}$$

$$\sigma_{xz}^{(1)} = -\phi'(x)z, \tag{4}$$

$$\sigma_{xz}^{(2)} = \left(\frac{t_1}{t_2}\right)\phi'(x)(z-h), \tag{5}$$

$$\sigma_{zz}^{(1)} = \frac{1}{2}\phi''(x)(z^2 - ht_1), \tag{6}$$

$$\sigma_{zz}^{(2)} = -\frac{1}{2}\left(\frac{t_1}{t_2}\right)\phi''(x)(h-z)^2. \tag{7}$$

3.2 Variational formulation

The complementary energy U_c associated with the admissible stresses in a laminate subject to traction boundary conditions is defined by:

$$U_c = \frac{1}{2}S_{ijkl}^{*}\sigma_{ij}^{0}\sigma_{kl}^{0}V + \sigma_{ij}^{0}\alpha^{0}\Delta T, \tag{8}$$

where S_{ijkl}^{*} are the effective compliances of the composite and $V = hL$ is the volume of the model of unit depth. In general, for region (i) bounded by $x_i \le x \le x_{i+1}$, the complementary energy is given by

$$U_{ca}{}^{(i)} = \int_{x_i}^{x_{i+1}} \left[\int_0^{t_1} W_1^{(i)}\, dz + \int_{t_1}^{h} W_2^{(i)}\, dz\right] dx, \tag{9}$$

$W_m^{(i)}$ is the energy density for ply m $(m = 1,2)$ in region (i). Substitution of expressions in Eq. (2)-(7) for the resulting stresses into the energy density $W_m^{(i)}$ and integration over the laminate thickness in z-direction in Eq. (9) yields the complementary energy for each region:

$$U_{ca}{}^{(i)} = \frac{1}{2}\int_{x_i}^{x_{i+1}} \left[\psi_i - C_0^{(i)}\phi^{(i)} + C_{00}^{(i)}\phi^{(i)^2} + C_2^{(i)}\phi^{(i)''} + C_{02}^{(i)}\phi^{(i)}\phi^{(i)''} + C_{22}^{(i)}\phi^{(i)''^2} + C_{11}^{(i)}\phi^{(i)'^2}\right] dx, \tag{10}$$

where primes denote derivatives with respect to x. C are the coefficients from the expression. In conjunction with the principle of minimum complementary energy, Euler-Lagrange equation was used thus gives the solution of the system as

$$\phi^{(i)}(x) = A_1^{(i)}\, e^{\eta_1^{(i)}x} + A_2^{(i)}\, e^{\eta_2^{(i)}x} + A_3^{(i)}\, e^{\eta_3^{(i)}x} + A_4^{(i)}\, e^{\eta_4^{(i)}x} + B^{(i)}, \tag{11}$$

where $A_1, A_2, A_3,$ and A_4 are the constants to be determined from the boundary conditions and $B^{(i)}$ is the far-field stress in ply 1 of region i. Summing up the complementary energy for the whole unit cell, we have the total complementary energy,

$$U_{ca}^{total} = \sum_{i=1}^{N} 2U_{ca}^{(i)}. \tag{12}$$

Here, N is the total number of regions.

3.3 Determining the region boundary stresses that minimize the complementary energy

By some mathematical means of integration by parts and rearranging it according to the order of derivatives, we can write the total complementary energy in Eq. (10) in the terms of regions' boundary stresses as:

$$U_{ca}^{(total)} = \{\boldsymbol{a}\}^T[\boldsymbol{L}]\{\boldsymbol{a}\} + \{\boldsymbol{l}\}^T\{\boldsymbol{a}\} + \sum_{i=1}^{N} K_0^{(i)}, \tag{13}$$

where $\boldsymbol{a} = \{\bar{\boldsymbol{a}}_{\boldsymbol{1}}, \hat{\boldsymbol{a}}, \bar{\boldsymbol{a}}_{\boldsymbol{2}}\}^T$,here, $\bar{\boldsymbol{a}}_{\boldsymbol{1}} = \{\phi_1, \phi_1', \psi_1\}^T$, $\bar{\boldsymbol{a}}_{\boldsymbol{2}} = \{\phi_{N+1}, \phi_{N+1}', \psi_{N+1}\}^T$ are the vectors of known stresses at the tips of the specimen while $\hat{\boldsymbol{a}} = \{\phi_2, \phi_2', \psi_2, \dots\dots, \phi_N, \phi_N', \psi_N\}^T$ is the vector of unknown internal region boundary stresses that will be determined by minimizing the total complementary energy. In this case, $[\boldsymbol{L}] = \begin{bmatrix} \boldsymbol{L_{11}} & \boldsymbol{L_{12}} & \boldsymbol{L_{13}} \\ \boldsymbol{L_{21}} & \boldsymbol{L_{22}} & \boldsymbol{L_{23}} \\ \boldsymbol{L_{31}} & \boldsymbol{L_{32}} & \boldsymbol{L_{33}} \end{bmatrix}$ and $\{\boldsymbol{l}\} = \{\boldsymbol{l_1}, \boldsymbol{l_2}, \boldsymbol{l_3}\}^T$. $\boldsymbol{L_{ij}}$ and vector $\boldsymbol{l_i}$ are the corresponding coefficients matrices/vectors. Minimizing the total complementary energy in respect to the unknown boundary stress vector, $\hat{\boldsymbol{a}}$,

$$\frac{\partial U_{ca}^{(total)}}{\partial \hat{\boldsymbol{a}}} = \left[\boldsymbol{L_{22}} + \boldsymbol{L_{22}}^T\right]\{\hat{\boldsymbol{a}}\} + 2[\boldsymbol{L_{21}}]\{\bar{\boldsymbol{a}}_{\boldsymbol{1}}\} + 2[\boldsymbol{L_{23}}]\{\bar{\boldsymbol{a}}_{\boldsymbol{2}}\} + \{\boldsymbol{l_2}\} = 0, \tag{14}$$

we have,

$$\{\hat{\boldsymbol{a}}\} = -\left[\boldsymbol{L_{22}} + \boldsymbol{L_{22}}^T\right]^{-1}\langle 2[\boldsymbol{L_{21}}]\{\bar{\boldsymbol{a}}_{\boldsymbol{1}}\} + 2[\boldsymbol{L_{23}}]\{\bar{\boldsymbol{a}}_{\boldsymbol{2}}\} + \{\boldsymbol{l_2}\}\rangle. \tag{15}$$

Solution of Eq. (15) determines constants A (Eq. (11)), which provide the final expressions for the stress functions $\phi^{(i)}$ (Eq. (11)) and consequently defines the entire admissible stress field that gives the minimum complementary energy. However, it is to be noted that the dependency

on the interval lengths in Eq. (13) disappears only in case the intervals near to the tips are long enough, so the interfaces do not interact.

3.4 Calculation of energy release rate (ERR) associated with cracking

The energy release rate (ERR) associated with the crack formulation, $G(x)$ is defined by the difference between the energies of a cracked laminate, $U_{ca}^{(cr)}$ and the uncracked laminate, $U_{ca}^{(0)}$, assuming the effect of curvature on the energy release and crack length is small,

$$G(x) = \frac{U_{ca}^{(cr)} - U_{ca}^{(0)}}{t_1}. \quad (16)$$

For secondary cracks prediction, a model representing a laminate with more than one crack in the resin pocket is shown in Fig. 4. Once the first crack was formed, the stress field and the ERR as a function of the potential crack location were recalculated.

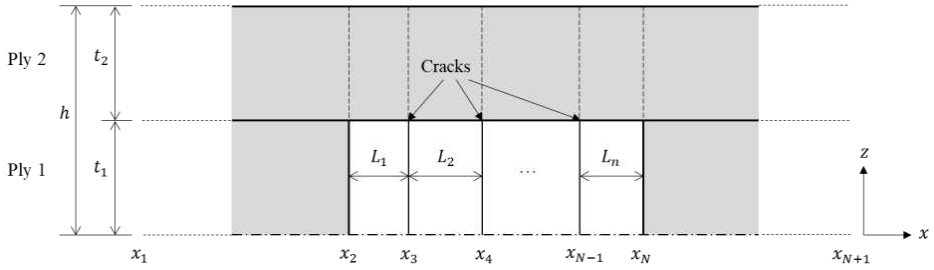

Figure 4. Analysis model with cracks

4. Analysis results

The models in Fig. 3 and Fig. 4 are analyzed, where the length of the specimen is 100 mm, t_1 = t_2 = 0.3 mm and L_0 = 1.24 mm. The material properties used were quoted from Fikry et al. [4]. An axial stress of σ = 451 MPa corresponding to the first crack formation in the specimen described in Section 2 was applied, as well as a temperature change of cooling down to room temperature, ΔT = −106°C.

Fig. 5 (a) shows the axial and first principal stress while Fig. 5 (b) shows the ERR as functions of location within the resin region for various values of chemical shrinkage. When no considerations of chemical shrinkages of the resin in the resin pocket, the maximum axial and principal stress in the resin region are at the corners/interfaces with the UD region. Besides, the ERR reaches its maximum also at the ends of the interval occupied by the resin pocket, hence, cannot explain the observed cracking pattern in our experiments as the cracks appear within the resin region and away from the interfaces. It can be seen that at higher values of chemical shrinkage, the energy release rate becomes higher at a distance from the interfaces than at the interfaces.

To predict the cracking in this study, a free strain due to the chemical shrinkage of ε_{ep}^{ch} = 0.0126 was then assumed in this study. The resultant stress distribution and the ERR as a function of the first crack occurrence are shown in Fig. 6 (a) and (b), respectively. Although the method of calculation of the ERR presented here was based on the simple geometry of a plane crack, the variational stress analysis could be used to visualize the curved crack shape by assuming that the crack would run normal to the first principal stress, i.e., along the trajectory of the second principal stress. Therefore, the slope of the crack can be determined by:

  doi:10.5075/epfl-298799_978-2-9701614-0-0 published under CC BY-NC 4.0 license

$$\frac{dx}{dz} = tan\,\theta\,(x, z), \tag{17}$$

where $\theta(x, z)$ is the angle between the direction of the second principal stress at (x, z) and z-direction. The resultant location and trajectory of the first crack is shown in Fig. 6 (d). It can be seen from the figure that the crack was slightly curved towards the center of the region, which agreed with the optical observation (Fig. 6 (c)).

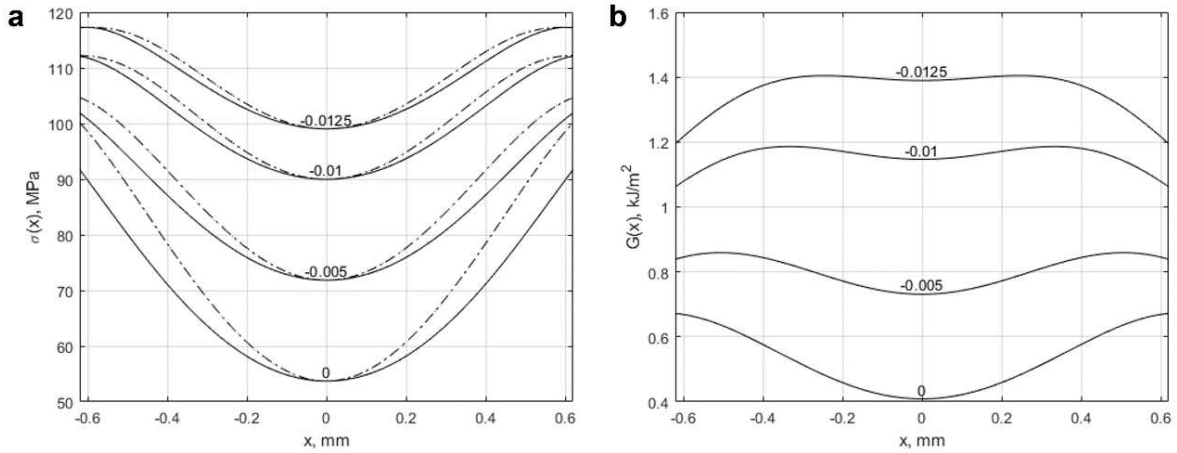

Figure 5. (a) Axial stress σ_{xx}(solid line) and the maximum principal stress (dashed line) plotted along the top interface $z = t_1$, (b) ERR, as a function of x-distance in resin of the uncracked laminate. Labels indicate the corresponding values of chemical shrinkage

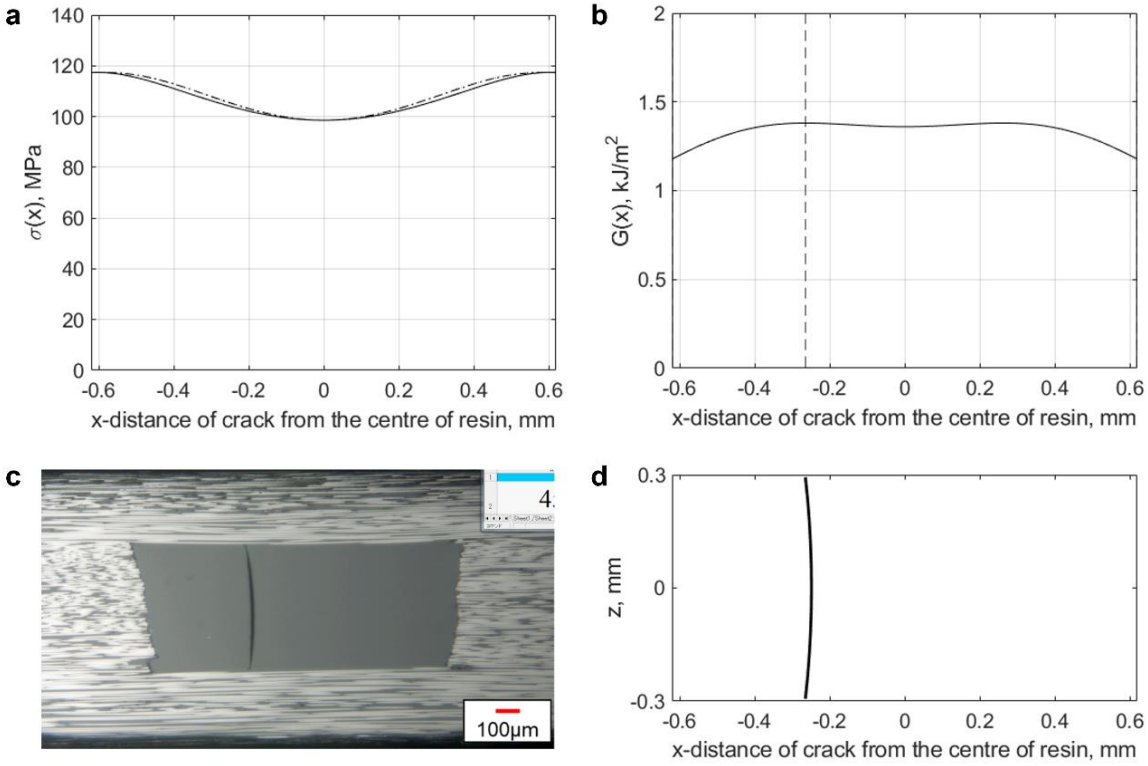

Figure 6. Prediction of first crack in the resin region, (a) axial stress σ_{xx} (solid line) and the maximum principal stress (dashed line) as a function of location along $z = t_1$, (b) ERR, (c) observed crack, (d) predicted crack

In accordance with the maximum ERR criterion, the value of a calculated maximum ERR associated with the first crack location determines the critical ERR. For the specimen in this study, the calculated maximum ERR was estimated to be $G_C \approx$ 1.38 kJ/m^2. It was expected that the subsequent cracks could form at the same value for the ERR. Fig. 7 shows the ERR as a function x-distance in the resin pocket, predicted location and curvature of the second and third cracks. The location of the crack based on the predicted maximum ERR, had good agreement with the observed location. In addition, the calculated curvature was higher than of the first crack, which also agreed with the observation.

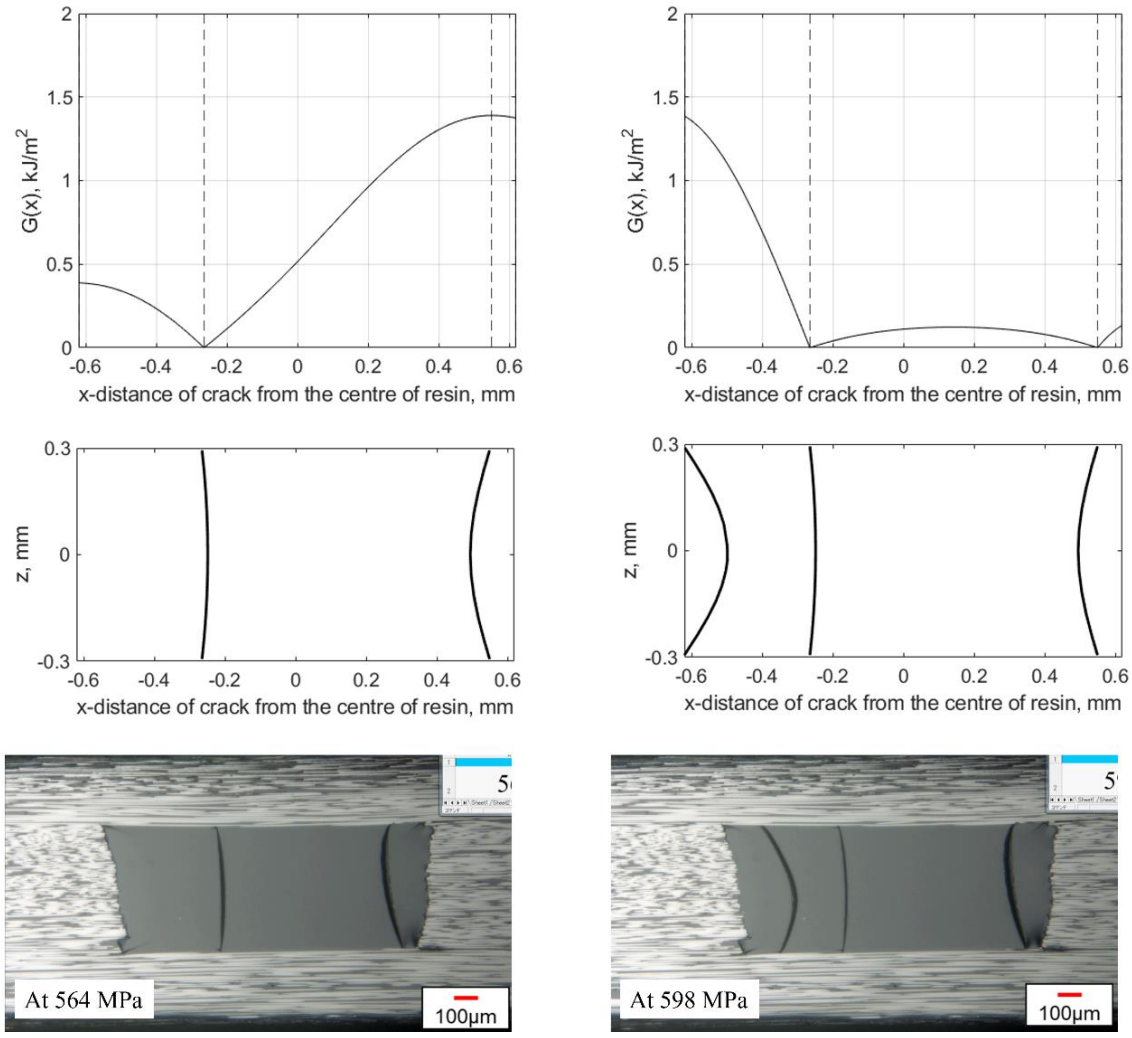

Figure 7. Prediction of cracking in the resin region with increasing applied stress. Columns left to right: second crack at the critical load 564 MPa; third crack at the critical load 1024 MPa. Rows top to bottom: ERR; predicted crack shapes; observed cracks

5. Conclusion

A variational model for analysis of stress fields in laminates with regions of different material properties along the longitudinal direction (such as ply discontinuity) subjected to uniaxial loading was developed based on the original variational model of Hashin's analysis. The spectrum of applications also includes estimation of the effect of cracks on the approximate stress distribution and effective Young's modulus of laminates. The critical energy release rate associated with cracking was calculated using the complementary energy of the model to predict

  doi:10.5075/epfl-298799_978-2-9701614-0-0

crack in the resin-rich region. It has been shown that the trajectories of the principal stress, based on the developed stress analysis, also replicate the experimentally observed crack shapes. We should emphasize the importance of the effect of chemical shrinkage on the results as the value was assumed in this study. Development of additional residual stresses due to chemical shrinkage in the confined geometry, assumed herein, deserves further attention.

6. References

1. Fikry M, Nur Atikah Z, Ogihara S. Microscopic Damage Behavior of Angle-ply CFRP Laminates with Fiber Discontinuous Plies. Materials System 2020; 37:65-72.
2. Hashin Z. Analysis of cracked laminates: a variational approach. Mechanics of Materials 1985; 4:121-136.
3. Hashin Z. Analysis of stiffness reduction of cracked cross-ply laminates. Engineering Fracture Mechanics 1986; 25:771-778.
4. Fikry M, Ogihara S, Vinogradov V. The effect of matrix cracking on mechanical properties in FRP laminates. Mechanics of Materials 2018; 4:3:1-16.

  doi:10.5075/epfl-298799_978-2-9701614-0-0

Composites Meet Sustainability – Proceedings of the 20th European Conference on Composite Materials,
ECCM20. 26-30 June, 2022, Lausanne, Switzerland

ENERGY AND STRENGTH-BASED CRITERIA FOR INTRALAMINAR CRACK GROWTH IN REGIONS WITH HIGH STRESS GRADIENTS

Anish Niranjan, Kulkarni[a,b], Andrejs, Pupurs[a], Patrik, Fernberg[b]

a: Riga Technical University, 1658 Riga, Latvia – anish-niranjan.kulkarni@edu.rtu.lv
b: Luleå University of Technology, 971 87 Luleå, Sweden

Abstract: *Composite laminates can develop high density of intralaminar cracks upon severe mechanical or thermal loading. When the distance between two adjacent intralaminar cracks reduces to a very small value normalized with respect to the ply thickness, local stress perturbations caused by these cracks start to interact resulting in the formation of regions with high stress gradients in 90-layer. In the present study, stress state in such regions is analyzed for glass-fiber and carbon-fiber epoxy cross-ply laminates using finite element modeling. The high stress gradients are seen to influence growth characteristics of new intralaminar cracks. The growth characteristics are studied using FEM models and fracture mechanics, with the available energy release rate calculated by virtual crack closure technique and J-Integral method.*

Keywords: Intralaminar cracking; finite element modeling; energy release rate; virtual crack closure technique; J-Integral

1. Introduction

Cross-ply composite laminates develop intralaminar cracks in off-axis layers (90-layers) when loaded mechanically in the longitudinal direction. These cracks lead to a stepwise decrease in laminate properties, and thus need to be studied in detail to predict the behavior of such laminates under mechanical and thermal loading conditions.

Weibull strength distribution [1] is one of the most common approaches to characterize intralaminar cracking in laminates, and it requires stress in a composite ply as an input parameter. To calculate the ply stress, various models have been developed. According to classical laminate theory (CLT) [2], stresses developed in a k^{th} layer can be calculated according to Eq. (1).

$$\{\sigma\}_k = [\bar{Q}]_k(\{\varepsilon_0\} - \{\varepsilon^{th}\}_k) + z[\bar{Q}]_k\{k\} \quad (1)$$

In Eq. (1), ε_0 is applied linear mechanical strain, ε^{th} is thermal strain and k is applied curvature. Stress is calculated using the applied strain values and global stiffness matrices. In the absence of applied curvature, classical laminate theory predicts that stress generated along any direction in any ply is constant throughout a ply and is independent of longitudinal (X) or transverse (Y, Z) coordinates (For coordinate system, refer to Fig. 1). CLT provides accurate results for a laminate with undamaged layers, but with shear lag model [3], one can calculate stresses in a laminate with damaged layers. This model states that the longitudinal stress (σ_x) in 90-layer can vary along X axis, but it remains constant through ply thickness (Z axis) (refer Eq. (2)).

$$\sigma_x = E_x\varepsilon_c\{1 - \frac{\cosh\beta x}{\cosh\beta l}\} \quad (2)$$

  doi:10.5075/epfl-298799_978-2-9701614-0-0

In Eq. (2), l is half-distance between two adjacent intralaminar cracks and β is known as shear lag parameter, which depends on the shear modulus of 90-layer and the thickness of 90-layer.

In addition to these primary models, there are variational models developed by Hashin [4], which use principle of minimum complementary energy to calculate stiffness reduction and stress distribution in damaged cross-ply composites. However, Hashin's model is also based on the assumption that σ_x in a 90-ply remains constant along Z axis. As demonstrated in the present work, this assumption is not applicable when 90-ply is severely damaged. Thus, the above-mentioned models cannot be used to characterize the stress state in 90-layers with high intralaminar crack density. In the present work, finite element modeling is used to calculate two-dimensional stress state in highly damaged cross-ply composite laminates.

To study intralaminar cracking and crack growth, various failure criteria can be applied, which are divided into strength-based or energy-based criteria. A basic failure criterion such as maximum stress criterion predicts failure based on a condition that the resolved stress in a composite ply along a particular direction exceeds the maximum permissible stress value for failure i.e., the strength of material in that direction. This approach assumes a uniform intralaminar strength distribution in a damaged 90-ply of a loaded composite. Manders et.al. [1] showed that damaged 90-plies do not show uniform strength distribution. They considered 90-ply as a layer with statistically distributed defects, whose strength can be described by a two-parameter Weibull distribution. With this criterion, the risk of rupture or probability of failure can be calculated by Eq. (3).

$$P_f = 1 - \exp\left(\frac{\sigma_T^{90}}{\sigma_0}\right)^m \tag{3}$$

In Eq. (3), P_f is probability of failure, σ_T^{90} is transverse stress in 90-ply, and σ_0 and m are Weibull scale and shape parameters respectively. The strength-based failure criteria work well in prediction of intralaminar cracking, however the use of them under presence of stress singularities or high stress concentrations is doubtful.

Energy-based failure criteria offer an appropriate solution in such cases, as these criteria are based on change in surface energy of the crack face during the crack growth. Wang [5] used linear elastic fracture mechanics (LEFM) and Griffith criterion [6] to predict crack growth in structural composite laminates. Griffith postulated that at the instance of crack growth, the stored elastic strain energy, *U*, is converted into crack surface energy, *S*, such that, during a virtual crack extension, by Eq. (4),

$$\frac{\partial U}{\partial a} = \frac{\partial S}{\partial a} \tag{4}$$

The ratio mentioned in Eq. (4) or the rate of change of stored elastic strain energy is termed as available energy release rate (ERR), which is denoted by the symbol *G*. The present work uses *G* as a parameter to characterize growth of an intralaminar crack in a damaged laminated composite material.

2. Procedure

A finite element model of a cross-ply composite laminate with [0,90]s layup was generated using ANSYS software. The model was generated in ANSYS APDL module and was meshed with two-dimensional 8-node type elements with plane strain behavior. Each layer was assigned uniform

  doi:10.5075/epfl-298799_978-2-9701614-0-0

material properties individually. The material properties of a unidirectional ply for glass-fiber epoxy composite (GFEP) and carbon-fiber epoxy composite (CFEP) are given in Table 1. Properties of GFEP UD composite ply were obtained from literature [7], whereas CFEP UD mechanical properties were determined from experimental tests (E_L, E_T, η_{LT}, α_T) or assumed according to typical values (η_{TT}, G_{LT}, α_L). For manufacturing of CFEP laminates, the materials used were Pyrofil TR50S carbon fibers from Grafil Inc, and epoxy resin Araldite LY556, with Aradur HY917 by Huntsman. The manufacturing was performed using filament winding technique and vacuum infusion of resin.

Table 1. Material Properties of UD ply.

Material Property	GFEP	CFEP
Longitudinal Modulus (E_L)	44.73 GPa	138.00 GPa
Transverse Modulus (E_T)	12.76 GPa	8.10 GPa
Longitudinal Poisson's Ratio (η_{LT})	0.30	0.25
Transverse Poisson's Ratio (η_{TT})	0.42	0.45
Longitudinal Shear Modulus (G_{LT})	5.80 GPa	5.00 GPa
Transverse Shear Modulus (G_{TT})	4.49 GPa	2.79 GPa
Longitudinal CTE (α_L)	8.60 e^{-6}	0
Transverse CTE (α_T)	22.10 e^{-6}	27.00 e^{-6}

A uniform meshing was done across the model, except at the crack tip, where mesh was highly refined to accurately capture the stress and displacement distributions in its vicinity. Purely mechanical strain of 1% was applied in the longitudinal direction to simulate mechanical loading and a temperature body force of -100K was applied to simulate curing induced thermal stresses. Refer to Fig. 1 for description of coordinate system, geometrical model, and applied boundary conditions. The solutions were obtained for material deformation under given loading conditions and the results were post-processed to obtain displacement and stress distributions.

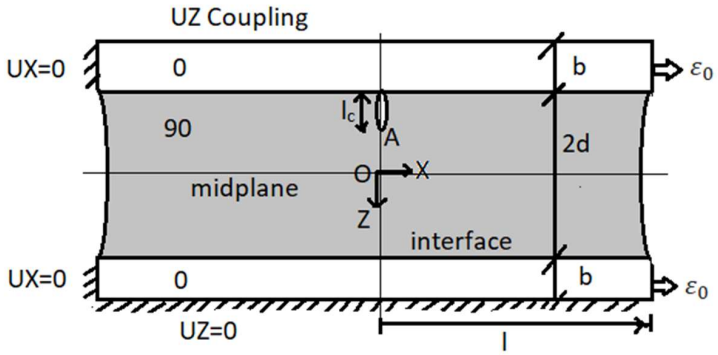

Figure 1. Model Description

For strain energy release rate studies, a small crack was created at 0-90 interface along the line x=0 as shown in Fig. 1, and the crack length was increased stepwise to obtain ERR values. The ERR values were calculated using built-in VCCT (virtual crack closure technique) and J-Integral method in ANSYS APDL.

  doi:10.5075/epfl-298799_978-2-9701614-0-0

3. Observations

3.1 Stress Analysis

Stress analysis is carried out to determine the potential for formation of new intralaminar cracks in a damaged 90-layer of cross-ply laminate. Longitudinal stress (Sxx) is plotted across half the region between two intralaminar cracks (considering symmetry in the other half), and the variation in Sxx is studied along longitudinal (X) and thickness (Z) directions using path operations post-processing function in ANSYS APDL. Note that the finite element model used for stress analysis consists only of two terminal intralaminar cracks at x=±l (refer to Fig. 1) and does not include the intralaminar crack at x=0.

Fig. 2 shows longitudinal stress distribution for GFEP [0,90]s laminates plotted along the midplane (line z=0) and just near the 0-90 interface (line z=0.95*d*). Note that 2*d* is 90-ply thickness and *b* is 0-ply thickness (refer to Fig. 1). The stress values in Fig. 2 and Fig 3 are normalized with respect to the far-field stress value in 90-layer and values along X axis for all the graphs in the present work are normalized with respect to *d*. Note that RON denotes the normalized crack density, which is obtained by multiplying actual crack density with the 90-ply thickness.

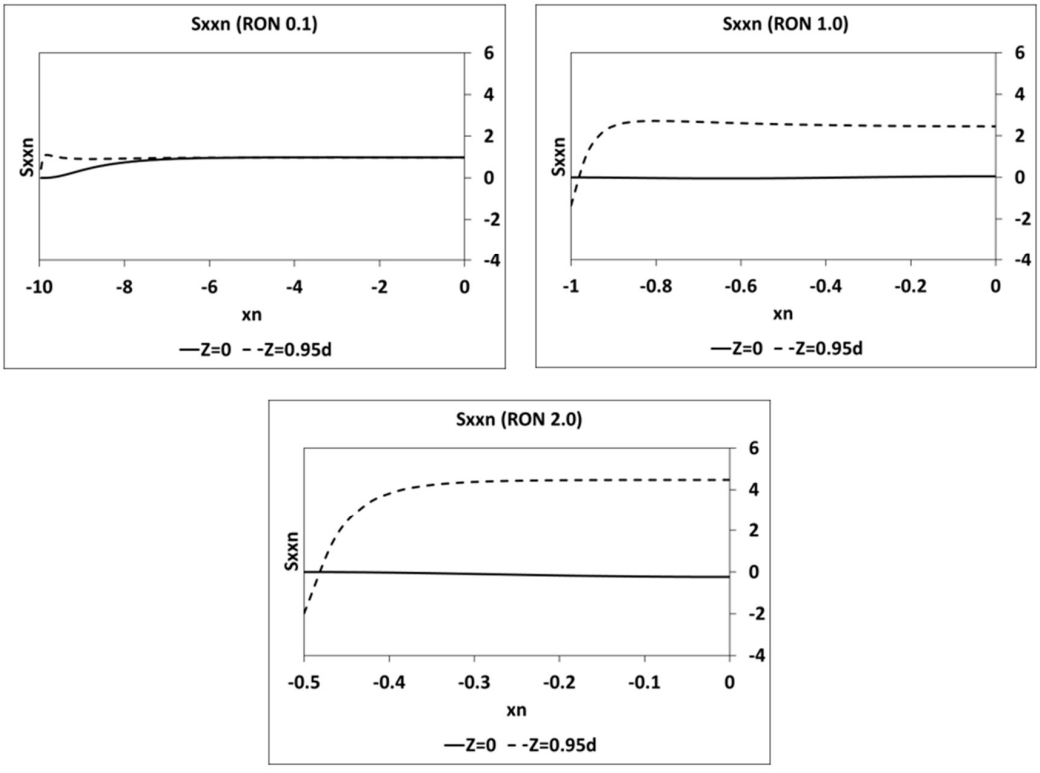

Figure 2. GFEP Longitudinal stress distribution along X-axis

Longitudinal stress plots in Fig. 2 show that the trends in Sxxn change significantly with changes in crack density. When the cracks are relatively far apart and crack density is low (RON 0.1), longitudinal stress along the midplane and that near 0-90 interface show very similar trends.

  doi:10.5075/epfl-298799_978-2-9701614-0-0

Both the graphs reach far-field stress value at some distance away from the intralaminar crack face.

Such behavior is not observed in the case of high crack densities (RON 1.0 and RON 2.0). When intralaminar cracks are very close to each other, the longitudinal stress near 0-90 interface reaches a very high value at xn=0, whereas the longitudinal stress along midplane stays zero or even becomes compressive at xn=0.

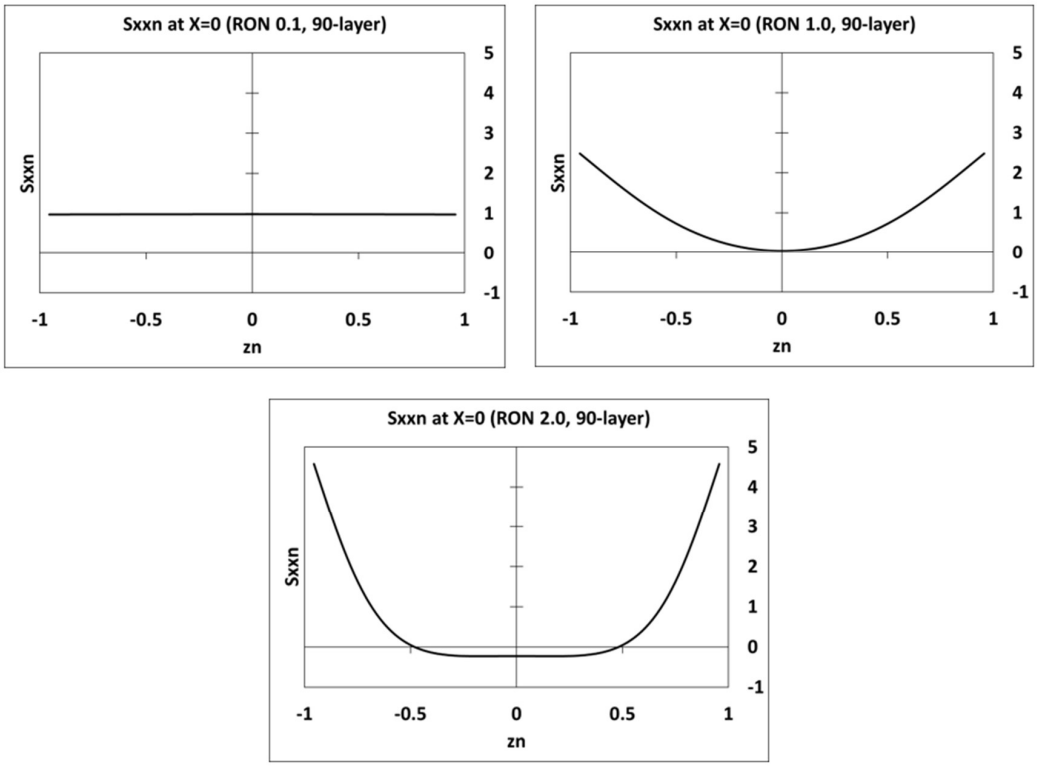

Figure 3. GFEP Longitudinal Stress Distribution along Z-axis in 90-layer

The gradient in longitudinal stress at x=0 is more clearly seen in Fig. 3, where longitudinal stress distribution through 90-layer thickness is shown. At low crack density (RON 0.1), longitudinal stress is seen to remain constant through 90-layer thickness. However, at high crack densities, stress perturbations near intralaminar crack faces start to interact with each other and a stress gradient is seen to be developed between 0-90 interface and midplane. Comparing stresses at these two locations, stress is considerably higher at the interface. Thus, a new intralaminar crack is more likely to initiate at the 0-90 interface than at the midplane.

3.2 Energy Release Rate Analysis

For ERR analysis with FEM, a small intralaminar crack with length lc is created at 0-90 interface along Z axis at x=0 (refer to Fig. 1) and the available energy release rate is calculated for increasing crack lengths using built-in virtual crack closure technique and J-Integral method in ANSYS APDL. The two methods are compared in Fig. 4 for a representative case of GFEP with normalized crack density of 0.1, where ERR is plotted v/s normalized crack length. Note that ERR

  doi:10.5075/epfl-298799_978-2-9701614-0-0

values for both the plots in Fig. 4 are normalized with respect to the first values of their respective series.

ERR observations in Fig. 4 indicate that *G* values obtained with J-Integral show a similar trend to *GI* (mode-I) values obtained with VCCT. The observations are in unison with all the other cases studied by varying both material properties and normalized crack densities. Note that all the ERR trends further shown in this work consist of values obtained with the method of J-Integral.

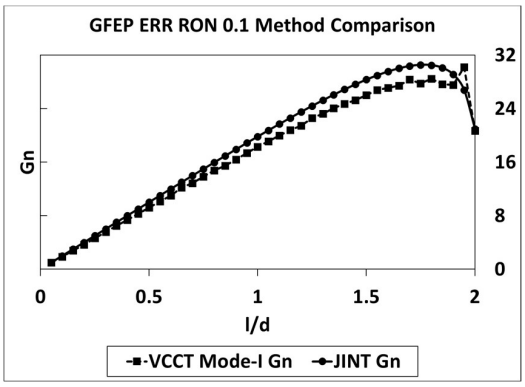

Figure 4. GFEP ERR Method Comparison

Fig. 5 shows ERR analysis in GFEP for cases with different normalized crack densities. Each point on the graph represents ERR for a crack, which has initiated at 0-90 interface (zn=-1) and has grown along Z axis at x=0 inside 90-layer until the corresponding zn value.

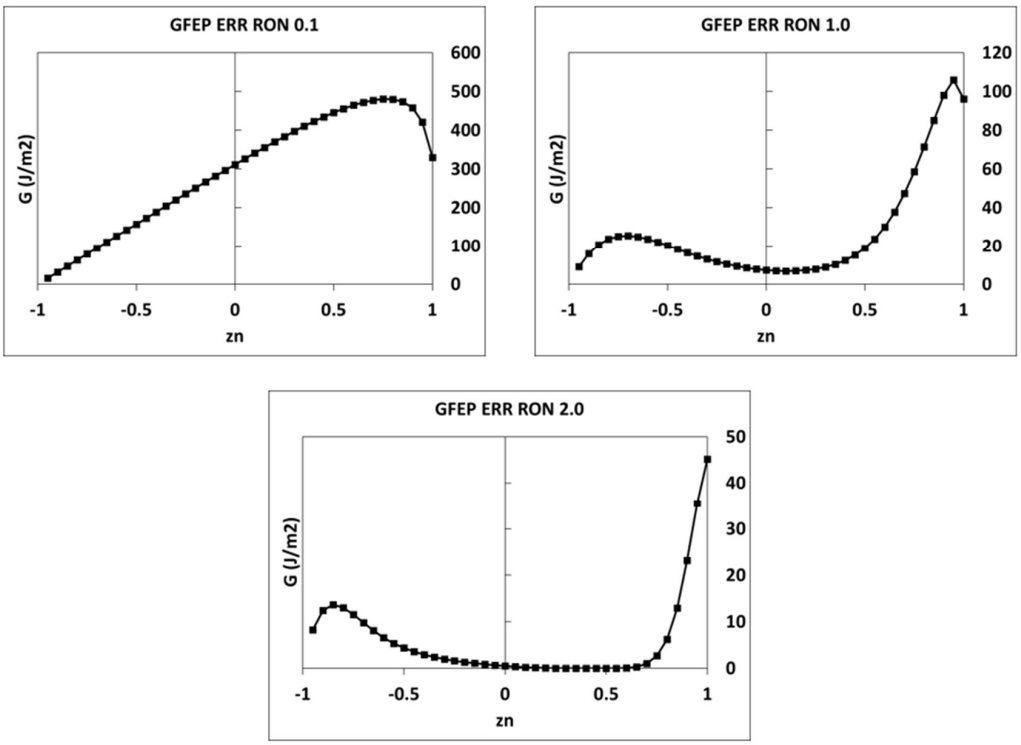

Figure 5. ERR Trends for crack growth through 90-layer

For the case of RON 0.1, available ERR increases linearly with increasing crack length except for the cases when crack tip is near 90-0 interface (zn=1). Assuming a simple energy-based failure criterion stating that a crack would propagate when the available ERR reaches critical ERR (fracture toughness or G_{Ic}), the positive gradient in available ERR trend mostly indicates an unstable crack growth.

The cases with higher crack densities (RON 1.0, RON 2.0) show a decrease in ERR trend near zn=0. For these cases, the available ERR reaches a very small value, or even reaches zero for RON 2.0 at zn=0, before it rises again and reaches a maximum near 90-0 interface. Once again assuming the crack propagation when ERR reaches G_{Ic}, negative gradients in ERR trends indicate that the crack growth would mostly be stable in these cases, except when approaching the 90-0 interface near zn=1. For the extreme case of RON 2.0, the crack growth would be arrested, since ERR becomes zero.

4. Results and Discussion

The trends in available energy release rate for a partially grown intralaminar crack are closely related to the stress distribution through 90-layer thickness. Referring to Fig. 3 and Fig. 5, observations for cases with high crack densities (RON 1.0 and RON 2.0) in GFEP show that the available ERR decreases when local transverse stress goes to a low value. In the extreme case of RON 2.0, available ERR becomes null when the stress becomes compressive. This is an expected ERR behavior considering that a positive stress i.e., tensile stress is needed to open an intralaminar crack in mode-I.

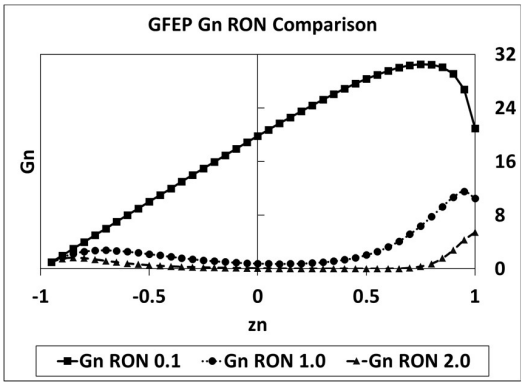

Figure 6. GFEP ERR Comparison

Fig. 6 and Fig. 7 represent ERR trends for GFEP and CFEP respectively, with plots for various crack densities shown together on one graph for comparison. For these figures, ERR values for each RON case, denoted as *Gn*, are normalized with respect to the first value of the corresponding series. ERR for GFEP and CFEP follow a similar pattern, with ERR trends for low crack density (RON 0.1) showing more variation and ERR trends for high crack densities (RON 1.0 and RON 2.0) staying closer to zero, when the three RON cases are compared among themselves. In future, a similar analysis can be done for different composite materials to generalize the growth characteristics of intralaminar cracks in regions with high stress gradients in any cross-ply laminate.

  doi:10.5075/epfl-298799_978-2-9701614-0-0

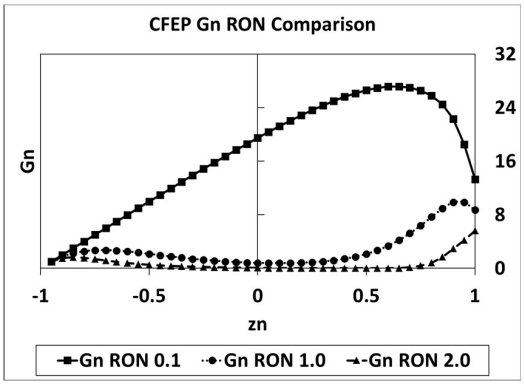

Figure 7. CFEP ERR Comparison

Acknowledgements

Part of this work was supported by Latvian Council of Science, project LZP-2019/1-0357 "Development and behavior analysis of novel textile composite/metal joints with enhanced mechanical properties".

5. References

1. Manders PW, Chou TW, Jones FR, Rock JW. Statistical analysis of multiple fracture in 0/90/0 glass fibre/epoxy resin laminates. Journal of Materials Science. 1983 Oct;18(10):2876-89.
2. Tsai SW, Hahn HT. Introduction to composite materials. Routledge; 2018 May 2.
3. Garrett KW, Bailey JE. Multiple transverse fracture in 90 cross-ply laminates of a glass fibre-reinforced polyester. Journal of materials science. 1977 Jan;12(1):157-68.
4. Hashin Z. Analysis of cracked laminates: a variational approach. Mechanics of materials. 1985 Jul 1;4(2):121-36.
5. Wang AS. Fracture Mechanics of Sublaminate Cracks in Composite Laminates. DREXEL UNIV PHILADELPHIA PA DEPT OF MECHANICAL ENGINEERING AND MECHANICS; 1983 Feb 1.
6. Griffith AA. VI. The phenomena of rupture and flow in solids. Philosophical transactions of the royal society of london. Series A, containing papers of a mathematical or physical character. 1921 Jan 1;221(582-593):163-98.
7. Pakkam Gabriel VR, Loukil MS, Varna J. Analysis of intralaminar cracking in 90-plies of GF/EP laminates with distributed ply strength. Journal of composite materials. 2021 Nov;55(26):3925-42.

  doi:10.5075/epfl-298799_978-2-9701614-0-0

DATA DRIVEN DAMAGE AND ANALYTICAL CAI MODELS FOR RAPID STRENGTH PREDICTION

Dr. James, Evans[a], Prof. Richard, Butler[b] , Dr. Karim Anaya-Izquierdo[c] ,Dr. Andrew, Rhead[d]

a: jamesglynnevans@gmail.com
b: r.butler@bath.ac.uk
c: k.anaya-izquierdo@bath.ac.uk
d: a.t.rhead@bath.ac.uk

Abstract: *An extensive laminate damage database has been constructed through in-house impact testing and non-destructive damage inspection methods. Generalised Additive Models (GAMs) are applied to the resulting dataset, using material and laminate properties, to produce a predictive model for both delamination diameter at a given interface and total plan area. Damage tolerant strain limits are often the design driver for safety-critical parts such as those used in aerospace structures. In such cases, compressive failure following damage is dominated by propagation of delaminations following localised buckling of surface sub-laminates A closed-form analytical expression for the strain energy release rate (SERR) has been expanded to better account for the complexity of damage morphology. The GAM models accurately predict delamination data including examples outside the range of the in-house dataset. The compression model is verified using experimental and GAM model damage input data. For both inputs there is a good agreement between prediction and compression test results.*

Keywords: Delamination; CAI; Modelling; Damage; Impact;

1. Introduction

Barely visible impact damage (BVID) is a major concern to the aerospace industry. This is due to the resulting reduction in strength of components and the difficulties identifying this during component inspection. Considerable effort and resources have been dedicated to the construction of detailed Finite Element (FE) models that can be used to predict the outcomes of specific impact events. However, such models require significant compute time. An empirical approach, utilizing Generalised Additive Models (GAMs) is taken owing to the complexity of damage and failure, so far, of analytical models. GAMs have a predictive advantage over machine learning as they enable stable extrapolation outside of the dataset, provided the correct variables have been specified.

Rapid damage prediction models are most useful if they can be paired with an equivalent residual strength model, enabling fast predictions of strength loss without the need for prototype testing. Choudhry et al. [2], have presented a semi-analytical method for predicting the strain at which initial delamination will propagate following sub-laminate buckling when compressed after impact. This study enhances the Compression After Impact (CAI) model, proposing improvements in how the model assess the compressive failure mode based on sub laminate layup. The critical sub-laminate identification method is also revised, allowing the model to consider the fractional sub-laminate combinations observed in experimental impact damage morphology.

  doi:10.5075/epfl-298799_978-2-9701614-0-0

2. Methodology – Empirical Data Collection

Forty-three unique layups employing HTS/977-2 and T800/M21 material systems and three laminate thicknesses were subjected to dynamic and quasi-static impacts of 6J-30J over a circular test window which owing to its symmetric nature allowed multiple stacking sequences to be considered in each impact test. 76 dynamic impact events were recorded, as well as 24 quasi-static indentation processes, with each process yielding impact data up to the equivalent of 10 impact events. Stacking sequences were selected to cover the greatest possible range of possible total miss-match angles (TMMA) that could be achieved in quasi-isotropic laminates, where. TMMA is the sum of the angles between plies across a given laminate. The purpose of having a spread of TMMA values was to facilitate assessment of the impact of this variable on delamination growth, both rate and morphology. It has been seen [3,4] that a greater TMMA can result in a comparatively slower growth rate of delaminations for a given material and thickness. Delamination damage is assessed via ultrasonic C-scans and MATLAB code was written to extract individual delamination diameters as well as total delamination plan area from each scan of an impact event.

CAI tests were performed, using the ASTM D 7137 standard, on the dynamically impacted coupons using an Instron 5585 Universal Testing Machine (UTM). The laminates were loaded at a displacement rate of 2 mm/min until propagation and/or failure occurred.

3. Methodology – GAM Construction

Generalised additive models (GAMs) [5] are computationally efficient, data-driven methods to produce models that accurately model a dataset, given relevant variables are supplied. These models are also strong predictive tools, capable of extrapolating outside of the original dataset. An exhaustive testing method is constructed to ensure the modelling process produces the optimal model for the dataset by considering all possible variable combinations. This process is then used to identify the optimal model distribution and model framework using the given initial variables. These initial variables are: Total ply miss-match angle, Interface miss-match angle, Fracture toughness, Laminate thickness, Relative ply orientation, Interface fractional depth and Impact energy. Delamination area is modelled using an appropriate variable selection as the input into the exhaustive method. GAM implementation is performed in the statistical programming language R easily [5], with the package 'mgcv' facilitating GAM implementation.

4. Methodology – CAI Model Modifications

The basis for the current CAI model is that of Choudhry et al. [2], which uses a comparison of the difference in energy before and after crack propagation to the Strain Energy Release Rate (SERR) in Mode I or II to determine the applied strain at which delamination propagation will occur. Specifically, bending energy is evaluated assuming

  doi:10.5075/epfl-298799_978-2-9701614-0-0

that no post-buckled stiffness is developed in the sub-laminate, exaggerating the Mode I bending energy available for propagation. The model can be applied to all loadings and non-standard angle designs. A limitation of the model is that it is unable to account for all forms of stiffness coupling and that the complexity of impact damage is likely to provide mechanics that bypass assumptions of this model. Therefore, conservative results are prioritised. This contrasts with potential adjustments to the model which aim to for closer match to mean experimental data.

4.1. Critical Strain Modification

To identify the laminate's Threshold Strain in the existing CAI model each potential delamination interface and accompanying sub-laminate (surface plies that are separated from the main body of the laminate by delamination) in the outer 25% of the laminate is considered individually. The calculation of the Threshold Strain is detailed in Equations 1.1 and 1.2. The full derivation of these equations can be found in Choudhry et al. (2019) [2].

$$\epsilon_{th}^{*} = \epsilon_{c}^{*}\left(\sqrt{4 + \frac{G_{1C}}{\mu_T}} - 1\right) \tag{1.1}$$

Where:

$$\mu_T = \epsilon_{c}^{*2}(A_{11}^{*} - 2(1 + \mu_L)A_{12}^{*} + A_{22}^{*}\mu_L^2) \tag{1.2}$$

A* represents the A-matrix of the sub-laminate, μL is the Poisson's ratio of the laminate, ε_C* is the critical sub-laminate strain (determined using the infinite strip program VICONOPT [6]) and ε_{th}* is the threshold sub-laminate strain. These equations are considered for each sub-laminate in the outer 25% of a laminate in the original method, which does not consider the possibility of fractional sub-laminates that may have formed due to delaminations 'stepping' down across interfaces via intra-ply cracks.

The outer 25% is considered as below this depth sub-laminates will not buckle before failure. The Threshold Strain is identified for each interface using each of the sub-laminates' A-matrix and Critical Strain values and identifying the lowest. This method relies on the assumption that each damaged interface acts independently of any others and that delaminations do not cross between interfaces. However, the critical sub-laminate is generally a fractional combination of sub-laminates where a crack has opened which is composed of both inter and intra-ply damage. Figure 1 details an updated delamination diagram to take this into account.

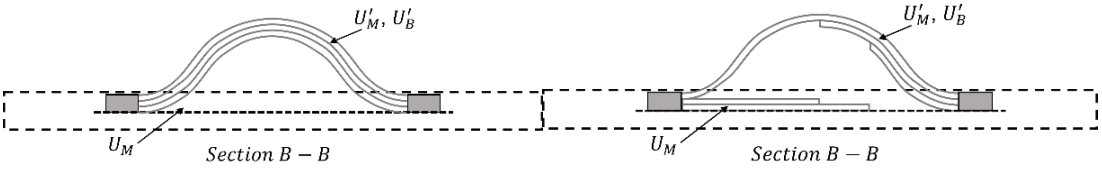

Figure 1. (Left) Original method for assuming delamination buckles with no intra-ply cracking. (Right) Updated delamination diagram, highlighting the uneven breaking of sub-laminates within the buckling region.

To consider this behaviour a different approach to identifying the laminate Threshold Strain was developed. Instead of considering each interface as independent integers, fractional coefficients were introduced. The coefficients were applied to the sub-laminate A-matrices and ε_c^* values. These coefficients range from 0 to 1, with each iteration increasing the coefficient by 0.01 to cover a range of every fractional combination of every sub-laminate. In each iteration, the coefficients of the sub-laminate's A-Matrix were set the same as the Threshold Strain for continuity in Eqn. (1.2) - e.g. if the fractional sub-laminate in question is 40% ε_c^* of sub-laminate one and 60% ε_c^* sub-laminate two then the considered A-matrices will be 40% and 60% of their respective values.

4.2. Fracture Toughness Modification

It was theorised that the manner of laminate buckling may be different for layups with 0^o orientated plies in the outer 25% of the laminate than those without, and therefore the GIC term in Eq. (1.1) may be the incorrect mode of fracture toughness to model this with. This vertical reinforcement in the outer 25% sub-laminate causes the critical sub-laminate to form a 'closing' post-buckling failure mode, rather than opening away from the remainder of the laminate - as is assumed in a Mode 1 failure. The 'closing' post-buckling mode would be governed by shear and would therefore be more accurately modelled using the second mode of fracture toughness, G_{2C}. To test this theory the model was run twice with G_{1C} and then with G_{2C} as the input fracture toughness values.

5. Results

Figure 2 shows results for the delamination diameter and area GAM models, with the red model data points overlayed onto the grey raw data. Figure 3 compares predictions of the Choudhry et al. CAI model with the improved CAI model and experimental CAI data. Figure 4 shows the CAI results of the updated CAI model when fed both raw data and the output of delamination models for both delamination diameter and area. Figure 5 details a Bland-Altman plot of the selective fracture toughness results, detailing a strong relationship between model and experimental results and low data variance.

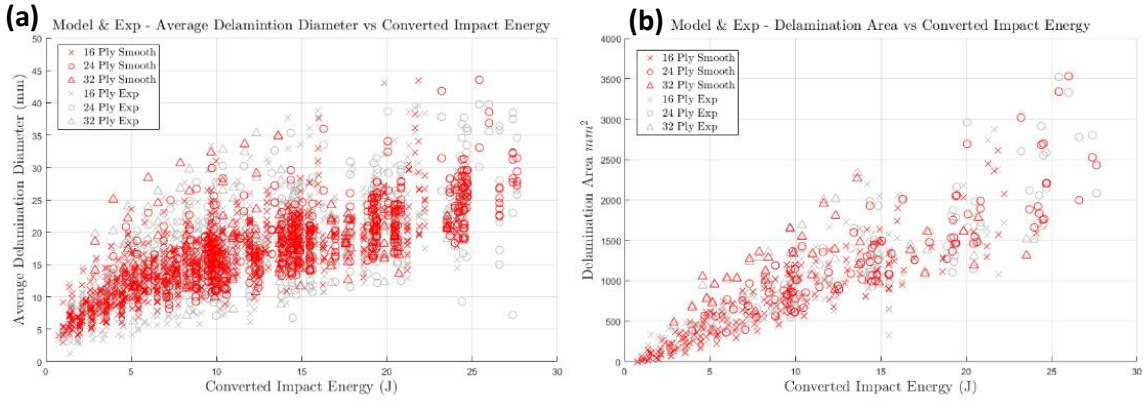

Figure 2. (a) Delamination diameter smooth model results. (b) delamination area smooth model results.

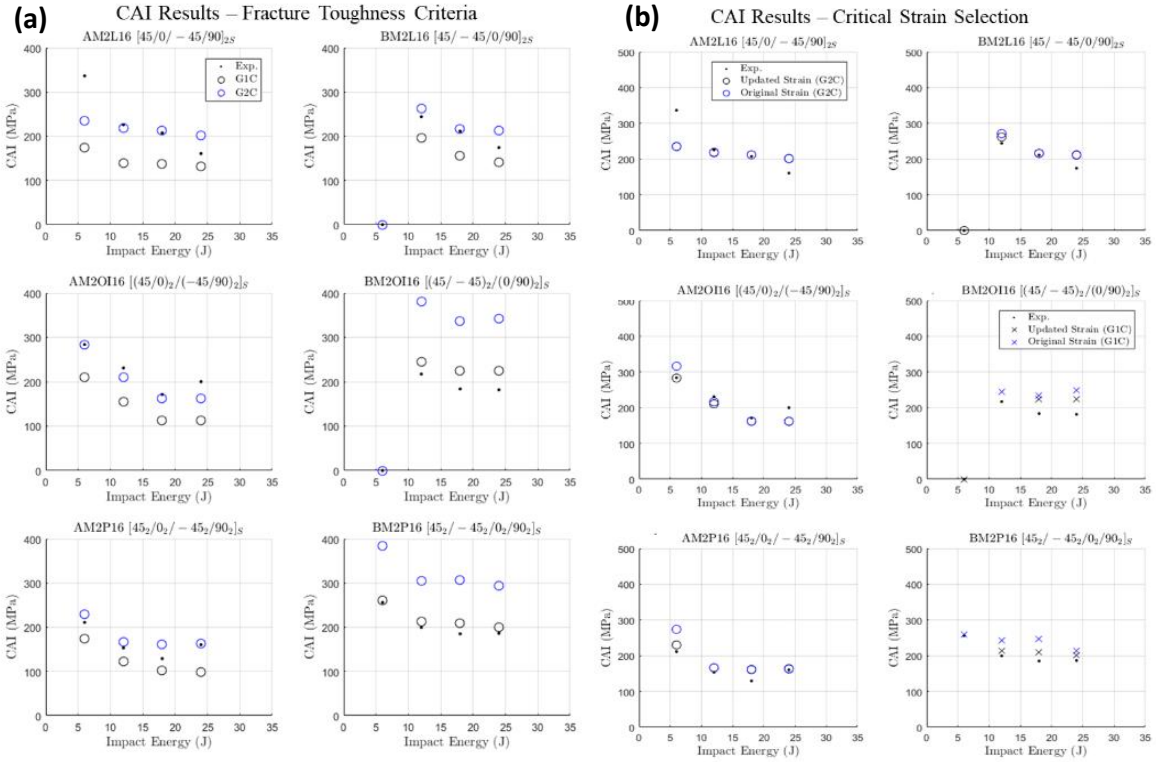

Figure 3. (a) Fracture toughness criteria implementation results – black data points are G_{1C}, blue are G_{2C} and red are the experimental results. (b) Critical strain selection inclusion results – black data points are the updated strain method, blue are the original method and red are the experimental results. Model predictions are from experimentally obtained delamination size data.

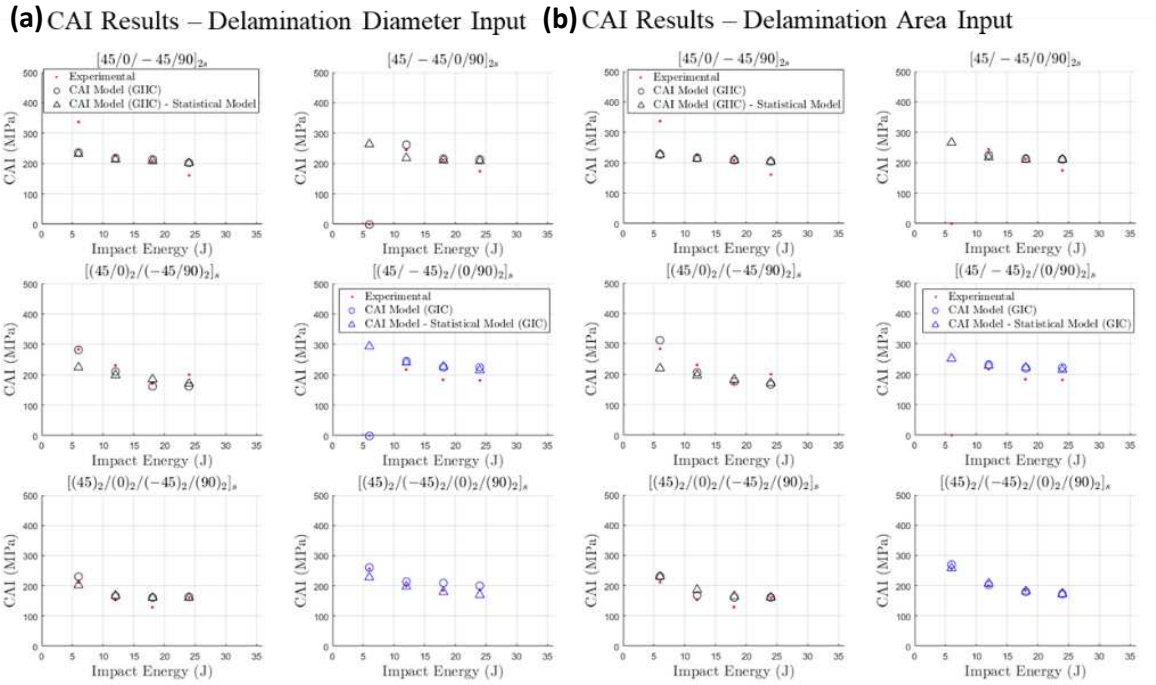

Figure 4. (a) delamination diamater as input to damage data CAI model results. (b) delamination area data as input to CAI model results. Both experimental and smooth model damage data input results shown. The black data points are predicted using G2C while the blue data point are predicted using G1C. Red data points are the experimental CAI results.

  doi:10.5075/epfl-298799_978-2-9701614-0-0

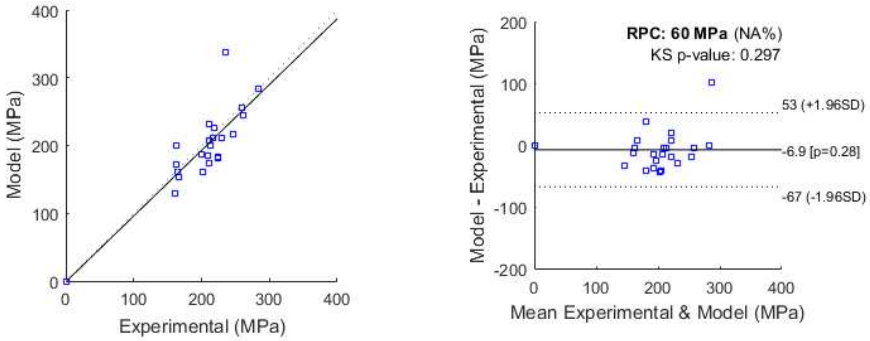

Figure 5. Bland-Altman plot detailing the results of using the selective fracture toughness method for the 16 ply CAI tested laminates.

6. Discussion

Figure 2 (a) shows the Average Delamination Diameter model results overlaid over the original data. For lower impact energies the model often slightly over predicts damage size. This will result in more conservative predictions being made for laminates in this damage range, however as damage in this range is so small (<8mm), and as such is not likely to lead to sub-laminate buckling driven failure, it is unlikely that this would impact the design process. At the higher end of the X-axis (higher impact energies) the trends of the model's predictions are well matched to the experimental data. This behaviour is also observed in the Delamination Area model figures, displayed in Figure 2 (b). The variation of the area data is more closely match by the area model than the diameter data is by the diameter model, but the latter still lies within the spread of the experiential data.

To assess the choice in fracture toughness the CAI model was modified to estimate laminate CAI strength using first G_{1C} and then G_{2C} in modelling delamination propagation. Figure 3 (a) details the results of the CAI model with both G_{1C} and G_{2C} using experimental input data. The layups can be clearly split into two categories - those that fit well with G_{1C} and those that fit well with G_{2C}. The CAI results for layups AM2 L16, AM2 OI16, AM2 P16 & BM2 L16 are all predicted closest using G_{2C}, while BM2 OI16 & BM2 P16 are better predicted using G_{1C}. Reason for this is found in the ply composition of the outer 25% of each of these laminates. Note that for the BM2 OI16 and BM2 P16 only the 12J, 18J & 24J could be averaged due to no damage observed for the 6J impact. The ply composition of the outer 25% of the laminates that are predicted most accurately with G_{1C} do not contain a 0^o orientated ply. This can be explained by the initial post-buckling response of the laminate - opening or closing. Laminates that do not contain a 0^o ply in the outer 25% buckle via the critical delamination opening away from the remainder of the laminate below. Hunt et al. (2004) in the paper 'Non-linear Modelling of Delaminated Struts' discuss the phenomenon of opening and closing in post-buckling [7]. Here, a four degree of freedom Rayleigh-Ritz formulation is used to study the behaviour of partially delaminated struts during buckling and post-buckling. They conclude that the governing factor that initiates either an opening or closing buckling

response is the depth of the critical delamination. In the current study it was seen that laminates that do not contain a 0° ply in the outer 25% of plies behave like the thin sub-laminate buckling observed in [7] opening as they buckle. Presence of a 0° ply in the outer 25% of plies determines whether the opening or closing buckling modes observed in [7] paper occur, implying that the presence of a 0° ply in the sub-laminate has the same effect as the laminate being thinner.

The presence of a 0° ply in the outer 25% of the laminate has the effect of creating a 'hard'/thin, therefore stiff, surface on the laminate. The 'hard' surfaces result in the laminate bending in a closing failure mode, more akin to a thin plate. In contrast, the laminates which do not contain a 0° ply in the outer 25% have relatively 'soft'/thin surfaces. As axial loading is applied to the laminate these interfaces bow outward, opening. The neutral plane is therefore shifted deeper into the laminate as the laminate buckles. Figure 5 shows a Bland-Altman plot of the results of this method for 16 ply laminates; a strong correlation between model and experimental results is seen.

Figure 3 (b) shows how the original method of critical strain calculation would often over predict the CAI strength of damaged laminates, particularly at lower impact energies. The improvement seen can be assessed by layup, with the AL16 layup showing very little change in the predicted CAI values compared to the BP16 laminates. The updated model is therefore choosing around 100% of a sub-laminate as the critical sub-laminate for the AL16 laminate and a selection of connected sub-laminates in the BP16 case. This implies that the original assumption of no connected delaminations through the sub-laminate likely hold true for some layups more than others, however the updated method only improves the model prediction if it changes the prediction.

The 16 ply CAI HTS/977-2 predictions generally mirror experimental results, as seen in Figure 4. However, there is little difference in the accuracy of the predictions obtained from the use of delamination diameter or area as the input to the CAI model for either experimental or smooth model inputs. This behaviour holds for T800/M21 16 ply laminates and 24 ply HTS/977-2 laminates but these results are omitted for brevity.

7. Conclusions

An extensive composite damage database was constructed from quasi-static and dynamic impact testing on 12, 24 and 32 ply laminates from two material systems - HTS/977-2 and T800-M21. This resulted in over 40 unique layups being manufactured and impacted with over 1400 unique delamination observations being recorded.

As the Generalised additive models (GAMs) used to model the experimental impact are data-driven models, prior knowledge prior of relationships between variables is not required, allowing previously unknown variable relationships to surface. This gives GAMs an advantage over traditional polynomial models that are model-driven. GAMs are also stable predictive tools, performing well when extrapolating outside of the original dataset (providing the correct variables have been identified). GAM

  doi:10.5075/epfl-298799_978-2-9701614-0-0

distributions and model variables have been optimised to produce high quality models that can predict both delamination diameter and delamination area sizes given layup, material, and impact energy properties. Models display a strong correlation to the database and to external data that requires model extrapolation implying that the correct variables have been identified and their relationships well modelled.

This study has successfully implemented two major improvements to the model CAI model in Choudhry et al. (2019) [2] that was designed to predict CAI strength following BVID created by out-of-plane impacts. The Choudhry model was adjusted to consider both opening and closing failure modes observed during compression after impact (CAI) by introducing a criterion for fracture toughness selection based on outer sub-laminate ply angles. The compression model was also updated by altering the critical sub-laminate identification process to consider fractional sub-laminates to allow for the fact critical sub-laminate in CAI failure is not generally delaminated at only a single interface. Model updates were tested on twenty-two 16 ply and nineteen 24 ply laminates and improved the predictive accuracy of the model whilst keeping it conservative in nature.

Finally, the coupled GAM impact damage model and the updated CAI model (with fractional sub-laminate buckling considerations) can rapidly and accurately predict CAI coupon strength given inputs of stacking sequence, standard material properties and impact energy for a range of stacking sequences and impact energies.

Acknowledgements

Butler, Anaya-Izquierdo, and Rhead gratefully acknowledge support from EPSRC Programme Grant ‘Certification for Design – Reshaping the Testing Pyramid’ (CerTest, EP/S017038/1).

8. References

[1] Olssen, ‘Analytical prediction of damage due to large mass impact on thin ply composites’, ‘Composites Part A: Applied Science and Manufacturing’ p184-p191, 2015.

[2] Choudhry, ‘A plate model for compressive strength prediction of delaminated composites’, ‘Composite Structures’ p509-517, 2019.

[3] Pernice, Rhead, ‘Ply-By-Ply Delamination Morphology In Composite Laminates Under Low-Velocity Impact’, ‘ECCM17-17th European Conference on Composite Materials’, 2016.

[4] Pernice, Rhead & Jiangiang, ‘Delamination growth rate in composite laminates under increasing low-velocity impact energy’, ‘21st International Conference on Composite Materials, ICCM 2017’, 2017.

[5] Wood, ‘Generalized Additive Models: An Introduction with R’, 2006.

[6] Williams et al., ‘VICONOPT – Program for exact vibration and buckling analysis or design of prismatic plate assemblies’, ‘AIAA JOURNAL’, 29 (11), p1927-1928, 1991.

[7] Hunt, ‘Nonlinear Modeling of Delaminated Struts’, ‘AIAA JOURNAL’, 2004.

  doi:10.5075/epfl-298799_978-2-9701614-0-0

CHARATERISATION AND MODELLING OF CRACK-INDUCED DELAMINATION IN COMPOSITE LAMINATES SUBJECTED TO CYCLIC LOADINGS

Lucio, Maragoni[a], Paolo Andrea, Carraro[a], Mirko, Simonetto[a], Marino, Quaresimin[a]

a: University of Padova – lucio.maragoni@unipd.it

Abstract: *In the present work, some recent experimental findings by the authors are presented concerning the initiation and propagation of crack-induced delamination in glass/epoxy composite laminates subjected to tensile-tensile loadings. The damage evolution was investigated both from a macroscopic and a microscopic point of view. In the former analysis, a quantitative measurement of the crack density, the delamination ratio and the stiffness drop were carried out along the fatigue life of the laminates. Concerning the micro-scale, edge micrographs took in interrupted tests allowed to understand the interactions between different damage mechanisms. Based on experimental evidence, a procedure was developed to include crack-induced delamination in a discrete damage modelling framework, showing a satisfactory prediction of the experimental trends.*

Keywords: Fatigue, delamination, crack, characterization, prediction

1. Introduction

To define damage-tolerant approaches for the fatigue design of composite structures implies the need to properly understand and predict the different damage events that cause the progressive material stiffness loss well before the final failure. In multidirectional laminates such damage events are, from a macroscopic point of view, represented by matrix cracks, delamination, and fibre failure. The authors worked intensively to characterise and model the progressive matrix cracking in composite laminates, reaching satisfactory results (see Ref. [1] and works quoted therein). With the objective to build a comprehensive damage predictive framework, the next logical step consists of adding also delamination to the scenario.

In the literature, delamination was often studied as an isolated phenomenon, through DCB, ENF, MMB and ELS tests [2-6]. However, in multidirectional laminates the delamination behaviour is affected by the presence of matrix cracks. Although several works have been carried out to study the delamination onset and progression in laminates subjected to static loadings (see, among others, Refs [7-11]), its fatigue behaviour received far less attention [12-15]. In particular, only a few works dealt with the delamination onset and growth away from the edges, in the so-called bulk material [16-17], reporting only the fraction of delaminated area during the fatigue life.

Moving from delamination characterization to modelling, the delamination growth rate (DGR) was seen to be linked to its energy release rate (ERR) with a power-law both for isolated delamination and delamination propagating inward from the edges of a laminate [2-6,15]. No observations of such a kind were reported for a crack-induced delamination propagating in the bulk material. Such an understanding would be extremely useful also when Cohesive Zone

  doi:10.5075/epfl-298799_978-2-9701614-0-0

Models (CZM) [18,19] are used, as they proved to be more robust if the cycle-dependent damage function consists of a DGR-ERR power law [19].

Finally, concerning the simultaneous prediction of crack density and delamination during the fatigue life of a laminate, both *distributed* [20-22] and *discrete* [23-25] damage models were proposed in the literature: the former kind consider damage as an average entity within a volume, while the latter considers damage events individually, including their exact location and mutual interaction. Both distributed and discrete damage models can be readily implemented into commercial finite element (FE) codes, the latter using CZM for delamination propagation. However, they both present some drawbacks, as the applicability in regions with high stress gradients (distributed models), or the computational cost, mesh-dependence, and parameters calibration (discrete models).

In this scenario, with the objective to understand the crack-induced delamination phenomenon and to properly include it in an efficient damage predictive framework, recent experimental findings [26] by the authors are first reported in the present work. Then, the experimental observations are used to develop a novel methodology to include delamination in a predictive procedure based on discrete damage modelling, showing a satisfactory prediction of the available experimental data.

2. Testing methods

In order to characterise crack-induced delamination from an experimental viewpoint, $[0_2/90_4]_S$ and $[0/90_2]_S$ glass/epoxy laminates were produced by vacuum resin infusion, cured at room temperature for 72 hours and then post-cured at 60°C for 12 hours. After an appropriate edge polishing procedure, specimens cut from the panels were tested at different load levels with a frequency of 10 Hz and a load ratio R = 0.05. Damage progression was quantified with a linear camera placed in front of the sample [27]. The crack density was measured through an in-house developed Matlab® image analysis tool based on Gabor filtering, using a backlight to increase contrast; delamination progression could instead be quantified directly via image binarization and the aid of a front light. To carry out microscopic damage observations, some tests were periodically interrupted, and the specimen edges observed under an optical microscope. Finally, a biaxial extensometer was used to track the trend of the laminate longitudinal modulus and Poisson's ratio during the fatigue life.

3. Damage characterisation

Figure 1 shows representative trends of the damage evolution and elastic property for $[0_2/90_4]_S$ (Fig. 1a) and $[0/90_2]_S$ (Fig 1b) laminates, respectively. Matrix crack and delamination are quantified by the weighted crack density and the delamination ratio, defined as:

$$\rho_w = \frac{\sum_{i=1}^{n_c} c_i}{w \cdot L} \quad (1)$$

$$d_r = \frac{A_d}{A_{tot}} \quad (2)$$

where n_c is the total number of cracks, c_i the length of the i-th crack, w the laminate width, L the length of the observation area, A_d the delaminated area and A_{tot} the total observation area.

For both lay-ups, most of the change in elastic properties is due to the fast crack density saturation. A progressive diminishing trend can still be observed after crack density saturation is reached, which can be attributed to the continuous delamination growth. Delaminations were seen to involve the whole laminate width and not to start from the edges, and their growth rate diminishes in time due to mutual shielding that decreases their ERR.

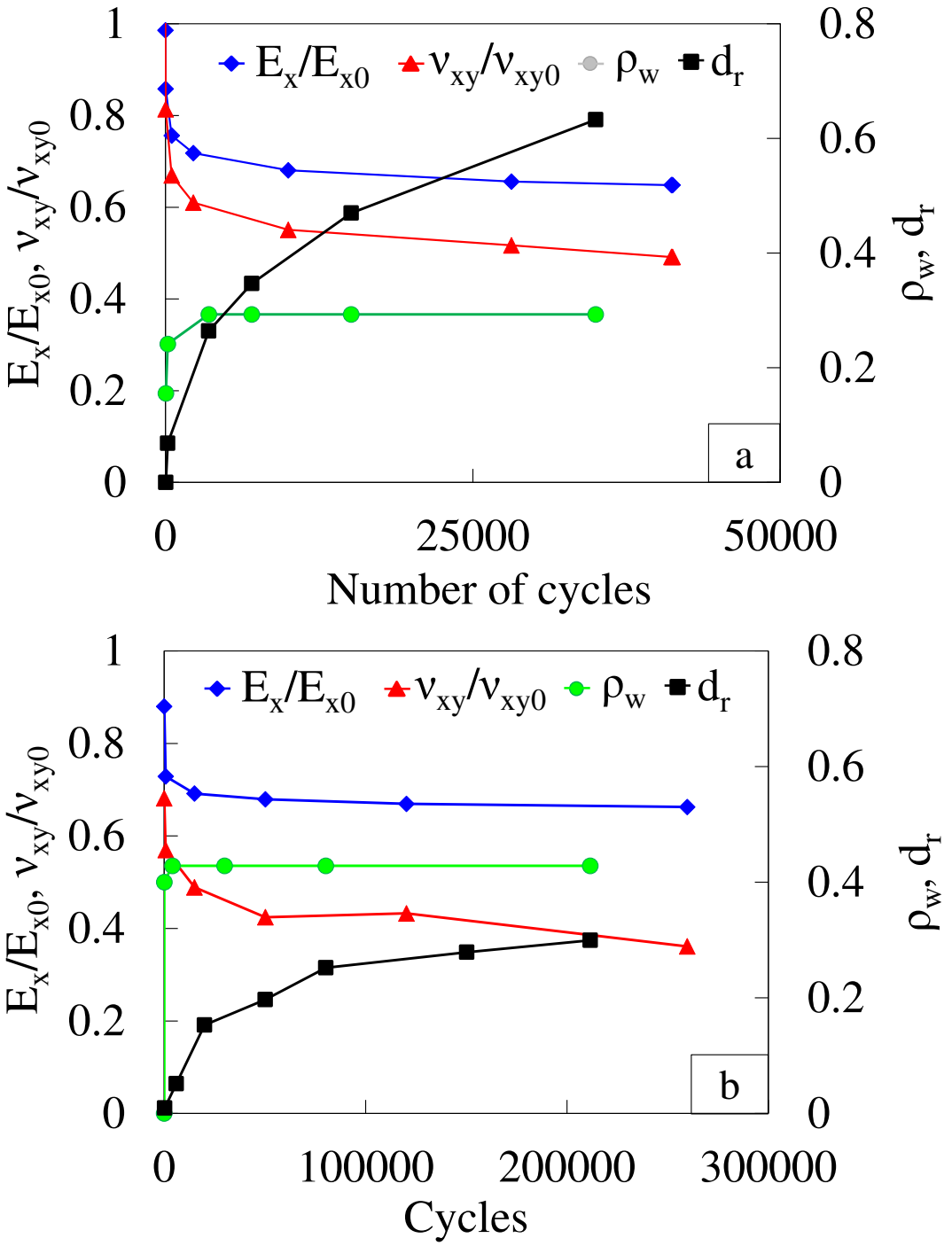

Figure 1. Damage and elastic properties trends for (a) $[0_2/90_4]_S$ laminate under $\sigma_{x,max}$= 120 MPa, (b)) $[0/90_2]_S$ laminate under $\sigma_{x,max}$= 120 MPa.

Thicker laminates are characterized by a much lower crack density saturation level (due to the more pronounced shielding effect between cracks) and by a much faster delamination

  doi:10.5075/epfl-298799_978-2-9701614-0-0

propagation (as their ERR increases with the ply thickness). This produces a faster fibre failure rate, as confirmed by microscopic edge observations, which leads to a shorter fatigue life. As expected, the elastic properties drop faster for the thicker laminate, while the plateau level is similar for both laminates, being it related to the crack density times the ply thickness, which is similar for the two stacking sequences.

Representative microscopic observations of the damage evolution are reported in Figure 2 for a $[0_2/90_4]_S$ laminate subjected to $\sigma_{x,max}$ = 90 MPa, being them qualitatively similar for laminate $[0/90_2]_S$ and for other load levels. First, it was possible to notice that a small delamination appears as soon as a crack initiates, although not visible by naked eye. This evidence was found for all the observed cracks. Second, the interaction between damage mechanisms appears to be clear, with the transverse crack inducing the delamination and both of those mechanisms promoting fibre failure due to stress concentration in the 0° ply. Last, but not less important, most of the delamination were found to initiate on both 90° ply interface and to propagate in both directions from the crack ("H-shaped" configuration).

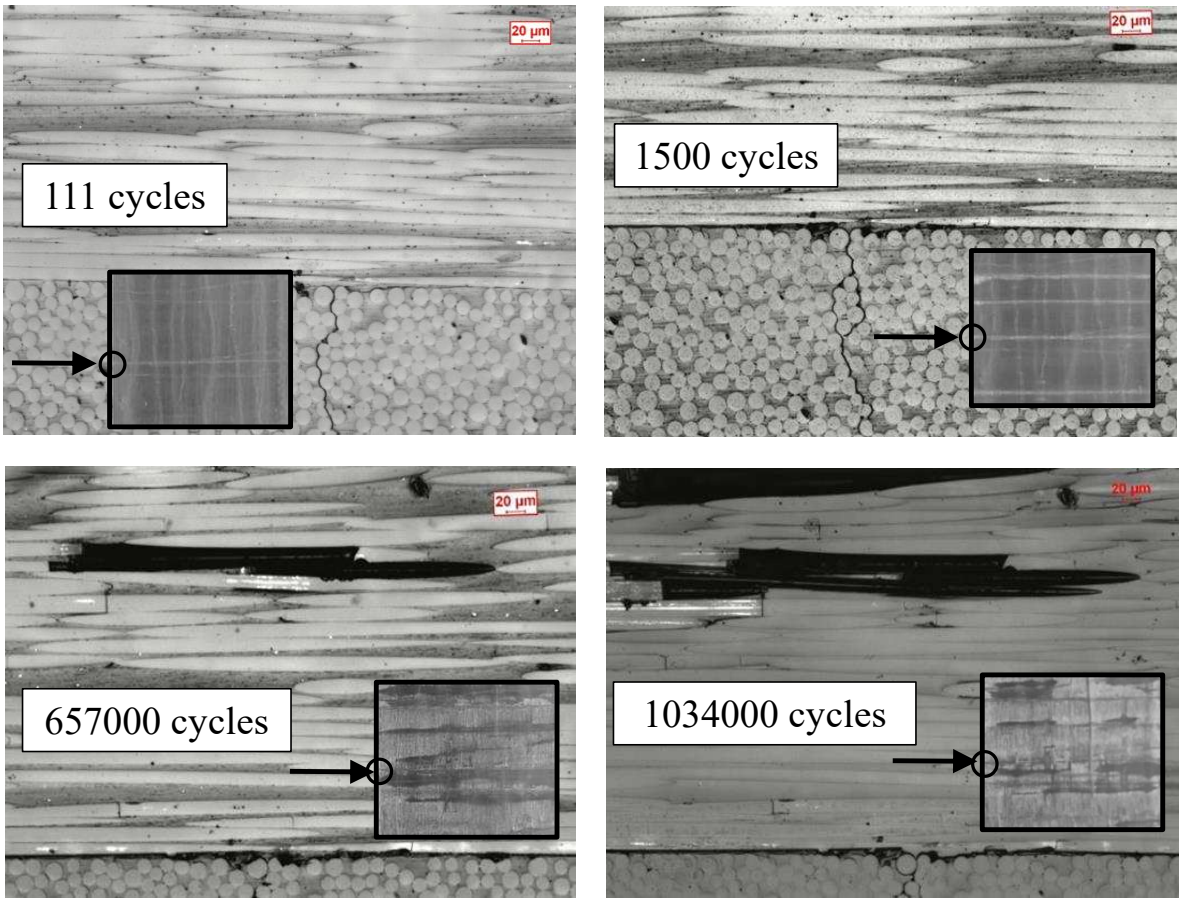

Figure 2: Representative damage evolution from front and edge view at increasing number of cycles ($[0_2/90_4]_S$ laminate, $\sigma_{x,max}$ = 90 MPa)

4. Modelling strategy

A first modelling steps consisted of understanding the relation between the crack-induced delamination ERR to its DGR. To do so, an average delamination length was calculated as:

$$d = \frac{l \cdot d_r}{2} = \frac{d_r}{2 \cdot \rho_w} \quad (3)$$

Then, the DGR was calculated according to the 7-point incremental polynomial method [28]. The delamination ERR was instead calculated from FE analyses carried out on laminate representative volume elements (RVEs) using the VCCT technique as indicated in Ref. [29], assuming a H-shaped configuration. As shown in Figure 3, a power-law relation was found to be suitable to relate the delamination ERR to its propagation speed, at least for the thicker laminate. For the thinner laminate, the data resulted much more scattered. The reason could lie in the fact that for those laminates the delamination length was always extremely short, so that its ERR remained influenced by the local microstructure, thus a fracture mechanics approach based on homogenized plies and a self-similar propagation could not be reasonably applied.

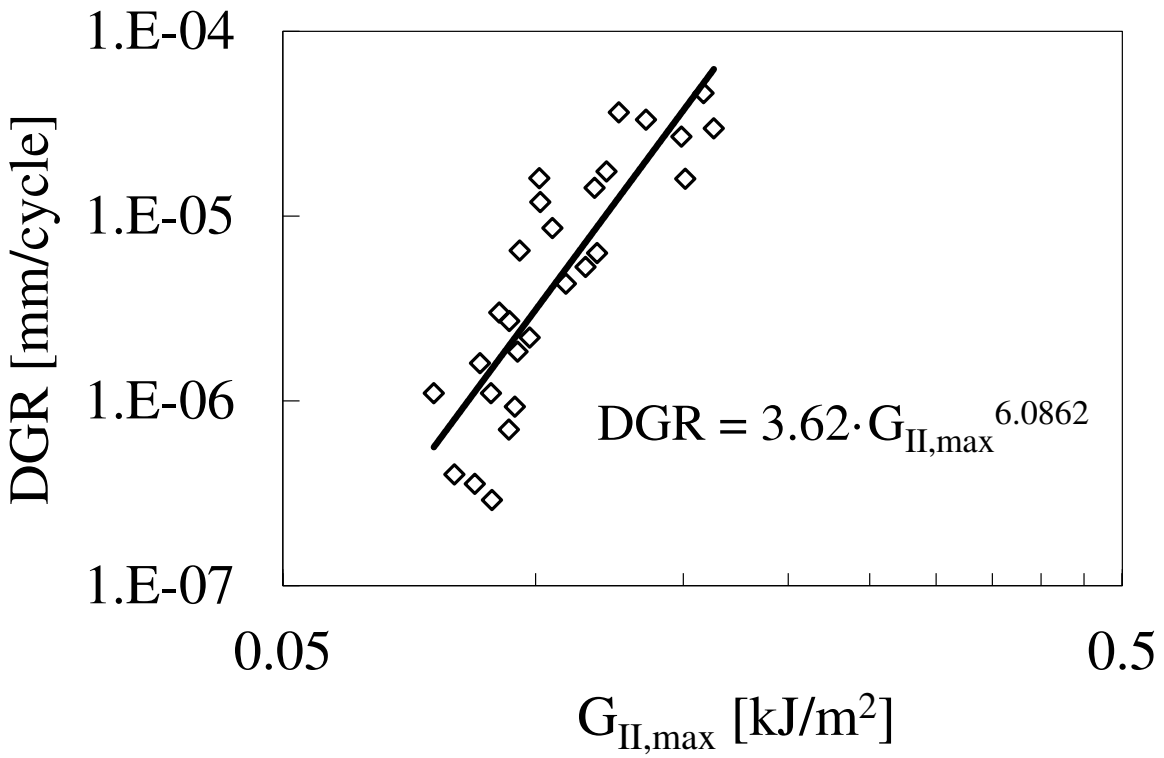

Figure 3: Relation between crack-induced delamination ERR and DGR for $[0_2/90_4]_S$ laminates

With the objective to develop a comprehensive damage predictive framework, delaminations at cracked ply interfaces were added to the procedure to predict the crack density evolution developed in Ref. [1], taking into account the experimental observations here reported concerning both their initiation and propagation behaviour [30]. As shown in Figure 4, a satisfactory agreement was found between the experimental values and the prediction of both weighted crack density and delamination ratio. Worth of mention is the computational efficiency of the overall framework, that allowed the damage evolution simulations to be run in a few minutes with a common desktop machine.

  doi:10.5075/epfl-298799_978-2-9701614-0-0

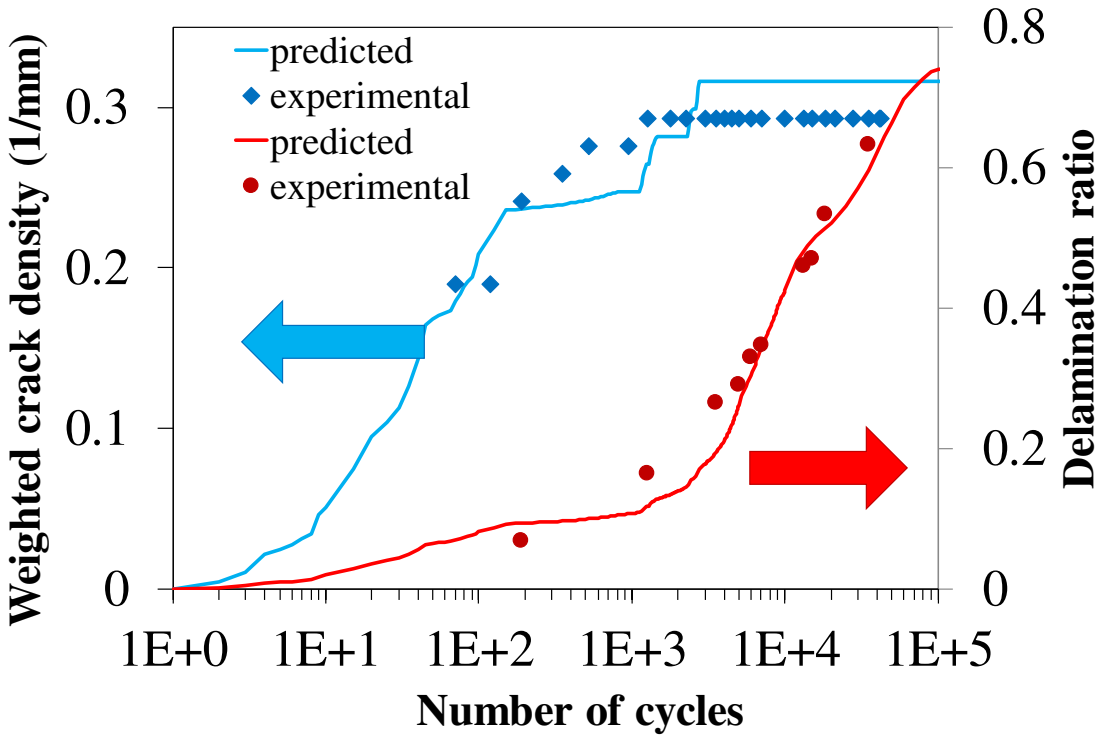

Figure 4: Comparison between experimental and predicted trends of weighted crack density and delamination ratio in a $[0_2/90_4]_S$ laminate subjected to $\sigma_{x,max}$ = 120 MPa

5. Conclusions

In this work, an analysis was carried out on the tensile fatigue behaviour of crack-induced delamination. Experimental observations on glass/epoxy cross-ply laminates showed that a very short delamination appears when a transverse crack initiate reaching the ply interfaces. Then, the delamination stably grows promoting fibre failure and leading to the final separation. The faster delamination growth rate for thicker laminate resulted in a much shorter fatigue life, thus highlighting a strong thickness effect on the overall fatigue life of a composite laminate.

From a modelling point of view, a power-law was observed to hold for crack-induced delamination propagating in the bulk material (i.e.: far from the edges), at least for long enough delamination. For the propagation of very short delamination, instead, care must be taken in applying fracture mechanics tools that consider homogeneous plies, as the delamination propagation was found to be largely affected by the local microstructure. The experimental observations were considered to include delamination in a damage predictive framework based on discrete damage modelling, showing satisfactory predictive capabilities.

Acknowledgements

The authors wish to acknowledge the support and the computational resources made available by the High Performance Computing Lab at the Department of Management and Engineering (DTG), co-funded by the University of Padova in the framework of the program “Scientific research instrumentation 2015”. The financial support to the activities, received from the

  doi:10.5075/epfl-298799_978-2-9701614-0-0

project “CARR_SID_03 - Advanced methods for health monitoring in primary composite structures” by the University of Padova, is also acknowledged.

6. References

1. Carraro PA, Maragoni L, Quaresimin M. Prediction of the crack density evolution in multidirectional laminates under fatigue loadings. Composites Science and Technology 2017; 145:24-39.
2. Hojo M, Ochiai S, Gustafson CG, Tanaka K. Effect of matrix resin on delamination fatigue crack growth in cfrp laminates. Engineering Fracture Mechanics 1994; 49:35-47.
3. Tanaka H, Tanaka K, Tsuji T, Katoh H. Mixed-mode (I+II) propagation of delamination fatigue cracks in unidirectional graphite/epoxy laminates. Transactions of the Japan Society of Mechanical Engineers, Part A 1999; 65:1676–83.
4. Asp L, Sjögren A, Greenhalgh E. Delamination growth and thresholds in a carbon/epoxy composite under fatigue loading. Journal of Composites Technology and Research 2001; 23:55-68.
5. Hojo M, Ando T, Tanaka M, Adachi T, Ochiai S, Endo Y. Modes I and II interlaminar fracture toughness and fatigue delamination of CF/epoxy laminates with self-same epoxy interleaf. International Journal of Fatigue 2006; 28:1154–1165.
6. O’Brien TK, Johnston WM, Toland GJ. Mode II interlaminar fracture toughness and fatigue characterization of a graphite epoxy composite material. NASA/TM–2010-216838. Hampton: 2010.
7. Crossman FW, Warren WJ, Wang ASD, Law GE. Initiation and Growth of Transverse Cracks and Edge Delamination in Composite Laminates Part 2. Experimental Correlation. Journal of Composite Materials 1980; 14:88-108.
8. O'Brien TK. Characterization of delamination onset and growth in a composite laminate. In: Reifsnider KL, editor. Damage in composite materials, ASTM STP 775. Philadelphia: American Society for Testing and Materials; 1982, p.140-167.
9. Takeda N, Ogihara S. Initiation and growth of delamination from the tips of transverse cracks in cfrp cross-ply laminates. Composites Science and Technology 1994; 52:309–18.
10. Zubillaga L, Turon A, Renart J, Costa J, Linde P. An experimental study on matrix crack induced delamination in composite laminates. Composite Structures 2015; 127:10-7.
11. Carraro PA, Novello E, Quaresimin M, Zappalorto M. Delamination onset in symmetric cross-ply laminates under static loads: Theory, numerics and experiments. Composite Structures 2017; 176:420–32.
12. O’Brien TK. Local delamination in laminates with angle ply matrix cracks: part II delamination fracture analysis and fatigue characterization. In: Proceedings of the 4th ASTM Conference on Composite Materials: Fatigue and Fracture, Indianapolis, Indiana, May 6-7, 1991.
13. Wharmby AW, Ellyin F. Damage growth in constrained angle-ply laminates under cyclic loading. Composites Science and Technology 2002; 62:1239–47.
14. Wharmby AW, Ellyin F, Wolodko JD. Observations on damage development in fibre reinforced polymer laminates under cyclic loading. International Journal of Fatigue 2006; 25:437–46.
15. Hosoi A, Sato N, Kusumoto Y, Fujiwara K, Kawada H. High-cycle fatigue characteristics of quasi-isotropic CFRP laminates over 108 cycles (Initiation and propagation of delamination considering interaction with transverse cracks). International Journal of Fatigue 2010; 32:29–36.

  doi:10.5075/epfl-298799_978-2-9701614-0-0

16. Adam TJ, Horst P. Fatigue damage and fatigue limits of a GFRP angle-ply laminate tested under very high cycle fatigue loading. International Journal of Fatigue 2017;99:202–14.
17. Adam TJ, Nolte F, Begemann B, Horst P. Selective laser illumination method for enhanced damage monitoring of micro cracking and delamination in GFRP laminates. Polymer Testing 2018; 65:125–33.
18. Bak BLV, Serrado C, Turon A, Costa J. Delamination under fatigue loads in composite laminates: a review on the observed phenomenology and computational methods. Appl Mech Rev 2014; 66:1-24.
19. Bak BLV, Turon A, Lindgaard A, Lund E. A benchmark study of simulation methods for high-cycle fatigue-driven delamination based on cohesive zone models. Compos Struct 2017;164:198–206.
20. Nairn J. A., Microcracking, Microcrack-Induced Delamination, and Longitudinal Splitting of Advanced Composite Structures. NASA CR 4472, 1992.
21. Pakdel H, Mohammadi B. Stiffness degradation of composite laminates due to matrix cracking and induced delamination during tension-tension fatigue. Engineering Fracture Mechanics 2019; 21:106489.
22. Cristiani D, Sbarufatti C, Giglio M. An interactive damage progression model for cross-ply laminates subject to fatigue load cycles. Composites: Part A 2021; 151:106658.
23. Bak BLV, Turon A, Lindgaard E, Lund E. A simulation method for high-cycle fatigue-driven delamination using a cohesive zone model. International Journal for Numerical Methods in Engineering 2016; 106:163–91.
24. Zhu M, Gorbatikh L, Lomov SV. An incremental-onset model for fatigue delamination propagation in composite laminates. Composites Science and Technology 2020; 200:108394
25. C.G. Dávila. From S-N to the Paris law with a new mixed-mode cohesive fatigue model for delamination in composites. Theoretical and Applied Fracture Mechanics 2020; 106:102499.
26. Carraro PA, Maragoni L, Quaresimin M. Characterisation and analysis of transverse crack-induced delamination in cross-ply composite laminates under fatigue loadings. International Journal of Fatigue 2019; 129:105217.
27. Maragoni L, Carraro PA, Peron M, Quaresimin M. Fatigue behaviour of glass/epoxy laminates in the presence of voids. International Journal of Fatigue 2017; 95:18–28.
28. ASTM E647-00. Standard test method for measurement of fatigue crack growth rates. ASTM International; 2000.
29. Maragoni L, Carraro PA, Quaresimin M. Periodic boundary conditions for FE analyses of a representative volume element for composite laminates with one cracked ply and delaminations. Composite Structures 2018; 201:932–41.
30. Maragoni L, Carraro PA, Simonetto M, Quaresimin M. A novel method to include crack-induced delamination in a fatigue damage predictive procedure for composite laminates. In preparation.

  doi:10.5075/epfl-298799_978-2-9701614-0-0

NUMERICAL STUDY OF THE DELAMINATION TOUGHENING EFFECT OF WEAKENING AND TOUGHENING PATCHES

Guillem Gall Trabal[a], Brian Lau Verndal Bak[a], Boyang Chen[b], Simon Mosbjerg Jensen[a],Esben Lindgaard[a]*

a: CraCS research group (cracs.aau.dk), Department of Materials and Production, Aalborg University, Fibigerstræde 16, Aalborg, Denmark *(elo@mp.aau.dk)
b: Faculty of Aerospace Engineering, Delft University of Technology, Kluyverweg 1, 2629HS Delft, Netherlands

Abstract: *A numerical study on the feasibility of using patches of interface weakening or toughening material to trigger multiple delaminations toughening laminated composite structures against delamination is presented. The studies use an adaptive refinement formulation that uses cohesive elements to model delamination initiation and propagation. A DCB specimen is loaded under displacement control with two cohesive interfaces and a single pre-crack is introduced in one of them. The studies show that multiple delaminations can be initiated in the secondary originally uncracked interface by placing interface toughening patches at the main pre-cracked interface or interface weakening patches at the secondary one. The energy dissipation significantly increases compared to a standard DCB specimen featuring a single delamination.*

Keywords: Delamination toughening; multiple delamination, adaptive refinement, cohesive zone modelling; Floating Node Method

1. Introduction

Several methodologies have been introduced in the literature to toughen composite laminated structures against delamination propagation. Current strategies include modifying the constituent materials by improving the interface between fibre and matrix using fibre sizing [1,2] or obtaining tougher matrix materials. Interface toughening can also be obtained by procedures such as stitching [3,4], z-pinning [5], interlocking mechanisms [6], or using 3D woven fabrics [7]. However, the aforementioned techniques provoke unwanted side effects such as a decrease in the wettability of the laminate or a decrease in the in-plane strength of the structure [5].

Another option is to toughen the structure by defusing the damage into multiple delamination fronts. This idea, presented in [8], implemented using a weakened interface, increases the amount of energy dissipated. However, creating a weakened plane may induce premature damage initiation from e.g., intralaminar damage. Another option noticed for toughened interfaces in co-cured laminates [9] is using a local toughening of the interface to initiate damage in a secondary adhesive interface.

In this article, the possibility of onsetting multiple delaminations in laminated composites using patches of interface toughening or weakening material is explored with a set of numerical tests featuring different interface toughening or weakening materials. The analyses are performed with a modified version of the adaptive refinement formulation from [10].

  doi:10.5075/epfl-298799_978-2-9701614-0-0

2. Methods and numerical testing protocol

This section introduces the methodology and numerical testing protocol used to study the interface patching induced multiple delamination initiation, and the toughening effect it has on the structure.

2.1 Adaptive refinement formulation

The adaptive Floating Node Method (FNM) based formulation presented in [10] is composed of the Adaptive Refinement Scheme (ARS) and the Adaptive FNM (A-FNM) element. Together, the ARS and the A-FNM element efficiently refine the model as required, obtaining a computationally efficient formulation for the accurate analysis of delamination propagation using Cohesive Zone Models (CZM). The adaptive formulation presented in [10] does not consider damage initiation in pristine interfaces, a feature needed for the numerical tests presented in this work. All the modifications to the adaptive formulation necessary for the work presented in this paper are restricted to the ARS. Therefore, the A-FNM element is not presented in this section, and the reader is instead referred to [10] for details.

The formulation presented in [10] allows the discretisation of an entire 2D laminate with a single A-FNM element through the thickness, as shown in Figure 1a. Each of the A-FNM elements contains a set of interfaces that can be at 4 different states: 1) Fully damaged, 2) Refined, 3) Coarse, or 4) Pristine. For the cases analysed in this paper, only states 1), 2) and 3) are relevant.

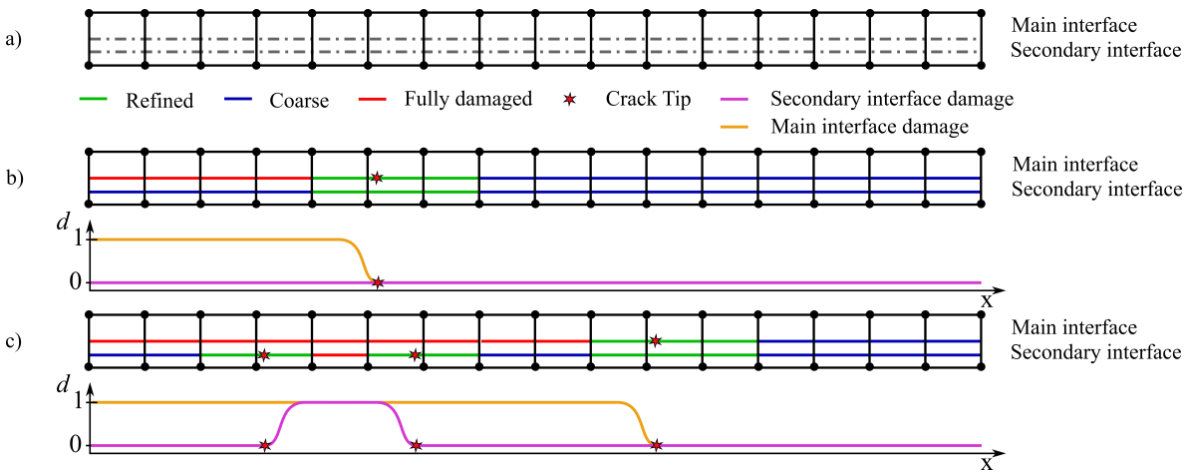

Figure 1: Adaptive Floating Node Method (A-FNM) element interface states of the specimen shown in a), after the application of the ARS for a single delamination b), and after the initiation of multiple delaminations c).

The ARS algorithm continuously monitors the damage in the structure to allocate the correct state at each A-FNM element interface in the model. As visualised in Figure 1b, the ARS sets all the A-FNM elements containing damage and its immediate neighbours to a refined state. The A-FNM element interfaces that have been fully damaged are set at a damaged state, and the remaining A-FNM element interfaces are set as coarse. With this approach, the damaged interfaces and their surroundings are effectively refined, leaving the remaining ones with a coarse discretisation of damaged or undamaged cohesive elements.

The fact that all the undamaged A-FNM element interfaces of the model contain at least a coarse cohesive element allows damage initiation in pristine interfaces. This is exemplified by the

  doi:10.5075/epfl-298799_978-2-9701614-0-0

scenario shown in Figure 1, which is encountered in the studies presented in this article. Initially, a single delamination propagates through the structure, as seen in Figure 1b. Notice how the secondary interface near the crack tip is at a refined state. This refinement allows for the accurate initiation of damage, which can eventually form two new independent crack tips, as seen in Figure 1c. Thus, the only necessary change to the ARS is allowing the preallocation of coarse CEs at any interface (pre-cracked or pristine) selected by the user.

2.2 Underlying standard element formulations

The calculation of the A-FNM element stiffness matrix is done by assembling stiffness matrices calculated for each of the sub-elements. The subelements are shown in Figure 2 for the relevant configurations of the presented numerical studies. The solid sub-elements stiffness matrices are calculated following a 4-node Enhanced Assumed Strains plane strain layered formulation detailed in [10]. This formulation enables the use of coarse discretisations under bending dominated situations and the use of a single sub-element to model several layers. The cohesive sub-elements are formulated as cohesive interface elements following the formulations presented in [11,12] adapted to a 4-node interface configuration.

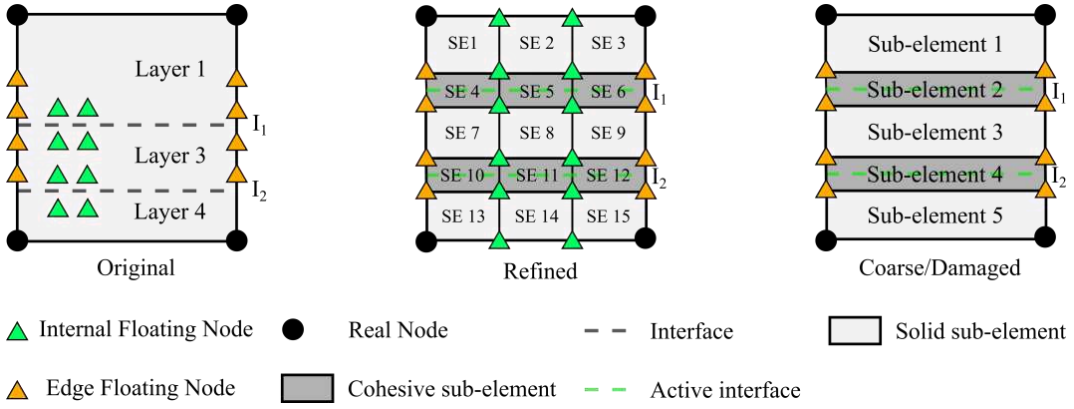

Figure 2: The A-FNM element's three configurations in the numerical tests.

2.3 Numerical testing protocol

A set of tests are performed with the specimen shown in Figure 3. The specimen contains either a toughening or a weakening interface material patch. The base material used for the analyses is listed in

Tabel 1. An initial mesh of 90 A-FNM elements is used, resulting in the initial mesh shown in Figure 4. A cohesive sub-element size of 0.084 mm is chosen in the refined area to ensure that a minimum of 4 cohesive sub-elements are present in the damage process zone.

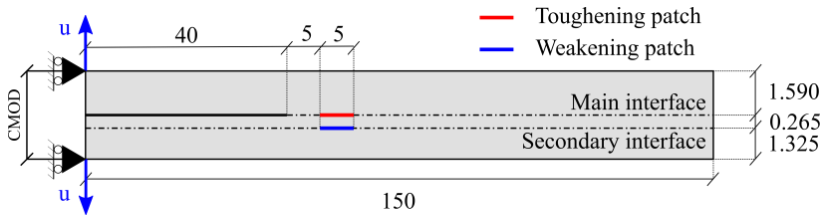

Figure 3: Specimen used in the numerical tests. Dimensions in [mm]

Tabel 1: Base material and interface properties used in the numerical tests [13,14].

	Material properties			Interface properties	
E_{11}	120	[GPa]	G_{Ic}	260	[N/m]
$E_{22} = E_{33}$	10.5	[GPa]	G_{IIc}	1002	[N/m]
$G_{12}=G_{13}$	5.3	[GPa]	τ_{I0}	30	[N/m]
G_{23}	3.5	[GPa]	τ_{II0}	60	[N/m]
$\nu_{12}= \nu_{13}$	0.3	[-]	η	2.73	[-]
ν_{23}	0.51	[-]	K	30e6	[N/mm^3]

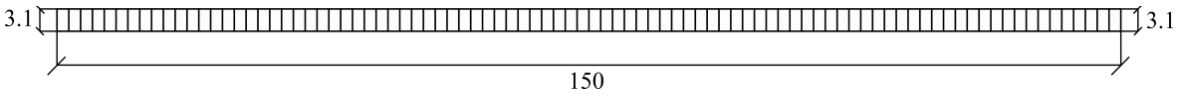

Figure 4: Initial coarse mesh of A-FNM elements. Dimensions in mm.

A total of 50 numerical tests are performed. These are grouped in 2 categories featuring either an interface toughening patch or an interface weakening patch. The interface patches are modelled by changing the interface properties at the designated patched areas. This is done by multiplying or dividing the onset tractions (τ_{I0}, τ_{II0}) by an integer scalar *n,* and the critical energy release rates (G_{Ic}, G_{IIc}) by an integer scalar *m*:

$$(G_c \cdot n, \tau_0 \cdot m) \rightarrow \text{Interface toughening patch}$$
$$(G_c/n, \tau_0/m) \rightarrow \text{Interface weakening patch}$$

The 25 analyses for each category are built by varying *n* and *m* from 1 to 5 in unity steps.

3. Results

3.1 General response

The force-displacement equilibrium curve for the analyses featuring an interface toughening patch and those with an interface weakening patch are displayed in Figure 5 and Figure 6, respectively.

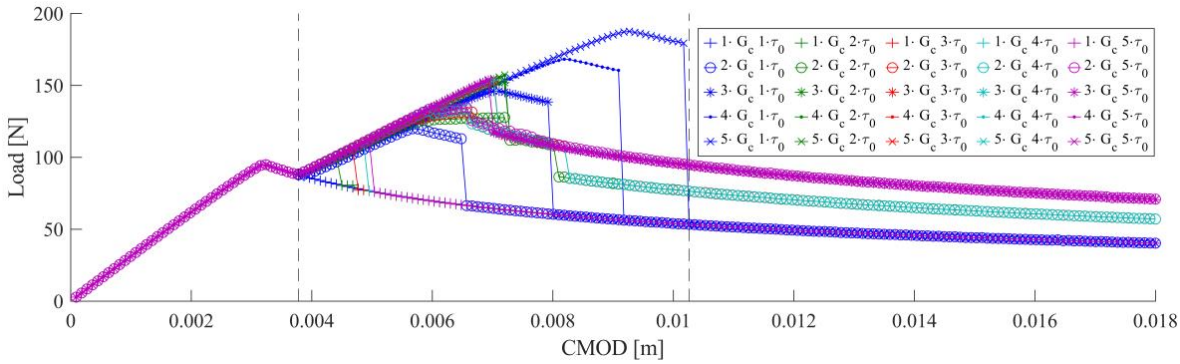

Figure 5: Force-displacement equilibrium curves for the analyses featuring an interface toughening patch.

Notice, that cases where multiple delaminations are initiated, display a response with higher force level than the single delamination reference case ($1\cdot\tau_0$,$1\cdot G_c$) during the crack propagation phase. In that regard, both interface toughening and weakening patches can initiate multiple delaminations. Figure 5 also shows that the interface toughening patch approach results in a higher force peak than the interface weakening patch strategy results from Figure 6.

  doi:10.5075/epfl-298799_978-2-9701614-0-0

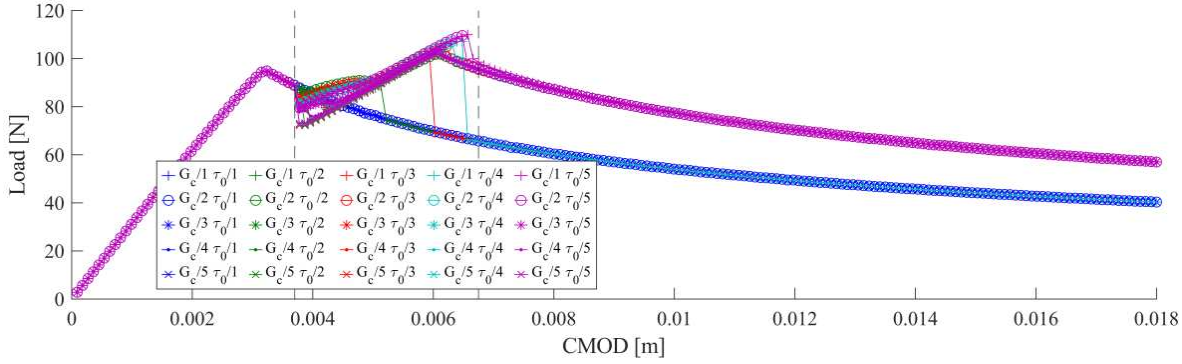

Figure 6: Force-displacement equilibrium curves for the analyses featuring an interface weakening patch.

3.2 Multiple delamination initiation

To study the delamination initiation phase, the normalised traction $\tilde{\mu}$, and the energy-based damage variable D_e [14] are defined as:

$$\tilde{\mu} = \frac{\mu}{\mu_0} \quad where \;\; \mu_0 = \sqrt{\tau_{I0}^2 + (\tau_{II0}^2 - \tau_{I0}^2)B^\eta}$$

$$D_e = \frac{G_c - \omega_r}{G_c} = 1 - \frac{\lambda_c(1-D)K\lambda_D}{2G_c}$$

where ω_r is the specific remaining ability to do non-conservative work, and λ_D, λ_c are defined as in [14]. Figure 7 shows the multiple delaminations initiation process. When the traction profile enters the patched area, the increase in the traction peak produced by the interface toughening patch initiates the damage at the secondary interface. This happens because the secondary interface properties are unmodified, unlike in the main interface. The same case also holds for the interface weakening patch, but in this case, the main interface traction profile is not varied when entering the patched area. The decrease in the interface onset traction value produces the damage initiation. In both cases, the toughness of the interface at the patched area needs to be modified to extend the damage in an area sufficiently large to initiate the two new delamination fronts.

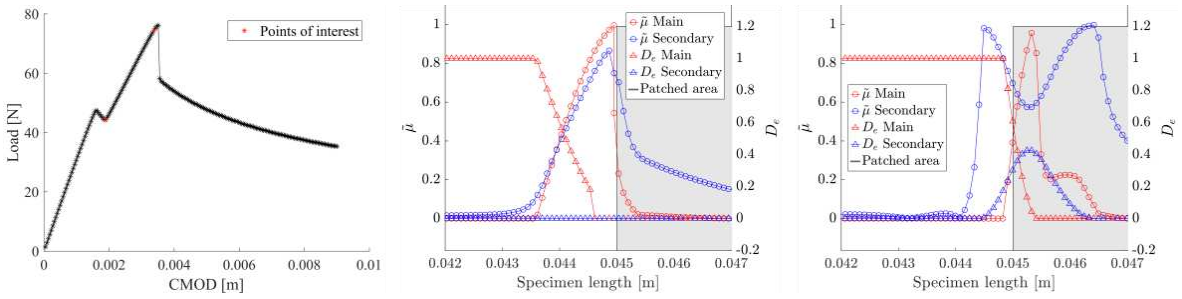

Figure 7: Normalized traction and damage D_e for a toughening patch of (G_c·3,τ_0·3) at selected points of interest.

3.3 Multiple delaminations propagation phase

The propagation phase of the analyses shown in Figure 5 andFigure 6 is determined by whether multiple delaminations are initiated and if so which crack tips are propagating. Figure 8 shows the energy dissipation rate defined as the energy dissipated per crack mouth opening (CMOD).

  doi:10.5075/epfl-298799_978-2-9701614-0-0

In both cases, the analyses with multiple delaminations initiation (curves 2 and 3) provide higher energy dissipation than the single delamination cases (curve 1).

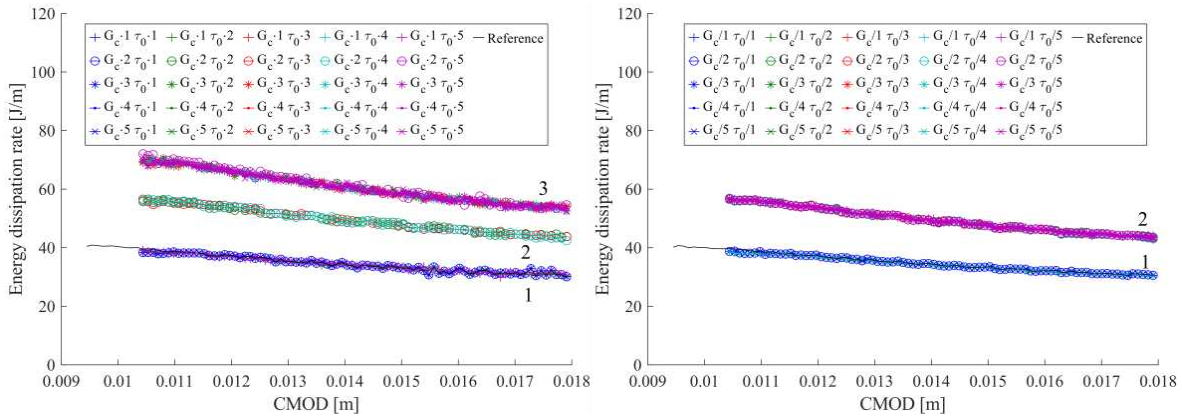

Figure 8: Energy dissipation rate for the interface toughening (left) and weakening (right) analyses.

The three different curves displayed in Figure 8 are linked to the three outcomes displayed in Figure 9. Outcome 1 is the reference case with a single delamination, where multiple delaminations is not initiated. Outcome 2 occurs when multiple delaminations are onset in the interface weakening cases, and in the interface toughening cases where the main crack is not arrested. For interface toughening cases with a high G_{Ic} and G_{IIc}, outcome 3, the main crack tip is successfully arrested, leaving the crack tips at the secondary interface as the only ones propagating. This situation results in more energy dissipation due to the local mode mixity conditions, which have a higher mode II component.

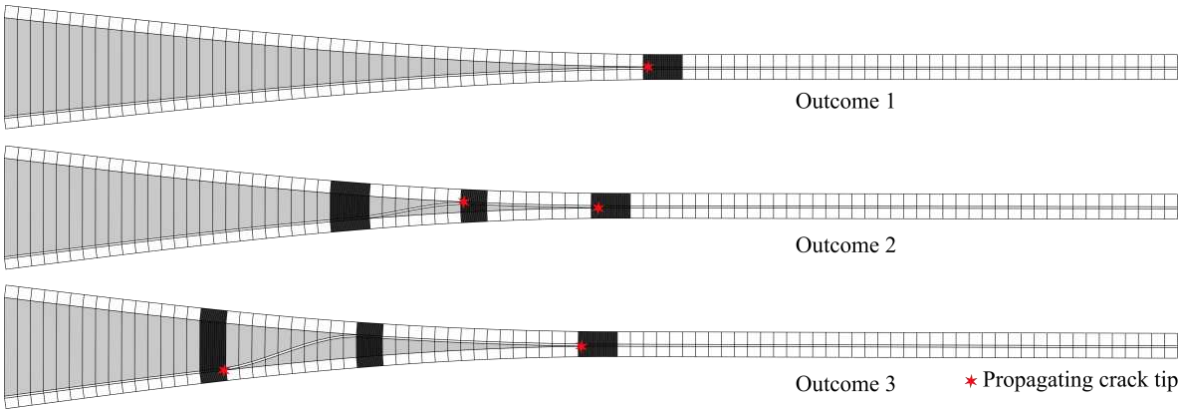

Figure 9: Deformed mesh at the end of selected analyses.

4. Discussion and Conclusions

A study on the toughening effect against delamination propagation produced by initiating multiple delaminations by including interface toughening or weakening patches in the structure is presented. A set of numerical tests is performed using a slightly modified version of the FNM adaptive formulation from [10]. The studies show that multiple delaminations can be initiated with both interface weakening and toughening patches, with overall higher load carrying capabilities provided by the analyses featuring a toughening patch. Moreover, the studied traction profiles identify that the multiple delaminations initiation is driven by a combination of onset traction and toughness modification of the patched area. Different outcomes depending on the values of the patched area onset traction and toughness are observed. The different

outcomes are a consequence of the multiple delaminations initiation, and of which crack tips propagate afterwards. Each of the outcomes corresponds to a different level of energy dissipation. The presented studies for quasi-static loading show promising results for increasing the toughness and load carrying ability. As a next step, the authors would like to explore how significant these effects will be for more advanced cohesive law formulations able to capture the effects of fibre bridging [15,16]. Furthermore, the authors would like to explore the effects of the interface weakening and toughening patches on fatigue-driven damage initiation and propagation. To accomplish this, the authors will use the fatigue simulation framework [17,18,19] which has recently been implemented into the A-FNM framework.

Acknowledgements

This work is supported by the Talent Management Programme at Aalborg University, Denmark (Internal grant number: 771120). This support is gratefully acknowledged.

References

1. Wu Z, Yi XS, Wilikinson A. Interlaminar fracture toughness of carbon fibre/RTM6-2 composites toughened with thermoplastic-coated fabric reinforcement. Composites Part B: Engineering. 2017 December; 130: 192-199.

2. Downey MA, Drzal LT. Toughening of carbon fiber-reinforced epoxy polymer composites utilizing fiber surface treatment and sizing. Composites Part A: Applied Science and Manufacturing. 2016 November; 90: 687-698.

3. Göktaş D, Kennin WR, Potluri P. Improvement of Mode I Interlaminar Fracture Toughness of Stitched Glass/Epoxy Composites. Appl Compos Mater. 2017 April; 24: 351-375.

4. Ravandi M, Teo WS, Tran LQN, Yong MS, Tay TE. The effects of through-the-thickness stitching on the Mode I interlaminar fracture toughness of flax/epoxy composite laminates. Materials & Design. 2016 November; 109: 659-669.

5. Mouritz AP. Review of z-pinned laminates and sandwich composites. Composites Part A: Applied Science and Manufacturing. 2020 December; 139: 106-128.

6. Pascoe JA, Pimenta S, Pinho ST. Interlocking thin-ply reinforcement concept for improved fracture toughness and damage tolerance. Composites Science and Technology. 2019 September; 181: 107681.

7. Mouritz AP, Bannister MK, Falzon PJ, Leong KH. Review of applications for advanced three-dimensional fibre textile composites. Composites Part A: Applied Science and Manufacturing. 1999 December; 30(12): 1445-1461.

8. Goutianos S, Sørensen BF. Fracture resistance enhancement of layered structures by multiple cracks. Engineering Fracture Mechanics. 2016 January; 151: 92-108.

  doi:10.5075/epfl-298799_978-2-9701614-0-0

9. Tao R, Li X, Yudhanto A, Alfano M, Lubineau G. Laser-based interfacial patterning enables toughening of CFRP/epoxy joints through bridging of adhesive ligaments. Composites Part A: Applied Science and Manufacturing. 2020 December; 139: 1069094.

10. Trabal GG, Bak BLV, Chen B, Lindgaard E. An adaptive floating node based formulation for the analysis of multiple delaminations under quasi-static loading. Composites Part A: Applied Science and Manufacturing. 2022 May; 156: 106846.

11. Turon A, Camanho P, Costa J, Dávila C. A damage model for the simulation of delamination in advanced composites under variable-mode loading. Mechanics of Materials. 2006 November; 38(11): 1072-1089.

12. Lindgaard E, Bak BLV, Glud JA, Sjølund JH, Christensen ET. A user programmed cohesive zone finite element for ANSYS Mechanica. Engineering Fracture Mechanics. 2017 July; 180: 229-239.

13. Juntti M, Leif AE, Olsson R. Assessment of evaluation methods for the mixed-mode bending test. Journal of Composites, Technology and Research. 1999; 21(1): 37-48.

14. Bak BLV, Turon A, Lindgaard E, Lund E. A simulation method for high-cycle fatigue-driven delamination using a cohesive zone model. Numerical Methods in Engineering. 2016 August; 106(3): 163-191.

15. Mosbjerg SJ, Martos MJ, Bak BLV, Lindgaard E. Formulation of a mixed-mode multinlinear cohesive zone law in an interface finite element for modelling delamination with R-curve effects. Composite Structures. 2019 May; 216: 477-486.

16. Mosbjerg SJ, Martos MJ, Lindgaard E, Bak BLV. Inverse parameter identification of n-segmented multilinear cohesive laws using parametric finite element modeling. Composite Structures. 2019 October; 225: 111074.

17. Bak BLV, Lindgaard E, Lund E. A simulation method for high-cycle fatigue-driven delamination using a cohesive zone model. Internation al Journal for Numerical methods in Engineering. 2015 August; 106(3): 163-191.

18. Carreras L, Turon A, Bak BLV, Lindgaard E, Renart J, Martin de la Escalera F, et al. A simulation method for fatigue-driven delamination in layered structures involving non-negligible fracture process zones and arbitrarily shaped crack fronts. Composites Part A: Applied Science and Manufacturing. 2019 January; 122: 107-119.

19. Carreras L, Bak BLV, Turon A, Renart J, Lindgaard E. Point-wise evaluation of the growth driving direction for arbitrarily shaped delamination fronts using cohesive elements. European Journal of Mechanics. 2018 March; 72: 464-482.

  doi:10.5075/epfl-298799_978-2-9701614-0-0

EXPERIMENTAL AND NUMERICAL STUDY OF THE INTRA/INTER LAMINAR DAMAGE COUPLING OF LAMINATED COMPOSITES

Ping HU and Gilles Lubineau

King Abdullah University of Science and Technology (KAUST), Physical Science and Engineering Division, Mechanics of Composites for Energy and Mobility Lab.,
Thuwal 23966-6900, Saudi Arabia
ping.hu@kaust.edu.sa

Abstract: *Coupling between intralaminar and interlaminar damage largely influences the evolution of damage in laminated composites. A well-known example is the transverse crack induced local delamination. In the early stage of loading, the matrix is prone to diffuse matrix damage, followed by macroscopic transverse cracks. Stress concentration in the crack tip would then leads to local delamination in the interlaminar region. In this work, we implemented both experimental and numerical study to dig into the intra/inter laminar coupling mechanism. Our experiments indicated that preset intralaminar damage could be both detrimental and helpful to the interlaminar damage performance [1]. In one aspect, the transverse crack induced delamination will decrease the delamination resistance. In the other aspect, the preset intralaminar damage could cause crack branch inside the layers during delamination progress. The arrested delamination crack would pull out fiber bridging in mode I fracture. Both the wavy delamination crack and pulled out fiber bridging will, in the end, prohibit delamination propagation and dissipate more energy. Furthermore, we proposed a hybrid cohesive element to involve the coupling mechanism [2]. In this hybrid cohesive element, we not only use the classical displacement jump, but also the displacement field of the top and bottom surface of the cohesive element. The displacement field of the cohesive element's top and bottom surface is used to estimate the strain and damage level of the adjacent layers of this interested interface. The estimated in-plane strain could then be used to operate an appropriate strategy.*

Keywords: intralaminar; interlaminar; damage coupling; experiments; simulation

1. Introduction

Carbon fiber reinforced polymers (CFRPs) are widely used in current advanced industries, like airplanes and automotive. CFRPs are usually made by two components: fiber and matrix. Fibers are used to reinforce the mechanical strength and matrix combines fibers as a whole material, which lead to laminar composites. By stacking composite layers with different fiber orientation, a composite laminate with a good in-plane strength is obtained. Fig. 1 shows a schematic of composites from different length scales. Because of the two-component constitution and layered structure, CFRP materials behave as heterogeneous and anisotropic behavior. The damage evolution inside a laminated composites evolve in different forms, and can be divided into two branches: intralaminar damage and interlaminar damage.

  doi:10.5075/epfl-298799_978-2-9701614-0-0

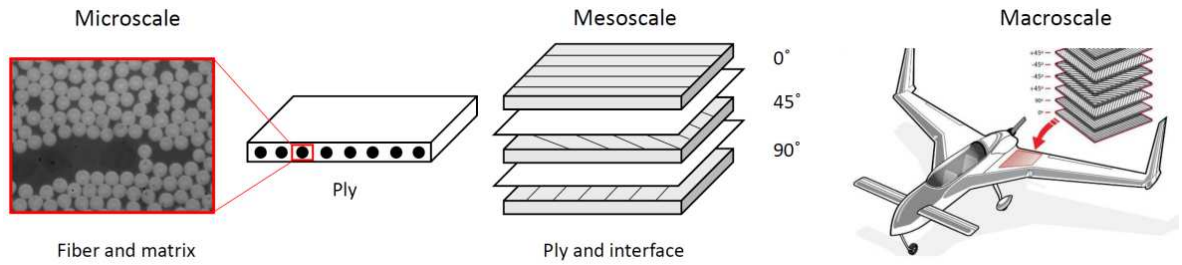

Figure 1. CFRP materials observed from different length scales

Intralaminar damage happens inside the layer, including fiber/matrix debonding, diffuse matrix damage, matrix cracking and fiber breakage. Interlaminar damage is also referred as delamination, which happens between different fiber-oriented plies due to the mismatch of mechanical properties of different fiber-oriented layers. Fig. 2 illustrates different damage forms happening in laminated composites. At the initial stage of loading, the first occurred damage is usually fiber/matrix debonding [3] and diffuse matrix damage. Matrix cracking [4] will occur with the accumulation of fiber/matrix debonding and diffuse matrix damage. Laminated composites are still safe usually at the stage of matrix cracking. With further loading, the saturation of matrix cracking will lead to the next stage of damage forms, i.e., delamination damage between different oriented layers [5]. The stress concentration in the matrix crack tip will transfer the damage from the intra-ply to the inter-lay region. Local delamination occurs in this stage. The local delamination damage coalesced to a macro ply delamination, which could lead to a catastrophic failure.

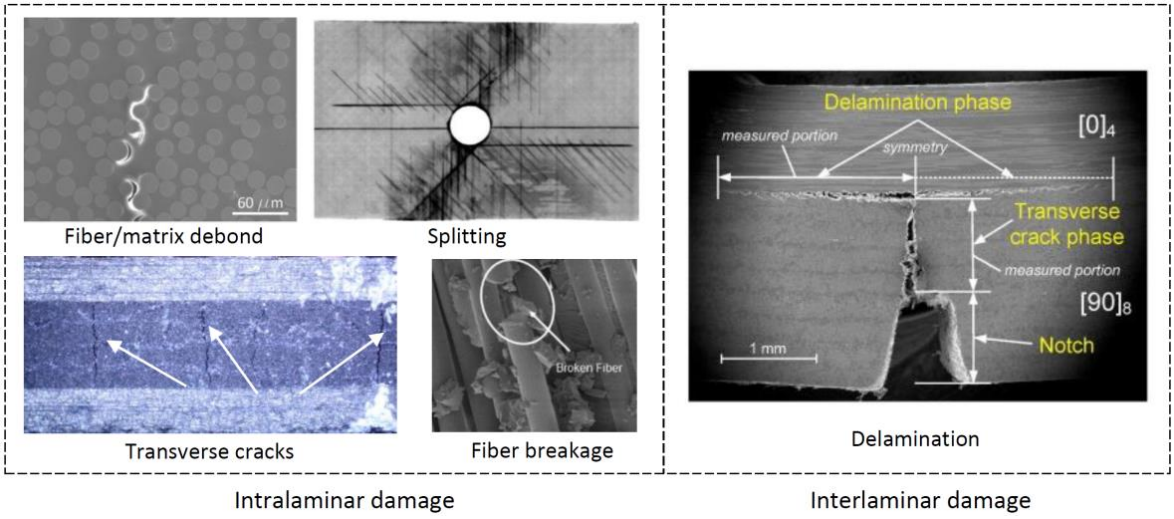

Figure 2. Intralaminar and interlaminar damage [3-5]

The different damage modes can strongly couple with each other, making the damage monitoring and service life prediction of composites structures difficult. One of the well-known damage coupling in laminated composites happens between intralaminar and interlaminar damage. Fig. 3 (a) shows that the delamination area is surrounded by matrix cracks of adjacent layers for a laminate under impact loading [6]. Fig. 3 (b) shows that the delamination crack kinks into the plies when delamination direction is misaligned with the fiber orientation of the adjacent layers in a double cantilever beam (DCB) test [7].

  doi:10.5075/epfl-298799_978-2-9701614-0-0

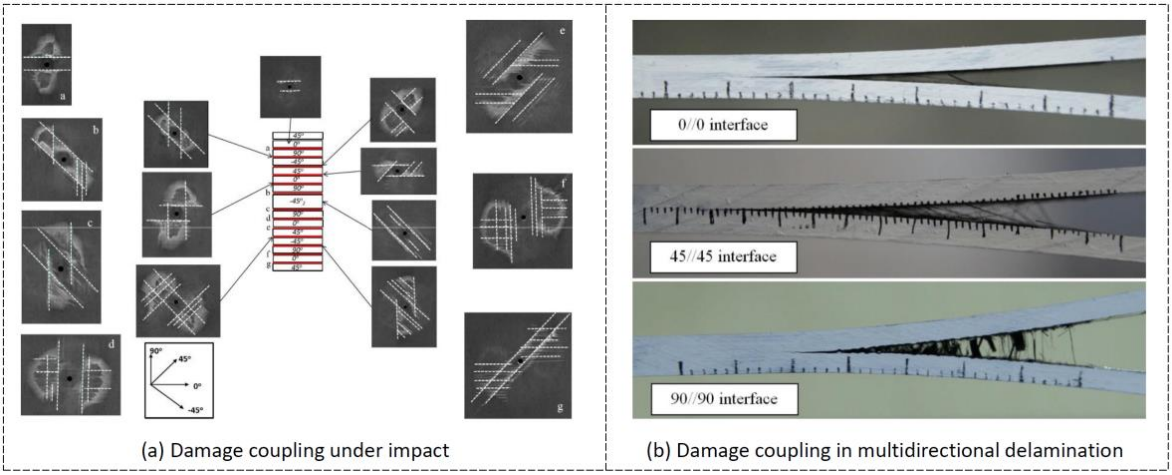

Figure 3. Intralaminar and interlaminar damage coupling under impact and mode I delamination [5,6]

Proper simulation tools to encounter the intralaminar and interlaminar damage coupling are necessary to predict the damage evolution of laminated composites. Two classes of simulation methods have been developed. The first class of methods is to explicitly introduce cracks in the form of displacement jump, such as extended finite element method (X-FEM) and floating node method (FNM). The stress concentration at the local crack tip can be well captured using these methods. However, these crack modeling techniques require high quality of finite mesh and could be computational expensive. More importantly, the crack path may not be known a priori in some complex structures. The other class of methods is based on continuum damage mechanics (CDM), in which the crack effect is replaced with the smeared damage variables to represent degradation of some mechanical properties like stiffness. Meshing difficulty and computational cost is less compared to the cracking modeling techniques. The disadvantage is that, without the explicit introduction of the displacement jump in the simulation, the interaction between intralaminar and interlaminar damage is lost. Without the explicit form of stress concentration in the matrix crack tip, the delamination damage prediction is usually underestimated in such CDM based method.

This paper explores the intralaminar and interlaminar damage coupling from both experiments and numerical simulations. Experimental strategy to reveal the influence of intralaminar damage on interlaminar performance is proposed. Besides, a numerical tool that considers the coupling effect in a pragmatic way is also developed and used to simulate the experiments, which shows a good agreement between experimental and numerical results.

2. Experimental method

2.1 Experimental method

Fig. 4 presents a two-step test (Tensile-DCB), which studies the influence of intralaminar damage on interlaminar performance. In the first step, cross-ply $[0_2/90_2]_s$ is pulled at different in-plane strain levels (0% - 1.4% with a step of 0.2%). Thus, the $90°$ plies undergo different extents of intralaminar damage. In the second step, two backing adherends $[0_8]_s$ are bonded to each side of the pre-loaded cross-ply $[0_2/90_2]_s$ samples. The backing adherend can provide extra bending stiffness for the following DCB test. A preset aluminum foil is inserted before the tensile loading, which is used as a crack starter for the DCB test. The DCB test evaluates the propagation

toughness using the compliance calibration method. Through this method, quantitative data can be achieved to study the intralaminar and interlaminar damage coupling.

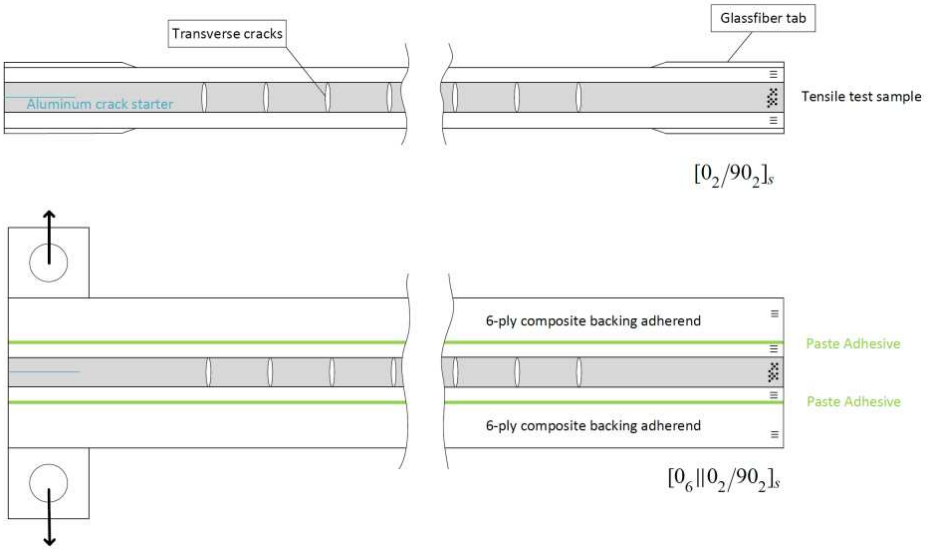

Figure 4. Tensile-DCB method

2.2 Experimental results

Fig. 5 (a) shows the transverse crack density and propagation toughness evolution with the increase of in-plane strain. The transverse crack initiates at the in-plane strain of ~0.2%, and increase dramatically from 0.2% - 0.8%. After 0.8% in-plane strain, the crack density gradually saturates. The propagation toughness increases from 0.2% - 0.8% in-plane strain, which corresponds to the transverse crack density increasing stage. After 0.8% in-plane strain, the propagation toughness decreases slightly.

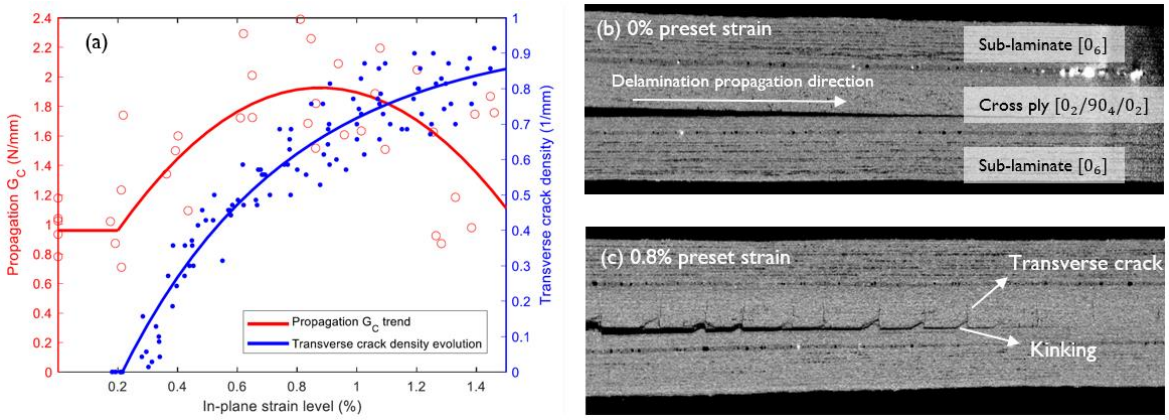

Figure 5. Tensile-DCB experimental results

Fig. 5 (b) and (c) explain the phenomenon when propagation toughness increases with transverse crack density. The existence of transverse cracks will allure the delamination crack kink inside the 90° plies, which pulls out fiber bridging during the delamination propagation stage. The matrix cracking and fiber bridging dissipates extra energy, which increase the apparent propagation toughness.

  doi:10.5075/epfl-298799_978-2-9701614-0-0

3. Numerical method

3.1 Hybrid cohesive modeling

A hybrid cohesive element is proposed to consider the intralaminar and interlaminar damage coupling. Except the classical out-of-plane separation (Eq. (1)), the in-plane strain (Eq. (2)) of the top and bottom surface of the interface element is also calculated, which is used to estimate the adjacent layers damage state. When laminate undergoes limited bending, the in-plane strain of cohesive element can be used to well estimate the in-plain strain of the adjacent layers. Fig. 6 shows the schematic of the hybrid cohesive element.

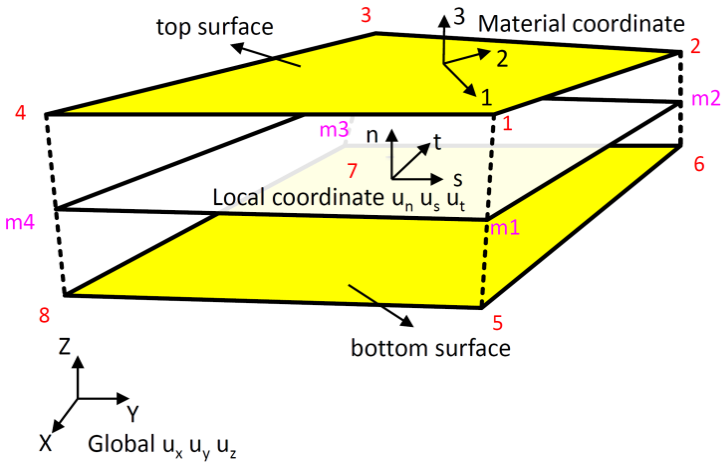

Figure 6. Schematic of the hybrid cohesive element

$$\underline{\delta} = (\delta_n, \delta_s, \delta_t)^T \tag{1}$$

$$\varepsilon_{ij} = \frac{1}{2}\left(\frac{\partial u_i}{\partial x_j} + \frac{\partial u_j}{\partial x_i}\right) \quad i,j = s,t \tag{2}$$

3.2 Simulation results

Fig. 7 shows the comparison between simulation and experimental results. The simulation results can well fit the mean value of the experimental results because we calibrate the hybrid cohesive model using the propagation toughness from the experiments. The fluctuation of the experimental curve is due to the unstable of fiber bridging and matrix crack branching during delamination propagation process.

4. Conclusions

This work reveals that the intralaminar damage has a two-fold influence on the interlaminar performance. On one hand, the preset intralaminar damage can lead to delamination crack branching, which pulls out fiber bridging and toughen the interface. On the other hand, the transverse crack induced delamination will also decrease the interlaminar toughness.

The hybrid cohesive element proves its efficiency and robustness to capture the intralaminar and interlaminar damage coupling. Further development on this hybrid cohesive element can address more industry subjects.

  doi:10.5075/epfl-298799_978-2-9701614-0-0

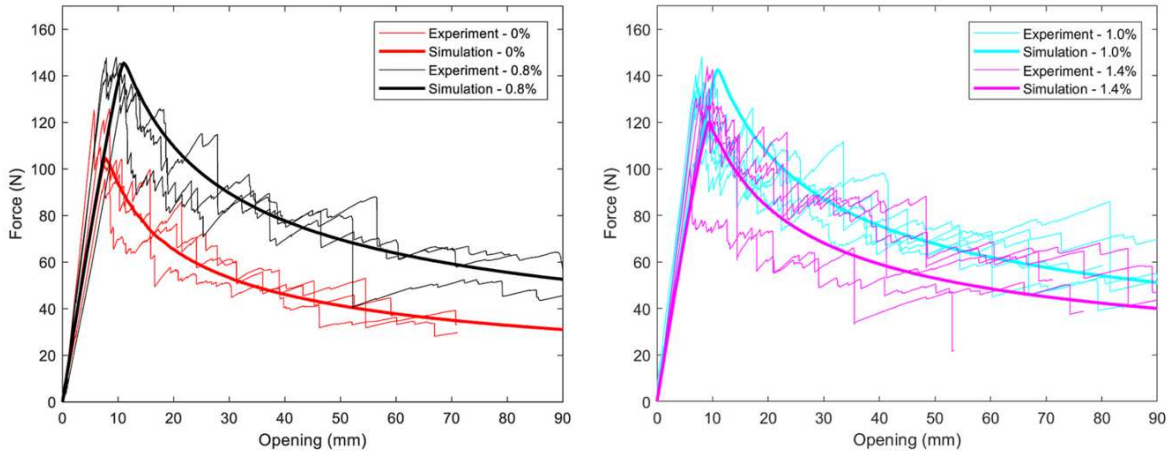

Figure 7. Comparison between simulation and experimental results

Acknowledgements

The research reported in this publication was supported by funding from King Abdullah University of Science and Technology (KAUST) Baseline Research Funds, under award number BAS/1/1315-01-01.

5. References

1. Hu P, Pulungan D, Tao R, Lubineau G. An experimental study on the influence of intralaminar damage on interlaminar delamination properties of laminated composites. Composites Part A 2020; 131:105783.
2. Hu P, Pulungan D, Lubineau G. An enriched cohesive law using plane-part of interfacial strains to model intra/inter laminar coupling in laminated composites. Composites Science and Technology 2021; 200:108460.
3. Canal L P, Gonzalez C, Segurado J, Lorca J. Intraply fracture of fiber-reinforced composites: Microscopic mechanisms and modeling. Composites Science and Technology 2012. 72:1223-1232.
4. Hallett S R, Green B G, Jiang W G, Wisnom M R. An experimental and numerical investigation into the damage mechanisms in notched composites. Composites Part A 2009; 50:613-624.
5. Wafai H, Yudhanto A, Lubineau G, Mulle M, Alghamdi T, Thoroddsen S T, Yaldiz R, Verghese N. In situ micro-scale high-speed imaging for evaluation of fracture propagation and fracture toughness of thermoplastic laminates subjected to impact. Composite Sturctures 2019; 210:747-754.
6. Abisset E, Daghia F, Sun X C, Wisnom M R, Hallett S R. Interaction of inter- and intralaminar damage in scaled quasi-static indentation tests: Part 1 – Experiments. Composite Structures 2016; 136:712-726.
7. Bin Mohamed Rhan M S, Rousseau J, Fontaine S, Gong X J. Experimental study of the influence of ply orientation on DCB mode-I delamination behavior by using multidirectional fully isotropic carbon/epoxy laminates. Composite Structures 2017; 161:1-7.

INCREASING DELAMINATION RESISTANCE THROUGH TAILORED DEFECTS IN LAYERED COMPOSITES

*M. Herráez, N. Pichler, J. Botsis**

École Polytechnique Fédérale de Lausanne (EPFL), STI, Lausanne, Switzerland
*john.botsis@epfl.ch

Abstract: *Delamination is a well-known damage mode exhibited by laminated composites which has been extensively studied in unidirectional laminates (UD). In this work, a novel strategy consisting of the introduction of a small interlaminar defect to enhance the fracture resistance to delamination of UD composites is presented. This toughening concept is based on the simultaneous propagation of multiple interlaminar cracks along different interfaces predicted by finite element analyses. An experimental campaign to prove the toughening concept with one defect at the adjacent interface of the pre-crack was carried out and compared against a reference configuration under two different applied mode mixities ($\phi_{glob} = 0.4$ and 0). The single defect configuration reached an improvement in the fracture resistance of +300% under applied pure mode I, and +100% for applied mixed mode of 0.4.*

Keywords: Delamination; Mechanical testing; Numerical modeling; Enhanced toughness

1. Introduction

Since *fiber-reinforced polymer* (FRP) composite materials are commonly used as laminated architectures, they often suffer from interlaminar damage or delamination. Although this damage mechanism may not be critical at the structural level, flexural stiffness and damage tolerance of the laminate are dramatically reduced. Thus, improving interlaminar fracture toughness of FRP laminates is crucial to prevent and/or control delamination growth and design more damage-tolerant structures.

Several works published in the literature in the last decades aimed at improving delamination resistance and can be grouped in two categories: *extrinsic* and *intrinsic* toughening of the interface. In the first group, reinforcement methods include stitching (1), z-pinning (2), tufting (3) and interlocking systems at the ply level (4). Among the extrinsic procedures to achieve higher interlaminar toughness, resins toughened with rubbers (5), and thermoplastics (6–8) are proposed. Lately, these toughened resins have been dispersed following special patterns along the interface exhibiting better performance (9).

A different philosophy, based on the custom tailoring of the microstructure of the composite to optimize a particular property, has become popular recently. For instance, the longitudinal tensile toughness of a conventional carbon/epoxy UD system was increased by a factor of 3 by making micro-cuts following a certain pattern along the crack path (10). This concept was further exploited to enhance the damage tolerance response of orthotropic laminates (11) and polypropylene/carbon hybrid composites (12) under in-plane loading of notched specimens. Therefore, the introduction of defects or discontinuities at certain locations can increase the

  doi:10.5075/epfl-298799_978-2-9701614-0-0

effective toughness of the material. Inspired by these works and other works (13,14), the present study proposes the pre-insertion of small interlaminar defects along the laminated composite to enhance the delamination resistance of the system.

The aim of this work is to demonstrate numerically and experimentally the effect of introducing an interlaminar defect on the interlayer adjacent to the main delamination plane under different mode mixities in a *unidirectional* (UD) laminate.

2. Experimental methods

2.1 Material and specimens

The material system employed throughout this work was Gurit™ SE84, a UD carbon/epoxy prepreg system with ply thickness $t = 0.2\,mm$. In this study, 20-ply UD laminates were considered, having a total thickness of $2h = 4\,mm$.

A reference laminate with no inserts followed by a laminate with one insert were manufactured. In all cases a precrack, $a_0 = 45\,mm$, was introduced by inserting a $13\,\mu m$ thick PTFE release film at the midplane during layup. The single insert laminate has a $\ell_d = 5\,mm$ wide PTFE insert placed one ply above and $\delta_d = 15\,mm$ ahead of the pre-crack, see Figure 1b. The plates were cut into $280 \times 25\,mm^2$ specimens using a diamond-coated disk saw as shown in Figure 1a. At least 2 specimens were tested under each applied mode mixity.

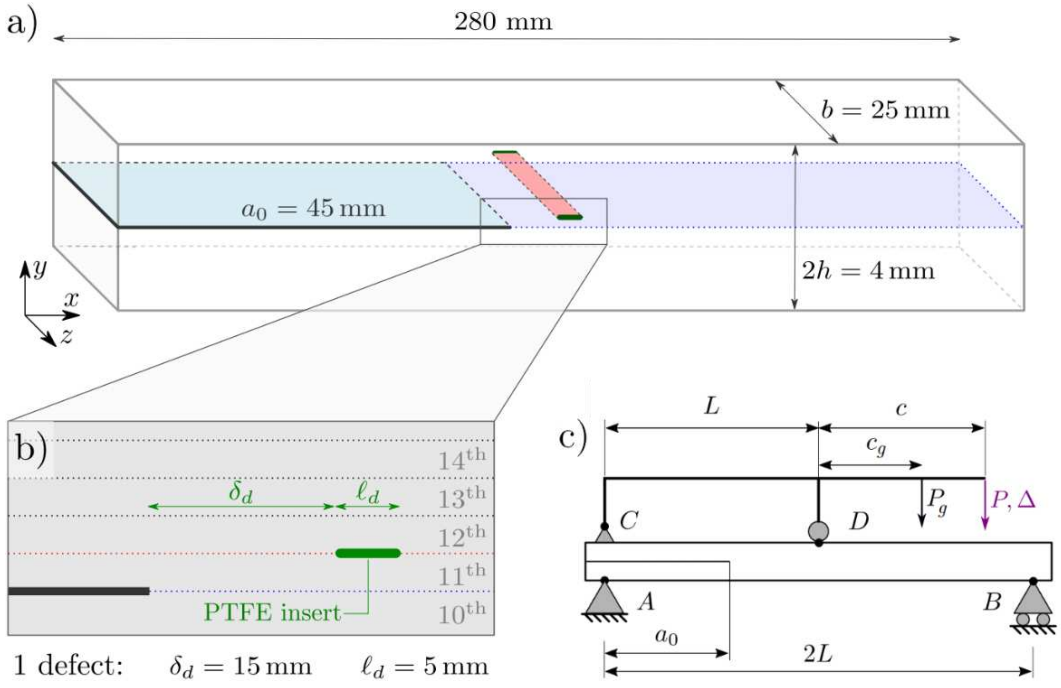

Figure 1. a) Schematic of the coupons manufactured with one defect, b) including a detailed side view of the relative position of the insert. c) Schematic of the MMB test.

2.2 Experimental setup

The *mixed-mode bending* test (MMB) used in this work is described in the standard ASTM D6671/D6671M. This procedure allows to apply a controlled global mode I/II mixity loading. The ratio of mode II or mode mixity, $\phi_{glob} = G_{II}/(G_I + G_{II})$, is controlled by the relative length of

the lever, c/L. For this experimental campaign the length between the bending rollers was chosen as $L = 100\ mm$ and the lever length, c, was varied to obtain the mode mixity desired.

The *energy release rate* (ERR) was computed based on the J-integral (15). In the MMB case, the integral can be reduced to the following expression,

$$J = \frac{P}{2b}\left[\left(\frac{1}{2} - \frac{c}{2L}\right)\theta_A + \left(\frac{c}{2L} + \frac{1}{2}\right)\theta_B - \frac{c}{L}\theta_C - \left(\frac{c}{L} + 1\right)\theta_D\right] \quad (1)$$

where b is the specimen width, P is the applied load and θ_j the local rotations at the rollers contact points for $j \to A, B, C, D$, as illustrated in Figure 1c.

For the characterization under pure mode I ($\phi_{glob} = 0$), DCB tests (*double cantilever beam*) were carried out according to ASTM D5528 along with J-integral data reduction method (16).

3. Numerical model

3.1 Model description

A 2D FE model was developed to investigate the fracture process during propagation of the primary and secondary cracks. The model, whose dimensions are shown in Figure 2a, represents a UD coupon with the loading conditions of the MMB test described previously.

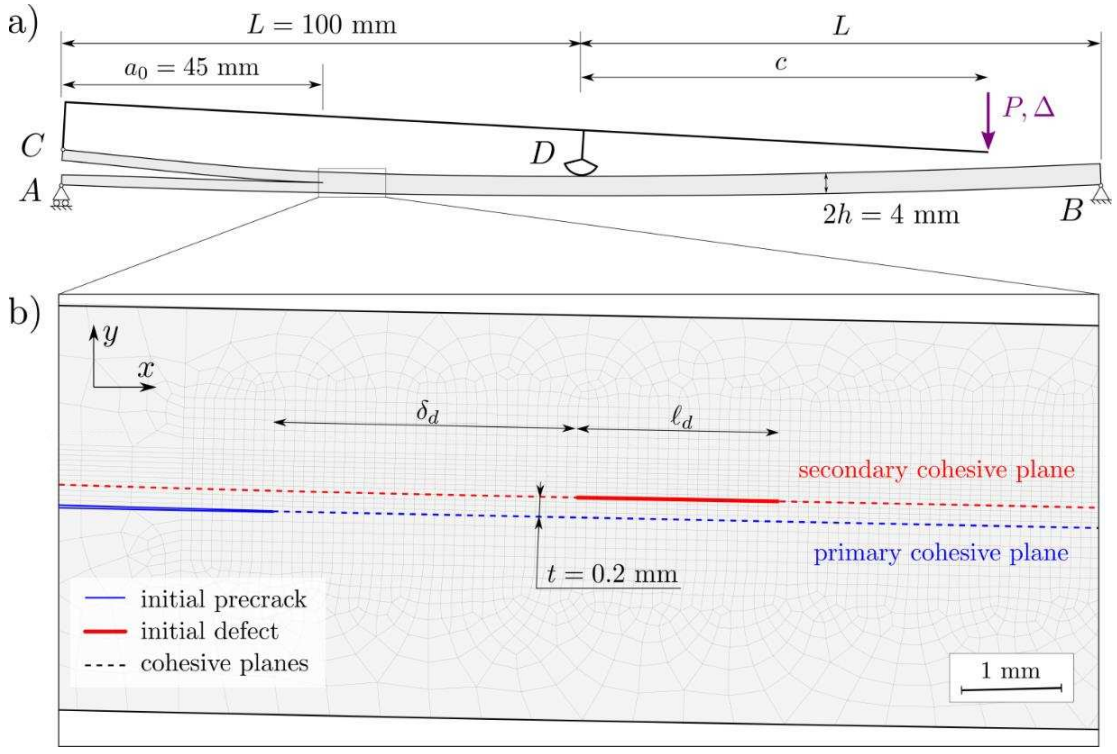

Figure 2. a) Global view of the FE model of a specimen with one defect during the MMB test, and b) detail of the cohesive planes: initial precrack (blue) and adjacent interface (red).

The coupon was simply supported at points A and B ($u_y = 0$), as shown in Figure 2a. The lever of the MMB test was rigid and attached to the coupon at point C and to the rigid roller D. A hard, friction-less contact was defined between roller D and the upper face of the coupon. Load, P, was recorded as a result of the applied vertical displacement downwards of the tip of the lever. The relative length of the lever, c/L, was varied between simulations to modify the applied

mode mixity during the crack propagation process, as explained in Section 2.2. Delamination was represented by adopting a *cohesive zone model* (CZM) approach by means of cohesive elements in Abaqus/Standard (17). In this manner, 2D cohesive elements (COH2D4) were inserted along the predefined fracture planes of the model. Two cohesive planes are identified: a primary plane along the initial precrack plane (dashed blue line) and a secondary plane along the adjacent upper interply (dashed red line), shown in Figure 2b. A defect was introduced to promote secondary crack propagation, by removing the cohesive elements along this region. The location of the defect was the same as in the experiments: for the one defect case $\delta_d = 15\ mm$ and $\ell_d = 5\ mm$. A hard, friction-less contact was defined along the initial precrack and defect free surfaces to prevent penetration and permit slippage between faces. The mesh size along the cohesive planes was $0.1\ mm$, which is fine enough to represent the fracture process zone accurately.

The cohesive planes followed a traction-separation law with linear softening. Damage initiation is controlled by a quadratic stress criterion and damage evolution follows a BK law (18) with the following cohesive properties: $G_I^f = 0.15\ kJ/m^2$, $G_{II}^f = 1.25\ kJ/m^2$ and $\eta = 1.5$. The UD plies were represented using solid elements of incompatible modes assuming plane strain (CPE4I). The composite plies were assumed to be linear elastic transversely isotropic with the following properties: $E_L = 124.8\ GPa$, $E_T = 9.0\ GPa$, $G_L = 4.0\ GPa$, $\nu_L = 0.314$ and $\nu_T = 0.47$.

3.2 Data reduction

The ERR was obtained by computing the J-integral around the outermost contour of the FE model, analogous to the experimental method following eq. (1). The position of the crack tip, Δa, was considered as the furthest damaged cohesive element in the x-direction, with the damage variable greater than 0.001.

4. Experimental results

4.1 Applied mixed mode, $\boldsymbol{\phi_{glob} = 0.4}$

The behavior of the reference specimen is shown through the dotted lines in Figure 3a-1. The response is linear elastic until reaching the peak load followed by a pop-in and subsequent small increase in load and progressive softening that corresponds to the propagation of a single crack along the initial precrack plane. In this case, the R-curve exhibits a plateau from the very beginning of the crack propagation at $0.39 \pm 0.02\ kJ/m^2$, see Figure 3a-2.

For the case with one defect, solid black line in Figure 3a-1, the initial response is similar to the reference configuration: after the linear part, a pop-in and stick-slip are recorded for the primary crack until its arrest, see point *i*. Upon additional loading the crack does not grow, due to the shielding effect of the adjacent defect, until a maximum is reached, indicated by the highlighted blue section in Figure 3a-1. Afterwards, both cracks propagate giving rise to significant toughening increase from 0.39 to $0.8\ kJ/m^2$, as observed in Figure 3a-2 at points *ii* and *iii*.

Figure 4 shows a schematic side view of the fracture process where the blue and red lines represent the primary and secondary cracks, respectively. The fracture process following secondary crack propagation (stages *ii* and *iii*) is illustrated through Figure 4ii-2 and iii-2, where the simultaneous propagation of both cracks is ascertained.

  doi:10.5075/epfl-298799_978-2-9701614-0-0

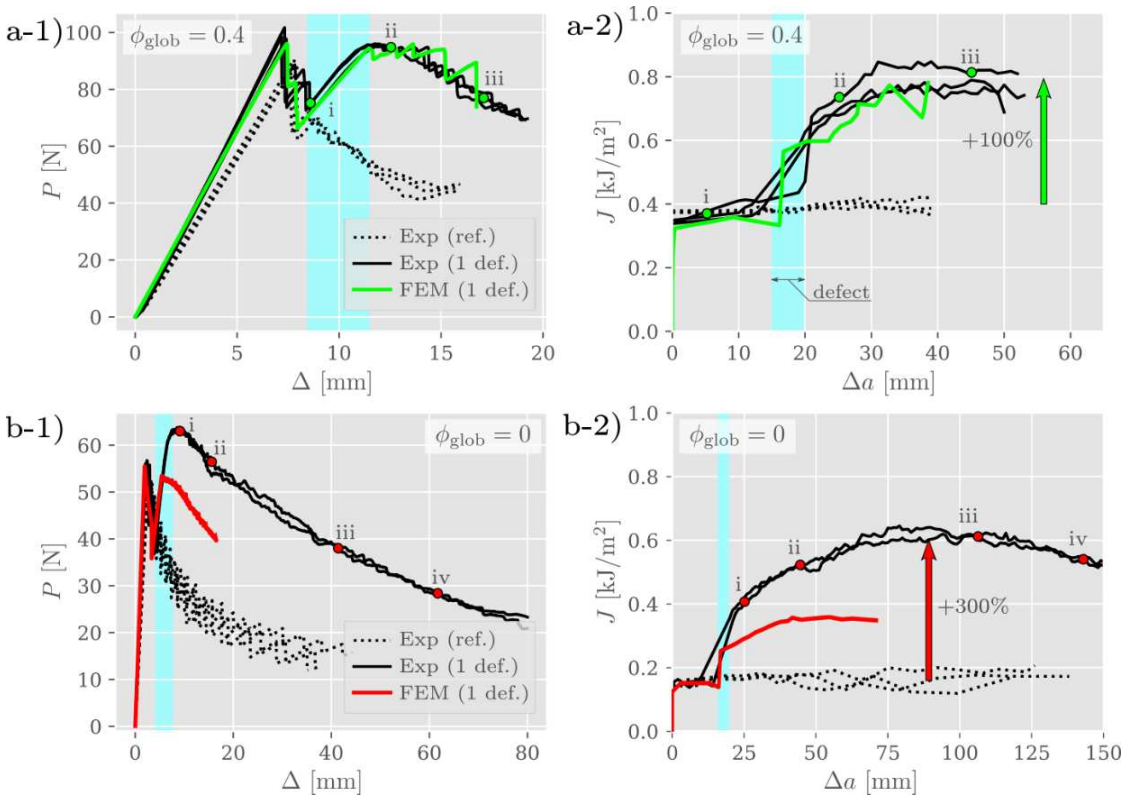

Figure 3. Experimental and numerical load vs. displacement curves (1) and R-curves (2) for a) $\phi_{glob} = 0.4$ and b) pure mode I ($\phi_{glob} = 0$)

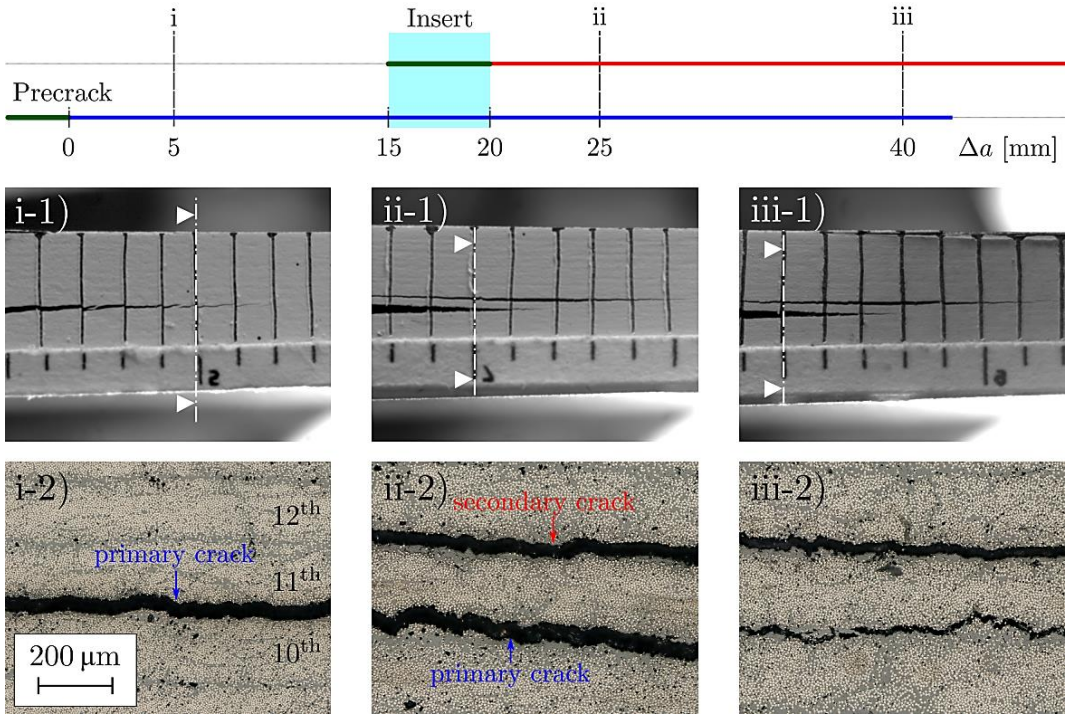

Figure 4. Schema on top shows the side view of a single insert specimen tested under $\phi_{glob} = 0.4$. Side views (1) and micrographs of the corresponding cross sections (2) for i) $\Delta a = 5$ mm, ii) 25 mm, iii) and 40 mm.

  doi:10.5075/epfl-298799_978-2-9701614-0-0

The numerical model was able to capture the whole fracture process including the delamination propagation from the initial precrack, arrest of the primary crack when approaching the defect, and the toughened response of the system during the simultaneous propagation of the primary and secondary cracks, see green lines in Figure 3a.

4.2 Applied pure mode I, $\phi_{glob} = 0$

The baseline configuration, without any defect exhibits the well-known linear response until a peak load with subsequent pop-in, a growth to a maximum load followed by progressive softening due to crack propagation along a brittle interface, as shown by the dotted black lines in Figure 3b-1. It should be noted that the flat shape of the R-curve of the reference case is due to the absence of toughening mechanisms such as fiber bridging, see dotted lines in Figure 3b-2. Therefore, the absence of any bridging mechanism explains the poor fracture toughness of the interlamina under pure mode I, $G_I^f = 0.15 \pm 0.03\ kJ/m^2$.

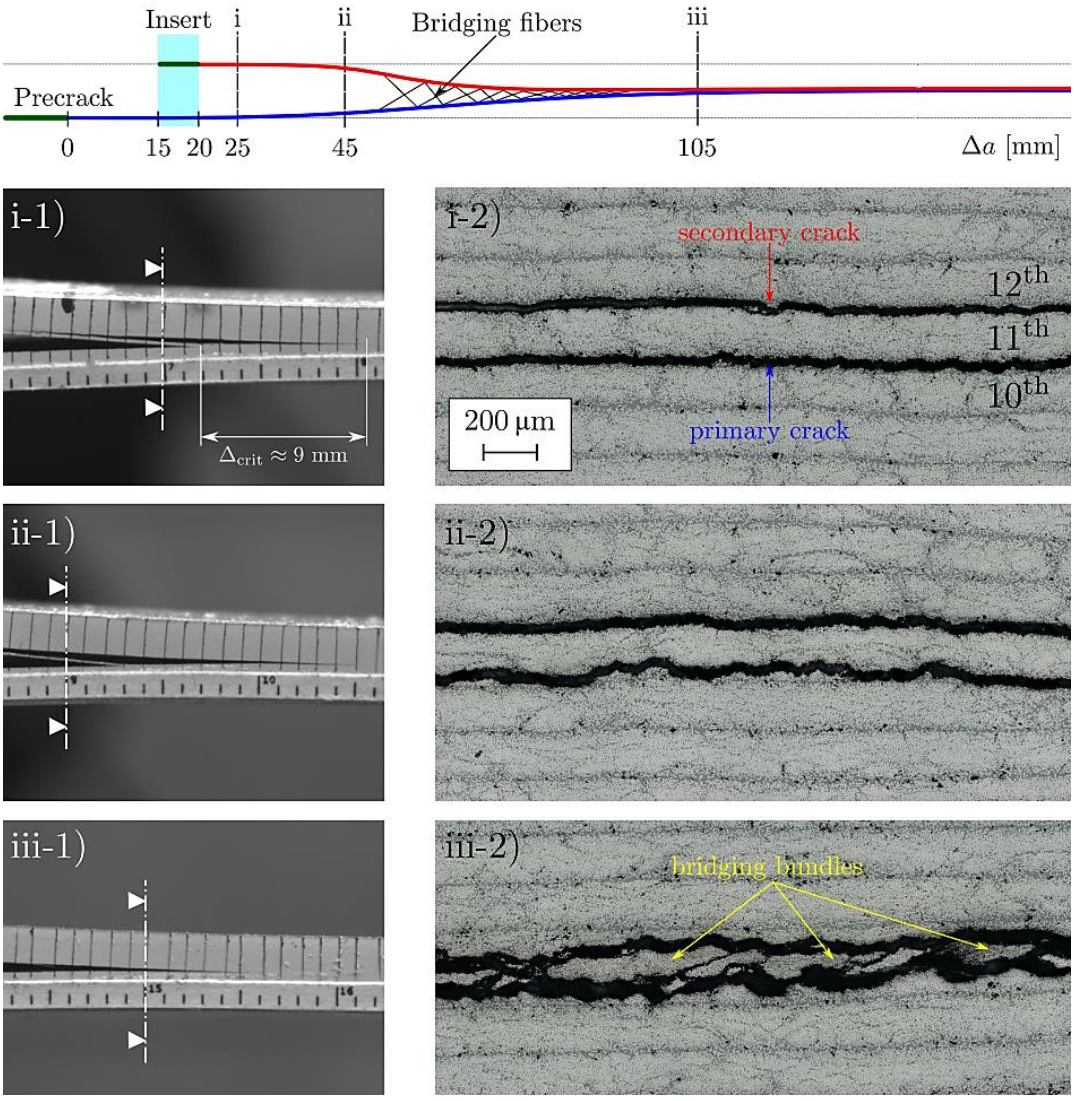

Figure 5. Schema on top shows the side view of a single insert specimen tested in pure mode I (DCB) with the propagation of the primary (blue) and secondary (red) cracks. Side views (1) and micrographs of the cross sections (2) for i) $\Delta a = 25$ mm, ii) 45 mm and iii) 105 mm.

  doi:10.5075/epfl-298799_978-2-9701614-0-0

The experimental results obtained from the DCB tests of the coupons with one defect are summarized in Figure 3b-1 and b-2. The overall response is similar to the case described before: an initial linear elastic regime until a peak load followed by a pop-in that corresponds to the propagation of the precrack, which arrests when it approaches the defect, see highlighted region in Figure 3b-1. Afterwards, load increases without crack advance up to a higher peak load around 65 N. At point *i*, both cracks start propagating giving rise to a progressive decay in the load, while dissipating a tremendous amount of fracture energy, i.e. up to 4 times the reference case, from 0.15 to $0.61 \pm 0.03\ kJ/m^2$, as shown in Figure 3b-2.

Although, the numerical model predicts a similar qualitative behavior, it underestimates the toughening enhancement obtained from the experiments, see red line in Figure 3b-2. This lower prediction corresponds to the simultaneous propagation of two interlaminar cracks without fiber bridging, as measured from the reference DCB tests. However, fiber bridging was experimentally observed under applied pure mode I from the analysis of the fracture process for the 1-defect case, based on the micrograph of the cross section shown in iii-2.

The sequence of events of the fracture process is described in detail in . As shown schematically in , the fracture process initiates with the propagation of the primary crack along the precrack plane, between plies 10 and 11 (blue line), until arrest when it approaches the defect at the adjacent interply, as also recorded in Figure 3b-1. The fracture process continues with both cracks propagating simultaneously keeping a constant distance between crack tips, Δ_{crit} as shown in i-1 and i-2. As both cracks keep advancing, it is observed that the primary crack ascends and starts propagating through the upper ply (11th ply), see ii-2, whereas the secondary crack descends to dive into that same ply. After 105 mm of crack propagation, in iii-2, the transition from interlaminar to intralaminar fracture of both cracks is evidenced. In this manner, fiber bundles that bridge the fracture process are formed by the coalescence of the primary and secondary cracks through the 11th ply thus, increasing the fracture resistance of the sample as shown in Figure 3b-2.

5. Conclusions

The ERR at crack propagation increased notably with the inclusion of an adjacent interlaminar defect. The delamination resistance of the material increased +300% under applied pure mode I. Whereas for $\phi_{glob} = 0.4$, the relative gain was around +100%, i.e. fracture resistance is doubled as compared to the reference case. A complete description of the full experimental campaign addressing the inclusion of more defects under a full range of mode mixities, and including a numerical preliminary study can be found in (19).

6. References

1. Dransfield K, Baillie C, Mai YW. Improving the delamination resistance of CFRP by stitching-a review. Compos Sci Technol. 1994;50(3):305–17.

2. Pegorin F, Pingkarawat K, Mouritz AP. Comparative study of the mode I and mode II delamination fatigue properties of z-pinned aircraft composites. Mater Des. 2015;65:139–46.

3. Martins AT, Aboura Z, Harizi W, Laksimi A, Khellil K. Analysis of the impact and compression after impact behavior of tufted laminated composites. Compos Struct. 2018;184:352–61.

  doi:10.5075/epfl-298799_978-2-9701614-0-0

4. Pascoe J-A, Pimenta S, Pinho ST. Interlocking thin-ply reinforcement concept for improved fracture toughness and damage tolerance. Compos Sci Technol. 2019 Sep;181:107681.

5. Bagheri R, Marouf BT, Pearson RA. Rubber-toughened epoxies: A critical review. Polym Rev. 2009;49(3):201–25.

6. Hodgkin JH, Simon GP, Varley RJ. Thermoplastic toughening of epoxy resins: A critical review. Polym Adv Technol. 1998;9(1):3–10.

7. Nash NH, Young TM, McGrail PT, Stanley WF. Inclusion of a thermoplastic phase to improve impact and post-impact performances of carbon fibre reinforced thermosetting composites - A review. Mater Des. 2015;85:582–97.

8. Sela N, Ishai O. Interlaminar fracture toughness and toughening of laminated composite materials: a review. Composites. 1989;20(5):423–35.

9. Narducci F, Lee KY, Pinho ST. Interface micro-texturing for interlaminar toughness tailoring: a film-casting technique. Compos Sci Technol. 2018;156:203–14.

10. Bullegas G, Pinho ST, Pimenta S. Engineering the translaminar fracture behaviour of thin-ply composites. Compos Sci Technol. 2016;131:110–22.

11. Bullegas G, Benoliel J, Fenelli PL, Pinho ST, Pimenta S. Towards quasi isotropic laminates with engineered fracture behaviour for industrial applications. Compos Sci Technol. 2018 Sep;165:290–306.

12. Mencattelli L, Tang J, Swolfs Y, Gorbatikh L, Pinho ST. Bio-inspired design for enhanced damage tolerance of self-reinforced polypropylene/carbon fibre polypropylene hybrid composites. Compos Part A Appl Sci Manuf. 2019;

13. Kachanov M, Montagut ELE, Laures JP. Mechanics of crack—microcrack interactions. Mech Mater. 1990 Nov;10(1–2):59–71.

14. Chudnovsky A, Wu S. Effect of crack-microcracks interaction on energy release rates. Int J Fract. 1990;44(1):43–56.

15. Rice JR. A Path Independent Integral and the Approximate Analysis of Strain Concentration by Notches and Cracks. J Appl Mech. 1968;379–86.

16. Anthony J, Paris PC. Instantaneous evaluation of J and C*. Int J Fract. 1988;38:19–21.

17. Simulia, editor. Abaqus Analysis User's Guide. Version 6.13. 2013.

18. Benzeggagh ML, Kenane M. Measurement of mixed-mode delamination fracture toughness of unidirectional glass/epoxy composites with mixed-mode bending apparatus. Compos Sci Technol. 1996;56(4):439–46.

19. Herráez M, Pichler N, Botsis J. Improving Delamination Resistance Through Tailored Defects. Compos Struct. 2020 May;112422.

  doi:10.5075/epfl-298799_978-2-9701614-0-0

ANALYSIS OF THE MECHANICAL AND FRACTURE BEHAVIOR OF RECYCLED CARBON STAPLE FIBER YARN UNDER STATIC LOAD

Christian Becker [a], Nicole Motsch-Eichmann [a], Joachim Hausmann [a]*

a: *Leibniz-Institut für Verbundwerkstoffe GmbH, Kaiserslautern, Germany,*
**corresponding author: christian.becker@ivw.uni-kl.de*

Abstract: *In this work, the mechanical behavior of unidirectional (UD) reinforced plates out of recycled carbon fiber (rCF)-rovings is investigated. The mechanical properties are determined by tensile tests in fiber direction. This will proof the usability of this material for load carrying structures. Afterwards the fracture surface is analyzed by scanning electron microscopy (SEM) to characterize the fiber matrix adhesion and get first indications of possible failure mechanisms. Smaller samples will be tested under predefined load levels (parallel and perpendicular to the fiber direction) and the failure behavior is investigated in-situ using X-Ray microscopy. With this, the failure behavior of the staple fibers is visualized in order to detect fiber pull out, fiber- or inter-fiber failure and to draw first conclusions about the damage behavior in comparison to classic fiber composites.*

Keywords: CFRP recycling, rCF-Roving, in situ X-Ray Microscopy, Failure mechanism

1. Introduction

The use of fiber-reinforced components for lightweight constructions is rapidly increasing over the past decade. The rising amount of waste per year leads to an increasing requirement to develop new techniques of recycling and reuse of carbon fiber. [1] To fulfill environmental and economic goals, upcycling of end-of-life products and production waste into structural components must be achieved. Several techniques have been developed to extract the fibers out of the matrix. The fiber length is reduced differently trough these processes and new pre-products have to be made out of this shorten fibers (non-woven, woven or staple fiber yarn (rovings)). [2][3] The separation of fibers can be done chemically (solvolysis) or thermally (pyrolysis) [4]. The pyrolysis is actually the most commonly used process. All processes lead to a loss of fiber length because of cutting the components to smaller parts, which can be handled during the treatment [5].

Recycling of carbon fiber reinforced plastics (CFRP) is challenging both in isolating the fibers from the matrix and reusing the receiving fibers in a technical or constructive application with load bearing requirements. Continuous fiber reinforcement afterwards, as in components out of new fibers, is not possible anymore because of the shortened fibers. The shortened rCF fibers have to be converted to other kinds of semi-finished products like woven or non-woven fabrics. Another way is to ply them into a continuous staple fiber yarn [6]. One product, which is commercially available, is a rCF-roving from the Wagenfelder Spinnerei GmbH (Germany) [7]. This product (seen in Fig 1. a) stands out due to the fixation trough a binding yarn and variation of fiber amount by adding PA 6 fibers into the stable yarn (from 30/70 % (rCF/PA6) up to 90/10 %). In this work a 90/10 rCF-roving is used with a single fiber length of 60 – 80 mm. Because of the fixation of the staple fibers through a binding yarn, undulations are applied to the dry rCF-

  doi:10.5075/epfl-298799_978-2-9701614-0-0

roving structure and have to be compensated during processing. Through this, a pre-stressing of the fibers is generated to get an optimal uni-directional (UD) orientation and equalized undulations in the roving structure. The aim is also to achieve a high fiber volume content (>50 %). The plates are manufactured with a bio-based resin (Envirez 70301, Ashland Performance Materials; 40 % bio amount [8]) in an adapted plate winding process. The fibers were wound dry on a metal plate, impregnated afterwards with tempered resin and cured in the autoclave. For the samples a fiber volume content of ≈ 50 % in the plate is reached. A micro section of the final plate is seen in Fig. 1 (b). It can be seen, that the individual structure of every single roving remains and the matrix fills both the gaps between the rovings and the gaps in the roving structure.

An important point for designing components is the knowledge about the mechanical and also damage behavior. The characterization of the mechanical properties trough standardized tests (tensile, compression, etc.) is well established [6]. More complex tests have to be performed if the damage behavior has to be analyzed. In situ X-ray experiments are in this case an excellent method of performing mechanical tests and detecting the structural changes in the meantime. Especially for rCF fibers it can be an important gain of information, e.g. of the exact fiber orientation, the crack initiation and propagation, the pull-out and post-failure behavior. [9, 10]

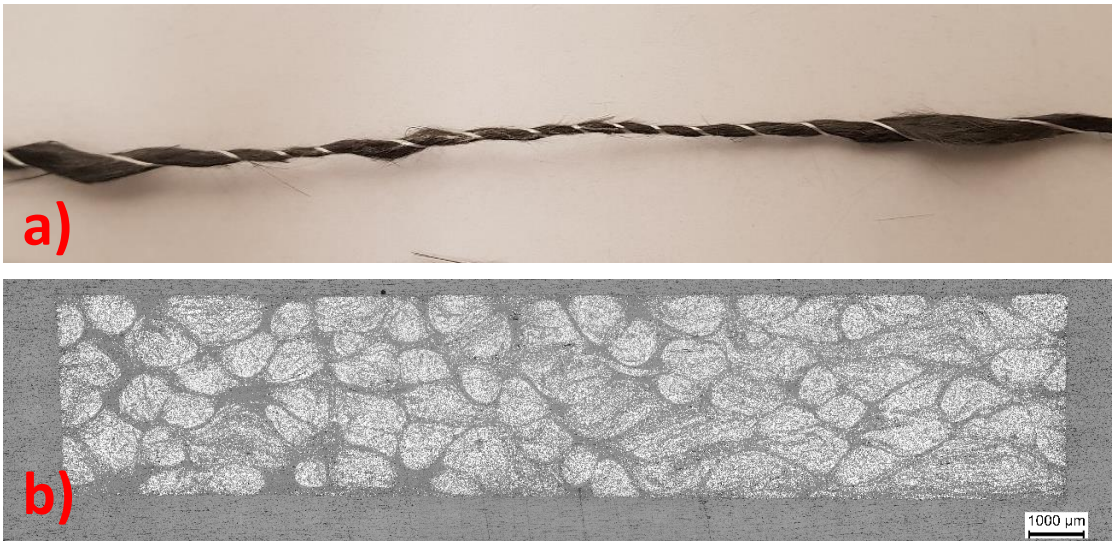

Figure 1. (a) rCF Roving with binding yarn; (b) micro section of impregnated plate

2. Mechanical tests and material characterization

The mechanical tests were performed at a Universal Testing Machine (Zwick 1485, 250 kN). The resulting stress-strain diagram of one test series is shown in Fig. 2 (a). Out of this a Young's Modulus of 85 GPa, a strength of 855 MPa and fracture strain of 1.06 % is calculated. Because of the inhomogeneity of the material itself, some specimen reached a Young's Modulus of over 100 GPa.

A sudden breaking event in the roving structure occurs during the test followed by a constant fiber pullout without any additionl load apply (not visible in the diagram). The failure mechanism seems to be Inter-Fiber-Failure of the matrix followed by fiber pullout (Fig.2 (b)). A fiber failure

  doi:10.5075/epfl-298799_978-2-9701614-0-0

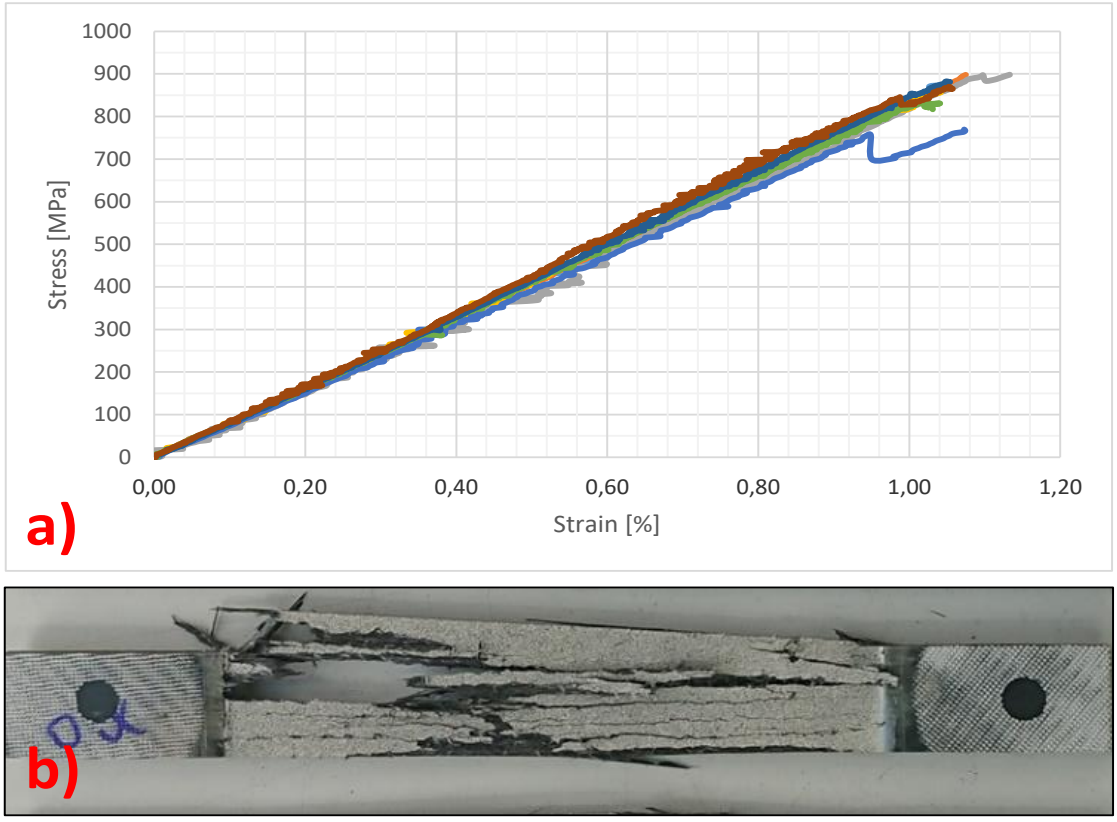

Figure 2 (a) Stress-Strain diagram of rCF-plate with 50 % fibre volume content.
(b) rCF-sample after tensile test; inter-fiber failure visible

could not be identified. A SEM analysis of the fracture surface (Fig. 3) proves this thesis. It can be observed, that single fibers are intact but pulled out of the matrix (fiber canal can clearly be seen) and the crack propagation expands trough the matrix.

Also a low fiber-matrix adhesion can be detected because of missing matrix residuals on the exposed fibers. It could be assumed, that a missing sizing of the pyrolyzed fibers leads to a low adhesion. Nevertheless, the properties of the compound are near to applications with new fibers. But this effects promotes the effect of fiber pullout after the failure of the sample.

The unidirectional orientation of shortened but stapled fibers leads to a high strength in load direction but also causes a failure of the matrix system because the single fibers have the ability to slip against each other before breaking. In comparison to normal unidirectional reinforced compounds a fiber failure in load direction has not be seen.

The SEM analysis, micro sections and a computer tomography (CT) overview scan also show that nearly unidirectional orientation of the fibers is present but because of the inhomogeneity of the roving several single fibers vary from this orientation. In the mechanical tensile test it can be observed, that this “misaligned” fibers prohibit a burst of the specimen although a failure event took place. The results of the mechanical tests lead to the question, what exactly happens inside of the specimen and in which way does the microstructure behave during a tensile loading.

  doi:10.5075/epfl-298799_978-2-9701614-0-0

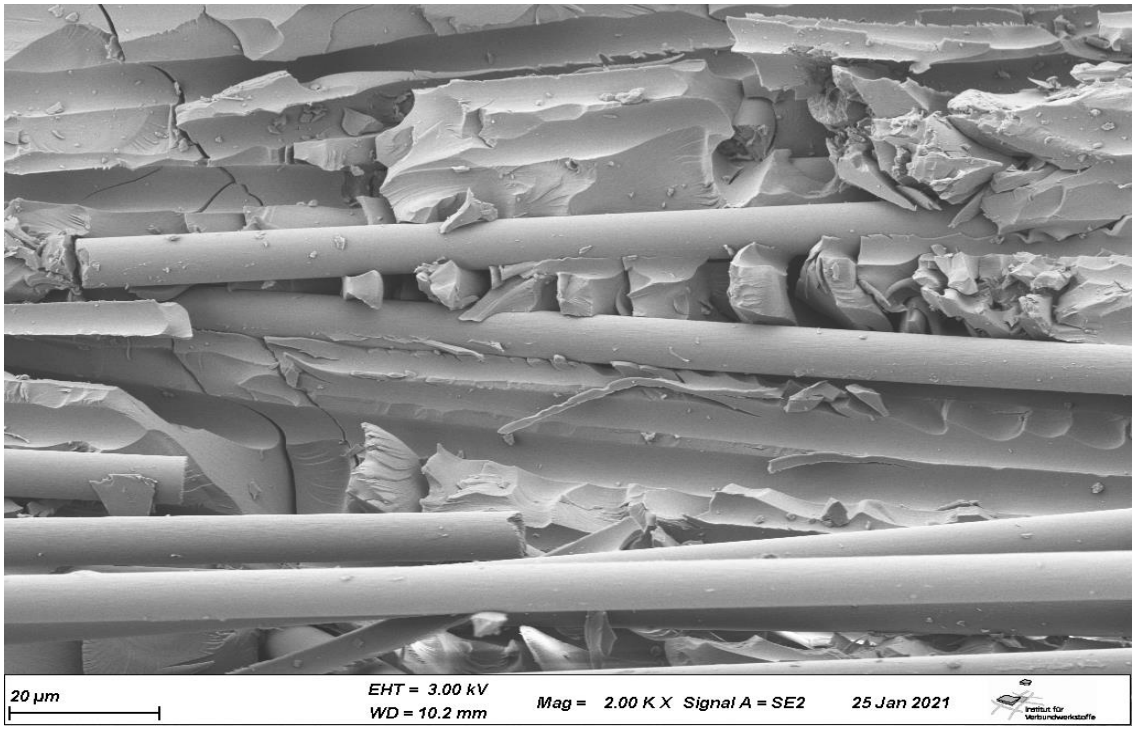

Figure 3. SEM image (magnification 2000 X) of the fracture surface of an rCF-sample with fibre pull-out, crack through the matrix and low fibre-matrix adhesion

3. In situ X-ray Microscopy

The test setup for the in situ experiment is shown in Fig. 4. At first the tensile properties of small in situ samples were measured ex situ with the in situ test machine to determine the load stages for the actual measurements. During this test it could be seen, that the sample geometry for the UD samples in fiber direction leads to several problems. First the diameter of the samples was too high to reach a consistent failure over all samples. Second the fixture of the sample with extra bolts in the clamping area leads to a failure of the sample at these holes. Third, when fixing

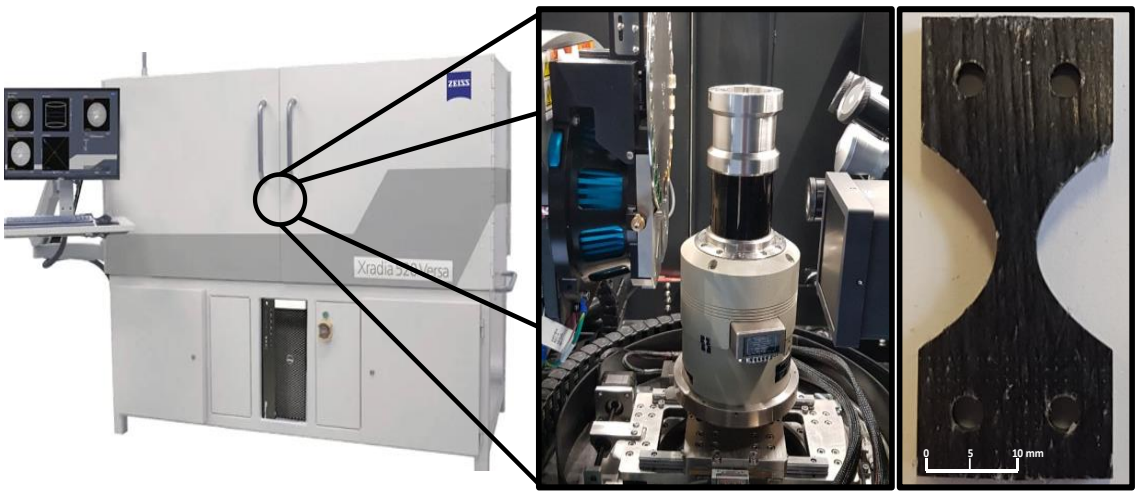

Figure 4. X-Ray Microscope Zeiss Xradia 520 Versa with In situ Module Deben CT 5000 and used sample geometry

the samples only by clamping, the reached surface pressure was not high enough to fix the sample; slipping of the sample out of the clamps at higher loads occured. Because of several non-successful tests with different sample geometries the in situ experiments in fiber direction couldn't be accomplished. However, the pre-tests with the samples normal to the fiber orientation were successful. The results are shown in Fig. 5 (a).

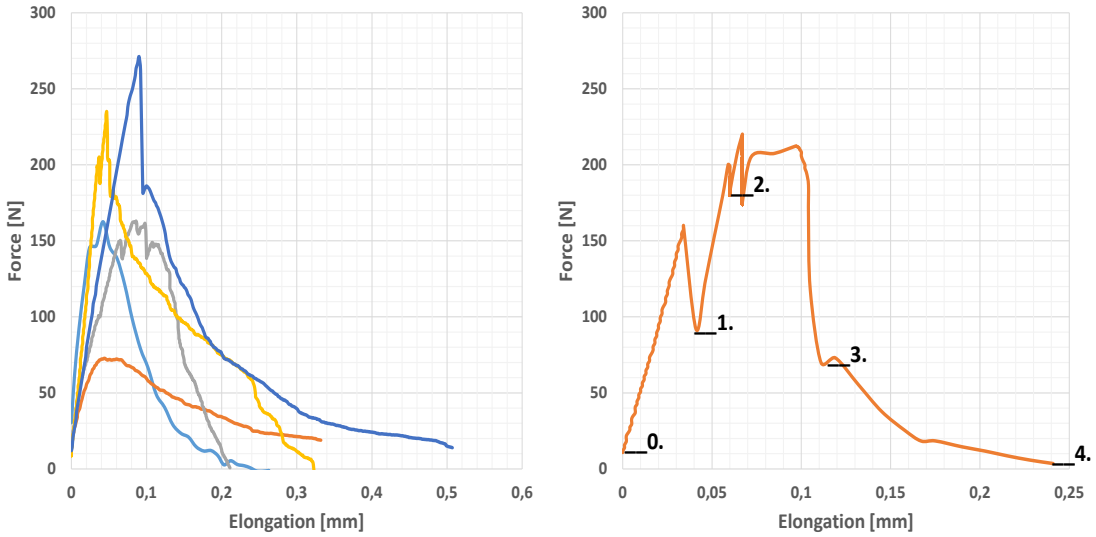

Figure 5. (a) Force-Elongation diagram from the pre-tests of the rCF-in situ samples normal to the fiber orientation. (b) Measurement diagram during in situ experiment with load levels; relaxation of sample visible

Out of these tests 5 load levels were selected and the relaxation span and time at this stages were defined, to get a stable force and elongation at the defined levels. This is necessary to prevent not wanted movement in the sample during the CT-scan to avoid artifacts in reconstruction. Challenging is the variation of the test results in the maximum ultimate load range because of the inhomogeneity of the material. It is possible, that the failure occurs in a load step, where no failure is expected and the crack propagation is not detected clearly.

An important result of the pre-tests is, that after failure the samples are not separated into two parts. It can be seen, that the parts are connected through "misaligned" fibers and a fiber pullout post-failure occurs. The following levels were set due to the pre-tests (cf. Fig. 5 (b)):

0. 20 N (pre stressing); no relaxation detected
1. 100 N; relaxation from 150 N
2. 170 N; relaxation from 200 N
3. > 200 N; break event; no relaxation
4. Crack opening of 0.1 mm after failure

Each CT scan took around 9 hours with 2400 images with an image size of 3.3 x 3.3 mm and a resulting voxel size of 1.5 µm. With a fiber diameter of 7 µm it is possible to get around 5 voxels per fiber, which is enough to reconstruct the fibers sharply. In Fig. 6 the resulting images of the CT scans are presented (volume rendering of the CT images; every image displays the same plane of the volume). For better visibility in the first two levels, the crack is marked in red on the image.

  doi:10.5075/epfl-298799_978-2-9701614-0-0

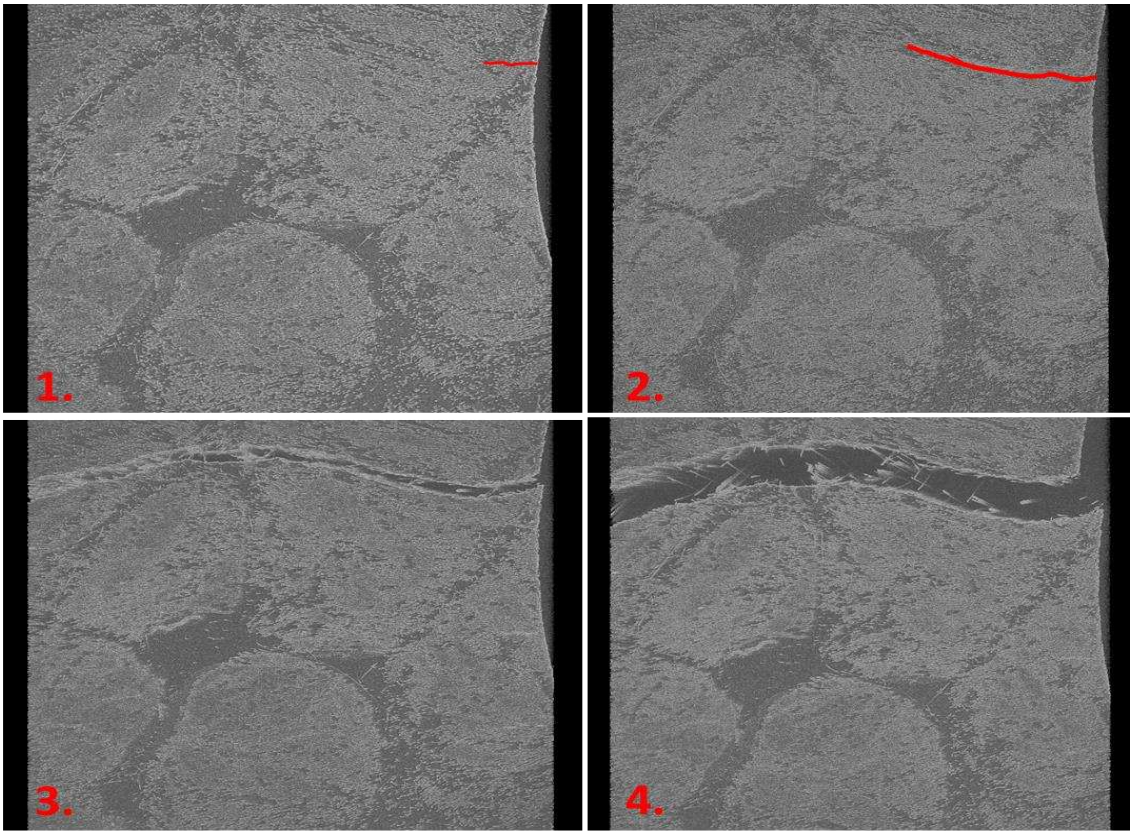

Figure 6. Volume rendering images of the different load levels (unloaded level not shown): 1) 100 N; small crack (red line) at the edge. 2) 170 N: crack propagation (red line) between the fibres. 3) 220 N: failure of the sample. 4) Crack opening of 0.2 mm; some bridging fibres visible

In the first load step (100 N) a small crack (30 µm) appears at the edge of the specimen. This crack spread through the matrix with higher load (crack length of 124 µm at 170 N). It can be seen, that the crack propagates between the roving structure. Also bigger parts of resin were not affected by crack initiation or propagation. At the third load level (220 N) a nearly horizontal crack through the whole specimen at the smallest diameter of the sample geometry can be observed. A reason for crack propagation from load level one to three is, that the crack propagation is independent of the material structure (parts of higher/ lower fiber content) and a defined failure event at the middle of the sample is introduced by the tailored shape of the specimen. The sample geometry is therefore suitable to receive a defined failure event at the center plane and can be reliably detected in the region of interest in the X-ray microscope.

At the fourth load level the crack opening of 0.1 mm is performed to reconstruct the fiber pullout while post-failure. Here it can be seen clearly, that isolated fibers cross the crack and connect the two separated parts. A fiber pullout because of free fiber tails in the crack zone cannot clearly be detected because of the small elongation of the sample (overlapping length of the fibers up to 50 mm). This will always lead to a compromise: by increasing the field of view to detect larger pullout length the resolution will downgrade and single fibers cannot be detected. Only an estimation can be made with the in situ tests and have to be proved in standard tensile tests.

  doi:10.5075/epfl-298799_978-2-9701614-0-0

4. Conclusions

The tensile properties in fiber direction of components out of rCF-Rovings are close to components out of new fibers. With a Young's modulus of > 100 GPa it is possible to design load carrying structures and to "upcycle" the recycled carbon fibers. The strength of 850 MPa and a fracture strain of 1 % is also comparable to composites with standard carbon fibers. Tensile tests transverse to the fiber, pressure and bending tests are planned for future analysis to substantiate the mechanical properties.

Major differences can be observed in the failure behavior of the rCF material compared to new material. With tensile loading in fiber direction fiber failure is expected. In this test series (standard and in situ tests) an inter-fiber failure with a parallel proceeding fiber-slipping and –pullout of the rCF-staple fibers occurs. In synergy with the friction between the fibers still a high bearable load (despite low fiber-matrix adhesion) can be applied to the material before the sample fails. A similar behavior can be seen in transverse loading. An inter-fiber failure occurs but because of "misaligned" fibers a separation of the broken parts is not induced. These fibers bridge the crack and a fiber pullout during post-failure takes place. At transverse loading in general an inter-fiber failure is expected and detected here, too. But there is a large elongation span at low load in the post-failure without sample separation in which the fiber pullout takes place before total failure. This could be interesting for apllications, which need a higher structural integrity. This first conclusion onthe failure behavior has to be be proved for other matrix systems and for larger samples/parts.

Questionable is, whether the low fiber-matrix adhesions is responsible for the fiber-pullout behavior. It is possible, that a higher adhesion probably leads to fiber failure as well in fiber direction as in transversal direction (in misaligned fibers parallel to the load direction). Another matrix system has to be used to confirm or refute the results. A sizing of the fibers could also improve the fiber-matrix adhesion and should therefore be investigated. Both adjustments could affect the mechanical properties and can lead to better performance of the material.

The detection of the failure in in situ X-ray experiments has to be adjusted. Maybe there have to be more load steps, especially in the post-failure region to clearly show the crack propagation, fiber slipping and pullout. To detect possible fiber failure the resolution has to be raised (< 1µm). This includes a reduction of the sample size. Problematically with this point could be, that the validity in comparison to larger structures could not be given. This has to be proved through separate mechanical tests. Generally the development of a defined in situ sample geometry especially for test in fiber direction is another necessary next research step. A defined load introduction and the prevention of slipping or damaging the sample in the clamping area are crucial for convincing in situ measurement results.

In conclusion for the performed experiments in this work it can be said, that the fracture behavior of rCf staple fiber yarn cannot be put into classical failure mechanisms. A superposition of inter fiber failure and fiber pullout without any visible fiber failure occurs. Because of the stapled fibers the material can also be declared as long fiber reinforced but the fiber concentration is packed in many defined areas (Rovings) which leads to a nearly endless fiber, unidirectional structure. The material properties prove the comparability to endless fiber reinforced compounds but classical failure theory cannot be adapted one-on-one onto this behavior. For exact interpretation of the failure mechanism more tests have to be performed

  doi:10.5075/epfl-298799_978-2-9701614-0-0

and the above-mentioned difficulties in sample geometry, sizing and material properties have to be solved.

5. References

1. Goergen C. Quasi-plastic deformation behavior of organic sheets made of recycled carbon staple fibers. TU Kaiserslautern. PhD thesis. 2020.
2. Schürmann H. Designing with Fiber Polymer Compounds. Berlin Heidelberg. Springer Verlag. ISBN 978-3-540-72189-5. 2007.
3. Pimenta S, Pinho S. Recycling carbon fiber reinforced Polymers for structural applications: Technology review and market outlook. Waste management 3. Pp 378-392. 2011.
4. Goergen C, Baz S, Reichert O, Mitschang P, Gresser G. Organic sheets with deep-drawing ability made of recycled carbon fibers. Journal of Plastics Technology 15. 2019.
5. Meiners D, Eversmann B, Recycling von Carbonfasern. Recycling und Rohstoffe –Band 7. TK Verlag Karl Thome-Kozmiensky. ISBN 978-3-944310-09-1. 2014.
6. Hengstermann M, Raithel N, Abdkader A, Hasan MMB, Cherif Ch. Development of new hybrid yarn construction from recycled carbon fibers for high performance composites. Part I-4. Textile Research Journal. Vol 86. 2016.
7. https://www.wagenfelder-spinnereien.de/produkte.html
8. https://www.ulprospector.com/plastics/de/datasheet/280099/envirez-70301
9. Garcea SC, Wang Y, Withers PJ. X-ray computed tomography of polymer composites. Composites Science and Technology 156. Pp 305-319. 2018.
10. Garcea SC, Sinclair I, Spearing SM. Withers PJ. Mapping fibre failure in situ in carbon fibre reinforeced polymers by fast synchrotron X-ray computed tomography. Composites and Technology 149. Pp 81-89. 2017.

  doi:10.5075/epfl-298799_978-2-9701614-0-0

AN ANALYSIS OF MODIFIED CT SPECIMENS FOR THE DETERMINATION OF THE LONGITUDINAL INTRALAMINAR FRACTURE TOUGHNESS IN COMPOSITE LAMINATES USING SHPB CONFIGURATION

*A. Cimadevilla[a], A. Vaz-Romero[a], J. Pernas-Sánchez[a], **J. A. Artero-Guerrero**[a],P. Maimí[b], E. V. González[b], E. De Blanpre[c], V. Jacques[c]*

a: Department of Continuum Mechanics and Structural Analysis, Universidad Carlos III de Madrid, Leganés, Madrid, Spain – jartero@ing.uc3m.es

b: AMADE - Escola Politècnica Superior, Universitat de Girona, Girona

c: Dassault Aviation, Paris, France

Abstract: *Composite materials subjected to dynamic conditions exhibit significant strain rate sensitivity. Several experimental methodologies has been proposed to analyse its influence. In this work, it has been studied the original configuration of a CT specimen in a SHPB. A numerical model has been generated in the commercial FEM code ABAQUS/Explicit. The results shows that the asymmetrical opening of the specimen induces inertial forces that produces a non-unidimensional stress wave propagation in the bars. New design of the specimen has been proposed to reduce the asymmetrical effects of the original CT configuration in the SHPB. The new geometry guarantees a correct property characterization under dynamic loadings since avoids the emergence of inertial effects on the data reduction analysis. This study has been developed within the framework of the European Clean-Sky project BEDYN (reference number 886519).*

Keywords: Dynamic Characterization; SHPB; CT specimen; FEM; Intralaminar behavior

1. Introduction

The material characterization of composite materials under dynamic loading has been researched over the last two decades. Composite materials subjected to dynamic conditions exhibit significant strain rate sensitivity. Several experimental methodologies has been proposed to analyse its influence. Taking into account the strain rates ranges representative for an impact (50-1000s-1), Split Hopkinson Pressure Bars (SHPB) is the preferred experimental method to evaluate the dynamic behavior [1]. Most of the scientific work has been focused on the determination of the variance of the mechanical properties of the composite material in this range of strain rate loadings, including properties of individual constituents, failure mechanisms and fracture toughness for both intralaminar and interlaminar behaviour. There are only few works concerning fracture toughness analysis. The work of McCarroll (2011) [2] was one of the fisrt analyising this aspect. In this publication, the data reduction is performed without the force history input due to the strong oscillations of the signal. The applied force is obtained by measuring the compressive strain in the vicinity of the specimen's back. The strain is related to the force by means of a stiffness parameter obtained by a numerical model using cohesive elements. The strain and the crack growth are measured experimentally and the FE model is based on the quasi static properties. The same FE model is used to determine the compliance. Both, the compliance and the stiffness parameter are assumed rate independent, however these parameters depend on the elastic properties, which are rate dependant. Therefore, the

  doi:10.5075/epfl-298799_978-2-9701614-0-0

data reduction method can be potentially improved by including this dependence in the material model. Few years after the work of Hoffmann et al. [3] appeared, where the typical Compact Tension (CT) specimen has been used for characterizing the intralaminar longitudinal fracture toughness of IM7/8552 under tensile loading conditions. After the study, it is reported more than a 50% reduction of the property analysed. Also, the double edge notched tensile (DENT) specimen is commonly used in the SHPB [4]. Conclusions are divergent between both techniques, even for the same material [3,4]. This clearly indicates that the optimal technique to characterize this property under high-rate loading is still a question unresolved.

In this work, it has been studied the original configuration of a CT specimen in a SHPB based on the work of Hoffmann et al. [3]. A numerical model has been generated in the commercial FEM code ABAQUS/Explicit. The numerical model has been validated with the results of the referenced paper. The asymmetrical opening of the specimen induces inertial forces that produces a non-unidimensional stress wave propagation in the bars. New design of the specimen has been proposed to reduce the asymmetrical effects of the original CT configuration in the SHPB. The new geometry guarantees a correct property characterization under dynamic loadings since avoids the emergence of inertial effects on the data reduction analysis.

2. Numerical methodology

The simulation is based in the work of Hoffman et al. [3] where the original CT specimen has been used in a tensile SHPB to analyse the dynamic crack propagation of the tensile failure mode. The numerical simulation has been carried out by means of Abaqus/Explicit software. The main aim of the simulation is to analyse the behaviour of both specimen and bar during the dynamic fracture process. In the following subsections are included the detail of the exact geometry of the specimen and the SHPB device.

2.1 Geometry and test setup

The geometry of the specimen considered the regular CT specimen (a_0=26mm and w=51mm). In order to analyse the SHPB tests the geometry of the device from the Uc3m laboratory, where the experimental tests will be performed are used. A sketch of the test setup is included in *Figure 1*, showing also the detail of the numerical model of the projectile-pulse shaper impact position and the CT specimen –bar connection. The model consists of 6 different parts: The projectile, the input bar, the output bar, a pulse shaper, two bolts and the specimen.

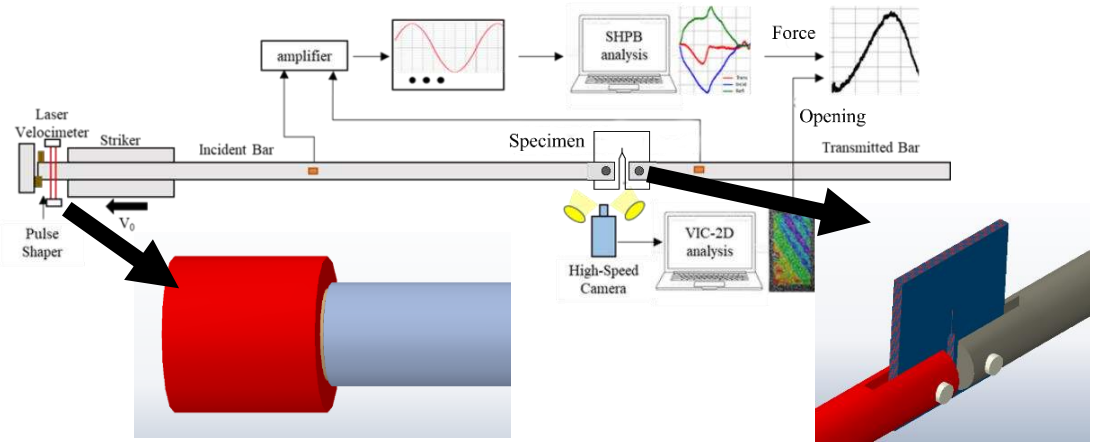

Figure 1 Test setup for dynamic CT test

2.2 Material models

Projectile, input bar, output bar and bolts are considered as linearly elastic steel material, while for the pulse shaper a Johnson-Cook material model is considered. The following properties are used: ρ = 8960 kg/m^3, E = 124 GPa, ν = 0.3, A = 90MPa, B = 292MPa, n = 0.31, m = 1.09, Tm = 385, and c = 0.025.

For the composite material used in this simulation the unidirectional IM7/8552 Carbon-Epoxi composite (lay-up sequence: [(90,0)8,90]symm) is selected. Table 1 shows the elastic properties used:

Table 1: Composite elastic properties.

Property	Value	Property	Value
E_1[GPa]	162	ν_{12}=0.26	0.36
E_2[GPa]	9.72	G12=G23=G13[GPa]	4.68

A Hashin damage criterion has been used. Following properties have been considered for the definition of damage initiation (Table 2):

Table 2: Composite strength properties

Property	Value	Property	Value
X_T [MPa]	1800	Y_C [MPa]	250
X_C [MPa]	1350	S_L [MPa]]	95.7
Y_T [MPa]	75.2	S_T [MPa]	125.7

For the Hashin damage evolution model, the Table 3 contains the required fields:

Table 3: Composite fracture properties

Property	Value	Property	Value
G_{1+} [kJ/m^2]	82	G_{2+} [kJ/m^2]]	0.3
G_{1-} [kJ/m^2]	37.13	G_{2-} [kJ/m^2]	0.87

A VUFIELD type of subroutine has been used to achieve a proper element deletion. This subroutine allows the removal of those elements that had reached a certain principal deformation value. This value has been considered regarding Hashin damage evolution theory. The value when the element is totally damaged and must be deleted has been calculated by using the values shown above.

Test sample has been defined using SC8 elements (quadrilateral continuum shell). All layers are bonded by means of a cohesive interaction definition in order to reproduce possible

  doi:10.5075/epfl-298799_978-2-9701614-0-0

delaminations. Damage in the interaction has been defined using a quadratic stress criterion. Once the damage stars, the evolution of it is based on the amount of energy dissipated during the damaging process. The dependence between the energy fracture in mixed mode is defined by the Benzeggagh-Kenane fracture criterion.

2.3 Data reduction

The investigation of the notch effect on the composite structure under dynamic loading will be conducted via Compact Tension (CT) tests in a SHPB system, following the methodology of Hoffman et al. [3]. The intra-laminar fracture toughness will be also obtained through this test. The data reduction is based on the area method, since not require the composite elastic properties (which are rate dependant) for calibration. Obtaining GIc using the area method is based on relating the dissipated mechanical energy ΔU to the newly generated free surface area due to crack tip advancement Δa. The force history used for the data reduction process was the arithmetic average of the bar forces Fin and Fout determined based on the classical SHB analysis (equation 1)

$$G_{IC} = \frac{1}{2t_{lam}N\Delta a}\sum_{i=1}^{N}(F_{1i}X_{i2} - F_{2i}X_{1i}) \quad (1)$$

The displacement is recorded with DIC since the conventional SHBPA not accounts for the additional compliance of the loading train under high rate loadings. The intra-laminar fracture toughness is determined based on the work of Pinho et al. [5], considering no interaction between 0-90 plies and neglecting other dissipation mechanisms. The fracture toughness needs to be related with some strain rate in order to use this value as an input parameter in a continuum damage mechanics-based (CDM) modelling approach, i.e. to feed the material model of a FE analysis. The strain rate is measured across a reference length perpendicular to the advancing crack tip.

3. Numerical methodology

3.1 Analysis of the original CT geometry

The comparison between the experimental results obtained by Hoffmann and the results obtained by the simulation can be seen in *Figure 2*. It can be pointed that the behaviour of both curves is similar on the early stages. The initial crack fracture point occurs when the sample has reached 1.2 mm of opening displacement and being 5.5kN the maximum load withstood. It could be stated that the prediction of the experimental results can be accurately predicted since the behaviour of the curves have a remarkable match. Moreover the strain- strain-energy release rate calculated is very similar one to the other (Numerical results = 89kJ/m^2 vs experimental results = 82 kJ/m^2).

  doi:10.5075/epfl-298799_978-2-9701614-0-0

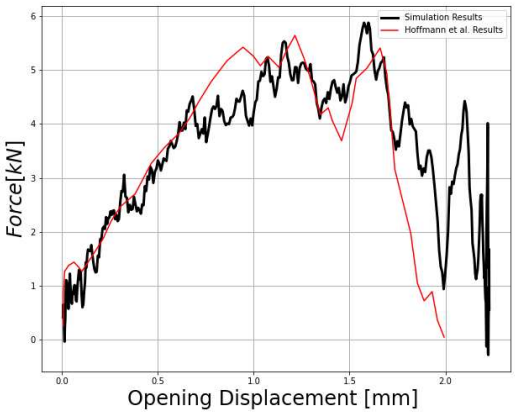

Figure 2 Representative force vs. opening displacement curves

It is worth to mention that the usage of a pulse shaper clearly improves the load curves extracted (*Figure 3*). Pulse shaper is a ring-shaped part of a ductile material placed in the touchpoint in-between the projectile and the incident bar. Due to the deformation experimented by the pulse shaper during the impact process, the incident signal shows smoother, enhancing mechanical equilibrium of the sample and obtaining more accurate results.

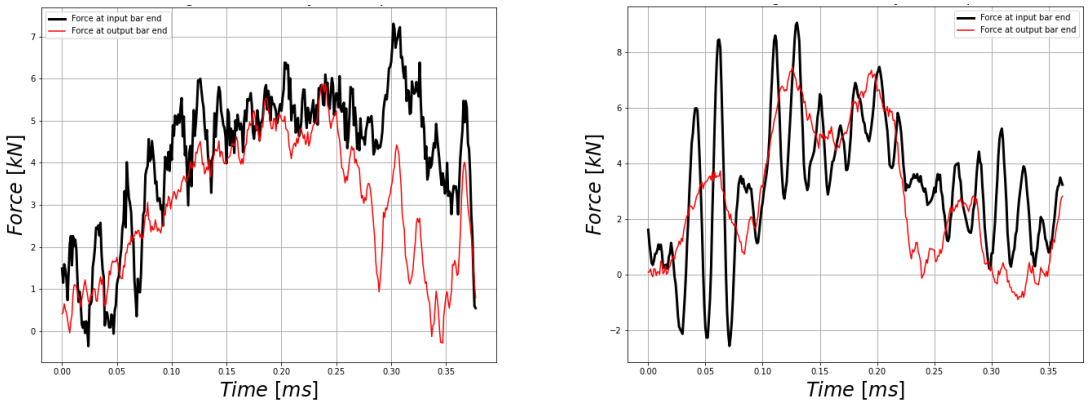

Figure 3 Left: Dynamic equilibrium with Pulse Shaper. Right: Dynamic equilibrium without Pulse shaper

In the analysis of the behaviour of the specimen and the Hopkinson bar, it has been observed that due to the CT specimen geometry and its lack of symmetry in the direction of the load application, a bending process is appearing on the bars during the experiment. This leads to a necessary correction and compensation of the taken measure. This compensation is done by placing different strain gauges all along the diameter of the bar. Afterwards, an average of all gauges is calculated. If the compensation adjustment wasn't done the obtained results would be over-dimensioned, considering SHPB theory, as shown in Figure 4.

  doi:10.5075/epfl-298799_978-2-9701614-0-0

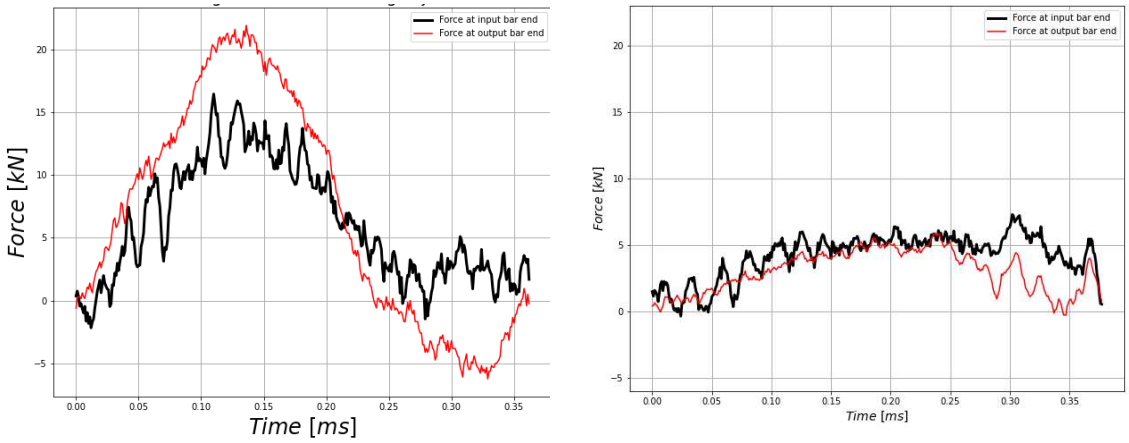

Figure 4 Left: Dynamic equilibrium with 1 gauge data. Right: Dynamic equilibrium with 4 strain gauge data

In order to carry out a more exhaustive study of the inertia effect, different impact projectile velocities has been simulated. It has been analysed the horizontal forces experienced in the bars (produced by the opening of the specimen) and the vertical forces (induced by the bending phenomena). *Figure 5* left shows the horizontal forces for different test speeds. The behaviour of the specimen is very similar for all tests. The maximum load point occurs for the same opening, and the fracture initiates at the same point. This indicates that inertia does not affect these results. *Figure 5* right shows the vertical forces generated by the specimen during the dynamic test. The influence of the impact velocity on the behaviour of the specimens can be seen. The higher the velocity, the more these forces increase, which generate more bending in the bars. For this reason, a redesign of the specimen is carried out in order to reduce these vertical forces.

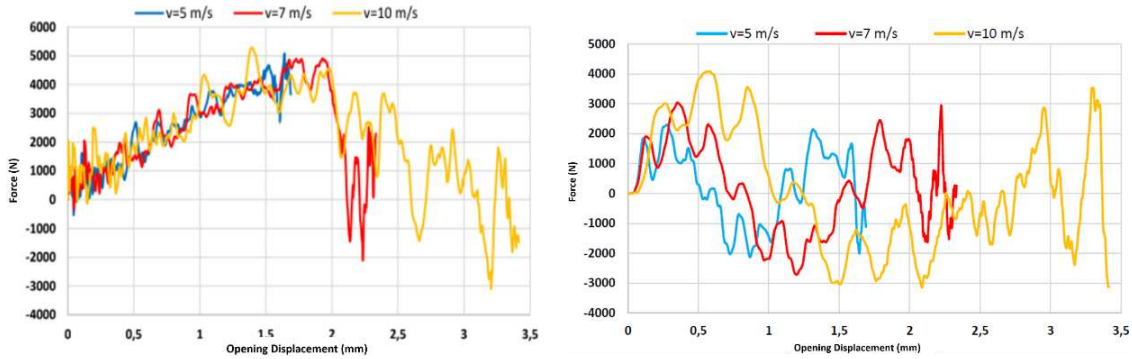

Figure 5 Left: Horizontal forces. Right: Vertical forces

3.1 Analysis of the modified CT geometry

In a first approach to the problem, an attempt was made to align the center of mass (COM) of the specimen with the axis of application of the loads. This idea was discarded after observing how the specimen deforms at the initial instant. The end of the specimen does not move solidly with the point of application of the load, generating oscillations in the horizontal force that is generated. An inertia effect is also observed in these forces, something that did not occur in the original specimen (*Figure 6*).

  doi:10.5075/epfl-298799_978-2-9701614-0-0

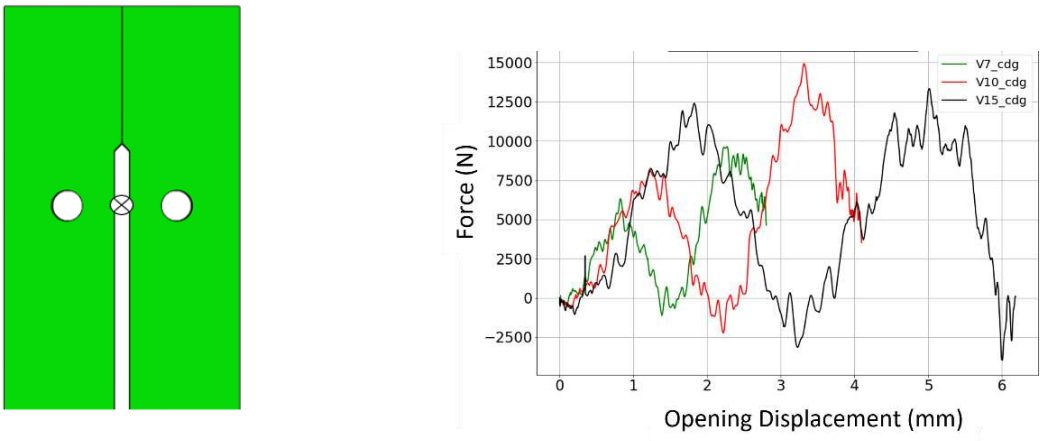

Figure 6 Left: Modified CT specimen (Aligned COM). Right: Horizontal forces on the test

Therefore It was decided to study the influence of the initial crack size (a_0). For this purpose, a simulation was carried out with a zero initial crack (*Figure 7*). In this specimen, it can be seen that there is no inertia effect on the horizontal forces. The behaviour is practically the same for different crack velocities. It can also be seen that the vertical forces have been reduced by half compared to the values obtained in the original specimen. However, a considerable increase in the maximum value of the horizontal force is observed. Due to this increase, an analysis of the possible occurrence of bearing during the test should be carried out. In the case of the original specimen, no type of defect was observed in the load application zone. On the other hand, for the modified cases, a clear structural failure is observed, making it impossible to carry out the complete test for these geometries

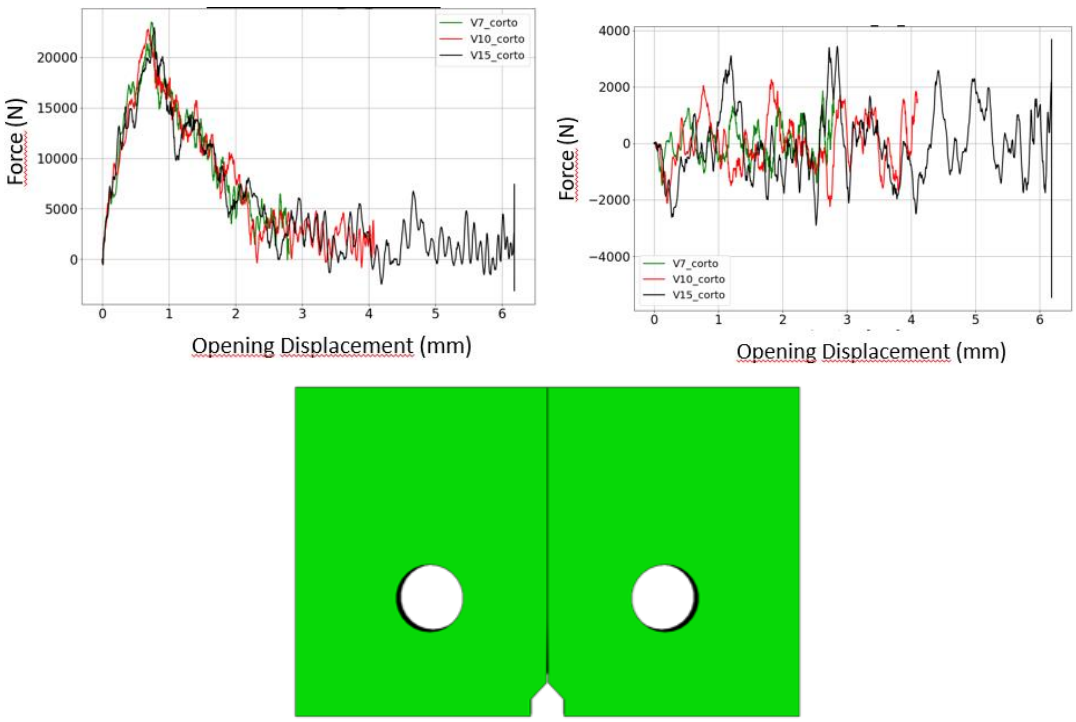

Figure 7 Upper Left: Horizontal forces on the test.Upper Right: Vertical forces on the test. Lower: Modified CT specimen (a_0=0mm)

4. Conclusions

In this work it has been analysed the behaviour of CT specimen under dynamics loadings. It has been seen that original geometry due to its non-symmetrical shape induces bending effect in the Hopkinson bars that present inertial effects. This inertial effect has been reduced with the used of modified CT specimen with lower initial crack length. However an increase of the horizontal forces are produced compared to the original CT that may induce bearing effects. Therefore it is recommended that for the design of dynamic fracture toughness test a preliminary study of the appropriate geometry with the specific material and stacking sequence is considered in order to find an optimum geometry where bending effect and therefore inertial forces are reduced while bearing phenomena is not induced.

Acknowledgements

This project has received funding from the Clean Sky 2 Joint Undertaking (JU) under grant agreement No. 886519. The JU receives support from the European Union's Horizon 2020 research and innovation programme and the Clean Sky 2 JU members other than the Union.

5. References

[1] Koerber H, Camanho P. P. High strain rate characterisation of unidirectional carbon–epoxy IM7-8552 in longitudinal compression. Composites Part A: Applied Science and Manufacturing 2011; 42 : 462–470

[2] McCarroll C.A. High Rate Fracture Toughness Measurement of Laminated Composites PhD thesis, 2011.

[3] Hoffmann J, Cui H, Petrinic N. Determination of the strain-energy release rate of a composite laminate under high-rate tensile deformation in fibre direction. Composites Science and Technology 2018; 164 :110–119.

[4] Kuhn P., Catalanotti G., Xavier J., Ploeckl M., Koerber H. Determination of the crack resistance curve for intralaminar fiber tensile failure mode in polymer composites under high rate loading. Composite Structures 2018 ; 204 : 276–287

[5] Pinho S T, Robinson P, Iannucci L. Fracture toughness of the tensile and compressive fibre failure modes in laminated composites. Composite Science and Technology 2006: 66 (13) 2069-2079.

  doi:10.5075/epfl-298799_978-2-9701614-0-0

MODELLING DELAMINATION RESISTANCE OF COMPOSITE LAMINATES REINFORCED WITH NOVEL Z-PINS THROUGH AN ENERGY-EQUIVALENT BRIDGING MAP FORMULATION

Luís F. Varandas[a], António R. Melro[b], Giuliano Allegri[c], and Stephen R. Hallet[d]

a: Bristol Composites Institute, University of Bristol, Queen's Building, University Walk, Bristol BS8 1TR, UK – luis.varandas@bristol.ac.uk
b: Bristol Composites Institute, University of Bristol, Queen's Building, University Walk, Bristol BS8 1TR, UK
c: Bristol Composites Institute, University of Bristol, Queen's Building, University Walk, Bristol BS8 1TR, UK
d: Bristol Composites Institute, University of Bristol, Queen's Building, University Walk, Bristol BS8 1TR, UK

Abstract: *The bridging action in through-thickness reinforced (TTR) composite laminates performed by standard and novel z-pins is modelled using an adaptation of a new multi-scale framework. Firstly, single z-pin experimental data is obtained at different mode-mixity loading cases, which is then used to calibrate a semi-analytical constitutive bridging model. This model is then able to generate a library of bridging maps for the different z-pin materials and/or geometries. At the structural-level, a user-defined cohesive constitutive model is used, following either a tri-linear or a trapezoidal cohesive law, to model initiation and propagation of interlaminar damage in the presence of low- and high-deformation z-pins, respectively. The computational efficiency of the presented methodology enables for a fast assessment of the performance of both brittle and ductile z-pins when used as reinforcement in laminated carbon fibre-reinforced polymer (CFRP) structural components.*

Keywords: Through-thickness reinforcement; Damage tolerance; Delamination; Finite Element Analysis (FEA); Constitutive modelling

1. Introduction

Interlaminar damage, also known as delamination, is recognised to be the precursor to ultimate failure in laminated carbon fibre-reinforced polymers (CFRPs) [1]. Z-pinning is a well-established technique for the insertion of small rods through the thickness into uncured prepreg laminates, as a delamination propagation restraining mechanism. Standard BMI-based CFRP z-pins are most commonly used as reinforcement [2], since a good bonding is ensured between the z-pin and the surrounding laminate, thus withstanding the complete pull-out process under opening displacements. However, the quasi-brittle nature of such z-pins leads to poor energy dissipation when delamination is propagating under shear-driven loads.

Other z-pin material types that are able to dissipate larger amounts of energy via plastic deformation, such as stainless steel, can also be considered as reinforcement [3]. Due to their increased ductility, a full pull-out of the z-pin occurs, even under high mode-mixity loadings, in contrast to CFRP z-pins.

  doi:10.5075/epfl-298799_978-2-9701614-0-0

In this work, the bridging action of next generation more ductile z-pins is evaluated using an adaptation of an already validated multi-scale modelling framework [4]. Figure 1 shows a representative diagram of the energy equivalent bridging map (EEBM) formulation. Single z-pin experiments were firstly conducted to obtain the individual z-pin energy dissipation for different mode-mixity ratios. Appropriate modifications to a previously proposed semi-analytical bridging model [5] were undertaken, in order to account for the high deformation of the z-pins. Finally, the z-pin dissipated energy and displacement at failure, as computed by the new semi-analytical bridging model, are used as input data for structural-level finite element models that are able to evaluate macroscopic interlaminar crack propagation using a user-defined enhanced cohesive constitutive model.

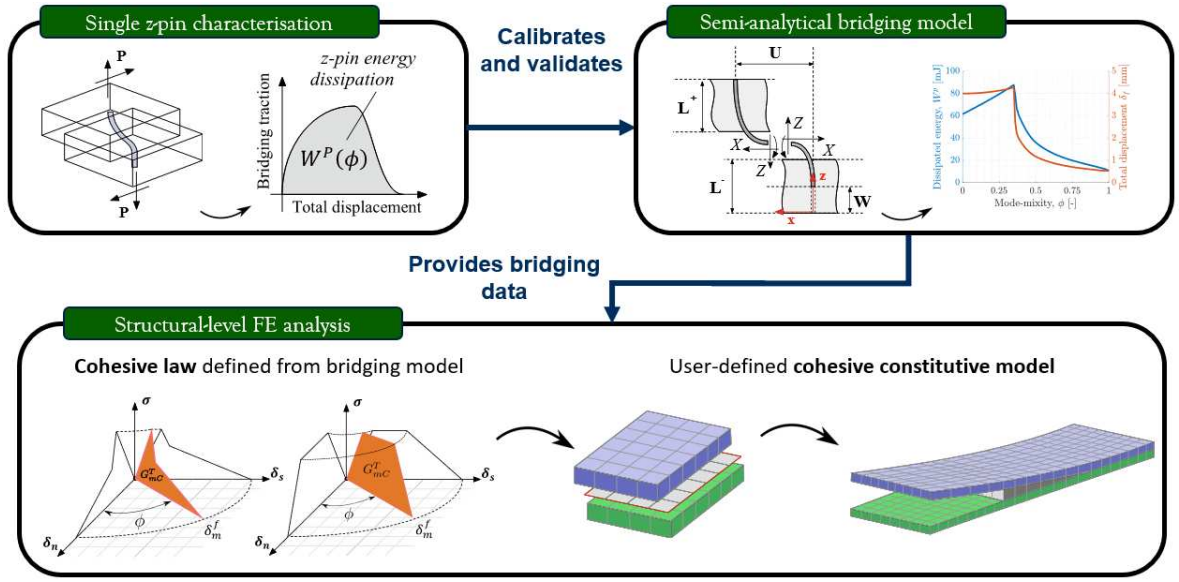

Figure 1. Multi-scale framework for modelling delamination in TTR composite laminates.

2. Single z-pin experimental testing

In-house experimental testing was carried out using a mixed-mode test fixture [6]. Three different z-pin materials were considered: BMI-based CFRP, a novel fibre-matrix combination, and stainless steel. Under small mode-mixities, all z-pins pulled-out completely of the embedded laminate. However both CFRP and novel z-pins showed a good adhesion with the laminate, whereas the stainless steel z-pins did not. Under high mode-mixities, CFRP z-pins sheared-out, showing a clear transition region from pull-out to failure when increasing mode-mixity [6], whereas both metallic and novel z-pins still exhibited full pull-out, leading to a high energy dissipation when compared to standard CFRP z-pins.

The results assessing the dissipated energy by each individual z-pin are shown in Section 3 along with numerical predictions.

3. Constitutive bridging model

The bridging model presented in [5] describes z-pins as Euler-Bernoulli beams embedded in an elastic foundation undergoing small but finite rotations. Z-pin fracture is taken into account by using a Weibull strength criterion, allowing for the transition from complete pull-out to final rupture, with increasing mode-mixity, ϕ. Furthermore, this algorithm requires the input of five

  doi:10.5075/epfl-298799_978-2-9701614-0-0

different parameters that are identified through model calibration using a Genetic Algorithm (GA).

The aforementioned formulation is suitable to model quasi-brittle z-pins that fracture under medium to high mode-mixity loadings. By contrast, high-deformation z-pin materials, such as stainless steel do not fail across the mode-mixity range. To take that into account, appropriate modifications were made to the original formulation of the semi-analytical bridging model. The beams are now modelled following a Timoshenko formulation, thus taking into account shear deformation and rotational bending effects, making it more suitable for describing the behaviour of thick beams, in which the shear modulus of the material is more pronounced. The calculation of the normal displacement, W, was also implemented for $\phi > \sqrt{2}/2$, using as input the mode-mixity and the sliding displacement, U:

$$W = \frac{\sqrt{1-\phi^2}}{\phi} U. \tag{1}$$

Yielding of the z-pin was here considered by reducing the Young's modulus as soon as the yield stress of the material is reached, leading to a decrease on the computed resultant forces along the z-pin, thus achieving a better calibration with the experimental data.

Figure 2 shows the generated bridging maps for the different z-pin materials calibrated with the single z-pin experimental data through the GA.

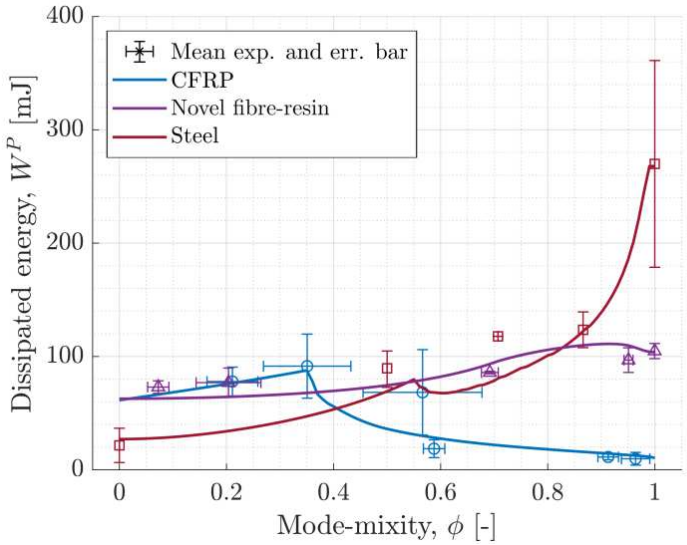

Figure 2. Calibrated bridging maps for the different z-pin materials: Blue – CFRP; purple – novel fibre-resin; red – stainless steel.

The experiments on the CFRP z-pins show a transition region from complete pull-out to z-pin rupture, a feature captured by the bridging model, in which, after the first z-pin breakage occurs, the associated dissipated energy decreases when increasing mode-mixity. By contrast, both the novel fibre-matrix and stainless steel materials have shown an overall increase of the dissipated energy when increasing mode-mixity, in which the latter yields at an approximate mode-mixity of 0.55, leading to a decrease in the computed dissipated energy. Out of these three different material types, the novel z-pins are the ones that demonstrated the most balanced performance

  doi:10.5075/epfl-298799_978-2-9701614-0-0

across the mode-mixity range, given the low adhesion between stainless steel z-pins and CFRP laminate for mode I dominated delaminations.

Overall, the bridging model is capable of generating bridging maps which are in excellent agreement with the experimental data.

4. Macro-scale analysis

The user-defined enhanced cohesive constitutive model used here to model the interlaminar region takes into account the energy dissipated by delamination growth along the interface, plus the energy contributed by the z-pin smeared over the delamination area, thus not requiring the modelling of each individual z-pin (as in [4]). This is achieved by using as input data the two outputs from the bridging model, i.e. the total displacement at failure/pull-out and dissipated energy by an individual z-pin over the mode-mixity range, to model the pinned region of the structure.

The models presented here for macro-level analysis are representative of interlaminar characterisation tests, such as double cantilever beam (DCB), mixed-mode bending (MMB), and end-loaded split (ELS), all aimed at assessing the performance of the presented z-pins under mode I, mixed mode I/mode II, and mode II loadings, respectively. These are composed of homogenised laminate-level QI IM7/8552 blocks and of a single interfacial layer in the mid-plane, having pinned and unpinned regions, where the latter is modelled with a standard cohesive zone model (CZM) [7]. Tables 1 and 2 show the material properties used to model the composite laminate and interlaminar region, respectively.

For more details on the user-defined cohesive element formulation, capturing the interfacial behaviour of both resin-rich unpinned interlaminar regions, as well as the large-scale bridging mechanism due to the presence of z-pins, the reader is referred to [4].

Table 1: Laminate properties [4].

Material property	Composite laminate
$E_{11} = E_{22}$ [GPa]	61.60
E_{33} [GPa]	13.61
G_{12} [GPa]	23.37
$G_{13} = G_{23}$ [GPa]	4.55
ν_{12} [-]	0.32
ν_{31} [-]	0.07
ν_{32} [-]	0.1

  doi:10.5075/epfl-298799_978-2-9701614-0-0

Table 2: Cohesive elements properties [4, 7].

Material property	Cohesive elements
$K_I = K_{II}$ [N/mm³]	10^5
σ_I^{0M} [MPa]	60
σ_{II}^{0M} [MPa]	90
G_{IC}^{M} [N/mm]	0.21
G_{IIC}^{M} [N/mm]	0.78
η_{BK} [-]	1.94
η [-]	0.7

A comparison between the quantitative load-displacement responses of the different unpinned and pinned models is shown in Figure 3.

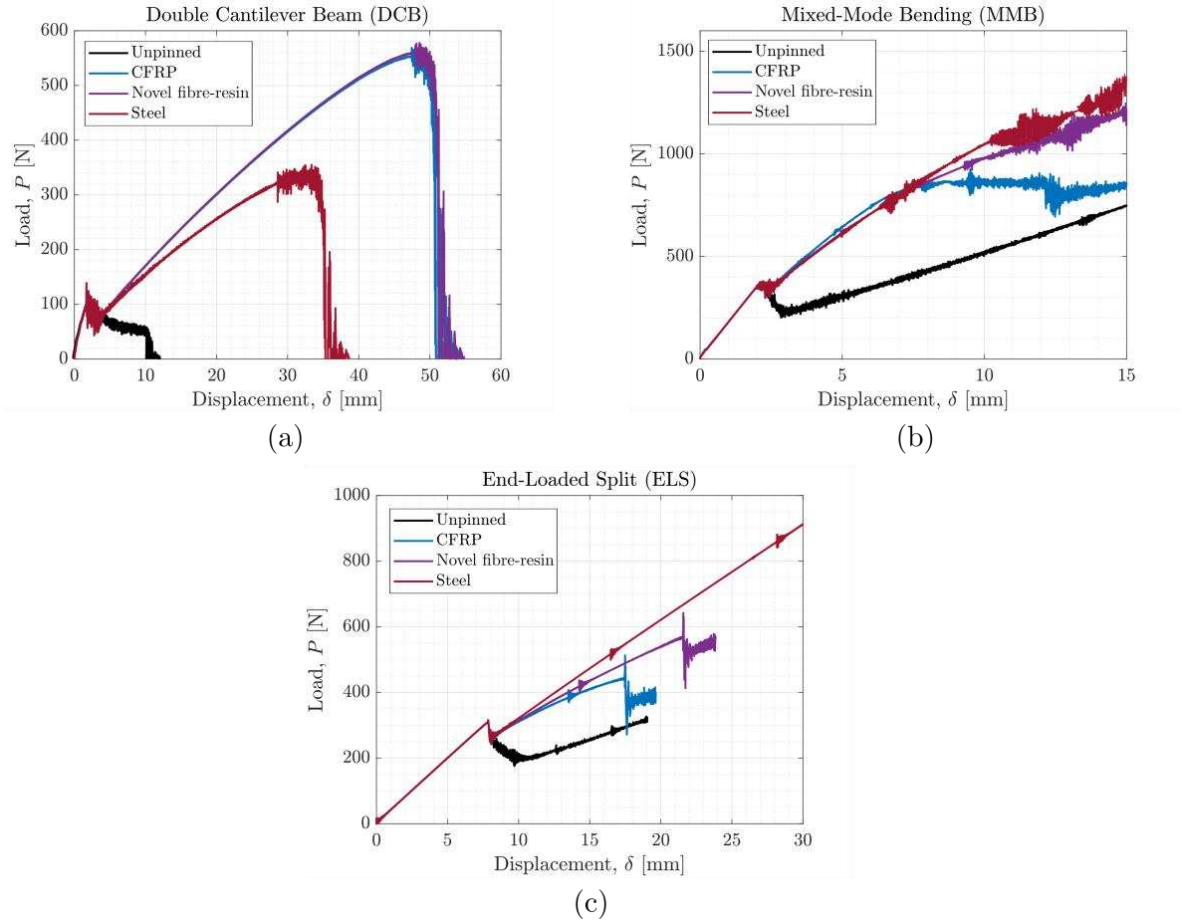

Figure 3. Coupon-level numerical predictions of the load-displacement curves associated to different z-pin materials.

As expected, for the pure mode I case (Figure 3a), the biggest improvement in comparison to the unpinned response was provided by both CFRP and novel z-pins, since both materials have exhibited an excellent adhesion with the surrounding composite laminate.

The MMB 47% mode II simulation (Figure 3b) has shown that the novel and stainless steel z-pins perform better under these stress-states, since shear failure after some pull-out of the z-pin is likely to occur for CFRP z-pins causing less energy to be dissipated during the bridging process.

When simulating a mode II loading scenario (Figure 3c), the simulations were stopped when the crack front reached the clamped end of the specimen, except for the stainless steel case, given its very high capability to deform plastically and continue bridging delamination for high deformations. Both the novel and stainless steel z-pins have exhibited promising results when compared to the unpinned samples, since under these conditions, CFRP z-pins tend to shear off and provide a small enhancement of the apparent fracture toughness of the interlaminar region.

5. Conclusions

A numerical framework has been presented to assess the performance of different z-pin materials under a variety of mixed-mode loadings through an adaptation of an already validated energy-equivalent bridging map formulation [4]. Modifications were undertaken to a semi-analytical bridging model [5] in order to describe the bridging actions exerted by both quasi-brittle and ductile z-pins.

Calibration of the bridging model was performed using single z-pin experimental data for the successful generation of bridging maps associated to different z-pin materials.

Coupon-level FE models were created to assess the effectiveness of the interaction of multiple z-pins under three different mode-mixities. For that, user-defined enhanced cohesive elements were developed following a tri-linear and a trapezoidal law and were used to model the pinned region with low- or high-energy z-pins, respectively.

From the single z-pin analysis and the structural-level simulations, it is clear that the z-pin material that ensures the most balanced mechanical performance along the mode-mixity range is a novel combination of fibre and matrix types, since this not only yields the same adhesion-level as the CFRP to the outer laminate providing good bridging effect for mode I dominated load cases, but also ensures a full pull-out under mode II shear-driven loads, leading to high levels of energy being dissipated along the entire mode-mixity range.

Acknowledgements

The authors wish to acknowledge the support of Rolls-Royce plc through the Composites University Technology Centre (UTC) at the University of Bristol, UK.

6. References

1. Kashtalyan, M., Soutis, C., 2005 – Analysis of composite laminates with intra- and interlaminar damage. Progress in Aerospace Sciences. 41, 152-173.
2. Mouritz, A.P., 2020 – Review of z-pinned laminates and sandwich composites. Composites Part A. 139, 106128.

  doi:10.5075/epfl-298799_978-2-9701614-0-0

3. M'membe, B., Yasaee, M., Hallett, S.R., Partridge, I.K., 2019 – Effective use of metallic Z-pins for composites' through-thickness reinforcement. Composites Science and Technology. 175, 77-84.
4. Melro, A., Serra, J., Allegri, G., Hallett, S.R., 2020 – An energy-equivalent bridging map formulation for modelling delamination in through-thickness reinforced composite laminates. International Journal of Solids and Structures. 202, 153-165.
5. Allegri, G., Yasaee, M., Partridge, I.K., Hallett, S.R., 2014 – A novel model of delamination bridging via Z-pins in composite laminates. International Journal of Solids and Structures. 51, 3314-3332.
6. Yasaee, M., Lander, J.K., Allegri, G., Hallet, S.R., 2014 – Experimental characterisation of mixed mode traction-displacement relationships for a single carbon composite Z-pin. Composites Science and Technology. 94, 123-131.
7. Li, X., Hallet, S.R., Wisnom, M.R. – Predicting the effect of through-thickness compressive stress on delamination using interface elements. Composites Part A. 39, 218-230.

  doi:10.5075/epfl-298799_978-2-9701614-0-0

GEOMETRIC CONDITIONS FOR PURE MODES I AND II IN INTERLAMINAR FRACTURE TESTS OF BI-MATERIAL SPECIMENS

Faustino, Mujika[a], Nagore, Insausti[a], Miren, Isasa[a], Ana I., Boyano[b]

a and b: MECMAT Group, Department of Mechanical Engineering, University of the Basque Country (UPV/EHU), Spain
a: faustino.mujika@ehu.eus, Faculty of Engineering of Gipuzkoa
b: Faculty of Engineering of Vitoria-Gasteiz

Abstract: *Double Cantilever Beam (DCB) and End Notched Flexure (ENF) tests were designed to characterize interlaminar fracture of composite materials in pure modes I and II. In both cases, specimens have an initial crack length in the middle of the thickness. In the case of bi-material specimens, if the crack is located in the middle of the thickness, mixed-mode could exist, due to the material asymmetry. The objective of the present study is to propose geometric conditions in order to obtain pure mode conditions when bi-material specimens are tested in DCB and ENF configurations.*

Keywords: Interlaminar fracture; pure mode; bi-material specimen.

1. Introduction

Double Cantilever Beam and End Notched Flexure tests were designed for the determination of interlaminar fracture behavior in mode I and mode II of composite materials. The same configurations were used also in the characterization of adhesive joints in modes I and II. When geometric or material symmetry does not exist, mixed mode fracture appear. The problem of the decomposition of fracture modes has been analyzed by several authors [1-6]. In the present study, the geometric conditions to obtain pure modes in bi-material joints are studied in the case of Asymmetric Double Cantilever Beam (ADCB) and Asymmetric End Notched Flexure tests (AENF).

2. Strain energy release rate and cohesive zone

A body is acted on by generalized concentrated forces F_i. The generalized displacement of the application point of that force in its direction is δ_i. In a small crack advance, the work carried out in infinitesimal displacements $d\delta_i$ is:

$$dW = dU + Gbda \tag{1}$$

where dW is the work done by the applied forces; dU is the change in strain energy; G is the energy needed for the crack advance per unit area; b is the width of the crack; and da is the differential crack advance.

The differential work done by the external forces F_i in their respective displacements d_i, assuming the repeated index convention, is $dW = F_i d\delta_i$. Thus, Eq. (1) becomes in:

$$dU = F_i d\delta_i - Gbda \tag{2}$$

  doi:10.5075/epfl-298799_978-2-9701614-0-0

Assuming that the strain energy is a state function that depends on the displacements δ_i and the crack length *a*:

$$dU = \left(\frac{dU}{d\delta_i}\right)_a d\delta_i + \left(\frac{dU}{da}\right)_{\delta_i} da \tag{3}$$

Identifying terms in Eqs. (2) and (3) it results:

$$F_i = \left(\frac{dU}{d\delta_i}\right)_a \tag{4}$$

$$G = -\frac{1}{b}\left(\frac{dU}{da}\right)_{\delta_i} \tag{5}$$

Eq. (4) is the first theorem of Castigliano and Eq. (5) gives the Strain Energy Release Rate.

The complementary strain energy or *coenergy* is defined as:

$$C = U^* = F_i\delta_i - U \tag{6}$$

The name coenergy is usually applied in the case of magnetic forces [7]. In the present study, it is adopted for the complementary strain energy in the mechanical case, using the letter *C* for denoting it. Differentiating Eq. (6) and replacing Eq. (2) it results:

$$dC = \delta_i dF_i + Gbda \tag{7}$$

Assuming that the coenergy is a state variable of the generalized forces F_i and the crack length *a*:

$$dC = \left(\frac{dC}{dF_i}\right)_a dF_i + \left(\frac{dC}{da}\right)_{F_i} da \tag{8}$$

Identifying terms in Eqs. (7) and (8) it results:

$$\delta_i = \left(\frac{dC}{dF_i}\right)_a \tag{9}$$

$$G = \frac{1}{b}\left(\frac{dC}{da}\right)_{F_i} \tag{10}$$

Eq. (9) is the theorem of Engesser-Castigliano and Eq. (10) gives the Strain Energy Release Rate. In the present study, coenergy is used to consider the independent generalized forces as state variables.

3. J integral and pure modes

Rice defined the *J* integral independent of the path in a closed curve including the crack tip. It is shown that in the case of elastic material, *J* = *G*. Taking into account relative displacements and stresses in a zone near the crack tip named cohesive zone, it results [8]:

  doi:10.5075/epfl-298799_978-2-9701614-0-0

$$J = G = \int_0^{\delta_n} \sigma d\delta_n + \int_0^{\delta_t} \tau d\delta_t \tag{11}$$

where σ is the normal stress; δ_n the associated relative displacement; τ the shear stress; and δ_t the associated relative displacement. All of them correspond to the crack tip.

Therefore, the first integral in Eq. (11) is related to mode I, and the second integral, is related to modes II and III. Mode III is not considered in the present study. Cohesive zone is related to different factors as plasticization, fiber bridging and micro-cracking.

In the case of pure modes, only one relative displacement exists as state variable. Relative displacements δ_n and δ_t are the addition of displacements of homologous points at the crack tip. Homologous points are defined as those that were the same point before crack advance. Then, in the fracture process zone, they are acted on by the same stress.

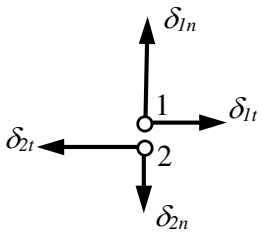

Figure 1. Normal and tangential displacements in two homologous points

According to Figure 1 where 1 and 2 are homologous points in the crack tip corresponding to the upper and lower parts, respectively, the relative displacements are:

$$\begin{aligned} \delta_n &= \delta_{1n} + \delta_{2n} \\ \delta_t &= \delta_{1t} + \delta_{2t} \end{aligned} \tag{12}$$

When pure mode I occurs the second integral of Eq. (11) is null. Then, it is assumed that the relative tangential displacement at the crack tip is null. Consequently, pure mode I occurs when:

$$\delta_t = 0 \Rightarrow \delta_{1t} = -\delta_{2t} \tag{13}$$

Assuming that mode III is not present, when pure mode II occurs, the first integral of Eq. (11) is null. Then, it is assumed that the relative normal displacements at the crack tip is null. Consequently, pure mode II occurs when:

$$\delta_n = 0 \Rightarrow \delta_{1n} = -\delta_{2n} \tag{14}$$

In the present study, if the relative tangential and normal displacements are null at the crack tip, it is assumed that they are null near the crack tip at the cracked side.

4. Asymmetric Double Cantilever Beam Test: ADCB

Figure 2 shows the configuration of an Asymmetric Double Cantilever test. The asymmetry could be due to different thicknesses of the same material or due to the joint of two different materials. The rotation of the straight part of the specimen indicates the presence of mode II.

  doi:10.5075/epfl-298799_978-2-9701614-0-0

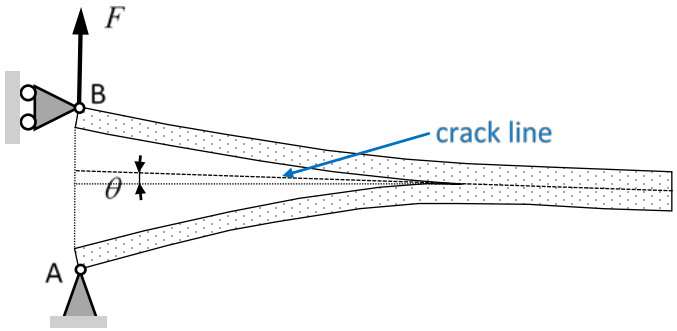

Figure 2. Asymmetric Double Cantilever Beam (ADCB) test configuration

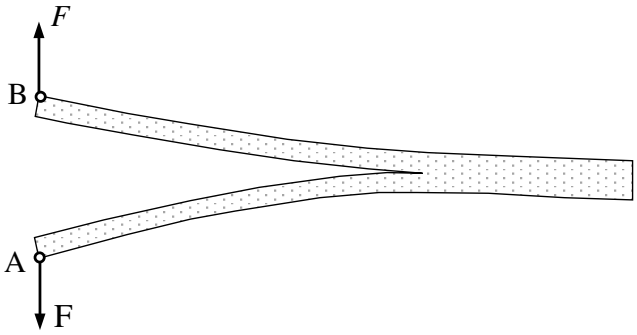

Figure 3. Forces acting on the ADCB test

The rotated angle of the non-cracked zone can be determined as a first approach without taking into account the crack tip rotations, that is, assuming that both cracked arms are perfectly clamped at the crack tip. Figure 3 shows the free-body diagram of the specimen and Figure 4 shows the free-body diagram corresponding to the application of a unit moment in the non-cracked zone. This diagram is used to calculate the derivatives of bending moments.

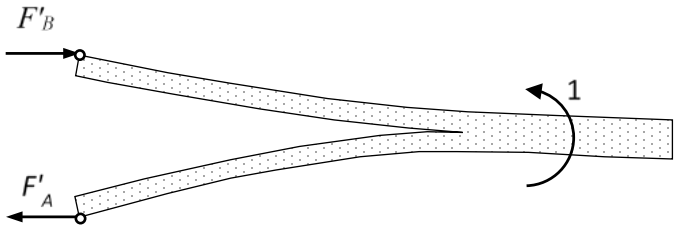

Figure 4. Unit moment and resulting reactions in ADCB test

According to the Engesser-Castigliano's theorem:

$$C' = d_1 \int_0^a M_1 M_1' dx + d_2 \int_0^a M_2 M_2' dx \tag{15}$$

where M_i and M'_i are bending moments and their derivatives, respectively.

  doi:10.5075/epfl-298799_978-2-9701614-0-0

After determining bending moments from Figure 3 and their derivatives from figure 4, replacing in Eq. (15) the rigid body rotation is given by:

$$\theta = \frac{Fa^2}{4h}\left(h_1 d_1 - h_2 d_2\right) \tag{16}$$

Where h is the total thickness; h_i are the thicknesses of each arm; F is the applied load; a is the crack length; d_i are bending flexibilities, being: $d_i = \left(E_i I_i\right)^{-1}$; E_i is the bending modulus of arm i; I_i is the moment of inertia or arm i; being i = 1, 2 the upper and lower cracked arms, respectively.

By a rigid body rotation, the test configuration is that shown in Figure 5. In this case, the crack line is horizontal and the relative tangential displacement between the load application points A and B is:

$$\delta_t^{A,B} = \theta h = \frac{Fa^2}{4}\left(h_1 d_1 - h_2 d_2\right) \tag{17}$$

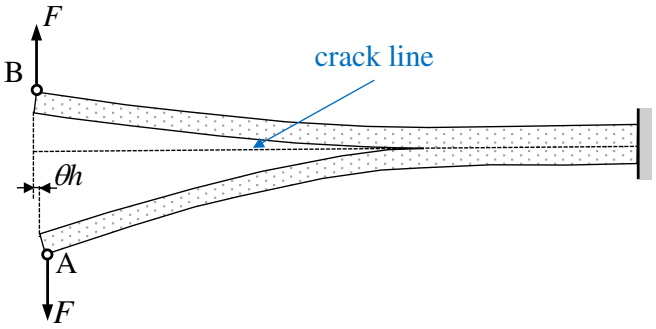

Figure 5. Rotated ADCB configuration with horizontal crack line

The crack line remains horizontal and the relative tangential displacement between two homologous points can be determined using the unit loads of Figure 6.

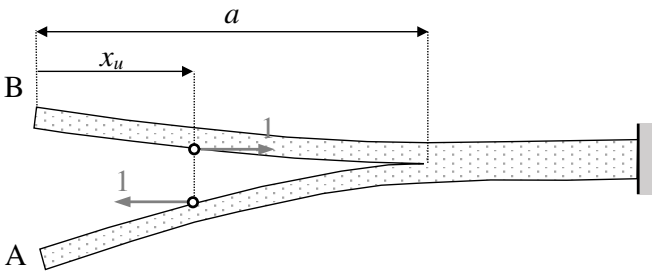

Figure 6. Unit loads to determine the relative tangential displacement

Introducing the moments of Figure 5 and the derivatives of Figure 6 in Eq. (15), the relative tangential displacements between two homologous points is:

$$\delta_t\left(x_u\right) = \frac{P}{4}\left(x_u^2 - a^2\right)\left(h_1 d_1 - h_2 d_2\right) \tag{18}$$

  doi:10.5075/epfl-298799_978-2-9701614-0-0

when x_u = 0, the displacement agrees with that of Eq. (17). For any point, the relative displacement is null if

$$h_1 d_1 - h_2 d_2 = 0 \tag{19}$$

This condition is equivalent to impose the equality of strains at homologous points. It is worth noting that the condition for null displacement agrees also with the condition of null rotation angle. The condition of Eq. (19) becomes in:

$$\frac{h_2}{h_1} = \sqrt{\frac{E_1}{E_2}} \tag{20}$$

5. Asymmetric End Notched Flexure Test

5.1 Force between cracked arms

Figure shows the configuration of an AENF test satisfying the condition that the contact between cracked arms occurs only above the left support. This condition is depicted by a roller of negligible radius. Thus, it is assumed that the load transfer is concentrated above the support and both cracked arms are subjected to an unknown load *Y*. In order to calculate that force, only the cracked part should be analyzed. Taking into account bending and shear effects, this load can be determined by the Engesser-Castigliano theorem:

$$C_{,Y} = 0 \Rightarrow d_1 \int_0^a M_1 M_{1,Y} dx + s_1 \int_0^a Q_1 Q_{1,Y} dx + d_2 \int_0^a M_2 M_{2,Y} dx + s_2 \int_0^a Q_2 Q_{2,Y} dx = 0 \tag{21}$$

where M_i, Q_i are bending moments and shear forces of part i; $M_{i,Y}$ and $Q_{i,Y}$ are derivatives of bending moments and shear forces of part *i* with respect to *Y*; s_i are shear flexibilities, being: $s_i = \frac{6}{5}\left(G_i A_i\right)^{-1}$; G_i is the out-of-plane shear modulus of arm *i*; A_i is the area of part *i*; being *i* = 1, 2 the upper and lower cracked arms, respectively.

Eq. (21) is equivalent to impose that the normal relative displacement is null at A, B points. The force *Y* is:

$$Y = \frac{P}{2} \frac{d_2 a^2 + 3 s_2}{a^2 \left(d_1 + d_2\right) + 3\left(s_1 + s_2\right)} \tag{22}$$

The force in Eq. (22) can be decomposed in two components related to bending and shear effects, respectively:

$$\begin{aligned} Y &= Y_b + Y_s \\ Y_b &= \frac{P}{2} \frac{d_2}{d_1 + d_2} \\ Y_s &= \frac{P}{2} \frac{s_2 d_1 - s_1 d_2}{\left(d_1 + d_2\right)\left[a^2 \left(d_1 + d_2\right) + 3\left(s_1 + s_2\right)\right]} \end{aligned} \tag{23}$$

The bending component of Eq. (23) is obtained considering only bending effects in Eq. (21). Then, the shear component is obtained as:

  doi:10.5075/epfl-298799_978-2-9701614-0-0

$$Y_s = Y - Y_b \tag{24}$$

The component due to shear effects is null when the following condition is satisfied:

$$Y_s = 0 \Rightarrow s_2 d_1 - s_1 d_2 = 0 \Rightarrow \frac{h_2}{h_1} = \sqrt{\frac{G_2 E_1}{G_1 E_2}} \tag{25}$$

5.2 Relative normal displacements

Otherwise, the relative normal displacement between two homologous points of the crack can be determined by the Engesser-Castigliano's theorem:

$$C' = \delta_n = d_1 \int_0^a M_1 M_1' dx + s_1 \int_0^a Q_1 Q_1' dx + d_2 \int_0^a M_2 M_2' dx + s_2 \int_0^a Q_2 Q_2' dx \tag{26}$$

Derivatives of moments and shear forces are obtained by applying vertical forces, as shown in Figure 7.

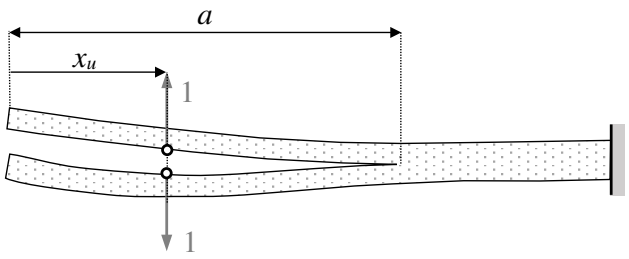

Figure 7. Unit loads to determine the relative normal displacement

The condition to avoid interaction between both arms is:

$$\delta_n \geq 0 \tag{27}$$

After calculating Eqs. (26) and imposing condition (27) it results:

$$\left[\left(s_1 + s_2\right)\left(1 + \frac{Y_s}{Y_b}\right) - s_2 \frac{d_1 + d_2}{d_2} \right] I_s \geq \left[-\left(d_1 + d_2\right)\left(1 + \frac{Y_s}{Y_b}\right) + \left(d_1 + d_2\right) \right] I_b \tag{28}$$

Being I_b and I_s in Eq. (28) integrals related to shear and bending terms, respectively:

$$\begin{aligned} I_s &= \int_{x_u}^a dx = a - x_u \\ I_b &= \int_{x_u}^a x\left(x - x_u\right) dx = \tfrac{1}{6}\left[x_u^3 + a^2\left(2a - 3x_u\right) \right] \end{aligned} \tag{29}$$

Assuming that $\frac{Y_s}{Y_b} \ll 1$ Eq. (28) becomes in:

$$\delta_n \geq 0 \Rightarrow \frac{h_2}{h_1} \leq \sqrt{\frac{G_2 E_1}{G_1 E_2}} \tag{30}$$

  doi:10.5075/epfl-298799_978-2-9701614-0-0

If the inequality of Eq. (30) is not satisfied, there is contact between both cracked arms. The interaction between them cannot be assumed to be concentrated above the support. Otherwise, pure mode II occurs when the equality is satisfied. This condition is the same as that obtained in Eq. (25). Then, in pure mode II, the interaction between both cracked arms is concentrated above the support and depends only on bending effects.

6. Conclusions

Being 1 and 2 the upper and lower cracked arms, the thickness ratios for obtaining pure modes I and II in Asymmetric DCB and ENF test of bi-material joints have been obtained. Using those geometric relations, standard methodologies of testing in pure modes I and II can be used for determining strain energy release rates in modes I and II of bi-material joints.

Acknowledgements

The financial support of the University of the Basque Country (UPV/EHU) in the Research Group GIU20/060 “Mechanics of Materials” is gratefully acknowledged.

7. References

1. Williams JG. On the calculation of energy release rates for cracked laminates. International Journal of Fracture 1988; 36: 101-119.
2. Charalambides M, Kinloch AJ, Wang Y, Williams JG. On the analysis of mixed-mode failure. International Journal of Fracture 1992; 54: 269-291.
3. Bennati S, Colleluori M, Corigliano D, Valvo PS. Composites Science and Technology 2009; 69: 1735-1745.
4. Mollón V, Bonhomme J, Argüelles A, Viña J. Influence of the crack plane asymmetry over G_{II} results in carbon epoxy ENF specimens. Composite Structures 2012; 94: 1187-1191.
5. Valvo PS. On the calculation of energy release rate and mode mixity in delaminated laminated beams. Engineering Fracture Mechanics 2016; 165: 114-139.
6. Maimí P, Renart J, Sarrado C, González EV. Characterization of debonding between two different materials with beam like geometries. Engineering Fracture Mechanics 2021; 247: 107661.
7. Mawardi OB. On the concept of coenergy, Journal of the Franklin Institute 1957, 264: 313-332.
8. Arrese A, Boyano A, De Gracia J, Mujika F. A novel procedure to determine the cohesive law in DCB tests. Composites Science and Technology 2017; 152: 76-84.

  doi:10.5075/epfl-298799_978-2-9701614-0-0

ANALYSIS OF THE RATE-DEPENDENCY OF THE MODE I INTERLAMINAR FRACTURE TOUGHNESS IN COMPOSITE LAMINATES USING DIFFERENT DATA REDUCTION STRATEGIES

Sergio A., Medina[a], Emilio V., González[a], Norbert, Blanco[a], Jesús, Pernas-Sánchez[b], José A., Artero-Guerrero[b], Vincent Jacques[c], Elisabeth E. de Blanpré[c]

a: AMADE - Escola Politècnica Superior, Universitat de Girona, Girona, Spain – sergio.medina@udg.edu
b: Department of Continuum Mechanics and Structural Analysis, Universidad Carlos III de Madrid, Leganés, Madrid, Spain
c: Dassault Aviation, 78 Quai Marcel Dassault, 92210 Saint-Cloud, France

Abstract: *This work investigates the rate-dependency of the Mode-I interlaminar fracture toughness in a thermoset-matrix CFRP composite at different displacement rates. The tests have been carried out using a Guided Double Cantilever Beam (GDCB) test set-up. This is an in-house developed test set-up for the characterisation of mode I fracture toughness at different loading rates that guarantees a symmetric crack opening and pure mode I propagation during the test. Three different data reduction methods have been used: a displacement-based formulation taking into account the dynamic contribution, a near-crack-tip displacement formulation and a numerical assessment based on the arms displacements. The testing method and the different data reduction strategies have allowed to investigate the rate-sensitivity of the Mode-I fracture toughness of the material for the applied opening displacement rate. Small differences between the three different methods can be noticed, meanwhile no clear rate-dependency for the material used has been evidenced.*

Keywords: Fracture toughness; Mode-I; testing method; high rates; rate-dependency

1. Introduction

The use of composite structures has continually attracted interest in automotive, aerospace and military applications. Despite being a matter of research during the last decades, the rate-dependency of the fracture toughness of fibre reinforced composites still needs to be well understood and characterised to improve the reliability of numerical predictions in dynamic events.

Interlaminar damage has been extensively studied under quasi-static loading conditions [1-4]. Nevertheless, for dynamic loading cases there is not much information available about the behaviour of polymer-based composite materials. When the damage is induced by dynamic loading, the material properties used in the analysis tools, such as Finite Element simulations, should take into account the effect of high strain rates and/or high speed propagation of cracks. The study of this kind of dynamic induced damage has increased during the last decade, using experimental and numerical analysis. However, most studies carried out need to be improved since the base hypotheses are not adequate (such as the use of strain-rate independent material properties or the use of governing equations without taking into account a dynamic framework). In fact, different studies carried out by different authors with the same material combination

  doi:10.5075/epfl-298799_978-2-9701614-0-0

obtained different results and contradictory conclusions, showing that there is a lack of comprehensive characterisation methods. This work investigates the rate-dependency of the Mode-I interlaminar fracture toughness in a thermoset-matrix CFRP composite at different displacement rates. The results of the fracture toughness using tree different data reduction methods are compared. Quasi-static fracture tests are performed using a standard DCB method for normalisation.

2. Test set-up

The tests have been carried out using a Guided Double Cantilever Beam (GDCB) test method. This is an in-house developed test set-up for the characterisation of mode I fracture toughness at different loading rates. The device for the GDCB testing has been patented with international application number PCT/ES2021/070415 and publication number WO/2022/003219. One of its main characteristics is that, in contrast to other methods reported in the literature [5,6], it guarantees a symmetric crack opening and pure mode I propagation during the test. Additionally, when it is used in a dynamic servo-hydraulic testing machine with controllable displacement velocity, a constant opening velocity can be obtained. As seen in Fig. 1, the device introduces the load through a V-shape guidance system that allows to reach a constant velocity (after the acceleration period of the machine). The tool also includes a pair of hinges clamped to the arms of the specimen that transfer the load/displacement from the main part of the tool. It includes a simple, fast and reliable design avoiding adhesive joints and overcomes the problems associated to end blocks and piano hinges.

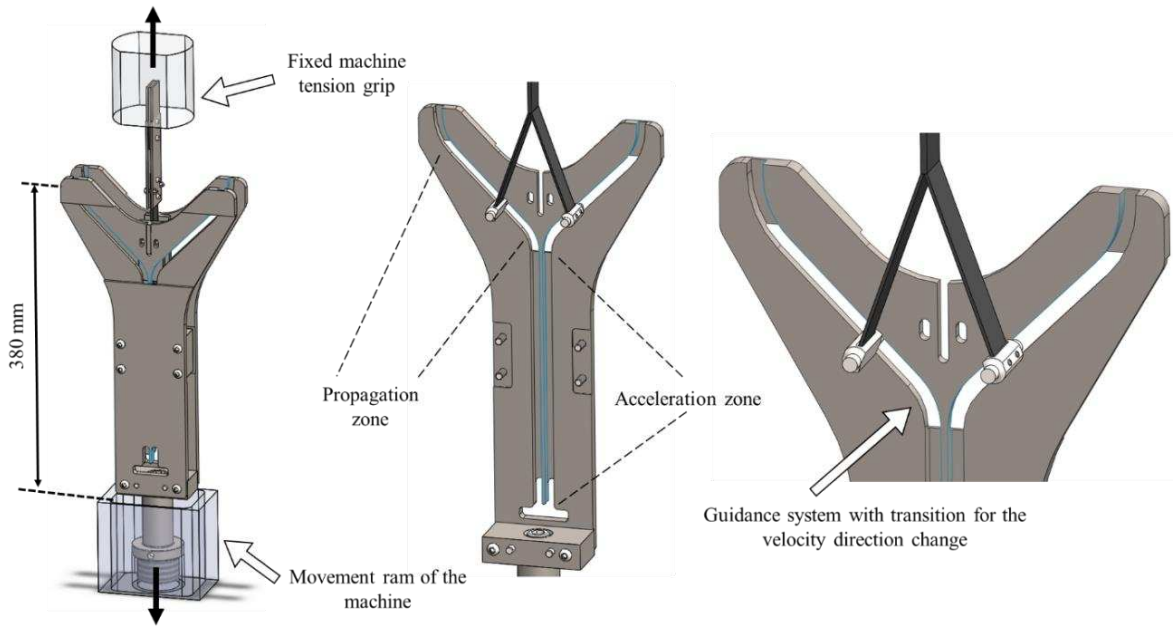

Figure 1. Guided Double Cantilever Beam (GDCB) test method parts and way of loading.

The specimen geometry used with this test method is similar to the one defined for the Double Cantilever Beam (DCB) test (ISO 15024:2001) for the characterisation of the mode I interlaminar fracture toughness in laminated materials in quasi-static loading. However, the initial crack length and the total length of the specimen are longer than the standard DCB specimen.

The dynamic study has been carried out at three specimen opening displacement rates: 1, 6 and 30 m/s using an Instron VSH dynamic servo-hydraulic testing machine. For the reduction of the experimental data and determination of the energy release rate, the tests have been monitored with a high-speed video system. One Photron SA-Z high-speed camera has been used to measure the displacements and rotations at the loading points. Another one has been used to monitor the crack tip location and the openings and rotations of the specimen's arms close to the crack tip area. The image frames were analysed using an in-house Matlab algorithm to obtain the required data for each of the data reduction methods.

3. Data reduction methods

Three different data reduction methods have been used for the analysis of the mode I interlaminar fracture toughness. Each method is explained next.

3.1 Method 1: Displacement-based formulation

The GDCB configuration including an axial-tensile loading due to the guiding system is shown in Fig. 2.

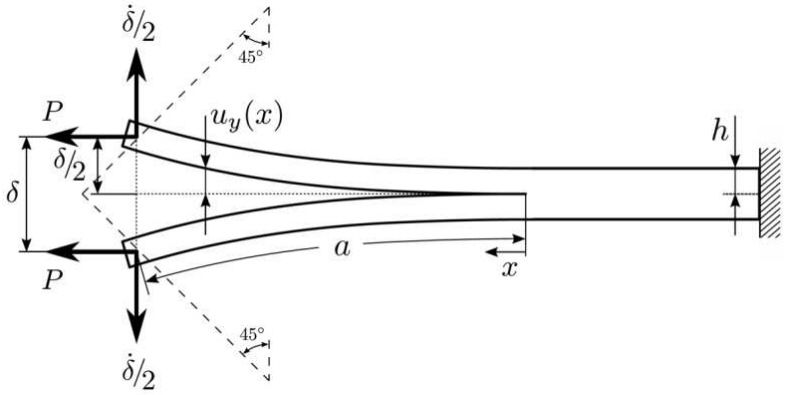

Figure 2. Mode I GDCB test method configuration.

Taking into account that it is convenient to avoid the use of the load signal for high loading rates testing, a displacement-based equation for the fracture toughness for the GDCB test method can be obtained based on the first order beam theory. The complete deduction of this data reduction method can be found in [7]. The equation can be described as:

$$G_I = \frac{3E_{11}h^3\delta^2}{16(a_{ef})^4}\left[\frac{\left(1-\frac{\delta}{2a_{ef}}\right)^2}{\left(1-\frac{3\delta}{5a_{ef}}\right)^2}\right] \quad (1)$$

where E_{11} is the Young's modulus, h is the thickness of one arm of the specimen, δ is the opening displacement at the load-point, a_{ef} is the crack length corrected for the rotation of the arms at the crack tip by adding a length χh, where χ is a constant given by the elastic properties of the material as described in [8].

Eq. (1) is valid for quasi-static cases. However, as the GDCB tests are performed under high loading rates, a correction for the inertia effects by means of the kinetic energy must be

considered. Taking into account the contribution of the kinetic energy to the energy release rate, the final equation for the mode I interlaminar fracture toughness is

$$G_I = \frac{3E_{11}h^3\delta^2}{16\left(a_{ef}\right)^4}\left[\frac{\left(1-\frac{\delta}{2a_{ef}}\right)^2}{\left(1-\frac{3\delta}{5a_{ef}}\right)^2}\right] - \frac{33\rho bh\dot{\delta}^2}{560} \tag{2}$$

where $\dot{\delta}$ is the opening loading rate at the load-point, b is the specimen width and ρ is the density of the material (see [7] for further reference).

3.2 Method 2: Near-crack-tip displacement formulation

For the local solution data reduction method, which considers the near-crack-tip displacement, the analysis is focused as close as possible on the crack tip. In this way, the dynamic effects affecting the arms of the specimen can be neglected during the analysis.

The fracture toughness can be described in terms of the load P and the crack length a or in terms of the equivalent moment M as

$$G_I = \varphi P^2 a^2 = \varphi M^2 \tag{3}$$

where $M = Pa$ and $\varphi = E_{11}I$, being I the second moment of area of the cross section.

Then, the equation for the energy release rate can be obtained using the theory of Euler-Bernoulli where $\varphi M = \frac{d\phi}{dx}$ and $\frac{d\omega}{dx} + \phi = 0$, being $\omega(x)$ the displacement of the arms near the crack tip (polynomial equation of n-grade) and $\phi(x)$ the rotation of the arm near the crack tip. For the case where the analysis is carried out sufficiently close to the crack tip, i.e., when $x \to 0$, the fracture toughness can be expressed as

$$G_I = \frac{12M^2}{Eb^2h^3} = \frac{Eh^3\omega_2^2}{3} \tag{5}$$

3.3 Method 3: Numerical assessment method

The numerical assessment method for the data reduction strategy is done using Finite Element simulations with the commercial software Abaqus™/Explicit [9]. A linear elastic model is used with the boundary conditions represented in Fig. 3. The two beams of the specimen are loaded imposing prescribed displacement profile in a characteristic segment from the crack tip. For each case, the displacement profile is obtained using a polynomial curve fitting of the images recorded during the tests. Finally, the VCCT theory defined by Krueger [10] is applied to obtain the value of the fracture toughness in every specific point of the crack propagation.

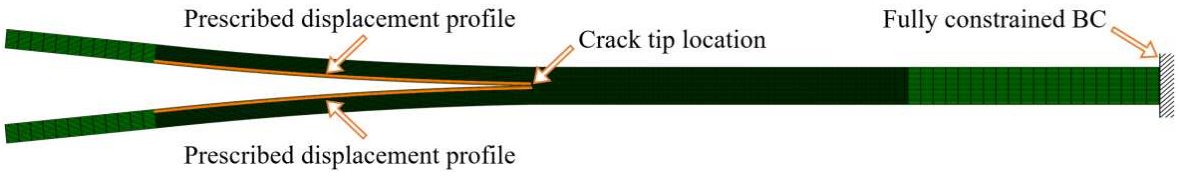

Figure 3. Boundary condition for the FE model for the VCCT solution method.

4. Material and specimen geometry

For this study a Hexply® M21EV/34%/UD200/IMA/150ATL thermoset-matrix composite material has been used. The average specimen thickness is 3.165 mm. This thickness corresponds to the mean value of cured specimens, counting six measures per specimen at different locations with a thickness variation within the limits established by the standard.

The specimen dimensions have been determined to ensure the specimens ability to have the initiation propagation only once the constant velocity is reached during the propagation zone (see Fig. 2) without interference in the form of plastic deformation or failure in the arms of the specimen due to excessive bending or low stiffness. Hence, samples of 350×20 mm^2 size are obtained. The starter crack length in the specimens is 150 mm. The specimens have been subjected to a pre-cracking using the DCB setup in quasi-static loading. Once the specimens are placed into the grips, after the pre-cracking, the initial crack length is around 146 mm. Four specimens per configuration of loading rate have been tested.

5. Results and discussion

Fig 4. shows the normalised fracture toughness results for each of the three different data reduction methods. The dynamic fracture toughness is normalised by the fracture toughness value from the DCB quasi-static tests.

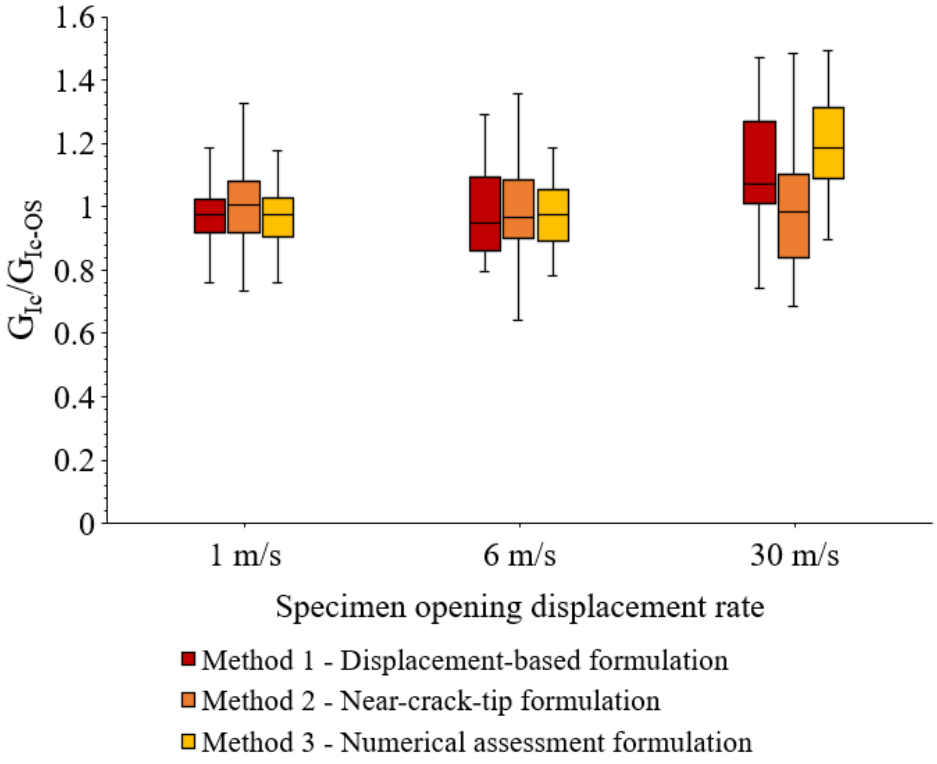

Figure 4. Normalised fracture toughness for the different tester displacement rates using the different data reduction methods.

For the case of 1 m/s opening displacement the results of the fracture toughness are similar between them with a relative small dispersion. Besides, the results can be assumed as equal to

the quasi-static value. At this displacement rate, the inertia effect is low and can be neglected, giving results consistent with the quasi-static results. For the case of 6 m/s, the results are similar to those of the previous case but with higher dispersion. Even so, the difference respect to the quasi-static value is small. However, for the 30 m/s opening displacement rate, the results present a high dispersion and a certain difference with respect to the quasi-static results. This may be explained by the inertia effect and the accuracy in the analysis of the images to obtain the data for the different data reduction methods. At high displacement rates like this one, the resolution of the images is limited to the test set-up and the cameras used. Additionally, the mean values of the fracture toughness for the opening displacement rate of 30 m/s are higher that the quasi-static values. However, due to the scatter of the data, it cannot be assumed a clear rate-dependency of the fracture toughness for high displacement rates, being necessary to perform additional tests using different materials.

From Fig. 4, it can be seen that the near-crack-tip fata reduction method is the one that gives higher dispersion of results. This is linked to the accuracy to read the displacement profile near the crack tip. These results may be improved by improving the test set-up by means of a better resolution of the images obtained through the high-speed camera.

6. Conclusions

The rate-dependency of the Mode-I interlaminar fracture toughness in a thermoset-matrix CFRP composite has been studied at different displacements rates. Three different methods have been compared to obtain the rate-dependency obtaining that the results are similar between the methods with small differences between the three different methods for low displacement rates. Meanwhile no clear rate-dependency for the material used has been evidenced.

The near-crack-tip formulation is the one that gives a higher dispersion in the results. However, this can be improved by improving the resolution of the image acquisition. The GDCB test method has proven to work appropriately for opening velocities between quasi-static to 30 m/s.

Acknowledgements

This project has received funding from the Clean Sky 2 Joint Undertaking (JU) under grant agreement No. 886519. The JU receives support from the European Union's Horizon 2020 research and innovation programme and the Clean Sky 2 JU members other than the Union. The first author acknowledges the grant for doctoral studies IFUdG2017/43 and the financial support from the Spanish Ministerio de Ciencia, Innovación y Universidades through the project RTI2018-099373-B-100.

7. References

1. N. Sela, O. Ishai, Interlaminar fracture toughness and toughening of laminated composite materials: a review, Composites 20. 1989; 423-435. doi:10.1016/0010-4361(89)90211-5.
2. A. Brunner, B. Blackman, P. Davies, Mode i delamination, in: D. Moore, A. Pavan, J. Williams (Eds.), Fracture Mechanics Testing Methods for Polymers, Adhesives and Composites, volume 28 of European Structural Integrity Society, Elsevier. 2001; 277-305. doi:10.1016/S1566-1369(01)80038-8.

3. N. Nasuha, A. I. Azmi, C. L. Tan, A review on mode-I interlaminar fracture toughness of fibre reinforced composites, Journal of Physics: Conference Series 908. 2017; 012024. doi:10.1088/1742-6596/908/1/012024.
4. A. Siddique, S. Abid, F. Sha_q, Y. Nawab, H. Wang, B. Shi, S. Saleemi, B. Sun, Mode I fracture toughness of fiber-reinforced polymer composites: A review, Journal of Industrial Textiles 50. 2021; 1165-1192. doi:10.1177/1528083719858767.
5. P. B. R. K. Blackman, J. P. Dear, A. J. Kinloch, H. Macgillivray, Y. Wang, J. G. Williams, P. Yayla. The failure of fibre composites and adhesively bonded fibre composites under high rates of test. Part I Mode I loading - experimental studies. Journal of Materials Science, 30(23). 1995; 5885–5900. doi:10.1007/BF01151502.
6. C. M. Colin de Verdiere, A. A. Skordos, M. May, A. C. Walton. Influence of loading rate on the delamination response of untufted and tufted carbon epoxy non crimp fabric composites: Mode I. Engineering Fracture Mechanics, 96. 2012; 11–25. doi:10.1016/j.engfracmech.2012.05.
7. S.A. Medina, E.V. González, N. Blanco. Guided Double Cantilever Beam test method for intermediate and high loading rates in composites. To be submitted to Composites Part A.
8. S. Hashemi, A. J. Kinloch, J. G. Williams. The analysis of interlaminar fracture in uniaxial fibrepolymer composites, Proceedings of the Royal Society of London. Series A, Mathematical and Physical Sciences 427. 1990; 173-199.
9. Dassault Systemes Simulia Corp., Abaqus Analysis User's Manual, in: Abaqus documentation 6.14, Simulia Worldwide Headquarters, Providence, RI, USA. 2014.
10. R. Krueger. Virtual crack closure technique: History, approach, and applications. ASME. Appl. Mech. Rev. 57(2). 2004; 109–143. doi: 10.1115/1.1595677.

COOLING RATE EFFECTS ON CONSOLIDATION QUALITY OF CARBON FIBER REINFORCED POLYAMIDE6 (CF/PA6) LAMINATED COMPOSITES

Sepehr Simaafrookhteh [a, b], Stepan V. Lomov [c], and Jan Ivens [a]

a: Department of Materials Engineering, KU Leuven Campus De Nayer, J. De Nayerlaan 5, BE-2860 Sint-Katelijne-Waver, Belgium - sepehr.simaafrookhteh@kuleuven.be

b: SIM M3 program, Technologiepark 48, B-9052 Zwijnaarde, Belgium

c: Department of Materials Engineering, KU Leuven, Kasteelpark Arenberg 44 Box 2450, 3001, Leuven, Belgium

Abstract: Carbon fiber/polyamide6 (CF/PA6) tapes are investigated for thermal and microstructural characteristics. Flat laminates ($[0°]_4$) are consolidated using two cycles that result in slow (~ 40 °C/min) and fast (~ 830 °C/min) cooling rates. Performing wedge peel test, a significant increase in peel resistance was observed for increasing processing temperature and the cooling rate. This behavior can be correlated to a lower degree of crystallinity (Xc) in the sample processed at a higher cooling rate. X-ray diffraction (XRD) is implemented to investigate crystalline structure and Xc. A double cantilever beam (DCB) test is used to find interlaminar fracture toughness and corroborate the trend with the peel resistance results. Fracture toughness of 1.6 and 2.4 kJ/m2 were obtained for slow and fast cooled specimens that indicates a higher crack growth resistance for laminates produced at a higher cooling rate.

Keywords: CF/PA6; Wedge peel test; DCB test; X-ray diffraction; Thermoplastic composites

1. Introduction

Continuous carbon fiber (CF)-reinforced thermoplastics (CFRTP) has gained a lot of interest among researchers and industry in the past decades due to their advantageous properties, including their high strength-to-weight ratio, high fracture toughness, long pot life, and recyclability [1,2]. These properties made them ideal for use in the sports, aerospace, and automobile industries. Among CFRTPs, unidirectional (UD) carbon fiber-reinforced polyamide 6 (CF/PA6) has been massively used recently [3–5] due to their relatively low cost, good processability, chemical resistance, and high mechanical performance [4].

However, the production of thermoplastic composites is costly because of using low-speed and conventional manufacturing processes like autoclaving and vacuum bagging, high cost of the preparation and the high processing temperatures of thermoplastics. The use of UD CF/PA6 well-impregnated prepreg tapes can increase productivity and lower costs. A tape can be applied for automated on-line consolidation processes such as automated tape placement (ATP), or automated fiber placement (AFP) based on the width of the tape. Moreover, fiber-reinforced thermoplastics have the advantage of being thermoformed quickly into a variety of structural shapes. Flat laminates with the desired number of layers must be produced as a prerequisite to thermoforming. To this end, a hot compression molding setup can be used to consolidate the prepared blank.

Two primary steps that contribute to the consolidation and bond strength development of these UD fiber reinforced thermoplastic tapes are intimate contact and autohesion (healing). During

  doi:10.5075/epfl-298799_978-2-9701614-0-0

intimate contact, surface asperities of the tape are flattened due to pressure at elevated temperatures (above the melting point, Tm, for semi-crystalline polymers such as PA6). Simultaneously, autohesion develops over the interface between two plies that come into intimate contact. During autohesion, intermolecular diffusion and polymer chain entanglement occur across the interface. Autohesion is independent of the applied pressure and will progress with time at elevated temperatures to remove the bond line between plies and increase the bond strength [6]. Based on the current models developed to estimate the degree of intimate contact [1,7], we know that a combination of process temperature (thus, material viscosity), applied pressure, time, and surface geometry (roughness) play a prominent role in the evolution of intimate contact. Hence, to better understand the underlying behavior of tape materials during processing, it is essential to assess their microstructural, thermal, and rheological characteristics. Nevertheless, what is missing here and often overlooked in publications related to the bond strength of thermoplastic composite laminates are the manufacturing process cooling rate and its effect on the crystalline structure and the degree of crystallinity.

In the current investigation, we initially examine the as-received CF/PA6 thermal and microstructural characteristics to assess the tape quality. Then using the compression molding process, we induce two cooling rates to produce UD flat laminates at different processing temperatures. Subsequently, the laminates will be investigated using X-ray diffraction (XRD) for their crystalline structure. The interlaminar peeling strength and mode-I fracture toughness will be investigated using the wedge peel test (WPT) and double cantilever beam (DCB) test, respectively. The goal is to assess the peel resistance and opening mode fracture toughness of the thin specimens as a result of the different manufacturing conditions.

2. Material Characteristics and Experimental Methods

2.1 CF/PA6 Tape Characteristics

The material used for the current investigation is the commercial UD CF/PA6 tapes from Toray (Toray Cetex® TC910) with a width of 166 mm, the thickness of 0.16 mm, and composite density of 1.45 g/cm3. The tape has a fiber weight content of 60 % [8]. Figure 1 shows the tapes microstructure, observed by optical microscopy.

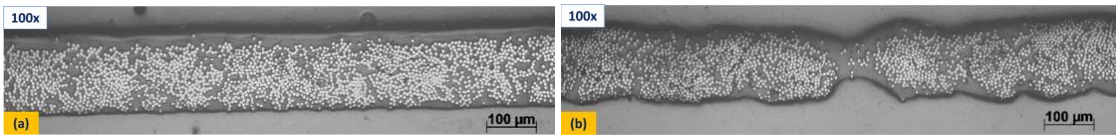

Figure 1. Cross-sectional micrographs of UD CF/PA6 Toray tapes: a) smooth surface; b) rough surface.

Figure 1 depicts examples of smooth and rough surface quality of the tape used in this investigation. A majority of the cross-sectional micrographs showed qualities similar to Figure 1a. It can be concluded that the current tape has a good impregnation quality and distribution of fibers with relatively low roughness at the surface. As shown in Figure 1, there is a thin resin-rich on one side of the tape. The resin-rich layer was previously illustrated in literature and proved to improve bond strength development due to better resin flow and chain entanglement [1,9]. Research has also demonstrated that a thin layer of resin-rich material can effectively increase the mode-I fracture toughness and wedge peel strength [2,5].

Thermal characteristics of the tape are investigated using differential scanning calorimetry (DSC) and dynamic mechanical analysis (DMA). A few milligrams of tape specimens are used for DSC measurements with a heating-cooling ramp of 10 °C/min. Since the glass transition temperature (Tg) endothermic peak was not detectable in the DSC heating curve, DMA is applied on 20 mm × 11.3 mm × 1.1 mm specimens with a ramp of 3 °C/min up to 260 °C, 1 Hz frequency, and 20 µm amplitude. Some samples were dried before being tested for 72 h at 85 °C. Thermogravimetric analysis (TGA) is used to burn the polymer content up to 500 °C to find the residue content of the tape material that would be the weight fraction of fibers. The results are listed in Table 1. The weight fraction (Wf) measured for the tape is consistent with the tape Wf = 60 %, mentioned in Toray's datasheet [8].

Table 1. CF/PA6 characteristics obtained using DSC, DMA, TGA.

Sample	Melting peak Tm [°C]	Crystallization peak Tc [°C]	Glass transition temp. Tg [°C]	Fibers weight fraction (Wf) [%]
CF/PA6 dried	223.1	191.6	-	60.5
CF/PA6 undried	222.7	196.3	73.4	

2.2. Laminate Manufacturing

Blank preparation is done by using four plies of CF/PA6 tapes to produce $[0°]_4$ laminates. Two different press machines are used to induce different thermal cycles for processing. However, four different processing temperatures are applied to produce laminate for both conditions. In the first method, using a Fontijne press, cooling down the plates is done on the same press platens used for heating. Contrary to this, for the second method, a Pinette press is used with an additional cold and insulated stage that is always at room temperature. Therefore, after placing the blank on the hot stage and allowing sufficient time to reach the desired processing temperature, we wait for the chosen holding (dwell) time. Subsequently, the press platens are opened, and the blank is moved immediately to the cold stage to cool down under the same pressure but using the cold platens. The second method can induce a considerably higher cooling rate than the first one using the Fontijne press. The thermal cycles for both setups are shown in Figure 2 that are recorded by embedding thermocouple wires into the blank mid-plane. The recorded cooling rates are 37 °C/min and 830 °C/min for the Fontijne and Pinette press methods, respectively.

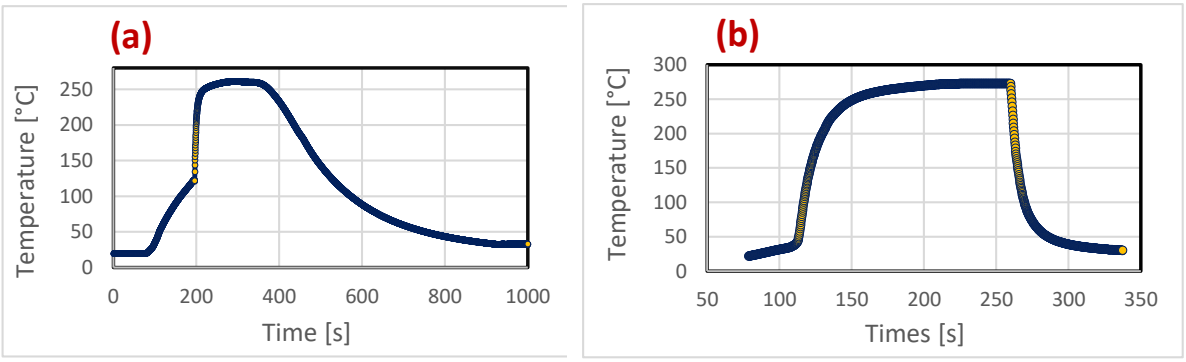

Figure 2. Thermal cycle for two different press machines used: a) Fontijne press with in a slower cooling down, b) Pinette press in a fast cooling down condition.

Regarding the consolidation pressure that can ensure complete intimate contact, as shown in [4], a few kPa of pressure should be enough for full intimate contact to occur between CF/PA6 plies due to relatively low viscosity of CF/PA6 at elevated temperature. Therefore, here we tried to apply the minimum possible pressure in the operating range of the press machines. Furthermore, for the autohesion to be completed when intimate contact is achieved at elevated temperatures (> Tm), only a few milliseconds should be enough for the polymer chains to diffuse across the interface and entangle with other chains. Different processing conditions are used to produce laminates, as listed in Table 2. The plates size is 280 mm × 166 mm and a polyimide film (Kapton 50 HN) with a length of 80 mm is used on the mid-plane as a crack starter to create a non-bonded region. The plates are then cut into 15 mm width for the tests. It should be mentioned that zero holding time for plate #5 and #10 means that the cool down of the press immediately started when the temperature reached the desired processing temperature (220 °C in this case)

Table 2. List of the processing conditions used to manufacture ten $[0°]_4$ *laminates.*

Sample number	Processing temperature [°C]	Pressure [bar]	Holding time [s]	Press	Cooling rate
1	220	2.5	30	Fontijne	Slower
2	240		30		
3	260		30		
4	280		30		
5	220		0		
6	220		30	Pinette	Faster
7	240		30		
8	260		30		
9	280		30		
10	220		0		

2.3. Bond Strength Quality

Different mechanical testing methods can be employed to assess the interlaminar bond strength [1]. In the past years, the wedge peel test (WPT) method started to draw much positive attention among researchers. This is primarily due to its simplicity in sample preparation and data reduction. In addition, tests such as short beam strength or DCB require relatively thick samples. Here, the objective is to produce thin samples (four plies), so we can assume that the cooling rate in the through-thickness direction of the laminate remains constant. The WPT setup and different regions on the sample are shown in Figure 3. Based on the previous research by Schaëfer [4], a wedge with a thickness of 3.2 mm and a 20° opening angle is considered.

Since WPT is not a standard test method and the fact that there is an unknown friction coefficient between the wedge and specimen legs, the DCB test is implemented here as a standard method based on the modified beam theory method and guidelines of ASTM D5528 [10]. One sample from each cooling condition will be investigated to find interlaminar fracture toughness and corroborate the trend with the peel resistance results. In the current investigation, it was essential to process thin laminates (four plies with a thickness below 1 mm) to keep a constant cooling rate across the thickness of the samples. Hence, to perform DCB and

  doi:10.5075/epfl-298799_978-2-9701614-0-0

avoid beams yielding and plastic failure, aluminum beams (3 mm thickness) are used to increase the stiffness of the beam and prevent undesired failure.

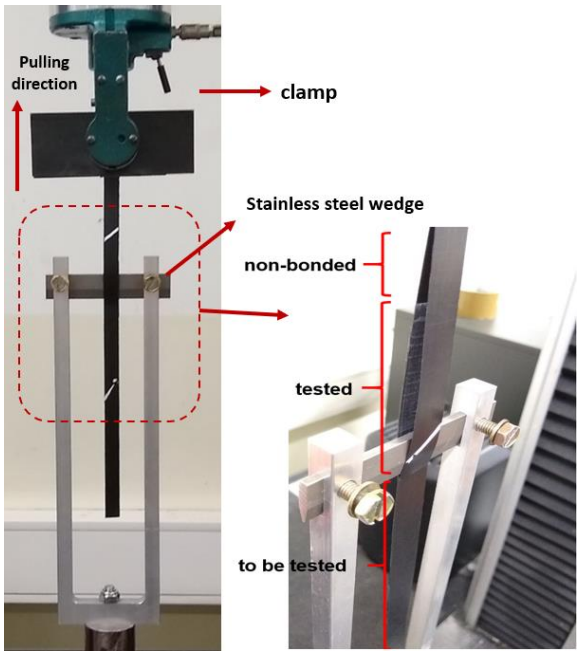

Figure 3. Wedge peel test setup and different regions of the specimen.

2.3. X-ray Diffraction

X-ray diffraction pattern of the samples manufactured with two different cooling rates is recorded using D2 phaser XRD (Bruker AXS GmbH, Germany) to investigate the crystalline structure and the degree of crystallinity (Xc). X-ray source is CuKα, and the scan is performed in the sliding range of 5° - 50° with a speed of 0.5 °/min. Xc can be measured by the ratio between the areas below crystalline peaks and the total area below the amorphous halo and the crystals.

3. Results and Discussions

Wedge peel tests are performed on five or six specimens out of each laminate depending on the case to obtain force-crack extension curves. Specimens are numbered from left to right on the plates from one to ten. The curves coming from the tensile machine for six specimens coming from different regions of plate #2 are shown in Figure 4.

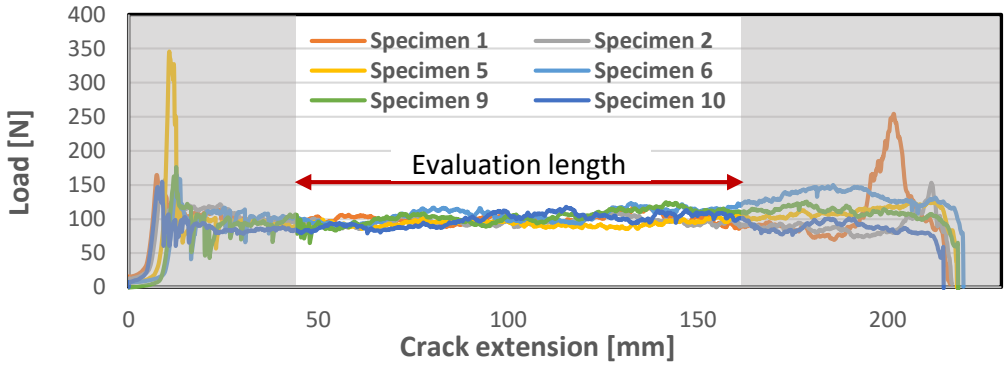

Figure 4. Load versus crack extension (delaminated length) for six specimens of plate #2 processed using Fontijne press at 240°C with 30 seconds of holding time.

The obtained peeling forces for six specimens out of one plate show stable results. Figure 5 shows the results for all tested specimens processed at different temperatures with two cooling rates where T and H denote processing temperature and holding time, respectively. Standard deviation comes from the variation between the peeling forces of six specimens tested out of each plate. Plates #5 and #10, which were processed at 220 °C with two different cooling rates with zero holding time, still exhibit competitive peel resistances compared to the samples held for 30 seconds. Hence, it can be inferred that autohesion will be completed in a fraction of a second when intimate contact is achieved. It is also evident that by increasing processing temperature, the peel resistance is growing at both cooling rates. In addition, there is a pronounced increase in peel resistances by switching from the slower cooling rate to the specimens processed at the higher cooling rate.

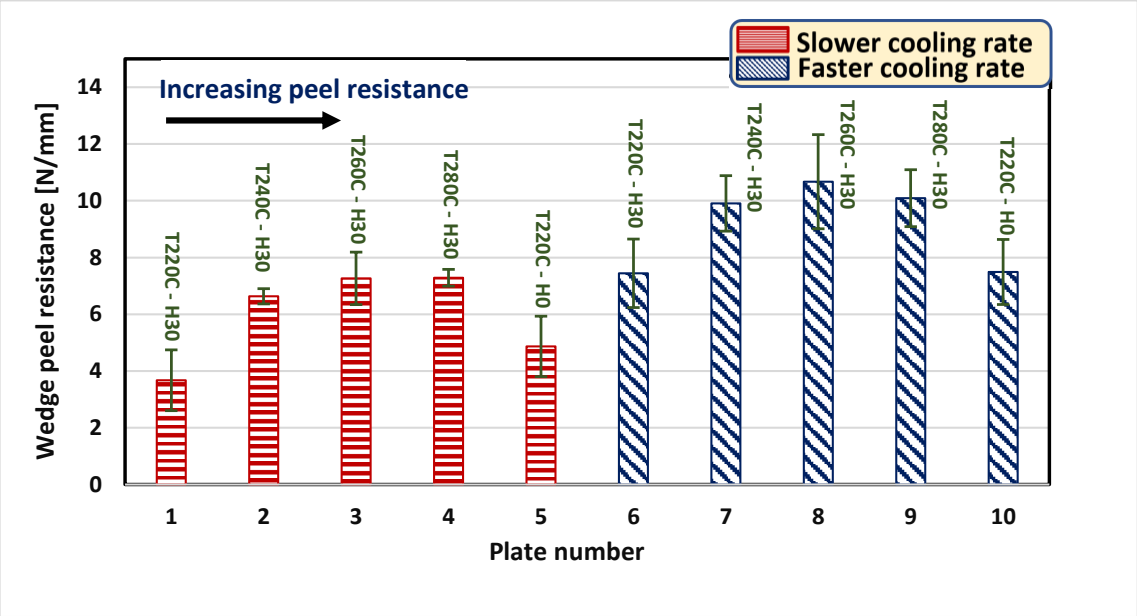

Figure 5. Average wedge peel resistance for different specimens of each plate processed at various temperatures and cooling rates based on the processing conditions in Table 1.

This behavior is primarily correlated to the different levels of crystallinity in the sample. The degree of crystallinity is lower for the faster cooling rate, and there should be less brittle crystalline structure available in the structure. Hence, their higher content of the more ductile amorphous region could result in a higher peel resistance.

To further investigate the samples crystalline structure, XRD patterns are obtained. As previously indicated in the literature [11], PA6 exhibits polymorphism behavior and could form alpha and gamma phases. A deconvolution procedure is followed using Gaussian functions to separate crystalline peaks and amorphous halo. Finally, the Xc is calculated to be 40 % for the slow cooling rate sample and 35 % for the faster cooling rate. Finding an absolute value for Xc using an XRD pattern is not straightforward for CF-reinforced composite materials since carbon fibers and their semi-crystalline structure can affect the results. Moreover, baseline correction and fitting parameters during deconvolution can alter the results. Another difficulty is the differences between the density of each crystalline structure at different cooling rates since the density will change based on the degree of order. Therefore, more investigations and maybe other techniques such as DSC are still needed to measure Xc for different conditions.

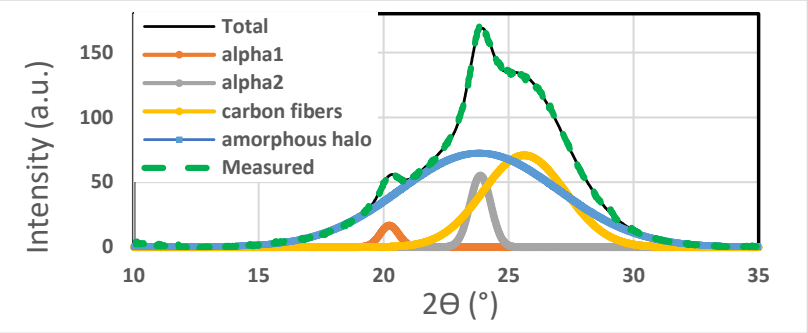

Figure 6. XRD pattern of plate #3 and deconvoluted amorphous halo and crystalline peaks.

The DCB force-displacement curves of two specimens processed using different cooling rates are shown in Figure 7. The result shows that crack initiation happens at almost the same displacement. Stick-slip growth of cracks is also observed in both cases. This indicates that the crack growth is not continuous but contains steps of rapid growth followed by crack arrest. Moreover, initiation points might be affected by the presence of a blunt crack tip and resin pockets in the vicinity of the crack starter tip. Therefore, to calculate G_{Ic}, an average is taken among the G values after initiation, which corresponds to the peak forces before each sudden drop in force. Based on the results shown in Figure 7, the average G_{Ic} for the fast cooling rate sample is measured to be 2.4 kJ/m2, while 1.6 kJ/m2 for the slower cooled sample.

We would like to emphasize that performing the DCB test on thin CF-reinforced thermoplastic laminates is challenging. This is because the fracture toughness of the PA6-PA6 interface here is much higher than the fracture toughness of adhesively bonded CFRTP-Aluminum. Thus, the crack can readily jump to the Al-composite interface. Hence, specific preparation and test procedure must be taken to avoid undesired failure, which would be our focus for future studies.

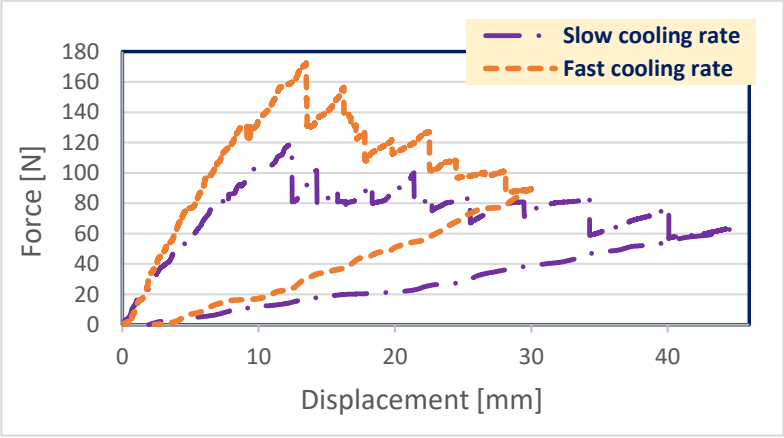

Figure 7. Force-displacement curves obtained using DCB setup for $[0°]_4$ thin laminate attached to Al beams. Two laminates processed at different cooling rates are compared.

4. Conclusion

The effect of different processing temperatures and cooling rates on the consolidation and bond strength development of the CF/PA6 laminates is investigated. Using the WPT, the interlaminar peeling resistance (strength) of the 4-ply UD laminates showed an increase from 3.7 to 7.3 N/mm by increasing processing temperature from 220 °C (melting temperature) to 260 °C and

280 °C (almost the same range recommended by the supplier). Comparing two different processing methods having different cooling rates, it was deduced that peel resistance could increase substantially by increasing the cooling rate. This finding agrees with what was reported previously in the literature and results from a lower degree of crystallinity or an increased amount of ductile amorphous phase. The crystalline structure of the CF/PA6 composites is assessed using XRD measurements. $\alpha 1$ and $\alpha 2$ phases, and the peak for CFs are detected at the expected sliding angles. Mode-I fracture toughness for slow and cooling rate is found to be 1.6 kJ/m2 and 2.4 kJ/m2 for slow and fast cooling rate specimens, respectively, which confirms the higher fracture toughness of the fast-cooled samples.

Acknowledgements

The work leading to this paper has been funded by the ICON project “ProPeL”, which fits in the MacroModelMat (M3) research program, coordinated by Siemens (Siemens Digital Industries Software, Belgium), and funded by SIM (Strategic Initiative Materials in Flanders) and VLAIO (Flemish government agency Flanders Innovation & Entrepreneurship).

5. References

1. Yassin K, Hojjati M. Processing of thermoplastic matrix composites through automated fiber placement and tape laying methods: A review. Journal of Thermoplastic Composite Materials 2018;31:1676–725.
2. Qureshi Z, Swait T, Scaife R, El-Dessouky HM. In situ consolidation of thermoplastic prepreg tape using automated tape placement technology: Potential and possibilities. Composites Part B, 2014; 66:255–67.
3. Uematsu H, Mune K, Nishimura S, Koizumi K, Yamaguchi A, Sugihara S, et al. Fracture properties of quasi-isotropic carbon-fiber-reinforced polyamide 6 laminates with different crystal structure of polyamide 6 due to surface profiles of carbon fibers. Composites Part A, 2022;154:106752.
4. Schäfer PM. Consolidation of carbon fiber reinforced polyamide 6 tapes using laser-assisted tape placement. PhD Thesis. Technische Universität München, 2017.
5. Stokes-Griffin CM, Kollmannsberger A, Compston P, Drechsler K. The effect of processing temperature on wedge peel strength of CF/PA 6 laminates manufactured in a laser tape placement process. Composites Part A, 2019;121:84–91.
6. Yang F, Pitchumani R. Nonisothermal healing and interlaminar bond strength evolution during thermoplastic matrix composites processing. Polym Compos 2003;24:263–78.
7. Çelik O, Peeters D, Dransfeld C, Teuwen J. Intimate contact development during laser assisted fiber placement: Microstructure and effect of process parameters. Composites Part A, 2020;134:105888.
8. Toray Advanced Composites. Toray Cetex® TC910 PA6: Product Data Sheet 2019. https://www.toraytac.com/product-explorer/products/r2Vf/Toray-Cetex-TC910.
9. Lamontia MA, Gruber MB, Systems A, Drive S. Remaining developments required for commercializing in situ thermoplastic ATP. Proceedings of the 2007 SAMPE Conference and Exhibition, Baltimore, MD 2007.
10. ASTM. D5528-13. Standard test method for mode I interlaminar fracture toughness of unidirectional fiber-reinforced polymer matrix composites. ASTM International; 2013.
11. Preda FM. Dynamics of polyamide in the solid state in presence of solvents and in the molten state. PhD Dissertation. University of Lyon, 2016.

  doi:10.5075/epfl-298799_978-2-9701614-0-0

AN EXPERIMENTAL STUDY OF CRACK PROPAGATION IN STIFFENED OVER-HEIGHT COMPACT TENSION (SOCT) SPECIMENS

Xiaoyang, Sun[a], Xiaodong, Xu[a,b], Shimizu, Takayuki[c], Michael R. Wisnom[a]

a: Bristol Composites Institute, Queen's Building, University Walk, Bristol BS8 1TR, UK – xiaoyang.sun@bristol.ac.uk
b: University of the West of England, Coldharbour Lane, Bristol BS16 1QY, UK
c: Research & Innovation Centre, Mitsubishi Heavy Industries, LTD. 10, Oye-cho, Minato-ku, Nagoya, 455-8515, Japan

Abstract: *In this paper, three Stiffened Over-height Compact Tension (SOCT) specimens were tested to investigate the damage mechanism when a crack encounters a stringer in Quasi-Isotropic (QI) laminates, where the stringer is simulated by a strip representative of a stringer foot. SOCT specimens consist of a 4 mm thick skin sandwiched by a 2 mm stringer on each side of the skin at the rear of the specimen, the stringers were co-cured to the skin. It was found that severe skin-stringer debonding occurred while no stringer breakage was observed. It is believed that as the crack propagates in the skin and causes skin-stringer debonding, load is transferred to the stringers. Skin fracture did not induce crack propagation in the stringer, but rather large areas of skin-stringer debonding.*

Keywords: Fracture; Debonding; Stiffener; Stringer; Delamination.

1. Introduction

With the desire for more efficient design of composite structures, detailed knowledge for the onset and subsequent propagation of damage is very important. Designing large composite structures is a complex task of balancing many design drivers - with notched strength being one of the critical ones. Large load-carrying notched composite structures used in aerospace applications often consist of a skin and stringers which may act as crack stoppers. Hence an accurate understanding of the interaction between trans-laminar fracture propagating in the skin and stringers and stringer debonding is of vital importance. Previously, we reported the damage evolution [1] and initial R-curves [2] for translaminar fracture of laminates using three different sized in-plane Over-height Compact Tension (OCT) specimens. In this study, two stringer feet are co-cured to the rear end of the OCT specimen on either side to form a new Stiffened OCT (SOCT) specimen. The aim is to investigate the interaction between trans-laminar fracture and stringer debonding.

2. Test method

The SOCT specimen geometry is shown in Figure 1. SOCT specimens were manufactured with Hexcel's HexPly® IM7/8552 carbon/epoxy unidirectional prepreg with a 0.125 mm nominal cured ply thickness. The stacking sequence was $[45/90/-45/0]_{4s}$ for the skin and $[45/90/-45/0]_4$ and $[0/-45/90/45]_4$ respectively for the 2 mm stringers on either side of the specimen, creating a symmetric layup. The location of the stringers is highlighted in Figure 1. The stringers were laid-up on the skin prior to curing, with 2 mm spacers also made from IM7/8552 pre-preg placed adjacent to the stringers to ensure the whole laminate panel stays flat during curing. The laminate panel, including the skin, stringers and spacers were all cured in one session according

  doi:10.5075/epfl-298799_978-2-9701614-0-0

to the manufacture's specifications. Individual SOCT specimens were cut from the large laminate using a diamond coated saw cutter. The SOCT specimens were tested in a hydraulic-driven Instron 100kN test machine under displacement control at a rate of 1 mm/min. No anti-buckling guides were necessary as no overall buckling of the specimen was observed. Figure 2 shows the test set-up, with the loads being applied via loading arms and pins. The loads were measured at the test machine, and the displacements were measured at the pins which were connected to the crossheads. It was found that the crosshead displacement is very close to the video extensometer measured displacement at the loading pins, so crosshead displacements are used throughout this paper for the Pin Opening Displacement (POD).

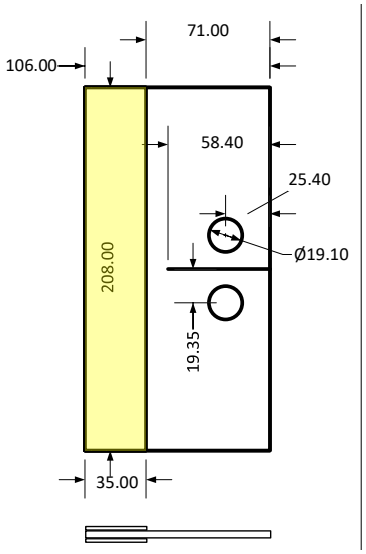

Figure 1. SOCT specimen dimensions, all dimensions in mm.

Figure 2. A photo showing the test set-up.

  doi:10.5075/epfl-298799_978-2-9701614-0-0

3. Test results

Three uninterrupted tests have been carried out with the SOCT specimens. Loads increased linearly at the beginning. A high degree of resemblance can be found in these three cases during the initial linear portion of the test, followed by a number of small load-drops – caused by crack propagation in the skin. Load increases overall during these small load drops, reaching a maximum load of approximately 18kN. All three cases suffered from compressive failure at the rear of the specimen underneath the stringers at the final stage of the tests. None of the cases showed stringer fracture. Figure 3 shows the load-displacement curves from the three tests.

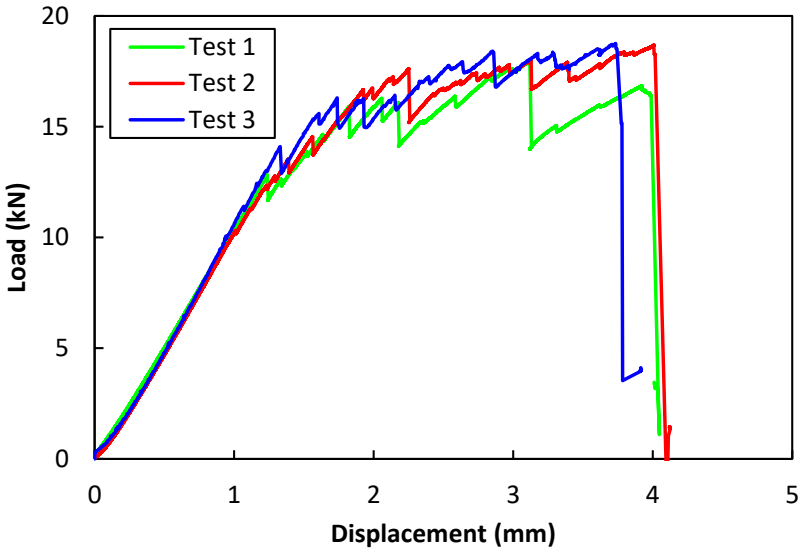

Figure 3. Load-displacement curves of the three SOCT specimens.

The peak load is approximately the same for all three specimens tested, with test 1 and test 2 having the same displacement at ultimate failure. The ultimate failure of the specimen for all three cases was induced by the compressive failure of the skin at the rear end. Special care has been taken during the testing phase to observe any potential buckling occurring of the specimen, and none was found.

4. Results Analysis

By observing the specimens both during testing and the failed specimens after testing has finished, shown in Figure 4 to Figure 6, a few observations can be made –

1. All three specimens exhibited severe skin-stringer debonding, the debonding is especially apparent within the area at the rear of specimen.
2. No stringer fracture or breakage has been observed and given all specimens have been tested to ultimate failure, it can be concluded that stringer fracture does not occur for this specimen geometry and material combination.
3. When fracture in the skin propagates towards the stringer it does not promote fracture in the stringers, rather, the skin fracture continues in the skin and causes skin-stringer debonding.
4. Compressive failure at the rear of the specimen occurs only in the skin, while the stringers avoid the compressive failure issue as they debond from the skin and locally buckle out.

  doi:10.5075/epfl-298799_978-2-9701614-0-0

Figure 4 to figure 6 show the surface damage morphologies of the failed specimens. All three specimens are in very similar damage states – stringers showing no surface damage while skin-stringer debonding is apparent. Through these observations, the proposed damage mechanism of the SOCT specimens is as follows – as the load applied to the specimen increases, a crack starts to propagate from the machined notch towards the rear of the specimen. Such crack propagation in the skin is accompanied by growth of a damage process zone which includes local delamination and splitting of the 45° and 90° plies. As the crack and splitting reaches the stringer, skin-stringer debonding takes place. The debonded area increases as the displacement increases which allows the crack in the skin to open-up. The load-bearing capacity of the skin decreases as the crack propagates, resulting in the load being transferred to the stringers. Due to stringers being 2 mm thick on each side of the skin, their load bearing capacity is relatively high, hence compressive failure occurs at the rear of the skin prior to the stringers exhibiting tensile failure.

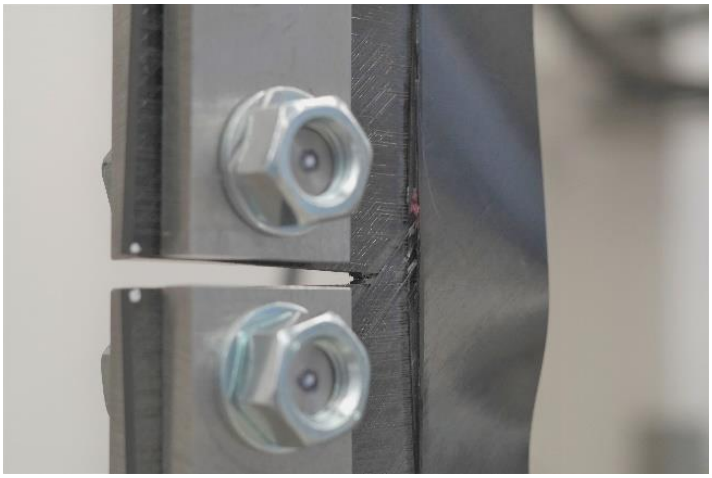

a) Test 1 after compressive failure showing large area of skin-stringer debonding without stringer failure.

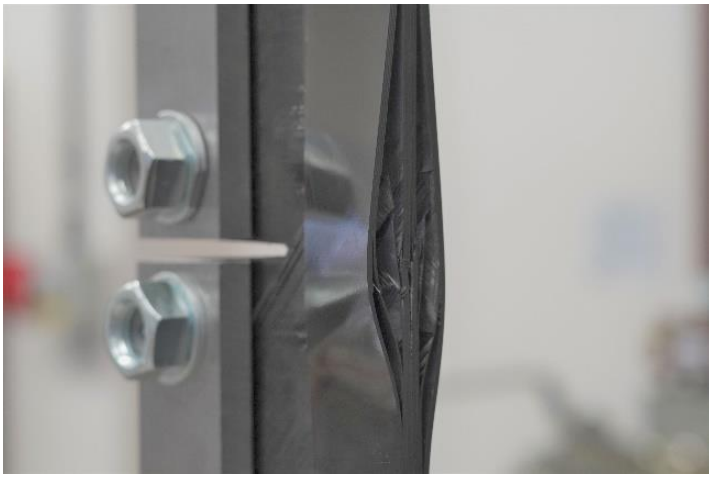

b) Test 1 specimen showing compressive failure at the rear without stringer failure. Stringers at the rear of the specimen have bulged out due to compression, no stringer cracking observed.

Figure 4. Photos taken from SOCT Test 1.

  doi:10.5075/epfl-298799_978-2-9701614-0-0

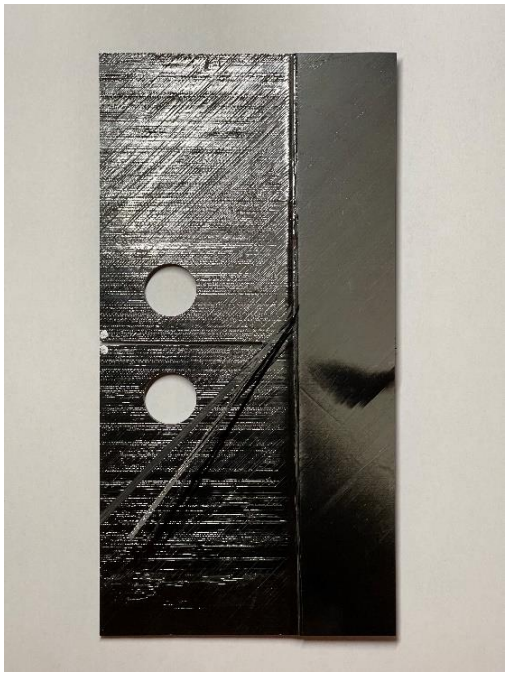

Figure 4. Test 2 specimen showing no stringer damage after compressive failure at the rear. Triangular black area on the stringer is the stringer bulging out as compressive failure in the skin underneath it has created a thicker damage zone in the skin.

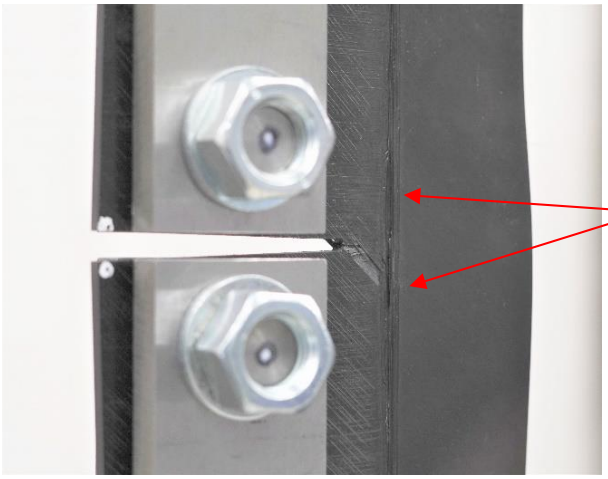

a) Test 3 specimen showing skin surface splitting and skin-stringer debonding.

  doi:10.5075/epfl-298799_978-2-9701614-0-0

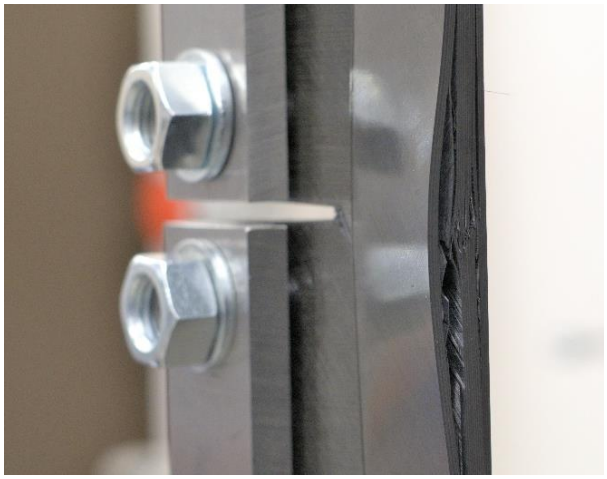

b) Test 3 specimen showing skin compressive failure at the rear and skin-stringer debonding.

Figure 6. Photos taken from SOCT Test 3.

5. Discussion

Xu et al. [1] published tensile test results of unstiffened OCT specimens of three different sizes – scaled down, baseline, and scaled up. The baseline set is of value to the current study as the specimen geometry is identical to the SOCT specimen tested, except without the stringers. Figure 7 shows a comparison between the typical SOCT and baseline OCT load-displacement curves. SOCT results exhibit approx. 50% higher peak load values and a lack of the gradual load decreasing trend that is present in the baseline OCT specimens. The higher peak load shows that the SOCT specimen is much tougher than the OCT specimen. The lack of the load decreasing trend can be attributed to the load being transferred to the stringers as the crack propagates in the skin, a mechanism which does not exist in the baseline OCT specimens. Both the SOCT specimens and the baseline OCT specimens fail in compression at the rear at approx. 4 mm displacement.

  doi:10.5075/epfl-298799_978-2-9701614-0-0

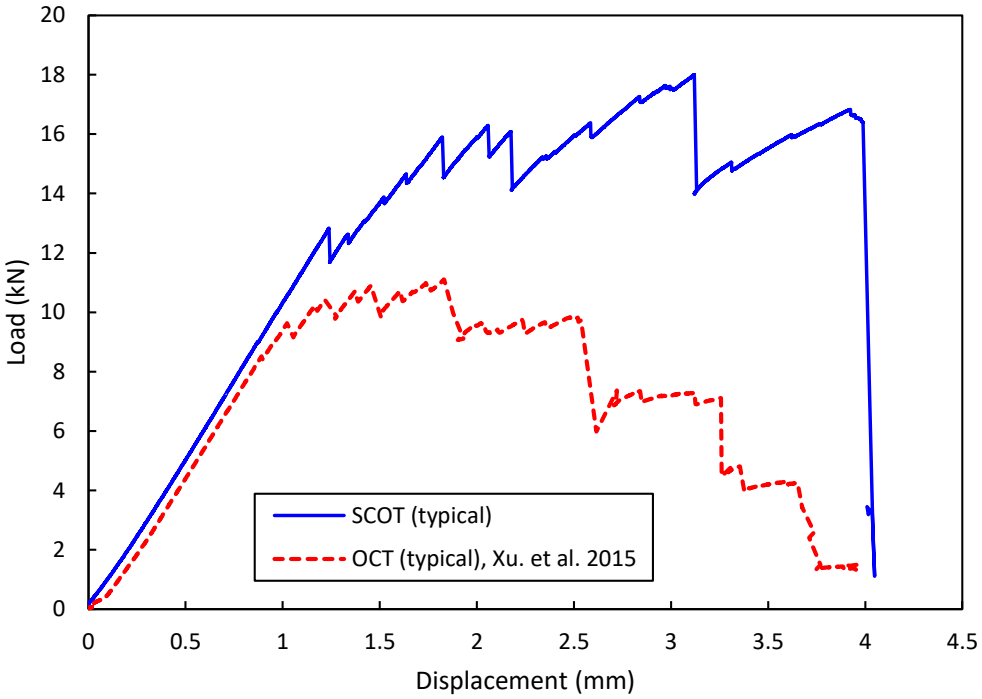

Figure 5. Comparison of typical load-displacement curves of SOCT specimens and OCT specimens of same in-plane dimensions, [1].

6. Conclusions

Compared to the same specimens without stringer feet, the SOCT specimens yielded substantially higher peak loads and were able to maintain the high load for much more of the displacement range. A closer inspection of the failed specimens showed a severe skin-stringer debonding – in all three cases, the stringer feet have debonded from the skin over a large part of the initially bonded area. No stringer foot failure was observed in any of the three specimens. Acting as a crack stopper, the stringer feet lead to a significantly delayed crack propagation even after skin-stringer debonding has initiated.

References

[1] Xu X, Wisnom MR, Mahadik Y & Hallett SR, Scaling of fracture response in over-height compact tension tests, Composites, Part A: Applied Science and Manufacturing, 2015;69: 40-48. https://doi.org/10.1016/j.compositesa.2014.11.002

[2] Xu X, Sun X & Wisnom MR. Initial R-curves for trans-laminar fracture of quasi-isotropic carbon/epoxy laminates from specimens with increasing size. Composites Science and Technology. 2021;216:109077. https://doi.org/10.1016/j.compscitech.2021.109077

MODELING MICRO-DAMAGE DEVELOPMENT IN FUNCTIONALLY GRADED KNITTED AND WOVEN CARBON/STEEL FIBRE COMPOSITES

Olga, Kononova[a], Vladislavs, Jevstignejevs[a], Andrejs, Pupurs[a], Anish Niranjan, Kulkarni[a]

a: Riga Technical University – olga.kononova@rtu.lv

Abstract: *Mechanical joining of composite and metal components is an increasing necessity in various engineering applications for improved efficiency and minimal structural weight. Mechanical joints such as bolted and adhesive joints have been widely implemented in aerospace, automotive and wind power applications. However, they possess some significant drawbacks such as stress concentrations, abrupt change of stiffness and brittleness of failure. To overcome these disadvantages a novel type of composite/metal joint with textile mesostructure was investigated in the present study, where carbon fiber and steel fiber yarns are gradually interwoven obtaining a functionally graded composite material. The present work presents results of numerical simulations performed in ANSYS FEM software and their comparison with experimental results of mechanical elastic properties of knitted and woven carbon/steel fiber composites. Results show good agreement between numerical predictions and experimental results.*

Keywords: composite/metal joint; knitted composites; woven composites; FEM simulation

1. Introduction

Polymeric composite materials, especially carbon fiber reinforced plastics, have become widespread for a variety of civil and military applications due to their advantageous properties such as low weight, high strength and thermomechanical stability. The necessity of metal/composite joints has increased with the growth of production to ensure structural integrity between metal and composite structural parts. Traditional mechanical joints such as bolted, selfpiercing rivet (SPR), adhesive joints [1, 2] have some significant drawbacks. Mechanical properties of SPRs are influenced by geometrical features, die pressure and shape. This has a significant impact on fatigue life and static strength of SPR composite/metal joints [3]. SPR joints can cause damage in both the fiber reinforcement and in the matrix, introduce stress concentration points and consequently cause reduction of structural integrity. Another disadvantage of such joints is that the additional joining elements increase the weight. Adhesive bonding offers light-weighted structures with respect to other joint types providing improved fatigue life and damage tolerance. However, the stress concentrates at the edege of the bond-line causing failure, which is often catastrophic.

To overcome these disadvantages a novel type of composite/metal joint with textile mesostructure is proposed in the present study, where carbon fiber and steel fiber yarns are gradually interwoven obtaining a functionally graded composite material. Given the gradual transition between the dissimilar materials, the proposed textile joint leads to reduced stress concentrations and residual stresses compared with conventional composite/metal joints thus also achieving an improvement in mechanical strength of the joint.

  doi:10.5075/epfl-298799_978-2-9701614-0-0

The novel type of composite materials was obtained on the base of knitted fabric and woven fabric reinforcements. For the production of reinforcement, the most easy-to-manufacture methods of weaving yarns were chosen: single jersey method for knitted fabric and plane weave for woven fabric.

In some cases textile reinforced composites are competitive with traditionally fabricated composites which uses the prepregging, layers stacking and autoclave manufacturing methods. Layered composites have relatively low tensile and shear strength in thickness direction leading to low wearability and impact resistance. All these problems can be solved replacing them by 3D textile reinforced composites. The knitting process leads to the formation of a high degree of curvature of yarn in the knitted fabric compared to other textile manufacturing processes [4–6]. Knitted fabrics have a high porous structure, which reduce fiber volume fracture of composite material [7].

Several studies have analysed the dimensional properties of knitted structures, prevailing from Chamberlain, Peirce, Leaf and Glaskin, Munden and Kawabata, Choi [8 – 9]. These studies presented either formulated geometrical models consisting of curves of known analytical description, for example circular arcs and straight lines, or the results of measurements that have been carried out on a series of knitted structures. The Leaf and Glaskin model was preferred due to the ease of measuring a series of knitted structures and obtaining a smooth 3-D continuous structure of knitted fabric. The structural geometry of the fabric can be defined if three geometric parameters, the wale number W, the course number C and the yarn diameter d are given. The wale number can be described as the step of fabric's loops per unit length along the width (in the course) direction and the course number can be described as the step along the length (in the Wale direction).

Weaving is the production of fabric by interlacing two sets of yarns: the warp yarn and the weft yarns. The form of interlacing of warp and weft yarns can be divided into three categories- plain, twill and satin weave. The simplest plain weave reinforcement was used in this study. The main advantages of these materials are high strength to weight ratio, possibility of obtaining any shape and easy production [10]. The most popular geometrical model of woven fabric is Peirce's model with different modification for cross-section of warp and weft yarn: circular, elliptical and race track cross-section [11].

2. Knitted carbon fiber / steel fiber yarn composite materials

2.1 Geometrical model

Weft-knitted fabrics or single jersey, which are produced by interlacing one yarn, was used for investigation. The weft-knitted fabric reinforcement and its main geometrical characteristics are shown in Figure 1. The vertical and horizontal row of loops in knitted fabrics are known as wale and course, W – wale spacing, C – course spacing. Due to the symmetrical and repeating distribution of yarn loops, instead of focusing on entire fabric, 3D unit cell is analysed in order to efficiently use the computational resources. The Leaf and Glaskin 3D geometrical model was used for obtaining of x, y and z coordinates for spatial curve of a loop.

3D curves defining the yarn positions were generated using the spline function in CAD software. Yarns were generated as homogenized rods. The rest of the unit cell was filled with solid material representing epoxy resin.

  doi:10.5075/epfl-298799_978-2-9701614-0-0

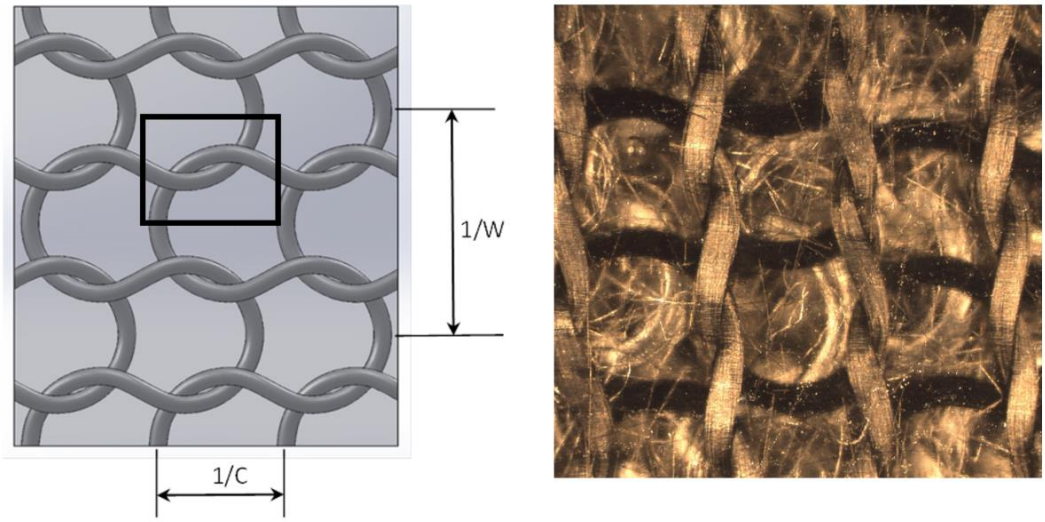

Figure 1. The knitted fabric reinforcement and its main geometrical characteristics, 3D unit cell of knitted fabric

Two types of carbon fiber filaments and one type of stainless steel fibers (in continuous yarns) were selected and purchased from the commercially available assortment to perform the experimental work of the present project. Following types of carbon fibers were selected: Toray T300-1K 50A (Japan) and Toray FT300B-3K-50B (France) fibers.

Regarding metallic fibers, stainless steel yarn SY 11/1 (91 tex) filaments manufactured and provided by Bekintex (Belgium) were used.

Four different types of knitted fabrics as a reinforcement were used for composite materials production: steel fiber yarn SY11/1 reinforcement, carbon fiber yarn T300-1000 (1000 filaments) reinforcement, hybrid reinforcement steel fiber yarn SY11/1 and carbon fiber yarn T300-1000 reinforcement, steel fiber yarn SY11/1 reinforcement (three yarns). The main geometrical characteristics as wale spacing W, course spacing C and fiber yarn diameter d were determined after the production of composite materials specimens (Table 1), since the weft-knitted fabrics is easily subject to deformation.

Table 1: Geometrical characteristics of knitted fabric

Number	Reinforcement	W, loop/cm	C, loop/cm	d, cm
1	SY11/1	2.69	5.36	0.012
2	T300-1000	2.18	5.21	0.022
3	hybrid SY11/1+T300-1000	2.50	5.00	0.012/0.022
4	SY11/1x3	2.72	5.10	0.012x3

To ensure the necessary hybridity of composite materials, the reinforcements were produced both from one type of fiber yarn and from two, while carbon and steel fibers yarns being woven together as it shown on Figure 2a. In addition, a reinforcement consisting on three fiber yarn of

  doi:10.5075/epfl-298799_978-2-9701614-0-0

the same type - steel fiber yarn (Figure 2b), was produced to increase fiber volume fraction of knitted fiber yarn composite material, which is usually quite low.

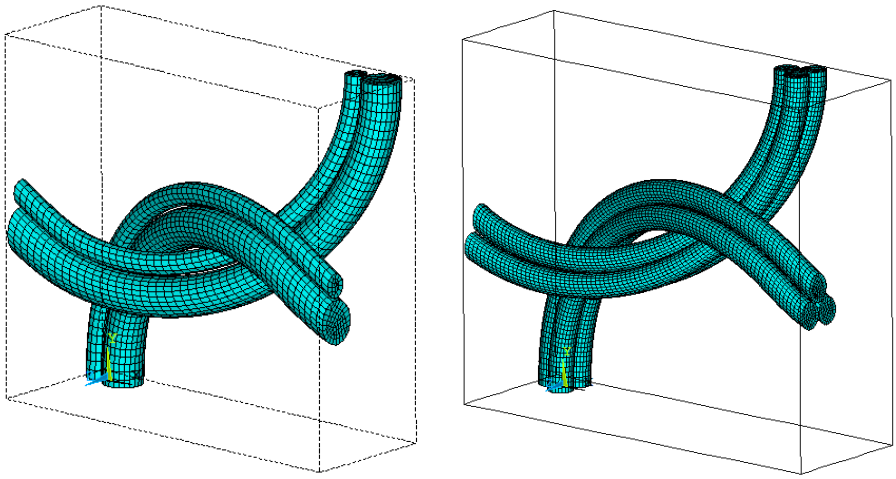

Figure 2. 3D unit cell of knitted fabric a) hybrid two-yarn SY11/1+T300-1000 ; b) three-yarn SY11/1x3

2.2 Material model and boundary conditions

3D unit cells geometry created in SolidWorks software was exported to ANSYS FEM software for further analysing. Epoxy resin LY1564 was used for composite material fabrication, epoxy matrix assumed as isotropic elastic material with following constants: Elastic modulus E = 3 GPa and Poisson's ratio ν = 0.29.

Carbon fiber and steel fiber reinforced yarns were represented as homogenized bundles impregnated with epoxy, hence their properties were defined as for transversally isotropic materials following the spline geometry of the yarn. The elastic properties of impregnated fiber yarns are given in Table 2.

Table 2: The elastic properties of impregnated fiber yarns

Fibre	E1, GPa	E2, GPa	G12, GPa	v12	G23, GPa	v23
SY11/1	105.00	105.00	40.38	0.30	40.38	0.30
T300	230.00	20.00	12.00	0.18	7.04	0.42

Boundary conditions applied to unit cell are presented in Figure 3. Left, bottom and front faces of the unit cell have symmetry boundary conditions, top face has coupling condition in y-axis direction, right face is displaced in positive x-axis direction to produce 1% strain, and rear face is free. Additionally, one node is fixed as shown in Fig.3. Hexahedral elements were used for the yarns and tetrahedral ones for the matrix.

  doi:10.5075/epfl-298799_978-2-9701614-0-0

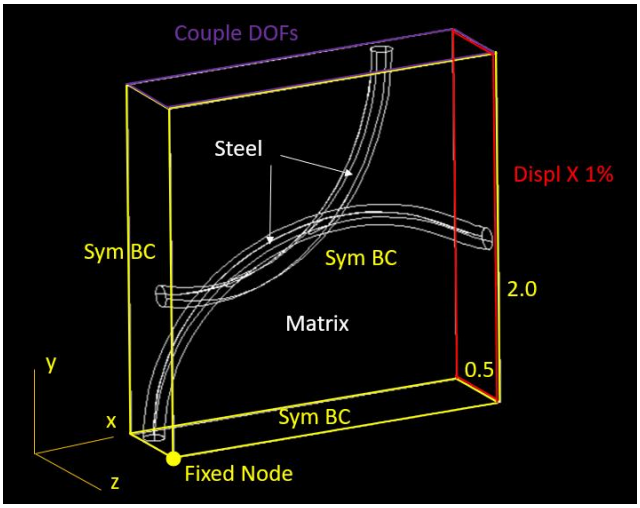

Figure 3. Applied boundary conditions

3. Woven carbon fiber / steel fiber yarn composite materials

3.1 Geometrical model

The simplest plain weave fabric was used for investigation. The woven fabric reinforcement and its main geometrical characteristics are shown in Figure 4. The Peirce's geometrical model was used: circular cross-section for steel fiber yarn and race track cross-section for carbon fiber yarn. The Peirce's model consists of straight and curved segments, straight yarn – weft and curved yarn warp; A – weft spacing, B – warp spacing. 3D curves defining the yarn positions were generated using the spline function in CAD software. Yarns were generated as homogenized rods. The rest of the unit cell was filled with solid material representing epoxy resin.

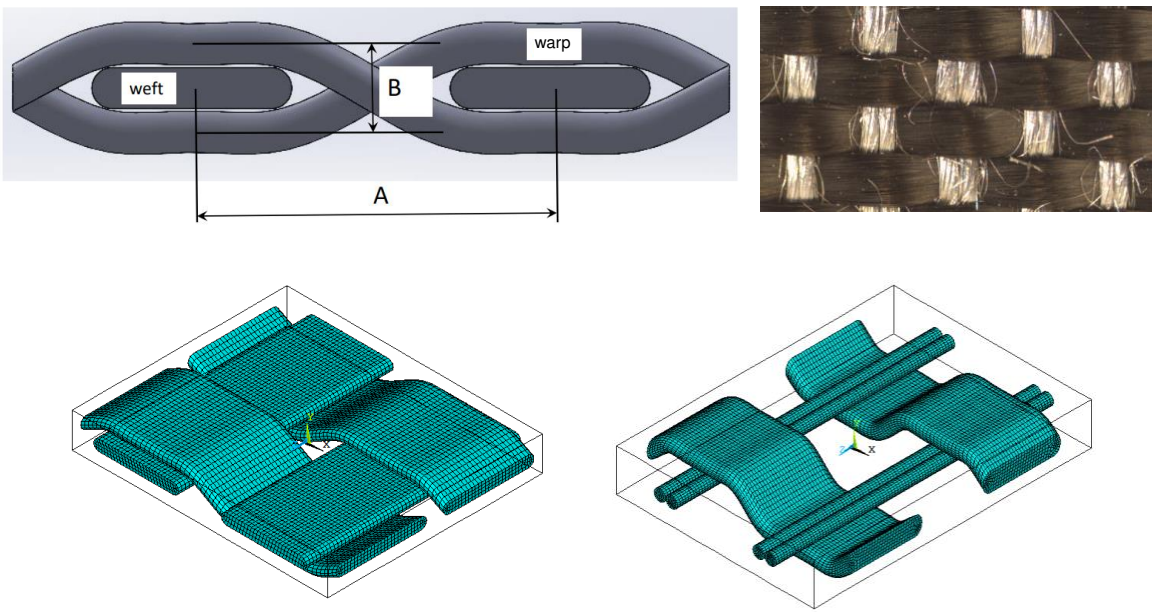

Figure 4. 3D unit cell of woven fabric and its main geometrical characteristics

  doi:10.5075/epfl-298799_978-2-9701614-0-0

Four different types of woven fabrics as a reinforcement were used for composite materials production: steel fiber yarn SY11/1 (weft and wrap), carbon fiber yarn T300-3000 (weft and wrap), hybrid reinforcement steel fiber yarn SY11/1 (warp) and carbon fiber yarn T300-3000 (weft), hybrid reinforcement carbon fiber yarn T300-3000 (warp) and steel fiber yarn SY11/1 (weft) . The main geometrical characteristics as weft spacing A, warp spacing B and fiber yarn diameter d are shown in Table 3.

Table 3: Geometrical characteristics of woven fabric

Number	Reinforcement	A, cm	B, cm	d, cm
1	SY11/1	0.146	0.034	0.012
2	T300-3000	0.144	0.121	0.038
3	hybrid SY11/1(warp)+T300-3000(weft)	0.09	0.145	0.012/0.038
4	hybrid T300-3000(warp)+SY11/1(weft)	0.104	0.146	0.038/0.012

4. Comparison of Simulation and Experimental Results

Longitudinal elastic moduli obtained experimentally according to the ASTM D3039 and by finite element simulation are shown in Table 4 for knitted carbon fiber / steel fiber yarn composite materials and in Table 5 for woven carbon fiber / steel fiber yarn composite materials.

Table 4: Longitudinal elastic modulus of knitted fabric composite materials

Nr.	Composite material, lay-up	Experimental E_L, GPa	Standard deviation, %	Simulation result E_L, GPa
1	$[T300\text{-}1000]_8$	13.41	8.47	11.94
2	$[SY\ 11/1]_8$	6.14	21.21	6.86
3	$[SY\ 11/1\ 3x]_8$	7.67	5.42	6.51
4	$[Hybrid\ SY11/1+T300\text{-}1000]_8$	11.09	4.70	11.13
5	$[T300\text{-}1000/SY11/1]_{2s}$	7.73	12.99	7.01
6	$[(T300\text{-}1000)_2/(SY11/1)_2]_s$	10.00	0.99	7.01
7	$[(T300\text{-}1000)/(\ SY\ 11/1\ 3x)]_{2s}$	6.78	25.52	5.80

Elastic moduli of symmetric and balanced composite materials with mixed lay-up Nr. 5 – 7 (Table 5) and Nr. 5 (Table 6) were calculated according to the theory of laminated composites [12].

  doi:10.5075/epfl-298799_978-2-9701614-0-0

Table 5: Longitudinal elastic modulus of woven fabric composite materials

Nr.	Composite material, lay-up	Experimental EL, GPa	Standard deviation, %	Simulation result EL, GPa
1	$[SY\ 11/1\ 2x]_3$	7.11	7.45	12.42
2	$[T300\text{-}3000]_4$	44.89	4.99	35.99
3	$[SY\ 11/1\ 2x\ (warp)+ T300\text{-}3000(weft)]_4$	9.87	5.23	8.04
4	$[T300\text{-}3000(warp) + SY\ 11/1\ 2x(weft)]_4$	35.83	4.58	16.36
5	ply Nr.3/ply Nr.4/ply Nr.3/ply Nr.4/ply Nr.3	24.93	15.30	11.46

5. Conclusions

In this study the results of initial stage of micro-damage modelling, as creation of 3D finite element models and obtaining from the linear elastic FEM simulations tensile elastic moduli, in knitted and woven carbon fiber / steel fiber yarn composite materials are presented. Woven fiber yarn composite materials expectedly showed higher elastic properties compared to knitted fiber yarn composites due to their meso-structure with less waveness of yarns and due to greater fiber volume fracture.

An analysis of the results for knitted fiber yarn composites shows that, in general, the simulation results are in good agreement with experimental values of elastic moduli, difference is within 15%. Higher values of the moduli, with respect to experimental ones, obtained for the composite reinforced with steel fiber yarn, and lower values for composite reinforced with carbon fiber yarn. A possible reason for this is the discrepancy between the real value of the transverse modulus of elasticity of the carbon fiber yarn and the value used in the finite element simulation.

The same tendency, and for the same reason, persists for woven composites - the results are close to experimental in cases where a steel fiber yarn runs along the warp, and differs significantly if a carbon fiber yarn used for the warp.

Satisfactory simulation results allow us to calculate the optimal architecture of knitted and woven fabric to obtain the required stiffness of the final composite material. The presented work demonstrates the potential benefits of application a novel type of composite/metal joint with textile mesostructure, where carbon fiber and steel fiber yarns are gradually interwoven obtaining a functionally graded composite material.

Acknowledgements

This work has been supported by Latvian Council of Science, project LZP-2019/1-0357 “Development and behavior analysis of novel textile composite/metal joints with enhanced mechanical properties”

  doi:10.5075/epfl-298799_978-2-9701614-0-0

6. References

1. Jahn J, Weber M, Boehner J, Steinhilper R. Assessment Strategies for Composite-metal Joining Technologies-A Review. Procedia CIRP. 2016;50:689–94.
2. Pramanik A, Basak AK, Dong Y, Sarker PK, Uddin MS, Littlefair G, et al. Joining of carbon fibre reinforced polymer (CFRP) composites and aluminium alloys – A review. Composites Part A: Applied Science and Manufacturing. 2017 Oct 1;101:1–29.
3. Pickin CG, Young K, Tuersley I. Joining of lightweight sandwich sheets to aluminium using self-pierce riveting. Materials & Design. 2007 Jan 1;28(8):2361–5.
4. Kyosev Y, Angelova Y, Kovar R. 3D Modeling of Plain Weft Knitted Structures of Compressible Yarn. Research Journal of Textile and Apparel. 2005 Feb 1;9(1):88–97.
5. Tong L, Mouritz AP, Bannister MK. 3D fibre reinforced polymer composites. 2002;241.
6. Huysmans G, Verpoest I, van Houtte P. A damage model for knitted fabric composites. Composites Part A: Applied Science and Manufacturing. 2001 Oct 1;32(10):1465–75.
7. Duhovic M, Bhattacharyya D. Simulating the deformation mechanisms of knitted fabric composites. Composites Part A: Applied Science and Manufacturing. 2006 Nov;37(11):1897–915.
8. Kurbak A. Geometrical models for weft-knitted spacer fabrics: http://dx.doi.org/101177/0040517516631320 [Internet]. 2016 Feb 15;87(4):409–23.
9. Huang ZM, Zhang Y, Ramakrishna S. Modeling of the progressive failure behavior of multilayer knitted fabric-reinforced composite laminates. Composites Science and Technology. 2001 Nov 1;61(14):2033–46.
10. Ravandi M, Moradi A, Ahlquist S, Banu M. Numerical Simulation of the Mechanical Behavior of a Weft-Knitted Carbon Fiber Composite under Tensile Loading. Polymers 2022, 14, 451.
11. Behera BK, Militky J, Mishra R, Kremenakova D. Modeling of Woven Fabrics Geometry and Properties, Woven Fabrics 2012, Prof. Han-Yong (Ed.), ISBN: 978-953-51-0607-4, In Tech
12. Halpin JC Primer on Composite Materials analysis. Lancaster (USA): Tehnomic Publishing Company, Inc.; 1992.

  doi:10.5075/epfl-298799_978-2-9701614-0-0

ANALYSING AND PREDICTING FAILURE OF INJECTION-MOULDED SHORT-FIBRE COMPOSITE COMPONENTS

Yuki Fujita[a,b,d], Satoshi Noda[b], Junichi Takahashi[c], Emile S. Greenhalgh[d], Soraia Pimenta[a]

a: Department of Mechanical Engineering, Imperial College London, South Kensington Campus, SW7 2AZ London, United Kingdom
Email: y.fujita@imperial.ac.uk

b: Polymers R&D Planning and Business Development, Asahi Kasei Corporation, 210-0863, 1-3-1, Yako, Kawasaki, Japan

c: Asahi Kasei Plastics Vietnam Co.,Ltd, 29 Le Duan, Ben Nghe Ward, District 1, HCMC, Vietnam

d: Department of Aeronautics, Imperial College London, South Kensington Campus, SW7 2AZ London, United Kingdom

Abstract: *Injection-moulded short-fibre composites are lightweight materials suitable for high-volume applications; however, current simulation methods for these materials cannot yet predict failure accurately. This work proposes a methodology to predict failure of injection-moulded short-glass-fibre reinforced PA66 composite components, based on experimentally measured properties. The material's fracture toughness was characterized for different fibre orientations, and these values were used as the input for cohesive zone modelling in Finite Element analyses of the components, coupled with simulations of the injection-moulding process. The coupled process/structural simulations using cohesive zone modelling presented excellent agreement with the experimental data of the component tests, highlighting the importance of accounting for the finite fracture toughness of the material to accurately predict the ultimate failure of injection-moulded short-fibre reinforced PA66 composite components.*

Keywords: Injection moulded components; Fracture toughness; Finite element modelling; Cohesive zone modelling; Fractography.

1. Introduction

Injection-moulded short-glass fibre reinforced thermoplastics (SFRPs) have three key advantages over conventional materials: they are lightweight, they have short production cycles, and they can be moulded into complex 3D-shaped components. These SFRPs are composed by short glass fibres (200-400 µm long) in a polymeric matrix; the injection-moulding process creates a core-shell structure with complex fibre orientation states, as fibres align along the flow direction in the shell, and along the transverse direction or randomly in the core. This microstructure leads to anisotropic and heterogeneous mechanical properties and failure modes, which complicates the design of SFRP components.

  doi:10.5075/epfl-298799_978-2-9701614-0-0

When designing SFRP components, it is necessary to predict when and where failure will occur. However, failure criteria for SFRPs are not well established; the industry faces challenges associated with the under-prediction or over-prediction of failure, leading to overly conservative design, and hence excessively heavy and costly components. The objective of this work is to develop a methodology to analyse and predict the failure of injection-moulded components manufactured with short glass-fibre reinforced polyamide 6.6.

2. Manufacturing and characterization of PA66GF components

2.1 Manufacturing and testing

Polyamide 6.6 reinforced by 50% (wt) glass-fibres (deemed as *PA66GF50*) from Asahi Kasei Corporation (Leona™14G50) was used to manufacture the components shown in Figure 1 (left) by injection moulding. Some of these components were conditioned based on ISO1110 [1] to prepare for testing under 50% of relative humidity (RH50). These PA66GF50 components were tested through quasi-static (1.0 mm/min) indentation at room temperature, under two moisture conditions: dry as moulded (DAM) and RH50. Figure 1 (right) shows the load-displacement curves of the PA66GF50 components at 23°C-DAM and 23°C-RH50 conditions. Unstable failure was seen under 23°C-DAM, while under 23°C-RH50 the components presented a more plastic behaviour and stable failure progression after reaching the peak load.

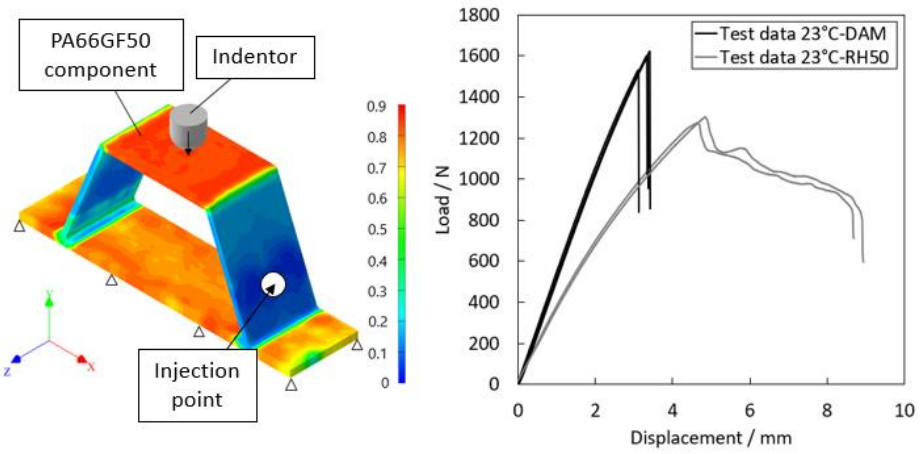

Figure 1. Left: Geometry of PA66GF50 components (contour: fibre orientation along the x direction predicted by simulating the injection-moulding process). Right: Load-displacement curves of PA66GF50 components tested under 23°C-DAM and 23°C-RH50 conditions.

2.2 Fractography

The damage mechanisms in the PA66GF50 components were investigated using scanning electron microscopy (SEM). Figure 2 shows the fracture surfaces of PA66GF50 components in the shell region near the bottom surface of the top wall directly under the indentation point. Brittle matrix failure with fibre pull-out was observed in components tested at 23°C-DAM, while ductile matrix deformation with fibre failure was observed in components tested at 23°C-RH50.

The next section reports on the characterization of the fracture toughness associated with the initiation and progression of fracture under 23°C-DAM and 23°C-RH50.

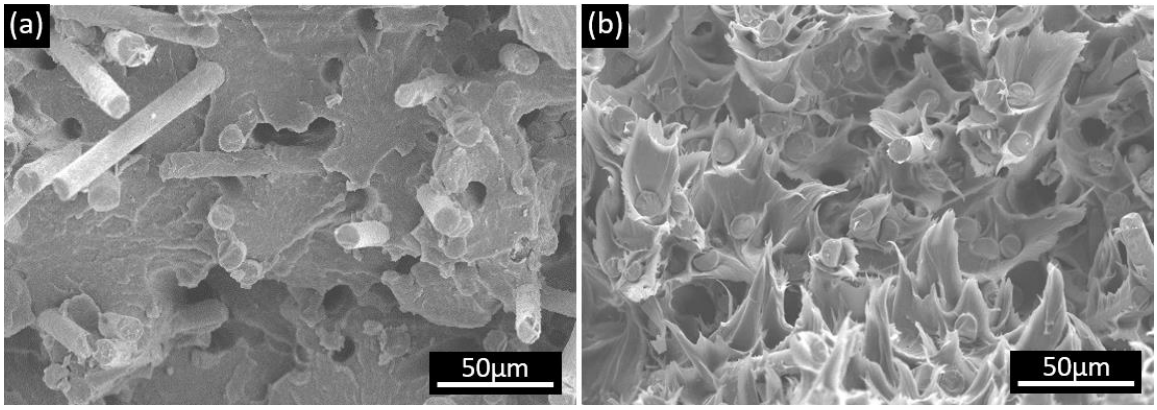

Figure 2. SEM images of the fracture surfaces of PA66GF50 components in the shell region at the centre of bottom face at tested at 23°C-DAM (a, left) and 23°C-RH50 (b, right)

3. Fracture toughness testing

3.1 Design and manufacturing of Compact Tension specimens

Since there are no established standards to characterise the initiation and propagation fracture toughness of SFRPs, modified Compact-Tension (CT) specimens [2] were designed using Finite Element (FE) simulations. Full details of the design process are shown in Reference [3], and the final geometry used is shown in Figure 3.

The CT specimens were machined from the centre of injection-moulded plates (thickness: 2mm) at several angles with respect to the flow direction (Figure 3). As with the components, some of these CT specimens were conditioned based on ISO1110 [1] to prepare them for testing at RH50 conditions.

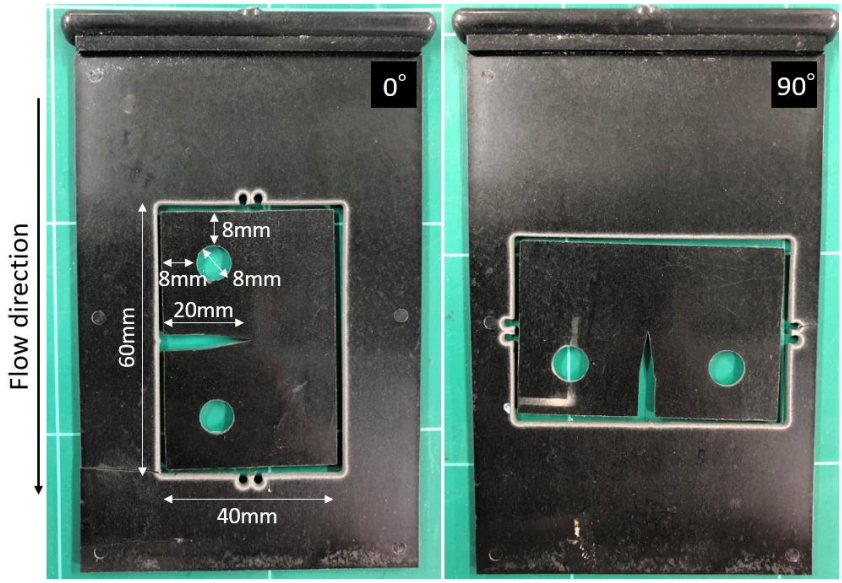

Figure 3. Photograph of CT specimens machined from injection-moulded plates.

3.2 Fracture toughness measurements

The tensile fracture toughness was measured using CT tests under static conditions. Figure 4 shows representative load-displacement curves of tested CT specimens at different machining angles. The specimens showed stable crack propagation with a progressive decrease in load for all angles and moisture conditions, and this behaviour was repeatable (full details are shown in Reference [3]).

These load-displacement curves of CT specimens were transformed into R-curves using an FE-based compliance calibration method [2-4], and the propagation fracture toughness for each specimen was determined as the plateau of its R-curve. Figure 5 shows the propagation fracture toughness (or critical strain energy release rate) (Gc) as a function of the machining angle. The fracture toughness is maximum for fracture along a plane perpendicular to the main flow direction (i.e. at 0°), and decreases progressively as the machining angle increases, reaching a minimum when the fracture plane and the main flow direction are aligned (i.e. at 90°). Moreover, the fracture toughness of specimens tested under RH50 is higher than that under DAM, which is consistent with the more ductile behaviour observed in the latter in Section 2.3.

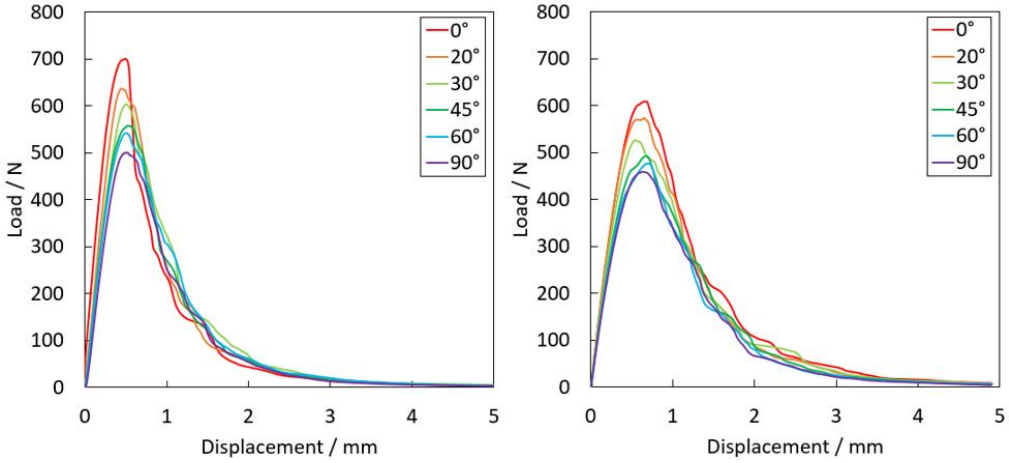

Figure 4. Representative load-displacement curves of CT specimens machined at several angles. Left: specimens tested at 23°C-DAM. Right: specimens tested at 23°C-RH50.

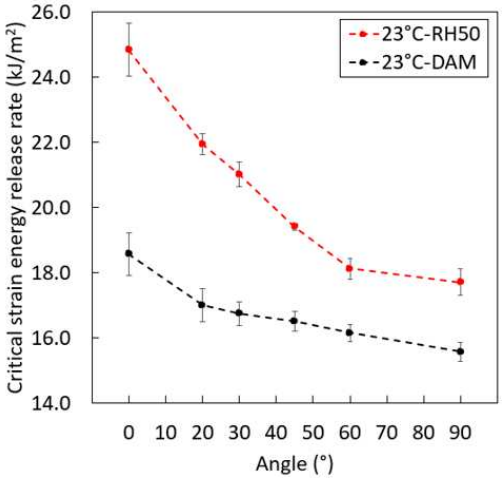

Figure 5. Propagation fracture toughness as a function of machining angles of CT specimens.

4. Finite Element modelling

4.1 Coupled process/structural simulations

Moldflow software [5] was used to simulate the injection-moulding process and to predict the fibre orientation in the components. The fibre orientation tensor was then mapped onto an Abaqus [6] Finite Element Analysis (FEA) model of the component under quasi-static indentation, using Digimat-MAP [7]. Digimat's elastic-plastic material model (which is based on Mori-Tanaka mean-field homogenization and J_2-plasticity model) was calibrated with tensile stress-strain curves obtained by testing dog-bone specimens under several machining angles, thus accounting for the anisotropy and material nonlinear response. We present full details of these coupled process/structural simulations ("coupled FEA") elsewhere [8].

Figure 6 (left) compares load-displacement curves obtained from the experiments (reported in Section 2.1) and from the coupled FEA described in the previous paragraph; for the latter, the failure point corresponds to the moment when the Tsai-Hill failure criterion is first met. A good agreement was observed regarding the initial stiffness and progressive softening, although the coupled FEA based on the Tsai-Hill criterion predicts failure initiation about 25% earlier than the failure point actually observed in the experimental results.

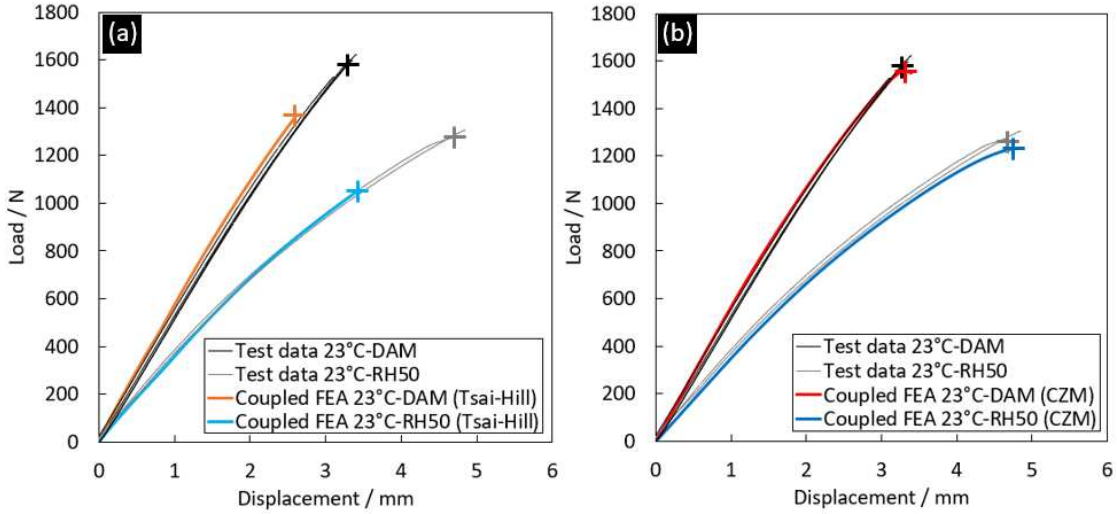

Figure 6. Comparison of load-displacement curves of PA66GF50 components. Left: experiments and coupled FEA using the Tsai-Hill criterion. Right: experiments and coupled FEA using CZM.

4.2 Cohesive zone modelling

Figure 6 (left) clearly demonstrates that the failure models currently implemented in commercially-available software based on failure initiation criteria (e.g. Tsai-Hill) is not sufficient to accurately predict the maximum observed experimental load. Therefore, to improve failure predictions, the finite fracture toughness of the material was then introduced in the simulations. The fracture toughness obtained from the experiments in Section 3.2 was used as the input for cohesive zone modelling (CZM) to predict ultimate failure of the components. This required accounting for (i) the relationship between fracture toughness and fibre orientations (derived from Figure 5), and (ii) the distinct fibre orientations in the skins and the core of the material at the fracture plane; further details are presented elsewhere [8].

  doi:10.5075/epfl-298799_978-2-9701614-0-0

Figure 6 (right) shows the comparison between load-displacement curves obtained from the experiments and those from the improved coupled FEA using CZM (with experimentally-measured fracture toughnesses). These curves show excellent agreement of the predicted failure point (with less than 1% error in failure load) under both 23°C-DAM and 23°C-RH50 conditions. This demonstrates that accounting for the finite fracture toughness of the material is essential to accurately predict the failure load of some injection-moulded SFRP components.

5. Conclusions

PA66GF50 components were tested under static indentation at room temperate in dry and wet conditions; fractography demonstrated that the presence of moisture promoted ductile failure mechanisms, which led to an increase in fracture toughness as quantified through compact tension testing. Coupled FEA using cohesive zone modelling calibrated with experimentally-measured fracture toughnesses showed excellent agreement with the experimental observations, and predicted the failure load within 1% for both dry and wet conditions. As a conclusion, accounting for the finite fracture toughness of the material in coupled simulations is required to overcome the limitations of current methodologies and accurately predict the ultimate failure of injection-moulded SFRP components.

Acknowledgements

This research was funded by Asahi Kasei Corporation under the “Material Modelling of Short-Fibre Reinforced Composites” project.

References

1. BS EN ISO 1110:2019 Plastics - Polyamides - Accelerated conditioning of test specimens.
2. Pinho S, Robinson P, Iannucci L. Fracture toughness of the tensile and compressive fibre failure modes in laminated composites. Composite Science and Technology 2006; 66:2069-2079.
3. Fujita Y, Noda S, Takahashi J, Greenhalgh E, Pimenta S. Initiation and propagation fracture toughness of injection-moulded short fibre composites under different environmental conditions. Manuscript submitted for publication, 2022.
4. Pimenta S, Pinho S, Robinson P, Wong K, Pickering S. Mechanical analysis and toughening mechanisms of a multiphase recycled CFRP. Composite Science and Technology 2010; 70:1713-1725.
5. Autodesk. Moldflow. Plastic injection and compression mould simulation for design and manufacturing (https://www.autodesk.co.uk/products/moldflow/overview, accessed on March 8th 2022).
6. Dassault Systemes. Abaqus Analysis User’s Guide Version 6.14.
7. e-Xstream engineering. Digimat USER’S MANUAL 2019.1.
8. Fujita Y, Noda S, Takahashi J, Greenhalgh E, Pimenta S. Combining fractography, fracture mechanics and FE modelling to improve the failure prediction of injection-moulded short fibre composite components. Manuscript submitted for publication, 2022.

  doi:10.5075/epfl-298799_978-2-9701614-0-0

AN ENERGY METHOD FOR PHYSICS-BASED PROGRESSIVE DAMAGE MODELLING IN COMPOSITE LAMINATES UNDER MULTIAXIAL FATIGUE LOADING

M. Hajikazemi[a,b], J. Sommer[a,b], W. Van Paepegem[a]*

a: Department of Materials, Textiles and Chemical Engineering, Faculty of Engineering and Architecture, Ghent University, Technologiepark Zwijnaarde 46, Ghent, Belgium
b: Dutch Polymer Institute (DPI), P.O. Box 902, 5600 AX, Eindhoven, Netherlands
*Corresponding author: (Mohammad.Hajikazemi@UGent.be)

Abstract: *In this paper, the estimation of energy release rates under different deformation modes is provided, for statically loaded ply cracks in multiple off-axis plies of general symmetric laminates. Such relations are provided using the variational approach which is enhanced by a homogenization approach to consider the effects of ply cracks in more than one orientation. These relations are then used in conjunction with an extended version of the energy-based fatigue crack growth law to predict the progressive development of ply cracks in several plies of a laminate under multiaxial fatigue loading. A new version of the variational approach is implemented to consider the effects of different fatigue damage mechanisms (ply cracking and delamination) on the effective properties of symmetric laminates. The comparison of the results with available experiments shows good agreement.*

Keywords: Ply cracking; Delamination; fatigue loading; homogenization

1. Introduction

The estimation of the fatigue life for a composite structural element is a very difficult task. If failure is defined to be the separation of a composite into two or more separate pieces, then it has to be considered that composite failure is preceded by progressive formation of several damage mechanisms, such as fiber/matrix debonding, matrix cracking, ply cracking, delamination, and fiber fracture, that are highly interactive, and subject to statistical uncertainty [1, 2]. As the prediction of fatigue damage initiation in composites is extremely difficult, it is usual to consider fatigue damage growth assuming that pre-existing defects of known size are already present in the material [1].

The main objective of this work is, to revisit the ply cracking fatigue energy methods developed by McCartney for $[0_m/90_n]_s$ cross-ply laminates under uniaxial fatigue loading [1], and to extend the approach to deal with more complex lay-ups and loading conditions. To do so, ply cracking energy release rates under different deformation modes are estimated, in terms of macroscopic laminate properties, for general symmetric laminates under multiaxial loading conditions. A previously developed variational approach [3] is implemented to calculate the laminate macroscopic properties in terms of crack density. It is discussed that a homogenization approach [4] can be applied to consider the effects of ply cracks in more than one orientation. A new version of the variational approach [5] is also introduced to consider the effects of interactive fatigue damage mechanisms (e.g. ply cracking and delamination) on the laminate properties

  doi:10.5075/epfl-298799_978-2-9701614-0-0

where the results are compared with fatigue experiments on Glass/epoxy [6, 7] laminates with microscopic observation of both ply crack and delamination growth under cyclic loading. A new fatigue crack growth law considering the effects of mixed mode deformations is suggested. To verify this model, fatigue experimental results on carbon/epoxy [8] laminates with microscopic observation of ply crack growth under cyclic loading are used. It is shown that the model can successfully predict the propagation of ply cracks under multiaxial fatigue loading conditions together with the impact of fatigue driven damage modes (both ply cracks and delamination) on the laminate properties.

2. Theoretical formulations

2.1 Effective stress-strain-temperature relations of a damaged symmetric laminate

Consider a symmetric laminate subject to a general triaxial loading condition involving effective uniform in-plane (σ_A, σ_T, τ_A), through-thickness (σ_t), out-of-plane shear (τ_a, τ_t) applied stresses and thermally induced residual stresses due to the temperature difference ΔT. Under the applied loading conditions, ε and γ are the corresponding axial and shear strain terms. When the effects of damage modes can be effectively homogeneous at the macroscopic laminate level, the effective stress-strain-temperature relations of a damaged symmetric laminate can be written as follows [4, 5]:

$$\varepsilon_A(\omega) = \frac{1}{E_A(\omega)}\sigma_A - \frac{\nu_A(\omega)}{E_A(\omega)}\sigma_T - \frac{\nu_a(\omega)}{E_A(\omega)}\sigma_t - \frac{\lambda_A(\omega)}{E_A(\omega)}\tau_A + \alpha_A(\omega)\Delta T, \quad (1)$$

$$\varepsilon_T(\omega) = -\frac{\nu_A(\omega)}{E_A(\omega)}\sigma_A + \frac{1}{E_T(\omega)}\sigma_T - \frac{\nu_t(\omega)}{E_T(\omega)}\sigma_t - \frac{\lambda_T(\omega)}{E_A(\omega)}\tau_A + \alpha_T(\omega)\Delta T, \quad (2)$$

$$\varepsilon_t(\omega) = -\frac{\nu_a(\omega)}{E_A(\omega)}\sigma_A - \frac{\nu_t(\omega)}{E_T(\omega)}\sigma_T + \frac{1}{E_t(\omega)}\sigma_t - \frac{\lambda_t(\omega)}{E_A(\omega)}\tau_A + \alpha_t(\omega)\Delta T, \quad (3)$$

$$\gamma_t(\omega) = \frac{1}{G_t(\omega)}\tau_t - \frac{\lambda_S(\omega)}{G_a(\omega)}\tau_a, \quad (4)$$

$$\gamma_a(\omega) = -\frac{\lambda_S(\omega)}{G_a(\omega)}\tau_t + \frac{1}{G_a(\omega)}\tau_a, \quad (5)$$

$$\gamma_A(\omega) = -\frac{\lambda_A(\omega)}{E_A(\omega)}\sigma_A - \frac{\lambda_T(\omega)}{E_A(\omega)}\sigma_T - \frac{\lambda_t(\omega)}{E_A(\omega)}\sigma_t + \frac{1}{G_A(\omega)}\tau_A + \alpha_S(\omega)\Delta T. \quad (6)$$

where the parameters E, G, υ and α specify, respectively, Young's moduli, shear moduli, Poisson's ratios and thermal expansion coefficients. The parameters λ are ratios associated with the effect of shear stress on in-plane and transverse shear strains. The upper case subscripts A, T are attached to axial and transverse thermo-elastic constants to specify that they refer to axial and transverse deformations while the corresponding lower case subscripts (a and t) denote thermo-elastic constants that involve through-thickness stress and deformations. Moreover, the parameter ω is introduced to denote the state of damage in the laminate. For each laminate property, the quantity f(ω) denotes its value when the damage state is defined by ω. If ply cracking is the only damage mode and only one ply is cracked, then ω is crack density ρ in that ply.

2.2 Energy balance for quasi-static ply crack formation in a 90° ply of general symmetric laminates

Let's assume that the crack surfaces are assumed to form quasi-statically under conditions of fixed effective multi-axial applied tractions and fixed temperature. From energy balance considerations and the fact that the kinetic energy is never negative, the criterion for crack formation under these conditions has the form

$$G = G_c, \tag{7}$$

where G specifies the energy release rate resulting from ply crack formation and G_c is the critical energy release rate of the laminate material for the formation of the new ply cracks (ω ≡ ρ) which characterizes the effective "fracture energy" of the ply, i.e. its resistance to ply crack growth. If the growth of ply cracks in the 90° ply is considered, the energy release rates in different deformation modes, resulting from ply crack formation can be obtained from the following equations in terms of effective laminate properties [4]

$$G_I(\rho) = \frac{\left(\varepsilon_A^*(\rho) - \varepsilon_A^*\right)^2}{2\left(\frac{1}{E_A^*(\rho)} - \frac{1}{E_A^*}\right)} \frac{h}{\rho h^{90}}, \tag{8}$$

$$G_{II}(\rho) = \left(\frac{1}{2} G_A(\rho) \gamma_A^{\,2}(\rho) - \frac{1}{2} G_A \gamma_A^{\,2} \right) \frac{h}{\rho h^{90}}, \tag{9}$$

$$G_{III}(\rho) = \frac{1}{2} \tau_a^{\,2} \left(\frac{1}{G_a(\rho)} - \frac{1}{G_a} \right) \frac{h}{\rho h^{90}}. \tag{10}$$

where h is the half-thickness of the laminate and h^{90} is the thickness of the 90 ply in half of the laminate (above or below symmetry plane). It is noted that subscripts I, II and III correspond to the different deformation modes. Moreover, where ε_A^* is the in-plane axial strain for a symmetric laminate that is constrained so that the shear strains are zero, and E_A^* is the reduced axial stiffness modulus, defined by

$$\varepsilon_A^*(\rho) = \varepsilon_A(\rho) + G_A(\rho) \frac{\lambda_A(\rho)}{E_A(\rho)} \gamma_A(\rho), \qquad \frac{1}{E_A^*(\rho)} = \frac{1}{E_A(\rho)} \left(1 - \lambda_A^2(\rho) \frac{G_A(\rho)}{E_A(\rho)} \right). \tag{11}$$

It is noted that having ply cracks in the 90° ply is not a limitation as general loading is considered so that if cracks form first in another single orientation, the laminate can be rotated so that the crack planes are parallel to the fiber direction of that ply and the applied stresses and effective properties transformed to appropriate values for the new orientation. Moreover, it is noted that while considering cracks in a specific ply, other plies might be already cracked and the effects of those cracks will have been taken into account using the homogenization technique [4, 9]. The homogenization methodology involves smoothing the effective properties of a cracked ply in a laminate into the equivalent properties of a homogeneous ply, having reduced properties.

2.3 Fatigue crack growth law

Following the method developed by McCartney [1], the concept of using an energy balance approach for the prediction of unstable crack growth can be extended to the case of fatigue crack growth. It is first necessary to consider the energy balance that must be applied when cyclic deformation is occurring in the crack tip region. Much of the cyclic deformation will be contributing to localized heating but some will lead to the degradation of the material lying within the fracture process zone. As fatigue crack growth has been argued as resulting from energy dissipation (or energy absorption) in the crack tip failure process zones, energy concepts are used to define the effective energy release rate range ΔG. One can assume the following definition for the effective energy release rate range ΔG under cyclic loading

$$\Delta G = \Delta G_I + \Delta G_{II} + \Delta G_{III}, \ \textit{where} \tag{12}$$
$$\Delta G_I = \left(\sqrt{G_I(\rho)} - \sqrt{G_{\min,I}(\rho)}\right)^2,$$
$$\Delta G_{II} = \left(\sqrt{G_{II}(\rho)} - \sqrt{G_{\min,II}(\rho)}\right)^2,$$
$$\Delta G_{III} = \left(\sqrt{G_{III}(\rho)} - \sqrt{G_{\min,III}(\rho)}\right)^2,$$

where G_I, G_{II} and G_{III} are the strain energy release rates at the maximum load of the cycle for different deformation modes and G_{min} is the energy release rate at the minimum load of the stress cycle. A useful feature of the above definition for effective energy release rate range is that the effects of R-ratio or both maximum and minimum applied stresses are taken into account. Another desirable feature of this definition is that $\Delta G \to 0$ as $\sigma \to \sigma_{\min}$.

Finally, for ply cracks in the 90° plies of general symmetric laminates, a fatigue crack growth law can be assumed of the form

$$\frac{d\rho}{dN} = C_I \left(\Delta G_I\right)^{n_I} + C_{II} \left(\Delta G_{II}\right)^{n_{II}} + C_{III} \left(\Delta G_{III}\right)^{n_{III}}, \tag{13}$$

where C_I, C_{II}, C_{III}, n_I, n_{II} and n_{III} are material constants that should be calibrated using fatigue experiments on laminates with microscopic damage quantifications.

2.4 Fatigue crack growth law for the uniaxial cyclic loading of a cross-ply laminate

It is now useful to consider a specific loading condition and a basic lay-up to obtain simpler form of the equations that were introduced in the previous sub-sections. To do so, consider a symmetric cross-ply laminate which is under in-plane uniaxial σ_A cyclic mechanical loading with $R=0=\sigma_{min}/\sigma_{max}$ and that $\sigma_T=\tau_A=\sigma_t=\tau_a=\tau_t=0$. By assuming isothermal conditions, residual thermal stresses are fixed during stress cycling. On the basis of linear elastic stress analysis, it can be concluded that

$$\Delta G(\Delta\sigma, \Delta T) = G(\Delta\sigma, 0), \tag{14}$$

For a cross-ply laminate, the coupling between the in-plane and shear deformations is vanished, thus, the energy release rates for the considered loading condition can be simplified as follows:

$$\Delta G_I = \sigma_A \sqrt{\frac{h\left(\frac{1}{E_A(\rho)}\right) - \left(\frac{1}{E_A}\right)}{2\rho h^{90}}}, \tag{15}$$

$$G_{II}(\rho) = 0 \tag{16}$$

$$G_{III}(\rho) = 0. \tag{17}$$

Which is exactly the development derived by McCartney [1]. By replacing the above equations in (13), the crack growth law can be simplified as follows for uniaxial loading of a cross-ply laminate:

$$\frac{d\rho}{dN} = C_I \left(\sigma_A \sqrt{\frac{h\left(\frac{1}{E_A(\rho)}\right) - \left(\frac{1}{E_A}\right)}{2\rho h^{90}}} \right)^{n_I} \tag{18}$$

3. Results and discussions

The first step for validation of the approach is to assess its quality in predicting the laminate effective properties as a function of fatigue damage mechanisms. For comparison with experiments, a $[0_2/90_4]_s$ laminate and a $[0_2/45_4]_s$ laminate made of Glass/epoxy, which were tested in Refs. [6, 7], are considered. These laminates were tested under uniaxial fatigue loading with different amplitude loads. For each case and at specific loading cycles, the normalized in-plane axial stiffness E_A/E_{A0} and normalized in-plane axial Poisson's ratio υ_A/υ_{A0} were measured together with the average value of crack density in the off-axis ply and delamination length at the interface between the off-axis ply and the 0° ply. We have used exactly the reported average crack densities and delamination lengths [6, 7] together with the provided input material properties to predict elastic constants (see Eqs. (1-6)) as a function of loading cycles. Fig. 1, shows the variation of the normalized in-plane axial stiffness E_A/E_{A0} for two samples with $[0_2/90_4]_s$ lay-up which were tested under uniaxial cycling load with amplitude $\sigma_{A,\max} = 120MPa$ and load ratio $R = 0.05$. The results of the new variational approach [5] are also depicted for each sample separately as slightly different crack densities and delamination lengths were reported for each sample at different cycles. Fig. 2 shows the variation of the normalized in-plane axial stiffness E_A/E_{A0} and the normalized in-plane axial Poisson's ratio υ_A/υ_{A0} for the $[0_2/45_4]_s$ laminate which was tested under a uniaxial cycling load with amplitude $\sigma_{A,\max} = 120MPa$ and load ratio $R = 0.05$. It is noted that only the results for one sample were reported [7] for the $[0_2/45_4]_s$ laminate. It can be seen in Fig. 1 that the predictions of the variational approach for the in-plane axial stiffness of $[0_2/90_4]_s$ samples are in a rather good accordance with experiments although there is some scatter between the experimental results for different samples of the same type. The predictions in Fig. 2 are also in a good agreement with experiments for the $[0_2/45_4]_s$ laminate.

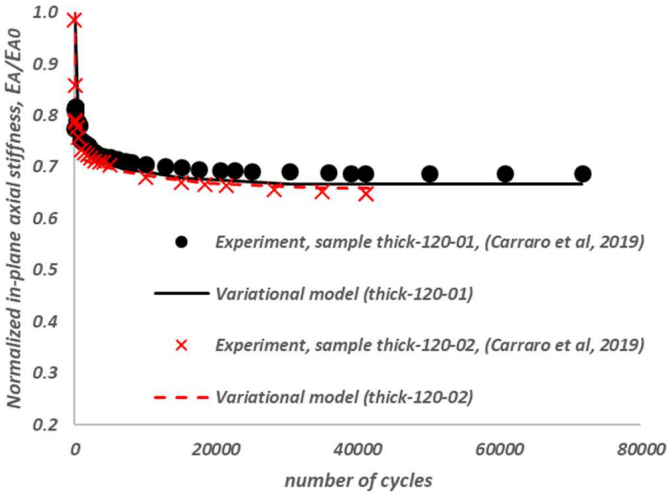

Fig. 1. Variation of normalized in-plane axial stiffness E_A/E_{A0} in two samples with $[0_2/90_4]_s$ lay-up which both were tested under a cyclic load $\sigma_{A,\max} = 120MPa \;\; and \;\; R = 0.05$ as a function of cycles.

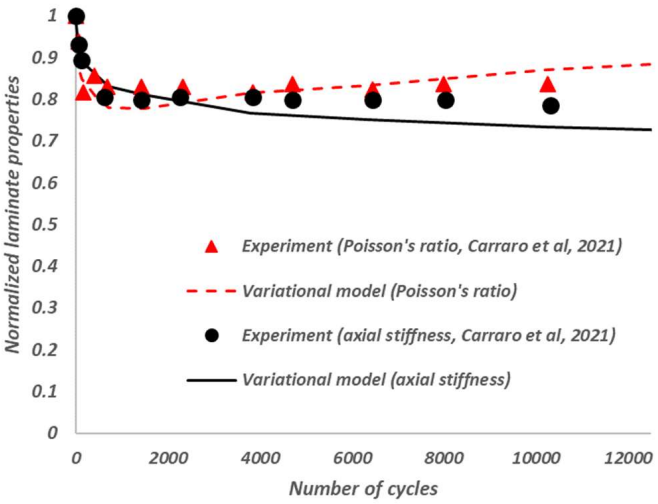

Fig. 2. Normalized In-plane axial stiffness E_A/E_{A0} and in-plane Poisson's ratio υ_A/υ_{A0} in one sample with $[0_2/45_4]_s$ lay-up which was tested under a cyclic load $\sigma_{A,\max} = 120MPa \;\; and \;\; R = 0.05$ as a function of cycles.

  doi:10.5075/epfl-298799_978-2-9701614-0-0

In Ref. [8], ply cracking propagation is characterized experimentally, in the off-axis plies of $[0/90_2]_s$, $[0/75_2]_s$, $[0/60_2]_s$ and $[0/75_3]_s$ laminates under uniaxial cyclic loading with different amplitudes. Therefore, the crack density in the off-axis plies is quantified versus the applied cycles. For the unbalanced laminates, ply cracks will grow under a mixed mode conditions while for the cross-ply laminates, cracks form under mode I deformation under a uniaxial loading condition. Therefore, experiments on the cross-ply laminate and an arbitrary laminate with an off-axis ply rather than 90-degree are needed to completely calibrate the model. The experimental crack density measurements on the $[0/90_2]_s$ and $[0/75_2]_s$ samples are used, respectively, to calibrate C_I, n_I and C_{II}, n_{II} in Eq. (13). Having the model calibrated, it can predict the evolution of crack density in other laminates. An example of ply crack modeling in $[0/60_2]_s$ laminate is provided in Figure 3. It can be clearly seen that the model can accurately predict the evolution of crack density under cyclic loading when cracks are propagating under a mixed mode loading condition.

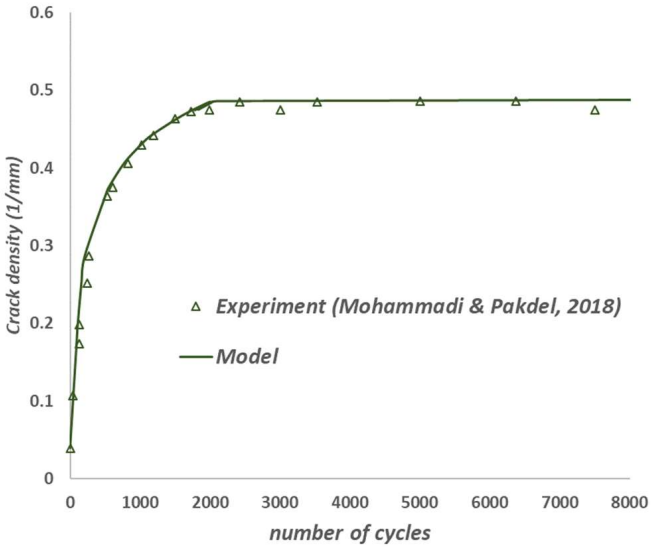

Figure. 3: Variation of crack density as a function of cycles in a carbon/epoxy $[0/60_2]_s$ laminate tested under a cyclic load .

4. Concluding remarks

A variational approach is developed to estimate the laminate effective properties as a function of damage state in the laminate. The model can predict the dependence of laminate properties on crack density and delamination lengths at the tips of ply cracks. When ply cracking is the only existing damage mechanism, the energy release rates in different deformation modes, resulting from ply crack formation are obtained in terms of laminate properties. A fatigue crack growth law is suggested that incorporates the energy release rates as the fatigue driving force and can predict the growth of ply cracks in laminates under multiaxial loading conditions considering the effects of mixed mode deformations.

  doi:10.5075/epfl-298799_978-2-9701614-0-0

Acknowledgements

M. Hajikazemi acknowledges the financial support of Fonds voor Wetenschappelijk Onderzoek (Grant No. 1202522N).

The work of M. Hajikazemi and J. Sommer forms part of the research programme of DPI, project 812T17.

5. References

1. McCartney LN. Energy methods for fatigue damage modelling of laminates. Composites Science and Technology 2008; 68: 2601-15.
2. Talreja R. Fatigue of composite materials: damage mechanisms and fatigue life diagrams. Proc Roy Soc Lond 1981; A378:461–75.
3. Hajikazemi M, Sadr MH. A variational model for stress analysis in cracked laminates with arbitrary symmetric lay-up under general in-plane loading. International Journal of Solids and Structures 2014; 51:516-29.
4. Hajikazemi M, McCartney LN, Van Paepegem V. Matrix cracking initiation, propagation and laminate failure in multiple plies of general symmetric composite laminates. Composites Part A: Applied Science and Manufacturing 2020; 136: 105963.
5. Hajikazemi M, Ahmadi H, McCartney LN, Van Paepegem W. A variational approach for accurate prediction of stress and displacement fields and thermo-elastic constants in general symmetric laminates containing ply cracking and delamination under general triaxial loading. Under review at the International Journal of Solids and Structures.
6. Carraro PA, Maragoni L, Quaresimin M. Characterisation and analysis of transverse crack induced delamination in cross-ply composite laminates under fatigue loadings. International Journal of Fatigue 2019; 129: 105217.
7. Carraro PA, Maragoni L, Quaresimin M. Stiffness degradation of symmetric laminates with off-axis cracks and delamination: an analytical model. Int. J. Solids Struct. 2021; 213, 50–62.
8. Mohammadi B, Pakdel H. Fatigue driven matrix crack propagation in laminated composites. Materials & Design 2018; 146: 108-15.
9. McCartney LN. Energy-based prediction of progressive ply cracking and strength of general symmetric laminates using an homogenisation method. Compos Part Appl Sci Manuf 2005;36:119–28.

STOCHASTIC ANALYTICAL AND NUMERICAL MODELLING OF INTERFACE STRESSES FOR GENERALLY LAYERED 3D-PRINTED COMPOSITES

Efstratios Polyzos[a] and Lincy Pyl[a]

a: Department of Mechanics of Materials and Constructions, Vrije Universiteit Brussel (VUB), BE-1050, Brussels, Belgium - efstratios.polyzos@vub.be

Abstract: Generally layered 3D-printed composite laminates are promising for engineering applications but exhibit insufficient bonding. To aid the understanding of the bond capacity, a stochastic analytical and numerical modelling procedure of the interface stresses of such laminates is presented in this paper. The specific case of the end-notched flexure test is considered and a novel formulation is developed for the evaluation of the contact force between the two sub-laminates. This formulation accounts for the different boundary conditions of the bonded interface. Three analytical models, the rigid, the semi-rigid, and the flexible joint models, are implemented for the determination of the interface stresses for a 3D-printed composite laminate of nylon reinforced with carbon fibres and compared with finite element analysis results. The present formulation considers residual thermal stresses, a common problem in 3D-printed structures.

Keywords: 3D-printed composites; Polynomial Chaos Expansion; Interface joint model; Mode II delamination; Contact force

1. Introduction

Additive manufacturing (or 3D-printing) is a relatively new manufacturing process that offers distinct advantages due to the freedom of design and the possibility of producing high-performing parts. 3D-printed materials with continuous reinforced filament, containing carbon, glass, or aramid fibres, exhibit properties close to those of metals and are prominent candidates for many engineering applications [1].

During the manufacturing of a 3D-printed part, single beads (printed filaments) are printed successively side-by-side and form laminas with different orientations (Figure 1). The final structure is similar to conventional composite laminates but exhibits certain problems. For instance, the bond between the adjacent is insufficient and leads to delamination. This is especially pronounced when the orientation of adjacent plies differs largely. Estimating the magnitude and the distribution of interface stresses can shed light on the capacity of the interface bond.

The 3D-printed laminated composites present geometrical similarities to the conventional composite laminates and can be treated as such in numerical and analytical models [2,3]. As in many engineering structures, special care is needed to correctly represent the presence of residual hygrothermal stresses. The latter are especially pronounced in 3D-printed composites. Note that only the thermal stresses are considered in the present study. The hygroscopic effects can be added by analogous processes and are neglected hereafter.

Following the above, a novel analytical formulation of the interface stresses is introduced in this paper based on the first-order shear deformation theory (FSDT). The formulation is applied to the end-notched flexure (ENF) test (Figure 2 (a)) of a generally layered laminate of 3D-printed nylon with continuous carbon fibres. Focus is given to the evaluation of the contact force

  doi:10.5075/epfl-298799_978-2-9701614-0-0

Figure 1 Manufacturing process of 3D-printed composite laminates with various orientations ϑ.

between the upper and lower (relatively to the crack) sub-laminates because of its importance in mode II delamination tests [4]. The contact force is evaluated considering three assumptions for the interface bond [5] (Figure 2 (b)): a rigid bond where both the translations and rotations are restricted, a semi-rigid bond where the translations are restricted, but the rotations are allowed, and a flexible bond where both translations and rotations are allowed. The solutions of the contact force are used for the estimation of the interface stresses (Figure 2 (c)). Notably, the contact force has been previously either neglected [6] or modelled following the rigid joint model [4,7]. The analytical results for the interface stresses are compared with numerical finite element (FE) models developed using the Virtual Crack Closure Technique (VCCT) [8].

Finally, both the analytical and the numerical models are implemented stochastically using a non-intrusive uncertainty quantification technique, the polynomial chaos expansion (PCE) [9]. The PCE is used to capture the dimensional uncertainties which are mostly related to the tolerances of the 3D printer and are common in 3D-printed structures [3].

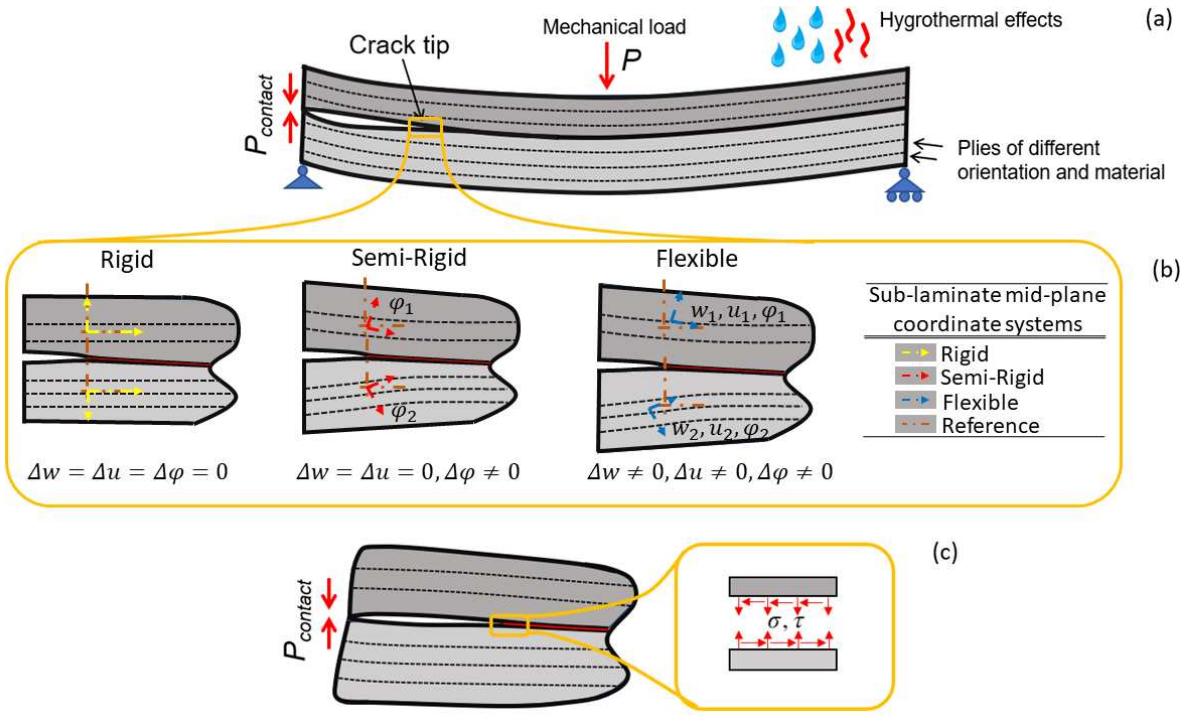

Figure 2 ENF test of a generally layered composite laminate with residual hygrothermal stresses (a). Assumptions for the interface bond for the relative transverse Δw and axial Δu displacements and the rotation Δφ (b). Development of interface stresses σ and τ (c).

2. Analytical formulation of the interface stresses

2.1 Background

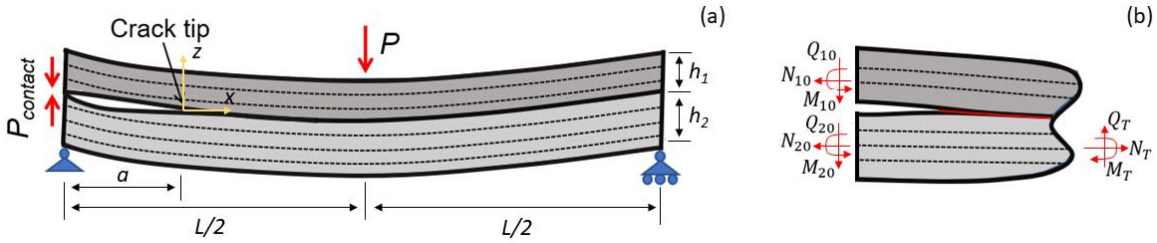

Figure 3 Representation of the ENF specimen (a). Free-body diagram of the crack-tip element and force equilibrium (b).

Consider a generally layered laminate of length *L* with a through-the-width crack of length *a* embedded between the upper and the lower sub-laminates (Figure 3). A solution of the interface axial N_{10} and transverse shear Q_{10} forces of the upper sub-laminate (denoted by subscript 1) is given in the work of Zhang and Wang [6] as a function of the distance in front of the crack tip *x* for the case of the rigid, the semi-rigid, and the flexible joint model, as:

Rigid joint model (superscript *(r)*):

$$N_1^{(r)}(x) = A_{NN}N_T + A_{NM}M_T + A_{NT}\Delta T,\ Q_1^{(r)}(x) = A_Q Q_T \tag{1}$$

Semi-rigid joint model (superscript *(sr)*):

$$N_1^{(sr)}(x) = ce^{-kx},\ Q_1^{(sr)}(x) = -\left(\frac{\eta_1}{\xi_1} + \frac{h_1}{2}\right)cke^{-kx} \tag{2}$$

Flexible joint model (superscript *(f)*):

$$N_1^{(f)}(x) = \sum_{f=1}^{3} c_f\, e^{-R_f x},\ Q_1^{(f)}(x) = \sum_{f=1}^{3} c_f\, T_f e^{-R_f x} \tag{3}$$

where $A_{NN}, A_{NM}, A_{NT}, A_Q, c, k, \eta_1, \xi_1, c_f, T_f$ are given in [6], h_1 is the thickness of the upper sub-laminate (Figure 3 (a)) and ΔT the thermal difference. N_T, M_T, and Q_T denote the total applied resultant axial force, bending moment, and transverse shear force around the midplane of the lower sub-laminate, evaluated using the crack-tip element concept (Figure 3 (b)) as demonstrated in [10]. The R_f coefficients are the roots of the characteristic equation of the flexible joint model which for real material and geometry parameters are expressed for two cases as: case (1) $\pm R_1, \pm R_2, \pm R_3$ or case (2) $\pm R_1, \pm R_2 \pm iR_3$ and are real, positive constants [10].

The interface stresses τ_1 and σ_1 can be derived by differentiating the interface forces N_1 and Q_1, respectively, with respect to x as:

$$\tau_1^{(r)}(x) = A_{NM}Q_T\ ,\ \sigma_1^{(r)}(x) = -\left[\left(b_2 + \frac{h_2}{2}d_2\right) - \left(\frac{\eta_1}{\xi_1} + \frac{h_1}{2}\right)A_{NM}\right]\frac{dQ_T}{dx} \tag{4}$$

$$\tau_1^{(sr)}(x) = -cke^{-kx} + \tau_1^{(r)}(x),\ \sigma_1^{(sr)}(x) = \left(\frac{\eta_1}{\xi_1} + \frac{h_1}{2}\right)ck^2e^{-kx} + \sigma_1^{(r)}(x) \tag{5}$$

$$\tau_1^{(f)}(x) = -\sum_{f=1}^{3} c_f R_f\, e^{-R_f x} + \tau_1^{(r)}(x),\ \sigma_1^{(f)}(x) = -\sum_{f=1}^{3} c_f\, T_f R_f e^{-R_f x} + \sigma_1^{(r)}(x) \tag{6}$$

The use of Eqs. (1)-(3) in the derivation of Eqs. (4)-(6) ensures that the formulation considers extension-bending coupling phenomena, and it is an extension of the one presented in [10].

The evaluation of the c_f coefficients for the flexible joint model is closely related to the assumptions of the displacement and rotation along the bonded portion of the two sub-laminates which influences the contact force in mode II tests. To guarantee a physically accurate analytical modelling, the previous formulation for the derivation of the c_f coefficients [6] requires reconsideration.

2.2 Evaluation of the c_f coefficients

Following [6], the formalism of self-balanced N, M, Q is used. The latter appear at the crack tip in order to satisfy the equilibrium equations and can be evaluated as:

$$N = N_{10} - N_1^{(r)}, \quad M = M_{10} - M_1^{(r)}, \; Q = Q_{10} - Q_1^{(r)} \tag{7}$$

with N_{10}, M_{10}, Q_{10} the mechanical loads applied at the left end of the upper sub-laminate (Figure 3 (b)) expressed as $N_{10} = 0, M_{10} = aQ_{10}$, $Q_{10} = -P_{contact}$ for the case of the ENF test.

The c_f coefficients can be evaluated as functions of the N, M, Q for the two cases presented in section 2.1., as:

$$\begin{pmatrix} c_1 \\ c_2 \\ c_3 \end{pmatrix} = \begin{pmatrix} 1 & 1 & 1 \\ S_1 & S_2 & S_3 \\ T_1 & T_2 & T_3 \end{pmatrix}^{-1} \begin{pmatrix} N \\ M \\ Q \end{pmatrix} case\ (1), \; \begin{pmatrix} c_1 \\ c_2 \\ c_3 \end{pmatrix} = \begin{pmatrix} 1 & 0 & 1 \\ S_1 & S_2 & S_3 \\ T_1 & T_2 & T_3 \end{pmatrix}^{-1} \begin{pmatrix} N \\ M \\ Q \end{pmatrix} case\ (2) \tag{8}$$

and, therefore, depend on the contact force. All coefficients S_i, T_i are presented in [10].

2.3 Evaluation of the contact force

The contact force rises when the relative displacement along the z-axis Δw of the two sub-laminates at the left tip is zero, i.e, $\Delta w|_{x=-a} = (w_2 - w_1)|_{x=-a} = 0$. By superimposing the displacement of the cracked and the bonded portion, Δw can be expressed as:

$$\Delta w = \Delta w_{cracked} + \Delta w_{bonded} = \Delta w_{cracked} + \Delta\varphi|_{x=0}(a - x) + \Delta w|_{x=0}, \quad x \in [-a, 0] \tag{9}$$

with $\Delta w_{cracked}$ given in [7] as the generalized Nairn's approach to Timoshenko beams' displacement and $\Delta\varphi|_{x=0}$ and $\Delta w|_{x=0}$ given in [10] as the relative rotation and displacement at the crack tip. Replacing in Eq. (9) the mechanical loads of the ENF test at *x=-a,* the contact force can be estimated as:

$$P_{contact} = \frac{Q_{20}\left(l_2 a + d_2\frac{a^3}{3}\right) - (a_{m2} - a_{m1})\frac{a^2}{2} - a\Delta\varphi|_{x=0} - \Delta w|_{x=0}}{\left[(l_1 + l_2)a + (d_1 + d_2)\frac{a^3}{3}\right]} \tag{10}$$

and accounts for the different boundary conditions of displacement and rotation at the crack tip. The coefficients $l_1, l_2, d_1, d_2, a_{m1}, a_{m2}$ are derived from the FSDT in [7] and physically represent the shear and bending compliance and the curvature due to residual thermal stresses of the upper and lower sub-laminates denoted by the subscript *1* and *2*, respectively. Q_{20} denotes the transverse force acting on the left side of the lower sub-laminate (Figure 3 (b)).

Considering the above, for the evaluation of the interface stresses according to the rigid and the semi-rigid joint models, Eqs. (4) and (5) are used. For the flexible joint model Eqs. (6), (7), (8), and (10) are used.

3. Case study

3.1 Geometry and material properties

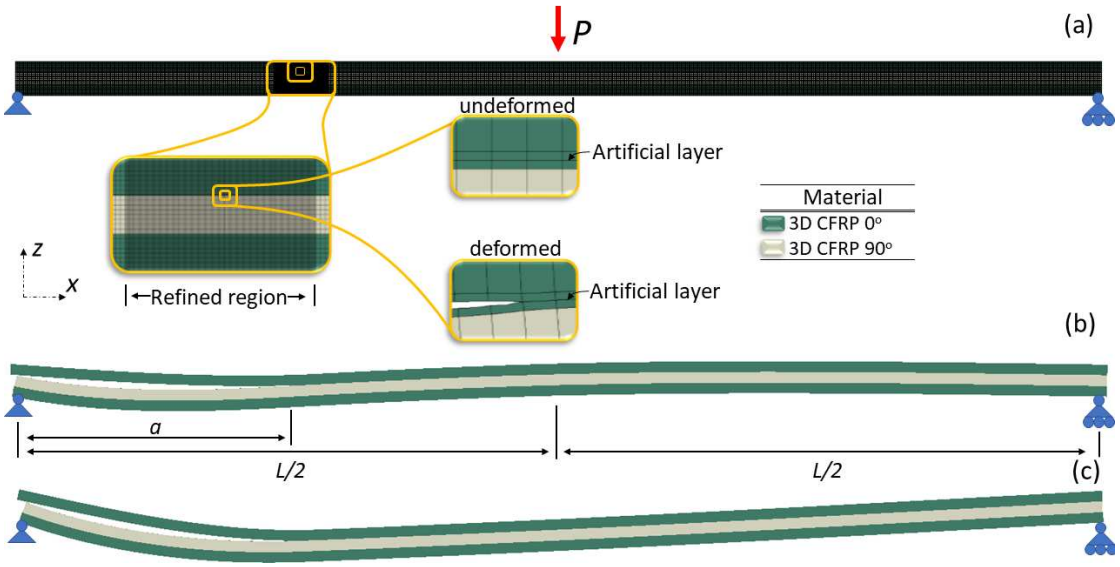

Figure 4 Meshed specimen in the undeformed state (a). Deformed specimen only with thermal stresses (b). Deformed specimen with thermal stresses and mechanical load (c). The mesh is removed from (b) and (c) to offer a clearer view.

A 3D-printed composite laminate $[0_8/90_8/0_8]_T$ of nylon reinforced with continuous carbon fibres (Figure 4) is chosen since it is formed of laminae with large difference in orientation. The upper sub-laminate is considered as the $[0_8]_T$ and the lower sub-laminate as the $[0_8/90_8]_T$. A through-the-width crack of length *a* is embedded between them.

Following the measurements provided in [3], the crack length, the thickness of each lamina, and the total width (out-of-plane dimension), are taken as 25±1 mm, 0.125±0.004 mm, and 20±0.2 mm, respectively. The length of the laminate *L* is taken as 100 mm and the load *P* as 1000 N. All loads and stresses presented hereafter are reduced over the specimen's width. The thermal difference is taken as the difference between printing (275°C) and room temperature (25°C), i.e, ΔT= -250°C. The elastic properties of a unidirectional (UD) lamina are evaluated using the Mori-Tanaka homogenization scheme as illustrated in [11] considering the effective volume fraction (see [12]) of carbon fibres (0.17) which accounts for the imperfect matrix-fiber adhesion in flexural problems such as the present one [13]. The elastic properties of the UD lamina are calculated as E_{11}=40 GPa, E_{22}=1.67 GPa, G_{12}=0.54 GPa, and ν_{12}=0.38. The thermal expansion coefficient is estimated following the homogenization process described in [14] as $a_{11}=3.03\cdot10^{-6}$/°C, $a_{22}=1.27\cdot10^{-6}$/°C. The elastic properties and the thermal expansion coefficient of the T300 carbon fibres [15] and of nylon white [16] are used for the homogenization.

3.2 Numerical modelling

The numerical modelling is performed using the ABAQUS software. The problem is that of a 1D delamination with a stationary crack. The VCCT [8], one of the most decorated methods for delamination problems is implemented. According to the VCCT, the laminate is created by rigidly joining together the common nodes on the bonded surface of the two sub-laminates, created as 2D Planar Shells. The contact between the two sub-laminates is modelled as 'hard contact' and frictionless. An artificial layer of reinforced nylon is added between the two sub-laminates

to prevent stress oscillation, as in [7]. The mesh is determined by mesh convergence studies considering the stresses and the strain energy release rate. A region close to the crack tip is refined to offer a better approximation of the stresses. Approximately 9000 and 17000 elements are used for the upper and the lower sub-laminates, respectively. The eight-node quadrilateral reduced integration plane-strain elements are employed to avoid shear locking. The stresses are evaluated at the common nodes of the two sub-laminates in front of the crack tip. The final model in a meshed, undeformed and in an unmeshed, deformed state is illustrated in Figure 4.

3.3 Uncertainty quantification

The uncertainty quantification is performed using the Point Collocation (PC) method, a non-intrusive PCE method. A short description of the implementation of the PC method is provided here and the reader is referred to [9] for more information.

Firstly, samples are generated from the joint distribution as in [3], considering stochastically independent uncertain parameters and using the Korobov low-discrepancy sequence and the hyperbolic truncation scheme. Then, the deterministic models (here the analytical (section 2) and numerical (section 3.2) models) are evaluated for each sample and a polynomial expansion is selected following the three terms recurrence method. Finally, the models' approximation is constructed as the solution of the linear regression problem defined by the model's evaluations (dependent variables) and the evaluations of the polynomials at the samples (independent variables) using the least squares method.

4. Results and discussion

The distribution of the mean and the standard deviation of the interface stresses $\tau_1$and σ_1 in front of the crack tip for the cases without ((a), (c)) and with ((b), (d)) thermal stresses is illustrated in Figure 5 for the analytical rigid (RJM), semi-rigid (SRJM), and flexible (FJM) joint models and the numerical FE model (FEM). Note that the distance from the crack tip (*x*-axis) is reduced over the thickness of the upper sub-laminate. For the FEM, the markers account for the position of each node in front of the crack tip.

The results demonstrate that only the flexible joint model is able to capture the radical increase of the interface stress close to the crack tip, whereas both the rigid and the semi-rigid models drastically underestimate the crack tip stress. This is a direct result of the consideration of a deformable interface between the two sub-laminates and has been reported before in [10]. For τ_1, converge comes after a relatively short distance of $0.5h_1$ (case without thermal stresses) - $1.5h_1$ (case with thermal stresses). σ_1 converges after $0.5h_1$ for both without and with thermal stresses.

Notably, the thermal effects can radically modify the stresses near the crack tip, as well as influence the ratio of the maximum values of τ_1 and σ_1. This result can be also related to modification of the strain energy release rate, exhibited in various studies [4,5,7,17]. Furthermore, note that for the presented geometry, $a_{m2} - a_{m1} < 0$, which results in inwards bending of the sub-laminates' arms, as explained in [4], and a direct contact even without mechanical load (Figure 4 (b)). The contact is maintained after the imposition of the mechanical loads (Figure 4 (c)), making the formulation of the contact force a necessity for the analytical modelling of the ENF test.

Finally, the PCE demonstrates that the uncertainty of the dimensional parameters (crack length, thickness, width) does not drastically influence the model's estimation. The area very close to the crack tip is mostly affected, as illustrated by the increased scattering of the models. The models evaluations converge to the expected one after a distance of $0.5h_1$ to $1.5h_1$.

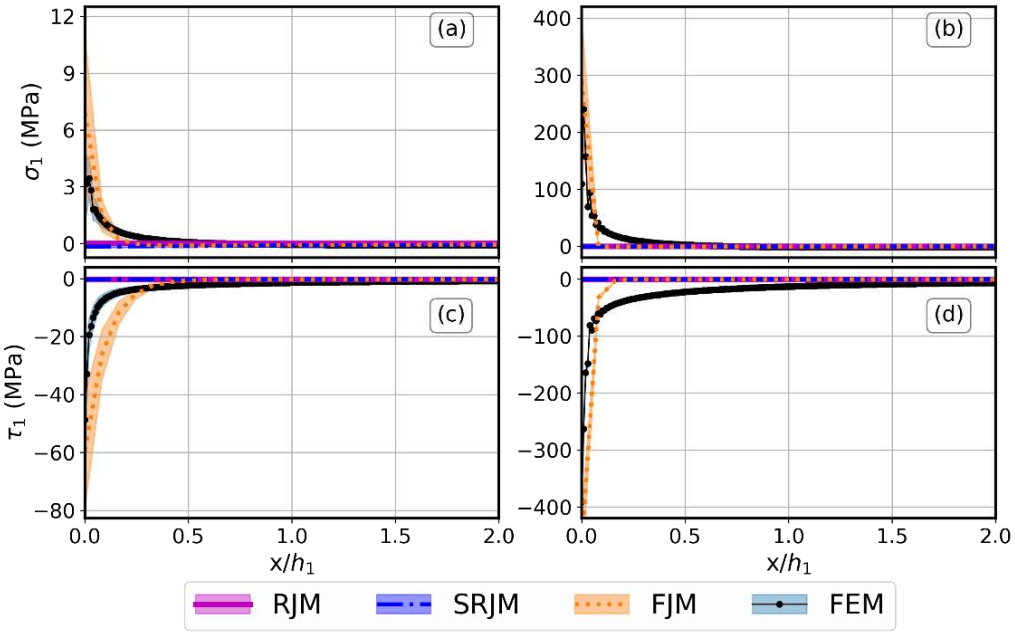

Figure 5 Comparison of the distribution of interface stresses along the x-axis between analytical and numerical models without (a), (c) and with (b), (d) residual thermal stresses.

5. Conclusions

The stochastic analytical and numerical modelling of the interface stresses in generally layered 3D-printed composite laminates is presented in this paper. The ENF test is considered, and emphasis is given to the evaluation of the contact force between the two sub-laminates. The later is estimated using a novel formulation that accounts for the different boundary conditions of the bonded interface between the two sub-laminates. Three analytical models of interface stress evaluation are implemented for a 3D-printed composite laminate nylon reinforced with carbon fibres and compared with numerical models.

Three major conclusions can be drawn from the results of this study. Firstly, the only analytical model that is able to capture the crack tip stresses is the flexible joint model. Secondly, the influence of the thermal stresses is high and can drastically modify the amplitude and the ratio between τ_1 and σ_1 and should be considered during the modelling of such structures. Finally, the dimensional uncertainties for the considered geometry influence the area close to the crack tip, but do not highly affect the models' predictions.

Acknowledgements

The financial contribution of FWO Research Foundation–Flanders (file number 1102822N) is gratefully acknowledged.

6. References

1. van de Werken N., Tekinalp H., Khanbolouki P., Ozcan S. Additively manufactured carbon fiber-reinforced composites: State of the art and perspective. Additive Manufacturing 2020; 31:100962.
2. Polyzos E., Van Hemelrijck D., Pyl L. Numerical modelling of the elastic properties of 3D-printed specimens of thermoplastic matrix reinforced with continuous fibres. Composites Part B: Engineering 2021; 211:108671.
3. Polyzos E., Katalagarianakis A., Van Hemelrijck D., Pyl L. Delamination analysis of 3D-printed nylon reinforced with continuous carbon fibres. Additive Manufacturing 2021; 46:102144.
4. Nairn J. A. On the calculation of energy release rates for cracked laminates with residual stresses, International Journal of Fracture 2006; 139:267–293.
5. Qiao P., Liu Q., Energy release rate of beam-type fracture specimens with hygrothermal influence, International Journal of Damage Mechanics 2016; 25:1214–1234.
6. Zhang C., Wang J. Delamination analysis of layered structures with residual stresses and transverse shear deformation. Journal of Engineering Mechanics 2013; 139:1627-1635.
7. Tsokanas P., Loutas T. Hygrothermal effect on the strain energy release rates and mode mixity of asymmetric delaminations in generally layered beams. Engineering Fracture Mechanics 2019; 214:390–409.
8. Krueger R., The virtual crack closure technique for modelling interlaminar failure and delamination in advanced composite materials. Elsevier Ltd. 2015.
9. Sudret B. Polynomial chaos expansions and stochastic finite element methods. Risk and Reliability in Geotechnical Engineering, CRC Press. 2015.
10. Qiao P., Wang J. Mechanics and fracture of crack tip deformable bi-material interface. International Journal of Solids and Structures 2004; 41:7423–7444.
11. Polyzos E., Katalagarianakis A., Polyzos D., Van Hemelrijck D., Pyl L. A multi-scale analytical methodology for the prediction of mechanical properties of 3D-printed materials with continuous fibres. Additive Manufacturing 2020; 36:101394.
12. Papanicolaou G.C., Portan D.V., Kontaxis L.C. Interrelation between fiber–matrix interphasial phenomena and flexural stress relaxation behavior of a glass fiber–polymer composite. Polymers 202; 13:978.
13. Polyzos E., Ravidranath S.B., Van Hemelrijck D., Pyl L. Analytical and numerical modelling of voids in additively manufactured thermoplastic parts. Additive Manufacturing 2021; 48:102356.
14. Nadeau J.C., Ferrari M. Effective thermal expansion of heterogeneous materials with application to low temperature environments. Mechanics of Materials 2004; 36:201-214.
15. Zhiguo R., Ying Y., Jianfeng L., Zhongxing Q., Lei Y. Determination of thermal expansion coefficients for unidirectional fiber-reinforced composites. Chinese Journal of Aeronautics 2014; 27:1180-1187.
16. Faust J.L., Kelly P.G., Jones B.D., Roy-Mayhew J.D. Effects of coefficient of thermal expansion and moisture absorption on the dimensional accuracy of carbon-reinforced 3D printed parts. Polymers 2021; 13:3637.
17. Polyzos E., Van Hemelrijck D., Pyl L. Analytical model for the estimation of the hygrothermal residual stresses in generally layered laminates. Engineering Fracture Mechanics 2021; 247:107667.

NUMERICAL SIMULATION OF MICROCRACK-INDUCED DELAMINATION IN CROSS-PLY-LAMINATES UNDER STATIC LOADING USING COHESIVE ZONE MODELS

G. Hacker[a,], M. Brod[a], G. Just[b], S. Scheffler[a], I. Koch[b], R. Rolfes[a], M. Gude[b]*

a: Leibniz Universität Hannover, Institute of Structural Analysis, Appelstr. 9A, 30167 Hannover, Germany
b: Technische Universität Dresden, Institute of Lightweight Engineering and Polymer Technology, Holbeinstr. 3, 01307 Dresden, Germany
*Corresponding author: g.hacker@isd.uni-hannover.de

Abstract: *In this contribution, the delamination behaviour in cross-ply glass fiber reinforced composites under static tensile loading is investigated numerically using both cohesive elements and contact cohesive surfaces in the commercial finite element software ABAQUS. The laminates studied contain predefined microcracks in the embedded 90° ply, which serve as the source of delamination. Particular attention is paid to the connection of the pre-existing matrix crack tips to the cohesive zone in the [0/90] interfaces, which have a strong influence on delamination initiation and growth. The presented analysis includes different modelling approaches of microcrack-induced delamination (MCID), which are compared and critically discussed. In this relation, the different modelling approaches partly show a strong influence on the simulation results. The static MCID model can be converted to a fatigue MCID model by using a cyclic cohesive zone model.*

Keywords: Fiber Reinforced Plastics, Microcrack-induced Delamination, Cohesive Zone Model

1. Introduction

The importance of structural components made of fiber reinforced plastics (FRP) is continuously growing in several engineering branches as aircraft or automotive industry. The initiation of micro cracks, followed by microcrack-induced delamination (MCID) growth, are one of the most important fatigue damage mechanisms in composite materials [1,2]. They lead to a significant loss of stiffness, cause stress concentrations and can be the reason for subsequent damage events like buckling or fiber fractures events.

For an efficient and safety-relevant design of a cyclically loaded component, the initiation and propagation of MCID has to be accurately investigated experimentally and numerically. From the numerical point of view, a well-established method for the simulation of delamination processes is the use of cohesive zone models (CZM) [3-5] describing the traction separation behaviour of an interface in form of cohesive elements or contact cohesive behaviour.

The objective of this contribution is to investigate and evaluate different approaches of modelling MCID in cross-ply laminates by applying a well-established CZM [4,5]. At first, the implemented and applied CZM is described. Afterwards, the different modelling options of MCID are presented and compared. Based on that, selected simulation results are presented and critically discussed. Finally, a summary of the conducted investigation as well as some concluding remarks are given.

  doi:10.5075/epfl-298799_978-2-9701614-0-0

2. Numerical modeling of MCID

2.1 Cohesive zone model

The formulation of a three-dimensional cohesive zone model (CZM) presented in this section was developed closely oriented towards the work of Turon et al. [5]. It differs from this work in the definition of the equivalent displacement jump where the equivalent stress and equivalent stiffness can be derived from.

The cohesive interface behaviour is described by the bilinear traction separation law,

$$\tau_i = K_{ij}(1-d)\,\Delta_j \qquad \text{with} \qquad K_{ij} = \begin{pmatrix} K_n & 0 & 0 \\ 0 & K_s & 0 \\ 0 & 0 & K_s \end{pmatrix} \tag{1}$$

where τ_i represents the stress vector, Δ_j the displacement jump vector and d the damage parameter taking values between 0 and 1. The mode dependent penalty stiffness matrix K_{ij} contains the penalty stiffness in normal direction K_n (Mode I) and the penalty stiffness in shear direction K_s, whereby no distinction is made between Mode II shear and Mode III shear. The equivalent displacement jump λ is defined by,

$$\lambda = \sqrt{\langle\lambda_1^2\rangle + \lambda_2^2 + \lambda_3^2} = \sqrt{\langle\lambda_n^2\rangle + \lambda_s^2} \tag{2}$$

where $\lambda_n = \lambda_1$ is the displacement jump in normal direction, λ_s is the equivalent displacement jump in shear direction and <> are the Macaulay brackets defined as $\langle x\rangle = 0.5(x + |x|)$. According to Turon et al. [5], the equivalent stress τ_{eq} and penalty stiffness K_{eq} have to be chosen in such a way that they satisfy the following two equations:

$$\tau_{eq} = (1-d)K_{eq}\lambda \tag{3}$$

$$\psi_{coh} = \frac{1}{2}\tau_{eq}\lambda = \frac{1}{2}(1-d)\Delta_i K_{ij}\Delta_j - K_{11}\langle-\Delta_1\rangle^2 \tag{4}$$

Here ψ_{coh} represents the cohesive contribution to the Helmholtz free energy. The equivalent stress τ_{eq} and penalty stiffness K_{eq} are obtained by substituting Eq. (2) and Eq.(3) into Eq. (4):

$$K_{eq} = \frac{K_s\Delta_s^2 + K_n\langle\Delta_n\rangle^2}{\lambda^2} \tag{5}$$

$$\tau_{eq} = \frac{\tau_s\Delta_s + \tau_n\langle\Delta_n\rangle}{\lambda} \tag{6}$$

The damage parameter d is defined as follows:

$$d = \frac{D_A\lambda^f}{D_A\lambda^f + (1-D_A)\lambda^0} \tag{7}$$

D_A represents a further damage parameter taking values between 0 and 1 which can be interpreted as the damaged area referred to the area of the cohesive surface. It is defined by,

$$D_A = \max_s\left\{\min\left\{\frac{\lambda-\lambda^0}{\lambda^f-\lambda^0}\right\}, 1\right\} \quad 0 \le s \le t \tag{8}$$

where t represents pseudo time in an implicit analysis. λ^0 and λ^f are the equivalent displacement jumps corresponding to damage initiation respectively damage propagation. λ^f is derived from the propagation criterion of Benzeggagh and Kenane [6],

$$\lambda^f = \frac{2G_{Ic}+2(G_{IIc}-G_{Ic})B^\eta}{K_{eff}\lambda^0} \tag{9}$$

where G_{Ic} and G_{IIc} are the fracture toughnesses for pure mode I respectively pure mode II loading, η is a fitting parameter and B represents the mixed mode ratio specifying the ratio of mode II energy release rate G_{II} to the total energy release rate $G_I + G_{II}$:

$$B = \frac{G_{II}}{G_I+G_{II}} = \frac{K_s\Delta_s^2}{K_s\Delta_s^2+K_n\langle\Delta_n\rangle^2} \tag{10}$$

The initiation criterion is defined in [5] as follows:

$$\lambda^0 = \sqrt{\frac{\frac{{\tau_n^0}^2}{K_n}+\left(\frac{{\tau_s^0}^2}{K_s}-\frac{{\tau_n^0}^2}{K_n}\right)B^\eta}{K_{eq}}} \tag{11}$$

τ_n^0 and τ_s^0 represent the interface strengths in normal and shear direction. Following the thermodynamic consistency conduction in [5], the penalty stiffnesses in normal and shear direction have to fulfil:

$$\frac{K_s}{K_n} = \frac{G_{Ic}}{G_{IIc}}\left(\frac{\tau_s^0}{\tau_n^0}\right)^2 \tag{12}$$

While the penalty stiffness is just a numerical parameter, in reality tending towards infinity for an interface of zero thickness, the interface strengths τ_n^0 and τ_s^0 as well as fracture toughness G_{Ic} and G_{IIc} are material parameters usually determined from pure mode I double cantilever beam (DCB) test and pure mode II end notched flexure (ENF) test. The additional fitting parameter η can be determined from mixed mode bending (MMB) tests. The CZM therefore requires six independent input parameters, which were chosen as listed in Table 1. The interface strengths τ_n^0 and τ_s^0 were approximated by the values of experimentally determined tensile strength (90°) respectively shear strength of a single layer, while the values for strain energy release rates G_{Ic} and G_{IIc} as well as for mixed mode parameter η were taken from [3]. The CZM was implemented in commercial finite element solver ABAQUS/Standard by means of a subroutine UMAT for cohesive elements and UINTER for contact cohesive behaviour.

Table 1: Input parameters for cohesive zone model (partly taken from [3])

K_n [N/mm³]	τ_n^0 [MPa]	τ_s^0 [MPa]	G_{Ic} [kJ/m²]	G_{IIc} [kJ/m²]	η
10^6	33.58	48.78	0.969	1.719	2.284

2.2 Finite element model of a cross-ply-laminate with discrete microcracks

A finite element model of a $[0_n/90_m]_s$ cross-ply-laminate with a length of 100 mm and a width of 25 mm was built in commercial software ABAQUS/Standard. The overall thickness is 2 mm for each of the external 0° layers and 6 mm for the embedded 90° layer. Four predefined microcracks were introduced in the 90° layer in form of equidistantly distributed seams which run perpendicular to the interface. The general geometrical design of the cross-ply-laminate model is illustrated in Figure 1 (a). Due to the symmetric stacking direction of the laminate, only one half of it was represented in the FE model using a symmetric boundary condition.

  doi:10.5075/epfl-298799_978-2-9701614-0-0

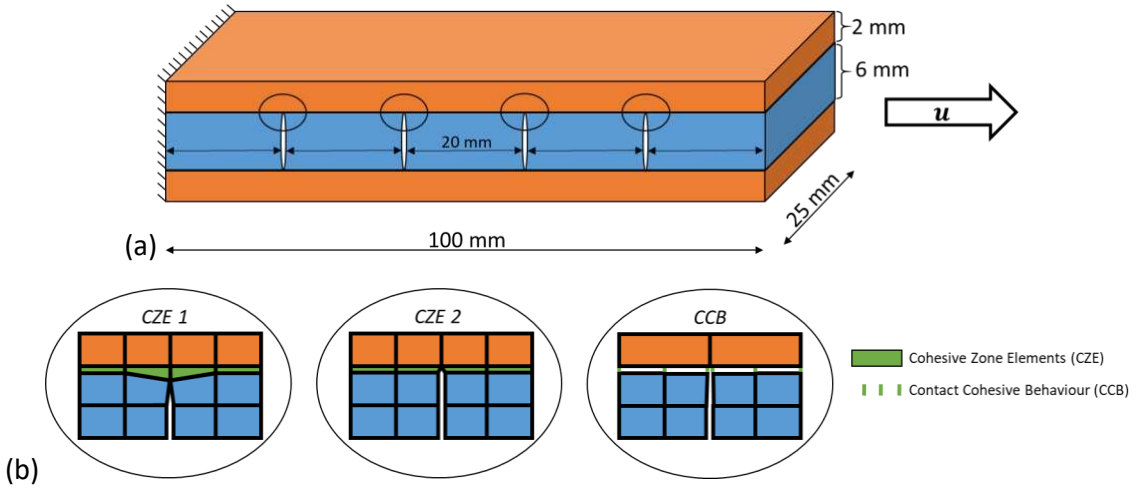

Figure 1: Cross-ply-laminate model: (a) General design (b) detailed presentations of connection between the microcracks and the cohesive zone in three different variants

The 0° and the 90° layers were represented by linear eight-node solid elements with a transversely isotropic material behaviour. The corresponding material properties were derived from a material characterization of a glass fibre reinforced plastic consisting of SIGRATEX G U220-0/SO e-glass fibre and MGS RIMR135 / RIMH137 epoxy resin. The parameters were determined according to the applying standards ISO 527 [7] and ASTM D 7078 [8] for tension and shear, respectively. Tests were carried out at room temperature and 50% relative humidity. with at least 4 samples per loading direction. Additionally, the fibre volume fraction φ_f has been examined by burn-off tests. The derived parameters are listed in Table 2.

Table 2: Transversal isotropic material properties for glass fibre reinforced plastic

E_{11} [GPa]	E_{22} [GPa]	ν_{12} [-]	G_{12} [GPa]	G_{23} [GPa]	φ_f [%]
37.2	9.045	0.292	3.09	3.277	48.96

The interface between the 0° and 90° layers was modelled by means of the CZM described in section 2.1. Three different approaches were made to model the connection and interaction between the microcracks and the cohesive zone resulting in three different types of mesh. The three variants are visualized in detail in Figure 1. In the first approach (further referred to as CZE 1) the interface consists of cohesive zone elements (CZE) with a thickness of 10^{-3} mm sharing their nodes with the adjacent linear solid elements of the 0° and 90° layer. The seams run through the 90° layer only and stop at the cohesive zone. This type of mesh forces the microcrack tips to stay always sharp while crack opening. A mesh convergence study showed a strong dependency of the results on the element length and the number of elements in the 90° layer in thickness direction for this approach, while the influence of element width and the number of elements in the 0° layer in thickness direction was weak. Therefore, a fine mesh with an element length of 0.125 mm, an element width of 2.5 mm as well as a number of 20 elements in the 90° layer and 3 elements in the 0° layer in thickness direction was chosen here. The second approach (further referred to as CZE 2) differs from CZE 1 in terms of the extended lengths of the seams so that the microcracks run through the cohesive zone and stop at the 0° layer. This mesh allows the crack tip to become blunt due to large deformations of the adjacent cohesive

  doi:10.5075/epfl-298799_978-2-9701614-0-0

zone elements. The same modelling approach was made by Reiner et al. in [9]. The mesh convergence study showed that for this approach an element length of 1 mm and a number of elements in the 90° layer in thickness direction is sufficient. In the third approach (further referred to as CCB) contact cohesive behaviour is applied between the interface surfaces, where the coarser meshed surface of the 0° layer (element length and width of 5 mm) acts as the master surface and the finer meshed surface of the 90° layer (element length 1 mm, element width 2.5 mm) acts as the slave surface. In thickness direction, three elements were used in the 0° layer and five elements in the 90° layer, which is also result of a mesh convergence study.

In order to take into account the manufacturing induced residual stresses in the finite element model a thermal expansion analysis was conducted in a first step. Starting from an initial temperature of 80°C the laminate was cooled down to room temperature (20°C). The doubled nodes at the seams were stuck together by means of tie constraints, so that no crack opening can occur during the cooling process. As a consequence residual stresses in normal and shear direction can be observed in the cohesive zone, especially at the edges. The residual stress field was used as initial state for the following analysis step. In this step, a displacement of 2 mm was applied to one end of the laminate while the other end was clamped.

3. Results and Discussion

The total delaminated area A_{del} was measured during the loading process by evaluating,

$$A_{del} = \sum_{i=1}^{n} D_{A,i} A_i \tag{14}$$

where n is the number of integration points for CZE 1 and CZE 2 respectively the number of nodes for CCB in the interface and A_i is the area represented by the integration point or node. The delaminated area A_{del}, referred to the total interface area, is plotted against the applied tensile strain in Figure 2. Obviously, the approach CZE 1 leads to significantly less delamination than the other approaches CZE 2 and CCB. All curves can be divided into three stages: In the first stage MCID takes place. The rate of delamination is relatively low. The following second stage shows a rapid delamination propagation. The propagation rate decreases again in the third stage, when the delaminated area gets closer to the total interface area, which is the maximal possible delamination area. In the first stage, the approach CCB shows more delamination than the approach CZE 2. In the second stage, the curves of CCB and CZE 2 become aligned.

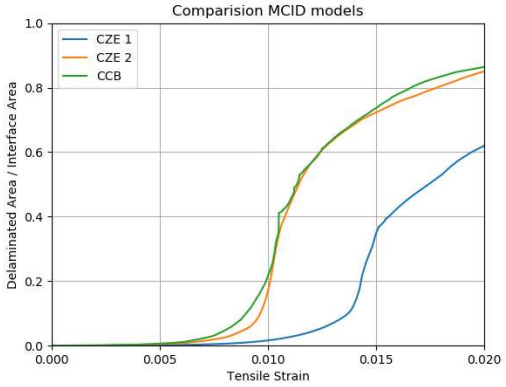

Figure 2: Comparison of delaminated area for different model approaches

In Figure 3, the spatial distribution of the damage parameter D_A is visualized in a contour plot for all three approaches at different strain states. In all cases damage initiation takes place at

the location of the microcracks starting from the free edges which is the place of the highest stress caused by stress concentrations at the crack tips and the superimposed residual stresses. As already observed in Figure 2 the time of initiation as well as the rate of propagation differ for each approach. This different damage behavior can be explained by different occurring fracture modes for this MCID as visualized in Figure 4. While approach CZE 2 leads to a mode II dominated delamination initiation occurring at higher tensile strains due to a higher interface strength in shear direction τ_S^0, the approach CZE 1 shows a mode I dominated delamination initiation occurring at lower tensile strains because of the lower interface strength in normal direction τ_n^0. However, this mode I dominated region is strongly bounded to the elements connected with the microcrack tips. The loading applied to the adjacent elements is pure mode II. Thus, the lower fracture toughness for mode I G_{Ic} has no impact on the further delamination rate. On the contrary, the applied mesh seems to slow down propagation. For both approaches using cohesive zone elements, the occurring fracture mode is mainly predefined by the mesh, while the CCB approach allows the whole range of possible mixed mode ratios. At the locations of the microcracks a mixed mode delamination initiation can be observed. During delamination propagation, the mixed mode ratio increases until it reaches pure mode II delamination.

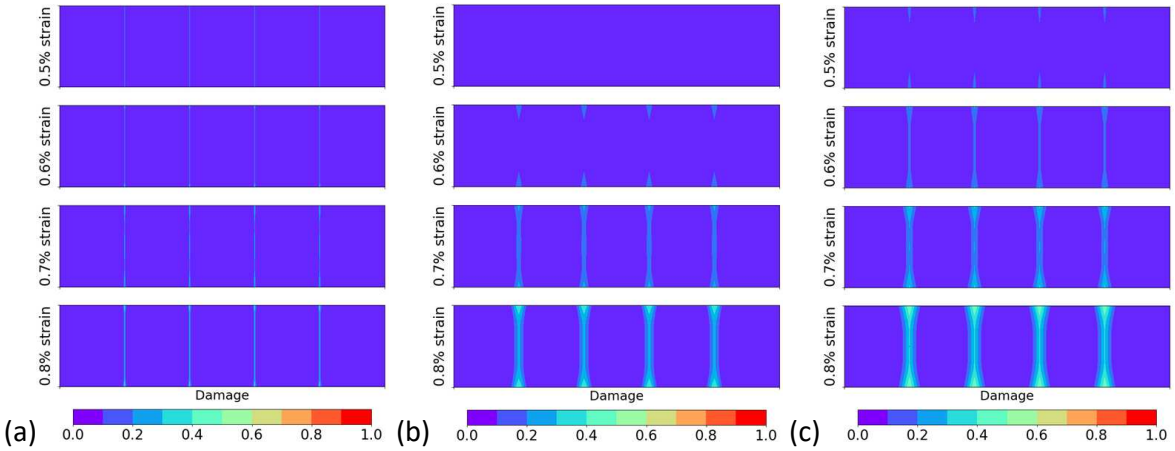

Figure 3 : Damage Initiation (a) CZE1, (b) CZE2 and (c) CCB

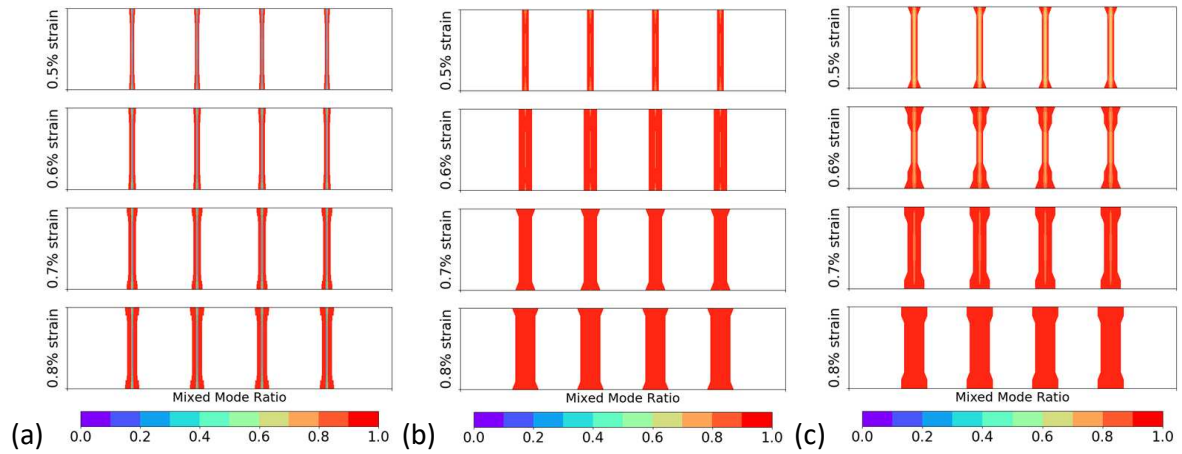

Figure 4: Mixed mode ratio for MCID for (a) CZE1, (b) CZE2 and (c) CCB

The further delamination propagation is visualized by means of contour plots of damage parameter D_A in Figure 5. It can be observed, that in case of approach CZE 1 the delamination starting from the microcracks mainly propagates to one side of loading direction. Concerning

the other approaches CZE 2 and CCB delamination propagates to both sides of loading direction. Considering the applied symmetric boundary conditions, the predicted shapes of delamination were a C-shape for CZE 1 and a H-shape for CZE 2 and CCB. Such H-shaped delaminations were also found in microscopic investigations of cross-ply-laminates under cyclic tensile loading in [10] to an amount of about 45%, whereas C-shaped delaminations could not be overserved in the study. The remaining amount consists of Z-shaped delaminations (about 17%) and mixed shaped delaminations (26%). However, due to the choice of symmetric boundary conditions a prediction of Z-shaped or mixed shaped delaminations by the numerical model was impossible.

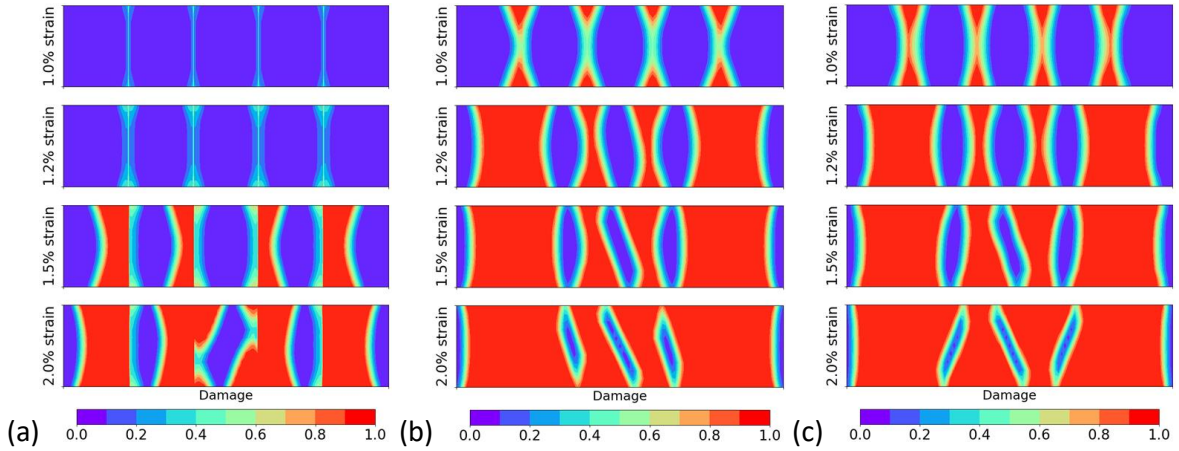

Figure 5: Damage propagation for (a) CZE1, (b) CZE2 and (c) CCB

The mixed mode ratio B for delamination propagation is visualized in a contour plot in Figure 6. Obviously, the occurring fracture mode for delamination propagation is pure mode II regardless of the modelling approach.

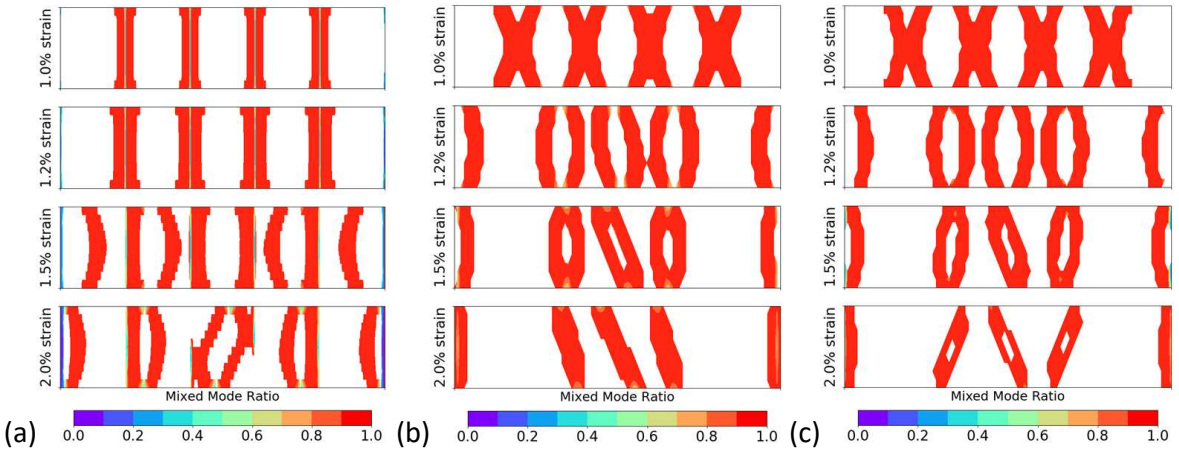

Figure 6: Mixed mode ratio for damage propagation for (a) CZE1, (b) CZE2 and (c) CCB

4. Concluding remarks and outlook

In this contribution, microcrack-induced delamination (MCID) in cross-ply laminates was simulated numerically by means of a mesoscopic finite element model containing predefined microcracks in the embedded 90° layer. These microcracks could interact in different ways with the [0/90] interface represented by a cohesive zone model (CZM) which is mainly influenced by the applied mesh. Three different modelling approaches were presented resulting in different

  doi:10.5075/epfl-298799_978-2-9701614-0-0

delamination behaviour. In the stage of delamination initiation, these differences could be explained by differently occurring fracture modes caused by various meshes. Although all approaches showed a pure mode II fracture mode in the later stage of delamination propagation, one approach showed a much lower rate of propagation than the other two approaches.

In future works a CZM taking into account fatigue damage behaviour due to cyclic loading should be included into the presented MCID model. This CZM needs to be verified experimentally by means of cyclic DCB and ENF tests. In order to verify the MCID model as well, cyclic tests on cross-ply laminates are planned, where the delaminated area can be measured and compared to the simulation results.

Acknowledgements

The authors gratefully acknowledge the financial support of the German Research Foundation (DFG) within the Research Grant 457043708.

References

1. Just G, Koch I, Brod M, Jansen E, Gude M, Rolfes R. Influence of reversed fatigue loading on damage evolution of cross-ply carbon fibre composites. Materials 2019; 12(7):1153.
2. Koch I, Just G, Brod M, Chen J, Doblies A, Dean A, Gude M, Rolfes R, Hopmann C, Fiedler B. Evaluation and modeling of the fatigue damage behavior of polymer composites at reversed cyclic loading. Materials 2019; 12(11):1727.
3. Camanho PP, Dávila CG, De Moura MF. Numerical Simulation of Mixed-mode Progressive Delamination in Composite Materials. Journal of Composite Materials 2003; 37(16):1415-1438.
4. Turon A, Camanho PP, Costa J, Dávila CG. A damage model for the simulation of delamination in advanced composites under variable-mode loading. Mechanics of Materials 2006; 38(11):1072-1089.
5. Turon A, González EV, Sarrando C, Guillamet G, Maimí P. Accurate simulation of delamination under mixed-mode loading using a cohesive model with a mode-dependent penalty stiffness. Composite Structures 2018; 184:506-511.
6. Benzeggagh ML, Kenane M. Measurement of mixed-mode delamination fracture toughness of unidirectional glass/epoxy composites with mixed-mode bending apparatus. Composite Science and Technology 1996; 56(4):439-449.
7. DIN EN ISO 527-5 - Kunststoffe - Bestimmung der Zugeigenschaften, Beuth, 2010
8. ASTM D 7078 - Standard Test Method for Shear Properties of Composite Materials by V-Notched Rail Shear Method, ASTM International, 2005
9. Reiner J, Veidt M, Dargusch M, Gross L. A progressive analysis of matrix cracking-induced delamination in composite laminates using an advanced phantom node method. Journal of Composite Materials 2017; 51(20):2933-2947.
10. Carraro PA, Maragoni L, Quaresimin M. Characterisation and analysis of transverse crack-induced delamination in cross-ply composite laminates under fatigue loadings. International Journal of Fatigue 2019; 129:105217

  doi:10.5075/epfl-298799_978-2-9701614-0-0

MODELLING THE DAMAGE EVOLUTION IN UNIDIRECTIONAL ALL-CARBON HYBRID LAMINATES

Amaury, Ollic[a], Fariborz, Sheibanian[b], Babak, Fazlali[c],
Yentl, Swolfs[c], Stepan V., Lomov[c], Valter, Carvelli[a]

a: Department A.B.C., Politecnico di Milano, Milan, Italy – amaury.ollic@gmail.com
b: Department of Aerospace Engineering, Amirkabir Univ of Technology, Tehran, Iran
c: Department of Materials Engineering, KU Leuven, Leuven, Belgium

Abstract: *A finite element model was developed to simulate the damage evolution in unidirectional (UD) all-carbon hybrid composites subjected to tensile loading. The finite element model exploits translaminar embedded cohesive elements governed by a unimodal Weibull strength distribution in the Low-Strain (LS) plies to simulate fragmentation. Interlaminar cohesive elements simulate the Low-Strain (LS) and High-Strain (HS) plies interfaces. The numerical analyses highlighted the evolution of the tensile behavior from pseudo-ductile to catastrophic delamination by changing the LS/HS thickness ratio. The distribution of translaminar strength of the LS material and the number of cracks simulated have a key role in the numerical mechanical response. The model had good agreement to experimental data for tensile behavior of thin-ply all-carbon hybrid laminates.*

Keywords: all-carbon hybrid laminates; pseudo-ductility; numerical model; damage evolution

1. Introduction

The lack of ductility of fiber reinforced composite materials can be overcome by interlayer hybridization where Low Strain (LS) material is sandwiched between High Strain (HS) material. Hybridization tends to improve composite properties but induces complex failure mechanisms, including multiple interacting damage modes, such as ply fragmentation and delamination [1]. Therefore, modelling the damage evolution of hybrid composites is more complex than that of non-hybrid composites. Few mechanical numerical models of fiber hybrid composites are available in the literature, to the authors' knowledge, and they are mainly dedicated to unidirectional reinforcements (see e.g. [2–4]).

Intrayarn random fiber packings have been considered to build three-dimensional finite element models in [3]. The models simulated the effect of the hybridization on the stress concentration around a broken carbon fiber. Modelling UD interlayer carbon/glass hybrid laminates has been detailed in [4], which concluded that one of the most important parameters influencing the damage is the ratio of LS thickness and the overall laminate thickness. The variation of this ratio allows to depict a damage mode map and to predict the failure behavior of new hybrid fiber reinforced composite configurations.

  doi:10.5075/epfl-298799_978-2-9701614-0-0

In this context, the present study was dedicated to the development of a finite element model to predict the tensile response of unidirectional all-carbon hybrid laminates. The numerical results were compared to experimental data available in [5].

2. Finite element modelling approach for tensile loading of UD hybrid laminates

The model considers an interlayer hybrid laminate configuration made of one layer of LS material and two layers of HS material. 3D cohesive elements are used at the LS/HS interface to simulate delamination. Fragmentation is simulated by cohesive elements embedded between two bulk elements of the LS layer, which properties are not affected [4]. The thickness of the cohesive elements is set to 0.3 µm. In real tensile tests, multiple fragmentation density and distribution may affect the damage evolution. However, in this work, a uniform distribution of possible fragmentation is supposed considering 319 cohesive elements along the specimen length (X), and, consequently, the length of the LS bulk element is 0.25 mm, which lead to a length of the specimen $l = 80$ mm. As discussed in [4], the distribution of cohesive elements alongside the length could cause unrealistic material softening behavior. To prevent it, a large penalty stiffness ($K = 10^9\ MPa/mm$) and a low viscosity parameter ($\mu = 10^{-6}\ Pa \cdot s$) have been used. Hence, the dimensions of the interface cohesive elements are 0.25 mm x 0.25 mm and thickness 0.3 µm, which is coherent with the suggestions in [6]. To simplify the approach, the stiffness and the fracture energy are assumed the same for all embedded cohesive elements. The random nature distribution of the fiber strength is represented by Weibull distribution.

The model geometry and boundary conditions represent a unidirectional tensile test. The model constraints are summarized in Figure 1, where U_X, U_Y and U_Z are the displacement component along X, Y and Z direction, respectively. To reduce the computation cost, symmetry was applied along the length and the thickness.

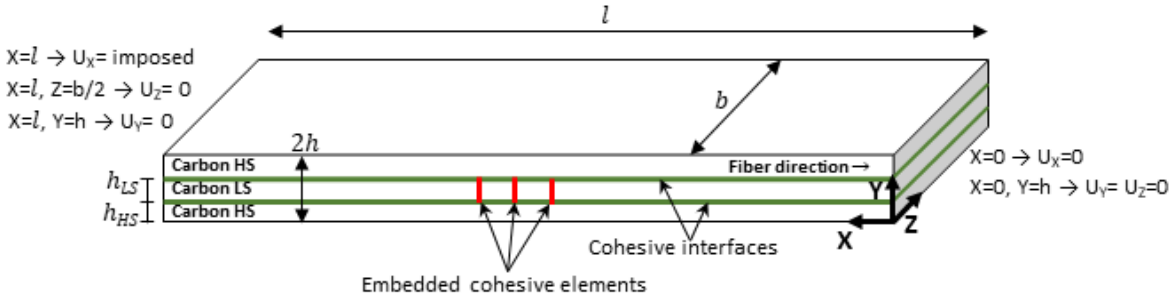

Figure 1. Sketch of the geometry, boundary conditions and multi-fragmentation of the all-carbon hybrid laminate3D model.

The length of the bulk element, namely the distance between two embedded cohesive elements, is 0.25 mm, which is lower than the recovery length of the LS layer. When failure occurs at a cohesive element position, the stress in nearby LS elements decreases. Hence, damage in some cohesive elements located within the recovery length is not activated due to the low stress level [7].

  doi:10.5075/epfl-298799_978-2-9701614-0-0

3. Numerical predictions of UD thin-ply all-carbon hybrid laminate

A UD thin-ply all-carbon hybrid laminate was experimentally investigated in [5]. It was produced with T1000 (T) carbon fibers for the high-strain (HS) layer (cured ply thickness 0.032 mm), and M55 (M) carbon fibers for the low-strain (LS) layer (cured ply thickness 0.031 mm). It had stacking sequence $[T_2/M/T_2]$. The geometry (with symmetries) and materials properties considered for the model of the thin-ply all-carbon hybrid laminate under tensile loading are listed in Table 1 [5].

Table 1: Features of the UD all-carbon thin-ply hybrid laminate finite element model.

Mechanical properties of HS and LS layers

	E_{11} [b]	$E_{22} = E_{33}$ [b]	$G_{12} = G_{13}$ [b]	G_{23} [b]	$v_{12} = v_{13}$ [b]	v_{23} [b]	V_f [a]
HS	143 GPa	6.5 GPa	3.1 GPa	2.6 GPa	0.25	0.23	0.481
LS	277 GPa	4.7 GPa	2.7 GPa	2.0 GPa	0.25	0.12	0.513

Properties of the cohesive elements embedded in LS layer

$G_{Ic} = G_{IIc} = G_{IIIc}\ (N/mm)$	$\sigma_n^0 = \tau_{tn}^0 = \tau_{sn}^0 (MPa)$	$K(MPa/mm)$
1	$2217 - 2618$	10^9

Properties of the cohesive elements at the HS/LS interface

$G_{Ic}\ (N/mm)$	$G_{IIc} = G_{IIIc}\ (N/mm)$	$\sigma_n^0 = \tau_{tn}^0 = \tau_{sn}^0 (MPa)$	$K(MPa/mm)$
0.199	0.5	67	10^5

Geometric parameters

$l\ (mm)$	$b\ (mm)$	$h\ (mm)$	$h_{HS}\ (mm)$	$h_{LS}\ (mm)$
80.0	20×0.5	0.160×0.5	2×0.0323	0.5×0.0308

Finite elements mesh details

Elements number	*Elements in the length / type*	*Elements in the width*	*Elements in the HS thickness*	*Elements in the LS thickness*
230040	320 / C3D8 319 / COH	40	5	3

[a] Based on manufacturer's data [5]
[b] Calculated using manufacturer's data and Chamis model [9]

According to the literature, the range for the interlaminar shear strength is 67 - 100 MPa [4,10]. Since no data on the interlaminar shear strength was provided in [5], 67 MPa was adopted as conservative value. The fracture energy of the cohesive interface was set to 0.5 N/mm using the failure criterion proposed in [5].

As in [4], the modulus of the Weibull distribution is set to m = 41, which allows the distribution to match the experimentally observed scatter of carbon ply failure strain [10]. The characteristic strength of the LS layer for the Weibull distribution is set to 2342 MPa in order to have the first failure at 2217 MPa, which was calculated by the Hooke's law and reference data [5]. Then, the strength is randomly assigned among the cohesive elements in the range 2217 MPa - 2618 MPa (Table 1).

Table 1 also details the mesh features of the model. The specimen is discretized as follows, considering symmetries: 639 bulk elements along the length of the HS layer; 320 bulk elements and 319 cohesive elements simulating cracks in the LS layer; the LS layer has 3 elements in the

  doi:10.5075/epfl-298799_978-2-9701614-0-0

thickness direction (Y), and each of the two HS layer has 5 elements with bias ratio of 10 in the thickness direction (Y); one element composes the thickness of the remaining cohesive layer, which brings the total of 9 elements along the thickness; the width has 40 elements of 0.25 mm, a typical dimension for cohesive elements [7,10].

The results of the modelling of the UD thin-ply all-carbon hybrid laminate [T_2/M/T_2] are presented in the Figure 2. The map of the stress component in the X direction in Figure 2b has been taken at a global stress level of 1400 MPa, which is almost in the middle of the pseudo-ductile plateau.

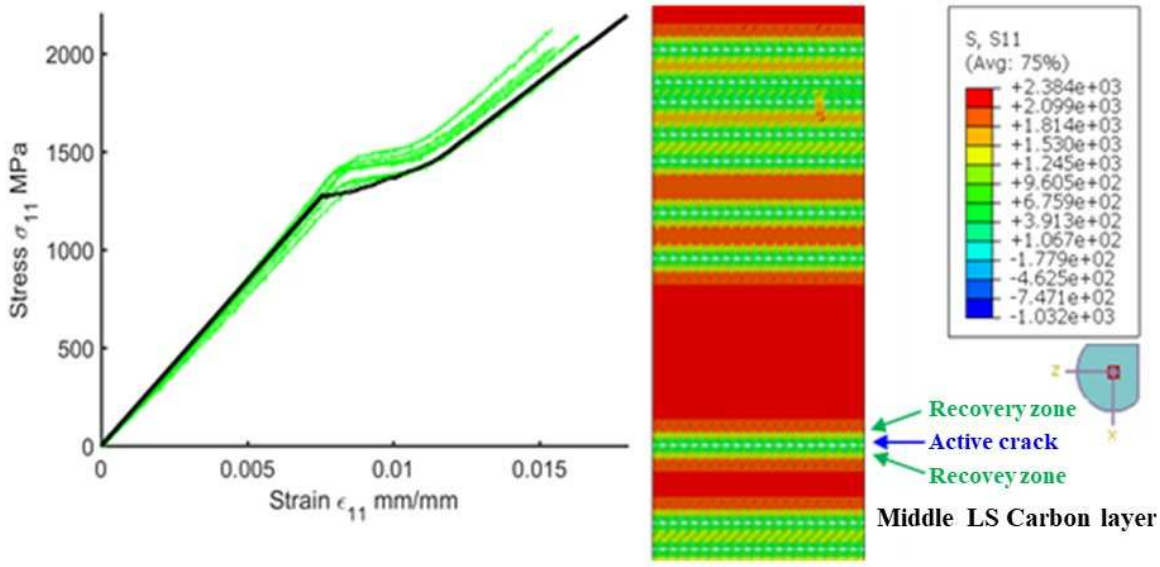

(a) (b)

Figure 2. UD thin-ply all-carbon hybrid laminate: (a) tensile stress-strain comparison, experimental data (green curves) and FE model prediction (black curve); (b) prediction of the fragmentation distribution for a global stress level of 1400 MPa.

In the elastic region, the load is mostly carried by the LS material, being stiffer than the HS material. The first ply fails at stress of 1386 MPa. Then, the plateau region starts. Activation of each new crack transfers stress from the LS layer to the HS layer via the interface. The interlaminar fracture toughness is high enough to avoid catastrophic delamination and to transfer the load to the HS layer without damage. So, the stress keeps increasing in the LS layer, leading to more fragmentation. In other words, a high interlaminar fracture toughness hinders the onset and propagation of delamination. This progressive transfer of load creates the pseudo-ductile behavior of the laminate.

According to the criterion proposed in [7], the recovery length $l_c/2$ of the laminate [T_2/M/T_2] is about 1.11 mm. Since the bulk element length is 0.25 mm, at least 8 neighbor cohesive elements (cracks) are not activated due to the low stress level. This also depends on the strength random distribution. This event is shown in Figure 2b with activated crack, recovery zone (green) and far-field stress zone (red).

  doi:10.5075/epfl-298799_978-2-9701614-0-0

The same approach was used to determine the mechanical response of different layups, varying the LS thickness ratio. The LS thickness ratio corresponds to the ratio between the LS thickness and the thickness of the laminate. According to the results in Figure 3, the laminate $[T_9/M_4/T_9]$ and $[T_2/M/T_2]$ have a LS thickness ratio relatively close, 17% and 19%, respectively, while the thickness of the $[T_9/M_4/T_9]$ laminate is 4.5 times higher than the $[T_2/M/T_2]$ laminate. The thinner laminate $[T_2/M/T_2]$ results in pseudo-ductile behavior and the thicker laminate $[T_9/M_4/T_9]$ in catastrophic delamination.

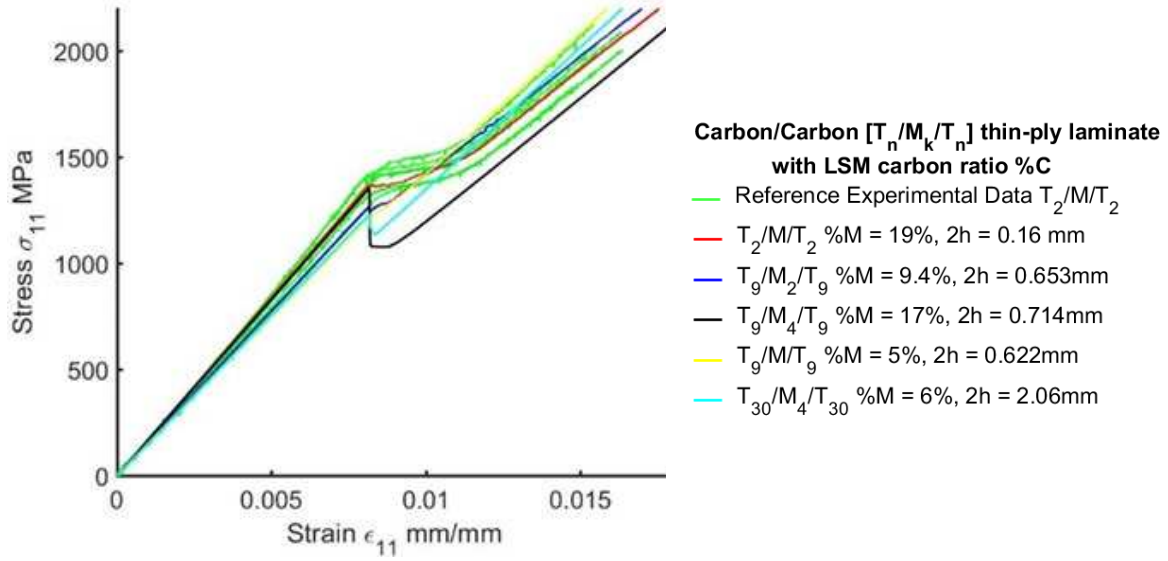

Figure 3. UD thin-ply all-carbon hybrid laminate: tensile stress-strain comparison, green curves are experimental data $[T_2/M/T_2]$ and other colored curves are the FE model response of different layups $[T_n/M_k/T_n]$. The legend gives the laminate layup, the LS thickness ratio and the total thickness of the laminate.

4. Conclusions

This study was devoted to the numerical modelling of the tensile damage evolution of interlayer-hybrid laminates. The results obtained by the FE model are consistent with the experimental reference data of thin-ply all-carbon hybrid laminate [5]. The achievement of the pseudo-ductile behavior is only possible using a tough interface [5] and a sufficiently high number of embedded cohesive elements with a realistic strength distribution. The latter considerably increases the computational cost of the simulation. Convergence issues may be faced if the interface stiffness is too high and if the viscosity of the interface is too low. The selected values (Table 1) allow us to obtain a consistent numerical solution in an acceptable computational time.

Further analyses, assuming the featured of the present finite element model, will be dedicated to thick-ply all-carbon hybrid laminates and the construction of damage mode maps by modelling new layups of the interlayer hybrid laminates. The maps will help to distinguish catastrophic delamination and pseudo-ductile behavior as function of the LS thickness ratio.

  doi:10.5075/epfl-298799_978-2-9701614-0-0

Acknowledgements

The work leading to this publication was performed within the framework of HyFiSyn project and has received funding from the European Union's Horizon 2020 research and innovation programme under the Marie Skłodowska-Curie grant agreement No. 765881. Amaury Ollic acknowledges KU Leuven partial support of his research stay in Leuven and the access to the Vlaams Supercomputer Centrum.

5. References

[1] Swolfs Y, Gorbatikh L, Verpoest I. Fibre hybridisation in polymer composites: A review. Compos Part Appl Sci Manuf 2014;67:181–200. https://doi.org/10.1016/j.compositesa.2014.08.027.
[2] Dong C, Duong J, Davies IJ. Flexural properties of S-2 glass and TR30S carbon fiber-reinforced epoxy hybrid composites. Polym Compos 2012;33:773–81. https://doi.org/10.1002/pc.22206.
[3] Swolfs Y, Gorbatikh L, Verpoest I. Stress concentrations in hybrid unidirectional fibre-reinforced composites with random fibre packings. Compos Sci Technol 2013;85:10–6. https://doi.org/10.1016/j.compscitech.2013.05.013.
[4] Jalalvand M, Czél G, Wisnom MR. Numerical modelling of the damage modes in UD thin carbon/glass hybrid laminates. Compos Sci Technol 2014;94:39–47. https://doi.org/10.1016/j.compscitech.2014.01.013.
[5] Czél G, Jalalvand M, Wisnom MR, Czigány T. Design and characterisation of high performance, pseudo-ductile all-carbon/epoxy unidirectional hybrid composites. Compos Part B Eng 2017;111:348–56. https://doi.org/10.1016/j.compositesb.2016.11.049.
[6] Turon A, Dávila CG, Camanho PP, Costa J. An engineering solution for mesh size effects in the simulation of delamination using cohesive zone models. Eng Fract Mech 2007;74:1665–82. https://doi.org/10.1016/j.engfracmech.2006.08.025.
[7] Jalalvand M, Czél G, Wisnom MR. Damage analysis of pseudo-ductile thin-ply UD hybrid composites – A new analytical method. Compos Part Appl Sci Manuf 2015;69:83–93. https://doi.org/10.1016/j.compositesa.2014.11.006.
[8] Kaw AK. Mechanics of Composite Materials. 0 ed. CRC Press; 2005. https://doi.org/10.1201/9781420058291.
[9] Balzani C, Wagner W. An interface element for the simulation of delamination in unidirectional fiber-reinforced composite laminates. Eng Fract Mech 2008;75:2597–615. https://doi.org/10.1016/j.engfracmech.2007.03.013.
[10] Wisnom MR. Relationship between strength variability and size effect in unidirectional carbon fibre/epoxy. Composites 1991;22:47–52. https://doi.org/10.1016/0010-4361(91)90102-M.

  doi:10.5075/epfl-298799_978-2-9701614-0-0

Multiscale analysis of an aircraft wingbox

S. T. Pinho[a], R.O.S.S. Costa[b], M. Matos[c,d], A. Ibbotson[d], M. Ostergaard[d]

a: Dept. Aeronautics, Imperial College London, UK – silvestre.pinho@imperial.ac.uk
b: Dept. Aeronautics, Imperial College London
c: Airbus, Filton, UK

Abstract: This paper presents results of a methodology for structural simulation of very large structures. It does not assume the use of a specific failure model, but rather focuses on establishing a framework that enables failure analyses on full-wing models with a complexity comparable to real wings in large passenger aircraft.
Keywords: Structural simulation, multi-scale modelling

1. Introduction

Modern composite structures, such as aircraft wings, are typically very complex structures 10s of meters long (Figure 1). This is the scale at which design engineers insist that numerical damage models are required, with the constraint of being as accurate as possible.

The damage tolerance of these large structures is often the consequence of damage processes that become unstable at very small ply-level scales of o(0.1 mm) (Figure 2). Researchers therefore often insist that damage models need to be developed at this scale, with the constraint of being as scalable as possible.

There is a wide gap between the two positions described above, and the outcome is that failure models for composites, including those available in commercial software, tend not to be readily usable for the design and analysis of very large composite structures (such as an entire aircraft wingbox).

However, to enable multiscale analyses, hot-spots need to be identified at the large scale. This paper demonstrates this, as well as proposing, detailing and verifying a viable alternative multiscale composite material model failure assessment methodology.

  doi:10.5075/epfl-298799_978-2-9701614-0-0

Figure 1. Very large aircraft wingbox (Airbus A350) [1]

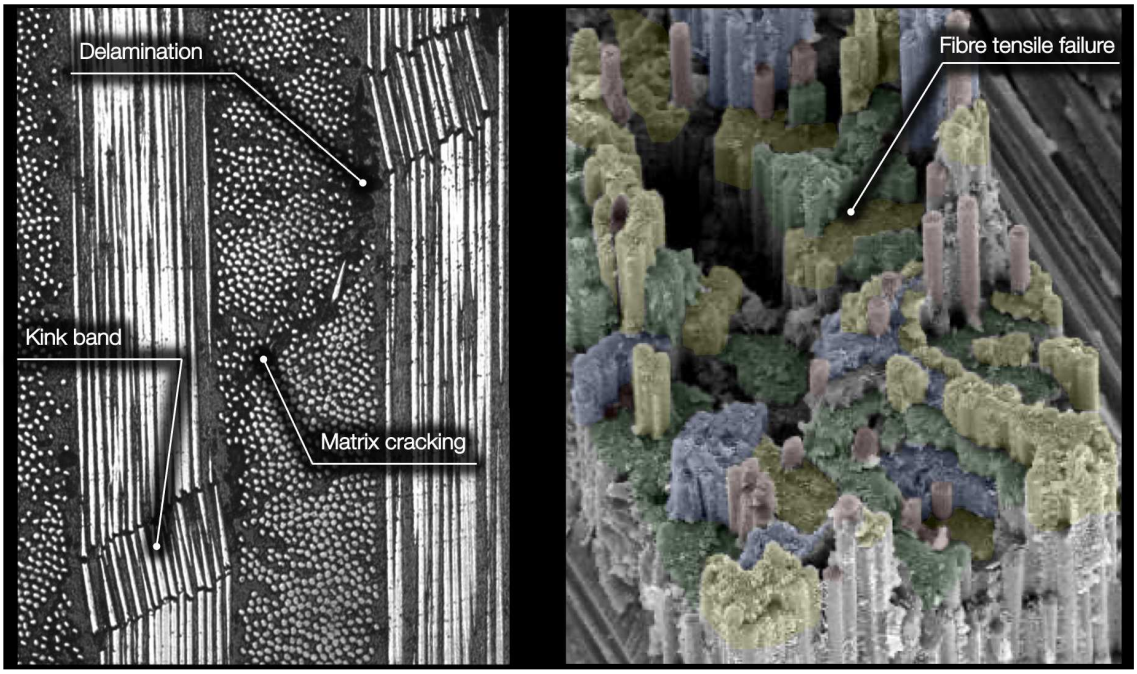

Figure 2. Typical failure modes in composites at the ply scale [2]

2. Modelling framework for very large models

We propose a framework (Figure 3) whereby high-value data is calculated directly in the HPC cluster during the analysis, and the design engineer only needs to render high-value data suitable for decision making, including identifying hot-spots for sub-modelling. So that these hot-spots are modelled using the exact same material models regardless of the scale and

  doi:10.5075/epfl-298799_978-2-9701614-0-0

material idealisation in the analysis, the implementation of material models does not assume any specific interface (Figure 4).

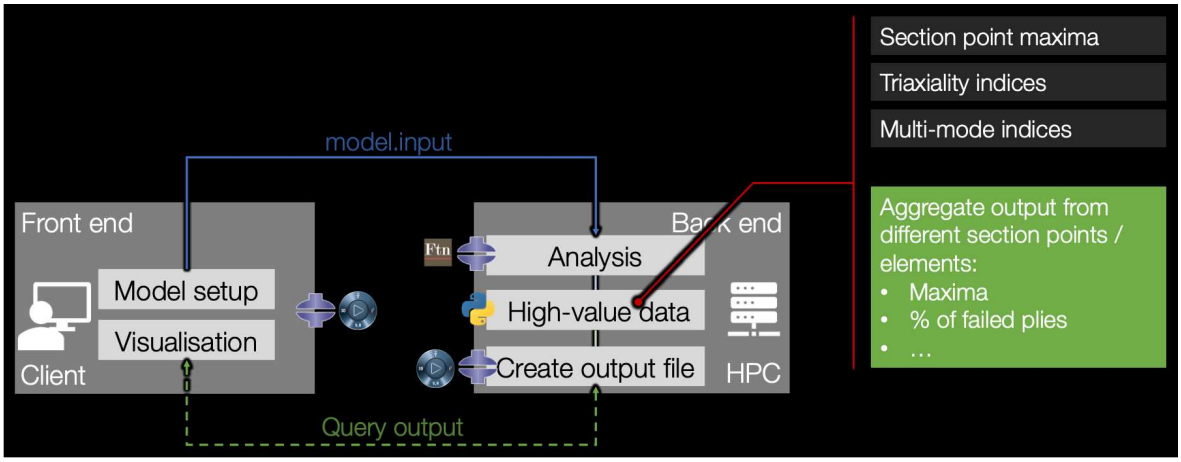

Figure 3. Modelling framework designed around the need to extract high-value data in HPC

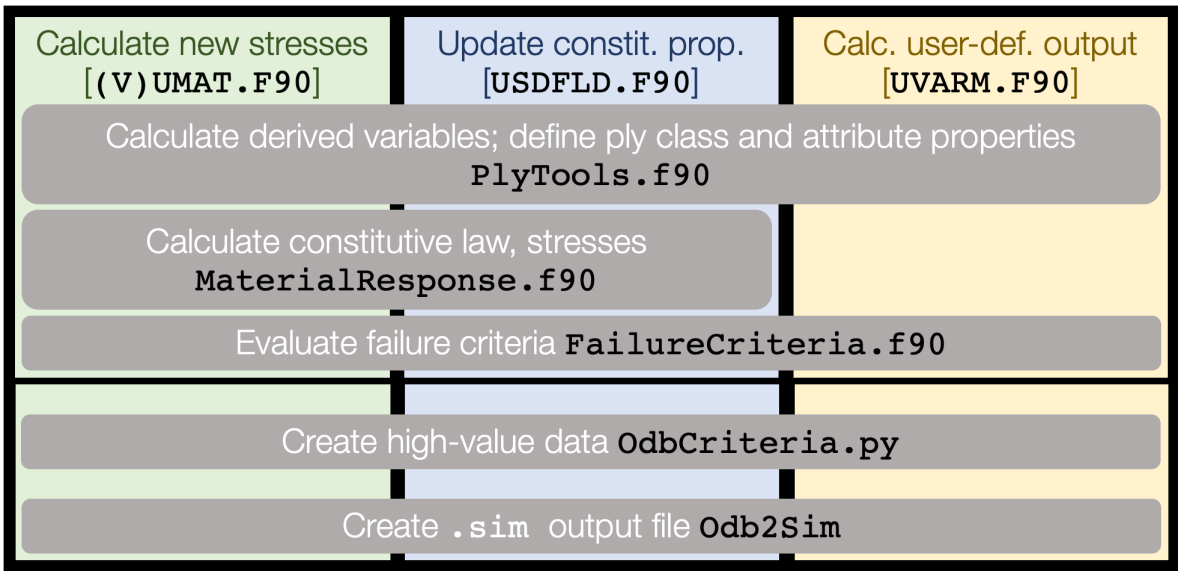

Figure 4. While different interfaces are differently suited for different scales of analysis and for different idealisations of the material, the modelling framework is designed to always use the same underlying code, hence ensuring a harmonised modelling approach across the various scales.

3. Application: wingbox

We created a detailed CAD model of an aircraft wingbox based on the Airbus A350 and using only data that is publicly available (Figure 5). The model contains 81 full-sized components. These include CFRP parts (upper and lower covers, front and rear spars, 22 upper and 22 lower stringers) and aluminum parts (33 ribs).

  doi:10.5075/epfl-298799_978-2-9701614-0-0

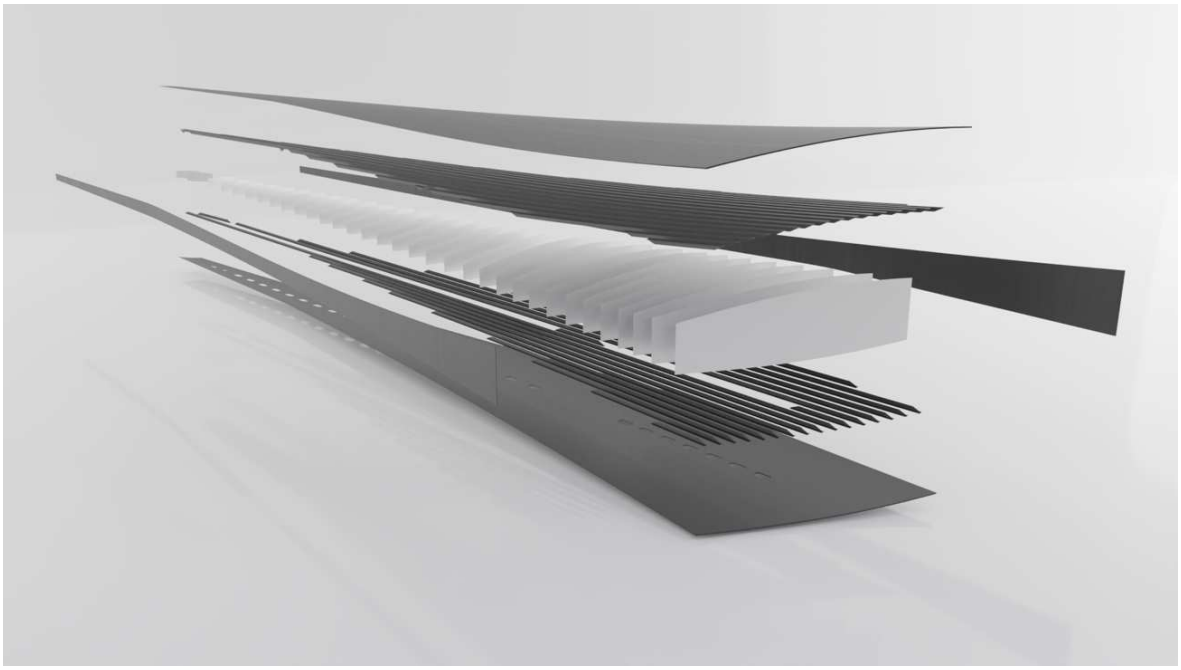

Figure 5. CAD model of a realistic aircraft wing

We fixed the wing at the root and applied a uniform distributed normal pressure to the covers. We ran the FE analysis using Abaqus Implicit with non-linear geometric behaviour on an HPC cluster.

4. Results for full wingbox model

The full wingbox model ran successfully up to complete structural collapse. We found that the wing collapsed due to unstable compressive failure of the upper cover near the root of the wing (Figure 6), and that this failure started due to local buckling near the rear spar.

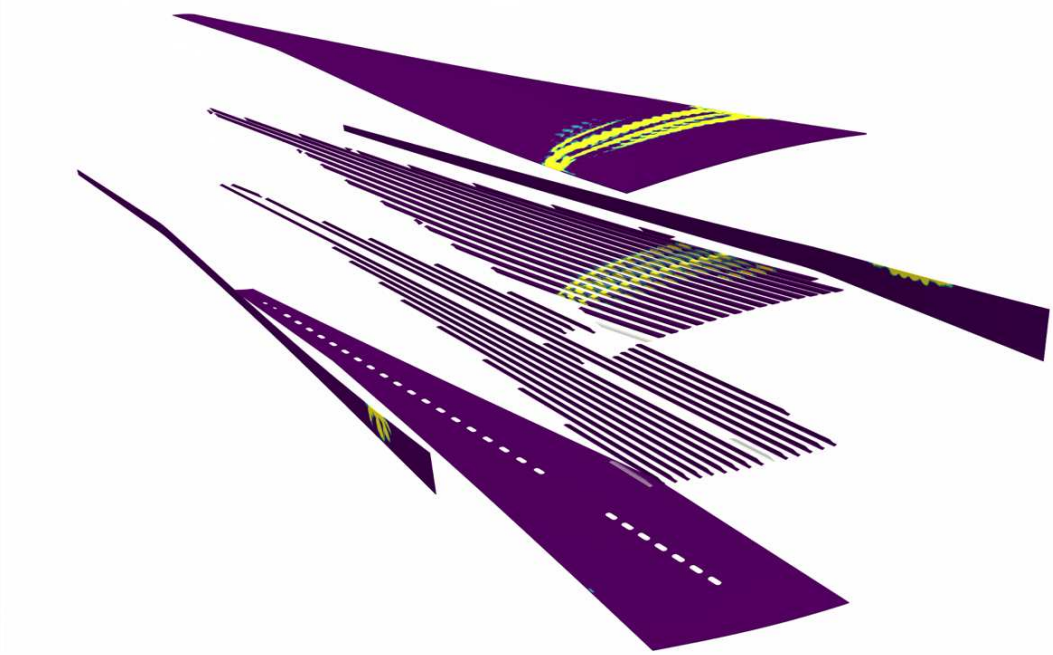

Figure 6. Fibre kinking damage variable (maximum cross section) at end of analysis for the full wingbox model

5. Multiscale analysis: setup

Based on the hotspot identified by the full wingbox model (Figure 6), we created models at two further scales (Figure 7).

We ran all models using sub-modelling so that the boundary conditions came from a suitable larger-scale model.

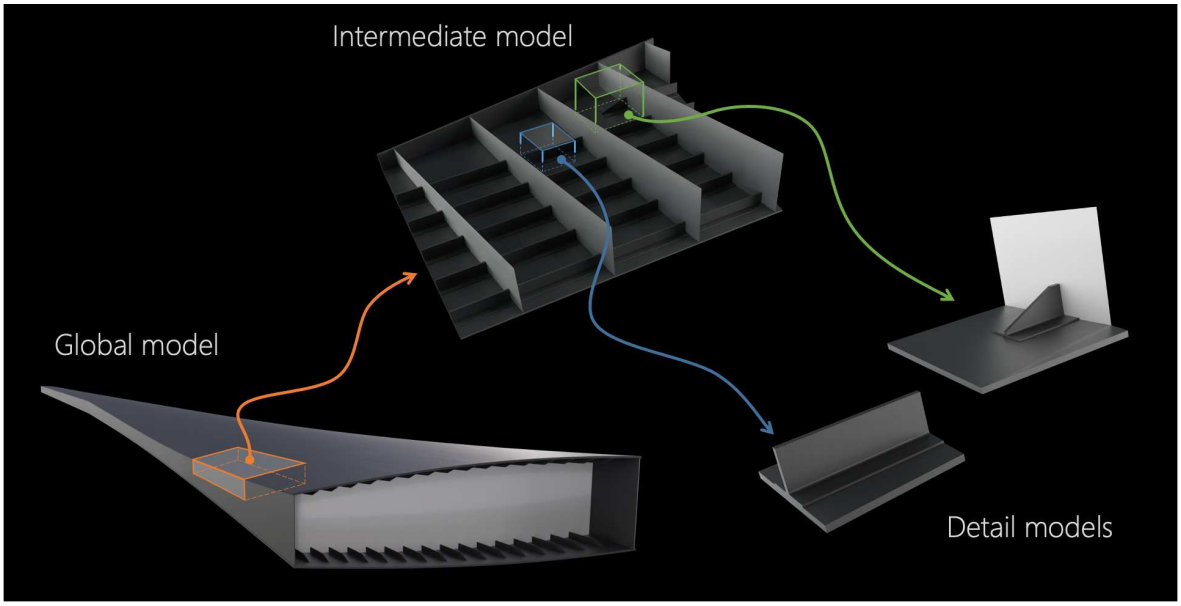

Figure 7. Multiscale analysis with 3 scales

6. Multiscale analysis: results

The intermediate-scale model with surface *tied* contact interactions (between stringers and cover) exhibited a structural failure mode very similar to that of the full-scale

We ran each detail-scale model three separate times using suitable boundary conditions coming from all larger-scale models (Figure 8).

To compare quantitatively the results all multiscale simulation settings, we plotted in Figure 9 the load experienced by the wing, as a function of the displacement of a suitable point in the cover chosen for experiencing large deflections due to the local buckling which initiated the failure process.

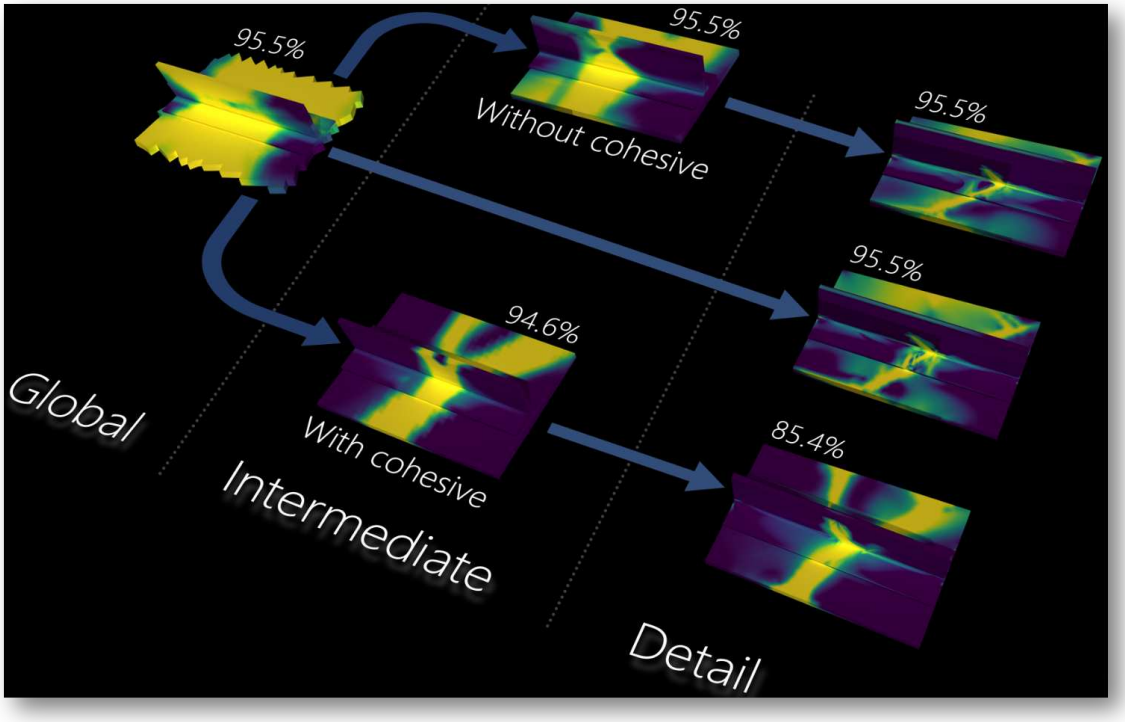

Figure 8. All multiscale simulation settings considered (the field shown is kink-band damage (maximum across section))

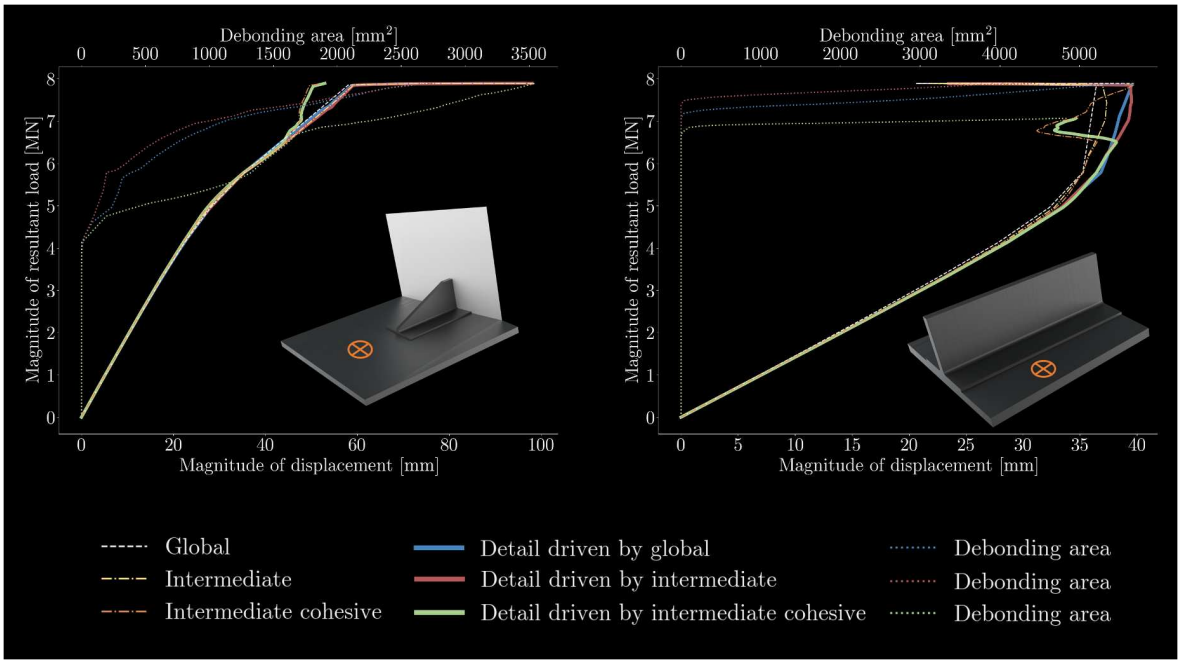

Figure 9. The various simulation settings lead to similar mechanical responses, even in the regions most affected by non-linear deformations. However, modelling debonding at the intermediate scale is needed to fully capture the deformation state in the cover during the later stages of the analysis.

7. Conclusions

In this work, we implemented a modelling framework for analysis of very large composite structures. Its key characteristics are:

- the numerical implementation works across various user interfaces;
- it employs back-end high-value data calculation (e.g. proportion of failed plies; coded output).
- it leads to manageable output files + data for decision making; and
- it is agnostic to actual failure model used.

We can conclude that this framework can be successfully used in models with 15M DOF for:

- extending predictions of full-wing models into the non-linear region, including full collapse of the wing;
- identifying hot-spots in the wing; i.e. regions which merit more detailed attention; and
- driving meaningful multiscale analyses for the hot-spots.

This work provides a foundation for (and constitutes a significant step towards) achieving virtual twins of very large composite structures. The interface for high-value data can be extended to include a plethora of specific types of high-value data suitable for the most varied situations. The multiscale analysis, sequential in this work, can be extended to be made concurrent or even adaptive [3].

  doi:10.5075/epfl-298799_978-2-9701614-0-0

8. References

1. Airbus, https://www.airbus.com/, last accessed 20-April-2022
2. Pinho ST, Darvizeh R, Robinson P, Schuecker C, Camanho PP, 2012, Material and structural response of polymer-matrix fibre-reinforced composites, JOURNAL OF COMPOSITE MATERIALS, Vol: 46, Pages: 2313-2341, ISSN: 0021-9983
3. E.S. Kocaman, B.Y. Chen, S.T. Pinho, 2019, A polymorphic element formulation towards multiscale modelling of composite structures, Computer Methods in Applied Mechanics and Engineering, Vol: 346, Pages 359-387, ISSN 0045-7825

CONSIDERATION OF ORTHOTROPIC THERMAL PROPERTIES OF SHORT FIBRE REINFORCED PLASTICS

Reza, Afsharnia[a], Andreas, Primetzhofer[b], Gerald, Pinter[a,b], Beate, Oswald-Tranta[c], Gabriel, Stadler[a]

a: Montanuniversität Leoben, Chair of Material Science and Testing of Polymers, Otto-Glöckel-Strasse 2, 8700 Leoben, Austria – reza.afsharnia@unileoben.ac.at
b: Polymer Competence Center Leoben GmbH, Roseggerstrasse 12, 8700 Leoben, Austria
c: Montanuniversität Leoben, Chair of Automation, Peter-Tunner-Strasse 27, 8700, Leoben, Austria

Abstract: *In this study a multiscale modelling has been performed to predict the orthotropic thermal expansions in short fibre reinforced plastics (SFRP). For the simulation, thermal conductivity as well as specific heat of the chosen materials as a function of temperature was measured experimentally by Light Flash Analysis (LFA) respectively by Differential Scanning Calorimetry (DSC). A first order Mori-Tanaka homogenization scheme have been utilized for material homogenization and an average fibre orientation matrix provided the fibre distribution data. E-Module of each matrix was defined temperature dependent and the E-Module of the fibre materials (glass and carbon) considered to be constant in the investigated temperature interval. Simulation has been performed for PA6-GF50, PPA-GF50, PEEK-GF30 and PEEK-CF30 from -40°C to 200°C. PP-GF-35, PP-GF40 and PP-GF50 was simulated from -25°C to 150°C. To validate the achieved results from the simulation, thermal strains were measured experimentally by Digital Image Correlation (DIC) method in two directions.*

Keywords: short fibre reinforced plastics; thermal strains; orthotropic material properties

1. Introduction

The demand for thermoplastics is increasing rapidly, especially in automotive industry. Some of the most deciding advantages of polymers are their low weight character, chemical stability and the possibility of producing complex geometries. However, they do not exhibit high mechanical properties like common engineering materials, which are partly improvable by adding fibres, in this case short fibres, typically with a length less than 1 mm (1–4).

The most common method for producing parts from SFRP is injection moulding technique which causes a fibre orientation in components (5, 6). There are two typical models for describing fibre distribution in the composite:

- Skin-core-skin model: The model is valid for thicker parts and consist of different regions with different fibre orientation over the thickness direction.
- Quasi-uniform model: This model considers a quasi-uniform fibre distribution in the direction of the thickness and the fibres are mostly in the direction of flow oriented (6).

As mentioned in several studies, mechanical and thermomechanical properties of SFRP are strongly depending on the fibre orientation distribution (7–10). Components from SFRP have in most cases joints with metals and the coefficient of thermal expansion of metals is significantly

  doi:10.5075/epfl-298799_978-2-9701614-0-0

smaller compared to polymers. Just this phenomenon shows the importance of having a deeper understanding of the thermomechanical behaviour of SFRPs to avoid undesired thermal stresses in the structure. Coefficient of thermal expansion (CTE) of SFRPs is a function of thermomechanical matrix and fibre properties as well as the fibre orientation, the aspect ratio and the fibre length distribution (11).

Fibre orientation data can be extracted experimentally from computer tomography measurements by processing voxel data (12) or by segmenting the fibres and calculating the mean fibre orientation based on this segments (13). Another possibility to get the fibre orientation matrix for the simulation is injection moulding simulation (14). Lusti et al. have shown in (15), the accuracy of a finite element simulation will not be lost if the mean fibre length is used instead of the measured fibre length distribution.

2. Experiments

For this study several materials have been chosen to investigate the effect of matrix, the effect of fibre, fibre weight fraction and fibre orientation on the thermal expansion of SFRPs. Table 1, illustrates the matrix material and the fibre material as well as the fibre fraction by weight of the investigated materials.

Table 1: Characteristic of the investigated materials

Matrix	Fibre type	Fibre mass fraction	Notation
Polypropylene	Glass fibre	35%	PP-GF35
Polypropylene	Glass fibre	40%	PP-GF40
Polypropylene	Glass fibre	50%	PP-GF50
Polyamide 6	Glass fibre	50%	PA6-GF50
Polyphetalamide	Glass fibre	50%	PPA-GF50
Polyetheretherketone	Glass fibre	30%	PEEK-GF30 (VESTAKEEP® 2000 GF30)
Polyetheretherketone	Carbon fibre	30%	PEEK-CF30 (VESTAKEEP® 2000 CF30)

For this study, the short fibre reinforced polymers, have been injected moulded to plates. An effect of such production method is a skin-core-skin structure, which is already published in earlier publications (5, 16) and shown in Fig. 1 (a). The required samples for the tests have been extracted out from 120 x 80 x 2 mm (L x W x H) plates (according to ISO294-4), see Fig. 1 (b).

  doi:10.5075/epfl-298799_978-2-9701614-0-0

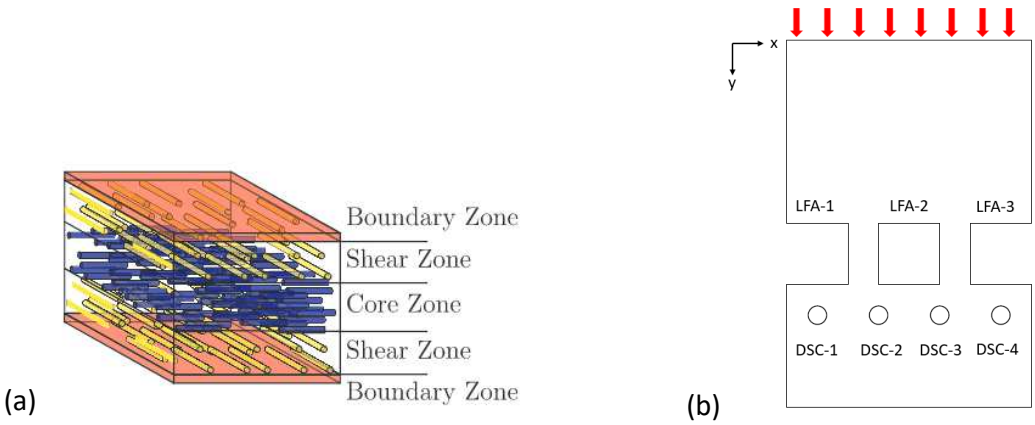

Figure 1: (a) Characteristic of micro structure of the plates (5)(b) Position and geometry of the extracted samples from the primary plate

2.1 Differential scanning calorimetry (DSC)

To measure the specific heat capacity of the chosen materials as a function of temperature, a DSC test have been performed for each one of the materials on the sample from the same position (DSC-3), see Fig. 1 (b). The tests have been performed in a wide temperature spectrum to cover the maximum possible operating temperature of the materials. For PP-base composites the tests were performed from -25°C to 150°C and for the other materials from -40°C to 200°C. Additionally, the specific heat was measured during heating and cooling processes. Heating/cooling rate was set to 10°C/min, since it is the most common heating rate according to literature (17).

2.2 Light Flash Analysis (LFA)

For measuring thermal conductivity of each material against temperature, two LFA tests have been performed for two different positions on the sample (LFA-1 and LFA-3), see Fig. 1 (b). Generally, the LFA device provides thermal diffusivity for the calculation of the thermal conductivity by using Equ. 1.

$$\lambda(T) = Cp(T) * \rho(T) * \kappa(T) \quad (1)$$

There, $\lambda(T)$ is the thermal conductivity, $Cp(T)$ the specific heat, $\rho(T)$ the density and $\kappa(T)$, the thermal diffusivity, as a function of temperature (T).

To investigate if the thermal conductivity changes from one plate to another plate from the same material, LFA tests have been performed on a second plate for each one of the materials as well. The measurements didn't show a remarkable change in the thermal diffusivity between different plates. However, for the simulation the average value of the driven thermal conductivities has been used.

3. Simulation working chain

3.1 Flow analysis

As mentioned earlier, fibre orientations in the parts from SFRPs are highly depended of the production method and process parameters. In (14), Primetzhofer et al. explained that, in the injection moulding process, melt flows in a cavity whereby the flow is depending on several

  doi:10.5075/epfl-298799_978-2-9701614-0-0

parameters like, injection pressure, geometry of the component and the temperature. It is also mentioned that, because of the temperature transfer from melt to the mould, a thin layer of the meld, known as frozen layer, will form on the mould in earlier stage. The localized flows in the plate will lead to a so-called skin-core-skin structure in the plate (Fig 1 (b)) (14, 5). There are several models available for predicting the fibre orientation in the composites and also it could be calculated by injection moulding simulation. The fibre orientation can be characterized by a second order symmetric tensor, equation 2 (14).

$$a^2 = a_{ij} = \begin{bmatrix} a_{xx} & a_{xy} & a_{xz} \\ a_{yx} & a_{yy} & a_{yz} \\ a_{zx} & a_{zy} & a_{zz} \end{bmatrix} \quad (2)$$

While the entities on the main diagonal represent the fibre orientation along the three main directions (x, y and z) and the other entities represent the rotation along the axes.

3.2 Mesh mapping

Due to numerical advantages, the elements used in processing simulation are different from the elements used in structural simulation. Therefore, a mesh mapping is necessary to transfer the processing data like residual stresses and fibre orientation data from processing mesh to the structural mesh (14). In this study, the processing simulation have been performed in MOLDFLOW® with tetrahedral meshes and the structural simulation have been performed in ABAQUS® with a hexahedral mesh type.

3.3 Homogenization

Since fibre distribution in SFRPs is not uniform, mechanical properties of the components made of SFRPs will change significantly in the component. Therefore, considering the fibre-matrix interaction, or more general the inclusion-matrix interaction, is necessary. On the other hand, calculating mechanical problems in micro scale is too time-consuming and therefore not suitable (18, 13) for a complex part. A solution for this problem is a homogenization, which provides a homogeneous material with non-isotropic material properties (18). For the homogenization several theorems are provided to bridges the gap between micro and macro solutions. One of the most famous homogenization methods is Mori-Tanaka scheme (19–21). A common approach for homogenization in commercial software is representative volume elements (REVs). In this approach software calculates the homogenized material properties in restricted elements and then the mechanical properties of the whole part will be presented in the form of a homogenized element, see Fig 2. Materials homogenization in this study have been performed in the software package DIGIMAT® using a first order mean field homogenization with Mori-Tanaka scheme with a temperature dependent E-Modulus for the matrix materials. The fibre E-Modulus, poison ratio as well as thermal expansion of both fibre and matrix materials are defined as temperature independent. Carbon and glass fibres considered to be spheroidal with an aspect ratio of 30, as defined in previous studies.

  doi:10.5075/epfl-298799_978-2-9701614-0-0

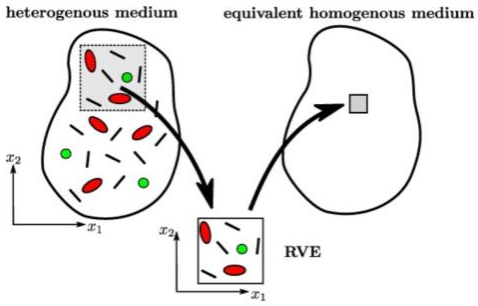

Figure 2:Micro-macro transition in a representative volume element (REV) (14)

4. Validation method

To validate the performed simulations, thermal strains of the prepared specimens, see Fig 1 (b), have been measured in two directions using a DIC. Thermal strains in the direction of thickness are not measured in the experimental tests. Thermal strains have been measured by a **DanTec®** solid mechanics DIC device, which uses two cameras for measuring the thermal strains in a 2D format. Fig 3, shows the setup, used for measuring the thermal strains. The measurements are performed in discrete temperature intervals from -40°C to 200°C (for PP from -40°C to 150°C), with a heating rate of 10°C/min and a dwell time of 5 min in each temperature level, and thermal strains between the measured temperatures are interpolated linearly.

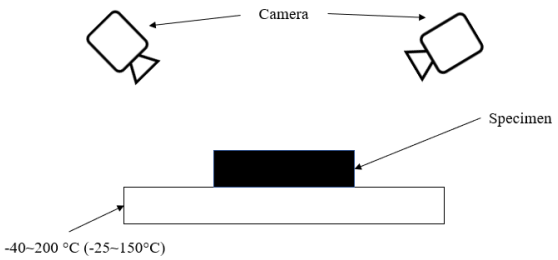

Figure 3: DIC setup for measuring thermal strains

5. Results and discussion

Fig 4, compares the simulated thermals strains and the thermal strains measured by DIC method. In Fig 4, direction “xx” represents the transvers direction of mould direction and “yy” represents the mould flow direction, see Fig 1 (b).

(a)

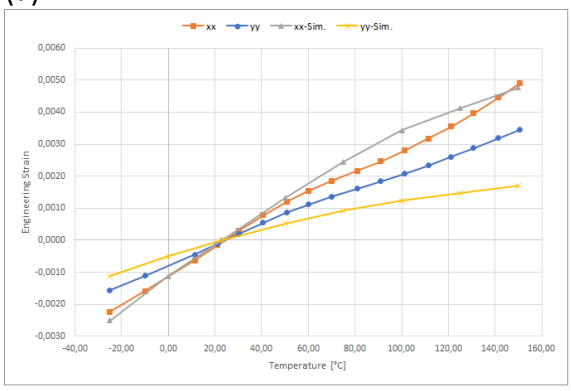

(b)

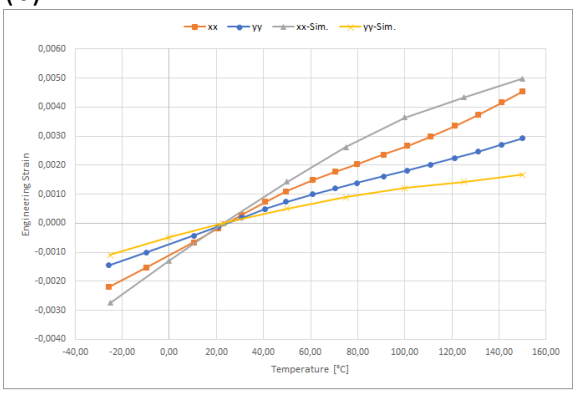

  doi:10.5075/epfl-298799_978-2-9701614-0-0 published under CC BY-NC 4.0 license

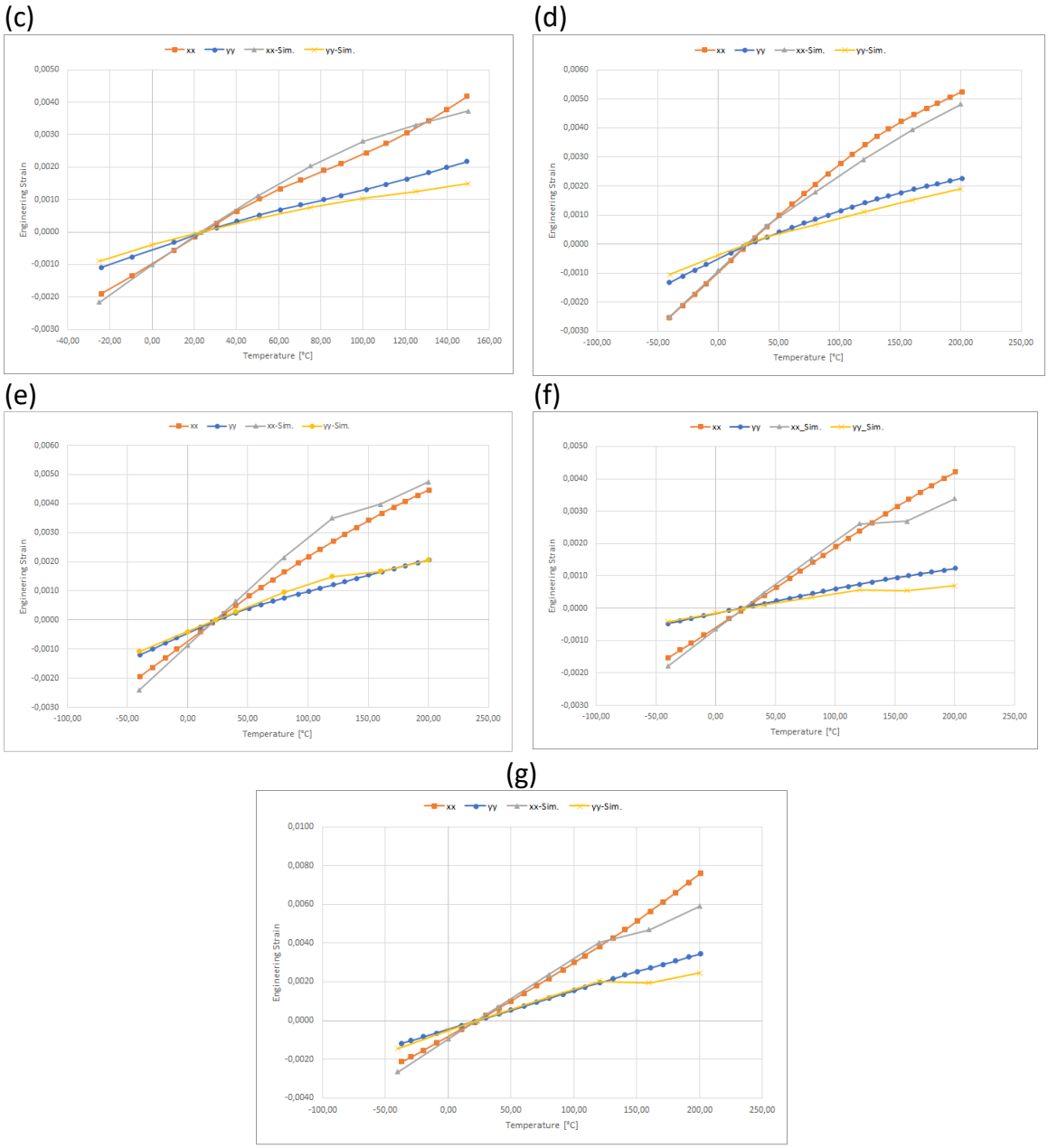

Figure 4: comparison between simulation results and experimental thermal strains for: (a)PP-GF35, (b)PP-GF40, (c)PP-GF50, (d)PA6-GF50, (e)PPA-GF50, (f)PEEK-GF30 and (g)PEEK-CF30

Fig 4 (a-c) shows that the deviation of thermal strain in the mould flow direction for Polypropylene decreases as the mass fraction of the fibres increases, the deviation of simulated thermal strain from measurements for PP-GF35 at 150°C is about 51% and the deviation decrease to 36% for PP-GF50 at 150°C, while the deviation of thermal strains in the direction transvers to the mould flow direction for all three PP-base composites is the same. The deviation of simulated thermal strains in the mould flow direction for PA6-GF50 at 200°C is roughly 22% and for the direction transverse to the mould flow direction about 7%, Fig 4 (d). For PPA-GF50, a sudden change in the thermal strains occurs in a temperature range 120°C -130°C, see Fig 4 (e), which is caused by material softening after glass transition temperature in PPA. Although, material softening is clearly observable in the simulation, it is not visible in the optical measurement. Regarding to Fig 4 (f and g), and similar to PPA-GF50 the glass transition for PEEK (140°C-150°C) is only to be seen in the simulation. For PEEK-CF30 and PEEK-GF30, the effect of

  doi:10.5075/epfl-298799_978-2-9701614-0-0

fibre materials on thermal strains in both, simulation and optical measurements, is clearly recognizable and carbon fibre reduces the thermal strains in both longitudinal and transversal directions extremely.

6. Discussion

In this study a simulation has been performed for predicting the thermal expansion in SFRPs. In the simulation a first order Mori-Tanaka scheme has been used for material homogenization. To validate the simulation, thermal expansion of the investigated materials has been measured experimentally in a wide temperature range in two directions. Comparing the results form simulation and the measured thermal strains, it could be concluded that the simulation could not predict the thermal strains for PP-base composites especially in the flow direction. However, by increasing the portion of the glass fibre the deviation between simulation and the measurement decreases. Since the simulation for PP-base composites has been performed in a temperature range higher than glass transition temperature, defining a temperature dependent CTE would be suggested to improve the accuracy of simulation. For PPA-GF50, PEEK-CF30 and PEEK-GF30 thermal strains could be predicted by the simulation accurately, although around the glass transition temperature a deviation between the simulation and the measurements has been observed. For PA6-GF50 simulation can predict thermal expansion accurately in the whole investigated temperature interval.

7. Acknowledgement

This research was funded by FFG grant number 854178. The research work of this paper was performed Polymer Competence Center Leoben GmbH (PCCL) in collaboration with the Chair of Mechanical Engineering and the Chair of Science and Testing of Polymers at the Montanuniversitaet Leoben within the framework of the COMET-program of the Austrian Ministry of Traffic, Innovation and Technology with contribution by BOREALIS AG, Brose Fahrzeugteile GmbH & Co. KG, Engineering Center Steyr GmbH (MAGNA Powertrain ECS), Evonik Operations GmbH, Hilit AG and Multi Wing international A/S. The PCCL is founded by the Austrian Government and the State Governments of Styria, Lower and Upper Austria.

References

1. Campo EA. Mechanical Properties of Polymeric Materials. In: Selection of Polymeric Materials. Elsevier; 2008. p. 41–101.

2. Röhrig C, Scheffer T, Diebels S. Mechanical characterization of a short fiber-reinforced polymer at room temperature: experimental setups evaluated by an optical measurement system. Continuum Mech. Thermodyn. 2017; 29(5):1093–111.

3. Mallick PK. Thermoplastics and thermoplastic–matrix composites for lightweight automotive structures. In: Materials, Design and Manufacturing for Lightweight Vehicles. Elsevier; 2021. p. 187–228.

4. Fu S, Lauke B, Mai Y. Introduction to short fibre-reinforced polymer composites. In: Science and Engineering of Short Fibre-Reinforced Polymer Composites. Elsevier; 2019. p. 1–7.

5. Stadler G, Primetzhofer A, Pinter G, Grün F. Investigation of fibre orientation and notch support of short glass fibre reinforced thermoplastics. International Journal of Fatigue 2020; 131:105284.

  doi:10.5075/epfl-298799_978-2-9701614-0-0

6. Dean A, Sahraee S, Reinoso J, Rolfes R. A new invariant-based thermo-plastic model for finite deformation analysis of short fibre reinforced composites: Development and numerical aspects. Composites Part B: Engineering 2017; 125:241–58.

7. Mortazavian S, Fatemi A. Fatigue behavior and modeling of short fiber reinforced polymer composites including anisotropy and temperature effects. International Journal of Fatigue 2015; 77:12–27.

8. Brunbauer J, Mösenbacher A, Guster C, Pinter G. Fundamental influences on quasistatic and cyclic material behavior of short glass fiber reinforced polyamide illustrated on microscopic scale. J. Appl. Polym. Sci. 2014; 131(19).

9. Hao X, Zhou H, Mu B, Chen L, Guo Q, Yi X et al. Effects of fiber geometry and orientation distribution on the anisotropy of mechanical properties, creep behavior, and thermal expansion of natural fiber/HDPE composites; 2020. (vol 185).

10. Dong C, Li K, Jiang Y, Arola D, Zhang D. Evaluation of thermal expansion coefficient of carbon fiber reinforced composites using electronic speckle interferometry. Opt Express 2018; 26(1):531–43.

11. Fu S, Lauke B, Mai Y. Thermal conductivity and expansion of short fibre-reinforced polymer composites. In: Science and Engineering of Short Fibre-Reinforced Polymer Composites. Elsevier; 2019. p. 213–40.

12. Bernasconi A, Cosmi F, Dreossi D. Local anisotropy analysis of injection moulded fibre reinforced polymer composites. Composites Science and Technology 2008; 68(12):2574–81.

13. Müller V, Brylka B, Dillenberger F, Glöckner R, Kolling S, Böhlke T. Homogenization of elastic properties of short-fiber reinforced composites based on measured microstructure data. Journal of Composite Materials 2016; 50(3):297–312.

14. Primetzhofer A, Stadler G, Pinter G, Grün F. Lifetime assessment of anisotropic materials by the example short fibre reinforced plastic. International Journal of Fatigue 2019; 120:294–302.

15. Lusti H. Direct numerical predictions for the elastic and thermoelastic properties of short fibre composites. Composites Science and Technology 2002; 62(15):1927–34.

16. Primetzhofer A, Stadler G, Pinter G, Grün F. Model Calibration and Data Set Determination Considering the Local Micro-Structure for Short Fiber Reinforced Polymers. J. Compos. Sci. 2021; 5(2):40.

17. Menczel JD, Prime RB. Thermal analysis of polymers. Oxford: Wiley; 2009.

18. Digimat: User documentation. Version 2021.2.

19. Mori T, Tanaka K. Average stress in matrix and average elastic energy of materials with misfitting inclusions. Acta Metallurgica 1973; 21(5):571–4.

20. Hessman PA, Welschinger F, Hornberger K, Böhlke T. On mean field homogenization schemes for short fiber reinforced composites: Unified formulation, application and benchmark. International Journal of Solids and Structures 2021; 230-231.

21. Ghossein E, Lévesque M. A comprehensive validation of analytical homogenization models: The case of ellipsoidal particles reinforced composites. Mechanics of Materials 2014; 75:135–50.

  doi:10.5075/epfl-298799_978-2-9701614-0-0

MODELLING AND EXPERIMENTAL TESTING OF HEAT TRANSFER DURING ELECTROFUSION WELDING OF GLASS-PE THERMOPLASTIC COMPOSITE PIPES

Ameen AL Obedan[a], Rachel Tomlinson[a] and Abderrazak Traidia[b]
a: Department of Mechanical Engineering, University of Sheffield, United Kingdom – ameen.obedan@gmail.com
b: Aramco Overseas Company UK Ltd, London, United Kingdom

Abstract: *Electrofusion welding (EW) is investigated as an alternative solution to replace the metallic connectors currently used to join reinforced thermoplastic composite pipes (TCP) with a cheaper non-metallic system. Using COMSOL Multiphysics software, a 2D finite element model was developed to simulate the unsteady heat transfer during electrofusion welding of TCP. The thermal conductivity and specific heat capacity were determined using Flash laser analysis and differential scanning calorimetry (DSC) was used to define the melting temperature. An experimental test was conducted to verify the accuracy of the developed model. A new procedure was used to install 30 thermocouples in various axial locations and radial depths in 180 mm fitting and 6"* glass fibre reinforced polyethylene *(GF-PE) pipes. The total heating time was 203 seconds and the maximum input power was 2.0 kW. The results show an acceptable level of agreement in the behaviour of the simulated and measured temperatures.*

Keywords: Electrofusion welding; composite pipes; heat transfer; modelling and simulation.

1. Introduction

Reinforced thermoplastic composite pipes (TCP and RTP) are increasingly used as a more sustainable replacement for conventional carbon steel pipes in the oil and gas industry. On average, 60% reduction in lifecycle carbon footprint could be achieved if glass fibre reinforced thermoplastic composite pipes were adopted instead of carbon steel in onshore flowlines [1]. TCP (being here defined as fully bonded RTP structures) offer superior corrosion protection [2], excellent mechanical strength, and are lightweight, which facilitates storage, transportation, and installation [3].

Solutions are sought to replace the metallic connectors used currently for joining TCP, with a corrosion-free joining method. Electrofusion welding (EW) is a well-developed joining technique used since the 1950s for conventional single-layer polyethylene (PE) pipes [4]. It is believed that this technique can be further enhanced to suit the operational requirements of reinforced TCP.

A considerable number of numerical modelling studies have been published on the electrofusion welding of PE pipes. These models were designed to study the effect of various welding parameters such as welding power, cooling time, air gap, phase change material and thermal contact resistance on the EW simulated temperature profile [5-7]. To date, no previous study has explored electrofusion welding of reinforced pipes.

This study investigates the feasibility of utilising EW as a potential solution for joining TCP and focuses on the heat transfer and temperature profiles during welding. Both modelling and experimental test results will be analysed to understand the behaviour of TCP under thermal loading.

  doi:10.5075/epfl-298799_978-2-9701614-0-0

2. Background

2.1 Thermoplastic composite pipes

Reinforced TCP comprises three layers: an internal liner, a middle reinforcement layer, and an external cover. The liner is made from thermoplastic material and functions as a barrier to contain the transported fluid [8]. This study uses pipes with high-density polyethylene (HDPE) liners. The reinforcement layer is made from multiple layers of high-quality GF-HDPE tapes and provides the pipe with the required strength to withstand internal and external pressure. The protective cover is made from HDPE and its primary function is to protect the pipe from environmental damage [9].

2.2 Electrofusion welding

Joining pipes by electrofusion welding requires three main elements: an electrofusion fitting, a power source and an electrofusion control unit (ECU). Welding for the electrofusion fitting, shown in Figure 1, is accomplished by the heat generated from circulating an electrical current from the control unit to the embedded resistance coil, usually at a fixed voltage. The energy supplied to the fitting raises the temperature of the heating wire for a specified length of time until the surrounding PE melts. The material is then allowed to cool and solidify.

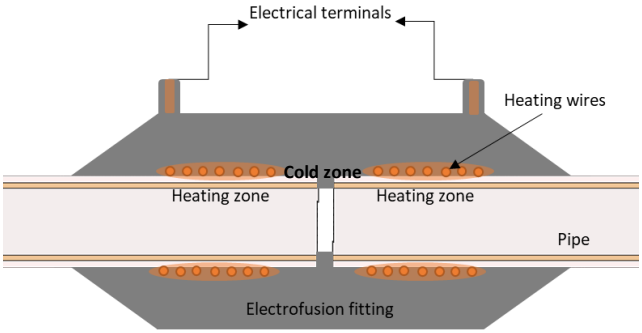

Figure 1. Electrofusion joint

Earlier studies established the required conditions to achieve successful welding of PE. To limit any thermal degradation, the maximum allowable welding temperature is 270 °C [10]. The minimum required temperature at the welding interface is 160 °C. To avoid thermal degradation around the heating wires, their temperature should not exceed 350 °C [11]. More information about reinforced composite pipes and EW can be found in a review article by Gierulski et al. [12].

3. Modelling

3.1 Model setup

Electrofusion welding is a transient heat transfer problem. This problem utilizes the heat conduction equation in cylindrical coordinates, presented in Eq. (1), to predict the temperature distribution considering the thermal contact conductivity of the contact surfaces.

$$\rho C_P \frac{\partial T}{\partial t} = k\left(\frac{\partial^2 T}{\partial z^2} + \frac{1}{r}\frac{\partial T}{\partial r} + \frac{\partial^2 T}{\partial r^2}\right) + \dot{q} \qquad (1)$$

where ρ is the density, C_P is the specific heat capacity, k is the thermal conductivity and $\dot{q}$ is the heat rate to the heating wires and can be determined from actual welding test.

The electrofusion joint being symmetric at both ends, only half of the joint is analysed in the model, as shown in Figure 2. The basic model for EW of TCP can be divided into three bodies: fitting, heating wires and pipe. The wires are made from copper, the fitting is made from HDPE and the pipe materials are as specified in section 2.1.

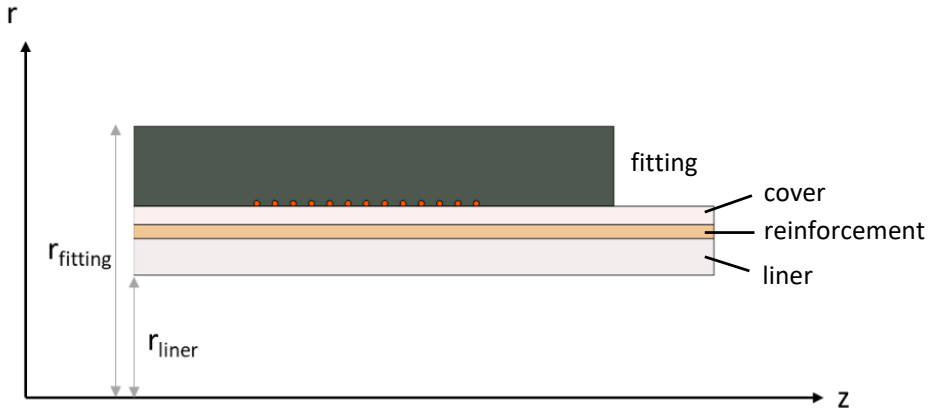

Figure 2. Schematic of the modelled joint.

The basic dimensions for the modelled joint are as follows: pipe liner radius (75 mm), liner thickness (8 mm), reinforcement thickness (3 mm), external cover (4 mm), fitting outer radius (210 mm), heating wires diameter (1.3 mm), number of wires (13 turns), distance between heating wires (4 mm), and half cold zone length (27 mm).

3.2 Model assumptions

A 2D axisymmetric model was designed to represent the heat transfer to the pipe and fitting during EW. The model considers a three-layer TCP pipe with temperature-dependent thermal properties. The model assumptions are as follows:

- perfect contact between the pipe and electrofusion fitting (no air gap),
- heat imposed as input power per unit volume in the heating wires,
- negligible radiation heat transfer,
- constant thermal properties for GF-HDPE,
- isothermal initial condition with a temperature equal to ambient temperature,
- free convection boundary condition with heat transfer coefficient of 10 $W/m^2 \cdot k$.

3.3 Material thermal properties

In the temperature range investigated in this study, the thermal properties of HDPE are nonlinear and temperature-dependent. A rapid change in the value of the thermal properties of HDPE occurs close to the melting temperature. Therefore, the values for the thermal properties of HDPE were taken as a function of temperature as measured by Shi et al. [6]. Measurement of thermal properties was carried out for the GF-HDPE with 0.42 glass volume fraction. Laser Flash Analysis (LFA) was conducted on a 10x10x3 mm sample to determine the corresponding thermal conductivity and specific heat capacity of the reinforcement. Differential scanning calorimetry (DSC) was used to measure the heat flow on the pipe samples to determine their melting temperature. All thermal properties for HDPE, GF-HDPE and copper heating wire are listed in Table 1.

  doi:10.5075/epfl-298799_978-2-9701614-0-0

Table 1: Material thermal properties.

Property	HDPE	GF-HDPE	Copper
Thermal conductivity k $(W/m \cdot K)$	$k(T)$	0.477	400
Specific heat capacity Cp $(J/kg \cdot K)$	$Cp(T)$	0.993	385
Density ρ (kg/m^3)	$\rho(T)$	1,690	8,960
Melting temperature °C	130.59	131.27	-

4. Experimental Testing

4.1 Preparation

A new procedure was developed to measure the temperature evolution at different locations in the pipe and in the electrofusion fitting using k-type thermocouples. The following steps were taken to prepare the pipe segments and the fitting before testing:

- straighten the pipe segments,
- cut the pipe segments to produce square ends,
- scrape the pipe ends and ensure proper alignment between the pipe and the fitting,
- cut each pipe segment into two segments of equal length,
- drill from the inner surface to the location of interest in the cut pipe,
- drill from the outer surface to the location of interest in the electrofusion fitting,
- weld the pipe segments back together by extrusion welding and
- insert the thermocouples in the drilled holes and seal them properly.

4.2 Test setup

Two 1 m long 6” TCP pipe segments were inserted in a 180 mm electrofusion fitting, as shown in figure 3. The pipe segments were fixed in place using clamps to limit their movements during the welding process. Thirty thermocouples were installed in different positions and at various depths into both pipe segments and the fitting. None of the thermocouples was installed in the cover layer to avoid any possible short circuit with the heating wire. The thermocouples were connected to a data logger that recorded the temperature at half-second intervals.

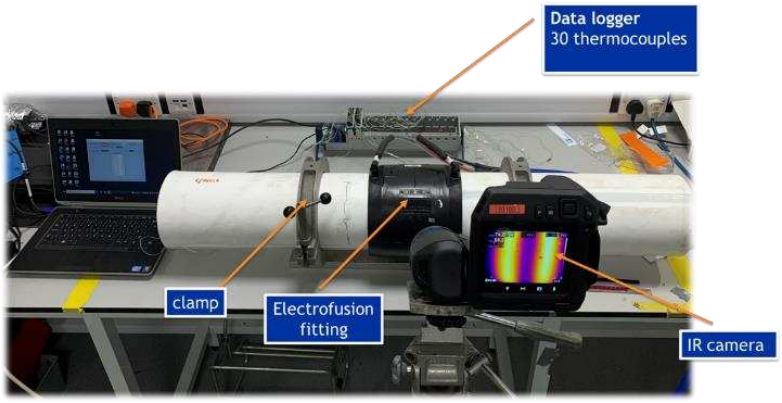

Figure 3. Electrofusion welding test setup

4.3 Input power

The welding control unit input voltage and current were recorded at one-second intervals during the welding process. The input power shown in Figure 4 was obtained by multiplying the output voltage by the current from the welding machine. The total heating time for the welding was 203 seconds and the cooling time was 30 minutes.

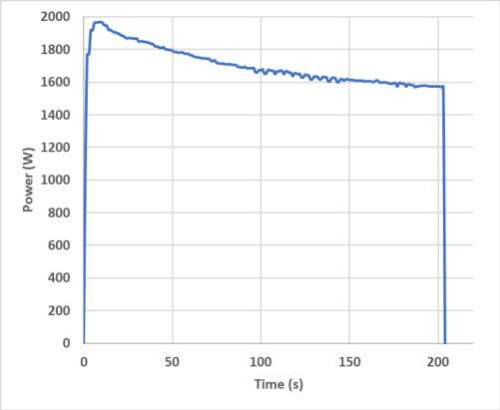

Figure 4. Input power for TCP electrofusion test

4.4 IR camera

A thermal infrared (IR) camera was used to capture the temperature profile on the fitting's external surface during the EW process. Correlation between the simulated temperature and the thermocouples temperature readings was established using the data generated by thermography. The polyethylene emissivity was assumed to be 0.96. The IR camera is capable of capturing live temperatures at a speed rate of 30 frames per second. The thermography indicated that the temperature profile on the external surface of the fitting reaches peak temperature around 888 seconds.

4.5 CT scan

A detailed computed tomography (CT) scan of the electrofusion joint was conducted post-welding. The CT scan aimed to verify the axial location and radial depth of all inserted thermocouples, as shown in the sample picture in Figure 5. Unfortunately, the scans showed that some of the thermocouples became displaced and others fell during transit; so only partial data could be collected. The gathered information was used to identify the actual location and depth of the thermocouples in the developed model.

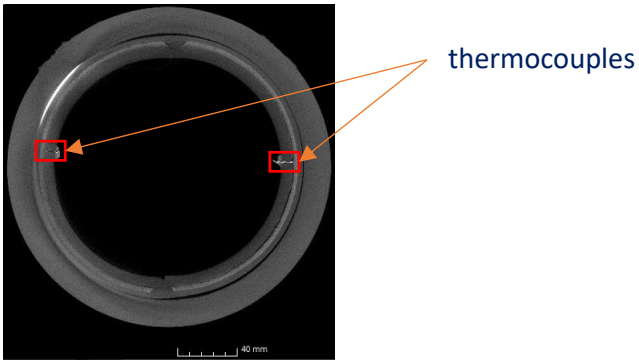

Figure 7. CT scan of the electrofusion joint of TCP

5. Results and Discussion

The electrofusion welding problem was solved by finite element modelling using COMSOL Multiphysics with a Heat Transfer Module and a step size of one second. A physics-controlled extra-fine mesh with 40,658 elements and 2,317 boundary elements was used to model the geometric domain. Using the power input from Section 4.3, the simulation profile taken in the centre of the heating zone for various points in the electrofusion joint, is shown in Figure 6. The temperature peaks at 300 °C in the heating wires, at 121 °C in the reinforcement layer, at 81.5 °C on the pipe inner surface and at 72 °C on the fitting external surface.

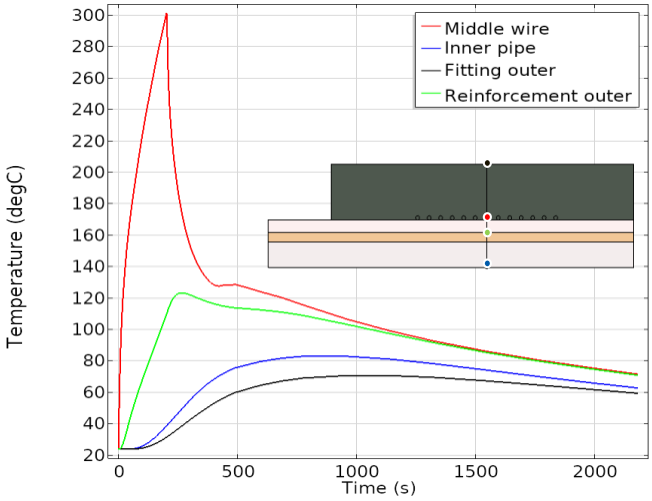

Figure 6. Simulated temperature profile over time for the power input given in section 4.3

An essential condition for the TCP welding to be successful is the temperature at the reinforcement layer of the pipe. To maintain the mechanical properties of the reinforcement and hence, the overall pipe strength, this temperature should not exceed the HDPE melting temperature. Figure 6 shows clearly that the maximum temperature in the reinforcement at the centre of the heating zone does not exceed the HDPE melting temperature. The simulated melted region at different times in the welding process was analysed in Figure 7 to display the region where HDPE melting may occur. Figure 7(a) shows the melting region at 50 seconds, Figure 7(b) at 101 seconds (half the heating time), Figure 7(c) at 203 seconds (end of the heating time) and Figure 7(d) at 6 minutes after the heating.

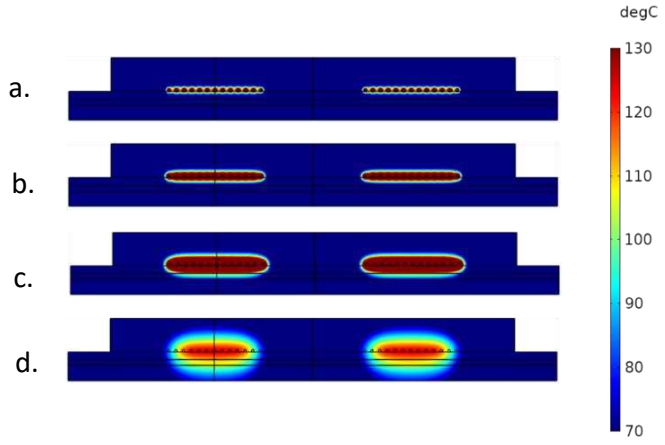

Figure 7. Melted region temperature at a) t=50 s, b) t= 101 s, c) t=203 s and d) t= 563 s.

  doi:10.5075/epfl-298799_978-2-9701614-0-0

The maximum measured temperature in the reinforcement layer was 96.8 °C at the centre of the heating zone. This temperature is lower than the HDPE melting temperature and should not substantially affect the quality of the reinforcement. The results from the simulation, thermocouple readings and thermography were compared to assess the quality of the current model. The temperature profiles of two points at the centre of the heating zone are presented in Figure 8. On the external fitting surface (Figure 8(a)), the temperature profiles are approximately matching in the heating phase and start to deviate, up to a maximum of almost 5 °C temperature difference, before the reversal point. Comparing the simulated and thermocouples profiles at the reinforcement layer, a variation between the simulated and experimental results can be seen (Figure 8(b)). However, thermocouple readings and simulated temperature during heating and cooling behave similarly, with a maximum temperature difference of 20 °C prior to the reversal point.

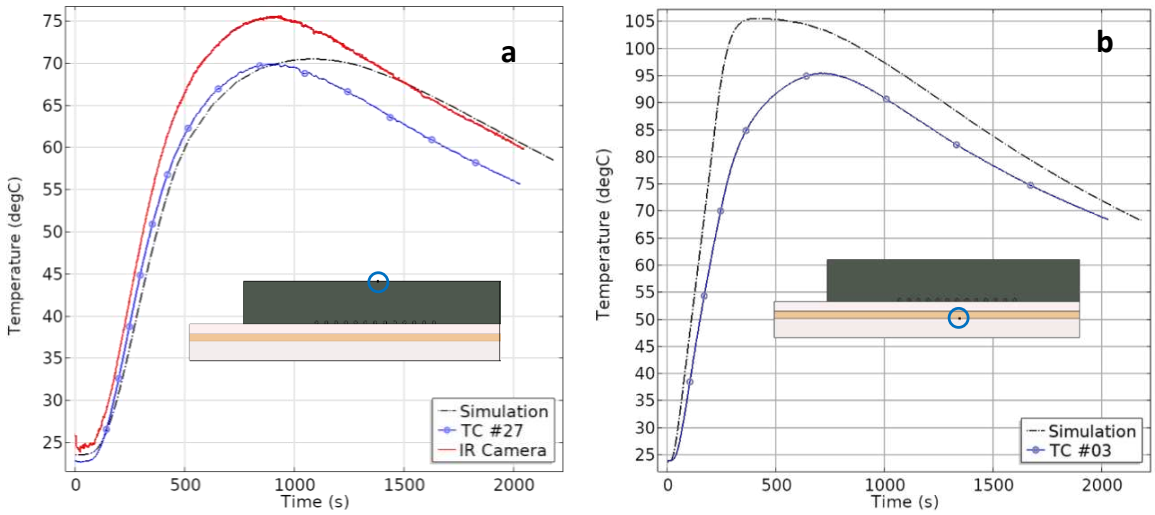

Figure 8. Temperature profile for selected locations at a) fitting and b) reinforcement

Overall, these results indicate that the numerical model can successfully estimate the ideal welding conditions. However, the simulated temperature — especially in the reinforcement layer — is always higher than the temperature measured experimentally. The reason for this discrepancy remains unclear. It could be related to the contact resistance between the welded surfaces or to a thermal barrier to the heat flow introduced by the cracks between the cover and reinforcement.

6. Conclusion and Future Work

A finite element heat transfer model was developed to simulate the temperature evolution during electrofusion welding of GF-HDPE TCP. The results show an acceptable level of agreement in the behaviour of the simulated and measured temperatures. Electrofusion welding shows promising potential for joining reinforced TCP. However, several enhancements to the numerical model are required to correlate the model results with those obtained from experimental testing. Future work will focus on improving the model to validate the experimental readings and coupling the current heat transfer model with a structural mechanics model (under development) to predict the operating envelop of the pipe-coupler system. Consideration should be given to the effects of the phase change behaviour of HDPE and the impacts of cracks and air gaps introduced from the ovality of TCP which could play during heat transfer.

  doi:10.5075/epfl-298799_978-2-9701614-0-0

Applying numerical optimisation methods could improve the estimation of some of the assumed parameters. Finally, this model will be used as a baseline to design new electrofusion fittings better suited to joining TCP.

Acknowledgements

This publication was made possible by the sponsorship of Saudi Aramco and the support of the Non-metallic Innovation Centre (NIC)

References

1. Zubail, A., Traidia, A., Masulli, M., Vatopoulos, K., Villette, T., & Taie, I. (2021). Carbon and energy footprint of nonmetallic composite pipes in onshore oil and gas flowlines. Journal of Cleaner Production, 305, 127150.
2. Kruijer, M. P., Warnet, L. L., & Akkerman, R. (2005). Analysis of the mechanical properties of a reinforced thermoplastic pipe (RTP). Composites Part A: Applied Science and Manufacturing, 36(2SPEC.ISS.), 291–300.
3. Hastie, J. C., Kashtalyan, M., & Guz, I. A. (2019). Failure analysis of thermoplastic composite pipe (TCP) under combined pressure, tension and thermal gradient for an offshore riser application. International Journal of Pressure Vessels and Piping, 178(August), 103998.
4. Tayefi, P., Beck, S.B.M., Tomlinson, R.A. (2015). Fatigue Failure of Polyethylene Electrofusion Joints Subject to Contamination. In: Carroll, J., Daly, S. (eds) Fracture, Fatigue, Failure, and Damage Evolution, Volume 5.
5. Rosala, G. F., Day, A. J., & Wood, A. S. (1997). A finite element model of the electrofusion welding of thermoplastic pipes. Proceedings of the Institution of Mechanical Engineers, Part E: Journal of Process Mechanical Engineering, 211(2), 137–146.
6. Shi, J., Zheng, J., Guo, W., Xu, P., Qin, Y., & Zuo, S. (2009). A model for predicting temperature of electrofusion joints for polyethylene pipes. Journal of Pressure Vessel Technology, Transactions of the ASME, 131(6).
7. Chebbo, Z., Vincent, M., Boujlal, A., Gueugnaut, D. and Tillier, Y. (2015), Numerical and experimental study of the electrofusion welding process of polyethylene pipes. Polym Eng Sci, 55: 123-131.
8. Bai, Y., Tang, J., Xu, W., Cao, Y., & Wang, R. (2015). Collapse of reinforced thermoplastic pipe (RTP) under combined external pressure and bending moment. Ocean Engineering, 94, 10–18.
9. Wang, S. Q., Yao, L., & Meng, X. J. (2018). Bending mechanical behavior analysis of glass-fiber reinforced thermoplastic pipe based on a nonlinear solid element model. Journal of Marine Science and Technology (Taiwan), 26(4), 575–586.
10. Zheng, J., Zhong, S., Shi, J., & Guo, W. (2015). Study on the allowable temperature for preventing over welding during thermal welding of polyethylene pipe. Journal of Pressure Vessel Technology, Transactions of the ASME, 137(2).
11. Fujikake, M., Fukumura, M., & Kitao, K. (1997). Analysis of the electrofusion joining process in polyethylene gas piping systems. Computers and Structures, 64(5–6), 939–948.
12. Gierulski, M. P., Tomlinson, R., & Troughton, M. (2022). Electrofusion welding and reinforced thermoplastic pipes – A review. Journal of Reinforced Plastics and Composites, 41(3–4), 147–163.

  doi:10.5075/epfl-298799_978-2-9701614-0-0

MULTIPHYSICS SIMULATION OF COOLING-RATE-DEPENDENT MATERIAL PROPERTIES OF THERMOPLASTIC COMPOSITES

Ryo, Higuchi[a], Masaya, Kato[b], Yutaka, Oya[c], Sota, Oshima[d], Shu, Minakuchi[b], Tomohiro, Yokozeki[b], Takahira, Aoki[b]

a: The University of Tokyo – higuchi@aastr.t.u-tokyo.ac.jp
b: The University of Tokyo, c: Tokyo University of Science, d: Tokyo Metropolitan University

Abstract: *The aim of this study is to establish a numerical simulation scheme that can predict the crystal morphology and resultant mechanical properties of semi-crystalline thermoplastic resin and carbon fiber reinforced thermoplastics (CFRTPs) from the manufacturing condition. To this end, this study develops a multiscale and multiphysics simulation scheme combining the phase-field simulation and homogenization simulation. Firstly, the crystal morphology development of thermoplastics depending on the manufacturing condition is predicted using the phase-field simulation. Then, the homogenization simulation on the predicted morphology is performed using the extended finite element method to predict the mechanical properties of thermoplastic resin. The developed scheme is demonstrated by simulating the crystal morphology and equivalent Young's modulus of neat thermoplastic resin solidified in an isothermal process.*

Keywords: Thermoplastics; Carbon fiber reinforced thermoplastics; Phase-field simulation; eXtended Finite Element Method (XFEM); Homogenization Method

1. Introduction

Carbon fiber reinforced thermosetting and thermoplastic resins (CFRTSs and CFRTPs) have been increasingly applied to the structural components of aircraft, automobiles, and wind turbines thanks to their superior specific stiffness and strength. So far, CFRTSs with an epoxy resin have been mainly applied to the structural component. During these application processes, the material and structural design process and manufacturing process have been developed for CFRTSs. However, CFRTSs are not environment-friendly since they require a long molding time with high pressure. Furthermore, cured CFRTSs are difficult to recycle, which causes a problem with the disposal of CFRTSs. Therefore, CFRTPs, which are sustainable materials with short molding time and recyclability, have been partially applied in aircraft components as an alternative material to CFRTS [1].

Among the types of CFRTPs, semi-crystalline thermoplastic resins are promising as structural materials because their stiffness, strength, and heat resistance are superior to those of amorphous resin. Semi-crystalline resins can be regarded as resin composites consisting of crystalline and amorphous phases having different mechanical properties. Additionally, the manufacturing conditions such as temperature and pressure histories highly affect the crystal morphology and resultant properties of resin. For example, the longer the holding time in the crystallization temperature range, the higher the crystallinity, the higher the elastic modulus, and the lower the ductility [2-6]. These uncertainties make the design and manufacturing processes difficult. Although some theoretical and empirical models have been proposed for the

  doi:10.5075/epfl-298799_978-2-9701614-0-0

relationships between cooling rate and crystallinity, or crystallinity and mechanical properties, no model can bridge from various molding conditions to mechanical properties.

The objective of this study is to establish a numerical scheme for the design of thermoplastic resin and CFRTPs considering the effect of manufacturing conditions. For this purpose, a multiscale and multiphysics simulation scheme is developed that links manufacturing conditions, microscopic crystal morphology, and macroscopic mechanical properties of thermoplastic resin and CFRTP, as shown in Fig. 1. Firstly, the phase-field simulation [7] is carried out to predict the crystal morphology of thermoplastic resin from the manufacturing condition. Then, the homogenization simulation [8, 9] on the predicted crystal morphology is performed to predict the equivalent mechanical properties of thermoplastic resin. In this paper, the developed scheme is applied to an isothermal crystallization of neat thermoplastic resin as the simplest example.

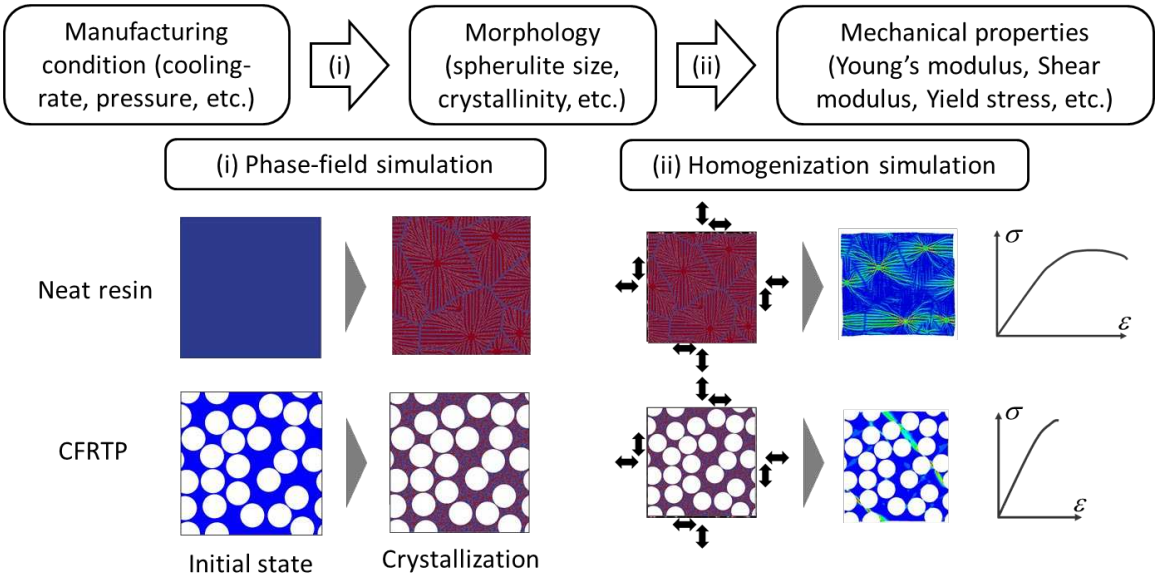

Fig. 1 Proposed numerical scheme for the prediction of mechanical properties of thermoplastic resin and CFRTPs based on the manufacturing condition.

2. Numerical procedure

2.1 Phase-field model for polymer crystallization

In this study, a phase-field method is used to predict crystal morphology of thermoplastics and CFRTP based on molding conditions. In the phase-field method for the polymer crystallization, the total free energy of the system $F(\psi)$ is described in terms of a local free energy density $f_{\mathrm{local}}(\psi)$ and a nonlocal free energy density describing the interface gradient $f_{\mathrm{grad}}(\psi)$ involving a nonconserved crystal order parameter ψ as follows.

$$F(\psi) = \int \left[f_{\mathrm{local}}(\psi) + f_{\mathrm{grad}}(\psi) \right] \mathrm{d}V. \tag{1}$$

where ψ represents the amorphous phase at ψ = 0 and the crystalline phase at ψ = 1. The temporal evolution of the order parameter ψ can be expressed as

$$\frac{\partial \psi(\boldsymbol{x}, t)}{\partial t} = -M_{\psi} \frac{\delta F(\psi)}{\delta \psi(\boldsymbol{x}, t)}. \tag{2}$$

  doi:10.5075/epfl-298799_978-2-9701614-0-0

Here, M_ψ is the mobility which is inversely proportional to the melt viscosity. According to the literrature, the local free energy density for polymer crystallization can be defined as follows.

$$f_{\mathrm{local}}(\psi,T) = W\int_0^{\psi}\psi\left(\frac{1}{2}-\ \psi - m(T)\right)(1-\psi)\mathrm{d}\psi, \quad \text{with: } m(T) = \frac{a_k}{\pi}\arctan\big(\gamma(1-T)\big). \tag{3}$$

W is a dimensionless coefficient describing the height of energy barrier for surface nucleation. m(T) is a function of temperature that controls the stable state between amorphous and crystal phases. The nonlocal free energy density can be defined in terms of the gradient free energy density describing the growth process as follows:

$$f_{\mathrm{grad}}(\psi) = \frac{1}{2}\varepsilon^2(\nabla\psi)^2, \tag{4}$$

where ε is the coefficient of interface gradient. In polymer crystallization, the self-generated temperature field created by the liberation of latent heat is important. Thus, heat conduction is taken into account by,

$$\rho C_{\mathrm{p}}\frac{\partial T}{\partial t} = k_{\mathrm{t}}\nabla^2 T + \rho\Delta H_{\mathrm{c}}\frac{\partial\psi}{\partial t}. \tag{5}$$

Here, ρ is density, C_{P} is heat capacity, k_{T} is thermal conductivity, and ΔH_{u} is latent heat during the crystallization. In order to derive the dimensionless forms of Eqs. (2) and (5), the variables are rescaled as $\mathrm{d}\hat{x}_1 = \mathrm{d}x_1/D,\ \mathrm{d}\hat{x}_2 = \mathrm{d}x_2/D,\ \mathrm{d}\hat{t} = \mathrm{d}t/\tau$ using the characteristic length D and time $\tau = D^2\rho C_{\mathrm{p}}/k_{\mathrm{t}}$. In this study, the following dimensionless governing equations are solved by the finite differential method.

$$\tau^*\hat{\varepsilon}^2\frac{\partial\psi}{\partial\hat{\mathrm{t}}} = \left[\hat{\nabla}\cdot\left(\frac{1}{2}\big(\hat{\nabla}\psi\big)^2\frac{\partial(\hat{\varepsilon}^2)}{\partial\hat{\nabla}\psi}\right) + \hat{\nabla}\cdot\big(\hat{\varepsilon}^2\hat{\nabla}\psi\big)\right] - W\psi(\psi-1)\left(\psi-\frac{1}{2}+m(\hat{T})\right) + a\psi(1-\psi)R_{\mathrm{v}}, \tag{6}$$

$$\frac{\partial\hat{T}}{\partial\hat{t}} = \hat{\nabla}^2\hat{T} + \hat{K}\frac{\partial\psi}{\partial\hat{t}}. \tag{7}$$

$$\text{with: } \hat{T} = (T-T_{\mathrm{c}})/(T_{\mathrm{m}}-T_{\mathrm{c}}),\ \tau^* = k_{\mathrm{t}}/\rho C_{\mathrm{p}}\varepsilon^2 M_\psi,\ \hat{K} = \Delta H_{\mathrm{c}}/C_{\mathrm{p}}(T_{\mathrm{m}}-T_{\mathrm{c}}).$$

In polymer crystallization, it is well known that the crystallization rate G varies with the crystallization temperature T_{c} and is expressed by the Lauritzen-Hoffman equation as [11]

$$G(T_c) = G_0\exp\left(-\frac{U}{k(T_{\mathrm{c}}-T_\infty)}\right)\exp\left(-\frac{K}{T_{\mathrm{c}}(T_m^0-T_{\mathrm{c}})}\right), \tag{9}$$

According to Ref. [11], Eq. (9) is implemented into the phase-field model via modifications of τ^* and $\hat{K}$ as to be functions of T_{c} as follows:

$$\tau^*(T_{\mathrm{c}}) = \begin{cases} {\tau^*}_0 & (T_{\mathrm{g}} \le T_{\mathrm{c}} \le T_{\mathrm{c\,max}}) \\ {\tau^*}_0/H(T_{\mathrm{c}}) & (T_{\mathrm{c\,max}} \le T_{\mathrm{c}} \le T_{\mathrm{m}}^0) \end{cases}, \tag{10}$$

$$\hat{K}(T_{\mathrm{c}}) = \begin{cases} \hat{K}_0/H(T_{\mathrm{c}}) & (T_g \le T_{\mathrm{c}} \le T_{\mathrm{c\,max}}) \\ \hat{K}_0 & (T_{\mathrm{c\,max}} \le T_{\mathrm{c}} \le T_{\mathrm{m}}^0) \end{cases}, \tag{11}$$

where $H(T_{\mathrm{c}}) = G(T_{\mathrm{c}})/G(T_{c\,\mathrm{max}})$, and $T_{\mathrm{c\,max}}$ represents the temperature at which the crystallization rate is maximum.

For the crystal nucleation, this study assumes the uniform nucleation and employs the following nucleation rate model proposed by Pantani et al. [13].

$$\frac{\mathrm{d}N\big(T(t)\big)}{\mathrm{d}t} = N_0\exp\left[-\frac{C_1}{(T(t)-T_\infty)}\right]\exp\left[-\frac{C_2(T(t)+T_{\mathrm{m}})}{T(t)^2\big(T_{\mathrm{m}}-T(t)\big)}\right]. \tag{12}$$

Here, N is the number of nucleation per unit volume

2.2 Homogenization Simulation Using eXtended Finite Element Method

This study utilizes an eXtended Finite Element Method (XFEM) homogenization simulation framework [15, 16] to efficiently evaluate the equivalent mechanical properties of predicted crystal morphology by the phase-field method. The XFEM can handle the discontinuity within one element by enriching of conventional shape function and introducing an additional degree of freedoms (DoFs). These additional DoFs, so-called enriched DoFs, are introduced to construct enrichment function. For the weak (strain) discontinuity that happens at material interface, the approximated displacement field $\boldsymbol{u}^{\mathrm{h}}$ at arbitrary position $\boldsymbol{x}$ near the interface is expressed as

$$\boldsymbol{u}^{\mathrm{h}} = \sum_{I=1}^{m} N^I(\boldsymbol{x})\boldsymbol{u}^I + \sum_{I\subseteq M} N^I(\boldsymbol{x})R(\boldsymbol{x})\boldsymbol{a}^I, \tag{13}$$

where, N^I is the conventional shape function, $\boldsymbol{u}^I$ and $\boldsymbol{a}^I$ are nodal degrees of freedom assigned to node I, M is the set of enriched nodes (see Fig. 2 (a)). $R(\boldsymbol{x})$ is the ramp function defined as [14] (see Fig. 2 (b))

$$R(\boldsymbol{x}) = \sum_{I=1}^{3} |\phi^I| N^I(\boldsymbol{x}) + \left| \sum_{I=1}^{3} \phi^I N^I(\boldsymbol{x}) \right|, \tag{14}$$

Here, ϕ^I is defined based on the phase-field variable ψ^I as follows.

$$\phi^I = 2\psi^I - 1. \tag{15}$$

This means that the contour lines at $\psi = 0.5$ are regarded as interfaces between amorphous and crystalline phases.

On each model of crystal morphology, the periodic boundary conditions (PBCs) are imposed. The detail about the PBCs in XFEM-based homogenization can be found in the literature [16].

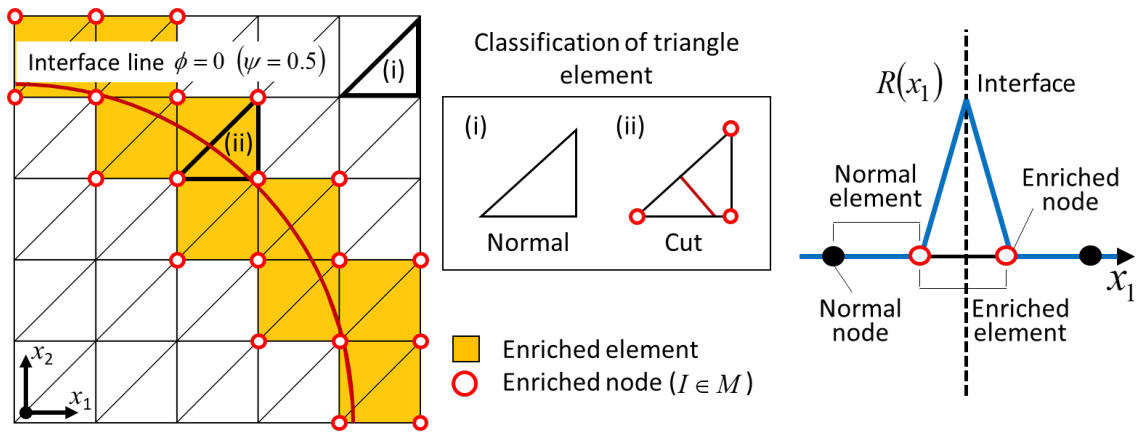

(a) 2D interface modelling using $\phi(\boldsymbol{x})$ (b) Enrichment function

Fig. 2 Modelling of material interface by XFEM.

3. Verification

In this section, the crystallization simulation and homogenization simulation of the isothermal crystallization of neat resin are carried out as a simple example. The model parameters used in the phase-field simulation are shown in Table 1 [11, 16], and the mechanical properties of the

  doi:10.5075/epfl-298799_978-2-9701614-0-0

crystalline and amorphous phases used in the homogenization analysis are shown in Table 2 [17-19]. Here, both crystalline and amorphous phases are assumed to be isotropic.

Table 1: Parameters for phase field simulation [11, 16].

$W = 2.0$	$\hat{\varepsilon} = 1/3$	$\widehat{K}_0 = 1.4$
$T_{\mathrm{m}}^0 = 280.5℃$	$T_{\mathrm{g}} = 100℃$	$T_{\mathrm{c\,max}} = 180℃$
$\tau^*{}_0 = 3.0$	$a_{\mathrm{k}} = 0.9$	$\gamma = 10$
$a = 0.02$	$D = 10^{-7}$ m	$N_0 = 1.44 \times 10^7$
$\mathrm{d}\hat{x} = \mathrm{d}\hat{y} = 1.0$	$\mathrm{d}\hat{t} = 0.1$	

Table 2: Material properties for crystal and amorphous phases.

	Crystal phase	Amorphous phase
E (MPa)	81040	103.84
ν	0.3*	0.49

* Assumed value

3.1 Case (I) Single Crystal System

This subsection performs the two-dimensional single crystal growth simulations by omitting the nucleation model in Eq. (12). As an initial condition, a single nucleus is placed at the center. The crystal structures obtained by the phase-field method at crystallization temperatures of $T_c = 155, 180, 205℃$ are illustrated in Fig. 3 (a)-(c). Here, the crystal structures having the same radii are compared. Because the crystal growth rates are different at each crystallization temperature, the required times for development are different. It can be seen from Fig. 3 that the thicker lamella (crystalline phase) grows with the lower supercooling (i.e., higher crystallization temperatures). This means that the higher crystallinity emerged in the lower supercooling and is consistent with the experimental trend reported in the literature. The stress distributions of each structure under unit tensile strain in the x_1 direction are summarized in Fig. 4 (a)-(c). All stress distributions in the homogenization simulations are reasonable since high stress happens in the stiff crystal phase in the loading direction and no spurious stress concentration on the periodic boundary.

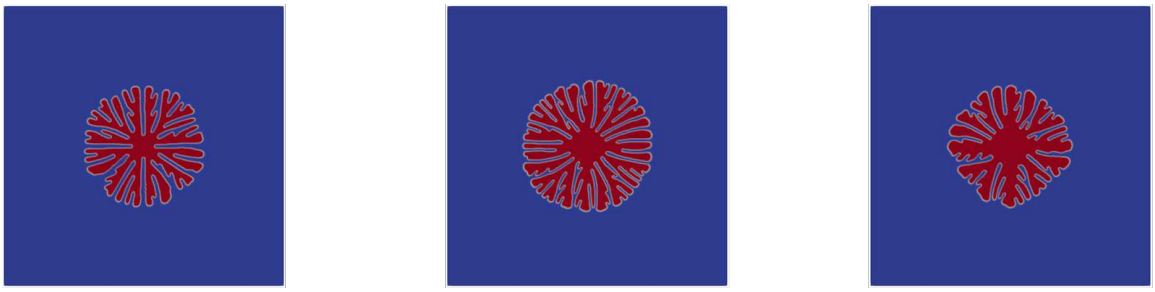

(a) $T_c = 155℃$ (b) $T_c = 180℃$ (c) $T_c = 205℃$

Fig. 3 Crystal morphologies at each crystallization temperatures.

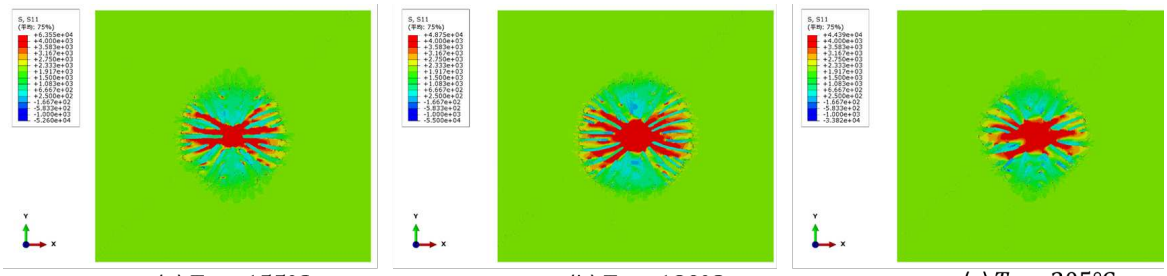

(a) $T_c = 155°\mathrm{C}$ (b) $T_c = 180°\mathrm{C}$ (c) $T_c = 205°\mathrm{C}$

Fig. 4 Stress distributions when unit strain is applied to the crystal structure at each crystallization temperatures.

3.2 Case (II) Multiple Crystal System

In this subsection, the two-dimensional multiple crystal growth simulation is conducted incorporating the nucleation model in Eq (12), and the equivalent mechanical properties are evaluated by homogenization simulation. The multiple crystal growth behaviors at each time increment at the crystallization temperature $T_c = 180°\mathrm{C}$, and the stress distributions in these crystal structures subjected to unit tensile strain in the x_1 direction are summarized in Fig. 5. Furthermore, the relationship between the volume fraction of crystal and the equivalent Young's moduli is shown in Fig. 6. In this graph, the vertical axis is normalized by Young's modulus of the crystalline phase. Notations (a) to (d) in Fig. 6 are corresponding to those in Fig. 5. At $\hat{t} = 11000$ (Fig. 5 (a)), the crystal-rich and amorphous-rich regions are observed. This is because the crystal nucleation rate in Eq. (12) is a function of temperature and time. After nucleation of some crystals, new crystal nuclei are likely to form around the existing crystals due to heat generated by the liberation of their latent heat. Because of the low load transfer capability of the amorphous-rich region, the equivalent Young's modulus is relatively low. On the other hand, Figs. 5 (b)-(d) shows that the load paths increase with the growth of existing crystals and the nucleation of crystals in the amorphous-rich region. This results in a significant increase in equivalent Young's modulus. As a result, the equivalent Young's modulus is not linearly increased with the volume fraction of the crystalline phase but is strongly affected by the spatial arrangement of the crystals as shown in Fig. 6.

4. Conclusion

This study developed a multiscale and multiphysics simulation scheme to bridge the manufacturing conditions, microscopic crystal morphology, and mechanical properties of thermoplastic resins and CFRTPs. The proposed scheme utilizes the phase-field simulation to predict the microscopic crystal morphology from the manufacturing process, and the XFEM-based homogenization simulation to predict the mechanical properties from the crystal morphology. The simulation of a single crystal system demonstrated that the proposed scheme can predict the reasonable crystal structure depending on the temperature. Moreover, the simulation of a multiple crystal system verified that the proposed scheme can predict the equivalent mechanical properties depending on the detailed crystal morphology. For more quantitative prediction, the identification of the mechanical properties of crystalline and amorphous phases is necessary in future work.

  doi:10.5075/epfl-298799_978-2-9701614-0-0

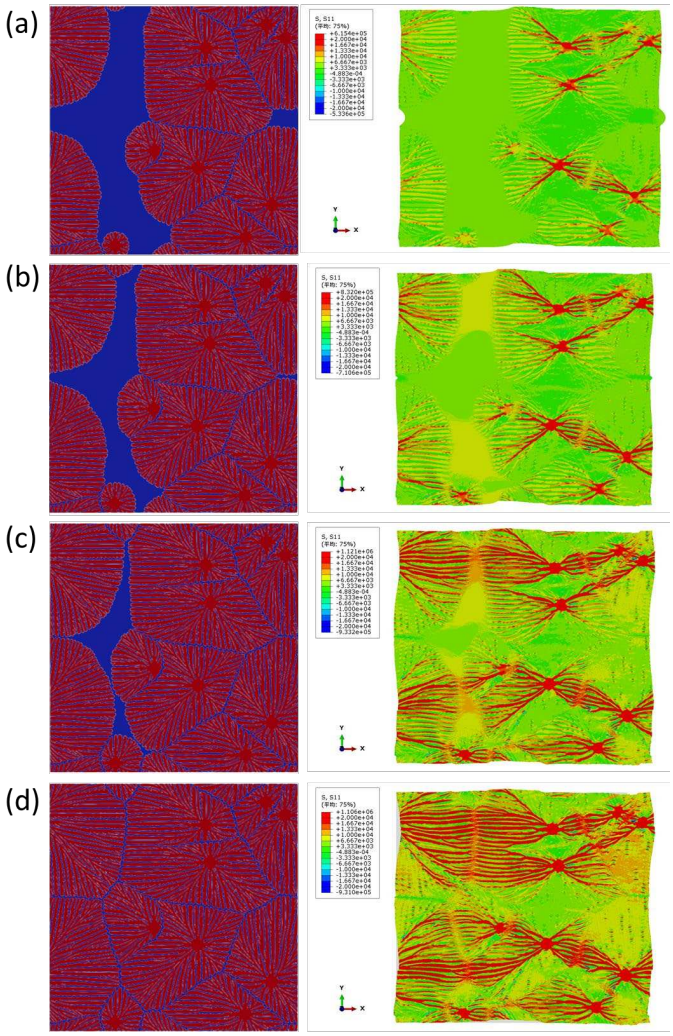

Fig. 5 Stress distribution when unit strain is applied to the crystal structure at each time increments; (a) $\hat{t} = 11000$, (b) $\hat{t} = 12000$, (c) $\hat{t} = 13000$, and (d) $\hat{t} = 15000$.

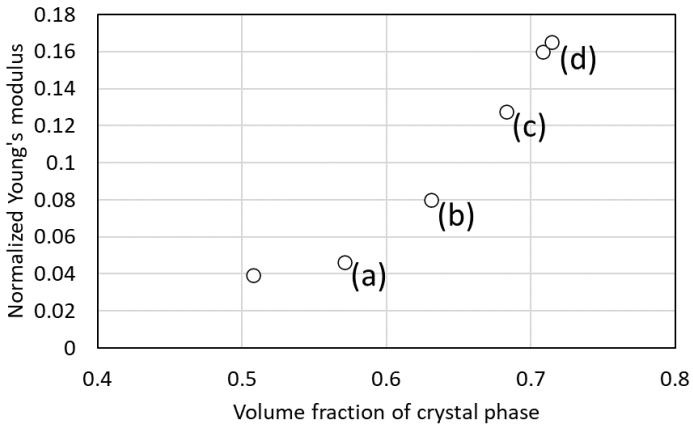

Fig. 6 Relationship between crystal volume fraction and equivalent Young's modulus.

Acknowledgements

This study was partially supported by the Japan Society for the Promotion of Science (JSPS) KAKENHI (Grant Number 18K13921, 22K14489).

  doi:10.5075/epfl-298799_978-2-9701614-0-0

5. References

1. Miaris A, Edelmann K, Sperling S. Thermoplastic Matrix Composites: Xtra complex, Xtra Quick, Xtra Efficient. In: Proc. 20th Int. Conf. Compos. Mater., Copenhagen, Denmark, 2015.
2. Gao SL, Kim JK. Cooling rate influences in carbon fibre/PEEK composites. Part 1: Crystallinity and interface adhesion. Compos. Part A-Appl. S. 2000; 31(6): 517-530.
3. Gao SL, Kim JK. Cooling rate influences in carbon fibre/PEEK composites. Part II: interlaminar fracture toughness. Compos. Part A-Appl. S. 2001; 32(6): 763-774.
4. Gao SL, Kim JK. Cooling rate influences in carbon fibre/PEEK composites. Part III: impact damage performance. Compos. Part A-Appl. S. 2001; 32(6): 775-785.
5. Ye L, Scheuring TBAUK, Friedrich KBAUK. Matrix morphology and fibre pull-out strength of T700/PPS and T700/PET thermoplastic composites. J. Mater. Sci. 1995; 30(19), 4761-4769.
6. Higuchi R, Oshima S, Minakuchi S, Yokozeki T, Aoki T. Study on Cooling Rate-Dependent Mechanical Properties of Thermoplastic Composites. In: Proc. American Society for Composites 36th Tech. Conf., Virtual, 2021.
7. Kobayashi R. Modeling and numerical simulations of dendritic crystal growth. Physica D. 1993; 63(3-4): 410-423.
8. Belytschko T, Black T. Elastic crack growth in finite elements with minimal remeshing, Int. J. Numer. Meth. Eng. 1999; 45(5): 601-620.
9. Moës N, Dolbow J, Belytschko T. A finite element method for crack growth without remeshing, Int. J. Numer. Meth. Eng. 1999; 46(1): 131-150.
10. Sanchez-Palencia E. Non-Homogeneous Media and Vibration Theory, Lecture Notes in Physics, 1980; 127, Springer-Verlag Berlin Heidelberg.
11. Bahloul A, Doghri I, Adam L. An enhanced phase field model for the numerical simulation of polymer crystallization. Polym. Cryst., 2020; 3(4): e10144.
12. Pantani R, Coccorullo I, Speranza V, Titomanlio G. Modeling of morphology evolution in the injection molding process of thermoplastic polymers. Prog. Polym. Sci. 2005; 30(12): 1185-1222.
13. Moës N, Cloirec M, Cartraud P, Remacle JF. A computational approach to handle complex microstructure geometries, Comput. Methods Appl. Mech. Eng. 2003; 192(28): 3163–3177.
14. Nagashima T, Sawada M. Development of a damage propagation analysis system based on level set XFEM using the cohesive zone model. Comput. Struct. 2015; 174: 42-53.
15. Higuchi R, Yokozeki T, Nagashima T, Aoki T. Evaluation of mechanical properties of noncircular carbon fiber reinforced plastics by using XFEM-based computational micromechanics. Compos. Part A-Appl. S. 2019; 126: 105556.
16. Lovinger AJ, Davis DD, Padden Jr FJ. Kinetic analysis of the crystallization of poly (p-phenylene sulphide). Polymer. 1985; 26(11): 1595-1604.
17. Lee BJ, Parks DM, Ahzi S. Micromechanical modeling of large plastic deformation and texture evolution in semi-crystalline polymers. J. Mech. Phys. Solids. 1993; 41(10): 1651-1687.
18. Van Dommelen JV, Parks DM, Boyce MC, Brekelmans WAM, Baaijens FPT. Micromechanical modeling of the elasto-viscoplastic behavior of semi-crystalline polymers. J. Mech. Phys. Solids. 2003; 51(3): 519-541.
19. Tomita Y, Adachi T, Tanaka S. Modelling and application of constitutive equation for glassy polymer based on nonaffine network theory. Eur. J. Mech. A/Solids. 1997; 16(5): 745-755.

  doi:10.5075/epfl-298799_978-2-9701614-0-0

STOCHASTIC MODELLING OF RANDOMLY ORIENTED TAPES THERMOPLASTIC COMPOSITES IN NET-SHAPED SPECIMENS

Deniz Ezgi Gulmez[a], Jos Sinke[a], Clemens Dransfeld[a]

a: Aerospace Manufacturing Technologies, Faculty of Aerospace Engineering, Delft University of Technology - D.E.Gulmez@tudelft.nl

Abstract: *Discontinuous tape composites have considerable attention due to their high formability and tailorable structures. Despite their advantages, this discontinuity leads to complex structures and makes it difficult to predict their mechanical properties. On the other hand, they have high orientational and dimensional sensitivity, which causes spatial variability and complexity in the structure to predict the mechanical properties. This spatial variability is also related to the mould cavity. A constitutive model was improved to explain the relationship between DT orientations and the mould cavity. According to the modelling technique, a random DT distribution was generated by Random Sequential Adsorption then, the Set Voronoi Tessellation was implemented to obtain DT layers. Afterwards, the Classical Laminate Theory and Finite Element Method were applied to compare the virtual net-shaped DT specimens. The results of both methods showed high stiffness at the edges of the specimens.*

Keywords: Discontinuous reinforcements; cavity edge effect; stiffness model; finite element modelling

1. Introduction

The tendency to use composite materials in the aircraft industry due to their lightweight and durable structures causes massive waste such as the out-of-date prepreg rolls, end of life aircraft structures and manufacturing cut-offs (1). Recycling, reuse and zero-waste manufacturing technologies have attracted considerable attention in reducing these wastes. Discontinuous thermoplastic composites minimize waste and offer recyclability. Besides their environmental advantages, they show high formability due to their discontinuous structure. This discontinuity helps to tailor mechanical properties such as increasing pseudo-ductility, which retards failure due to the shear lag between tapes (2).

On the other hand, they have high orientational and dimensional sensitivities, which cause spatial variability and complexity in the structure to predict the mechanical properties. This spatial variability is also related to the mould cavity. Experimental results of Discontinuous Tape (DT) composites have shown higher tensile modulus at the edges of the specimens than at the centre (3). Therefore, the mechanical properties of DT composites can be enhanced by using the edge effect of the mould. However, the relationship between mould cavity and tape orientation hasn't been well defined to understand the mechanical response of the DT composites and to improve the manufacturing routes.

The study aims to improve a modelling technique to explain the relationship between DT orientations and the mould cavity. The stiffness of the DT net-shaped specimens is calculated Classical Laminate Theory (CLT) and Finite Element Method (FEM) to evaluate and compare both results according to the width of the specimens.

  doi:10.5075/epfl-298799_978-2-9701614-0-0

2. Modelling

2.1 Randomization and Homogenization Algorithm

The Random Sequential Adsorbtion (RSA) algorithm (4) was modified by defining the distribution frame to generate a random distribution as seen in Fig. 1(a). According to this algorithm, random seed points and random angles between 0^0 and 179^0 in 2D were generated by considering a non-overlapped DT distribution inside the frame (Fig. 1(b)). The algorithm was continued for 4000 iterations to obtain a high filling ratio. DTs of 2.5 mm by 10 mm were placed in the virtual specimen dimensions of 150 by 60 mm in this study.

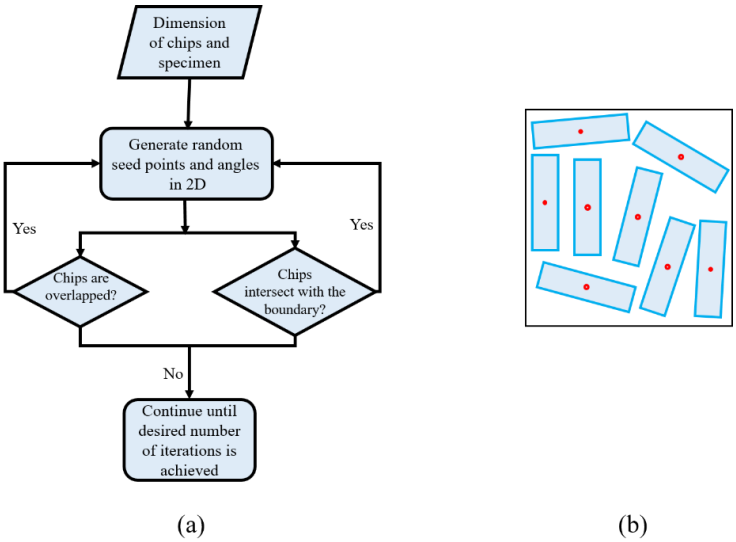

Figure 1. (a) Flowchart of the bounded-RSA algorithm and (b) the deposition result

After obtaining a DT distribution, the Set Voronoi tessellation (5) was implemented to define the local properties of each DTs layer and obtain full coverage of the DTs in the net-shaped frame. Elastic properties of the DTs were scaled according to the Set Voronoi Tessellation to implement the local variability to mechanical properties. the ratio between the tape area (A_t=l_t*w_t) and its cell area (A_c) was calculated (6). This ratio is called the local packing density (ϕ) as given in Eq. (1).

$$\phi = \frac{A_t}{A_c} \tag{1}$$

Elastic properties of AS4/PPS unidirectional (UD) prepreg tapes are scaled according to the local packing density (Table 1) and Eq. (2-5).

Table 1: Elastic Properties of UD AS4/PPS composite with a fibre volume ratio of 59% (7)

Longitudinal modulus, E_{11}	128 GPa
Transverse modulus, E_{22}	10.1 GPa
Shear modulus, G_{12}	5.7 GPa
Longitudinal Poisson's ratio, υ_{12}	0.37

$$E_{1i} = E_1 * \frac{\phi_i}{\phi_{avg}} \tag{2}$$

$$E_{2i} = E_2 * \frac{\phi_i}{\phi_{avg}} \tag{3}$$

$$G_{12i} = G_{12} * \frac{\phi_i}{\phi_{avg}} \tag{4}$$

$$\upsilon_{12i}, \upsilon_{21i} = \upsilon_{12}, \upsilon_{21} * \frac{\phi_i}{\phi_{avg}} \ (\upsilon_{12i}, \upsilon_{21i} \leq 0.49) \tag{5}$$

2.2 Laminate Analogy and Finite Element Model

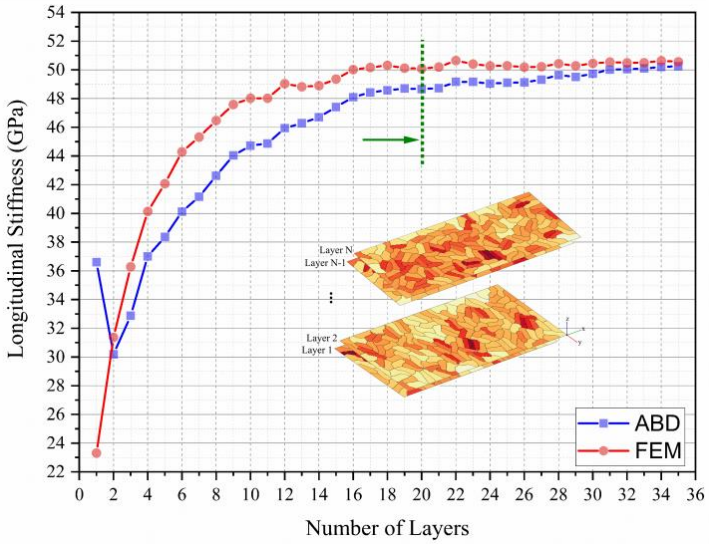

Figure 2. Convergence analysis for FEM and CLT models

A discretization process is necessary to implement CLT and FEM for each heterogeneous layer. The grid size is 1mm by 1mm. After the discretization of representative layers, the determination of the number of layers is another parameter to generate a representative specimen. As seen in Fig. 2, a convergence study was conducted to decide the number of layers for both CLT and FEM. In addition, the second-order orientation tensors in the two-dimension were calculated (8,9).

A, B, D matrices in CLT were calculated (Eq. (6-8)) by assuming each grid is an independent laminated composite:

$$A_{ij} = \sum_{k=1}^{n} Q_{ij}\,(z_k - z_{k-1}) \qquad i,j = 1,2,6 \tag{6}$$

$$B_{ij} = \frac{1}{2}\sum_{k=1}^{n} Q_{ij}\left(z_k^2 - z_{k-1}^2\right) \qquad i,j = 1,2,6 \tag{7}$$

$$D_{ij} = \frac{1}{3}\sum_{k=1}^{n} Q_{ij}\left(z_k^3 - z_{k-1}^3\right) \qquad i,j = 1,2,6 \tag{8}$$

The laminate compliance matrix (S), the longitudinal (E_x) and the transverse Modulus (E_y) were evaluated regarding (Eq. (9, 10)):

$$S = \begin{bmatrix} \alpha & \beta \\ \beta & \delta \end{bmatrix} = \begin{bmatrix} A & B \\ B & D \end{bmatrix}^{-1} \tag{9}$$

$$E_x = \frac{1}{t_s \alpha_{11}}\,, E_y = \frac{1}{t_s \alpha_{22}} \tag{10}$$

For Finite Element (FE) modelling of the virtual DT specimen, each partition assumed a FE and has an orientation angle after the discretization process. However, the elastic properties weren't scaled according to the tessellation approach to simplify the model. Tape angles are the only variable parameter for each FE. Therefore, an element size is 1 mm x 1 mm x 0.1 mm. Nodes are known and 8-node quad continuum shell elements (SC8R) can be obtained easily by using node data. Continuum shell elements have stacked through the thickness and one lamina is assigned for each SC8R element. A constant displacement is applied along the y-direction from one edge, encastre boundary condition is applied at the opposite edge, as seen in Fig. 3. ABAQUS/Standard (Implicit) input file is generated by using node and element data and defining boundary conditions and Hashin failure criteria (10) was implemented to evaluate the tensile response of the virtual specimens. Failure limits and fracture properties are given in Table 2. Viscous regularization factor was chosen at 0.00075.

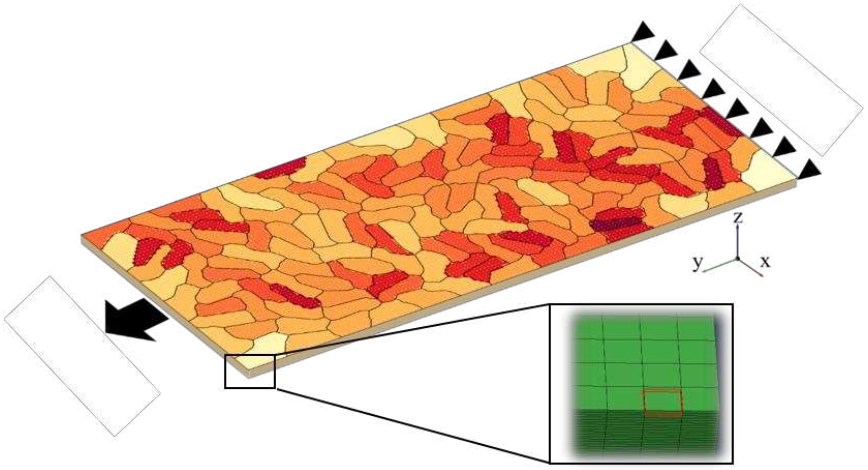

Figure 3. Boundary conditions of the representative virtual specimen

Table 2: Failure Limits and Fracture Properties of UD AS4/PPS composite (11,12)

Longitudinal tensile strength, X_t	2045 MPa
Longitudinal compressive strength, X_c	1117 MPa
Transverse tensile strength, Y_t	50 MPa
Transverse compressive strength, Y_t	90 MPa
Longitudinal shear strength, $S_{12}=S_{13}$	77 MPa
Fracture Energy, G_I	12.5 kJ/m^2
Fracture Energy, G_{II}	1.0 kJ/m^2

A net-shaped specimen was divided into regions as left, centre and right to understand the edge-orientations relationships as seen in Fig. 4. The size of the specimens was 60 mm by 150 mm. The width of the specimens at the edges was chosen as 8 mm considering the material loss due to the blade thickness for potential experimental validation. The width of the centre specimens was 40 mm. The length of all regional specimens was 150 mm.

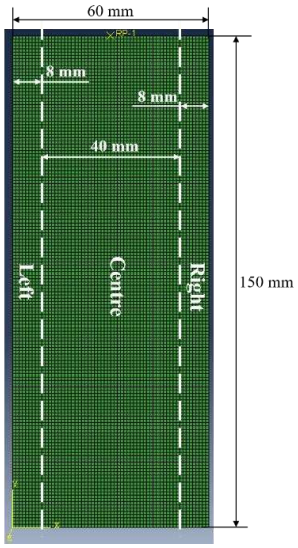

Figure 4. A representative virtual specimen, its regions and dimensions

3. Results and Discussion

Longitudinal Young Modulus distribution showed a high variability from 15 GPa to 95 GPa. However, the Young modulus in the longitudinal direction was the highest at the edges of the specimen, as given in Fig. 5 (a). When we look at Fig. 5 (b), matrix failure at 6.8 % global strain shows local variability due to the stiffness distribution all over the specimen. However, the result isn't related to the region of the specimen.

  doi:10.5075/epfl-298799_978-2-9701614-0-0

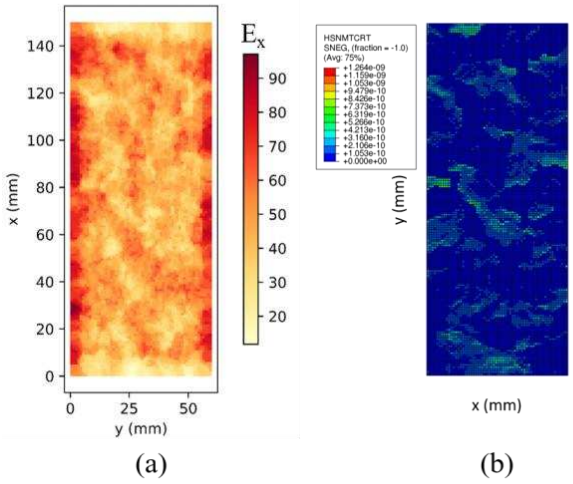

Figure 5. (a) Longitudinal stiffness and (b) Matrix failure (@6.8% strain) distribution in one virtual specimen

Longitudinal Young Modulus associated with orientation tensor in Fig. 6 (a). It was shown that the orientations of tapes were aligned length of the specimen. Thus, this alignment increases the stiffness at the edge of the net-shaped specimens. FEM results agreed with the high stiffness at the edges compared with the centre of the specimen as seen in Fig. 6 (b). In addition, matrix damage patterns were similar even though the specimens are cut according to the regions. However, their global mechanical response was variable. Specimens at the edges showed high tensile stress but low failure strain while low tensile stress and high failure strain were observed in the centre of the specimen.

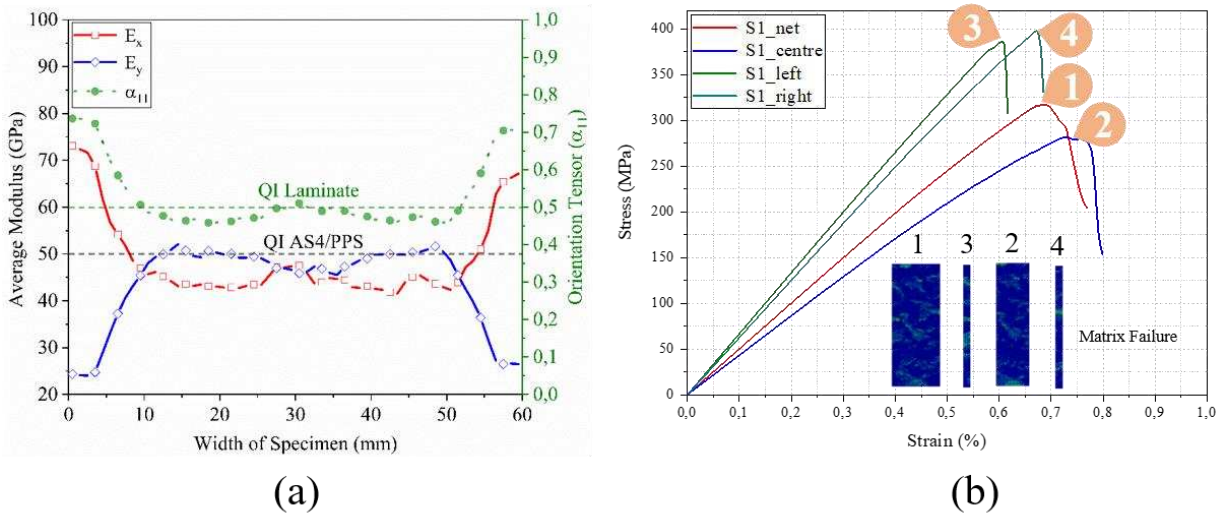

Figure 6. (a) Orientation tensor and elastic modulus through the width of one virtual specimen (b) Stress-Strain curve of one virtual specimen

Six virtual specimens were generated by using the modelling technique for both CLT and FEM evaluations to investigate the results statistically. Normalised stiffness results are given in Fig. 7. In general, both approaches showed high stiffness and a high range between minimum and maximum stiffness values at the edges. DTs are placed randomly and aligned at the edges

  doi:10.5075/epfl-298799_978-2-9701614-0-0

whereas DTs are highly random in the centre of the specimens. Thus, this range reduces in the centre for both CLT and FEM results.

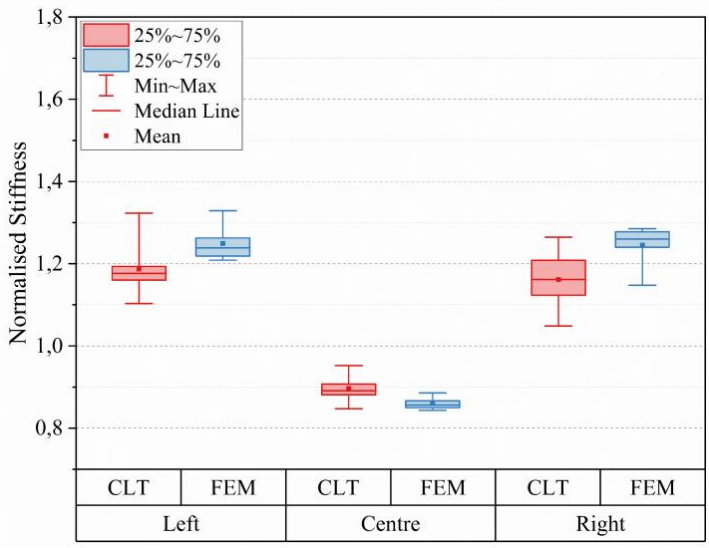

Figure 7. Comparison of normalized stiffness according to CLT and FEM

4. Conclusion

In this study, a modelling technique to predict the stiffness and strength of DT composites in net-shaped specimens was improved. The model generation starts with the RSA algorithm which is a defined frame of the distribution area to define the DT orientations. After that, a tessellation algorithm is implemented to obtain full coverage in the distribution area for discretization. According to the discretization, CLT and FEM are applied to evaluate the stiffness and strength of DT composites in net-shaped specimens. The results showed that stiffness at the edges of specimens is higher than in the centre of the specimens due to the high local alignment of DTs. This study demonstrates improving the mechanical properties of DT composites by controlling the DT orientations with the mould cavity.

Acknowledgements

We would like to thank Fraunhofer-Gesellschaft for their financial support.

5. References

1. Pimenta S, Pinho ST. Recycling carbon fibre reinforced polymers for structural applications: Technology review and market outlook. Waste Manag. 2011;31(2):378–92.

2. Czél G, Jalalvand M, Wisnom MR. Design and characterisation of advanced pseudo-ductile unidirectional thin-ply carbon/epoxy-glass/epoxy hybrid composites. Compos Struct [Internet]. 2016;143:362–70. Available from: http://dx.doi.org/10.1016/j.compstruct.2016.02.010

3. Tuttle M, Shifman T, Boursier B. Simplifying certification of discontinuous composite material forms for primary aircraft structures. In: International SAMPE Symposium and Exhibition (Proceedings). 2010.

  doi:10.5075/epfl-298799_978-2-9701614-0-0

4. Feder J. Random sequential adsorption. J Theor Biol. 1980;87(2):237–54.

5. Schallerab FM, Kapferac SC, Evansa ME, Hoffmanna MJF, Asted T, Saadatfare M, et al. Set Voronoi diagrams of 3D assemblies of aspherical particles. Philos Mag. 2013;93(31–33):3993–4017.

6. Völkel S, Huang K. Set Voronoi Tessellation for Particulate Systems in Two Dimensions. Springer Proc Phys. 2020;252(8):429–37.

7. Pappas G, Canal LP, Botsis J. Characterization of intralaminar mode I fracture of AS4/PPS composite using inverse identification and micromechanics. Compos Part A Appl Sci Manuf [Internet]. 2016;91:117–26. Available from: http://dx.doi.org/10.1016/j.compositesa.2016.09.018

8. Advani SG, creasy TS, Shuler SF. Chapter 8 Rheology of long fiber-reinforced composites in sheetforming. Compos Mater Ser. 1997;11(C):323–69.

9. Kravchenko SG, Pipes RB. Progressive Failure Analysis in Discontinuous Composite System of Prepreg Platelets with Stochastic Meso-Morphology. Sci Age Exp (SIMULIA User Meet. 2018;(June):1–14.

10. Hashin Z. Failure criteria for unidirectional fiber composites. J Appl Mech Trans ASME. 1980;47(2):329–34.

11. Pps- C. for Thermoplastic Composites. 2013.

12. Lapczyk I, Hurtado JA. Progressive damage modeling in fiber-reinforced materials. Compos Part A Appl Sci Manuf. 2007;38(11):2333–41.

A MULTI-SCALE APPROACH TO ANALYSIS OF SHORT-FIBER REINFORCED THERMOPLASTIC ADDITIVELY MANUFACTURED STRUCTURES

Troy Zangle, Britt Helten, Nicholas Garfield, Kyle Warren

Advanced Structures and Composites Center
University of Maine
troy.zangle@maine.edu

Abstract: *A method for structural analysis of thermoplastic additively manufactured structures is presented that captures the multi-scale properties of parts printed with fiber reinforced thermoplastics. This method captures the physics of the multiple property scales using a homogenization method that combines the anisotropic filament properties in larger elements for efficient analysis. This allows for mesh elements to be used that are much larger than the filament cross-sections in the manufacturing process, providing an effective approach for including print properties in the analysis of large-scale structures. Models were run in the finite element analysis software Simulia Abaqus and were compared with similar models with constant material properties.*

Keywords: Multiscale analyses; Large-Scale Additive Manufacturing; Modeling; Design Tools; Software

1. Introduction

Additive manufacturing (AM) is rapidly transitioning from small-scale prototype development to large-scale production manufacturing. Printer size and extrusion rates are rapidly increasing, with such large-scale manufacturing systems as the Cincinnati Inc. BAAM and the Ingersoll MasterPrint offering immense print volumes and high extrusion rates. These print volumes have been used to manufacture large objects and parts including a full-size automobile [1] and a center console boat [2]. Build techniques in these systems commonly employ fiber reinforcement with the extruded thermoplastic to allow for higher part strength and improved material characteristics [3]. Many pellet-fed AM systems use short fiber reinforced thermoplastics to increase part performance with minimal added complexity to the print system. This transition requires accurate and efficient additive manufacturing analysis methods during the design process as the trial-and-error process of prototype development does not scale well to large-scale manufacturing.

Modeling of AM with fiber reinforced thermoplastics requires accounting for the multiple property scales of the print. Properties of the microscale, mesoscale, and macroscale must be considered when modeling AM structures. Microscale structure accounts for the performance of the fiber reinforced polymer that makes up the individual printed filaments. Next, mesoscale properties account for filament strength resulting from the as-printed contact efficiency and resulting void space between filaments [4]. Finally, the macroscale properties deal with the overall part performance. Numerical modeling to the microscale and mesoscale levels requires very finely discretized meshes for these large-scale additively manufactured parts. Therefore,

  doi:10.5075/epfl-298799_978-2-9701614-0-0

efficient numerical models must appropriately approximate these properties and include them at the macroscale level.

This paper presents a method for informing numerical analyses with manufacturing information. Directed properties of a given printed structure are captured to make up the microscale (material type) and mesoscale (print process) properties of the AM structure. These directed properties are then associated with the manufacturing directions of the part and intersected with the macroscale mesh for finite element analysis (FEA). A homogenization scheme then combines the directional print information and void locations within each mesh element to generate an analysis that efficiently captures the multiple property scales.

2. Approach

Modeling of thermoplastic AM processes must account for the multiscale nature of the material and manufacturing method. This modeling approach accomplishes this during a preprocessing step in which a directed volume representing the printed filament of a given material is intersected with the elements of a solid element FEA mesh. Part analysis with this method requires printing instructions for the part in the form of a G-code file, a FEA model of the part, and a material definition describing the extruded material's properties. The resulting intersection components are directionally averaged and adjusted based on the amount of void space left in the element. The resulting homogenized material in the element is generated as a unique material, which is then input to an FEA solver to generate a macroscale analysis of the given part that is informed by the print process and material properties.

The following sections describe the constituent pieces of the preprocessing steps and provide details of the intersection and homogenization method. These include the material representation of the extruded material, G-code conversion to a volume-mesh, and interaction with the FEA model. Next the intersection and homogenization methods and assumptions for each are discussed.

2.1 Material Definition

This method requires a material definition of the mesoscale filament performance. Properties must be matched to the extruded materials type and print. To simplify the method, material properties are assumed to be constant throughout the printing process, and that the tested lattice of the filaments are representative of the larger print. This latter assumption is largely true for large-scale AM as prints typically make less use of infill and largely feature print strategies that stack similarly directed filaments on top of each other.

This approach concentrates on defining the filament stiffness matrix of the mesoscale material sample. Material data can be generated in a multitude of ways including manufacturer material data, material coupon testing of as-printed material [5][6], or from modeling of a representative volume element (RVE) generated with the print parameters [7]. Results in this paper focus on the stiffness properties of the part, but this homogenization method is being investigated for use with other directional material properties such as coefficient of thermal expansion and thermal conductivity. These expansions will be developed further in a later paper.

  doi:10.5075/epfl-298799_978-2-9701614-0-0

2.2 Print Representation

The part structure is represented by a set of volume meshes and is generated from manufacturing instructions stored as a G-code. These meshes are simplified representations of the actual extruded filament shape to reduce the computational complexity of the intersection calculation. These volume meshes are used to approximate the volume of filaments and voids of a given print. The goal of this mesh is to approximate the shape and volume of the print defined by the G-code using a minimal number of mesh faces.

Defining the mesh requires a user-defined rectangular cross-section that is then swept along the filament path. This cross-section should match the height and width dimensions of the bead. This simplification from the ellipsoidal shape of the actual printed bead to the approximated rectangular cross-section is shown in *Figure* 1. By reducing the cross-section to a rectangular definition the number of bounding volume mesh triangles is greatly reduced.

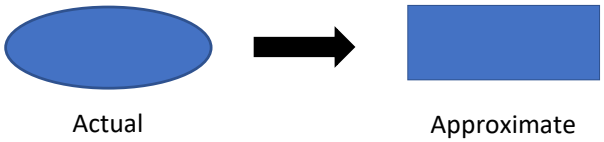

Figure 1: Cross-section simplification from ellipsoidal to rectangular

With the filament cross-section defined, the volume mesh is then generated by sweeping this area along the nozzle path. The nozzle path is obtained from the manufacturing instructions produced by an external slicing program that converts a 3D model into a layer-by-layer set of printer-specific instructions. These instructions specify the nozzle movements as a set of straight line moves. Each individual straight-line nozzle movement is then converted into an individual volume mesh as shown in Figure 2. By handling each individual nozzle movement separately, the nozzle direction can be stored along with the volume mesh and used later in the homogenization calculation. Continuous print segments of the filament are connected with a simple corner approximation to avoid overlaps. With this process, the G-code polyline instructions are then converted from polylines to a set of volume meshes that store the underlying nozzle movement direction as shown in Figure 3.

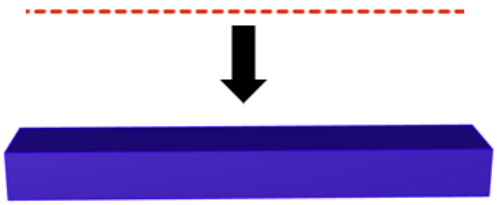

Figure 2: GCode segment conversion to a closed volume mesh

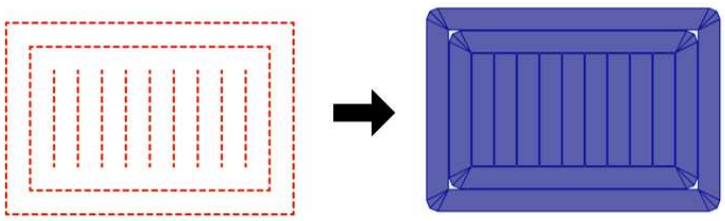

Figure 3: Layer of GCode polylines converted to a 3D volume mesh representation

  doi:10.5075/epfl-298799_978-2-9701614-0-0

2.3 Finite Element Analysis

Simulia Abaqus was chosen as an initial solver for this preprocessing method. A user-defined finite element model with mesh and boundary conditions applicable to the desired model is used as an input to the preprocessing method. The FEA mesh is setup to capture the macroscale aspects of the part and should ignore the layout and geometry of the additive manufacturing process. By modeling at the macroscale level, the model greatly reduces the number of elements and preprocessing in the analysis that would be required to capture the filament scale phenomena.

Interfacing with Abaqus is done using the program's input file. This file gives access to the Abaqus mesh elements and material definitions. These can then be modified outside of the Abaqus user interface. The analysis mesh is loaded into the method and each element of the mesh is represented as a closed volume mesh. With this closed volume representation of the elements, the FEA model can then be intersected with the filament mesh.

2.4 Intersection

The filament-FEA element intersection is accomplished by using a mesh Boolean intersection algorithm [8]. All filament segment meshes are intersected with each element of the FEA mesh and the resulting components retain the parent filament's directionality and material properties. This is the most computationally expensive algorithm in the method, but this calculation is highly scalable. An example case of the intersection is shown below in Figure 4.

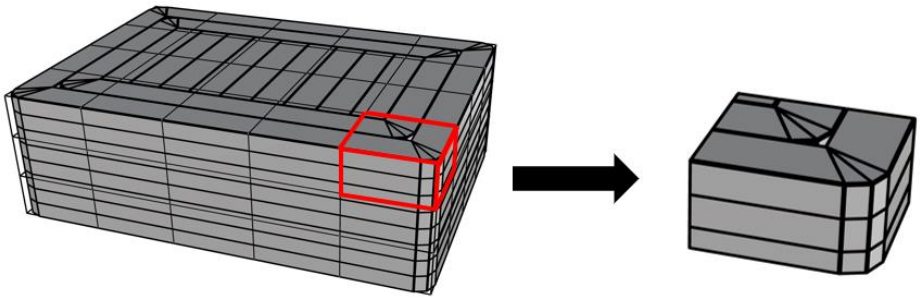

Figure 4: Example of the intersection of element and filament meshes

2.5 Homogenization

A volume homogenization scheme then operates on the directed components found in the intersection. The stiffness of each element can be calculated by

$$C = \frac{1}{V}\sum_{i=1}^{N} V_i K_i C_i {K_i}^T \tag{1}$$

where V is the volume of the element, V_i is the volume of the current component, K_i is the rotation matrix between the component's local coordinate system and the global coordinate system, and C_i is the stiffness of the component material in local coordinates. Voids are accounted for in this step by reducing the volume averaged material properties by the volume fraction. The resulting homogenized material property is then written to the input file as a new material definition and is defined for each element of the simulation

  doi:10.5075/epfl-298799_978-2-9701614-0-0

3. Results and Analysis

3.1 Setup

Testing was completed on a tensile coupon run in the FEA program Abaqus with multiple slicing approaches and compared to a coupon generated with homogenous properties. The tensile coupon geometry and coordinate system used is shown in *Figure* 5. This geometry was chosen as it presents a small-scale test case that can be manufactured with different strategies that highlight how the method works. A displacement is applied to the coupon in the X-direction at the ends of the coupon in the simulation.

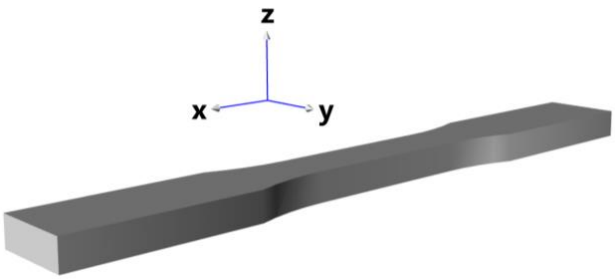

Figure 5: Tensile coupon geometry and coordinate definition

Two separate slicing strategies were used in this analysis: a perimeter only case and a 45-degree infill strategy Figure 6. The perimeter only strategy was chosen to show the capture of void effects in the print, while the 45-degree infill coupon was chosen to show the directionality of the homogenized print properties. These were compared with a solid part of homogenous material properties.

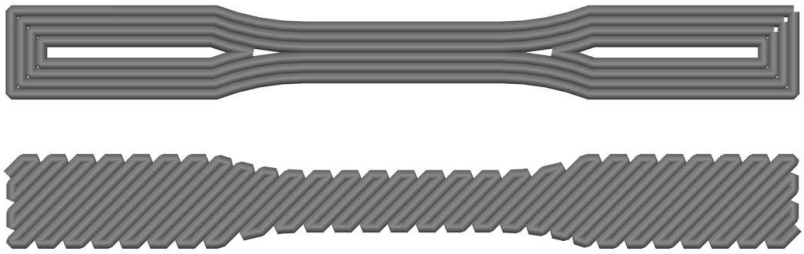

Figure 6: Tensile coupon slicing with four perimeters (top) and 45-degree infill (bottom)

Carbon fiber reinforced PETG was used to define the material properties of the filament for testing. The principal coordinate directions for the filament properties are shown in *Figure* 7. These properties were defined as transversely isotropic from material coupon testing [5][6] and are shown in Table 1. The transversely isotropic material definition treats properties in the 2 and 3 direction as equal and are denoted by the subscript p for in plane, while the transverse property is denoted by the subscript t.

  doi:10.5075/epfl-298799_978-2-9701614-0-0

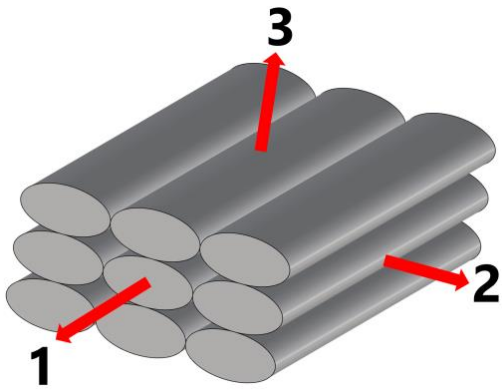

Figure 7: Local coordinate definition for filament properties

Table 1. Transversely isotropic material properties of PETG-CF [5][6]

Property	Unit	Value
E_t	MPa	12197
E_p	MPa	2705.2
ν_p		0.375
ν_{pt}		0.375
G_t	MPa	1118.7
ρ	kg/m^3	1080

3.2 Comparison Test Results

Comparison testing was completed with the tensile coupon and results were acquired for two mesh sizes with seed sizes of 3mm and 1mm. The finite element mesh is comprised solely of hex elements. The 3mm mesh represents a typical mesh size for this analysis and is sized such that the large voids created in both the four-perimeters and the 45-degree schemes are not fully included in elements. Results from the 3mm test can be seen in Table 2. Results are shown in the global X-direction for stress and strain and a homogenous tensile coupon is shown that is modeled with constant properties over the entire model for comparison.

Table 2: Comparison of Abaqus results with a mesh seed size of 3mm.

Scheme	σ_x	ε_x
Homogenous	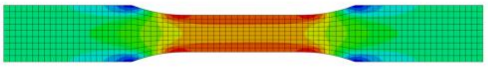	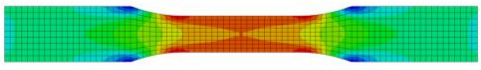
4-Perimeters		
45-Degree	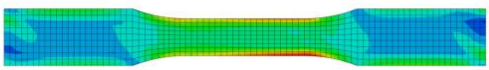	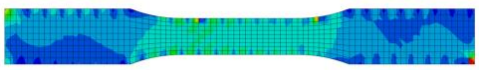
		

For the four-perimeters scheme the effect of the voids can be seen most clearly in the stress plot near the wider ends of the tensile coupon. Stress is decreased in the large void areas created

by the printing strategy in this case, which matches the predictions for this method. The area of the analysis of most concern for this case is where the perimeters begin converging to form the middle section of the coupon and produces a very low strain value.

The 45-degree case seems to capture the directionality of the filaments and the location of the voids in both plots. This is most easily seen in the strain plot, where the locations of voids from the filament turning along the perimeter of the coupon are matching with the location of low strain values. Two pieces of these plots should be noted. First, there is a strain concentration in the bottom right corner of coupons. This corresponds to the start of the print where a larger void area is produced. Also, locations along the perimeter in the center of the coupon produce have increases in strain magnitude and will require inspection of the method's void handling algorithm to smooth results.

Next the results from the refined 1mm seed size mesh are shown in Table 3. With the finer mesh discretization of the tensile coupon the capture of the void elements with the mesh can be further investigated. The two issues from the 3mm mesh size runs were enhanced in these cases The plot limits were kept constant to filter out extrema.

Table 3: Comparison of Abaqus results with a mesh seed size of 1mm.

Scheme	σ_x	ε_x
Homogenous		
4-Perimeters		
45-Degree		
	Min  Max	

Plots produce largely the same patterns as the 3mm case, but add more refinement in the capture of void geometries. For the 4-perimeter case, the second void location can now be identified in the stress and strain analysis that is caused by a small overlap of filaments. For the 45-degree scheme the directionality of the filaments also is apparent and produces a similar pattern. However, the finer mesh in both cases produces more issues with the zero-stiffness values of void elements when no filament passes through an element.

4. Conclusions

A method is presented for the analysis of short fiber reinforced thermoplastic AM by combining material information with specific print processes. The method emphasizes the capture of void elements and the direction of filament properties in a macroscale FEA model by modifying the material definition of elements based on directed mesoscale properties. It also adds the capability of including properties of the directed filament segments throughout the print that can be gathered from either coupon testing of similar prints or from RVE modeling of mesoscale filament properties.

  doi:10.5075/epfl-298799_978-2-9701614-0-0

Results show that the method can successfully capture the directionality and void geometry of a filament and apply this to a macroscale FEA mesh using transversely isotropic properties of the filament structure. This is displayed in the testing of the tensile coupon, with comparison of two printing schemes to an injection molded solid tensile coupon of the same properties. Additional work is required to address the capture of voids more accurately as well as adjusting their treatment within the volume homogenization scheme.

Acknowledgements

This research was funded by the Accelerating Rapid Prototyping: Process and Modeling project from the U.S. Army Engineer Research and Development Center (ERDC). Contract number: W912HZ21C0005.

5. References

1. Talagani M.R., DorMohommadi S., Dutton R., Godines C., Baid H., Abdi F., Kunc V., Compton B., Simunovic S., Duty C., Love L., Post B., Blue C. Numerical simulation of big area additive manufacturing (3D printing) of a full size car. SAMPE Journal 2015, 51:27-36
2. Saltonstall P. University of Maine: 3Dirigo; Maine Boats Homes & Harbors 2020, 162: 1:36-39
3. Blok L.G., Longana M.L., Yu H., Woods B.K.S An investigation into 3D printing of fibre reinforced thermoplastic composites; Additive Manufacturing 2018, 22:176-186
4. Helten B., Warren K. Homogenization of additively manufactured materials; ECCM20 2022 Pre-Print
5. Seigars C., Warren K., Steva B., Murphy C., Helten B. Characterizing the tensile and compressive behavior of PETG/CG and PC/CF manufactured using large scale additive processes; ECCM20 Pre-Print
6. Steva B., Warren K., Seigars C., Helten B. Evaluation of the shear behavior of CF-PETG and CF-PC coupons manufactured using large-scale additive manufacturing processes; ECCM20 Pre-Print
7. Gupta A., Hasonov S., Fidan I., Zhang Z. Homogenized modeling approach for effective property prediction of 3d-printed short fibers reinforced polymer matrix composite material; The International Journal of Advanced Manufacturing Technology February 2022, 118:4161-78
8. Jacobson A., Panozzo D. LibIGL: A simple C++ geometry processing library; https://libigl.github.io/ 2018

  doi:10.5075/epfl-298799_978-2-9701614-0-0

NUMERICAL MODELLING OF INTERFACE FORMATION DURING THE INJECTION OVERMOULDING PROCESS

Ruaraidh. MacLennan[a], M. Ali. Aravand[a,b]

a: Advanced Composite Research Group, School of Mechanical and Aerospace Engineering, Queen's University Belfast, UK – rmaclennan01@qub.ac.uk
b: Northern Ireland Advanced Composites and Engineering (NIACE) Centre, Airport Road, Belfast, BT3 9DZ, United Kingdom

Abstract: *There is currently a demand for numerical tools to support the design process of overmoulded structures as determination of interface strength may currently only be determined reliably from experimentation, which is limiting due to tooling costs. Simulation of the injection overmoulding process represents a complex challenge as the final interface strength is dictated by polymer bonding mechanisms and the microstructure of the interface which are dependent on material characteristics and processing conditions. In this work a multi-phase Computational Fluid Dynamics (CFD) simulation is presented which shows the initial micro-scale development of the interface during overmoulding using the volume of fluid (VOF) method to further understand and simulate the development of the interface morphology. Thus far the numerical model has captured the solidification/melting process and the subsequent development of a stratified flow phenomenon which can explain the formation of complex interfacial features that have been observed experimentally.*

Keywords: *Injection Overmoulding; Interface Formation; Simulation; Thermoplastic Composites; Computational Fluid Dynamics;*

1. Introduction

Composite injection overmoulding is a relatively new manufacturing process, through which a wide range of complex composite structures may be produced which may be expensive or impossible through alternative methods [1, 2]. It is performed by injection of a polymer melt directly onto the surface of a Carbon Fibre Reinforced Polymer (CFRP) laminate which is contained within a mould tool. The injected polymer is then consolidated under pressure before cooling and subsequent ejection, with the output resulting in a new complete structure. Additionally, thermoforming may be performed before overmoulding, depending on product requirements and manufacturing capabilities.

A considerable advantage of the overmoulding process is the benefits offered by composite structures produced through continuous fibre reinforcement composites (such as their superior strength to weight ratio) may be retained for load-bearing sections of a structure while using the advantage of high productivity and dimensional accuracy brought by the injection moulding process for any complex features. This allows considerable flexibility and allows for a wide range of composite structures to be produced that may not be feasible through alternative means [3]. Furthermore, with a growing need to produce structures through sustainable means, the use of thermoplastics to produce composites offers the potential for recyclability. However, there are

  doi:10.5075/epfl-298799_978-2-9701614-0-0

still challenges facing the overmoulding process: One of these is that the interface between the CFRP laminate and the injected polymer is a complex process that is not yet fully understood. Furthermore, the interface is frequently a point of weakness in the final structure and (particularly in the event of an unsuccessful bond formation) the strength of the interface may define the ultimate strength of the overmoulded structure [3]. Due to the complexity of this process and the resulting changes in the interface morphology due to interactions between the CFRP insert and the injected polymer, the interface strength may currently only be determined by direct measurement through mechanical testing. The following interface morphology, produced in related work [4], shows the presence of interfacial irregularities that were found to arise as a result of the overmoulding process during a successful overmoulding case of 30 wt% CF filled injected Polyether ether ketone (PEEK) over CF reinforced Polyphenylene sulfide (PPS) laminate [5]. It can be seen in this image that a considerably larger surface area is produced between the injected polymer and substrate than a flat separation between phases. Due to an observed correlation between the formation of interface irregularities and interface strength, it is expected that these features impact the final interface strength. Suspected mechanisms to aid interface strength are thought to occur from mechanical interlocking in addition to an increased contact area through which interdiffusion of polymer molecules occurs. Interdiffusion of polymers has long been found to be which is important for the development of strength and has been implemented in previous work for calculating interface strength [6-8].

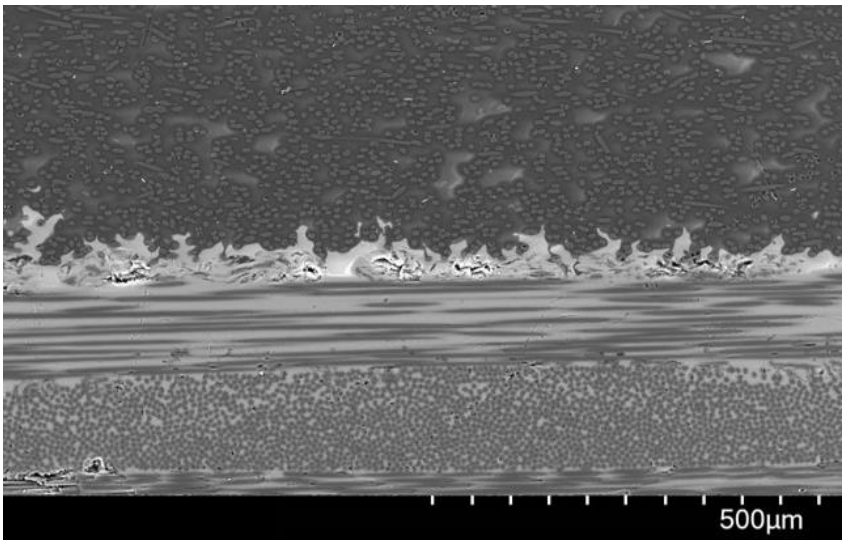

Figure 1: interface morphology following overmoulding of CF filled PEEK (above) injected over a CF reinforced PPS substrate, related to Aravand et al (5).

With the motivation of further understanding the formation of the interface during overmoulding, a numerical simulation has been developed that captures the resulting change in morphology that occurs at the micro-scale during the overmoulding process.

2. Simulation method

A multi-phase fluid simulation was developed within Ansys Fluent (v2020 R2) to capture the interactions between injected polymer and substrate at the micro-scale, with explicit interface tracking using the Volume of Fluid (VOF) method. The domain of the simulation has been prepared to reflect the formation of the interface at the micro-scale during the overmoulding of a rectangular specimen. Due to computational cost restraints for resolving micro-scale flow, it

  doi:10.5075/epfl-298799_978-2-9701614-0-0

was deemed necessary to simplify the full interface formation process to a representative 2D domain as seen in Figure 2 below. Through this simplification, it was assumed that a section of the insert is modelled in such a way that it remains outside the direct influence of the mould walls in the thickness direction. Also, a reduced section of the interface was considered. In the simulation case, the simulation parameters are used such that the output is comparable to the case in Figure 1 where CF reinforced PEEK is considered as the injected polymer over a PPS matrix.

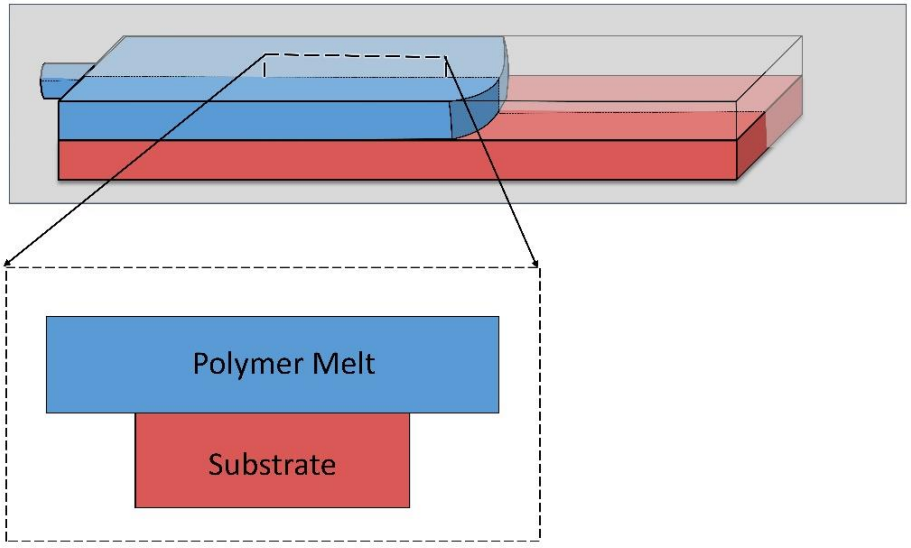

Figure 2: Simplification of the full injection overmoulding procedure to a representative 2D model

Currently, the air initially contained within the mould has been neglected upon initialization of the model. This simplification has been made due to the complex micro-scale interactions between the three fluid phases: the injected melt, substrate and air initially contained within the domain. Thus the initial condition of the current simulation is as seen in the simplified domain in Figure 2. Through neglecting the air within the domain it is assumed that perfect contact is initially made between the polymer melt and the insert. It was also considered necessary to preserve the channel height while reducing the area of contact between the injected melt and substrate for simulation feasibility.

The Cross-WLF model has been implemented to reflect the non-Newtonian behaviour of the viscosity [9]. This model is obtained through a combination of the Cross model and Williams-Landel-Ferry (WLF) equation which model viscosity for a shear-thinning fluid and the change in viscosity due to temperature shift, respectively. The following form of the Cross model is used [10]:

$$\mu = \frac{\mu_0}{\left[1+\left(\frac{\mu_0 \cdot \dot{\gamma}}{\tau}\right)^{1-n}\right]} \quad (1)$$

Where, μ is the polymer viscosity (Pa s), μ_0 is the zero-shear viscosity, $\dot{\gamma}$ is the shear rate (1/s), τ is the critical stress upon transition to shear-thinning, and n is the power-law index.

The variation in μ_0 due to temperature is provided by the WLF equation in the following [10]:

  doi:10.5075/epfl-298799_978-2-9701614-0-0

$$\mu_0 = D_1 \exp\left[\frac{-A_1(T-D_2)}{A_2+(T-D_2)}\right] \quad (2)$$

Where, T is the temperature (K), and A_1, A_2, D_1 and D_2 are constants determined through curve fitting, along with τ and n.

Since semi-crystalline polymers are primarily used within high-performance thermoplastic CFRPs it was necessary to consider the effect of phase change within the simulation model, as these have a distinct melting point. Thus, a solidification/melting model was implemented, constraining the movement of solidified material.

Table 1: Parameters used within overmoulding simulation

Parameters	Value
Insert temperature	200℃
Melt temperature	385℃
Injection velocity	0.1 ms^{-1}

3. Discussion

3.1 Development of interface irregularities

In the current work, the developed numerical simulation was able to reproduce features similar to those seen above, which have aided in the explanation of the generation of such features. A current simulation of the interaction between the injected polymer and substrate can be seen below in Figure 3. In the following representation, the injected melt phase (phase 0), can be seen to transfer heat to the substrate (phase 2), resulting in mass transfer to an additional phase (phase 3) representing the melted substrate. In this case, the criteria for transfer to this additional phase are dictated by the melting point of the PPS substrate. Phase 3 is unconstrained from movement and allowed to behave as a viscous fluid within the simulation. The melting depth can be seen to progressively increase over time.

In Figure 3 there can also be observed the development of microscopic features at the interface between the melted substrate phase and the injected polymer, leading to the initiation of wave-like instabilities that develop over time due to drag forces that occur between the respective phases. This is akin to the initiation of a Kelvin-Helmholtz instability which occurs as a result of velocity shear between stratified layers of flow [11]. The injected melt and the substrate phase are considered stratified layers in this case. It is proposed that this is a mechanism of importance in the development of interfacial features as observed experimentally in Figure 1.

  doi:10.5075/epfl-298799_978-2-9701614-0-0

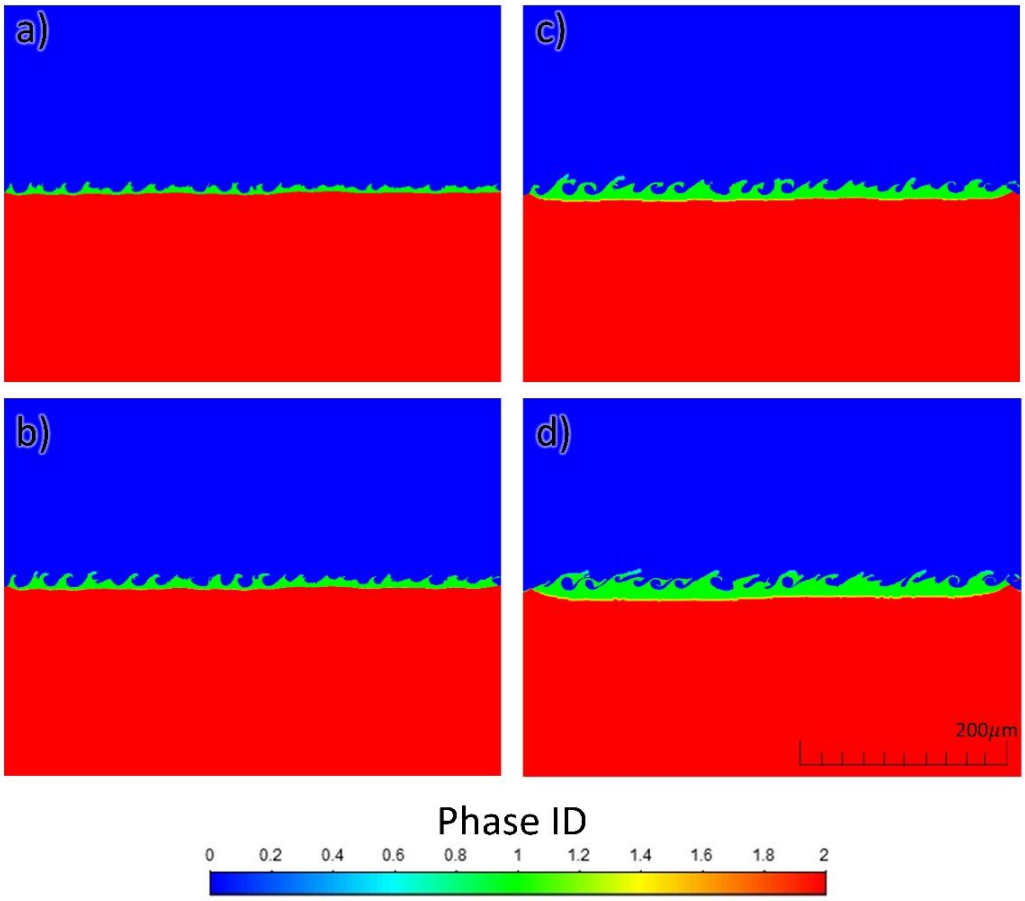

Figure 3: Contours of phase ID, showing heat transfer and subsequent melting of the substrate and the development of a Kelvin-Helmholtz instability, shown at time intervals a) t=0.001, b) t=0.002, c) t=0.005, and d) t=0.01, where phase ID 0, 1 and 2 refer to the injected melt, melted substrate and solidified substrate, respectively.

In the current work, it has been found that the development of interfacial irregularities is influenced considerably by the non-Newtonian viscosity of the respective polymer phases. The development of features at the interface is dependent upon the velocity shear between phases. The velocity field is affected by the non-Newtonian viscosity, leading to its influence on the generation of interfacial features. As seen in Figures 3 and 4, the development of interface features primarily occurs within a short time of contact between the injected melt and the substrate phases (in this case between 0.001 and 0.002s, images a and b). Outside of this period, although the features continue to evolve, they are primarily developed and do not continue to grow in magnitude considerably. Since the viscosity of the injected melt can be seen to progressively increase with simulation time within the bulk flow of the molten polymer due to heat transfer, this results in the formation of an increasingly thick layer of viscous polymer melt adjacent to the interface. Upon sufficient heat transfer, local areas of freezing, seen as regions of high viscosity within the injected melt can be seen to occur in this case due to the injected polymer cooling below its melt temperature.

Freezing of the features at the interface of the specimen may explain why these features are observable through microscopy following cooling of the sample and may explain why further intermixing of the injected melt and the substrate has not yet been observed at the interface

  doi:10.5075/epfl-298799_978-2-9701614-0-0

following overmoulding. Further intermixing may be expected upon initiations of a Kelvin-Helmholtz instability within a Newtonian flow.

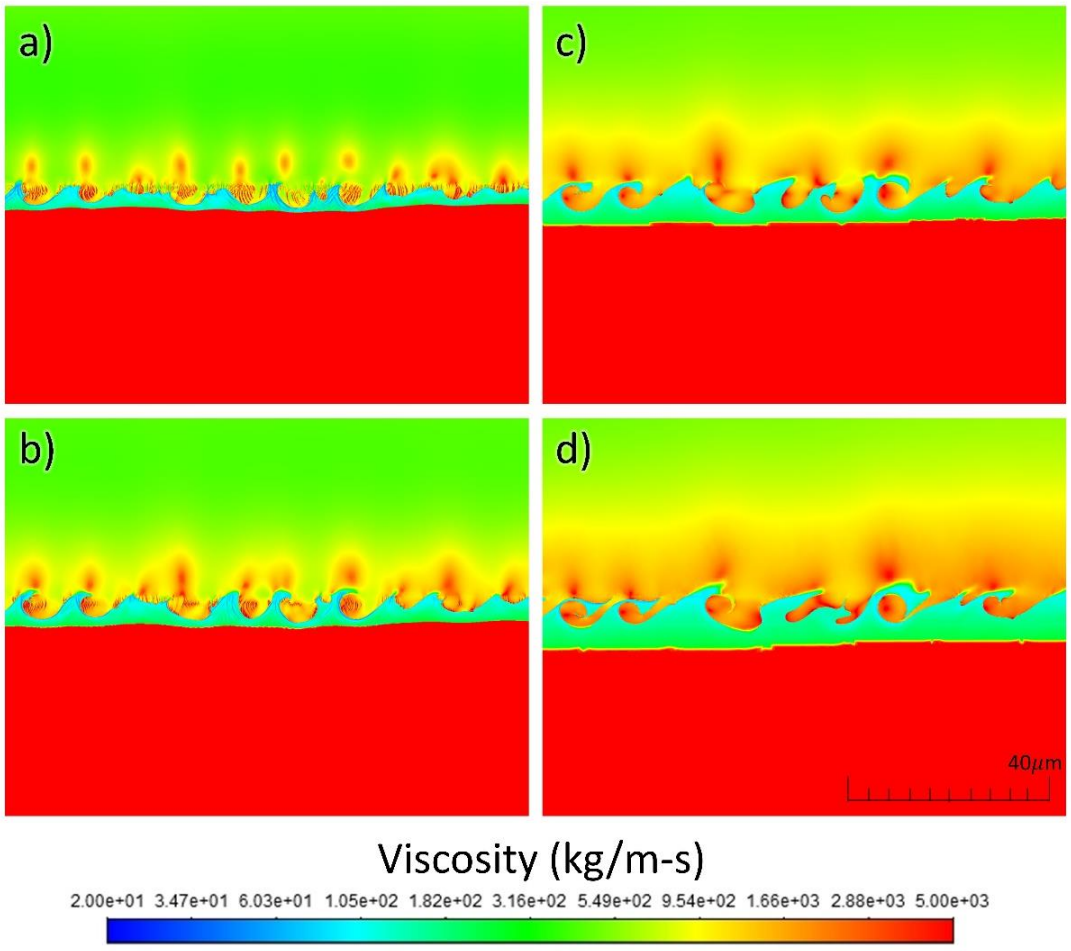

Figure 4: Viscosity contours during the development of interface over time. Shown at time intervals a) t=0.001, b) t=0.002, c) t=0.005, and d) t=0.01.

It is noted, that while there are similarities in the morphology between these two cases, the interface instability becomes increasingly complicated when considering 3D space and as such, it is expected that this would more accurately reflect the overmoulding scenario in Figure 1.

4. Conclusion

A simulation is presented to describe the formation of irregularities that influence the interfacial strength of an overmoulded component. It has been found thus far that irregularities qualitatively similar to those observed experimentally can be generated through simulation of the melting/solidification process that occurs between injected polymer and the insert and the subsequent drag forces that are generated between phases, resulting in a stratified flow phenomenon. Additionally, non-Newtonian viscosity was found to influence the formation of irregular features.

Acknowledgements

  doi:10.5075/epfl-298799_978-2-9701614-0-0

The authors gratefully acknowledge the support from Department for Economy (DfE) for funding the project.

5. References

1. Knox MP. Continuous Fiber Reinforced Thermoplastic Composites In The Automotive Industry. 2001.
2. Hanser C. From Laminate to Component. Kunststoffe International. 2013.
3. Akkerman R, Bouwman M, Wijskamp S. Analysis of the Thermoplastic Composite Overmolding Process: Interface Strength. Frontiers in Materials. 2020;7(27).
4. Aravand A. Composite Injection Overmoulding (COMINO). 2016-2019.
5. Aravand MA, Falzon BG, editors. Characterisation of the interfacial bonding at solid/melt interfaces in multiphase carbon fibre reinforced thermoplastic composites. International Conference on Composite Materials (ICCM21); 2017.
6. Wool RP, Yuan B-L, McGarel OJ. Welding of polymer interfaces. Polymer Engineering & Science. 1989;29(19):1340-67.
7. Yang F, Pitchumani R. Healing of Thermoplastic Polymers at an Interface under Nonisothermal Conditions. Macromolecules. 2002;35(8):3213-24.
8. Bastien LJ, Gillespie Jr. JW. A non-isothermal healing model for strength and toughness of fusion bonded joints of amorphous thermoplastics. Polymer Engineering & Science. 1991;31(24):1720-30.
9. Cross MM. Rheology of non-Newtonian fluids: A new flow equation for pseudoplastic systems. Journal of Colloid Science. 1965;20(5):417-37.
10. Cross-WLF Viscosity Model | Moldflow Insight Support and Learning 2017 [Available from: https://knowledge.autodesk.com/support/moldflow-insight/learn-explore/caas/CloudHelp/cloudhelp/2017/ENU/MoldflowInsight/files/GUID-7BC3A8F0-8B41-4FCB-BDF1-F1159E4DD175-htm.html.
11. De Silva IPD, Fernando HJS, Eaton F, Hebert D. Evolution of Kelvin-Helmholtz billows in nature and laboratory. Earth and Planetary Science Letters. 1996;143(1):217-31.

  doi:10.5075/epfl-298799_978-2-9701614-0-0

IN-SITU MEASUREMENT OF L-SHAPED CFRP DEFORMATION BEFORE GELATION BY A FIBER-OPTIC-BASED SHAPE SENSOR

Toshiyuki, Tamagawa[a], Shu, Minakuchi[b], Shoma, Niwa[b], Nobuo Takeda[b]

a: The University of Tokyo – tamagawa@smart.k.u-tokyo.ac.jp
b: The University of Tokyo

Abstract: *A prepreg-based composite part changes its geometry during consolidation as the uncured prepreg is soft enough to be compacted by high pressure. In an L-shaped part, this often causes defects like fiber wrinkle, resin-rich areas, and non-uniform laminate thickness. Several studies to establish the prediction models have been conducted, but the model validation relied on the cured part's dimension. The deformation history was unavailable for the validation because there were no experimental techniques to monitor the consolidation. The present study developed an embeddable fiber-optic-based shape sensor and conducted in-situ deformation measurements for tightly and softly stacked L-shaped parts. The shape sensor provided new insights into the deformation mechanism.*

Keywords: consolidation; L-shape; fiber wrinkling; shape sensing; in-situ measurement

1. Introduction

CFRP laminate is prone to deformation at corners during consolidation, and these defects degrade its mechanical properties [1-3]. In addition, dimensional changes affect the assembly and require machining. Various deformation models have been proposed, but the validity of the models is evaluated by comparing the shapes before and after curing due to the limited methods for measuring the deformation process during consolidation. One approach to measuring the deformation process is to embed an optical fiber sensor in the prepreg. This sensor can measure the internal strain caused by cure shrinkage and thermal contraction during curing in a severe environment in an autoclave. However, the strain cannot be measured during consolidation, in which the resin has not been cured, because the optical fiber and CFRP are not integrated yet. Since the deformation during consolidation determines the final shape and the presence of most defects, it is necessary to establish a measurement method for the deformation process of uncured prepreg in an autoclave.

The present study developed an embeddable fiber-optic-based shape sensor to monitor the consolidation process (Fig. 1). This shape sensor consists of a thin layer resin sheet and an optical fiber, which is on both the upper and lower surfaces of the resin sheet. The shape sensor can output the shape of itself by measuring the compressive and tensile strains caused by bending with the optical fiber sensor. To evaluate the usefulness of this sensor, the deformation of L-shaped CFRP laminates before curing was measured. In Automated Fiber Placement (AFP) process, compaction conditions at corners sometimes vary. Therefore, to observe the difference in the deformation mechanism depending on the degree of compaction at the stage of prepreg layup, two cases were set for the experiments: prepregs were stacked tightly and softly.

  doi:10.5075/epfl-298799_978-2-9701614-0-0

2. Deformation measurement of prepreg before curing

The method of shape calculation by the shape sensor is shown in Fig. 2. The direction along the shape sensor is defined as the s-axis. The radius of curvature R at each point is expressed from Euler-Bernoulli beam theory as follows,

$$R = \frac{\Delta t}{\Delta \varepsilon} \tag{1}$$

where $\Delta\varepsilon$ is the strain difference between the upper and lower surfaces and Δt is the distance between the optical fiber cores. The shape can be constructed by smoothly connecting micro-arcs of radius R and length ds, where ds is the sampling interval of the fiber-optic strain measurement system. The shape is expressed in x-y coordinates by accumulating the increments between the starting and ending points of each micro-arc. The increments in x and y directions are expressed as follows

$$dx = 2R \sin\left(\frac{d\theta}{2}\right) \cos\left(\theta + \frac{d\theta}{2}\right) \tag{2}$$

$$dy = 2R \sin\left(\frac{d\theta}{2}\right) \sin\left(\theta + \frac{d\theta}{2}\right) \tag{3}$$

where θ is the angle between the tangent line of micro-arc and the x-axis and $d\theta$ is the incriment of θ.

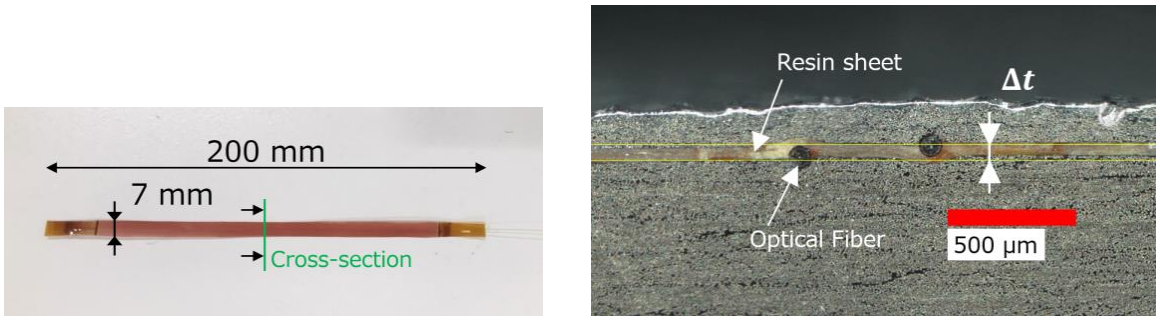

(a) *(b)*

Figure 1. Embeddable fiber-optic-based shape sensor (a) Photo of the whole (b) Cross-sectional micrograph after curing within CFRP laminate.

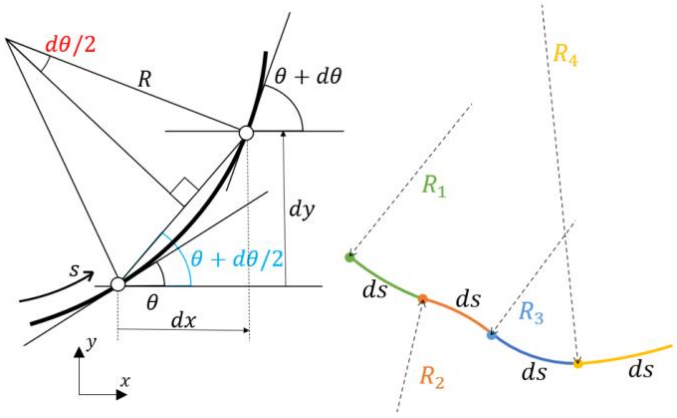

Figure 2. Schematic of shape calculation.

The shape sensor was fabricated by placing optical fiber sensors on both surfaces of an uncured thin-layer resin sheet and integrating them by curing process. In this experiment, we used polyimide-coated optical fibers (Fujikura Ltd.) with an outer diameter of 94 μm and 60 μm-thick thin-layer resin sheet (ES-3310KA, Risho Kogyo Co., Ltd.), which is composed of glass cloth impregnated with polyimide resin. First, the thin-layer resin sheet was cut into a strip of 7 mm wide and 170 mm long, and one optical fiber was placed on both surfaces by turning the optical fiber at one side of the resin sheet. The optical fiber and the resin sheet were sandwiched between aluminum plates covered by 0.05 mm thick Teflon films, and the whole was bagged. Curing was performed in an autoclave (Ashida MFG Co., Ltd.) under high pressure of 1.0 MPa so that the optical fiber is fully embedded in the thin-layer resin. The temperature was raised to 130°C at 2°C/min and maintained for 60 minutes, then raised to 200°C at 2°C/min and maintained for 60 minutes, and cooled to room temperature at -2°C/min.

The distributions of Δt for each shape sensor were calculated from the strain measured while the sensor was wrapped around a disk of constant curvature. A distributed optical fiber sensor based on Rayleigh backscattering (Luna Innovations Inc., ODiSI) was used for strain measurement, and the sampling interval ds was set to 1 mm.

3. Experiment method

Carbon/epoxy prepreg (Toray, T700SC/2592) with a thickness of approximately 145 μm was cut to a length of 200 mm in the fiber direction and a width of 100 mm in the fiber orthogonal direction, and 42 plies were laminated on a convex aluminum L-shaped tool covered with a 0.05 mm thick Teflon film. The fiber orientation of each ply was along the circumferential direction of the corner. Since the corner of the tool has a radius of 6 mm and the thickness of the 42 prepreg plies was about 6 mm, the outside corner of the L-shaped CFRP laminate has a radius of about 12 mm. After 40 plies were laminated, a shape sensor was placed at the center along the fiber direction, and prepregs were stacked on either side of the sensor as the 41st ply. Finally, the 42nd ply was stacked on covering the 41st ply and the shape sensor.

When stacking each ply, prepreg was temporarily heated over the release paper with iron to soften it. To demonstrate the impact of the layup method on the deformation mechanism, two manufacturing trials were conducted. In the first case, the iron was repeatedly pressed on each ply with a strong force by hand (this was referred to as the “tight layup” case); in the second case, the iron was pressed on each ply softly only once in one direction (this was referred to as the “soft layup” case). The laminated prepregs were covered with Teflon film, surrounded by sealant tape on all four edges to prevent resin flow, bagged by bagging film, and vacuumed in 5 minutes. In an autoclave, first the pressure was increased from 0.1 MPa to 0.4 MPa in 10 minutes, followed by the temperature rise from 24°C to 130°C in 45 minutes. After 60 minutes, the cured CFRP laminate was cooled to room temperature in 45 minutes. The shape sensor monitored the deformation from before vacuuming to after cooling.

To evaluate the relationship between the consolidation deformation and the resin viscosity, the change in resin viscosity was measured using a rheometer during the same temperature cycle as during the curing. The resin was obtained by compressing and squeezing heated prepreg sheets.

  doi:10.5075/epfl-298799_978-2-9701614-0-0

4. Result

Fig. 3 shows the thickness distribution calculated from the 3D scan data of the cured L-shaped laminates. In the tight layup case, the laminate was thinner at the corners. On the other hand, in the soft layup case, the downstream side in the layup direction at the corner became thicker.

Fig. 4 shows the cross-sectional images of the cured CFRP laminates. The red lines are the shape lines calculated by the shape sensor, indicating that the deformation at the corners can be measured accurately in the proposed monitoring method. In the tight layup case, no noticeable unevenness in thickness or wrinkles were observed. On the other hand, in the soft layup case, a wrinkle was observed at the corner, which corresponds with the thicker area. Fig. 5 shows the curvature distributions of each shape after curing. For comparison with the ideal shape (Ideal L-shape), the curvature distribution of an L-shape with a constant thickness of 6 mm is shown, for which the corner is arcs with a radius of 12 mm and the flanges are straight lines. The distribution of curvature is wide for the tight layup case, while it is tall and uneven for the soft layup case. Fig. 6 shows the curvature distribution from before vacuuming to 20 minutes after the temperature reached 130°C. The curvature distribution at the corner became taller and narrower through the pressurization process. However, the heating process reverted the distribution to the initial state. In the soft layup case, the pressurization induced a sharp peak and valleys in the curvature distribution, but the heating process moderated them.

Fig. 7 shows the curvature histories at characteristic positions for each condition. For the tight layup case, the mean curvature history of the corner area (s = -6 – 6 mm) and the curvature

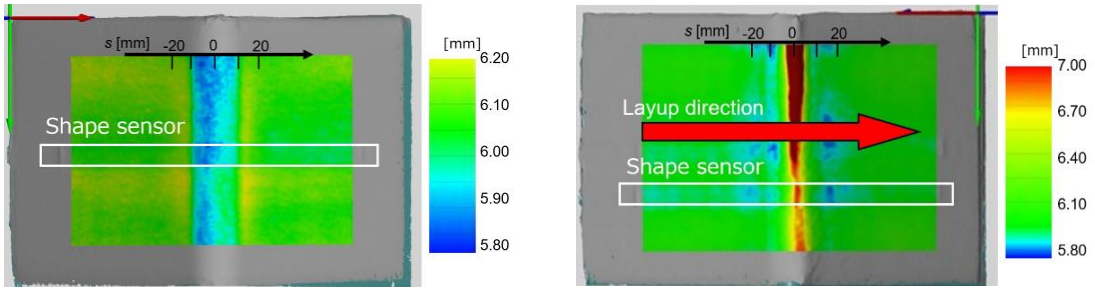

(a) Tight layup. *(b) Soft layup.*

Fig. 3 Thickness distribution of L-shaped CFRP.

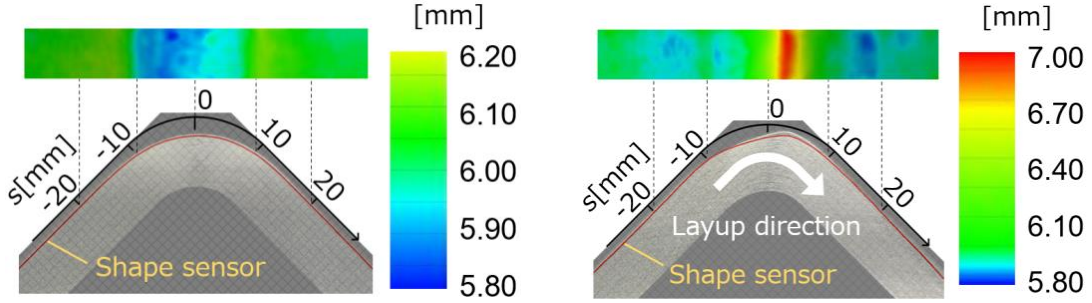

(a) Tight layup. *(b) Soft layup.*

Fig. 4 Cross-sectional micrograph of L-shaped CFRP with a shape line calculated by the shape sensor and thickness distribution of corresponding area.

histories at the outside of the corner (around s = -6, 6 mm) are shown. In both histories, the changes induced by the applied pressure seemed to relax after heating. During the heating, the changes accelerated with the temperature rise, and the changes stopped about 10 minutes after the temperature reached 130°C. For the soft layup case, the curvature history of the peak (s = 3 mm) and two valleys (around s = -3, 9 mm) are shown. As in the tight layup case, the change due to the applied pressure relaxed with heating, but the relaxation at the curvature peak was almost constant, while the relaxation at the valley was almost completed in the early stage of heating and the change after 50°C was relatively negligible.

The history of the resin viscosity measured by the rheometer shows that the viscosity decreases with increasing temperature, but begins to increase around 100°C (see Fig. 8). This indicates that curing has started at 100°C, and the deformation gradually stopped as the viscosity increases.

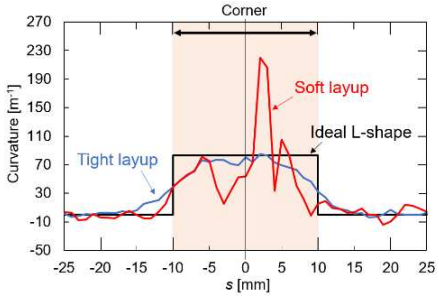

Fig. 5 Calculated curvature distribution after curing process.

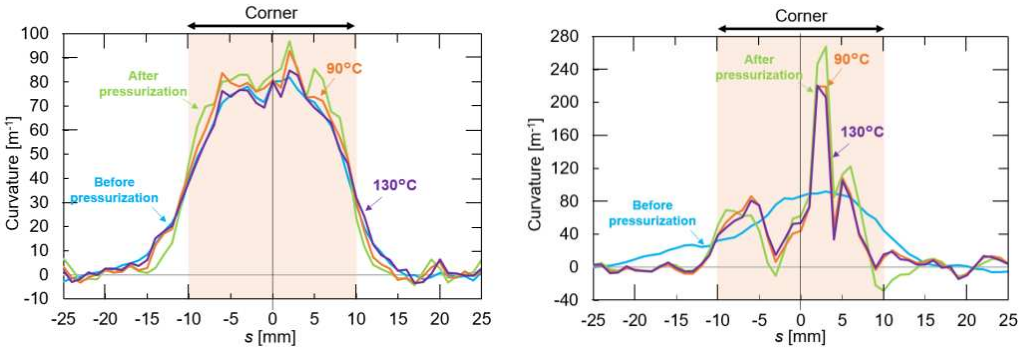

(a) Tight layup. *(b) Soft layup.*

Fig. 6 History of calculated curvature distribution.

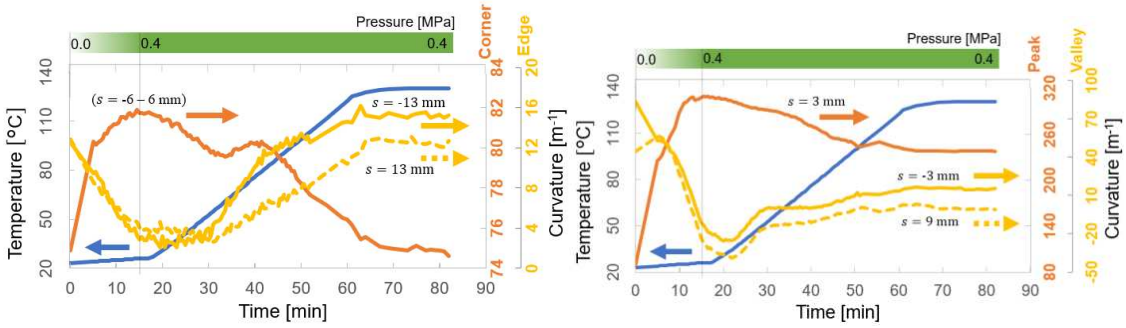

(a) Tight layup. *(b) Soft layup.*

Fig. 7 History of calculated curvature distribution.

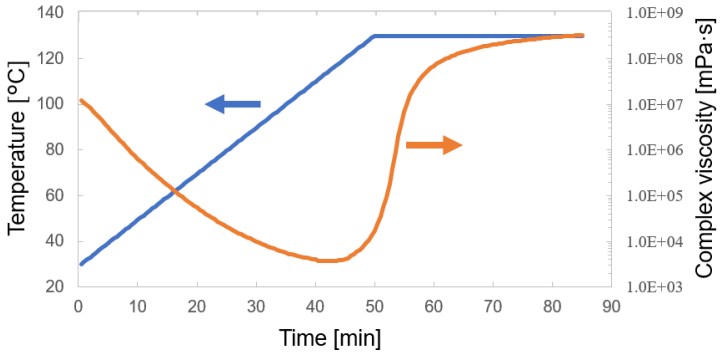

Fig. 8 Complex viscosity of the resin during cure cycle.

5. Discussion

5.1 Tight layup

From the experimental results, the following characteristics were observed.

- The curvature distribution was wide before and after curing.
- The curvature distribution became taller and narrower by pressurization.
- The curvature distribution became lower and wider by heating.
- The deformation rate during heating increased with temperature rise.
- The thickness after curing in the corner was thinner than in the flanges.

These indicate that the corner part was thin during layup, but the flange parts became as thin as the corner part by applying pressure, and then the corner part became thinner again by subsequent heating.

Firstly, the convex corners were compressed more strongly than the planar flanges due to pressure concentration, resulting in a relatively smaller thickness (see Fig. 9 (a)). Therefore, the curvature was more widely distributed than that of an ideal L-shape. When the prepreg was subsequently pressurized, the thickness of the flange, which still has room for compression, decreased (see Fig. 9 (b)), and thereby the curvature at the corner became taller and narrower. When heating started, the resin became less viscous and started to flow. It is known that the pressure at the corner increases due to the difference in area between the tool side and the bag side [4]. Therefore, the resin flowed out from the corner to the flange, and the thickness of the corner decreased. Since the deformation was accelerated as the viscosity of the resin decreased, this deformation was considered to be caused by resin flow. Through these processes, the final curvature distribution became wider than that of the Ideal L-shape.

5.2 Soft layup

From the experimental results, the following characteristics were observed.

- The curvature distribution became steeply concavo-convex by pressurization.
- The curvature at the peak decreased and the curvature distribution at the valleys became smooth by heating.
- The deformation rate was constant or decreased when heated.

  doi:10.5075/epfl-298799_978-2-9701614-0-0

These indicate the following deformation mechanism. First, at the time of layup, the prepregs were weakly compressed and contain a large number of inter-ply gaps, and the curvature was gently biased due to asymmetry in the layup direction. When the prepreg was pressurized in an autoclave, the thickness decreased significantly due to the elimination of the inter-ply gaps. The inter-ply friction restrained the inter-ply sliding of the prepregs, resulting in excess circumferential length at the corner. Thereby, the prepreg became wavy and had a sharply convex shape (see Fig. 10 (a)). When the resin was heated, the viscosity of the resin decreased and the inter-ply became slippery, and the circumferential length excess caused by the pressurization was eliminated to some extent and the unevenness became gentle (see Fig. 10 (b)). As the excess length eliminated, the force to slide the prepreg in-plane direction weakened, and the deformation was decelerated.

6. Conclusion

In this study, a shape sensor using an optical fiber sensor was fabricated to monitor the consolidation deformation of L-shaped laminates laminated under two different conditions.

In the tight layup case, deformation due to resin flow caused by the pressure gradient at the corners was observed. In the soft layup case, the thickness of the laminate decreased significantly during the pressurization, resulting in excess circumferential length, and the prepreg waviness was observed. By focusing on the relationship between the rate of deformation and viscosity, the difference in the deformation mechanism was discussed. This can only be achieved by measuring the deformation process from before the resin curing.

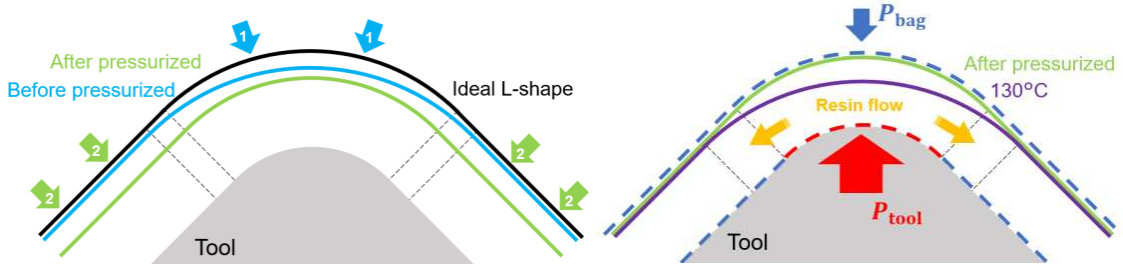

(a) Debulk. *(b) Thinning by resin flow.*

Fig. 9 Deformation mechanism of the tight layup.

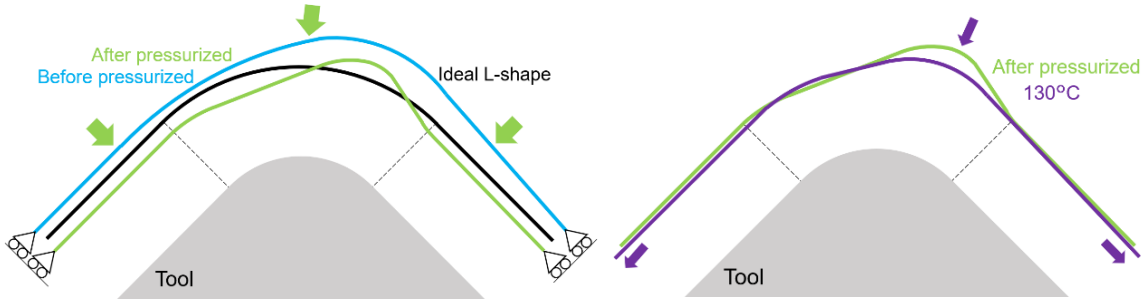

(a) Debulk. *(b) Ply slipping.*

Fig. 10 Deformation mechanism of the soft layup.

7. References

1. Potter K, Khan B, Wisnom M, Bell T, Stebens J. Variability, fibre waviness and misalignment in the determination of the properties of composite materials and structures. Composites Part A: Applied Science and Manufacturing 2008; 39(9):1343-1354.
2. Mukhopadhyay S. Jones MI. Hallett SR. Compressive failure of laminates containing an embedded wrinkle; experimental and numerical study. Composites Part A: Applied Science and Manufacturing 2015; 73:132-142.
3. Mukhopadhyay S. Jones MI. Hallett SR. Tensile failure of laminates containing an embedded wrinkle; numerical and experimental study. Composites Part A: Applied Science and Manufacturing 2015; 77:219-228.
4. Hubert P. Kratz J. Tool interface pressure during the forming of model composite corners. Composites Part A: Applied Science and Manufacturing 2021; 151:106639.

  doi:10.5075/epfl-298799_978-2-9701614-0-0

CHARACTERIZATION AND MODELING OF THE IMPREGNATION PROCESS OF ELECTRIC ENGINES' ROTORS WITH A REACTIVE THERMOSETTING RESIN

Amélie Moisy[a,b,c], Sébastien Comas-Cardona[a], Nicolas Désilles[b], Pascal Genevée[c], Jere Kolehmainen[c]

a: Nantes Université, Ecole Centrale Nantes, CNRS, GeM, UMR 6183, F-44000 Nantes, France - amelie.moisy@ec-nantes.fr
b: Normandie Université, INSA Rouen Normandie, CNRS, PBS, UMR 6270, F-76801 Saint Etienne-du-Rouvray, France
c: Renault, F-76410 Cléon, France

Abstract:

In the mobility electrification context, the Renault Group assembles its own electric engines. The rotor is the mobile part of the motor, mainly composed of a steel core wound by insulated copper wires. Then the winding is immersed into a liquid acrylate-based thermosetting resin bath which role is to ensure the performance and durability of the motor.
The impregnation occurs under controlled temperature settings to facilitate the flow and the polymerization. This process does not involve any pressurization to facilitate the resin flow between the wires. This suggests that capillary and gravity forces play a significant role on the impregnation. The global objective is to evaluate the impregnation quality. It requires to characterize and simulate a multi-materials and multi-physics process in which heat transfer, polymerization kinetics and resin flow are strongly coupled. This paper presents a unidirectional thermo-regulated capillary rise set-up, developed to validate an analytical model at various temperatures.

Keywords: Impregnation; capillary effect; experimental; modeling

1. Introduction: Context and objectives

As part of its development in the electric mobility market, the Renault Group assembles its own electric engines. The rotor is the rotating component of the electric motor. A rotor is mainly composed of a laminated steel core wound by insulated copper wires. Then the winding is immersed into a liquid acrylate-based thermosetting resin bath which role is to:

- Bind the wires (resist to vibrational, electromagnetic and centrifugal forces: rotation speed rises up to 12000 rpm),
- improve the insulation,
- resist to chemical attacks and moisture,
- improve the thermal conductivity.

The impregnation occurs under controlled temperature settings to facilitate the flow and the polymerization. Contrary to many composite processes, it does not involve a pressurization to facilitate the resin flow between the fibers (of a few millimeters of diameter). This suggests that capillary and gravity forces play a significant role on the impregnation. The objective of the study is to evaluate the windings' impregnation quality within such processing conditions. It requires

  doi:10.5075/epfl-298799_978-2-9701614-0-0

to characterize and to simulate a multi-materials and multi-physics process in which phenomena such as heat transfer, polymerization kinetics and resin flow are strongly coupled.

Before addressing the full scale and fully coupled case, an intermediary step needs to be implemented to understand the phenomena and validate the observations at small scale. The objectives to address in this paper are to define an impregnation set-up (representative sample, adapted impregnation follow-up method, repeatable protocol) and to model the phenomena observed in the experiments. This will include hypotheses choice and material characterization to be able to find a model fitting the experiments at three different temperatures.

2. Impregnation set-up and results

2.1. Impregnation follow-up method

Several methods can be used to follow-up an impregnation between fibers. Among the available methods, the visual front follow-up and the weight intake through a balance could be considered. The copper wires being opaque, the weight intake method was naturally chosen. The weight intake can be measured only if the sensitivity of the balance and the resin intake are properly chosen.

2.2. Sample geometry

The main target in the geometry choice was to obtain a hexagonal compact stacking similar to the rotor one in a simplified configuration to perform a vertical impregnation thanks to capillary effect. The capillaries' shape and size are a major influencing factor on the capillary rise.
After several trials to obtain a homogeneous stacking with repeatable capillaries, it has been chosen to aim at a rectangle shape for the section of the porous sample (Figure 1 (a)). The sample dimensions were chosen to represent approximately half a rotor pole in all the directions. Preliminary tests prove that the fluid does not impregnate into the larger capillaries in contact with the mold if the latter is not in contact with the resin. For the first tests a PVC reusable mold has been machined (Figure 1(b) at the background) and then replaced by a thermo-regulated aluminum one (Figure 2). The wires, straightened and cut are deposited one by one in the mold to obtain the most regular arrangement possible. The mold is then tightly closed with screws.

(a) *(b)* *(c)*

Figure 1. (a) Target arrangement of wires – (b) and (c) Wires' arrangement on the cut polymerized copper bar after polishing

The obtained profile (Figure 1(c)) confirms that the mold system enables to obtain a quite compact stack as targeted. The considered porosity in the modeling section will be $\varepsilon \cong 0.0931$ which is the theoretical value for a hexagonal compact stacking.

  doi:10.5075/epfl-298799_978-2-9701614-0-0

2.3. Test set-up

The balance needed to detect the resin weight evolution has a sensitivity of 10^{-4} g and a maximum mass of 200 g. Consequently the sample in the equipped aluminum mold is too heavy for this balance: the follow-up is done on the resin tank mass evolution.
The mold is attached to a bar linked to a height adjustment system to plunge into the microbalance crankcase. The target is to perform these tests at controlled high temperatures close to the process. To obtain a good homogenization of the temperature inside the copper bar, 4 long heaters are positioned in the aluminum mold. A sensor is placed between the heaters and the copper bar at mid-height to obtain a smooth regulation. Finally three temperature sensors record the temperatures along the copper bar. The 4 heaters and the regulation sensor are linked to a PID regulation system (Figure 2).

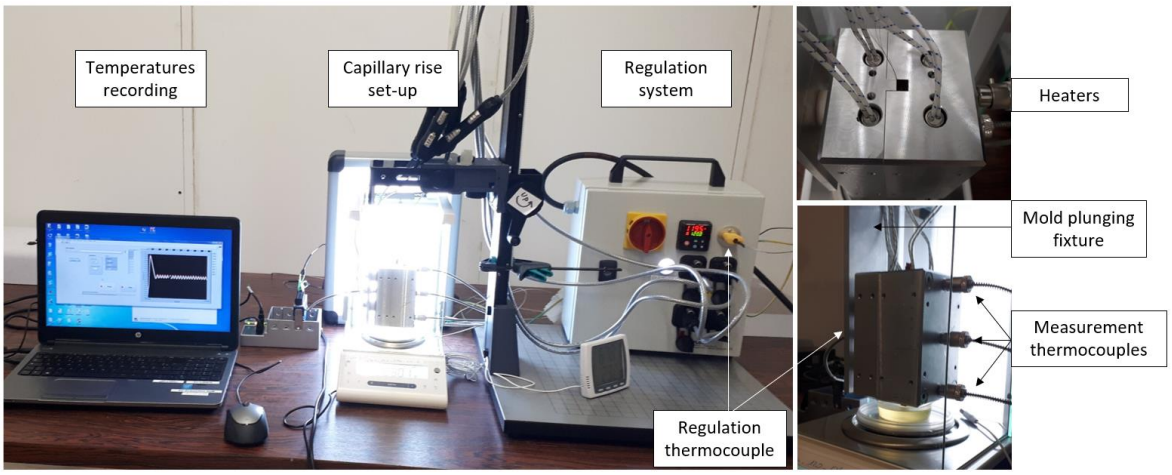

Figure 2. Global thermo-regulated capillary rise impregnation set-up

The resin is brought in the testing room the day before the test to ensure a homogeneous temperature. Before each test, the resin viscosity is controlled with a Brookfield viscosimeter and the temperature and hygrometry are recorded. The mold is heated and maintained at the test temperature during the impregnation. The resin container is put on the balance and the tare is made. The weight evolution is recorded and post-treated thanks to a Matlab code converting the removed mass of resin from the tank into a height of capillary rise. The sample is progressively brought closer to the resin and stopped as soon as the contact is created. The contact is precisely detected thanks to the backwards lighting and to a mirror put under the resin tank.

2.4. Results

Tests were performed at 20°C, 60°C and 120°C. Two repetitions have been done for each temperature. Once the weight converted into capillary rise height, the results can be analyzed in Figure 3. The results are quite repeatable and the behavior is clearly different for each isotherm. The quicker initial rise occurs at 120°C, however the higher equilibrium is reached at 60°C. For the three isotherms an equilibrium asymptote is visible, suggesting that capillary and gravitational forces are balancing while the resin columns become higher. A singular phenomenon occurs between 30 s and 2000 s at 120°C: the capillary rise slows down, not following the progressive behavior observed for the two other temperatures. To understand and validate these experimental results, a modeling phase is now required.

  doi:10.5075/epfl-298799_978-2-9701614-0-0

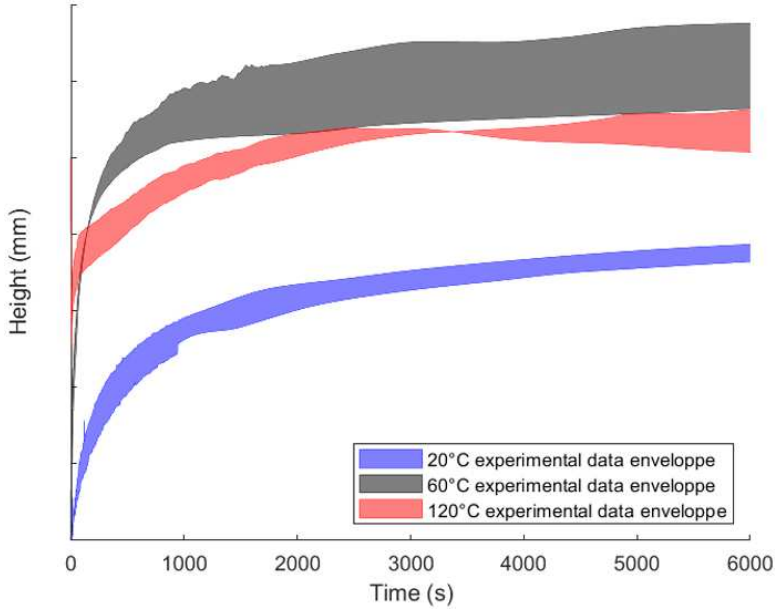

Figure 3. Capillary rise test results

3. Capillary rise modeling

3.1. Analytical solution of capillary rise in porous media when neglecting inertia

To confirm the experimental observations and include the capillary phenomena in the global simulation of the process, an analytical model must be found.
[1] describes a one-dimensional resolution of the momentum equation in the case of a capillary rise in a porous medium as described by Figure 4. The target is to solve Eq. (1), that is to say the momentum law with Darcy's law hypothesis and neglecting the inertia, with signs adapted to our case:

$$\boldsymbol{v} = \frac{1}{\eta}\boldsymbol{K}.(-\nabla p_i - \rho_r \boldsymbol{g}) \quad (1)$$

as $\boldsymbol{v}$ is the Darcy velocity, phase average of the resin velocity, η the resin viscosity, $\boldsymbol{K}$ the porous medium permeability tensor, p_i the intrinsic phase average of the resin pressure and $\boldsymbol{g}$ the gravity vector.

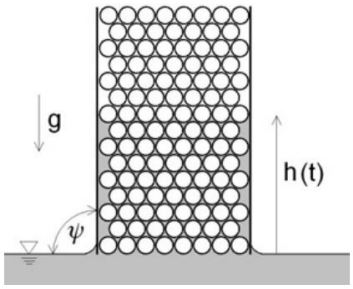

Figure 4. Capillary rise in a porous medium from [1]

An analytical solution can then be found by integrating and manipulating Eq. (1) using the Lambert function W. For a vertical column the capillary rise can then be described by:

$$h(t) = \frac{2\sigma cos\theta}{r_{cap}\rho g}\left[1 + W\left(-e^{-1-\frac{K_z(\rho g)^2 r_{cap}}{2\varepsilon\eta\sigma cos\theta}t}\right)\right] \quad (2)$$

with σ the surface tension liquid/gas, θ the contact angle at the triple line resin-wire-air, ε the medium porosity, K_z the permeability component on the *z* axis, and r_{cap} the equivalent capillary radius.
These properties have then to be evaluated to use the analytical model.

3.2. Material properties characterization

Using this model then requires characterizing the materials in temperature. Regarding the density of the resin, it has been evaluated with a densimeter between 20°C and 90°C and then extrapolated until 120°C. In a first step of study, the viscosity before gelation was also measured between 20°C and 90°C with a Brookfield rheometer and extrapolated until 120°C, neglecting then the impact of the polymerization.

The target is to characterize surface tension between the liquid resin and air σ and the contact angle at the triple line resin-wire-air θ. These measurements are done thanks to a Dataphysics OCA15 goniometer equipped with a thermal chamber rising to 100°C in the air of the chamber. Specific Teflon-ending needles were needed to avoid the resin to come up on the needle.

For the surface tension evaluation, a drop is dispensed until a pear-shape is reached (Figure 5 (a)) and the picture is taken before the falling of the drop for analysis by the software. As a given drop goes bigger and the viscosity lower when the temperature rises, the drop is falling when the temperature is increasing. The dosing of a new drop is then needed for each measurement. The results are given in Figure 5 (b). The surface tension is linearly decreasing with temperature, which is consistent with literature results for similar polymers [2].

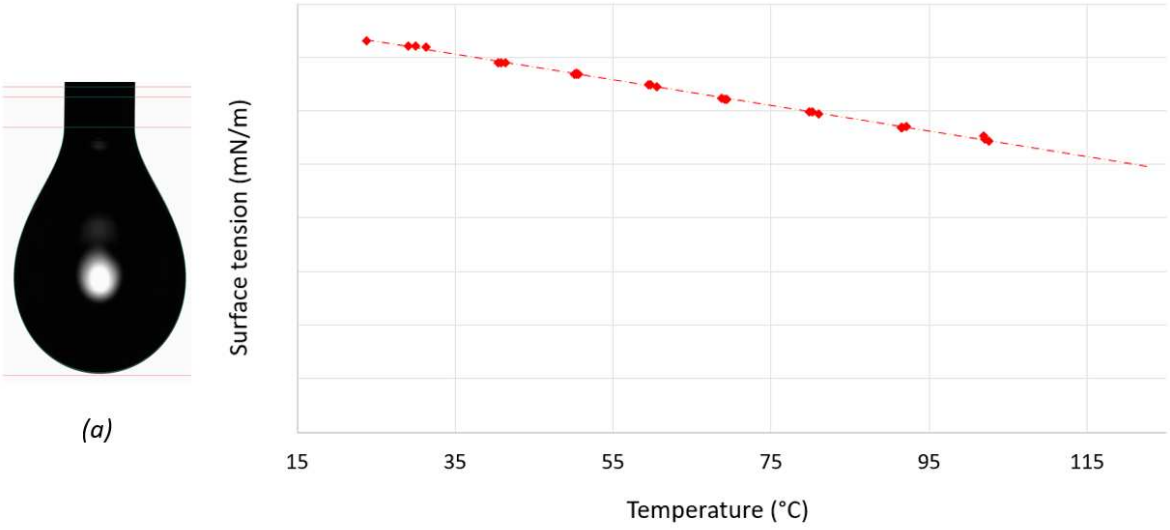

(a) *(b)*

Figure 5. (a) Pear-shaped drop to evaluate the surface tension (b) Surface tension evolution according to temperature - marks: experimental data points - dotted line: linear regression extrapolated until 120°C

Contact angles are usually measured on plane surfaces, so the method must be adapted for deposit on round wires. First, the wire has to reach the equilibrium temperature of the air of the chamber. Consequently the fixture on which it is put must insulate it from the Peltier heater. Second, a good centering of the drop on the wire has to be ensured: some trials enabled to secure this risk optically and a sensitivity evaluation revealed a low impact on the results. Finally,

  doi:10.5075/epfl-298799_978-2-9701614-0-0

the variability linked to the size of the drop was evaluated: as it was significant it has been chosen to consider only drops surfaces between 1 and 5 mm² (Figure 6 (b)) in the final results.

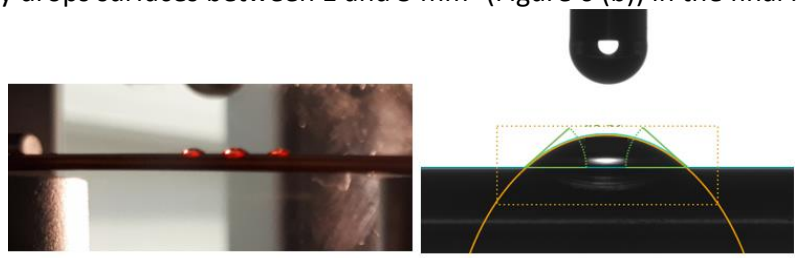

(a) (b)

Figure 6. (a) Several drops deposited on the insulated copper wire (b) Contact angle measurement, the drop surface considered is the surface inside the green contour

The obtained results are available in Figure 7. The contact angle decreases when the temperature increases: high temperatures improve the wettability.

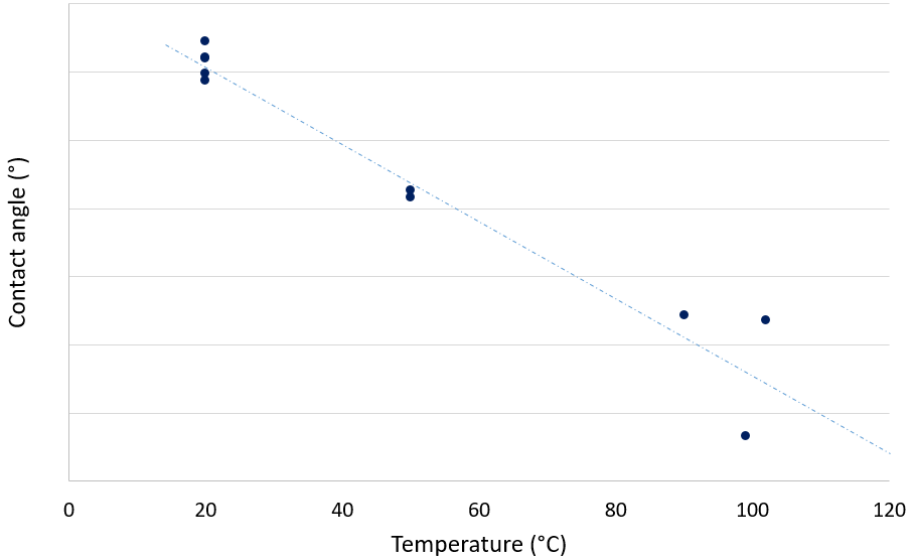

Figure 7. Contact angle resin / wire evolution according to temperature. Experimental data points and linear regression extrapolated until 120°C

3.3. Geometric parameters' definition

The porosity value ε is given in section 2.2. The longitudinal permeability K_z is defined thanks to Gebart's model in parallel wires case [3].
Finally, the analytical model requires to define an equivalent capillary radius. Several models exist for porous media. Two possibilities seemed to be applicable to this case.
A first method, presented by [4] consists in defining an equivalent section between the fibers and calculating the radius r_{cap} of a fictive capillary tube having this same section. The result would be for a hexagonal compact stacking of wires:

$$r_{\text{cap}} = \sqrt{\left(\frac{\sqrt{3}}{\pi} - \frac{1}{2}\right)}\, r_{\text{f}} \tag{3}$$

with r_{f} the fiber radius.
A second definition is described by [5], giving an expression of r_{cap} for a flow in unidirectional fibrous preforms in the direction of fibers:

$$r_{\text{cap}} = \left(\frac{\varepsilon}{1-\varepsilon}\right) r_{\text{f}} \tag{4}$$

  doi:10.5075/epfl-298799_978-2-9701614-0-0

A general form for the capillary radius would then be:

$$r_{cap} = C\, r_f \quad (5)$$

with C a constant to adjust to this case. In Eq. (3) $C \cong 0.23$ and in Eq. (4), for a fully compact staking of wires $C \cong 0.11$.

3.4. Modeling results and discussion

Using the analytical model defined by Eq. (2), the material properties characterized, and the equivalent capillary radius model with a compromise value of $C \cong 0.14$, the modeling results can be compared to experimental data in Figure 8. The relative behaviors are confirmed by the analytical models: the initial speeds of capillary rise are quite well fitting for the three temperatures. After 2000 s the equilibrium height is fitting well for 60°C and 120°C. The C parameter has been adjusted to fit better high temperatures than ambient one to be closer to the process conditions: taking a higher value would fit better the asymptote of 20°C but keeping the relative behaviors.

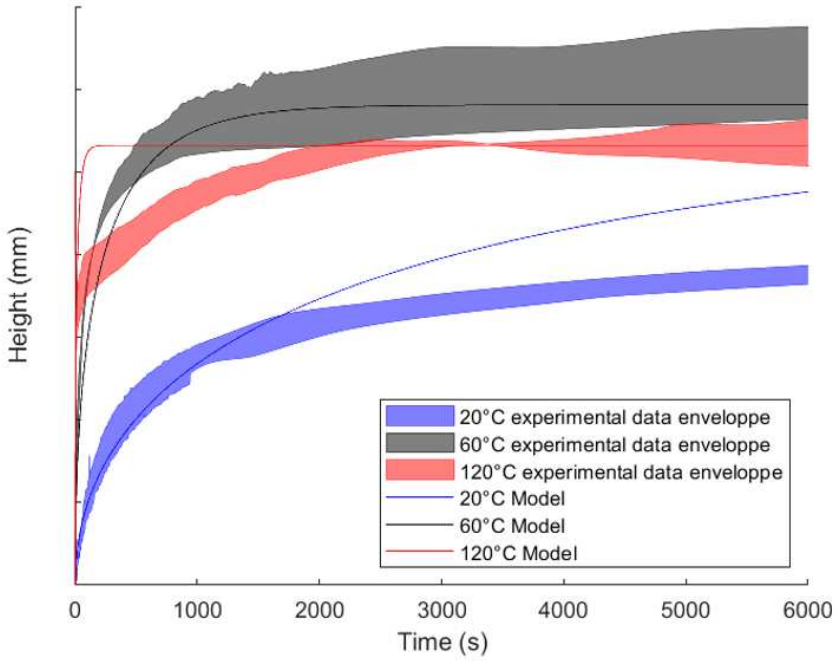

Figure 8. Comparison of experimental data and analytical model for capillary rise impregnation

However the model does not follow the singular behavior at 120°C between 30 s and 2000 s. The extrapolated material properties until 120°C may be wrong, particularly the viscosity. Indeed, the polymerization advancement has not been considered until now whereas it influences the viscosity especially when gelation starts. To do so, a chemo-rheology study must be performed and a multi-physics simulation has to be implemented.

Acknowledgements

The authors acknowledge the ANRT (Association Nationale Recherche Technologie) for funding part of this study under CIFRE program (2019/0089).

4. References

1. Fries, N., & Dreyer, M. (2008). An analytic solution of capillary rise restrained by gravity. Journal of Colloid and Interface Science, 320(1), 259–263.
2. Wu, S. (1970). Surface and interfacial tensions of polymer melts. II. Poly(methyl methacrylate), poly(n-butyl methacrylate), and polystyrene. Journal of Physical Chemistry, 74(3), 632–638.
3. Gebart, B. R. (1992). Permeability of Unidirectional Reinforcements for RTM. Journal of Composite Materials, 26(8), 1100–1133.
4. Senecot, J-m. (2002). Etude de l ' imprégnation capillaire de tissus de verre. PhD thesis, Université de Haute-Alsace, France.
5. Ahn, K., Seferis, J., & Berg, J. C. (1997). Simultaneous Measurements of Permeability and Capillary. Polymer Composites, 12(3), 146–152.

  doi:10.5075/epfl-298799_978-2-9701614-0-0

NOVEL MANUFACTURING PROCESSES AND NUMERICAL SIMULATION METHODS ENABLING THE TRANSITION FROM SPECIAL APPLICATIONS TO SERIAL PRODUCTION THROUGH THE USE OF ADDITIVE MANUFACTURED CONTINUOUS FIBRE COMPOSITE PARTS

Igor Zhilyaev[a], Stefan Grieder[a], Marco Küng[a], Michael Akermann[b], Jonas Bosshard[b], Yannick Willemin[b], Martin Eichenhofer[b], Petra Inderkum[b], Christian Brauner[a]

a: Institute of Polymer Engineering, FHNW University of Applied Sciences and Arts Northwestern Switzerland, Klosterzelgstrasse 2, 5210 Windisch, Switzerland;
igor.zhilyaev@fhnw.ch
b: 9T Labs, Badenerstrasse 790, 8048 Zürich, Switzerland;

Abstract: *High performance polymers such as PA12, PPS, PEEK and PEKK could be combined with industrial-grade carbon fibre to achieve a high fibre volume ratio of up to 60% allowing a weight reduction of over 40% compared to the classic metal construction. The production cycle of such load-bearing structural applications requires a proper consolidation process, the so-called additive fusion technology, following the printing process. By upfront digital modeling of the process, a highly optimized composite component can be produced while decreasing the expensive prototyping iterations. In this study advanced numerical methods are presented to describe the consolidation process of additive manufactured continuous composite parts. The simulation of the additive fusion step allows being first time right with the final degree of crystallization, process induced deformations and residual stresses, final engineering constants and porosity. The simulation workflow is demonstrated and validated with experimental data from the consolidation tests.*

Keywords: Fibre-reinforced composites; multi-material 3D-printing; composites consolidation; composites additive fusion simulation.

1. Introduction

Additive manufacturing is one key driver which combines digital automated manufacturing, flexibility and on demand production, enables lightweight design and as well near net shape manufacturing. For polymer materials several methods exist such as Fused Filament Fabrication (FFF), Stereolithography (SLA) and Selective Laser Melting (SLM). The disadvantage is that most of the time a pure polymer is limited to non-load bearing applications. Using classical FFF methods in combination with endless fibers, the challenge is to manufacture primary load carrying structures. Similar to classical composite manufacturing methods like Automated Fibre Placement (AFP), Automated Tape Laying (ATL) or Tailor Fibre Placement (TFP) pre-impregnated fibre reinforced materials are used in the continuous fibre additive manufacturing, mainly high-performance thermoplastic polymers like PA12, PPS, PEEK or PEKK in combination with carbon or glass fibers. The company 9T Labs has developed a unique set of methods to design the part using the fibrify® Design Suite, to print the part with the Build Module and to consolidate the part by the so-called Fusion Module (see Figure 1).

  doi:10.5075/epfl-298799_978-2-9701614-0-0

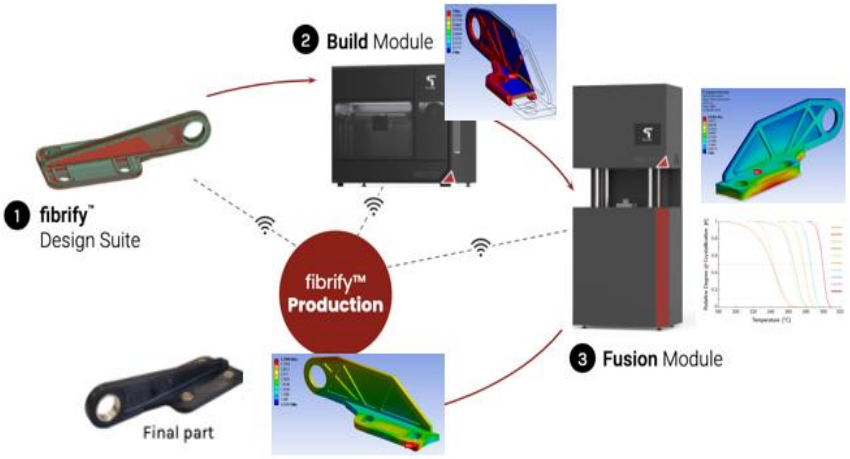

Figure 1. 9T Labs production cycle of the composite part.

However, the disadvantage of any additive manufacturing method is that if the print speed is increased the level of porosity increases and the requirements for a load bearing part are not fulfilled anymore. Therefore, a consolidation step is necessary. The following study presents a novel method to represent this fusion (consolidation) step to analyze the dependence of the final mechanical properties and residual stresses on the process conditions. The method is implemented by a sequential thermo-mechanical coupled, transient implicit analysis in Ansys R2022 based on user subroutines. In the thermal part the local temperature distribution is calculated considering temperature-dependent heat capacity, density and thermal conductivity. Using these local temperatures inside the part the phase transition behavior of the polymer from solid to molten and back to a solid is modeled considering a crystallization approach, a modified Nakamura model. In the mechanical part all engineering properties like Young`s modulus or thermal shrinkage coefficients are dependent on temperature, fibre volume content and crystallization. That allows precise simulation of the process induced deformations and residual stresses formation. The simulation workflow is presented in Figure 2.

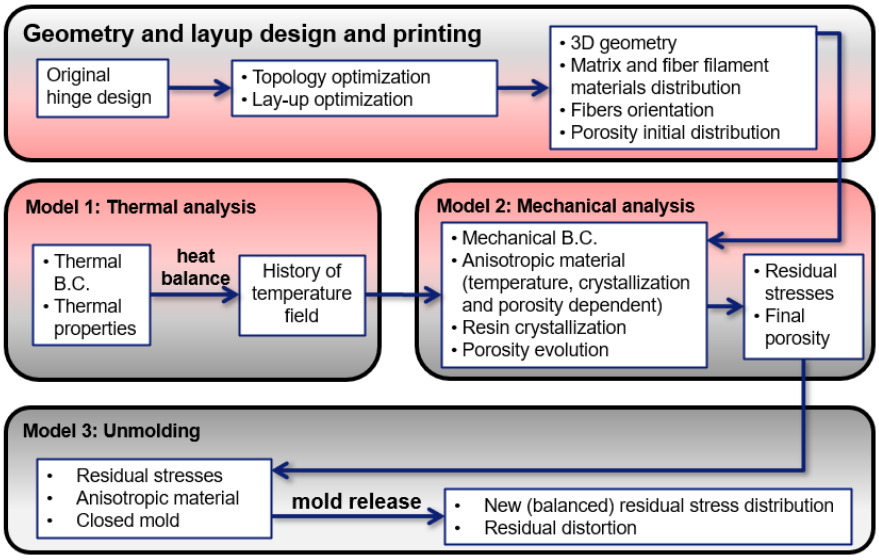

Figure 2. Simulation workflow.

In the following study the focus lies on process induced deformations validated on an aerospace part, namely the so-called helicopter hinge, a bracket to assemble the helicopter door.

  doi:10.5075/epfl-298799_978-2-9701614-0-0

2. Material characterization

The material used in this study is a carbon fibre reinforced material with a PA12 matrix provided by 9T Labs. The composite`s properties at room temperature are presented in Table 1.

Table 1: Measured composite properties for PA12-CF at room temperature.

Property at RT	Identifier and value	Unit
Young's modulus in fibre direction	$\mathrm{E}_1 = 132632$	MPa
Young's modulus transverse to the fibre direction	$\mathrm{E}_2 = 6568$	MPa
Shear modulus	$\mathrm{G}_{12} = 2043$	MPa
Poisson's ratio	$\upsilon_{12} = 0.298$	-
Coefficient of thermal expansion (CTE) in fibre direction	$\alpha_1 = -1.609 \cdot 10^{-6}$	K^{-1}
CTE transverse to fibre direction	$\alpha_2 = 67.417 \cdot 10^{-6}$	K^{-1}
CTE in out of plane direction	$\alpha_3 = 90.257 \cdot 10^{-6}$	K^{-1}
Fibre relative volume ratio	$\varphi_0 = 0.573$	-

The composite part consists of two individual components, the matrix and the fibres. The properties for the matrix and the fibre are presented in Table 2 and Table 3, respectively.

Table 2: Measured matrix properties for PA12 at room temperature.

Property	Identifier and value	Unit
Young's modulus	$\mathrm{E}_\mathrm{m} = 1372$	MPa
Poisson's ratio	$\upsilon_\mathrm{m} = 0.43$	-
CTE	$\alpha_\mathrm{m} = 136.833 \cdot 10^{-6}$	K^{-1}
Glass transition temperature	$\mathrm{T}_\mathrm{g} = 93.923$	°C
Melting temperature	$\mathrm{T}_\mathrm{m} = 179.38$	°C

Table 3: Fibre properties at room temperature.

Property	Identifier and value	Unit
Young's modulus in fibre direction	$\mathrm{E}_{\mathrm{f},1} = 231000$	MPa
Young's modulus transverse to fibre direction	$\mathrm{E}_{\mathrm{f},2} = 28000$	MPa
Shear modulus	$\mathrm{G}_{\mathrm{f},12} = 28600$	MPa
Poisson's ratio	$\upsilon_\mathrm{f} = 0.23$	-
CTE in fibre direction	$\alpha_{\mathrm{f},1} = -2.23 \cdot 10^{-6}$	K^{-1}
CTE transverse to fibre direction	$\alpha_{\mathrm{f},2} = 15.7 \cdot 10^{-6}$	K^{-1}

2.1 Characterization of the crystallization and melting behavior

A crystallization process that occurs during a transition from a liquid into a solid state can be described using generalized empirical rate equations or mechanistic models. Mechanistic models describe the crystallization process at an atomic scale by examining the growing

  doi:10.5075/epfl-298799_978-2-9701614-0-0

macromolecules. The empirical rate approach derives a phenomenological mathematical description of the process from the results of experimental studies using Differential Scanning Calorimetry (DSC). Using this method, the endothermic heat flow is measured and interpreted with respect to the assumption that the heat flow is proportional to the relative crystallization. The relative crystallization $\theta_{rel}(t)$ is a conversion factor varying from 0 (no crystallisation network) to 1 (maximum relative degree of crystallization). Based on the DSC measurements, crystallization kinetics can be derived to predict the formation and growth of the relative crystallization parameter as a function of time and temperature for various experimental conditions.

To determine crystallization kinetic parameters to fit all situations during cooling, DSC experiments were performed. During crystallization, the fibres serve as initial nuclei and thereby influence the formation of the crystalline network. The material was positioned in the DSC oven and heated to 70 °C above melting temperature to a final temperature of 250 °C, which was realized by a heating rate of 10 °C/min. The sample was held for 5 minutes at isothermal conditions to ensure that it was completely melted. Afterwards, the sample was cooled down at various rates: 1, 5, 10, 20 and 50 °C/min. The measured data and the crystallization kinetics fit are shown in Figure 3.

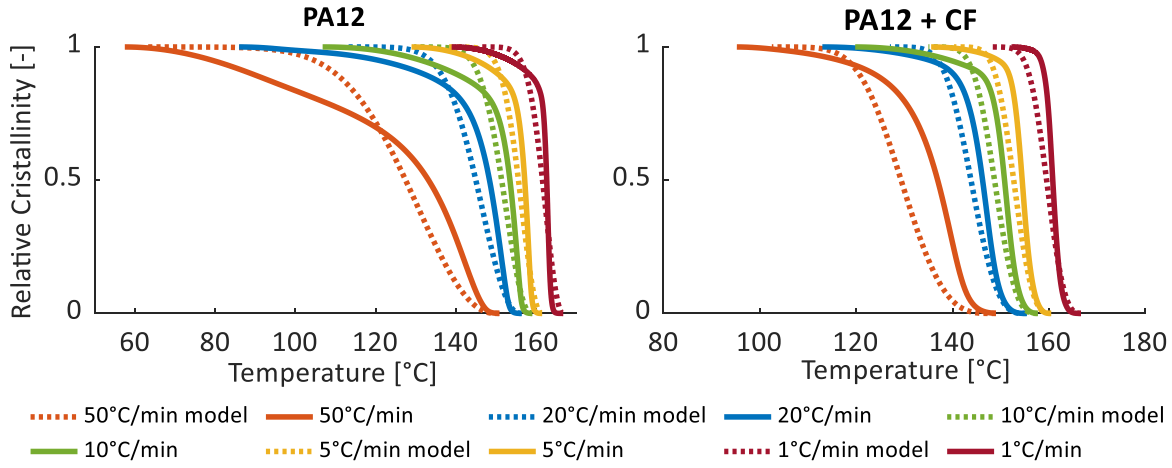

Figure 3. Diagram of relative crystallization according to different constant cooling rates.

The crystallization kinetics during the cooling phase is described by the Nakamura equation [2]:

$$\frac{\partial\theta}{\partial t} = n \cdot K(T) \cdot (1-\theta)[-\ln(1-\theta)]^{\frac{n-1}{n}} \quad (1)$$

Where T is temperature, θ is the crystallization degree. $K(T)$ is the Avrami coefficient:

$$K(T) = \left(\frac{\ln(2)}{{t_{1/2}}^n}\right)^{\frac{1}{n}} \quad (2)$$

Where $t_{1/2}$ is half-crystallization time:

$$t_{1/2} = a \cdot \left(\frac{\partial T}{\partial t}\right)^b + c \quad (3)$$

The parameters n, a, b, c are defined on the basis of the experimental data by fitting the crystallization vs temperature dependencies for the various cooling rates.

  doi:10.5075/epfl-298799_978-2-9701614-0-0

Table 4: Equation parameters for the crystallization kinetics.

Material	Parameter	Value [-]
PA12	a	3.63
	b	-1.31
	c	0.37
	n	2.00
PA12-CF	a	5.50
	b	-1.02
	c	0.18
	n	2.85

The initial material state is solid, therefore melting behavior is introduced as material phase change from 1 (solid state) to 0 (molten state) according to [3]:

$$\frac{\partial\theta}{\partial T} = k_{mb} \cdot e^{-k_{mb}(T-T_m)}\left[1 + (d-1)e^{-k_{mb}(T-T_m)}\right]^{\frac{d}{1-d}} \quad (4)$$

Where $k_{mb} = 0.55$ and $d = 5.0$ are model parameters tuned to fit to DSC measurement. The same melting model parameters are used for both PA12 and PA12-CF materials.

2.2 Temperature dependent mechanical stiffness

For the neat PA12 polymer the Dynamic Mechanical Analysis (DMA) was performed to measure the dependence of the elastic modulus in solid state on temperature. The obtained data was processed through the polynomial curve fitting with a 10th degree polynomial dependence on the temperature. Measured data and corresponding fit are shown in Figure 4.

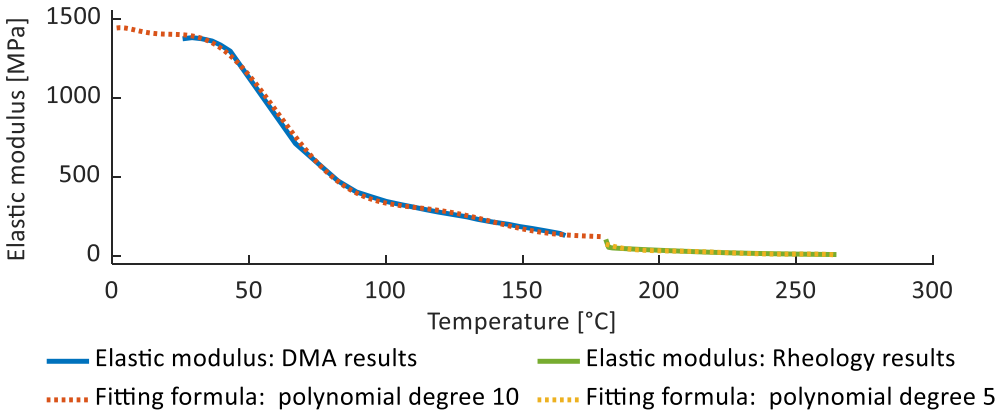

Figure 4. DMA and rheology analysis results and corresponding fits.

The matrix elastic modulus E_m depends on the temperature according to DMA experiment, on the crystallization degree and porosity ϕ according to the following [4, 5]:

$$E_m = \begin{cases} E_{m,s} \cdot 2 \cdot (\theta - 0.5) \cdot (1-\phi)^S + E_{m,l} \cdot 2 \cdot (1-\theta) \cdot (1-\phi)^M, \theta \geq 0.5 \\ E_{m,l} \cdot 2 \cdot (1-\theta) \cdot (1-\phi)^M, \theta < 0.5 \end{cases} \quad (5)$$

Here $E_{m,l}$ and $E_{m,s}$ are matrix elastic moduli in the molten and solid phase, respectively; $S = 2$ and $M = 5$ are model parameters; $\theta = 0.5$ is the borderline between solid and molten state [6].

  doi:10.5075/epfl-298799_978-2-9701614-0-0

Porosity is evaluated as a function of bulk strain ε_{bulk} [7]:

$$\phi = \phi_0 + \varepsilon_{bulk} \tag{6}$$

Where ϕ_0 is initial porosity, which is equal to 10% for PA12 and 18% for PA12-CF according to the Computer Tomography (CT) analysis of the unconsolidated composite part.

2.3 Process dependent composite properties

Fiber volume ratio depends linearly on porosity using the following assumption:

$$\varphi = \varphi_0(1 - \phi) \tag{7}$$

Where φ_0 is the measured fiber volume ratio, which corresponds to the fully consolidated PA12-CF. Composite material transversal isotropic mechanical properties are evaluated according to the mixing rules. Elastic modulus in the fiber direction is defined as follows [8]:

$$E_1 = E_{f,1}\varphi + E_m(1 - \varphi) \tag{8}$$

The elastic modulus in the transverse and thickness direction is defined as follows [9]:

$$E_2 = E_3 = E_m \frac{1+3.3\varphi(E_{f,2}-E_m)/(E_{f,2}+3.3E_m)}{1-(E_{f,2}-E_m)/(E_{f,2}+3.3E_m)\varphi} \tag{9}$$

Poisson`s ratio is defined according to [8]:

$$v_{12} = v_{13} = v_f\varphi + v_m(1 - \varphi) \tag{10}$$

$$v_{23} = v_f\varphi + v_m(1 - \varphi)\frac{\left(1 + v_m - v_{12}\,E_m/E_{f,2}\right)}{\left(1 - {v_m}^2 + v_m v_{12}\,E_m/E_{f,2}\right)} \tag{11}$$

Shear moduli are defined as follows [10, 11]:

$$G_m = \frac{E_m}{2(1 + v_m)} \tag{12}$$

$$G_{12} = G_{13} = G_m \frac{1 + 1.675 \cdot \varphi \cdot \frac{G_{f,12} - G_m}{G_{f,12} + 1.675 \cdot G_m}}{1 - \varphi \cdot \frac{G_{f,2} - G_m}{G_{f,12} + 1.675 \cdot G_m}} \tag{13}$$

$$G_{23} = \frac{E_2}{2(1 + v_{23})} \tag{14}$$

The presented mixing rules (7)-(14) are hold for the PA12-CF composite filament in the solid material state, while in the molten state the composite material is considered as isotropic with material properties corresponding to the pure PA12 material.

Coefficients of thermal expansion are defined according to the following equations [8]:

$$\alpha_1 = S_1 \frac{\alpha_m \cdot E_m \cdot (1 - \varphi) + \alpha_{f,1} \cdot E_{f,1} \cdot \varphi}{E_m \cdot (1 - \varphi) + E_{f,1} \cdot \varphi} \tag{15}$$

  doi:10.5075/epfl-298799_978-2-9701614-0-0

$$\alpha_2 = S_2\left(\varphi \cdot \alpha_{f,2} + (1-\varphi)\cdot \alpha_m\right) \quad (16)$$

$$\alpha_3 = S_3\alpha_2 \quad (17)$$

$$\alpha_m = \begin{cases} 1.37\cdot 10^{-4}, T < T_g \\ 2.5\cdot 10^{-4}, T \geq T_g \end{cases}; \quad (18)$$

$$S_1 = \begin{cases} 1, T < T_g \\ 1.16, T \geq T_g \end{cases};\ S_2 = \begin{cases} 1, T < T_g \\ 2.74, T \geq T_g \end{cases};\ S_3 = \begin{cases} 1.34, T < T_g \\ 2.74, T \geq T_g \end{cases} \quad (19)$$

Here α_m and $\alpha_{f,1}$ $\alpha_{f,2}$ are coefficients of thermal expansion for matrix and fibre (in longitudinal and transverse direction). The CTE of PA12 α_m is modified above T_g according to the performed Thermomechanical Analysis (TMA). The coefficients $S_{1,2,3}$ are implemented into the material model according to the measured difference between the expansion of the composite in transverse and thickness directions and observed increase of the composite`s CTE above T_g. All CTE coefficients are equal to 0 in the molten material state.

The composite material shrinkage is defined according to the following mixing rules [4]:

$$\beta_1 = (1-\varphi)\cdot E_m \cdot \beta \,/\, \left(\varphi \cdot E_{f,1} + (1-\varphi)E_m\right) \quad (20)$$

$$\beta_2 = \beta_3 = (1-\varphi)\cdot(1-v_m)\cdot\beta - \left(v_{13}\cdot\varphi + v_m\cdot(1-\varphi)\right)\left(\frac{\beta}{\varphi\cdot E_{f,1}+(1-\varphi)E_m}\right) \quad (21)$$

Here $\beta = 3\%$ is the crystallization shrinkage of PA12.

3. Finite-element model application and solution validation

3.1 Application setup

Hinge sub-parts are printed separately (see Figure 5a), then combined and inserted into the mold. All the sub-parts consist of a PA12 matrix reinforced by the PA12-CF filaments. The location and orientation of the reinforcing plies are designed via the composite design tool fibrify® (see Figure 5b). The average temperature on the heating elements and the pressure applied in the experiment are presented in Figure 5c.

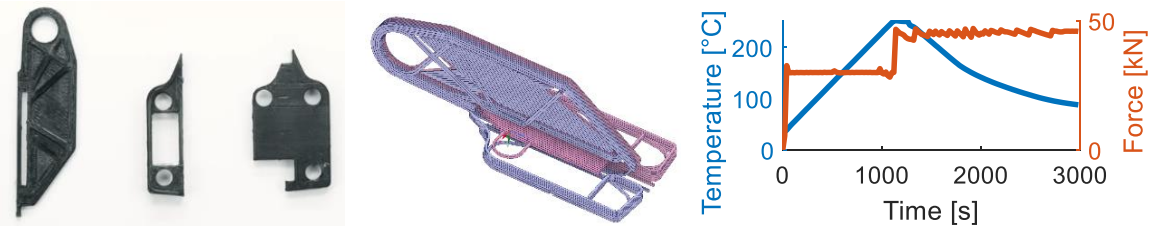

a) *b)* *c)*

Figure 5. a) 3D-printed hinge sub-parts: vertical plate (left sub-part) and base plate (central and right sub-parts); b) Composite layup; c) Temperature and pressure applied in the experiment.

The finite element thermal model considers three phases of the consolidation process for the whole mold and composite part inside: heating, molten and cooling. Heating is set by the PID controllers attached to the heating and cooling channels in the mold, which provides temperature regime corresponding to the experimental setup. A free convection of the hinge with air is simulated after 3000 seconds for the hinge released from the mold. Boundary

  doi:10.5075/epfl-298799_978-2-9701614-0-0

conditions for the thermal model are convection of all the outer mold`s surfaces with the surrounding air as well as radiosity of the outer walls.

The mechanical model resolves the problem for the composite part only. In the presented approach a sequentially coupled thermal-stress analysis is performed, in which the temperature field does not depend on the stress field. Boundary conditions are shown in Figure 6. Release from the mold is simulated after 3000 seconds by removing all the boundary constraints and forces applied and providing a 3-point fixation of the hinge.

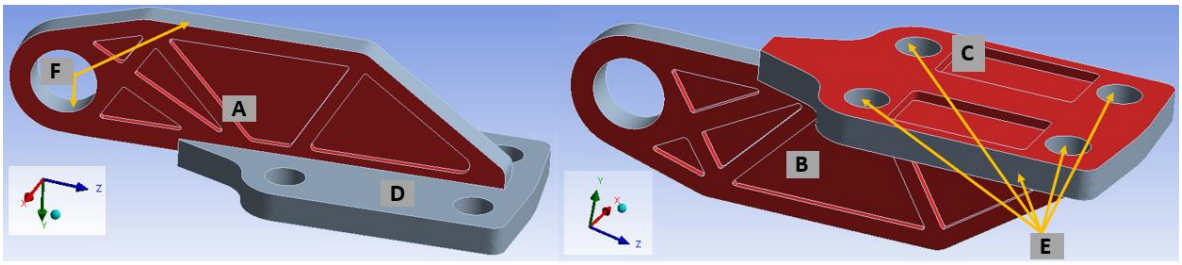

Figure 6. Boundary conditions for the mechanical problem: Pressure is applied to the sets of surfaces A, B and C (marked with red); Surfaces E have free displacement only in y-direction, D and F have free displacement only in x-direction.

3.2 Numerical solution

In Figure 7 the solution for the temperature and crystallization inside the hinge is presented.

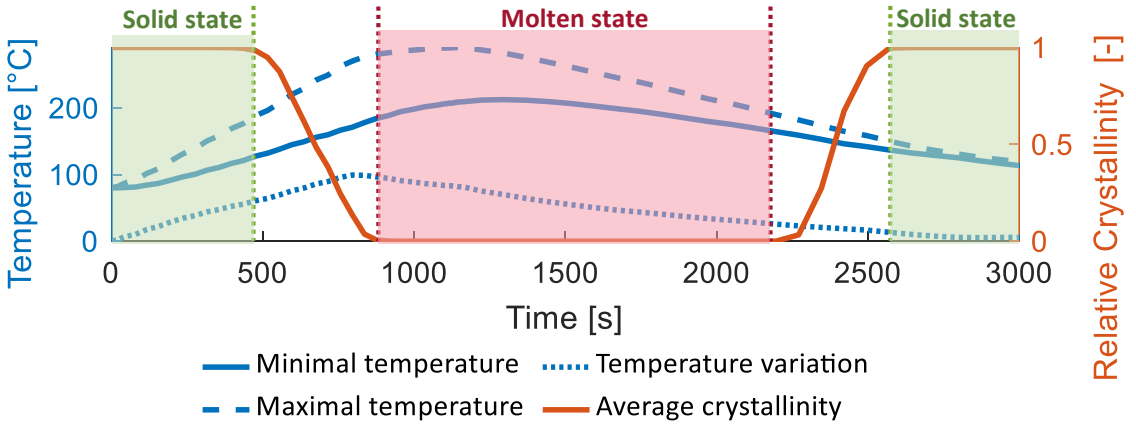

Figure 7. Minimal, maximal, variation of the temperature and average crystallization in the hinge

PA12 and PA12-CF elastic moduli are presented in Figure 8.

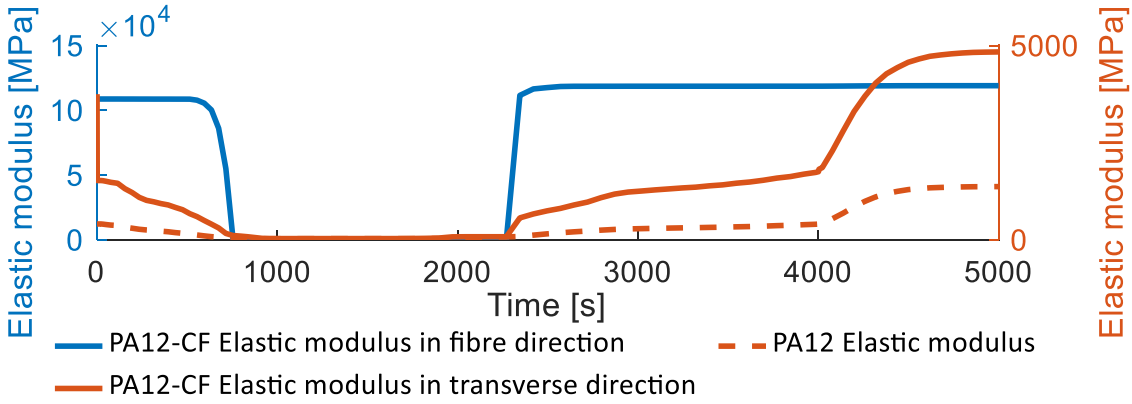

Figure 8. PA12 matrix elastic modulus and PA12-CF anisotropic elastic modulus.

  doi:10.5075/epfl-298799_978-2-9701614-0-0

The directional stresses in PA12-CF element are presented in Figure 9. Stresses are relieved at 3000 seconds due to the release from the mold.

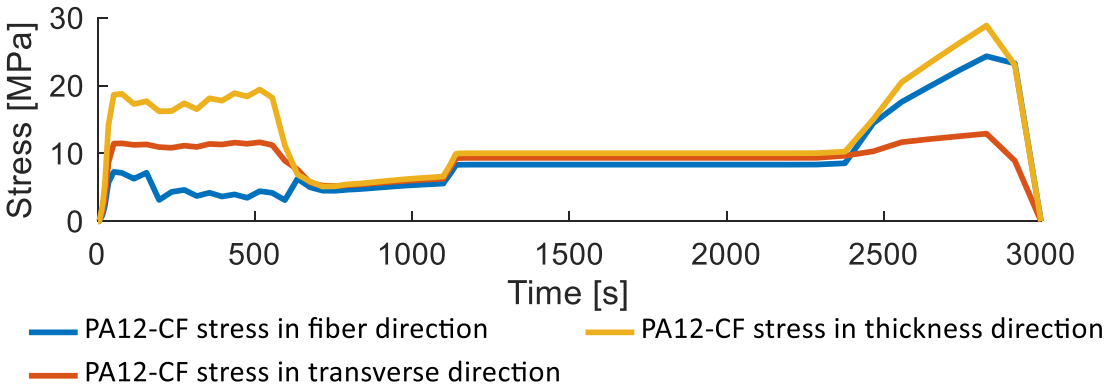

Figure 9. PA12-CF stress in fiber, transverse and thickness direction.

Final part`s total deformations are presented in Figure 10, black contour lines show the original shape of the hinge. Figure 11 describes warpage measurement method used for the model validation: deformations were measured using CT-data in a set of representative points on the base plate. Table 5 provides the comparison of the simulated and experimentally observed process induced deformations.

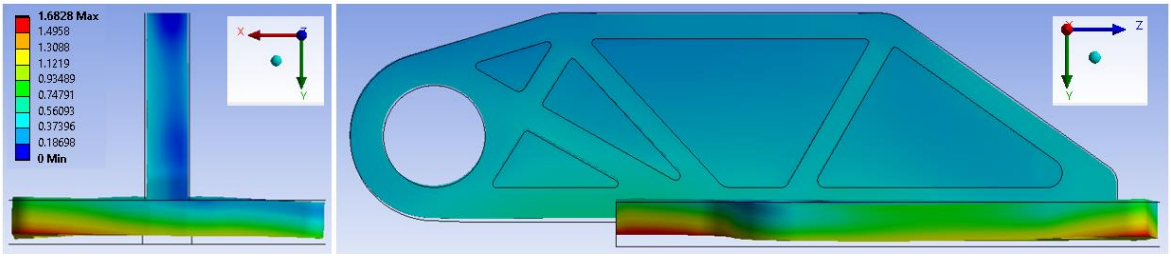

Figure 10. Simulated final process induced deformations in mm.

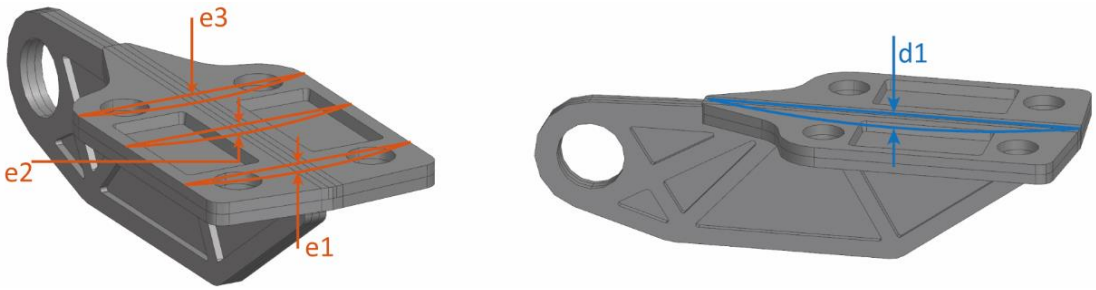

Figure 11. Warpage measurement description.

Table 5: Measured and simulated deformations.

Reference deformation / thickness	Initial	Experiment	Model
d1, mm	0	0.33	0.28
e1, e2, e3, mm	0, 0, 0	-0.53, 0.21, 0.44	0.09, 0.52, 0.69
Average final thickness of base plate, mm	6.15	4.82	4.89
Average final thickness of vertical plate, mm	6.23	5.28	5.41

Proposed model allows to predict final compaction of the part with high accuracy. Predicted warpage shows the same trend as the observed one. However, the absolute values are significantly different. This difference could be caused by multiple reasons such as inaccuracy of the thermal simulation, limitations of the assumptions made or the mixing rules, imprecision of the initial data provided to the model or the measurements of the consolidated hinge.

Conclusions

The proposed finite-element model allows to predict the final process induced deformations of the consolidated part considering orthotropic composite properties depending on temperature and crystallization. The presented approach provides digital modeling of the consolidation process decreasing the expensive prototyping iterations. The highly accurate 3D-printing and post-printing consolidation together with ANSYS` finite-element model and fibre filament layup design enables the transition from special applications to serial production of additive manufactured continuous fibre composite parts.

Acknowledgements

This study was supported by the national funded project Addfu [grant number 38729.1 IP-ENG], which was supported by Innosuisse, Switzerland.

References

1. Eichenhofer M., Wong J., Ermanni P. Continuous lattice fabrication of ultra-lightweight composite structures. Additive Manufacturing, 2017; 18: 48-57
2. Nakamura K. Some aspects of nonisothermal crystallization of polymers I – relationship between crystallization temperature, crystallinity, and cooling conditions. J Appl Polym Sci, 1972; 16: 1077–1091.
3. Greco A., Maffezzoli A. Statistical and kinetic approaches for linear low-density polyethylene melting modeling. J. Appl. Polym. Sci., 2003; 89: 289–295
4. Wijskamp S. Shape distortion in composite forming. PhD Thesis, Enschede, Netherlands, University of Twente, 2005
5. Wang X., Zhao L., Fuh J., Lee H. Effect of Porosity on Mechanical Properties of 3D-Printed Polymers: Experiments and Micromechanical Modeling Based on X-Ray Computed Tomography Analysis. Polymers, 2019; 11(7):1154
6. Brauner C., Peters C., Brandwein F., Herrmann A. Analysis of process-induced deformations in thermoplastic composite materials. Journal of Composite Materials, 2014; 48:2779-2791
7. Barari B., Simacek P., Yarlagadda S., Crane R., Prediction of process-induced void formation in anisotropic fiber-reinforced autoclave composite parts. International Journal of Material Forming, 2020; 13:143–158
8. Schürmann H. Konstruieren mit Faser-Kunststoff-Verbunden, Springer, 2007
9. Osoka E., Onukwuli O. A Modified Halpin-Tsai Model for Estimating the Modulus of Natural Fiber Reinforced Composites. International Journal of Engineering Science Invention, 2018; 7:63-70
10. Younes R., Hallal A., Fardoun F., Chehade F., Comparative Review Study on Elastic Properties Modeling for Unidirectional Composite Material. Composites and Their Properties, 2012
11. Halpin J., Kardos J. The Halpin-Tsai equations: A review. Polymer Engineering and Science, 1976; 16: 344-352

  doi:10.5075/epfl-298799_978-2-9701614-0-0

ARTIFICIAL NEURAL NETWORK-BASED CHARACTERISATION OF THE BOND BETWEEN FRP BAR AND CONCRETE UNDER ENVIRONMENTAL CONDITIONS

Keyvan, Aghabalaei Baghaei[a], S. Ali, Hadigheh[a]

a: School of Civil Engineering, Faculty of Engineering, The University of Sydney, Sydney, New South Wales 2006, Australia – keyvan.baghaei@sydney.edu.au

Abstract: *The durability of the interfacial bond between fibre-reinforced polymer (FRP) bar and concrete is a determining factor in the long-term performance of the FRP-reinforced concrete beams. It has experimentally been shown in previous durability studies that exposure to chemical conditions, such as acidic, alkaline, and saline environments, can degrade the bond performance. Hence, it is necessary to quantify the bond strength for the long-term performance study of FRP-reinforced concrete members. In the current paper, a data-driven machine learning-based approach was developed based on 320 observations of bond strength tests performed under aggressive environment. Using Bayesian optimisation, an artificial neural network (ANN) model was created to examine the strength of the bond between FRP bar and concrete, coupled with environmental durability. As a result of this study, it has been found that machine learning can accurately and efficiently predict the long-term performance of composite structures that are exposed to different environmental conditions.*

Keywords: Fibre-reinforced polymer (FRP) bar; Long-term durability prediction; Bond strength; Artificial neural network (ANN); *Bayesian optimisation*

1. Introduction

FRP bars are increasingly being explored as a replacement for conventional steel reinforcement in concrete structures due to their properties, notably strong resistance to corrosion and harsh environmental conditions [1]. The integrity of the FRP-concrete bond is the key factor determining the efficiency of these bars for use in concrete [2]. The long-term performance of the bond depends on different parameters, varying from the geometrical and mechanical characteristics of FRP and concrete to the environmental conditions affecting the FRP-reinforced concrete members [3]. International design guidelines along with recent scholarly works have provided equations of bond strength by including some of the mentioned parameters into their formulations [1, 4, 5]. However, a practical equation which accounts for the environmental impact on bond strength between bar and concrete is still missing in the literature.

Recently, Aghabalaei Baghaei and Hadigheh [6], [7] implemented a data-centric approach to model the bond degradation of FRP-to-concrete connections. Their work demonstrated the capability of machine learning methods in developing accurate models to predict the long-term performance of the bond under moisture conditions.

The present study addresses the application of artificial neural networks (ANNs) in modeling the bond degradation under environmental conditions. A dataset of 320 test results from 13 references is compiled and used to develop the ANN prediction model. Bayesian optimisation

  doi:10.5075/epfl-298799_978-2-9701614-0-0

method is implemented to search for the ANN architecture with best prediction performance. A practical equation is also proposed based on the ANN algorithm to predict the bond strength under environmental conditions. The impact of environmental parameters on the bond strength is also studied by the developed ANN model. It is demonstrated that the proposed data-driven machine learning-based model can accurately predict the bond strength taking into account the geometrical and mechanical properties as well as the aggressive conditioning regimes.

2. Artificial neural network model development

Despite classical machine learning, ANN has become a most widely used model in theory and practice owing to its capability to manage big-data analytics [8]. Because of this, it can represent both complex and simple models, and its calculation cost can be adjusted to meet the problem requirements [9]. ANN can be interpreted as a mathematical representation of the behaviour of organic neurons. Figure 1a and Figure 1b depict the mathematical implementation and structure of ANN. An architecture of ANN is composed of networks of neurons working interactively to make predictions about a real phenomenon. This is possible through feed-forward (FF) and backpropagation (BP) iterations in the network. During FF, the computation of each neuron is passed through layers to make the prediction. The prediction error is then deployed during BP to update the parameters and minimise the cost function. The process is iterated until a desired minimum error is obtained.

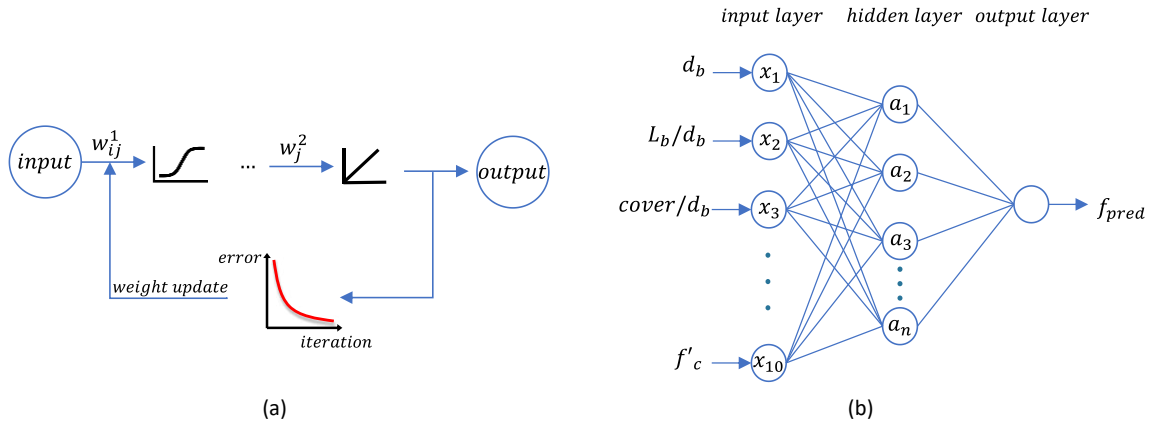

Figure 1. (a) ANN mathematical model; (b) ANN architecture

In order to deploy ANN in this study, data was cross-validated to confirm the model's generalisation ability to new data. Moreover, to automate the ANN model selection, Bayesian optimisaiton was implemented together with the 10-fold cross validation (CV) technique, and the accuracy of the model was validated by the out-of-fold predictions. Figure 2 shows the framework for the development and evaluation of ANN. It is seen that 10-fold CV is integrated with Bayesian optimisation to search for an architecture with minimum prediction error. In the model evaluation, the accuracy of the selected ANN is validated with experimental values. The impact of environmental agents on the bond was also evaluated under conditioning regimes.

  doi:10.5075/epfl-298799_978-2-9701614-0-0

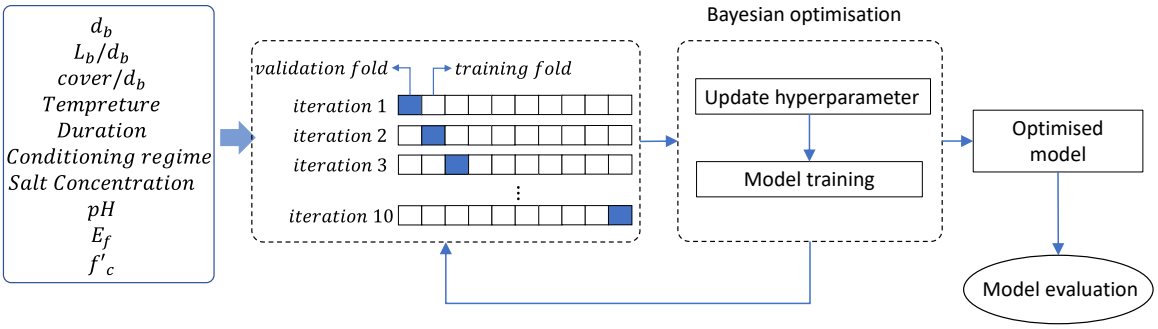

Figure 2. Flowchart of ANN optimisation and development

Figure 2 also shows the list of input variables in the dataset, which were obtained from pull-out tests on the FRP-reinforced concrete samples under environmental conditions. In this figure, d_b is the bar diameter; L_b denotes bar embedment length; $cover$ implies the concrete cover above the bar; E_f and f'_c represent the FRP elastic modulus and concrete compressive strength, respectively. The schematic arrangement of the test setup is depicted in Figure 3. During the test, the conditioned sample is placed in the test rig while the tensile force (f) is applied to the end of the bar until the bond failure occurs. The expected failure modes are normally shear or concrete splitting.

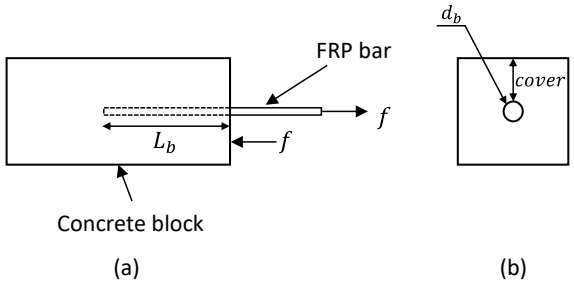

Figure 3. Pull-out test set up: (a) side view (b) front view

The frequency and range of the data for each input parameter are shown in Figure 4. It is seen that the scale and distribution of data are different between the parameters. Since during the training process of ANN, the weights are updated, it is possible that the features with smaller scales attain lower weight values, thus undermining their importance while making predictions. Therefore, it is common to standardise data by removing the mean and scaling it to a unit variance. Eq. (1) was used to scale the data before training the machine learning model.

$$x_i' = \frac{x_i - \mu_i}{\sigma_i} \tag{1}$$

where, x'_i is the scaled variable; μ_i is the mean, and σ_i denotes the standard deviation of data for each input parameter.

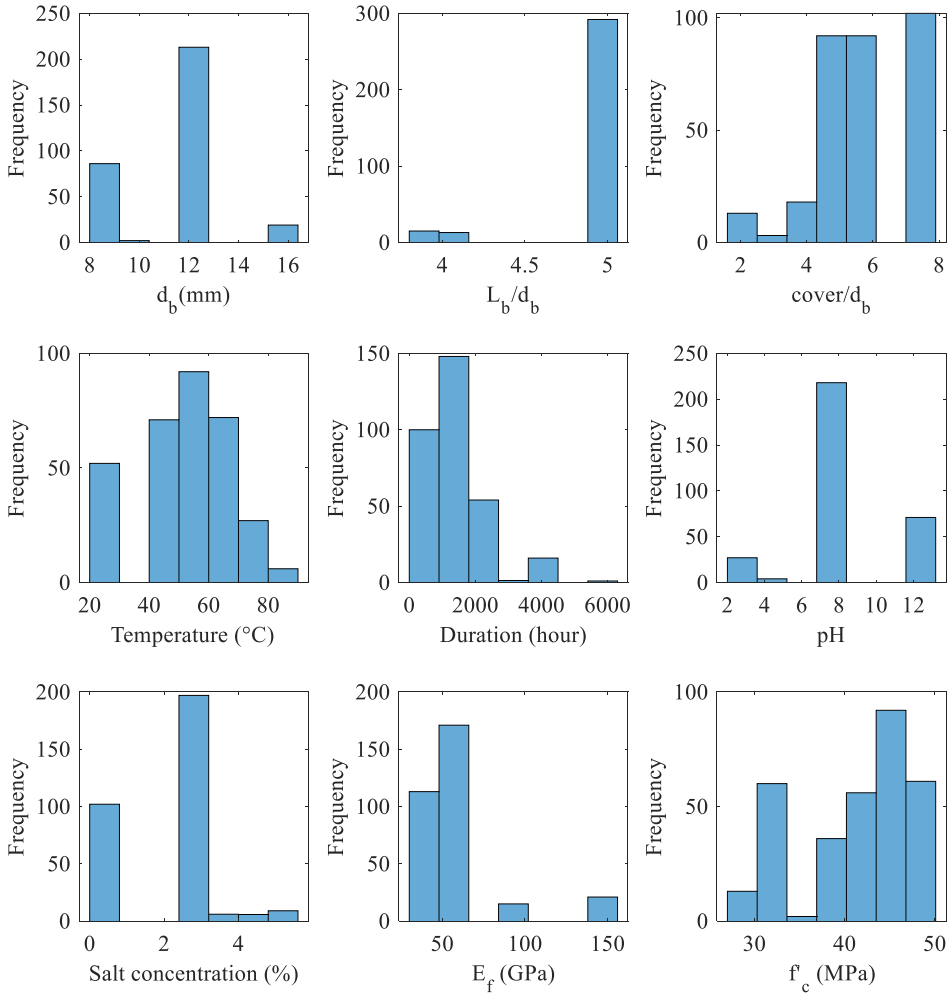

Figure 4. Distribution of input parameters

3. Analysis of Results

A regression analysis by ANN was performed in this paper to make bond strength predictions. Due to the importance of hyperparameters in developing accurate models, their values were tuned by Bayesian optimisation. Table 1 presents the list and range of hyperparameters together with their optimised values. In this table, activation function indicates the shape of the function used to transform the weighted sum of the input to an output during FF; λ denotes the generalisation term used in the loss function equation; and weight initializer describes the functions used to sample the weights from either a uniform or normal distribution by Glorot or He functions, respectively[10, 11].

The tuning process of the hyperparameters is also shown in Figure 5a. Each point in this figure shows the minimum of the estimated objective function for the ANN model after it has been trained using the hyperparameters discovered in each iteration. The best point in this figure implies the set of hyperparameters for which the minimum loss is derived. Based on this figure, a minimum error of 3.36 was obtained at iteration 32 during the hyperparameter tuning. Figure 5b shows the learning curve of the ANN model during training. This figure shows a steep

decrease in the error within 100 learning iterations. It is also seen that there is a constant change in training loss after 400 iterations, indicating that the model was able to converge to a minimum error value while fitting well to the data.

Table 1. List of hyperparameters with selected values for ANN

Hyperparameter	Search range	Optimal value
Number of layers	1 – 3	1
Layer size	1 – 300	8
Activation function	relu, tanh, sigmoid	tanh
λ	3.12e(-8) – 312.5	0.0185
Weight initialiser	Glorot, He	Glorot

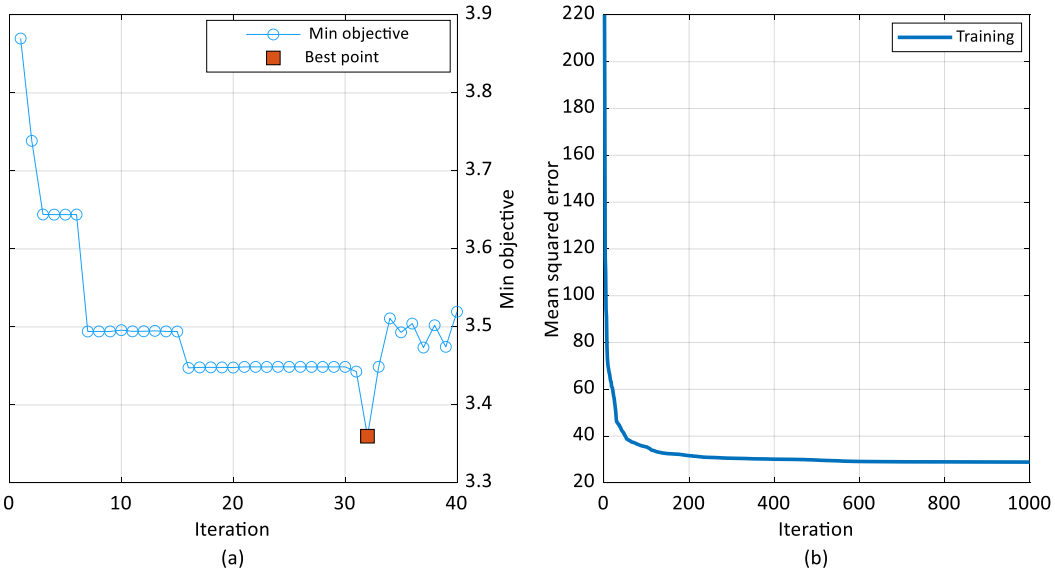

Figure 5. (a) Bayesian optimisation process; (b) Learning curve of training process

Furthermore, the out-of-fold prediction accuracy of the ANN model was evaluated by root mean square error (RMSE) and Pearson correlation coefficient (R) evaluation criteria. These metrices are written in Eqs. (2) and

(3) as:

$$RMSE = \sqrt{\frac{1}{N}\sum_{i=1}^{n}(f_i - (f_{pred})_i)^2} \tag{2}$$

$$R = \frac{\sum_{i=1}^{n}(f_i - \bar{f})((f_{pred})_i - \bar{f}_{pred})}{\sqrt{\sum_{i=1}^{n}(f_i - \bar{f})^2 \sum_{i=1}^{n}((f_{pred})_i - \bar{f}_{pred})^2}} \tag{3}$$

where f, f_{pred} and $\bar{f}$ denote the experimental, the prediction, and the mean value of bond strength in the dataset. Table 2 shows the mean values of the metrices for training and validation folds. It is seen that there is a low error and a high correlation between the predicted and real bond strength values. This demonstrates that ANN is capable to accurately predict bond strength under exposure to environmental conditions based on the geometrical, mechanical, and

  doi:10.5075/epfl-298799_978-2-9701614-0-0 published under CC BY-NC 4.0 license

environmental parameters. In addition, to visualise the accuracy of the model, the correlation between the experimental and out-of-fold predictions was depicted in Figure 6. This figure compares the experimental values with the predicted ones. It is seen that the ANN predictions of unseen data are located almost within $\pm 30\%$ of the real values.

Table 2. Mean evaluation criteria of training and validation folds

Model	Training fold		Validation fold	
	RMSE	R	RMSE	R
ANN	4.538	0.937	4.498	0.935

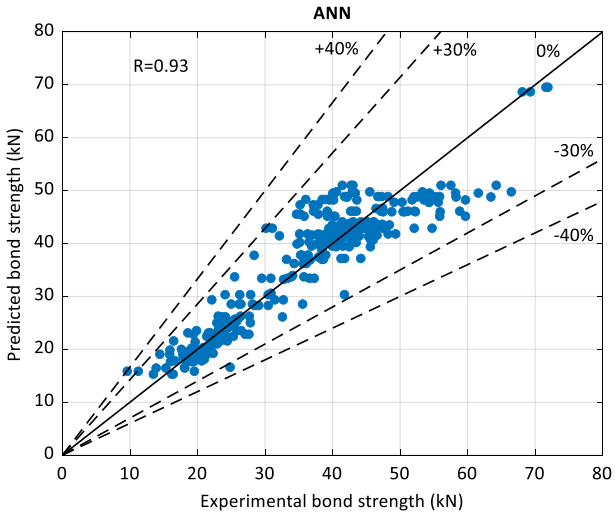

Figure 6. Experimental versus predicted bond strength

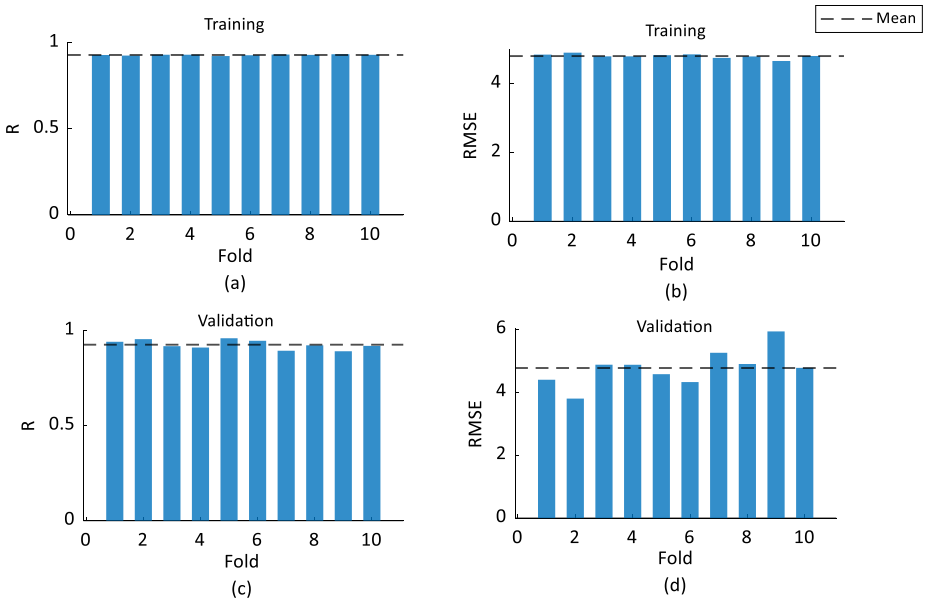

Figure 7. 10-fold CV measurements: (a, c) R; (b, d) RMSE

Figure 7 includes the statistical measures of the ANN model. The RMSE and R values for the training and validation folds together with their corresponding mean values are depicted in this figure. The agreement of the values between the training and validation folds implies that the model was able to accurately perform out-of-fold-prediction without overfitting to the training set.

A practical equation was also extracted based on the mathematical expression of the ANN algorithm with one hidden layer. Eq. (4) introduces the output of the trained ANN, which is a function of weight and bias values obtained at the $1000th$ step of learning curve.

$$f_{pred} = \sum_{j=1}^{j=8} W_j^2 \left(tanh\left(\sum_{j=1}^{j=8} \sum_{i=1}^{i=12} W_{ij}^1 x_i + b_j^1 \right) \right) + b^2 \quad (4)$$

In Eq. (4), i and j are indices for the input variable and the neuron in the hidden layer; W^1 and W^2 are the weight matrices of the first and second layers, respectively. Similarly, b^1 and b^2 denote the bias vectors for the input and hidden layers, respectively. The weight and bias values for the first and second layers are shown in Table 3 and Table 4, respectively. Therefore, by substituting these values into the ANN formulation in Eq. (4), the bond strength can be predicted directly.

Table 3. Weight and bias values of the first layer

N	W^1												b^1
	Input variable												
	d_b	$\frac{L_b}{d_b}$	$\frac{cover}{d_b}$	T^a	D^b	AC^c	AL^d	SA^e	pH	$Salt\ Conc.$	E_f	f'_c	
	X												
	x_1	x_2	x_3	x_4	x_5	x_6	x_7	x_8	x_9	x_{10}	x_{11}	x_{12}	
1	-0.96	-0.30	0.82	-1.77	-0.07	0.28	-0.13	-0.06	-0.31	-0.46	2.19	-0.67	-2.08
2	0.70	0.39	-0.44	1.33	-0.22	-0.39	0.17	0.10	0.50	-0.42	-0.29	-0.82	-0.31
3	-0.41	-0.12	-0.36	0.24	1.07	0.25	0.39	-0.51	0.12	0.04	-0.37	0.14	-0.45
4	-0.18	-0.94	0.50	-1.29	-0.09	0.30	0.79	-0.89	0.42	-0.91	1.05	2.69	0.66
5	-0.30	-0.06	-0.27	-0.16	-0.84	-0.02	0.20	-0.17	0.16	-0.32	0.21	-0.13	-2.21
6	2.16	1.15	0.20	-0.69	-0.21	-0.20	0.36	-0.19	0.32	-0.32	-0.50	-2.58	2.04
7	-0.26	-0.44	0.92	0.34	-0.47	0.10	-0.26	0.17	-0.27	0.09	-0.19	-0.80	-1.85
8	-1.22	0.81	-1.28	-1.11	0.19	0.06	-0.33	0.25	-0.30	-0.52	-1.09	-1.30	-0.37

[a] Temperature; [b] Duration; [c] Acidic condition; [d] Alkaline condition; [e] Saline condition

Table 4. Weight and bias values of the second layer

N	W^2	b^2
1	-8.82	8.76
2	-5.06	
3	-6.14	
4	7.55	
5	-8.69	
6	8.64	
7	-8.70	
8	-7.68	

In order to measure the contribution of input parameters to the bond strength, a weight-based feature selection was used to rank the importance of environmental parameters in governing

  doi:10.5075/epfl-298799_978-2-9701614-0-0

the bond strength. Howes and Crook [12] introduced a general method to rank the importance of features based on the weight and bias values in a neural network. Eq. (5) defines the method as:

$$rank(x_i) = \frac{\sum_{j=1}^{j=8} \left| \left(\frac{W_{ij}^1}{b_j^1 + \sum_{i=1}^{12} W_{ij}^1} \right) W_j^2 \right|}{b^2 + \sum_{j=1}^{8} W_j^2} \quad (5)$$

where $rank(x_i)$ measures the importance of the feature x_i. Using the values in Table 3 and Table 4, the contribution of environmental parameters in percentage is shown in Figure 8. It is seen that the duration of exposure has the highest impact on the bond, followed by the temperature, pH, and salt concentration for the conditioned samples.

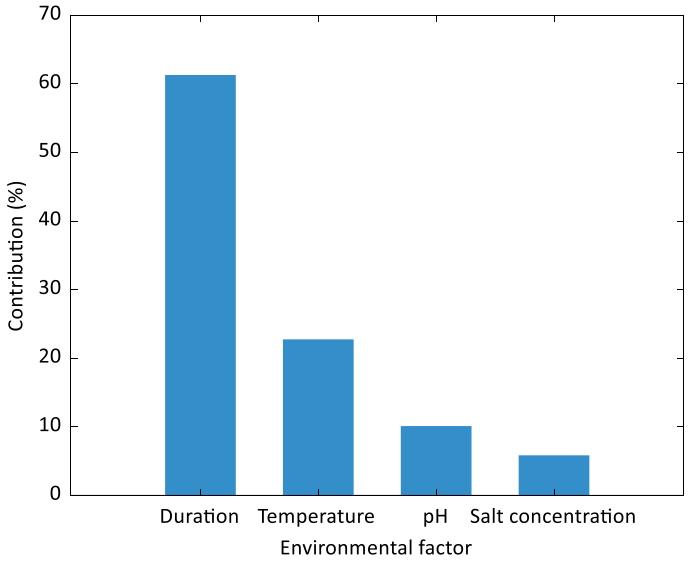

Figure 8. Contribution of environmental factors on the bond strength

4. Conclusion

This study presented a data-driven analysis of the durability of the interfacial bond between FRP bars and concrete. A total of 320 pull-out test results of samples under acidic, alkaline, and saline conditions were collated and used to train an ANN model and test its prediction performance. The dataset included information on the geometrical and mechanical properties as well as the environmental conditions of the FRP bar and concrete. Bayesian optimisation was used to tune the model hyperparameters. Furthermore, a 10-fold CV technique was used to avoid the overfitting of ANN to the training set. The prediction results indicated that ANN was able to accurately predict the bond strength with high accuracy. In addition, a practical equation was extracted from the ANN algorithm to predict the long-term degradation of the bond while avoiding computational and experimental costs. Finally, an evaluation of the environmental impacts on the bond was performed using a weight-based feature selection method. It was seen that, exposure duration highly impacts the bond compared to temperature, pH, and salt concentration factors. The findings of this study demonstrate the potential of machine learning to model the long-term performance of composite structures accurately and rapidly.

  doi:10.5075/epfl-298799_978-2-9701614-0-0

Acknowledgements

Authors would like to thank the School of Civil Engineering at the University of Sydney for supporting this project. Hadigheh would like to acknowledge supports that he received through the Australian Research Council's Discovery Early Career Researcher Award (DECRA) fellowship scheme (project DE200100406).

5. References

1. ACI 440.1R-15. Guide for the Design and Construction of Structural Concrete Reinforced with Fiber-Reinforced Polymer (FRP) Bars. MI, USA: American Concrete Institute; 2015.
2. Hadigheh SA, Gravina RJ, Smith ST. Effect of acid attack on FRP-to-concrete bonded interfaces. Constr Build Mater. 2017;152:285-303.
3. Gravina RJ, Li J, Smith ST, Visintin P. Environmental Durability of FRP Bar-to-Concrete Bond: Critical Review. J Compos Constr. 2020;24(4):03120001.
4. CSA S806-02. Design and construction of building components with fibre-reinforced polymers. Canada: Canadial Standards Association; 2002.
5. Basaran B, Kalkan I, Bergil E, Erdal E. Estimation of the FRP-concrete bond strength with code formulations and machine learning algorithms. Compos Struct. 2021;268:113972.
6. Aghabalaei Baghaei K, Hadigheh SA. Durability assessment of FRP-to-concrete bonded connections under moisture condition using data-driven machine learning-based approaches. Compos Struct. 2021:114576.
7. Aghabalaei Baghaei K, Hadigheh SA. A Machine Learning Approach to Modelling the Bond Strength of Adhesively Bonded Joints Under Water Immersion Condition. 10th International Conference on FRP Composites in Civil Engineering; Cham: Springer International Publishing; 2022. p. 738-49.
8. Chiroma H, Abdullahi UA, Abdulhamid SM, Alarood AA, Gabralla LA, Rana N, et al. Progress on Artificial Neural Networks for Big Data Analytics: A Survey. IEEE Access. 2019;7:70535-51.
9. Snoek J, Larochelle H, Adams RP. Practical bayesian optimization of machine learning algorithms. Advances in neural information processing systems. 2012;25.
10. Glorot X, Bengio Y, editors. Understanding the difficulty of training deep feedforward neural networks. Proceedings of the thirteenth international conference on artificial intelligence and statistics; 2010: JMLR Workshop and Conference Proceedings.
11. He K, Zhang X, Ren S, Sun J, editors. Delving deep into rectifiers: Surpassing human-level performance on imagenet classification. Proceedings of the IEEE international conference on computer vision; 2015.
12. Howes P, Crook N. Using input parameter influences to support the decisions of feedforward neural networks. Neurocomputing. 1999;24(1):191-206.

  doi:10.5075/epfl-298799_978-2-9701614-0-0

REDUCED-ORDER MODELLING OF COMPOSITE RESIN INJECTION REPAIR

Ahmed Asiliskender[a], Koon-Yang Lee[a,b], Joaquim Peiró[a]

a: Imperial College London – Email Address: ahmed.asiliskender14@imperial.ac.uk
b: Institute for Molecular Science and Engineering (IMSE)

Abstract: *Resin injection repair of composites is beneficial in circumstances where the damage has minimal fibre fracture. However, implementation to practical scenarios presents some challenges. The main aim of this work is to develop a two-dimensional reduced-order digital reconstruction, simulation and injection strategy in order to reliably conduct an efficient resin injection repair. A key objective is to ensure the repair strategy is scalable and remains practical. After establishing the basis for this method, we show a proof-of concept simulation and assess the predicted efficacy of resin injection under two injection configurations. We observe that filling efficiency is significantly improved by utilising knowledge of the reconstructed cavity to place ports and vents such that the area covered by resin flow paths are increased.*

Keywords: Composite laminate repair; Multiphase flow; Finite Element Analysis (FEA); Process Modelling; Porosity

1. Introduction

The constituent material and architecture of composite materials often leads to highly complex damage mechanisms after impact that make their repair challenging and costly. There is a range of repair methods that are efficient and reliable in restoring the mechanical properties of composite structures such as fastening methods, bond scarf and patching repairs [1]. Compared to these more traditional composite repair methods, resin injection repair (RIR) can be more cost effective and faster to apply on site with or without vacuum support [1-2]. A schematic of a representative RIR set up is shown in Fig. 1. Current RIR practices are based on basic guidelines, intuition, and/or trial-and-error experience [3] and therefore offer significant potential for improvement.

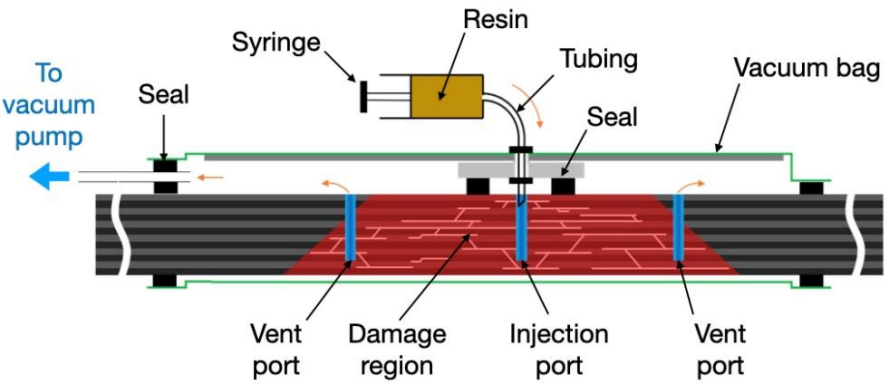

Figure 1: A cross-sectional view of a representative resin injection repair setup.

To address these issues, we propose the use of a “virtual twin” to simulate the RIR process and to assess its efficacy, with the ultimate aim of allowing end users to achieve optimal repair efficiencies in practical applications.

  doi:10.5075/epfl-298799_978-2-9701614-0-0

2. Proposed Reduced-Order Method

Finding an optimal or near-optimal repair configuration for RIR in practice is difficult for repair operators because the geometry and characteristics of damaged zones are both intricate and intrinsically different from case to case. This is the main reason why current RIR procedures are based on intuition or operator experience obtained by trial-and-error. The availability of computational techniques for simulating of a "virtual injection" process offers an option to use them to guide the operator in the search for porting and venting configurations that would lead to increased cavity filling efficacy or, by combining simulations with optimal control, to automatically find optimal (or near-optimal) configurations.

Since high-fidelity three-dimensional (3D) simulations of the virtual injection process are impractical because their high cost and their reliance on high-resolution scanning equipment, such as CT scanners, we advocate the use of a more cost effective reduced-order model. The model views the damaged cavity as a two-dimensional porous medium characterised by a depth-averaged porosity field that can be reconstructed using simpler, and more accessible, scanning methods such as ultrasound. Furthermore, the reduction of the dimensions of the problem to two significantly reduces the computational cost.

On that account, we propose a novel reconstruction-simulation-injection strategy to RIR. More precisely, we propose a methodology that first creates a two-dimensional reconstruction of a damaged composite through ultrasonic testing. This 2D reconstructed geometry is assumed to have a porous damage zone. The porosity is linked to flow properties by means of a constitutive equation, allowing for computational simulations of resin flow through this damage area. The aim of this strategy is to provide repair operators with a cost-effective way to carry out RIR by analysing alternative configurations, assessing the suitability of the adopted porting and venting locations, and calculating estimates of their filling efficiency. The availability of such estimates, if accurate, could ultimately allow repair operators to find optimal or near-optimal repair configurations.

The proposed modelling assumes that the thickness of the composite panel is small compared with the other dimensions and that the damage zone to be injected with resin behaves like a porous material.

The key steps of the proposed approach are:

- The injection process is modelled as a two-dimensional (2D) flow through porous material governed by the Darcy equation.
- The permeability of the material is calculated from the porosity through a semi-empirical constitutive relation.
- Ultrasonic C-scan measurements are used to determine the geometry of the damaged area, and to calculate the porosity from the thickness distribution of the composite panel.
- The resin flow is simulated via the numerical solution of Darcy's equation of two-phase flow of resin and air.
- The flow simulation predicts the fill ratio of the damaged area given the injection flow rate and the position of the porting and venting holes.

  doi:10.5075/epfl-298799_978-2-9701614-0-0

The methodology proposed is a proof-of-concept for predicting the effectiveness of injection configurations in a given repair process. It has been verified against an analytical solution of the axisymmetric Darcy's equation (not shown for brevity), but due to the current lack of available data, there is no rigorous comparison to experimental or field studies for validation.

3. Modelling the RIR process as a 2D flow through porous media

In order to model the resin flow, we must first note that the flow is slow and dominated by viscosity. We also assume the resin to behave as a Newtonian fluid thus neglecting viscoelastic effects, which is reasonable if the duration of the resin flow is shorter than the resin gel-time. Furthermore, we neglect gravity, capillarity, and inertial effects.

3.1 Governing Equation: 2D Darcy's Law

The flow in a porous material with the mentioned assumptions follows Darcy's law:

$$\mathbf{q} = -\frac{\mathbf{k}}{\mu} \cdot \boldsymbol{\nabla} P, \quad \mathbf{q} = \phi \boldsymbol{u} \tag{1}$$

where $\mathbf{q}$ is the fluid flux vector, ϕ is the (isotropic) porosity, $\boldsymbol{u}$ is the velocity vector, $\mathbf{k}$ is the permeability tensor, P is the pressure and μ is the fluid viscosity. In the case of the assumptions taken in this paper, the permeability tensor is assumed to be isotropic and a function of the porosity, ϕ, namely

$$\mathbf{k} = k(\phi)\boldsymbol{I} \tag{2}$$

where $\boldsymbol{I}$ is the identity matrix, and $k(\phi)$ is the permeability modulus. The porosity values are obtained from measurements of the thickness field, described later in Section 4. The permeability values are obtained by using a permeability-porosity relation, discussed next.

3.2 Constitutive Relation for $k(\phi)$

There are several semi-empirical equations that can be adapted to characterize the damage zone as a porous material such as the Kozeny-Carman (KC) equation, the formulation of Bruschke and Advani [4] and Gebart's formulas [5].

For brevity, a comparison of these formulations is not discussed here. We have selected the Kozeny-Carman (KC) equation (Eq. (3)) for use in our simulations, where β is a parameter dependent on the microgeometry of the porous material. A simple sensitivity study shows the final filling efficiency (volume of cavity filled/total cavity volume) to be insensitive to the permeability magnitude. The filling efficiency is the primary quantity of interest.

$$k(\phi) = \beta \frac{\phi^3}{(1-\phi)^2} \tag{3}$$

4. 2D Reconstruction from C-scans

4.1 Porosity Evaluation

As a specimen may be deformed due to damage, its thickness is different prior to, and after, damage has occurred. We use two key assumptions needed to evaluate the porosity. The first is a 0% porosity assumption for an undamaged composite specimen as structural composites are produced with minimal voids and any existing voids are negligible in comparison to the amount

  doi:10.5075/epfl-298799_978-2-9701614-0-0

introduced due to damage. The second is that there is no significant loss of composite material due to damage, as such this evaluation will not be accurate in cases such as those of heavy impact damage or perforation where significant material is lost around the impact zone or behind the impacted surface.

The assumption of material conservation is essentially that the amount of composite material remains the same along the thickness prior to and after damage

$$(1 - \phi_{pre})t_{pre} = (1 - \phi_{post})t_{post} \tag{4}$$

where the subscripts *pre* and *post* indicate pre-damage and post-damage states, respectively. Rearranging Eq. (4) and applying the initial 0% porosity assumption provides the post-damage porosity equation:

$$\phi_{post} = 1 - \frac{t_{pre}}{t_{post}} \tag{5}$$

4.2 Data Sourcing

The pre-damage thickness field is obtained by utilising the knowledge of the specifications of the designed composite structure. The post-damage thickness field is obtained by using ultrasonic C-scan testing where both the front and back faces of the specimen are scanned, in separate instances, in order to give a complete view of any displacements on either side (note that this may not always be possible in the field which could result in loss of accuracy). The C-scan data is put through processing in order to obtain the post-damage thickness field, which is discussed in Section 4.4. Following this, the porosity is obtained as per Section 4.1.

4.3 Material Sourcing

The composite specimen used as a case study here was provided by Queen's University Belfast [6]. The specimen was created using an IM7/HexPly® 8552 fibre/resin composite composed of 24 laminae of $[45/0/-45/90]_{3s}$ layup with a laminar thickness of 0.131 mm for a total of 3.14 mm.

The damage was applied according to the ASTM D7136/D7136M-15 standard with a hemispherical impactor of 5.74 kg and an impact energy of 25 J. Of note was the barely visible dent in the centre of the composite on the front face of the panel and the broken plies on the back face.

4.4 Data Processing

The C-scan data must be processed in order to provide a porosity field. The specimen is scanned on the front face and turned over to scan the back face to obtain the surface displacement (i.e. distance-to-probe) data, as ultrasonic signal is lost or too noisy to reliably read the back surface from the front face through the damage zone. This means one scan dataset will be initially flipped and must be flipped back accordingly.

Information regarding the specimen size, scan parameters (such as the size of the scan pixels in mm) and the processing parameters are required. Using these, the background data is omitted. After this, the specimen scan images are corrected for in-plane rotation (and orientation). This correction is necessary in-order to align the scans of the front and back face of a specimen in order to prevent 'smearing' of the porosity values.

  doi:10.5075/epfl-298799_978-2-9701614-0-0

There is also the possibility of slanting (out-of-plane rotation) which can significantly affect the apparent values and accuracy of the result. The slant correction was performed by creating 4 point probes that assess the apparent distance from the C-scan probe to the specimen surface. As these probes are on locations without damage, the correction is constrained to equalise these values. Such a correction is applied in bilinear interpolation fashion.

Once the slant is corrected for, the values must be scaled to represent the correct distance between the ultrasonic probe and the specimen surface. The scans are then aligned at their centres and the surface values shifted so that the distance between the slant probes of both scans is set to the pre-damage thickness. The values of the two scans are then subtracted from each other to provide the post-damage thickness and the porosity obtained through Eq. (5) provided in Section 4.1.

After obtaining the porosity there could be points or regions with negative porosity values (possibly due to the corrections applied in previous steps or errors in scanning), this is adjusted for by setting them to zero. Finally, if there are still notable artefacts around the damage zone (porosity values in such areas could approach values of the damage zone), a simple value filtering of non-zero porosity would be applied to cut out such artefacts.

5. Application of the Reduced-Order Methodology

5.1 Damage Zone Porosity Field Reconstruction

The composite specimen scans as described in Section 4.2 of the front (impacted) and back face of the panel are shown in Figs. 2(a) and 2(b) respectively. Both scans show evidence of being rotated (in-plane) and slanted (out-of-plane). The application of post-processing as described in Section 4.4 results in the porosity map shown in Fig. 2(c).

The parameter β in Eq. (3), is obtained through additional assumptions about the characteristics of the damage zone, the geometry and distribution of the fibre tows within it. These assumptions and the pertinent calculations, not described here, result in the final form of the permeability-porosity relation used, shown in Eq. (6), with the resulting permeability field is shown in Fig. 2(d).

$$k = 2.59 \times 10^{-9} \frac{\phi^3}{(1-\phi)^2} \ \mathrm{m}^2 \tag{6}$$

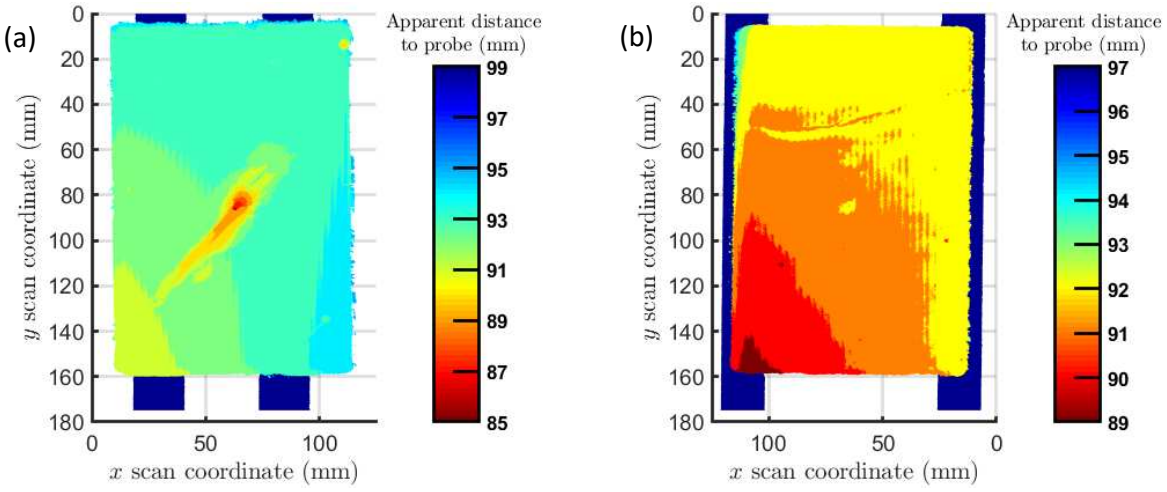

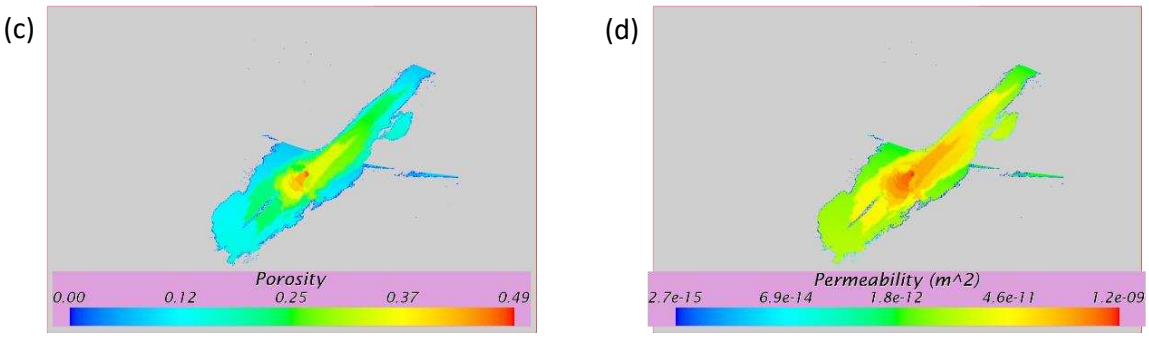

Figure 2: An ultrasonic scan (C-scan) time-of-flight data of the outer surfaces of the composite specimen provided by QUB [8] – (a) scan data of the front (impacted) surface; (b) scan data of the back surface; (c) porosity field obtained after the post-processing steps and; (d) The permeability field of the damage zone (in a logarithmic colour scale).

A potential source of errors was identified in the coarse resolution of the measured depth data from time-of-flight (±1 mm). The porosity field showed artefacts arising because the bilinear correction for the observed slant was smooth while the depth data resolution much coarser. These artefacts, despite being mostly filtered, may have polluted the porosity field. One example would be the isolated slender 'cavity' on the right side of the specimen in Fig. 2(c).

5.2 Resin Injection Simulations

The filling efficiency is defined as the ratio of the volume occupied by the resin to the volume of the damage zone (which excludes the unconnected zones). The pressure difference used to simulate the flow between the injection port and outlet vent(s) is 1 kPa. To avoid potential numerical oscillations, the pressure difference was gradually and smoothly increased over a period of 12.5 s, from 0 Pa to its final value. This value corresponds to a very low Reynolds number, Re ≈ 0.02, at the time when the resin initially reaches an outlet vent.

In the simulations shown (Figs. 3(a) and 4(a)), orange indicates resin, light grey indicates air and dark grey indicates unconnected regions. The red dot is the injection port and the blue dot is the outlet vent. This convention is used in both cases.

5.2.1 Simulation Case 1

The injection port and outlet vent locations in this case, shown in Fig. 3(a), were selected through direct visual inspection of the damaged specimen. The distance between the inlet and outlet holes is approximately 35 mm.

Fig. 3(a) shows the degree of resin infiltration. It also shows that the cavity is not filled uniformly, with resin infiltrating the bulk of the side of the outlet vent following both direct and wrap-around paths to the vent. Alongside the unfilled cavity on the top right, some areas near the boundary on the filled side of cavity are also unfilled. A possible explanation of this is that firstly there is no direct flow path to the unfilled boundary as the vent is not in its immediate vicinity, and secondly that the permeability near the boundary drops to values that are about a 4 to 5 order of magnitude lower than that in areas closer to the centre of the damage zone. Also noticeable is the presence of a few regions of trapped air, which we will refer to as air bubbles, within the resin bulk arising from the pockets of air being compressed and enveloped between the growing resin front and the domain boundary.

  doi:10.5075/epfl-298799_978-2-9701614-0-0

(a) 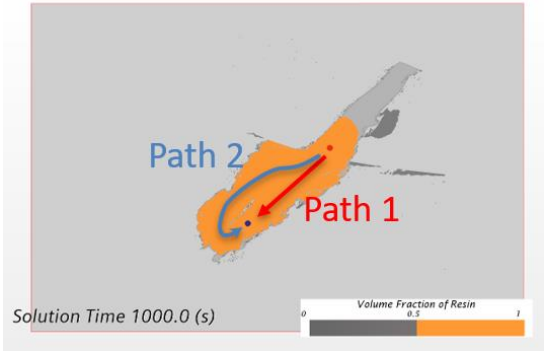

(b) 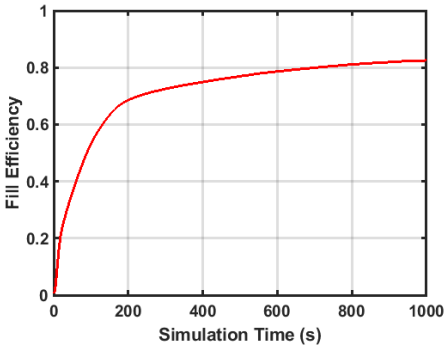

Figure 2: Case 1 – (a) Final state of the injection simulation with the indicated direct (path 1, red) and wraparound (path 2, blue) resin flow paths, and; (b) time evolution of fill ratio for the first scenario.

Fig. 3(b) shows the ratio of the volume of the domain that has been infiltrated by the resin. Much of the infiltration happens quickly, approximately in the first quarter and then some of the remaining volume is filled at a much slower rate with the fill efficiency eventually stagnating at a value of around 82.5%.

5.2.2 Simulation Case 2

For this case, information on the geometry was used to purposefully place an outlet vent in a possibly sub-optimal location, namely near a corner close to the centre and injection port as shown in Fig. 4(a). The injection vent is in the same location as in the first case. The main aim of this configuration is to reduce the likelihood of the resin front travelling across the damage zone and infiltrating the cavity.

Fig. 4(a) shows that the resin front has travelled some distance from either of the two holes but has not infiltrated either end of the damage zone. The number of air bubbles in this case is larger than in Case 1 perhaps due to the flow being subject to a greater pressure gradient: the pressure difference has not changed but the holes are closer. This negatively impacts the filling efficiency.

(a) 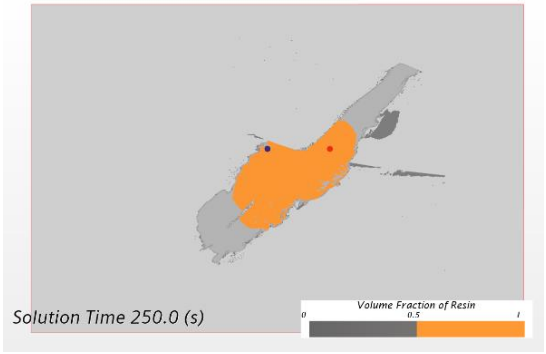

(b) 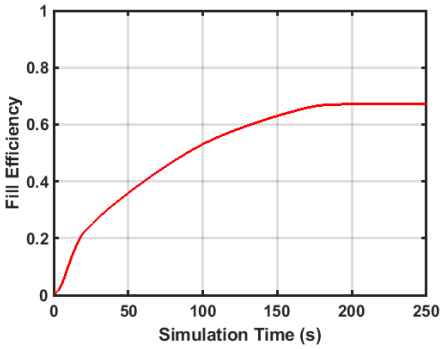

Figure 3: Case 2 – (a) Final state of the injection simulation and; (b) time evolution of the fill ratio for the second scenario.

The filling efficiency plot in Fig. 4(b) and the resin distribution in Fig. 4(a) show an achieved fill efficiency of 67.1% which is worse than the value of 82.5% of the Case 1. On the other hand, the simulation time of 200 s is noticeably shorter compared to 1000 s from Case 1.

  doi:10.5075/epfl-298799_978-2-9701614-0-0

In comparison, this case exhibits a reduction of filling efficiency due to poor hole placement as the paths available for the resin to flow to the outlet cover a smaller portion of the damage zone, but the injection time is reduced due to the proximity of the outlet vent to the injection port.

6. Key Findings and Conclusions

We have proposed a simulation-based strategy that aims at improving the reliability and efficacy of the resin injection repair (RIR) process. The strategy incorporates 2D flow simulation with available technologies for reconstruction and injection to devise a practical method for assessing filling efficiencies for a given set of ports and vents. In our view, this demonstrated proof-of-concept has the potential to lead to significant improvements in reliability and efficacy and thus to a more robust and appealing approach to RIR.

We have also studied two injection configuration scenarios to ascertain key findings relating to resin flow behaviour and the repair methodology. For RIR to be effective and improve cavity filling, the position of ports and vents should permit the creation of paths within the damage zone for the resin to flow from injection ports to outlet vents such that the resin can infiltrate the damage zone in a widespread manner.

It should be noted that our choice of permeability-porosity relation and related assumptions are based on rough approximations. Therefore, further systematic validation against real case scenarios is required to determine its suitability for accurately reproducing flow injection behaviour within damaged composite structures.

Acknowledgements

We would like to thank Apostolos Parlamas, Brian Falzon and Zafer Kazancı from Queen's University Belfast (QUB) for providing the composite specimen used in this study, and also for their feedback and insightful discussions about this work.

This research was supported by a grant from Dstl for a 3 Year Research PhD titled "Design and Optimisation of Nano-Modified Liquid Resin Injection Strategy for Maximum Composite Repair Efficiency". The research was monitored by Luke Rumsey and Kevin Denham to whom we are thankful for arranging the fruitful collaboration with QUB, and for their support, encouragement, expert advice and feedback.

7. References

1. Halliwell S. Repair of fibre reinforced polymer (FRP) structures. National Composites Network. 2012.
2. Pierce RS, Campus N, Falzon BG. Injection repair of composites for automotive and aerospace applications. 21st International Conference on Composite Materials. Xi'an; 2017.
3. FAA. Aviation Maintenance Technician Handbook-Airframe, Volume 1 (FAA-H-8083-31A). 2018.
4. Bruschke MV, Advani SG. Flow of generalized Newtonian fluids across a periodic array of cylinders. Journal of Rheology 1993; 37:479-498.
5. Gebart BR. Permeability of Unidirectional Reinforcements for RTM. Journal of Composite Materials 1992; 26:1100-1133.
6. Parlamas A. PhD Student; QUB. Personal Communication. 2019.

  doi:10.5075/epfl-298799_978-2-9701614-0-0

ANALYTICAL, COMPUTATIONAL AND EXPERIMENTAL STUDY OF 3D PRINTED POLYMERIC LATTICE STRUCTURES

Maedeh, Amirpour[a], Mark, Battley[a]

a: Department of Engineering Science, Centre for Advanced Composite Materials (CACM). the University of Auckland, New Zealand- m.amirpourmolla@auckland.ac.nz

Abstract: *This paper investigates theoretical, numerical and experimental studies on static compression behaviour of polymeric Body-Centred Cube (BCC) lattices manufactured using the Selective Laser Sintering (SLS) method. In the theoretical formulation, the influence of manufacturing defects such as material overlapping in the vicinity of strut joints is taken into consideration to provide predictions of mechanical properties of a macro lattice cube. Finite Element models of the BCC lattices are performed to predict the compressive behaviour of filaments. Compression experiments were conducted utilising digital image correlation echniques in order to capture deformations and validate the material properties obtained by the analytical modelling and numerical simulations. Good agreements are observed among the analytical, numerical and experimental results.*

Keywords: Imperfections; SLS Additive Manufacturing; Analytical Model; Finite Element; Compressive behaviour

1. Introduction

3D printing is a form of additive manufacturing that is revolutionising the manufacturing industry by providing an efficient method for producing complex, customised and lightweight structures such as lattices [1] that cannot feasibly be fabricated by conventional manufacturing methods . A lattice is a type of cellular structure which has been widely used in aerospace [2] and medical industries [3] with excellent properties, such as high specific stiffness and strength, heat insulation and energy damping attenuation. One of the most common strut arrangements in lattice structures is Body-Centred Cube (BCC) which has been extensively used for energy absorption applications [4]. Moreover, open-lattices have specific advantages compared to conventional foam cores such as the capability of core ventilation that eliminates the property degradation caused by moisture absorption [5]. Thus, the BCC lattices have a great potential and flexibility for structural design. The mechanical properties of BCC lattices are determined by the size of the unit cell and the arrangement and connectivity of the struts . Along with advances in additive manufacturing methods of BCC lattices and efficient design of these structures, efforts are underway to accurately describe the mechanical properties of BCC lattices. Lee et al. [6] studied elastic modulus of stainless steel BCC lattices using an analytical model for a single unit cell without considering shear effects. They implemented a 2D FE simulation to validate analytical studies. They concluded that discrepancies between FE simulation and experimental results are caused by the inconsistent lattice strut diameter and the 2D simplification in the FE modelling. Compressive properties of stainless steel micro lattices using Euler–Bernoulli assumption were defined by Ushijima et al. [7]. They found that the predicted analytical model had good agreement with experimental results for low strut aspect ratio (d/l<0.1). However, these studies focused on metallic micro lattices without considering influence of strut joints and

  doi:10.5075/epfl-298799_978-2-9701614-0-0

material overlapping effect. Moreover, to the best of our knowledge, material parameters of an individual 3D printed polymeric microstructure have been rarely determined for analytical models and FE simulation of lattice structures. Though several analytical and FE simulation models have been developed for micro lattices, one should note that the strut joints at higher aspect ratio (d/l) impact overall mechanical properties of a lattice structure. FE simulation of large-scale lattice structures containing material overlapping effect at joints are computationally intensive. Therefore, further investigation on the geometries of struts and connectivities should be carried out to accurately design the lattice structures. In this paper, we aim to develop a combination of an analytical formulation, FE simulation and experimental tests to elucidate the impact of connectivity and material overlapping on static mechanical properties such Young' modulus and plastic collapse strenght of a polymeric macro lattice structure. An analytical approach utilising Timoshenko's beam theory and the impact of material overlapping at nodes for a micro lattice structure under compressive loading is proposed. The propagation of strut-deformation patterns of a macro lattice constrained between two rigid platens is shown to represent the sections with different elastic constants. FE simulation with 3D solid hexahedral elements is used to predict compressive behaviour of a macro lattice structure. The stress–strain curve and material properties of an individual 3D printed single strut is experimentally determined using a custom-made experimental setup and inverse calibration approach. To verify the analytical model and FE simulation and gain insight to mechanical behaviour of lattices, the compressive experimental tests using digital image correlation technique are also carried out. Results are evaluated in terms of initial stiffness and plastic collapse strength and deformation modes for lattice cubes. These findings provide a combination of predictive analytical model, simulation and experiments to investigate the effect of imperfections and material overlapping effect on static compressive behaviour and failure modes of 3D-printed macro lattice structures.

2. Theoretical formulation

The geometry of a Body Centre Cubic (BCC) unit cell and individual lattice strut are given in Figure 1. The main assumption in this work is to consider the material overlapping at the strut joint. Since the joint connecting struts to each other were assumed to be rigid, deformations are expected to occur in a place near to the joint which require a new moment arm or effective length $l_{eff.}$. The geometrical parameters of the unit cell are defined as follows in equations 1 to 4.

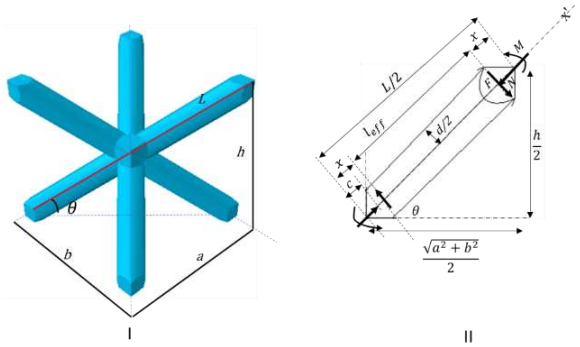

Figure 1: I) 3D representation of BCC unit cell (II) individual strut geometry.

Analytical model of compressive stiffness of a micro lattice block with considering the effect of strut joints is presented in the authors' work [8]:

$$E_y = \frac{2h}{ab\left(\frac{l_{eff}}{AE}sin^2\theta + \left(\frac{{l_{eff}}^3}{12EI_{y'}} + \frac{l_{eff}}{kAG}\right)cos^2\theta\right)} \quad (5)$$

Figure 2 shows the macro lattice block constrained with upper and lower rigid platens. As it can be seen we have a distribution of elastic modulus within a structure [9].

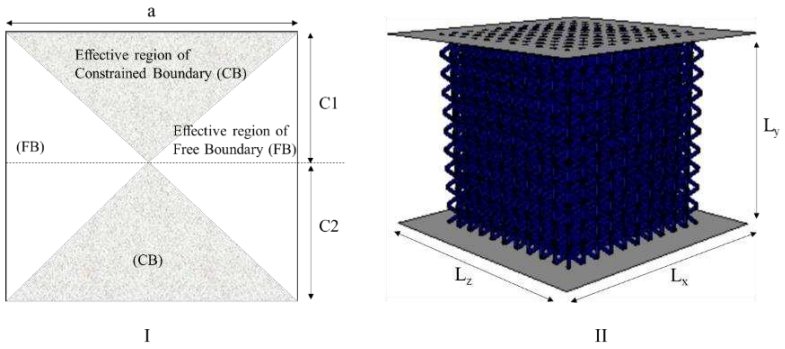

Figure 2: (I) sketches of distributions of unit cells, (II) CAD model, 10×10×10 unit cells

Yang (2019) developed the effective Young's modulus of a macro sandwich BCC lattice with different dimensions (regular and irregular lattices) [9]. It is noted that they did not consider the effect of imperfections such as material overlapping effect at the vicinity of the joints. It is also recommended to use the formulation when the number of unit cells along sides are larger than 5. They showed effective E for a cubic regular structure is formulated as follows:

$$E_{eff} = -\frac{2E_{CB}\left[1+\frac{ln\left(\frac{E_{CB}}{E_{FB}}\right)}{1-\frac{E_{CB}}{E_{FB}}}\right]}{1-\frac{E_{CB}}{E_{FB}}} \quad (7)$$

where E_{CB} and E_{FB} are elastic modulus of unit cell with the constrained and free boundary conditions, respectively.

3. Computational modelling

To simulate the deformation behaviour of the macro lattice cubes, finite element analysis was performed using ABAQUS 2019. The regular BCC configuration has a isotropic material behaviour with three independent parameters including elastic modulus (Ex=Ey=Ez), Poisson's ratio and Shear modulus. The dimension of a single unit cell is 5×5×5 mm with strut diameter 1 mm and lattice structure is composed of 10 unit cells in directions x, y and z. The BCC unit cell and lattice structures are designed and meshed using Micromechanics as a plugin in ABAQUS (shown in Figure 3). A single filament compaction experimental set up was developed at Centre for Advanced Composite Materials (CACM) [8]. An inverse calibration method using MCalibration software version 5.1.2 was used in combination with a FEA model of a single filament under transverse compaction test. The inverse method was used to determine an appropriate material constitutive model and input parameters for the 3D-printed Nylon lattices which included permanent plasticity deformation under compression tests.

  doi:10.5075/epfl-298799_978-2-9701614-0-0

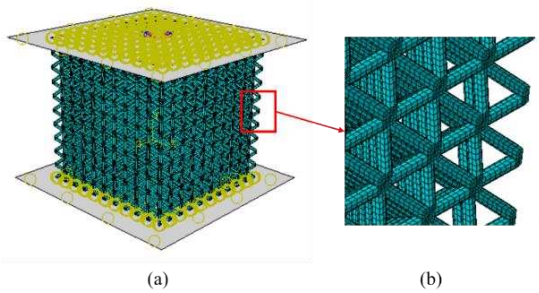

Figure 3: (a) applied boundary condition and constrains (b) hexahedral mesh

4. Experimental Tests

In order to design the lattice structures in cubes of dimensions 50 ×50×50 mm PTCTM Creo Parametric 5.0.2.0 software was used. The cell strut diameter was selected as 1mm for a relative density of 0.17. To capture deformation response of the fabricated lattice structures, uniaxial compression experiments were performed using an Instron 1185 universal testing machine with 100kN load capacity. During the tests, the lattice structures were centrally located between two platens as shown in the experimental compression rig (Figure 4). Macroscopic engineering strains were calculated through Digital Image Correlation (DIC) using an in-house developed system called MODEM (MATLAB Optical Displacement and Strain Measurement) [8].

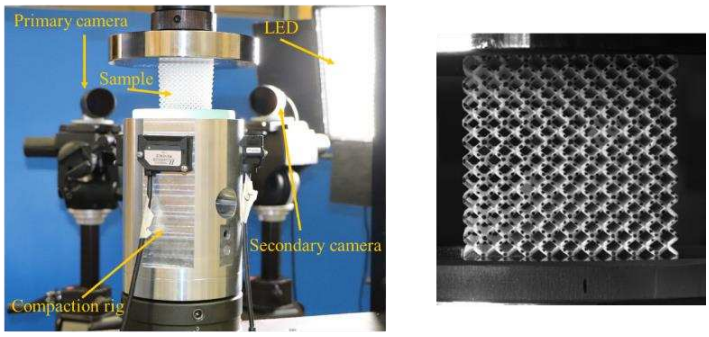

Figure 4: (a) DIC setup for compression test (b) lattice structure with speckle pattern

5. Results

The values of initial stiffness from theories and experiments from literature according to aspect ratio for stainless steel with modulus of elasticity 97 GPa are shown in Figure. The proposed analytical model matches well with experimental data form Gumruk et al. [9] for all aspect ratio ranges. Ushijima considered only axial and bending effects showing a deviation of up to 42% with increase of aspect ratio [6]. In Figure , a comparison of initial Young's modulus from analytical formulation, numerical simulation and experimental data of lattice structure with relative density of 17% is given. It can be seen that analytical modelling overestimates the stiffness of the lattice structure by 6.2% as it is based on fully constrained boundaries at the top and the bottom of the lattice structure which fully restricts the transverse displacement in the YZ plane. Due to the undesired unprocessed materials during 3D printing and post processing, the 3D printed lattice cube shows higher stiffness than the FE simulation with a difference of less than 2%.

  doi:10.5075/epfl-298799_978-2-9701614-0-0

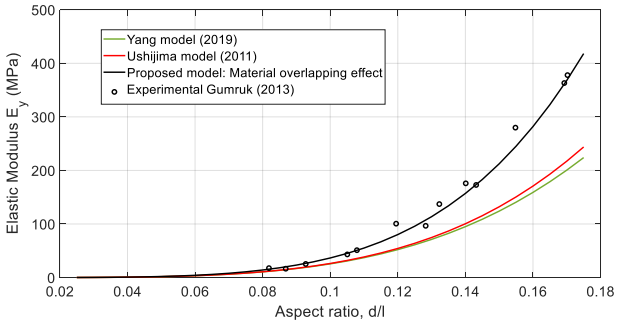

Figure 5: Variation of compressive Young's modulus versus aspect ratio

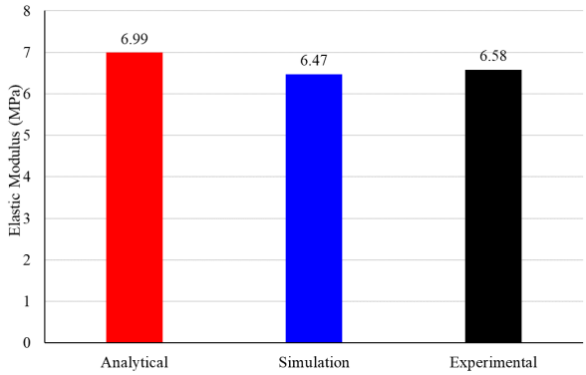

Figure 6: Comparison of initial Elastic modulus from analytical, simulation and experimental data

The photos in Figure show typical images at macroscopic deformation $\sigma_{elastic}$, $\sigma_{plastic}$ collapse and an image at the final frame (12 mm displacement) which are compared with the simulation results at the same time frame. The final frame shows a barrel shape deformation for the lattice block. Also, the middle horizontal row shows the highest distortion compared to the other rows. As mentioned earlier (refer to Figure) when considering the top and the bottom surfaces as constrained boundaries, the external boundary conditions of the entire lattice structure affect not only the mechanical properties of boundary unit cells but also those of internal unit cells which leads to a nonuniform Y-component of displacement under compression load along the Y- axis. The deformation patterns of boundary struts will be propagated to internal struts, as indicated in the FE simulation displacement plot which causes variations of mechanical properties such as stiffness.

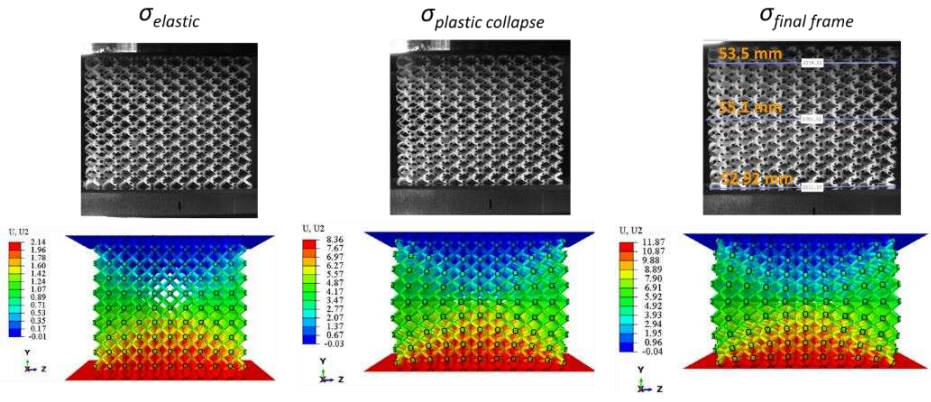

Figure 7: Comparison of deformation between optical images obtained from DIC at increasing compression steps, σelastic, σcollapse, and σfinal frame (circles in ***Erreur ! Source du renvoi introuvable.****) and FE simulation*

  doi:10.5075/epfl-298799_978-2-9701614-0-0

6. Conclusion

- The effect of shear and strut joints are much more important for large aspect ratios (d/l>0.1) rather than small aspect ratios.
- A series of simulations confirmed the capability of the parent material model obtained from a single filament compression and inverse calibration method in replicating the nonlinear response of real 3D printed lattices.
- The developed analytical predictions for stiffness and collapse strength showed a very close agreement to the numerical and experimental results.

7. Acknowledgements

The first author wishes to thank New Zealand Royal Society Te Aparangi for providing her Rutherford Fellowship RFT-UOA1903-PD. She would also like to thank Dr. Juan Schutte (Creative Design and Additive Manufacturing Lab , the University of Auckland) and Dr. Willsen Wijaya for the technical assistance in 3D printing of the sample and experimental setup.

8. References

1. Nazir, A. and J.-Y. Jeng, Buckling behavior of additively manufactured cellular columns: Experimental and simulation validation. Materials and Design, 2020. 186: p. 108349.
2. Vasiliev, V.V., V.A. Barynin and A.F. Razin, Anisogrid composite lattice structures– Development and aerospace applications. Composite Structures, 2012. 94(3): p. 1117–27.
3. Obaton, A.-F., J. Fain, M. Djemaï, D. Meinel, F. Léonard, E. Mahé, B. Lécuelle, J.-J. Fouchet and G. Bruno, In vivo XCT bone characterization of lattice structured implants fabricated by additive manufacturing. Heliyon, 2017. 3(8): p. E00374.
4. Bai, L., J. Zhang, X. Chen, C. Yi, R. Chen and Z. Zhang, Configuration Optimization Design of Ti6Al4V Lattice Structure Formed by SLM. Materials, 2018. 11(10): p. 1856.
5. Ptochos, E. and G. Labeas, Elastic modulus and Poisson's ratio determination of microlattice cellular structures by analytical, numerical and homogenization methods. Journal of Sandwich Structures & Materials, 2012. 14(5): p. 597–626.
6. Lee, K.-W., S.-H. Lee, K.-H. Noh, J.-Y. Park, Y.-J. Cho and S.-H. Kim, Theoretical and numerical analysis of the mechanical responses of BCC and FCC lattice structures. Journal of Mechanical Science and Technology, 2019. 33(5): p. 2259-2266.
7. Ushijima, K., W.J. Cantwell, R.A.W. Mines, S. Tsopanos and M. Smith, An investigation into the compressive properties of stainless steel micro-lattice structures. Journal of Sandwich Structures and Materials, 2010. 13(3): p. 303-329.
8. Amirpour, M. Battley, M, Study of imperfections on compressive deformation of 3D printed polymeric lattices, Submitted in J. of Composite Structure.
9. Gumruk, R. and R.A.W. Mines, Compressive behaviour of stainless steel micro-lattice structures. International Journal of Mechanical Sciences 2013. 68: p. 125–139.
10. Yang, Y., M. Shan, L. Zhao, D. Qi and J. Zhang, Multiple strut-deformation patterns based analytical elastic modulus of sandwich BCC lattices. Materials and Design, 2019. 181: p. 107916.

  doi:10.5075/epfl-298799_978-2-9701614-0-0

A COMPUTATIONALLY EFFICIENT MULTI-SCALE STRATEGY FOR PREDICTING THE ELASTO-PLASTIC BEHAVIOUR OF SHORT FIBER COMPOSITES

Hossein Ahmadi[a,b], Mohammad Hajikazemi[a,c], Ehsan Rashidinejad[a], Yuriy Sinchuk[a],

Wim Van Paepegem[a]

a: Department of Materials, Textiles and Chemical Engineering, Faculty of Engineering and Architecture, Ghent University, Technologiepark 46, Zwijnaarde 9052, Belgium
b: SIM Program M3, Technologiepark 48, Zwijnaarde B-9052, Belgium
c: Dutch Polymer Institute (DPI), P.O. Box 902, 5600 AX, Eindhoven, Netherlands
Email: Hossein.Ahmadi@UGent.be

Abstract: *In this study, a multi-scale strategy is presented to address the nonlinear mechanical response of short fiber reinforced polymers (SFRPs) under in-plane and out-of-plane loading conditions while the effects of microstructural details are taken into account. To do so, a three-dimensional unit cell with intrinsic physical properties of the constitutive materials is adopted to predict the elasto-plastic response of SFRPs with fully aligned fibers. The homogenized response of the SFRPs unit cell is linked to an anisotropic plasticity model to represent the mechanical response in the continuum domain. Moreover, a multi-step homogenization strategy is introduced to estimate the nonlinear mechanical response of SFRPs with misaligned fibers. Finally, the validity of the suggested model is thoroughly investigated using RVEs with complex microstructures.*

Keywords: Short fiber reinforced polymers (SFRPs); Anisotropic plasticity; Periodic boundary conditions (PBCs); Unit cell; Homogenization

1. Introduction

Short fiber reinforced polymers (SFRPs) are gaining widespread popularity in many industrial applications [1]. Predicting the nonlinear mechanical behavior of SFRPs is an essential step for understanding the performance of such composite systems. However, due to the intricacy of SFRPs' microstructures, evaluating their mechanical behavior is not an easy task and requires much effort.

Various analytical and numerical homogenization approaches have been developed to predict the mechanical behavior of SFRPs and link the effective material properties to their underlying microstructure. The mean-field homogenization approaches are well-known closed-form techniques for estimating the homogenized response of composite materials [2, 3]. Although these strategies lead to good predictions for the elastic behavior of the SFRPs, their accuracy in the nonlinear regime is still a challenging topic [4, 5]. On the other hand, the finite element method has been widely employed to obtain the mechanical behavior of composite materials in different length scales [6]. This method can model RVEs having complex microstructures with the possibility to consider different types of nonlinearity. Nevertheless, the main limitation of this approach is high computational costs for predicting the effective mechanical response of complex microstructures. To overcome this problem, it is useful to replace the complex and time-consuming FEM RVE modeling with a simplified unit cell. For this reason, various numerical studies have utilized the single fiber unit cell to determine the homogenized response of fully aligned SFRPs [7-9]. However, the mechanical response of such

microstructure is highly dependent on their packing configuration [10]. Considering a simplified multi-fiber unit cell can help to reduce the effects of fiber packing configuration. In order to be able to use the nonlinear mechanical response of material for structural level analysis, there is a requirement to link the obtained microscopic results to an anisotropic constitutive law. Hill's plasticity model [11] has attracted a lot of attention for predicting the nonlinear mechanical response of heterogeneous materials in the literature.

The main aim of this study is to suggest a simplified numerical multi-scale framework to evaluate the nonlinear mechanical response of SFRPs with complex microstructure under the in-plane and out-of-plane loading conditions. In this regard, an efficient unit cell is introduced to represent the nonlinear mechanical behavior of SFRPs with fully aligned fibers. Then, the homogenized responses of such unit cells are coupled with anisotropic plasticity models to describe the mechanical behavior of materials at the continuum level. The resulting anisotropic plasticity model is used in a multi-step homogenization strategy [3] to predict the homogenized response of SFRPs with complex microstructures. Finally, various complex RVEs are analyzed to show the efficiency and accuracy of the proposed methodology.

2. Methodology

2.1 Microstructural analysis

In order to investigate the nonlinear mechanical behavior of SFRPs, the microscale analysis is performed using finite element modeling. The periodic boundary conditions (PBCs) are efficient numerical tools to reduce the computational cost of numerical simulation in different length scales [12]. This approach relies on coupling the nodal displacement fields of parallel boundaries via a linear equation as [13]

$$u_j^{i+} - u_j^{i-} = \varepsilon_{ij} l_i \quad (i\ and, j = x, y, z) \tag{1}$$

where u and l indicate the displacement fields and the length of RVE, respectively. The average stress and strain responses of the composite material can be determined using data from the integration points of the whole RVEs, which are provided as

$$\bar{\sigma}_{ij} = \frac{1}{V}\int_V \sigma_{ij} dV \tag{2}$$

$$\bar{\varepsilon}_{ij} = \frac{1}{V}\int_V \varepsilon_{ij} dV \tag{3}$$

In this work, a multi-fiber unit cell is considered to predict the nonlinear mechanical response of aligned SFRPs. Fig. 1 demonstrates the utilized geometry and mesh for such unit cells.

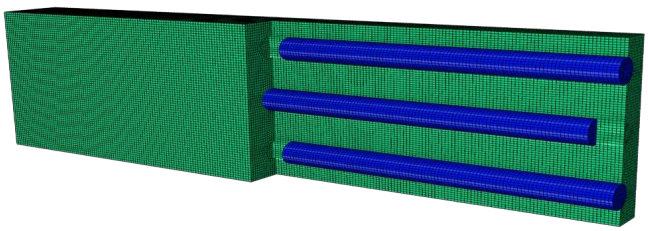

Figure 1. Selected unit cell to obtain the nonlinear mechanical response of SFRPs.

2.2 Plasticity model

  doi:10.5075/epfl-298799_978-2-9701614-0-0

It is well-known that the SFRPs demonstrate anisotropic mechanical response under different loading conditions. Due to the high computational cost of micro-scale modeling, microstructural analysis cannot be directly used for the structural level analysis of materials. For this reason, there is a requirement to benefit from the existing anisotropic constitutive laws. In this study, Hill's plasticity model, which is already implemented in a wide range of finite element commercial software, is employed.

$$f(\sigma) = \sqrt{F(\sigma_{22} - \sigma_{33})^2 + G(\sigma_{33} - \sigma_{11})^2 + H(\sigma_{11} - \sigma_{22})^2 + 2L\sigma_{23}^2 + 2M\sigma_{31}^2 + 2N\sigma_{12}^2} \quad (4)$$

where *F*, *G*, *H*, *L*, *M* and *N* are the anisotropic plasticity parameters that are usually calibrated based on the experimental or numerical data.

2.3 Multi-step homogenization

Different two-step homogenization strategies have been reported by researchers [3, 14-16] to estimate the mechanical response of composite materials with complex microstructures using numerical and analytical approaches. In this work, a multi-step homogenization strategy is suggested to take into account the effects of microstructural details in the effective mechanical response. Based on this strategy, the multi-step homogenization is directly performed in the finite element analysis without the requirement to use analytical approaches. To do so, the anisotropic plasticity model is linked to the Pseudo-grain and a meso-scale laminate analogy to consider the effects of fiber misalignment as well as the core and shell structure.

3. Results

It is undeniable that simplification of micro-scale modeling and reducing the computational cost in this scale provide a useful instrument for obtaining the nonlinear mechanical response of SFRPs. To this end, a multi-fiber unit cell is considered to predict the mechanical response of SFRPs with aligned fibers while the interactions between the fibers are considered. On the other hand, a multi-fiber RVE is selected to examine the efficiency of the utilized unit cell (see Fig. 2). *Fig. 3* indicates the prediction of the nonlinear mechanical response of glass SFRPs based on the generated RVE and the utilized unit cell.

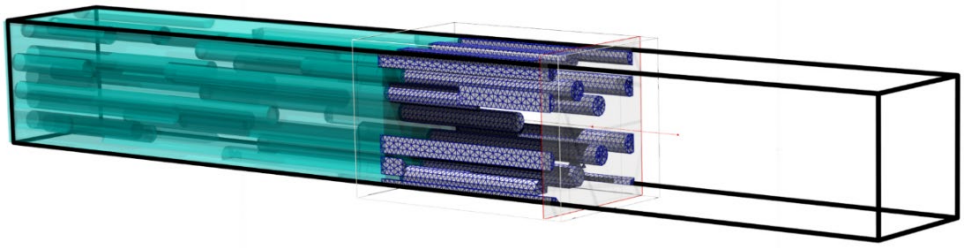

Figure 2. Sample of generated RVE to demonstrate the validation of selected unit cell.

  doi:10.5075/epfl-298799_978-2-9701614-0-0

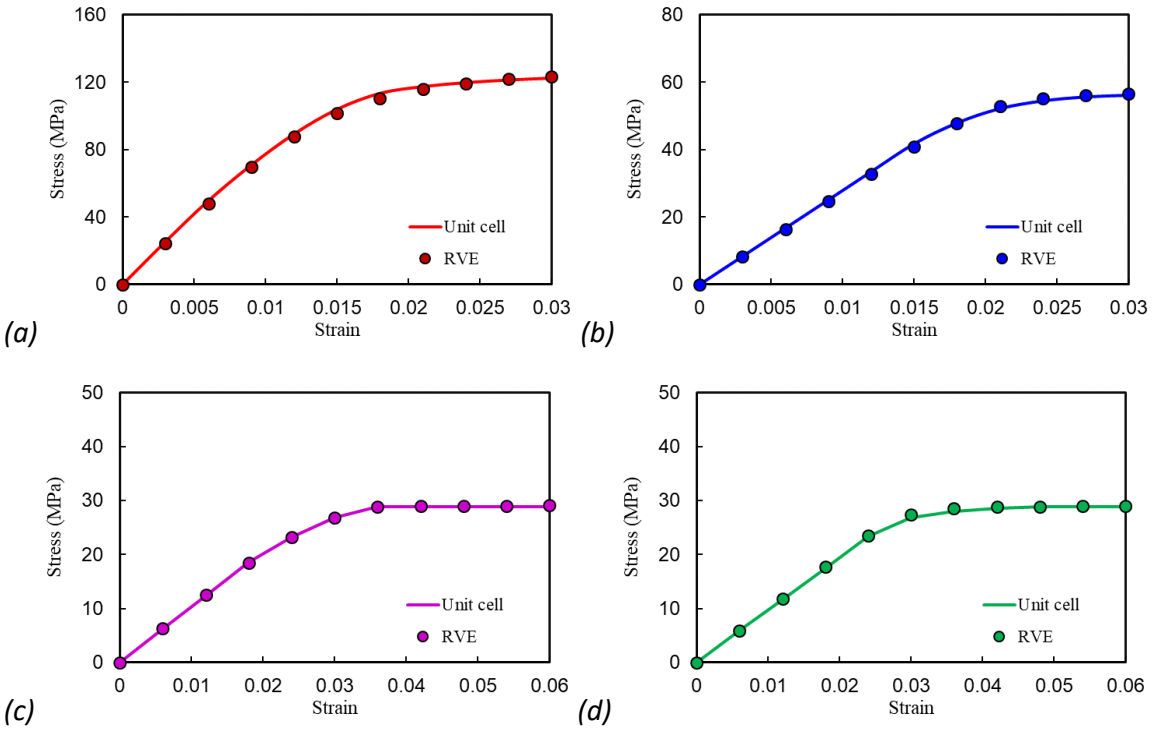

Figure 3. Evaluated stress-strain response of glass SFRPs with aligned fibers under different loading conditions; (a) tensile load in the fiber direction, (b) tensile load in the transverse direction, (c) In-plane shear load and (d) out-of-plane shear load.

It is clear from the results that the employed unit cell provides good predictions for the nonlinear response of aligned SFRPs in different loading conditions. The homogenized mechanical response is then bridged to the anisotropic constitutive law to describe the nonlinear response with low computational costs. In this regard, the material parameters of Hill's plasticity are identified using the obtained microscopic results. Afterward, the anisotropic material response is utilized in the multi-step homogenization strategy based on numerical method to address the nonlinear mechanical response of complex microstructures. To investigate the validity of the proposed multi-scale approach, an RVE with misaligned fiber is selected (see Fig. 3).

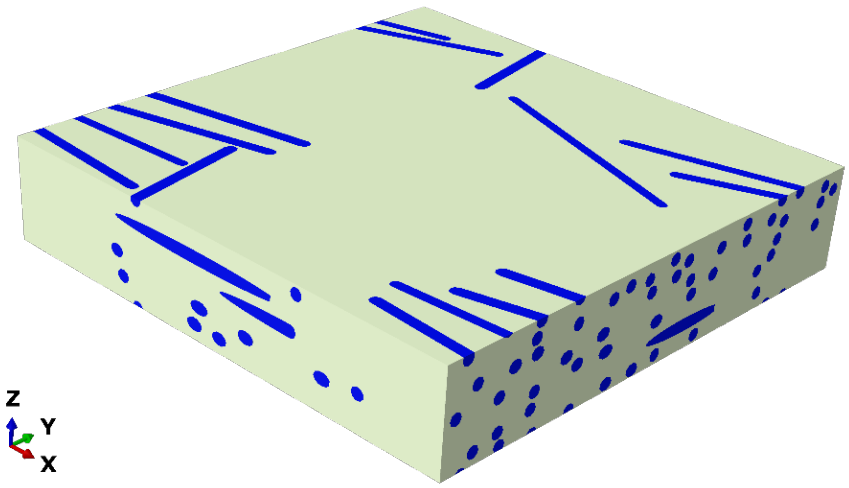

Figure 4. Sample of generated RVE with misaligned fiber to demonstrate the potential of the proposed multi-scale strategy.

Fig. 5 presents the results of different approaches in predicting the nonlinear mechanical response of glass SFRPs with misaligned fibers.

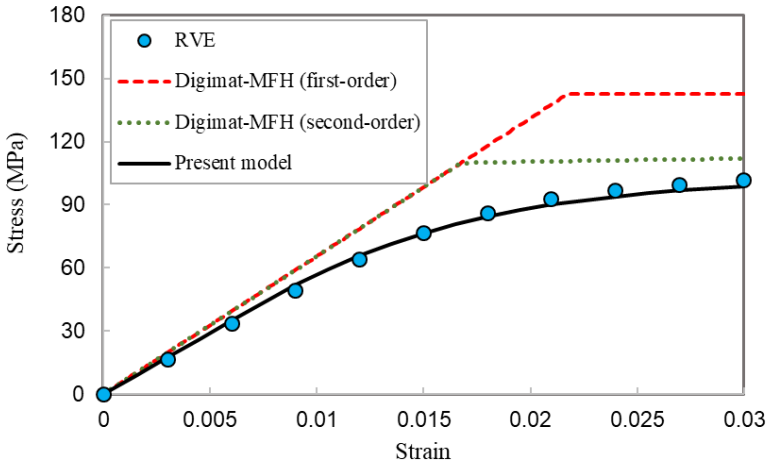

Figure 5. Evaluated stress-strain response of glass SFRPs with misaligned fibers under tensile load.

The evaluated data illustrates that there is a good agreement between the RVE generated results and the obtained results from the proposed strategy. In addition to the results obtained from the FEM RVE analysis and those obtained from the present model based on calibaration of Hills' plasticity model with simplified FEM unit cells, the results of mean-field homogenization approach with first and second-order Mori-Tanaka [17] are provided. Considering the time-consuming FEM RVE results as the benchmark, it can be clearly seen that the current approach is providing much more accurate results in comparison to the different MFH approaches.

4. Conclusion

The following conclusions can be drawn from this work:

- A simplified multi-fiber unit cell was introduced to predict the nonlinear mechanical behavior of SFRPs.
- A straightforward numerical multi-scale framework was suggested to evaluate the nonlinear mechanical response of SFRPs at structural levels.
- Finite element analysis was performed to obtain the effective mechanical response of SFRPs at micro-and meso-scale.
- Hill's anisotropic plasticity model was employed to bridge the microscopic response of the material to the continuum domain.
- A multi-step homogenization strategy is introduced to take into account the microstructural information.

Acknowledgments

The work leading to this publication has been funded by the ICON project "ProPeL", which fits in the MacroModelMat (M3) research program, coordinated by Siemens (Siemens Digital

Industries Software, Belgium), and funded by SIM (Strategic Initiative Materials in Flanders) and VLAIO (Flemish government agency Flanders Innovation & Entrepreneurship). M. Hajikazemi acknowledges the financial support of Fonds voor Wetenschappelijk Onderzoek (Grant No. 1202522N). The work of M. Hajikazemi forms part of the research programme of DPI, project 812T17.

5. References

1. Xu H, Kuczynska M, Schafet N, Welschinger F, Hohe J. Modeling the anisotropic temperature-dependent viscoplastic deformation behavior of short fiber reinforced thermoplastics. Composites Science and Technology. 2021;213:108958.
2. Benveniste Y. A new approach to the application of Mori-Tanaka's theory in composite materials. Mechanics of Materials. 1987;6(2):147-57.
3. Ahmadi H, Hajikazemi M, Rashidinejad E, Sinchuk Y, Van Paepegem W. A hierarchical multi-scale analytical approach for predicting the elastic behavior of short fiber reinforced polymers under triaxial and flexural loading conditions. Composites Science and Technology. 2022:109452.
4. Doghri I, Brassart L, Adam L, Gérard JS. A second-moment incremental formulation for the mean-field homogenization of elasto-plastic composites. International Journal of Plasticity. 2011;27(3):352-71.
5. Doghri I, Ouaar A. Homogenization of two-phase elasto-plastic composite materials and structures: Study of tangent operators, cyclic plasticity and numerical algorithms. International Journal of Solids and Structures. 2003;40(7):1681-712.
6. Ahmadi H, Jahanshahi M, Khoei AR, Bordas S. Mechanical behavior of multilayer graphene reinforced epoxy nano-composites via a hierarchical multi-scale technique. Carbon Trends. 2021;4:100048.
7. Breuer K, Stommel M. RVE modelling of short fiber reinforced thermoplastics with discrete fiber orientation and fiber length distribution. SN Applied Sciences. 2019;2(1):91.
8. Huang Z-M, Zhang C-C, Xue Y-D. Stiffness prediction of short fiber reinforced composites. International Journal of Mechanical Sciences. 2019;161-162:105068.
9. Mirkhalaf SM, Eggels EH, van Beurden TJH, Larsson F, Fagerström M. A finite element based orientation averaging method for predicting elastic properties of short fiber reinforced composites. Composites Part B: Engineering. 2020;202:108388.
10. Rashidinejad E, Ahmadi H, Hajikazemi M, Van Paepegem W. Modeling of geometric configuration and fiber interactions in short fiber reinforced composites via new modified Eshelby tensors and enhanced mean-field homogenization. Mechanics of Materials. 2021:104059.
11. Hill R. A Theory of the Yielding and Plastic Flow of Anisotropic Metals. Proceedings of the Royal Society of London Series A, Mathematical and Physical Sciences. 1948;193(1033):281-97.
12. Ahmadi H, Hajikazemi M, Van Paepegem W. A computational study about the effects of ply cracking and delamination on the stiffness reduction of damaged lamina and laminate. International Journal of Damage Mechanics. 2022;31(3):325-47.
13. Ahmadi H, Hajikazemi M, Van Paepegem W. Closed-form analytical formulae for prediction of homogenized ply properties and laminate thermo-elastic constants in symmetric laminates containing ply cracks in multiple orientations. Composite Structures. 2020;241:112061.

14. Pierard O, Friebel C, Doghri I. Mean-field homogenization of multi-phase thermo-elastic composites: a general framework and its validation. Composites Science and Technology. 2004;64(10):1587-603.
15. Kammoun S, Doghri I, Adam L, Robert G, Delannay L. First pseudo-grain failure model for inelastic composites with misaligned short fibers. Composites Part A: Applied Science and Manufacturing. 2011;42(12):1892-902.
16. Mirkhalaf SM, van Beurden TJH, Ekh M, Larsson F, Fagerström M. An FE-based orientation averaging model for elasto-plastic behavior of short fiber composites. International Journal of Mechanical Sciences. 2022;219:107097.
17. Digimat A. Software for the Linear and Nonlinear Multi-Scale Modeling of Heterogeneous Materials; e-Xstream Engineering: Louvain-la-Neuve. Belgium; 2011.

BUCKLING TEST OF STIFFENED PANELS: EVALUATION OF POST-BUCKLING AND FAILURE BY TESTING AND LAYERWISE MODELS

R. Augello[a], A. Pagani[a], E. Carrera[a], D. M. J. Peeters[b], A. Prado[c], H. E. A. A. Santos[d], P. H. Galeb[e], P. H. Cabral[c]

[a] MUL2, Department of Mechanical and Aerospace Engineering, Politecnico di Torino, Torino, Italy

[b] Delft University of Technology, faculty of Aerospace Engineering, section: Aerospace Structures and Computational Mechanics, Delft, Netherlands

[c] Embraer S.A., São José dos Campos, Brazil

[d] Instituto Tecnológico de Aeronáutica, São José dos Campos, Brazil

[e] Universidade Federal de Itajubá, Itajubá, Brazil

Abstract: *The present paper deals with the buckling and post-buckling analysis of a multilayered composite reinforced panel. The panel, designed for aeronautical applications, results in a complex stacking sequence, and the development of a refined model able to describe its geometrical nonlinear behavior is mandatory to avoid the usage of highly computational effort-required 3D finite elements. The proposed approach is a finite element analysis based on the Carrera Unified Formulation (CUF). Thanks to CUF, a 1D model of the composite panel can be formulated and complicated stress fields within the structure can be evaluated, so that the nonlinear behavior is fully described. A refined Equivalent Single Layer (ESL) technique is employed, making use of Lagrange polynomials for the description of the stacking sequence. The results clearly demonstrate the reliability of this approach, comparing the linearized buckling and nonlinear post-buckling solutions with those from Nastran (1D, 2D and 3D) and experiments.*

Keywords: Post-Buckling; Reinforced Panel; Multilayered structure; Geometrical Nonlinear Analysis; Carrera Unified Formulation.

1. Introduction

The design of reinforced composite aerospace structures and the choice of safety margins are strongly affected by our predictive capability. The analysis of buckling and many other failure mechanisms require~~s~~ the use of mathematical models able to capture 3D complex internal stress states, which is a major concern in composite laminates and represents a challenge of today structural simulations. For this reason, scientists have focused on the development of mathematical models able to cut down the computational effort required for the analysis while maintaining a high level of accuracy.

In the present work, we use a detailed model to characterize the post-buckling behavior and the stress state of a stringer-reinforced composite wing panel subjected to uniform compression. The model under consideration has layerwise capabilities and is based on the Carrera Unified Formulation (CUF) [1]. According to CUF, refined structural theories can be formulated automatically as a generalization of the three-dimensional equilibrium equations and by making use of arbitrary expansion of the primary unknowns, which can be either distributed along 1D

  doi:10.5075/epfl-298799_978-2-9701614-0-0

(CUF beam models) or 2D (CUF plate models) supports. Depending on the choice of the expansion functions, low- to high-order structural theories can be used in a unified manner. In this work, for example, we employ a piecewise description of the cross-section kinematics by Lagrange polynomials. These models have been demonstrated to be highly efficient and effective for the simulation of laminates in both linear and nonlinear regimes [2,3] and satisfy the C_z^0requirements [4].

2. Numerical model of the reinforced panel

The geometry of the numerical model of the analyzed reinforced panel is presented in Fig. 1, where h_1= 9.52 mm, h_2= 39.3 mm, h_3 = 3.66 mm, t = 7.3 mm, b = 270 mm, b_1 = 70 mm, l_1 = 50 mm and l = 690 mm. The dark gray zones shown in Fig. 1 represent the experimental blocks which were used to apply the external load and to constrain the panel. Moreover, Fig. 1 shows the stacking sequence of the material, which properties are E_1 = 119 GPa, E_2 = 9.8 GPa, E_3= 4.67 GPa, ν_{12}= 0.316, ν_{13}= 0.26, ν_{23}= 0.33, G_{12}= 4.7 GPa, G_{13} = G_{23} = 1.76 GPa and ρ = 1580 kg/m³. It should be noted that the out-of-plane properties were assumed, since they were not available from the manufacturer.

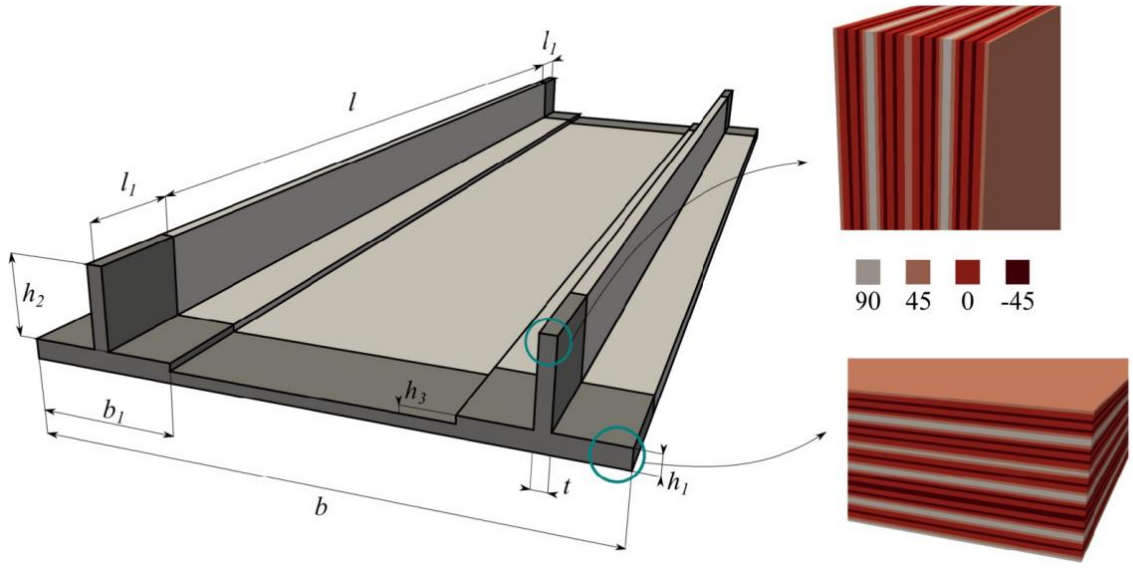

Figure 1. Geometry and stacking sequence of the composite stiffened panel.

In order to develop the Finite Element (FE) model of the stiffened composite panel, the Carrera Unified Formulation (CUF) is recalled. CUF is used in this paper for the derivation of the geometrical nonlinear governing equation. According to CUF and Fig. 2, the three-dimensional displacement field $\boldsymbol{u}(x, y, z)$ of the panel can be written as follows:

$$\boldsymbol{u}_k(x, y, z) = F_\tau(x, z) N_i(y) \boldsymbol{q}_{k\tau i} \qquad \tau = 1, 2, \dots M \quad i = 1, 2, \dots N_n$$

where y is placed in the longitudinal direction of the panel, (x, z) are the coordinates of the cross-section, $\boldsymbol{q}_{k\tau i}$ is the vector of the nodal unknowns evaluated at each of the Nn node at the $k-th$ layer level; $N_i(y)$, shown in blue in Fig. 2, represents the shape functions in the y direction; and $F_\tau(x, z)$, shown in red in Fig. 2, are the expansion functions of the cross-sectional area. Repeating indexes denote summation.

  doi:10.5075/epfl-298799_978-2-9701614-0-0

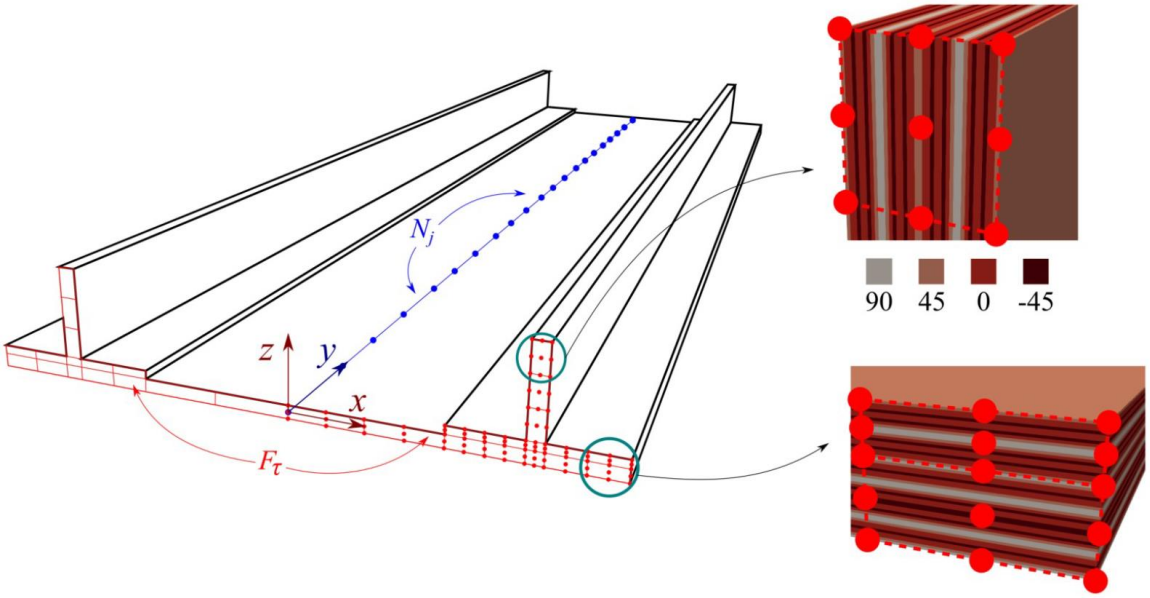

Figure 2. Mathematical 1D CUF model of the composite stiffened panel.

In this work, refined models are employed by using quadratic Lagrange Expansions. This expansion function, introduced in [2], makes use of opportune quadratic interpolation of the variables evaluated at the Lagrange Point (the red circles in Fig. 2). The interpolation functions are based on Lagrange polynomials, and they denote the order of the expansion (quadratic in this work). The Lagrange points can be used to define any geometric shape and, as in this work, to denote the domain of each layer in the classical Layer-Wise (LW) approach and of a group of plies in the refined Equivalent Single Layer (ESL) approach, as shown in Fig. 2.

2.1 Nonlinear governing equations

The stress, **σ**, and strain, **ε**, components are expressed in vectorial form with no loss of generality,

$$\boldsymbol{\sigma} = \{\sigma_{xx}\ \sigma_{yy}\ \sigma_{zz}\ \sigma_{xz}\ \sigma_{yz}\ \sigma_{xy}\}^T \qquad \boldsymbol{\varepsilon} = \{\varepsilon_{xx}\ \varepsilon_{yy}\ \varepsilon_{zz}\ \varepsilon_{xz}\ \varepsilon_{yz}\ \varepsilon_{xy}\}^T$$

As far as the geometrical relations are concerned, the Green-Lagrange nonlinear strain components are considered. Therefore, the displacement-strain relations are expressed as

$$\varepsilon = \varepsilon_l + \varepsilon_{nl} = (\boldsymbol{b}_l + \boldsymbol{b}_{nl})\boldsymbol{u}$$

where $\boldsymbol{b}_l$ and $\boldsymbol{b}_{nl}$ are the linear and nonlinear differential operators. Regarding the constitutive relations, linear elastic material is assumed in this work, thus Hooke's law can be employed:

$$\boldsymbol{\sigma} = \boldsymbol{C}\boldsymbol{\varepsilon}$$

where **C** is the material matrix, whose complete form can be found in [5].
In this work, the principle of virtual work is recalled for the derivation of the FE governing equations, which, for a generic structure, can be expressed as:

$$\delta L_{int} = \delta L_{ext}$$

where δL_{int} is the virtual variation of the work of the internal loads (i.e., the strain energy) and δL_{ext} is the virtual variation of the work of the external loads.
The first term of the previous equation can be written as:

$$\delta L_{int} = \int_V \delta \boldsymbol{\varepsilon}^T \boldsymbol{\sigma} \, dV$$

where V is the volume of the body. Introducing the geometrical and constitutive relations, it takes the following form:

$$\delta L_{int} = \delta \boldsymbol{q}_{sj}^T \boldsymbol{K}_S^{ij\tau s} \boldsymbol{q}_{\tau i}$$

The argument of the integral represents the so-called secant stiffness matrix $\boldsymbol{K}_S^{ij\tau s}$. Its complete form is omitted here for the sake of brevity, but can be found in [3,6].
The right term of the principle of virtual work, omitting some mathematical steps that can be found in Carrera et al. [1], can be written as:

$$\delta L_{ext} = \delta \boldsymbol{q}_{sj}^T \boldsymbol{p}_{sj}$$

so that

$$\boldsymbol{K}_S^{ij\tau s} \boldsymbol{q}_{\tau i} - \boldsymbol{p}_{sj} = 0$$

The previous equation can be arbitrarily expanded to reach any desired theory, from low- to higher-order ones, by choosing the values for $\tau, s = 1, 2, \dots, M$ and $i, j = 1, 2, \dots, p + 1$ to give:

$$\boldsymbol{K}_s \boldsymbol{q} - \boldsymbol{p} = 0$$

where $\boldsymbol{K}_s$, $\boldsymbol{q}$, and $\boldsymbol{p}$ are the global, assembled finite element arrays of the final structure. The final equation represents a nonlinear algebraic system of equation for which an alternative method is needed. We employ here the same procedure detailed in the work by Pagani and Carrera [6], where a Newton-Raphson scheme is derived by making use of a path following constraint. The main steps of the procedure are explained in this work. This procedure demands for the linearization of the nonlinear governing equations. As a result, we need to introduce the so-called tangent stiffness matrix $\boldsymbol{K}_T = \frac{d(\boldsymbol{K}_s \boldsymbol{q} - \boldsymbol{p})}{d\boldsymbol{q}}$. The explicit form of $\boldsymbol{K}_T$ is not given here, but it is derived in a unified form in [7]. The resultant system of equations needs to be constrained. In this work, an opportune arc-length path-following constraint is adopted. More detail about the arc-length method adopted can be found in the works by Carrera [8] and Crisfield [9,10].

2.2 Refined equivalent single layer

In this paper, a refined equivalent single layer technique for the description of the composite panel is proposed. This approach makes use of the variable kinematics characteristics of CUF formalism. In fact, one can introduce refined mechanical theories with computational efficiency by opportunely using Lagrange polynomials. In this technique, the model of the composite structure is built to have a group of plies with the ESL assembling approach (homogenizing the mechanical properties), as depicted in Fig. 2. In addition, Fig. 3 summarizes the assembling technique using ESL. Clearly, despite the larger number of plies, the assembling procedure does

  doi:10.5075/epfl-298799_978-2-9701614-0-0

not require a huge computational effort, compared to the LW assembling, which is described in Fig. 4.

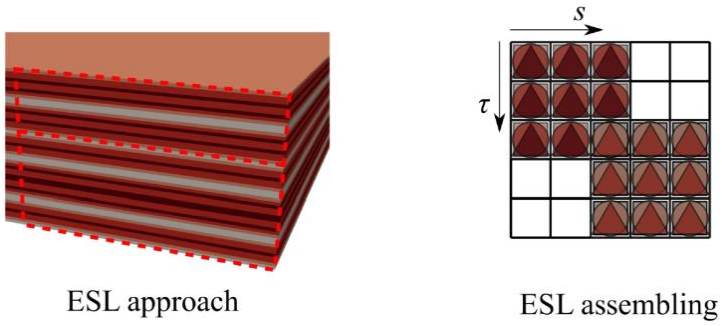

Figure 3. ESL approaches for the composite stiffened panel.

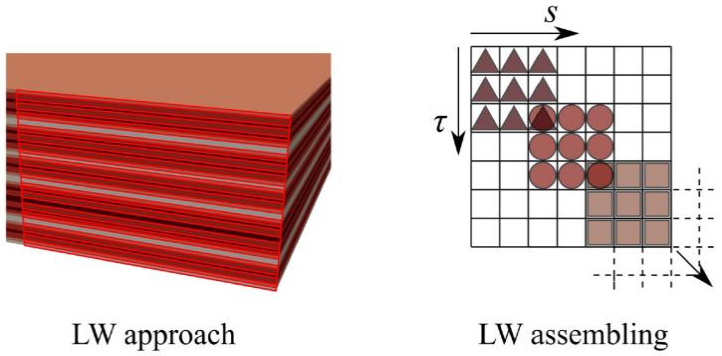

Figure 4. LW approaches for the composite stiffened panel.

3. Numerical results

The numerical results report the linearized buckling analysis of the stiffened panel, comparing the results from experiments to those obtained using LW and refined ESL models. Finally, the main post-buckling solutions, using the refined ESL model, are given and compared to the experimental results and those using Nastran 2D, 2D (skin) +1D (stringers), and 3D formulations. The details of the experimental setup are given in [11]. Briefly, 3 panels were manufactured, as depicted in Fig. 5. and the shortening was measured using two linear vertical displacement transducers (LVDT): one was placed on each side of the panel to ensure the panel was loaded in pure compression and no moment was induced on it.

Figure 5. Three manufactured stiffened panel and experimental buckling setup.

  doi:10.5075/epfl-298799_978-2-9701614-0-0

3.1 Linearized buckling

The first buckling load evaluated with experimental data, LW and refined ESL models is reported in Table 1.

Table 1: Measured buckling load and comparison between experimental results and numerical simulation.

Model	Buckling load, kN	DOF	Error %
Experimental	744.68	-	-
LW	739.17	715365	0.03 %
Refined ESL	744.12	10521	0.64 %

The buckling load is perfectly evaluated by the proposed model, compared to the experimental results, and with a significant gain on the computational cost, compared to the LW model. Moreover, Table 2 reports the first four buckling modes numerically evaluated with LW and refined ESL. Error % is obtained comparing to the average of tests.

Table 2: Measured buckling load and comparison between LW and refined ESL models.

Model	Buckling mode 1	Buckling mode 2	Buckling mode 3	Buckling mode 4
LW	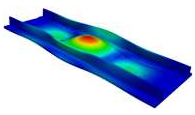	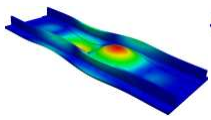	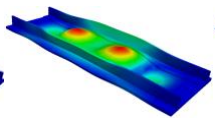	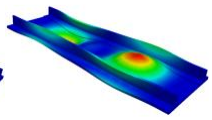
	739.17 kN	744.86 kN	809.42 kN	829.87 kN
Refined ESL	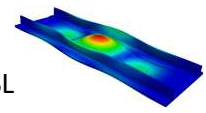	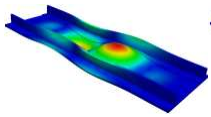	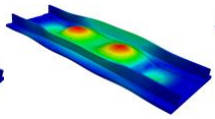	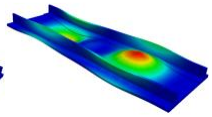
	744.12 kN	749.96 kN	815.78 kN	836.96 kN
Diff %	0.67 %	0.68 %	0.79 %	0.85 %

It can be concluded that the proposed refined ESL model can evaluate the buckling behavior of the structure with a reliable accuracy while increasing the computational cost.

3.2 Nonlinear post-buckling

Post-buckling results are discussed hereafter. The described refined ESL model is used for the geometrical nonlinear analysis. The results are compared with those from experiments and Nastran models. The adopted Nastran models are 3:

- Mixed 1D and 2D model for the modelling of the stringers and the skin, respectively. Degrees of Freedom (DOFs): 16746;

  doi:10.5075/epfl-298799_978-2-9701614-0-0

- Full 2D model. DOFs: 22146;
- Full 3D model. DOFs: 159570.

Nastran sol400 was used for the analysis. The results in terms of end shortening are depicted in Fig. 6 and listed in Table 3. Clearly, Nastran 1D and 2D models are not able to describe the buckling and post-buckling behavior of the stiffened panel, as the estimated buckling load is higher than the one from experimental setup. On the contrary, Nastran 3D, CUF and experimental results are close to each other

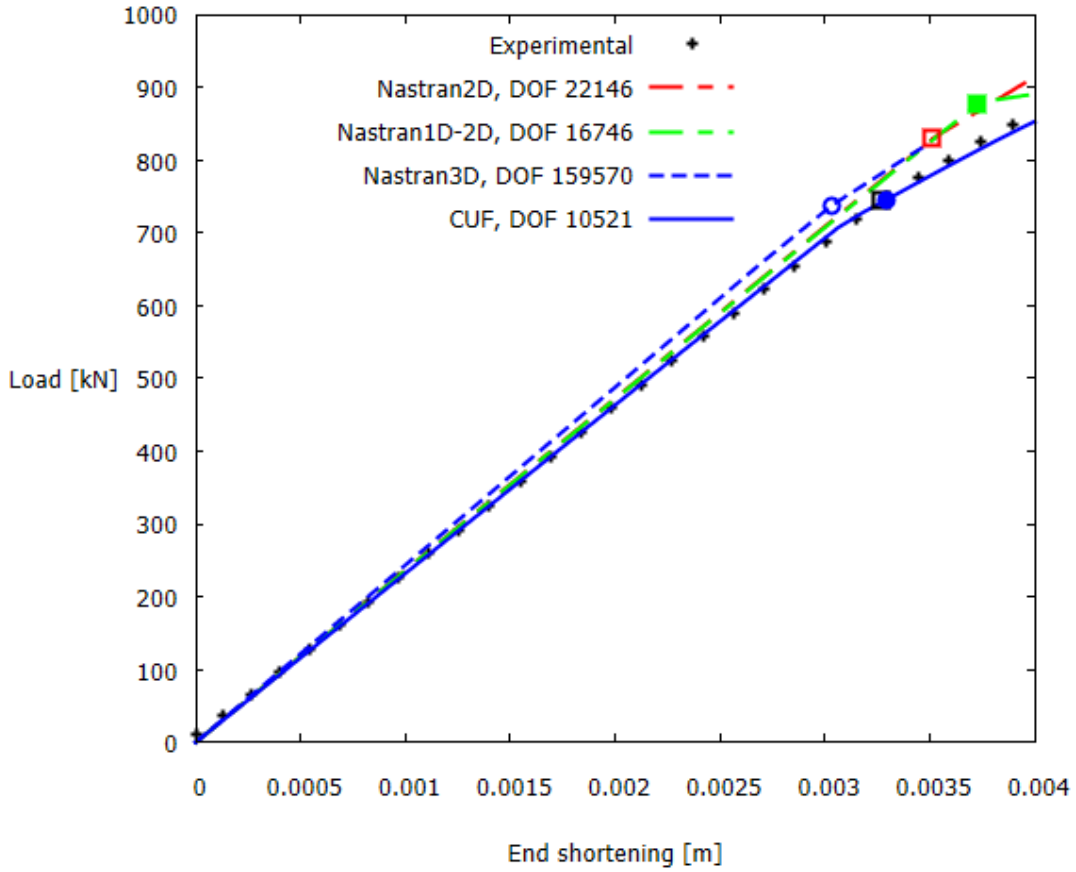

Figure 6. End-shortening vs applied load with Nastran, CUF and experimental results. Points and square indicate the buckling.

Table 3: Critical buckling load correspondent to the points and squares on Fig. 6.

Model	Shortening, m	Load, kN	DOF
Experimental	0.00327	744.676	-
Nastran 2D	0.00351	829.130	22146
Nastran 1D-2D	0.00372	877.694	16746
Nastran 3D	0.00309	729.498	159570
CUF	0.00329	728.819	10521

In addition, the post-buckling curves are reported in Fig. 7. Once again, the agreement between the refined ESL (denoted by CUF in the figure), Nastran 3D and Experimental results are close.

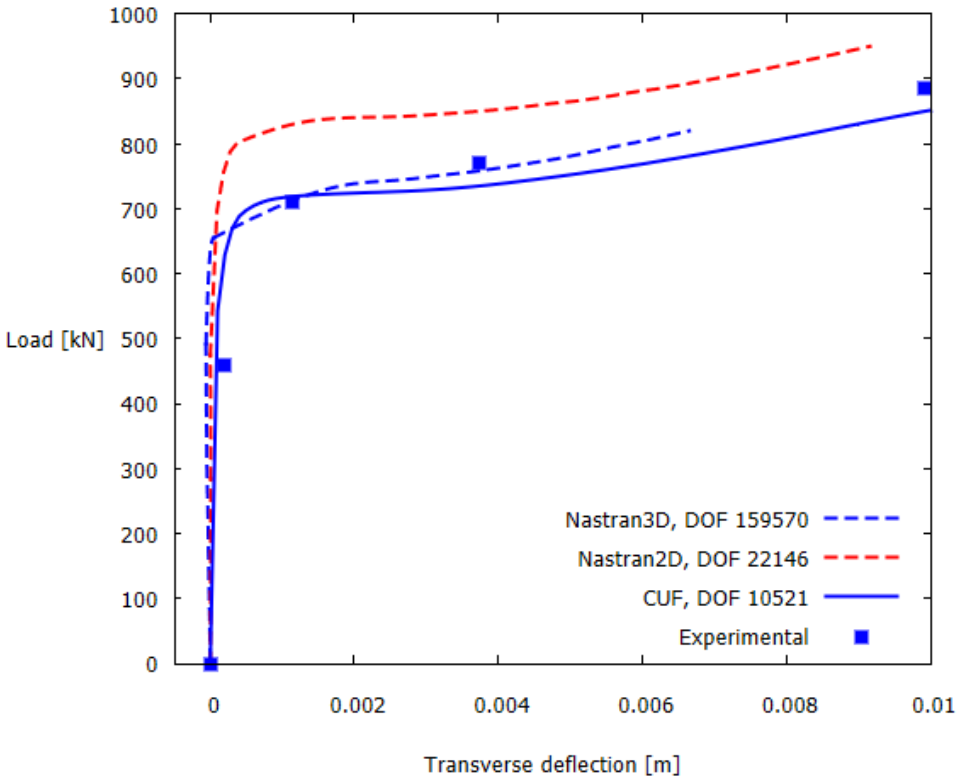

Figure 7. Transverse deflection vs load of the composite stiffened panel. Nastran, CUF and experimental results.

Finally, the refined ESL model is adopted for the evaluation of the post-buckling behavior, as reported in Fig. 8. Clearly, the model is demonstrated to be reliable.

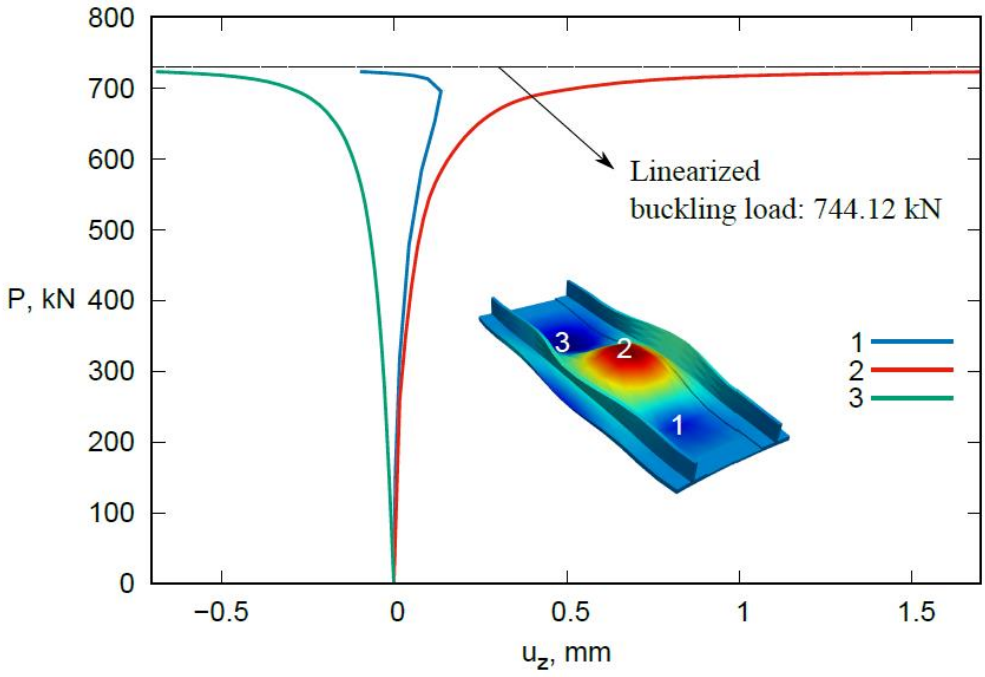

Figure 8. Numerical simulation of the post-buckling of the reinforced panel.

4. Conclusions

The present paper has the aim of analyzing the buckling and post-buckling behavior of a multilayered composite stiffened panel of aeronautical interest. Due to the complex stacking sequence, low-order mathematical models are not able to describe the 3D stress field and, thus, the post-buckling behavior. For a proper design of such structures, one must rely on heavy 3D models, which require a huge effort in terms of computational cost. However, the proposed refined ESL approach succeeds in correctly evaluating the critical point and the post-buckling behavior. This is possible thanks to CUF and its capability of developing 1D models while accounting for complicated stacking sequences by using refined expansion functions, which are based on Lagrange polynomials in this case. Results clearly show the advantage in terms of DOF gained and demonstrate that the present method can be used for the design of this kind of structures.

5. References

1. E. Carrera, G. Giunta, and M. Petrolo. *Beam structures: classical and advanced theories.* John Wiley & Sons, New York, USA, 2011.
2. E. Carrera and M. Petrolo. Refined one-dimensional formulations for laminated structure analysis. *AIAA journal*, 50(1):176-189, 2012.
3. A. Pagani and E. Carrera. Unified formulation of geometrically nonlinear refined beam theories. *Mechanics of Advanced Materials and Structures*, 25(1):15-31, 2016.
4. E. Carrera. C^0_z requirements-models for the two-dimensional analysis of multilayered structures. *Composite structures,* 37(3-4), 373-383, 1997.
5. E. Carrera and M. Filippi. Variable kinematic one-dimensional finite elements for the analysis of rotors made of composite materials. *Journal of Engineering for Gas Turbines and power*, 136(9):029501, 2014.
6. E. Carrera, A. Pagani and R. Augello. Evaluation of geometrically nonlinear effects due to large cross-sectional deformations of compact and shell-like structures. *Mechanics of Advanced Materials and Structures*, pages 1-9, 2018.
7. A. Pagani and E. Carrera. Large-deflection and post-buckling analyses of laminated composite beams by Carrera unified formulation. *Composite Structures*, 170:40-52, 2017.
8. E. Carrera. A study on arc-length type methods and their operation failures illustrated by a simple model. Computers & Structures, 50(2):217-229, 1994.
9. M. A. Crisfield. A fast incremental/iterative solution procedure that handles “snap- through". In *Computational Methods in Nonlinear Structural and Solid Mechanics*. Elsevier, Amsterdam, Netherlands, 1981.
10. M. A. Crisfield. An arc-length method including line searches and accelerations. *International journal for numerical methods in engineering*, 19(9):1269-1289, 1983.
11. P.H. Cabral, E. Carrera, H.E.A.A. dos Santos, P.H.G. Galeb, A. Pagani, D. Peeters, and A.P. Prado. Experimental and numerical vibration correlation of pre-stressed laminated reinforced panel. *Mechanics of Advanced Materials and Structures*, pages 1-13, 2020.

  doi:10.5075/epfl-298799_978-2-9701614-0-0

EFFICIENT SIMULATION OF DUAL-SCALE FLOW IN RTM PROCESSES BY DOMAIN SKELETONIZATION

S. Bancora[a], C. Binetruy[a,b], S. Advani[b,a], S. Comas-Cardona[a], A. Leygue[a], E. Syerko[a]

a: Nantes Université, Ecole Centrale Nantes, CNRS, GeM, UMR 6183, F-44000 Nantes, France – simone.bancora@ec-nantes.fr
b: Center for Composite Materials, University of Delaware, Newark, Delaware 19716, USA

Abstract: *In this work we present a novel Dual-Scale Skeleton model (DSS) to simulate the mesoscopic dual-scale flow inside a fibrous layup at an affordable computational cost. Instead of using a traditional Stokes-Brinkman model to govern the flow inside and around the tows, the flow domain is separated into three interconnected subdomains. For each subdomain, the three-dimensional mesoscale geometry of yarns and channels is replaced by their medial axis representation, on which the flow is simulated by FE method. The generation of a Hybrid Skeleton mesh (2D and 1D elements) allows to reduce the computational cost of the problem while still accounting for three-dimensional effects in the flow. This allows one to carry out mesoscale simulations on relatively large domains. Although further refinements are desirable, the DSS model shows potential for application in composites process modeling.*

Keywords: dual-scale flow; RTM process modeling; skeletonization; efficient simulation

1. Introduction

In Resin Transfer Moulding (RTM) processes, a fibrous preform is compacted inside a mould and impregnated with a polymeric resin, which is later cured to obtain a structural composite part. Simulating the flow of resin as it impregnates the empty spaces within the porous preform is of great interest to process engineers, as it allows one to predict defects that may arise and/or optimize the location of the gates and vents. The flow of a resin infiltrating a dry preform is traditionally modeled at the macroscale using Darcy's law. This model, which relies on the permeability tensor of the material to compute the volume averaged velocity of the resin, is suitable for the numerical simulation of the filling of industrial scale parts. However, there are cases when this macroscale model falls short: for instance, when the upscaled permeability tensor of a certain stack cannot be characterized a priori, or when the effect of local features such as defects is to be studied. In such cases, one possibility is to model the dual-scale flow of the resin at the scale of the tows (mesoscale) to account for any local feature which is present in the input geometry. Provided that the mesoscale geometry of the preform is modeled with enough accuracy, the dual-scale flow of resin inside and around the tows can be directly simulated using the Stokes-Brinkman model [1], effectively bypassing the need for permeability characterization. However, the high computational cost of this detailed approach strongly limits the size of the domain that can be computed numerically. Consequently, the simulation of a 3D dual-scale flow is not suitable for application to entire parts, leaving the macroscale simulation the only option available to the process engineer [2]. In this work we introduce a new method to model the dual-scale filling of an RTM process at the mesoscale, at a reduced computational

  doi:10.5075/epfl-298799_978-2-9701614-0-0

cost when compared to a full 3D solution. To reduce the computational cost of the problem a series of assumptions are adopted, notably the lubrication approximation and topological skeletonization of 3D geometries. Such model, referred to as Dual Scale Skeleton (DSS) model, is introduced and validated over a simple test case before demonstrating an example application.

2. Methodology

The Dual Scale Skeleton (DSS) model is based on a series of assumptions that allow one to simplify both the governing equations and the geometrical dimension of the problem. Typically, the dual-scale flow of a resin in porous media such as dry textiles is modeled by combining Stokes and Darcy-Brinkman flow models, each describing the flow in a specific domain [1]. Stokes flow is generally accepted to model the flow of resin in the clear-fluid domain (the spaces in-between tows) under the assumption of creeping flow. Darcy's law models are conveniently applied to the flow inside the yarns [2] which are seen as porous domains and the velocity of the resin is phase averaged. Adding an additional term yields the Brinkmann's equation, which allows one to have stress continuity at the interface between the channels and the tows. Instead of solving the classical Stokes-Brinkman dual-scale problem, the DSS model is formulated through a series of assumptions: i) Lubrication approximation is adopted in the channels subdomain. ii) Darcy's law is valid in the tows subdomain. iii) A special "interface" domain ensures the interaction between channels and tows in the computation of the pressure solution. A key element in the DSS model is the topological skeletonization of the domains. Reynolds and Darcy equations adopt a gap-averaged or phase-averaged velocity definition, allowing one to reduce the geometrical representation of the channel and tow volumes from a three-dimensional volume to a two-dimensional surface, neglecting the dimension transverse to the characteristic direction of flow. Such surface is referred to as medial surface skeleton, or in its discrete representation as medial skeleton mesh.

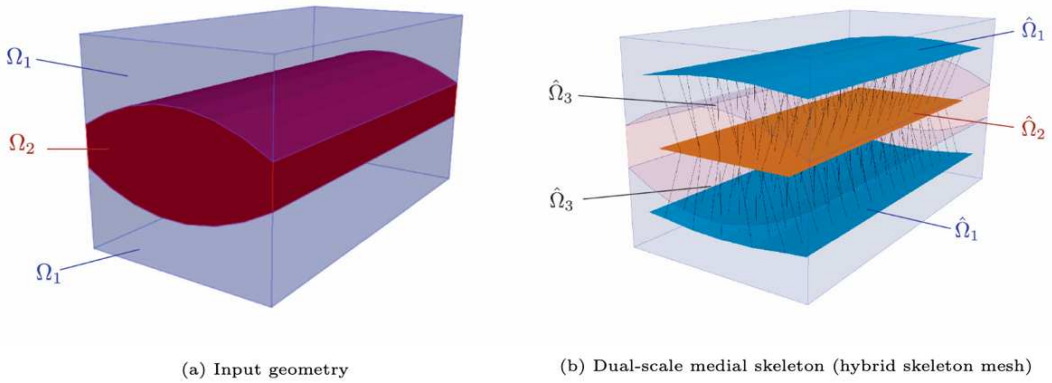

Figure 1. Yarn immersed in a channel: original three-dimensional geometry and corresponding hybrid skeleton mesh

  doi:10.5075/epfl-298799_978-2-9701614-0-0

2.1 Skeletonization

Flow models in porous media based on medial skeletons have been developed before. The permeability of rock fractures was estimated using Reynolds equation and the medial skeleton in [4, 5], for 2D and 3D skeletons. Wong et al. in [6] solved lubricated flow on a 1D medial axis mesh to compute the upscaled permeability of textiles. In the DSS model, the 3D geometries of channel and tow subdomains are replaced by a 2D medial skeleton mesh which is assigned the gap height ($h(\boldsymbol{x})$) at every node from the original boundaries. The interaction between the channel and tow domains is obtained by introducing a third "interface" subdomain composed by one-dimensional elements which connects them. Such mixed element skeleton mesh is named Hybrid Skeleton mesh. In Fig.1a an example of input domain is shown. The channel and tow subdomains are labeled as Ω_1 and Ω_2 respectively. In Fig.1b the corresponding Hybrid Skeleton mesh is shown. The physical subdomains Ω_1 and Ω_2 are reduced to their 2D skeleton versions $\widehat{\Omega}_1$ (channels), $\widehat{\Omega}_2$ (tows) and linked through the 1D elements $\widehat{\Omega}_3$ (interface).

2.2 DSS model

The DSS model is formulated as an assembly of three different subdomains under the principle of mass conservation (continuity equation). For each one, different modeling assumptions are adopted.

Channels domain ($\widehat{\boldsymbol{\Omega}}_{\boldsymbol{1}}$) Flow in the channel domain is modeled using Reynolds equation, under the assumption of lubricated flow. Continuity equation can be expressed for the gap-averaged Reynolds velocity $\langle \mathbf{u} \rangle$ by applying the volume averaging theorem of the divergence operator [7].

$$\nabla \cdot \left\langle -\frac{1}{\mu}\frac{h^2}{12}\nabla p \right\rangle + \frac{1}{V}\int_{\Gamma} q \; dx = 0 \tag{1}$$

where h denotes the channel gap height. The second term in Eq.1 is used to account for the transverse flow at the interface with the tows.

Tows domain ($\widehat{\boldsymbol{\Omega}}_{\boldsymbol{2}}$) Flow in the tow domain is modeled using Darcy's law. As in Eq. 1, the interface extra term is present:

$$\nabla \cdot \left\langle -\frac{k}{\mu}\nabla p \right\rangle + \frac{1}{V}\int_{\Gamma} q \; dx = 0 \tag{2}$$

where k denotes the longitudinal permeability of the tow.

Interface domain ($\widehat{\boldsymbol{\Omega}}_{\boldsymbol{3}}$) The interface element couples the flow of resin between the mesh of the channel domain $\widehat{\Omega}_1$ and the mesh of the tow domain $\widehat{\Omega}_2$. The lubrication approximation is adopted in the channels, therefore the pressure gradient in the direction of the interface element is null in the region $\widehat{\Omega}_1$. On the other hand, the pressure gradient in the direction of the interface element is not null in the region $\widehat{\Omega}_2$. Therefore, the flow velocity in the interface element is defined using Darcy's law, but the pressure gradient is not null only in the portion of the element inside $\widehat{\Omega}_2$.

$$q = u \cdot n = -\frac{K_t}{\mu}\frac{\partial p}{\partial s} \tag{3}$$

  doi:10.5075/epfl-298799_978-2-9701614-0-0 published under CC BY-NC 4.0 license

where K_t is the yarn transverse permeability, $\boldsymbol{n}$ is the interface normal and s denotes the curvilinear coordinate of the 1D element.

The pressure derivative is defined as a linear pressure gradient so that only the tow region is considered:

$$\frac{\partial p}{\partial s} = \frac{p_i - p_j}{L_e \, \delta_e} \tag{4}$$

where L_e is the total length of the element, and δ_e is a scalar coefficient corresponding to the fraction of the element length which is immersed in the tow domain. Finally, Eqs. 1-3 expressed in FE weak form are combined into a global linear system that can be solved given appropriate boundary conditions.

2.3 Validation

The traditional Stokes-Brinkman model is adopted as a reference solution to compare against the result yielded by the DSS model. A test case used for validation consists of a two-layer domain, representing a channel (Ω_1) and a tow (Ω_2). The test case is shown in Fig. 2. Resin flow is introduced with inlet/outlet pressure boundary conditions and Stokes-Brinkman model is solved numerically by finite elements method. Conversely, the same flow scenario is solved using the DSS model after extracting the hybrid skeleton mesh from the input geometry. The error for velocities computed for this simple test case is ≈ 12%. The large gain in CPU time for solution on the same machine shows the potential of the model.

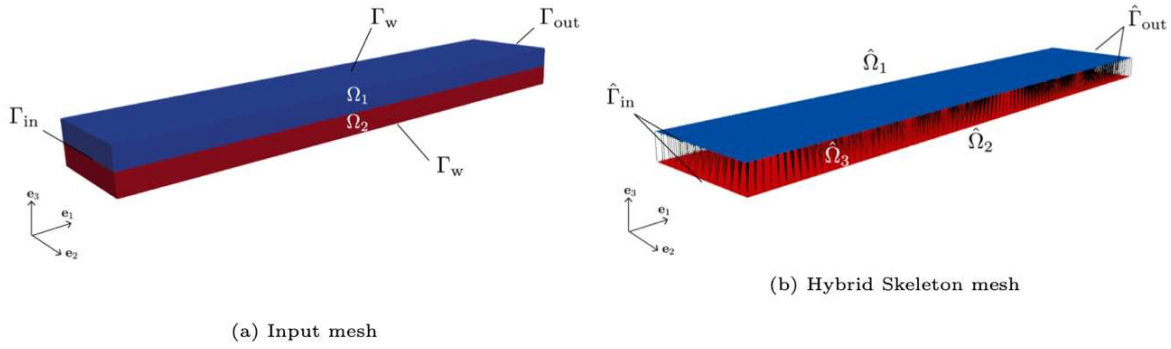

Figure 2. The geometry used for DSS model validation

Table 1: Results from DSS model validation test case

Case	N_{elem}	CPU t [s]	$\langle u \rangle_{\Omega_1}$ [m/s]	$\langle u \rangle_{\Omega_2}$ [m/s]
Stokes-Brinkman	63316	97	7.72E-04	2.00E-05
DSS model	9354 (2D + 1D)	0.04	6.75E-04	2.02E-05

  doi:10.5075/epfl-298799_978-2-9701614-0-0

2.4 Filling simulation

By extracting the hybrid skeleton mesh from the input geometry of a multi- layer stack of fabrics, it is possible to simulate the unsaturated filling of the preform using the DSS model. For the purpose, the DSS model was implemented in the commercial filling simulation software LIMS [8, 9]. As an example, the dual-scale filling of an array of tows is simulated in Fig. 3. One can see the plug flow in the channel region as well as the partially saturated flow front in the tows because of the transverse flow from the channels. Although no full-3D validation is available in this case, the pattern observed in the flow front advancement qualitatively agrees with expected behavior.

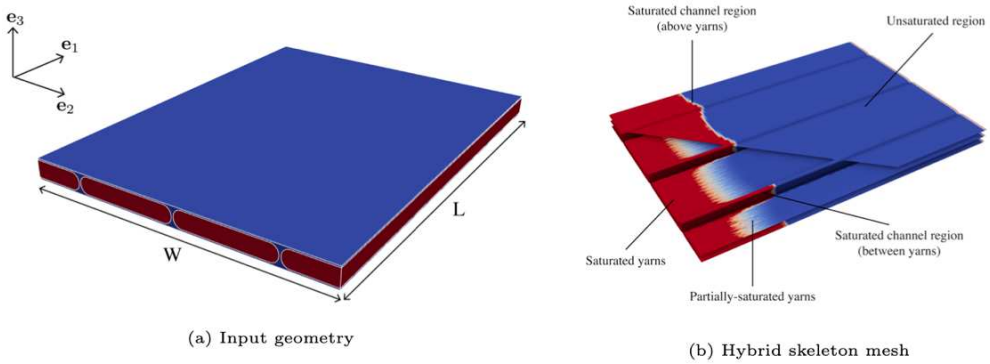

Figure 3. Input geometry and sliced view of the dual-scale flow front

3. Discussion and Conclusions

We have presented a new Dual-Scale Skeleton (DSS) model which can handle the dual-scale flow of a resin onto a novel Hybrid Skeleton mesh. The model can be used to compute both saturated and unsaturated RTM filling simulations at a reduced computational cost when compared to 3D solutions. The accuracy of the DSS model was assessed by comparison against a full-dimensional Stokes-Brinkman solution. The results show large gains in computational cost, while the tradeoff error is below 15%. This value cannot be assumed as representative of more complex scenarios: at the current level of development the model requires further validation, which could be achieved only by either experimental measurement or by solving the same scenarios numerically using a high-computing Stokes-Brinkman transient flow solver. It is worth to note that experimental validation is still very challenging. The dual scale flow in fabrics is very difficult to monitor and is subjected to experimental errors. However, several different test cases were solved using the DSS model and all the results show good qualitative agreement with how the flow is expected to behave in presence of some distinctive features (racetracks, low/high transverse yarn permeability...). Although still far from the possibility to simulate full-scale parts, the current state of work can be considered a first successful attempt at applying the novel Dual-Scale Skeleton model to the direct meso-scale simulation of RTM processes.

4. Acknowledgements

This research was partially funded by Conseil Regional Pays de la Loire, France (grant number TEU29). The authors also acknowledge the DGAC for the funding of the AVATAR Project.

  doi:10.5075/epfl-298799_978-2-9701614-0-0

5. References

[1] H. C. Brinkman. “A calculation of the viscous force exerted by a flowing fluid on a dense swarm of particles”. In: Flow, Turbulence and Combustion 1.1 (1949), pp. 27–34.

[2] F. Desplentere et al. “Micro-CT characterization of variability in 3D textile architecture”. In: Composites Science and Technology 65.13 (2005), pp. 1920–1930.

[3] V. Michaud. “A review of non-saturated resin flow in liquid composite moulding processes”. In: Transport in porous media 115.3 (2016), pp. 581–601.

[4] X. Li et al. “A pore-skeleton-based method for calculating permeability and capillary pressure”. In: Transport in Porous Media 124.3 (2018), pp. 767–786.

[5] Z. Jiang et al. “Extraction of fractures from 3D rock images and net- work modelling of multi-phase flow in fracture-pore systems”. In: International Symposium of the Society of Core Analysts, Aberdeen, Scotland. Citeseer. 2012.

[6] C. Wong et al. “Comparisons of novel and efficient approaches for permeability prediction based on the fabric architecture”. In: Composites Part A: Applied Science and Manufacturing 37.6 (2006), pp. 847–857.

[7] K. M. Pillai. “Governing equations for unsaturated flow through woven fiber mats. Part 1. Isothermal flows”. In: Composites Part A: Applied Science and Manufacturing 33.7 (2002), pp. 1007–1019.

[8] M. Bruschke and S. G. Advani. “A finite element/control volume approach to mold filling in anisotropic porous media”. In: Polymer composites 11.6 (1990), pp. 398–405.

[9] P. Simacek and S. G. Advani. “Desirable features in mold filling simulations for liquid composite molding processes”. In: Polymer Composites 25.4 (2004), pp. 355–367.

  doi:10.5075/epfl-298799_978-2-9701614-0-0

SCALABLE AND LOCALISED MODEL ORDER REDUCTION APPLIED TO COMPOSITE AERO-STRUCTURES

Jean Bénézech[a], Linus Seelinger[b], Peter Bastian[c], Tim Dodwell[d,e], Richard Butler[a] and Robert Scheichl[b]*

a: Material & Structure Research Centre, University of Bath, Bath, UK.
b: Institute for Applied Mathematics, Heidelberg University, Heidelberg, Germany.
c: Interdisciplinary Center for Scientific Computing, Heidelberg University, Heidelberg, Germany.
d: Institute of Data Science and AI, University of Exeter, Exeter, UK.
e: The Alan Turing Institute, The British Library, London, UK.
jb3285@bath.ac.uk

Abstract: *Due to the interaction of structural meso-scale and geometric macro-scale features, composite aero-structures are inherently multi-scale in nature. In addition, complex manufacturing processes lead to the appearance of defects at multiple scales. These defects bring extra dimensions to the multi-scale problem which discourage the use of a scale separation hypothesis. Despite the growing knowledge of the types of composite characteristic defects, for large scale aerostructures, their location and exact geometry remain unknown or are only observable with difficulty. Hence, a large-scale uncertainty quantification (UQ) problem must be solved. The primary challenge is the cost of the associated numerical simulation. Therefore, to tackle this problem, an efficient multiscale generalized finite element (FE) method has been developed within the open-source software package DUNE (https://www.dune-project.org/). Thanks to its modularity, our method has been integrated into an Offline/Online framework allowing a very efficient exploration of defects in of the material parameters.*

Keywords: GMsFEM; A-harmonic GenEO; Offline/Online; Composites; Material Defects.

1. Introduction

Introduced by Spillane et al. [1], the Generalized Eigenvalue problem in the Overlaps (GenEO) method is a robust preconditioner for iterative PDE solvers. The fine domain and the associated discretized global finite element space are divided into overlapping subdomains. On each subdomain, a generalized eigenvalue problem (GEVP) is solved in order to obtain local eigen-vectors. The lowest energy modes, i.e., eigenvectors corresponding to the smallest eigenvalues, are exported to form a local basis which represents locally the principal deformation modes of the structure. Solving GEVPs on an overlapping subdomain partition ensures compatibility of local bases across subdomains. They are then combined to generate a coarse global space using a partition of unity approach [2]. A reduced order approximation of the fine scale problem is hence constructed. This method has recently been implemented in DUNE and extended to strongly anisotropic linear elasticity applications in aerospace composites in the module *dune-composites* [3,4], where the scalability of the GenEO preconditioner has been shown on the UK national high-performance computer (HPC) cluster ARCHER with up to 15,360 cores.

The GenEO coarse space has clearly demonstrated its efficiency and accuracy as a preconditioner for iterative solvers. It reduces drastically the number of iterations used by the

  doi:10.5075/epfl-298799_978-2-9701614-0-0

fine scale solver [3] in challenging problems where established methods like Algebraic Multigrid fail. However, one can ask if the coarse approximation space could supplant the fine scale model for aero-space composite applications and be used as a Generalized Multi-scale Finite Element Method (GMsFEM) [5]. Independently in [6], Babuska and Lipton have constructed an optimal generalized finite element space by constraining the local eigenproblems with an A-harmonicity condition. Ma, Dodwell and Scheichl [7] have used this as the basis for a new optimal coarse space that incorporates the A-harmonic constraint into the local eigenproblems, so fitting directly into the GenEO framework. The applicability of the new method to composite aero-structures and its performance have recently been assessed in [8]: The method is shown to provide a hierarchy of models of increasing complexity and accuracy, and to scale optimally to entire aero-space components.

Furthermore, the modularity of our method makes it suitable to be used in an Offline/Online framework, as described by Efendiev et al. [5]. In the Offline phase a first coarse approximation space for a 'pristine' material model is constructed within a parallel setting. A database is initiated, where the components involved in the coarse space construction are stored. Then Online, in order to assess the effect of a localized defect (i.e., a wrinkle), the approximation space needs to be updated only in a small region of the structure affected by the defect. The computational savings are huge, as the approximation update and the solve can be handled by a single processor, freeing parallel resources for multiple and simultaneous defect assessments.

The proposed developments are part of the CerTest project (https://www.composites-certest.com/), which aims at designing a new certification process, adapted to composites for aerospace application. Indeed, the building of an understanding and the quantification of uncertainties, e.g., arising from composite material variabilities, experimental measurements and approximation of in-service conditions, form the critical challenge. As a result, the new certification process needs to promote more confidence in virtual testing, which must assess more efficiently the effect of those uncertainties. Our approach has been designed to be applicable to very large aero-space components while representing the composite meso-structure without scale separation. The method is automatic and applicable to any structural design and can efficiently evaluate local defects that may occur in the structure. To demonstrate the novel CerTest methodologies, a 500 mm long C-spar, embedded with a tapered region [8] has been chosen and will exemplify the method also in this paper.

2. A-Harmonic GenEO as a GMsFEM

2.1 Model solver

A clear description of the approximation space construction, detailing each step as well as the implementation details, is available in [8]. A brief summary of the main points is provided here. Figure 1 depicts the main components of the method.

We begin with a decomposition of the domain Ω into non-overlapping subdomains $\{\widehat{\Omega}_j\}_{j=1}^{N}$. The GenEO coarse space requires overlapping subdomains. We thus define overlapping subdomains Ω_j by extending each non-overlapping subdomain $\widehat{\Omega}_j$ by several layers of neighbouring elements to achieve a prescribed overlap. We define V_h and $V_h(\Omega_j)$ as the (local) finite element space, restricted to Ω and to Ω_j respectively.

  doi:10.5075/epfl-298799_978-2-9701614-0-0

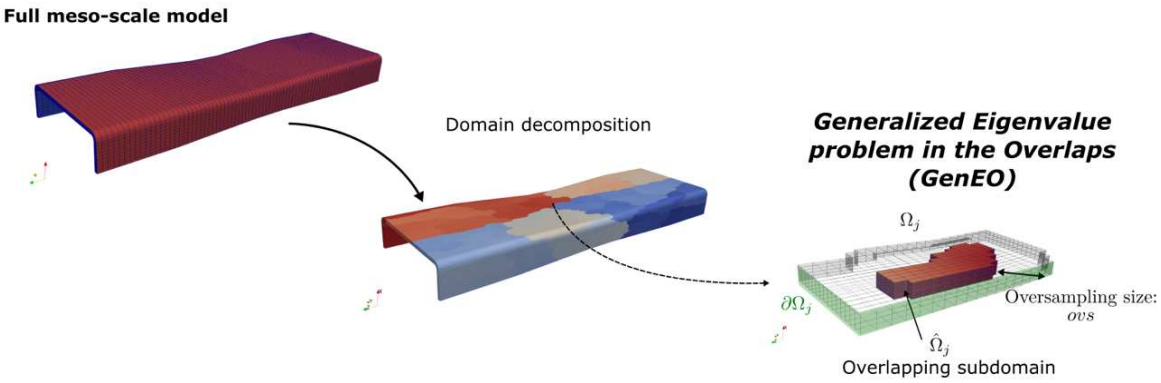

Figure 1. Domain decomposition of fine scale C-spar model and schematic of GenEO approach.

The local GEVPs consist of finding $\lambda \in \mathbb{R}, \varphi_h \in V_h(\Omega_j)$, such that

$$a_{\Omega_j}(\varphi_h, v_h) = \lambda a_{\Omega_j}(\Xi_j \varphi_h, \Xi_j v_h), \quad \text{for all} \quad v_h \in V_h(\Omega_j), \tag{1}$$

where a_{Ω_j} is the bilinear form of the elasticity problem restricted to the subdomain Ω_j and Ξ_j denotes the partition of unity operator on Ω_j. Then, the GenEO space is defined as

$$V_H := span\{R_j^\top \Xi_j(\varphi_h^{j,k}) : k = 1, \dots, m_j, \quad j = 1, \dots, N\}. \tag{2}$$

Here, $R_j^\top : V_h(\Omega_j^o) \to V_h$ is the prolongation operator from subdomain to full domain, m_j is the size of the local basis (corresponding to the number of eigenvectors included) and N is the number of subdomains Ω is decomposed into.

To introduce the A-harmonicity condition [7] we first define two further subspaces:

$$V_{h,D}(\Omega_j) = \{v \in V_h(\Omega_j) : v = 0 \text{ on } (\partial\Omega_j \cap \Gamma_D)\}, \tag{3}$$

$$V_{h,DI}(\Omega_j) = \{v \in V_h(\Omega_j) : v = 0 \text{ on } (\partial\Omega_j \cap \Gamma_D) \cup (\partial\Omega_j \cap \Omega)\}, \tag{4}$$

where Γ_D denotes the Dirichlet boundary of Ω and $\partial\Omega_j$ (visible in Fig. 1) the (artificial) interior boundary of the subdomain. Then, the A-harmonic finite element sub-space is defined as:

$$V_A(\Omega_j) = \{u \in V_{h,D}(\Omega_j) : a_{\Omega_j}(u, v) = 0 \quad \forall \quad v \in V_{h,DI}(\Omega_j)\}. \tag{5}$$

Under the A-harmonicity condition, the eigenvectors are solutions of the homogenous partial deferential equation on Ω_j. The transformation of the GEVP (Eq. 2) to fulfill the A-harmonicity condition is provided in [7] and the implementation used for composite elasticity problems is described in [8]. In addition, the coarse space is enriched with some additional local 'particular' solutions in subdomains that intersect Γ_D or where the source term is nonzero.

For scalar elliptic problems, the relative approximation error between the fine-scale solution u_h and its approximation $u_H \in V_H$ is proven in [7, Thm. 3.4] to be bounded in energy norm $||.||_a$ by:

$$\frac{||u_h - u_H||_a}{||u_h||_a} \leq \kappa \max_{1 \leq j \leq N} \frac{1}{\sqrt{\lambda_j^{m_j+1}}}, \tag{6}$$

where κ denotes the maximum number of subdomains overlapping at any point in Ω and $\lambda_j^{m_j+1}$ is the eigenvalue corresponding to the first eigenvector that is not included in the local

  doi:10.5075/epfl-298799_978-2-9701614-0-0

basis. This result extends also to the linear elasticity equation considered here, and the decay of the bound on the right of eqn. (6) is faster the wider the gap between the support of the partition of unity operator Ξ_j and the boundary of Ω_j. See [8] for details.

2.2 Application to the C-spar

The accuracy of the coarse approximation is driven by the maximum of $1/\lambda_j^{m_j+1}$ in the error bound, as well as by the size of the overlaps. On the other hand, the efficiency of the method is mainly driven by the model order reduction factor $dof(\Omega_H)/dof(\Omega)$, which depends on the local basis sizes $\{m_j\}$ and on the number of subdomains N.

Thus, for a given target accuracy, there is a necessary and sufficient m_j^{opt} (for each subdomain) that guarantees the target accuracy for minimal coarse space size. The A-harmonicity condition ensures a nearly exponential decay of $1/\lambda_j^{m_j+1}$ and thus reasonably small values of m_j. In practice, one applies a threshold on $\{1/\lambda_j^{m_j+1}, i = 1, \ldots, m_j\}$ to obtain the minimal m_j^{opt}. However, prior knowledge of the local distribution of the material parameters can help to estimate this optimal m_j^{opt}, and thus to reduce the computational cost of solving the GEVPs [8]. As each GEVP is independent from the others, this step is fully parallelizable and optimal weak scalability of the Offline step has been demonstrated in [8].

In order to assess the accuracy of the reduced order model on the C-spar, its deformation under a compressive load has been simulated, with the results shown in Figure 2. The threshold for the error bound (of u_h) has been chosen to be $1/\lambda_j^{m_j+1} \leq 1e-6$, the number of subdomains was $N = 256$, leading to a reduction factor of $dof(\Omega_H)/dof(\Omega) = 32$ (here $dof(\Omega) = 1.2M$). The compression failure criterion:

$$\phi_{1-} = \frac{\left\langle \left|\widetilde{\sigma_{12}^R}\right| + \eta^L \widetilde{\sigma_{22}^R} \right\rangle}{s_L}. \tag{7}$$

outlined in detail in Furtado et al. [10] is plotted in Figure 2 (normalized). The preferential zone where the damage may appear, the deformation of the structure, as well as a high variation of the failure criterion through thickness can be observed. The error on the failure criterion is very low (bounded by $3e-3$), which demonstrates the ability of the reduced order model to approximate the full meso-scale model.

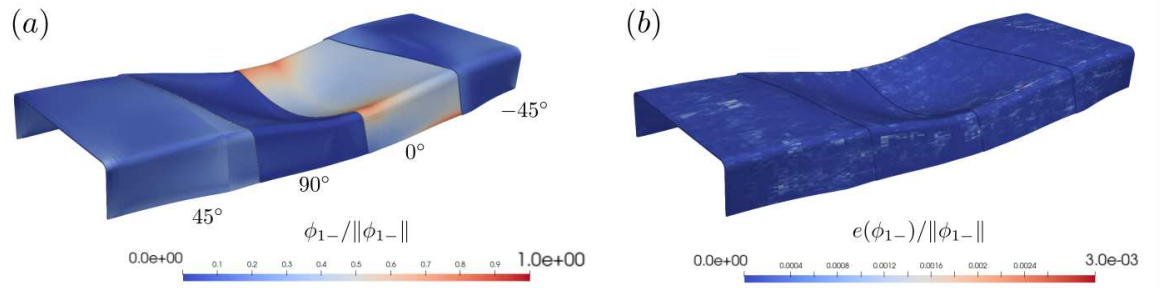

Figure 2. Compressive failure criterion (a) and relative error w.r.t the full meso-scale model (b).

At this target accuracy, the model took 20 minutes on 256 processors to run (15 minutes for the GEVP phase and 5 minutes for the coarse space creation and solution). The first strength of this

  doi:10.5075/epfl-298799_978-2-9701614-0-0

method is the ability to build a hierarchy of models of increasing complexity and accuracy, e.g., a crude reduced order model of a fine-scale problem with $4.6M$ degrees of freedom can be solved in 6 seconds [8]. The second strength of the method is the modularity of the coarse space V_H. Indeed, the proposed GMsFEM has been designed to fit into an Offline/Online framework that increases dramatically the efficiency to assess of localized defects inside the structure.

3. Offline/Online approach

In order to statistically evaluate a potential defect, uncertainty quantification algorithms need large numbers of similar simulation runs. To integrate the GMsFEM in a stochastic framework, one suitable idea - already advanced by Efendiev et al. [5] - consists of using an Offline/Online approach. In the Offline phase, the A-harmonic GenEO approximation space is generated for a given set of parameters within a parallel setting, e.g., for composites this Offline phase could consider generating the approximation space for a pristine part (such as the one presented in Figures 1 and 2). During this phase, information (subdomain grid, material properties, local bases, connectivity graphs, etc.) will be stored; a data base is initiated.

Then, in the Online phase, the effect of one or multiple changes in the parameters are assessed. For instance, a new parameter choice could correspond to adding a localized defect into the structure. New local eigenbases are computed, but crucially only in the affected regions, and the coarse space is updated. This offers huge computational savings for large components, since most basis vectors are simply loaded from the offline data base.

In Figure 3, the capabilities of the Offline/Online approach are depicted. Firstly, a thickness measurement of the C-spar tapered region is shown (a). The stacking sequence in this sample has been chosen to cause wrinkles, explaining their severity [9]. Nevertheless, similarly shaped wrinkling defects of similar amplitude can occur during the fabrication process of large-scale laminated composite structures.

Figure 3 (b) shows, for a given wrinkle, the representation via grid transformation [3] of the wrinkle in the model (left), the subdomains which require new eigenbases (middle) and the effect of the defect on the compression failure criterion of the ply oriented in 0° (lengthwise of the C-spar; right). We observe a local variation of the failure criterion around the defect, but also a change of the global deformation of the structure under compression. Local and global effects are both handled in the approximation space despite the localized re-computation.

Finally, Figure 3 (c) shows the potential of the Offline/Online approach: the efficient assessment of four different wrinkling defects in the structure. It demonstrates the relative effect of wrinkles on the compressive behaviour of the C-spar, highlighting the necessity of a statistical study involving many parameters to be tested. In fact, each run has been performed on only a few processors (depending on the size of the defect) and defects are completely independent on how the domain is partitioned. The ratio of the number of subdomains to be recomputed (t) over the number of subdomains used Offline (N) will determine the gain factor between Offline and Online runs; necessarily, this depends on the ratio between defect size and part size. As the GEVP step of the method is scalable, larger parts can be simulated Offline within the same amount of time while providing more parallel resources. Online, the ratio t/N can then be drastically reduced. In this way, parallel resources can be used to assess hundreds of wrinkle configurations simultaneously. In addition, each Online run serves to increment the data base for future Online runs, making the assessment of a combination of defects even more efficient.

  doi:10.5075/epfl-298799_978-2-9701614-0-0

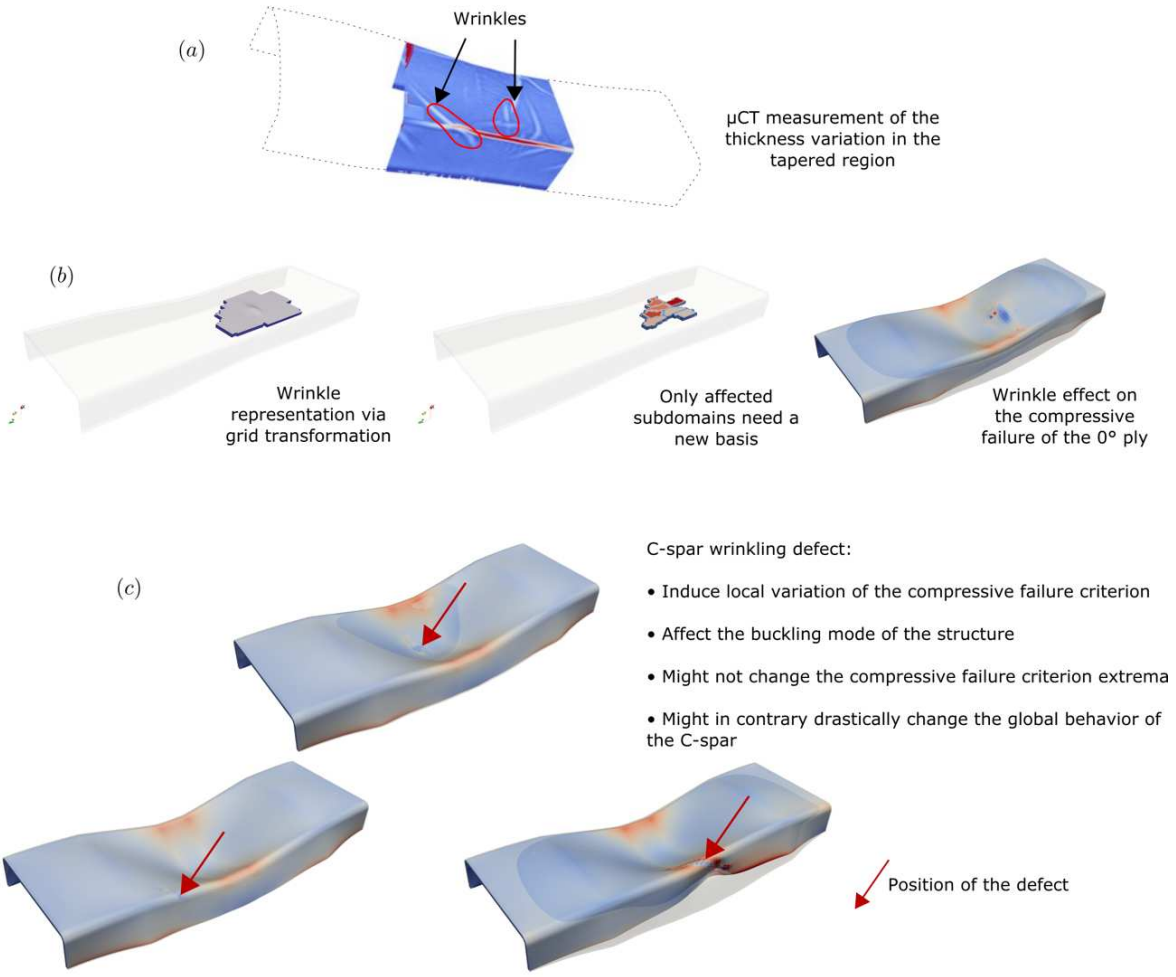

Figure 3. Assessment of wrinkling defects in a C-spar. In each case, the failure criterion is plotted on the deformed shape (exaggerated) of the defective C-spar and over the deformed shape (same scale factor) of the pristine C-spar.

A forthcoming paper will describe in detail the Offline/Online framework, the implementation, as well as an application to an engineering problem: namely, the statistical evaluation of wrinkling defects inside a C-spar structure.

4. Conclusion

In this paper, a new scalable and localized model order reduction approach in the form of a GMsFEM has been proposed that can be used in an Offline/Online framework. Based on the theory of generalized finite elements, this method (related to GenEO) is designed to provide an efficient assessment of meso-scale uncertainties in composite aero-structure applications (such as wrinkles). The method is applicable to any composite structure, as no scale separation assumption is required.

The components and parameters of the solver (domain decomposition, subdomains sizes, local basis sizes) are automatically chosen for a given target accuracy, allowing the creation of a

  doi:10.5075/epfl-298799_978-2-9701614-0-0

hierarchy of models of increasing complexity. This modelling framework is then suitable to be integrated in a Multilevel Markov chain Monte Carlo (MLMCMC) algorithm [11] for uncertainty quantification, answering reverse engineering questions and allowing a classification of defect severity that may occur in large composite structures.

Future work will focus on the implementation of non-linear behavior, such as geometric non-linearities and progressive failure mechanisms.

Acknowledgements

The research was supported by the UK Engineering and Physical Sciences Research Council (EPSRC) through the Programme Grant: "Certification of Design: Reshaping the Testing Pyramid" EP/S017038/1 (https://gow.epsrc.ukri.org/NGBOViewGrant.aspx?GrantRef=EP/S017038/1). The funding received is gratefully acknowledged.

This work has made use of the Hamilton HPC Service of Durham University.

5. References

1. N. Spillane, V. Dolean, P. Hauret, F. Nataf, C. Pechstein, R. Scheichl, Abstract robust coarse spaces for systems of PDEs via generalized eigenproblems in the overlaps, *Numerische Mathematik,* **126**, 741–770, 2014.
2. A. Toselli, O. Widlund, Domain decomposition methods-algorithms and theory, Vol. 34, Springer Science & Business Media, 2004.
3. A. Reinarz, T. Dodwell, T. Fletcher, L. Seelinger, R. Butler, R. Scheichl, dune-composites–A new framework for high-performance finite element modelling of laminates, *Composite Structures,* **184**, 269–278, 2018.
4. R. Butler, T. Dodwell, A. Reinarz, A. Sandhu, R. Scheichl, L. Seelinger, High-performance dune modules for solving large-scale, strongly anisotropic elliptic problems with applications to aerospace composites, *Computer Physics Communications*, **249**, 106997, 2020.
5. Y. Efendiev, J. Galvis, T. Y. Hou, Generalized multiscale finite element methods (GMsFEM), *Journal of Computational Physics,* **251**, 116–135, 2013.
6. I. Babuska, R. Lipton, Optimal local approximation spaces for generalized finite element methods with application to multiscale problems, *Multiscale Modeling & Simulation*, **9** (1), 373–406, 2011.
7. C. Ma, R. Scheichl, T. Dodwell, Novel design and analysis of generalized FE methods based on locally optimal spectral approximations, *SIAM Journal on Numerical Analysis,* **60**, 244-273, 2022.
8. J. Bénézech, L. Seelinger, P. Bastian, T. Dodwell, R. Butler, C. Ma, R. Scheichl, Scalable local model order reduction applied to composite aerostructure. To be submitted.
9. K. J. Johnson, R. Butler, E.G. Loukaides, C. Scarth, A.T. Rhead, Stacking sequence selection for defect-free forming of uni-directional ply laminates, *Composites Science and Technology*, **171**, 34-43, 2019.
10. C. Furtado, G. Catalanotti, A. Arteiro, P. Gray, B. Wardle, P. Camanho, Simulation of failure in laminated polymer composites: Building-block validation, *Composite Structures,* **226**, 111168, 2019.
11. T. J. Dodwell, C. Ketelsen, R. Scheichl, A. L. Teckentrup, Multilevel Markov chain Monte Carlo, *SIAM Review,* **61**, 509–545, 2019.

  doi:10.5075/epfl-298799_978-2-9701614-0-0

STRESS INTENSITY FACTOR OF A FIBRE EMBEDDED IN A MATRIX

M. Barzegar[a], J. Costa [a], D. Trias[a], J. M. Guerrero[a], C. Gonzalez[b]

a: AMADE, Polytechnic School, University of Girona, 17073 Girona, Spain –
m.barzegar@udg.edu
b: IMDEA Materials Institute, 28906 Getafe, Madrid, Spain

Abstract: *The current methods of stress intensity factor (SIF) in cracked fibres usually assume the fibre to be isolated. Moreover, current fragmentation models in composites rely on the experimental characterization of the fibre strength using a Weibull distribution, performed on dry isolated fibres. However, in composites the fibre, as the main load carrying component, is embedded in a matrix. To clarify the effect, the embedding matrix has on the SIF of the fibre we propose a 3D computational model of an orthotropic fibre embedded in an isotropic matrix, and compute the SIF using the J-integral method. A parametric analysis investigates the effect of the fibre-matrix stiffness ratio, and the effect of the degree of elastic orthotropy of the fibre. The results show that the SIF is highly influenced by both factors and that the matrix reduces the SIF by constraining the crack opening.*

Keywords: Stress intensity factor; Finite element method; Fibre reinforced polymer; Micro-mechanics modelling; Linear elastic fracture mechanics

1. Introduction

Fibre Reinforced Polymer (FRP) composites are widely used in many industrial sectors, especially in lightweight aerospace structures, thanks to their high specific mechanical properties such as stiffness and strength. However, their low fracture toughness translates into brittle behaviour that often leads to catastrophic failure without prior damage symptoms [1].

In order to fully utilise the potential of modern composite materials it is necessary to predict their behaviour in the presence of crack-like flaws which frequently exist, often due to manufacturing defects or mechanical damage [2]. According to Linear Elastic Fracture Mechanics (LEFM), the growth rate of a crack is governed by the Stress Intensity Factor (SIF) in the crack tip [3]. Thus, understanding the SIF especially at crack tip, which is a function of applied loads and crack geometries, is essential to predict the behaviour of crack propagation.

The SIF of fibres has been investigated by combining experimental methods and some type of analytical and numerical approaches [4-8]. The most common experimental methodology to estimate the SIF is the determination of the initial crack size by observing fracture mirror size on a tensile fracture surface of un-notched specimens, which is difficult and expensive especially for small diameter components. Purely analytical solutions are the products of highly sophisticated mathematical analysis for idealized crack geometries and loading conditions, which can be applied to cracks with simple and regular configurations. However, the cracks in real structures have a three-dimensional nature and are often both complex and irregular, which makes it challenging to compute an analytical closed-form solution for the SIF. These Limitations make these methods unsuitable for the model with complex cracks and boundary conditions.

  doi:10.5075/epfl-298799_978-2-9701614-0-0

Over the last few years, increased use of composite materials has motivated the researchers to conduct more exclusive study on the fibres. Ogihara et al. [4] proposed a method to create various types of notches with straight front crack on carbon fibre mono-filaments using a focused ion beam machining system. Then he used the virtual crack closure method to calculate the SIF of free carbon fibre under tensile load in both isotropic and orthotropic cases and compared with experimental results. Heraez et al. [5] characterized strength and toughness of carbon AS4, E-glass and Kevlar KM2 by tensile tests on notched and un-notched fibres. The strength of the un-notched fibres was characterized in terms of the Weibull statistics, whereas the residual strength of the notched fibres was used to determine their apparent toughness and the SIF was computed by means of the finite element method for different crack lengths. These studies have been conducted on a mono-filament free fibre and effect of the matrix was not considered.

In FRP composites, the fibres are surrounded by the matrix which maintains the orientation of the fibres according to specific design directions and also protects fibres from environmental destructive effects. Hence, the properties of composites are essentially controlled by the corresponding properties of their constituents, including fibre, matrix and fibre/matrix interfaces [9,10]. Nonetheless, it is unclear how the SIF of a fibre embedded into a matrix differs from that of the isolated fibre. The clarification of this issue is relevant for the prediction of the strength of unidirectional composites.

To the best of the authors' knowledge, there is no work to date studying the effect of the matrix on the SIF of fibre, at the micromechanical level. The present research explores the use of high-fidelity computational micromechanics modelling to compute the SIF variation along the crack front for a straight-fronted edge crack in a fibre subjected to tension loading. In a first set of simulations, a parametric study was performed on an isotropic fibre embedded in a matrix to comprehend the overall effects of the existence of the matrix and the fibre-matrix stiffness ratio on the SIF. Finally, we investigated the influence of the fibre longitudinal-transverse stiffness ratio on the SIF for an orthotropic fibre to capture the orthotropy effect.

2. Methodology

This section describes the general computational micromechanics framework used throughout the present research. The modelling and simulation were performed in Abaqus/Standard [11].

2.1 Finite element modelling

Figure 1 illustrates a 3D geometry of the model including a notched fibre embedded in a matrix, subjected to a tensile axial force. The length of the model (L) = 10D, thickness of matrix (t) = D, wherein D is the fibre diameter. A straight-fronted edge crack was introduced on one side surface of the fibre at $x_1 = L/2$, with various depths (a). The size of model was decided based on parametric studies that targeted the best trade-off between computational effort and accurate capturing of the relevant deformation phenomena with minimum interference of model boundaries.

  doi:10.5075/epfl-298799_978-2-9701614-0-0

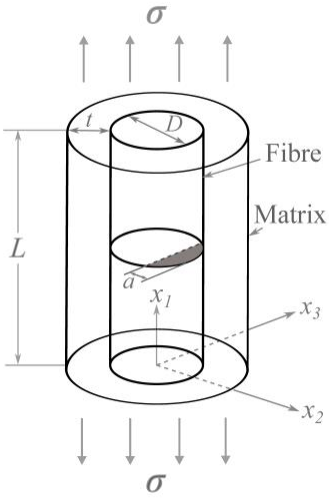

Figure 1. A notched fibre with straight-fronted edge crack (indicated in grey) embedded in a matrix.

To reduce the computational costs, only one-quarter of the model was modelled by taking advantage of symmetry boundary conditions in x_1 and x_3 axis. The fibre and matrix are meshed separately. In order to enrich the discretization and capture the high stress gradients at crack tip, swept and structured meshes were used, respectively, to discretize the region around the crack. This discretization is judged, after parametric analysis, to be fine enough to capture the high stress gradients around the crack tip.

The stress intensity factor evaluation through this study was carried out based on the J-integral [12] method, which is the standard approach in characterizing the energy release rate associated with a potential crack growth in LEFM. In this approach, the energy release rate is obtained by integration along the contour Γ around the crack tip as:

$$J = \int_{\Gamma} \left(W dx_1 - t.\frac{\partial u}{\partial x_2} ds \right) \quad (1)$$

where x_1 and x_2 are rectangular coordinates to the crack front, W is the elastic strain density, t is the traction vector, u is the displacement vector, and ds is an increment of arc length along any contour Γ. Due to the geometry of the model, the J-integral values are not constant along the crack front. Thus, this work concentrated on the maximum value attained at the crack tip. The non-dimensional stress intensity factor (f) is calculated by:

$$f(a, D) = \frac{K_I}{\sigma\sqrt{\pi a}} \quad (2)$$

where K_I the stress intensity factor in mode I, σ is the far-field stress, and a is the crack length.

3. Results and Discussion

3.1 Isotropic fibre embedded in a matrix

Figure 2 plots the evolution of the non-dimensional SIF for an isotropic fibre embedded in an elastic matrix for different fibre/matrix stiffness ratios (E_f / E_m) and relative crack lengths (a/D equal to 0.07, 0.1, 0.2, 0.3, 0.4, and 0.45). The SIFs of an isotropic free fibre (grey continuous

line) were added as a baseline, for comparison and to have a better understanding of the impact of matrix on the SIF.

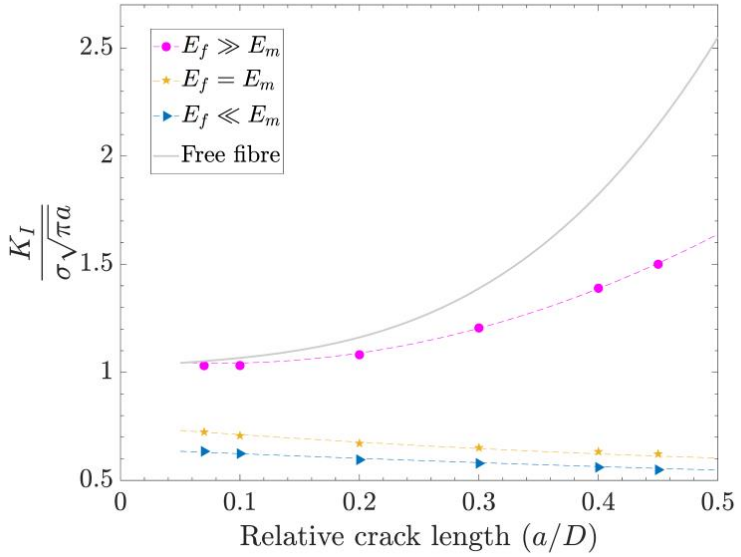

Figure 2. Non-dimensional SIF for an isotropic fibre embedded in a matrix for different fibre/matrix stiffness ratios. The dots refer to the FEM results and the dashed lines indicate the fitting results.

The trend is that an increase in matrix stiffness (E_m) leads to a significant drop in the SIF of the cracked fibre, especially for longer cracks. For better visualization, Figure 3 shows a 3D surface plot of non-dimensional SIF with respect to the crack lengths and fibre/matrix stiffness ratios (E_f/E_m).

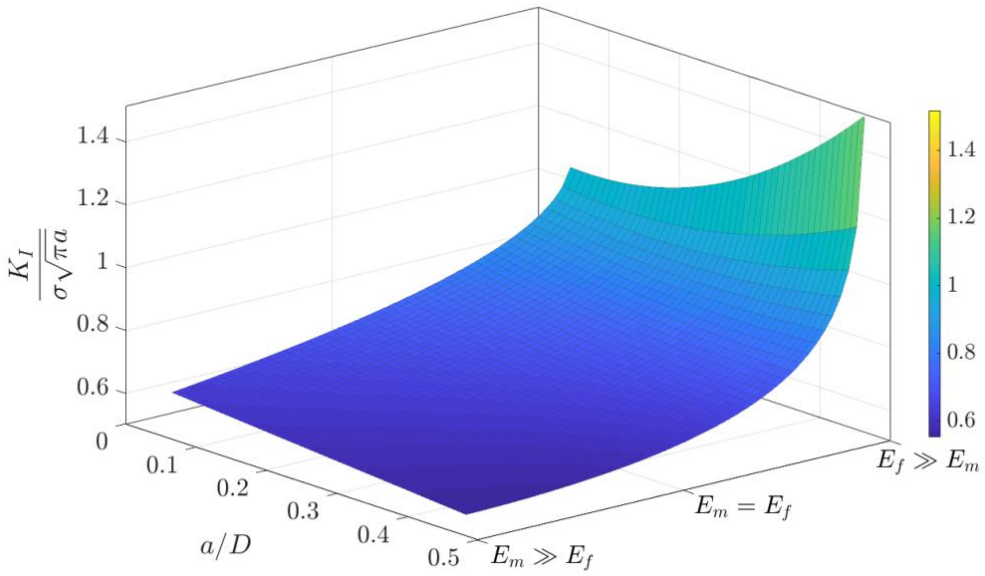

Figure 3. 3D surface plot of non-dimensional SIF for an isotropic fibre embedded in a matrix for different fibre/matrix stiffness ratios and crack lengths.

3.2 Effect of elastic orthotropy on SIF

  doi:10.5075/epfl-298799_978-2-9701614-0-0

Figure 4 shows the non-dimensional SIF for an orthotropic free-fibre, for different longitudinal/transverse stiffness ratios (E_1/E_2) and relative crack lengths (a/D equal to 0.07, 0.1, 0.2, 0.3, 0.4, and 0.45).

The curves indicate that the degree of orthotropy has a strong influence on the SIF, and that the trend is opposite depending on whether the transverse modulus (E_2) is smaller or higher than the axial modulus (E_1). For better visualization, Figure 3 shows a 3D surface plot of non-dimensional SIF with respect to the crack lengths and longitudinal /transverse stiffness ratios (E_1/E_2).

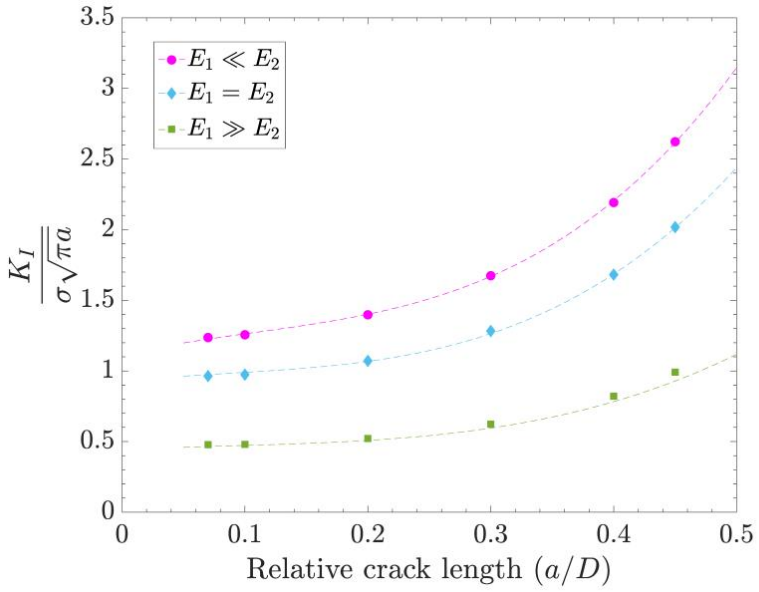

Figure 4. Comparison of non-dimensional SIF of an orthotropic free fibre for different longitudinal/transverse stiffness ratio.

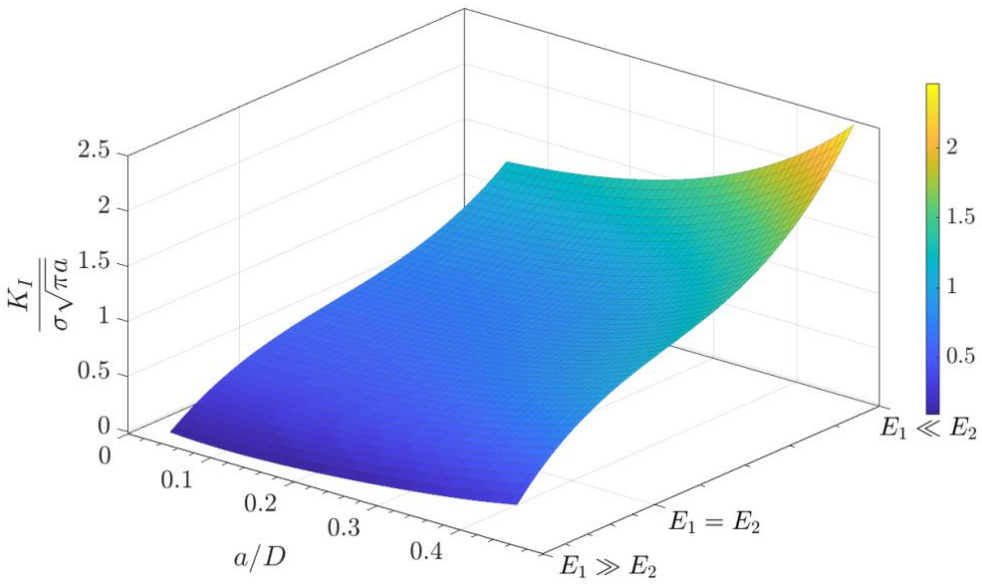

Figure 3. 3D surface plot of non-dimensional SIF for an orthotropic free fibre for different longitudinal/transverse stiffness ratios and crack lengths.

4. Conclusions

This research presented a computational micromechanics analysis of the stress intensity factor of a single fibre with a straight-fronted edge crack. The fibre was considered elastic, either isotropic or orthotropic, and free or embedded in an elastic material. The influence of embedding in a matrix, fibre/matrix stiffness ratio, and fibre longitudinal/transverse stiffness ratio on the SIF were studied. The stress intensity factor evaluation was carried out using the *J*-integral.

It was found that embedding the fibre in an elastic matrix reduced the SIF over the free fibre case. The higher the matrix stiffness was, the more substantial the decrease in SIF. This effect is due to the constraint of the matrix over the fibre crack opening. The elastic orthotropy of the fibre greatly affected the SIF in that it increased for the case of a transverse stiffness higher than that of the axial, and decreased for the opposite case.

Acknowledgements

The research leading to this publication received financial support from the Spanish Ministry of Science, Innovation and Universities through projects MAT2015-69491-C3-2-R, RTI 2018-097880-B-I00 and FPI grant BES-2016–076544.

5. References

1. Rangappa S, Satishkumar T, Cuadrado M, Siengchin S, Barile C. Fracture failure analysis of fiber reinforced polymer matrix composites, Springer Singapore 2021.
2. Tsai S, Melo J. Composite materials design and testing. Department of Aeronautics & Astronautics, Stanford University 2015.
3. Paris P, Erdogan F. A critical analysis of crack propagation laws. ASME Journal of Basic Engineering 1963; 85:528-533.
4. Ogihara S, Imafuku Y, Yamamoto R, Kogo Y. Direct evaluation of fracture toughness in a carbon fiber. 17th International Conference on Composite Materials, ICCM-17, Edinburgh, United Kingdom 2009.
5. Herraez M, Fernandez A, Lopes C, Gonzalez C. Strength and toughness of structural fibres for composite material reinforcement, Philosophical Transactions of the Royal Society A 2016; 374:20150274.
6. Daoud E. K. O, Cartwright J. D, Carney M. Strain-energy release rate for a single-edge-cracked circular bar in tension, Journal of Strain Analysis for Engineering Design 1978; 13:83-89.
7. Bush J, Stress intensity factors for single-edge-crack solid and hollow round bars loaded in tension. Journal of Testing and Evaluation 1981; 9:216-223.
8. Ouchterlony F. Extension of the compliance and stress intensity formulas for the single edge crack round bar in bending, Fracture Mechanics for Ceramics, Rocks and Concrete 1981; 745:237-256.
9. Barzegar M, Costa J, Lopes S. C. High-fidelity computational micromechanics of first-fibre failure in unidirectional composites: Deformation mechanisms and stress concentration factors. International Journal of Solids and Structures 2020; 204-205:18-33.
10. Barzegar M, Costa J, Lopes S. C. Effects of dynamic fibre failure in unidirectional composites. Materiales Compuestos 2020; 4:24-29.
11. Simulia. Abaqus/standard user's manual 2020.

  doi:10.5075/epfl-298799_978-2-9701614-0-0

12. Rice R. J. A path independent integral and the approximate analysis of strain concentration by notches and cracks, J. Appl. Mech. 1968; 35(2):379-386.

  doi:10.5075/epfl-298799_978-2-9701614-0-0

APPLICATION OF A TENSOR INTERPOLATION METHOD ON THE DETERMINATION OF FIBER ORIENTATION TENSORS FROM COMPUTED TOMOGRAPHY IMAGES

Juliane Blarr[a], Noah Kresin[a], Constantin Krauß[b], Kay A. Weidenmann[c,d], Wilfried V. Liebig[a,d], Peter Elsner[a,d]

a: juliane.blarr@kit.edu, Karlsruhe Institute of Technology (KIT), Institute for Applied Materials (IAM-WK), Hybrid and Lightweight Materials, Engelbert-Arnold-Straße 4, 76131 Karlsruhe, Germany
b: Karlsruhe Institute of Technology (KIT), Institute of Vehicle System Technology - Division Lightweight Technology, Rintheimer Querallee 2, 76131 Karlsruhe, Germany
c: Universität Augsburg, Institute of Materials Resource Management, Universitätsstr. 2, 86159 Augsburg
d: Fraunhofer Institute for Chemical Technology ICT, Joseph-von-Fraunhofer Strasse 7, 76327 Pfinztal, Germany

Abstract: *When investigating the mechanical behavior of fiber-reinforced polymers, fiber orientation plays a decisive role concerning anisotropy. Fiber orientation distributions are typically measured in the form of fiber orientation tensors. In order to measure orientation tensors, computed tomography scans and consecutive image processing methods have become one of the leading non-destructive testing methods. The conflict between scan resolution and sample size limits the volume that can be scanned. To obtain the fiber orientation behavior across an entire plate, a direct interpolation of orientation tensors computed from CT scans of smaller volumes at selected coordinates of the plate is implemented. Rather than a component-based interpolation, the authors chose a decomposition and reassembly method interpolating shape and orientation of the tensors separately. While this approach has been implemented and used for e.g. diffusion tensors in medical imaging, the authors consider the application to sparse but measured CT-based data to be a novelty.*

Keywords: tensor mapping; tensor algebra; quaternions; non-destructive testing; image processing

1. Introduction and state of the art

Fiber orientation distributions (FOD) are one of the various characteristic quantities evolved over time in order to quantify the microstructure of long- and short-fiber-reinforced polymers (FRP). Fiber orientation specifically has a high impact on anisotropy as the fiber orientation is typically a function of the position since orientation is defined by process (compression molding) induced material flow. FOD are described in scalar distribution functions. However, in the use cases of process or structural simulations the most common and compact form of representation are fiber orientation tensors (FOT) [1]. FOT can be determined from µCT images via structure tensor approach [2]. While fiber volume contents (FVC) and fiber length distributions (FLD) can also be determined experimentally by eliminating the matrix material [3], validating FOT determined via image processing depicts a challenge. Furthermore, the conflict

  doi:10.5075/epfl-298799_978-2-9701614-0-0

between image resolution and sample size in CT images limits the volume that can be scanned in order to still detect carbon fibers (diameter of 5 µm - 7 µm) massively. These small volumes often do not represent the microstructure sufficiently well and additionally, the coverage of a full plate is resource-intensive. However, full-field information on FOT is of elevated interest when analyzing and trying to improve the preceding manufacturing process and corresponding process simulation. The alternative to a high amount of scans and orientation analyses, i.e. considering less measured tensors and ascertaining predicted values in between, constitutes a classical interpolation problem. While interpolation for scalar values is well-known and various approaches exist, interpolation of tensors represents a more challenging, less well-explored field. The fact that orientation tensors are received via closure approximations of the orientation distribution function (ODF) might be considered as an advantage. A scalar interpolation for discrete directions is thereby possible (e.g. in contrast to strain or stress tensors). The easiest way of interpolating fiber orientations would then be a Euclidean interpolation of the scalar valued function $\bar{\phi}$. The result is a weighted arithmetic averaging of the tensor components. Interpolating the tensor components lead to a kind of "shape shift" instead of sufficient rotation of the interpolated tensors in former studies, particularly showing an "artificial" isotropy [4-6]. There are further "global" interpolation methods, which could be applied to symmetric positive-definite (SPD) tensors. The Riemannian Interpolation has been used e.g. in [7]. However, as soon as more than two input arguments are used, the underlying computations can only be solved implicitly, necessitating an iterative and computationally expensive method, which is why this method is not pursued any further in this work. As another logarithmic, yet explicitly solvable approach, Arsigny et al. [4] introduced the Log-Euclidean tensor interpolation method. As a completely different kind of concept, decomposition-based methods have been made use of. These approaches are grounded on the idea of the generally acknowledged spectral decomposition of tensors (cf. Eq. (3)). This is followed by a separate interpolation of shape (e.g. invariants like Eigenvalues) and of orientation (e.g. Eigenvectors or quaternions) and a subsequent reassembly to a then interpolated tensor. This method particularly provides the possibility of a smoother behavior in-between two differently oriented tensors and has been used successfully for diffusion tensors in medical imaging [5]. However, the specific interpolation of shape and orientation can be realized in multiple, different ways. The chosen methods for the implementation of the decomposition method in this work are explained in detail in the "Methods" chapter. Sabiston et al. [8] have explored the use of artificial intelligence (AI) for FOT interpolation. The authors used ground truth fiber orientation data from µCT measurements - as also used in this work. They then trained an artificial neural network with this data, which was subsequently able to predict tensor components within ranges smaller than the variability of the orientation of neighboring microstructural units.

This work focuses on determining a full-field distribution of fiber orientation tensors across an entire carbon long-fiber-reinforced polyamide 6 plate by interpolating orientation tensors determined from small samples at specific positions. Therefore, nine samples were scanned in the CT and the orientation tensor was determined for each scanned volume. Following, the nine computed tensors of second order were interpolated via a decomposition-based interpolation method and the results were discussed both visually and quantitatively with the help of the Frobenius norm.

  doi:10.5075/epfl-298799_978-2-9701614-0-0

2. Notation

Symbolic tensor notation is preferred in this work. Scalar values are denoted by standard Latin and Greek letters, e.g. c, λ. Tensors of first order are represented by bold lowercase letters, e.g. $\boldsymbol{x}, \boldsymbol{p}$ and bold uppercase letters are used for tensors of second order such as $\boldsymbol{R}, \boldsymbol{S}$. Fourth-order tensors are denoted by double-struck letters like $\mathbb{C}, \mathbb{S}$.

Sets, i.e., collections of quantities, are denoted by calligraphic symbols, e.g. $\mathcal{A}$ and are constructed by curly braces. In them, the elements typically are given explicitly or expressed by conditions to be fulfilled by each element contained in the set. The special orthogonal group $SO(3)$ represents all 3D rotations. Four-dimensional quaternions are represented by an arrow-head above the Latin letter, such as in $\vec{q}$.

The terms $tr()$ and $det()$ are the trace and determinant operators respectively, $|\boldsymbol{D}|$ represents the Frobenius norm of the tensor $\boldsymbol{D}$ defined by $|\boldsymbol{D}| = \sqrt{tr(\boldsymbol{D}\boldsymbol{D}^T)}$. The rotation of a tensor is denoted by the Rayleigh Product ★.

3. Methods

4.1 General

The interpolation method was mainly implemented in Python 3.8. SPD tensors can be visualized as tensor glyphs [9]. This method was used in this work as it constitutes a descriptive and interpretable way of assessing the success of the implemented interpolation method. The authors implemented the visualization in Matlab R2020b with the help of the “plotDTI” function of the fanDTasia ToolBox by Barmpoutis et al. [10].

4.2 Scan acquisition and determination of fiber orientation tensors

The authors used the YXLON-CT precision µCT system with a flat panel PerkinElmer Y.XRD1620 detector with 2048 px x 2048 px. 1950 projections were made per scan and an accelerating voltage of 150 kV and a current of 0.25 mA were chosen with an integration time of 500 ms and a frame binning of two. The resulting volumetric images are reconstructed applying the Feldkamp cone-beam algorithm [11]. The scans had a voxel size of 0.00857123 mm/voxel.

In this study, carbon fiber-reinforced polyamide 6 is investigated. This material is manufactured in the so-called "long-fiber thermoplastic direct process" (LFT-D) introduced by Krause et. al [12]. This is a compression molding process in which a so-called plastificate, an elongated, cross-sectionally oval mix of C-fibers and polymer blend, comes out of the extruder and is placed sideways in a press, which then closes in and produces CF-PA6 plates. Out of one of these manufactured plates, which have dimensions of 400 mm x 400 mm x 4 mm, nine samples of 10 mm x 10 mm x 4 mm were cut via waterjet cutting and scanned with the described parameters.

Subsequently, the reconstructed scans were processed in VG Studio Max 3.4.2. If necessary, brightness and contrast were adjusted in the ImageJ (FIJI) software. In addition, the individual gray value threshold was determined for each scan. To determine the FOT from the scan data, the method introduced by Pinter et al. [13] was used. The algorithm (implemented in C++ with the help of the ITK library) makes use of the structure tensor (cf. Eq. (1)):

  doi:10.5075/epfl-298799_978-2-9701614-0-0

$$\boldsymbol{S} = \begin{bmatrix} \left(\frac{\delta I}{\delta x}\right)^2 & \frac{\delta I}{\delta x}\frac{\delta I}{\delta y} & \frac{\delta I}{\delta x}\frac{\delta I}{\delta z} \\ \frac{\delta I}{\delta y}\frac{\delta I}{\delta x} & \left(\frac{\delta I}{\delta y}\right)^2 & \frac{\delta I}{\delta y}\frac{\delta I}{\delta z} \\ \frac{\delta I}{\delta z}\frac{\delta I}{\delta x} & \frac{\delta I}{\delta z}\frac{\delta I}{\delta y} & \left(\frac{\delta I}{\delta z}\right)^2 \end{bmatrix} \quad (1)$$

The structure tensor calculation is combined with a Gaussian blur of a width of $\sigma = 0.2$ and a mask size of 2. The FOT calculated with this algorithm constitute the foundation or ground truth that is fed into the interpolation method. They are henceforth called "measured values", implicitly including that these FOT are subject to a certain error as well.

4.3 Decomposition-based interpolation method

Determining values between a set of measured values, here the set $\mathcal{T}_m = \{\boldsymbol{UL}, \boldsymbol{UM}, \boldsymbol{UR}, \boldsymbol{ML}, \boldsymbol{MM}, \boldsymbol{MR}, \boldsymbol{LL}, \boldsymbol{LM}, \boldsymbol{LR}\}$ (respectively denoting “Upper Left, Upper Middle, Upper Right, Middle Left, …, Lower Left, etc.”) of measured FOT computationally, based on the set of measured values, describes the interpolation problem at hand. An interpolation scheme $\bar{\phi}$ is defined as a mapping f, which connects its arguments, on the one hand a set of $N \geq 1$ discrete values ϕ_i and on the other hand their associated weights $w_i \in [0; 1]$: $\bar{\phi} = f(\phi_i, w_i)$. For the chosen decomposition approach, the shape and orientation of the tensors are to be interpolated separately. Therefore, the well-known spectral decomposition resulting from the Eigenvalue problem is used:

$$\boldsymbol{A} = \boldsymbol{R}\boldsymbol{\Lambda}\boldsymbol{R}^T = \boldsymbol{R} \bigstar \boldsymbol{\Lambda}. \quad (2)$$

$\boldsymbol{\Lambda}$ denotes the tensor containing the Eigenvalues on the principal diagonal and $\boldsymbol{R}$ is defined as the orthogonal rotation matrix consisting of the normalized Eigenvectors.

4.3.1 Orientation

The rotation matrix $\boldsymbol{R}$ can be interpreted as a rotation around a rotation axis and therefore be transformed into a quaternion:

$$q = \cos\frac{\theta}{2} + \left(u_x\,\boldsymbol{i} + u_y\,\boldsymbol{j} + u_z\,\boldsymbol{k}\right)\sin\frac{\theta}{2} \quad \text{with} \quad \text{rotation axis } \boldsymbol{u} = (u_x,\ u_y,\ u_z)^T \text{ and rotation angle } \theta. \quad (3)$$

Following, the quaternion is calculated from the given rotation matrix $\boldsymbol{R}$ via:

$$t = tr(\boldsymbol{R}), r = \sqrt{1+t} \quad \text{and} \quad a = \frac{r}{2} \quad \text{with}$$

$$b = sgn(R_{zy} - R_{yz})\left|\frac{1}{2}\sqrt{1 + R_{xx} - R_{yy} - R_{zz}}\right|,$$

$$c = sgn(R_{xz} - R_{zx})\left|\frac{1}{2}\sqrt{1 - R_{xx} + R_{yy} - R_{zz}}\right| \text{ and}$$

$$d = sgn(R_{yx} - R_{xy})\left|\frac{1}{2}\sqrt{1 - R_{xx} - R_{yy} + R_{zz}}\right|. \quad (4)$$

This is followed by the actual interpolation:

$$q_{ges} = \sum_i w_i\, q_i \quad \text{with weights yielding} \quad \sum_i w_i = 1. \quad (5)$$

  doi:10.5075/epfl-298799_978-2-9701614-0-0

The retransformation of the resulting quaternion in the rotation matrix $\boldsymbol{R}$ is realized with

$$\boldsymbol{R} = \begin{bmatrix} a^2+b^2-c^2-d^2 & 2(bc-ad) & 2(bd+ac) \\ 2(bc+ad) & a^2-b^2+c^2-d^2 & 2(cd-ab) \\ 2(bd-ac) & 2(cd+ab) & a^2-b^2-c^2+d^2 \end{bmatrix}. \quad (6)$$

4.3.2 Shape

For the interpolation of the shape, three linear independent invariants are formed of each tensor and interpolated separately. Of the orthogonal K- and R-invariants introduced by Ennis et al. [6] K_1, R_2 and R_3 will be used (based on the approach of Gahm et al. [5]) as they apparently work well for physical problems, instead of working on the Eigenvalues or $\boldsymbol{\Lambda}$ respectively, with $\boldsymbol{A}'$ denoting the deviatoric (anisotropic) part of $\boldsymbol{A}$:

$$K_1 = tr(\boldsymbol{A}),\ R_2 = \sqrt{\frac{3}{2}}\frac{|\boldsymbol{A}'|}{|\boldsymbol{A}|} \text{ and } R_3 = 3\sqrt{6}\det\left(\frac{\boldsymbol{A}'}{|\boldsymbol{A}'|}\right). \quad (7)$$

The invariants are then interpolated individually:

$$K_{1,ges} = \sum_i w_i K_{1,i}, \qquad R_{2,ges} = \sum_i w_i R_{2,i} \qquad \text{and} \qquad R_{3,ges} = \sum_i w_i R_{3,i}. \quad (8)$$

The authors used the following formula to calculate the associated eigenvalues from the interpolated invariants (cf. [5]):

$$\text{For } i = 1,2,3 \text{ holds: } \lambda_i = \frac{1}{3}K_1 + \frac{2K_1R_2}{3\sqrt{3-2{R_2}^2}}\cos\left(\frac{\cos^{-1}(R_3)+P_i}{3}\right) \text{ with } P_i = 0, 2\pi, -2\pi \quad (9)$$

With these Eigenvalues, Λ can then be created again. Shepard's inverse distance weighting method is used as weight function in all cases with $p = 2$: $w_i = \frac{1}{|\boldsymbol{x}_i-\boldsymbol{x}|^p}\frac{1}{\sum_j |\boldsymbol{x}_j-\boldsymbol{x}|^{-p}}$.

4. Results

The set of "measured" orientation tensors via CT scan and subsequent calculation via structure tensor $\mathcal{T}_m$ is represented by the blue tensor glyphs in Figure 1, the set of interpolated tensors $\mathcal{T}_i = \{\boldsymbol{T}_{xy}\ \forall\ x \in 1,\dots,13\ \cap y\ \in 1,\dots,13\}$ by the orange tensor glyphs. The origin of the global coordinate system is located in the lower left corner of the plate. The original LFT charge covered almost the entire left side of the 400 mm x 400 mm mold with a width of about x = 90 mm (to the right), a length of about y = 350 mm (up) and a height of about z = 60 mm. Thus, when the press closes, one would expect a quasi 1D flow to the right. However, in the picture at the top of Figure 1, a clear curve can be seen in the fiber orientation. Instead of a distinct preferred direction in the positive x-direction, the fibers align in a curve to the upper right after clear preferred direction in the left region resulting from the plastificate, i.e. from the last extrusion step in the LFT-D process. As for the interpolation method as such, the visual results are for the most part very appealing. Interpolation between the individual measured FOT is good and the transition between two adjacent tensors also appears reasonable. The anisotropy is not basically lost between two differently oriented tensors by "rounding the tensor". The rotation of two adjacent tensors occurs with small angles and therefore smoothly. The only exception to this can be seen at the upper right edge: The interpolated tensor $\boldsymbol{T}_{10,13}$ in the middle of $\boldsymbol{UM}$ and

  doi:10.5075/epfl-298799_978-2-9701614-0-0 published under CC BY-NC 4.0 license

$\boldsymbol{UR}$ behaves somewhat strangely as far as the behavior of the row is concerned. Instead of closing the estimated angle of 20° between the measured tensors to its left and right by a 10° change, this one rotates around the larger 170°. However, the tensor $\boldsymbol{MM}$ is also taken into account for the calculation of this tensor, even if weighted less strongly than $\boldsymbol{UM}$ and $\boldsymbol{UR}$. Furthermore, the behavior in this column looks much better than could be expected if the tensor had rotated in the other direction. In order to be able to approach quantitative error analyses and to better assess the interpolation behavior, one measured tensor of $\mathcal{T}_m$ was omitted in each case and also determined with the interpolation method. The visualization results are shown in the nine lower pictures in Figure 1. There are definite changes in the orientation course. For example, the behavior of $\boldsymbol{T}_{10,13}$ changes significantly when $\boldsymbol{UM}$ or $\boldsymbol{UR}$ are omitted.

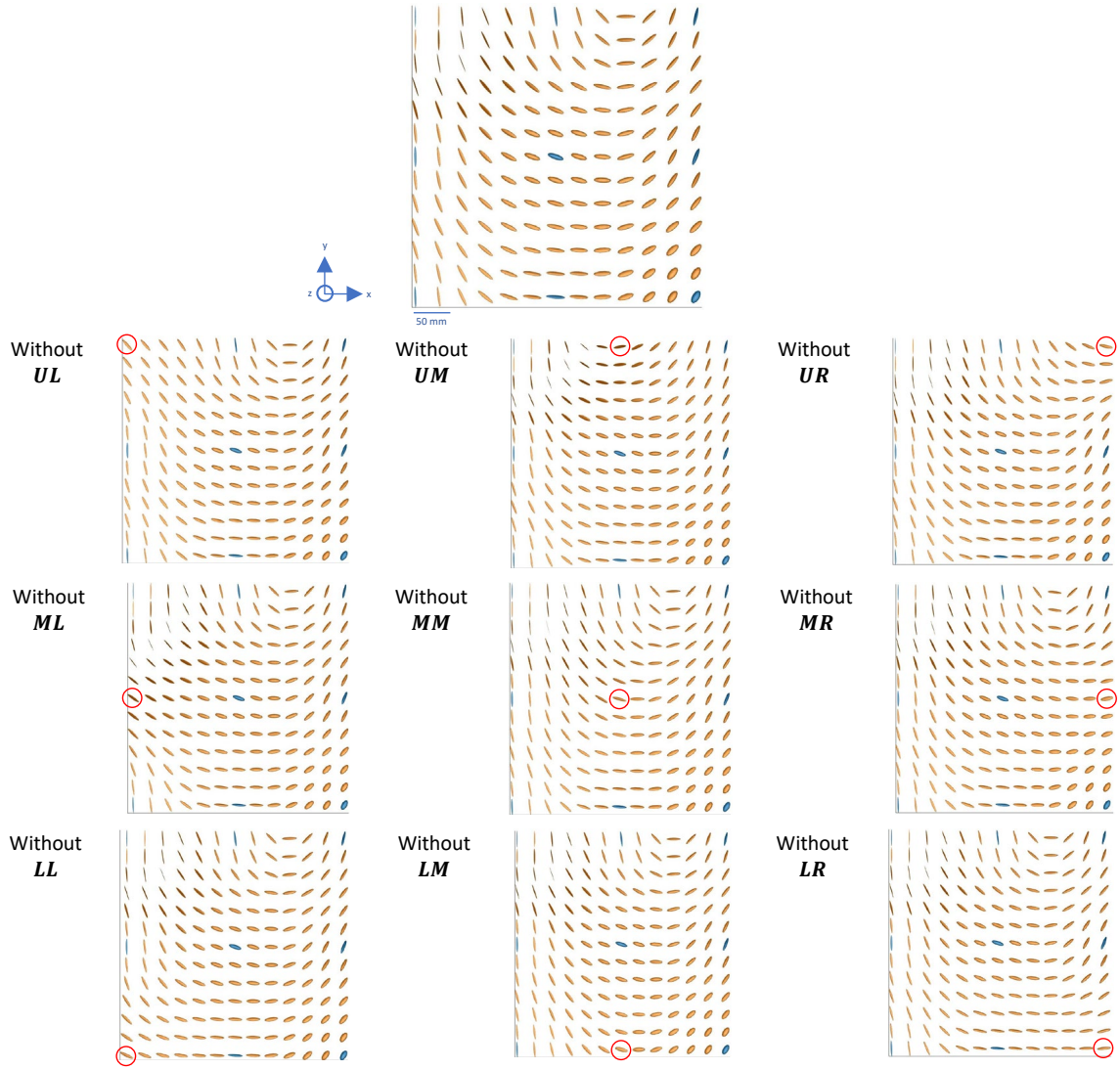

Figure 1. Picture at the top: Visualization of interpolated (orange) and measured (blue) tensors when using the decomposition-based interpolation method described in this paper. Lower nine pictures: Result when leaving one measured tensor out of the calculation and interpolating it instead respectively.

To obtain a quantitative error value, the Frobenius norm of the measured tensors and their respective interpolated substitutes was formed. The result can be seen in Figure 2. The rather

  doi:10.5075/epfl-298799_978-2-9701614-0-0 published under CC BY-NC 4.0 license

poorer interpolation at the left and upper edges and the relatively good performance in the middle of the plate (and lower right) are noticeable.

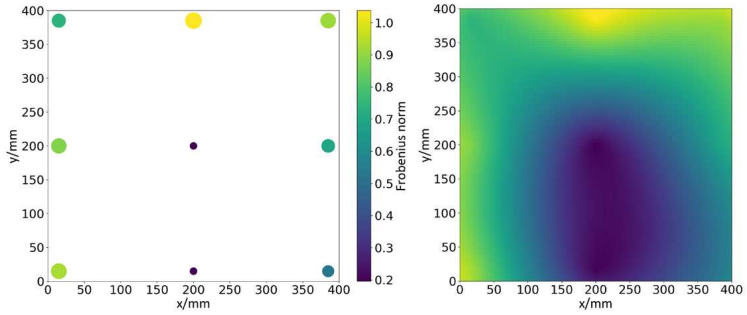

Figure 2. Visualization of the discontinuous (left image) and continuous (right image) error across the plate of the interpolated tensor in comparison to the measured one when leaving this specific tensor out of the computation. Value determined via Frobenius norm.

5. Discussion

Uneven height or dimensions of the plastificate and uneven temperatures in the tool could explain the curve in the orientation tensor field. The authors distinctively measured variations in both temperature and geometry, presumably causing the flow front to start prematurely in one edge. Furthermore, the plastificate is inserted in the mold manually, resulting in skewed/angular position of the plastificate when the press closes.

The interpolation behavior at the top right could be artificially prevented by restricting the possible angle. This could be implemented via comparing the results of the scalar products of the specific quaternions involved and taking the one providing the maximum scalar product. However, the authors tried to implement as little artificial restrictions as possible. Furthermore, as described before, the visual smoothness of rotation highly depends on whether one considers the row or the column course of rotation. In addition, the use of projectors instead of invariants might simplify the shape interpolation due to its uniqueness for a given tensor.

6. Conclusion

The implemented method provides for good macroscopic interpolation results for fiber orientation tensor fields interpolating measured FOT determined from microscopic X-ray computed tomography scans. Especially the observed isotropy behavior is satisfying. The quantitative error is higher towards the edges of the plate. Further research approaches should consist of testing this method with more sampling points (or with less of them being at the borders of the plate) and with plates that show different orientation behavior, as well as implementing a sensible angle restriction or using projectors. The use of a convolutional neural network instead of an algebraic solution could prevent the necessity of incorporating physical phenomena.

  doi:10.5075/epfl-298799_978-2-9701614-0-0

Acknowledgements

The research documented in this manuscript has been funded by the German Research Foundation (DFG) within the International Research Training Group “Integrated engineering of continuous-discontinuous long fiber reinforced polymer structures” (IRTG 2078). The support by the German Research Foundation (DFG) is gratefully acknowledged. Furthermore, the authors would also like to thank the Fraunhofer ICT for their support by providing the LFT plates, which were manufactured under the project leadership of Christoph Schelleis.

7. References

1. Advani SG, Tucker CL. The Use of Tensors to Describe and Predict Fiber Orientation in Short Fiber Composites. Journal of Rheology 1987; 31(8): 751–84.
2. Krause W, Henning F, Tröster S, Geiger O, Eyerer P. LFT-D — A Process Technology for Large Scale Production of Fiber Reinforced Thermoplastic Components. Journal of Thermoplastic Composite Materials 2003; 16(4): 289–302.
3. Terada M, Yamanaka A, Shimamoto D, Hotta Y, Shiraki K, Kimoto Y et al. Carbon fiber sampling method for determining the fiber length distribution. Advanced Composite Materials 2021; 30(sup1): 59–76.
4. Arsigny V, Fillard P, Pennec X, Ayache N. Log-Euclidean metrics for fast and simple calculus on diffusion tensors. Magn Reson Med 2006; 56(2): 411–21.
5. Gahm JK, Wisniewski N, Kindlmann G, Kung GL, Klug WS, Garfinkel A et al. Linear invariant tensor interpolation applied to cardiac diffusion tensor MRI. Medical image computing and computer-assisted intervention: MICCAI (International Conference on Medical Image Computing and Computer-Assisted Intervention) 2012; 15(Pt 2): 494–501.
6. Ennis DB, Kindlmann G. Orthogonal tensor invariants and the analysis of diffusion tensor magnetic resonance images. Magn Reson Med 2006; 55(1): 136–46.
7. Hiai F, Petz D. Riemannian metrics on positive definite matrices related to means. Linear Algebra and its Applications 2009; 430(11-12): 3105–30.
8. Sabiston T, Inal K, Lee-Sullivan P. Application of Artificial Neural Networks to predict fibre orientation in long fibre compression moulded composite materials. Composites Science and Technology 2020; 190: 108034.
9. Schultz T, Kindlmann GL. Superquadric glyphs for symmetric second-order tensors. IEEE Trans Vis Comput Graph 2010; 16(6): 1595–604.
10. Barmpoutis A, Vemuri BC, Shepherd TM, Forder JR. Tensor splines for interpolation and approximation of DT-MRI with applications to segmentation of isolated rat hippocampi. IEEE Trans Med Imaging 2007; 26(11): 1537–46.
11. Feldkamp LA, Davis LC, Kress JW. Practical cone-beam algorithm. Journal of the Optical Society of America A 1984; 1(6): 612–9.
12. Krause W, Henning F, Tröster S, Geiger O, Eyerer P. LFT-D — A Process Technology for Large Scale Production of Fiber Reinforced Thermoplastic Components. Journal of Thermoplastic Composite Materials 2003; 16(4): 289–302.
13. Pinter P, Dietrich S, Bertram B, Kehrer L, Elsner P, Weidenmann KA. Comparison and error estimation of 3D fibre orientation analysis of computed tomography image data for fibre reinforced composites. NDT & E International 2018; 95: 26–35.

  doi:10.5075/epfl-298799_978-2-9701614-0-0

FATIGUE LIFE PREDICTION OF FLAX-EPOXY COMPOSITES USING A 3D PROGRESSIVE FATIGUE DAMAGE MODEL (3D-PFDM)

Kamal, Kolasangiani[a], Habiba, Bougherara[b]

a: Department of Mechanical & Industrial Engineering, Ryerson University, Toronto, ON, Canada
b: Department of Mechanical & Industrial Engineering, Ryerson University, Toronto, ON, Canada- Habiba.bougherara@ryerson.ca

Abstract: *A three-dimensional (3D) finite element model that is based on 3D progressive fatigue damage model (PFDM) is developed to predict the fatigue life of Flax-epoxy (FE) laminates with $[0]_{16}$ and $[\pm45]_{4S}$ layups under strain-controlled loading conditions. As the input for PFDM, the material properties are characterized under static and fatigue loadings in all directions. A double-notched shear test is used to characterize the out-of-plane shear properties of laminate. The 3D PFDM including stress analysis, failure analysis, sudden material properties degradation and gradual coupled stiffness/strength degradation is implemented thorough a user-defined material subroutine UMAT in ABAQUS. The finite element analysis was performed for laminates containing voids by considering a number of weak elements randomly distributed in 3D model. The predicted fatigue life is in good agreement with the experimental results.*

Keywords: Flax-epoxy composite; Progressive fatigue damage model; 3D finite element model; Fatigue life prediction.

1. Introduction

In the last two decades, the use of natural fibers as an alternative to synthetic fibers in composite materials for engineering applications has gained more attention due to the concern about environment and sustainability issues. Flax is one of the most widely studied natural fibers and is often used as reinforcement in composite structures. An important issue in the design of flax-composites is fatigue behavior of laminates under cyclic loading, which is the responsible for many, if not most, failures in composite structures. Most available fatigue studies to date on flax-composites are based on stress-controlled conditions [1]. These studies have reported an unusual stiffening behavior of flax-epoxy (FE) laminates with certain configurations. Mahboob and Bougherara [2] attributed the stiffening behavior of FE composites to the variation in strain rate during stress-controlled loading conditions. They showed that all FE specimens under strain-controlled loading conditions demonstrated a stiffness degradation over fatigue life.

A considerable number of models and methodologies emerged to predict the fatigue behavior of examined composites. Refs [3-5] are the only attempts concerning the fatigue life prediction of Flax-composites which are based on stiffness/strength degradation, temperature variation and energy dissipation. Among the models, progressive fatigue damage model (PFDM) is the most advanced model which could be employed to predict the fatigue life as well as the material property degradation in the composite materials. Numerical methods e.g. finite element method are suitable to apply a PFDM on laminated composite under cyclic loading. The authors of the present study have recently investigated the fatigue life prediction of FE laminate using

  doi:10.5075/epfl-298799_978-2-9701614-0-0

2D finite element model [6]. However, in order to incorporate the delamination effects and achieve a realistic stress analysis, a 3D model is developed to analyze the 3D state of stress of FE laminate. In this research, a 3D finite element model that is based on PFDM is performed thorough UMAT subroutine in ABAQUS to predict the fatigue life of on FE composites.

2. 3D progressive fatigue damage model (3D PFDM)

A 3D PFDM is applied in this study in order to predict fatigue damage accumulation and fatigue life of FE composites. This model includes stress analysis, failure analysis and material property degradation.

2.1 Failure analysis

In this research, seven 3D polynomial stress-based failure criteria were used to detect seven failure modes. Specifically, for detecting the matrix cracking in tension and compression, fiber failure in compression and fiber/matrix shear failure a set of 3D Hashin failure criterion [7] was used. The maximum stress criterion was used to identify the fiber breakage in tension [8]. Also, Ye-delamination criterion [9] was applied in order to detect delamination in tension and compression. The fatigue failure criteria with regard to failure modes are depicted in Table 1. In the equations of Table 1, F, M, FMS and DEL are fiber failure, matrix failure, fiber/matrix shear failure and delamination failure indices respectively. A mode of failure occurs when the corresponding failure index exceeds 1. X_r, Y_r, Z_r and S_r are residual strengths of unidirectional ply under uniaxial cyclic loading in the longitudinal, transvers, normal and shear (i.e., in-plane or out-of-plane) directions, respectively. Subscripts t and c represent tension and compression components of residual strength. σ_{ij} is the layer stress component in the i-j direction. Notations i and j in σ_{ij} and S_{rij} refer to a local layer coordinate system in which the 1-axis is parallel to the fibers, 2-axis is transverse to the fibers, and 3-axis coincides with the normal direction.

Table 1: Fatigue failure criteria.

Failure mode	Failure criterion
Fiber tensile failure ($\sigma_{11} > 0$)	$F^2 = \frac{\sigma_{11}}{X_{rt}}$
Fiber compressive failure ($\sigma_{11} < 0$)	$F^2 = -\frac{\sigma_{11}}{X_{rc}}$
Matrix tensile failure ($\sigma_{22} > 0$)	$M^2 = \left(\frac{\sigma_{22}}{Y_{rt}}\right)^2 + \left(\frac{\sigma_{12}}{S_{r12}}\right)^2 + \left(\frac{\sigma_{23}}{S_{r23}}\right)^2$
Matrix compressive failure ($\sigma_{22} < 0$)	$M^2 = \left(\frac{\sigma_{22}}{Y_{rc}}\right)^2 + \left(\frac{\sigma_{12}}{S_{r12}}\right)^2 + \left(\frac{\sigma_{23}}{S_{r23}}\right)^2$
Fiber/matrix shear failure ($\sigma_{11} < 0$)	$FMS^2 = \left(\frac{\sigma_{11}}{X_{rc}}\right)^2 + \left(\frac{\sigma_{12}}{S_{r12}}\right)^2 + \left(\frac{\sigma_{13}}{S_{r13}}\right)^2$
Delamination tension failure ($\sigma_{33} > 0$)	$DEL^2 = \left(\frac{\sigma_{33}}{Z_{rt}}\right)^2 + \left(\frac{\sigma_{13}}{S_{r13}}\right)^2 + \left(\frac{\sigma_{23}}{S_{r23}}\right)^2$
Delamination compression failure ($\sigma_{33} < 0$)	$DEL^2 = \left(\frac{\sigma_{33}}{Z_{rc}}\right)^2 + \left(\frac{\sigma_{13}}{S_{r13}}\right)^2 + \left(\frac{\sigma_{23}}{S_{r23}}\right)^2$

  doi:10.5075/epfl-298799_978-2-9701614-0-0

2.2 Material property degradation

For composite laminates subjected to fatigue loading with lower stress or strain than the static failure stress or strain, the material properties are degraded gradually until the level where the degraded residual strength reaches the applied stress. At this moment, a sudden mode of failure and a sudden degradation of material properties occur. In this study, the independent stiffness degradation rule as a function of fatigue life fraction in all directions established by Lian and Yao [10] is utilized. The stiffness degradation rule for unidirectional laminates is expressed as:

$$\frac{E_0-E_r}{E_0-E_{rc}} = \frac{\left(\frac{n}{N}\right)^u + a\left(\frac{n}{N}\right)^v}{1+a} \tag{1}$$

where E_0 is the initial stiffness; n and N are number of cycles and fatigue life; E_r and E_{rc} are the residual stiffness after n cycles and critical residual stiffness at failure respectively. u, v and a are material parameters obtained by curve fitting of the experimental data. Furthermore, Lian and Yao [10] presented a coupled residual stiffness and strength model to eliminate the required experiments for characterization of residual strength. The residual strength proposed by [10] is as follows:

$$S_r = S_0 - (S_0 - S_{rc})\left(\frac{\left(\frac{n}{N}\right)^u + a\left(\frac{n}{N}\right)^v}{1+a}\right)^w \tag{2}$$

In the above equation, the parameter w is a function of load level. S_0 is the static strength and S_r is the residual strength after n cycles. S_{rc} is the critical residual strength at failure which is equal to the maximum applied stress ($S_{rc} = \sigma_{max}$).

Sudden material degradation rules of unidirectional ply are summarized in Table 2. If the laminate fails in fiber direction, the catastrophic failure takes place and all material properties are reduced. The matrix failure only affects the material properties in transverse direction. The fiber/matrix shear failure only influences the in-plane shear properties. When delamination failure is detected by failure criteria, it is assumed that the material cannot sustain load in normal direction, and the normal properties are reduced.

2.3 Stress analysis

The stress analysis and fatigue life prediction of the FE laminate is performed for a 3D finite element model using the software ABAQUS, and the 3D PFDM is implemented via a subroutine UMAT that is written in FORTRAN. Fig. 1 illustrates dimensions and boundary conditions of 3D model comprising 16 layers. One end of the specimen was fixed in all directions and the other end was constrain in all but loading directions. A total of 30400 elements of C3D8 which is an

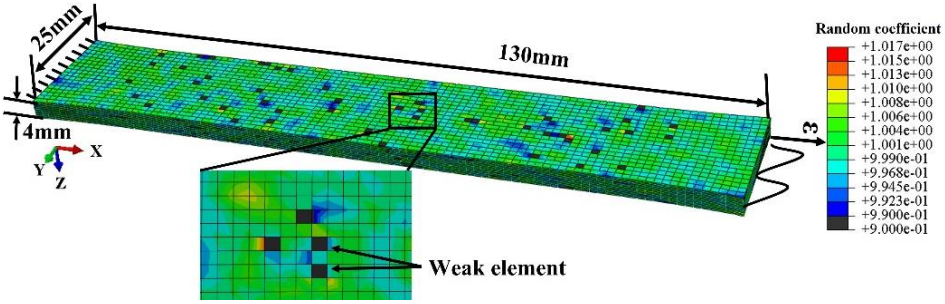

Figure 1. 3D finite element model with random coefficients and weak elements.

  doi:10.5075/epfl-298799_978-2-9701614-0-0

Table 2: Sudden material property degradation rule.

Failure mode	Sudden material properties degradation rule
Fiber failure	$E_{11} = E_{22} = E_{33} = E_{12} = E_{13} = E_{23} = \nu_{12} = \nu_{13} = \nu_{23} = \nu_{21} = \nu_{31} = \nu_{32} \rightarrow 0$ $\frac{\sigma_{11}}{X_{rt}} = \frac{\sigma_{11}}{X_{rc}} = \frac{\sigma_{22}}{Y_{rt}} = \frac{\sigma_{22}}{Y_{rc}} = \frac{\sigma_{33}}{Z_{rt}} = \frac{\sigma_{33}}{Z_{rc}} = \frac{\sigma_{12}}{S_{r12}} = \frac{\sigma_{13}}{S_{r13}} = \frac{\sigma_{23}}{S_{r23}} \rightarrow 0$
Matrix failure	$E_{22} = \nu_{23} = \nu_{21} \rightarrow 0$ $\frac{\sigma_{22}}{Y_{rt}} \rightarrow 0\ (tension),\ \frac{\sigma_{22}}{Y_{rc}} \rightarrow 0\ (compression)$
Fiber/matrix shear failure	$E_{12} = \nu_{12} = \nu_{21} \rightarrow 0$ $\frac{\sigma_{12}}{S_{r12}} \rightarrow 0$
Delamination failure	$E_{33} = \nu_{31} = \nu_{32} \rightarrow 0$ $\frac{\sigma_{33}}{Z_{rt}} \rightarrow 0\ (tension),\quad \frac{\sigma_{33}}{Z_{rc}} \rightarrow 0\ (compression)$

eight-node trilinear hexahedral element with full integration was employed. The numerical procedure and stochastic distribution of material properties assigned to elements are similar to that developed previously and reported in [6]. In order to consider the voids in model, a number of weak elements was chosen randomly and a coefficient 0.9 was assigned to them (see Fig. 1). The number of weak elements was calculated based on the void contents.

3. Material characterization

As the input for 3D PFDM, the material properties of FE laminate are fully characterized under static and fatigue loading conditions in the longitudinal (1-1), transvers (2-2), normal (3-3), in-plane shear (1-2) and out-of-plane shear (1-3 and 2-3) directions. The static and fatigue properties of FE laminates in longitudinal, transvers, normal and in-plane shear directions were characterized by authors previously and reported in [2,6,11]. The initial mechanical properties and fatigue parameters of FE laminate in coupled residual stiffness/strength degradation rules in longitudinal, transverse, normal and in-plane shear directions are summarized in Table 3. Superscript 0 in Table 1 denotes the initial material property. Moreover, The linear equations fitted to experimental strain-life ($\varepsilon - N$) data in all direction are presented in Table 3.

There are four main methods for performing the out-of-plane shear experiments [12]. Among these methods, the double-notched shear (DNS) test requires no extensive set-up fixture and the specimen is simple. Moreover, some studies on DNS test showed that the specimen fails in shear. These features make the double-notched test method attractive for out-of-plane shear testing. In this research, the DNS test method was used for characterizing the out-of-plane shear properties. The geometry of DNS specimen with $[90]_{16}$ layup is shown in Fig. 2(a). Due to out-of-plane deformation caused by compressive loading, a supporting jig was placed in the middle of the specimen to prevent from buckling (Fig 2(b)). All out-of-plane static and fatigue tests were performed using MTS 370 test frame under strain-controlled conditions with cross head speed

  doi:10.5075/epfl-298799_978-2-9701614-0-0

Table 3: Longitudinal, transverse, normal and in-plane shear parameters of FE laminates in PFDM [2,6,11].

Longitudinal		Transverse and normal		In-plane shear	
E_{11}^0 (GPa)	31.42	$E_{22}^0 = E_{33}^0$ (GPa)	5.58	E_{12}^0 (GPa)	2.07
X_t (MPa)	286.7	$Y_t = Z_t$ (MPa)	33.86	S_{12} (MPa)	37.35
X_c (MPa)	127.11	$Y_c = Z_C$ (MPa)	79.94	ν_{12}	0.353
$\varepsilon_{11}^{\text{fail}}$ (%)	1.53	$\varepsilon_{22}^{\text{fail}} = \varepsilon_{33}^{\text{fail}}$ (%)	1.36	$\gamma_{12}^{\text{fail}}$ (%)	14.92
u	0.12	u	0.12	u	0.45
v	39.6	v	37.6	v	0.17
a	0.3	a	0.25	a	1.79
$w = 4.22e^2 - 1.99e + 0.36$		$w = 3.21e^2 - 1.2e + 0.33$		$w = 68.62e^2 - 8.57e + 0.49$	
$\log(N) = 7.47 - 402.42\varepsilon_{max}$		$\log(N) = 7.81 - 585.84\varepsilon_{max}$		$\log(N) = 9.85 - 289.42\gamma_{max}$	

of 1.3 mm/min in static test, and strain ratio of 0.1 and loading frequency of 5Hz in fatigue test. Strain measurement was carried out using digital image correlation (DIC) setup. The out-of-plane shear properties obtained from static test are tabulated in Table 4.

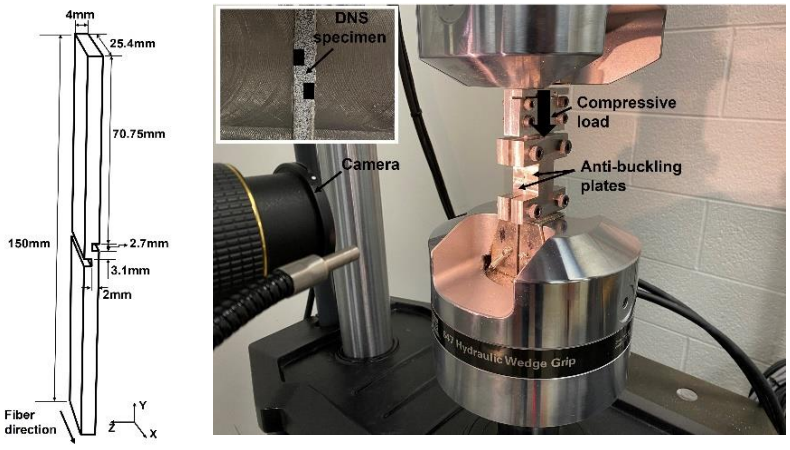

(a) (b)

Figure 2. (a) Geometry of DNS specimen, (b) Out-of-plane shear test setup.

Table 4: Out-of-plane shear parameters of FE laminates in PFDM.

E_{23}^0 (GPa)	S_{23} (MPa)	$\gamma_{23}^{\text{fail}}$ (%)	u	v	a	w
0.955	27.07	7.5	13.4	0.2193	4.85	$60.731e^2 - 9.09e + 1.42$

Fig. 3(a) shows the out-of-plane shear residual stiffness degradation normalised by the initial modulus under different maximum shear strain levels. The normalised residual stiffness degradation results are fitted using Eq. (1). The curve fitting parameters u, v and a for stiffness degradation rule in out-of-plane shear direction were listed in Table 4. The parameter w was

  doi:10.5075/epfl-298799_978-2-9701614-0-0

calculated from Eq. (2) at failure moment using experimental critical residual stiffness and corresponding critical residual strength for each strain level. The curve fitting function for parameter *w* versus relative shear strain level $e = \frac{\gamma_{max}}{\gamma^{\text{fail}}}$ in 2-3 direction is given in Table 4. The fatigue life results of out-of-plane shear test for DNS specimen are plotted in Fig. 3(b). A linear equation was curve fitted to the experimental strain-life data and shown in this figure. This equation is used in the simulation to determine the fatigue life of the elements under specific constant amplitude loading at each cycle jump.

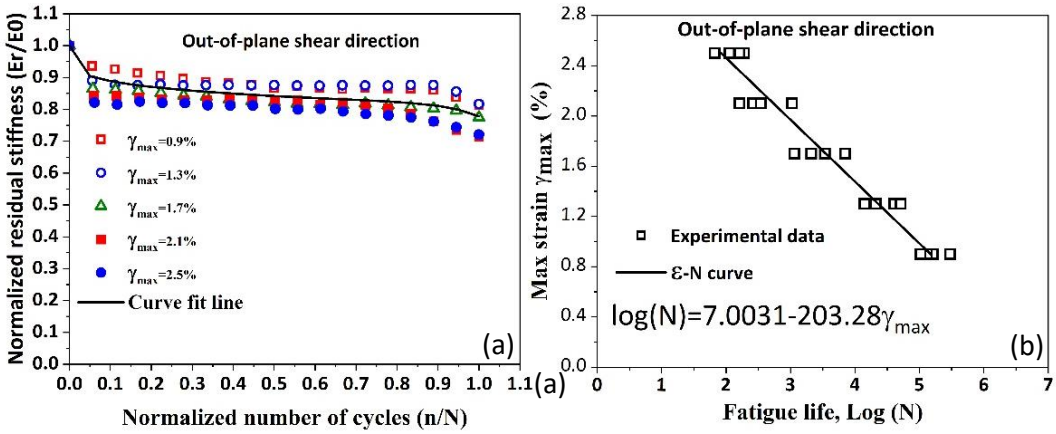

Figure 3. Out-of-plane fatigue test results (a) Residual stiffness degradation, (b) strain-life curve.

4. Validation of numerical results using experimental data

The finite element analysis was performed on $[0]_{16}$ and $[\pm45]_{4S}$ layups, and the results were compared with experimental findings (see Fig. 4). The numerical analysis for $[0]_{16}$ layup was carried out for void contents of 0.72% and 3.35%. The number of weak elements for void contents 0.72% and 3.35% were calculated to be around 176 and 800. The numerical results showed that the fatigue life is similar for $[\pm45]_{4S}$ with different porosities and the failure occurs in the lower or upper part of specimens irrespective of the number of weak elements. As such, the predicted $\varepsilon - N$ curve of $[\pm45]_{4S}$ with only void content of 0.3% (72 weak elements) is shown in Fig. 4(b). As seen, predicted fatigue life is in a good correlation with those obtained experimentally. However, it is observed that at high strain levels, the simulation and experiment have some deviation. The reason can be attributed to plasticity of the FE composites caused by several mechanisms at higher load levels [11], and use of single fitting function and parameters for stiffness/strength degradation rules for all strain levels. In order to investigate the effect of presence of the voids (weak elements) on the simulation results, the predicted fatigue life of $[0]_{16}$ laminate with 3.35% void content is compared to the laminate without voids for all loading levels in Fig. 5. It is observed that the presence of weak elements has minimal effect (between 11-14%) on the fatigue life at lower strain loading levels. On the other hand, the fatigue life reduces by about 27% at highest strain loading level ($\varepsilon_{max} = 1.08\%$).

Fig. 6(a) depicts the variation of failure indices for a weak element in the $[\pm45]_{4S}$ laminate under a 1.1% maximum strain loading. It observed that the matrix in 45 plies failed at around 70% of fatigue life and the load is carried out by fiber in the rest of fatigue life. The delamination failure index is negligible until 50% of fatigue life, after which it increases until the final failure. A microdamage analysis was performed to validate the simulation results. $[\pm45]_{4S}$ laminate was

imaged across the longitudinal section after it was loaded up until 75% of fatigue life under 1.1% maximum strain loading (Fig. 6(b)). SEM image shows matrix cracking before 75% of fatigue life, a corroboration of the simulation results.

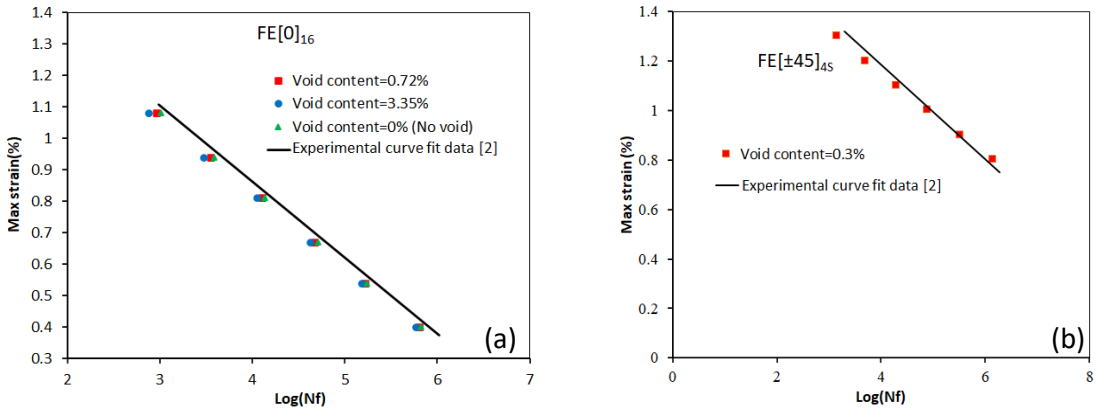

Figure 4. Comparison of numerical and experimental $\varepsilon - N$ curves for FE laminates (a) $[0]_{16}$ and (b) $[\pm45]_{4S}$.

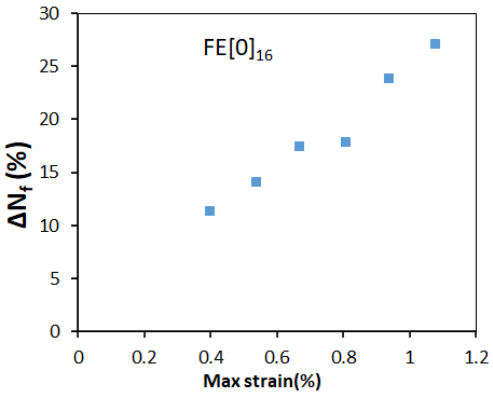

Figure 5. Variation in the fatigue life of $[0]_{16}$ laminate with 3.35% void content compared to one with no voids.

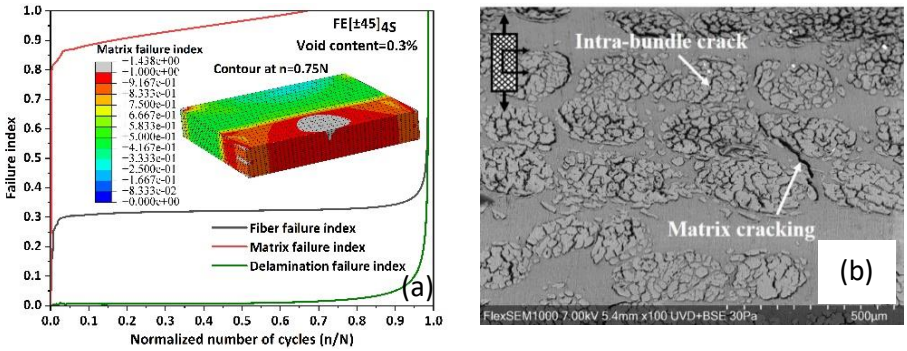

Figure 6. Results of fatigue analysis for [±45] laminate under a 1.1% maximum strain loading (a) Failure indices evolution versus number of cycles, (b) SEM micrograph after 75% of fatigue life.

5. Conclusion

In this paper, a three-dimensional progressive fatigue damage model (3D PFDM) is implemented via a user-defined material subroutine UMAT in finite element software ABAQUS to predict the fatigue life of flax/epoxy (FE) composites with $[0]_{16}$ and $[\pm45]_{4S}$ layups. The 3D PFDM includes

stress analysis, sudden material property degradation as identified by failure criteria, and gradual stiffness degradation coupled with residual strength degradation. The finite element analysis was performed for laminates containing voids by considering a number of weak elements randomly distributed in 3D model. The numerically predicted fatigue life and experimental results show good agreement. It was shown that the effect of void content on the predicted fatigue life was more considerable for $[0]_{16}$ layup under a higher load. From SEM images, matrix cracking in $[\pm45]_{4S}$ laminates starts before 75% of fatigue life corroborating the simulation results.

6. References

1. Mahboob Z, Bougherara H. Fatigue of flax-epoxy and other plant fibre composites: Critical review and analysis. Compos Part A Appl Sci Manuf. 2018; 109:440–62.
2. Mahboob Z, Bougherara H. Strain amplitude controlled fatigue of Flax-epoxy laminates. Compos Part B Eng. 2020; 186:107769.
3. El Sawi I, Fawaz Z, Zitoune R, Bougherara H. An investigation of the damage mechanisms and fatigue life diagrams of flax fiber-reinforced polymer laminates. J Mater Sci. 2014 ;49(5):2338–46.
4. Islam MZ, Ulven CA. A thermographic and energy based approach to define high cycle fatigue strength of flax fiber reinforced thermoset composites. Compos Sci Technol. 2020; 196:108233.
5. Seghini MC, Touchard F, Sarasini F, Chocinski–Arnault L, Ricciardi MR, Antonucci V, et al. Fatigue behaviour of flax-basalt/epoxy hybrid composites in comparison with non-hybrid composites. Int J Fatigue. 2020; 139:105800.
6. Kolasangiani K, Oguamanam D, Bougherara H. Strain-controlled fatigue life prediction of Flax-epoxy laminates using a progressive fatigue damage model. Compos Struct. 2021; 266:113797.
7. Tserpes K., Papanikos P, Labeas G, Pantelakis S. Fatigue damage accumulation and residual strength assessment of CFRP laminates. Compos Struct. 2004; 63(2):219–30.
8. Tsai SW, Hahn HT. Introduction to Composite Materials. Stability and Vibrations of Thin Walled Composite Structures. Routledge; 2018.
9. Lin Ye. Role of matrix resin in delamination onset and growth in composite laminates. Compos Sci Technol. 1988; 33(4):257–77.
10. Lian W, Yao W. Fatigue life prediction of composite laminates by FEA simulation method. Int J Fatigue. 2010; 32(1):123–33.
11. Mahboob Z, El Sawi I, Zdero R, Fawaz Z, Bougherara H. Tensile and compressive damaged response in Flax fibre reinforced epoxy composites. Compos Part A Appl Sci Manuf. 2017; 92:118–33.
12. Shokrieh MM, Lessard LB. An Assessment of the Double-Notch Shear Test for Interlaminar Shear Characterization of a Unidirectional Graphite/Epoxy under Static and Fatigue Loading. Appl Compos Mater. 1998;5(1):289–304.

  doi:10.5075/epfl-298799_978-2-9701614-0-0

COMPOSITE PROCESS SIMULATION COMPARATIVE STUDIES AND INTEGRATION IN THE DESIGN WORKFLOW

W.M. van den Brink, Senne Sterk, T. Koenis, T. Panis
NLR - Royal Netherlands Aerospace Centre)

Abstract: *Composite material for lightweight structures has become the standard in aerospace. Still the manufacturing of accurate composite components does often provide challenges and trial and error is needed to dial in the process and to achieve first time right parts. Currently during the assembly steps, parts often do not align correctly and reshaping (inducing further residual stress) or shimming is needed. Also in case of repairs of composite structures the residual stress developed during the process can cause undesired distortions and reduce the service life. In recent years process simulation of composite manufacturing processes has gained more traction. In this paper the work performed at Royal NLR in the field of process simulation for thermoplastic and thermoset composites will be presented.*

Keywords: composites, process simulation, thermoplastic

1. Introduction

Current advanced computational tools enable, apart from structural analyses, also evaluation and analysis of the manufacturing process of high performance CFRP aerospace components. By combining manufacturing process parameters with interface behaviour and thermo-mechanical-chemical material behaviour in the simulation, the manufacturing and the design processes are combined in the so-called “virtual manufacturing”, which can support the production of “first time right” parts [1]. In previous work by Royal NLR this has been addressed for composite braiding [2], fibre placement manufacturing of thermoplastic composite, see Figure 1 [3, 4] and thermoset curing [5].

In this paper, an overview of the broad experience developed in the field of virtual manufacturing is presented. Such experience ranges from using virtual manufacturing to support design and manufacturing of composite components, to the development of new virtual manufacturing models, both analytical and via finite element models. This knowledge has been developed via joint cooperation in several European projects.

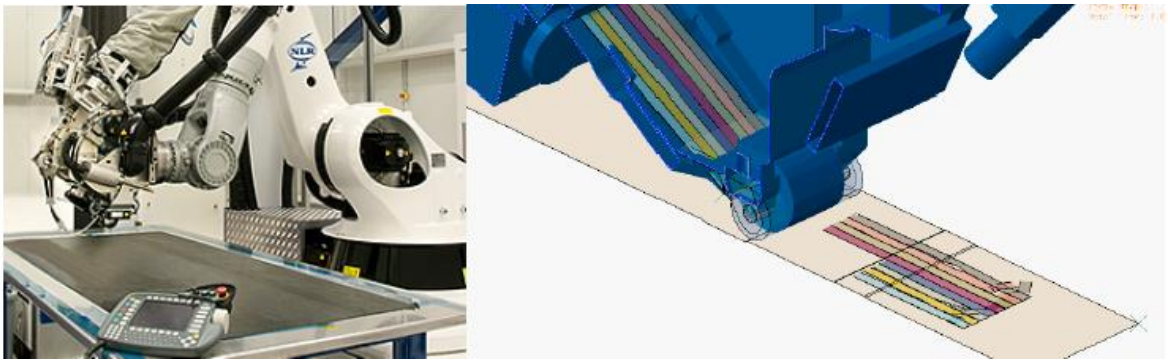

Figure 1 : Fibre placement facility at NLR and virtual manufacturing tow head simulation. In the simulation the placement, wrinkling and cutting of tows is simulated

  doi:10.5075/epfl-298799_978-2-9701614-0-0

More projects are currently ongoing to build on the existing knowledge and to expand into making more manufacturing processes “virtual”. Several challenges and opportunities are still open in this field of research. One of the most intriguing concerns the determination of the material properties of the virtually manufactured components and of the process parameters required to achieve pre-determined material properties. A fundamental step to fully implement virtual manufacturing solutions in support of development and certification activities is to develop a framework for the validation of virtual manufacturing models and results, as currently no clear virtual manufacturing test standard is available.

An active research field for virtual manufacturing is in composite draping [6] which is also the focus of this paper. There has been extensive research and also commercial software offerings are available among which Aniform, SimuDrape, ESI PAM FORM. In research by Dorr [7] the different approaches are compared for a thermoplastic composite example case. This interesting overview shows the possibilities and challenges of these types of advanced analyses. One of the main challenges is accurate characterization of the material for processing conditions, i.e. at elevated temperature. While the mentioned examples are physics based analyses, in work by Maymard [8] one kinematic approach for draping of prepreg is presented. This method is faster and can thus be used in design approaches.

For the approach of characterising the manufacturing process for aerospace parts the following steps were taken, see Figure 2. On material and coupon level the characterisation is performed. This is then validated on the element and component level.

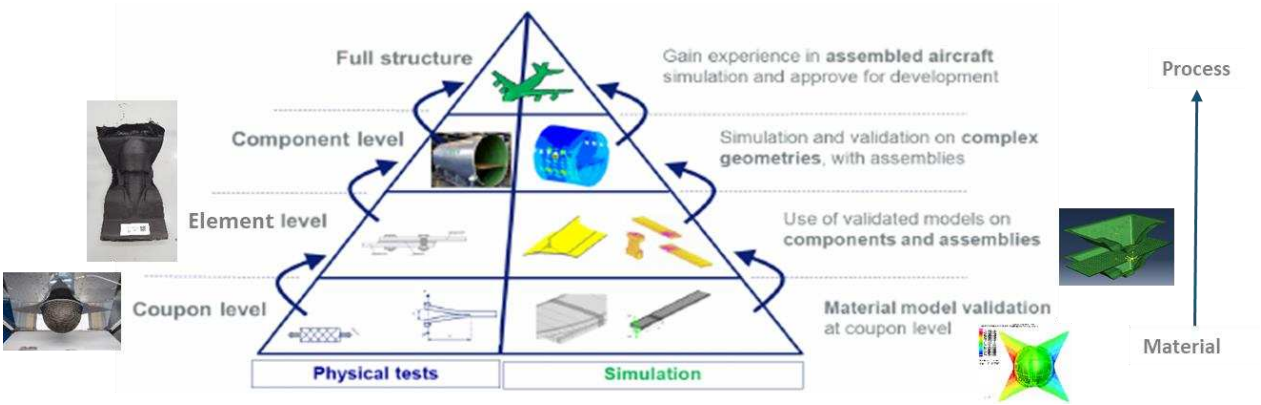

Figure 2 : Overview of the building block approach to characterise the manufacturing process. On material and coupon level the characterisation is performed. This is then validated on the element and component level

In the next section the setup for the analyses of draping of thermoplastic prepreg is shown.

2. Simulation of half sphere draping

The draping behaviour has initially been investigated using the standard draping model available in Abaqus and on a double curved half sphere case. Draping test result of a double curved half sphere is shown in Figure 3.

  doi:10.5075/epfl-298799_978-2-9701614-0-0

Figure 3 : Draping of dry carbon fibre fabric into the double curved sphere shape. This is a common test shape to investigate the shear of the individual yarns of the fabric. At NLR the test was performed with the fabric between two transparent plastic sheets with a central hole and a 3D printed sphere mould was lowered through the transparent plates.

For this the stiffness of the resin and the fibres have been adjusted. Also the shear stiffness of the resin has been set low to simulation elevated temperature behaviour. The following inputs were chosen;

- Rho: 1.6E-6 kg/mm3
- Warp direction: alfa_1 = 0 degrees, E1=10 GPa
- Weft direction: alfa_2 = 90 degrees, E2=10 GPa
- Shear coupling: G=1E-5 GPa
- Thickness 0.3 mm
- Friction sphere-blank: Coefficient 0.2
- Friction blankholder-blank: Coefficient 0.2
- Blank size: 300 x 300 mm
- Pressure on blank holder: 4E-5 GPa
- Imposed velocity sphere: 0.5 m/s
- Quarter model
- Element size: 1 mm

The results that are obtained are shown below. It appears that with large deformation it becomes more difficult to decouple the membrane stiffness of the material and the bending stiffness. During draping the laminate has a low bending stiffness but a high membrane stiffness in warp and weft directions.

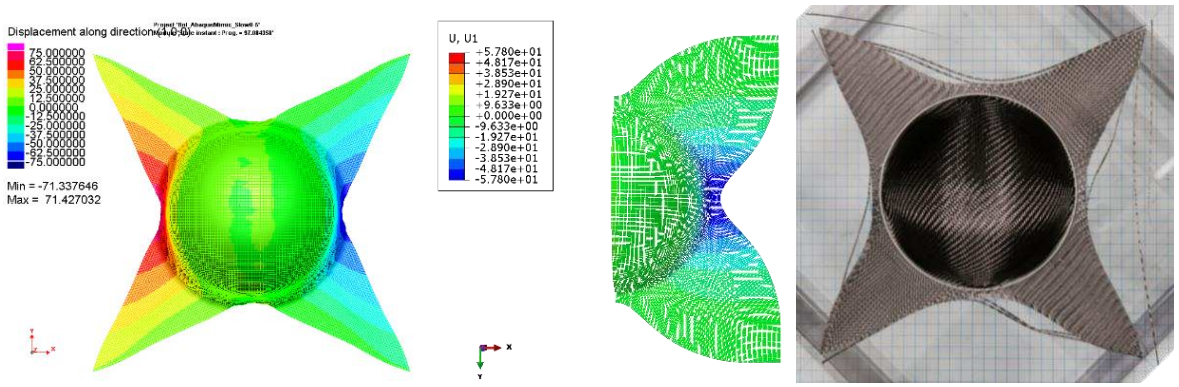

Figure 4 : Comparison of the predicted draping distortions with dry fabric and the tested half sphere. On the left the PAM FORM results and in the middle the standard Abaqus material results. Clear differences can be observed between the methods with more shear present in the actual test and PAM FORM model.

From this it was concluded that the standard Abaqus elastic material model is not suitable to predict draping behaviour of dry fabric and probably prepregs. Therefore the focus was on the specific methods for predicting draping.

  doi:10.5075/epfl-298799_978-2-9701614-0-0

3. Simulation of CFRTP draping

In this section two demonstrators will be shown with complex shapes to determine the added value of virtual manufacturing simulations. Especially the focus lies on the added value of virtual manufacturing in the design process. For these demonstrators the material AS4D-PEKK was used. The characterisation of the material was done together with SimuTence and Fraunhofer institute, see Figure 5, including rheometer bending, frictions and shear tests. Also Modulated Differential Scanning Calorimetry (MDSC) measurements have been done in-house. Before implementing the virtual manufacturing methods in the design process, first the method has to be validated.

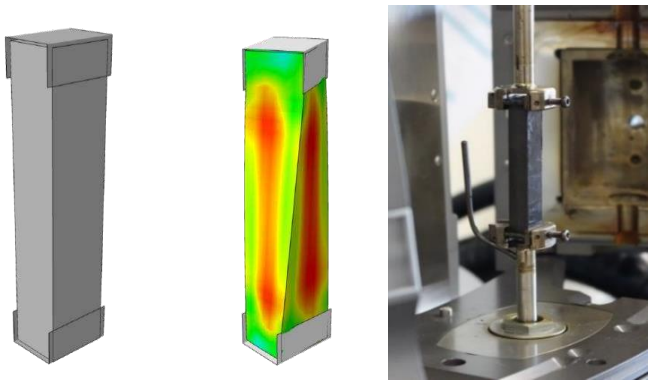

Figure 5 : Torsion bar test configuration to determine shear rate effects with on the left the CAD model where the central part is the thermoplastic carbon reinforced material. In the middle the finite element verification of the test . On the right the test setup to apply shear rate effects

Complex draping simulations are performed in ABAQUS using the Simudrape plugin [9]. One beneficial application of virtual manufacturing in draping is for the development of the process and mould/stamp geometries. Criteria for the process development mainly include the circumvention of manufacturing defects such as wrinkles. However, the advanced draping simulations can also be used to determine the fibre orientation in the final part. These orientations can be used to determine the performance (using structural analyses) of the draped component after manufacturing. In this way, virtual manufacturing can be employed to ensure that the component is manufactured first time right and will behave as intended.

To develop the process by virtual manufacturing, fast iterations are preferable, as this could require many iterations. Therefore, isothermal simulations are performed, not taking into account any thermal effects occurring during the draping process. In the mechanical simulations, the material properties are taken at a constant temperature. In molten condition, the stiffness of the matrix material is assumed to be zero. However, because the material can rapidly cool down during the draping process, it is necessary to determine an effective matrix stiffness, see Figure 6.

  doi:10.5075/epfl-298799_978-2-9701614-0-0

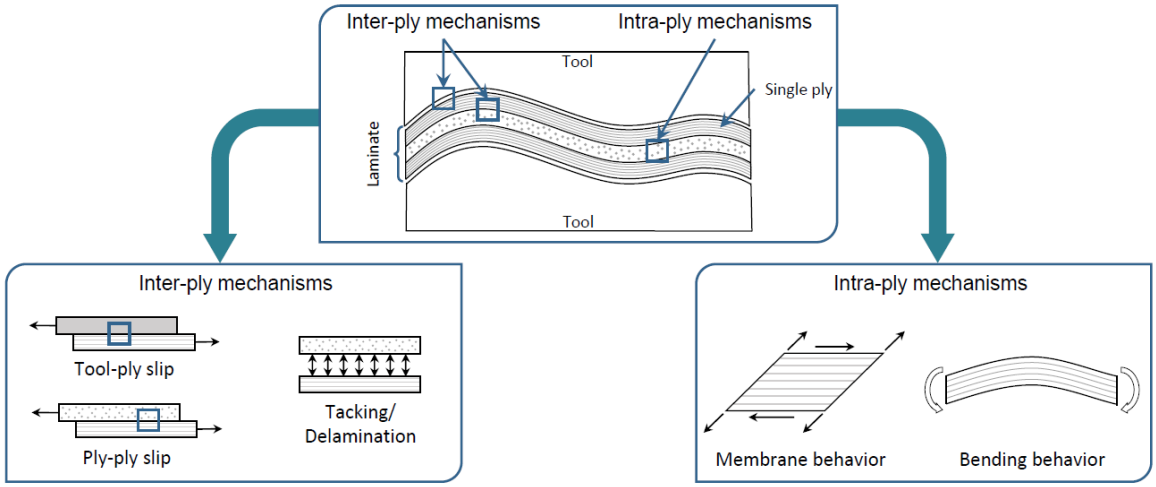

Figure 6 : Overview of the interactions and mechanisms at play during the draping of thermoplastic material. It is very important to characterize these interactions and properties to achieve accurate predictions [9]

In this paper, the simulation approach is verified and calibrated using a generic CFRTP component. In the calibration, the effective value for the matrix stiffness during the draping process is determined. The calibrated draping simulations are subsequently used for the analysis and improvement of the draping process for a CFRTP component. Within this process development, different designs of mould geometry and the use of grippers are analysed by virtual manufacturing.

Figure 7 displays the generic CFRTP component used to validate and calibrate the mechanical simulations. This component is manufactured from $[90/45/0/-45/90]_s$ UD AS4D-PEKK blank of 200 x 400 mm, at a stamp velocity of 200 mm/s. The same blank and draping settings will be used to manufacture the CUPID component displayed in Figure 7. In the draping simulations, de stamp and mould are assumed rigid, and the blanks are modelled individually with 3 mm triangular (S3R) elements.

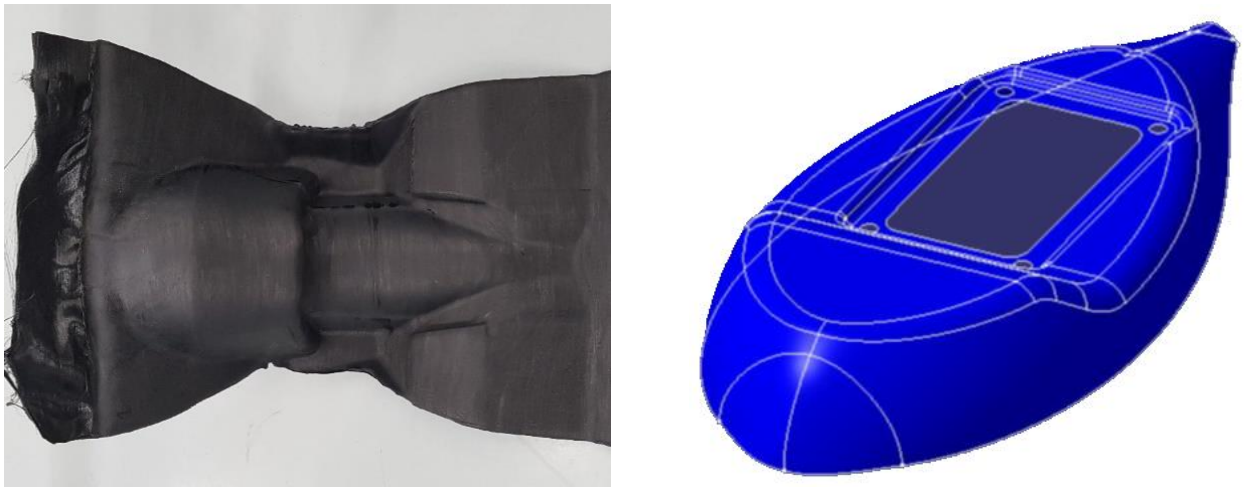

Figure 7 : Photo of the generic complex CFRTP components used to validate and calibrate the draping simulations

  doi:10.5075/epfl-298799_978-2-9701614-0-0

4. Comparison of CFRTP draping results

Figure 8 displays the results of the calibrated isothermal simulations of the generic draping component. It is observed that with a low matrix stiffness of 50 MPa the contour and wrinkles in the final component can be accurately predicted. The predicted wrinkles displayed in Figure 8b clearly indicate critical areas also observed experimentally. The comparison of the contour in Figure 8c displays the numerically predicted and experimentally observed contours, illustrating very good correlation between the simulations and experiments.

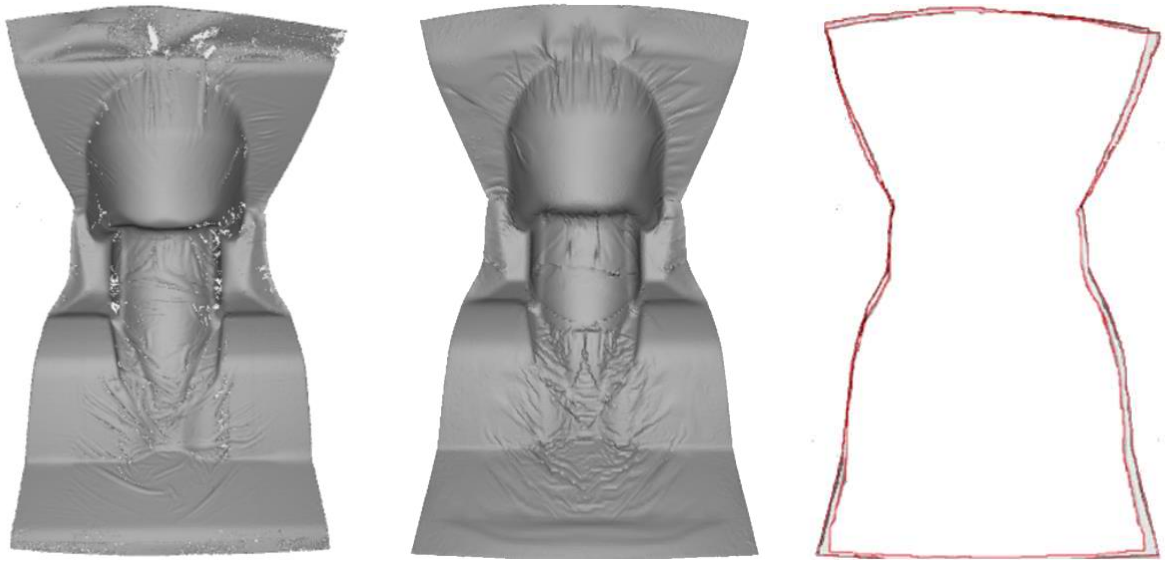

(a) **(b)** **(c)**

Figure 8 : Results of the isothermal simulations of the generic draping component, (a) is the experimental results as scanned, (b) the analyses result and (c) the comparison of the contour between the experiment and simulation

Figure 9a displays the result of a draping analysis of the CUPID component with the initial stamp and mould geometry. Many manufacturing defects are observed in the form of wrinkles. After multiple virtual iterations on gripper location and mould geometry, a component was obtained without any manufacturing defects as displayed in Figure 9b. A combination of grippers located on the corners and a mould geometry with a gradual transition into the final shape was found to result in a correctly manufactured component.

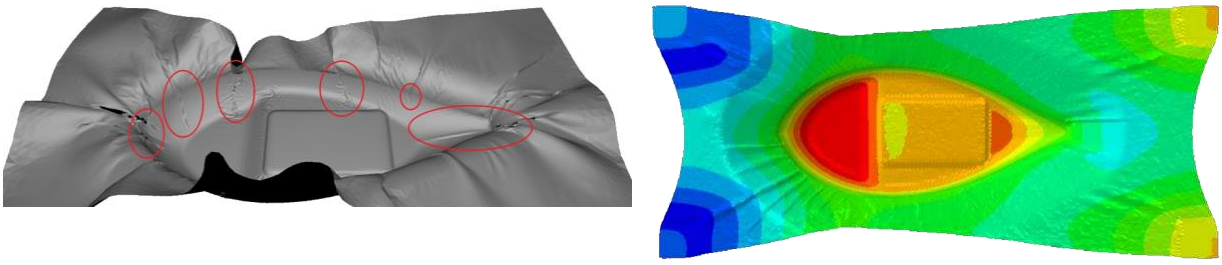

(a) **(b)**

Figure 9 : Result of a draping analysis of the CUPID component

  doi:10.5075/epfl-298799_978-2-9701614-0-0

It should be noted that the contour and wrinkle predictions are strongly depended on the employed matrix stiffness. Further experimentation will be required to observe if the single value for the matrix stiffness is still valid when following different draping procedures, or when other components are manufactured. However, if this method remains predictive for these different situations, it is a strong tool for process development without costly and time consuming experimental work.

5. Results and future developments

The results shown in the previous section are part of a continuous development in the field of virtual manufacturing. It shows the capabilities of current tools to predict material behaviour and draping behaviour. This can only be achieved with gathering accurate material property and interaction data.

The ambition for future development is to use these tools more often to support the actual manufacturing and reduce trial and especially expensive errors. Ideally the whole manufacturing process from raw material to the final product is simulated and can be predicted including capturing and storing data. The data can also be integrated in digital twin models to simulate the as-built product. Currently it is not feasible to include all manufacturing steps in simulations and for some areas also the added value is minimal. The focus of current and future developments lies on the manufacturing steps that are most critical and sensitive to process parameters. Examples are the draping analyses (thermo-mechanical), thermoplastic welding (thermo-mechanical-electromagnetic), thermoplastic material model including crystallisation kinetics, curing analyses (thermo-chem-mechanical), composite braiding analyses (mechanical) and fibre placement simulation (thermo-mechanical).

6. Conclusion and discussion

In this paper the results have been presented of virtual manufacturing projects at Royal NLR. The aim is to gain insight in the manufacturing process of high performance CFRP aerospace components. With this insight the manufacturing process can be optimized to achieve first time right parts.

The draping simulations and comparison between software and experiments showed that material inputs are a current challenge. There are no standards yet to obtain these material inputs such as material stiffness as function of time and temperature for thermoplastics. Also to obtain the level of expertise required for use of the tools can take considerable time and some have quite a steep learning curve. Despite these challenges the current tools are very well capable to predict the global behaviour of CFRTP draping and fibre orientations. However the local effects such as wrinkling are more sensitive to the inputs and boundary conditions.

Other work on thermoplastic material model developments and welding is currently ongoing. The ambition is to combine the models to have a workflow to predict the material and part behaviour during the most critical steps of the manufacturing of aerospace components.

  doi:10.5075/epfl-298799_978-2-9701614-0-0

Acknowledgements

The support of the Netherlands ministry of Economic Affairs and Climate (EZ) is kindly acknowledged in the project – ‘ Strategische ambitie’.

7. References

1 K. Potter, “Towards a design for manufacture capability in composites – tying together manufacturing research to maximise impact”, ACCIS Annual Conference 2013.

2 E.H. Baalbergen, S. Voskamp, A.A. ten Dam, W. Gerrits, Innovating the overbraiding design process to optimise the development of composite aircraft structural components, NLR-TP-2012-498, 2012

3 W.M. van den Brink, W.J. Vankan, G. van de Vrie, Manufacturing process simulation and structural evaluation of grid stiffened composite structures, NLR-TP-2014-442, 2015.

4 J.M. Muller, W.M. van der Brink, Comparison of integrated rib stiffened and L-blade stiffened composite panels manufactured using simple tooling methods, NLR-TP-2016-201, 2016.

5 F.P. Grooteman, Inverse probabilistic analyses of composite part distortion, NLR-TP-2015-303, 2015.

6 Akkerman, R., Haanappel, S., Thermoplastic composites manufacturing by thermoforming. Enschede: University of Twente & TPRC, 2015

7 Dörr, D., Brymerski, W., Ropers, S., Leutz, D., Joppich, T., Kärger, L., & Henning, F., A benchmark study of finite element codes for forming simulations of thermoplastic UD-tapes. Karlsruhe: Karlsruhe Institute of Technology, 2017

8 Maynard, V., A new approach to simulating the draping of prepreg composites manufactured by hand layup, Master Thesis, Sweden, 2017

9 Dörr, D., Simudrape User's guide. Karlsruhe, Simutence, 2021

  doi:10.5075/epfl-298799_978-2-9701614-0-0

MACHINE VISION FOR DIGITAL TWIN SIMULATION OF COMPOSITE STRUCTURES

Oliver, Döbrich[a,]; Christian, Brauner[a]*

a: FHNW University of Applied Sciences and Arts Northwestern Switzerland,
Institute of Polymer Engineering, 5210 Windisch, Switzerland – *oliver.doebrich@fhnw.ch

Abstract: *Whereas the structural design of composite structures is already carried out on a virtual level, composites mechanical properties remain sensitive to the fiber orientation and therefor to the quality of the production process. The ideal design layout and the actual achieved fiber orientation may differ locally in dependance to the preforms production process. To account on this problem, an innovative approach is achieved by the usage of Microsoft's Azure Kinect camera. With this contribution a vision system is introduced which digitalizes the composites preform configuration during the production by evaluating the achieved local fiber orientation by digital image processing as result of the complex preform draping process from optical image data.*

Keywords: Composite, Simulation, Digital-Twin, Machine-Vision

1. Introduction

1.1 Motivation

Composite components have excellent mechanical properties at a low specific density compared with conventional construction materials. This combination results in a wide range of applications for those components in the high-performance sector. For composite components with oriented fibers, the orientation of the fiber is crucial for the mechanical properties. Nevertheless, due to the high cost and effort, fiber orientation is rarely digitally verified in practice. Hand-held systems or local checks at critical locations are known. However, current systems are expensive, time-consuming and rely on specific hardware which is mostly offered by the system provider in a closed environment.

In this paper, a system is presented that determines the fiber orientation on the ply level of a composite part using an inexpensive RGB-D camera. The Azure Kinect camera, launched by Microsoft initially for entertainment purpose, can provide both a depth measurement for providing geometry and texture information.

The point cloud captured by the camera is used to detect the structural geometry. Based on the color image taken by the camera, the local texture is projected onto the component geometry and the orientation of the fiber is determined using image analysis. The system presented in the contribution convinces by low investment costs and a high degree of automation as well as open-source Python libraries which make a customization of the system easy and enhances the systems flexibility.

  doi:10.5075/epfl-298799_978-2-9701614-0-0

1.2 State of the art

Since the manufacturing of complex shaped parts from composite materials is a sequential process characterized by ether manual or automated handling of unstable and limb reinforcement fabrics, deviations from an ideal “as-planed” configuration are likely to be observed. The design of composite parts is regularly carried out with only small reserves in mechanical capacity due to the general lightweight motivation when using fiber reinforced composites. Deviations in fiber orientation and defects from the manufacturing process may result in reduced structural stiffness or unpredicted failure. Therefore, the use of machine vision to digitalize the quality assessment of the composite production is aspired.

Different systems are already known for providing information on the fiber orientation. Common camera images have also been used for mapping fiber orientation in numerical composite models [1]. The introduced systems mostly rely on expensive hardware, specific software packages and are vulnerable to changes in environmental conditions. Hand-guided or robotic guided camera systems are known [2,3]. These systems can easily adapt to the shape of the structural part. However, the process is time consuming and requires ether manual guidance or the teaching of the robotic guidance system. Another setback is that generally only the top layer is evaluable. This requires a sequential examination of every single layer that may be draped over or added to a stack of reinforcement layers. Time and labor consuming evaluation methods are directly increasing the assessment time when they must be carried out multiple times. Systems that can evaluate a stack of reinforcement layers are known as well. Micro-CT scans [4] as well as X-Ray Micro-CT scans [5] have been used to build composite unit cell models to predict the mechanical properties. An application of this technique on structural scale is hard to carry out and limited by the sample size, the duration of the method and the cost. Eddy current sensor data can be used to evaluate the result of the preforming process [6]. Unfortunately, this technique is limited to carbon fibers due to the need of conductivity within the material.

Therefore, a system is aspired that does not rely on manual or guided camera/sensor movement but offers an environment observed by a static camera array able to capture the geometry as well as the texture information in a single shot. The system should be so fast, that a sequential evaluation of multiple layers can be carried out without additional expense in process time and therefore be applicable in mass consumer industry.

1.3 Novel approach for composite quality evaluation by stationary Machine Vision

Our approach presented in this contribution introduces an evaluation system based on the Microsoft Azure Kinect camera. The Kinect cameras have been published for entertainment and gaming purpose but are distributed in their recent version for industrial applications, only. The third generation is equipped with a 1 MP depth sensor (infrared time of flight) and a 12 MP 4K webcam for color image capturing. The Azure cameras are, especially compared to existing composite evaluation products, low priced and come with a sync port to build up camera array, as shown in Figure 1.

  doi:10.5075/epfl-298799_978-2-9701614-0-0

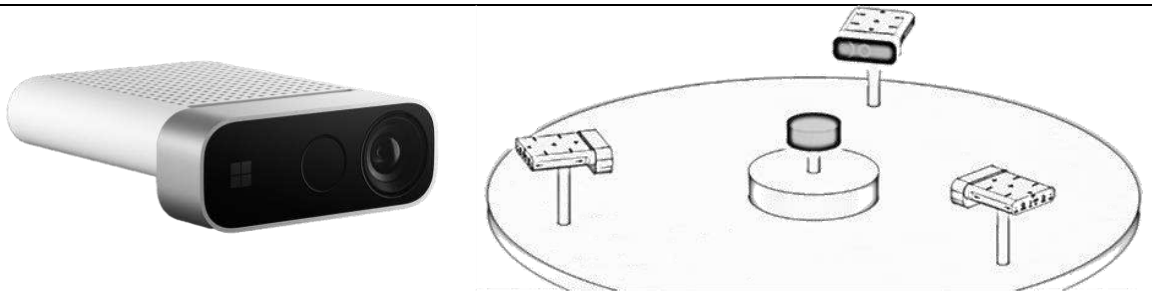

a) Microsoft Azure Kinect b) Microsoft Azure Kinect camera array

Figure 1 Principle of Microsoft Azure Kinect camera array

The developed method to apply the Microsoft Azure Kinect camera to detect fiber orientation can be found in Figure 2. The array is capturing a single point cloud per camera which is put together respecting the positioning of the camera by performing a rigid body transformation related to the master camera position. This procedure is shown in Figure 3. The combined point cloud contains all points captured by the camera. These are points from the part itself but also points related to the surroundings. Exceeding points can be cleaned by the definition of a space of interest. All points outside this space are deleted. The remaining point cloud can be cleaned and simplified regarding the parts size. The simplified cloud will be meshed using ball pivot meshing algorithms, as shown in Figure 4.

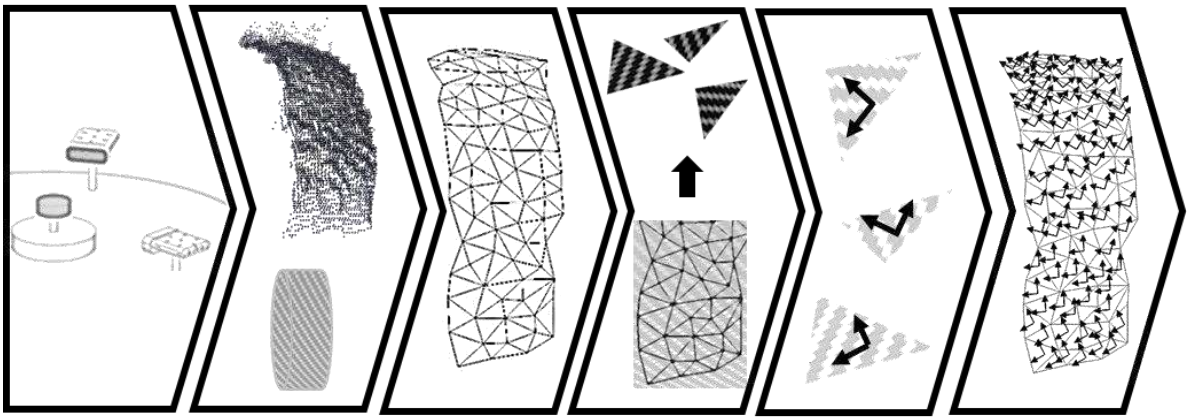

Figure 2 Procedure to evaluate local fiber orientation by stationary Machine Vision

By using UV-transformation (Section 2.2), the texture image related to every element of the generated mesh is generated from the captured color image and cropped to the size of interest related to the element size. For these images the main orientations, not in regard of fiber orientation, but in regard of gradients within the picture, are determined using image processing methods like the Histogram of oriented gradients (HOG) [7] or edge detection algorithms [8]. Especially for continuous fiber surface textures, the color gradient, and the main trace of the edges correlate with the main fiber orientations. The established orientation vector (or several vectors) must be transformed regarding the positioning of the surface element towards the camera to account for tilted surfaces causing distortions in the captured image.

  doi:10.5075/epfl-298799_978-2-9701614-0-0

2. Experimentation

2.1 Capture structural geometry

To use the Microsoft Azure Kinect cameras as camera array, a rigid transformation matrix must be found for every slave camera to transform the captured information into the master cameras coordinate system according to Eq. 1. For this, a calibration pattern is captured with every camera and the specific parameters $\vec{t}$ (transformation vector) and R (rotation matrix) must be determined. After this, the points captured by every slave camera can be transformed into the master camera coordinate system which results in a single cloud containing every point captured by the camera array, as seen in Figure 3 b).

$$T(\vec{v}) = R\,\vec{v} + \vec{t} \qquad (1)$$

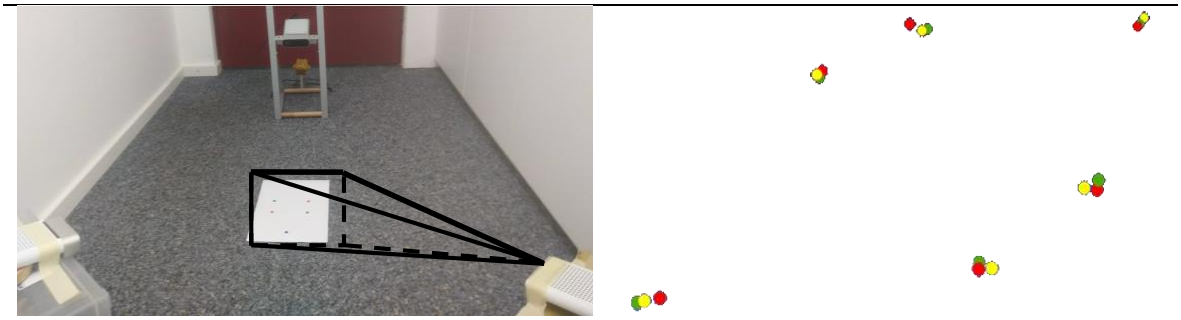

a) Azure Kinect array with calibration pattern

b) Calibration pattern captured by camera array

Figure 3 Determination of rigid transformation matrix from slave to master camera

For converting the point cloud into a surface mesh ball pivoting [9] is used as part of Open3D library. [10] The meshing can be adjusted by parameters to regulate the point distance and the element size. The result of this step is shown exemplarily in Figure 4.

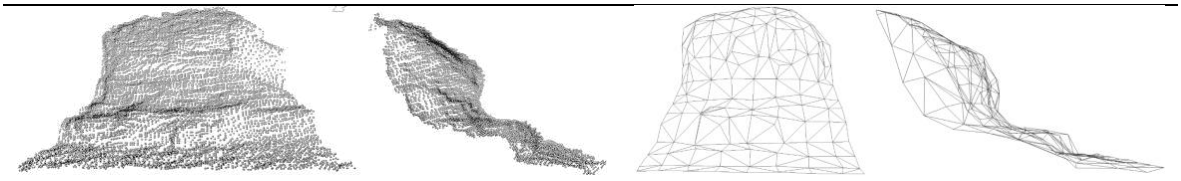

a) Captured point cloud

b) Meshed point cloud

Figure 4 Point cloud and meshed surface derived from ball pivot meshing algorithms

2.2 UV transformation of surface texture

To map the surface texture onto the specific mesh element, a pre-evaluation is done to determine the orientation of the elements towards the camera. The texture that is to be evaluated must not be tilted too much to guaranty a successful examination of the fiber orientation. Therefore, the element normal vector $\vec{n}$ is calculated from the element node coordinates. The angle towards the specific camera, that shot the image that need to be

mapped, is calculated and the “element quality” is evaluated by ranking the element as shown in Figure 5.

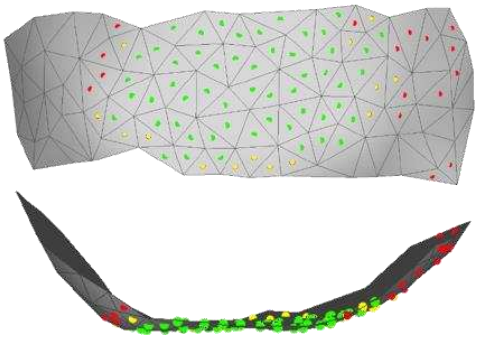

$$\sphericalangle(\vec{n}_{element}, \vec{n}_{camera}) < 20°$$

$$20° < \sphericalangle(\vec{n}_{element}, \vec{n}_{camera}) < 30°$$

$$30° < \sphericalangle(\vec{n}_{element}, \vec{n}_{camera}) < 40°$$

Figure 5 Evaluation of element orientation towards camera

The texture that is corresponding to the location of every element must be determined by UV-transformation. In general, the captured color image is 2D, containing texture information in an UV-system. The point cloud and the derived mesh exist in a XYZ-cartesian coordinate system. By performing UV-transformation, every location in XYZ-space gets related to the specific area in the UV-image. For this, the center of the elements is used as reference. By using the intrinsic parameters (specific for every camera) and the focal length of the camera setting, the position of every point in XYZ-space can be found on the UV-image on the camera’s digital sensor as illustrated in Figure 6 and explained in Eq. 2.

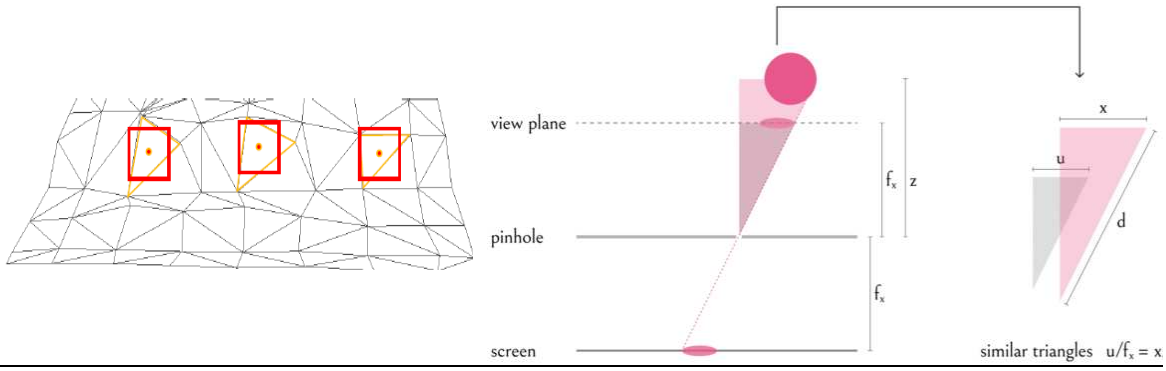

a) Center of element (red dot) and size of texture derived from UV-image

b) Determination of UV-coordinates [10]

Figure 6 Basic parameters used in UV-transformation

$$With:\ x = \frac{u\,z}{f_x}\ ,\ u = \frac{x}{z}f\ ,and\ v = \frac{y}{z}f \qquad (2)$$

2.3 HOG Descriptor

The Histogram of oriented gradients is formed from feature vectors of images or image sections. In contrast to pure edge detection methods, the feature vector of the HOG primarily contains information about the color gradient in discrete directions within a certain evaluation cell. These direction vectors are displayed in a histogram or by plotting them onto the specific area of the image (Figure 7 c)). The HOG-plot represents the main orientation of lines in the test image (Figure 7 b)) for every evaluation cell (Figure 7 a)). For textile textures, the main orientation of

surface texture gradients is assumed to be in correlation with the trace of the reinforcement yarns, namely the local fiber orientation. The orientation gradients are classified by a defined number of angles. Therefore, the number of existing main orientations can be evaluated by investigating the histograms local maxima. The number of local maxima corresponds with the number of local fiber systems (1 – UD reinforcement, 2 – weave, 3 - ORW). The algorithms used for the presented results are part of the OpenCV library. [10]

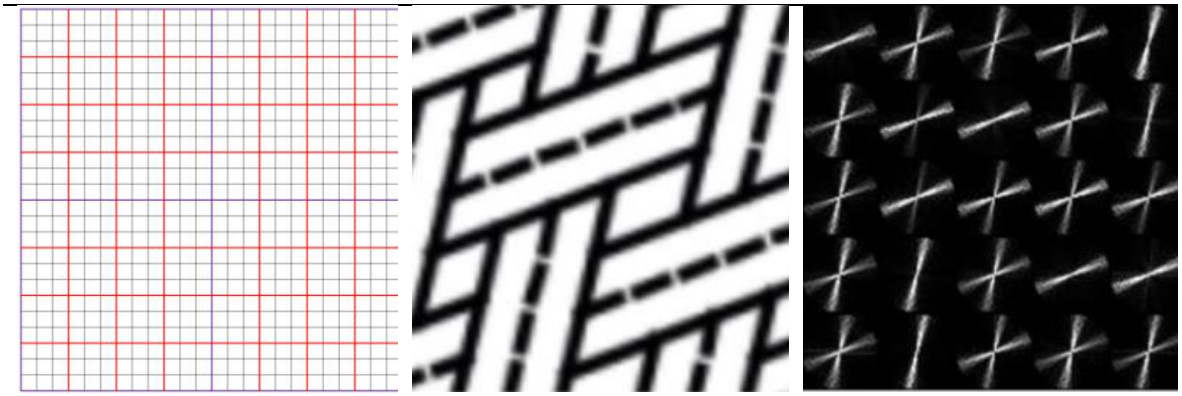

Cells (3x3), Blocks (4x4) | Test image | HOG Visualization

Figure 7 Histogram of oriented gradients

3. Results

The evaluation of image sections captured by the Microsoft Azure Kinect camera can be seen in Figure 8 c) and d). The quality of data that is provide by the application of the HOG algorithm depends strongly on the image quality. Therefore, adequate illumination (strong, diffuse) and a certain maximal distance (depending on the size of the reinforcements rapport) for capturing texture images are required. However, the main orientations could be evaluated successfully even for fuzzy images, but the system is also flexible in the regard, that Microsoft Azure Kinects embedded RGB camera may be substituted with an even better camera to capture more detailed images of the texture in the first place. The main orientations have been determined by finding the local maxima along the histogram. For the test image Figure 8 a), one main direction is assigned, whereas two directions have been found for the images showing weave textures.

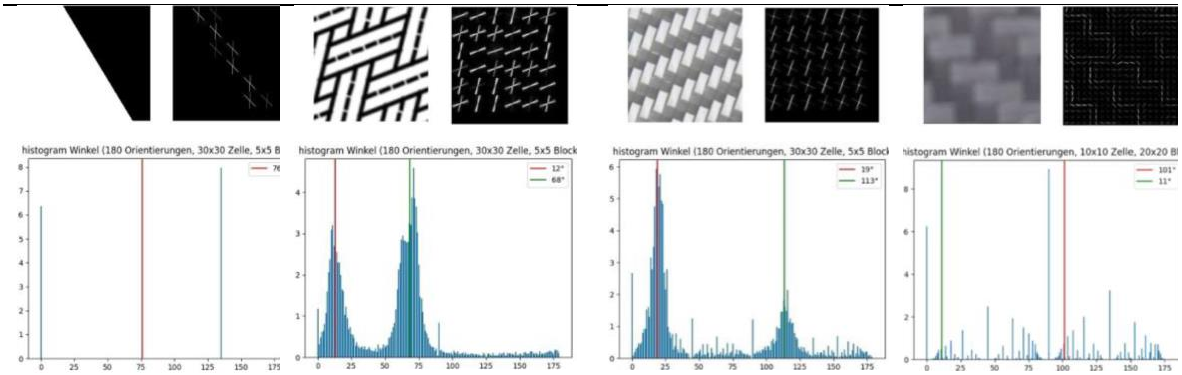

a) Simple line | *b)* Weave sketch | *c)* Clear image | *d)* Fuzzy image

Figure 8 Detection of fiber orientation with HOG-descriptor

  doi:10.5075/epfl-298799_978-2-9701614-0-0

Figure 9 shows the result of the evaluation system. The geometry of the robot limb made from carbon fiber twill weave is determined by the infrared depth sensor and a meshed surface topology could be generated. Texture evaluation is only carried out for elements that are oriented towards the camera within the introduced tolerances. The local fiber orientations are determined by the HOG algorithm and mapped onto the discrete elements of the meshed surface. The result presented was created with a single shot and covers most of the structural parts surface visible by the camera.

a) Azure Kinect color image b) Evaluation result

Figure 9 Result of established Machine Vision system for assessing the composite fiber orientation

4. Conclusion

A method is introduced that enables the evaluation of composite materials local fiber orientation along with the corresponding location on the structure by scanning the surface texture as well as the geometry at a single shot. The introduced methods are efficient for the quantification of the orientation values and can be used as input for FEA simulation to carry out “as-built” numerical simulations, digitalize processes, asses the production quality and archiving production data. The low investment costs and the availability of the introduced methods by relying on Open-Source libraries can boost the application in composite industry, especially for small and middle businesses, and helps to increase the digitalization by enabling the digital twin preprocessing.

The simple, fast and supervision free method is suitable for mass consumer production since production processes can be observed without handling of cameras or manually initiating the scanning process. The system mainly targets the sequential processes found in draping of complex composite structures or the stacking of reinforcement layers. In future, continuous production processes are targeted.

  doi:10.5075/epfl-298799_978-2-9701614-0-0

5. Acknowledgement

This research received external funding. The results presented were carried out within the NextGenCoMan project that received funding from Innosuisse-Swiss Agency for Innovation Promotion under grant number 35197.1 IP-ENG.Michels J, Sena-Cruz J, Czaderski C, Motavalli M. Structural strengthening with prestressed CFRP strips with gradient anchorage. Journal of Composites for Construction 2013; 17:651-661.

6. References

1. S. Stender et al.: Function-orientated Production of FRP Components. Lightweight design worldwide 12, 18–25 (2019)
2. Döbrich, Oliver, et al.: "Machine Vision for As-Built Modelling of Complex Draped Composite Structures." Materials 14.3 (2021): 682
3. Kunze, Eckart, et al.: "Forming analysis of internal plies of multi-layer unidirectional textile preforms using projectional radiography.", Procedia Manufacturing 47 (2020): 17-23.
4. F. Desplentere, et al.: Micro-CT characterization of variability in 3D textile architecture, Composites Science and Technology, Volume 65, Issue 13, 2005, Pages 1920-1930
5. Focke, Oliver, et al.: "Multiscale non-destructive investigations of aeronautic structures: from a single fiber to complex shaped fiber-reinforced composites." 8th Conference on Industrial Computed Tomography. Wels,, 2018.
6. G. Bardl, et al.: Automated detection of yarn orientation in 3D-draped carbon fiber fabrics and preforms from eddy current data, Composites Part B: Engineering, Volume 96, 2016, Pages 312-324, ISSN 1359-8368
7. T. Lindeberg: "Edge detection and ridge detection with automatic scale selection," Proceedings CVPR IEEE Computer Society Conference on Computer Vision and Pattern Recognition, San Francisco, CA, USA, 1996, pp. 465-470
8. N. Dalal and B. Triggs: "Histograms of oriented gradients for human detection," 2005 IEEE Computer Society Conference on Computer Vision and Pattern Recognition (CVPR'05), San Diego, CA, USA, 2005, pp. 886-893 vol. 1
9. F. Bernardini, et al.: "The ball-pivoting algorithm for surface reconstruction." IEEE transactions on visualization and computer graphics 5.4 (1999): 349-359.
10. Bradski G.: The OpenCV Library. Dr Dobb's Journal of Software Tools. 2000
11. Q.-Y. Zhou, P. Jaesik, K. Vladlen: "Open3D: A modern library for 3D data processing." arXiv preprint arXiv:1801.09847 (2018).

COMPUTER VISION & MACHINE LEARNING TECHNIQUES FOR NON-DESTRUCTIVE TESTING OF COMPOSITES

Ruslan Vorobyev[a, b], *Mile Mitrovic*[a, b], *Ivan Kremnev*[a]

a: Composite Vision – info@composite.vision

b: Skolkovo Institute of Science & Technology

Abstract: *In this study, we analyze data from microCT of carbon fiber-reinforced polymer composite (CFRP) samples to detect production structural defects, e.g. voids and delaminations, using deep neural networks for computer vision. To carry out experiments, we collected data from a laboratory experiment and manually labeled defects. We showed that a deep learning based data processing pipeline can be effectively used to automate defectoscopy inspection, leaving space to further optimizations. Collected data was put in open access.*

Keywords: composite, non-destructive evaluation, computer vision, machine learning, CFRP

1. Introduction

In recent years, significant efforts have been made by the scientific and technical community to disseminate simulation models based on the concepts of artificial intelligence (AI) and machine learning (ML) in the sectors related to the production of fiber. Such algorithms open up revolutionary opportunities for such areas of science and technology as continuum mechanics and mechanics of gasses and liquids, allowing you to automatically process data sets and find implicit dependencies in them. In particular, machine learning and computer vision technologies can be used to analyze representative volumes of material reconstructed with non-destructive evaluation techniques for different anomalies [1, 2]. This study has two aims. First aim is to present a task of locating and characterizing structural defects such as voids and delaminations in CFPR specimens. Second aim is to assess deep learning methods viability for processing non-destructive testing data with the eventual goal of time and cost optimization for non-destructive evaluation of fiber reinforced composite materials. Non-destructive testing procedures such as computed tomography (CT), thermography, and ultrasound are suitable for inspecting FRP parts. Nowadays, software packages that are customized to the employed sensor or specialized to the type of gathered data are used to evaluate the acquired measurement data. There are just a few software platforms that can handle and visualize various measurement data sets generated by thermography, ultrasonography, or CT. The current work focuses on the creation of a system prototype for data processing of CT scans of FRP specimens.

When dealing with CT imaging, it is worth mentioning that deep learning-based computer vision is mainly applied to CT images in the field of medical imaging. In [3] and [4], Convolutional Neural Networks (CNNs) are applied to finger and lung CT images. Recent studies [5] use the same approach for the inspection of defect evolution in metal binder jetting additive manufacturing. Therefore, it is natural to apply the same techniques for the segmentation of defects in CFRP. As a result, proposed techniques can be used by manufacturers to optimize their operations related to non-destructive inspections.

  doi:10.5075/epfl-298799_978-2-9701614-0-0

In this paper, we examine a CT image data processing pipeline. All related code and links to the dataset are available in our official repository https://github.com/CompositeVision/ECCM20.

2. Data, dataset description

We collected a dataset of microscopic computed X-ray tomography images of 4 CFRP composite specimens glued together with structural defects in them. Each specimen is a cylindrical part with 1 mm radius and 4 mm height, imaged on an X-ray tomograph GE Phoenix v|tome|x L 24 with volumetric resolution of 2.5 microns. The CT scan dataset is presented as a sequence of 16-bit integer TIFF images, 6579 in total. Each image is a reconstructed slice of the CT scan in the axial projection of the sample. A high-contrast view of a slice is presented in Figure 1.

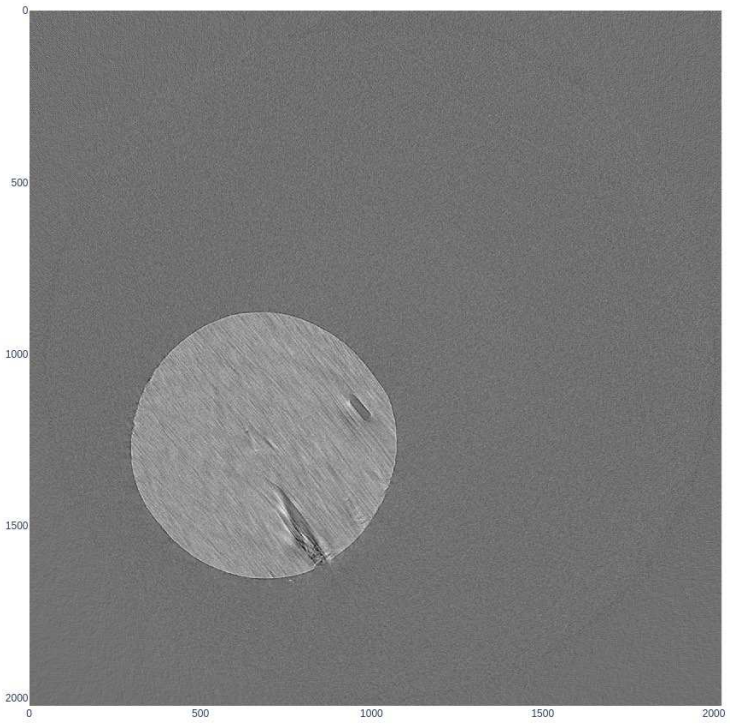

Figure 1. CT scan slice with visible CFRP sample and defects

CT scan contains two informative region types: sample body and inner structural defects. Two non-informative region types are outer volume and glue binding. Structural defects typically span a number of slices, constituting delaminations.

In order to convey and evaluate experiments with the data, we took a random sample of 190 slices and annotated them manually with polygons corresponding to the informative region types described previously. No cross-annotation performed, so the quality of the annotations is subject to further improvement.

The whole dataset with selected annotations is available for download via link provided in the official repository. We plan to release updates to the annotations, hopefully covering a bigger percentage of the CT slice images.

  doi:10.5075/epfl-298799_978-2-9701614-0-0

3. Experiment setup

The natural way to approach the problem of semantic segmentation of defects on images is to employ a deep learning model. To be able to use one, we train it on a subset of the annotated data and then test it on the remaining data. Therefore, our experiment setup is organized in two steps: training and testing the model.

3.1 Network architecture

In our experiment, as the central deep learning model we used a modified U-Net [6] architecture, which is a standard baseline for semantic segmentation tasks. The proposed architecture is illustrated in Fig. 2 and consists of two parts: a contracting path (left side) and an expansive path (right side). The contracting path processes and downsamples input images while extracting hierarchically meaningful feature maps from an input image. In contrast, the expansive path upsamples the feature maps to the original input image size, adding features from corresponding levels of the contracting path, and completes the semantic segmentation task.

Both contracting and expanding paths consist of 4 convolutional blocks, each block consists of two padded 3x3 convolution layers, followed by batch normalization (BN) and a rectified linear unit (ReLU) function. In the contracting path, downsampling is performed using a 2x2 max pooling operation with stride 2. For upsampling of the feature map in the expansive path, 2x2 transposed convolution operator with stride 2 was applied. The expansive path is concatenated with the corresponding feature map from the contracting path to add extra information that might be lost during downsampling. Both the input image and output layer are interpolated to permit a seamless tiling of the output segmentation map. The proposed architecture has 23 convolutional layers and 16.5 million trainable parameters.

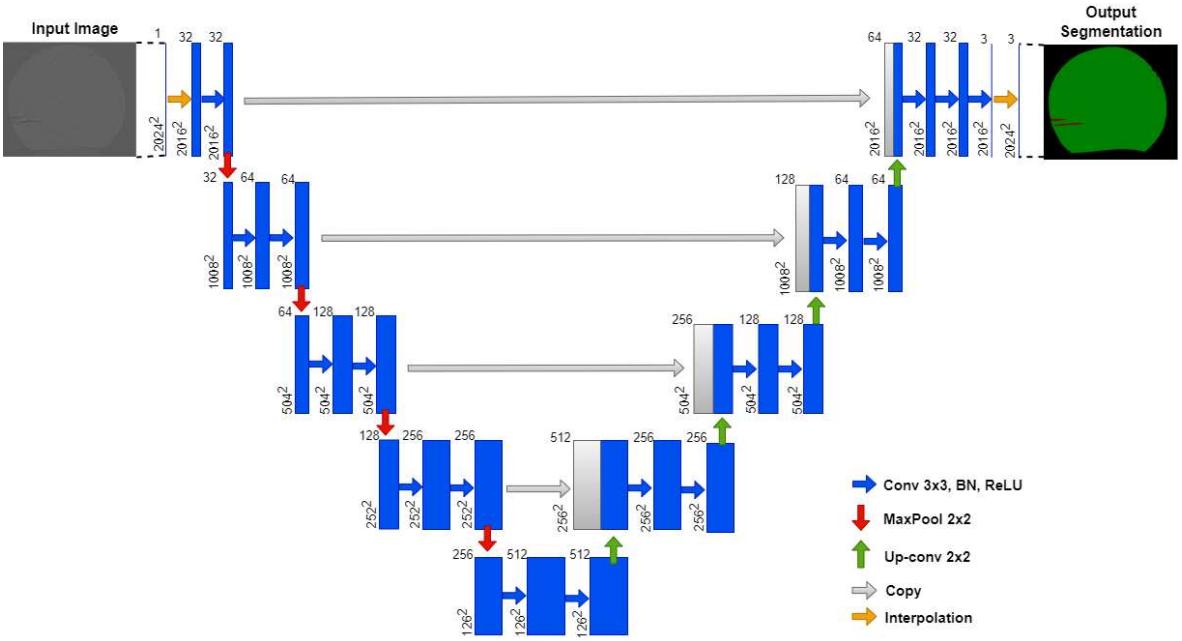

Figure 2. Modified U-Net architecture

3.2 Training

Model training based on input images and corresponding segmentation maps is performed using a stochastic optimization method based on a first-order gradient, the so-called Adam [7]. The learning rate of the optimizer was set to 1e-3, while weight decay (L2 penalty) was set to 1e-6. Additionally, the cosine annealing scheduler [8] was used to restart the learning rate for every 10 epochs and thus improve optimization results. The mini-batch size was set to 18 in order to make maximum use of the GPU memory and minimize the overhead. A total of 51 epochs were cycled.

The output feature map is computed by a softmax function combined with the cross entropy loss function. The softmax is a normalized exponential function and is defined as:

$$s_i(x) = \frac{exp(a_i(x))}{\sum_{i=1}^{C} exp(a_i(x))} \quad (1)$$

where $s_i(x)$ denotes the approximated maximum function; $a_i(x)$ is the activation function in feature channel i at the pixel position $x \in \Omega$ ($\Omega \subset Z^2$); and C represents the number of classes. The deviation at each pixel position is penalized using cross-entropy function as follow:

$$l = \sum_{j=1}^{C} w_j(x) log(s_{p(x)}(x)) \quad (2)$$

where l denotes the cross-entropy function; $p(x)$ represents the true label of each pixel; and $w_j(x)$ is a weight map.

The model was trained on a single Nvidia GeForce RTX 2060 GPU machine with Pytorch-Lightning library.

3.3 Validation

At the validation step, the trained model infers semantic segmentation masks from CT images. One of the challenges of dealing with CT images is their high spatial resolution which causes big images to be produced. Since the targeted defects in these images can be quite small, we can't just resize and interpolate those images and risk losing these defects. Therefore, patch-based inference must be adapted. We used a sliding window of 255×255 pixels to infer from 2024×2024 images.

We measured mean class accuracy and mean intersection over union for train and test parts of the dataset. The results are presented in Table 1. More detailed results can be found as tensorboard logs in the official repository.

Table 1: Quality metrics of the trained model.

Metric	Train set	Test set
Mean class acc	0.81	0.76
Mean IoU	0.72	0.69

  doi:10.5075/epfl-298799_978-2-9701614-0-0

3.4 Data Augmentation

Usually, deep networks require many thousands of annotated samples for successful model training. Since the annotated part of our dataset consists of 190 images, we used data augmentation to artificially increase variability of the training data. Augmentations include random transforms of image and label data and are implemented through the albumentations library package.

In our experiment, we used RandomResizedCrop augmentation with a minimum scale of 0.2 of the original image, and RandomRotate90. Our experiments show that too low scale of the RandomResizedCrop can detriment the quality for underfitted models. Other augmentations are considered excessive, since CT images tend to be of low variability but of great resolution.

In both training and validation steps data normalization is performed by scaling data to zero mean and unit standard deviation. Typical original distribution of pixel values is presented on histogram in Figure 3.

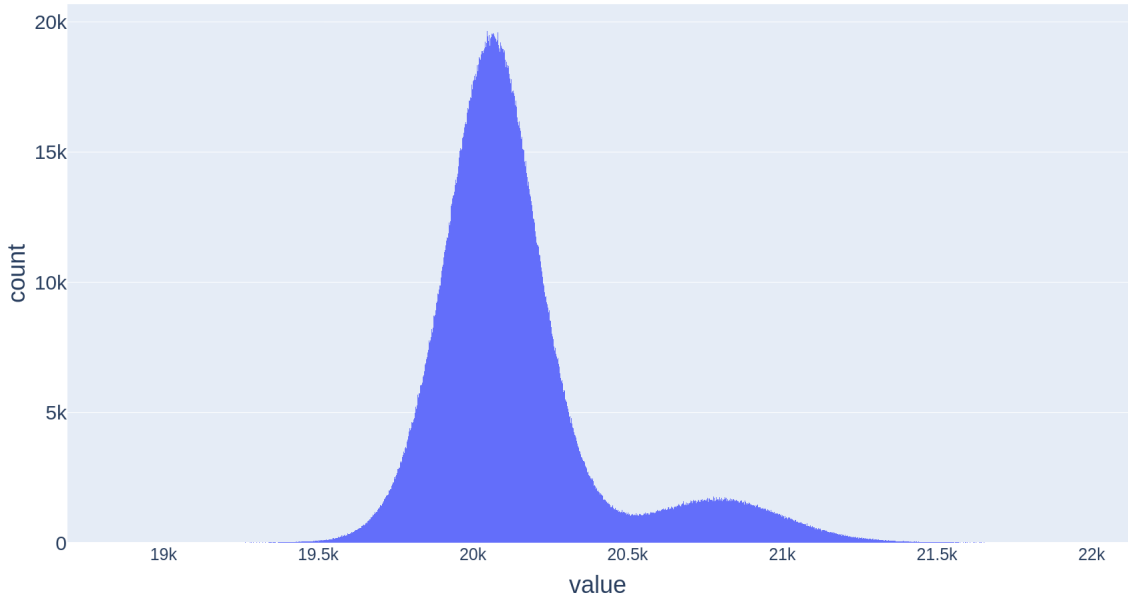

Figure 3. Typical pixel intensity distribution on CT images

4. Results and conclusion

We collected and annotated a series of micro CT images of CFRP specimens and provided open access to the dataset, which we consider as the main contribution of our work.

We developed a data pipeline able to perform a task of semantic segmentation of CT image via slice-patch-based inference. It consists of two steps: data preprocessing, and deep learning model inference. This approach can be seen as a general pipeline for dealing with CT images and can be extended with additional post-processings, such as morphological closing operations for false positive region filtering or volumetric prediction aggregation. The latter is of most interest in regard to the practical task of identifying and describing structural defects in CFRP specimens.

  doi:10.5075/epfl-298799_978-2-9701614-0-0

Our pipeline demonstrates suboptimal quality in terms of the measured metrics. This can be attributed to data and annotations quality and deep learning model training procedure. Possible improvement is expected from architecture tweaks, longer training and further data annotation, covering more CT image slices.

The code and dataset links are available at https://github.com/CompositeVision/ECCM20.

5. References

1. Sacco C, Radwan AB, Anderson A, Harik R, Gregory E. Machine learning in composites manufacturing: A case study of automated fiber placement inspection. Composite Structures 2020, v. 250, pp. 112514.
2. Maran Ri, Palumbo D, Galietti U, Stella E, D'Orazio T. Automatic detection of subsurface defects in composite materials using thermography and unsupervised machine learning. IEEE 8th International Conference on Intelligent Systems (IS), 2016, pp. 516–521.
3. Chandrasekaran AC, Fu Z, Kraniski R, Wilson FP, Teaw S, Cheng M, et al. Computer vision applied to dual-energy computed tomography images for precise calcinosis cutis quantification in patients with systemic sclerosis. Arthritis Res Ther, 2021, 23 (1):6.
4. Ginneken BV., Setio AA, Jacobs C, Ciompi F. Off-the-shelf convolutional neural network features for pulmonary nodule detection in computed tomography scans. In: Proceedings of the IEEE International Symposium on Biomedical Imaging, 2015, pp. 286–289.
5. Zhu Y, Wu Z, Hartley WD, Sietins JM, Williams CB, Yu HZ. Unraveling pore evolution in post-processing of binder jetting materials: X-ray computed tomography. Comput Vision Mach Learn Addit Manuf, 2020::10118.
6. Ronneberger O, Fischer P, Brox T. U-net: Convolutional networks for biomedical image segmentation. In Proc. Med. Image Comput. Comput.-Assisted Intervention (MICCAI) 2015, pp. 234–241.
7. Kingma DP, Ba JL. Adam: A method for stochastic optimization. In International Conference on Learning Representations (ICLR), 2015.
8. Loshchilov I, Hutter F. SGDR: Stochastic gradient descent with warm restarts. In Proceedings of the International Conference on Learning Representations (ICLR). 2017.

  doi:10.5075/epfl-298799_978-2-9701614-0-0

COMPUTATIONAL METHODOLOGY TO ESTABLISH RELATIONSHIP BETWEEN VOLUME FRACTION AND COMPRESSION STRENGTH OF CERAMIC FOAM

Vinit Vijay, Deshpande[a], Romana, Piat[b]

a: Department of Mathematics and Natural Sciences, University of Applied Sciences Darmstadt, Schöfferstraße 3, Darmstadt 64295, Germany – vinit-vijay.deshpande@h-da.de
b: Department of Mathematics and Natural Sciences, University of Applied Sciences Darmstadt, Schöfferstraße 3, Darmstadt 64295, Germany

Abstract: *A numerical method to study effect of volume fraction on the compression strength of ceramic foam is presented. A recently developed reconstruction procedure is used to create artificial microstructures statistically equivalent to a real foam sample obtained from µCT. A finite element-based compression failure simulation is conducted and the results are compared with the experimental results obtained for a foam of a particular volume fraction. The length scale of the microstructural features is determined by calculating 2-point correlation function. The effect of length scale on compression strength of the ceramic foam is determined by studying the variations in compression strength with increase in volume element (VE) size. For different volume fractions, sets of artificial microstructures are created for three different VE sizes. The same simulation is performed on these microstructures. Finally, the relationship between volume fraction and compression strength is determined and compared with the Gibson-Ashby model.*

Keywords: Ceramic foam; compression strength; finite element analysis; microstructure reconstruction; 2-point correlation function.

1. Introduction

Cellular ceramics are lightweight materials that offer unique properties like high hardness and strength, low thermal expansion, good stability at elevated temperatures. As a result, they have been a predominant choice of materials in high temperature applications like metal filtering during casting, thermal insulation as well as energy absorption devices. However, since the ceramics are brittle, their susceptibility to mechanical damage has always been a point of concern. Limited experimental data exists in literature that studies the failure mechanisms involved in compression failure of ceramic foams and the effect of volume fraction on the compression failure behavior. [1,2] performed compression strength measurements on silicon carbide foams of volume fraction in the range of 0.15-0.3. [3] measured the compression strength of two alumina foams having volume fraction 0.05 and 0.1. [4] studied effect of loaded area, rate of applied load and pore size of alumina foam on its compression strength.

The ceramic foam studied in this article was manufactured by mechanical stirring of a ceramic slurry as detailed in the article [5]. The resulting foam displayed high compression strength and was utilized as a preform for manufacturing interpenetrating phase composite.

The random nature of the foam microstructure requires a large number of foam samples for performing any useful simulations. We have recently developed a microstructure reconstruction procedure [6] that can generate statistically equivalent microstructures for a given distribution

  doi:10.5075/epfl-298799_978-2-9701614-0-0

of pore sizes and volume fraction. Using this procedure, artificial microstructure was generated that was equivalent to a real one in terms of their statistical correlation functions as well as the effective elastic properties calculated by homogenizing the reconstructed and the real microstructures. The calculated properties also fared well in comparison with the experimental measurements.

The Gibson and Ashby model detailed in [7] provides a theoretical basis for understanding the failure mechanisms involved in crushing of the open-cell and closed-cell foams. The model formulates proportionality laws with respect to relative density based on the mode of failures observed in cellular solids.

The current work demonstrates a numerical framework to determine the effect of volume fraction (relative density) on compression strength of the ceramic foam. It also studies the effect of length scale on the compression strength by developing microstructural volume elements of different edge lengths and calculating scatter of compression strength for each VE size. Finally, the numerical results are compared with the Gibson-Ashby model to check the relevance of the simulated results and also discuss the assumptions of the theoretical model.

2. Microstructure generation

The microstructure reconstruction algorithm described in [6] is based on Yeong-Torquato (YT) method [8] in which a trial microstructure is perturbed till the statistical correlation functions of the trial microstructure match to that of the target microstructure. The objective function is defined as an energy functional as shown in Eq. (1).

$$E = \sum_r \left[f(r) - \bar{f}(r) \right]^2 \quad (1)$$

In Eq. (1), $f(r)$ and $\bar{f}(r)$ indicate statistical correlation functions of trial and target microstructures as a function of distance measured r. The correlation functions utilized in this study were 2-point correlation function, 2-point cluster correlation function and lineal path function. Instead of choosing an initial microstructure as a random distribution of voxels as described in YT method, we utilized the available information of pores size distribution to create a much more realistic initial microstructure that accelerated the optimization process. In the present research work, this algorithm has been employed to create microstructures of different volume fractions. Fig. 1. shows three such reconstructed microstructures for volume fractions 0.25, 0.5 and 0.75 where black color phase indicates pores and white color phase is alumina.

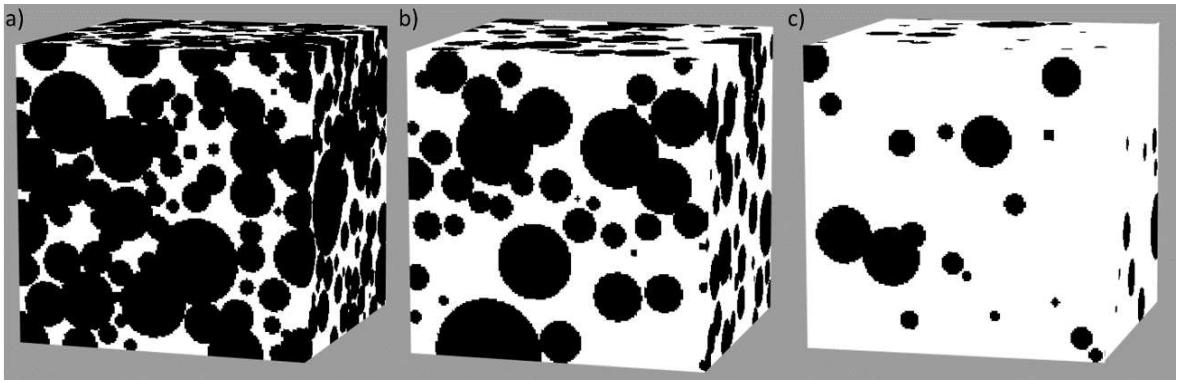

Figure 1. Reconstructed microstructures of volume fraction a) 0.25; b) 0.5; c) 0.75

  doi:10.5075/epfl-298799_978-2-9701614-0-0

3. Simulation of compression failure

3.1 Finite element model of a real preform sample

In article [6], appropriate size of volume elements of a real preform sample (with volume fraction 0.25) obtained from µCT was determined through calculation of statistical functions. A ranking method was developed to shortlist a few volume elements which were the most representative of the entire material. One of these volume elements (refer Fig.2a) was meshed using linear tetrahedral elements and subjected to a quasi-static compression. The constitutive behavior of the ceramic base material was modelled using Johnson Holmquist-2 material model [9] which is particularly suited for simulating damage in brittle materials. The material parameters of the JH-2 model were adopted from [10]. The maximum compression strength and shear modulus was tuned so that the compression strength obtained from FE simulation correspond to the one obtained experimentally (refer Fig.2c). Fig. 2a shows microstructure volume element subjected to boundary conditions. In order to simulate compression failure in a particular direction, one face normal to that direction was completely constrained while the other one was subjected to normal displacement such that the foam sample is compressed. The damage in the material was modelled by deleting the finite elements when the failure criteria of JH-2 model was fulfilled. Fig. 2b shows the ceramic foam model at the end of the simulation. The red color regions indicate failed struts in the ceramic foam. Fig. 2c shows effective compression stress-strain curves along the three orthogonal directions of the specimen obtained from simulations. The three experimentally measured curves (reported in [11]) are also given for reference.

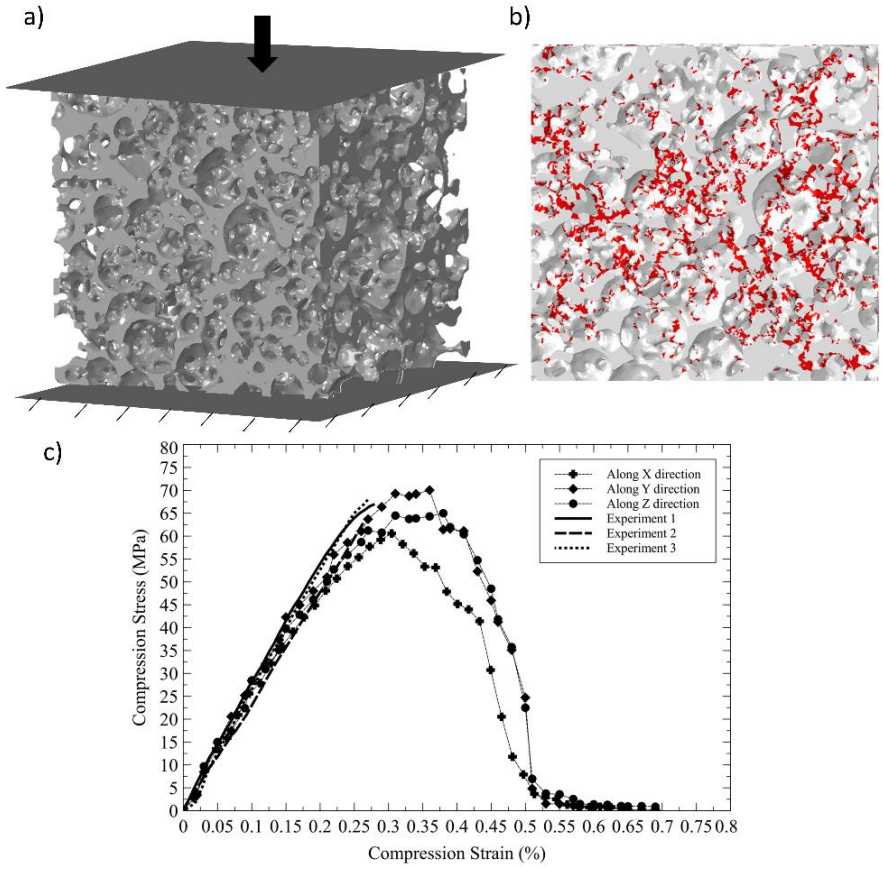

Figure 2.a) Boundary conditions on real VE; b) Failed struts (red) at the end of simulation; c) Compression stress-strain curves from FE simulations of SVE44 and experiments [11].

  doi:10.5075/epfl-298799_978-2-9701614-0-0 published under CC BY-NC 4.0 license

3.2 Effect of length scale

In order to study the effect of length scale on compression failure behavior of the material, artificial microstructures equivalent to the real one described in section 3.1 were reconstructed for three different sizes as shows in Fig. 3a. The characteristic length of the microstructural features was selected as the length (in voxels) at which the 2-point correlation function became long-ranged (refer Fig. 3b). This value was 15 voxels. FE simulations for compression failure were conducted on five reconstructed samples of each size in all three orthogonal directions.

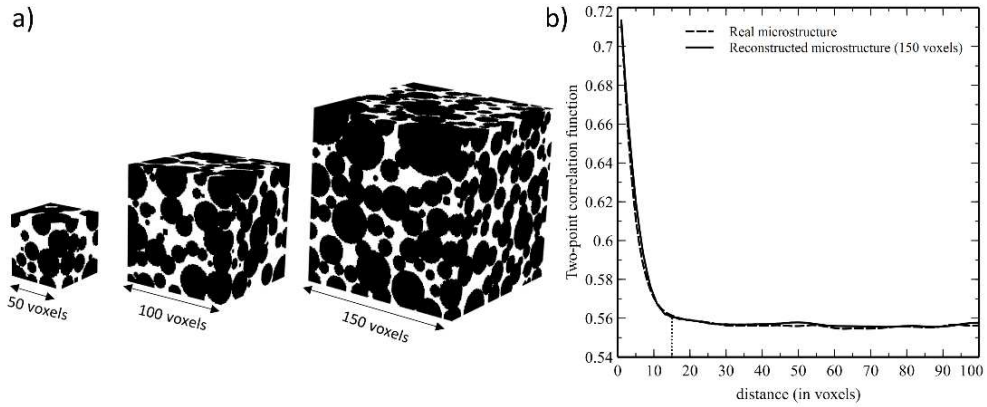

Figure 3. a) Reconstructed microstructures of three different sizes; b)2-point correlation function of real and reconstructed microstructure.

Fig. 4a shows shadow curves of compression stress-strain formed by enveloping all the fifteen curves (three curves for five samples each) and three experimentally measured curves. The article [11] describes that the measurements were conducted till the maximum stress is reached. Hence, the softening region after the maximum stress was not captured. Fig. 4a shows that as the VE size is increased the deviation in the results is reduced and is converging towards the experimental values. The term 'size factor' is defined in Eq. (2).

$$Size\ factor = \frac{edge\ length\ of\ volume\ element}{characteristic\ length\ of\ microstructure} \tag{2}$$

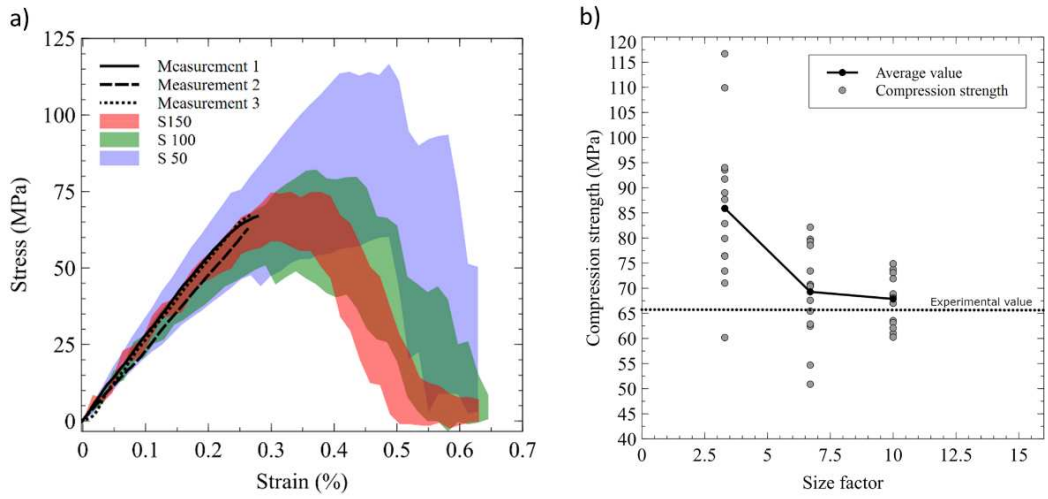

Figure 4. a) Shadow diagrams of volume elements with edge length 50 voxels (S 50), 100 voxels (S 100) and 150 voxels (S 150) along with three experimental results; b) Scatter of compression strength with size factor along with the mention of experimentally measured value.

Fig. 4b shows the variation in compression strength with size factor. As the size is increased, the variation is reduced with the mean value converging towards the experimental value.

4. Relationship between volume fraction and compression strength

4.1 Scatter in results

Artificial microstructures were reconstructed for a series of volume fractions (0.25-0.875) and FE simulations were performed to determine the relationship between ceramic volume fraction and compression strength. It was observed that for all volume fractions, the average compression strengths obtained from VEs with edge lengths 100 and 150 voxels were very close to each other. The scatter in the results decreased as size of VE was increased from 100 to 150 voxels. Fig. 5a-b show shadow diagrams for volume fractions 0.5 and 0.75 respectively.

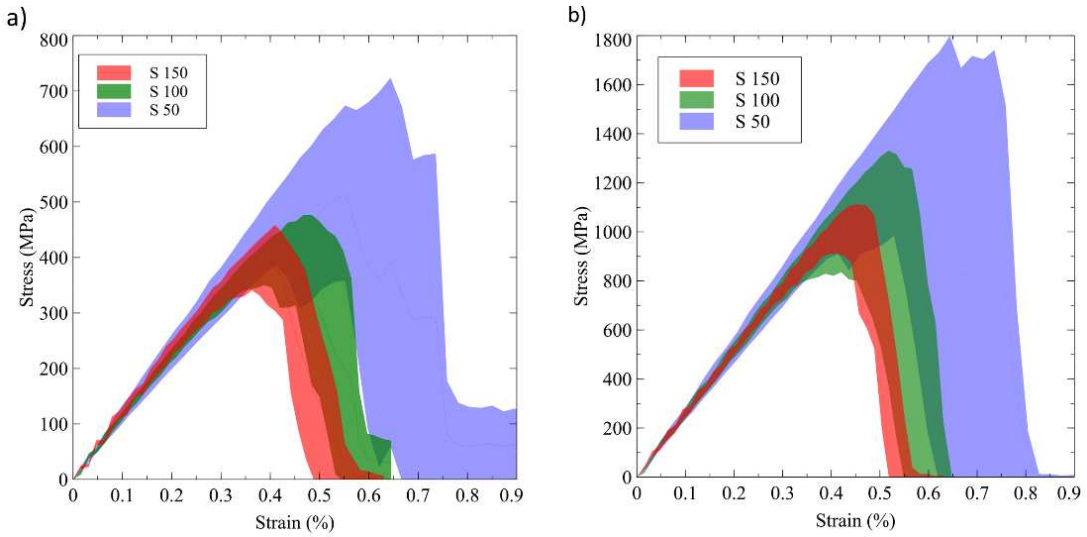

Figure 5. Shadow diagrams of volume elements having volume fraction a) 0.5 and b) 0.75

Table. 1 gives information about average compression strength, its standard deviation and normalized standard deviation for each volume fraction. The results correspond to volume element of edge length 150 voxels.

Table 1: Average compression strength, its standard deviation and normalized standard deviation for each volume fraction of the ceramic foam.

Volume fraction	Average compression strength [MPa]	Standard deviation [MPa]	Normalized standard deviation
0.25	67.9	5.1	0.07
0.375	200.4	17.6	0.09
0.5	399.3	35.3	0.09
0.625	646.8	60.1	0.09
0.75	1040.1	85.4	0.08
0.875	1602.6	102.1	0.06

  doi:10.5075/epfl-298799_978-2-9701614-0-0

The normalized standard deviation results in Table. 1 show that for the studied volume fractions, the scatter in compression strength results is similar for all volume fractions. It was decided to accept this value of scatter and use this size of volume element (edge length 150) for studying relationship between volume fraction and compression strength of ceramic foam.

4.2 Volume fraction vs. compression strength

Fig. 6a shows shadow curves of compression stress-strain (obatined from VE size of 150 voxels) for all the studied volume fractions. Fig. 6b shows average compression strength with respect to volume fraction along with the results of the analytical model Gibson-Ashby.

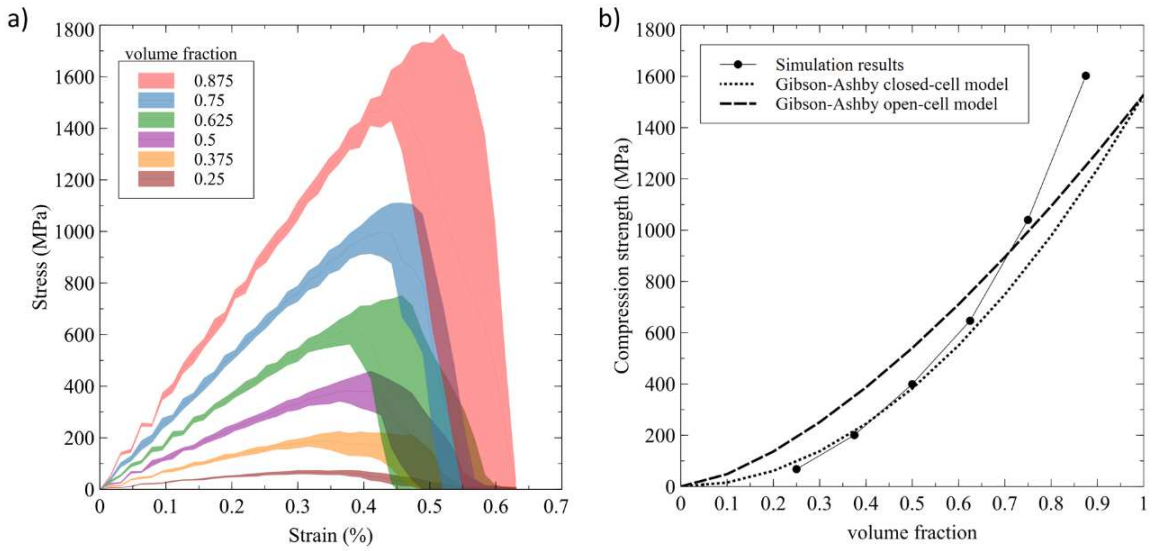

Figure 6. a) Shadow cures of compression stress-stain for all studied volume fractions from VE size of 150 voxels; b) average compression strength versus volume fraction from simulation results and Gibson-Ashby model.

Gibson and Ashby in articles [7,12] developed the proportionality laws for stiffness and strength of cellular solids. The compression strength relations developed for open-cell and closed-cell cellular solids are given in Eq. (3).

$$\sigma_s = C\sigma_{base}\left(\frac{\rho_{cellular}}{\rho_{base}}\right)^{\pi} \tag{3}$$

In Eq. (3), σ_s and σ_{base} indicate compression strength of cellular solid and base material respectively. ρ_{foam} and ρ_{base} indicate density of cellular solid and base material respectively. The exponent π takes value of $\frac{3}{2}$ for open-cell and value of 2 for closed-cell cellular solids. The constant C was predicted as 0.65 from experimental measurements in [7]. From Fig. 6b, it can be seen that for volume fraction less than 0.6, the simulation results are in close agreement with the theoretical results of the closed-cell Gibson-Ashby model. Above 0.6, the simulation results predict higher strength values and are diverging from the theoretical estimates. [7] stated that the theoretical models are applicable only below 0.6 volume fraction as the failure modes of beam (for open-cell) and plate (for closed-cell) bending assumed for the failure of the cellular solids are no longer valid as the volume fraction of the solid phase is increased beyond a certain value. Above this point, the heterogeneous medium becomes a distribution of pores within a solid medium rather than a cellular solid. The failure modes beyond this point are strut

  doi:10.5075/epfl-298799_978-2-9701614-0-0

compression and shear rather than strut bending. The simulation results are closer to closed-cell model rather than open-cell possibly because the cell walls in the real foam microstructure resembled more as closed walls with small holes rather than a network of connected edges (which would be closer to an open cell architecture).

5. Conclusions

The research work describes study of compression failure of ceramic foam particularly the relationship between volume fraction and compression strength. A finite element model of a real foam sample was developed to simulate compression failure. Artificial microstructures (equivalent to the real sample) of different sizes were reconstructed to study length scale effect on the compression strength. Microstructures of different volume fractions were developed and FE simulations were performed to determine effect of volume fraction on the compression strength. Finally, the results were compared with the theoretical model of Gibson-Ashby and the assumptions of the theoretical model were validated through the simulation results.

Acknowledgements

The financial support of the Darmstadt University of Applied Sciences and the Hessian Ministry of Higher Education, Research, Science and the Arts by Program “Forschung für die Praxis” is gratefully acknowledged. Special thanks go to Joél Schukraft and Kay Weidenmann for the experimental support.

6. References

1. Colombo P, Hellmann JR, Shelleman DL. Mechanical properties of silicon oxycarbide ceramic foams. Journal of the American Ceramic Society 2001; 84(10):2245-2251.
2. Colombo P, Modesti M. Silicon oxycarbide ceramic foams from a preceramic polymer. Journal of the American Ceramic Society 1999; 82(3):573-578.
3. Seeber BSM, Gonzenbach UT, Gauckler LJ. Mechanical properties of highly porous alumina foams. Journal of Materials Research 2013; 28(17):2281-2287.
4. Voigt C, Storm J, Abendroth M, Aneziris CG, Kuna M, Hubálková. The influence of the measurement parameters on the crushing strength of reticulated ceramic foams. Journal of Materials Research 2013; 28(17):2288-2299.
5. Schukraft J, Lohr C, Weidenmann KA. 2D and 3D in-situ mechanical testing of an interpenetrating metal ceramic composite consisting of a slurry-based ceramic foam and AlSi10Mg. Composite Structures 2021; 263, 113742.
6. Deshpande VV, Weidenmann KA, Piat R. Application of statistical functions to the numerical modelling of ceramic foam: From characterisation of CT-data via generation of the virtual microstructure to estimation of effective elastic properties. Journal of the European Ceramic Society 2021; 41(11):5578-5592.
7. Maiti SK, Gibson LJ, Ashby MF. Deformation and energy absorption diagrams for cellular solids. Acta metallurgica 1984; 32(11):1963-1975.
8. Jiao Y, Stillinger FH, Torquato S. Modeling heterogeneous materials via two-point correlation functions. II. Algorithmic details and applications. Physical Review E 2008; 77(3): 031135.
9. Johnson GR, Holmquist TJ. An improved computational constitutive model for brittle materials. In AIP conference proceedings. American Institute of Physics 1994; 309(1):981-984.

  doi:10.5075/epfl-298799_978-2-9701614-0-0

10. Guo G, Alam S, Peel LD. Numerical analysis of ballistic impact performance of two ceramic-based armor structures. Composites Part C: Open Access 2020; 3:100061.
11. Schukraft J, Lohr C, Weidenmann KA. Mechanical characterization of an interpenetrating metal-matrix composite based on highly homogeneous ceramic foams. In Hybrid 2020-Materials and Structures proceedings 2020; 33-39.
12. Gibson IJ, Ashby MF. The mechanics of three-dimensional cellular materials. Proceedings of the royal society of London. A. Mathematical and physical sciences 1982; 382(1782):43-59.

  doi:10.5075/epfl-298799_978-2-9701614-0-0

HOMOGENIZATION OF ADDITIVELY MANUFACTURED MATERIALS

Britt Helten, Kyle Warren

University of Maine Advanced Structures and Composites Center, Orono, ME, USA – britt.helten@maine.edu

Abstract: *Structures manufactured via extrusion-based additive manufacturing processes are comprised of a multitude of extrudates deposited in a successive manner. These extrudates bond to form the 'material' of the structure. The morphology of these extrudates directly impacts the resulting mechanical performance and is dependent upon both processing parameters and manufacturing instruction algorithm settings. An understanding regarding the significance of these effects as they correspond to the selection of settings during the generation of manufacturing instructions can be of importance during design efforts.*

These effects have been investigated via the development of a numerical homogenization scheme based on the utilization of representative volume elements to predict elastic mechanical behavior. This scheme utilizes the assumption that extrudate morphologies can be analytically represented with truncated superellipses. The homogenization scheme was compared with the Mori-Tanaka method and an analytical model proposed in literature. Recommendations for their respective use cases have been discussed.

Keywords: Additive manufacturing; homogenization; anisotropy; Mori-Tanaka

1. Introduction

Advancements in additive manufacturing (AM) technologies have continued to expand its applications into increasingly complex and high-value areas. Such application areas require design and engineering methods capable of predicting part performance. These predictions are predicated on the availability of constituent material properties which can be utilized in analysis methods such as finite element analysis (FEA).

The constituents of extrusion-based and Fused Filament Fabrication (FFF) AM processes consist of extrudates which are deposited in a predetermined geometrical arrangement. Modeling each of these extrudates at part-scale would be infeasible in many applications and therefore requires methods for incorporating extrudate-scale performance on the part-scale.

Multiscale modeling methods have been utilized in a variety of applications to reduce computational costs while incorporating effects on scales lower than those of immediate interest to designers and engineers [1]. These result in homogenized properties which can be applied en masse or per region of a given model. AM provides opportunities for low-cost variations of the extrudate morphology throughout the structure to form, whether intentionally designed or a product of the manufacturing process, functionally graded materials. The effects of such morphology variability can be an important consideration during design and require methods to evaluate and integrate them into analysis workflows. A numerical homogenization scheme was developed to evaluate such effects.

  doi:10.5075/epfl-298799_978-2-9701614-0-0

2. Homogenization

2.1 Extrudate Geometry

The geometry of extrudates manufactured via AM processes such as extrusion-based, FFF [2–5], and bound metal deposition (BMD) [6] often exhibit an elliptical cross-section as shown in Figure 1.

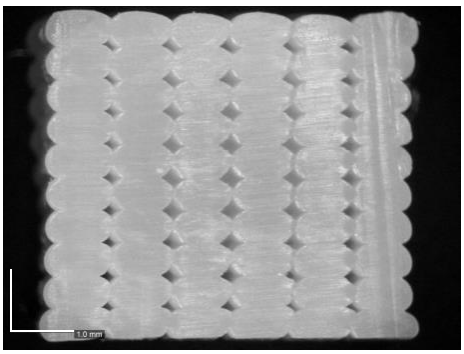

Figure 1. Representative cross-sectional extrudate geometry produced via FFF

The cross-sectional geometry can vary as a function of the print parameters and manufacturing instruction generation algorithms settings such as layer height, extrusion width, and path separation/overlap used to convert a geometry into machine instructions. The repeating pattern of such a system of unidirectional extrudates has been modeled with a representative volume element (RVE) consisting of a single extrudate. The extrudate geometry has been described as a superellipse which can be expressed in the YZ-plane of a cartesian coordinate system as

$$\left|\frac{y}{a}\right|^n + \left|\frac{z}{b}\right|^n = 1 \tag{1}$$

where a is the major axis dimension, b is the minor axis dimension, and n is the shape parameter.

The contact between adjacent extrudates has been described here in terms of contact efficiency. Contact efficiency has been defined as the ratio of the area of the contact region to the effective area of the extrudate's major and minor axes. These relations have been expressed as

$$\eta = \frac{w}{2a} \tag{2}$$

$$\mu = \frac{h}{2b} \tag{3}$$

for the major and minor contact efficiencies, respectively. Where η is the major contact efficiency, w is the width of contact along the major axis, μ is the minor contact efficiency, and h is the height of contact along the minor axis. The truncated geometry with a given combination of major and minor contact efficiencies can then be described using a truncation rectangle with the dimensions y_r and z_r as shown in Figure 2(a). A truncated superellipse with contact regions defined by contact efficiencies and corresponding contact dimensions is show in Figure 2(b).

  doi:10.5075/epfl-298799_978-2-9701614-0-0

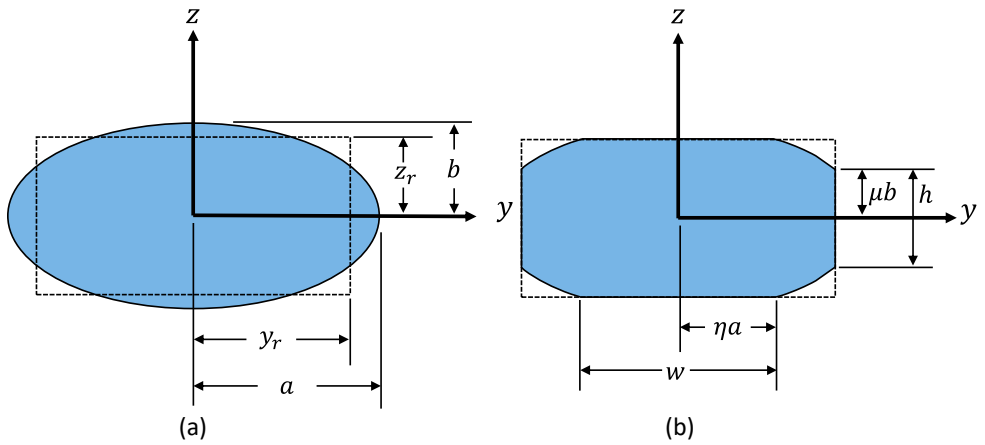

Figure 2. (a) Superellipse and truncation rectangle (dashed line) dimensions and (b) a truncated superellipse with contact efficiency dimensions

The truncation rectangle dimensions can then be expressed as a function of the contact efficiencies as

$$y_r = \mathrm{a}\sqrt[n]{1-\mu^n} \tag{4}$$

$$z_r = \mathrm{b}\sqrt[n]{1-\eta^n} \tag{5}$$

When using an elliptical cross-sectional geometry, i.e. n=2, the area of the truncated ellipse can be expressed as

$$A = 4ab\left[\eta\sqrt{1-\eta^2} + \left(\frac{t}{2} + \frac{\sin 2t}{4}\right)\Big|_{\sin^{-1}\eta}^{\cos^{-1}\mu}\right] \tag{6}$$

and the effective area represented by the truncation rectangle is given as

$$A_{eff} = 4ab\sqrt{1-\mu^2}\sqrt{1-\eta^2} \tag{7}$$

The volume fraction of the void can then be expressed as

$$V_{void} = 1 - \frac{\eta\sqrt{1-\eta^2} + \left(\frac{t}{2} + \frac{\sin 2t}{4}\right)\Big|_{\sin^{-1}\eta}^{\cos^{-1}\mu}}{\sqrt{1-\eta^2}\sqrt{1-\mu^2}} \tag{8}$$

and has a value of zero when the following expression is satisfied

$$\eta^n + \mu^n \geq 1 \tag{9}$$

These analytical approximations of the as-manufactured extrudate geometry were then used to inform the evaluated homogenization methods in a parametric form.

2.2 Homogenization

The analytical definition of extrudate cross-sectional geometry was used to obtain effective properties via a numerical homogenization implemented in Abaqus, the Mori-Tanaka method [7], and the Mechanics of Materials method proposed by Rodriguez et al. [8]. The principal coordinate system used throughout this work is shown in Figure 3.

  doi:10.5075/epfl-298799_978-2-9701614-0-0

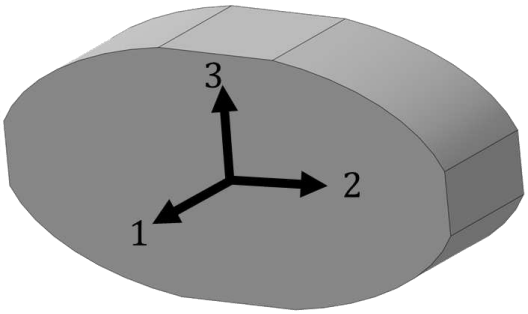

Figure 3. Principal coordinate system of the extrudate RVE

2.2.1 Modeling assumptions

The implemented homogenization methods have assumed bulk properties for the contact between adjacent extrudates. This assumption has been demonstrated to be reasonable for some materials [9]. Potential effects caused by the manufacturing method, e.g. residual stresses, were also neglected. The use of a linearly elastic material model assumes a negligible amount of nonlinear/plastic deformation. The neglect of nonlinear behavior could result in stiffer responses due to artificially low strains in the regions of high stress.

2.2.2 Material

The material properties used in this study were obtained from [2,5] and consist of an isotropic definition for acrylonitrile butadiene styrene (ABS) feedstock which is shown in Table 1.

Table 1. ABS mechanical properties [2,5]

Property	Unit	Value
E	MPa	2230 ± 15
G	MPa	833 ± 7.6
ν	-	0.34 ± 0.02

2.2.3 Numerical Model

The extrudate geometry was generated in Abaqus using the built-in geometry tools to create the ellipse and truncation rectangle using the equations outlined in Section 2.1. An example of the resulting mesh generated from such a geometry is shown in Figure 4.

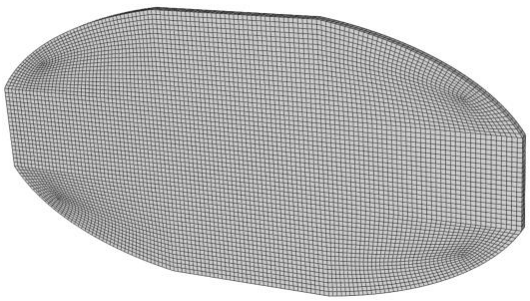

Figure 4. Representative FE mesh of an extrudate with an aspect ratio of 2, η=0.3, and μ=0.3

Loads and periodic boundary conditions for the 6 load cases required to characterize the elastic response of the RVE were applied using the Micromechanics Plugin for Abaqus [10].

  doi:10.5075/epfl-298799_978-2-9701614-0-0

2.2.4 Analytical Models

The Mori-Tanaka method [7] was implemented with void inclusions modeled as elliptic cylinders for which closed-form solutions for Eshelby's tensor are available [11]. The use of an elliptic cylinder allowed for the incorporation of the void morphology to yield orthotropic properties. The void fraction was calculated using Eq. (8) and the aspect ratio of the voids was calculated by

$$ar = \frac{a\left(\sqrt{1-\mu^2}-\eta\right)}{b\left(\sqrt{1-\eta^2}-\mu\right)} \tag{10}$$

The Rodriguez Mechanics of Materials method [8] expresses the transversely isotropic engineering constants as a function of the corresponding matrix property and a void fraction. Void fraction, referred to as void density, ρ_1, in the text, and was also calculated using Eq.(8).

3. Results

The cross-sectional geometry of the aligned mesostructured coupon from [2] was modeled using the truncated superellipse parameters of a/b=1.59, n=2, η=0.575, and μ=0.446. The resulting void fraction was 6.76%. The property predictions from the numerical approach were within 10% of the reported in-plane values. These results, along with the predictions from the Mori-Tanaka and Rodriguez methods, are shown in Table 2.

Table 2. Prediction comparisons with experimental values in literature

Property	Unit	Exp. [2]	Numerical		Mori-Tanaka		Rodriguez	
			Pred.	Δ_{exp}	Pred.	Δ_{exp}	Pred.	Δ_{exp}
E_1	MPa	1972	2079	(+5.44%)	2079	(+5.44%)	2079	(+5.44%)
E_2	MPa	1762	1826	(+3.64%)	1953	(+10.8%)	1650	(-6.34%)
ν_{12}	-	0.376	0.340	(-9.57%)	0.340	(-9.57%)	0.317	(-15.7%)
G_{12}	MPa	676.0	724.3	(+7.14%)	748.4	(+10.7%)	686.6	(+1.57%)

The resulting stress fields for each load case, presented as stress in the corresponding principal loading direction, are shown in Figure 5.

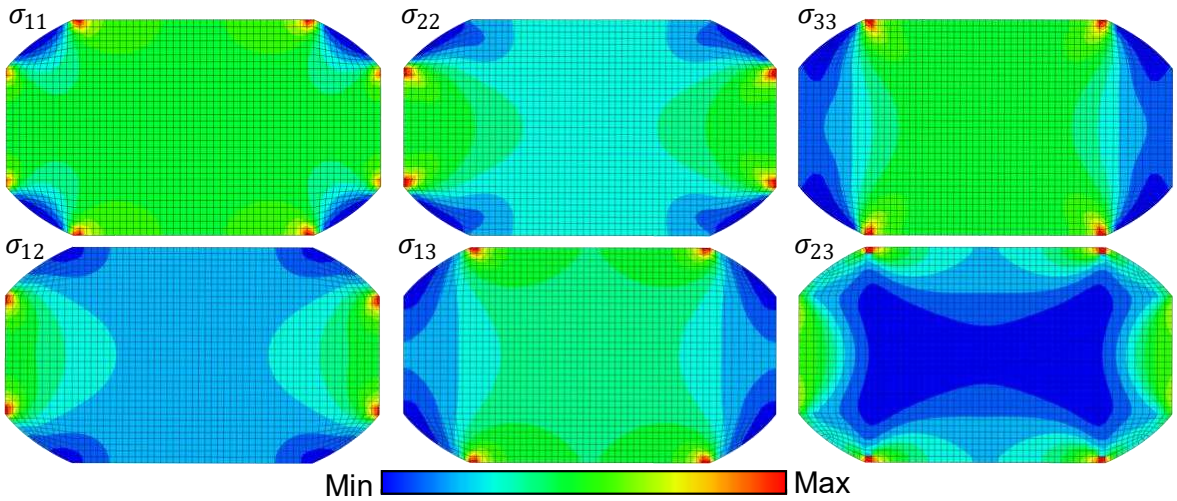

Figure 5. Representative stress fields for each load case, ε_{ij}, denoted by σ_{ij}

  doi:10.5075/epfl-298799_978-2-9701614-0-0

The numerical model consisted of 5,328 C3D8R elements and was solved in approximately 2 seconds using a single CPU. The model was evaluated throughout the range of potential contact efficiencies to generate response surfaces for each of the nine orthotropic engineering constants. An example of the E_{22} response surface for each homogenization method is shown in Figure 6. The plane $\eta = \mu$ was selected for 2D evaluation where all nine engineering constants were normalized by the corresponding constituent property. These are shown in Figure 7.

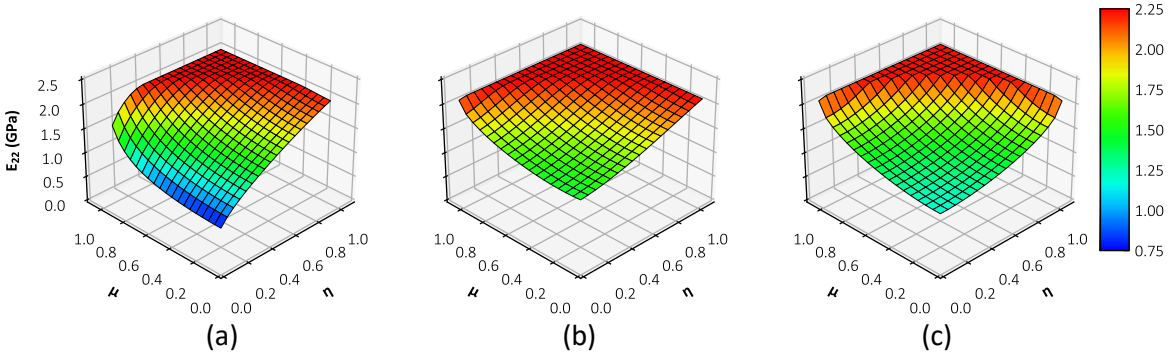

Figure 6. E_{22} vs major, η, and minor, μ, contact efficiencies for (a) numerical, (b) Mori-Tanaka, and (c) Rodriguez homogenization methods

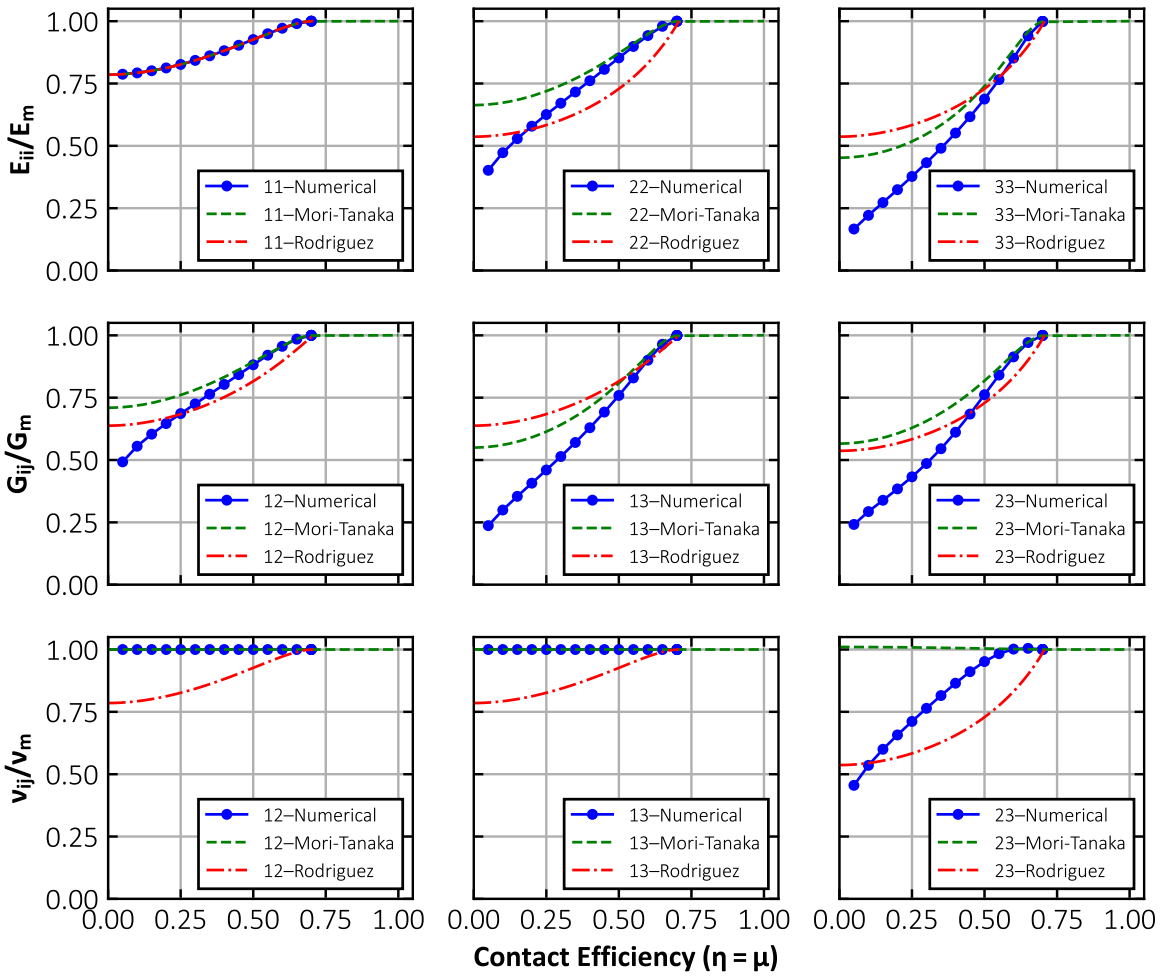

Figure 7. Engineering constants vs contact efficiency for numerical, Mori-Tanaka, and Rodriguez homogenization methods

  doi:10.5075/epfl-298799_978-2-9701614-0-0

The predictions of E_{11} were consistent among all evaluated homogenization methods. The predictions of the Mori-Tanka method were found to consistently yield values greater than those of the numerical method. The predictions of the Rodriguez method were found to generally yield values lower than the numerical results at higher contact efficiencies, i.e. lower void fractions, and higher values at lower contact efficiencies, i.e. higher void fractions. Predicted differences of the Mori-Tanaka and Rodriguez methods with respect to the numerical results for tensile and shear moduli are shown in Figure 8.

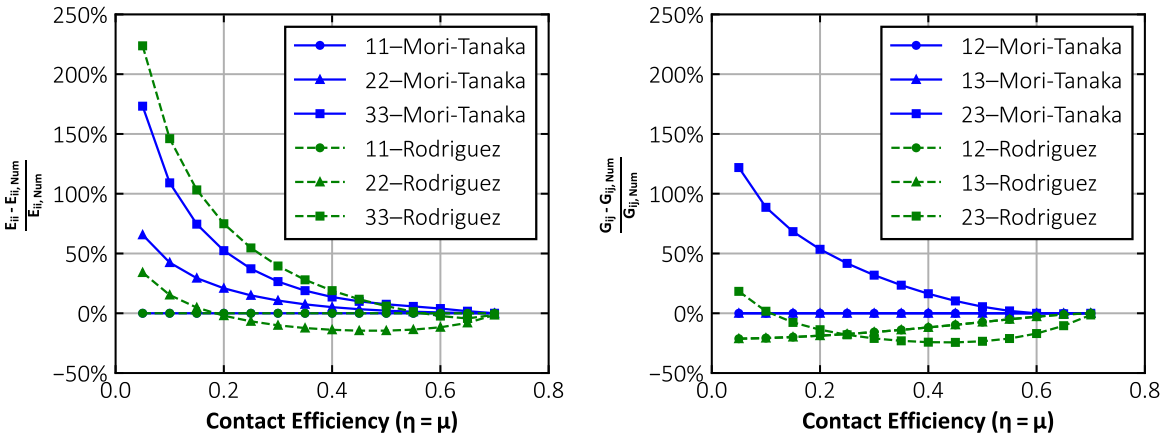

Figure 8. Analytical prediction difference with respect to the numerical result vs contact efficiency for tensile (left) and shear (right) moduli

The Mori-Tanaka and Rodriguez predictions for tensile and shear moduli also tended towards a non-zero value as the contact efficiencies approached zero. At this point the moduli would be expected to approach zero as contact between adjacent extrudates approaches zero. This phenomenon was found to be better predicted by the numerical method.

4. Conclusions

The results of this study have demonstrated the cross-sectional geometry can have significant effects on the predicted performance of AM extrudates. Preliminary comparisons with results in the literature indicate that a truncated ellipse is a viable parametric model for the as-manufactured geometry of extrusion-based and FFF AM processes.

The results also indicated that design efforts which primarily rely on the first principal extrudate direction, such as unidirectional beam bending, can utilize the simple Rules of Mixtures approach. Design efforts with more complex load cases which require load transfer between extrudates in the 2 and 3-directions would benefit from the use of a homogenization method to more accurately model the performance of such a part or structure.

The Mori-Tanaka method with void inclusions modeled as elliptic cylinders was found to result in predictions within 10% of the numerical method at contact efficiencies above 50%, i.e. void fractions below approximately 8%, for the evaluated response plane. Predictions within 10% of the numerical method for the Rodriguez model were observed at contact efficiencies at 65% and above for the evaluated response plane, i.e. void fractions below approximately 1%. These results indicate that these methods could be utilized when the contact efficiencies are above 50% and 65% for reasonable approximations using the Mori-Tanaka and Rodriguez methods, respectively.

  doi:10.5075/epfl-298799_978-2-9701614-0-0

The numerical homogenization scheme implemented herein has demonstrated the need for careful consideration of homogenization methods as they relate to the as-manufactured geometries of interest. While analytical methods can produce reasonable approximations for elastic extrudate behavior in the 23-plane, consideration of their limitations with regards to extrudate morphology and void content are important and should not be neglected.

The methods evaluated in this work can also serve as tools of varying fidelity to be integrated into optimization and/or functionally graded material design schemes. One such application would be the integration of performance predictions to inform the placement and spacing of extrudates to yield a desired set of properties by controlling contact efficiencies in a manufacturing instructions generation algorithm like a slicer.

Acknowledgements

This work was funded by the Accelerating Rapid Prototyping: Process and Modeling project from the U.S. Army Engineer Research and Development Center. Contract number: W912HZ21C0005

5. References

1. Kanouté P, Boso DP, Chaboche JL, Schrefler BA. Multiscale Methods for Composites: A Review. Arch Comput Methods Eng. 2009 Mar 1;16[1]:31–75.

2. Rodríguez JF, Thomas JP, Renaud JE. Mechanical behavior of acrylonitrile butadiene styrene (ABS) fused deposition materials. Experimental investigation. Rapid Prototyp J. 2001 Jan 1.

3. Li L, Sun Q, Bellehumeur C, Gu P. Composite modeling and analysis for fabrication of FDM prototypes with locally controlled properties. J Manuf Process. 2002;4[2]:129–41.

4. Somireddy M, Czekanski A. Mechanical characterization of additively manufactured parts by FE modeling of mesostructure. J Manuf Mater Process. 2017;1[2]:18.

5. Rodriguez Matas JF. Modeling the mechanical behavior of fused deposition acrylonitrile-butadiene-styrene polymer components: University of Notre Dame; 1999

6. Watson A, Belding J, Ellis BD. Characterization of 17-4 PH Processed via Bound Metal Deposition (BMD). In: TMS 2020 149th Annual Meeting & Exhibition Supplemental Proceedings. Cham: Springer International Publishing; 2020. p. 205–16..

7. Benveniste Y. A new approach to the application of Mori-Tanaka's theory in composite materials. Mech Mater. 1987;6[2]:147–57.

8. Rodríguez JF, Thomas JP, Renaud JE. Mechanical behavior of acrylonitrile butadiene styrene fused deposition materials modeling. Rapid Prototyp J. 2003 Oct 1;9[4]:219–30.

9. Allum J, Moetazedian A, Gleadall A, Silberschmidt VV. Interlayer bonding has bulk-material strength in extrusion additive manufacturing: New understanding of anisotropy. Addit Manuf. 2020 Aug 1;34:101297.

10. McLendon R. Micromechanics Plugin for Abaqus [Internet]. LinkedIn; 2017.

11. Mura T. Micromechanics of defects in solids. Springer Science & Business Media; 1982.

  doi:10.5075/epfl-298799_978-2-9701614-0-0

A DETERMINISTIC DIGITAL TWIN-BASED METHOD FOR DAMAGE DETECTION OF COMPOSITES SUBJECTED TO IMPACT LOADING: DEVELOPMENT AND VALIDATION

Efthymios, Giannaros[a], Vassilis, Kostopoulos[a], Athanasios Kotzakolios[a]

a: Applied Mechanics & Vibrations Laboratory, Department of Mechanical Engineering and Aeronautics, Greece – efthimisgian@upatras.gr

Abstract: *Both monolithic and sandwich composites are highly susceptible to impact loading. Despite of their inherent strength-to-weight ratio benefits, this vulnerability constitutes a major concern related to structural integrity. Although structures designed with fail-safe principles can withstand in theory partial system failure, the early detection of in-service damage is useful for supplementing regular inspections. The development and validation of a time-efficient predictive method for the localization and quantification of damage to composites can bring numerous benefits such as rapid post-damage strength estimation. In the current study, a deterministic digital twin-based algorithm for the damage localization and quantification of a composite sandwich panel subjected to soft body impact is developed. The effectiveness and robustness of developed algorithm is highlighted, whilst proposals for enhancement of time-efficiency of algorithm are provided.*

Keywords: Multi-Fidelity Modeling; Impact Simulation; Structural Health Monitoring; Composites; Fibre Bragg Gratings.

1. Introduction

The constant requirement of aerospace industry to enhance the structural efficiency has driven to the usage of high-performance composite materials, either monolithic or sandwich. However, aerospace composite structures are prone to damage due to high-velocity impact events such as bird strike, hail impact, etc. These impact events can result in extensive damage including structure perforation, which will eventually degrade its post-impact residual strength. Therefore, the early detection of damage in composite structures is imperative to avoid catastrophic failure. The development and validation of a time-efficient predictive method for the localization and quantification of damage to composites can bring numerous benefits such as rapid post-damage strength estimation; however, the detection and estimation of composites damage using digital twin (DT) technology is a brand-new technique that has not been widely used in aerospace industry yet.

A few attempts for the integration of digital twin concept to aerospace and space industry are shown below. Tuegel et al. [1] presented a conceptual model using digital twin to predict the aircraft structural life prediction and to assure the structural integrity in flight conditions. Later, in 2012, Glaessgen and Stargel [2] proposed a digital twin paradigm for the prediction of the health and the remaining life of future NASA and U.S air force vehicles. Despite all of that, the digital twin technology is not mature enough for use in the aerospace industry and more development is required in several sectors such as data transmission, collection and processing, communication-interaction technology, modeling-simulation technology and sensing-measurement technology. The modeling technology is the main research focus of this study,

  doi:10.5075/epfl-298799_978-2-9701614-0-0

nevertheless important conclusions can be extracted for the data recording device (interrogator) and the FBG sensing technology.

In the current study, a deterministic digital twin-based algorithm for the damage localization and quantification (named Damage Evaluation Algorithm-DEA) of a composite sandwich panel subjected to soft body impact is developed. The principle of its operation is based on the comparison of the strain histories recorded by FBG sensors with the numerically calculated ones. More specifically, high-fidelity (HF) and low-fidelity (LF) finite element (FE) models are employed as digital replicas of actual structure; firstly, the low-fidelity model is used as a computationally efficient tool for the identification of impact loading conditions and damage localization based on strain measurements recorded by the FBG sensors, and afterwards the high-fidelity model is employed for damage quantification considering known the position and load-time profile. For the better comprehension of general idea, a schematic of digital-twin-assisted damage diagnosis concept including the function of developed models is shown in figure 1.

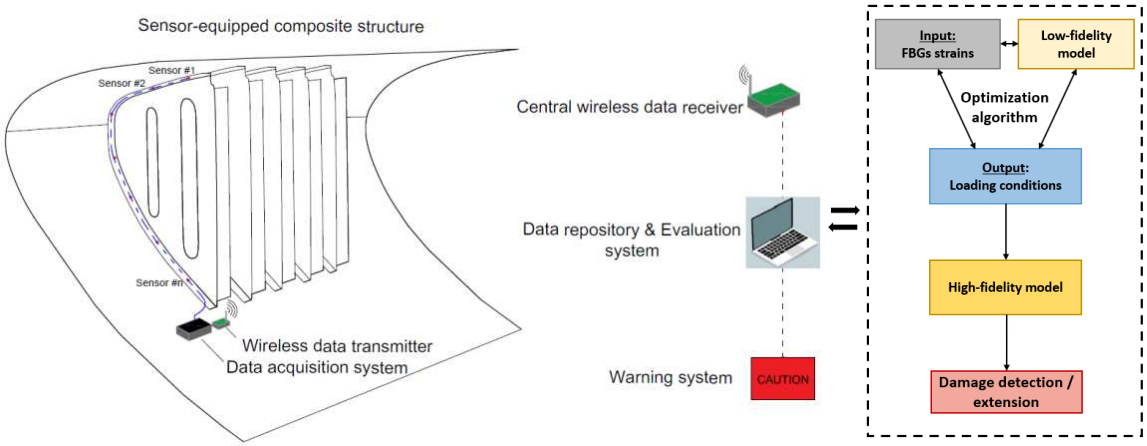

Figure 1. A schematic of digital-twin-assisted damage diagnosis concept

2. Modelling tools

This section briefly describes the physical-based FE models with different fidelity levels which were developed for a specific curved sandwich panel in a previous authors' investigation [3]. It should be mentioned that the creation and validation of these modeling tools constitute a preparatory and prerequisite step for the development of the DEA algorithm. In this study, the examined sandwich panel is 500 mm in length, 470 mm in width and about 26 mm in thickness. In essence, it is a slightly curved rectangular panel with a radius of 400 mm, whilst it is assumed that it consists of two symmetric quasi-isotropic lay-up [(45/0/-45/90)2]s) CFRP faces with 2.88 mm thickness and a 20 mm thick polymer foam layer.

In the case of high-fidelity model, ply-based method (stacked-solid method) with 3D solid elements was adopted for the laminated skins. This technique can predict the separation of laminated plies on the grounds that each lamina is explicitly modelled. For delamination initiation and propagation modelling, a fracture-based contact algorithm is utilized at each lamina interface since it eliminates the drawbacks of cohesive elements. In the case of foam core modeling, the three one-integration point solid elements in through the thickness direction are considered adequate for capturing the bending and shear stiffness of panel. For the intralaminar damage, a modification of Hashin criterion is applied.

  doi:10.5075/epfl-298799_978-2-9701614-0-0

Regarding the LF model, it targets to reduce the high computational time of HF one keeping the modeling accuracy to an acceptable level. It is well known that the most representative the model is, the most time consuming is. Therefore the relegation of accuracy of damage modeling is applied using layered solid elements for skin modeling. The 8-node layered solid elements in LS-DYNA use one integration point per layer for computational efficiency capturing efficiently the bending stiffness and the through the thickness stresses like a 3D solid element. The second modification in relation to the HF model is that no cohesive elements are implemented into the CFRP faces for the capturing of interlaminar damage. Thus, the running time was significantly reduced (98%). In parallel, impulse-equivalent loading technique was implemented for the further mitigation of computational time. In essence, it is used a time-variable, distributed and impulse-equivalent load for the representation of bird impact force. The equivalent load is applied on a rectangular area whose the edge length is equal to the projectile's diameter (50mm). Regarding the loading shape, it is observed that it looks like a symmetrical bell for 45° oblique soft-body impact; therefore, it is simplified as a tri-linear loading curve. The figure 2 shows the model with the explicit SPH model of soft projectile and the model with the equivalent load. Detailed discussion about the modeling approach, the computational time and the validation process of modelling tools using experimental impact tests is given in [3].

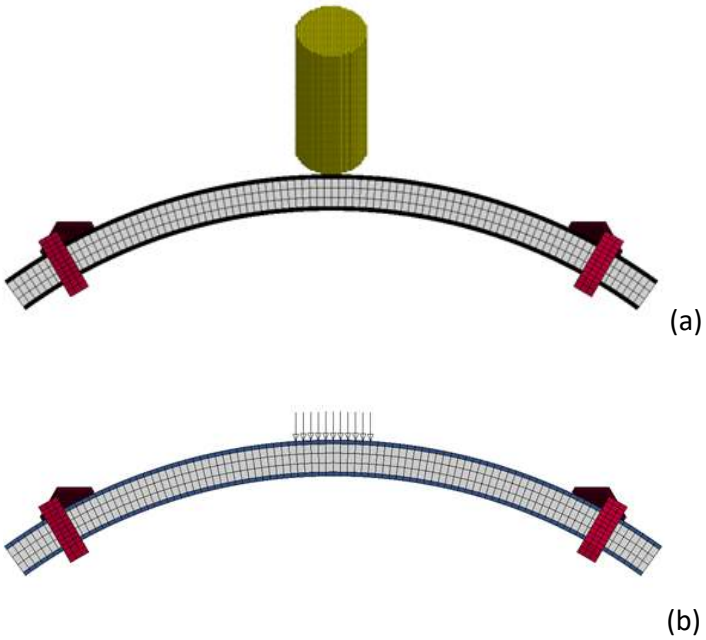

Figure 2. Model including SPH soft projectile (a), and Impulse-equivalent model (b)

In previous authors' study [3], it has been concluded that the high-fidelity model can sufficiently approximate the experimental strain histories recorded by the FBG sensors, with the experimental delamination area accurately predicted. On the other hand, the LF model can rapidly predict the global vibrational response of sandwich panel, whereas the further transformation of the LF model based on applying an impulse-equivalent loading instead of SPH model of the soft projectile reduced the total computational time by 68%. In current research, all employed models were set using simplified equivalent loading due to a) the necessity for time efficiency and b) the parametrization of tri-linear loading curve in terms of loading rate, the magnitude, the unloading rate, and the impact duration.

  doi:10.5075/epfl-298799_978-2-9701614-0-0

3. Description of DEA algorithm

The MATLAB developed DEA algorithm consists of six (6) steps, which are in parallel the targets of current study, and they are executed in series. In the first step, the algorithm roughly estimates the position of the applied load by providing an initial arbitrary pair of values for load magnitude and impact duration. In essence, the LF model is running for different load positions and the algorithm evaluates the strain-time histories at the two measuring points. The target here is the minimization of root-mean-square (RMSE) error between the experimental values and the numerical ones, whereas the used searching algorithm of the 1st step is based on a user-defined logic scanning 35 points on the panel's surface. The output of 1st step is the rough estimation of load location and constitutes also the input of 2nd step. In the 2nd step, a fine searching procedure of load location follows and is based on the Pattern-search method [4]. The position of load is determined with an accuracy equal to the element size (i.e. 5mm in current research). When the location of loading has been defined, the 3rd step of algorithm is being activated for the calculation of loading rate changing the slope of loading curve at each running. The optimum value of loading rate is defined using the derivative-free Nelder-Mead Simplex optimization method [5] and the target experimental strain-time histories. Afterwards, the 4th step deals with the definition of loading magnitude, whereas the 5th step calculates the total impact duration using again the Nelder-Mead Simplex method. All the above steps are executed using only the LF modeling tool. Finally, the 6th step is a single running of HF model knowing the location and the time-variance of applied load. The necessary inputs for the running of algorithm are the FBG sensors data and an initial pair of values for the load magnitude and impact duration. The flow chart of DEA algorithm is illustrated in figure 3.

Regarding the assumptions of the proposed methodology, the current framework is formulated for high-velocity soft body impact and is restricted to the 45^o oblique impact due to the available experimental tests; nevertheless, it can easily be modified for a normal impact scenario. The second assumption is that the area of applied pressure load is constant assuming that the projectile size is known, and the load is spatially static during the analysis. Therefore, the effect of projectile flattening cannot be captured due to the fact that it is an inherent limitation of modeling method.

As far as the execution time is concerned, both the numerical models and the DEA algorithm is highly improved for the minimization of running time. The execution time for a single run of LF model is 25 s, whereas for the HF model is 2hr and 19 min using an 12th Gen Intel i7-12700K 3.6 GHz processor and a 64 GB RAM. The total computational time of DEA algorithm is 3hr and 49min. Furthermore, it is necessary to be mentioned that the DEA algorithm is executed without any user intervention during the process.

  doi:10.5075/epfl-298799_978-2-9701614-0-0

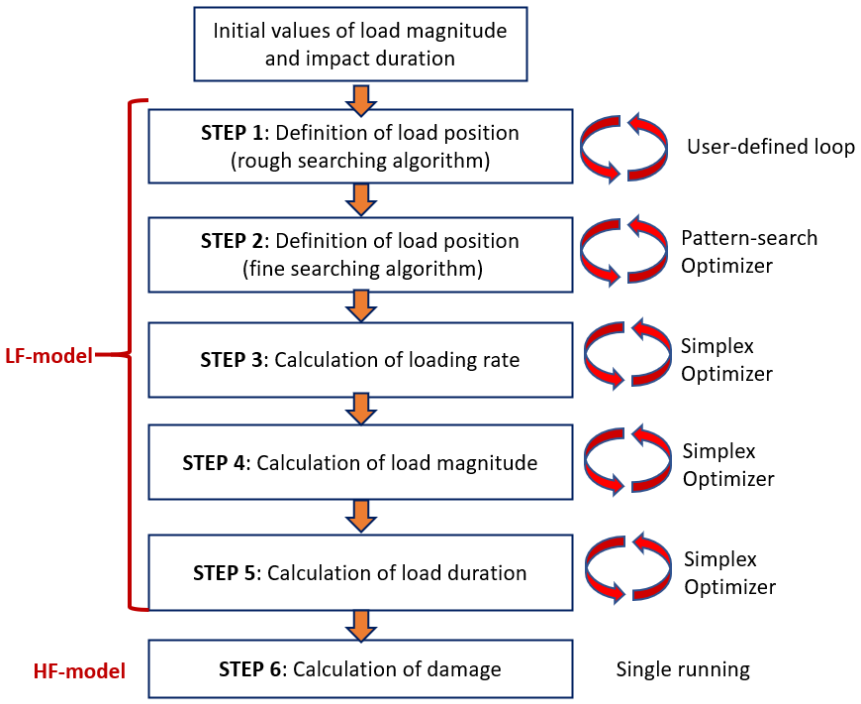

Figure 3. Flow chart of DEA algorithm

4. Results and Discussion

4.1 DEA algorithm's effectiveness

As described above, the execution of damage evaluation procedure is a stepwise process starting from the definition of load position. The distribution of RMSE error between numerical and target strain-time profiles on the panel surface for the 1st step is depicted in figure 4. The error minimizes at the point with coordinates X=260 mm and Y=-50mm which shows the location of the right-back corner of pressure load, whereas the fine searching routine finds the global minimum RMSE error at point with X=268 mm and Y=-50 mm which is extremely close to the experimental impact point.

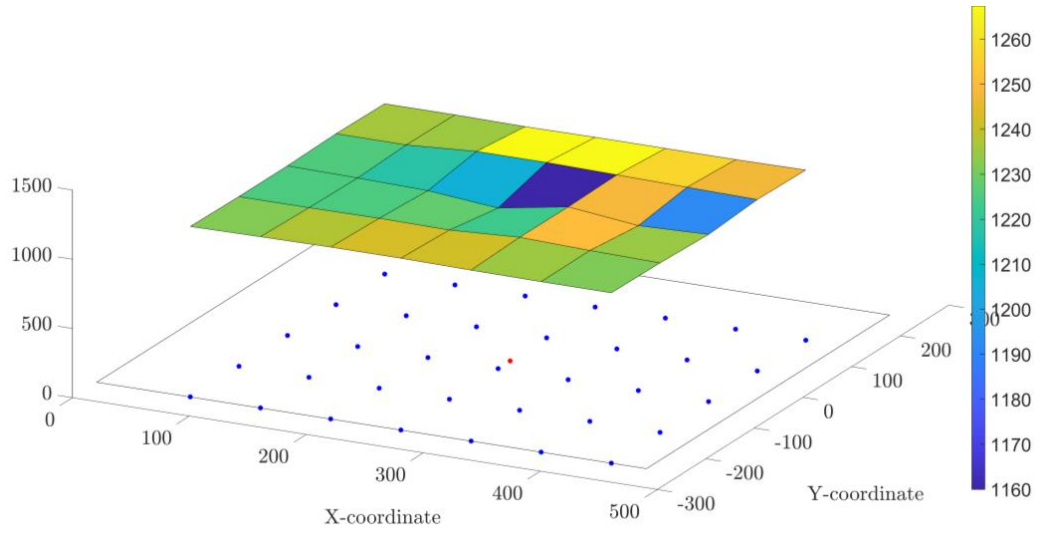

Figure 4. RMSE between numerical and target strain-time histories for 1st step of algorithm

The figure 5 compares the applied load versus time derived by HF/SPH model [3] with the time-varying load calculated from DEA algorithm. The HF/SPH model, showed in [3], is the high-fidelity numerical impact model created using SPH method for soft projectile representation.

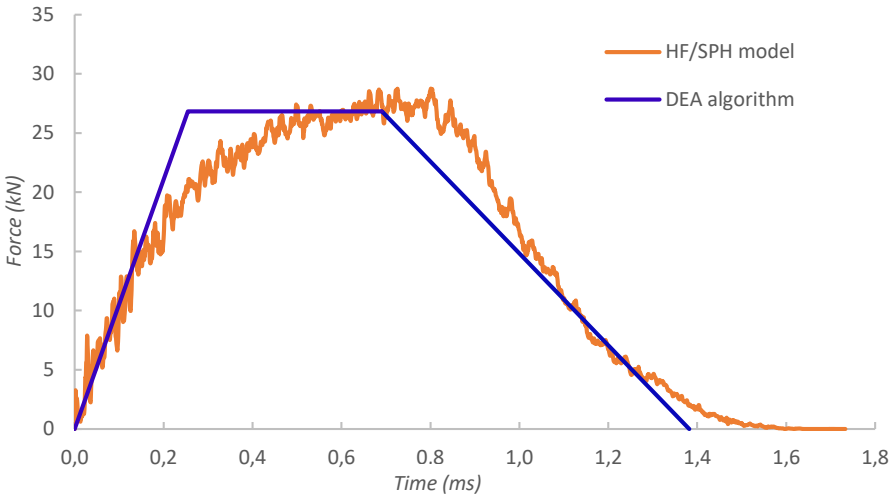

Figure 5. Comparison of the contact force-time response derived from LF/SPH model [3] and the calculated one from the DEA algorithm

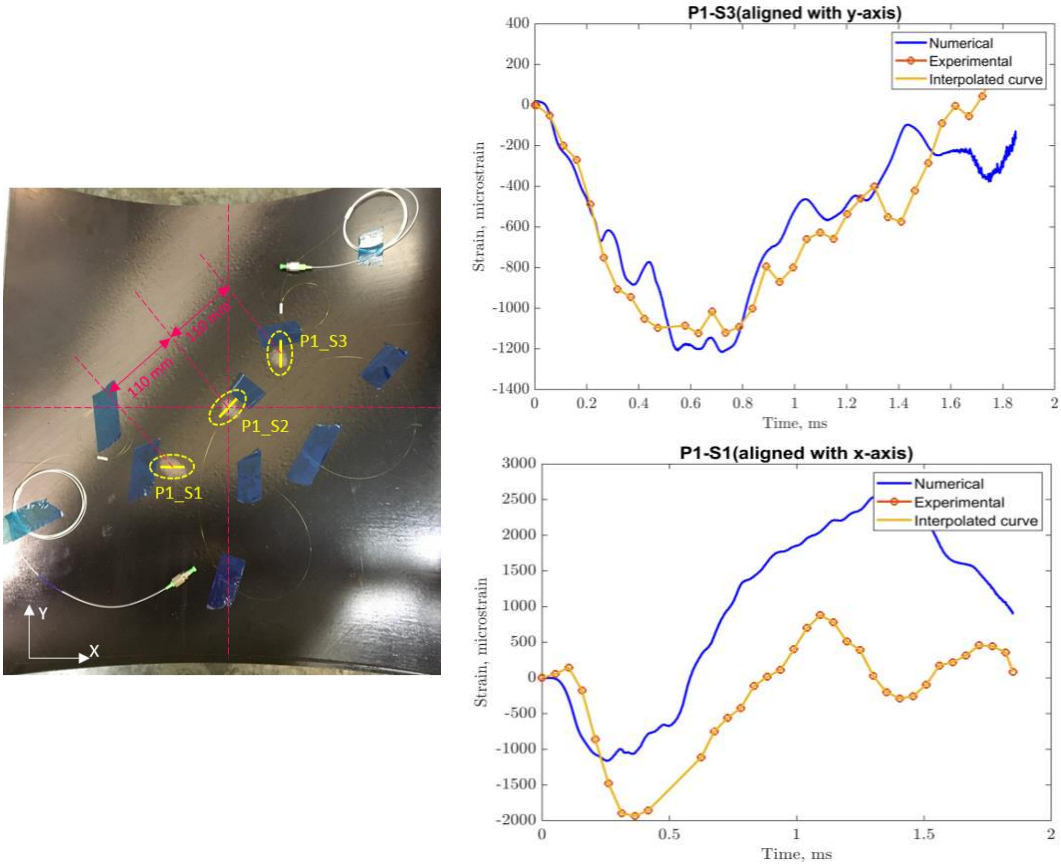

Figure 6. Comparison of experimental and numerical (DEA algorithm) strain-time profiles

In the case of HF/SPH model, the force-time curve of figure 5 is the applied force-time profile derived from the contact between composite panel and soft projectile. Comparing the responses, it is noted that the impulse difference is only 1.2 %. In particular, the impulse for

HF/SPH model is 24.6 Ns, whereas for DEA algorithm equal to 24.3 Ns.In parallel, the loading rate, the magnitude of load and the impact duration are on agreement with those of HF/SPH model of [3]. Consequently, it is infered that the DEA alogorithm has accurately calculated the impulse-equivalent load of impact event. The figure 6 shows the numerical strain-time profiles for the two measuring points P1_S1 and P1_S3 derived from DEA algorithm and the corresponding experimental ones [3]. From numerical point of view, each numerical strain-time profile was calculated from the output strain data of corresponding solid element located on the back side of target structure. In the case of P1_S3 point, the numerical profile is identical to the experimental one in terms of a) the initial slope of strain curve, b) the maximum strain during the impact event, c) the rise time at which the maximum strain occurs, d) the decay time and e) the trend of strain-time profile. Looking the result for P1_S1 point, it is infered that the numerical strain-time profile diverges from the experimental ones due to the load simplification according to the previous author's investigation [3]. However, it is in good agreement from the trend point of view. The conclusion here is that a pair of measuring points is necessary for better convergence of DEA algorithm and therefore more accurate results. Concerning the interlaminar damage, the total delaminated area by non-destructive evaluation is calculated equal to 16,875 mm^2, whereas the cumulative numerical damage is slightly larger and equal to 19,228 mm^2 (Figure 7). This discrepancy is due to the asymmetric delamination pattern observed in the experimental results. Acccording to [3], a heterogeneity of gelatine projectile and an imperfection in the target material might be possible reasons. However, the location and the extent of the actual damage in both directions have been precisely captured from the DEA algorithm, as shown in figure 7.

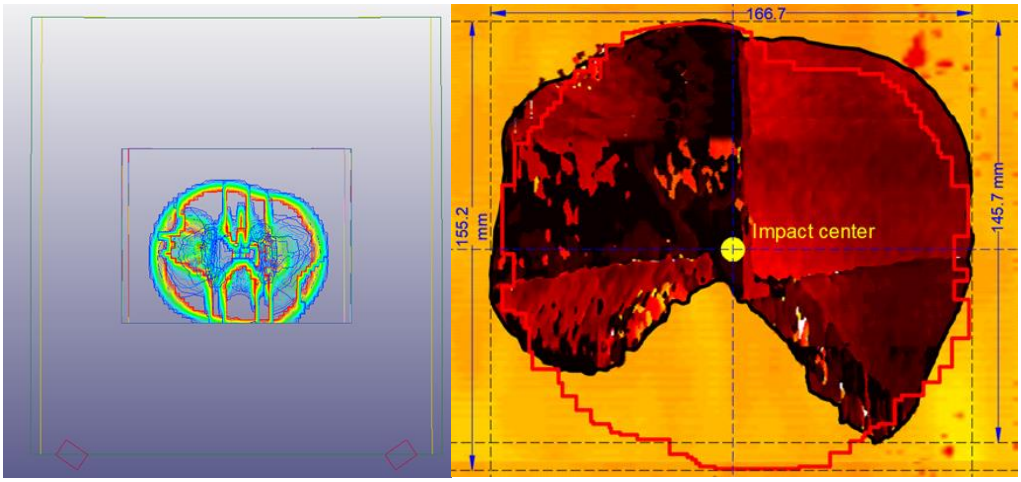

Figure 7. Comparison of total numerical delamination damage (red line) with the experimental one (black line) (right) and model with numerical delamination damage (left).

4.1 DEA algorithm's robustness

Apart from the algorithm's effectiveness, the robustness of methodology was assessed regarding the effect of the initial input values of load magnitude and impact duration. More specifically, 85 combinations of load magnitude-impact duration, which were derived from Latin-Hypercube Sampling (LHS) method, were studied. The influence of initial values on the load localization is presented in figure 8. 79 samples (viz. 92.9% of sampling) showed that the right-back corner of distributed load is placed at point with X=260mm and Y=-50mm; 4 samples (4.7%) locate the corner of load at X=440mm and Y=-50 mm; whereas, 2 samples (2.4%) provide

the minimum error at X=260mm and Y=-150mm. Therefore, the DAE algorithm demonstrates high level of robustness.

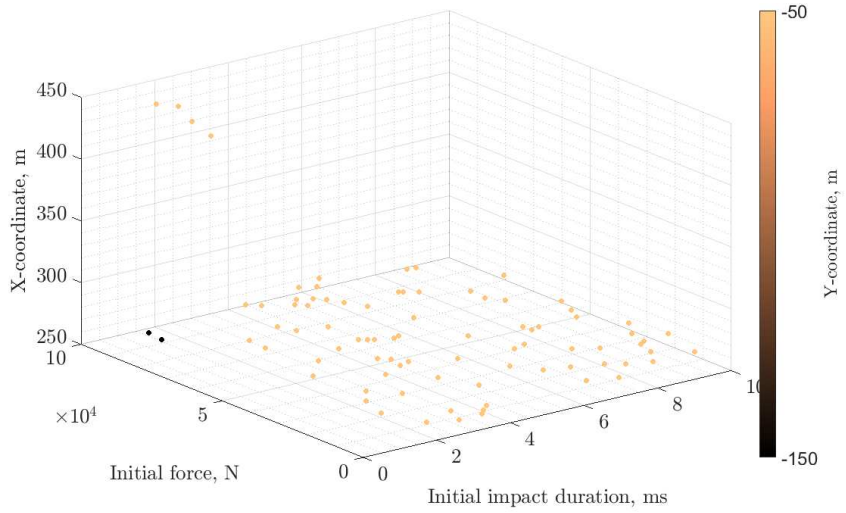

Figure 8. Incluence of load magnitude-impact duration combination on the load localization

5. Conclusions

In the current study, an effective and highly robust digital-twin based algorithm for composite structure damage evaluation was developed. The damage localization and quantification with high precision is feasible using as input the FBG sensors strain-time profiles and without any user-intervention. The level of robustness of methodology can be maximized using multi-point strain data, whereas the time-efficiency can be increased implementing a surrogate model to the process.

Acknowledgements

This work is funded in the context of ODOS 2020, co-funded by the European Regional Development Fund of the European Union and National Resources through the Operational Programmed Competitiveness, Entrepreneurship and Innovation “RESEARCH-CREATE-INNOVATE” (T1EDK-03081).

6. References

1. Tuegel E.J, Ingraffea A, Eason T, Spottswood S.M. Reengineering aircraft structural life prediction using a digital twin. Int. J. Aerospace Eng., 2011; 154798. https://doi.org/10.1155/2011/154798
2. Glaessgen E, Stargel D. The digital twin paradigm for future NASA and U.S. Air Force Vehicles. 53rd AIAA/ASME/ASCE/AHS/ASC Conf., Honolulu, Hawaii, April 2012. https://doi.org/10.2514/6.2012-1818
3. Giannaros E, Kotzakolios A, et.al. Low- and high-fidelity modeling of sandwich-structured composite response to bird strike, as tools for a digital-twin-assisted damage diagnosis. Int. J. Impact Eng., 2022; 104058. https://doi.org/10.1016/j.ijimpeng.2021.104058
4. Matlab R2022a documentation, Mathworks.
5. Lagarias, J. C., et.al. “Convergence Properties of the Nelder-Mead Simplex Method in Low Dimensions.” SIAM Journal of Optimization. Vol. 9, Number 1, 1998, pp. 112–147.

  doi:10.5075/epfl-298799_978-2-9701614-0-0

HYBRID DATA DRIVEN MULTISCALE MODELLING OF COMPLEX COMPOSITES STRUCTURES

Bassam El Said [a]

a: University of Bristol – bassam.elsaid@birstol.ac.uk

Abstract:

The behaviour of composite structures is dominated by complex interactions of the materials' internal architecture, structure geometry, loads and boundary conditions. Damage initiation and progression occur at the lower scales and is dependent on the local internal material architecture, as well as the local strain state. Data-driven multiscale modelling has emerged as an efficient approach to capturing this complex behaviour in composite structures. However, data-driven modelling often come with major limitations such as model opacity, over fitting and lack of robustness. Data-driven models operate as an opaque black box where the underlying physical behaviour is hidden from the model output. Hybrid-data driven models embed knowledge about the physical behaviour of composites in a data-driven framework. A new hybrid data-driven modelling approach is proposed in this paper. This approach utilises a pre-computed response database constructed on the lower length scales which is used to inform the material behaviour on the structural scale.

Keywords: Multiscale Modelling; Data-Driven Modelling; Machine Learning; 3D Woven Composites; Damage

1. Introduction

The term "composite materials" covers a wide variety of material architectures such as: unidirectional pre-preg, woven (2D-3D), Non-Crimp Fabrics (NCF) and short fibres materials. Within each architecture there are a wide array of matrix and fibre choices, with each combination leading to different material behaviour. Additionally, for some composite categories, there are multiple manufacturing methods which have an impact on the composite mechanical behaviour. To design and optimize composite structures, engineers often embark on expensive testing campaigns to characterize a given materials systems behaviour for each matrix type, fibre type and manufacturing method. However, even when the high cost and time of extensive experimental testing is not a barrier, the presence of material variabilities can render the experimental measurements insufficient for developing a complete understanding of the materials' behaviour. Material variabilities are an integral part of the design and manufacture of composites. From a modelling point of view, these variabilities can be classified into two main categories. First, are variabilities introduced by design were the structural requirements forces a change in the internal material architecture. This can be seen in laminated composites around tapered regions where plies are dropped in order to achieve a thickness transition. These terminations are often associated with the presence of local variabilities such as matrix pockets. The presence of local variabilities and the stress redistribution around the terminated plies would lead to a change in mechanical performance [1, 2]. This change in behaviour is often not captured as part of a conventional testing campaign. Similar design variabilities can be seen in woven composites as result of draping over curved surfaces. During

  doi:10.5075/epfl-298799_978-2-9701614-0-0

draping, woven composites undergo shearing and compaction resulting in a local change in the material architecture and the associated mechanical properties [3]. Design variability of the type described here lead to a coupling between the material architecture and the structural geometry which cannot be captured using copoun testing.

The second category of material variabilities are manufacturing variabilities. These can be inherent to the manufacturing process as is the case with gaps and overlap in Automated Fibre Placement (AFP)[4], or can result from suboptimal manufacturing as is the case with wrinkles and voids [5]. From a modelling perspective, this category of variability, often termed (defects), differ in that their presence is not known deterministically during design. Factors such as the void volume fraction or the location of a wrinkle differ from one part to another, even if the two parts are of the same design and are manufactured using the same processes. Here, models need to consider impact of these manufacturing variabilities in a statistical manner by establishing ranges of confidence in the material and design of a given composite structure. This is unlike the design variability which are known beforehand, and their location and morphology are similar in every part of the same design.

This coupling between structural geometry, material architecture and the manufacturing process can be a significant challenge to models on the component scale. Capturing the impact of all variabilities in each structure would require models which explicitly describe the material architecture but are of a structural size. This will always lead to a computationally unfeasible model. Additionally, when including manufacturing variabilities, which are indeterministic, a large number of models will be needed to quantify mechanical performance uncertainty [6, 7]. To mitigate these limitations, in this current work, a novel Hybrid Data-Driven modelling paradigm is introduced. In this hybrid approach, data-driven modelling is used to enrich and accelerate physics based deterministic models operating on the macro-scale. To achieve this goal, an integrated suite of multiscale modelling capabilities has been developed. This suite consists of a set of tools for modelling periodic materials such as laminated composites and closely related set for non-periodic materials. For periodic materials, computational homogenisation tools are used to generate a database of non-linear responses of the composites on the meso-scale, considering the effect of defects and features. For non-periodic materials, such as 3D woven composites, data clustering techniques are used to identify repeatable patterns existing on the sub-unit cell scale which are then used as basis for homogenisation and data-transfer between the length scales. Associated with the non-linear response database, a parametrised representation for both the material architecture and loading condition is employed. This parametrised representation allows for efficient sampling of the design space and for the construction of parametric response manifolds [8, 9]. In a structural scale simulation, the variables controlling the lower-scale material behaviour are predicted using the parametric manifolds with no need to run co-simulations on the lower scales.

The hybrid data-driven approach provides key advantages over conventional multiscale approaches originating from the use of a precomputed response database which leads to highly efficient large-scale simulation. Additionally, the framework retains all key information relating to the physical damage behaviour of the structure being simulated. Moreover, the framework can operates using a fully parametrised representation of both the structure and material on the macroscale which is valuable for design and optimisation problems. Figure 1 shows an overview of the proposed framework.

  doi:10.5075/epfl-298799_978-2-9701614-0-0

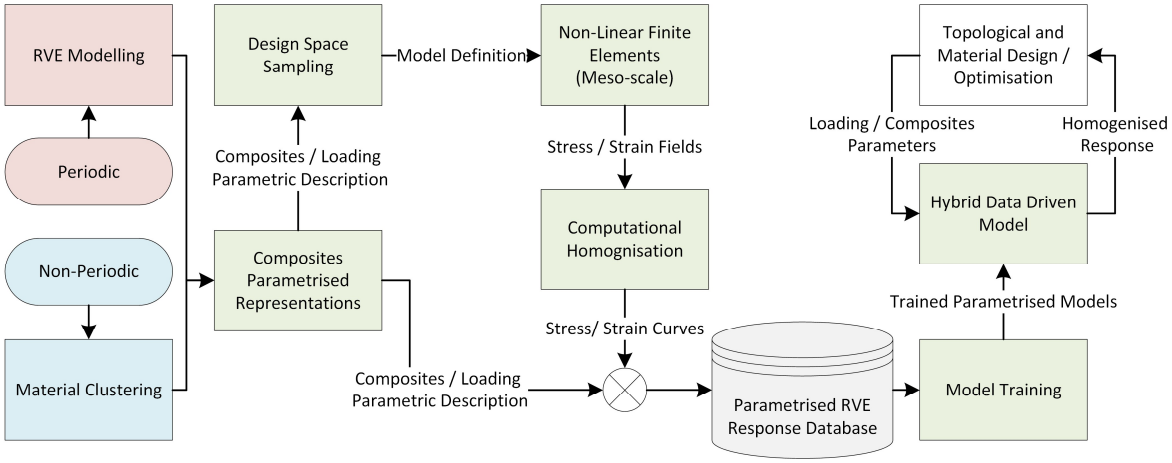

Figure 1. A schematic of the propsoed Hybrid Mutliscale Framework.

2. Representing Material Non-Linearity in a Structural Scale Simulation

Multiscale modelling of composites requires the establishment of a two-way link between the finer length scale and the structural scale (Figure 2). In general, composites are hierarchal structures constructed on several length scales from nano toughening particles on the nan-scale to the full components on the macro-scale. While all length scales should be taken into account, the link between the meso-scale and macro-scale is the most challenging to establish. The meso-scale is the scale of the induvial composite layer in case of laminated composites and is the scale of the yarn/tow in woven, braided and NCF materials. The dimensions of these architectural features are often in the order of fractions of a millimetre in size. Thickness of composite components is often in the order of millimetres. The relatively close size of the two-length scales means that scale separation using homogenisation can be hard to achieve and that local variations in the material architecture might lead to significant change of a structure mechanical response.

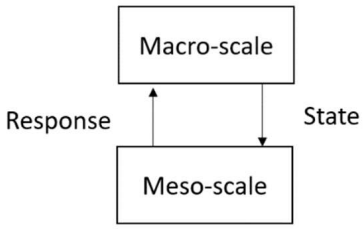

Figure 2. Two - way non-linear multiscale link

There are two main multiscale modelling paradigms that has been applied to composites to deal with this two-way link. The first are the bottom-up approaches in which the high-fidelity meso-scale models are examined to select the most important modes of deformation. These modes of deformation are then used to build a macro-scale model of a reduced fidelity. The Proper Generalized Decomposition (PGD) family of methods [10] and the Generalized Eigen problem in Overlaps (GENEO) methods [11], are among the most notable in this paradigm. The other paradigm is a top-down approach which starts from an engineering judgment about the material behaviour on the structural scale. In this family, meso-scale modelling is used to calculate key performance controlling parameters on the macro-scale such as stiffness, damage initiation stresses and fracture energy. An example of this family of approaches is the parametric failure manifolds [9] where a macro-scale damage law is informed by precomputed manifolds representing damage initiation and progression. Bottom-up approaches are intuitive and transparent to implement for linear problems since they follow the natural order of the material construction. However, non-linear problems can be a challenge as they would require special treatment or the continues reconstruction of the macro-scale model with damage progression.

  doi:10.5075/epfl-298799_978-2-9701614-0-0

The top-down approaches can cope with damage induced non-linearity as long as the assumed macro-scale behaviour takes this into account. The proposed framework is primary concerned with damage initiation and progression in composites and consequently follows a top-down approach.

3. Computational Homogenisation Schemes and Parametrisation for Composite Materials

Laminated composites are often assumed to be periodic on the meso-scale which allows them to be modelled using periodic RVE Models. These RVE models are used to investigate the effect of the ply orientation and loading conditions on the composite behaviour. The output of an RVE model is full 3D stress and strain fields. In order to use an RVE in a multiscale model, the full field response needs to be homogenised into an equivalent response. There are two classes of computational homogenisation that are often used to generate this equivalent response. Both classes rely on establishing an energetic equivalence between the finer and coarser length scales. First order computational homogenisation links a volume on the meso-scale to a single point on the macro-scale, often and integration point in an FE model. The outcome of this homogenisation is the equivalent response of an RVE in 3D including axial and shear responses. Another more recent approach is 2nd order computational homogenisation which links a volume on the meso-scale to an equivalent volume on the macro-scale[12, 13]. This 2nd order approach has the advantage of including the strain gradients of an RVE during homogenisation. Consequently, 2nd order homogenisation can be used to capture the bending behaviour of a composite which are not included 1st order schemes.

Computational homogenisation and RVE modelling can be utilised in a number of ways to characterise a composite behaviour. Firstly, an RVE model can be subjected to several different loading cases in an elastic simulation to calculate an equivalent homogeneous stiffness tensor for the composite. Alternatively, an RVE model with damage models included can be used to predict the full non-linear response under a specific sets of strain conditions. Key information about the material behaviour can then be extracted from the stress/strain curves such as the damage initiation stresses. Several types of defects and variabilities can be included in these models to predict their impact on a composite performance. Figure 3 shows an RVE model of a composite containing a wrinkle with the associated failure patterns. Figure 4 shows the homogenised stress/ strain curves from a 1st order homogenisation of an RVE with the effect of variabilities.

4. Periodic Composites

Data-driven modelling of materials often starts with sampling the design space to understand the material behaviour. For periodic composites, such as laminated composites, the design space is sampled in terms of the feasible layups, loading conditions and any variabilities. It is often desirable to sample the design space using a fixed number of variables. However, since each layer in a composite can have a different orientation, sampling the design space using the ply angles will result in a variable number of parameters describing each design point.

  doi:10.5075/epfl-298799_978-2-9701614-0-0

Consequently, sampling the laminated composites design space is often done using a parametrised representation.

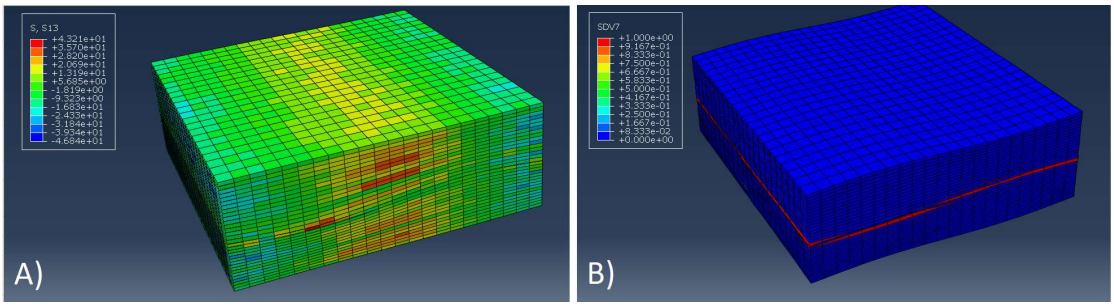

Figure 3 RVE Model of a composite containing a wrinkle, A) Through thickness shear stresses, B) Delamination damage around the wrinkle.

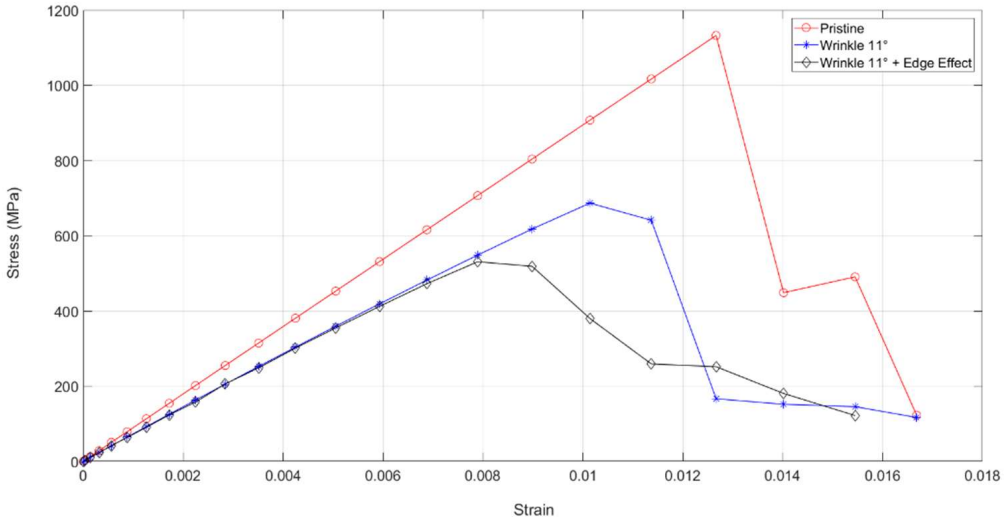

Figure 4 RVE stress / strain response under tension vs wrinkle severity

Two parametrisation approaches are available in literature. The first approach is based on Classical Laminate Analysis (CLA) and is well suited for applications involving shell elements on the macro-scale. In this approach, the stiffness tensor of a composite is divided into two sets of parameters, the Lamination Parameters which are described as a function of the ply orientations through thickness and the material invariants which are dependent on the material system used. There are 12 CLA lamination parameters which fully describe all the possible layup combination in for any composite layup. The other type of Lamination Parameters is based on the first order homogenisation and is more suited for thick composite structure modelled using solid elements. In both approaches, an equivalent stiffness tensor can be calculated for a layup to describe the elastic response. Surrogate models can then be used to correct the elastic stiffness tensor to include the impact of defects and variabilities such as the presence of a wrinkle [8]. This is often done using a surrogate model taking the form of:

$$Q^X = Q_K^X - \Delta(\zeta) \quad (1)$$

Here Q^X is the homognised stiffness tensor compoent. Q_K^X is the analytical stiffness tensor component calculated from homogenisation of a pristine layup. $\Delta(\zeta)$ is a surrogate model described as a function of the lamination parameters. This approach has been used successfully

  doi:10.5075/epfl-298799_978-2-9701614-0-0

to model the impact of variabilities on laminated composites stiffness behaviour. A parametrised map of the change of the change in stiffness due to the presence of a sever wrinkle in IM7/8552s is shown in Figure 5. Similar parametrised maps can be built for damage initiation and progression. This is done by assuming the composite failure can be represented as a Gaussian surface in the stress/strain space. These parametrised surfaces can describe the composites failure under multi-axial loading and include the impact of defects and variabilities. In a macro-scale FE model, each integration point is assigned a failure surface based on the local layup and any variabilities present at this location. Since these surfaces are pre-computed there is no runtime overhead to the macro-scale simulation as result of including these information on the structural scale. The quick runtime of these macro-scale models allows these models to be used efficiently in design and optimisation problems. Figure 6 shows a parametrised failure manifold with the effect of an embedded wrinkle and results from a structural scale optimisation example.

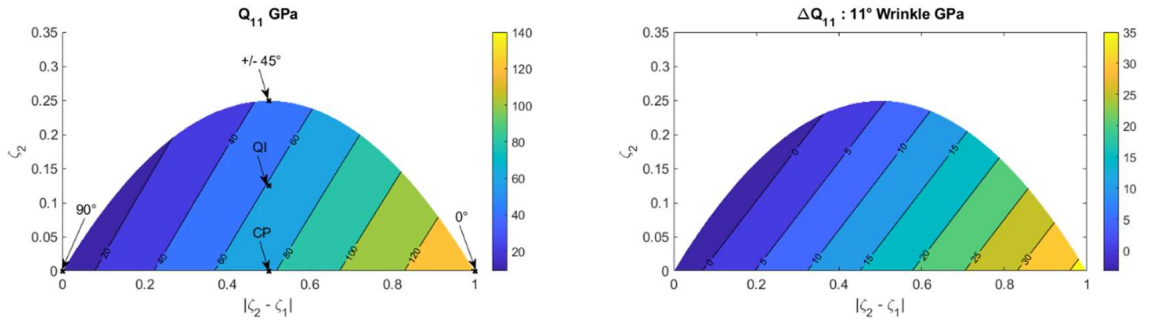

Figure 5 Parametrised map of a wrinkle impact on thick laminated composites

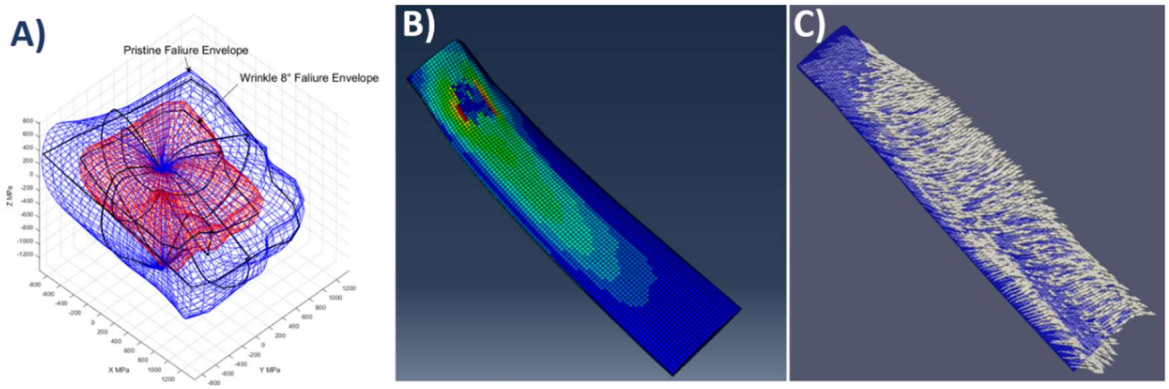

Figure 6 A) Tri-axial parametric failure manifold with the effect of an embedded defect, B) Non-linear multiscale simulation of a composites blade with progressive damage, C) Strength optimised fibre steering direction over the blade.

5. Loss of Periodicity due to Material Architecture / Geometry Interaction

As has been discussed in earlier sections, one of the more common tools in multiscale modelling is the use of RVE models. These models can be used to sample the design space of a given composite system and are often assumed to be periodic. The purpose is to use these models to calculate equivalent responses of the different material architectures under different loading conditions. These models can include the stiffness and damage initiation/ progression. Once these properties have been calculated they are then used to inform the macro-scale models.

  doi:10.5075/epfl-298799_978-2-9701614-0-0

However, in materials such as 3D woven composites or in laminated composites around tapered regions. The internal material architecture tends to interact with geometric features leading to a geometry depend on behaviour [14]. An example is the open hole interaction with the weave architecture (Figure 7). Different parts of a woven unit cell architecture will interact with the stress concentration around an open hole leading to different damage response. A similar form of coupling between geometry and material happens in curved 3D woven structures which undergoes differential shearing and compaction. The same effect can be observed around regions of thickness transition in laminated composite structures. While RVE modelling and periodicity are powerful assumptions for a wide array of applications, it is not the correct assumption when there is material / geometry coupling. Consequently, non-periodic composites require a special treatment in multiscale models.

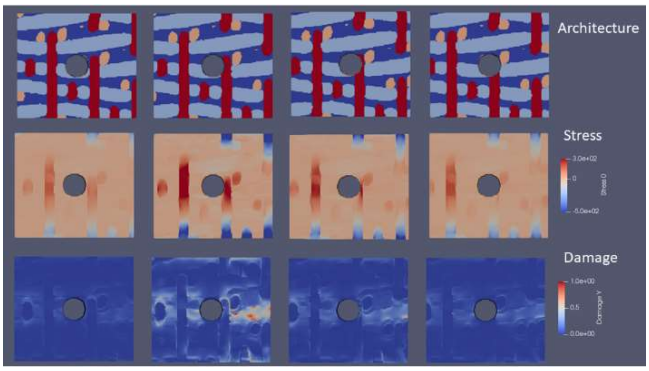

Figure 7 Woven architecture interaction with an open hole.

6. Non-Periodic Composites

The loss of periodicity in woven composites means that RVE modelling is no longer representative of the material behaviour on the structural scale. In this case, its desirable to create and intermediate length scale for homogenisation that is independent from the structural geometry and consequently will not be affected by the geometry/ material architecture coupling. Tessellation based techniques such as Voronoi tessellation and data-clustering are used to generate "Materials Clusters" which are repeatable patterns on the sub-unit cell scales. These material cluster then serve as basis for homogenisation in place of the unit cell. However, due to the irregular shapes of these material clusters, developing a reliable parametrisation approach is non-trivial and is still an ongoing research effort. Figure 8 shows a schematic for a proposed material clustering approach which combines both data clustering and Voronoi Tessellation [3]. In these approaches, the design space is no longer sampled systematically using RVE models. Instead, the design space is sampled using representative feature models which are each clustered into sets of material clusters. The homogenised response from the clusters are then stored in a response database replacing the RVE responses used in periodic composites. The strength of this approach comes from its independence from the structural geometry but also that its computational efficient since it relies on pre-computing the material cluster responses.

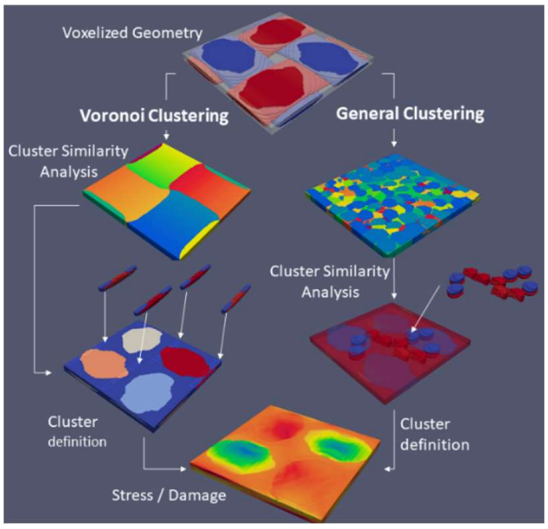

Figure 8 Material clustering approaches for Woven Composites.

  doi:10.5075/epfl-298799_978-2-9701614-0-0

7. Summary

In this paper, the challenges associated with multiscale modelling of complex composite structures has been discussed which include the representation of material non-linearity on the macro-scale, the presence of defects and variabilities and the loss of periodicity. Hybrid physics-based/ data-driven approaches has been proposed as promising paradigm for multiscale modelling of composites.

8. References

1. Bender JJ, Hallett SR, Lindgaard E. Parametric study of the effect of wrinkle features on the strength of a tapered wind turbine blade sub-structure. Composite Structures. 2019;218:120-9.
2. Zhang B, Kawashita LF, Jones MI, Lander JK, Hallett SR. An experimental and numerical investigation into damage mechanisms in tapered laminates under tensile loading. Composites Part A: Applied Science and Manufacturing. 2020;133:105862.
3. El Said B, Ivanov D, Long AC, Hallett SR. Multi-scale modelling of strongly heterogeneous 3D composite structures using spatial Voronoi tessellation. Journal of the Mechanics and Physics of Solids. 2016;88:50-71.
4. Li X, Hallett SR, Wisnom MR. Modelling the effect of gaps and overlaps in automated fibre placement (AFP)-manufactured laminates. Science and Engineering of Composite Materials. 2015;22(2):115-29.
5. Mehdikhani M, Gorbatikh L, Verpoest I, Lomov SV. Voids in fiber-reinforced polymer composites: A review on their formation, characteristics, and effects on mechanical performance. Journal of Composite Materials. 2018;53(12):1579-669.
6. Bessa MA, Bostanabad R, Liu Z, Hu A, Apley DW, Brinson C, et al. A framework for data-driven analysis of materials under uncertainty: Countering the curse of dimensionality. Computer Methods in Applied Mechanics and Engineering. 2017;320:633-67.
7. Sandhu A, Reinarz A, Dodwell TJ. A Bayesian framework for assessing the strength distribution of composite structures with random defects. Composite Structures. 2018;205:58-68.
8. El Said B, Hallett SR. Multiscale surrogate modelling of the elastic response of thick composite structures with embedded defects and features. Composite Structures. 2018;200:781-98.
9. El Said B, Hallett SR. Parametric failure manifolds for laminated composites. Composite Structures. 2020;253:112798.
10. Ladevèze P, Passieux J-C, Néron D. The latin multiscale computational method and the proper generalized decomposition. Computer Methods in Applied Mechanics and Engineering. 2010;199(21):1287-96.
11. Butler R, Dodwell T, Reinarz A, Sandhu A, Scheichl R, Seelinger L. High-performance dune modules for solving large-scale, strongly anisotropic elliptic problems with applications to aerospace composites. Computer Physics Communications. 2020;249:106997.
12. Kouznetsova V, Geers MG, Brekelmans WM. Multi-scale constitutive modelling of heterogeneous materials with a gradient-enhanced computational homogenization scheme. International Journal for Numerical Methods in Engineering. 2002;54(8):1235-60.
13. Coenen E, Kouznetsova V, Geers M. Computational homogenization for heterogeneous thin sheets. International Journal for Numerical Methods in Engineering. 2010;83(8-9):1180-205.
14. El Said B, Ivanov D, Long A, Hallett S. Multi-scale modelling of strongly heterogeneous 3D composite structures using spatial Voronoi tessellation. Journal of the Mechanics and Physics of Solids.2016.

  doi:10.5075/epfl-298799_978-2-9701614-0-0

TEMPERATURE DISTRIBUTION DETERMINATION OF THERMOPLASTIC COMPOSITES SAMPLES IN BIAS EXTENSION TESTS USING A DIGITAL TWIN

Ramak Hossein Abadi, Javane Karami, Ali Shivaie Kojouri, Kalliopi-Artemi Kalteremidou, Danny Van Hemelrijck

Department of Mechanics of Materials and Constructions (MeMC), Vrije Universiteit Brussel (VUB), Brussels, Belgium – ramak.hossein.abadi@vub.be

Abstract: *Designing a production process such as thermoforming for thermoplastic composites might be challenging as it requires material characteristics at high temperatures. Material characterization tests (e.g., bias extension) in the molten state can encounter several difficulties, one of the most important ones is maintaining a uniform temperature distribution on the sample. Accordingly, during this research, a set of thermal tests has been initially done at different temperature levels. During these tests, the temperature was measured at several locations. Next, we developed a finite element model for both the sample and the clamp. In the final step, the boundary conditions of the FE model have been determined by coupling the experimental results and the numerical model. Results show the strong dependency of the sample temperature gradient on the clamps, which has been ignored in the previous studies. Moreover, a sensitivity study is done to select the best location for the temperature sensor for future studies.*

Keywords: thermoplastic composites; bias extension test; molten state; finite element method; digital twin.

1. Introduction

There are multiple applications for thermoplastic composites, such as automobiles and the construction industries. In addition to their several advantages regarding their thermo-mechanical behavior, they are cost-effective, and thanks to their thermoplastic matrix, they can be shaped into a desired complex geometry at high temperatures by forming techniques such as thermoforming. In the mentioned process, thermoplastic composite components are formed by melting a consolidated product above the melting point of the matrix and pressing it into the desired shape [1]. Despite several advantages of these forming methods, utilizing them requires a detailed design of the process to prevent defects such as wrinkles [2] or intra-ply slippage [3]. Accordingly, it is essential to carry out numerical simulations of the forming process to minimize the product defects and in turn, increase its mechanical performance [4, 5]. One of the main requirements of these simulations is the material characteristics of the component at high temperatures, which can be determined by coupling experimental tests and numerical models [6]. The tests should be designed according to the dominant deformation mode of composite reinforcement during forming, which is in-plane shear [7].

The bias extension test is one of the most common experiments in this field. It is noteworthy that due to the high-temperature nature of the thermoforming process and the strong dependency of thermoplastic materials' behavior on temperature [8], the mentioned test should be performed at high temperatures where the material is in its molten state. A successful test

  doi:10.5075/epfl-298799_978-2-9701614-0-0

requires having a desired temperature balance within the sample. If the temperature is low, the thermoplastic will not form properly [6-8], and if it is high, the specimen will be decomposed and damaged [7]. Moreover, determining temperature distribution is vital in performing thermo-mechanical simulations and computing the thermal stresses.

Although simulating the test can have a critical influence on determining the accurate material characteristics, most studies have ignored that, and computing the temperature gradients, corresponding thermal stresses, and their effect has been limited to process modeling. As an example, Lee et al. have investigated the formability of CFRTPs by considering the heat transfer between tool and laminate and have performed an inverse analysis to define the heat transfer coefficient for the process [6]. Studies simulating the bias-extension test have generally ignored the sample temperature gradient and assumed a uniform distribution over the sample.

Behrens et al. have determined the temperature dependency for the shear angle and shear stress relation in the bias extension test of woven thermoplastics by linking the experimental results with the numerical model [9]. In another study, an anisotropic hyperelastic constitutive model was proposed by Gong et al. for thermoplastic woven composite prepregs. They have validated the model by performing the bias extension test at elevated temperatures [4].

Maldonado et al. have used the bias extension test to identify the in-plane shear properties of thermoplastic composites at different temperatures. Later, they used these properties to simulate thermoforming of the composite part. It has been shown that the temperature field changes significantly during the forming, and since the mechanical behavior of the material strongly depends on temperature, the assumption of constant temperature is not sufficient in the case of thermoforming [10]. In another study by Machado et al., a series of isothermal bias extension tests are simulated to analyze the rate and temperature dependency of the proposed model [11].

Although a more detailed study by Maldonado et al. confirms the existence of a temperature gradient on the sample during bias extension tests [12], and most of the papers indicate the strong temperature dependency of in-plane shear behavior of thermoplastic composites, the temperature gradient under the clamps has been ignored [8, 12-14] by most researchers in simulating the test or calculating the required time to obtain a more uniform temperature. In the previous publications, the required time to reach the uniform temperature distribution in the bias extension test has been determined experimentally based on some selective areas [8, 15, 16]. However, having a finite element model can be beneficial in determining this period more accurately and based on the whole temperature distribution on the test sample.

This paper presents a thermal digital twin of the bias extension test by considering the effect of the chamber and clamps (Figure 1). For this purpose, a finite element model is developed and linked to the experiments. Having proper knowledge of the applied experimental conditions is crucial in building a valid numerical model. For this reason, it is necessary to determine the applied temperature and thermal boundary conditions.

2. Experimental Setup

A set of thermal tests at 210 and 220 degrees Celsius has been performed and repeated once for each temperature level on woven thermoplastic composites. For this purpose, an Instron tensile test machine with a TA Instrument climate chamber has been used (Figure 2). The

  doi:10.5075/epfl-298799_978-2-9701614-0-0

samples were cut out from a 2-ply composite sheet made of PA6 matrix and reinforced with woven glass fibers (45% fiber volume fraction). The composite layup was ±45° and the samples had a nominal thickness of one millimeter. The dimensions of the samples were chosen based on ASTM D3518 [17], as illustrated in Figure 2. Three type-K thermocouples were connected at different locations to measure the temperature of the mid sample, under the clamp, and at a three-millimeter distance above the clamp, as shown in Figure 4. The temperatures were logged using the 8000 Micro-Measurements data logger with a data sampling frequency of 10 Hz.

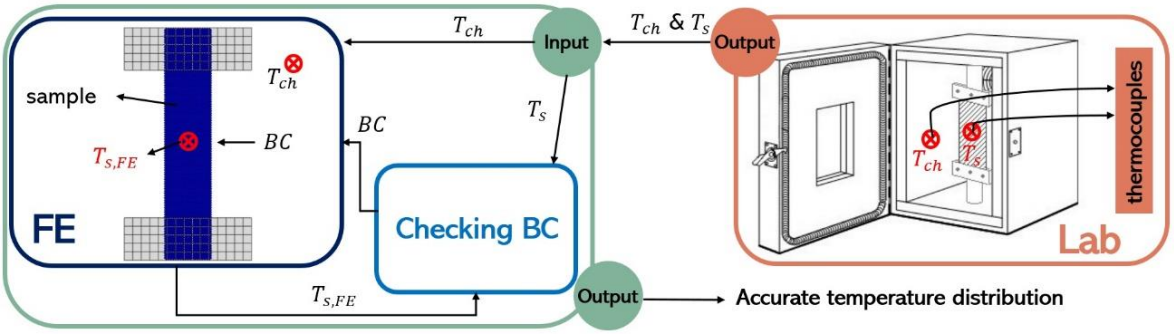

Figure 1. The thermal digital twin for the bias extension test.

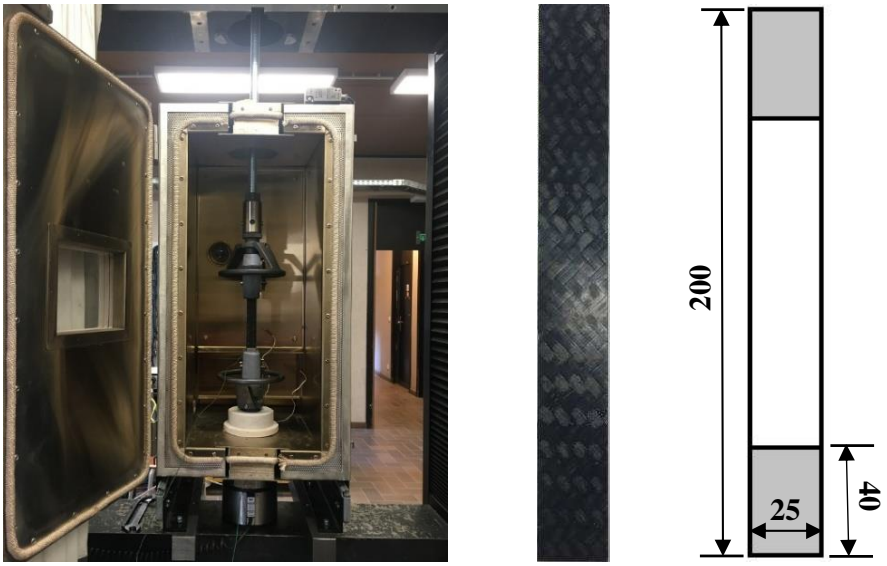

Figure 2. Experimental set-up and test sample with dimensions.

3. Numerical Model

A detailed finite element model for the sample and the clamps has been developed in ABAQUS (Figure 3). The symmetry line is used to model half of the sample-clamp structure and reduce computational time. The mesh sensitivity test is done to ensure that the solution is independent of mesh size, resulting in a model of 80257 elements. Table 1 summarizes the thermophysical material properties used in the FE model. The rule of mixture has been used to define the equivalent properties of the composite [11].

The initial and boundary conditions should be set to finalize the model. In this regard, the initial temperature is set to room temperature as it was in the experiment. Based on Newton's law of

  doi:10.5075/epfl-298799_978-2-9701614-0-0

cooling, one should specify the heat transfer coefficient to define the boundary condition in a thermal problem with convection. We compared the finite element solution and the experimental results to minimize the difference and identify an average heat transfer coefficient. It is worth mentioning that we used the measured chamber temperature as the ambient temperature for this aim.

Table 1: Thermal properties employed in the FE model.

	Density [kg/m^3]	Specific heat [J/kg.K]	Thermal Conductivity [W/m.K]
Composite	1775.50	1116.03	0.57

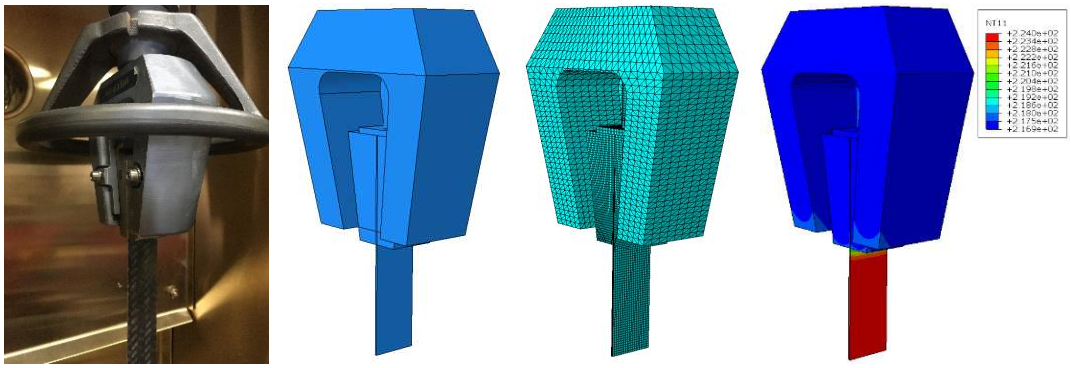

Figure 3. Physical product and the finite element model.

4. Results and Discussion

In this part, the experimental results have been combined with the FE model to identify the boundary conditions. As mentioned, the experimentally measured ambient temperature of the chamber has been imported into the FE model, and the heat transfer coefficient has been changed to have maximum alignment between the numerical and experimental results. The results show that the heat transfer coefficients for 210 and 220 degrees Celsius are 32 and 35 W/m.K, respectively. As shown in Figure 4, based on the mentioned values, the numerical solution aligns well with the experimental results at different points. The numerical and experimental results show that, during the test, at first, the temperature gradient starts to rise. The temperature difference between points A and C reaches its maximum value of 111.5 and 116.5 degrees Celsius for 210 and 220 degrees Celsius temperature levels at 18 minutes. After this point, the temperature difference decreases to about 5.5 degrees Celsius for both temperature levels at 60 minutes.

Additionally, the finite element solution has been used to determine the sensitivity of the introduced locations (A, B, and C) to a variation in the heat transfer coefficient (Figure 5). Based on the results, point A has the maximum sensitivity to the mentioned parameter, and it can be the best location to measure the temperature during the test. Since point A is under the clamp, it is easier to attach a thermocouple to this point during a tensile test as it does not have a relative movement.

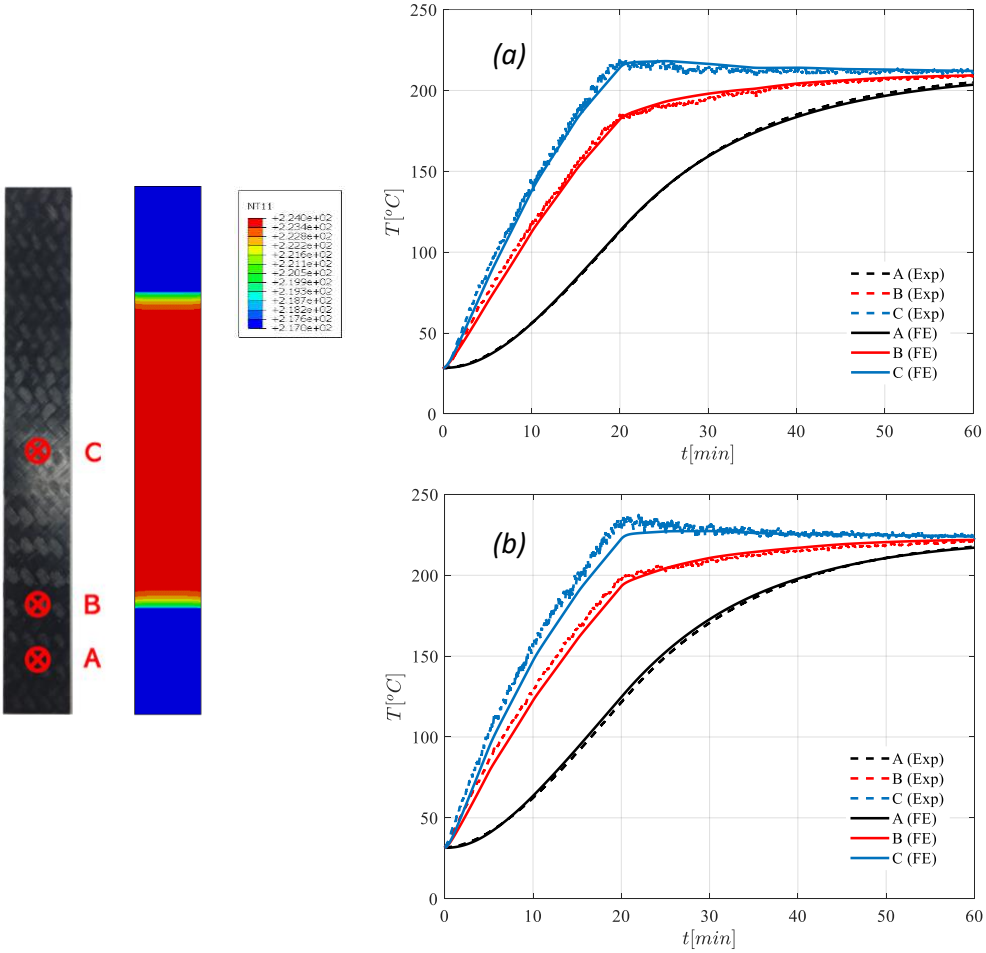

Figure 4. The experimental measurements compared to the FE results for (a) 210 and (b) 220 °C

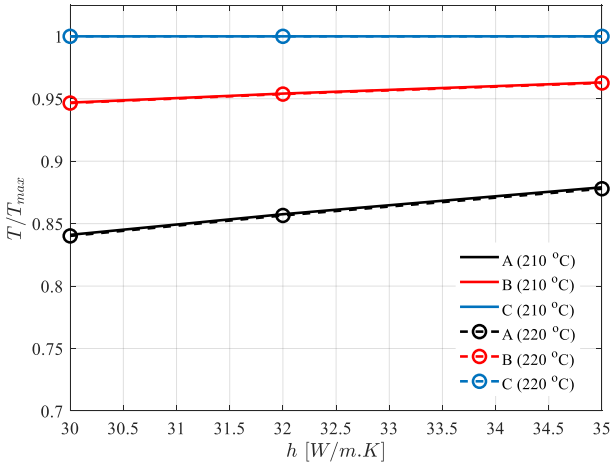

Figure 5. Sensitivity of different locations to a variation in the heat transfer coefficient.

5. Conclusions

In this paper, first, a set of tests has been done at 210 and 220 degrees Celsius on the PA6 matrix and reinforced with woven glass fibers (±45°) with an overall thickness of one millimeter. The temperature is measured at three points on the sample (under the clamp, three millimeters above the clamp, and the mid-sample). In the next step, we developed a finite element model for the sample and clamp. Later, by coupling the experimental results and the numerical model,

the heat transfer coefficient for the FE model is determined (32 and 35 W/m.K for 210 and 220 degrees Celsius, respectively). The experimental and numerical results show the strong dependency of the sample temperature gradient on the clamps, which was ignored in previous studies. Moreover, the sensitivity study shows that locating the temperature sensor under the clamp and coupling that with the FE model can be the best preference to determine the entire temperature distribution within the bias extension test specimen.

Acknowledgements

The authors acknowledge the support of the STOEMP project "Stamping of thermoplastic composite materials" funded by Innoviris and coordinated by Solvay.

6. References

1. Baumard T, Menary G, de Almeida O, Schmidt F, Bikard J. Characterisation and modelling of the temperature and rate dependent shear behaviour of a non-consolidated powder impregnated fabric. In ECCM18-18th European Conference on Composite Materials 2018; 24-28.
2. Chen H, Li S, Wang J, Ding A. A focused review on the thermo-stamping process and simulation progresses of continuous fibre reinforced thermoplastic composites. Composites Part B: Engineering. 2021; 224:109196.
3. Harrison P, Alvarez MF, Anderson D. Towards comprehensive characterisation and modelling of the forming and wrinkling mechanics of engineering fabrics. International Journal of Solids and Structures. 2018; 154:2-18.
4. Gong Y, Peng X, Yao Y, Guo Z. An anisotropic hyperelastic constitutive model for thermoplastic woven composite prepregs. Composites Science and Technology. 2016; 128:17-24.
5. Rashidi A, Montazerian H, Milani AS. Slip-bias extension test: A characterization tool for understanding and modeling the effect of clamping conditions in forming of woven fabrics. Composite Structures. 2021; 260:113529.
6. Lee JM, Kim BM, Min BJ, Park JH, Ko DC. Formability of CFRTP prepreg considering heat transfer. International Journal of Precision Engineering and Manufacturing-Green Technology. 2017; 4(2):161-8.
7. Boisse P, Hamila N, Guzman-Maldonado E, Madeo A, Hivet G. The bias-extension test for the analysis of in-plane shear properties of textile composite reinforcements and prepregs: a review. International Journal of Material Forming. 2017; 10(4):473-92.
8. Wang P, Hamila N, Pineau P, Boisse P. Thermomechanical analysis of thermoplastic composite prepregs using bias-extension test. Journal of Thermoplastic Composite Materials. 2014; 27(5):679-98.
9. Behrens BA, Chugreev A, Wester H. Experimental and numerical characterization method for forming behavior of thermoplastics reinforced with woven fabrics. Procedia Manufacturing. 2019; 29:443-9.
10. Guzman-Maldonado E, Hamila N, Naouar N, Moulin G, Boisse P. Simulation of thermoplastic prepreg thermoforming based on a visco-hyperelastic model and a thermal homogenization. Materials & Design. 2016; 93:431-42.

11. Machado M, Murenu L, Fischlschweiger M, Major Z. Analysis of the thermomechanical shear behaviour of woven-reinforced thermoplastic-matrix composites during forming. Composites Part A: Applied Science and Manufacturing. 2016; 86:39-48.
12. Guzman-Maldonado E, Hamila N, Boisse P, Bikard J. Thermomechanical analysis, modelling and simulation of the forming of pre-impregnated thermoplastics composites. Composites Part A: Applied Science and Manufacturing. 2015; 78:211-22.
13. Chen Q, Boisse P, Park CH, Saouab A, Bréard J. Intra/inter-ply shear behaviors of continuous fiber reinforced thermoplastic composites in thermoforming processes. Composite Structures. 2011; 93(7):1692-703.
14. Nishi M, Kaburagi T, Kurose M, Hirashima T, Kurasiki T. Forming simulation of thermoplastic pre-impregnated textile composite. Int J Mater Text Eng. 2014; 8:779-87.
15. Brands D, Grouve W, Wijskamp S, Akkerman R. Intra-ply shear characterization of unidirectional fiber reinforced thermoplastic tape using the bias extension method. ESAFORM, 24th International Conference on Material Forming. 2021.
16. Gendre L, Williams G, Hughes D, Reynolds N. In-Plane Shear Characterisation of UD Tape based Thermoplastic Composite Laminates for Automotive Applications. ICCS20. 2017.
17. Standard Test Method for In-Plane Shear Response of Polymer Matrix Composite Materials by Tensile Test of a ±45° Laminate. ASTM D3518/D3518M-18. [in English] 2013.

  doi:10.5075/epfl-298799_978-2-9701614-0-0

DESIGN AND DIMENSIONING OF AERODYNAMIC AND STRUCTURAL VANES FOR JET ENGINES MADE OF MULTI-AXIAL AND VARIABLE-AXIAL CFRP AND COMPARISON WITH TITANIUM VANES

Jonas Kluger[a], Sebastian Spitzer[a], Axel Spickenheuer[b], Lars Bittrich[b], Christoph Klaus[c], Maik Gude[a]

a: Institute of Lightweight Engineering and Polymer Technology, Technische Universität Dresden, 01307 Dresden, Germany – jonas.kluger@tu-dresden.de
c: Leibniz-Institut für Polymerforschung Dresden e. V., Hohe Straße 6 Dresden D 01069
b: Complex Fiber Structures GmbH, Wigardstraße 21, Dresden D 01097
c: Rolls-Royce Deutschland Ltd & Co KG, Eschenweg 11, Blankenfelde-Mahlow D 15827

Abstract: *Aerodynamical and structural outlet guide vanes for jet engine intermediate cases can be made out of titanium, multi-axial or variable-axial CFRP. The absolute and density specific stiffnesses of the material approaches and the engine structures are compared. The lightweight potential for different 1- to 3-directional load scenarios are shown. Application-oriented boundary conditions of the aerodynamical and structural component are developed and defined. Furthermore, design and simulation methods (e.g. for variable-axial CFRP) are presented in order to elaborate suitable fiber architectures for different composite design methods in a given design space. The relative density specific stiffnesses of the component using the three different lightweight material approaches are compared and evaluated under both 1- to 3-dimensional idealized load scenarios and with a real engine reference load case.*

Keywords: composite vane; design-methods; variable-axial CFRP; jet engine guide vane

1. Structural Outlet Guiding Vanes for Future Engine Intermediate Casings

The utilization of lightweight materials and new technologies in aviation industry can contribute to reach the goal of reducing CO_2 emissions by 2050 as announced by the European Green Deal [1]. In consideration of current geopolitical conflicts and their influence on the worldwide availability of resources carbon fiber reinforced polymers (CFRP) can substitute lightweight metals e.g. titanium. Additionally the application of CFRP can reduce the weight of load-bearing jet engine structures and thereby increase the engine efficiency and reduce the CO_2 and NO_x emissions. While conventional structural designs with isotropic materials show high stiffness even when bearded with three-dimensional loads, carbon fiber reinforced materials shell be engineered in specific load adapted designs to utilize the superior material properties. However, design of composite structures is complex and assessment of its load-bearing capacity is challenging due to a strong interaction between design, manufacturing and material engineering.

2. The Intermediate Case as a Highly Load-bearing Aerodynamic Structure

The generated thrust in the engine is transferred to the airframe via the intermediate case (IMC, cf. Figure 1, left, main function 1). Simultaneously, while transferring the generated loads, the IMC needs to provide a sufficient overall stiffness to ensure a certain tip clearance of the fan blades mounted onto the engine shaft and thus to realize a high efficiency of the engine. In

  doi:10.5075/epfl-298799_978-2-9701614-0-0

addition to this mechanical function of load transfer and stiffness, intermediate cases of new generations are also performing an aerodynamic task (main function 2). The airflow swirled by the fan is realigned into an axially oriented flow by structurally integrated guide vanes in the IMC. This synthesis of functions creates a component with structural and aerodynamic functionality within a minimal design space (cf. Figure 1, centre). CFRP can be used in the aerodynamic and load-bearing vanes (cf. Figure 1, right) as well as in the undisturbed areas of the outer ring structure (ring, cf. Figure 1, middle). A robust design process of composite guide vanes requires a consistent validation strategy, to ensure the structural integrity of the component in case of rare dynamic impact loading conditions like hail stone impacts [2]. To ensure the high structural and aerodynamic requirements for the vanes in the IMC, the design of composite materials needs an increased flexibility in the alignment of fibers and demand a systematic and digitally supported development process [3].

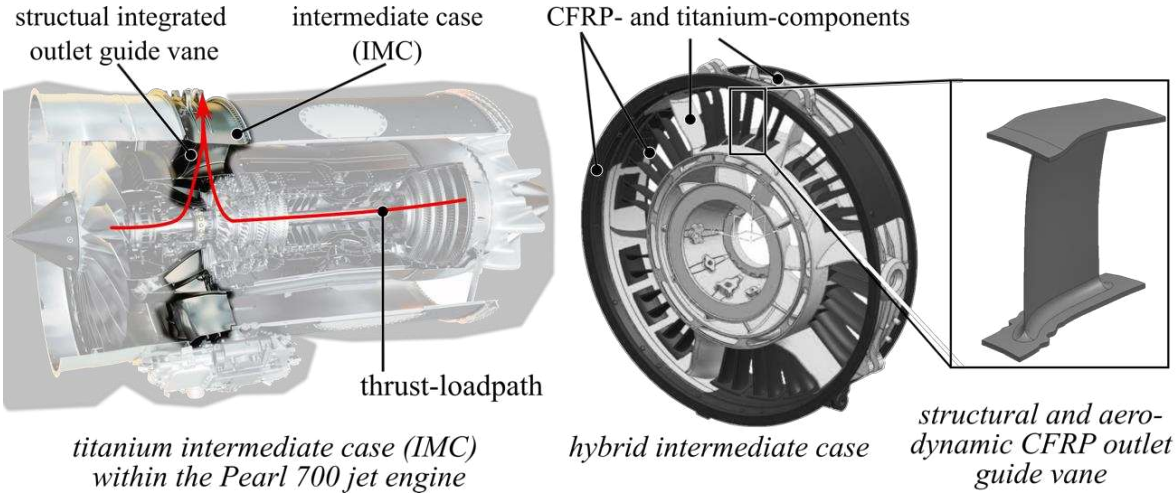

Figure 1. Rolls-Royce Pearl 700 (left) with function-integrated metallic Intermediate Case, hybrid composite-metal intermediate case of future jet engine generations (middle) and CFRP outlet guide vane (right)

3. Lightweight Materials and their theoretical Lightweight Design Potential

In order to meet the high mechanical as well as aerodynamic functionality of a structural engine guide vane, it is necessary to utilize the high structural-mechanical properties of fibers in the composite almost entirely through a load-adapted orientation by means of a variable-axial fiber placement.

Figure 2 illustrates the potential of the density specific stiffness of CFRP compared to a titanium alloy. The figure shows the density specific Youngs-modulus of CFRP-laminates in longitudinal direction. The laminates consist of an intermediate modulus carbon fiber (E-modulus approx. 290 GPa) with aviation certified epoxy resin and a thickness of 2 mm. When loaded with a one-directional load in the longitudinal direction, the unidirectional fiber-layup provides four times the density specific stiffness. Due to complex or different load scenarios it is often necessary to align fibers in multiple direction to cope with these load scenarios and its induced states of stresses. With a constant defined boundary condition on the overall thickness of the specimen, this leads directly to a decreased density specific stiffness. Overall, the quasiisotropic CFRP specimen still shows a higher lightweight potential regarding the laminate Youngs-modulus and underlines the potential for application in aviation propulsion systems.

  doi:10.5075/epfl-298799_978-2-9701614-0-0

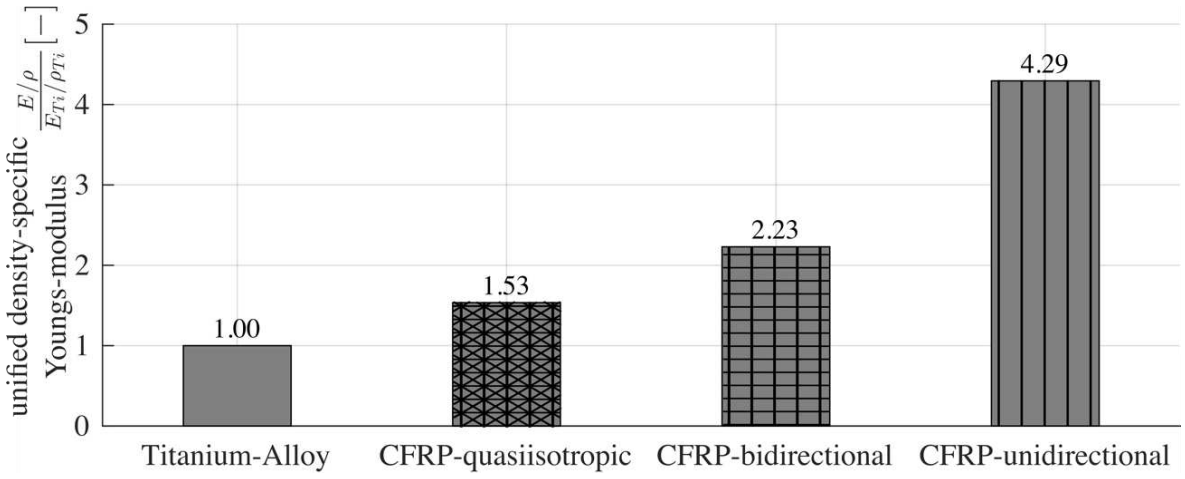

Figure 2. Unified density specific stiffness in the longitudinal direction of specimens acc. [4]

Figure 3 gives an indication of the stiffness of the specimens under one-directional, two-directional and a three-directional load, calculated by numerical models and representing different stress conditions. The loads are to be considered as unit loads and have the same absolute value. The sum of the displacement of the rectangular specimen is used as a value for its stiffness and is referenced to the titanium specimen using the inverse value. The model is constained at the oposite edges of the force introduction. The short edge is fixed in every degree of freedom, while the longitudinal edge fixes the degree of freedom in the lateral direction.

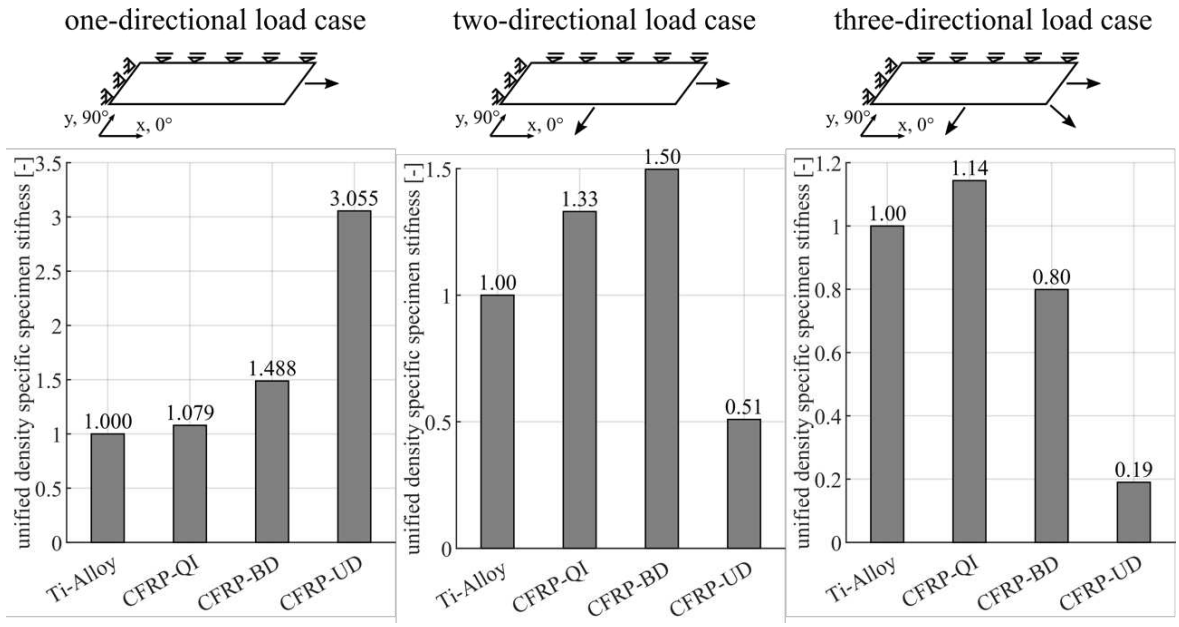

Figure 3. Theoretical lightweight design potential via the unified density specific overall stiffness of simplified specimen under 1-to-3-directional load cases

The evaluation of the calculated results of the one-directional load case agrees with the theoretical stiffnesses shown in Figure 3. However, when a further lateral force component is considered, a rapid drop of the normalized density specific stiffness of the unidirectional CFRP laminate becomes apparent. The additional fibers in the 90° direction in the bidirectional and quasiisotropic laminate show a positive effect on the overall specimen stiffness. When a three-directional load case is considered, the quasiisotropic composite laminate is the only composite

  doi:10.5075/epfl-298799_978-2-9701614-0-0

layup which shows a higher density specific stiffness than the titanium specimen. Based on the large difference of the density specific stiffness of the unidirectional laminate relative to titanium between a one and three-directional load scenario, the optimization potential of fiber composites becomes visible if a specific load case is given.

4. Structural Outlet Guide Vane Realization and Modeling Concept

Structural outlet guide vanes need to provide sufficient stiffness to assure the overall engine efficiency while also aligning the airflow in the bypass duct. The aerodynamic requirement for the vane results in an aerodynamic cross section and an overall design space restriction, which must be considered during the design and dimensioning process.

Conventional structural outlet guide vanes are made of titanium alloys. To substitute the conventional titanium design, with state-of-the-art composite solutions, a multi-axial laminate with unidirectional plies can be used. An optimized variable-axial CFRP layup, manufactured with the Tailored Fiber Placement (TFP), can improve the lightweight-potential of the multi-axial CFRP.

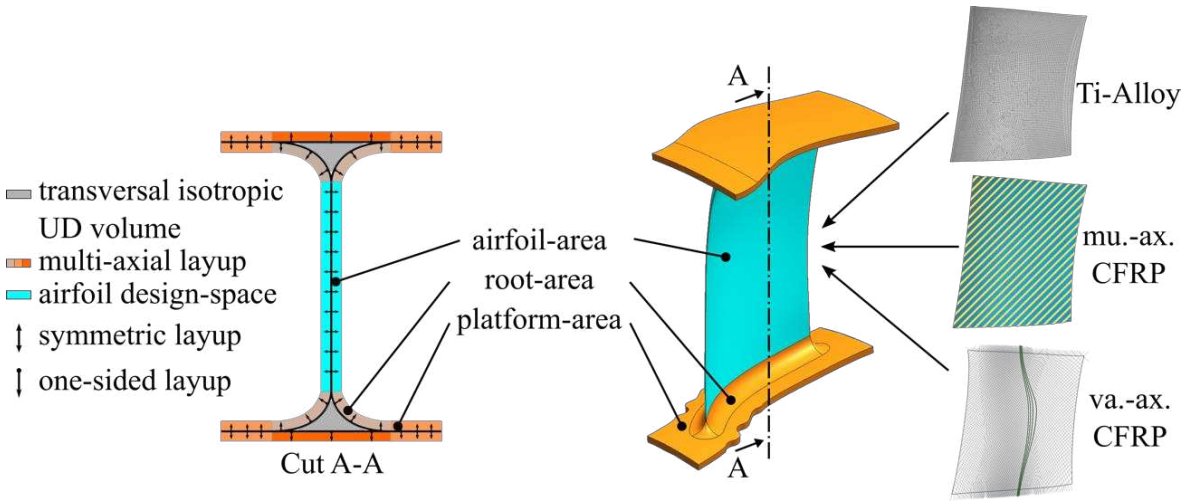

Figure 4. Composite concept (left) and structural vane geometry model (middle) with different lightweight material opportunities (right)

Based on a composite concept developed in earlier works [5] and the design space model of the vane geometry, a simulation model is developed which can be calculated using different models of the airfoil's design space (cf. Figure *4*). The upper and lower platform and root areas are defined as a constant boundary condition and modeled with constant material specifications. The airfoil is initially modeled using solid volume elements with isotropic material behavior of a titanium alloy. Another model of the airfoil's design space is represented using conventional unidirectional laminate modeling methods. The fiber path mapping method using the EDOstructure software is used to represent the variable-axial fiber architecture. The three models derived in this way show the same structural mechanical properties for platform and root areas. Thus, a statement can be made regarding the effect of the different lightweight material concepts on the stiffness of the guiding vane.

  doi:10.5075/epfl-298799_978-2-9701614-0-0

5. Simulation Methodologies for Different Airfoil Concepts

To conceive numerical representation of the available airfoil design space under consideration of thickness restrictions and the intended material behavior, different FE modelling approaches are necessary. To enable a neutral comparison between the different models, constant numerical conditions are defined. Accordingly, all models were derived from an identical mid-surface model and meshed with two-dimensional (2D) shell elements within the software Siemens NX-Simcenter. The obtained 2D shell model was subsequently used as the initial mesh for solid models of the airfoil design space (cf. Figure *5*). The model parts of the upper and lower platform areas are modeled with the same material behavior and numeric conditions for every vane model. Added boreholes at the upper and lower platform serve as load introduction via a master-node and RBE3 elements while the nodes at boreholes of the lower platform are fixed.

To model a multi-axial quasiisotropic composite airfoil, thickness profile iso-lines is projected onto the 2D mid-surface and unidirectional single plies with corresponding contour edges are defined. The single layer thickness corresponds to the thickness parameters of the derived iso-lines. Afterwards a symmetric laminate is defined, using 2D layers and contours to meet the defined thickness profile of the given design-space. The laminates ply configuration is optimized with a simplified plate-model loaded with a multi-dimensional engine reference load case. Subsequently, a 3D laminate structure is extruded from the defined quasiisotropic laminate using modeling approaches supplied within the Siemens NX-Simcenter software.

To represent the titanium airfoil the same derived solid volume mesh is used and in parallel calculated with material properties of a titanium-alloy.

Figure *5*

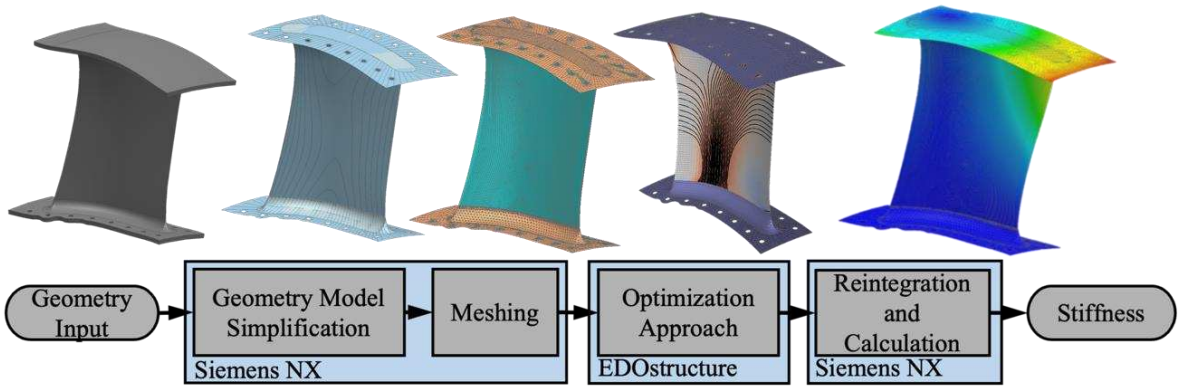

Figure 5. Efficient and robust modelling and dimensioning process for stiffness driven variable-axial composite vane airfoil

To model and calculate the structural behavior of a variable-axial composite laminate, the special TFP-modelling software EDOstructure is used, to cover the special manufacturing parameters of the TFP process. Therefore, the existing 2D-shell model is imported and a symmetric variable-axial layup for the airfoil is initially designed. The software considers specific TFP-parameters and interactions between them as for example the roving width, curvature and its influence on the local layer thickness. The definition of an initial layup is part of a special modelling methodology and optimization approach (cf. Figure 5). The modelling methodology considers the given thickness restriction at every node of the airfoil 2D shell mesh by using the

functions of the software EDOstructure [6]. An especially for this use-case developed fiber path optimization approach according to the direct fiber path optimization (DFPO) is used to optimize the initially designed layup for a real, dominating reference engine load case. Within the optimization the fiber orientation serves as design-variable, while the defined thickness distribution of the design-space is a restriction which must be fulfilled. Target of the optimization is the minimal displacement of the master node at the upper platform. After an optimum is found, a 3D-FE-model is derived, which allows the export of optimized fibre patterns for manufacturing [5].

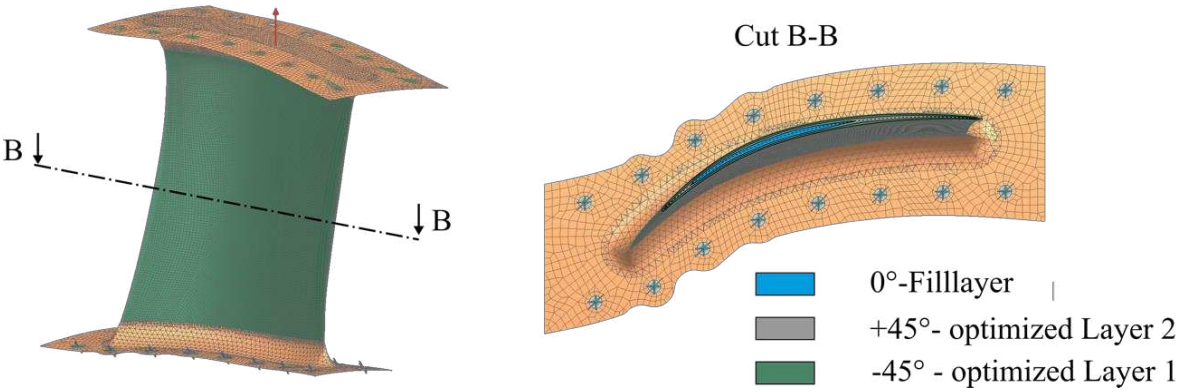

Figure 6. Derived analysis FE-model with 3D variable-axial airfoil model (left) and the variable-axial symmetric layup setup (right)

6. Calculations and Result Comparison

The generated models of the airfoils are integrated into the model environment of the original initial FE model using assembly FE models and calculated under the load scenarios (cf. Table *1*). The considered load scenarios differ in their complexity and the resulting stress states induced in the airfoil. Finally, a real engine load case is considered. The engine load case served as optimization load case for both, the multi-axial and variable-axial CFRP layup.

load case	one-dimensional	two-dimensional	three-dimensional	engine load case
representation		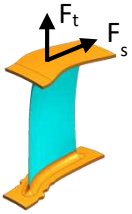	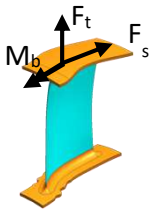	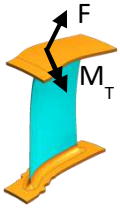

Table 1. Considered load cases and their schematic representations within the scope of the stiffness analysis

The created and calculated models are analyzed, and the total sum of displacement at the force introducing mater node is evaluated. The information about the compliance of the component is inverted and specified on the density of the used materials. The density of the used CFRP laminates and titanium is directly related to the component mass, since the design space with the defined thickness distribution represents a constant volume which needs to be filled. In this context, the mass influence of TFP manufacturing aids is initially neglected in the context of the variable axial CFRP laminate and only the density of the CF fibers and matrix is considered, which

  doi:10.5075/epfl-298799_978-2-9701614-0-0 published under CC BY-NC 4.0 license

are dominant in terms of the component mass. Finally, the calculation results are normalized to the stiffness of the titanium airfoil and plotted in Figure *7*.

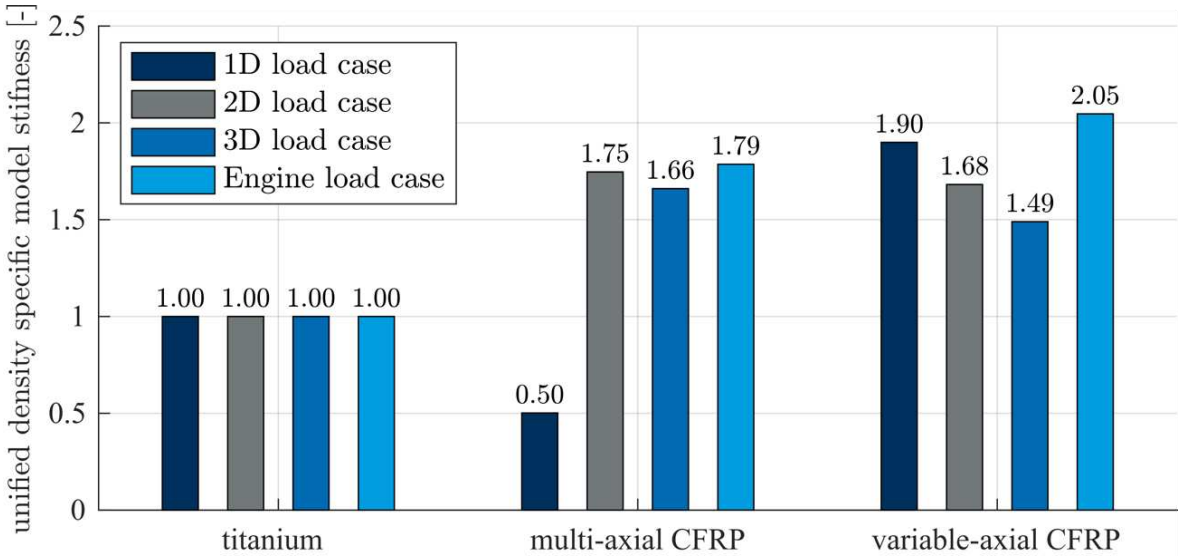

Figure 7. Relative density specific stiffness of different vane FE-model configurations evaluated at the force introducing master-node

The diagram visualizes the lightweight potential of the composite airfoils compared to an airfoil made of titanium via the unified density specific stiffness. The quasiisotropic multi-axial laminate offers a higher lightweight potential in all load cases except for the one-dimensional load case. In response to the one-dimensional load case, it exhibits only half the density specific stiffness. A possible explanation for this phenomenon might be the low proportion of fiber reinforcement in the loading direction of the quasiisotropic laminate.

The unified density specific stiffness of the variable-axial model shows a significantly higher lightweight potential compared to an airfoil made of titanium. The density specific stiffness of the model is almost two times higher than titanium, and the density specific stiffness is 0.3 times higher than the multiaxial, quasiisotropic composite airfoil in terms of the optimization load case originating from the engine environment. A lower density specific stiffness is also evident compared to the multiaxial quasiisotropic composite vane under the 2D and 3D unit load cases.

7. Conclusion

This paper presented three possible lightweight material and construction solutions for the realization of a structural and aerodynamic outlet guide vanes for future jet engine intermediate cases. An investigation on the main functions of outlet guide vanes defined the main requirements for the design and dimensioning process. Therefore, the density specific stiffness as measurement for the lightweight design potential of titanium and different CFRP laminates was theoretically shown and evaluated on multi-directional load cases with simplified FE-models.

Afterwards an overall FE-model setup approach to model three possible lightweight material solutions within the given design space of the airfoil area is presented. To model the material behavior design and simulation methods for titanium, a quasiisotropic multi-axial CFRP-layup

and variable-axial CFRP-layup are shown. The derived airfoil models are reintegrated in the vane assembly FE-model framework and the stiffness at a predefined master-node is analyzed.

The use of variable-axis CFRP in combination with material-appropriate design and dimensioning methods allows a substitution of resource-intensive titanium with the same or increased functionality at lower structural mass.

Acknowledgements

The work took place as part of the project "Development of a highly efficient linked product engineering process (PEP) for hybrid lightweight structures in the context of Industry 4.0" (PEP4.0, funding code 20X1717B). The project is funded as part of the fifth Luftfahrforschungsprogramm of the Bundesministerium für Wirtschaft und Klimaschutz BMWK.

References

1. European Commission. Flightpath 2050: Europe's vision for aviation ; maintaining global leadership and serving society's needs ; report of the High-Level Group on Aviation Research. Luxembourg: Publ. Off. of the Europ. Union; 2011.
2. König R, Spitzer S, Böhm, Holger, Bätzel, Tim, Rao, Reyya Nitin, Gude, Maik. Ice hail stone impact testing of tailored fibre placed variabel axial composite structural guide vanes for novel CFRP-Ti intermediate cases of future jet engines. In: ECCM20; 2022.
3. Spitzer S, Folprecht F, Dargel A, Klaus C, Langkamp A, Gude M. Effiziente und Robuste Entwicklung Komplexer Faserverbund-Triebwerkstrukturen (Presentation); 17.06.2021.
4. Spickenheuer A. Zur fertigungsgerechten Auslegung von Faser-Kunststoff-Verbundbauteilen für den extremen Leichtbau auf Basis des variabelaxialen Fadenablageverfahrens Tailored Fiber Placement [Dresden, Technische Universität Dresden, Diss., 2014]. Dresden: Saechsische Landesbibliothek- Staats- und Universitaetsbibliothek Dresden; Technische Universität Dresden; 2014.
5. Dargel A, Kluger J, Klaus C, Spickenheuer A, Bittrich L, Spitzer S, et al. Design, modelling and manufacturing of variable-axial composite structural guide vane for a jet engine intermediate case in the context of industry 4.0. In: SAMPE Europe Conference Baden/Zürich; September 24-28, 2018; Baden (Switzerland); 2021.
6. Bittrich L, Spickenheuer A, Almeida JHS, Müller S, Kroll L, Heinrich G. Optimizing Variable-Axial Fiber-Reinforced Composite Laminates: The Direct Fiber Path Optimization Concept. Mathematical Problems in Engineering. 2019;2019:1–11. doi:10.1155/2019/8260563.

  doi:10.5075/epfl-298799_978-2-9701614-0-0

EFFICIENT COMPUTATION OF THE FREE-EDGE EFFECT IN COMPOSITE LAMINATED SHELLS

A. Kappel[a], C. Mittelstedt[a]*

a: Department of Mechanical Engineering, Institute for Lightweight Construction and Design, Darmstadt University of Technology, Otto-Berndt-Str. 2, D-64287 Darmstadt, Germany
* andreas.kappel@klub.tu-darmstadt.de

Abstract: *The accurate, yet efficient prediction of the state variables in composite shells subjected to four-point bending is a major challenge especially when the free-edge effect has to be considered. To remedy this problem, this paper introduces a higher-order semi-analytical approach for the computation of the three-dimensional stress field in cylindrically curved composite laminated shells with arbitrary layups undergoing a uniform bending moment. The computational model superimposes a closed-form analytical solution with a displacement-based layerwise approach and the governing equations are derived by means of the principle of minimum elastic potential. A comparison of the numerical results of the presented semi-analytical method with finite element simulations for* $[\theta/0°/-\theta/90°]$ *composite laminates indicates that the developed method works with high accuracy, although being extremely efficient in terms of computational resources.*

Keywords: Curved composites; Free-edge effect; Layerwise analysis; Finite element method; Four-point bending

1. Introduction

Driven by the demand for high-performance lightweight structures, composite technologies have experienced a remarkable development in the last decades. Thus, it was only a matter of time until fibre-reinforced plastics could be employed as primary load-bearing components. Experimental studies [1,2] of composite laminated shells under four-point bending, however, demonstrated that those safety-critical structures potentially exhibit complex failure modes with an interaction of matrix cracking and delamination stemming from the different orientations of the unidirectional reinforced laminate layers. Further on, the different deformation properties of the plies lead to three-dimensional stress concentrations at the traction-free edges of laminated shells, commonly referred to as the free-edge effect [3], which complicates the unambiguous identification of the dominating reason for failure.

While there exists a considerable amount of two-dimensional analytical models [4] which enable a depiction of the state variables at a sufficient distance from the traction-free edges of laminated shells, the assessment of the stress concentrations in the boundary-layer region is usually carried out by means of full-scale three-dimensional finite element computations which, however, are often unfavourable in terms of computational resources. An alternative way to quantify the impact of the free-edge effect is to utilize higher-order displacement-based layerwise approaches [5,6] which deliver results of similar quality in a more efficient fashion.

The present study extends the scope of the semi-analytical model by Kappel and Mittelstedt [5] by introducing a novel closed-form analytical solution that is combined with a layerwise

  doi:10.5075/epfl-298799_978-2-9701614-0-0

approach in order to enable the assessment of the free-edge stress fields in general composite laminated shells subjected to a uniform bending moment. The accuracy of the numerical results is verified by comparison with three-dimensional finite element computations carried out using the commercial tool Abaqus FEA.

2. Structural situation

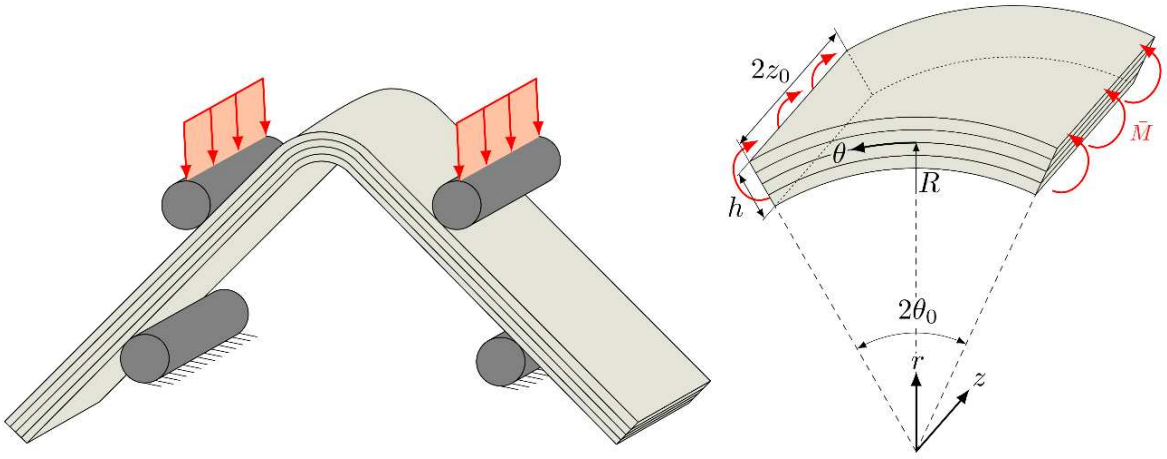

Figure 1. Four-point bending of an L-shaped composite angle bracket (l.) and specification of the region under consideration (r.)

The problem under study in this contribution is the curved segment of an L-shaped composite angle bracket (see Fig. 1). Hence, we consider thick, circular cylindrical laminated shells of finite length with N perfectly bonded, homogeneous laminate layers reinforced by unidirectional fibres. Herein, the radial position of the mid-plane and the total thickness are specified by means of R and h, while $2\theta_0$ characterizes the opening angle and $2z_0$ refers to the length of the considered composite shells. It is stated that the fibres of a $0°$-ply run along the circumferential direction θ and that the laminate layers are numbered sequentially starting from the innermost one at the inner radius $R_i = R - h/2$. All laminate layers are expected to have the same ply thickness $d_L = 0.25\ \mathrm{mm}$. It should be noted that in order to depict the structural situation during four-point bending, the considered composite laminated shells will have traction-free edges at the axial positions $z = 0, 2z_0$ and are subjected to a uniform bending moment flux $\bar{M}$ at its circumferential ends $\theta = \pm\theta_0$.

3. Semi-analytical model

The upcoming section discusses the derivation of the semi-analytical approach which can be subdivided into a closed-form analytical solution and a displacement-based layerwise approach.

3.1 Three-dimensional theory of elasticity

The kinematics of a circular cylindrical composite laminated shell with fibre-reinforced layers that are arbitrarily tailored can be described as follows, provided that the displacements $u^{(l)}(r,\theta,z)$, $v^{(l)}(r,\theta,z)$ and $w^{(l)}(r,\theta,z)$ in the radial, circumferential and axial direction are expected to be infinitesimal small:

$$\varepsilon_{rr}^{(l)} = \frac{\partial u^{(l)}}{\partial r}, \quad \varepsilon_{\theta\theta}^{(l)} = \frac{1}{r}\left(\frac{\partial v^{(l)}}{\partial \theta} + u^{(l)}\right), \quad \varepsilon_{zz}^{(l)} = \frac{\partial w^{(l)}}{\partial z},$$

  doi:10.5075/epfl-298799_978-2-9701614-0-0

$$\gamma_{\theta z}^{(l)} = \frac{\partial v^{(l)}}{\partial z} + \frac{1}{r}\frac{\partial w^{(l)}}{\partial \theta}, \quad \gamma_{rz}^{(l)} = \frac{\partial w^{(l)}}{\partial r} + \frac{\partial u^{(l)}}{\partial z}, \quad \gamma_{r\theta}^{(l)} = \frac{1}{r}\left(\frac{\partial u^{(l)}}{\partial \theta} - v^{(l)}\right) + \frac{\partial v^{(l)}}{\partial r} \tag{1}$$

Hooke's generalized law, on the other hand, is written as:

$$\begin{pmatrix} \varepsilon_{rr}^{(l)} \\ \varepsilon_{\theta\theta}^{(l)} \\ \varepsilon_{zz}^{(l)} \\ \gamma_{\theta z}^{(l)} \\ \gamma_{rz}^{(l)} \\ \gamma_{r\theta}^{(l)} \end{pmatrix} = \begin{bmatrix} S_{11}^{(l)} & S_{12}^{(l)} & S_{13}^{(l)} & S_{14}^{(l)} & 0 & 0 \\ S_{12}^{(l)} & S_{22}^{(l)} & S_{23}^{(l)} & S_{24}^{(l)} & 0 & 0 \\ S_{13}^{(l)} & S_{23}^{(l)} & S_{33}^{(l)} & S_{34}^{(l)} & 0 & 0 \\ S_{14}^{(l)} & S_{24}^{(l)} & S_{34}^{(l)} & S_{44}^{(l)} & 0 & 0 \\ 0 & 0 & 0 & 0 & S_{55}^{(l)} & S_{56}^{(l)} \\ 0 & 0 & 0 & 0 & S_{56}^{(l)} & S_{66}^{(l)} \end{bmatrix} \begin{pmatrix} \sigma_{rr}^{(l)} \\ \sigma_{\theta\theta}^{(l)} \\ \sigma_{zz}^{(l)} \\ \tau_{\theta z}^{(l)} \\ \tau_{rz}^{(l)} \\ \tau_{r\theta}^{(l)} \end{pmatrix} \tag{2}$$

Herein, $S_{ij}^{(l)}$ represent the compliance constants of the underlying material while the strain and stress components of each lamina in a cylindrical $r\theta z$-coordinate system are specified by $\underline{\varepsilon}^T = \left(\varepsilon_{rr}^{(l)}, \varepsilon_{\theta\theta}^{(l)}, \varepsilon_{zz}^{(l)}, \gamma_{\theta z}^{(l)}, \gamma_{rz}^{(l)}, \gamma_{r\theta}^{(l)}\right)$ and $\underline{\sigma}^T = \left(\sigma_{rr}^{(l)}, \sigma_{\theta\theta}^{(l)}, \sigma_{zz}^{(l)}, \tau_{\theta z}^{(l)}, \tau_{rz}^{(l)}, \tau_{r\theta}^{(l)}\right)$.

3.2 Closed-form analytical solution

Numerical computations indicate on the one hand, that remote from the traction-free edges of the considered composite laminated shells, the impact of the free-edge effect on the stress field vanishes and thus, a plane state of strain with respect to the axial direction is obtained. On the other hand, the state variables show no dependency concerning the circumferential direction due to the axisymmetric loading condition. Consequently, the governing equations [7] can be reduced to:

$$\begin{aligned} L'^{(l)}_4 F^{(l)} + L'^{(l)}_3 \Psi^{(l)} &= 0 \\ L''^{(l)}_3 F^{(l)} + L'^{(l)}_2 \Psi^{(l)} &= 0 \end{aligned} \tag{3}$$

Herein, $L'^{(l)}_4$, $L'^{(l)}_3$, $L''^{(l)}_3$ and $L'^{(l)}_2$ are ordinary differential operators

$$\begin{aligned} L'^{(l)}_4 &= \tilde{S}_{22}^{(l)}\frac{d^4}{dr^4} + 2\tilde{S}_{22}^{(l)}\frac{1}{r}\frac{d^3}{dr^3} - \tilde{S}_{11}^{(l)}\frac{1}{r^2}\frac{d^2}{dr^2} + \tilde{S}_{11}^{(l)}\frac{1}{r^3}\frac{d}{dr} \\ L'^{(l)}_3 &= -\tilde{S}_{24}^{(l)}\frac{d^3}{dr^3} + \left(\tilde{S}_{14}^{(l)} - 2\tilde{S}_{24}^{(l)}\right)\frac{1}{r}\frac{d^2}{dr^2} \\ L''^{(l)}_3 &= -\tilde{S}_{24}^{(l)}\frac{d^3}{dr^3} - \left(\tilde{S}_{14}^{(l)} + \tilde{S}_{24}^{(l)}\right)\frac{1}{r}\frac{d^2}{dr^2} \\ L'^{(l)}_2 &= \tilde{S}_{44}^{(l)}\frac{d^2}{dr^2} + \tilde{S}_{44}^{(l)}\frac{1}{r} \end{aligned} \tag{4}$$

while $F^{(l)}$ and $\Psi^{(l)}$ are stress functions which satisfy the equations of equilibrium of each laminate layer (l). The reduced compliance constants, on the other side, are defined as follows:

$$\tilde{S}_{ij}^{(l)} = S_{ij}^{(l)} - \frac{S_{i3}^{(l)} S_{j3}^{(l)}}{S_{33}^{(l)}} \tag{5}$$

The solution of the system of coupled, homogeneous ordinary differential equations (3) is obtained by means of the following approaches for the stress functions:

$$F^{(l)}(r) = C_1^{(l)} r^2 + C_2^{(l)} r + C_3^{(l)} r^{1+\lambda^{(l)}} + C_4^{(l)} r^{1-\lambda^{(l)}} \tag{6}$$

  doi:10.5075/epfl-298799_978-2-9701614-0-0

$$\Psi^{(l)}(r) = 2C_1^{(l)}\eta_1^{(l)} r + C_2^{(l)}\eta_2^{(l)} \ln(r) + C_3^{(l)}\eta_\lambda^{(l)} r^{\lambda^{(l)}} + C_4^{(l)}\eta_{-\lambda}^{(l)} r^{-\lambda^{(l)}} \tag{7}$$

wherein the material parameters $\lambda^{(l)}$, $\eta_1^{(l)}$, $\eta_2^{(l)}$ and $\eta_{\pm\lambda}^{(l)}$ are specified as:

$$\lambda^{(l)} = \sqrt{\frac{\tilde{S}_{11}^{(l)}\tilde{S}_{44}^{(l)} - \tilde{S}_{14}^{(l)}\tilde{S}_{14}^{(l)}}{\tilde{S}_{22}^{(l)}\tilde{S}_{44}^{(l)} - \tilde{S}_{24}^{(l)}\tilde{S}_{24}^{(l)}}}$$

$$\eta_1^{(l)} = \frac{\tilde{S}_{14}^{(l)} + \tilde{S}_{24}^{(l)}}{\tilde{S}_{44}^{(l)}}, \qquad \eta_2^{(l)} = \frac{\tilde{S}_{11}^{(l)}}{\tilde{S}_{14}^{(l)}}, \qquad \eta_{\pm\lambda}^{(l)} = \pm\frac{\tilde{S}_{14}^{(l)} \pm \tilde{S}_{24}^{(l)}\lambda^{(l)}}{\tilde{S}_{44}^{(l)}} \frac{1 \pm \lambda^{(l)}}{\lambda^{(l)}} \tag{8}$$

The stress components are obtained through the following relations

$$\sigma_{rr}^{(l)} = \frac{1}{r}\frac{dF^{(l)}}{dr}, \quad \sigma_{\theta\theta}^{(l)} = \frac{d^2F^{(l)}}{dr^2}, \quad \tau_{\theta z}^{(l)} = -\frac{d\Psi^{(l)}}{dr},$$

$$\sigma_{zz}^{(l)} = -\frac{1}{S_{33}^{(l)}}\left(S_{13}^{(l)}\sigma_{rr}^{(l)} + S_{23}^{(l)}\sigma_{\theta\theta}^{(l)} + S_{34}^{(l)}\tau_{\theta z}^{(l)}\right), \tag{9}$$

while the displacement components $U_\infty^{(l)}(r)$, $V_\infty^{(l)}(r,\theta)$ and $W_\infty^{(l)}(r,\theta)$ can be specified by utilizing the kinematics (1) and the underlying material law (2).

The $4N$ constants $C_j^{(l)}$ are determined via $4N-4$ continuity conditions

$$\sigma_{rr}^{(l)} = \sigma_{rr}^{(l+1)}, \quad U_\infty^{(l)} = U_\infty^{(l+1)}, \quad V_\infty^{(l)} = V_\infty^{(l+1)}, \quad W_\infty^{(l)} = W_\infty^{(l+1)} \tag{10}$$

in the corresponding interfaces and the following 4 boundary conditions:

$$\sigma_{rr}^{(1)}(r = R - h/2) = \sigma_{rr}^{(N)}(r = R + h/2) = 0,$$

$$\sum_{l=1}^{N}\left(\int_{r_{l-1}}^{r_l} \sigma_{\theta\theta}^{(l)} r \, dr\right) = -\bar{M}, \quad \sum_{l=1}^{N}\left(\int_{r_{l-1}}^{r_l} \tau_{\theta z}^{(l)} \, dr\right) = 0 \tag{11}$$

3.3 Layerwise approach

In order to depict the impact of the free-edge effect on the stress field, the radial, circumferential and axial displacements $U_\infty^{(l)}(r)$, $V_\infty^{(l)}(r,\theta)$ and $W_\infty^{(l)}(r,\theta)$ of the closed-form analytical solution have to be upgraded by layerwise displacement functions which can be formulated after discretizing the laminate layers into M mathematical layers. Thus, the displacement field of a material point located at (r,θ,z) in the k^{th} mathematical ply is defined as [5,6]:

$$u^{(k)}(r,\theta,z) = U_\infty^{(l(k))}(r) + \sum_j U^{(j)}(z)\Phi^{(j)}(r) + u_0(r,\theta) \tag{12}$$

$$v^{(k)}(r,\theta,z) = V_\infty^{(l(k))}(r,\theta) + \sum_j V^{(j)}(z)\Phi^{(j)}(r) + v_0(r,\theta) \tag{13}$$

$$w^{(k)}(r,\theta,z) = W_\infty^{(l(k))}(r,\theta) + \sum_j W^{(j)}(z)\Phi^{(j)}(r) + w_0 \tag{14}$$

with $j \in \{I(k)+1, I(k)+2, \dots, I(k)+\Psi+1\}$. Herein, Ψ characterizes the order of the global Lagrangian interpolation vector $\Phi^{(j)}(r)$ and $I(k) = \Psi(k-1)$ describes the last grid point of the

  doi:10.5075/epfl-298799_978-2-9701614-0-0 published under CC BY-NC 4.0 license

$(k-1)^{\text{th}}$ mathematical layer [5,6]. While the rigid-body displacements $u_0(r,\theta)$, $v_0(r,\theta)$ and w_0 can be neglected for a pure stress analysis, the a priori unknown displacement functions $U^{(j)}(z)$, $V^{(j)}(z)$ as well as $W^{(j)}(z)$ have to be determined by virtue of the principle of minimum elastic potential of the composite laminated shell [5]:

$$\delta\Pi^{(k)} = \delta\Pi_i^{(k)} + \delta\Pi_e^{(k)} = 0 \tag{15}$$

with

$$\delta\Pi_i^{(k)} = \frac{1}{2}\sum_k \int_0^{2z_0} \int_0^{\theta_0} \int_{r_{(k-1)}}^{r_{(k)}} \delta\underline{\varepsilon}^{(k)^T}\,\underline{\sigma}^{(k)} r \; dr\, d\theta\, dz \tag{16}$$

$$\delta\Pi_e^{(k)} = -\frac{1}{2}\sum_k \int_0^{2z_0} \int_{r_{(k-1)}}^{r_{(k)}} \overline{M}\,\delta\left(\frac{\partial v^{(k)}}{\partial r}\right) dr\, dz \tag{17}$$

By employing the fundamental lemma of calculus of variations, the equilibrium equations of the cylindrical composite laminated shell for each grid point (i) are obtained as (the definition of the abbreviations can be found in section 6):

$$\begin{aligned}\delta U^{(i)}\colon \sum_j & -A_{55}^{ij(k)}\frac{d^2U^{(j)}}{dz^2} + (\overline{A}_{14}^{ji(k)} - \overline{A}_{56}^{ij(k)} + B_{24}^{ij(k)} + B_{56}^{ij(k)})\frac{dV^{(j)}}{dz} + (\overline{A}_{13}^{ji(k)} - \overline{A}_{55}^{ij(k)} \\ & + B_{23}^{ij(k)})\frac{dW^{(j)}}{dz} + (\tilde{A}_{11}^{ij(k)} + \overline{B}_{12}^{ij(k)} + \overline{B}_{12}^{ji(k)} + D_{22}^{ij(k)})U^{(j)} = -M_{r,0}^{(i)} - N_{\theta,0}^{(i)}\end{aligned} \tag{18}$$

$$\begin{aligned}\delta V^{(i)}\colon \sum_j & -A_{44}^{ij(k)}\frac{d^2V^{(j)}}{dz^2} - A_{34}^{ij(k)}\frac{d^2W^{(j)}}{dz^2} + \left(-\overline{A}_{14}^{ij(k)} + \overline{A}_{56}^{ji(k)} - B_{24}^{ij(k)} - B_{56}^{ij(k)}\right)\frac{dU^{(j)}}{dz} \\ & + \left(\tilde{A}_{66}^{ij(k)} - \overline{B}_{66}^{ij(k)} - \overline{B}_{66}^{ji(k)} + D_{66}^{ij(k)}\right)V^{(j)} + \left(\tilde{A}_{56}^{ij(k)} - \overline{B}_{56}^{ij(k)}\right)W^{(j)} = -\overline{M}^{(i)}\end{aligned} \tag{19}$$

$$\begin{aligned}\delta W^{(i)}\colon \sum_j & -A_{34}^{ij(k)}\frac{d^2V^{(j)}}{dz^2} - A_{33}^{ij(k)}\frac{d^2W^{(j)}}{dz^2} + \left(\overline{A}_{55}^{ji(k)} - \overline{A}_{13}^{ij(k)} - B_{23}^{ij(k)}\right)\frac{dU^{(j)}}{dz} \\ & + \left(\tilde{A}_{56}^{ij(k)} - \overline{B}_{56}^{ji(k)}\right)V^{(j)} + \tilde{A}_{55}^{ij(k)}W^{(j)} = 0\end{aligned} \tag{20}$$

with $j \in \{I(k)+1, I(k)+2, \dots, I(k)+\Psi+1\}$. Equations (18) - (20) characterize a system of coupled ordinary differential equations that can be solved numerically [5,6].

For the boundary conditions at the traction-free edges, on the other hand, the following formulations are derived:

$$\delta U^{(i)}\big|_{z=0}^{z=2z_0}\colon \sum_j \left(A_{55}^{ij(k)}\frac{dU^{(j)}}{dz} + \left(\overline{A}_{56}^{ij(k)} - B_{56}^{ij(k)}\right)V^{(j)} + \overline{A}_{55}^{ij(k)}W^{(j)}\right)\Bigg|_{z=0}^{z=2z_0} = 0 \tag{21}$$

$$\delta V^{(i)}\big|_{z=0}^{z=2z_0}\colon \sum_j \left(A_{44}^{ij(k)}\frac{dV^{(j)}}{dz} + A_{34}^{ij(k)}\frac{dW^{(j)}}{dz} + \left(\overline{A}_{14}^{ij(k)} + B_{24}^{ij(k)}\right)U^{(j)}\right)\Bigg|_{z=0}^{z=2z_0} = -R_{\theta z,0}^{(i)} \tag{22}$$

$$\delta W^{(i)}\big|_{z=0}^{z=2z_0}\colon \sum_j \left(A_{34}^{ij(k)}\frac{dV^{(j)}}{dz} + A_{33}^{ij(k)}\frac{dW^{(j)}}{dz} + (\overline{A}_{13}^{ij(k)} + B_{23}^{ij(k)})U^{(j)}\right)\Bigg|_{z=0}^{z=2z_0} = -M_{z,0}^{(i)} \tag{23}$$

with $j \in \{I(k)+1, I(k)+2, \dots, I(k)+\Psi+1\}$.

  doi:10.5075/epfl-298799_978-2-9701614-0-0

4. Verification of accuracy

In the scope of the current section, the accuracy of the introduced semi-analytical method is studied by the example of the unsymmetric $[\theta/0°/-\theta/90°]$ composite laminated shells. Herein, the numerical results, which have been carried out by means of the following material properties [6]

$$E_1 = 143 \text{ GPa}, E_2 = E_3 = 9.1 \text{ GPa},$$
$$G_{23} = 4.82 \text{ GPa}, G_{12} = G_{13} = 4.9 \text{ GPa},$$
$$\nu_{12} = \nu_{13} = \nu_{23} = 0.3,$$

will be directly compared to detailed three-dimensional finite element computations. All numerical results are presented using the following non-dimensional quantities:

$$\overline{\sigma}_{ii} = \frac{2z_0 h}{\overline{M}}\sigma_{ii}, \qquad \overline{\tau}_{ij} = \frac{2z_0 h}{\overline{M}}\tau_{ij}$$
$$\overline{r} = \frac{r-R}{h}, \qquad \overline{z} = \frac{z-z_0}{2z_0}$$

with $(i,j = r,\theta,z)$. Fig. 2 provides an insight into the stress field of the unsymmetric $[45°/0°/-45°/90°]$ composite laminated shell remote from the boundary-layer regions while Fig. 3 and Fig. 4 illustrate the decaying behavior of the interlaminar stress gradients in close proximity to the traction-free edges for another two laminate lay-ups. To sum up, it can be concluded that the numerical results of both methods show a remarkable agreement which confirms the good quality of the presented semi-analytical model.

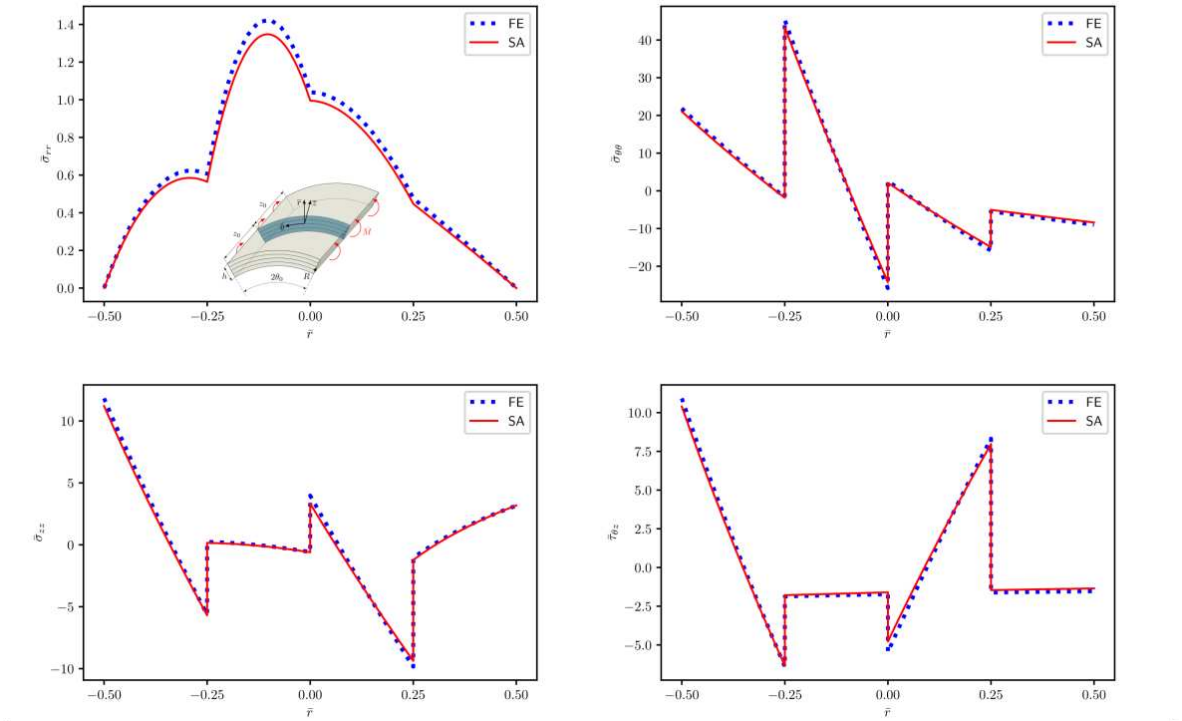

Figure 2. Non-dimensional stress components $\overline{\sigma}_{rr}, \overline{\sigma}_{\theta\theta}, \overline{\sigma}_{zz}$ and $\overline{\tau}_{\theta z}$ evaluated at $(\theta, \overline{z}) = (0,0)$ for the unsymmetric $[45°/0°/-45°/90°]$ composite laminate ($R/h = 4$, $2z_0/h = 4$, $2\theta_0 = \pi/2$) subjected to a uniform bending moment flux $\overline{M} = 10\ N$

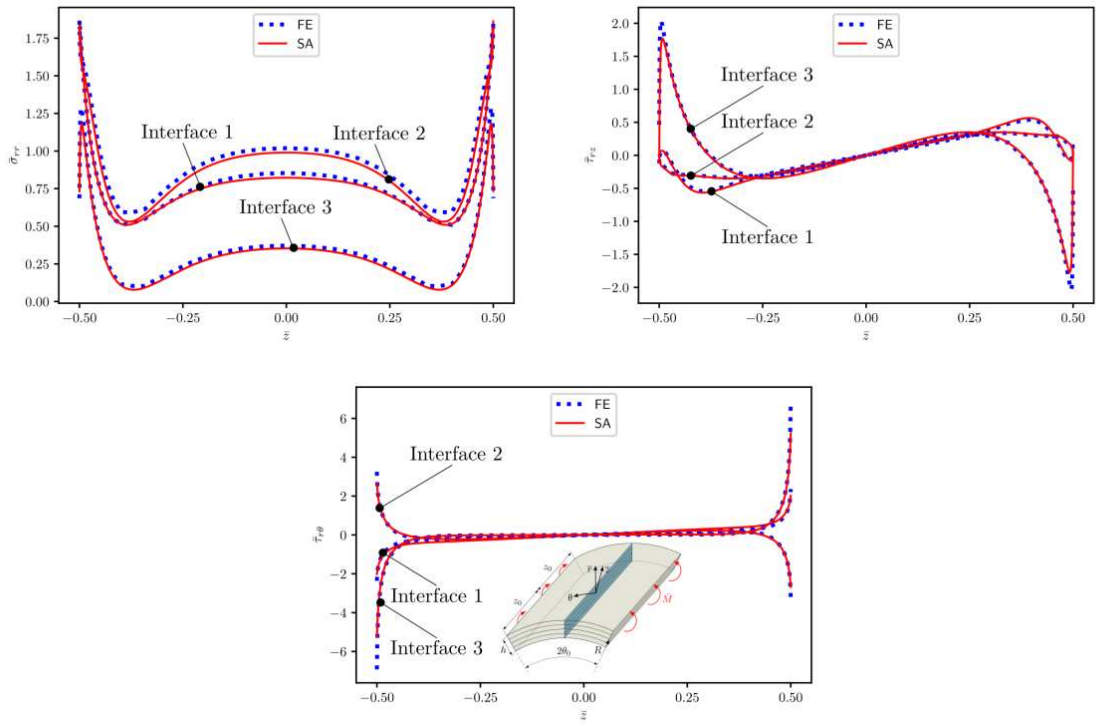

Figure 3. Non-dimensional interlaminar stress components $\overline{\sigma}_{rr}$, $\overline{\tau}_{rz}$ and $\overline{\tau}_{r\theta}$ evaluated in all interfaces at $\theta = 0$ for the unsymmetric $[30°/0°/-30°/90°]$ composite laminate ($R/h = 4$, $2z_0/h = 4$, $2\theta_0 = \pi/2$) subjected to a uniform bending moment flux $\overline{M} = 10\ N$

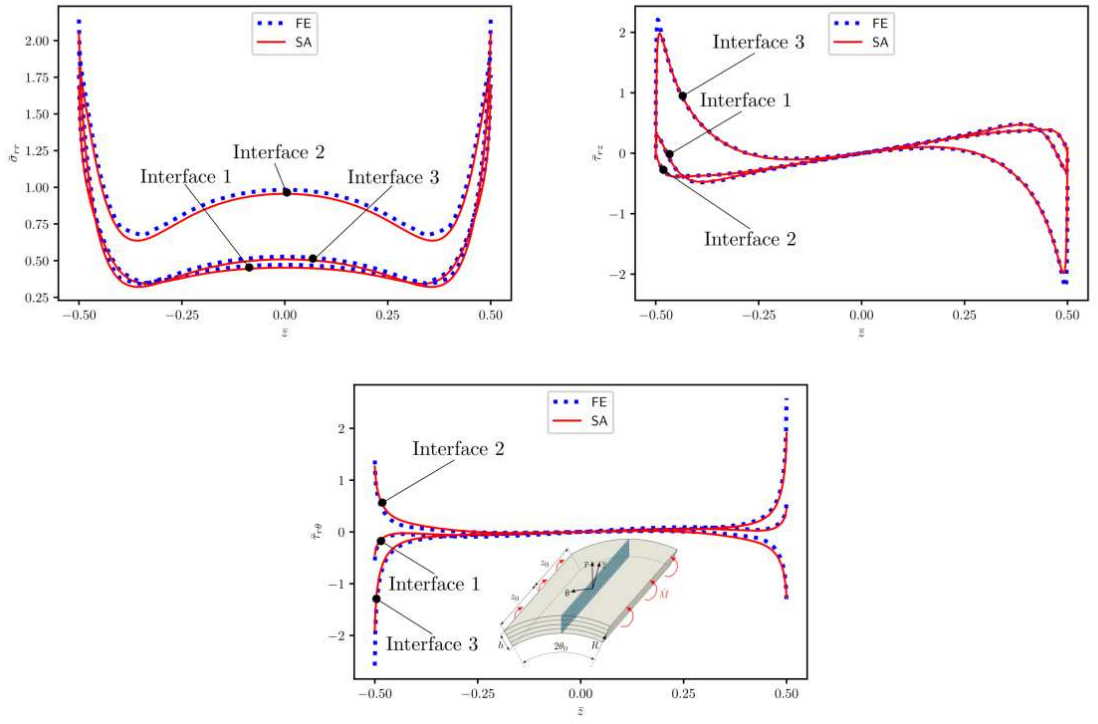

Figure 4. Non-dimensional interlaminar stress components $\overline{\sigma}_{rr}$, $\overline{\tau}_{rz}$ and $\overline{\tau}_{r\theta}$ evaluated in all interfaces at $\theta = 0$ for the unsymmetric $[60°/0°/-60°/90°]$ composite laminate ($R/h = 4$, $2z_0/h = 4$, $2\theta_0 = \pi/2$) subjected to a uniform bending moment flux $\overline{M} = 10\ N$

  doi:10.5075/epfl-298799_978-2-9701614-0-0

5. Concluding remarks

In this contribution, a semi-analytical approach for the computation of the stress fields in circular cylindrical composite laminated shells undergoing four-point bending has been introduced. The comparison of the numerical results with three-dimensional finite element computations outlined the excellent accordance of both models.

Further research concerning the extension of the current semi-analytical method should be conducted to assess the prediction of the free-edge stress field in general composite laminated shells undergoing arbitrary mechanical loadings.

6. Abbreviations

$$\begin{aligned}
\left\{A_{op}^{mn(k)}, \overline{A}_{op}^{mn(k)}, \tilde{A}_{op}^{mn(k)}\right\} &= \int_{r_{(k-1)}}^{r_{(k)}} C_{op}^{(k)} \left\{\Phi^{(m)}\Phi^{(n)}, \Phi^{(m)}\Phi_{,r}^{(n)}, \Phi_{,r}^{(m)}\Phi_{,r}^{(n)}\right\} r dr \\
\left\{B_{op}^{mn(k)}, \overline{B}_{op}^{mn(k)}, D_{op}^{mn(k)}\right\} &= \int_{r_{(k-1)}}^{r_{(k)}} C_{op}^{(k)} \left\{\Phi^{(m)}\Phi^{(n)}, \Phi^{(m)}\Phi_{,r}^{(n)}, \Phi^{(m)}\Phi^{(n)}\frac{1}{r}\right\} dr \\
\left\{N_{\theta,0}^{(i)}, M_{z,0}^{(i)}, R_{\theta z,0}^{(i)}, \overline{M}^{(i)}\right\} &= \int_{r_{(k-1)}}^{r_{(k)}} \left\{\sigma_{\theta\theta,0}^{(k)}, r\sigma_{zz,0}^{(k)}, r\tau_{\theta z,0}^{(k)}, \overline{M}\right\} \Phi^{(i)} dr \\
\left\{M_{r,0}^{(i)}\right\} &= \int_{r_{(k-1)}}^{r_{(k)}} \left\{r\sigma_{rr,0}^{(k)}\right\} \Phi_{,r}^{(i)} dr
\end{aligned} \tag{24}$$

Acknowledgements

This work was supported by the German Research Foundation DFG [PNO 427624054].

References

1. González-Cantero JM, Graciani E, López-Romano B, París F. Competing mechanisms in the unfolding failure in composite laminates. Composites Science and Technology 2018;156:223-30.
2. Cao D, Hu H, Duan Q, Song P, Li S. Experimental and three-dimensional numerical investigation of matrix cracking and delamination interaction with edge effect of curved composite laminates. Composite Structures 2019;225:111154.
3. Mittelstedt C, Becker W, Kappel A, Kharghani N. Free-Edge Effects in Composite Laminates - A Review of Recent Developments 2005–2020. Applied Mechanics Reviews 2022;74(1): 010801.
4. Ko WL, Jackson RH. Multilayer theory for delamination analysis of a composite curved bar subjected to end forces and end moments. Composite Structures 1989;5:173-98.
5. Kappel A, Mittelstedt C. Free-edge stress fields in cylindrically curved cross-ply laminated shells. Composites Part B: Engineering 2020;183:107693.
6. Kappel A, Dillen S, Mittelstedt C. Hygrothermomechanical analysis of the free-edge stress fields in cylindrical cross-ply laminated shells. Mechanics of Advanced Materials and Structures 2021;1-18.
7. Yuan FG. Thermal stresses in thick laminated composite shells. Composite Structures 1993;26(1-2):63-75.

  doi:10.5075/epfl-298799_978-2-9701614-0-0

REDUCED ORDER MODEL FOR MICRO-SCALE PERMEABILITY PREDICTION OF A FIBRE TOW

Roman Kandinskii[a,b,c,d], Wim Desmet[c,d], Frank Naets[c,d], Yentl Swolfs[a], Stepan V. Lomov[a]

a: Department of Materials Engineering, KU Leuven, Belgium
b: SIM M3 program, Belgium
c: Department of Mechanical Engineering, KU Leuven, Belgium
d: DMMS core group, Flanders Make @ KU Leuven, Belgium

Abstract: *The ever-growing complexity of numerical simulations creates the demand for acceleration. Model order reduction (MOR) methods use the algebraic properties of linear systems underlying a simulation to seek for solution to a problem on a smaller subspace. This work explores applicability of the classical reduced basis method to the problem of permeability assessment of a composite fibre tow. The proposed algorithm is based on solving Stokes-Brinkman flow in the fictitious-domain manner, allowing for using any geometry for training. The key to calculation speed-up here is the geometric variability and training on flows through different geometries.*

It is shown that the model's performance strongly depends on the variability. For one or two deterministic parameters, the new design points can be calculated 10 times faster with 2% relative error. For random fibre distribution, the model is not more effective than regular numerical analysis. However, this framework can be applied to flows where the local shape changes are limited.

Keywords: permeability, Brinkman flow, model order reduction

1. Introduction

Many composite manufacturing techniques such as resin transfer moulding, vacuum-assisted resin infusion and others are based on impregnation of a preform with a liquid resin under pressure. A crucial parameter defining the impregnation quality is permeability of the preform. Usually derived from the Darcy's law, estimation of this purely geometric parameter is hard for several reasons. First, it is hard to measure. A series of international experimental benchmarks has shown [1] that predicted permeability value for the same textile preform can vary by 50 %. Second, it depends on the local character of the flow and thus is spatially variable. The imperfections of alignment of fibre tows of a fabric might not be well seen with a naked eye, but in fact the little wrinkles contribute to a significant inhomogeneity [2]. Third, it is multi-scale. The non-uniformity of the fibre distribution inside a single tow (micro-scale) impacts the flow pattern on the fabric unit cell level (meso-scale), which makes it hard to analyse permeability with flow simulations.

In this work, we would like to pay attention to theoretical estimation of the micro-scale permeability. In the field of composites, this task has been in the spotlight for several decades. The first practical analytical models which are still in frequent use are Kozeny-Karman (1927/1956), Berdichevsky-Kai (1993), Gebart (1992) [3,4,5]. All these models assume some level of idealisation of the fibre arrangement, thus tend to over- or underestimate the

  doi:10.5075/epfl-298799_978-2-9701614-0-0

permeability. The main reliable tool for calculation of permeability on both scale levels is computational fluid dynamics (CFD). Even though they are precise, simulations of Navier-Stokes equations become costly and timely when the geometric domain reaches a representative size. To overcome this, different alternatives have been proposed, such as Lattice-Boltzmann method, which, however, did not become an industry standard [6]. The latest trend in estimation of micro-scale permeability is building surrogate models which can use or bypass the actual CFD stage [7, 8].

In this study we explore a different strategy to tackle the permeability estimation problem. The basic idea is to formulate the problem as a set of flow simulations with parameterised geometry of the domain. Flexible geometric description will allow for acceleration of the simulations using some of the established methods such as model order reduction (MOR) [9]. MOR methods employ algebraic properties of a discretized system of equations to significantly reduce dimensionality of the problem, thus reducing computational time by orders of magnitude.

This paper is organised as follows: first, we describe the physical problem of interest in terms of the partial differential equations (PDEs); then the numerical model including full and reduced order models (FOM and ROM) are described in detail; finally, the performance of the model is analysed for two types of numerical tests.

2. A fictitious-domain model of flow with arbitrary geometry

2.1 Governing system of partial differential equations

We consider stationary Brinkman flow in a rectangular domain. The velocity-pressure formulation and a mixed set of boundary conditions are used.

The full system of PDEs consists of the Brinkman momentum equation (1.1), continuity equation for an incompressible fluid (1.2) and boundary conditions. For simplicity, we restrict this paper to the case of 2D flow between two no-slip walls (Fig. 1). The boundary conditions for this problem include typical inlet-outlet conditions: Dirichlet for pressure and Neumann for velocity (1.3, 1.4). No-slip conditions are applied to the horizontal walls (1.5).

$$\Delta \boldsymbol{v} - R(\rho)\boldsymbol{v} - \frac{1}{\mu}\nabla p = 0 \quad on\ \Omega \tag{1.1}$$

$$\nabla \cdot \boldsymbol{v} = 0 \quad on\ \Omega \tag{1.2}$$

$$p_{\Gamma in} - p_{\Gamma out} = P_{drop} \tag{1.3}$$

$$\frac{\partial \boldsymbol{v}}{\partial n} = 0 \quad on\ \Gamma_{in}, \Gamma_{out} \tag{1.4}$$

$$\boldsymbol{v} = 0 \quad on\ \Gamma_{wall} \tag{1.5}$$

Here $\boldsymbol{v}$ is velocity vector field, k – permeability, $R = 1/k$ – flow resistance or inverse permeability (assumed isotropic), ρ – the parameter set, μ – dynamic viscosity, p – pressure, P_{drop}– prescribed pressure drop, n – normal unit vector. We will use the flow resistance instead of permeability in the model definition for convenience (permeability of the free-fluid region is infinite).

  doi:10.5075/epfl-298799_978-2-9701614-0-0

The spatial distribution of flow resistance R defines the partitioning of the domain into fluid and porous parts. The geometric parameterisation is realised through the dependence $R(\rho)$. For simplicity, we limit ρ to be a single scalar parameter.

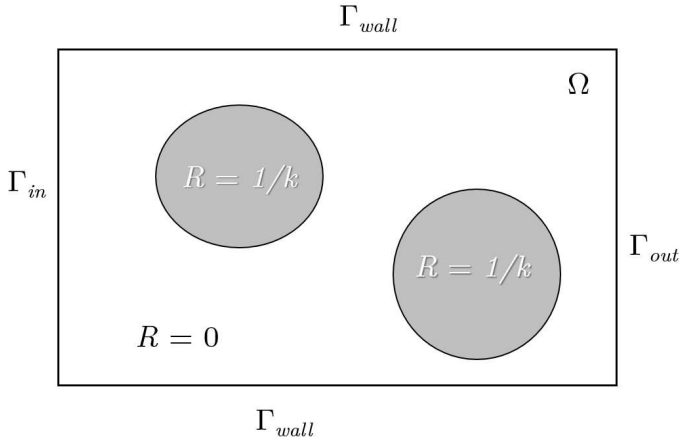

Figure 1. Sketch of the computational domain

Angot [10] theoretically proved convergence of Brinkman solution to a Stokes solution, given the permeability of the porous part tends to zero. This convergence allows for calculating flow with impermeable inclusions by prescribing their permeability to be zero.

2.2 Resistance distribution function

The flow resistance R is a scalar function of coordinates. Its spatial distribution defines the position and shape of the obstacles and/or additional boundaries. This distribution is physical and at the same time plays the role of the fictitious-domain penalty. To ensure smoothness of the solution in the vicinity of the fluid-porous interface, the R is defined continuously using a level-set function. The distribution along a line, normal to the interface, can be expressed as:

$$R = \frac{{}^{2}/_{k}}{1+\exp(a\exp(lx))} \tag{2.1}$$

$$a = \ln(0.1\sqrt{{}^{1}/_{k}} - 1) \tag{2.2}$$

Here k is permeability of the porous region, l – steepness of the logistic curve, and x is the coordinate along the line, $x = 0$ on the interface (Fig. 2). The steepness l defines the width of the transition region between the fluid and porous parts.

3. Numerical model

3.1 Full order model

The equations (1) are discretised via the finite difference method. It matches well with the employment of the regular structured mesh which provides the ease of programming. The marker-and-cell centred difference scheme (MAC) is used to ensure numerically stable

  doi:10.5075/epfl-298799_978-2-9701614-0-0

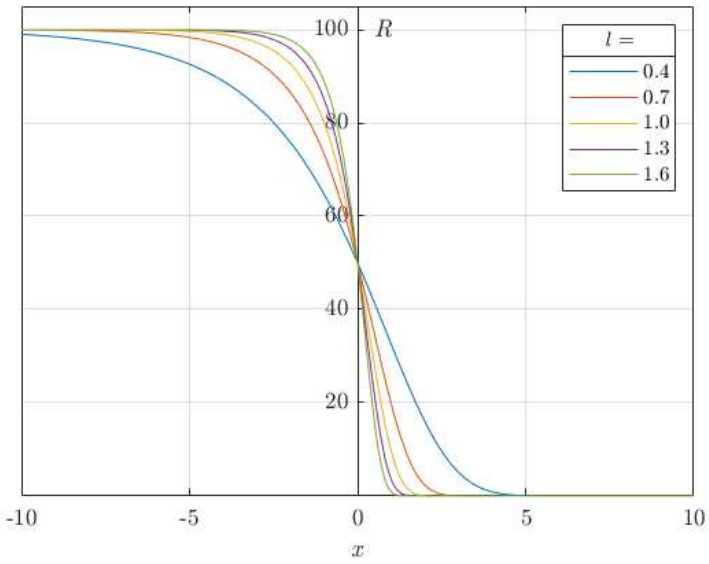

Figure 2. Flow resistance distribution along a normal to the fluid-porous interface
The resistance is equal to 1/ k, $k = 0.01$ inside the porous part, and is zero elsewhere

discretisation. It is based on assigning the variables – velocity components and pressure – to mutually shifted grids (Fig. 3). This helps to meet the inf-sup condition also called Ladyzhenskaya-Babuska-Brezzi condition.

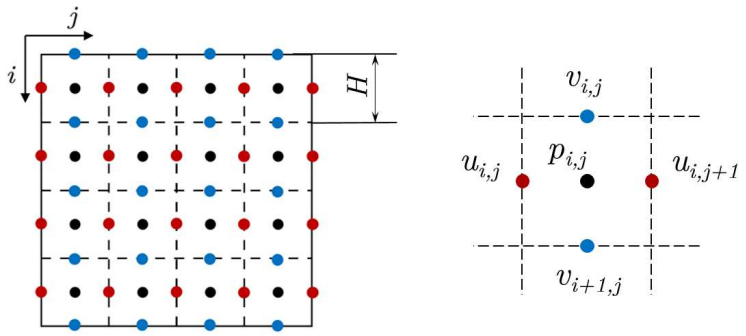

Figure 3. Staggered grid in two dimensions

i, j – row and column indices;
u and v – horizontal and vertical velocity components; p – pressure; H – cell size

The discretised linear system of equations has the following saddle-point form:

$$A\,x = b \tag{3.1}$$

$$\begin{bmatrix} D_U & & B_U \\ & D_V & B_V \\ B_U^T & B_V^T & \end{bmatrix} \begin{bmatrix} u \\ v \\ p \end{bmatrix} = \begin{bmatrix} b \end{bmatrix} \tag{3.2}$$

D_U and D_V are the discrete Laplace operators for horizontal and vertical velocity components respectively, B_U and B_V – the discrete gradient operators, B_U^T and B_V^T – the discrete divergence operators, u, v and p – velocity and pressure distributions stacked in a column-vector, b – the right-hand side containing the boundary condition values. It is important to emphasise that A, x and b depend on the parameter set ρ. The B -blocks correspond to the velocity divergence and

  doi:10.5075/epfl-298799_978-2-9701614-0-0

the pressure gradient, which do not depend on the permeability distribution, so these blocks are ρ-independent.

3.2 Reduced order model

The proposed ROM consists of the offline and online stages. The offline stage is training – running FOM for the chosen parameter values, *sampling points*. During the online stage, approximate solutions for new parameter values are calculated via orthogonal projection of the linear system.

The offline stage starts with choosing the sampling points. At each such point, the flow solution, called *snapshot*, is collected to construct the basis later in the online stage. The parameter ρ may represent position, shape or size of an obstacle (fibre). Here we assume that ρ is a scalar and deterministic. Consider an *m*-size set of sample points: [ρ_1, ρ_2, … , ρ_m]. The FOM is called *m* times to solve the system

$$A(\rho_i)\, x(\rho_i) \;=\; b(\rho_i) \tag{4}$$

The *m* snapshots x_i are stored in the snapshot matrix X = [x_1, …, x_m] of size $N \times m$ (*N* is the number of degrees-of-freedom).

$$X \;=\; [x_1, \ldots, x_m] \;=\; \begin{bmatrix} u_1, \ldots, u_m \\ v_1, \ldots, v_m \\ p_1, \ldots, p_m \end{bmatrix} \;=\; \begin{bmatrix} U \\ V \\ P \end{bmatrix} \tag{5}$$

In the online stage, a new parameter value is passed to the ROM to calculate the approximate solution. For each new query point, the reduced order system $A_r\, x_r \;=\; b_r$ is solved. The reduced coefficient matrix A_r and the right-hand side b_r are obtained via orthogonal projection using the basis Φ:

$$A_r \;=\; \Phi^T\, A\, \Phi, \quad b_r \;=\; \Phi^T\, b \tag{6}$$

The reduced solution vector x_r is then projected back to the original space using the same basis

$$x \;=\; \Phi\, x_r \tag{7}$$

Construction of the basis Φ involves several techniques important for the most accurate approximation of the solution manifold. First, the separate variable parts of the snapshot matrix must be arranged in block-diagonal shape. This will ensure the structure-preserving projection and establish individual approximation spaces for each variable.

$$\begin{bmatrix} U \\ V \\ P \end{bmatrix} \rightarrow \begin{bmatrix} U & & \\ & V & \\ & & P \end{bmatrix} \tag{8}$$

The flow patterns in the snapshots may contain values of very different magnitude – 0 in the porous region and some significant value in the fluid region. Numerically, this can lead to prevalence of zero elements during projection, which can cause the locking effect when the projected matrix becomes singular. To separate the approximation subspaces regarding fluid or porous part the flow appeared to be in, the regional basis splitting is used for velocity bases Φ_U and Φ_V. The splitting consists simply in duplicating the snapshot matrices U and V making them twice as wide but zeroing all the elements pointing to the porous region of the current geometry

  doi:10.5075/epfl-298799_978-2-9701614-0-0

in one block – U_f, V_f , and zeroing all the elements pointing to the fluid region – U_p, V_p. Finally, the basis takes the following shape:

$$\Phi = \begin{bmatrix} U_f\ U_p & & \\ & V_f\ V_p & \\ & & P \end{bmatrix} = \begin{bmatrix} \Phi_U & & \\ & \Phi_V & \\ & & P \end{bmatrix} \tag{9}$$

The projection and the reduced linear system can be expressed as

$$A_r = \Phi^T A\, \Phi = \begin{bmatrix} \Phi_U^T\, D_U\, \Phi_U & & \Phi_U^T B_U\, P \\ & \Phi_V^T\, D_V\, \Phi_V & \Phi_V^T\, B_V\, P \\ P^T\, B_U^T\, \Phi_U & P^T\, B_V^T\, \Phi_V & \end{bmatrix} = \begin{bmatrix} D_{Ur} & & B_{Ur} \\ & D_{Vr} & B_{Vr} \\ B_{Ur}^T & B_{Vr}^T & \end{bmatrix} \tag{10.1}$$

$$b_r = \Phi^T\, b = \begin{bmatrix} b_{Ur} \\ b_{Vr} \\ b_{Pr} \end{bmatrix} \tag{10.2}$$

4. Numerical tests

4.1 Flow over one fibre

The ROM was tested in two numerical experiments. In the first one, we look at flow over one fibre. There is one deterministic parameter – the vertical coordinate of the fibre centre. During the training, 34 snapshots of flow solutions were taken. Following the procedure described in section 3.2, the ROM was solved for different positions of the fibre along the vertical line.

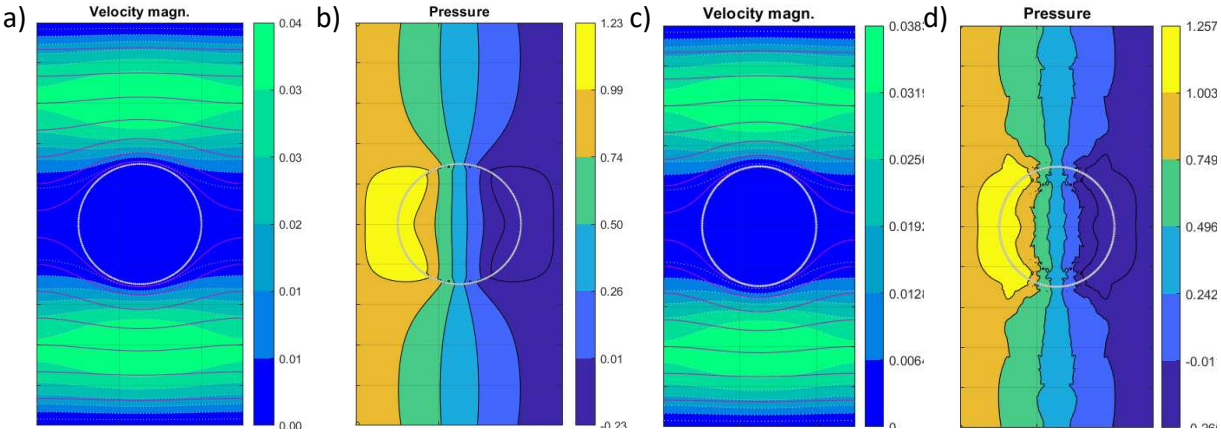

Figure 4. Example solutions for one-parameter problem
a) FOM velocity, b) FOM pressure, c) ROM velocity, d) ROM pressure

Example solutions of the full and reduced order models are showed in Fig. 4. The pressure plot contains distinctive noise, while the velocity field is rather smooth. As a quantitative error metric, we use the following error measure $\varepsilon_i = 100\% \cdot \|i - i^r\|/\|i\|$. Here i denotes a solution variable. The following error values correspond to the solution from Fig. 4: $\varepsilon_{\mathrm{U}} = 0.8\%, \varepsilon_{\mathrm{V}} = 3\%,\ \varepsilon_{\mathrm{P}} = 4\%, \varepsilon_{\mathrm{K}} = 0.2\%$. The last metric stands for the error of homogenised permeability of the whole domain.

Fig. 5 shows errors at all possible parameter points. The values spreading along the horizontal axis correspond to the sample points. The average values for the errors are $\langle\varepsilon_{\mathrm{U}}\rangle = 1.3\%, \langle\varepsilon_{\mathrm{V}}\rangle = 2.4\%, \langle\varepsilon_{\mathrm{P}}\rangle = 4.0\%, \langle\varepsilon_{\mathrm{K}}\rangle = 2\%$.

  doi:10.5075/epfl-298799_978-2-9701614-0-0

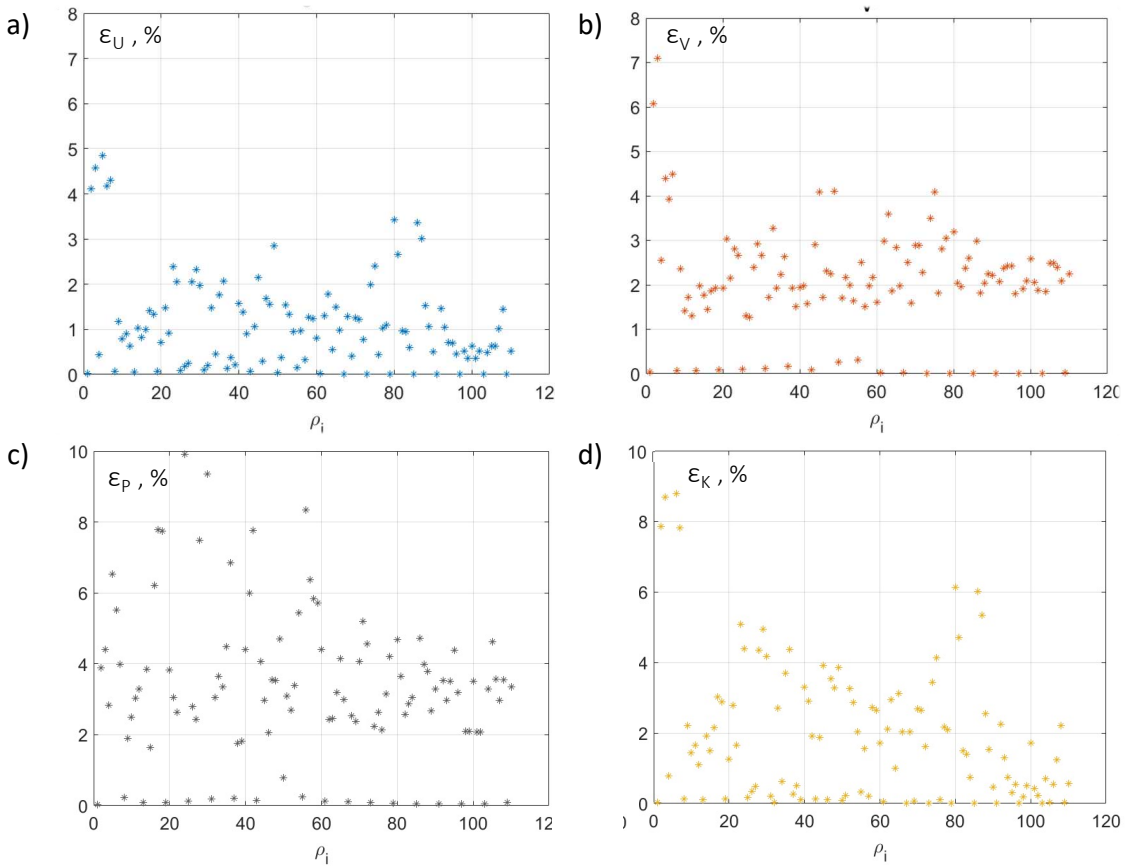

Figure 5. Error plots for all parameter values
a) horizontal velocity, b) vertical velocity, c) pressure, d) homogenised permeability

4.2 Flow over array of fibres

In the second test, random fibre distributions were considered. In this case, no explicit parameter was defined. The training has been performed on sets of randomly distributed arrays of fibres with fixed diameter. First, arrays with 5 fibres and volume fraction of 35% were used.

Building a basis from more than 150 snapshots, the resulting ROM was able to reconstruct the velocities with less than 15% accuracy. The average error in homogenised permeability was 12%, which leaves much to be desired. Given that, one ROM calculation was 3 times slower than FOM.

Running an analogous test with three fibres showed slight increase in accuracy. The average errors for velocity and permeability were now 10 and 7%. An increase in speed of calculation, however, did not take place.

5. Conclusions

The present work proposed a numerical approach for estimation of fibre tow permeability. The approach is based on sequential flow simulations with geometric parameterisation, used to apply model order reduction for acceleration. Numerical tests showed that the potential of the approach in this instalment is limited to not-so-varied geometries. Velocity, pressure fields and permeability for a problem with one moving fibre could be predicted with relative errors of 1-4%. Random fibre arrangements contain too much variability of possible flow patterns, which substantially limit possibilities of this approach.

  doi:10.5075/epfl-298799_978-2-9701614-0-0

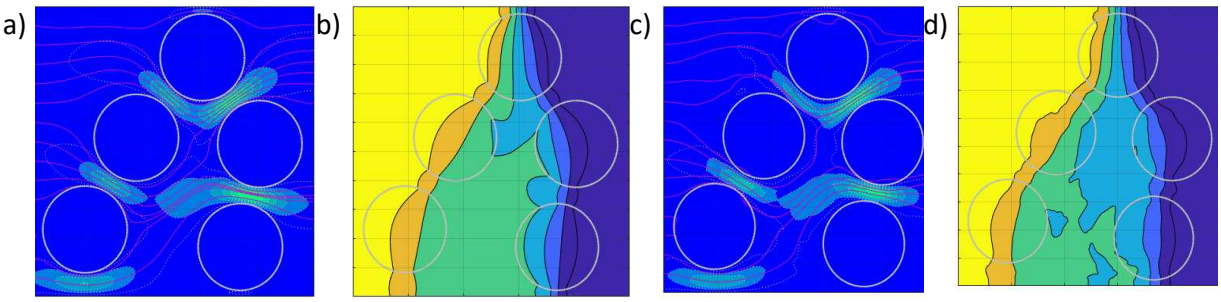

Figure 6. Example solutions for random array problem
a) FOM velocity, b) FOM pressure, c) ROM velocity, d) ROM pressure

Acknowledgements

The work has been funded by the project "MOR4MDesign", which is part of the MacroModelMat (M3) research program coordinated by Siemens (Siemens Digital Industries Software, Belgium) and funded by SIM (Strategic Initiative Materials in Flanders) and VLAIO (Flanders Innovation & Entrepreneurship)

6. References

1. Vernet N, Ruiz E, Advani S, Alms JB, Aubert M, Barburski M, Barari B, Beraud JM, Berg DC, Correia N, Danzi M. Experimental determination of the permeability of engineering textiles: Benchmark II. Composites Part A: Applied Science and Manufacturing. 2014 Jun 1;61:172-84.
2. Swery EE, Allen T, Kelly P. Capturing the influence of geometric variations on permeability using a numerical permeability prediction tool. Journal of Reinforced Plastics and Composites. 2016 Dec;35(24):1802-13.
3. Carman PC. Fluid flow through granular beds. Trans. Inst. Chem. Eng.. 1937;15:150-66.
4. Berdichevsky AL, Cai Z. Preform permeability predictions by self-consistent method and finite element simulation. Polymer Composites. 1993 Apr;14(2):132-43.
5. Gebart BR. Permeability of unidirectional reinforcements for RTM. Journal of composite materials. 1992 Aug;26(8):1100-33.
6. Belov EB, Lomov SV, Verpoest I, Peters T, Roose D, Parnas RS, Hoes K, Sol H. Modelling of permeability of textile reinforcements: lattice Boltzmann method. Composites Science and Technology. 2004 Jun 1;64(7-8):1069-80.
7. Gommer F, Endruweit A, Long AC. Influence of the micro-structure on saturated transverse flow in fibre arrays. Journal of Composite Materials. 2018 Aug;52(18):2463-75.
8. Endruweit A, Gommer F, Long AC. Stochastic analysis of fibre volume fraction and permeability in fibre bundles with random filament arrangement. Composites Part A: Applied Science and Manufacturing. 2013 Jun 1;49:109-18.
9. Schilders WH, Van der Vorst HA, Rommes J. Model order reduction: theory, research aspects and applications. Berlin: springer; 2008 Aug 27.
10. Angot P. Analysis of singular perturbations on the Brinkman problem for fictitious domain models of viscous flows. Mathematical methods in the applied sciences. 1999 Nov 10;22(16):1395-412.

  doi:10.5075/epfl-298799_978-2-9701614-0-0

Composites Meet Sustainability – Proceedings of the 20th European Conference on Composite Materials,
ECCM20. 26-30 June, 2022, Lausanne, Switzerland

MICROMECHANICAL MODELING OF RATE-DEPENDENT OFF-AXIS FAILURE IN THERMOPLASTIC COMPOSITES

Dragan Kovačević [a,b], Frans P. van der Meer [c]

a: Delft University of Technology, P.O. Box 5048, 2600 GA Delft, The Netherlands
d.kovacevic-1@tudelft.nl
b: DPI, P.O. Box 902, 5600 AX Eindhoven, The Netherlands
c: Delft University of Technology, P.O. Box 5048, 2600 GA Delft, The Netherlands

Abstract: *A micromechanical finite deformation framework for modeling failure in unidirectional composites under rate-dependent off-axis loading is presented. The onset of global softening in the micromodel corresponds to macroscopic matrix crack formation. A thin slice representative volume element with periodic boundary conditions is used, which enables representation of three-dimensional stress states. A constant prescribed strain-rate is applied in the model with a dedicated arclength control method. Two failure mechanisms are included in the polymer matrix: visco-plasticity and microcracking. A cohesive surface methodology represents the microcracking process. Cohesive elements are added on the fly with a stress-based initiation criterion. For this purpose, a power law microcrack initiation criterion is proposed. The model is validated with experimental data from tensile tests on unidirectional carbon/PEEK composite material at prescribed strain-rate and different off-axis angles. The obtained maximum stress levels are used to generate Tsai-Hill failure envelopes for macroscopic transverse crack initiation.*

Keywords: thermoplastic composites; plasticity; microcracking; off-axis loading; strain-rate

1. Introduction

Modeling of failure processes in continuous fiber reinforced composite materials has drawn a lot of attention in the past decades. The customizable microstructure of composites offers more freedom to design the lightweight structures as compared to monolithic engineering materials such as steel and aluminum. Furthermore, the application of thermoplastic polymers as the composite matrix provides an opportunity for recycling of the deteriorated structural components. However, the heterogeneous structure of composites combined with the viscous nature of the polymer resin makes the prediction of the nonlinear material behavior under different loading scenarios more difficult. The majority of the theories proposed to study failure in composites do not explicitly account for the rate dependency of the process, but rather the strength parameters must be determined separately for every considered strain-rate. The micromechanical framework offers a good environment to readily accommodate rate dependent effects, providing that a suitable rate dependent material model is used for the matrix part. In this way the rate dependent failure of composites was studied by Govaert et al. [1], Bai et al. [2], Sato et al. [3], to name a few.

In this paper we propose a micromechanical model to study the rate dependent failure in unidirectional (UD) composites exposed to off-axis loading. The model is a Representative Volume Element (RVE), defined in local coordinate system aligned with carbon fibers. Being

  doi:10.5075/epfl-298799_978-2-9701614-0-0

defined in three-dimensional (3D) space, the RVE allows for the stress states in composites under general off-axis loading. The model undergoes finite deformations including two sources of nonlinearity in the matrix part. Visco-plasticity is included by the Eindhoven Glassy Polymer material model, whereas microcracking process is represented by a cohesive zone model. The onset of softening in the RVE response is taken as the point of failure and corresponds to the macroscopic crack formation. The model results are compared with experiments on unidirectional carbon/PEEK composite system subjected to a prescribed strain-rate under different off-axis angles.

2. Experiment

The experimental benchmark consists of UD C/PEEK laminates with different orientation of the reinforcement relative to the loading direction, tested at room temperature conditions until complete failure is observed [4], see Fig. 1. Because of the macroscopically uniform stress distribution in these tests, the test can be simulated with a single-scale microscopic model.

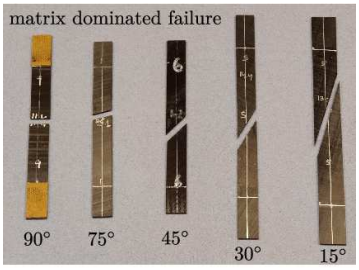

Figure 1. Fractured UD composite laminates under constant strain-rate, for different off-axis angles

The extensometer was used to measure the exact strain for the off-axis angle χ=90° at different strain-rates, and angles of: 75°, 45° and 30° at the strain rate of 10^{-4}/s. In all other cases, including χ=15° the extensometer was not utilized. In those cases, therefore, the compliance of the testing machine affects the results.

3. Micromechanical model

3.1 Problem definition

In order to develop the RVE model, first the homogenized deformation and stress state of the composite material exposed to a prescribed strain-rate is considered, see Fig. 2.

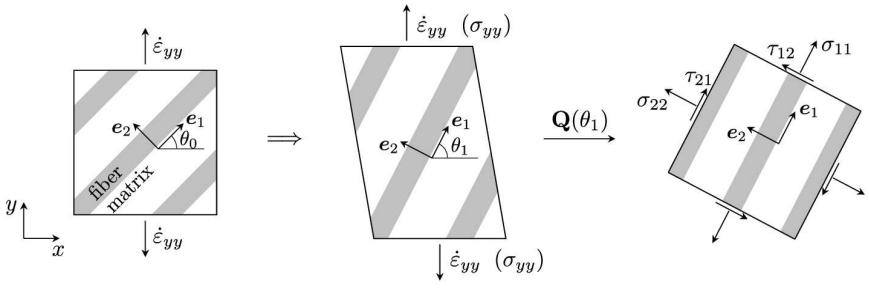

Figure 2. Strain-rate applied on UD composite material (left); deformation of the material due to applied strain-rate (middle); stress components in local coordinate system (right)

  doi:10.5075/epfl-298799_978-2-9701614-0-0

There is no restriction on the magnitude of strains in the material, implying that the local coordinate frame aligned with fibers may change orientation from the initial angle θ_0 to a new angle θ_1. Given this new angle, the transformation of the Cauchy stress to the local frame leads to the stress components acting on the material as shown in Fig. 2 (right).

Further analysis is done on the microlevel. The RVE with periodic boundary conditions is considered [5], such that one of its sides coincides with the reinforcement direction, see Fig. 3. The deformation and stress state of the RVE must be equivalent to that shown in Fig. 2. This means that the homogenized stresses on the RVE are equal to the corresponding components in Fig. 2 (right), and the deformation pattern of the RVE must correspond to the strain-rate applied in the global loading direction.

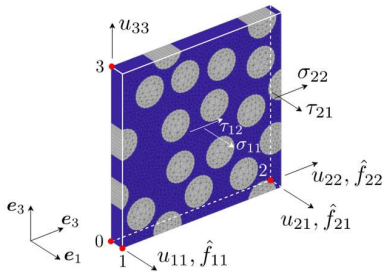

Figure 3. RVE with active displacements on master nodes and applied unit force components; master node displacements not indicated in the figure are set to zero; σ_{ij}, τ_{ij} required homogenized stress components on RVE

To satisfy these requirements a strain-rate based arclength model was formulated [6]. The constraint equation of the arclength model ensures that the RVE deforms according to the strain-rate imposed in global loading direction. In order to capture the finite strains in the material exactly, the unit force components of the arclength model are updated in every time step, accounting for the previous deformation and the change in orientation of the local frame from θ_0 to θ_1.

3.2 Material model for polymer matrix

Visco-plastic effects in the polymer matrix are included in the RVE by the Eindhoven Glassy Polymer (EGP) material model [7]. The EGP is an isotropic, elasto-viscoplastic material model that allows for the finite strains in the material. In the model, the stress is additively decomposed in three components: the hydrostatic stress, the hardening stress and the driving stress. The driving stress component introduces viscosity as well as plasticity in the model. It can also distinguish between different relaxation processes in the material, and for every relaxation process there might be multiple relaxation modes represented by different Maxwell elements connected in parallel. Material parameters used for the EGP model as described in [7] are listed in Table 1. The relaxation spectrum of one process, α, is considered and specified in Appendix.

Table 1: Material parameters for the EGP model

K [MPa]	G_r [MPa]	$\tau_{0\alpha}$ [MPa]	μ_α	$S_{\alpha\alpha}$	$r_{0\alpha}$	$r_{1\alpha}$	$r_{2\alpha}$
2600	14.2	1.386	.08	3	.95	1	-5

  doi:10.5075/epfl-298799_978-2-9701614-0-0

3.2 Material model for carbon fibers

It is assumed that carbon fibers do not undergo any failure process, therefore, the reinforcement responds elastically to the loading. A hyperelastic transversely isotropic material model [8] is selected to model this behavior, with a small modification as presented in [6]. The parameters of the material model are listed in Table 2. E_1 is the Young's modulus in the preferential stiffness direction, E_2 and v_{23} are the Young's modulus and Poisson's ratio in the plane of isotropy, G_{12} and v_{12} are the shear modulus and the Poisson's ratio defining behavior in the planes perpendicular to the isotropic plane. The modulus G_{12} has a value larger than usually reported [9], in order to achieve a good match in the initial slope between the experiment and the model.

Table 2: Material parameters for transversely isotropic material model

E_1 [GPa]	E_2 [GPa]	G_{12} [MPa]	v_{12}	v_{23}
125	15	45	.05	.3

3.3 Cohesive law for microcracking processes

Beside visco-plasticity, microcracking will also take place in the matrix part at higher stress levels. It is represented by means of a cohesive zone model that is governed by a mixed-mode damage cohesive law as explained by Liu et al. [10], and extended to 3D. Cohesive segments are added on the fly [11], when a stress-based initiation criterion is satisfied. At every time step the traction vector is computed on a potential cohesive surface, which may be any surface between two adjacent finite elements in the matrix part, or interface between carbon fibers and the matrix. The traction vector is decomposed in a component perpendicular to the fiber direction $t_\perp$ and a component parallel with the fibers $t_\parallel$. Then we propose an initiation criterion in the power law form:

$$\left(\frac{t_\perp}{f_\perp}\right)^m + \left(\frac{t_\parallel}{f_\parallel}\right)^n < 1 \tag{1}$$

where m and n are the power law coefficients, and $f_\perp$ and $f_\parallel$ are the strength parameters in the corresponding directions. In this study the following values are adopted: $m = 3$, $n = 2$, $f_\perp = 130$ MPa, $f_\parallel = 60$ MPa. For the fiber/matrix interface, the strength in direction parallel with the fibers is set higher, $f_\parallel = 75$ MPa.

The cohesive model also requires the fracture energy G_c as an input parameter. Observing the fractured specimens in Fig. 1, a conclusion arises that the mode of fracture changes for different off-axis angles. Hence, the value provided to the model interpolates between a value G_{cI} calibrated for χ=90° and a value G_{cII} calibrated for χ=15°, see Fig. 4. The G_c value provided to the model depends on the ratio between $t_\parallel$ and $t_\perp$ at the moment of initiation. For the problem at hand, this ratio provides a sufficient insight in the mode of fracture that will follow after the initiation takes place. This is because the load on the RVE increases almost proportionally, and there cannot be a huge variation in direction of the displacement jump. The value $\bar{t}_r$, after which the fracture energy cannot increase, represents the ratio between the initial homogenized shear stress τ_{21} and normal stress σ_{22} acting on the RVE for χ=15°, see Fig. 3.

  doi:10.5075/epfl-298799_978-2-9701614-0-0

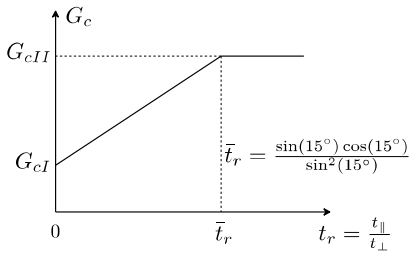

Figure 4. Fracture energy provided to cohesive law

The cohesive zone model also accounts for geometric nonlinear effect on the fracture process. This part is based on the work of Reinoso and Paggi [12], which is extended to 3D.

4. Results and discussion

In this section the simulation results are compared with the experiment. Homogenized stress-strain curves in the global loading direction are considered, see Fig. 2. The onset of softening in the RVE response is taken as the point of failure, and that point is compared with experimentally observed failure.

The strain-rate of 10^{-4}/s is applied on the RVE under several different off-axis angles. The obtained results are plotted in Fig. 5, together with the experimental stress-strain curves.

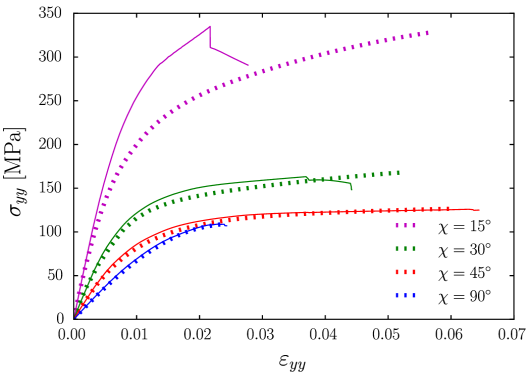

Figure 5. RVE response (solid) versus experiment (dotted) for strain rate 10^{-4}/s and different off-axis angles

For the off-axis angles in the range 30°-90° there is a good match with the experiments. For the off-axis angle χ=15°, there is an offset. One reason for this difference might be the fact that the extensometer was not used in this case. Also, the clamps of the testing machine introduce a restraining effect such that fibers close to the boundaries cannot freely rotate in an attempt to align with the loading direction. This is not the case with the RVE model, where the change in orientation of the RVE from the angle θ_0 to the angle θ_1 is allowed, see Fig. 2. This discrepancy in the kinematics implies a difference in the stress state. The difference gets more pronounced for lower off-axis angles, when a small variation in the angle makes a significant change in the stress taken by the fibers.

The fractured RVE for χ=30° is shown in Fig. 6. The contour plot indicates the distribution of the equivalent plastic strain in the model. The fracture plane is parallel with the reinforcement as is observed in the experiment, see Fig. 1. Also due to the higher strength of the interface in

direction parallel with the fibers, microcracking process is completely in the matrix. To support this fact, it is reported in the reference experiments that the interface mostly remains intact and the failure is indeed in the resin.

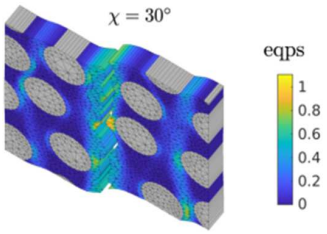

Figure 6. Example of fractured RVE with distribution of equivalent plastic *strain*

Now we make an attempt to construct a failure envelope based on the micromechanical simulations. The envelope intends to represent a stress at which the macroscopic crack forms for different off-axis angles. The Tsai-Hill failure criterion is considered [13]. Since the material is loaded in tension, this failure criterion gives reasonably accurate estimation of the material behavior. The idea presented in [14] is followed, such that the failure stress is a product of a reference failure stress $\sigma_{\text{ref}} = \sigma_{90^0}$ and a function depending on the off-axis angle $g(\chi)$. Coefficients needed to construct the function $g(\chi)$ are as follows: $R_{11} = \sigma_{0^0} / \sigma_{\text{ref}} = 18.94$, $R_{22} = R_{33} = \sigma_{90^0} / \sigma_{\text{ref}} = 1$, $R_{12} = 1.3$. The strength at χ=0°, $\sigma_{0^0} = 2063$ MPa was determined experimentally. The coefficient R_{12} is calibrated to achieve a good fit with the trend observed in the simulations. The Tsai-Hill failure criterion is compared with the failure stresses obtained from the RVE in Fig. 7.

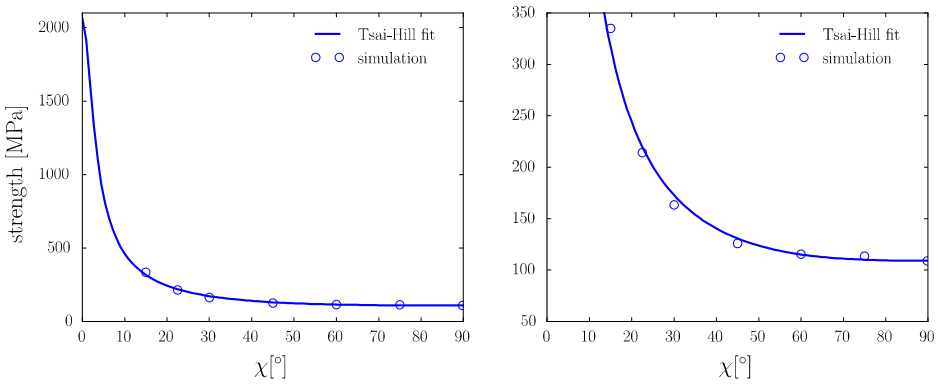

Figure 7. Tsai-Hill failure envelope versus simulation results; close-up view of the range covered by the RVE model (right)

Since no failure takes place in the carbon fibers, the model cannot accurately represent failure at low off-axis angles when the fibers bear most of the loading. Nevertheless, in the range that is covered by the present simulations a good fit is possible.

5. Conclusion

In this contribution a micromechanical framework to study rate-dependent failure in unidirectional composites under off-axis loading is introduced. The onset of softening in the micromodel represents macroscopic crack formation. The micromodel is a 3D RVE defined in the local coordinate frame aligned with the carbon fibers. This way, the stress states encountered

  doi:10.5075/epfl-298799_978-2-9701614-0-0

in off-axis loading scenarios can be reproduced in the RVE. A strain-rate is imposed on the RVE by means of a proper arclength model. The arclength model ensures that the homogenized kinematics of the RVE correspond with the strain-rate applied in the global loading direction. Finite deformations are allowed in the homogenized kinematics of the RVE as well as at every integration point, where appropriate constitutive models are used to represent the matrix part and the fibers. In the matrix part two different failure processes are included: visco-plasticity and microcracking. A cohesive zone model is utilized for the microcracking process in which geometric nonlinear effects are also included. The performance of the RVE model is compared with experiments on thermoplastic C/PEEK composite system at one prescribed strain-rate and different off-axis angles, at room temperature conditions. Based on the simulation results obtained, the Tsai-Hill failure fit is constructed. In the future work, failure of the model at different strain-rates will be considered and compared with experiments to validate the model.

6. Acknowledgement

This research forms part of the research programme of DPI, project #811t17.

The experimental work as part of the same project, performed at the University of Twente by Bharath Sundararajan and Leon Govaert is greatly acknowledged.

7. Appendix

Table 3: Relaxation spectrum of the EGP model

mode	$G_{\alpha,j}$ [MPa]	$\eta_{0\alpha,j}$ [MPa·s]	mode	$G_{\alpha,j}$ [MPa]	$\eta_{0\alpha,j}$ [MPa·s]
1	1045.52	$7.590 \cdot 10^{21}$	9	50.61	$9.198 \cdot 10^{10}$
2	400.03	$8.502 \cdot 10^{16}$	10	83.94	$2.272 \cdot 10^{10}$
3	46.06	$2.570 \cdot 10^{14}$	11	77.28	$8.756 \cdot 10^{8}$
4	87.28	$1.843 \cdot 10^{13}$	12	60.61	$2.874 \cdot 10^{7}$
5	72.43	$5.912 \cdot 10^{12}$	13	56.67	$1.127 \cdot 10^{6}$
6	63.03	$1.992 \cdot 10^{12}$	14	4.64	$3.851 \cdot 10^{4}$
7	45.46	$5.520 \cdot 10^{11}$	15	53.03	$1.840 \cdot 10^{3}$
8	42.43	$1.987 \cdot 10^{11}$	16	3.42	$4.961 \cdot 10^{1}$

8. References

1. Govaert LE, Schellens HJ, Thomassen HJM, Smit RJM, Terzoli L, Peijs T. A micromechanical approach to time-dependent failure in off-axis loaded polymer composites. Composites Part A 2001, 32:1697–1711.

2. Bai X, Bessa MA, Melro AR, Camanho PP, Guo L, Liu WK. High-fidelity micro-scale modeling of the thermo-visco-plastic behavior of carbon fiber polymer matrix composites. Composite Structures 2015, 134:132–141.

  doi:10.5075/epfl-298799_978-2-9701614-0-0

3. Sato M, Shirai S, Koyanagi J, Ishida Y, Kogo Y. Numerical simulation for strain rate and temperature dependence of transverse tensile failure of unidirectional carbon fiber-reinforced plastics. Journal of Composite Materials 2019, 53:4305–4312.

4. Sundararajan B, Govaert LE. Experimental part of the research programme of DPI, project #811t17, 2020.

5. Van der Meer FP. Micromechanical validation of a mesomodel for plasticity in composites. European Journal of Mechanics – A/Solids 2016, 60:58–69.

6. Kovačević D, Van der Meer FP. Strain-rate based arclength model for nonlinear microscale analysis of unidirectional composites under off-axis loading. Under review.

7. Van Breemen LCA, Klompen ETJ, Govaert LE, Meijer HEH. Extending the EGP constitutive model for polymer glasses to multiple relaxation times. Journal of the Mechanics and Physics of Solids 2011, 59:2191–2207.

8. Bonet J, Burton AJ. A simple orthotropic, transversely isotropic hyperelastic constitutive equation for large strain computations. Computer Methods in Applied Mechanics and Engineering 1998, 162:151–164.

9. Miyagawa H, Sato C, Mase T, Drown E, Drzal LT, Ikegami K. Transverse elastic modulus of carbon fibers measured by Raman spectroscopy. Materials Science and Engineering: A 2005, 412:88–92.

10. Liu Y, Van der Meer FP, Sluys LJ, Ke L. Modeling of dynamic mode I crack growth in glass fiber-reinforced polymer composites: Fracture energy and failure mechanism. Engineering Fracture Mechanics 2021, 243:107522.

11. Camacho GT, Ortiz M. Computational modelling of impact damage in brittle materials. International Journal of Solids and Structures 1996, 33:2899–2938.

12. Reinoso J, Paggi M. A consistent interface element formulation for geometrical and material nonlinearities. Computational Mechanics 2014, 54:1569–1581.

13. Azzi VD, Tsai SW. Anisotropic strength of composites. Experimental Mechanics 1965, 5:283–288.

14. Amiri-Rad A, Pastukhov LV, Govaert LE, Van Dommelen JAW. An anisotropic viscoelastic-viscoplastic model for short-fiber composites. Mechanics of Materials 2019, 137:103141.

  doi:10.5075/epfl-298799_978-2-9701614-0-0

SCALER NONLINEAR CONTINUUM DAMAGE MODELS FOR CERAMIC MATRIX COMPOSITES WITH SIGNIFICANT IN PLANE PLY ANISOTROPY

Craig Przybyla[a], Antoine Débarre[b], Jean-François Maire[b], Emmanuel Baranger[c], Frédéric Laurin[c]

a: Air Force Research Laboratory, Wright-Patterson AFB, OH, USA – craig.przybyla@us.af.mil
b: l'Office National d'Études et de Recherches Aérospatiales, Châtillon, France
c: Laboratoire de Mécanique Paris-Saclay, Gif-sur-Yvette, France

Abstract: *Continuous fiber reinforced ceramic matrix composites (CMCs) are increasingly being employed in safety critical applications and the need the need for damage models to support the design, certification and sustainment has increased. In this work, we propose a simple but robust formulation for a 2D continuum damage model derived via a thermodynamics-based approach called openDM. Specifically, we consider a model with two scalar damage parameters that account for damage as a result of matrix cracking in the ply in both the fiber and transverse directions. The applicability of this model is considered for both a balanced 2D woven based SiC fiber reinforced composite and a 2D unidirectional ply based SiC fiber reinforced composite with predominately SiC matrices. While the response of the 2D woven composite was captured well with the two parameter model, the more anisotropic unidirectional ply based CMC was more difficult to capture unless a hybrid [0,90] ply was assumed in the model.*

Keywords: Continuum damage model; ceramic matrix composites; anisotropic damage response

1. Introduction

As the use of continuous fiber reinforced ceramic matrix composites (CMCs) has rapidly accelerated, particularly in aero-propulsion, the need for damage models to support the design, certification and sustainment of safety critical CMC components has increased. One CMC variant with continuous SiC fibers embedded into a predominately SiC matrix has been of particular interest for components in the hot section of gas turbine engines. Recently, CFM started selling their new LEAP® engine with SiC/SiC CMC shrouds (1). Despite these successes, the requirements for insertion of these types of materials in critical applications such as gas-turbine engines for aerospace require extensive testing for design, certification and sustainment. Progressive damage modelling tools that can better inform designs, provide accurate life assessments for certification and address sustainment issues after systems have been fielded have the potential to greatly reduce the required amount of testing, reduce conservatism in design, and provide sustainment engineers with the ability to perform performance prognosis in the presence of defects or in service damage.

Typically SiC/SiC CMCs are designed with a weak fiber coating or interphase of pyrolytic carbon or boron nitride that promotes a toughened response (2,3). The architecture of the fiber reinforcement can be stacks of 2D plys, 3D woven preforms or unidirectional laminate based layups (4). They are typically processed either using a mixture of chemical vapour infiltration/deposition (CVI/CVD) and polymer infiltration and pyrolysis or densified using a melt infiltration (MI) process with silicon melted into a carbon preform. Several studies have characterized the mechanical behavior. At the microscale, the cracks appear to initially form

  doi:10.5075/epfl-298799_978-2-9701614-0-0

near the weak interphase or defects and grow dependent on local microstructural conditions (5). In dense MI based systems, the cracks have been observed to initiated near the interphase and coalesce into larger matrix cracking with increasingly large loads (6,7). At larger scales, damage in the laminate based MI SiC/SiC CMCs appears in bands (8,9). In the more porous PIP derived matrices with 2D woven plies, the damage appears to depend on the weave architecture with the major cracks forming at specific cross over points in the tows (10). These observations indicate that there is a strong influence of microstructure on initiation and propagation and that damage propagation is very dependent on the direction of loading.

Continuum damage modelling (CDM) approaches that estimate an effective or average damage state over a given volume have been frequently employed to model the mechanical response of CMCs. Chaboche et. al. (11) introduced a CDM model for brittle materials that employed a tensorial damage variable that accounts for damage deactivation and irreversible strains. Later Chaboche and Maire (12) expanded on the approach include deactivation due to closure in compression. In this model, Chaboche and Maire employed both scalar damage variables corresponding with microcracks oriented by the orientation of the fibre reinforcement and a second rank damage tensor that evolves with the maximum principal strain directions. Marcin et. al. (13) employed the same framework developed earlier by Chaboche and Maire, but used five scalar damage variables to account damage in the direction of the primary reinforcement, transverse to the direction of the primary reinforcement, in the ±45° directions and in the out of plane direction. Baranger (14) and Friderikos and Baranger (15) showed that reduced order models (such as the scaler model by Marcin et. al. (13)) can be as accurate as complex models with tensorial damage variables for a wide range of loading cases.

In this work we follow the approach of Marcin et. al. (13) to develop a simple two parameter model to capture the in plane effects effects of the primary damage modes observed in 2D ply based layups including woven and unidirectional laminates but limit our analysis to two scale damage variables for the in plane response.

2. Methods

2.1 Model Formulation

In this approach the continuum damage formulation is based on the Helmholtz free energy to derive a thermodynamically consistent relationship for the deformation response. A simple 2D damage model can be formulated such that the Helmholtz free energy is defined according to

$$\psi = \frac{1}{2\rho}\left(\varepsilon^{*}\colon \tilde{\mathbf{C}}\colon \varepsilon^{*}\right) \tag{1}$$

where

$$\boldsymbol{\varepsilon}^{*} = \boldsymbol{\varepsilon} - \boldsymbol{\varepsilon}^{th} \tag{2}$$

The compliance is related to the stiffness according to

$$\tilde{\mathbf{C}} = \left(\tilde{\mathbf{S}}\right)^{-1} \tag{3}$$

The effective compliance is defined as

  doi:10.5075/epfl-298799_978-2-9701614-0-0

$$\tilde{\mathbf{S}} = \mathbf{S}^0 + \Delta\mathbf{S}^m \tag{4}$$

such that $\Delta\mathbf{S}^m$ is the variation of the initial compliance tensor $\mathbf{S}^0$ as a result of the matrix damage.

For a thin plate we can assume either plane stress or plane strain boundary conditions. The resulting compliance tensor can be expressed as

$$\mathbf{S}^0 = \begin{bmatrix} \frac{1}{E_{11}} & \frac{-\nu_{12}}{E_{11}} & 0 \\ \frac{-\nu_{21}}{E_{22}} & \frac{1}{E_{22}} & 0 \\ 0 & 0 & \frac{1}{G_{12}} \end{bmatrix} \tag{5}$$

with a total of four independent elastic constants including the elastic moduli in the two orthogonal directions E_{11} and E_{22}, the in-plane Poisson ratio ν_{12} and the in-plane shear modulus G_{12}. Note that the Poisson ratio ν_{12} is related to ν_{21} according to $\nu_{12}/E_{11} = \nu_{21}/E_{22}$. The elastic stiffness is defined as $\mathbf{C}^0$ and ρ is the material density. It follows then that the behavior law is

$$\boldsymbol{\sigma} = \rho\frac{\partial\psi}{\partial\boldsymbol{\varepsilon}} = \tilde{\mathbf{C}}\colon\boldsymbol{\varepsilon}^* \tag{6}$$

The strain is determined according to

$$\boldsymbol{\varepsilon} = \tilde{\mathbf{S}}\colon\boldsymbol{\sigma} + \boldsymbol{\varepsilon}^{th} \tag{7}$$

The total strain tensor is defined as $\boldsymbol{\varepsilon}$ and the thermal strain tensor $\boldsymbol{\varepsilon}^{th}$ is defined such that

$$\boldsymbol{\varepsilon}^{th} = \boldsymbol{\alpha}(T - T^0) \tag{8}$$

where $\boldsymbol{\alpha}$ is the symmetric thermal expansion tensor, T is the current or test temperature and T^0 is the reference temperature. We employ two scalar damage variables (d_1^m, d_2^m) to account for matrix damage in the 0° and 90° loading directions. The superscript m indicates damage in the matrix and not in the fibers. The change in compliance based on damage $\Delta\mathbf{S}^m$ can be simplified to as

$$\Delta\mathbf{S}^m = \sum_{i=1}^{2} d_i^m\mathbf{H}_i^m \tag{9}$$

where $\mathbf{H}_i^m$ is the fourth-order damage-effect tensor. Here we assume a simple deactivation index η_i^m as defined previously. As the behavior in the transverse direction (relative to the loading axis) remains linear, the form of the fourth order damage-effect tensor is expressed as

$$\mathbf{H}_1^m = \begin{pmatrix} \eta_1^m S_{11}^0 & 0 & 0 \\ 0 & 0 & 0 \\ 0 & 0 & h_{66}^1 S_{66}^0 \end{pmatrix} \tag{10}$$

and

$$\mathbf{H}_2^m = \begin{pmatrix} 0 & 0 & 0 \\ 0 & \eta_2^m S_{22}^0 & 0 \\ 0 & 0 & h_{66}^2 S_{66}^0 \end{pmatrix} \tag{11}$$

  doi:10.5075/epfl-298799_978-2-9701614-0-0

The model parameter h_{66}^1 and h_{66}^2 correspond to the effect of the stress acting parallel to the plane of the crack and parallel to the crack front, respectively.

The deactivation index η_i^m is defined such that

$$\eta_i^m = h(\sigma_i) \tag{12}$$

where h is the Heaviside step function. This indicates that the cracks are closed under compressive stresses. The driving forces y_i^m associated with the two scalar damage variables d_i^m are defined as a function of the positive part of the total strain tensor such that:

$$\begin{cases} y_1^m = \frac{1}{2}(E_{11}\langle\varepsilon_1^*\rangle_+^2 + b_1 G_{12}(\varepsilon_6^*)^2) \\ y_2^m = \frac{1}{2}(E_{22}\langle\varepsilon_2^*\rangle_+^2 + b_2 G_{12}(\varepsilon_6^*)^2) \end{cases} \tag{13}$$

where $\langle . \rangle_+$ are the Macaulay Brackets. The model parameter b_1 define the coupling between tension and in plane shear. We then define

$$\begin{cases} y_1^{max} = \max\limits_{0<\tau\leq t}(y_1^m(\tau)) \\ y_2^{max} = \max\limits_{0<\tau\leq t}(y_2^m(\tau)) \end{cases} \tag{14}$$

Finally, we define an exponential form of the scalar function that accounts for saturation effects such that

$$g_{s(i)}^{max}(y) = \frac{\left\langle \sqrt{y_{(i)}^{max}} - \sqrt{y_{0(i)}^m} \right\rangle_+}{\sqrt{y_{c(i)}^m}} \tag{15}$$

and the damage variables d_i can be calculated as

$$d_i = d_{c(i)}^m \left[1 - \exp\left\{-\left(g_{s(i)}^{max}\right)^{p_i^m}\right\}\right] \quad \text{for } i \in \{1,2\} \tag{16}$$

where the model parameter $d_{c(i)}^m$ describes the saturation damage parameter, $y_{0(i)}^m$ is the damage threshold, $y_{c(i)}^m$ describes the influence of the damage rate, and p_i^m accounts for the curve shape. The parameters for the 2D damage model are summarized in Table 1.

2.2 Model Implementation

Here we employ generalized non-linear composite laminate theory to solve the material model for thin composites with 2D plys oriented at various angles relative to the sample reference frame. Following the Kirshoff-Love theory, we assume that the total mesoscopic strain relative to the global reference frame is linear in the thickness of the laminate such that

$$\boldsymbol{\varepsilon} = \boldsymbol{\varepsilon}^0 + \mathrm{z}\boldsymbol{\kappa}^0 \tag{17}$$

where $\boldsymbol{\varepsilon}^0$ and $\boldsymbol{\kappa}^0$ are the membrane strain and the curvature of the laminate and z is the perpendicular distance to the middle plane of the laminate. It is assumed here that the deformed shape remains normal to the middle-plane during loading and that the out-of-plane shear strains are negligible. The governing equilibrium equations for the composite layup are

$$\mathbf{N} + \mathbf{N}^g + \mathbf{N}^{th} = \mathbf{A}\colon \boldsymbol{\varepsilon}^0 + \mathbf{B}\colon \boldsymbol{\kappa}^0 \tag{18}$$

and

  doi:10.5075/epfl-298799_978-2-9701614-0-0

$$\mathbf{M} + \mathbf{M}^{g} + \mathbf{M}^{th} = \mathbf{B}\colon \boldsymbol{\varepsilon}^{0} + \mathbf{D}\colon \boldsymbol{\kappa}^{0} \tag{19}$$

where $\mathbf{N}$ and $\mathbf{M}$ are the Loads and bending moments applied to the laminate. The superscript g denotes the loads and moments associated with the non-linear strains, and the superscript th indicates those associated with the thermal strains. The nonlinear strains in the ply coordinate system can be calculated such that

$$(\boldsymbol{\varepsilon}^{\boldsymbol{g}})^{p} = \left[\mathbf{I} - \mathbf{S}(T_0)^{p}\colon \tilde{\mathbf{C}}(T, \boldsymbol{d})^{p}\right]\colon \left[\boldsymbol{\varepsilon}^{\boldsymbol{p}} - \left(\boldsymbol{\varepsilon}^{th}\right)^{\boldsymbol{p}}\right] \tag{20}$$

and the thermal strains were defined previously. The matrices $[\mathbf{A}]$, $[\mathbf{B}]$, and $[\mathbf{D}]$ in equations (18) and ((19) are called the extensional stiffness, the coupling stiffness and the bending stiffness, respectively, and are defined elsewhere (16). Schematics explaining the resultant forces $\mathbf{N}$ and resultant moments $\mathbf{M}$ are given in Figure 1.

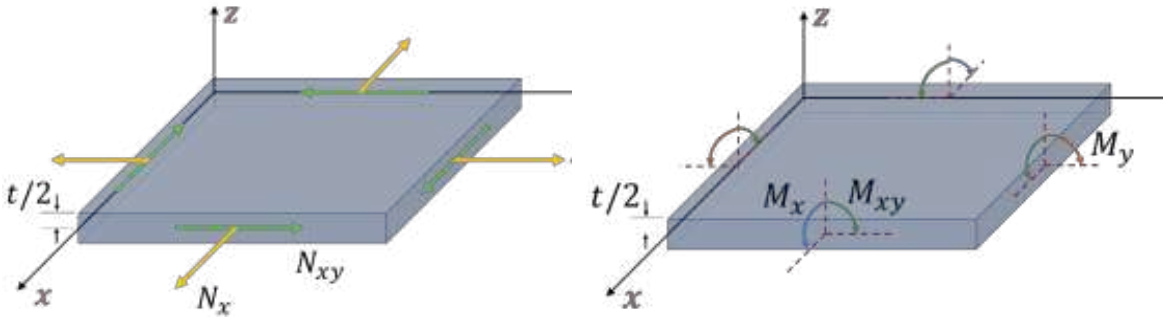

(a) (b)

Figure 1 Schematic showing the definitions of the (a) force and (b) moment resultants

3. Results and Discussion

3.1 2D woven SiC/SiC composite

The first material that was considered was a 2D continuous woven SiC fiber CMC with a predominately SiC matrix. The weave was balanced with equal fiber volume fraction in the 0° and 90° directions with no off angle plies in the layup. Data were available for tensile tests in both the 0° and 45° degree direction relative to the direction of the warp tows. The experimental data and model results are both given in Figure 2.

Several iterations were employed by adjusting the model parameters for calibration. Specifically, this calibration was performed using a specific procedure such that

1. Estimate elastic parameters based on constituents and rule of mixtures (E_{11}^{0}, E_{22}^{0}, ν_{12}^{0}, G_{12}^{0}, α_i, T_o)
2. Calibrate Elastic Parameters for 0°tests (E_{11}^{0}, E_{22}^{0})
3. Calibrate Elastic Parameters for 45°tests (G_{12}^{0})
4. Calibrate damage parameters for 0°tests ($y_{0(i)}^{m}$, $y_{c(i)}^{m}$, p_i^{m}, $d_{c(i)}^{m}$)
5. Calibrate damage parameters for 45°tests (h_{66}^{i}, b_i)
6. Iterate parameters to find best fit for 0°and 45°tests

The calibrated parameters are given in Table 1.

  doi:10.5075/epfl-298799_978-2-9701614-0-0

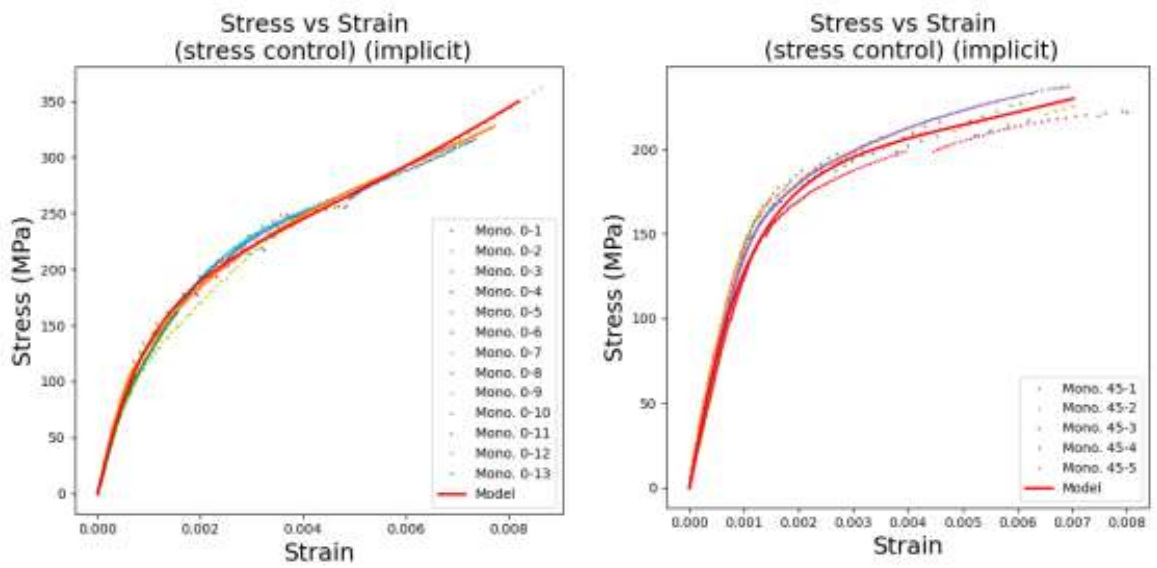

(a) (b)

Figure 2: Experimental stress versus strain response with the openDM model predicitons for 2D woven SiC/SiC (a) oriented 0° relative to the loading direction, (b) oriented 45° relative to the loading direction.

Table 1: Calibration parameters for 2D woven SiC/SiC CMC

Elasticity	$E_{11}^0 = E_{22}^0 = 180GPa$ $\nu_{12}^0 = 0.1$ $G_{12}^0 = 68GPa$	Young Modulus Poisson ratio Shear modulus
Thermal behavior	$\alpha_1 = \alpha_2 = 3.7x10^{-6}$ 1 /°C $T_o = 20$°C	Thermal expansion Reference Temperature
Damage effects	$h_{66}^1 = h_{66}^2 = 1.35$	"Shear" Damage Effect
Thermodynamic forces	$b_1 = b_2 = 0.3$	Traction / Shear Coupling
Damage Kinetics	$y_{0(1)}^m = y_{0(2)}^m = 0.003$ $y_{c(1)}^m = y_{c(2)}^m = 2.2$ $p_1^m = p_2^m = 1.3$ $d_{c(1)}^m = d_{c(2)}^m = 3.8$	Damage Thresholds Damage Evolution Celerity Damage Evolution Exponents Damage Saturations

3.2 Unidirectional Laminate based SiC/SiC CMC

The second material considered was a laminate based material with unidirectional SiC fibers embedded in a SiC matrix produced via the MI process. In all cases the material considered here was laid using an eight ply $[0,90]_{4s}$ layup. To accommodate the significant anisotropy between the 0° and 90° loading it was helpful to model each ply as a hybrid [0,90] ply stack instead of individual plies. The experimental data relative to the calibrated model are shown in Figure 3. The calibrated model parameters are in Table 2

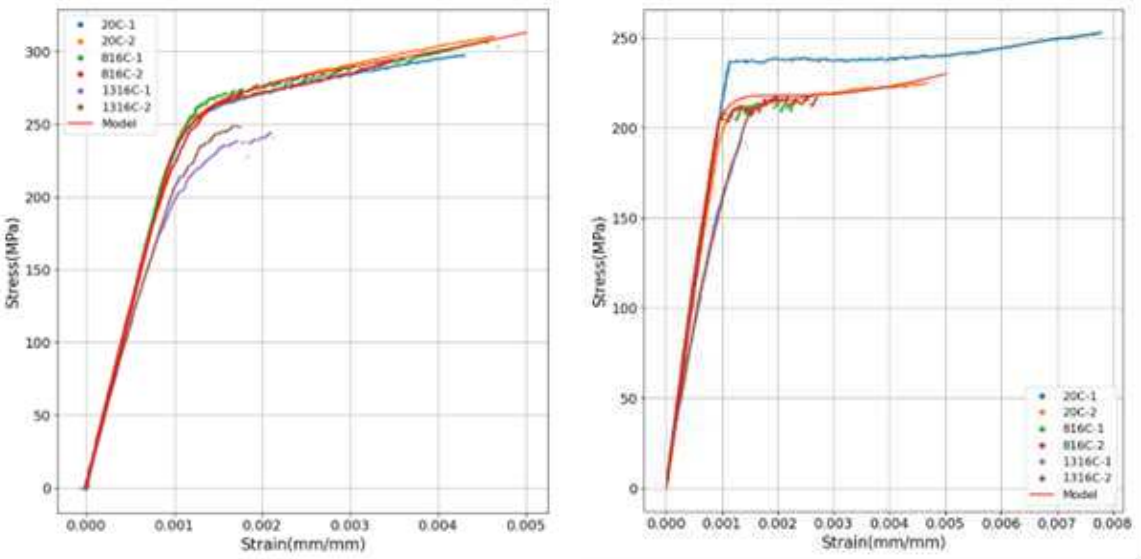

Figure 3: Experimental stress versus strain response with the openDM model predicitons for (a) the GE SiC/SiC CMC oriented 0° relative to the loading direction and (b) the GE SiC/SiC CMC oriented 45° relative to the loading direction.

Table 2: Calibration parameters for Laminate based

Elasticity	$E_{11}^0 = E_{22}^0 = 290GPa$ $\nu_{12}^0 = 0.17$ $G_{12}^0 = 95.36GPa$	Young Modulus Poisson ratio Shear modulus
Thermal behavior	$\alpha_1 = \alpha_2 = 8.6x10^{-7}$ 1/℃ $T_o = 20$℃	Thermal expansion Reference Temperature
Damage effects	$h_{66}^1 = h_{66}^2 = 0.8$	"Shear" Damage Effect
Thermodynamic forces	$b_1 = b_2 = 2.4$	Traction / Shear Coupling
Damage Kinetics	$y_{0(1)}^m = y_{0(2)}^m = 0.13$ $y_{c(1)}^m = y_{c(2)}^m = 6.3$ $p_1^m = p_2^m = 1.16$ $d_{c(1)}^m = d_{c(2)}^m = 6.3$	Damage Thresholds Damage Evolution Celerity Damage Evolution Exponents Damage Saturations

4. Conclusion

A simple 2D two parameter scaler continuum damage model was introduced to model the stress strain response in 2D CMC layups. The model is able to match the behavior well when the response of the plies is similar in the 0° and 90° directions such as is the case with a CMC with balance 2D woven plies. Unidirectional ply based CMCs can also be modeled using the simple two scale damage parameter model as stacks of coupled [0/90] degree plies. In this manner, it the same calibration proceeded can be employed with the coupled coupled [0/90] degree plies that was employed for the 2D balanced woven based CMC. However, it is likely that to model the highly anisotropic response of a single ply in a unidirectional ply based layup a more complex damage model will be required.

  doi:10.5075/epfl-298799_978-2-9701614-0-0

References

1. Steibel J. Ceramic matrix xomposites taking flight at GE Aviation. American Ceramic Society Bulletin. 2019; 98: 30-33.
2. DiCarlo JA, Yun HM, Morscher GN, Bhatt RT. Handbook ofCeramic Composites. In Bansal NP, editor..: KLUWER ACADEMIC PUBLISHERS; 2005. p. 77-98.
3. Corman GS, Luthra KL. Handbook ofCeramic Composites. In Bansal NP, editor..: KLUWER ACADEMIC PUBLISHERS; 2005. p. 99-115.
4. DiCarlo JA. Ceramic matrix Composites: materials, Modeling and Technology. In Bansal NP, Lamon J, editors..: Wiley; 2015. p. 217-235.
5. Swaminathan B, McCarthy NR, Almansour AS, Sevener K, Pollock TM, Kiser JD, et al. Microscale characterization of damage accumulation in CMCs. Journal of the European Ceramic Society. 2021; 41: 3082-3093.
6. Tracy J, Daly S, Sevener K. Multiscale damage characterization in continuous fiber ceramic matrix composites using digital image correlation. Journal of Materials Science. 2015/08/; 50: 5286-99.
7. Sevener KM, Tracy JM, Chen Z, Kiser JD, Daly S. Crack opening behavior in ceramic matrix composites. Journal of the American Ceramic Society. 2017; 100: 4734-4747.
8. Whitlow T, Jones E, Przybyla C. In-situ damage monitoring of a SiC/SiC ceramic matrix composite using acoustic emission and digital image correlation. Composite Structures. 2016; 158: 245-251.
9. Whitlow T, Pitz J, Pierce J, Hawkins S, Samuel A, Kollins K, et al. Thermal-mechanical behavior of a SiC/SiC CMC subjected to laser heating. Composite Structures. 2019; 210: 179-188.
10. Rossol MN, Rajan VP, Zok FW. Effects of weave architecture on mechanical response of 2D ceramic composites. Composites Part A: Applied Science and Manufacturing. 2015; 74: 141-152.
11. Chaboche JL, Lesne PM, Maire JF. On the constitutive damage modelling of composite systems. In ; 1995; Boulder. p. 223-226.
12. Chaboche JL, Maire JF. A new micromechanics based CDM model and its application to CMC's. Aerospace Science and Technology. 2002; 6: 131-145.
13. Marcin L, Maire JF, Carrere N, Martin E. Development of a Macroscopic Damage Model for Woven Ceramic Matrix Composites. International Journal of Damage Mechanics. 2011/08/; 20: 939-57.
14. Baranger E. Building of a reduced constitutive law for ceramic matrix composites. International Journal of Damage Mechanics. 2013; 22: 1222-1238.
15. Friderikos O, Baranger E. Automatic building of a numerical simplified constitutive law for Ceramic Matrix Composites using Singular Value Decomposition. International Journal of Damage Mechanics. 2016/05/; 25: 506-37.
16. Berthelot JM. Mécanique des Matériaux et Structures Composites: Institut Supérieur des Matériaux et Mécaniques Avancés; 2010.
17. Talreja R. Continuum modelling of damage in ceramic matrix composites. Mechanics of Materials. 1991; 12: 165-180.

  doi:10.5075/epfl-298799_978-2-9701614-0-0

18. Corman GS, Luthra KL. Melt infiltrated ceramic composites (HIPERCOMP®) for gas trubine engine applications. Tech. rep. United States Deptartment of Energy; 2006 January.
19. Corman GS, Luthra KL. Handbook of ceramic composites. In Bansal N, editor..: Springer; 2010.
20. Whitlow T, Jones E, Przybyla C. In-situ damage monitoring of a SiC/SiC ceramic matrix composite using acoustic emission and digital image correlation. Composite Structures. 2016; 158: 245-51.
21. Zawada LP, Carson LE, Przybyla C. MICROSTRUCTURAL AND MECHANICAL CHARACTERIZATION OF 2-D AND 3-D SiC/SiNC CERAMIC MATRIX COMPOSITES. 2018/02/;: 148p -.
22. Evans AG, Zok FW. The physics and mechanics of fibre-reinforced brittle matrix composites. Journal of Materials Science. 1994; 29: 3857-96.
23. Rossol MN, Fast T, Marshall DB, Cox BN, Zok FW. Characterizing in-plane geometrical variability in textile ceramic composites. Journal of the American Ceramic Society. 2015; 98: 205-213.
24. Ben Ramdane C. Étude et Modélisation du Comportemement Mécanique de CMC Oxyde/Oxyde. Ph.D. dissertation. , L'Université de Bordeaux; 2014 June.
25. Marcin L. Modélisation du Comportement, de L'Endommagement et de la Rupture de Matériaux Composites Á Renforts Tissés pour le Dimensionnement Robuste de Structures. Ph.D. dissertation. , L'Université Bordeaux 1; 2010.

  doi:10.5075/epfl-298799_978-2-9701614-0-0

MULTISCALE SIMULATION OF DECONSOLIDATION IN THERMOPLASTIC COMPOSITE USING A LEVEL FINITE ELEMENT APPROACH

Lorys, Le Gohebel[a], Luisa, Silva[a], Steven, Le Corre[a], Hugues, Digonnet[a], Tuan-Linh, Nguyen[a], Stéphanie, Colliou[a]

a: Nantes Université, CNRS, Ecole Centrale Nantes, GeM, UMR 6183, Laboratoire de Thermique et Energie de Nantes, LTeN, UMR 6607, IRT Jules Verne, Programme PERFORM, F-44000 Nantes, France

Abstract: *During the forming processes of thermoplastic composites, deconsolidation phenomenon can occur, particularly in the heating phase [1]. This phenomenon can be observed by the appearance and growing of porosities [2]. These phenomena are due to the thermal or mechanical stresses generated by forming conditions. To better understand these phenomena, this work therefore aims to develop advanced simulation tools at two scales; At the macroscopic scale, a model is developed to simulate the evolution of a laminate composite behavior during the manufacturing process [3, 4, 5]; At the microscopic scale, this work consists of modelling the nucleation and growth of porosities under process conditions given by the simulations at the macroscopic scale [6, 7]. The goal of this work is thus to establish a new model of evolution of the rate of porosity, usable at the scale of the process, starting from direct simulations and experimental observations [8].*

Keywords: Finite Elements; Composite materials; Parallel Simulations; Anisotropic Solver; Multiphysics Solver

1. Introduction

In many industrial fields, materials such as steel are being replaced by composites. These new materials offer equivalent and sometimes even better mechanical properties for a weight significantly lower than that of steel. Those studied in this thesis are thermoplastic composites which bring many advantages: such as recyclability. Many studies are underway to understand the physical mechanisms during the creation of the various composite parts. This work focuses on the mechanisms during the shaping of these composites, from a numerical point of view. This study is done on two scales, the macroscopic scale allowing having the thermo-mechanical state of the part, and the microscopic scale where we simulate the nucleation and the growth of the porosities. This paper will focus on simulations at the macroscopic scale. The first part presents the chosen models and their implementation in the massively parallel finite element solver of the Ecole Centrale de Nantes, IciTech. The second part presents the results of the intermediate simulations used to validate the solver. These results are compared with experimental cases or simulations made under Abaqus.

2. Numerical Model

The shaping of a composite will lead to the appearance of various physical phenomena due to the temperature, the pressure and the geometry of the part. This shaping can be separated into two phases, consolidation and deconsolidation. Deconsolidation is the phase where the temperature exceeds a threshold, which will lead to the appearance of defects in the part. These defects may be due to delamination, deformations, or porosities. These defects will likely to be

  doi:10.5075/epfl-298799_978-2-9701614-0-0

removed during the consolidation phase when the pressure is applied and the material is viscous state. The simulation of these phenomena can hep to predict the final state of the part and to modify design defects. The studied material here is a thermoplastic matrix reinforced with unidirectional carbon fibers. The already-existing solver is taken as a basis in order to be enriched to obtain a solver adapted to the case study. This solver is apllied to solving the Stokes equations in velocity/pressure for viscous flows. This gives equation (1) where p represents the hydrostatic pressure and ε the velocity-dependent strain tensor.

$$\begin{cases} \nabla.\left(2\eta\underline{\underline{\varepsilon}} - p\underline{\underline{I}}\right) = 0 \\ -Tr(\varepsilon) = 0 \end{cases} \quad (1)$$

This solver, which was previously used for isotropic viscous flow, must thus be adapted to more complex cases, here anisotropic cases. The initial choice was not to go through the stiffness or flexibility tensors. These tensors being of order 4. A possiblility consists of passing these tensors to second order tensors. However, its implementation into our solver remains difficult. The studied case has the advantage, moreover, of being a transverse isotropic case. Each layer can therefore be described with the orientation of the fibers and 5 constants, defined by the properties of the matrix and the fibers. These criteria are therefore taken into account in the form of the equation.

2.1 Thermoelastic Model

Since the parameters involved in the manufacturing processes of these composites are temperature and pressure, a thermoelastic model was chosen. The pure elastic case of a UD was described by Rogers using the following constitutive equation [4].

$$\underline{\underline{\sigma}} = \left(\lambda Tr\left(\underline{\underline{\varepsilon}}\right) + \alpha Tr\left(\underline{\underline{A}}.\underline{\underline{\varepsilon}}\right)\right)\underline{\underline{I}} + 2\mu_T\underline{\underline{\varepsilon}} + 2(\mu_L - \mu_T)\left(\underline{\underline{A}}.\underline{\underline{\varepsilon}} + \underline{\underline{\varepsilon}}.\underline{\underline{A}}\right) + \left(\alpha Tr\left(\underline{\underline{\varepsilon}}\right) + \beta Tr\left(\underline{\underline{A}}.\underline{\underline{\varepsilon}}\right)\right)\underline{\underline{A}} \quad (2)$$

The equation is characterized by 5 constants, α , β , λ , μ_L and μ_T which can be recalculated using the more often used engineering constants. These constants characterize the mechanical properties of the unidirectional composite. The tensor of order 2 $\underline{\underline{A}}$, meanwhile, characterizes the orientation of the fibers. From this equation, it is possible to obtain the Stokes equations with two tensors of order 2 $\underline{\underline{\mu}}$ and $\underline{\underline{\lambda}}$ and a constant K whose form is similar to that in the isotropic case.

$$\begin{cases} \nabla.\left(\underline{\underline{\mu}}.\underline{\underline{\varepsilon}} + \underline{\underline{\varepsilon}}.\underline{\underline{\mu}} - \frac{2}{3}Tr\left(\underline{\underline{\mu}}.\underline{\underline{\varepsilon}}\right)\underline{\underline{I}} - \frac{Tr\left(\underline{\underline{\lambda}}\right)}{3}Tr\left(\underline{\underline{\lambda}}.\underline{\underline{\varepsilon}}\right)\underline{\underline{I}} + Tr\left(\underline{\underline{\lambda}}.\underline{\underline{\varepsilon}}\right)\underline{\underline{\lambda}} - p\underline{\underline{I}}\right) = 0 \\ -Tr\left(\underline{\underline{\varepsilon}}\right) - \frac{2}{3K}Tr\left(\underline{\underline{\mu}}.\underline{\underline{\varepsilon}}\right) - \frac{Tr\left(\underline{\underline{\lambda}}\right)}{3K}Tr\left(\underline{\underline{\lambda}}.\underline{\underline{\varepsilon}}\right) - \frac{1}{K}p = 0 \end{cases} \quad (3)$$

With

$$\underline{\underline{\mu}} = \mu_T\underline{\underline{I}} + 2(\mu_L - \mu_T)\underline{\underline{A}}; \underline{\underline{\lambda}} = \frac{\alpha}{\sqrt{\beta}}\underline{\underline{I}} + \sqrt{\beta}\underline{\underline{A}}; K = \lambda - \frac{\alpha^2}{\beta} \quad (4)$$

  doi:10.5075/epfl-298799_978-2-9701614-0-0

The non-isothermal case, meanwhile, is taken into account by adding a source term characterizing the thermal expansion. These equations are implemented in IciTech as "contributors", which represent different parts of the variational formulation. This formulation allows the use of solver of the equations of Stokes in displacement/pressure.

2.2 Thermoviscous Model

During the manufacturing processes, the matrix is changed to viscous state as the temperature exceeds a threshold (fusion on-set temperature). This matrix will therefore be able to flow and thus create adhesions between layers, but also leave free the porosities which will increase and decrease during this cycle. The model chosen in this case is a thermo-viscous model, it is based on the constitutive equation presented by Beaussart and Hearle [5] drawn from that of Rogers [4].

$$\underline{\underline{\sigma}} = 2\eta_T\underline{\underline{\varepsilon}} + 2(\eta_L - \eta_T)\left(\underline{\underline{A}}.\underline{\underline{\varepsilon}} + \underline{\underline{\varepsilon}}.\underline{\underline{A}}\right) + \gamma Tr\left(\underline{\underline{A}}.\underline{\underline{\varepsilon}}\right)\underline{\underline{A}} - p\underline{\underline{I}} \quad (5)$$

This equation describes a viscous model for a UD characterized by the same orientation tensor of order 2 $\underline{\underline{A}}$, as well as 3 constants, γ , η_L and η_T. The same method as for the elastic equation is used and makes it possible to obtain a similar shape with two tensors of order 2 $\underline{\underline{\eta}}$ and $\underline{\underline{\gamma}}$.

$$\begin{cases} \nabla.\left(\underline{\underline{\eta}}.\underline{\underline{\varepsilon}} + \underline{\underline{\varepsilon}}.\underline{\underline{\eta}} + Tr\left(\underline{\underline{\gamma}}.\underline{\underline{\varepsilon}}\right)\underline{\underline{\gamma}} - p\underline{\underline{I}}\right) = 0 \\ -Tr\left(\underline{\underline{\varepsilon}}\right) = 0 \end{cases} \quad (6)$$

With

$$\underline{\underline{\eta}} = \eta_T\underline{\underline{I}} + 2(\eta_L - \eta_T)\underline{\underline{A}}; \underline{\underline{\gamma}} = \sqrt{\gamma}\underline{\underline{A}} \quad (7)$$

The link with equation (3) can easily be made by replacing the constants β , μ_L and μ_T respectively by γ , η_L and η_T. It is also necessary to take $\alpha = 0$ and the constant $K = 0$, which is equivalent to $\lambda = \infty$ which characterizes the incompressibility in the viscous case. The thermoviscous allows the use of solver of the equations of Stokes in velocity/pressure. The viscous case is therefore a particular case of the elastic case which does not require the implementation of new contributors. The final solver implemented therefore theoretically makes it possible to simulate a complete composite forming cycle.

3. Numerical Simulations

The solver being now implemented, must be validated in simple cases in order to see the effect of the anisotropy on the solver. The elastic model is thus validated initially by simulating a case of simple tensile test. The simulation is done in 2D then in 3D on an isotropic plate, and finally on a transverse isotropic plate with different orientations. The thermal part is also validated by a case of thermal expansion directly in 3D, on an isotropic and transverse isotropic plate. The viscous part, meanwhile, is validated by simulating a 3D Poisseuille flow case. The conclusion of these preliminary cases will lead to the presentation of future simulations at the macroscopic scale.

  doi:10.5075/epfl-298799_978-2-9701614-0-0

3.1 Validation of the elastic part

The elastic solver will be firstly validated in a case of tensile test. A thick plate of dimensions 1m x 1m x 0.2m on which a displacement of 0.05m is imposed at both ends is simulated (Figure 1).

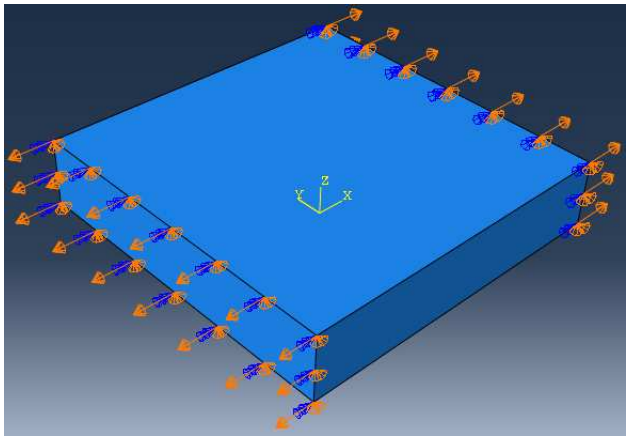

Figure 1. Boundary conditions for the 3D tensile case.

The simulations are made with the IciTech solver, as well as with Abaqus in order to be able to compare the results. In the 3D isotropic case, the results coincide between Abaqus and IciTech. The plate stretches well in the x direction and contracts in other directions due to the bare Poisson's ratio = 0.25 (Figures 2 and 3). The scales of values between IciTech and Abaqus are identical.

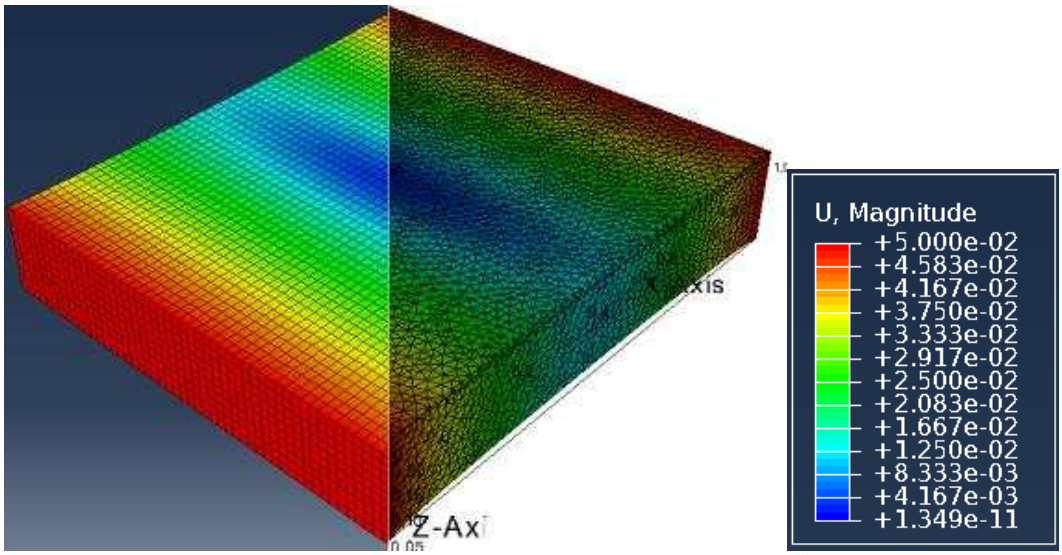

Figure 2. Magnitude of displacement in meters (m) with Abaqus (left) and with IciTech (right) in the isotropic plate in tensile according to x axis.

  doi:10.5075/epfl-298799_978-2-9701614-0-0

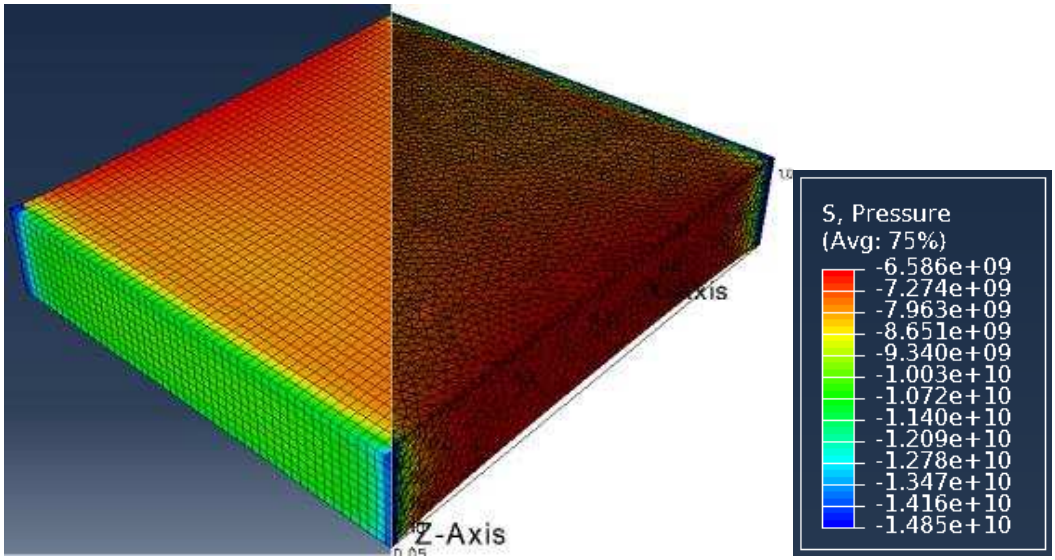

Figure 3. Pressure in Pascals (Pa) with Abaqus (left) and with IciTech (right) in the isotropic plate in tensile according to x axis.

The simulations in the transverse isotropic case were carried out in different directions (0°, 45°, 90°, -45°). The 45° case is presented here and again shows the correlation between the results under Abaqus and IciTech (Figure 4 and 5). The displacement again shows a stretch along x and a contraction along y and z. The displacement is, however, oriented according to an angle corresponding well to the imposed 45° angle. The pressure also clearly shows this orientation with a greater pressure at 45° due to the fibers which are more rigid.

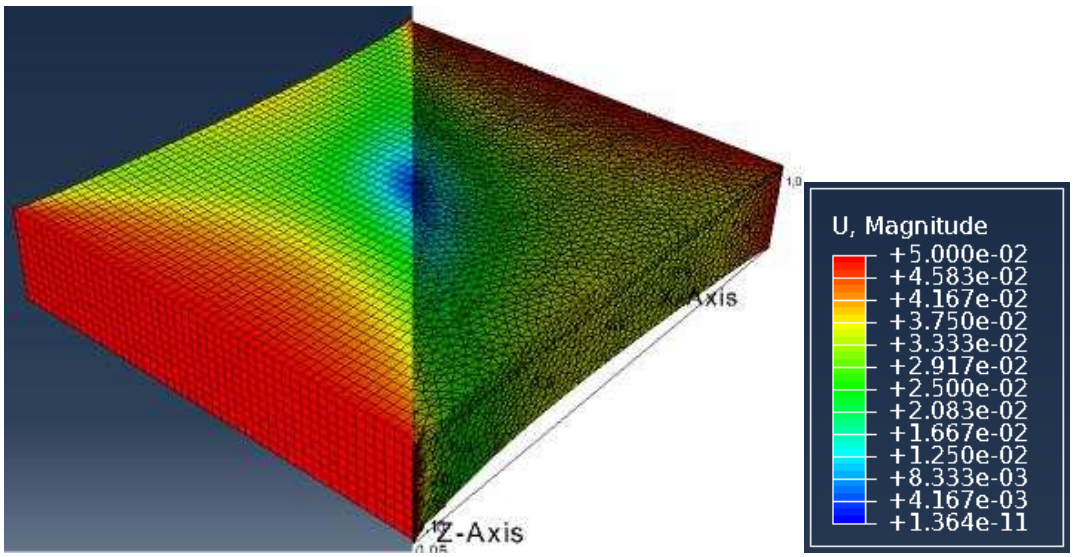

Figure 4. Magnitude of displacement in meters (m) with Abaqus (left) and with IciTech (right) in the UD plate at 45° in tensile along x axis.

  doi:10.5075/epfl-298799_978-2-9701614-0-0

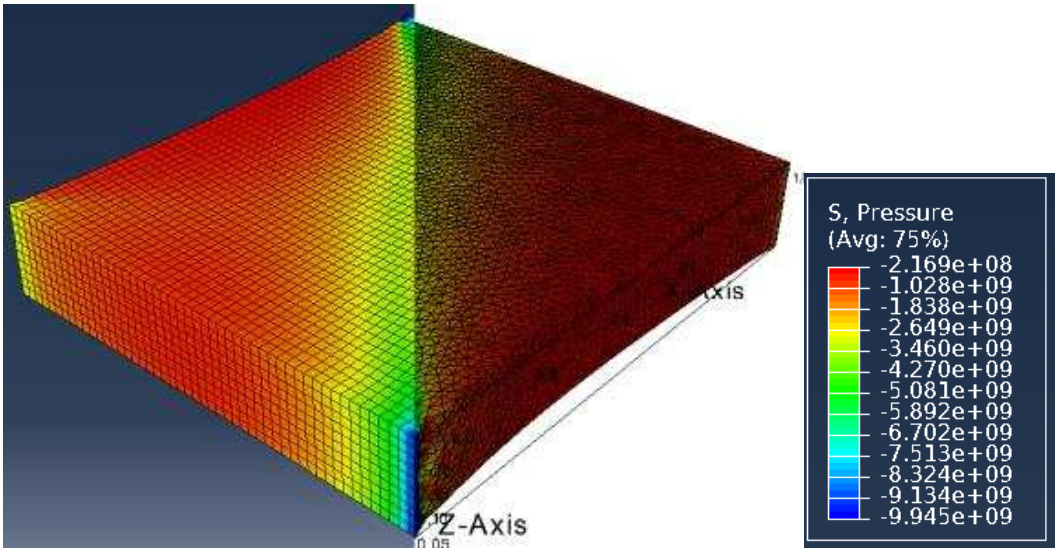

Figure 5. Pressure in Pascals (Pa) with Abaqus (left) and with IciTech (right) in the UD plate at 45° in tensile along x axis.

The results obtained for the isotropic and transversely isotropic simulations show a correlation between Abaqus and IciTech. This allows a first validation of the IciTech solver in the isothermal elastic case.

3.2 Validation of the thermal part

The thermal part of the solver must also be validated, for this, the same thick plate is simulated. The part is subjected to a uniform temperature variation from 24°C to 144°C. It is also constrained in order to block displacements in the x and y directions, leaving only possible expansion according to the thickness. The simulations are again carried out under Abaqus and IciTech in order to compare the results. The isotropic case gives the following results:

$$\begin{cases} p = 0.269\ GPa \\ u_z = 0.0024z\ m.s^{-1} \end{cases}$$

These results are the same between Abaqus and IciTech, they have also been calculated analytically and correspond to the results obtained in the simulation. The transverse isotropic case is again tested with different orientations, the example at 45° gives the following results:

$$\begin{cases} p = 0.123\ GPa \\ u_z = 0.00244z\ m.s^{-1} \end{cases}$$

These results are obtained with Abaqus and IciTech and give us a first validation of the thermoelastic solver in the non-isothermal case.

3.3 Validation of the viscous part

The viscous part is simulated using a Poiseuille flow, by imposing a pressure of 1 bar at one end and zero pressure at the other. This boundary condition will induce a stationary flow with a parabolic flow velocity, stronger in the center. The isotropic case (Figure 6) clearly shows this pressure which decreases linearly from 1 bar to 0 bar from one end to the other. The velocity also corresponds to the predictions with a stronger speed in the center.

  doi:10.5075/epfl-298799_978-2-9701614-0-0

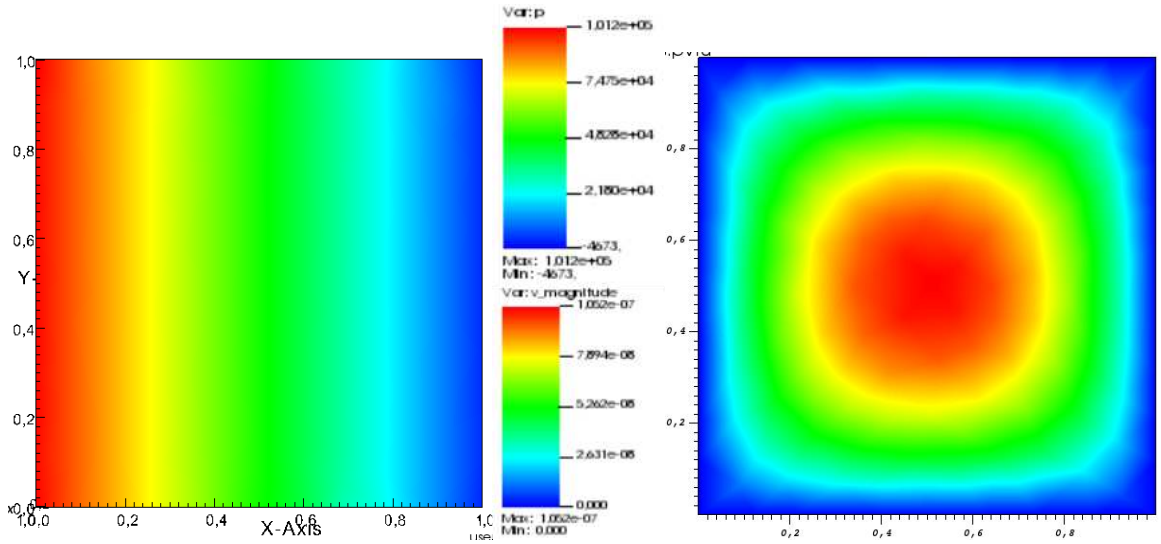

Figure 6. Pressure in Pascals (Pa) (left) and magnitude of velocity in meters (m) (right) in the isotropic part in steady state flow along x axis.

The transverse isotropic viscous case, in the 45° case, shows (Figure 7) a pressure oriented at 45° due to the orientation of the fibers. The flow will also present an orientation with a more important flow on the thickness which is not influenced by this orientation.

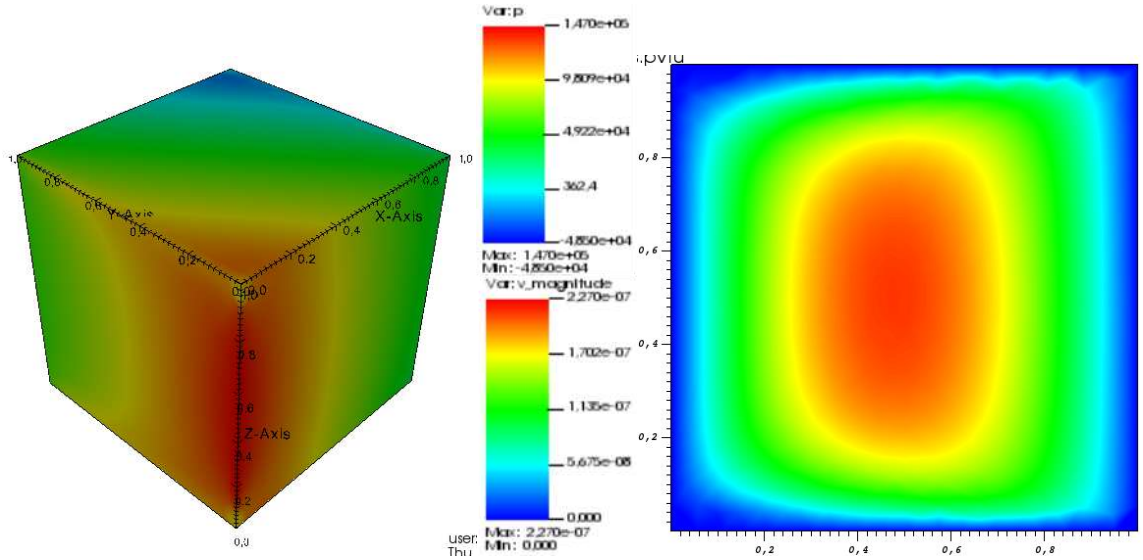

Figure 7. Pressure in Pascals (Pa) (left) and magnitude of velocity in meters (m) (right) in the UD part at 45° in steady state flow along x axis.

These results seem consistent with expectations and give a first validation of this viscous solver.

3.4 Conclusions

In conclusion, the proposed FE solver has the advantage of being able to solve a problem in both thermoelasticity and thermoviscosity. This is an advantage in the simulation of the consolidation and deconsolidation cycle of composites where the temperature will change the matrix from a solid state to a viscous state. A transition between the two solvers will therefore make it possible to simulate the entire cycle without multiplying the solvers. The future work to be done is

  doi:10.5075/epfl-298799_978-2-9701614-0-0

therefore to create a temporal solver which will calculate the velocity and the pressure at each point of the domain, and this at each time step.

4. References

1. T.K. Slange. Rapid Manufacturing of Tailored Thermoplastic Composites by Automated Lay-up and Stamp Forming, 2018.
2. B. Parscau du Plessix and all. In situ real-time 3D observation of porosity growth during composite part curing by ultra-fast synchrotron X-ray microtomography, 2019.
3. J. M. Berthelot. Mécanique des matériaux et Structures Composites, 2010.
4. T.G. Rogers. Rheological characterization of anisotropic materials, Composites, Volume 20 Number 1, 1989.
5. A. J. Beaussart, J. W. S. Hearle, R. B. Pipes. Constitutive relationships for anisotropic viscous materials, Composites Science and Technology, 0266-3538/93, 1993.
6. Y. Ledru. Etude de la porosité dans les matériaux composites stratifiés aéronautiques, 2009.
7. B. Parscau du Plessix, S. Le Corre, F. Jacquemin, P. Lefebure, and V. Sobotka. Improved simplified approach for the prédiction of porosity growth during the curing of composites parts, 2016.
8. J.F. Zaragoci. Simulation numérique directe multiphasique de la déformation d'un alliage Al-Cu à l'état pâteux – Comparaison avec des observations par tomographie aux rayons X in situ en temps réel, 2012.

  doi:10.5075/epfl-298799_978-2-9701614-0-0

MODELLING THE MICROSCALE RESPONSE OF UNIDIRECTIONAL CARBON FIBER REINFORCED PVDF

Tom Lenders[a], Joris J.C. Remmers[a], Tommaso Pini[a], Peter Veenstra[b], Leon E. Govaert[a], Marc G.D. Geers[a]

a: Department of Mechanical Engineering, Eindhoven University of Technology
b: Shell Global Solutions International B.V.
email: t.lenders@tue.nl

Abstract: *In this study, we develop a numerical model of unidirectional carbon fiber reinforced PVDF based on experimental data. The microscale behaviour of the composite is described using a plane strain finite element model of a carbon fiber embedded in a PVDF matrix, connected by a cohesive zone interface. The intrinsic behaviour of the PVDF matrix is modelled using an elasto-viscoplastic constitutive model which is able to represent the rate-dependent behaviour of PVDF. Numerical simulations of uniaxial tensile tests of the composite show the interaction between the rate-dependent response of PVDF and the cohesive zone interface response. The microscale failure mechanisms are governed by the competing mechanisms of the matrix model and the cohesive interface model at the fiber/matrix interface.*

Keywords: Microscale modelling; polyvinylidene fluoride; cohesive zone method; finite element model; elasto-viscoplastic behaviour

1. Introduction

The worldwide increasing demand for energy in combination with the decrease of fossil energy resources presents a challenge for many industries, in particular for the energy industry. The offshore energy industry can be divided into the fossil fuel branch and the green fuel branch. The fossil fuel branch is facing the problem of a decrease of oil and gas fields, both in number and in size. Therefore, these fields are becoming harder to access and new transport solutions are required. On the other hand, the green fuel branch is expanding with large wind parks and exploring the possibility for on-site green hydrogen production [1]. Both branches face a common challenge which is related to the transport of the energy, i.e., transporting hydrocarbons from the bottom of the sea to the oil rig or transporting the produced hydrogen from the wind parks to the mainland.

A method that is already used for oil and gas transport but may also be applied for the transport of hydrogen, is the so called thermoplastic composite pipeline (TCP) which is a multilayered flexible pipe. A novel material that may be used in these pipes is continuous carbon fiber reinforced polyvinylidene fluoride (PVDF). The high strength carbon fibers are used for their excellent mechanical properties, while the semi-crystalline PVDF matrix shows outstanding thermal and chemical characteristics, interesting for offshore applications [2].

To assess the potential of carbon fiber reinforced PVDF in offshore applications, its complex short- and long-term behaviour must be well understood. This requires a proper description of the deformation and failure behaviour at the microscale. At the microscale, one can distinguish two different constituents of the composite, being the carbon fiber and the PVDF matrix. In this

  doi:10.5075/epfl-298799_978-2-9701614-0-0

study, a numerical finite element model is defined to describe the micromechanical behaviour of unidirectional carbon fiber reinforced PVDF. The response of the semi-crystalline PVDF matrix is rate- and temperature dependent and therefore a suitable elasto-viscoplastic constitutive model is used to describe its intrinsic behaviour. The interaction between the fiber and the matrix is described by a cohesive zone model. The micromechanical behaviour is analyzed by means of uniaxial tensile simulations on a transversely loaded composite.

2. Modelling the intrinsic behaviour of PVDF

True stress strain curves from uniaxial compression tests performed at different temperatures and applied strain rates are shown in Fig. 1a. The data in this plot is obtained from [3]. The time- and temperature dependence of the yield stress was successfully described using Eyring's flow theory in [3]. It was concluded that the yield kinetics can be described by two relaxation processes acting in parallel. To model this behaviour in a finite element environment, the Eindhoven Glassy Polymer (EGP) constitutive model is used [4], which is a constitutive model that adequately describes the elasto-viscoplastic behaviour of glassy and semi-crystalline polymers by incorporating a stress-activated Eyring viscosity.

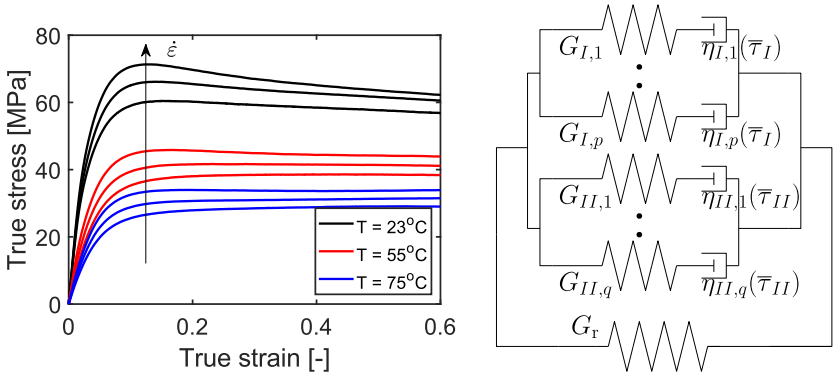

(a) (b)

Figure 1: True stress-strain response of bulk PVDF obtained from uniaxial compression tests (a). Data is obtained from [3]. Mechanical analogue of the EGP-model in its multi-mode multi-process form as described in [4] (b).

2.1 Constitutive model

To describe the intrinsic behaviour of PVDF, the Eindhoven Glassy Polymer (EGP) model is employed. From [3] it was concluded that multiple relaxation processes act simultaneously within the tested range of applied strain rates and temperatures. Therefore, the EGP-model in its multi-process multi-mode form will be used [4], of which the mechanical analogue is shown in Fig. 1b. The total stress response is composed of the strain hardening stress $\boldsymbol{\sigma}_{\mathrm{r}}$ and the driving stress $\boldsymbol{\sigma}_{\mathrm{s}}$, which are additive as represented in Fig. 1b. The elastic strain hardening stress is represented by a single spring, related to the intramolecular response of the polymer chains, and governed by the elastic strain hardening modulus G_{r}. The elasto-viscoplastic driving stress is represented by parallel connected nonlinear Maxwell elements, related to the intermolecular interactions of the polymer chains. The two relaxation processes observed in PVDF can be modelled by two sets of parallel linked Maxwell elements. Each set corresponds to a relaxation process indicated by the subscripts I and II. The nonlinear pre-yield response of the polymer is described by incorporating multiple nonlinear Maxwell elements for each process.

  doi:10.5075/epfl-298799_978-2-9701614-0-0

The main equations used in the constitutive model are given in the following. The total stress is decomposed in the driving stress $\boldsymbol{\sigma}_{\mathrm{s}}$ and the hardening stress $\boldsymbol{\sigma}_{\mathbf{r}}$

$$\boldsymbol{\sigma} = \boldsymbol{\sigma}_{\mathrm{s}} + \boldsymbol{\sigma}_{\mathrm{r}} \tag{1}$$

The driving stress can be split into the hydrostatic part $\boldsymbol{\sigma}_{\mathrm{s}}^{\mathrm{h}}$, described by the constant bulk modulus κ, and the deviatoric part $\boldsymbol{\sigma}_{\mathrm{s}}^{\mathrm{d}}$. To account for the multiple relaxation processes acting simultaneously, the deviatoric driving stress is decomposed into the contributions of processes I and II, resulting in the following expression for the driving stress.

$$\boldsymbol{\sigma}_{\mathrm{s}} = \boldsymbol{\sigma}_{\mathrm{s}}^{\mathrm{h}} + \boldsymbol{\sigma}_{\mathrm{s}}^{\mathrm{d}} = \kappa(J-1)\mathbf{I} + \sum_{i=1}^{p} G_{I,i}\widetilde{\mathbf{B}}_{\mathrm{e}_{I,i}}^{\mathrm{d}} + \sum_{j=1}^{q} G_{II,j}\widetilde{\mathbf{B}}_{\mathrm{e}_{II,j}}^{\mathrm{d}} \tag{2}$$

Here, $G_{r,k}$ and $\widetilde{\mathbf{B}}_{\mathrm{e}_{r,k}}^{\mathrm{d}}$ are the elastic shear modulus and the deviatoric part of the elastic isochoric left Cauchy Green strain tensor, respectively, corresponding to the k^{th} mode of process r. The total number of modes corresponding to process I and II are p and q, respectively. The volume change ratio is denoted by J and $\mathbf{I}$ is the second-order unit tensor. The deviatoric driving stress $\boldsymbol{\sigma}_{\mathrm{s}_{r,k}}^{\mathrm{d}}$ and the modified Eyring viscosity $\eta_{r,k}$ of mode k are related via the plastic rate of deformation tensor $\mathbf{D}_{\mathrm{p}_{r,k}}$as described in Eq. (3).

$$\mathbf{D}_{\mathrm{p}_{r,k}} = \frac{\boldsymbol{\sigma}_{\mathrm{s}_{r,k}}^{\mathrm{d}}}{2\eta_{r,k}} \tag{3}$$

where the modified Eyring viscosity of mode k in process r is defined as

$$\eta_{r,k} = \eta_{0_{r,k}}(T)\frac{\frac{\bar{\tau}_r V_r^*}{k_{\mathrm{B}}T}}{\sinh\left(\frac{\bar{\tau}_r V_r^*}{k_{\mathrm{B}}T}\right)}\exp\left(\frac{\mu_r p V_r^*}{k_{\mathrm{B}}T} + S_r\left(\bar{\gamma}_{\mathrm{p}}\right)\right) \tag{4}$$

Here, $\eta_{0_{r,k}}(T)$ is the temperature-dependent reference viscosity, $\bar{\tau}_r$ the equivalent shear stress, V_r^* the activation volume, k_{B} Boltzmann's constant, μ_r a pressure-dependence parameter, p the hydrostatic pressure and S_r a term accounting for the intrinsic strain softening, dependent on the equivalent plastic strain $\bar{\gamma}_{\mathrm{p}}$.

2.2 Characterization of material properties

The characterization of the parameters for the EGP-model is described extensively in [5]. Unfortunately, characterizing a single set of parameters for modelling the response of a semi-crystalline polymer over a wide range of temperatures proved unsuccessful for the application to PVDF. Therefore, a set of material parameters was characterized at three individual temperatures: 23°C, 55°C and 75°C. As this work focuses on the interaction between the PVDF matrix and the cohesive zone, only the PVDF behaviour at $T = 23$°C is discussed here. Although it was stated in [3] that at least two relaxation processes are active at 23°C, the yield kinetics at this temperature can be described using only one relaxation process. Therefore, only one process is incorporated in this study, i.e. $r = I$.

First, the hardening modulus G_{r} is determined from the PVDF response at large strains as discussed in [6], which is equal to 0.6 MPa. The shear activation volume V^* is determined from the slope of the yield stress as a function of the applied strain rate $\dot{\varepsilon}$ and is equal to 2.936e^{-27} m^3. The pressure dependence term μ is derived from the difference in yield stress between uniaxial compression and tension at a single constant applied strain rate $\dot{\varepsilon}$ and equals 0.175. The shear

moduli and reference viscosities are determined from a uniaxial compression test performed at a single constant applied strain rate $\dot{\varepsilon}$ = 1e^{-3} s^{-1}, adopted from [7]. This results in a spectrum of relaxation moduli and viscosities of which the total relaxation modulus is shown in Fig. 2a. The total viscosity at this strain rate equals 2.453e^{13} MPa·s. The large-strain response is modeled using a deformation-dependent evolution of the parameters V^* and $\eta_0(T)$, as proposed in [5]. The evolution of the parameters is modelled as a bi-linear dependence of the parameters on the equivalent plastic strain $\bar{\gamma}_{\mathrm{p}}$. Finally, the characterized material parameters are used to compute the compressive stress-strain response at different strain rates which is shown in Fig. 2b. The characterized material parameters have been validated on uniaxial tensile simulations and creep simulations at conditions that were not used during the characterization of the material [5]. This set of material parameters is now used in the micromechanical finite element model of the composite, where the EGP-model is implemented as a UMAT user subroutine [8].

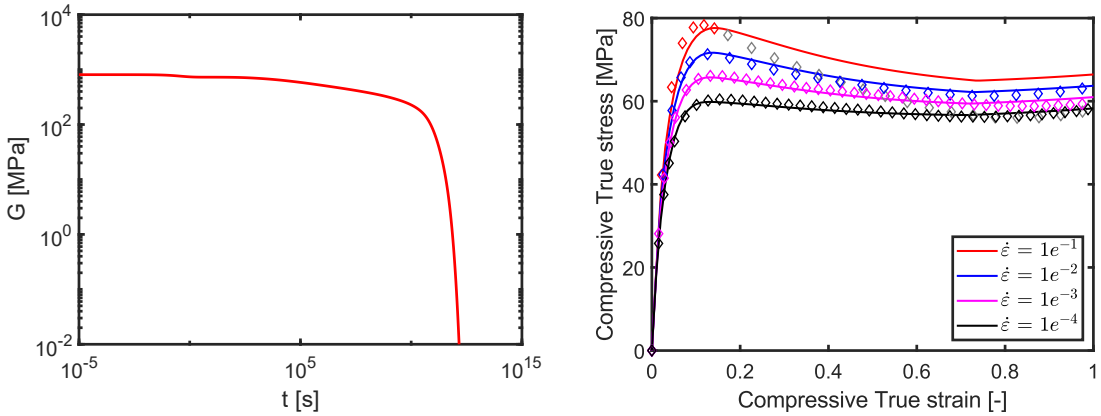

Figure 2: Shear relaxation modulus fit to the uniaxial compression data obtained at a constant applied strain rate $\dot{\varepsilon}$=1e^{-3} s^{-1} (a) and the compressive stress-strain response at different applied constant strain rates obtained from numerical simulations denoted by the solid lines, compared to experiments, denoted by the markers [3] (b).

3. Micromechanical model CFR PVDF

Uniaxial tensile tests were performed on bulk PVDF and on carbon fiber reinforced PVDF with fiber orientation perpendicular to the loading direction. The tests were performed at different applied strain rates and showed a large deviation in the stress-strain response between bulk PVDF and the transversely loaded composite. The off-axis loaded composite response was weaker than the bulk PVDF, which indicates that the composite is failing at the interface between the fiber and matrix for the current loadcase. To this extent, an interface is incorporated in the micromechanical model by means of a cohesive zone. With the numerical micromechanical model, the interaction between the rate-dependent response of the PVDF matrix and the cohesive interface model is investigated by means of uniaxial tensile simulations.

3.1 Geometry and boundary conditions

To model the micromechanical behaviour of the composite, the geometrical microstructural properties must be known. In Fig. 3a, a microscopic image of a cross section of the composite is shown, where the fiber and the matrix can be clearly distinguished. The average fiber area fraction A_{f} and fiber radius r_{f} are determined as $A_{\mathrm{f}} \approx 0.55$ and $r_{\mathrm{f}} \approx 3.5\mu$m, respectively. These microscopic dimensions are used to create the micromechanical model of the composite. In Fig.

3b, the schematic representation of the model is shown. A quarter of a fiber is embedded in a PVDF matrix, connected by a cohesive zone interface. The width and height of the model are chosen such that the fiber volume fraction is equal to $A_\mathrm{f} = 0.55$.

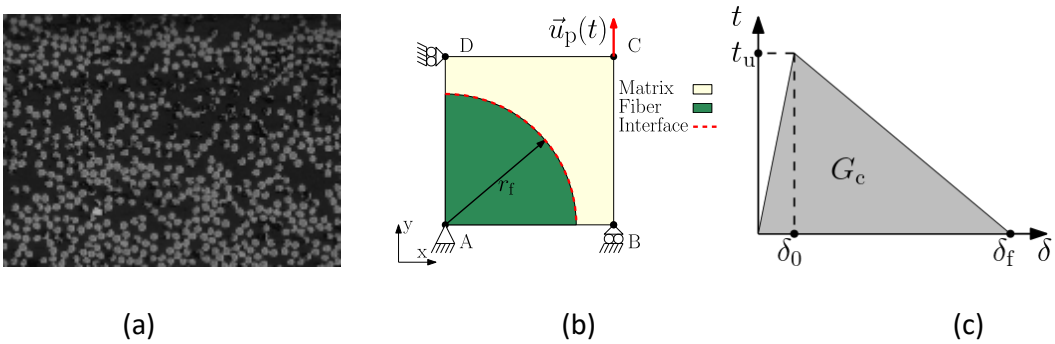

Figure 3 : Microscopic image of a cross-section of the carbon fiber reinforced PVDF (a) and the schematic representation of the finite element model of the composite (b). Double linear traction separation law describing the constitutive behaviour of the cohesive zone elements at the fiber/matrix interface (c).

The finite element model is implemented in ABAQUS® 2019 and discretized under the plane strain assumption using 4-node bilinear plane strain elements CPE4, where mesh refinement has been applied near the fiber/matrix interface. The model is fixed in point A and symmetry conditions have been applied to edges AB (fixed displacement in y-direction) and AD (fixed displacement in x-direction) to create a periodic square stacking. The displacement in x-direction of edge BC is tied to the x-displacement of point C, whereas the displacement in y-direction of edge CD is tied to the y-displacement of point C. A prescribed time-dependent displacement $\vec{u}_\mathrm{p}(t)$ is applied in point C in the y-direction to simulate a tensile loadcase [9]. The average stress-strain behaviour of the model is computed by extracting the displacements and reaction forces at point C.

3.2 Cohesive zone model

The fiber is modelled using a linear elastic transversely isotropic material with the highest stiffness along the out-of-plane direction. For the cohesive zone, interface elements are used of which the constitutive response is modelled according to the double linear traction-separation law as shown in Fig. 3c [8]. This traction separation law relates the relative opening δ between two opposing edges of the element to the traction t between these edges. The linear elastic behaviour at small opening is followed by the initiation of damage. Damage initiation is governed by the ultimate traction t_u after which the damage evolution is modelled linearly. Complete damage of the cohesive zone element is achieved, once the opening is equal to δ_f. The evolution of damage is governed by the fracture toughness G_c which is a measure for the dissipated energy in the cohesive zone element. No distinction is made between normal and shear deformation of the interface elements.

3.3 Numerical analysis

The influence between the rate dependent PVDF matrix and the cohesive interface model is studied in the next chapter by varying the ultimate traction t_u between 45 and 90 MPa at constant G_c, which is well below and above the yield stress of the bulk PVDF. Furthermore, the fracture toughness G_c is varied between 3 J/m^2 and 10 J/m^2 at constant t_u [10]. Two outer limits for the fiber/matrix interface are used for comparison. For the upper limit, the interaction

  doi:10.5075/epfl-298799_978-2-9701614-0-0

between fiber and matrix is modelled as fully bonded, denoted in the results as *Full Adhesion (FA)*. For the lower limit, the interaction is modelled as a frictionless contact, denoted as *Contact (C)*.

4. Results

The micromechanical response of the finite element model is analyzed. The global response is analyzed by computing the average stress of the model and the local response is analyzed by means of local deformation plots.

4.1 Global response of the micromechanical model

The average stress-strain behaviour of the micromechanical model is computed and compared to the limit solutions *Full Adhesion (FA)* and *Contact (C)* that are displayed by the symbols in Fig 4. The influence of varying the ultimate traction on the average stress-strain response is shown in Fig. 4a. If the ultimate traction is much lower than the yield stress of the PVDF matrix, interface failure is dominant in the micromechanical response, resulting in a much lower overall yield stress of the composite. If the ultimate traction is higher than the yield stress of the matrix, the average response of the composite will approach the upper limit being the fully adhered fiber/matrix interaction. As a result, the height of the ultimate traction determines the onset of interface failure. Furthermore, the competition between matrix yield stress and ultimate traction of the interface determines the average yield stress under uniaxial tension for the unidirectional composite considered here.

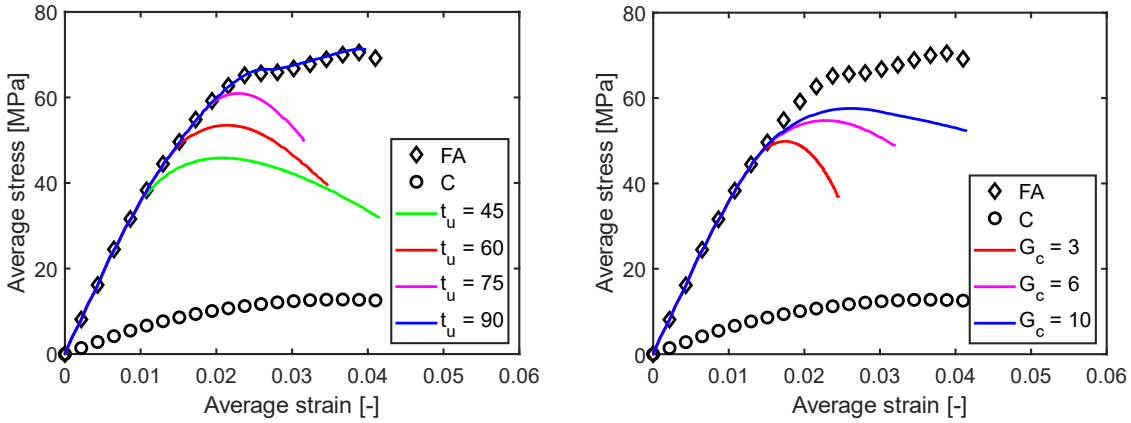

Figure 4: Average stress-strain response of the micromechanical model for varying ultimate traction (a) and fracture toughness (b).

The fracture toughness has a more pronounced effect on the failure evolution along the interface, as can be seen in Fig. 4b. A low fracture toughness means that complete failure of the cohesive zone element is achieved at a relatively small opening of the cohesive zone element compared to a higher value of the fracture toughness. In other words, the amount of energy required for complete failure of the element is less for a lower value of the fracture toughness, which is also confirmed by Fig. 4b. A low value of the fracture toughness results in a fast evolution of the interface damage and a sudden load drop. A higher value of the fracture toughness, on the other hand, results in a more gradual evolution of the interface damage.

  doi:10.5075/epfl-298799_978-2-9701614-0-0

4.2 Local response of the micromechanical model

The local response is shown in Fig. 5 for two different ultimate tractions, i.e. 45 MPa in Fig. 5a and 90 MPa in Fig. 5b. For the lowest ultimate traction, the interface between the matrix and the fiber has opened under the influence of the prescribed displacement at the top edge. A mode I opening initiates at the left edge which evolves to a mixed-mode opening as the interface failure evolves along the interface. For an ultimate traction which is well below the yield stress of the bulk PVDF, the interface failure is initially dominant in the micromechanical deformation and strains in the matrix remain relatively small as shown in Fig. 5a. On the other hand, when the ultimate traction of the interface is well above the yield stress of PVDF, the deformation in the matrix becomes dominant in the micromechanical response. This is also supported by the shear band in the matrix along the fiber/matrix interface in Fig. 5b in which the strain values are much higher compared to the interface dominant deformation.

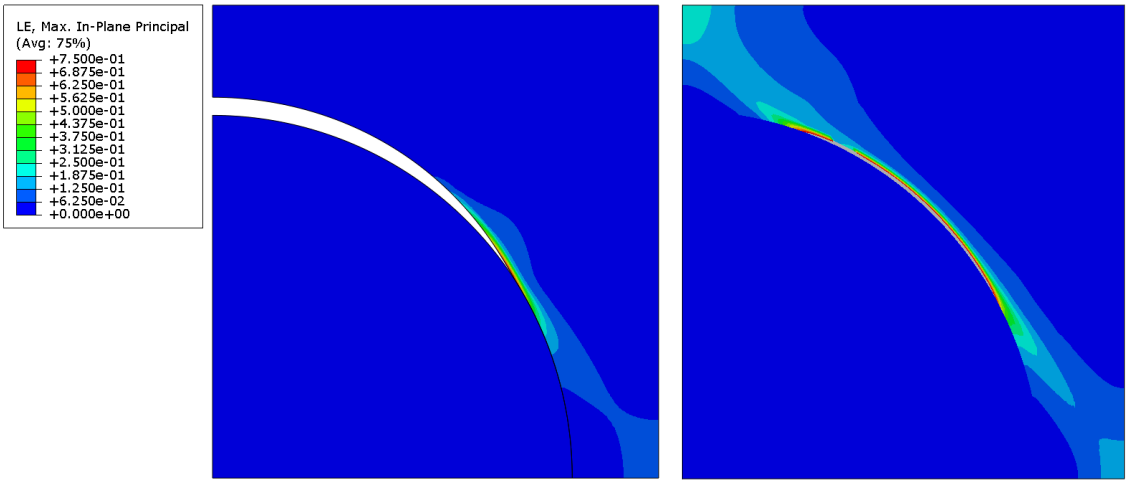

Figure 5: Deformation plot of the finite element model with an ultimate traction in the cohesive zone model of 45 MPa (a) and 90 MPa (b). Colors indicate the maximum in-plane principal strain.

5. Conclusion

To describe the micromechanical behaviour of carbon fiber reinforced PVDF, a micromechanical finite element model was defined. The EGP-model was used to describe the elasto-viscoplastic behaviour of the PVDF matrix. The interface between the carbon fiber and the PVDF matrix was modeled using cohesive zone elements of which the behaviour was described by a double-linear traction-separation law. There is a clear influence between the rate-dependent behaviour of the PVDF matrix and the cohesive interface model employed at the fiber/matrix interface. It was shown that the ultimate traction in combination with the yield stress of the PVDF matrix determines whether the micromechanical response is dominated by failure of the cohesive zone interface or large matrix deformations, while the fracture toughness determines the rate at which failure along the interface evolves.

Acknowledgements

The authors would like to thank Shell Global Solutions International B.V. for their financial support.

  doi:10.5075/epfl-298799_978-2-9701614-0-0

6. References

1. NorthH2. About NorthH2 [Internet]. Available from: https://www.north2.eu/en/about-north2/. [Accessed 10th March 2022].
2. Challier M, Besson J, Laiarinandrasana L, Piques R. Damage and fracture of polyvinylidene fluoride (PVDF) at 20 ˚C: Experiments and modelling. Engineering Fracture Mechanics 2006; 73:79-90.
3. Pini T, Van Drongelen M, Remmers J, Geers M, Govaert L. Deformation and failure kinetics of polyvinylidene fluoride: Influence of crystallinity. Journal of Polymer Science 2021; 59:1209-1220
4. Van Breemen L, Engels T, Klompen E, Senden D, Govaert L. Rate- and temperature-dependent strain softening in solid polymers. Journal of Polymer Science, Part B: Polymer Physics 2012; 50:1757-1771.
5. Lenders T, Pini T, Remmers J, Veenstra P, Govaert L, Geers M. Describing the time-dependent behaviour of polyvinylidene fluoride using an elasto-viscoplastic constitutive model [In preparation].
6. Senden D, Krop S, Van Dommelen J, Govaert L. Rate- and temperature-dependent strain hardening of polycarbonate. Journal of Polymer Science, Part B: Polymer Physics 2012; 50:1680-1693.
7. Van Breemen, Klompen E, Govaert L, Meijer H. Extending the EGP constitutive model for polymer glasses to multiple relaxation times. Journal of the Mechanics and Physics of Solids 2011; 59:2191-2207.
8. Dassault Systèmes Simulia Corp. ABAQUS USER MANUAL 6.14.
9. De Kok J, Meijer H. Deformation, yield and fracture of unidirectional composites in transverse loading 1. Influence of fibre volume fraction and test-temperature. Composites: Part A 1999; 30:905-916.
10. Varna J, Berglund L, Ericson M. Transverse single-fibre test for interfacial debonding in composites: 2. Modelling. Composites Part A 1997; 28:317-326.

  doi:10.5075/epfl-298799_978-2-9701614-0-0

MULTI-SCALE FATIGUE MODEL TO PREDICT STIFFNESS DEGRADATION IN SHORT-FIBER REINFORCED COMPOSITES

Nicola Magino[a], Jonathan Köbler[a], Heiko Andrä[a], Fabian Welschinger[b], Ralf Müller[c], Matti Schneider[d]

a: Fraunhofer Institute for Industrial Mathematics (ITWM)–
nicola.magino@itwm.fraunhofer.de
b: Robert Bosch GmbH
c: TU Darmstadt
d: Karlsruhe Institute of Technology (KIT)

Abstract: *The prediction of stiffness degradation in short-fiber reinforced composites under high-cycle fatigue loading is studied. To reduce the experimental characterization effort involved, we propose a computational multi-scale method to model the stiffness degradation under fatigue loading of fiber-reinforced polymer composites. First, we introduce a damage model for the thermoplastic matrix directly resolved in time scale. In contrast to formulations in cycle space, this enables us to predict damage evolution of the material accounting for vavrious stress ratios.*
For industrial-scale components, fully coupled FE²-simulations are currently infeasible with conventional hardware. Thus, we employ a model order reduction for the time scale model. For the high cycle regime, the computational costs for the prediction of an engineering component are still unfeasible using the time scale model. We thus use a cycle jump technique for sinusoidal loading. The reformulation of the model yields a cycle-dependent damage evolution with a driving effective stress dependent on stress ratio and stress amplitude.

Keywords: Fatigue damage; cycle jump; model order reduction; convex damage

1. Introduction

Under fatigue loading, short-fiber reinforced polymers show a stiffness degradation prior to failure [1,2]. This degradation depends on the local fiber-orientation in the fatigue specimen, the loading amplitude, the stress ratio and the geometry of the macroscopic specimen. Due to this multitude of influencing parameters, a complete characterization of a newly developed short-fiber reinforced material by experimental procedures is a time and cost intensive task. Complementary simulative tools aim to reduce this effort.
Our approach to simulate short-fiber reinforced composites is based on a convex damage model for the thermoplastic matrix and a linear-elastic material model for the fiber [3]. With these rather simple ingredients on the microscale, we aim to predict the composite material behavior. To reach models feasible for the computation on macroscopic components without loss of accuracy, we firstly make use of a model order reduction strategy specifically introduced for the convex damage model. Secondly, we introduce a cycle jump technique [4] for periodic loadings leading to an effective stress model in cycle space.

2. Time scale model for fatigue damage in thermoplastic matrix

2.1 Time scale model

  doi:10.5075/epfl-298799_978-2-9701614-0-0

We use a damage model based on a free energy density

$$w(\boldsymbol{\varepsilon}, D) = \frac{1}{2(1+D)}\boldsymbol{\varepsilon}\colon \mathbb{C}_0 \colon \boldsymbol{\varepsilon}. \tag{1}$$

Here, the symbol $\boldsymbol{\varepsilon}$ refers to the strain, D denotes the scalar damage variable and $\mathbb{C}_0$ is the undamaged stiffness tensor. Damage is only evolving under loading and is defined by

$$\dot{D}(\boldsymbol{\varepsilon}, D, q) = \begin{cases} \alpha_{\mathrm{q}}(q) \ \frac{1}{2}\boldsymbol{\sigma}\colon \mathbb{C}_0^{-1} \colon \boldsymbol{\sigma}, & \text{if } \frac{\mathrm{d}}{\mathrm{d}t}(\boldsymbol{\sigma}\colon \mathbb{C}_0^{-1} \colon \boldsymbol{\sigma}) \geq 0, \\ 0, & \text{otherwise.} \end{cases} \tag{2}$$

The parameter $\alpha_{\mathrm{q}}(q)$ is a time-dependent material parameter governing the damage evolution speed. Motivated by experimental results we set

$$\alpha_{\mathrm{q}}(q) = \frac{4\alpha_{\mathrm{t}}}{q}, \tag{3}$$

$$\dot{q} = K_{\mathrm{t}}. \tag{4}$$

Under fatigue loading the resulting damage evolution of single material point is shown in Fig. 1. The Young's modulus is 3.35 GPa, the Poison's ratio is 0.4. We set $\alpha_{\mathrm{t}} = 0.1$ 1/MPa and $K_{\mathrm{t}} = 5.0$ 1/s. For periodic loading with $\sigma_{\max} = 60$ MPa, the damage evolution for stress ratios $R = 0$ and $R = -1$ are shown. We observe that damage only increases under loading. The damage evolution for $R = -1$ is faster.

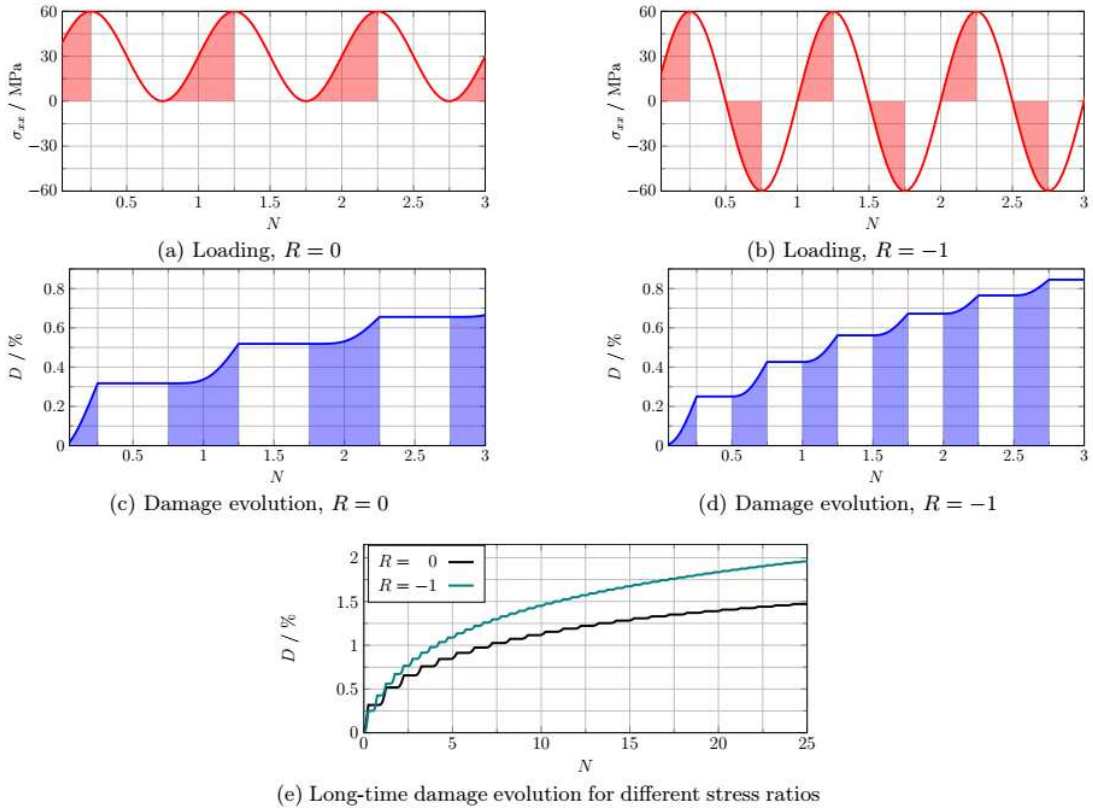

Figure 1. Damage evolution under periodic loading with different stress ratios

2.2 An effective stress model for damage evolution under sinusoidal loading conditions

For sinusoidal loading conditions, commonly used in fatigue experiments

$$\boldsymbol{\sigma} = (\sin(2\pi t/T) + c)\boldsymbol{\sigma}_{\mathrm{a}} \tag{5}$$

with the cycle duration T, the stress amplitude $\boldsymbol{\sigma}_{\mathrm{a}}$ and the stress ratio dependent parameter c, a reformulation of the damage evolution equation dependent on the cycle number N instead of the time variable t is possible. Details can be found in [4]. The damage model in cycle space reads

$$\frac{\partial D}{\partial N} \equiv D' = \frac{\alpha_{\mathrm{t}}}{q_0 + KTN}\boldsymbol{\sigma}_{\mathbf{a}} : \mathbb{C}_0^{-1} : \boldsymbol{\sigma}_{\mathbf{a}}\left(\frac{1}{2} + c\right) \tag{6}$$

with the initial condition $q(0) = q_0$.

3. Model order reduction

To study the effect of damage evolution on a structure typical for an injection-molded short-fiber reinforced structure, we make use of the generic structure shown in Fig. 2. It comprises of a polymer matrix modeled with material parameters of polyamid: $E = 3.35\,\mathrm{GPa}$, $\upsilon = 0.38$, $\alpha_{\mathrm{t}} = 0.1$ 1/MPa and $K_{\mathrm{t}} = 5.0$ 1/s for the damage model. The matrix is reinforced by 17.8 vol% of short fibers with an aspect ratio of 23 and eigenvalues of the fiber orientation tensor $\lambda_1 = 0.77$, $\lambda_2 = 0.21$ and $\lambda_3 = 0.02$. The fiber reinforcements are modeled as a linear-elastic material with $E = 72$ GPa and $\upsilon = 0.22$.

Figure 2. Generic fiber structure with 128^3 voxels to study damage evolution

We investigate the strain evolution of the homogenized strain tensor of the fiber structure under cyclic loading. We apply a uniaxial stress driven load with a loading amplitude of 60 MPa in the *xx*-component of the stress amplitude tensor $\boldsymbol{\sigma}_{\mathbf{a}}$**.** The stress ratio is $R = 0$.

To enable efficient computation, we make use of a model order reduction approach based on the non-uniform transformation field analysis (NTFA) [5,6]. For details on the model order reduction, we refer to [3]. It enables us to model the composite material as a single material point with a set of internal variables.

In Fig.3, the full-field and the reduced order model computed for the generic structure shown in Fig. 2 are compared. In Fig. 4, the evolution of the peak strain in the *xx*-component $\varepsilon_{xx}^{\max}$ is plotted. We observe that the order-reduced model can reproduce the increasingly large strain amplitude of the full-field model due to damaging effects. More precisely, the peak strain at

cycle 200 is $\varepsilon_{xx}^{\max}$= 6.50x10^{-3} in the full-field model and $\varepsilon_{xx}^{\max}$= 6.49 x10^{-3} in the reduced order model, which amounts to a relative error of about 0.15 %.

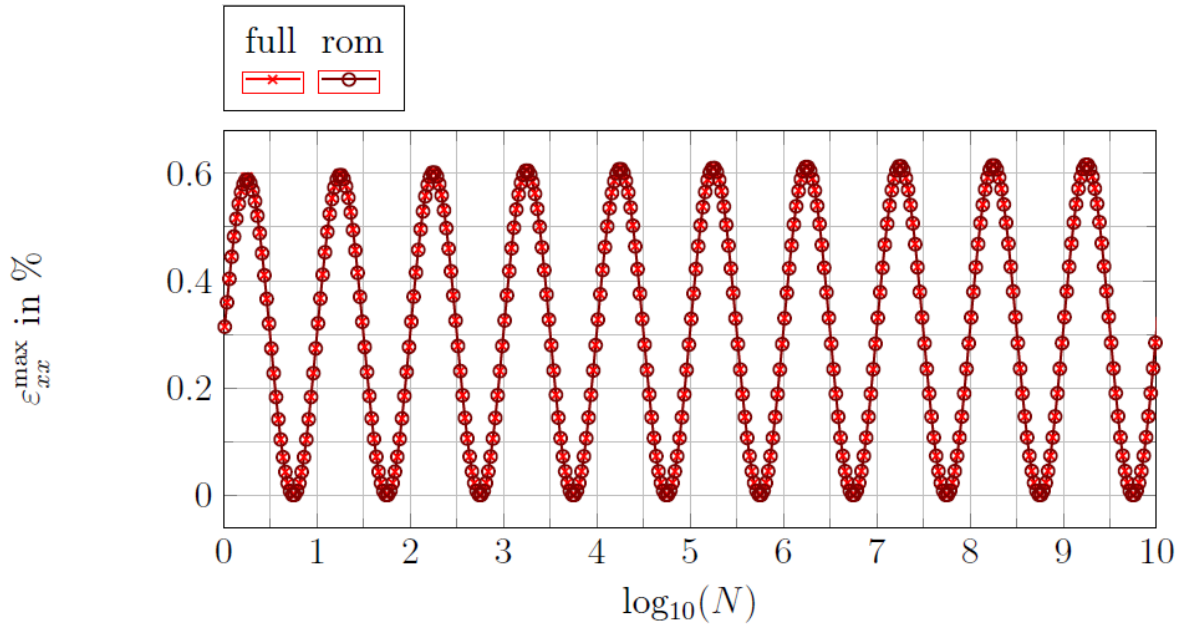

Figure 3. Evolution of the strain ε_{xx} for the first 10 cycles in full field and reduced order model

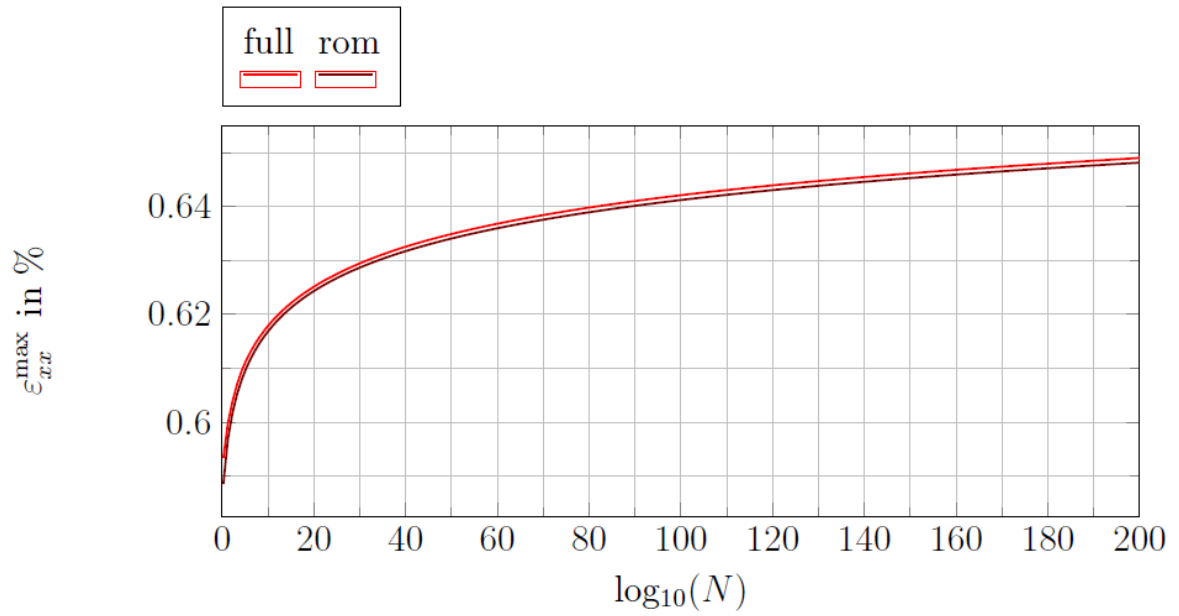

Figure 4. Evolution of the peak strain $\varepsilon_{xx}^{\max}$ over 200 cycles in full field and reduced order model

4. Comparison to effective stress models in fatigue literature

By replacing the time scale model introduced in section 2.1 and exposed in section 3 with the cycle scale model of section 2.2 further speed up in computations is achieved. When modeling the damage evolution in cycle space, we consider an effective driving stress

$$\boldsymbol{\sigma}_{\text{eff}} = \boldsymbol{\sigma}_{\text{a}}\sqrt{1+2c^2} \tag{7}$$

with

$$D' = \boldsymbol{\sigma}_{\mathrm{eff}} : \mathbb{C}_0^{-1} : \boldsymbol{\sigma}_{\mathrm{eff}} \tag{8}$$

to model stiffness degradation *prior to failure* in the material.

Using an appropriate effective stress to predict fatigue *failure* dependent on mean stress and stress amplitude is a well-studied approach in the literature. In fact, the Goodman [7] and Gerber [8] relations are known since the end of the 19th century. Many authors have studied empirical relations to predict mean-stress-dependent failure in fatigue and we refer to suitable overviews [9,10]. The fundamental difference between these methods and the proposed approach is that the former are empirical relations for failure while the latter emerges from a cycle-jump technique and aims at predicting the stiffness degradation during the fatigue *process*. Yet, to investigate whether the stiffness degradation is the main factor driving failure process in these materials, it is interesting to compare the equivalent stress in fatigue-life prediction methods and the effective stress obtained from the time-scale integration approach for the model at hand.

In the one-dimensional version of the proposed model, the equivalent stress may be expressed in terms of the mean stress σ^{mean} and the stress amplitude σ^{a} in the form

$$\sigma_{\mathrm{eq}} = \sqrt{\sigma_{\mathrm{a}} + 2\sigma_{\mathrm{mean}}}. \tag{9}$$

For σ_{eq}=50MPa, this relation is plotted in black in Fig. 5.

Mean-stress effects in short-fiber reinforced polymers were studied by several authors. Mallick et al. [11] performed fatigue experiments on short glass-fiber reinforced PA6.6 with R-values between 0.1 and 0.8. Oka and coworkers [12] characterized short-fiber reinforced polybuthylene terephthalate (PBT) at R-values between -1 and 0.9. Both Mallick et al. [11] and Oka et al. [12] suggested a modified Gerber-type equation to model the experimental data. The data of Mallick et al. [11] is shown in blue in Fig. 5.

Mortazavian and Fatemi [13] studied several short-fiber reinforced polymers under different orientations at stress ratios of *R = -1*, *R = 0.1* and *R = 0.3*, including polyamide 6 at room temperature. They suggest using the Walker equation or its special case, the Smith-Watson-Topper (SWT) model. Lu et al. [14] similarly studied several materials, including PA6 with 30 wt% fiber reinforcement, at R-values between -1 and 0.3. They suggested using the Walker equation

$$\sigma_{\mathrm{eq}} = (\sigma_{\mathrm{a}} + \sigma_{\mathrm{mean}})^{1-\gamma} \sigma_{\mathrm{a}}^{\gamma} \tag{10}$$

with exponent γ = 0.4. Both the SWT-model and the Walker equation with exponent γ = 0.4 are shown for an equivalent stress σ_{eq} = 50 MPa in Fig. 5 in bright red and green, respectively.

For low-cycle fatigue, Bailey et al. [15] suggested a Goodman relation. This was also discussed in Mallick et al. [11] for high cycle fatigue, but not recommended due to larger deviations than obtained with the SWT-model. The Goodman relation is shown in dark red in Fig. 5.

In the work at hand we are interested in R-values between *R = 0* and *R = -1*. The respective range is marked by the solid black line, while the extrapolation to higher *R*-values is dashed. The mean-stress dependence of the proposed model is higher than for the fatigue-failure

models in the literature. Taking the stiffness degradation modeled in the work at hand as the sole indicator to predict failure leads to comparatively conservative predictions compared to the relations recommended in the literature. Yet, the deviation of the current model from the Walker equation is at maximum 17 %, while the deviation between Walker and modified Gerber equation is of about 28 % for *R*-values below 0. Thus, we consider the proposed model to be able to reproduce the *general trend* for modeling fatigue with reasonable accuracy. However, care has to be taken when extending the model to higher R-values. We reiterate that the model at hand is primarily designed to model the stiffness degradation and not the failure under fatigue of polymers.

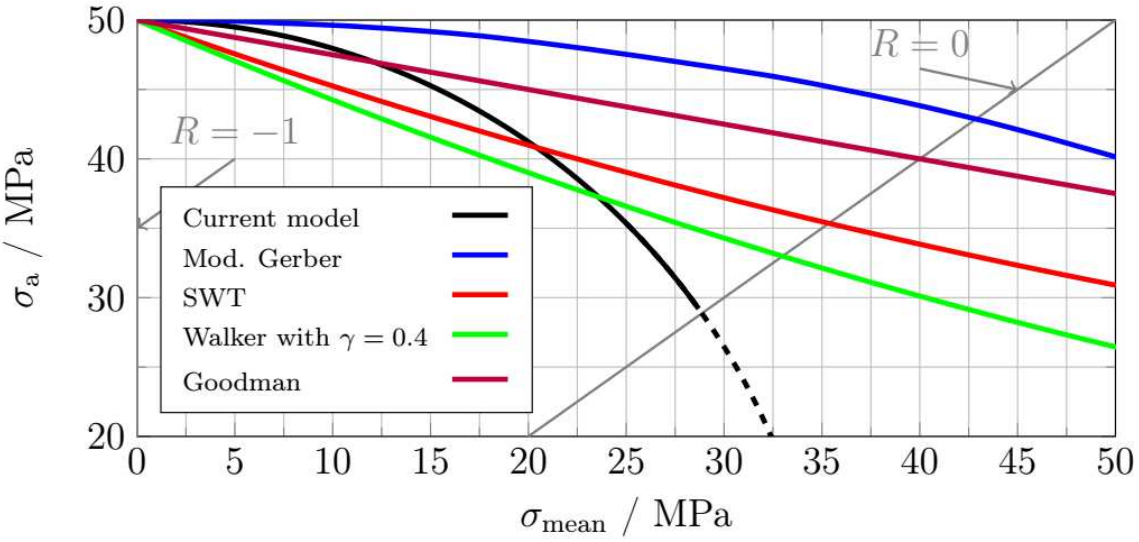

Figure 5. Relationship between stress amplitude and mean stress using different correlations

5. Conclusion

The presented fatigue-damage model is based on a simple isotropic matrix damage material, with a minimal number of parameters to be determined experimentally. Using advanced computational methods, i.e., model order reduction and a reformulation in cycle space, complex microstructures and components can be simulated efficiently. The nonlinear mechanical behavior of the damage evolution for the cycle scale model depends on the effective stress. This effective stress was compared to effective stress models for fatigue *failure* in the literature. For stress ratios between $R = -1$ and $R = 0$, the effective stresses to predict failure are similar to the effective stress driving fatigue damage prior to it. Thus a prediction of fatigue failure based on the proposed fatigue damage appears to be reasonable for this range.

Acknowledgements

MS acknowledges financial support of the German Research Foundation (DFG) within the International Research Training Group “Integrated engineering of continuous-discontinuous long fiber reinforced polymer structures” (GRK 2078).

6. References

1. Nouri H., Meraghni F., Lory P. Fatigue damage model for injection-molded short glass fiber reinforced thermoplastics. International Journal of Fatigue, 2009; 31:934-942.
2. Van Paepegem W., Degrieck J. A new coupled approach of residual stiffness and strength for fatigue of fibre-reinforced composites. Composites Part B: Engineering, 2002; 24:747-762.
3. Magino N., Köbler J. et al. A multiscale high-cycle fatigue-damage model for the stiffness degradation of fiber-reinforced materials based on a mixed variational framework. Computer Methods in Applied Mechanics and Engineering, 2022; 388:114198.
4. Magino N., Köbler J. et al. A space-time upscaling technique for modeling high-cycle fatigue-damage of short-fiber reinforced composites. Composites Science and Technology, 2022; Accepted.
5. Michel J.-C., Suquet P. Non-uniform transformation field analysis. International Journal of Solids and Structures, 2003; 40(25):6937-6955.
6. Fritzen F., Leuschner M. Reduced basis hybrid computational homogenization based on a mixed incremental formulation. Computer Methods in Applied Mechanics and Engineering, 2013; 260:143-154.
7. Goodman J. Mechanics of Applied Engineering. Longmans, Green & Co. 1899.
8. Gerber H. Bestimmung der zulässigen Spannungen in Eisen-Constructionen. Wolf. 1874.
9. Papuga J., Vízková I., et al. Mean-stress effect in stress-life fatigue prediction re-evaluated. MATEC Web Conf., 2018; 165:10018.
10. Böhm M., Glowacka K. Fatigue life estimation with mean stress effect compensation for light weight structures – the case of glare 2 composite. Polymers, 2020; 12(2):10018.
11. Mallick P. K., Zhou Y. Effect of mean stress on the stress-controlled fatigue of a short E-glass fiber reinforced polyamide-6,6. International Journal of Fatigue, 2004; 26:941-946.
12. Oka H., Narita R., et al. Effect of Mean Stress on Fatigue Strength of Short Glass Fiber Reinforced Polybthyleneterephthalate. Key Engineering Materials, 2007; 340-341:537-542.
13. Mortazavian S., Fatemi A. Effects of mean stress and stress concentration on fatigue behavior of short fiver reinforced polymer composites. Fatigue and Fracture of Engineering Materials and Structures, 2016; 39(2):149-166.
14. Lu Z., Feng B., Loh C. Fatigue behaviour and mean stress effect of thermoplastic polymers and composites. Frattura ed Integrità Strutturale, 2018; 46:150-157.
15. Bailey P.B.S., Wilson P.R. Investing the Goodman diagram for short-fibre carbon reinforced polypropylene composites. 21st International Conference on Composite Materials, 2017

FIBER BREAKAGE MODELING BASED ON HYDRODYNAMIC FORCES IN MACROSCOPIC PROCESS SIMULATIONS

Florian Wittemann[a], Robert Maertens[b], Frank Henning[a,b], Luise Kärger[a]

a: Karlsruhe Institute of Technology (KIT), Institute of Vehicle System Technology, Karlsruhe, Germany – florian.wittemann@kit.edu
b: Fraunhofer Institute for Chemical Technology (ICT), Pfinztal, Germany

Abstract: *Injection molding is one of the most important processes for manufacturing parts from discontinuous fiber reinforced polymers. Fiber length and orientation do not only influence the final structural behavior in an anisotropic way, but also the flow field and hence the mold filling process. Therefore, fiber length distribution and fiber breakage modeling are important aspects of an adequate process simulation. For fiber breakage modeling, hydrodynamic forces from matrix on fibers are considered within this work. Knowing the flow field and fiber orientation distributions of the homogenized material, flow-induced hydrodynamic forces on the fibers can be calculated. The fiber orientation tensor is used to determine reference fibers in every element. Based on this information an advanced approach for fiber breakage modelling is proposed. The fiber length distribution in the final part is compared to experimental data of a reactive injection molding process, showing good agreement.*

Keywords: Discontinuous fiber reinforced polymers; injection molding simulation; hydrodynamic forces; fiber breakage

1. Introduction

Injection molding of fiber reinforced polymers is one of the most important processes for manufacturing discontinuous reinforced polymer parts. Due to the option of full automatization in combination with realizing complex geometries, it is widely used in industry and was in the focus of several scientific publications in the last decades [1]. The process is transient and non-isothermal, and the materials show a complex chemo-thermal viscosity behavior, which is in case of fiber reinforcement also anisotropic. To ensure and optimize the manufacturing process, simulation is an important tool. An adequate process simulation has to focus on the non-Newtonian and chemo-thermal matrix material behavior, but also on the fibers [2]. Fiber orientation influences the mechanical behavior during mold filling and in the final part. This also applies to the fiber length, having crucial impact on viscosity and impact strength.

Fibers may break during processing. In literature, buckling is named as dominant phenomena for fiber breakage, although there are other effects [3, 4]. The shortening of fibers influences the viscosity behavior of the material and hence the flow field, which vice versa influences the forces acting on the fibers and therefore fiber breakage. Consequently, an adequate process simulation must include both anisotropic, fiber dependent flow modeling and fiber breakage modeling [5].

Since the numerical effort for performing a process simulation with individual fibers on part level is too high, the fiber orientation distribution is represented by an orientation tensor in most cases [6]. Unfortunately, no information on individual orientation and position of fibers is known by applying this tensorial approach. Hence, forces depending on position, orientation and

  doi:10.5075/epfl-298799_978-2-9701614-0-0

contact of fibers, must be approximated. Our previous work [5, 7] presents approaches to calculate hydrodynamic and fiber-contact forces in macroscopic simulations with orientation tensors, by using eigenvectors of the orientation tensor as reference fibers. These forces are used in the present work to approximate the occurrence of fiber breakage.

Today's fiber breakage simulation approaches focus on buckling as phenomenon for fiber breakage. One of the most applied models in macroscopic simulations is the one presented by Phelps et al. [8]. Here, the acting forces are based on the work of Dinh and Amstrong [9], representing forces with slender body analysis. Based on this, a buckling index is determined and an empirical function describes the amount of buckling fibers, which break within a control volume. Within this work, a novel approach for fiber breakage simulation in macroscopic process simulations is presented. The approach is based on the work of Phelps et al., but with a different approach for force calculation and with the use of eigenvectors as reference fibers.

2. Theory

The fiber breakage modeling is based on reference fibers, which are represented by the eigenvectors ϑ_i of the second order orientation tensor. Hydrodynamic forces acting from the flow field on the fibers are approximated with the eigenvectors and are used for force calculation in the fiber breakage model. The hydrodynamic force F_i^{hyd} is split into a drag part, due to the relative velocity between fibers and polymer and a lift part, since the fibers are non-spherical. Based on Stokes law, the drag force F_i^{d} is approximated by

$$F_i^{\mathrm{d}} = 3\pi\eta_{\mathrm{M}} d_{\mathrm{f}} k_{\mathrm{d}} \Delta U_i, \tag{1}$$

with η_{M} being the matrix viscosity, d_{f} the fibers diameter, k_{d} a geometry-dependent fitting factor and ΔU_i the relative velocity. The fitting factor is given by

$$k_{\mathrm{d}} = 1 - \alpha(r_{\mathrm{f}} - 1)\cos(2\phi) + \beta(r_{\mathrm{f}} - 1), \tag{2}$$

with $\alpha = 0.09$, $\beta = 0.3125$, r_{f} being the aspect ratio of the fibers and ϕ the angle between ϑ_i and ΔU_i. A derivation for Eq. (1) and (2) is given by Meyer et al. [10, 11]. The definition of the relative velocity ΔU_i is given in our previous work [5, 7].

Similar to the drag force, the lift force F_i^{li} is approximated by

$$F_i^{\mathrm{li}} = 3\pi\eta_{\mathrm{M}} d_{\mathrm{f}} k_{\mathrm{li}} \|\Delta U_i\| [\![p_i]\!], \tag{3}$$

with

$$k_{\mathrm{li}} = \alpha(r_{\mathrm{f}} - 1)\sin(2\phi) \tag{4}$$

and

$$p_i = (\vartheta_i \times [\![\Delta U_i]\!]) \times [\![\Delta U_i]\!]. \tag{5}$$

The operator $[\![\cdot]\!]$ indicates that the vectors are normed. The derivation of the lift force is also given by Meyer et al. [10, 11]. In summary it is

$$F_i^{\mathrm{hyd}} = F_i^{\mathrm{d}} + F_i^{\mathrm{li}} = 3\pi\eta_{\mathrm{M}} d_{\mathrm{f}} (k_{\mathrm{d}} \Delta U_i + k_{\mathrm{li}} \|\Delta U_i\| [\![p_i]\!]). \tag{6}$$

  doi:10.5075/epfl-298799_978-2-9701614-0-0

This eigenvector-based approach for calculating hydrodynamic forces in the homogenized material is verified with numerical experiments in our previous work [7].

The assumptions for fiber breakage are:

- Fibers break due to buckling.
- Fibers break only in one point, so one fiber breaks only in two parts.
- Until buckling, fibers are perfect, rigid cylinders.
- There is a defined minimum fiber length, which cannot be undercut.
- There is a defined number of possible fiber lengths.
- Fiber-fiber contact forces are neglected.

The fiber forces, induced by the hydrodynamic load may lead to fiber buckling, and an amount of the fibers which buckle will also break. The forces are calculated on reference fibers, represented by the eigenvectors, therefore the fiber breakage modeling is also applied on the eigenvectors. In a first step it is determined if the fibers are under compression or tension, so if they may buckle or not, by checking if they are in the so-called Jeffery orbit, defined as

$$D_{ij}\vartheta_i\vartheta_j < 0, \tag{7}$$

with D_{ij} being the strain rate tensor. This is performed three times, once for each eigenvector. Afterwards it is determined if the forces are large enough to enable buckling in the fibers by

$$B = \frac{\hat{F}^{\mathrm{hyd}}}{F^{\mathrm{bu}}} \geq 1, \tag{8}$$

where $\hat{F}^{\mathrm{hyd}} = \vartheta_i F_i^{\mathrm{hyd}}$ since only the force component in fiber direction is relevant for buckling. The critical force for buckling is defined as

$$F^{\mathrm{bu}} = \pi^3 E_{\mathrm{f}} d_{\mathrm{f}}^4 / \left(64 L_{\mathrm{f}}^2\right), \tag{9}$$

with fiber Youngs modulus E_{f} and fiber length L_{f}. F^{bu} is determined independently for each fiber length. The buckling index B is calculated three times for each fiber length, once for every eigenvector. The ongoing calculations for fiber breakage modeling are adapted from the procedure presented by Phelps et al. [8]. Based on the buckling index, a breaking probability P_k is defined as

$$P_k = \begin{cases} 0, & B_k < 1 \quad \text{or} \quad D_{ij}\vartheta_{ik}\vartheta_{jk} \geq 0 \\ C\dot{\gamma}\left(1 - \exp(1 - B_k)\right), & B_k \geq 1 \quad \text{and} \quad D_{ij}\vartheta_{ik}\vartheta_{jk} < 0' \end{cases} \tag{10}$$

with the breakage coefficient C and the scalar shear rate $\dot{\gamma}$. The index $k \in \{1,2,3\}$ indicates the different eigenvectors ϑ_{ik}. To sum up the breakage probability within one cell, the eigenvector-specific probabilities are weighted with the corresponding eigenvalues,

$$P = \lambda_k P_k. \tag{11}$$

Whenever fibers break, new and shorter fibers are created. This 'child generation' must be considered in a constitutive modeling approach. It is assumed that fibers break only into two smaller parts within this work. Phelps et al. [8] define the child generation rate R_{nm} as probability density function (PDF), representing the position of the breaking point, so

  doi:10.5075/epfl-298799_978-2-9701614-0-0

$$R_{nm} = \varrho_m \mathrm{PDF}\left(L_n^{\mathrm{f}}, \frac{L_m^{\mathrm{f}}}{2}, S\right), \tag{12}$$

where S is the standard deviation, L_m^{f} the parent fiber length, L_n^{f} the child fiber length and the scaling factor ϱ_m is defined to fulfill the constitutive condition, as described in [8]. The indices n and m represent the number of possible fiber lengths. It is $R_{nm} = R_{(m-n)m}$ since the initial fiber length and one length of a child define the length of the other child. Furthermore, it is $R_{nm} = 0$ for $L_n^{\mathrm{f}} \geq L_m^{\mathrm{f}}$, so short fibers cannot combine to longer fibers again.

Finally, the number of fibers N_n^{f} with corresponding length L_n^{f} within a control volume is given by

$$\frac{\partial N_n^{\mathrm{f}}}{\partial t} + U_i \frac{\partial N_n^{\mathrm{f}}}{\partial x_i} = -P_n N_n^{\mathrm{f}} + \sum_m R_{nm} N_m^{\mathrm{f}}, \tag{13}$$

where U_i is the velocity vector of the regarded cell.

3. Results and discussion

The novel fiber breakage modeling approach is validated with reactive injection molding experiments of a 190 mm × 480 mm rectangular plate with 4 mm thickness as presented in [5, 12]. The material is injected via a 185 mm long cone sprue with a start and end diameter of 9 mm and 15.5 mm, respectively, ending at the plate's center. The machine used for experiments is a KraussMaffei 550/2000 GX injection molding machine equipped with a standard 60 mm thermoset screw. A part of the screw chamber is also considered in the simulation model to enable a better modeling of the initial material state with respect to fiber orientation and fiber length distribution. The simulation model with part of the screw chamber and position of the fiber length measurement is shown in Figure 1. The material enters the cavity in the blue highlighted area.

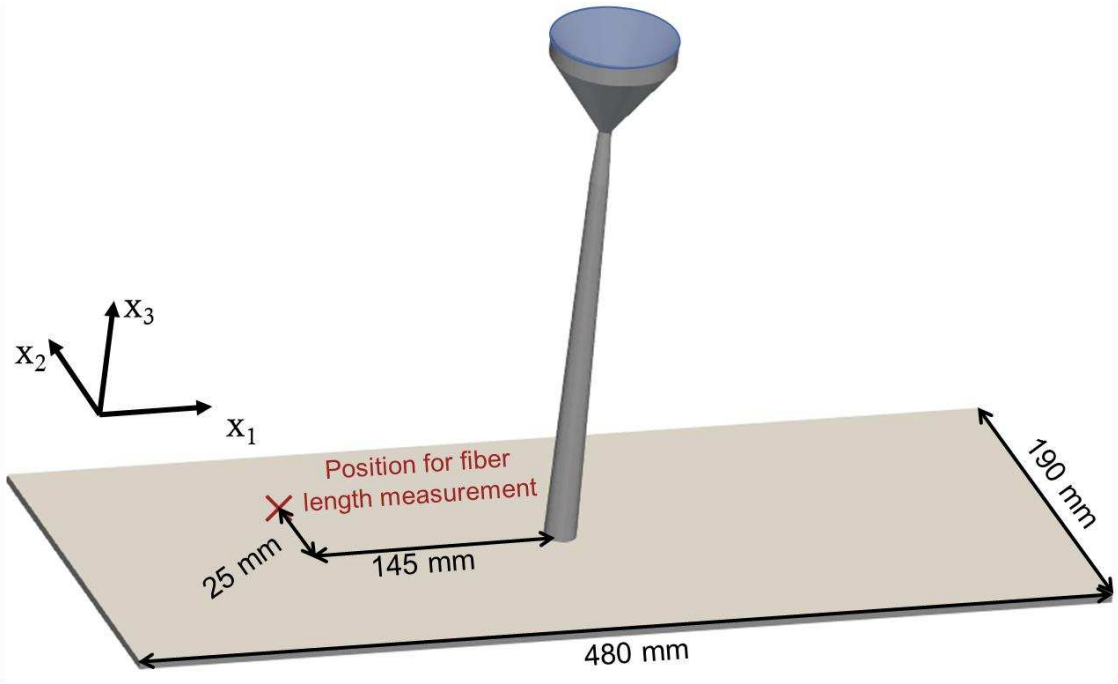

Figure 1. Simulation model for validation with inlet area highlighted in blue

  doi:10.5075/epfl-298799_978-2-9701614-0-0

The material used for the experiments is phenolic long-fiber compound of the novolac type, called Porophen GF9201L12a by Sumitomo Bakelite Co., Ltd [13]. The material is reinforced with 55 %-wt. glass fibers, having an initial length of 12 mm. The fiber length measurement is performed with pyrolysis and the commercially available FASEP system by IDM Systems as described in [12].

As shown in [5, 12] only a small amount of fibers remains with a length of 12 mm after plastification (about 5 % by weight). The majority of fibers is already broken to less than 1 mm, being about 75 % in summary. The fiber length distribution after plastification (screw chamber) is shown in Figure 2 by the black, dotted curve. It represents the initial state of the simulation model. The material is injected in the cavity with an injection speed of 150 cm³/s, the mold has a temperature of 185 °C. The considered fiber lengths in the simulation are 0.25 mm to 11.75 mm in 0.5 mm steps, resulting in 24 possible fiber lengths. The measurements are also clustered in 0.5 mm steps. The simulation is performed with the finite-volume based open-source software OpenFOAM. The simulation method and material models are described in [2, 5]. The model parameters for fiber breakage calculation are given in Table 1. The values for C and S are identical to the ones used by Phelps et al. [8].

Table 1: Parameters used for fiber breakage calculation.

Parameter	Value	Unit
E_f	73	GPa
d_f	$17 \cdot 10^{-6}$	m
C	0.025	-
S	1	-

Figure 2 shows the averaged experimental results of five measurements with corresponding standard deviation for the screw chamber and the plate. As can be seen, only a small amount of fibers with less than 25 % has a length of more than 1 mm after plastification, i.e. in the screw chamber. However, there are some longer fibers with 5-8 mm and about 5 % still have a length of 12 mm. During the injection, nearly all fibers break to lengths of 1 mm or less, as shown by the measurements in blue in Figure 2. The position in the plate, where the specimens were taken, is shown in Figure 1. Comparing the experimental results in the plate (blue) to the simulation results (red) shows a good agreement between simulation and experiments for the complete length distribution. Also in the simulation nearly all fibers break to less than 1 mm and the amounts of fibers with 0.25 mm and 0.75 mm are quite similar in simulation and measurements. The good agreement validates the presented approach to be able to predict reasonable fiber length distributions in injection molding simulation, with respect to process conditions and material properties.

  doi:10.5075/epfl-298799_978-2-9701614-0-0

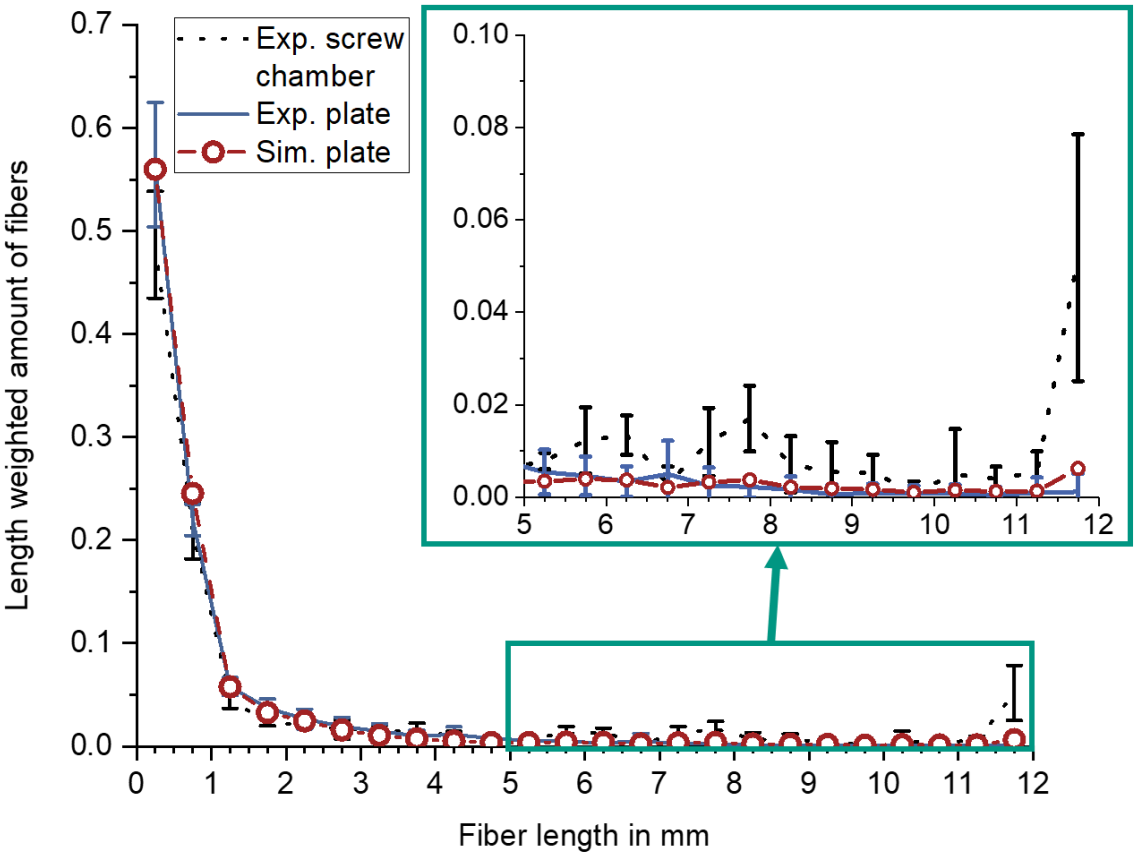

Figure 2. Comparison of fiber length for experimental results in screw chamber (black, dotted), plate (blue, lines) and simulation in plate (red, circles), experimental results are shown with standard deviation

4. Conclusion and outlook

A novel approach for simulation of fiber breakage in macroscopic injection molding simulations is presented. The approach focuses on reference fibers, represented by the eigenvectors of the second order orientation tensor. Hydrodynamic drag and lift force are calculated individually for all eigenvectors. Based on hydrodynamic load and buckling, a constitutive fiber breakage model predicts the fiber length distribution during injection molding with respect to process conditions and material properties. The method is validated with experimental fiber length distribution measurements of an injection molded plate, showing good agreement.

The main difference between this approach and the one presented by Phelps et al. [8] is the procedure of the force calculation, which has two effects. One is that the forces within this work are related to the eigenvectors and hence there are three forces for three representative fibers with different orientations in each cell. Due to different orientation and the weighting with the eigenvalues it is possible that only an amount of fibers within the control volume is able to buckle and break, which increases the orientation dependence of the breakage modeling. The second point is the reduction of empirical parameters, since the calculation of the hydrodynamic forces can be performed without empirical parameters, reducing the necessary parameters from three to two compared to [8].

  doi:10.5075/epfl-298799_978-2-9701614-0-0

Hydrodynamic load is not the only effect which may lead to fiber damaging. One other important aspect are fiber contact forces like normal, friction and lubrication forces, as investigated by Meyer et al. [14] in a mesoscopic fiber bundle simulation approach. Such forces are especially relevant for highly filled materials and influence fiber movement, orientation and damaging. However, the exact effects of these forces on the material behavior, particularly on macroscopic scale, are not well understood at this point of time, whether on the experimental side, nor on the numerical. More investigation in fiber-fiber interactions needs to be done to create a better understanding of these phenomena and the influence on material behavior and properties.

Acknowledgements

We would like to thank the 'Deutsche Forschungsgemeinschaft' (DFG) for funding the research project 'MeproSi' (project number: 464119659), which enabled this work. Furthermore, we are grateful for the experimental process data, generously provided by the DFG project 'LFD-Spritzgussprozess' (project number: 400343062), led by Prof. Peter Elsner and Prof. Kay Weidenmann.

5. References

1. Osswald TA, Beaumont JP. Injection molding handbook. 2. ed. Munich: Hanser; 2008.

2. Wittemann F, Maertens R, Kärger L, Henning F. Injection molding simulation of short fiber reinforced thermosets with anisotropic and non-Newtonian flow behavior. Composites Part A: Applied Science and Manufacturing 2019; 124:105476.

3. Durin A, Micheli P de, Ville J, Inceoglu F, Valette R, Vergnes B. A matricial approach of fibre breakage in twin-screw extrusion of glass fibres reinforced thermoplastics. Composites Part A: Applied Science and Manufacturing 2013; 48:47–56.

4. Hernandez JP, Raush. T., Rios A, Strauss S, Osswald TA. Theoretical analysis of fiber motion and loads during flow. Polym. Compos. 2004; 25(1).

5. Wittemann F. Fiber-dependent injection molding simulation of discontinuous reinforced polymers: Doctoral Thesis. Karlsruhe, Germany; 2022.

6. Advani SG, Tucker CL. The Use of Tensors to Describe and Predict Fiber Orientation in Short Fiber Composites. Journal of Rheology 1987; 31(8):751–84.

7. Wittemann F, Kärger L, Henning F. Theoretical approximation of hydrodynamic and fiber-fiber interaction forces for macroscopic simulations of polymer flow process with fiber orientation tensors. Composites Part C: Open Access 2021; 132(53):100152.

8. Phelps JH, Abd El-Rahman AI, Kunc V, Tucker CL. A model for fiber length attrition in injection-molded long-fiber composites. Composites Part A: Applied Science and Manufacturing 2013; 51:11–21.

9. Dinh SM, Armstrong RC. A Rheological Equation of State for Semiconcentrated Fiber Suspensions. Journal of Rheology 1984; 28(3):207–27.

  doi:10.5075/epfl-298799_978-2-9701614-0-0

10. Meyer N, Schöttl L, Bretz L, Hrymak AN, Kärger L. Direct Bundle Simulation approach for the compression molding process of Sheet Molding Compound. Composites Part A: Applied Science and Manufacturing 2020; 132:105809.

11. Meyer N. Mesoscale simulation of the mold filling process of Sheet Molding Compound: Doctoral Thesis. Karlsruhe, Germany; 2021.

12. Maertens R, Hees A, Schöttl L, Liebig W, Elsner P, Weidenmann KA. Fiber shortening during injection molding of glass fiber-reinforced phenolic molding compounds: fiber length measurement method development and validation. Polymer-Plastics Technology and Materials 2021:1–14.

13. Datasheet Porophen GF 9202 L12; 2013 [cited 2021 Jan 11]. Available from: URL: https://sbhpp-static.s3.amazonaws.com/documents/ds_2124_e.pdf.

14. Meyer N, Hrymak AN, Kärger L. Modeling Short-Range Interactions in Concentrated Newtonian Fiber Bundle Suspensions. International Polymer Processing 2021; 36(3):255–63.

  doi:10.5075/epfl-298799_978-2-9701614-0-0

CHARACTERISTIC LENGTH-INSENSITIVE PHASE-FIELD DAMAGE MODELING OF CRACKS IN FIBER-REINFORCED COMPOSITES WITH FFT SOLVER

X. Ma[a], M. Shakoor[a], Y. Chen[b], D. Vasiukov[a], S.V. Lomov[c], C.H. Park[a]

a: IMT Nord Europe, Institut Mines-Télécom, Univ. Lille, Center for Materials and Processes, F-59000 Lille, France
xiao.ma, modesar.shakoor, dmytro.vasiukov, chung-hae.park@imt-nord-europe.fr
b: Materials and Structures Centre, Department of Mechanical Engineering, University of Bath, Claverton Down, Bath, United Kingdom, BA2 7AY
c: Department of Materials Engineering, KU Leuven, Belgium

Abstract: *Using an FFT-based solver for phase-field modeling of damage is attractive because it can enable massive parallelization. Before applying it for complex analysis, the characteristic length, an important parameter of phase-field damage models, needs a prudent discussion. This parameter is commonly treated as a material parameter since it can hugely affect the predicted mechanical behavior. However, for heterogeneous materials, our recent studies have shown that the choice of the characteristic length affects not only the macroscopic mechanical behavior but also the local crack patterns. This makes it difficult to get proper macro-responses and local crack patterns simultaneously. Consequently, this work addresses the implementation of a length-insensitive phase-field model with an FFT solver to deal with the above issue. Meanwhile, a criterion for choosing a proper characteristic length for this phase-field model is also proposed in this work.*

Keywords: Fast Fourier Transform (FFT); phase-field; damage modeling; composites

1. Introduction

Prediction of the strength of heterogeneous materials such as composites is a challenging task. In recent years phase-field modeling has gained increased attention for failure modeling of composite materials. Similar to continuum damage models, phase-field models use a damage variable d, which varies in the range $[0, 1]$, to describe the effect of a crack or material damage. Thus a sharp crack (Fig. 1(a)) is regularized as a diffusive crack band (Fig. 1(b)) by a function of d [1,2]. The phase-field models are closely related to the variational approach to brittle fracture [2,3] that seeks the displacement field and the cracks by minimizing the total potential energy of the cracking solid. A compact formulation of the phase-field model was outlined by Miehe in [4,5]. This comprehensive formulation description has promoted the application of phase-field models in the engineering community.

In the phase-field model, there are two important parameters: the critical energy release rate (G_c) and the characteristic length (l_c). G_c is widely accepted as a material damage property while l_c describes the diffusive crack bandwidth as illustrated in Fig. 1(c). The smaller the l_c is, the narrower the crack band is. If $l_c = 0$, a sharp crack is fully recovered. Nevertheless, in the literature, discussions and arguments were presented about the choice of l_c value.

  doi:10.5075/epfl-298799_978-2-9701614-0-0

The Finite Element Method (FEM) is the most widely used numerical tool to solve phase-field problems. It raises the question of the relation between l_c and the mesh size. Although phase-field models are non-local damage models in nature, generally considered mesh independent, a condition on element size still should be ensured. Miehe et al. [5] have proven that the characteristic length of the phase-field model needs to be twice larger than the element size of the fractured zone. In this context, especially for 3D simulations, conventional FEM solvers can be cumbersome hence requiring an efficient parallel implementation to avoid the computational limits.

Recent works have focused their interest on the Fast Fourier Transform (FFT) for material modeling. This method, which was proposed initially in [6], uses image-type (voxel) meshes that make the meshing of complex fibrous reinforcements less complicated and give results in agreement with FEM voxel-based models. Compared with conventional FEM, the FFT method does not need to assemble a global stiffness matrix and is easier to parallelize, contributing to its high computational efficiency. Thus, the FFT-based method can be an interesting alternative to the conventional FEM for modeling heterogeneous materials such as fibrous composites.

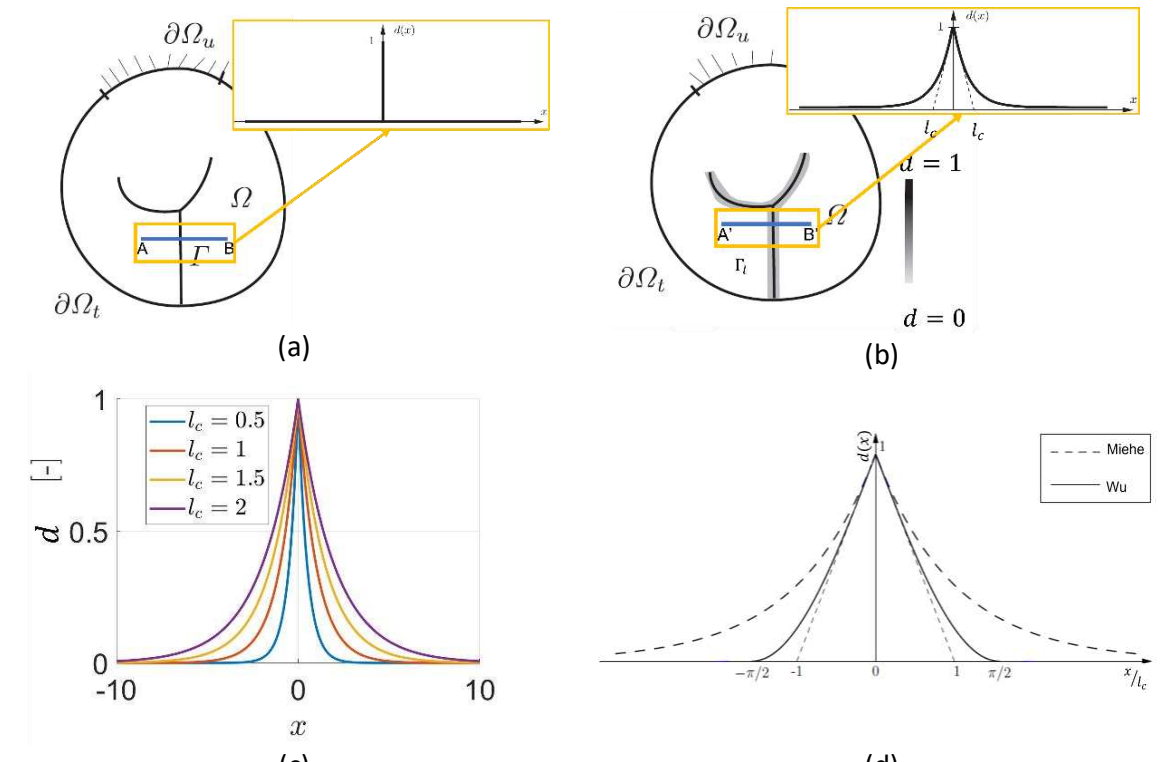

Figure 1. A solid body Ω with the crack set Γ/Γ_{l_c}: (a) sharp crack and (b) diffuse crack band. (c) Illustration of the damage profile of a diffusive crack at $x = 0$ for various length parameters l_c. (d) The damage profiles of Miehe's and Wu's phase-field model.

The second discussion has focused on the relationship between l_c and the predicted material's mechanical behavior. Although the initial intention was to use l_c as a numerical parameter to describe the degree of crack diffusion, Some works [7,8] found that it can significantly impact the simulated material's behavior in some phase-field models, such as Miehe's phase-field model [5]. In line with this finding, this parameter is commonly treated as a material parameter nowadays [9,10]. In the literature, two main approaches can determine l_c values. One is from

  doi:10.5075/epfl-298799_978-2-9701614-0-0

an analytical calculation of a 1D bar problem with a homogeneous crack phase-field [8], while another is from the inverse analysis of experiments [11].

Even though these techniques can give satisfactory results in some cases, they complicate the calculation. Furthermore, Mandal et al. [12] have shown that these l_c estimations can be sometimes too large compared with the model size, which leads to some bizarre phenomena. Our recent studies on composite materials have shown that the choice of the characteristic length affects not only the macroscopic mechanical behavior but also the local crack propagation patterns. Hence, it is difficult to choose an appropriate l_c that both gets proper macroscopic responses and local-crack patterns. Consequently, the l_c insensitive phase-field model proposed by Wu [13] is implemented in the FFT solver in this work, which can avoid or reduce the above issue.

As aforementioned, two representative phase-fields exist in the literature, and both were studied in this work. One is Miehe's phase-field model [5], which is l_c sensitive, while another is Wu's phase-field model [13], which is considered as l_c insensitive. Section 2 will present a brief introduction of these two phase-field models. The numerical results will be presented in section 3, and the conclusions are in section 4.

2. Review of Miehe's and Wu's phase-field model

The first characteristic of phase-field is using a diffusive crack function to smear the sharp crack. The diffusive crack functions of Miehe's and Wu's phase-field model can be written as follows,

$$d^M = \exp\left(-\frac{|x|}{l_c}\right) \text{(Miehe)}, \quad d^W = 1 - \sin\left(\frac{|x|}{l_c}\right) \text{(Wu)}, \tag{1}$$

and their graphical presentations are illustrated in Fig. 1(d). With Eq. (1), it is straightforward to figure out the diffusive crack surface (Γ_l) and its density (γ), where their generic forms can be expressed as follows,

$$\Gamma_l = \int_{-\infty}^{+\infty} \gamma dV, \qquad \gamma = \frac{1}{c_0}[\alpha(d) + l_c(\nabla d)^2], \tag{2a}$$

$$\alpha(d) = \zeta d + (1-\zeta)d^2. \tag{2b}$$

In Eq. (2), the c_0 and ζ are parameters that depend on different phase-field models. As for Miehe's and Wu's models, their values and expressions are shown in Table 1.

Table 1: The parameters of different phase-field models.

Model name	ζ	$\alpha(d)$	c_0	$d(x)$
Miehe [5]	0	d^2	2	$\exp\left(-\frac{\|x\|}{l_c}\right)$
Wu [13]	2	$2d - d^2$	π	$1 - \sin\left(\frac{\|x\|}{l_c}\right)$

This description (Eq. 2(a)) of the diffusive crack surface can then be incorporated into the variational framework [3] to deduce the governing equations evolving the damage and

displacement fields. This variational approach is based on Griffith's energy principle for a cracked body.

$$\Pi = \Phi_s + \Phi_d, \tag{3a}$$

$$\Phi_s = \int_\Omega \varphi(\varepsilon, d)\mathrm{d}V = \int_\Omega g(d)\varphi_0(\varepsilon)\mathrm{d}V, \tag{3b}$$

$$\Phi_d = \int_{\Gamma_l} G_c \mathrm{d}\Gamma_l = \int_{\Gamma_l} G_c\, \gamma(d, \nabla d)\mathrm{d}V, \tag{3c}$$

where Φ_s denotes the strain energy stored in the cracked body, and $g(d)$ and $\varphi_0(\varepsilon)$ present the energetic degradation function and initial strain energy, respectively. Φ_d describes the energy dissipated due to the opening of the crack. The problem can then be solved by minimizing Griffith's energy function (Eq. (3)). With this step, we can get the local governing equations to solve the mechanical and damage fields by applying weak or strong coupling schemes.

$\varphi_0(\varepsilon)$ is calculated based on the stress and strain fields of the model, while $g(d)$ should be defined for different phase-field models. As illustrated in Eq. (4), a simple quadradic energetic degradation function is applied for Miehe's model. Concerning Wu's model with a linear softening law, the simple degradation function is replaced by a more complicated form. According to the detailed mathematical description in [14,15], the key point making Wu's model l_c insensitive is the introduction of σ_c.

$$g(d) = (1-d)^2 \text{(Miehe)}, \tag{4a}$$

$$g(d) = \frac{(1-d)^2}{(1-d)^2 + a_1 d(1-0.5d)}, \quad a_1 = \frac{E_0 G_c}{\sigma_c^2} \cdot \frac{4}{\pi l_c} \text{ (Wu)}. \tag{4b}$$

In summary, the damage evolution equations of Miehe's and Wu's model are written as:

$$g'(d)H + \frac{G_c}{c_0 l_c}\alpha'(d) - \nabla \cdot \left(\frac{2G_c l_c}{c_0}\nabla d\right) = 0 \text{ (Generic form)}, \tag{5a}$$

$$-2(1-d)H + \frac{G_c}{l_c}d - \nabla \cdot (G_c l_c \nabla d) = 0 \text{ (Miehe)}, \tag{5b}$$

$$-\frac{4a_1(1-d)}{(2a_1 d - 4d - a_1 d^2 + 2d^2 + 2)^2}H + \frac{2}{\pi}\cdot\frac{G_c}{l_c}(1-d) - \nabla \cdot \left(\frac{2G_c l_c}{\pi}\nabla d\right) = 0 \text{ (Wu)}. \tag{5c}$$

where H is called the history field, which describes the maximum initial strain energy from [0, t_n], and t_n is the current time. Since the compressive part of strain energy does not contribute to the damage evolution in phase-field models, the H functions of these two phase-field models are defined as:

$$\mathrm{H}(x, t_n) = \max_{0 \le t \le t_n}[\varphi_0^+(x,t)] \text{ (Miehe)}, \tag{6b}$$

$$\mathrm{H}(x, t_n) = \max_{0 \le t \le t_n}\left[\varphi_0^+(x,t),\ \frac{1}{2}\frac{\sigma_c^2}{E_0}\right] \text{ (Wu)}, \tag{6c}$$

where $\varphi_0^+(x,t)$ describes the initial tensile strain energy at time t. Solving Miehe's phase-field with the FFT method, detailed in [16], uses a fixed-point algorithm and weak coupling scheme. However, due to the complexity of Wu's model, Newton-Krylov and alternating minimization algorithms are applied in our work. The flowchart is shown in Fig. 2. As shown in Fig. 2, first, we have the FFT mechanical solver to calculate the stress and strain fields at the current time (t_n).

  doi:10.5075/epfl-298799_978-2-9701614-0-0

These values can then be entered into the Newton-Krylov loop to calculate the local damage fields with an iteration number <<i>>. Finally, the alternating minimization is applied to ensure that all damage and mechanical fields are well updated in the current time increment, and the iteration number is denoted as <<alt>>.

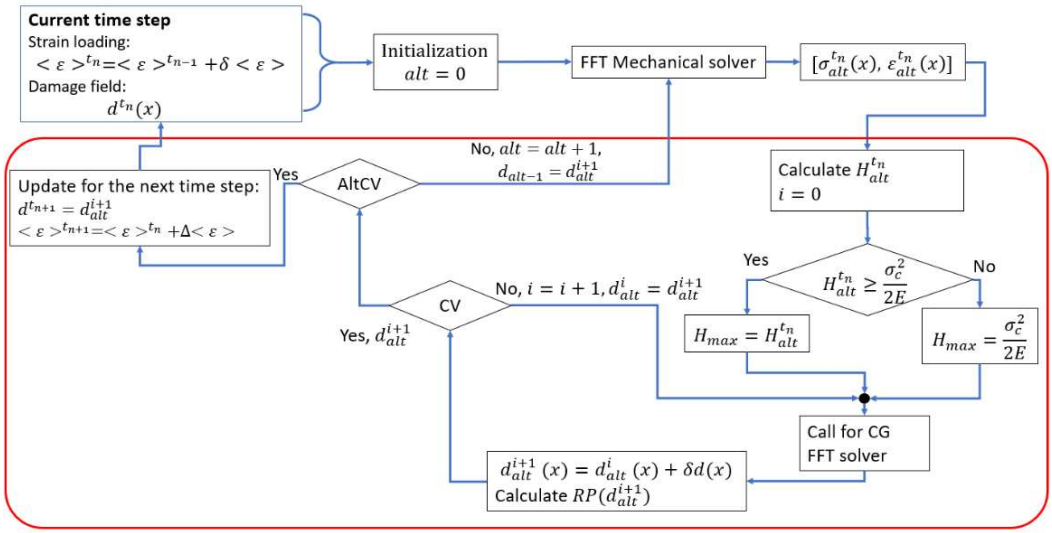

Figure 2. The flow chart of the implementation of Wu's phase-field method with an FFT solver. (Remark: CV is the damage variable convergence check. AltCV is the alternating minimization convergence check. CG is the conjugate gradient algorithm. The part in the red rectangular is the main algorithm for solving the damage field.)

3. Results and discussions

The model chosen in this work is presented in Fig. 3, a 3D model with a thickness of one voxel size. The resolution of the model is $\mathrm{N} = 225$ with an element size of $h = 8.9 \cdot 10^{-5}$ mm. The blue part is fiber for which the material is E-glass with properties: $E_f = 74000\,\mathrm{MPa}$, $\upsilon_f = 0.20$, $G_c^f = 60\,\mathrm{N/mm}$. The red part is the matrix for which the material is Epoxy with properties: $E_m = 4650\,\mathrm{MPa}$, $\upsilon_m = 0.35$, $G_c^f = 3.0 \cdot 10^{-3}\,\mathrm{N/mm}$. The total fiber volume fraction of this model is 0.15.

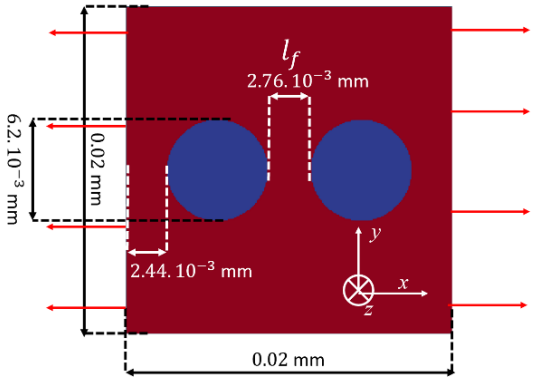

Figure 3. The presentation of the model under x-direction tensile loading (blue part: fiber and red part: matrix). (Remark: periodic boundary conditions are applied.)

  doi:10.5075/epfl-298799_978-2-9701614-0-0

In the present studies, the l_c is varied to study its impact. Fig. 4 shows the results of Miehe's phase-field model with different l_c values. As illustrated in Fig. 4(a), the results of the stress-strain relation confirm the conclusion in [7,8]. Increasing l_c will reduce the maximum stress and accelerate the damage evolution. That is the reason why l_c is linked to the mechanical response. Furthermore, from Fig. 4(b-c), the crack pattern in Fig. 4(b) is in the center zone, while that in Fig. 4(c) is on the model borders. Sakata et al. [17] have shown that stress/strain concentration can depend on the inter-fiber distance (l_f). The smaller the inter-fiber distance is, the higher concentration is. In the present case, the inter-fiber distance (l_f) of the periodic unit-cell implies the strain concentration is not expected to be on the boundaries neither for crack initiation position. Thus, the crack pattern in Fig. 4(c) may not be physical. However, as aforementioned, l_c is linked to the mechanical response, which cannot be freely chosen. Hence, for Miehe's model, it is difficult to choose an appropriate l_c that both gets proper macro-responses and local-crack patterns.

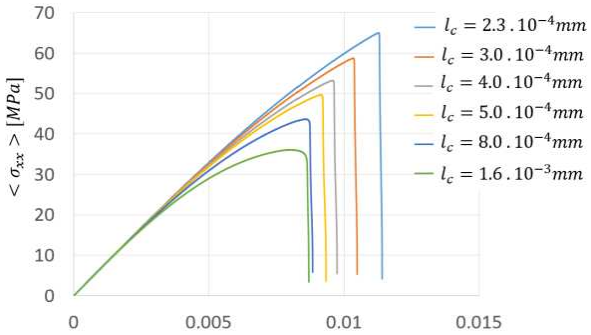

(a)

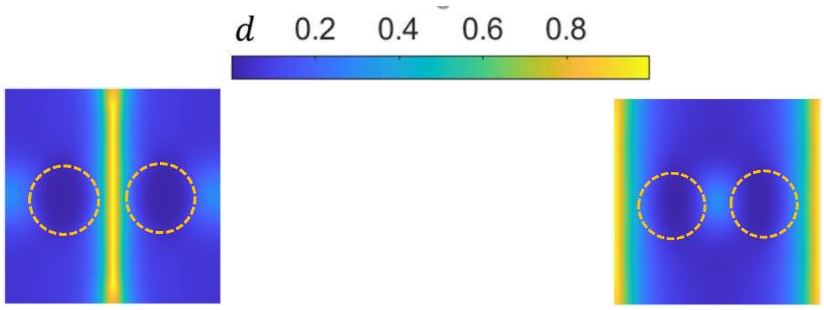

(b) (c)

Fig. 4: (a) The macroscopic stress-strain curves. The local damage fields at final failure when (b) $l_c = 8.0 \cdot 10^{-4}$ mm and (c) $l_c = 1.6 \cdot 10^{-3}$ mm.

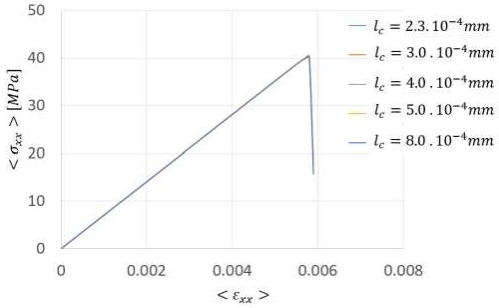

Fig. 5: The macroscopic stress-strain curves of Wu's model.

  doi:10.5075/epfl-298799_978-2-9701614-0-0

In contrast, if we look at the results of Wu's model in Fig. 5, the results show much less sensitivity to the l_c values. In Wu's phase-field model, the l_c values and material mechanical response are uncoupled. However, based on our studies, especially for heterogeneous models, there still exists a criterion for the choice of l_c. Because heterogeneous models are generally multi-phase systems, it needs to ensure that other phases do not enter the fracture zone of the damaged phase. If it is not the case, the macroscopic mechanical response can be affected. Moreover, if the ratio l_f/l_c is too small, the local crack patterns may not be physical as well.

As shown in Fig. 1(d), the fracture zone of Wu's phase-field model is limited at a value of πl_c. Thus, for a composite model, the proposition of l_c is $l_c \leq l_f/\pi$. However, the phase-field also needs a sufficiently large l_c/h ratio to ensure its non-locality. In [4], this ratio should be larger than two, while [14] proposed $l_c/h > 5$. Based on our studies shown in Fig. 5, a proper result can also be obtained when$l_c/h = 2.5$. Thus, the present work would prefer the proposition in [4] in terms of l_c/h ratio. In summary, the proposed criterion of l_c for Wu's phase-field is $2h \leq l_c \leq l_f/\pi$ without the need of adjusting G_c values.

4. Conclusions

Two groups of conclusions can be formulated. The first group shows that the choice of the characteristic length (l_c) in Miehe's phase-field model affects not only the macroscopic mechanical behavior but also the local crack propagation patterns. Sometimes, the crack pattern for a certain l_c value is not physical. Hence, it is not easy to choose an appropriate l_c that both get proper macroscopic responses as well as local-crack patterns.

The second conclusion deals with Wu's phase-field method in the FFT solver. Due to the complexity of Wu's model, a Newton-Krylov algorithm with an alternating minimization scheme is applied in the present work. The results show that the sensitivity to l_c is hugely reduced in Wu's phase-field model. However, heterogeneous materials are often multi-phase systems, like composite materials. Hence, a criterion of l_c should be set to ensure that one phase does not enter the fracture zone of another phase. Meanwhile, the ratio between l_c and mesh size (h) should be sufficiently large. One work proposed that this ratio is larger than two, while another set it to five. Based on our studies, the present work prefers the first proposition. In summary, it can be concluded that Wu's phase-field model is l_c insensitive for composites in case of satisfying the criterion presented in section 3.

5. References

1. Bourdin B, Francfort GA, Marigo JJ. Numerical experiments in revisited brittle fracture. J Mech Phys Solids. 2000 Apr 1;48(4):797–826.

2. Bourdin B, Francfort GA, Marigo J-J. The Variational Approach to Fracture. J Elast 2008 911 [Internet]. 2008 Mar 15;91(1):5–148.

3. Francfort GA, Marigo JJ. Revisiting brittle fracture as an energy minimization problem. J Mech Phys Solids. 1998 Aug 1;46(8):1319–42.

4. Miehe C, Welschinger F, Hofacker M. Thermodynamically consistent phase-field models of fracture: Variational principles and multi-field FE implementations. Int J Numer Methods Eng. 2010 Sep 3;83(10):1273–311.

5. Miehe C, Hofacker M, Welschinger F. A phase field model for rate-independent crack

propagation: Robust algorithmic implementation based on operator splits. Comput Methods Appl Mech Eng. 2010;199(45–48):2765–78.

6. Moulinec H, Suquet P. A fast numerical method for computing the linear and nonlinear mechanical properties of composites. 1994;

7. Zhang X, Vignes C, Sloan SW, Sheng D. Numerical evaluation of the phase-field model for brittle fracture with emphasis on the length scale. Comput Mech 2017 595 [Internet]. 2017 Jan 21;59(5):737–52.

8. Nguyen TT, Yvonnet J, Bornert M, Chateau C, Sab K, Romani R, et al. On the choice of parameters in the phase field method for simulating crack initiation with experimental validation. Int J Fract 2016 1972. 2016 Feb 2;197(2):213–26.

9. Espadas-Escalante JJ, van Dijk NP, Isaksson P. A phase-field model for strength and fracture analyses of fiber-reinforced composites. Compos Sci Technol. 2019;174(September 2018):58–67.

10. Espadas-Escalante JJ, Isaksson P. Mesoscale analysis of the transverse cracking kinetics in woven composite laminates using a phase-field fracture theory. Eng Fract Mech. 2019;216(May).

11. Nguyen TT, Yvonnet J, Bornert M, Chateau C. Initiation and propagation of complex 3D networks of cracks in heterogeneous quasi-brittle materials: Direct comparison between in situ testing-microCT experiments and phase field simulations. J Mech Phys Solids. 2016 Oct 1;95:320–50.

12. Mandal TK, Nguyen VP, Wu JY. Length scale and mesh bias sensitivity of phase-field models for brittle and cohesive fracture. Eng Fract Mech. 2019 Aug 1;217:106532.

13. Wu JY, Nguyen VP. A length scale insensitive phase-field damage model for brittle fracture. J Mech Phys Solids. 2018 Oct 1;119:20–42.

14. Wu JY. A unified phase-field theory for the mechanics of damage and quasi-brittle failure. J Mech Phys Solids. 2017 Jun 1;103:72–99.

15. Ma X. The elastic and damage modeling of heterogeneous materials based on the Fast Fourier Transform. IMT Nord Europe; 2022.

16. Chen Y, Vasiukov D, Gélébart L, Park CH. A FFT solver for variational phase-field modeling of brittle fracture. Comput Methods Appl Mech Eng. 2019;

17. Sakata SI, Sakamoto T. A Local Sensitivity-Based Multiscale Stochastic Stress Analysis of a Unidirectional Fiber-Reinforced Composite Material Considering Random Location Variation of Multifibers. ASCE-ASME J Risk Uncertain Eng Syst Part B Mech Eng. 2019 Sep 1;5(3).

  doi:10.5075/epfl-298799_978-2-9701614-0-0

A VARIATIONAL APPROACH FOR MODELLING THE EFFECT OF TRANSVERSE CRACKS AND DELAMINATIONS ON THERMOELASTIC PROPERTIES OF LAMINATES

Vladimir Vinogradov

School of Engineering, Newcastle University, Newcastle upon Tyne, NE2 2NP, UK
vladimir.vinogradov@newcastle.ac.uk

Abstract: *An approximate stress field in laminates with parallel intralaminar crack induced delamination is derived based on the principle of minimum complementary energy. Simple matrix expressions are obtained that define the effective compliance matrix, thermal expansions and curvatures, and specific heat of a cracked laminate. The method allows to analyze laminates with various stacking sequences and cracking patterns at negligible computational costs. Results for the stress distribution perturbations and changes in the effective laminate properties due to delamination cracks are presented for symmetric and non-symmetric crack patterns for varying delamination lengths.*

Keywords: Laminates; Transverse cracks; Delamination; Stress analysis; Effective properties

1. Introduction

Delamination cracks in fiber reinforced composite laminates can form at various stages of the laminate service and often present the main reason for final failure. Whether the delamination cracks are formed due to monotonous, cyclic or thermal loadings, it is desirable to know their effect on the mechanical properties of the cracked laminate and the stress distribution perturbation due to the cracks.

The variational approach adopted in this paper was originated by Hashin [1] for a symmetric cross-ply $[0_n/90_m]_S$ is one of the most accurate methods to analyze the stress fields in a cracked laminate. The main idea of the approach consists of developing a stress state that satisfies all equilibrium, boundary and traction continuity conditions, and minimizes the complimentary energy of the laminate in attempt to have the best approximation for the stresses. It has been widely used and extended to different cases. One can refer to work by Nairn, who has extensively used the variational analysis, extended it to thermal loading, and used it with an energy based fracture criterion to describe crack accumulation in cross-ply laminates (see, e.g. [2] and references therein). Li and Hafeez [3] looked at a general symmetric cross-ply with symmetric periodic arrangement of transverse cracks. Vinogradov and Hashin [4] looked at an angle-ply laminate with cracks in the middle ply. Recently, the method has gained more attention, e.g. [5,6]. Vinogradov [7] expanded the approach to estimate the effective thermoelastic properties of generic laminates with parallel but not necessarily coplanar matrix cracks. Fikry et. al. [8] developed a variational analysis to explain an experimentally observed crack pattern in unidirectional laminate with a resin pocket.

The variational analysis has also been applied to study effects of delamination cracks [9,10] on the effective properties of cross-ply laminates and associated energy release rate. The present work extends the approach to generic laminates and in-plane loadings.

  doi:10.5075/epfl-298799_978-2-9701614-0-0

2. Admissible stress field

Consider an *n*-ply laminate sample in the xy plane under a uniform in-plane membrane forces N_x, N_y, N_{xy} and moments M_x, M_y, M_{xy}. We next impose an arbitrary state of damage in a family of plies defined by a certain fibre orientation θ^*, when the intralaminar cracks are parallel to the fiber direction, but are not necessarily coplanar. One can then rotate the coordinate system by $(\pi/2 - \theta^*)$ about the z-axis, such that the crack surfaces are all normal to the x-axis and the cracked plies become $90°$ plies (see Fig. 1). The front of interlaminar cracks are assumed to be parallel to axis y.

For an arbitrary orientation of plies in the laminate, when there are no cracks, the in-plane stresses $\sigma_1^{0(m)} \equiv \sigma_{xx}^{0(m)}$, $\sigma_2^{0(m)} \equiv \sigma_{yy}^{0(m)}$ and $\sigma_6^{0(m)} \equiv \sigma_{xy}^{0(m)}$ in any ply (m) are linear function of the transverse coordinate z, which can be obtained from a simple analysis using the classical laminate theory, and the rest of the stress tensor components $\sigma_4^0 \equiv \sigma_{yz}^0$, $\sigma_5^0 \equiv \sigma_{xz}^0$ and $\sigma_3^0 \equiv \sigma_{zz}^0$ are equal to zero. The cracks introduce stress perturbations, which are denoted $\sigma_i^{(m)}$, where i ranges over 1 to 6.

Let us represent the stresses in the m-th ply of the cracked material as a superposition of the stresses in the uncracked material and perturbation stresses due to the presence of the cracks

$$\sigma_i^{C(m)}(x,z) = \sigma_i^{0(m)}(z) - \sigma_i^{(m)}(x,z). \tag{1}$$

It is assumed that the in-plane perturbation stresses $\sigma_1^{(m)}$, $\sigma_2^{(m)}$ and $\sigma_6^{(m)}$ in ply m are linear functions of z everywhere in the cracked laminate, i.e. for every coordinate x. According to this assumption the in-plane perturbation stresses can be expressed in terms of yet unknown functions $\phi_i^{(m)}(\xi)$ and $\psi_i^{(m)}(\xi)$:

$$\sigma_i^{(m)}(\xi,z) = \phi_i^{(m)}(\xi) + \psi_i^{(m)}(\xi)\,\zeta, \qquad i = 1,2,6, \tag{2}$$

where $\xi = x/t_0$ is the dimensionless x-coordinate, t_0 is an arbitrary normalization thickness, which is chosen as the thickness of a lamina. ζ is the dimensionless z-coordinate, defined as

$$\zeta = (z - \bar{z}_m)\,/t_m, \tag{3}$$

and varying between -1/2 to 1/2 within each ply, z_m is the z-coordinate of the middle of ply m, t_m is the thickness of the ply m.

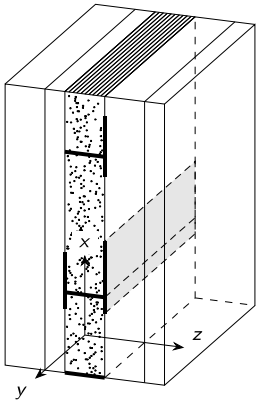

Figure 1. Schematic presentation of a cracked laminate with matrix and delamination cracks.

  doi:10.5075/epfl-298799_978-2-9701614-0-0

It can be shown [7] that the resultant stresses that satisfy Eq. (4), zero traction at $z = -h/2$ and traction continuity at the interfaces between plies have the form:

$$\sigma_5^{(m)}(\xi,\zeta) = -\lambda_m \frac{1}{2}(1+2\zeta)\phi_1'^{(m)} + \lambda_m \frac{1}{8}(1-4\zeta^2)\psi_1'^{(m)} - \sum_{i=1}^{m-1}\lambda_i\,\phi_1'^{(i)},$$

$$\sigma_4^{(m)}(\xi,\zeta) = -\lambda_m \frac{1}{2}(1+2\zeta)\phi_6'^{(m)} - \lambda_m \frac{1}{8}(1-4\zeta^2)\psi_6'^{(m)} - \sum_{i=1}^{m-1}\lambda_i\phi_6'^{(i)}, \quad (4)$$

$$\sigma_3^{(m)}(\xi,\zeta) = \lambda_m^2 \frac{1}{8}(1+2\zeta)^2\phi_1''^{(m)} + \lambda_m^2 \frac{1}{24}(1+2\zeta)^2(1-\zeta)\psi_1''^{(m)} + \frac{1}{2}\sum_{i=1}^{m-1}\lambda_i\left(\lambda_i + 2\sum_{j=i+1}^{m-1}\lambda_j + \lambda_m(1+2\zeta)\right)\phi_1''^{(i)} - \frac{1}{12}\sum_{i=1}^{m-1}\lambda_i^2\psi_1''^{(i)}.$$

where $\lambda_m = t_m/t_0$. It should be noticed that the above general form of the stress distribution is valid for the case of a laminate with delamination cracks as well, since at the delaminated interfaces the traction vector vanishes and hence continuous.

Independently of the membrane loading applied to the laminate, the total forces and moments formed by the perturbation stresses should vanish. This implies that for perturbation forces

$$t_0 \sum_{m=1}^{n}\lambda_m \int_{-\frac{1}{2}}^{\frac{1}{2}} \sigma_i^{(m)}(\xi,\zeta)\,d\zeta = 0, \quad i = 1,2,6, \quad (5)$$

and for perturbation moments

$$t_0^2 \sum_{m=1}^{n}\lambda_m^2 \int_{-\frac{1}{2}}^{\frac{1}{2}} \sigma_i^{(m)}(\xi,\zeta)\,\zeta\,d\zeta = 0, \quad i = 1,2,6 \quad (6)$$

Eq. (5) and (6) form six constraints that must hold for any coordinate x. It is follows that these constraints are sufficient to satisfy zero traction condition at the external surface $z = h/2$ [7].

In the intervals where delamination cracks are present, the zero-traction condition must hold on the delaminated surfaces, which is ensured if the axial force $N_1^{(d)}$and shear force $N_6^{(d)}$ in the delaminated sublaminate remain constant along the delaminated region, while the bending moment $M_1^{(d)}$ is a linear function of ξ

$$N_1^{(d)} = t_0 \sum_{m=1}^{n_d}\lambda_m \int_{-\frac{1}{2}}^{\frac{1}{2}} \sigma_1^{(m)}(x,\zeta)\,d\zeta = c_1,$$

$$N_6^{(d)} = t_0 \sum_{m=1}^{n_d}\lambda_m \int_{-\frac{1}{2}}^{\frac{1}{2}} \sigma_6^{(m)}(\xi,\zeta)\,d\zeta = c_2, \quad (7)$$

$$M_1^{(d)} = t_0^2 \sum_{m=1}^{n_d}\lambda_m^2 \int_{-\frac{1}{2}}^{\frac{1}{2}} \sigma_1^{(m)}(\xi,\zeta)\,\zeta\,d\zeta = c_3 + c_4\xi,$$

where the sum is over n_d plies in the delaminated sub-laminate.

In view of linearity of the perturbation stresses in the unknown functions and their derivatives, the stresses can be written in a matrix form:

$$\boldsymbol{\sigma}^{(m)} = \mathbf{A}_0^{(m)}\,\mathbf{f} + \mathbf{A}_1^{(m)}\,\mathbf{f}' + \mathbf{A}_2^{(m)}\,\mathbf{f}'', \quad (8)$$

where $\boldsymbol{\sigma}(\xi,\zeta) = (\sigma_1,\sigma_2,\sigma_3,\sigma_4,\sigma_5,\sigma_6)^T$ is a (6×1) vector of the stress tensor components, $\mathbf{f}(\xi)$ is a $(6N\times 1)$ vector of unknown functions:

  doi:10.5075/epfl-298799_978-2-9701614-0-0

$$\mathbf{f}(\xi) = \left(\phi_1^{(1)}, \phi_2^{(1)}, \phi_6^{(1)}, \psi_1^{(1)}, \psi_2^{(1)}, \psi_6^{(1)}, \phi_1^{(2)}, \dots\right)^T, \tag{9}$$

and the matrices $\mathbf{A}_0^{(m)}$, $\mathbf{A}_1^{(m)}$, $\mathbf{A}_2^{(m)}$ are the ζ-dependant coefficient matrices of the functions of ξ and their first and second derivatives, respectively. The elements of these matrices are simple polynomials of ζ that are defined by Eqs. (2) and (4). Correspondingly, the six constraints of Eqs. (5) and (6) can be written in the matrix form

$$\mathbf{B}_{\mathrm{eq}} \cdot \mathbf{f} = 0, \tag{10}$$

where $\mathbf{B}$ is a $(6 \times 6N)$ matrix, whose elements follow from substituting (2) and (4) into Eqs. (5) and (6). Constraints (7) are written as

$$\mathbf{B}_{\mathrm{d}} \cdot \mathbf{f} = \mathbf{c}_{\mathrm{d}}(\xi), \tag{11}$$

where $\mathbf{B}_d$ is a $(3 \times 6N)$ matrix and $\mathbf{c}_{\mathrm{d}}(\xi)$ represents the combination of right-hand sides of Eq. (7). Additional constraints as in Eq. (11) must be appended if the interval contains several delaminated interfaces. Eqs. (10) and (11) are now combined

$$\mathbf{B} \cdot \mathbf{f} = \mathbf{c}(\xi), \tag{12}$$

3. Variational solution

According to the variational approach, employed in the present paper, the unknown functions $\mathbf{f}(\xi)$ are determined using the principle of minimum complementary energy. The complementary energy in terms of the perturbation stresses is given as:

$$U_C = U_C^0 + \frac{1}{2}\int_V \boldsymbol{\sigma}^T \mathbf{S}\, \boldsymbol{\sigma}\, dV = U_C^0 + \frac{t_0^2}{2}\int_L \sum_{p,1=0,1,2} \mathbf{f}^{(p)^T} \mathbf{M}_{pq} \mathbf{f}^{(q)} d\xi\,, \tag{13}$$

where U_C^0 is the complementary energy of the uncracked laminate, $\mathbf{S}(\mathbf{x})$ is the local compliance tensor, $\mathbf{f}^{(p)}$ denotes the *p*-th derivative of $\mathbf{f}(\xi)$, and

$$\mathbf{M}_{pq} = \sum_{m=1}^{n} \lambda_m \mathbf{P}_{pq}^{(m)}\,, \qquad \mathbf{P}_{pq}^{(m)} = \int_{-\frac{1}{2}}^{\frac{1}{2}} \mathbf{A}_p^{(m)^T}(\zeta)\, \mathbf{S}^{(m)} \mathbf{A}_q^{(m)}(\zeta)\, d\zeta \tag{14}$$

Elements of the integrand matrix in (14) represent polynomials of ξ of order up to six and can be calculated numerically with any degree of accuracy. Explicit expressions for elements of matrices $\mathbf{P}_{pq}$ can be found in [7].

Minimization of the complementary energy reduces to the problem of determining functions $\mathbf{f}$ that minimize the integral in Eq. (13)

$$I = \min_{\mathbf{f}(\xi)} \int_L F(\xi) d\xi, \tag{15}$$

with the integrand having the following form:

$$F(\xi) = \mathbf{f}^T \mathbf{M}_{00} \mathbf{f} + \mathbf{f}^T \mathbf{M}_{02} \mathbf{f}'' + \mathbf{f}''^T \mathbf{M}_{20} \mathbf{f} + \mathbf{f}' \mathbf{M}_{11} \mathbf{f}' + \mathbf{f}''^T \mathrm{M}_{22} \mathbf{f}'' \tag{16}$$

subject to constraints (12), which are added to the Lagrangian forming a new augmented functional:

  doi:10.5075/epfl-298799_978-2-9701614-0-0

$$I = \min_{\mathbf{f},\boldsymbol{\omega}} \int_L [F(\xi) + 2\boldsymbol{\omega}^T(\xi)(\mathbf{B}\,\mathbf{f}(\xi) - \mathbf{c}(\xi))]d\xi, \tag{17}$$

where $2\boldsymbol{\omega}(\xi)$ is the vector of Lagrange multipliers.

The Euler-Lagrange equations for this functional lead to the system

$$\begin{bmatrix}\mathbf{M}_0 & \mathbf{B}^T\\ \mathbf{B} & \mathbf{0}\end{bmatrix}\begin{bmatrix}\mathbf{f}\\ \boldsymbol{\omega}\end{bmatrix} + \begin{bmatrix}\mathbf{M}_2 & \mathbf{0}^T\\ \mathbf{0} & \mathbf{0}\end{bmatrix}\begin{bmatrix}\mathbf{f}''\\ \boldsymbol{\omega}''\end{bmatrix} + \begin{bmatrix}\mathbf{M}_4 & \mathbf{0}^T\\ \mathbf{0} & \mathbf{0}\end{bmatrix}\begin{bmatrix}\mathbf{f}^{(iv)}\\ \boldsymbol{\omega}^{(iv)}\end{bmatrix} = \begin{bmatrix}\mathbf{0}\\ \mathbf{c}(\xi)\end{bmatrix}, \tag{18}$$

where $\mathbf{M}_0 = \mathbf{M}_{00}$, $\mathbf{M}_2 = \mathbf{M}_{02} + \mathbf{M}_{20} - \mathbf{M}_{11}$ and $\mathbf{M}_4 = \mathbf{M}_{22}$. Eliminating the Lagrange multipliers one obtains:

$$\mathbf{M}_0\mathbf{f} + \mathbf{H}\mathbf{M}_2\mathbf{f}'' + \mathbf{H}\mathbf{M}_4\mathbf{f}^{(iv)} = \mathbf{B}^T(\mathbf{B}\,\mathbf{M}_0^{-1}\mathbf{B}^T)^{-1}\mathbf{c}(\xi), \tag{19}$$

where $\mathbf{H} = \mathbf{I} - \mathbf{B}^T(\mathbf{B}\mathbf{M}_0^{-1}\mathbf{B}^T)^{-1}\mathbf{B}\mathbf{M}_0^{-1}$ is the projection matrix onto the set of solutions satisfying Eq. (12). The general solution is a combination of the homogeneous and particular solutions. The homogeneous part satisfies the equation

$$\mathbf{M}_0\mathbf{f}_h + \mathbf{H}\mathbf{M}_2\mathbf{f}_h'' + \mathbf{H}\mathbf{M}_4\mathbf{f}_h^{(iv)} = 0, \tag{20}$$

which reduces to an eigenvalue problem and is solved by the same way as without delamination cracks [7] to give

$$\mathbf{f}_h = \sum_i c_{h,i}\mathbf{u}_i \exp(r_i\xi) = \mathbf{U}_h(\xi)\mathbf{c}_h, \tag{21}$$

where r_i is the *i*-th eigenvalue, $\mathbf{u}_i$ is the corresponding eigenvector and $\mathbf{c}_h$ is a vector of constant coefficients.

The right-hand side of Eq. (19) is a linear function of x, hence the particular solution is

$$\mathbf{f}_p = \mathbf{M}_0^{-1}\mathbf{B}^T(\mathbf{B}\,\mathbf{M}_0^{-1}\mathbf{B}^T)^{-1}\mathbf{c}(\xi) = \mathbf{U}_p(\xi)\mathbf{c}_p, \tag{22}$$

where $\mathbf{c}_p$ are in general unknown constants, in case of one delamination surface, the constants follow from Eq. (7): $\mathbf{c}_p = [c_1, c_2, c_3, c_4]^T$. Finally, the solution of the Euler Lagrange equations can be written in the form

$$\mathbf{f} = \mathbf{f}_p + \mathbf{f}_h = \mathbf{U}_h(\xi)\mathbf{c}_h + \mathbf{U}_p(\xi)\mathbf{c}_p = \mathbf{U}(\xi)\mathbf{c}, \tag{23}$$

where the coefficients $\mathbf{c}$ are defined using boundary conditions at the planes of transverse cracks, continuity of traction between intervals and other possible boundary conditions at the end planes of the intervals, such as periodicity or reflection symmetry.

Typically, the number of boundary conditions above is insufficient to determine all the coefficients. In order to obtain them, the complementary energy is minimized considering constraints (12). Substitution (23) into (15), leads to the following quadratic form in terms of independent constants $\mathbf{c}$:

$$\min_{\mathbf{c}}[I = \sum_{k=1}^{n}\mathbf{c}_k^T\mathbf{W}_k(L_k)\mathbf{c}_k = \mathbf{c}^T\mathbf{W}\mathbf{c}], \qquad \text{s.t. } \mathbf{B}_{\mathrm{bc}}\,\mathbf{c} = \mathbf{b}, \tag{24}$$

where the sum is over all the joined intervals of lengths L_k having different delamination pattern or separated by transverse cracks. Matrices $\mathbf{W}_k(L_k)$ have a closed form expression in terms of matrices $\mathbf{U}$ and $\mathbf{M}$ (omitted here). Using again the method of Lagrange Multipliers, the solution of the problem can be derived to be

  doi:10.5075/epfl-298799_978-2-9701614-0-0

$$\mathbf{c} = \mathbf{W}_{\text{sym}}^{-1}\mathbf{B}_{\text{bc}}^{T}\left(\mathbf{B}_{\text{bc}}\mathbf{W}_{\text{sym}}^{-1}\mathbf{B}_{\text{bc}}^{T}\right)^{-1}\mathbf{b}, \tag{26}$$

which leads to the final stress distribution and the complementary energy in the form

$$U_C = U_C^0 + \frac{t_0^2}{2}\mathbf{b}^T\left(\mathbf{B}_{\text{bc}}\mathbf{W}_{\text{sym}}^{-1}\mathbf{B}_{\text{bc}}^{T}\right)^{-1}\mathbf{b}. \tag{27}$$

The complementary elastic energy can be written in terms of its effective compliance matrix $\mathbf{ABD}^*$, thermal expansions and specific heat of the cracked laminate, and the effect of the cracks on the effective properties/engineering constants can be investigated.

4. Numerical examples

Although the derived solution for the stress distribution and effective properties of a laminate is concise and requires negligible computational efforts, it is very robust and applicable to a variety of crack geometries and laminate systems. It has also been shown [7] that the results for effective thermomechanical properties of laminates with transverse cracks (no delamination cracks) agree very well with experimental data. Figs. 2 and 3 show an example of two different crack patterns in a symmetric laminate $[45/90_2/\text{-}45/90]_S$ and the axial stress distribution due to axial tension. The left figures show the unit cell, while free surfaces (external and cracks) are indicated by thicker solid lines. The cell is bounded by transverse cracks (horizontal) and is split into three intervals containing different delamination crack pattern: the top and bottom intervals contain delamination cracks originated from the tips of matrix cracks in the transverse plies, while the middle interval is uncracked.

The approximate distribution of the axial stress shown in the right columns of Figs. 2 and 3 demonstrate some stress concentration close to crack tips. More detailed stress analysis is achieved if the plies are subdivided and different stress functions are introduced in each sub-

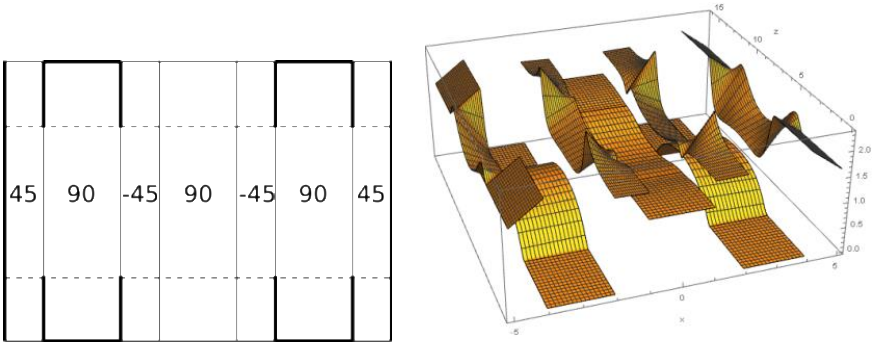

Figure 2. Stress distribution σ_{xx} in symmetrically cracked $[45/90_2/\text{-}45/90]_S$.

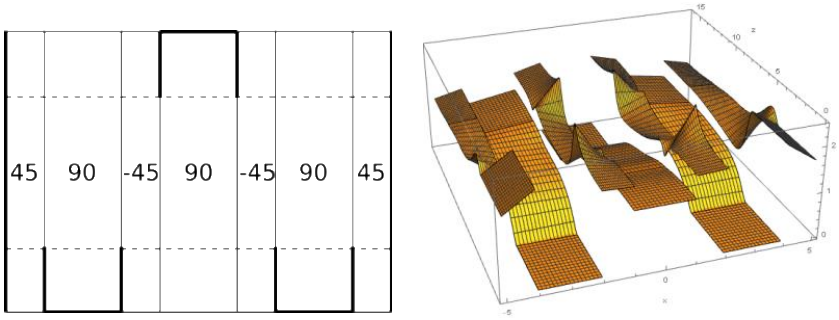

Figure 3. Stress distribution σ_{xx} in non-symmetrically cracked $[45/90_2/\text{-}45/90]_S$.

  doi:10.5075/epfl-298799_978-2-9701614-0-0

ply. In Fig. 4 the results of the axial stress formed in $[\pm 45/90_2]_S$ laminate due to axial tensile loading. The thick black solid line indicates the location of a matrix transverse crack, and the delamination cracks are shown by dashed lines. The left figure shows the stress distribution for a symmetric crack pattern, while the right figure shows the stress distribution for the so-called Z-delamination type. In these examples, the plies are subdivided, and more nonlinear stress distribution along the thickness direction is revealed, with clear stress singularities at the tips of the delamination cracks.

Figs. 5 and 6 show the results for the effective axial Young's modulus and coefficient of thermal expansion of the cracked $[\pm 45/90_2]$ as functions of delamination length. The normalized spacings between transverse cracks in 90 ply is indicated in Figs. 5 and 6 for a pair of curves, when the solid lines correspond to the symmetric pattern and the dashed lines correspond to the non-symmetric delamination pattern (Z-delamination). It is interesting to note that due to the nature of the developed solution, it is possible to analyze laminates with very short delamination cracks, as well as cracks that extend to almost the entire length of a laminate, which is quite difficult to implement using FE.

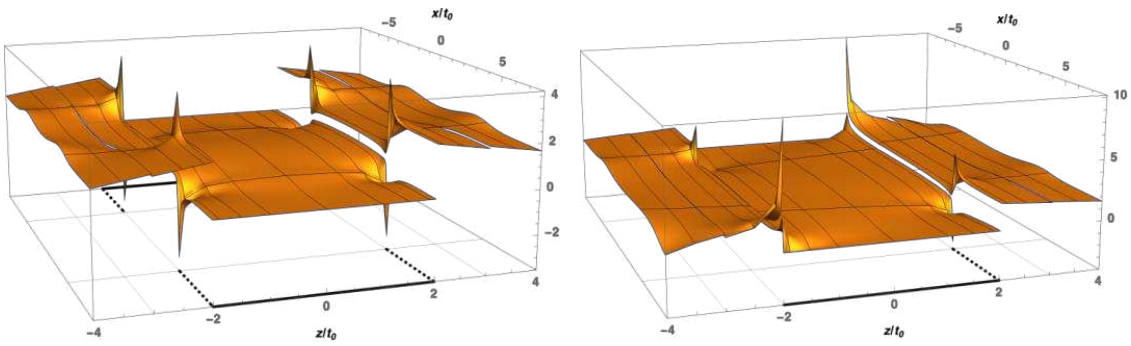

Figure 4. Stress distribution σ_{xx} in cracked $[\pm 45/90_2]_S$.

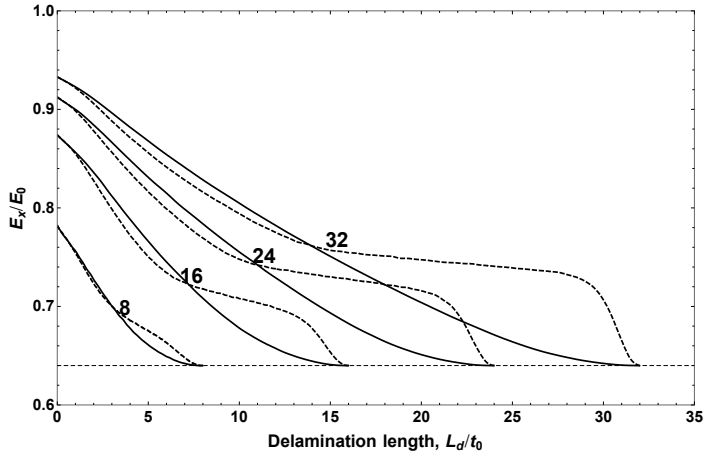

Figure 5. Effective axial Young's modulus vs delamination length in cracked $[\pm 45/90_2]_S$ for various initial transverse crack densities.

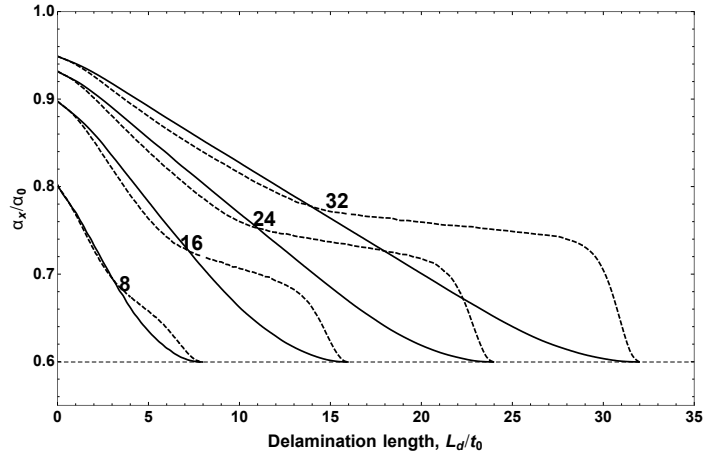

Figure 6. Effective axial thermal expansion coefficient vs delamination length in cracked $[\pm 45/90_2]_S$ for various initial transverse crack densities.

5. References

1. Hashin Z. Analysis of cracked laminates: a variational approach. Mechanics of Materials. 1985; 4(2):121–36.
2. Nairn JA, Hu S. Matrix microcracking. In: Talreja R, editor. Damage Mechanics of Composite Materials. Elsevier Science; 1994. p. 187–243.
3. Li S, Hafeez F. Variation-based cracked laminate analysis revisited and fundamentally extended. International Journal of Solids and Structures. 2009; 46(20):3505–15.
4. Vinogradov V, Hashin Z. Variational analysis of cracked angle-ply laminates. Composites Science and Technology. 2010; 70(4):638–46.
5. Hajikazemi M, Sadr MH. A variational model for stress analysis in cracked laminates with arbitrary symmetric lay-up under general in-plane loading. International Journal of Solids and Structures. 2014; 51(2):516–29.
6. Huang ZQ, Zhou JC, He XQ, Liew KM. Variational analysis for angle-ply laminates with matrix cracks. International Journal of Solids and Structures. 2014; 51(21):3669–78.
7. Vinogradov V. A variational method for analysis of laminates with parallel arrays of intralaminar cracks. International Journal for Numerical Methods in Engineering. 2019; 120(5):666–705.
8. Fikry MJM, Vinogradov V, Ogihara S. Experimental observation and modeling of resin pocket cracking in unidirectional laminates with ply discontinuity. Composites Science and Technology. 2022; 218:109175.
9. Nairn JA, Hu S. The initiation and growth of delaminations induced by matrix microcracks in laminated composites. International Journal of Fracture. 1992; 57(1):1–24.
10. Lim SH, Li S. Energy release rates for transverse cracking and delaminations induced by transverse cracks in laminated composites. Composites Part A: Applied Science and Manufacturing. 2005;36(11):1467–76.

  doi:10.5075/epfl-298799_978-2-9701614-0-0

NUMERICAL SOLUTION FOR SECOND- AND THIRD-ORDER COMPOSITE DOUBLY-CURVED SHELLS WITH DELAMINATION BY DIFFERENTIAL QUADRATURE METHOD

András, Szekrényes[a]

a: Budapest University of Technology and Economics, Faculty of Mechanical Engineering, Department of Applied Mechanics – szeki@mm.bme.hu

Abstract: *This work deals with the development and extension of higher-order models for delaminated doubly-curved composite shells with constant radii of curvatures. The mechanical model is based on the method of four equivalent single layers and the system of exact kinematic conditions. A remarkable addition of this work - compared to some previous ones – is that the shell edges are fully clamped. Using the principle of virtual work, the equilibrium equations of the shell system is brought to the stage and solved by using the differential quadrature method. The differential quadrature results are compared to 3D finite element calculations and excellent agreement was obtained for the displacement components and normal stresses. The distributions of the J-integral components are also determined and compared to energy release rates obtained by the virtual crack closure technique. The agreement in this respect is also good. In the final stage the decomposition of the J-integral is performed and it is shown how the order of the applied theory affects the results.*

Keywords: Second-order shell; Third-order shell; Delamination; J-integral; Differential quadrature.

1. Introduction

Engineering structures made of advanced composite materials are prone to various damage modes. One of the major damage modes is delamination or interlaminar fracture [1]. The delaminations and cracks reduce significantly the stiffness and load-bearing capacity of the structure. Besides, even the vibration behavior of the system may change essentially [2]. The primary quantity characterizing the cracks and delaminations is the energy release rate (ERR) [3]. If the structure obeys a linear elastic material law, then the well-known J-integral is equivalent to the ERR [3]. While the ERR can be calculated relatively easily in the commercial finite element packages, like ANSYS and ABAQUS, the J-integral is not available in these codes if the material behavior becomes anisotropic. The mentioned codes offer the virtual crack closure technique (VCCT) on the other hand [4]. The main contribution of this work is that it makes it possible to determine the J-integral in shells with orthotropic material behavior.

In some previous papers the author investigated and solved many related problems including composite plates [4,5] and shells [6] with delamination. The so-called semi-layerwise model is applied to doubly curved shells and the edges of the shells are rigidly fixed and not simply-supported as they used to be in many works [4-6].

  doi:10.5075/epfl-298799_978-2-9701614-0-0

The main points detailed are the following. Section 2 presents the governing equations of the delaminated shell system. Section 3 is dedicated to the applied numerical method very briefly. Section 4 presents the results and section 5 contains the conclusions.

Figure 1 shows four cases of a laminated composite shell structure element. The element represents the transition between the delaminated and intact parts of the shell. In this work only case I is documented. The acronym ESL means equivalent single layer. The four cases differ from each other in the through-thickness position of the delamination.

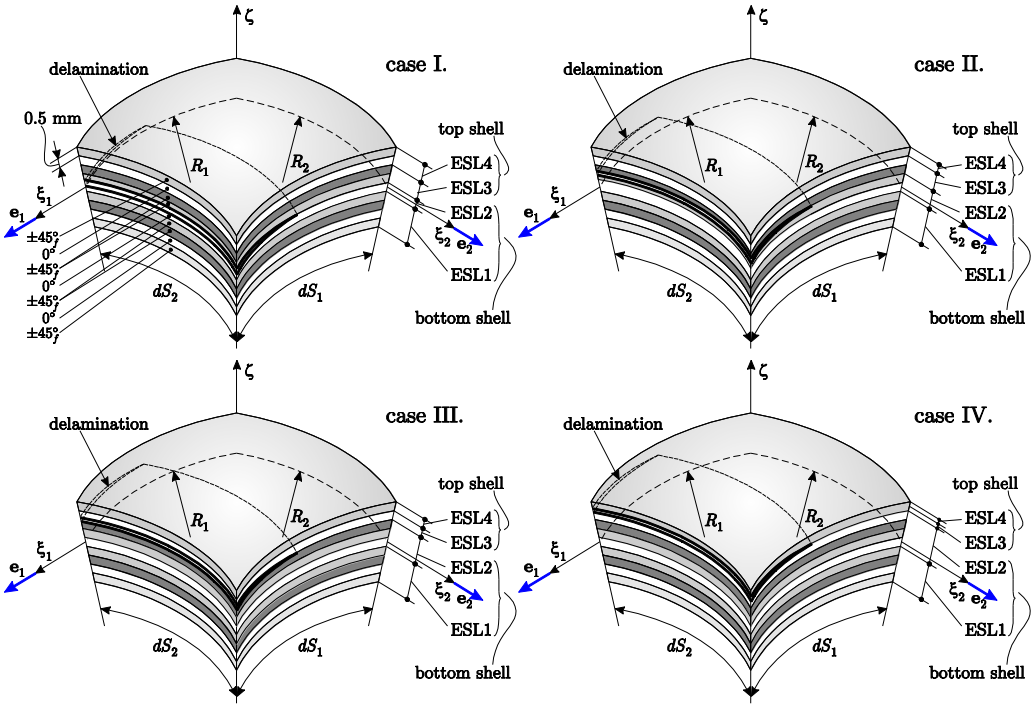

Figure 1. The four different scenarios of the doubly-curved delaminated composite shells and the lay-up of the structure

2. Governing equations

The governing equations of the applied model for the delaminated shells are available in [6] using the first-, second- and third-order shear deformable shell theories (FST, SST and TST) and the so-called semi-layerwise approximation [6]. The equations have been derived using the principle of virtual work for both the intact and delaminated shell regions. Here only the equations of the intact part are shown for brevity:

$$\delta u_0 : \sum_{i=1}^{4} \hat{\nabla} \cdot \mathbf{N}^{(1,12)} + \frac{a_1 a_2}{R_1} Q_{1(i)} + \frac{a_1}{2}\left(\frac{1}{R_1} - \frac{1}{R_2}\right) M_{12(i),2} = 0, \tag{1}$$

$$\delta v_0 : \sum_{i=1}^{4} \hat{\nabla} \cdot \mathbf{N}^{(12,2)} + \frac{a_1 a_2}{R_2} Q_{2(i)} - \frac{a_1}{2}\left(\frac{1}{R_1} - \frac{1}{R_2}\right) M_{12(i),1} = 0, \tag{2}$$

where δu_0 and δv_0 are the membrane displacements, $\hat{\nabla} = a_2(..)_{,1}\mathbf{e}_1 + a_1(..)_{,2}\mathbf{e}_2$ is the Hamilton differential operator, $\mathbf{N}^{(1,12)}$ and $\mathbf{N}^{(12,2)}$ are the vectors of in-plane forces [6], a_1 and a_2 are the scale factors of the curvilinear coordinate system. Moreover, $R_1$and R_2 are the principle radii of curvature, $Q_{1(i)}$ and $Q_{2(i)}$ are the transverse shear forces, M_{12} is the twisting moment, respectively. The second set of equations is obtained by separating the terms of the

total potential energy with respect to the virtual primary displacement parameters of the model [6]:

$$\begin{matrix}\delta\psi_{(1)j}:\\ \delta\psi_{(2)j}:\end{matrix}\Big\} \sum_{i=1}^{4} K_{ij}^{(0)} \begin{pmatrix} \hat{\nabla}\cdot\mathbf{N}^{(1,12)} \\ \hat{\nabla}\cdot\mathbf{N}^{(12,2)} \end{pmatrix} + K_{ij}^{(1)} \begin{pmatrix} \hat{\nabla}\cdot\mathbf{M}^{(1,12)} \\ \hat{\nabla}\cdot\mathbf{M}^{(12,2)} \end{pmatrix} + K_{ij}^{(2)} \begin{pmatrix} \hat{\nabla}\cdot\mathbf{L}^{(1,12)} \\ \hat{\nabla}\cdot\mathbf{L}^{(12,2)} \end{pmatrix} +$$
$$K_{ij}^{(3)} \begin{pmatrix} \hat{\nabla}\cdot\mathbf{P}^{(1,12)} \\ \hat{\nabla}\cdot\mathbf{P}^{(12,2)} \end{pmatrix} - a_1 a_2 \begin{pmatrix} (R_1 K_{ij}^{(1)} - K_{ij}^{(0)})/R_1 \cdot Q_{1(i)} \\ (R_2 K_{ij}^{(1)} - K_{ij}^{(0)})/R_2 \cdot Q_{2(i)} \end{pmatrix} - 2a_1 a_2 K_{ij}^{(2)} \begin{pmatrix} R_{1(i)} \\ R_{2(i)} \end{pmatrix} -$$
$$a_1 a_2 \begin{pmatrix} (3R_1 K_{ij}^{(3)} + K_{ij}^{(2)})/R_1 \cdot S_{1(i)} \\ (3R_2 K_{ij}^{(3)} + K_{ij}^{(2)})/R_2 \cdot S_{2(i)} \end{pmatrix} = \begin{pmatrix} 0 \\ 0 \end{pmatrix}, \tag{3}$$

where ψ is the primary displacement parameter, K_{ij} is the so-called displacement multiplicator matrix, $\mathbf{L}^{(1,12)}$ and $\mathbf{P}^{(1,12)}$ are the vectors of higher-order stress resultants, $R_{1(i)}$, $R_{2(i)}$, $S_{1(i)}$ and $S_{2(i)}$ are the higher-order shear forces. Finally, in each equation *i* means the index of the actual equivalent single layer (refer to Figure 1). The last equation captures the equilibrium of transverse forces [6]:

$$\sum_{i=1}^{4} \hat{\nabla}\cdot\mathbf{Q}_i - a_1 a_2 \sum_{i=1}^{k} \left(\frac{N_{1(i)}}{R_1} + \frac{N_{2(i)}}{R_2}\right) + q = 0, \tag{4}$$

where *q* is the external load of the shell. As mentioned before these are the governing equations of the intact part only. For the delaminated part quite similar equations can be derived, refer to [6].

3. Numerical solution – differential quadrature method

Herein, the basic concept of the DQ method is presented [7]. The governing equations contain directly the partial derivatives of the membrane displacement and the primary displacement parameters. Any of these parameters is approximated by:

$$f(x,y) = \sum_{p=1}^{N} \sum_{q=1}^{M} f(x_p, y_q) r_p(x) s_q(y), \tag{5}$$

where *p* and *q* are indexes meaning the grid point position of the shell surface, *N* and *M* are the number of grid points along the *x* and *y* coordinates. Furthermore, $r_p(x)$, $s_q(y)$ are the so-called Lagrange interpolation functions defined by [7]:

$$r_p(x) = \prod_{\substack{k=1 \\ k\neq p}}^{N} \frac{x - x_k}{x_p - x_k}, \quad s_q(y) = \prod_{\substack{k=1 \\ k\neq q}}^{M} \frac{y - y_l}{y_q - y_l}. \tag{6}$$

The grid points are distributed in accordance with Chebyshev-Gauss-Lobatto scheme [5]:

$$x_k = x_1 + \frac{1}{2}\left(1 - \cos\frac{k-1}{(N-1)\pi}(x_N - x_1)\right), \; y_l = y_1 + \frac{1}{2}\left(1 - \cos\frac{l-1}{(M-1)\pi}(y_M - y_1)\right). \tag{7}$$

The derivatives of any displacement parameter are approximated by:

$$\left.\frac{\partial^n f(x,y)}{\partial x^n}\right|_{\substack{x=x_p \\ y=y_q}} \cong \sum_{k=1}^{N} a_{pk}^{(x,n)} f(x_k, y_q), \; a_{pk}^{(x,n)} = \frac{\partial^n r_p(x)}{\partial x^n}, \tag{8}$$

$$\left.\frac{\partial^m f(x,y)}{\partial y^m}\right|_{\substack{x=x_p \\ y=y_q}} \cong \sum_{l=1}^{M} a_{ql}^{(y,m)} f(x_p, y_l) \quad , a_{ql}^{(y,m)} = \frac{\partial^m s_q(y)}{\partial y^m}, \tag{9}$$

$$\left.\frac{\partial^{n+m} f(x,y)}{\partial x^n \partial y^m}\right|_{\substack{x=x_p \\ y=y_q}} \cong \sum_{k=1}^{N} \sum_{l=1}^{M} a_{pk}^{(x,n)} a_{ql}^{(y,m)} f(x_k, y_l), \tag{10}$$

where a_{pk} and a_{ql} are the weighting coefficients, the superscripts refer to the coordinate the differentiation is performed with respect to and the order, respectively [7]. Thus, the stress resultants in Eq.(1)-(4) and their derivatives should be determined in terms of the derivatives of membrane and primary displacement parameters. Then, by using the DQ method each parameter and its derivative should be approximated by Eqs.(5-10). The equations mentioned should be satisfied at the internal grid point values. The grid points at the edges are dedicated to the boundary conditions [7].

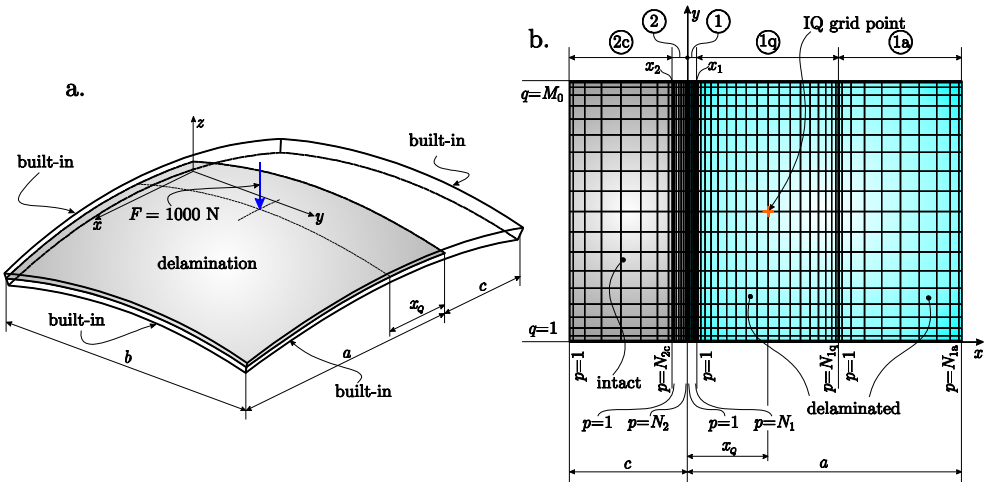

Figure 2. Schematic draw of an elliptic composite shell with delamination and the applied DQ grid structure with refinements.

Figure 2a shows the problem considered (elliptic shell with through-width delamination) and the applied DQ grid structure. The geometrical and material parameters of the shell are given in [6]. The model was loaded by 1000 N in the middle point. The 3D FE model was created by using SOLID elements, documented in [6]. The applied grid structure in Figure 3b was created by using the following parameters: N_{1a}=10, N_1=8, N_2=8, N_{2c}=10, N_{1q}=13 and M_0=27, which are the number of grid points over the different regions. For the other data refer to [5-6].

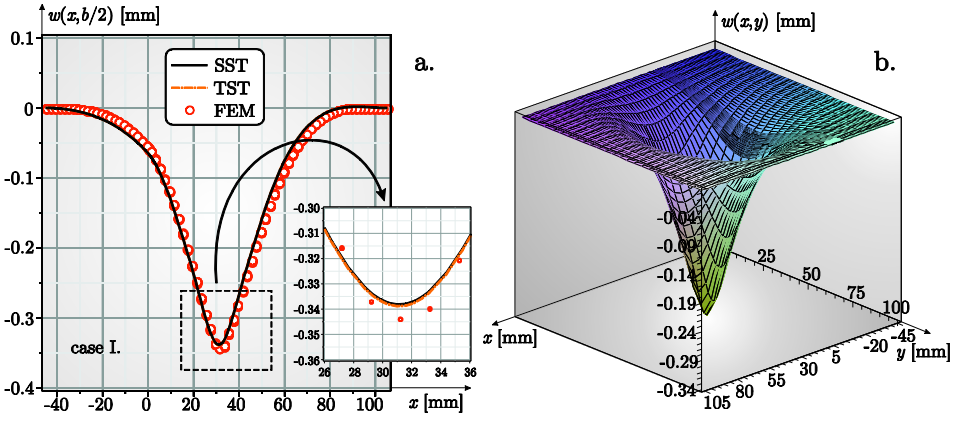

Figure 3. Deflections by DQ method (SST and TST) and FE solution for a composite shell with delamination, case I (a.). Deflection of the shell by the SST solution (b.).

4. Results and discussions

The results consist of the distribution of mechanical field parameters along some material lines. Figure 3a indicates the deflection of the delaminated shell along the middle parallel to *x*. A thumbnail view is also added and it can be seen that although the TST provides slightly higher deflection than the SST, the difference between the two theories is negligible. The agreement with the result of 3D FE analysis is quite good. In Figure 3b the complete deflection function determined by the SST is shown.

Figure 4 presents the in-surface displacements and the stresses along some specified material lines over the thickness. Considering the *u* and *v* displacements it can be observed that the lines do not fit exactly the set of points by FE solution. In other words there are certain offsets between the DQ and FE solutions which is because of the different constraints applied for the DQ models and the FE one [5,6]. The DQ method involves the imposition of the dynamic boundary conditions, too, apart from the kinematic ones. For the FE model only the latter is required. Otherwise, it is the slope and the nature of the displacement distributions that are comparable to the FE solution. From this standpoint, the DQ solution agrees well with the FE points.

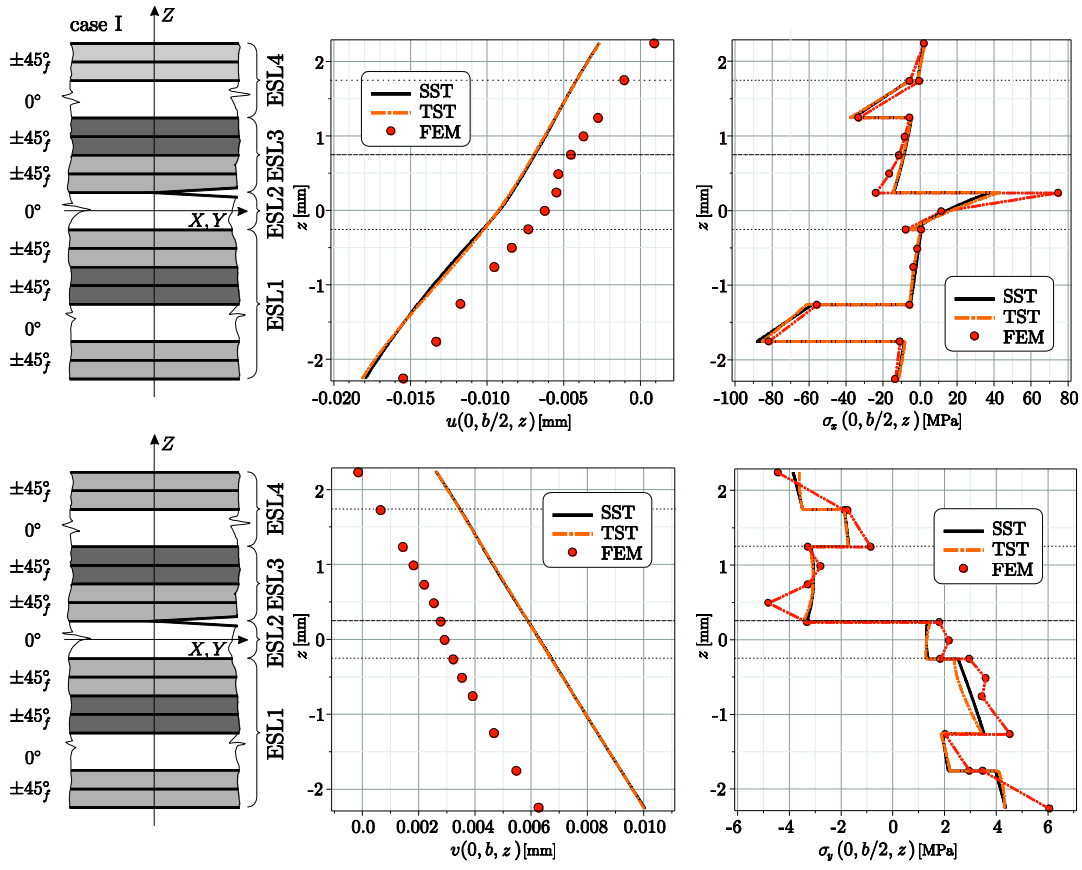

Figure 4. Distribution of the in-surface displacements (u and v) and the normal stresses (σ_x and σ_y) *over the thickness of the shell.*

The normal stresses (σ_x and σ_y) are plotted on the right side of Figure 4. The agreement with the FE solution is very good, although the FE solution provides some peaks at the delamination tip.

This singular nature of the FE solution becomes more and more pronounced as the mesh is refined [4-6].

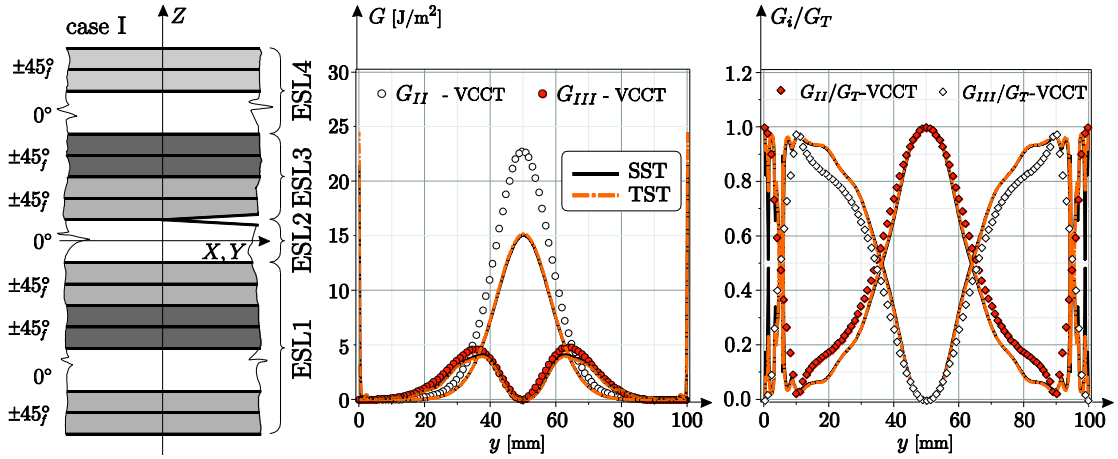

Figure 5. Distribution of the energy release rates and mode mixity along the delamination front for a composite shell with delamination, case I.

Under quasi/static loading and linear elastic material the J-integral is equivalent to the ERR [3]. The J-integral has been determined for delaminated composite shells in [5] and thus the relevant equations are not shown here. Figure 5 indicates how the ERRs (mode-II and mode-III components) are distributed over the delamination front. The DQ solution is compared again to the FE results by the VCCT method [5]. The mode-II ERR by DQ solution is approximately 30% smaller in the middle point ($y=b/2$) than the FE one. The agreement of the mode-III component by the two methods is on the other hand outstanding. A complete agreement between the two methods cannot be expected, because they are based on different considerations. The J-integral is based on the stress resultants and strain field components, the VCCT involves the nodal forces and displacements. It can be seen in Figure 5 that at the sides, the DQ (J-integral solution) provides significant peaks. The VCCT on the other hand ends up in zero at the sides. The conclusion is that the boundary conditions of the problem affects the results of the applied method and vice versa. The mode ratios are presented on the right side of Figure 5. The agreement is moderate and some waviness is clearly observable at the sides.

An interesting issue is to show how the different stress resultants and corresponding strains by the SST and TST contribute the ERRs. Figures 6-7 show some kind of decomposition to answer the former question. In Figure 6a the contribution by the normal forces is shown. An immediate observation is that the J-integrals (both mode-II and mode-III) by the SST and TST are quite different and the solution by TST for the mode-III component is more wavy than that by the SST. The J-integrals by the moments are plotted in Figure 6b. This time the SST involves larger values (approximately twice) than the TST. The tremendous differences are maintained also if the *L* stress resultants are taken into consideration (Figure 7a). Finally, the J-integrals by the *P* stress resultants in Figure 7b are provided only by the TST. Although the contributions by the different stress resultants (*N*, *M*, *L* and *P*) are essentially not the same, the sum of the distributions by SST and TST in Figures 6-7 leads almost the same as it has already been shown in Figure 5. The conclusion is that accuracy of the J-integral cannot be improved by increasing the order of the applied theory only, something more is required. This issue should be solved in the near future.

  doi:10.5075/epfl-298799_978-2-9701614-0-0

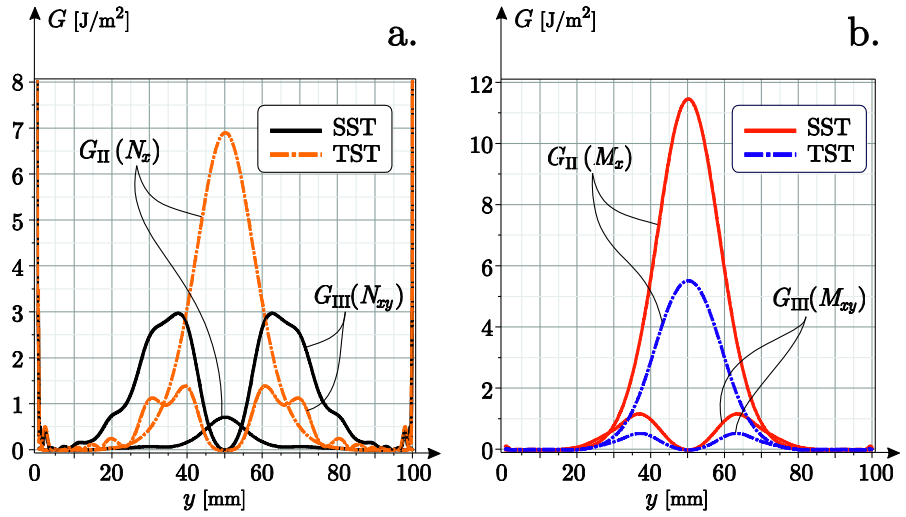

Figure 6. Distribution of the energy release rates by normal forces (N_x and N_{xy}) and moments (M_x and M_{xy}) along the delamination front of a composite shell.

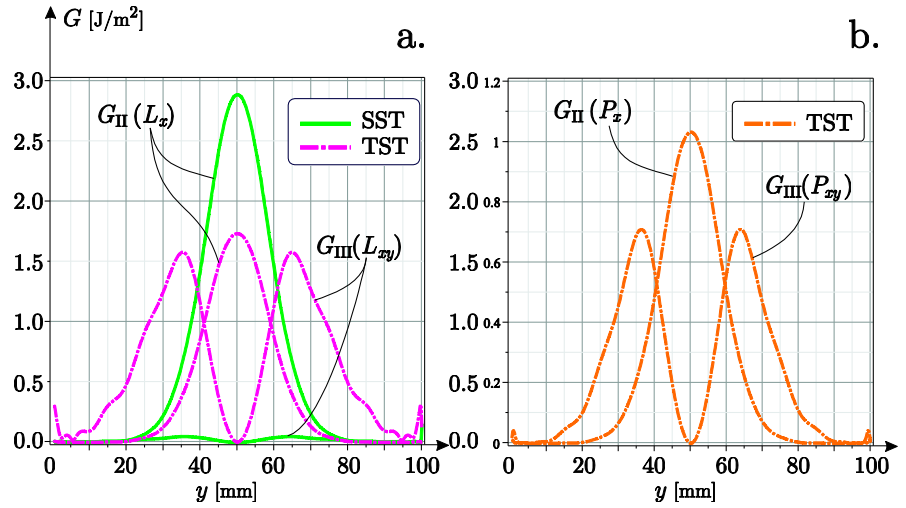

Figure 3. Distribution of the energy release rates by higher-order stress resultants (L_x and L_{xy} , P_x and P_{xy}) along the delamination front of a composite shell.

5. Conclusions

This work briefly presents the governing equations of doubly-curved composite shells with delamination using the so-called semi-layerwise model. The governing equations are solved using the differential quadrature method and the results are compared to spatial finite element solution. The mechanical fields indicated a good agreement between the two in each case, however, the thin-walled nature of the applied model leads to some differences compared to the finite element solution. The energy release rate distributions over the delamination front were determined and showed that the mode-II and mode-III J-integrals are quite similarly distributed to those calculated by the virtual crack closure technique and the finite element method. The most important conclusion is that a complete agreement between the J-integral and the energy release rates by cannot be expected and the decomposition of the total J-integral

with respect to the different stress resultants makes it clear that the accuracy cannot be increased by enhancing the order of applied theory only.

Acknowledgements

This work has been supported by the National Research, Development and Innovation Office (NKFI) under grant No.128090. The research reported in this paper and carried out at BME has been supported by the NRDI Fund (TKP2020 IES, Grant No. BME-IE-NAT) based on the charter of bolster issued by the NRDI Office under the auspices of the Ministry for Innovation and Technology.

6. References

1. Reddy JN. Mechanics of laminated composite plates and shells: theory and analysis. CRC Press, 2003.
2. Hirwani CK, Panda SK, Mahapatra TR. Nonlinear finite element analysis of transient behavior of delaminated composite plate. Journal of Vibration and Acoustics 2018; 140(2): 021001.
3. Anderson TL. Fracture mechanics: fundamentals and applications. CRC press, 2005.
4. Szekrényes A. Nonsingular crack modelling in orthotropic plates by four equivalent single layers. European Journal of Mechanics-A/Solids 2016; 55: 73-99.
5. Szekrényes A. Application of differential quadrature method to delaminated first-order shear deformable composite plates. Thin-Walled Structures 2021; 166:108028.
6. Szekrényes A. Higher-order semi-layerwise models for doubly curved delaminated composite shells. Archive of Applied Mechanics 2021; 91(4):1-30.
7. Shu C. Differential quadrature and its application in engineering. Springer, 2000.

Composites Meet Sustainability – Proceedings of the 20th European Conference on Composite Materials,
ECCM20. 26-30 June, 2022, Lausanne, Switzerland

CHARACTERIZATION OF MODE-II DELAMINATION FRACTURE ENERGY VIA COMPUTATIONAL HOMOGENIZATION

Lu Ke, Frans P. van der Meer

Delft University of Technology – Faculty of Civil Engineering and Geosciences
l.ke@tudelft.nl, f.p.vandermeer@tudelft.nl

Abstract: *It is well-known that the fracture energy for delamination is a function of the mode of fracture. Mode II delamination crack growth is accompanied with significantly higher energy dissipation than mode I delamination crack growth. It is not completely understood which physical processes drive this difference. In this study, a multiscale model based on computational homogenization (FE^2) is developed to shed light on the sources of energy dissipation for mode II crack growth. Distinction is made between matrix plasticity, matrix cracking and fiber/matrix debonding. In this paper, a study on a simplified micromodel is presented which allows for the validation of the results obtained with computational homogenization through comparison with direct numerical simulation (DNS) in which the microstructure is explicitly modeled in a monolithic model. In both DNS and FE^2 simulations, the amount of plastic energy dissipation that accompanies crack growth is quantified.*

Keywords: Micromechanics; multiscale modeling; delamination; plasticity; mode II

1. Introduction

The amount of energy required to grow a delamination crack in mode II is higher than it is in mode I. On the mesoscale, where the plies of composite laminates are modeled as homogeneous orthotropic material and the interface between the plies is modeled as a zero-thickness plane, this is usually accounted for by using phenomenological relations for the fracture energy as function of the mode of fracture. Although these models can describe the mode-dependence of the fracture energy, they do not offer an explanation for this phenomenon, which gives rise to the question whether the models generalize well to loading cases that are different from the fundamental experimental setups. In fact, there is evidence that the generalization lacks accuracy in the observation that different experimental setups that describe the same mode of fracture provide different values for the fracture energy as has been observed for the two different mode II setups of the end-notched flexure (ENF) test and the transverse crack tensile (TCT) test.

To gain more insight in the dissipative processes that constitute the fracture energy, it is relevant to zoom in to the microscale, where processes as fiber/matrix debonding, matrix microcracking and matrix plasticity can be explicitly accounted for. Micromechanical models have been proposed in literature to predict the nonlinear response up to failure of composite materials. The idea is that a representative volume element (RVE) can be subjected to a fundamental loading scenario to compute the homogenized stress/strain response. However, in fracture tests, the local strain history that is seen is not as simple as in fundamental loading scenarios like simple tension or pure shear. The strain path that a macroscopic material point near the crack plane follows in a fracture test is not monotonic. The nonlinear interaction between

  doi:10.5075/epfl-298799_978-2-9701614-0-0

neighboring material points in and around the fracture process zone makes it impossible to know the strain path at any point before solving the full macroscale problem. Therefore, in order to use a micromodel for describing the material response in a fracture test, a fully coupled approach is needed. This can be achieved either by explicitly modeling the microstructure in (part of) the macroscopic domain with an embedded model in a direct numerical simulation (DNS), or by coupling an RVE simulation to every macroscopic integration point using computational homogenization (or FE^2).

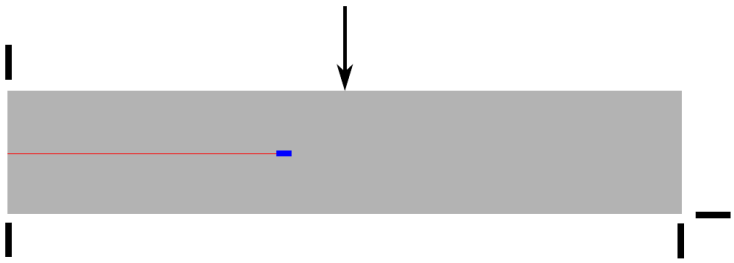

Figure 1. Geometry and boundary conditions. The red line indicates the notch, the blue line shows a region in which the nonlinear response is modeled, either with DNS or with FE^2. Figure not to scale.

With FE^2 no assumptions on the constitutive response of the homogenized material are needed—the micromodel replaces the macroscopic constitutive model. The strain from the macroscale is translated to microscale boundary conditions, after which the micromodel is solved and averaged stresses are passed back to the macromodel. When localization takes place, the standard homogenization approach in which the micromodel is used to compute macroscopic stress from macroscopic strain breaks down because the averaged response becomes pathologically dependent on the size of the micromodel. However, it is possible to repair this by using a discontinuous approach on the macroscale, such that the micromodel is used to provide a traction separation relation. The size of the micromodel can then be included in the scale transition to recover RVE-size independence in the macroscopic response.

In this work, FE^2 for crack growth is applied to the study of energy dissipation for a delamination crack. To establish the suitability of the framework for describing crack growth in an elasto-plastic medium under mode II conditions comparison with DNS is performed. Because DNS of an actual fiber/matrix composite for the case where the crack grows in direction parallel to the fibers is not computationally feasible, a simplified layered microstructure is devised with alternating thin layers of elastic and elasto/plastic material and with the possibility of debonding along the interface between the layers. Mode II crack growth in the layered material is investigated with DNS as well as with FE^2 and results are compared. The influence of plasticity on the total energy dissipation per unit crack length is assessed for the ENF setup.

2. Methods

In this paper, we show results for an ENF test. Like in most delamination tests, the ENF operates on unidirectional laminates. On the macroscale, the test can be simulated quite accurately in two dimensions. However, when considering a microstructure of fiber-reinforced composite material, a three-dimensional micromodel is needed, because the plane in which the

microstructural geometry can be described (the transverse plane) is perpendicular to the plane in which the macroscopic geometry and boundary conditions can be described. Under the assumption that fibers are straight and perfectly aligned, a three-dimensional RVE can be obtained by extruding a two-dimensional RVE with random fiber direction to a single element in fiber direction. Such thin-slice RVE can be used in FE^2 and capture the interaction between longitudinal shear and stress in fiber direction [1]. Notably, the slice itself does not experience crack growth. However, in line with the concept of separation of scales, a series of thin slice RVEs representing different stages of material degradation can be representative for the fracture process zone.

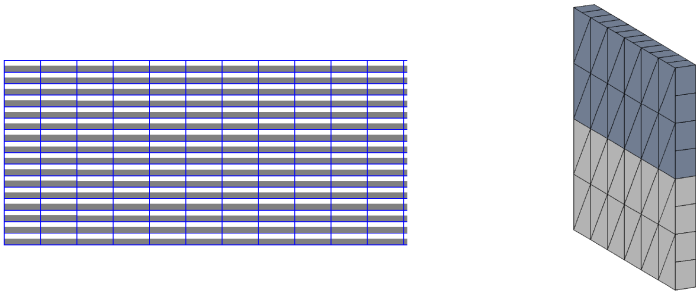

Figure 2. Region with layered microstructure for DNS (left) and bimaterial RVE used for FE^2 (right)

In order to validate the FE^2 approach with a thin slice RVE for mode II crack growth through a comparison with DNS is made. It is computationally not feasible to run a DNS through an embedded model of fiber-reinforced material. Therefore a simplified microstructure is considered in this paper. A layered microstructure is modeled with alternating stiff elastic layers and softer elasto/plastic layers. For this microstructure, a two-dimensional DNS can be performed and a representative micromodel can be constructed of two materials. The RVE response for this simple micromodel will be independent of the RVE dimensions, just as it is at least in statistical sense for the more realistic heterogeneous RVE [2].

In mode II crack growth, there is a thin layer of material around the crack in which crack growth is accompanied by significant plastic deformations. In a homogenized model, and therefore also on the macroscale in FE^2, a sufficiently refined mesh is needed to capture this accurately [3]. Furthermore, the FE^2 model relies on the principle of separation of scales, meaning that every macroscopic integration point represents a region with uniform deformation apart from a microscopic fluctuation that can be modeled as periodic. For agreement between DNS and FE^2 sufficiently thin layers in the DNS and a sufficiently refined mesh in the FE^2 are required. Therefore, a twofold convergence study is performed on these two aspects. The results are compared in terms of global force-displacement response and predicted plastic energy dissipation.

For the elasto/plastic 'matrix'-material, we use Melro's model developed for pressure dependent plasticity in polymers [4, 1]. The 'fibers' are modeled as isotropic linear elastic. For matrix microcracking and fiber/matrix debonding, interelement cohesive elements are inserted on the fly based on a stress-based criterion [5, 6].

For computational homogenization we use framework by Ke and Van der Meer [2]. In this approach, localization is detected by analysis of the sign of the determinant of the acoustic tensor. Prior to localization, standard first order homogenization is applied, where strain is imposed on the micromodel with periodic boundary conditions and stress is defined as the average of the microscale stress over the RVE domain. Upon detection of localization in an RVE, a discontinuity is inserted through the corresponding macroscale element, using the phantom node version of XFEM. The softening RVE with its history variables is then cloned to be used in the integration points along the discontinuity. To define the boundary conditions for the RVEs corresponding to these integration points, an equivalent strain is computed that is composed of the bulk strain in the material right next to the crack and a regularized strain measure related to the magnitude of the displacement jump. The relation between the displacement jump and the equivalent strain accounts for the size of the RVE to remove pathological RVE size dependence in the homogenized response. To compute the macroscale cohesive traction from the RVE response, macroscale stresses obtained through the standard averaging procedure are multiplied with the normal to the discontinuity.

3. Results

Two different ENF simulations are performed in which a short thin region is defined over which the microstructure is modeled, either with FE^2 or with an embedded model, see Fig. 1. Figure 2 shows the layered microstructure modeled in the DNS and the thin slice RVE used for FE^2. Load-displacement results are shown in Figure 3 where for the DNS the layer thickness is progressively reduced and for FE^2 the macroscale mesh is refined by changing the number of element layers in the refined region. Because only a short region of crack growth is modeled, the load-displacement graphs start to increase very soon after a small drop. However, the refined region is of sufficient length to get stable crack growth, meaning that the position of the small load drop is governed by the effective fracture energy consisting of a cohesive contribution and a plastic contribution. For both refinement studies, the results tend to converge to a unique one. However, although not far apart, they do not converge to exactly the same results.

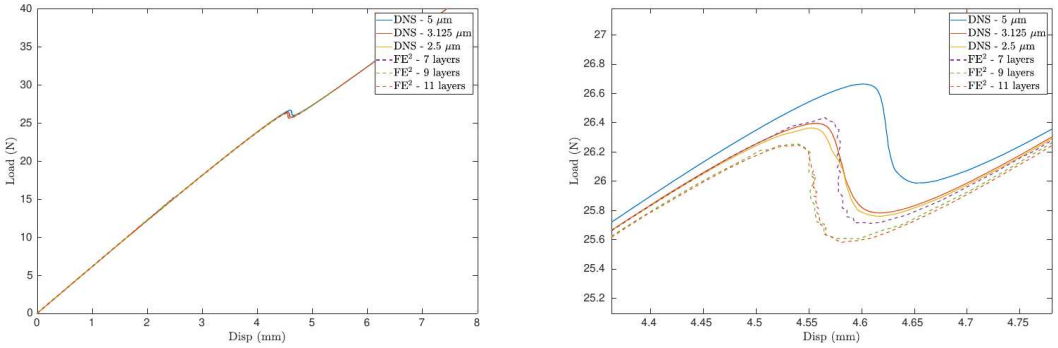

Figure 3. Load-displacement response in DNS with different layer thicknesses and in FE^2 with different macroscale element sizes

In Figure 4, the evolution of plastic energy dissipation across the height of the refined region is visualized. For this figure, a single column of integration points across the height of the refined domain is selected and dissipation for each integration point is plotted for each time step.

Results from both simulations show a similar profile with localized plastic deformation adjacent to the crack and a wider region of diffuse plasticity. It is evident from these results that a fine discretization of layers in the DNS is needed to get a response that can be homogenized and that a fine mesh in the FE^2 is needed to capture this homogenized response accurately.

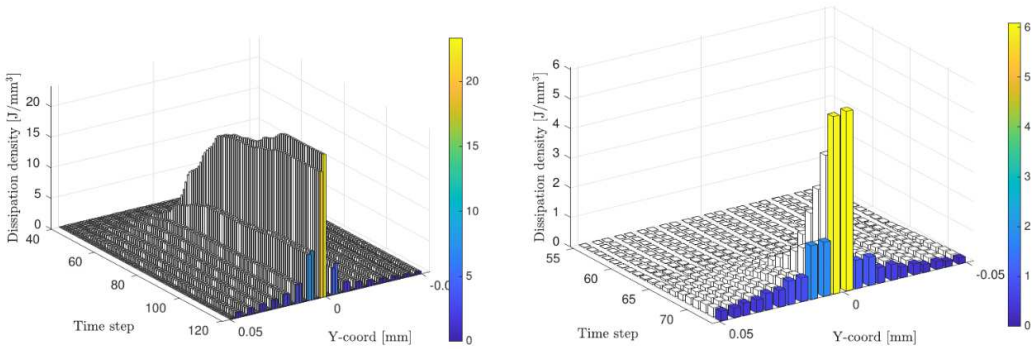

Figure 4. Evolution of dissipation across the height of the refined region as the crack passes: DNS vs FE^2

There remains a significant difference between the results from the two models. A difference can be expected from the fact that in the DNS results the two phases are separately present while in the FE^2 results the averaged dissipation from the complete micromodel is shown. However, dividing the peak values from the DNS by a factor of two to perform the averaging still does not lead to a perfect match with the FE^2 results. A more detailed investigation of the local stress and strain history may shed light on the cause for this difference.

4. Conclusions

A multiscale framework for modeling mode II delamination in unidirectional composites has been developed. In this paper, it is shown through comparison with DNS on a material with simplified microstructure that the FE^2 framework can capture plastic energy dissipation around a growing crack with reasonable accuracy. The multiscale model response is independent from the RVE size as shown in earlier work [2], and here it is also shown that the model response is independent on the macroscale element size although much refinement is needed to obtain an objective response. The need for extreme refinement exacerbates the need for acceleration techniques to speed up microscale simulations for instance with the approach presented elsewhere in this conference [7].

Acknowledgement

Financial support from the Dutch Research Council (NWO) under Vidi grant 16464 is acknowledged by the authors.

5. References

1. F. P. van der Meer. Micromechanical validation of a mesomodel for plasticity in composites. Eur J Mech Solids, 60:58–69, 2016.

2. L. Ke and F. P. van der Meer. A computational homogenization framework with enhanced localization criterion for macroscopic cohesive failure in heterogeneous materials. J Theor Comput Appl Mech, page 7707, 2022.
3. F. P. van der Meer and L. J. Sluys. A numerical investigation into the size effect in the transverse crack tensile test for mode II delamination. Compos Part A, 54:145–152, 2013.
4. A. R. Melro, P. P. Camanho, F. M. Andrade Pires, and S. T. Pinho. Micromechanical analysis of polymer composites reinforced by unidirectional fibres: Part I - Constitutive modelling. Int J Solids Struct, 50:1897–1905, 2013.
5. G. T. Camacho and M. Ortiz. Computational modelling of impact damage in brittle materials. Int J Solids Struct, 33(20-22):2899–2938, 1996.
6. Y. Liu, F. P. van der Meer, L. J. Sluys, and L. Ke. Modeling of dynamic mode I crack growth in glass fiber-reinforced polymer composites: Fracture energy and failure mechanism. Eng Fract Mech, 2021.
7. M. A. Maia, I. B. C. M. Rocha, P. Kerfriden, and F. P. van der Meer. Neural networks meet physics-based material models: accelerating concurrent multiscale simulations of path-dependent composite materials. In Proceedings of 20th European Conference on Composite Materials, Lausanne, Switzerland, June 2022.

MODELLING THE STIFFNESS DEGRADATION AND STRESS REDISTRIBUTION IN CRACKED LAMINATES UNDER IN-PLANE AND BENDING LOADS

Mirko, Simonetto[a], Paolo Andrea, Carraro, Lucio, Maragoni, Marino, Quaresimin

a: Department of Management and Engineering, University of Padova, Stradella S. Nicola 3, Vicenza, 36100 (VI) – mirko.simonetto@phd.unipd.it

Abstract: *Laminates with intralaminar cracks exhibit stiffness loss; knowing this reduction is useful in the assessment of the fatigue life of a composite component. The aim of this research is to develop a model that can describe the stiffness and stress trends of cracked laminates with generic layup configurations subjected to tension and bending loads. This was done by extending the shear lag model and considering at first an asymmetric [0/90] laminate, which is reported in this paper. Obtained curvature trends are compared with results from the finite element model.*

Keywords: Laminate; Cracks; Stress redistribution; Analytical modelling; Bending stiffness.

1. Introduction

Models capable of determining stress trends in cracked laminates are useful for a variety of purposes; this one, like the model developed by the authors [1], was developed with mechanism-based damage prediction models in mind. Several methods for analyzing cracked laminates in symmetric layup configurations have been developed, including variational models, shear lag models [2], or numerical models. Barbero et al. [3] developed a shear-lag model capable of determining the stiffness loss for symmetric laminates under bending loads, but it does not consider asymmetric laminates. In some cases, the symmetric shear lag model is adopted to calculate the reduced ply proprieties, later used in the classical laminate theory [4,5]. More sophisticated variational models have been developed to model generic cracked laminates under bending conditions [6]. Finite element unit cells could also be adopted, as was done in [7,8]. In this work, the shear lag approach, already adopted by the authors for in-plane loads [1], is extended to include non-symmetric lay-ups and bending loads. Only the case study of a [0/90] laminate with cracks in the 90° ply is described in this paper.

2. Model definition

2.1 Starting assumptions

The reference system adopted refers to the x-axis as the loading direction, normal to the crack face. The y axis refers to the out of plane direction of laminate. Only normal and bending loads are considered. To simplify the model and make the treatise and its basic principles clearer, the Poisson effect is not considered. The shear load is taken in account using the Reissner-Mindlin hypothesis, with correction factor k_s equal to 5/6. For both laminae the following constitutive relations can be written as:

  doi:10.5075/epfl-298799_978-2-9701614-0-0

$$N_i = E_{x,i} h_i \frac{\partial u_i}{\partial x} \tag{1}$$

$$Q_i = k_s G_{xy,i} h_i \left(\frac{\partial w_i}{\partial x} + \varphi_i \right) \tag{2}$$

$$N_i = E_{x,i} \frac{h_i^3}{12} \frac{\partial \varphi_i}{\partial x} \tag{3}$$

Where h_i is the thickness of the lamina, E_{xi} and G_{xyi} elastic parameters for the two laminae in the direction of load. N_i is normal load, Q_i shear load and M_i is bending load, with positive direction as depicted in Figure 1. u_i and ϕ_i are displacement and rotation in the x direction, while w_i is the displacement in the y direction.

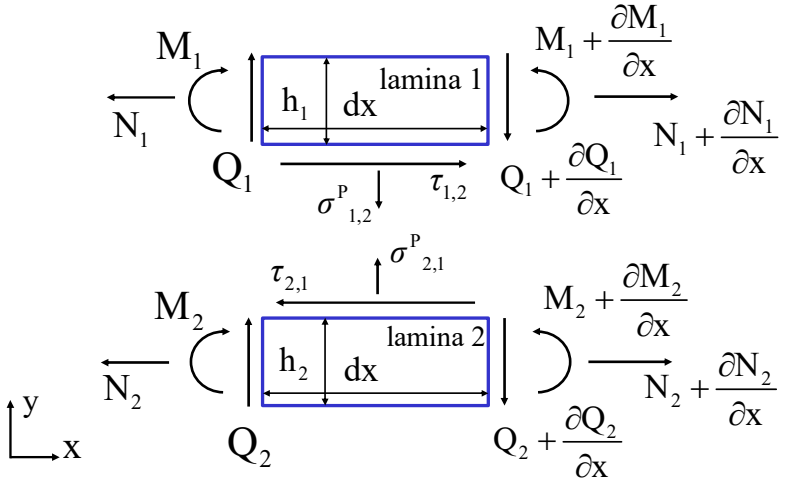

Figure 1. Representation of a 2 laminae laminate with infinitesimal length, with variation of loads per each lamina and stresses at interface between the laminae.

The loads are influenced by the presence of cracks and thus they vary along the x direction, as shown in Figure 1. The translational and rotational equilibrium equations for an infinitesimal length dx of the i-th lamina read as:

$$\begin{cases} \dfrac{\partial N_i}{\partial x} + \tau_{i,i+1} - \tau_{i,i-1} = 0 \\ \dfrac{\partial Q_i}{\partial x} + \sigma^P{}_{i,i+1} - \sigma^P{}_{i,i-1} = 0 \\ \dfrac{\partial M_i}{\partial x} + \dfrac{h_i}{2}\left(\tau_{i,i+1} + \tau_{i,i-1} \right) - Q_i = 0 \end{cases} \tag{4}$$

Based on global equilibrium, the relations between the internal loads and external load must be the following, where b_i is the distance between the lamina midplane and the laminate midplane:

$$\begin{cases} N_1 + N_2 = N_{ext} \\ Q_1 + Q_2 = Q_{ext} \\ M_1 + M_2 - N_1 \cdot b_1 - N_2 \cdot b_2 = M_{ext} \end{cases} \tag{5}$$

The relations at the interface between the two laminae need to considered. First, shear lag equation are obtained as in [1] where displacements along the thickness of laminae are considered to have a quadratic trend described by a polynomial form. Then the relationship between the in plane displacement and the shear stress is added. Eventually, an equation system is set between the two laminae by setting an equal shear stress at the shared interface and null on the top and bottom interfaces of the laminate. An integral mean of the in-plane displacements is carried over the lamina thickness obtaining:

$$\tau_{1,2} = \frac{3 \cdot G_{23} G_{13}}{h_1 G_{23} + h_2 G_{13}} \cdot \left(\bar{u}_2 - \bar{u}_1 - \frac{h_2}{2} \varphi_2 - \frac{h_1}{2} \varphi_1 \right) \tag{6}$$

The same approach has been adopted to describe the behavior of the out of plane stress between the laminae, generally identified as peel stress. In writing this it is assumed that both laminae have the same out of plane stiffness E_3.

$$\sigma^{P}_{1,2} = \frac{3 \cdot E_3}{h_1 + h_2} \cdot \left(\bar{w}_2 - \bar{w}_1 \right) \tag{7}$$

2.2 Elaboration

These conditions need to be put together to form a general system. Interface relation (6) and (7) are differentiated along the x direction and the deformations are substituted using the constitutive equation from (1), (2) and (3), obtaining a new set of functions, not reported here for brevity. To take in account the global equilibrium equation, one lamina must be excluded using equations (5), in this case the first lamina was chosen. Expressions including shear loads are derived once more. Now these relations could be substituted into the shear and peel stresses contained in the indefinite equilibrium relations (4) of the second lamina. Hence a differential system as a function of the loads is obtained, which can be rearranged and written as:

$$[m_1] \frac{\partial^3}{\partial x^3} \begin{Bmatrix} N_2 \\ Q_2 \\ M_2 \end{Bmatrix} + [m_2] \frac{\partial^2}{\partial x^2} \begin{Bmatrix} N_2 \\ Q_2 \\ M_2 \end{Bmatrix} + [m_3] \frac{\partial}{\partial x} \begin{Bmatrix} N_2 \\ Q_2 \\ M_2 \end{Bmatrix} + [m_4] \begin{Bmatrix} N_2 \\ Q_2 \\ M_2 \end{Bmatrix} = \begin{Bmatrix} T_v \end{Bmatrix} \tag{8}$$

Where m_i are matrices of constant coefficients and T_v a vector of known terms. To get the roots λ_j of the homogeneous part of the differential system the following condition is set:

$$\det\left([m_1] \cdot \lambda^3 + [m_2] \cdot \lambda^2 + [m_3] \cdot \lambda + [m_4] \right) = 0 \tag{9}$$

Then eigenvectors U_j can be calculated by evaluating the polynomial for the different λ_j and imposing it equal to zero, with unknown coefficients multiplying each row minus one which is set to one. Load trends can be computed as a solution in the form below

  doi:10.5075/epfl-298799_978-2-9701614-0-0

$$\begin{Bmatrix} N_2 \\ Q_2 \\ M_2 \end{Bmatrix} = \sum_j P_j \cdot e^{\lambda_j \cdot x} \cdot \begin{Bmatrix} U_j \end{Bmatrix} + \begin{Bmatrix} C_{N_2} \\ C_{Q_2} \\ C_{M_2} \end{Bmatrix} \tag{10}$$

Where constant terms C_{N2} and C_{M2} are equal to the lamina loads obtained with the classical laminate theory for the uncracked laminate. Since an external shear action is not applied C_{Q2} is set to zero. P_j are unknown coefficients that need to be found imposing the correct boundary conditions.

The laminate has been considered as centered at the x-axis coordinate equal to zero. By doing so, the symmetry can be exploited by having null in plane displacement, out of plane displacement and rotation at x=0, so eventually integration coefficients related to those displacements became null. In a cracked laminate, loads on the cracked face, which is a free end, must be equal to zero, so considering a crack spacing of length L:

$$\begin{cases} N_2(\pm L/2) = 0 \\ Q_2(\pm L/2) = 0 \\ M_2(\pm L/2) = 0 \end{cases} \tag{11}$$

By imposing these conditions, the system can be solved to obtain the coefficients P_j. The loads on the first lamina are obtained using the global equilibrium equations (5), the displacements are obtained trough integration of loads using the constitutive equations. Particularly the rotation of the laminate is obtained from (3) as:

$$\varphi_x(x) = \frac{12}{E_{x,1} \cdot h_1} \cdot \int \left(M_{ext} - M_2(x) + N_2(x) \cdot b_2 + \left(N_{ext} - N_2(x) \right) \cdot b_1 \right) dx \tag{12}$$

3. Numerical comparison

3.1 Model setup

A simple 2D model of a [0/90] laminate with cracks in the transverse layer has been developed in ANSYS© APDL mechanical to compare the stress trends and curvature with the presented model. The laminate, represented with a regular mesh with PLANE183 element type with generalized plain strain option, has been symmetry-constrained in the middle position. To maintain the congruence of displacements with a subsequent periodic representative element, the nodes at the free end of the uncracked lamina has been constrained with an equation producing a straight line.

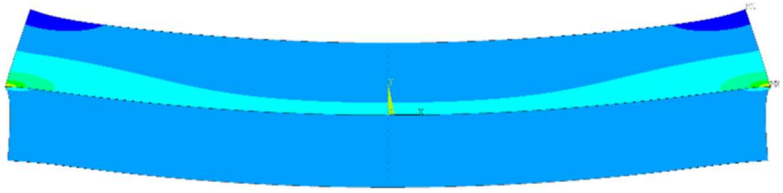

Figure 2. Contour plot of the σ_x stresses about the FE model of a [0/90] laminate subject to tension.

For the normal load loading condition, a displacement is applied to the uncracked face, with deformed shape shown in Figure 2, while for the bending load loading condition a rotation of the uncracked face was applied. For both cases the resulting curvature have been normalized to the global stress in the direction of load (σ_X).

3.2 Results

The analyzed laminate stacking sequence of [0/90] is characterized by a tension-bending coupling, due to its asymmetricity. When it is loaded, an out of plane displacement is obtained, which is higher in the presence of cracks if the applied load has positive sign. A panel with no curvature at room temperature is considered, condition met manufacturing it with room temperature-curing epoxies. The material proprieties adopted for both the numerical simulation and analytical model are reported on Table 1. The thickness considered is 0.3 mm for both laminae.

Table 1: Material parameters adopted for the simulation.

E_1 [MPa]	E_2 [MPa]	G_{12} [MPa]	ni_{12}
51595	15220	5590	0

The curvature has been compared at the crack spacing boundary. This is calculated for the analytical model using the following relation:

$$k_{xx,\text{model}} = \frac{\varphi_x(L/2)}{L} \tag{13}$$

For the numerical model, given two points on the uncracked face with y coordinate y_i and displacement along the x direction $u_{x,i}$, the curvature is obtained as:

$$k_{xx,FEM} = \frac{u_{x,2} - u_{x,1}}{y_1 - y_2} \tag{14}$$

The same laminate has been compared under tension loading and bending loading, results are reported in Figure 3 and Figure 4.

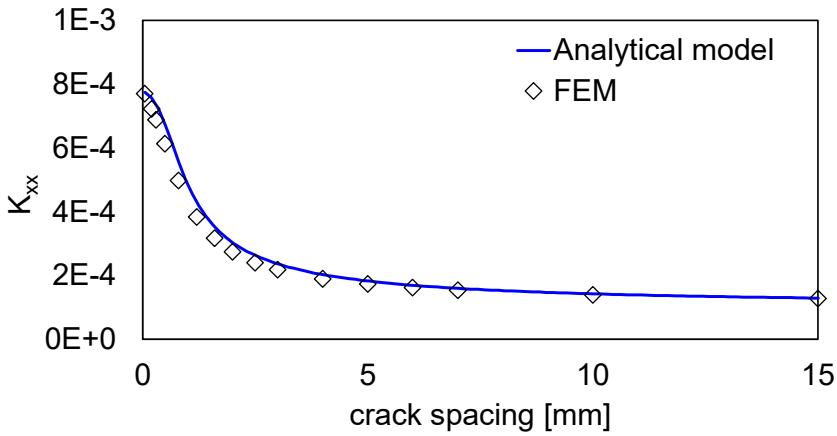

Figure 3. Curvature for a [0/90] laminate subject to 1 MPa tension loading

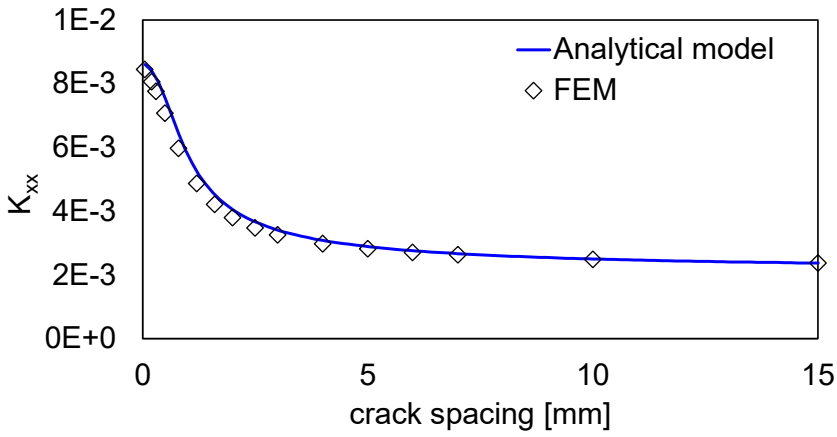

Figure 4. Curvature for a [0/90] laminate subject to 1 Nmm bending loading

4. Conclusions

An analytical model has been developed using shear lag relations to determine the stress trends and stiffness of a cracked [0/90] laminate. To take in account of the asymmetry a relation between the out of plane displacements and the peel stress is considered. The obtained results are comparable respect to a numerical FE model. Further work is needed to consider a multi lamina configuration, the Poisson effect and the presence of generically oriented laminae.

5. References

1. Carraro PA, Quaresimin M. A stiffness degradation model for cracked multidirectional laminates with cracks in multiple layers. International Journal of Solids and Structures 2015; 58:34-51.
2. Kashtalyan M, Soutis C. Stiffness degradation in cross-ply laminates damaged by transverse cracking and splitting. Composites Part A - Appl Sci 2000; 31:335–351.
3. Barbero EJ, Barbero JC. Analytical Solution for Bending of Laminated Composites with Matrix Cracks. Composite Structures 2016; 135:140-155.
4. Shabani P, Shokrieh MM, Saeedi A. A novel model to simulate the formation and healing of cracks in self-healing cross-ply composites under flexural loading. Composite Structures 2020; 35:111750.
5. Pupurs A, Varna J, Loukil M, Kahla HB, Mattsson D. Effective stiffness concept in bending modeling of laminates with damage in surface 90-layers. Composites Part A: Applied Science and Manufacturing 2016; 82:244-252.
6. Hajikazemi M, McCartney LN, Ahmadi H, Paepegem WV. Variational analysis of cracking in general composite laminates subject to triaxial and bending loads. Composite Structures 2020; 239:111993.
7. Schmitz A, Horst P. A finite element unit-cell method for homogenised mechanical properties of heterogeneous plates. Composites Part A: Applied Science and Manufacturing; 2014; 61:23-32.
8. Garoz D, Hajikazemi M, Dinh TD, Paepegem WV. Mesoscale finite element analysis of cracked composite laminates under out-of-plane loads using 3D periodic boundary conditions. Composite Structures 2020; 235:111699.

  doi:10.5075/epfl-298799_978-2-9701614-0-0

THE EFFECT OF MODELLING NANOPLATELET AND NANOTUBE CURVATURE ON THE REPRESENTATIVITY OF NANOCOMPOSITE VOLUME ELEMENTS

Alessandro, Pontefisso[a]

a: Department of Management and Engineering, University of Padova, IT – alessandro.pontefisso@unipd.it

Abstract: *This article presents a methodology to model curved CNTs and Graphene nanoplatelets for generating nanocomposite volume elements. The focus is placed on comparing the effect of curvature on isolated reinforcements and on cubic VEs where the interparticle distance is of interest, such as in the case of detecting percolation. The results support the idea that curvature reduces the 3D span of both reinforcements in the same way, whereas percolation appears affected only in the case of CNTs. However, for GNPs the difficulties in generating Volume Elements with a sufficiently high volume fraction could support only preliminary considerations.*

Keywords: CNT; Graphene; Numerical modeling; Curvature;

1. Introduction

Nowadays, the use of polymer nanocomposites is a consolidated tool in the hands of material designers and manufacturers, following the thousands of publications setting out their ability to improve polymers functional and mechanical properties. Given the number of parameters involved while dealing with nanocomposites, it comes as no surprise that the scientific community devolved great efforts in developing tools for predicting their properties. Among the parameters of interest, the curvature of reinforcements is one of those that attracted the interest of many researchers. Following this interest, many authors proposed approaches for generating Volume Elements, VEs, able to account for CNTs curvature [1-3], whereas to the best of the author knowledge, curvature in Graphene NanoPlatelets, GNPs, is either disregarded, or it is just modelled in 2D. This limitation is very likely due to the difficulties characterizing the generation of 3D VEs with curved GNPs. The goal of the present article is to propose a solution to fill this gap, providing an approach and references to software libraries that allow the generation of such VEs. Then, these VEs are used to compare the effects of curvature on CNTs and GNPs VEs. Eventually, the effects of nanoreinforcement curvature are studied in terms of the reinforcement own isotropy and in the definition of the interparticle distance that defines the percolation condition in the VE.

2. Numerical model

2.1 Generation of curved reinforcements

The curvature in a nanotube is obtained by splitting the nanotube straight cylinder according to a given number of equally long segments, concatenated to each other. Then, one of the two ending segments is fixed in space in a random position within the VE. After that, the segment

  doi:10.5075/epfl-298799_978-2-9701614-0-0

concatenated to it is tilted by a solid angle randomly picked from 0 to a given maximum angle, α_{max}, equal to 45 degrees and then it is fixed in place. The process is iterated for each segment of the chain, one after the other, until all segments are positioned. Figure 1a represents the case of a CNT of 4 segments.

Concerning nanoplatelets, their curvature is generated by slicing each initially flat circular platelet with a parallel sheaf of planes, equally spaced and orthogonal to the platelet flat surface. Then, a procedure like that of nanotubes is proposed: one of the two ending slices of the platelet is fixed in space in a random position. Then, the slice next to it is randomly tilted by a planar angle defined on the plane orthogonal to the planes of the sheaf and passing through the vector normal to the previous slice surface. The tilting angle is randomly chosen within an interval [0; ± 45 deg], where 0 refers to the flat surface of the former slice. The slice is then fixed in space and the process is iterated for each of the remaining slices, in turn. With this procedure, the curvature cannot result in skewed geometries, but it can represent rolled platelets. Figure 1b represents a GNP composed of 6 slices. For the rest of the article, GNP slices and CNT segments are referred as segments.

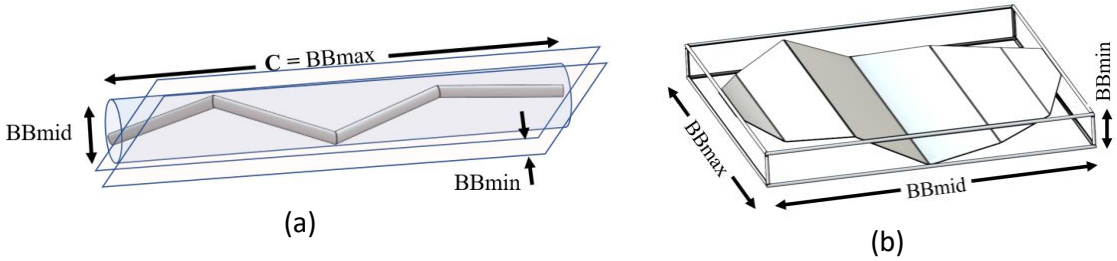

Figure 1. (a) represents geometric dimensions for a curved-CNT description, while (b) represents the same for a curved nanoplatelet.

2.2 Reinforcement isotropy indexes

The reinforcement own isotropy expresses the ability of the reinforcement in creating connections within its surrounding space without a preferred direction. Among the possible isotropy indexes, one is the ratio between the radius of the sphere enveloping the CNT and the CNT length: high values of this ratio indicate that the reinforcement is stretched in one direction. Another index is the ratio between the dimensions of the smallest bounding box enveloping the reinforcement: if these ratios are close to one, it suggests that the reinforcement is homogeneously filling the space around it. The first index is used in this article to study the isotropy of nanotubes: this choice is coherent with that of other researchers who used the ratio between a nanotube maximum span, C, and its theorical length, W, giving rise to index C/W [4]. The second index is used for nanoplatelets: this choice is based on the fact that C loses its meaning with a platelet that is bended in only one direction, since in the other direction it is still straight. Hence, the ratio between the platelet bounding box middle-size edge dimension, BBmid, and its maximum dimension, BBmax, (which is close to the platelet diameter) seems a valid alternative that relies on the same underlying rationale. Another index of the same family is the ratio between the bounding box minimum dimension, BBmin, and BBmax. Representations of these geometrical dimensions are reported in Figure 1a-b.

  doi:10.5075/epfl-298799_978-2-9701614-0-0

2.3 Percolation

The identification of the percolation condition is based on the application of the graph theory [5]: reinforcements and VE faces are considered as nodes in a graph whose edges are represented by inter-nodal distances. The graph is screened for the minimum value in inter-reinforcement distance that allows two VE opposite faces to be connected by a continuous network of reinforcements. Since percolation distances may differ in the three directions of the cubic VE, their average value is regarded as the percolation minimum distance of the given VE.

2.4 Implementation details

Volume elements were generated by the so-called Random Sequential Adsorption, RSA, algorithm [6], while the concepts described in the previous section were implemented in a code written in C++. This choice gave access to already developed libraries, open source and free to use. In more detail, the Computational Geometry Algorithms Library, CGAL, [7] contains many useful sub-libraries that were employed:

- A library named Optimal Distances, dedicated to the calculation of distances between convex hulls. Thanks to this library, it is possible to evaluate the distance between two polyhedrons, thus calculating inter-segment distances and verifying if intersections occur. This library is the core of the Random Sequential Adsorption algorithm, where a reinforcement segment is approximated with an inscribed polyhedron.
- A library named Bounding Volumes, which provides algorithms for computing optimal bounding volumes of point sets. This library was used to generate the envelope spheres around nanotubes.
- A library named Optimal Bounding Box, which provides functions to compute tight oriented bounding boxes around a point set. This library was used to generate bounding boxes around nanoplatelets.

Another useful library is Boost (www.boost.org), which provides free peer-reviewed portable C++ source libraries. In particular, the Boost Graph Library [8] was used in this research activity, relying on its easy-to-use data structures and algorithms implementing the graph theory.

For matrix manipulation, Eigen3 library [9] was used.

3. Results and discussions

To better appreciate the effect of segmentation on CNT and GNP isotropy, 50 independent realizations of each reinforcement were generated at different number of segments. Results for CNTs are reported in Figure 2, where the average ratios BBmin/BBmax and C/W are plotted for different number of segments. Results for GNPs are reported in Figure 3, where the ratio BBmin/BBmax and BBmid/BBmax are plotted.

It emerges that the two kinds of nanoreinforcements exhibit a remarkably similar trend: in both cases, the increase in the reinforcement curvature results in a decrease in the reinforcement span. On the other hand, CNTs show a more relevant increase in the minor bounding box dimension, as compared to GNPs.

  doi:10.5075/epfl-298799_978-2-9701614-0-0

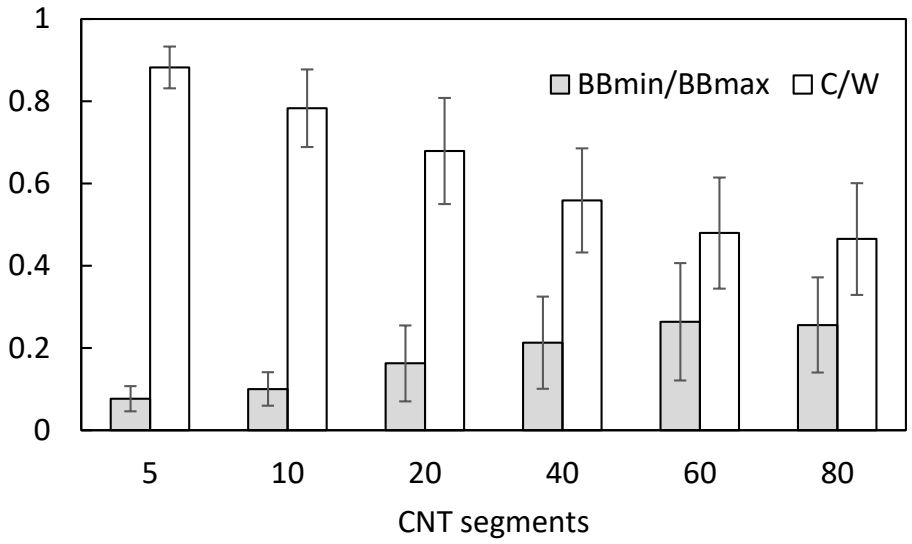

Figure 2. Distribution of envelopes dimensions for 50 independent realizations of CNTs with different number of segments, but same maximum tilt angle (45 deg). The scatter band represents standard deviation.

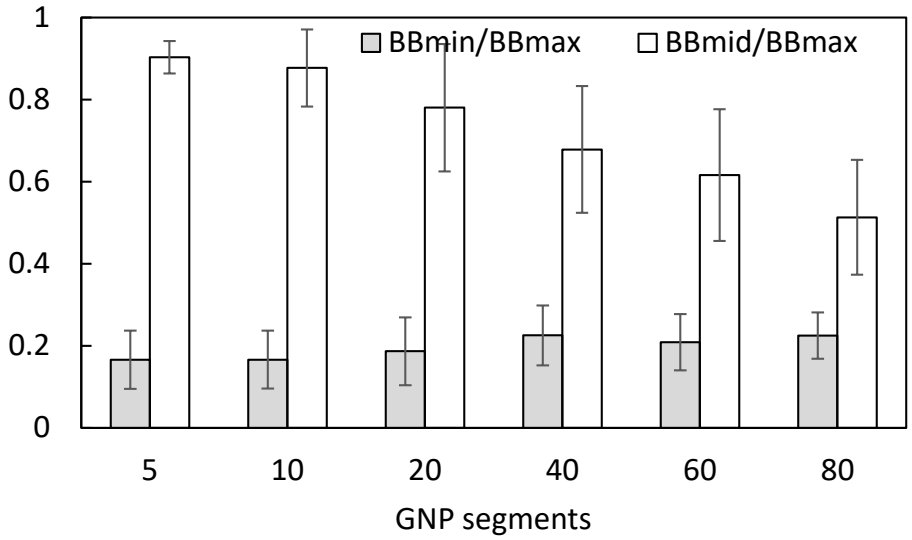

Figure 3. Distribution of envelopes dimensions for 50 independent realizations of GNPs with different number of segments, but same maximum tilt angle (45 deg). The scatter band represents standard deviation.

As a further step in the analysis, volume elements were generated with straight or curved reinforcements.

As far as CNTs are concerned, results for VEs of size 2400nm and with CNTs of length 1200nm and diameter 6nm are reported in Figure 4 for different values of volume fraction and curvature. Four different conditions are considered:

  doi:10.5075/epfl-298799_978-2-9701614-0-0

- Straight CNTs.
- Curved CNTs, with 20 segments each and maximum tilt angle 45 degrees.
- Curved CNTs, with 80 segments each and maximum tilt angle 45 degrees.
- Straight CNTs without the constraint of no-overlapping during the RSA iterations.

What emerges from the analysis is that increasing the curvature an increase in the interparticle distance appears. This increase in interparticle distance implies that the percolation condition is reached at higher volume fractions, and this result agrees with the literature, where curved CNTs are deemed less effective than straight ones [10].

The case of no-overlapping constraint was used in the literature by some authors who chose to model the CNTs just in terms of their axis, and for this reason it seemed worthy to add that case to the analysis. It appears that such a choice affects deeply the identification of percolation conditions, and results from articles making use of different approaches may be difficult to compare.

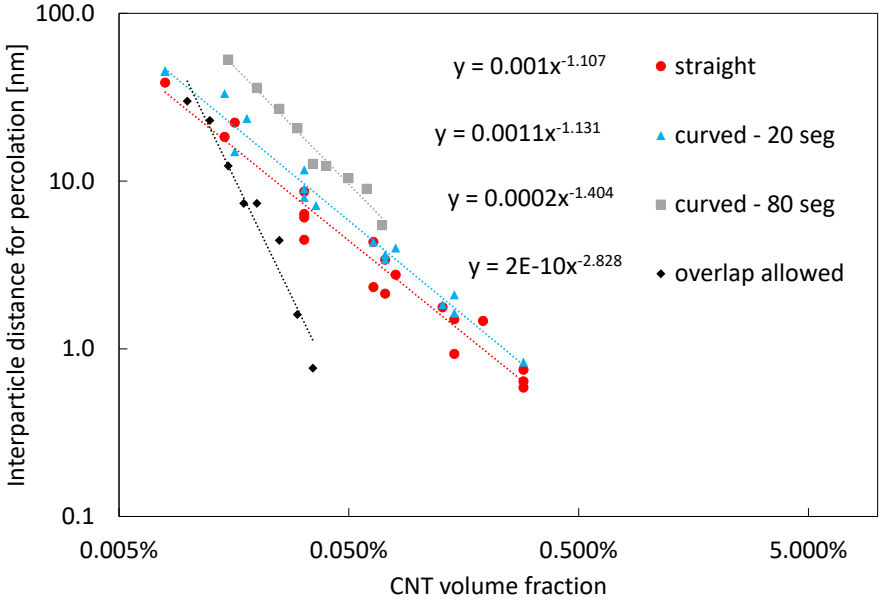

Figure 4. Each point is an independent VE realization which plots the relation between the interparticle distance from which percolation is detected.

As far as GNPs are concerned, results for VEs of size 2400nm and with GNPs of diameter 1000nm and thickness 2nm are reported in Figure 5 for different values of volume fraction and curvature. Three different conditions are considered:

- Straight GNPs.
- Curved GNPs, with 20 segments each and maximum tilt angle 45 degrees.
- Curved GNPs, with 60 segments each and maximum tilt angle 45 degrees.

Different from the case of CNTs, with GNPs the effect of curvature is not clear. This outcome may be the result of an insufficient number of reinforcements in the VE, that promotes the high dispersion in numerical results.

  doi:10.5075/epfl-298799_978-2-9701614-0-0

It is important to stress that the attempts to increase the filler volume fraction resulted in a computational time that exceeded the computational resources available. The RSA algorithm seemed not suitable for the task of adding curved high aspect ratio platelets.

This outcome is not surprising: as it was proved in a previous publication [6] nanoplatelets enforce a local anisotropy, where platelets suffer a short-range self-alignment with increasing filler amount. However, the inclusion of GNPs exhibiting a random curvature makes it difficult to increase the volume fraction. Eventually, the outcome is VEs that are unable to increase their number of particles, and that is an obstacle to collecting enough research data.

A work-around that will be attempted in the next future is the generation of platelets where the platelets themselves are absorbed incrementally, segment by segment. This should allow self-alignment within the VE and overcome the difficulties in increasing the volume fraction.

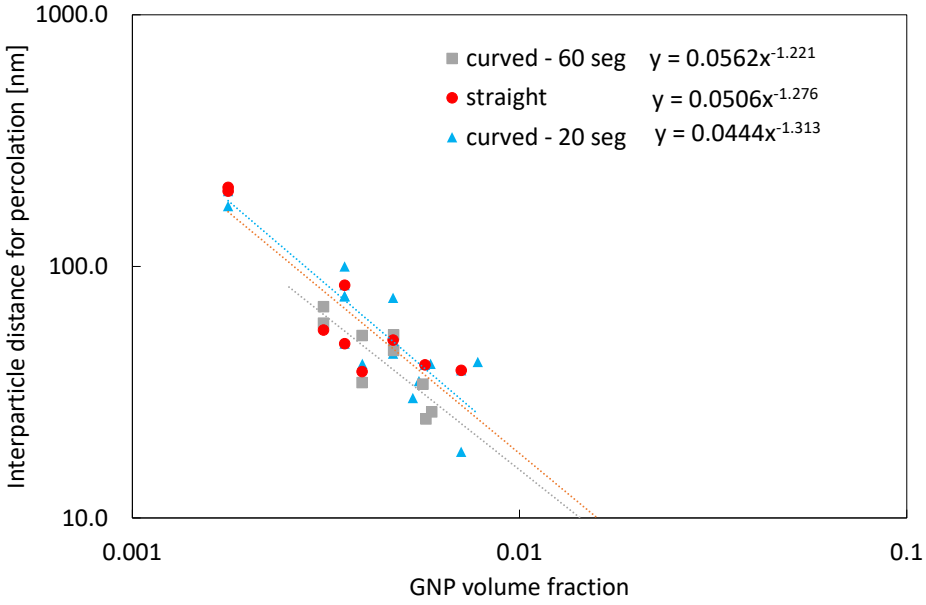

Figure 5. Each point is an independent VE realization which plots the relation between the interparticle distance from which percolation is detected.

4. Conclusions

This article presents a methodology to generate volume elements with curved nanotubes and nanoplatelets. Studying the shape of reinforcements generated by this approach, it emerged that CNTs and GNPs behave in a comparable manner and they reduce their volumetric span with increasing curvature with a remarkably similar trend. When considering volume elements, straight CNTs have a lower percolation threshold than curved ones. Considering the case of GNPs, the presence of a curvature did not result in appreciable differences from the case of straight GNPs. The last consideration should be regarded preliminary, as the proposed approach in generating curved GNPs is still in an initial release and it will benefit from future improvements.

  doi:10.5075/epfl-298799_978-2-9701614-0-0

5. References

1. Zare Y, Rhee KY. A simple methodology to predict the tunneling conductivity of polymer/CNT nanocomposites by the roles of tunneling distance, interphase and CNT waviness. RSC advances, 7(55), 2017; 34912-34921.
2. Matos MA, Tagarielli VL, Baiz-Villafranca PM, Pinho ST. Predictions of the electro-mechanical response of conductive CNT-polymer composites. Journal of the Mechanics and Physics of Solids 2018; 114, 84-96.
3. Dalmas F, Dendievel R, Chazeau L, Cavaillé JY, Gauthier C. Carbon nanotube-filled polymer composites. Numerical simulation of electrical conductivity in three-dimensional entangled fibrous networks. Acta materialia 2006; 54(11), 2923-2931.
4. Panozzo F, Zappalorto M, Quaresimin M. Analytical model for the prediction of the piezoresistive behavior of CNT modified polymers. Composites Part B: Engineering 2017; 109, 53-63.
5. Cormen TH, Leiserson CE, Rivest RL, Stein C. Introduction to algorithms. MIT press. 2022.
6. Pontefisso A, Zappalorto M, Quaresimin M. Effectiveness of the random sequential absorption algorithm in the analysis of volume elements with nanoplatelets. Computational Materials Science 2016; 117, 511-517.
7. The CGAL Project, CGAL User and Reference Manual, 5.3.1, 2021. https://doc.cgal.org/5.3.1/Manual/packages.html.
8. Siek JG, Lee LQ, Lumsdaine A., Boost Graph Library, The: User Guide and Reference Manual, 1st ed., Addison-Wesley Professional. 2001.
9. Guennebaud G, Benoît J, Eigen v3. 2010. http://eigen.tuxfamily.org.
10. Yi YB, Berhan L, Sastry AM. Statistical geometry of random fibrous networks, revisited: waviness, dimensionality, and percolation. Journal of applied physics 2004; 96(3), 1318-1327.

  doi:10.5075/epfl-298799_978-2-9701614-0-0

A STREAMLINE-INTEGRATION TECHNIQUE FOR SIMULATING BUILD-UP OF PROCESS-INDUCED STRESSES AND SHAPE DISTORTIONS IN THERMOSET PULTRUSION PROCESSES

Michael Sandberg[a], Jon Spangenberg[b], Jesper H. Hattel[b]*

a: Department of Mechanical and Production Engineering, Aarhus University, Denmark
(*ms@mpe.au.dk)
b: Department of Mechanical Engineering, Technical University of Denmark, Denmark

Abstract: *Limiting shape distortions and residual stresses are of utmost importance when ensuring the structural integrity and the quality of fibre-reinforced thermoset composites. This paper presents a novel method for 3D thermo-chemical-mechanical analysis of pultrusion processes to analyse process-induced stresses and deformations. As opposed to established methods that rely on coupling a 3D transient Eulerian thermo-chemical analysis with a Lagrangian mechanical analysis, this framework presents a novel method to simultaneously solve for all variables in the same Eulerian domain. As demonstrated in the paper, the framework benefits from significant improvements in computation times (a reduction of 95% compared to established methods) without sacrificing solution accuracy.*

Keywords: *Thermo-chemical-mechanical modelling; composite processing; residual stresses;*

1. Introduction

Pultrusion is a continuous process for the manufacture of composite profiles with a constant cross-section. In conventional thermoset pultrusion processes [1–4], the fibre material is drawn through a resin bath or an impregnation chamber, directly followed by a heating die. During impregnation, the fibre material is saturated with resin and in the heating die, an exothermic chemical curing reaction is initiated. As the resin crosslinks, it shrinks and contracts. The chemical shrinkage, the thermal history of the composite part, as well as mismatches in the constitutive properties of the profile layup, all contribute to process-induced stresses and shape distortions in the profile. To limit process defects such as curing cracks and excessive warpage, thermo-chemical-mechanical (TCM) simulation models of pultrusion processes are of high importance to investigate this multiphysical behaviour.

State-of-the-art TCM simulation models for the assessment of process-induced stresses and strains in pultrusion processes couple a 3D transient Eulerian thermo-chemical analysis together with a 2D plane strain or 3D Lagrangian mechanical analysis (Baran et al. [5, 6]). This approach allows one to perform a segregated mechanical analysis by letting a cross section or part of the profile travel through the thermal and cure history. This approach is pioneering of I is kind, but it relies on interpolation between two separate domains, and it is inherently limited to a reduction of the actual 3D displacement field.

In the present study, we present a novel numerical framework for coupled TCM analysis in full 3D. In this novel method, the stress, as well as the thermal and chemical strain increments, are accumulated by integrating along the streamlines of the material flow (see Fig. 1). While this essentially resembles the traditional Eulerian approach typically reserved for fluid mechanics,

  doi:10.5075/epfl-298799_978-2-9701614-0-0

similar concepts have already been used for a variety of other continuous manufacturing processes such as friction stir welding [7], wire drawing [8], etc.

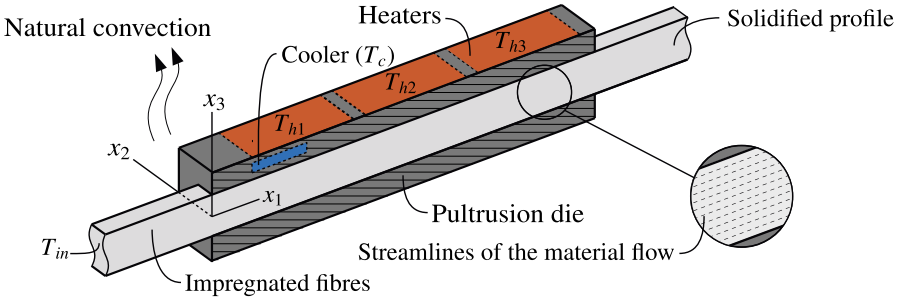

Figure 1. Cut-view of the pultrusion setup that served as the test case for the simulation model. The setup was originally developed by Chachad et al. [9] and later adapted by Baran et al. [5, 6]. The profile was drawn from left to right.

2. Method

The test case for the numerical framework in this paper was based on the experimental studies by Chachad et al. [9] that also served as the basis for Baran et al. [5, 6]. The test case concerned the pultrusion of a 25.4 × 25.4 mm^2 epoxy profile that was reinforced with unidirectional glass fibres. In this case study, the profile was pre-impregnated in a resin bath before entering the 0.915 m long die and it was advanced with a pulling speed of 20 cm/min. The temperature of the die was controlled using three individual heater units as well as a cooler. The configuration is depicted in Fig. 1. Since the test case in this paper does not deviate in any way from Baran et al. [5, 6], we only summarise the already established methods and list the most essential input data. Therefore, the reader is referred to [5, 6] for the extensive amount of input data needed from material values, process conditions, and relevant die and profile dimensions.

2.1 Material derivative

The material derivative that relates the rate of change of a physical quantity moving along a streamline with velocity, v_i, is the starting point for the steady-state Eulerian formulation:

$$\dot{(\,)} = \frac{\partial (\,)}{\partial t} = v\frac{\partial (\,)}{\partial x_i} = (\,)_{,t} + v_i(\,)_{,i} \tag{1}$$

where repeated indices imply summation and $(\,)_i = \partial(\,)/\partial x_i$ denotes partial differentiation as Eq. (1) indicates. In this paper, we seek a stationary solution, meaning that the temporal term, $\partial(\,)/\partial t = (\,)_{,t} = 0$, is omitted. In pultrusion processes, only the profile-advancing pulling speed contribute to the velocity tensor $v_1 = v_{pull}$ once the fibre material has entered the straight part of the pultrusion die. As such, all streamlines of the material flow are parallel to the x_1-axis as Fig. 1 indicates. The same principle applies to resin-injection pultrusion when considering parts of the profile that are some distance away from inlet ports.

2.2 Thermo-chemical model

Utilising the material derivative, conservation of energy and species (degree-of-cure) implies:

$$\frac{\partial}{\partial x_i}\left(K_{ij}\frac{\partial T}{\partial x_j}\right) + v_{pull}\rho c_p\frac{\partial T}{\partial x_1} = S_T, \qquad v_{pull}\frac{\partial \alpha}{\partial x_1} = R\_\alpha \tag{2}$$

  doi:10.5075/epfl-298799_978-2-9701614-0-0

where T is the temperature and α is the degree of cure. K_{ij} and ρc_p are the effective thermal conductivity tensor and thermal capacity of the composite profile. Finally, R_α is the cure rate given by an Arrhenius equation and S_T is the heat generated from the exothermic cure reaction (cf. Eqs. (3-4) in [5]).

2.3 Mechanical model

In the steady-state formulation, equilibrium is based on stress rates rather than total stress. Accordingly, we seek to find velocities (displacement rates) instead of displacements. The stress rates must fulfil a conventional static equilibrium condition:

$$\dot{\sigma}_{ij,j} + \dot{p}_i = 0 \tag{3}$$

where $\dot{p}_i$ is the rate of any external forces. A conventional constitutive law is used to establish a relationship between the strain rates and displacement rates (velocities):

$$\dot{\sigma}_{ij} = L_{ijkl}\left(\dot{\epsilon}_{kl} - \dot{\epsilon}_{kl}^{pr}\right), \qquad \dot{\epsilon}_{ij} = \frac{1}{2}(v_{i,j}+) \tag{4}$$

where $\dot{\epsilon}_{kl}^{e} = \dot{\epsilon}_{kl} - \dot{\epsilon}_{kl}^{pr}$ denotes the elastic part of the strain rate and $\dot{\epsilon}_{kl}^{pr}$ is the rate of the process-induced strains. The instantaneous stiffness tensor, L_{ijkl}, was based on the self-consistent field micromechanics (SCFM) for orthotropic composites by Bogetti and Gillespie [10], while the resin modulus was characterised with a modified cure-hardening instantaneous linear elastic (CHILE) approach that included thermal softening [5, 6] (see Eq. (11) and Appendix A in [5]).

2.3.1 Process-induced strain rates

Instead of formulating process-induced strains as incremental quantities as in Baran et al. [5, 6], the chemical shrinkage and thermal expansion/contraction were expressed as rate-measures, $\dot{\epsilon}_{kl}^{pr} = \dot{\epsilon}_{kl}^{ch} + \dot{\epsilon}_{kl}^{th}$. By utilising the principle of the material derivative (Eq. (1)), the contribution to the process-induced strain rate from thermal expansion was given by the relation:

$$\dot{\epsilon}_{ij}^{th} = \alpha_{ij}^{th}\dot{T} = \alpha_{ij}^{th} v_{pull}\frac{\partial T}{\partial x_i} \tag{5}$$

while thermal expansion coefficients, α_{ij}^{th}, are given in Eqs. (18-19) in [5]. The strain rate introduced by the chemical shrinkage rate is given by:

$$\dot{\epsilon}_r^{ch} = \sqrt[3]{1 + V_{sh}\dot{\alpha}} - 1 = \sqrt[3]{1 + V_{sh} v_{pull}\partial\alpha/\partial x_1} - 1, \qquad \dot{\epsilon}_{ij}^{ch} = \alpha_{ij}^{ch}\dot{\epsilon}_r^{ch} \tag{6}$$

where V_{sh} is the total volumetric shrinkage of the resin after complete cure. The coefficients, α_{ij}^{ch}, relating the isotropic resin shrinkage and the anisotropic shrinkage, can be derived from Eqs. (16-17) in [5].

2.4 Numerical framework and solution method

The commercial simulation software package COMSOL Multiphysics®[11] was used to solve the governing equations. The first part of the solution scheme was to solve for the conservation of energy and species in Eq. (2). Equivalent to Baran et al. [5, 6], we assumed a one-way coupling to the subsequent mechanical analysis, so the first solution step did not deviate from the established literature [12, 13]. Once the thermal and cure histories were calculated, the process-

  doi:10.5075/epfl-298799_978-2-9701614-0-0

induced strain rates were estimated based on Eqs. (5-6). As the total process-induced strains were needed to evaluate the constitutive properties of the profile, the strain increments were integrated along streamlines of the material flow (Eq. (1)). As an example, the operation for obtaining the thermal strain is resembled by the integral:

$$\epsilon_{ij}^{th} = \frac{1}{v_{pull}} \int_0^{x_1} \dot{\epsilon}_{ij}^{th} \, \mathrm{d}x \tag{7}$$

which was determined by solving a convective equation where the strain rate entered as a source term:

$$v_{pull} \frac{\partial \epsilon_{ij}^{th}}{\partial x_1} = \dot{\epsilon}_{ij}^{th} \tag{8}$$

Basically, this step is equivalent to the procedure for obtaining the degree of cure in Eq. (2) based on the material derivative. Once the process-induced strain and strain rates were determined, the displacement rates (velocities) were calculated by solving the equilibrium condition in Eq. (3). As appropriate boundary and contact conditions to the pultrusion die needed to be enforced, the equilibrium condition coupled to the streamline integration operation for accumulating the strain rates.

3. Results

Fig. 2 (Page 5) illustrates the thermal and cure histories of the profile. Fig. 3 (Page 6), depicts the process-induced thermal and chemical strain as well as the associated stresses. Figs. 2-3 present results for both the top and centre of the profile and compare to all data available in Baran et al. [6] for verification. Fig. 4 (Page 6) illustrate stress fields throughout the cross section for the location $x = 7.3$ m that correspond to Fig. 15 in Baran et al. [6]. Finally, Table 1 lists elapsed computation times for the framework presented in Section 2 compared to state-of-the-art methods [5, 6].

The thermal and cure histories presented in Fig. 2 together with the process-induced stresses and strains in Fig. 3 confirm that the new framework presented in Section 2 reached the same results as the established methods. This includes all strain and stress components in and outside the pultrusion die.

Based on the elapsed computation times in Table 1, it is clear that the new numerical framework presents a significant improvement in efficiency compared to existing 3D methods. The calculation time was reduced by 95% when the two 3D methods were compared in the case study. While the 3D-2D method that relied on a reduction of the displacement field based on a plane-strain assumption (Baran et al. [5]) was still significantly faster (45 s), the new framework enabled fast 3D simulation with reasonable computation times on a laptop.

Table 1: Calculation times for all steps (16 GB, 2.8 GHz, Core i7, 7700HQ laptop). Pre- and post-die regions were excluded from this example. The full 3D mesh was composed of 20,000 2nd-order brick elements, which was used as the basis for all three examples.

	2D-3D, Baran et al. [5]	3D-3D, Brain et al. [6]	3D (This paper)
Calculation time	45 s	1920 s	98 s

  doi:10.5075/epfl-298799_978-2-9701614-0-0

4. Conclusion

This study concerned the development of a new numerical framework for the simulation of process-induced stress and deformation in thermoset pultrusion processes. The framework is based on stationary formulations where increments are accumulated by integration along streamlines. We observed a reduction in computation times of 95% compared to the existing frameworks that rely on coupling Eulerian and Lagrangian methods.

The framework presented enables fast 3D computation of process-induced stress and strains even on a laptop computer. This new achievement is important as it allows for future studies of how out-of-plane effects such as the profile-advancing pulling force affect process-induced stress and strains.

Acknowledgements

This work was funded by the Danish Council for Independent Research, Technology and Production Sciences (Grant no. DFF-6111-00112: Modelling the multi-physics in resin injection pultrusion (RIP) of complex industrial profiles).

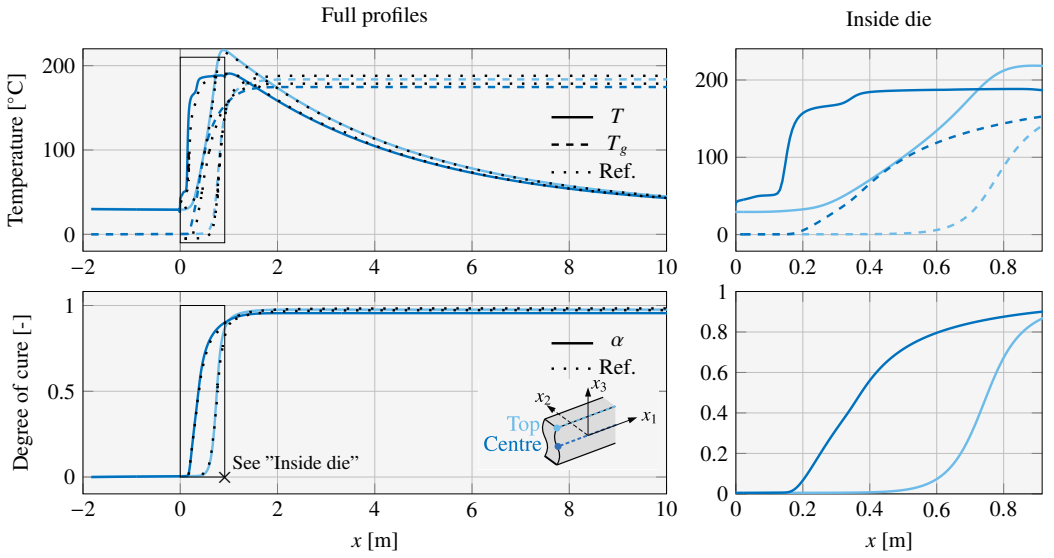

Figure 2. Full temperature and cure histories at the centre (dark blue) and at top (light blue) of the profile. Ref. refers to data obtained from Baran et al. [6] in which the same example was calculated.

  doi:10.5075/epfl-298799_978-2-9701614-0-0

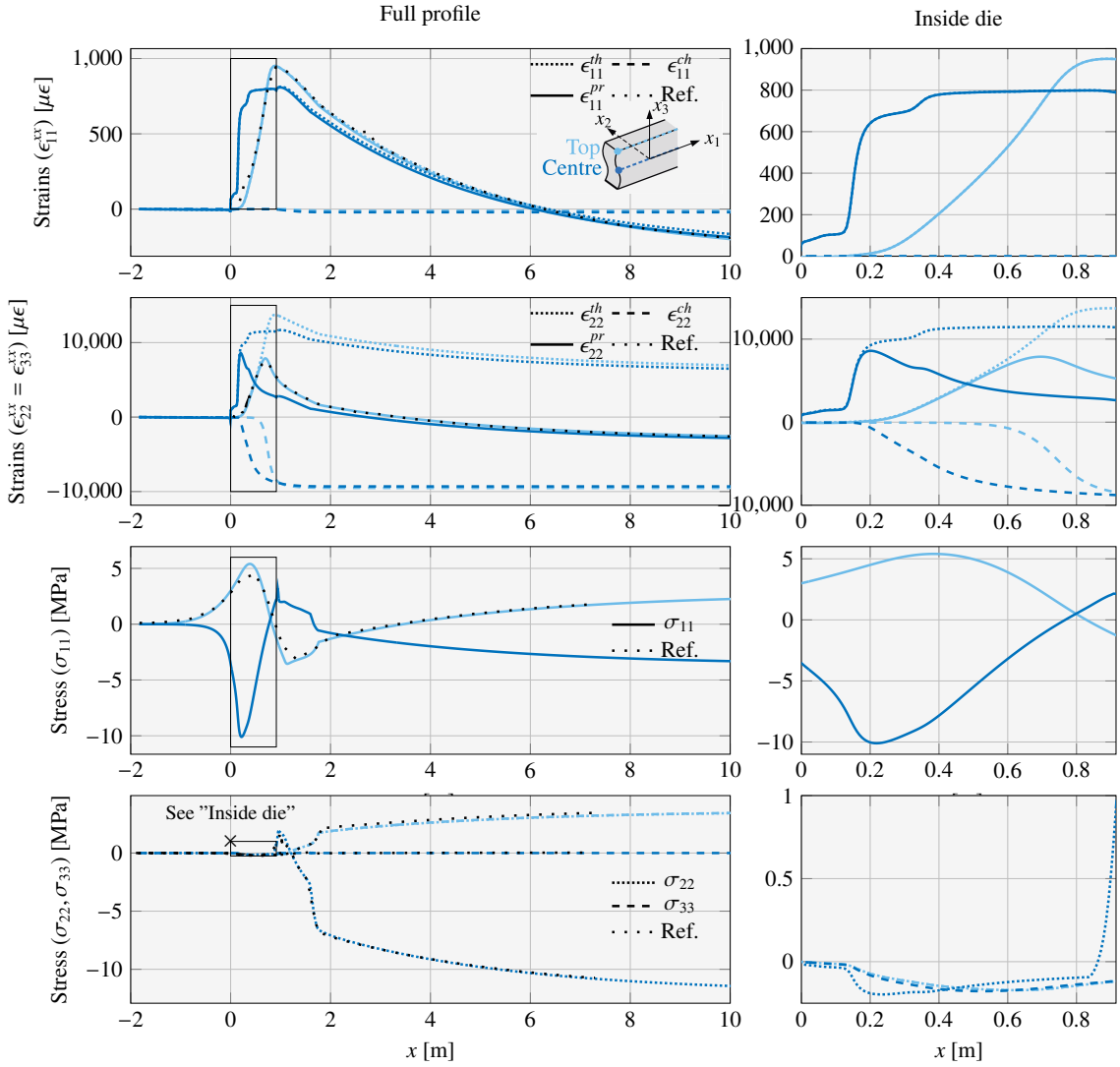

Figure 3. Full strain and stress histories at the centre (dark blue) and at top (light blue) of the profile. The $(\ )_{11}$- component is the longitudinal direction, while $(\ )_{11}$- and $(\ )_{11}$-components are the transversal directions. Ref. refers to data obtained from Baran et al. [6] in which the same example was calculated.

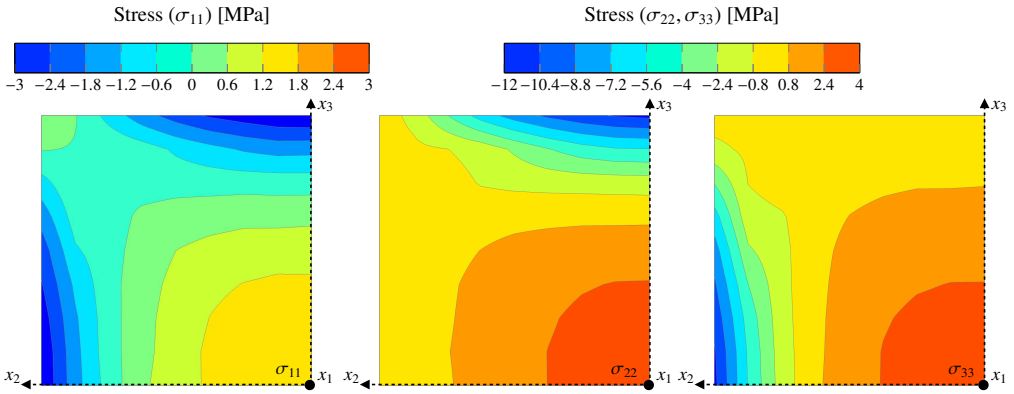

Figure 4. Stationary stress fields at $x_1 = 7.3$ m *(measured from the entrance to the die). For reference, the same stress fields can be seen in Fig. 15 in Baran et al. [6].*

  doi:10.5075/epfl-298799_978-2-9701614-0-0

5. References

1. M. Sandberg, J. H. Hattel, J. Spangenberg, Simulation of liquid composite moulding using a finite volume scheme and the level-set method, International Journal of Multiphase Flow 118 (2019) 183–192.
2. M. Sandberg, O. Yuksel, I. Baran, J. H. Hattel, J. Spangenberg, Numerical and experimental analysis of resin-flow, heat-transfer, and cure in a resin-injection pultrusion process, Composites Part A: Applied Science and Manufacturing 143 (2021) 106231.
3. M. Sandberg, O. Yuksel, I. Baran, J. Spangenberg, J. H. Hattel, Steady-state modelling and analysis of process-induced stress and deformation in thermoset pultrusion processes, Composites Part B: Engineer- ing 216 (2021) 108812.
4. O. Yuksel, M. Sandberg, J. H. Hattel, R. Akkerman, I. Baran, Mesoscale process modeling of a thick pultruded composite with variability in fiber volume fraction, Materials 14 (2021) 3763.
5. I. Baran, C. C. Tutum, M. W. Nielsen, J. H. Hattel, Process induced residual stresses and distortions in pultrusion, Compos Part B-Eng 51 (2013) 148–161.
6. I. Baran, J. H. Hattel, R. Akkerman, C. C. Tutum, Mechanical modelling of pultrusion process: 2d and 3d numerical approaches, Appl Compos Mater 22 (2015) 99–118.
7. A. Bastier, M. Maitournam, K. Dang Van, F. Roger, Steady state thermomechanical modelling of friction stir welding, Sci Technol Weld Joi 11 (2006) 278–288.
8. K. J. Juul, K. L. Nielsen, C. F. Niordson, Steady-state numerical modeling of size effects in micron scale wire drawing, J Manuf Process 25 (2017) 163–171.
9. Y. Chachad, J. Roux, J. Vaughan, E. Arafat, Three-dimensional characterization of pultruded fiberglass- epoxy composite materials, J Reinf Plast Comp 14 (1995) 495–512.
10. T. A. Bogetti, J. W. Gillespie, Process-Induced Stress and Deformation in Thick-Section Thermoset Com- posite Laminates, J Compos Mater 26 (1992) 626–660.
11. COMSOL Multiphysics® v. 5.4. www.comsol.com. COMSOL AB, Stockholm, Sweden, 2019.
12. I. Baran, J. H. Hattel, C. C. Tutum, Thermo-chemical modelling strategies for the pultrusion process, Appl Compos Mater 20 (2013) 1247–1263.
13. M. Sandberg, O. Yuksel, R. B. Comminal, M. R. Sonne, M. Jabbari, M. Larsen, F. B. Salling, I. Baran, J. Spangenberg, J. H. Hattel, Numerical modeling of the mechanics of pultrusion, in: Mechanics of materials in modern manufacturing methods and processing techniques, Elsevier, 2020, pp. 173–195.

  doi:10.5075/epfl-298799_978-2-9701614-0-0

GENERATION OF INITIAL FIBER ORIENTATION STATES FOR LONG FIBER REINFORCED THERMOPLASTIC COMPRESSION MOLDING SIMULATION

Louis Schreyer[a], Juliane Blarr[b], Katja Höger[c], Nils Meyer[a], Luise Kärger[a]

a: Institute of Vehicle System Technology, Karlsruhe Institute of Technology, Karlsruhe, Germany; louis.schreyer@kit.edu
b: Institute for Applied Materials - Materials Science and Engineering IAM-WK, Karlsruhe Institute of Technology, Karlsruhe, Germany
c: wbk Institute of Production Science, Karlsruhe Institute of Technology, Karlsruhe, Germany

Abstract: *The prediction of the fiber orientation state (FOS) is of utmost interest for compression molded long fiber reinforced thermoplastics as the part's properties strongly depend on it. Besides the position of the initial plastificate in the mold cavity and the process settings, detailed knowledge of the initial FOS is essential. During compounding, the fibers align depending on the extruder screw configuration yielding a non-uniform local FOS. For process simulation, a common approach is to neglect this effect and assume an isotropic or planar-isotropic FOS of the initial plastificate. A more sophisticated approach consists of micro-computed tomography (µCT-) scans of slices of the initial plastificate and the derivation of the initial FOS from the three-dimensional image data. This approach can yield accurate predictions but is quite cumbersome and expensive. In this paper, we present a novel approach to account for the FOS of the initial plastificate. The approach is motivated by experimental observations and based on geometric assumptions. Depending on the extruder type and the dimensions of the initial plastificate, the developed tool generates a three-dimensional data set containing the mesh information alongside the initial FOS in a tensorial representation. To investigate the influence of the initial FOS for different flow regimes, we conducted compression molding simulations on a planar part.*

Keywords: thermoplastic; compression molding; fiber orientation; plastificate; process simulation

1. Introduction

Compression molded long fiber reinforced thermoplastics (LFT) are widely used for large semi-structural parts in the automotive and aerospace industry. The main advantage of compression molded LFT compared to injection molded LFT is the final part's longer average fiber length due to lower shear forces during processing [1]. Its popularity increased with the introduction of the direct LFT in-line compounding (D-LFT-ILC) process, which offers additional degrees of freedom. Instead of semi-finished LFT pellets, thermoplastic granulate, additives and fibers are compounded in-line, reducing the supply chain. In the D-LFT-ILC process, the thermoplastic granulate and the additives are fed via a hopper to the first extruder, where they mix, and the thermoplastic material melts. In the second extruder (single or double screw extruder), fiber rovings are then fed continuously. Due to the shear forces introduced by the extruder screw(s), the fibers break and disperse, yielding a non-uniform local FOS. The compound is extruded into a predetermined shape via a nozzle and cut. When using a double screw extruder, the general fiber orientation of the plastificate resembles two swirls [2]. However, the fibers align in extrusion direction in the outermost layer. Finally, the extruded plastificate is transferred to a compression molding press and compressed into shape.

  doi:10.5075/epfl-298799_978-2-9701614-0-0

To predict a LFT part's mechanical properties accurately, the local FOS must be considered. Further, the FOS critically influences the part's dimensional stability. Therefore, detailed knowledge of the initial FOS in the plastificate and the reorientation phenomena during molding are of utmost interest, with this work focusing on the former. The FOS can be expressed in form of a probability density function $\psi(\cdot)$ [3]. A more convenient and computationally efficient tensorial representation based on moments of the probability density function was introduced by Advani and Tucker [4]. The second-order fiber orientation tensor (FOT) is defined as:

$$\boldsymbol{A} = \oint \boldsymbol{p} \otimes \boldsymbol{p} \psi(\mathbf{p}) \mathrm{d}\mathbf{p} . \tag{1}$$

$\boldsymbol{p}$ denotes the unit vector characterizing the direction of a single fiber and $\otimes$ denotes the outer product. Non-destructive methods to determine the local FOS are micro-computed tomography (µCT) [5-7] and terahertz spectroscopy [8], where the latter is only suitable for thin cross-sections (therefore not applicable for LFT plastificates). A general challenge with µCT scans depicts the conflict between the scan resolution and the sample size. With increasing scan resolution, the permissible sample size decreases and vice versa. This effect especially applies to carbon fibers (CF) due to their small diameter (5 – 7 µm). Further, the contrast between CF and thermoplastics is unpronounced on µCT images, due to their respective molecular structures. As a result, meaningful µCT scans of larger volumes (especially for CF) are time-consuming and storage-intensive. To partially circumvent this problem, at least for glass fibers (GF), Perez et al. [2] assumed that fiber bundles describe the local FOS in GF plastificates adequately, allowing a scan resolution lower than the diameter of the fiber (> 15 µm). The latter requires that the individual fibers stay in bundle-like configurations during compounding, which must be resolved by the µCT scan. A comparison by Perez et al. [2] with the FOS results from high-resolution scans (4 µm/voxel) at sample locations showed an average relative deviation of 23 percent when using VGStudio Max software to determine the FOS. Song et al. [9] additionally assumed periodicity of the FOS in the extrusion direction due to the nature of the flow. Further, they scanned a plastificate with a smaller cross-section (resolution: 50 µm/voxel) and mapped the FOS onto the simulated plastificate mesh. The simulation results showed the best agreement with the investigated GF reinforced LFT part's final FOS at sample locations compared to an isotropic and planar-isotropic initial FOS. In a later work, Song et al. [10] applied the latter workflow with an identical scan resolution to a CF plastificate (from a single screw extruder). The scanned volume was divided into (1 x 1 x 1) mm cells to determine the local FOS, corresponding to only (20 x 20 x 20) voxels per cell. However, the detection of CF bundles is unlikely due to the low resolution and the mentioned difficulties that arise in µCT scans with CF. The postprocessing algorithm more likely examines the FOS based on the local orientation of the matrix material. Nevertheless, the authors achieved good agreement with the experimental results. However, the good agreement is probably due to the simpler initial FOS caused by the used single screw extruder.

This work focuses on developing a novel method to consider the FOS of an LFT plastificate in compression molding simulations. The method approximates the averaged expected FOS based on the geometric construction of artificial fiber vectors (FV) rather than the local FOS, which is subjected to statistical variations. We compare the FOS from the plastificate generator with those from µCT scans qualitatively at selected locations. The influence of the initial FOS is discussed based on compression molding simulations for different initial FOS and flow regimes.

  doi:10.5075/epfl-298799_978-2-9701614-0-0

The investigated D-LFT-ILC plastificate was manufactured using a double screw extruder with the same direction of rotation and a (75 x 35) mm rectangular nozzle. The material of the investigated plastificate was 25 vol.% carbon fiber reinforced polyamide 6 (PA6).

2. Methods

2.1 Plastificate generator

The plastificate generator generates a three-dimensional data set (VTK file) containing the mesh information alongside the second-order FOT as cell data. The method was implemented in Python 3.8. An ideal plastificate is assumed with the cross-section dimensions of the nozzle. Consequently, voids resulting from extrusion and lofting (swelling of the plastificate after extrusion) are neglected. The second-order FOT (cf. Eq. (1)) is approximated by the weighted summation of artificial unit FV $\boldsymbol{p}$ for each cell:

$$\boldsymbol{A} = \frac{1}{\sum_k w_k} \sum_k \boldsymbol{p}_k \otimes \boldsymbol{p}_k w_k \,. \tag{3}$$

w denotes the k-th weight function of the individual FV. The FV correspond to the tangent and normal of the ellipses, respectively. Three ellipses are constructed with respect to the position of the two extruder screws and the center of the plastificate's cross-section (cf. Figure 1). We choose the semi-major (horizontal) and semi-minor (vertical) axis (a, b) according to the plastificate's width and height to (width/4, height/2) and (width/2, height/2), respectively. The tangent FV $\boldsymbol{p}^c_{\mathrm{t},1}$ and $\boldsymbol{p}^c_{\mathrm{t},2}$ of the lateral ellipses approximate the swirl-like fiber orientation. The notation $(\cdot)^c$ denotes the c-th cell. The tangent FV $\boldsymbol{p}^c_{\mathrm{t},3}$ of the center ellipse increases the degree of orientation in the circumferential direction in the outer area. The degree of isotropy is adjusted by the normal FV $\boldsymbol{p}^c_{\mathrm{n},1}$ and $\boldsymbol{p}^c_{\mathrm{n},2}$ of the lateral ellipses.

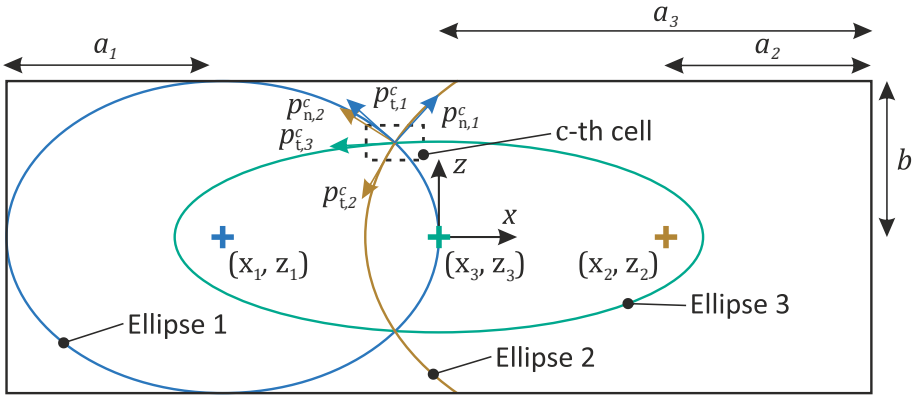

Figure 1. Geometric construction of artificial FV based on the tangent and normal of the three ellipses for the c-th cell. (x_k, z_k) denote the respective ellipse centers.

In the following, it is assumed that the coordinate system is in the middle of the plastificate's cross-section and that the y-axis corresponds to the extrusion direction, see Figure 1. The weight functions for the tangent FV $\boldsymbol{p}^c_{\mathrm{t},1}$ and $\boldsymbol{p}^c_{\mathrm{t},2}$ are defined as:

$$w_{\mathrm{t},1} = \frac{(d_1+d_2)}{d_1}\,,\quad \mathrm{w}_{\mathrm{t},2} = \frac{(d_1+d_2)}{d_2}, \tag{4}$$

with d_1 and d_2 being the Euclidean distance from the cell center to the respective ellipse center.

  doi:10.5075/epfl-298799_978-2-9701614-0-0

The weight function of the FV $\boldsymbol{p}_{\mathrm{t},3}^{c}$ are defined by scaling the latter weight functions depending on the cell coordinates:

$$w_{\mathrm{t},3} = \begin{cases} w_{\mathrm{t},1}\ \mathrm{argmax}\left(\frac{|z|}{b}, \frac{|x|}{a_3}\right)^4, & x \leq 0 \\ w_{\mathrm{t},2}\ \mathrm{argmax}\left(\frac{|z|}{b}, \frac{|x|}{a_3}\right)^4, & x > 0 \end{cases}. \tag{5}$$

The weight functions of the normal FV $\boldsymbol{p}_{\mathrm{n},1}^{c}$ and $\boldsymbol{p}_{\mathrm{n},2}^{c}$ are chosen to increase the degree of isotropy in the area between the extruder screw. The latter are defined as:

$$w_{\mathrm{n},i} = w_{\mathrm{t},i}\ \mathrm{argmin}\left(1 - \frac{|z|}{\mathrm{b}}, 1 - \frac{|x|}{\mathrm{a}_3}\right)^2, \quad i = 1, 2. \tag{6}$$

So far, only planar FOT were defined in the (x, z)-plane. To account for the orientation in the extrusion direction, the weighted summation of the in-plane FOT and a unidirectional FOS with $A_{yy} = 1$ are calculated, with the ratio of the respective weight factors defining the degree of orientation in the extrusion direction. The strong anisotropy in the boundary layer of the plastificate was considered by assigning a unidirectional orientation state in the extrusion direction (A_{yy} = 1) to the outermost cells. The approximation of the artificial FOT is independent of the extrusion direction, which is why all cells with identical (x, z)-coordinates have identical FOT.

2.2 Compression molding simulation

The numerical investigation was conducted on a (400 x 400 x 3) mm plate tool. The (75 x 200 x 35) mm plastificate was placed in the center of the mold. The plate was meshed with 20 elements in the thickness direction, corresponding to a total of 4,156,197 tetrahedrons. The compression molding simulations were conducted using Moldflow 2021.1. The used CF/PA6 material "OnForce™ LFT-NN40LCF001" was given in the Moldflow material database. We used the RSC [11] model to account for the reorientation of fibers. To elaborate the influence of the initial FOS for different flow regimes, we conducted simulations with different values for the retarding rate κ and the interaction coefficient C_{i}. Namely, κ = 0 and C_{i} = 0, reducing the model to Jeffery's equation [12], κ = 0.1 and C_{i} = 0, and κ = C_{i} = 0.1. We ran simulations with those parameter sets for the following initial FOS: artificial (plastificate generator), planar-isotropic (A_{xx} = A_{yy} = 0.5) and isotropic (A_{xx} = A_{yy} = A_{zz} = 1/3). The weight factors for the extrusion direction of the artificial FOT were chosen so that A_{yy} = 0.3, which corresponds to the averaged A_{yy} of the evaluated µCT volumes.

2.3 Fiber orientation measurement

The Zeiss Metrotom 800 (cone-beam) µCT system with the flat panel detector PaxScan2520V with (1536 x 1920) pixels was used to scan a section of the plastificate. The scan resolution was 73 µm/voxel, which corresponds to the maximal resolution. The resulting volumetric images were reconstructed applying the Feldkamp cone-beam algorithm [13] and the Shepp-Logan noise reduction filter. Subsequently, the reconstructed scans were processed in VG Studio Max 3.4.2. A grid of 36 (3.33 x 3.33 x 3.33) mm cubes was superimposed around the left swirl. Each cell was evaluated individually in the further process of the FOT determination. If necessary,

  doi:10.5075/epfl-298799_978-2-9701614-0-0

brightness and contrast were adjusted within the software ImageJ (FIJI). In addition, the individual gray value threshold was determined for each cell using Otsu's method [14]. To determine the FOT from the scan data, the method introduced by Pinter et al. [7] was used. The algorithm makes use of the structure tensor:

$$\boldsymbol{S} = \begin{bmatrix} \left(\frac{\delta I}{\delta x}\right)^2 & \frac{\delta I}{\delta x}\frac{\delta I}{\delta y} & \frac{\delta I}{\delta x}\frac{\delta I}{\delta z} \\ \frac{\delta I}{\delta y}\frac{\delta I}{\delta x} & \left(\frac{\delta I}{\delta y}\right)^2 & \frac{\delta I}{\delta y}\frac{\delta I}{\delta z} \\ \frac{\delta I}{\delta z}\frac{\delta I}{\delta x} & \frac{\delta I}{\delta z}\frac{\delta I}{\delta y} & \left(\frac{\delta I}{\delta z}\right)^2 \end{bmatrix}, \tag{2}$$

with I being a discrete function describing the grey-value intensity of the reconstructed image. The structure tensor calculation is combined with a Gaussian blur of a width of σ = 0.2 voxels and a mask size of 2 voxels. As a result, the second-order FOT was obtained for each cell.

3. Results

Figure 2 shows the estimated FOT of µCT volumes around the left extruder screw and the FOT of the plastificate generator of the right half of the plastificate in the (x, z)-plane perpendicular to the extrusion direction represented by tensor glyphs [15]. Unidirectional FOT, e.g., A_{yy} = 1, are represented as lines by tensor glyphs and are therefore not visible in Figure 2 (concerns boundary layer of artificial FOS). The FOT of the µCT volumes as well as the artificial ones show a swirl-like pattern, as reported by [2]. However, individual FOT from µCT volumes have strongly deviating orientation states compared to their adjacent cells. As expected, the artificial FOT map the averaged expected fiber orientation of the investigated extrusion process. The latter tensors show a significant alignment of the fibers in the circumferential direction in the outer area, which is to be expected due to the concurrent extruder screws. The lateral artificial FOT exhibit a stronger alignment than near the top and bottom, which is caused by the chosen weight functions.

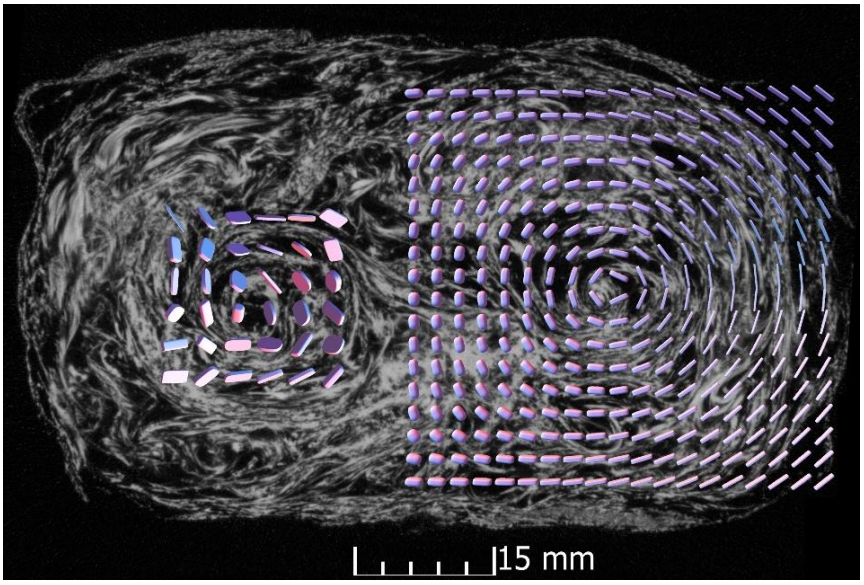

Figure 2. FOT from µCT images (left) and from the plastificate generator (right) represented by tensor glyphs [15] in front of a µCT image of the evaluated volume.

  doi:10.5075/epfl-298799_978-2-9701614-0-0

The fiber orientation results for A_{xx} and A_{yy} of the compression molding simulations of the different initial FOS are shown in Figure 3. The A_{zz} component is omitted since it is given by tr(A_{ii}) = 1. The evaluation was carried out at Position A close to the plastificate's initial position and Position B near the end of the flow. The results using Jeffery's equation show significant fiber alignment in the flow direction, however, the influence of the initial FOS is pronounced. The introduction of the retarding rate κ reduces the rate of reorientation. The influence of the initial FOS is insignificant when using a high interaction coefficient C_i. Further, the fiber orientation of the latter is more random in the (x, y)-plane.

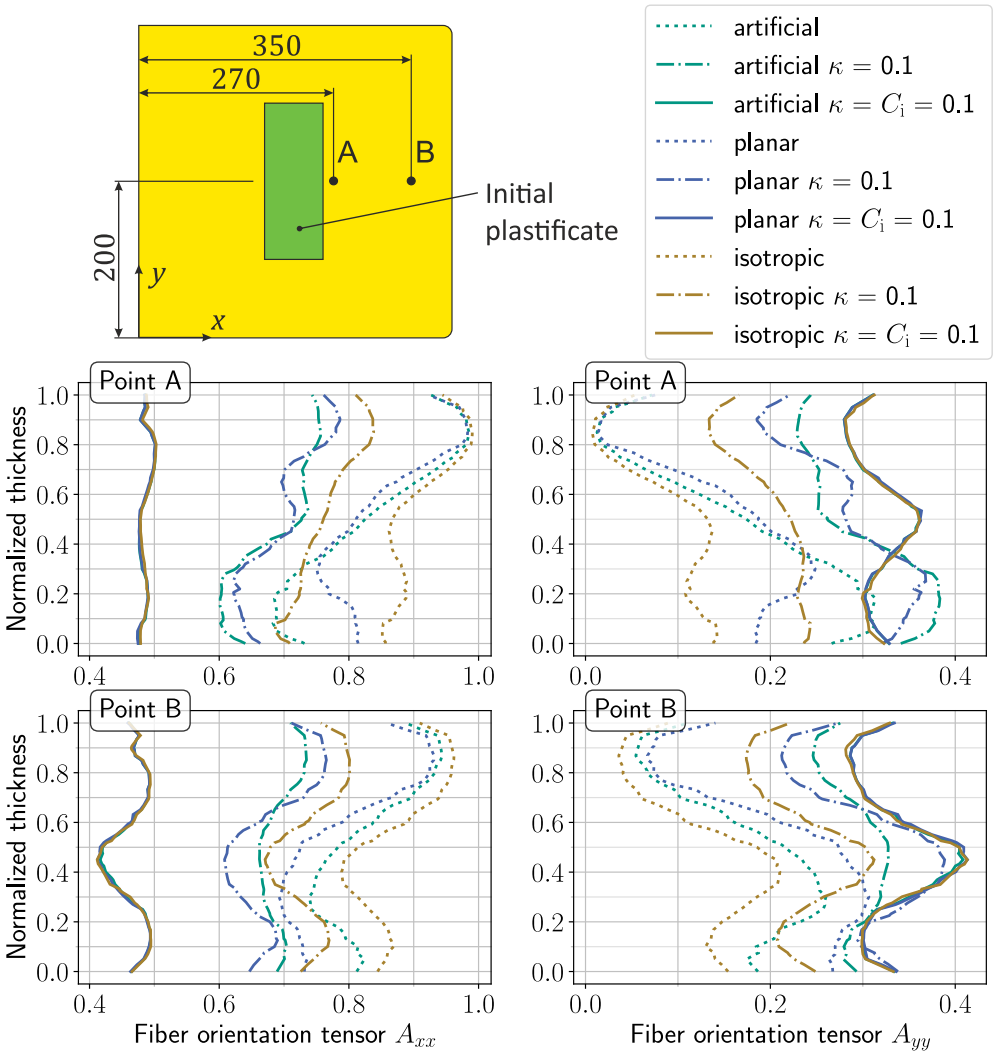

Figure 3. Comparison of FOT components A_{xx} and A_{yy} at locations A (upper graphs) and B (lower graphs) through the thickness for different initial FOS and RSC model parameters.

4. Discussion

There are limits to the comparison of the fiber orientation state determined from the µCT volumes and the artificially generated one. While the plastificate generator outputs deterministic FOT, the physical plastificate is subjected to strong statistical variations, e.g., voids, presence and distribution of fiber bundles (relevant for low µCT resolution) and fiber breakage. This leads to strong local deviations from the averaged expected fiber orientation, caused by too few voxels per cell (compare for example the FOT in the upper left tensor glyph in Figure 2 on

  doi:10.5075/epfl-298799_978-2-9701614-0-0

the left), not to mention the resolution problem. If the cell size is increased, however, the FOS tends to be more isotropic and therefore not reasonable. The same applies to the idea of averaging orientation tensors, e.g., in extrusion direction, to reduce the statistical variations. On the one hand, this touches on the well-known problem of finding representative volume elements, which have often been converted into statistical volume elements for fiber-reinforced plastics. On the other hand, this depicts the problem to correctly interpolate or average tensors for larger volumes and areas. The question of a suitable error measure also arises for the direct comparison of tensors, since neither a direct component comparison nor, e.g., the use of the Frobenius norm has proved particularly useful. Furthermore, the large number of voids in the plastificate complicate the identification of fiber bundles, because the gray value drop between CF and thermoplastic is much smaller compared to the drop to air. This effect does not apply to finished parts as the air escapes during molding. Therefore, the estimated FOT from µCT images of the plastificate can only be considered correct under the condition of the uniform behavior of the fibers to the matrix in the flow. Consequently, the comparison of FOT from µCT volumes of the plastificate (independent of the scan resolution) and the plastificate generator is not suitable for validation. Rather, the validation must be based on the comparison of a compression molded part's final virtual and physical fiber orientation.

The results of the compression molding simulations illustrate the influence of the initial FOS for different flow regimes. Jeffery's equation retains the information of the initial FOS most, as the fiber reorientation only depends on the rotation and rate of deformation of the surrounding thermoplastic. On the other hand, the influence of the initial FOS is negligible for high interaction coefficients C_i as the state of equilibrium is more random and therefore reached faster (compare results for C_i = 0.1 in Figure 3). However, a high value of this coefficient does not approximate the physical process as the fibers exhibit a significant alignment in the flow direction dependent on the flow path. Consequently, the interaction coefficient must be sufficiently small so that the resulting state of equilibrium has a strong orientation in the flow direction.

5. Conclusion

In this work a novel approach based on the construction of artificial fiber vectors (FV) from ellipses is developed to consider the initial FOS of an LFT plastificate in compression molding simulation. Qualitative comparison with µCT images shows that the proposed FOS generator maps the expected averaged FOS of the physical plastificate. However, quantitative comparison with FOS from µCT volumes depict several challenges, which impedes validation, especially for CF. The results of the compression molding simulations show a non-negligible influence of the initial FOS for long fiber reinforced polymers. Therefore, the approach must be validated based on a physical part's final fiber orientation at sample locations.

6. Contributions

LS: Conceptualization, Methodology, Software, Writing – original draft. **JB**: Investigation, Resources, Writing - review & editing. **KH**: Investigation, Resources. **NM**: Conceptualization, Writing – review & editing. **LK**: Supervision, Writing - review & editing.

7. Acknowledgements

The research documented in this manuscript has been funded by the German Research Foundation (DFG) within the International Research Training Group "Integrated engineering of

continuous-discontinuous long fiber reinforced polymer structures" (IRTG 2078). The support by the German Research Foundation (DFG) is gratefully acknowledged. Furthermore, the authors would also like to thank the Fraunhofer ICT for their support by providing the LFT plastificates, which were manufactured under the project leadership of Christoph Schelleis.

8. References

1. Ning H, Lu N, Hassen AA, Chawla K, Selim M, Pillay S. A review of Long fibre thermoplastic (LFT) composites. International Materials Reviews 2020; 65:164-188.
2. Perez C, Osswald T, Goris S. Study on the fiber properties of a LFT strand. 2013.
3. Folgar F, Tucker C. Orientation Behavior of Fibers in Concentrated Suspensions. Journal of Reinforced Plastics and Composites 1984; 3(2):98-119.
4. Advani S, Tucker C. The Use of Tensors to Describe and Predict Fiber Orientation in Short Fiber Composites. Journal of Rheology 1987; 31(8):751-784.
5. Gandhi U, Sebastian DB, Kunc V, Song Y. Method to measure orientation of discontinuous fiber embedded in the polymer matrix from computerized tomography scan data. Journal of Thermoplastic Composite Materials 2016; 29(12):1696-1709.
6. Schladitz K, Büter A, Godehardt M, Wirjadi O, Fleckenstein J, Gerster T, Hassler U, Jaschek K, Maisl M, Maisl U, Mohr S, Netzelmann U, Potyra T, Steinhauser MO. Non-destructive characterization of fiber orientation in reinforced SMC as input for simulation based design. Composite Structures 2017; 160:195-203.
7. Pinter P, Dietrich S, Bertram B, Kehrer L, Elsner P, Weidenmann KA. Comparison and error estimation of 3D fibre orientation analysis of computed tomography image data for fibre reinforced composites. NDT & E International 2018; 95: 26–35.
8. Jördens C, Scheller M, Wietzke S, Romeike D, Jansen C, Zentgraf T, Wiesauer K, Reisecker V, Koch M. Terahertz spectroscopy to study the orientation of glass fibres in reinforced plastics. Composites Science and Technology 2010; 70(3):472-477.
9. Song Y, Gandhi U, Pérez C, Osswald T, Vallury S, Yang A. Method to account for the fiber orientation of the initial charge on the fiber orientation of finished part in compression molding simulation. Composites Part A 2017; 100:244-254.
10. Song Y, Gandhi U, Sekito T, Vaidya UK, Vallury S, Yang A, Osswald T. CAE method for compression molding of carbon fiber-reinforced thermoplastic composite using bulk materials. Composites Part A 2018; 114:388-397.
11. Wang J, O'Gara JF, Tucker CL. An objective model for slow orientation kinetics in concentrated fiber suspensions: Theory and rheological evidence. Journal of Rheology 2008; 52(5):1179-1200.
12. Jeffery GB. The Motion of Ellipsoidal Particles Immersed in a Viscous Fluid. Proceedings of the Royal Society of London. Series A, Containing Papers of a Mathematical and Physical Character 1922; 102:161-179.
13. Feldkamp LA, Davis LC, Kress JW. Practical cone-beam algorithm. Journal of the Optical Society of America A 1984; 1(6): 612–9.
14. Otsu N. A Threshold Selection Method from Gray-Level Histograms. IEEE Trans. Syst., Man, Cybern. 1979; 9(1): 62–6. https://doi.org/10.1109/TSMC.1979.4310076.
15. Schultz T, Kindlmann GL. Superquadric glyphs for symmetric second-order tensors. IEEE Trans Vis Comput Graph 2010; 16(6): 1595–604.

  doi:10.5075/epfl-298799_978-2-9701614-0-0

CHALLENGES OF VIRTUAL TESTING FOR THE COMPREHENSION OF IMPACT PHENOMENA

Maxime Pouliquen[a], Olivier Allix[b], Roland Ortiz[c], Juan Pedro Berro Ramirez[d]

a: Altair Engineering – ONERA DMAS/CRD – LMPS / ENS Paris-Saclay –
maxime.pouliquen@ens-paris-saclay.fr
b: LMPS / ENS-Paris-Saclay
c: ONERA DMAS/CRD
d: Altair Engineering

Abstract: *Delamination is one of the most critical damage mechanisms taking place in composite structures. Its modeling is challenging and its observation even more. Numerical modeling allows us to study these phenomena in a new way and make it possible to study the influence of different parameters on the damage mechanics taking places during an impact loading. In this article, we propose to use virtual testing of complex composite structures subjected to low and high velocity impact loading and to study the effect of different mechanisms on the damage induced in the composite.*

Keywords: Impact modeling; Delamination; Virtual testing; Cohesive zone modeling

1. Introduction

Composite materials are widely used in aeronautics for their high strength coupled with their low density. Such materials can mainly be found in the fuselage, the wings and the tailplanes. These structures will be subjected, throughout their entire life cycle, to a certain number of impacts. These impacts, ranging from low velocity and low energy (e.g., tool drop, hail) to high velocity and high energy (e.g., birds, debris from the track), can cause significant damage. Among the major damage types appearing in composite laminates, delamination is the most critical for low velocity and low energy impacts [1,2]. Indeed, such damage can then reduce drastically the residual compression strength of the structure [3].

Studies on the behavior of the interface under varying loading rates showed very mixed results. Some authors noticed an increase in the critical energy release rate G_c when the loading rate increased [4-7]. Their explanation for this behavior is that the fracture surfaces of the samples tested seemed to have absorbed more energy when the loading rate increased [7]. Others noticed a decrease of the G_c [8-12], attributing it to smoother rupture profiles and a lesser number of shear cusps. Finally, some did not notice any effect of the strain rate on the G_c [13-14]. This discrepancy between the results seems partly due to the complexity of the phenomena studied, of the tests and of the analyses.

In order to understand and characterize these effects, the tests are chosen so that such effects are amplified. However, composite structures chosen for industrial purposes are chosen to minimize the possible damages. A question comes then to determine how these effects translate to such complex laminates. This is an important question as some models can require several parameters that will require extensive testing and analysis to calibrate it.

  doi:10.5075/epfl-298799_978-2-9701614-0-0

In this study, we focus on a few simple aspects of numerical models of composite layups. We studied the influence of impactor velocity and layup on delamination using a simple model with elastic plies. We then looked at the influence of friction between the plies on delamination and stability.

2. Material properties

2.1 Ply

The ply is considered purely elastic in this first study. The properties chosen are that of T700/M21 as presented in Table 1. E_l and E_t represent the longitudinal and transverse modulus respectively, ν_{lt} and ν_{tt}, represent the Poisson coefficients, G_{lt} is the shear modulus and ρ is the density. An improved material law will later be used to implement fiber rupture, matrix damage and strain rate effects.

Table 1: Ply properties (T700/M21)

E_l [MPa]	E_t [MPa]	ν_{lt} [-]	ν_{tt}, [-]	G_{lt} [MPa]	ρ $[kg/mm^3]$
115000	8500	0.28	0.4	4500	1.58×10^{-6}

2.2 Interface

Cohesive zone modeling is used for the interface behavior with a simple bilinear law, as represented in Figure 1. The law chosen is an elastoplastic bilinear cohesive law called CONNECT (MAT59) available in the Radioss solver. In this law, both modes (normal and shear) are defined separately by an initiation displacement δ_0 and a critical displacement δ_c. When δ_0 is reached, stress is reduced as displacement increases through a negative hardening plasticity. A coupling is then introduced for the rupture of the element based on a power law for the displacement as presented in Eq. 1:

$$\frac{\delta_N}{\delta_{cN}} + \frac{\delta_S}{\delta_{cS}} = 1 \quad (1)$$

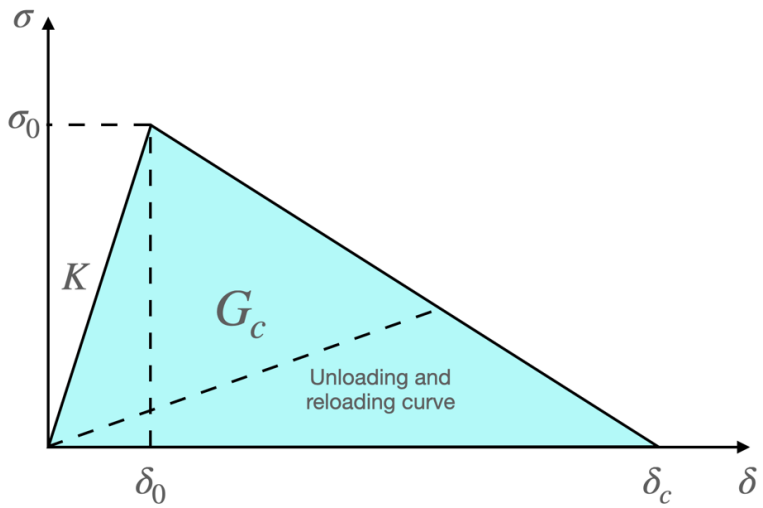

Figure 1. Bilinear law

The properties chosen for the interface are presented in Table 2.

Table 2: Interface properties

K [MPa/mm]	σ_{ON} [MPa]	σ_{OS} [MPa]	G_{Ic} $[J/m^2]$	G_{IIc} $[J/m^2]$
10^5	45	75	400	1200

3. Simulations

The impact simulations were based on an experimental setup found in [14]. A 16 plies composite is supported by two cylinders. The hemispherical impactor is dropped on the composite with an energy of $10\,J$. The different layups and impactor velocities used in the simulations are presented in Table 3.

Table 3: Layups and impactor velocities

Layups				
$[0_{16}]$	$[90_{16}]$	$[0_5/90_6/0_5]$	$[(45/90/-45/0)_2]_s$	$[(0/-45/90/45)_2]_s$
Impactor velocities (m/s)				
1.7	3.5	8.9	17.7	

Supports were modeled by blocking nodes displacement ($u_z = 0$) along two lines, representing the cylinders, set parallel to the fiber in the 0° direction. The numerical model used for the simulations is represented in Figure 2.

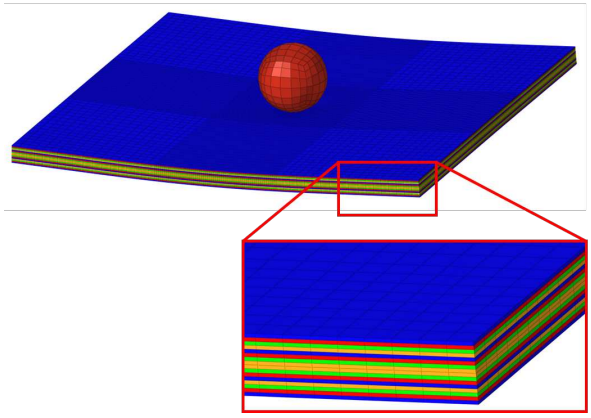

Figure 2. Numerical model for the impact simulations

A fine mesh was used for elements in the center of the model (where most of the delamination takes place) and became coarser further from the center. This mesh size was determined by approximating the cohesive zone length, which corresponds to the size of the process zone where damage occurs. An approximation presented in [15] was used and displayed in Eq.2.

$$l_{cz} = \frac{E_t G_{Ic}}{\sigma_0^2} \tag{2}$$

  doi:10.5075/epfl-298799_978-2-9701614-0-0

In this equation, l_{cz} is the cohesive zone length, and with our values for E_t, G_{Ic} and σ_{0N}, we obtain a cohesive zone length of $1.67\ mm$. It is recommended to have a mesh size at least three times smaller than this value, leading to a sufficient mesh size of $0.5\ mm$. This value was confirmed after conducting a sensibility analysis.

4. Results

4.1 Influence of impactor velocity and layup

The influence of impactor velocity and layup on delamination was first studied. This was done so that it could be isolated in further studies where strain rate effects will be implemented. Looking at the results on each layup for the different impactor velocities, a clear trend appears for the dissipated energy in the interfaces due to delamination: as the impactor velocity increases, the dissipated energy increases too. This is clearly visible for unidirectional layup as shown is Figure 3. This is however not the case for quasi-isotropic layups where the total delaminated area stayed almost constant over the range studied, as seen in Figure 4.

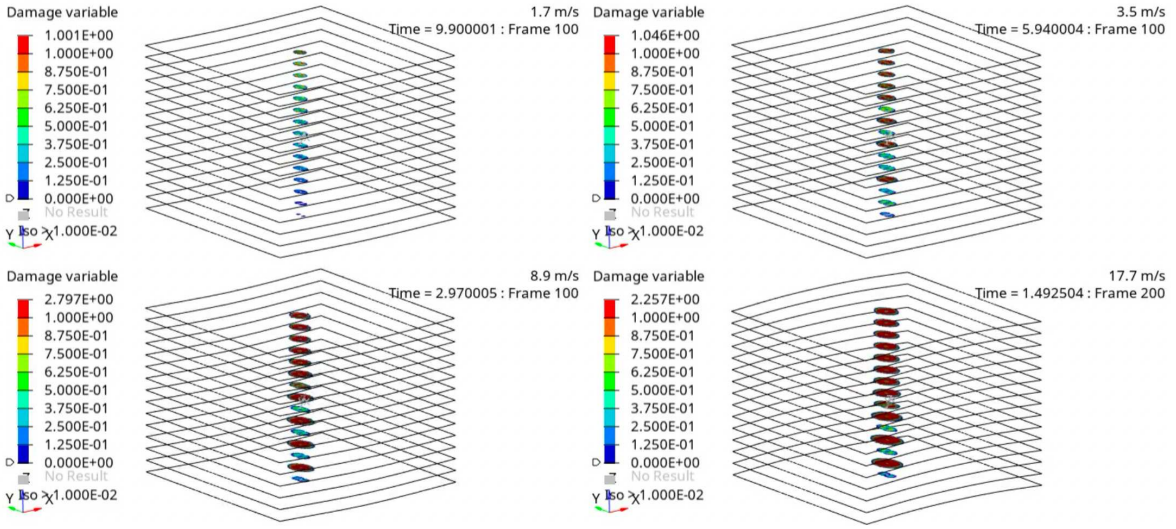

Figure 3. Delamination on a $[0_{16}]$ composite with increasing impactor velocity

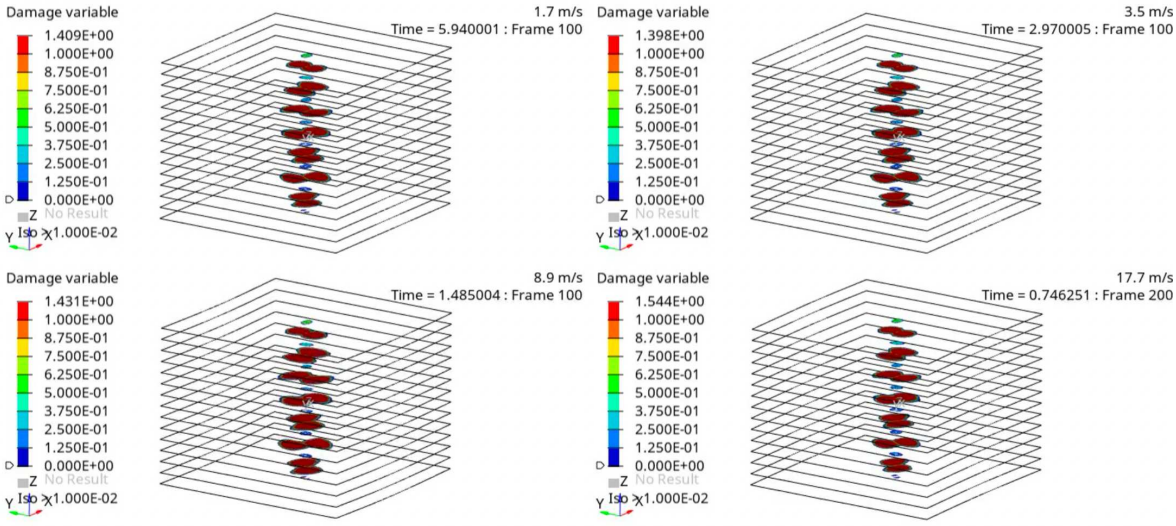

Figure 4. Delamination on a $[(45/90/-45/0)_2]_s$ composite with increasing impactor velocity

  doi:10.5075/epfl-298799_978-2-9701614-0-0

The layup also has a strong influence on delamination. Based on the orientation of the plies, the delamination orientation and shape changes. But it has also been observed that when the layup rigidity increases, so does the dissipated energy. This tendency is clearly visible in Figure 5.

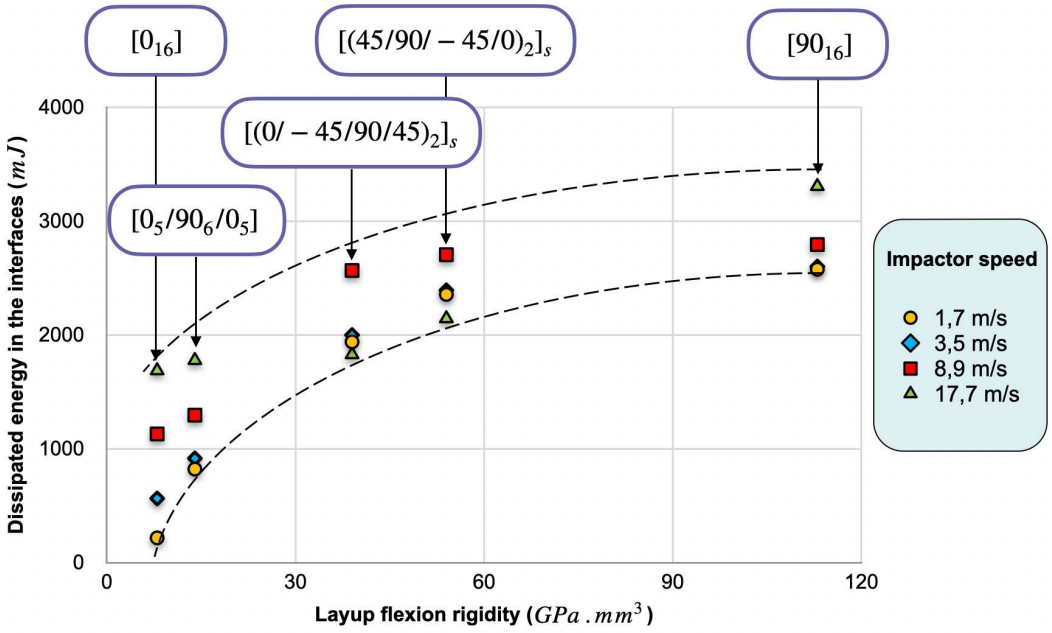

Figure 5. Impactor velocity and layup influence on delamination

4.2 Influence of friction between the plies

A second law based on the work of Camanho and Dávila [16] was implemented in a User Subroutine to be then used in the explicit solver Radioss. This law implements better coupling definition for mixed modes loading as well as introducing damage instead of plasticity.

The initiation displacement δ_0 (indicating the start of damage) is determined through a quadratic formula (Eq. 3), with indices N and S corresponding to normal and shear loading respectively:

$$\left(\frac{\sigma_N}{\sigma_{0N}}\right)^2 + \left(\frac{\sigma_S}{\sigma_{0S}}\right)^2 = 1 \tag{3}$$

The final displacement δ_c,corresponding to rupture of the interface, is then deduced through a power law criterion defined in Eq. 4:

$$\left(\frac{G_I}{G_{Ic}}\right)^\alpha + \left(\frac{G_{II}}{G_{IIc}}\right)^\alpha = 1 \tag{4}$$

Damage evolution is then given by:

$$d = \frac{\delta_c}{\delta} \cdot \frac{\delta - \delta_0}{\delta_c - \delta_0} \tag{5}$$

Finally, the stresses can be computed:

$$\sigma = K(1-d).\delta \tag{6}$$

  doi:10.5075/epfl-298799_978-2-9701614-0-0

Using this new law, delaminations appeared to become asymmetrical. This was unexpected, considering every component of the model (mesh, boundary conditions) are all symmetrical. Adding a general surface/surface contact with penalty and a Coulomb friction coefficient showed a strong influence on delamination symmetry. Increasing the friction coefficient brought symmetry to the delaminations as shown in Figure 4.

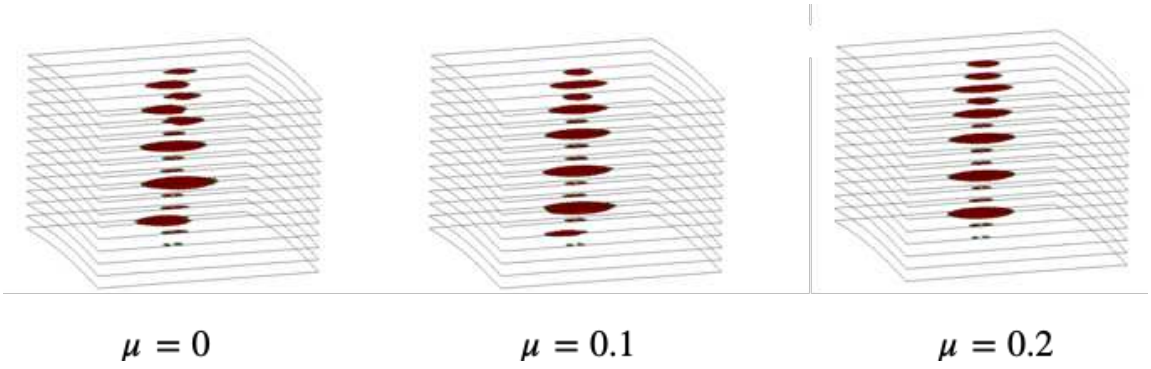

Figure 6. Influence of friction coefficient μ on delamination on a $[0_{16}]$ layup

On top of gaining symmetry, friction also changes the delamination shapes, which has also been noted by other authors [17]. This result led us to believe the use of friction between plies could help with instabilities, as well as give better results.

5. Conclusion

The main goal of this study was to isolate effects of impactor velocity and strain rate before introducing strain rates in the material laws. It has been shown that layup greatly changes how the impactor velocity influences the delamination. Moreover, a difference appears between quasi-isotropic layups and the other layups. This behavior remains however to be seen when a more realistic ply behavior is introduced. Two different ply models are being implemented in our simulations: an elastoplastic model available in Radioss (COMPSH) and a viscoelastic model with damage developed at ONERA called OPFM [18] (ONERA Ply Failure Model). Comparison between these models and with the current results are our primary focus. Strain rate effects will then be introduced in both the ply and the interface models.

Friction influence on simulation stability and delamination shape is obvious in the results obtained. An improvement currently in the works is the inclusion of friction in the cohesive law. A formulation based on the work of Alfano and Sacco [19, 20] is currently studied and its influence will be covered in future work.

6. References

1. Trousset E. Prévision des dommages d'impact basse vitesse et basse énergie dans les composites à matrice organique stratifiés. ENSAM; 2013
2. Guinard S, Allix O, Guédra-Degeorges D, Vinet A. A 3D damage analysis of low-velocity impacts on laminated composites. Composites Science and Technology. 2002; 62(4):585-9.
3. Lopes C, Seresta O, Coquet Y, Gürdal Z, Camanho P, Thuis B. Low-velocity impact damage on dispersed stacking sequence laminates. Part I: Experiments. Composites Science and Technology. 2009; 69(7-8):926-936.

  doi:10.5075/epfl-298799_978-2-9701614-0-0

4. Aliyu AA, Daniel IM. Effects of strain rate on delamination fracture toughness of graphite/epoxy. Delamination and Debonding of Materials. 1985.
5. You H, Yum YJ. Loading Rate Effect on Mode I Interlaminar Fracture of Carbon/Epoxy Composite. Journal of Reinforced Plastics and Composites. 1997; 16(6):537-49
6. Cantwell WJ. The influence of loading rate on the mode II interlaminar fracture toughness of composite materials. Journal of Composite Materials. 1997; 31(14):1364-80
7. Berger L, Cantwell WJ. Temperature and Loading Rate Effects in the Mode II Interlaminar Fracture Behavior of Carbon Fiber Reinforced PEEK. Polymer Composites. 2001; 22(2):271-81
8. Smiley AJ, Pipes RB. Rate effects on mode I interlaminar fracture toughness in composite materials. Journal of Composite Materials. 1987 Juillet; 21
9. Chapman TJ, Smiley AJ, Pipes RB. Rate and temperature effects on mode II interlaminar fracture toughness in composite materials. In: ICCM6/ECCM2. London, UK; 1987.
10. Zabala H, Aretxabaleta L, Castillo G, Aurrekoetxea J. Loading rate dependency on mode I interlaminar fracture toughness of unidirectional and woven carbon fibre epoxy composites. Composite Structures. 2015; 121:75-82
11. Dagorn N, Portemont G, Joudon V, Bourel B. Fracture rate dependency of an adhesive under dynamic loading. Engineering Fracture Mechanics. 2020; 235
12. Ekhtiyari A, Alderliesten R, Shokrieh MM. Loading rate dependency of strain energy release rate in mode I delamination of composite laminates. Theoretical and Applied Fracture Mechanics. 2021; 112
13. Gillespie Jr JW, Carlsson LA, Smiley AJ. Rate-Dependent ModeI Interlaminar Crack Growth Mechanisms in Graphite/Epoxy and Graphite/PEEK. Composites Science and Technology. 1987; 28:1-15
14. Tsai JL, Guo C, Sun CT. Dynamic delamination fracture toughness inunidirectional polymeric composites. Composites Science and Technology. 2001; (85):87-94.
15. Turon A, Dávila CG, Camanho PP, Costa J. An engineering solution for mesh size effects in the simulation of delamination using cohesive zone models. Engineering Fracture Mechanics. 2007; 74:1665-82
16. Camanho PP, Dávila CG. Mixed-mode decohesion finite elements for the simulation of delamination in composite materials. NASA; 2002. TM211737
17. Su Z, Wu F. Simulation for laminate's Delamination under out-of-Plane Impact with Modification of Interface Friction Effect. Applied Composite Materials. 2019
18. Laurin F, Carrere N, Huchette C, Maire JF. A multiscale hybrid approach for damage and final failure predictions of composite structures. Journal of Composite Materials. 2013; 47(20-21):2713-47
19. Alfano G, Sacco E. Combining interface damage and friction in cohesive-zone model. International Journal for Numerical Methods in Engineering. 2006 10; 68:542 582
20. Catalanotti G, Furtado C, Scalici T, Pitarresi G, van der Meer F P, Camanho P P. The effect of through-thickness compressive stress on mode II interlaminar fracture toughness. Composite Structures. 2017; 182:153-63

  doi:10.5075/epfl-298799_978-2-9701614-0-0

MODELLING THE FORMING OF TAILORED FIBRE PLACEMENT PREFORMS ON A TETRAHEDRAL PUNCH

Jessy, Simon[a], Nahiene,Hamila [b], Christophe, Binétruy[a], Sébastien, Comas-Cardona[a]

a: Nantes Université, Centrale Nantes, GeM, UMR CNRS 6183, 1 rue de la Noë, Nantes, 44321, France
b: ENI Brest, IRDL, UMR CNRS 6027, F-29200 , Brest, France
hamila@enib.fr

Abstract: *The experimental and numerical forming of a Tailored Fibre Placement preform on a tetrahedral punch with orthotropic final orientation is addressed. The forming simulation is based on a finite element model where the fibre tows are modelled explicitly using beam elements. The stitching yarn, which is implicitly modelled, is supposed to act as a hinge connection between intersecting fibre tows of adjacent layers. An embedded element formulation is implemented to model the hinge connection which allows meshing independently the fibre tows in the adjacent layers. Optical measurements are carried out to measure the inter-layer angles on one face of the tetrahedron. The simulation results show good agreement with the experimental one. This work demonstrates the ability to combine the TFP technology and forming to manufacture doubly-curved part with orthotropic final orientations.*

Keywords: Tailored Fibre Placement; Forming; Preform; Embedded element;

1. Introduction

Reducing production costs and its environmental impact while maintaining or increasing the mechanical properties of engineered fibre-reinforced composite (FRC) parts is the challenge faced by aeronautic, automotive or energy industrie. Manufacturing 3D optimized FRC requires exploiting the potential of fibrous reinforcements by taking full advantage of the intrinsic anisotropy of fibres. Optimization of parts made from conventional textiles obtained by weaving, knitting or stitching often lead to quasi-isotropic parts due to the complexity of the loading path and the intrinsic limitation of unidirectional reinforcements' stacking. Fibre placement technologies like Automated Fibre Placement (AFP), Continuous Tow Shearing (CTS) or Tailored Fibre Placement (TFP) technologies are a class of additive manufacturing process that allow the manufacture of nearly net-shape preforms with continuously varying orientations and thickness by depositing fibres only where necessary.

More precisely, flat TFP preforms are made of one continuous tow laid down on a backing material and following prescribed curvilinear paths. This tow remains in place thanks to a zigzag stitching. TFP offers a large choice of combinations for the backing material, fibre tows and stitching yarn. A single TFP preform can be made of several tow materials and the backing material can be a polymer film or woven or non-woven fabrics for example. Dry or commingled tow is used depending on the forming process involved. The stitching yarn material is usually polyester although higher performance materials are possible. This technology allows a whole

  doi:10.5075/epfl-298799_978-2-9701614-0-0

preform to be manufactured or can be used to locally reinforce a flat preform made of a conventional textile.

During forming, fibre motion inevitably occurs. The proposed work focused on modelling the forming of flat TFP preforms using the finite element method. To the best of the authors' knowledge, this is the first contribution to the numerical forming of flat TFP preforms. Some works [1, 2] investigated the experimental folding of flat TFP preforms or the influence of cuts in the backing material to avoid formability issues for complex varying orientations on doubly-curved shapes [3]. In this work, 2-layer TFP preforms without backing material are considered. To validate the proposed modelling strategy and highlight the advantages of combining TFP preform with forming, a dry TFP preform is formed on a tetrahedral punch both experimentally and numerically. The design of the TFP preform allows obtaining orthotropic final configurations which is impossible using conventional textiles.

2. Semi-discrete model of the TFP preform

2.1 TFP preform characteristics

A TFP preform is composed of a continuous fibre tow whose cohesion is ensured by a stitching yarn. Non-Crimp Fabrics (NCF) are conventional textiles whose architecture is most similar to TFP preforms that can be considered as a generalization of NCF to multi-directional plies.

The fibre tows constitute the core of the reinforcement. They have a preponderant tensile stiffness and a low bending stiffness. The latter has to be taken into account for an accurate prediction of wrinkles during forming [4].

The stitching yarn is responsible for the cohesion between adjacent layers. This cohesion depends on the stitching length, width and tension which are manufacturing parameters. The stitching yarn is generally made of polyester but higher performance material such as aramid can be used for a better through-the-thickness reinforcement. In the proposed model, it is assumed that the stitching yarn remains during forming (it does not melt).

2.2 Objectives of the modelling

Accurate prediction of the final fibre orientations and distribution in the final 3D part are the main objectives of the modelling. Since TFP offers a high degree of design freedom, the model must allow for all its capabilities, such as curvilinear fibre placement and heterogeneity of the fibre tow density.

2.3 Explicit discretization of the fibre tows

To take into account the main feature of TFP preforms, namely, the continuous varying orientations, the fibre tows are modelled explicitly with 1D elements. More precisely, beam elements are used to take into account the bending stiffness required to predict defect such as wrinkles. A 2-node shear-flexible beam as formulated by [5, 6, 7] is implemented. Since a fibre tow is not a continuum medium, uncoupled generalized stress stiffnesses are used. Therefore, the forces $\vec{F}$ and moments $\vec{M}$ of the cross-section are related to the strains $\vec{\Gamma}$ and curvatures $\vec{\mathrm{K}}$ by the following equation:

$$\vec{F} = \begin{bmatrix} C_E & 0 & 0 \\ 0 & C_{G_1} & 0 \\ 0 & 0 & C_{G_2} \end{bmatrix} \vec{\Gamma} \qquad \vec{M} = \begin{bmatrix} C_T & 0 & 0 \\ 0 & C_{K_1} & 0 \\ 0 & 0 & C_{K_2} \end{bmatrix} \vec{\mathrm{K}} \tag{1}$$

where C_E is the tensile stiffness, $C_{G_1}$and $C_{G_2}$are the transverse shear stiffnesses, C_T is the torsional stiffness and C_{K_1} and C_{K_2} are the bending stiffnesses.

2.3 Implicit modelling of the stitching yarn

Modelling explicitly the stitching yarn would require high computational efforts to model the contact interactions with the beam elements representing the fibre tows. Since the stitching yarn ensures a strong cohesion of the fibre tows between adjacent layers, it is modelled implicitly using an embedded element formulation. This approach assumes that fibre tows of adjacent layers which intersect each other are bonded together at their intersection. Consequently, the fibre tows of the second layer are embedded by the fibre tows of the first layer. Fig.1 illustrates the proposed model considering two fibre tows of adjacent layers which intersect. The bonding between intersected fibre tows is modelled as a hinge connection. To mesh independently the adjacent layers, an embedded formulation is used and briefly presented hereafter.

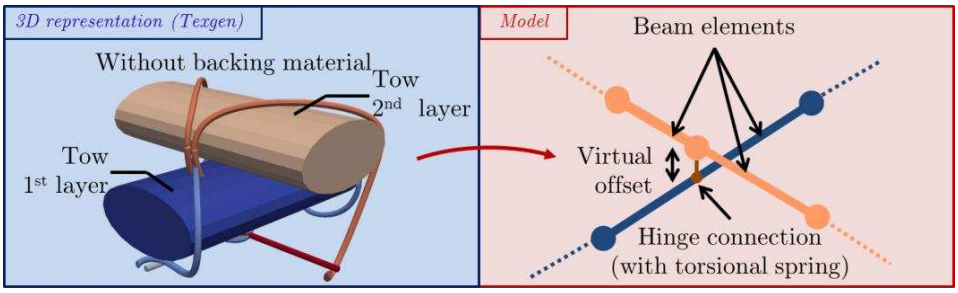

Figure 1. Representation of the TFP preform model

The embedded element approach has been applied to the modelling of fibre-reinforced concrete [8] but also to simulate forming of interlock fabrics [9]. This strategy consists in embedding a body of lower dimension (embedded body) into a body of higher dimension (host body). In a finite element model, the position of a node $\overrightarrow{x^e}$ discretizing the embedded body is defined from the nodes of the host element in the host body according to this equation:

$$\overrightarrow{x^e} = \sum_i N_i(\vec{\chi})\, \overrightarrow{x_i^h} \tag{2}$$

where $\overrightarrow{x_i^h}$ and N_i are the position and shape function of the i^{th} node of the host element. The natural coordinates $\vec{\chi}$ of the embedded node is determined during the meshing procedure.

Therefore, an embedded node is kinematically driven by its host element. As a consequence of this kinematic constraint, the internal forces at the embedded node are transferred to the host element nodes. Therefore, the internal forces of a host node $\vec{F}_{int}^h$ are composed of the contribution from the material behavior of the host element $\vec{F}_{int}^{hb}$ and the contribution from the embedded node $\vec{F}_{int}^{he}$ as expressed in Eq.3:

$$\vec{F}_{int_i}^h = \vec{F}_{int_i}^{hb} + \vec{F}_{int\_i}^{he} \tag{3}$$

  doi:10.5075/epfl-298799_978-2-9701614-0-0

where: $\vec{F}^{he}_{int\_i} = \sum_k N_i(\vec{\chi})\ \overrightarrow{F^e_{int_k}}$ is the sum of the contribution from the k-embedded nodes.

The transfer of internal forces is illustrated in Fig.2. Since a hinge connection is used for the bonding between intersecting fibre tows, only the internal forces associated to the displacement degrees of freedom are transferred to the host element nodes. Consequently, the rotation degrees of freedom of the beam elements are independent from the host element. To take into account the resistance to the rotation between intersecting fibre tows due to the friction and the stitching yarn, a linear torsional spring is added at the intersection.

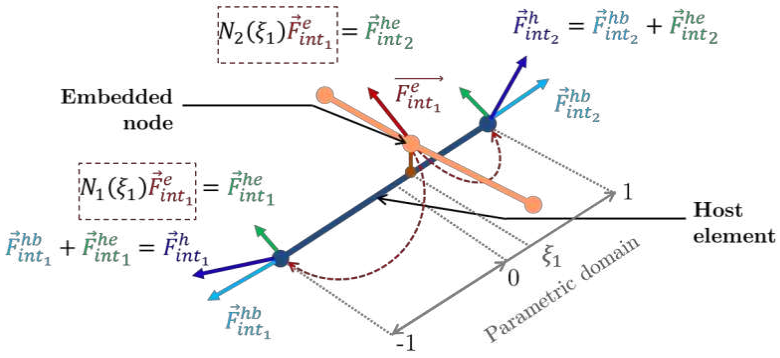

Figure 2. Transfer of the internal forces of the embedded node to the host element nodes

3. Experimental forming

3.1 Materials

The 2-layer preform is made of 2690 tex PET/Eglass continuous tow (from P-D-Glasseiden GMBH, Oschatz, Germany) stitched with using a 24 tex PET stitching yarn (Serafil fine, Amman). A water soluble polyvinyl alcohol (PVA) film (Gunold® Solvy film 80, Stecker) was used as backing material for the stitching before being washed out. The TFP preform has been manufactured at IRT Jules Verne using the TFP ZSK © CMCW 0200-900D-2500 embroidery machine. A stitching length and width of 2.5 mm were used.

3.2 Forming device

The forming device is composed of a tetrahedral punch mounted on the cross head of a universal testing machine (AG-Xplus by Shimadzu). Two square plates (550 mm x 550 mm x 10 mm) made of poly(methyl methacrylate) were used as blank-holder. One plate is fixed to a metallic frame and the other is placed directly onto the preform. A pin system prevents the movable plate of the blank-holder from moving in the plane. No pressure is applied on the movable plate so that only its weight is distributed on the TFP preform at the contact surface. The punch consists of a tetrahedral part, which is 120 mm high, and a 20 mm thick base. The punch controlled by the testing machine has a stroke of 140 mm with a speed of 15 mm/min.

3.3 Measurements

Quantitative measurements were carried out to compare the results with the forming simulations presented in section 4. A camera positioned along the displacement axis of the punch takes a picture every 2 mm. The camera allows visualizing the 2D displacement field orthogonal to the punch displacement. An EOS Canon Mark II camera was used with a constant focal length of 15 mm and initially set at 52 mm from the TFP preform. At the end of

  doi:10.5075/epfl-298799_978-2-9701614-0-0

the experiment, a picture was taken after placing the camera according to the normal of one of the face of the tetrahedral punch. This picture allows measuring the final angles between the two layers on one side of the part. Red-ink markers were drawn and an image processing algorithm using sparse optical flow was used to compute the 2D field displacement orthogonal to the punch stroke.

3.4 Results

The final configuration of the TFP preform is shown in Fig.3 (left). No defects such as wrinkles or fibre slippage were observed. Fig.3 (right) shows the 2D displacement field. The angles between the layers on one face have been computed. Fig.4 (right) shows the distribution of these angles around 90°. Considering a normal distribution of the angles, a mean angle of 90.72° with a standard deviation of 4.31° is obtained. However, parallel fibre tows are present in the middle of the faces (Fig.4 (left)) due to the chosen deposition strategy of the layers. It was noticed too late that this orientation defect can be eliminated by modifying the deposition strategy without impacting the initial orientations in the rest of the preform.

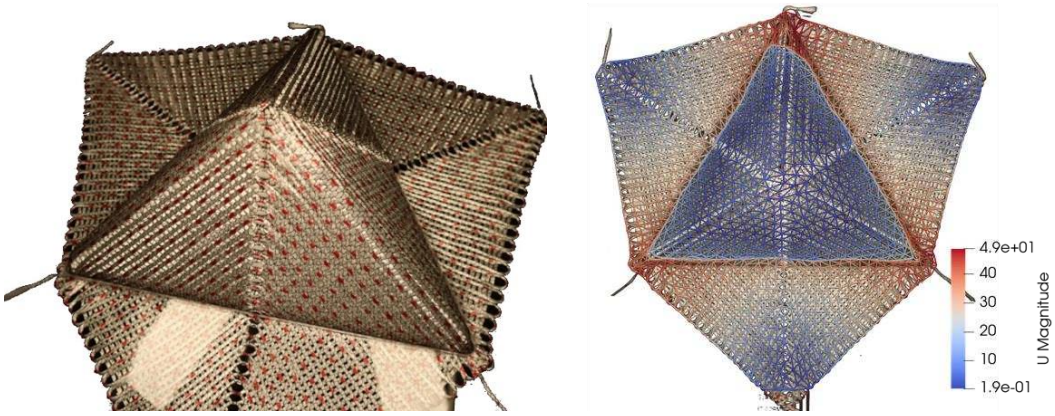

Figure 3. Final configuration of the tetrahedral forming (left) and 2D displacement (mm) (right)

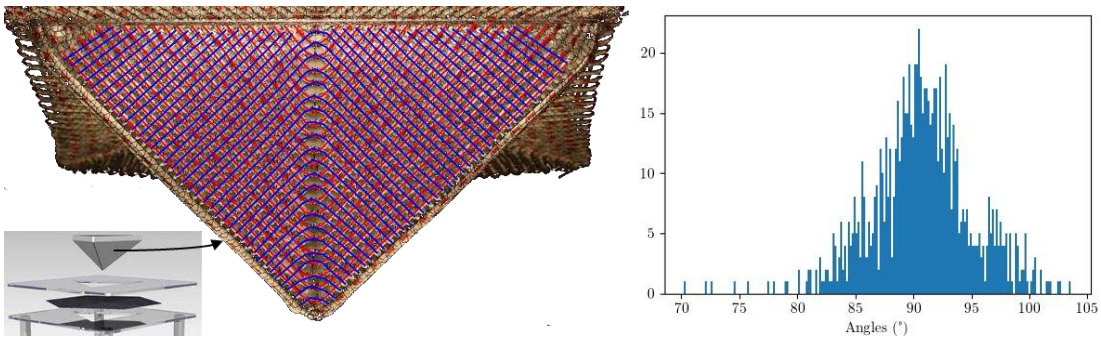

Figure 4. Final fibre tows orientation on one face: layer 1 (blue color), layer 2 (red color) (left) and inter-layer angle distribution (right)

4. Simulation

4.1 Material parameters

The TFP preform model depends on seven material parameters. The beam element required six material parameters, namely, the tensile stiffness (C_E), the transverse shear stiffnesses C_{G_1}, C_{G_2}), the torsional stiffness (C_T) and the bending stiffnesses (C_{K_1}, C_{K_2}). Besides, the linear

coefficient of the torsional springs at intersections between fibre tows of different layers is C_{T_s}. Due to a lack of resources, the characterization of these material parameters has not been carried out. Consequently, the values of the material parameters given in Table 1 have been estimated and are supposed to give an acceptable order of magnitude. In particular, the tensile stiffness C_E is estimated from the Young's modulus of E-glass fibres taken equal to 72.5 GPa. The value of the transverse shear stiffness is taken as half the value of the axial stiffness. The torsional and bending stiffness have non zero but low values.

Table 1: Material parameters of the finite element model.

Parameter	C_E	C_{G_1}	C_{G_2}	C_T	C_{K_1}	C_{K_2}	C_{T_s}
Value	1400	700	700	1	0.1	0.1	1
Unit	kN	kN	kN	kN.mm²	kN.mm²	kN.mm²	N.mm

4.2 Finite element model

Layer 1 is first meshed with an element size of 2.5 mm. Then, layer 2 is meshed with the same element size and nodes are appended at intersections with the first layer. These additional nodes are embedded in the corresponding host elements of layer 1. The adjacent nodes of the nodes located at the intersections are deleted if the element size is lower than half the initially prescribed size. The total number of beam elements is 22190 and the simulation runs in 12 hours using four cores of an Intel(R) Core(TM) i7-8750H CPU 2.20GHz processor. The friction coefficient between the fibre tows and the forming tools is equal to 0.2, even though it might be different since the blank-holders are made of PMMA and the punch of PLA. A displacement of 140 mm is imposed to the punch. Regarding the blank-holder, the fixed part is clamped and the movable part can only move along the punch axis.

4.3 Results

Fig.5 shows the final angles between the two layers on a face of the tetrahedral shape. The angles are very close to 90° at every position on the face. Fig.6 shows the final configuration of the simulation which is superimposed on the experimental result. The predicted contour matches well the experimental one. In the TFP path of the simulation, the curved paths connecting the straight ones have been removed for simplicity. It might contribute to the differences observed between the contours.

5. Conclusion

The forming of dry and thin TFP preforms without backing material has been investigated both experimentally and numerically on a tetrahedral shape. It was shown that an orthotropic final configuration, which cannot be achieved using conventional textiles, can be obtained by combining TFP and forming. Therefore, this work demonstrates the ability to improve the mechanical properties of structural part using TFP preform forming.

A finite element model of TFP preforms is proposed and based on an embedded element formulation where the stitching yarn acts as a bond between intersecting fibre tows of adjacent layers. The fibre tows are modelled using beam elements with independent

  doi:10.5075/epfl-298799_978-2-9701614-0-0

generalized stress stiffnesses. The fibre tows of the next layer are embedded in the tows of the previous layer. The model assumes quasi-inextensibility of the fibre tows and no slip between the components of the TFP preform. The forming simulations of the tetrahedral shape gave results in good agreement with the experimental ones.

The modelling strategy proposed in this work allows the modelling of TFP preforms without backing material. However, it would also be interesting to investigate the forming of preforms made from conventional textiles that are locally reinforced with TFP. For instance, continuous tows can be added in some regions to remove stress concentration, especially around holes. Stitching a continuous tow on top of conventional textiles will modify their behaviour during forming and could lead to defects. Consequently, extending the proposed work to TFP preforms with backing material is a challenge to be addressed.

In the example addressed in this work, the determination of the flat TFP pattern leading to an orthotropic configuration in the final 3D parts was achieved intuitively. To address the orthotropic design of parts with even more complex geometries, a numerical method performing the "flattening" of the 3D orthotropic design needs to be developed. An interesting approach has been proposed in [10] which is based on the reverse numerical modelling of double diaphragm forming and was applied to a single layer CTS preform.

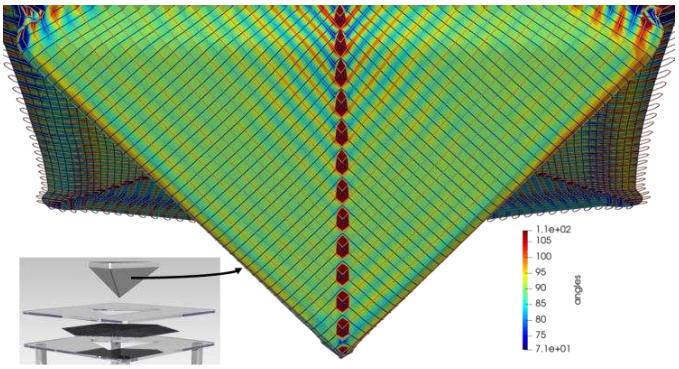

Figure 5. Inter-layer angles in the final configuration of the simulation displayed on a surface mesh built from triangulation of the intersections of the fibre tows

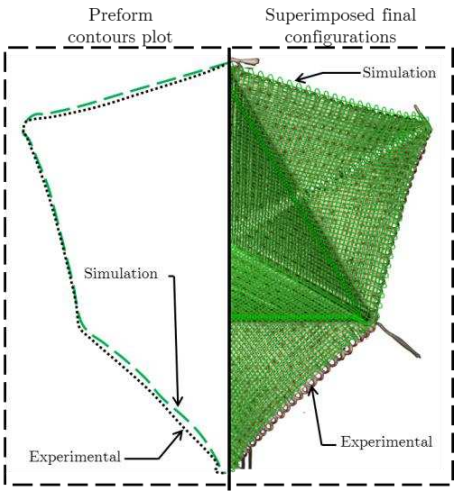

Figure 6. Comparison of the final preform contour

Acknowledgements

This work was funded by IRT Jules Verne as part of the Ph.D program PERFORM.

6. References

1. Fial, J, Harr, M, Böhler, P, Middendorf, P, 2018. Automated wet compression moulding of load-path optimised TFP preforms with low cycle times. IOP Conference Series: Materials Science and Engineering 406, 012018.
2. Rihaczek, G, Klammer, M, Başnak, O, Petrš, J, Grisin, B, Dahy, H, Carosella, S, Middendorf, P., 2020. Curved Foldable Tailored Fiber Reinforcements for Moldless Customized Bio-Composite Structures. Proof of Concept: Biomimetic NFRP Stools. Polymers 12, 2000.
3. Takezawa, M, Otoguro, Y, Matsuo, K, Shibutani, T, Sakurai, A, Maekawa, T, 2021. Fabrication of doubly-curved CFRP shell structures with control over fiber directions. Computer-Aided Design 136, 103028.
4. Hamila N, Boisse P, Sabourin F, Brunet M. A semi-discrete shell finite element for textile composite reinforcement forming simulation. International Journal for Numerical Methods in Engineering. 2009;79(12):1443-66.
5. Géradin M, Cardona A. Flexible Multibody Dynamics: A Finite Element Approach. New York: Wiley–Blackwell; 2001. 340 p.
6. Ibrahimbegović A, Frey F, Kožar I. Computational aspects of vector-like parametrization of three-dimensional finite rotations. International Journal for Numerical Methods in Engineering. 15 nov 1995;38(21):3653-73.
7. Ritto-Corrêa M, Camotim D. On the differentiation of the Rodrigues formula and its significance for the vector-like parameterization of Reissner-Simo beam theory: DIFFERENTIATION OF RODRIGUES FORMULA. International Journal for Numerical Methods in Engineering. 30 nov 2002;55(9):1005-32.
8. Cunha VMCF, Barros JAO, Sena-Cruz JM. A finite element model with discrete embedded elements for fibre reinforced composites. Computers & Structures. mars 2012;94-95:22-33.
9. De Luycker E, Morestin F, Boisse P, Marsal D. Simulation of 3D interlock composite preforming. Composite Structures. mai 2009;88(4):615-23.
10. Sun X, Belnoue JPH, Wang WT, Kim BC, Hallett SR. “Un-forming” fibre-steered preforms: Towards fast and reliable production of complex composites parts. Composites Science and Technology. nov 2021;216:109060.

  doi:10.5075/epfl-298799_978-2-9701614-0-0

INVESTIGATION OF NOVEL FE-BASED MODELING APPROACHES FOR STIFFENED CFRP AIRCRAFT STRUCTURES

L. Reichert[a], T. Tiemann[b], C. Schmidt[b], S. Heimbs[a], P. Horst[a]

a: Institute of Aircraft Design and Lightweight Structures, Technische Universität Braunschweig, Ottenbecker Damm 12, 21684 Stade, Germany
Email: lisa.reichert@tu-braunschweig.de
b: Institute of Production Engineering and Machine Tools, Leibniz Universität Hannover, Ottenbecker Damm 12, 21684 Stade, Germany

Abstract: *Reduced representations of stiffened shell structures are required for an efficient FE-based evaluation of different unconventional fuselage stiffener layouts for example in layout optimizations. The use of omega profiles adapted to fiber placement technologies introduces additional challenges. Three different modeling approaches are introduced, each combining a numerical and an analytical model. Two approaches are based on existing numerical models and are combined with analytical models. In the novel third approach, extra shell elements to explicitly model the width of the omega stiffener are added. In an evaluation, the calculated displacements of four characteristic load cases for different wide omega profiles are compared to a reference. The results show small deviations for the new modeling approach. Under tension and bending loads, mean deviations below 1 % are achieved. For torsional loads, the mean deviation can be reduced to 3 % compared to 30 % using a conventional approach.*

Keywords: omega stiffener; fuselage structure; composite design; FE-modeling, shell structures

1. Introduction

The aircraft industry in particular has set high emission targets for itself. Going along with a general trend toward lightweight design in all areas of transportation, efforts to reach these targets rely on an increased use of lightweight materials, primarily carbon fiber-reinforced plastics (CFRP) and new structural layouts, specifically adapted to local loads. The application of these changes to stiffened aircraft structures such as the fuselage causes an increasing complexity in the design of these structures as well as in the design process.

The use of CFRP in itself causes an increase in design parameters due to the necessary layup design. By deviating from the conventional black-metal design approach and adapting the structure to CFRP requirements, even more design parameters are introduced. An example of this is the double curved stiffener described by Kolesnikov et al. (1). The reconfiguration of stiffener layouts provides another way to reduce the structural weight both dependent and independent of the material. Current research into novel stiffener layouts mainly focuses on specific types of periodical grid structures such as anisogrid structures described by Belardi et al. (2) and Boldyrev et al. (3), or orthogrid structures as analyzed by Deniz et al. (4). To be able to efficiently compare different configurations and expand research into non-periodical structures, the computational efforts of the finite element (FE)-models on a panel level have to be reduced as much as possible without significant loss of accuracy. An example of a current

  doi:10.5075/epfl-298799_978-2-9701614-0-0

model used for the analysis of a specific unconventional layout can be seen in Figure 1a). This model is built up from a high number of shell elements to accurately represent the complex geometry.

In general, the computational effort can be decreased by reducing the degrees of freedom (DOF) of the model. This is achieved by reducing the number of elements itself but also by reducing the DOFs per element by combining them with analytical models to derive simplified structural properties from the detailed geometry. The most common approach for setting up such a reduced model relies on substituting one beam element for each stiffener and one shell element for each skin segment. Grihon (5) applies this approach in the early design process to analyze trade-offs between different stiffener geometries on a fuselage level. Schuster et al. (6) apply this concept in a multidisciplinary design optimization of a complete aircraft structure. Another approach is described by Nemeth (7), where an ABD matrix is set up for general stiffeners, based on beam theory, which can be used to add a smeared influence of the stiffener to the skin and model both components using shell elements in the skin plane. This approach is used by Dähne and Hühne (8, 9) to optimize the orientation of blade stiffeners on a wing panel.

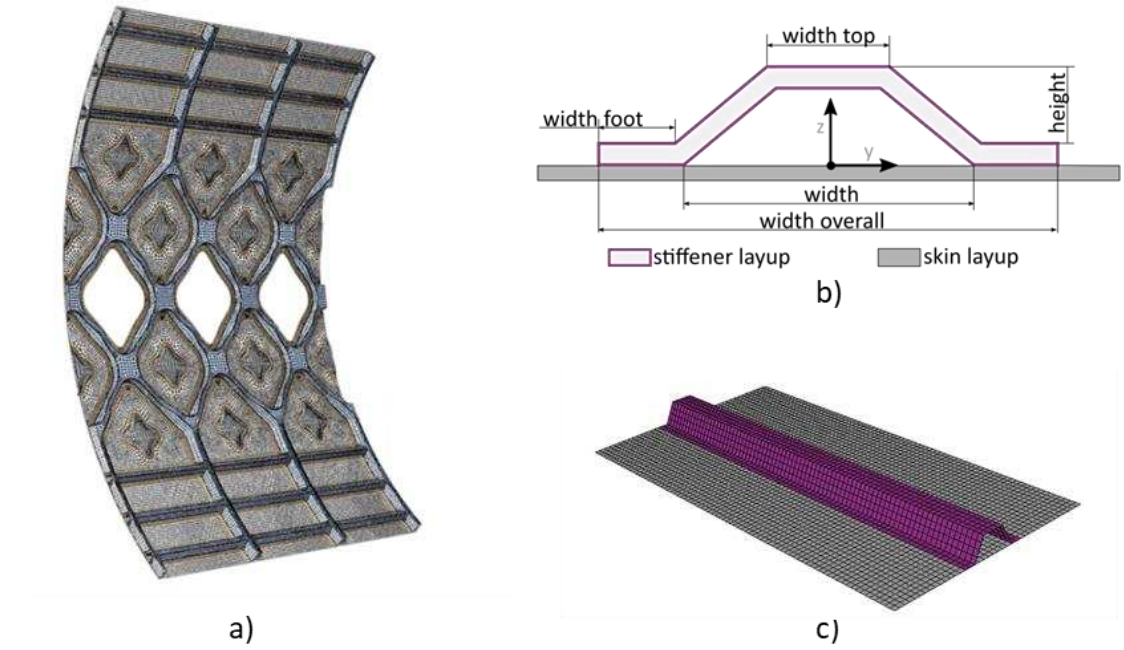

Figure 1. Omega stiffener in a grid structure (a), parameters of the omega profile (b) and the detailed FE-model used as a frame of reference (c).

A typical profile used for unconventional grid structures is an omega profile as shown in Figure 1b). This profile differs in certain key characteristics from conventional profile shapes such as I- and Z-profiles. The width is typically higher and, therefore, the interaction with the skin more complex. For this study, the focus is placed on extra wide omega profiles (width up to 100 mm). This is done to address manufacturing challenges resulting from typically highly integrated grid designs and by designing the profiles according to manufacturing constraints of an automated fiber-placement process. For a representative grid stiffener length of 400 mm this violates the fundamental beam assumption of a small cross-section in comparison to the length. Additionally, the omega profile forms a closed profile in combination with the skin underneath, prohibiting a straight-forward application of analytical equations derived from beam theory.

  doi:10.5075/epfl-298799_978-2-9701614-0-0

The applicability of the simple beam approach to standard omega profiles was already analyzed by Reichert et al. (10). It showed good results under tensile and bending loads, torsion and shear were not considered. In this work, a novel reduced FE-model for a wide omega stiffener on a skin segment is introduced and compared to existing approaches, which are adapted to the specific requirements of the omega profile. Each modeling approach consists of a numerical and an analytical part. The numerical modeling approach describes, which and how many FE-elements are used for the model. Depending on this approach, different parameters are required to completely define the model. These parameters are derived from the detailed geometry using the analytical models. The different modeling approaches are applied to a series of differently sized omega profiles and assessed by their ability to model the structural behavior under characteristic loads.

2. Different Modeling Approaches

2.1 Conventional Beam Approach

The first modeling approach is based on the conventional beam approach. A single beam element is used to model the omega stiffener, including the foot section but excluding the skin underneath. This part of the skin is included in the two shell elements on both sides of the stiffener, representing the skin segment. The resulting FE-model is shown in Figure 2, along with the partitioning of the detailed structure. The analytically calculated mechanical properties used to define each FE-element are also indicated. All analytical models use beam theory and assume thin-walled profiles. The different stiffness parameters for the profiles are calculated using the equations set up by Krieglsteiner et al. (11) unless specified otherwise. For now, it is assumed that the shear center coincides with the elastic center ($c_e = c_s$).

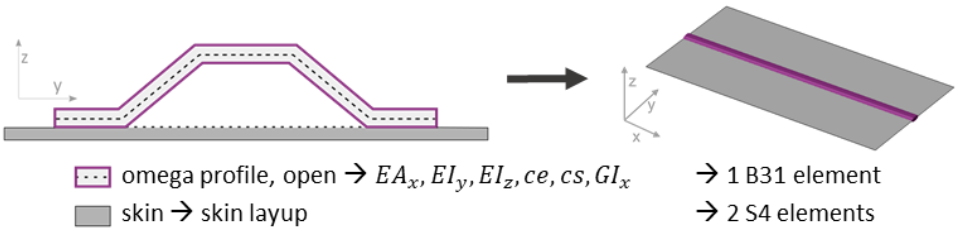

Figure 2. Analytical basis and resulting FE-model for the conventional beam approach.

In this conventional beam approach, most of the equations can be applied directly to the omega profile. A slight adaption is only necessary to calculate the torsional stiffness. For the torsional stiffness, a differentiation between open and closed profiles is necessary as closed profiles have a significantly higher stiffness. Applying the torsional stiffness of the open omega profile and, thereby, neglecting the fact that it forms a closed profile with the skin would significantly underestimate the torsional stiffness in the reduced model. The torsional stiffness of a closed profile is given by:

$$GI_x = \frac{4A^2 \cdot G}{\sum \frac{l_i}{t_i}} \tag{1}$$

Here the area A refers to the area enclosed by the profile; t is the thickness and l the length of the centerline of all profile segments. This centerline is indicated in Figure 2 by the dashed line. In order to avoid overestimating the torsional stiffness by directly applying Eq. (1) to the open

  doi:10.5075/epfl-298799_978-2-9701614-0-0

profile geometry, the length l is increased by the width of the skin segment underneath the profile, as indicated by the dashed line.

2.2 Shell Approach

The second modeling approach, see Figure 3, uses a third shell element to model the stiffener profile combined with the skin underneath.

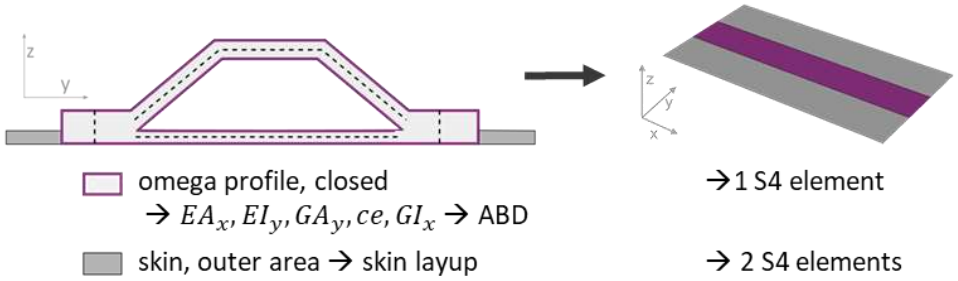

Figure 3. Analytical basis and resulting FE-model for the shell approach.

This model is based on the smeared stiffener approach presented by Nemeth (7), where the ABD matrix for the stiffener is defined as follows:

$$A = \begin{pmatrix} \frac{EA_x}{d} & 0 & 0 \\ 0 & 0 & 0 \\ 0 & 0 & \frac{\kappa_s GA}{4d} \end{pmatrix}, B = \begin{pmatrix} \frac{EA_x \cdot c_e}{d} & 0 & 0 \\ 0 & 0 & 0 \\ 0 & 0 & \frac{\kappa_s GA \cdot c_e}{4d} \end{pmatrix}, D = \begin{pmatrix} \frac{EI_y}{d} & 0 & 0 \\ 0 & 0 & 0 \\ 0 & 0 & \frac{GI_x}{4d} \end{pmatrix} \quad (2)$$

Apart from typical stiffness parameters, this approach relies on a length d, which represents the distance between two stiffeners. Originally, d is used to smear a number of regularly spaced stiffeners over an entire panel. With the goal of modeling irregularly spaced stiffeners in mind, this has to be adapted for this work. The stiffener is only smeared over the profile width and used to define the middle shell element; the outer shells are only defined by the skin layup. Therefore, d is set to the total profile. By using a shell element to model the stiffener, the width can now be modeled explicitly. The partitioning of the geometry for this approach is shown in Figure 3. The part of the skin underneath the stiffener is included in the profile model, allowing a direct application of the closed profile model to calculate the torsional stiffness. The interpretation of the foot section in terms of Eq. (1) is highlighted by the dashed line as centerline. For the foot section of the profile, the foot width is used as profile width t. Therefore, the orientation of the centerline is vertically in this section and the length is the sum of foot and skin thickness. The shear correction factor is assumed to be $\kappa_s = 0.5$ based on the profile shape.

2.3 Novel Shell-Beam Approach

To address the issues of the first two approaches, the third approach is set up as shown in Figure 4. By introducing an additional shell element on each side of the stiffener beam, the foot section (stiffener layup and skin underneath) can be excluded from the beam element. The omega profile represented in the beam element is now a simple, closed profile without complicated sections in the foot region. This allows the direct use of thin-walled, closed profile models. Additionally, the two shell elements enhance the model by explicitly modeling the profile width.

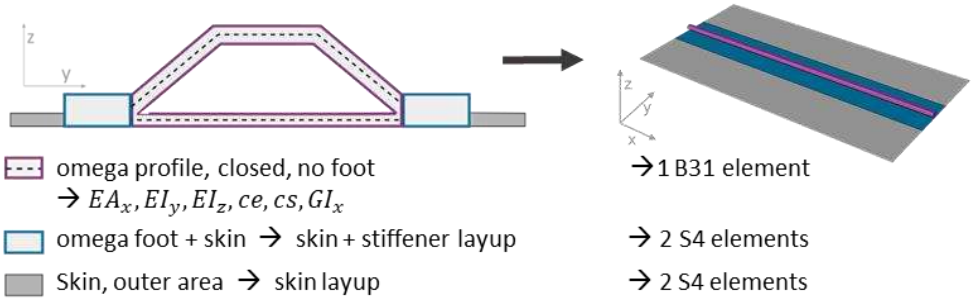

Figure 4. Analytical basis and resulting FE-model for the shell-beam approach.

To model the foot section, a composite layup is defined in *Abaqus* based on the stiffener and the skin layup. To compensate for the increase in width in the reduced model, the height of each layer is adjusted to achieve the same cross-sectional area as in the geometry definition.

$$h_{new} = \frac{2 \cdot width_{foot} \cdot h_{old}}{width_{overall}} \tag{3}$$

The resulting number of DOFs is relatively high, compared to the conventional beam approach (60 vs. 30). In comparison to the approximately 25.000 DOFs in the detailed model, depending on the exact geometry, this is still a significant reduction and acceptable to achieve the required accuracy on a panel level.

3. Evaluation of the Approaches and Comparison with Detailed FE-Results

3.1 Model Setup

In order to analyze the quality of the different modeling approaches, their response to four characteristic load cases is compared to the response of the detailed model as shown in Figure 1c). Around 4.000 shell elements are used in the detailed model, depending on the exact geometry. This way the shape of the omega profile is modeled explicitly. The element size used was determined through a mesh convergence study. Identical load and boundary conditions are applied to both the detailed and the reduced model. The setup for each load case is shown in Figure 5 using a simplified detailed mesh.

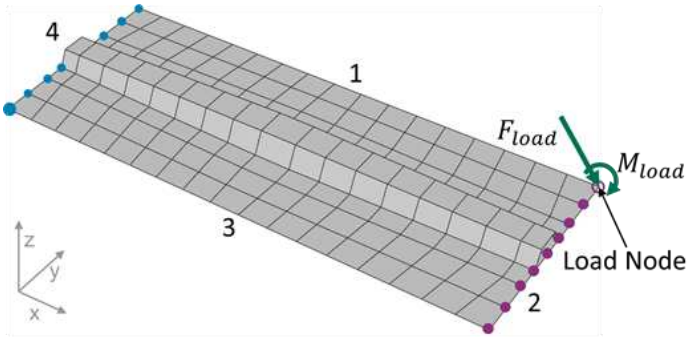

LC 1 – Tension
$F_{load} = N_x$
$u_x^2 = u_x^{load}$
$r_y^2 = r_y^{load}$
$u_x^4 = 0$
$r_y^4 = 0$

LC 3– Shear
$F_{load} = N_y$
$u_y^2 = u_y^{load}$
$r_{x,z}^2 = r_{x,z}^{load}$
$u_{x,y,z}^4 = 0$
$r_{x,y,z}^4 = 0$

LC 2 – Bending
$M_{load} = M_y$
$u_x^2 = u_x^{load}$
$r_y^2 = r_y^{load}$
$u_x^4 = 0$
$r_y^4 = 0$

LC 4 – Torsion
$M_{load} = M_x$
$r_x^2 = r_x^{load}$
$u_{x,y}^4 = 0$
$r_{x,y,z}^4 = 0$

Figure 5. Loads and boundary conditions used for the analysis.

  doi:10.5075/epfl-298799_978-2-9701614-0-0

In general, the left side “4” of the panel is fixed by constraining specific DOFs of the respective nodes. The loads are applied to the right side “2” via an external node, which is then coupled to all nodes on the right side. The specific DOFs to which the couplings and constraints are applied differ with each load case and are listed in Figure 5. No boundary conditions are applied to the top “1” or bottom “3” edge.

The resulting displacements of the lower right corner node are compared to evaluate the modeling capabilities of the different approaches. Two different parameter studies are carried out using the FE-software *Abaqus*. In a first study, 250 different omega profiles are analyzed to compare the resulting accuracy of the three reduced modeling approaches over a range of parameters. For this, all profile parameters except the foot width are varied. In all cases different aircraft laminates ($[\pm 45°_x, 0°_x, 90°_x]_s$) are applied to the skin and the stiffener. In the second study, only the profile height and width are varied to test the sensitivity of the most accurate approach to these main design parameters.

3.2 Results

The resulting deviations of the reduced model displacements from the detailed model displacements are calculated as follows:

$$d = \left(1 - \frac{disp_{red}}{disp_{det}}\right) \cdot 100\,\%. \tag{4}$$

The resulting minimum, maximum and mean deviations for each reduced modeling approach are listed in Table 1. Under tension and bending loads, all approaches produce good results. The conventional beam approach reaches the highest accuracy with deviations significantly under 1 %. For the shear load case, the deviations are widely distributed. The most constant deviation is achieved by the conventional beam approach with values around 30 %. The smallest deviation over the range of profiles is obtained by the shell-beam approach. The shell approach does not show good ability to model the shear behavior in this setup. Under torsion, all three modeling approaches exhibit significantly different behavior. Especially the conventional beam and the shell approach show large deviations, differing greatly over the range of profiles. Acceptable results are only obtained using the shell-beam approach, with deviations around 3 % and maximum values under 8 %.

Table 1: Resulting deviations for the different modeling approaches.

Deviation	$u_1^{tension}$	$r_2^{bending}$	u_2^{shear}	$r_1^{torsion}$
Conventional Beam Approach				
d_{min} [%]	-0.20	-0.15	25.43	-0.02
d_{max} [%]	-0.63	-0.51	37.94	-81.86
d_{mean}[%]	0.44	0.34	29.24	23.52
Shell Approach				
d_{min}[%]	-0.90	-0.14	0.02	-119.02
d_{max}[%]	-6.17	-2.33	-253.60	-153.39
d_{mean}[%]	4.27	1.24	52.88	568.36
Shell-Beam Approach				
d_{min}[%]	0.01	-0.02	-0.10	0.03
d_{max}[%]	1.72	1.54	27.10	7.76
d_{mean}[%]	0.55	0.56	11.7	3.26

  doi:10.5075/epfl-298799_978-2-9701614-0-0

Based on these findings, the shell-beam approach is selected for further analysis. Figure 6a) shows the influence of profile height on the deviation for each of the four load cases. All other profile parameters are kept constant. The influence of the profile width is shown in Figure 6b), here the width is the only profile parameter being varied. In both cases, the influence on the deviation under tension and bending loads is negligibly small, as was shown by the previous study.

For the study of different profile heights, the deviation under torsion increases with increasing profile height only up to a height of 35 mm. However, since the deviation only increases from 2 % to 4 %, this influence is rather insignificant. As expected, the width has a larger influence on the behavior in general. Under torsion, a higher order dependency between the width and the resulting deviation can be observed. Both profile height and profile width have a significant influence on the shear behavior. With the overall deviation under shear being so large in all cases, further investigation is necessary.

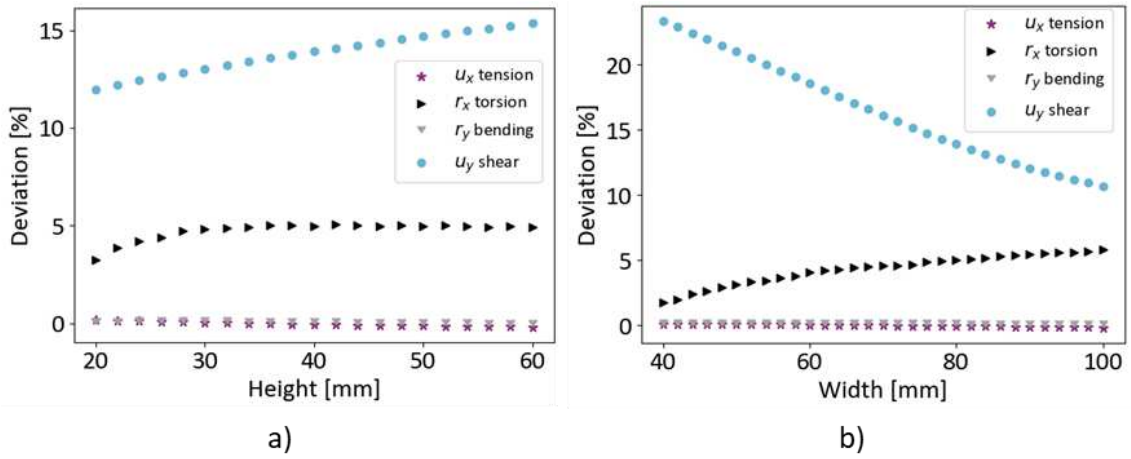

Figure 6. Resulting deviations for the shell-beam approach over different profile heights (a) and profile widths (b).

4. Conclusion and Outlook

Three different approaches for a reduced FE-model of a wide omega profile were introduced and compared in their ability to accurately model the structural behavior of a conventional detailed model. Under tension and bending loads, good agreement in the resulting displacements could be found for all approaches with deviations being mostly below 1 %. The novel shell-beam approach showed the best ability in modeling the torsional stiffness, with a mean deviation of 3 %. For the other two approaches, the resulting deviations were significantly larger. In both cases, this could be caused by the adaptions to the profile model in combination with the application of the closed, thin-walled assumption. Hence, it was shown that an enhancement of the numerical model is required in order to apply a suitable analytical model as done in the shell-beam approach. All approaches show significant deviation under shear loading, which can be attributed to shear locking due to the small number of elements, the element type used here and the simplification of the shear center location. A qualified comparison of the different approaches is therefore not possible in this regard. An additional study on the sensitivity of the shell-beam approach to profile height and width showed significant influence of the profile width on the behavior under torsion only. Due to the general issues in modeling the shear behavior, the sensitivity in this case should be reevaluated in the future.

  doi:10.5075/epfl-298799_978-2-9701614-0-0

Future work will focus on improving the modeling of the shear behavior by analyzing the influence of shear locking and the calculation of the shear center. This will include studies of larger structures containing a higher number of stiffeners under the introduced characteristic load cases as well as representative fuselage loads. Additionally the approach will be extended to non-rectangular setups and stability analyses.

Contributions

Conceptualization, L.R., T.T. and C.S; methodology, L.R.; formal analysis, L.R.; data curation, L.R.; writing – original draft, LR., T.T., writing – review & editing, C.S., P.H., S.H.; visualization, L.R., supervision, C.S., P.H., S.H., project administration, P.H., S.H., funding acquisition, P.H., C.S.

Acknowledgements

The authors would like to thank the German Research Foundation for the support of the project *Layout Topology Optimization of Unconventionally Stiffened CFRP-Structures Considering Manufacturing Constraints (OptiFee*, HO 2122/33-1).

5. References

1. Kolesnikov B, Fink A, Herbeck L, Kleineberg M, Kruse T, inventors. Semimonocoque-Bauweise, Double Curved Stringers.
2. Belardi V-G, Fanelli P, Vivio F. Structural Analysis and Optimization of Anisogrid Composite Lattice Cylindrical Shells. Composites Part B: Engineering 2018; 139:203–15.
3. Boldyrev A-V, Kozlov D-M, Pavelchuk M-V. Evaluation of Anisogrid Composite Lattice Structures Weight Effectiveness Using the Load-Carrying Factor. Procedia Engineering 2017; 185(19):153–9.
4. Deniz O, Horst P, Schmidt C. Production-based Multi-criteria Design Optimisation of an Unconventional Composite Fuselage Side Panel by Evolutionary Strategies and a Surrogate Model of Manufacturability Analysis. 11th World Congress on Structural and Multidisciplinary Optimisation 2015.
5. Grihon S. Structure Sizing Optimization Capabilities at AIRBUS. In: Advances in Structural and Multidisciplinary Optimization. Cham: Springer International Publishing; 2018. p. 719–37.
6. Schuster A, Scherer J, Führer T, Bach T, Kohlgrüber D. Automated Sizing Process of a Complete Aircraft Structure for the Usage within a MDO Process. Deutscher Luft- und Raumfahrtkongress 2016.
7. Nemeth MP. A Treatise on Equivalent-Plate Stiffnesses for Stiffened Laminated-Composite Plates and Plante-Like Lattices. No. NASA/TP-2011-216882 2011.
8. Dähne S, Hühne C. Efficient Gradient Based Optimization Approach of Composite Stiffened Panels in Multidisciplinary Environment. 5th Aircraft Structure Design Conference 2016.
9. Dähne S, Hühne C. Gradient Based Structural Optimization of a Stringer Stiffened Composite Wing Box with Variable Stringer Orientation. In: Advances in Structural and Multidisciplinary Optimization. Cham: Springer International Publishing; 2018. p. 814–26.
10. Reichert L, Krieglsteiner J, Schmidt C, Horst P. Simplified Representation of Complex Structural Components for Finite-Element-Analysis. European Conference on Composite Materials 2018.
11. Krieglsteiner J, Horst P, Schmidt C. Characterization of Fiber-Reinforced Stiffener Profiles for Aircraft Fuselage Preliminary Structural Design. European Conference on Composite Materials 2014.

  doi:10.5075/epfl-298799_978-2-9701614-0-0

MOISTURE EFFECTS IN NANOCOMPOSITES OF 2D GRAPHENE OXIDE IN CELLULOSE NANOFIBER (CNF) MATRIX – A MOLECULAR DYNAMICS STUDY

Hanieh Mianehrow [a], Lars A Berglund [a] and Jakob Wohlert [a]*

a: Department of Fibre and Polymer Technology, Wallenberg Wood Science Center, KTH Royal Institute of Technology, Teknikringen 56, 100 44 Stockholm, Sweden

Abstract: *Moisture largely affects properties in nanocellulose-based nanocomposites. Despite this fact, in-depth studies on moisture effects at the interface in such nanocomposites is missing. In this work, molecular dynamics (MD) simulation is used to study effects from moisture at cellulose nanofibril (CNF)-graphene oxide (GO) interfaces on atomistic level. Two nanocellulose models with different surface chemistry are used as models for native cellulose nanofibrils (NCNF) and TEMPO-oxidized cellulose nanofibrils (TCNF). Work of adhesion and interfacial shear strength at CNF-GO interface is calculated and compared with CNF-graphene interface to study interaction mechanisms. Simulations are done in the presence and absence of water to study the effect of moisture. Interfacial adhesion mechanism between CNF and GO is also investigated.*

Keywords: Graphene Oxide; Cellulose nanofibrils; Interfacial adhesion; Moisture

1. Introduction

Cellulose-based biocomposites are interesting as sustainable materials with different functional and structural performances [1, 2]. However, moisture sensitivity is a major drawback in such materials and has great effects on their mechanical properties [3-6]. 2D platelets such as graphene [7, 8], graphene oxide (GO) [9], montmorillonite (MTM) [10], molybdenum disulfide (MoS2) [11] and boron nitride (BN) nanosheets [12] are of interest as they bring different functionalities to the nanocomposite materials such as strong mechanical reinforcement [8, 13, 14], and electrical [13, 15] or thermal conductivity [16, 17]. The highest potential of a reinforcement nanomaterial is not achieved until it is well-dispersed in the matrix and makes strong interfacial adhesion with it. Therefore, the extent of interfacial adhesion becomes very important.

Nanocomposites based on cellulose nanofibrils (CNF) and graphene/GO have shown strong mechanical reinforcement and improved Oxygen barrier properties at very low graphene/GO content (0.1-0.5 wt%) [18-20]. This makes such nanocomposites an interesting candidate for different applications. However, in-depth investigation of interface properties, especially in the presence of moisture, is often neglected. There are a few studies in which cellulose-graphene/GO interfaces are discussed on the atomistic scale by MD simulations [21-25]. The main focus in these studies has been either on the effect of graphene aspect ratio and surface chemistry on CNF/cellulose matrix-graphene interface [22, 25] or on the extent of interactions between different cellulose crystal planes and graphene/GO [23, 24]. In the present study, the focus is on moisture effects on the extent of molecular interactions at NCNF-GO and TCNF-GO

  doi:10.5075/epfl-298799_978-2-9701614-0-0

interfaces. This is done by potential of mean force calculations and interfacial shear force experiment in both the presence and absence of water. Molecular mechanisms responsible for work of adhesion and shear strength are investigated by comparing CNF-GO interfaces with CNF-graphene.

2. Methodology

2.1 Model development and molecular dynamics simulations:

A graphene sheet with 1472 carbon atoms with lateral size 7 nm × 6 nm was made by VMD software. It was then randomly functionalized by adding hydroxyl and epoxy groups to make GO (Fig. 1a). A Native CNF model was made from 18 glucan chains, each with 8 Glucose unites, which were arranged in a hexagonal cross-section (Fig. 1b). For TEMPO-Oxidized cellulose nanofibril (TCNF), every other glucose unit in the surface chains was substituted for a glucuronic acid unit. Central chains of the TCNF crystal remained chemically identical to NCNF (Fig. 1c). MD simulations were performed using GROMACS 2019.4. The pressure was 1 atm and temperature was 298 K. GLYCAM06 parameters were used for CNF, GAFF for graphene/GO, and the TIP3P water model.

2.2 Potential of mean force calculations for work of adhesion

The potential of mean force (PMF) between the CNF and the GO was calculated using umbrella sampling. 105 intermediate states were prepared by starting from each equilibrated structure and then pull the CNF-GO apart by varying the reference distance continuously during 50 ns of MD (Fig. 1d). Weighted histogram analysis (WHAM) 64 was used to make the full PMF for each system.

2.3 Interfacial shear strength calculations for shear slippage

Shear slippage between the GO platelet and the CNF matrix was induced by applying constant force on the CNF. The force was applied to the CNF centre-of-mass in the longitudinal CNF direction (Fig. 1e), so that shear is induced at the interface. Interfacial shear strength was determined as the minimum force required to slide the CNF on the GO, divided by the initial contact area.

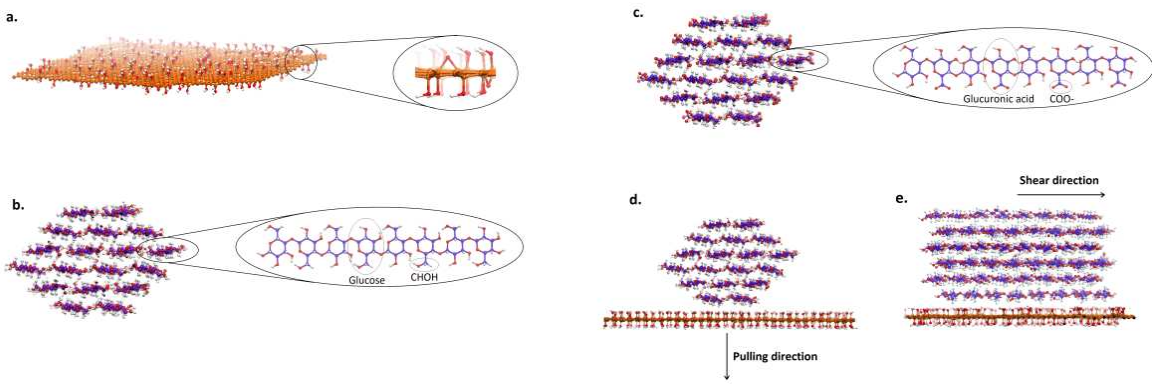

Figure 1. Graphene Oxide (a), TEMPO-CNF (b) and Native CNF models (c). Cross-section of CNF-GO system and pulling direction for Potential of Mean Force and work of adhesion (WA) calculations (d) and side view of CNF-GO system during interfacial shear loading (h). Reproduced from Ref [26] with permission from the Royal Society of Chemistry

3. Results and discussions

3.1 The CNF-GO interface

Fig. 2a and 2b show the final CNF-GO configurations after 10 ns simulation in water. Spontaneous adsorption of both CNFs to the GO is observed. However, water is present at the CNF-GO interface for both NCNGF-GO and TCNF-GO. At TCNF-GO interface there is more water due to the Na+ ions surrounding TCNF in water. Fig. 2c and 2d show the configurations after 100 ns simulation in water. Now the water layer has disappeared for NCNF-GO, but it remains at the TCNF-GO interface even after 100 ns. When simulation was done in vacuum (Fig. 2e and 2f), the CNF quickly adheres to the GO, and since there is no water, the CNF and GO can immediately form a tight interface. Finally, the dry nanocomposites in vacuum were wetted (Fig. 2g and 2h). These dry-wetted nanocomposites hold the tight interfaces formed in the dry state and only a few water molecules are observed at the interface.

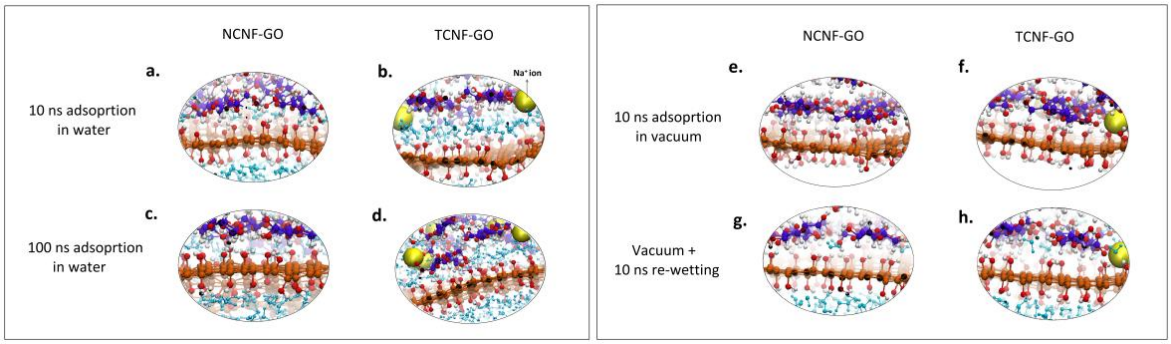

Figure 2. Zoomed-in interfaces of NCNF-GO and TCNF-GO systems at different states and simulation times. Reproduced from Ref [26] with permission from the Royal Society of Chemistry

3.2 Interfacial adhesion

The work of adhesion between CNF and GO is investigated in this section to see which state is more stable and lower in energy. Fig. 3 shows PMF graphs for different systems at different states. The effect of water at the CNF-GO interface is obvious in Fig. 3. The WA for NCNF-GO after 100 ns in water is much higher than for NCNF-GO after 10 ns in water (Fig. 3a). After 10 ns, there is still water at the interface, but this has disappeared after 100 ns. The dry-wetted interface gives similar WA as for the 100 ns NCNF-GO case for simulation in water. A similar trend is observed for TCNF-GO (Fig. 3b). However, even after 100ns there is water at TCNF-GO interface, therefore, the WA is still low for TCNF-GO after 100 ns simulation in water. This indicates that the hydrated interface is a meta-stable state and that the stable state is a dry interface.

To compare CNF-GO and CNF-Graphene interfaces, simulations of NCNF-Graphene and TCNF-Graphene were performed in water and WA values were calculated. Fig. 3c compares the PMF curves for NCNF-Graphene and TCNF-Graphene. Here, 10 ns of simulation was enough to achieve a dry interface. The meta-stable state is observed as a small dent at around 1.7 nm separation. This corresponds to one hydration layer between CNF and graphene. Both NCNF-graphene and TCNF-graphene exhibit similar behavior, although TCNF-graphene has lower WA, possibly due to the presence of Na+ counter ions. The main conclusion in this section is that

  doi:10.5075/epfl-298799_978-2-9701614-0-0

water at the interface acts as a contaminant and reduces WA. Once it is removed from the interface, the surface chemistry of CNF or GO/Graphene does not make a big difference on the WA.

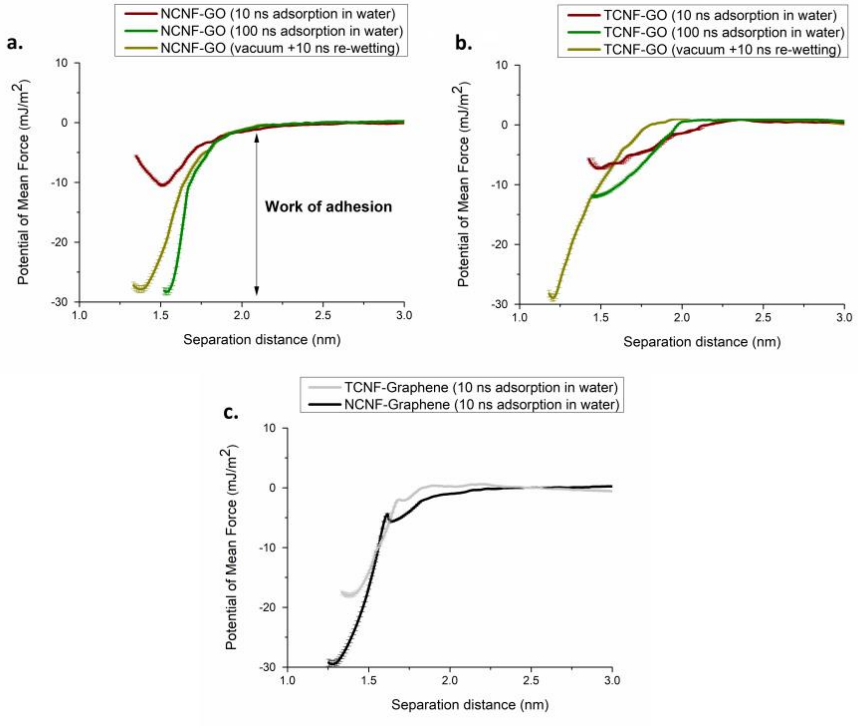

Figure 3. PMF graphs for NCNF-GO (c), TCNF-GO (d) and NCNF/TCNF-Graphene (e) in different states. Reproduced from Ref [26] with permission from the Royal Society of Chemistry

3.3 Interfacial shear strength

Interfacial shear strength between the CNF and the GO was calculated from the minimum force required to initiate sliding of CNF on the GO. The simulated interfacial shear strength is higher for NCNF-GO than for TCNF-GO in water (55.3 MPa and 41.5 MPa respectively). The NCNF-GO nanocomposite shows so-called stick-slip behavior during sliding. This effect is very weak for TCNF-GO, since there is more water at this interface (Fig. 4a and 4b).

In vacuum, the interfacial interactions are so strong that both NCNF and TCNF deform under shear forces rather than sliding on the GO (Fig. 4c and 4d). Fig. 4e and 4c shows CNF-GO interfaces after vacuum + 10ns wetting and again the CNFs deform under shear forces. The reason is that the strong interface between CNF and GO stays mostly intact and only a few water molecules can penetrate into the interface. This shows that the presence of water is necessary for the CNF to slide on the GO.

A comparison between interfacial shear strength of CNF-GO systems and CNF-Graphene systems shows that the presence of functional groups on the GO is necessary for having high interfacial shear strength (Table 1). This shows that hydrogen bonding is important for shear strength and lack of hydrogen bonding in CNF-Graphene system results in an order of magnitude less shear strength compared with CNF-GO systems. However, the WA is not governed by hydrogen bonding and CNF-Graphene interfaces show as high WA as CNF-GO. The mechanism of

  doi:10.5075/epfl-298799_978-2-9701614-0-0 published under CC BY-NC 4.0 license

interfacial adhesion could be related to entropy gain by releasing interfacial water molecules from the interface and making a dry interface.

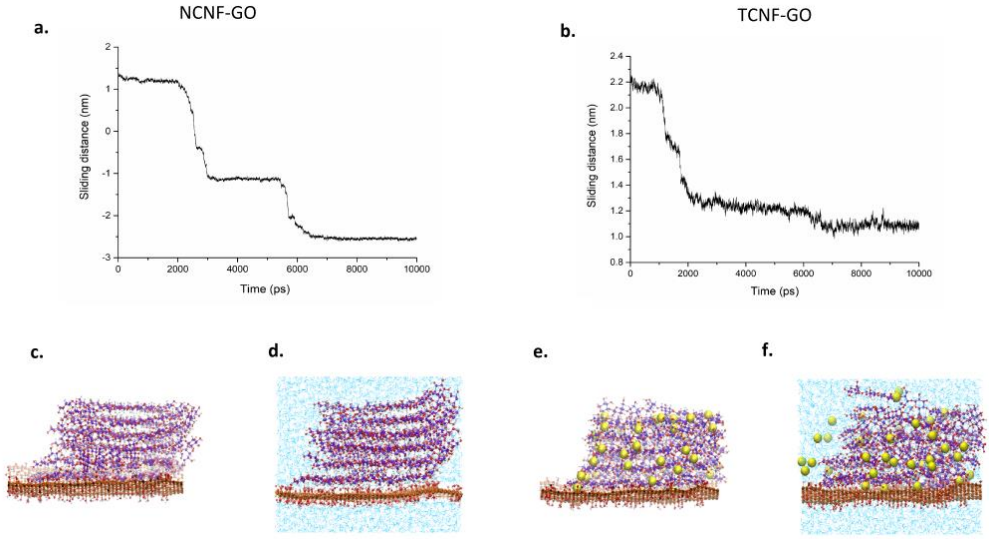

Figure 4. Sliding profiles for NCNF-GO and TCNF-GO after 10 ns in water (a and b). NCNF-GO under shear forces in vacuum (c) and after vacuum + 10 ns in water (d). TCNF-GO under shear forces in vacuum (e) and after vacuum + 10 ns in water (f). Reproduced from Ref [26] with permission from the Royal Society of Chemistry

Table1. Calculated work of adhesion and interfacial shear strength for CNF-GO and CNF-Graphene systems. *Reproduced from Ref [26] with permission from the Royal Society of Chemistry*

System	State	Number of CNF-GO Hydrogen Bonds	Work of Adhesion (mJ/m^2)	Interfacial Shear Strength (MPa)
NCNF-GO	10 ns in water	6 ± 2.0	10.5 ± 1.8	55.3 ± 1.8
	100 ns in water	11 ± 4.0	28.3 ± 1.8	-
	10 ns dry/vacuum	31 ± 5.0	≥ 120	-
	Dry/vacuum +10 ns wetted	17 ± 3.0	27.6 ± 2.5	-
TCNF-GO	10 ns in water	1 ± 1.0	7.7 ± 0.5	41.5 ± 1.3
	100 ns in water	6 ± 2.0	12.0 ± 1.2	53.4 ± 1.8
	10 ns dry/vacuum	36 ± 4.0	≥ 120	-
	Dry/vacuum +10 ns wetted	31 ± 2.0	28.8 ± 3.2	-
NCNF-Graphene	10 ns in water	0	29.2 ± 1.7	4.8 ± 0.2
TCNF-Graphene	10 ns in water	0	17.0 ± 1.0	3.7 ± 0.1

Conclusions

Nanocellulose-GO interface was studied in the presence and absence of water by MD simulation. Effects from moisture and cellulose oxidation on the properties of CNF-GO interface were investigated in details. Results showed that there is a meta-stable state where the water is present at CNF-GO/Graphene interface. This state is very stable for TCNF-GO and may be thus influenced by drying procedure. For NCNF-GO this state is short lived and giving the system enough time results in a solvent-excluded interface. Once the water is removed from the interface, the adhesion is the same for TCNF-GO, NCNF-GO and NCNF-Graphene provided by a tight formed interface. The adhesion is very strong and exceeds the cohesive energy of the CNF itself. Even after re-wetting, the pre-formed tight interface was not significantly affected by moisture. Such observation suggests that the drying history has a great effect on the interface properties. In addition, the re-wetted state is considered to be the equilibrium state where water molecules have to overcome a large energy barrier to penetrate into the interface.

We showed that hydrogen bonding does not drive the adhesion between CNF and GO and propose that CNF-GO adhesion in the wet state is dominated by gain in free energy from the reduction of water molecules at the interface. However, hydrogen bonds play an important role in shear strength and the constant breakage and formation of them results in higher interfacial shear strength. If there is no water at the interface, CNF deforms under shear forces and it does not slide on the GO. This is due to strong cohesive forces between CNF and GO and the absence of water at the interface to lubricate CNF sliding. The same deformation behavior was observed even after re-wetting which again shows the importance of drying history on CNF-GO interface properties.

Acknowledgements

The authors acknowledge Wallenberg Wood Science Centre for the financial support and the Swedish National Infrastructure for Computing (SNIC) at the PDC Centre for High Performance Computing, KTH, partially funded by the Swedish Research Council through grant agreement no. 2016-07213.

References

1. Eichhorn SJ, Dufresne A, Aranguren M, Marcovich N, Capadona J, Rowan S, et al. Current international research into cellulose nanofibres and nanocomposites. Journal of materials science. 2010;45(1):1-33.
2. Klemm D, Kramer F, Moritz S, Lindström T, Ankerfors M, Gray D, et al. Nanocelluloses: a new family of nature-based materials. Angewandte Chemie International Edition. 2011;50(24):5438-66.
3. Berglund LA, Peijs T. Biocomposites—from bulk moldings to nanostructured systems. MRS Bull. 2010:201-7.
4. Moon RJ, Martini A, Nairn J, Simonsen J, Youngblood J. Cellulose nanomaterials review: structure, properties and nanocomposites. Chem Soc Rev. 2011;40(7):3941-94.
5. Walther A, Lossada F, Benselfelt T, Kriechbaum K, Berglund L, Ikkala O, et al. Best Practice for Reporting Wet Mechanical Properties of Nanocellulose-Based Materials. Biomacromolecules. 2020.
6. Benítez A, Walther A. Cellulose nanofibril nanopapers and bioinspired nanocomposites: a review to understand the mechanical property space. J Mater Chem A. 2017;5(31):16003-24.

7. Stankovich S, Dikin DA, Dommett GH, Kohlhaas KM, Zimney EJ, Stach EA, et al. Graphene-based composite materials. Nature. 2006;442(7100):282-6.
8. Rafiee MA, Rafiee J, Wang Z, Song H, Yu Z-Z, Koratkar N. Enhanced mechanical properties of nanocomposites at low graphene content. ACS nano. 2009;3(12):3884-90.
9. Suk JW, Piner RD, An J, Ruoff RS. Mechanical properties of monolayer graphene oxide. ACS nano. 2010;4(11):6557-64.
10. Das P, Malho J-M, Rahimi K, Schacher FH, Wang B, Demco DE, et al. Nacre-mimetics with synthetic nanoclays up to ultrahigh aspect ratios. Nature communications. 2015;6(1):1-14.
11. Wang X, Xing W, Feng X, Song L, Hu Y. MoS2/polymer nanocomposites: preparation, properties, and applications. Polym Rev. 2017;57(3):440-66.
12. Song WL, Wang P, Cao L, Anderson A, Meziani MJ, Farr AJ, et al. Polymer/boron nitride nanocomposite materials for superior thermal transport performance. Angew Chem Int Ed. 2012;51(26):6498-501.
13. Huang T, Lu R, Su C, Wang H, Guo Z, Liu P, et al. Chemically modified graphene/polyimide composite films based on utilization of covalent bonding and oriented distribution. ACS applied materials interfaces. 2012;4(5):2699-708.
14. Li Z, Young RJ, Wilson NR, Kinloch IA, Vallés C, Li Z. Effect of the orientation of graphene-based nanoplatelets upon the Young's modulus of nanocomposites. Composites Science Technology 2016;123:125-33.
15. Kumar P, Yu S, Shahzad F, Hong SM, Kim Y-H, Koo CM. Ultrahigh electrically and thermally conductive self-aligned graphene/polymer composites using large-area reduced graphene oxides. Carbon. 2016;101:120-8.
16. Saeidijavash M, Garg J, Grady B, Smith B, Li Z, Young RJ, et al. High thermal conductivity through simultaneously aligned polyethylene lamellae and graphene nanoplatelets. Nanoscale. 2017;9(35):12867-73.
17. Zeng X, Sun J, Yao Y, Sun R, Xu J-B, Wong C-P. A combination of boron nitride nanotubes and cellulose nanofibers for the preparation of a nanocomposite with high thermal conductivity. ACS nano. 2017;11(5):5167-78.
18. Mianehrow H, Re GL, Carosio F, Fina A, Larsson PT, Chen P, et al. Strong reinforcement effects in 2D cellulose nanofibril–graphene oxide (CNF–GO) nanocomposites due to GO-induced CNF ordering. J Mater Chem A. 2020;8(34):17608-20.
19. Malho J-M, Laaksonen Pi, Walther A, Ikkala O, Linder MB. Facile method for stiff, tough, and strong nanocomposites by direct exfoliation of multilayered graphene into native nanocellulose matrix. Biomacromolecules. 2012;13(4):1093-9.
20. Laaksonen P, Walther A, Malho JM, Kainlauri M, Ikkala O, Linder MB. Genetic engineering of biomimetic nanocomposites: diblock proteins, graphene, and nanofibrillated cellulose. Angew Chem Int Ed. 2011;50(37):8688-91.
21. Zhu C, Monti S, Mathew AP. Cellulose Nanofiber–Graphene Oxide Biohybrids: Disclosing the Self-Assembly and Copper-Ion Adsorption Using Advanced Microscopy and ReaxFF Simulations. ACS nano. 2018;12(7):7028-38.
22. Rahman R, Foster J, Haque A. Molecular dynamics simulation and characterization of graphene–cellulose nanocomposites. J Phys Chem A. 2013;117(25):5344-53.
23. Alqus R, Eichhorn SJ, Bryce RA. Molecular dynamics of cellulose amphiphilicity at the graphene–water interface. Biomacromolecules. 2015;16(6):1771-83.
24. Mao Q, Yang L, Geng X, Chen L, Sapkota B, Zhao H, et al. Interface Strain Induced Hydrophobic Facet Suppression in Cellulose Nanocomposite Embedded with Highly Oxidized Monolayer Graphene Oxide. Adv Mater Interfaces. 2017;4(23):1700995.
25. Xiong R, Kim HS, Zhang L, Korolovych VF, Zhang S, Yingling YG, et al. Wrapping nanocellulose nets around graphene oxide sheets. Angew Chem Int Ed. 2018;57(28):8508-13.

26. Mianehrow H, Berglund LA, Wohlert J. Interface effects from moisture in nanocomposites of 2D graphene oxide in cellulose nanofiber (CNF) matrix–a molecular dynamics study. J Mater Chem A. 2022;10:2122-32.

  doi:10.5075/epfl-298799_978-2-9701614-0-0

A NEW VIRTUAL FIBER MODELING APPROACH TO PREDICT THE KINEMATIC AND MECHANICAL BEHAVIOR OF THROUGH-THICKNESS FABRIC COMPRESSION

Lode Daelemans[a], Tien Dung Dinh[a], Baris Caglar[b], Véronique Michaud[c], Wim Van Paepegem[a].

a: Ghent University (Belgium), Lode.Daelemans@UGent.be;
b: Delft University of Technology (The Netherlands);
c: Ecole Polytechnique Fédérale de Lausanne (Switzerland);

Abstract: *We propose a new modeling strategy based on hybrid elements for virtual fiber modeling (also known as the digital element method) to predict both kinematics as well as mechanics of woven fabrics. In virtual fiber modeling, yarns are modeled consisting of a number of discrete fibers. We show that through the development of a modeling strategy based on hybrid elements, we are able to impose correct properties in the fiber direction, as well as out-of-plane properties thanks to the inclusion of fiber bending stiffness. This approach accurately predicts the through thickness compression of a 2x2 twill glass fiber woven fabric. Both kinematically, as well as mechanically, good agreement between experiment and simulation is obtained. Ultimately, these kinds of models could allow faster virtual prototyping as the amount of experimental input is very low and can usually be found in the datasheet.*

Keywords: finite element modelling; textile mechanics; predictive simulation; forming

1. Introduction

Liquid Composite Molding (LCM) processes such as Vacuum Assisted Resin Transfer Molding (VARTM), Resin Transfer Molding (RTM), or Injection Compression Molding (ICM), are composite manufacturing processes in which a dry fibrous reinforcement is infused with liquid resin. The reinforcement is often compressed between two mold halves (or between a mold and a vacuum bag) in these processes and its microstructure hence changes because of the applied pressure (e.g. tow compaction). Hence, understanding and predicting the through-thickness compression behavior of reinforcements is one of the crucial factors in the manufacturing of high-quality composite parts through LCM processes.

Modeling techniques would provide a good alternative to cumbersome experimental techniques such as high-resolution X-ray microcomputed tomography (µCT). One of the main goals is to gain insight into microstructural changes of the fiber reinforcements that could for example influence the permeability of the reinforcements [1]. Although macro- and mesoscale models exist, these are usually fitted with specific constitutive laws based on experimentally determined through-thickness input properties [2]. In addition, they do not reveal conclusions about the micro-level which would be relevant for microscale permeability.

Microscale models offer the possibility to analyze the through-thickness compression at the reinforcement level while taking into account the microscale deformation mechanisms. Most notably, the virtual fiber modeling method, initially conceived by Wang et al. [3,4], is proving to be one of the most viable options. Often referred to as the digital element method, this method is centered around the modeling of fibers through a chain of truss-like elements (digital

  doi:10.5075/epfl-298799_978-2-9701614-0-0

elements), simulating the textile material as made up of a relatively small amount of such "virtual" fibers (up to 100-200). The virtual fiber method thus explicitly takes into account the fibrous behavior of the reinforcements at near-microscale, see Figure 1.

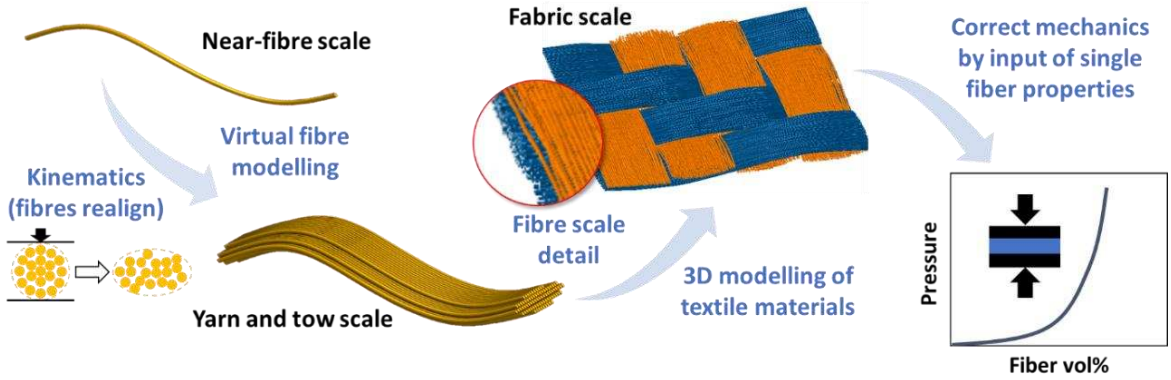

Figure 1 – Concept of virtual fiber modelling to determine the through thickness compression of textile materials.

The virtual fiber modeling method has recently been applied to through-thickness compression of woven fabrics with successful validation of the microstructure (e.g. yarn compaction, yarn paths, …) to experimental data [5,6]. Yet in both cases, the modeling is kinematic only in that the compaction in the models is realized without taking the actual pressure level into account. Although this enables meso-scale models to include the correct mechanical behavior by using the predicted microstructures [6], virtual fiber modeling with correct out-of-plane mechanics might provide a more efficient route for virtual mechanical analysis of textile reinforcements. In the case of in-plane loadings, the response is dominated by tensile loading in the fiber directions and we have previously reported a successful correlation between kinematics and mechanics for these cases [7,8].

In this work, we describe a framework to enable the correct inclusion of fiber bending into the virtual fiber modeling approach, to predict the through-thickness compression of a twill woven glass fiber fabric reinforcement. It is based on an overlay mesh-element technique, combining both (i) finite elements that determine the in-plane fiber properties as well as (ii) finite elements that determine out-of-plane fiber bending. This method is applied to the through-thickness compression of a single layer of dry fabric reinforcement to exclude any effects by the nesting of multiple layers. To validate the model, two different test methods are used to determine the pressure-compaction relationship for a single reinforcement ply with adequate resolution.

.

2. Simulation set-up

The simulation details are fully explained in Ref. [9]. Briefly, an idealized and "loose" unit cell geometry is created within the Abaqus 2019 Finite Element Analysis environment. A shrinkage step then creates tensile forces in the yarns similar to those present in an actual weaving step. By tensioning the yarns, the fibers will realign and spread out, creating the typical lenticular yarn cross-sectional shapes. This results in the as-woven state of the fabric. Periodicity of the unit cell is ensured using periodic boundary conditions proposed by Green et al. [10], consisting of

  doi:10.5075/epfl-298799_978-2-9701614-0-0

periodicity imposed at individual fiber ends as well as slave yarns that provide a contact surface at the unit cell edges. This is illustrated in Figure 2.

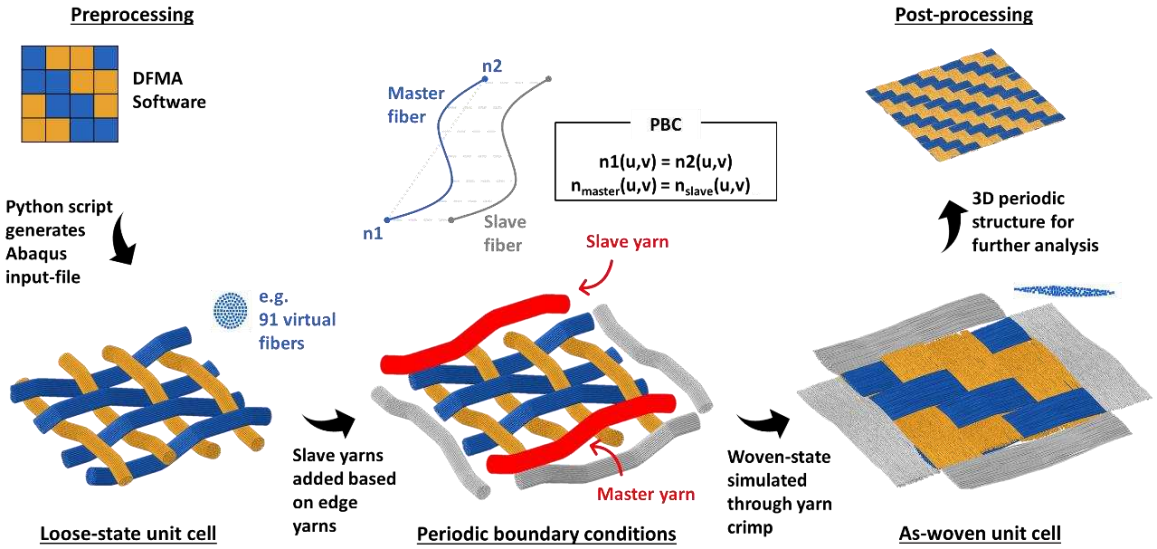

Figure 2 – Conceptual overview of the as-woven fabric generation using the virtual fiber principle and periodic boundary conditions (figure taken from Ref. [9])

Here, the virtual fibers consist of chains of linear elastic truss elements (T3D2 elements, Abaqus/Explicit) with properties representing glass fiber properties. All input properties that are used are related to actual physical and measurable parameters (see Table 1). Note that the majority of these parameters can already be found in the datasheets of the fiber and fabric material, making extended experimental characterization unnecessary. The idealized unit cell geometry is created through the Dynamic Fabric Mechanical Analyzer (DFMA, www.fabricmechanics.com) from the Fabric Mechanics group at Kansas State University (Wang et al.). The DFMA software was used only as a pre-processor; the idealized geometry is generated in DFMA and then exported through a dedicated python script to an Abaqus 2019 input file for the as-woven simulation.

Bending stiffness is imposed on the virtual fibers by overlaying the truss elements with beam elements (B31, Abaqus/Explicit) using the same nodes, see Figure 3. This creates hybrid virtual fibers in which the truss elements will determine the properties in the fiber direction (tensile stiffness), while the beam elements are chosen such that they do not affect those properties (negligible Young's modulus), but have a certain bending stiffness EI. The value of that bending stiffness can be set to the required value by changing either the Young's modulus E or the beam element radius which defines its second moment of inertia I ($= \pi r^4$). Here we opted to fix the Young's modulus such that $E_{truss} = 100\ E_{beam}$ to suppress any effects that might rise from the stiffness of the beam elements. For the range of EI considered, the beam radius was similar to that of the truss elements, ensuring that the overall tensile stiffness of the virtual fibers was barely affected by the superimposed beam elements. The virtual fiber bending stiffness was set as follows

$$n_{vf} E_{beam} I_{vf,beam} = (EI)_{measured} \quad (1)$$

  doi:10.5075/epfl-298799_978-2-9701614-0-0 published under CC BY-NC 4.0 license

The through-thickness compression is simulated by two rigid platens (rigid shell elements R3D4, Abaqus/Explicit) which move towards each other (displacement-controlled) with the fabric reinforcement in between, see Figure 3. The simulation is performed under quasi-static conditions in Abaqus 2019 Explicit (the internal energy is much higher than the kinetic energy). Contact between the virtual fiber surfaces and their surroundings (other fibers and compression platens) is imposed on the truss elements only and is defined by Abaqus' *General Contact* algorithm. The beam elements are excluded from any contact definition as their radius is dependent on the required bending stiffness and does not represent the fiber radius, the fiber radius is equal to the truss element radius. During compression of the as-woven fabric, the reaction forces on the platens and the distance between them are used to determine the pressure-thickness and pressure-volume fraction curves. The same periodic boundary conditions as before are used.

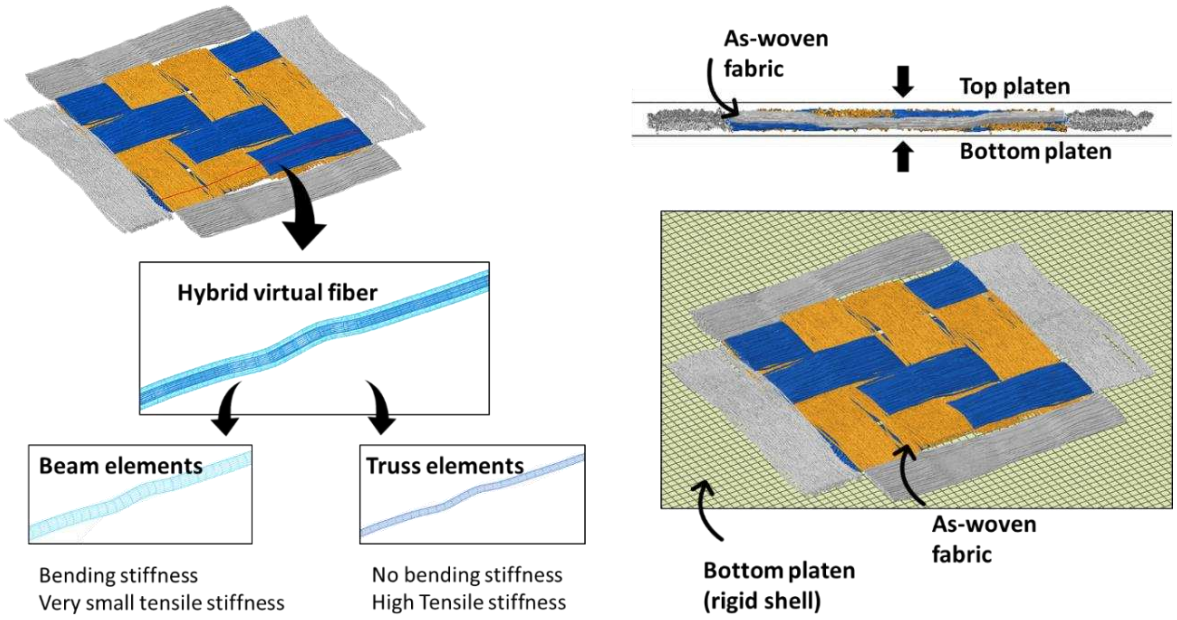

Figure 3 – (a) The fabric is constructed of hybrid virtual fibers that consist of a chain of beam elements for bending stiffness and truss element for tensile stiffness. (b) Overview of the through-thickness compression setup (figure taken from Ref. [9]).

3. Experimental details

Table 1 gives an overview of all the properties of the dry glass fiber twill fabric (Interglas 92140 aero, finish FK 144, 2x2 twill woven, 390 g/m², purchased through R&G Faserverbundwerkstoffe GmbH, Waldenbuch, Germany) that serve as input for the simulations.

Table 1 – Input properties used in the simulations.

Property	Warp	Weft	Property determination
FIBERS Linear density (dTex)	1.57		Measured according to ISO 1973 (vibroscope)

Average fiber diameter (μm)	8.9 (9)		Calculated from linear density and volumetric density.
Volumetric density (kg m^{-3})	(2550)		Datasheet value.
E-modulus (cN/dTex | GPa)	292 | 74.6		Measured according to ASTM D3822.
YARNS			
Linear density (Tex)	338 (340)	269 (272)	Measured according to ISO 7211-5.
Fibers per yarn (-)	2148	1708	Calculated from linear densities of yarn and fiber.
Bending stiffness (10^{-7} Nm^2)	1.49	0.99	Measured according to ASTM D1388.
FABRIC			
Areal density (g m^{-2})	387 (390)		Measured.
Thread count (cm^{-1})	6.1 (6.0)	6.5 (6.7)	Measured according to ISO 7211-2.
Yarn spacing (cm)	0.164	0.154	Calculated from thread count.
Crimp (%)	0.55	0.75	Measured according to ISO 7211-3.

4. Results and discussion

The need to add virtual fiber bending stiffness to the simulation is illustrated in Figure 4 by the difference in the compression reaction force of the fabric when bending stiffness is and is not present. Simulations performed without any bending stiffness mainly show a kinematic response where initially the reaction force is predominantly determined by the ease with which the (virtual) fibers can be rearranged in the structure by the compression platens (densification). The reaction force on the platens only increases at high compression levels when fiber realignment becomes obstructed and the fibers become transversally loaded. On the other hand, when including fiber bending stiffness, the kinematics remain fairly similar, but an additional compressive reaction force is noted, especially in the low pressure range. At this stage, the platens deform the virtual fibers by bending – as well as realigning – them. The compressive response shows better agreement with the experimentally determined curve, both in terms of its shape and its position.

  doi:10.5075/epfl-298799_978-2-9701614-0-0

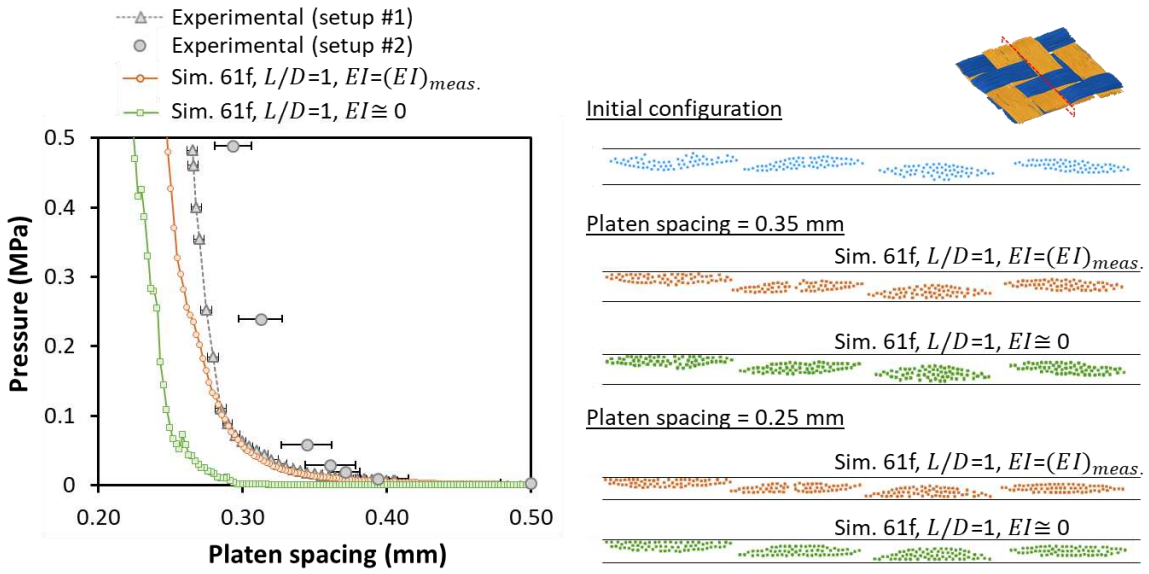

Figure 8 – Compressive response of fabric simulated with and without bending stiffness of the virtual fibers show that while kinematically similar (yarn cross-sections are visualized on the right-hand side), the mechanical response (left-hand side) is better predicted when bending stiffness is considered (figure taken from Ref. [9]: *61f means 61 virtual fibres, L/D is the truss element length over diameter ratio, and EI is the implemented bending stiffness of the virtual fibres).*

5. Conclusion

The results clearly show the potential for the virtual fiber modeling method including fiber bending stiffness as a general textile modeling framework. Taking our previous work on in-plane properties into account, the addition of out-of-plane property simulation capabilities indicates that a large range of textile-relevant loadings can be considered. This approach, fully implemented in the commercial finite element software package Abaqus using the standard element, material and contact libraries, allows research groups with FEA experience but without dedicated virtual fiber tools to implement this type of modeling. Good agreement is obtained between the experimental and the numerical determined pressure-compression behavior. The macroscopic compressive response of the fabric is well predicted for the right set of input parameters.

6. Acknowledgements

Financial support from Research Foundation – Flanders (FWO) is gratefully acknowledged. Results in this paper were obtained within the framework of the FWO grant 12ZR520N. We also acknowledge the Swiss Competence Center for Energy Research (SCCER) Mobility of the Swiss Innovation Agency (Innosuisse) and the Swiss National Science Foundation (SNF - 182669) for financial support.

  doi:10.5075/epfl-298799_978-2-9701614-0-0

7. References

[1] Y. Mahadik, K.A.R. Brown, S.R. Hallett, Characterisation of 3D woven composite internal architecture and effect of compaction, Compos. Part A Appl. Sci. Manuf. 41 (2010) 872–880. doi:10.1016/j.compositesa.2010.02.019.

[2] M. Valkova, D.B. Anthony, A.R.J. Kucernak, M.S.P. Shaffer, E.S. Greenhalgh, Predicting the compaction of hybrid multilayer woven composite reinforcement stacks, Compos. Part A Appl. Sci. Manuf. 133 (2020) 105851. doi:10.1016/j.compositesa.2020.105851.

[3] Y. Wang, X. Sun, Digital-element simulation of textile processes, Compos. Sci. Technol. 61 (2001) 311–319. doi:10.1016/S0266-3538(00)00223-2.

[4] G. Zhou, X. Sun, Y. Wang, Multi-chain digital element analysis in textile mechanics, Compos. Sci. Technol. 64 (2004) 239–244. doi:10.1016/S0266-3538(03)00258-6.

[5] Z. Yousaf, P. Potluri, P.J. Withers, D. Mollenhauer, E. Zhou, S. Duning, Digital element simulation of aligned tows during compaction validated by computed tomography (CT), Int. J. Solids Struct. 154 (2018) 78–87. doi:10.1016/j.ijsolstr.2017.05.044.

[6] A.J. Thompson, B. El Said, D. Ivanov, J.P.H.P.-H. Belnoue, S.R. Hallett, High fidelity modelling of the compression behaviour of 2D woven fabrics, Elsevier Ltd, 2018. doi:10.1016/j.ijsolstr.2017.06.027.

[7] L. Daelemans, J. Faes, S. Allaoui, G. Hivet, M. Dierick, L. Van Hoorebeke, W. Van Paepegem, Finite element simulation of the woven geometry and mechanical behaviour of a 3D woven dry fabric under tensile and shear loading using the digital element method, Compos. Sci. Technol. 137 (2016) 177–187. doi:10.1016/j.compscitech.2016.11.003.

[8] T.D. Dinh, A. Rezaei, L. Daelemans, M. Mollaert, D. Van Hemelrijck, W. Van Paepegem, A hybrid micro-meso-scale unit cell model for homogenization of the nonlinear orthotropic material behavior of coated fabrics used in tensioned membrane structures, Compos. Struct. 162 (2017) 271–279. doi:10.1016/J.COMPSTRUCT.2016.12.027.

[9] L. Daelemans, B. Tomme, B. Caglar, V. Michaud, J. Van Stappen, V. Cnudde, M. Boone, W. Van Paepegem, Kinematic and mechanical response of dry woven fabrics in through-thickness compression: Virtual fiber modeling with mesh overlay technique and experimental validation, Compos. Sci. Technol. 207 (2021) 108706. doi:10.1016/J.COMPSCITECH.2021.108706.

[10] S.D. Green, A.C. Long, B.S.F. El Said, S.R. Hallett, Numerical modelling of 3D woven preform deformations, Compos. Struct. 108 (2014) 747–756. doi:10.1016/j.compstruct.2013.10.015.

Composites Meet Sustainability – Proceedings of the 20th European Conference on Composite Materials,
ECCM20. 26-30 June, 2022, Lausanne, Switzerland

VIRTUAL CHARACTERIZATION AND NEURAL NETWORK BASED HOMOGENIZATION OF COMPOSITE MATERIALS

Sebastian, Müller[a]

a: ESI Group, Germany – Sebastian.mueller@esi-group.com

Abstract: *The formulation of macroscopic constitutive relations that reflect the effective material behaviour of composite materials is a persistent challenge for structural design engineers. The number of potential constituents as well as the manifold material structures makes it cumbersome to define a universal relation for all possible combinations and commonly leads to expensive experimental test campaigns. Virtual material characterization based on multiscale approaches has been found to overcome or ease the latter. Based on representative models of the material structure and calibrated material models for the constituents they allow for a prediction of the effective material behaviour. The gathered information is easy to generate and can be used to feed machine learning algorithms in order to learn the relations of the material behaviour. The present contribution outlines the approach based on a feed forward neural network. The generation of training data as well as the subsequent implementation of the material model is based on the commercial FEM package ESI Virtual Performance Solution and allows for an application to industrial relevant topics.*

Keywords: Neural network; Homogenization; 3D composite; Constitutive model

1. Introduction

The macroscopic performance of modern composite materials is determined by the material behaviour of the individual constituents as well as the material architecture. The discrepancy in length scale between the latter and the composite part dimensions prevent a direct modelling of the material structure in an industrial relevant part simulation. Multiscale based analysis in combination with homogenization techniques are commonly used to determine the effective material properties. The subsequent macro-scale simulation however requires the availability of suitable constitutive models. The sheer variability in the possible constituents as well as in the material micro- and meso-structure hinder the formulation of universal material models.

Machine learning based material modelling has therefore gained increasing attention [1]. Approaches like neural networks allow for a fast implementation of complex relations and have been proven to give good accuracy in predicting the effective mechanical response of complex material micro-structures [2] and inelastic material behaviour [3].

The generic implementation of the neural network evaluation functions in a commercial Finite Element code, such as ESI *Virtual Performance Solution* (VPS) [4] allows for the direct application of the method to industrial relevant problems. In the present contribution a feed forward neural network is used to describe the effective material behaviour of composites. A principal sketch of the network architecture is given in Fig. 1 (a). To demonstrate the potential of the method, the effective inelastic material behaviour of a 3D textile reinforced composite (e.g. Fig. 1 (b)) is analysed. The complete workflow, including characterization, neural network training and validation as well as macroscopic structural simulations will be shown.

  doi:10.5075/epfl-298799_978-2-9701614-0-0

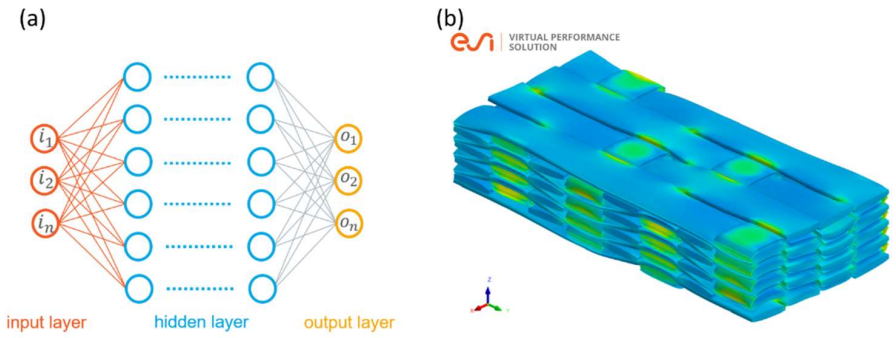

Figure 1. (a) Feed forward neural network architecture, (b) 3D textile reinforced composite - unit cell of the mesoscopic material structure

2. Virtual Material Characterization

The multi scale homogenization approach used in the present contribution is based in the FEM analysis of a representative part of the material structure. The size of this so called Representative Volume Element (RVE) is determined by the periodic repetition of the internal material geometry. An example of a RVE for a 3D textile is shown in Fig. 1 (b).

The prediction of effective mechanical properties for the local heterogeneous material structure requires the definition of an averaging assumption. For the derivation of effective elastic properties this can be accomplished using Hill-Mandel condition [5, 6]. It is an energy equivalence theorem, which relates local effective virtual work on the macro-scale (M) to the volume average of the variation of work on the sub-scale (m)

$$\boldsymbol{\sigma}^M : \delta\boldsymbol{\varepsilon}^M = \frac{1}{V^{RVE}} \int_{\Omega^{RVE}} \boldsymbol{\sigma}^m : \delta\boldsymbol{\varepsilon}^m dV \tag{1}$$

It can be shown that for certain boundary conditions, namely constant traction, linear displacement or periodic displacement, the macroscopic virtual work can be calculated from the product

$$\boldsymbol{\sigma}^M : \delta\boldsymbol{\varepsilon}^M = \langle\boldsymbol{\sigma}^m\rangle : \langle\delta\boldsymbol{\varepsilon}^m\rangle = \delta E \tag{2}$$

of the averaged stress- and strain-field on the subscale

$$\langle\boldsymbol{\sigma}^m\rangle = \frac{1}{V^{\mathrm{RVE}}} \int_{\Omega^{\mathrm{RVE}}} \boldsymbol{\sigma}^m dV, \qquad \langle\delta\boldsymbol{\varepsilon}^m\rangle = \frac{1}{V^{\mathrm{RVE}}} \int_{\Omega^{\mathrm{RVE}}} \delta\boldsymbol{\varepsilon}^m dV \tag{3}$$

Motivated by the periodicity of the reinforcement structure of the considered 3D textiles, periodic displacement and antiperiodic traction boundary conditions are used for the determination of the effective stress-strain relations.

3. Artificial Neural Network

3.1 Basic relations

Artificial neural networks (ANN) can be considered as a system of signal processing units. The units are thereby arranged in layers, where each layer l can have a distinct number of units

  doi:10.5075/epfl-298799_978-2-9701614-0-0

$\mathrm{n_N}^{(l)}$. Each unit is also commonly referred to as neuron. The signal processing of each layer is governed by an activation function $A^{(l)}$. Assuming a neural network of n_L layers, the first layer $l = 1$ is often referred to as input layer, whereas the last layer $l = n_L$ is considered as the output layer. However, neural networks can be designed with arbitrary complexity what go beyond such classification. More details and information about neural networks and their design and implementation can be found in [7].

A sketch of a simple feedforward neural network is shown in Fig. 2. The signal at k-th neuron of the l-th layer is defined as

$$p_k^{(l)} = A^{(l)}\left(z_k^{(l)}\right) \tag{4}$$

with $A^{(l)}$ the activation function of the corresponding layer. The function argument $z_k^{(l)}$ is a composure of the weighted signals $p_s^{(l-1)}$ of the precedent layer $l-1$

$$z_k^{(l)} = \sum_{s=1}^{n_N^{(l-1)}}\left(w_{ks}^{(l)} p_s^{(l-1)}\right) + b_k^{(l)} \tag{5}$$

with $w_{ks}^{(l)}$ and $b_k^{(l)}$ the corresponding weighting and bias factors, respectively.

The network parameters (weight and bias factors) are identified in an iterative optimization or training process. To this end, a sufficiently large number of input and output data-sets needs to be provided as training data. In addition, the user can provide validation data to check the learning progress and the accuracy throughout the training. The progress is thereby monitored by one or several loss functions.

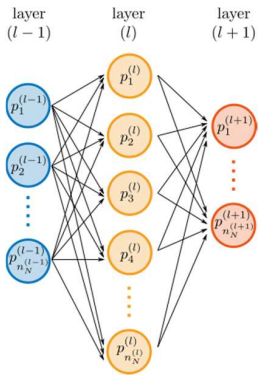

Figure 2. Signal flow between the layers of a feed forward artificial neural network

3.2 Network gradients

The computation of the output of a neural network can be seen as a sequence of evaluations of analytic functions. Given that they are differentiable, it is possible to calculate the derivative of the output with respect to the input. With respect to the input signal i_r , the the derivative of the k-th neuron of the l-th layer is derived from Eq. (4) as

$$\frac{\partial p_k^{(l)}}{\partial i_r} = A'^{(l)}\left(z_k^{(l)}\right)\frac{\partial z_k^{(l)}}{\partial i_r} \tag{6}$$

with $A'^{(l)}$ the first order derivative of the activation function. The second term follows from Eq. (5) as

$$\frac{\partial z_k^{(l)}}{\partial i_r} = \sum_{s=1}^{n_N^{(l-1)}} w_{ks}^{(l)} \frac{\partial p_s^{(l-1)}}{\partial i_r} \tag{7}$$

and incorporates the gradients from the precedent layer.

In a similar fashion second order gradients can be derived as

$$\frac{\partial^2 p_k^{(l)}}{\partial i_r \, \partial i_t} = A''^{(l)}\left(z_k^{(l)}\right) \frac{\partial z_k^{(l)}}{\partial i_r} \frac{\partial z_k^{(l)}}{\partial i_t} + A'^{(l)}\left(z_k^{(l)}\right) \frac{\partial^2 z_k^{(l)}}{\partial i_r \partial i_t} \tag{8}$$

with

$$\frac{\partial^2 z_k^{(l)}}{\partial i_r \, \partial i_t} = \sum_{s=1}^{n_N^{(l-1)}} w_{ks}^{(l)} \frac{\partial^2 p_s^{(l-1)}}{\partial i_r \partial i_t}. \tag{9}$$

It can be seen that the order of the network gradients is directly related to the order of the activation functions and if they are differentiable.

4. Neural network based homogenization

4.1 Basic principle

The energy equivalence theorem from section 2 can be used as a basis for the formulation of a neural network that relates the internal work E of a system with the macroscopic effective strain $\bar{\boldsymbol{\varepsilon}}$. Both quantities are standard outputs of a FEM simulation and can therefor easily be recorded during a RVE based virtual characterization simulation. Making use of fundamental thermodynamic principles as outlined in [3] and the inherent differentiation of the neural network with respect to its input quantities allows for the automated derivation of the effective stress $\bar{\boldsymbol{\sigma}}$ as well as the effective material tangent stiffness $\bar{\mathbf{C}}$ (cf. Fig. 3). The same authors introduced the term Thermodynamics-based Artificial Neural Networks (TANNs) which will be used subsequently for this type of network.

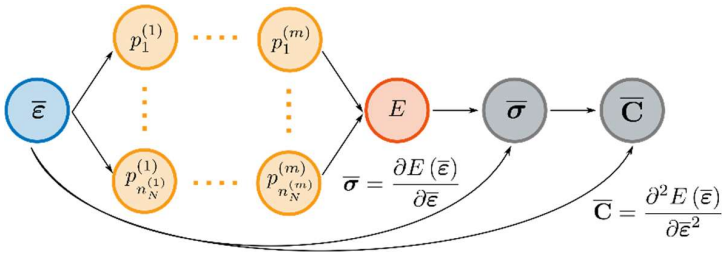

Figure 3. Thermodynamics-based Artificial Neural Network (TANN) of the internal work and its gradients

4.2 Inelastic homogenization

The homogenization principle illustrated in Fig. 3 can be used to describe the effective material behaviour of a composite material. An example can be given considering the RVE of an unidirectional fibre reinforced polymer (cf. Fig. 4 (a)). While the fibres are transversely-isotropic elastic, the polymeric matrix shows isotropic elasto-plastic behavior. The resulting internal work and effective stress-strain curve for uniaxial shear loading is shown in Fig. 4 (b).

  doi:10.5075/epfl-298799_978-2-9701614-0-0

The TANN response curve has been obtained based on a single layer network with 10 neurons and a swish activation function.

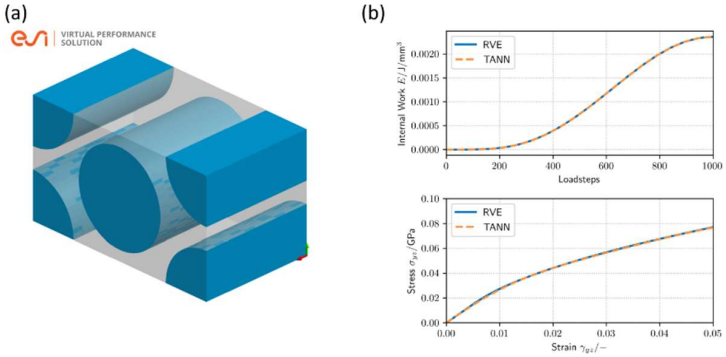

Figure 4. (a) UD RVE model and (b) comparison of internal work and stress response between RVE and TANN under monotonic uniaxial shear loading

The TANN stress response is calculated in an incremental scheme from the predicted effective material tangent stiffness. It can be seen that the network is capable of learning the energy-stress-stiffness relation of this material.

Predicting the response under cyclic loading and unloading (cf. Fig. 5 (a)) however shows that the network is not capable of predicting the hysteresis of the material following the plastification of the polymeric matrix. This is due to the insufficient input to the network for this type of history dependent material behaviour. It can be overcome by an extension of the input with a set of history functions $\underline{h}(\bar{\boldsymbol{\varepsilon}})$ that monitor the evolution of the effective strain components. A sketch of the resulting network is given in Fig. 5 (b).

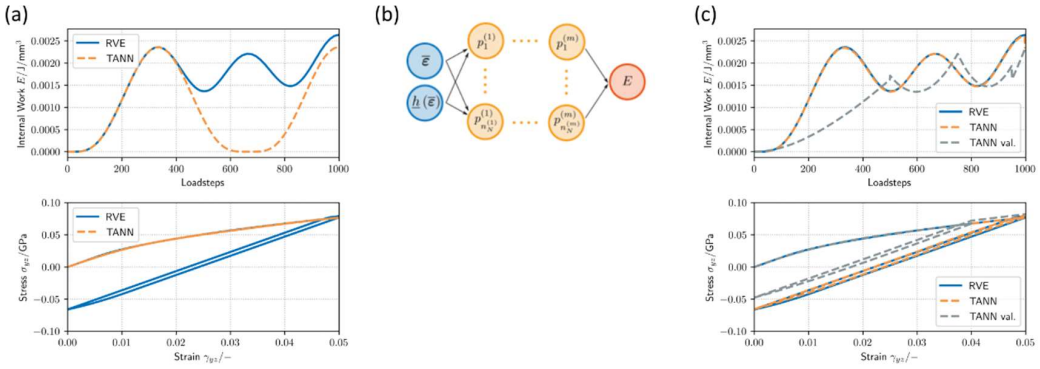

Figure 5. (a) RVE and TANN response under cyclic shear loading (b) extended TANN with history functions $\underline{h}(\bar{\boldsymbol{\varepsilon}})$ and (c) response of the extended TANN for two different cyclic loading scenarios

The additional input and the resulting logic that needs to be trained to the network require a further extension of the hidden layers. In the present case, two hidden layers with 10 neurons each and the swish activation function are used. The response of the extended TANN is given in Fig. 5 (c) and shows good agreement with the RVE results. A second validation set shows that the un and reloading is properly captured for different loading scenarios too.

5. TANN based 3D composite homogenization

The increasing complexity of the reinforcement architecture of woven 3D composite materials as well as the variability in the weave pattern make it cumbersome to formulate a universal macroscopic constitutive model. The previously introduced TANN approach in combination with virtual testing has the potential to overcome this issue. The RVE based prediction of the effective material behaviour allows for the analysis of arbitrary loading scenarios and the creation of all relevant training data to feed the neural network based constitutive model. A demonstration is given based on the layer-to-layer 3D woven composite material shown in Fig. 6.

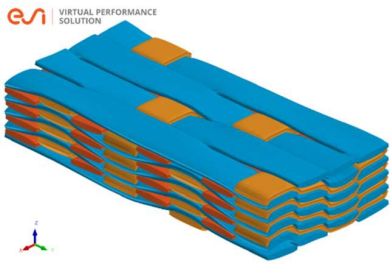

Figure 6. RVE of a woven 3D composite material with a layer-to-layer architecture

The effective elasto-plastic material behaviour is analysed based on a combination of uni-axial and multi-axial loading-scenarios. Exemplary effective strain load-paths are shown in Fig. 7. In total 15000 datasets have been generated from 9 uni-axial and 6 multi-axial load cases, which builds the basis for the network training.

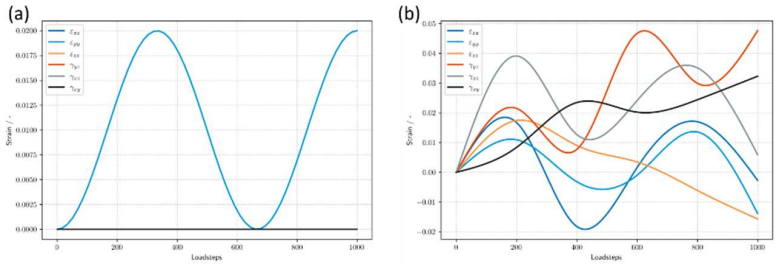

Figure 7. Virtual testing load cases, applied effective strain functions: (a) cyclic uni-axial strain loading (e.g. tension y-direction) (b) cyclic random multi-axial loadings

The extended TANN shown in Fig. 5 (b) is applied to learn the effective material behaviour. 2 hidden layers with 40 neurons each and the swish activation function are defined.

The effective stress-strain curves retrieved from the RVE simulations are compared with the TANN response in Fig. 8 and 9 for an exemplary uni-axial and multi-axial load case, respectively.

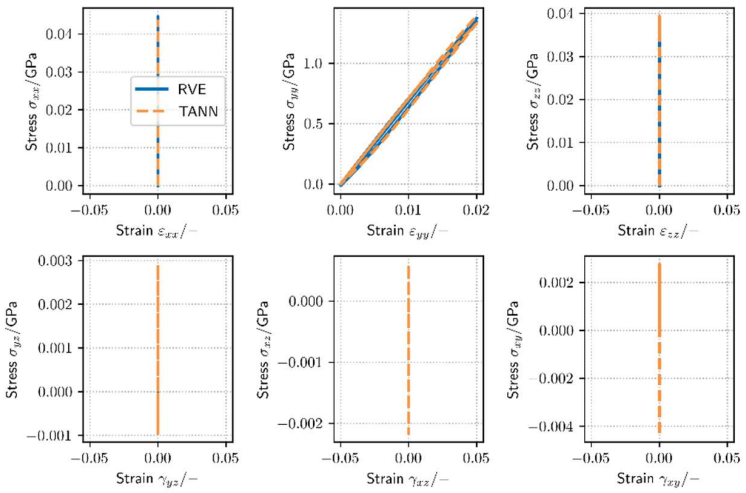

Figure 8. Effective material behaviour of a woven 3D composite under cyclic uni-axial strain loading (tension y-direction)

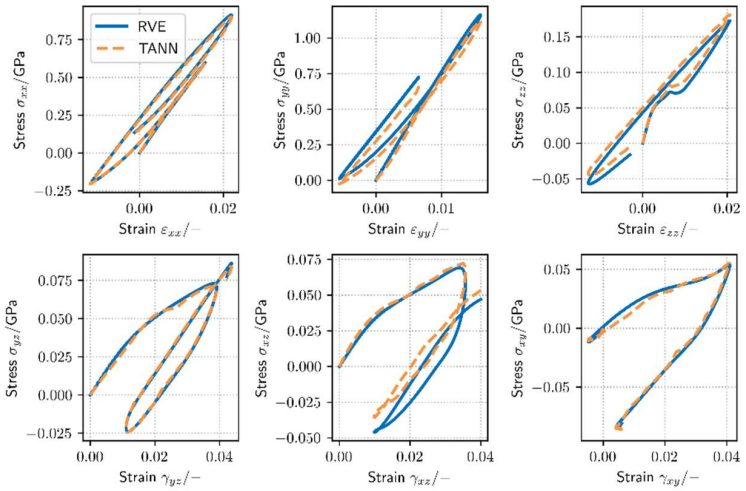

Figure 9. Effective material behaviour of a woven 3D composite under cyclic random multi-axial loading

The extended TANN is capable of learning the effective inelastic and anisotropic material behaviour of the 3D composite material. The hysteresis generated by the un- and re-loading is properly captured by the neural network.

Once trained, the TANN attributes and parameters are exported into a user defined material model for the commercial finite element package ESI Virtual Performance Solution (VPS). This subsequently allows for the simulation of large composite structures.

6. Summary

In the present contribution a Thermodynamics-based Artificial Neural Network (TANN) has been formulated to describe the effective inelastic material behaviour of composite materials. The inherent differentiability of the neural network output with respect to its input quantities

  doi:10.5075/epfl-298799_978-2-9701614-0-0

allows for an straightforward calculation of the effective stress response and material tangent stiffness from the primary network output (e.g. the internal work). A virtual characterization approach based on representative volume elements has been used to generate the necessary training data for the determination of the network parameters. Comparisons of the predicted effective behaviour of the TANN with the RVE simulations show good agreement for both uni-axial and multi-axial loading conditions. The extension of the neural network input by a set of history functions further allows the network to learn the hysteresis generated by un- and reloading scenarios. The trained TANN constitutive model can easily be ported into a material routine of a finite element code, such as ESI Virtual Performance Solution (VPS), and therefore be used for large structural analysis models.

7. References

1. Liu X., Tian S., Tao F., Du H. and Yu W. How machine learning can help the design and analysis of composite materials and structures. ArXiv: Materials Science. 2020.
2. Liu Z., Wei H., Huang T. and Wu C. Intelligent multiscale simulation based on process-guided composite database. ArXiv, abs/2003.09491. 2020.
3. Masi F., Stefanou I., Vannucci P. and Maffi-Berthier V. Thermodynamics-based Artificial Neural Networks for constitutive modeling. ArXiv abs/2005.12183. 2020.
4. ESI Group, Virtual Performance Solution, https://www.esi-group.com.
5. Hill R. Elastic Properties of Reinforced Solids: Some Theoretical Principles. J.Mech. Phys. Solids 11:357–372. 1963.
6. Hill R. On constitutive macro-variables for heterogeneous solids at finite strain. Proc. R. Soc. Lond. A.: 131–147. 1972.
7. Géron A. Hands-On Machine Learning with Scikit-Learn, Keras, and TensorFlow, 2nd Edition. O'Reilly Media, Incorporated. 2019.

  doi:10.5075/epfl-298799_978-2-9701614-0-0

TOWARDS A UNIFIED NUMERICAL MODELING OF FORMING AND CONSOLIDATION OF THERMOPLASTIC COMPOSITES WITH PREPREG PATCHES: A SHELL ELEMENT BASED APPROACH

Paris Dilip, Mulye[a,b], Lionel, Morançay[a], Christophe, Binetruy[b], Sébastien, Comas-Cardona[b], Adrien, Leygue[b]

a: Altair Engineering France, 1300, Route des Crêtes, WTC Bâtiment 4, Entrée M, 06560, Valbonne, France (Paris-Dilip.Mulye@ec-nantes.fr)
b: GeM - Research Institute of Civil Engineering and Mechanics, UMR 6183, CNRS - École Centrale de Nantes, 1 Rue de la Noë, 44321, Nantes, France

Abstract: *The "Quilted Stratum Process" (QSP®) shares several features with the standard composite thermostamping process. But at the same time there are some additional challenges in the physical process and its numerical modeling because of the usage of thermoplastic prepreg patches, inability to use a blank holder, possible long distance sliding of prepreg patches during forming and the transverse squeeze flow occurring during consolidation especially for UD prepregs. In this work, the existing formulation of a full integration shell element of Altair Radioss™ (QBAT) was extended in order to have a functionality of transverse normal (pinching) stress. Further, an elastoplastic constitutive model for this new shell element was developed based on the global plasticity approach to model the behavior of melt thermoplastic polymer during consolidation. Finally, the unified modeling of forming and consolidation of QSP® was achieved using these developments and validated on a semi-industrial part developed by CETIM.*

Keywords: process simulation; forming; consolidation; shell element; plasticity

1. Introduction

A modified version of the standard thermoplastic composite forming process called "Quilted Stratum Process" (QSP®) [1] has been developed in 2012 by CETIM, Centrale Nantes and other partners. The main idea behind this process is to use UD/woven thermoplastic prepreg patches instead of using uniformly shaped prepreg stack as is the case with standard thermostamping process. Thus, even components with complex geometries and curvatures can be formed by using near-rectangular prepreg patches while still maintaining a short cycle time of about a minute. A stack of such prepreg patches (Fig. 1a) can be formed and then overmolded into the final component (Fig. 1b) using QSP®. The main advantage of QSP® over the classical thermostamping process is the use of near-rectangular prepreg patches. With this approach, one can use the material more efficiently and produce more components compared to the classical composite forming process. This reduction, or even absence of material wastage not only decreases the production cost but also reduces the environmental impact.

Driven by the anisotropic nature of fabric coupled with its interaction with the polymer in case of prepregs, numerical simulation of a standard composite forming process itself poses several challenges. But for QSP®, there are some additional challenges in the physical process and its numerical modeling because of the usage of thermoplastic prepreg patches, inability to use a

  doi:10.5075/epfl-298799_978-2-9701614-0-0

blank holder, possible long distance sliding of prepreg patches during forming [2,11] and the transverse squeeze flow occurring during consolidation especially for UD prepregs.

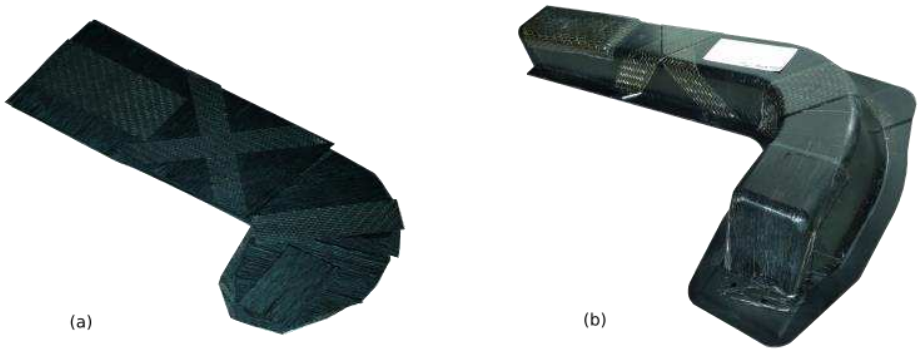

Figure 1. (a) Flat two dimensional stack of prepregs before QSP® (b) Final formed part

2. A full-integration shell with transverse normal stress (QBATP)

During the consolidation process of thermoplastic prepregs, there exists a through-thickness normal (transverse) stress also referred to as 'Pinching Stress' [3] which in fact is the main driving mechanism. This three-dimensional state of stress cannot be modeled with the classical 5-parameter Mindlin shells which are built with a plane stress assumption. To overcome this, the existing hourglass-free full-integration shell element in Altair Radioss™ (known as QBAT [4]) has been extended to add the functionality of pinching stress by introducing additional nodal degrees of freedom. This new element is referred to as QBATP element.

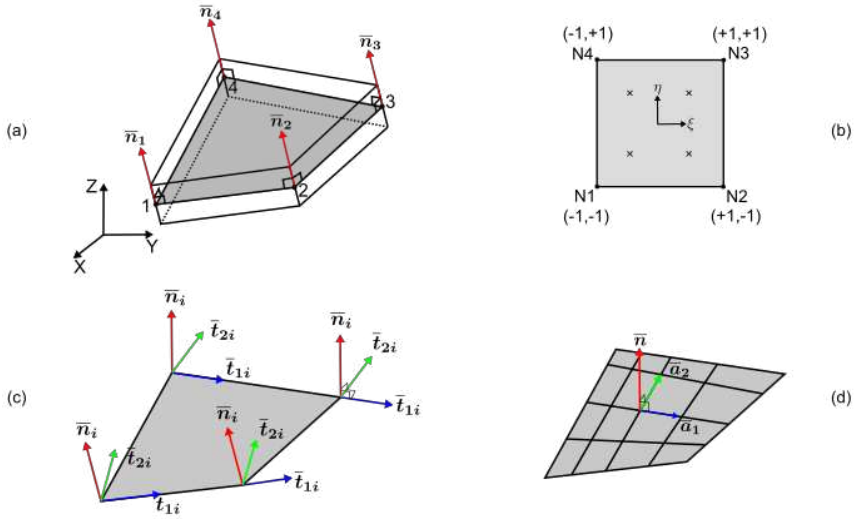

Figure 2. QBATP element (a) Geometry (b) Reference element (c) Nodal orthogonal coordinate systems (d) Covariant basis

The geometry of this shell is shown in Fig. 2 which consists of 4 nodes on the mid-surface of the shell. The corresponding reference element in the isoparametric space along with the local node numbering convention is shown in Fig. 2b. Classical bilinear shape functions and their derivatives are used for the interpolation of a nodal degree of freedom. Within the element, each node (*i*) has 6 local degrees of freedom; 3 for standard mid-surface displacements (U_{1i}, U_{2i}, U_{3i}), 2 for rotations (θ_{1i}, θ_{2i}) and additionally 1 for the pinching displacement (U_{pi}) as follows:

  doi:10.5075/epfl-298799_978-2-9701614-0-0

$$\underset{(6\times 1)}{[Ui]} = \begin{bmatrix} U_{1i} & U_{2i} & U_{3i} & \theta_{1i} & \theta_{2i} & U_i^p \end{bmatrix}^T \quad (1)$$

which are defined with respect to the orthonormal coordinate system ($\bar{\boldsymbol{t}}_{\boldsymbol{1i}}, \bar{\boldsymbol{t}}_{\boldsymbol{2i}}, \bar{\boldsymbol{n}}_{\boldsymbol{i}}$) defined at each node as shown in Fig. 2c. Additionally, one must define the covariant basis vectors ($\bar{\boldsymbol{a}}_{\boldsymbol{1}}$ and $\bar{\boldsymbol{a}}_{\boldsymbol{2}}$) as shown in Fig. 2d, which are not necessarily orthogonal to each other. The calculation of strain rates is split into four strain interpolation matrices (1) Membrane **[B_m]** (2) Curvatures **[B_b]** (3) Pinching **[B_p]** and (4) Transverse shear **[B_{ts}]** (Refer to [5] for more details). The assembly of internal and external forces, moments and pinching forces results in the following global dynamic system of equations. It consists of three sets of equations each corresponding to displacements, rotations and pinching displacements respectively.

$$\boldsymbol{M}\,\ddot{\boldsymbol{U}} = \boldsymbol{F_{ext}} - \boldsymbol{F_{int}} \quad ; \quad \boldsymbol{I}\,\ddot{\boldsymbol{\theta}} = \boldsymbol{M_{ext}} - \boldsymbol{M_{int}} \quad ; \quad \boldsymbol{M^p}\,\ddot{\boldsymbol{U}}^{\boldsymbol{p}} = \boldsymbol{F_{ext}^p} - \boldsymbol{F_{int}^p} \quad (2)$$

Where $\boldsymbol{M}$ and $\boldsymbol{M^p}$ are lumped mass matrices corresponding to the displacements and pinching displacements. $\boldsymbol{I}$ is the diagonal moment of inertia. $\boldsymbol{F_{ext}^p}$ and $\boldsymbol{F_{int}^p}$ correspond to the external and internal forces due to pinching.

Further, a selective mass scaling has been added for this element to increase its critical time-step. In the case of QBATP element; an approach inspired from the technique of the acceleration filtering for solid elements [6] and the selective mass scaling for solid-shell elements [7] was used. With this, one can selectively increase the mass corresponding only to the pinching DoFs ($\boldsymbol{M^p}$) without changing the mass for the mid-surface DoFs ($\boldsymbol{M}$). The validation tests for this element, along with the discussion of interaction between contact interfaces and pinching DoFs can be found in [5] and is not discussed here.

Overall, this QBATP element with selective mass scaling serves as a first step towards a unified full-scale simulation of both forming and consolidation phases in a generic composite forming process as well as a more specific one such as QSP®.

3. An elasto-plastic constitutive model for QBATP element

Through-thickness compression is required to ensure proper consolidation of multi-layered thermoplastic composites. Through-thickness compression force applied during the consolidation of composite prepregs is the driving force for various mechanisms such as squeeze flow [8]. During consolidation, the squeeze flow not only affects the in-plane dimensions of the prepreg as a whole (Fig. 3a and Fig. 3b) but also affects the spatial field of fibre orientations within the prepreg (Fig. 3c). The influence of the squeeze flow effect becomes even more important in case of thermoplastic unidirectional (UD) prepregs since the in-plane transverse behavior is predominantly governed by the melt polymer which is nearly incompressible.

Thus, in order to model the behavior of the nearly incompressible melt polymer during consolidation; following the approach used predominantly by composite forming community; viscous effects are not modeled within the prepreg. A plasticity-based approach is chosen in order to emulate the flow of melt polymer and a new elastoplastic constitutive model has been developed that is compatible with the QBATP shell element. This is inspired from the global plasticity model proposed by Ilyushin [9] for classical shells where the Von-Mises yield criterion (f) is defined directly in terms of deviatoric stress resultants ($\widetilde{N}^{dev}$) and stress couples ($\widetilde{M}$) as follows,

  doi:10.5075/epfl-298799_978-2-9701614-0-0

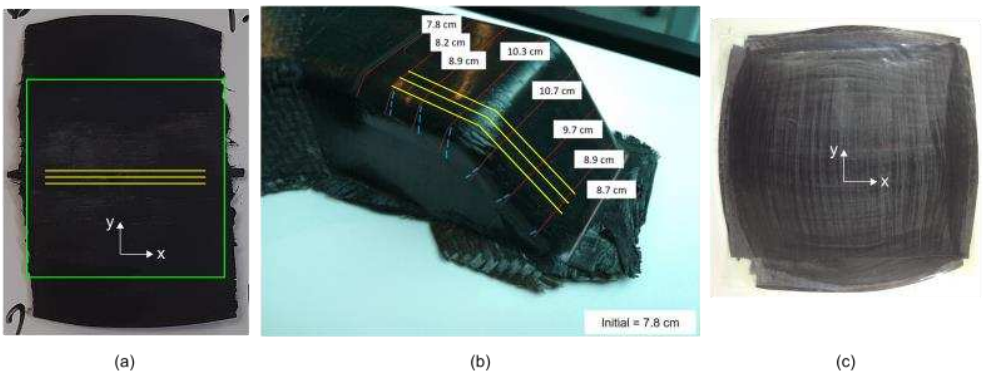

Figure 3. Impact of transverse squeeze flow: (a) In-plane deformed shape of a $[0^o]_5$ laminate after consolidation (initial geometry is shown by green rectangle and the initial fibre orientation is shown by yellow colored lines) (b) Width measurements for a UD prepreg patch of a component manufactured using QSP® (the fibre orientation is shown by yellow colored lines). (c) Changes in the fibre orientations for a stack $[0^o/90^o]_6$ (reproduced Fig. 5 from [8])

$$f = \sqrt{16\,(\tilde{M}_{eq}^{t})^2 + (\tilde{N}_{eq}^{t})^2} - \sigma_y \tag{3}$$

$$(\tilde{M}_{eq})^2 = (\tilde{M}_x)^2 + (\tilde{M}_y)^2 - \tilde{M}_x\,\tilde{M}_y + 3\,(\tilde{M}_{xy})^2 \tag{4}$$

$$(\tilde{N}_{eq})^2 = 1.5\,[\,(\tilde{N}_x^{dev})^2 + (\tilde{N}_y^{dev})^2 + (\tilde{N}_z^{dev})^2 + 2\,(\tilde{N}_{xy})^2\,] \tag{5}$$

The model uses linear isotropic hardening with radial return and a linear equation of state is used to correlate pressure, specific volume and bulk modulus. A selective reduced integration is performed for the spherical part of stress in order to avoid volumetric locking.

The model requires 4 parameters: Young's modulus (*E*), Poisson's ratio (*v*), Yield stress (σ_y) and isotropic hardening modulus (*HM*). Due to the very low stiffness of the melt polymer and absence of fibres in the in-plane transverse direction; the classic uniaxial tensile test could not be used. Therefore, an alternate approach was considered (Fig. 4). The parameters *E* and *v* were obtained using the Tait equation and the incompressibility of the melt polymer whereas the parameters σ_y and *HM* were obtained using an experimental campaign based on a UD consolidation test. The main idea was to use the flat sections of the actual mold directly to characterize the model thereby avoiding the need to develop a dedicated test setup [5].

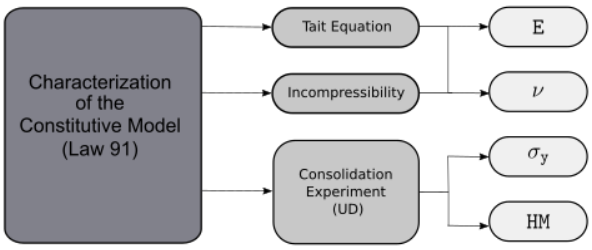

Figure 4. Representation of the characterization procedure for the elasto-plastic constitutive model proposed in this work

  doi:10.5075/epfl-298799_978-2-9701614-0-0

3.1 Flat $[0^o]_5$ Case

To demonstrate the capability of the QBATP shell with the new constitutive model; a flat UD ply that is made up of glass fibres impregnated with PA-66 polymer (Celestran® CFR-TP PA-66 GF60-02 Supplier: TICONA) and of dimensions 60 mm × 60 mm with a thickness of 1.55 mm was modeled between two flat molds. The punch and die are given elastic material properties. The prepreg ply is modeled as two overlapping shell element components, one modeling the UD fibres and the other modeling the melt polymer. The initial fibre orientation is along X axis as shown in Fig. 5a. An imposed displacement is applied on the flat punch which induces a transverse squeeze flow in the prepreg stack whereas the die is fixed in all DoFs. The simulation is run until a final average thickness of 1.161 mm was obtained which corresponds to a total consolidation of 25.1%. The displacement field along direction Z at various stages of the consolidation is shown in Fig. 5b to Fig. 5f.

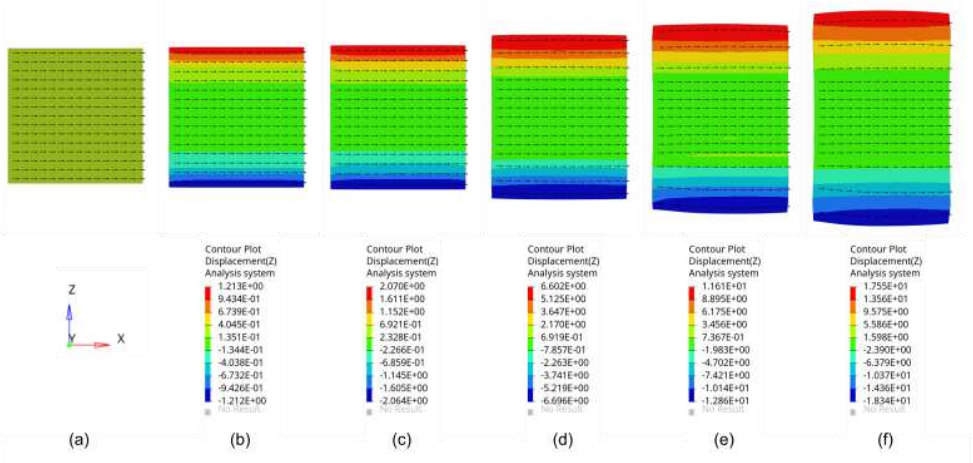

Figure 5. Flat UD $[0^o]_5$ case: (a) Initial geometry and mesh (b) Displacement Z (mm) at 5% consolidation (c) Displacement Z (mm) at 10% consolidation (d) Displacement Z (mm) at 15% consolidation (e) Displacement Z (mm) at 20% consolidation (f) Displacement Z (mm) at 25.1% consolidation

The final deformed shape obtained from the simulation is compared to the experiment in Fig. 6. Fibres being nearly inextensible, the displacements along X are very small as indicated by the measurements at various locations. It can be observed that even though some curvature is seen in the simulation depicting the barreling effect, it does not match exactly with the experiment. This difference could have come from the ply-mold interaction and the heat transfer happening at their interface which is not modeled in the simulation.

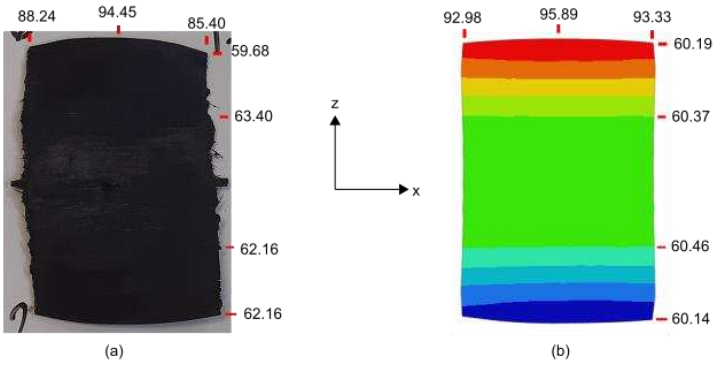

Figure 6. Flat UD $[0^o]_5$ case: (a) Deformed shape from experiment (b) Deformed shape from simulation

3.2 Flat $[0^o/90^o]_2$ Case

Another consolidation test with the same UD prepreg is conducted but with a stack of the configuration $[0^o/90^o]_2$ where each ply is of the size 60 mm × 60 mm × 0.31 mm. This is motivated by a similar previous work discussed in [10]. Starting with an initial average stack thickness of 1.225 mm; a consolidation operation was performed until the final average stack thickness of 1.187 mm was achieved. The loading and boundary conditions are exactly the same as that of the $[0^o]_5$ case. Also, the material properties are same (except the direction of the fibres).

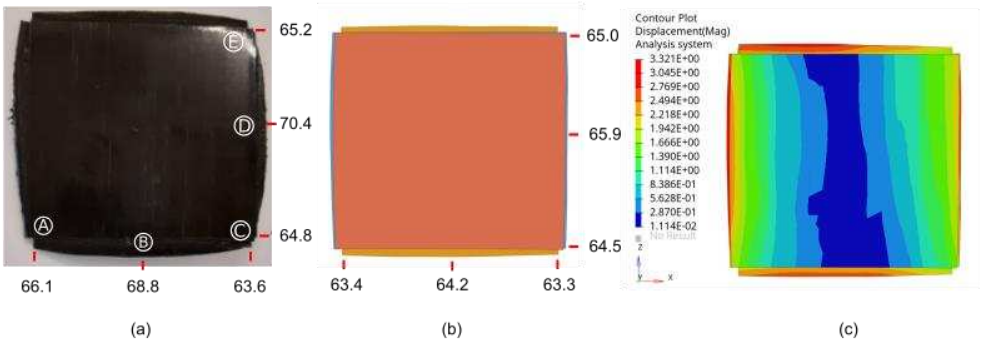

Figure 7. Flat $[0^o/90^o]_2$ case: (a) Measurements on the final deformed shape from experiment (b) Measurements on the final deformed shape from simulation (c) Field of the magnitude of displacement from simulation

The in-plane deformations observed from the simulations are compared with those obtained from the experiments in Fig. 7. The width predictions at the corners (locations **A**, **C** and **E** in Fig. 7) are predicted quite well from the simulation (with a difference of less than 1 mm). Also, the deformation patterns at the corners are predicted with a good accuracy. However, the amount of widening predicted by the simulation at the midpoints of sides of the stack (locations **B** and **D** Fig. 7) is less than what has been observed in the experiments which requires further investigation.

4. The unified approach of modeling forming and consolidation

The modeling strategy for the shell based unified approach is schematically represented in Fig. 8 for a general stack consisting of 4 plies. Each ply contains two shell element components with shared coincident nodes. One of these two components represents fibres whereas the other represents the polymer. The shell for fibres is modeled using a full integration standard shell element (QBAT) of Altair Radioss™ and uses an anisotropic material model (Law 58). On the other hand, the shell for the polymer is modeled using the QBATP element. The elasto-plastic constitutive model (Law 91 of Altair Radioss™) is assigned to this polymer shell. The ply-ply interaction is modeled with Type 25 contact law with interply adhesion as discussed in [11].

To validate this unified approach, a semi-industrial model designed by CETIM was considered. It consists of a flat UD ply stack $[0^o]_4$ of dimensions 420 mm×60 mm and thickness of 0.31 mm each resulting in a total stack thickness of 1.21 mm. The fibres are oriented along the X direction (Fig. 9). The UD ply tapes used in this work consist of Glass fibres impregnated with PA-66 polymer Celestran® CFR-TP PA-66 GF60-02 (Supplier: TICONA). The blank is formed into a dissymmetric omega-shaped mold.

  doi:10.5075/epfl-298799_978-2-9701614-0-0

In order to quantitatively compare the results of simulation with the experiments, the final widths (in mm) were measured at various locations of the ply both in experiments (Fig. 9a) and in simulation (Fig. 9b).

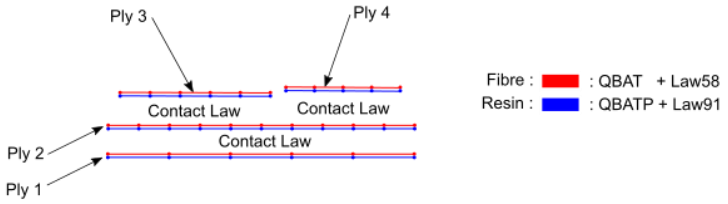

Figure 8. Schematic representation of the modeling strategy for unified approach

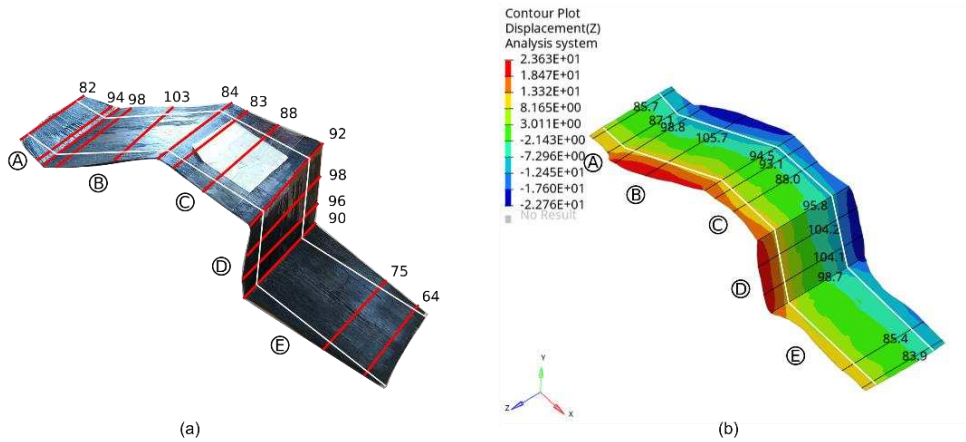

Figure 9. Unified simulation of a UD ply on Omega mold: Width comparison between experiments and simulation (measurements are in mm) (initial width is shown with the white colored lines)

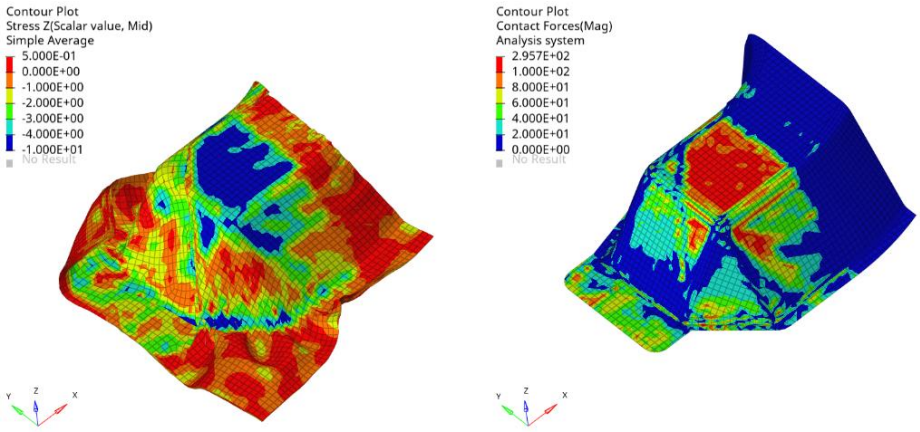

Figure 10. Final stage after the consolidation phase (a) Plot of transverse normal stress σ_{zz} (MPa) for all plies (b) Magnitude of contact force (N) on the punch

Based on the comparison, several observations can be made. With the exception of face **E**, all other faces have comparable results. Considering all faces, the average of absolute errors in the widths calculated from simulation and obtained from the experiments was found to be 7.1 mm. Also, the maximum width predicted by the simulation is 105.7 mm (on face **B**) which is close to the experimentally observed value which is 103 mm.

  doi:10.5075/epfl-298799_978-2-9701614-0-0

5. Conclusion

In summary, it has been shown that the simulation of forming and consolidation phases of QSP® can be performed using a shell element based unified approach. With the use of QBATP shell element and the elasto-plastic constitutive model for the melt polymer, one can simulate and predict the squeeze flow behavior to a reasonable accuracy. Additionally, due to the use of pinching shell elements in this approach; one has access to some additional ply level information such as transverse normal stress (Fig. 10) which can be used to design the mold and the stack itself by incorporating the effects of the consolidation phase along with the forming phase.

Acknowledgements

The authors would like to express their gratitude towards ANRT (CIFRE #2017/1621) for the financial support. The authors would also like to thank CETIM for their inputs, feedback and support.

6. References

1. Guillon D, Lemasçon A, Callens C. QSP®: An innovative process based on tailored preforms for low cost and fast production of optimized thermoplastic composite parts. In: Proceedings of the 17th European Conference on Composite Materials ECCM17. ICM – International Congress Center Munich; 2016. p. 5.607-5.614.
2. Schell J, Amory L, Guillon D. Movement of patches during thermoforming: Experiment and simulation. In: AIP Conference Proceedings. vol. 1769. AIP Publishing; 2016. p. 170032.
3. Soulat D, Cheruet A, Boisse P. Simulation of continuous fibre reinforced thermoplastic forming using a shell finite element with transverse stress. Computers & structures. 2006;84(13-14):888-903.
4. Altair Engineering. Radioss Theory Manual. 2018.
5. Mulye P. Unified numerical modeling of forming and consolidation of thermoplastic composites with prepreg patches. Ecole centrale de Nantes; 2021.
6. Olovsson L, Unosson M, Simonsson K. Selective mass scaling for thin walled structures modeled with tri-linear solid elements. Computational Mechanics. 2004;34(2):134-6.
7. Cocchetti G, Pagani M, Perego U. Selective mass scaling and critical time-step estimate for explicit dynamics analyses with solid-shell elements. Computers & Structures. 2013;127:39-52.
8. Sorba G, Binetruy C, Leygue A, Comas-Cardona S. Squeeze flow in heterogeneous unidirectional discontinuous viscous prepreg laminates: Experimental measurement and 3D modeling. Composites Part A: Applied Science and Manufacturing. 2017;103:196-207.
9. Ilyushin A. Plasticity [in Russian], gostekhizdat. Moscow–Leningrad. 1948.
10. Sorba G. Experimental study and numerical modelling of squeeze flow in laminate viscous discontinuous composites. Ecole centrale de Nantes; 2017.
11. Mulye P, Hemmer J, Moran¸cay L, Binetruy C, Leygue A, Comas-Cardona S, et al. Numerical modeling of interply adhesion in composite forming of viscous discontinuous thermoplastic prepregs. Composites Part B: Engineering. 2020;191:107953.

  doi:10.5075/epfl-298799_978-2-9701614-0-0

IMPROVING CREDIBILITY OF COMPOSITES DAMAGE MODELS

S. Miot[a], L. Barrière[a], J. Camacho Casero[a] and M. De Lozzo[a]
a: IRT Saint Exupéry, Adv. Manuf. Technologies, Toulouse, France
stephanie.miot@irt-saintexupery.com

Abstract: *IRT Saint Exupéry is developing a software solution called VIMS to ensure a robust and reliable use of modelling and simulation (M&S) techniques to generate material allowables or design values. VIMS offers a framework to integrate, evaluate and use advanced composites models in association with experimental data post-processing, decision-making support and an innovation-friendly environment that facilitates the deployment within design offices.*

Keywords: Verification, Validation, Uncertainties Quantification & Management, Damage model

1. Introduction

Reducing uncertainties and therefore risks in structural design implies determining accurate statistically-based properties of the material. Large experimental test campaigns are required to evaluate material properties distributions and compute design values. However, these campaigns are costly and the number of tested samples can be limited leading to excessive conservatism, unexplored solutions and limitation in term of weight saving and performance improvement.

Virtual testing could help to obtain more accurate and less conservative predictions. Despite the growing interest for simulation-informed decision-making, a lack of confidence in modelling and simulation methods remains. A hybrid and integrated method, combining physical and virtual testing, is proposed here to overcome the difficulty of generating virtual allowables.

2. VIMS – Virtual testing Integration for decision Making Support

IRT Saint-Exupéry has been developing a software solution called VIMS that uses the GEMSEO open source python library [1] to generate material allowables. VIMS offers a framework to integrate, evaluate and use advanced modelling methods to simulate the mechanical response of composite materials up to failure. Combined with integrated techniques such as experimental data post-processing, sensitivity analysis or surrogate modelling and dedicated workflows for model verification and validation or design value computation, VIMS aims at driving modelling capabilities maturity to the required level that will support decision-making.

  doi:10.5075/epfl-298799_978-2-9701614-0-0

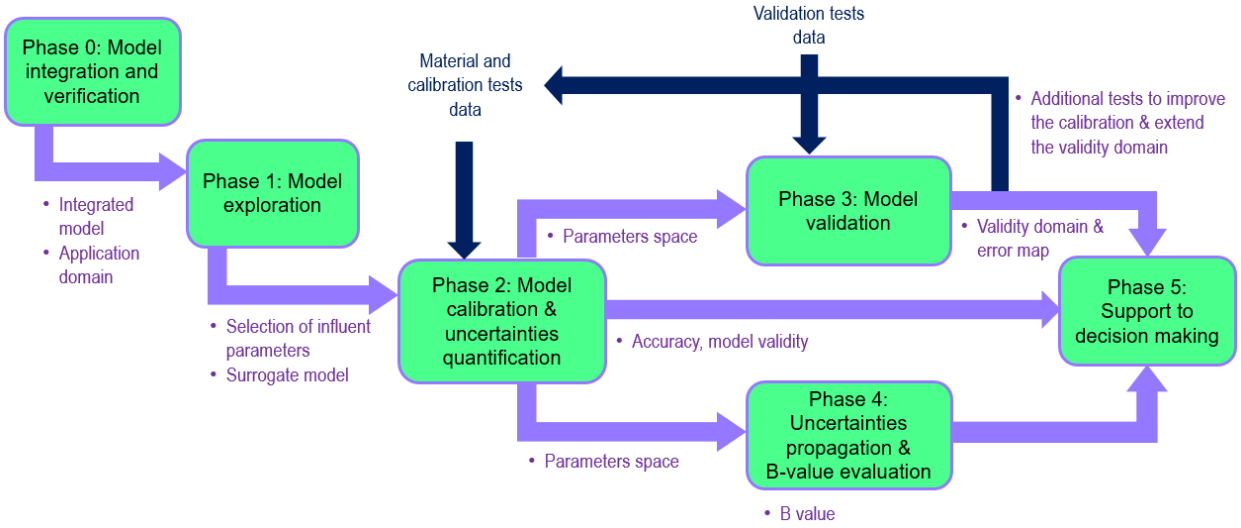

Figure 1. VIMS' concept and workflow

Figure 1 illustrates the strategies implemented into VIMS. Models for predicting damage and failure in composite materials are integrated and their usage is automated. Specific tools are provided to facilitate the following tasks:

- Model exploration through sensitivity analyses and surrogate modelling
- Model calibration, i.e. the identification of the model parameters from experimental data stored within the tests database
- Model verification and validation associated to a maturity assessment model (Predictive Capability Maturity Model – PCCM [2])
- Decision making supported by error maps and additional tests recommendations to improve confidence for a series of predictions on an specific application domain
- Generation of design values – A or B-basis allowables for instance – relying on various approaches including the Composite Material Handbook-17 methods (CMH-17 [3]).

3. Application

3.1 Model exploration

The composite damage models developed by Onera [4], the University of Girona [5] and the University of Porto [6] have been integrated into VIMS. The model exploration coupled with uncertainties propagation methods allow the most influent parameters and the most accurate surrogate model to be identified. An example of the results obtained with Onera's Progressive Damage Model (OPFM) is presented in Figure 2. The test case considered is a tensile test on a (+45,-45)s specimen corresponding to an in-plane shear test. As expected, the sensitivity study identified the shear modulus (G_{12}) and the shear strength (S_{12}) as influent parameters.

The analysis also highlighted the coupling between the shear and the transverse responses through the influence of the transverse modulus (E_2) and the tensile strength in the transverse direction (Y_T). Other influent parameters include damage parameters (α_2, h_{22t}, h_{66iff2}) and viscoelasticity parameters (γ, n_0). For more information about OPFM, please refer to [4].

  doi:10.5075/epfl-298799_978-2-9701614-0-0

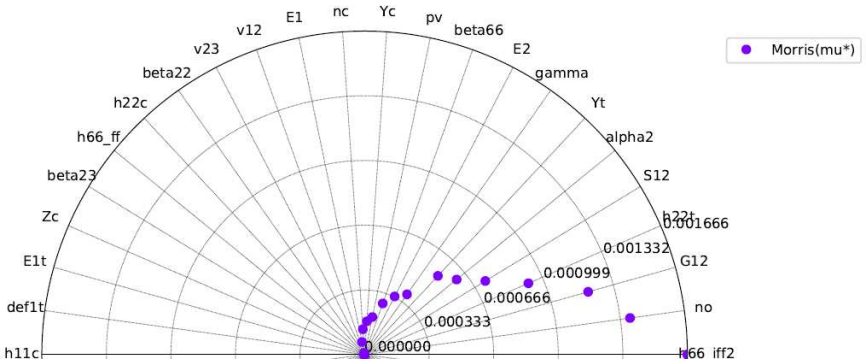

Figure 2. Morris indices highlighting the influent parameters of a tensile test on a (+45,-45)s simulated with Onera's model (OPFM)

The model exploration phase allows the identification of the relevant parameters that will be considered during the calibration phase. Automated processes have been implemented to assist the user in the identification of the model parameters from standardised tests. These calibration processes rely on direct and inverse measurement methods, local and global optimisation schemes included into sequences of material properties evaluations and physical tests data extraction. Figure 3 shows the three parameter spaces considered in the exploration phase, in combination with the calibration phase. At first, the material is unknown and the model is analysed over its entire domain: the global parameter space. Then a material is defined and the calibration process will allow the bounds to the reduced, first through direct measurements and finally using inverse methods. Further exploration of the model is performed at each stage, considering the whole domain or reduced parameter spaces, allowing general and material- or load case-specific parameters to be highlighted.

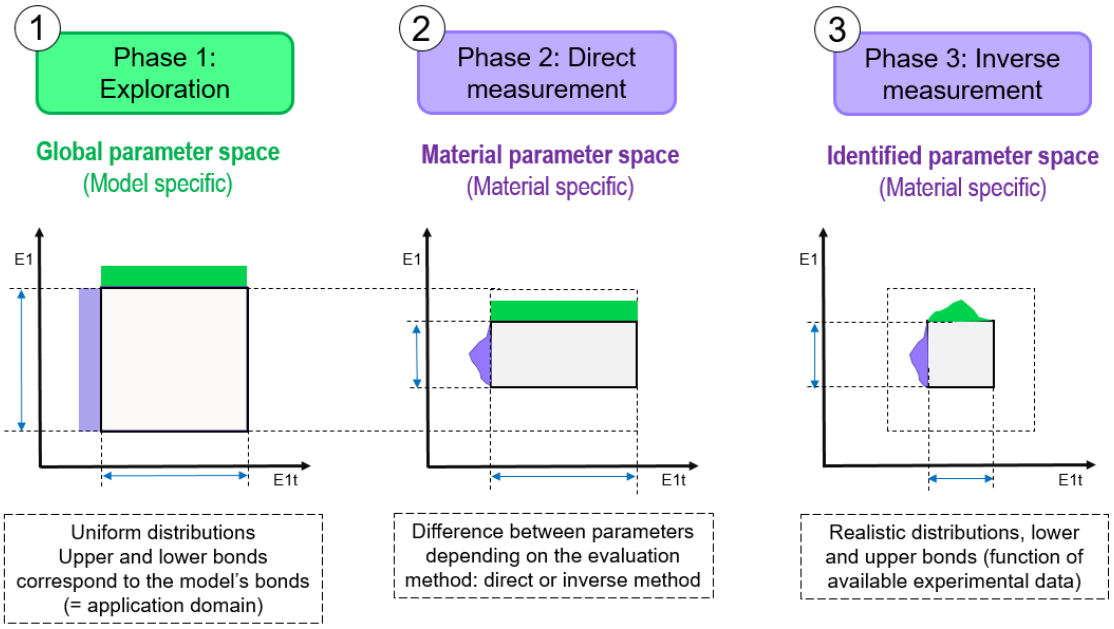

Figure 3. Towards the identification of realistic distributions of the model parameters for a specific material from the global parameter space representing the validation domain

  doi:10.5075/epfl-298799_978-2-9701614-0-0

3.2 Model calibration

Model calibration and model exploration are two inter-connected phases. As described in the previous section, knowledge about the material is required to refine the parameter space used for sensitivity analysis or surrogate model building. A simple example of the calibration process is illustrated in Figure 4. Three sets of parameters are considered:

- Non-influent parameters that can be set to a constant value (α_0)
- Influent parameters that can be measured directly from experimental data (longitudinal modulus E1 and longitudinal tensile strength Xt). If the results of multiple tests are available, distributions can be estimated.
- Influent parameters that require an inverse method to evaluate their value and distribution (model's specific parameters α_1 and α_2).

The third set of model's parameters include:

- Parameters that describe physical phenomena that cannot be fully characterised due to a lack of experimental data (missing specific test or specific test output)
- Parameters that describe complex physics that may not be fully understood, or rely on lower scale models to be identified.
- Numerical parameters than are inherent to the method chosen to solve the problem.

Methods to evaluate the uncertainties related to these parameters are being investigated [7,8].

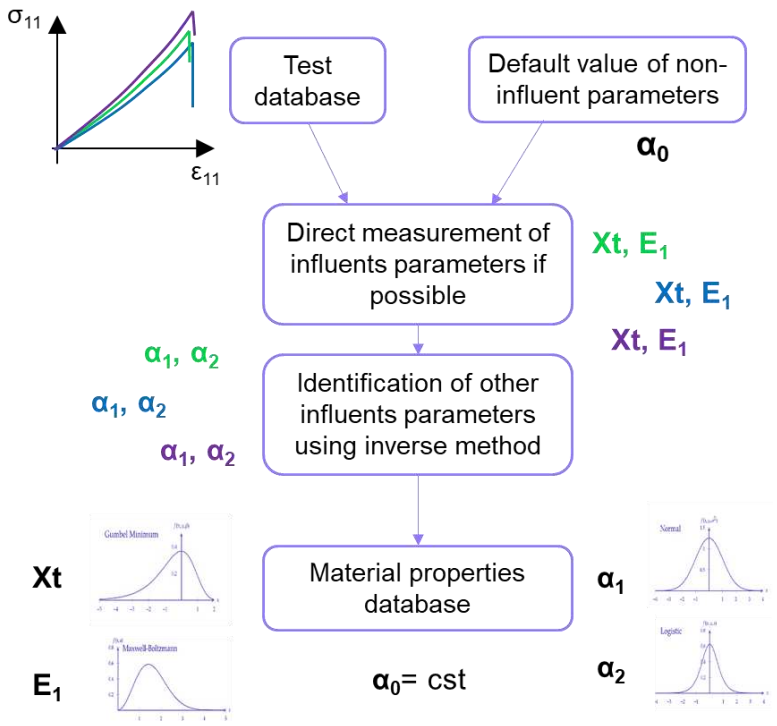

Figure 4. Automated calibration process managing data from/to databases and using direct and inverse measurement tools according to pre-defined sequences

  doi:10.5075/epfl-298799_978-2-9701614-0-0

3.3 Model validation and design value computation

Validation process may cover three aspects as described in [3] and shown in Figure 5. The first aspect covers the assessment of model accuracy by comparison with experimental data. In order to increase maturity level, uncertainty should be considered assuming the models parameters have been calibrated and their uncertainty quantified as a distribution. Methods and criteria to evaluate the statistical distances between reference data and model predictions are being investigated. Alternatively, the error can be computed as the distance between statistical quantities of interest such as the B-basis allowable.

The second and third aspects are related to the difference between the validation domain and the application domain and the estimation of the error made when using model's predictions. An estimator could be a surrogate model of the error built to interpolate between the points where reference data is available. The authors proposed to use a Kriging (Gaussian process regression) model of the error and more specifically, the Kriging standard deviation of the model error prediction to highlight the uncovered areas of the application domain.

Finally, methodologies to generate material allowables have been implemented into VIMS including, for instance:

- CMH-17 based method
- A new method based on adaptive surrogate models and active training accounting for uncertainties more efficiently.

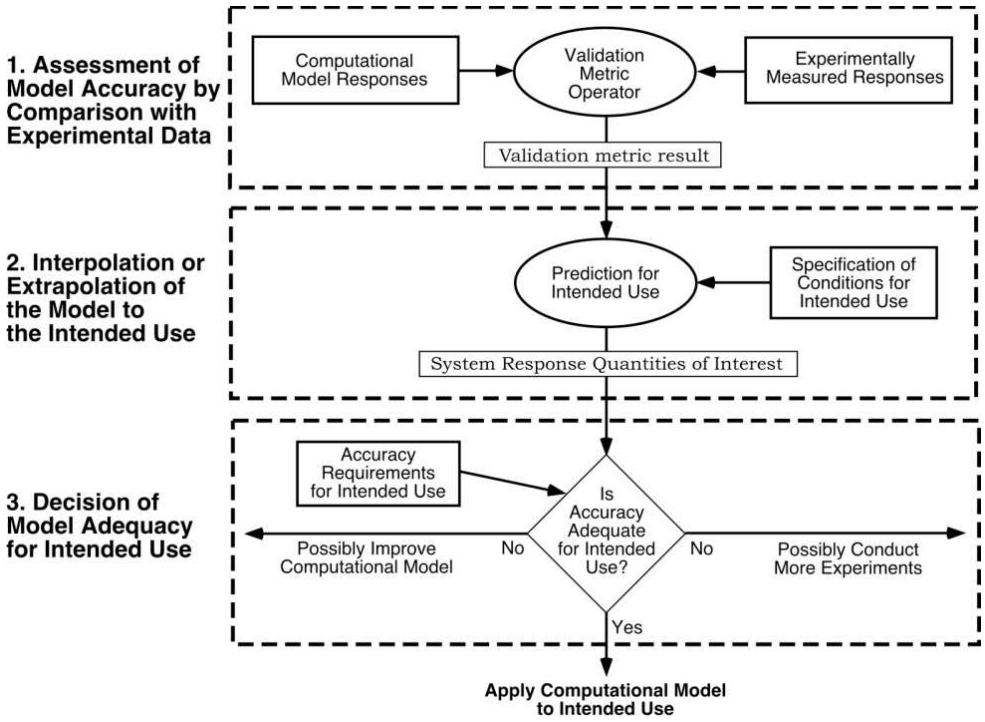

Figure 5. Three aspects of model validation [3]

  doi:10.5075/epfl-298799_978-2-9701614-0-0

4. Conclusion

Composite damage models [4,5,6] have been integrated into a software solution called VIMS. VIMS provides toolboxes to facilitate the models exploration through sensitivity analyses and surrogate model building. Automated workflows are being implemented to assist the user in the calibration phase, i.e. the identification of the model parameters including their distributions, from experimental tests. Further work will allow the calibration efficiency to be improved using new and richly instrumented tests. The model validation phase provides the user with error maps and guidance on the supplementary experimental tests that could enhance the confidence in the model predictions. The generation of B-basis allowables can be based on different methods including the CMH-17 method [2] and a new efficient UQ&M methodology based on adaptive surrogate models and active learning techniques. Further work will include the development of the last phase: the decision-making support by providing a dashboard collecting and presenting to the user all relevant information from the preceding phases.

5. Acknowledgements

The authors acknowledges the members of the VITAL project: University of Porto, University of Girona, ONERA, Airbus and Airbus Atlantic.

6. References

1. F. Gallard, GEMS: a Python library for automation of multidisciplinary design optimization process generation. In SCITECH Forum, AIAA/ASCE/AHS/ASC Str., Str. Dyn. & Mat. Conf., Kissimmee, USA, Jan. 2018.
2. U. S. D. of Defense., Military Handbook–MIL-HDBK-17-1F: Composite Materials Handbook, Volume 1, US Department of Defense, 2002.
3. W.L. Oberkampf et al., Predictive Capability Maturity Model for Computational Modeling and Simulation, Sandia National Laboratories, SAND2007---5948, Oct. 2007.
4. F. Laurin, et al., A multiscale hybrid approach for damage and final failure predictions of composite structures. *J of Composite Materials*, vol.47(20-21), pp.2713-2747, 2013.
5. E.V. González, et al., Simulation of drop-weight impact and compression after impact tests on composite laminates. *Composite Structures*, vol.94(11), pp.3364–3378, 2012.
6. C. Furtado, et al. Simulation of failure in laminated polymer composites: Building-block validation. *Composite Structures*, vol.226, 2019.
7. C. Laboulfie, et al. Calibration of material model using mixed-effects models. *4th International Conference on Uncertainty Quantification in Computational Sciences and Engineering* (UNCECOMP 2021), Jun 2021, Athens, Greece.
8. M. V. Rama Rao, R. L. Mullen and R. L. Muhanna. A new interval finite element formulation with the same accuracy in primary and derived variables. International Journal of Reliability and Safety. July 2011. DOI:10.1504/IJRS.2011.041184

MULTI-SCALE VISCOELASTIC BENDING ANALYSIS OF LAMINATED COMPOSITES WITH SOFT INTERFACES

Vu An Le[a,b], Sanjay Nimbalkar[a], Navid Zobeiry[c], Sardar Malek[d,]*

[a] School of Civil and Environmental Engineering, University of Technology Sydney, Ultimo NSW 2007, Australia

[b] Department of Civil Engineering, The University of Danang, University of Science and Technology, Da Nang, Vietnam

[c] Department of Materials Science and Engineering, University of Washington, Seattle, WA 98195, United States

[d] Department of Civil Engineering, University of Victoria, Victoria, BC V8P 5C2, Canada

[*] Corresponding author, smalek@uvic.ca

Abstract: *This study investigates the bending behaviour of the orthotropic elastic and viscoelastic multi-layered plates with resin rich inter-plies to improve our understanding of the effects of shear deformation and ply slippage on wrinkle formation. This is accomplished by employing a three-dimensional (3D) multi-scale modelling framework that incorporates analysis at different scales (micro-, meso-, and macro-scale). The variation of resin viscoelastic characteristics at the early stage of cure and its effect on the bending properties of the composite is investigated numerically. The results highlight the importance of considering the material's rate dependency in describing the bending behaviour of composite prepregs accurately. Moreover, the bending response of the thin uncured prepregs is found to be dominated by their ply bending stiffness rather than inter-ply friction.*

Keywords: Bending; Viscoelasticity; Multi-scale modelling; Orthotropic properties; Resin.

1. Introduction

Wrinkle formation during the forming process of laminated composite components poses obstacles to fully exploiting the potential of advanced composites. In literature, much attention has been paid to deformation mechanisms behind wrinkle formation during consolidation such as in-plane shear, out-of-plane bending and inter-ply slippage [1, 2]. It is now well-understood that bending properties of uncured thin laminates can influence the occurrence of wrinkles including the shape, magnitude and intensity of wrinkles [3]. Analyzing the bending and buckling deformations of uncured thermoset composites is crucial to understand contributing mechanisms and underlying physics of the wrinkle formation during hot drape forming process of laminated composites [4, 5]. Recently, Le et al. [4] developed an efficient multi-scale approach for viscoelastic analysis of single-ply woven composites under bending. In addition to from bending stiffness, inter-ply slippage has been considered as an important deformation mechanism during the process of forming composites, particularly for multi-layered textile composites [2]. Therefore, the proposed method has been expected to expand the investigation into the bending behaviour of multi-layered textile composite separated by relatively soft interfaces.

  doi:10.5075/epfl-298799_978-2-9701614-0-0

Recently, some researchers (e.g. [2]) have employed Aniform Finite Element (FE) software with shell elements to model the viscoelastic bending behaviour of composite plies under conditions relevant to the forming process. Several time-consuming characterization tests (i.e. bias extension, bending) are required to determine the material parameters for a suitable constitutive model. Unlike previous studies, the influence of various parameters including fibre stiffness, ply anisotropy, resin properties, and loading rates on the viscoelastic bending behaviour of laminated composites are analyzed in this study. The weaving pattern and the stacking sequence of plies are considered at the meso-scale while the effect of ply slippage is captured by introducing a thin interface layer between the plies at the macro-scale. Section 2 briefly introduces the methodology for simulating the bending behaviour of prepregs using the analytical homogenization techniques at micro- and meso-scale for material properties combined with the DF of viscoelasticity at macro-scale for numerical analysis. The details of the FE model and its verification are provided in Section 3. The capabilities, limitations of the developed model, and future work are discussed in Section 4.

2. Methodology

The viscoelastic behaviour of multi-layered cantilever plates subjected to tip displacements has been modelled using the multi-scale approach proposed in Malek [6] for orthotropic composites. At the micro-scale, the analytical micromechanics equations described in Malek [6] are used to predict the effective viscoelastic properties of a representative volume element (RVE) of a composite with circular long fibres (see Fig. 1).

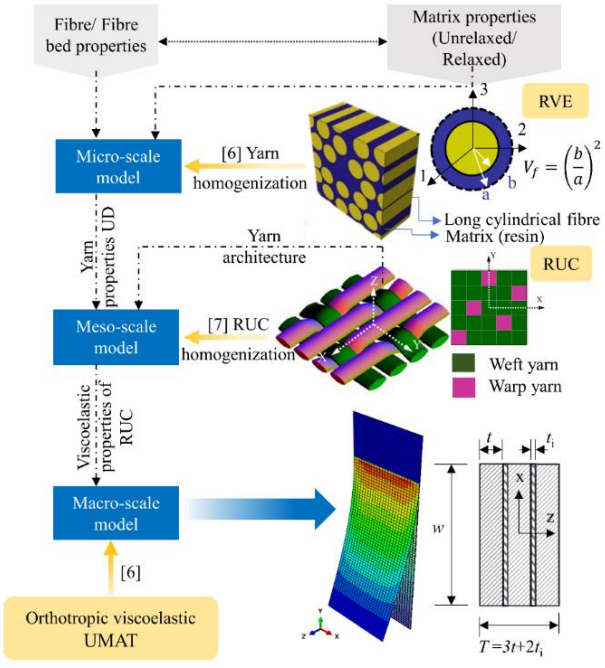

Figure 1: Schematic of the multi-scale modelling approach for bending behaviour of 5-harness satin weave multilayered composites from micro-scale to macro-scale.

The fibre's elastic and resin's viscoelastic properties are required as inputs for the micro-scale model. Since fiber-bed characteristics are essential in describing the behaviour of prepregs at the early stage of cure, the fibre-bed properties are incorporated into the micromechanics equations [6]. The effective properties obtained from the micromechanics model along with

  doi:10.5075/epfl-298799_978-2-9701614-0-0

fabric architecture are then used to estimate the properties of a representative unit cell (RUC) of a woven fabric at the meso-scale. The method for calculating three-dimensional effective parameters was adapted from Naik [7]. Once the effective meso-scale properties of the composite are obtained, they are employed directly for structural analysis at the macro-scale. A differential form (DF) of orthotropic viscoelasticity implemented as a UMAT is used for structural level (macro-scale) simulations. For further details, the reader is referred to [4].

3. Results

The composite plate selected for this study is based on a bending test of a three-layer textile composite conducted by Alshahrani & Hojjati [2]. Each ply has dimensions of 50 mm in width (w), 0.55 mm in thickness (t) and an un-gripped length of 120 mm, out of 150 mm in total length (L). Assuming that each ply is separated by a very thin interface, t_i = 0.01 mm (see Fig. 2). The three-layer cantilever plate is restrained from all displacements in a length of 30 mm as it was gripped along this distance [2]. A 20-node solid quadratic brick element with reduced integration elements (C3D20R) is used. A tip displacement of 30 mm is applied to introduce high curvature in the sample [2].

For simplicity, the effective material properties of the uncured layers under bending are assumed isotropic (E_p =700 MPa and υ_p = 0.4) first. Such effective bending stiffness were computed employing the in-plane properties of uncured prepreg under bending with known compressive and tensile moduli based on the transformation method discussed in [4]. The Young's modulus of the interface, E_i may vary within a range of values shown in Table 1. Identical Poisson's ratios are used for plies and the interface (i.e. $\upsilon_p = \upsilon_i$). The laminated plate has an overhang that may be treated as a cantilever wide beam subjected to a uniform displacement at the free end. Using Roark's formulas [8] for wide beams, the force, F, required to reach the tip displacement of 30 mm is calculated and results are presented in Table 1. Calculations for the upper and lower bound are obtained by assuming the layers to be fully bonded or disconnected. As shown in Table 1, the FE results for the homogeneous and isotropic case ($E_i = E_p$) are very close but below the upper bound. This verifies the present FE model in terms of mesh size, applied load and boundary conditions.

To better understand the role of ply anisotropy on the plate's bending response, parametric studies with transversely isotropic layers were conducted. The elastic constants of such layers for two specific transversely isotropic sets are listed in Table 2. As noted in Fig. 3, irrespective of very low interface stiffness (e.g. 70 kPa), the effect of shear deformation on the bending behaviour is less than 6.5% for the dimensions of the selected multi-layered plates. In other words, bending is the dominating deformation mechanism in this case study. Also, it seems that the anisotropy nature of plies affects the bending behaviour of laminated plates with thin and soft interfaces more considerably than their shear properties. The ply anisotropy nature (assumed in Table 2) reduces the apparent flexural rigidity of the entire plate up to 14 % (see Fig. 3). Recognizing the role of the ply's anisotropy as mentioned above along with the variation of resin viscoelastic characteristics [9] at the early stage of cure that may affect the deformation behaviour, the orthotropic viscoelastic properties are considered in the followings.

The mechanical properties of the resin, fibre and fibre-bed that have been used for viscoelastic analysis at micro-scale are listed in Table 3 [4]. It should be noted that the selected low value for fibre bending stiffness (i.e. 1.5 GPa) is an apparent value based on the micro-buckling of

  doi:10.5075/epfl-298799_978-2-9701614-0-0

individual fibres arising from the low compressive modulus of the uncured composites [4]. It should be highlighted that such a low value of the longitudinal fibre modulus considered here (1.5 GPa) is in agreement with data previously reported in the literature [4].

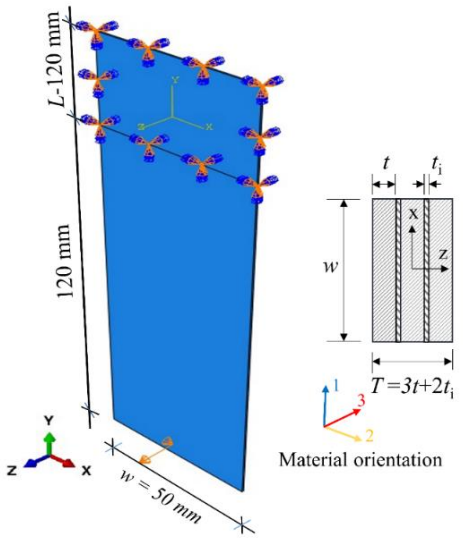

Figure 2: Bending model of a three-layer plate

Table 1: Comparisons between current FE predictions and analytical estimates [8].
E_p = 700 MPa, $\upsilon_p = \upsilon_i = 0.4$

E_i (MPa)	F (N)		
	FE (Isotropic)	Upper bound	Lower bound
700	9.372×10^{-1}		
70	9.335×10^{-1}		
7	9.317×10^{-1}	9.324×10^{-1}	9.993×10^{-2}
0.7	9.232×10^{-1}		
0.07	8.757×10^{-1}		

Due to the lack of experimental data for uncured resin (i.e. Cycom 5320), Prony series constants for MTM45-1 [9] are assumed to validate the model against the experimental data reported in [2]. First, the fibre-bed elastic properties are incorporated into the micromechanics equations [6] at micro-scale to estimate the effective viscoelastic properties of the uncured UD prepreg. The effective properties obtained from analytical homogenization at this scale are then used to predict the properties of the fabric at the meso-scale [7]. The estimated mechanical viscoelastic constants for 5-harness satin weave composite ply are provided in Table 4. Similar to previous cases for assumed elastic constants, five interface properties, E_i, ranging from 70 kPa to 700 MPa are introduced to investigate the influence of interface stiffness on the overall bending behaviour. Fig. 3 compares the required loads for the multi-layered plates with five different interface properties to reach a tip displacement of 30 mm at room temperature. As seen in Fig.

  doi:10.5075/epfl-298799_978-2-9701614-0-0

3, the apparent flexural rigidity of the viscoelastic plates is reduced by almost 30% compared to the corresponding elastic cases while the effect of ply-slippage on the overall bending behaviour is still negligible.

Table 2: Input properties of transversely isotropic plies.

Properties	Set[a]	Set[b]	Unit
$E_{1p} = E_{2p}$	700	700	MPa
E_{3p}	136	13.6	MPa
G_{12p}	40	4.0	MPa
$G_{13p} = G_{23p}$	40	4.0	MPa
υ_{12p}	0.2	0.2	-*
$\upsilon_{13p} = \upsilon_{23p}$	0.7	0.7	-*

Notes: The 12-plane is the plane of woven fabric

As a next step towards validating the proposed model, bending of four fabrics with different layups (as shown in Fig. 4) published in the literature were investigated. Note that by employing the analytical technique [7] for the homogenization technique at the meso-scale, the stiffnesses in warp and weft direction are assumed the same for simplification. Therefore, this study neglects the difference between weft and warp yarns in woven fabric structure as concerned in [2]. The load value required to achieve a tip displacement of 30 mm is used to calculate the bending moment along the length of the beam. By capturing the bending curve corresponding to the maximum displacement reached, deflection profile $z(y)$ is fitted using a proper polynomial function. The expression for the curvature is subsequently calculated as $\kappa = z''(y)/(1 + z(y)'^2)^{3/2}$[10]. Finally, the moments at each point can be plotted against the corresponding curvature values as shown in Fig. 5.

As shown in Fig. 5, the stacking 1 [0°/0°/0°] with respect to fibre direction requires the highest load to reach the desired displacement. Fig. 5 also demonstrates that rotating ply 2 and ply 3 by 45° (stacking 3) decreases the bending stiffness by approximately 15% compared to stacking 1. Stacking 2 and stacking 4 give slight differences from stacking 1 and stacking 3, respectively. It is noted that FE simulations of multiple plies under bending are considered at room temperature with a speed of 3 mm/s and assumed the interface stiffness of 7 MPa for all cases. Nevertheless, the moment against curvature relation captured by the experiment for selected stacking sequences [2] was conducted at 70°C only, hence, they are not included in Fig. 5 for comparison purposes. At room temperature, the maximum bending moment for stacking 1 with a speed of 3 mm/s was measured about 55 N.mm in [2], compared to the present FE prediction of 75 N.mm (see Fig. 5). This discrepancy can be attributed to the assumed input parameters for the fibre bending stiffness, resin viscoelastic characteristics and yarn architecture due to the lack of experimental data for material properties at micro- and meso-scale. However, the proposed multi-scale approach should be emphasized as a rapid method for estimating the effect of various parameters on wrinkle formation. Moreover, it appears to be rather difficult to precisely predict the bending behaviour of uncured laminated prepregs using FE analysis because the simulation outcome is dependent on precise material inputs at smaller scales that may be

  doi:10.5075/epfl-298799_978-2-9701614-0-0

missing in the literature. It should be noted that the simulation model using Aniform software in [2] underestimates the maximum bending moment for stacking 1 at room temperature .

Table 3: Input material properties of fibre, resin and fibre bed used in the bending simulation of textile prepregs [4].

V_f =	0.600				
Property	Unit	Fibre	Resin		Fibre bed
			Relaxed	Unrelaxed	
E_1	GPa	1.50×10^{0}	3.00×10^{-6}	1.65×10^{-1}	1.50×10^{0}
$E_2 = E_3$	GPa	1.72×10^{-1}	3.00×10^{-6}	1.65×10^{-1}	1.12×10^{-4}
$G_{12} = G_{13}$	GPa	27.60	1.00×10^{-6}	5.52×10^{-2}	1.13×10^{-4}
G_{23}	GPa	0.07	1.00×10^{-6}	5.52×10^{-2}	4.49×10^{-5}
$v_{12} = v_{13}$	-	0.2	0.495	0.495	
v_{23}	-	0.25	0.495	0.495	0.250

Table 4: Meso-scale predictions of 5HS prepreg mechanical properties under bending using the analytical technique of Naik [7].

Laminate type	Material	E_{xx}, E_{yy}	E_{zz}	G_{xz}, G_{yz}	G_{xy}	v_{xz}, v_{yz}	v_{xy}
		MPa	MPa	MPa	MPa		
5HS	Relaxed resin	412.60	8.40	5.10	3.80×10^{-1}	0.800	2.94×10^{-4}
	Unrelaxed resin	680.20	394.10	126.20	187.20	0.676	0.212

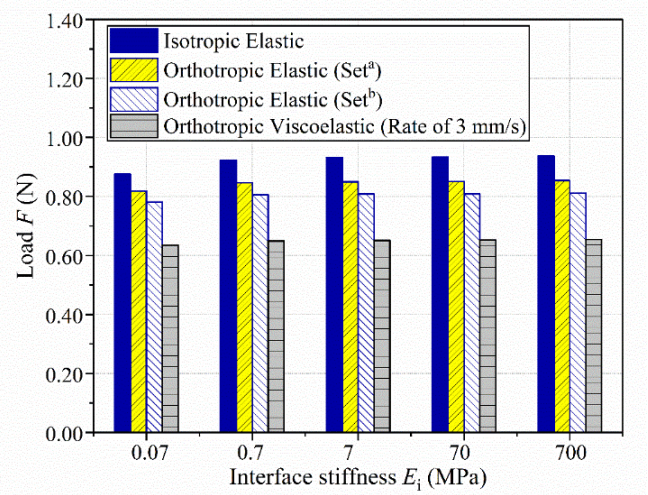

Figure 3: The effect of interface properties on the bending loads. Required loads to reach a tip displacement of 30 mm at room temperature are compared using various material models. Resin viscoelastic properties selected for the orthotropic viscoelastic material model are provided in [9]. The composite has the length of 150 mm, the width of 50 mm and the thickness of 1.67 mm.

  doi:10.5075/epfl-298799_978-2-9701614-0-0

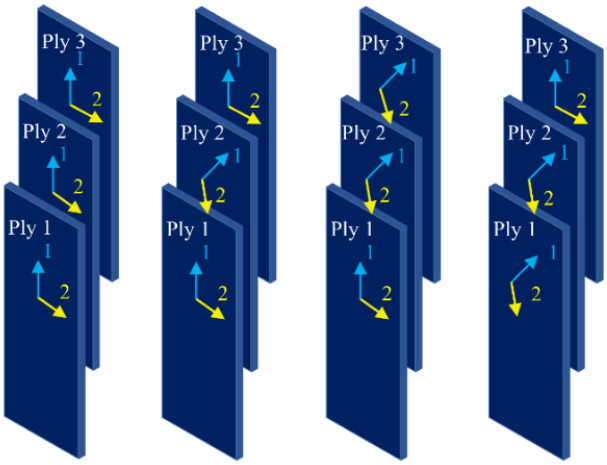

Figure 4: Stacking sequences of three-layer plate (a) Stacking 1 [0°/0°/0°]; (b) Stacking 2 [0°/45°/0°]; (c) Stacking 3 [0°/45°/45°]; (d) Stacking 4 [45°/45°/0°].

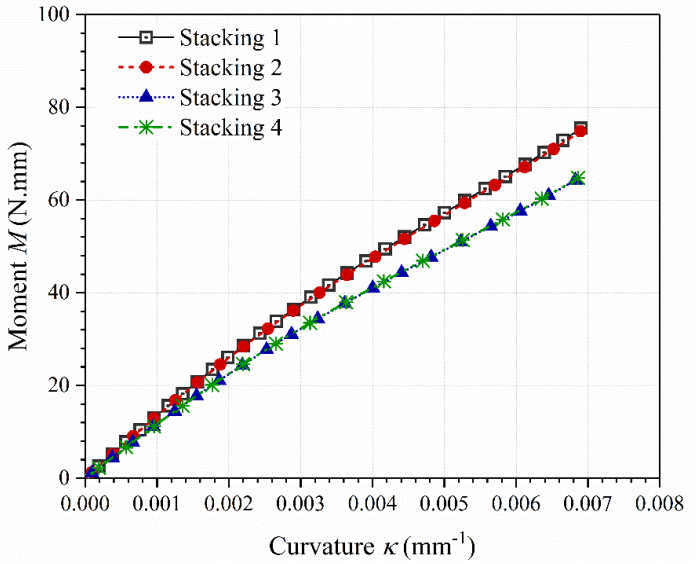

Figure 5: Moment vs curvature for all selected stacking sequences at room temperature. A loading rate of 3 mm/s and an interface modulus, Ei, of 7 MPa were considered for all cases. Resin viscoelastic properties are similar to those provided in [9].

4. Conclusions and discussion

The viscoelastic bending behaviour of multi-layered composite plates with thin and soft interfaces was analyzed using an efficient multi-scale modelling approach. The effect of ply slippage was captured by introducing a thin interface layer between the plies at the macro-scale. Some discrepancies between the numerical result and the experimental data were noted that may be attributed to the assumed input parameters for the fibre bending stiffness, resin viscoelastic characteristics and yarn architecture due to the lack of experimental data for material properties at micro- and meso-scale. Therefore, conducting additional experimental study on the viscoelastic characteristics of composites at the small scales will advance our understanding of the bending response of composites during manufacturing and, ultimately, enhance the accuracy of the proposed method.

  doi:10.5075/epfl-298799_978-2-9701614-0-0

As the bending response of the uncured prepregs was found to be dominated by their ply bending stiffness rather than inter-ply friction, further investigation on the bending mechanism of thicker laminated composites is suggested to ascertain the limitations and validity range of the viscoelastic multi-scale model predictions for wrinkle formation in large composite parts. Finally, it should be highlighted that temperature effect was ignored in the paper. As temperature is a critical parameter during forming, studying the variation of resin viscoelastic properties with temperature and their effect on wrinkle formation will be investigated in the future.

Acknowledgements

This research was supported by Vietnam International Education Cooperation Department – Ministry of Education and Training, University of Technology Sydney (Australia) and University of Victoria (Canada).

5. References

1. Long AC. Design and manufacture of textile composites. Cambridge: Woodhead Publishing Limited; 2005.
2. Alshahrani H, Hojjati M. Bending behavior of multilayered textile composite prepregs: Experiment and finite element modeling. Materials & Design. 2017;124:211-24.
3. Belnoue JPH, Nixon-Pearson OJ, Thompson AJ, Ivanov DS, Potter KD, Hallett SR. Consolidation-Driven Defect Generation in Thick Composite Parts. J Manuf Sci Eng. 2018;140(7).
4. Le VA, Nimbalkar S, Zobeiry N, Malek S. An efficient multi-scale approach for viscoelastic analysis of woven composites under bending. Submitted to Composite Structures, minor revision. 2022.
5. Le VA, Zobeiry N, Erkmen E, Malek S. Buckling behaviour of laminated viscoelastic composites under axial loads. Mech Mater. 2021.
6. Malek S. Efficient multi-scale modelling of viscoelastic composites with different microstructures [PhD Thesis]. Canada: University of British Colombia; 2014.
7. Naik RA. Analysis of woven and braided fabric reinforced composites. Washington DC: National Aeronautics and Space Administration; 1994. Contract No.: NASA CR-194930.
8. Warren CY, Richard GB. Roark's formulas for stress and strain. Seventh Edition ed. United States of America: McGraw-Hill; 2002.
9. Thorpe R. Experimental characterization of the viscoelastic behavior of a curing epoxy matrix composite from pre-gelation to full cure. Canada: University of British Colombia; 2012.
10. Gere J, M,., Goodno BJ. Mechanics of material. 7th, editor: Global Engineering; 2009. 1184 p.

  doi:10.5075/epfl-298799_978-2-9701614-0-0

BUCKLING TEST OF STIFFENED PANELS: MODELING AND VIBRATIONAL CORRELATION TESTING

Daniël, Peeters[a], Alfonso, Pagani[b], Riccardo, Augello[b], Erasmo, Carrera[b], Alex, Pereira do Prado[c], Pedro, Higino Cabral[c], Henrique, Dos Santos[d]

a: Delft University of Technology, faculty of Aerospace Engineering, section: Aerospace Structures and Computational Mechanics – d.m.j.peeters@tudelft.nl
b: MUL2, Department of Mechanical and Aerospace Engineering, Politecnico di Torino, Torino, Italy
c: Embraer S.A., São José dos Campos, Brazil
d: Instituto Tecnologico de Aeronautica, São José dos Campos, Brazil

Abstract: *Representative stiffened panels are optimized such that multiple buckling modes and failure (using open hole allowables) occur within a range of 10% of the lowest buckling load. This implies the panels cannot be loaded up to the buckling load without risking failure, hence vibrational correlation testing was used to estimate the buckling loads and modes. At the same time, a finite element model was created using the Carrera Unified Formulation. This model was validated using the tests and a good correlation between both was observed. Three panels were manufactured and each panel was put in place for testing twice. Each time a panel was put in place, the test was repeated three times. This allowed us to get a ballpark estimate for the variation due to replicas of the panel, the test set-up and repeating the tests.*

Keywords: vibrational correlation; buckling; stiffened panel

1. Introduction

The uncertainty or spread in properties is usually checked at the coupon level in terms of the material properties. However, it is not the spread in the material properties, but the spread of the performance of the resulting structure that is of interest to the user. In this work, the buckling load of a panel will be investigated using Vibration Correlation Testing (VCT). The outcome will lead to insights in the cause of the scatter, besides material scatter which is already studied more frequently.

The key assumption of VCT is that the vibration modes are similar to the buckling modes. By using that assumption, one can plot the relationship between the natural frequencies and the progressively higher applied (compression) loading. By extrapolating this relationship, the buckling load can be estimated as the load where the natural frequency is zero [1]. The advantage of VCT is that the buckling load can be estimated without the need to buckle the structure, which may lead to panel failure.

In the ideal case of stable buckling (i.e., Euler buckling), the natural frequency squared and the compressive load are linearly dependent [2], so that:

$$\left(\frac{f}{f_0}\right)^2 + \left(\frac{P}{P_{cr}}\right) = 1 \tag{1}$$

where f is the natural frequency of the structure under load P, f_0 is the natural frequency of the unloaded structure, and P_{cr} is the critical buckling load. In [3] it was shown that eq. (1) works

  doi:10.5075/epfl-298799_978-2-9701614-0-0

well for simply supported columns, but for other types of structures or boundary conditions, the curve becomes curved rather than the straight line predicted by eq. (1). One of the more advanced formulations reads [4,5]

$$\left(1-\frac{P}{P_{cr}}\right)^2+(1-\xi^2)\left(1-\left(\frac{f}{f_0}\right)^4\right)=1 \tag{2}$$

where ξ represents the experimental knock-down factor. In the present work, the VCT method used is similar to eq. (2).

In this work, we aim to investigate the influence of different parts (called replica's in the current work), the influence of the test set-up and the repetition of the same test with the same test set-up. For this purpose three stiffened panels are manufactured. The tests done are compression test where VCT is used to assess the panel's response and estimate the buckling load and buckling mode. This type of test allows us to accurately estimate the buckling load, without risking to break the panel.

2. Design and manufacturing

2.1 Design and analysis

The panels were optimized using the slice and swap method [6] in terms of lamination parameters, in such a way that multiple buckling modes happen within 10% of the lowest buckling load. Furthermore, failure of the panel (using open-hole allowables) also happened in this load region. Next to the lamination parameters also the width, height and thickness of the stiffener and the thickness of the panel were changed during the optimization. The 50 mm on each side (which in reality is encapsulated in a resin block), shown on the left in Figure 1, is not taken into account in this optimization, instead a simply supported line load is used.

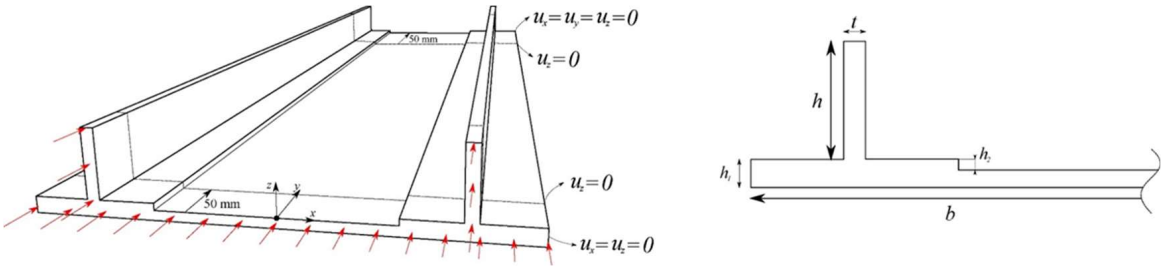

Figure 1. Panel dimensions (left) and stiffener dimensions (right)

The end result of the optimization is a two-stringer reinforced panel with a length of 690 mm (free length) and width b of 270 mm. On the right of Figure 1 the dimensions of the final cross-section are shown. Here, the stringer height and thickness are h = 39.3 mm and t = 7.3 mm, respectively, whereas h_1=9.52 mm and h_2=3.66 mm. Afterwards, the design is transferred into a stacking sequence using 0/90/45/-45 degree plies. Since failure and buckling happen so close together, the VCT method is used to estimate the buckling load to allow multiple repetitions of the test without risk of braking the panel.

After design, more detailed analysis of the panel is performed, including the 50 mm resin blocks that are used on the outside. This detailed analysis is performed using the Carrera Unified Formulation (CUF) [7]. The main advantage of this method is that classical to higher-order models can be implemented with ease in an automated way. In fact, the governing equations

and the related finite element arrays are written in terms of theory-independent fundamental nuclei (kernels) in CUF. When extended to laminated composite structures, it is therefore possible to formulate advanced models with layer-wise kinematics [8]. CUF-based layerwise models are computationally efficient and provide accurate through-the-thickness stress states [9], which are of fundamental importance in the nonlinear analysis and whenever a rigorous estimation of the tangent (incremental) stiffness is required, such as in the case of VCT simulations. The buckling modes predicted are shown in Figure 2.

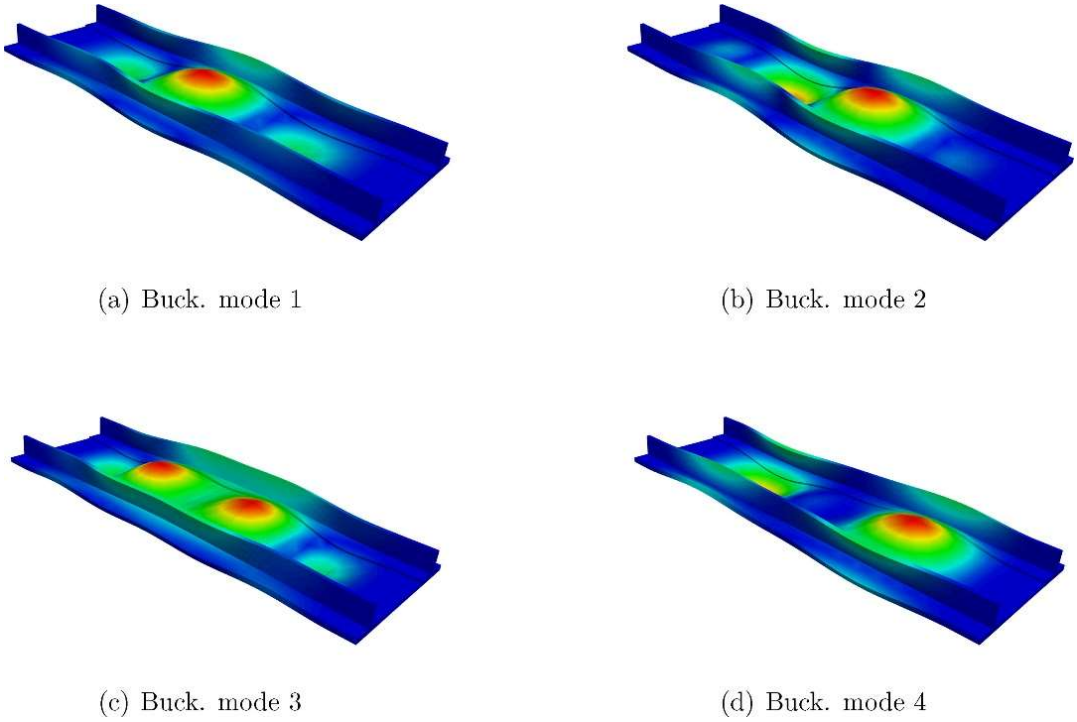

Figure 2. buckling modes from finite element simulations

2.2 Manufacturing

The reinforced composite panels were manufactured at the Delft Aerospace Structures and Materials Laboratory. The AS4 unidirectional prepreg employed has the following material properties: E_1=119 GPa, E_2=9.8 GPa, E_3=4.67 GPa, ν_{12}=0.316, ν_{13}=0.026, ν_{23}=0.33, G_{12}=4.7 GPa, G_{13}=G_{23}=1.76 GPa, and ρ=1580kg/m3. Note that the properties in the out-of-plane directions (13 and 23) are assumed and not available from the manufacturer.

As a first step, the layers of the skin were stacked on top of each other, regularly debulking to ensure good bonding between the layers. The stiffeners were manufactured by making two parts from the same layup, again often debulking them. One of the two parts was flipped before being bent in L format to guarantee that the stringer web was symmetric, and finally the two L-parts were put back-to-back, obtaining the T-stringer. The noodle at the bottom between the two L-parts was filled up using unidirectional 0 degree material. Finally, the stiffeners were carefully placed on the panel and the stiffened composite panel was co-cured as a whole. During curing, care was taken to ensure that the pressure was evenly distributed, the stiffeners did not fall over and stayed in their intended position on the panel.

After curing, all sides of the panel were trimmed to their final dimensions. To provide the clamped boundary conditions on the short edges, the outer 50 mm were molded in an epoxy.

This epoxy was flattened to ensure the compression load is applied perfectly in line with the panel. The final dimension of the panel used for the simulation is the 'free' length: the part molded in the epoxy is not modeled. The three finished panels are shown in Figure 3.

Figure 3. Manufactured panels

3. Testing

3.1 Test plan

Since the main goal is to get a grip on the source of variation, we have used a nested or hierarchical design of experiments [10]. In our case there are two levels we want to investigate: the influence of replica's and the test set-up, and both may have an influence on the result. We have set up three replica's, and each replica will be put in the test set-up twice in a random order. For each set-up, three measurements are performed to check the influence of the measurement accuracy. A graphical representation of the test plan can be seen in Figure 4.

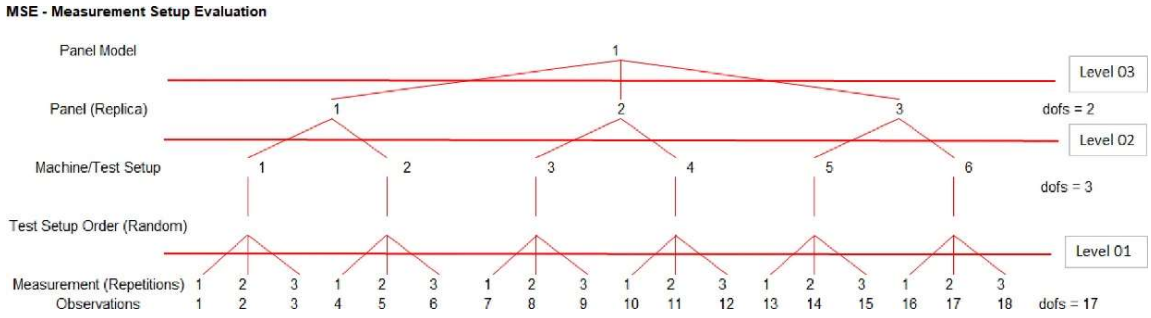

Figure 4. Test plan

3.2 Test preparation

The compression tests were performed using a MTS machine with a maximum force of 3500 kN and an accuracy of 1 kN. One of the panels placed in this machine is shown in Figure 5. During the compressive loading, VCT was performed with loads up to 600 kN; i.e. approximately 80% of the expected buckling load. A Polytec laser vibrometer was used for the data acquisition. A shaker was used as excitation device, using a frequency sweep between 0 and 1000 Hz. The load was gradually changed to ensure the panel does not fail due to dynamic defects. A measurement

with the vibrometer was performed every 100 kN, leading to six measurements. The shortening was measured using two linear vertical displacement transducers (LVDT): one was placed on each side of the panel to ensure the panel was loaded in pure compression and no moment was induced on it. The test set-up is shown in Figure 5.

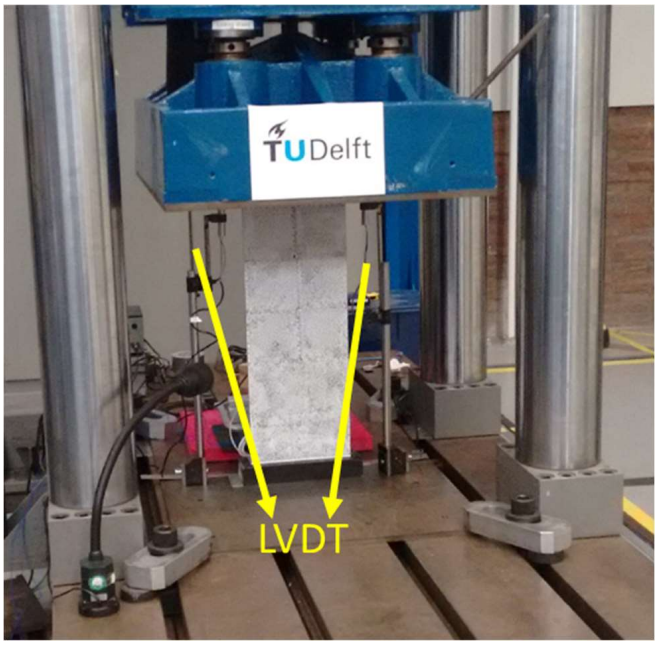

Figure 5. Test set-up

The VCT was performed using a 7x3 mesh, which allows to track the expected buckling modes. During the test the first four frequency response function peaks were tracked. By tracking the mode shapes, we can determine the frequency change at each loading level. This information is then extrapolated to predict the linear static buckling load (i.e., the location with zero frequency) in a nondestructive way, reducing the chance of introducing defects in the panel during the repeated loading tests.

4. Results and discussion

Before diving into the VCT result and buckling, first the stiffness in compression of the panels is checked, by comparing the E-modulus of the different panels with the finite element models. The Nastran model was built by using 2D CQUAD elements, based on a first-order shear approximation theory and homogenized properties across the thickness. The results are shown in Table 1. It can be seen that very little scatter is present between the panels, and a good correlation with the finite element models exists. As demonstrated previously in literature, the Nastran model is appropriate for linear static considerations, but should be avoided when the evaluation of the internal stress state is of fundamental importance, for example for failure and buckling calculations.

The results of the VCT calculation for the different modes is shown in Table 2. The average of all tests is used in this table to compare to the CUF model. The Nastran model is not used for these calculations. For frequency 4, there is no data for the first measurement loads since this mode is not one of the lowest 4 modes measured at the lower loads, the frequency at these loads is unknown. In general, a good match between the experiments and the CUF model is observed. The small differences will not affect the conclusions.

  doi:10.5075/epfl-298799_978-2-9701614-0-0

Table 1: Compression test: stiffness results.

	Shortening [mm]	Loading [kN]	Compression modulus [MPa]
Panel 1	2.61	599.97	229.9
Panel 2	2.61	599.82	229.8
Panel 3	2.61	599.98	229.9
Nastran	2.41	600	249.0
CUF model	2.41	600	249.0

Table 2: Vibration analysis: comparison of CUF model and experiments.

Load [kN]	f_1 [Hz] CUF	f_1 [Hz] exp.	F_2 [Hz] CUF	f_2 [Hz] exp.	f_3 [Hz] CUF	f_3 [Hz] exp.	f_4 [Hz] CUF	f_4 [Hz] exp.
100	349	348	462	459	550	555	622	—
200	330	339	447	457	537	553	578	—
300	308	324	431	449	523	546	532	—
400	284	304	415	436	513	535	476	514
500	258	281	398	420	499	522	414	462
600	225	253	381	407	487	505	336	394

The measured frequencies, as a function of the compression load is graphically shown in Figure 6. Here also the confidence interval of the tests is provided. On the graph on the left it can be observed that the first two buckling modes are also with the VCT method predicted to be very close together. The fourth frequency, which is only measured from 400 kN onwards, is rapidly decreasing and is the second buckling mode expected. The second and third frequency decrease slower and are linked to a much higher buckling load. On the right, the predictions with the CUF model and the extrapolated experimental data can be seen, which both lead to two buckling loads being close together, but the experiments over-estimate the buckling load.

The measured modes using VCT are shown in Figure 7. The first and fourth mode, which are expected to be the first two buckling modes based on the extrapolation, show a good match with the buckling modes expected based on the simulation. Modes 2 and 3 are related to the stiffener or outsides of the plate buckling, which does not match the expected buckling modes. This is however expected since the extrapolated load at which these modes reach a zero frequency is a lot higher than the first buckling load.

  doi:10.5075/epfl-298799_978-2-9701614-0-0

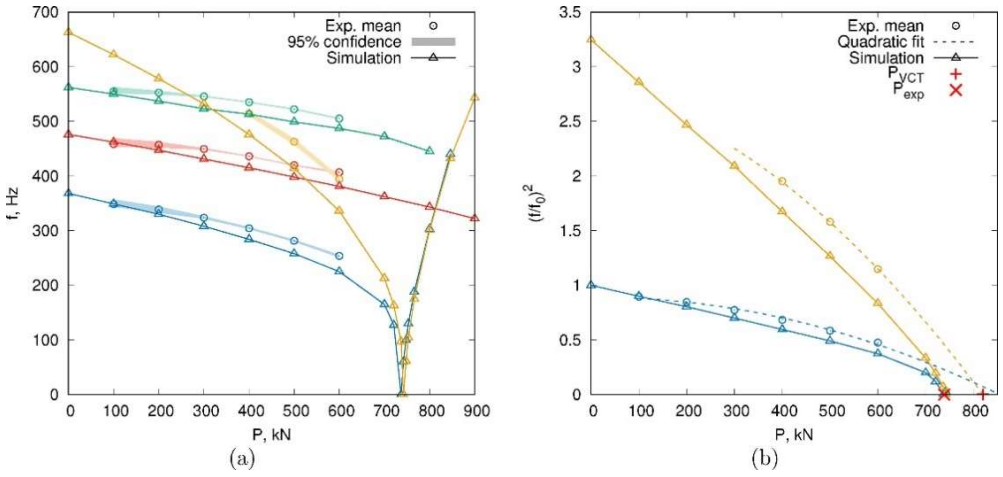

Figure 6. VCT results

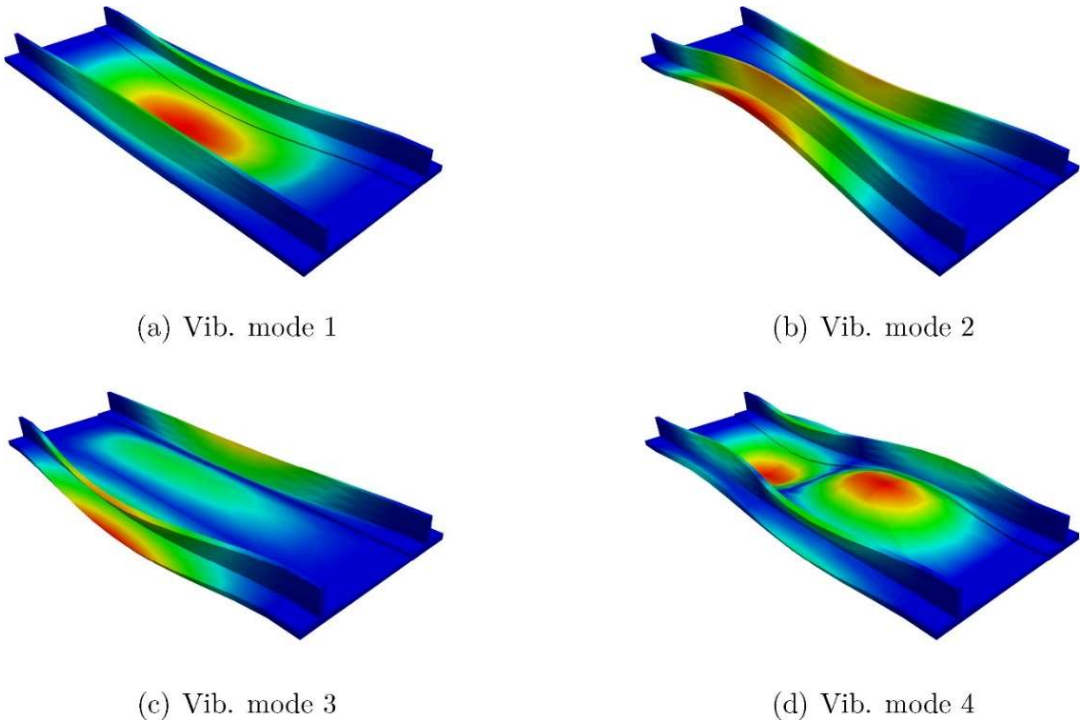

Figure 7. vibrations modes obtained from CUF model

Based on the different tests, it was found that the different set-ups could not be distinguished from each other at 200 kN since the natural variation of the measurements (i.e., repeating the same test without changing the set-up) has the same magnitude as the variance between test set-ups. This shows that the test set-ups cannot be distinguished from each other, and that the test set-up gives a very good repeatability.

5. Conclusion

The current work shows a first step towards getting a grip on the variation between structural parts and where they come from. A stiffened panel was optimized to have multiple buckling modes and failure within a margin of 10% of the lowest buckling load. Using CUF, the stiffness, buckling loads/modes and natural frequencies at different compressive loads were predicted.

The finite element results and experiments showed a good match, highlighting the potential of this method to be used during design.

The influence of the test set-up and replicas could not be distinguished in this case due to the relatively low number of tests. The results do give a ballpark figure for the variation due the replica's and the test set-up. With this information, we can expand our experimental configuration in order to improve the standard variation estimates to also include other important factors such as different material batches and/or parts suppliers, for example.

6. References

1. J. Singer, J. Arbocz, and T. Weller. Buckling experiments, shells, built-up structures, composites and additional topics, volume 2. John Wiley & Sons, 2002.
2. L.N. Virgin and R.H. Plaut, Effect of axial load on forced vibrations of beams, Journal of Sound and Vibration, 168(3):395-405, dec 1993
3. H. Abramovich, D. Govich, and A. Grunwald. Buckling prediction of panels using the vibration correlation technique. Progress in Aerospace Sciences, 78:62-73, 2015.
4. M.A. Souza, W.C. Fok, and A.C. Walker. Review of experimental techniques for thinwalled structures liable to buckling, Part I - neutral and unstable buckling. Experimental Techniques, 7(9):21-25, sep 1983.
5. M.A. Souza, W.C. Fok, and A.C. Walker. Review of experimental techniques for thinwalled structures liable to buckling, Part II - stable buckling. Experimental Techniques, 7(10):36-39, oct 1983.
6. G. H. C. Silva, A. P. do Prado, P. H. Cabral, R. De Breuker, and J. K. S. Dillinger, Tailoring of a composite regional jet wing using the slice and swap method, J. Aircraft., vol. 56, no. 3, pp. 990–1004, 2019
7. E. Carrera, M. Cinefra, M. Petrolo, and E. Zappino, Finite Element Analysis of Structures through Unified Formulation. John Wiley & Sons, Chichester, West Sussex, UK, 2014.
8. A. Pagani, A. G. de Miguel, M. Petrolo, and E. Carrera, Analysis of laminated beams via unified formulation and Legendre polynomial expansions, Compos. Struct., vol. 156, pp. 78–92, 2016
9. A. G. de Miguel, I. Kaleel, M. H. Nagaraj, A. Pagani, M. Petrolo, and E. Carrera, Accurate evaluation of failure indices of composite layered structures via various Fe models, Compos. Sci. Technol., vol. 167, pp. 174–189, 2018
10. D. C. Montgomery, Design and Analysis of Experiments, Wiley Hoboken, NJ, 1984

PREDICTING THE EFFECTIVE THERMAL CONDUCTIVITY OF INJECTION MOULDED SHORT GLASS FIBRE REINFORCED POLYAMIDE USING DIFFERENT EFFECTIVE MEDIUM THEORIES

Majid Mokarizadehhaghighishirazi [a,b], Bart Buffel [a], Stepan Lomov [c], and Frederik Desplentere [a]

a: Department of Materials Engineering, KU Leuven Campus Bruges, Research Group ProPoliS, Spoorwegstraat 12, 8200 Bruges, Belgium
b: SIM M3 program, Technologiepark 48, B-9052 Zwijnaarde, Belgium
c: Department of Materials Engineering, KU Leuven, Kasteelpark Arenberg 44 Box 2450, 3001, Leuven, Belgium
(majid.shirazi@kuleuven.be)

Abstract: *This paper deals with predicting the effective thermal conductivity (ETC) of injection moulded short fibre reinforced polymers (SFRPs) using different homogenisation schemes: a scheme which is a reformulated model for electric permittivity, described by the same equations as the heat transfer, and a two-step homogenisation model. In both cases, the fibre orientation tensor (FOT) obtained from Autodesk Moldflow simulation is used. Concerning the two-step homogenisation, the Mori-Tanaka model is used in the first step for calculating the ETC in the hypothetical case of complete fibre alignment, followed by an orientation averaging based on the FOT inside each element. The ETCs predicted with both methods are compared with each other, and evaluated against the experimental measurements for the injection moulded Polyamide reinforced with short glass fibre. The values predicted by both approaches are found to be in good agreement with that of ETCs measured on a flat coupon. Both schemes can be hence used for homogenisation of the ETC of injection moulded SFRPs.*

Keywords: effective thermal conductivity; homogenisation; fibre orientation tensor

1. Introduction

Several models have been developed to predict the ETC of composites. Generally, they can be categorised in two different groups: methods based on numerical modelling and models based on analytical approaches [1]. Concerning the numerical methods, which are mainly represented by the Finite Element method (FEM), they can predict the effective properties of composites quite accurately if the complex microstructure is provided in detail [2]. However, generating and meshing a representative volume element (RVE), that accurately describes the fibre´s placement and orientation in the injection moulded SFRP is not feasible. The computational process might be inefficient, time-consuming and costly [3]. Regarding the analytical models, one can distinguish between two categories: Models on the basis of the Eshelby´s single inclusion problem and methods based on the Laplace`s heat transfer equation [4]. These two analytical approaches have been used separately to obtain effective medium properties. Regarding homogenisations based on the Laplace`s heat transfer equation, which is also called the Maxwell's homogenisation scheme, early works considered dispersion of spheres or ellipsoids embedded in a matrix. In the context of the electric properties, this theory is called Maxwell´s theory for spherical inclusions and Fricke´s theory for ellipsoidal

  doi:10.5075/epfl-298799_978-2-9701614-0-0

inclusions. Sometimes the term Maxwell-Garnett theory is used for both geometries [5]. In any case, this approach is perfectly equivalent to the so called mean-field homogenisation scheme (Mori-Tanaka, etc.), which is based on the Eshelby´s problem. When the volume fraction of inclusions is higher than a given threshold, differential methods are introduced in both thermal/electric and elastic contexts. This differential approach is summarised in [6] and [7] for predicting the effective permittivity (based on the Maxwell's homogenisation scheme) and elastic moduli (based on the mean-field homogenisation approach), respectively.

The orientation of ellipsoidal inclusions can affect the effective properties of the composite significantly. The orientation of fibres within the matrix can be expressed via the FOT, which is defined by forming the dyadic products of the unit vectors along fibre´s axis and then integrating over all possible directions using the orientation distribution function (ODF). It has been shown that the second-order orientation tensor (a_{ij}) is the only knowledge about the orientation distribution function which is needed to perform the orientation averaging, which is defined as taking an average of unidirectional properties over all directions, weighted by the ODF [8]. The FOT of injection moulded parts can be obtained via conducting simulation using different commercially available software packages such as Autodesk Moldflow, Moldex3d, etc. as well as employing experimental techniques like X-ray computed tomography [9]. Concurrently, Giordano [10] has introduced a scalar parameter to determine the state of order (orientation) of inclusions for electrical characterisation of a heterogeneous medium, which can be also used in predicting the fibre orientation-dependent ETC of the SFRPs.

The relationship between the components of the FOT and the scalar orientation parameter in Giordano´s model [10] has not been stated explicitly. This will be clarified in this research by three simple equations. Subsequently, the Giordano model is coupled with the FOT results obtained from Autodesk Moldflow simulation via a MATLAB script. To the best of our knowledge, this approach has not been employed in modelling the local ETC of injection moulded SFRPs so far. Apart from the Giordano´s model, a two-step homogenisation method using orientation averaging is developed to find the local ETC of injection-moulded SFRPs. Firstly, the Mori-Tanaka model is used for calculating the ETC in the hypothetical case of perfectly aligned fibres. Giordano´s simplified model for this case is also used to check the results. In the second step, the actual misaligned fibre orientation inside each element (FOT on elements) is taken into account for homogenising the ETC using an orientation averaging approach.

2. Theories, Procedures and Materials

2.1 Maxwell´s homogenisation scheme: Giordano´s model

Based on the model proposed by Giordano [10], which is originally developed for predicting effective electric permittivity, the Maxwell´s solution is expanded based on the Bruggeman´s differential approach to consider the orientational order/disorder of ellipsoidal particles in composite by introducing a scalar parameter, S. The main results which have been reformulated to calculate the ETC of SFRPs are as follows:

$$1-\nu_f = \frac{k_f-k_{zz}}{k_f-k_m}\left(\frac{k_m}{k_{zz}}\right)^{\frac{3L(1-2L)}{2-3L+S-3SL}}\left[\frac{(1+3L-S+3SL)k_m+(2-3L+S-3SL)k_f}{(1+3L-S+3SL)k_{zz}+(2-3L+S-3SL)k_f}\right]^{\frac{(1-3L)^2(2+S)(1-S)}{(2-3L+S-3SL)(1+3L-S+3SL)}}, \quad (1a)$$

$$1-v_f = \frac{k_f-k_{xx}}{k_f-k_m}\left(\frac{k_m}{k_{xx}}\right)^{\frac{3L(1-2L)}{2-3L-2S+6SL}}\left[\frac{(1+3L+2S-6SL)k_m+(2-3L-2S+6SL)k_f}{(1+3L+2S-6SL)k_{xx}+(2-3L-2S+6SL)k_f}\right]^{\frac{2(1-3L)^2(2S+1)(1-S)}{(2-3L-2S+6SL)(1+3L+2S-6SL)}}. \quad (1b)$$

In Eq. (1a) and (1b), v_f, k_m and k_f are fibre volume fraction, thermal conductivity of the matrix and thermal conductivity of fibres, respectively. L is the shape factor, which is dependent on the aspect ratio of fibres (the length of each fibre divided by its diameter, $e = l/d$) , which can be computed from

$$L = \frac{e}{4(\sqrt{e^2-1})^3}\left[2e\sqrt{e^2-1} + ln\frac{e-\sqrt{e^2-1}}{e+\sqrt{e^2-1}}\right]. \quad (2)$$

The shape factor is calculated based on the assumption that we are dealing with ellipsoids of rotation as inclusions which means that the length of ellipsoid´s axes along y- and z-direction are the same and the ellipsoid is invariant under a rotation around the x-axis. Therefore, the composite is assumed to be transversely isotropic whose thermal conductivity tensor is

$$[k] = \begin{bmatrix} k_{xx} & 0 & 0 \\ 0 & k_{zz} & 0 \\ 0 & 0 & k_{zz} \end{bmatrix}. \quad (3)$$

Concerning the orientational factor S, it can be shown that it is related to the diagonal components of the FOT (a_{ij}) as in:

$$S = (3\,a_{xx} - 1)/2 = 1 - 3a_{yy} = 1 - 3a_{zz}. \quad (4)$$

When $S = 1$, the state of complete order is considered; i.e. all fibres are assumed to aligned with x direction ($a_{xx} = 1$). In this case, Eq. (1) will be simplified for obtaining the ETC in the case of complete order, regarded as simplified Giordano´s model in this paper. $S = 0$ refers to a random orientation in which fibres have no preferential direction ($a_{xx} = a_{yy} = a_{zz} = 1/3$). The deviation from the complete ordered condition increases as S takes values from 1 to 0. It should be noted that assuming the condition of transverse isotropy requires two conditions to be satisfied in the FOT; $a_{yy} = a_{zz}$ and $a_{ij} = 0 \text{ when } i \neq j$. That is the off-diagonal components of the tensor are zero.

2.2 Mean-field homogenisation scheme: Mori-Tanaka model

A family of models for composite materials with no-dilute concentration of inclusions has been developed from a proposal originally made by Mori and Tanaka [11]., which is then reformulated for predicting the ETC of SFRPs. The ETC of the composite can be expressed as a second-order tensor, $\boldsymbol{k}$, which can be calculated from

$$\boldsymbol{k} = \boldsymbol{k}_m + v_f\big(\boldsymbol{k}_f - \boldsymbol{k}_m\big)\boldsymbol{A}, \quad (5)$$

where $\boldsymbol{A}$ is the intensity-concentration tensor (similar to the strain-concentration tensor in elasticity). Different models in the mean-field homogenisation scheme have suggested various formulae for obtaining $\boldsymbol{A}$**.** Based on Mori-Tanaka, we have:

$$\boldsymbol{A}^{MT} = \boldsymbol{A}^{ES}\big[\big(1-v_f\big)\boldsymbol{I} + v_f\boldsymbol{A}^{ES}\big]^{-1}. \quad (6)$$

$\boldsymbol{I}$ is the second-order identity tensor, and $\boldsymbol{A}^{ES}$ is the Eshelby concentration tensor, which can be calculated by

$$\boldsymbol{A}^{ES} = \left[\boldsymbol{I} + \boldsymbol{S}\boldsymbol{k}_m^{-1}\left(\boldsymbol{k}_f - \boldsymbol{k}_m\right)\right]^{-1}. \quad (7)$$

$\boldsymbol{S}$ is called the interior-point Eshelby thermal conductance tensor, which is dependent on the inclusions size and its detailed expressions is given in [4]. The Mori-Tanaka approach will be used for obtaining the ETC of the unidirectional oriented SFRPs.

2.3 Fibre orientation averaging

In order to incorporate the effect of the fibre orientation on the ETC, consider $\boldsymbol{k}(\boldsymbol{p})$ as a tensorial property of the composite associated with a unidirectional microstructure aligned in the direction of $\boldsymbol{p}$, which is a unit vector along each fibre´s axis. The orientation average of $\boldsymbol{k}$ is denoted by $\langle \boldsymbol{k} \rangle$ and is defined as:

$$\langle \boldsymbol{k} \rangle = \oint \boldsymbol{k}(\boldsymbol{p})\psi(\boldsymbol{p})d\boldsymbol{p}, \quad (8)$$

where $\psi(\boldsymbol{p})$ is the ODF.

According to [8], $\boldsymbol{k}$ must be a transversely-isotropic tensor with $\boldsymbol{p}$ as its axis of symmetry. Assuming $\boldsymbol{k}(\boldsymbol{p})$ as a second-order tensor, so that it can be expressed as: $\boldsymbol{k}(\boldsymbol{p}) = \begin{bmatrix} k_x & 0 & 0 \\ 0 & k_z & 0 \\ 0 & 0 & k_z \end{bmatrix}$. On the other hand, this tensor must also have the form:

$$k_{ij}(\boldsymbol{p}) = cp_ip_j + d\delta_{ij}, \quad (9)$$

where c and d are two scalar constants and δ_{ij} is the Kronecker delta. If we take the orientation average of the property, $\langle k \rangle_{ij}$, we get:

$$\langle k \rangle_{ij} = c\langle p_ip_j \rangle + d\langle \delta_{ij} \rangle = ca_{ij} + d\delta_{ij}. \quad (10)$$

In other words, the orientation average of a second-order tensor is completely determined by the second-order orientation tensor, and by the underlying unidirectional property tensor [8]. Now we aim to find the relationship between the constants (c and d) and unidirectional properties ($k_x$and k_z) . For this purpose, the first and second tensor invariants, $I_1$and I_2, of two expressions of $\boldsymbol{k}$ based on Eq. (3) and (10) are used to form a system of equations:

$$I_1 = trace(\boldsymbol{k}) = k_x + 2k_z = c + 3d \quad (11a)$$

$$I_2 = 1/2\left[(trace(\boldsymbol{k}))^2 - trace((\boldsymbol{k}^2))\right] = 2k_xk_z + k_z^2 = 2cd + 3d^2. \quad (11b)$$

Solving the system of equations results in:

$$d = k_z \; and \; c = k_x - k_z. \quad (12)$$

Substituting Eq. (12) in Eq. (10), and the orientation average of the second-order tensorial property of the composite (for example the ETC) can be derived using the FOT and unidirectional properties:

$$\langle k \rangle_{ij} = (k_x - k_z)a_{ij} + k_z\delta_{ij}. \quad (13)$$

2.4 Sample preparation, injection moulding simulation and the ETC measurements

DOMAMID 6LVG50H2BK, a commercial grade of polyamide 6 (PA6) composite reinforced with 50 weight percent short glass fibre (which is equivalent to around 30.8 volume percent), is injection moulded to produce dog-bone shaped samples originally used for tensile testing based on the ISO 527 1A standard. Thermal conductivity of PA6 is measured at 0.26 $Wm^{-1}K^{-1}$ and the conductivity of glass fibres assumed to be 1.30 $Wm^{-1}K^{-1}$[12]. Cylindrical fibres with aspect ratio of around 20 are assumed. Autodesk Moldflow is used to simulate the injection moulding process. Fibre orientation on elements result is used to find the FOT (a_{ij}) at each location of the part. It has been shown that injection moulding software packages can accurately predict the actual fibre orientation distribution in injection moulded parts [13], particularly for non-complex geometries like a tensile bar. Therefore, we can rely on the simulation results for the FOT on elements. C-therm Trident equipment is used to measure the thermal conductivity of unfilled PA6, as well as the injection-moulded composite samples along transversal (k_{zz}) and longitudinal (k_{xx}) directions. The Modified Transient Plane Source (MTPS) sensor is used for carrying out the measurements.

3. Results and discussions

3.1 Prediction of the ETC in the case of unidirectional fibre alignment

We begin our discussion by calculating the shape factor (L) in the Giordano´s model, which is only dependent on the fibres aspect ratio (e). The major mechanism in glass fibre breakage during the compounding process is buckling, as the tensile stresses developed in the melt are not high enough to fracture glass fibres in tension. The typical $e >= 20$ for commercial SFRPs is due to the fact that buckling is no longer possible below this value [14]. Figure 1 shows how L is changing with different values of e. It is evident that when e takes values above 10, L can be approximated at 0.5. Therefore, in our case, the shape factor can be assumed to be 0.5.

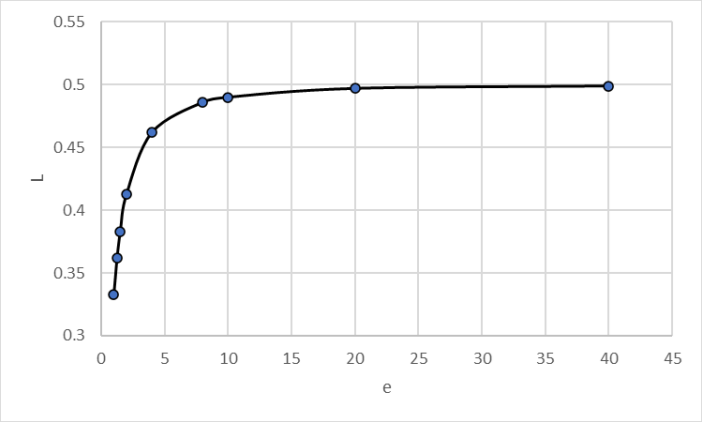

Figure 1. The variation of the shape factor versus the aspect ratio of fibres.

As we are dealing with predicting the unidirectional ETC in this part, the orientational factor in Giordano´s model is unity, $S = 1$. Hence, Eq. (1a) and (1b) can be expressed as:

$$1 - v_f = \frac{k_f - k_z}{k_f - k_m}\left(\frac{k_m}{k_z}\right)^{\frac{1}{2}}, k_x = (1 - v_f)k_m + v_f k_f \quad (14)$$

Regarding the Mori-Tanaka approach, the procedure starts with calculating the interior-point Eshelby thermal conductance tensor, $\boldsymbol{S}$. We are dealing with fibres with relatively high aspect ratios. So, they can be assumed as cylinders with circular cross section aligned along the flow direction (x axis). Then according to [4], $\boldsymbol{S}$ is calculated as:

$$\boldsymbol{S} = \begin{bmatrix} 0 & 0 & 0 \\ 0 & 0.5 & 0 \\ 0 & 0 & 0.5 \end{bmatrix} \tag{15}$$

Substituting Eq. (15) and thermal conductivities of the constituents in Eq. (7), $\boldsymbol{A}^{ES}$ would be obtained. $\boldsymbol{A}^{MT}$ could be also calculated using Eq. (6). Then, the ETC of the composite is predicted by Eq. (5). The calculations are done and the results are plotted against the fibre content in Figure 2 for the PA6/glass fibre composite. Moreover, this figure compares the predicted ETC based on Mori-Tanaka's approach to that of Giordano´s model. In the case of the particular composite studied in this paper in which $v_f = 0.308$, the results based on the simplified Giordano´s model and Mori-Tanaka are summarised in Table 1, which will be used for the orientation averaging in the next step.

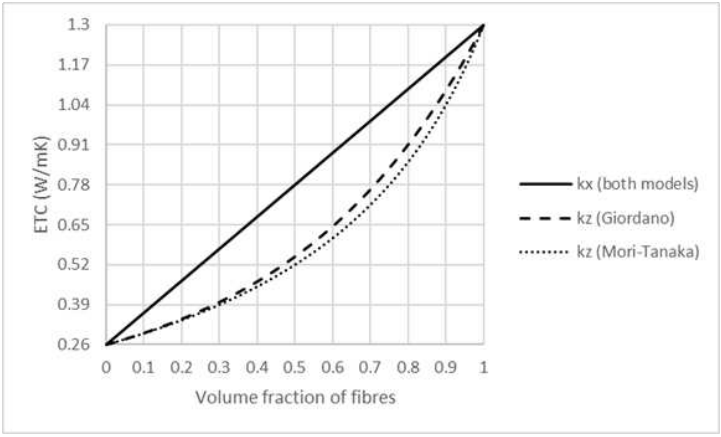

Figure 2. The variation of transversal (k_z) and longitudinal (k_x) ETCs versus v_f.

Table 1: comparison between k_z and k_x of DOMAMID 6LVG50H2BK for unidirectional fibre alignment predicted by the Giordano and Mori-Tanaka models.

Model	$\boldsymbol{k_x}$ $(Wm^{-1}K^{-1})$	$\boldsymbol{k_z}$ $(Wm^{-1}K^{-1})$
Giordano	0.580	0.403
Mori-Tanaka	0.580	0.394

Taking a glance at Figure 2 indicates that both models present the same values for the ETC along the fibre direction, which is also consistent to the Voigt upper bound model [11]. On the other hand, the ETCs perpendicular to the fibre´s direction are not identical. It seems that Giordano´s model predicts slightly higher values for k_z compared to Mori-Tanaka. The difference becomes more significant at higher volume fractions of fibres.

3.2 Prediction of the ETC in the case of misaligned fibre orientation

In this study, we will focus on predicting the ETC at the gauge length of the injection moulded tensile sample. The average values for diagonal components of the FOT in this region are reported in Table 2. Because of the converging flow, strong fibre alignment along the flow direction is seen in the gauge length, while little shares of fibres are aligned along other two axes. However the case certainly differs from perfect uniaxial alignment. Regarding the use of the Giordano model to predict the ETC, a MATLAB script is written to select elements that comply with the transverse isotropy conditions. Around 1500 elements are selected to form a volume of interest of 10 x 10 x 4 mm^3 in this region. 92% of the elements satisfies the transverse isotropy conditions. Using Eq. (1a) and (1b), the longitudinal and transversal ETC can be computed for each element, and then averaged for the region. Turning into the two-step homogenisation approach, firstly $k_x = 0.580$ and $k_z = 0.394\ Wm^{-1}K^{-1}$ will be used in Eq. (13) based on the Mori-Tanaka´s prediction in the case of complete order, according to Table 1. Afterwards, by having the FOT for each element from the Moldflow analysis and using Eq. (13), the orientation averaged ETC can be computed along each direction for every element and then volume-averaged for the region. These data are reported in Table 2 and compared to the measured ETC obtained from experiments.

Table 2: Comparison between the predicted and measured ETC for misaligned fibre orientation (ETCs are expressed in $Wm^{-1}K^{-1}$).

Average FOT components			**Two-step homogenisation**			**Giordano**		**Experiment**	
a_{xx}	a_{yy}	a_{zz}	k_{xx}	k_{yy}	k_{zz}	k_{xx}	k_{zz}	k_{xx}	k_{zz}
0.87	0.08	0.05	0.555	0.409	0.403	0.563	0.418	0.464±0.009	0.398±0.003

The measured k_{zz} and k_{xx} are found to be consistent with the predicted results, yet shows a small decrease in transversal ETC, possibly due to assuming perfect interfaces between the fibre and matrix in the models, and a more pronounced drop in the longitudinal ETC, which may be because of the gaps between samples when merging them for performing thermal conductivity measurements along the flow direction to cover the sensor surface.

4. Conclusions

Two different analytical methods based on the Maxwell`s homogenisation scheme and mean-field homogenisation method are used to predict the ETC of an injection-moulded SFRP part. When unidirectional fibre alignment is assumed, both models predict nearly identical longitudinal and transversal ETC. For predicting the ETC in case of misaligned fibres, the gauge length of an injection-moulded part is used. the process is firstly simulated via the Autodesk Moldflow in order to obtaining the FOT associated to each element. A MATLAB script is written to find elements whose FOT satisfies the transverse isotropy criteria, as required for the Giordano´s model. Regarding the two-step homogenisation, the Mori-Tanaka results for unidirectional fibre alignment are used to find the constants associated to the orientation averaging formulation. The predicted ETCs based on these two approaches are fairly consistent, while the Giordano's model predicts slightly higher values. Also, experimental measurements of the transversal and longitudinal ETC are found to be in good agreement with the predicted values.

Acknowledgements

The work leading to this paper has been funded by the ICON project “ProPeL”, which fits in the MacroModelMat (M3) research program, coordinated by Siemens (Siemens Digital Industries Software, Belgium), and funded by SIM (Strategic Initiative Materials in Flanders) and VLAIO (Flemish government agency Flanders Innovation & Entrepreneurship).

5. References

1. Zhai S, Zhang P, Xian Y, Zeng J, Shi B. Effective thermal conductivity of polymer composites: Theoretical models and simulation models. International Journal of Heat and Mass Transfer. 2018 Feb 1;117:358-74.
2. Tian W, Qi L, Zhou J, Liang J, Ma Y. Representative volume element for composites reinforced by spatially randomly distributed discontinuous fibers and its applications. Composite Structures. 2015 Nov 1;131:366-73.
3. Mirkhalaf SM, Eggels E, Anantharanga AT, Larsson F, Fagerström M. Short fiber composites: Computational homogenization vs orientation averaging. Melbourne, VIC: Engineers Australia. 2019 Jan:3000-7.
4. Tian W, Fu MW, Qi L, Ruan H. Micro-mechanical model for the effective thermal conductivity of the multi-oriented inclusions reinforced composites with imperfect interfaces. International Journal of Heat and Mass Transfer. 2020 Feb 1;148:119167.
5. Duan HL, Karihaloo BL, Wang J, Yi X. Effective conductivities of heterogeneous media containing multiple inclusions with various spatial distributions. Physical Review B. 2006 May 5;73(17):174203.
6. Giordano S. Effective medium theory for dispersions of dielectric ellipsoids. Journal of electrostatics. 2003 May 1;58(1-2):59-76.
7. Giordano S. Differential schemes for the elastic characterisation of dispersions of randomly oriented ellipsoids. European Journal of Mechanics-A/Solids. 2003 Nov 1;22(6):885-902.
8. Advani SG, Tucker III CL. The use of tensors to describe and predict fiber orientation in short fiber composites. Journal of rheology. 1987 Nov;31(8):751-84.
9. Baradi MB, Cruz C, Riedel T, Régnier G. Frontal weld lines in injection-molded short fiber-reinforced PBT: Extensive microstructure characterization for mechanical performance evaluation. Polymer Composites. 2019 Dec;40(12):4547-58.
10. Giordano S. Order and disorder in heterogeneous material microstructure: Electric and elastic characterisation of dispersions of pseudo-oriented spheroids. International journal of engineering science. 2005 Sep 1;43(13-14):1033-58.
11. Tucker III CL, Liang E. Stiffness predictions for unidirectional short-fiber composites: review and evaluation. Composites science and technology. 1999 Apr 1;59(5):655-71.
12. Bansal NP, Doremus RH. Handbook of glass properties. Elsevier; 2013 Oct 22.
13. Foss PH, Tseng HC, Snawerdt J, Chang YJ, Yang WH, Hsu CH. Prediction of fiber orientation distribution in injection molded parts using Moldex3D simulation. Polymer Composites. 2014 Apr;35(4):671-80.
14. Inceoglu F, Ville J, Ghamri N, Durin A, Valette R, Vergnes B. A Study of Fiber Breakage During Compounding of Glass Fiber Reinforced Composites. InProceedings of the Polymer Processing Society 26th Annual Meeting, Banff, AB, Canada 2010 Jul (pp. 4-8).

A NEW TEST FOR VALIDATING MODELS OF LIGHTNING STRIKE DAMAGE ON CFRP LAMINATES

Tim, Harrell[a], Ole, Thomsen[b], Janice, Dulieu-Barton[b]

a: University of Virginia, Department of Mechanical and Aerospace Engineering, Charlottesville, USA
b: Bristol Composites Institute, University of Bristol, Bristol, United Kingdom
* Corresponding author email: janice.barton@bristol.ac.uk

Abstract: *The structural response of Carbon Fibre Reinforced Polymer (CFRP) panels damaged by lightning strikes are evaluated using a new "Compression After Lightning Strike (CALS)" test procedure. CALS can accommodate the full scale of actual lightning damage in a large CFRP panel, enabling the load response and buckling/failure behaviour to be determined experimentally at a representative scale using stereo Digital Image Correlation (DIC).*

Keywords: Full-field imaging; Digital Image Correlation (DIC); Compression; Lightning strike; Model validation

1. Introduction

Assessing the efficiency of lightning protection is an integral part of the testing/qualification of new wind turbine (WT) blade and aircraft designs. The introduction of conductive Carbon Fibre Reinforced Polymer (CFRP) composites has made lightning protection more challenging for these structures. CFRP materials, which are used due to their high specific stiffness and strength properties, are also effectively semi-conductors with strongly anisotropic electrical and thermal properties. Thus, CFRP materials exhibit properties different from conductive materials like e.g. metal alloys, making CFRPs more susceptible to lightning damage. The main reasons for this are the limited electrical and thermal conductivity transverse to the fibres. Lightning strikes can lead to damage in the CFRP especially due to elevated temperatures which cause loss of resin, fibre breakage, and delamination [1], [2]. In WT blades direct strikes occur when lightning attaches to the CFRP normal to the blade surface. This causes large current densities, which result in large temperature rises and damage in zones near the lightning attachment point. The compressive behaviour of CFRP sparcaps in WT blades is a crucial design driver. The Compression After Lightning Strike (CALS) test investigates the buckling response of a CFRP panel damaged by lightning. The CFRP laminate considered represents a WT blade sparcap near the tip of the blade, where the probability of the occurrence of a lightning strike is the most severe [3]. In these regions UD material configurations with a relatively small laminate thickness in the range of 5 to 10 mm is used. If the CFRP sparcap is damaged by a high enough intensity lightning strike, the blade tip structural support cannot withstand normal operational loading conditions. The stiffness reduction promotes premature buckling-like behaviour leading to collapse in a worst-case scenario. Thus, the buckling/post-buckling load response of WT blade CFRP structures subjected to lightning strike events is of crucial importance [4], [5].

  doi:10.5075/epfl-298799_978-2-9701614-0-0

A description of the design of the CALS test apparatus [6] is briefly described alongside the overall test methodology. A comparison with model data presented in [7] is provided and the validation procedure assessed.

2. Experimental setup

2.1 Test Specimens

Ten CFRP unidirectional (UD) eight ply laminate specimens were manufactured using a carbon/epoxy material system. The carbon fibres are an 800 gsm fabric from Panex-35 by Zoltek and the epoxy system is Epilox ER5300 resin/EC5310 hardener. The eight laminates were manufactured using vacuum liquid resin infusion. The laminates were manufactured to a dimension of 550 mm long x 500 mm wide x 7 mm thick. The plates were post cured at 70°C for 6 hours. The top edge was chamfered to an approximate 4:1 taper to expose the fibres for electrical grounding. An example of a laminate is shown in Figure 1(a). Two of the samples were used as control specimens, and eight samples were subjected to direct lightning strike tests. The CFRP panel specimens were subjected to electrical current with a unipolar 10/350µs waveform simulating the first return stroke during a direct strike according to IEC 61400-24 Ed1.0 [7]. The current was injected by a large current generator and an electrode with a gap of 20 mm. The peak current subjected to the samples was 50, 75, 100, and 125 kA. Two of the damage samples are shown in Figure 1(b) and 1(c). The lightning strike damaged and control specimens were cut using a waterjet cutter to a final plate dimension of 500 mm square, as shown in Figure 1.

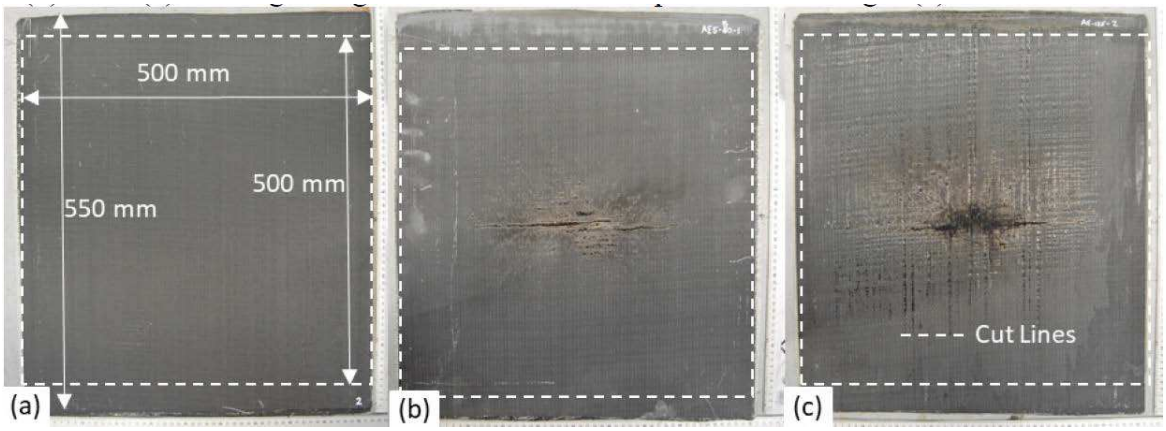

Figure 1 Test specimens: (a) Control, (b) 50kA damaged and (c) 125kA damaged.

2.2 CALS test rig

To capture the effects of lightning strike induced damage on the structural scale, the traditional compression after impact was upscaled and redesigned. The new CALS test rig configuration and rig is shown in Fig. 2. The upscaling was done to fit a variety of plate widths and lengths (larger than 500 mm). The rig is designed with interchangeable supports, and in the present work a simple support was used. The CFRP plates were loaded in the fibre direction with a 0.5mm/min loading rate in compression. Cameras for stereo 3D digital image correlation (DIC) were positioned both front and back of the test machine to capture the full field strains and displacements on both sides of the plate.

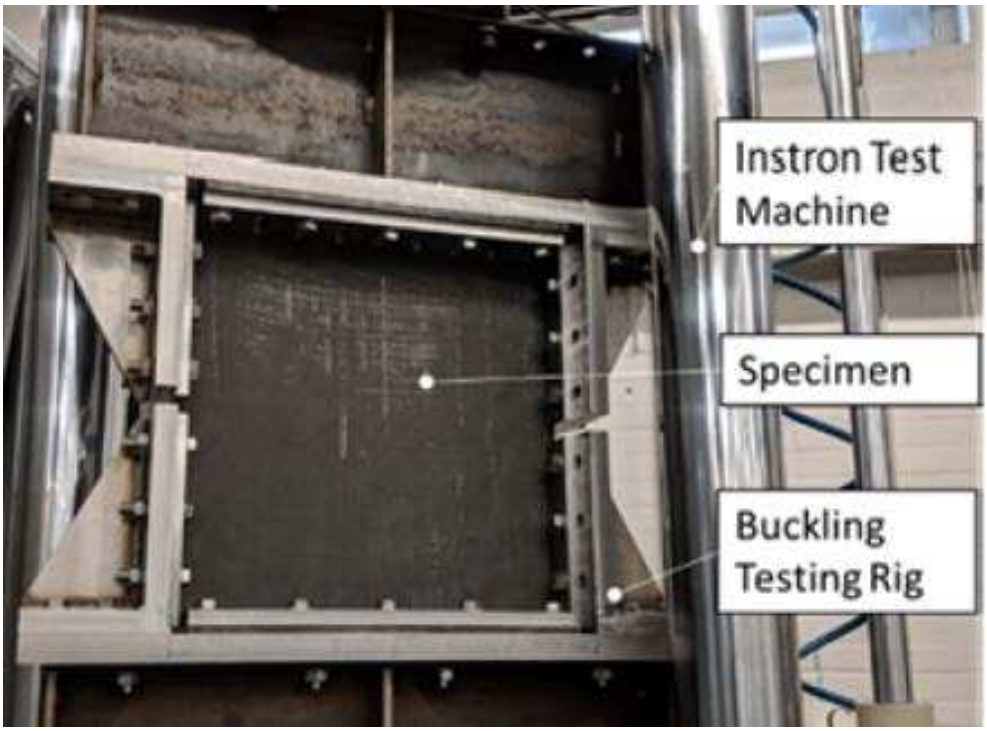

Figure 2 CALS test rig

3. Results and Discussion

Typical results from the DIC are shown in Figure 3 there are significant differences between the control specimens and the damaged specimens. The out-of-plane displacements are clearly much larger for the damaged sample specimen. The most severely damaged specimen gave the highest displacement levels, with the maximum displacement occuring away from the damaged region. This indicates that the stiffness in the damaged regions was significantly reduced by the lightning strike.

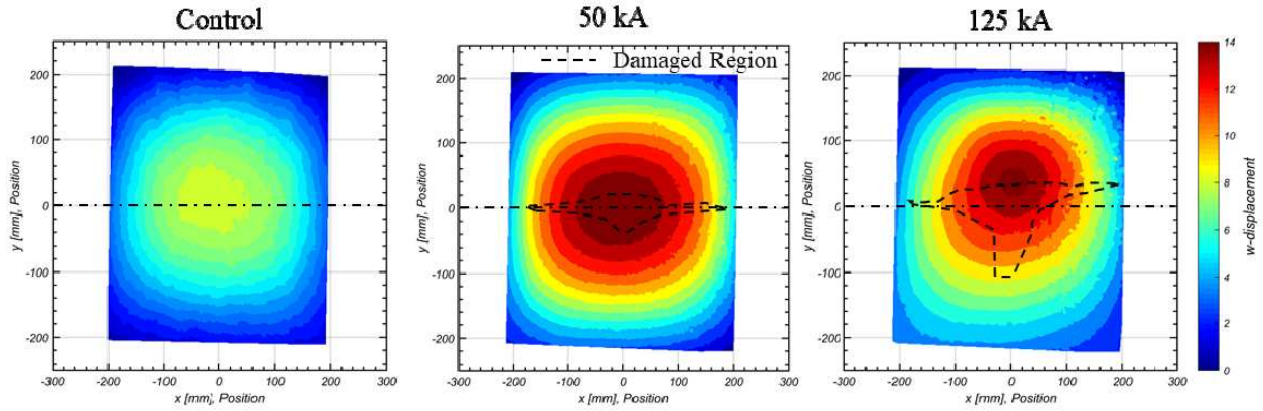

Figure 3 Out-of-plane displacement for the control specimen and lightning damaged specimens

The experimental results were compared with a 3D shell post-buckling finite element model constructed in Abaqus 6.14 using shell elements that represented the laminate. The damage

induced by the lightning strike was taken into account by altering the material properties to have essentially no stiffness. The extent (area and depth) of the damaged zones was estimated based on visual inspection and X-ray computed tomography (CT) of the damaged plate samples as described in detail in [7]. The damage regions were modelled by assuming an elliptical shape with equal area to the damage seen on the surface. The number of plies to remove in the modelling was determined using a technique described in [7] based on the X-ray CT data. Figure 4 shows comparable model data to the experimental results shown in Figure 3. Considering the simplicity of this modelling approach, the predicted out-of-plane displacement field match well with the DIC results. In the work described in [7], an improved model of the damage is presented which in future work will be incorporated into a multiscale structural model.

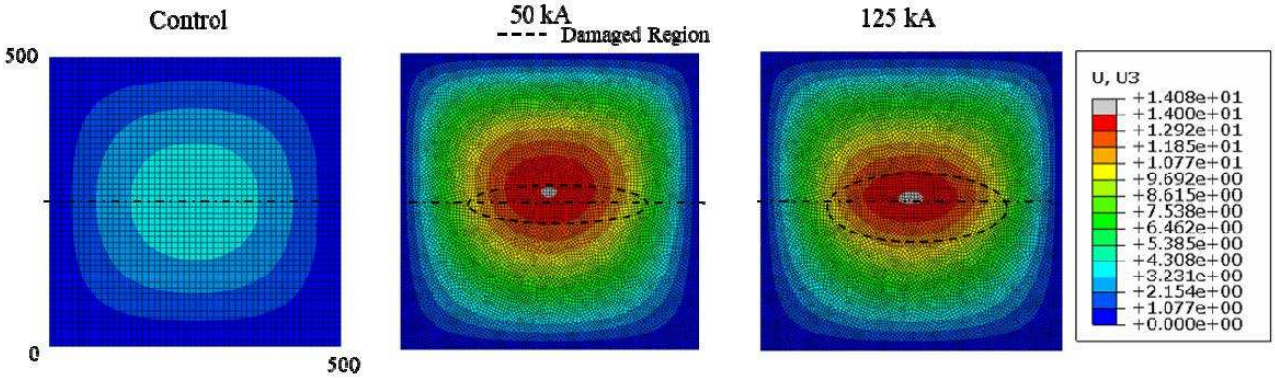

Figure 4 Predicted out of plane displacement

4. Conclusions

The behaviour of CFRP plate panels representative for wind turbine blade sparcap laminates impacted with simulated lightning strikes has been studied. A specially adapted compression loading test, the Compression After Lightning Strike (CALS) is proposed and commissioned to include important structural scale effects not included in conventional Compression After Impact test apparatus. The full field out-of-plane displacements were measured using DIC at different load levels for undamaged and lightning strike damages laminate specimens. The measured displacement fields were benchmarked against FEM predictions that include the damaged zones and a reasonable match was found. Hence the CALS procedure provides a new means of validation that increases confidence in complex models of the effect of lightning strike on wind turbine blade structures.

Acknowledgements

The authors acknowledge the Marie Skłodowska Curie Action, Innovative Training Networks (ITN), H2020-MSCA-ITN-2014, as part of the 642771 SPARCARB project. The simulated lightning strike tests were conducted with Poly-Tech A/S, Denmark.

References

[1] L. Chemartin *et al.*, “Direct Effects of Lightning on Aircraft Structure : Analysis of theThermal , Electrical and Mechanical Constraints”, *J. Aerosp. Lab*, no. 5, pp. 1–15, 2012. [

2] T. M. Harrell, O. T. Thomsen, S. F. Madsen, and L. Carloni, “Lightning protection of CFRPwind turbine blades - What is the dominant cause of failure : Specific Energy or Charge?”, in *International Conference on Lightning and Static Electricity*, 2017, pp. 1–5.

[3] A. C. Garolera, S. F. Madsen, M. Nissim, J. D. Myers, and J. Holboell, “Lightning Damage to Wind Turbine Blades From Wind Farms in the U.S.”, *IEEE Trans. Power Deliv.*, vol. 31, no. 3, pp. 1043–1049, 2016, doi: 10.1109/TPWRD.2014.2370682.

[4] X. Li, W. Gao, and W. Liu, “Post-buckling progressive damage of CFRP laminates with a large-sized elliptical cutout subjected to shear loading”, *Compos. Struct.*, vol. 128, pp. 313–321, 2015, doi: 10.1016/j.compstruct.2015.03.038.

[5] T Y. Feng, H. Zhang, X. Tan, Y. He, T. An, and J. Zheng, “Effect of impact damage positions on the buckling and post-buckling behaviors of stiffened composite panel”, *Compos. Struct.*, vol. 155, pp. 184–196, 2016, doi: 10.1016/j.compstruct.2016.08.012.

[6] T. M. Harrell, J.M. Dulieu-Barton and O. T. Thomsen, "Buckling behaviour of ud carbon/epoxy panelssubjected to direct lightning strike" ICCM22, Melbourne, Austrailia

[7] T.M. Harrell, , O.T. Thomsen, S.F. Madsen and J.M. Dulieu-Barton,., “On the effect of dielectric breakdown in UD CFRPs subjected to lightning strike using an experimentally validated model”, Applied Composite Materials, 2022, 28 pages. https://doi.org/10.1007/s10443-022-10014-7

STOCHASTIC UPSCALING OF TRANSIENT TRANSVERSE MULTI-PHASE FLOW WITHIN FIBROUS MEDIA FOR MODELLING COMPOSITE MANUFACTURING PROCESSES

Sylvain Drapier [a], Aubin Geoffre [a], Julien Bruchon [a], Nicolas Moulin [a]

a: Hexcel Chair & Mines Saint-Étienne, Université de Lyon, CNRS, UMR 5307 LGF, Centre SMS
158 Cours Fauriel 42023, Saint-Étienne, France. drapier@emse.fr

Abstract: Direct elaboration processes of composite materials, such as *LCM* processes, induce transient two-phase flows within multi-scale fibrous media. Based on stabilized finite element simulations of such flows at the fibre scale, statistical descriptions of the responses of randomly generated representative volume elements are proposed. For modelling resin infusion at the preform scale, upscaled properties are identified through data science analyses. With this objective of homogenization, this work addresses in particular the influence of boundary conditions, the resultant of capillary effects, and the flow dynamics in both fully and partially saturated regimes. An explicit stochastic permeability is first proposed for stationary regimes. Then, capillary pressures and local saturation dynamics are identified for transient two-phase flows with surface tension effects.

Keywords: Liquid Infusion; Numerics; Capillarity; Upscaling; Gaussian Process Regression

1. Introduction

Out-of-autoclave direct elaboration processes stand now as very attractive alternatives to dry routes processes (pre-impregnated) for manufacturing structural materials with significant energy and economic gains. This work concerns more particularly the infusion processes in which dry preforms, made up of architectured long fibers reinforcement, are laid on a half-mold before being impregnated by a liquid resin under the action of a vacuum – Figure 1.

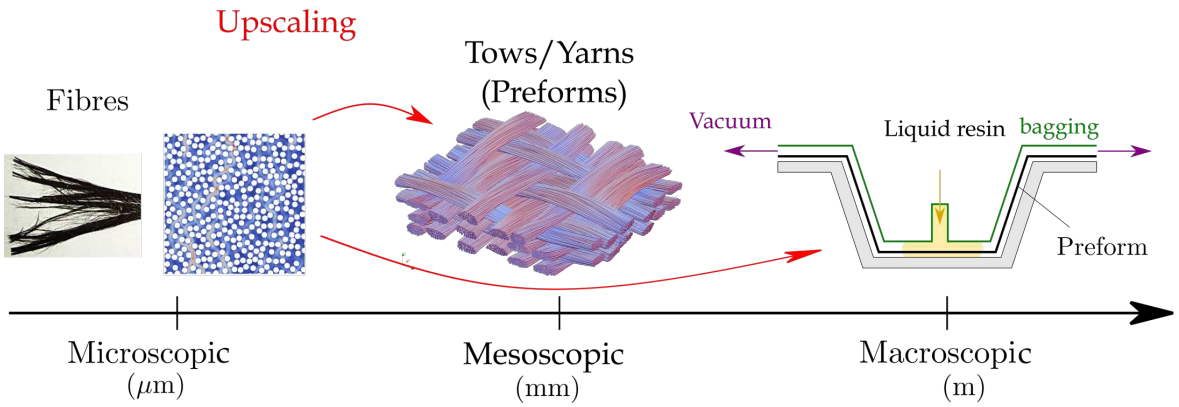

Figure 1. Scales of observation and flows in infusion-based processes

Usually, the impregnation stage is modelled through simulations at the part scale but involving somehow complex 'material parameters' carrying more and more fine descriptions to try and approach reality. Indeed, the industrial part can reach several meters, while it consists of fibers of only a few microns in diameter - Figure 1. Obviously, this rises lots of questions about the

  doi:10.5075/epfl-298799_978-2-9701614-0-0

upscaling of local information obtained at the fibre scale, potentially stochastic, to larger scales, *i.e.* the homogenization methods that can be applied for upscaling saturated as well as partially saturated flows. In a more global view, we prefer to see impregnation as a transient two-phase flow within a geometrically complex and multi-scale fibrous medium.

This work encompasses both flow regimes that can be met in infusion-based processes. Computations are carried out, within a stabilized Finite Element framework, on validated Representative Volume Element (RVEs) and averaged over the volume in order to establish a probabilistic response that can be used at upper scales. First is presented the case of a permanent single-phase flow [1]. In this framework, the notion of permeability introduced in the Darcy's law is generally sufficient to characterize the scale-up [2]. Through a statistical study of dimensionless randomly generated RVEs, the factors controlling these local flows are identified. A versatile explicit stochastic permeability is then proposed which includes the most significant morphological descriptors, along with the effect of fluid/fiber contact slip. Then, keeping a similar statistical approach, a more realistic situation with respect to the process is studied, in which the liquid resin drives out the air initially contained in the medium. Modeling such a transient two-phase flow at the microscopic scale requires absolutely to consider the capillary effects originating from the surface tensions acting at the fibre-fluid-air level. During transient flows, these capillary effects are in competition with the viscous effects. This greatly controls the observed flow [3] in terms of saturation dynamics, preferential flow paths, residual porosities, ...

2. Materials and methods

2.1 Modelling saturated and transient flows

In accordance with the regime met in LCM processes, fluid flows are modelled here in laminar regime through the Stokes' equations: $\nabla \cdot \boldsymbol{v} = 0$ and $\mu \, \Delta \boldsymbol{v} - \nabla p = 0$ complemented by Dirichlet's and Neuman's boundary conditions, with $\boldsymbol{v}$ the fluid velocity, p the fluid pressure and μ the fluid viscosity. A complementary condition can be introduced which models the contact between both fluid and solid phases, characterized by a slip length ℓ_s [4]. This Navier's slip condition [5] is prescribed on the liquid/solid interface Γ_{LS}, it relates the fluid tangential velocity to shear components of the fluid Cauchy stress tensor $\boldsymbol{\sigma}$ (Figure 2) and reads:

$$\boldsymbol{v} \cdot \boldsymbol{t} = -\left(\ell_S \,/\, \mu\right) \boldsymbol{t} \cdot \boldsymbol{\sigma} \cdot \boldsymbol{n} \text{ on } \Gamma_{LS} \tag{1}$$

where $\boldsymbol{t}$ (resp. $\boldsymbol{n}$) is a unit tangential (resp. normal) vector to Γ_{LS}. This generalizes no-slip ($\ell_s \to 0$) and free- slip conditions ($\ell_s \to \infty$). It will be shown that this condition has a large influence on the flow. In saturated regime, knowing the fluid velocity and pressure fields computed, the solution is then upscaled to extract permeability from the Darcy's law [2]:

$$\boldsymbol{v}_D = -\left(\boldsymbol{K} / \mu\right) \cdot \nabla p_D \tag{2}$$

where $\boldsymbol{v}_D$ (resp. p_D) is the upscaled velocity (resp. pressure) and $\boldsymbol{K}$ the second order permeability tensor. That upscaling procedure must be performed on RVE that is the smallest geometry for which permeability, and other characteristics associated, become independent of the domain size [1, 6].

For transient regimes, schematically depicted in Figure 2, the physics to be modelled is more complex, it implies two phase-flows in the poral structure. These fluids are named here as vapor (or air) and liquid, defined respectively by their viscosity: μ_V and μ_L. Moreover, surface tension

  doi:10.5075/epfl-298799_978-2-9701614-0-0

effects must be accounted for in two ways so that capillary effects are properly represented since they can reach 1/3 of the driving pressure [5, 7]. First, due to the presence of 3 phases - liquid, fluid, and solid- at triple points (lines in 3D) menisci will form to enforce surface tension equilibrium (Eq. 3a). Second, the liquid-vapor interface will experience this surface tension equilibrium also, accounted for through the Laplace's law (Eq. 2) [5] which relates the normal stress vector jump $[[\boldsymbol{\sigma}\cdot\boldsymbol{n}]]_j$ at interface j to the mean curvature $\mathscr{C}$ of this interface (Eq. 3b). These 2 conditions introduce interfacial discontinuities which translate into some driving forces usually referred to as wicking force and capillary pressure. They summarise as:

$$\gamma_{LS}\boldsymbol{t}_{LS}+\gamma_{LV}\boldsymbol{t}_{LV}+\gamma_{SV}\boldsymbol{t}_{SV}=0 \qquad \text{at } \Gamma_{LS}\cap\Gamma_{LV}\cap\Gamma_{SV} \qquad (3\text{-a})$$

$$[[\boldsymbol{\sigma}\cdot\boldsymbol{n}]]_{LV}=-\gamma_{LV}\mathscr{C}\boldsymbol{n} \qquad \text{on } \Gamma_{LV} \qquad (3\text{-b})$$

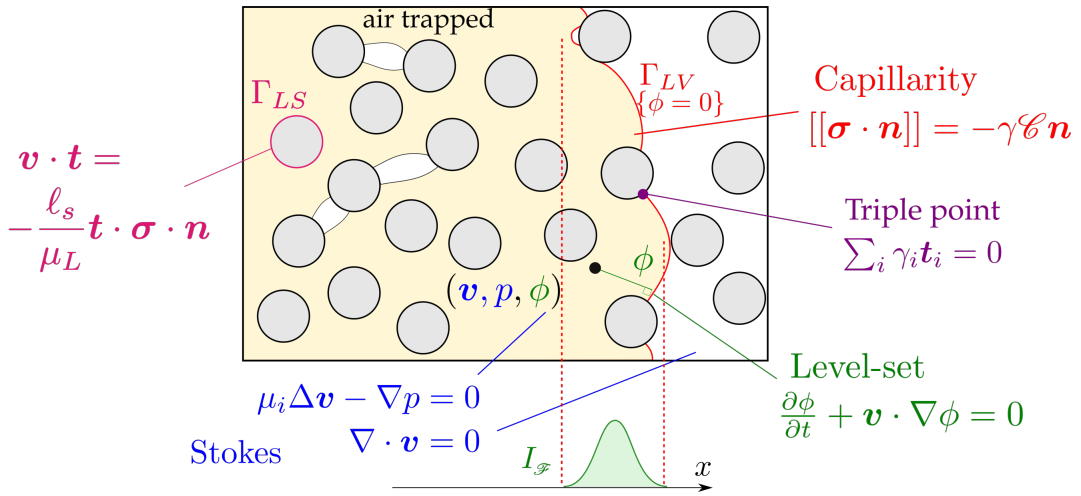

Figure 2. Schematic of transient flow descriptions.

Let us finally remark that the saturated regime may be seen as a particular case of the transient regime: 'sufficiently' behind the flow front, a steady quasi-saturated regime will be reached. One can anticipate that a proper representation of transient flows in 'sufficiently' large RVEs may permit to characterize transient and steady flows, and hence both responses of the medium.

2.2 Numerical modelling approach

Before concentrating on the flow characterization, the numerical framework used for solving this problem numerically has to be recalled briefly; all the details can be found in the publications of our group, for instance [5, 8] … In few words, Stokes' flows (liquid and vapor) are solved in a monolithic approach, using the same mixed velocity-pressure P1/P1 finite elements stabilized by an *Algebraic SubGrid Scal*e method. The Navier's condition is implemented in this FE approach [1] along with the weak enforcement of the surface tension equilibria (Eqs 3-a and 3-b) as described in [5]. For transient flows, a method must be implemented to capture the flow front for transient regimes. Among the various existing methods, the *Level-set* method [9] has been selected for its numerous capabilities, and under the constraint applying as precisely as possible some conditions on interfaces such as the surface tension effects described above that depend on the interface curvature (Eq. 3b). Basically, this method consists in defining a scalar field ϕ, usually the signed distance to the interface -Figure 2 -, and describe the interface as the 0 iso-value of this level-set. This field is convected in a velocity field, here the computed fluid

velocity, through the same linear FE scheme but stabilized with a SUPG method [5]. A staggered weak coupling is considered, where fluid velocity is computed on a fixed domain and then used to update the flow front position and properties. All these methods are implemented in a robust environment validated on lots of test cases along the past and recent years [1, 5, 8, …], in the finite element code Zset[1].

Eventually, the RVEs are to be generated for these simulations. A specific generation scheme has been developed [1] which permits to generate random RVEs with periodic boundaries, statistically representative of the fibre distribution that can be actually measured in long fibre micro-structures [10]. Given variable fibre radii following a normal distribution, typically $r = \mathcal{N}(\bar{r}, 0.1\bar{r})$, and a target fibre fraction, microstructures are generated and optimal finite element meshes are produced that ensure a proper description of the fluid flow together with minimum number of elements. All this is summarized in Figure 3.

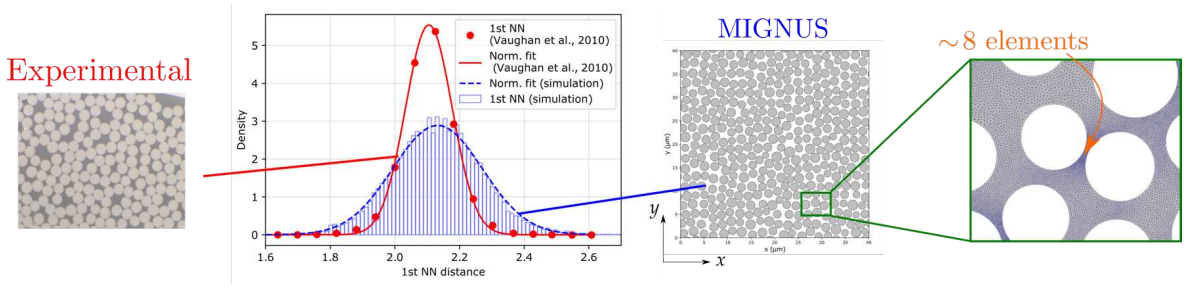

Figure 3. MIGNUS scheme for the generation of random elementary volumes statistically representative and associated finite element mesh [1].

For the simulations, typical materials have been considered: mean fibre radius $\bar{r}$ =3.5 µm, resin as liquid and air as vapor, fibre volume fractions (V_f the volume of fibre over the total volume) from 0.3 to 0.65. The corresponding material data are given in Table 1.

Table 1: Material data.

μ_L (Pa.s)	μ_V (Pa.s)	γ_{LS}(N/m)	γ_{SV}(N/m)	γ_{LV}(N/m)
2.76 x 10^{-3}	1.71 x 10^{-5}	54.7 x 10^{-3}	25.9 x 10^{-3}	50.8 x 10^{-3}

2.4 Upscaling methods

Saturated cases consist typically in applying a pressure gradient in a direction (x or y in Figure 3) and measuring the fluid velocity (flux) across the boundaries in both directions to identify the corresponding permeability tensor components – tensor not necessarily diagonal nor symmetric [6] - through the Darcy's law (Eq. 2). For the flows in transient regimes, the upscaling procedure is not so standard, and the first questioning comes about the relevant physically-sound characteristics that can be upscaled. Looking at literature, in composite materials [3, 7, 11, 12] but also in hydrogeology for instance [6], transient permeabilities may be extracted from transient flows but overall the question is : " is it relevant to estimate a transient permeability

[1] http://www.zset-software.com/

to feed simulations at the upper scale ? ” Indeed, we do believe that other local descriptors may be more relevant for transient flows, such as the equivalent capillary pressure acting overall on the fluid front, or some more informative characteristics such as saturation in the RVE or describing the flow front. In both regimes, Gaussian Regression Processes (GPR) / Machine learning is considered to capture the inherent stochastic character of the physics in play.

As stated previously, a pressure discontinuity appears at the liquid-vapor interface (Eq. 3-a) generally called capillary pressure. In a homogenization context, the overall contribution P^{cap} can characterize the capillary action at an upper scale [13, 14]. Two methods can be considered to evaluate the capillary pressure (Eq. 5): measure directly the average pressure drop at the liquid-vapor interface Γ_{LV} [13], and from the interface curvature from Eq. 3-a [6, 14] :

$$P^{cap} = \langle |p_L - p_V| \rangle_{\Gamma_{LV}} \qquad P^{cap} = \gamma_{LV} \langle \mathcal{C} \rangle_{\Gamma_{LV}} \tag{5}$$

where $\langle . \rangle_{\Gamma_{LV}} = \frac{1}{|\Gamma_{LV}|} \int_{\Gamma_{LV}} . \, \mathrm{d}S$ is the aerial average over Γ_{LV}.

Another key feature of transient flows in porous media is the saturation which represents the ratio between the volume of fluid and the total poral space ($S_L \in [0,1]$). This information can be local or global, but for a spatialized information one may prefer to define the section saturation $S_L(t; x(A))$, *i.e.* the saturation that measures at a given position along the flow – say along $\boldsymbol{x}$ -, the ratio of liquid over the RVE 'height' – along $\boldsymbol{y}$ - *see* Figure 2.

Let us note that for saturation as well as P^{cap} the liquid-vapor interface must be carefully processed to extract the non-contiguous interface pieces of the moving flow front, disregarding the 'bubbles' trapped in the fibre network, downwards the flow – *see* Figure 2 for illustration of the concept.

3. Results

3.1 Saturated flows

For selected fibre volume fractions ranging from 0.3 to 0.6, some sets of 150 microstructures were generated using the MIGNUS procedure (Figure 3) and studied; all the details can be found in Geoffre e*t al.* [1]. The optimum RVE size was shown to depend directly on the fibre volume fraction: the higher the volume fraction, the smaller the RVE size; if V_f varies 0.3 → 0.6, $\ell_{RVE}/\bar{r}$ ($\bar{r}$ is the mean fiber radius) varies 100→ 60. A statistical study demonstrated that (Figure 4):

- the permeability tensor is symmetric, isotropic, and follows a normal distribution – Figure 4-a
- among the various morpho-mathematical descriptors, the fibre volume fraction carries 95% of the statistical information on its own - Figure 4-a
- permeabilities computed are consistent with literature predictions - Figure 4-b
- variability of the microstructure induced by both fibre radius variability and randomness of fibre placements yields only 3% of permeability variability - Figure 4-a,b.

Second, other physical parameters were considered. The most relevant effect comes from the slip length which represents the fiber-fluid affinity: between the extreme bounds corresponding to no-slip and slip conditions the permeability varies by a decade - Figure 5 ! Let us recall that theoretically upscaling local Stokes' flow in fibrous arrangements to Darcy's flow requires to assume a no-slip condition of the fluid [5]. From these results an explicit stochastic expression

  doi:10.5075/epfl-298799_978-2-9701614-0-0

bounding the saturated permeability has been proposed, it is composed of 2 terms: one related to the intrinsic variability induced by radius and generation variability, and a second one related to the slip length. The coefficients identified - Figure 5 right - carry a very exhaustive information:

$$\mathrm{K}(V_f, \bar{r}, \ell_s) = \bar{r}^2\ \mathcal{N}(1, 3\%)\ e^{c_1 + c_2 V_f}\left[1 - \frac{1 - e^{\beta V_f}}{1 + \frac{1}{2}\frac{\bar{r}}{l_s}}\right] \qquad (6)$$

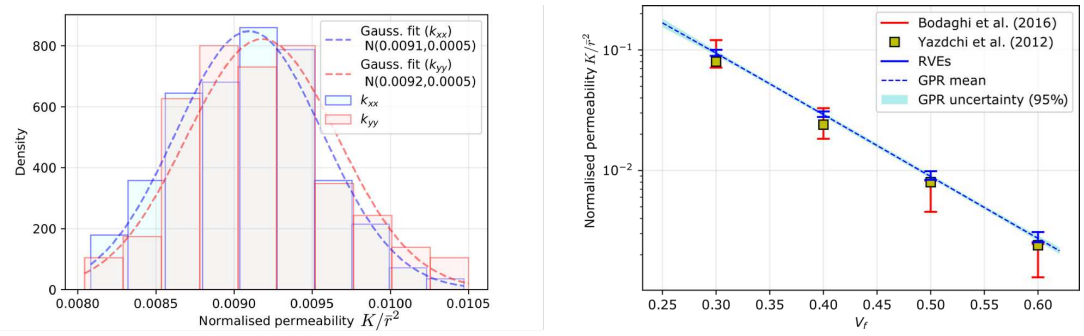

(a) (b)

Figure 4. saturated normalized permeability results [1]*: (a) principal permeabilities distributions for V_f= 0.5, and (b) normalized permeability compared to literature.*

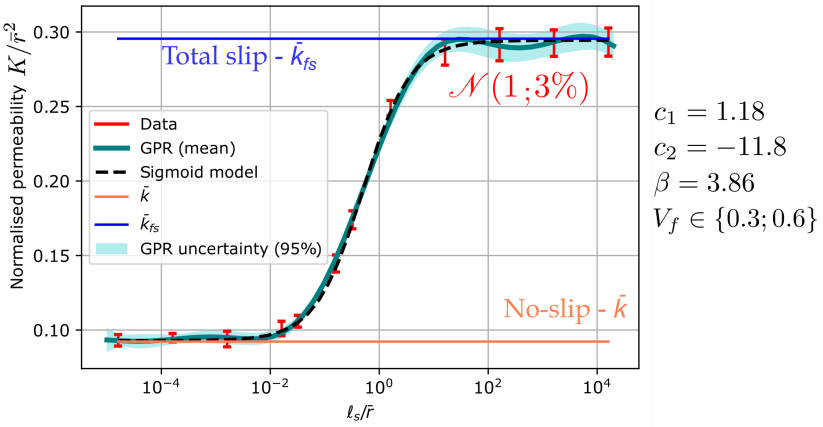

Figure 5. Saturated stochastic normalized permeability as a function of the normalized slip length $\ell_S/\bar{r}$ for V_f= 0.3 (30 RVEs at every $\ell_S/\bar{r}$) from [1].

3.2 Transient regime

Simulations were carried out in transient regime on the same RVEs, optimized in terms of computation costs and representativity, with a size $\ell_{RVE}/\bar{r}$=40. As commonly admitted, the flow is characterized by its capillary number [3, 6], the ratio of viscous effects to the surface tension effects : $\mathrm{Ca} = \mu_L \bar{v} / \gamma_{LV}$ with $\bar{v}$ is the fluid inlet velocity. We have shown that sufficiently high capillary numbers must be prescribed for the flow to be stable, of the order of $\mathrm{Ca} \approx 10^{-3}$.

Macroscopically, saturation reaches a plateau corresponding to maximum poral space that the fluid finally occupies. This can be also cast from the change in the section saturation $\mathrm{S_L(t}; x(\mathrm{A}))$, as shown in Figure 6 -a,b : saturations of the 4 sections $\mathrm{A_i}$ are sigmoids that reach a plateau $\mathrm{S_{L,max}} = \mathrm{S_L(t{=}\infty}; x(\mathrm{A}))$ [11]. The transition time τ_A provides some information about the dynamics of infusion. One can verify that the RVE size is sufficient, *i.e.* a large part of the RVE can be filled

before the flow front reaches the outlet. This saturation can be also converted to a saturation length which is, for our material configurations, of the order of ℓ_{sat} ≈12 $\bar{r}$ (Figure 6-c).

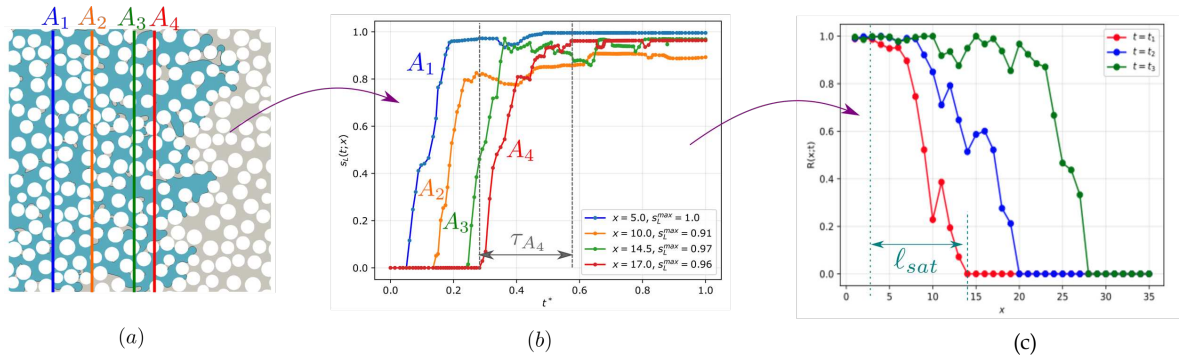

Figure 6. Section saturation: (a & b) 4 section saturations vs normalised time, and (c) saturation spatial distribution for 3 times.

Saturation study for numerous RVEs shows that the upscaled flow front position can be seen as the realization $I_{\mathcal{F}}(x,t)$ of a random process - Figure 2 : its mean value corresponding to the section saturation is linear in time for constant inlet flux - Figure 7-a, and its standard deviation corresponds to the saturation length (span) - Figure 7-b : $I_{\mathcal{F}}(x,t) \sim \mathcal{N}(\alpha\, S_L(t),\ \ell_{sat}/2)$.

Eventually, the capillary pressure can be estimated through the 2 methods presented previously (Eqs. 5) : using the Laplace's law and integrating the interfacial pressure. In Figure 7-v, one can verify that both methods yield the same trend, with an asymptotic pressure when the flow reaches steadiness. For the material configuration chosen here – Table 1 – the capillary pressure is estimated at P^{cap} = 12.5 kPa. Although direct comparisons with measurements have to be carefully achieved, these results are in accordance with capillary pressures reported in the literature, for instance in [7] P^{cap} = 32.1 kPa ± 11.6 kPa for carbon quasi-UD at V_f= 0.4.

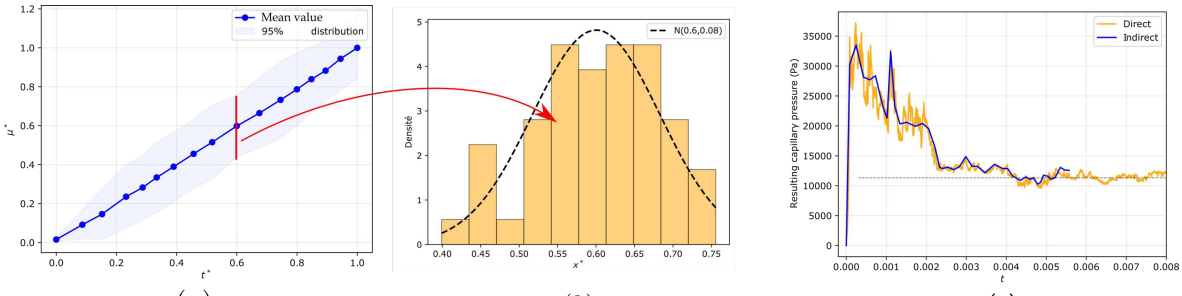

Figure 7. Flow front (a) mean position over normalised time, (b) position distribution and normal fit, and (c) capillary pressure over time for V_f= 0.5.

4 Conclusions

Relying on very robust simulation capabilities and well-grounded upscaling statistical approaches, we have explored the infusion of resin in long-fibre composite microstuctures. Numerous computations carried out on various RVEs have permitted to optimize the RVE size in saturated regime, and above all to propose an explicit stochastic relation between permeability and fibre volume fraction, but which accounts in the meantime for the resin-fibre affinity as well as the micro-structure variability induced by both fibre radius and RVE randomness – *see* [1].

Second, transient flows have been considered, incorporating all the surface tension effects which largely control these flows. In that case, relevant local descriptors of the flow appear to be first the saturation (time and length), a precious indicator that will measure the scales separation: the saturation length permits to wisely build homogeneous equivalent media for upscaled flows. Also, the flow front position over time can be described through a normal law, built on the change in section saturation over time and geometrically spanning over a bandwidth corresponding to the saturation length. Eventually, another precious data extracted from these transient flows is the capillary pressure, consistently calculated using 2 methods, the results of which are in accordance with literature. The transient flows are further explored in details, based on complementary simulations covering a wide range of material configurations.

5 References

1. Geoffre A, Ghestin M, Moulin N, Bruchon J, Drapier S. Bounding transverse permeability of fibrous media: a statistical study from random representative volume elements with consideration of fluid slip. Int J Multiph Flow. 2021;143(March):103751.
2. Darcy H. Les fontaines publiques de la ville de Dijon. Dalmont; 1856.
3. Michaud V. A Review of Non-saturated Resin Flow in Liquid Composite Moulding processes. Transp Porous Media. 2016;115(3):581–601.
4. Rougier V, Cellier J, Gomina M, Bréard J. Slip transition in dynamic wetting for a generalized Navier boundary condition. J Colloid Interface Sci. 2021;583:448–58.
5. Chevalier L, Bruchon J, Moulin N, Liotier PJ, Drapier S. Accounting for local capillary effects in two-phase flows with relaxed surface tension formulation in enriched finite elements. Comptes Rendus - Mec. 2018;346(8):617–33.
6. Whitaker S. Flow in porous media I: A theoretical derivation of Darcy's law. Transp Porous Media. 1986;1(1):3–25.
7. Pucci MF, Liotier PJ, Drapier S. Capillary wicking in a fibrous reinforcement - Orthotropic issues to determine the capillary pressure components. Compos Part A Appl Sci Manuf. 2015;77:133–41.
8. Pacquaut G, Bruchon J, Moulin N, Drapier S. Combining a Level-Set method and a stabilized mixed formulation P1 / P1 for coupling Stokes-Darcy flows: application to the resin infusion-based processes. 2010;
9. Sussman M, Smereka P, Osher S. A Level Set Approach for Computing Solutions to Incompressible Two-Phase Flow. J Comput Phys. 1994;114(1):146–59.
10. Vaughan TJ, McCarthy CT. A combined experimental-numerical approach for generating statistically equivalent fibre distributions for high strength laminated composite materials. Compos Sci Technol. 2010;70(2):291–7.
11. Gueroult S, Lebel-Lavacry A, Park CH, Bizet L, Saouab A, Bréard J. Analytical modeling and in situ measurement of void formation in liquid composite molding processes. Adv Compos Mater. 2014;23(1):31–42.
12. Caglar B, Tekin C, Karasu F, Michaud V. Assessment of capillary phenomena in liquid composite molding. Compos Part A Appl Sci Manuf. 2019;120(October 2018):73–83.
13. Konangi S, Palakurthi NK, Karadimitriou NK, Comer K, Ghia U. Comparison of pore-scale capillary pressure to macroscale capillary pressure using direct numerical simulations of drainage under dynamic and quasi-static conditions. Adv Water Resour. 2021;147.
14. Starnoni, M and Pokrajac D. On the concept of macroscopic capillary pressure in two-phase porous media flow. Adv Water Resour. 2020;135.

A DEEP ENCODER-DECODER NEURAL NETWORK FOR SURROGATE MODELLING OF LIQUID MOULDING OF COMPOSITES

Joaquin Fernandez-Leon[a,b], Keayvan Keramati [a,c], Luis Baumela[b], Carlos Gonzalez[a,c]

a: IMDEA Materials, C/Eric Kandel 2, 28906, Getafe Madrid, Spain.
joaquin.fernandez@imdea.org
b: Departamento de Inteligencia Artificial, Universidad Politécnica de Madrid, E.T.S. de Ingenieros Informáticos, 28660 Madrid, Spain
c: Departamento de Ciencia de Materiales, Universidad Politécnica de Madrid, E.T.S. de Ingenieros de Caminos, 28040 Madrid, Spain

Abstract: *Since fluid dynamic simulations are high-cost computational processes and time-consuming, it presents a drawback during the design process when a wide variety of parameters need to be simulated. In this work, we propose a surrogate deep learning-based model that generates an outcome faster but sacrifices some accuracy in the process. In other words, our surrogate model can find an approximation of a fluid dynamic simulation without the need to solve all partial differential equations. Thus, it speeds up the process almost 36 times for a simple simulation and loses just 1.3% of precision. Such a problem is solved as an image-to-image regression. A fully convolutional encoder-decoder network was designed to capture the complex boundaries set by the engineer from the high-dimensional input field and generates the output fields without using any explicit intermediate method. This structure is used to build the feature extractor within the encoder and decoder paths. Intuitively, in the first step, the encoder part extracts essential features from the input data, and all this information is given to the decoder network. After that, the decoder will try to learn how to reconstruct the output fields and get the complete simulation.*

Keywords: Deep Learning; Surrogate Modeling; Liquid Moulding Simulations; Computer Vision; Composite Materials.

1. Introduction

Computational Fluid Dynamics (CFD) is the science that produces simulations of fluid-flow phenomena based on the conservation laws (conservation of mass, momentum, or energy) governing fluid motion and computing it by employing a multiprocessor in a computer. Thus, when a free-stream flow of a fluid is required, boundary conditions are defined, creating a simulation model for being developed. The computer is used to carry out calculations to simulate the interaction of the fluid in this process. However, CFD simulations present some drawbacks currently. The first one is the need for high-speed computers, which sometimes are expensive; the second one is that such CFD techniques are time-consuming since they must solve partial differential equations of the problem, which are complex; the last one is that some CFD software requires either tedious installations or its manageability is not trivial. For that reason, many researchers started developing surrogate models to simulate the reality while avoiding the main drawbacks that CFD presents.

Surrogate models arise in the engineering field as solutions when an outcome of interest is expensive, time-consuming, or otherwise difficult to measure. Previous works related to the

  doi:10.5075/epfl-298799_978-2-9701614-0-0

development of surrogate models can be found in the literature. *Yinhaou Zhu et al.* [1] develop a surrogate model for uncertainty quantification and propagation in problems governed by stochastic PDEs. They get an excellent surrogate model performance even though no underlying structure is shared between the input (permeability) and output (flow/pressure) fields. *Shaoxing Mo et al.* [2] design a surrogate methodology based on an image-to-image regression strategy to link their high-dimensional input permeability fields images using an encoder with the output pressure/saturation field images through a decoder. Also, output has a time dimension which is treated as an additional input to the network trained as pairs in the input. *Freitas et al.* [3] present another surrogate model for seismic imaging to map the subsurface reflectivity under uncertainty. Their inputs are a set of velocity fields expressing the uncertainty and output of the seismic images.

This work presents a methodology to create a surrogate model based on Deep Learning (DL) to obtain very accurate fluid simulations throughout a porous media. DL mainly implements multilayer neural networks trained throughout an iteration process. In this process, the different trainable parameters are modified in the proper direction according to an optimizer and the proposed data problem. This process ends in a set of convergence parameters, which mimics the problem's purpose and links a data set of inputs (boundary conditions) with another dataset of outputs (flow and pressure advance). We have based on the universal approximation theorem [4]. It says that any DL architecture, seen as a $y = f(x, \theta, w)$, can map input attributes x together with model parameters θ to output simulations, denoted as (y), given a set of w weights standing for learning parameters in the neural network. The iteration finds patterns in a training set of simulations previously computed. For new unseen input parameters, it predicts their corresponding simulations without the need to solve the fluid-flow equations in a high-speed computer.

2. Problem Definition

2.1 Darcy's Law

According to fluid theory, Darcy's law determines the flow through a porous medium. That law finds a linear relationship between the pressure gradient $\nabla p(x,t)$ and the average fluid velocity through the fiber preform $v(x,t)$, with the proportionality factor being related to the fabric permeability tensor $K(x)$ and the fluid viscosity μ as $v(x,t) = -\frac{K(x)}{\mu}\nabla p(x,t)$. Particularly, x and t represent the position of a given point in the fabric and the time, respectively. If flow continuity is assumed, $\nabla \cdot v(x,t) = 0$, the governing equation for the pressure field can be obtained as: $\nabla \cdot \left(-\frac{K(x)}{\mu}\nabla p(x,t)\right) = 0$.

An initial time (t = 0) and boundary conditions should be given to determine the evolution of the pressure and velocity fields. That problem can be defined as a moving boundary problem because the flow front position Γ(x, t) evolves during the time until the preform is filled. In that case, simulation tools must implement numerical methods that can determine the flow front's position for a given time t and, consequently, the pressure and velocity fields according to standard finite element modeling. Once such information is obtained, updating the flow front's position for time t + Δt can be acquired. Furthermore, a two-phase flow appears due to a flow transition from air to resin due to different external pressure between the inlet and the outlet.

  doi:10.5075/epfl-298799_978-2-9701614-0-0

That fact must be simulated, and that is possible by employing the volume of fluid (VOF) approach by using α as a phase variable. This variable ranges between α = 1 and α = 0 for the resin and air fluids, respectively. α variable is continuously updated during simulation time using the equation given by K(x) tensor stands for fabric permeability, and μ represents fluid viscosity. Both are set in the experiment initially and will simulate the liquid moving boundary throughout the mold.

2.2 CFD Model Definition

Simulations are generated using a well-known CFD program called OpenFoam (Open source Field Operation And Manipulation) [5] in Python according to a specific model defined. It makes it possible to perform the calculations required to simulate the free-stream flow of the fluid. Flow simulations represent physical RTM injections virtually given a mold definition with its characteristic. At that stage, different types of imperfections are set and run by OpenFoam. It generates simulations with flow-front pressure evolution information throughout an RTM injection.

In this work, we have studied the development of a surrogate model to mimic the pressure and flow-front simulation during an RTM injection in a rectangular mold that may contain different permeability. Particularly, dry square regions' appearance.

Figure 1 a) stands for a bi-dimensional square of dimensions $L \times L \times t$ mold, which may contain random disturbances of dry region. For simplicity, macroscopic unidirectional flow is induced by applying a constant pressure condition p_0 at $x = 0$. In contrast, $p = 0$ is set on the opposite edge at $x = L$. Slip-free conditions are applied in the remaining faces of the mold and assume that, at a solid boundary, the fluid will have zero velocity relative to the border.

The OpenFoam outputs are represented in Figure 2 a) for particular boundary conditions. It shows the simulation process generated by a CFD program at different relative times.

2.3 Simulated dataset for a supervised learning approach

A simulated dataset is used in this work to train a surrogate deep learning model in a supervised approach. The goal is to prepare a DL structure that learns how to map the input boundary condition data with their corresponding output conditions for different instants of time and initial injection pressure in RTM. For this purpose, the scope of boundary conditions of interest must be identified and set for study. Such boundary conditions are encapsulated in a sequence of different variables. Some of them may be modified to achieve different software situations for each realization, while the rest conditions remain constant for the model in each completion. The adjustable variables are the imposed dry region's permeability map (its (x, y) center, l size), their permeability, and their initial injection pressure for resin impregnation. The remaining perpetual variables stand for the mold size and the fabric's permeability. This division makes it easier to cover the whole scope in terms of the number of samples and the range adopted and obtaining, in consequence, a more balanced dataset. It is trivial that exploring the whole space of possibilities is a prohibitive approach from a computational viewpoint. For that reason, a uniform distribution of these variables is generated to ensure that all disturbances are equally measured.

The input data structure is a 96 × 96 pixels-size image standing for the permeability map and two additional data, representing the instant t of time and the initial pressure in the RTM injection. The output is a 96 × 96 pixels-size image standing for the pressure map field for a particular instant t of time. In particular, a 96 × 96 pixels-size input image contains one random

  doi:10.5075/epfl-298799_978-2-9701614-0-0

uniform distribution variable, generating this so-called permeability map. That configuration generates a 96 × 96 pixel-size output image in which each pixel includes a specific value of pressure map for a particular instant t of time and initial injection pressure. This time-dependent methodology is trained with discrete array of time since a time is continuous, and it was discretized. OpenFoam ran a wide bunch of simulations for each combination for feeding the neural networks in the following steps. Once the data set of simulations has finished, the data is scrapped and transformed into a particular format for training the DL model.

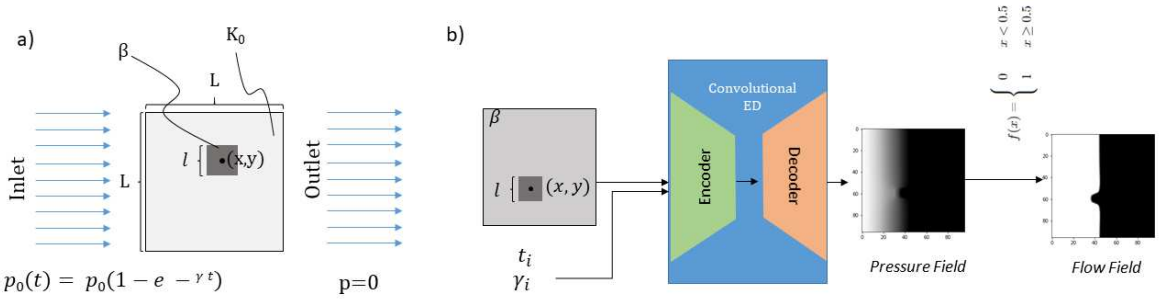

Figure 1. The physical model is represented for the dry region disturbance in a). It stands for the configuration for the center position, height, width permeability, and initial pressure. In b), the surrogate deep learning based-model links the structure of inputs and outputs.

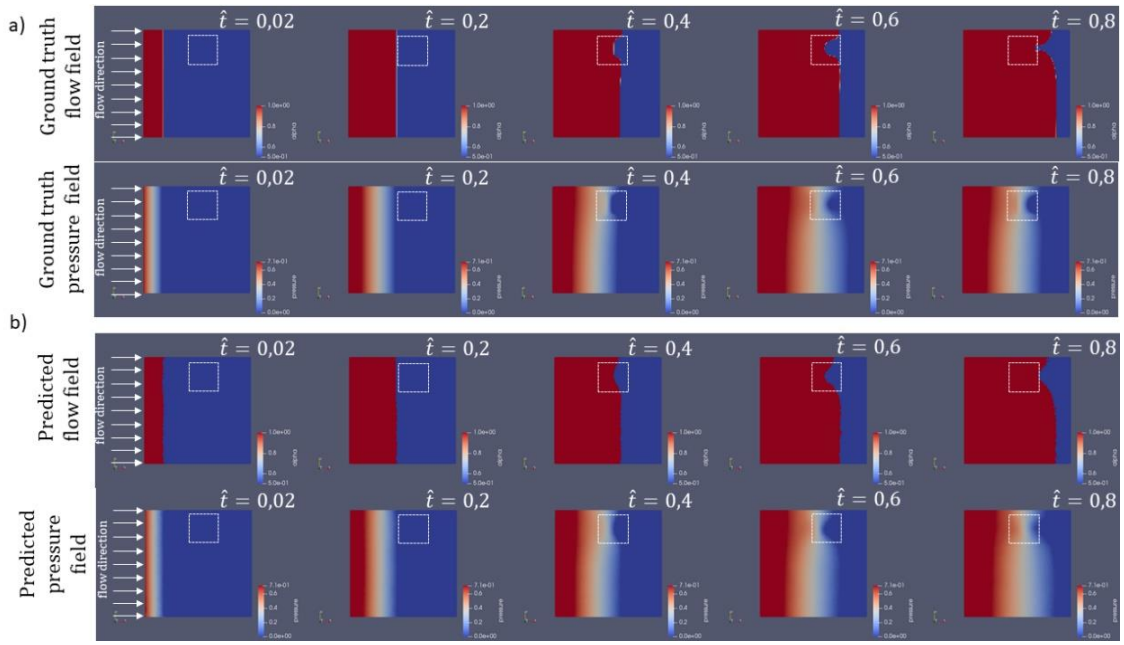

Figure 2. Dry region of 5 uniform instant of times computed by OpenFoam and for our surrogate model are represented in a) and b), respectively. The dashed lines visualize the defect position for each case. Time is non-dimensional from t0 until tn. Resin progress from left to right. Blue and red colors correspond to fill phase values of α=0 and α=1, respectively, and the scale denotes the continuous pressure value from 0 to 1. In b)

3. The Deep Convolutional Encoder-Decoder Model

The surrogate problem is modeled in this work as an image-to-image regression. An encoder-decoder structure was selected to address this formula from a DL viewpoint and can be seen in Figure 1 b). The main idea behind an encoder-decoder architecture is to link one high-dimensional input to a high-dimensional output throughout a coarse-refined process iteratively. The encoder section focuses on learning and transforming the broad patterns coming from the

  doi:10.5075/epfl-298799_978-2-9701614-0-0

input to encode them into middle latent space. However, the decoder's target is to retransform the information found in the latent space to reconstruct it in an output similar to the output ground truth corresponding to its time and initial pressure

The information input-output pipeline is described as follows. The boundary conditions, represented by a 96 x 96 image, feed the encoder together with its time t_i and its γ_i, transforming them into a latent space codification. Then, the decoder receives all this information by continuously operating over this information to obtain outputs similar to the ground truth, the pressure field particularly. Since the alpha flow is related to the pressure flow, a step function was implemented to convert it into a flow field. It allows to train a smaller model with fewer parameters, backpropagating just the pressure field errors and, consequently, saving time in the convergence process.

4. Deployment and results

The training process is essential in DL since it determines the convergence and precision of our model. The training process amounts to optimizing the network parameters θ iterating throughout a training data set to minimize a loss function or objective function. Mean Square Error (MSE) is a quadratic loss function used in this work for neural network training. Stochastic Gradient Descent (SGD) [6] was the iterative method that guided the minimization of the MSE function.

The training process starts with a random neural network weights initialization, and the data is divided into two sets: training and validation. Training data feeds the model in the forward neural network. After that, the MSE is computed and the error committed is backpropagated, changing the network parameters θ according to the SGD optimizer. It changes the parameters in the proper direction. After that, the validation data is presented to the model without inferring the network's parameters to validate the rules learned in the training set. This iteration process finalizes when the MSE losses for the training and validation sets are calculated and get stuck. Our model has been trained with 430 epochs.

We have to remark that our model is trained with the pressure data. The alpha field is a binary output obtained from the pressure field prediction by applying a step function to transform them with a threshold of 0.5. Alpha field ground truth is just used to quantify the error committed in the alpha field predicted from the pressure field transformation. After the model has converged, it is tested over unseen data corresponding to dry region disturbances. Table 1 represents the model's accuracy in quantifying the error according to the F1 Score and the Mean Absolute Error (MAE). Also, we can see the 95th and 99th percentile MAE errors. F1 Score is a classification metric that measures the misunderstanding between wet and dry regions in the flow field. At the same time, MAE is a regression metric that reflects the distance between the pressure field predicted and the ground truth. Figure 2 visualize the ground truth versus de predicted for the completion of the analysis.

Table 1: Surrogate Deep Encoder-Decoder model performance for unseen data.

Simulations	F1 Score	MAE	95th percentile MAE error	99th percentile MAE error
Dry Region	0.987	0.006	0.019	0.026

  doi:10.5075/epfl-298799_978-2-9701614-0-0

5. Discussion and conclusions

A robust and straightforward surrogate deep learning-based model is presented in this work for defects simulation by the nonhomogeneous flow. The presence of different map permeabilities can be induced dry regions disturbances. The need to perform simulations without solving any PDE can lead the designers to study the problem solving the main drawbacks of CFD. This surrogate model performs a simulation in 5 seconds while an OpenFoam simulation delays around 180 seconds, being our model 36 times faster. It could be argued that some accuracy may be reduced with this paradigm. However, the results obtained in Table 1 denote that the errors are minimal, and it is a robust model. The flow front is a binary field where each pixel stands for wetness or dryness in this zone. Our model wrongs, on average, just in 1.3% of the pixels with 9216 pixels for the image (96x96 = 9216). The pressure field is more complicated. It comprehends continuous values. On average, it performs a $6e^{-3}$. It means that our model pollutes the ground truth pressure signal in those quantities. However, the industry could argue for the need for uncertainty for the worst pixel predictions since it is an image regression task. We show 95th and 99th percentile errors to quantify the residual errors. Surprisingly, those errors are not far from the mean, and we can be sure that the remaining errors are below 0.026 MAE for whatever unseen example.

We have to remark that only a limited data sets were needed to feed the surrogate model and replicate Darcy's flow through a porous medium by OpenFoam since DL techniques require a significant amount of data for training purposes. Random distributions allowed the generation of different realizations that covered different instants of flow, pressure fields given a particular permeability map, and initial pressure.

Acknowledgments

The research leading to the results presented in this paper received funding from the Regional Government of Madrid through the research and Innovation Hubs 2018 through the TEMACOM project.

6. References

1. Yinhao Zhu and Nicholas Zabaras. Bayesian deep convolutional encoder–decoder networks for surrogate modeling and uncertainty quantification. Journal of Computational Physics, 366:415– 447, 2018.Sims FA. Applications of resins in bridge and structural engineering. International Journal of Cement Composites and Lightweight Concrete 1985; 7:225-32.
2. Shaoxing Mo, Yinhao Zhu, Nicholas Zabaras, Xiaoqing Shi, and Jichun Wu. Deep convolutional encoder-decoder networks for uncertainty quantification of dynamic multiphase flow in heterogeneous media. Water Resources Research, 55(1):703–728, 2019.
3. Rodolfo SM Freitas, Carlos HS Barbosa, Gabriel M Guerra, Alvaro LGA Coutinho, and Fernando A Rochinha. An encoder-decoder deep surrogate for reverse time migration in seismic imaging under uncertainty. arXiv preprint arXiv:2006.09550, 2020.
4. HORNIK, Kurt; STINCHCOMBE, Maxwell; WHITE, Halbert. Multilayer feedforward networks are universal approximators. Neural networks, 1989, vol. 2, no 5, p. 359-366.

  doi:10.5075/epfl-298799_978-2-9701614-0-0

5. H. G. Weller, G. Tabor, H. Jasak, C. Fureby, A tensorial approach to computational continuum mechanics using object-oriented techniques, COMPUTERS IN PHYSICS, VOL. 12, NO. 6, NOV/DEC 1998.

6. ROBBINS, Herbert; MONRO, Sutton. A stochastic approximation method. The annals of mathematical statistics, 1951, p. 400-407.

  doi:10.5075/epfl-298799_978-2-9701614-0-0

GAUSSIAN PROCESS REGRESSION FOR THE PREDICTION OF MATERIAL ALLOWABLES

Roberta, Cumbo[a], Antonio, Baroni[b], Alfredo, Ricciardi[c], Alessandro, Nicolosi[d], Stefano Giuseppe, Corvaglia[b]

a: Leonardo Labs, Via dell'Aeronautica, 80038 Pomigliano d'Arco, Italy
b: Leonardo Aerostructures, Via per Monteiasi 83, 74023 Grottaglie, Italy
c: Leonardo Aerostructures, Zona ASI- Località Incoronata, 71122 Foggia, Italy
d: Leonardo Labs, Via Tiburtina Km 12.400, 00131, Roma, Italy

Abstract: *The certification of composite laminates requires a statistical approach estabilished by the Composite Material Handbook (CMH-17) which defines the guidelines for the evaluation of material allowables. The accuracy of their estimation is highly important in order to guarantee the integrity of the structure and a high number of experimental tests are performed in order to consider most of the uncertainties associated to the entire manufacturing process. Several methodologies have been explored in literature by combining simulation solutions with a reduced set of test data. In the recent years, Gaussian Process Regression (GPR) applied to Machine Learning has been tested, demonstrating to be a powerful alternative to existing approaches and requiring a low number of data. The presented paper aims to test the GPR for different testing conditions by considering noisy features and outputs.*

Keywords: Design allowables; Composite materials; Fracture Mechanics; Gaussian Process Regression; Machine Learning

1. Introduction

The certification process of aerospace composite structures is normally established by the Composite Material Handbook (CMH-17) [1] which defines the guidelines for the evaluation of material allowables. The allowables are conservative values of ultimate strain or strength defined in a statistical manner in order to take into account for the uncertainties of composite materials identified in the constituent's properties, manufacturing process and testing. The CMH-17 requires a minimum number of 18 specimens to be tested for a single layup and a single test case. The repetition of physical tests leads to delay in the certification and in the design of a new structure. Nowadays, simulation-based solutions supported by a reduced set of experimental data are not accepted by the certification office even if several approaches proved to reach good accuracy on the prediction of material allowables. Among the proposed solutions, Machine Learning (ML) algorithms show more benefits: reduced set of experimental data required and reduced computational time if compared to other standard simulation approaches. Recent studies on data-driven solutions for the prediction of composite laminates consider the estimation of delamination phenomena and stress/strain field on small coupons or on full-scale structural elements [2-6]. In ref. [6], different algorithms are tested for the prediction of first-ply failure strength based on simulated data and shows that the Gaussian Process Regression (GPR) [7] can reach very low regression error for a small number of data samples (less than 500)

  doi:10.5075/epfl-298799_978-2-9701614-0-0

with a short computation time. The authors show the application of GPR on an Open Hole Tension (OHT) test case and approach the choice of input features by considering the analytical formulation provided by Finite Fracture Mechanics (FFM). Given the positive results reached by GPR, this paper aims to test the same approach on multiple test cases as Unnotched Tension (UNT), Unnotched Compression (UNC), Open Hole Compression (OHC) and OHT. The material IM7/8552 [8] is considered and the experimental data at lamina-level are used to calibrate the model in Digimat [9] in order to simulate different stacking sequences. The paper is structured as follows: Sec. 2 provides a brief summary about the used methodology i.e. GPR and analytical models for OHT/OHC, Sec. 3 shows the simulated Design of Experiments (DOEs) over the lamination space, Sec. 4 shows estimation through GPR when the features are considered deterministic or statistic values. Conclusions will follow in Sec. 5.

2. Methodology

2.1 Gaussian Process Regression applied to Machine Learning

A Gaussian Process (GP) is a non-parametric model used to define distribution over function $\mathrm{f}(\mathrm{x})$ [7], which is identified by mean $\mathrm{m}(\mathrm{x})$ and covariance $\mathrm{k}(\mathrm{x},\mathrm{x}')$. In the framework of supervised learning, a Bayesian regression approach can be formulated: the GP is used as *prior*, which is updated with training samples $\mathrm{x}_{\mathrm{train}}$ resulting in the *posterior*, i.e. prediction of $\mathrm{f}(\mathrm{x}^*)$ corresponding to the unobserved samples data x^*. The GP *posterior* can be summarized with the following set of equations:

$$\begin{cases} \mathrm{m_p}(\mathrm{x}) = \mathrm{m}(\mathrm{x}) + \Sigma(\mathrm{x_{train}},\mathrm{x})^{\mathrm{T}}\Sigma(\mathrm{x_{train}},\mathrm{x})^{-1}\left(\mathrm{f}(\mathrm{x_{train}}) - \mathrm{m}(\mathrm{x_{train}})\right) \\ \mathrm{k_p}(\mathrm{x},\mathrm{x}') = \mathrm{k}(\mathrm{x},\mathrm{x}') - \Sigma(\mathrm{x_{train}},\mathrm{x})^{\mathrm{T}}\Sigma(\mathrm{x_{train}},\mathrm{x})^{-1}\Sigma(\mathrm{x_{train}},\mathrm{x}') \end{cases} \quad (1)$$

From Eq. 1, the *prior* mean and covariance function are updated with training data and the uncertainty on the estimation identified by $\mathrm{k_p}(\mathrm{x},\mathrm{x}')$ is always less than the *prior* covariance $\mathrm{k}(\mathrm{x},\mathrm{x}')$. Normally, the estimation of functions close to the training data will return a small covariance, which is instead very high for samples located in the space of features out of the training domain. In the case of noisy inputs, more considerations are needed in order to take into account features uncertainties. The formulation, i.e. noisy input Gaussian Process (NIGP), presented in ref. [10] is adopted in this paper.

2.2 Analytical models for open hole testing

2.2.1 Fracture Mechanics for Open Hole Tension strength [11,12]

The Finite Fracture Mechanics model for OHT is based on the stress and energy balance as follows:

$$\begin{cases} \frac{1}{\mathrm{l}}\int_{\mathrm{R}}^{\mathrm{R+l}} \sigma_{\mathrm{xx}}(0,\mathrm{y})\mathrm{dy} = \mathrm{X_L} \\ \frac{1}{l}\int_{\mathrm{R}}^{\mathrm{R+l}} \mathrm{K_I^2}(\mathrm{a})\mathrm{da} = \mathrm{K_{IC}^2} \end{cases} \quad (2)$$

where the first equation put in relation the stress distribution $\sigma_{\mathrm{xx}}(0,\mathrm{y})$ averaged over a distance l from the hole with radius R, with the unnotched material strength $\mathrm{X_L}$. This condition is supported by the second equation which imposes that the failure occurs when the energy release rate or fracture toughness $\mathrm{K_I}$ reaches the critical value $\mathrm{K_{IC}}$. This formulation is considered in [6] in combination with other models in order to build an analytical framework

which is able to predict the unknown variables of Eq. 2. The notched strength of an open hole coupon in tension results to be function of longitudinal Young's modulus of the ply E_1, unnotched strength X_T, critical energy release rate K_{IC} of laminate with plyes at 0°, width to diameter ratio W/D, stacking sequence [6]. The framework has been applied both on OHT and OHC tests resulting in high accuracy on tension but poor results on compression [13]. In this paper, K_{IC} is evaluated for each laminate by solving Eq. 2, where:

$$K_I = \sigma\sqrt{(\pi a)} \tag{3}$$

Eq. 3 is valid for coupons with large ratio W/D. In this paper, coupons with sizes in agreement with ASTM D5766 are considered and the assumption of Eq. 3 can be applied. The notched strength of coupons with fixed geometry and material will result as function of:

$$\sigma_{OHT} = f(\sigma_{UNT}, K_{IC}, layup) \tag{4}$$

where the layup is identified by the lamination parameters introduced in Sec. 3.

2.2.2 Analytical model for Open Hole Compression strength [14]

Ref. [14] proposed an analytical approach for the evaluation of ultimate strength of open hole coupons under compression. In this condition, failure occurs in the plies oriented at 0° with the initiation of fibers micro-buckling close to the edge of the hole. The linear softening cohesive zone law can reach high correlation with experimental data [14] and it defines the ultimate compressive strength as function of:

$$\sigma_{OHC} = g(l_{cr}, \sigma_{UNC}, v_c, E, R, W) \tag{5}$$

where l_{cr} is the critical value of buckled length, E is the laminate elastic modulus, R is the radius of the center hole, W is the width of the coupon and v_c is the crack closure displacement. v_c is expressed as function of (d_f, V_f, E_f, τ_y) with d_f fiber diameter, V_f volume fraction, E_f fiber elastic modulus and τ_f in-plane shear yield strength of the laminate. The notched strength of coupons with fixed geometry and material can be considered from Eq. 5 as function of:

$$\sigma_{OHC} = g(\sigma_{UNC}, v_c, layup) \tag{6}$$

3. Design of Experiments over the lamination space

This paper aims to replicate and extend the work presented in [6] on different test cases. The lamination space used here is the one identified by lamination parameters [15] ζ_1, ζ_2. In [6], 27133 unique balanced laminates with the number of plies ranging between 0 and 32 are used to define the DoE. However, this set of laminates do not consider the symmetry and additional manufacturing constraints as:

1. Maximum orientation gap between two consecutive plies no more than 45°;
2. No more than 4 successive plies with same orientation;
3. Percentage of plies oriented at ±45°, 0°, 90° usually less than 8% and higher than 70%.

Table 1 shows the number of possible laminates for some combinations of constraints. In this paper, a number of plies ranging between 12 and 24 is considered and only symmetric laminates are retained. The total number of points without repetitions of ζ_1, ζ_2 is 179 (Fig. 1). This set of laminates will be used to perform GPR over lamination space but particular attention will be

  doi:10.5075/epfl-298799_978-2-9701614-0-0

given to the estimation of laminates in the subspace defined by all the mentioned constraints, identifying a subset of 79 stacking sequences.

Table 1: Number of possible laminates with respect to manufacturing constraints. Constraints 4 and 5 indicate respectively balanced and symmetric laminates and n. plies between 12 and 24.

Constraints	n. laminates
Balanced with 126 plies	27133
4, 5	179
3, 4, 5	83
1-5	79

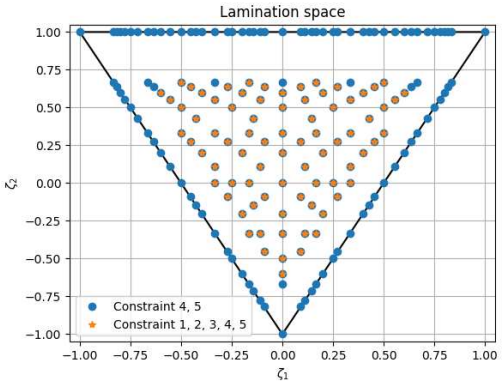

Figure 1. Lamination space ζ_1,ζ_2.

A database of 716 (179 laminates x 4 test cases) simulated data has been created for the material IM7/8552. The laminates are modelled in Digimat and the geometry is chosen in agreement with the ASTM (Table 2).

Table 2: Geometry of coupons for each test case with reference to ASTM standards.

Test case - ASTM		size [mm]
UNT – ASTM D3039	Length	254
	Width	25.4
UNC – ASTM D6641	Length	139.7
	Width	12.7
OHT – ASTM D5766 OHC – ASTM D6484	Length	177.8
	Width	38.1
	Hole diameter	6.35

The Progressive Failure Analysis (PFA) is considered for the evaluation of ultimate strength. For each sample, 18 simulations have been performed by varying the physical parameters of the material with a normal distribution. The uncertain parameters have been selected from the output of the sensitivity analysis of ultimate strength carried out for a subset of laminates with respect to constituent's parameters. The results of this analysis are not shown here because already presented in [6] and similar results are obtained. However, since the main source of variability of material allowables comes from a small perturbation of fiber volume fraction and tension/compression fiber strength, a normal distribution of these variables with uncertainty of

6% with respect to the baseline value is considered for the creation of the database. The statistical values of the ultimate strength for UNT and OHT are used in Eq. 2 to get $\mathrm{K_{IC}}$ for each laminate. The trend of $\mathrm{l_{cr}}$ and $\mathrm{K_{IC}}$ is shown in Fig. 2. The value of $\mathrm{l_{cr}}$ is oscillating around a mean value of 3.6 mm, except for $\zeta_1 = 0, \zeta_2 = -1$, which is a laminate with only plies oriented at ±45°. Given this result, $\mathrm{l_{cr}}$ is considered to be constant for any laminate with fixed geometry and material.

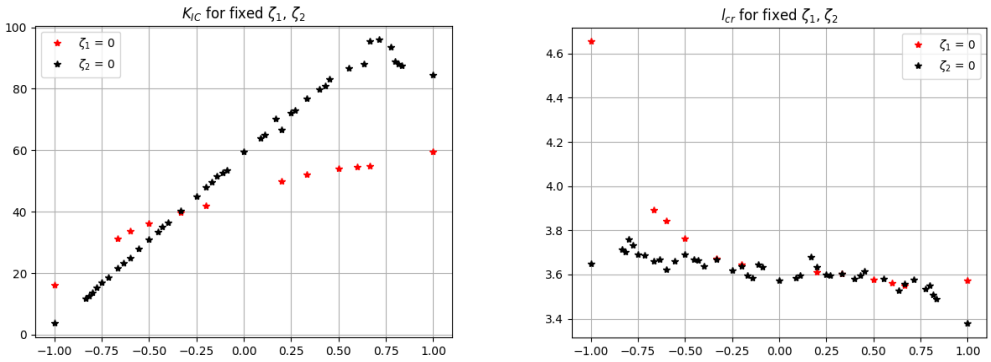

Figure 2. Trend of l_{cr} $[mm]$ and K_{IC} $[MPa\sqrt{mm}]$ for fixed ζ_1, ζ_2.

4. Gaussian Process Regression over lamination space for UNT, UNC, OHT, OHC

The application of GPR on unnotched tests requires less attention than open hole cases. Indeed, for a single material with same specimen sizes, the ultimate strength of UNT and UNC will be a Gaussian distribution, function of the lamination parameters:

$$\sigma_{UNT} = h(\zeta_1,\zeta_2) \sim N(\bar{\sigma}_{UNT}, \Sigma_{UNT})$$
$$\sigma_{UNC} = k(\zeta_1,\zeta_2) \sim N(\bar{\sigma}_{UNC}, \Sigma_{UNC}) \quad (7)$$

Where $\bar{\sigma}$ and Σ are respectively the mean and variance. Recalling Eq. 4 and Eq. 6, the notched strength is function of experimental variables, thus the input features will not be deterministic but statistic values identified with mean and standard deviation. For open hole tests, NIGP will be thus applied.

4.1 Selection of training data

In order to reduce the number of experiments, an instance selection algorithm has been applied to select a limited number of training data. In this case, a simple algorithm based on random sampling has been adopted. The optimization criterion was chosen by training a GPR for each instance subsets and by evaluating the Mean Absolute Error (MAE) on a predefined test data which has been chosen ad-hoc (red samples in Fig. 3) including the most significant laminates with mixed plies at 0°, ±45° and 90°. The size of training instances has been fixed as a percentage of the full set of data (Table 3). However, a more sophisticated instance selection algorithm should be implemented in order to find a better solution which gives the highest performance on the test set in terms of MAE.

  doi:10.5075/epfl-298799_978-2-9701614-0-0

Table 3: Number of training samples and mean absolute error (MAE) for each test case.

Test case	n. training samples	MAE [MPa]
UNT	**16**	**33**
UNC	**16**	**47**
OHT	**16**	**10.5**
OHC	**16**	**20**

4.1 Results and discussion

The results of the estimation in terms of allowables and relative percentage error with respect to simulated reference data are shown in Fig. 3 for each analyzed test case. The error maps for all the cases show a value less than 15% for the center of the lamination space, which is a good result since the most of the laminates used in aerospace applications are located in that area. The upper area and the vertices are instead the ones with higher uncertainty and this can be also explained with real test data because the first one is represented by laminates with high percentage of plies oriented at 0° and 90° and the vertices are identified by laminates fully oriented at 0°, 90° or ±45°. The training set has been set equal to 10% of the full dataset. Ideally, we could increase the number of training samples for OHT/OHC since, on a real test case, the estimation of UNT/UNC can be used for the estimation of OHT/OHC without the knowledge of additional experimental tests.

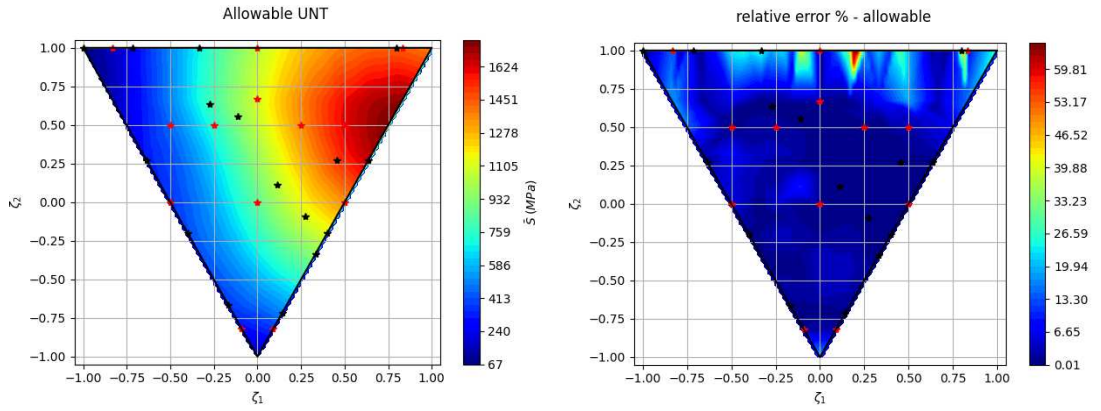

(a) Estimation UNT

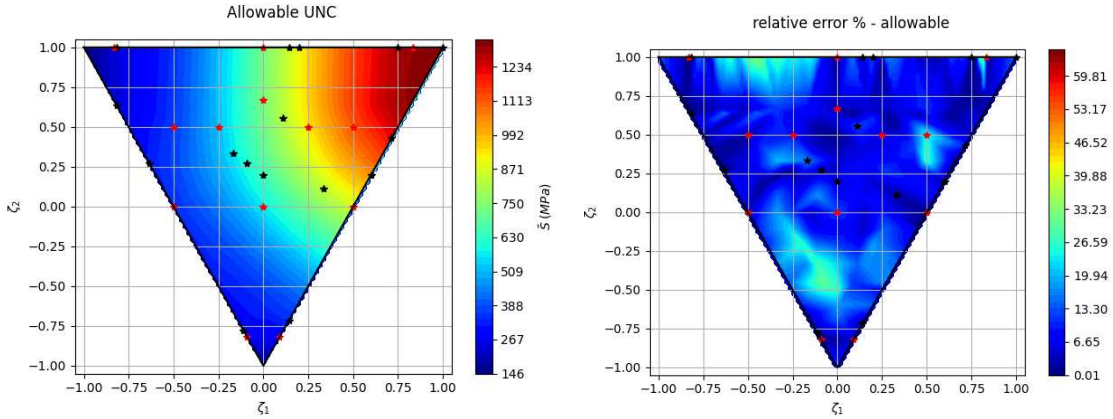

(b) Estimation UNC

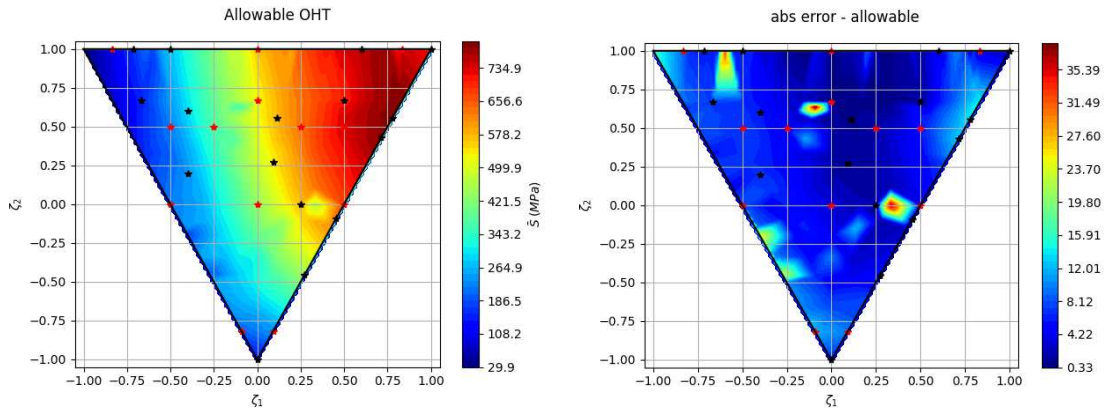

(c) Estimation OHT

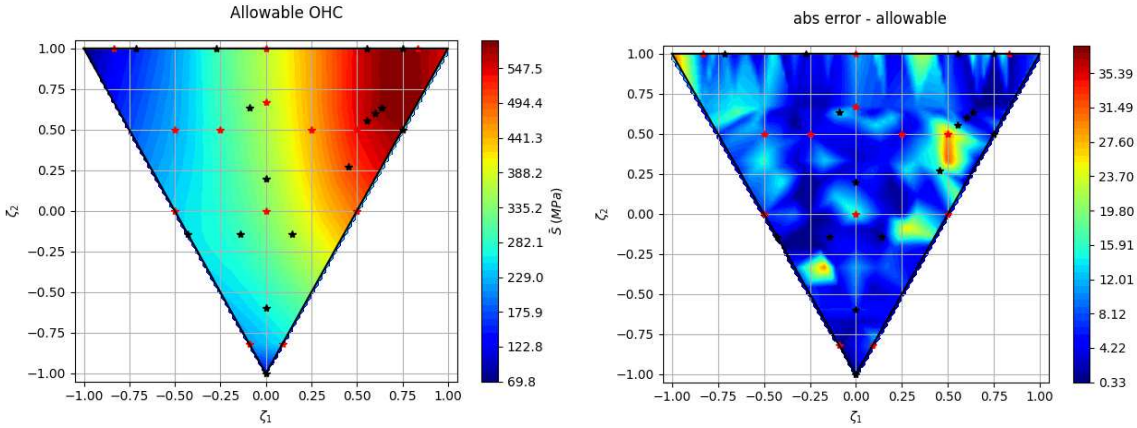

(d) Estimation OHC

Figure 3. Estimated allowable values [MPa] (left) and relative percentage errors with respect to simulated data (right) for each point of the lamination space. Red samples: validation set – Black samples: training set.

5. Conclusions

The application of GPR for the estimation of material allowables has been tested in this paper on simulated data for the material IM7/8552. The aim was to study the performances of GPR on multiple testing cases, i.e. UNT, UNC, OHT, OHC, in order to reduce the number of experimental tests needed during the design phase of a composite structure. The input features are selected on the knowledge of analytical formulation that have been already experimentally validated in literature. The advantage of the proposed investigation is that the good accuracy of the unnotched strength allows to use the estimated values as inputs for the estimation of open hole strengths. This results in testing only a small number of coupons for UNT/UNC. However, the proposed approach can be improved and needs more investigation as future steps: i) optimal selection of the training set, ii) study of the uncertainty propagation of the estimation of unnotched allowables on the estimation of open hole strength.

  doi:10.5075/epfl-298799_978-2-9701614-0-0

Acknowledgements

We thank Pasquale Paolella (Università degli Studi Federico II – Naples) for supporting the data analysis, Davide Chirico (Leonardo) for useful comments, Daniele Malacrida, Ivan Spisso, Alessandro Russo (Leonardo) for assistance in running simulations on HPC Davinci-1.

6. References

1. Composites material handbook, Polymer Matrix Composites, Volume 1: Guidelines for characterization of structural materials. 1997.
2. ZACARIA, Marco; YAZDANI, Hamed; PONNUSAMI, Sathiskumar. Machine Learning for Predicting Interlaminar Stresses in Composite Panels. 2021.
3. ZHANG, Zilan, et al. Machine Learning for Accelerating the Design Process of Double-Double Composite Structures. *Composite Structures*, 2022, 115233.
4. MOJUMDER, Satyajit, et al. Mechanistic Data Science for Modeling and Design of Aerospace Composite Materials. *arXiv preprint arXiv:2112.00968*, 2021.
5. GUO, Jianchao; ZHANG, Yongbo; CHEN, Ke. Algorithm for Compression Design Allowable Determination of Composite Laminates with Initial Delaminations. *Machines*, 2021, 9.12: 307.
6. Furtado, C., Pereira, L. F., Tavares, R. P., Salgado, M., Otero, F., Catalanotti, G., Arteiro, A., Bessa, M.A., Camanho, P. P. A methodology to generate design allowables of composite laminates using machine learning. *International Journal of Solids and Structures*, 2021, 233: 111095.
7. Rasmussen, C. E. Gaussian processes in machine learning. In: *Summer school on machine learning*. Springer, Berlin, Heidelberg, 2003. p. 63-71.
8. K. Marlett, et al., Hexcel 8552 IM7 Unidirectional Prepreg 190 gsm & 35%RC Qualification Material Property Data Report, CAM-RP-2009-015 Rev. A, NIAR, Wichita State University, 2011.
9. Digimat Virtual Allowables, https://www.e-xstream.com/ (2020, accessed 10 January 2022)
10. MCHUTCHON, Andrew; RASMUSSEN, Carl. Gaussian process training with input noise. *Advances in Neural Information Processing Systems*, 2011, 24.
11. Furtado, C., Arteiro, A., Bessa, M. A., Wardle, B. L. and Camanho, P. P. Prediction of size effects in open-hole laminates using only the Young's modulus, the strength, and the R-curve of the 0 ply. *Composites Part A: Applied Science and Manufacturing*, 2017, 101: 306-317.
12. Cornetti, P., Pugno, N., Carpinteri, A. and Taylor, D. Finite fracture mechanics: a coupled stress and energy failure criterion. *Engineering Fracture Mechanics*, 2006, 73.14: 2021-2033.
13. Camanho, P. P., Erçin, G. H., Catalanotti, G., Mahdi, S., & Linde, P. (2012). A finite fracture mechanics model for the prediction of the open-hole strength of composite laminates. *Composites Part A: Applied Science and Manufacturing*, *43*(8), 1219-1225.
14. Soutis C, Fleck NA, Smith PA. Failure prediction technique for compression loaded carbon fibre–epoxy laminate with an open hole. J Compos Mater 1991;25:1476–98.
15. Tsai SW, Pagano NJ. Invariant properties of composite materials. Tech. Rep.; Air force materials lab Wright-Patterson AFB Ohio; 1968.

  doi:10.5075/epfl-298799_978-2-9701614-0-0

DEEP LEARNING BASED PREDICTION OF FIBROUS MICROSTRUCTURE PERMEABILITY

Baris Caglar[a], Guillaume Broggi[b], Muhammad A. Ali[c], Laurent Orgéas[d], Véronique Michaud[b]

a: Aerospace Manufacturing Technologies, Faculty of Aerospace Engineering, Delft University of Technology, Kluyverweg 1, Delft 2629HS, Netherlands – b.caglar@tudelft.nl
b: Laboratory for Processing of Advanced Composites (LPAC), Institute of Materials (IMX), Ecole Polytechnique Fédérale de Lausanne (EPFL), Station 12, 1015 Lausanne, Switzerland
c: Department of Aerospace Engineering, Khalifa University of Science and Technology, Abu Dhabi, United Arab Emirates
d: CNRS, Univ. Grenoble Alpes, 3SR Lab, F-38000 Grenoble, France

Abstract: *Knowledge of permeability of fibrous microstructures is crucial for predicting the mold fill times and resin flow path in composite manufacturing. Herein we report a method to rapidly predict the permeability of 3D fibrous microstructures. Our method relies on predicting the permeability of 2D cross-sections via deep neural networks and extending this capability to 3D microstructures via circuit analogy as a means of reduced order modeling. Approximately 50% of the permeability predictions of 2D cross-sections have 10% or less deviation from the permeability results obtained via flow simulations in Geodict. Computational time required for predicting the permeability of 3D microstructures is reduced from hours to less than 10 seconds. This framework enables fast and accurate prediction of micro-permeability and serves as the first building block towards prediction of fabric mesostructures' permeability via deep learning based methods.*

Keywords: Deep Learning; Permeability; Microstructures; Numerical analysis

1. Introduction

Permeability, a 3D tensor defined by the pore structure within the fabrics, is a key set of input parameters to predict mold-filling times and filling patterns in Liquid Composite Molding (LCM) [1]. Nowadays, numerical flow simulations in virtual fabric structures is on its way to replace experimental characterization techniques [2,3], and these efforts are further refined owing to X-ray computed microtomography based representation of 3D geometric information within and between individual tows [4,5]. However, the flow simulations in such structures still require substantial computational power and computations typically take hours in parallelized systems. On the other extreme, analytical models provide rapid predictions of permeability and these models range from models based on the isotropic porous media to models that take into account the fiber orientation and tortuosity [6–9]. However, these models are limited in accounting for the local variability in fabric structures.

Convolutional neural networks (CNNs), a type of deep learning algorithm, provide powerful alternatives for detecting patterns in images and linking these features to a property (such as permeability). In materials science, they have been used for many purposes such as for predicting mechanical, thermal and hydraulic properties of material systems [10,11] and also for predicting the permeability of isotropic porous media such as those found in soil sciences [12,13]. This work aims to provide a fast and accurate method for predicting the permeability of

  doi:10.5075/epfl-298799_978-2-9701614-0-0

highly oriented anisotropic media, more specifically the fibrous microstructures encountered in advanced composites. To this end, we propose a method based on the following steps: 1- generate 3D fibrous microstructures, 2- estimate the transverse permeability of individual slices (along the fiber direction) and the full 3D structures using FlowDict module of Geodict software, 3- train a 2D CNN using the simulation results to predict the permeability of 2D slices, 4- predict the 2D permeability in the slices of 3D structures previously unseen by CNN, 5- use the circuit analogy between 2D slices to predict the permeability of 3D structures. The outlined methodology enables us to reduce the computational time from hours required for running 3D flow simulations to estimate the permeability in less than 10 seconds.

2. Methods

2.1 Elementary volume (EV) generation

We generated 400x400 pixels images with 1 µm2/pixel correspondence where fibers had radii, r,: 6, 8, 10, 12, or 14 pixels and fiber volume fraction, vf, was between 0.25 and 0.70, by increments of 0.05. We used a modified version of the Monte-Carlo procedure by Chen and Papathanasiou [14,15], to account for the short-range tortuosity. Figure 1 shows two EVs generated by the modified fiber generator.

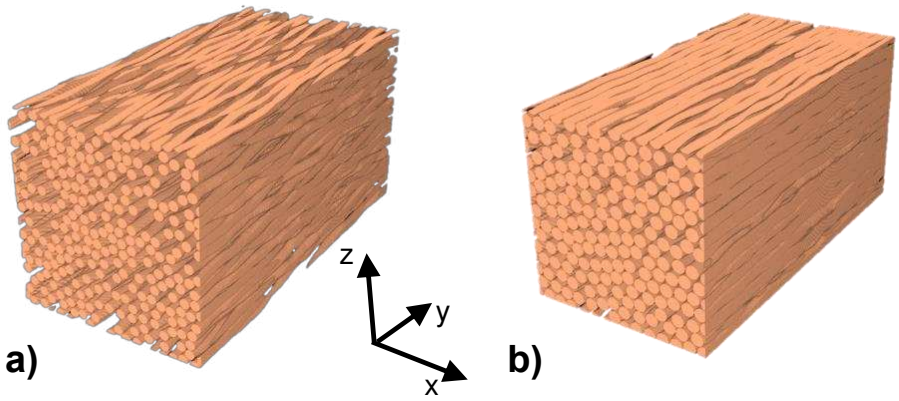

Figure 1. Two examples of generated 3D structures. a) r = 10 pixel, v_f = 0.5, b) r = 14 pixel, v_f = 0.7.

2.2 Flow simulations

We performed flow simulations to extract the transverse permeability (along x- and z-directions) of the generated EVs. These simulations included those where the EVs had a depth of one in y-direction (i.e., on 2D slices) to train the 2D CNN, and simulations on full EVs (which consisted of 800 slices with 400x400 pixels). 3D simulations were used for validating our approach based on combining both the circuit analogy as an upscaling technique.

We used FlowDict module of the Geodict software to perform the flow simulations. The choice was based on Geodict's capability to perform the simulations directly on the binarized images and its suitability for automation as we performed the simulations on thousands of 2D binary images. We defined the boundary conditions as depicted in Figure 2 following the suggestions by Rimmel et al. [16] that were reported for similar simulations using the same software module.

  doi:10.5075/epfl-298799_978-2-9701614-0-0

We solved the governing Stokes flow equations (*i.e.*, at negligible or zero-valued Reynolds number) using the Explicit Jump-Stokes solver, as reported in earlier work for permeability characterization [4,5].

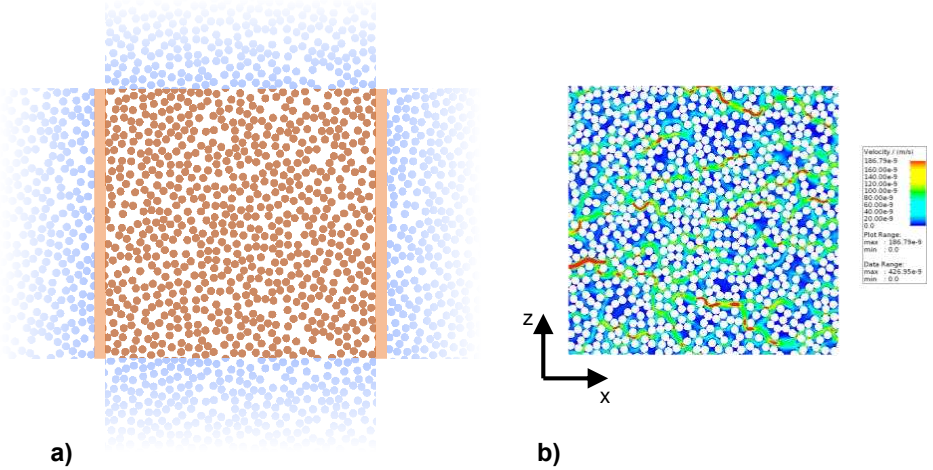

Figure 2. a) Boundary conditions and b) corresponding flow field in x-direction. In a) boundary conditions highlight the implicit inlet/outlet voxels in orange and periodic tangential boundaries in blue.

2.3 CNN architecture and training

We implemented a modified version of AlexNet [17] in Matlab's Deep Learning toolbox. The design of the CNN is outlined in Figure 3. It takes an image with 400×400 pixels as input and outputs the permeability. Each convolutional block in Figure 3 consists of the following: a convolutional layer, followed by an activation via a rectified linear unit (ReLU), followed by batch normalization and max pooling layers. The last block is connected to a dropout layer and a fully connected layer for the regression task. The filters of convolution layers have a size of 7×7, 5×5, and 3×3 respectively. Filters have a stride of 1 and paddings of 3, 2, and 1 and number of filters is 16, 32 and 64 respectively. Max pooling layers' size and stride are as follows: the first two of them have a size of 4×4 and a stride of 4 while the last one has a size of 2×2 and a stride of 1.

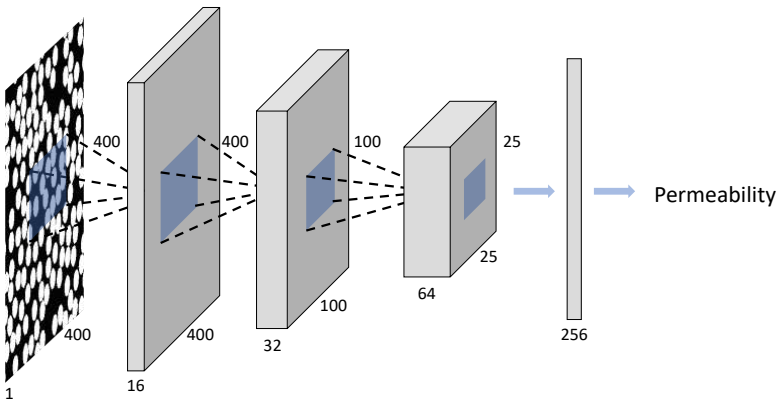

Figure 3. Architecture of the used convolutional neural network where each convolutional block is made up of a convolution, activation, batch normalization and max pooling layers

  doi:10.5075/epfl-298799_978-2-9701614-0-0

5 different pixel counts per r and 10 different fiber content combination (v_f) results in 50 unique microstructures, and each microstructure has 1000 slices along the fiber direction. 1280 of the 50000 unique 2D slices are selected randomly and used in the CNN training. 2D microstructure permeability is flip-invariant, and we exploited this characteristic to augment the number of images during CNN training and used the resulting database with a split of 3:1 between training and validation images.

We mapped the logarithm of permeability between -1 and 1 using the minimum and maximum values and used it as the output of the CNN. We trained the CNN for 500 epochs using the ADAM optimizer via Matlab Deep Learning Toolbox on an Nvidia Quadro RTX6000 with 24GB memory; the training lasted approximately 14 hours.

3. Results and Discussion

3.1 2D transverse permeability

3000 randomly selected images' predicted permeability along x-direction and the corresponding simulation results are shown in Figure 4a. CNN predictions seem to be well-aligned with the simulation results in general, some scatter is observed at the low permeability regime - approximately for permeability values lower than 1×10-13 m^2 obtained at high v_f. This is suspected to originate from 0 permeability results returned by the flow simulation at high v_f range. Another trend is the relatively more pronounced scatter in the images where fiber radius is 14 pixels. Figure 4b shows the cumulative distribution of relative deviation of neural network predictions (NN) from the Geodict results (GD), $(GD - NN)/GD$. This is suspected to originate from the disparity between the individual fiber size (and thus the spacing between neighboring fibers) and the filter sizes in the convolutional layers. We note that, even in the case of 14 pixel radius fibers, more than 50% of predictions have 10% or less deviation from the simulation results.

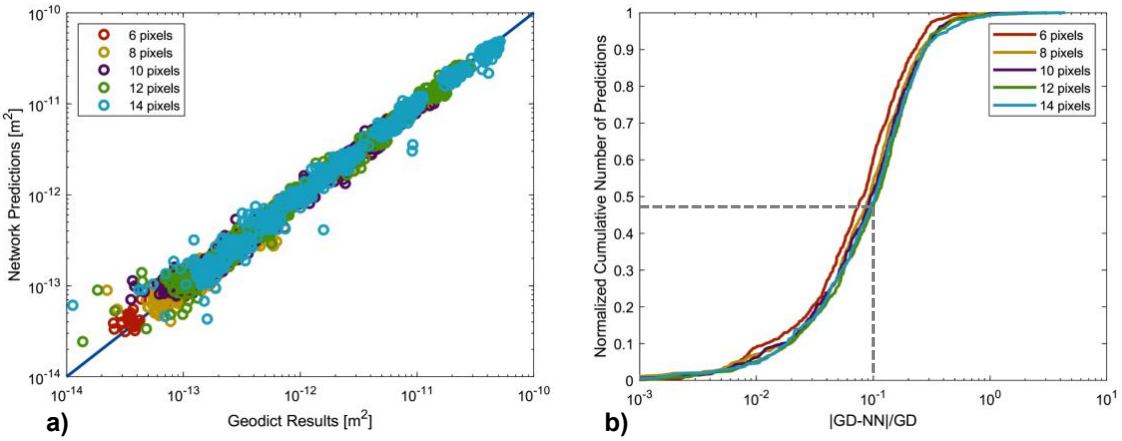

Figure 4. a) Neural network predictions for permeability in x-direction vs. corresponding Geodict results, b) normalized number of predictions as a function of the predictions' deviation from simulation results

3.2 3D permeability: circuit analogy based on 2D predictions

To test the suitability of upscaling the 2D predictions via circuit analogy, we generated 15 new microstructures with 400x800x400 voxel dimensions (800 slices along the fiber direction with 400x400 pixels). These microstructures consisted of images where the fiber radii were represented by 6, 10 or 14 pixels and v_f was 0.3, 0.4, 0.5, 0.6, or 0.7. Flow simulations to obtain the transverse permeability values took between 1675 seconds and 8118 seconds with an average of 4305±1839 seconds. The equivalent transverse permeability (in both x- and z-directions) is calculated via circuit analogy of 800 resistances ($1/K_x$) in parallel using the arithmetic mean of individual slices' permeability. Complete operation, including the pre-processing and post-processing operations, to predict the permeability of individual slices and the equivalent permeability took 8.56 seconds.

Figure 5 shows the permeability values obtained via 3D flow simulations (GD-3D), as well as the resulting circuit analogy results (NN-circuit) for both x- and z-directions. Results show that most of the GD-3D and NN-circuit results fall in a small range for all the studied pixel per radius correspondence and v_f combinations. Departure of both GD-3D and NN-circuit from Gebart's permeability predictions [6] at high v_f is another distinct characteristic of these results and these are in agreement with the observations reported in literature [18] further validating our approach where we achieve reasonable accuracy with significantly smaller computational effort.

The reader is referred to our paper [19] for more detailed description of the methodologies we relied on and for more detailed validation of the proposed approach, also extended for prediction of longitudinal permeability. The said paper also explores the suitability of pre-processing strategies to enable predicting the permeability of images that have different pixel dimensions than what the CNN expects that can be made up of finer or coarser 2D square slices as well as rectangular slices.

4. Conclusion

This work presents a mixed and fast numerical-analytical strategy to predict the transverse permeability of 3D fibrous microstructures. To that end, we treated the images of 3D microstructures as a series of 2D slices. After generating such microstructures and performing flow simulations on 2D and 3D images, we trained a 2D Convolutional Neural Network for predicting the transverse permeability of individual 2D slices. These highly accurate predictions were then used in a circuit analogy to predict the transverse permeability of full 3D microstructures. Results show that predictions in both 2D and 3D are in good agreement with their counterparts obtained via flow simulations and require only a fraction of the computational effort needed for flow simulations. Our approach serves as the first building block towards accurate and fast prediction of fabric mesostructures' permeability where local fiber volume fraction and dual-scale effects are prominent.

  doi:10.5075/epfl-298799_978-2-9701614-0-0

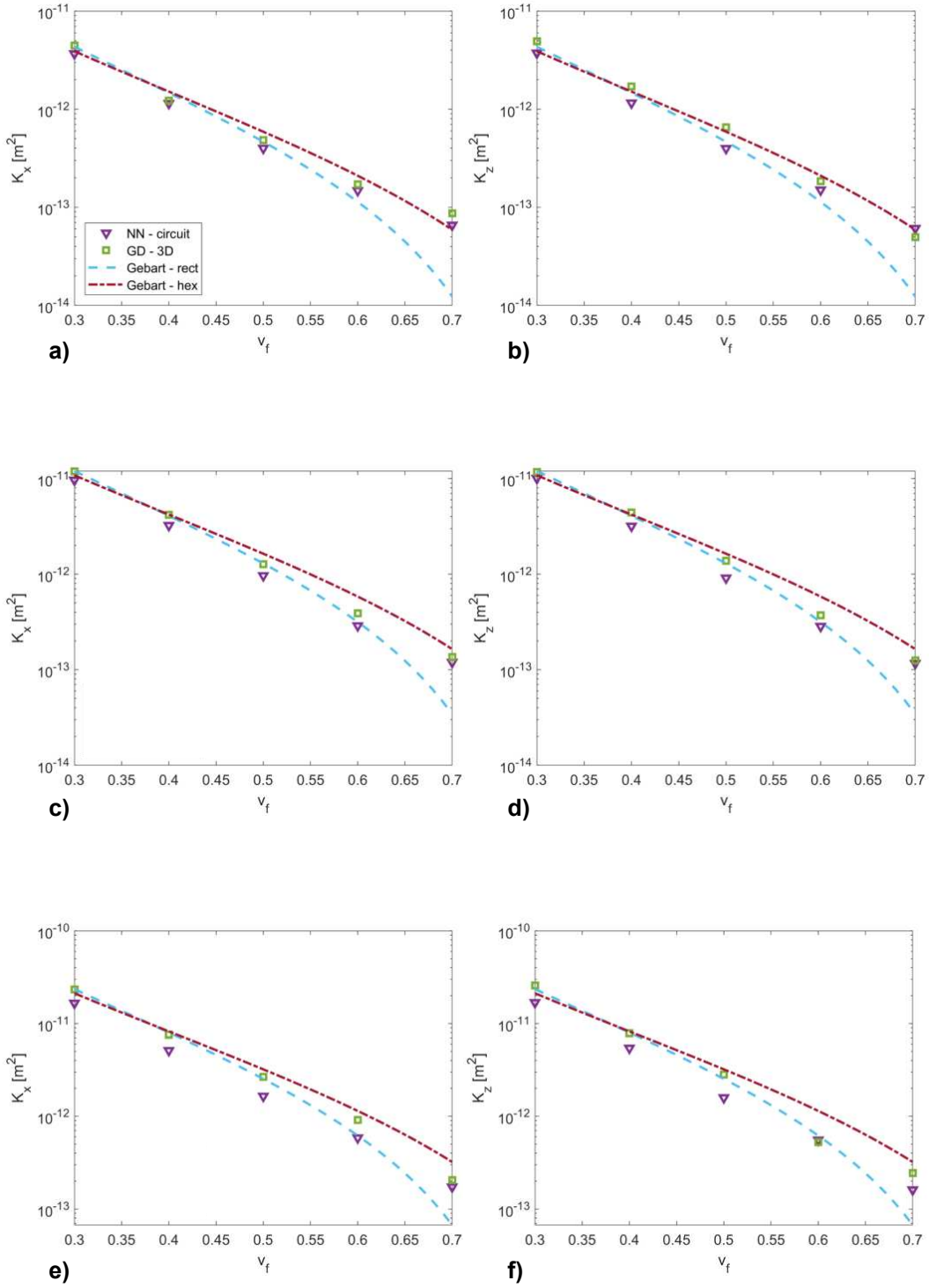

Figure 5. Permeability results obtained via 3D simulations and circuit analogy of the neural network predictions, on images with r = 10 pixel. Top, middle, and bottom rows correspond to the results along the x-, y-, and z-directions, respectively.

Acknowledgements

This research was financially supported by the Swiss National Science Foundation (SNF-182669). The 3SR Lab is part of the LabEx Tec 21 (Investissements d'Avenir - grant agreement n◦ANR-11-LABX-0030) and the Carnot Institute Polynat (ANR16-CARN0025).

5. References

[1] Advani SG, Sozer EM. Process Modeling in Composites Manufacturing. CRC Press; 2010.

[2] Verleye B, Lomov S V., Long AC, Verpoest I, Roose D. Permeability prediction for the meso-macro coupling in the simulation of the impregnation stage of Resin Transfer Moulding. Compos Part A Appl Sci Manuf 2010;41:29–35.

[3] Xiao X, Endruweit A, Zeng X, Hu J, Long AC. Through-thickness permeability study of orthogonal and angle-interlock woven fabrics. J Mater Sci 2015;50:1257–66.

[4] Caglar B, Orgéas L, Rolland du Roscoat S, Sozer EM, Michaud V. Permeability of textile fabrics with spherical inclusions. Compos Part A Appl Sci Manuf 2017;99:1–14.

[5] Ali MA, Umer R, Khan KA, Cantwell WJ. In-plane virtual permeability characterization of 3D woven fabrics using a hybrid experimental and numerical approach. Compos Sci Technol 2019;173:99–109.

[6] Gebart BR. Permeability of unidirectional reinforcements for RTM. J Compos Mater 1992;26:1100–33.

[7] Kuwabara S. The forces experienced by randomly distributed parallel circular cylinders or spheres in a viscous flow at small Reynolds numbers. J Phys Soc Japan 1959;14:527–32.

[8] Tamayol A, Bahrami M. Transverse permeability of fibrous porous media. Phys Rev E - Stat Nonlinear, Soft Matter Phys 2011;83:1–9.

[9] Wu H, Fang WZ, Kang Q, Tao WQ, Qiao R. Predicting Effective Diffusivity of Porous Media from Images by Deep Learning. Sci Rep 2019;9:1–12.

[10] Rong Q, Wei H, Huang X, Bao H. Predicting the effective thermal conductivity of composites from cross sections images using deep learning methods. Compos Sci Technol 2019;184:1–19.

[11] Jung K, Chang S. Advanced deep learning model-based impact characterization method for composite laminates. Compos Sci Technol 2021;207:108713.

[12] Araya-Polo M, Alpak FO, Hunter S, Hofmann R, Saxena N. Deep learning–driven permeability estimation from 2D images. Comput Geosci 2019.

[13] Wang Y Da, Chung T, Armstrong RT, Mostaghimi P. ML - LBM : Predicting and Accelerating Steady State Flow Simulation in Porous Media with Convolutional

  doi:10.5075/epfl-298799_978-2-9701614-0-0

Neural Networks. Transp Porous Media 2021.

[14] Chen X, Papathanasiou TD. Micro-scale modeling of axial flow through unidirectional disordered fiber arrays. Compos Sci Technol 2007;67:1286–93.

[15] Chen X, Papathanasiou TD. On the variability of the Kozeny constant for saturated flow across unidirectional disordered fiber arrays. Compos Part A Appl Sci Manuf 2006;37:836–46.

[16] Rimmel O, May D. Modeling transverse micro flow in dry fiber placement preforms. J Compos Mater 2019.

[17] Krizhevsky A, Sutskever I, Hinton GE. ImageNet classification with deep convolutional neural networks. Commun ACM 2017;60:84–90.

[18] Endruweit A, Gommer F, Long AC. Stochastic analysis of fibre volume fraction and permeability in fibre bundles with random filament arrangement. Compos Part A Appl Sci Manuf 2013;49:109–18.

[19] Caglar B, Broggi G, Ali MA, Orgéas L, Michaud V. Deep learning accelerated prediction of the permeability of fibrous microstructures. Compos Part A Appl Sci Manuf 2022.

  doi:10.5075/epfl-298799_978-2-9701614-0-0

UNCURED OUT-OF-AUTOCLAVE COMPOSITE PREPREGS CHARACTERIZATION VIA DEEP LEARNING

Pedro Galvez-Hernandez[a], James Kratz[b]

[a]Department of Aerospace Engineering, University of Bristol, Bristol, United Kingdom – pedro.galvezhernandez@bristol.ac.uk

Abstract: Six Deep Learning state-of-the-art architectures have been implemented to segment interlaminar voids and dry areas in an X-Ray micrograph of an uncured composite laminate. The performance of this novel segmentation approach is compared to the standard thresholding method in three sub-volumes containing different porosity levels (1%, 6% and 26%). All Deep Learning architectures outperform the conventional thresholding method in the segmentation of both phases regardless of the porosity content. Of the Deep Learning models considered here, U-Net and FCN-8s exhibited the best and poorest performance, respectively. Deep Learning models showed a high accuracy in the segmentation of voids in low porosity volumes (<2%), whereas thresholding achieves comparable performance as the ground truth porosity increases. Deep Learning models, unlike thresholding, were able to handle moderate levels of noise and provide an accurate segmentation directly on the raw scan, without requiring a denoising step.

Keywords: micro-CT, deep learning, voids, dry areas, prepreg

1. Introduction

During composite manufacturing, defects in the form of porosity are likely to appear, negatively affecting the mechanical properties of the final component [1]. Autoclave manufacturing is the standard process to produce defect-free parts, where the high temperature and pressure facilitate the fibre bundle impregnation and the porosity evacuation. Alternatively, Out-of-Autoclave (OoA) is a cost-effective manufacturing process where the atmospheric pressure acts as the driving force to extract the entrapped air and impregnate the dry areas. However, because of the pressure being an order of magnitude lower than in an autoclave, the properties of the final component are increasingly dependent on the initial state of the uncured laminate Therefore, an accurate characterization of its main phases (interlaminar voids and dry areas) is deemed necessary [2].

X-Ray CT (XCT) is a powerful tool to visualize the 3D microstructure of composites [3]. In a typical XCT image, each phase is displayed with a characteristic greyscale value linked to its density. In uncured samples, interlaminar voids are represented by darker pixels because of the low density of air, whereas fibres and resin-saturated areas are illustrated with brighter pixels. The greyscale intensity of the dry areas is determined by the fraction of air and fibres contained in its volume.

Following the data acquisition, each phase must be segmented prior to its analysis. Deep Learning, based in the training of a convolutional neural network featuring millions of trainable parameters, has recently gained attention as a powerful alternative to segment features in

  doi:10.5075/epfl-298799_978-2-9701614-0-0

different composite applications, such as defect detection [4] or virtual specimens generation [5].

In this study, the performance of six state-of the-art Deep Learning architectures is evaluated against the thresholding segmentation, in the characterization of the main phases in X-Ray micrographs of an out-of-autoclave uncured laminate.

2. Materials and Methods

2.1. Sample Preparation and X-Ray CT Setup

The selected out-of-autoclave prepreg for this study was Hexcel HexPly® M56 epoxy matrix with IM7 unidirectional fibres as reinforcement, having a resin content and a fibre areal weight of 35% and 268 g/m^2, respectively. An initial laminate of 30 plies at 0° with dimensions 100 x 100 mm was manually laid-up and consolidated under vacuum during 10 minutes at room temperature. Three test samples of 6 x 100 mm were cut from the central part of the initial laminate. The samples will be referenced as: *Training Sample 1*, *Training Sample 2,* and *Validation Sample*.

The three samples were scanned in independent sessions under the same conditions in a lab-based Nikon XTH-320 CT Scanner at 103kV, 9.5W and a voxel size of 8.24µm. The scan time for each sample was 1h 06min. Following the data acquisition, the scans were reconstructed with Nikon CT Pro. ImageJ [6] was used for the subsequent image preprocessing applied to the resulting raw images, including 8-bit conversion and sub-volume selection after cropping out the air surrounding the sample captured in the scan.

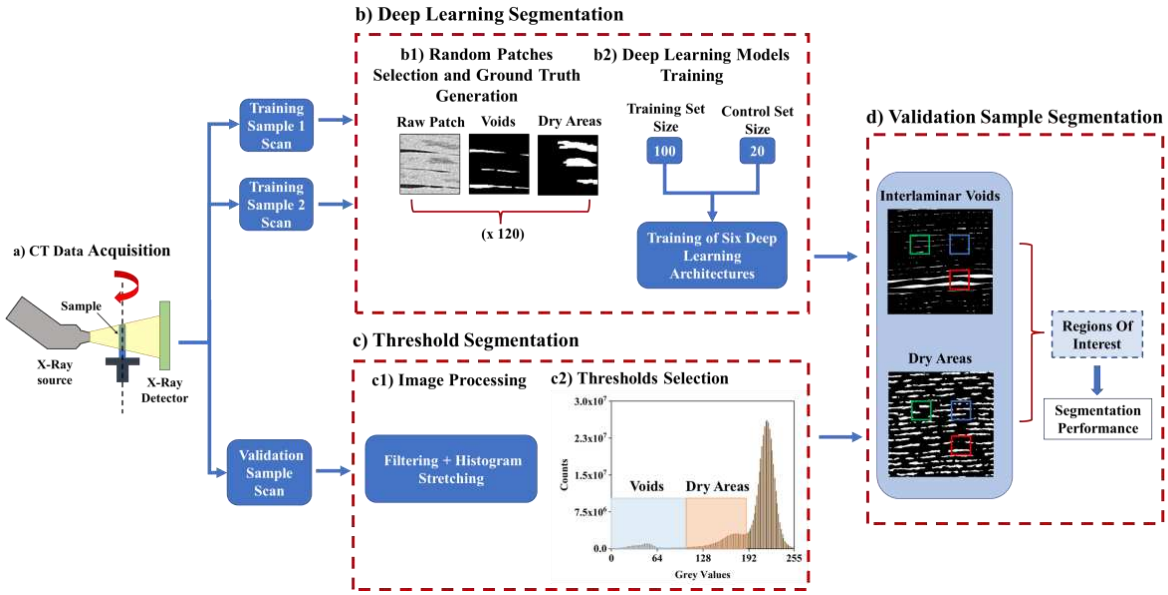

Figure 1: Flowchart of the data acquisition (a), implementation of the Deep Learning and thresholding segmentation methods (b-c) and segmentation of the Validation Sample scan (d).

2.2. Segmentation methods

2.2.1. Thresholding Segmentation

A tailored image processing methodology was implemented to improve the overall quality of the *Validation Sample* scan prior to the selection of the threshold, involving denoising with a

  doi:10.5075/epfl-298799_978-2-9701614-0-0

median filter of size 2 and histogram stretching to improve the visual contrast. From the resulting histogram, the peaks corresponding to the interlaminar voids, dry areas and resin-saturated areas were identified and the following thresholds were selected:

- *Th1:* It is selected as the mid-greyvalue of two adjacent peaks [7].
- *Th2*: The minimum greyvalue between two consecutive peaks is selected as the threshold [8].

2.2.2. Deep Learning Segmentation

The following six state-of-the-art Deep Learning architectures were selected for their demonstrated ability of segmenting features of interest in a wide range of applications: *FCDenseNet* [9], *FCN-8s* [10], *LinkNet* [11], *DeepLabv3+Xception* [12, 13] and *U-Net* [14]. All architectures were implemented in Tensorflow 2.5 and Python 3.6.

The process to train each architecture and segment the *Validation Sample* is described hereafter.

Firstly, an image set was prepared after selecting 120 patches of 128 x 128 pixels from random locations at the *Training Sample 1* and *Training Sample 2* scans. The interlaminar voids and dry area ground truths were manually annotated in each image using specific software [15, 16], resulting in each greyscale image having two associated binary masks, one per each phase, where white pixels would denote the phase of interest for a given mask, and black pixels represent the background.

Secondly, the initial image set is split into the training and control set prior to training. The training set contains 100 images, with their corresponding binary masks, and it is used to train the parameters, also called weighs, of the models. The control set, containing 20 images, is used to evaluate the models performance in unknown data after each iteration or *epoch*. The following hyperparameters were used for the models training: 300 epochs, Adam optimizer with learning rate of 0.0001, batch size of 1 image and categorical cross-entropy as the loss function.

Finally, the model weights after the epoch that minimizes the control set loss are saved and will be used for the segmentation of the *Validation Sample* scan, consisting of one thousand 2D slices of dimensions 700 x 700 pixels. A detailed explanation of the segmentation process of the entire scan can be found in [17].

2.4 Performance Evaluation

Three Regions of Interest (ROI) were selected in the central volume of the segmented *Validation Sample* scan provided by each of the methods to assess the performance of the segmentation methods in detecting interlaminar voids and dry areas. The dimensions of each ROI are 128 x 128 pixels spanning twenty consecutive slices. The same ROIs were selected from the raw *Validation Sample* scan and manually annotated to produce the associated interlaminar voids and dry areas ground truths.

After comparing the segmentation of both phases provided by the segmentation methods to their ground truths counterparts, each pixel within the ROI is assigned a category depending on the correctness of the segmentation. The pixel would be considered a True Positive (TP) or True Negative (TN) if its correctly segmented as the phase of interest or background, and it would be labelled as False Positive (FP) or False Negative (FN) if the category assigned by the segmentation

  doi:10.5075/epfl-298799_978-2-9701614-0-0

method does not match the ground truth segmentation. From the pixelwise classification, the following metrics to evaluate the segmentation method are defined:

$$Precision = \frac{TP}{TP + FP} \quad (1)$$

$$Recall = \frac{TP}{TP + FN} \quad (2)$$

$$MCC = \frac{TP\ x\ TN - FP\ x\ FN}{\sqrt{(TP + FP)\ x\ (TP + FN)\ x\ (TN + FP)\ x\ (TN + FN)}} \quad (3)$$

Precision and *Recall*, defined in the range [0,1], inform about the amount of noise (FP) in the segmentation and the ability of the segmentation method to capture the ground truth information, respectively. *The Matthews Correlation Coefficient (MCC)*, defined in the range [-1,1], provides information about the overall segmentation performance as it integrates the four-pixel categories.

3. Results

Qualitative segmentation results are illustrated in Figure 2. Notable differences can be identified in the segmentation provided by the thresholding and Deep Learning approaches. Th1 and Th2 provide a noisy segmentation of dry areas as they incur in a high level of misclassification of voids pixels. These methods also fail to correctly classify pixels belonging to dry areas displaying darker grey levels typical of interlaminar voids as pointed by the black arrow in Figure 1. Deep Learning models greatly reduce noise in the segmentation and provide a cleaner and more accurate segmentation of both phases. U-Net provides the best correlation of interlaminar voids and dry areas when compared to the raw scan, and it correctly labels ambiguous regions within the dry areas. FCN-8s, although being the model providing the poorest segmentation, it also provides a noise-free segmentation and reduces the mislabeling of ambiguous dry areas with respect to the thresholding segmentation. Both approaches accurately capture large interlaminar voids. However, only Deep Learning models successfully segments small voids, whereas thresholding methods either miss them or incorrectly classify them.

From a quantitative standpoint, Table 1 summarizes the performance of the segmentation methods in the segmentation of interlaminar voids in each of the ROIs.

ROI 1 contains the lowest ground truth porosity (1.07%). Thresholding segmentation exhibits the lowest MCC score (Th1: 0.43, Th2: 0.37), mainly due to a poor recall value in both methods contribute to this value, indicating that both methods fail to detect ground truth voids in this region. It is worth noting that Th2 achieves the perfect precision score as it does not capture noise in the segmentation. Deep Learning models show stronger segmentation results in this region, with U-Net reaching an MCC score of 0.89. The significant increase of the Deep Learning g models recall values (>0.68) with respect to the thresholding results drives the improvement of the overall performance metric.

The performance of both thresholding and Deep Learning methods improves in the segmentation of voids in ROI 2 and ROI 3, containing a ground truth porosity of 6.09% and 26.43%, respectively. Th2 provides the lowest MCC score in ROI 2 (0.59), although it represents a three times improvement with respect to its ROI 1 values. The rest of the methods achieve

  doi:10.5075/epfl-298799_978-2-9701614-0-0

high precision (>0.82), recall (>0.78) and MCC (>0.81). All approaches achieve their best performance in the ROI 3, containing large voids and a ground truth porosity of 26.43%.

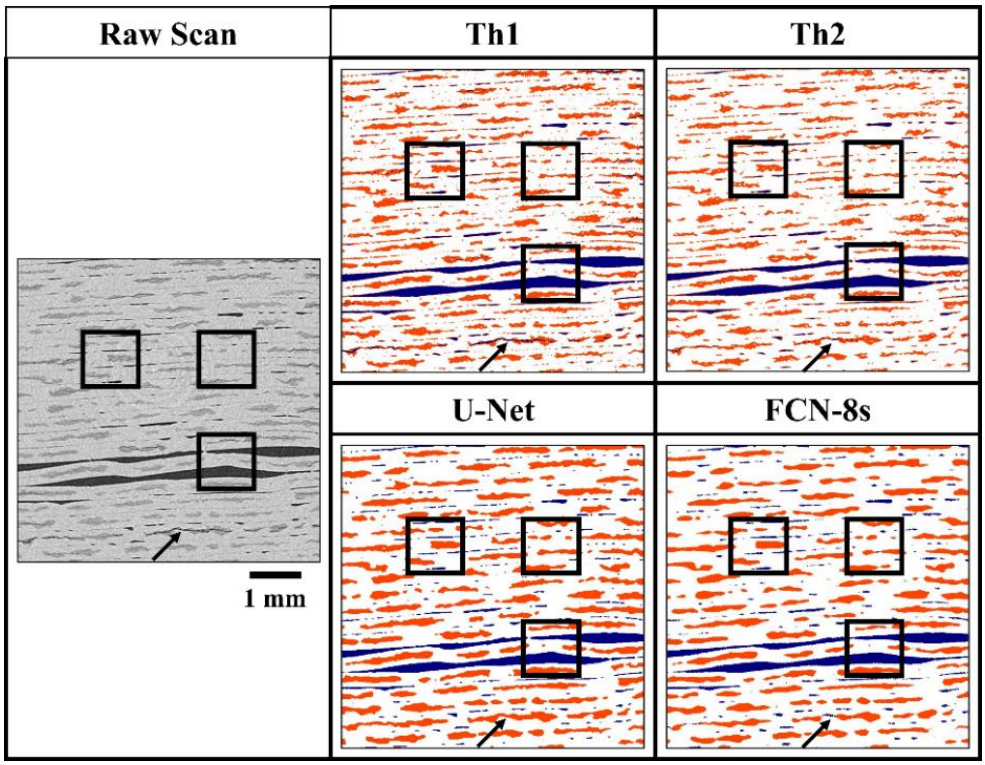

Figure 2: Raw scan and segmentation of interlaminar voids (blue) and dry areas (red) provided by the thresholding methods and the Deep Learning models providing the highest (U-Net) and lowest (FCN-8s) MCC score. ROIs location is displayed in black: ROI 1 (top-right), ROI 2 (top-left) and ROI 3 (bottom-right). Areas displaying ambiguous greyscale values are pointed with a black arrow.

Table 1: Quantitative results relative to the segmentation of the interlaminar voids in the three Regions of Interest provided by the different methods.

ROI Id	Segmentation Method	(%)	Precision	Recall	MCC
ROI 1	Ground Truth	1.07	1.00	1.00	1.00
	Th1	0.53	0.62	0.31	0.43
	Th2	0.15	1.00	0.14	0.37
	FCDenseNet	0.88	0.97	0.80	0.88
	FCN-8s	1.16	0.63	0.68	0.65
	LinkNet	0.98	0.78	0.71	0.74
	SegNet	0.84	0.93	0.73	0.83
	U-Net	0.92	0.96	0.82	0.89
	Xception	1.17	0.72	0.80	0.76
ROI 2	Ground Truth	6.09	1.00	1.00	1.00
	Th1	4.88	0.98	0.78	0.87

  doi:10.5075/epfl-298799_978-2-9701614-0-0

	Th2	3.63	1.00	0.59	0.76
	FCDenseNet	6.02	0.95	0.94	0.94
	FCN-8s	6.12	0.82	0.82	0.81
	LinkNet	5.81	0.89	0.85	0.86
	SegNet	5.63	0.94	0.87	0.90
	U-Net	5.72	0.97	0.91	0.93
	Xception	5.57	0.92	0.84	0.87
ROI 3	Ground Truth	26.43	1.00	1.00	1.00
	Th1	25.42	0.99	0.95	0.96
	Th2	24.17	1.00	0.91	0.94
	FCDenseNet	25.28	1.00	0.95	0.97
	FCN-8s	25.30	0.99	0.95	0.96
	LinkNet	24.91	1.00	0.94	0.96
	SegNet	23.98	0.99	0.90	0.93
	U-Net	25.04	1.00	0.95	0.96
	Xception	25.90	0.98	0.96	0.96

Regarding the segmentation of dry areas, as the three ROIs contain a similar dry area ground truth percentage (18.9 ± 1,6%), Table 2 summarizes the average performance values of each segmentation approach across the three ROIs.

All segmentation methods show a strong performance in the segmentation of the dry areas (>0.65). However, there is a notable difference of approximately 0.2 points between the MCC score provided by the thresholding and Deep Learning segmentation, mainly driven by the high number of false positives captured by the thresholding approach. The best thresholding method, Th1, provides an MCC score of 0.7, which is 21% lower than the best performing Deep Learning model (U-Net: 0.89).

Table 2: Quantitative results relative to the segmentation of the dry areas in the three Regions of Interest provided by the different methods.

Segmentation Method	**(%)**	**Precision**	**Recall**	**MCC**
Th1	16.29 ± 1.07	0.81 ± 0.06	0.7 ± 0.03	0.7 ± 0.02
Th2	14.53 ± 1.26	0.81 ± 0.09	0.62 ± 0.03	0.65 ± 0.03
FCDenseNet	15 ± 1.03	0.97 ± 0	0.77 ± 0.02	0.84 ± 0.01
FCN-8s	17.07 ± 1.71	0.91 ± 0.02	0.82 ± 0	0.84 ± 0.01
LinkNet	18.51 ± 0.95	0.88 ± 0.01	0.87 ± 0.02	0.84 ± 0.02
SegNet	16.89 ± 1.67	0.91 ± 0	0.81 ± 0.02	0.83 ± 0.01
U-Net	19.22 ± 1.85	0.9 ± 0.01	0.92 ± 0.02	0.89 ± 0.01
Xception	16.59 ± 0.26	0.92 ± 0.02	0.81 ± 0.04	0.83 ± 0.02

  doi:10.5075/epfl-298799_978-2-9701614-0-0

4. Summary

Interlaminar voids and dry areas have been segmented via Deep Learning in an X-Ray micrograph of an uncured out-of-autoclave composite laminate. The performance of the Deep Learning approach has been compared to the conventional thresholding segmentation.

Interlaminar voids and dry areas have been successfully segmented by all six Deep Learning models, being U-Net the best model in this task. Deep Learning has shown its ability to segment interlaminar voids in volumes containing a wide range of porosity contents, whereas thresholding segmentation achieves a low segmentation accuracy in low porosity volumes (<2%) as can be noted from Figure 3a. As the ground truth interlaminar porosity increases, thresholding and Deep Learning segmentation converge to similar MCC scores. However, important differences persist between the two approaches in the segmentation of dry areas and interlaminar voids displayed with ambiguous greyscale intensities, as shown in Figure 2. This behavior leads to a noisy and incomplete segmentation of dry areas generated by the thresholding segmentation compared to the sharp and clean segmentation provided by the Deep Learning models. Because of the high rate of false positives and negatives of the thresholding segmentation, the MCC value is approximately 0.2 points lower than the Deep Learning score (Figure 3b).

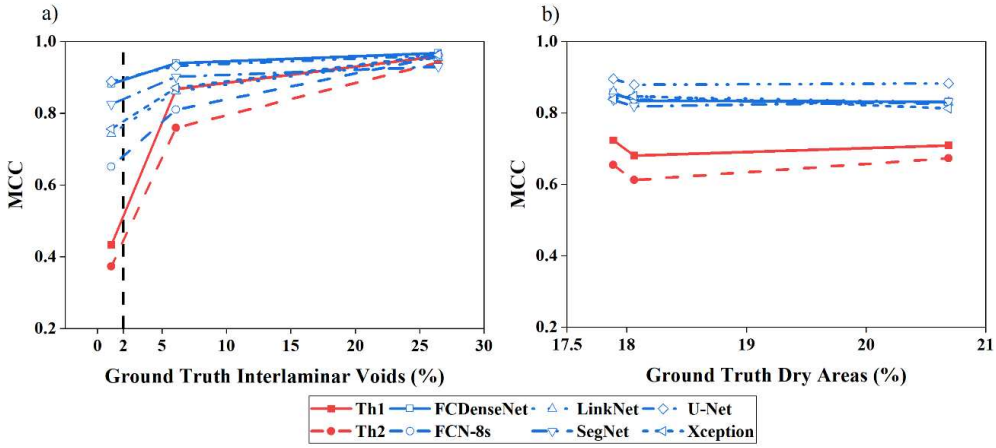

Figure 3: Dependency of the MCC score with the interlaminar void (a) and dry area (b) percentage ground truth.

Finally, Deep Learning provides a high segmentation performance directly segmenting the raw scan and despite the presence of moderate levels of noise. On the other hand, the thresholding segmentation requires the application of denoising filters to improve the overall scan quality and facilitate the selection of a threshold. This preprocessing step would eventually lead to an information loss.

Acknowledgements

The authors would like to acknowledge the Engineering and Physical Sciences Research Council (EPSRC) for their support of this research through Investigation of Fine-Scale Flows in Composites Processing [EP/S016996/1]. A PhD studentship for P. Galvez-Hernandez was supported through the Rolls-Royce Composites University Technology Centre at the University of Bristol.

  doi:10.5075/epfl-298799_978-2-9701614-0-0 published under CC BY-NC 4.0 license

5. References

1. Lambert J, Chambers AR, Sinclair I, Spearing SM. 3D damage characterisation and the role of voids in the fatigue of wind turbine blade materials. Composites Science and Technology. 2012;72(2):337-43.
2. Centea T, Grunenfelder LK, Nutt SR. A review of out-of-autoclave prepregs – Material properties, process phenomena, and manufacturing considerations. Composites Part A: Applied Science and Manufacturing. 2015;70:132-54.
3. Dilonardo E, Nacucchi M, De Pascalis F, Zarrelli M, Giannini C. High resolution X-ray computed tomography: A versatile non-destructive tool to characterize CFRP-based aircraft composite elements. Composites Science and Technology. 2020;192:108093.
4. Djavadifar A, Graham-Knight JB, Körber M, Lasserre P, Najjaran H. Automated visual detection of geometrical defects in composite manufacturing processes using deep convolutional neural networks. Journal of Intelligent Manufacturing. 2021.
5. Ali MA, Guan Q, Umer R, Cantwell WJ, Zhang T. Deep learning based semantic segmentation of µCT images for creating digital material twins of fibrous reinforcements. Composites Part A: Applied Science and Manufacturing. 2020;139:106131.
6. Schindelin J, Arganda-Carreras I, Frise E, Kaynig V, Longair M, Pietzsch T, et al. Fiji: an open-source platform for biological-image analysis. Nature Methods. 2012;9(7):676-82.
7. Kruth JP, Bartscher M, Carmignato S, Schmitt R, De Chiffre L, Weckenmann A. Computed tomography for dimensional metrology. CIRP Annals. 2011;60(2):821-42.
8. Gélébart L, Chateau C, Bornert M, Crépin J, Boller E. X-Ray Tomographic Characterization of the Macroscopic Porosity of Chemical Vapor Infiltration SIC/SIC Composites: Effects on the Elastic Behavior. International Journal of Applied Ceramic Technology. 2010;7(3):348-60.
9. Jégou S, Drozdzal M, Vazquez D, Romero A, Bengio Y. The One Hundred Layers Tiramisu: Fully Convolutional DenseNets for Semantic Segmentation2016 November 01, 2016:[arXiv:1611.09326 p.]. Available from: https://ui.adsabs.harvard.edu/abs/2016arXiv161109326J.
10. Long J, Shelhamer E, Darrell T. Fully Convolutional Networks for Semantic Segmentation2014 November 01, 2014:[arXiv:1411.4038 p.]. Available from: https://ui.adsabs.harvard.edu/abs/2014arXiv1411.4038L.
11. Chaurasia A, Culurciello E. LinkNet: Exploiting Encoder Representations for Efficient Semantic Segmentation2017 June 01, 2017:[arXiv:1707.03718 p.]. Available from: https://ui.adsabs.harvard.edu/abs/2017arXiv170703718C.
12. Chen L-C, Zhu Y, Papandreou G, Schroff F, Adam H, editors. Encoder-Decoder with Atrous Separable Convolution for Semantic Image Segmentation. Computer Vision – ECCV 2018; 2018 2018//; Cham: Springer International Publishing.
13. Zakirov E. keras-deeplab-v3-plus. GitHub; 2019.
14. Ronneberger O, Fischer P, Brox T, editors. U-Net: Convolutional Networks for Biomedical Image Segmentation. Medical Image Computing and Computer-Assisted Intervention – MICCAI 2015; 2015 2015//; Cham: Springer International Publishing.
15. Breheret A. Pixel Annotation Tool. 2017.
16. Dutta A, Zisserman A. The VIA Annotation Software for Images, Audio and Video2019 April 01, 2019:[arXiv:1904.10699 p.]. Available from: https://ui.adsabs.harvard.edu/abs/2019arXiv190410699D.
17. Galvez-Hernandez P, Gaska K, Kratz J. Phase segmentation of uncured prepreg X-Ray CT micrographs. Composites Part A: Applied Science and Manufacturing. 2021;149:106527.

  doi:10.5075/epfl-298799_978-2-9701614-0-0

EXPERIMENTALLY TRAINED PHYSIC-INFORMED NEURAL NETWORK AS MATERIAL MODEL

Alberto, Ciampaglia[a,b], Andrea, Ferrarese[a], Davide, Paolino[a], Giovanni, Belingardi[a], Wing Kam, Liu[b]

a: Department of Mechanical and Aerospace Egineering, Politecnico di Torino, Torino, Italy – alberto.ciampaglia@polito.it
b: Northwestern University, Evanston, IL

Abstract:

The authors propose a new approach for the data-driven discovery of composite material models leveraging on physic informed mechanistic neural networks. The methodology is unsupervised since the surrogate neural network can learn the unexplicit constitutive law from the strain field and global force data of mechanical tests, that can be easily collected with digital image correlation technique. The approach integrates the distinctive characteristics of both mechanistic data science and physic informed neural networks: the neural network architecture is designed to predict a constitutive law respecting the material symmetry and decoupling of the axial and shear response; the data-driven model is trained with a custom loss function enforcing the equilibrium constraints between external and internal energy. The results of the training is a physic-informed neural network predicting the response of composite. Using experimental data on tensile tests of carbon fiber woven reinforced epoxy specimens, authors demonstrate the capability of the data-driven method to efficiently discover the mechanical response of composite material with a reduced set of experiments.

Keywords: mechanistic; digital image correlation (DIC); machine learning; material law; surrogate model;

1. Introduction

Experimental characterization of composite materials requires an extensive set of experiments to properly assess their mechanical properties. Especially in applications where the post-failure behavior must be experimentally investigated, the experimental campaign is expensive and the characterization and material model selection is perpetuated through trial and error loops guided by the engineer's expertise. This work propose a methodology to learn constitutive laws from Digital Image Correlation measurements by a mechanistic Physic Informed Neural Network (PINN). Recently, [1-6] has proven the capability of standard and PINN to capture the constitutive behavior of complex material systems from artificial dataset. The proposed approach is tested with experimental data of carbon fiber twill fabric reinforced epoxy subjected to tensile test.

2. Materials and experimental tests

  doi:10.5075/epfl-298799_978-2-9701614-0-0

The composite under study is a prepreg made of GG630T-37 12K carbon fiber woven by Microtex Composites with a 2 by 2 twill fabric pattern and the E3-150N series thermosetting epoxy resin prepreg. Specimens are cut by a plate manufactured in autoclave with a maximum pressure of 6 bars and curing temperature of 125° C. Coupons have been visually inspected and no evident defect or milling induced delamination was visible.

Cross-ply specimen are made of 3 layers with 0°/90°, while angle-ply coupons have +45°/-45° orientated layers. All specimen have a total length of 250 mm, while the with is either 12, 24 or 36 mm. Plate thickness has been measured before milling in six different locations of the plate, showing an average value of 2.05 mm. For sake of brevity, the coupons will be referred as LWD_# with: L indicating if it is a cross-ply (C) or an angle-ply (A), W indicating the width (1: 12mm, 2: 24mm, 3: 36mm), D indicating the hole diameter over width ratio (0: no hole, 1: 1/12, 2: 1/6, 3: 1/4), followed by the trial number. As example, C23_2 will refer to the second trial of the cross-ply (C) lay-up test with a width of 24mm (2) and an D/W ratio of 1/4 , yielding to a 3 mm hole diameter.

Tensile tests are performed with the hydraulic powered testing machine Instron 8801, with a maximum load capability of 150 kN. Tensile tests are performed following D6390 standards, with a constant displacement rate of 2 mm / min.

Every test has been recorded with high-precision cameras and processed with Digital Image Correlation (DIC) system synchronized with the testing machine digital acquisition system.

As results of the experimental campaign, for each tensile test the following data are available:

- Crosshead displacement sampled every 0.05 seconds
- Crosshead tensile load sampled every 0.05 seconds
- Longitudinal, orthogonal and shear strain measures on the coupon surface every 0.5 second

Thanks to the synchronous measurements system, each strain map can be associated to the crosshead displacement and measured load at the instant of the acquisition (Figure 1).

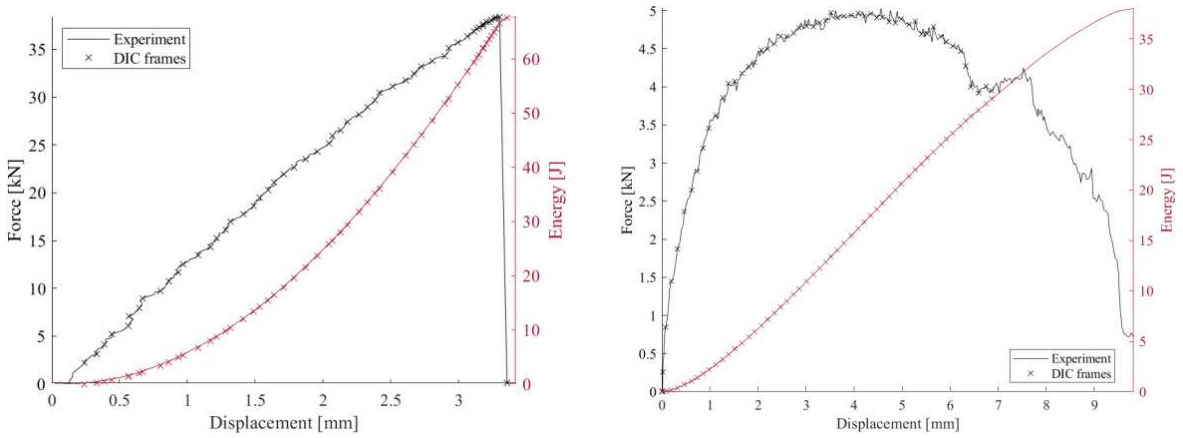

Figure 1. Force displacement curve for cross-ply (a) and angle ply (b) laminate with cross marks indicating the DIC acquisition frames

3. Method

The simplest constitutive models are a causal relation between a measurable quantity ε , the strain, and an engineering abstraction σ, the stress. In fact, the mechanical stress is not experimentally measurable; it is a indirectly measured quantity that can be computed from the experimental tests results following calculations usually described by the standards. Training a neural network to learn a constitutive equation from experimental data is not a trivial task, since the output of the network should be first computed from the measured force, according to pre-defined equations with assumptions that inevitably introduce bias in the learning process. To overcome this issue, [7] proposed a framework for learning indirectly measurable relation and applied to it for learning the failure surface of composite from analytical data. In this work, authors want to extend the capability of the network, not only learning the failure limit, but the complete constitutive law. [8] demonstrated that a parametric constative law for hyperplastic materials can be trained on strain field and force-displacement curve of experiments and validated their work on artificially simulated experiments. The presented research, aim at training a Neural Network to learn the constitutive equation of fiber reinforced composite, by only constraining the solution with physical knowledge on composite materials, letting the machine learning structure to find the best feasible interpolation on the experimental data.

2.1 Time and space filters

When Neural Network are used to perform regression over observed data, there is the risk of overfitting the training data. Especially when dealing with experimental measures, the signal noise could worsen the performance of the minimization algorithm, yielding to an overfitting of the noisy data. In this regard, data preprocessing is a crucial step in mechanistic machine learning pipelines, where mechanistic principles could be violated by non-physical noisy observation. The strain measured with DIC during the tensile tests is affected by both space and time domain noise. These can be separately processed to remove signal information that are not descriptive of the observed phenomena. In this work, each strain component time history of each element is fitted with a cubic function as shown in Figure 2.

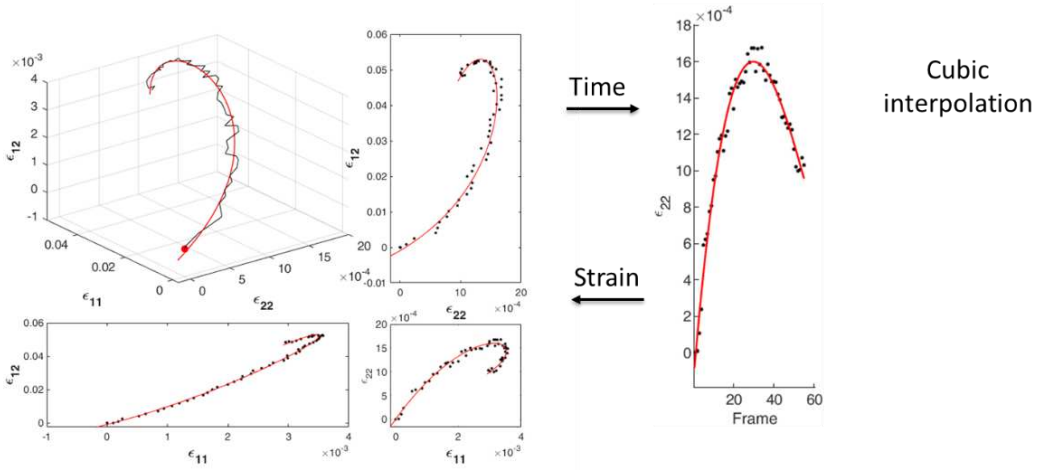

Figure 2. The three components of the strain history of each element are fitted with a cubic function of the time to remove the signal noise.

The spatial resolution of DIC depends on the camera resolution, distance from the object, subset size and other prost-processing parameters (e.g., displacement interpolation function). For the here presented experiments, the spatial resolution is approximately 0.2 mm. Since the final goal of the work is to find a surrogate material law of the homogenized material, it is mandatory to compare the resolution of the strain field with the Representative Volume Element (RVE) of the fiber reinforced material under study. Figure 3 shows the size of a Twill 2x2 RVE compared with the specimen dimension.

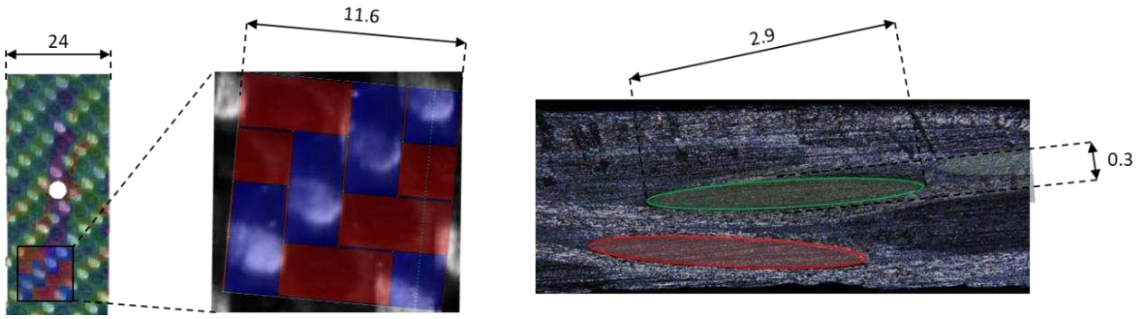

Figure 3. a) Magnification of the specimen surface with woven architecture scale length, b) cross-section of the woven specimen

Being the resolution of the DIC acquisition system lower than the RVE size, the strain is not representative of the homogenized materials. To pass the Neural Network a strain field it can learn an homogenized material law from, a spatial convolutional filter is applied to strain maps.

2.2.1 Feed-forward neural networks (FFNN)

Supervised Feed-forward neural networks (FFNN) are traditionally trained with a set of input and output observation that the network will relate through a general operator $\mathbb{N}(w_i, b_i)$, where trainable parameters w and b are the weights and biases of the network, respectively. Since the final goal of the research is to train the network on experimental data and the stress is not measurable, the network is trained to predict a local plane stress vector $\boldsymbol{\sigma_e}$ in each point of the structure from the local strain state $\boldsymbol{\varepsilon_e}$ as described in equation (1):

$$\boldsymbol{\sigma_e} = \mathbb{N}(\boldsymbol{w}, \boldsymbol{b}; \boldsymbol{\varepsilon_e}) \tag{1}$$

the total internal energy Π_i is computed at each observation i by summing the internal energy of all the N elements of the domain Ω_e using equation (2):

$$\Pi_i = \sum_{elem}^{N} \frac{1}{2} \int_{\Omega_e} \boldsymbol{\varepsilon}_e^T \boldsymbol{\sigma_e} d\Omega_e \tag{2}$$

The loss function over N_f observations, is defined by equation (3) as the root mean squared error:

$$\mathcal{L} = \sum_{i}^{N_f} \sqrt{\frac{\left(\Pi_i - \int_0^{d_i} f dx\right)^2}{N_f}} \tag{3}$$

  doi:10.5075/epfl-298799_978-2-9701614-0-0

Where f is the load as function of displacement, d_i is the crosshead displacement at the observation instant i and the integral is the external work. The integral is computed using the trapezoidal rule.

The network is optimized with a stochastic gradient descent method (Kingma et al.) and the trainable parameters are upgraded with a back-propagation procedure, to minimize the loss function. Since the constitutive equation is the same for every material point, $\mathcal{N}$ is unique: to properly train it on the presented data, the number of element in each batch is set equal to the number of element in the structure and the loss function is computed at each batch.

2.2.2 Physic-informed FFNN

Neural networks have been demonstrated to be universal approximators of any functions, but the accuracy of the interpolation is strongly dependent on the amount data. For this reason, the implementation of such methods has been for a long while rarely adopted in scientific application, where dataset are usually small. In last decades, researcher has proposed a new approach for training machine learning algorithm on physic data: physic informed neural network. Several studies demonstrated that coupling the prior physical knowledge of the observed phenomena, with the approximation capability of the neural network can give good results even with small datasets. Along that line, authors propose a Physic-informed FFNN (PI-FFNN) trained on the experimental data of tensile tests coupled with the physic principles of material symmetry and energy conservation.

Starting from the first law of thermodynamic in equation (4):

$$\Delta \mathrm{U} = Q + W \tag{4}$$

Where ΔU is the change in internal energy, Q the heat added to the system and W is the work done on the system by the surrounding. Considering an adiabatic system, the change in the strain of the material is equal to the work done by the testing machine, leading to equation (5):

$$\sum_{elem}^{N} \frac{1}{2} \int_{\Omega_\mathrm{e}} \boldsymbol{\Delta\varepsilon}_e^T \Delta \boldsymbol{\sigma_e} d\Omega_\mathrm{e} = W_i \tag{5}$$

Imposing the strain energy convexity constraints formulated in equation (6):

$$\boldsymbol{\varepsilon}^T \boldsymbol{C} \boldsymbol{\varepsilon} \geq 0 \tag{6}$$

The constitutive equation matrix C must be semi-positive definite, it could be decomposed into the Cholesky triangular matrix L with equation (8):

$$C = LL^T \tag{8}$$

The PINN is designed to predict a positive definite matrix C by predicting the Cholesky triangular matrix L, later used to get the constitutive matrix C.

The aforementioned assumptions restrict the solution domain, enhancing the machine learning capabilities of finding the best weight and bias by training the network on the experimental database. The final formulation of the problem is reported in equation (9):

  doi:10.5075/epfl-298799_978-2-9701614-0-0

$$\overline{w},\ \bar{b} = \min_{w,\,b} \sqrt{\sum_i^N \frac{\left(\int_0^{d_i} \boldsymbol{f}\, dx - \frac{\sum_j^{n_x \cdot n_y} t_j A_j \boldsymbol{\varepsilon}_j^T \cdot \mathbb{N}(\boldsymbol{\varepsilon}_j;\boldsymbol{w},\boldsymbol{b}) \mathbb{N}^T(\boldsymbol{\varepsilon}_j;\boldsymbol{w},\boldsymbol{b}) \varepsilon}{n_x n_y} \right)^2}{N}} \quad (9)$$

Where n_e is the total number of DIC elements.

2.2.3 Unit-consistent data normalization

It is known that the normalization of input and output data facilitates the training process of Neural Networks. When the gradient of the prediction error is of different order of magnitude respect to the input parameters, the convergence of the optimization algorithm is slow and unstable. More specifically, unscaled input data can slow down the learning process and requires small learning rates, whereas unscaled outputs can results in exploding gradients causing the learning process to fail. The NN designed in this study learns the constitutive equation of composite materials, linking the applied strains, which magnitude is 10^{-4}, to the material stress, with magnitude of 10^2 (expressed in MPa); thus, the network weights will be in the order of 10^6, leading to unstable learning and higher generalization error. The natural conclusion follows that both input and output data should be scaled within the same, small range (e.g., between 0 and 1); however, the structure of the mechanistic PI-NN contains physic equations, whose validity is preserved by the unit consistency. Scaling the data would stretch the strain and energy values, affecting the physical consistency of equation (9):

$$\mathcal{L} = \sum_i^{N_f} \sqrt{\frac{\left(\frac{1}{2} \sum_e^N \int_{\Omega_e} \boldsymbol{\varepsilon}_e^T \boldsymbol{C} \boldsymbol{\varepsilon}_e d\Omega_e - E_i \right)^2}{N_f}} \quad (9)$$

If both the input, $\boldsymbol{\varepsilon}_e$, and the output, E_i, are scaled within the range [0, 1] through equations (10):

$$\bar{\varepsilon}_e = \frac{\varepsilon_e - \varepsilon_{min}}{\varepsilon_{max} - \varepsilon_{min}};\ \ \bar{E}_i = \frac{E_i - E_{min}}{E_{max} - E_{min}} \quad (10)$$

For each frame, the error will be computed by equation (11) as:

$$\frac{1}{2} \sum_e \int_{\Omega_e} \bar{\varepsilon}_e^T C \bar{\varepsilon}_e \, d\Omega_e - \bar{E}_i \quad (11)$$

Where the left and right term are no longer compliant in units. To overcome this issue, while both preserving the advantage of scaling the database and preserving the physical meaning of the mechanistic PI-NN, the network is passing the scaled input only to the layers predicting the constitutive law. The computation of the loss function is performed with the unscaled values and the predicted energy is later scaled consistently with the output, yielding to equations (12).

$$\bar{E}_i^{pred} = \frac{\frac{1}{2} \sum_e^N \int_{\Omega_e} \boldsymbol{\varepsilon}_e^T \boldsymbol{C}(\bar{\boldsymbol{\varepsilon}}_e) \boldsymbol{\varepsilon}_e d\Omega_e}{E_{max}} \quad (12)$$

$$\mathcal{L} = \sum_i^{N_f} \sqrt{\frac{(\bar{E}_i^{pred} - \bar{E}_i)^2}{N_f}}$$

Since every test starts from the undeformed configuration with zero load applied, E_{min} is equal to zero and the constitutive matrix C can be rescaled to restore the real units.

2.2.4 Neural network structure

Once the optimization problem for the training of the PINN has been defined, the network is built stacking multiple layers of neurons as described in Table (1).

Table 1: Neural Network structure.

Layer	Type	Neurons	Activation function	Output dimension
1	Input	0	-	(3, 1)
2	Normalization	0	-	(3, 1)
3	Dense	10	Linear	(10, 1)
4	Physic	10	Linear	(4, 1)
5	Reshape	0	-	(3, 3)

4. Results

As discussed in Section 3, the proposed PINN is not learning a material law from a ground truth stress measurements, hence a direct comparison with the reference stress can not be analysed. Figure 4 shows the training curve of the PINN trained on the A20_1 specimen on the left, and the variation of the term of the constitutive matrix in position (3,3) with the shear strain on the right.

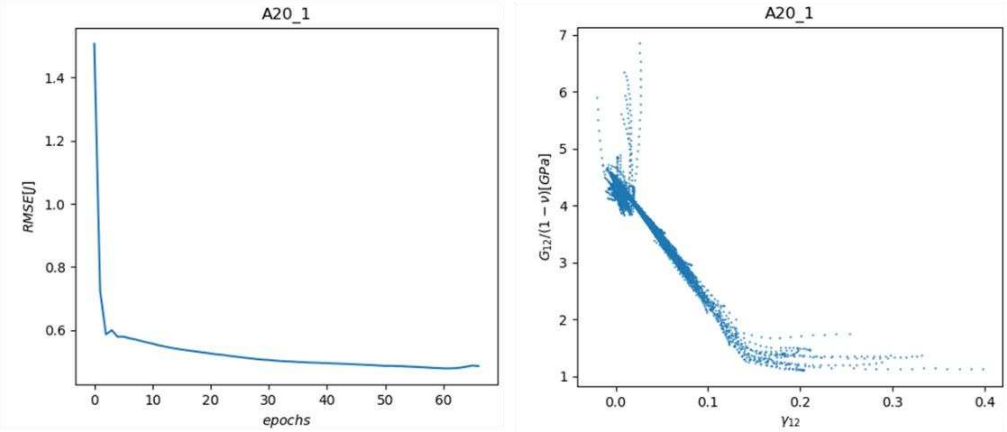

Figure 4. On the left, the training history of the PINN; on the right, the variation of the shear term of the constitutive matrix with the applied shear strain.

The regression error on the prediction of the variation of internal energy is lower than 0.5 J over a total energy variation of 35 J. From the angle-ply tensile test, the networks learned a damage law with a linear degradation of the shear modulus, until a plateau of residual stiffness of 1 GPa after an engineering shear strain of 0.15 . The right graph on Figure 4 shows the capability of the PINN to learn a material law accounting for the local strain state of each element in the structure.

  doi:10.5075/epfl-298799_978-2-9701614-0-0

5. References

1. Mozaffar, M., R. Bostanabad, W. Chen, K. Ehmann, Jian Cao, and M. A. Bessa (2019). “Deep Learning Predicts Path-Dependent Plasticity.” Proceedings of the National Academy of Sciences of the United States of America
2. As’ad, Faisal, Philip Avery, and Charbel Farhat (2022). *International Journal for Numerical Methods in Engineering*
3. Zhang, Annan and Dirk Mohr (2020). “Using neural networks to represent von Mises plasticity with isotropic hardening", *International Journal of Plasticity*
4. Shen et al. (2020). "Prediction of plastic yield surface for porous materials by a machine learning approach " *Materials Today Communications*
5. Yang et al. (2020). “Learning material law from displacement fields by artificial neural network", *Journal of Applied Mechanics, Transactions ASME* 87, no. 9 (2020)
6. Ge, Weijian, and Vito L Tagarielli (2021). “A computational framework to establish data-driven constitutive models for time-or path-dependent heterogeneous solids", Nature: Scientific reports (2021)
7. Liu, Xin, Fei Tao, and Wenbin Yu. “A Neural Network Enhanced System for Learning Nonlinear Constitutive Law and Failure Initiation Criterion of Composites Using Indirectly Measurable Data,” 2020.
8. Flaschel, Moritz, Siddhant Kumar, and Laura De Lorenzis. “Unsupervised Discovery of Interpretable Hyperelastic Constitutive Laws.” Computer Methods in Applied Mechanics and Engineering 381, 2021.

SEMANTIC SEGMENTATION OF µCT IMAGES OF 3D WOVEN FABRIC USING DEEP LEARNING

Muhammad A. Ali[a], Tayyab Khan[a], Muhammad S. Irfan[a], Rehan Umer[a]

a: Department of Aerospace Engineering, Khalifa University of Science and Technology, Abu Dhabi, United Arab Emirates – muhammad.ali@ku.ac.ae

Abstract: *In this work, we have used deep convolutional neural networks (DCNN) for segmenting µCT images of a 3D fabric with orthogonal architecture with a focus on improving the segmentation of the binder yarn. A set of raw 2D slices were extracted from the gray-scale volume of the fabric. Each pixel in these slices was then annotated as voids/pores and weft/warp/binder yarns. A DCNN was implemented in MATLAB® and trained using the set of raw and annotated images. The trained network was then tested against the segmented ground truth images, and the segmentation accuracy and network performance metrics were thoroughly analyzed. The results confirm that the weight balancing improved the accuracy of binder yarn segmentation, however, at the expense of losing accuracy on the remaining classes.*

Keywords: Fabrics/Textiles; CT Analysis; Deep Learning; Meso-structures

1. Introduction

The greatest challenge in creating realistic computational models from µCT images is the lack of a robust and versatile tool for segmenting µCT images [1]. In the case of 3D woven composites with binder yarns, further work is necessary due to the similarities they share with warp yarns (e.g., the same orientation). The challenges associated with the segmentation process can be addressed by using deep-learning approaches such as, the deep convolutional neural network (DCNN) [2]. Recently, deep-learning approaches have been successfully applied in segmenting both 2D [3] and 3D fabrics [4].

In applying DCNN on segmenting the µCT images of 3D fabrics, the binder yarn is poorly segmented. The issue is known as "class imbalance" segmentation and refers to the low representation of one of the classes as compared to the others, which biases the learning process in favor of the dominant class [5, 6]. The results can be improved by class weight balancing which increases the weight given to underrepresented classes. The common scheme involves assigning to each class a cost equal to the inverse of the proportion of this class in the dataset. This leads to higher penalization for the underrepresented classes.

Here, we have used deep convolutional neural networks (DCNN) for segmenting µCT images of a 3D fabric with orthogonal architecture with a focus on improving the segmentation of the binder yarn. A set of raw 2D slices were extracted from the gray-scale volume of 3D fabric. Each pixel in these slices was then annotated as voids/pores and weft/warp/binder yarns. A DCNN, DeepLab v3+ network [7] with ResNet18 as the backbone [8], was implemented in MATLAB® Deep Learning Toolbox [9, 10] and trained using the set of raw and annotated images. The effect of using class weight balancing on the accuracy of binder yarn segmentation was tested. Also, a number of layers were removed from the original ResNet18 network to analyze its accuracy. The trained network was then tested against the segmented ground truth images, and the

  doi:10.5075/epfl-298799_978-2-9701614-0-0

segmentation accuracy and network performance metrics were thoroughly analyzed. The results confirm that the weight balancing does improve the accuracy of binder yarn segmentation, however, at the expense of losing accuracy on the remaining classes.

2. Materials and methods

2.1 Materials

The test material used here was a woven carbon fabric with a 3D orthogonal architecture (GSM = 3260) [11]. The fabric consists of alternate cross-layers (0°/90°) of warp and weft yarns with 12K carbon filaments. In total, there are eight warp and nine weft yarns interlaced by a z-binder yarn with 12K carbon filaments. The test fabric was cut into a circular geometry of diameter 40 mm and then scanned using the GE Phoenix Nano-tom laboratory-sized µCT machine [12]. During the image acquisition process, the applied voltage on the X-ray tube was 120 kV with a current of 200 µA [11]. A total of 3600 projections, with a size of 2400 × 1600 pixels, were captured at a resolution of 25 µm. The tomographic projections were reconstructed into grayscale 3D raw volumes.

2.2 Data preparation

Two dimensional slices, in the form of grayscale raw images (400×400×200) were extracted from the reconstructed 3D raw volume. A set of labeled images (400×400×200) were also created from these raw images, where pixels were labeled/annotated manually as weft, warp, z-binder and voids/pores by using the MATLAB® Image Labeler Tool [9, 10]. These raw and labeled volumes were divided into four sub-volumes (225×225×200). Two of these sub-volumes were selected as the training volumes and the remaining two as the validation and test volumes. Each image had a size of 225×225 pixels as the built-in ResNet18 network requires a minimum size of 224×224 pixels. The total number of training image pairs (raw and labeled images) was 400 (200 each from the two training sub-volumes).

2.3 Implementation and training

For the segmentation of µCT images, the DeepLab v3+ model [37] in MATLAB® Deep Learning Toolbox [39, 40] was used. The DeepLab v3+ model DCNN has an encoder-decoder architecture and requires input features extracted using a base network. Here we have usedResNet18 as a base network, which comprises 18 layers with skip connections to enable residual learning [38]. The first layer of ResNet18 is a typical convolutional layer with 64 kernels of size (7×7). The remaining layers are grouped into four “residual blocks”. All the residual blocks have convolution, batch normalization and ReLu activations stacked into four layers with two identity/skip connections between the alternate layers. The Residual Block I has a 1×1 convolution, followed by batch normalization, instead of the first skip connection.

The features extracted by the base network are passed through the Atrous Spatial Pyramid Pooling (ASPP) module. The ASPP module encodes multi-scale contextual information by applying atrous/dilated convolutions with different rates. Atrous/Dilated convolution is a tool that enables refining/enlarging the effective field of view of the convolution by inserting rows/columns of zeros in the convolution filters. The number of rows/columns of zeros added is known as the atrous rate. The encoder features are then up-sampled and then concatenated with the corresponding low-level features. The low-level features are extracted by the initial

  doi:10.5075/epfl-298799_978-2-9701614-0-0

layers of the base network (by the Residual Block I in the current case). The complete architecture of the DCNN is shown in Figure 1.

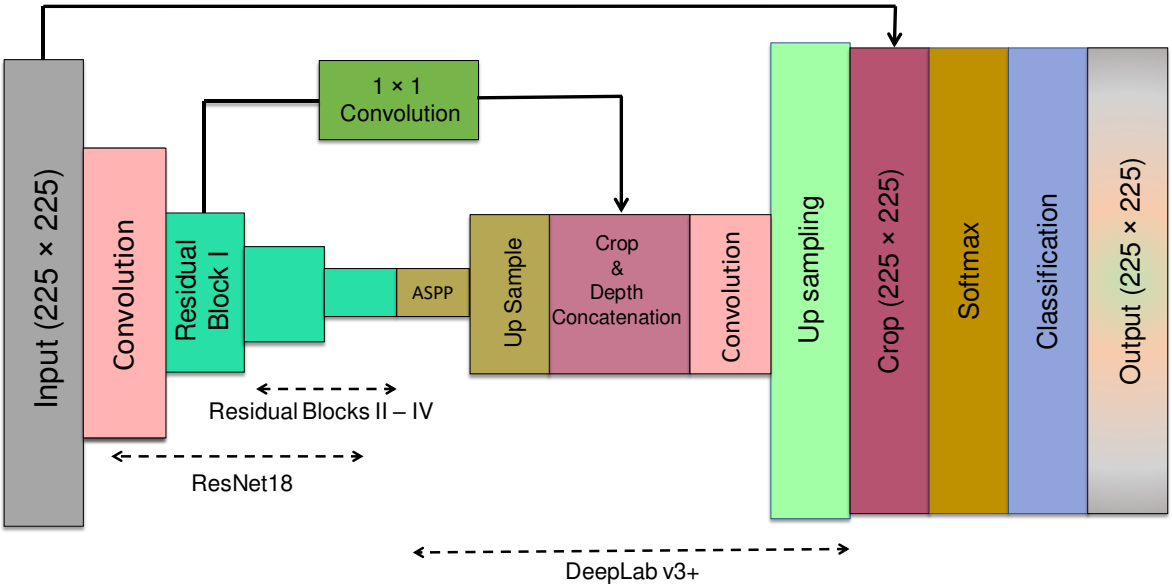

Figure 1. The architecture of the DCNN used in this study.

The final segmentation results are achieved in terms of the probability distribution of each pixel in the class that is matrix, warp, weft or binder. The pixel classification layer assigns each image pixel a categorical label which has the highest probability. Usually the probability of each class computed is used directly. To counter the class imbalance, the probability of each class needs to be modified. Here, we have used class weights for this purpose. The probability of each class is scaled by the corresponding class weight. The class weights were calculated as the inverse class frequency by counting the total number of pixels of each class. This makes sure that the probability if underrepresented class is scaled up.

By using raw and labeled training sub-volumes, three versions of the DCNN were trained on a single NVIDIA GeForce GTX 1650 GPU mounted on a laptop with a dual-core Intel i7 hexa-core processor. First, the original ResNet18 was trained without any weight balance. Then, the same network was trained by incorporating the weight balance. Finally, the last 2 Residual Blocks III and IV were removed from the network and then trained. By removing these blocks, the depth of the networks is reduced. In order to add diversity to the images, and improve the generalization, data augmentation with a random rotation of ±5° and translation of ±10 pixels was performed on the training images.

3. Results and discussions

3.1 Training process

During the training process, the networks converged exponentially, with the accuracy and loss reaching stable values after the fifth epoch (50 iterations). As shown in Figure 2, it can be observed that the training and validation curves are very similar, mainly because the images in the training and validation sets are highly correlated. It was expected that the reduced network may take less computational time but the results suggest otherwise. All the networks were trained within 12-14 minutes with a final validation accuracy of ~94%.

  doi:10.5075/epfl-298799_978-2-9701614-0-0

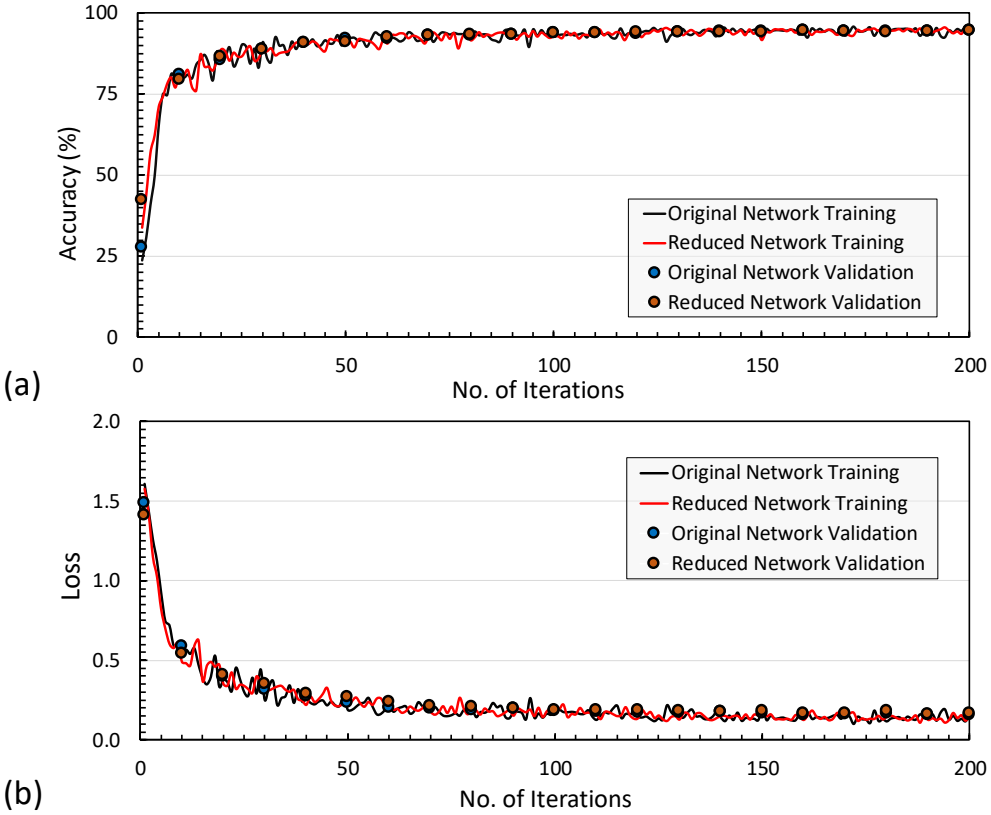

Figure 2. The convergence history of the accuracy and loss of the original and reduced networks.

3.2 Model performance

The primary performance indicator of the trained network is the Confusion Matrix, also known as the error matrix, which is the summary of the number of correctly and incorrectly classified pixels. It is presented class wise and shows how the trained model gets confused while making predictions. It is a tabular comparison of the predicted class of each pixel against the true class (ground truth). The diagonal and off-diagonal cells of the matrix correspond to the number of correctly and incorrectly classified pixels, respectively. The confusion matrix for the three networks trained in this work is given in Table 1 below. The results confirm that the weight balancing does improve the accuracy of binder yarn segmentation, however, at the expense of losing accuracy on the remaining classes. It can be seen that including weight balancing has improved the accuracy of the binder yarn from 89% to 98%. Similarly, the accuracy of the weft yarn is also slightly improved. The penalty of this improvement is minor loss of accuracy of the pores/matrix and warp yarn. Also, the reduced network produces similar results and also uses similar computational time.

  doi:10.5075/epfl-298799_978-2-9701614-0-0

Table 1: Confusion matrix for different networks.

		Predicted Class											
		Original ResNet18				ResNet18 with Weight Balance				Reduced ResNet18 with Weight Balance			
		Pores	Warp	Weft	Binder	Pores	Warp	Weft	Binder	Pores	Warp	Weft	Binder
True Class	Pores	97.5	0.8	0.9	0.7	94.7	0.9	1.4	2.9	95.8	1.2	1.0	2.0
	Warp	1.2	95.8	2.5	0.5	0.9	93.6	3.7	1.8	0.9	95.8	2.5	0.8
	Weft	1.9	2.5	94.8	0.8	1.2	1.8	95.5	1.5	1.9	2.8	93.6	1.7
	Binder	6.2	2.4	2.3	89.0	1.0	0.1	0.5	98.4	1.5	0.5	0.6	97.4

Apart from the confusion matrix, the other performance metrics include accuracy; intersection over union (IoU) and boundary F1 contour matching score (BFScore). These metrics are usually presented as mean or weighted-by-class values. The accuracy is perhaps the simplest metric, and defined as the number of correct predictions divided by the total number of predictions. The accuracy of the model gives only an overview by merely counting the number of pixel correctly identified. For multiclass semantic segmentation, the intersection over union (IoU) is the most commonly used metric. The IoU is the number of pixels common between the ground truth and predicted segmentation divided by the total number of pixels of a given class. The boundary F1 contour matching score (BFScore) indicates how well the predicted boundary of each class aligns with the true boundary and is calculated as the harmonic mean of the precision and recall values. The overall performance metrics of the trained network are summarized in Table 2. The metrics indicate that around 95% of the four classes were correctly segmented by all the three trained networks. The high accuracy is because the images in the training and test sets are highly correlated. Mainly, pixels at the boundary of the yarns were classified inaccurately as indicated by the lower values of the BFScore. This can also be improved by defining specialized loss function such as the “boundary loss function”.

Table 2: Overall performances of the different networks.

Network	Global Accuracy	Mean Accuracy	Mean IoU	Weighted IoU	Mean BFScore
Original ResNet18	0.958	0.943	0.891	0.919	0.847
ResNet18 with Weight Balance	0.949	0.955	0.858	0.905	0.796
Reduced ResNet18 with Weight Balance	0.952	0.957	0.875	0.911	0.824

3.3 Post-processing

Although the performance metrics (listed in Table 2) showed reasonably good accuracy, visual inspection reveal that the segmented volume is still full of noises, as shown in Figure 3.

  doi:10.5075/epfl-298799_978-2-9701614-0-0

Fortunately, simple filtering techniques were able to remove these noises. The segmented and cleaned volumes representing the binder yarn are shown in Figure 3. The entire raw and segmented volumes are shown in Figure 4. It can be seen that all the yarns are separated in the segmented volume.

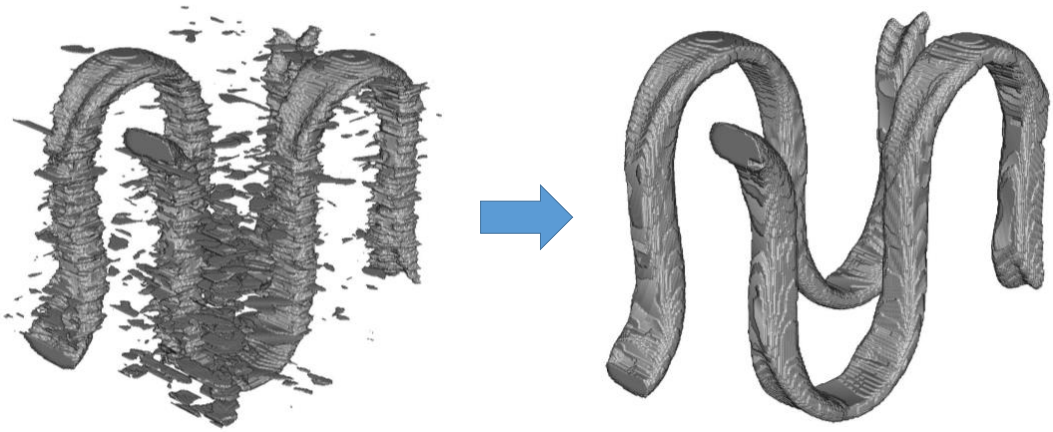

Figure 3. Cleaning of the binder yarn.

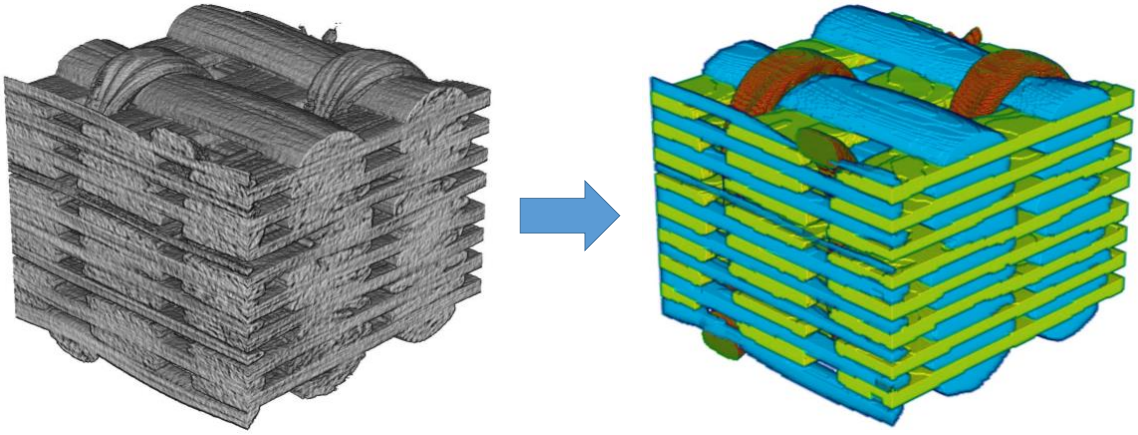

Figure 4. Segmentation of the raw volume.

4. Conclusion

The work presented here provides a robust framework of segmenting µCT images of 3D fabrics capable of segmenting the binder yarn accurately. The results confirm that the weight balancing does improve the accuracy of binder yarn segmentation, however, at the expense of losing accuracy on the remaining classes. It was found that including weight balancing improved the accuracy of the binder yarn from 89% to 98%. The training process for the three networks used here were almost the same. The trained networks struggled to correctly classify the pixels at the boundary of the yarns. A clean-up operation is also required to remove the noise generated during the segmentation process.

Acknowledgements

This publication is based on work supported by the Khalifa University of Science and Technology internal grants CIRA-2020-007 and FSU-2019-08.

  doi:10.5075/epfl-298799_978-2-9701614-0-0

5. References

[1] M.A. Ali, R. Umer, K.A. Khan, W.J. Cantwell, Application of X-ray computed tomography for the virtual permeability prediction of fiber reinforcements for liquid composite molding processes: A review, Composites Science and Technology 184 (2019).
[2] M.A. Ali, Q. Guan, R. Umer, W.J. Cantwell, T. Zhang, Deep learning based semantic segmentation of μCT images for creating digital material twins of fibrous reinforcements, Composites Part A: Applied Science and Manufacturing 139 (2020).
[3] M.A. Ali, Q. Guan, R. Umer, W.J. Cantwell, T. Zhang, Efficient processing of μCT images using deep learning tools for generating digital material twins of woven fabrics, Composites Science and Technology 217 (2022) 109091.
[4] A. Mendoza, R. Trullo, Y. Wielhorski, Descriptive modeling of textiles using FE simulations and deep learning, Composites Science and Technology 213 (2021).
[5] J.M. Johnson, T.M. Khoshgoftaar, Survey on deep learning with class imbalance, Journal of Big Data 6(1) (2019).
[6] M. Buda, A. Maki, M.A. Mazurowski, A systematic study of the class imbalance problem in convolutional neural networks, Neural Networks 106 (2018) 249-259.
[7] L.-C. Chen, Y. Zhu, G. Papandreou, F. Schroff, H. Adam, Encoder-decoder with atrous separable convolution for semantic image segmentation, Proceedings of the European Conference on Computer Vision (ECCV), 2018, pp. 801-818.
[8] K. He, X. Zhang, S. Ren, J. Sun, Deep residual learning for image recognition, Proceedings of the IEEE Conference on Computer Vision and Pattern Recognition, 2016, pp. 770-778.
[9] MathWorks,The MathWorks, Inc. https://www.mathworks.com. (Accessed Jan, 06 2021).
[10] Help Center,The MathWorks, Inc. https://www.mathworks.com/help/index.html. (Accessed Jan, 06 2021).
[11] M.A. Ali, R. Umer, K.A. Khan, W.J. Cantwell, In-plane virtual permeability characterization of 3D woven fabrics using a hybrid experimental and numerical approach, Composites Science and Technology 173 (2019) 99-109.
[12] M.A. Ali, R. Umer, K.A. Khan, A virtual permeability measurement framework for fiber reinforcements using micro CT generated digital twins, International Journal of Lightweight Materials and Manufacture 3(3) (2020) 204-216.

  doi:10.5075/epfl-298799_978-2-9701614-0-0

PREDICTION OF IMPACT-INDUCED INTERNAL DAMAGES OF COMPOSITES LAMINATES USING MULTITASK LEARNING

Saki, Hasebe[a], Ryo, Higuchi[b], Tomohiro, Yokozeki[b], and Shin-ichi, Takeda[c]

a: Department of Aeronautics and Astronautics, The University of Tokyo, Japan– hasebe-saki866@g.ecc.u-tokyo.ac.jp
b: Department of Aeronautics and Astronautics, The University of Tokyo, Japan
c: Aeronautical Technology Directorate, Japan Aerospace Exploration Agency (JAXA), Japan

Abstract: *In order to aim for easier maintenance of impact damage on the composite structures in aircraft, such as dropping of a tool, the possibility of inferring low-velocity impact (LVI) information in CFRP laminates from the surface damage profiles is verified. This study conducts low-velocity impact tests considering three factors (stacking sequence, impactor shape, and impact energy). Subsequently, a tree-based multi-task learning algorithm is founded for the estimation. This model is characterized by several hyperparameters, especially on the depth of trees. As a result of using this new model and manually designed features, the close relations among variables on impactor shape and delamination are verified.*

Keywords: CFRP; Low-velocity impact; Machine learning; Multi-task learning

1. Introduction

In recent years, it has been necessary to deal with CO2 emissions, concerning environmental threats, and various improvements have taken in the aerospace industry aiming for weight saving, for example. Carbon fiber reinforced plastics (CFRPs) have great material characteristics, and have been increasingly adopted as a primary structural material for aircraft, such as Boeing 787 or Airbus 380. Materials used for airframes must be impact-resistant, since objects of various shapes, like tools, stones, and birds, can impact on aircraft surfaces during manufacturing and operation. CFRP is strong against in-plane loads, however, it does not have enough resistance against out-of-plane loads. Therefore, research on impact events on CFRP laminates has been reported by many researchers.

Once objects impact on CFRP laminates, there are various defects, such as surface dents, matrix cracks, and fiber fractures on the impacted and non-impacted side layers, and delamination, transverse cracks inside laminates, which is difficult to recognize from the outer surface. Even if the impact damage does not look very large, like barely visible impact damage (BVID), internal damage in CFRP laiminates can reduce their residual compressive strength by 30 % [1].

Airlines mainly perform visual inspections since current CFRP aircraft are designed to tolerate even if BVID exists [2]. Although non-destructive testing is necessary to determine the degree of internal damage, it is not always performed due to the significant cost problem. To overcome this situation, the relationship between dent depth and internal damage, which is one of the information that can be easily obtained externally, has been studied, but no clear relationship has yet been found [3].

  doi:10.5075/epfl-298799_978-2-9701614-0-0

This study investigates the possibility of estimating impact-related information such as shapes of impacted objects and internal damage from impact damage profiles of CFRP laminates using a machine learning approach. The authors have studied using a conventional machine learning model [4], and found that the estimation is possible to a certain extent. This study has introduced a new multitask learning approach to damage prediction. This presentation will provide an overview of the new model and compare results and features with previous models.

2. Experiments

2.1 Low-velocity impact tests

Low-velocity impact (LVI) tests were performed to collect both surface profiles and internal damage data, and to discuss the impact phenomena caused by various tool-drop on CFRP laminates. The material system was T800S/3900-2B, manufactured by Toray Industries Inc. The specimen size was 80 mm x 80 mm, and the specimen was placed between two plates with 60 mm x 60 mm cutouts, which were tightened with four screws. The CEAST 9350 Drop Tower Impact System (Instron) was used for this testing.

The impact test was conducted under three different impact factors. The first factor was stacking sequence: cross-ply laminates C8($[0/90]_{2s}$), C16($[0/90]_{4s}$), and C24($[0/90]_{6s}$), quasi-isotropic laminates Q8($[45/0/-45/90]_{s}$), Q16($[45/0/-45/90]_{2s}$), and Q24($[45/0/-45/90]_{3s}$), and 0˚ and 45˚-dominant laminates R0($[0/45/0/90/0/-45/0/45/0/-45]_{s}$) and R45($[45/-45/0/45/-45/90/45/-45/45/-45]_{s}$) were used. The average ply thickness is almost 0.1875 mm. The second factor was impactor shape. As foreign objects with different shapes collide on the aircraft's skin in an actual situation, the LVI test was performed considering six types of impactor shapes, namely HemiA, HemiB, HemiC, Coni60, Coni120, and Flat, as shown in Figure 1. The third factor was the impact energy level. Considering that the specimen size is smaller than that mentioned in ASTM D7136[5], and the conical impactors are used in this study, these experimental environments can induce serious damage on the specimens. Therefore, this study adopts less than the standard energy level 6.7 J/mm, i.e., 4.4, 3.35, 2.7, 2.2, 1.6, and 1.1 J/mm.

A wide-area 3D measurement system (Keyence VR-5000) was used to measure the surface profile of the specimens, and an ultrasound C-scanning (KJTD HIS3) was performed to confirm the in-plane damage propagation in the specimens.

Figure 1. Impactor shape

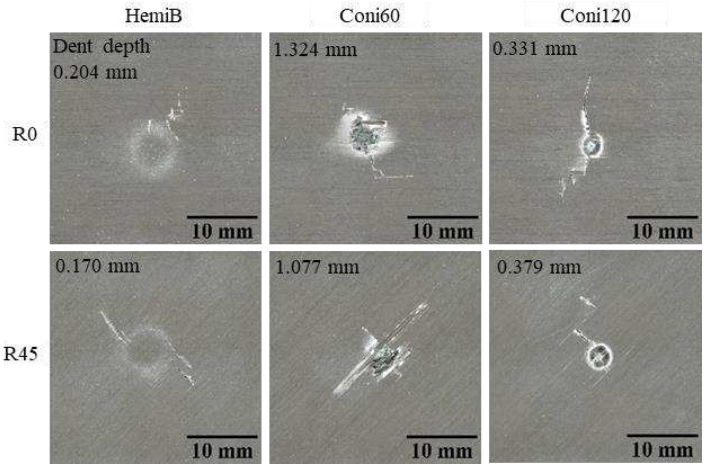

Figure 2. External damage (impact energy of 3.35 J/mm)

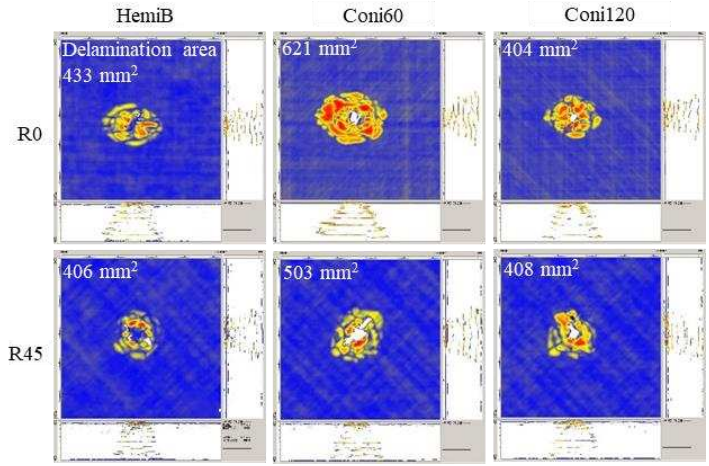

Figure 3. Internal damage (impact energy of 3.35 J/mm)

2.2 Experimental result

Figure 2 depicts the external damage of R0 and R45 specimens. In the case of Coni60, the dents and surrounding bulges are observed around the impact point. This is because the impactor penetrated through the impact side of the specimen during the impact test. In the case of Coni120, in addition to the indentation, matrix cracks and fiber fractures around the dent are observed. On the other hand, HemiB induced matrix cracks and fiber breakage around the shallow indentation area. Comparing the damage of R0 and R45, the surface damage of R45 spreads extensively. As R45 contains more 45-degree layers than R0, the specimens are likely to generate global deformation during the impact test. Therefore, the compressive stress generated on the impact side of the specimen was more extensive, which caused wide area damage.

Figure 3 depicts the internal damage of the same specimen as shown in Figure 2. Comparing the damage of R0 and R45 impacted with the same impactor shape, the delamination area is larger in R0 except for the case of Coni120. Considering the difference of the fiber angle rotation between adjacent plies, the delamination in R0 is likely to spread between the plies. In addition, the delamination of R45 is more concentrated near the top layer, which indicates that the external damage induces it.

From the experiment, the impact damage is found to depend highly on the impact condition, which means that impact information can be estimated using machine learning by designing appropriate features from the surface profile.

3. Multi-task learning

3.1 Introduction of multi-task learning

In our previous research [4], we verified that it is possible to estimate impactor shape, delamination area, and delamination length only from impact surface damage using a single-task learning model (Figure 4(a)). Single-task learning models are very common machine learning algorithms, which can estimate only one objective variable in one model. However, in the previous research, there were two problems:

- The number of samples is small, compared to that of data that is required for machine learning.
- Single-task models cannot consider the close relationship between the objective variables, such as impactor shape and internal damage.
- Even though the inputs or models are changed, it is difficult to improve the results of models better than 80%, especially the impactor shape and delamination area models.

In order to address these problems, a multi-task learning is introduced in this study [6]. Multi-task learnings (Figure 4(b)) can estimate multiple objective variables simultaneously, regardless of whether they are classification or regression problems.

3.2 Algorithm

The previous study [6] did not introduce any restrictions on the depth of the model, which can lead to overfitting. Therefore, this study defined five new hyperparameters, which determine the shape of the model, including the constraints on the depth: $max\_features$, $min\_samples\_split$, max_depth, max_depth_each, max_leaf_nodes (see Table 1). Figure 5 depicts the flowchart of the multi-task learning algorithm as follows;

1. Extract $max\_features$ features, the number of candidate features used in the branch, and store them in the list fea_list.
2. Store the values of each feature fea in the input samples into the list val_list.

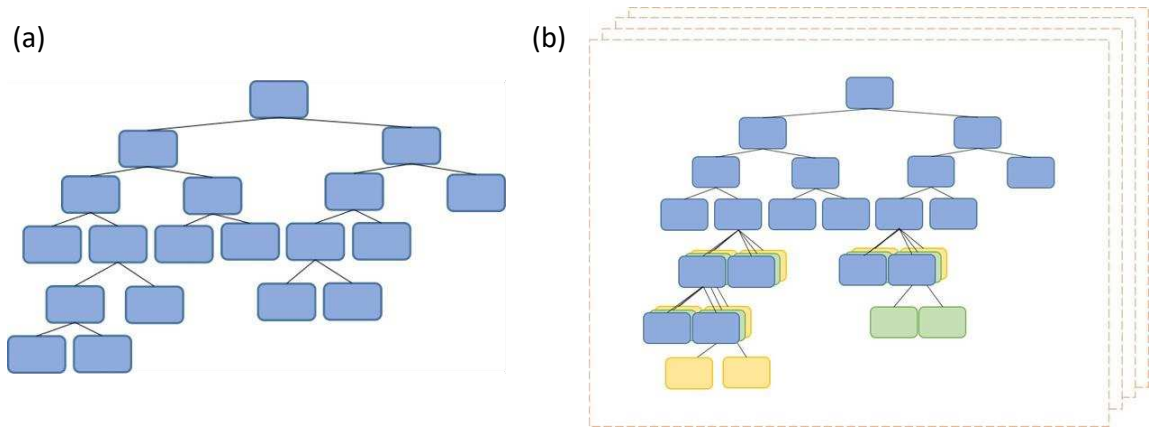

Figure 4. Overview of the two model (a) single-task learning, and (b) multi-task learning (three objective variables)

Table 1: Hyperparameters of the multi-task learning model

Hyperparameter	Explanation
$max\_features$	The number of features to reference in splitting an internal node
$min\_samples\_split$	The minimum number of samples required to split an internal node
max_depth	The maximum number of layers of a common part
max_depth_each	The maximum number of layers of a single part
max_leaf_nodes	The maximum number of leaves

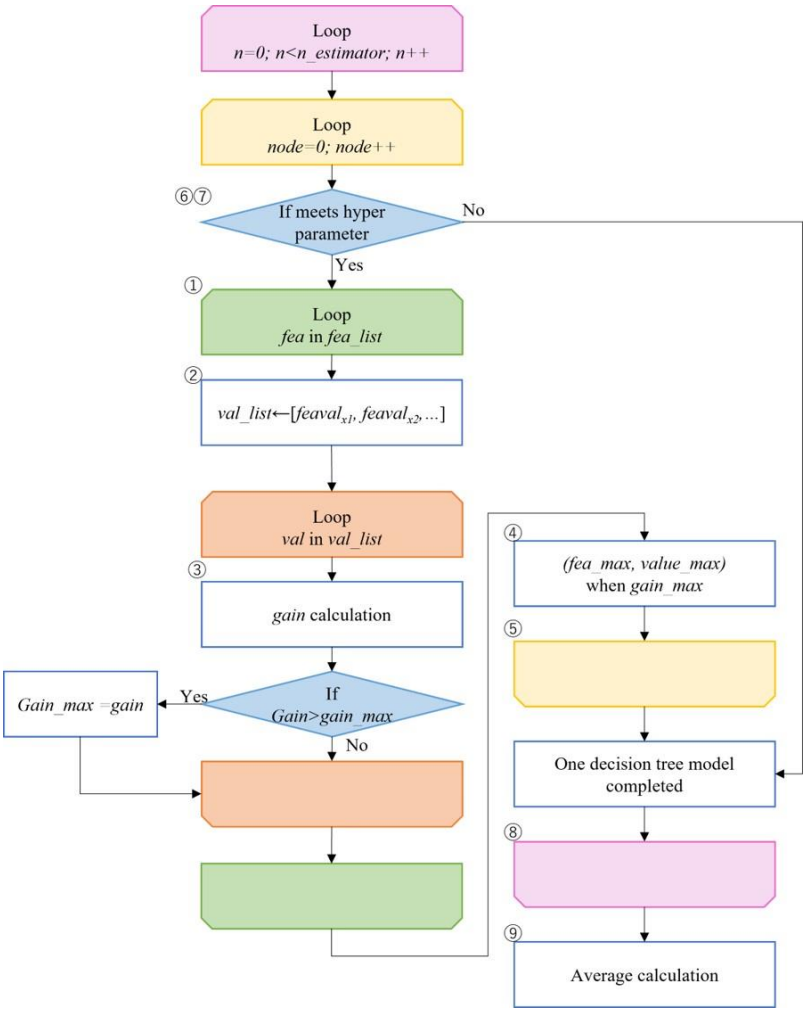

Figure 5. Overview of the multi-task learning algorithm

3. Calculate $gain$ when dividing the samples in the parent node into the two child nodes using the feature fea and the value val.
   In the case of a classification problem, entropy will be,
   $H_c(t) = -\sum p\,(c|x)\,log\,p(c|x)$ (1)
   where $p(c|x)$ is the probability when the class c samples are in the node x. In the case of a regression problem, entropy will be
   $H_{\{r|c\}}(t) = \sum p(c|x)\,(-\int p(r|c,x) log\,p(r|c,x)dx)$ (2)

Using the calculated entropies, the importance of three nodes of each objective variable imp_parent_obj, imp_left_obj and imp_right_obj will be

$$imp\_left\_obj = \frac{H\_left\_obj}{H\_all\_obj} \quad (3)$$

$$imp\_right\_obj = \frac{H\_right\_obj}{H\_all\_obj} \quad (4)$$

$$imp\_parent\_obj = \frac{H\_parent\_obj}{H\_all\_obj} \quad (5)$$

The gain of the focusing node for each objective variable $gain\_obj$ will be calculated as follows:

$$gain\_left\_obj = \frac{n\_left}{n\_parent} \cdot (imp\_parent\_obj - imp\_left\_obj) \quad (6)$$

$$gain\_right\_obj = \frac{n\_right}{n\_parent} \cdot (imp\_parent\_obj - imp\_right\_obj) \quad (7)$$

$$gain\_obj = gain\_left\_obj + gain\_right\_obj \quad (8)$$

where $gain\_left\,(right)\_obj$ is the gain of the left (right) child node, $n\_left\,(right, parent)$ is the number of samples in the left (right) child or parent node. The average value of the gains of each objective variable will be regarded as the gain of the focusing split.

$$gain = mean(gain\_obj) \quad (9)$$

4. After calculating all of the gains using every combination in fea_list and val_list, decide the combination of the feature and the value which generate the maximum $gain$ for the focusing split.
5. Create splits, repeating from 1. to 4..
6. Once the depth of the decision tree is equal to max_depth, splits after this will be decided for each objective variable. In addition, once the number of samples in parent nodes is less than $min\_samples\_leaf$, the nodes will be leaf nodes, i.e., no more splits after them.
7. Once the model satisfies the constraints on the hyperparameters as follows, exit from all loops and complete one decision tree for the objective variable.
    - The number of samples is less than $min\_samples\_split$.
    - The depth of the non-common layers of the decision tree is equal to max_depth_each.
    - The number of leaf nodes is equal to max_leaf_nodes.
8. Create $n\_estimator$ decision trees, repeating from 1. to 6..
9. When a testing phase, the majority decision for classification problems and the average value for regression problems of the results of $n\_estimator$ tree will be the output of the multi-task leaning algorithm.

In order to reinforce the versability of this model, the K-fold method was introduced to this research, and Optuna, the optimization library in python, was used to decide the best hyperparameters. After first learning, the feature selection was performed by selecting the features whose gain was higher than the median value. Again, the K-fold method was used using the selected features, and finally, the verification was conducted.

3.3 Input and output

The features designed from the surface profile data are the inputs to learn and verify the model. The objective variables are the categorized impactor shape, contact area, and contact radius, which are introduced as the quantified impactor shape, delamination area, length, and peak

load. Although the peak load is not the final target, this study treated it as a pseudo-objective variable considering the learning algorithm of the multi-task learning model.

4. Verification results

4.1 Results of learning

The results of the classification problem are shown in Table 2. Accuracy is the percentage of correctly classified data, and recall is the percentage of correctly classified data without missing the category data. As a result of introducing the multi-task learning model, recall exceeded 80% in addition to accuracy, which means that the new model is able to find out the impactor shape without mistakes.

The results of the regression problems are listed in Table 3 using r2 score and RMSE. R2 score is used to evaluate the performance of the model, and RMSE (Root Mean Square Error) shows the error of the model. As for delamination area, although RMSE was larger than that of the previous study, r2 score exceeds 80 % using the new model, which was one of the problems to be solved.

4.2 Essential information for the estimation

The top five most essential features are plotted in Figure 6. In the single task, dent depth is the most essential feature to estimate impactor shape, and local volumes are the almost only essential features to estimate delamination area and delamination length. In the present model, dent depth was included due to the common layer of the multi-task learning model. In Figure 6(a), unlike the single-task learning, the most essential feature is not dent depth but local deformed area. In the present model, max_depth is 2, and max_depth_each of the impactor classification is 6, i.e., the model has 8 layers. Therefore, in addition to dent depth used in the common layer, the feature representing the two-dimensional impact damage is regarded as essential.

Table 2: Results of the multi-task learning (the classification problem)

Objective variable	Accuracy	Recall
Impactor shape	0.862	0.813

Table 3: Results of the multi-task learning (the regression problem)

Objective variable	R2 score	RMSE
Delamination area	0.801	75.9
Delamination length	0.780	4.75
Contact radius	0.935	0.558
Contact area	0.906	17.4

  doi:10.5075/epfl-298799_978-2-9701614-0-0

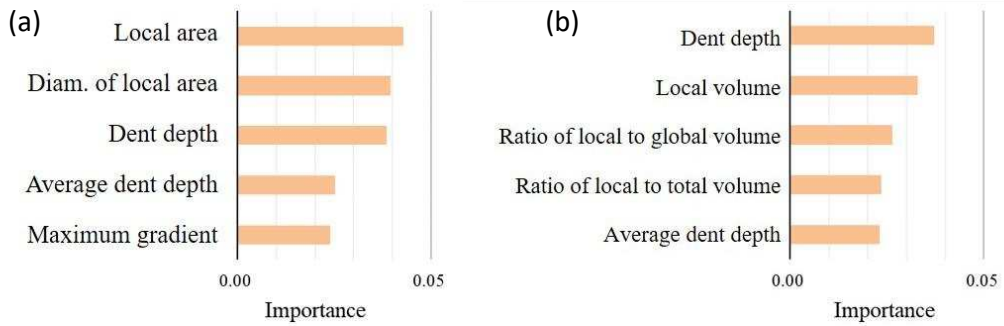

Figure 6. Essential features of the learning (a) impactor shape, and (b)delamination area

Focusing on Figure 6(b), the contribution of dent depth is the top of the other features and local volume is included due to the common layer. Considering that local volume is not included in Figure 6(a), it was confirmed again that delamination area is highly related to local volume.

5. Conclusion

This study applied a new multi-task learning algorithm to estimate low-velocity impact information and verified its feasibility.

First, a low-velocity impact test was conducted under the various impact conditions, and the impact damage profile data of the CFRP specimens was obtained. A decision tree-based multi-task learning model was founded, and the main feature of the new model was the introduction of a common depth max_depth and individual depths max_depth_each to account for the relationship among the objective variables. The results showed that the accuracy or r2 score is as high as or higher than that of the single-task, indicating that the new algorithm with a common layer is effective. In addition, dent depth and local volume are found to have a high relationship with the impact damage.

As future work, the multi-task learning model will be improved to apply for the residual compressive strength prediction, which is one of the critical issues for low-velocity impacts on CFRP laminates.

6. References

1. Davies GAO, Olsson R, Impact on composite structures. Aeronaut J. 2004; 108(1089):541-63.
2. Federal Aviation Administration. AC20-107B. Composite Aircraft Structure.2009.
3. Delaney MP, Fung SYK, Kim H. Dent depth visibility versus delamination damage for impact of composite panels by tips of varying radius. J Compos Mater. 2018;52(19):2691–705.
4. Hasebe S, Higuchi R, Yokozeki T, Takeda S. Internal low-velocity impact damage prediction in CFRP laminates using surface profiles and machine learning. Composites Part B: Engineering 2022;237:109844.
5. ASTM D7136. Standard test method for measuring the damage resistance of a fiber-reinforced polymer matrix composite to a drop-weight impact event. ASTM International 2007.
6. Linusson H. Multi-output random forests. PhD Thesis. 2013.

PREDICTION OF STRESS-STRAIN CURVES OF WOVEN CARBON FIBER REINFORCED PLASTICS COMPOSITE THROUGH MULTI-SCALE ANALYSIS

Gyu-Won Kim[a], Dug-Joong Kim[a], and Hak-Sung Kim[a,b]

a: Department of Mechanical Convergence Engineering, Hanyang University, 222, Wangsimni-ro, Seongdong-gu, Seoul, Republic of Korea
b: Institute of Nano Science and Technology, Hanyang University, 222, Wangsimni-ro, Seongdong-gu, Seoul, Republic of Korea
*E-mail: Kima@hanyang.ac.kr

Abstract: *In this study, the method to predict the mechanical properties of woven carbon fiber reinforced plastics (CFRP) using multi-scale analysis was proposed. Recently, woven CFRP composites have been widely applied to structures due to their high strength and excellent fracture toughness. As the properties of these composites are determined by various factors such as yarn width, space, thickness, it has been difficult and time-consuming to evaluate their properties through experiments for each condition. We developed multi-scale analysis method of plain and twill woven composites using stress amplification factor (SAF) to predict the stress-strain curves of composites. Then, mechanical tests of composite specimens fabricated by resin transfer molding (RTM) were performed, and the results of tests were compared with multi-scale simulation result. With the proposed simulation modeling, it is expected to predict the mechanical properties of composites in a fast time and with high accuracy.*

Keywords: Carbon fiber reinforced plastics; multi-scale analysis; stress amplification factor; stress-strain curve; progressive damage analysis

1. Introduction

Carbon fiber reinforced plastics (CFRP) have been widely used in various fields such as aircraft, automobiles, and medical devices [1]. Especially, woven CFRP composites have been widely applied in structures due to their high strength and superior fracture toughness [2]. The properties of woven CFRP composites are determined by various factors. The mechanical properties of composites are directly affected by the properties of the fiber and matrix such as stiffness and strength. Additionally, the structural factors of textile such as yarn width, space, and thickness also have an effect on the mechanical properties of woven composites. It takes much time to set up the mechanical tests to estimate the mechanical properties of woven CFRP composites considering all these various factors

In this study, the mechanical properties of woven composites were predicted using multi-scale analysis utilizing the interaction of micro-scale and meso-scale modeling. The micromechanics of failure criteria were applied to each constituent and the stress amplification factor (SAF) was adopted to transfer stress between micro-scale and meso-scale simulation [3]. A representative volume element (RVE) of micro-scale and meso-scale models was generated, and meso-scale RVE models were produced by classifying them into plain and twill types according to the weaving pattern. All meso-scale RVE was modeled with open-source software TexGen. Then, finite element analysis (FEA) was performed with ABAQUS software to obtain multi-scale simulation data. To validate the multi-scale simulation results, they were compared

  doi:10.5075/epfl-298799_978-2-9701614-0-0

with data obtained through tensile, compressive, and shear tests of woven CFRP. The specimens of tests were manufactured by resin transfer molding (RTM). Finally, it was confirmed that stress-strain curve data obtained through multi-scale simulation showed good agreement with the experimental results, and it is considered that multi-scale analysis showed high accuracy [3]. In addition, the distribution of damage factors based on progressive damage analysis was observed [4]. Then, the tendency of damage propagation in fiber and matrix was analyzed in relation to the stress-strain curve.

2. Theoretical background

2.1 multi-scale analysis

Multi-scale analysis was performed through the interaction of micro-scale and meso-scale models. Because their yarns are composed of fiber and matrix with different properties from the point of view of micro-scale, woven CFRP composites are inhomogeneous. Therefore, in the process of multi-scale modeling, homogenizations of material properties between micro-scale and meso-scale models were performed [5]. As a result of finite element analysis (FEA) of micro-scale modeling, effective material properties that can be substituted as mechanical properties of yarn in the meso-scale model were derived. In this process, the periodic boundary condition (PBC) method was applied to analyze the micro-scale RVE model, and can be expressed as follows [6]:

$$u_i{}^{j+}(x,y,z) - u_i{}^{j-}(x,y,z) = c_i{}^{j} \qquad (i,j = 1,2,3) \tag{1}$$

Where $u_i{}^{j+}$ and $u_i{}^{j-}$ are displacements of on pair of nodes at opposite boundary faces. $i = x,y,z$ indicates the normal direction to three pairs of boundary surfaces, and $j = x,y,z$ indicates three directions of nodal displacement. $c_i{}^{j}$ is constants defined by displacement difference. The effective material properties derived from micro-scale simulation were substituted for the yarn part of meso-scale model. In addition, for accurate simulation using multi-scale modeling, progressive damage model theory was introduced, and stress amplification factor (SAF) matrix was applied to connect between micro-scale and meso-scale analysis. A detailed description of progressive damage model and SAF is introduced in the next section. Fig. 1 shows the overall multi-scale analysis algorithm performed in this study.

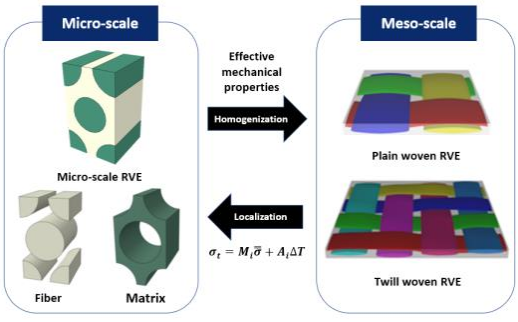

Figure 1. Schematic view of multi-scale analysis

2.2 Stress amplification factor (SAF)

As mentioned before, multi-scale simulation enhances the accuracy of the. analysis through the interconnection between micro-scale and meso-scale modeling. For this process, stress

  doi:10.5075/epfl-298799_978-2-9701614-0-0

amplification factor (SAF) links the models of two scales through the correlation of micro-scale and meso-scale constituent stress. SAF formula can be expressed as [3]:

$$\sigma_i = M_i\bar{\sigma} + A_i\Delta T \tag{2}$$

Where σ_i and $\bar{\sigma}$ are the micro-scale stress and the meso-scale stress in fibers and the matrix, respectively. M_i is the stress amplification factors that express transfer of the micro-scale stress and the meso-scale stress. A_i indicates the thermal stress amplification factors for the temperature influence. In this study, since there is no effect of temperature, these temperature variables are ignored, and the above formula is expressed as a determinant as follows [4]:

$$\begin{pmatrix}\sigma_1\\ \sigma_2\\ \sigma_3\\ \sigma_4\\ \sigma_5\\ \sigma_6\end{pmatrix} = \begin{bmatrix}M_{11} & M_{12} & M_{13} & M_{14} & 0 & 0\\ M_{21} & M_{22} & M_{23} & M_{24} & 0 & 0\\ M_{31} & M_{32} & M_{33} & M_{34} & 0 & 0\\ M_{41} & M_{42} & M_{43} & M_{44} & 0 & 0\\ 0 & 0 & 0 & 0 & M_{55} & M_{56}\\ 0 & 0 & 0 & 0 & M_{65} & M_{66}\end{bmatrix}\begin{pmatrix}\overline{\sigma_1}\\ \overline{\sigma_2}\\ \overline{\sigma_3}\\ \overline{\sigma_4}\\ \overline{\sigma_5}\\ \overline{\sigma_6}\end{pmatrix} + \begin{pmatrix}A_1\\ A_2\\ A_3\\ A_4\\ A_5\\ A_6\end{pmatrix}\Delta T \tag{3}$$

The values in M_i matrix can be derived through the micro-scale analysis described in the previous section.

2.3 progressive damage model

The progressive damage model is applied in the finite element analysis of woven composites exhibiting non-linear behavior. From a micro-scale point of view, the modified von mises failure criterion was introduced into the matrix, and the formula is as follows [7]:

$$\frac{{\sigma_{VM}}^2}{C_m T_m} + \left(\frac{1}{T_m}\frac{1}{C_m}\right) I_1 = 1 \tag{4}$$

$$\sigma_{VM} = \sqrt{{I_1}^2 - 3I_2} \tag{5}$$

$$I_1 = \sigma_{m1} + \sigma_{m2} + \sigma_{m3} \tag{6}$$

$$I_2 = \sigma_{m1}\sigma_{m2} + \sigma_{m2}\sigma_{m3} + \sigma_{m3}\sigma_{m1} - ({\sigma_{m12}}^2 + {\sigma_{m23}}^2 + {\sigma_{m13}}^2) \tag{7}$$

where $I_1\ and\ I_2$ are the first stress invariant, and second stress invariant of micro-scale stress of the matrix, and σ_{VM} is the von mises equivalent stress. C_m and T_m indicate compression and tensile strength of the matrix, respectively. In addition, this failure criterion can be expressed as a function of equivalent stress, σ_{eq} [4]:

$$\sigma_{eq} = \frac{(\beta-1)I_1 + \sqrt{(\beta-1)^2{I_1}^2 + 4\beta{\sigma_{VM}}^2}}{2\beta} \tag{8}$$

where β is the ratio of compression strength to the tensile strength of the matrix. The equivalent stress σ_{eq} is also expressed with matrix failure index, k_m, and the equation is expressed as follows [4]:

$$k_m = \frac{\sigma_{eq}}{T_m} \tag{9}$$

If fracture occurs in the matrix, the stiffness of the matrix gradually decreased, and this micro-scale failure model is expressed as following [4]:

  doi:10.5075/epfl-298799_978-2-9701614-0-0

$$D_m = \begin{cases} 1 - exp[\gamma(1 - k_m)] & (1 < k_m < \alpha) \\ 0.99 & (\alpha < k_m) \end{cases} \quad (10)$$

when σ_{eq} is greater than the final strength of the matrix, D_m is set to 0.99 to complete fracture of the matrix. γ is matrix damage factor that can be determined through the experiment of shear deformed woven composites. α is fixed to 1.5 with the reference data.

For the fiber, matrix longitudinal stress failure criterion was introduced, and the formula expressed as follow [4]:

$$k_f = \frac{T_f}{\sigma_{f11}} \quad (11)$$

where k_f, T_f, σ_{f11} indicate the fiber failure index, the tensile strength of the fiber, and the micro stress of the fiber. If k_f was larger than 1, the fiber failed, and its stiffness decreased. The fiber damage factor can be expressed as follows [4]:

$$D_f = \begin{cases} 0 & (k_f \leq \alpha) \\ 0.99 & (1 < k_f) \end{cases} \quad (12)$$

3. The experiment and finite element analysis

3.1 Experimental process (Tensile/compression/shear test for stress-strain curve)

Specimens for each condition of woven composites were prepared to perform the mechanical tests. The plain woven CFRP specimens were fabricated with $123\ g/m^2$ and $200\ g/m^2$ areal density 1/1 plain fabric, and twill woven CFRP specimens were fabricated with $160\ g/m^2$ and $285\ g/m^2$ areal density 2/2 twill fabric. After each fabric was laminated, the resin was injected using VARTM process and then cured. Finally, the tests were conducted through ASTM D 3039 for tensile test, ASTM D 6641 for compression test, and ASTM D 5379 for shear test. Fig. 2 shows the experimental set-up of each test.

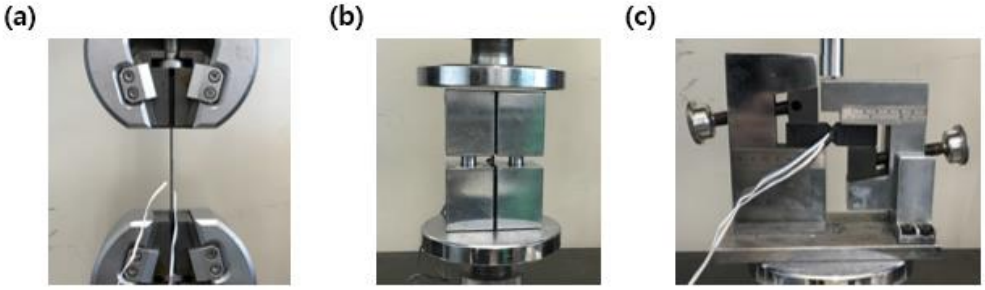

Figure 2. experimental set-up of (a) Tensile, (b) Compression, and (c) Shear test

3.2 the textile structural dimension

As a process for multi-scale analysis, meso-scale model should reflect the textile structure parameters (yarn width, yarn space, and yarn thickness). In this study, yarn space, width and thickness were measured using a microscope. Fig. 3 summarized the cases for each weaving pattern and areal density condition, and the measured textile structure dimensions for each case. These values were substituted into meso-scale model using textile geometric modeling software TexGen.

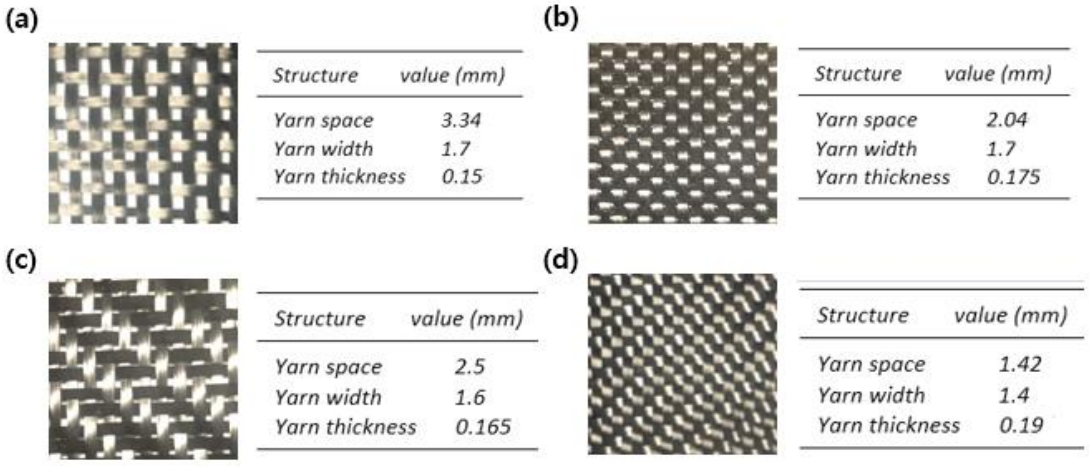

Figure 3. Fabric for (a) case 1-1. $123\ g/m^2$ *areal density plain, (b) case 1-2.* $200\ g/m^2$ *areal density plain, (c) case 2-1.* $160\ g/m^2$ *areal density twill, and (d) case 2-2.* $285\ g/m^2$ *areal density twill, and value of the textile structure dimensions (yarn width, space, thickness)*

3.3 Finite element analysis

In this study, multi-scale simulation was performed through finite element analysis (FEA) using ABAQUS software with UMAT (user material subroutine) [3]. The effective material properties substituted for the mechanical properties of yarn and stress amplification factor (SAF) values were derived through micro-scale RVE model with 0.6 fiber volume fraction. The fiber and matrix properties were reflected in the micro-scale RVE model, and the periodic boundary condition (PBC) method was introduced. As mentioned in the previous section, the yarn properties and resin properties were respectively substituted for the meso-scale RVE model using TexGen software. Table 1. includes the mechanical properties applied to micro-scale and meso-scale RVE models. For each model, the displacement conditions suitable for tensile, compression, and shear analysis were substituted.

4. Results and discussion

To validate the multi-scale modeling, the simulation results were compared with experimental data. Fig. 4 shows the stress-strain curves of the simulations compared with the experimental data for each condition (weave type, areal density, test type), and it showed good agreement in all conditions.

  doi:10.5075/epfl-298799_978-2-9701614-0-0

Table 1. mechanical properties for (a) fiber, (b) matrix, and (c) effective material properties.

(a)

Property	value
$E_{11}\ (GPa)$	230
$E_{22}\ (GPa)$	15
$G_{12}\ (GPa)$	27
$G_{23}\ (GPa)$	7
υ_{12}	0.2
υ_{23}	0.07
σ_{Tm} (GPa)	1.6
σ_{Cm} (GPa)	1.2

(b)

Property	value
$E_m\ (GPa)$	3
υ_m	0.35
σ_{Tm} (GPa)	50
σ_{Cm} (GPa)	100

(c)

Property	value
$E_{11}\ (GPa)$	139.67
$E_{22}\ (GPa)$	8.62
$G_{12}\ (GPa)$	4.26
$G_{23}\ (GPa)$	2.96
υ_{12}	0.25
υ_{23}	0.35

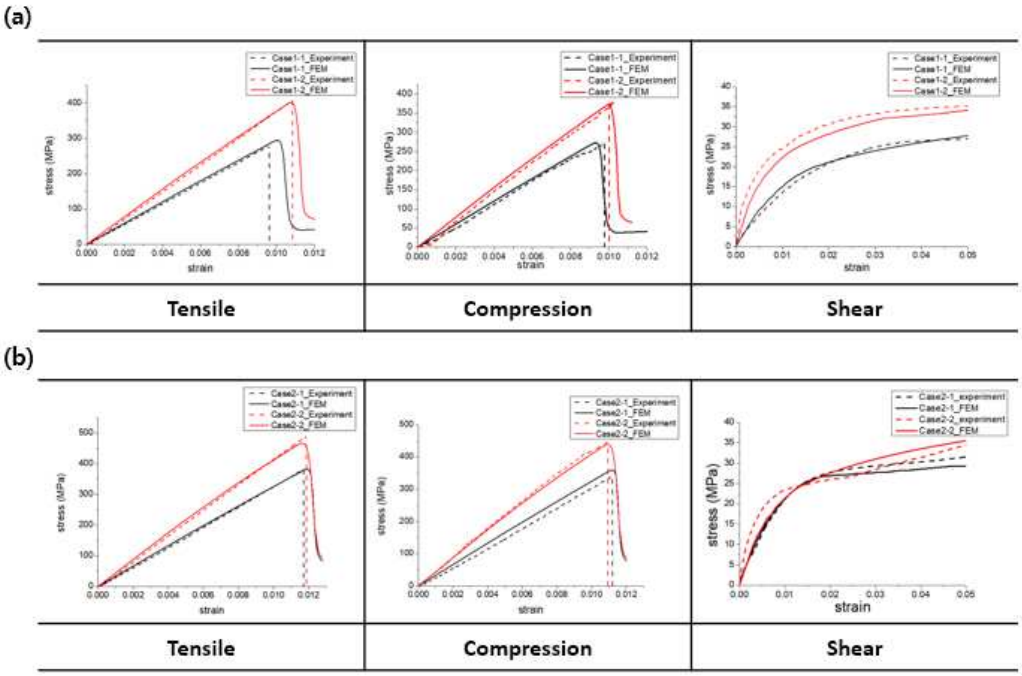

Figure 4. strain-stress curve by conditions (weave type, areal density, test type)

It was found that the multi-scale simulation could predict the experimental stress-strain curve for each tensile, compression, and shear simulation. Fig. 5 shows the damage propagation with respect to the damage factor at each point of the stress-strain curve of the case 1-2 model [4]. The point (a) of Fig. 5 is the damage status before the failure occurs, the point (b) of Fig. 5 is the damage status just before the failure occurs, and the point (c) is the damage status after the failure. As shown at point (b) of Fig. 5, the failure occurred in the fiber yarn and propagated rapidly, and then the damage to the pure matrix and the matrix in yarns occurred in the vicinity of the failure of the fiber. Same tendency was also found in the compression simulation. Meanwhile, in the shear simulation, which was conducted up to 0.5% strain condition, as shown at Fig. 7, the matrix was gradually damaged, and there was almost no damage in the fiber. As a result, in the tensile and compression simulations, it can be concluded that the damage to the fiber had a great effect on the overall failure of the woven CFRP composite, and in the shear simulation, the damage in the matrix accumulated slowly.

  doi:10.5075/epfl-298799_978-2-9701614-0-0

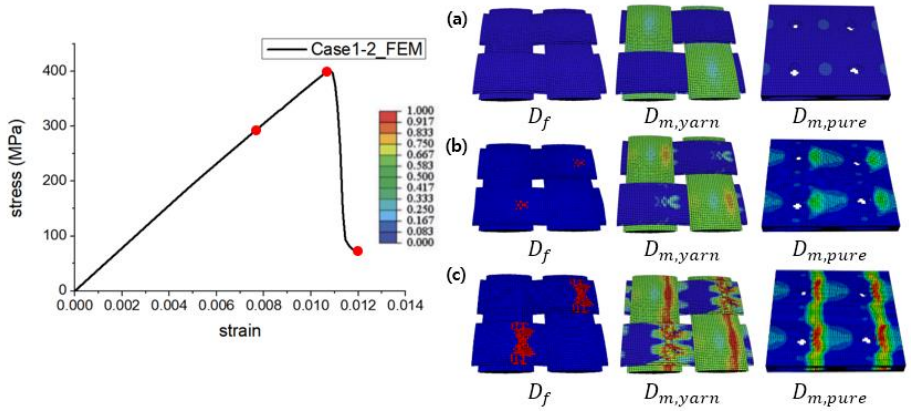

Figure 5. damage propagation with the stress-strain curve of case 1-2 model (Tensile)

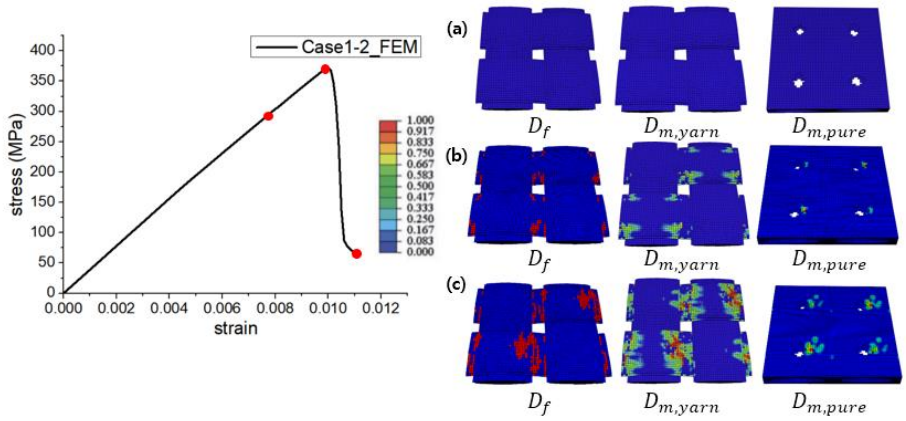

Figure 6. damage propagation with the stress-strain curve of case 1-2 model (Compression)

5. Conclusion

In this study, multi-scale analysis based on the correlation of micro-scale and meso-scale modeling was proposed to predict the stress-strain curve of woven CFRP composites. Micro-scale RVE model was composed of fiber and matrix, and effective material properties and SAF values were derived through finite element analysis of this model. Meso-scale RVE model was created by reflecting the textile structure dimensions derived through microscopic measurements and the effective material properties of yarn. The stress-strain curve of the simulation for each condition (weave type, areal density, test type) was derived and compared with the experimental data. Also, based on the progressive damage analysis, the damage propagation according to the stress-strain curve was observed. Conclusively, the curves showed good validation in all conditions, and the damage mechanism of the woven CFRP composites for each test type was identified. The multi-scale modeling in this work could be a good approach to predict the mechanical properties and damage propagation of woven composites.

  doi:10.5075/epfl-298799_978-2-9701614-0-0

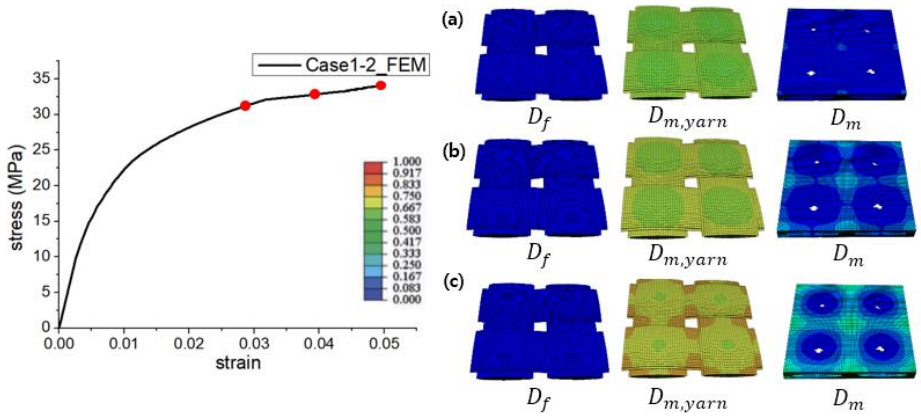

Figure 7. damage propagation with the stress-strain curve of case 1-2 model (Shear)

Acknowledgements

This work was supported by Korea Institute of Energy Technology Evaluation and Planning(KETEP) grant funded by the Korea government(MOTIE)(20212020800090, Development and Demonstration of Energy-Efficiency Enhanced Technology for Temperature-Controlled Transportaion and Logistics Center)

6. References

1. ZHEN MJ. A multiscale modeling approach for the progressive failure analysis of textile composites. 2013.
2. Ullah H, Harland AR, Silberschmidt VV. Damage and fracture in carbon fabric reinforced composites under impact bending. Composite Structures. 2013;101:144-56.
3. Hwang Y-T, Choi K-H, Kim J-I, Lim J, Nam B, Kim H-S. Prediction of non-linear mechanical behavior of shear deformed twill woven composites based on a multi-scale progressive damage model. Composite Structures. 2019;224:111019.
4. Xu L, Huang Y, Zhao C, Ha SK. Progressive failure prediction of woven fabric composites using a multi-scale approach. International Journal of Damage Mechanics. 2018;27(1):97-119.
5. Lomov SV, Bernal E, Ivanov DS, Kondratiev SV, Verpoest I. Homogenisation of a sheared unit cell of textile composites: FEA and approximate inclusion model. Revue Européenne des Eléments. 2005;14(6-7):709-28.
6. Xia Z, Zhang Y, Ellyin F. A unified periodical boundary conditions for representative volume elements of composites and applications. International journal of solids and structures. 2003;40(8):1907-21.
7. Ernst G, Vogler M, Hühne C, Rolfes R. Multiscale progressive failure analysis of textile composites. Composites Science and Technology. 2010;70(1):61-72.

GENERATION OF REALISTIC 2D TRANSVERSE MICROSTRUCTURES OF UNIDIRECTIONAL FIBRE-REINFORCED COMPOSITES USING A GENERATIVE ADVERSARIAL NETWORK

Rui Guo[1], Marco Alves[2], Mahoor Mehdikhani[1], Christian Breite[1], Yentl Swolfs[1]*

[1]Department of Materials Engineering, KU Leuven, Kasteelpark Arenberg 44 box 2450, 3001 Leuven, Belgium, rui.guo1@kuleuven.be
[2]Move.ai,14 Adeline Pl, London WC1B 3AJ, UK

Abstract: *Microstructure generators for unidirectional fibre-reinforced composites are a crucial step for the prediction and optimisation of their mechanical properties. The purpose of this study is to generate 2D realistic transverse microstructure of these composites using a deep convolutional generative adversarial network (DCGAN). To make detailed statistical comparisons between the real and synthetic microstructures in terms of the geometric characteristics, a fibre segmentation method based on the watershed segmentation was developed to separate each fibre. The results show a good agreement between the real and synthetic microstructures, which illustrate the capability and potential of the DCGAN to generate realistic transverse microstructures.*

Keywords: deep learning; microstructure generator; materials design; microstructural analysis; generative adversarial network

1. Introduction

Fibre-reinforced composites are used in a wide range of applications due to their excellent mechanical properties and low density [1]. To assess the effect of microstructural variability on their mechanical properties, the industry largely relies on experimental characterisation. This approach hampers the adoption of new material combinations and production processes. To overcome this issue, advanced virtual characterisation techniques are needed to bridge the relevant scales starting from the microscale.

Models that start at the microscale often need a reliable method to generate random fibre packings. Pyrz et al. [2] proposed a hard core method to simulate the actual random fibre packings, however, this method cannot generate packings with fibre volume fractions greater than 50% [3]. To address this limitation, more advanced algorithms have been proposed. Melro et al. [3] proposed a stirring method that can effectively overcome the jamming limit problem for fibre-reinforced composites and the fibre volume fraction can even marginally exceed 65%. Yang et al. [4] proposed a random sequential expansion algorithm that can generate microstructure with fibre volume fraction up to 68% when fibres are allowed to contact each other. However, these algorithms only consider the stochastic placement of the fibre. In real microstructures, resin-rich areas exist [5], which have important effects on the mechanical properties [5,6]. Therefore, algorithms, which can fully capture real microstructural features, like non-circular fibres, resin-rich areas, and diameter variations, are in ongoing research.

Due to the availability of copious amounts of image data, deep learning methods have become popular to create representations of material microstructures. Compared to traditional generation methods, methods based on the generative adversarial networks (GAN) do not have

  doi:10.5075/epfl-298799_978-2-9701614-0-0

assumptions of the features and patterns represented in the image data. Therefore, such models can learn the underlying data distribution from their input dataset directly and can generate large datasets of unique realistic microstructures, which follow the same characteristics. Currently, GANs have been applied for microstructural generation of porous media [7] [8] and energy materials [9][10], resulting in microstructures representative of the real ones.

In this work, we use a Deep Convolutional Generative Adversarial Network (DCGAN) [11] to generate realistic 2D representations of transverse microstructures of unidirectional fibre-reinforced composites. A fibre segmentation method was built based on the watershed. Detailed statistical methods were employed to compare the synthetic microstructures with the real microstructures in terms of the fibres' geometric characteristics.

2. Materials and method

2.1 Experimental microstructures

The material used was a thin-ply carbon fibre/epoxy prepreg consisting of GRAFIL 34-700WD-24 K-1.4%A carbon fibres (Mitsubishi, Japan) and a proprietary 736LT resin (North Thin Ply Technology, Switzerland). Specimens were produced by stacking multiple plies on top of each other and curing them using a computerised autoclave at KU Leuven, as previously described in [12]. The specimens were water-jetted to the desired cross-section and scanned at the ID19 beamline of the ESRF synchrotron. Imaging settings were chosen to ensure high-contrast and high-resolution reconstructed images. For the here used data, the CT projections were acquired using a mono-chromatic beam at 20 keV paired with a 10x optical magnification lens and the pco.edge 5.5 camera available at ID19. This resulted in a final voxel size of 0.65 µm. The raw data was cropped to focus on the centre region of the reconstructed CT image. The input dataset became thereby a volume of 1100 x 550 x 1800 pixel^3, which corresponds to 715 x 357.5 x 1170 µm^3.). A sample image for a transverse slice of the CT volume is shown in Fig. 1. The images show the non-uniform distribution of the fibre due to the layered structure of the thin plies. Especially on the ply boundaries, some resin-rich areas are captured.

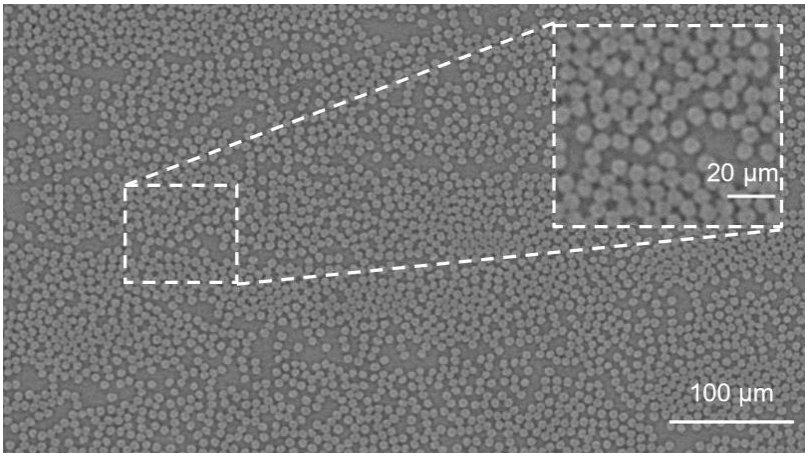

Fig. 1. A sample image for a transverse slice of the CT volume showing the cross-section of carbon fibres in an epoxy matrix

2.2 DCGAN implementation

Goodfellow et al. [13] first proposed the GAN. These networks are used to implicitly learn the probability distribution of a given data and then generate data with a similar probability distribution.

DCGAN can generate good results on small-sized images by introducing the convolutional neural networks [11]. Therefore, the large-sized input images were further cropped to the final 41.6 x 41.6 μm^2 (64 x 64 $pixel^2$) images. To obtain a sufficiently large training dataset, sampling of the cropped images with overlap was performed with a stride of 8 pixels as proposed in [9]. In addition, data augmentation methods were applied [14]. In total, 32390 images were obtained to train the DCGAN.

Table 1. summarises the specific networks and hyperparameters used for the DCGAN. The slope for all Leaky ReLU activations was 0.2, and batch normalisation was applied before the activation function. In the training process, the Adam optimum and a classic non-saturating GAN loss function [13] were used. The parameter $from\_logits$ in this loss function was set as True. The learning rates for discriminator and generator were both 0.0002 and the momentum constants were $\beta_1 = 0.5, \beta_2 = 0.99$. The batch size was set to 64.

Table 1. The architecture of the DCGAN model for 2D transverse microstructures of unidirectional fibre-reinforced composite

Layer	Operations	Output	Kernel	Stride	Padding	Batch	Activation
	Input shape	(1*1*128)	-	-		-	-
G_1	Conv2DTranspose	(4*4*512)	4	1	Valid	Yes	ReLU
G_2	Conv2DTranspose	(8*8*256)	4	2	Same	Yes	ReLU
G_3	Conv2DTranspose	(16*16*128)	4	2	Same	Yes	ReLU
G_4	Conv2DTranspose	(32*32*64)	4	2	Same	Yes	ReLU
G_5	Conv2DTranspose	(64*64*1)	4	2	Same	No	Tanh
	Input shape	(64*64*1)	-	-		-	-
D_1	Conv2D	(32*32*64)	4	2	Same	No	LeakyReLU
D_2	Conv2D	(16*16*128)	4	2	Same	Yes	LeakyReLU
D_3	Conv2D	(8*8*256)	4	2	Same	Yes	LeakyReLU
D_4	Conv2D	(4*4*512)	4	2	Same	Yes	LeakyReLU
D_5	Conv2D	(1*1*1)	4	1	Valid	No	No

DCGAN was trained on a workstation based on the TensorFlow framework with a high-performance GPU (Nvidia RTX A5000). The training took around 16 minutes (25300 iterations).

  doi:10.5075/epfl-298799_978-2-9701614-0-0

After training, we were able to generate 100 microstructures in a few seconds only using the CPU.

2.3 Segmentation

To perform a statistical analysis of real and synthetic microstructures, an image-based fibre segmentation was implemented in MATLAB R2020b. The main steps are:

1. A Gaussian filter with a 2-D Gaussian smoothing kernel with standard deviation of 0.5 was used to remove the noise and smoothen the images. The Otsu threshold method was applied to automatically select a global threshold for converting grayscale images to binary images (see Fig. 2b).
2. A morphological opening operation with a disk-shaped kernel of radius 4 was used to remove artefacts (see Fig. 2c). It is worth noting that if the radius of the disk-shaped kernel is small, artefacts cannot be removed and if the kernel radius is too large, some fibres can be mistakenly removed as noise.
3. The image was eroded with the same disk kernel size as in step 2 first and then the Euclidean distance transformation was applied. After this, watershed ridge lines were found by using the watershed transformation. Based on these watershed ridge lines, most touching fibres were separated effectively. (See Fig. 2d).

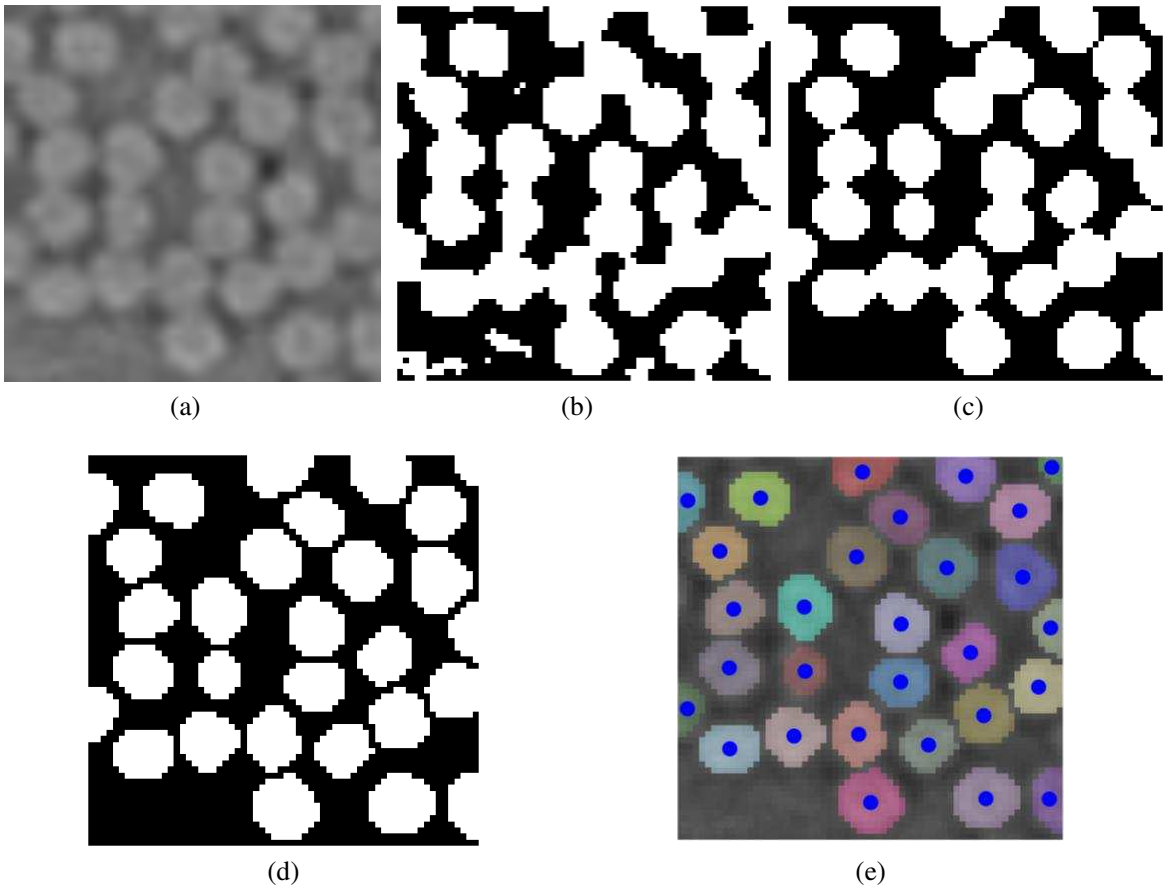

Fig. 2. Fibre segmentation methods based on watershed: (a) grayscale images, (b) binary images with some noises, (c) binary images after removing the noise, (d) binary image after separating the touching fibres, (e) overlay of the grayscale images and individual fibres

  doi:10.5075/epfl-298799_978-2-9701614-0-0

Fig. 2e shows the overlay of a binary sample image and the corresponding grayscale image. Each individual fibre is represented by a different colour. The blue points indicate the centre of each fibre, which were extracted according to the image moment method. These two functions and all further statistical analyses were implemented in Python code.

3. Results

3.1 Visual similarity

In contrast to the microstructures of porous media and energy materials, which are interconnected and irregular in shape, the fibres in the unidirectional fibre-reinforced composite studied have close to an ideal circular shape and there are no overlapping regions between the fibres. In addition, resin-rich areas and fibre clusters (densely packed fibres) exist in the real microstructure (see Fig. 3a). Nine randomly picked the synthetic microstructures were given in Fig. 3b. The synthetic microstructures visually capture the complex patterns in the real experimental data well. However, upon careful examination, a few unrealistic fibres can be detected, as is highlighted in Fig. 3b.

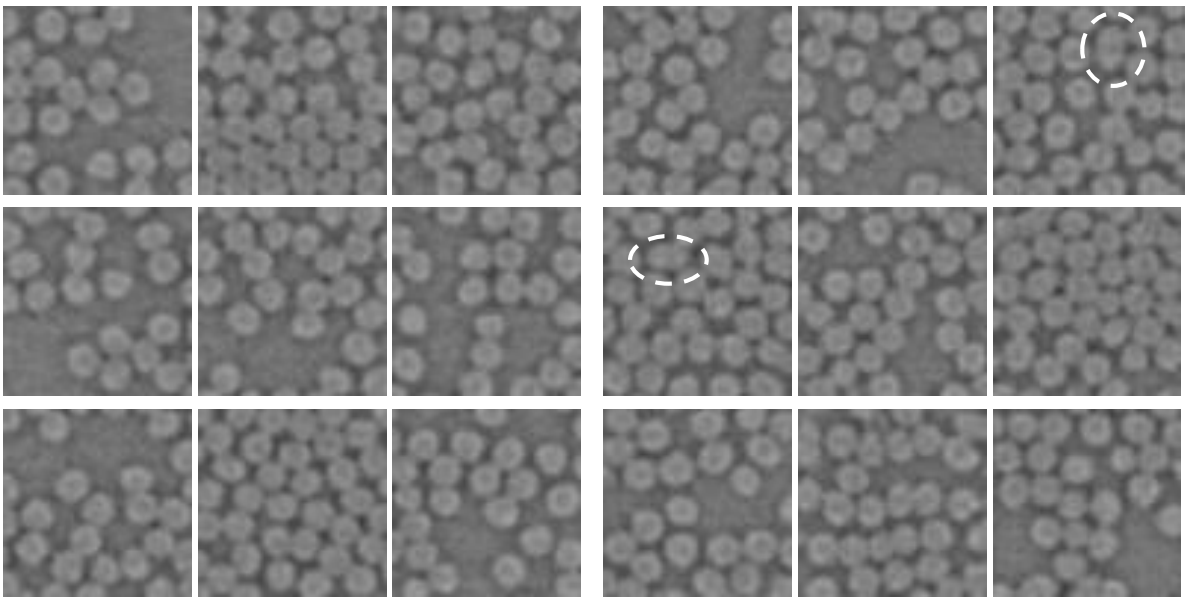

(a) (b)

Fig. 3. Comparison of samples of (a) real and (b) DCGAN-synthetic microstructures.

3.2 Statistical analysis

It is known that mechanical properties are affected by microstructural parameters, such as amongst others the fibre volume fraction, fibre diameter and clustering of fibres. All of these are captured in the synthetic images. To assess how well the synthetic data represents reality, a sample of 120 synthetic images generated by DCGAN was compared with 120 real images. The real images are unique without using any overlap and data augmentation to crop them from the input data.

The diameter of the same fibres type and even produced in the same batch by the manufacturer as the ones cured into composite and imaged using CT (our input data) was measured using a laser diffraction system (LDS) in [15]. The mean value and standard deviation of diameters for 89 fibres are 6.52 μm, 0.45, respectively. We assume the measurements using the LDS to be

  doi:10.5075/epfl-298799_978-2-9701614-0-0

precise and the ground truth for the following comparisons. 2050 fibres were extracted from the real images (64*64 pixel^2) after removing the fibres at the borders. The fibres at the image borders have to be excluded as their cross-section is often only partly included in the cropped CT image. The mean equivalent diameter for these fibres measured after segmentation is 6.25 µm with a standard deviation of 0.50, using Eq. (1), where f is equal to 1. Comparing to the LDS measurement value, this underestimated mean value is most likely due to the still low resolution of the images [16]. Assuming that the ground truth value should be obtained from the CT image if this limitation would be overcome, the actual fibre diameter can be reasonably obtained by applying an empirical factor f, as in Eq. (1), on the single fibre area. This factor is the ratio of the square of the average of the fibre diameters measured with LDS and the CT image measurements. It is around 1.088 for the current case.

$$D_{sing\_fibre} = \sqrt{\frac{4 * S_{single\_fibre} * f}{\pi}} * unit \tag{1}$$

Where D_{sing_fibre} is the equivalent diameter of a single fibre. S_{single_fibre} is the sum of the number of pixels in the fibre with pixel value equal to 255 in the binary images. f is the empirical factor considering the effect of the low-resolution images, and it is equal to 1 if no modifications is used on the fibres area. $unit$ is equal to the 0.65 µm.

For the 120 synthetic images, 1970 fibres were extracted. Some unrealistic fibres with equivalent diameters less than 4 µm and larger than 8 µm were found in the synthetic images. These unrealistic fibres accounted for about 1.4% of the fibres (=28 fibres) and thus were removed. Fig. 4a plots the histogram of the equivalent fibre diameter in both the real and synthetic images, and confirm the similarity of the distributions.

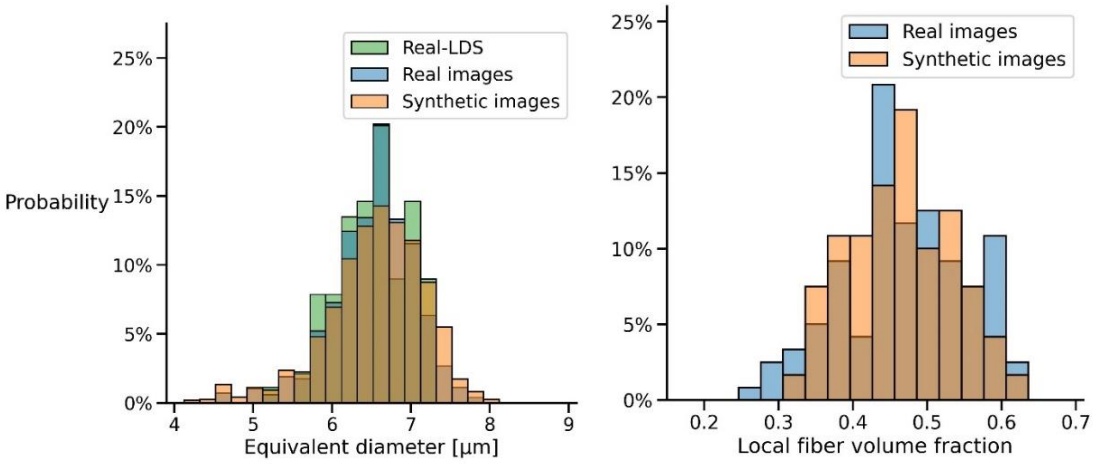

Fig. 4. The histogram of the (a) equivalent diameter after removal of 28 unrealistic fibres for synthetic images and (b) local fibre volume fractions

After establishing the empirical factor f, the local fibre volume fraction was calculated using the Eq. (2) for sub-images of 1100 x 550 pixel^2. The mean value of the real images is varying from 43.1% to 46.9% after applying the empirical factor. This means the accuracy of resolving the correct equivalent fibre diameter has a significant effect on the local fibre volume fraction. Inspection of Fig. 4b confirms the similarity of the distributions of the local fibre volume fractions for the real and synthetic microstructures.

$$V_f = \frac{S_{all\_fibres} * f}{S_{all\_pixels}} \quad (2)$$

Where S_{all_fibres} is the sum of the number of pixels belonging to all fibres with pixel value equal to 255, and S_{all_pixels} is the sum of the number of all pixels, which is also equal to the image size.

4. Conclusions

We implemented a DCGAN model to generate realistic 2D transverse microstructures of unidirectional fibre-reinforced composites. The synthetic microstructures were verified versus the real microstructure in term of visual appearance and fibre statistical characteristics. This is a necessary step for the application of GAN-synthetic microstructures in future studies. Future work will expand this generator to 3D and will automate the creation of finite element models based on the synthetic images.

5. Acknowledgements

For provision of the synchrotron CT data, we kindly acknowledge I. Sinclair, M. N. Mavrogordato and E. Schöberl from University of Southampton μ-VIS lab. The related synchrotron experiment was conducted at ESRF ID19 with the help of L. Helfen. R. Guo would like to acknowledge his PhD scholarship from China Scholarship Council (202006430010). M. Mehdikhani would like to acknowledge his FWO Postdoc Fellowship, project ToughImage (1263421N). C. Breite would like to acknowledge FWO for the funding of his Postdoctoral Fellowship project COCOMI (1231322N).

6. References

[1] Biswal A, Swain SK. Smart composite materials for civil engineering applications. Elsevier Ltd; 2020. https://doi.org/10.1016/b978-0-08-103013-4.00011-x.

[2] Pyrz R. Quantitative description of the microstructure of composites. Part I: Morphology of unidirectional composite systems. Compos Sci Technol 1994;50:197–208. https://doi.org/10.1016/0266-3538(94)90141-4.

[3] Melro AR, Camanho PP, Pinho ST. Generation of random distribution of fibres in long-fibre reinforced composites. Compos Sci Technol 2008;68:2092–102. https://doi.org/10.1016/j.compscitech.2008.03.013.

[4] Yang L, Yan Y, Ran Z, Liu Y. A new method for generating random fibre distributions for fibre reinforced composites. Compos Sci Technol 2013;76:14–20. https://doi.org/10.1016/j.compscitech.2012.12.001.

[5] Huang F, Pang X, Zhu F, Zhang S, Fan Z, Chen X. Transverse mechanical properties of unidirectional FRP including resin-rich areas. Comput Mater Sci 2021;198:110701. https://doi.org/10.1016/j.commatsci.2021.110701.

[6] Sharifpour F, Montesano J, Talreja R. Micromechanical assessment of local failure mechanisms and early-stage ply crack formation in cross-ply laminates. Compos Sci Technol 2022;220:109286. https://doi.org/10.1016/j.compscitech.2022.109286.

[7] Mosser L, Dubrule O, Blunt MJ. Stochastic reconstruction of an oolitic limestone by generative adversarial networks 2017:1–22.

[8] Mosser L, Dubrule O, Blunt MJ. Reconstruction of three-dimensional porous media using generative adversarial neural networks. Phys Rev E 2017;96. https://doi.org/10.1103/PhysRevE.96.043309.

[9] Gayon-Lombardo A, Mosser L, Brandon NP, Cooper SJ. Pores for thought: generative adversarial networks for stochastic reconstruction of 3D multi-phase electrode microstructures with periodic boundaries. Npj Comput Mater 2020;6:1–11. https://doi.org/10.1038/s41524-020-0340-7.

[10] Hsu T, Epting WK, Kim H, Abernathy HW, Hackett GA, Rollett AD, et al. Microstructure Generation via Generative Adversarial Network for Heterogeneous, Topologically Complex 3D Materials. Jom 2021;73:90–102. https://doi.org/10.1007/s11837-020-04484-y.

[11] Radford A, Metz L, Chintala S. Unsupervised representation learning with deep convolutional generative adversarial networks. ICLR 2016:1–16.

[12] Breite C, Gorbatikh L, Lomov S V, Swolfs Y. Automated image analysis of ultrafast synchrotron CT scans to experimentally characterize the fibre break development during in-situ tensile tests. ICCM22 22nd Int Conf Compos Mater Melb 2019.

[13] Goodfellow I, Pouget-Abadie J, Mirza M, Xu B, Warde-Farley D, Ozair S, et al. Generative adversarial networks. NIPS 2014. https://doi.org/10.1145/3422622.

[14] Tran N, Tran V, Nguyen N, Nguyen T, Cheung N-M. On Data Augmentation for GAN Training. IEEE Trans Image Process 2021;30:1882–97.

[15] Mesquita F, Bucknell S, Leray Y, Lomov S V., Swolfs Y. Single carbon and glass fibre properties characterised using large data sets obtained through automated single fibre tensile testing. Compos Part A Appl Sci Manuf 2021;145:106389. https://doi.org/10.1016/j.compositesa.2021.106389.

[16] Emerson MJ, Dahl VA, Conradsen K, Mikkelsen LP, Dahl AB. Statistical validation of individual fibre segmentation from tomograms and microscopy. Compos Sci Technol 2018;160:208–15. https://doi.org/10.1016/j.compscitech.2018.03.027.

PREDICTION OF MECHANICAL BEHAVIOR OF WOVEN COMPOSITE VIA DEEP NEURAL NETWORK

Dug-Joong, Kim[a], Jeong-Hyeon, Baek[a], Gyu-Won, Kim[a] and Hak-Sung, Kim[a,b]

a: Department of Mechanical Engineering, Hanyang University, Republic of Korea
b: Institute of Nano Science and Technology, Hanyang University, Republic of Korea
– kdj9207@gmail.com

Abstract: *The mechanical behavior of CFRP was trained by deep-neural-network (DNN). For an accurate analysis of composite properties, micromechanics of failure based multi-scale simulation method was introduced for progressive damage analysis of composite materials. The meso-scale and micro-scale representative volume was used for multi-scale simulation, and stress transfer between meso-micro scale model, was performed by applying stress amplification factor (SAF). With the developed simulation method, stress-strain curves of CFRP were derived depending on constituent properties and yarn structures. The databases of mechanical behavior were trained by deep-neural-network, which use stress-strain curves as training output, and mechanical, geometrical properties as training input, respectively. As a result, mechanical behavior of CFRP could be predicted by the developed method in a very fast time with high accuracy.*

Keywords: Carbon fiber-reinforced plastics (CFRP); Finite-element-method (FEM); Deep-neural-network (DNN); Deep-learning;

1. Introduction

In recent years, carbon fiber reinforced plastics (CFRP) have been widely used in many fields such as automotive, aerospace, sports and marine due to their superior mechanical properties. Particularly, woven composites, which have weaving patterns along warp and weft directions, have got increasing attention due to their high out-of-plane stiffness, toughness and manufacturability. In order to design and fabricate reliable and superior structures with woven composite materials, it is important to analyze and predict the mechanical properties of them. However, it is hard to predict the mechanical properties because of their complex structures and many factors affecting mechanical behavior such as volume fraction, modulus and strength of their constituents (fiber and matrix). In recent years, finite element method (FEM) has been investigated and developed to predict mechanical behavior of composite structures [1-3]. These methods have been cost-effective and promising method with high reliability because the mechanical properties of composite could be predicted without experimental method. Although many FEM methods have been developed, it is still hard and costly because many simulations were demanded to predict each case which have a lot of variables. Moreover, complicated processes to set up simulation model by expert engineer is required to obtain reliable simulation result. In this study, the deep-neural-network (DNN) based prediction method to predict stress-strain curves of woven CFRP was developed. The DNN was trained by a lot of data from multi-scale simulations of composite. For multi-scale simulations, the micro-mechanics failure criteria, which analyze failure of fiber and matrix respectively, was applied to simulate damage accumulation of composite. Also, the stress amplification factor (SAF) was applied to connect

  doi:10.5075/epfl-298799_978-2-9701614-0-0

micro and meso-scale stresses. To gather database of multi-scale simulation, simulation results were obtained depending on mechanical properties of constituents (fiber and matrix), and structures of fiber yarns (width, space and thickness of fiber bundle). Then, the databases were trained by deep-neural network. The structures and mechanical properties of fiber and matrix were used as training input and several points on tensile stress-strain curves were used as training output. As a result, the mechanical behavior of CFRP depending on constituents properties and yarn structures was successfully predicted by developed neural network. In addition, it is expected that the compressive and shear behavior can be also predicted by similar method (FEM trained DNN) by training additional data of compressive and shear tests simulations. Moreover, other composite structures having a various kind of weaving pattern (twill, satin and etc.) will be trained by developed approaches.

2. Multi-scale simulation based on micro-mechanics failure

2.1 Multi-cale simulation using SAF

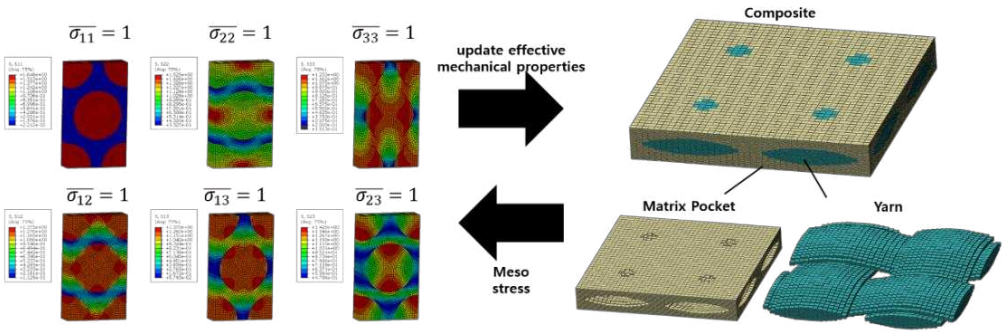

Figure 1. Stress transfer between meso-scale and micro-scale representative volume element

In this study, multi-scale simulation of CFRP was conducted by commercial FEM software ABAQUS. The correlation of stresses between meso-scale and micro-scale was performed as shown in Fig. 1. The meso-scale stresses were transferred to micro-scale by using stress amplification factor (SAF) as following Eq. (1):

$$\sigma_{micro} = M\sigma_{meso} \tag{1}$$

where, σ_{micro}, σ_{meso} and M are the micro-scale stress, meso-scale stress, and the SAF, respectively. For meso- and micro-scale simulation, the reperesentative volume element (RVE) were modelled as shown in Fig. 1, which express the unit structures of textile and tow, respectively. In sequence, the periodic boundary conditions were applied to describe the six normalized stress conditions with following Eq. (2) [4] :

$$u_i^{j+}(x,y,z) - u_i^{j-}(x,y,z) = c_i^j \tag{2}$$

where, pair of u indicate the displacement of one pair of nodes set of opposite boundary surfaces and i, j indicates the normal direction of boundary surfaces, respectively.

2.2 Micromechanics of failure

After stress transformation, the respective failure criteria were adopted for each constituent (fiber and matrix), respectively. For the matrix, a modified von Mises criteria was used as following eq. (3) and (4):

$$\frac{\sigma_{mises}^2}{T_{matrix}C_{matrix}} - (\frac{1}{T_{matrix}} - \frac{1}{C_{matrix}})I_1 = 1 \quad (3)$$

$$\sigma_{mises}^2 = I_1^2 - I_2^2 \quad (4)$$

Where, σ_{mises}, I_1 and I_2 are the von Mises stress, first stress invariant and second stress invariant, respectively. T_m and C_m indicate the tensile and compressive strength respectively.

Above equations is same with the equivalent stress reaching the function of tensile stresses as follows:

$$\sigma_{eq} = \frac{(\beta-1)I_1 + \sqrt{(\beta-1)I_1^2 + 4\beta\sigma_{VM}^2}}{2\beta} = k_m T_m \quad (5)$$

where, k_m is the matrix failure index and β is the ratio of compressive to tensile strength of matrix. Finally, the matrix gradually decreased with the damage progression as following eq. (6).

$$D_m = \begin{cases} 1 - \exp(\gamma - \gamma k_m) \ (1 < k_m < \alpha) \\ 0.99 \ (k_m > \alpha) \end{cases} \quad (6)$$

By applying matrix damage factor, the damage of matrix has been gradually progressed and finally reached the final rupture.

For the fiber, a maximum longitudinal stress failure criterion was used as the fiber have the brittle properties. Therefore, when the k_f was larger than a certain level, the fiber failed completely and stiffness degradation occurred as depicted in eq. (7) and eq. (8).

$$D_f = \begin{cases} 0 & (k_f < 1) \\ 0.99 & (k_f > 1) \end{cases} \quad (7)$$

$$k_f = \frac{T_f}{\sigma_{f11}} \quad (8)$$

where, k_f, T_f, and σ_{f11} are the fiber failure index, fiber tensile strength and micro stresses of fiber in the longitudinal direction.

3. Deep-neural-network for training multi-scale simulation

3.1 Database of multi-scale simulation

With the developed multi-scale simulation method, database was constructed depending on various factors affecting mechanical behavior of composites. To obtain huge amount of simulation results, the simulation was automated by python script code. The input files of ABAQUS were automatically generated and result extraction was followed. Tensile stress-strain curves were obtained depending on geometrical factors (yarn width, space and thickness) and mechanical properties of constituents. The value of geometries and mechanical properties were randomly sampled as shown in Table. 1. The range of parameters were determined according to commercial fiber, matrix and CFRP products.

Table 1: Range of mechanical and geometrical parameters

Properties	Range of properties

  doi:10.5075/epfl-298799_978-2-9701614-0-0

Mechanical Properties	Modulus of fiber [GPa]	50~300
	Tensile strength of fiber [GPa]	2~7
	compressive strength of fiber [GPa]	2~7
	modulus of matrix [GPa]	2~4
	tensile strength of matrix [MPa]	40~120
	compressive strength of matrix [MPa]	60~240
Geometrical parameters	volume fraction of yarn [%]	55~80
	yarn width [mm]	1.0~5
	yarn space [mm]	1.05~8
	yarn thickness [mm]	0.12~0.6

2.2 Deep-learning of multi-scale simulation

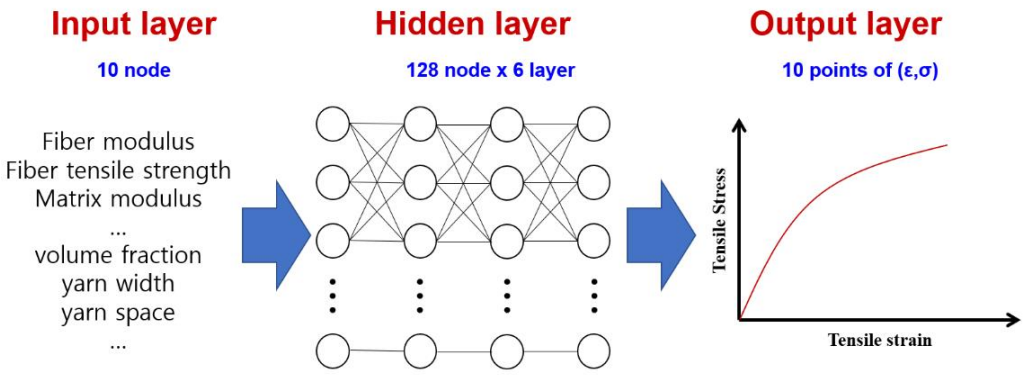

Figure 2. Schematic of Deep-neural-network

The multi-scale simulation results were trained by deep neural network (DNN). DNN, of which structure is similar to the biological brain of human, trained the relationship between input and output of the network. The network consists of several layers of neurons and they transfer signals between each other. DNN for training multi-scale simulation was composed of input layer, hidden layer and output layers as shown in Fig. 2. In this work, mechanical and geometrical parameters in Table. 1 were used as training input. These parameters are transferred through several hidden layers and finally derive the output parameters. The 10 points of stress-strain curves were used as output parameters. In hidden layers, signals are calculated with the bias and weight of each neuron as following Eq. (9):

$$y = \sum_{k=1}^{n} w_k x_k + b \quad (9)$$

where, x and y are the input and output of each neuron. w_k and b indicates the weight and bias of neurons. The w and b are optimized to maximize the R^2 value by back propagation algorithm [5]. The 5,000 data-sets were obtained and used for training DNN. Finally, the random stress-strain curve was predicted and generated with the developed DNN with non-trained random input parameters (geometries and mechanical properties).

  doi:10.5075/epfl-298799_978-2-9701614-0-0

4. Results and Discussion

Tensile stress-strain curves from both multi-scale simulation and DNN are shown in Fig. 3. The tensile behaviors were predicted based on three random cases of input parameters (geometries and parameters) in Table 2, and compared with results of FEM. The DNN successfully predicted the stress-strain curves of CFRP which have any kinds of input variables.

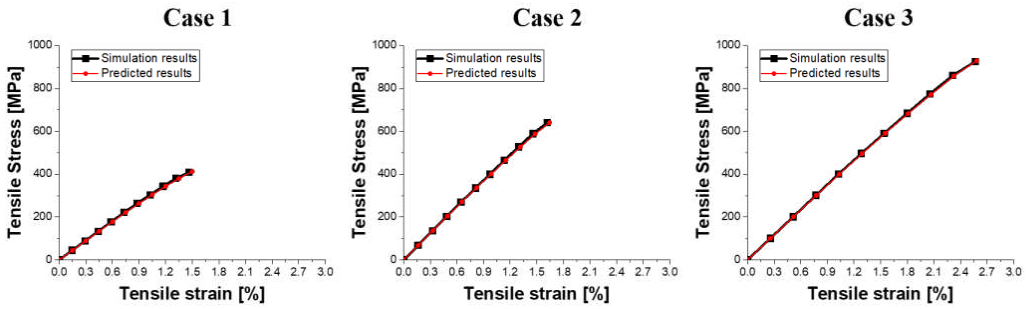

Figure 3. Schematic of Deep-neural-network

Table 2: Random input parameters for DNN

Properties	Input parameters		
	Case 1	Case 2	Case 3
Modulus of fiber [GPa]	220	270	245
Tensile strength of fiber [GPa]	3.5	4.7	6.7
compressive strength of fiber [GPa]	2.7	4.6	6.0
modulus of matrix [GPa]	3.8	2.1	2.4
tensile strength of matrix [MPa]	80	50	75
compressive strength of matrix [MPa]	130	90	135
volume fraction of yarn [%]	55	75	60
yarn width [mm]	2.8	2.5	3.3
yarn space [mm]	3.8	4.2	3.9
yarn thickness [mm]	0.5	0.25	0.35

In addition, the training process are shown in Fig. 4. The training was progressed until 1000 epochs, where the loss does not decrease (Fig. 4(a)). Fig. 4(b) shows the predicted results of stress-strain points at each epoch. After the 1000 epoch, the network started to capture the tendency of stress behavior. Finally, the DNN predicted the stress-strain curves that highly correlated with true data (simulation result) at final epoch 1000.

5. Conclusion

Conclusively, the FEM trained deep neural network successfully predicted the mechanical behavior of composite material. It has high accuracy and require only a few seconds to predict any kinds of composite with various structures and properties. As a

  doi:10.5075/epfl-298799_978-2-9701614-0-0

result, it is expected to expend to predict behavior of other kinds of materials with different type of structures such as twill and satin.

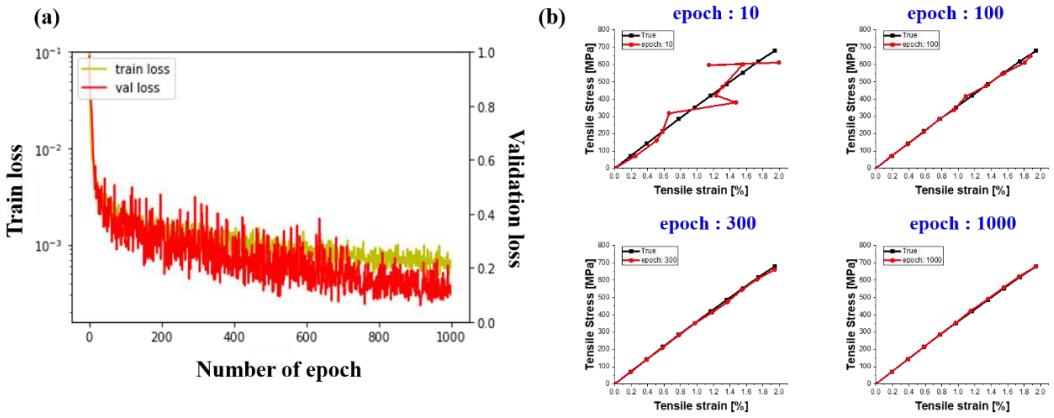

Figure 4. Schematic of Deep-neural-network

Acknowledgements

This work was supported by Korea Institute of Energy Technology Evaluation and Planning(KETEP) grant funded by the Korea government(MOTIE)(20212020800090, Development and Demonstration of Energy-Efficiency Enhanced Technology for Temperature-Controlled Transportation and Logistics Center). This work was supported by Korea Institute of Energy Technology Evaluation and Planning(KETEP) grant funded by the Korea government(MOTIE)(20202020800360, Innovative Energy Remodeling Total Technologies(M&V, Design, Package Solutions, and Testing & Verifications Technologies) for the Aging Public Buildings)

6. References

1. Ha SK, Jin KK, Huang Y. Micro-mechanics of failure (MMF) for continuous fiber reinforced composites. Journal of Composite materials. 2008;42(18):1873-95.Sims FA. Applications of resins in bridge and structural engineering. International Journal of Cement Composites and Lightweight Concrete 1985; 7:225-32.
2. Hwang Y-T, Choi K-H, Kim J-I, Lim J, Nam B, Kim H-S. Prediction of non-linear mechanical behavior of shear deformed twill woven composites based on a multi-scale progressive damage model. Composite Structures. 2019;224:111019.
3. Xu L, Huang Y, Zhao C, Ha SK. Progressive failure prediction of woven fabric composites using a multi-scale approach. International Journal of Damage Mechanics. 2018;27(1):97-119.
4. Xia Z, Zhang Y, Ellyin F. A unified periodical boundary conditions for representative volume elements of composites and applications. International journal of solids and structures. 2003;40(8):1907-21.
5. Hecht-Nielsen R. Theory of the backpropagation neural network. Neural networks for perception: Elsevier; 1992. p. 65-93.

  doi:10.5075/epfl-298799_978-2-9701614-0-0

GENERATION OF DESIGN ALLOWABLES ON THE OPEN HOLE TENSILE STRENGTH OF COMPOSITE LAMINATES USING SENSITIVITY ANALYSIS AND UNCERTAINTY QUANTIFICATION FRAMEWORK

Aravind Sasikumar[a], Joan Ninyerola[a], Ivan Ruiz[a], Miguel Bessa[b], Albert Turon[a]

[a]AMADE, Polytechnic school, University of Girona, Campus Montilivi s/n 17071, Girona, Spain
[b]Department of Materials Science and Engineering, Delft University of Technology, 2628 CD Delft, The Netherlands

Abstract: *Aeronautical industries are concerned about the cost effective generation of design allowables for composite laminates. Design allowables take into account the variabilities arising from different sources (material, manufacturing, defects etc.,) which are determined using expensive and time consuming experimental campaigns. For rapid certification and costs reduction, it is of high interest for the aeronautical industries to use high fidelity numerical models to compliment the testing. In this work, we use a high fidelity numerical model to simulate open hole tension (OHT) of composite laminate, followed by an efficient global sensitivity analysis and uncertainty quantification and management framework to generate design allowables. In a first step, Morris sensitivity analysis is used to screen the sensitive input material properties that affect the OHT strength. In the second step, machine learning technique is used to create a surrogate model, which is used to obtain the B basis design allowable on the OHT strength.*

Keywords: Design allowables, Virtual testing, Sensitivity analysis, Machine learning, Uncertainty quantification and propagation

1. Introduction

Aeronautical industries confront the challenge of accounting for the various uncertainties related to composite material response. Uncertainties related to composite materials can arise from material properties, manufacturing processes, test setup, specimen geometry, loading conditions, manufacturing defects etc., and need to be quantified to evaluate their influence on the structural performance. Hence, uncertainty quantification and management (UQ&M) approach is used to provide the variability from each input parameter and provide the design allowables on the output (for e.g., strength of the laminate), which adds confidence and robustness to the design and certification process. Contrary to the conventional method of obtaining design allowables through extensive experimental campaigns, industries have started to supplement the experimental tests with virtual tests using high fidelity numerical models that can predict with good accuracies, and also reduces the recurring and non-recurring costs, thereby leading to cost efficient and shorter certification processes.

The failure strength of a laminate depends on the material properties of the fiber-matrix system, laminate configuration, specimen geometry etc. Material properties account to the elastic, strength and fracture properties of both fiber and matrix and the variability in these material properties can significantly affect the structural response of the laminate. To quantify the variability associated to each material property, a statistical distribution of the property is

  doi:10.5075/epfl-298799_978-2-9701614-0-0

obtained through experimental testing. Here it is beneficial to screen the sensitive material properties that affect the output, where the identified sensitive parameters can be well characterized experimentally by testing more specimens and thereby obtaining a better statistical distribution.

Global sensitivity analysis has been widely applied over different fields with the idea of identifying the key input parameters that affect the output. Variance based methods are suitable for non-linear complex models but with the drawback of high computational costs. Screening based method is optimum for models demanding high computational cost since these methods require less model evaluations, but with the drawback of providing only qualitative effects. Different authors [1, 2] have performed local sensitivity analysis to identify the key material properties that affects the open hole strength, impact delamination area etc., where the identified sensitive parameters where used to build a response surface for the calculation of the design allowables using UQ&M approach [2].

Recent advances on machine learning has made its way into the virtual testing of composite materials, where the computational expensive numerical simulations can be represented by surrogate models that can predict the response at a relatively cheaper cost [3]. At first, an input test matrix is created using a sampling approach from a defined design space and further, using FEM simulations the output data is generated. This obtained data is used for training and testing the surrogate model using a defined approach. Different machine learning techniques such as Gaussian Process, Random Forest, Artificial neural network have gained prominence towards the building of surrogate models.

In this paper, we aim to define a framework to generate the design allowables on the open hole tensile strength of composite laminate, taking into account of the variability in the material properties. At first, we define a cheap and efficient global sensitivity analysis based on 3D FE numerical model where we identify the sensitive material properties that influence the OHT strength from a total of 21 input material properties. Further, a surrogate model is created from a design space where only the sensitive material properties are varied, where the other parameters are kept constant at their mean values. Gaussian process was used to build the surrogate model, where the relation between the R score and the number of FE simulations required was studied. Once an accurate model was generated, this was employed to estimate the B basis design allowable using the Monte Carlo approach, and was also compared with the Composite Material Handbook 17 (CMH17) [8] approach.

2. Methodology

2.1 Numerical model

We used a mesoscale FE model to simulate the open hole tensile response, where Abaqus/Explicit [6] 3D solid elements (C3D8R) were used to model the plies. The interfaces were modeled using Abaqus finite thickness cohesive elements (COH3D8) [ref]. Progressive intra-ply damage was accounted for with the continuum damage model proposed by Maimi et al. [4,5] The damage activation functions are based on LARC04 failure criteria. The intralaminar model was implemented in a VUMAT user-written subroutine. An intralaminar element was deleted once the fiber damage variable (d1) reached 1. A uniform in-plane element size of 0.5 mm was used for all the elements (both inter and intralaminar) throughout the study. Each ply was modeled as a solid layer with one element through the ply thickness, while the thickness of the

  doi:10.5075/epfl-298799_978-2-9701614-0-0 published under CC BY-NC 4.0 license

cohesive elements was set to 0.01 mm as recommended in the Abaqus documentation. Tensile load was introduced by applying a pre-de displacement at one of the specimen edges while keeping the other edge constrained.

The laminate modeled is a quasi-isotropic laminate with 24 plies of 0.131 mm per ply. The nominal thickness is 3.12 mm and the hole diameter is selected as 2 mm with the in-plane dimensions of 12 mm (width), 24 mm (length) and maintaining a with-to-diameter ratio of 6. The selected material is IM7/8552 and the FE model considers 21 material properties that includes the elastic, strength and fracture properties of both fiber and matrix.

2.2 Sensitivity analysis

In this work, we used the Morris One-At-a-Time (MOAT) [7] screening based sensitivity analysis in order to filter the key material properties. In each model evaluation, only one input parameter is varied at a time and is varied across a selected *p* levels in the grid space. An elementary effect is calculated which provides the ratio of the change in the model output to the input parameter variation. Morris provides two sensitivity measures: μ*, which provides the overall influence of the input parameter on the output, and σ, which assesses the non-linear or interaction effect of that input parameter with the rest of the parameter. MOAT uses hyper parameters such as p and r which are denoted as the number of levels in the design grid space and the number of repetitions/trajectories, respectively. All the input material properties follow a normal distribution and are varied within ±3 standard deviations for the creation of the input matrix of the sensitivity analysis. We used Morris hyper parameters p=16 and r =20 (defined through a preliminary study) and with 21 material properties, this leads to a total of 440 FE simulations.

2.3 Metamodel and UQ&M

Latin hypercube sampling (LHS) approach (with max_min criteria) is used for design of experiments, where the identified sensitive material properties from the previous step are the input parameters. The material properties were varied within ±3 standard deviations from their mean value, and the LHS sampling with a 75% of the total samples following a uniform distribution and the remaining 25% following a normal distribution. This will ensure that there are more sample points added to the tail of the normal distribution. An input matrix of 2000 samples (varying the sensitive material properties) was created and then subjected to virtual testing to obtain the OHT strengths. With this data generated, a Gaussian process regression was performed with a train to test ratio of 0.75. This was performed progressively for different number of simulations to obtain the dependence of R score with respect to the number of simulations required. Once an accurate model was obtained, the B basis design allowable was calculated using two approaches: (a) CMH17 [8] approach (b) Monte Carlo simulations (MCS) of n samples to obtain the 10th percentile Empirical Cumulative Distribution Function (ECDF), followed by repeating the process N times and then obtaining the B value as the 5th percentile of the ECDF of the N 10 percentiles.

3. Results and Discussion

3.1 Morris sensitivity analysis

Figure 1 (a) presents the Morris μ* vs σ plot for the 21 material properties and Figure 1(b) presents the μ* values along with 95% confidence interval obtained from bootstrapped

  doi:10.5075/epfl-298799_978-2-9701614-0-0

resampling. Material properties placed on the right top are considered as the sensitive parameters that have a high μ* and σ values. Fiber longitudinal tensile strength (XT), fiber tensile fracture toughness (GXT), mode II interlaminar fracture toughness (GIIC) and fiber tensile cohesive law parameters (fXT and fGT, ratios of XT and GXT in the first branch of the cohesive law) are the sensitive parameters identified through Morris approach.

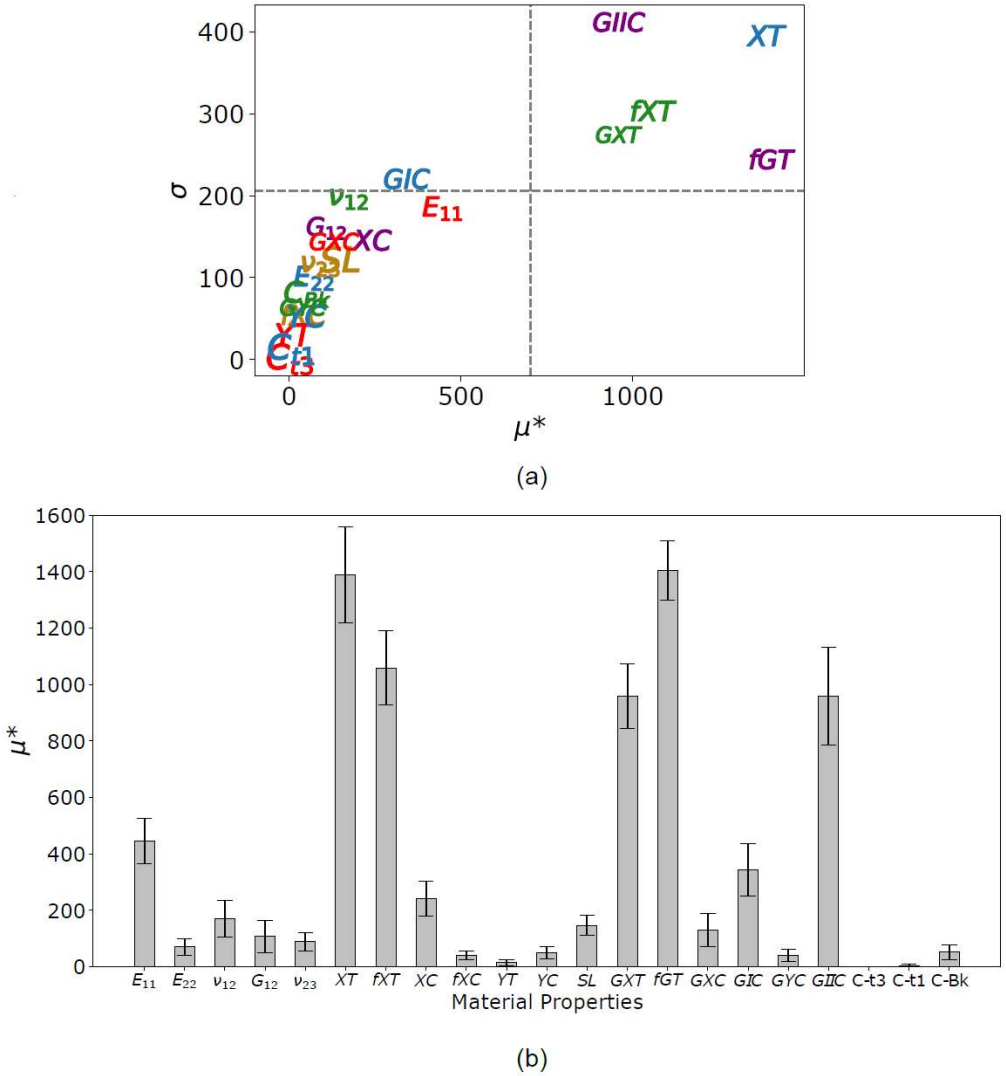

Figure 1. (a) Morris sensitivity analysis results (p=16, r=20) and (b) Morris plot with 95% confidence interval on the absolute mean values obtained through bootstrapped re-sampling.

3.2 Metamodel and Design allowable

As mentioned before, a total of 2000 OHT simulations were performed, where the input matrix was obtained through Latin hypercube sampling (LHS) of the above-mentioned five sensitive material properties. Once the OHT strengths were obtained, this data is used for training the metamodel. The evolution of R score with respect to the number of samples (simulations) was performed as shown in Figure 2. For example, 100 samples (input matrix as well as the OHT strengths) were selected randomly out of the total 2000 samples available. Out of this 100, 75 samples were used to train the model and 25 for the test, which will provide a R score. This

process was repeated 100 times, which thus provides 100 R scores and hence Figure 2 shows a box plot of the R-scores for different number of samples selected (ranging from 100 to 2000). Figure shows that the even with a low a number of samples, a good prediction is obtained with an R score more than 0.95. With increased number of samples, the bounds of the R-score keep decreasing (except for the last case).

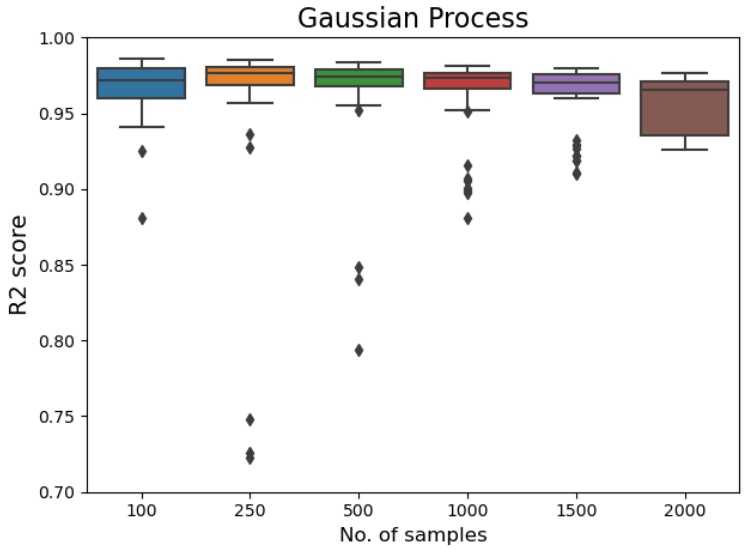

Figure 2. Box plot of the metamodel R-score for increasing number of samples

To estimate the design allowables, two approaches are used. First one is to use the metamodel and perform Monte Carlo simulations (MCS). Here, metamodel built from a sample size of 200 was selected (from Figure 2) and using this metamodel, MCS were performed. At first, MCS of n samples were performed to obtain the 10th percentile Empirical Cumulative Distribution Function (ECDF), followed by repeating this process N times and then obtaining the B value as the 5th percentile of the ECDF of the N 10 percentiles. Figure 3 shows the B value obtained using metamodel and the MCS approach represented using the black dashed line, with $N=10^3$ and $n=10^5$.

In addition, this B value is compared with the CMH17 approach, where the mean and standard deviation of the n samples can be used to calculate the B value (following the guidelines in the Composite Material Handbook 17). Figure 3 shows the B value obtained from the CMH17 approach for different number of samples. For example, for 100 samples case, 100 OHT strengths are randomly selected out of the 2000 simulations to obtain one B value, and this process is repeated 100 times, which provides the box plot of the B value for each case. With increasing number of samples/simulations, the B basis value increases. For a lower number of samples, it provides a conservative B value in contrary to increasing the number of samples. Hence, it's important to find a balance in the approach to have a reasonable computational time and not to have a very low or conservative B basis value.

  doi:10.5075/epfl-298799_978-2-9701614-0-0

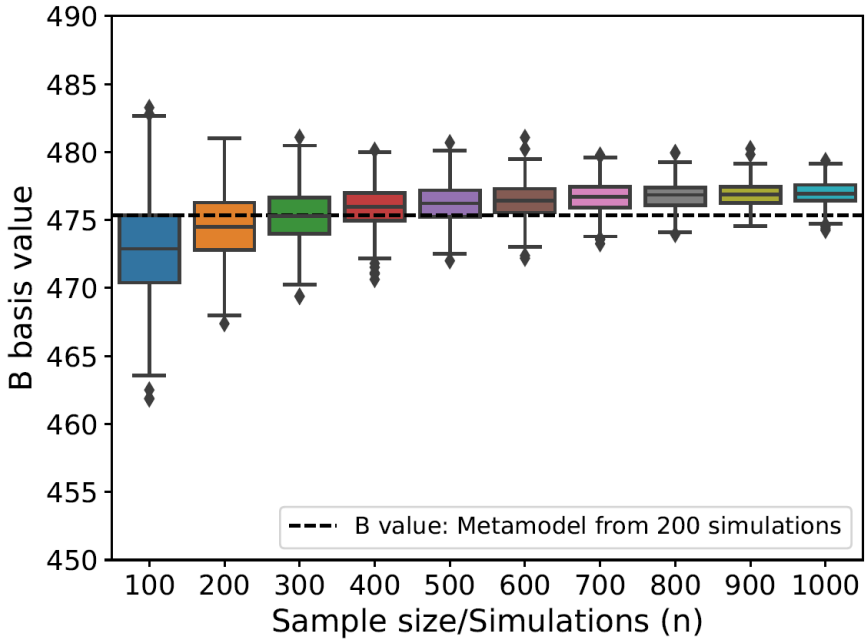

Figure 3. Box plots of B basis values (using CMH17 approach) for n simulations, whereas the dashed line represents the B value obtained from the Monte Carlo simulations of the metamodel (from 200 samples)

4. Conclusion

Aeronautical industries are trying to quantify the various uncertainties associated with composite materials response. Within the framework of uncertainty quantification and management (UQ&M), industries aim to obtain statistical design allowables for different composite tests to quantify the confidence on the design & certification process and structural performance. In this aspect, we propose a framework of sensitivity analysis followed by UQ&M approach to estimate the design allowable on the open hole tensile strength accounting for the uncertainty from the material properties. Morris sensitivity analysis method identified five sensitive material properties out of 21 properties that are influencing the open hole strength. Further to estimate the design allowable on the open hole tensile strength, two approaches were used where the first one is to build a surrogate model (accounting for the variability of the sensitive material properties identified) and compute the B basis value using Monte Carlo simulations, and the second one to use the Composite Military Handbook approach. The results are compared and it is observed that for a low number of samples, CMH approach provides a conservative B value and on the other hand using metamodel approach, there has to be a balance on the computational time required for the creation of the metamodel, which depends on the test case. This proposed framework can help to estimate design allowables, where the experimental tests can be complimented by virtual testing and leading to a more robust and cost efficient designs and more importantly helping to achieve rapid certification processes.

  doi:10.5075/epfl-298799_978-2-9701614-0-0

Acknowledgements

This work has been accomplished within the framework of an ongoing EU Horizon 2020 CleanSky 2 Project TREAL (Thermoplastic material allowable generation using a reliability-based virtual modelling platform). This work has received funding from the Clean Sky 2 Joint Undertaking (JU) under grant agreement No. 864723. The JU receives support from the European Union's Horizon 2020 research and innovation programme and the Clean Sky 2 JU members other than the Union. The project consortium is formed between Amade (University of Girona), University of Porto and MSC-Xstream, with Airbus as the topic manager.

5. References

1. Vallmajó O, Cózar IR, Furtado C, Tavares R, Arteiro A, Turon A, Camanho PP. Virtual calculation of the B-value allowables of notched composite laminates. Composite Structures. 2019 Mar 15; 212:11-21.
2. Cózar, I. R., Turon, A., González, E. V., Vallmajó, O., & Sasikumar, A. (2020). A methodology to obtain material design allowables from high-fidelity compression after impact simulations on composite laminates. Composites Part A: Applied Science and Manufacturing, 139(April), 106069.
3. Furtado C, Pereira LF, Tavares RP, Salgado M, Otero F, Catalanotti G, Arteiro A, Bessa MA, Camanho PP. A methodology to generate design allowables of composite laminates using machine learning. International Journal of Solids and Structures. 2021 Dec 15; 233:111095.
4. Maimí P, Camanho PP, Mayugo JA, Dávila CG. A continuum damage model for composite laminates: Part I–Constitutive model. Mechanics of materials. 2007 Oct 1;39(10):897-908.
5. Maimí P, Camanho PP, Mayugo JA, Dávila CG. A continuum damage model for composite laminates: Part II–Computational implementation and validation. Mechanics of materials. 2007 Oct 1;39(10):909-19.
6. Abaqus, inc, abaqus version 6.14 user manual, simulia, providence, Ri, usa.
7. Morris MD. Factorial sampling plans for preliminary computational experiments. Technometrics. 1991 May 1;33(2):161-74.
8. Composites material handbook 17g. vol. 1 guidelines for characterization of structural materials (2012)

  doi:10.5075/epfl-298799_978-2-9701614-0-0

BAYESIAN CALIBRATION OF A FINITE ELEMENT STIFFENED PANEL MODEL USING EXPERIMENTAL COMPRESSION TEST DATA

Carl Scarth[a], Andrew T. Rhead[a], Richard Butler[a]

a: Materials and Structures Centre, Department of Mechanical Engineering, University of Bath, Claverton Down, Bath, BA2 7AY, UK.
Email: c.scarth@bath.ac.uk

Abstract: *Bayesian calibration is a statistical framework for combining experimental and numerical data to make predictions using computer models, while formally accounting for uncertainty associated with: i) experimental observation error, ii) inaccuracies in the model and assumed physics, and iii) variability in the physical parameters of the test specimen. The ability to accurately quantify such uncertainty will enable certification processes to be better informed by mathematical models and component-level structural tests.*

In this paper, Bayesian calibration is applied to a finite element stiffened panel model implemented in Abaqus, using strain gauge data from experimental compression tests. In this preliminary investigation, the elastic properties of the AS4/8552 prepreg lamina from which the panel was manufactured are inferred. Such parameters cannot be precisely controlled in the experiment during to inherent variability in manufacturing processes. A Gaussian Process Emulator is used in the calibration for the sake of computational efficiency.

Keywords: Model calibration; Finite Element Analysis; Bayesian inference; Uncertainty Quantification; Gaussian Process Emulators

1. Introduction

Certification of composite aerospace structures is currently undertaken via a series of tests of increasing size and complexity known as a “test pyramid”. Empirical knockdown factors based-upon data from coupon tests are used alongside relatively few tests at higher length-scales, leading to conservative strain limits and limiting the benefits of tailoring in composite structures. Over-dependence upon coupon tests may be overcome through virtual testing using mathematical models, with data from both models and component-level tests used to predict structural behaviour. To ensure consistency across datasets in such an approach it is, however, necessary to quantify the effects of myriad sources uncertainty associated with model inputs (e.g. due to defects and features [1], variability in material properties [2]), accuracy of the experimental observations, and discrepancies [3] in the model predictions.

Uncertainty quantification using Finite Element models can be computationally expensive due to the large number of required model evaluations. It is common to use nonparametric regression methods such as Gaussian Processes [4], Quantile Regression [5] or Kernel approaches [6] in place of expensive models. Gaussian Process Emulators are beneficial as these not only make predictions in quantities of interest, but also give a pointwise estimate of uncertainty in these predictions [4,7]. Gaussian processes have, for example, been used in stochastic finite element analysis [8], to model vibration of composite shells [9] and aeroelastic stability of composite plate wings [10] with uncertain material properties, and in preliminary design of aircraft wings with uncertain design parameters [11].

  doi:10.5075/epfl-298799_978-2-9701614-0-0

Bayesian model calibration [12,13] is an approach which enables predictions to be informed by both experimental and numerical data, while formally accounting for numerous sources of uncertainty. This procedure is an inverse problem, the aim of which is to learn about inputs upon which both the mechanical model and physical system depend, but which cannot be controlled or observed in physical experiments. For instance, material properties of test specimens cannot be precisely controlled due to inherent variability in manufacturing processes, and as such it is necessary to learn about material property values associated with specific tests. The approach originally proposed by Kennedy and O'Hagan in [12] and built upon by Higdon et al. in [13], uses Gaussian Process Emulators to efficiently approximate computer models during calibration, and also explicitly incorporates uncertainty due to model discrepancy and observation error.

In this paper, Bayesian model calibration is applied to a Finite Element model of a blade-stiffened composite panel, implemented in commercial software ABAQUS, using historic compression test data from [14]. Strain gauge data taken from a fixed point in the load history are combined with solution data from a (linear) static analysis to learn about the elastic properties of the AS4/8552 prepreg from which the tested panel was manufactured. A Gaussian Process Emulator is fitted to the finite element model for computationally efficiency. This preliminary case study is intended as a simplified demonstration of calibration, which will later be applied to the full experimental dataset and more complex models. The experimental data and model are introduced in Sections 2. and 3. respectively. The calibration methodology is subsequently described in Section 4., and results of the case study presented in Section 5.

2. Experimental Data

Experimental data was taken from compression tests of a blade-stiffened panel previously published in [14]. An image of the panel geometry is shown in Figure 1. The panel was designed to investigate a "Discrete Stiffness Tailoring" concept, wherein strips of prepreg are laid up with varying angle in the transverse direction, resulting in tapered skin thickness.

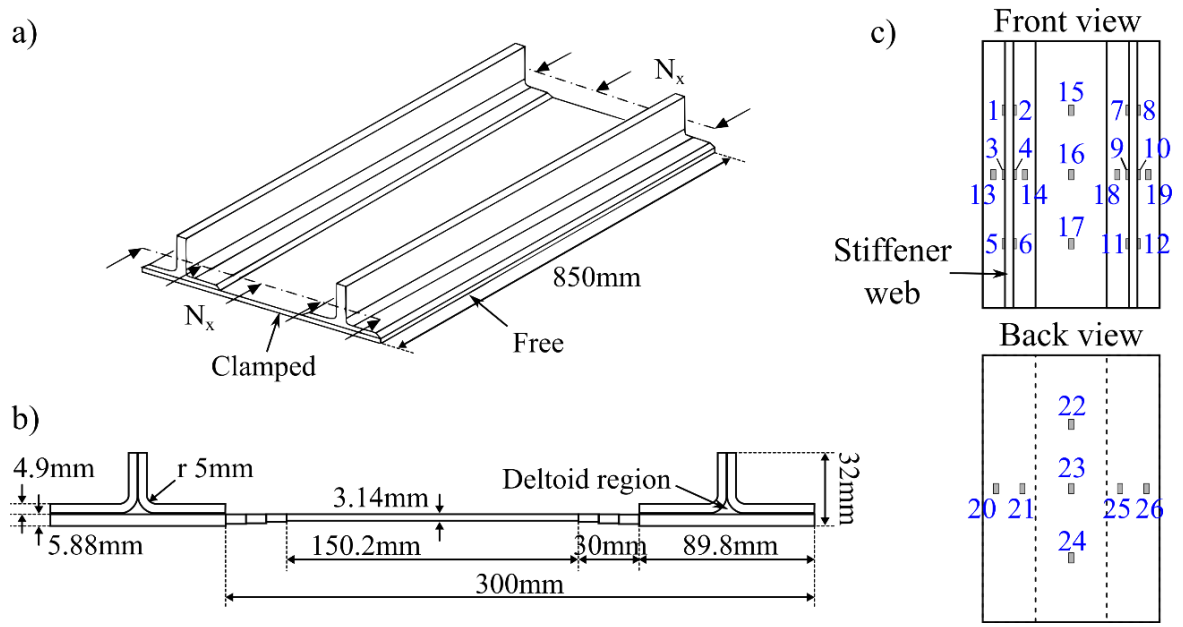

Figure 1: a) Geometry of panel indicating applied load and boundary conditions, b) cross-section dimensions, and c) map of strain gauges bonded to panel.

  doi:10.5075/epfl-298799_978-2-9701614-0-0

Skin and stiffeners were laid up and cured separately, then secondary bonded using Hexcel Redux liquid shim. All components of the panel were manufactured from a Hexcel AS4/8552 prepreg. The panel height, from skin base to web top, was trimmed to 32mm. The panel was potted in 25 mm deep resin blocks at both loading edges to prevent end brooming, resulting in an effective length of 800 mm. For stacking sequences of the different components, the reader is referred to [14]. Compression tests were undertaken using a Dartec 2000 kN testing machine under displacement control, at a rate of 0.4 mm/min. Thirteen pairs of axial strain gauges were used to monitor strain during the test, bonded to the panel surface in accordance Figure 1c). Strain gauges on the stiffener webs are located 3mm from the web tops.

Strain data is illustrated in Figure 2. Across the entire dataset there are 123,040 measurements for each strain gauge, which is more data than can be handled by the calibration framework used in this paper without further processing or thinning. In this preliminary study strain gauge data is extracted for a fixed load of 175kN to reduce the quantity of data; a relatively low load is chosen to enable calibration of a linear model with rapid runtime. Due to noise in the dataset the median strain corresponding to this load is extracted for each gauge.

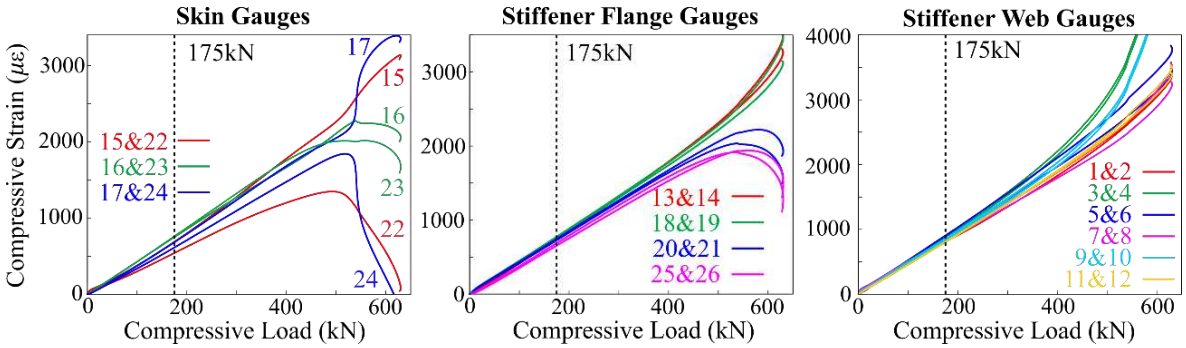

Figure 2: Strain gauge data from the compression test. Gauge numbers are indicated in colour.

3. Model Data

A Finite Element model of the above compression test has been implemented in ABAQUS. To replicate the experiment the two stiffeners and skin are modelled as illustrated in Figure 3. In this preliminary work a (linear) static analysis is undertaken; the approach will be applied in the nonlinear regime in future work. The skin and stiffener are modelled using four node general purpose shell elements (S4R), with three integration points within each ply and a target element size of 5 mm. Bonding of the stiffeners to the skin is simulated using tie constraints. The panel is restrained in all degrees to freedom at one end to achieve a clamped boundary condition, and in all degrees of freedom except longitudinal displacement (u_x) on the loading edge to allow for crosshead displacement, as shown in Figure 3. Longitudinal displacements along this edge are constrained to the same value to ensure that the load of 175kN is uniformly distributed. A Python script is used to output element strains on the outer (front and back) faces of the shells, outputting the component aligned with the longitudinal axis of the panel, ε_x, such that strains are comparable with the strain gauge data. Example strain output is illustrated in Figure 3.

4. Bayesian Calibration Methodology

A univariate, fully Bayesian calibration framework is used in this paper as described in [13], based upon that originally proposed in [12]. In this framework, it is assumed that for a given physical experiment there are n observations of a scalar quantity of interest

  doi:10.5075/epfl-298799_978-2-9701614-0-0

$$y(\boldsymbol{x}_i) = \zeta(\boldsymbol{x}_i) + \epsilon_i, \quad i = 1, \dots, n \tag{1}$$

where $y(\boldsymbol{x}_i)$ is the i^{th} experimental observation, y_i, and $\zeta(\boldsymbol{x}_i)$ is the "true" value of the quantity of interest. This true value cannot be known exactly as all observations are subject to some error, ϵ_i. All observations are grouped into vector $\boldsymbol{y} = \{y_1, \dots, y_n\}^T$. The $\boldsymbol{x}_i$ terms denote the i^{th} setting of some inputs which were controlled in the experiment. In this work, experimental observation y_i is the strain measured by the i^{th} strain gauge and $n = 26$. Each observation is indexed by controlled variable, $\boldsymbol{x} = \{x, y, z\}$, the Cartesian coordinates at which the strain measurement is taken, and $\boldsymbol{x}_i$ contains the centroid coordinates of the i^{th} strain gauge as illustrated in Figure 1c).

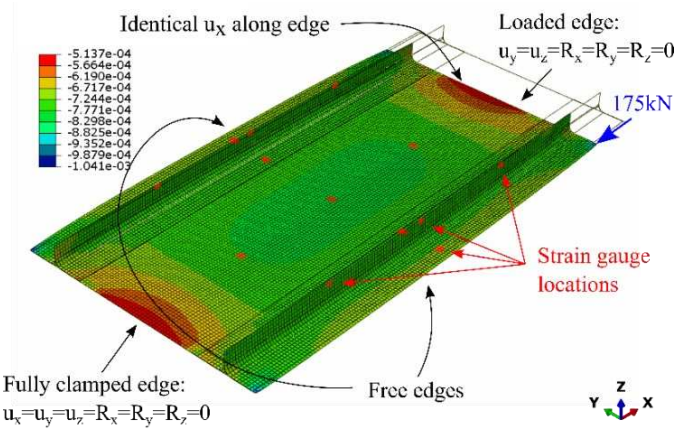

Figure 3 : Example model longitudinal strain output (ε_x) for the first data point, illustrating applied load and boundary conditions

In addition to the experimental data, it is assumed that there are m model output observations,

$$\eta\left(\boldsymbol{x}_j^*, \boldsymbol{t}_j^*\right), \quad j = 1, \dots, m \tag{2}$$

where $\boldsymbol{t}$ denotes a vector of model inputs upon which the physical system also depends, but which were not controlled during the experiment, and $\boldsymbol{x}$ is as used in Eq. (1). $\boldsymbol{x}_j^*$ and $\boldsymbol{t}_j^*$ are the values of $\boldsymbol{x}$ and $\boldsymbol{t}$ used to train the emulator. In this study, $\boldsymbol{t}$ is selected as elastic lamina properties, with $\boldsymbol{t} = \left\{E_{11}, E_{22}, \nu_{12}, G_{12}, G_{23}, t_{ply}\right\}$, containing the longitudinal and transverse moduli, Poisson's ration, in-plane and transverse shear moduli, and ply thickness respectively. These properties were not controlled in the physical experiment due to inherent variability in the prepreg from which the panel was manufactured. Training data were obtained by running the ABAQUS model for 60 different $\boldsymbol{t}_j^*$ settings, selected using Latin Hypercube Sampling, resulting in a total of $m = 2{,}629{,}760$ training data points from all elements, across all simulations. Note that the number of elements varies between simulations due to geometric variations caused by different t_{ply} values. Values of $\boldsymbol{x}_j^*$ are taken as the element centroids, with through-thickness coordinates used for both the outer faces of the shell, matched to the corresponding strain output. These coordinates therefore also have dependence upon t_{ply}.

The purpose of calibration is to learn the values of uncontrolled inputs $\boldsymbol{t}$ in the experiment, and in this application, to learn the elastic properties of the stiffened panel test specimen. The "best" calibrated value of these inputs is denoted $\boldsymbol{\theta}$. The statistical model for each experimental data point, dependent upon these calibrated values, is stated as [12,13]

$$y(\boldsymbol{x}_i) = \eta(\boldsymbol{x}_i, \boldsymbol{\theta}) + \delta(\boldsymbol{x}_i) + \epsilon_i \tag{3}$$

  doi:10.5075/epfl-298799_978-2-9701614-0-0

such that the observed data is given by the model output at the matching coordinate given the calibrated inputs, adjusted by the model discrepancy, $\delta(\boldsymbol{x}_i)$, and observation error, ϵ_i. The model discrepancy accounts for inaccurate or incomplete physics in the model which may explain the differences between model output and experimental data. Following [13], a Gaussian Process Emulator is used in place of the model, with prior distribution

$$\eta(\boldsymbol{x},\boldsymbol{t}) \sim \mathrm{GP}\left(0, c_\eta\big((\boldsymbol{x},\boldsymbol{t}),(\boldsymbol{x}',\boldsymbol{t}')\big)\right) \tag{4}$$

$$\text{where,}\quad c_\eta\big((\boldsymbol{x},\boldsymbol{t}),(\boldsymbol{x}',\boldsymbol{t}')\big) = \frac{1}{\lambda_\eta}\prod_{k=1}^{p_x}\rho_{\eta k}^{4\left(x_k-x_k'\right)^2} \times \prod_{k=1}^{p_t}\rho_{\eta,p_x+k}^{4\left(t_k-t_k'\right)^2}$$

where $\boldsymbol{x}'$ and $\boldsymbol{t}'$ are alternative realisations of $\boldsymbol{x}$ and $\boldsymbol{t}$ which may take different values, and p_x and p_t are the number of dimensions of $\boldsymbol{x}$ and $\boldsymbol{t}$ respectively. Eq. (4) is conditional upon hyperparameters, λ_η, the emulator precision, and $\rho_{\eta k}$, which governs the strength of the dependence upon input k. This covariance function results in a smooth and infinitely differentiable emulator. All inputs are transformed onto the unit hypercube, and outputs scaled to have zero sample mean and unit standard deviation, ensuring that a zero prior mean model is reasonable, and to standardize the magnitude of the correlation parameters. The discrepancy is also modelled as a zero-mean Gaussian process, with dependence only upon $\boldsymbol{x}$ [13]:

$$\delta(\boldsymbol{x}) \sim \mathrm{GP}\big(0, c_\delta(\boldsymbol{x},\boldsymbol{x}')\big) \tag{5}$$

$$\text{where,}\quad c_\delta(\boldsymbol{x},\boldsymbol{x}') = \frac{1}{\lambda_\delta}\prod_{k=1}^{p_x}\rho_{\delta k}^{4\left(x_k-x_k'\right)^2}$$

Following [12], the observation error at each point is assumed to be drawn from identical Gaussian distributions with, $\epsilon_i \sim \mathcal{N}(0, 1/\lambda_\epsilon)$, where λ_ϵ is the precision of the observation error.

Grouping all model output values into a vector, $\boldsymbol{\eta} = \{\eta(\boldsymbol{x}_1^*,\boldsymbol{t}_1^*),\dots,\eta(\boldsymbol{x}_m^*,\boldsymbol{t}_m^*)\}^T$, and combining this with the experimental observations as $\boldsymbol{\mathcal{D}} = \{\boldsymbol{y}^T,\boldsymbol{\eta}^T\}^T$, the first n components of which correspond to inputs $(\boldsymbol{x}_1,\boldsymbol{\theta}),\dots,(\boldsymbol{x}_n,\boldsymbol{\theta})$ and the remaining m components to $(\boldsymbol{x}_1^*,\boldsymbol{t}_1^*),\dots,(\boldsymbol{x}_m^*,\boldsymbol{t}_m^*)$, the likelihood function may be expressed as

$$\mathcal{L}\big(\boldsymbol{\mathcal{D}}\big|\boldsymbol{\theta},\lambda_\eta,\boldsymbol{\rho}_\eta,\lambda_\delta,\boldsymbol{\rho}_\delta,\lambda_\epsilon\big) \propto |\Sigma_\mathcal{D}|^{-1/2}\exp\left\{-\frac{1}{2}\boldsymbol{\mathcal{D}}^T\Sigma_D^{-1}\boldsymbol{\mathcal{D}}\right\} \tag{6}$$

$$\text{where,}\quad \Sigma_\mathcal{D} = \Sigma_\eta + \begin{pmatrix}\Sigma_\delta + 1/\lambda_\epsilon \times I_n & 0\\ 0 & 0\end{pmatrix}$$

where $(n+m)\times(n+m)$ matrix Σ_η is populated by calculating c_η (Eq. (4)) for each pair of inputs in $\boldsymbol{\mathcal{D}}$, $n\times n$ matrix Σ_δ is similarly populated by evaluating c_δ (Eq. (5)) for each pair of experimental inputs, and I_n is the $n\times n$ identity matrix.

The described calibration is an inverse problem, the aim of which is to find distributions in $2(p_x+p_t)+3$ unknown quantities (21 in this example). In a Bayesian approach it is necessary to define distributions which quantify prior beliefs about each quantity. Prior distributions for the statistical model hyperparameters are taken from previously published values [15]. Prior distributions for the material properties are taken from published coupon test data [16,17]. These prior distributions are summarised in Table 1.

The posterior distribution in the unknown parameters is obtained using Bayes' formula as

  doi:10.5075/epfl-298799_978-2-9701614-0-0

$$\pi\left(\boldsymbol{\theta}, \lambda_\eta, \boldsymbol{\rho}_\eta, \lambda_\delta, \boldsymbol{\rho}_\delta, \lambda_\epsilon \middle| \boldsymbol{\mathcal{D}}\right) \propto \mathcal{L}\left(\boldsymbol{\mathcal{D}} \middle| \boldsymbol{\theta}, \lambda_\eta, \boldsymbol{\rho}_\eta, \lambda_\delta, \boldsymbol{\rho}_\delta, \lambda_\epsilon\right) \pi(\boldsymbol{\theta}) \pi\left(\lambda_\eta\right) \pi\left(\boldsymbol{\rho}_\eta\right) \pi(\lambda_\delta) \pi(\boldsymbol{\rho}_\delta) \pi(\lambda_\epsilon) \quad (7)$$

where $\pi(\boldsymbol{\theta})$, $\pi\left(\lambda_\eta\right)$, $\pi\left(\boldsymbol{\rho}_\eta\right)$, $\pi(\lambda_\delta)$, $\pi(\boldsymbol{\rho}_\delta)$ and $\pi(\lambda_\epsilon)$ are prior distributions in the bracketed parameters. There is no closed form expression for Eq. (7) and so this is instead explored using Markov Chain Monte Carlo, undertaken using the No U-turn Sampler (NUTS) in Stan, based upon a modification of the implementation in [15]. It may be noted from Eq. (6) that evaluating the Likelihood requires inversion of a $(n+m) \times (n+m)$ matrix, where $n+m = 2{,}629{,}786$ if all data points are used. To ensure computational efficiency, a subset of 250 model data points is used in the simulation. A space-filling set of points are selected using the maximin package in R.

Table 1 : Details of prior distributions used in the calibration. Parameters of distributions are indicated in brackets under distribution, where COV is the Coefficient of Variation (%), and a and b are shape parameters for a Beta distribution.

Input/Parameter	Distribution	Parameter 1	Parameter 2	Source
E_{11} (GPa)	Gaussian (mean, COV)	115.6 GPa	6	[16]
E_{22} (GPa)	Gaussian (mean, COV)	9.24 GPa	6	[16]
ν_{12}	Gaussian (mean, COV)	0.302	12*	[16]
G_{12} (GPa)	Gaussian (mean, COV)	4.82 GPa	6	[16]
G_{23} (GPa)	Gaussian (mean, COV)	2.959 GPa†	12*	[17]
t_{ply} (mm)	Gaussian (mean, COV)	0.196 mm	10*	[14]
$\rho_{\eta k}, \rho_{\delta k}$	Beta (*a*, *b*)	1.0	0.3	[15]
λ_η	Gamma (shape, scale)	10.0	10.0	[15]
λ_δ	Gamma (shape, scale)	10.0	0.3	[15]
λ_ϵ	Gamma (shape, scale)	10.0	0.03	[15]

5. Preliminary Results

Four chains were used to draw 5000 samples from the posterior distribution described in Eq. (7). Chains were run in parallel, with an average run time of 5995 seconds per chain on a standard laptop. Resulting marginal distributions of the calibration inputs are shown in Figure 4.

Reductions in uncertainty are visible in E_{11} and the ply thickness with updated Coefficients of Variation of 4.4% and 5.4% respectively, and a decrease in the modes to 113.1GPa and 0.19mm respectively, with distributions skewed towards lower values in both cases. Clearly the model over-predicts the panel stiffness compared with the experimental data when using nominal values. There is also a small shift in the distribution of ν_{12} which has a mode of 0.34. Posterior distributions in all other inputs are unchanged by the inference. This result may be explained by examining emulator correlation parameters $\rho_{\eta k}$, which are a measure of the sensitivity of model outputs to a given input. Mean and standard deviations for the parameters which correspond to the calibration inputs are shown in Table 2, wherein values of $\rho_{\eta k}$ near 1 indicate insensitivity to input *k*, and lower values indicate higher sensitivity. The correlation parameters associated with E_{22}, G_{12} and G_{23} are located very close to 1 with low uncertainty, indicating that these inputs are unlikely to affect model output and it may be possible to remove them from the calibration.

* Large Coefficient of Variation used in the absence of published data (higher levels of prior uncertainty).
† Estimated from reference assuming $G_{23} = E_{22}/2(1+\upsilon_{23})$.

  doi:10.5075/epfl-298799_978-2-9701614-0-0

The model is most sensitive to variations in the ply thickness, explaining the more significant reductions in uncertainty in this input. The higher sensitivity to ply thickness may be attributed to the fact that this not only influences laminate stiffness, but also the stiffener geometry and height, noting that this was defined as a fixed value from skin base to web top.

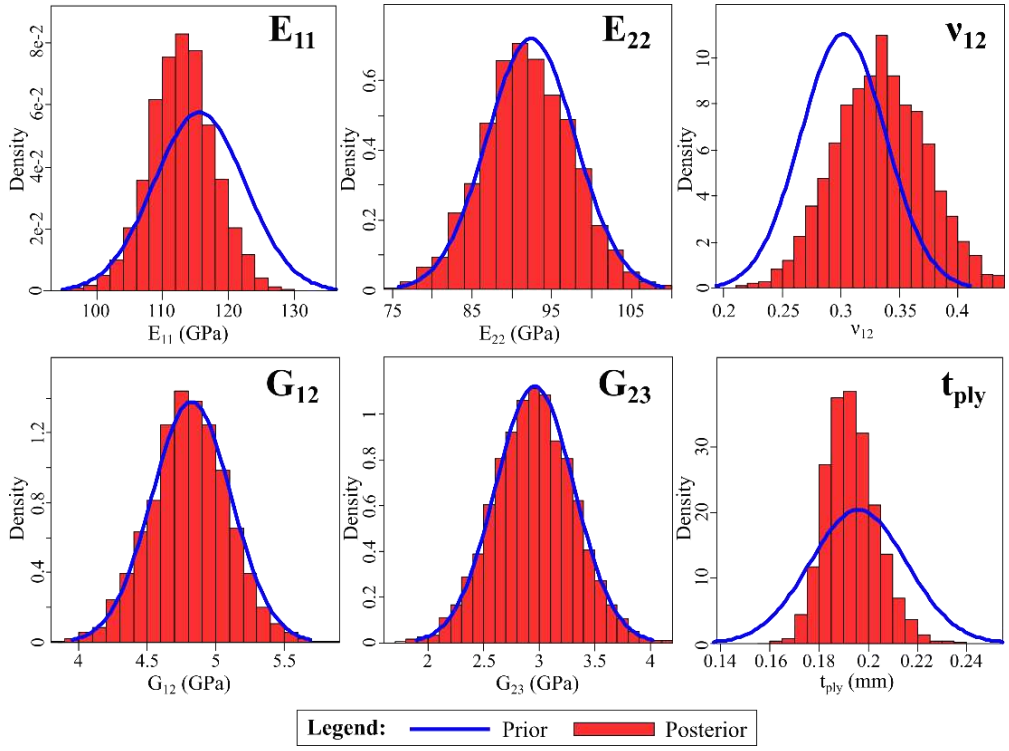

Figure 4. Marginal posterior distributions for the calibration parameters.

Table 2 : Posterior statistics of emulator correlation parameters in the calibration inputs.

	$\rho_{\eta 4}\ (E_{11})$	$\rho_{\eta 5}\ (E_{22})$	$\rho_{\eta 6}\ (\nu_{12})$	$\rho_{\eta 7}\ (G_{12})$	$\rho_{\eta 8}\ (G_{23})$	$\rho_{\eta 9}\ (t_{ply})$
Mean	0.81	1.00	0.99	1.00	1.00	0.74
Standard deviation	0.055	0.002	0.007	0.0008	0.0004	0.069

It is also likely that the lack of updating in E_{22}, G_{12} and G_{23} is due to the experimental data not being sufficiently informative about these inputs, noting that these are longitudinal surface strains measurements, and the properties in which no updating has occurred are resin dominated. This issue may perhaps be overcome by using full-field experimental data such as Digital Image Correlation data from [14]. It is also possible that the reduced set of points used as emulator training data are not sufficiently informative, which may be overcome by using the full-field model output. Incorporating full-field data from either source is a significant challenge due to the poor scalability of the univariate emulator-based framework discussed in Section 4. A multivariate framework such as that proposed in [13] may help address this challenge.

6. Conclusions

Bayesian model calibration has been applied to a finite element stiffened panel model using strain gauge data from compression tests. The calibration resulted in modest reductions in uncertainty in the longitudinal modulus with larger reductions in uncertainty in the ply thickness, and an average decrease in these inputs, indicating that the model previously over-predicted

  doi:10.5075/epfl-298799_978-2-9701614-0-0

panel stiffness. The limited reductions in uncertainty are attributed to the fact that experimental data and emulator training data are not sufficiently informative in these parameters, reflected in low emulator sensitivity to variations in these parameters. Future work will focus upon a multivariate calibration framework to enable use of more informative full-field data.

Acknowledgements

The presented research was supported by the EPSRC Programme Grant 'Certification for Design – Reshaping the Testing Pyramid' (CerTest, EP/S017038/1).

7. References

1. Potter K, Khan B, Wisnom M, Bell T, Stevens J. Variability, Fibre waviness and misalignment in the determination of the properties of composite materials and structures. Compos. Part A Appl. Sci. Manuf. 2008; 39(9):1343–54.
2. Sriramula S, Chryssanthopoulos MK. Quantification of uncertainty modelling in stochastic analysis of FRP composites. Compos. Part A Appl. Sci. Manuf. 2009; 40(11):1673–84.
3. Brynjarsdóttir J, O'Hagan A. Learning about physical parameters: the importance of model discrepancy. Inverse Probl. 2014;30(11):114007.
4. Rasmussen CE, Williams CK. Gaussian processes for machine learning. MIT Press. 2006.
5. Davino C, Furno M, Vistocco D. Quantile regression: theory and applications. Wiley. 2013.
6. Schölkopf B, Smola AJ, Bach F. Learning with kernels: support vector machines, regularization, optimization, and beyond. MIT press. 2002.
7. Oakley JE, O'Hagan A. Bayesian inference for the uncertainty distribution of computer model outputs. Biometrika 1999; 89(4):769-84.
8. DiazDelaO FA, Adhikari S. Gaussian process emulators for the stochastic finite element method. Int. J. Numer. Methods Eng. 2011; 87(6):521–40.
9. Dey S, Mukhopadhyay T, Adhikari S. Stochastic free vibration analyses of composite shallow doubly curved shells - a Kriging model approach. Compos. Part B Eng. 2015; 70:99–112.
10. Scarth C, Sartor PN, Cooper JE, Weaver PM, Silva GHC. Robust and reliability-based aeroelastic design of composite plate wings. AIAA J. 2017;55(10):3539-52.
11. Paiva RM, Crawford C, Suleman A. Robust and reliability-based design optimization framework for wing design. AIAA J. 2014;52(4):711–24.
12. Kennedy MC, O'Hagan A. Bayesian calibration of computer models. J. R. Stat. Soc. Ser. B Statistical Methodol. 2001; 63(3):425–64.
13. Higdon D, Gattiker J, Williams B, Rightley M. Computer model calibration using high-dimensional output. J. Am. Stat. Assoc. 2008; 103(482):570–83.
14. Culliford LE, Scarth C, Maierhofer T, Jagpal R, Rhead AT, Butler R. Discrete stiffness tailoring: optimised design and testing of minimum mass stiffened panels. Compos. Part B Eng. 2021; 221:109026.
15. Chong A, Menberg K. Guidelines for the Bayesian calibration of building energy models. Energy Build. 2018; 174:527–47.
16. Clarkson E. Hexcel 8552 AS4 unidirectional prepreg qualification statistical analysis report: FAA special project number SP4614WI-Q. National Institute for Aviation Research, Wichita, Kansas. Report NCP-RP-2010-008 Rev. D, 2011.
17. Falcó O, Ávila RL, Tijs B, Lopes CS. Modelling and simulation methodology for unidirectional composite laminates in a Virtual Test Lab framework. Compos. Struct. 2018; 190:137–59.

  doi:10.5075/epfl-298799_978-2-9701614-0-0

DENSITY BASED CLUSTERING AS A TOOL TO ANALYZE ACOUSTIC EMISSION SIGNALS

Johannes, Wiener[a], Maria, Gfrerrer[a], Christian, Schneider[b], Gerald, Pinter[a]

a: Montanuniversitaet Leoben, Material Science and Testing of Polymers –
johannes.wiener@unileoben.ac.at
b: Exel Composites GmbH, R&D

Abstract*: In this contribution, the performances of two different clustering algorithms, namely K-means and hierarchical density-based spatial clustering of applications with noise (HDBSCAN), are compared. Features extracted from acoustic emission measurements are chosen as dataset. Acoustic emission data is typically challenging due to noise and the uneven shape of clusters in the feature space. The latter turns out to be problematic for K-means, where affiliation to clusters is solely based on the distance of data points to the centers of clusters. HDBSCAN overcomes this problem by recognizing continuously dense regions as one cluster. Additionally, far outliers are correctly detected as noise. As a result, HDBSCAN may yield better results compared to the classical K-means, especially when the data is challenging.*

Keywords: non-destructive testing, acoustic emission, machine learning, clustering

1. Introduction

Structural health monitoring and lifetime modeling have become an important part in designing composite parts. Established methods include finite element simulations, linear-elastic fracture mechanics or the construction of lifetime diagrams (e.g. Wöhler lines or the Haigh diagram) [1-4]. These approaches usually predict if the specimen is broken or intact, but no information can be given on the progression of damage. Moreover, the variance between predicted and measured lifetime may be considerable for individual specimens.

Innovative methods have gained popularity in recent years, where the state of damage is monitored throughout the loading process. These approaches may also be applied to monitor components during service life. One such method is the detection of acoustic emissions (AE): Elastic waves that are created by breaking fibers, cracking matrix, debonding between fiber and matrix or the friction between pre-existing crack flanks are measured. AE techniques can detect even microscopic damage events due to the high sensitivity and, when using more than one sensor, it is also possible to locate damage sources via triangulation.

In a first approach, the number of AE events can be used as indication of overall damage processes within the material. AE activity usually strongly increases towards the end of life due to the heavy damage shortly before failure (e.g. large cracks opening or fibers breaking). However, individual damage mechanisms may not follow this pattern. Matrix cracking, for example, is known to increase initially, but stagnates later on when the matrix is saturated with cracks. Detailed analysis of the underlying damage mechanisms is possible by extracting features from the AE signals. Parameters such as duration or maximum amplitude are used to characterize the individual waveforms. Since these signals are rather complex in the time domain, Fourier transformation is often used to transform the spectra to the frequency domain

  doi:10.5075/epfl-298799_978-2-9701614-0-0

before further investigation. Several frequency based features can be generated from the Fourier spectra. The activity in certain frequency bands, so-called partial powers, offer additional features for characterization [5,6].

AE measurements can produce an excessive amount of data points. Machine learning techniques are an excellent tool for handling and analyzing these signals in a fast and efficient manner. Specialized algorithms exist for dividing the feature space into clusters, which may then be correlated with certain failure mechanisms. As a result, the progression of damage can be illustrated in greater detail and the structural integrity can be monitored. Two algorithms, namely K-means [7] and HDBSCAN (hierarchical density-based spatial clustering of applications with noise [8]), are investigated more closely in this contribution.

K-means is a popular method due to its ease of use, good scalability to large datasets and high computational speed [9]. The number of clusters is usually predefined by the user and an equal number of data points are assigned as initial centers for the individual clusters. Subsequent data points are assigned the cluster with the smallest Euclidean distance between data point and the center of that cluster. Throughout the process, the centers are re-calculated as clusters grow and affiliations are re-evaluated until certain convergence criteria are met. A more detailed explanation of the algorithm can be found in [7,10].

On the other hand, HDBSCAN uses density instead of distance to evaluate affiliation with individual clusters. A region in the feature space is rated as dense, if all included points have a minimum number of neighbors within a certain radius. Continuous regions that satisfy this criterion are recognized as cluster, while stand-alone points are labelled as noise. While the radius may be calibrated manually, automated approaches are also implemented. Therein, the number of resulting clusters is screened for various radii and a radius is chosen, where the number of clusters is the most stable. An in-depth explanation of this method as well as other details concerning HDBSCAN are given in [8,11].

These two algorithms shall be applied to an AE-dataset and compared regarding the quality of clustering as well as their overall performance and applicability.

2. Methods

2.1 Material and specimen preparation

Test specimens were manufactured from an unidirectional carbon fiber fabric (fabric type HS 15-50/250 by G. Angeloni srl., Quarto d'Altino, Italy), which was arranged in a 0° layup in 8 layers. The epoxy resin EPIKOTE™ RIM R135 with EPIKURE™ MGS® RIMH1366 as a curing agent served as matrix (both by Lange + Ritter GmbH, Gerlingen, Germany). The material was cured at 80°C for 5 hours in a vacuum assisted resin transfer moulding process. The cured pates had a fiber volume content of 55% and an areal weight of 250 g/m^2. Prismatic specimens were then cut from the cured plates with dimensions of 200x20x2.2 mm^3. Shafted aluminum tabs with a thickness of 1 mm were used to ensure proper introduction of the load.

  doi:10.5075/epfl-298799_978-2-9701614-0-0

2.2 Tensile testing

The specimens were tested under monotonic tensile load on a Zwick Z250 universal testing machine (ZwickRoell GmbH & Co. KG, Ulm, Germany), which offered a load cell of 250 kN. Testing was performed at a crosshead speed of 0.5 mm/min until specimen failure.

2.3 Acoustic emission

AE measurements were performed using a system by MISTRAS Group Inc. (Princeton, USA) with two broad band sensors, which were applied to the specimen with a gauge length of 75 mm. The sensors were secured in place using spring clamps and proper transmission from the specimen to the sensors was ensured by applying a thin layer of silicone free vacuum grease as coupling medium. Only AE signals which could pass a Δt-filter were considered for further evaluation. Such a filter requires the acoustic wave to be detected at both sensors within a certain time difference, which ensures that the AE originated within the specimen and does not stem from the surroundings. Hits with an amplitude lower than 35 dB_{AE} were not recorded in order to avoid registering excessive amounts of noise data. The software AEwin™ by MISTRAS Group Inc. was used for signal acquisition, where a peak definition time of 10, hit definition time of 80 and hit lockout time and 300 µs were employed.

2.4 Data treatment and clustering

From all recorded waveforms, various features were extracted utilizing the software nAExtor by BCMtec GmbH (Augsburg, Germany). A preliminary screening was performed to choose a promising pair of features. As is illustrated in Figure 1, some combinations are not suitable for clustering due to their random nature (Figure 1a) or because a function-like relation exists between the two features (Figure 1b). Fortunately, some pairs of features showed good separation (e.g. Figure 1c), so that signal amplitude and weighted peak frequency, $\langle f_{peak} \rangle$, were ultimately chosen for further analysis. The weighted peak frequency was calculated from Fourier spectra of the waveforms according to Eq. (1) and Eq. (2) [5,6]:

$$f_{centroid} = \frac{\int_{f_{start}}^{f_{end}} f \cdot U(f) df}{\int_{f_{start}}^{f_{end}} U(f) df} \tag{1}$$

$$\langle f_{peak} \rangle = \sqrt{f_{peak} \cdot f_{centroid}} \tag{2}$$

Therein, the peak frequency, f_{peak}, is the frequency with the maximum magnitude in the frequency space, U is the magnitude and $f_{centroid}$ is the frequency centroid.

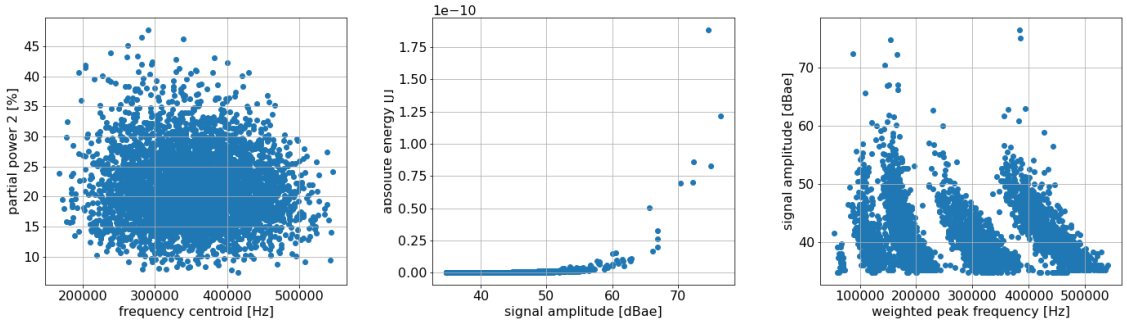

(a) (b) (c)

Figure 1 : Preliminary screening of features reavealing (a) random, (b) function-like and (c) cluster-shaped correlations between parameters.

Before clustering, parameters were normalized according to Eq. (3) and Eq. (4) to confine the feature vectors, *x*, between plus and minus 1.

$$x_{\,center} = x - \bar{\bar{x}} \tag{3}$$

$$x_{\,norm} = \frac{x_{center}}{\max\left(\left|x_{center}\right|\right)} \tag{4}$$

Therein, the normalized feature vector, x_{norm}, is obtained through centering the data by subtracting the mean value, $\bar{\bar{x}}$, and then dividing by the maximum absolute value of x_{center}. This was done to remove size dependent influences, which may occur when absolute values of the features have different orders of magnitude. However, the normalization was reverted after clustering, so the real values are shown in all figures.

Both clustering algorithms were performed in Python 3.8 using the packages “scikit-learn” for K-means and “hdbscan” for the density based approach. The K-means computations were attempted with predefined numbers of clusters ranging from 3 to 8, where the best results were obtained using 3 clusters. For HDBSCAN, the minimum number of points per cluster and the minimum number of samples for the density evaluation were set to 30 and 10, respectively. The remaining parameters were left at their default values for both methods [10,11].

The growth rates of clusters determined by HDBSCAN were obtained by calculating the first derivative of the counts over time. However, due to the stochastic nature of AE events throughout the experiment, the data had to be resampled and processed with a Savitzky-Golay filter in order to obtain a smooth curve for derivation.

Especially for industrial applications, the processing time of an algorithm may be of importance. Thus, both algorithms were run a total of 100 times and the averaged time for one run was considered as measure for the speed of clustering. In order to avoid dataset-specific artifacts, random subsets of the original data including 90% of the 4218 data points were used for these timed repetitions.

  doi:10.5075/epfl-298799_978-2-9701614-0-0

3. Results and discussion

The outcome of K-means and HDBSCAN clustering are presented in the following section. The investigation focuses on the advantages and drawbacks of the two algorithms.

3.1 Quality of clustering

Figure 2a shows the results of the K-means computation, which divided the feature space into 3 clusters. The procedure appears to yield a decent separation at first sight. However, some peripheral regions, e.g. in cluster 1 and 2 at amplitudes of 50 dB_{AE}, are falsely categorized as the neighboring clusters. These errors are caused by the distance based approach of K-means. Due to the elongated shape of the clusters, remote areas are in fact closer to the center of a neighboring cluster than to their own. Three separate clusters can be distinguished visually for frequencies <240000 Hz. Unfortunately, these could not be detected properly by K-means due to their proximity and shape. Increasing the total number of clusters did not improve the result, but led to further division of clusters 1 and 2 instead. In addition to that, even far outliers have to be affiliated with one of the clusters due to the lack of a noise category. Thus, the model could not distinguish between valid data and background noise. Despite these drawbacks, K-means exhibits high speed with an average of only 4.9 ms for the present dataset.

HDBSCAN is better equipped to deal with the challenges of the presented AE dataset. On the one hand, the slim shapes of the clusters are recognized by the density-based approach and even points at the corners of clusters are assigned correctly. On the other hand, far outliers as well as transition regions between clusters are labelled as noise. This ensures that all non-noise data definitely correlates with the core regions of the corresponding clusters. These advantages come at the cost of computation time, which was determined as 120.5 ms on average.

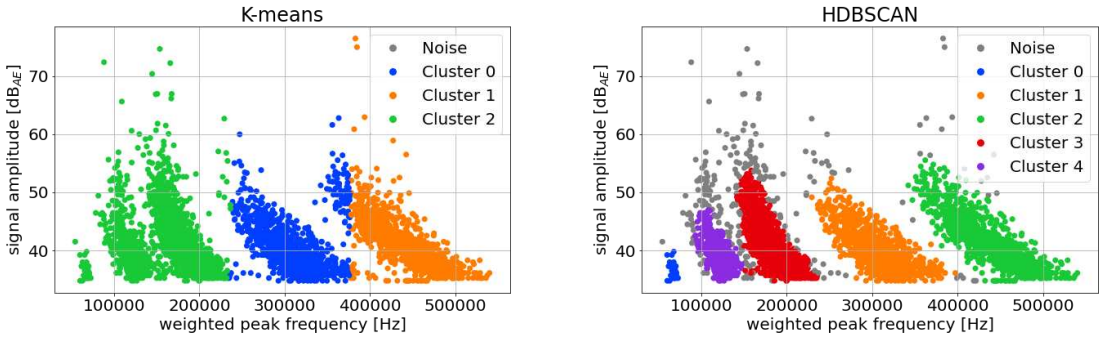

(a) (b)

Figure 2: Clustering of AE data with (a) K-means and (b) HDBSCAN using signal amplitude and weighted peak frequency as features.

3.2 Interpretation of clustering data

The results of the HDBSCAN algorithm are investigated more closely in this section. The final counts are listed in **Fehler! Verweisquelle konnte nicht gefunden werden.**, while individual cluster sizes as well as the force over the course of the experiment are shown in Figure 3a. Since the slope of the curves is more sensitive to changes, the growth rate is also shown in Figure 3b.

After an initial settling process, the force progresses in a linear fashion with no warning signs of imminent failure. Thus, detailed analysis of AE data is vital to analyze structural integrity.

Table 1: Total number of counts for clusters and noise.

Affiliation	Total counts [-]
Noise	220
Cluster 0	40
Cluster 1	1002
Cluster 2	1170
Cluster 3	1322
Cluster 4	464

A decent signal-to-noise ratio could be achieved with only 5.2% of data not having a cluster label. The detected noise shows exponential increase of counts and growth rate, which reflects the general AE activity during the experiment.

Cluster 0 shows a low amount of affiliated data points. A low absolute amount of counts does not necessarily mean that the mechanism is less important for the failure process. For example, the specimen may be able to endure several matrix cracks, while a single breaking fiber could have significant consequences. However, cluster 0 is located at low frequencies, which are often associated with machine noise. Moreover, the sensors used in this example are less sensitive at these frequencies. Therefore, cluster 0 is not considered in the further discussion.

Cluster 1 shows more activity at early stages of the test, so that counts and growth rate are larger than for the other clusters. However, the growth slows down at a later stage and almost stagnates as a plateau region of counts is reached. Such a behavior correlates well with matrix cracking, which is known to progress rapidly at first, but is strongly reduced later on, when crack saturation is reached.

The clusters 2 and 3 show the characteristics of an exponential function, where counts and their derivative are almost identical. This behavior may be explained by friction effects, where counts increase more rapidly, the more crack flanks are already present in the material. A plateau in the growth rate can only be seen near the end of the experiment in cluster 3. An explanation would be the saturation of matrix cracks, so that no additional sources are created and the growth rate remains constant. An alternative explanation may be increased damping of the material, which has a reduced ability to transfer acoustic waves as a result of being heavily damaged in later stages.

Cluster 4 exhibits very low activity during the earlier stages. However, counts and growth rate increase steadily between 225 and 380 s. At this point, a small plateau of growth rate is reached, which coincides with the maximum in growth rate of cluster 1. This section is followed by a significant increase in growth rate until specimen failure. These trends may be associated with

  doi:10.5075/epfl-298799_978-2-9701614-0-0

fiber breakage, which becomes the dominant mechanism after matrix crack saturation and ultimately leads to the destruction of the specimen.

It should be noted, that these interpretations are solely based on a comparison of cluster size and growth rate with well-known descriptions of damage phenomena. The presented assumptions should be validated by additional investigation. Imaging techniques such as X-ray computed tomography or scanning electron microscopy are good candidates. Confirming the assumed damage mechanisms in such a way is part of ongoing research.

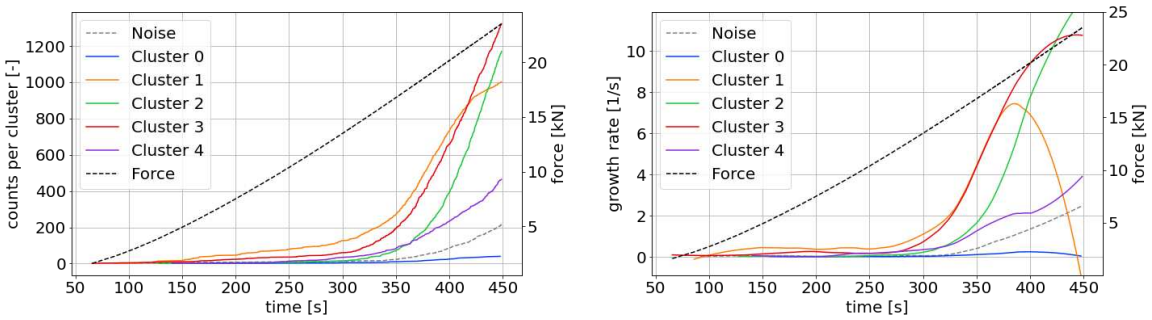

(a) (b)

Figure 3: (a) Absolute cluster size and (b) growth rate over the course of the experiment based on results from HDBSCAN.

4. Conclusions

Two different clustering algorithms are used to analyze a dataset from acoustic emission measurements.

The commonly used K-means method operates at high speed, but can not always assign data points to the correct clusters due to their elongated shapes in the feature space. Additionally, the detection of noise is not possible using K-means.

Alternatively, HDBSCAN accomplishes clustering based on point density in the feature space. This approach performs well in clustering the investigated dataset at moderate speed. In addition to that, far outliers can be recognized as noise.

Based on the labelling from HDBSCAN, cluster size and growth rate are investigated and compared to well-known damage phenomena in composites. Cluster 1 matches the characteristics of matrix cracking, which starts early but reaches saturation before specimen failure. Cluster 4 may be associated with fiber breakage, which is not detected at early stages but becomes more prominent before specimen failure.

Acknowledgements

Special thanks go to Clemens Sperling for experimental work and to Andreas Brunner for fruitful discussions and most useful advice.

5. References

1. Schürmann H. Konstruieren mit Faser-Kunststoff-Verbunden. 2. bearb. u. erw. Aufl. Berlin, Heidelberg: Springer Berlin Heidelberg; 2007.

2. Haibach E. Betriebsfestigkeit: Verfahren und Daten zur Bauteilberechnung. 3rd ed. Berlin, Heidelberg: Springer Berlin Heidelberg; 2006.

3. ASTM Standard E739-91. Standard Practice for Statistical Analysis of Linear or Linearized Stress-Life (S-N) and Strain-Life (ε-N) Fatigue Data. West Conshohocken: ASTM International; 1998.

4. Brunbauer J, Arbeiter F, Stelzer S, Pinter G. Stiffness Based Fatigue Characterisation of CFRP. Advanced Materials Research 2014; 891-892:166–71.

5. Sause MGR. In Situ Monitoring of Fiber-Reinforced Composites: Theory, Basic Concepts, Methods, and Applications. Cham: Springer International Publishing AG; 2016.

6. Trauth A, Pinter P, Weidemann KA. Investigation of Quasi-Static and Dynamic Material Properties of a Structural Sheet Molding Compound Combined with Acoustic Emission Damage Analysis. Journal of Composites Science 2017; 1(2):18.

7. Lloyd SP. Least squares quantization in PCM. Information Theory, IEEE Transactions 1982; 129-137

8. Campello RJGB, Moulavi D, Sander J. Density-Based Clustering Based on Hierarchical Density Estimates. Berlin, Heidelberg: Springer Berlin Heidelberg; 2013.

9. Xu D, Tian YA. A comprehensive Survey of Clustering Algorithms. Annals Data. Science 2015; 2:165-193.

10. https://scikit-learn.org/stable/modules/generated/sklearn.cluster.KMeans.html (last visited: 17.04.2022)

11. https://hdbscan.readthedocs.io/en/latest/how_hdbscan_works.html (last visited: 17.04.2022)

Composites Meet Sustainability – Proceedings of the 20th European Conference on Composite Materials,
ECCM20. 26-30 June, 2022, Lausanne, Switzerland

NEURAL NETWORKS MEET PHYSICS-BASED MATERIAL MODELS: ACCELERATING CONCURRENT MULTISCALE SIMULATIONS OF PATH-DEPENDENT COMPOSITE MATERIALS

Marina, A. Maia[a], Iuri, B. C. M. Rocha[a], Pierre, Kerfriden[b,c], Frans P., van der Meer[a],

a: Delft University of Technology, P.O. Box 5048. 2600GA Delft, The Netherlands
b: Mines ParisTech (PSL University), Centre des Matériaux, 63-65 Rue Henri-Auguste Desbrueres BP87, F-91003, Évry, France
c: Cardiff University, School of Engineering, Queen's Buildings, The Parade, Cardiff, CF24 3AA, United Kingdom
e-mail: m.alvesmaia@tudelft.nl

Abstract: *In a concurrent multiscale (FE^2) modeling approach the complex microstructure of composite materials is explicitly modeled on a finer scale and nested to each integration point of the macroscale. However, such generality is often associated with exceedingly high computational costs in real-scale applications. In this work, a novel Neural Network (NN) is used as the constitutive model for the microscale to tackle that issue. Unlike conventional NNs, the proposed network employs the actual material models used in the full-order micromodel as the activation function of one of the layers. The NN's capabilities are assessed (i) for a single micromodel level, where its performance is compared to that of a Recurrent Neural Network (RNN), and (ii) for an FE^2 example. A highlight of the proposed network is the ability to predict unloading/reloading behavior without ever seeing it during training, a stark contrast with highly popular but data-hungry models such as RNNs.*

Keywords: Neural Networks (NNs); Multiscale; Path-dependency

1. Introduction

Machine learning techniques are an increasingly popular alternative to time-consuming simulations in various fields. Recognizing this potential, the development and application of such methods gained traction in recent years in the field of concurrent multiscale analysis. However, a critical limitation of data-driven models is that they do not perform as well in extrapolation as they do within their training space. This can be especially critical when they are used as constitutive models in FE^2 where the lack of basic physics-related constraints can cause numerical instabilities and convergence issues.

On top of that, devising a sampling plan to train Neural Networks (NN) to capture path-dependent behavior is itself a convoluted task. This is because stresses depend on the strain history of the material. Thus, independent pairs of strains and stresses cannot fully describe how the material should evolve. A common approach to handle that is to augment the feature space with an extra variable that carries information about the history of stress and/or strain:

$$\widehat{\boldsymbol{\sigma}}^t = f_{NN}(\mathbf{W}, \mathbf{b}, \boldsymbol{\varepsilon}^t, \boldsymbol{\alpha}) \tag{1}$$

where $\mathbf{W}$ and $\mathbf{b}$ are the model parameters of a NN, $\boldsymbol{\varepsilon}^t$ and $\widehat{\boldsymbol{\sigma}}^t$ are the macroscopic strain and the approximated stress tensors at time step t, respectively, and $\boldsymbol{\alpha}$ is the history variable vector.

  doi:10.5075/epfl-298799_978-2-9701614-0-0

Typically, the previous strain state $\boldsymbol{\varepsilon}^{t-1}$ or the accumulated absolute strain are chosen for that [1].

Another highly popular alternative is to use Recurrent Neural Networks (RNNs). These networks can account to some extent for the typical loading/unloading by incorporating information from previous inputs as in the following parametric regression:

$$\widehat{\boldsymbol{\sigma}}^{t} = f_{RNN}(\mathbf{W}, \mathbf{b}, \mathbf{W}_h, \mathbf{b}_h, \boldsymbol{\varepsilon}^{t}) \tag{2}$$

where $\mathbf{W}_h$ and $\mathbf{b}_h$ represent additional model parameters shared across time to keep track of history-dependent materials in an implicit way. These parameters describe the evolution of the so-called hidden state and can capture information from previous iterations without the need to include previous strain states in the input vector as shown in Eq. (1). This way, the network ca learn how to process and predict a sequence of strains. As such, RNNs rapidly became a popular choice to model composite materials with path-dependency [2-4].

Despite their popularity, RNNs are still severely limited by the curse of dimensionality associated with sampling arbitrarily long strain paths. In this work, a physics-infused network is proposed to overcome this issue and accelerate concurrent multiscale simulations. In Section 2, the computational bottleneck in FE^2 is briefly discussed, while in Section 3 the main features of the novel NN are described. Finally, results are presented in Section 4 and conclusions are shown in Section 5.

2. Multiscale analysis

Let M define the macroscopic domain being modeled subjected to a set of Neumann and Dirichlet boundary conditions acting on the body surface. To find the internal stresses and displacement field of such body, a boundary value problem that satisfies the following equilibrium equation is defined:

$$\mathrm{div}\left(\boldsymbol{\sigma}^{\mathrm{M}}\right) = 0 \tag{3}$$

where $\mathrm{div}(\cdot)$ is the divergence operator. To relate strains and stresses, a constitutive model $\mathcal{D}$ is required:

$$\boldsymbol{\sigma}^{\mathrm{M}} = \mathcal{D}\left(\boldsymbol{\varepsilon}^{\mathrm{M}}, \boldsymbol{\alpha}^{\mathrm{M}}\right) \quad \text{with} \quad \boldsymbol{\varepsilon}^{\mathrm{M}} = \frac{1}{2}\left(\nabla \mathbf{u}^{\mathrm{M}} + (\nabla \mathbf{u}^{\mathrm{M}})^{\mathrm{T}}\right) \tag{4}$$

where $\boldsymbol{\alpha}^{\mathrm{M}}$ is a history term that accounts for path-dependency and $\mathbf{u}^{\mathrm{M}}$ is the macroscopic displacement field. However, in the concurrent multiscale approach, $\mathcal{D}$ is not directly formulated but is instead obtained by nesting a lower scale model to each integration point, as illustrated in Fig. 1. In that scale, complex materials can be explicitly modeled using simpler constitutive models and a geometrical representation of the microstructure.

The computational bottleneck arises from the fact that to obtain the internal forces and the tangent stiffness matrix of a single integration point of the macroscale, an entire FE model is run instead of a single evaluation of a homogenous material model. To alleviate that, the alternative explored in this work consists in replacing the solution of a Representative Volume Element (RVE) subjected to a periodic boundary value problem with a physics-based neural network.

  doi:10.5075/epfl-298799_978-2-9701614-0-0

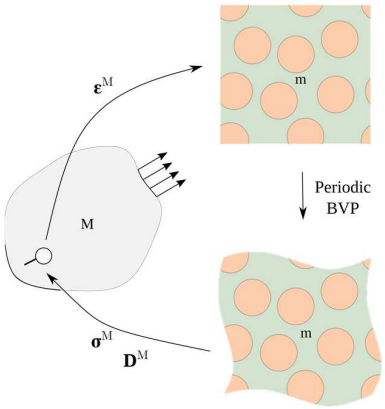

Figure 1. FE² scheme

3. Neural networks

Consider the parametric regression model in Eq. (2). When training a neural network for $\boldsymbol{\sigma}^{\mathrm{M}}$, strains are fed its first layer (input) and the values are propagated until the final layer (output) to give the predicted stresses $\widehat{\boldsymbol{\sigma}}^{\mathrm{M}}$, which are in turn compared to the ground truth value using the loss function:

$$\mathcal{L} = \frac{1}{N}\sum_{i=1}^{N}\frac{1}{2}\left\|\boldsymbol{\sigma}^{\mathrm{M}}(\boldsymbol{\varepsilon}_i^{\mathrm{M}}) - \widehat{\boldsymbol{\sigma}}^{\mathrm{M}}(\boldsymbol{\varepsilon}_i^{\mathrm{M}})\right\|^2 \tag{5}$$

where N is the number of pairs of $\boldsymbol{\varepsilon}^{\mathrm{M}} - \boldsymbol{\sigma}^{\mathrm{M}}$ obtained from microscopic simulations. Eq. (5) is then minimized by updating the model parameters according to an optimization algorithm.

3.1 Bayesian Recurrent Neural Network

In practice, RNNs struggle with vanishing gradient problems and are not suitable for long-term dependent problems. Among other architectures, the Gated Recurrent Unit (GRU) has become a widely used alternative to circumvent that issue. The GRU contains more operations and parameters than a regular RNN and can control more precisely the flow of information, being able to retain or forget information in a long sequence. In this work, a GRU with Variational dropout (i.e., Gaussian dropout where the rates are learned implicitly by the network) [5], also referred as Bayesian Recurrent Neural Network (BNN), is used for comparison purposes.

3.2 Adding physics-based material models

The proposed regression model consists of a neural network composed of one fully-connected material layer followed by a Dense layer, as illustrated Fig. 2. The material layer is responsible for explicitly incorporating into the network the same physics-based material model used in the homogenization of the RVE.

  doi:10.5075/epfl-298799_978-2-9701614-0-0

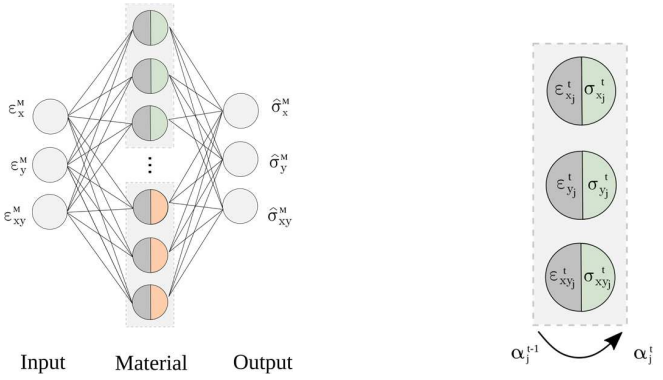

(a) Proposed neural network (b) Fictitious integration point *j*

Figure 2. Physics-infused neural network

Two different material models are used to describe the fibers and the matrix of the composite microscopic models in this work: the first consists of a linear elastic model and the second is an elastoplastic model $\mathcal{M}$. Since the latter is more complex, it is used to illustrate how its features are incorporated into the network. Model $\mathcal{M}$ takes as input the current strain $\boldsymbol{\varepsilon}^t \in \mathbb{R}^{n_\varepsilon}$ and the internal variables from previous time step $\boldsymbol{\alpha}^{t-1} \in \mathbb{R}^{n_{IntVar}}$, where n_ε and n_{IntVar} are the number of strain components and number of internal variables of the material model, respectively.

First, neurons are grouped in sets of the size of the input layer (light grey boxes in Fig. 2a) and only then activated as a subgroup, or *fictitious material point*. To store the internal variables used as input/output of the material model, an auxiliary vector $\mathbf{h}_j \in \mathbb{R}^{n_{IntVar}}$ is defined. For the first time step, $\mathbf{h}_j$ is initialized as zero for all subgroups.

As information reaches the material layer and the material model is evaluated (or updated), three features are obtained: the stresses $\boldsymbol{\sigma}_j^t$, the updated internal variables $\boldsymbol{\alpha}_j^t$,and the tangent stiffness matrix $\mathbf{D}_j^t \in \mathbb{R}^{n_\varepsilon \times n_\varepsilon}$. Then, stresses are propagated forward, and the updated internal variables $\boldsymbol{\alpha}^t$ are stored in $\mathbf{h}_j^t$ so that when new strains $\boldsymbol{\varepsilon}_j^{t+1}$ are fed to the fictitious material point *j* in the next time step, the material model is aware of its own history so far, as illustrated in Fig. 2b. Finally, to obtain the stiffness matrix, a full backwards differentiation pass is required.

3.3 Decoders

The decoder converts the outputs from the Material layer and combines them into the predicted macroscopic stress $\widehat{\boldsymbol{\sigma}}^{\mathrm{M}}$. In that sense, the decoder acts as the averaging operator in the multiscale approach. Therefore, weights of the output layer can be seen as the relative contribution of each fictitious material point to the average macroscopic stress as if they were obtained from a Gaussian quadrature, which are always positive.

Based on that, four different approaches are investigated: (i) first, no constraints are applied and the weights can be positive and negative, then weight positivity is enforced either with (ii) a penalty approach or by applying the (iii) *relu* function or the (iv) *softplus* function on the weights. For the decoder with the penalty (ii), an extra term is added to the loss function in Eq. (5):

$$P\,(w_k) = \begin{cases} 0.0, & w_k \geq 0 \\ \theta\,|w_k|, & w_k < 0 \end{cases} \tag{6}$$

where θ is a penalty parameter term introduced to penalize negative weights w_k in the output layer. Finally, for the approaches (iii) and (iv), the transformation functions are applied element-wise on the weight matrix.

It is worth mentioning that the first two decoders are shown as reference results since only (iii) and (iv) guarantee that, after the transformation, weights will be positive. This is an important outcome for the FE^2 framework because by constraining the decoder to be positive, the spectral properties of the Jacobian of the material model $\mathcal{M}$ are inherited by the network when calculating the tangent stiffness matrix.

4. Results

In this section, the performance of the proposed physics-infused network, or Material Neural Network (MNN), is compared to a Bayesian Recurrent Neural Network (BNN). The MNN was implemented in an in-house Finite Element code using the open-source Jem/Jive C++ numerical analysis library, while PyTorch was used to construct the BNN. The goal is to demonstrate the capabilities of the proposed network to capture path-dependent behavior in comparison to a popular method using exclusively monotonic data for training. The maximum number of epochs for both networks is 60000. For the BNN, an early stopping criterion of 5000 epochs is used.

The microscopic model consists of an RVE with 9 elastic fibers with properties $E = 74000$ MPa and $\nu = 0.2$ embedded in an elastoplastic matrix with isotropic hardening. The latter is modeled using the von Mises yield criterion with properties $E = 3130$ MPa, $\nu = 0.3$ and yield stresses given by:

$$\sigma_t = \sigma_c = 64.8 - 33.6\, e^{-\varepsilon_{\mathrm{eq}}^{\mathrm{p}}/0.003407} \tag{7}$$

where $\varepsilon_{\mathrm{eq}}^{\mathrm{p}}$ is the equivalent plastic strain. Plane strain conditions are assumed.

For training the MNN, 18 curves with *a priori* known directions (black lines in Fig. 3a) are generated. Each curve consists of 60 pairs of $\boldsymbol{\varepsilon}^{\mathrm{M}} - \boldsymbol{\sigma}^{\mathrm{M}}$ with monotonic loading (solid line in Fig. 3b). These directions comprehend typical loading cases used for calibrating mesomodels and comprise pure uniaxial, shear, biaxial and biaxial with shear cases. The validation set consists of another 54 monotonic curves in random directions (red lines in Fig. 3a).

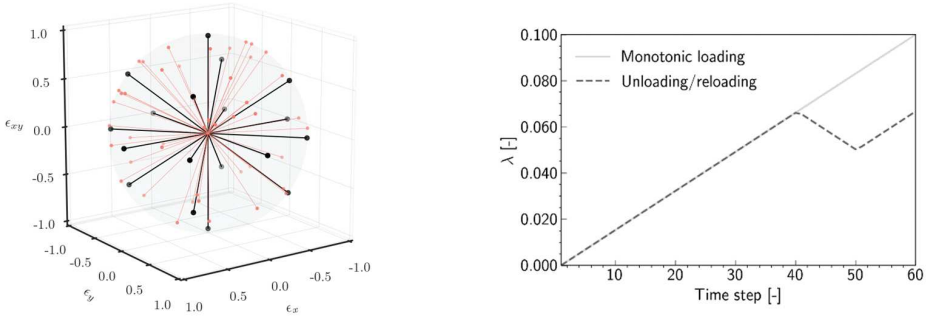

(a) Directions as unit load vectors (b) Monotonic and non-monotonic loading

Figure 3. Loading directions in (a) and loading function in (b)

Based on that, a preliminary study with 10 different initializations was carried out for each decoder and size of the material layer as shown in Fig. 4. It is clear from the results that using only 3 fictitious integration points (in contrast, the original FE micromodel comprises 7088 integration points) is enough to accurately represent the homogenized material behavior. We, therefore, adopt a layer size of 3 points (9 units) with softplus-activated weights for the sake of parsimony. A similar procedure is followed for the BNN, and a network with a single GRU layer with 128 units is selected.

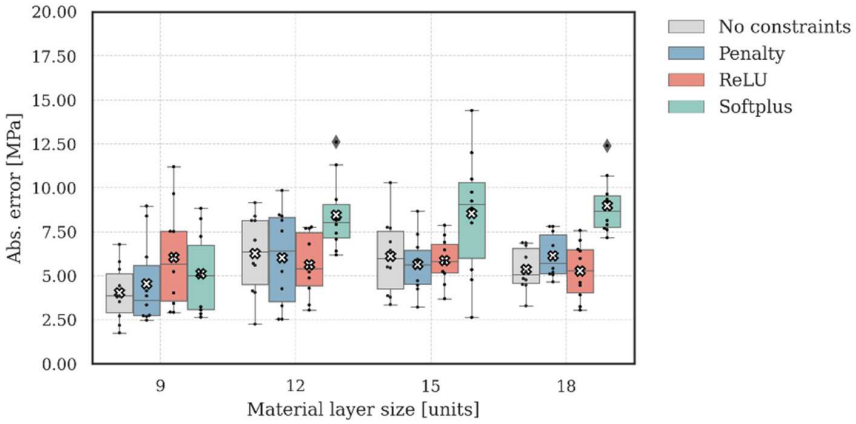

Figure 4. Abs. error for validation set with different combinations of decoder and layer size

4.1 Single scale

In this section, the 18 curves with known directions are kept as a fixed part of the dataset of both networks, while the BNN is trained with additional random monotonic curves for different training dataset sizes. The test set consists of 100 random curves with unloading/reloading as shown in Fig. 3b. Again, 10 different initializations were considered for each case, but only the best performance is depicted in Fig. 5.

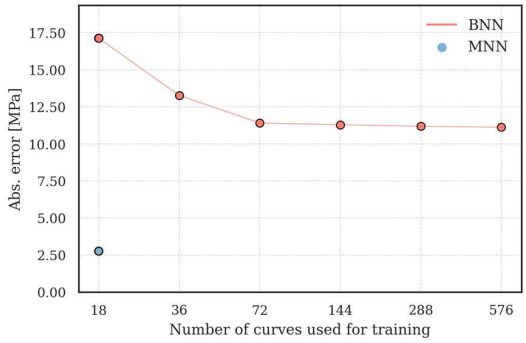

Figure 5. Networks trained on monotonic data and tested for curves with unloading/reloading

Note that as more curves are added, the BNN's error decreases, but around 144 curves, the addition of more monotonic data is no longer useful to the network in this scenario. The initial error decrease is actually associated with the points before the unloading. Once that part of the curve is accurate enough, the error in the unloading will remain unchanged (and high) while the MNN can capture accurately the entire strain path, as illustrated in Fig. 6. Although this is a simplified scenario, it helps in elucidating the ability of the proposed network to predict non-

  doi:10.5075/epfl-298799_978-2-9701614-0-0

monotonic data without the need to extend the training dataset with curves with arbitrary unloading/reloading cycles, as typically done for RNNs.

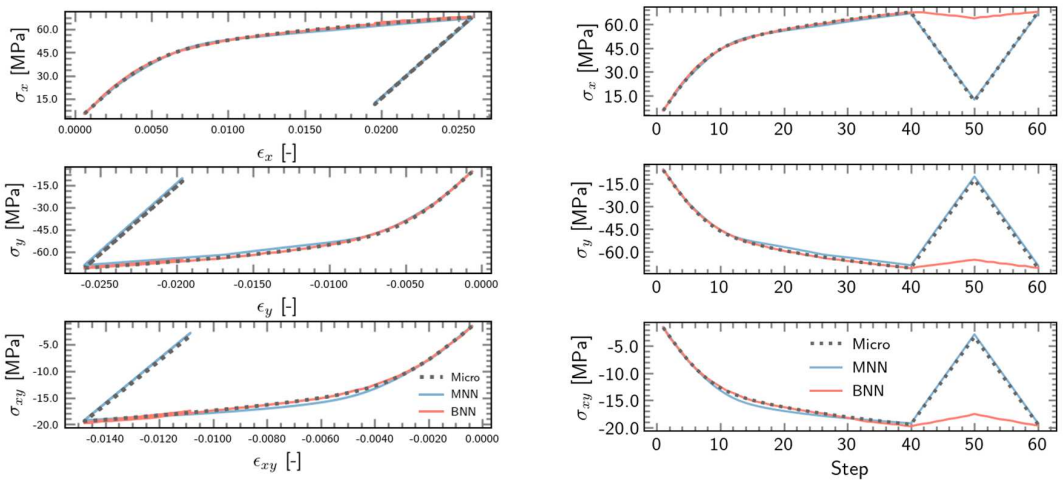

(a) Strain-stress view (b) Time step-stress view

Figure 6. BNN trained on 144 monotonic curves cannot capture unloading/reloading behavior

4.2 Multi-scale

Here, the MNN trained in the previous section is tested as the constitutive model in a multiscale application. The structure consists of a composite tapered specimen with a length of 128 mm and a height of 8 mm loaded in transverse tension. The boundary and loading conditions are shown in Fig. 7, where the load-displacement curve using the full-order solution is plotted along with the network's response. Good agreement is observed between the curves.

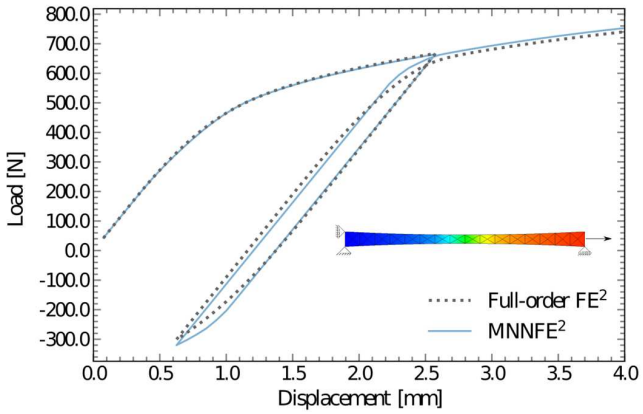

Figure 7. Load-displacement curves using the full-order solution and the MNN

5 Conclusions

A network with embedded physics-based constitutive models was presented. The network captures unloading without ever seeing it during training, which is not observed in the BNN regardless of the number of monotonic curves considered. In the multiscale example, the

proposed approach showed good accuracy in an structure subjected to different strain states and reduced the CPU time from 9077 s to 3 s (excluding training and data generation times). Further details on the training of the networks and results over a broader range of test cases will be presented in a future publication.

Acknowledgements

The authors acknowledge the TU Delft AI Initiative for their support through the SLIMM AI Lab. FM acknowledges financial support from the Dutch Research Council (NWO) under Vidi grant 16464.

6 References

1. Huang D, Fuhg JN, Weißenfels C, Wriggers P. A machine learning based plasticity model using proper orthogonal decomposition. Computer Methods in Applied Mechanics and Engineering 2020; 365:113008.
2. Ghavamian F, Simone A. Accelerating multiscale finite element simulations of history-dependent materials using a recurrent neural network. Computer Methods in Applied Mechanics and Engineering 2019; 357:112594.
3. Wu L, Nguyen VD, Kilingar NG, Noels L. A recurrent neural network-accelerated multi-scale model for elasto-plastic heterogeneous materials subjected to random cyclic and non-proportional loading paths. Computer Methods in Applied Mechanics and Engineering 2020; 369:113234.
4. Mozaffar M, Bostanabad R, Chen W, Ehmann K, Cao J, Bessa MA. Deep learning predicts path-dependent plasticity. Proceedings of the National Academy of Sciences 2019; 116:26414–26420.
5. Kingma DP, Salimans T, Welling M. Variational Dropout and the Local Reparameterization Trick. arXiv 2015; arXiv:1506.02557.

  doi:10.5075/epfl-298799_978-2-9701614-0-0

MACHINE LEARNING BASED TAPE WIDTH PREDICTION FOR THE THERMOPLASTIC AUTOMATED TAPE PLACEMENT PROCESS

Alexander Legenstein, Ralf Schledjewski

Processing of Composites Group, Department of Polymer Engineering and Science,
Montanuniversität Leoben, Otto Glöckel-Straße 2/III, 8700 Leoben, Austria
Email: ralf.schledjewski@unileoben.ac.at

Abstract: The thermoplastic automated tape placement process offers the possibility to replace the currently in the aerospace industry mostly used thermoset automated tape placement process. Due to in-situ consolidation no autoclave curing is necessary, which reduces manufacturing time and costs. Though, the processing of thermoplastic materials is a challenging task due to many different input variables and processing conditions. It is of great importance to understand the influence of the input and processing variables on the consolidated tape width. Varying conditions in the tape quality and processing conditions can lead to gaps or overlaps, which reduce the mechanical properties of the laminate. In this study a Neural Network modeling approach is used to predict the tape width after consolidation based on processing conditions. The Neural Network showed a not satisfactory performance based on the current data.

Keywords: Automated Tape Placement; Machine Learning; Fiber-Reinforced Plastics; Thermoplastic Prepreg

1. Introduction

The demand for Fiber Reinforced Plastics (FRP) has been increasing over the past decades, especially in the aerospace industry. Airplanes like the Airbus A350 XWB consist of over 50% FRP. Continuous fiber laminates not only offer excellent lightweight properties due to their high specific stiffness and strength, but can also increase the lifespan of parts due to non-corrosive behavior. [1–4] The Automated Tape Placement (ATP) process offers a highly automated processing of unidirectional fiber reinforced semi-finished tape materials. Either thermoplastic or thermoset tapes can be processed with ATP. To this day the processing of thermoset tapes is the state of the art due to challenges in the in-situ consolidation of thermoplastic tapes [4, 5]. Besides the consolidation of the tapes, the tape width after consolidation is of great importance. The width after consolidation is affected by process variability and variations in tape quality [6]. Due to these variabilities in width, gaps or overlaps of the individual tapes during the lay-up can occur, which reduces the mechanical properties of the laminate [7–9]. Besides these challenges the thermoplastic ATP process offers significant advantages over the thermoset ATP process. Due to the in-situ consolidation, no autoclave cycle after the lay-up is needed. This reduces manufacturing time and enables the manufacturing of bigger structures. [5, 10]. Currently, different approaches exist to detect errors in the laminate in-line, but no efforts have been made so far in controlling the tape-width with Machine Learning (ML) based process control [11–13]. Data driven approaches like ML are able to learn and predict complex behaviors based on data [14]. The ATP process has many inputs like consolidation force, lay-up speed, tool temperature, consolidation roller temperature and hardness or nip-point temperature. Furthermore there are

  doi:10.5075/epfl-298799_978-2-9701614-0-0

also numerous properties of the tape material, which effects the tape width after consolidation like surface roughness, cross section shape, fiber volume fraction or fiber distribution within the matrix [15, 16]. Due to the vast number of possible influences on the tape width after consolidation, a data driven model is used in this work. Wanigasekara et al. [15] has shown, that ML approaches can be used to predict mechanical properties of laminates manufactured in the ATP process based on processing conditions. In a later work Wanigasekara et al. [17] demonstrated, that a ML based inverse model can predict the necessary processing conditions to reach the desired mechanical characteristics of the laminate. Both studies enhanced the experimentally generated dataset with virtually generated samples [15, 17]. This study aims to utilize solely experimentally generated data for predicting the tape width after consolidation with the help of ML.

2. Machine Learning

Machine learning is a subset of artificial intelligence. Mitchell [18] defined ML as follows "A computer program is said to learn from experience E with respect to some class of tasks T and performance measure P, if its performance at tasks in T, as measured by P, improves with the experience E". ML unfolds its full potential when there are complex tasks, which cannot be easily solved by traditional programming or when there is a vast amount of data available which is at a first glance not connected among themselves. The most common form of ML is supervised learning, where the training set for the algorithm includes the solutions to the known inputs. The algorithm learns the connections between the inputs and outputs based on this labeled data. [19, 20] In unsupervised learning the algorithm aims to discover patterns to gain hidden information in the data set, as no labels are presented to the algorithms [20]. Supervised learning algorithm include linear regression, decision trees or neural networks. Neural Networks (NN) have a similar structure compared to the human brain. A basic neural network consists of multiple layers of neurons. The strength of the connections between the layers is determined by a weight. The weights are updated during the learning process. The first layer of neurons gets activated by inputs from the environment, whereas all the other layers get activated through the weighted connections. [21] The output layer compares the predicted value with the label and calculates the difference with a loss function. With the help of backpropagation, the neural network can adapt the weights based on the loss [20].

3. Experimental setup and material

The placement rig used is shown in Figure 1. It consists of Light Section Sensors (LSS) (Micro-Epsilon LLT2900-25/BL) to measure the tape width before and after the lay-up. The LSS can measure up to 1280 points with a point spacing of 19.5 µm at a sampling rate of 300 Hz and can measure widths up to 29.1 mm. For the consolidation force measurement, a multi-component sensor (K6D40 500N/20Nm/MP11) from ME-Messsysteme is used. This sensor has an accuracy of 0.2% and can measure force and torque, with a force of up to 2000 N in z-direction. The rig is equipped with a steel consolidation roller, with an internal water cooling. The PID controller of the system can operate with an accuracy of +/-1°C. On the heating plate an aluminum tool is placed (EN-AW 5083). The humidity and room temperature are measured with a hygrometer (608-H1) from Testo. It has a temperature measurement accuracy of +/-0.5°C and a resolution of 0.1°C. The measurement accuracy for the humidity measurement is +/-3% with a resolution of 0.1%.

  doi:10.5075/epfl-298799_978-2-9701614-0-0

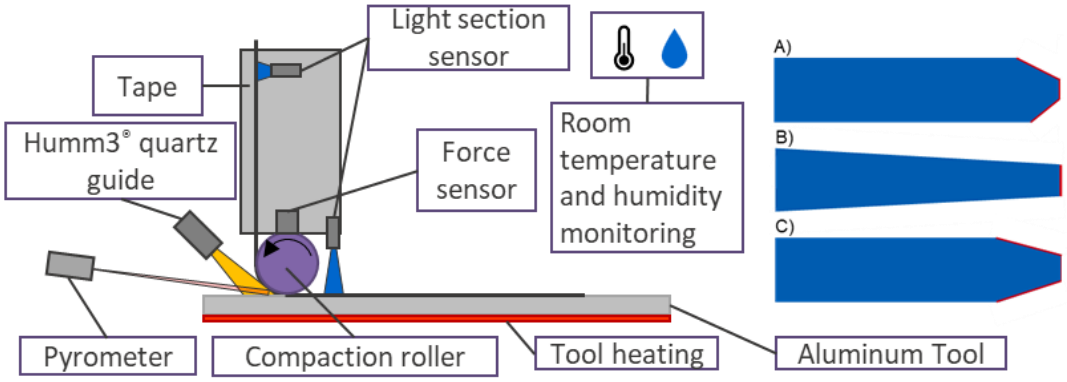

Figure 1: Tape placement rig and the different quarz guides used in this study

For heating up the tape, there are numerous systems available like laser systems, hot gas torch, infrared, ultrasonic or induction [4, 10]. Heraeus Noblelight developed a new heating system which uses a flashlamp for heating. [22] The Humm3® system is based on a pulsed light technology and utilizes high-energy pulsed flashes for the heating of the tape material. High voltage is used to ionize the xenon gas in the lamp to conduct electricity. At regular intervals the capacitators are discharged to generate flashes. A quartz light guide is used as an optical medium for focusing the flashes. Different chamfered quartz guides are available to distribute the energy on the tape and substrate. [23–25]. The red displayed areas mark the radiating surfaces. The energy is distributed equally based on the length of the surfaces. The energy of the system is controlled with three parameters. The pulse energy, pulse duration und pulse frequency (Figure 1). The main benefits of this system compared to laser or IR emitters are the fast heating and cooling time, high energy capability, low safety requirements, scalable width and a compact design. [22] Di Francesco [26] has shown that the system is capable to deposit thermoset and thermoplastic prepregs and bindered dry fibers.

The tapes used for the experiments were fully impregnated unidirectional prepreg tapes (Celstran® CFR-TP PA6-CF60-01-275-0.13 CF2). The material has a thickness of 0.13 mm and a fiber volume ratio of 48.5%. The melting point is 220°C and the glass transition temperature is 57°C.

4. Model and data preprocessing

The initial dataset consists of 231 samples. In a first step all outliers were removed from the dataset, with the help of the Interquartile Range (IQR) of the tape width after consolidation. All tape widths which fall below Eq. (1) or above Eq. (2) are considered outliers and were removed from the dataset.

$$Lower\ bound = Q1 - 1.5\ IQR \tag{1}$$

$$Upper\ bound = Q3 + 1.5\ IQR \tag{2}$$

Whereas Q1 is the 25th percentile Q3 is the 75th percentile. This results in a reduced dataset of 206 samples. No duplicates or missing values were found in this data. Three samples with lay-up speed of 30 mm/s were also removed, because there are just three samples with this speed. After this step, the dataset was split into a training and test set at an 80/20 split resulting in 162 training data samples and 41 test samples.

  doi:10.5075/epfl-298799_978-2-9701614-0-0

To select the most important features for the ML algorithm the influence of the different parameters on the tape width after the consolidation was investigated via a scatter matrix. A clear positive trend can be seen for all parameters except the quartz, the ambient room temperature, and the ambient humidity. Those three parameters show a negative influence on the tape width after consolidation. The scatter matrix is shown in Figure 2. The Pearson Correlation Coefficient (PCC) for all values is shown in Figure 3. The PCC for the power is the highest with a value of PCC=0.36, followed by the pulse width (PCC=0.27), the tape width before consolidation (PCC=0.18) and the lay-up speed (PCC=0.15).

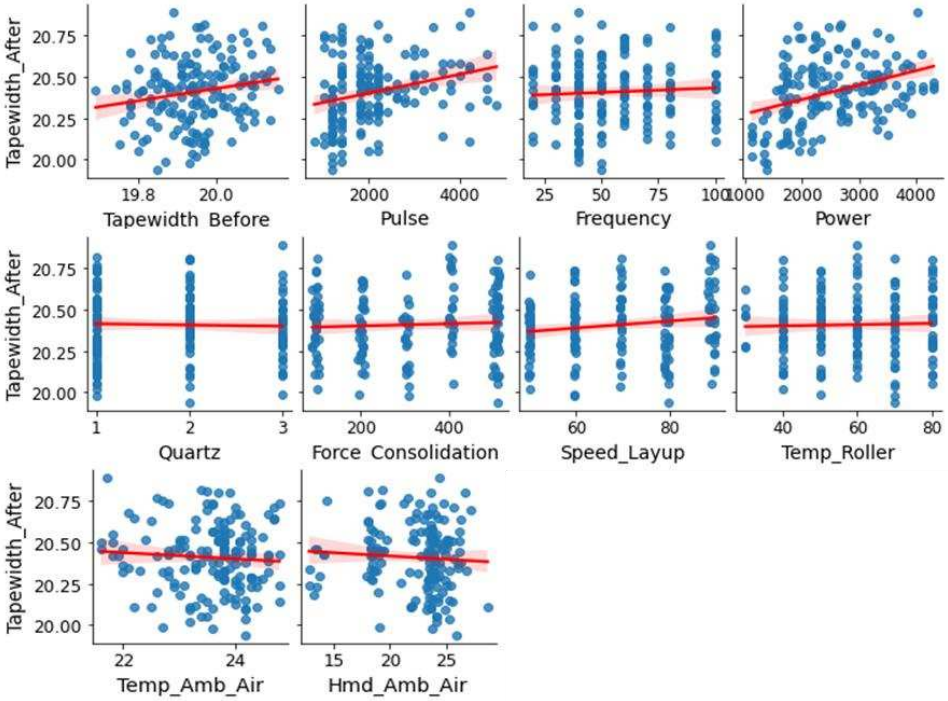

Figure 2: Scatter matrix of all parameters on the tape width after consolidation

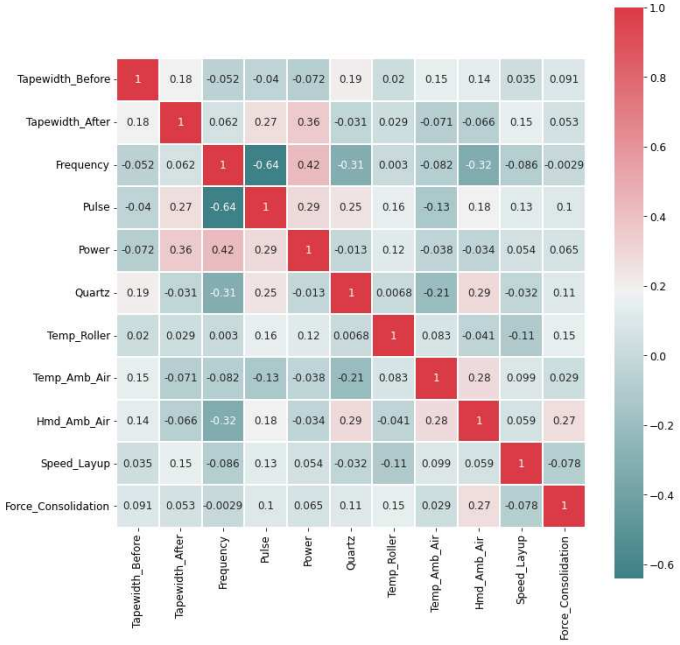

Figure 3: Correlation Matrix

The tape width before and after consolidation, and the power follow a normal distribution. The pulse width was transformed via a Box-Cox transformation to make it normally distributed, to help getting a better result for the linear regression model. All other parameters were not modified. Due to different ranges of the parameters, the parameters were scaled with a standardization approach. The formula for the standardization can be seen as follows in Eq. (3):

$$X' = \frac{X - \mu}{\sigma} \tag{3}$$

Whereas σ is the standard deviation of the feature value and μ is the mean of the feature value. X is the current feature value and X' is the value after standardization.

To compare the performance of the Neural Network to a baseline model, a linear regression model was chosen. The NN consists of the input layer followed by 3 hidden layers, where the first layer has 20 nodes, the second layer 10, the third layer 5. The output layer consists of one node. The hidden layers use L2 regression to compensate overfitting. As evaluation metric, the Mean Squared Error (MSE) was chosen for both the NN and the linear regression. The formula for the mean squared error is shown in Eq. (4):

$$MSE = \frac{1}{N}\sum_{i=1}^{N}(y_i - \widehat{y_i})^2 \tag{4}$$

Where N are the number of samples, y_i is the predicted target value and $\widehat{y_i}$ is the true value.

As input for both models, a study with all features is conducted to find the optimal number of features for both models. More features do not always lead to a better results and therefore special care must be taken in selecting the features. This reduces the risk of the model getting to complex without having a better accuracy, due to a lack of data. Both the linear regression and the NN use a learning rate of 0.0005 and a batch size of 50. The NN is trained for 1500 epochs and the linear regression for 500. All layers of the neural network use a regularization factor of 0.075 and a rectified linear unit activation function, except the first and last layer. The rectified linear unit is defined in Eq. (5):

$$f(x) = \max(0, x) \tag{5}$$

Whereas x is the input to the neuron.

5. Results

Figure 4 shows the mean squared error for different feature combinations. A minimal mean squared error of MSE=0.585 can be achieved with 6 features. Those six features include the tape width before consolidation, the frequency, the pulse width, the lay-up speed, and the consolidation force. The features with the smallest positive PCC and all features with a negative PCC impact increase the MSE again after reaching the minimum. The linear regression baseline model has a MSE of 0.824 with the chosen 6 features. A further optimization of the linear regression is not conducted in this study, due to the better performance of the NN.

The best MSE for the NN with 0.585 indicates, that the model does not predict the data well. Figure 5 shows the absolute tape width change of 21 experiments at the same processing parameters. As seen in Figure 5 the absolute tape width change results in a range of 0.8 mm. This indicates that there is a large variability present in the data, which cannot be explained with varying processing conditions.

  doi:10.5075/epfl-298799_978-2-9701614-0-0

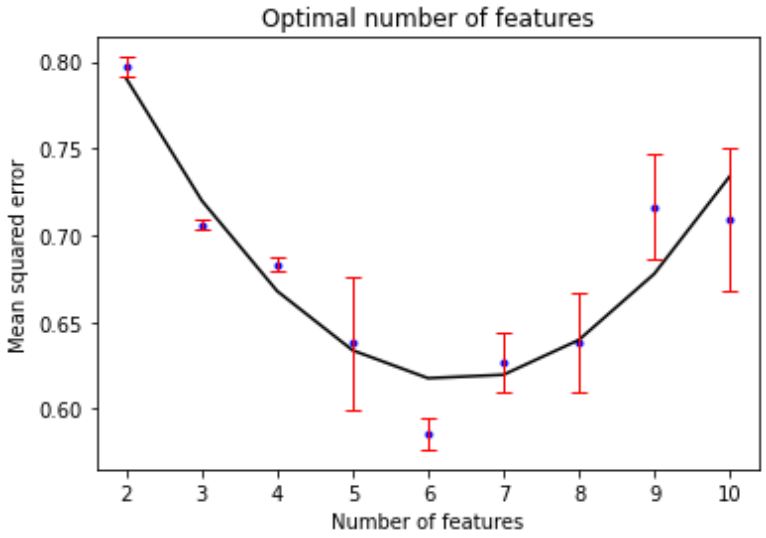

Figure 4: Optimal number of labels for the Neural Network

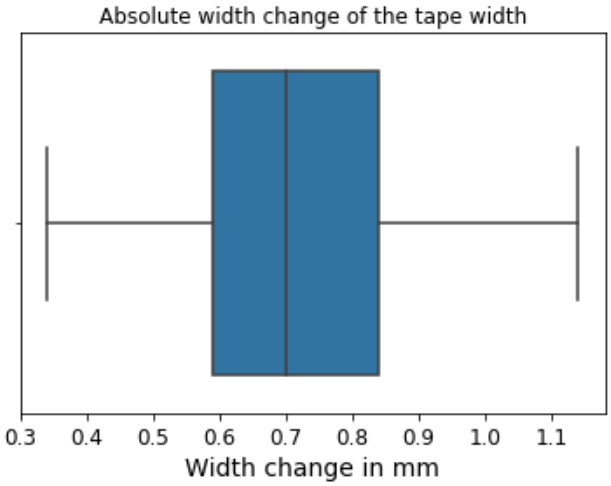

Figure 5: Boxplot of the absolute tape width change after the consolidation

6. Discussion

This study shows that the ambient room temperature and humidity as well as the different quartz guides and the consolidation roller temperature have a negative impact on the model performance. The NN based on the best features is not able to predict the tape widths after consolidation well enough. The bad performance can be led back to the variability in the training and test data. In the future work a special emphasis will be taken to reduce the variability in the data. It is important, that the variability in tape width before consolidation is kept smaller, than the variability which is induced based on the processing. Furthermore, the topography of the NN will be refined and hyperparameter tuning will be carried out. Another aspect, worth noting is that in this study no temperature data of the nip point was included, and the data is solely experimental. An enhancement of the data with simulation-based results would introduce a physical description of the problem to the model. This could increase the accuracy of the NN. The temperature data is important to determine if the energy provided by the heating source is high enough to melt the tape. Therefore, emphasis on the consolidation should also be placed to achieve high quality laminates.

  doi:10.5075/epfl-298799_978-2-9701614-0-0

7. References

1. Wiedemann M. CFK - Status der Anwendung und Produktionstechnik im Flugzeugbau. 2013. https://elib.dlr.de/61319/1/Vortrag_Faszination_Karosserie.pdf. Accessed 16 Jul 2021.
2. Bachmann J, Hidalgo C, Bricout S. Environmental analysis of innovative sustainable composites with potential use in aviation sector—A life cycle assessment review. Sci. China Technol. Sci. 2017;60:1301–17. doi:10.1007/s11431-016-9094-y.
3. Airbus. Composites: Airbus continues to shape the future. 2017. https://www.airbus.com/newsroom/news/en/2017/08/composites--airbus-continues-to-shape-the-future.html. Accessed 16 Jul 2021.
4. Neitzel M, Mitschang P, Breuer U, editors. Handbuch Verbundwerkstoffe: Werkstoffe, Verarbeitung, Anwendung. 2nd ed. München: Hanser; 2014.
5. Denkena B, Schmidt C, Kaczemirzk M, Schwinn M. Influence of a Dynamic Consolidation Force on In Situ Consolidation Quality of Thermoplastic Composite Laminate. J. Compos. Sci. 2021;5:88. doi:10.3390/jcs5030088.
6. Lukaszewicz DH-J, Ward C, Potter KD. The engineering aspects of automated prepreg layup: History, present and future. Composites Part B: Engineering. 2012;43:997–1009. doi:10.1016/j.compositesb.2011.12.003.
7. Croft K, Lessard L, Pasini D, Hojjati M, Chen J, Yousefpour A. Experimental study of the effect of automated fiber placement induced defects on performance of composite laminates. Composites Part A: Applied Science and Manufacturing. 2011;42:484–91. doi:10.1016/j.compositesa.2011.01.007.
8. Woigk W, Hallett SR, Jones MI, Kuhtz M, Hornig A, Gude M. Experimental investigation of the effect of defects in Automated Fibre Placement produced composite laminates. Composite Structures. 2018;201:1004–17. doi:10.1016/j.compstruct.2018.06.078.
9. Sawicki A, Minguett P. The effect of intraply overlaps and gaps upon the compression strength of composite laminates. In: 39th AIAA/ASME/ASCE/AHS/ASC Structures, Structural Dynamics, and Materials Conference and Exhibit; 20 April 1998 - 23 April 1998; Long Beach,CA,U.S.A. Reston, Virigina: American Institute of Aeronautics and Astronautics; 1998. doi:10.2514/6.1998-1786.
10. Schledjewski R. Thermoplastic tape placement process – in situ consolidation is reachable. Plastics, Rubber and Composites. 2009;38:379–86. doi:10.1179/146580109X12540995045804.
11. Meister S, Möller N, Stüve J, Groves RM. Synthetic image data augmentation for fibre layup inspection processes: Techniques to enhance the data set. J Intell Manuf 2021. doi:10.1007/s10845-021-01738-7.
12. Sacco C, Baz Radwan A, Anderson A, Harik R, Gregory E. Machine learning in composites manufacturing: A case study of Automated Fiber Placement inspection. Composite Structures. 2020;250:112514. doi:10.1016/j.compstruct.2020.112514.
13. Schmidt C, Hocke T, Denkena B. Deep learning-based classification of production defects in automated-fiber-placement processes. Prod. Eng. Res. Devel. 2019;13:501–9. doi:10.1007/s11740-019-00893-4.
14. Samuel AL. Some Studies in Machine Learning Using the Game of Checkers. IBM J. Res. & Dev. 1959;3:210–29. doi:10.1147/rd.33.0210.
15. Wanigasekara C, Oromiehie E, Swain A, Prusty BG, Nguang SK. Machine Learning Based Predictive Model for AFP-Based Unidirectional Composite Laminates. IEEE Trans. Ind. Inf. 2020;16:2315–24. doi:10.1109/TII.2019.2932398.

16. Schledjewski R. Inline Control of Tape Width during Automated Tape Placement. In: ECCM18-18th European Conference on Composite Materials; 24-28 June 2018; Athens, Greece; 2018.
17. Wanigasekara C, Oromiehie E, Swain A, Prusty BG, Nguang SK. Machine learning-based inverse predictive model for AFP based thermoplastic composites. Journal of Industrial Information Integration. 2021;22:100197. doi:10.1016/j.jii.2020.100197.
18. Mitchell TM. Machine learning. New York, NY: McGraw-Hill; 2010.
19. Chen C-T, Gu GX. Machine learning for composite materials. MRC. 2019;9:556–66. doi:10.1557/mrc.2019.32.
20. Géron A. Hands-on machine learning with Scikit-Learn, Keras, and TensorFlow: Concepts, tools, and techniques to build intelligent systems. Sebastopol CA: O'Reilly; 2020.
21. Schmidhuber J. Deep learning in neural networks: an overview. Neural Netw. 2015;61:85–117. doi:10.1016/j.neunet.2014.09.003.
22. Heraeus Noblelight. humm3® - intelligent heat for composites. https://www.heraeus.com/en/hng/products_and_solutions/arc_and_flash_lamps/humm3/humm3.html. Accessed 22 Jul 2021.
23. Di Boon Y, Joshi SC, Bhudolia SK. Review: Filament Winding and Automated Fiber Placement with In Situ Consolidation for Fiber Reinforced Thermoplastic Polymer Composites. Polymers (Basel) 2021. doi:10.3390/polym13121951.
24. Danezis A, Williams D, Edwards M, Skordos AA. Heat transfer modelling of flashlamp heating for automated tape placement of thermoplastic composites. Composites Part A: Applied Science and Manufacturing. 2021;145:106381. doi:10.1016/j.compositesa.2021.106381.
25. Monnot P, Williams D, Di Francesco M. Power Control of a Flashlamp-based Heating Solution for Automated Dry Fibre Placement. In: ECCM18-18th European Conference on Composite Materials; 24-28 June 2018; Athens, Greece; 2018.
26. Di Francesco M. Laser-assisted Automated Fibre Placement Process Development [PhD Thesis]: University of Bristol; 2018.

  doi:10.5075/epfl-298799_978-2-9701614-0-0

A NOVEL CLOSED-LOOP TESTING FRAMEWORK FOR DECODING CONSOLIDATION DEFORMATION MECHANISMS IN MANUFACTURING

Anatoly Koptelov[a], Jonathan P.-H. Belnoue[a], Ioannis Georgilas[b], Stephen R. Hallett[a], and Dmitry S. Ivanov[a]

a: Bristol Composites Institute, University of Bristol, Bristol, United Kingdom,
anatoly.koptelov@bristol.ac.uk
b: Department of Mechanical Engineering, University of Bath, Bath, United Kingdom

Abstract: *The introduction of new materials in industrial practice goes through cumbersome processes with very long lead times and huge cost of manufacturing trials. Modern materials are complicated and require tailored characterisation testing programmes. The benchmarking exercises for materials in manufacturing, the first steps towards standardisation of testing practices, often show remarkable discrepancy when identical materials are tested on similar rigs at different labs. The proposed approach reinvents the entire process of composites testing. Autonomous Testing Framework intelligent system designs test programmes independently of human intervention and enables fast screening of material properties on the go. It decides on the loading programme reacting on feedback data received from the material in real-time. The developed testing tool was previously tested for two prepreg systems. This research focuses on the characterisation testing of dry materials.*

Keywords: consolidation characterisation; compaction; resin flow

1. Introduction

The consolidation of composite precursors is a key mechanism in the manufacturing of laminate structures. Due to the complex flow and deformation mechanisms of a composite, conventional approach requires a number of tests to be conducted to gather enough data for further material characterisation. However, manufacturing and testing is both expensive and time consuming. Therefore, there is a need in a predictive tool capable of designing testing programs based on the material's viscoelastic behaviour, thus reducing the total number of experiments to a minimum.

A typical material's characterisation process involves a training of a chosen phenomenological model by fine-tuning its parameters. The goal is to achieve model's output similar to a material's actual behaviour. Plain experimental program or low number of conducted tests could be insufficient for material's characterisation. In such case, the derived model might perform deceptively well within data provided for training but completely fail to adapt to changing processing conditions. The research question is how complex loading program should be and how many experiments is enough. The idea of the proposed approach is to build such a testing system, which will not be bound by any predefined assumptions about material's behaviour and have no bias towards any supposed phenomenological consolidation model. Such a system is implemented within the current project and is called Adaptive Testing Framework (ATF).

The proposed Adaptive Testing Framework deploys a set of material models (referred to as candidate models) in the pre-coded library. Based on the material feedback, the ATF is able to

  doi:10.5075/epfl-298799_978-2-9701614-0-0

pick the best performing candidate model and to build a test programme in real-time without any human involvement. Such programme is aimed to facilitate an extraction of the characteristic features of the material behaviour. This work continues the research presented in [1,2], where the proposed system was tested for different toughened prepreg materials. This paper explores the application of the ATF to dry materials. Thorough description of the ATF structure and used candidate material models can be found in [1,2].

2. Adaptive testing framework

The concept of the Adaptive Testing Framework

The concept of the ATF is presented in Figure 1.a. The framework is connected to the compression test machine through the data acquisition hardware. The incoming compression evolution data from the machine is processed by the ATF. The framework fits candidate models to the received compaction data and picks the best performing ones. Then, the loading command for the next step is built to distinguish between candidate models as the experimentation goes on. The loading command for the load step 2 is submitted back to the test machine. After the completion of every load step, the last registered load level is dwelled to give the framework time to process the data as shown in Figure 1.b (shown in pink colour).

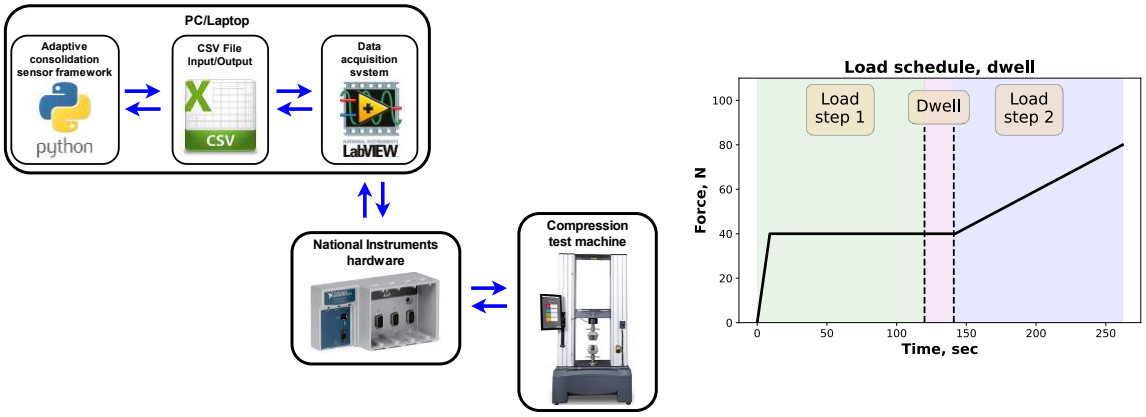

a b

Figure 1 - a - Autonomous real-time testing setup overview; b – Transition between load steps

Although, the compaction data is still received by the framework during the “dwell stage”, it is necessary to minimise the time delay. The reason for that is that the employed load schedule at this stage is not designed to distinguish between candidate models (as opposed to the “controlled” load schedule at the other stages of the test). It is present purely for computational purposes. The time delay between load steps is present purely for computational purposes. The excessive duration of such “dwell stages” in the resulting load schedule defeats the purpose of a material-driven experimental programme. In such case, the compaction history data used for the load step definition would contain regions which were not aimed for the efficient material characterisation. Moreover, introduction of dwell stages may affect the resulting path of the load curve, because the framework’s algorithm might find a different set of favourable candidate models for the provided compaction dataset. The duration of the time delay for the load dwell stage reflects the processing speed of the consolidation framework and depends on several factors:

  doi:10.5075/epfl-298799_978-2-9701614-0-0

- The complexity of the candidate material models (the number of model parameters, the complexity of data fitting related to model's non-linearity).
- The number of the candidate material models in the library.
- The chosen methods for optimisation.
- The available hardware for running the framework (PC/laptop).
- The size of the input experimental compaction dataset.

Data acquisition setup

The connecting interface of the data acquisition hardware is shown in Figure 2. The main parts of the setup include:

- A compact data acquisition chassis cDAQ-9174 which serves to create portable sensor measurement systems. The chassis has four slots for inserting measuring input/output modules. It controls the synchronisation, timing, and data transfer between measuring modules and an external host (PC/laptop). The chassis has 9-30 V power supply port and USB port for connection with the PC/laptop.
- A voltage output module NI 9263. The module is attached to the port №3 of the chassis. Its purpose is to transmit a voltage signal to the compression machine. The signal is transmitted through one channel only, as only the load value is sent. The connection with the testing machine is implemented through the BNC cable.
- A voltage input module NI 9201. The module is attached to the port №1 of the chassis. This module receives a voltage signal from the compression machine. There are two channels employed, as both load and displacement data are received from the compression machine. Similar to the output module, the connection is performed through the BNC cable (2 cables as there are 2 channels).

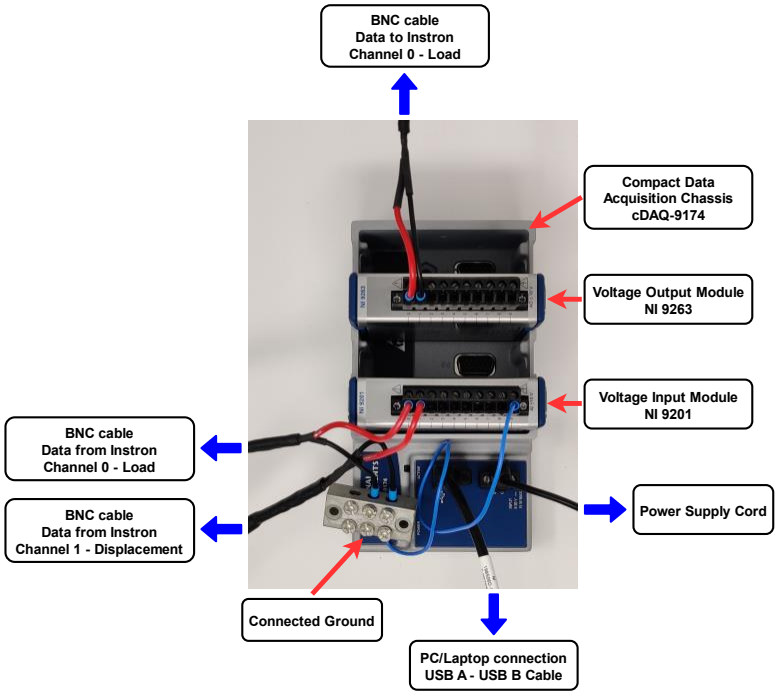

Figure 2 – Data acquisition setup. Input/output modules and connection interfaces.

Studied materials

In previous work [2] the experimentation was performed for IMA/M21 [3] and IM7/8552 [4] toughened prepregs. The real-time characterisation testing within the current research was performed for dry material systems. This type of the material was chosen to trial the consolidation framework within the material which is not represented in the consolidation library. It is important to emphasise, that due to the absence of resin phase there was no particular reason to manufacture dry specimens in a crucifix shape. Nevertheless, it is done for the sake of consistency with the previous experimentation [1,2]. Two material textile systems were trialed:

- ampliTex 5040 flax fibre twill weaved fabric [5] with a ply thickness of 0.48 mm. The specimens were laid-up in 8 plies cross-ply (CP) configuration $[90/0]_4$. The specimen is demonstrated in Figure 3.a.

- Carbon fibre non-crimp fabric (NCF) with a ply thickness of 0.86 mm. The specimens were laid-up in 6 plies cross-ply (CP) configuration $[90/0]_3$. The specimen is demonstrated in Figure 3.b.

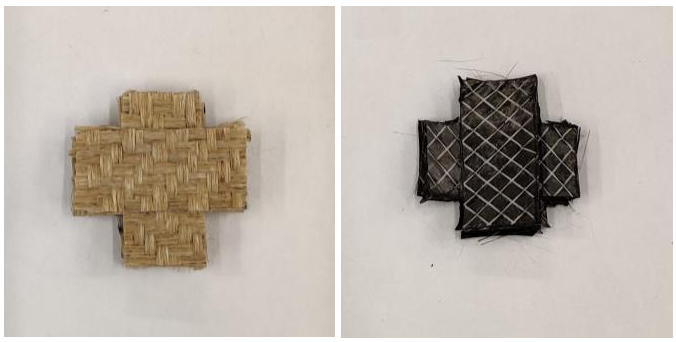

a b

Figure 3 –a - ampliTex 5040 flax fibre twill weaved fabric; b – carbon fibre NCF test sample

For the sake of consistency with previous work [1,2], the geometry and the layup of the cross-ply specimen remained unchanged. The compaction area of the crucifix specimens was chosen to be 15 x 15 mm.

3. Results and discussion

The purpose of this exercise was to put the autonomous testing framework in challenging conditions, when the candidate material models in the consolidation library are not designed for the studied material system specifically. The idea was to demonstrate the existing limitations of the proposed approach. As the definition of a loading programme is based on the difference between two best performing candidate models, there is a compulsory requirement for the presence of at least two comprehensive models in the library relevant to the studied material. All considered candidate models [1,2] are formulated for two-phase materials (e.g. shear thinning flow of the reinforced fluid, resin's percolation through the fibrous network, the transition between squeezing and bleeding flow modes). It is possible to assume why the current set of material models in the library could potentially reflect the behaviour of a dry fibre material:

- Air represents a fluid in the material system. In this case, the range of viscosities would be significantly different in comparison with the conventional two-phase material system (e.g. prepregs IMA/21, IM7/8552 etc.). Such development presents a potential challenge for the framework to derive the optimal set of material parameters.

- There are certain aspects of the considered candidate models which could reflect characteristic features of dry material's behaviour. For instance, the set of material parameters can be defined in a way, which makes resin's contribution negligible. For percolation model it would mean that only elastic reaction of fibrous network contributes to the compaction response. For shear models it could be the distortion of fibre network's structure (widening of yarns) during compaction.

Real-time experimentation approach was described in [2]. To explore different loading scenarios, the initial and following load steps' amplitudes were varied in ranges 40 - 80N and 30 - 50N respectively. The summary of al performed tests is presented in Table 1. The resulting test programmes and samples' compaction feedback for flax and NCF samples are shown in Figure 4.a and Figure 4.b respectively.

Table 1 Explored test settings for the real-time testing of dry material. RTT stands for real-time test.

Test id	Material	Initial load step		Further load steps		
		Load amplitude, N	Loading regime	Max. load amplitude, N	Step duration, sec	Number of load options
RTT_DRY 1	Flax	40	Ramp-dwell	30	100	5
RTT_DRY 2	Flax	80	Ramp-dwell	50	100	5
RTT_DRY 3	NCF	80	Ramp-dwell	50	100	5
RTT_DRY 4	NCF	40	Ramp-dwell	30	100	5

Both material systems demonstrated a significant drop in thickness within the first seconds of the test. Loading programmes for flax samples showed a trend for a constant increase of the load level up to 250 N with several dwell stages (RTT_DRY 2). The programmes for NCF samples demonstrated a different trend. The load reached a plateau (100 N for the test RTT_DRY 4 and 200 N for the test RTT_DRY 3) and held steady up until the end of the experimentation. The framework selected both monotonic and ramp-dwell loading options for the test RTT_DRY 4.

  doi:10.5075/epfl-298799_978-2-9701614-0-0

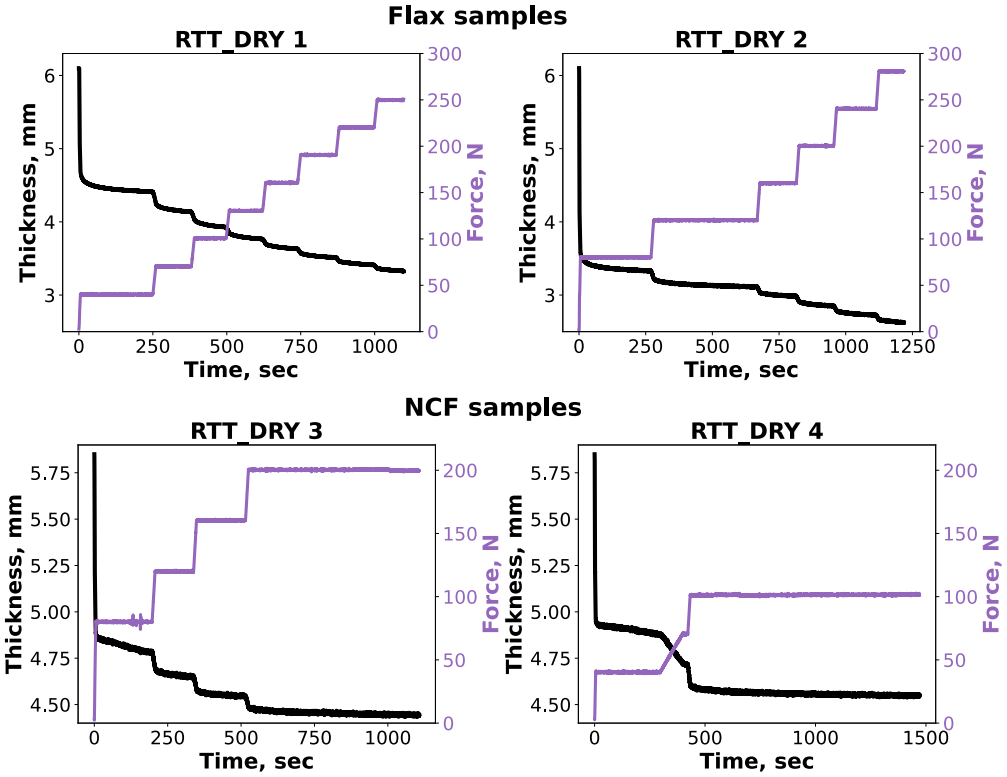

Figure 4 - Dry material testing. Resulting loading programmes and compaction curves for flax and NCF samples.

The step-by-step parameter extraction routine breakdown for both types of dry material samples is shown in Figure 5 (due to the volume of data, only two steps for each material system are shown). The set of favourable candidate models evolved during the testing of flax samples. After the initial load step, the DefGen and percolation models were able to fit the data very well (the prediction curves overlapped with the experimental data). But in the last steps of the test the second-best candidate changed from the percolation to the shear model. Within this research, this was the first instance when the shear model was selected as one of the top two candidates upon the completion of a characterisation test. For the NCF material the best candidates were consistent throughout the test – DefGen and percolation models (purple and orange curves). Both models demonstrated high accuracy in thickness prediction – the DefGen model showcased the perfect fit to the experimental data and overlapped with the actual compaction curve (the thin purple "DefGen" curve can be seen on top of the thick blue "experimental data" curve). The second-best percolation candidate was able to fit the experimental data with an offset at the stage of the initial load raise (orange curve). The deviation in final thickness prediction for both models was less than 0.1%.

  doi:10.5075/epfl-298799_978-2-9701614-0-0

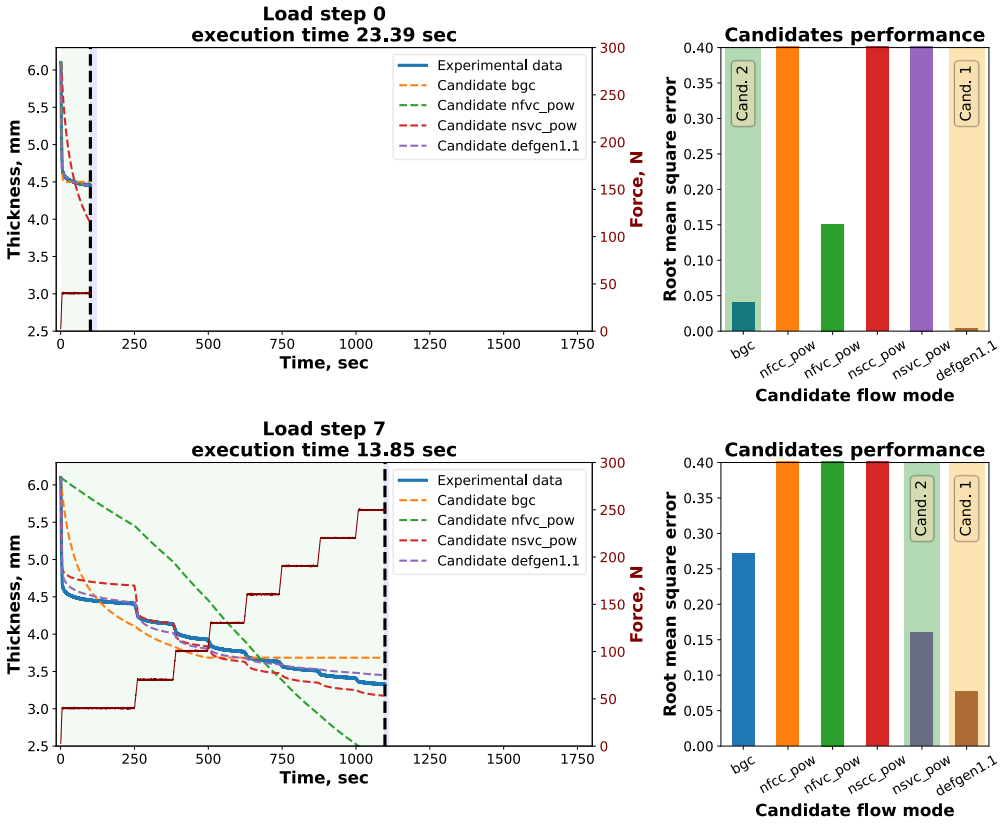

a

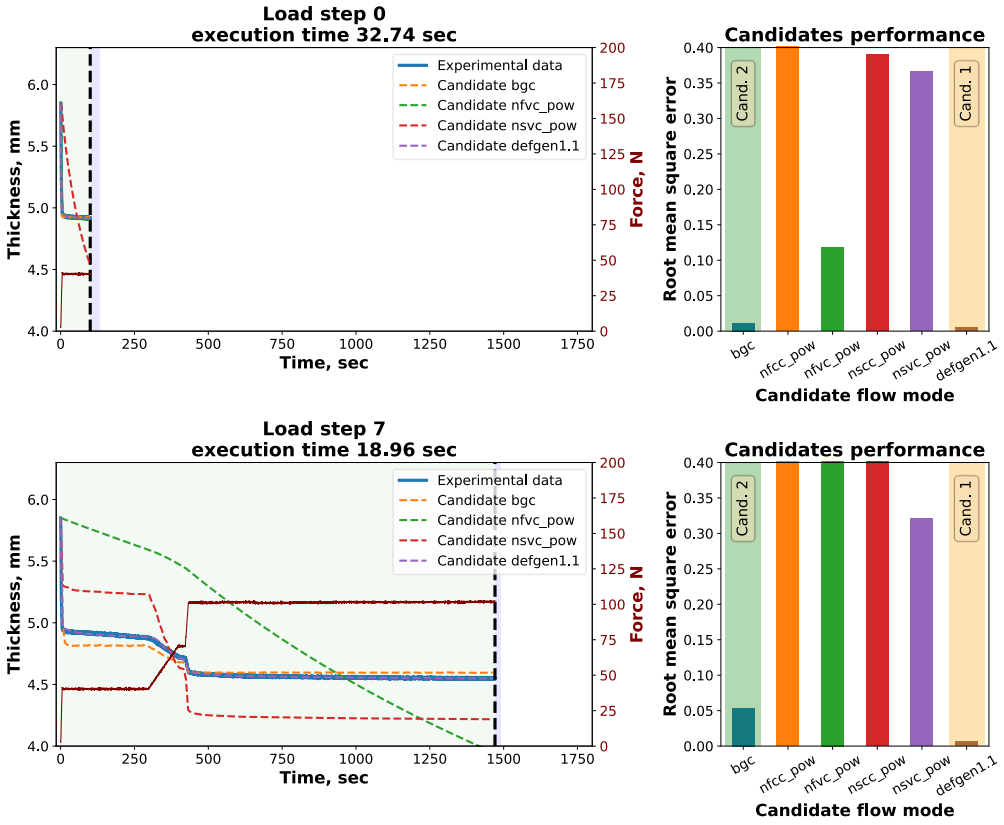

b

Figure 5 - Dry material real-time experimentation step by step routine. a) Flax material; b) NCF material. Green region – all previously received data. Blue region (on the right from the vertical black dashed line) – required processing time.

  doi:10.5075/epfl-298799_978-2-9701614-0-0

The validation (see [2]) of the obtained models was not performed for this set of materials. The main reason for that is the variability of the specimens. There was no resin which could keep separate plies in place. Inconsistencies in experimentation (in the equipment, specimens' preparation, methodology etc.) for obtaining training or validation compaction datasets may lead to misleading results. In such case, the obtained material model is trained or trialled within features of material behaviour which are not represented in the validation/training sets. As a result, it will perform poorly either due to the insufficiency or irrelevancy of the training dataset.

4. Conclusions

The characterisation of dry materials was performed to explore the limitations of the proposed approach. The framework showcased a robust performance during training stage by fitting the candidate models to the material's thickness data with no visible offset. Formidable performance of a candidate model at the training stage is a necessary condition. However, it alone does not provide sufficient cause for making a conclusion about model's feasibility. Even though for certain test/materials scenarios (NCF sample, test RTT_DRY 4) the error in thickness prediction is next-to-zero, there is no guarantee that the derived model would uphold its performance for changed processing conditions. The validation of the obtained models was not performed due to the imperfections in dry samples preparation process.

Acknowledgements

This work was supported by the Engineering and Physical Sciences Research Council (EPSRC) through the Centre for Doctoral Training in Advanced Composites Collaboration for Innovation and Science (grant number EP/L016028/1) and SIMulation of new manufacturing PROcesses for Composite Structures (SIMPROCS) (grant number EP/P027350/1).

5. References

[1] Koptelov A, Belnoue JP-H, Georgilas I, Hallett SR, Ivanov DS. Revising testing of composite precursors – A new framework for data capture in complex multi-material systems. Compos Part A 2022;152:106697. https://doi.org/10.1016/j.compositesa.2021.106697.

[2] Koptelov A, Belnoue JP-H, Georgilas I, Hallett SR, Ivanov DS. Adaptive Real-Time Characterisation of Composite Precursors in Manufacturing. Front Mater 2022;9:1–18. https://doi.org/10.3389/fmats.2022.864584.

[3] HEXCEL Corporation. HexPly ® M21 180°C (350°F) curing epoxy matrix. Epoxy Matrix Product Datasheet. 2015.

[4] HEXCEL Corporation. HexPly 8552 ® Epoxy matrix (180°C/356°F curing matrix). Epoxy Matrix Product Datasheet. 2020.

[5] Bcomp Ltd. ampliTex™ 5040 flax fibres fabric. Fabric Product Datasheet. n.d.

  doi:10.5075/epfl-298799_978-2-9701614-0-0

Neural Network Assisted Ga Optimization of Adhesively Bonded Composite Joints

Edore G. Arhore*, Mehdi Yasaee, Iman Dayyani

School of Aerospace, Transport and Manufacturing, Cranfield MK43 0AL, UK

edore.arhore@cranfield.ac.uk

Abstract

Accurate prediction of an adhesive bonded joint performance with numerical analysis requires the inclusion of nonlinear and damage modelling such as cohesive zone modelling (CZM) and continuum damage modelling (CDM) which is computationally expensive. Therefore, using these nonlinear modelling methods in finite element analysis (FEA) during an optimisation process is often impractical. This investigation presents a new method to improve a genetic algorithm optimisation of adhesively bonded joints using a convolutional neural network (CNN) to replace/augment the computationally intensive FEA portion of the process. The proposed methods use trained CNN to predict adhesive joints' performance (strength). Training has been conducted on a database of random joint designs that have been analysed with high fidelity nonlinear FEA. The trained CNN is then used to predict joint strength during the optimisation process. The proposed methods reduced the computational cost by up to 93% compared to the current GA method that uses FEA.

Declaration of Interest: None

Keywords

Adhesive joints, Convolutional neural network, Genetic algorithm, Cohesive zone modelling (CZM), Continuum damage model (CDM)

1 Introduction

Recent advancements in machine learning (ML) a subset of artificial intelligence (AI) have led to the capability of computers to labelling and classify images, detecting objects and scenes among others [1]. Convolutional neural network (CNN) has exhibited ground-breaking performance in the field of object detection and image classification [2]. It can be defined as a deep learning method that is comprised of neurons utilising learnable weight values to perform convolution mathematical operations to carry out an assigned task [3]; [4]. It can also be described as the standard for image classification and has the potential to deal with problems involving data analysis [5].

ML can be described as a computer algorithm that uses experience and performance measures to perform specific tasks [3]. Deep learning and therefore CNN is a specific type of ML. An example of the specific task performed by CNN includes classification in which the CNN is trained to identify the class an input belongs to [6]. For this task type, the CNN will map the input to a class from a predefined list of classes. Another task type is regression, in which the CNN produces a number as a prediction for the given input [3]. Therefore, unlike in the case of classification, the regression task does not require the CNN to identify the input with a distinct

  doi:10.5075/epfl-298799_978-2-9701614-0-0

class from a predefined list. Instead, it uses its experience and performance measures to estimate or predict a numerical value to classify/identify the input. Other task types which include anomaly detection, denoising, and transcription among others are extensively explained by Bengio et. al [3].

The use of CNN in engineering, although initially limited, has increased recently displaying some promising results. This includes the research performed by Kim et. al [7] on the use of CNN for the prediction of mechanical behaviour of unidirectional composites. The results showed that the CNN exhibited high accuracy in its predictions displaying a potential to identify the behaviour of composites based on their microstructure. Zhu and Wang [8] proposed the use of CNN in the prediction of long-term deformation of concrete due to creep. They showed that the use of CNN, resulted in the prediction of creep failure to a higher level of accuracy when compared to classical numerical and analytical analysis techniques. The only caveat is that their method required a large database to train the CNN.

Although research has been carried out to improve the properties of adhesively bonded joints, most of these studies are focused predominantly to modify a single feature during the optimisation process and focus predominantly on the elastic stiffness of the joint [9]. The dominant failure mechanism in adhesively bonded joints is the cohesive failure [10] which can be computationally expensive to capture during finite element analysis (FEA.) Therefore, most studies performed on the optimisation of these joints do not include failure and progressive damage modelling in the FEA. Studies have shown the possibilities of carrying out FEA analysis with progressive damage modelling of the adhesive interface with cohesive zone modelling (CZM) [9] as well as the implementation of these advanced FE models with an optimisation process [11]; [12]; [13]; [14]. A disadvantage of these methods is the high computational cost which therefore limits its application, often with a single analysis during the optimisation iteration requiring more than 10 minutes for completion on a standard desktop PC. To complete an optimisation process that may require upwards of thousands of iterations, the implementation of finite element models with progressive damage is, therefore, not practical.

To overcome this problem, CNN using regression was trained to predict the strength of adhesively bonded joints using only an image representation of the joint. In this paper, 2 new CNN assisted optimisation process will be proposed for the optimisation of adhesively bonded joints. The results of the different methods would be discussed and compared with emphasis on the computational cost of each method as well as the accuracy of the optimisation process in terms of the properties of the generated optimum joint.

2 Methodology

The objective of this study is to minimise the computational cost in the optimisation of adhesively bonded joints with the use of CNN. The three different joint types used in this study are shown in Figure 2-1 which also highlights the applied loading and boundary conditions. The joints are comprised of composite inner adherends, modelled with Hashin failure initiation criterion and progressive damage properties given in Table 1, and metallic outer adherend which were modelled using Johnson-Cook plasticity and failure properties given in Table 2. The interface interaction between the adherends (bonded region) was modelled using CZM. The CZM was created using surface interaction between the bonded surfaces, it was modelled as a

  doi:10.5075/epfl-298799_978-2-9701614-0-0

bi-linear cohesive behaviour using Benzeggagh-Kenane (BK) mixed-mode fraction criteria. The parameters applied to the CZM are listed in Table 3. A legacy (GA-FEA) optimisation process Figure 2-2a was performed on the different joint types to produce a benchmark optimum design for comparison. It would also be used for the comparison of the computational cost.

Table 1
Composite IM7/8552 Material Properties [15]

Parameter	Value
Young modulus, fibre direction (E_1)	$161GPa$
Young modulus, transverse direction (E_2, E_3)	$11.38GPa$
In-plane shear modulus (G_{12}, G_{13})	$5.17GPa$
Transverse shear Modulus (G_{23})	$3.92GPa$
Poisson's ratio (v_{12})	0.32
Poisson's ratio (v_{13})	0.32
Poisson's ratio (v_{23})	0.3813
Tensile strength, fibre direction (X_T)	$2.3GPa$
Compressive strength, fibre direction (X_C)	$1GPa$
Tensile strength (Y_T)	$62.3MPa$
Compressive strength (Y_C)	$253.7MPa$
Shear strength (in-plane), (S_{12})	$89.6MPa$
Shear strength (S_{23})	$126.9MPa$
α	0

Structural optimisation process using convolutional neural network (GA-CNN)

The GA-FEA process Figure 2-2a was modified by replacing the FEA segment with a trained CNN as shown in Figure 2-2b. The trained CNN was tasked with the function of predicting the strength of the joint design generated by the optimiser. To perform this task, an image representation of the joint was generated based on the design variable produced by the GA optimiser. This generated image was sent to the CNN which predicted a specific reaction force (SRF_N) value for it. The objective of the optimisation was set to maximise this value, as such the design variable for which the CNN predicted the maximum SRF_N value would be classified as the optimum.

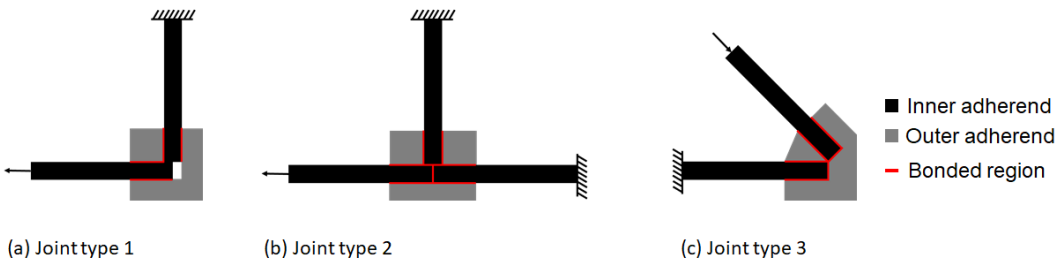

Figure 2-1 Illustration of the analysed joints design space

Figure 2-2a shows the GA-FEA optimisation process described by Arhore et. al [9] used to obtain the optimum geometry of the outer adherend. The entire optimisation process is fully autonomous requiring no user input and limited to a maximum of 120 hours of runtime.

Table 2
Aluminium 7075-T6 material properties [15]

Parameter	Value
Young's modulus (E)	$71.7GPa$
Poisson's ratio (v)	0.33
Mass density (ρ)	$2810kgm^{-3}$
A	$473MPa$
B	$210MPa$
n	0.3813
d_1	0.3714
d_2	-0.1233
d_3	-1.9354

Table 3

Bonded joint adhesive interface cohesive damage property [9]

Parameter	Value
G_{IC}	$210Jm^{-2}$
G_{IIC}, G_{IIIC}	$663m^{-2}$
σ_I	15
$\sigma_{II}, \sigma_{III}$	$340MPa$
$BK\ exponent$	2.1

Structural optimisation process augmented with convolutional neural network (GA-FEA-CNN)

The accuracy of the trained CNN is dependent on factors which include the training data and the CNN architecture, among others. The GA-CNN optimisation procedure may produce non-optimal designs, purely due to the training dataset resulting in a poor performing CNN. To overcome this, in this section, an alternative approach is proposed, where the GA-FEA optimisation process is augmented with CNN. The flowchart shown in Figure 2-2c shows the combination of the GA-FEA (Figure 2-2a) and GA-CNN (Figure 2-2b) optimisation processes producing the GA-FEA-CNN process.

In this method, the design variable generated by the optimiser is used to produce an image representation of the joint which is used by the trained CNN to predict its strength value. However, unlike in the case of the GA-CNN optimisation process, if the design is classified as good, that is, the predicted SRF_N value is greater or equal to 60% of the SRF_N value of the GA-FEA optimum, an ABAQUS model would be generated, and FEA performed to validate the predicted SRF_N value. After verification, the calculated SRF values are normalised using the same method used to create the CNN training. This ensured the values returned to the optimiser are the same order of magnitude.

  doi:10.5075/epfl-298799_978-2-9701614-0-0

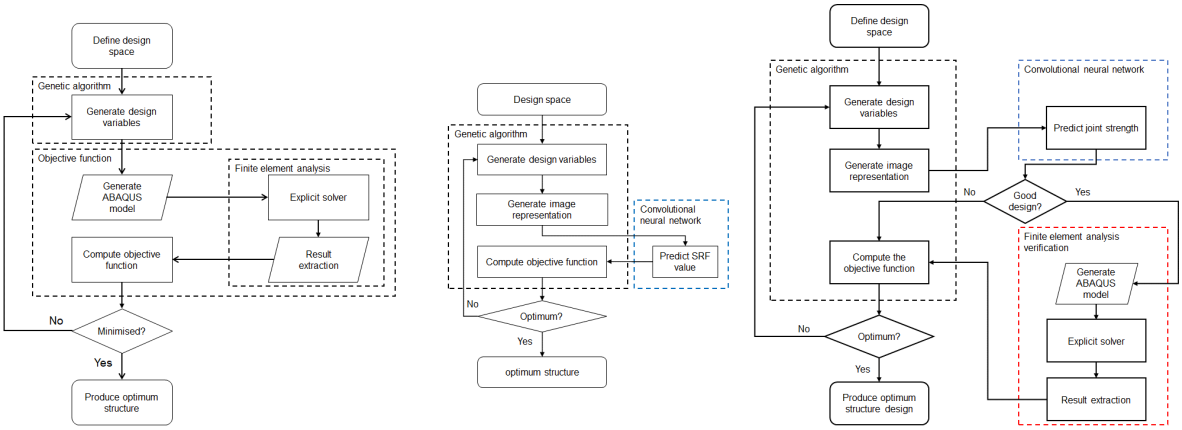

(a) GA-FEA (b) GA-CNN (c) GA-FEA-CNN

Figure 2-2 Proposed optimisation methods

3 Results

Joint Type 1

The results obtained from the different optimisation methods is shown in Figure 3-1a outlining the maximum and minimum values. It also shows the average SRF_N value (the objective function) from multiple optimisation runs with the error bars indicating the maximum and minimum values obtained.

The computational cost for the GA-FEA process in terms of runtime peaked at a value of 95 hours. The GA-CNN method produced an optimum design that matched the GA-FEA optimum. The computational resource in terms of runtime required by the GA-CNN process was, on average 7 hours. This equated to a percentage reduction of up to 92% of the resources required by the GA-FEA process (Figure 3-1a). The GA-FEA-CNN optimisation process produced an optimum design exhibiting a SRF value 1% higher than that of the GA-FEA optimisation process. This was achieved with a reduction of up to 86% in computational cost (Figure 3-1) in comparison to the GA-FEA method.

Joint Type 2

The average runtime for the optimisation process was 35 hours with a high of 36 hours as illustrated in Figure 3-1b. The optimum joint designs produced by the GA-CNN method matched that produced by the GA-FEA. It required approximately 2.3 hours of computational time. This equated to a 93% reduction in computational cost in comparison to the GA-FEA method. The GA-FEA-CNN process also produced an optimum that matched that produced by the GA-FEA method requiring on average 6.7 hours of runtime for completion.

Joint Type 3

Figure 3-1c shows the results of the optimisation process outlining the consistency of the GA-FEA process in terms of its optimum joint design. The computational cost of this process fluctuated between the values of 110 and 120 hours. The GA-FEA-CNN method produced an optimum joint design matching the GA-FEA method. It required on average 18 hours which equated to an 84% drop in computational cost in comparison to the GA-FEA method. The

  doi:10.5075/epfl-298799_978-2-9701614-0-0

optimum joint produced by the GA-CNN closely resembles the optimum produced by the other methods requiring on average 6 hours for completion. This design however exhibited a SRF value which was 6% lower than the optimum from the other methods.

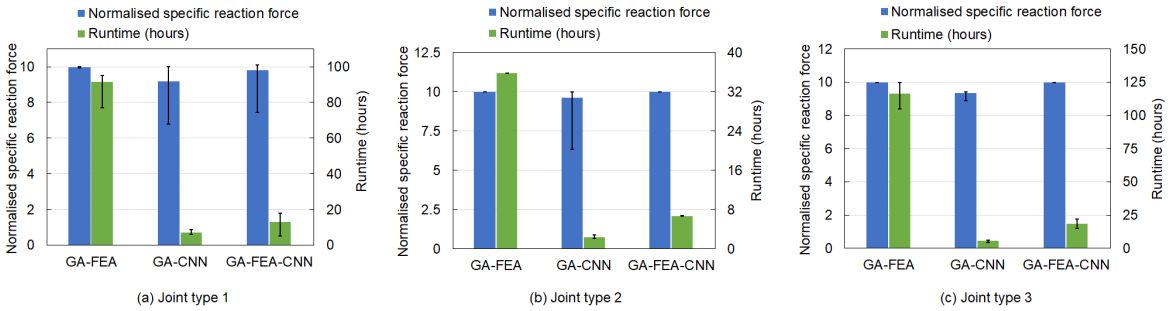

Figure 3-1 Optimisation results *error bars indicate the maximum and minimum values

4 Discussions and Conclusion

This paper presents new methods of improving the structural optimisation process of adhesively bonded joints for strength improvements. For the study, two different optimisation procedures were proposed to minimise the computational cost without negatively affecting the optimisation process. The first method (GA-CNN) proposed is the implementation of a convolutional neural network (CNN) with the task of completely replacing finite element analysis (FEA) within the optimisation process. This means that the CNN is the only means of obtaining the strength properties of joint designs generated during the optimisation process. For the second method (GA-FEA-CNN), a trained CNN was added to the optimisation process to function as a filter limiting the requirement to perform FEA.

The results showed that the GA-FEA-CNN method offered the best in terms of overall performance. Using this method, the computational cost was reduced by up to a maximum of 84% when compared to the GA-FEA method. Although the accuracy of the CNN was dependent on the availability of training data, the fact that this method allowed, the limited use of FEA to validate the predictions made by the CNN, accounts for its high efficiency. This validation step played a pivotal role when the accuracy of the CNN was less than ideal when deployed to perform the optimisation process. This proposed method was noticed to produce optimum designs which were even better than those produced by the current method in a fraction of the runtime. This behaviour can be attributed to many factors, for example, the legacy optimisation process (GA-FEA) in some cases is terminated autonomously at a maximum computational cost. This might be limiting the design search and therefore leaving the optimiser trapped at a local optimum. The proposed optimisation process with CNN augmented FEA was able to counteract this limitation.

The proposed CNN only method (GA-CNN) offered the best reduction in computational cost performing the optimisation process in approximately half the time the GA-FEA-CNN method. However, this method was heavily dependent on the accuracy of the CNN which was again dependent on the availability of data for training. As a result, the accuracy of this method could

  doi:10.5075/epfl-298799_978-2-9701614-0-0

not be guaranteed at the start. Getting the CNN to achieve the level of accuracy needed to produce correct optimum design, requires a high number of reasonably distributed data for training as well as distinguishable features in the dataset for the CNN to capture. In cases where joints with dissimilar features behaved similarly, the CNN struggled to predict the properties accurately which resulted in the poor overall performance of the optimisation process. In other cases, the CNN struggled to identify subtle differences in similar geometries which also affected the accuracy of the CNN.

The key advantage of the proposed methods is the minimisation of the computational cost. This allowed the selected optimiser to better search through the design space obtaining better performing models. However, a major disadvantage lies with the accuracy of the CNN which is dependent on the availability of training data. This training data could be computationally expensive to create but will only be needed once, if not already available. Although the GA-FEA-CNN method mostly counteracted the dependency on the CNN's accuracy, in some cases, the optimiser was misdirected by bad CNN predictions resulting in low performing optimum designs. For the GA-FEA-CNN method, the threshold for which the FEA validation step is triggered can also be adjusted to suit the accuracy of the CNN and thereby limit the dependency on its accuracy. Increasing the threshold for a more accurate CNN will result in a reduction in computational cost while reducing it for a less accurate CNN will result in an increased computational cost.

References

[1] Garcia-Garcia, A., Orts-Escolano, S., Oprea, S., Villena-Martinez, V. and Garcia-Rodriguez, J. (2017) 'A Review on Deep Learning Techniques Applied to Semantic Segmentation'. Available at: http://arxiv.org/abs/1704.06857.

[2] Sharma, N., Jain, V. and Mishra, A. (2018) 'An Analysis of Convolutional Neural Networks for Image Classification', *Procedia Computer Science*. Elsevier B.V., 132(Iccids), pp. 377–384. doi: 10.1016/j.procs.2018.05.198.

[3] Bengio, Y., Goodfellow, I. and Courville, A. (2016) *Deep learning*. MIT Press.

[4] Habib, G. and Qureshi, S. (2020) 'Optimization and acceleration of convolutional neural networks: A survey', *Journal of King Saud University - Computer and Information Sciences*. doi: 10.1016/j.jksuci.2020.10.004.

[5] Traore, B. B., Kamsu-Foguem, B. and Tangara, F. (2018) 'Deep convolution neural network for image recognition', *Ecological Informatics*. Elsevier, 48(September), pp. 257–268. Available at: https://doi.org/10.1016/j.ecoinf.2018.10.002.

[6] Dreiseitl, S. and Ohno-Machado, L. (2002) 'Logistic regression and artificial neural network classification models: a methodology review', *Journal of Biomedical Informatics*, 35(5–6), pp. 352–359. doi: 10.1016/S1532-0464(03)00034-0.

[7] Kim, D.-W., Lim, J. H. and Lee, S. (2021) 'Prediction and validation of the transverse mechanical behavior of unidirectional composites considering interfacial debonding through convolutional neural networks', *Composites Part B: Engineering*, 225, p. 109314. doi: 10.1016/j.compositesb.2021.109314.

[8] Zhu, J. and Wang, Y. (2021) 'Convolutional neural networks for predicting creep and shrinkage of concrete', *Construction and Building Materials*, 306, p. 124868. doi:

10.1016/j.conbuildmat.2021.124868.

[9] Arhore, E. G., Yasaee, M. and Dayyani, I. (2021) 'Comparison of GA and topology optimization of adherend for adhesively bonded metal composite joints', *International Journal of Solids and Structures*, 226–227, p. 111078. doi: 10.1016/j.ijsolstr.2021.111078.

[10] Khosravani, M. R., Soltani, P., Weinberg, K. and Reinicke, T. (2021) 'Structural integrity of adhesively bonded 3D-printed joints', *Polymer Testing*, 100, p. 107262. doi: 10.1016/j.polymertesting.2021.107262.

[11] Imran, M., Shi, D., Tong, L. and Waqas, H. M. (2019) 'Design optimization of composite submerged cylindrical pressure hull using genetic algorithm and finite element analysis', *Ocean Engineering*, 190, p. 106443. doi: 10.1016/j.oceaneng.2019.106443.

[12] Wang, L., Kolios, A., Nishino, T., Delafin, P.-L. and Bird, T. (2016) 'Structural optimisation of vertical-axis wind turbine composite blades based on finite element analysis and genetic algorithm', *Composite Structures*, 153, pp. 123–138. doi: 10.1016/j.compstruct.2016.06.003.

[13] Almeida, F. S. and Awruch, A. M. (2009) 'Design optimization of composite laminated structures using genetic algorithms and finite element analysis', *Composite Structures*, 88(3), pp. 443–454. doi: 10.1016/j.compstruct.2008.05.004.

[14] Muc, A. and Gurba, W. (2001) 'Genetic algorithms and finite element analysis in optimization of composite structures', *Composite Structures*, 54(2–3), pp. 275–281. doi: 10.1016/S0263-8223(01)00098-8.

[15] Arhore, E. G. and Yasaee, M. (2020) 'Lay-up optimisation of fibre–metal laminates panels for maximum impact absorption', *Journal of Composite Materials*, 54(29), pp. 4591–4609. doi: 10.1177/0021998320937396.

STRUCTURAL MODELING OF THREE-DIMENSIONAL WOVEN PREFORM CONSIDERING ITS MANUFACTURING PROCESS

Kyeong Mo Kang[a], Hyeon Joon Yang[a], Woong-Ryeol Yu[a]*

a: Department of Materials Science and Engineering and Research Institute of Advanced Materials (RIAM), Seoul National University, Gwanak-ro 1, Gwanak-gu, Seoul 08826, Korea – *E-mail: woongryu@snu.ac.kr

Abstract: *In this paper, we develop a modeling process of 3D woven preform considering it's weaving mechanism. By analyzing the weaving mechanism, three design control parameters are defined. With various combinations of the parameters, a lot of random 3D woven composites are predictively modeled automatically. This modeling process makes it possible to generate 3D woven patterns of representative volume element (RVE) of composites, which are going to be used to establish a neural network to obtain relationship between the structure of the textile reinforcement and the mechanical properties of composite materials. The patterns are converted to input data of the neural network by the featurization inspired by the handwritten digit classification. The output data, nine elastic engineering constants, is calculated by finite element methods from the RVE of composites. Finally, a simple neural network model is constructed and evaluated with respect to prediction performance.*

Keywords: Modeling; 3D woven structure; fabric structure; neural network;

1. Introduction

Three-dimensional (3D) woven composites have attracted much attention in various fields because of their superior mechanical properties compared to conventional two-dimensional laminated composites. According to the yarn pattern in the thickness direction, various 3D woven preforms can be manufactured, e.g., layer-to-layer interlocked, through-the-thickness interlock, angle-interlocked, and so on [1]. The 3D woven composites can have various mechanical properties according to the patterns and the preform structures. The establishment of relationship between the structure of the textile reinforcement and the mechanical properties of composite materials is essential as the properties are significantly affected by the structures, and the textile reinforcement can be freely tailored by development of weaving techniques and 3D printing. This kind of work is aiming to obtain optimal textile structures for desired mechanical properties. The more diverse structures are adopted to be related with the properties, the better optimization we can achieve. Therefore, it is important to generate numerous 3D structures practically. However, there are limitations because of the randomness and complexity of the 3D architecture.

In this research, a strategy is proposed for geometrically modeling 3D woven structures considering a new weaving process [2]. Considering the weaving mechanism, the three main weaving parameters (layer, section, basis unit) which control the yarn patterns and structures are defined. Then, according to the main parameters, the yarn paths are calculated and actual yarn geometry is added, finally modeling various 3D woven preforms. All the modeling procedures are performed in TexGen, open-source software for modeling the geometry of

  doi:10.5075/epfl-298799_978-2-9701614-0-0 published under CC BY-NC 4.0 license

textile, by scripting Python code. Some critical modeling problems, like distortion of modeled structures, are solved by analyzing the source code of TexGen. Using this modeling method, not only conventional 3D woven structures but also new 3D structures are generated randomly and automatically. Then, the elastic engineering constants of such 3D woven composites were calculated through finite element analysis using ABAQUS. A neural network is constructed to relate the elastic constants with the three main parameters and will be used to explore specific 3D woven structures, e.g., the mechanical properties of which exhibit isotropic behavior in 3D.

2. Geometric modeling of 3D woven composites

2.1 Weaving mechanism

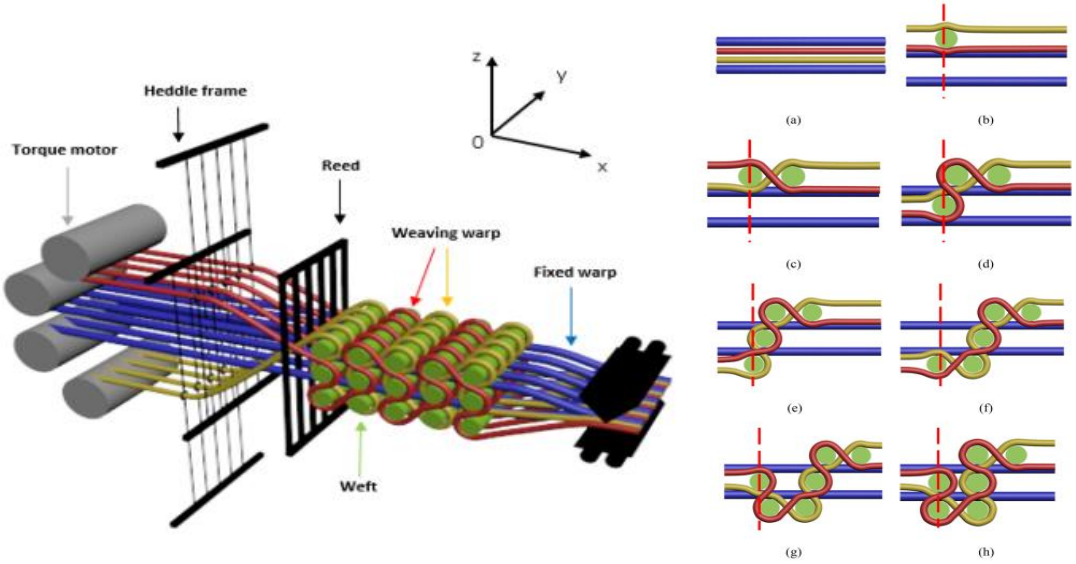

Figure 1. Weaving machine (Left) and weaving mechanism (a-h) [2]

Yang et al. have developed a new weaving technique that makes it possible to produce three-dimensional woven preforms continuously and rapidly [2]. Fig. 1 describes the manufacturing mechanism schematically. The weaving warps (binder yarns) bind the weft yarns in some repeating units. Then the weft yarns in 2D plane get folded by beating up. The layers are finally formed by the fixed warps. From this manner, three design parameters are determined. Fig 2. shows the parameters and the relationship. *Basis unit* means the repeating bound units and *Layer* means the number of layers. The two parameters make one *Section*. *Section* just signifies the number of combinations of *Basis unit* and *Layer*. One Section composes of two fixed warps and two weaving warps.

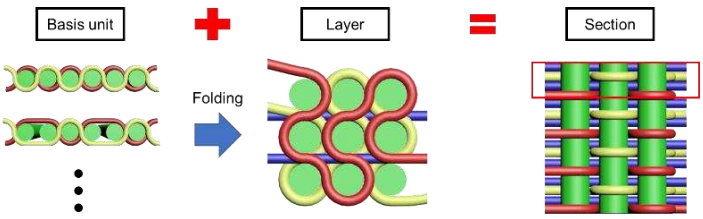

Figure 2. Three design parameters (Basis unit, Layer, Section)

2.2 Modeling strategy

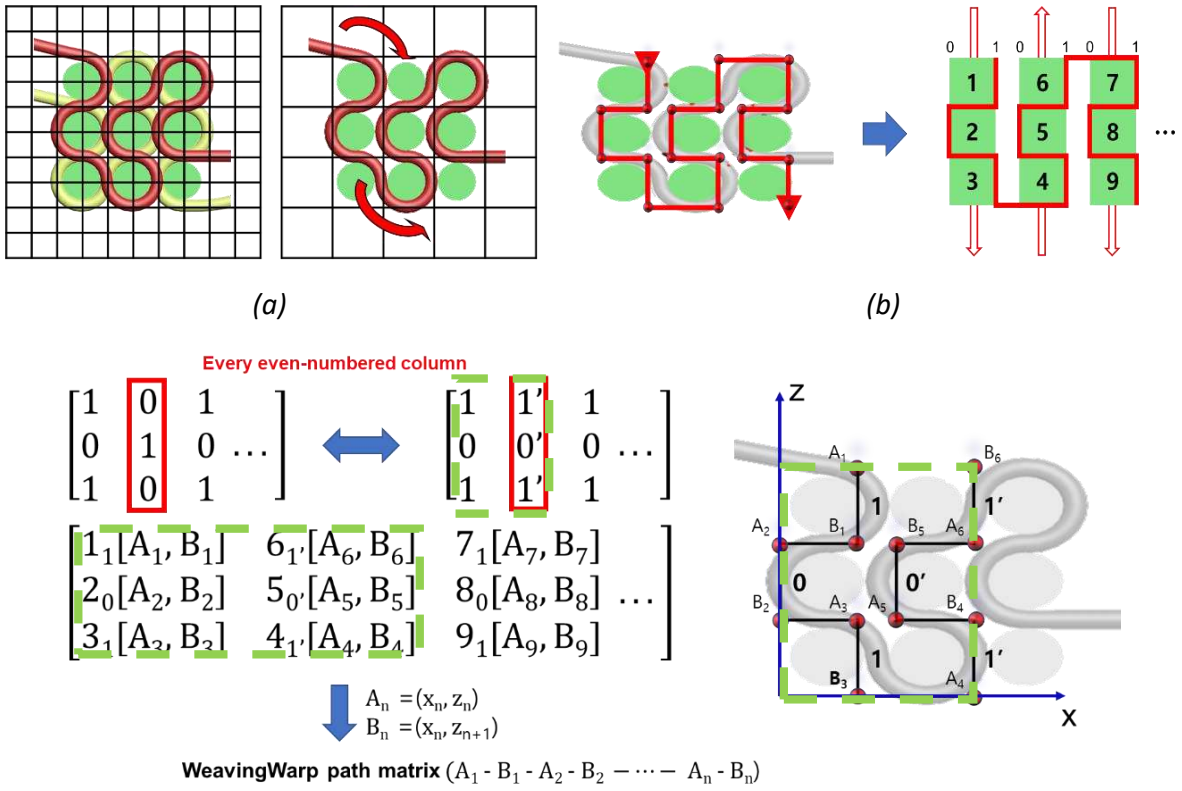

Figure 3. Scheme of weaving yarn path extraction, (a) assignment of coordinate information to weaving warp (b) binary weft path of weaving warp (c) weaving warp path matrix (unit cell in green dash line)

To model 3D textile structures, TexGen was used. In TexGen, yarn paths are defined with connecting master node points. Once the paths are defined, corss-section and surface of yarns are generated on the slave nodes in the path [3]. Considering the weaving mechanism, the paths of wefts and fixed warps are predetermined. Therefore only the paths of weaving warps have to be calculated like in Fig. 3. In the end, weaving warp path matrices with node coordinate information are formed and they make yarn paths in TexGen. Fig. 4 shows one example of 3D textile modeling. Within feasible ranges of three parameters, TexGen generated random 3D textile structures automatically by Python sctipting.

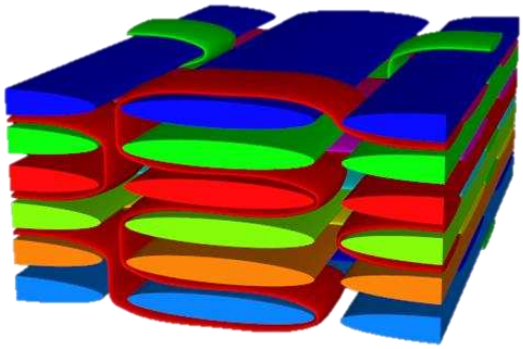

Figure 4. 3D textile with Basis unit = [1,2], Layer = 6, and Section = 1

  doi:10.5075/epfl-298799_978-2-9701614-0-0 published under CC BY-NC 4.0 license

3. Data processing and establishment of a neural network

3.1 Pattern featurization

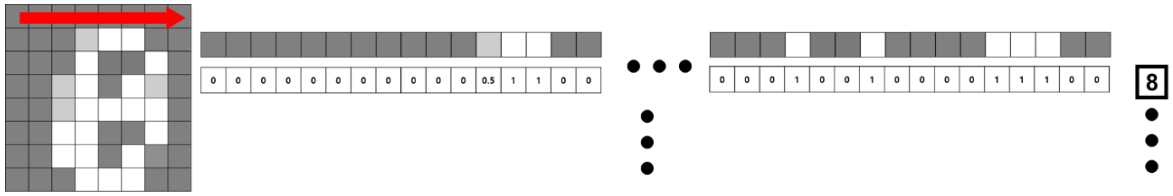

Figure 5. scheme of featurization of hand-written digit(8) classification

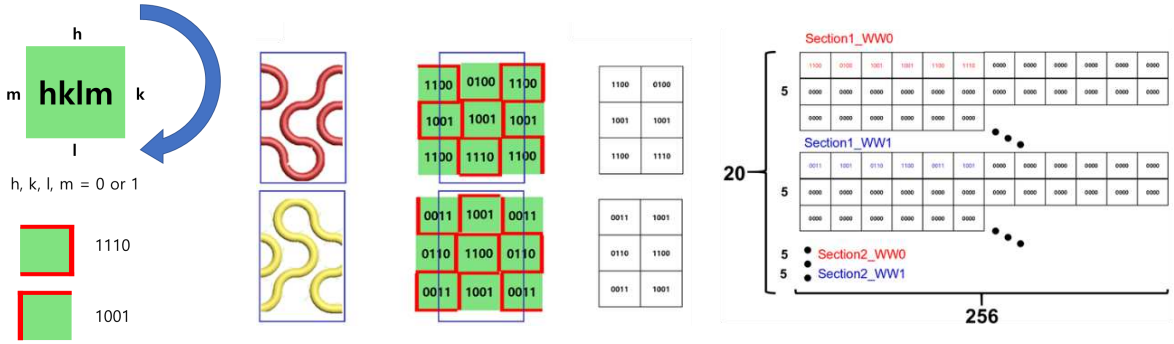

Figure 6. Featurization of patterns of weaving warps

Like the way of featurization of hand-written digit classification in Fig. 5, the patterns of weaving warps are featurized by splitting the paths with unit path elements. One element contains the specific weft-wrapping path information, which is written in four-digit binary number. For example, 1110 element wraps a weft in three sides as shown in Fig. 6. In this manner, a weaving warp is divided into the number of wefts it is wrapped in in a unit cell. Then all the four-digit binary number are extracted in 2D matrices. Finally, 2D matrices are converted to 1D arrays, and each array represents each 3D textile structure.

3.2 Elasticity of 3D woven composites

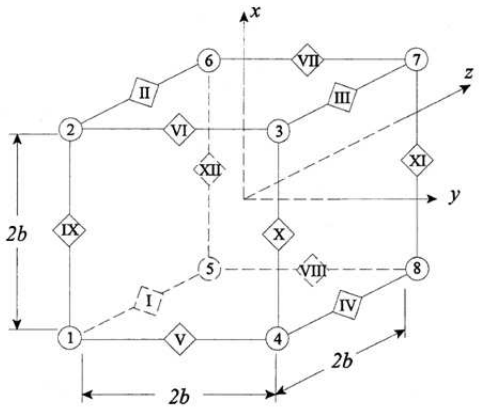

Figure 7. Edges and vertices in the cubic unit cell for simple cubic packing [4]

3D woven composites have anisotropic mechanical behavior, so to define the behavior twelve elastic engineering constants are needed. Among twelve constants, only nine independent constants are required to define the elasticity because of the reciprocity relations. According to Li et al. [4] and Section 4.2 of his paper, they assigned the periodic boundary conditions in a unit

  doi:10.5075/epfl-298799_978-2-9701614-0-0

cell by using translational symmetry transformation neglecting the involvement of reflectional or rotational symmetry transformations (Fig. 7). Then Li et al. used simple energy equivalence consideration. For example, the work done by the concentrated force($\mathrm{F_x}$) is expressed by

$$W = \frac{1}{2} F_x \varepsilon_x^0. \tag{1}$$

The strain energy in a unit cell is

$$E = \frac{1}{2}\int_V \sigma_x^0 \varepsilon_x^0 \, dV = \frac{1}{2} \mathrm{V} \sigma_x^0 \varepsilon_x^0 \tag{2}$$

where V is the volume of the unit cell. Equating W to E results in a relationship between the applied concentrated force $\mathrm{F_x}$ and the macroscopic stress σ_x^0. Applying the procedure to the degree of freedom, the following simple relationships can be obtained

$$\sigma_x^0 = F_x / V. \tag{3}$$

Finally, the elastic property (E_x^0) are then obtained by:

$$E_x^0 = \sigma_x^0 / \varepsilon_x^0 = F_x / V \varepsilon_x^0 \text{ when } F_y = F_z = F_{yz} = F_{zx} = F_{xy} = 0. \tag{4}$$

In the same manner, other elastic properties can be obtained. More detailed information is shown in [4]. These are implemented in TexGen, so the generated unit cells of 3D structures can be imported to ABAQUS/Standard Version 6.13 and simulated under six load conditions. Consequently, after post-processing, nine elastic engineering constants can be obtained as output for neural networks.

3.3 Neural network

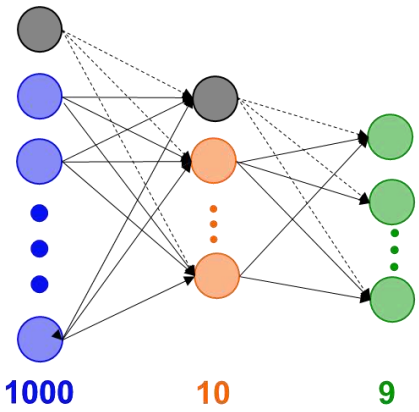

Figure 8. A simple neural network model (one input layer, one hidden layer, one output layer)

Neural networks are widely used as a powerful tool to optimize the relationship between input-output datasets $\{x_k, y_k\}$. In this case, input data (x_k) means a 1D array, and output data (y_k) is the corresponding nine elastic engineering constants. Each unit in a layer, called *neuron*, has a function which is *activation function* (f^l), and the *weights* (Θ) are assigned to the input value to units with function g^l. The layer can be expressed by $f^l(g^l)$. The neural networks are optimized by minimizing the cost, which is termed *loss function (L)*:

$$loss = \sum_k L\big(y_k, \hat{y}(x_k)\big). \tag{5}$$

$\hat{y}$ denotes the set of expected output data. To minimize the cost, gradient descent methods are usually used with many optimizer algorithms. For this neural network model, sigmoid hidden neurons and linear output neurons are selected with Levenberg-Marquardt algorithm [5].

4. Results of neural network training

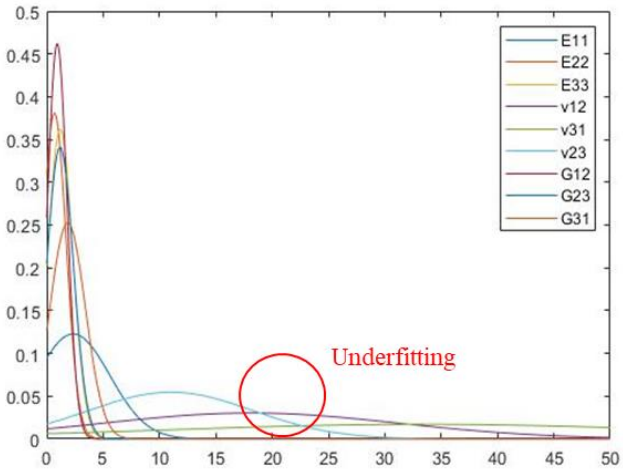

Figure 9. Probability density function of the Error rate with nine elastic engineering constants

All the training process was done in MATLAB, and the number of training datasets is 1,668. Originally, the number of input features was 5,120, but the longest 1D array had smaller number of valid features than 1,000. For this reason, the input features had to be adjusted for efficiency and reducing computing cost. In conclusion, total trained number of *weights* is 4,869. To assess the quality of neural network, *Error rate (%)* was calculated like below:

$$Error\ rate\ (\%) = \frac{|y_k - \hat{y}(x_k)|}{y_k} * 100. \quad (6)$$

For all the data samples, the *Error rate (%)* was obtained, and the distribution is shown in Fig. 9.

Table 1: mu (μ) and sigma (σ) results of each elastic engineering constant

Eng. Const.	mu (μ) [0.95]	sigma (σ)
E11	2.34239 [2.18621, 2.49857]	3.2521
E22	0.679551 [0.62929, 0.729812]	1.04657
E33	1.19214 [1.13924, 1.24504]	1.10144
V12	18.111 [17.4789, 18.743]	13.1609
V31	33.4728 [32.353, 34.5926]	23.3169
V23	11.0029 [10.6521, 11.3538]	7.3056
G12	0.929819 [0.888381, 0.971257]	0.862851
G23	1.17715 [1.12098, 1.23333]	1.16969
G31	1.85356 [1.77771, 1.92942]	1.57953

  doi:10.5075/epfl-298799_978-2-9701614-0-0

The more detailed information about the distribution is in Tab. 1. *μ (mu)* indicates the center position (location parameter) of the distribution and the values in square brackets imply the range which 95% of samples belong to. *σ (sigma)* value denotes the sharpness or broadness (scale parameter) of probability density function. As shown in Fig. 9 and Tab. 1, almost all the constants display sharps distribution near zero value, which means the AI model was trained well. However, in case of poisson's ratios, they showed significantly broad and far from zero distribution. The biggest reason might be the scale difference of output value. Actually, the ratios are less than 1 at all time, whereas the moduli always have 10 to the 3rd or 4th power. With further work on this research, this kind of underfitting problem is looking forward to be disappeared.

5. Conclusion

By analyzing a weaving technique, an innovative 3D pattern generation mechanism was created and the automation modeling procedure built by the method was performed well. Also, the finite element method in ABAQUS was successfully integrated to the modeling in TexGen. Eventually a fully automatic process *from design parameters to elasticity* was produced. Moreover, through the 3D pattern featurization inspired by conventional hand-written digit classification, 3D textile structures were able to turn into input data format for neural networks. The possibility and applicability of the new pattern featurization method were validated. In the future, we shall focus on achievement enough amount of training datasets and optimization of the architecture of the neural network model. Furthermore, several strategies will be studied to make the neural network suggest any optimized structures under arbitrary conditions.

Acknowledgements

This work was supported by the National Research Foundation of Korea (NRF) grant funded by the Korea government(MIST)(No. NRF-2020R1A5A6017707)

1. References

1. Huang, Tao, Yanling Wang, and Gang Wang. Review of the mechanical properties of a 3D woven composite and its applications. Polymer-Plastics Technology and Engineering 2018; 57.8: 740-756.
2. Yang, Hyunjoon, et al. Continuous and rapid production of three-dimensional woven fabric preforms using a new weaving technique. Functional Composites and Structures 2020; 2.1: 015005.
3. Lin, Hua, Louise P. Brown, and Andrew C. Long. Modelling and simulating textile structures using TexGen. Advanced Materials Research. Trans Tech Publications Ltd, 2011; Vol. 331.
4. Li, Shuguang, and Anchana Wongsto. Unit cells for micromechanical analyses of particle-reinforced composites. Mechanics of materials 2004; 36.7: 543-572.
5. Marquardt, Donald W. An algorithm for least-squares estimation of nonlinear parameters. Journal of the society for Industrial and Applied Mathematics 1963; 11.2: 431-441.

  doi:10.5075/epfl-298799_978-2-9701614-0-0

A NOVEL TOPOLOGY OPTIMISATION METHODOLOGY FOR ROBUST DESIGN OF STRUCTURAL COMPONENTS CONSIDERING MATERIAL DEFECTS

Rui O. S. S. da Costa[a], Silvestre T. Pinho[a]

a: Department of Aeronautics, Imperial College London, UK – r.costa18@imperial.ac.uk

Abstract: *This work outlines a new Topology Optimisation methodology whereby material defects are introduced at the earliest stage of the structural design process, leading to more robust final design solutions. We couple the Levelset Method and the Floating Node Method to capture a moving material boundary explicitly on the Finite Element mesh. A continuum design sensitivity analysis scheme based on a measure of the energy release rate is used to quantify the impact of the defect. We show how the structure is optimised to reduce this measure and mitigate the impact of the material defect on the overall response.*

Keywords: Floating node method; Topology optimization; Levelset method; Energy release rate; Material defect

1. Introduction

Material defects – such as delamination, debonding, inclusions or internal cracks – occur during the manufacturing of composite structures. The smallest defects can be undetectable to current non-destructive testing techniques and may lead to premature structural collapse [1]. It is therefore imperative to account for such defects as early as possible in the design stage of a component.

The pre-inclusion of defects within a component during its design amounts to a quantification of the uncertainty relating to the impact of the defect on the response of the component; the uncertainty quantification allows for more robust design solution that mitigate the effects of the included defect.

The design of intricate structural components – such as a skin-stringer assembly of an aircraft (Figure 1) – is often sequential and iterative in nature; such a component must be studied under varied loading scenarios and with various material and geometric configurations, all of these constitute design variables that influence and depend on each other. Introducing into the design workflow material defects such as kissing bonds can make the already complex workflow to costly and time consuming.

  doi:10.5075/epfl-298799_978-2-9701614-0-0

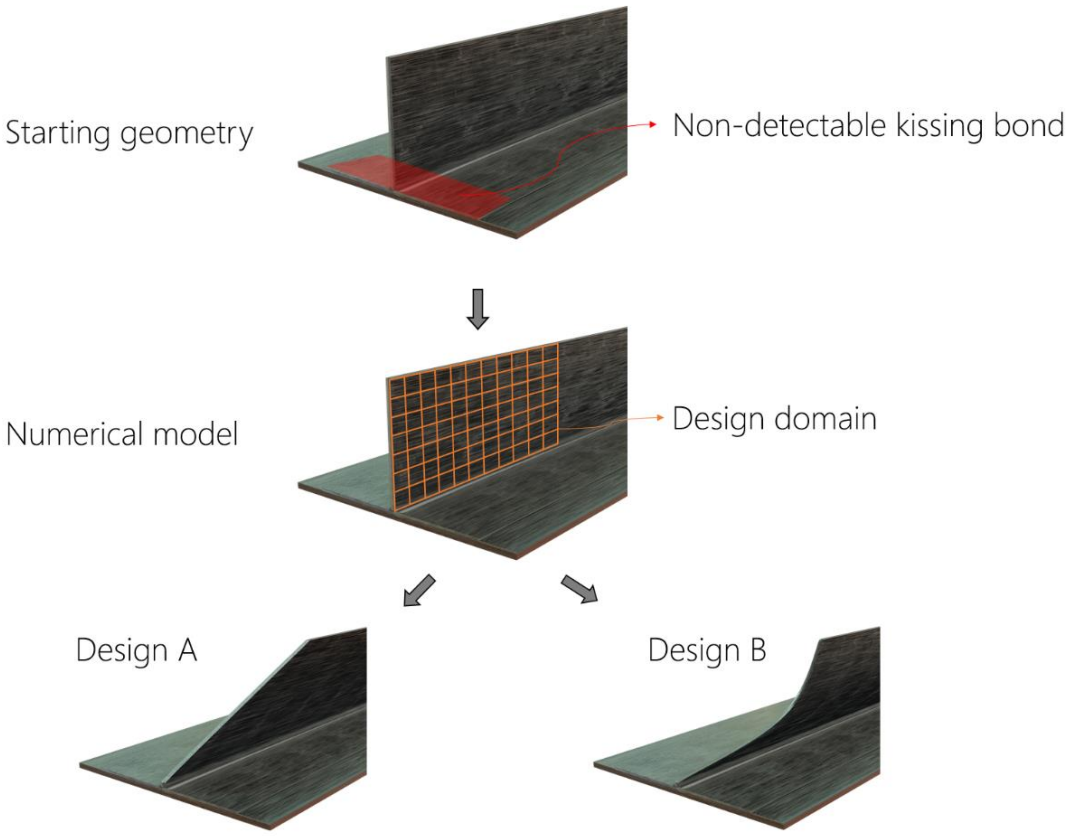

Figure 1. Optimisation concept of skin-stringer assembly with a kissing bond defect

Therefore, to alleviate these shortcomings a Structural Optimisation methodology can be used. Such a methodology can abstract design allowables and requirements as optimisation objectives allowing for multiple objectives to be included in a single design study.

Topology Optimisation (TO) is a Structural Optimisation methodology whereby the material distribution of a domain is optimized. The literature often categorizes TO methods based on the nature of the design variables; for example, density-based TO methods use cell densities to determine the solidity of a given region in space, and Levelset (LS) based TO methods use a scalar field that represents the moving material boundary and therefore dictates the regions within the solid domain [2].

Density-based TO methods have seen a recent proliferation in the literature and commercial applications but it suffers from a fundamental drawback – one that is more critical when we want to study the inclusion of material defects. Because the design variables are cell densities the material boundary resolution is limited to the density of the mesh and will often result in a blurry transition between material and void. In contrast, LS-based TO methods capture the material boundary through every design iteration as a scalar field [2] providing more granular design control.

Furthermore, LS-based TO methods allows us to employ continuum design sensitivity analysis based on the concept of shape derivative [3]. In this work we use this ability to develop a formulation based on the crack energy release rate and inform the optimisation algorithm of an embedded defect in the structure.

  doi:10.5075/epfl-298799_978-2-9701614-0-0

2. Methodology

2.1 Implicit boundary tracking

The Levelset Method (LSM) is a numerical method capable of representing and manipulating any arbitrary boundary as a scalar field embedded in a Finite Element (FE) formulation. The LS field, ϕ, can be define, depending on its value, whether a region in space is considered solid or void (Figure 2).

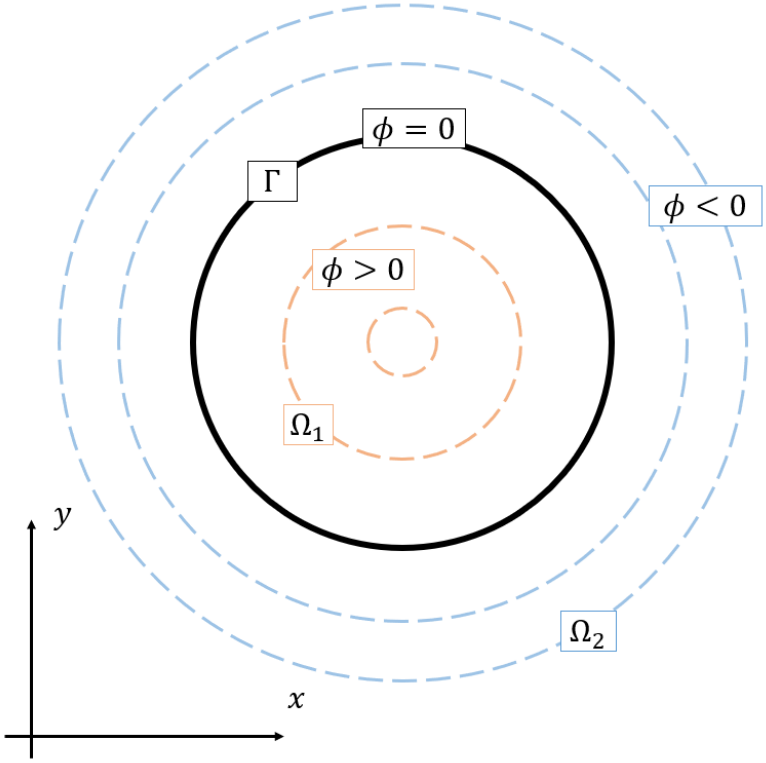

Figure 2. A 2D representation of the Levelset field, ϕ, of an arbitrary shape

The LS field, ϕ, can be manipulated in any way through an advection equation. This equation takes a velocity field as an input to move the boundary in the domain. The velocity field can be defined through the optimisation problem such that the LS field moves according to the design variables.

2.2 Element partitioning

The Floating Node Method (FNM) was initially developed to model crack propagation. It is a numerical method based on the Finite Element Method (FEM) that introduces extra nodes without a coordinate position at the start of the analysis – floating nodes (Figure 3).

These floating nodes can be tied to topological features such as edges, areas, or other nodes, although this is not mandatory. The connectivity of the element reflects the inclusion of floating nodes such that the element formulation does not change, and the partitioning algorithm is only tasked with activating/deactivating the correct combination of floating nodes.

  doi:10.5075/epfl-298799_978-2-9701614-0-0

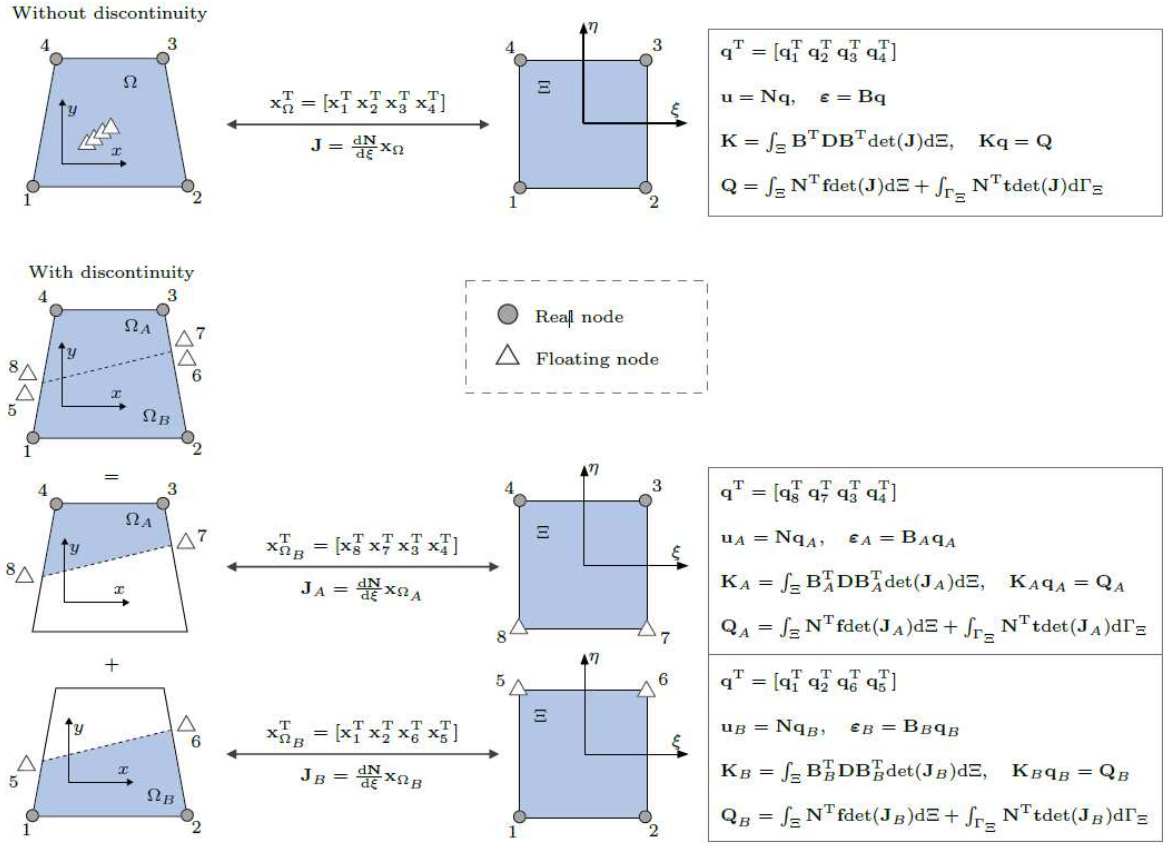

Figure 3. The Floating Node Method

2.3 Boundary-conforming mesh update

By coupling the LSM and FNM one can get both the implicit capabilities of boundary tracking and explicit element-wise partitioning. The partitioning can be done base on the LS field so as to capture the zero LS curve within each element (Figure 4).

To that end, each real node will have an additional degree of freedom (apart from the displacement ones) that represents the LS field in that point in space. The position at which each edge should be partitioned can then be computed by means of linear interpolation.

The partitioning algorithm is performed at the element level. So long as a given element has knowledge of its LS degrees of freedom it can partition itself independently of others. Therefore, the algorithm is highly parallelisable and scalable.

The partitioning cases are defined before the analysis and optimisation begin and can be as simple or as complex as the problem necessitates. The examples shown in Figure 4 are but an

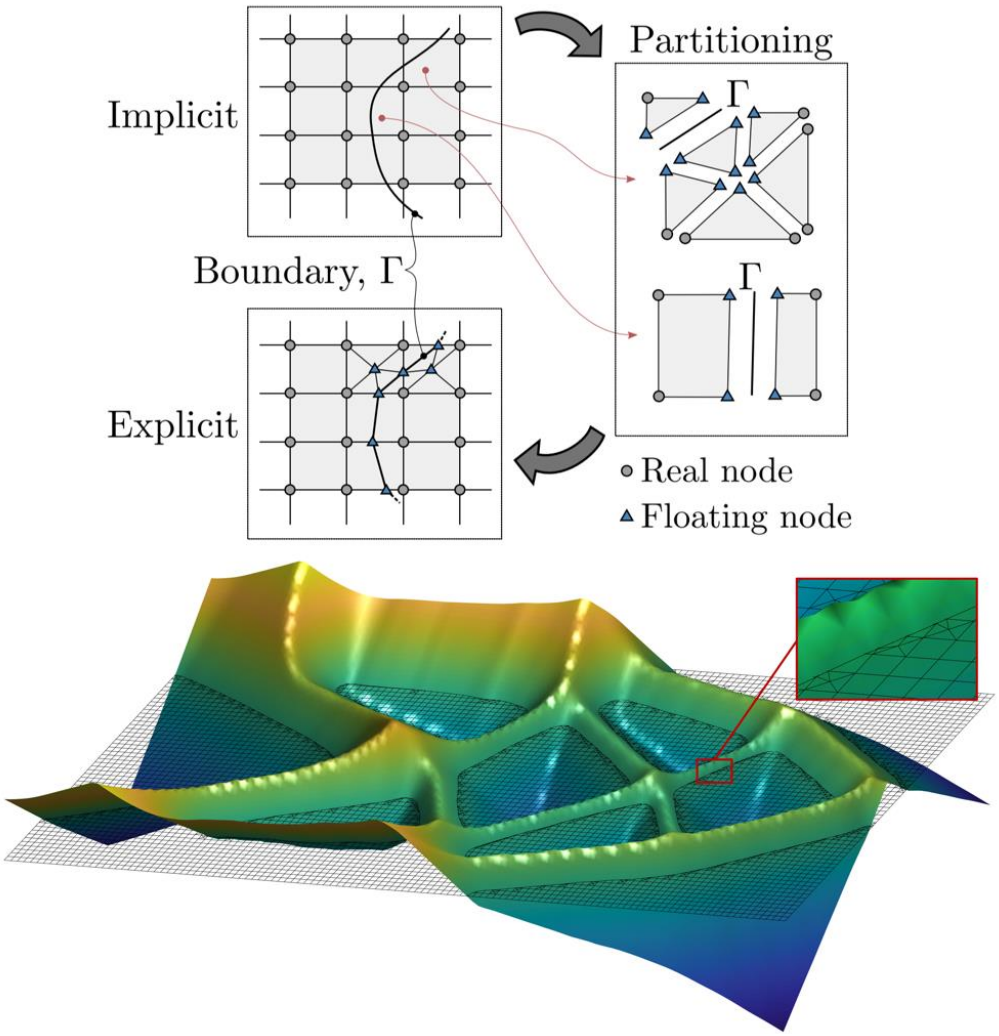

Figure 4. Coupling of the Levelset Method (implicit) and Floating Node Method (explicit) to achieve a conformal mesh partitioning scheme

example of the simplest cases – single partition linearly representing the boundary within the element.

3. Results

The proposed methodology was assessed on a variety of problems with embedded cracks. The problems are variations of the MBB beam problem which is a common benchmark in topology optimisation problems.

Figure 5 contains the results for the MBB variation with a centred crack, specifically it shows the final design solutions for different weights of the energy release rate term. It is possible to observe that for higher weights of energy release rate the structure creates weakened structural members to divert load away from the crack tip – effectively reducing the effect of the crack on the overall response.

Figure 6 shows the evolution of the design measures through the design iterations and showcases the convergence of both of the measures.

  doi:10.5075/epfl-298799_978-2-9701614-0-0

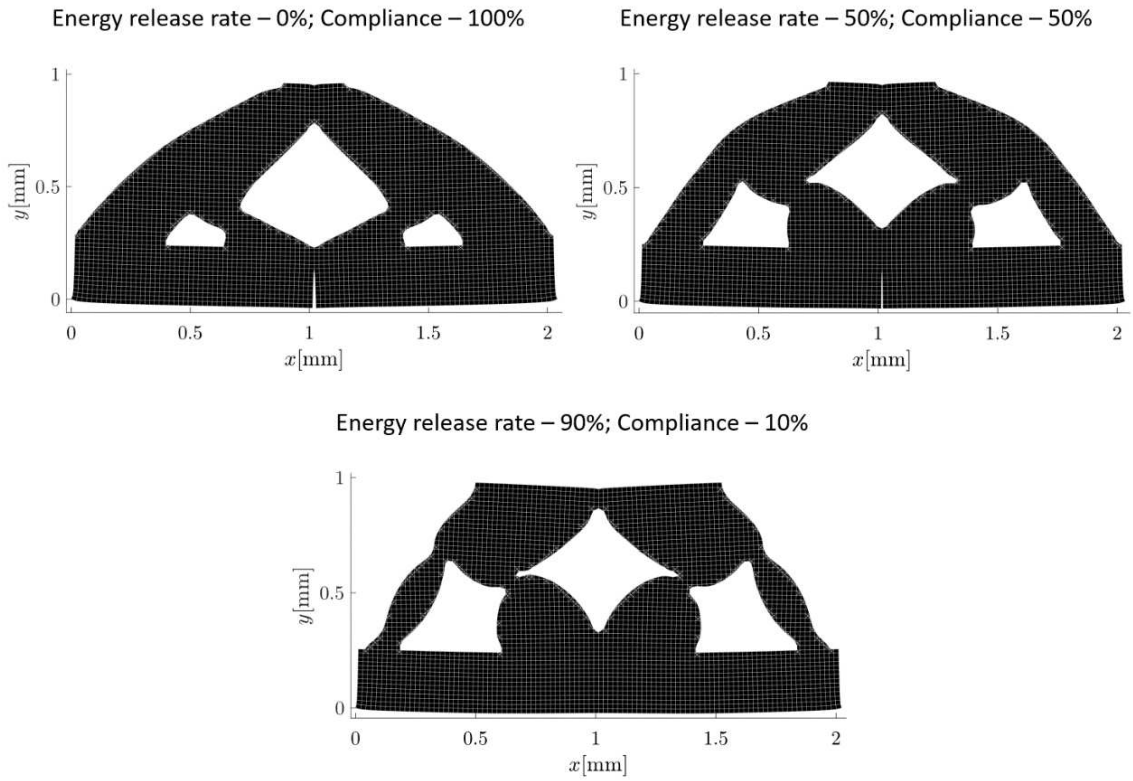

Figure 5. Design evolution of a MBB beam with a centred embedded crack for various weights of the energy release rate objective function

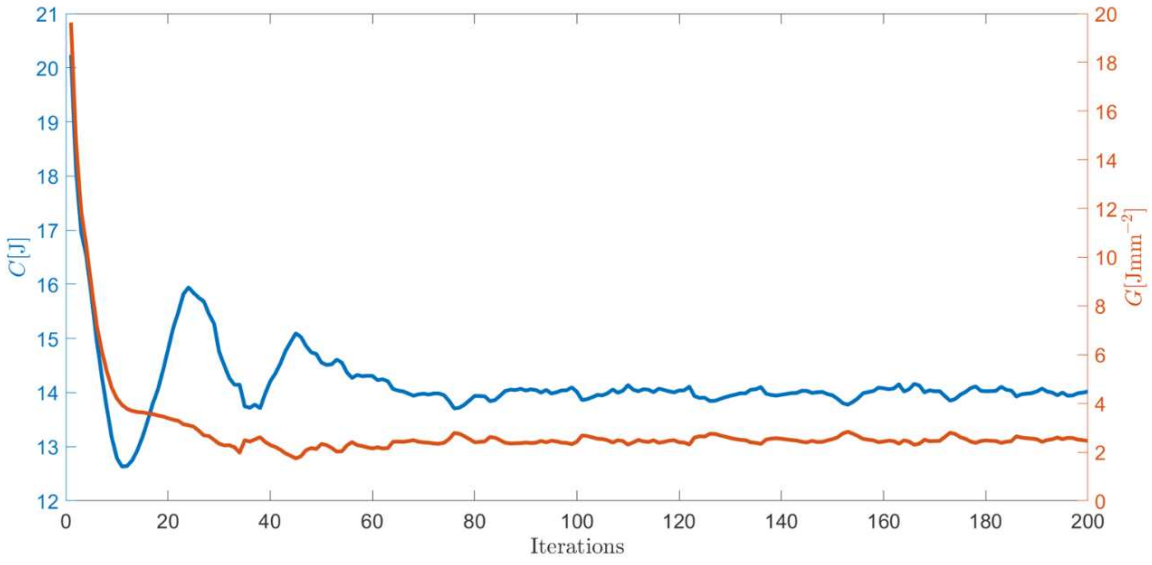

Figure 6. Evolution of the compliance (C) and energy release rate (G) terms as the design iterations evolve

Figure 7 contains the results for the MBB variation with an offset crack, specifically it shows the final design solutions for different weights of the energy release rate term. It is possible to observe that for higher weights of energy release rate the structure creates weakened structural

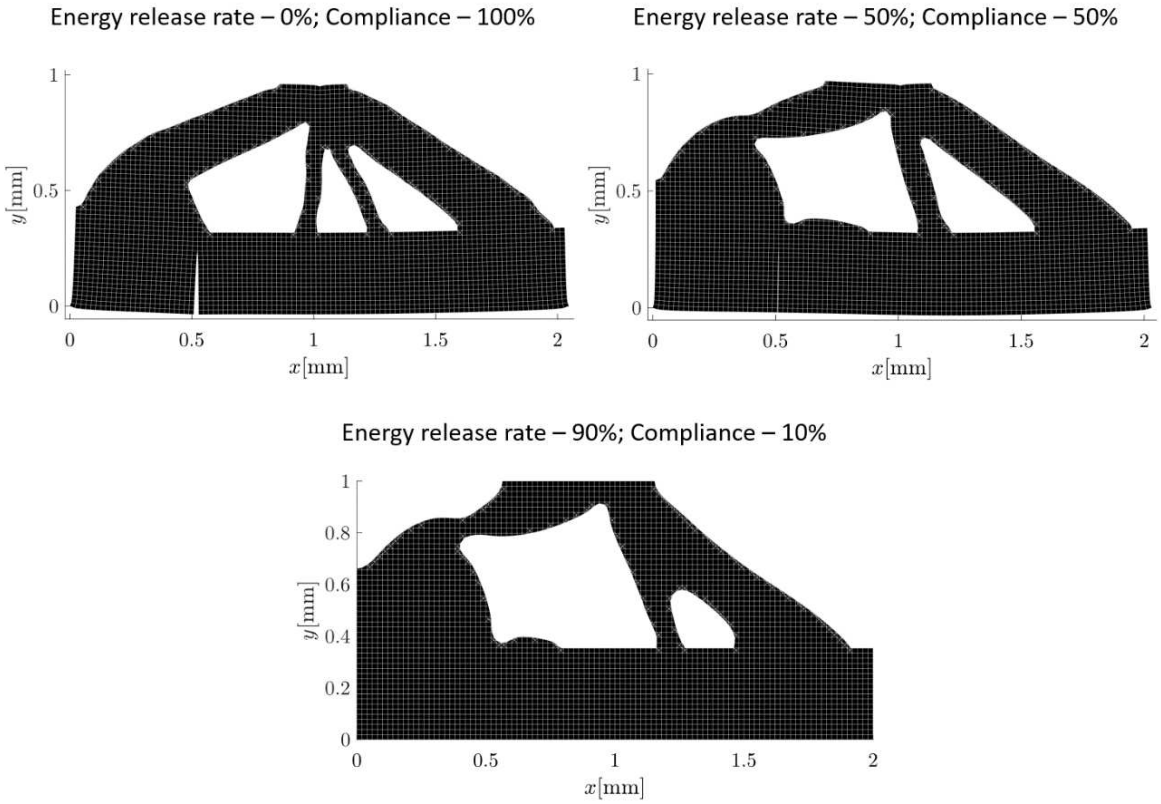

Figure 7. Design evolution of a MBB beam with an offset embedded crack for various weights of the energy release rate objective function

members to divert load away from the crack tip – effectively reducing the effect of the crack on the overall response.

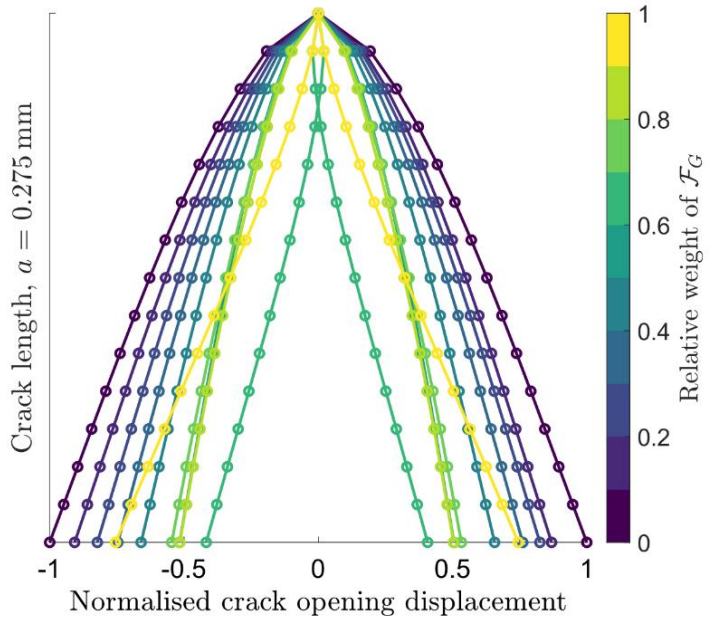

Figure 8. Effect of the energy release rate objective function (Fg) on the crack opening displacement

It can be observed from Figures 5 and 7 that the crack seems to close for the bigger weights of energy release rate. Figure 8 shows this effect in more detail and highlights the effect of the energy release rate term on the crack opening displacement

4. Conclusions

In this work we developed a Topology Optimisation methodology that couples the Levelset Method and Floating Node Method with a design sensitivity analysis formulation based on the energy release rate. Its key features include:

- the ability to include material defects in the model definition;
- an optimisation algorithm capable of reducing the impact of the material defects;
- an element partitioning algorithm capable of tracking the material boundary of the different designs;

We can conclude that this methodology can be applied to domains with embedded material defects for:

- studying design solutions that mitigate the impact of the defect while satisfying other design objectives and constraints;
- achieving more robust design solutions;
- simplifying the design process of intricate structures;

In summary, the proposed methodology provides a new framework for the robust design of composite structures with embedded material defects such as cracks and kissing bonds. This is achieved in a way that is highly scalable and easily configurable to fulfil unique design requirements and allowables.

5. References

1. R. Vijaya Kumar, M. Bhat and C. Murthy, "Evaluation of kissing bond in composite adhesive lap joints using digital image correlation: Preliminary studies", International Journal of Adhesion and Adhesives, vol. 42, pp. 60-68, 2013. Available: 10.1016/j.ijadhadh.2013.01.004Sims FA. Applications of resins in bridge and structural engineering. International Journal of Cement Composites and Lightweight Concrete 1985; 7:225-32.
2. N. van Dijk, K. Maute, M. Langelaar and F. van Keulen, "Level-set methods for structural topology optimization: a review", Structural and Multidisciplinary Optimization, vol. 48, no. 3, pp. 437-472, 2013. Available: 10.1007/s00158-013-0912-y
3. R. da Costa and S. Pinho, "A novel formulation for the explicit discretisation of evolving boundaries with application to topology optimisation", Computer Methods in Applied Mechanics and Engineering, vol. 367, p. 113077, 2020. Available: 10.1016/j.cma.2020.113077

THE EFFECT OF FAILURE CRITERIA CHOICE ON OPTIMISED COMPOSITE PANELS

Tobias, Lorimer[a], Tom, Allen[a]

a: Centre for Advanced Composite Materials, University of Auckland, Auckland, New Zealand – t.lorimer@auckland.ac.nz

Abstract: *With every effort to create structures that are lighter, stiffer, and stronger, there must be further exploration of the design space in which these structures exist. Composite design increasingly requires more structurally efficient architecture, and it is this need that drives the search for more effective design methodology. One significant aspect that influences design methodology development is the impact of the employed material failure criteria (FC). FC that can accurately depict the failure mechanism and loading capacity of a material are an invaluable tool and vital for understanding the limits of a material's use.*

This paper investigates the impact of FC choice on the optimisation of a bi-axially loaded composite plate. A genetic algorithm is used to design the stacking sequence and number of plies in a plate subject to a range of in-plane loads. The optimisation target is minimum mass subject to a minimum safety factor. Tsai-Wu, Tsai-Hill, Hashin damage criteria, Puck, and the maximum strain criteria have all been tested. Results highlight Hashin as being, on average, the least conservative of the FC, with a 7% average difference from the lowest optimal structural efficiency. A comparison between unconstrained laminate optimisation and traditional laminate design is also undertaken, and results indicate that choice of FC has a noteworthy impact on the similarity between resulting laminates. Tsai-Wu, Hashin, and Puck all show a close correlation between free and constrained optimisation, but Puck is the only FC to outperform constrained laminates in non-trivial loading scenarios.

Keywords: Composite materials; Bi-axial loading; Anisotropic Failure Criteria; Optimisation

1. Introduction

Accurately predicting the failure of composite materials is necessary for maximising the efficient use of composite structures. The outcomes of the World Wide Failure Exercise (WWFE) [1] indicated there remains uncertainty as to the reliability of even the most widely used Failure Criteria (FC) currently employed. In high-performance and competitive applications, where maximum structural efficiency is highly sought after, uncertainty makes accurate predictions and therefore maximising efficiency challenging [2]. There is no shortage of FC to choose from as composites design is a state-of-the-art field. However, the existence of these many FC can encumber the design process as there may be confusion as to what theoretical material strength limits in bi-axial loading should be. This uncertainty is exacerbated for multi-axial loads, for which experimental strengths are rarely obtained. Robust analytical or numerical tools still need developing, something which the misrepresentation of feasible composite design and failure limits does not aid. Part I of the WWFE [1] suggested that out of the 19 FC tested, only three theories reliably predicted failure within *±50%* of experimental results.

Optimisation is increasingly gaining recognition as the most efficient method for generating maximally structural efficient configurations. One major aspect that influences the development

  doi:10.5075/epfl-298799_978-2-9701614-0-0

of optimisation theories is the impact of the employed material failure criteria within the cost function. This paper investigates the effect of FC choice on the results of an optimised laminate plate in a range of biaxial loading states. A Genetic Algorithm (GA) has been employed to search a design space characterised by the limits that each FC imposes. The key objective is to identify the influence of FC choice on the proposed 'optimal' solution and the variation in weight and structural efficiency that can occur through the selection of different FC for various loading scenarios.

2. Failure Criteria

Failure criteria have been used for centuries to predict the loading capacity of structural materials [3]. However, many of the FC currently employed for composite materials are extensions of those used for isotropic materials and can struggle to accurately capture the varied and complex modes of failure that composites can experience [4], [5]. This means that many FC for composites are approximations, and there are currently no clearly superior criteria [1].

The function of any failure criteria is to allow designers to evaluate the theoretical risk of failure. This value is essential, as designating a safety factor to a design must be based on the ultimate strength of the material from which it is constructed. Of course, other considerations such as the application, commercial factors such as regulations, or danger of part failure also apply. A structure designed with this approach can then be rated as 'safe' for use and appropriately designed for expected loads [5].

2D stress fields in laminates are typically evaluated layer by layer for laminates. However, this process generally oversimplifies complex failure mechanisms such as matrix cracking which is not fully understood. It also ignores any non-linear 3D failure mechanisms introduced by delamination or free-edge singular stresses. Unfortunately, any attempt to capture all failure behaviours would result in a FC so complicated as to be prohibitive if it were even possible. Therefore, 3D effects are generally ignored for practical purposes [6].

Furthermore, there is some discussion that the *'in situ'* performance of laminae is under-estimated by lamina properties and that significant strength increases observed in physical testing can be attributed to the architecture of a laminate, e.g., adjacent layers of *0˚* and *90˚* will prevent each other suffering from transverse crack propagation [7]. However, this complex behaviour is not yet quantified in the literature and is not considered in this analysis. While many structures can remain fit for purpose after sustaining some limited amount of damage, this research has been limited to just considering First Ply Failure (FPF). Classical Lamination Theory (CLT) is employed for stress calculation and is not strictly valid for damaged or broken laminates.

Based on their performance in the WWFE I [1] and common use in industry, including within commercial software [8]–[10], the following five FC have been chosen:

Tsai-Wu *Tsai-Hill* *Maximum strain* *Puck* *Hashin*

The FC tested here cover three different types: Non-interactive (Max strain), interactive (Tsai-Wu, Tsai-Hill), and failure mode-based theories (Puck, Hashin). Interactive theories use strains/ stresses in both the $x, \text{and } y$ directions to contribute to the measure of the point of failure; non-interactive theories only consider the direction of direct loading. Failure mode theories tend to focus on the initiation of damage features such as micro-cracking, crack propagation, and micro-

  doi:10.5075/epfl-298799_978-2-9701614-0-0

buckling. These theories attempt to use material strength limits to signal the beginning of one or more of these secondary failure methods.

3. Methods

An optimisation approach has been developed within MATLAB to determine a composite laminate's optimal configuration. The approach utilises Classical Lamination Theory (CLT) to calculate a stress state based on applied running loads and moments. A Genetic Algorithm (GA) is used to search a constrained design space (as described later) for the most structurally efficient laminate with a Safety Factor (SF) greater than or equal to one. The GA uses Eq. (1) as the target function, thereby minimising the structure's mass while maximising the SF.

$$S_{EFF} = Mass + \frac{1}{SF} \tag{1}$$

The optimisation scheme has been tested across a range of biaxial loading states applied to a unit square Carbon Fibre Reinforced Plastic (CFRP) panel constructed from layers of the unidirectional lamina with properties presented in Table 1. A grid of points in (N_x, N_y) have been assessed and the mass, SF, and number of layers have been recorded for each point for each FC. N_x and N_y refer to the running loads applied to the composite plate in the x and y directions and are taken to be principal loads. The loading ranges from - *500* to *500 kN/m* with a step size of *50 kN/m*.

Table 1 Intermediate modulus CFRP lamina properties

E_{11}	E_{22}	G_{12}	ν_{12}	ρ
$147Gpa$	$9\ GPa$	$3.3Gpa$	0.31	$1850\ kgm^{-3}$
S_{1T}	S_{1C}	S_{2T}	S_{2C}	τ_{12}
$2.260\ GPa$	$1.2\ GPa$	$0.05\ GPa$	$0.9\ GPa$	$0.1\ \ Gpa$
X_{1T}	X_{1C}	X_{2T}	X_{2C}	γ_{12}
0.015	0.008	0.005	0.21	0.015

A separate optimisation run is undertaken for each FC, returning the minimum number of layers to fulfil the requirement of SF ≥ 1 at FPF and the laminate mass. FC are applied at the lamina level, and the resulting SF for the laminate is found by taking the minimum SF from any one layer. The GA is allowed simultaneous control over the following design parameters for the CFRP plate:

- Stacking sequence: This is the order of stacking and the orientation of the fibres within each lamina in the ply stack
- Layer thickness: The thickness of each lamina up to a bound of 6 layers, each layer being $0.127\ mm$ thick

The size of the design space for the optimisation is limited to a laminate made of up to *8* discrete orientations (from a range -90˚ to 90˚, with an increment of 1˚), each with an allowable thickness up to *6* layers. The GA may use fewer angles and a lower number of layers if they are not required. This bounds the optimisation, increasing accuracy and limiting the computational resource needed to complete the optimisation in a practical length of time. Laminate data takes the form:

$$[\alpha_1, \alpha_2, \alpha_3, \alpha_4, \alpha_5, \alpha_6, \alpha_7, \alpha_8, t_1, t_2, t_3, t_4, t_5, t_6, t_7, t_8]$$

  doi:10.5075/epfl-298799_978-2-9701614-0-0

where α_{1-8} are the angles that the GA selects, and t_{1-8} are the number of layers thick that one angle stack, $\alpha_i$ls assigned. For example, in the case of unidirectional tension, $N_x = 100kNm^{-1}$, the GA returns: [*0,4*], which denotes a laminate containing four layers at *0˚*.

A laminate with eight possible angles and a thickness for each angle corresponds to an optimisation with $2.4E^{13}$ possible combinations. It is important to set up the GA with an appropriate search formulation. The key parameters that influence search time are the start population size and the number of allowable generations. The population size controls the diversity of the initial test space. The larger the population, the greater the variation in the points that make up the test solutions. As in evolutionary *'survival of the fittest'*, the greater the variation in a population, the higher the likelihood that an individual will survive. The same principle is applied here. MATLAB documentation suggested that for GAs, a sensible population size is the number of points that the optimisation is dealing with [11]. Still, this yielded results that did not very thoroughly search the design space for this application in practice. Alternative documentation suggests that a suitable population size for an optimisation with a similar number of variables to what is present in this study is 2000 [12]. Therefore, the population size used in this optimisation scheme is *2000*. In the authors' experience, most optimisations of this size have required fewer than 250 generations to reach a solution, so *300* is selected as an appropriate number of allowable generations.

4. Results and Discussion

The minimum S_{EFF} at each load-point may be seen in Figure 1. To simplify analysis and discussion, the upper right, upper left, lower left, and lower right are referred to as quadrants 1,2,3 and 4. Quadrants 1,2,3, and 4 represent tension-tension, -ve N_x, +ve N_y, compression-compression, and +ve N_x, -ve N_y loading respectively. As expected, the S_{EFF} increases as the load increases. Of note, the largest vales for S_{EFF} occur in the tension-tension quadrant (1st), this appears to contradict established failure knowledge of composites, which is that compressive failure strengths are lower, requiring more mass to achieve a *SF > 1*. There is also some slight unexpected asymmetry between the 2nd and 4th quadrants.

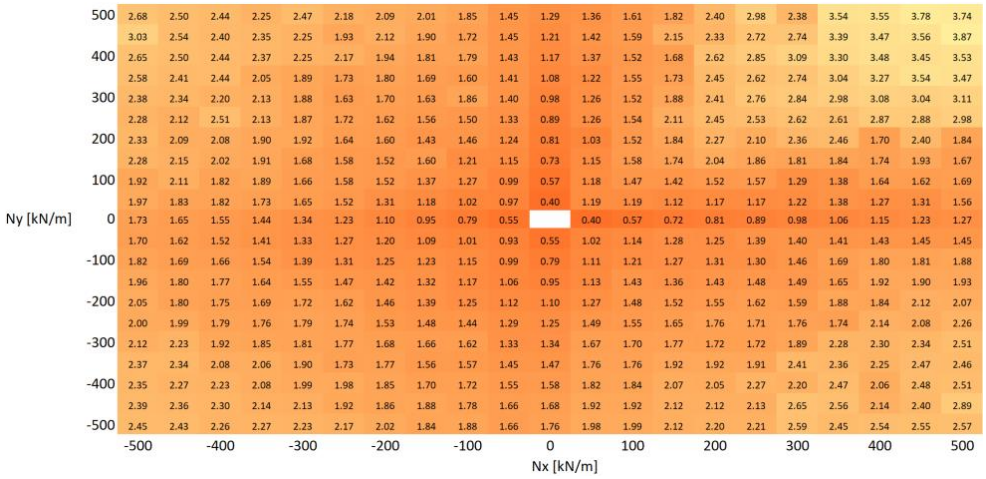

Figure 1 Minimum possible S_{EFF}

The FC that corresponds with the minimum S_{EFF} at each point is plotted in Figure 2. This plot shows that in the compression-compression sector (3rd quadrant), the overwhelming majority of minimum S_{EFF} solutions are found using Tsai-Wu. This implies that Tsai-Wu is the least

  doi:10.5075/epfl-298799_978-2-9701614-0-0 published under CC BY-NC 4.0 license

conservative estimation of strength for this type of loading. Tsai-Wu is noted as being likely to overpredict compression-compression strength [1], and Figure 2 agrees with this, along with the unexpectedly low S_{EFF} values in this quadrant in Figure 1.

Hashin dominates the 2 and 4 quadrants: 42% and 45%, respectively. Quadrant 1 tends to have a greater spread in terms of the dominant FC.

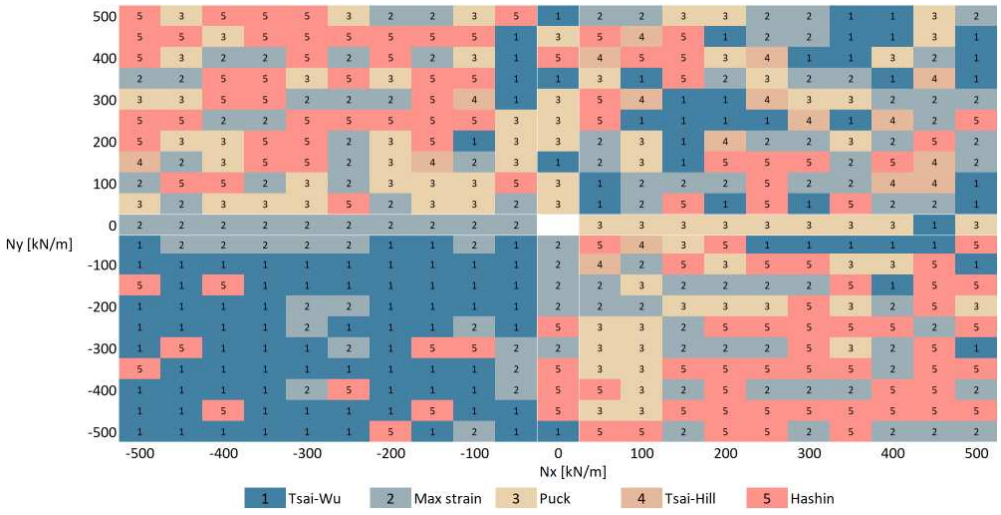

Figure 2 Index of minimum S_{EFF} FC

Figure 3 shows the percentage difference between the highest and lowest predicted mass across the 5 FC considered. Interestingly, there appears to be large differences in unidirectional tension, where the difference is as much as 100%. All FC share the minimum mass for the largest unidirectional load case in either direction except Puck, which includes some additional interaction terms in its criterion for unidirectional failure. Some of the stepwise changes in variation as the load increases are attributed to the discrete nature of the mass increases, where the minimum mass increase is one lamina. If two FC provide similar solutions, but one requires a single extra layer, this can significantly affect the increase in mass. These results indicate how significant the choice of failure criteria can be on final structural mass. However, all quadrants have a similar variation in predicted mass; 46 ±3%. The choice between two criteria can result in an up to 167% variation when applying them via a GA.

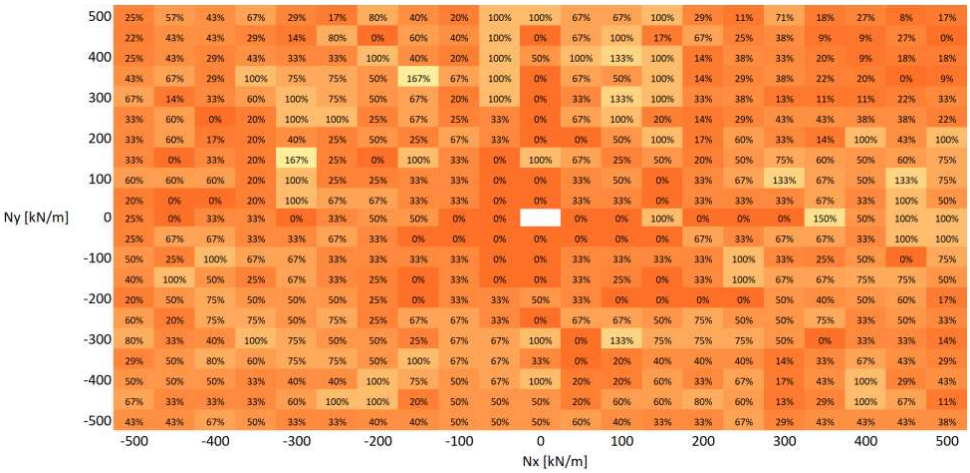

Figure 3 Optimal mass – spread

Figure 4 shows the difference between the first and second lowest S_{EFF}. It may be seen that in the unidirectional load cases (where either N_x or N_y = 0) that there is minimal difference between the predictions of the first two failure criteria and that they will provide similar if not identical results. This makes sense for FC, where the unidirectional SF is calculated using $\mathrm{SF} = \frac{\sigma_{T/C}}{X_{T/C}}$ as is the case for the majority. The small differences in S_{EFF} can be attributed to optimal angles having slight variation between GA runs (< 3°). The maximum recorded difference is 40%, where the max strain criteria predict the lowest S_{EFF}, and Hashin predicts the second lowest. Figure 4 illustrates many scenarios where the variation between two FC is minimal (<5%), which explains the scatter seen in Figure 2, particularly in quadrant 1. If there is a slight variation in S_{EFF}, this may easily be less that the variation due to the implication of a GA, rather than a brute force optimisation scheme.

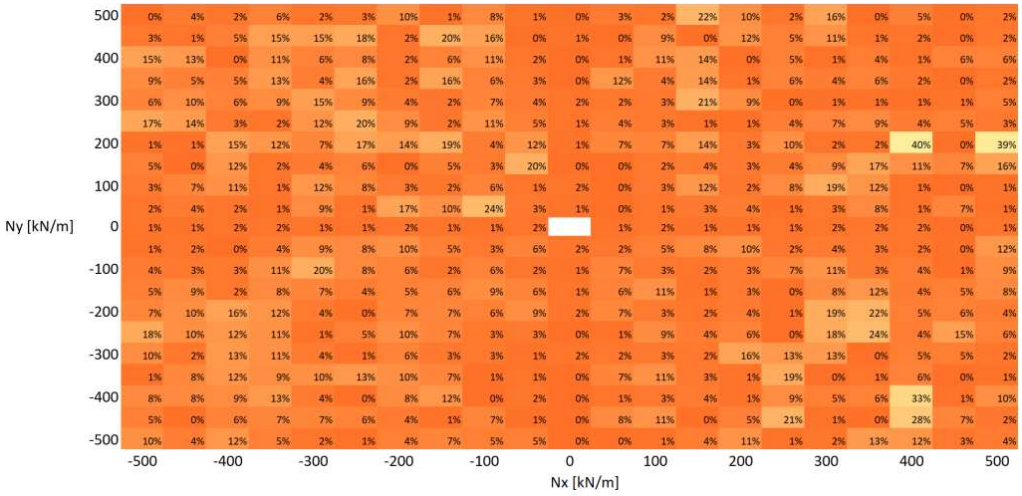

Figure 4 Percentage change required to move to the second smallest S_{EFF}

The average S_{EFF} for each of the FC is recorded in Table 2. Average $S_{EFF,min}$ is the average minimum S_{EFF} across all FC (Figure 1) and Average S_{EFF} is the average of all FC at all points. Hashin has the closest percentage difference in S_{EFF} (7%) across all tested loading scenarios and so gives the least conservative estimation of failure points. Standard deviation = 0.056. Puck gives the greatest average S_{EFF}, 15% higher than the minimum on average. Interestingly, despite such significant variation in the minimum mass (up to 167%), there is only a 7.6% difference between the most and least conservative criteria, on average. This indicates that within different quadrants, the relative conservatism changes between FC. It should also be noted that these averages will be more heavily weighted to higher load cases where the mass and, therefore, S_{EFF} will be higher.

Table 2 Average S_{EFF} and average difference inS_{EFF} for each FC

	Minimum	Average	H	TW	MS	TH	P
S_{EFF}	1.85	2.05	1.98	2.02	2.03	2.11	2.13
% Diff	-	11%	7%	9%	10%	14%	15%

Specific load cases were used to test which laminates were predicted for common loading scenarios. The loading chosen ensured that all quadrants of the failure envelope were tested as well as some unidirectional loading and $N_x = 2/N_y$. These are also compared with laminates optimised for the same load cases but with possible angles constrained to between *-90˚* and *90˚* with a *15˚* step size. This allows comparison between a free reign approach and a 'traditional'

approach using a standard set of angles (Table 3). The optimisations with a full range of angles available have greater variation in the laminates they returned compared with the constrained angle laminates. On average, the free laminates are *80gsm* or *8%* lighter. Tsai-Wu has the lowest average reduction at *20gsm* and Hashin the largest at *100gsm*. The free laminates, on average, had a *2%* lower SF than the constrained. This is assumed to be due to redundancy in the constrained laminates.

Table 3 Specific loading laminates 100kN load

N_x[kN/m] N_y[kN/m]	100 100	100 −100	−100 −100	−100 100	100 0	−100 0	100 50
Tsai-Wu	0.94 [-27/63$_2$/-27]	0.70 [-85$_3$]	0.70 [29/-61/29]	0.70 [-87/-11/-90]	0.24 [0]	0.47 [-4$_2$]	0.70 [15/-65/15]
	0.94 [-60/30$_2$/-60]	0.70 [-60/-15/-60]	0.70 [-60/30/-60]	0.70 [90/0/90]	0.24 [0]	0.47 [0$_2$]	0.94 [0/90$_2$/0]
Max strain	1.64 [37/-33$_2$/75$_2$/39/-21]	0.70 [13/64/14]	0.94 [-36/55$_2$/-35]	0.70 [-76/-24/-76]	0.24 [-1]	0.47 [-2$_2$]	0.94 [32/-46$_2$/32]
	0.94 [0/-90$_2$/0]	0.70 [0/-90/0]	0.70 [30/-45/30]	0.70 [-90/0$_2$/-90]	0.24 [0]	0.47 [0$_2$]	0.70 [-45/3-/-45]
Puck	0.94 [-54/39$_2$/-52]	0.70 [-1/86/-3]	0.94 [-12/78$_2$/-9]	0.70 [11 85 12]	0.24 [-2]	0.47 [0$_2$]	0.70 [-27/44/-31]
	0.94 [-30/45/75/-30]	0.94 [90/0$_2$/90]	0.94 [90/0$_2$/90]	0.94 [90/0$_2$/90]	0.24 [0]	0.47 [0$_2$]	0.70 [30/-45/30]
Tsai-Hill	1.41 [-9/80$_3$/-39/6]	0.94 [-7/-79$_2$/-10]	0.70 [-32/58/-32]	0.94 [73/22$_2$/72]	0.24 [0]	0.47 [0$_2$]	0.70 [36/-44/36]
	0.94 [-30/60$_2$/-30]	0.94 [0/-90$_2$/0]	0.94 [-30/-60$_2$/-30]	0.70 [90/0/90]	0.24 [0]	0.47 [0$_2$]	0.94 [90/0$_2$/90]
Hashin	0.94 [-27/62/-29]	0.70 [-13/-64/-19]	0.94 [-38/58$_2$/-38]	0.94 [-87/-6$_2$/-90]	0.24 [0]	0.47 [4$_2$]	0.70 [-32/42/-32]
	0.94 [90/0$_2$/90]	0.94 [90/0$_2$/90]	0.94 [90/0$_2$/90]	0.70 [90/0/90]	0.24 [0]	0.47 [0$_2$]	0.94 [-30/45/-30]

In Table 3, as expected, most of the FC achieve similar laminates for both the free and constrained optimisations. Hashin and Tsai-Wu appear to have the most similar mass for both optimisations; however, the constrained laminates outperform the free. However, Puck free laminates regularly outperform constrained laminates. Max strain in tension-tension appears to be an outlier; the free mass (*1.64kg*) is unusually large compared with the constrained mass (*0.94kg*). This has been put down to potential premature GA convergence.

Throughout the data collection for this analysis, several issues were encountered. They are discussed here; Firstly, GAs do not use a brute force approach to determining optimum laminates and therefore cannot search all possible combinations of laminates and layer numbers. This means that in any given result, there is the possibility that the algorithm has experienced premature convergence and returned a local optimum rather than the intended global optimum. This is one of the perils of using this type of optimisation scheme, but this analysis would not have been possible within the given timeframe with a brute force method.

Secondly, there has been no tuning of the equation used to calculate S_{EFF} (Eq. 1), so it is unduly affected by the mass at higher loads. The mass component dominates the cost function once the laminate reaches more than five layers. Once the mass of the laminate becomes roughly equal to the SF, further increases in the mass mean the effect of the SF on the S_{EFF} becomes a smaller proportion, and so the solution becomes mass focused. The orientation does not impact the result as much as the number of plies. Similarly, below five layers, the SF is the dominant factor and has more impact on the optimal laminate. This is thought to pose less of an issue as laminates with a SF closer to one will inherently be lighter, and even for a *1*-layer laminate, *20%* of the response is provided by the mass.

  doi:10.5075/epfl-298799_978-2-9701614-0-0

5. Conclusions

This paper investigates the effect of Failure Criteria (FC) choice on the result of an optimisation scheme for a CFRP plate structure subject to in-plane loading. The stacking sequence and thickness of a *1x1m* plate are optimised using a GA that employs each of five FC, separately, as the cost function. A range of bi-axial loads have been applied to the plate, and the resulting structural efficiency (S_{EFF}) and mass have been compared for laminates employing each of the FC. In general, across all test cases, Hashin has the lowest average difference from the minimum S_{EFF} at *7%*. The difference in mass between FC at each test point is, on average, *7.6%* and the average difference between the two least conservative FC is 6%; however, the maximum differences are up to 167% and 40%, respectively. Significant differences in S_{EFF} can be attributed to scenarios where less conservative FC demand a larger number of layers which dictates a discrete step in laminate mass, alongside the potential for premature GA convergence. Laminates optimised using Tsai-Wu, Puck, and Hashin best conform to 'traditional' laminate design.

6. References

[1] A. S. Kaddour, M. J. Hinton, and P. D. Soden, "Predictive capabilities of nineteen failure theories and design methodologies for polymer composite laminates. Part B. Comparison with experiments.," *Fail. Criteria Fibre-Reinforced-Polymer Compos.*, pp. 1073–1221, 2004.

[2] A. S. Kaddour, M. J. Hinton, S. Li, and P. A. Smith, "The world-wide failure exercises: How can composites design and manufacture communities build their strength," *16th Eur. Conf. Compos. Mater. ECCM 2014*, no. June, pp. 22–26, 2014.

[3] S. W. Tsai, "Survey of Macroscopic Failure Criteria for Composite Materials.," *J. Reinf. Plast. Compos.*, vol. 3, no. 1, pp. 40–62, 1984.

[4] W. E. Wolfe and T. S. Butalia, "A strain-energy based failure criterion for non-linear analysis of composite laminates subjected to biaxial loading," *Fail. Criteria Fibre-Reinforced-Polymer Compos.*, pp. 353–378, 2004.

[5] G. C. Eckold, "Failure criteria for use in the design environment," *Fail. Criteria Fibre-Reinforced-Polymer Compos.*, pp. 121–139, 2004.

[6] C. T. Sun and J. Tao, "Chapter-3-9-Prediction-of-failure-envelopes-and-stress-strain-behavior-of-composite-laminates-_2004_Failure-Criteria-in-Fibre-Reinforced-Polymer-Compo.pdf," pp. 316–333, 2004.

[7] H. Dong, J. Wang, and B. L. Karihaloo, "An improved Puck's failure theory for fibre-reinforced composite laminates including the in situ strength effect," *Compos. Sci. Technol.*, vol. 98, pp. 86–92, 2014.

[8] "Siemens Documentation." [Online]. Available: http://www2.me.rochester.edu/courses/ME204/nx_help/index.html#uid:id1196302. [Accessed: 24-Mar-2022].

[9] "Tsai-Wu Failure Criterion - 2017 - SOLIDWORKS Help." [Online]. Available: http://help.solidworks.com/2017/english/SolidWorks/cworks/r_tsaiwu_failure_criterion.htm. [Accessed: 24-Mar-2022].

[10] D. Zenkert and M. Battley, *Foundations of fibre composites : notes for the course: Composite lightweight structures*. DTU, 2006.

[11] "Population Diversity - MATLAB & Simulink - MathWorks Australia." [Online]. Available: https://au.mathworks.com/help/gads/population-diversity.html. [Accessed: 03-Dec-2021].

[12] "Tips for specifying Population Size, No. of Generations, and other Options for GA with large nvars -." [Online]. Available: https://au.mathworks.com/matlabcentral/answers/105754-tips-for-specifying-population-size-no-of-generations-and-other-options-for-ga-with-large-nvars?s_tid=srchtitle. [Accessed: 03-Dec-2021].

DISCRETE MATERIAL AND THICKNESS OPTIMIZATION OF LAMINATED COMPOSITES USING AGGREGATED HIGH-CYCLE FATIGUE CONSTRAINTS

Sebastian M. Hermansen[a], Erik Lund[b]

a: Aalborg University, Department of Materials and Production, Fibigerstraede 16, DK-9220 Aalborg East, Denmark
b: Aalborg University, Department of Materials and Production, Fibigerstraede 16, DK-9220 Aalborg East, Denmark, Email: el@mp.aau.dk

Abstract: *This work presents an efficient approach for gradient-based structural optimization of multi-material laminated composites where high-cycle fatigue constraints are included by a novel approach. The parameterization of the structure is done by the Discrete Material and Thickness Optimization approach, such that an optimized combination of material, fiber orientation, layup sequence, and layer thickness can be obtained. The high-cycle fatigue analysis approach used takes offset in methods typically applied in the wind turbine industry for blade design. The variable-amplitude loading is quantified by rainflow counting assuming proportional loading. A constant life diagram approach is used to calculate equivalent stresses from the amplitude and mean components, taking into account mean stress of various magnitudes by interpolating between their respective S-N curves. Reversals to failure are computed from the S-N curves, and damages are summed using cumulative methods such as the linear Palmgren-Miner damage rule. The high number of local fatigue constraints is reduced by use of aggregation functions. This also enables efficient design sensitivity analysis using the adjoint method. The potential of the optimization approach will be demonstrated by a number of examples.*

Keywords: Multi-material optimization; Topology optimization; High-cycle fatigue; Laminated composites.

1. Introduction

Laminated composite structures consisting of Glass or Carbon Fiber Reinforced Polymers (GFRP/CFRP) make it possible to achieve efficient and lightweight structural designs due to their superior strength and stiffness characteristics. Due to the large design freedom associated with these structures, it is attractive to apply structural optimization techniques in the design process, and many different approaches have been developed. An overview of optimization methods for laminated composites can be found in [1-3]. Gradient-based structural optimization of composites is well developed for response functions like stiffness, displacements, buckling load factors, eigenfrequencies, static strength criteria, etc., but the inclusion of general fatigue constraints is a new area. This paper will focus on an efficient approach for including high-cycle fatigue constraints in a gradient-based optimization procedure.

2. Parameterization

The parameterization of the structure is done by the Discrete Material and Thickness Optimization (DMTO) approach [4], such that an optimized combination of material, fiber orientation, layup sequence, and layer thickness can be obtained. This parameterization takes offset in multi-material topology optimization formulations, in particular in the family of Discrete

  doi:10.5075/epfl-298799_978-2-9701614-0-0

Material Optimization (DMO) approaches [5-6]. In the DMO method a number of candidate materials are defined, which could be different fiber-reinforced polymer materials oriented at chosen fiber angles combined with core materials in case of sandwich structures. The discrete problem of choosing the best candidate material *c* is converted to a continuous problem that can be solved efficiently using gradient-based optimizers. Multi-material interpolation functions with penalization of intermediate design variable values are applied, such that the effective element constitute matrix for a given layer *l* in a given shell element is obtained by interpolation between constitutive matrices $\boldsymbol{E}_c$ of the candidate materials. In DMTO this interpolation is combined with topology (density) variables that govern the presence of material in given layers, such that simultaneous material and thickness optimization can be performed, see Figure 1 where a 3-layer laminated plate is divided into 4 domains with individual topology variables, such that a varying thickness laminate can be obtained.

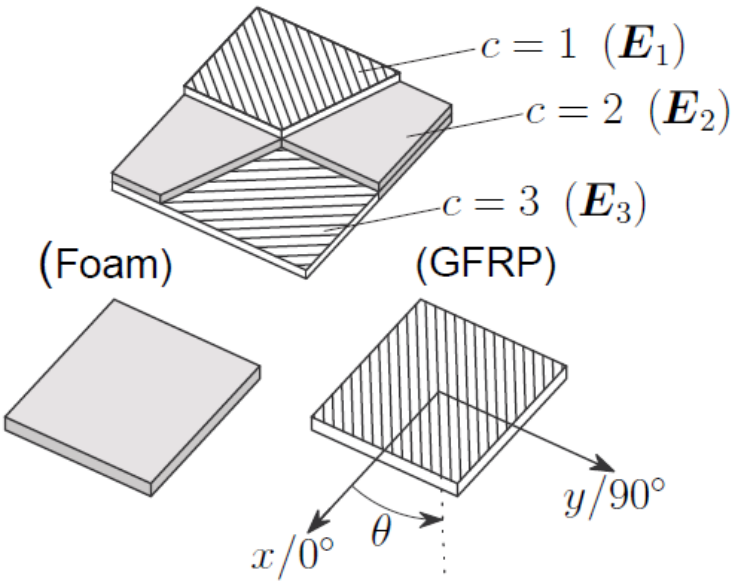

Figure 1. Potential outcome of a tapered laminated plate example.

The DMO/DMTO parameterization approach can be applied for a number of structural response functions like compliance, displacements, eigenfrequencies, and buckling load factors [4-10], and recently also for local failure criteria [11].

3. Fatigue Analysis

The high-cycle fatigue analysis approach in this work takes offset in methods typically applied in the wind turbine industry for blade design, see e.g. [12]. The variable-amplitude loading is quantified by rainflow counting yielding a set of scaling factors for determining amplitude and mean stress. Proportional loading is assumed, such that the computationally expensive rainflow counting only needs to be performed once during the optimization. In the general case when loads are non-proportional, a new stress state has to be determined at each time step in the load history, which is computationally expensive. For an approach for efficient computation of non-proportional stress states including evaluation of gradients using the adjoint approach, the reader is referred to [13].

  doi:10.5075/epfl-298799_978-2-9701614-0-0

A constant life diagram (CLD) approach is used to calculate equivalent stresses from the amplitude and mean components, taking into account mean stress of various magnitudes by interpolating between their respective S-N curves.

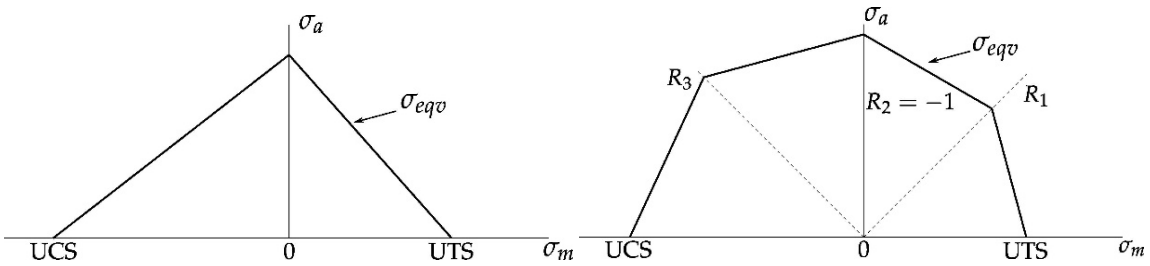

Figure 2. Left: CLD formulated with bilinear Goodman. Right: Example of a CLD with interpolation between three S-N curves.

Many equivalent stress models exist with varying accuracy. The modified Goodman expression is commonly used for isotropic materials based on R = -1, i.e. fully-reversed loading, as it generally yields conservative results, in particular if neglecting the beneficial effect of positive mean stress. It is illustrated in Figure 2 left, where UTS is the tensile strength and UCS is the compressive strength of the material. However, for composites alternating compressive stresses are damaging and are therefore not negligible [14]. Furthermore, due to the orthotropic behavior of fiber-reinforced polymer layers, it is not sufficient to perform mean stress correction based on an isotropic equivalent stress criterion such as the signed von Mises or Sines methods. Instead, mean stress correction has to be performed in each load direction, i.e. for each amplitude and mean stress component. Here, the Goodman correction is applied as it is a simple expression. The fatigue evaluation is performed on each stress component in material coordinates, thus neglecting stress interaction effects, however, this is commonly used in industry.

Reversals to failure are computed from the S-N curves, which are constructed using a data-fitted power law (Basquin's expression). Damages are summed using a cumulative method. Here, the linear Palmgren-Miner damage rule is used for simplicity.

The Goodman correction is formulated from a fully-reversed loading case, i.e. at R = -1, where R is the stress ratio defined as

$$R = \frac{\sigma_{min}}{\sigma_{max}} = \frac{\sigma_m - \sigma_a}{\sigma_m + \sigma_a} \quad (1)$$

For laminated composites the different failure behavior exhibited by the material in tension and compression can be better included in the fatigue prediction by including more data in the CLD [14]. A simple approach to this is by linear interpolation between available data at different R-ratios. Despite its simplicity, [15] concludes that this method seems to perform quite well. An improved piece-wise non-linear formulation has since been presented in [16], and this can replace the piece-wise linear formulation if increased accuracy is required. Commonly, data for stress ratios of R = 10 and R = 0.1 is included for laminated composites as demonstrated in [17], which yields a CLD as illustrated in Figure 2 right. Analytical expressions for all sections of the CLD can be found in [14,17]. In this work, it is chosen to pre sample a number of S-N curves before performing the fatigue calculation to reduce the amount of data.

  doi:10.5075/epfl-298799_978-2-9701614-0-0

4. Design Sensitivity Analysis and Optimization Approach

In a gradient-based optimization context, the high number of local fatigue constraints combined with many design variables is challenging. Therefore, the number of local fatigue constraints is reduced by use of aggregation functions, such that a single global fatigue constraint is applied when solving the optimization problem, see also a similar approach for topology optimization with stress constraints in [18]. This also enables efficient design sensitivity analysis using the adjoint method where one adjoint problem needs to be solved for each aggregated constraint. In this work a P-norm function is used as aggregation function. Furthermore, fatigue damage constraints have inherent difficulties, which require reformulation of the problem in order to stabilize the optimization and be able to achieve a good solution. These difficulties include singularities in the design domain as a consequence of the stress-based formulation and an exponential dependence of the fatigue damage on stress, making it difficult for the problem to converge. The singularity issue is treated using the qp-method introduced for topology optimization with stress constraints for isotropic materials in [19] and demonstrated for the DMO/DMTO method in [11]. The exponential dependence of the fatigue damage on the stress is handled by making use of scaling of the damage values. In this work the inverse P-mean scaling also presented in [20] is used.

The optimization problems are solved using Sequential Linear Programming techniques. Such approaches are very efficient for the applied DMO/DMTO parameterization where many linear equality constraints on design variables are needed [4, 7]. The aggregated P-norm damage constraint will overestimate the maximum local damage in the model, and this overestimation typically would result in a design where the true damage constraint is not active. Therefore, the adaptive constraint scaling scheme proposed in [21] is used. With this approach the constraint is scaled according to the ratio of the current maximum local damage value and the P-norm value together with history information about the constraint scaling, see details about our implementation in [18]. This adaptive constraint scaling scheme has the advantage that lower values of penalization power P can be applied, which makes the optimization problem easier to solve.

5. Example

In this paper only one small illustrative example is included while several other examples including mass minimization of a main spar from a wind turbine blade with fatigue constraints will be presented at the conference. The fatigue properties used are based on the OPTIDAT database [22].

The example demonstrates fatigue optimization with the DMO parameterization. The problem considered is finding the optimal fiber distribution of a clamped plate subject to distributed pressure load p = 1 MPa, see Figure 3. The objective is to minimize the P-norm aggregated fatigue damage. It is a standard benchmark example where the optimal fiber distribution for stiffness and strength problems are known to be symmetric.

The plate is discretized using 32x32 regular 9-node isoparametric shell finite elements. The material used in the model is GFRP with four DMO candidates constituted by different fiber orientations of -45°, 0°, 45° and 90°. A fatigue load spectrum of 10^6 cycles has been applied for a zero-based constant amplitude loading, i.e. $R = 0$ for all load combinations. Only the S-N curve

  doi:10.5075/epfl-298799_978-2-9701614-0-0

at *R* = -1 is used for the fatigue evaluation, and the bilinear Goodman expression is applied for mean stress correction. An 8x8 patch parametrization is used, such that the same candidate design variable is assigned to each 4x4 square of finite elements.

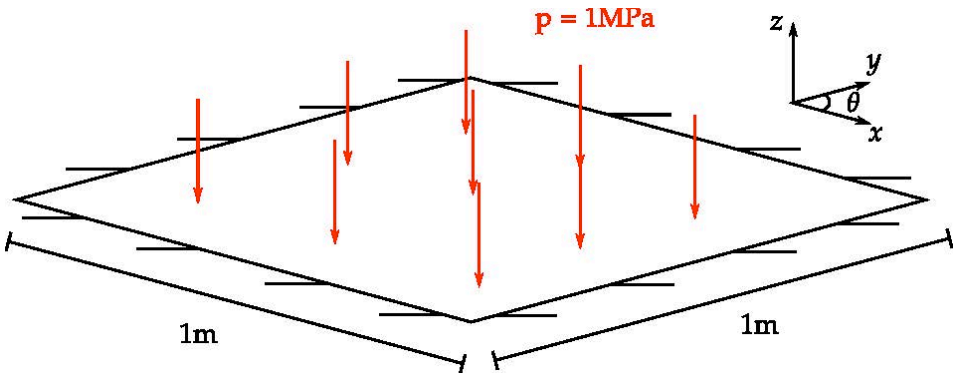

Figure 3. Clamped plate subjected to uniform pressure.

In each of the finite elements the damage is computed at the top and bottom, and each damage value is scaled with an inverse P-mean norm approach as described in Section 4. All damage values are aggregated to one global damage value using a P-norm function with P=12. The gradient-based optimization needs 88 design iterations until the relative change in design variables between iterations is less than of 0.1%, which is used as convergence measure.

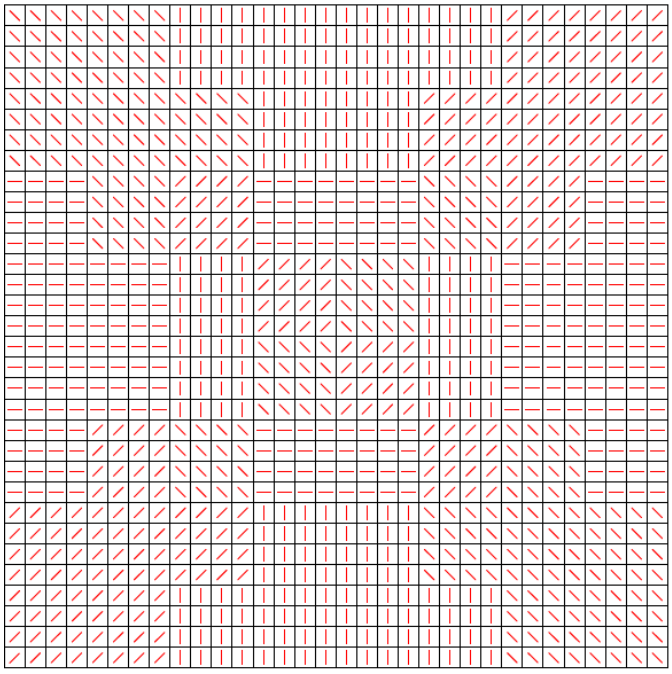

Figure 4. Resulting fiber distribution.

The resulting fiber distribution for the 8x8 patch parameterization can be seen in Figure 4, and it resembles the fiber orientations obtained for stiffness and strength design. In a similar way, the distributions of damages resemble the distributions of failure indices for this academic benchmark example, see [11]. The distributions of scaled damages D_{11} and D_{22} (damages in the two principal material directions) at the bottom of the plate can be seen in Figure 5.

  doi:10.5075/epfl-298799_978-2-9701614-0-0

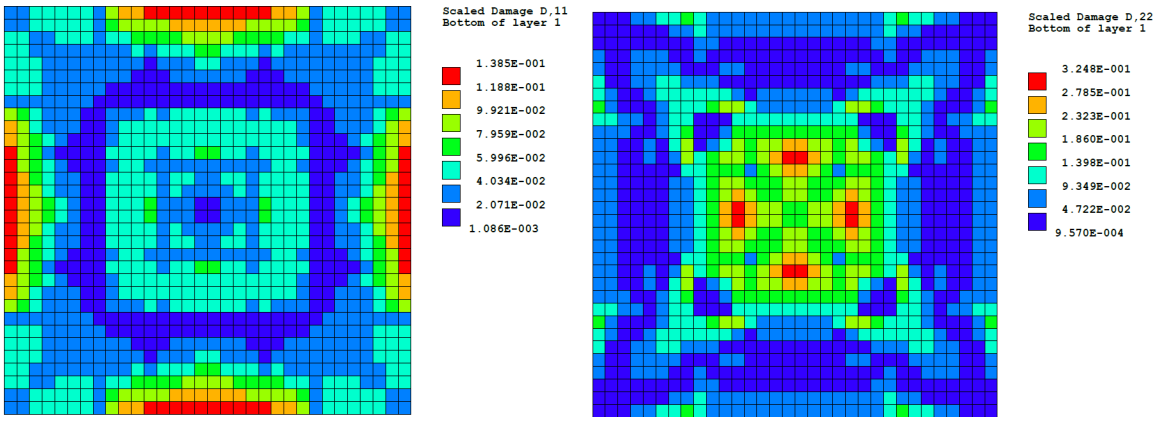

Figure 5. Resulting scaled damage distributions D_{11} *and* D_{22} *at the bottom of the plate.*

The iteration history can be seen in Figure 6. The optimization is rather stable despite the highly non-linear fatigue equations, which is attributed to the use of damage scaling. The penalization powers in the DMO parameterization are increased at iteration 20 and 40, and the two continuation steps are clearly seen in the iteration history. The choice of fiber orientation is distinct at the end of the optimization.

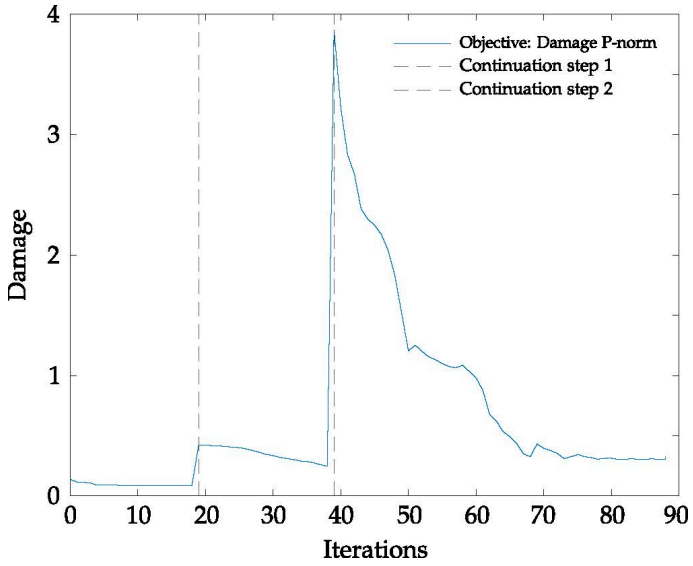

Figure 6. Iteration history for plate example.

6. Conclusions

This work has demonstrated a gradient-based framework for high-cycle fatigue optimization, simultaneously considering material and thickness optimization of laminated composite structures. The high-cycle fatigue analysis is based on methods applied in the wind turbine industry for blade design. The variable-amplitude loading is assumed proportional, and it is quantified by rainflow counting. A constant life diagram approach is used, taking into account mean stress of various magnitudes by interpolating between their respective S-N curves. Reversals to failure are computed from the S-N curves, which are constructed using a data-fitted power law. Damages are summed using cumulative methods such as the linear Palmgren-Miner damage rule. The high number of local fatigue constraints is reduced by use of aggregation functions, which also enables efficient design sensitivity analysis using the adjoint method. A

  doi:10.5075/epfl-298799_978-2-9701614-0-0

benchmark example of optimal fiber orientations for a clamped plate has been used to demonstrate the approach, and the potential of the optimization approach will be demonstrated by an example of mass minimization of a main spar from a wind turbine blade with fatigue constraints at the conference.

Acknowledgements

The work was supported by the MADEBLADES project funded by the Energy Technology Development and Demonstration Program, Grant No. 64019-0514. This support is gratefully acknowledged.

7. References

1. Ghiasi H, Pasini D, Lessard L. Optimum stacking sequence design of composite materials Part I: Constant stiffness design. Composite Structures 2009; 90(1):1-11.
2. Ghiasi H, Fayazbakhsh K, Pasini D, Lessard L. Optimum stacking sequence design of composite materials Part II: Variable stiffness design. Composiste Structures 2010; 93(1):1-13.
3. Nikbakt S, Kamarian S, Shakeri M. A review on optimization of composite structures part I: Laminated composites. Composite Structures 2018; 195:158-185.
4. Sørensen SN, Sørensen R, Lund E. DMTO - a method for Discrete Material and Thickness Optimization of laminated composite structures. Structural and Multidisciplinary Optimization 2014; 50:25-47.
5. Stegmann J, Lund E. Discrete material optimization of general composite shell structures. International Journal for Numerical Methods in Engineering 2005; 62:2009-2027.
6. Lund E, Stegmann J. On structural optimization of composite shell structures using a discrete constitutive parametrization. Wind Energy 2005; 8:109-124.
7. Hvejsel CF, Lund E. Material interpolation schemes for unified topology and multi-material optimization. Structural and Multidisciplinary Optimization 2011; 43(6):811-825.
8. Sørensen SN, Lund E. Topology and thickness optimization of laminated composites including manufacturing constraints. Structural and Multidisciplinary Optimization 2013; 48(2):249-265.
9. Sørensen R, Lund E. Thickness filters for gradient based multi-material and thickness optimization of laminated composite structures. Structural and Multidisciplinary Optimization 2015; 52(2):227-250.
10. Sjølund JH, Peeters D, Lund E. A new thickness parameterization for discrete material and thickness optimization. Structural and Multidisciplinary Optimization 2018; 58:1885-1897.
11. Lund E. Discrete Material and Thickness Optimization of laminated composite structures including failure criteria. Structural and Multidisciplinary Optimization 2018; 57:2357-2375.
12. Nijssen R. Fatigue Life Prediction and Strength Degradation of Wind Turbine Rotor Blade Composites. Knowledge Centre Wind Turbine Materials and Constructions (KCWMC), Ph.D. Thesis 2006.
13. Zhang S, Le C, Gain AL, Norato JA. Fatigue-based topology optimization with non-proportional loads. Computer Methods in Applied Mechanics and Engineering 2019; 345:805-825.
14. Vassilopoulos AP, Keller T. Fatigue of Fiber-reinforced Composites. ISBN: 978-1-84996-180-6, Springer 2011.

  doi:10.5075/epfl-298799_978-2-9701614-0-0

15. Vassilopoulos AP, Manshadi BD, Keller T. Influence of the constant life diagram formulation on the fatigue life prediction of composite materials. International Journal of Fatigue 2010; 32:659-669.
16. Vassilopoulos AP, Manshadi BD, Keller T. Piecewise non-linear constant life diagram formulation for FRP composite materials. International Journal of Fatigue 2010; 32:1731-1738.
17. Philippidis TP, Vassilopoulos AP. Life prediction methodology for GFRP laminates under spectrum loading. Composites Part A: Applied Science and Manufacturing 2004; 35(6):657-666.
18. Oest J, Lund E. Topology optimization with finite-life fatigue constraints. Structural and Multidisciplinary Optimization 2017; 56(5):1045–1059.
19. Bruggi M. On an alternative approach to stress constraints relaxation in topology optimization. Structural and Multidisciplinary Optimization 2008; 36:125-141.
20. Olesen AM, Hermansen SM, Lund E. Simultaneous optimization of topology and print orientation for transversely isotropic fatigue. Structural and Multidisciplinary Optimization 2021; 64:1041-1062.
21. Le C, Norato J, Bruns T, Ha C, Tortorelli D. Stress-based topology optimization for continua. Structural and Multidisciplinary Optimization 2010; 41:605-620.
22. Nijssen R, van Wingerde A, van Delft D. The OptiDAT materials fatigue database. In: Polymer composite materials for wind power turbines, Riso national Laboratory 2006; 257-263.

  doi:10.5075/epfl-298799_978-2-9701614-0-0

DESIGN AND OPTIMISATION OF A 3D PRINTED COMPOSITE PROSTHETIC FOOT: A FINITE ELEMENT FEASIBILITY STUDY

Luca M. Martulli[a], Abdel Rahman Al Tahabi[a], Andrea Sorrentino[b], Marino Lavorgna[b], Emanuele Gruppioni[c] , Andrea Bernasconi[a]

a: Politecnico di Milano, Via La Masa 1, I-20156 Milano, Italy
andrea.bernasconi@polimi.it
b: Polymer, Composites and Biomaterials Institute, National Research Council (CNR), Via Previati 1/E, 23900 Lecco (LC), Italy
c: INAIL, Centro Protesi Inail, Via Rabuina 14, 40054 Vigorso di Budrio (BO), Italy

Abstract: *Currently, the most traditional manufacturing process for composite prosthetic feet is lamination. While allowing the production of light high-performance structures, the process is very expensive and limits both production rate and customisability. Additive manufacturing can be an alternative solution to cope with these limitations. This work explores the possibility to additively manufacture a prosthetic foot with the same stiffness of a laminated one. To this end, a commercially available foot is first analysed via numerical simulations. Using this reference case, a beam elements-based tool is developed and validated. The tool was then used to optimise four different designs of a possible additively manufactured prosthesis. This preliminary work resulted in two possible 3D printed foot designs that could be further analysed to potentially substitute the laminated prosthesis.*

Keywords: 3D printing; additive manufacturing; prosthesis; optimisation; composite structures

1. Introduction

Modern commercially available prosthetic feet for amputees belong to two categories [1]. The first, the Solid Ankle Cushion Heel (SACH), is relatively inexpensive and reliable, but generally displays poor performance: it is thus indicated for people with limited activity on standard terrains. The second, the Energy Storage And Return (ESAR) prosthesis mimics more accurately the human foot by storing and releasing energy during the different phases of the walk; it is therefore more comfortable and allow for a higher level of activity. The ESARs, however, are often made of laminated carbon fibre composites, making them very expensive for the final user.

Additive manufacturing can potentially allow for cheaper, faster, and customised manufacturing of high-performance composite structures [2]. The objective of this work is to assess the feasibility of an ESAR prosthetic foot made by Fused Filament Fabrication (FFF), one of the most popular additive manufacturing techniques for polymeric composites [2].

A reference prosthetic foot was defined, inspired by commercially available models (e.g. [3]) was assumed. Finite Element (FE) simulations were first performed on this geometry. These simulations aimed to define target prosthesis stiffnesses in the different analysed configuration. Moreover, a beam element-based modelling approach is developed and validated on the

  doi:10.5075/epfl-298799_978-2-9701614-0-0

reference prosthesis. Thanks to the fewer geometrical descriptors it requires, this modelling approach is adopted in the optimisation process of the newly developed 3D printed prosthesis.

2. Modelling methodologies and approaches

2.1 Reference prosthesis models

Figure 1a shows a 3D CAD model of the reference prosthesis. Shell element simulations were performed on Abaqus software by extracting the mid surface of the two springs and the plantar (see Figure 1b). The connection gasket was modelled with tie constraints between the interested surfaces. A rigid coupling was applied to the upper end of the springs to a fixed node-top to simulate the connection to the pylon. Moreover, vertical displacements Δu were applied to the lowest points, as shown in Figure 1b, to simulate the mid-stance phase of the walk [4]. After a mesh sensitivity analysis, a mesh seed of 5 mm was used.

A beam elements model was also obtained by projecting the shell model on the X-Z plane (see Figure 1c). Rigid connections were used as shown. A constant width of 55 mm was assumed for this model, because this approximated best the width of the springs and of the central part of the plantar. The boundary conditions mimic the ones of the shell model: the node-top is fixed, while vertical displacements are applied to nodes A and node B.

The prosthesis was assumed to be made of a Carbon Fibre Reinforced Plastic (CFRP) laminate, with stacking sequences $[(\pm 45°)_3(0°)_{24}]_s$ and $[(\pm 45°)_2(0°)_{16}]_s$ for the plantar and the springs, respectively. The CFRP material properties are reported in Table 1 as obtained from [5]. For the shell simulations, the composite laminate tool of Abaqus was used. Regarding the beam model, Chou's theory [6] was used to homogenise the laminates and obtain their engineering constants. The reaction force at the node-top was extracted as function of the applied displacement Δu. The slope of this load-displacement curve was considered as the stiffness of the reference prosthesis.

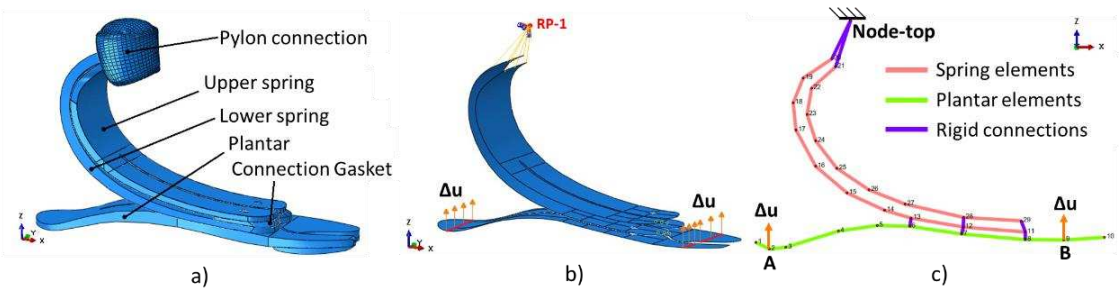

Figure 1: Reference prosthesis: a) real object, b) 3D CAD, c) shell model and d) beam model.

Table 1: CFRP properties [5]. Moduli are in GPa, Poisson's ratio are dimensionless.

E11	E22	E33	G12	G13	G23	v12	v13	v23
121	7.46	7.46	5.2	5.2	2.6	0.13	0.13	0.44

2.2 3D printed prosthesis models

The 3D printed prosthesis will take advantage of the 3D printed sandwich structures concept [7]: the sandwich skins will be made of continuous carbon fibres layers, while the infill will make

  doi:10.5075/epfl-298799_978-2-9701614-0-0

the sandwich core. The infill is made of Onyx, a micro-carbon fibres reinforced polyamide developed by Markforged [8]. The geometrical complexity of the prosthesis requires it to be printed on the X-Z plane. Therefore, the carbon fibre layers will all be oriented along the local material x-axis (0° orientation). Considering the inherent geometry of sandwich structures and the different stiffness of skins and core, the skins were assumed to bear all the bending stresses, while the core was assumed to bear all the shear stresses. This was possible since Timoshenko beam elements were considered, so to include the shear flexibility of the sandwich beams. For the full theory on Timoshenko's beam elements, the reader is referred to [9].

To fully exploit the additive manufacturing potentials, a unique integrated structure will be considered for the prosthesis. To keep the biomechanical properties of the prosthesis as close as possible to the reference prosthesis, the plantar was left unchanged. Two different spring geometries were considered, namely C-shaped or J-shaped. The exemplificative case of a C-shaped prosthesis is shown in Figure 2a. Moreover, considering similar works on the subject [10], the possible presence of a heel support was evaluated (see Figure 2b and 2c). The spring and heel elements were imposed to have a total thickness of 75% of the thickness of the plantar (as was approximately the case for the springs of the reference prosthesis).

The optimisation procedure was thus performed on four different geometries. Seventy configurations per geometry were considered in the optimisation procedure. This is schematically illustrated in Figure 2a: different configurations per geometry were obtained by varying the parameter ε, which thus becomes an optimisation variable. Configurations 1, 35 and 70 are shown for all geometries in Figure 3, as examples. The other optimisation variables were the thickness of the core *c* and the thickness of the skins *t* of the spring elements. Weight was set as the objective function to minimise, while the design constraint was to have an equal stiffness of the reference prosthesis. The stiffnesses of the 3D printed prostheses were obtained by applying the same boundary conditions as those shown in Figure 1c, with a fixed note-top and applied displacement Δu to both nodes A and B.

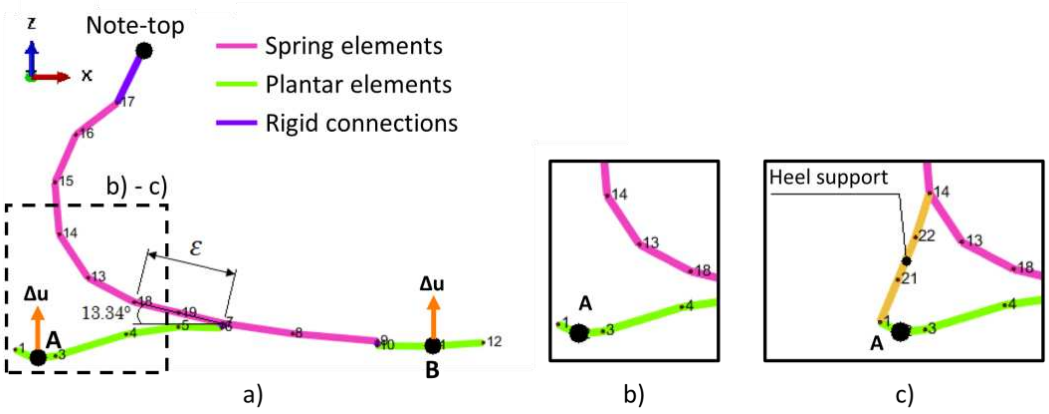

Figure 2: a) Example of the beam model of a 3D printed prosthesis with a C-shaped spring. The optimisation variable ε is shown. Details of the prosthesis b) without and c) with the heel support are also shown.

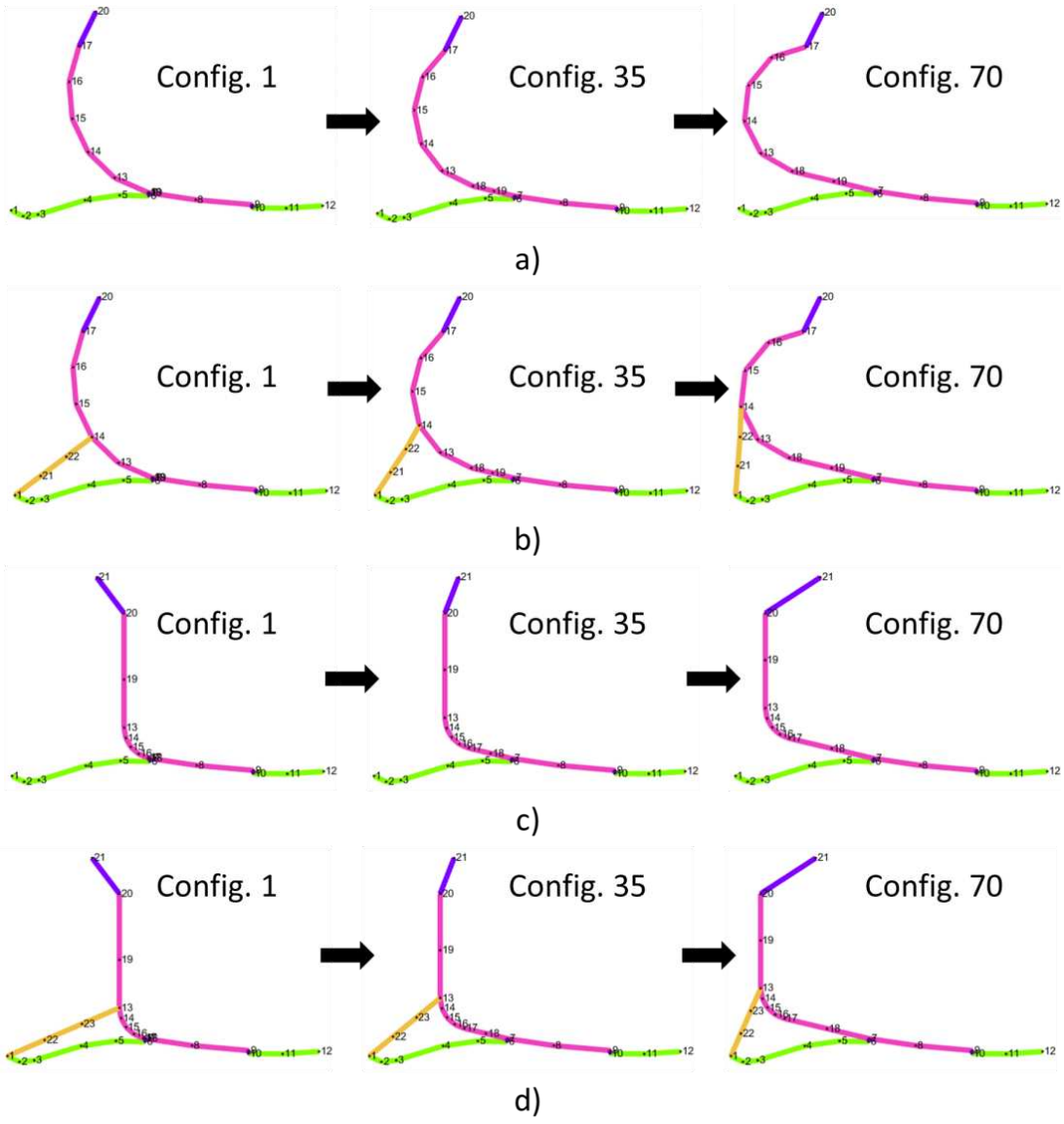

Figure 3: Configurations 1, 35 and 70 for the a) C-shaped spring prosthesis, b) C-shaped spring prosthesis with heel support, c) J-shaped spring prosthesis and d) J-shaped spring prosthesis with heel support.

Finally, Table 3 reports the remaining material and geometrical details adopted in the optimisation procedure, as well as the considered material densities for the weight calculations.

Table 3: Material and geometrical details adopted in the optimization procedure.

Parameter	Value
Young's modulus of the skins E_s [8]	45.0 GPa
Shear modulus of the core G_c [7]	122.0 MPa
Width of all the beam elements b	55 mm
Density of the carbon fibre skins ρ_s [8]	1200 kg/m^3
Density of the core ρ_c (20% rectangular infill) [7]	418 kg/m^3

  doi:10.5075/epfl-298799_978-2-9701614-0-0

3. Results and discussion

3.1 Beam model validation

Table 4 reports the comparison of the stiffnesses obtained with the shell FE model on Abaqus and the developed beam FE model. As shown, the developed beam elements-based model overpredicts the stiffness predicted by the shell element model by less than 8%. This is coherent with the different width of the two models. As mentioned, the beam elements-based model considers a constant width equal to the central width of the reference prosthesis. However, the front and rear portions of the prosthesis present a reduction of width, which is considered only by the shell model. Overall, the beam model is thus considered a reliable tool for the optimisation of the 3D printed prosthesis.

Table 4: Comparison of stiffnesses obtained in the shell and beam FE model.

Simulated stiffness	Value
Shell FE model (Abaqus)	294.5 N/mm
Beam FE model	317.1 N/mm

3.2 Optimisation of the new prostheses

Figure 3 reports the results of the optimisation procedure, showing for each design the best configuration and the core and skins thickness *c* and *t*, respectively. As expected, the presence of a heel support significantly increases the stiffness of the prosthesis: the foot with the heel support thus requires much thinner core and skins (see Figure 3c and 3d). However, the thickness of these two designs is likely not to be printable, as printing with continuous fibres usually requires layers of about 1 mm [8]. Moreover, such thin structures may result in too high stresses in the structure. For these reasons, the presence of the heel support must be discarded. The difference between the other two feet (Figure 3a and 3b) highlights the different contributions of the spring shape, with the J-shaped one being stiffer than its C-shaped counterpart. Both designs show skins layers thicker than 1 mm, and can thus be printed. Interestingly, for both these designs the best configuration was the first one, with ε=0.

  doi:10.5075/epfl-298799_978-2-9701614-0-0

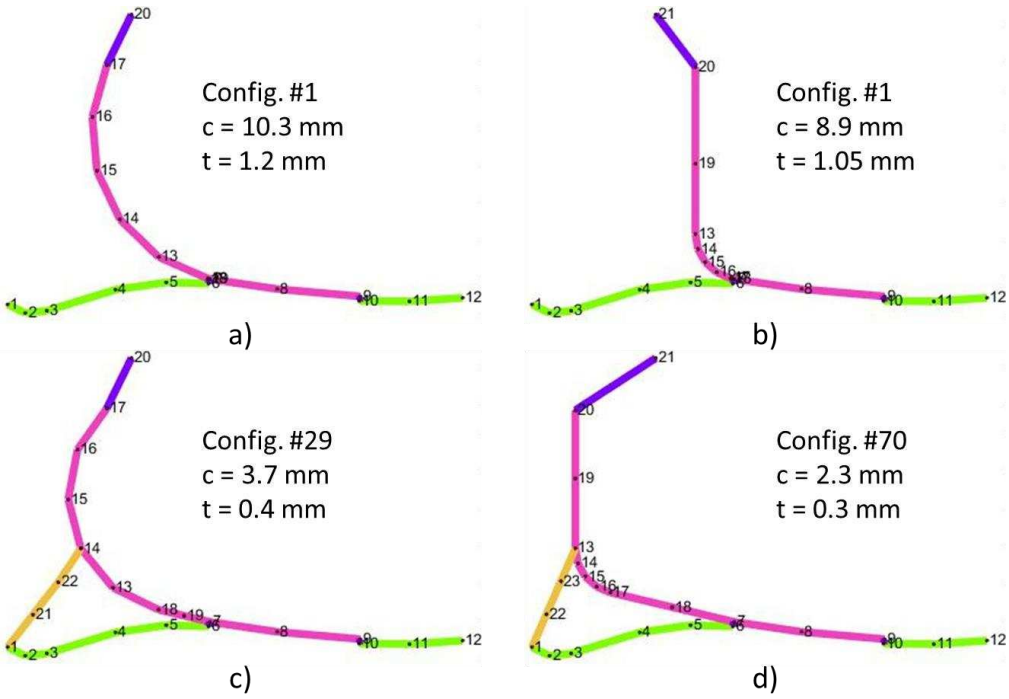

Figure 3: Results of the four optimisations

Considering the above, both prostheses without the heel support could match the vertical stiffness of the laminated structure with reasonable geometrical parameters. Therefore, these geometries can be further analysed to design a 3D printed prosthetic foot with performance similar to that of a commercially available one.

4. Conclusions and future works

The present work aimed to explore possible designs for a 3D printed prosthesis as an alternative to laminated ones. A beam elements-based numerical tool was developed to allow for an efficient optimisation of different prosthesis shapes. The tool was first validated against a reference case, namely a commercially available laminated prosthesis. This prosthesis was also analysed to predict its vertical stiffness. The beam elements-based tool was then used to optimise four different 3D printed prosthesis designs. The reference vertical stiffness was set as optimisation constraint, while weight was the objective function. It was found that the presence of a heel support made the prosthesis too stiff. On the other hand, it was possible to obtain two different designs matching the vertical stiffness of the reference prosthesis.

This work supports the feasibility of a 3D printed prosthetic foot as replacement for a laminated one. This work can thus be the basis for a future design phase, that would require a deeper analysis. First, the vertical stiffness was considered as optimisation constraint: this is equivalent to consider the response of the prosthesis in the mid-stance phase of the gait [4]. However, it is also important to evaluate the overall stiffness of the prosthesis in the other phases of the gait cycle [4]. Once this is done, an assessment on the strength of the obtained 3D printed prosthesis design must also be performed, considering both static, fatigue and creep loading conditions.

  doi:10.5075/epfl-298799_978-2-9701614-0-0

Finally, the overall design of the prosthesis should also consider a proper connection device to the upper structures of the prosthesis.

5. References

1. Wezenberg, Cutti AG, Bruno A, Houdijk H. Differentiation between solid-ankle cushioned heel and energy storage and return prosthetic foot based on step-to-step transition cost. J Rehabil Res Dev. 2014;51(10):1579-90.
2. Brenken B, Barocio E, Favaloro A, Kunc V, Byron Pipes R. Fused filament fabrication of fiber-reinforced polymers: A review. Addit Manuf 2018;21:1–16.
3. Össur catalogue, "Pro-Flex® XC." https://www.ossur.com/en-us/prosthetics/feet/pro-flex-xc (accessed Jan. 15, 2022)
4. Versluys R, Beyl P, Van Damme M, Desomer A, Van Ham R, Lefeber D. Prosthetic feet: state-of-the-art review and the importance of mimicking human ankle-foot biomechanics. Disabil Rehabil Assist Technol. 2009 Mar;4(2):65-75
5. Turon A, Camanho PP, Costa J, Davila CG. A damage model for the simulation of delamination in advanced composites under variable-mode loading. Mech of Mat 2006; 38: 1072-1089.
6. Chou P, Carleone J, Hsu C. Elastic constants of layered media. J Compos Mater 1972; 80-93.
7. Martulli LM, Barriga Ruiz P, Rajan A, Bárnik F, Ságа M, Bernasconi A. Infill shape effects on bending stiffness of additively manufactured short fibre reinforced polymer sandwich specimens. J Reinf Plast and Compos 2021; 40: 927-938.
8. Markforged datasheets, https://markforged.com/it/datasheets (Accessed on March 2022).
9. Fogang V. Timoshenko beam theory: exact solution for bending, second order analysis, and stability. Preprints 2020, 2020110457.
10. Rochlitz B, Pammer D. Design and Analysis of 3D Printable Foot Prosthesis. Period. Polytech. Mech. Eng. 2017; 61(4):282-7.

  doi:10.5075/epfl-298799_978-2-9701614-0-0

TOPOLOGY-OPTIMIZED DESIGN TO MANUFACTURE FOR WET FIBER PLACEMENT

Maximilian Eckrich[a], Peter Arrabiyeh[a], Anna Dlugaj[a], David May[a]

a: Leibniz-Institut für Verbundwerkstoffe GmbH, Erwin-Schrödinger-Str. 58,
67663 Kaiserslautern, Germany – maximilian.eckrich@ivw.uni-kl.de

Abstract: *In Wet Fiber Placement (WFP) continuous fiber rovings are in situ impregnated with a thermoset resin and then placed along load-adapted paths. For efficient design of corresponding structures, topology optimization is very promising. However, topology optimization as well as the subsequent derivation of actual placement paths must take the process-specific manufacturing and material restrictions into account. In this context, a holistic workflow is presented: The parts topology and its fiber orientation are simultaneously optimized, while a dilate filter prevents features smaller than roving width and non-manufacturable undercuts. Placement paths are automatically derived by a modified streamline algorithm, which e. g. ensures a defined and constant path distance. The final design is then established by manual re-work of the streamlines to actually manufacturable paths. For manufacturing, the paths are transferred into a WFP machine-readable G-Code.*

Keywords: Topology optimization; Wet fiber placement; Manufacturing restrictions; Placement paths

1. Introduction

By tension-free placement of in situ impregnated rovings, WFP offers high geometric flexibility and material efficiency: Material can be placed only where needed and the fiber orientation can be aligned with the load paths [1]. In numerical topology optimization, inefficient material is iteratively removed from the design space of a part, which results in truss-like structures that are reduced to the main load paths. Such structures are well suited for being manufactured by WFP. However, WFP is subject to certain manufacturing restrictions, e.g. the width of the rovings has to be considered and undercuts cannot be manufactured. Those restrictions and the material anisotropy should be addressed when designing corresponding structures. Furthermore, the topology optimization result must be transferred to actual fiber placement paths as required for manufacturing. Based on a topology optimization algorithm that already accounts for material anisotropy [2], this approach is extended in order to consider manufacturing restrictions. For the derivation of placement paths for 3D printing, streamline algorithms have been proposed [3]. Yet, the resulting paths may not be parallel to adjacent ones resulting in unwanted gaps or overlaps. Therefore, the target of this work is to improve parallelism of placement paths by modifying the streamline algorithm.

2. Materials

All calculations in this work are based on the properties of a typical carbon fiber reinforced polymer composite (CFRPC), given in Table 1. Here, E is the Young's modulus, G is the shear modulus and μ is the Poisson's ratio. The subscript numbers denote the material direction, where "1" is the longitudinal fiber direction.

  doi:10.5075/epfl-298799_978-2-9701614-0-0

Table 1: Elastic material properties used for topology optimization

E_{11} [MPa]	E_{22} [MPa]	E_{33} [MPa]	G_{12} [MPa]	G_{13} [MPa]	G_{23} [MPa]	μ_{12} [-]	μ_{13} [-]	μ_{23} [-]
139960	8800	8800	4600	4600	3200	0.02	0.02	0.37

For manufacturing of samples, the carbon fiber roving TORAYCA T700SC with 24000 filaments was used, together with the epoxy resin system EPIKOTE™ Resin 04976 + EPIKURE™ Curing Agent 04976 + EPIKURE™ Catalyst 04976 provided by Westlake Epoxy.

3. Methods

3.1 Test cases

In order to investigate several features in topology optimization and for the derivation of placement paths, a 2D and a 3D test case are required. For both, a cantilever beam subjected to a bending load is selected (Fig. 1).

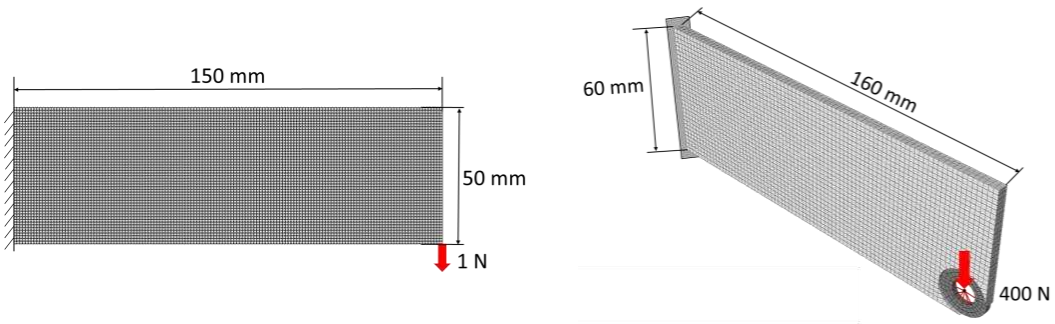

Figure 1: 2D and 3D test case for topology optimization

3.2 Manufacturing tolerant topology optimization

As a starting point, the anisotropic Bi-directional Evolutionary Structural Optimization (BESO) algorithm from Mehl et al. [2] is used. In this algorithm, the decision whether an element will be solid or void material is made based on the element sensitivity α_i, which is calculated according to Eq. (1):

$$\alpha_i = -p\frac{E_i}{x_i} \tag{1}$$

In Eq. (1), E_i is the element strain energy, x_i is the element density (which is one for solid elements and zero for void elements) and p is the penalty exponent, which is set to 1.5 for our studies. To account for the fact that in WFP features smaller than the actual roving width cannot be manufactured, a dilate filter from Sigmund [4] was integrated into the BESO procedure. The filtered sensitivity $\tilde{\alpha}_i$ is given by Eq. (2):

$$\tilde{\alpha}_i = \frac{\log(\sum_j w_{ij} e^{\beta \alpha_j})}{\beta} \tag{2}$$

Here, β is a constant and set to six. The element's filtered sensitivity $\tilde{\alpha}_i$ is calculated based on the sensitivity of all surrounding elements α_j, for which the distance between the elements'

  doi:10.5075/epfl-298799_978-2-9701614-0-0

centers r_{ij} is smaller than the so-called filter radius r_{min}. By setting r_{min} to the roving width, the dilate filter will prevent smaller features. Finally, w_{ij} are weight factors given by Eq. (3):

$$w_{ij} = \begin{cases} \frac{1}{|N_i|} & for\ j \in N_i \\ 0 & for\ j \notin N_i \end{cases} \tag{3}$$

In Eq. (3), N_i is the number of elements within the filter radius.

In order to investigate, whether the integration of the dilate filter into anisotropic BESO is suitable to adapt the topology optimization results to a minimum feature width corresponding to the roving width, topology optimizations for the 2D case (Fig. 1 a)) are performed using several filter radii ranging from 2 mm up to 6 mm. In all cases, the compliance is optimized for a constant target volume fraction of 40%.

In 3D topology optimization, the dilate filter is not only applied in the XY-plane, but combined with a three-dimensional projection scheme in order to prevent undercuts, which cannot be manufactured by WFP (Fig. 2).

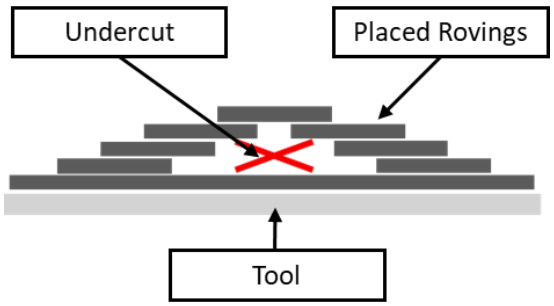

Figure 2: Example of a non-manufacturable undercut transverse to the placement plane

According to the proposed scheme, the filtered sensitivity $\tilde{\alpha}_i$ from Eq. (2) is calculated based on the elements' sensitivities α_j from those elements that fulfill the criteria given in Eq. (4).

$$j \in N_i \qquad \text{if } r_{ij} \leq r_{min} \text{ and } |z|_j \geq |z|_i \tag{4}$$

For verification, whether the three-dimensional dilate filter can be used to prevent undercuts transverse to the placement plane, the three-dimensional test case (Fig. 1 b)) is used.

3.3 Derivation of placement paths

For automated derivation of placement paths, the streamline algorithm developed by Jobard and Lefer [5] is applied and combined with a clustering algorithm to improve the parallelism of adjacent placement paths. As indicated in Fig. 3, where the clusters are shown in different colors to visualize their borders and which vectors belong to the same cluster, the orientation vectors from topology optimization are grouped into clusters with respect to their position and their orientation angle.

In addition, the algorithm was modified, so that seeding points are not arbitrarily chosen as starting points. Instead, the first streamline starts at the point of the highest longitudinal stress and the second streamline starts at the point of the next highest stress and so on. It is expected that this will result in placement paths that are more likely to follow the main load paths. To investigate, whether the clustering strategy improves parallelism of adjacent placement paths,

  doi:10.5075/epfl-298799_978-2-9701614-0-0

results with and without clustering are compared, for a 2D structure and a path distance of 2 mm and 4 mm.

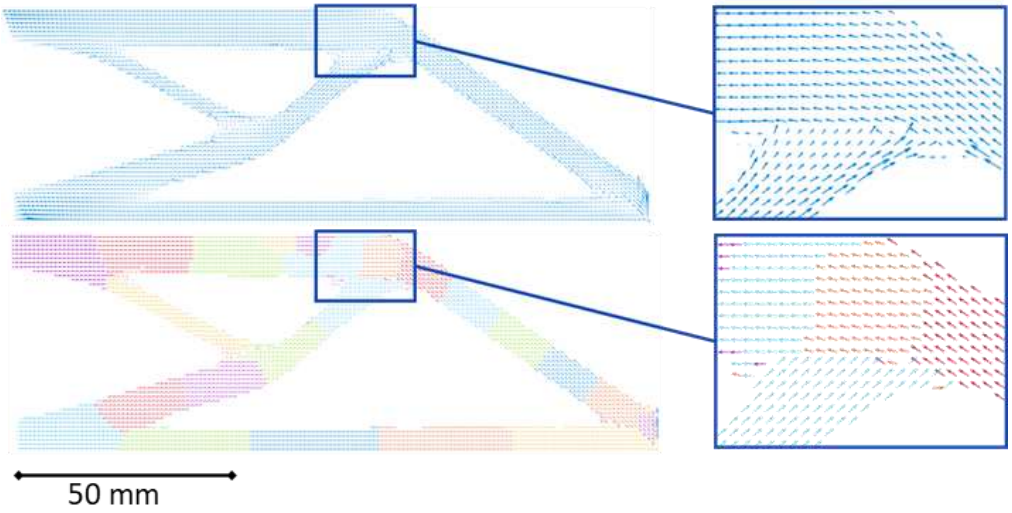

Figure 3: Element orientation vectors before and after clustering

Furthermore, the method is extended to 2.5D problems and placement paths for the 3D test case are derived. The final design of the part is then established by manual re-work of the placement paths – especially in intersection areas – by using a standard CAD-software.

3.4 Demonstrator manufacturing

For the 2D test case, the final placement paths are transferred to a G-code, which contains all the machine commands for manufacturing the part by WFP. In WFP, the roving is impregnated in-line by a thermoset resin, conveyed by a special arrangement of driven rollers and finally placed by using a placement head that is movable in the Z-direction and that can be rotated. The tool is mounted on the driven XY-table (Fig. 4).

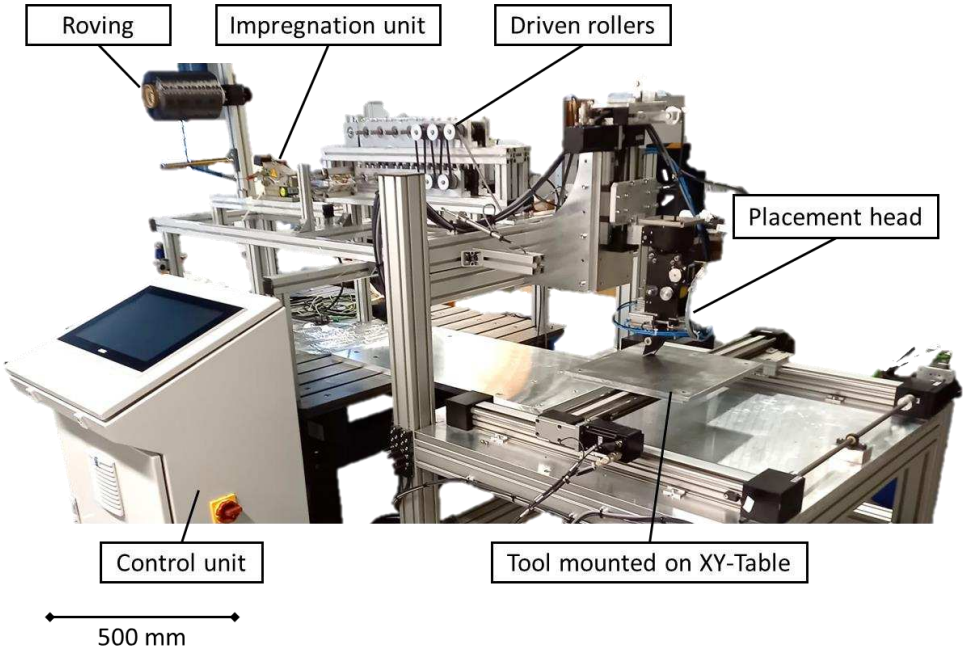

Figure 4: Wet fiber placement system

After placement, the tool was demounted. The part was then covered with a vacuum bag and placed on a heated plate. For curing, vacuum and a heating plate temperature of 80°C were applied for 4 hours.

4. Results

4.1 Topology optimization

The results from topology optimization of the 2D test case with several filter radii are shown in Fig. 5. By comparing those results, it is found, that – as expected – with an increasing filter radius the width of the beams increases. For all the results, the minimum width within the optimized structure is equal or higher than the filter radius applied. Therefore, the dilate filter is suitable for controlling the minimum width and to avoid features that are smaller than the roving width being used in WFP.

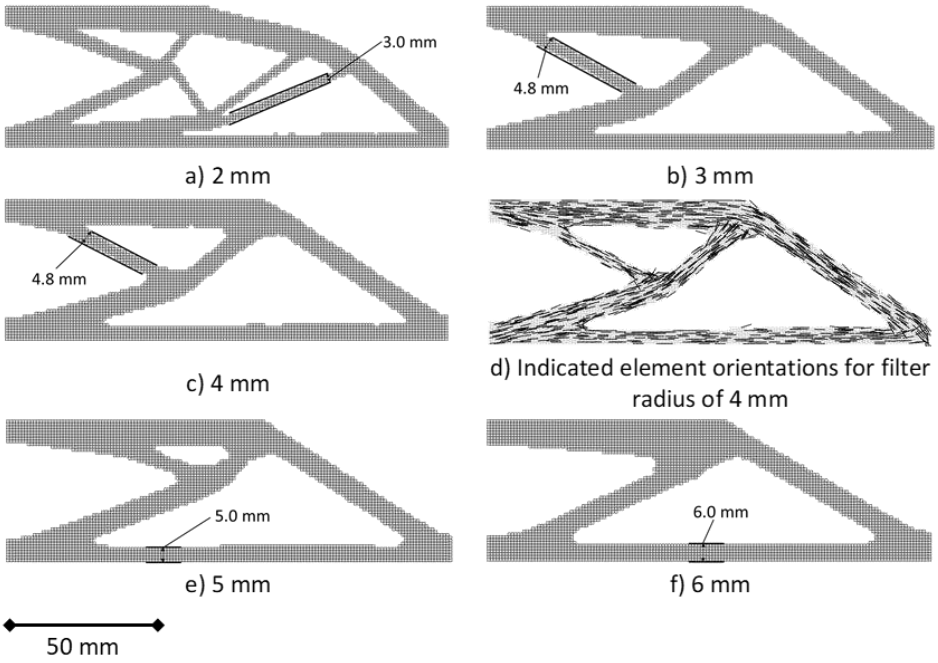

Figure 5: 2D topology optimization results for several filter radii

In Fig. 6, the structure resulting from 3D topology optimization is presented. The resulting structure does not contain any undercuts transverse to the placement plane and could therefore be manufactured by WFP.

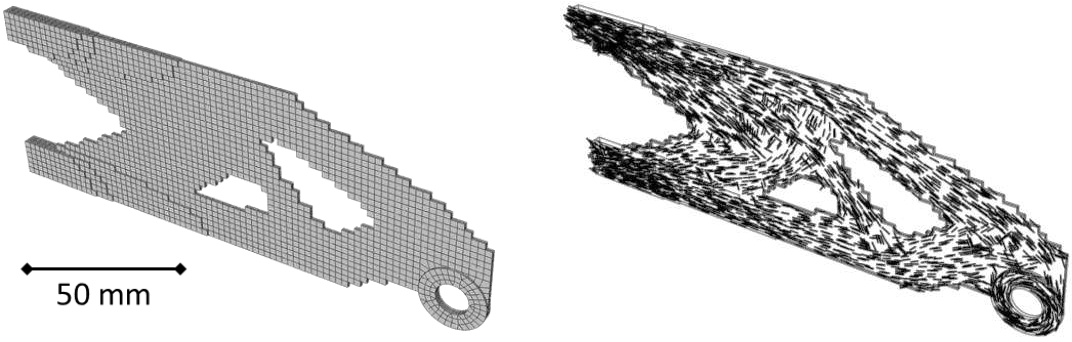

Figure 6: Topology optimization result and corresponding fiber orientation for 3D test case

  doi:10.5075/epfl-298799_978-2-9701614-0-0

4.2 Placement paths

For comparison, placement paths derived automatically with the 2D streamline algorithm with and without the clustering method are given in Fig. 7. A higher setting for the minimum distance between the paths results in a lower number of placement paths within the structure. Furthermore, clustering the orientation field before applying the streamline leads the streamlines to be straighter and an increased parallelism of adjacent lines occurs, which is beneficial for manufacturing and reduces the need for manual rework.

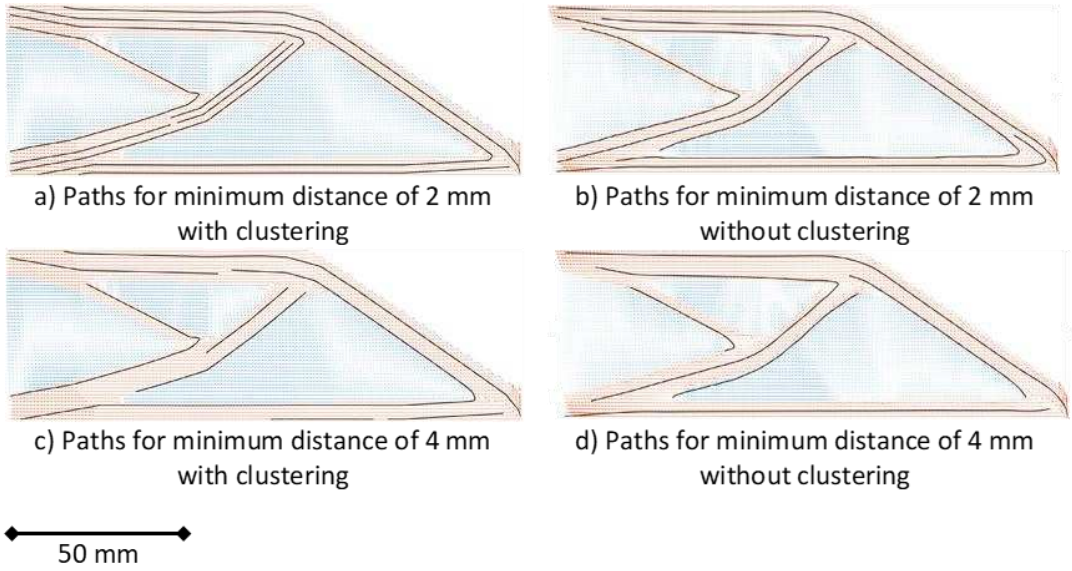

Figure 7: Placement paths derived for 2D structure with and without clustering and with different settings for path distance

For the example given in Fig. 7 c), the streamlines are extruded to roving width. This allows to check for gaps and overlaps. The streamlines are then manually re-worked in a CAD-software for manufacturing. The original, extruded paths and the paths after manual post-processing are presented in Fig. 8. From the post-processed paths, a G-code program is written for manufacturing by WFP.

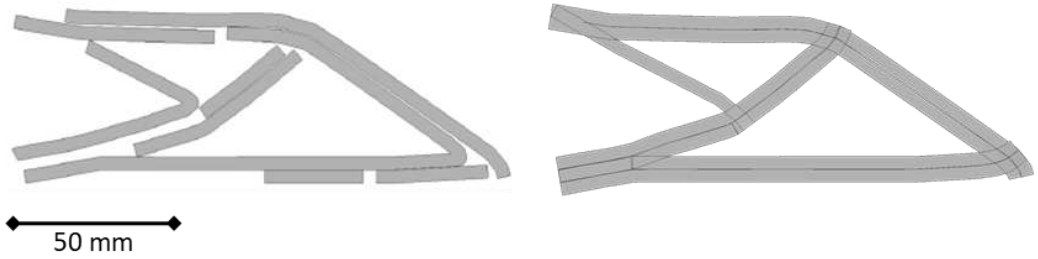

Figure 8: Placement paths for 2D structure before and after manual post-processing

Automatically created streamlines and manually processed placement paths for the 3D structure are shown in Fig. 9. Again, the streamlines are mostly parallel, but a small amount of manual re-work is necessary – especially for designing intersection areas.

  doi:10.5075/epfl-298799_978-2-9701614-0-0

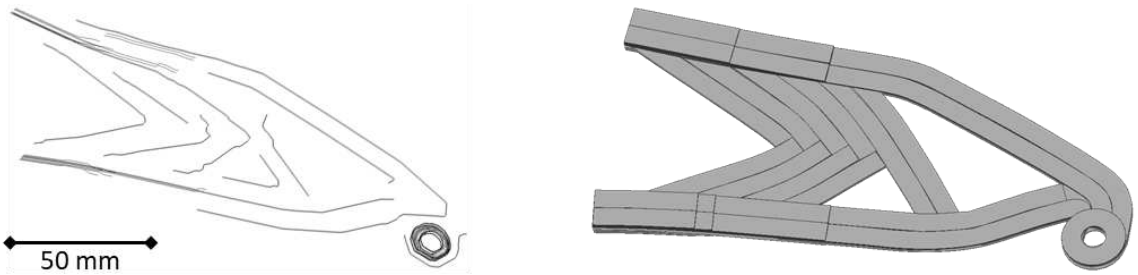

Figure 9: Automatically obtained paths from the modified streamline algorithm and manually post-processed fiber paths

4.3 Wet fiber placement

In Fig. 10, the 2D structure (Fig. 8) manufactured by WFP and cured under vacuum and temperature is presented. This shows that WFP is suitable for manufacturing complex, topology-optimized components.

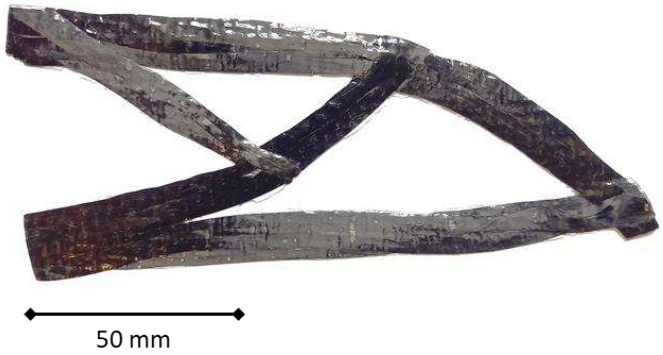

Figure 10: Topology-optimized 2D structure manufactured by WFP

5. Conclusions

Within this study, methods to integrate WFP-specific manufacturing restrictions into topology optimization and for the derivation of manufacturing-suitable placement paths were investigated. Results show, that implementing a dilate filter within anisotropic BESO is suitable to account for the roving width that is used for manufacturing and to prevent undercuts that cannot be manufactured by using WFP. Furthermore, it could be observed that combining clustering strategies with streamline algorithms leads to an improved parallelism of the derived placement paths.

Acknowledgements

The project “TopComposites – Topology-optimized and resource efficient composites for mobility and transport” is funded by the Federal Ministry of Education and Research (Funding reference 03XP0259).

We thank our advisory board members: ACE Advanced Composite Engineering GmbH, AVK – Industrievereinigung Verstärkte Kunststoffe e.V., BMW Group, Innomat GmbH, Leibniz-Institut für Verbundwerkstoffe GmbH, The University of Auckland, Westlake Epoxy.

  doi:10.5075/epfl-298799_978-2-9701614-0-0

6. References

1. May D, Domm M, Mitschang P. Wet Fiber Placement: A novel manufacturing technology for continuous fiber reinforced polymer composites. Journal of Composite Materials 2019; 53(4):521-533.
2. Mehl K, Schmeer S, Motsch-Eichmann N, Bauer P, Müller I, Hausmann J. Structural optimization of locally continuous fiber-reinforcements for short fiber-reinforced plastics. Journal of Composites Science 2021; 5(5):118-133.
3. Kubalak JR, Wicks AL, Williams CB. Deposition path planning for material extrusion using specified orientation fields. Procedia Manufacturing 2019; 34:754-763.
4. Sigmund O. Morphology-based black and white filters for topology optimization. Structural and Multidisciplinary Optimization 2007; 33:401-424.
5. Jobard B, Lefer W. Creating Evenly-Spaced Streamlines of Arbitrary Density. In: Visualization in Scientific Computing ’97. Springer. 1997.

  doi:10.5075/epfl-298799_978-2-9701614-0-0

DYNAMIC FE MODEL UPDATING USING PARTICLE SWARM OPTIMISATION METHOD: A METHODOLOGY TO DESIGN CRITICAL MECHANICAL COMPOSITE STRUCTURES

R., Figueiredo de Sá[a], J. P., Nunes[b], A. I., F. Vaz[c] F. W. J, van Hattum [d]

a: Institute of Polymers and Composites/I3N, Minho University, Portugal email: sa.ricardof@gmail.com
b: Inst. of Polymers and Composites, Polymer Engineering Dept., Minho University; Portugal
c: ALGORITMI Research Center, University of Minho, Campus of Gualtar, Portugal
d: Saxion University of Applied Sciences, 7513 AB Enschede, The Netherlands

Abstract:

To increase the performance of an industrial cutting machine, this work studied the possibility of replacing its current main steel gantry by a Carbon Fibre Reinforced Polymer (CFRP) composite solution. This component strongly influences the most relevant characteristics of the equipment, namely accuracy and maxima allowed accelerations.

The flexibility of composites in terms of number, thickness and orientation of layers and the challenging trade-offs between weight and stiffness motivated the development of an optimisation process. The Particle Swarm Optimisation method (PSO) was used to develop a solution able to ensure higher accelerations and the required accuracy of the equipment, by optimizing continuously the FE model algorithm input and output assessment and updating it. The process resulted in a near optimal solution allowing a 43% weight reduction and an increase of the maximum allowed acceleration in 25%, while ensuring the same accuracy.

Keywords: Optimisation process; Particle Swarm Optimisation; Composites; Fibre-reinforced polymers, Laser cutting

1. Introduction

The ever-growing trend of global consumption leads to the continuous increase of products produced to meet human needs and desires. The current situation is characterized by a mix of huge product portfolios, reduced lead-time, and increased quality standards and competitive costs, which leads to the need to the immediately development of faster cutting systems able to overcome these roadblocks. Such high demands of consumption led almost whole currently market to choose to use just only plasma, laser and waterjet cutting machinery using computer numerical control (CNC) or programmable logic control (PLC). In between these processes, laser-cutting is the latest among the sheet and plate metal-cutting technologies and one of the most widely used thermal energy based non-contact type advanced machining method [1, 2].

The combination of low density, high stiffness, strength, toughness, design flexibility, corrosion resistance and faster assembly have led to a continuous growth on the application of Polymer Matrix Composites (PMCs) in the past 50 years. Nowadays, CFRPs and other composite materials, which were early just predominantly used in high advanced applications and prototypes, are rising their number of applications among most common industrial markets [3].

  doi:10.5075/epfl-298799_978-2-9701614-0-0

CFRP lightweight structures improve the basic functions of a machine tooling: the manufacture of a workpiece having the required geometric form, acceptable surface finish and imperative accuracy at the highest feasible production-rate and lowest possible cost [4]. Achieving maximum positioning accuracy is only feasible if machine moving parts present high stiffness and low mass. One main reason for reducing productivity is the large mass of the moving parts of machine tools, which cannot afford high accelerations and decelerations during working operations and simultaneously maintaining the same accuracy [5]. Thus, the importance of structural optimisation and lightweight design is evident [6]. Also, it leads to energy efficiency, reduces the environmental impact, cost, and increases the performance of structures [7].

Analysing the mechanical behaviour of fibre-reinforced laminates and composite structures presents huge modelling challenges. As they are not homogeneous and isotropic, anisotropic laminated composite structures present unique phenomena at different geometric scales: the global (or laminate), the ply and the fibre-matrix levels. Hence, the global deformation of composite laminate structures is often characterised by complex couplings between extension, bending, and shearing modes. Due to the study complexity, Finite Elements Analysis (FEA) is a common methodology used in the analysis of composite structures mechanical behaviour.

As many variables can be manipulated in composite structures, they also need to be evaluated to determine the best design configuration [8]. Therefore, an optimisation process becomes of great value and complexity when such a high number of variables are involved. For problems with hard and complex numerical procedures for objective function evaluation, the optimisation by derivative calculation might be deemed as undesirable because computer simulations usually do not return derivative information [9].

Metaheuristic algorithms offer an alternative by using combination of heuristics, making the method a more general framework and not problem-specific [10, 11]. This type of techniques includes both simple (such as local search procedures) and complex processes (ranging up to sophisticated learning processes) [11]. Amongst them, Swarm algorithms demonstrated to present better results in problems presenting larger design vectors or a larger number of local optima, reaching global optima with less evaluations and requiring less computational resources [12, 13].

The machine studied in the present work is a 2-dimensional $C0_2$ Industrial laser cutting machine, having 2-axis flying optics powered by linear motors, produced by the manufacturer Adira. The Finite Element Analysis (FEA) was used to simulate the effect of the machine operation on its structure. A formal optimisation process is implemented, resorting to a population-based optimisation algorithm having the objective function (focused on the acceleration and part stiffness) evaluated through FEA. The result of the optimisation process is to obtain a composite gantry able to ensure the same level of accuracy at an acceleration 25% higher and having less 43% weight than the current conventional metallic one.

2. Methods

2.1 Part Geometry

The simulated gantry geometry is displayed in Figure 1. The domain of the simulation comprises two parts: the CFRP beam (in grey) and the metallic mask along which the laser cutting head moves (in green).

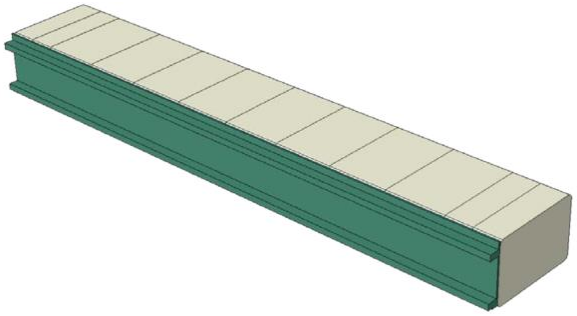

Figure 1 . Part geometry used for thickness optimisation

As the external shell and ribs were represented in a single part and the connection between them considered rigid. These simplifications, adopted to keep the model simple and lighter, means that details such as tabs from ribs and external shell connections (by adhesion and/or other process) and other production process features coming were not considered. The metallic and composite parts were also considered linked by a rigid connection. This simplification means that load will be transmitted throughout all contact surface and that is not possible splitting the two components.

The composite gantry is 2385 mm long and has a cross section of 382.5 mm x 246 mm. The outer ribs (3 on each end) were spaced by 110 mm and the middle ones by 243 mm. These ribs are responsible for ensuring that the loads are effectively distributed to the entire beam section. The metallic mask has overall thickness of 7 mm and the rails considered to have the same configuration and positioning as in the original metallic part.

2.2 Finite Elements Model

When the gantry suffers acceleration (as it is moved towards the cutting spot), it becomes subjected to forces and suffers deformations, which have implications in the precision of the optical path components attached to the gantry. As these components suffer displacements in the 6 degrees of freedom, the precision of the machine and the point of incidence differs from the desired one. The deviations from the target must be minimum, as to ensure a precise cut. In the study, the analysis considered as mostly critical case in term of accuracy loss, the laser head localised at the centre of the gantry when the maximum acceleration was applied to it.

The numerical model emulates the working conditions while not considering geometrically represented the surrounding components. Instead, they were replaced by all their weight located in a point localised in each centre of gravity. All loads applied to those components were also considered localised in the previously mentioned centres of gravity. The connection between the centres of gravity of components and gantry were replaced by kinematic coupling.

Table 1 summarises the properties considered for laminates, which were used in the thickness optimisation process.

Table 1. Properties of the laminate layers

Fabric Type	Property					
	E1 (MPa)	E2 (MPa)	v1	G12 (MPa)	G13 (MPa)	G23 (MPa)
Unidirectional 0º	134	7	0.1	4.2	4.2	3.85
Plainweave ±45º	15	15	0.1	34.5	34.5	3.85

The properties described above were the basis of the definition of the sections to all composite components. Because the gantry was represented by shell elements (which have no graphic representation of thickness), different properties can be given to different regions, resorting to the thickness and section definitions. Such method has a huge advantage for the optimisation process as a geometry does not have to be defined each time a different configuration needs to be considered. The geometric part is kept the same when its section is changed before each utility function evaluation. The layup definition requires the definition of mechanical properties of each layer (resorting in those listed in Table 1), the number and order of plies, their thickness and orientation and how the layup is placed relative to the surface defined by the shell elements.

2.3 Optimisation

The optimisation has aimed therefore to determine the optimal layup of CFRP at each section of the gantry, which was considered produced by vacuum infusion. Therefore, the number of layers with a given fibre orientation can vary from section to section. The layers were considered to have fibres orientated just at 0º (along the beam's axis) and ±45º. Layers with fibres at 90º were also considered, mainly due to local loadings. A total of six sections was considered, as displayed in *Figure 2*.

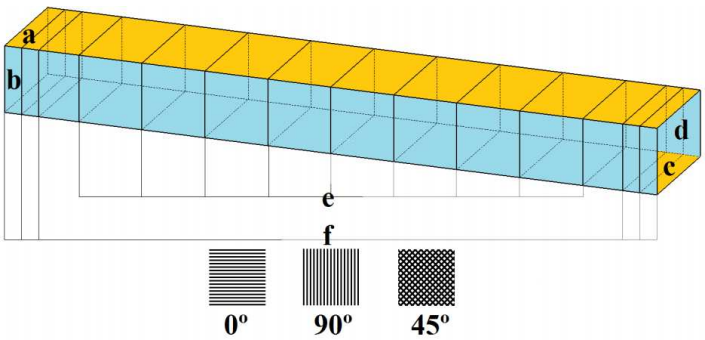

Figure 2. Different sections to be optimised, resulting in different variables

The sections considered are: the top horizontal face (a), the frontal vertical face on which the rails are applied (b), the bottom face (c), the back opposite vertical face (d)), one for the central ribs positioned throughout the gantry (e) and one for the ribs in the extremity (f). As result, a total of 18 variables were created, each denominated by a letter corresponding to the region and by the fibre orientation, for example e45 relates to the thickness of the ±45º fibres in the internal ribs of the gantry. These account for most of the considered variables, having being added one more variable to account the maximum acceleration. This variable was introduced to evaluate the objective function as the loads applied to the centres of gravity of the surrounding objects were calculated based on the value assumed by the acceleration in each run.

The optimisation loop consists of a PSO algorithm that resorts to FEM to evaluate the objective function. The selected algorithm was PSwarm, a Pattern Search and Particle Swarm hybrid algorithm. PSwarm is a derivative free, optimisation algorithm and, therefore, suitable for working with FEA as a method to evaluate the objective function. It aims at the minimization of a function with variables restricted to upper and lower bounds. Being PSwarm a hybrid algorithm, it has the ability of initiating a poll step resorting to pattern search, to determine the direction that the population should follow based on the best element from the previous search (particle swarm) step [14, 15].

2.4 Constraints

To ensure that the machine's behaviour is analogous to the performance with the metallic gantry, this component was firstly analysed by using a FEA similar to the one used for the composite gantry. The displacement suffered by a critical component carrying the optical system (cutting head) resulting of this analysis will serve as a maximum limit for dimensioning the composite part, thus ensuring the current accuracy is respected.

Also, if the acceleration imprinted to a given configuration exceeds the maximum force the linear motors are capable of exerting, the solution parametrized by those 19 variables is deemed not viable. In this case, and since PSwarm is a minimisation algorithm, a high value of the objective function is returned, as a penalty is imposed to the solutions that violate the rigidity or acceleration constraints. Regarding the thickness variables, each is constrained to a maximum thickness of 12 mm and a minimum of 0 mm, allowing the inexistence of a given type of orientation in each section. However, any section must have, at least 0.01mm.

2.5 Objective function

Given that the goal is to maximise the acceleration and PSwarm is a minimisation algorithm, the value to be evaluated is the symmetric of the acceleration (-a). With this in mind, and to input the penalties for breaching the maximum mass possible for a desired acceleration or the rigidity constrains, the objective function is represented by the following equation:

$$f = \begin{cases} -a & if\ dof_i \leq dof_{i_{max}}, i \in [1,6]\ and\ m \leq m_{max}(a) \\ 1E+20 & if\ dof_i > dof_{i_{max}}, i \in [1,6]\ or\ m > m_{max}(a) \end{cases} \quad (1)$$

where, f is the objective function, *a* is the acceleration, dof_i is translation or rotation in any of the six degrees of freedom of the centre of mass of the cutting head for the composite part, $dof_{i_{max}}$ is translation or rotation in any of the six degrees of freedom of the center of mass of the cutting head for the metallic part, *m* is the mass of the composite gantry and m_{max} is the maximum mass the linear motor can apply the defined acceleration to.

Based on the knowledge from previous optimisation processes, the population size was set to 40 elements. Each evaluation corresponds to changing the 19 variables, inputting those changes in the FEA, performing the simulation for each of the population elements, and extracting the relevant outputs. Each run requires a maximum of 2000 evaluations to ensure convergence to a near optimal value.

3. Results and discussion

The output of the optimisation process is presented in the form of the plot shown in Figure 3. As can be seen, the initial configuration presents an acceleration of 2.3 G, as the one provided as best guess. As the optimisation process evolved, the system tended to present best solutions with higher maximum accelerations, meaning the algorithm is able to extract values from the simulations run and generate new configurations based on the population elements that present better results. One can see that the search step, performed resorting to the swarm population, results in discontinuous improvements in the results. However, it then has difficulties in converging to higher accelerations, as happens, for example, after iteration ten. When this is verified, the algorithm creates a poll step that, starting from the best value obtained, tries to find the direction that will be more prone to lead to better results. With the

first objective function, the maximum acceleration achieved is just below 2.45 G, which is already an improvement regarding the current machine's performance.

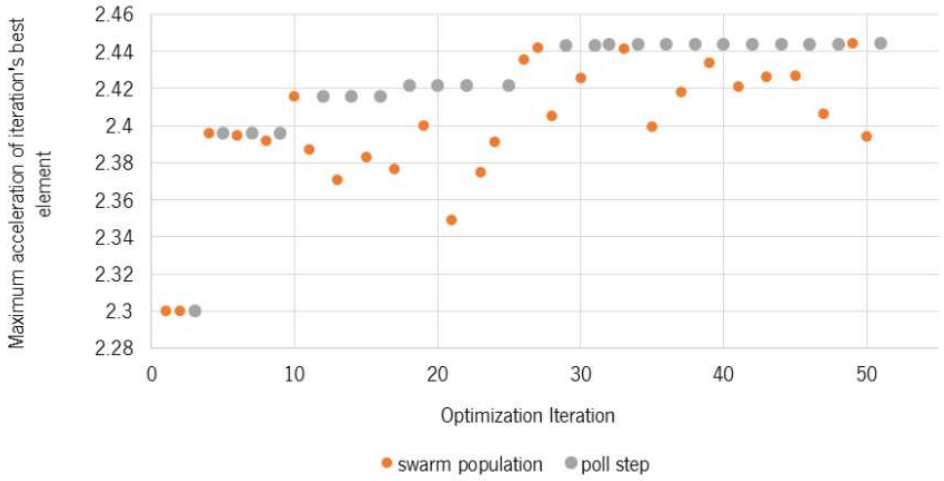

Figure 3. Results of initial optimisation process

Nevertheless, it was deemed as interesting to test new objective functions as to understand if other performance indicators are also introduced in the objective function. Another reason as why this could be interesting was the fact that the best element for each optimisation process was not suffering a steady decrease, as initially expected. The mass of the best element of each iteration is plotted in *Figure 4*.

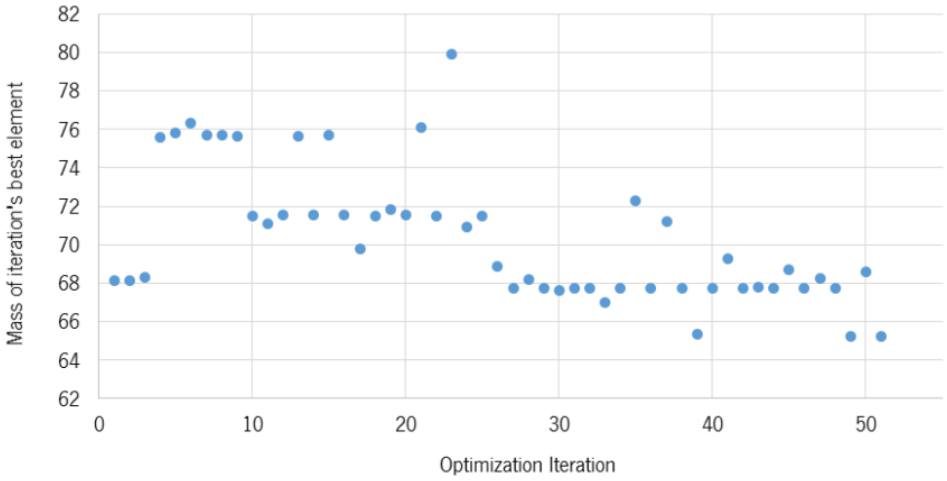

Figure 4. Mass of the best elements of each iteration as optimisation process evolves

At this stage, the hypothesis that the inclusion of the system's mass in the objective function would lead to better optimisation results was formulated. This comes from the fact that including mass in the objective function will increase the tendency of lower mass solutions being selected. On the other hand, lower mass solutions can be subjected to higher acceleration without compromising the limitations imposed by the force required from the linear motors. To test this, the objective function was formulated to force the algorithm to consider not only the acceleration, but also the mass of each configuration tested. Because PSwarm is a single objective optimisation algorithm, both objectives must be combined in a single one. To do this, each of the objectives (acceleration and mass) were multiplied by a factor that will represent

the relative importance of each factor. The new objective function is expressed in the following equation:

$$f = \begin{cases} -a \times \alpha + m \times \beta \; if \; dof_i \leq dof_{i_{max}}, i \in [1,6] \; and \; m \leq m_{max}(a) \\ 1E+20 \qquad if \; dof_i > dof_{i_{max}}, i \in [1,6] \; or \; m > m_{max}(a) \end{cases} \quad (2)$$

where α is the factor attributed to the acceleration and β is the factor attributed to *m*, the mass of the gantry. The ratio between α and β dictate the relative importance of each of the two system properties considered.

The best results were obtained for α=1 and β=0.1. The results obtained are shown in *Figure 5*.

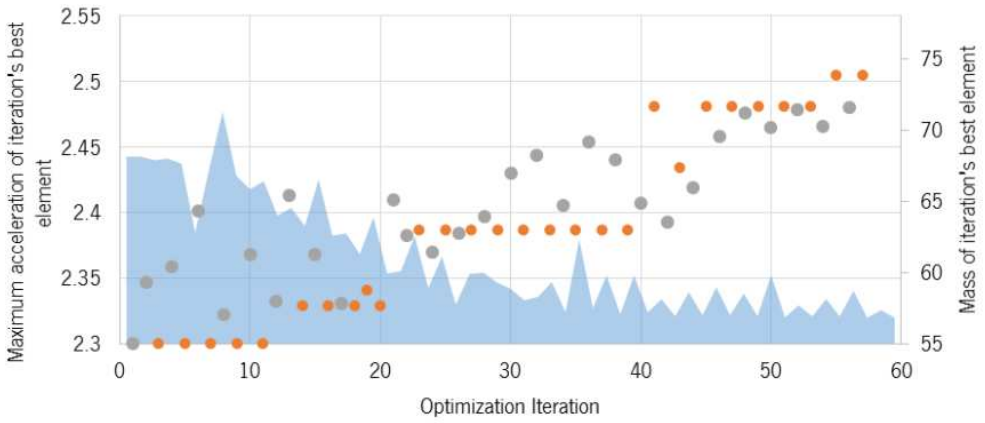

Figure 5. Acceleration and mass evolution for an α = 1 and a β = 0.1

As may be seen, not only the mass decreased faster, the maximum acceleration reached is also above 2.5 G. Overall, the optimisation seemed to converge in a smoother manner and reach better acceleration results. Thus, it was possible to achieve CFRP gantry dimensioned using optimisation resulting in a part that presents 43% lower mass than the current metallic part and allowing for a maximum acceleration increase of 25% without accuracy loss or the need to reconfigure the linear motors that are responsible for moving the gantry.

4. Conclusions

The optimisation process implemented allows to develop a laser cutting machine capable of withstand a higher acceleration with minimal impact on the structure and present the same cutting accuracy level. The optimisation loop implemented consisted in (I) a population-based derivative-free metaheuristic optimisation algorithm, and (II) an objective function evaluation based in FEA. The objective function addressed the deformation of the system and the variation in the 6 degrees of freedom of the laser cutting head, which were critical to assess the accuracy of the machine. The variables considered were related to the thickness of different fibre orientations in different areas of the part and to the maximum acceleration. From the first trials of the new method implemented it was possible to get to a viable near-optimal solution that presents capability for being subjected to higher accelerations while reducing the mass. There was a clear tendency in the algorithm output to increase the acceleration within allowed values. However, the mass variation did not present such a clear trend. The strategy to overcome this was introducing the mass as part of the objective function. Because the optimisation algorithm is single objective, the relative relevance between accuracy and mass had to be defined. Among

the several ratios tested, the one with better results lead to the selection of a configuration capable of sustaining an allowed maximum acceleration 25% higher than the current one without loss of accuracy. Regarding mass, the gantry dimensioned by the optimisation process presented 43% lower weight than the current metallic part.

5. Acknowledgements

This work has been supported by FCT – Fundação para a Ciência e Tecnologia within the R&D Units Project Scope: UIDB/00319/2020 and the scholarship SFRH / BD / 51106 / 2010.

6. References

1. Nallusamy, D., Enhancement of Productivity and Efficiency of CNC Machines in a Small Scale Industry Using Total Productive Maintenance. International Journal of Engineering Research in Africa, 2016. 25: p. 119-126.
2. Radovanovic, M. and M. Madic. EXPERIMENTAL INVESTIGATIONS OF CO2 LASER CUT QUALITY: A REVIEW. 2011.
3. Möhring, H.C., Composites in Production Machines. Vol. 66. 2017. 2-9.
4. Lee, C.S., et al., Novel applications of composite structures to robots, machine tools and automobiles. Composite structures, 2004. 66(1): p. 17-39.
5. Lucisano, G., M. Stefanovic, and C. Fragassa, Advanced design solutions for high-precision woodworking machines. International Journal of Quality Research, 2016. 10(1): p. 143-158
6. Möhring, H.-C., et al., Materials in machine tool structures. CIRP Annals-Manufacturing Technology, 2015. 64(2): p. 725-748.
7. Reddy, J.N. and J.D.H. Robbins, Theories and Computational Models for Composite Laminates. Applied Mechanics Reviews, 1994. 47(6): p. 147-169.
8. Paluch, B., M. Grédiac, and A. Faye, Combining a finite element programme and a genetic algorithm to optimize composite structures with variable thickness. Composite Structures, 2008. 83(3): p. 284-294.
9.Holmstrom, A., Derivative-free Algorithms in Engineering Optimization. 2000, Chalmers University of Technology: Goteborg. p. 43.
10. Bianchi, L., et al., A survey on metaheuristics for stochastic combinatorial optimization. Natural Computing, 2009. 8(2): p. 239-287.
11. Blum, C. and A. Roli, Metaheuristics in combinatorial optimization: Overview and conceptual comparison. ACM Comput. Surv., 2003. 35(3): p. 268-308.
12. Duan, Y., R.G. Harley, and T.G. Habetler. Comparison of Particle Swarm Optimization and Genetic Algorithm in the design of permanent magnet motors. in Power Electronics and Motion Control Conference, 2009. IPEMC '09. IEEE 6th International. 2009.
13. Hassan, R., et al., A Comparison of Particle Swarm Optimization and the Genetic Algorithm, in 46th AIAA/ASME/ASCE/AHS/ASC Structures, Structural Dynamics & Materials Conference. 2005, American Institute of Aeronautics and Astronautics, Inc.: Austin, Texas.
14. Vaz, A.I.F. and L.N. Vicente, PSwarm: a hybrid solver for linearly constrained global derivative-free optimization. Optimization Methods and Software, 2009. 24(4-5): p. 669-685.
15. Vaz, A.I.F. and L.N. Vicente, A particle swarm pattern search method for bound constrained global optimization. Journal of Global Optimization, 2007. 39(2): p. 197-219.

NUMERICAL ANALYSIS OF A MANUFACTURING PROCESS FOR HYBRID STRUCTURES COMBINING EXTRUDED ALUMINUM PROFILES AND ADDITIVE MANUFACTURING

Frederic Timmann[a], André Hürkamp[a], Klaus Dröder[a]

a: Technische Universität Braunschweig, Institute of Machine Tools and Production Technology, Langer Kamp 19b, 38106 Braunschweig – frederic.timmann@tu-braunschweig.de

Abstract:

One of the primary challenges for the manufacturing of hybrid components continues to be the bonding of metal and plastic components. The proposed method yields a form fit connection by foaming the metal structure. Within this framework, the bonding mechanisms of aluminum foam and additive manufactured plastic parts are investigated. For this purpose, a virtual foam model with random distributed Voronoi cells is developed in order to parametrize the aluminum foam geometry. This model is used in a subsequent structural finite element analysis of a representative volume element for the bonding interface of the hybrid structure. Based on the simulation results, the investigation aims to find the optimum aluminum foam structure for a high bond strength by varying parameters such as the pore size. Assuming a complete pore filling during the additive manufacturing process, this research verifies the positive contribution of smaller pores towards a higher bond strength.

Keywords: Hybrid structures; bond strength; virtual foam model; aluminum foam;

1. Introduction

Lightweight design concepts offer promising solutions for the resource-efficient and sustainable development as well as production of technical functional structures. A promising lightweight strategy is the combination of different materials such as metal and polymers to manufacture integrated hybrid structures. For these hybrid composites the growing market demands flexible production processes [1]. A robot-based process chain is introduced in Dröder et al. as an approach for a flexible manufacturing system [2]. Within this contribution, geometrically determined undercuts are created in the metal structures to obtain a mechanical interlocking effect and thus an increase of the strength of the metal-plastic compound. The process envisioned for the flexible manufacturing of hybrid structures examined in this publication is shown in Fig. 1.

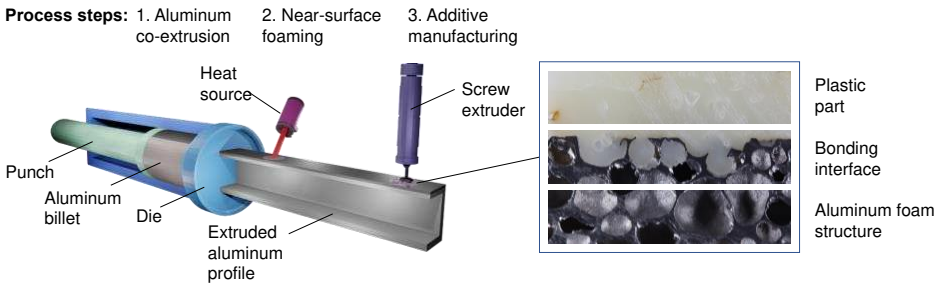

Figure 1. Schematic illustration of a manufacturing process for hybrid structures

  doi:10.5075/epfl-298799_978-2-9701614-0-0

Here, the interlocking of aluminum and polymer material is created by the geometrically undefined surface of aluminum foam. This process combines continuous and additive manufacturing technologies. Continuous processes, such as the extrusion of aluminum profiles, are examples for manufacturing processes enabling the production of semi-finished products in high batch sizes at low production costs [3]. The manufacturing of individualized components in low quantities requires a high adaptability and flexibility of the production environment. Additive or generative manufacturing offer a high potential for these specifications. The examined combined process involves local near-surface foaming of co-extruded aluminum profiles to create the undercuts suitable for bonding and interlocking with polymer material. The billet for the extrusion process and the resulting profile consists of two aluminum alloys, one for the core profile structure and one for the foamable boundary layer. Currently, material sciences is still investigating the optimal conditions for these foamable aluminum alloys [4]. The surface of the aluminum foam is cut by milling, allowing the filling of pores during a screw extrusion additive manufacturing (SEAM) process with thermoplastics.

The focus of the present research is on the bonding interface of the hybrid compound and its bonding mechanisms. Due to the foam structure, there are two effects with positive contribution on bond strength, the created undercuts and the enlargement of the bonding surface. Whereas the mechanical interlocking is not only located at the macroscale pores, as shown in Fig. 2. In this micrograph of an aluminum foam plastic compound, the microscale and macroscale pores are marked.

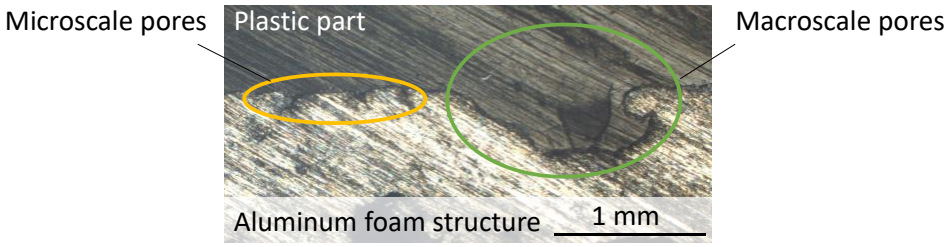

Figure 2. Micrograph of an aluminum foam plastic composite

To investigate the interlocking effect of the macroscale pores and the area of the bonding surface, a virtual foam model is developed. These models are geometrically analyzed for different parameters, such as pore size and density. Furthermore, structural finite element analysis are performed for a representative volume element (RVE) under uniaxial loading. The resulting displacements are used to study the contribution of interlocking aluminum foam cells. For this purpose acrylonitrile butadiene styrene (ABS) is considered as material for the additive manufactured plastic part.

2. Virtual foam model

A virtual foam model is used to model aluminum foam structures with arbitrary foaming parameters in order to numerically investigate the interlocking effects for the bond strength of the hybrid structure. Here, the approach is based on a closed-cell aluminum foam, which is produced by heating an aluminum alloy and using titanium hydride as a foaming agent [5]. In the literature, there are already several approaches to model the geometry of aluminum foams. In Giorgi et al. Kelvin cells and ellipsoidal cells are used for this purpose [6]. Another approach for modeling general foams structures is the usage of Voronoi diagrams. These decompose a

978/1045 doi:10.5075/epfl-298799_978-2-9701614-0-0

surface (in 2D) or the space (in 3D), by a given set of points into individual regions, called Voronoi cells [7, 8]. Thus, the convex Voronoi cells are therefore used to model the pores in the foam. The generation of meshes for the finite element method using Voronoi diagrams has been well established in various studies [9–11].

The here presented virtual foam model is built in Matlab according to the approach of Michailidis et al. [12]. The methodology is illustrated in Fig. 3. Starting from randomly distributed points, the Voronoi diagram is constructed in a fixed volume. Here, the factor of pore density ρ_{pore} can be used to influence the number of Voronoi cells and thus their size. Since in this study only the boundary layer of the hybrid composite is considered, a plane is defined to select the Voronoi cells which lies at the height of the boundary layer. This plane defines the location where the aluminum foam is exposed by the milling process. Furthermore, only the internal pores are considered in the modeling, so that no clipped and half pores are created in the model. Hence, the total number of Voronoi cells is n_{cells}. These convex polyhedra are iteratively modeled to the final pore geometry in the following step. By scaling the Voronoi cell, the wall thickness between the pores in the aluminum foam is determined. For this purpose, the scale factor sf_{cell} is introduced. Scaling is done by moving the points of the polyhedron along the vector to the center of the cell. Before a smoothing algorithm rounds off the sharp corners of the polyhedron geometry, the larger faces are remeshed into uniform smaller triangles. At the level of the defined plane, the upper half of the pore is cut off. Triangles of the mesh, which are connected with points above the cutting plane, are eliminated.

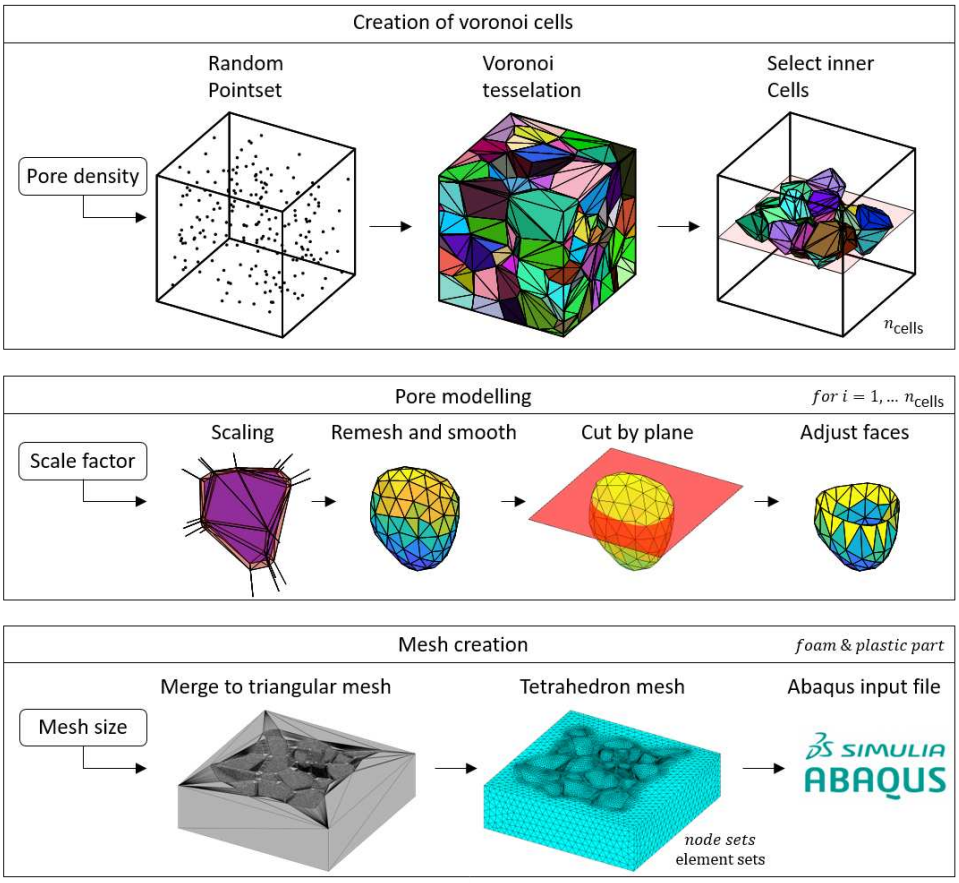

Figure 3. Modelling approach for the virtual foam models

  doi:10.5075/epfl-298799_978-2-9701614-0-0

The points of the intersected triangles are set to the height of the cutting plane and moved to the outer contour of the cells. This avoids the distortion of the modeled cell. In a final step, the opened cells are merged into a triangular mesh using the Matlab triangulation algorithm including the points of a basic structure. The thickness of the basic structure is determined by the minimum z-component of the deepest cell, in order to ensure the existance of at least one cell wall thickness between the lower surface of the basic structure and the cell. Given a minimum and maximum element size, a tetrahedral mesh is created. By inverting the elements of the triangular mesh and mirroring the basic structure at the cutting plane, the plastic part is modeled analogously to a tetrahedral mesh. The meshes are further exported to Abaqus for the subsequent numerical investigations.

3. Simulation model for a cross tension test

A structural mechanics FEM analysis in Abaqus Standard is used to determine the part displacement of the hybrid material composite as shown in Fig. 4.

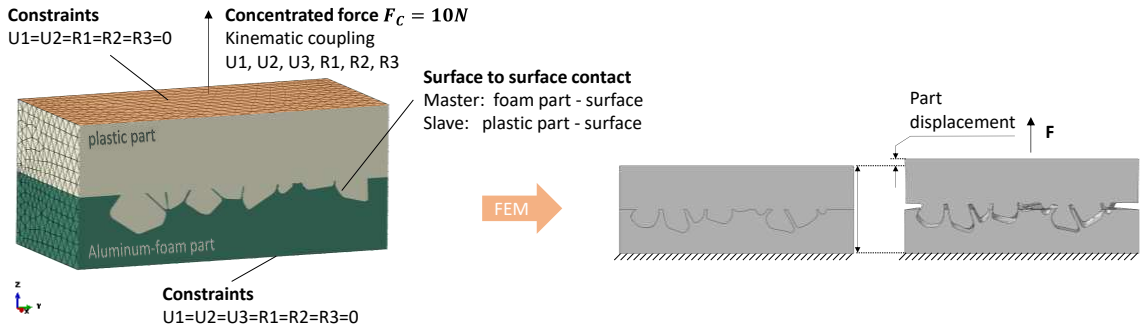

Figure 4. Boundary conditions for FEM-Analysis and part displacement

A normal force on the top surface of the plastic part is applied representing a cross tension test. The concentrated force $F_C = 10N$ is applied at a reference node linked to the top surface. The kinematic coupling distributes the force uniformly to all nodes on the upper surface of the plastic part. In addition, only displacement in the direction of force application is permitted. All displacements and rotations are blocked at the nodes of the bottom surface of the aluminum foam part. To model the contact between the aluminum foam and the plastic part, the surface-to-surface interaction is chosen. Since the simulation is only intended to investigate the geometric contribution of the pores to the interlocking effect, no adhesion of the surfaces is considered. A friction coefficient of 0.1 dampens the detachment of the plastic structure from the aluminum foam. The material behavior is linear-elastic and the material data from Table 1 are used.

Table 1: Material data used in the numerical analysis

Material	Density	Young's modulus	Poisson's ratio
ABS	1.07 g/cm^3	2300 MPa	0.39
Aluminum	2.7 g/cm^3	70 GPa	0.35

Automated execution and result export allows performing a high number of simulations to determine the influence of the stochastic distributed cells in the virtual foam model. For each parameter set, 40 models are created within a full factorial experimental design, with a variation

  doi:10.5075/epfl-298799_978-2-9701614-0-0

of the scale factor $sf_{cell} = \{0.7, 0.8, 0.9\}$ in three steps and at six different pore densities $\rho_{pore} = \{ 200, 400, 600, 800, 1000, 2000 \}$, which describes the number of generation points for the Voronoi diagram in a cube with an edge length of 25 mm.

4. Results

4.1 Geometrical analysis of the virtual foam model

First, the virtual foam model is compared to real aluminum foam structure. Thereafter the total surface area of virtual foam models in dependency of the foam parameters is calculated. Therefore, the sum of all triangles in the surface mesh is used. In Fig. 4, the comparison of the virtual foam model with an x-ray microscopy (XRM) of an aluminum foam structure is shown. Due to the geometry of the specimen, a cylinder is used as the basic structure for the virtual foam model. The sample of foaming tests with aluminum alloys for extrusion processes is based on current research for the presented process for the production of hybrid functional structures. The XRM data of the aluminum foam test specimen is provided by Schäfke et al. as part of the continuation of the ongoing research [4]. While the comparison of the pores in the cut view shows a high similarity in the inner region, the edge region differs. The distribution of the points for generating the Voronoi diagram and the scaling factor for the outer Voronoi cells need to be adjusted for a more accurate match of the complete aluminum foam structure.

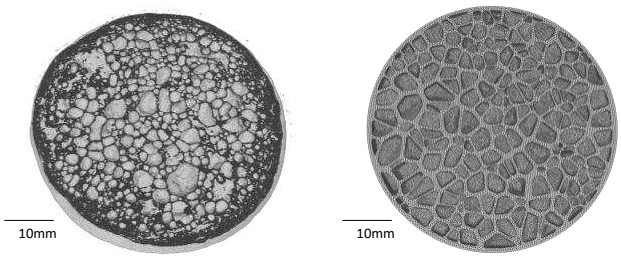

Figure 4. Comparison of real aluminum foam structure (left) with virtual foam model (right)

For the surface calculation of the virtual foam models, a smaller section of the model is considered in order to avoid the lack of pores at the edge regions. For this purpose, a rectangle with an edge length of 15 mm is centered as shown in Fig. 6. The projected area is therefore 225 mm^2. The figure shows variants of a virtual foam model with the same pore density and for varying scale factors. The calculated surface area compared to the projected area is about twice as large. The surface area decrease with the lower scaled cells.

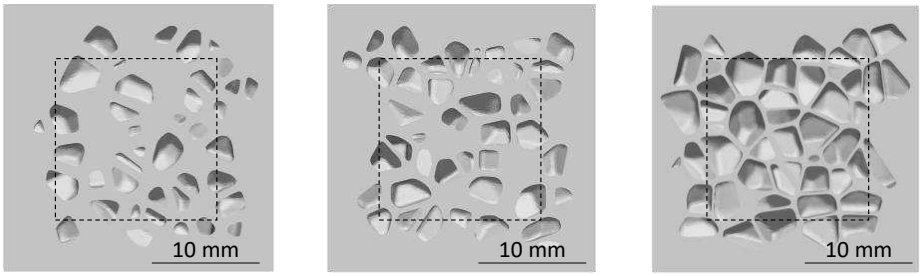

Pore density:	600	Pore density:	600	Pore density:	600
Scale factor:	0.70	Scale factor:	0.80	Scale factor:	0.90
Surface:	427.24 mm^2	Surface:	539.13 mm^2	Surface:	555.83 mm^2

Figure 6. Virtual foam models with varying scale factor

  doi:10.5075/epfl-298799_978-2-9701614-0-0

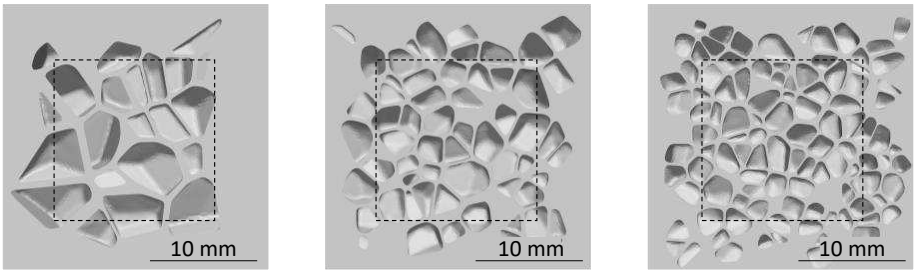

Pore density:	200	Pore density:	1000	Pore density:	2000
Scale factor:	0.90	Scale factor:	0.90	Scale factor:	0.90
Surface:	629.68 mm²	Surface:	579.56 mm²	Surface:	527.61 mm²

Figure 7. Virtual foam models with varying pore density

For different pore densities, three virtual foam models are shown in Fig. 7. The largest surface area was calculated for a pore density of 200, which is due to the larger volumes of the pores. The average value of the true surface for all 40 variants, as well as the corresponding standard deviation, can be seen in the diagram in Fig. 8. The influence of the scaling factor on the bonding surface reaches the maximum for small pore densities and decreases with increasing pore density. For the virtual foam models with a pore density of 2000, the statistical means for the surfaces are almost identical for all scaling factors.

4.1 Numerical analysis of the hybrid structure

The part displacement as the central result of the FEM analysis is shown in the diagram on the right in Fig. 8. The minimum displacements are obtained for virtual foam models with the highest pore densities and scaling factors. The standard deviation of the part displacement is lowest for these models. This is due to the amount of pores with undercuts. As can be seen in Fig. 7, smaller pore densities model larger, but also fewer cells in the RVE, decreasing the probability of generated undercuts. By visualizing the nodal displacements of the plastic part, which are shown in Fig. 9, the contribution of the different pores as a result of interlocking effects can be gauged visually. Of the 45 modeled cells in this virtual foam model, 15 cells interlock in the aluminum foam structure. This value was determined by studying the Von Mises stresses of the elements at the top of the cell walls of the aluminum foam part.

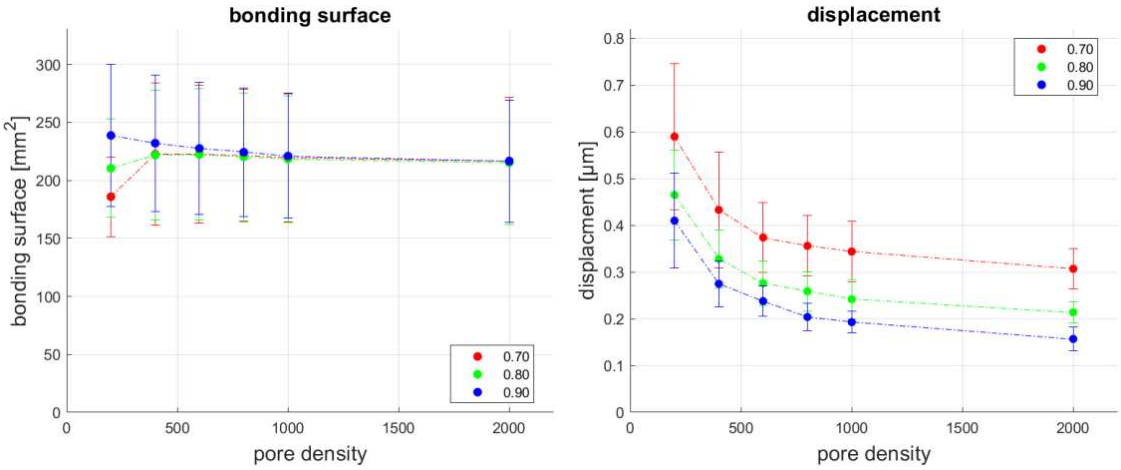

Figure 8. Bonding surface and part displacement for different foam parameters

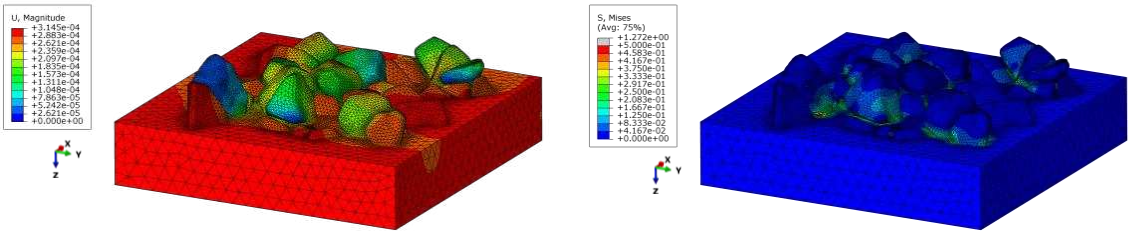

Figure 9. Node displacement (left) and Von Mises stress (right) in the plastic part

As can be seen in Fig. 10, the highest stresses occur in the cell walls of the aluminum foam, which is due to the higher Young's modulus of the aluminum. In the plastic part, higher stresses occur through smaller pore openings in case of interlocking pores. Since the number of undercuts is higher in virtual foam models with smaller pores, the load is also distributed to multiple cells. Geometric analysis confirmed that in virtual foam models with larger pore densities and therefore smaller pores, the total area of the pore openings is higher. This results in higher stresses in the plastic part for the variants of the virtual foam model with larger pores. This assumption is also confirmed by the calculated stresses of the structural mechanics FEM analysis. The higher stresses lead to failure at lower forces in virtual foam models with low pore density. Whereby with the linear-elastic approach it is not feasible to make a conclusive statement about the critical force and the failure behavior.

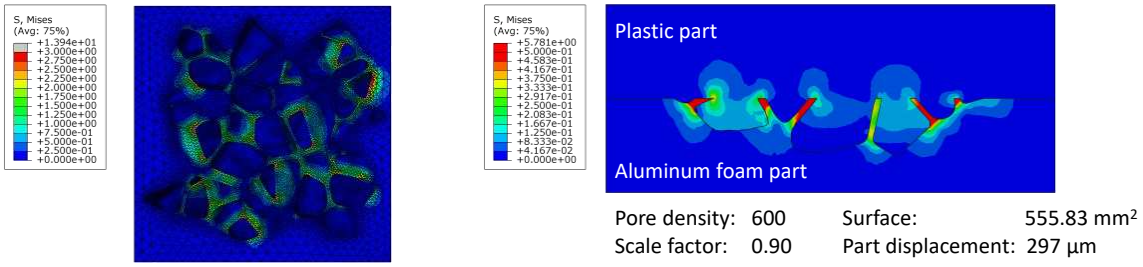

Figure 10. Von Mises stress in aluminum foam (left) and in the hybrid structure (right)

5. Conclusion and future work

The proposed method for the investigation of the bonding mechanisms of hybrid functional structures in aluminum foam-plastic composites opens up new possibilities for the analysis of bond strengths for these hybrid components and could therefore expand their usage widely. The foam parameters defined in this paper are the pore density and the scaling factor, which are used to create virtual foam models using a Voronoi diagram. By analyzing real aluminum foam structures, the virtual model should be modified to represent the pore size distribution of cells of real aluminum foams. The surfaces for joining the dissimilar materials were determined, however the surface adhesion between the aluminum foam surface and the polymers applied in the SEAM process is still unknown. The numerical analysis of the hybrid structure have shown an increase in undercuts for aluminum foams with smaller pores, and thus a lower part displacement is observed. However, complete filling of the aluminum foams is assumed. The degree of filling in relation to the pore size is to be determined by experimental and numerical investigation. In order to predict the pore filling, the next steps of research in this field should focus on a numerical model for the additive manufacturing process of polymers.

  doi:10.5075/epfl-298799_978-2-9701614-0-0

Acknowledgements

The support of the German National Science Foundation (Deutsche Forschungsgemeinschaft DFG) through the funding of the research project “Experimental and numerical investigations of locally foamable extruded profiles for additive manufacturing of hybrid functional structures” (442092412) is gratefully acknowledged.

6. Reverences

1. Witten E, Mathes V, Sauer M, Kühnel M (2018) Composites market report 2018: market developments, trends, outlooks and challenges
2. Dröder K, Reichler A-K, Mahlfeld G et al. (2019) Scalable Process Chain for Flexible Production of Metal-Plastic Lightweight Structures. Procedia CIRP 85:195–200. https://doi.org/10.1016/j.procir.2019.09.045
3. Ostermann F (2014) Anwendungstechnologie Aluminium. Springer Berlin Heidelberg, Berlin, Heidelberg
4. Schäfke FP, Thürer SE, Maier HJ et al. (2021) Development of an Aluminum-Based Hybrid Billet Material for the Process-Integrated Foaming of Hollow Co-Extrusions. Metals 11:1382. https://doi.org/10.3390/met11091382
5. Miyoshi T, Itoh M, Akiyama S et al. (2000) ALPORAS Aluminum Foam: Production Process, Properties, and Applications. Adv Eng Mater 2:179–183. https://doi.org/10.1002/(SICI)1527-2648(200004)2:43.3.CO;2-7
6. Giorgi M de, Carofalo A, Dattoma V et al. (2010) Aluminium foams structural modelling. Computers & Structures 88:25–35. https://doi.org/10.1016/j.compstruc.2009.06.005
7. Lautensack C, Zuyev S (2008) Random Laguerre tessellations. Advances in Applied Probability 40:630–650. https://doi.org/10.1239/aap/1222868179
8. Imai H, Iri M, Murota K (1985) Voronoi Diagram in the Laguerre Geometry and Its Applications. SIAM J Comput 14:93–105. https://doi.org/10.1137/0214006
9. Zhang X, Tang L, Liu Z et al. (2017) Yield properties of closed-cell aluminum foam under triaxial loadings by a 3D Voronoi model. Mechanics of Materials 104:73–84. https://doi.org/10.1016/j.mechmat.2016.10.007
10. Tekoglu C, Gibson LJ, Pardoen T et al. (2011) Size effects in foams: Experiments and modeling. Progress in Materials Science 56:109–138. https://doi.org/10.1016/j.pmatsci.2010.06.001
11. Redenbach C, Shklyar I, Andrä H (2012) Laguerre tessellations for elastic stiffness simulations of closed foams with strongly varying cell sizes. International Journal of Engineering Science 50:70–78. https://doi.org/10.1016/j.ijengsci.2011.09.002
12. Michailidis N, Smyrnaios E, Maliaris G et al. (2014) Mechanical Response and FEM Modeling of Porous Al under Static and Dynamic Loads. Adv Eng Mater 16:289–294. https://doi.org/10.1002/adem.201300039

  doi:10.5075/epfl-298799_978-2-9701614-0-0

TEXGEN – GEOMETRICAL MODELLING OF BIAXIAL BRAIDED FABRICS

Matthew Thompson[a], Louise Brown[a], Kishen Rengaraj[a], Nick Warrior[a]

a: Composites Research Group, Faculty of Engineering, University of Nottingham, Nottingham, UK – matthew.thompson@nottingham.ac.uk

Abstract: Newly developed functions within TexGen allow users to model 2D biaxial braided fabrics as both flat and curved unit cells. Key parameters of the braid such as braid angle, coverage and yarn paths are predicted using established models. Custom refinement functions have been implemented to accurately model the changes in the cross-section of the fibre along the undulations of the yarns within the fabric. Differences in elastic mechanical properties between flat and curved unit cells have been investigated for a range of curvatures, demonstrating up to a 10.5 % reduction in the longitudinal elastic modulus for curved unit cells, for a radius of 8 mm, reducing with larger radii. Similar effects have been demonstrated for shear modulus.

Keywords: Braid; TexGen; Unit Cells; Mechanical Properties

1. Introduction

Braided composite tubes are used in a wide variety of industries. Some current applications involve automotive shafts and chassis components, aircraft structural components and medical applications such as braided catheters. Recent developments have seen braided composite components replace other materials due to their intrinsic advantages, and for structural applications it is critical to accurately predict the mechanical properties. A wide range of techniques are available, from analytical models and volume averaging methods to complex finite element (FE) modelling. The effects of braid angle, coverage, yarn undulation and braid pattern have all been investigated. However, within much of this research the curvature of the braid is neglected and the fabric is assumed to be flat. This has led to the requirement to characterise how the curvature of the tube effects the stiffness predicted from these meso-scale models.

Ayranci et al. [1] evaluated the effect of the radius of curvature on the longitudinal and shear elastic modulus and in-plane Poisson's ratio based on volume averaging of the constituent stiffness, showing up to a 7 % reduction in both longitudinal and shear modulus for curved unit cells. This work showed good agreement with their experimental values. This has been echoed in work by Nagaraju et al. [2] investigating the effect of the curvature on the extensional stiffness matrix of 2D braided tubes. This work focused on SiC/SiC composite and carbon/epoxy composite tubes, researching the effect of the ratio of thickness to inner radius on the stiffness. Models were produced as flat unit cells within TexGen [3] and exported as voxel meshed FE models. The curvature was then implemented as the models were mapped into a polar coordinate system to model the representative unit cell (RUC).

The present work shows the development of tools within TexGen for the modelling of 2D braided fabrics in both flat and curved RUC's and the effect this has on the prediction of the elastic properties.

  doi:10.5075/epfl-298799_978-2-9701614-0-0

2. Braid Modelling

When modelling fabrics, the fibre architecture is typically represented by the RUC. Due to the process of producing a braided fabric there are levels of variation in yarn geometry as detailed by Czichos et al. [4]. Therefore, the unit cell geometry is an idealised model of the fabric. This study shows the fundamental steps needed to create a RUC of biaxial braided fabric and the automated process within TexGen.

New classes have been developed within TexGen, CTextileBraid and CTextileBraidCurved, both derived from CTextile. By building this system within the TexGen source code the models can take advantage of the current systems such as meshing, exporting and yarn building functions. Building of braided unit cells can be conducted through two routes: GUI (Graphical User Interface) or Python scripting. Previously it has been possible to create a custom braided fabric through the Python scripting method, however no analytical models were included, and yarn locations, paths and cross sections were required to be manually programmed, limiting its usage. CTextileBraid uses process parameters such as braider speeds and mandrel size to predict the key characteristics of the braid such as braid angle and coverage factor. The techniques for producing a biaxial braided unit cells within TexGen will be discussed in the following sections.

2.1 Model and Node Locations

Prediction of braid angle based on experimental machine parameters is given by Potluri et al. [5] in Eq. (1), linking braid angle to machine input parameters such as the average angular velocity of the horn gears around their own centres, ω_h, and the number of horn gears, N_h. The model was analysed by the authors against braids on a 48 carrier Steeger axial braider and showed a maximum error of 2 degrees for stabilised fabrics.

$$\alpha = tan^{-1}\left(\frac{2\omega_h R}{N_h v}\right) \tag{1}$$

Further to braid angle, the coverage of the fabric needs to be calculated in order to determine the spacing between the fibres. Ravenhorst [6] defines cover factor, CF, as the fraction of the substrate area covered by bias yarns. An expression for biaxial fabrics is presented in Eq. (2) with terms outlined in *Figure 1*. For mono material axisymmetric braids where, $w_{y,X,1} = w_{y,O,1} = w_{y,X,2} = w_{y,O,2} = w_y$, $p_x = p_O = p$ and $a_x = a_O$ this can be simplified to Eq. (3).

$$CF = 1 - \frac{(2p_x - w_{y,X,1} - w_{y,X,2})(2p_o - w_{y,o,1} - w_{y,0,2})}{\sin(\alpha_x + \alpha_o)} \tag{2}$$

$$CF = 1 - \left(1 - \frac{w_y n_c}{4\pi R cos(\alpha)}\right)^2 \tag{3}$$

This model is valid whilst the fabric has not jammed. This is identified when $\frac{w_y n_c}{4\pi R cos(\alpha)} \leq 1$. At this point the fabric is assumed to have 100% coverage. Further customisation can be done to model jammed fabrics with fibre overlap. Assuming the spacing between the weft and warp yarns is equal the spacing between yarns, x_g is defined by Eq. (4).

$$x_g = \frac{\frac{1}{1-CF} - {w_y}^2}{2w_y} \tag{4}$$

  doi:10.5075/epfl-298799_978-2-9701614-0-0 published under CC BY-NC 4.0 license

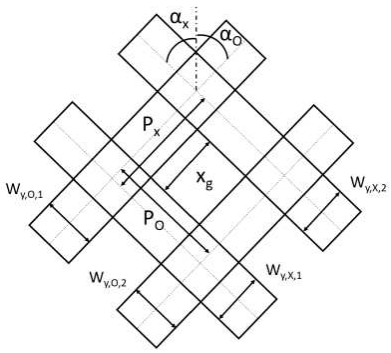

Figure 1: Definition of coverage factor for biaxial braided composite fabric.

Using both fibre angle and coverage the location of the nodes within the model can be determined. A node is located at each of the cross-over points between the yarns, with there being assumed no gap between the fibres. The yarn path is then interpolated using a Bezier spline between the nodes for each yarn. This ensures there is periodicity within the yarn as well as maintaining the required thickness of the fabric.

2.2 Cross Section

At each node location the cross-section of the yarn is constructed. Through optical microscopy analysis of braids the cross-sectional shape of the yarn can be defined through a power ellipse defined in Eq. (5-6), where w_y represents the yarn width, t_y represents yarn thickness, assumed to be half the thickness of the fabric, and the exponent, n, is the shape of the power ellipse. This can be varied within the model to represent a range of yarn shapes. This is required as the yarn shape will change if an infused or dry fabric is being modelled. Boundary conditions are applied to both the start and end of the yarns to ensure periodicity within the length.

$$x(v) = \frac{w_y}{2}\cos(2\pi v) \quad 0 \le v \le 1 \tag{5}$$

$$y(v) = \begin{Bmatrix} \frac{t_y}{2} sin(2\pi v)^n \\ -\frac{t_y}{2}(-\sin(2\pi v))^n \end{Bmatrix} \begin{matrix} if\ 0 \le v < 0.5 \\ if\ 0.5 \le v \le 1 \end{matrix} \tag{6}$$

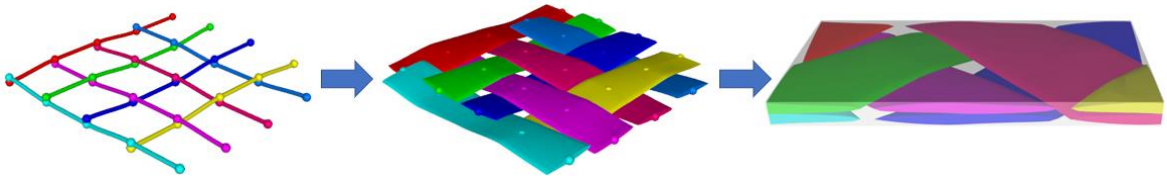

Figure 2: Formation of braided unit cell within TexGen. Node and path locations, cross-sections and interpolation applied and domain assigned for periodicity.

2.3 Refinement

Although in general the cross-section of the yarn can be defined through the power ellipse equations, small distortions in the cross-sectional shape have been identified due to the interactions between fibres during the braiding process. In order to represent this within TexGen a custom refinement function has been implemented, without which intersections between the yarns can arise leading to unrealistic geometries and problems post-processing the model. This function iterates through each yarn and applies small changes, where appropriate, to the cross-section using two operations. Firstly, rotation in the yarns was observed due to undulations in

the fabric. If a rotation is required, the angle is determined using Eq. (7) from the thickness of the fabric, t_f, and the spacing between the centres of the yarns, P. Secondly, small changes to the cross-sectional shape are applied through the '*CorrectInterference*' operation. This redefines the cross-section as a polygon and deforms small sections of this to reduce the interference between the yarns. *Figure 3* shows the results for both an unrefined and a refined model compared to the optical microscopy, showing a good agreement in yarn shape and rotation for the refined model.

$$\theta = \tan^{-1}\left(\frac{t_f}{2P}\right) \tag{7}$$

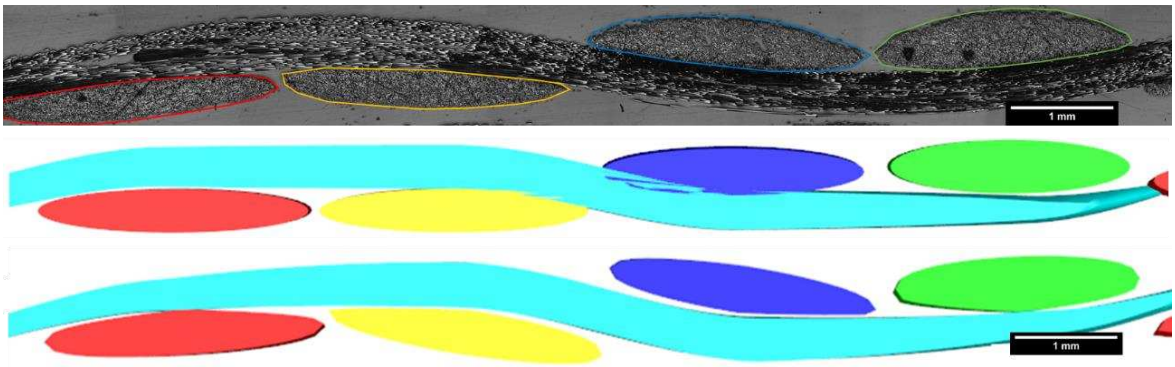

Figure 3: Comparison of microscopy image of braid to predicted TexGen model built with unrefined (top) and refined fabric (bottom).

2.4 Curved Unit Cell

In order to investigate the effect of curvature, a novel function CTextileBraidCurved has been developed to allow for the modelling of a braid on a circular mandrel. CTextileBraidCurved uses the same equations to calculate the braid angle and coverage factor, then uses a polar coordinate system within TexGen to produce a fabric curved around a central radius. Similar to the flat fabric construction the cross-sections are applied at the nodes, however with an initial rotation applied to match the slope of the mandrel at the node location, with a refinement function implemented to further rotate and alter the cross-section of the nodes to match more closely that of the sample fabrics. The process of the fabric construction with the new domain applied to match the curvature can be seen in *Figure 4*. Nagaraju et al. [2] mapped a flat unit cell from TexGen after generating the FE mesh. Through this procedure distortion in the elements can have an impact on the local properties such as local yarn volume fraction, although it is expected to remain constant in respect to global properties. Within this study the unit cells are produced curved from the construction of the fabric, resulting in the correct local properties within each element of the FE mesh.

Figure 4: Formation of braided curved unit cell within TexGen. Node and path locations, cross-sections and interpolation applied and domain assigned for periodicity.

  doi:10.5075/epfl-298799_978-2-9701614-0-0

3. Prediction of Elastic Properties

3.1 Micromechanics of flat unit cell

The method for evaluating the mechanical properties of flat RUC's has been given in detail by Li and Sitnikova [7]. Periodicity within the unit cells is assumed to be translational along the x-plane and y-plane. The boundary faces normal to this, in the z-plane, have no displacement restrictions in this analysis. This assumption is valid for single layer unit cell analysis, however further restrictions can be applied to calculate mechanical properties within the z direction.

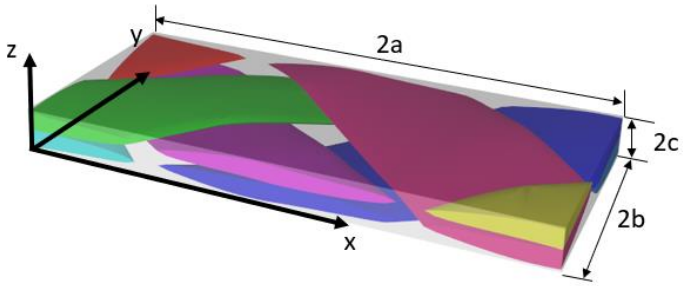

Figure 5: Flat unit cell of braided composite with rectangular coordinate system.

3.2 Micro-Mechanics of curved unit cell

The boundary conditions assumed in the previous section are valid for unit cells with translational symmetry. Due to the presence of rotational symmetry within the curved RUC alternative constraints are required. This section outlines those boundary conditions and the method to calculate the effective elastic properties of the unit cells. The rotational symmetry can best be presented in a cylindrical coordinate system shown in *Figure 6*.

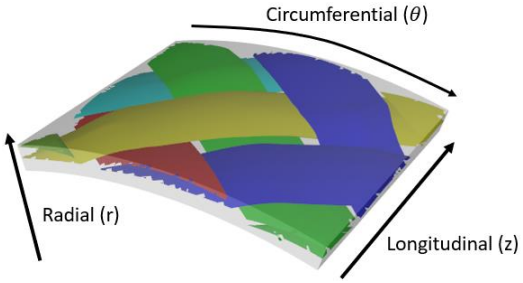

Figure 6: Curved unit cell of braided fabric with polar coordinate system.

Unlike within a rectangular coordinate system, in a cylindrical coordinate system with a strain field periodic in the circumferential direction, the in-plane displacements, u_r and u_θ will have the same periodic characteristics. Therefore the following periodic boundary conditions can be applied.

$$u_x|_{\theta=\alpha} = u_x|_{\theta=-\alpha}$$
$$u_r|_{\theta=\alpha} = u_r|_{\theta=-\alpha} \quad (8)$$
$$u_\theta|_{\theta=\alpha} = u_\theta|_{\theta=-\alpha}$$

Within the longitudinal direction the periodicity leads to the following relative displacement boundary conditions.

$$u_x|_{x=b} - u_x|_{x=-b} = 2b\varepsilon_x^0$$

$$u_r|_{x=b} - u_r|_{x=-b} = 0 \quad (9)$$

$$u_\theta|_{x=b} - u_\theta|_{x=-b} = 2\phi r$$

Where ϕ is the relative angle of twist about the z-axis and *b* is half the length of the unit cell in the longitudinal direction. The longitudinal modulus can be calculated using the same procedure as outlined in the previous section. However, the shear modulus is obtained using Eq. (10).

$$G = \frac{nT}{J\phi/2b} \quad (10)$$

Where *n* is the number of periods over the circumference, *T* is the torque applied and *J* is the polar moment of inertia.

3.3 Meshing

TexGen has been used to generate a voxel mesh of the RUC. This method is used to ensure the mesh is homologous which is necessary for the successful implementation of the periodic boundaries outlined in the previous sections. The node sets have been identified for opposite faces, edges and vertices, with the required boundary conditions written into the Abaqus input file. An eight-node brick element (linear hexahedron, C3D8) was used within the analysis. Both flat and curved fabrics have been meshed using this technique. While exporting the FE mesh TexGen generates two additional files. The orientation file (.ori extensions) contains the fibre orientation data for each element and the element data file (.eld extension) which contains the local yarn volume fraction data for each element. Elastic properties of each element within the yarns were calculated using Chamis' equations [8]. This semi-empirical approach does not require any modelling and is often used for its simplicity.

4. Applications

In this section the proposed curved unit cell model is compared against equivalent flat fabrics for the longitudinal modulus and shear modulus using Eq. (8-10). Four braid angles were chosen, 35, 40, 45 and 50 degrees at a radius of 10 mm. Yarns within the study were modelled as AS4 fibres with a yarn width of 2.7 mm and yarn thicknesses of 0.35 mm and 0.5 mm. The properties of the fibres and matrix used within the study are given in Table 1.

Table 1: Elastic properties used for analysis. Data adopted from Carey et al. [9]

	E_{11}(GPa)	E_{22}(GPa)	E_{33}(GPa)	G_{12}(GPa)	G_{13}(GPa)	G_{23}(GPa)	ν_{12}	ν_{13}	ν_{23}
Carbon Fibre	228	40	40	24	24	24	0.26	0.24	0.1
Matrix	4.2	-	-	1.62	-	-	0.3	-	-

  doi:10.5075/epfl-298799_978-2-9701614-0-0

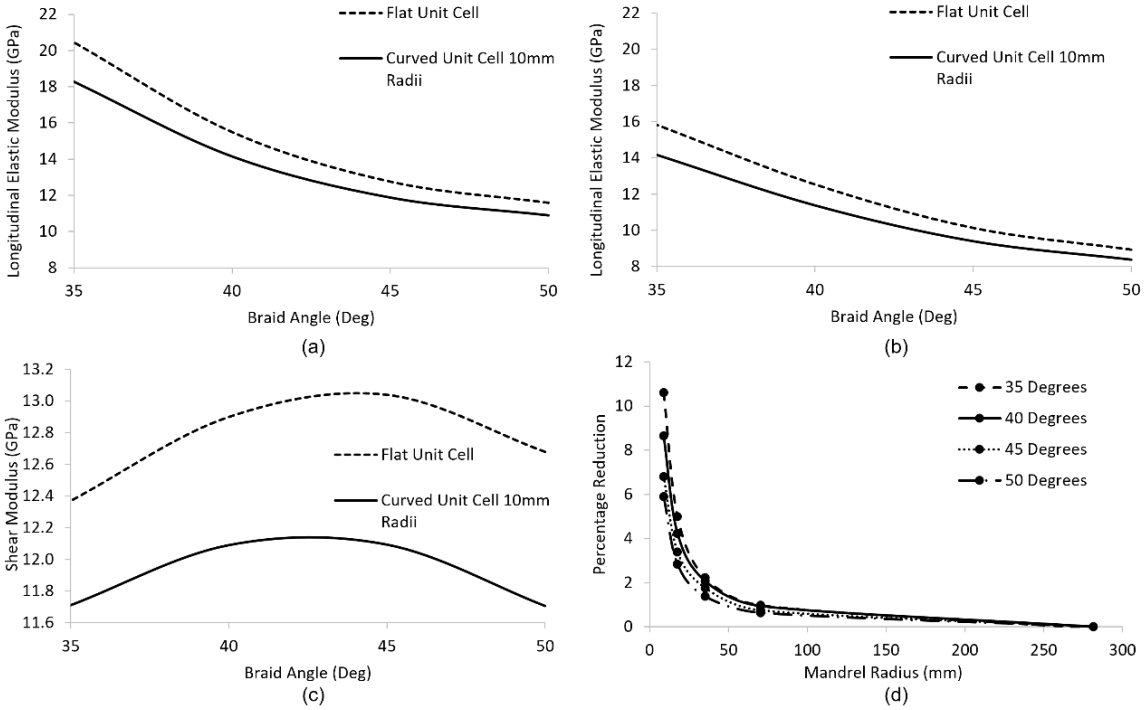

Figure 7: Effect of curvature on mechanical properties (a) Longitudinal Modulus for yarn thickness = 0.35 mm, (b) longitudinal modulus for yarn thickness = 0.50 mm, (c) shear modulus for yarn thickness = 0.35 mm and (d) difference between flat and curved calculated longitudinal modulus at varied radius.

The effect of curvature on the longitudinal elastic modulus can be seen in *Figure 7*(a), showing a reduction in the predicted modulus for curved unit cells. Yarns with a thickness of 0.35 mm were modelled giving a yarn volume fraction of 0.67. Up to 10.5 % difference in the modulus has been predicted, with greater effects seen in lower braid angles. By changing input parameters to the TexGen model similar fabrics were produced with an increase in yarn thickness to 0.50 mm, leading to a decrease in yarn volume fraction to 0.47. *Figure 7*(b) shows the effect this has on the longitudinal elastic modulus, showing a similar trend of a reduction in the modulus for the curved unit cell compared to the equivalent flat fabric. The effect of shear modulus has additionally been investigated with a similar outcome of a reduction in the predicted values for the curved unit cell. This is demonstrated in *Figure 7*(c), showing up to an 8 % difference in shear modulus. To evaluate the effect of this curvature a range of radii were modelled from 8 mm to 280 mm. A comparison to the flat unit cell is shown in *Figure 7*(d), with the percentage reduction in the longitudinal elastic modulus displayed. This shows a clear trend for a greater difference at smaller radii, alongside negliable difference for mandrel radii greater than 280 mm.

The results presented here show a reduction in the stiffness of the composite when modelled with a small radius. This agrees with work reported in [2], and care should be taken when using data from flat specimens to design such components. To further this work experimental validation Is to be undertaken.

5. Conclusions

The present work outlines the effects of curvature on the elastic mechanical properties of 2D biaxial braided tubular composites. TexGen has been expanded to predict and build 2D biaxial braided unit cells in both flat and curved domains with custom refinement functions to accurately model the variations in yarn cross-section. This has been shown to have good agreement with optical microscopy images. Elastic mechanical properties have been evaluated for curved domain composites and equivalent flat unit cells. This has shown a significant reduction in longitudinal elastic modulus with up to 10.5 % reduction for fabrics with a 35 degree braid angle. Similar results were seen for shear modulus with up to 8 % difference. The effect of radius was investigated showing a reduction in difference in longitudinal elastic modulus for larger radii, with negliable difference at a 280 mm radius.

6. Acknowledgments

This work was funded by the Engineering and Physical Sciences Research Council [Grant number: EP/P006701/1], as part of the “EPSRC Future Composites Manufacturing Research Hub”. Software engineering support was funded by the Engineering and Physical Sciences Research Council RSE Fellowship [Grant number: EP/N019040/1].

7. References

1. Ayranci C, Carey JP. Predicting the longitudinal elastic modulus of braided tubular composites using a curved unit-cell geometry. Composites Part B: Engineering. 2010;41(3):229-35.
2. Thandaga Nagaraju H, Sankar BV, Subhash G, Kim NH, Haftka RT. Effect of curvature on extensional stiffness matrix of 2-D braided composite tubes. Composites Part A: Applied Science and Manufacturing. 2021;147:106422.
3. TexGen [Available from: http://texgen.sourceforge.net]
4. Czichos R, Bareiro O, Pickett AK, Middendorf P, Gries T. Experimental and numerical studies of process variabilities in biaxial carbon fiber braids. International Journal of Material Forming. 2021;14(1):39-54.
5. Potluri P, Manan A, Francke M, Day RJ. Flexural and torsional behaviour of biaxial and triaxial braided composite structures. Composite Structures. 2006;75(1):377-86.
6. Van Ravenhorst JH. Design Tools for Circular Overbraiding of Complex Mandrels [Dissertation]: University of Twente; 2018.
7. Li S, Sitnikova E. Chapter 6 - Formulation of unit cells. In: Li S, Sitnikova E, editors. Representative Volume Elements and Unit Cells: Woodhead Publishing; 2020. p. 107-87.
8. Chamis C C. Mechanics of Composite Materials: Past, Present and Future. Journal of Composites Technology & Research. 1989;11:3-14.
9. Carey J, Munro M, Fahim A. Longitudinal Elastic Modulus Prediction of a 2-D Braided Fiber Composite. Journal of Reinforced Plastics and Composites. 2003;22(9):813-31.

  doi:10.5075/epfl-298799_978-2-9701614-0-0

ANISOTROPIC TOPOLOGY OPTIMIZATION OF CARBON FIBER REINFORCED COMPOSITE MATERIALS ENGINEERED WITH NOVEL MANUFACTURING TECHNOLOGIES

Vinay Nagaraj[a], Nicole Motsch-Eichmann[b], Joachim Hausmann[c]

a: Leibniz-Institut für Verbundwerkstoffe GmbH – vinay.nagaraj@ivw.uni-kl.de

Abstract: *Nowadays, more and more industries are opting topology optimization to arrive at an optimal design layout at very early stages of product development. Although the origins of topology optimization dates back to late 1980s, even today, there is less insight in translating the optimized topology into engineering application [1]. This field is actively evolving around design of composite structures to obtain high-performing lightweight structures.*

The focus here is on the development of components consisting of a 3D printed metallic insert, which acts as a load introduction element into the surrounding carbon fiber reinforced plastic. Thanks to the novel technologies like TFP (tailored fiber placement) by which fiber bundles can be custom placed and stitched along the optimized path determined using FE simulations. The rough surface nature of additive manufactured parts supports the load carrying capacity at component level because of its superior interface bond strength. Challenges involved here are to simulate the component behavior without neglecting the physics, manufacturing restrictions and complexities. This paper is aimed at comparing the application of two composite topology optimization strategies/algorithms offered by ABAQUS Tosca®, namely condition-based and the most applied continuous and density based, Solid Isotropic Material with Penalization (SIMP) approach [6]. The stack up configurations were predefined as per the design rules [5] and the best fiber topology along the load path was determined by minimizing its compliance. In our study, we attempt to address the simulation challenges encountered in the context of the optimization of anisotropic 3D topology applied to composites. Using the voxel-based Finite Element (FE) approach, some of these numerical examples will be illustrated in this paper with the help of a simple toy model.

Keywords: Topology optimization, Condition-based, SIMP, Tailored fiber placement, quasi-isotropic layup, compliance, voxel-based FE

1. Introduction

In fiber-reinforced structures (e.g. made of CFRPs), it is possible to place the fibers in the component in layers according to the loading path. Lightweight constructions are of great worth as they can be tailored to take up loading in specific directions. Commercially available topology optimizers (e.g. TOSCA) are capable of considering anisotropic composite behavior, but simultaneous fiber orientation optimization is not possible using topology optimization.

Composite design optimization through topology optimization is computationally expensive and time-consuming. These complex simulations could be laborious, if the element count is not chosen wisely, especially with the voxel based 3D topology optimization. With calculated risks, it is possible to achieve a balance between accuracy and computational costs. Thus, in this study we begin with mesh refinement studies and quantifiable error indicators to help determine the size of the mesh for the problem in hand. Using this input in a simple toy model, we proceed on

  doi:10.5075/epfl-298799_978-2-9701614-0-0

to optimizing the design of a composite structure with predefined stack up configurations as per the design rules [5].

1.1 Background - Topology optimization

"Topology optimization is a mathematical method that optimizes material layout within a given design space, for a given set of loads, boundary conditions and constraints with the goal of maximizing the performance of the system" [8]. This method is widely used in the mechanical, aerospace, civil and bio-chemical engineering to optimize the designs during the conceptual phases. However, due to the free form nature the results from this optimization process is usually difficult to manufacture [8].

ABAQUS supports two algorithms for topology optimization, namely the efficient condition-based but with limitations and the other general algorithm, which is more flexible and most used [7]. In the following sections a brief introduction is given about the usage of both these topics. Detailed explanations of the described methods can be found in [7,9,10].

1.2 General algorithm

In general algorithms the density and stiffness of the design variables are updated in order to meet objective functions and constraints. These algorithms employ material interpolation schemes where the design variable (element density) is treated to be a continuous, allowing the relative element densities to have a value between 0 and 1. Thus results obtained from these algorithms generate elements with intermediate density values in the final design [7,10].

Under this category, ABAQUS Tosca structures provides two material interpolation schemes with penalization, SIMP (solid isotropic material with penalization) and RAMP (rational approximation of material properties). RAMP method is more suitable for dynamic problems [10]. In general algorithms, number of iterations/design cycles required to find an optimal topology is unknown to the user before the start of optimization, and is typically between 30-45 [7].

1.3 Condition-based

This algorithm was first developed at the University of Karlsruhe, Germany. Here the input data to the algorithm would be strain energy and the computed stress values at the nodes. Therefore, this algorithm is claimed to be more efficient as it avoids the calculation of local stiffness of design variables and computes the solution within the maximum number of design cycles (default-15). Nonetheless, this algorithm is less flexible since it is only applicable to strain energy minimization problems with material volume as equality constraints. Unlike the general algorithms, in this case the elements in the final design either take a value of 0 (no material) or 1 (solid) [7].

Both these strategies will be applied in the context of 3D and anisotropic composite topology optimization to study the influence of start configurations on the optimized design. Unfortunately, ABAQUS topology optimization does not support the variation of lamination parameters like fiber orientation in the composite laminate. Hence, this work lays the

  doi:10.5075/epfl-298799_978-2-9701614-0-0

foundation for future investigations on extending the functionality to simultaneous topology and fiber angle orientation optimization problems.

2. FE Modelling, results and discussions

2.1 Finite Element Modelling

In the following sections, we narrow our focus and try to solve the complexity of the model with a detailed investigation of a simple toy model. As shown in the fig. 1, the model chosen for the problem in hand is a half symmetric rectangular plate with a steel insert at the hole. The rectangular plate is to be modelled as a CFRP laminate. A 3D printed metallic steel insert acts as a load transferring element from the fastener into the composite part. The load case studied here is similar to the design of the tensile specimen to be optimized. This work forms the basis for a series of forthcoming investigations with the commercial finite element software package ABAQUS/CAE. Aforementioned optimization algorithms, the condition-based and the most popular general sensitivity based material interpolation technique, SIMP are applied to three different start configurations of stack up sequences. The optimized design output of these two algorithms are compared from different perspectives listing their advantages and disadvantages.

Usage of mesh dependent FE simulations in topology optimization may lead to suboptimal designs [4]. The adaptive mesh refinement (AMR) process helps one to arrive at a pragmatic mesh size by refining the elements at the sensitive areas and coarsening them at noncritical regions. This is achieved by reaching targets on selected error indicators and comparing these error indicators with the base results [2].

AMR in the field of topology optimization has received less research attention [4]. Initially the FE model depicted below was simulated using the automated adaptive mesh refinement technique available in ABAQUS to eliminate the mesh sensitivity with default re-meshing rules. Although AMR process seems to be quite promising, in ABAQUS it is unfortunately still limited to the tetrahedral elements, and it lead to localized stress singularities at the contact interfaces. Consequently, further research was conducted only using the continuum 3D, 8 noded hexahedral (C3D8) elements. Additionally in the case of topology optimization it is proven that optimization methods work extremely well with the voxel based approach [3]. It seems that a deep examination of this topic of the use of AMR in topology optimization is outside the scope of this paper, nevertheless it is very interesting in the author's opinion to apply AMR techniques with voxel based approach, which could help further accelerate the topology optimization process of large models with quantitative error estimates.

Table 1: Mesh refinement studies

Trial	Mesh size (mm)	Number of elements	Percentage error (CPRESS)
1	1	41852	33.9
2	0.8	41963	30.5
3	0.6	95769	28.4
4	0.25	1154457	28.8

Table 1 gives a quick view of manual mesh refinement process. Contact pressure (CPRESS) at the interface was selected as error indicator. Although the number of elements increased 12 times, there is no significant reduction in the calculated percentage error after the third test. Thus, the 0.6 mm mesh model was chosen to be the final mesh size for further investigations.

Fig. 1 (a) shows the half symmetry model and the Y plane symmetric boundary condition used in the simulation, also (b) depicts the applied tensile load through a structural coupling reference point at the center of the steel. The contact interaction between steel and composite material is currently penalty based friction formulation and could be improved further with cohesive zone modelling. Tensile load at the insert is applied through a continuum distributed coupling.

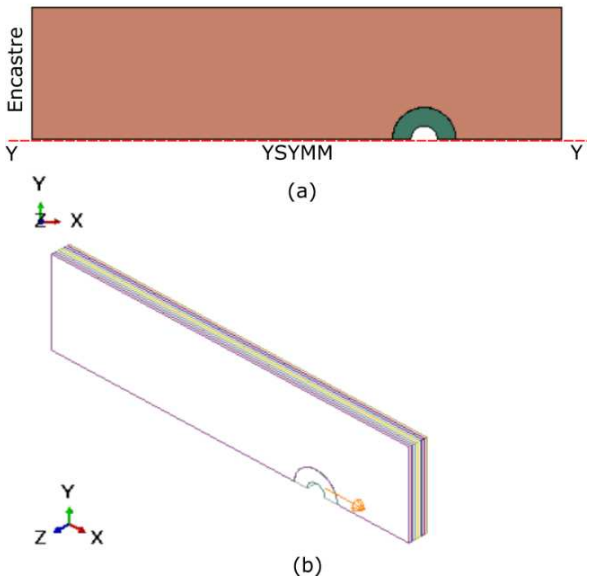

Figure 1. (a) Half symmetric toy model (full size: 100 mm × 50 mm × 5 mm) with Boundary conditions, (b) Tensile load of 1KN on the model in Isometric view

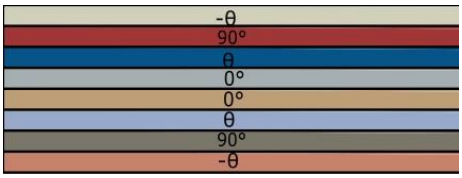

Figure 2. Illustration of symmetric and balanced composite laminate stack up (laminate configurations with $\Theta_1 = 30°$, $\Theta_2 = 60°$, $\Theta_3 = 45°$)

In order to understand the influence of start configurations on the final design, three different start configurations were selected as per the design rules as ~~is~~ represented in fig. 2.

2.2 Results and discussions

In this section, optimization results of a complete laminate material distribution with 65% volume constraint, using both the algorithms are discussed.

Fig. 3 and 4 compares the objective function (minimization of Strain Energy) versus number of iterations required to converge in both the methods. It can be derived from this graph that, the Θ = 30° design leads to the least strain energy (highest stiffness for the considered load case) in both the approaches. As expected 30° design, produced the stiffest topology in this case due to the axial tensile loading.

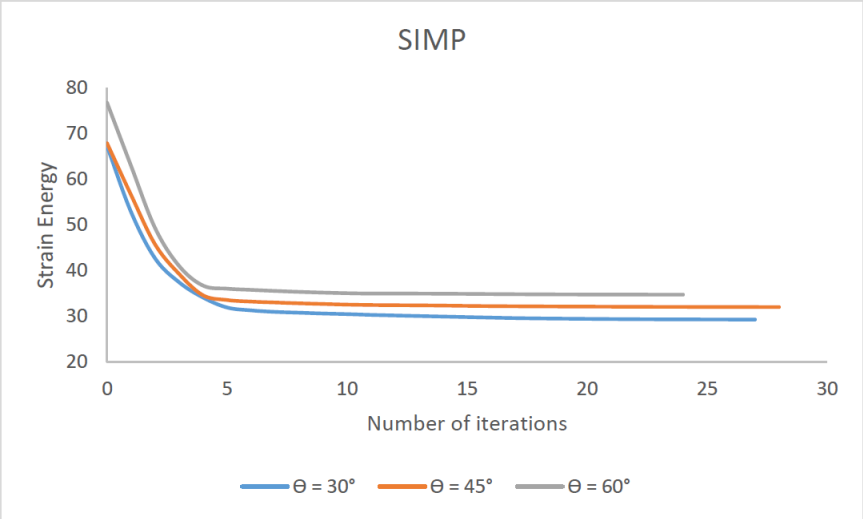

Figure 3. Convergence plot of SIMP algorithm for different start configurations

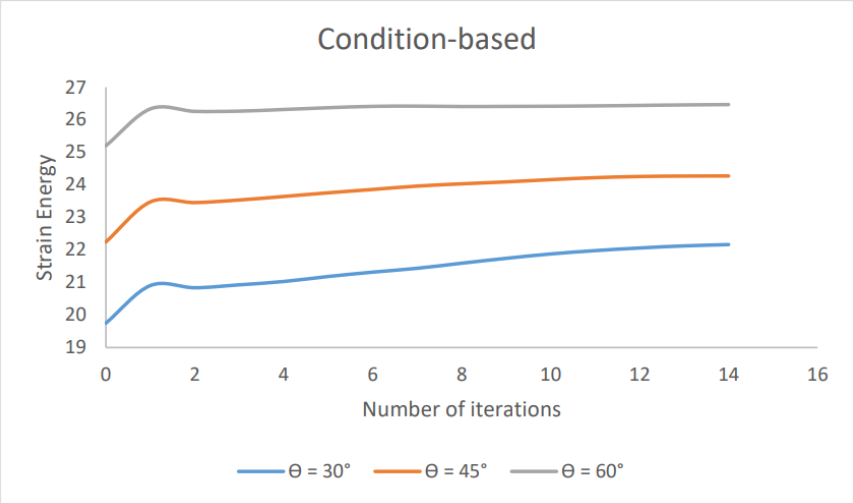

Figure 4. Convergence plot of condition-based algorithm for different start configurations

As stated above, because of its highest stiffness for Θ = 30° configuration, the following table was intendend to give a fair idea to the designer of material distribution in different layers. It is important to note that the table 2 is an illustration of material distribution in each layer, and in all cases, topology optimization was carried out considering the entire laminate as shown in fig.2 and not just the layers. Thus, each layer does not necessarily represent the same geometry as the entire laminate.

Table 2: Comparison of optimized material distribution of different layers between the two approaches

  doi:10.5075/epfl-298799_978-2-9701614-0-0

Case	Fiber layer	Material distribution
Cond-30	0°	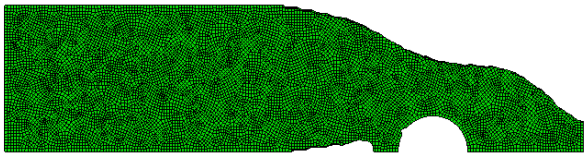
Cond-30	30°	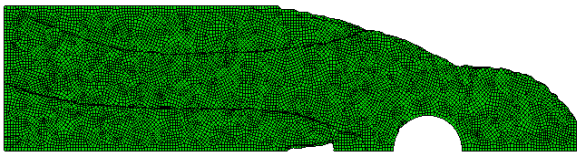
Cond-30	90°	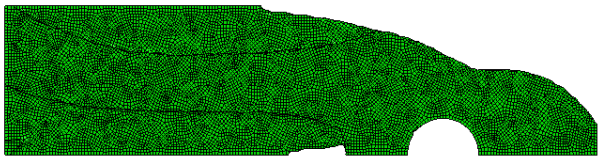
SIMP-30	0°	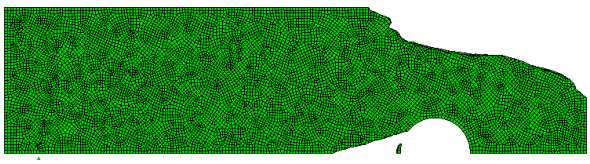
SIMP-30	30°	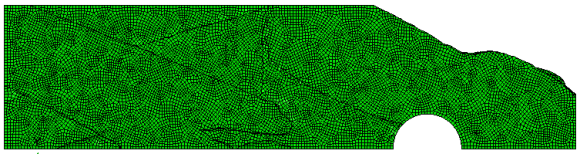
SIMP-30	90°	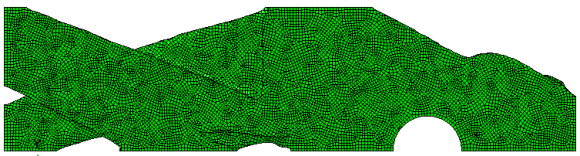

2.3 Conclusions

In this paper, 3D and anisotropic topology optimization of a composite laminate with a predefined stack up sequence was demonstrated. Applicability of advanced mesh refinement techniques like automated AMR were investigated in the context of composite topology optimization. Optimization trials using condition-based and SIMP methods, led to different material distributions. SIMP method required more iterations/design cycles to converge while the condition-based algorithm converged faster, but has its own limitations as discussed before. Optimized material distributions in different layers can be utilized as a guideline in the TFP method to fabricate load specific components.

2.4 Outlook

Current FE model can still be improved by extending AMR to hexahedral elements and including cohesive zone elements at the contact interface for topology optimization to capture the actual physics instead of frictional contact formulation. In author's opinion, simultaneously optimizing composite topology and fiber angle still remains challenging and can also be included in further extensions. As mentioned earlier methods studied here serves as a basis for further investigations in this direction.

Acknowledgements

This work is supported by the Central Innovation Programme for SMEs (ZIM) of the German Federal Ministry for Economic Affairs and Energy (BMWi) based on a resolution of the German Bundestag (funding code ZF4052329RU9).

3. Refernces

[1] Liu, S., Li, Q., Liu, J., Chen, W., & Zhang, Y. (2018). A realization method for transforming a topology optimization design into additive manufacturing structures. Engineering, 4(2), 277-285.

[2] Abaqus-docs.mit.edu. 2022. About adaptive remeshing. [online] Available at: <https://abaqus-docs.mit.edu/2017/English/SIMACAEANLRefMap/simaanl-c-adpover.htm> [Accessed 19 April 2022].

[3] Torigaki T, Fujitani K. Power of a voxel approach to structural analysis and topology-shape optimization in automobile industries. Japan journal of industrial and applied mathematics. 2000 Feb;17(1):129-47.

[4] De Sturler E, Paulino GH, Wang S. Topology optimization with adaptive mesh refinement. InProceedings of the 6th International Conference on Computation of Shell and Spatial Structures IASS-IACM 2008 May 28 (pp. 28-31).

[5] Werthen E, Dähne S. Design rules consideration within optimization of composite structures using lamination parameters (Doctoral dissertation).

[6] Tyflopoulos E, Steinert M. A Comparative Study of the Application of Different Commercial Software for Topology Optimization. Applied Sciences. 2022 Jan;12(2):611.

[7] About structural optimization [Internet]. Abaqus-docs.mit.edu. 2022 [cited 19 April 2022]. Available from: https://abaqus-docs.mit.edu/2017/English/SIMACAEANLRefMap/simaanl-c-

optover.htm#simaanl-c-optover-t-GeneralVersusConditionbasedTopologyOptimization-sma-topic4

[8] Topology optimization - Wikipedia [Internet]. En.wikipedia.org. 2022 [cited 19 April 2022]. Available from: https://en.wikipedia.org/wiki/Topology_optimization

[9] Bendsoe MP, Sigmund O. Topology optimization: theory, methods, and applications. Springer Science & Business Media; 2003 Dec 1.

[10] Material Interpolation [Internet]. Abaqus-docs.mit.edu. 2022 [cited 19 April 2022]. Available from: https://abaqus-docs.mit.edu/2017/English/TsoUserMap/tso-c-user-TopOpt-Sett-Sensi-MatInt.htm

SIMULTANEOUS TOPOLOGY AND ANISOTROPY OPTIMIZATION BY MEANS OF A GRADIENT-BASED ALGORITHM

Lander, Vertonghen[a], François-Xavier, Irisarri[a], Boris, Desmorat[b], Dimitri, Bettebghor[a]

a: DMAS, ONERA, Université Paris Saclay – lander.vertonghen@onera.fr
b: Sorbonne Université, CNRS, UMR 7190, Institut d'Alembert

Abstract:

Solutions to topology optimization problems are strongly influenced by the consideration and simultaneous anisotropy optimization. To broaden anisotropy consideration in topology optimization to other optimization objective and/or constraints, such as strength or buckling, this work introduces a novel way of incorporating 2D orthotropy in a gradient-based optimization routine. The orthotropy is represented by means of the polar formalism, and the optimization strategy uses a combination of the Method of Moving Asymptotes (MMA) and Global Convergent Method of Moving Asymptotes (GCMMA), whichever approximation is better suited to the variable type. As gradient-based optimization are prone to local minima, it is shown that with a proper initialization, the split "MMA" strategy obtains similar compliance values and variable distribution as the alternate directions benchmark algorithm, validating the strategy for further use.

Keywords: topology; optimization; polar parameters

1. Introduction

Topology optimization seeks to define the optimal material distribution of a structure for a defined load case. It is a well-documented problem for compliance minimization with an isotropic material [1], however other properties influence the final solution and topology. This effect can for example be seen in optimizations considering strength and/or buckling constraints [2]. The resolution of such optimization problems with additional constraint is either done with genetic [3] or gradient based [1,2,4] algorithms in literature.

Another influence on the optimized shape is the type and amount of material variables, such as incorporating material anisotropy. General material orthotropy was considered in topology optimizations by Ranaivomiarana *et al.* [5]. Another subset of anisotropy can be mentioned, being the composite laminate space, and having their equivalent stiffness represented and optimized by means of lamination parameters, as performed by Peeters *et al.* [4], with a subsequent fiber path retrieval step.

Ranaivomiarana *et al.* [5] demonstrated that the concurrent consideration of orthotropy in topology optimization resulted in different final topologies, being potential less bulky yet better designs than a sequential optimization of first the topology with an isotropic material, followed by the material orthotropy optimization. However, the optimization method used by Ranaivomiarana *et al.* [5] is based on the alternate directions (AD) method [6] which can only be used for compliance minimization.

  doi:10.5075/epfl-298799_978-2-9701614-0-0

In order to incorporate additional constraints in topology optimization whilst considering material anisotropy, the algorithm to solving the optimizations must be switched to a gradient-based method. This is the purpose of the presented work, and is done more specifically with the Methods of Moving Asymptotes (MMA) algorithm [7]. The material anisotropy is still characterized by means of the polar parameters [8], facilitating a comparison of the results of the proposed approach to the ones obtained by Ranaivomiarana *et al.* [5]. Moreover, this still leaves the later possibility to limit the design space to composite layups by means of the geometric bounds on the polar parameters [9].

This remainder of this abstract is setup as follow: Section 1 discusses the background of the topology and anisotropy modelling, the optimization strategy is laid out in Section 2, followed by the presentation and discussion of the results in Section 3 and finally the abstract is concluded in Section 4.

2. Methodology

2.1 Topology representation

The topology variables are the element densities ρ, which are used in the Solid Isotropic Material with Penalization (SIMP) [1] given in Eq. (1) to achieve distinct results. D is the elasticity tensor as used in the definition of an element's stiffness matrix in the finite element method (FEM) analysis, p is the penalization exponent and D_0 the pristine elasticity tensor of an element. Section 1.2 gives the definition of this elasticity tensor D_0 with anisotropy.

$$D = \rho^p D_0 \tag{1}$$

To prevent checkerboard instabilities, a linear filter is used to smoothen the density variables and obtain a length scale control, according to Eq. (2). Ω_i is the set of elements whose centroid distance lays within the filter radius R, and are given a filter weight w_{ij} according to Eq. (3). *x* represents each element's centroid location, and V the element's area.

$$\widetilde{\rho_i} = \frac{\sum_{j\in\Omega_i} w_{ij} V_j \rho_j}{\sum_{j\in\Omega_i} w_{ij} V_j} \tag{2}$$

$$\Omega_i = \{j \mid |x_j - x_i| \leq R\} \text{ and } w_{ij} = R - |x_j - x_i| \tag{3}$$

2.2 Anisotropic representation

The anisotropic behavior of the material is represented by means of the polar formalism [10]. In this communication, the anisotropy is restricted to orthotropy. The components of the pristine elasticity tensor D_0 are obtained by means of the polar parameters [8], expressed in Eq. (4) with normalized anisotropic modules η_0 and η_1. T_0 and T_1 are the isotropic modules, ϕ_1 is the direction of orthotropy. η_0 and η_1 are defined as $\frac{(-1)^K R_0}{T_0}$ and $\frac{R_1}{\sqrt{T_0 T_1}}$ respectively, where R_0 and R_1 are the anisotropic modules and K the orthotropic shape factor.

$$D_{1111} = T_0 + 2T_1 + \eta_0 T_0 \cos 4\phi_1 + 4\eta_1 \sqrt{T_0 T_1} \cos 2\phi_1$$

$$D_{1122} = -T_0 + 2T_1 - \eta_0 T_0 \cos 4\phi_1$$

$$D_{1112} = \eta_0 T_0 \sin 4\phi_1 + 2\eta_1 \sqrt{T_0 T_1} \sin 2\phi_1 \tag{4}$$

  doi:10.5075/epfl-298799_978-2-9701614-0-0

$$D_{2222} = T_0 + 2T_1 + \eta_0 T_0 \cos 4\phi_1 - 4\eta_1 \sqrt{T_0 T_1} \cos 2\phi_1$$

$$D_{2212} = -\eta_0 T_0 \cos 4\phi_1 + 4\eta_1 \sqrt{T_0 T_1} \sin 2\phi_1$$

$$D_{1212} = T_0 - \eta_0 T_0 \cos 4\phi_1$$

2.3 Thermodynamic bounds

To keep the elasticity tensor D_0 theoretically valid, meaning it remains positive definite, the thermodynamic bounds must be enforced on the anisotropic modules and orthotropic shape factor [8]. These bounds are expressed with the normalized anisotropic modules in Eq. (5), where the strict inequality has been relaxed by introducing $(1-\varepsilon)$. This relaxation is necessary, as the constraints in MMA are simple inequalities. The value of ε is taken as 0.05 in this communication.

$$\eta_0 \geq (1-\varepsilon)\left(2\left(\frac{\eta_1}{(1-\varepsilon)}\right)^2 - 1\right)$$

$$-(1-\varepsilon) \leq \eta_0 \leq (1-\varepsilon) \tag{5}$$

$$-(1-\varepsilon) \leq \eta_1 \leq (1-\varepsilon)$$

However, as the thermodynamic constraint must be considered for each separate element with its own variables, the number of optimization constraints quickly rises and becomes troublesome and slow to handle by the optimization algorithm. Therefore, the thermodynamic constraint is implicitly incorporated as a variable change in a similar way as suggested by Izzi *et al.* [11]. The variable change specific to Eq. (5) is given in Eq. (6), and means the optimization constraint now becomes a simple interval on these new variables.

$$\alpha = \frac{\eta_1 + (1-\varepsilon)}{2(1-\varepsilon)} \;;\; \beta = \frac{\eta_0 - (1-\varepsilon)}{2(1-\varepsilon)\left[\left(\frac{\eta_1}{(1-\varepsilon)}\right)^2 - 1\right]}$$

$$0 \leq \alpha \leq 1 \;;\; 0 \leq \beta \leq 1 \tag{6}$$

2.4 Optimization problem

The optimization problem treated is the minimization of the compliance (C), being the work of the external loads, and defined as the deformation energy ($U^T K U$). U is the displacement vector, obtained from the resolution of $KU = F$, where is K the global stiffness matrix and F the force vector. The optimization problem is stated in Eq. (7), and subjected to a volume V constraint to be lowered than a prescribed volume V_0.

$$\min_{\rho,\phi_1,\eta_0,\eta_1} \quad U^T K U$$

$$s.t.\ V \leq V_0$$

$$0 \leq \alpha \leq 1 \tag{7}$$

$$0 \leq \beta \leq 1$$

$$0.001 \leq \rho \leq 1 \quad ; \quad -\frac{\pi}{2} \leq \phi_1 \leq \frac{\pi}{2}$$

  doi:10.5075/epfl-298799_978-2-9701614-0-0

3. Optimization strategy

The MMA optimization algorithm class [7] is used to solve this optimization problem. MMA is an iterative method of solving a non-linear problem by solving a succession of approximate convex problems. These approximated convex problems are constructed based on the gradient information. As the response surface of the problem differs with respect to the nature of the variable, Bruyneel *et al.* [12] therefore suggested using different approximations for different variables [12], to influence on the convergence properties of the optimization. This inspired the following split "MMA" optimization strategy, where each variable type is optimized separately based on what better suits it characteristics.

The density variables are optimized with the standard MMA and its monotonous approximation, shown to behave well in literature [1,2]. Equally, the anisotropic modules and its change of variables are updated with a separate call of MMA and its monotonous approximation, giving good convergence. Having this separate MMA call allows to use a different optimization settings to guide the optimization of the anisotropic components. Finally, the orientations are optimized with the convex approximation of GCMMA, to help mitigate the influence of the periodicity of the variable, and again with its individual settings. An overview of the optimization strategy is given in Fig. (1).

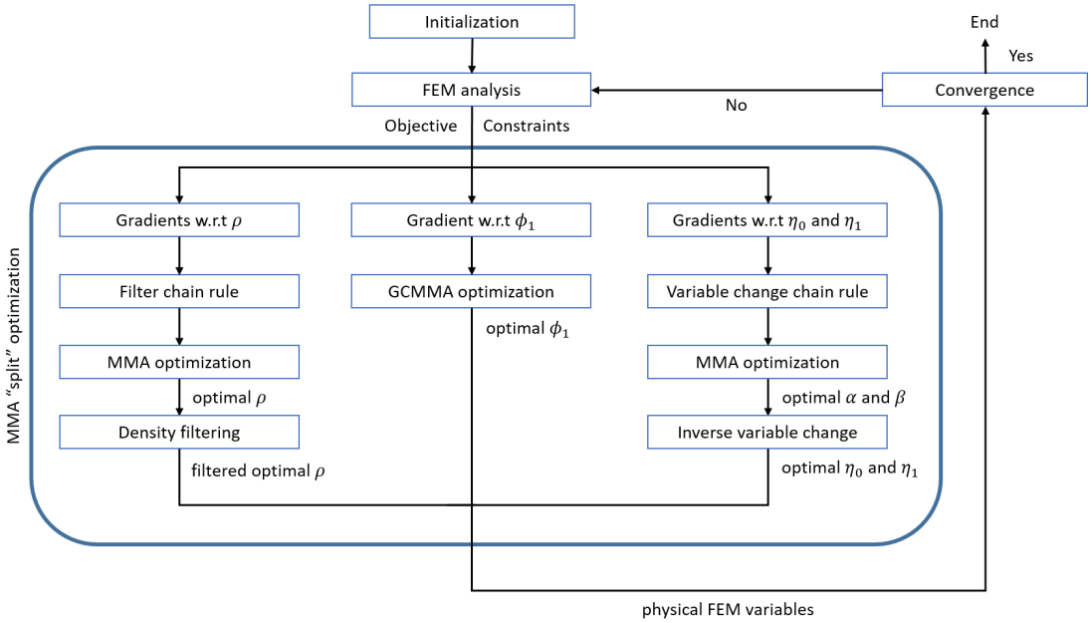

Figure 1. Optimization strategy.

3.1 Sensitivities

As a gradient optimizer is used, the sensitivities of the compliance and volume must be calculated with respect to each variable. The sensitivity with respect to the density is straightforward [1], given in Eq. (8) and Eq. (9), where k_i and u_i are the respective element's stiffness matrix and nodal displacement. V_i is an element's volume.

$$\frac{\partial C}{\partial \tilde{\rho}_i} = -p\tilde{\rho}_i^{p-1} u_i^T k_i u_i \tag{8}$$

$$\frac{\partial V}{\partial \tilde{\rho}_i} = V_i \tag{9}$$

  doi:10.5075/epfl-298799_978-2-9701614-0-0

Furthermore, to take the effect of the filter on the optimization variables into account, the chain rule must be applied according to Eq. (10), for any function *f*.

$$\frac{\partial f}{\partial \rho_i} = \sum_{e \in \Omega_i} \frac{\partial f}{\partial \tilde{\rho}_e} \frac{\partial \tilde{\rho}_e}{\partial \rho_i} \text{ , with } \frac{\partial \tilde{\rho}_e}{\partial \rho_i} = \frac{w_{ei} V_i}{\sum_{j \in \Omega_e} w_{ej} V_j} \tag{10}$$

Analogously to the gradient with respect to the density, and using the self-adjoint property of the compliance problem [1], the gradient with respect to the anisotropic components can be obtained as shown in Eq. (11) and Eq. (12) for the direction of orthotropy ϕ_1, and similarly for η_0 and η_1. The sensitivity of the elasticity tensor is obtained from the analytical derivation of Eq. (4), where B is the strain displacement matrix of the element used to setup the FEM analysis.

$$\frac{\partial C}{\partial \phi_i} = - u_i^T \frac{\partial k_i}{\partial \phi_i} u_i \tag{11}$$

$$\frac{\partial k_i}{\partial \phi_i} = -\rho_i^p \iint_\Omega B^T \frac{\partial D_{0i}}{\partial \phi_i} B d\Omega \tag{12}$$

Finally, to obtain the gradient with respect to the change of variable to incorporate the thermodynamic bounds, the chain rule as given in Eq. (13) must be applied.

$$\frac{\partial C}{\partial \alpha} = \frac{\partial C}{\partial \eta_0}\frac{\partial \eta_0}{\partial \alpha} + \frac{\partial C}{\partial \eta_1}\frac{\partial \eta_1}{\partial \alpha} \quad ; \quad \frac{\partial C}{\partial \beta} = \frac{\partial C}{\partial \eta_0}\frac{\partial \eta_0}{\partial \beta} + \frac{\partial C}{\partial \eta_1}\frac{\partial \eta_1}{\partial \beta} \tag{13}$$

4. Results and discussion

The suggested methodology and optimization strategy by means of a gradient-based algorithm is compared against reproduced results with the optimization strategy of Ranaivomiarana *et al.* [5], itself based on the alternate directions algorithm [6]. The treated optimization problem consists of a cantilever beam of aspect ratio 2:1, clamped at the left side, and loaded in the middle of the right side. The continuation on the SIMP exponent is p = 3 then p = 5, both exponents used for 100 iteration each for either algorithm.

Furthermore, the same filter radius is used with both algorithms. However, the AD algorithm in [5] is programmed with an energy filter [13], which filters the deformation energy instead of only the densities. The most notable difference from this comes as the energy filter with a given filter radius will result in a topology with little intermediate densities. On the contrary, the density filter with the same active filter radius will have intermediate densities due to the averaging and blurring effect on the boundary of the topology. These intermediate densities penalize the objective interpretation. Therefore, the density filter is removed for the last 25 iterations, to obtain distinct results. This removal results in similar intermediate density levels between both algorithms, measured by the measure of non-discreteness (M_{nd}) [14], and allows the comparison of the optimization objective value.

Gradient-based optimizations are prone to getting trapped in local minima. The optimization solutions are sensitive to the initialization of the variables, the settings of the (GC)MMA optimization algorithm, and continuation strategy on the SIMP exponent. Here, the split “MMA” optimization is initialized with the variable distributions obtained after five iterations with the energy filter and AD algorithm, given in Fig. (2). It can be seen that these variable distributions are still general, however, as discussed later, allow converging to a similar solution as the AD algorithm.

  doi:10.5075/epfl-298799_978-2-9701614-0-0

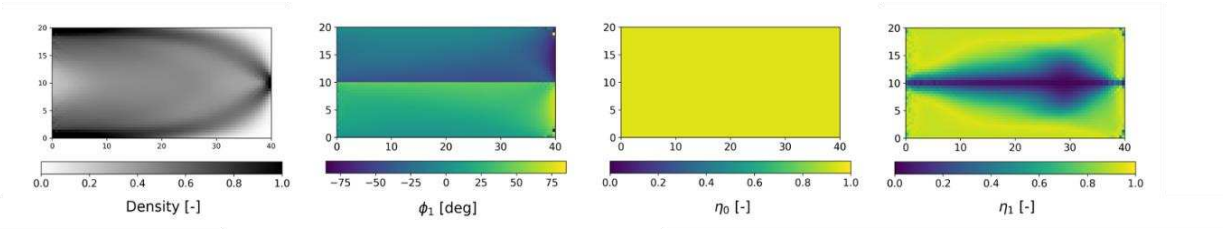

Figure 2. Initialization of the variables, obtained from five iterations with the AD algorithm [5], for the gradient-based optimization.

The results of both optimizations after the final iteration are given in Fig. (3). Similar topology and anisotropy variable distributions are obtained in both cases. Some chequerboard-like phenomenon is visible for η_1 with the gradient-based optimization. This difference could be filter related, where the energy filter in the AD optimization uses the deformation energy of neighboring elements into account, which in itself filters the orientation and anisotropic components. The filter used for the gradient-based optimization is only acting on the densities. Furthermore, comparing the compliance of both optimization reveals close values, with similar levels of M_{nd}: 13.8 mJ with 5.1% of M_{nd} for the AD optimization and 14.0 mJ with 2.9% M_{nd} for the suggested MMA gradient-based strategy.

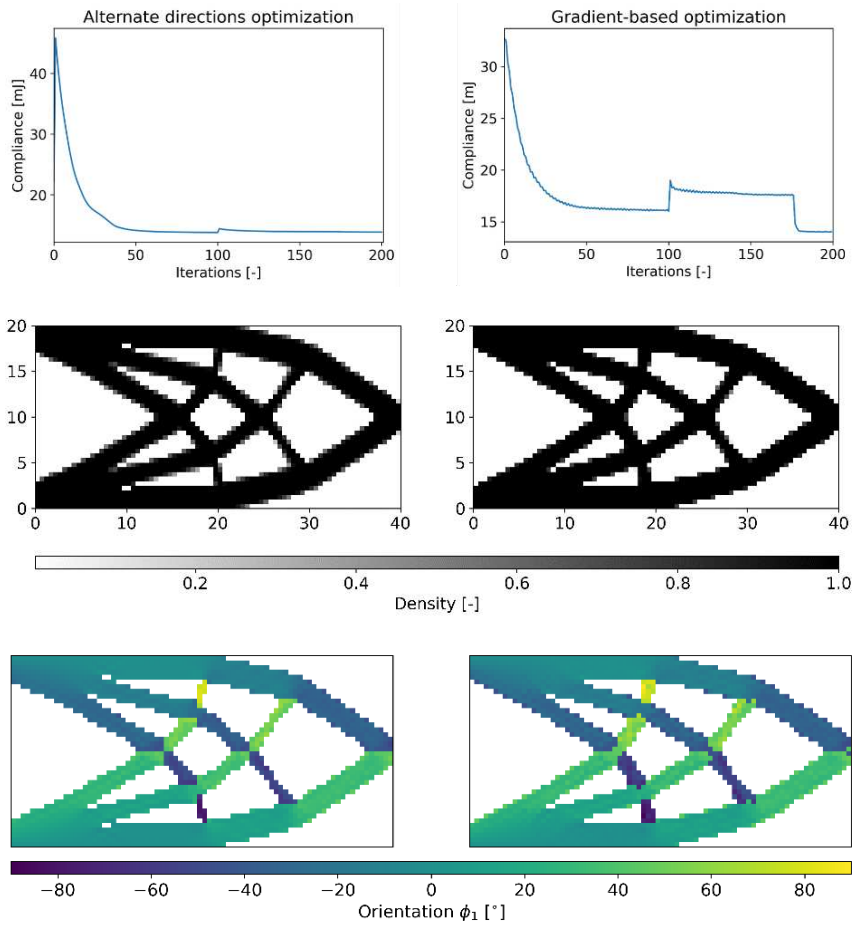

  doi:10.5075/epfl-298799_978-2-9701614-0-0

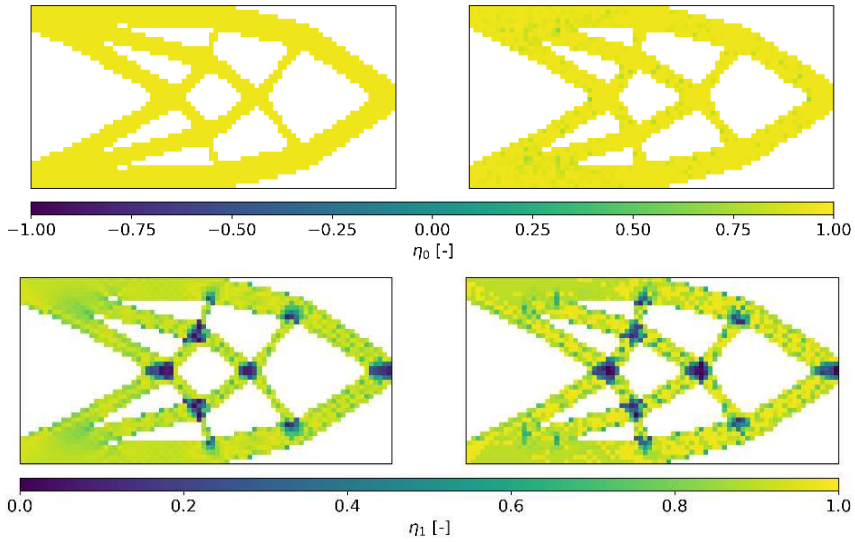

Figure 3. Final variable distribution, on the left for the AD algorithm [5] with energy filter (C = 13.8 mJ, M_{nd} = 5.1%), on the right with the current strategy with density filter (C = 14.0 mJ, M_{nd} = 2.9%). The orientations and anisotropic modules are shown for densities $\geq$ 0.8.

Analyzing the results more in details, it is particularly interesting to note that the gradient optimization manages to find a theoretical result directly exploited in the case of the AD algorithm, namely that the optimal orientations ϕ_1 are aligned with the maximum of the absolute value of the principal stresses. This observation and the good agreement between variable distributions and objective value allows to validate that the suggested gradient-based strategy is well suited to incorporating anisotropy in topology optimization, and converges to a similar solution to that of a simultaneous optimization with the AD algorithm.

5. Conclusion

The purpose of this paper is to describe a gradient-based optimization strategy capable of considering material anisotropy in topology optimization. The anisotropy is restricted to 2D orthotropy and characterized by means of the polar parameters. The anisotropic modules are bound by the thermodynamic bound, which applies to each separate element. To reduce the computational cost of considering the many thermodynamic constraints during the optimization, these bounds were therefore replaced as a variable change. This variable change results in an implicit optimization interval, furthermore ensuring the thermodynamic condition is always satisfied. Moreover, the optimization strategy relies on the adequate selection of the approximation type of the Method of Moving Asymptotes (MMA), depending on the nature of the variables. This results in the introduction of a “split” MMA strategy, where density and normalized anisotropic modules are optimized separately with each the standard MMA, while the orientations are optimized with GCMMA. Finally, as gradient-based optimization are prone to local minima, a specific initialization to the optimization problem is used to guide the “split” MMA optimization towards a similar topology and variable distribution as the alternate directions benchmark optimization. Furthermore, removing the density filter during the last few iterations reduces the amount of intermediate densities and boundary blurring, to obtain distinct topologies, whose compliance value can be compared to the alternate directions solution of Ranaivomiarana *et al.* [5]. The comparison of variable distribution and compliance between the benchmark and suggested strategy are in agreement. This successful comparison

validates the suggested split “MMA” strategy to consider anisotropy in topology optimization. Hence, this strategy allows for later incorporation of more versatile optimization constraints in topology optimization, such as buckling or strength.

Acknowledgements

The authors are thankful to Airbus Atlantic for funding this research project, and specifically Attilio Chiappini for his help and the interactions with him on the subject.

6. References

1. Bendsøe MP, Sigmund O. Topology Optimization. Berlin, Heidelberg: Springer Berlin Heidelberg; 2004.
2. Gao X, Li Y, Ma H, Chen G. Improving the overall performance of continuum structures: A topology optimization model considering stiffness, strength and stability. Computer Methods in Applied Mechanics and Engineering. 2020; 359:112660.
3. Montemurro M, Pagani A, Fiordilino GA, Pailhès J, Carrera E. A general multi-scale two-level optimisation strategy for designing composite stiffened panels. Composite Structures. 2018; 201:968-79.
4. Peeters D, van Baalen D, Abdallah M. Combining topology and lamination parameter optimisation. Structural and Multidisciplinary Optimization. 2015; 52(1):105-20.
5. Ranaivomiarana N. Simultaneous optimization of topology and material anisotropy for aeronautic structures [Thesis]. Sorbonne Université; 2019.
6. Allaire G, Belhachmi Z, Jouve F. The homogenization method for topology and shape optimization. Single and multiple loads case. Revue européenne de Mécanique Numérique. 2012 May;5(5).
7. Svanberg K. The method of moving asymptotes—a new method for structural optimization. International Journal for Numerical Methods in Engineering. 1987; 24(2):359-73.
8. Vannucci P. Plane Anisotropy by the Polar Method. Meccanica. 2005 Dec;40(4):437-54.
9. Vannucci P. A Note on the Elastic and Geometric Bounds for Composite Laminates. Journal of Elasticity. 2013; 112(2):199-215.
10. Verchery G. Les invariants des tenseurs d’ordre 4 du type de l’élasticité. Mechanical Behavior of Anisotropic Solids/Comportment Méchanique des Solides Anisotropes. 1982; 93-104.
11. Izzi MI, Catapano A, Montemurro M. Strength and mass optimisation of variable-stiffness composites in the polar parameters space. Structural and Multidisciplinary Optimization. 2021; 64(4):2045-73.
12. Bruyneel M, Duysinx P, Fleury C. A family of MMA approximations for structural optimization. Structural and Multidisciplinary Optimization. 2002; 24(4):263-76.
13. Desmorat B. Structural rigidity optimization with frictionless unilateral contact. International Journal of Solids and Structures. 2007; 44(3):1132-44.
14. Sigmund O. Morphology-based black and white filters for topology optimization. Structural and Multidisciplinary Optimization. 2007; 33(4):401-24.

  doi:10.5075/epfl-298799_978-2-9701614-0-0

CHARACTERIZATION AND SIMULATION OF THE MECHANICAL RESPONSE OF CO-CONSOLIDATED THERMOPLASTIC CRACKED LAP SHEAR JOINTS CONTAINING TWO NOVEL DISBOND ARREST FEATURES

Ioannis, Sioutis[a], Eirini, Tsiangou[b], Fabien, Allègre[c], Hugo, Boutin[c], Hugo, Plassot[c], Konstantinos, Tserpes[a], Maarten, Labordus[b], Michiel, Bruijkers[b], Rutger, Schutte[b]

a: Laboratory of Technology & Strength of Materials, Department of Mechanical Engineering & Aeronautics, University of Patras, Greece – *sioutis.i@upnet.gr*
b: KVE Composites Group, Laan van Ypenburg 56, 2497 GB Den Haag, The Netherlands
c: RESCOLL Société de Recherche, 8 Allée Geoffroy Saint Hilaire, 33615 PESSAC CEDEX, France

Abstract: *The mechanical response of co-consolidated thermoplastic joints containing Refill Friction Stir Spot Welds (RFSSW) as Disbond Arrest Features (DAFs) was characterized by mechanical tests and simulated by numerical analyses. Additionally, the technique of Induction Low Shear Friction Stir Riveting (ILSFSR) as DAF was numerically investigated. The thermoplastic substrates were manufactured from carbon fiber reinforced polyaryletherketone (PAEK) matrix prepregs and joined in Single Lap Shear (SLS) and Cracked Lap Shear (CLS) configurations via the co-consolidation technique. During testing, the crack propagation was monitored using frequent intermediate C-Scanning. Numerical simulations were performed using a FE model developed in the LS-Dyna code, where crack initiation and growth at the co-consolidated interface was simulated using the Cohesive Zone Modeling method. Installation parameters were examined for the DAFs with regards to their efficiency. Overall, the numerical study revealed the ability of both the DAFs to retard the crack growth, in contrast to the mechanical tests' results showing limited crack retardation effectiveness of the DAF.*

Keywords: Thermoplastic laminates; Disbond Arrest Features; Manufacturing; Characterization; Numerical Simulation

1. Introduction

The selection of thermoplastic matrix composites as structural materials has shown an increasing trend over the last decades. Their benefits over the more traditional thermosetting composites constitute the reason for this transition [1]. Apart from the ecological point of view, being easily recyclable, the thermoplastic composites generally offer higher fracture toughness properties and more flexible forming and joining capabilities, among others [2].

In the aerospace industry, non-perforative joining designs like adhesive and co-consolidation bonding have been established as effective and efficient ways to connect critical aircraft components, both in metals and in thermoset composites. However, the strict safety rules imposed by the international airworthiness organizations, like the European Union Aviation Safety Agency (EASA), make additional fail-safe design features mandatory in the case of such joining techniques [3]. Crack confinement features must be embedded along the bonded structure in all critical load bearing components. Many researchers have investigated and optimized the installation of crack stoppers, focusing however mainly on thermosetting composite joints [4].

  doi:10.5075/epfl-298799_978-2-9701614-0-0

The ability of thermoplastics to resolidify after melting at a certain temperature offers the potential for implementation welding techniques such as induction welding [5], ultrasonic welding [6], conduction welding [7] or resistance welding [8]. These welding processes all have the unique feature that there is a continuous, homogeneous presence of polymer over the joint interface. In fact, in a proper welded joint, there is no joint area to be identified when inspected under a microscope. Next to that, welding is not critical for surface preparation, mixing quality or curing parameters, as adhesive bonding is. This makes that welded joints are fundamentally different with respect to certification requirements, and basically much easier to certify. This allowed the qualification and certification of welded primary aircraft structures without the use of "chicken rivets" [9]. Still, damage arrest features could further improve the damage tolerance performance of welded joints. Considering the reformable nature of thermoplastics, there is potential for different approaches in the development of crack arresting techniques for these materials.

The present work focused on the investigation of ILSFSR and RFSSW as DAFs which can be installed in both welded and co-consolidated thermoplastic composite joints, with the latter having already been successfully used as a joint for both thermoplastic and metallic materials [10]. The manufacturing stage of the laminates and the concept of the DAFs installation are described, followed by an experimental campaign on mixed mode loaded bonded coupons. Eventually, numerical simulations were held to study further various installation parameters of the DAFs.

2. Manufacturing

The laminates were manufactured from CF/ low-melting PAEK TC1225 UD prepregs provided by Toray, in a quasi-isotropic lay-up. Two plates of 300 mm x 300 mm dimensions were consolidated with a 0.025 mm-thick polyimide (Kapton) insert that was previously coated with release agent LOCTITE® FREKOTE 700NC, in the appropriate position to produce the SLS and CLS coupon configurations (Fig. 1). The co-consolidation procedure was undertaken in a hot platen press at 350 ℃ at 6 bars for 20 min, with 7 ℃/min heating and cooling rate. Finally, the individual coupons were cut to the final dimensions table with a water-cooled circular diamond saw, with their longitudinal direction parallel to the 0 ° fibers.

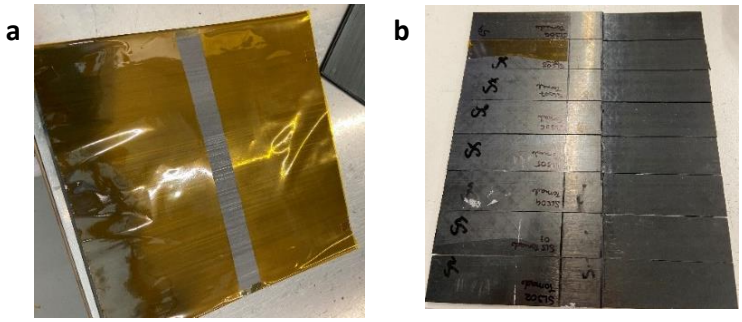

Figure 1 a. Plate before consolidation with the Kapton insert, b. SLS coupons after cutting

2.1 Refill Friction Stir Spot Welding (RFSSW)

RFSSW is a slightly modified technique to the Friction Spot Welding (FSW), employing the use of a multipart rotating tool to melt the material in a spot, preventing the formation of a cavity in the laminate usually referred as "key-hole". The tool is consisted of three coaxial rotating parts serving three different purposes (Fig. 2a). The outer hollow cylinder – clamp exerts downward

pressure to the substrates during the fusion procedure. The middle component – sleeve melts the material through friction, while the pin acts as the refilling mechanism, forcing the melted material to flow towards the center of the spot. This technique has already been studied as a stand-alone joint, however, the embedment of RFSSW as DAF is quite innovative.

This feature was installed in 4 CLS specimens for evaluation purposes in the current study as can be seen in Fig. 2b. Significant parameters were the 9mm diameter of the spot and the distance of the potential DAF's edge from the debonding initiation point, which was set at 10 mm.

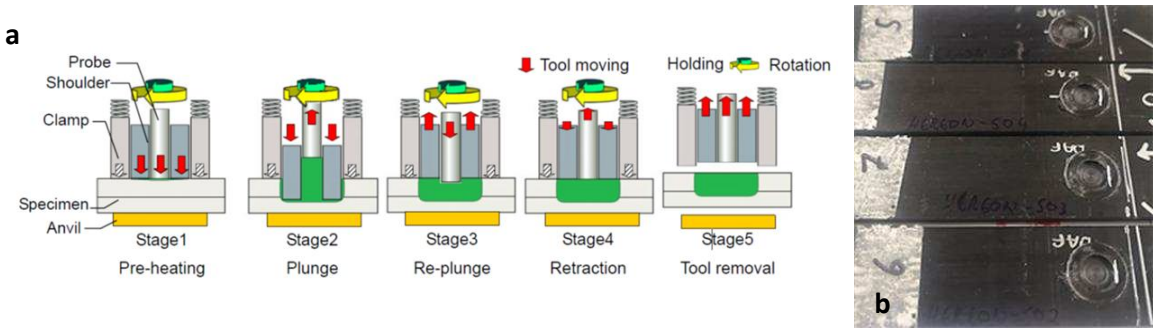

Figure 2 a. RFSSW installation procedure, b. CLS coupons with 9 mm RFSSW DAF

2.2 Induction Low Shear Friction Spot Welding (ILSFSR)

Induction Low-Shear Friction Stir Riveting (ILSFSR) is a KVE-patented approach, in which an end effector comprising an induction coil, a pressurizing body and a mechanism containing the DAF is used (Fig. 3a).

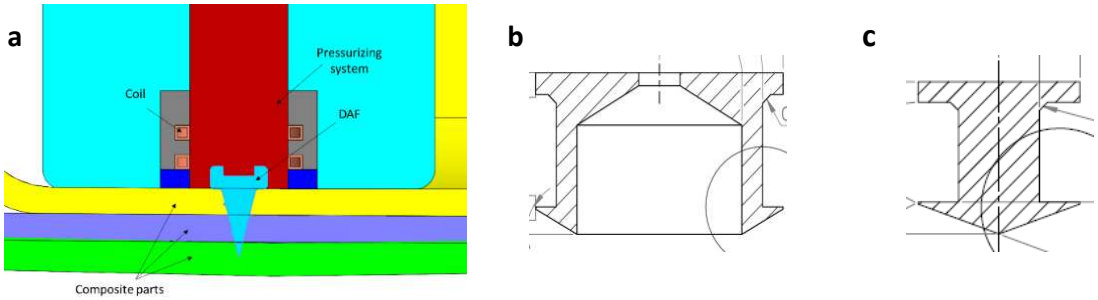

Figure 3 a. Schematic of the ILSFSR installation system b. Hollow DAF design, c. Solid DAF design.

The main principle of this approach is to firstly heat the DAF and the co-consolidated parts to a determined temperature via the electromagnetic field generated by the inductor and subsequently drive the DAF into the heated parts, until a predefined location, perpendicular to the contact surfaces. In this way, a spot-welded connection between the moulded parts that is also reinforced mechanically by the fastener is obtained. Heating of both composite and DAF is expected to i) limit composite damage during the installation, as well as ii) contribute to a dustless installation.

3. Experimental

The mechanical testing procedure of the SLS specimens was conducted in accordance with the ASTM D5868 – 01 standard [11]. The substrates' dimensions were 101.6 mm x 25.4 mm and 2 mm thick, following $[0^o/-45^o/45^o/90^o/45^o/-45^o]_s$ stacking sequence. The substrates had an overlap co-consolidation joined area of 25.4 mm x 25.4 mm. The tests were performed on an MTS Landmark hydraulic testing machine with a capacity in force of 250kN class 1 according to

ISO 7500-1, equipped with hydraulic jaws for regulated clamping during the test and diamond tips to prevent slippage. Loading rate was of 13 mm/min until final rupture. A microscopic fracture surface study was held after the mechanical tests to reveal the type of the substrates' separation.

The CLS coupons were selected to evaluate the efficiency of the DAFs. Thus, 6 reference coupons and 4 coupons with the 9 mm RFSSW DAF were cut in the length of 290 mm (bottom substrate), 230 mm (top substrate – strap), 25 mm wide and 3.6 mm in total thick. Tabs of the same material were installed on the one end of each specimen to ensure proper alignment and absence of unwanted secondary bending phenomena.

In order to monitor the crack propagation in the interface, the test was interrupted at predefined load steps which corresponded to 25%, 50%, 75% and 100% of the critical load. At each pause, C-Scans were performed in all the coupons and the loading procedure was then continued.

4. Finite Element Modelling

Numerical simulations were employed to explore further the capabilities of the 2 DAF designs, studying potentially crucial parameters such as the DAF's diameter alteration and topologies of installation. The FE models were developed in LS-Dyna commercial simulation software [12].

4.1 Damage Modelling

The failure sequence within the laminates, independently of the interface damage, was captured using progressive damage modeling. The LS-Dyna's MAT_162 material model was selected as it has been proven efficient and accurate in modeling interlaminar and intralaminar failure for thermoplastic laminates [13].

The co-consolidation joint's damage behavior was simulated with the Cohesive Zone Modeling technique, employing LS-Dyna's 8-noded solid cohesive elements (ELFORM 19). The most commonly used bi-linear traction-separation law was implemented.

4.3 Modelling of the DAFs

The RFSSW DAF was embedded in the numerical model as a cylindrical FE part, where short fiber composite properties were assigned to replicate the chopped fibers induced by the rotational direction of the processing tool. The micromechanical material model MAT_215 (MAT_4A_MICROMEC), provided by LS-Dyna, was selected to model this DAF, where distinguished material properties for the fibers and the matrix are required. Two diameters were investigated in terms of crack arresting capabilities, namely 6 mm and 9 mm.

The ILSFSR DAF was modeled in similar way as the RFSSW with the exception of the material model for the pin's response, where a simple isotropic elastic model was assigned to simulate the behavior of Stainless-Steel. The interface between the laminates and the metallic pin was assumed to remain the same as the actual co-consolidated joint. In this case two different installation parameters were examined, initiating with the diameter of the ILSFSR pin, set to 3 mm and 5 mm. While two 3 mm pins inserted in the laminates simultaneously in two different

topology configurations, were also a part of the simulation plan. The double pins were investigated positioned in row to the crack tip as well as side to side.

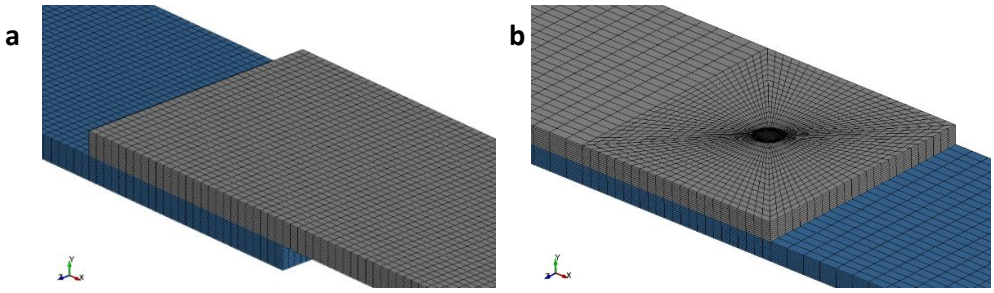

Figure 4. SLS typical FE mesh, b. CLS coupon with DAF typical FE mesh

5. Results

5.1 Experimental

The load-displacement curves obtained for the SLS mechanical tests are depicted in Fig. 5a. The first two coupons slipped from the grips during loading, and thus excluded from the final results. Overall, the curves show a very homogenous behavior, mostly linear, of the six SLS specimens. The load of rupture varied between 16 kN and 17 kN, while their stiffness was virtually the same.

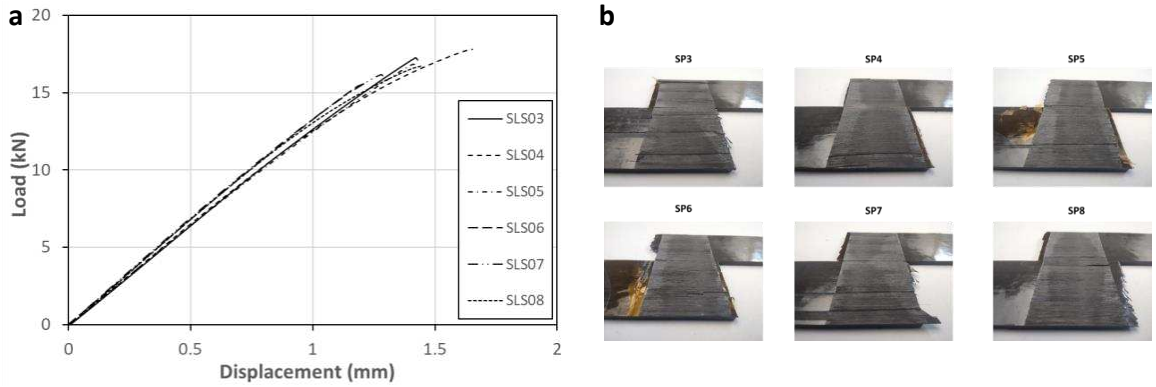

Figure 5. SLS experimental Load-Displacement curves, b. SLS fractured surfaces

In Fig. 6a, b the experimental load-displacement curves for both the reference CLS specimens and the 9 mm RFSSW DAF are presented.

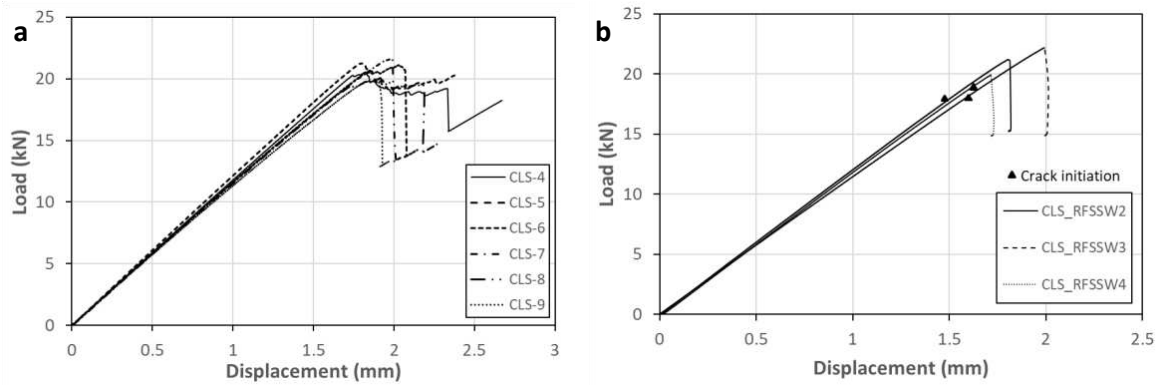

Figure 6 a, b. Experimental Load-Displacement curves for a. reference CLS, b. CLS with 9 mm RFSSW DAF

  doi:10.5075/epfl-298799_978-2-9701614-0-0

Regarding the reference CLS specimens, the response was quite close throughout the whole testing procedure. The crack propagation load variated between 20 kN and 21 kN. As for the coupons with the DAF installed a slight decrease in the crack initiation load can be noticed for the 3 tested coupons (around 18 kN). The peak of those curves shows the load where the crack propagates past the DAF and the variance is more important (20 kN to 23 kN).

In Fig. 7a, the images captured from the c-scanning during the loading-unloading procedure at the predefined load steps, are shown. It is clear that the crack showed the first noticeable initiation at about 15 kN while after the final failure (>20 kN) the crack propagated rapidly past the DAF. In Fig. 7b the fracture surfaces of the 3 CLS coupons with the 9 mm RFSSW DAF indicate the presence of the crack trace behind the DAF, most visible in the middle coupon (CLS_RFSSW3), which also resulted in the highest crack retardation.

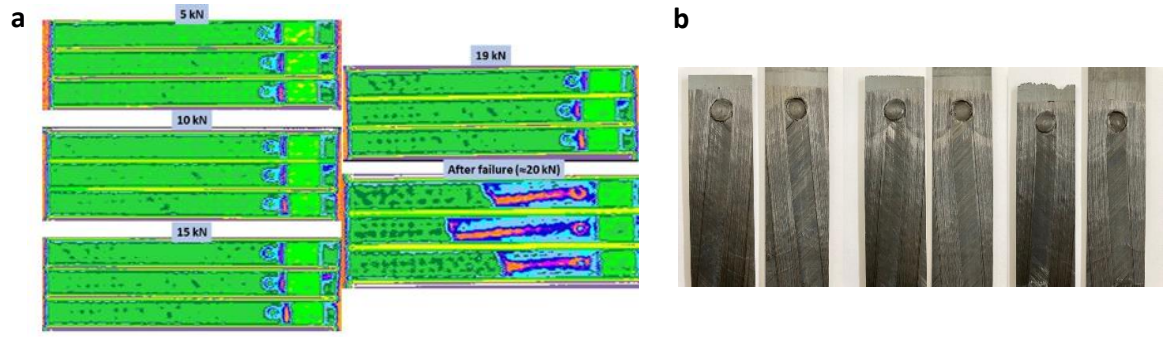

Figure 7. CLS coupons C-Scan images after each loading step, b. CLS final fractured surfaces

5.2 Numerical

Fig. 8a indicates the comparison between a typical experimental and the numerical load-displacement curve. Even though the stiffness is in good agreement, the rupture load is distinctively different. This difference is probably present due to the high amount of fiber bridging and interlaminar damage of the coupons tested, as shown from the fracture surface study (fig. 5b). The curve contains the interaction of both the joint and laminates' damage.

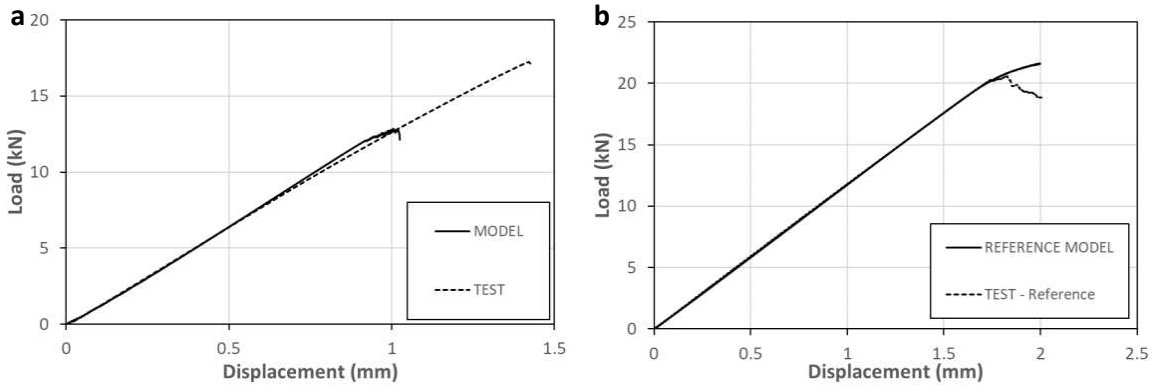

Figure 8. Numerical & experimental Load-Displacement curves for a. SLS, b. CLS

On the other hand, the numerical results for the reference CLS specimens come in good agreement with the test results. Both the stiffness and the crack initiation load are approximated quite well. This also can confirm the latter hypothesis about the large variance between the SLS

experimental and numerical rupture load, as the CLS coupons didn't show evidence of large-scale fiber bridging and thus the numerical model appears to be well calibrated.

The rest of the numerical simulation results concern the response of the CLS coupon, where different configurations of the two DAFs are examined. In Fig. 9a the numerical responses of the CLS are depicted for the two diameters considered (6 mm & 9 mm). The increment of the diameter results in obvious enhancement of the crack arresting capability, with the critical load for the crack to overcome the DAF, increases from 22 kN to 25 kN.

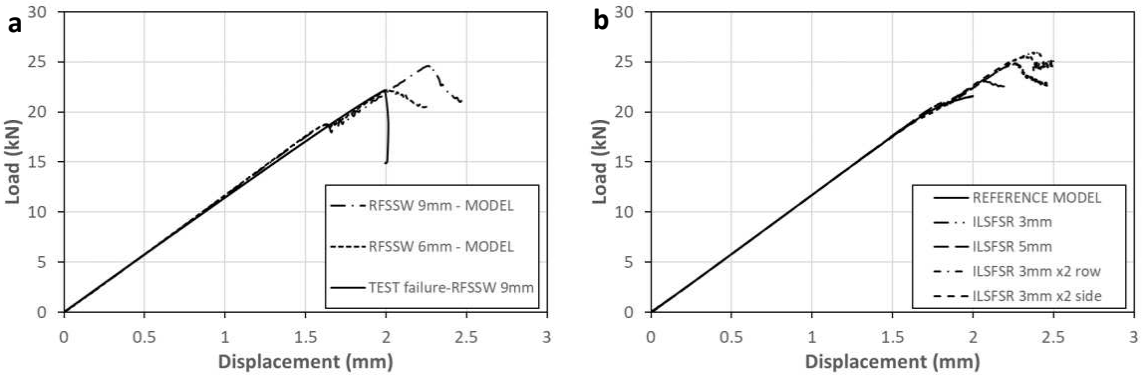

Figure 9. Numerical Load-Displacement curves for the studied parameters of a. RFSSW, b. ILSFSR

In the same principle, the larger the diameter of the ILSFSR pin the greater the DAF efficiency as shown in Fig. 9b. In this case though, the best results were obtained by the configuration where two pins were embedded simultaneously into the laminates in row, showing a critical load of about 26 kN.

5. Conclusions

In this work, manufacturing, experimental and numerical aspects of the RFSSW and ILSFSR techniques' implementation as DAFs in thermoplastic joints were described. The dustless installation provided by both these two novel processes gives the potential to be used quite efficiently in thermoplastic joints, though further study on their optimization is required.

The experimental results showed that the RFSSW in the studied configuration didn't manage to provide great crack retardation effectiveness. The two out of the three tested coupons failed at similar critical load as the reference specimens. This fact can arise from the quasi-static nature of the mechanical testing the DAF was submitted to. Previous studies have shown that in a more realistic approach, where the coupons are tested in fatigue, crack stoppers can behave much more efficiently [14].

Regarding the numerical simulation of the DAFs' behavior, the model developed appeared to approximate the testing results in a good degree. Apart from the SLS results' discrepancy, the CLS model proved to be a valuable tool for the evaluation of the DAFs' effectiveness. As accruing from the simulations, the diameters of both ILSFSR pins and RFSSW spots resulted as the most crucial parameters regarding their crack arresting capability. Moreover, the installation of multiple DAFs should also result in the enhancement of load bearing prior to crack propagation.

  doi:10.5075/epfl-298799_978-2-9701614-0-0

Acknowledgements

The present study was conducted in the frame of the European research project TORNADO Clean Sky 2: "Innovative Disbond Arrest Features for Long Thermoplastic Welded Joints" (Grant Agreement No.: 101007494). Partners: RESCOLL, KVE Composites Group and University of Patras. Topic Manager: GKN Fokker

Refill Friction Stir Spot Welding (RFSSW) is a patented thermoplastic joining technique by Helmholtz-Zentrum Hereon, Germany. The RFSSW DAF was installed by the Helmholtz-Zentrum Hereon.

References

1. Pantelakis S, Tserpes K, editors. Revolutionizing Aircraft Materials and Processes. Springer International Publishing; 2020. http://link.springer.com/10.1007/978-3-030-35346-9
2. Obande W, Mamalis D, Ray D, Yang L, Ó Brádaigh CM. Mechanical and thermomechanical characterisation of vacuum-infused thermoplastic- and thermoset-based composites. Materials & Design. 2019 Aug;175:107828.
3. Tserpes KI, Peikert G, Floros IS. Crack stopping in composite adhesively bonded joints through corrugation. Theoretical and Applied Fracture Mechanics. 2016 Jun;83:152–7.
4. Jeevan Kumar N, Ramesh Babu P. Analysis of Mode I and Mode II Crack Growth Arrest Mechanism with Z-Fibre Pins in Composite Laminated Joint. Appl Compos Mater. 2018 Apr;25(2):365–79.
5. Bach M, Labordus M. Qualification approach for induction welding of thermoplastic composites using UD-based materials. Webinar from Composites World; 2020 Nov 12. https://www.compositesworld.com/events/details/4f01d7a8-dabc-440e-b0b5-f64400356c78
6. Palardy G, Fernadez Villegas I. Smart ultrasonic welding of thermoplastic composites. In: Proceedings of the American Society for Composites - 31st Technical Conference. ASC 2016 DEStech Publications Inc.
7. Doldersum M, Offringa A, Teunissen J, Van Ingen JW. Conduction welding, Fokker Aerostructures BV.
8. Doldersum M. Welding technologies for thermoplastics, development and production. 2018 Apr 11; SAMPE Benelux.
9. Ingen J van, Wijngaarden M van, Buitenhuis A, Simmons F. Development of the Gulfstream G650 induction welded thermoplastic elevators and rudder. In 2010.
10. Huang Y, Meng X, Xie Y, Lv Z, Wan L, Cao J, et al. Friction spot welding of carbon fiber-reinforced polyetherimide laminate. Composite Structures. 2018 Apr;189:627–34.
11. D14 Committee. Test Method for Lap Shear Adhesion for Fiber Reinforced Plastic (FRP) Bonding. ASTM International. http://www.astm.org/cgi-bin/resolver.cgi?D5868-01R14
12. Hallquist JO, editor. LS-DYNA: theory manual. Livermore, Calif: Livermore Software Technology Corp; 2006.
13. Sioutis I, Tserpes K. A numerical evaluation of various damage models for thermoplastic composite materials subjected to quasi-static tensile loading. Pantelakis S, Lampeas G, Tserpes K, editors. MATEC Web Conf. 2021;349:01002.
14. Floros I, Tserpes K. Numerical simulation of quasi-static and fatigue debonding growth in adhesively bonded composite joints containing bolts as crack stoppers. The Journal of Adhesion. 2021 May 19;97(7):611–33.

FINITE ELEMENT ANALYSIS OF THICK CARBON COMPOSITE LAMINATES SUBJECTED TO LOW-VELOCITY IMPACT LOADS

Dongkuk Choi[a], Kyeonghan Lee[a], Seonwoo Byun[a], Sooyong Lee[a], Cheolju Lee[b]

a: Korea Aerospace University – dkchoi@kau.ac.kr/leesy@kau.ac.kr
b: Korea Aerospace Industry, LTD.

Abstract: *This paper deals with a numerical analysis for thick carbon composite laminates under low-velocity impact loads. The numerical studies have been carried out to predict the damaged area of composite laminates subjected to low-velocity impact loads. The composite laminates were modelled to shell elements with a 3-D strain-based interactive failure theory. The strain-based failure theory proposed in this paper was developed as a material model using a user-defined subroutine in commercial numerical solver. The material model had stiffness degradation modes based on individual failure modes of the maximum strain failure criteria. Several material models built in the commercial software were also employed to compare the accuracy of the proposed failure model. Finally, the proposed numerical model was predicted well the damaged area of thick composite laminates subjected to low-velocity impact loads.*

Keywords: Composite Materials; Failure Theory; Damage Prediction; Impact Analysis;

1. Introduction

Composite materials and structures generally sustain complex static loads as well as impact loads. Especially, composite laminates subjected to low-velocity impact loading suffer from several types of damage, such as delamination, fiber fraction, and matrix cracking. These damages are invisible and difficult to detect. Composite laminates damaged by impact loads are reduced in strength as well as stiffness.

Predicting the damage of composite laminates is important to estimate the reduction in strength and stiffness. To predict the damage, numerical analysis has commonly been used. Shah et al. [1] investigated previous research predicting the damage area of composite laminates subjected to low-velocity impact. Those previous researchers conducted numerical studies applying several failure theories as well as considered various modeling methods. Liu et al. [2] studied differences in accuracy between the three failure theories which were Puck, Hashin, and Chang-Chang criteria. They concluded that the numerical error from using Chang-Chang failure criteria was larger than the other two failure criteria because it did not include out-of-plane shear effects. Hashin criteria have been widely used to solve the impact problem because not only are its formulas simple but it also represents good results [3, 4].

The modeling method is also important to reduce the computing time for predicting the damaged area of composite laminates under low-velocity impact loading. Soto et al. [5] investigated a methodology to simulate large composite stiffened panels subjected to low-velocity impact comparing a shell element model and a solid element model. According to the paper, the conventional shell element model was lower accuracy than that of the solid element model on the low-velocity impact prediction because out-of-plane stress was neglected. Thus, it is important to consider out-of-plane stress for damage predictions in thick ply laminates.

1017/1045 doi:10.5075/epfl-298799_978-2-9701614-0-0 published under CC BY-NC 4.0 license ToC

In order to predict the damaged area of thick composite laminates under low-velocity impact loads, this paper deals with a numerical analysis model that can increase the accuracy developing a material model with both a 3-D strain-based interactive failure theory and stiffness degradation modes. The failure theory proposed in this paper considers out-of-plane strains to better reflect real-world results. The material model is deployed in the user-defined subroutine of the commercial solver. Several materials models built-in the commercial software are also employed to compare with the proposed failure model. Finally, it is confirmed that the proposed numerical model well predicts the damaged area of thick composite laminates subjected to low-velocity impact loads.

2. Material model

2.1 Failure Model

A failure model for composite materials was developed to improve the accuracy of shell elements for composite laminates subjected to low-velocity impact loads. The failure theory of Lee and Roh [6] was employed to the failure model. The theory is a 2-D strain-based interactive failure criteria which is expressed as follows:

$$F_{11}\varepsilon_1^2 + F_1\varepsilon_1 + \alpha_2(F_{22}\varepsilon_2^2 + F_2\varepsilon_2) + F_{66}\varepsilon_6^2 = 1 \tag{1}$$

$$F_{11} = \frac{1}{\varepsilon_1^T \varepsilon_1^C} \tag{2}$$

$$F_1 = \frac{1}{\varepsilon_1^T} - \frac{1}{\varepsilon_1^C} \tag{3}$$

$$F_{22} = \frac{1}{\varepsilon_2^T \varepsilon_2^C} \tag{4}$$

$$F_2 = \frac{1}{\varepsilon_2^T} - \frac{1}{\varepsilon_2^C} \tag{5}$$

$$F_{66} = \frac{1}{\varepsilon_S^2} \tag{6}$$

$$\alpha_2 = \frac{U_2}{U_1} = \frac{E_2 {\varepsilon_2^T}^2}{E_1 {\varepsilon_1^T}^2} \tag{7}$$

where F_{ii} and F_i indicate tensor quantities of the strength parameter. ε_1 is normal strain the in longitudinal direction and ε_2 is normal strain in the transverse direction. ε_6 is in-plane shear strain. ε_i^T are ultimate tensile strains in the normal direction. ε_i^C are ultimate compressive strains in the normal direction. ε_S is in-plane failure shear strain. The parameter α_2 is a ratio of tensile failure strain energy density in transverse and longitudinal directions; U_1 and U_2 represent longitudinal and transverse failure strain energy densities, respectively.

The 2-D failure theories for composite material such as the maximum strain failure criteria, Tsai-Wu, Chang-Chang failure, Hashin's 2-D failure, etc. including Eq. (1) have showed good static analysis results. However, the 2-D failure theories do not represent good prediction results in impact loading problems compared with 3-D failure theories. This is because the 2-D failure theories were not considered out-of-plane deformation effects [7, 8] which can be neglected in static analysis with small deformation, but not with impact behaviors.

1018/1045 ©2022 Lee et al. doi:10.5075/epfl-298799_978-2-9701614-0-0 published under CC BY-NC 4.0 license

The failure theory in Eq. (1) can be expanded to a 3-D strain-based interactive failure criterion considering the out-of-plane normal strain ε_3 as well as the out-of-plane shear strains ε_4 and ε_5. The 3-D failure criterion is expressed as:

$$F_{11}\varepsilon_1^2 + F_1\varepsilon_1 + \alpha_2(F_{22}\varepsilon_2^2 + F_2\varepsilon_2) + F_{66}\varepsilon_6^2 + \alpha_3(F_{33}\varepsilon_3^2 + F_3\varepsilon_3) + F_{44}\varepsilon_4^2 + F_{55}\varepsilon_5^2 = 1 \quad (8)$$

$$F_{33} = \frac{1}{\varepsilon_3^T \varepsilon_3^C} \quad (9)$$

$$F_3 = \frac{1}{\varepsilon_3^T} - \frac{1}{\varepsilon_3^C} \quad (10)$$

$$F_{44} = \frac{1}{\varepsilon_Q^2} \quad (11)$$

$$F_{55} = \frac{1}{\varepsilon_R^2} \quad (12)$$

$$\alpha_3 = \frac{U_3}{U_1} = \frac{E_3 {\varepsilon_3^T}^2}{E_1 {\varepsilon_1^T}^2} \quad (13)$$

where ε_Q and ε_R are two out-of-plane failure shear strains. The parameter α_3 is a ratio of tensile failure strain energy density in out-of-plane and longitudinal directions; U_3 represents out-of-plane failure strain energy densities.

2.2 Stiffness degradation modes

The 3-D failure theory in Eq. (8) has stiffness degradation modes based on individual failure modes of the maximum strain failure criteria which are expressed as:

- Longitudinal stiffness degradation mode:

$$F_{11}\varepsilon_1^2 + F_1\varepsilon_1 = 1 \ (or\ \varepsilon_1^C < \varepsilon_1 < \varepsilon_1^T) \quad (14)$$

- Transverse normal stiffness degradation mode:

$$F_{22}\varepsilon_2^2 + F_2\varepsilon_2 = 1 \ (or\ \varepsilon_2^C < \varepsilon_2 < \varepsilon_2^T) \quad (15)$$

- Out-of-plane normal stiffness degradation mode:

$$F_{33}\varepsilon_3^2 + F_3\varepsilon_3 = 1 \ (or\ \varepsilon_3^C < \varepsilon_3 < \varepsilon_3^T) \quad (16)$$

- In-plane shear stiffness degradation mode:

$$F_{66}\varepsilon_6^2 = 1 \ (or\ |\varepsilon_6| < \varepsilon_S) \quad (17)$$

- Out-of-plane shear stiffness degradation mode:

$$F_{44}\varepsilon_4^2 = 1 \ (or\ |\varepsilon_4| < \varepsilon_Q) \quad (18)$$

- Another out-of-plane shear stiffness degradation mode:

$$F_{55}\varepsilon_5^2 = 1 \ (or\ |\varepsilon_5| < \varepsilon_R) \quad (19)$$

Equation (8) can be described again as the combination of Eqs. (14)-(19). The 3-D failure theory and stiffness degradation modes are easily applicable for a failure prediction of composite

  doi:10.5075/epfl-298799_978-2-9701614-0-0

because the equations are simpler than other failure theories, such as the Hashin's 3-D failure criteria and Puck's failure criteria.

2.3 Material properties and behavior

The material used in this paper was unidirectional carbon composite IM7/977-3. The material properties are listed in Table 1. The behaviors in the normal direction were considered linear, but the shear behaviors were considered nonlinear. Considering the nonlinear shear behavior, the Ramberg-Osgood equation [9] was used for the tangential shear moduli G_{12} and G_{13}. The equation is expressed as:

$$G_{12} = \frac{d\sigma_6}{d\varepsilon_6} = \frac{G_o}{\left(1+\left(\frac{G_o\varepsilon_6}{\sigma_o}\right)^n\right)^{1+1/n}} \tag{20}$$

$$G_{13} = \frac{d\sigma_5}{d\varepsilon_5} = \frac{G_o}{\left(1+\left(\frac{G_o\varepsilon_5}{\sigma_o}\right)^n\right)^{1+1/n}} \tag{21}$$

where G_o is the initial shear modulus, σ_o is the asymptotic stress level, and n is a shape parameter for the stress and strain curve. The curve fitting result was presented in Fig. 1. The parameters G_o, σ_o, and n used in this paper were 5.15 GPa, 102 MPa, and 2.216, respectively.

3. Low-velocity impact analysis

3.1 Finite element model

The finite element model was composed of a composite laminate and an impactor as shown in Fig. 2. The thick composite laminate was modeled as layered shell elements in CQUAD4. The shell elements had a stacking sequence of the composite laminate. The layup pattern was $[45/-45/0/0/90/0/0/45/-45/0]_{3S}$, which is 60-ply laminate. The size of the laminate was 305 mm in length, 254 mm in width, and 7.95 mm in thickness. The impactor was modeled as solid element CTETRA. The properties of steel were used for the solid element. The tip diameter of the impactor was 10 mm. The boundary condition that was applied simply supported conditions near the edge of the laminate as shown in Fig. 2. The initial velocity of impactor applied was 4.68 m/s.

3.2 Analysis results

The impact analyses were conducted considering several failure theories: the maximum stress failure, the maximum strain failure, and the proposed failure in Eq. (8). Material models from the commercial solver, which is based on Chang-Chang failure criteria, were also employed for comparison. In addition, an experimental result was presented to verify the analysis results.

The numerical and the experimental results are presented in Fig. 3 and Fig. 4. The numerical results using 2D failure theories based on stress well predicted the damaged area, as shown in Fig. 3(a)-(c), compared with the experimental result in Fig. 3(h). However, the impactor behavior was not predicted as shown in Fig. 4(a). The 2D maximum strain failure also failed to estimate both the damaged area and the impactor behavior.

The numerical results based on 3D failure theories well predicted the damaged area represented in Fig. 3(e)-(g). Furthermore, the estimations of the impactor behavior showed relatively good results compared with the 2D based failure theories as shown in Fig. 4(b). The damaged area

  doi:10.5075/epfl-298799_978-2-9701614-0-0 published under CC BY-NC 4.0 license

estimated by the maximum stress and strain failure were larger than the experimental result, whereas the those of the proposed failure were similar to the experimental result. Therefore, it can be concluded that the proposed material model with the 3D strain-based interactive failure theory provides more accurate prediction results.

Table 1: Materials properties of IM7/977-3.

Modulus (GPa)		Strength (MPa)		Failure strain (%)	
E_1	165	X_T	2920	ε_1^T	1.629
E_2	9.25	X_c	1442	ε_1^C	0.901
E_3	9.25	Y_T	68.7	ε_2^T	0.761
G_{12}	5.15	Y_C	258	ε_2^C	1.993
G_{23}	2.49	Z_T	68.7	ε_3^T	0.761
G_{13}	5.15	Z_C	258	ε_3^C	1.993
v_{12}	0.3	S	95.7	ε_S	5.0
v_{23}	0.3	Q	29.4	ε_Q	1.211
v_{13}	0.3	R	95.7	ε_R	5.0

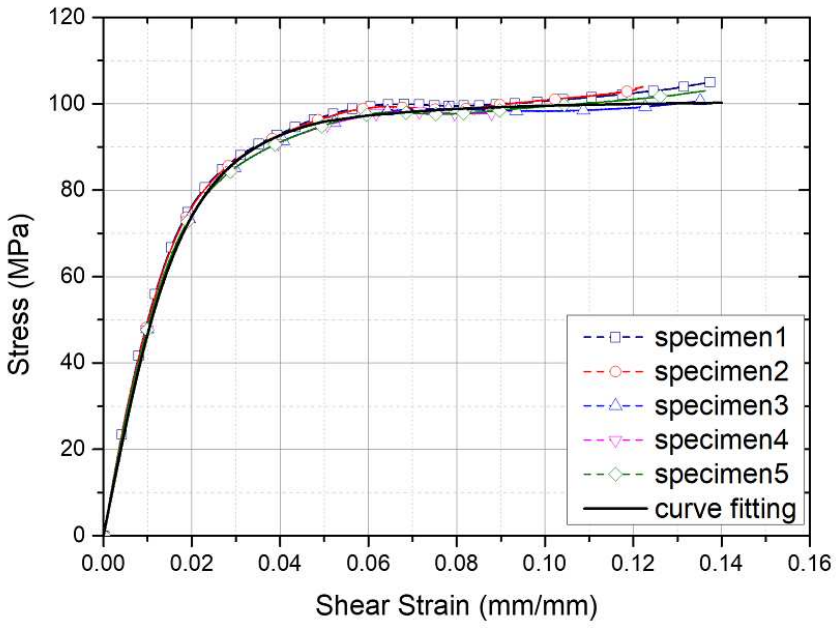

Figure 1. Curve fitting result of in-plane shear stress-strain

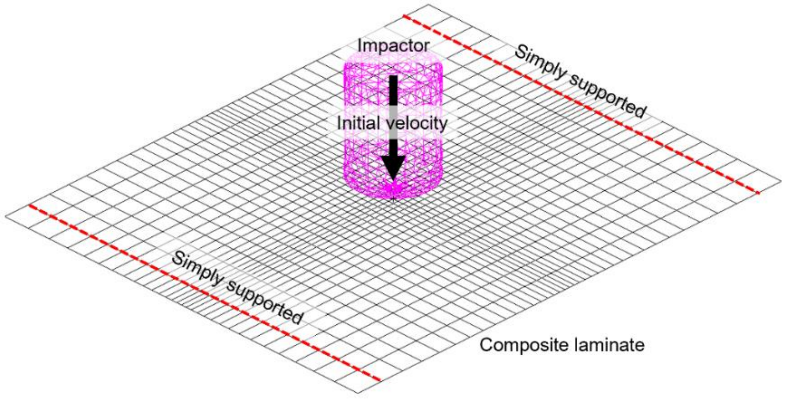

Figure 2. Finite element model for a low-velocity impact analysis

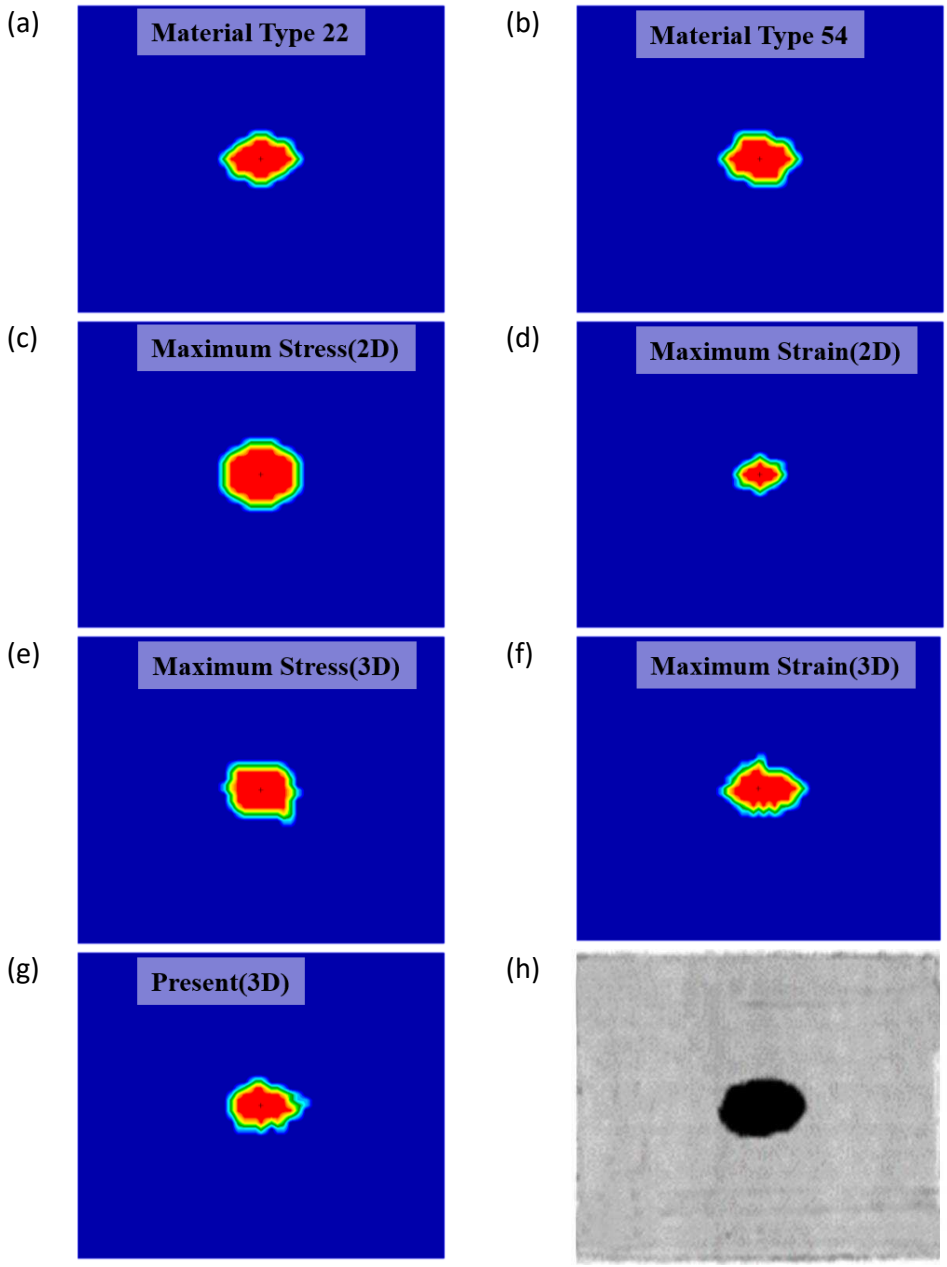

Figure 3. Damaged area prediction results of the 60-ply laminates

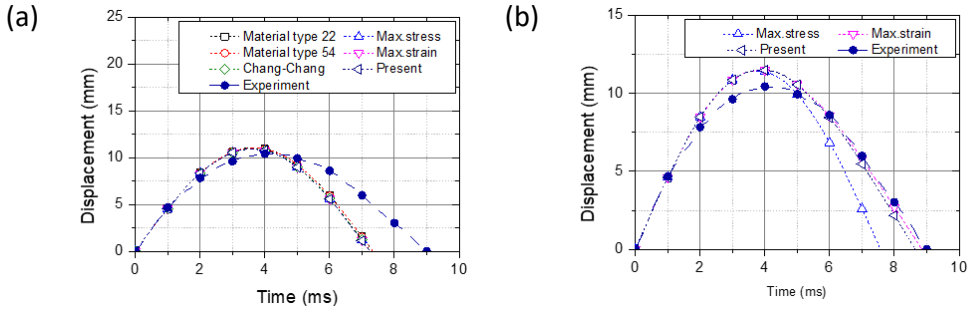

Figure 4. Impactor displacement prediction results: (a) 2D failure, (b) 3D failure

4. Conclusions

The finite element analysis of composite laminates subjected to low-velocity impact loads was investigated. To predict the damaged area, the proposed material model for composite laminates was developed using a user-defined subroutine. The 3D strain-based interactive failure theory and its stiffness degradation modes were employed in the material model. The numerical analysis result well predicted the damaged area compared with the experimental results. In addition, the proposed failure theory presented better results in the impactor behavior than other failure criteria. Therefore, it should be concluded that the proposed materials model with the 3D strain-based interactive failure theory provides better prediction results.

Acknowledgements

This work was supported under the Technology Innovation Program (No. 20011708) funded by the Ministry of Trade, Industry & Energy (MOTIE, Korea)

References

1. S.Z.H. Shah, S. Karuppanan, P.S.M. Megat-Yusoff, Z. Sajid. Impact resistance and damage tolerance of fiber reinforced composites: A review. Composite Structures. 2019; 217:100-121.
2. P.F. Liu, B.B. Liao, L.Y. Jia, X.Q. Peng. Finite element analysis of dynamic progressive failure of carbon fiber composite laminates under low velocity impact. Composite Structures. 2016; 149:408-422.
3. Ali Kursun, Mehmet Senel, and Halil M. Enginsoy. “Experimental and numerical analysis of low-velocity impact on a preloaded composite plate.” Advances in Engineering Software. 2015; 90:41-52.
4. Shivdayal Patel and C. Guedes Soares. “System probability of failure and sensitivity analyses of composite plates under low velocity impact.” Composite Structures. 2017; 180:1022-1031.
5. A. Soto, E.V. González, P. Maimí, J.A. Mayugo, P.R. Pasquali, and P.P. Camanho. “A methodology to simulate low velocity impact and compression after impact in large composite stiffened panels.” Composite Structures. 2018; 204:223-238.

  doi:10.5075/epfl-298799_978-2-9701614-0-0

6. Soo-Yong Lee, Jin-Ho Roh. Two-dimensional strain-based interactive failure theory for multidirectional composite laminates. Composite: Part B. 2015; 69:69-75.
7. Eun-Ho Kim, Mi-Sun Rim, In Lee, Tae-Kyung Hwang. Composite damage model based on continuum damage mechanics and low velocity impact analysis of composite plates. Composite Structures. 2013;95:123.134.
8. Yavuz Basar and Yunhe Ding. “Interlaminar stress analysis of composites: Layer-wise shell finite elements including transverse strains.” Composites Engineering. 1995; 5(5):485-499.
9. Travis A. Bogetti, Christopher P.R. Hoppel, Vasyl M. Harik, James F. Newill, Bruce P. Burns. Predicting the nonlinear response and progressive failure of composite laminates. Composites Science and Technology. 2004; 64:329-342.

  doi:10.5075/epfl-298799_978-2-9701614-0-0

PREDICTION OF ELASTIC PROPERTIES OF CERAMIC FOAM BY CREATING ARTIFICIAL MICROSTRUCTURES STATISTICALLY EQUIVALENT TO THE REAL ONE

Romana, Piat[a], Vinit Vijay, Deshpande[b]

a: Department of Mathematics and Natural Sciences, University of Applied Sciences Darmstadt, Schöfferstraße 3, Darmstadt 64295, Germany – romana.piat@h-da.de
b: Department of Mathematics and Natural Sciences, University of Applied Sciences Darmstadt, Schöfferstraße 3, Darmstadt 64295, Germany

Abstract: *The work describes an artificial microstructure reconstruction algorithm for ceramic foam material and its validation by calculating effective elastic properties. Firstly, the microstructure of a real foam sample obtained through microtomographic images is characterized by calculating statistical correlation functions. This is followed by development of a novel artificial microstructure reconstruction algorithm. It is an optimization-based algorithm in which the microstructure of the material is perturbed by changing location of the spherical pores within the foam till the correlation functions of perturbed microstructure match to those of the target microstructure. The choice of initial microstructure and the method of perturbation makes this algorithm unique and highly efficient. Effective elastic properties from both real and reconstructed microstructures are calculated through finite element simulations. The results are compared with experimental measurements to verify the accuracy of the reconstruction algorithm.*

Keywords: Ceramic foam, Elastic properties, Finite element analysis, Microstructure characterization, Reconstruction algorithm.

1. Introduction

Ceramic foams are peculiar materials that are used in a wide variety of high temperature and energy absorption applications due to their light weight, high strength and low thermal expansion. Further, these properties do not deteriorate at high temperatures. The shape and size distribution of the porous features within the foam microstructure control the behavior of this material. This provides an opportunity to extract desired behavior from the material by designing the microstructure accordingly. With this eventual goal in mind, this article studies the microstructure of a real foam material followed by development of an artificial microstructure reconstruction algorithm that can be used to generate variations of the microstructure in different shapes and sizes.

Statistical correlation functions have been extensively used to characterize the microstructure of random heterogeneous materials. [1,2] described in detail the variety of n-point correlation functions that can be used to define distribution of phases within the multiphase materials. This article calculates such correlation functions for the microstructure in question and utilize them in the microstructure reconstruction algorithm developed later.

  doi:10.5075/epfl-298799_978-2-9701614-0-0

In the next step, a microstructure reconstruction algorithm has been developed to create artificial microstructures statistically equivalent to the real ones. Review article [3] describes in detail the entire spectrum of microstructure reconstruction methods available ranging from those based on traditional optimization techniques to ones developed from machine learning and pattern recognition algorithms. The method developed in this article is inspired from Yeong-Torquato method [4] and takes advantage of the typical microstructure of the foam material to accelerate the reconstruction process.

The microstructures derived from the real material sample and from the reconstruction algorithm are utilized to determine effective linear elastic properties by applying mixed uniform boundary conditions [5] to the finite element models of these microstructures. The results are then compared with the experimental results available in [6] to verify the accuracy of the developed methods.

2. Microstructure characterization

A series of grayscale 2D images of cross-sections of a ceramic foam sample obtained through microtomography scanning were used as an input in this research. Detailed description of the material and the scanning parameters can be found in [6]. The grayscale images were stacked one on top of the other and binarized to obtained a 3D binary image as shown in Fig.1a. The black color region indicates pores and the white color region is ceramic material. In order to study shape of the individual pores in the microstructure, the pores were segmented using watershed algorithm. Sphericity ψ as defined in Eq. (1) was calculated for each segmented pore to determine how close the shape of each pore is to a sphere. Note that $\psi = 1$ indicate perfect sphere. V_p indicates volume of the pore and A_p indicates its surface area.

$$\psi = \frac{\pi^{1/3}\left(6V_p\right)^{2/3}}{A_p} \tag{1}$$

In Fig. 1b pore volume fraction indicates volume of a particular pore with respect to that of all the pores present in the material sample. Fig. 1b shows that all the pores have sphericity greater than 0.75. Also, 10 % of the pores have sphericity below 0.84, which means remaining 90 % of the pores have sphericity greater than 0.84.

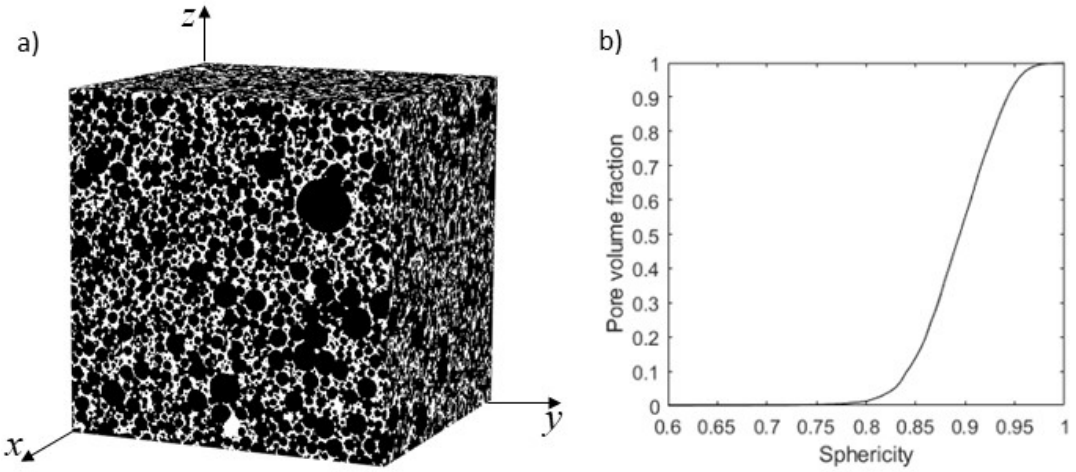

Figure 1. a) 3D binary image of foam microstructure; b) Graph of pore volume fraction versus sphericity ψ.

1026/1045 ©2022 Piat et al. doi:10.5075/epfl-298799_978-2-9701614-0-0 published under CC BY-NC 4.0 license

Four statistical correlation functions namely: 2-point correlation function, 2-point cluster correlation function, lineal path function and cumulative pore size distribution function were calculated for the entire foam sample (microstructure before segmentation). 2-point correlation function defines probability of occurrence of 2 points separated by a certain distance lying in the same phase of interest. 2-point cluster correlation function defines probability of occurrence of 2 points separated by a certain distance lying in the same connected region of the phase of interest. Lineal path function defines probability of occurrence of an entire line segment of a certain length lying in the phase of interest. Cumulative pore size distribution function defines probability of occurrence of a sphere of a certain radius lying entirely in the phase of interest. Detailed description of each of these functions along with the methods to calculated them have been described in [1]. The plots of these functions are shown in Fig. 2a-c.

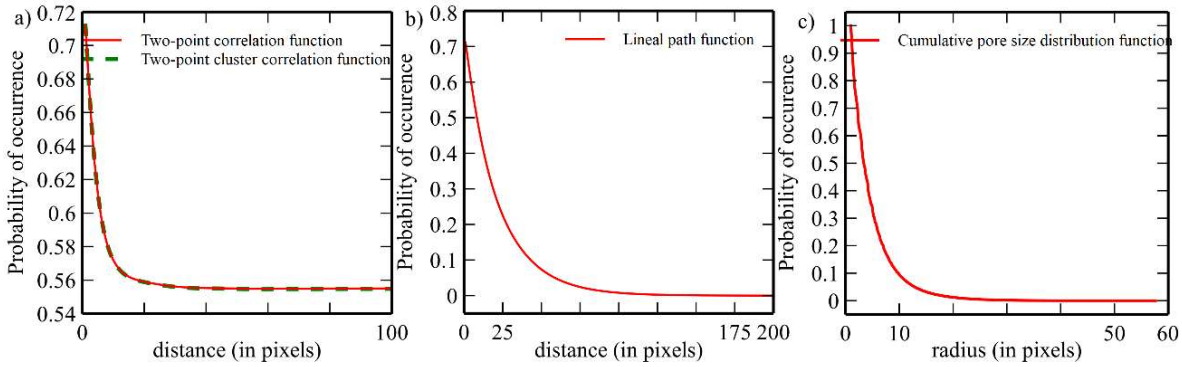

Figure 2. a) Two-point correlation function and Two-point cluster correlation function; b) Lineal path function; c) Cumulative pore size distribution function of the foam sample.

3. Microstructure reconstruction

Numerical creation of artificial microstructures is a fast and cost-effective way of studying the effect of microstructural features on the effective material properties. Large number of equivalent microstructures can be created so as to derive statistically acceptable results without resorting to extensive manufacturing of such samples. Yeong-Torquato [4] developed one of the mostly widely used microstructure reconstruction method. It is an optimization-based method in which the microstructure is represented as a 2D/3D image. An initial microstructure is assumed as a random distribution of black and white pixels (in case of two-phase system). In each iteration, the pixels of opposite color are switched and statistical correlation functions of the iterated microstructure are calculated. The iterations are continued till the statistical functions of the iterated microstructure match to that of the target microstructure. This process is robust as it starts with just the information of volume fraction of phases but is generally extremely time- consuming [7] as it takes tens of thousands of iterations to achieve optimum.

In this work, the peculiar microstructure of the ceramic foam was leveraged by selecting the initial microstructure for the optimization process as random distribution of spheres in a blank 3D space instead of random distribution of pixels. Since it was observed in Fig. 1b that most of the pores are almost spherical in shape this assumption is acceptable. The radius of each sphere was obtained from the size distribution of pores of the real foam microstructure after segmentation (refer Fig. 3a). Fig. 3b shows a single 2D slice of the real microstructure with pores replaced by spheres (circles in the 2D image).

1027/1045 ©2022 Piat et al. doi:10.5075/epfl-298799_978-2-9701614-0-0 published under CC BY-NC 4.0 license

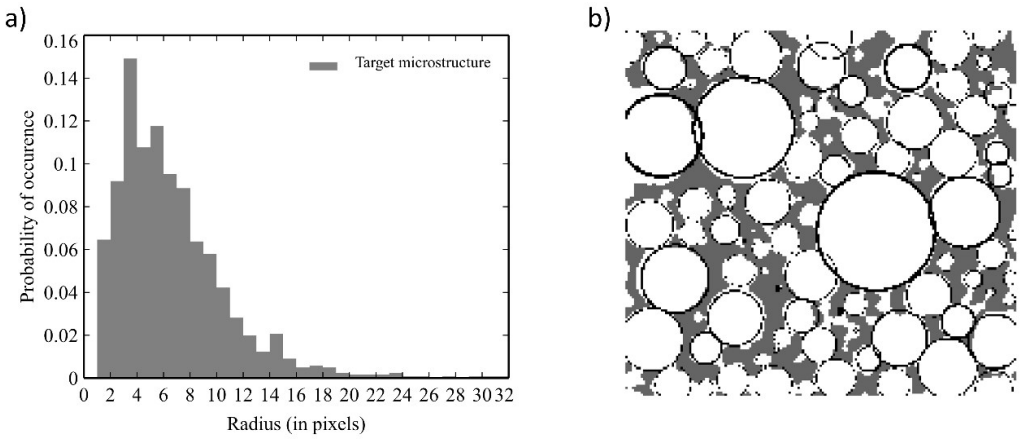

Figure 3. a) Size distribution of pores in real foam microstructure; b) 2D slice of the microstructure image with dark circles as approximated pores

The statistical functions shown in Fig.2a-b were chosen as target statistical functions. In each iteration, the microstructure was perturbed by selecting a random number of spheres and changing their location randomly by placing their centers in the region occupied by the solid phase. The volume fraction in each iteration was maintained constant by adding or removing the spheres from the system. Then, statistical functions were calculated followed by calculation of an energy functional, E as defined in Eq. (2).

$$E = \sum_r \sum_\alpha \left[f^\alpha(r) - \hat{f}^\alpha(r) \right]^2 \tag{2}$$

$f^\alpha(r)$ is the statistical correlation function of type α of the reconstructed microstructure. $\hat{f}^\alpha(r)$ is the corresponding function of the target (real) microstructure. The iterations were continued and the iterated microstructure was accepted with a probability of acceptance defined by the simulated annealing method. The iterations were terminated once the change in energy functional with number of iterations became negligible. The resulting reconstructed microstructure and the detailed procedure can be found in our published article [8].

The statistical functions of reconstructed microstructure and target microstructure are shown in Fig. 4a–c. It can be observed in Fig. 4d that below $E_{new} - E_{old} < 0.001$, the statistical functions closely matched to that of the target microstructure and further continuation of the optimization did not lead to any meaningful benefits. The histograms of size distribution of pores are shown in Fig. 4e. An ensemble of ten such reconstructions were created. They were further used to calculate the effective elastic properties.

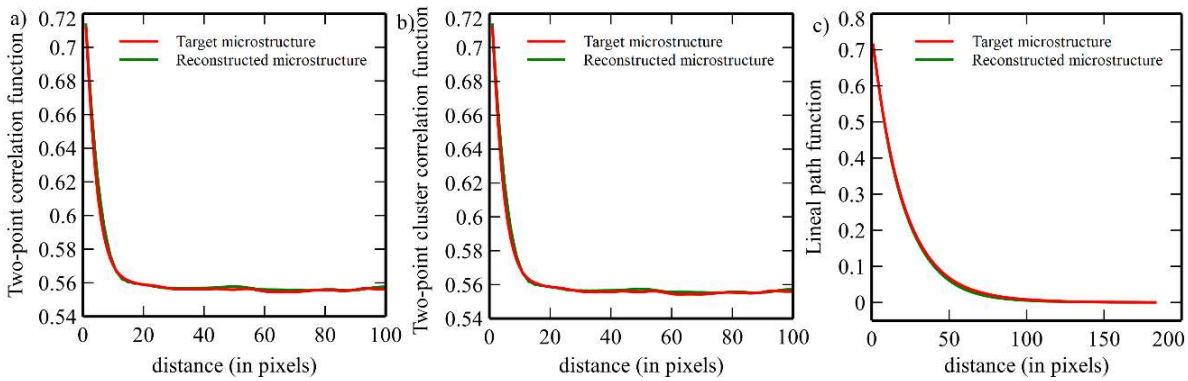

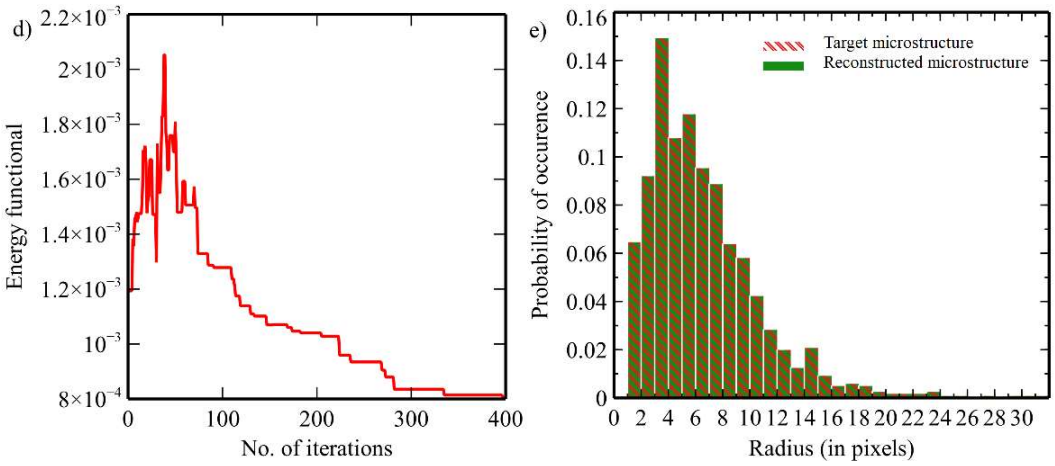

Figure 4. a) Two-point correlation function; c) Two-point cluster correlation function; d) Lineal path function; b) Evolution of energy functional with number of iterations; and e) size distribution of spheres of target and reconstructed microstructures (it can be seen, that both distributions are identical).

4. Determination of effective elastic properties

Determination of effective properties of a heterogeneous medium is based upon the idea that a heterogeneous medium can be converted into a homogeneous medium by utilizing the conservation of energy principle. The criteria in Eq. (3) given by Hill [9] needs to be satisfied:

$$\langle \sigma : \varepsilon \rangle = \langle \sigma \rangle : \langle \varepsilon \rangle \tag{3}$$

It states that average of the scalar product of stress σ and strain ε tensors over the heterogeneous medium should be equal to the scalar product of their individual averages. The boundary value problem defined to determine effective elastic properties is:

$$div(\sigma) = 0 \; in \; \Gamma \tag{4}$$

Γ is the boundary of the studied microstructure. The boundary conditions must satisfy Eq. (3). The real and the reconstructed microstructures were meshed using linear tetrahedral elements and subjected to periodically compatible mixed boundary conditions [5] to determine the effective stiffness tensor. Considering the isotropy of the microstructure, Table 1 shows average values of extension stiffness coefficients (C_{11}, C_{22}, C_{33}) and shear stiffness coefficients (C_{44}, C_{55}, C_{66}) obtained from the real microstructure, average of ten reconstructed microstructures and experimentally determined values [6]. The results obtained from two different types of microstructures are almost identical and are in fairly good agreement with the experimentally measured results. More details can be found in [8].

Table 1: Average stiffness coefficients (in GPa) from three different methods.

	C_{11}/ C_{22}/ C_{33} (GPa)	C_{44}/ C_{55}/ C_{66} (GPa)	Porosity (%)
Real microstructure	26.54	8.78	74.56
Reconstructed microstructure	26.15	8.46	74.45
Experimental measurement [3]	29.50	6.95	74.50

  doi:10.5075/epfl-298799_978-2-9701614-0-0

5. Conclusions

The research work describes a novel artificial microstructure reconstruction algorithm of the ceramic foam material. The artificial microstructure is reconstructed in such a way that its statistical correlation functions are equivalent that of the real microstructure. It is shown that the reconstructed microstructure has almost matching effective elastic properties to the real microstructure. The elastic properties calculated from finite element simulations correspond well with experimental measurements which prove the overall accuracy of the developed numerical procedure.

6. Acknowledgements

The financial support of the Darmstadt University of Applied Sciences is gratefully acknowledged. Special thanks go to J. Schukraft and Prof. K.A. Weidenmann for the experimental support.

7. References

1. Torquato S. Random Heterogeneous Materials: Microstructure and Macroscopic Properties. Springer, New York. 2002
2. Torquato S. Optimal design of heterogeneous materials. Annual review of materials research 2010; 40:101-129.
3. Bostanabad R, Zhang Y, Li X, Kearney T, Brinson LC, Apley DW, Liu WK, Chen W. Computational microstructure characterization and reconstruction: review of the state-of-the-art techniques, Progress in Materials Science 2018; 95:1–41.
4. Jiao Y, Stillinger FH, Torquato S. Modeling heterogeneous materials via two-point correlation functions. II. Algorithmic details and applications. Physical Review E 2008; 77(3), 031135.
5. Pahr DH, Zysset PK. Influence of boundary conditions on computed apparent elastic properties of cancellous bone. Biomechanics and modeling in mechanobiology 2008; 7(6):463-476.
6. Horny D, Schukraft J, Weidenmann KA, Schulz K. Numerical and experimental characterization of elastic properties of a novel, highly homogeneous interpenetrating metal ceramic composite. Advanced Engineering Materials 2020; 22(7), 1901556.
7. Xu H, Li Y, Brinson C, Chen W. A descriptor-based design methodology for developing heterogeneous microstructural materials system. Journal of Mechanical Design 2014. 136(5), 051007.
8. Deshpande VV, Weidenmann KA, Piat R. Application of statistical functions to the numerical modelling of ceramic foam: From characterisation of CT-data via generation of the virtual microstructure to estimation of effective elastic properties. Journal of the European Ceramic Society 2021; 41(11):5578-5592.
9. Hill R. Elastic properties of reinforced solids: some theoretical principles, Journal of the Mechanics and Physics of Solids 1963; 11(5):357–372.

UNCERTAINTY QUANTIFICATION OF THE DYNAMIC FRACTURE TOUGHNESS OF PARTICULATE POLYMER COMPOSITES USING A SURROGATE BASED METHODOLOGY

Aanchna, Sharma[a], Vinod, Kushvaha[a]*

a: Department of Civil Engineering, Indian Institute of Technology Jammu, J&K, India,
2018RCE0035@iitjammu.ac.in

Abstract: *This paper presents an efficient framework of quantifying the inherent uncertainties in determining the dynamic fracture toughness of particulate polymer composites. The size, shape and the volume fraction of the particles added as fillers are one of the key factors affecting the overall behaviour of these composite materials. For the accurate design and analysis of such composites, the uncertainties associated with these parameters must be taken into consideration. In this context, the present work has used an artificial neural network in conjunction with the Monte Carlo simulation approach to investigate the effects of uncertainty propagation onto the output space of dynamic fracture toughness. The results of this study indicate that among the different input parameters, the effect of uncertainty in the aspect ratio has the most prominent effect on the dynamic fracture toughness.*

Keywords: Dynamic fracture toughness; uncertainty quantification; monte carlo simulation; artificial neural network; particulate polymer composites.

1. Introduction

Direct relation between the weight and the energy consumption has led to the increasing development of polymer based composites that are lightweight, corrosion resistant and exhibit high strength [1]. Polymer composites are multiphase materials, wherein one phase is continuous, and the other phase is dispersed. The primary role of the continuous phase, more commonly known as matrix is to bind the dispersed phase together and transfer the load uniformly to the secondary phase, also known as reinforcement. Reinforcement is the main load-bearing element in the composite materials and different types of reinforcements result in different kinds of polymer composites. Particulate Polymer Composites (PPCs) are one such kind in which the reinforcement is used in the form of particles of different sizes in a polymeric matrix. The main advantage of using such composites is the manufacturing ease and the macroscopically isotropic nature [2]. These composites offer a great deal of flexibility to the user to design the composite as per the application requirement by choosing the constituent materials accordingly [3, 4]. Considering such wide range of striking properties of these composites, they have potential applications in aerospace, marine, automotive, medical and electronic industries [5]. To sustain the demand of these composites for commercial purposes, more research into the mechanical behavior under different exposure conditions is required. In this view, fracture toughness is one such critical property that needs to be thoroughly investigated prior to the industrial utilization of these composites. Fracture toughness of any material is indicative of its resistance to the propagation of crack [6]. Many researchers have looked into the quasi-static aspect of fracture toughness of polymer composites [7–10]

  doi:10.5075/epfl-298799_978-2-9701614-0-0

however, the dynamic fracture toughness of particulate polymer composites has been overlooked and hence requires more attention. Kushvaha et al. [11] studied the effect of filler particle shape, volume fraction and loading rate on the dynamic fracture toughness of polymer composites reinforced with three different shapes of glass particles. They used a gas-gun setup to experimentally characterize the material's resistance to crack growth and observed that the rod-shaped glass fillers were dominant in the enhancement of dynamic fracture toughness. Experimental investigation of dynamic fracture toughness is time consuming and laborious due to the complexities in the experimental and measurement setup. However, the advent of machine learning techniques has made it possible to make reliable predictions of material properties with limited experimentation [12]. Artificial Neural Network (ANN) is one such machine learning algorithm that has been successfully used to predict the material behavior [6, 13, 14]. However, for reliable predictions it is imperative to consider the inherent uncertainties associated with such predictive models. Also, the inevitable property uncertainty in the heterogeneous materials due to the manufacturing processes, exposure conditions, reinforcement distribution and measurement error, intensely affects the overall mechanical behavior [15]. The framework of uncertainty quantification enables one to predict these uncertainties in advance and assess their impact and hence increases the confidence in the obtained results. Researchers have used different approaches like perturbation techniques, Monte Carlo simulation and Karhumen-Loeve expansion to quantify uncertainties of different kinds [16–20]. Out of all these techniques, Monte Carlo is the most commonly used approach for the propagation of input uncertainty through the model and analyze the effect on the model response [21]. Although, this approach is computationally expensive, a large number of model evaluations can still be reduced using machine learning. In this view, this paper presents an ANN based framework for quantifying the uncertainties and assessing their effect on the dynamic fracture toughness of glass filled polymer composites.

2. Methodology

2.1 Experimental details

Specimens of particulate polymer composites used in this study were prepared using Bisphenol epoxy as the polymeric matrix and micron-sized glass particles. Three different shapes of glass fillers viz. spherical (aspect ratio = 1), flake (aspect ratio = 6), and rod (aspect ratio = 80), were used in a volume fraction of 0%, 5%, 10% and 15%. Using an amine based hardener, specimens were cured and then machined into the rectangular sheets of dimensions 60 mm X 30 mm X 9 mm. A 6 mm long notch was also created at the mid-span of the machined specimen. Then these specimens were tested for an impact of around 16 m/s using a gas-gun setup. A high speed camera was used to capture the entire event and consequently a set of images for the deformed and undeformed state at regular time intervals were recorded. Later these images were correlated using digital image correlation and displacement components along both the directions were obtained. Finally, using some asymptotic equations, Stress Intensity Factor (SIF) at each time instant was obtained. Please refer to [11] for the detailed description of the entire experimental procedure.

2.2 ANN approach

  doi:10.5075/epfl-298799_978-2-9701614-0-0

The working of artificial neural networks is inspired from the biological nervous system. It is essentially a network of interconnected layers that learns by finding the optimal connection weights to generate an output close to the target values. The advantage of using ANN is its ability to handle large datasets and solve complex problems using nonlinear mapping functions with utmost accuracy [22]. In the present work, ANN is implemented using the platform of SPSS version 23.0 wherein the input layer has four parameters namely, aspect ratio (*AR*), volume fraction (V_f), dynamic elastic modulus (E_d) and time (t). An automatic architecture is selected in which one hidden layer is used with hyperbolic tangent as the activation function and gradient descent is chosen as the optimization algorithm. Stress intensity factor is set as the dependent variable in this network. 70% of the available data was used to train the network and the remaining 30% was used as the teasing dataset. To measure the prediction accuracy the coefficient of determination (R^2) and the mean absolute percentage error (*MAPE*) were calculated using Eq. (1).

$$MAPE = \frac{100}{k}\sum_{i=1}^{k}\frac{T_i - P_i}{T_i} \quad (1)$$

Where k = no. of data points, T_i = target value, P_i = predicted value

2.2 Framework of uncertainty quantification (UQ)

The effect on the composite's dynamic fracture toughness due to the inevitable uncertainty in the aspect ratio, volume fraction and the dynamic elastic modulus is investigated. Four cases of parametric uncertainty are considered in this paper. The first one is when a stochasticity of 30 % is introduced only in the aspect ratio, second case is when a stochasticity of 10% is introduced in the dynamic elastic modulus in combination with the earlier introduced stochasticity in aspect ratio. Then the third case consists of uncertainty in the aspect ratio along with 20% stochasticity in the volume fraction. The final case studied in this work is when these uncertainties are introduced simultaneously in all the three parameters. This paper uses the framework of Monte Carlo Simulation (MCS) to generate the random fields of the input space as per the said degree of stochasticity and later the same has been integrated with ANN to account for their effects on the dynamic fracture toughness. The implementation of MCS approach is done using MATLAB. 10000 realizations are generated for each random input field corresponding to different time instants. The underlying ANN model was then executed for each instance drawn from the distribution and the model responses in terms of stress intensity factor are obtained. Then the output metrics are characterized and appropriate probabilistic estimates for the response's statistical representation are computed.

3. Results and discussions

3.1 Results of ANN model

The proposed model of neural network is used to predict the values of stress intensity factor corresponding to different time instants. Comparison of experimental and predicted SIF values is shown in Figure 1 and 2 and a good agreement can be seen within the two. The prediction accuracy is found to be ~94% and the R^2 is 0.9. The values of t<0 are indicative of the pre-crack initiation period, while at t = 0, the crack initiates and t>0 is suggestive of the post-crack initiation period. It is clear from the plots that SIF increases with increase in the volume fraction of the

  doi:10.5075/epfl-298799_978-2-9701614-0-0

fillers. Also, the highest values of SIF are exhibited by the rod-shaped glass fillers having aspect ratio = 80. Similar observation is obtained from the experimental results as well. The reason for this can be ascribed to the different failure mechanisms (matrix cracking, filler breakage, matrix-filler interfacial debonding and filler pull out) that these composites undergo and the corresponding dissipation of energy.

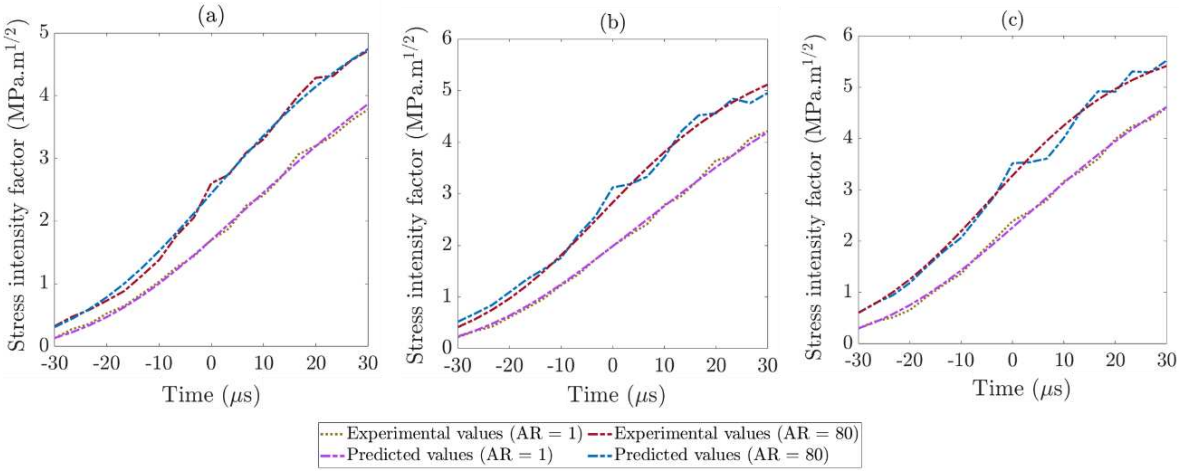

Figure 1. Comparison of predicted and experimental values at AR = 1 and 80 for (a) V_f = 5%, (b) V_f = 10%, (c) V_f = 15%

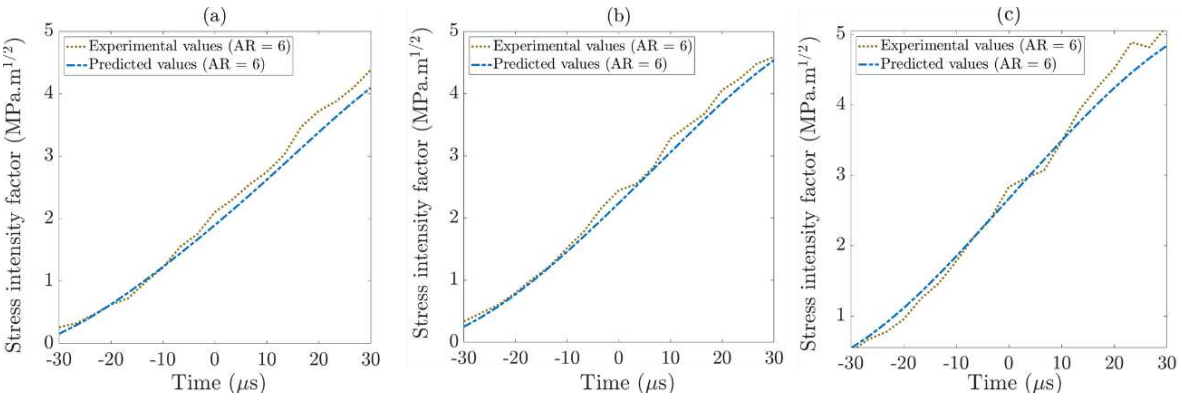

Figure 2. Comparison of predicted and experimental values at AR = 6 for (a) V_f = 5%, (b) V_f = 10%, (c) V_f = 15%

3.2 Uncertainty quantification

To estimate the random composite response based on the variability in the input parameters, Monte Carlo approach is used in conjunction with ANN. As observed from the results of ANN model, rod-shaped glass fillers show the highest values of SIF corresponding to different volume fractions. Therefore, UQ framework is applied only on the rod-shaped fillers for the sake of brevity. The framework of uncertainty quantification characterizes the parametric uncertainties by means of statistical analysis of the model responses resulting from the forward propagation

  doi:10.5075/epfl-298799_978-2-9701614-0-0

of the uncertainties through the model. This allows analysis of the induced probability distributions of the model outputs. In the present study, Probability Density Function (PDF) and the tolerance bounds for the uncertain responses of SIF are computed and shown in Figure 3 and 4. The SIF values obtained from the ANN model as mentioned in the section 3.1, are considered to be the deterministic SIF values. In the following figures, the stochastic SIF values are normalized with respect to the deterministic values. It is evident from both the figures that the effect of uncertainty is more pronounced in the period of pre-crack initiation, once the crack starts propagating, the variability effect follows a decreasing trend in all the cases. Also, the case wherein all the input parameters are simultaneously considered uncertain random fields, maximum variability in the SIF response is observed.

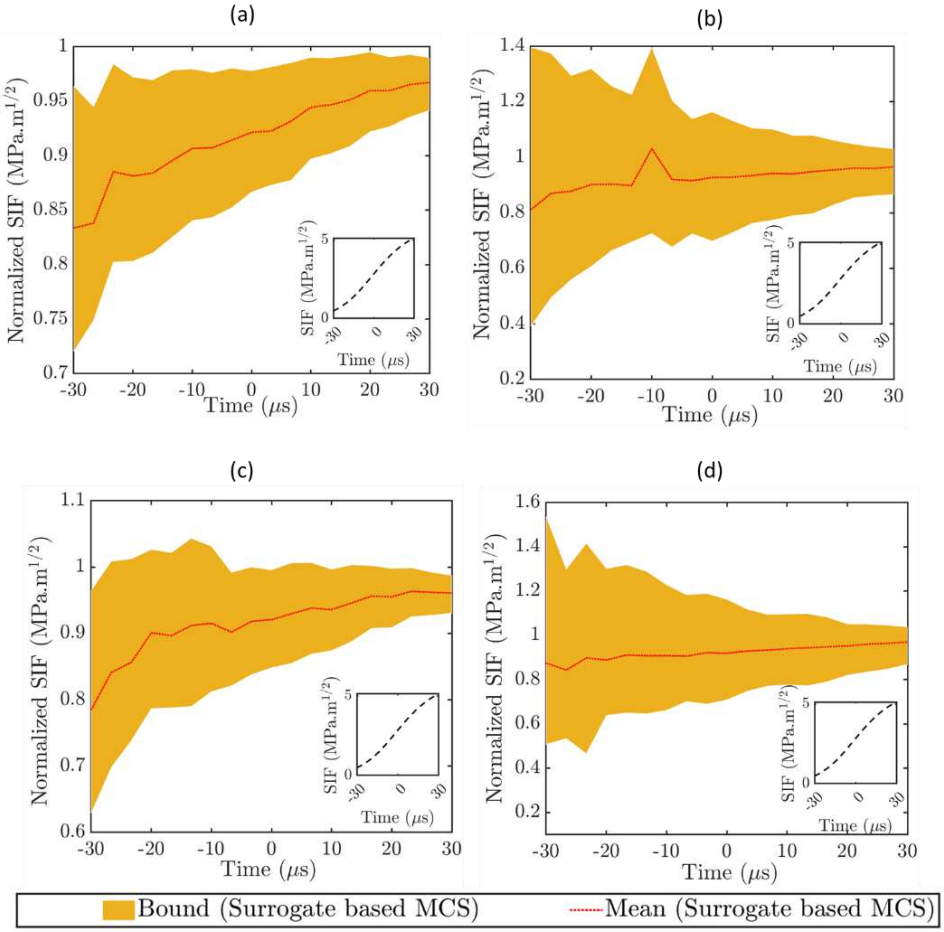

Figure 3. Tolerance bounds of SIF when (a) uncertainty is only in AR, (b) uncertainty is in AR and Ed, (c) uncertainty is in AR and Vf and (d) uncertainty is simultaneously in all three parameters

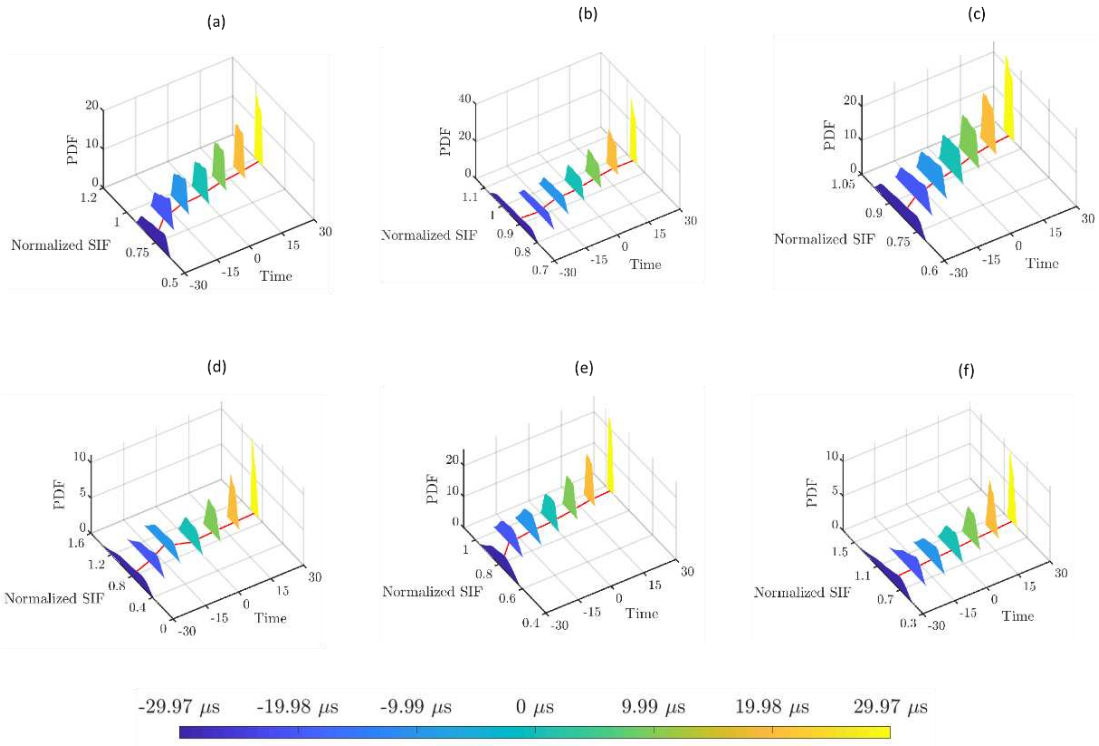

Figure 4. PDF plots for the stochastic response of SIF for variation in only aspect ratio (a) at 5% V_f, (b) at 15% V_f, and PDF responses of normalized SIF history for 10% V_f of rod shaped glass fillers when a stochastic variation is introduced (c) only in *AR*, (d) simultaneously in *AR* and E_d, (e) simultaneously in *AR* and V_f, (f) simultaneously in *AR*, E_d and V_f

4. Conclusion

The present work demonstrates a robust method of quantifying the uncertainties using the framework of ANN based methodology to model the uncertainties in the material properties of particulate polymer composites, forward propagate these uncertainties and assess their effect on the dynamic fracture toughness. As uncertainty quantification often requires a large number of model evaluations and computational effort, the proposed methodology creates a computationally efficient UQ framework. The experimental and predicted values of SIF are found to be in good agreement indicating the efficacy of the proposed neural network. Among the three filler types, rod-shaped fillers exhibited the highest values of SIF. Dynamic fracture toughness is affected more due to the combined uncertainty in aspect ratio and dynamic elastic modulus compared to the combined uncertainty in the aspect ratio and volume fraction.

  doi:10.5075/epfl-298799_978-2-9701614-0-0

5. References

1. Lyu M-Y, Choi TG (2015) Research trends in polymer materials for use in lightweight veicles. Int J Precis Eng Manuf 16:213–220. https://doi.org/10.1007/s12541-015-0029-x

2. Kushvaha V, Tippur H (2013) Effect of Filler Particle Shape on Dynamic Fracture Behavior of Glass-Filled Epoxy. In: Chalivendra V, Song B, Casem D (eds) Dynamic Behavior of Materials, Volume 1. Springer New York, pp 513–522

3. Aghadavoudi F, Golestanian H, Beni YT (2018) Investigating the effects of CNT aspect ratio and agglomeration on elastic constants of crosslinked polymer nanocomposite using multiscale modeling. Polymer Composites 39:4513–4523. https://doi.org/10.1002/pc.24557

4. DeArmitt C, Rothon R (2015) Particulate Fillers, Selection, and Use in Polymer Composites. In: Palsule S (ed) Encyclopedia of Polymers and Composites. Springer Berlin Heidelberg, Berlin, Heidelberg, pp 1–19

5. Oladele IO, Omotosho TF, Adediran AA (2020) Polymer-Based Composites: An Indispensable Material for Present and Future Applications. International Journal of Polymer Science 2020:e8834518. https://doi.org/10.1155/2020/8834518

6. Sharma A, Kushvaha V (2020) Predictive modelling of fracture behaviour in silica-filled polymer composite subjected to impact with varying loading rates using artificial neural network. Engineering Fracture Mechanics 239:107328. https://doi.org/10.1016/j.engfracmech.2020.107328

7. Cowley KD, Beaumont PWR (1997) The interlaminar and intralaminar fracture toughness of carbon-fibre/polymer composites: The effect of temperature. Composites Science and Technology 57:1433–1444. https://doi.org/10.1016/S0266-3538(97)00047-X

8. Prasad MSS, Venkatesha CS, Jayaraju T (2011) Experimental Methods of Determining Fracture Toughness of Fiber Reinforced Polymer Composites under Various Loading Conditions. Journal of Minerals and Materials Characterization and Engineering 10:1263

9. Lauke B, Fu S-Y (2013) Aspects of fracture toughness modelling of particle filled polymer composites. Composites Part B: Engineering 45:1569–1574. https://doi.org/10.1016/j.compositesb.2012.07.021

10. Sharafi S, Santare MH, Gerdes J, Advani SG (2021) A review of factors that influence the fracture toughness of extrusion-based additively manufactured polymer and polymer composites. Additive Manufacturing 38:101830. https://doi.org/10.1016/j.addma.2020.101830

11. Kushvaha V, Tippur H (2014) Effect of filler shape, volume fraction and loading rate on dynamic fracture behavior of glass-filled epoxy. Composites Part B: Engineering 64:126–137. https://doi.org/10.1016/j.compositesb.2014.04.016

12. Sharma A, Mukhopadhyay T, Rangappa SM, et al (2022) Advances in Computational Intelligence of Polymer Composite Materials: Machine Learning Assisted Modeling,

Analysis and Design. Arch Computat Methods Eng. https://doi.org/10.1007/s11831-021-09700-9

13. Sharma A, Subramaniyan AK, Kushvaha V (2020) Effect of aspect ratio on dynamic fracture toughness of particulate polymer composite using artificial neural network. Engineering Fracture Mechanics 228:106907. https://doi.org/10.1016/j.engfracmech.2020.106907

14. Farhangdoust S, Tashakori S, Baghalian A, et al (2019) Prediction of damage location in composite plates using artificial neural network modeling. In: Sensors and Smart Structures Technologies for Civil, Mechanical, and Aerospace Systems 2019. International Society for Optics and Photonics, p 109700I

15. Bostanabad R, Liang B, Gao J, et al (2018) Uncertainty quantification in multiscale simulation of woven fiber composites. Computer Methods in Applied Mechanics and Engineering 338:506–532. https://doi.org/10.1016/j.cma.2018.04.024

16. Zhang J (2021) Modern Monte Carlo methods for efficient uncertainty quantification and propagation: A survey. Wiley Interdisciplinary Reviews: Computational Statistics 13:e1539. https://doi.org/10.1002/wics.1539

17. Dey S, Mukhopadhyay T, Spickenheuer A, et al (2016) Uncertainty Quantification in Natural Frequency of Composite Plates - An Artificial Neural Network Based Approach. Advanced Composites Letters 25:096369351602500203. https://doi.org/10.1177/096369351602500203

18. Dey S, Mukhopadhyay T, Adhikari S (2015) Stochastic free vibration analysis of angle-ply composite plates – A RS-HDMR approach. Composite Structures 122:526–536. https://doi.org/10.1016/j.compstruct.2014.09.057

19. Sampaio L (Luiz) Eigenvector perturbation methodology for uncertainty quantification of turbulence models

20. Tipireddy R, Barajas-Solano DA, Tartakovsky AM (2020) Conditional Karhunen-Loève expansion for uncertainty quantification and active learning in partial differential equation models. Journal of Computational Physics 418:109604. https://doi.org/10.1016/j.jcp.2020.109604

21. Metropolis N, Ulam S (1949) The Monte Carlo Method. Journal of the American Statistical Association 44:335–341. https://doi.org/10.1080/01621459.1949.10483310

22. Kushvaha V, Kumar SA, Madhushri P, Sharma A (2020) Artificial neural network technique to predict dynamic fracture of particulate composite. Journal of Composite Materials 0021998320911418. https://doi.org/10.1177/0021998320911418

DEVELOPMENT OF ADDRESSABLE CONDUCTING NETWORK BASED DAMAGE SENSING AND SELF-HEALING SYSTEM OF CARBON FIBER REINFORCED POLYMER COMPOSITES USING DEEP-LEARNING

Myeong-Hyeon Yu[a], Ji-Seok Lee[a], Hak-Sung Kim[a, b]

a: Department of Mechanical Convergence Engineering, Hanyang University, 222, Wangsimni-ro, Seongdong-gu, Seoul, Republic of Korea – fatewithyou2@gmail.com
b: Institute of Nano Science and Technology, Hanyang University, 222, Wangsimni-ro, Seongdong-gu, Seoul, Republic of Korea

Abstract: In this work, damage sensing and self-healing of carbon fiber reinforced polymer composite (CFRP) was conducted based on an addressable conducting network (ACN). For the high accuracy of damage sensing, a deep-learning based damage sensing system was developed. The training data was generated through Kirchhoff's circuits laws. Then, the Artificial Neural Network (ANN) based deep learning algorithm was used for damage sensing. In addition, self-healing of the detected damage was performed. The self-healing was conducted by supplying an electric current to the damaged area. Supplied electric current generates joule heat in the damaged area. As a result, it was noteworthy that established deep-learning algorithm based on ACN exhibited high accuracy damage sensing resolution under compression test. In addition, the self-healing for damaged CFRP panels was also successfully performed.

Keywords: Carbon fiber reinforced polymer composite ; addressable conducting network ; damage sensing ; self-healing ; deep-learning

1. Introduction

Carbon fiber reinforced polymer composites (CFRP) are widely used in automobile, aircraft, space vehicle and sports equipment because of their lightweight, high specific strength and high specific stiffness [1-3]. Due to its benefits, many researchers are trying to replace the heavy metallic material of automobile components to lighter materials. Generally, CFRP has excellent mechanical properties in fiber direction. However, matrix cracking and delamination can be generated easily in structural application. These failures can cause serious accidents. Therefore, it is necessary to develop a damage detection technique to prevent them. In this work, deep learning-based damage sensing and self-healing system based on addressable conducting network (ACN) for CFRP was developed [4,5]. It uses grid metallic lines on upper- and bottom-surfaces of CFRP. Metallic lines of each surface are parallel, and bottom- and top- electrodes are perpendicular to each other. ACN utilizes installed metallic lines as conducting network, structural damage can be evaluated through by resistance change of composite. This method has strong benefits, including applicable to large area, no degradation of mechanical property, simple process, and low cost. In addition, by applying current to the installed electrode, resistance heat is generated in the damaged area. Using a thermoplastic resin as a matrix, the self-healing of CFRP can be performed using this joule heating [6]. In this study, by applying deep learning technology, the autonomous damage sensing was perfectly established and performed (Figure. 1). An analytical model using the Kirchhoff's circuits laws was developed to obtain the resistance change data due to damage of it. Deep-learning was performed using the artificial

  doi:10.5075/epfl-298799_978-2-9701614-0-0

neural network (ANN) algorithm. The resistance changes of the nodes were used as input signals. The signals passing through the ANN algorithm were classified as 0 or 1 depending on whether each area was damaged or not. The self-healing was conducted by supplying an electric current to the damaged area. The supplied electric current generates joule heat in the damaged area. Because it is a thermoplastic resin, it is melted by joule heat. The melted resin is cooled at room temperature and solidified. To verify the self-healing of CFRP, ultrasonic inspection was performed.

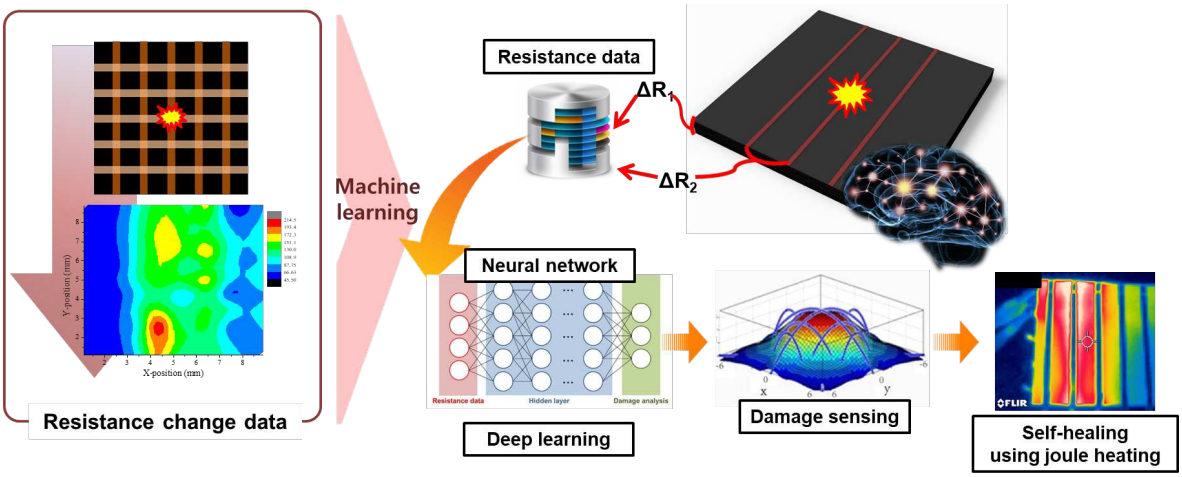

Figure 1. Addressable conducting network based damage sensing and self-healing using deep-learning.

2. Experiment

2.1 Fabrication of CFRP panel

The CFRP panel was fabricated by laminating 16 sheets of unidirectional carbon fiber/nylon prepregs (Kolon, thickness : 0.15 mm). The panel size was 100 mm X 100 mm X 2.4 mm. The stacking sequence was $[0_4/90_4]_s$. The 5 mm wide copper tapes were attached on the top and bottom prepregs for the electrodes of addressable conducting network (ACN). Then, the laminated prepregs were placed into a metal mold, compressed at a pressure of 1 MPa, and heated to 270° C using a hot press (Ocean Science, Korea). After holding for 10 minutes at a temperature of 270°C, it was cooled to room temperature at a rate of 1°C per minute (Figure. 2)

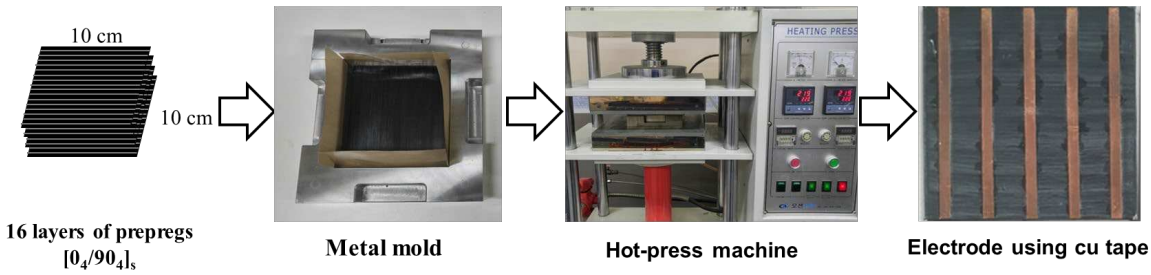

Figure 2. The photographs of the CFRP panel fabrication process

2.2 Measurement the electrical properties of CFRP

For analytical model using Kirchhoff's circuits laws, the electrical properties of CFRP were measured. To measure the resistance in the fiber direction, transverse direction and thickness

direction, the CFRP panel was manufactureded with a stacking sequence $[0_{16}]_T$. The resistance of each direction was measured using two-probe method. The contact resistance was calculated and removed from the results [4]. The resistivity of CFRP in the thickness direction, fiber direction, and transverse direction, were 79.17 Ω·mm, 0.048 Ω·mm and 68.35 Ω·mm, respectively. The resistivity of the copper tape was chosen as 1.6 x 10^{-5} Ω·mm [7].

2.3 Analytical model using Kirchhoff's circuits laws

To generate training data, Kirchhoff's circuits laws were used [8]. The CFRP panel was modeled as a 3D resistance network of 5x5x4 cube. The first Kirchhoff's circuit law is Kirchhoff's current law (KCL). It was applied to nodes of the resistor network. As shown in Eq. (1), this law means the numerical summations of currents are zero in every node.

$$\sum I_{node} = 0 \tag{1}$$

The second Kirchhoff's circuit law is Kirchhoff's voltage law (KVL), which was applied to closed loop in the resistance network. KVL means the total sum of voltages in the loop is zero (Eq. (2)).

$$\sum V_{loop} = \sum I_{loop} R_{loop} = 0 \tag{2}$$

The training data for deep learning were generated in the matrix form. Firstly, the damage location of the CFRP panel was marked with the damage status as a 5 x 5 matrix. The undamaged damage status was represented as 0. The damage status of the node perpendicular to the delamination was marked as 1. The thickness direction resistance of the damaged location was assumed as 100 times higher than the undamaged state [9]. The resistance change was calculated using analytical model based on Kirchhoff's Law.

2.4 Deep-learning for damage sensing

In this study, deep-learning technique was applied using Artificial Neural Network (ANN) algorithm. ANN is a deep learning algorithm immitated the biological brain [10]. ANN consists of multiple neurons and each neuron sends a signal to other neurons like a synapse in a biological brain. In the ANN algorithm, signals passed through a activation function. The signals passing through the activation function were classified according to their characteristics (Figure. 3 (a)). In this work, the ANN algorithm was coded using TensorFlow based on python script language. The algorithm was consist of 5 hidden layers, and ReLU function was utilized as activation function (Figure. 3 (b)). The resistance change data were classified as 1 or 0 depending on wheather each area was damaged or not. To increase optimization speed and accuracy, the Adam optimization algorithm was used [11]. In addition, to prevent overfitting, dropout rate was set as 0.5 [12].

  doi:10.5075/epfl-298799_978-2-9701614-0-0

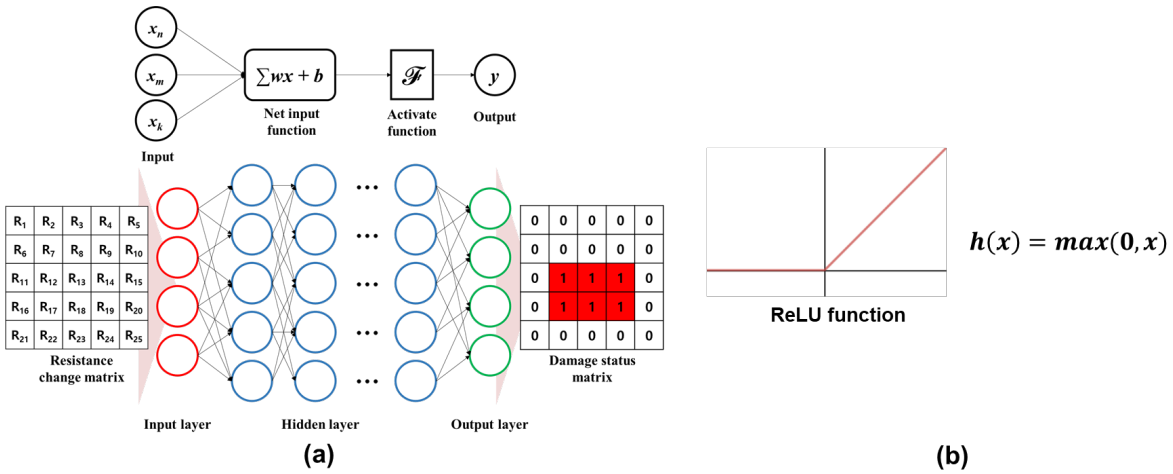

Figure 3. The schematic of (a) artificial neural network and (a) ReLU function

2.5 Damage sensing and verification

The experiment for CFRP damage sensing was conducted as follows. First, the thickness direction resistance of the undamaged CFRP panel was measured. Then, it was placed on a hemispherical jig with an empty center and compressed at a speed of 1 mm/min using a universal testing machine (RB 301 UNITECH-M, R&B, South Korea). After compress, the thickness direction resistance of the damaged CFRP panel was measured. Using these resistance change data, the damage location was predicted with ANN algorithm. An ultrasonic inspection (NAUT 21, JAPAN PROBE, Japan) was conducted to verify the real damage location and compared with the predicted damage sensing results.

2.6 Self-healing

In this work, nylon was used as matrix of CFRP. Nylon is a thermoplastic with a melting temperature of 205 °C. Therefore, self-healing of CFRP was performed by heating the damaged area using joule heat. The joule heat was calculated by Eq. (3) [13].

$$\frac{dP}{dV} = J \cdot E = \frac{J^2}{\sigma} \quad (1)$$

Where P is power converted from electrical energy to thermal energy, V is voltage, J is the current density, E is the electric field, and σ is conductivity. As shown in Eq. (3), joule heating was inversely proportional to the electrical conductivity. Therefore, Joule heat is higher in the damaged area. Based on these theoretical backgrounds, self-healing was performed by applying an electric current to the electrode passing through the damaged area.

3. Results and discussions

The damage sensing experiment of the CFRP panel was performed. To create damage, the center of the CFRP specimens were compressed at a rate of 1 mm/min at 1, 2, 3, and 4 mm displacements, respectively. The resistance changes were measured before and after damage. Based on the measured resistance changes, the damage locations were predicted using ANN based deep-learning algorithm. To verify the predicted damage location results, the ultrasonic inspection results were conducted and compared. Figure. 4 shows the comparison results [4]. In the case of 1 mm displacement, no delamination was detected in either the ultrasonic inspection

  doi:10.5075/epfl-298799_978-2-9701614-0-0 published under CC BY-NC 4.0 license

or the damage prediction using deep learning based ACN (Figure. 4 (a)). In the displacement of 2 mm and 3 mm cases, it was confirmed that the prediction results and the ultrasonic inspection results were similar (Figure. 4 (b), (c)). In the case of a displacement of 4 mm, it was confirmed that more than half of the CFRP panel was damaged.

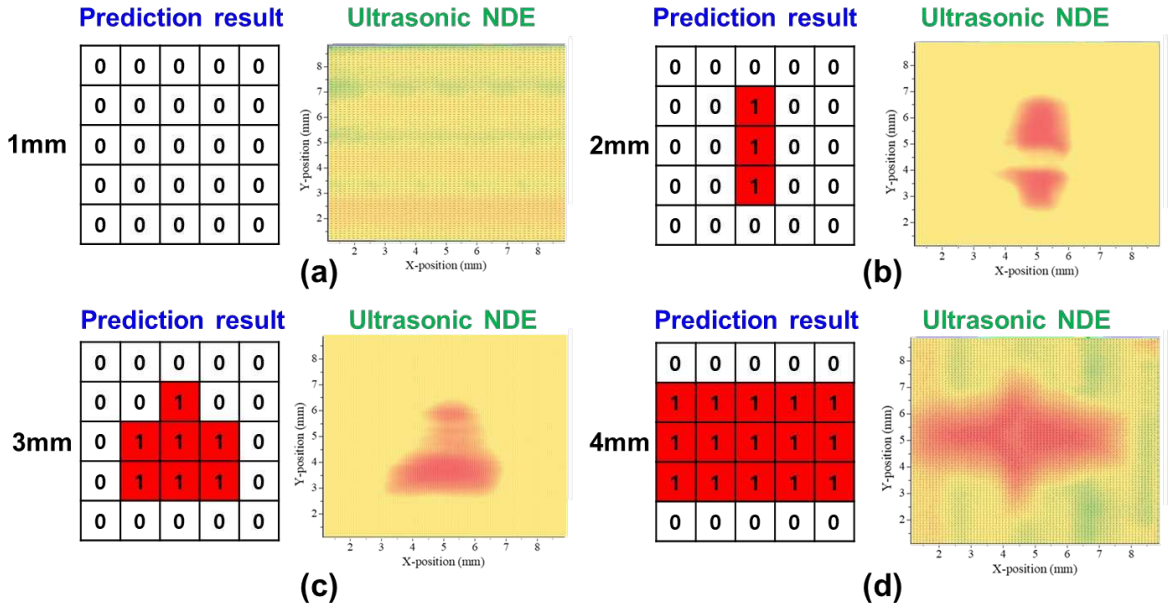

Figure 4. Comparison of damage location prediction results and ultrasonic inspection results of the stacking sequence $[0_4/90_4]_S$ specimen: (a) 1 mm, (b) 2 mm, (c) 3 mm and (d) 4mm pressed [4]

The self-healing of the damaged CFRP panel was performed by supplying electric current to the electrode passing through the damaged area. Figure. 5 shows the ultrasonic results before and after self-healing. . On ultrasonic inspection, It was confirmed that the damaged CFRP was completely healed. As a result, the damage sensing of CFRP with ACN could succesfully predict the damage location by combining deep learning based on the resist network model. Also, the damage of CFRP was perfectly healed.

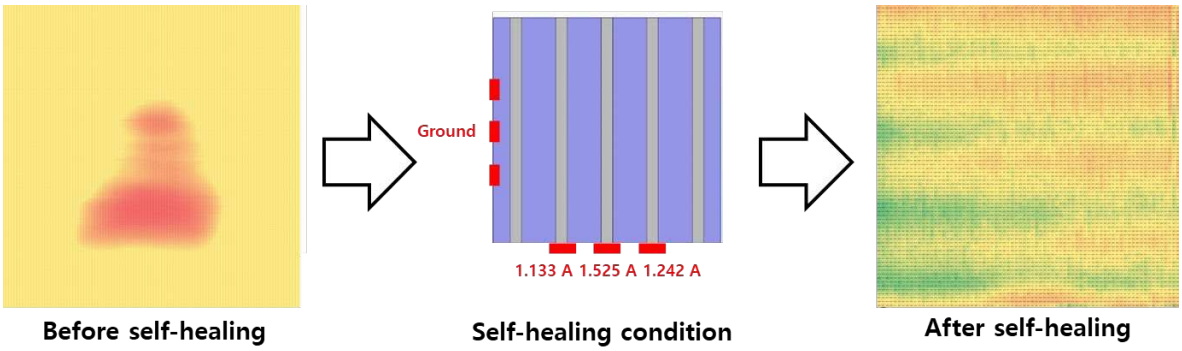

Figure 5. The self-healing condition and ultrasonic inspection results before and after self-healing

  doi:10.5075/epfl-298799_978-2-9701614-0-0

4. Conclusion

This work proposed the damage sensing method of carbon fiber reinforced polymer composite based on ACN. The damage detection was performed using the measured resistance in thickness direction. Deep-learning was also applied for the ACN method to improve the accuracy and speed of damage sensing. In order to obtain training data, a 3D resistance network of CFRP was modeled using Kirchhoff's circuits laws and the ANN deep learning algorithm was used. Damage detection of the locally compressed CFRP specimen was performed using a damage detection system, and it was verified through an ultrasonic inspection (NAUT21). Also, a study on self-healing using joule heat was conducted. The self-healing was conducted by supplying an electric current to the damaged area and it generates joule heat in the damaged area. As a result, it was noteworthy that established deep learning algorithm based on ACN exhibited high accuracy damage sensing resolution under compression test. In addition, the self-healing for damaged CFRP panels was also successfully performed. These damage detection and self-healing technologies are expected to be widely used in carbon fiber-based composite structures.

Acknowledgements

This work was partly supported by Korea Evaluation Institute of Industrial Technology (KEIT) grant funded by the Korea government (MOTIE) (Project No. 20014863, Development of 3D formable heating elements and forming technology for energy-efficient radiant heating of electric vehicles)

References

1. Lim AS, Melrose ZR, Thostenson ET, Chou T-W. Damage sensing of adhesively-bonded hybrid composite/steel joints using carbon nanotubes. Composites Science and Technology. 2011;71:1183-9.
2. Senthilnathan K, Hiremath CP, Naik N, Guha A, Tewari A. Microstructural damage dependent stiffness prediction of unidirectional CFRP composite under cyclic loading. Composites Part A: Applied Science and Manufacturing. 2017;100:118-27.
3. Wu Z, Cui H, Chen L, Jiang D, Weng L, Ma Y, et al. Interfacially reinforced unsaturated polyester carbon fiber composites with a vinyl ester-carbon nanotubes sizing agent. Composites Science and Technology. 2018;164:195-203.
4. Yu, Myeong-Hyeon, and Hak-Sung Kim. Deep-learning based damage sensing of carbon fiber/polypropylene composite via addressable conducting network. Composite Structures 267 (2021): 113871.
5. Takahashi K, Hahn HT. Towards practical application of electrical resistance change measurement for damage monitoring using an addressable conducting network. Structural Health Monitoring. 2012;11:367-77.
6. Joo, Sung-Jun, et al. Damage detection and self-healing of carbon fiber polypropylene (CFPP)/carbon nanotube (CNT) nano-composite via addressable conducting network. Composites Science and Technology 167 (2018): 62-70.
7. Matula RA. Electrical resistivity of copper, gold, palladium, and silver. Journal of Physical and Chemical Reference Data. 1979;8:1147-298.
8. Gerami A. 3D electrical resistivity forward modeling using the Kirchhoff's method for solving an equivalent resistor network. Journal of Applied Geophysics. 2018;159:135-45.

  doi:10.5075/epfl-298799_978-2-9701614-0-0

9. Viets C, Kaysser S, Schulte K. Damage mapping of GFRP via electrical resistance measurements using nanocomposite epoxy matrix systems. Composites Part B: Engineering. 2014;65:80-8
10. Chen Y-Y, Lin Y-H, Kung C-C, Chung M-H, Yen I. Design and implementation of cloud analytics-assisted smart power meters considering advanced artificial intelligence as edge analytics in demand-side management for smart homes. Sensors. 2019;19:2047.
11. Kingma DP, Ba JJapa. Adam: A method for stochastic optimization. 2014.
12. Srivastava N, Hinton G, Krizhevsky A, Sutskever I, Salakhutdinov RJTjomlr. Dropout: a simple way to prevent neural networks from overfitting. 2014;15:1929-58.
13. Fangohr H, Chernyshenko DS, Franchin M, Fischbacher T, Meier G. Joule heating in nanowires. Physical Review B. 2011;84:054437.

  doi:10.5075/epfl-298799_978-2-9701614-0-0

ECCM
26-30 JUNE
2022
LAUSANNE
SWITZERLAND

ECCM20 - Proceedings

ISBN: 978-2-9701614-0-0
DOI: 10.5075/epfl-298799_978-2-9701614-0-0